

# INTERNATIONAL SOCIETY FOR SOIL MECHANICS AND GEOTECHNICAL ENGINEERING



*This paper was downloaded from the Online Library of the International Society for Soil Mechanics and Geotechnical Engineering (ISSMGE). The library is available here:*

<https://www.issmge.org/publications/online-library>

*This is an open-access database that archives thousands of papers published under the Auspices of the ISSMGE and maintained by the Innovation and Development Committee of ISSMGE.*

# General report for TC 205 Safety and serviceability in geotechnical design: a reliability-based perspective

Rapport général du TC 205  
Sécurité et maintenance en conception géotechnique : une perspective fiabiliste

Salgado R.

School of Civil Engineering, Purdue University – West Lafayette, United States

**ABSTRACT:** A transition has been underway in geotechnical engineering from design based on analyses that treat problems as if every pertinent variable were deterministic only to recognize at the end that uncertainties exist by using a factor of safety to design based on probability concepts. In probabilistic design, key problem variables are treated, at least implicitly, as random variables, and probabilities of undesired outcomes (defined through the concept of limit states) are kept below certain maximum acceptable values. The ways to perform these analyses are many, depending on choices as to, for example, which variables to treat as random and which method of analysis (e.g., the limit equilibrium method, the finite element method) to use to solve the underlying boundary-value problem. Different approaches have been followed in North American and Europe, the two regions where use of probabilistic, limit states-based design is more common. Many unresolved issues remain. This paper highlights some of these issues in the context of papers submitted on the topic to the 18th ICSMGE.

**RÉSUMÉ:** Une transition s'est déroulée en géotechnique depuis une conception basée sur des analyses qui traitent les problèmes comme si chaque variable pertinente était déterministe vers la prise en compte des incertitudes par l'utilisation de facteurs de sécurité dans le cadre d'une conception basée sur des concepts probabilistes. Dans ce cadre probabiliste, les variables clés du problème sont traitées, au moins implicitement, comme des variables aléatoires et les probabilités des résultats attendus (définis par le concept d'état limite) sont maintenues en-dessous certaines valeurs maximales acceptables. Il y a de nombreux moyens de réaliser ces analyses, selon le choix, par exemple, des variables à traiter comme aléatoires et des méthodes d'analyse utilisée pour régler le problème aux limites considéré (e.g., la méthode des équilibres limites ou les éléments finis). Différentes approches ont été suivies en Amérique du Nord et en Europe, les deux régions où l'utilisation des méthodes probabilistes aux états-limites sont les plus répandues. De nombreuses questions restent posées. Cet article met en évidence ces questions dans le contexte des articles soumis au 18<sup>ème</sup> CIMSG sur ce thème.

**KEYWORDS:** stability, serviceability, geotechnical design, Eurocode 7, load factors, resistance factors, partial factors, characteristic and design values.

## 1 BACKGROUND

Development of the Eurocode started a large-scale effort to address geotechnical engineering problems in a more systematic manner from the point of view of the uncertainties present in these problems. One major theme of this effort has been to allocate uncertainties more precisely, e.g., between loads and resistances or, in the case of the Eurocode, between loads and the quantities that enable calculation of soil resistances. Another important theme has been to transition away from *ad hoc* measures of safety to probabilities of failure, with failure defined rather specifically. This emphasis on probability of failure has started an important debate concerning what probabilities of failure are acceptable given project importance and consequences of failure.

In Europe, the path followed was to account for uncertainties by dividing shear strengths or, more generally, soil properties controlling the specific resistance being calculated by material factors typically greater than one. Actions (defined in the code as loads or applied displacements) would be increased by factors also greater than one. This general approach is usually referred to as a partial factors approach. In North America, a different philosophy developed. In the still-evolving North American practice, an approach called Load and Resistance Factor Design (LRFD) is used. The main difference with respect to European practice is that design is based on the following inequality:

$$(RF)R_n \geq \sum (LF_i)Q_{i,n} \quad (1)$$

where  $R_n$  is the nominal resistance,  $RF$  is the corresponding resistance factor,  $Q_{i,n}$  are nominal loads (with dead load, live load, etc., identified each by a different value of  $i$ ), and  $LF_i$  are the corresponding load factors.

Both the Eurocode and its North American counterparts are based on the concept of Limit-States Design (LSD). Limit states exist on the boundary between acceptable and unacceptable states. They offer a solid conceptual basis for the definition of failure, which then becomes the achievement of an undesirable state as defined by the limit states. The probability of failure then becomes nothing more than the probability of achievement of an undesirable state. Figure 1 shows a hypothetical design problem involving two variables, resistance and load, both of which are random variables. The line in the figure separates acceptable pairings of  $Q$  and  $R$  ( $Q < R$ ) from those that would lead to failure. The line is the locus of limit states, and states above the line are failure states.

The advantage of use of inequality (1) over the European approach is that the resistance factor reflects all of the uncertainties involved in calculating resistance, including uncertainties in both soil property determination and the analysis used to calculate the resistance. This advantage is likely more of a conceptual nature, for it is possible to account for analysis uncertainty also in the European approach, but that must be done through the material factors dividing the strength parameters, which cease to be then pure factors on material properties.



Another important difference between Eurocode-related efforts and development of North American LRFD is in the process. The Eurocode started with an exclusive focus on buildings (Simpson and Driscoll 1998) but then developed into a code with broad application in geotechnical design. In North America, particularly in the United States, the effort targeted transportation infrastructure, leaving state DOTs and individual researchers with the task of developing load and resistance factors that made sense and could be used in a practical manner. This has in a way been an incentive for performing research in the subject.

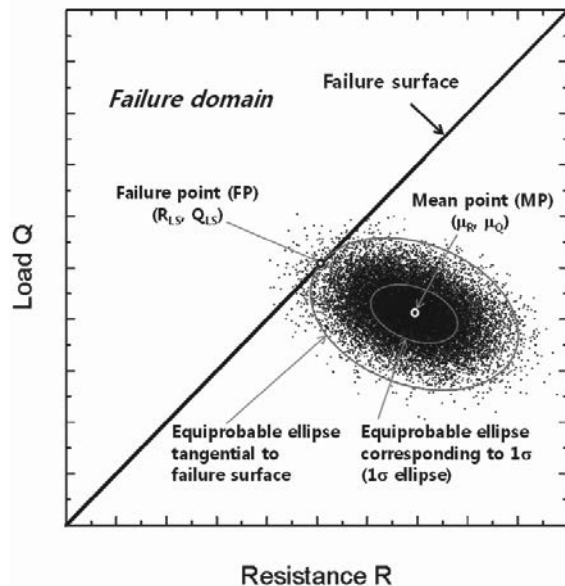


Figure 1– Design problem with load and resistance being random variables (after Salgado and Kim 2013).

The topic of safety and serviceability in geotechnical engineering, which involves design methods and approaches for a variety of geotechnical problems based on analyses that account for probabilities and variability in pertinent variables, is complex and should evolve over the years with the development of better methods of analyses and a greater understanding of variability in geotechnical problems. The following sections summarize current knowledge and challenges, together with the contributions of papers submitted to the XVIII ICSMGE.

## 2 RELIABILITY ANALYSIS

Research on limit-states design (LSD) in its various forms has ranged from simple calibrations of material factors (in the Eurocode framework) or resistance factors (in the LRFD framework) so that results would match those obtained using traditional methods with accepted values of factors of safety to reliability analysis performed with various levels of sophistication. The tools to perform sophisticated reliability analysis have evolved considerable in the last 20 years, and most advances that will be useful to code designers in the future are likely to result from this type of analysis.

Figure 1 shows a cloud of points representing pairings of load  $Q$  and resistance  $R$  around the mean point  $(\mu_R, \mu_Q)$  of these two variables. Each of these points is a simultaneous realization of random variables  $R$  and  $Q$ . Since  $Q$  and  $R$  are more likely to be close to their respective mean, there is a heavier concentration of points near  $(\mu_R, \mu_Q)$ ; however, if the load and resistance in a hypothetical problem deviate from their means by sufficiently large amounts,  $Q$  may end up exceeding  $R$ , which would, by definition, constitute failure. This cloud of points may be obtained using Monte Carlo simulations if the

probability distributions of  $Q$  and  $R$  are known. The probability of failure can be estimated from the ratio of the number  $n$  of points above the limit state line shown in the figure to the total number  $N$  of points. Mathematically:

$$p_f = \lim_{N \rightarrow \infty} \frac{n}{N} \quad (2)$$

where  $N$  must be large enough for  $p_f$  to converge.

Also shown in Figure 1 are dispersion ellipses. A dispersion ellipse represents the locus of the resistance-load pairings with the same level of deviation from the mean. Note that there is one dispersion ellipse that is tangential to the failure line at a point known as the most likely "failure point" FP, also known as the "design point". From the point of view of development of material factors or resistance factors, if the probability of failure calculated for the simulations of Figure 1 is the value that should be targeted in design, the relationship between the design point FP and the mean point MP yields directly the factors that would be used in design. This is easiest to show for LRFD, in which case the factors RF and LF shown in inequality (1) would follow from:

$$RF = \frac{R_{LS}}{\mu_R} \quad \text{and} \quad LF = \frac{Q_{LS}}{\mu_Q} \quad (3)$$

where  $R_{LS}$  and  $Q_{LS}$  are the resistance and load at the design point FP; and  $\mu_R$  and  $\mu_Q$  are the means of resistance and load.

For different reasons, code designers may set load factors  $LF_i^*$  that must apply to a range of design settings. If a resistance factor is developed using reliability analysis (calculated from an equation like (3)), this resistance factor is consistent with the load factor calculated using the same equation. If it is to be used with a different load factor specified in a code, it must be adjusted. If we refer to the adjusted resistance factor as  $RF^*$ , it may be computed by requiring that inequality (1) apply equally whether  $RF^*$  and  $LF_i^*$  or  $RF$  and  $LF_i$  are used:

$$RF^* = RF \frac{\sum (LF_i^*) Q_{i,n}}{\sum (LF_i) Q_{i,n}} \quad (4)$$

## 3 CODE DESIGN

The main goal of modern LSD-based codes is to prevent the occurrence of limit states or, more precisely, to guide or prescribe designs so as to keep the probability of such occurrence acceptably small. The concepts presented in Figure 1 apply equally to ultimate (ULS) and serviceability (SLS) limit states.

One of the key points in connection with LRFD and with partial factor design if model (analysis) uncertainty is included in the factors is that factors are specific to a given analysis. It is not possible to use resistance factors in an *ad hoc* manner or the purpose of LRFD or partial factor design is lost. This is a significant culture change for geotechnical engineers, for factors of safety have traditionally been used with considerable flexibility. This significant difference between practice as it is evolving at present and the practice of years back has important implications. It becomes difficult, for example, to use a method of analysis or design for which factors have not been developed. There are also ethical and professional conduct implications, as touched upon by Redaelli (2013), who points out that ethics should constrain engineers from selecting factors of safety based on financial motivations. In geotechnical engineering, Redaelli (2013) argues, the high level of uncertainty invites a reliance on judgment, which in turn enables geotechnical engineers willing to deliberately distort design outcomes for their own interests or for the interest of their direct employer to easily do so. Redaelli (2013) believes that honest and scrupulous engineers in a consulting company may meet with

resistance from clients and colleagues when attempting to incorporate into their design uncertainty that others may wish to ignore. It can be argued that codes containing partial factors or load and resistance factors determined carefully and scientifically would be of assistance in minimizing this problem.

Limit states design codes have not been and could not be based primarily on reliability analysis and research, largely because the research was not available. Many challenges remain, chiefly among them a proper assessment of soil variability both for code design and for specific projects. Although it is a stated goal of modern limit states codes to use acceptable probability of failure as a design reference and a basis to develop values of materials or resistance factors, the present reality is that codes have been largely developed based on calibrations, as noted by Länsivaara and Poutanen (2013), and code development committee deliberations. As results of better, more specific research become available, code designers may be able to take advantage of these results to modify values and recommendations in future editions of design codes.

Although this paper focuses on safety and serviceability as addressed by codes and design calculations, not every risk can be quantified; some are best avoided. For example, blunders can be avoided by having layers of checks on procedures and calculations put in place. Other risks may be avoided by taking a broad view of the project, looking for things that can go wrong and adapting designs and construction procedures based on this assessment. Robert (2013) discusses this type of project-management approach to risk management.

The next sections examine specific aspects of the design of slopes, foundations and retaining structures using modern limit states codes.

## 4 STABILITY OF SLOPES

### 4.1 General Remarks

Stability limit states, also known as ultimate limit states, are associated with dangerous outcomes. In mechanics terms, they would often be associated with collapse. A loss of slope stability would be associated with large slope movements after driving actions overcame available resistance. This is the primary design check for slopes, although more contained slope movement that would not be analyzed in the same manner are also sometimes critical.

Loads are, for the most widely used slope stability analysis methods, expressed through driving moments. The driving moment due to dead loads (self-weight of a potential sliding mass or permanent external loads acting on the boundary of the sliding mass) may be denoted by  $M_{d,DL}$ . The driving moment due to live loads (nonpermanent loads on the crest of the slope, such as vehicular loads) may be denoted by  $M_{d,LL}$ . Resistances are expressed through a resisting moment  $M_r$ . In terms of driving and resisting moments, inequality (1) becomes:

$$(RF)M_{rn} \geq (LF_{DL})M_{d,DL}|_n + (LF_{LL})M_{d,LL}|_n \quad (5)$$

Studies on probabilistic stability analysis of slopes and embankments started in the early 1970s and have continued (e.g., Cornell 1971, Tang et al. 1976, Christian et al. 1992). In early slope reliability analysis studies, the first-order second-moment method was popular for the assessment of probability of slope failure. More recent studies have made use of the first-order reliability method (FORM) and Monte Carlo simulations (MCSs) to assess the probability of slope failure (Christian et al. 1994, Tobutt 1982).

In probabilistic slope stability analysis, it is essential to consider the spatial variability of the soil in the slope. This is the most significant shortcoming of original studies on this topic. If a soil slope is assumed to remain homogenous when soil properties are varied (say, using Monte Carlo simulations)

in an analytical study, the reality that these properties in fact vary with some degree of independence across the slope is completely ignored, and probabilities of failure calculated in this manner will not be accurate. Salgado and Kim (2013) have used an advanced FORM method, coupled with random field modeling of the slope, to develop resistance factors for use in slope stability as a function of soil spatial variability. Although the results have been consolidated in terms of resistance factors, it would be possible to develop partial material factors from their reliability analyses. The fact that model uncertainty in slope stability analysis is small to negligible (Kim et al. 1999, Kim et al. 1992, Yu et al. 1998) makes it relatively easy to obtain Eurocode-like material factors from reliability analyses such as those performed by Salgado and Kim (2013).

As pointed out by Länsivaara and Poutanen (2013), use of (5) or another inequality like it requires the slope stability software to provide the values of moments from permanent, temporary and other loads separately. Although not yet common, this will not be an impediment for long (STABL WV, for example, is a slope stability software that already provides this level of information detail).

A key decision in performing reliability-based design or developing resistance or material factors is what the acceptable probability of failure  $p_f$  is. Christian (2004) characterized risk as a function of number of fatalities, referring to various efforts by regulators and others. Most slopes would be well designed with  $p_f = 10^{-3}$ , but lower values of  $p_f$  might be needed for structures whose failure would lead to large economic or human loss.

### 4.2 Papers

Länsivaara and Poutanen (2013) review the prescriptions of the Eurocode (EN-1997) regarding slope stability. The Eurocode prescribes three different ways of checking stability: design approaches DA1, DA2 or DA3.

According to these authors, DA1 with combination 2 and DA3 are most commonly used for slope stability analysis. There are also three different reliability classes (RC1, RC2 and RC3), which allow the accounting for consequences of attainment of a limit state, into which a slope would be fit before analyses are done. Another way allowed by the code to account for consequences of attainment of a limit state is to increase material factors for cases with more consequential failures.

As seen earlier, material strength is divided by a material factor, and this is supposed to account for uncertainties in shear strength and any analysis uncertainty. The material factor for effective stress analyses for soils modeled as Mohr-Coulomb materials is 1.25; for a total stress analysis of a slope with soil modeled as a Tresca material, it is 1.4. Self-weight is left unfactored but live (temporary) loads (actions) on the slope are factored by 1.3. Länsivaara and Potanen (2013) suggest that there is an "overestimation of safety" implied in typical factors of safety used in total stress analysis of the stability of clay slopes. Salgado and Kim (2013) also observed this possibility in the results of reliability analysis of slopes modeled using random fields.

Lechwicz and Wrzeński (2013) report on field-scale staged construction of an embankment on top of an organic soil deposit, the last stage built up until failure occurred. The shear strength of the soil profile on which the embankment was built was characterized using results of the vane shear test corrected according to the Swedish Geotechnical Institute method (Larsson et al. 1984) with correction factors determined based on triaxial compression (TC), triaxial extension (TE) and direct simple shear (DSS) testing of the materials in the laboratory. The shear strength data determined in this manner allowed estimation of the probability distributions of the undrained shear strength. Their analysis of the results of these field experiments focused on testing the Eurocode 7 DA1, DA2 and DA3 design approaches.

The embankment was constructed in three stages on organic subsoil from 1983 to 1987. The structure was then brought to failure by increasing the height of the fill (Wolski et al. 1988, 1989). The organic soil at the site, present as two separate layers (a 3.1-m-thick amorphous peat layer and a 4.7-m-thick calcareous-organic soil layer) is underlain by a sand layer. The water table is located near the ground surface, but the sand layer was subjected to artesian conditions, with the piezometric level as much as 1.5 meters above the ground surface. Effective stresses *in situ* were in the single digits (in units of kPa). The OCR of the organic soils was estimated to decrease from 5 near the surface to 2 at depth. The undrained shear strength was determined both before and after construction of the embankment. After consolidation, the strength was observed to increase below the embankment, with larger increases near the center. Interestingly, there seems to have been a slight reduction, on average, of the coefficients of variation of the shear strength from the values before embankment construction (all except one greater than 0.11 and as high as 0.19) after the embankment was constructed and consolidation completed; originally, these values were as low as 0.03, with several observations below 0.1. Consolidation may have evened out some spatial variability initially present.

The stability analysis performed for the third stage and the failure test assumed the organic subsoil to be divided into three different shear zones: A – below the embankment crest, B – below the embankment slope and C – to the side of the embankment. In these analyses, which relied on the Bishop Simplified Method, various approaches to account for uncertainty in shear strength were considered: direct use of mean values, use of characteristic values determined as the mean less 0.5 or one times the standard deviation, and application or not of a partial factor  $\gamma_m = 1.25$  to the mean and characteristic values of shear strength. This value is not the 1.4 prescribed by the Eurocode for Tresca materials, but the authors did not elaborate.

Based on comparisons between these different analyses and the results of the test embankment, the authors recommended use of design approach DA1 with combination 1 and use of characteristic values of undrained shear strength defined as a conservative mean (mean less a fraction of the standard deviation) for slope stability analysis under similar conditions. Design Approaches DA1 with combination 2 and DA3 were deemed excessively conservative.

One of the most challenging aspects of probabilistic stability analyses of slopes is that the spatial nature of the variability of slopes must be taken into account in order to produce reasonable results, as noted earlier. Lechwicz and Wrzesiński (2013) attempt to assess, using judgment, the degree of conservativeness of different approaches to determination of characteristic strengths and partial factors to use in design, but that appears to be a difficult task to complete until more rigorous analyses that fully consider spatial variability of the slope are properly done and scrutinized. The test to failure of the embankment slope that they describe is precisely the type of field result needed to combine with the rigorous reliability analyses done today to validate theoretical work. More information on spatial variability, which is difficult to assess, particularly in the horizontal direction, is certainly needed in field tests of this type.

## 5 FOUNDATIONS

### 5.1 General Remarks

Foundation engineering problems are interaction problems: a foundation element (e.g., a footing or a pile) or a collection of foundation elements interact with the soil around them through the interface between the elements and the soil. The presence of this interface can be exploited in probabilistic analyses of foundation limit states: the variability, spatial in nature, of soil

properties result in contact stresses at this interface that are a function of the response of the entire soil mass. It is customary to observe (directly measure or deduce from instrumentation using load cells and strain gauges) the values of these boundary loads on foundation elements, and the variability of these stresses can be used, combined with specific methods of analysis, to perform reliability analyses. This approach, as already discussed, is not viable for slope stability analysis.

Basu and Salgado (2012), for example, performed such an analysis for drilled shafts in sand. They placed the analyses of Loukidis and Salgado (2008) and Lee and Salgado (1999) on a probabilistic basis and used Monte Carlo simulations to determine the resistance factors corresponding to probability of failure equal to  $10^{-3}$  and  $10^{-4}$ . Rigorous reliability analysis combined with realistic and appropriate soil models, with a rigorous method of analysis of a particular boundary-value problem, and with careful accounting of variability of every random variable entering the calculation produces excellent and transparent results. The body of work of this type is still limited, but it is likely to produce results that will be useful to code designers.

Differently from slopes, which are most often checked for stability, deflection-based limit states, whether potentially leading to ultimate or serviceability limit states, are more frequent for foundations than a classical foundation plunge limit state. In more complex structures, such as piled rafts, analyses are more involved, often requiring numerical solutions, which makes a reliability analysis more challenging and makes it more difficult to consider spatial variability indirectly.

One of the hardest decisions for engineers to make in the context of reliability-based design is on the acceptable probability of failure. In every geotechnical design problem, the answer can be different. For example, in connection with pile foundations used in traditional solutions (not in a piled raft), a possible way to think of probability of failure  $p_f$  would be to pose a question such as "how often would an engineer be willing to deal with cracking of the superstructure (an indicator of a possible ULS) to keep initial foundations cost low?" A possible answer would be that no more often than would be the case if one pile in ten thousand settled too much, which could then lead to an acceptable probability of failure of  $10^{-4}$ .

### 5.2 Papers

Loehr et al (2013) discussed work that they have done for the Missouri Department of Transportation attempting to develop state-specific resistance factors for Missouri. The guidance offered by AASHTO on which resistance factors to use is very general, prompting this type of effort by individual states in the United States.

The work of Loehr et al (2013) aimed to develop prescriptions for drilled shaft design that would not be overly constraining. The authors worked with epistemic probabilities, which they however do not provide details on. One of the main advantages of LRFD, in these authors' view, is that LRFD enables placing a value on the marginal boring, CPT log or laboratory test, which in turn allows advocacy for a more complete site characterization. The authors illustrate this point with an example of drilled shaft design with site characterization done with different levels of detail. This potential use of LRFD, of facilitating the economic evaluation of site characterization and other decisions affecting design, has also been remarked on by other authors (e.g., Foye and Salgado 2005, Foye et al. 2011a and b).

Katzenbach et al. (2013) review a relatively new soil improvement method that resembles a piled raft. In this method, (usually unreinforced) concrete columns are installed beneath a raft (mat). The mat and columns do not actually touch, being separated by a layer of stone or gravel (Figure 2). The concrete columns, in effect piles, have diameter ranging from 0.25 to 0.80m.

A fundamental difference between design of this foundation solution and that of a piled mat is the presence of negative skin friction, as the layer of gravel pushes down on the soil, which compresses over time between the piles. The authors review French and German prescriptions for design of this type of foundation solution.

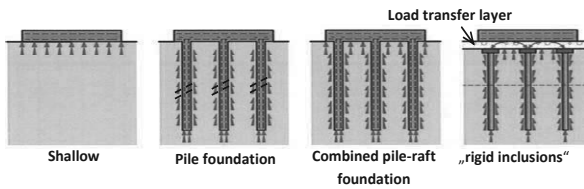


Figure 2 Comparison of common foundations solutions with pile-supported blanket solution (after Katzenback et al. 2013).

### 5.3 Discussion

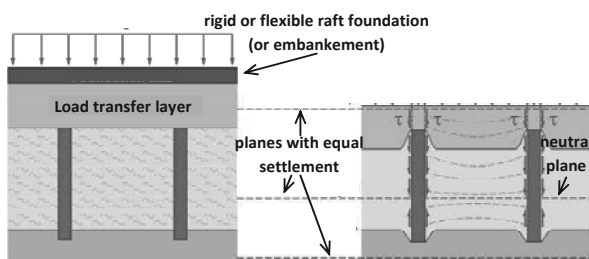


Figure 3 Occurrence of negative skin friction along unreinforced concrete piles caused by load applied by the layer of gravel on top of the column on the soil between the columns (after Katzenback et al. 2013).

## 6 EARTH RETENTION

### 6.1 General Remarks

Fundamental work on the probabilistic analysis of retaining walls has tended to focus on mechanically stabilized earth (MSE) walls. This work has resulted in part from the interest sparked by the AASHTO LRFD mandate in North America and the fact that MSE walls are widely used in transportation infrastructure.

While retaining wall limit states in general should be treated similarly to the slope stability limit state (because the pressure on the walls results from shear surfaces that develop in the backfill and that depend very much on spatial variability of shear strength in the backfill), the presence of an interface (the back of the wall) again allows the effects of the spatial variability of soil variables in the backfill to show as variability in contact pressure on the wall. Likewise, reinforcing elements in MSE walls will develop pullout resistance and exert stabilizing action on the backfill through the shear stresses (unit resistances) between them and the soil; variability of these unit resistances are then used in reliability analyses. In the case of MSE walls, instrumentation of reinforcements, including near the wall facing, provide data that can be used for estimation of both earth pressures and unit interface resistance of reinforcing elements (see, for example, Kim and Salgado 2012a,b).

An interesting issue in connection with retaining walls is the choice of limit states that must be checked in design. The traditional, idealized retaining wall limit states are sliding, overturning, bearing capacity failure and general instability. In MSE walls, the additional limit states of pullout and reinforcing element rupture must also be checked. However, as pointed out by Loukidis and Salgado (2012), realistic limit states tend to be a composition of these idealized limit states. Equally interesting, there is a relationship between mobilization of shear strength (and consequently pressures on the wall) and wall movement, and this relationship has implications for the setting up of

design situations. Merrifield et al. (2013) discuss aspects of this issue as well, as did Loukidis and Salgado (2012) and Simpson and Driscoll (1998).

### 6.2 Papers

Ho et al. (2013) used the design approach proposed in CIRIA Report C580 in the design of a permanent cantilevered, large-diameter, bored-pile wall (Figure 4) for the support of sloping ground bordering a new road, which now exists in front of the wall. This is the first known Hong Kong project in which a permanent retaining structure was designed using the C580 design approach. The wall, which is approximately 110m long, is made of 33 bored piles with diameter equal to 3.0m. Figure 5 shows a cross section of the wall as well as the original and post-construction ground profile.



Figure 4 Bored-pile wall in Hong Kong (after Ho et al. 2013).

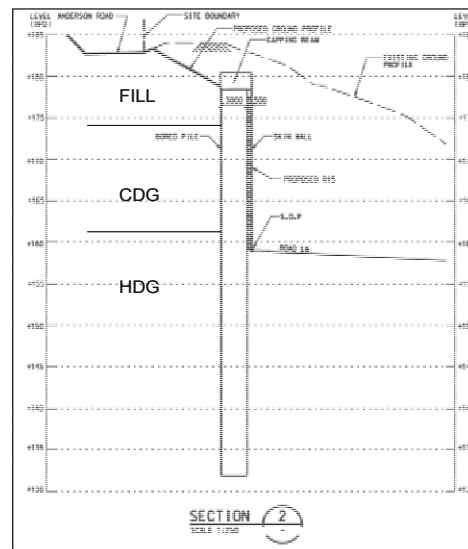


Figure 5 Cross section of bored pile wall in Hong Kong (after Ho et al. 2013).

The ground profile at the site consists essentially of fill and weathered granite. In the original ground profile, the fill had a maximum thickness of 8m and contained loose to medium dense, gravely silty sand or sandy clayey silt, with some rock and concrete fragments as well as domestic waste. Completely decomposed granite (CDG) and highly decomposed granite (HDG) are present below the fill. The granites in the area are commonly fine- to medium-grained and greyish pink to pinkish grey in their fresh state. The thickness of the CDG ranges from 5 m to 10 m with SPT blow counts ranging from 15 to 100. The HDG occurs with SPT blow counts greater than 100. The maximum depth to moderately to slightly decomposed granites (M/SDG) ranges from 15m to 40m below original ground level. The water level was assumed at the excavation level on the excavation side of the wall and within the the CDG layer on the

retained side. In the site characterization stage, a total of 105 consolidated undrained (CU) triaxial tests, with pore water pressure measurement, were carried out. Soil design parameters for the fill, CDG and HDG were determined based on this testing program.

Ho et al. (2013) used two methods to design the wall. One method is the traditional method used in Hong Kong. The other is the CIRIA C580 method. Use of the C580 design approach netted 10 % overall cost savings over what the wall would have cost if designed using the traditional method. This represented an amount of HK\$ 9.6 million saving on this project. This case history illustrates that geotechnical engineering still relies on design methods that may be too conservative, and that savings can be significant when more recent knowledge is put into use.

Merrifield et al. (2013) review the history of and difference in current practice of design and testing of ground anchors in Europe. Ground anchors were first used in rock applications, but found their way into soil retention systems in the 1950s. Ground anchors are routinely used in connection with embedded (cantilevered) walls and may be viewed as enablers of this type of retaining wall, which would otherwise be prohibitively expensive.

Merrifield et al. (2013) discuss the differences between the treatment of anchors in European national codes and provisional (draft) prescriptions in Eurocode (EN-1997:2004). Prescriptions must address the two primary limit states: an ultimate limit state that will prevent pullout of an anchor under the maximum expected load it will be subjected to during its service life and a serviceability limit state related to deflections, which may be stated in terms of loss of load or creep (in fact, an anchor is likely to both move or deform and see a degradation in the load it carries over its service life).

The authors call attention to an important, if not universally recognized, detail concerning definition of limit states for walls: serviceability limit states develop with retaining wall movement that is typically not sufficient to develop active or passive pressures historically assumed to act behind or in front of the wall. As a consequence, serviceability limit states must be defined separately from ultimate limit states. From the point of view of anchor design, anchor resistance must be sufficient to carry loads transferred to it by either serviceability or ultimate limit states, and the draft provisions do account for that as well.

In part because of the empirical basis for anchor design, proof loading has always been part of ground anchor design and installation practice. Again, each country handles testing and proof loads differently, a point that Merrifield et al. (2013) discuss in detail.

## 7 SUMMARY AND CONCLUSIONS

Safety and serviceability are the requirements that any geotechnical design must meet. These requirements are met through risk management, specific design checks and proper construction. The design checks are calculations that show that no limit state is achieved or exceeded. One of the main tasks of the geotechnical designer is to properly identify applicable limit states and then produce a design that keeps the probabilities of their occurrence below threshold levels. Guidance on identification of limit states and specific checks to be done in connection with these limit states are often prescribed by codes. Recent codes, such as the Eurocode and LRFD codes attempt to anchor the design process the notion of an acceptable probability of failure, which depends on the problem and consequences of achievement of a specific limit state. In the absence of specific guidance, definition of what these limiting probability values are sometimes must also be defined by the designer.

The papers submitted to the XVIII ICSMGE illustrate the complexity of probabilistic limit-states based design and encapsulation of it in design codes. Much work still remains for

researchers and code development agencies to produce codes and methods of analysis that will enable engineers to produce designs that achieve safety and serviceability in an optimal and economical manner.

## 8 REFERENCES

- Basu, D. and Salgado, R. 2012. "Load resistance factor design of drilled shaft in sand from soil variables." *Journal of Geotechnical and Geoenvironmental Engineering*, ASCE 138(12), 1455–1469.
- Christian, J. T. (2004). "Geotechnical engineering reliability: How well do we know what we are doing?" 39<sup>th</sup> Terzaghi Lecture, Journal of Geotechnical and Geoenvironmental Engineering, 130(10), 985–1003.
- Christian, J. T., Ladd, C. C., and Baecher, G. B. 1994. "Reliability applied to slope stability analysis." *J. Geotech. Eng. Div.*, 120(12), 2180-2207.
- CIRIA (Construction Industry Research and Information Association). 2003. *Embedded Retaining Walls – Guidance for Economic Design (C580)*, CIRIA.
- Cornell, C. A. 1971. "First-order uncertainty analysis of soils deformation and stability." Proc. 1<sup>st</sup> international Conference on Applications of Probability and Statistics in Soil and Structural Engineering, Hong Kong, 129-144.
- European committee for standardization, CEN. 2004. *EN 1997-1 Eurocode 7: Geotechnical design*. Brussels: European committee for standardization.
- Foye, K. C. and Salgado, R. 2005. "Soil Characterization for Consistent Reliability in the Load and Resistance Factor Design of Pile Foundations." International Symposium on Frontiers in Offshore Geotechnics. Perth, Western Australia, Australia.
- Foye, K. C., Prezzi, M., and Salgado, R. 2011 "Resistance Factors for Design of Piles in Sand: Tools to Understand Design Reliability." 3rd International Symposium on Geotechnical Safety and Risk. Munich, Germany.
- Foye, K. C., Prezzi, M., and Salgado, R. 2011 "Developing Resistance Factors for Design of Piles in Sand." GeoRisk 2011. Atlanta, Georgia.
- Ho, A., Wright, M. and Ng, S. 2013. "Deep Excavation in Hong Kong – Cantilever Bored Pile Wall Design Using CIRIA Report No. C580." *XVIII International Conference on Soil Mechanics and Geotechnical Engineering, September, Paris, France*.
- Katzenbach, R., Bohn, C. & Wehr, J. 2013. "Comparison of the safety concepts for soil reinforcement methods using concrete columns." *XVIII International Conference on Soil Mechanics and Geotechnical Engineering, September, Paris, France*.
- Kim, D.W. and Salgado, R. 2012a. "Load and resistance factors for external stability checks of mechanically stabilized earth walls." *Journal of Geotechnical and Geoenvironmental Engineering*, ASCE 138(3), 241–251.
- Kim, D.W. and Salgado, R. 2012b. "Load and resistance factors for internal stability checks of mechanically stabilized earth walls." *Journal of Geotechnical and Geoenvironmental Engineering*, ASCE, 138(8), 910-921.
- Kim, J., Salgado, R., and Yu, H. S. 1999. "Limit analysis of soil slopes subjected to porewater pressures." *J. Geotech. Geoenviron. Eng.*, 125(1), 49-58.
- Kim, J., Salgado, R., and Lee, J. 2002. "Limit analysis of complex soil slopes." *J. Geotech. Geoenviron. Eng.*, 128(7), 546-557.
- Lämsivaara, T. & Poutanen, T. 2013. "Slope stability with partial safety factor method." *XVIII International Conference on Soil Mechanics and Geotechnical Engineering, September, Paris, France*.
- Larsson R., Bergdahl U., Eriksson L. 1984. Evaluation of shear strength in cohesive soils with special reference to Swedish practice and experience. SGI Inf. Linköping. No. 3, 1-32
- Lechowicz, Z & Wrzesiński, G. 2013. "Assessment of embankment stability on organic soils using Eurocode 7." *XVIII International Conference on Soil Mechanics and Geotechnical Engineering, September, Paris, France*.
- Lee, J. and Salgado, R. 1999. "Determination of pile base resistance in sands." *Journal of Geotechnical and Geoenvironmental Engineering*, ASCE, 125(8), 673-683.
- Loehr, J.E., Bowders, J.J., Rosenblad, B.L., Luna, R., Maerz, N., Stephenson, R.W., Likos, W.J. & Ge, L. 2013. "Implementation of LRFD Methods to Quantify Value of Site Characterization Activities." *XVIII International Conference on Soil Mechanics and Geotechnical Engineering, September, Paris, France*.

# L'expérience française insolite d'un encadrement juridique : une certaine maîtrise du risque du sol

Unusual French experience of a legal frame: a certain mastery of ground risk management

Carrière M.-L.  
Avocat au Barreau de Paris

**RÉSUMÉ :** Au début des années 1990 la géotechnique est considérée aux yeux des juges comme une science quasi-occulte, affaire de spécialistes. En vertu d'une jurisprudence constante, les tribunaux et cours condamnent systématiquement le bureau d'étude spécialisé, au motif qu'il est le seul à connaître les règles de l'art géotechnique et doit le maîtriser. Pourtant, dans une science incertaine par nature, un risque du sol résiduel est inéluctable et d'autant plus, dans un contexte de recherche d'économie et de limitation des missions d'ingénierie. L'article montre comment le cadre juridique a pu évoluer par une formation réciproque des juges et des ingénieurs. Une formation géotechnique basique de l'avocat permet une vulgarisation de l'art géotechnique à l'attention du juge pour apprécier les limites de cette science naturelle. Une formation des ingénieurs sur les risques encourus et un accompagnement de la profession pour l'élaboration d'une norme délimitant les missions aident à encadrer juridiquement l'activité géotechnique. A l'aube du troisième millénaire la responsabilité du géotechnicien n'est plus une fatalité. Le juge est devenu familier de cette science et maîtrise désormais les contours des missions, pour imputer le risque du sol à qui de droit !

**ABSTRACT:** On the early 90's, the geotechnical matter is considered as occult from the jury's point of view: it's a business for specialist people. Under a law, tribunals and courts routinely condemn consulting firm specializing on the grounds that it is the only one to know the rules of the geotechnical art and should control it. However, in an uncertain science by nature, a residual risk due to soil is inevitable, even more in the context of limited budgets and missions. The article shows how the legal framework can evolve by a mutual training of the judge and the engineer. The judges must be taught on the particularity of this natural science to enable them to appreciate the limitations faced by these soil engineers, but also create a legal framework around geotechnical activity. A basic geotechnical training for the lawyer is necessary with a possible extension to geotechnical art to the attention of the judge. The training course for engineers on the risks and the accompaniment of the profession enable to develop a standard for a legal framework defining missions. At the dawn of the third millennium the responsibility of geotechnical is no longer inevitable. The judge became familiar with the science and now controls the contours of missions, to allocate the risk of soil to the one who is responsible.

**MOTS-CLÉS:** sol, risque du sol , vice du sol, norme géotechnique, responsabilité.

**KEYWORDS:** soil, soil risk ,standard geotechnical , responsibility

## 1 UN CONSTAT : UNE JUSTICE INJUSTE

Début des années 1990, en France, un constat : La géotechnique est une science quasi occulte aux yeux des juges ; elle est affaire de spécialistes.

Et avec un esprit quelque peu provocateur, il n'est pas interdit de penser que cette science demeure souvent mystérieuse pour l'homme de l'art lui-même.

En vertu d'une jurisprudence constante, les tribunaux et cours condamnent systématiquement le bureau d'étude spécialisé, au motif qu'il est le seul à connaître les règles de l'art géotechnique et doit le maîtriser.

Mission impossible.

### 1.1 *Un certain droit, « spécificité française »*

La société occidentale a vu naître le principe de précaution, consacré en droit communautaire. Ce concept flou vient satisfaire la société du risque : Le caractère plausible du risque dans l'incertitude scientifique, la proportionnalité entre l'objectif poursuivi et les mesures prises, mais des méthodes

finaleme nt définies pour évaluer les risques qui engendrent une mise en œuvre délicate et source d'interprétation.

Au-delà de ce droit, finalement européen, qui ne saurait susciter une quelconque envie de nos voisins puisqu'ils en bénéficient, où est la « spécificité française » ?

Dans un Etat qui se revendique « de droit », l'exigence du risque 0, pourtant inaccessible, se dessine. « Au commencement, la terre était déserte et vide... » La société exige désormais la sécurité ; la perception des risques évolue. Parallèlement, les risques en font de même : Une urbanisation massive, la perte de mémoire collective, le progrès comme facteur de risques, les risques naturels et technologiques...

On note également une extension de la notion de préjudice, des risques considérés classiques dans des temps anciens, étant plus difficilement acceptés.

Ainsi, la mutualisation se fait socialisation du risque pour répondre à un grand principe sans cesse réaffirmé en droit français : la réparation intégrale du préjudice.

Mais la socialisation du risque n'exclut pas la responsabilité, elle répond à un besoin d'indemnisation. La médiatisation ayant un effet important sur la perception du risque, la responsabilité sans faute est souvent la règle pour parvenir à une réparation aisée du préjudice et la « punition » pénale, recherchée en tant que sanction.

En droit de la construction, la justice est rendue dans un cadre législatif rigoureux pour les intervenants à l'acte de construire. Après réception de l'ouvrage et durant dix ans, le maître de l'ouvrage bénéficie d'une présomption de responsabilité de plein droit des constructeurs, pour les dommages graves, « même résultant du vice du sol », selon la terminologie de l'article 1792 du Code civil, en vertu d'une loi Spinetta édictée en 1978 difficile à exporter...

En matière de sol et fondations, les dommages sont toujours graves en ce qu'ils compromettent la solidité de l'ouvrage ou le rendent impropre à sa destination. Ces dommages engendrent d'ailleurs les sinistres les plus coûteux.

Mais le sol est-il réellement vicié ?

### 1.2 Une science incertaine par nature

Le sol, fondement de la construction, constitue un élément difficile à appréhender, tant eu égard aux limites scientifiques pour le prévenir, qu'au coût de cette prévention.

Les difficultés pour limiter l'incertitude liée à la nature du sol et déterminer par avance le comportement des ouvrages devraient inciter le maître d'œuvre, « chef orchestre » de l'opération, à prévoir l'intervention d'un spécialiste aux différentes phases de construction, et non uniquement en amont, souvent avant démolition. Le géotechnicien, intervenu au stade de la faisabilité du projet, pourrait ainsi contrôler son adéquation à la nature des terrains rencontrés après excavation et le cas échéant, modifier son étude préalable.

Souvent mal reconnu, ou d'une telle hétérogénéité difficilement appréhendable, le sol demeure un milieu empreint d'incertitudes. Sa connaissance, par sa reconnaissance, dépend en outre de l'investissement du maître de l'ouvrage, bénéficiaire de l'opération de construction, le plus souvent propriétaire du terrain.

A ce titre, selon une jurisprudence [Cass. 3<sup>e</sup> civ. 19 juin 2003] désormais bien établie, le propriétaire du terrain en est le gardien au sens de l'article 1384 al. 1<sup>er</sup> du Code civil.

Il est ainsi responsable du risque du sol, puisque contraint d'indemniser les dommages engendrés au fonds voisin par un glissement de terrain. Est-ce toujours aussi simple ?

Un cas d'école géotechnique sans force majeure pour le juge: selon Philippe Guillermain, éminent expert judiciaire, spécialiste en géotechnique, « ce constructeur n'avait aucune raison, ni obligation technique, d'aller rechercher la présence d'hypothétiques marnières inconnues sur ce site à l'époque, à une profondeur de 12 m » et « la maison s'est normalement comportée de 1990 à décembre 1999, délai d'épreuve technique probant, confirmant le bien fondé du choix initial de fondation. » Puis, l'expert précise : « L'effondrement s'est produit brutalement à la faveur de fortes précipitations de fin décembre 1999. On connaît par expérience l'effet néfaste de l'eau dans un tel contexte. Un arrêté de catastrophe naturelle a d'ailleurs été pris pour cette Commune. Il correspond très exactement à la nature du désordre "mouvement de terrain" et à la période d'apparition "du 25 au 29.12.1999" »

Comment le juge, en première instance, puis en appel, a-t-il pu condamner dans un tel contexte ? En l'occurrence, en l'absence d'étude de sol ! Mais cela n'est tout de même pas justifié, à défaut de lien de causalité, élément substantiel pour retenir la responsabilité.

## 2 UN PARADOXE : UN GÉOTECHNICIEN RESPONSABLE MAIS NON COUPABLE

Un paradoxe : Un bureau d'étude géotechnique spécialisé, donc très exposé en termes de responsabilité et pourtant intervenant le plus souvent en amont de l'opération, sans aucunement participer à la conception, ni à la réalisation de l'ouvrage et sans pouvoir influencer sur la nature et l'ampleur des études au cours de l'élaboration du projet.

### 2.1 Un certain art de construire...

Ces hommes d'un art si particulier savent que la géotechnique comporte des risques importants eu égard aux incertitudes naturelles et qu'une pratique trop audacieuse emporte inéluctablement la sanction du juge. Mais rien ne justifie qu'ils supportent abusivement les conséquences de choix techniques ou économiques qu'ils n'ont pas maîtrisés au seul prétexte qu'ils sont les spécialistes du sol et en sont garants à ce titre.

Or, le géotechnicien est souvent perçu à tort comme le maître d'œuvre des infrastructures même s'il s'est vu confier la réalisation de quelques sondages et a donné des principes généraux de fondation en fonction des caractéristiques des terrains, avant élaboration du projet. Il fut un temps, pas si ancien, où le contrat d'un tel bureau d'étude spécialisé se résumait à une liste « ésotérique » d'appellations savantes (pressiomètres, pénétromètres, carottages...), auxquelles le juge répondait par une simplification extrême de sa pensée : un sinistre de sol est imputable au spécialiste du sol.

Pourtant, à un stade très préalable, sans définition du projet et communication des descentes de charges, parfois dans un site partiellement inaccessible avant démolition, avec des moyens financiers restreints limitant les investigations, le géotechnicien ne peut sérier le risque du sol pour le rendre résiduel.

Si l'objet de la géotechnique est d'étudier le sous-sol, elle ne saurait pallier le « vice du sol », au sens de l'article 1792 du Code civil, expression considérée impropre par Jacques Catz [Les constructeurs et le risque du sol], *Editions du Moniteur*, 1985], car le sol n'est jamais vicié, il est seulement mal reconnu.

En effet, deux évidences s'imposent :

- Il est impossible de reconnaître l'intégralité du sous-sol et l'étude sera nécessairement fondée sur un nombre limité de sondages.

- Le risque 0 n'existe pas ; un aléa géologique ou une simple hétérogénéité entre deux sondages peut être décelé ultérieurement.

L'hétérogénéité est propre au sous-sol puisqu'il est constitué de sols et de roches de nature et de consistance très variées façonnés par le temps, le climat, les événements tectoniques à l'échelle géologique, mais aussi par l'action de l'homme qui en a tiré profit (exploitations de carrières et de mines).

La connaissance partielle du sous-sol acquise par l'étude à un instant donné peut également être remise en cause par une évolution dans le temps (variation du niveau des nappes – gonflement et retrait des argiles – dissolution de gypse et création de cavités...).

De surcroît, l'ouvrage lui-même peut avoir une incidence sur le comportement du sol (ex : paroi moulée qui crée un barrage à l'écoulement naturel des nappes).

Tous ces facteurs excluent une analyse trop simpliste en termes de responsabilité ; le juge doit apprendre à s'adapter à la complexité de la matière. Sinon, c'est le terrain juridique qui s'en trouvera vicié.

## 2.2 *Avec un risque délibérément accepté*

L'étude géotechnique, masquée dans le sous-sol, ne procure rien de concret au maître de l'ouvrage et il fut un temps – et parfois on s'y croirait encore de nos jours –, où elle n'était qu'un « ersatz » d'étude géotechnique.

En toute conscience, il s'agissait de passer le cap de la réception pour bénéficier d'une assurance tous risques durant la vie décennale de l'ouvrage. Quelquefois, même relativement souvent en la matière, la nature ne le permettait pas. Le sinistre résultant d'une inadaptation de l'ouvrage au sol survient en toute logique en cours de chantier sans même attendre la superstructure.

Alors le juge a pris conscience. Dans le cadre d'un régime juridique immuable, « exceptionnellement », de la garantie décennale, il a compris qu'il lui appartenait en quelque sorte de « moraliser » le secteur de la construction, en appréciant la prise de risques, en particulier celui relatif au sol, et de la sanctionner.

Ainsi est née la notion jurisprudentielle d'acceptation délibérée d'un risque par le maître de l'ouvrage. En l'espèce, il avait été informé du risque d'effondrement de la falaise par un précédent entrepreneur qui avait refusé le chantier [Cass. 3<sup>e</sup> civ. 19 janvier 1994].

Il est édifiant de constater que les arrêts de la Cour dite « suprême » consacrant cette notion sont très souvent relatifs au risque du sol. Cela ne peut surprendre que les juristes, car les ingénieurs sont nécessairement convaincus du caractère aléatoire de la géotechnique.

Toutefois, la reconnaissance d'une acceptation délibérée des risques par le maître de l'ouvrage reste réservée à un nombre infime de cas. En effet, le juge a quelques exigences à l'égard de l'homme de l'art : le maître de l'ouvrage doit avoir été parfaitement informé d'un tel risque [Cass. 3<sup>e</sup> civ. 11 déc. 2007]. Et la perfection n'est pas de ce monde...

Le devoir de conseil est apprécié de manière extensive et en devient « irrésistible » : Dans le cas d'un glissement de terrain, alors que le maître de l'ouvrage était passé outre les conseils des constructeurs pour une solution de confortement de talus, il a été jugé « ... qu'il n'était pas démontré que cette société employait du personnel ayant une expérience et des connaissances spécifiques lui permettant d'appréhender dans le détail l'ensemble des questions techniques... » [Cass. 3<sup>e</sup> civ. 14 mars 2007] Comment le juge peut-il imposer une telle condition alors qu'un maître de l'ouvrage, le plus souvent profane, doit s'en remettre à la compétence de ses constructeurs et suivre leurs conseils ?

## 3 UNE CONVICTION : "LA GÉOTECHNIQUE POUR LES NULS"

Une conviction : Il faut enseigner aux juges la particularité de cette science naturelle pour leur permettre d'apprécier les limites auxquelles se heurtent ces mécaniciens du sol, mais également encadrer juridiquement l'activité géotechnique.

Deux moyens : une formation géotechnique « basique » de l'avocat pouvant offrir ainsi une vulgarisation de l'art géotechnique à l'attention du juge ; un accompagnement de la profession pour l'élaboration d'une norme juridique délimitant les missions et une formation des ingénieurs sur les risques encourus.

### 3.1 *La formation réciproque*

Faire entrer la science dans les prétoires pour mettre fin à ce dialogue de sourds, apparut comme une évidence. Il fallut déjà acquérir quelques notions de ce langage scientifique auprès d'un consultant en géotechnique, Francis Blondeau, acceptant de délaissé quelque peu le prestige de l'Ecole Nationale des Ponts et Chaussées, pour une mission plus terre-à-terre, celle de servir la cause d'un avocat en quête de vérité. Ce fut le temps des

pâtés de sable et de l'apprentissage des formations géologiques, sans réelle cohésion...

Globalement, on aura compris l'incidence de l'eau dans le sol sans jamais maîtriser les calculs de perméabilité et encore moins, cette ignorance hydrogéologique revendiquée de manière péremptoire par des géotechniciens. A l'échelle des temps géologiques, la géotechnique est récente en tant que science rationnelle, même si la technique empirique doit être aussi vieille que l'humanité. Dès lors, il est raisonnable de penser que son exercice devrait encore évoluer.

L'expérience des sinistres aidant, les fondations posées, le langage acquis, il n'était pas encore temps de prétendre donner la leçon au juge, et encore moins à l'adversaire, tous deux empreints de certitudes acquises au fil de décennies passées dans le flou artistique de cette science quasi-occulte.

La communication entre deux mondes est d'autant plus aisée par le balbutiement réciproque : les géotechniciens devaient apprendre des bribes du langage juridique pour mieux appréhender leurs risques en termes de responsabilité, avec les aléas judiciaires, aussi inéluctables que les incertitudes terrestres de leur science.

Ce fut le temps de la formation juridique axée sur les risques à partir de la relecture de sinistres. Et là, l'avocat a perdu tout sentiment de fierté face à ses châteaux de sable, devant la maîtrise par les ingénieurs de l'emploi des adverbes, de la conjugaison au conditionnel et autres artifices cherchant à les prémunir contre toute certitude. Une belle leçon d'humilité par le géotechnicien, « maître » en modestie, car la nature le commande.

Enfin, la liste de sondages faisant office de devis a pris la forme plus adéquate d'un contrat en bonne et due forme, avec des conditions générales d'intervention annexées permettant de mettre en exergue les incertitudes inhérentes à la science géotechnique. Mais surtout, l'intervention du bureau d'étude est désormais encadrée par la normalisation des missions géotechniques, principal acquis du siècle dernier en la matière.

### 3.2 *L'élaboration d'une norme*

An 2000... A l'issue de plusieurs années d'application d'un projet de normalisation, le nouveau millénaire a vu la naissance de la norme géotechnique NF P 94-500, fruit du travail de recherche de l'homme de l'art pour préserver ses droits face à une justice plus rigoureuse à l'égard du spécialiste de sol, dans les limites d'une science incertaine par nature qui dépend de l'investissement du maître de l'ouvrage.

Par un avant-propos très explicite, la norme expose la problématique des risques liés aux aléas géologiques pour sensibiliser le maître de l'ouvrage, mais également tous les intervenants à l'acte de construire. Par analogie aux missions de maîtrise d'œuvre, l'objectif est de les convaincre de la nécessité d'un enchaînement des missions géotechniques G1, G2, G3 et G4, le cas échéant G5, à tous les stades d'élaboration et de réalisation du projet pour identifier les risques et prendre les dispositions qui s'imposent.

La norme ne donne aucune illusion : il demeure toujours des risques de sol résiduels. Mais elle permet d'en prendre conscience et de les limiter. Nul n'est censé l'ignorer. Lorsqu'un prétendu expert judiciaire feint de l'ignorer, la sagesse du juge rétablit la vérité.

Un autre cas d'école sur un terrain glissant : Chargé d'une mission de diagnostic G5 en cours de chantier, dans un laps de temps très bref de quatre jours, un géotechnicien a donné des principes généraux à partir d'hypothèses en émettant des réserves sur un problème d'emprise qui ne pouvait être respectée et sur la nécessité d'une adaptation du projet.

Un glissement de terrain étant survenu, le réquisitoire de l'expert fut dirigé exclusivement contre cet intervenant spécialiste du sol aux motifs : de ne pas avoir consulté la carte géologique et effectué de recherche bibliographique de PPR, de ne pas avoir exécuté de sondages carottés et d'essais de



laboratoire, de ne pas avoir respecté l'emprise initiale du projet, de ne pas avoir proposé d'ouvrages de collecte des eaux, de ne pas avoir suivi le chantier et enfin, de ne pas avoir exigé une mission complète, étant de ce fait un piètre commercial !

Bénéficiant d'une « vulgarisation » géotechnique acquise par l'expérience, le juge - pourtant souvent enclin à suivre l'expert judiciaire, d'ailleurs nommé à cet effet -, a analysé tous les reproches dans leurs « aspects scientifiques, d'abord : essais de laboratoire (carottages, triaxiaux), principes d'analyse d'un glissement de terrain (cisaillement et étude de la résistance des sols, courbes de glissement, coefficient de sécurité)... ». Par une logique rigoureuse, le juge a mis en exergue le défaut de lien causal entre les insuffisances relevées par l'expert, notamment au titre de l'étude des couches profondes, et, le sinistre, avec un cercle de glissement à 4 m de profondeur. De surcroît, le juge a également apprécié les limites du diagnostic géotechnique G5 au sens de la norme NF P 94-500 et écarté le reproche afférent à l'absence de qualité commerciale du géotechnicien qui n'avait pas su vendre une mission complète : « *Ce reproche, outre qu'il révèle un acharnement certain à vouloir trouver en dépit des faits un chef d'incrimination, méconnaît le rôle du maître d'œuvre... et voudrait en outre voir le spécialiste des sols se transformer en commis voyageur préoccupé de placer un produit ou un service...* »

#### 4 CONCLUSION

Troisième millénaire : La responsabilité du géotechnicien n'est plus une fatalité. Le juge est devenu familier de cette science et maîtrise désormais les contours des missions, pour imputer le risque du sol à qui de droit !

Et contrairement à la garantie décennale, la norme... nos voisins nous l'envient : « *la mission confiée se situe au stade de l'avant-projet (G1) et non au stade du projet définitif lequel tombe dans la mission G2* » [Tribunal civil de Luxembourg 2 juin 2010]. Une nouvelle étape : l'exportation de la norme...

# Ideas for improved geotechnical structures for natural disaster mitigation

## Idées pour l'amélioration des ouvrages géotechniques pour l'atténuation des catastrophes naturelles

Heerten G.

*Naue GmbH & Co. KG, Germany*

Vollmert L.

*BBG Bauberatung Geokunststoffe GmbH & Co. KG, Germany*

**ABSTRACT:** Floods, earthquakes, tsunamis, landslides or avalanches / rock fall are current threats to human beings around the world. Geotechnical structures can be improved or developed with the use of geosynthetics to mitigate the impact of these kinds of natural disasters and to minimize damage and casualties. With erosion-resistant dykes the impact of flooding can be significantly reduced when the overtopping of a dyke cannot lead to a dyke failure with a big gap in the dyke with concentrated discharge. Embankment dams reinforced with geosynthetics are much more resistant to earthquake loading than conventional concrete structures. Artificial tsunami shelters as artificial hills are currently discussed to establish safe places near the coast. Finally new model studies are showing that the behaviour of embankments against dynamic rock fall impact can be significantly improved by reinforcing the structure with geogrids

**RÉSUMÉ :** Les inondations, tremblements de terre, tsunamis, glissements de terrain ou avalanches / chutes de pierres, sont des menaces courantes pour les êtres humains partout dans le Monde. Les ouvrages géotechniques peuvent être améliorés ou développés par l'utilisation de géosynthétiques pour atténuer l'impact de ces catastrophes naturelles et minimiser les dommages et causalités. L'impact des inondations peut être considérablement réduit avec des digues résistantes à l'érosion, car en cas de débordement, un déversement concentré n'entraînerait pas de rupture dans la digue. Les digues en remblai renforcé par géosynthétiques sont beaucoup plus résistantes aux contraintes sismiques que les ouvrages conventionnels en béton. Les abris artificiels contre les tsunamis, tels que des collines artificielles, sont actuellement considérés pour établir des lieux sûrs à proximité des côtes. Enfin, les études menées sur de nouveaux modèles montrent que le comportement des remblais de protection contre les chutes de blocs à impact dynamique peuvent être considérablement améliorés par le renforcement de la structure avec des géogrilles.

**KEYWORDS:** geosynthetics /geogrids, natural disasters mitigation, dykes/levees, embankments, tsunami shelter, rock fall protection.

### 1 INTRODUCTION

World's population is growing further. Increasing numbers of people are living in mega cities close to flood plains of rivers and oceans endangered by floods or tsunamis, but also in areas endangered by earthquakes or landslides. Natural disasters have created and will create huge material damage and a high number of casualties. But already after a short time the experience is forgotten and the intention to spend money for improving the safety fades away. But it is the responsibility of governments and authorities to ensure that appropriate strategies and measures for risk mitigation are in place and applied. And it is our obligation as geotechnical engineers to communicate improved design and construction methods for geotechnical structures for natural disaster mitigation. Ideas for safer dykes of higher erosion resistance, for embankments with improved resistance to earthquake loading and/or higher protection against impacts from rockfall, avalanches or landslides and tsunami shelters are presented.

### 2 EROSION-RESISTANT DYKES / LEVEES

In the aftermath of past disastrous flood events in Germany and other European countries it became evident that levees are part of the society's infrastructure and need careful control and maintenance. Immediately after major flood events the willingness to improve flood protection structures is great and (tax) money is available. These programs to improve the flood protection should consider the present technical improvements e.g. for the construction of levees. The improvement of levee cross-sections by using different geosynthetics has developed to

be state-of-the-art (Heerten 2010). The use of nonwoven filter materials to form a filter-stable, erosion-resistant transition between levee core and the air-side drain and ballast body or the arrangement of geosynthetic clay liners (bentonite mats) as a water-side surface seal have already been included as established alternatives in current regulations and guidelines. Beyond the three-zone levee the effects of geosynthetics integrated into levees as safety measures have been investigated and documented to have a high resistance capability during overflow load conditions. Erosion processes on the inner embankment and the risks of unexpected levee breaches can be minimized with geosynthetic construction techniques; geosynthetics can also be employed as support facilities for emergency reinforcing measures. Internal erosion in the embankments and sudden breaches to the surface of dykes can be prevented with knowledge and implementation of geosynthetics. Thus, these technologies provide not just structural defences but more time for evaluating risk and providing emergency response to populated areas that are threatened by rising water levels.

Geosynthetic clay liners (GCL) as needle-punched bentonite mats have gained widespread acceptance for levee improvement projects in a lot of countries because these products create a simple, effective, economical seal for a levee that simultaneously provides erosion protection for the levee body (Heerten and Horlacher 2002). Following the Elbe River floods that took place in Germany between 2002 and the end of 2005, about 150 levee reconstruction projects are known, being carried out in this period, in which about 2.2 million m<sup>2</sup> of needle-punched nonwovens, about 300 000 m<sup>2</sup> of geogrids and about 700 000 m<sup>2</sup> of needle-punched geosynthetic clay liners

(bentonite mats) have been employed (Heerten and Werth 2006). One example is shown in Figure 1. In the meantime, needle-punched geosynthetic clay liners are considered as state-of-the-art construction materials in levee/dyke construction (DWA 2005) in Germany and show increasing acceptance and use also in other countries.

The installation of a GCL can be carried out in a simple manner with a minimum use of technical equipment. After construction of the profiled bedding the GCLs are unrolled and overlapped. Afterwards the GCL is covered with soil. According to DWA (2005), a cover layer thickness of 80 cm is recommended for both types of mineral sealing (GCL and compacted clay liner (CCL)) in order to withstand climatic influences like wet-dry or freeze-thaw cycles considering German climate conditions. Bentonite mats offer the advantages of low sensitivity to settling without degradation to seal characteristics (deformation up to 25 % for needle-punched GCLs), consistent quality even after installation as well as good friction behaviour for steeper embankment slopes. However, the potential effects of root penetration and/or rodent infestation must be given attention just the same as with classic compacted clay liner made of cohesive soil. These effects can be counteracted by the design of the levee's project-oriented cross-section geometry, the use of non-cohesive cover layers which are unattractive to burrowing animals (Figure 2) or by additional engineering measures. Further information about planning and building with geosynthetic clay liners can be found in Heerten and Werth (2010).

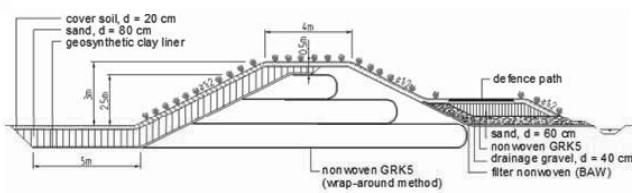


Figure 1. Cross-section of a levee after rehabilitation at Oder River, Poland (Heerten 1999).



Figure 2. Dyke rehabilitation Kinzig 2000 / 2001 - Needle-punched GCL as water-side lining covered with locally available sandy gravel and top soil for gras vegetation.

### 3 IMPROVING SEISMIC STABILITY OF STRUCTURES

#### 3.1 Geosynthetic reinforced soil structures (GRS structures)

In different regions of the world with potential high risks of earthquakes the advantages of geogrid reinforced embankments with reference to higher resistance to earthquake loading are well known and experienced. Based on the authors knowledge most know-how and experience with geogrid/geosynthetic

reinforced soil structures (GRS structures) under earthquake loading have been generated in Japan, where even fast train tracks are constructed on embankments by using GRS structures.

This development is based on the very positive experience with geosynthetic reinforced soil structures under seismic loading in Japan e.g. during the Kobe earthquake. Figure 3 is showing a GRS structure before and after the Kobe earthquake (Tatsuoka 2008).



Figure 3. Geosynthetic reinforced soil structure (GRS structure) as railway embankment after completion 1992 and after the Kobe earthquake 1995 (Tatsuoka 2008).

The synthetic polymeric materials used for soil reinforcement applications (mainly geogrids) are thermoplastic materials with visco-elastic material properties. The partial safety factor for creep (A1) is often the most important reduction factor to calculate the (long-term) design strength (F<sub>Bi,d</sub>) of a geosynthetic reinforcing element based on the characteristic (short-term) tensile strength (F<sub>Bi,K0</sub>) estimated for a given reinforcing product by lab testing.

It has to be pointed out again and again that creep of a synthetic reinforcing product is a product-specific visco-elastic material response and not a deterioration or damage to the product like e.g. corrosion for metal products. Therefore the special product characteristics of polymeric geogrids for soil reinforcement show that after a period of sustained loading in a soil structure an additional spontaneous dynamic load can be met by the original short-term tensile strength of the product. In a new seismic design code for Japanese railway structures this background is considered for the first time in geotechnical engineering. NO creep reduction factor is considered to obtain the design tensile strength of geosynthetic reinforcement under additional seismic loading.

The NO-creep-reduction-approach for seismic loading of geosynthetic reinforced structures (GRS) is part of the new concepts and procedures for the recent developed design code for Japanese railway structures reported by Tatsuoka (2009) with the following key elements:

- a) very high design seismic loads (i.e. , level 2), as those experienced during the 1995 Kobe earthquake;
- b) design against level 2 based on residual displacement;
- c) the use of both peak and residual shear strengths with well-compacted backfill;
- d) design based on the limit equilibrium stability analysis;
- e) control to high backfill compaction and good drainage;
- f) strong recommendation of GRS structures as highly earthquake-resistant soil structures;
- and
- g) no creep reduction to obtain the design tensile strength of geosynthetic reinforcement.

When following this design code, engineers naturally chose GRS structures.

### 3.2 Geogrid reinforcement for masonry walls in houses

It is also known that a lot of casualties during earthquakes are caused by falling bricks, when masonry walls in the houses e.g. between steel frames are collapsing. An important improvement of stability under seismic loading can be achieved by geogrid reinforcement of masonry walls (Figure 4) as investigated and developed in Germany at Bauhaus-University Weimar (Burkhardt et al 2005).

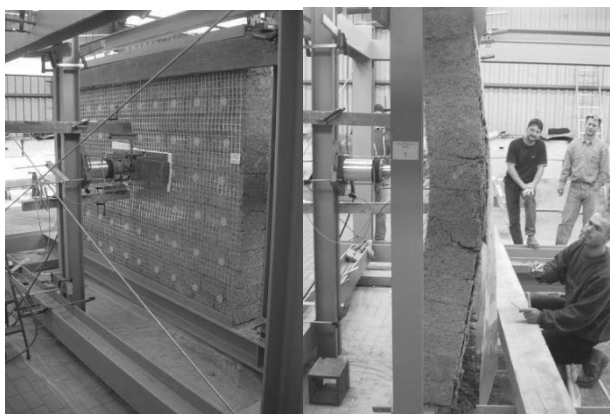


Figure 4. Strength test of geogrid reinforced masonry wall (Burkhardt et al 2005).

## 4 TSUNAMI SHELTER

When a tsunami warning is given people have to leave low coastal areas as quick as possible. After the devastating tsunami of 2004 in the Indian ocean in the meantime a “Tsunami Early Warning System” is in operation. But a big challenge still is the organization of an effective evacuation of the people living in the endangered big cities at the coast in the available very short time of about 30 minutes between “Tsunami Warning” and the arrival of the tsunami wave. In Indonesia for instance “raised earth parks” as cost effective tsunami shelter are discussed to establish safe places right at the coast. These artificial hills have to be high enough, stable against earthquake loading and erosion-resistant to the wash of the tsunami wave. It should also be easy for all people to get up to the safe top of the hill. Structures of geosynthetic-reinforced soil (GRS structures) can fulfil these requirements. Figure 5 is showing the idea of “TEREP – Tsunami Evacuation Raised Earth Park” as proposed for the city of Padang, Indonesia. For Padang five evacuation parks are discussed, each park as refuge for 15.000 people out of a 1.5 km radius. As of the author’s actual knowledge the construction of TEREP is still delayed. Let’s hope that fading away of the remembering of the last tsunami disaster is not the reason – the next tsunami will come!

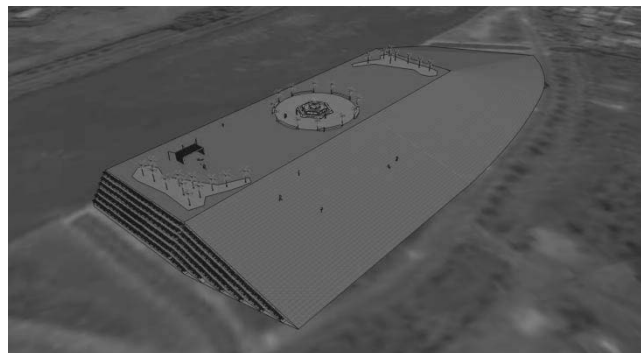


Figure 5. Idea of “Tsunami Evacuation Raised Earth Park” for the City of Padang, Indonesia (Tucker, 2010).

Tsunami defense systems can be separated into different “defense lines” as shown in Figure 6 (Recio, J. and Oumeraci, H. 2007). The artificial hills or “raised earth parks” are subject of the 4<sup>th</sup> defense line.

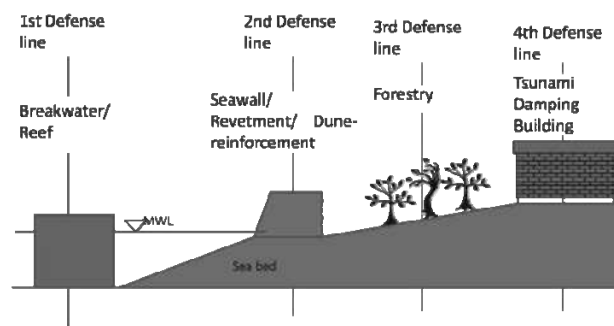


Figure 6. Different four defense lines for tsunami protection structures at endangered coast lines (Recio and Oumeraci 2007).

In the first off-shore defense line geosynthetic sand container which can be filled and placed with up to approx. 500 tons of sand have to be considered as cost efficient and environmental friendly solutions. The very positive results from e.g. the design and construction of the Narrowneck-Reef at the Goldcoast of Queensland, Australia with mega-sandcontainer made of needle-punched nonwoven staple-fibre geotextiles can be considered (Heerten 2010). At Narrowneck Reef the mega-sandcontainers have been hydraulically filled and installed with a special split-bottom hopper dredger (Figure 7).

In Japan geosynthetic reinforced structures for tsunami protection seawalls (defense line 2, Figure 6) are considered to improve the protection of nuclear power plants after the Fukushima disaster.

## 5 ROCKFALL-PROTECTION EMBANKMENTS

Much infrastructure buildings and densely populated areas with increasing population are located in rock fall areas. As rock fall protection by net-fences is restricted by the energy adsorption capacity (approx. 8000 kJ), embankments are built for higher design energies. New model studies to improve the prediction of dynamic rock fall impact on embankments have shown that the behaviour of embankments can be improved by reinforcing the structure with geosynthetics (geogrids). The lessons learned from the tests with geosynthetics are (Hofmann, R., Vollmert, L. and MÖlk, M. 2013):

- The model tests with the geosynthetics all showed a significantly larger lateral distribution (influence width) of the displacements. An influence width of at least 8 - 9 times the diameter of the sphere (the impact) can be estimated from the measurements and the pictures taken with the high-speed camera.

- Very slim constructions with uphill and downhill slope angles of 70° and 60° were also investigated. These exhibited a noticeably more elastic behaviour than pure soil embankments (Figure 8)
- However, they require a markedly greater freeboard than embankments with stacked-rock facing. For geogrid-reinforced structures, a freeboard of 1.5 times the sphere diameter can be considered as being on the safe side.

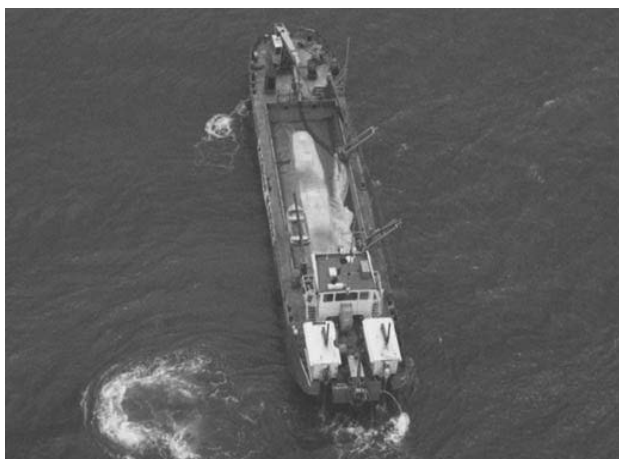


Figure 7. Hydraulic filling and placing of mega-sandcontainers with a split-bottom hopper dredger at Narrowneck Reef, Queensland, Australia (Heerten, 2010).

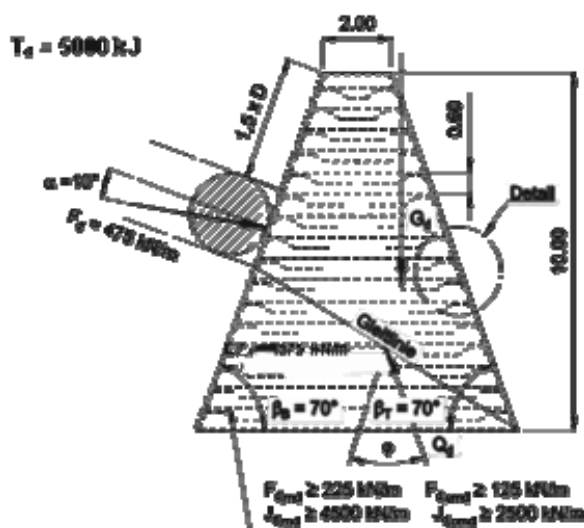


Figure 8. Possible slim and cost effective construction of rockfall embankments reinforced with geosynthetics. (Hofmann, R., Vollmert, L. and Molk, M. 2013).

Corresponding structures can also be used for torrent-control and avalanche-protection structures.

## 6 CONCLUSIONS

Considering geosynthetics for design and construction of dykes/levees, embankments in earthquake endangered areas, tsunamia protection structures and rockfall protection embankments can considerably improve the function of the structures. An important improvement of stability under seismic loading can also be achieved by geogrid reinforcement of masonry walls.

It is the task of the (geo)engineering community to inform the public about these improvements and the possible higher

level of safety for material goods and people in case of natural disasters. Let's hope that the last natural disaster experiences of earthquakes, tsunamis, floods and landslides and the need and intention to spend money for improving our safety does not fade away.

## 7 REFERENCES

Heerten, G. and Werth, K. 2010. Mitigation of flooding by improved dams and dykes. Proceedings of ICE-Ground Improvement, Volume 165, Issue 4.

Heerten, G. 1999. Erhöhung der Deichsicherheit mit Geokunststoffen. Proceedings of 6th Conference on Kunststoffe in der Geotechnik. Fachsektion Kunststoffe in der Geotechnik der Deutschen Gesellschaft für Geotechnik e. V. (DGGT) (ed), Technische Universität München, Germany.

Heerten, G., Horlacher, H.-B. 2002. Konsequenzen aus den Katastrophenhochwässern an Oder, Donau und Elbe. In geotechnik 25, No. 4, pp. 231ff, Verlag Glückauf (ed), Essen, Germany.

Heerten, G., Werth, K. 2006. Anwendung von Geokunststoffen bei der Deichertüchtigung. Proceedings of „Deichertüchtigung und Deichverteidigung in Bayern“. Department of Hydraulic and Water, Resources Engineering (ed), TU München, Wallgau, Germany.

DWA Report. Dichtungssysteme in Deichen. DWA Deutsche Vereinigung für Wasserwirtschaft, Abwasser und Abfall e.V. (German Association for Water, Wastewater and Waste) (ed), 2005.

Heerten G. 2010 Improved design methods for geogrid soil reinforcement and green-geo-engineering aspects. 14th Danube-European Conference on Geotechnical Engineering, Bratislava.

Tatsuoka F. 2008. Recent developments in practice and research of geosynthetic-reinforced earth structures in Japan. Keynote lecture, 30. Baugrundtagung, Dortmund, Germany.

Tatsuoka F. 2009: President's Corner, IGS News, Vol. 25, No. 3.

Burkhardt A., Friedrich T., Swain T.M., Schwarz J., Werner F., Nöthlich P., Batzke H. 2005. Sachbericht zum Verbund-Forschungsprojekt: "Steel Earthquake Design", Entwicklung eines Baukastensystems für kostengünstige erdbebengerechte Wohnbauten mit stählernem Tragwerk, Kooperation des Erdbebenzentrums und der Professur Stahlbau der Bauhaus-Universität Weimar mit der Rudolstädter Stahlbau GmbH, Weimar, Deutschland, Januar 2005.

Recio, J. and Oumeraci, H. 2007. Effect of deformations on the hydraulic stability of coastal structures made of geotextile sand containers. Geotextiles and Geomembranes, Volume 25, Issues 4-5.

Tucker, B. 2010. Seeking higher ground: A new approach to West Sumatra's Tsunami Risk. www.geohaz.org.

Heerten, G. 2010. "Geotextile containers for coastal and hydraulic engineering structures made of specially designed nonwoven geotextiles", 9<sup>th</sup> International Conference on Geosynthetics, Brazil.

Hofmann, R., Vollmert, L. and Molk, M. 2013. Rockfall –protection embankments – design model and construction. Proceedings of the 18th International Conference on Soil Mechanics and Geotechnical Engineering, Paris.

# Deep Excavation in Hong Kong – Cantilever Bored Pile Wall Design Using CIRIA Report No. C580

Excavation profonde à Hong Kong - Conception de mur cantilever à pieux forés suivant le rapport CIRIA n° C580

Ho A., Wright M., Ng S.

Ove Arup & Partners Hong Kong Ltd, Hong Kong Special Administrative Region, China

**ABSTRACT:** The design of cantilever retaining walls in Hong Kong is mainly carried out in accordance with Geoguide 1 (Second Edition) where a simplified model is adopted for the determination of the embedment depth of the pile. Following publication of CIRIA Report No. C580 (Embedded Retaining Walls – Guidance for Economic Design) several Hong Kong projects have adopted the design approach for temporary deep excavation works. This paper describes the first local application to a permanent cantilever wall approved by the Government of the Hong Kong Special Administrative Region, Geotechnical Engineering Office.

This paper compares the design approach of a large diameter bored pile cantilever wall for a large site formation development in Hong Kong using the traditional simplified model approach and the rational, safe and economic approach described in CIRIA C580. Detailed monitoring of the wall performance during construction is also described as a review of the C580 approach.

**RÉSUMÉ:** La conception des murs de soutènement cantilever à Hong Kong est principalement réalisée en conformité avec GeoGuide 1 (deuxième édition), où un modèle simplifié est adopté pour la détermination de la profondeur d'ancrage de la pile. Après la publication du rapport CIRIA C580 No. (incorporés Murs de soutènement - Lignes directrices pour la conception économique) plusieurs Hong Kong projets ont adopté l'approche de conception pour des travaux d'excavation temporaires profondes. Cet article décrit la première application locale d'un mur en porte à faux permanent approuvé par le Gouvernement de la RAS de Hong Kong, Bureau administratif du génie géotechnique.

Cet article compare la démarche de conception d'un diamètre foré grand mur en porte à faux poils pour un développement formation grand site de Hong Kong utilisant la méthode simplifiée modèle traditionnel et le rationnel, sûre et économique décrit dans CIRIA C580. Un suivi détaillé de la performance du mur en cours de construction est aussi décrit comme un examen de l'approche C580.

**KEYWORDS:** C580, Geoguide 1, cantilever retaining wall, case study, and cost saving.

## 1 INTRODUCTION

In Hong Kong, the CIRIA Report C580 – Embedded Retaining Walls – Guidelines for Economic Design (Gaba et al. 2003) has been critically reviewed by the Hong Kong industry and academic research community since its publication in 2003 and has been widely used in the design of temporary works for excavations and lateral support (ELS), (Sze et al 2005).

The authors have adopted the design approach of CIRIA Report C580 for the design of a permanent cantilever large diameter bored pile wall for the support of sloping ground and retaining around 20 m level difference for the construction of a new road in front of the wall. This is the first recorded Hong Kong project adopting the C580 design approach for a permanent application.

Analyses using the two design methods, Geoguide 1 (Second Edition) and CIRIA Report No. C580, for cantilever bored pile wall are discussed in this paper and the performance of the permanent cantilever wall during excavation is also presented.

## 2 SITE DESCRIPTION AND GROUND CONDITIONS

### 2.1 The Site

The Site is located at the north-eastern part of Kwun Tong, Kowloon, Hong Kong, see Figure 1. This Project comprises site formation works for a Public Housing development forming about 20 hectares of useable land on a sloping site. For the formation of the development platforms, retaining walls and slopes are required to create level platforms with significant level difference between platforms. Reinforced earth walls, reinforced concrete retaining walls as well as cut and fill slopes are proposed for retaining the level difference.

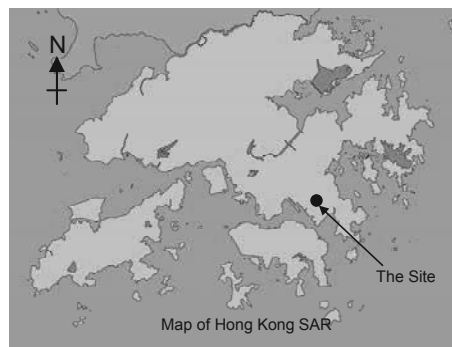


Figure 1. Site Location

The proposed works include construction of a new road as one of the principal vehicle accesses to the proposed development. The level difference between the proposed new road and an existing road and service reservoir varies from about 10m to 20m while the available horizontal clearance is approximately only 11m and 5m respectively. Different schemes were explored in the design stage including reinforced earth wall, reinforced concrete wall and steep cut slope with soil nails. These were found not feasible due to the extremely onerous space constraint. Therefore, a 3.0m diameter bored pile wall was eventually adopted. The proposed bored pile wall is approximately 110m long with 33 nos. of bored piles. The plan view of the proposed cantilever bored pile wall is illustrated in Figure 2 and the typical geological section is shown in Figure 3.

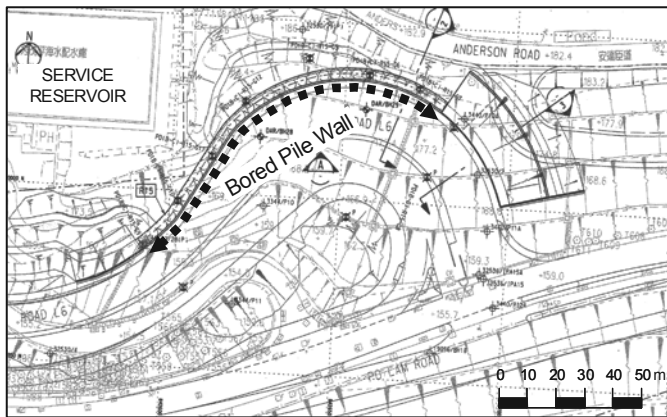


Figure 2. Layout of the bored pile wall with adjacent constraints

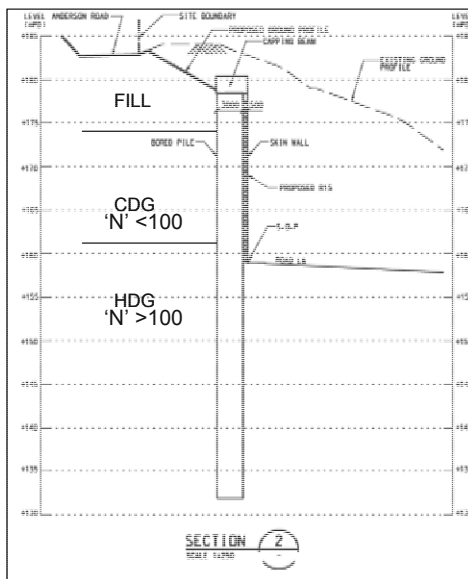


Figure 3. Geological section

### 2.2 Geological Conditions

The soil stratigraphy of the site comprises Fill and weathered granite. The fill was generally present within the Site with maximum thickness of fill up to 8m below existing ground level. The fill comprises loose to medium dense, gravely silty sand or sandy clayey silt, with some rock and concrete fragments and occasional domestic waste. The SPT 'N' values ranged from 5 to 15 indicating a loose state. Completely to highly decomposed granite is present beneath the superficial deposits. The granites are commonly fine to medium grained greyish pink to pinkish grey in colour in fresh state and the granite is weathered to varying depths. The thickness of completely decomposed granite (CDG) weathering Grade V ranges from 5 m to 10 m with SPT-N values from 15 to 100. Highly decomposed granites (HDG) of weathering Grade IV occurs with SPT 'N' value larger than 100. The maximum depth to moderately to slightly decomposed granites (M/SDG) encountered ranges from 15m to 40m below existing ground level. The uniaxial compressive strength of the M/SDG ranging from 40 to 135mPa. A geological section along the proposed cantilever bored pile wall is presented in Figure 4.

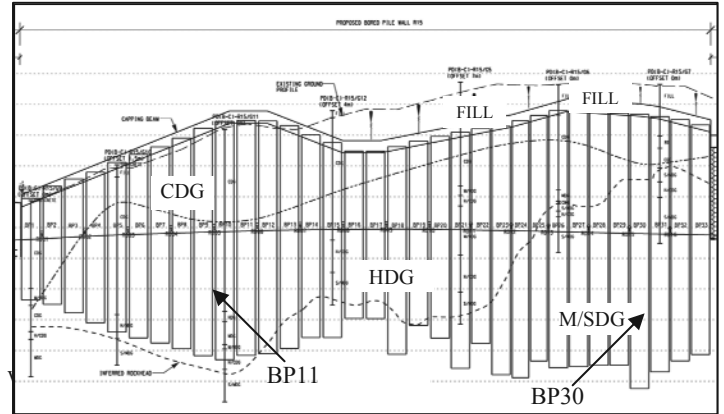


Figure 4. Geological long section

### 2.3 Geotechnical Design Parameters

The engineering properties of soils and rocks have been assessed using the field and laboratory test data. A total of 105 nos. consolidated undraining judgment with reference to the 'best fit', 'lower bound' and average values. The adopted design parameters are listed in Table 1.

Table 1. Summary of adopted soil parameters

Soil Stratum	Density ( $kN/m^3$ )	Cohesion, $c'$ (kPa)	Fictional Angle, (degree)	E value (MPa)
FILL	19	0	35	10
CDG	19	7	38	20
HDG	19	7	38	40

### 2.4 Groundwater levels

Piezometers and standpipes have been installed over the Site to provide groundwater information during construction. Generally, groundwater levels tend to be at or near the rockhead level and typically rise by up to about 3m after rainfall. The groundwater level is assumed to be +166 mPD on the retained side and at the excavation level (approximately +159 mPD) at the excavated side.

## 3 DESIGN OF CANTILEVER BORED PILE WALL

### 3.1 Design considerations

The results of analyses using the two design methods, Geoguide 1 (Second Edition) using a simplified model and CIRIA Report No. C580, for cantilever bored pile wall are presented. These calculations assume that the entire embedded portion of the cantilever bored pile wall is in soil. The effect of the capping beam is ignored in the analysis and the long term creep effect is to be controlled by the post construction of a 500mm thick skin wall.

### 3.2 Traditional Approach (Geoguide 1)

The traditional approach of the design of a cantilever bored pile wall was carried out in accordance with the recommendation given in Section 11.2.3 and Figure 50(c) of Geoguide 1 (Second Edition) where a simplified model was adopted for the determination of the embedment depth of the pile, (Pang et al 2005).

### 3.3 C580 Approach

In the CIRIA C580 design approach, the embedment depth is determined by achieving equilibrium in a soil-structure interaction analysis using a pseudo-finite element program FREW (Oasys 2007).

In the C580 design, partial factors as suggested in “Notes on Design of excavation and Lateral Support works Using the Limited State Partial Factor Method” (BD 2005) were adopted instead to reflect the application of limit state design.

The cantilever bored pile wall is subjected to the unbalanced loading of sloping ground and hydrostatic pressure. In both calculations, the pile heads deflections are controlled to be within 1% of the excavation depth.

### 4 DESIGN COMPARISON

Two sections are reviewed in this paper: BP11, which is the closest pile to the existing service reservoir, with retained height of 18.0 m and BP30, with retained height (deepest excavation) of 19.4 m.

The results of the deflection and internal structural force for both of the sections are presented in Figures 5 and 6 respectively.

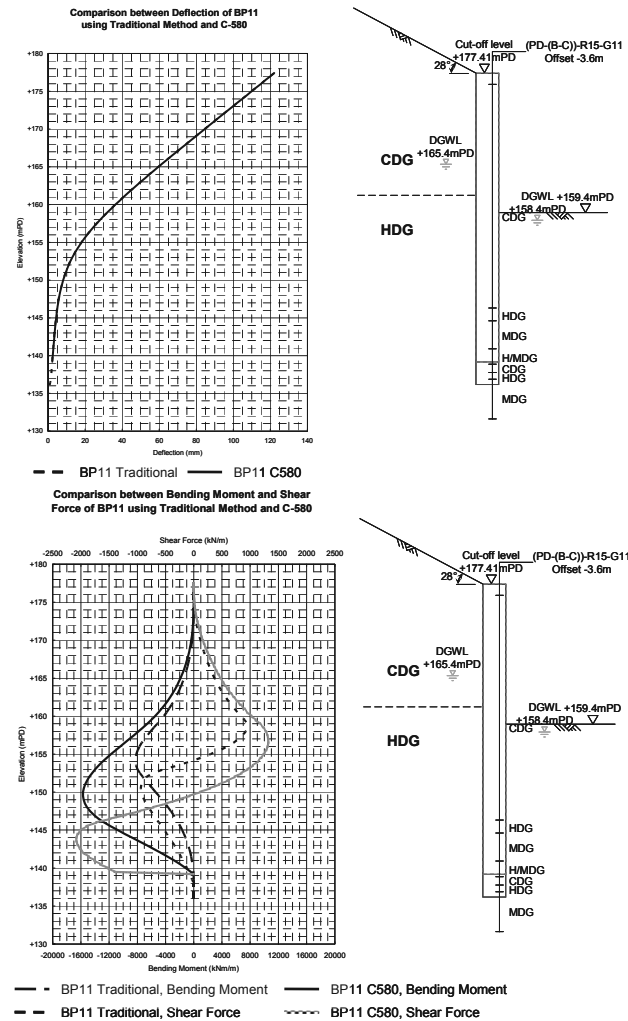


Figure 5. Calculated deflection, bending moment and shear force along cantilever bored pile wall (BP11)

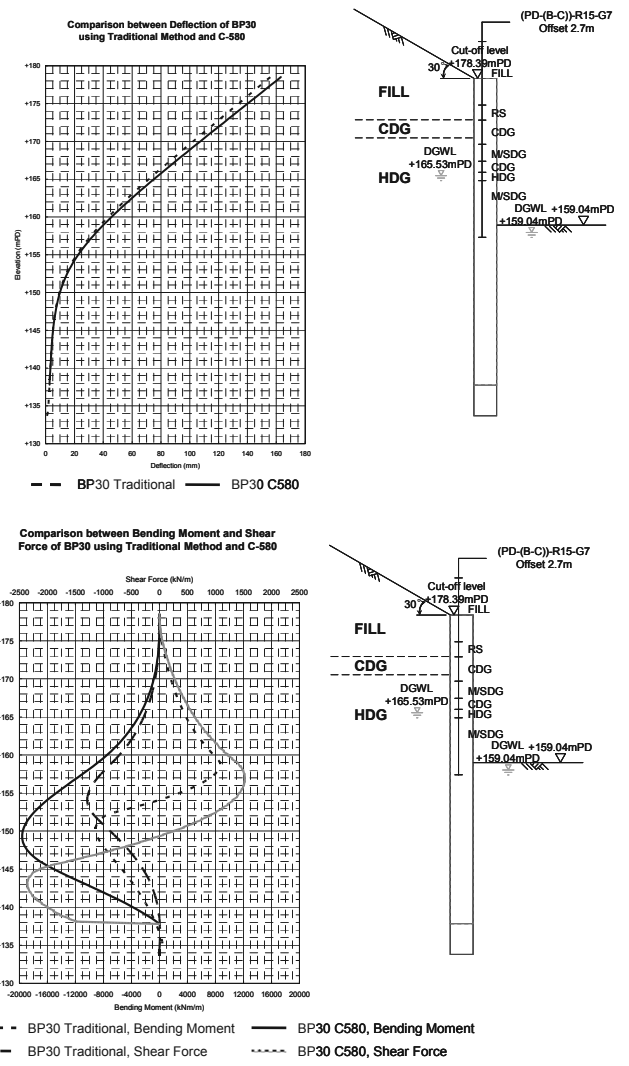


Figure 6. Calculated deflection, bending moment and shear force along cantilever bored pile wall (BP30)

The wall deflection, bending moment, and shear force of the two methods calculated using FREW at the final stage of the excavation were compared and summarized in Tables 2 and 3.

Table 2. Comparison of forces in wall and deflection (BP11\*)

	Embedment (m)	Bending Moment (kN-m/m)	Shear Force (kN/m)	Deflection (mm)
Traditional Approach (Geoguide 1)	23.21	8,267	1,041	146.7
C580	20.20	15,710	2,108	146.7
% Change	- 13%	+ 90%	+ 102%	No Change

\* BP11 is the closest pile to the existing service reservoir with retaining height of 18.0m



Table 3. Comparison of forces in wall and deflection (BP30#)

	<i>Embedment (m)</i>	<i>Bending Moment (kN-m/m)</i>	<i>Shear Force (kN/m)</i>	<i>Deflection (mm)</i>
Traditional Approach (Geoguide 1)	25.26	10,320	1,269	184.8
C580	21.24	19,610	2,403	193.9
% Change	- 16%	+ 90%	+ 89%	+ 5%

# BP30 is a pile with the highest retaining height of 19.4m

Based on the table above, there is an average decrease of 3m embedment by using C580 approach which is about 14% reduction to the original proposed embedment. However, the advantage of the reduction of embedment by using C580 results in a substantial increase in structural forces. Thus, it would require an increase of structural capacity by increasing the steel ratio in these cases.

## 5 COST SAVING

Although, the bending moment and shear force of the cantilever bored pile wall increased 90% in average as shown in Tables 2 and 3 above, the increase of the steel reinforcement percentage is only from 1.32% to 1.78% mainly due to the use of 3 m diameter bored pile with high bending capacity. The cost comparison using the two approaches is presented in Table 4.

Table 4. Summary of cost difference

	<i>Average pile length (m)</i>	<i>Steel percentage (%)</i>	<i>Total cost per pile (million HK\$)</i>
Traditional Approach (Geoguide 1)	43.0	1.32	3.03
C580	39.5	1.78	2.74
% Change	- 3.5	+ 0.46	- 0.29 (Saving of 10%)

The increase of the construction cost of the bored piles is not directly proportional to the increase of pile depth. Normally, it is an exponential increase with depth. Thus, the reduction of a pile embedment results in a saving in the overall construction cost. From the table above, there is about 10 % of overall cost saving on the cantilever bored pile retaining wall system when using C580 approach. This represents an amount of HK\$ 9.6 million saving on this project.

Besides the cost saving, there is also a non-quantified saving by using C580 approach such as the reduction of construction risk for deeper pile, (Sze et al 2005).

## 6 PERFORMANCE AND MONITORING

A 2.0 m deep capping beam was installed onto the pile heads before excavation and deformation markers were provided for the measurement of the wall top movement by land surveying methods. The excavation commenced in December 2011 and was completed by stages in June 2012, The condition of the cantilever wall during the excavation stage in January 2012 is shown in Figure 7.

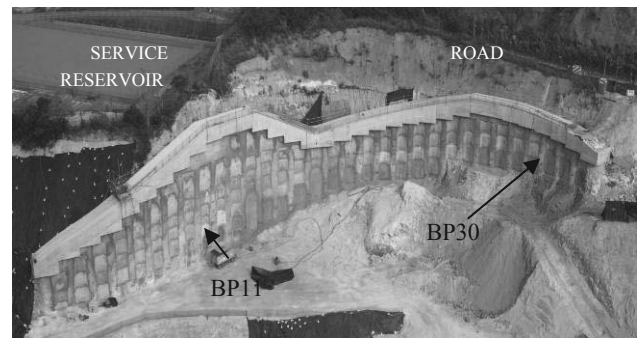


Figure 7: Excavation of the cantilever bored pile wall (January 2012)

The monitoring results of the wall top movement by land survey is compared with the design predictions are shown in the Table below. It is concluded that the use of C580 is a safe approach for the design of a permanent cantilever bored pile wall.

Table 5. Comparison of predicted and actual wall deflection

	<i>Traditional Approach (Predicted)</i>	<i>C580 (Predicted)</i>	<i>Actual lateral movement</i>
BP11	146.7 mm	146.7 mm	21 mm
BP30	184.9 mm	193.9 mm	20 mm

The actual movement from monitoring results maybe less than predicted due to:

1. the beneficial effect from the capping beam is not accounted for in the design
2. the slopping ground on the retaining side was significantly reduced in height due to the formation of a temporary piling platform and hence loading was reduced
3. local variations in the bedrock weathering profile was not accounted for in the design

A comprehensive and continuous monitoring of the wall movement was conducted throughout the construction period comprising the followings will be discussed in future:

1. Piezometers provided behind the wall to monitor the groundwater conditions.
2. Inclinometers and B-OTDR (Brillouin Optical Time Domain Reflectometer) optical fibres were installed into ducts reserved in the piles to monitor the behaviour of the cantilever bored pile wall.

## 7 CONCLUSIONS

The use of C580 design approach together with partial factors as suggested in "Notes on Design of Excavation and Lateral Support Works Using the Limit State Partial Factor Method" (BD 2005) is a safe and economic design for a cantilever bored pile wall. In general, there is a cost saving by using C580 design in comparison with the traditional design approach as described in Geoguide 1 (Second Edition)

However, the pile deflection profile and the long term effect (i.e creep effect) of a cantilever bored pile wall system using C580 design approach should be further reviewed.

## 8 ACKNOWLEDGEMENTS

Authors would like to thank Dr. P.L.R. Pang of Geotechnical Engineering Office, HKSAR for the review and guidance of the first C580 permanent cantilever wall design report.

9 REFERENCES

- BD (Buildings Department). 2011. Requirements for an Excavation and Lateral Support Plan Building (Administration) Regulation 8(1)(bc), APP-57. *Practice Note for Authorized Persons, Registered Structural Engineers and Registered Geotechnical Engineers.*
- CIRIA (Construction Industry Research and Information Association). 2003. Embedded Retaining Walls – Guidance for Economic Design (C580), *CIRIA.*
- Geotechnical Engineering Office (GEO). 1993. Guide to Retaining Wall Design (Geoguide 1, 2<sup>nd</sup> Edition). *Geotechnical Engineering Office, Hong Kong*
- Oasys Limited 2007. *Oasys FREW 18.2 User Manual*
- Pang, P.L.R., Lam, K.C., & Wong J.C.P. 2005. Introduction of the Limit State Partial Factor Method for Excavation and Lateral Support Works Design in Hong Kong. *Proceedings of Seminar On Excavation and Lateral Support, HKIE & HKGS, 2005.*
- Pappin, J.W., Endicott, John, & Clarke, John. 2005. Deep Excavation in Hong Kong – Design and Construction Control. *Proceedings of Seminar On The State-of-the-practice of Geotechnical Engineering in Taiwan and Hong Kong, HKIE, 2005.*
- Pappin, J.W., & Tham, T. 2005. Design Implications and Possibilities When Using C580. *Proceedings of Seminar On Excavation and Lateral Support, HKIE & HKGS, 2005.*
- Sze, James, & Lo, K.K. George. 2005. Case Histories to Illustrate the Saving of Using C580 Method of Design. *Proceedings of Seminar On Excavation and Lateral Support, HKIE & HKGS, 2005.*
- Yiu, Jack & Ko, M.C.Y. 2010. Comparison and Verification of Numerical Methods for Deep Excavation Design Adopting CIRIA Report C580. *Proceedings of Seminar On Geotechnical Aspects of Deep Excavation, HKIE & HKGS, 2010.*



# Comparison of the safety concepts for soil reinforcement methods using concrete columns

## Comparaison des concepts de sécurité pour les méthodes de renforcement de sol avec colonnes en béton

Katzenbach R., Bohn C.

Technical University Darmstadt, Institute and laboratory for geotechnics

Wehr J.

Keller Holding GmbH

**ABSTRACT:** The rigid inclusion concept is a soil reinforcement method using concrete columns with a small diameter compared to usual piles. The load bearing behaviour of such systems is presented in comparison to pile foundations and to combined pile-raft foundations. The safety concept developed in the French recommendations ASIRI for rigid inclusions is divided in two domains depending on the use of the columns, either to enhance the bearing capacity (analogy to piles) or only to reduce the settlements. The safety factors considered for the bearing capacity are compared with those in pile standards (Eurocode 7) and with those in different recommendations for similar reinforcement systems. The particular sensitivity of columns with small diameter is highlighted.

**RÉSUMÉ :** Les inclusions rigides sont une méthode de renforcement de sol avec colonnes en béton de diamètre faible par rapport aux pieux usuels. La répartition des charges au sein d'un tel système est présentée en comparaison avec les pieux et les fondations mixtes. Le concept de sécurité développé dans les recommandations ASIRI pour les inclusions rigides se divise en deux domaines d'utilisation, soit comme augmentation de la portance (analogie avec les pieux), soit uniquement comme réduction des tassements. Les facteurs de sécurité considérés pour la portance sont présentés en comparaison avec les normes de pieux (Eurocode 7) et avec différentes recommandations pour des systèmes similaires. On insiste sur la sensibilité particulière des colonnes de faible diamètre.

**KEYWORDS:** rigid inclusion, soil reinforcement, safety concept, Eurocode 7, column diameter, sensitivity

## 1 INTRODUCTION

One of the existing soil reinforcement methods with concrete columns is the so-called „rigid inclusions“ method, which has experienced a fast development in the last years, in particular in France (Briançon et al. 2004). This technique consists of a soil improvement method using in general non-reinforced concrete columns with a column diameter of 25 cm up to 80 cm with a soil displacement method. The rigid inclusions are in general separated from the structure by a granular load transfer layer (Figure 1).

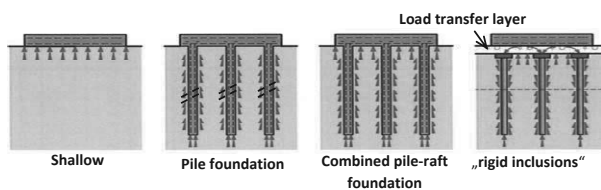


Figure 1. Rigid inclusions system in comparison with usual foundation systems

To some extent, these columns can be compared to usual piles. But in the case of rigid inclusions, the bearing capacity of the soil itself is taken into account in the design, like for combined pile-raft foundations (CPRF), which leads to considerable savings of concrete in the columns and of steel reinforcement in the foundation slab.

The technique with rigid inclusions is employed as well under shallow or raft foundations (e.g. industry halls, water tanks) as under embankments (e.g. high speed railway lines).

The French recommendations of the national research project ASIRI („Améliorations de Sols par Inclusions RIGides“), which have been published in 2012, provide a harmonization for the (in particular numerical) calculations (Jenck et al. 2004), for the safety requirements and for the execution of rigid inclusions. The initial point of the safety

theory is the European standardization, that is the French applications of the Eurocode 7 for the geotechnical safety checks, in general based on the pressuremeter design theory in France (Frank 2009), and the Eurocode 2 for concrete. Two different application cases are distinguished in ASIRI: the rigid inclusions can be either used to guarantee the stability of the structure or only as settlement reducers. These different application cases either in analogy to foundations systems or to soil reinforcement methods are reflected in the recommended safety concept in ASIRI.

## 2 LOAD BEARING AND DEFORMATION BEHAVIOUR OF RIGID INCLUSIONS

Rigid inclusions can both be embedded in a bearing layer or – in the general case – designed as floating elements in a compressible soil. The applied load from the structure on the system is distributed between the soil and the column heads. A so-called efficiency of the system can be defined from this load distribution as the ratio of the total load in the column head to the total vertical load. This definition corresponds to the pile-raft-coefficient for CPRF (Hanisch et al. 2002). The load distribution depends on different factors, in particular the rigidity of the foundation and of the soil, the thickness of the load transfer layer, the spacing between the columns and the rigidity of the columns (Okyay 2010).

The interactions between soil and columns in the case of a vertical load are presented in Figure 2. A negative skin friction affects the upper part of the columns due to the separation between slab and columns and because of the compressibility of the soil to be improved. This leads to a reduction of the load in the soil over the depth and to an increase of the force in the columns until the depth where the differential settlement between soil and column is equal to zero. Below this neutral plane, the force in the column is transferred to the soil through

positive skin friction and tip resistance, like for usual deep foundations.

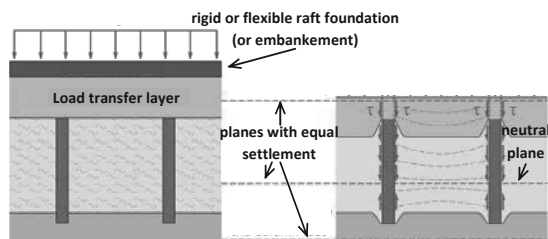


Figure 2. Load bearing and deformation behaviour of rigid inclusions

Horizontal loads can be supported by such systems as well, for example in the case of horizontally loaded isolated footings or when reinforced columns are used as nails against slope failure.

The usual applications of rigid inclusions are the following:

- Under large embankments or raft foundations to reduce settlements
  - At the border of embankments (slope) and potentially of raft foundations against slope failure, or to reduce settlements
  - Under isolated footings against failure of bearing capacity or sliding, or to reduce the settlements

### 3 SAFETY CHECKS IN THE FRENCH RECOMMENDATIONS ASIRI

First of all, the load distribution in the system without inclusions has to be determined, using the usual calculation methods for foundations or slopes. If the safety according to the French standards against failure of bearing capacity, sliding or slope failure in the ultimate limit state (ULS) is not guaranteed without columns, the subsequent safety checks correspond to the so-called „domain 1“ (Figure 3). Otherwise the columns can be used only to reduce the deformations („domain 2“). The required calculation of the load distribution with columns has to be carried out using comprehensive numerical models or using one of the recommended simplified models in ASIRI.

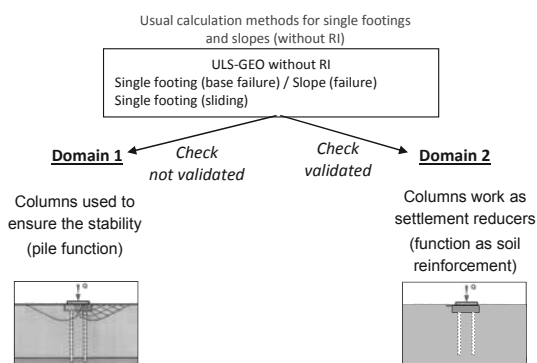


Figure 3. Classification in domain 1 and 2 in ASIRI

In the domain 1, the safety checks are carried out in analogy with the French Eurocode 7 application standards for deep foundations in addition to the standards for isolated footings and slope stability. The favourable action of the columns is taken into account by reducing the foundation load on the soil. Then, the checks of bearing capacity for the foundation or the slope are carried out normally with this reduced load. Besides, the bearing capacity of the columns has to be checked as well against ultimate limit states (ULS) against serviceability limit states (SLS) under the neutral plane (Figure 2), just like for piles after the French standard for deep foundations. The structural capacity of the columns, which are in general not reinforced,

has to be verified by means of a limitation of the compression and shear stresses in the column section in the ULS and SLS. The compatibility of the calculated vertical and horizontal deformations has to be checked in SLS.

In the domain 2, the columns are considered as pure settlement reducers. Therefore, no check of the bearing capacity is required in this domain, like in the design philosophy of the CPRF-guideline (Hanisch et al. 2002) or in the case of the so-called “creep piles”. Only SLS-checks have to be carried out here.

In both cases, compatibility verifications have to be done after the checks, in particular to verify the compatibility of the stresses in the load transfer layer.

### 4 COMPARISON WITH STANDARDS AND RECOMMENDATIONS

In this section, the recommended safety checks in ASIRI for the domains 1 and 2 are compared with the French and German piling standards and with recommendations for similar piles or columns systems, i.e. the German CPRF-Guideline (Hanisch et al. 2002) and the German guideline for stabilizing columns "Merkblatt für die Herstellung, Bemessung und Qualitätssicherung von Stabilisierungssäulen zur Untergrundverbesserung" (CSV-Merkblatt, DGGT 2002). Only the persistent load situation (BS-P in Germany) is considered here. The partial safety factors for the actions in this load case are the same in all regulations, that is 1,35 (respectively 1,5) for the permanent (respectively variable) loads in the case of foundations, and 1,0 (respectively 1,3) for the slope stability.

#### 4.1 External bearing capacity (GEO)

In ASIRI, only the domain 1, where the columns are necessary for the stability, is concerned by the safety checks in the ULS (Table 1). The verifications correspond to those of the French application standard of Eurocode 7 for compression piles (with a diameter of usually 1 m up to 3 m), in general with the use of empirical resistance values from pressuremeter tests (Table 2). The favourable effect of the columns in the checks of the footing or the slope is taken into account by reducing the total load by the force taken in the columns. After ASIRI, no pile loading test has to be done in the design phase for the determination of the bearing capacity. However, loading tests have to be carried out in the execution phase according to ASIRI to verify the previously determined bearing capacity.

In the CPRF-guideline (Hanisch et al. 2002), no distinction is made between a use as “settlement reducer” or as “resistance increaser”. The maximum characteristic resistance is defined here from the load-settlement curve of the global system, and divided by a safety factor to obtain the design value (Table 3). The bearing capacity of the piles themselves has not to be verified, since the whole system made of the slab, the piles and the soil has already to be stable. In the CSV-guideline on the contrary the bearing capacity of the single columns always has to be checked, with the additional assumption that the total applied load from the structure is taken by the columns (here diameter 12 cm up to 20 cm), which is on the safe side.

Table 1. Partial safety factors – ASIRI ULS-GEO

ULS-GEO (BS-P)	ASIRI (France)							
	Domain 1				Domain 2			
	Isolated footing		Slope	RI	Isolated footing		Slope	RI
Failure	Sliding	Failure			Sliding			
Partial safety factor for resistance	$\gamma_{R,v} \times \gamma_{R,d}$ = 1,4 x 1,2 = 1,68	$\gamma_{R,h} \times \gamma_{R,d}$ = 1,1 x 1,0 = 1,1	$\{\gamma_{\varphi} = \gamma_c\} \times \gamma_{R,d}$ = 1,25 x (1,1 bis 1,2) = 1,38 bis 1,5	$\{\gamma_b = \gamma_s\} \times \gamma_{R,d1} \times \gamma_{R,d2}$ = 1,1 x 1,15 x 1,1 = 1,39	/	/	/	/
Remark	load reduction due to RI (Slope only drained here model factor for reinforced soils depending on the sensitivity towards deformations)			like piles under the neutral plane empirical values (pressuremeter method)	no stability check	no stability check	no stability check	no stability check

Table 2. Partial safety factors – Eurocode ULS-GEO

ULS-GEO (BS-P)	Eurocode 7 Germany				Eurocode 7 France			
	Isolated footing		Slope	Piles	Isolated footing		Slope	Piles
	Failure	Sliding			Base failure	Sliding		
Partial safety factor for resistance	$\gamma_{R,v}$ = 1,4	$\gamma_{R,h}$ = 1,1	$\gamma_{\varphi} = \gamma_c$ = 1,25	$\gamma_b = \gamma_s$ = 1,4	$\gamma_{R,v} \times \gamma_{R,d}$ = 1,4 x 1,2 = 1,68	$\gamma_{R,h} \times \gamma_{R,d}$ = 1,1 x 1,0 = 1,1	$\gamma_{\varphi} = \gamma_c$ = 1,25	$\{\gamma_b = \gamma_s\} \times \gamma_{R,d1} \times \gamma_{R,d2}$ = 1,1 x 1,15 x 1,1 = 1,39
Remark			only drained here	with empirical values	with pressuremeter method		only drained here	with empirical values (pressuremeter method)

Table 3. Partial safety factors – Recommendations ULS-GEO

ULS-GEO (BS-P)	CPRF-Guideline (Germany)			CSV-Guideline (Germany)			
	Combined pile-raft foundation		Slope	Isolated footing		Slope	Columns
	Failure	Sliding		Failure	Sliding		
Partial safety factor for resistance	$\gamma_{R,v}$ = 1,4	$\gamma_{R,h}$ = 1,1	/	/	$\gamma_{\varphi} \times \lambda_{pv}$ = 1,25 x 1,15 = 1,43	$\gamma_{sp}$ = 1,25 bis 1,4	
Remark	as global system		/	not taken into account	only drained here $\lambda_{pv}$ against chain reaction of columns	Assumption: total load in the columns; depending on number of load tests (in execution phase)	

According to the French application standards of Eurocode 7, safety checks for the resistance have to be carried out in the SLS as well. This has been adopted in ASIRI for the domain 1. Therefore a so-called "pile creep load" has been defined in the French standards as 70% (for displacement piles) of the total resistance as a reference in the SLS. The safety against failure of bearing capacity of single footings also is increased in comparison with the ULS. In the domain 2, only the compatibility of the displacements has to be investigated. In the German application standards of the Eurocode 7, only the limits of deformation have to be controlled in the SLS.

#### 4.2 Internal structural capacity (STR)

The safety factors for the maximum compression in the section of the rigid inclusions in the ULS and SLS are similar to those for piles in Eurocode 7 (with reference to Eurocode 2 for the concrete). The safety factor for the resistance in ASIRI is up to approximately 2 to 11 depending on the limit state, the execution type, the slenderness of the column and the quality controls. In order to avoid very small column diameters, the mean compression stress in the section is in all cases limited to 7 MPa in the ULS (domain 1). Adapted values have to be considered for domain 2 (SLS).

Although the rigid inclusions are not used as tension piles, tension stresses can develop in the section resulting from bending moments. In the domain 1, the columns have to be

reinforced in the same way as piles according to Eurocode 2 as soon as tension stresses appear in the section. On the other hand, in the domain 2 tensile stresses up to the characteristic value of the tensile strength of the concrete are allowed. If this value is exceeded, the columns have to be reinforced as well.

The internal resistance can be particularly endangered in the case of unreinforced columns with very small diameter (Wehr & Sondermann 2011). For this reason, no shear stresses are allowed in ASIRI for unreinforced columns with a diameter smaller than 30 cm (cp. 40 cm for conventional piles). Buckling effects have to be analysed also for these small diameters and for very soft soils (pressuremeter modulus EM smaller than 3 MPa). The minimum allowed diameter in ASIRI for unreinforced columns is 25 cm.

In the CPRF-guideline (Hanisch et al. 2002) the internal resistance has to be checked in the same way as for conventional pile foundations.

According to the CSV-guideline (DGGT 2002), a safety factor of 2 has to be considered for the mean compression, in comparison with 2 up to 6 for the maximum compression stress in the ULS and 7 MPa for the mean compression stress in ASIRI. According to this guideline, the buckling has to be checked only in soft layers with an undrained cohesion smaller than 10 kPa. This is not in accordance with the present state of the art for slender piles: buckling effects can already appear for

soils with greater undrained cohesion (Vogt et al. 2005 and Eurocode 7 - DIN 1054 - 2010).

#### 4.3 Sensitivity of columns with small diameter

Two different design philosophies exist concerning the check of the bearing capacity of the column in the case of column diameters greater than 25 cm. The philosophy can be either without safety check (ASIRI in the domain 2 or CPRF-guideline, where the system is checked as a global system including slab, piles and soil), or with safety check in accordance with the piling standards (ASIRI in the domain 1). For smaller column diameters with a load transfer layer there is no recommendation for the use as pure settlement reducers, use which namely is only applicable for systems with a sufficient ductility and possibilities of load redistribution (flexible connection between piles and slab or relatively large column diameter).

Special attention must be paid to the particular sensitivity concerning the internal resistance of columns beneath the load transfer platform under horizontal loadings. Horizontal loads from the structure lead to shear, bending moments and thus possibly tension in the column section. Though the concrete design is regulated uniformly and with an adequate safety factor for all diameters, the particular importance of the interactions between the structure and the system made of soil and columns is not completely described in the current state of the art, in particular for very slender elements and under special temporary loading cases.

On the safe side, it can be assumed that the total horizontal load is taken by the columns, but this may lead to an uneconomical design. Furthermore, any execution imperfections in the position of the columns (eccentricity), in the column diameter or in their inclination can have a considerable influence in the case of small column diameters and induce undesigned shear stresses, even in compliance with the given tolerances. Attention must be paid to the execution stages too, where the top of the columns can be particularly endangered due to heavy vehicle traffic.

## 5 CONCLUSIONS

The soil reinforcement method with rigid inclusions is a soil stabilization system with columns which are separated from the structure by a load transfer layer, and which work either by analogy with a pile foundation or with a conventional soil reinforcement technique. The distinction between two application domains 1 and 2, either for an increase of the bearing capacity (1) or for a settlement reduction (2) reflects this difference. In the domain 1, the safety checks are similar to those for conventional pile foundations. In the domain 2, only SLS checks have to be carried out, including a control of the internal resistance of the columns.

The use of such column systems in the domain 2 corresponds to the design philosophy of the CPRF-guideline (Hanisch et al. 2002), in which no verification of the bearing capacity of single piles has to be done, and where only the stability of the global system and of course the structural capacity have to be checked.

In the CSV-guideline (DGGT 2002), a higher safety level than in ASIRI and in the CPRF-guideline is considered for the external resistance for the relevant small diameters. Indeed, the bearing capacity of single columns must always be carried out with the assumption of the total load in the columns, and the approach as settlement reducer without safety check for the single columns is not permitted for those diameters.

The internal resistance of columns with small diameters can be particularly threatened because of the significant influence of potential imperfections in the execution in this case. In the current state of the art of the soil-columns-structure interactions, an increased safety level should be taken into account for columns with small diameters under horizontal loads.

## 6 ACKNOWLEDGEMENTS

Special thanks go to Professor Roger Frank of Ecole des Ponts ParisTech (Navier-Cermes), Bruno Simon from the French company Terrasol and scientific director of ASIRI and Serge Lambert from the French company Keller Fondations Spéciales for the scientific and practical explanations of the recommendations ASIRI.

## 7 REFERENCES

- Briançon, L., Kastner, R., Simon, B. and Dias, D. 2004. Etat des connaissances – Amélioration des sols par inclusions rigides. *International Symposium on Ground Improvement ASEP-GI 2004*, Laboratoire Central des Ponts et Chaussées, Dhouib, A., Magnan, J.-P., Mestat, P., 15-43.
- DIN EN 1997-1:2009-09. Eurocode 7: Entwurf, Berechnung und Bemessung in der Geotechnik – Teil 1: Allgemeine Regeln.
- DIN EN 1997-1/NA:2010-12. Nationaler Anhang – National festgelegte Parameter – Eurocode 7: Entwurf, Berechnung und Bemessung in der Geotechnik – Teil 1: Allgemeine Regeln.
- DIN 1054:2010-12. Baugrund - Sicherheitsnachweise im Erd- und Grundbau - Ergänzende Regelungen zu DIN EN 1997-1.
- Deutsche Gesellschaft für Geotechnik (DGGT) e.V. 2002. Merkblatt für die Herstellung, Bemessung und Qualitätssicherung von Stabilisierungssäulen zur Untergrundverbesserung, Teil 1 – CSV („Combined Soil Stabilization with Vertical Columns“) Verfahren (CSV-guideline).
- Frank, R. 2009. Design of foundations in France with the use of Menard pressuremeter tests. *Soil Mechanics and Foundation Engineering* 46 (6), 219-231.
- Hanisch, J., Katzenbach, R. and König, G. 2002. Kombinierte Pfahl-Plattengründungen, Richtlinie für den Entwurf, die Bemessung und den Bau von Kombinierten Pfahl-Plattengründungen (CPRF-guideline)
- Institut pour la recherche appliquée et l'expérimentation en génie civil - IREX 2012. Recommendations of the national project ASIRI („Amélioration des Sols par Inclusions Rigides“) for soil improvement with rigid inclusions.
- Jenck, O., Dias, D. and Kastner, R. 2004. Modélisation physique bidimensionnelle de l'amélioration des sols compressibles par inclusions rigides verticales. *International Symposium on Ground Improvement ASEP-GI 2004*, Laboratoire Central des Ponts et Chaussées, Dhouib, A., Magnan, J.-P., Mestat, P., 175-182.
- NF EN 1997-1 2005. Eurocode 7: Calcul géotechnique – Partie 1: Règles générales.
- NF EN 1997-1/NA 2006. Annexe Nationale – Eurocode 7: Calcul géotechnique – Partie 1: Règles générales.
- Normenhandbuch Eurocode 7 2011. Geotechnische Bemessung, Band 1: Allgemeine Regeln, Beuth Verlag, Berlin.
- Okay, U.S. 2010. Etude expérimentale et numérique des transferts de charge dans un massif renforcé par inclusions rigides. Application à des cas de chargements statiques et dynamiques. PhD in the scope of ASIRI, INSA Lyon and Université Claude Bernard – Lyon 1.
- PR NF P94-261 2012. Norme d'application nationale de l'Eurocode 7 - Calcul géotechnique – Fondations superficielles.
- NF P94-262 2012. Norme d'application nationale de l'Eurocode 7 - Calcul géotechnique – Fondations profondes.
- Vogt, N., Vogt, S. and Kellner, C. 2005. Knicken von schlanken Pfählen in weichen Böden. *Bautechnik* 82 (12), 889-901.
- Wehr, J., Sondermann, W. 2011. Risiken bei der Bemessung von Baugrundverbesserungsmethoden und pfahlähnlichen Traggliedern. *Bauingenieur* 86, 459-463.

# Slope stability with partial safety factor method

## Stabilité des pentes à l'aide de la méthode de sécurité partielle

Lämsivaara T., Poutanen T.

*Tampere University of Technology, Tampere, Finland*

**ABSTRACT:** In most European countries Eurocode 7 (EN 1997) has been taken into use in geotechnical design. Although there are several design approaches in EN 1997, slope stability is commonly addressed by applying partial safety factors to material properties and variable loads. The outcome of such procedure has been evaluated with emphasis on uncertainty and consequences of failure. An attempt to improve the EN-1997 partial safety method by the introduction of consequence classes into stability analysis is then presented. Therein the partial safety factors for soil strength will be connected into consequence classes, i.e. the consequences of possible failure. Eurocode 1990 defines the minimum reliability index values for different Reliability Classes, which are then associated with the consequences classes. The result by the alternative method is then compared with results from the original approach.

**RÉSUMÉ :** Dans la plupart des pays européens, l' Eurocode 7 (EN 1997) a été mis en service dans la conception géotechnique. Bien qu'il existe plusieurs approches de conception de la norme EN 1997, la stabilité des pentes est généralement abordée en appliquant des facteurs de sécurité partiels pour les propriétés des matériaux et des charges variables. Le résultat d'une telle procédure a été évaluée en mettant l'accent sur l'incertitude et les conséquences de l'échec. Une tentative pour améliorer la méthode de sécurité EN-1997 partielle par l'introduction de classes de conséquence dans l'analyse de la stabilité est ensuite présentée. D'après celle-ci, les facteurs partiels de sécurité pour la résistance du sol seront connectés en classes de conséquence, c'est à dire les conséquences d'un échec possible. L' Eurocode 1990 définit les valeurs minimales indices de fiabilité pour les différentes classes de fiabilité, qui sont ensuite associées à des classes de conséquences. Le résultat par la méthode alternative est finalement comparé avec les résultats de l'approche originale.

**KEYWORDS:** slope stability, partial safety method, reliability, consequence class

## 1 INTRODUCTION

In most European countries, Eurocodes have been taken into use as the main design standard. Eurocodes are based on the principles of limit states design in conjunction with the partial factor of safety method. EN 1990 describes the principles and requirements for safety, serviceability and durability of structures for all materials, whilst EN 1997 sets the rules for geotechnical design. For ultimate limit states design, Eurocode requires the verification of various ultimate limit states by applying partial safety factors to actions or the effect of actions, material properties or resistances. For geotechnical design, it has so far been impossible to find a single way of combining factors between actions, ground properties and resistances, and thus three different design approaches (DA) are permitted in EN1997. However, for slope stability there seems to be a rather large consensus on how safety should be applied. Most countries have chosen either design approach 1 (DA1) or 3 (DA3) for slope stability. DA1 consists of two combinations of sets of partial factors, of which combination 2 is the one relevant for slope stability and analogous to DA3. As there is such a large agreement on applying safety for slope stability it could be considered that this part of the geotechnical design is well formulated in the Eurocodes. The intention of this article is to critically review the applied partial factor of safety method for the slope stability with respect to reliability and consequences of failure.

## 2 SHORT OVERVIEW ON THE EUROCODES

### 2.1 *Safety in Eurocodes*

According to EN-1990 the partial safety factors should account for the possible unfavourable deviation of the property from its characteristic value and the uncertainties in the model used in calculations. The consequences of the ultimate limit states are further considered based on three consequences classes. Therein the consequence of failure is accounted by multiplying the factors for actions by a separate factor depending on the consequence. In principle the partial factors of safety can be determined in two ways. One is the conventional method where the factors are calibrated to past experience. The other is to use probabilistic methods and calibrate the factors against a target reliability index value.

For the most common design situations, corresponding to the reliability class RC2, the recommended reliability index  $\beta$  for a 50 years reference period is 3.8. This corresponds to nominal probability for ultimate limit states of approximately 1/15 000. Whilst some of the partial factors for actions have been determined based on probabilistic methods, it is the understanding of the authors that material and resistance factors for geotechnical design has mainly been determined based on calibration to old codes.

### 2.2 *Slope stability in EN-1997 according to DA1 and DA3*

As previously discussed, most European countries have chosen either DA1 combination 2 or DA3 to be used in slope stability.



In practice this means, that safety is placed on material properties (strength) and on actions. The recommended values for partial factors on soils strength are  $\gamma_{\phi} = \gamma_c = 1.25$  for effective stress analysis and  $\gamma_{cu} = 1.4$  for total stress analysis. The largest action on slope stability comes often from the soil weight itself. It is often considered difficult to factor soil weight properly and thus permanent loads are, also in the Eurocodes, left unfactored. Actions from variable loads like e.g. traffic load are on the other hand factored. Accordingly, the recommended values for permanent actions in EN-1997 is  $\gamma_G = 1.0$  and for variable actions  $\gamma_Q = 1.3$ .

According to the principles of EN1997 the overall stability is checked by requiring that the design value of the effects of actions  $E_d$  driving instability is less than the design value of the resistances  $R_d$ , i.e.  $E_d \leq R_d$ . However, the common methods for slope stability don't usually provide these values, but rather their ratio as an overall factor of safety. Thus an over-design factor ODF is introduced (Frank et al.), and the requirement for overall stability for DA 1 combination 2 and DA 3 is written as the factor of safety calculated using design values equal to  $ODF \geq 1$ .

In short the recommended values mean that if only effective stress parameters are used for all soil layers, and there is no variable load, the total factor of the safety requirement is  $F = \gamma_{\phi} = \gamma_c = 1.25$ . Similarly, if only undrained shear strength is used and there is no variable load, the total factor of safety requirement is  $F = \gamma_{cu} = 1.4$ .

Traditionally, slope stability analysis is most commonly done applying the total safety factor approach. There is a lot of experienced based data on total safety factors and many engineers feel that it is easy to relate to a single safety factor. As discussed by Leroueil et al. (1990) based on the observations by Bourges et al (1969) a reduction of the total safety factor below a certain limit, increases the settlements due to increasing horizontal movements in the soil. The use of such empirical knowledge supports the continuous use of a total safety approach for slope stability.

The application of partial factors of safety in the Eurocodes is indirectly implying that safety is placed where uncertainty is found accounting also for the consequences of failure. It is the intention to evaluate how true this implication is in relation to slope stability and to consider what could be done to improve it.

### 3 RELIABILITY BASED PARTIAL SAFETY FACTORS

#### 3.1 Introduction

In the following material partial safety factors are calculated based on reliability theory. Firstly the theoretical bases and the assumptions made in the calculations will be presented. Thereafter the calculations will be done corresponding to the present system in the Eurocodes placing safety on both the variable action and on material properties. An alternative calculation will then be presented where both the uncertainty related to loads and material properties will be placed on the material partial safety factor. In both the influence of a general uncertainty will also be studied.

In the alternative approach, the influence of the consequence classes into stability analysis will also be considered. As for now, the reliability differentiation in Eurocodes is done by applying a multiplication factor  $K_{FI}$  to unfavourable loads. The recommended values for the factor are 0.9, 1.0 and 1.1 corresponding to Reliability classes RC1, RC2 and RC3. For slope stability problems the effect of external actions on the stability varies from zero to rather substantial. It seems thus rather random to apply safety related to reliability and consequence of failure on such basis. On the other hand it is also uncertain should the factor be applied only to variable loads or also for permanent loads. In the latter case the problem on how to treat ground weight arises again. However, in EN 1990 it is also stated that, quote "Reliability differentiation may also

be applied through the partial factors on resistance  $\gamma_M$ .". The material partial factors for the alternative approach will thus be calculated for different target reliability index values corresponding to the different reliability classes.

#### 3.2 Theoretical bases

Firstly, the design point, the target reliability, the uncertainty, load distributions and the basic parameters must be set. The design point is set at unity and the target reliability feasible in the reliability calculation is chosen according to EN 1990. The permanent load distribution is assumed to be normal, the coefficient of variation equal to 0.1, the cumulative distribution is  $FG(x, \mu_G, \sigma_G)$  and the density distribution is  $fG(x, \mu_G, \sigma_G)$ . For variable load a normal distribution is also used, although Gumbel distribution might also be considered. The distributions are  $FQN(x, \mu_{QN}, \sigma_{QN})$ ,  $fQN(x, \mu_{QN}, \sigma_{QN})$ , 0.98 fractile is set at the design point according to one-year load. The coefficient of variation used for the variable load is 0.4 as in EN 1990.

The material property distribution is assumed lognormal, the cumulative distribution is  $FM(x, \mu_M, \sigma_M)$  and the density distribution is  $fM(x, \mu_M, \sigma_M)$ , the characteristic value is a 5 % fractile value which is set at the design point.

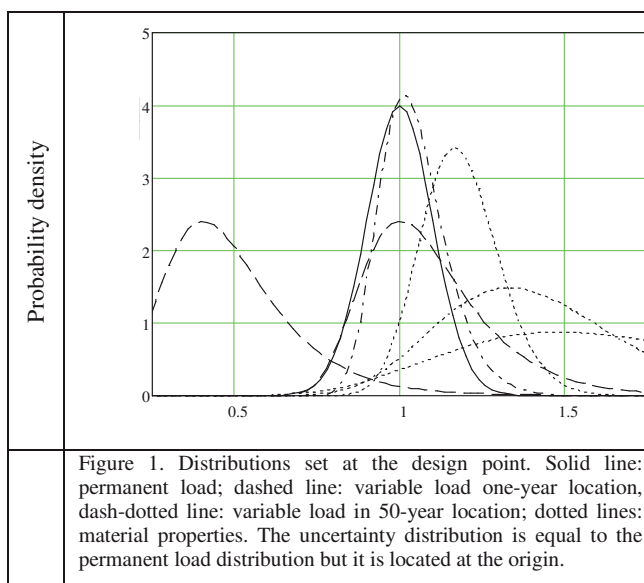
When the cumulative distribution of the load is  $FL(x, \mu_L, \sigma_L)$ , density distribution of the material property  $fM(x, \mu_M, \sigma_M)$ , the load safety factor is  $\gamma_L$  and the material safety factor  $\gamma_M$ , the formula for the failure probability  $P_f$  calculation is

$$1 - \int_0^{\infty} FL(x, \mu_L, \sigma_L) \cdot fM(x, \mu_M \cdot \gamma_L, \gamma_M \cdot \sigma_M \cdot \gamma_L, \gamma_M) dx = P_f \quad (1)$$

When two loads  $F_1(x, \mu_1, \sigma_1)$ ,  $f_1(x, \mu_1, \sigma_1)$  and  $F_2(x, \mu_2, \sigma_2)$ ,  $f_2(x, \mu_2, \sigma_2)$  with items  $x_{1,i}$  and  $x_{2,i}$  in fractile  $i$  are combined dependently in proportion  $\alpha$  and  $1-\alpha$ ,  $\alpha$  is the proportion of the load 1 in the total load, to obtain item  $x_{1,2,i}$  of the combination load in fractile  $i$ , is calculated by adding up the partial items:

$$\mu_{1,2,i} = \mu_{1,i} \cdot \alpha + \mu_{2,i} \cdot (1 - \alpha) \quad (2)$$

The graphs of the used distributions are presented in Figure 1.



#### 3.3 Calculated material factors for DA3

Herein the calculations are done to resemble the present partial safety factor approach DA3 in the Eurocodes. The loads are combined dependently and the partial safety factors for the

loads are  $\gamma_G = 1$  and  $\gamma_Q = 1.3$ . The load distribution for both permanent and variable loads is assumed to be normal. The variable load distribution is set at 50-year loads and the target reliability corresponds to RC2 of the Eurocodes, i.e.  $\beta_{50} = 3.8$ .

The calculations are done for material variation of  $V_M = 0.1$ ,  $V_M = 0.2$  and  $V_M = 0.3$ . In addition a general uncertainty following a normal distribution and 0.1 deviation is added into a parallel calculation. The results of the calculations are shown in Figure 2 as the function of the load ratio (the proportion of the variable load in the total load, %).

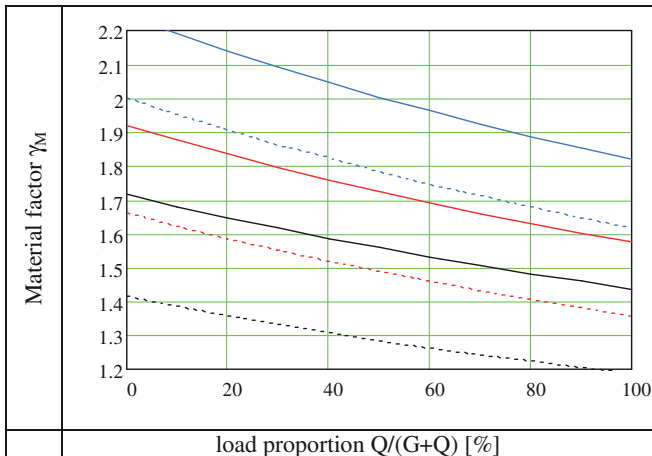


Figure 2. Material factors of the Eurocodes corresponding to  $\gamma_G = 1$ ,  $\gamma_Q = 1.3$  and  $\beta_{50} = 3.8$  as function of load ratio. The lowest, black lines denote to  $V_M = 0.1$ ; red lines, middle to  $V_M = 0.2$  and blue lines, highest to  $V_M = 0.3$ . The dotted lines correspond to values without uncertainty,  $V_U = 0$  and the solid lines with uncertainty,  $V_U = 0.1$ .

The results presented in Figure 1 are of course dependent on the assumptions made. It is though notable, that the material factors are not constant while they depend on the load ratio. For an independent load combination the material factors would also be highly non-linear. The application of a constant material factor as in EN 1997-1 does not thus result in a constant reliability index. Considering effective stress analysis, the variation of the parameter is according to data gathered by Abramson et al. (2002) in the range of 2-21%. On average one could use the value of 10 % corresponding to the black line in Figure 2. The recommended partial safety factor for friction in EN 1997-1 is 1.25, which corresponds to a load ratio of 60% in Figure 2. Stability problems are often less load driven while in some cases the external load has no significant effect on safety. For such cases DA3 would according to Figure 2 clearly overestimate the safety.

#### 3.4 Calculated material factors for alternative approach

Next an alternative approach will be presented where all uncertainty is placed on the material partial safety factor, i.e.  $\gamma_G = \gamma_Q = 1.0$ . In addition the material factors are calculated for three different reliability index values, corresponding to the three reliability classes in the Eurocodes. The target  $\beta$  values are  $\beta_{50} = 4.3$  (RC3),  $\beta_{50} = 3.8$  (RC2) and  $\beta_{50} = 3.2$  (RC1).

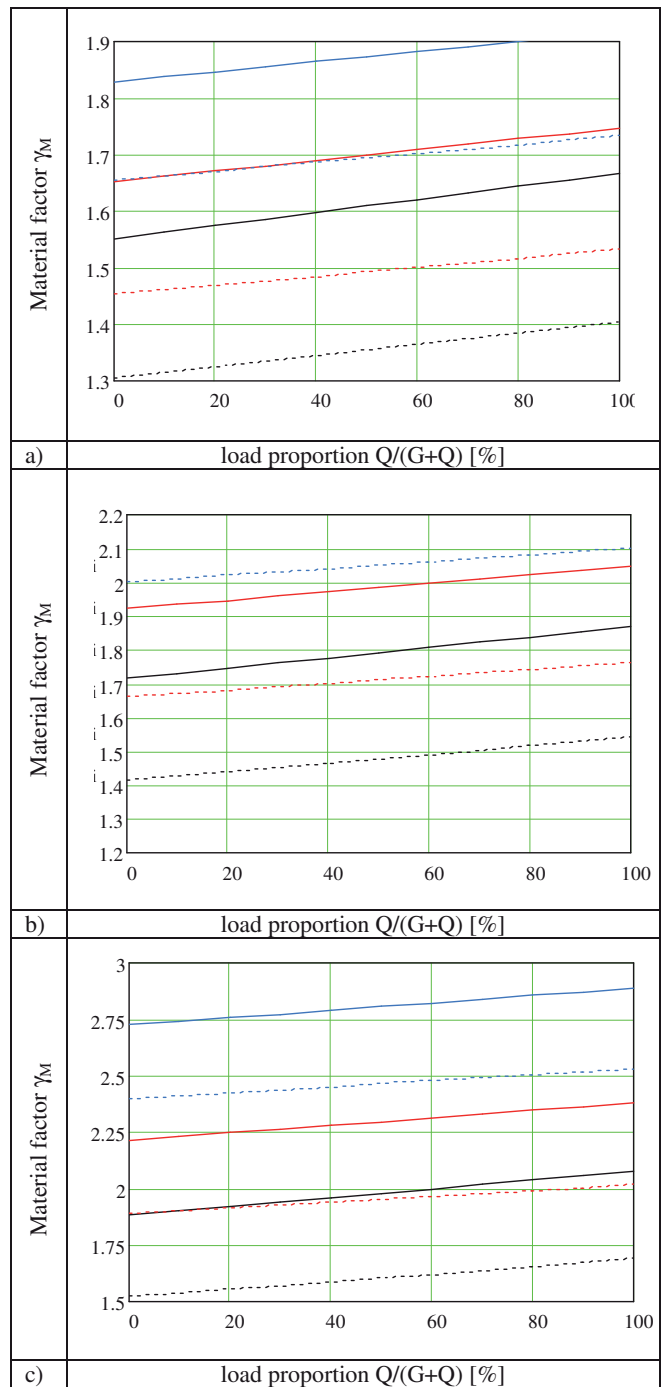


Figure 3. Material factors corresponding to  $\gamma_G = \gamma_Q = 1.0$  and a)  $\beta_{50} = 4.3$  (RC3), b)  $\beta_{50} = 3.8$  (RC2) and c)  $\beta_{50} = 3.2$  (RC1) as function of load ratio. The lowest, black lines denote to  $V_M = 0.1$ ; red lines, middle to  $V_M = 0.2$  and blue lines, highest to  $V_M = 0.3$ . The dotted lines correspond to values without uncertainty,  $V_U = 0$  and the solid lines with uncertainty,  $V_U = 0.1$ .

As can be seen, the material safety factors are the same as in Figure 2 for equal reliability index when the load proportion is zero. When Figure 2 and Figure 3 b) are compared we find out that an equal design outcome is obtained when the safety is set both in the action and in the resistance or in the resistance only (e.g. load proportion 60 %,  $V_M = 0.1$ , Figure 2:  $\gamma_M = 1.53$ , i.e.  $(0.4+0.6 \cdot 1.3) \cdot 1.53 = 1.81$  which is equal to the value of Figure 3 b).

#### 4 EXAMPLE OF APPLICATION

In the following the Eurocode EN 1997 will be applied in an example and compared to the alternative method presented in the previous section. The intention is to outline some issues the authors consider as problematic in a simplistic way. The example is thus very simplified and does not as such represent a true case study.

Let us consider the situation given in Figure 4. The soil conditions are the following. A 1m thick embankment is laid upon a dry crust layer. The unit weight of the embankment material is  $\gamma = 20\text{kN/m}^3$  and the characteristic friction angle is  $\phi = 38^\circ$ . The dry crust layer is 1m thick and has a unit weight of  $\gamma = 17\text{kN/m}^3$  and the characteristic undrained shear strength is 30kPa. Under the dry crust there is a layer of soft clay with a unit weight of  $\gamma = 16\text{kN/m}^3$  and a characteristic undrained shear strength of 10kPa at top of layer increasing with 1.4kPa/m depthwise. A 5m wide load of 40kPa is placed two meters from the crest of the embankment. The problem in question is much load driven. The total safety factor without any load is around 4 while the 40kPa load decreases it to 1.46 for a circular failure surface analysed by the Bishop method.

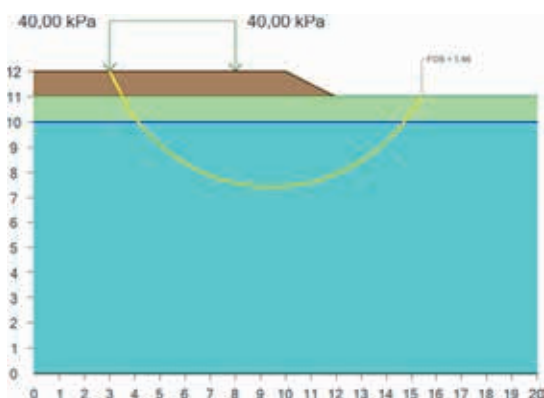


Figure 4. Geometry of the problem and calculated total factor of safety.

According to the recommended values to EN 1997 the partial safety coefficient for effective stress strength parameters is  $\gamma_{\phi} = \gamma_c = 1.25$  and for total stress analysis  $\gamma_{cu} = 1.4$ . Applying these yields for design values a friction angle of  $\phi = 32^\circ$  and undrained strength values of 21.4kPa for the dry crust and 7.1kPa + 1kPa/m for the soft clay. If the load comes from a permanent load, the recommended partial factor is 1.0 while it is 1.3 for variable loads. So in case of variable loads the design value entering the calculation is 52kPa.

In case of a permanent load the resulting over dimensioning factor is ODF = 1.04 indicating that the situation is safe. For the variable load case the ODF reduces to ODF = 0.88. To have enough safety, the characteristic initial value of undrained shear strength of the clay should increase by some 30 % to 13kPa. This corresponds to a total safety factor of 1.69 for the situation. Is it then reasonable to require a higher safety for the variable load case? A general argument in favour of this is that there might be more uncertainty for the variable load than for the permanent one. This is however not necessarily true. A typical high variable load representative to embankment stability would be train load from a heavy freight train. However, railway tracks are classified and there is an upper load allowed for a certain track part. So the characteristic load is rather a maximum load. In such cases the partial factor for action should rather be calculated using a log-normal distribution than a normal distribution. Also, there will always be uncertainty also in the permanent load which is disregarded in EN 1997-1. It is perhaps also more important to consider the consequences of failure. A permanent load might come from a residential building. The consequence of failure might thus be very severe with lots of casualties. On the other hand if the variable load is due to a

freight train carrying e.g. iron ore the consequences of failure in an uninhabited area are perhaps not that severe – at least the risk for loss of lives is minor. However, if a train with toxic material goes through an inhabitant area the consequences of failure are of course harsh.

The alternative approach presented in 3.4 allows for such considerations. It is emphasized that the results presented are aimed to give an example how safety could be applied. The assumed distributions, variations and target reliabilities needs of course careful consideration. However, if one assumes a variability of 0.1 for friction and 0.2 for the undrained shear strength one finds, that the recommended partial safety factors  $\gamma_{\phi} = \gamma_c = 1.25$  and  $\gamma_{cu} = 1.4$  in EN 1997-1 corresponds to the calculated one at approximately a load ratio of 80% assuming no additional uncertainty. While this is a very high load ratio its use is justified by the sake of comparison and the fact that the case is highly load driven. For the alternative approach corresponding safety factors for same  $\beta$  would be  $\gamma_{\phi} = \gamma_c = 1.52$  and  $\gamma_{cu} = 1.73$ . Applying this as a load factor on unity yields an ODF = 0.84. Now to have enough safety the undrained shear strength of the clay would need to increase to 13.3 kPa. This corresponds to on total safety factor of 1.71 i.e. close to the partial safety factor used for the undrained shear strength. Similarly the total safety requirement for a high consequence class (RC3) would be close to 2.0 and for a minor consequence class (RC1) approximately 1.5.

#### 5 CONCLUSIONS

The partial safety factor approach in EN 1997-1 adopted in most European countries for slope stability is reviewed. The author's conclusions are that risk and consequence of failure are not necessarily properly accounted for. For situation with no variable loads the safety level applied in EN 1997-1 does not correspond to the implied reliability index, but is below that. Also the consequence of failure is not properly addressed, as the load factor in EN 1990 have a negligible affect to safety for some slope stability problems. An alternative approach is presented, where all uncertainty is placed on the material partial safety factor and the consequence of failure is accounted by calculating the material safety factors separately for different consequence classes with different target reliability index values.

#### 6 REFERENCES

- Abramson, L., Lee, T. S., Sharma, S. and Boyce, G. M. 2002. Slope stability and stabilization methods. John Wiley & Sons, Inc.
- European committee for standardization, CEN. 2002. EN 1990 Eurocode: Basis of structural design. Brussels: European committee for standardization.
- European committee for standardization, CEN. 2004. EN 1997-1 Eurocode 7: Geotechnical design. Part 1: General rules. Brussels: European committee for standardization.
- Frank, R., Bauduin, C., Driscoll, M., Kavvasas, M., Krebs, Ovesen, N., Orr, T., Scuppener, B. 2004. Designer's guide to EN 1997-1 Eurocode 7: Geotechnical design-General rules. London: Thomas Telford Ltd.
- Leroueil, S., Magnan, J.-P. and Tavenas, F. 1990. Embankments of soft clays. Ellis Horwood. Darcy H. 1856. *Les fontaines publiques de la ville de Dijon*. Dalmont, Paris.
- Poutanen T., 2011. Calculation of partial safety factors, Applications of Statistics and Probability in Civil Engineering – Faber, Köhler & Nishijima (eds), Taylor & Francis Group, London

# Assessment of embankment stability on organic soils using Eurocode 7

## Évaluation de la stabilité des remblais sur sols organiques en utilisant l'Eurocode 7

Lechowicz Z., Wrzesiński G.

Department of Geotechnical Engineering, Warsaw University of Life Sciences - SGGW, Poland

**ABSTRACT:** A problem of the stability assessment of stage-constructed embankment on soft organic subsoil is discussed. Calculations were performed for the first and the third stage of embankment construction at the Antoniny site and for the failure test. The analysis contains measured and corrected shear strength values of organic soils obtained in the virgin and consolidated organic subsoil by staged construction. The statistical analysis of the field vane test results was performed to obtain mean values, standard deviations and probability distribution. Derived, characteristic and design values of undrained shear strength of organic soils were determined. The stability analysis according to design approaches of Eurocode 7 was carried out using mean values of undrained shear strength of organic soils. Additionally, the stability analysis was carried out using undrained shear strength reduced by 0.5 and 1.0 standard deviation. Based on probabilistic stability analyses the safety factor and the reliability index  $\beta$  were calculated.

**RÉSUMÉ:** Le problème présenté est celui de l'évaluation de la stabilité d'un remblai expérimental construit par étapes sur un sous-sol organique. Les calculs ont été effectués pour la première et la troisième étape de la construction du remblai sur le site d'Antoniny et pour l'essai de rupture. L'analyse contient les valeurs mesurées et corrigées des valeurs de résistance au cisaillement des sols organiques obtenus dans le sous-sol vierge et consolidé par les étapes de construction. L'analyse statistique des résultats d'essais sur le terrain a été réalisée pour obtenir des valeurs moyennes, l'écart-type et la loi statistique de distribution. Les valeurs, caractéristiques de la résistance au cisaillement non drainé des sols organiques ont été déterminées pour la conception. L'analyse de stabilité selon les approches de l'Eurocode 7 a été réalisée à l'aide des valeurs moyennes de la résistance au cisaillement des sols organiques. L'analyse de stabilité a été réalisée également en utilisant la résistance au cisaillement réduite de 0.5 et 1.0 écart-type. Les acteurs de sécurité et de fiabilité de l'indice  $\beta$  ont été calculés sur la base de l'analyse probabilistique de la stabilité.

**KEYWORDS:** organic soils, undrained shear strength, embankment stability, Eurocode 7, characteristic and design values.

### 1 INTRODUCTION

Geotechnical problems associated with embankments located on organic soils are more difficult than on soft mineral soils mainly due to their higher compressibility and very low virgin shear strength (Hartlen and Wolski 1996). The variability in the value of soil properties is a major contributor to the uncertainty in the stability of an embankment located on soft and highly compressible subsoil. This means that even construction of an embankment of only several meters height may lead to failure. As a result, the methods of design and construction that are normally used in other soft soils, may not be adequate in organic soils.

However, in many countries there are large areas with organic soils where different kinds of embankments have to be constructed. In such cases, the prediction of soil behaviour and the selection of a proper design method become an important as well as a difficult engineering task. In practice, embankment construction by stages utilizing the change in shear strength due to consolidation process is often selected solution. For such a stage constructed embankment, time and money can be saved if the embankment stability is accurately predicted.

Stability analysis according to Eurocode 7 can be performed using following Design Approaches: DA1 (Combination 1), DA1 (Combination 2), DA2 or DA3. Many countries as well as Poland accepted in 2010 Design Approach DA3 for design of slopes. In particular Design Approaches are applied different partial factors to characteristic values of parameters (Frank et al. 2004, Bagdahl 2005, Frank 2007, Bond and Harris 2008, Van Seters and Janses 2011, Orr 2012).

To assess the variability in the value of soil properties the statistical analysis should be performed. Statistical analysis allows to obtain mean values, standard deviations and

probability distribution. Thus, characteristic values of geotechnical parameters used in calculations can be obtained.

The characteristic value  $X_k$  used in geotechnical calculations corresponding to a 95% confidence level that the actual mean value,  $X_m$  is greater than this value, is given by Schneider (1999):

$$X_k = X_m(1 - k_n V) \quad (1)$$

where:

$k_n$  - the factor, depending on the type of statistical distribution and the number of test results,

$V$  - variation coefficient.

Schneider (1999), on the basis of calculations, has shown that a good approximation to  $X_k$  is obtained when  $k_n = 0.5$ ; i.e. if the characteristic value is chosen as one half a standard deviation below the mean value, as in the following equation:

$$X_k = X_m - 0.5SD \quad (2)$$

In this paper a problem of the assessment of embankment stability on soft organic subsoil is discussed based on the Antoniny test site. This is an adequate example to perform stability

analysis and research of organic subsoil under stage constructed embankment because each case of embankment construction, from loading of virgin subsoil to failure test can be considered.

### 2 DESCRIPTION OF THE ANTONINY SITE

The Antoniny test site is located in north-western Poland in the Noteć river valley. In 1980s the Department of Geotechnical Engineering of Warsaw University of Life Sciences in cooperation with the Swedish Geotechnical Institute performed extensive field and laboratory investigations.

At this test site the embankment was constructed in three stages on organic subsoil from 1983 to 1987. The structure was then brought to failure by increasing the height of the fill (Wolski et al. 1988, 1989). The schedule of construction is presented in Figure 1.

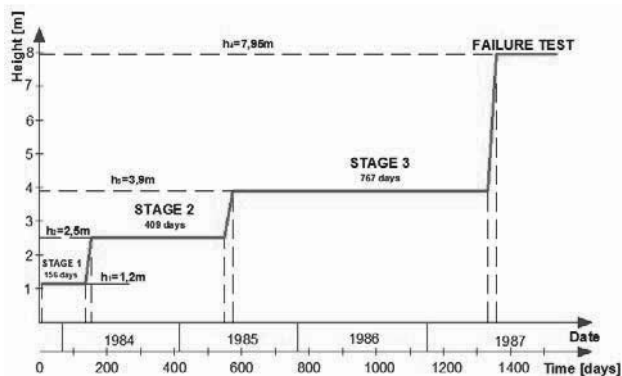


Figure 1. Construction schedule of embankment at the Antony site (Wolski et al. 1988).

At the Antony site the virgin subsoil consists of an amorphous peat layer and a calcareous-organic soil layer called “gyttja” underlain by a sand layer. The organic subsoil, 7.8 m thick, consists of 3.1 m peat and a 4.7 m gyttja. The results of the index properties of organic soils are summarized in Table 1 and Table 2. Based on the index properties the peat layer was divided into two layers: the first one being fibrous peat from the ground surface to depth 1.0 m and the second one amorphous peat below 1.0 m to depth 3.1 m. The gyttja layer was divided into three layers, the first one being calcareous-organic gyttja extending from 3.1 m to 4.5 m and the second and third layer calcareous gyttja from 4.5 m to 6.8 m and below 6.8 m, respectively. The ground surface is covered with grass vegetation. In the first layer of peat is an abundance of cracks and root channels.

Table 1. Index properties of peat at the Antony site (Wolski et al. 1988, 1989).

Properties	Peat	
	Fibrous	Amorphous
Water content $w_n$ [%]	420-450	310-340
Unit density $\rho$ [ $t/m^3$ ]	1.05-1.1	1.05-1.1
Specific density $\rho_s$ [ $t/m^3$ ]	1.4	1.45
Liquid limit $w_L$ [%]	-	305-310
Organic content [%]	8-85	65-75
CaCO <sub>3</sub> content [%]	5-10	10-15

Table 2. Index properties of gyttja at the Antony site (Wolski et al. 1988, 1989).

Properties	Gyttja		
	Calcareous-organic	Calcareous	Calcareous
Water content $w_n$ [%]	130-140	105-110	110-115
Unit density $\rho$ [ $t/m^3$ ]	1.25-1.30	1.35-1.40	1.40-1.45
Specific density $\rho_s$ [ $t/m^3$ ]	2.2	2.3	2.4
Liquid limit $w_L$ [%]	100-110	80-90	90-100
Organic content [%]	15-20	8-10	5-7
CaCO <sub>3</sub> content [%]	65-75	80-85	85-90

In the virgin subsoil the static ground water level was present in peat layer at the depth of 0.2 m below the ground surface. In the underlying sand at the 7.8 m depth the water pressure is artesian and has been measured to correspond to a water head of 1.0 to 1.5 meters above the ground surface. The high ground water level, combined with the artesian pore water pressure and with relatively low bulk densities of organic soils

resulted in the effective vertical stresses in organic soils being only a few kPa and almost constant in depth.

The preconsolidation pressure obtained from oedometer tests is higher than the initial values of effective vertical stresses, which shows that organic soils are overconsolidated with an overconsolidation ratio, OCR, decreasing from 5 to 2 with depth. However, in first stage the effective stress was only smaller than the initial preconsolidation pressure. During staged construction the effective vertical stress exceed the initial preconsolidation pressure several times.

### 3 UNDRAINED SHEAR STRENGTH

#### 3.1 Undrained shear strength from field vane tests

The field vane test is relatively simple and quick in situ method of shear strength measurement of organic soils. In order to evaluate undrained shear strength ( $\tau_{fu}$ ) from vane shear tests, the measured values of shear strength ( $\tau_{fv}$ ) have to be corrected using correction factor ( $\mu$ ).

In this paper the correction factors evaluated according to Swedish Geotechnical Institute method (Larsson et al. 1984) and average correction factors which was determined based on laboratory tests: triaxial compression (TC), triaxial extension (TE) and direct simple shear (DSS) (Lechowicz 1992). Values of correction factors are shown in Table 3.

Table 3. Correction factors for field vane tests obtained at the Antony site:  $\mu(w_L)$  – correction factor recommended by SGI,  $\mu(\text{lab})$  – correction factor based on laboratory tests.

Type of soil	$\mu(w_L)$	$\mu(\text{lab})$
Peat (0-3.1 m)	0.50	0.51
Gyttja 1 (3.1-4.5 m)	0.70	0.56
Gyttja 2 and 3 (4.5-7.8 m)	0.80	0.61

Mean values of corrected shear strength were calculated based on early corrected values of measured shear strength. Measured, corrected and mean values of undrained shear strength in the virgin organic subsoil before loading are shown in Figure 2.

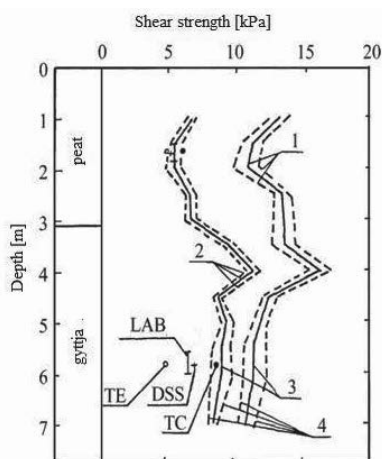


Figure 2. Profile of undrained shear strength based on field vane tests at the Antony site: 1 - results of field vane tests, 2 - values corrected according to SGI, 3 - mean values, 4 - mean values  $\pm$  standard deviation; TC - triaxial compression test, TE - triaxial extension test, DSS - direct simple shear test, LAB - mean value from laboratory tests.

Mean values of corrected shear strength ( $\tau_{fu}$ ) in the virgin organic subsoil before loading and in the consolidated organic subsoil before failure test are presented in Tables 4 and 5.

Table 4. Mean values, standard deviations and variation coefficients of undrained shear strength before loading at the Antony site (Lechowicz 1992, Batory 2004).



Layer	Undrained shear strength $\tau_{su}$ [kPa]	Standard deviation SD [kPa]	Variation coefficient V
peat 1	12.8	2.40	0.19
peat 2	6.4	0.71	0.11
gyttja 1	7.7	1.12	0.15
gyttja 2	7.0	0.49	0.07
gyttja 3	7.5	0.92	0.12

Table 5. Mean values, standard deviations and variation coefficients of undrained shear strength before the failure test at the Antony site. A - under embankment crest, B - under embankment slope, C - outside of embankment (Lechowicz 1992, Batory 2004).

Zone	Layer	Undrained shear strength $\tau_{su}$ [kPa]	Standard deviation SD [kPa]	Variation coefficient V
A	peat 1	28.0	2.40	0.09
	peat 2	24.5	0.71	0.03
	gyttja 1	20.2	1.56	0.08
	gyttja 2	18.7	1.38	0.07
	gyttja 3	22.3	2.62	0.12
B	peat 1	18.0	1.40	0.08
	peat 2	15.7	1.11	0.07
	gyttja 1	13.2	2.12	0.16
C	gyttja 2	12.6	1.84	0.15
	gyttja 3	13.4	1.29	0.10
	peat 1	12.5	2.40	0.19
	peat 2	7.7	0.73	0.09
	gyttja 1	10.3	1.53	0.15
	gyttja 2	9.9	1.23	0.12
	gyttja 3	10.2	0.91	0.09

Undrained shear strength values obtained by the field vane tests show a considerable increase in undrained shear strength due to the loading and subsequent consolidation. The highest strength increase was measured under the centre of the embankment and the increase was most evident in the peat layer. A smaller increase in undrained shear strength was obtained under the slope of embankment, while the measured shear strength values under the toes of slopes and outside the embankment remained practically unchanged.

### 3.2 Statistical analysis of the field vane test results

The statistical analysis of the field vane test results was performed to obtain mean values, standard deviations and probability distribution. For statistical analysis of shear strength normal distribution was used. Additionally, for comparison also other type of statistical distribution were tested (Lechowicz et al. 2004).

The statistical analysis was carried out using program Statgraphics Plus 4.1 (Batory 2004). In this program goodness-of-fit test is performing by the Kolmogorov-Smirnov test for a 95% confidence level.

The mean values, standard deviations and variation coefficients of corrected shear strength for each geotechnical layer are shown in Tables 4 and 5.

## 4 STABILITY ANALYSIS

### 4.1 Selection of shear zones and design parameters

In stability analysis performed for the first stage the same parameters for whole geotechnical layers were used. For the third stage and the failure test the organic subsoil was divided into three different shear zones: A - under embankment crest, B - under embankment slope, C - outside of embankment.

Division of organic subsoil into shear zones is presented in Figures 3 and 4.

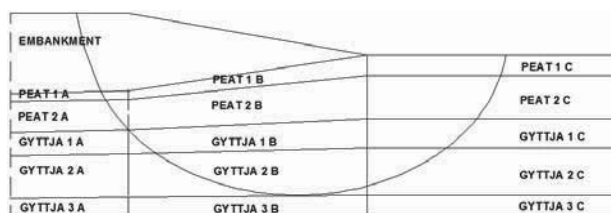


Figure 3. Division of organic subsoil into shear zones for the third stage at the Antony site.

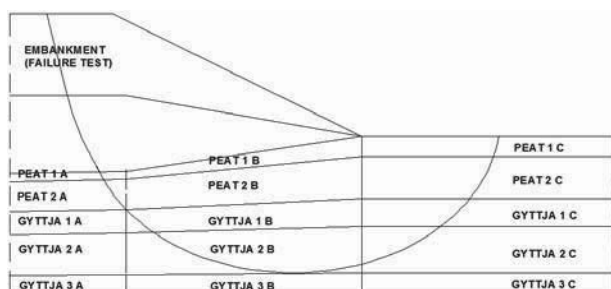


Figure 4. Division of organic subsoil into shear zones for the failure test at the Antony site.

In the stability analysis mean values of undrained shear strength were used. The characteristic values of undrained shear strength determined as mean values reduced by half and one standard deviation were also used. In stability analysis design values of undrained shear strength were received by using partial factors ( $\gamma_M$ ) to mean and characteristic values.

In Design Approach DA1(C1) partial factor recommended by Eurocode 7 is equal to 1.0 so values of design parameters used in calculations are the same as characteristic ones. In DA1(C2) and DA3 recommended partial factor ( $\gamma_M$ ) on undrained shear strength is equal to 1.25, so design parameters used in stability analysis are reduced by that factor.

### 4.2 Calculation results

The stability analysis was carried out for the first and the third stage as well as for the failure test of the embankment at the Antony site. The safety factor was calculated using the GeoSlope program with the use of Bishop's simplified method. The calculations were performed according to Eurocode 7 using Design Approaches: DA1(C1), DA1(C2), DA3 and also using probabilistic method. The stability analysis was carried out for subsoil divided into geotechnical layers and zones presented in Figures 3 and 4. Results of stability analysis performed according to Eurocode 7 of embankment at the Antony site are shown in Table 6.

Calculations performed for the first stage of embankment at the Antony site prove that the embankment was stable. Both for calculations carried out according to Eurocode 7 and using probabilistic method the safety factor was much higher than required. For DA1(C1) safety factor was equal to 1.82 assuming mean values while for DA1(C1) and DA3 was equal to 1.46. For comparison, safety factor using probabilistic method and normal distribution was equal to 1.52 assuming mean values of undrained shear strength. In this case reliability index  $\beta = 4.7$ . Using characteristic values of undrained shear strength evaluated based on Schneider's recommendation the safety factor for DA1(C1) was equal to 1.71, and for DA1(C2) as well as DA3 was equal to 1.39. For characteristic values reduced by one SD the safety factor was equal to 1.60 for DA1(C1) and 1.28 for DA1(C2) as well as DA3. Obtained values are less than permissible for this class of construction.

Table 6. Results of stability analysis performed according to Eurocode 7 at the Antony site.

Stage	Mean and characteristic values of undrained shear strength	Safety factor F	
		DA1(C1)	DA1(C2), DA3
1	$\bar{\tau}_{fu}$	1.82	1.46
	$\tau_{fu} - 0.5SD$	1.71	1.39
	$\tau_{fu} - SD$	1.60	1.28
3	$\bar{\tau}_{fu}$	1.41	1.12
	$\tau_{fu} - 0.5SD$	1.33	1.07
	$\tau_{fu} - SD$	1.26	1.01
Failure test	$\bar{\tau}_{fu}$	0.75	0.60
	$\tau_{fu} - 0.5SD$	0.71	0.57
	$\tau_{fu} - SD$	0.67	0.54

Calculation results show that after construction the first stage of embankment with a height of 1.2 m exists a large reserve of safety. In connection with it, for the embankment with a height of 1.7 m additional calculations were carried out using mean values of undrained shear strength. Then, safety factor was equal to 1.16 while  $\beta = 3.4$ . Using logistic type of distribution which better characterized distribution of shear strength the safety factor was close to one and  $\beta = 2.2$ . Performed calculations shows that the first stage of embankment could be constructed higher.

The stability analysis after consolidation of the third stage of embankment performed according to Eurocode 7 (Table 6) and probabilistic method assuming mean values of undrained shear strength shows that construction was stable. The safety factor using probabilistic method was equal to 1.48 and  $\beta = 8.9$ . Taking into consideration partial factors for undrained shear strength (DA1(C2) and DA3) the safety factor was insufficient.

During failure test the thickness of the fill was increased from 3.9 m to a final 7.95. The safety factor determined according to Eurocode 7 was less than permissible (Table 6) both using mean values of undrained shear strength and designed ones. Also calculations using probabilistic method prove that the construction was unstable.

It is important to pointed out the fill constructed in the failure test had approximately the shape of a truncated pyramid. The simplified Bishop's method modified to three-dimensional analysis to estimate the safety factor for the test fill during the failure test was used. Half of the sliding body of the fill was divided into cylindrical part with semi-ellipsoidal end. The three-dimensional calculations of stability for the final stage in the failure test indicate that the factor of safety was close to 1. The two-dimensional calculations carried out for the cross-section of the cylindrical part yielded a safety factor of about 0.75.

Performed stability analysis shows, that in case of Design Approach DA1(C1) the embankment stability in organic soils during construction can be assessed using the characteristic values of undrained shear strength determined according to Schneider's recommendation based on mean values and standard deviation of undrained shear strength derived from field vane tests.

Experience shows that in case of Design Approaches DA1(C2) and DA3 the assessment of embankment on organic soils based on the design values of undrained shear strength evaluated using partial factor  $\gamma_M = 1.25$ , characteristic values of  $\tau_{fu}$  from Schneider's recommendation, mean values of  $\tau_{fu}$  determined from undrained shear strength derived after correction of measured values of  $\tau_{fv}$  introduce too much safety for embankment during construction. The calculation results show that after third stage the safety factor form DA1(C2) and DA3 approaches is closed to one while in real case the embankment height was increased almost double, from 3.9 to 7.95 m in failure test.

## 5 CONCLUSIONS

The example of the determination of derived, mean, characteristic and design values of undrained shear strength of organic soils obtained from field vane tests for stage-constructed embankment at the Antony site was presented.

Performed stability analysis shows, that Design Approach DA1(C1) for stability assessment of embankment on organic soils during construction using the characteristic values of undrained shear strength evaluated based on Schneider's proposal from mean values and standard deviation of undrained shear strength derived from field vane test is recommended.

Experience indicates that Design Approaches DA1(C2) and DA3 introduce too much safety for the embankment on organic soils during construction. In this case the mean values of undrained shear strength evaluated based on corrected values from field vane tests, as characteristic values are recommended.

## 6 ACKNOWLEDGEMENTS

This research was supported by Grant N N506 218039 from the National Science Centre. Cracow, Poland.

## 7 REFERENCES

- Batory J. 2004. Application of probabilistic methods in stability analysis of embankment on organic subsoil. Doctoral thesis. Warsaw Agricultural University, (in Polish).
- Bagdahl U. 2005. Embankment design according to Eurocode 7. A compilation of different solutions on Example 10 – Road Embankment. Proc. of the International Workshop. Dublin, 159 – 163.
- Bond A. and Harris A. 2008. Decoding Eurocode 7. London and New York. Taylor & Francis.
- Frank R. 2007. Basic principles of Eurocode 7 on 'Geotechnical design'. Proc. of 18<sup>th</sup> EYGEC, Ancona.
- Frank R., Bauduin C., Driscoll R., Kawadas M., Krebs Ovesen N., Orr T., Schuppener B. 2004. Designer's Guide to EN 1997-1 Eurocode 7: Geotechnical design – general rules. Thomas Telford.
- Hartlen J. and Wolski W. 1996. Embankments on organic soils. Amsterdam. Elsevier.
- Larsson R., Bergdahl U., Eriksson L. 1984. Evaluation of shear strength in cohesive soils with special reference to Swedish practice and experience. SGI Inf. Linköping. No. 3, 1-32
- Lechowicz Z. 1992. An evaluation of the increase in shear strength of organic soils under embankment loading. Treatises and Monographs. Warsaw Agricultural University Press. No. 162, (in Polish).
- Lechowicz Z., Batory J., Hyb W. 2004. Variability assessment of undrained shear strength of organic soils obtained from field vane tests. Annals of Warsaw Agricultural University – SGGW. Land Reclamation No. 35a, 161-170.
- Orr T. L. L. 2012. How Eurocode 7 has affected geotechnical design: a review. Geotechnical Engineering. Vol. 156, Issue GE6, 337 – 349.
- Schneider H. R. 1999. Determination of characteristic soil properties. Geotechnical Engineering for Transportation Infrastructure, Barends et al. Balkema, Rotterdam. Vol. 1, 273 – 281.
- Van Seters A. and Janses H. 2011. Ground structures – Slope and Retaining wall design in the Netherlands. BGA Symposium, Eurocode 7 – Today and Tomorrow. Cambridge, England.
- Wolski W., Szymański A., Mirecki J., Lechowicz Z., Larsson R., Hartlen J., Garbulewski K., Bergdahl U. 1988. Two stage constructed embankments on organic soils. SGI. Report No. 32. Linköping.
- Wolski W., Szymański A., Lechowicz Z., Larsson R., Hartlen J., Bergdahl U. 1989. Full-scale failure test on a stage-constructed test fill on organic soil. SGI. Report No. 36. Linköping.

# Implementation of LRFD Methods to Quantify Value of Site Characterization Activities

Mise en œuvre des méthodes de conception LRFD pour quantifier la valeur des activités de caractérisation du site

Loehr J.E., Bowders J.J., Rosenblad B.L.  
*University of Missouri, Columbia, Missouri, U.S.A.*

Luna R., Maerz N., Stephenson R.W.  
*Missouri University of Science and Technology, Rolla, Missouri, U.S.A.*

Likos W.J.  
*University of Wisconsin, Madison, Wisconsin, U.S.A.*

Ge L.  
*National Taiwan University, Taipei, Taiwan*

**ABSTRACT:** A comprehensive research program was recently completed to develop "state specific" LRFD guidelines for the Missouri Department of Transportation in the United States of America (USA). The new guidelines implement improvements to current AASHTO LRFD specifications that provide minimum national standards for design of transportation projects in the USA. The most notable of these improvements are specification of resistance factors that are dependent upon the variability of input parameters. One product of these improvements is to produce designs that more closely achieve target levels of reliability. Perhaps more importantly, the guidelines provide designers with explicit means to quantify the potential value of site characterization activities during the design phase. The latter outcome allows designers to make more rational decisions regarding the type and scope of site characterization activities and provides quantitative support for such decisions so that designers can more effectively convey the value of site characterization to others.

**RÉSUMÉ :** Un vaste programme de recherche a été récemment mené pour adapter des directives LRFD spécifiques au Département des Transports du Missouri (USA). Les nouvelles recommandations apportent des améliorations aux normes actuelles nationales AASHTO LRFD qui fournissent des normes minimales pour la conception de projets de transport aux Etats-Unis. La plus notable de ces améliorations est la spécification de facteurs de résistance qui dépendent de la variabilité des paramètres d'entrée. Un résultat de ces améliorations est de produire des modèles qui permettent d'atteindre un plus grand niveau de fiabilité. Peut-être plus important encore, les directives fournissent aux concepteurs de moyens explicites pour quantifier le niveau de qualité des reconnaissances géotechniques permettant de caractériser un site. Le dernier résultat permet aux concepteurs de prendre des décisions plus rationnelles concernant le type et l'étendue des reconnaissances du site et leur offre un outil quantitatif pour évaluer et transmettre plus efficacement à d'autres la valeur de la qualité des investigations.

**KEYWORDS:** load and resistance factor design, geotechnical site characterization, variability, uncertainty.

## 1 INTRODUCTION

Current practice for geotechnical design of transportation infrastructure in the U.S. utilizes load and resistance factor design (LRFD) techniques. In these methods, load factors and resistance factors are respectively applied to different load effects and resistance components to produce designs intended to achieve some established target probability of failure. A national code developed by the American Association of State Highway and Transportation Officials (AASHTO) serves as a baseline for such design, but individual state transportation agencies are allowed to develop their own "state specific" LRFD methods to reflect differences in design practices.

This paper describes characteristics of one such state-specific code developed by the authors for the Missouri Department of Transportation (MoDOT). Unique features implemented in the new MoDOT design guidelines include:

- Resistance factors are explicitly selected based on variability and uncertainty in input parameters, and
- A practical technique to quantify uncertainty in design parameters from lab and field measurements is provided.

Practice using the new MoDOT design guidelines is compared to traditional design practice and current AASHTO practice. Methods used for calibration of resistance factors are then

described followed by description of the procedure recommended for quantifying variability and uncertainty from laboratory or field measurements. Finally, an example is provided to illustrate how the methods can be used to quantify the value of potential site characterization activities.

## 2 SOURCES OF VARIABILITY AND UNCERTAINTY

Variability and uncertainty arise from a multitude of sources in geotechnical design. However, these sources can be generalized into three broad categories:

- Variability and uncertainty in design input parameters,
- Variability and uncertainty in design methods, and
- Variability and uncertainty attributed to construction.

These sources are at times inter-related, especially for empirically based design methods. Nevertheless, it is useful to consider them as being separate because of the degree of influence that designers have over the different sources.

Designers generally have the greatest, and most direct, influence over variability and uncertainty in design parameters, principally through affecting the scope of site characterization activities. Designers can also affect variability and uncertainty in design methods by selecting from among several alternative



methods, but this influence often has a lesser effect on resulting designs. Designers can also influence variability and uncertainty in construction, by developing “constructable” designs, as well as by requiring and/or engaging in effective QC/QA. However, the influence is again generally smaller than what can be achieved through effective site characterization.

### 3 COMPARISON OF TRADITIONAL & LRFD PRACTICE

While traditional “allowable stress design” (ASD) and LRFD practices seek to account for variability and uncertainty introduced by all three sources, they do so differently. Differences among traditional geotechnical practice, current AASHTO specifications, and the new MoDOT guidelines arise primarily from differences in how these sources are addressed.

#### 3.1 Traditional ASD Practice

Traditional practice for geotechnical site characterization, in terms of the specific types of measurements made and the quantity of such measurements, is largely dictated by the judgment of the designer. In establishing the scope of site characterization activities, designers generally consider (often local) standards of practice for structures of similar complexity and importance as well as general characteristics about the site. The actual site characterization activities undertaken are also subject to the designer’s ability to “sell” the importance of the activities to those that are paying for the characterization. This task is often challenging because it can be difficult to quantify the potential value of site characterization activities in ways that are meaningful to those outside the profession.

Importantly, traditional geotechnical practice also provides some flexibility in selection of appropriate values for the factor of safety to be used in design. In selecting a specific value for a specific project, designers generally consider the importance and complexity of the structure, the complexity of the site, and the appropriateness of site characterization that has been performed. Thus, there is an implicit link between the quality and rigor of the site characterization and the safety margins that are employed in design. This link is clearly subjective, which introduces the potential for inconsistent application and inconsistent reliabilities for resulting designs. The subjectivity may also expose designers to substantial risk, since it can be difficult to justify specific design postures when performance does not meet expectations (e.g. if a problem occurs, one can often easily argue that site characterization was insufficient or that sufficient margins of safety were not used).

#### 3.2 AASHTO LRFD Practice

Design according to the AASHTO LRFD specifications largely follows traditional practice, but with two important distinctions. First, the AASHTO LRFD code explicitly establishes minimum standards for the quantity and type of site characterization that must be performed in order for the standards to be used. These minimum requirements enhance the designer’s ability to “sell” site characterization and provide some minimum level of confidence in the design parameters. However, the requirements also pose challenges for some regions of practice where traditional site characterization practices do not work well. Secondly, the AASHTO code stipulates fixed values for the margin of safety, via resistance factors. Table 1 shows a listing of resistance factors for side resistance of drilled shafts from the AASHTO LRFD specification (AASHTO, 2010). These “method specific” resistance factors are “lumped” factors in that they account for all three sources of variability and uncertainty collectively.

Fixing the magnitude of resistance factors results in more consistent designs and likely produces the intended effect of achieving more consistent reliability compared to ASD practice.

However, fixing the magnitude of resistance factors also eliminates the flexibility provided in ASD to select appropriate safety margins and limits the capability to improve design efficiency through improved site characterization. Conducting more tests, or higher quality tests, to improve confidence in design parameters does not allow one to use more advantageous resistance factors. Improving the scope or quality of site characterization may have a second order effect of changing predictions of nominal capacity, but it does not allow designers to exploit the improved confidence in design parameters.

Table 1. Resistance factors from AASHTO LRFD Specifications for side resistance of drilled shafts (AASHTO, 2010).

Soil/Rock Type	Design Method	Resistance Factor, $\phi$
Clay	O’Neill & Reese (1999)	0.45
Sand	O’Neill & Reese (1999)	0.55
IGM	O’Neill & Reese (1999)	0.60
Rock	Horvath and Kenney (1979)	0.55
	O’Neill & Reese (1999)	0.55
	Carter & Kulhawy (1988)	0.50

The AASHTO code may reduce the risk to geotechnical designers in the sense that they may have stronger defense against litigation as long as the minimum requirements are satisfied. However, the code also requires designers to employ judgment to expand the site characterization where conditions warrant so the practical truth for this is at least debatable.

#### 3.3 MoDOT LRFD Practice

The MoDOT design guidelines seek to address limitations in traditional ASD and AASHTO LRFD practices by linking the resistance factors used with the quality of site characterization performed, and simultaneously improving consistency by restricting this link so that the target reliability is more consistently achieved. The “link” in this case is formed by implementing resistance factors that depend on the variability and uncertainty in design input parameters, which in turn depends on the quality of the site characterization conducted. In implementing this link, the guidelines also provide designers with practical means to estimate the potential value of site investigation activities on a project specific basis so that more effective site characterization decisions can be made.

## 4 GUIDING PRINCIPLES

The principal objective for development of the MoDOT design guidelines was to provide procedures that would save agency funds by more precisely and consistently achieving target probabilities of failure in design (i.e. applying appropriate conservatism for the variability and uncertainty present for each specific project). The primary means for improving the precision of the procedures is by considering the variability and uncertainty in design input parameters separately from the variability and uncertainty in design and construction methods.

The predominant cost savings are expected to be savings in construction costs rather than savings in site characterization costs. However, it was recognized that conducting advanced or extensive site characterization to reduce variability and uncertainty in design parameters is not always justified and will not always produce net cost savings. The overall intent was therefore to provide the agency with practical procedures to identify conditions where more extensive investigations are likely to produce cost savings, considering the costs for site investigation, costs for construction, as well as potential future costs for maintenance and repair.

Conscious effort was also made to avoid overly prescriptive provisions. Rather, the intent was to provide methods that inform the judgment of the designer about the value of

alternative site characterization activities. In this way, the opportunity to apply sound judgment remains, but it can be made more knowledgeable and consistently.

In the context of the guidelines, the probabilities of failure considered were epistemic, or “degree of belief” probabilities, which reflect level of knowledge, rather than aleatory probabilities that are related to actual performance. Thus, the probabilities of failure considered are related to the level of knowledge and confidence in the design input parameters and design methods rather than an actual statement about performance rates, although the two are clearly related.

## 5 CALIBRATION OF RESISTANCE FACTORS

Calibration of resistance factors to separate consideration of variability and uncertainty in design and construction methods from variability and uncertainty in design parameters requires only minor changes to common procedures. The most significant change is to use a performance function,  $g$ , of the form:

$$g = R(x) \cdot M(\bar{x}) - LL - DL \geq 0 \quad (1)$$

where  $R(x)$  is a deterministic design relation for geotechnical resistance,  $x$  represents the probabilistic design input parameter(s),  $\bar{x}$  is the mean value of the design input parameter(s),  $LL$  is the probabilistic live load effect,  $DL$  is the probabilistic dead load effect, and  $M(\bar{x})$  is a probabilistic “model uncertainty” parameter used to represent the bias, variability and uncertainty attributed to design and construction.  $M(\bar{x})$  reflects the conditional variability of the design method established from load tests, from numerical analyses, or based on judgment, while  $x$  reflects the variability and uncertainty in the design input parameter(s). For design methods without substantial bias,  $M(\bar{x})$  is taken to have a mean value of 1.0 and a distribution that reflects the variability of the design method.

Given the performance function for a specific design method, calibrations are then performed for a range of assumed coefficients of variation ( $COV$ ) for the design input parameter(s). Figures 1 and 2 show results of calibrations conducted for two illustrative design methods: design for tip resistance of drilled shafts in clay and design for side resistance of drilled shafts in rock, respectively. In each figure, curves are shown for four categories of structures. Each of these curves represents resistance factors to achieve a target probability of failure established by agency policy. The curves reflect the magnitude of resistance factor needed to achieve the target probability of failure based on the variability and uncertainty present in relevant input parameters, as represented by the  $COV$ .

Simple observation of the curves shown in Figs. 1 and 2 provides valuable qualitative information regarding the importance of site characterization for the respective design methods. Comparison of resistance factors for  $COV = 0$  (corresponding to perfect information about the input parameters) reveals that the variability and uncertainty attributed to the method for side resistance in rock (Fig. 2) is substantially greater than that for tip resistance in clay (Fig. 1). Furthermore, the steepness of the curves in Fig. 1 indicate that the resistance factor needed to achieve a given target probability of failure is highly sensitive to the variability and uncertainty of the undrained shear strength, thus indicating that the quantity and quality of site characterization will have a substantial impact on the resulting design. Conversely, the curves shown in Fig. 2 are much flatter, indicating that reduction of the  $COV$  for uniaxial compressive strength via expanded testing will have a lesser effect on the resulting design. These simple qualitative comparisons can also be quantified if specific values of  $COV$  for the design input parameters are estimated as will be illustrated through a subsequent example.

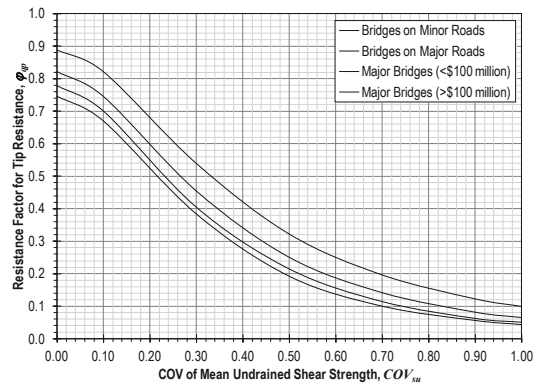


Figure 1. Resistance factors for tip resistance in clay.

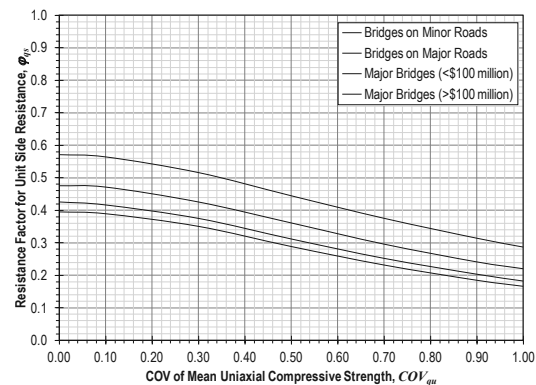


Figure 2. Resistance factors for side resistance in rock.

## 6 ESTIMATION OF PARAMETER UNCERTAINTY

Use of resistance factors established as described in the previous section is straightforward once  $COV$ -values for the input parameters are known. The primary complication introduced compared to current AASHTO specifications is that the MoDOT guidelines require estimation of parameter  $COV$ s. Fortunately,  $COV$  values can be established using practical means that introduce little complexity to the design process.

The general approach to establishing  $COV$  values closely follows conventional procedures for interpretation of design parameters. The process is based on establishing a “design profile” that reflects conditions present at a particular site. These design profiles establish a “model” describing how the magnitude of a design parameter varies with depth or elevation, as well as the variability and uncertainty of the model.

For the MoDOT guidelines, design profiles are assumed to be composed of a number of individual strata. The design parameter within an individual stratum is assumed to have values that are either constant, or linearly varying with depth or elevation as illustrated in Figure 3. As a practical matter, any design profile can be reasonably represented as some combination of strata that have either a constant or linearly varying property within each stratum. Regardless of whether the parameter value is assumed to be constant or linearly varying, the variability or uncertainty in the parameter within a single stratum is assumed to be constant, and represented by a constant value of the coefficient of variation ( $COV$ ).

Once individual strata are established, design values for parameters in a stratum judged to have constant values are taken to be the arithmetic mean of the available measurements:

$$y = \bar{y} = \frac{\sum_{i=1}^n \hat{y}_i}{n} \quad (2)$$

where  $y$  is the design, or “model” value of the parameter,  $\bar{y}$  is the mean value of the parameter measurements,  $\hat{y}_i$  is a measured value of the parameter, and  $n$  is the number of

measurements. The coefficient of variation of the mean value for the design parameter in a stratum with constant properties is established from available measurements as:

$$COV_y = \frac{\zeta \sigma_y}{y} = \frac{\zeta \sigma_y}{y} \quad (3)$$

where  $COV_y$  is the coefficient of variation of  $y$ ,  $\sigma_y$  is the standard deviation of  $y$ ,  $\zeta$  is an empirical modifier to account for the fact that  $COV_y$  may be underestimated for small numbers of tests, and  $\sigma_y$  is the standard deviation of the measurements.

Slightly different equations are used for strata where design parameters are deemed to vary linearly with depth (MoDOT, 2010). Fig. 3 illustrates results of such calculations.

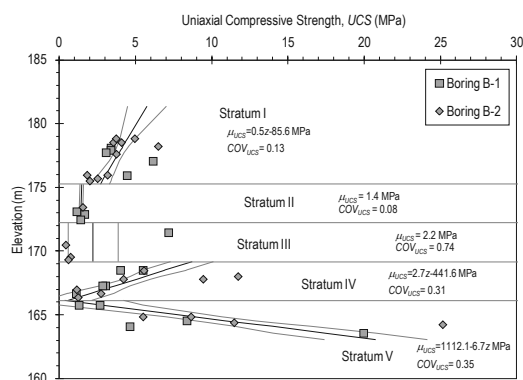


Figure 3. Example “site model” developed for design of drilled shafts.

### 7 EXAMPLE APPLICATION

To illustrate how the methods described can be used to quantify the potential value of site characterization activities, a conceptual design of drilled shafts for a highway bridge was conducted using measured values of uniaxial compressive strength for a shale site. Two designs were completed: the first using a small randomly selected subset of the available test measurements (Fig. 4) to reflect design based on a limited site investigation and testing program; the second was completed using a larger subset of the available measurements (Fig. 5) to reflect design based on a more typical site investigation for a bridge design. As shown in the figures, the more extensive investigation produces a slightly greater mean value for the uniaxial compressive strength in Maquoketa Formation C, but reduces the  $COV$  of the mean value by a factor of two. This, in turn, allows greater resistance factors to be used for design. Considering the same 13 MN axial load for both designs, the design completed based on the limited site investigation (Fig. 4) leads to use of 7.5 m long, 1200 mm diameter drilled shafts while the design completed based on the more typical site investigation (Fig. 5) leads to use of 5 m long, 1200 mm diameter drilled shafts. The estimated cost differences between these two designs is approximately \$5,000 per shaft. Thus, the value of the additional testing is approximately \$5,000 per shaft.

In practice, such direct comparisons are not possible *a priori*. However, designers can estimate how increasing the number of measurements will affect the  $COV$  of design parameters to develop estimates of potential costs savings as in the example. The estimated cost savings can, in turn, inform judgement regarding the scope of testing that may optimize final designs. If costs for additional characterization are not commensurate with estimated cost savings, then the additional characterization should not be undertaken as it is unlikely to “pay off”. While such estimation is unfamiliar, it is likely that one’s judgment regarding expected reductions in the  $COV$  with additional testing will improve with experience so that practices regarding effective scoping of site investigations will improve over time.

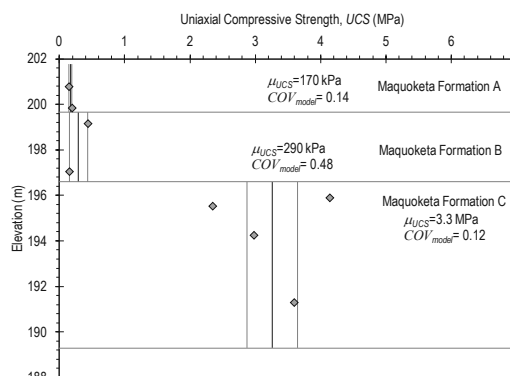


Figure 4. Uniaxial compressive strength measurements from site characterization with limited scope.

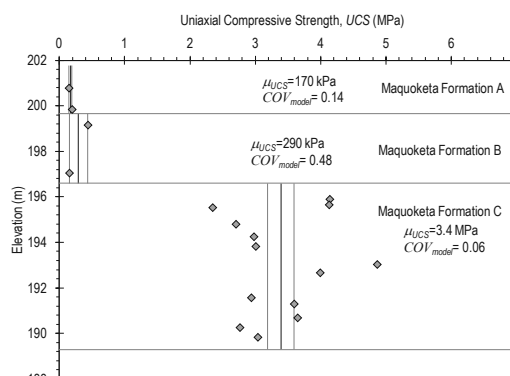


Figure 5. Uniaxial compressive strength measurements from more extensive site characterization.

### 8 CONCLUSION

Variability and uncertainty attributed to design parameters and due to design and construction methods can be practically separated within an LRFD framework by using resistance factors established as a function of the  $COV$  of the design parameter(s). Use of such resistance factors can improve the efficiency of geotechnical designs by more precisely and consistently achieving target probabilities of failure. This implementation also provides means to practically quantify the potential value of additional site characterization during design, which can improve design decisions and help convince owners/clients of the value of additional characterization.

### 9 ACKNOWLEDGEMENTS

The work presented was funded by MoDOT, The Center for Transportation Infrastructure and Safety at Missouri S&T, and the University of Missouri. Substantial in-kind support was also provided by members of ADSC: The International Association of Foundation Drilling. This support is gratefully acknowledged. The opinions, findings, and recommendations in this publication are not necessarily those of MoDOT or the U.S. Federal Highway Administration. This document does not constitute a standard, specification or regulation.

### 10 REFERENCES

AASHTO (2010), *AASHTO LRFD Bridge Design Specifications*, Fifth Edition, American Association of State Highway and Transportation Officials.  
 MoDOT (2010), “Guidelines for Estimation of Geotechnical Parameter Values and Coefficients of Variation”, *Engineering Policy Guidelines*, Section 321.3, Missouri Department of Transportation, <http://epg.modot.org/> (accessed January 10, 2013).

# European practice in ground anchor design related to the framework of EC7

## Pratique européenne pour le dimensionnement des tirants d'ancrage en application de l'EC7

Merrifield C.  
*Coffey Geotechnics, UK*

Møller O.  
*Aarsleff, Denmark*

Simpson B.  
*Arup, UK*

Farrell E.  
*AGL Consulting, and Trinity College, Ireland*

**ABSTRACT:** EN 1997-1:2004 (Eurocode7, Part 1 - EC7) is the European Standard for Geotechnical Design. Ground anchors are addressed in Section 8 of this standard, EN 1537:1999 (execution)(under revision) and it is planned that testing will be covered by prEN ISO 22477-5. EC7 Section 8 has been little used and is now under revision. Discussions between European experts on ground anchors have highlighted the diversity of current design practices used in different countries. This paper explores this diversity and highlights the variations in the approaches to the design and testing of ground anchors, dealing exclusively with grouted ground anchors which are able to be tensioned. The existing practices of Denmark, France, Germany, Ireland and the UK are considered in relation to the EC7 requirements for verification of ultimate and serviceability limit states. It is shown how the draft now proposed of EC7 for the design and testing of anchors accommodates the approaches currently used in European countries within a single framework.

**RESUME :** L'EN 1997-1:2004 (Eurocode 7, Par 1 - EC7) est la norme pour la conception des ouvrages géotechniques. Les tirants d'ancrage sont traités dans le chapitre 8 de cette norme, dans la norme d'exécution EN 1537 :1999 en révision et dans le projet de norme d'essais pr EN ISO 22477-5 en cours de rédaction. Le chapitre 8 de l'EC7 bien qu'encore peu utilisé, est en cours de révision. Les discussions entre les experts européens sur les tirants d'ancrage ont mis en lumière la diversité des pratiques couramment appliquées dans les différents pays. Cet article présente cette diversité et montre les différences d'approche tant au niveau de la conception que des essais, en particulier avec les tirants d'ancrage scellés au terrain qui peuvent être mis en tension. Les pratiques existantes au Danemark, en France, en Allemagne, en Irlande et au Royaume-Uni sont présentées selon les exigences de l'EC7 dans le cadre d'une vérification aux états limites ultimes et de service. L'article montre comment le projet proposé pour l'EC7 concernant la conception et les essais des tirants d'ancrage prend mieux en compte et de façon simple approches actuellement utilisées dans les pays européens.

**KEYWORDS:** Anchors, Eurocode, Standards, Design

### 1 INTRODUCTION AND HISTORICAL CONTEXT

Ground anchor design as it is today has been derived from many years of field tests, performance monitoring and field scale research, resulting in an empirical approach of anchor performance linked to soil parameters. Early use of anchors included the application of rock bolts for roof stability in Poland in 1918 and later in Czechoslovakia in 1926 to support an inclined shaft. The mining industry led the field in anchoring ground at this stage. Anchors were first introduced into civil engineering in 1934 by the French engineer André Coyne who devised strand anchors in sandstone to allow the raising of the Cheurfas dam in Algeria. The first use of anchors in soil was by Karl Bauer GmbH in Munich in 1958 to tie back retaining walls. The site agent, noting the difficulty in withdrawing steel drill casing developed a system which included 20m bars with 3m bond lengths installed with working loads of 25 tonnes. Development of anchor design accelerated between 1966 and 1969 with the use of anchors in stiff clays, marl, fine to medium sand and chalk (Littlejohn, 1970).

The developing design process was based on observations from field anchor tests taken to failure and long term behaviour of prestressed anchors. Empirical design rules with realistic factors of safety were being produced relating ultimate pull-out resistance to soil properties and anchor dimensions. The relationship between soil parameters and anchor performance was the basis of extensive research between 1970 and 1980, when many of the empirical relationships were developed upon which calculation of anchor/soil bond resistance, creep and multiple interface resistance are based (Littlejohn, 2012).

The methods of designing the anchor to contribute to the overall structural stability of, say, an anchored retaining structure were based on limit equilibrium stability analyses applying linear, active and passive pressure distributions. Where the design required the minimisation of wall displacement, the same approach was adopted using different pressure distributions. With the relatively recent availability of accessible FE approaches these conditions, taking into account the effect of anchor prestress, are examined routinely today.

With the expansion of anchor use throughout Europe, individual countries developed design guides and codes of practice (BS8081, DIN 4125, SIA V 191, TA95 for example) to promote safe design. Inevitably there were variations of design practice between these standards reflecting regional practices. In 1975, the Commission of the European Community initiated an action programme to develop a set of harmonised rules for the structural design of construction works based on Article 95 of the Treaty. This was transferred to CEN in 1989 guaranteeing them the status of European standards. EC7 (EN 1997-1:2004) was subsequently published and is intended to be used as a general basis for the geotechnical aspects of the design of buildings and civil engineering works. The design of anchors is accommodated in Section 8, for which a new draft has recently been prepared, which is referenced as EN 1997-1:2004/prA1, to be published. Alongside EC7 two further standards EN 1537 and prEN ISO 22477-5 have been developed to provide rules for the execution of anchors and the testing of anchors respectively. Whilst EN 1537 has been published for

some time and is now the subject of systematic review, prEN ISO 22477-5 has yet to be published.

## 2 DESIGN REQUIREMENTS OF EC7

The limit state framework adopted by EC7 requires that anchors are designed to ensure that:-

- Neither an ultimate limit state (ULS) nor a serviceability limit state (SLS) occur within the anchored structure or other supported structures.
- That an anchor has the required ULS and SLS resistance corresponding to these limit states.

The requirements of the new draft of Section 8 which are designed to satisfy these limit states for the anchor and structure are discussed in the following section.

### 2.1 Ultimate limit state (ULS) design force

Anchors are required to have an ULS design capacity ( $R_{ULS,d}$ ) to resist not only the force required to prevent an ULS in the anchored structure and supported structure ( $F_{ULS,d}$ ), but also must have the capacity to resist the maximum force that could be transferred to the anchor during its service life ( $F_{serv,k}$ ), with an adequate margin of safety. Thus the design of the anchor must consider the prestress or lock-off force applied and also any additional force attracted to the anchor during its design life. These safety requirements are expressed as Eq. 1 to 3 where  $\gamma_{serv}$  is a partial factor.

$$E_{ULS,d} \leq R_{ULS,d} \quad (1)$$

$$\text{where } E_{ULS,d} = \text{Max}(F_{ULS,d}; F_{serv,d}) \quad (2)$$

$$F_{serv,d} = \gamma_{serv} F_{serv,k} \quad (3)$$

### 2.2 Serviceability limit state (SLS) design force

Anchors are required to have the design capacity ( $R_{SLS,d}$ ) to resist the  $F_{serv,k}$  such that the limiting creep or load loss for a SLS are not exceeded. This requirement is not explicitly stated in all countries and may be covered in a ULS requirement. Assuming that the appropriate partial factor for this SLS is unity, this requirement is expressed as Eq. 4.

$$F_{serv,k} \leq R_{SLS,d} \quad (4)$$

### 2.3 Geotechnical ULS anchor resistance

EC7 requires that anchor tests be carried out to confirm that they have the resistance to satisfy Eq. 1. The value of the ULS resistance,  $R_{ULS}$ , is defined as the "value of the resistance of an anchor complying with ultimate limit state criteria". This means that tests must demonstrate that an anchor can provide a certain resistance while satisfying specified criteria of creep or load loss. The pull-out resistance will be greater than the value determined from the test. The design value of  $R_{ULS,d}$  and the characteristic resistance ( $R_{ULS,k}$ ) are determined from the minimum ( $R_{ULS,m}$ )<sub>min</sub> of measured values ( $R_{ULS,m}$ ) in investigation and suitability tests using the partial factor ( $\gamma_{a,ULS}$ ) and correlation factor ( $\xi_{ULS}$ ) and Eqs. 5 & 6.

$$R_{ULS,k} = \frac{(R_{ULS,m})_{min}}{\xi_{ULS}} \quad (5)$$

$$R_{ULS,d} = \frac{R_{ULS,k}}{\gamma_{a,ULS}} \quad (6)$$

### 2.4 Geotechnical SLS anchor resistance

In those countries which require that SLS of the anchor resistance be considered, it is necessary to verify that the anchors have at least the capacity to satisfy Eq. 4, satisfying SLS criteria of creep or load loss. Using the same symbols as in 2.3 but with SLS replacing ULS and a correlation factor of

unity, the design SLS resistance ( $R_{SLS,d}$ ) and characteristic SLS resistance are given by Eqs. 7 & 8.

$$R_{SLS,k} = (R_{SLS,m})_{min} \quad (7)$$

$$R_{SLS,d} = \frac{R_{SLS,k}}{\gamma_{a,SLS}} \quad (8)$$

## 3 CURRENT DESIGN PRACTICE

The amended Section 8 of EC7 only covers the design of anchors from load tests, hence only this aspect of anchor design is covered in this paper. Calculations using parameters derived from ground tests are considered to be for the estimation of the bond length only, and the design is then verified by load tests.

The discussion on current design practice is not as straightforward as it might appear due to the way anchor forces are determined for particular design situations in some countries and to the current lack of agreement on what precisely constitutes ULS and SLS failure criteria of an anchor. The design aspects include not only whether the SLS or ULS resistance of the anchor is verified but also whether the force used in this verification process is derived from analyses using factored ground properties or using characteristic values.

The derivation of ULS anchor forces is well developed and, for embedded walls, typically involves some type of Limit Equilibrium Analysis, although the use of finite elements is becoming more common. However the design of anchors in some countries is related to the 'working load'. This practice arose from the fact that earth pressures in the SLS condition (unfactored and considering compaction and at rest pressures) are greater than those at failure when the soil strength is fully mobilised, consequently can give rise to greater anchor force. Furthermore, as these are 'working loads', the anchor would be required to satisfy more onerous creep criteria at such loads. However, EC7 requires that in ULS design a more conservative view is taken of the ground strength and resistance, together with unexpected excavations and higher surcharges than considered for SLS and this situation must also be considered.

The methods used in the past to determine SLS forces, which are also called working forces, were very approximate for embedded walls. Typically the length required for ULS was derived by considering the wall as a beam with a length required for ULS, supported at the anchor and by passive earth pressure, on which act the active earth pressures determined using characteristic actions and soil parameters. Other approaches for simple walls were to calculate the anchor force using the characteristic actions and parameters but with the shortened pile length that is required for equilibrium. The advent of finite elements and other methods of analysis has allowed deformations to be considered more realistically thus providing a more reliable estimate of  $F_{serv,k}$ . The forces required to limit the movement of the structure and the supported ground are considered, including those forces attracted to the anchor after lock-off.

France has perhaps a design practice that can be most easily related to the proposed amendments of EC7 in that a  $F_{ULS,d}$  is determined from an ULS analysis of the structure and a 'service load', similar to  $F_{serv,k}$ , is also derived using characteristic values of actions and soil parameters. The testing is required to verify that the anchors have the required 'pull-out' resistance to satisfy the ULS requirements, including the required ULS resistance to ensure safety under  $F_{ULS,d}$  and that the creep requirements are satisfied under the service load.

Germany also calculates a value of  $F_{ULS,d}$ , however this value is calculated from characteristic values of the effects of permanent and variable actions, which are termed  $F_{Gk}$  and  $F_{Qk}$ . The anchor force for proof testing is related to  $F_{ULS,d}$  which is the maximum of  $1,35 F_{Gk} + 1,5 F_{Qk}$ , or 1,35 times the anchor force after lock-off if that is greater. The proof load has to satisfy a limiting creep criterion which is discussed in the

following section. The creep criterion is selected to represent a ULS anchor resistance.

The UK currently excludes Section 8 of EC7 from use in that country in its National Annex and requires anchors to be designed to BS8081 'Ground Anchorages'. The design of anchors in that standard is based on the 'working load',  $T_w$ , which is defined as 'The safe load of the anchorage'. No guidance is given in the standard as to whether  $T_w$  is determined using a ULS calculation or using characteristic values, however the terminology would suggest that it was originally considered to be similar to  $F_{Serv;k}$ . In practice, it is considered that for embedded walls,  $T_w$  is taken as the higher of that obtained using either a limit equilibrium or a bending moment and displacement analysis using appropriate pressure distributions. The proof load is related to  $T_w$ , as discussed in the following section, with different creep criteria to be satisfied which can be related to a SLS and to a ULS resistance.

Section 8 has not been specifically excluded in Ireland, nevertheless the practice is generally to adopt the BS8081 testing criteria with  $T_w$  based on a calculation using characteristic actions and parameters. However, given the general lack of specific guidance in this area prior to the publication of the amended Section 8, some designers also considered the value of  $F_{ULS;d}$  in the selection of  $T_w$  if that gave a greater value.

Denmark uses the present EC7, section 8. The anchor force is based on a ULS design force found from a calculation of the anchored structure with factored soil parameters. Some Danish designers compute a service load ( $F_{Serv;k}$ ), which considers prestress/lockoff of the anchor. This force is such as to resist a ULS if  $F_{Serv;k}$  is greater than  $F_{ULS;d}$ . This means that  $E_{ULS;d} = F_{Serv;k}$  if  $F_{Serv;k} > F_{ULS;d}$ . The Proof load is then based on  $E_{ULS;d}$  and must satisfy a limiting creep criterion. Previously Denmark used the German test method as described in DIN 4125. However, with the introduction of EN 1537:1999 Denmark has accommodated the incomplete test specifications stated in the informative annex E of EN 1537:1999. Test method 1 (TM1) is preferred because of the relationship to the former DIN 4125, but the creep rate limit measured in the acceptance test using TM1 in EN1537:1999 is so strict (0,8 mm), that often Test Method 3 (TM3) is adopted because of the more moderate creep rate limit (1,2 mm). Temporary anchors may be loaded to a lower proof load than permanent anchors, provided the consequence of failure justifies that. Similarly the effect of high or serious consequences of failure are governed by the reliability class concept as described in EC0, Annex B by introducing a  $K_{Ff}$  factor applied to the partial safety factor on the load or on the resistance.

#### 4 TESTING OF ANCHORS

Load testing of anchors has historically been an intrinsic part of the design and execution of anchors – in particular grouted ground anchors - and the mandatory acceptance testing of all grouted anchors is required in EN 1997-1:2004/prA1:2012 and in EN 1537:1999. The anchors are loaded to a proof load ( $P_p$ ) to verify limit state design requirements. The tests are categorised as:

1. Investigation Tests undertaken to establish the geotechnical ultimate resistance,  $R_{ULS;m}$ , of the anchor at the grout/ground interface and to determine the characteristics of the anchor within the working load range.
2. Suitability tests – carried out on site on anchors identical to those to be used in the works – to investigate some characteristics of the anchor and how the anchor performs under working conditions.
3. Acceptance tests – carried out on every anchor installed in the permanent works – to ensure that each anchor will perform as designed.

For Investigation and Suitability tests  $P_p$  is derived from:

$$P_p \geq \xi_{ULS} \times \gamma_{a;ULS} \times E_{ULS;d} \quad (8)$$

For Acceptance tests  $P_p$  is derived from  $E_{ULS;d}$  or  $F_{Serv;k}$ :

$$P_p \geq \gamma_{a;acc;ULS} \times E_{ULS;d} \quad (9)$$

or

$$P_p \geq \gamma_{a;acc;SLS} \times F_{Serv;k} \quad (10)$$

The method is to be stated in the National Annex of each country.

Table 1 - Limiting Criteria for investigation, suitability and acceptance tests for persistent and transient design situations at the ultimate and serviceability limit states (from EN 1997-1:2004/prA1:2012)

Test Method <sup>a</sup>	Limiting criterion	Investigation and Suitability tests	
		ULS	SLS
1	$\alpha_1$	2 mm	$0.01\Delta_e^b$
2	$k_1$ (per log cycle of time)	2%	2%
3	$\alpha_3$	5 mm	NA (use $P_c$ )
Test Method <sup>a</sup>	Limiting criterion	Acceptance tests	
		ULS	SLS
1	$\alpha_1$	2 mm	$0.01\Delta_e$
2	$k_1$ (per log cycle of time)	2%	2%
3	$\alpha_3$	NA	1.5 mm <sup>c</sup>

Note: NA = Not applicable

<sup>a</sup> Test methods are in accordance with Draft EN ISO 22477-5 Geotechnical investigation and testing - Testing of geotechnical structures - Part 5: Testing of anchorages

<sup>b</sup>  $\Delta_e = (F_{serv;k} \times \text{tendon free length}) / (\text{area of tendon} \times \text{elastic modulus of tendon})$

<sup>c</sup> Value given is for permanent anchors; for temporary anchors,  $\alpha_3 = 1.8$  mm

EN 1537:1999 provides for three methods to undertake the suite of tests, essentially following the traditions in testing developed and maintained in Germany, the UK and France. As stated in section 3, these test methods are referred to as Test Method 1, 2 and 3. This approach and test designation has been implemented in EN 1997-1:2004/prA1:2012 and Draft EN ISO 22477-5 expected to be published in 2013.

The provisional limiting criteria for ULS and SLS resistance for these tests to EN 1997-1:2004/prA1:2012 are given in Table 1. The methods of execution and interpretation of the tests are to be found in Draft EN ISO 22477-5. This standard makes no specific reference to testing for either SLS or ULS stating that proof loads are to be set in accordance with EN1997-1. Not all countries have the requirement to determine the limiting criteria for SLS of the anchor as this is considered to be satisfied if the test results meet the ULS criteria.

The test methods currently adopted in Germany, Denmark, France, Ireland and the UK are summarised below. It should be noted that some countries already use partial factors whilst others still adopt a more global safety factor approach.

#### Germany.

1. Follow Test Method 1
2. For all categories of test (investigation, suitability and acceptance), proof load is:
 
$$P_p = 1,1 \times 1,35 \times F_{Serv;k} \quad (11)$$
 or
 
$$P_p = 1,1 \times F_{ULS;d} \quad (12)$$
3. Limiting criteria based on value of  $\alpha_1$  for investigation, suitability and acceptance tests. Acceptance tests are required to satisfy the  $\alpha_1$  criterion, but the test is shorter than that required for suitability tests.

Denmark

1. Follow Test Method 1 and 3.
2. For all categories of test, proof load:

$$P_p = \xi (\gamma_a)^\alpha F_{ad} \quad (13)$$

where

$$F_{ad} = \max(F_{ULS;d}; F_{Serv;d}) \quad (14)$$

where all anchors are tested,  $\xi = 1,1$  and  $\gamma_a = 1,3$ .

$\alpha$  is a factor used to control reduced safety in temporary situations, provided the risk of the consequence justifies it. It may range from 0 to 1. For permanent anchors  $\alpha = 1$ . For temporary anchors – with small or no risk to human life or important infrastructure  $\alpha$  is typically set to 0,5. Thus for permanent anchors:

$$P_p = 1,1 \times 1,3 F_{ad} = 1,43 F_{ad} \quad (15)$$

For temporary anchors with less severe consequence of failure:

$$P_p = 1,1 \times (1,3)^{0,5} F_{ad} = 1,25 \times F_{ad} \quad (16)$$

3. Limiting criteria are based on a value of the creep rate according to (informative) values in EN 1537:1999

France

1. Follow Test Method 3
2. Proof load for Investigation and Suitability tests

$$P_p = 1,50 \times F_{serv;k} \quad (17)$$

where  $F_{serv;k}$  is derived from calculation.

3. Suitability tests should demonstrate that the critical creep load  $P_c \geq 1,2 \times F_{serv;k}$  (for permanent anchors) and  $P_c \geq 1,1 \times F_{serv;k}$  (for temporary anchors) where  $P_c$  is derived from the load corresponding to the end of the first pseudo-linear part of the creep rate versus anchor load plot found from an investigation or suitability test.
4. Proof load for Acceptance tests:

$$P_p = 1,25 \times F_{serv;k} \text{ (permanent anchors)} \quad (18)$$

or

$$P_p = 1,15 \times F_{serv;k} \text{ (temporary anchors)} \quad (19)$$

Given the limits on  $F_{serv;k}$  with respect to the critical creep load, at these proof loads the ratio between test load and creep load is independent of the application of the anchor. It will be constant and approximately 1,04.

5. Limiting criteria based on the value of  $\alpha_3$  at Proof load  $P_p$  and the value of  $P_c$  to check that  $P_c / F_{serv;k} > 1,2$ .

UK and Ireland

1. Follow Test Method 2 but also use Test Method 1.
2. Investigation tests - the anchor is normally loaded to the point where the vertical asymptote of the cumulative load loss  $k_l$  vs load relationship may be determined. An estimate of the anchor pull-out capacity may also be made.
3. Proof Load for the suitability and acceptance tests  $P_p = 1,5 \times T_w$  (20) where  $T_w$  is derived from the stability and serviceability requirements of the structure.
4. In both suitability and acceptance tests the limiting criteria are based on the values of  $k_l$  at a)  $P_p = 1,5 \times T_w$  and b)  $P_p = T_w$
5. Where Test Method 1 is adopted the limiting criterion  $k_l$  is translated into a creep displacement as shown in Table 1, note b.

5 CONCLUSIONS

The aim in developing a new Section 8 for EC7 has been to provide a rational framework for the design of ground anchors as elements within an overall ground-structure design, while accommodating the diverse practices of different countries. In the opinion of the group responsible for the drafting, which included the authors, this has been achieved. Some of the values of factors and criteria will probably be refined during the development of national annexes, though it is likely that national practices will remain distinct for the time being. Nevertheless, as with other aspects of Eurocodes, the existence of a single agreed text gives the possibility of clearer comparisons between national approaches, and so will hopefully contribute to the development of a more unified approach in the future.

6 ACKNOWLEDGEMENTS

The authors would like to acknowledge the contributions made by their fellow members of TC250/SC7/EG1, Klaus Dietz, Yves Legendre, Pierre Schmitt, Bernd Schuppener, Arne Schram Simonsen, in the development of the new draft of Section 8 of EC7.

7 REFERENCES

BS8081:1989. British Standard Code of practice for Ground Anchorages. *British Standards Institution, London*

DIN 4125 1990, Ground Anchorages – Design, construction and testing. *Deutsches Institut für Normung*

EN 1537:1999. Execution of special geotechnical work – Ground anchors. *CEN, Brussels*

EN 1997-1:2004/prA1:2012 Eurocode 7 – Geotechnical design – Part 1: General rules. *CEN, Brussels*

Littlejohn G.S. 1970. Soil anchors. *Proceedings of the Ground Engineering Symposium ICE, London, 33-44*

Littlejohn G.S. 2012. Personal communication

prEN ISO 22477-5 Geotechnical investigation and testing - Testing of geotechnical structures - Part 5: Testing of anchorages (in draft) *CEN, Brussels*

SIA V 191. 1995. Vorgespannte Boden- und Felsanker. *Schweizerischer Ingenieur- und Architekten – Verein.*

TA 95 1995. Ground Anchors – Recommendations for the design, calculation, execution and control. *Comité Français de la Mécanique des Sols et des Travaux de Fondations*

# Harmonising safety and profit: ethical issues in the geotechnical activity of major consulting companies

Harmoniser sécurité et profit: problèmes éthiques dans l'activité géotechnique de grosses entreprises de génie conseil

Redaelli M.  
*Halcrow (a CH2M Hill Company)*

**ABSTRACT:** Industrial enterprises aim at committing the lowest amount of resources and time to deliver a satisfactory product to the client. In the civil engineering industry failure to deliver a satisfactory product, in the form of structures and infrastructures which meet the required performance, may result in huge costs and loss of life. Conversely large uncertainties on the performance may also result in an unnecessarily safe and wasteful design. In the present time, considering the environmental impact of construction activities and the rapid depletion of finished resources, wasteful design is becoming ethically unacceptable. This paper discusses some issues that are specific of geotechnical engineering, where uncertainties are larger and the use of subjective engineering judgement and personal experience is more important than in other disciplines. Particular attention is given to problematic aspects of major projects, like the fragmentation of tasks in many sub-packages and the ensuing difficulty in managing the flow of information at the many interfaces. Practical suggestions are given to improve the compliance to ethical requirements in the geotechnical activity of large consulting companies.

**RÉSUMÉ :** Les entreprises industrielles désirent minimiser l'usage de ressources et de temps qui est nécessaire à obtenir un produit satisfaisant pour le client. Dans l'«industrie» du génie civil n'obtenir pas un produit satisfaisant, sous forme de structures ou infrastructures qui parviennent au comportement spécifiée, peut résulter en coûts énormes et même faire de victimes. Réciproquement, grandes incertitudes sur le résultat peuvent aussi produire un projet excessivement sûre et gaspilleuse. Aujourd'hui, à raison de l'impact de les activités de construction sur l'environnement et de l'épuisement rapide de ressources finies, les projets gaspilleurs deviennent éthiquement inacceptables. Ce papier discute des problèmes qui sont spécifiques de la géotechnique, où les incertitudes sont plus grandes, et l'usage du jugement subjectif et de l'expérience personnelle est plus important, que dans autres disciplines. Un' attention particulière est ici donnée aux aspects problématiques de gros projets, comme la fragmentation des actions dans beaucoup des sous-activités et la difficulté de gérer le flux d'informations a les nombreuses interfaces. Des suggestions pratiques pour améliorer la conformité aux critères éthiques de l'activité géotechnique dans les grosses sociétés de génie conseil sont, enfin, proposée.

**KEYWORDS:** ethics, decision making, risk, uncertainty, trust, communication, education, engineering judgement.

## 1 INTRODUCTION

This paper examines some ethical issues which are relevant to the practice of geotechnical engineering, with special attention to the activity of large, multidisciplinary consulting companies. The relevance of the subject arises from the peculiar nature of geotechnical engineering, which – in comparison with most other civil engineering disciplines – operates under higher levels of uncertainty and, necessarily, incorporates a remarkable amount of subjective judgement in the decision making process.

Moreover, the recent evolution of civil engineering, in its technical and commercial aspects, and the fast-paced changes our planet is experiencing, demand a constant re-evaluation and discussion of the principles of ethics applied to the civil engineering profession.

The content of this paper expresses the views of the author; it does not necessarily represent the position of the author's employer.

## 2 CODES OF CONDUCT, CORPORATE REPUTATION AND BEYOND

### 2.1 *Codes of professional conduct*

The “code of professional conduct” or “code of professional ethics” is generally the first - and often only - point of contact that civil engineering students and practitioners consciously have with their professional ethics. A code of conduct contains a set of rules of behaviour for civil engineers, established at national level by the relevant professional body. Such documents are essential cornerstones in the civil engineering ethical debate. However, due to the variety and complexity of the civil engineering profession, as well as its dynamic nature, the codes of conduct cannot be expected to always provide readily applicable rules for each and every real-life situation.

The review and discussion of specific national codes of conduct go beyond the scope of this paper. Since these documents are nowadays very accessible, the interested readers can easily expand their knowledge and understanding; for example the ICE Code of Professional Conduct (Institution of Civil Engineers 2008) and the ASCE Code of Ethics (American Society of Civil Engineers 2006) are freely available on-line.

The codes of conduct mentioned above regulate the practice of civil engineering in its entirety, as a macro-discipline. To the author's knowledge no specific code of conduct for specialist



disciplines, like geotechnical engineering, exists. The only exceptions apply to even more specific activities within a specialist discipline; for example the AGS Code of Conduct for Site Investigation (Association of Geotechnical Specialists 2007).

## 2.2 *Trustworthy corporation*

One of the functions of ethical behaviour is to protect the reputation of civil engineering professionals and corporations. This aspect is powerfully captured in the “Little Yellow Book” by Jim Howland (1982), whose *test to determine if a contemplated action is ethical is to ask: “Would I want to see it in the headlines tomorrow morning?”*. Although such an approach to ethics emphasises appearance over substance, the importance of corporate reputation and trustworthiness in the relationship with clients, contractors, third parties and society as a whole should not be underestimated. It is, in fact a key ingredient in developing successful projects which are capable of bringing benefits to the full range of stakeholders, as further discussed in Section 3.2.

## 2.3 *Full meaning of civil engineering ethics*

The full and deepest meaning of civil engineering ethics goes well beyond the straightforward application of the rules of behaviour contained in a code of conduct and the attempt to build and preserve corporate reputation.

Ethics involves the systematic study of moral norms and standards of behaviour, together with their underlying values and justifications (Armstrong *et al.* 1999). Applied ethics deals with the formulation of morally good decisions which can be made in a particular area of interest, for instance various professions (e.g. medical ethics, legal ethics, etc.) or particular issues of private and public interest (e.g. environmental ethics, bioethics, etc.). Part of the complexity of civil engineering ethics – which is one of the many branches of professional ethics – derives from the involvement of several ethical subjects and many different competing views of what is morally right or wrong. Those affected by the ethical decision-making of a geotechnical engineer for good or bad may include, for example:

- i the geotechnical engineer (and, where appropriate, their family and associates);
- ii the engineer’s colleagues (from the same discipline or from other disciplines);
- iii the engineer’s employer (in the present case a large engineering company);
- iv the engineer’s professional community (at national or international level);
- v the client;
- vi the society at large (ranging from a local community affected by a particular project, to larger groups of stakeholders at national and international level);
- vii the environment (the biosphere and its interaction with lithosphere, hydrosphere and atmosphere).

An extensive discussion of the philosophical theories of ethics is beyond the scope of this paper. The author agrees with Armstrong, Dixon and Robinson when they suggest that practical, real-life decision making requires a combination of the three main ethical theories: (a) deontological - to do with duty, (b) consequentialist - concerned with outcomes, (c) virtue ethics - concerned with moral excellence.

## 3 CIVIL ENGINEERING IN CONTEXT

### 3.1 *The intrinsic conflict between performance and profit*

Industrial enterprises aim at committing the lowest amount of resources and time to deliver a satisfactory product to their

clients. In the civil engineering industry failure to deliver a satisfactory product, in the form of a structure or infrastructure which meets the required performance, may result in huge costs and even loss of life.

In practice there is the need to strike the correct balance between a quick, cheap, approximate design of uncertain performance - on the one extreme - and slow, expensive, accurate design with much reduced uncertainty on the performance - on the other extreme. In a consulting company the “right” balance has to be satisfactory from both a commercial and an ethical point of view. Uncertainty in performance may result in either safer-than-required design (not dangerous but wasteful) or less-safe-than-required design, which is observed more rarely but may have extremely severe consequences.

In civil engineering, and particularly in geotechnics, a great deal of uncertainty in the final performance is associated with the human factor. Assigning tasks (including checking, reviewing and approving the design) to individuals with the appropriate level of competence and experience is of paramount importance. From a purely economic point of view a project manager or a project director wishes to see each task completed as quickly as possible by the available team member with the lowest hourly cost rate and therefore, most likely, level of experience. However, pushing tasks too far down the chain of competence/cost, has unacceptable implications on the quality of the design process and on the resulting uncertainty in the performance of the finished product.

There are no easy recipes to resolve this tension between cost control and profit, on one side, and quality in the form of performance of limited uncertainty (which avoids waste or lack of safety) on the other side. A useful strategy, however, consists of resisting short term pressures and “narrow framing” to embrace a long term view. Considering an oversimplified example, there is little use in containing the cost of project delivery if the final product is non-satisfactory and the client will therefore not be inclined to assign future commissions to the company. This elementary consideration can easily be suffocated by the pressure of working against tight programmes and budgets. More generally, whenever it is possible to avoid narrow framing and short term planning, commercial needs and quality assurance tend to become more compatible in an ethically satisfactory way.

### 3.2 *The problem of fragmentation*

A similar, often deleterious, tension between commercial and technical needs is connected to the problem of fragmentation, which affects the design process at many levels. From a purely technical point of view there is an obvious benefit in achieving continuity through the many phases of design and construction and in ensuring the same subject – same company and, ideally, same personnel – develops a project from inception to completion. This approach limits the need for knowledge transfer between different teams and individuals, thus minimising repetition and possible misunderstandings or loss of information. However, in some situations and in some forms of contract the continuity is discouraged or even prohibited. Such a choice is based on the principle of efficiency through competition and specialisation, which, in theory, should result in optimised cost and outcome. In practice there are other considerations which should complement, and in some cases overrule, these aspects. In a nutshell, commercial competition and specialisation push toward ever further fragmentation, while technical efficiency would require unity of vision and continuity of knowledge.

The author argues that, currently, the way major civil engineering projects are delivered is grossly unbalanced toward an excessive fragmentation which arises from the prevalence of commercially inspired principles over technical criteria. Often clients, and society at large, pay additional costs at the end of a

project due to mistakes or inefficiencies associated with this misguided approach.

It is here suggested that, without neglecting the value that project management and commercial specialists add to the delivery process, it is extremely important that high level decision-making incorporates sufficient input from technical experts. The subject deserves a richer and broader discussion than what is possible in this conference paper. The author agrees with Muir Wood (2004) on the detrimental role of discontinuity – sometimes deliberately enforced – between the functions of design and construction, and of the fragmentation of responsibility. Without reasonable continuity and unity a project is unlikely to meet satisfactory ethical standards with respect to impact on the society and the environment. Even the success in strictly engineering terms is endangered. In Muir Wood's words a successful engineering project comprises *a Client whose requirements have been understood and fulfilled; a Contractor who has been adequately reimbursed for a job well done; an Engineer who has fully understood the Client's need and has applied competence and creativity to a well-engineered project.* The final sign of success is *the rarity of unresolved dispute and litigation.* It is worth highlighting how this last point is largely dependent on the trustworthiness of the Engineer and all other parties. It is also strongly linked to the Engineers' reputation (see Section 2.2) and their conduct (Section 2.1).

A useful concept to inform the current and future discussion on successful forms of contract and procurement strategies is the Intelligent Market discussed by Muir Wood and Duffy (1991). This approach focuses on a holistic approach which avoids fragmentation and neglect of synergy, in summary taking generated value, not cost, as the main criterion for decision making.

## 4 SPECIFICITY OF GEOTECHNICS

### 4.1 *Uncertainty and judgement*

In geotechnical engineering uncertainties are typically larger than in other branches of civil engineering (structural engineering in particular). The analysis of geotechnical systems and the decision making associated with planning, designing and maintaining them often contains an unavoidable and significant component of engineering judgement. This can (and, when possible at all, should) be based on and informed by the existing literature, which condenses valuable and selected experience from others. However, in many circumstances individuals or teams of engineers have to introduce a considerable amount of subjective opinions in to the design process in order to achieve practical and usable solutions.

This consideration reveals how ethics, intended as good decision-making under uncertainty, bears particular relevance to the geotechnical discipline. The consequences of large uncertainty and reliance on judgement are numerous. On the one hand, geotechnical engineers willing to deliberately distort design outcomes for their own interests or for the interest of their direct employer can easily do so, when dealing with a client who is not familiar with ground behaviour and geotechnical works, by cherry-picking the most convenient results within the often large uncertainty band associated with different interpretations of site data and the selection of different models. On the other hand, the honest and scrupulous engineer in a consulting company may meet with resistance externally – with clients – and internally – with project managers and colleagues from other disciplines – when correctly trying to incorporate in to the design in a transparent way large levels of uncertainty which others may wish to ignore.

In this context helpful ethical behaviours from the geotechnical engineer include building trust by avoiding over-conservatism and by communicating risk accurately, also

highlighting which assumptions and hypotheses are judgement based. At the same time experienced geotechnical engineers need to hold their ground when unreasonably pressed to under-represent and under-communicate uncertainty. The author believes that in a discipline so closely associated with quantification of judgement a basic knowledge of the principles of cognitive psychology which are relevant to this task (Kahneman *et al.* 1982) should be more widespread.

Considering that large uncertainty on the performance of even very common geotechnical structures is not unusual, it is here suggested that national and international professional bodies and institutions should start recording statistical data on the key performance indicators for large numbers of structures.

### 4.2 *New challenges*

The constant evolution of geotechnics, and of the perception that mankind has of its own role and position on the planet, bring to light new ethical issues which should be incorporated in to the daily activity of geotechnical engineers. For example, the necessity of limiting greenhouse gasses emissions and of containing, as much as possible, the consumption of energy and other finite resources have never been so clear. These concepts need to become part of the basic consideration a geotechnical designer goes through when selecting and developing technical solutions (see for example Inui *et al.* 2011). Most importantly, the tendency to regard a large uncertainty in the performance of structures as tolerable and the inclination to deal with it by overdesigning, which implies producing a safer but potentially very wasteful structure, is becoming increasingly unacceptable. In fact such an approach cannot continue in the face of the new perception that the current generation must preserve the health of the environment and avoid resources depletion as much as reasonably practicable. Avoiding wasteful design is becoming an ethical imperative which cannot be achieved without credible understanding, accurate management and effective communication of uncertainties.

One more challenge currently presented to geotechnical engineers is the adoption of new, more complex and potentially more powerful, design codes. An obvious example is the suite of Eurocodes adopted by the European Union and other countries in recent years. The complexity of these codes requires particular attention to the communication between specialists of different disciplines if mistakes are to be avoided. Currently, in most consulting companies, the design of geotechnical structures (for example retaining walls) is jointly carried out by a geotechnical specialist and a structural specialist. The former verifies the geotechnical stability and provides structural actions from geotechnical considerations (for instance a soil-structure interaction analysis), whilst the latter provides the loading combinations to be studied and checks the structural safety on the basis of the geotechnical analysis results. This interaction, often iterative in its nature, requires particular attention to the communication across discipline boundaries. For example geotechnical engineers designing a structure according to Eurocode 7 – EN 1997 – will have to check and double check that they are fully understanding and using correctly the numerous load combinations that they receive from their structural colleagues. Similarly, when providing results in terms of structural actions, the geotechnical engineers need to carefully communicate to their structural colleagues the relevant explanations and clarifications about how the geotechnical calculations have been developed. A typically delicate situation is, for example, the incorporation of partial factors for the STR/GEO ultimate limit states (ULS) in soil-structure interaction analysis (for instance with the finite element method). In this specific circumstance the ULS partial factors from EN 1997-1 need to be rearranged (see for example Bond & Harris 2008) in a way which may be confusing. A discussion of such aspects and an additional effort to ensure the

correct understanding of the specific results communicated across the design team therefore becomes necessary.

## 5 CONCLUSIONS

In the process of civil engineering design there is an intrinsic tension between cost control, on one side, and quality - intended as confidence on the performance - on the other side. An excessive and uncontrolled effort to reduce costs would result in an unacceptably large uncertainty in the performance of engineering systems. Larger-than-expected uncertainty may produce an excessively safe and wasteful design or an unsafe design. Instances of unsafe design are relatively rare in civil engineering but the severity of the consequences of failure is often dramatic. In a world where we should be increasingly concerned with the human impact on the environment and with the rapid and irreversible depletion of finite resources a wasteful design is becoming increasingly unacceptable from the ethical point of view. A strategy to encourage an ethically balanced design is the avoidance of "narrow framing" and short term thinking, in favour of a long term view.

Fragmentation and discontinuity in civil engineering projects is detrimental to ethical choices and, in many cases, even to the basic success of the project in strict engineering terms (Muir Wood 2004). Procurement strategies and forms of contract should be discussed by the civil engineering community and rebalanced for a better harmony between commercial and technical needs.

The uncertainty affecting decision making in geotechnics is much higher than in other civil engineering disciplines. For this reason many ethical issues in geotechnics can be seen as ethical problems of uncertainty and risk communication. In the parts of codes of conduct concerned with communication the main focus and current interpretation is on restraining inappropriate communication. It is here argued that, still maintaining the integrity, objectivity, accuracy and sobriety requested by the codes of conduct, a new, urgent need to encourage the positive side of communication is emerging. This need for increased and improved communication acts at several levels:

- between geotechnical specialist and colleagues from other disciplines; to avoid misunderstandings (e.g. in the application of complex design codes)
- between design team and project management, to convey a realistic perception of uncertainty in the prediction of performance and programme;
- between Designer (or Engineer, depending on contract terminology), Contractor and Client (or Employer), in the various types of contractual arrangements (possibly including other parties, like checker, regulator, etc.), to maximise the probability of project success;
- between geotechnical as well as – more generally – civil engineers and multiple stakeholders and decision makers in the larger society; to ensure technical issues are understood by the public and rational decisions are made on the basis of credible and serious arguments.

The recognition of the key role that uncertainty plays in geotechnical engineering should result in practical steps being made to improve the capability of technical professionals in assessing and communicating risk. This paper suggests that the creation of databases recording the geotechnical performance of structures and infrastructures would offer valuable information, providing "base rates" to the professionals to support decision making during design.

Since a considerable amount of engineering judgement is integral to the activity of the geotechnical engineer it is here argued that the basic cognitive psychology principles associated with the quantification of expert opinion (Kahneman *et al.* 1982) should be taught to students enrolled in geotechnical engineering courses and offered to experienced engineers in continuous professional development training events.

Finally, the promotion of a culture of trust (Muir Wood 2004) is a fundamental ingredient for the success of civil engineering projects both in terms of commercial reward of the parties which are involved directly and in terms of benefit to society and the environment.

## 6 ACKNOWLEDGMENTS

The author is grateful to his employer for allowing this paper to be written. The content of this work is, in any case, an expression of the author's thoughts; it is not meant to represent the position of the author's employer. The author wishes to thank his colleague Dr Iain Tromans for the constructive discussion and the factual help which facilitated the preparation of this paper.

## 7 REFERENCES

- American Society of Civil Engineers, 2006. *Code of Ethics*. ASCE, Reston.
- Armstrong J., Dixon R. & Robinson S, 1999. *The decision makers: ethics for engineers*. Thomas Telford, London.
- Association of Geotechnical Specialists, 2007. *Code of Conduct for Site Investigation*. AGS, London.
- Bond A. & Harris A., 2008. *Decoding Eurocode 7*. Taylor & Francis, London.
- Howland J., 1982. *Little Yellow Book*. CH2M Hill, Englewood.
- Institution of Civil Engineers, 2008. *ICE Code of Professional Conduct*. ICE, London.
- Inui T., Chau C.Y.K, Soga K., Nicholson D. & O'Riordan N., 2011. Embodied energy and gas emissions of retaining wall structures. *Journal of Geotechnical and Geoenvironmental Engineering ASCE* 137(10):958-967.
- Kahneman D., Slovic P. & Tversky A., 1982. *Judgment Under Uncertainty: Heuristics and Biases*. Cambridge University Press, Cambridge, UK.
- Muir Wood A. & Duffy F., 1991. Society's needs. In *Education for the Built Environment*, Seminar, Madingley Hall, Cambridge, Arup.
- Muir Wood A., 2004. *Civil Engineering in Context*. Thomas Telford, London.

# La norme sur les missions d'ingénierie géotechnique, clé de voûte du management des risques géotechniques de tout projet

Geotechnical missions standard, the foundation of risk management for a project

Robert J.  
Arcadis France

**RÉSUMÉ :** Des ouvrages à construire de plus en plus complexes, des terrains disponibles de moins bonne qualité géotechnique, dans la Zone d'Influence Géotechnique (ZIG) une forte occupation du sol et du sous-sol par des ouvrages de plus en plus vulnérables, un voisinage plus sensible, tels sont les défis auxquels doit faire face l'ingénierie géotechnique pour satisfaire l'objectif fondamental du maître d'ouvrage qui est de réduire les risques techniques. Depuis 2000, la norme sur les missions d'ingénierie géotechnique a permis de définir une méthodologie d'intervention aussi bien pour la conception du projet que sa réalisation : ses révisions en 2006 et 2013 ont eu pour objectif de faciliter son application lors du déroulement d'un projet, condition indispensable pour assurer un bon management des risques géotechniques.

**ABSTRACT:** New constructions are more and more sophisticated, in a geotechnical context usually unfavourable and in an environment more and more sensitive. So, for the success of a project, it is necessary to reduce the geotechnical risk. As the soil conditions are not visible, complex and with a possibility of time-dependant modifications, the geotechnical risk reduction needs a geotechnical engineer intervention at each step of the design and during the construction to insure a good adaptation of the project to the actual soil conditions : it is the main aim of the geotechnical missions standard.

**MOTS-CLÉS :** norme, missions, zone d'influence géotechnique, maîtrise des risques

**KEY WORDS:** standard, geotechnical mission, risk management

## 1 INTRODUCTION

Tout projet de construction ou d'aménagement comporte des risques qui se sont amplifiés au fil des années. Ces risques, synonymes d'une maîtrise souvent difficile du délai de réalisation et du coût final de l'ouvrage, résultent de l'évolution défavorable de plusieurs facteurs : délais de conception et de réalisation de plus en plus courts, ouvrage de plus en plus complexe mettant en jeu des méthodes de construction sophistiquées qui s'adaptent mal aux incertitudes et aléas, environnement de plus en plus sensible à toute perturbation. Ce constat justifie l'intervention d'un nombre croissant de spécialistes, d'où des problèmes d'interfaces plus nombreux et une coordination plus difficile.

Devant cette complexité croissante des projets, le rôle joué par la géotechnique devient primordial car les exigences requises sur la qualité du sous-sol sont de plus en plus importantes notamment pour les fouilles profondes et les conditions de fondations. Le sous-sol étant non visible, complexe et évolutif dans le temps, la géotechnique permet de maîtriser au mieux l'inconnu en accompagnant le projet tout au long de sa conception et de sa réalisation par un enchaînement pertinent des missions conforme à la norme NF P 94-500.

## 2 SPÉCIFICITÉS DE LA GÉOTECHNIQUE

La géotechnique, discipline complexe qui étudie le comportement des terrains en relation ou non avec des ouvrages, s'appuie sur différentes sciences de la terre : géologie, hydrogéologie, mécanique des roches et des sols, géodynamique, rhéologie des géomatériaux, géochimie.

Sa première spécificité est d'étudier un milieu naturel non visible, donc mal connu : quelle que soit l'importance des investigations réalisées, la part du connu sera toujours faible par rapport au non reconnu. Ainsi, les observations et relevés faits lors de la réalisation de l'ouvrage sont capitaux car bien plus nombreux et mieux répartis que les investigations faites lors de sa conception. Sa deuxième spécificité est d'étudier un

milieu complexe. Le sous-sol est constitué de formations ni homogènes, ni isotropes, ni élastiques : elles sont nombreuses et de disposition spatiale aléatoire, une même formation pouvant présenter des lithologies très différenciées (voir Figure 1). Le resserrement du maillage des sondages permet de mieux approcher la complexité de la structure du sous-sol qui se prête mal à une modélisation toujours simplificatrice et réductrice, alors que le problème qui survient lors des travaux est souvent dû à une hétérogénéité locale non décelée à temps.

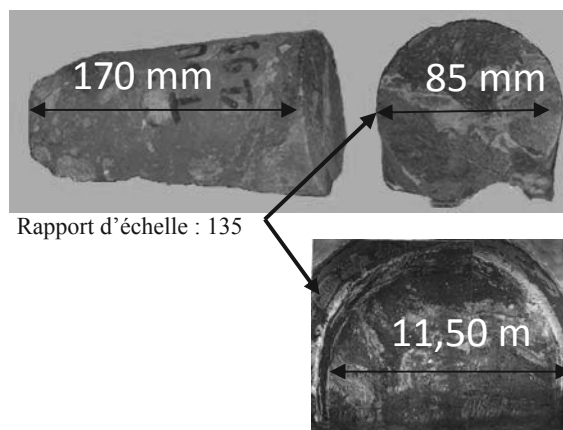


Figure 1 : Hétérogénéité à l'échelle de l'échantillon et du tunnel

Sa troisième spécificité est l'évolution possible de la constitution du sous-sol au fil du temps, évolution difficile à appréhender lors d'une étude limitée dans le temps. Les principaux facteurs d'évolution dans le temps sont :

- les perturbations apportées par l'homme : exploitation de matériaux, réalisation d'ouvrages souterrains, pollution de certaines formations, remblaiement de fouilles ultérieurement non détectables ;

- les phénomènes naturels liés à l'érosion et aux circulations d'eau, mettant en jeu la stabilité de versants (voir Figure 2) ;
- les secousses sismiques dont les effets sur certains terrains peuvent provoquer la perte de consistance ;
- la fluctuation des nappes contenues dans les formations, qu'elle soit naturelle (influence de la pluviométrie) ou artificielle (pompages industriels, création de barrages) ;
- le gonflement ou le retrait des terrains argileux ;
- la dissolution par l'eau de certaines formations (gypse, calcaire ...), créant un réseau karstique évolutif ;
- les entrainements de fines sous l'effet d'écoulements naturels ou non.



Figure 2 : Instabilité de versant due aux circulations d'eau

Face à cette complexité, le géotechnicien a pour principale arme les investigations ponctuelles, d'où le danger des interpolations entre sondages face aux anomalies locales difficilement détectables tels le puits perdu, le talweg fossile, la carrière.

### 3 SPÉCIFICITÉS DE L'OUVRAGE À CONSTRUIRE

Les principales spécificités de l'ouvrage à construire qui influent sur sa conception et l'interaction sol-structure sont :

- son emprise au sol et les charges qu'il apporte ;
- la sensibilité de sa structure vis à vis des incertitudes géotechniques (poussées, tassements différentiels par exemples) ;
- son implantation et sa profondeur dans le terrain ;
- ses phasages de construction qui imposeront des études d'interaction à chaque étape, même de courte durée.

L'optimisation des méthodes de construction nécessite l'étude de l'influence des incertitudes géotechniques, principalement en termes de délais de réalisation et de coût final de l'ouvrage : il faut choisir les méthodes les moins sensibles à ces incertitudes pour éviter des situations de crise. La méthode sophistiquée qui serait mise en échec par une variation de certains paramètres géotechniques est à proscrire si cette incertitude n'a pas pu être levée.

La méthode de construction elle-même peut avoir une influence sur les caractéristiques géotechniques du site : par exemples amélioration de sols, remontée de la nappe phréatique par effet de barrage, passage aux caractéristiques résiduelles par apparition de grandes déformations. Quelle que soit la méthode de construction retenue, les possibilités d'adaptations en cours de travaux doivent être étudiées, ainsi que leurs conditions de mise en œuvre : observations à faire, moyens de contrôle, dispositions conservatoires. La bonne maîtrise des méthodes de construction retenues suppose une vérification en continu de la bonne concordance entre prévision et réalité du comportement de l'ouvrage (auscultations), ainsi que de l'efficacité des procédés utilisés (pompages, soutènements, terrassements, améliorations de sol)

### 4 SENSIBILITÉ DE L'ENVIRONNEMENT

Pour mieux cerner les conséquences potentielles de la construction d'un ouvrage sur son environnement tant en surface qu'en sous-sol, la première étape est de définir sa zone d'influence géotechnique (ZIG). Sa ZIG correspond au volume du massif au sein duquel il y a interaction entre d'une part le sol et les avoisinants, d'autre part l'ouvrage du fait de sa réalisation et de son exploitation. Sa forme et son extension sont spécifiques à chaque site (contexte géotechnique, avoisinants) et à chaque ouvrage à construire (géométrie, phasage et méthodes d'exécution, conditions d'exploitation). Par exemple, un parking souterrain qui coupe un talweg fossile aquifère a une ZIG très étendue dans la direction du talweg (effet barrage).

La deuxième étape est l'identification de chaque avoisinant implanté dans la ZIG et l'analyse de sa vulnérabilité qui dépend des caractéristiques géotechniques des formations qu'il mobilise et de sa nature (structure, fondations). Cette analyse peut conduire à concevoir des dispositions préventives concernant l'avoisinant (reprises en sous œuvre, amélioration des sols) ou l'ouvrage à construire (adaptation locale de la méthode de construction), et éventuellement des dispositions correctives si le comportement réel du massif ou de l'avoisinant n'est pas conforme aux prévisions.

La vulnérabilité de l'environnement est de plus en plus importante au fil des années car d'une part il est de plus en plus dense et d'autre part il est constitué par des ouvrages vétustes (défauts de maintenance) ou complexes (nombreux sous-sols, grandes portées, fortes charges concentrées). Il est donc primordial de mettre en place une démarche conduisant à une maîtrise des risques géotechniques afin de limiter leurs conséquences potentielles sur l'environnement.

### 5 CARACTÉRISTIQUES PRINCIPALES DE LA NORME VERSION 2013

Face aux risques évoqués précédemment, la meilleure réponse est l'application rigoureuse de la norme NF P 94-500 sur la classification des missions types d'ingénierie géotechnique. Le reconnu en géotechnique est toujours modeste et les risques géotechniques dépendent non seulement des caractéristiques des terrains mais également de celles de l'ouvrage, de sa méthode de construction et de son environnement. Le projet sans risque n'existant pas, la maîtrise des risques géotechniques s'obtient par un enchaînement des missions d'ingénierie géotechnique tout au long des étapes de conception et de réalisation du projet, en coordination avec les missions de maîtrise d'œuvre générale.

Le retour d'expérience sur l'application de cette norme depuis 2000 permet de dégager quelques dysfonctionnements :

- Le non enchaînement des missions alors qu'il est obligatoire ;
- La réalisation d'une mission partielle sans que son complément soit fait ultérieurement ;
- Le contenu de la mission non adapté à l'état d'avancement du projet, parfois dû à une correspondance non évidente entre missions d'ingénierie géotechnique et phases de conception de la maîtrise d'œuvre générale.

L'objectif de la révision 2013 de la norme a été de faciliter son application en réduisant le nombre de missions pour faciliter leur enchaînement et en les calant au plus près des phases de maîtrise d'œuvre générale. Côté maître d'ouvrage et sa maîtrise d'œuvre, il y a trois missions à enchaîner de préférence par la même ingénierie géotechnique pour une plus forte valeur ajoutée dans la recherche des optimisations du projet tout en assurant une bonne maîtrise des risques.

L'étude géotechnique préalable G1, qui comprend deux phases :

- La phase étude de site ES, qui définit un modèle géologique préliminaire du site et ses principales caractéristiques géotechniques à partir de données pertinentes (investigations à réaliser si besoin), et établit une première identification des risques géotechniques majeurs du site (risques pouvant mettre en cause la faisabilité d'un projet non encore figé) ;
- La phase Principes Généraux de Construction PGC, qui contribue à la mise au point de l'étude préliminaire (ou APS) de l'ouvrage. Elle définit les données géotechniques à prendre en compte à ce stade (investigations à réaliser si besoin) et propose certains principes généraux de construction envisageables. Elle permet d'une part de compléter le modèle géologique et le contexte géotechnique, d'autre part de mieux identifier et hiérarchiser, en fonction de l'ouvrage projeté, les risques géotechniques majeurs afin d'en réduire les conséquences en cas de survenance ;

L'étude géotechnique de conception G2, qui comprend trois phases :

- La phase avant-projet AVP, qui contribue à la mise au point de l'AVP (ou avant-projet Détaillé APD) de l'ouvrage. Elle permet d'une part de compléter le modèle géologique et le contexte géotechnique (investigations en fonction du site et de la complexité de l'ouvrage projeté), d'autre part de mieux identifier les risques géotechniques importants et d'en réduire les conséquences en cas de survenance (risques pouvant nécessiter des mesures appropriées en phase conception et/ou un suivi spécifique en phase réalisation par mise en œuvre de mesures prédéfinies si besoin). Elle définit les hypothèses géotechniques à prendre en compte au stade AVP et les principes de construction des ouvrages géotechniques (terrassements, soutènements, pentes et talus, fondations, assises des dallages et des voiries, améliorations de sols, dispositions générales vis-à-vis des nappes et des avoisinants). Elle fournit une ébauche dimensionnelle par type d'ouvrage géotechnique, une première approche des quantités et conclut sur la pertinence d'application de la méthode observationnelle pour une meilleure gestion des risques résiduels.
- La phase projet PRO, qui contribue à la mise au point du projet de l'ouvrage. Elle définit les hypothèses géotechniques à prendre en compte au stade du projet, en particulier les valeurs caractéristiques des paramètres géotechniques (investigations en fonction de la complexité de l'ouvrage). Elle établit les notes techniques donnant les choix constructifs des ouvrages géotechniques (terrassements, soutènements, pentes et talus, fondations, assises des dallages et des voiries, améliorations de sols, dispositions vis-à-vis des nappes et des avoisinants), certaines notes de calcul de dimensionnement niveau projet, une approche des quantités et les valeurs seuils si l'application de la méthode observationnelle est conseillée. Si nécessaire, elle donne les principes de maintenance des ouvrages géotechniques.
- La phase DCE/ACT, qui contribue d'une part à l'établissement du Dossier de Consultation des Entreprises de l'ouvrage, d'autre part à l'Assistance pour l'établissement des Contrats de Travaux avec le ou les entrepreneurs retenus pour réaliser les ouvrages géotechniques. Elle participe à la rédaction des documents techniques nécessaires aux entreprises pour leurs études de réalisation des ouvrages géotechniques (dossier de la phase PRO avec plans, notices techniques, cahier des charges techniques particulières, cadre de bordereau des prix et d'estimatif, planning prévisionnel). Elle assiste le maître d'ouvrage ou la maîtrise d'œuvre pour la sélection des entreprises, analyse les offres techniques (projet de base et variantes éventuelles) et

participe à la finalisation des pièces techniques définitives des contrats de travaux concernés par les ouvrages géotechniques.

La supervision géotechnique d'exécution G4, réalisée en collaboration avec la maîtrise d'œuvre ou intégrée à cette dernière, qui comprend deux phases lors de la réalisation de l'ouvrage :

- La phase Supervision de l'étude géotechnique d'exécution, qui émet un avis pour le visa donné par la maîtrise d'œuvre. Elle donne un avis sur la pertinence des hypothèses géotechniques de l'étude géotechnique d'exécution, des dimensionnements et des méthodes d'exécution, des adaptations ou des optimisations des ouvrages géotechniques proposées par l'entrepreneur, du programme d'auscultation et des valeurs seuils en cas d'application de la méthode observationnelle.
- La phase Supervision du suivi géotechnique d'exécution. Par interventions ponctuelles sur le chantier, elle donne un avis sur la pertinence du contexte géotechnique et du comportement tels qu'observés par l'entrepreneur de l'ouvrage et des avoisinants concernés ainsi que de l'adaptation ou de l'optimisation éventuelle de l'ouvrage géotechnique proposée par l'entrepreneur. Elle permet de donner un avis sur le dossier des ouvrages exécutés (DOE) et sur le dossier d'interventions ultérieures sur l'ouvrage (DIUO) établis par l'entrepreneur.

Côté entrepreneur en charge de la réalisation d'un ouvrage géotechnique, la mission d'étude et suivi géotechniques d'exécution G3 est à réaliser par une ingénierie géotechnique (éventuellement intégrée à l'entreprise) : elle comprend deux phases interactives et indissociables :

- La phase Etude, qui contribue à l'étude d'exécution de l'ouvrage pour la part des ouvrages géotechniques. Elle établit la note d'hypothèses géotechniques sur la base des données fournies par la G2 phase Projet et des résultats d'investigations complémentaires si besoin. Elle donne le dimensionnement des ouvrages géotechniques, leur méthode et conditions d'exécution, leurs phasages généraux. Elle définit les suivis, les auscultations et les contrôles à prévoir, les valeurs seuils en cas d'application de la méthode observationnelle. Elle définit les moyens à mettre en œuvre pour sécuriser l'ouvrage et les avoisinants concernés ainsi que les adaptations du projet vis-à-vis des risques géotechniques identifiés en cas de survenance en cours de réalisation. Elle participe à l'établissement du dossier géotechnique d'exécution des ouvrages géotechniques provisoires et définitifs avec plans d'exécution, de phasage et de suivi.
- La phase Suivi, qui contribue fortement à la maîtrise des risques géotechniques résiduels pendant la réalisation des ouvrages géotechniques. Par un suivi en continu des travaux géotechniques (relevés) et des auscultations, elle permet d'une part de valider ou de mettre à jour le modèle géologique et les hypothèses géotechniques du site, d'autre part de s'assurer que le comportement en cours d'exécution de l'ouvrage et des avoisinants est conforme aux prévisions ou de mettre en œuvre à temps les adaptations nécessaires (mesures correctives prédéfinies) ou les optimisations possibles en cas d'application de la méthode observationnelle. Dans le cas de survenance d'un risque non identifié, elle permet de prendre les mesures sécuritaires qui s'imposent et d'alerter la maîtrise d'œuvre pour lancer en urgence un diagnostic géotechnique avec si besoin des investigations géotechniques pertinentes, et adapter en conséquence l'étude géotechnique d'exécution. Elle participe à l'établissement par l'entrepreneur du DOE et du DIUO.

## 6 MANAGEMENT DES RISQUES GEOTECHNIQUES

Dans le cadre de l'enchaînement des missions types d'ingénierie géotechnique, des risques géotechniques sont identifiés en fonction des données collectées et des spécificités de l'ouvrage géotechnique projeté, puis font l'objet d'une évaluation pour hiérarchisation et d'un traitement. Les risques géotechniques sont liés à une connaissance partielle des caractéristiques géotechniques du site susceptibles d'avoir des conséquences sur le comportement des ouvrages. Ils dépendent donc des incertitudes résiduelles (degré de connaissance limité malgré des investigations réalisées par étapes successives pendant les différentes phases de conception et un suivi géotechnique en phase de travaux), de la variabilité naturelle des paramètres et des accidents géologiques.

Les risques géotechniques identifiés sont classés selon une échelle de gravité pour apprécier leur impact sur le projet : les risques majeurs peuvent remettre en cause le projet, les risques importants peuvent nécessiter des mesures appropriées en phase conception et/ou un suivi spécifique en phase réalisation pour décider si nécessaire de la mise en œuvre d'adaptations ou de mesures prédéfinies, les risques mineurs peuvent justifier une optimisation en phase conception ou un suivi spécifique en phase réalisation pour aboutir à un faible impact en termes de qualité, sécurité, coût et délai.

Face à chaque risque identifié, il convient de définir les actions préventives possibles pour le réduire (réduction des incertitudes ou de l'impact potentiel de ces incertitudes), les dispositions à mettre en œuvre pour détecter sa survenance le plus tôt possible (programme de suivi et de contrôle avec valeurs seuils associées) et les actions correctives pour en minimiser l'impact s'il se réalise (adaptation du projet).

Le traitement des risques est adapté à chaque phase de déroulement du projet. Le canevas de traitement habituel est le suivant :

- le risque majeur identifié est réduit ou annulé par des recommandations appropriées pour le futur ouvrage dès la G1 ;
- le risque important identifié est réduit ou annulé par des mesures appropriées au stade de la G2 : adaptation du projet, suivi spécifique avec des mesures prédéfinies et des valeurs seuils associées, adaptations possibles en phase de réalisation ;
- le risque mineur identifié a un faible impact et peut justifier une solution d'optimisation au stade de la réalisation.

La gestion des risques (et donc de leur coût potentiel) est axée sur leur détection le plus tôt possible et sur le contrôle de l'efficacité des solutions correctives prédéfinies. Elle s'appuie sur les actions suivantes :

Au stade de la conception de l'ouvrage :

- évaluation des incertitudes et de la variabilité des paramètres influents, avec réalisation d'investigations géotechniques pour les réduire ;
- reconnaissance des avoisinants concernés (ZIG) ;
- définition des éventuelles dispositions constructives complémentaires à mettre en œuvre si le contexte géotechnique ou le comportement de l'ouvrage observé n'est pas conforme aux prévisions ;
- définition des adaptations possibles avec recherche d'opportunités ;
- prise en compte des risques inhérents par leur budgétisation et leur incidence sur les délais ;
- prise en compte de la maintenance inhérente à certains types d'ouvrages géotechniques (drains, tirants...).

Pendant la réalisation de l'ouvrage : suivi et contrôle géotechnique en continu (valeurs seuils associées).

Pendant l'exploitation de l'ouvrage : mise en œuvre de la maintenance inhérente à certains types d'ouvrages géotechniques.

## 7 CONCLUSION

L'application de la norme NF P 94-500 sur les missions types d'ingénierie géotechnique à réaliser dans le cadre de la conception puis de la réalisation d'un ouvrage est la clé de voûte du management des risques géotechniques. Le retour d'expérience montre que tout investissement fait par le maître d'ouvrage en phase conception pour la maîtrise des risques liés au site et aux sols est hautement rentable, l'approche quantitative faite pour les ouvrages souterrains en est une illustration (voir Figure 3). Comme disait Francis BACON, philosophe de la fin du 16<sup>ème</sup> siècle : « On ne commande à la nature qu'en lui obéissant ».

Les assureurs, qui mettent en place les polices d'assurance des intervenants pour couvrir les risques résiduels, sont les garants de l'application effective de cette norme qui consacre le rôle majeur joué par l'ingénierie géotechnique dans le management des risques. L'application de cette norme est une condition nécessaire pour répondre aux attentes du maître d'ouvrage qui recherche un ouvrage de qualité sans dépassement de délai et de coût.

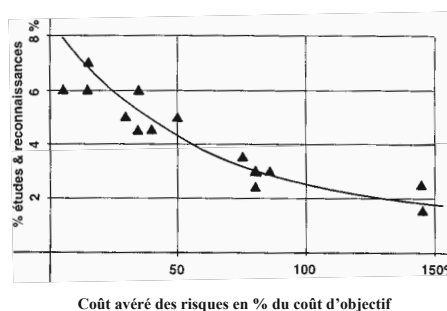


Figure 3 : Corrélation entre coût des études + investigations et coût avéré des risques pour plusieurs tunnels

## 8 REFERENCES

- AFNOR Norme NF P 94-500 décembre 2006, Missions d'ingénierie géotechnique – Classification et spécifications, révision en 2013.
- AFTES Recommandation sur la caractérisation des incertitudes et des risques géologiques, hydrogéologiques et géotechniques, TES n°232, 2012.
- GERMA Management des projets complexes de génie civil et urbain, janvier 2012.
- Motaz J. et al., Prévention des risques importants des grands ouvrages de bâtiment – guide pratique, AQC Editions 2010
- Breyse D., Maîtrise des risques en génie civil, Hermès, 2009
- Blondeau F. et al., Effets de l'encadrement juridique sur la pratique de la géotechnique, Revue Française de géotechnique n°123, 2008.
- Robert J., Le management des risques techniques pour la construction d'un tunnel en site urbain : la théorie et la pratique, AFTES Congrès de Monaco, 2008
- AFTES Recommandations Comment maîtriser les coûts de son projet, TOS n°201, 2007.
- Allagnat D. et al., La méthode observationnelle pour le dimensionnement interactif des ouvrages, Presses des Ponts et Chaussées, 2005.
- AFNOR Norme FD X50-117 Management des risques d'un projet, 2003.

# Embedding Geo Risk Management. The Geo-Impuls Approach

## L'implantation du management des risques géotechniques. L'approche Geo-Impuls

Staveren van M.Th.  
VSRM

Litjens P.P.T., Cools P.M.C.B.M.  
*Rijkswaterstaat Dienst Infrastructuur*

**ABSTRACT:** Geo-Impuls is a Dutch and industry wide geotechnical development programme. It aims to strengthen the geotechnical community by substantially reducing geotechnical failures in all types of construction projects. Over 40 Dutch organizations, including client organizations, contractors, engineering firms and knowledge institutes, work closely together in this programme that runs from 2009 up to 2015. All Geo-Impuls participants embraced geotechnical risk management (GeoRM) as leading working method to realize projects within budget and planning, as well as according to actual safety and quality standards. However, routinely applying GeoRM in projects requires embedding GeoRM in its organizations. This paper aims to present how the Dutch geotechnical community is currently embedding geotechnical risk management in its organizations. First, the Geo-Impuls program is introduced. The remaining part of this paper summarizes the four pillars of the Geo-Impuls program: (1) the process of geo risk management, (2) geo risk management principles, (3) geo risk management tools, and (4) geo risk management implementation. Finally, the main conclusions are drawn.

**RÉSUMÉ :** Geo-Impuls est un programme hollandais de développement géotechnique au niveau de l'ensemble de la profession. Son objectif est de renforcer la communauté géotechnique en réduisant les accidents géotechniques dans tous types les projets. Ce programme mis en œuvre de 2009 à 2015 regroupe plus de 40 organisations hollandaises (clients, entreprises, bureaux d'ingénieurs conseils et instituts d'enseignement et de recherche). Tous les participants au projet Geo-Impuls ont adopté le management des risques géotechniques (GeoRM) comme méthode principale pour réaliser des projets conformes aux budget et planning, et respectant les normes de sécurité et de qualité en vigueur. cependant, l'application routinière du GeoRM dans les projets exige son implantation dans les organisations. L'article vise à présenter de quel façon la communauté géotechnique hollandaise est en train d'implanter ce management des risques géotechniques. Tout d'abord, on présente le programme Geo-Impuls. Ensuite l'article fait une synthèse des quatre piliers du programme Geo-Impuls: (1) la processus de management des risques géotechniques, (2) les principes du management des risques géotechniques, (3) les outils du management des risques géotechniques, (4) l'implantation du management des risques géotechniques. Enfin, les conclusions les plus importantes sont tirées.

**KEYWORDS:** geotechnical risk, geotechnical risk management, project risk management, risk management implementation, tool box

### 1 INTRODUCTION

Building in, on, or with ground is risky. According to several assessments, on average geotechnical problems during engineering, construction, and operation of civil engineering projects result in cost increases of 5% of the original budgets. In the Netherlands only, this adds up to hundreds of millions of Euros, annually. So action within the geotechnical community is needed, which resulted in a major geotechnical development program in The Netherlands: Geo-Impuls.

First, the GeoImpuls program will be described, including three top geotechnical risks that drive the program, six dilemma's related to these top risks and three resulting research and development themes for providing effective and cost efficient risk remediation.

Next, the concept of geotechnical risk management or GeoRM will be presented, including an explanation what GeoRM is about and why GeoRM should be embraced by all geotechnical professionals.

An important element of GeoRM is provided by eight so-called Geo-Principles. These principles are derived from the generic risk management principles of the ISO 31000 risk management guideline (ISO 2009). By adopting these principles, Geo-Impuls decided to apply a modern principle-based risk management approach, rather than a more traditional rule-based one. The main advantage of a principle-based

approach is that any type of organization, in any type of construction project, is able to design its own tailor-made risk management activities and processes. This avoids a well known "one size fits nobody" situation. The Geo-Principles are introduced in the paper by a checklist, which is ready to be used in practice by any reader.

In addition to the principles, risk management tools are welcome and useful. Therefore, a Geo-Impuls risk management toolbox is in development. Together with already available techniques, this toolbox will be filled with the results of 12 working groups. It contains sub boxes for contractual matters, for geotechnical design and construction, as well as for dealing with the many project stakeholders and its environment. The latter is particular important for the growing number of complex underground projects in densely populated and sensitive build environments.

While having the risk management processes, principles, and tools, a fourth element proves to be of paramount importance: the organizations that have to deal with geotechnics. These are either client organizations, contractors, or engineers. Adapting geotechnical risk management activities to existing working procedures and process in these organizations is a key success factor for continuous GeoRM application. Rijkswaterstaat, executive agency of the Ministry of Infrastructure and the Environment and the largest Dutch



public client organization for construction projects, provides a pioneering role in embedding GeoRM in its entire organization. Their recent experiences with the GeoRM implementation will be shared.

Finally, the paper will draw some conclusions about the main experiences within the Geo-Impuls development programme with embedding geotechnical risk management in organizations. Any reader is invited to reflect on these experiences, and to use them for the benefits of his or her own geotechnical challenges.

## 2 GEO-IMPULS PROGRAM

Geo-Impuls is a Dutch and industry wide geotechnical development programme (Cools 2011). It aims to strengthen the geotechnical community, by substantially reducing geotechnical failures in all types of construction projects. Over 40 Dutch organizations, including client organizations, contractors, engineering firms and knowledge institutes, work closely together in this programme that runs from 2009 up to 2015. The two key objectives of the Geo-Impuls program are (1) a completed GeoRM toolbox, including guidelines and best-practices, and (2) a number of 100 projects that demonstrate GeoRM adoption by 2015. This requires embedding GeoRM principles and practices in organizations. Therefore, the implementation of GeoRM in (project) organizations is a key issue in the Geo-Impuls program.

During several sessions with program participants a number of infrastructural projects were analyzed regarding their geotechnical risks. The overall conclusion is that three top risks can be identified, which are related to Contracts, Geo-Engineering and Project Communication:

1. Top risk of Contracts: unforeseen soil conditions
2. Top risk of Geo-engineering: failure due to settlements or collapse
3. Top risk of Project communication: loss of public support

Managing these top risks involves dealing with several dilemmas, which are related to each specific top risk:

Ad 1 Contracts:

- A small or extensive scope of ground investigations during tendering?
- Do or don't apply contractual geotechnical risk allocation?

Ad 2 Geo-engineering:

- A robust design or flexibility during construction?
- Do or don't apply on site quality measurements?

Ad 3 Project communication:

- Do or don't inform the public on risks?
- Do or don't inform the public on nuisance?

So, there are three central development themes: Contracts for dealing with legal issues, Geo-engineering for dealing with technical issues, and Project communication for paying attention to the human factor. For each theme, the by the Dutch geotechnical community perceived most important topics are worked out in Working Groups.

Theme 1: Contracts

- Geotechnical risk allocation in projects by the geotechnical baseline approach
- Risk-based soil investigation planning, including tendering issues
- Process specifications for geo-engineering in contracts and contract management
- Geotechnical risk checklists for non-geotechnical decision makers

Theme 2: Geo-engineering

- Quality control for timely tracing imperfections of cast-in-place concrete elements

- Observational Method by using risk-based scenarios in combination with monitoring
- Reliable geotechnical modelling by revealing and presenting geological and geotechnical uncertainties and using sensitivity analysis
- Long-term geotechnical monitoring for better understanding of time-dependent geotechnical behaviour, by comparing monitoring results with predictive models

Theme 3: Project communication

- Communication of geotechnical risk to communities in project environments
- Closing the gap of misunderstanding between design and construction professionals
- International knowledge exchange on reduction of geotechnical failures and geotechnical risk management
- Geotechnical risk management education and training for students and professionals

Since 2009, an industry-wide Steering Committee takes responsibility for the Geo-Impuls programme. The day-to-day execution of the programme has been assigned to the Core Team comprising the leaders of the Working Groups. The Geo-Impuls Programme Office coordinates all administrative aspects and a program advisor focuses specifically on GeoRM and its implementation in (project) organizations.

## 3 GEO RISK MANAGEMENT

All Geo-Impuls participants embraced Geotechnical Risk Management (GeoRM) as the leading working method to realize projects within budget and planning, as well as according to pre-set safety and quality standards. Before explaining GeoRM, it helps to define the term geotechnical risk. According to ISO31000 (2009), a risk is the effect of uncertainty on realizing objectives.

Similarly, a geotechnical risk can be defined as the effect of geotechnical uncertainty on realizing objectives, such as settlements or horizontal deformations within pre-set limits. Geotechnical uncertainty may result from randomness, fuzziness, incompleteness or simply incorrect geotechnical information (Van Staveren 2006). A geotechnical risk has a probability of occurrence, one or more causes, and usually a number of effects when happening, such as damage, cost overruns and delay.

Geotechnical risk management or GeoRM is an explicit, structured, communicated, and continuous way of dealing with geotechnical risk, in order to achieve project objectives effectively and cost-efficiently. The process of geotechnical risk management is similar to the process of project risk management and involves the same sequence of steps.

Therefore, GeoRM fits well in any sort of project risk management. The difference is that GeoRM is a more detailed and in-depth approach of project risk management, for giving geotechnical risk the attention it requires in all phases of engineering and construction projects. Figure 1 presents the six GeoRM steps.

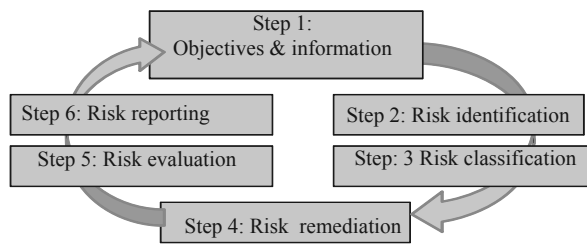


Figure 1. The GeoRM process in six steps.

While these six GeoRM steps are quite straightforward, it helps to take them according to so-called GeoRM principles. These are presented in the next section.

#### 4 GEO RISK MANAGEMENT PRINCIPLES

Basically, there are two main routes of doing risk management: rule-based and principle-based. The rule-based approach is using rules and results into one best way for managing risk. This is not appropriate for GeoRM, because of the large diversity of engineering and construction projects in complexity, size, location, and ground conditions.

For these reasons the Geo-Impuls takes the principle-based route for allowing fit-for-purpose geotechnical risk management. Based on the eleven generic risk management principles from ISO31000 (2009), eight specific geotechnical or GeoRM principles have been defined by a number of Geo-Impuls participants.

By definition, principles are abstract and need a translation into activities. Such a translation can be done for specific projects and even for specific project phases, again in a fit-for-purpose way. By this approach GeoRM is a mean for realizing project objectives and not an end in itself. Table 1 presents the eight GeoRM interrelated principles and a number of examples of related actions in the format of a simple checklist.

Table 1. GeoRM principles in a checklist format.

GeoRM Principles	GeoRM Actions	Done	
		Yes	No
1. Generate and protect value	Make all geotechnical risks in each project explicit, including all risk effects and the selected risk remediation measures.		
2. Participate in decision making in all project phases	Make a geotechnical risk file from the start if the project and use it for decision making.		
3. Make geotechnical uncertainty explicit	Include geotechnical sensitivity analyses with margins in project reports Use the geotechnical risk file for managing the consequences of any geotechnical changes during the project		
4. Work systematically, structured and in time	Include GeoRM explicitly in the project planning and reserve resources for it.		
5. Use all available information	Use all available historical and other relevant project information, right from the start of the project  Work from a general level to a detailed level, from		

		using geological maps to geotechnical monitoring
6. Work transparently together with all stakeholders	Asses the influence of the ground conditions on the critical success factors of the project stakeholders	Communicate clear about geotechnical risk with all parties involved
		Indicate and communicate any dependencies of geotechnics with other disciplines in the project
7. Include the role of the human factor	Make any differences in organizational culture of all involved project parties visible and feasible	
8. Use experiences and lessons for continuous improvement	Use all available and relevant project evaluations	Organize that geotechnical professionals participate in GeoRM courses and communities of practice

Table 1 can be used as a checklist, by simply tick boxing whether the principle-driven GeoRM actions have been executed in a project or not.

In summary, the main advantage of a principle-based approach is that any type of organization, in any type of construction project, is able to design its own tailor-made risk management activities and processes. This avoids a well known “one size fits nobody” situation.

#### 5 GEO RISK MANAGEMENT TOOLS

In addition to the GeoRM process and the GeoRM principles, a set of GeoRM tools is of great help for facilitating geotechnical risk management. Therefore, the Geo-Impuls program aims to provide a toolbox with tools for the three themes of contracts, geo-engineering and project communication. As a result of the Geo-Impuls program, the following tools examples become ready:

##### Theme 1: Contracts:

- Geotechnical Risk Allocation Reports, comparable to the concept of Geotechnical Baseline Report (GBR) from the United States. Recent project evaluations demonstrated that this concept is also beneficial to Dutch projects.
- Guideline for defining Risk-based Site Investigation programmes that provides explicit information and data for quantification of geotechnical risk
- Ground Risk Identification Checklists

##### Theme 2: Geo-Engineering

- Guideline with best practices for monitoring based design & construction by the Observational Method
- Long Term Subsoil Monitoring results for validation of existing numerical ground deformation models
- Techniques for checking the integrity of diaphragm-walls and in-situ made piled foundations. By using these techniques, weak spots can be detected and repaired before excavation

##### Theme 3: Project communication

- Communication strategies for managing expectations of the project stakeholders
- Intervention models for risk-based subsoil communication with in particular the public living and

working around projects in cities, by using tailor-made workshops

- Intervention models for effective communication from geotechnical designers to construction crews.

Together with already available techniques, these tools are part of the GeoRM toolbox. A study of 40 recent geotechnical failures shows that 90 % of these failures was caused by the fact that right knowledge and tools are available in the Dutch geotechnical community, but not used by the right engineer in the right way and at the right time (van Tol 2007).

## 6 GEO RISK MANAGEMENT IMPLEMENTATION

Routinely applying GeoRM in projects requires embedding GeoRM in its organizations. This implementation of risk management in general, and of GeoRM in particular, is not a spontaneous process (Van Staveren 2009). Organizational conditions, like the organizational structure and the organizational culture should facilitate, rather than frustrate, the routine application of GeoRM.

For this reason specific working sessions have been organized with the Geo-Impuls, for clients, contractors, and engineers. During these working sessions it has been made explicit to which degree four key conditions for GeoRM were available in the participating organizations. These key conditions are (1) shared GeoRM understanding, (2) GeoRM is formally embedded in existing procedures, (3) interdisciplinary application of GeoRM within the organizations, and (4) GeoRM cooperation with external parties and stakeholders. During the sessions it became clear that for most organizations considerable steps for optimizing these GeoRM conditions can be made. Therefore, each participant defined at least one specific GeoRM embedment action to be executed in his or her organization. This exercise provided in total 44 concrete actions for embedding GeoRM in client, contractor, and engineering organizations of the Dutch construction industry.

Regarding the development of a shared GeoRM understanding, examples of actions are including GeoRM in internal project management courses and explicitly discussing the main geotechnical risk in regular project meetings.

Examples of formally embedding GeoRM is providing a clear internal procedure GeoRM procedure and applying GeoRM products in projects.

Concerning the interdisciplinary application of GeoRM, it was for instance decided to involve a geotechnical engineer in tender-kick off and subsequent meetings and to integrate risk-based geotechnical engineering during tenders with design, quality, contracts and safety. With regard to the GeoRM cooperation with external parties, demonstrating to project stakeholders how to deal explicitly with geotechnical risk and embedding geotechnical risk in contracts were some of the actions. All of these actions are straightforward, concrete and relatively easy to execute in the going concern of projects. These activities demonstrate that implementing GeoRM in organizations is merely a matter of a lot of relatively small steps towards an explicit way of risk-based geotechnical engineering, than one major change management jump.

Rijkswaterstaat, the executive agency of the Ministry of Infrastructure and the Environment and the largest Dutch public client organization for construction projects, provides a pioneering role in embedding GeoRM in its entire organization. They work parallel on developing all of the four key conditions for implementing GeoRM in their organization. Developing a shared GeoRM understanding is ongoing by regular meetings of the geotechnical experts, where they exchange experiences and lessons how to apply their geotechnical activities in a risk-based way by taking the GeoRM process steps. Furthermore, a formal GeoRM procedure that fits in their project process is in

development. This GeoRM procedure is communicated to the project managers, contract managers and environment managers, in order to become accepted and used in an interdisciplinary way. Finally, Rijkswaterstaat is going to subscribe the application of GeoRM to the engineering consultancies and contractors, which involves the application of GeoRM together with external parties.

## 7 CONCLUSIONS

Due to the inherently uncertain nature of the subsoil, building in, on, or with ground remains risky. Nevertheless, modern risk management approaches are readily available for more explicitly and well-structured dealing with inherent ground uncertainty. Therefore, the Dutch industry wide geotechnical development programme Geo-Impuls has been started. It aims to substantially reduce geotechnical failures in all types of construction projects. Geotechnical risk management or GeoRM has been adopted as the main approach to achieve this objective by the forty organizations participating in Geo-Impuls.

The Geo-Impuls program is founded on four pillars: (1) the geo risk management process, (2) georisk management principles, (3) geo risk management tools, and (4) geo risk management implementation.

The process of geotechnical risk management is similar to the process of project risk management. Because it involves the same sequence of the similar risk management steps, GeoRM fits excellently in any sort of project risk management. By being geotechnically driven, GeoRM is simply a more detailed and in-depth approach of project risk management.

Geo-Impuls takes the principle-based route for allowing fit-for-purpose geotechnical risk management, which is worked out in eight specific GeoRM principles. These are based on generic ISO31000 risk management principles and translated into straightforward actions for geotechnical risk remediation. In addition to developing GeoRM tools, GeoImpuls dedicates considerable attention to routinely applying these tools by implementing the GeoRM processes and principles in organizations. These organizations are clients, contractors and engineering firms. This requires embedding GeoRM in the existing processes of organizations. Implementing GeoRM in (project) organizations is therefore considered the key success factor for effectively and cost-efficiently managing geotechnical risk. In final conclusion, applying GeoRM gives geotechnical risk the attention it requires, in all phases of engineering and construction projects, in order to realize project success.

## 8 ACKNOWLEDGEMENTS

The authors would like to thank all participants of the Geo-Impuls development program for sharing their knowledge and experience in the program, on which this paper is founded.

## 9 REFERENCES

- Cools, P.M.C.B.M. 2011. *The Geo-Impuls Programme reducing geotechnical failure in the Netherlands*. In: *Proc. of 3<sup>rd</sup> International Symposium on Geotechnical Safety and Risk*, München, pp 191-198.
- ISO 2009. *International Organization for Standardization 31000:2009 Risk management – Principles and guidelines*. ISO, Geneva.
- Van Staveren, M.Th. 2009. *Risk, Innovation & Change: Design Propositions for Implementing Risk Management in Organizations*. Thesis, University of Twente, Enschede.
- Van Staveren, M.Th. 2006. *Uncertainty and Ground Conditions: A Risk Management Approach*. Elsevier Publishers, Oxford.
- Van Tol, A.F., 2007, *Schadagevallen bij bouwputten*, Cement 2007 (in Dutch).

# General Report for TC206 Interactive Design

## Rapport général du TC206 Le dimensionnement géotechnique interactif

Ho A.  
*Ove Arup & Partners Hong Kong Ltd*

**ABSTRACT:** This General Report is to summarise the all papers submitted for TC206 – Interactive Design. A total of 15 papers were received and 6 papers were recommended for oral presentation and the rest for recommended for panel presentation at the 18<sup>th</sup> ICSMGE Paris, 2-6 September 2013. The submitted papers gave a general picture of the interactive design works around the Globe ranging from experimental and theoretical works from SWOT analysis to geoenvironmental application and potential risk detection for Slope failure to case report on some successful practical works from excavation of diaphragm wall to fibre optic instrumentation in reusing deep foundations. The papers are of good quality and will generate opportunities for the academia and practitioners to discuss and question on various different techniques and approaches to implement interactive design to their works.

**RÉSUMÉ :** Ce rapport général présente une synthèse des communications correspondant au TC206 – Dimensionnement géotechnique interactif. Un total de 15 articles ont été reçus, 6 ont été recommandés pour une présentation orale et les autres seront présentés lors de la conférence correspondant à ce rapport général au 18<sup>ème</sup> CIMSG Paris, 2-6 septembre 2013. Les communications donnent une description générale des travaux en dimensionnement interactif de par le monde, depuis les travaux expérimentaux et théoriques jusqu'aux analyses SWOT, aux applications géoenvironnementales et à la détection des risques potentiels dans la réutilisation des fondations profondes. La bonne qualité des communications créera des opportunités pour les universitaires et les praticiens de discuter et échanger sur les différentes techniques et approches permettant de mettre en œuvre le dimensionnement interactif dans leurs réalisations.

**KEYWORDS:** Observational method, SWOT analysis, monitoring, risk of slope failure, small-strain, fibre-optic sensing technology.

### 1 INTRODUCTION

A total of 15 papers were received by the TC 206 – Interactive design and 6 papers were selected for oral presentation and the other for panel presentation at the 18<sup>th</sup> ICSMGE, Paris, 2-6 September 2013. The submitted papers gave a general picture of the interactive design works around the Globe ranging from experimental and theoretical works from SWOT analysis to geoenvironmental application and potential risk detection for Slope failure to case report on some successful practical works from excavation of diaphragm wall to fibre optic instrumentation in reusing deep foundations.

The following section will highlight some keys in the various papers submitted.

#### 1.1 *Papers recommended for oral presentation*

Paper 1907 “Comparison of monitoring techniques for measuring deformations in an excavation” by DeVos, Van Alboon, Haelterman from Belgium. An online monitoring test set-up was realized in a railway-infrastructure project site in Anderlecht (Belgium). Both advanced and traditional monitoring equipment were installed to measure the deformation of a soil nailed jet grout wall, deformations behind the jet grout wall (on the railway tracks) and forces in the soil nails. The paper presents the results of the measurements in and behind the jet grout wall and on the comparison between the different techniques: FBGS; SAAF (in place inclinometer); Optical strands OSMOS; Traditional inclinometer; Draw Tower Grating; and BOTDR. It concluded that both new and traditional techniques can lead to the same result, when sufficient care is taken in the installation and interpretation. A significant advantage can be seen when continuous monitoring is applied, as the link with execution phases can be made.

The paper is clearly set out and well written and presents a real site monitoring case and compares predicted with actual deformation and bending moment results.

Paper 2397 “SWOT analysis Observational Method applications” by Korf, de Jong and Bles from Holland. A well set out account of Strengths, Weaknesses, Opportunities and Strengths of Observational Method and draws on a wide range of published work. This research is performed as part of “Geoimpuls” in the Netherlands; a joint industry programme, with the ambitious goal to half the occurrence of geotechnical failure in Dutch civil engineering projects by 2015. The Conclusion are given in the form of “Go”, “No Go” listed in terms of importance and “To be Overcome” items.

Paper 2029 “Experimental analyses on detection of potential risk of slope failure by monitoring of shear strain in the shallow section” by Tamate & Hori from Japan. The paper consider monitoring locations at shallow depth of slope and introduces a mean to monitor the failure of shallow portion of slope which is particularly important during temporary cut. It may attract discussions in how to bring this into practice so as to enhance safety control measures to safeguard the workers during actual construction stage. It would be good to have a paragraph summarizing their findings from the experiment and / or any further study that may be worthwhile, e.g. any suggested alert, alarm and action shear strain to quantify the potential risk level.

Paper 3059 “The role of fibre optic instrumentation in the re-use of deep foundations” by Bell, Soga, Ouyang, Yan and Wang from UK & China. This paper provided details of a recent project in London to further develop the understanding of foundation reuse by installing fibre optic sensors in both existing piles and a borehole to observe the impact of the demolition process on the changes in piles behavior and ground response. It explained how optical fibre instrumentation was used to monitor pile and ground response under demolition and presented the data captured by the fibre optic instrumentation during the demolition process. It also showed how the use of such instrumentation was fundamental to the successful reuse of the existing piles on this project. It would be good to include the limitations of fibre optic instrumentation; such as can it quantify the vertical extent of section changes or the lateral position of defects; the presence of vertical cracks. And percentage of

existing pile to be instrumented to assess the integrity of existing piles for reuse can also be discussed.

Paper 2971 "New Sensing Technology and New Applications in Geotechnical Engineering" by Wang, Ooi & Gao from Hong Kong. The paper described that soils are inherently a particulate medium, and relevant physical principles behind the macro-scale engineering properties originate from particle interactions. However, it is difficult in general to conduct measurements which can monitor soil particle movement and even characterize micromechanics behind different soil behaviour. The paper presented two examples of advancement of sensing technologies. The first is on using the tactile pressure sensor (film-like sensor) to monitor the evolution of contact normal forces among particles in aged sand. The measurement reveals that the contact forces are continuously redistributed during aging. This ultimately strengthens the soil structure and therefore increases the associated small-strain shear modulus. The second is on using the miniature 3D Micro-Electro-Mechanical-Systems (MEMS) accelerometer to characterize the soil movement in a laboratory flow landslide. The MEMS sensors demonstrate promising results in describing the rich features of local responses of soil movement in the shear zone, e.g. liquefaction, deceleration, contraction and dilation. Some comments on the paper: Are the sensors insensitive to any other property likely to be encountered in its application and to what extent the sensors influence the measured property? Are the sensors designed to be linear or linear to some simple mathematical function of the measurement, typically logarithmic? What is the dynamic error of MEMS accelerometer? A very relevant paper on application of the small-strain theory on flow slides.

Paper 1965 "Monitoring earthwork foundations by fibre optic sensors" by Artières from France. The paper presented that strain in earthworks is now easier to measure by using fibre optic sensing technologies combined with geotextile properties, such as very good soil friction interface enhancing the transfer of soil displacement to the sensors. More accurate measurements can be obtained due to their smaller and less intrusive size than those of the usual electro-mechanical strain gages. They have high sensing sensitiveness below 0.01% on strain measurement, but also temperature measurement with 0.1°C accuracy, that is combined with a high spatial resolution in the range of 1 m or less and a good durability of the sensors into soil. And they can be used to monitor either local earthworks such as walls and slopes or long infrastructures of several tenths of kilometers such as roads, railways and dikes, all with the same accuracy. Several tenths of earthworks are now monitored globally with this solution for more than 8 years demonstrating its durability. The detection of cavities in the foundation of a large polluted water storage basin was also described. Some comments on the paper: Are the sensors insensitive to any other property likely to be encountered in its application and to what extent the sensors influence the measured property? And are the sensors designed to be linear or linear to some simple mathematical function of the measurement, typically logarithmic? The paper was selected for oral presentation on its relevancy in the application of sensor technology in practical works.

## 1.2 Papers recommended for panel presentation

Paper 2253 "Development of Method for Evaluating and Visualizing 3-dimensional Deformation of Earth Retaining Wall for Excavation" by Matsumaru and Kojima from Japan. The paper described a System to evaluate and visualize retaining wall as three-dimensional curved surface. The validity was confirmed by the simulation of the loading test on the model wall and actual monitoring from the on-site measurement. It proposed to conduct monitoring of retaining walls using this analytical method and simple inclinometers. The paper

describes original research/application and would be interested to most researchers.

Paper 2669 "Geotechnical protection of engineering infrastructure objects in large cities under intense anthropogenic impact and long term operation" by Perminov, Zentsov, Perminov, Russia. This article describes more than 30-year experience of scientific and technical support, design, construction and reconstruction of water supply and sewage facilities in St. Petersburg, Sochi, etc. It includes experience of sinking of large diameter shaft/caisson and long term loadings on tunnels in urban areas. Could do with a thorough proof reading and some of the terms used are unfamiliar. It is recommended for Panel presentation as it will be of interest to those who would like to practice in Russia.

Paper 2535 "A geoenvironmental application of an optimisation model" by Azimi, Merrifield, Gallagher & Smith from UK. The paper summaries a network of monitoring wells installed in and around a refinery in mid 1990s as part of a research project aiming to investigate the impact of local groundwater on corrosion of buried foundations and underground storage facilities. A second research project was started in 2000 to delineate the extent of the oil contamination mound(s) beneath the refinery and devise appropriate remedial measures. This paper presented an optimisation technique which assisted with augmentation of the monitoring network, thereby the cost-effective delineation of the oil mounds beneath the refinery. An optimisation model, The Maximal Covering Location Problem (MCLP), was modified and applied to find the optimum number and locations of additional monitoring wells to assist with the cost-effective delineation of the oil contamination mound beneath the refinery.

It is recommended for panel presentation as it may provide further discussions on the degree of confidence in selection of the value of maximal service distance (S) in the order of 100m without consideration of field, laboratory and theoretical investigations.

Paper 2460 "Evaluation of diaphragm wall as-built data to determine the risk of leakage for the Kruisplein car park excavation in Rotterdam, The Netherlands" by Hannink & Thumann from Netherlands. This paper should give the geological profile of the site to let readers have a better understanding of the ground conditions. Representative pumping test results may be included to demonstrate the critical or potential locations of leakage and the contingency measures which shall be required. It is recommended for Panel presentation.

Papers 3083 "Preventive maintenance of water retaining structures based on fiber optic systems" by Fry, Courivaud, Beck & Pinettes from France. The Pare described that EDF develops the concept of preventive maintenance. It means design, building and operation of an early warning monitoring system (leakage and strains), plus model of interpretation and portfolio of technical or legal alarm and interventions. In that framework, EDF has been working since 1994 on the development of the use of the distributed measurements with fiber optic, to improve the monitoring of dykes and flood embankments. The fiber optic technology provides a remote control measurement of the distributed temperature and strain every meter along the embankment. This new technology strategically placed in the fill, allows to reinforce the hydraulic and mechanical behavior monitoring, which is provided to date by conventional instrumentation (leveling, piezometer, discharge rate), with simultaneously a global and detailed surveillance and an early warning system for extreme loadings and crisis (floods, earthquakes, vandalism). It introduces the principle of dikes monitoring using fiber optic and the validation results of this technology from both trial test sites and on EDF's real sites.

# Auscultation des fondations d'un ouvrage en terre par des capteurs à fibre optique

## Monitoring earthwork foundations by fibre optic sensors

Artières O.

TENCATE GEOSYNTHETICS, Bezons, France

**RÉSUMÉ :** La mesure des déformations dans un ouvrage en terre est maintenant plus facile à réaliser en utilisant la technologie des capteurs à fibres optiques, qui associée aux propriétés des géotextiles, comme par exemple leur excellent frottement d'interface avec les sols, permet un bon transfert des mouvements du sol vers le capteur. Leur faible taille moins intrusive que celle des capteurs électromécaniques classiques donne l'accès à des mesures plus fines. Ils ont une sensibilité élevée, inférieure à 0,01% en déformation, mais aussi de 0,1°C en température, combinée avec une haute résolution spatiale de l'ordre du mètre et une bonne durabilité des capteurs dans le sol. Ils sont polyvalents tant pour ausculter des ouvrages locaux, comme des murs ou des talus, que des infrastructures linéaires de plusieurs dizaines de kilomètres, comme les routes, les voies ferrées ou les digues avec la même résolution. Plusieurs dizaines d'ouvrages sont maintenant auscultés depuis plus de 8 ans, preuve de la durabilité de ces capteurs, comme des remblais sur cavité ou sur inclusions. La détection de cavités en fond d'un grand bassin de stockage d'eau industrielle est décrite

**ABSTRACT:** Strain in earthworks is now easier to measure by using fibre optic sensing technologies combined with geotextile properties, such as very good soil friction interface enhancing the transfer of soil displacement to the sensors. More accurate measurements can be obtained due to their smaller and less intrusive size than those of the usual electro-mechanical strain gages. They have high sensing sensitiveness below 0.01% on strain measurement, but also temperature measurement with 0.1°C accuracy, that is combined with a high spatial resolution in the range of 1 m or less and a good durability of the sensors into soil. They can be used to monitor either local earthworks such as walls and slopes or long infrastructures of several tenths of kilometres such as roads, railways and dikes, all with the same accuracy. Several tenths of earthworks are now monitored globally with this solution for more than 8 years demonstrating its durability, for example on foundations of embankments on piles, cavities or soft soils. The detection of cavities in the foundation of a large polluted water storage basin is described.

**MOTS-CLES:** Fontis, Cavité, Inclusion rigide, Fondation, Auscultation, Détection, Alerte, Géotextile, Capteur à fibre optique

**KEYWORDS:** Sinkholes, Piles, Foundation, Embankment, Monitoring, Detection, Warning, Geotextile, Fiber optic sensor.

## 1 INTRODUCTION

Les capteurs ponctuels de mesure des déformations des ouvrages en terre sont difficiles à installer et occasionnent parfois des problèmes de fiabilité à long terme. Les capteurs à fibre optique solutionnent ces inconvénients. Ils associent les propriétés des géotextiles, comme par exemple un frottement d'interface avec le sol élevé, avec plusieurs technologies de capteurs utilisant les fibres optiques pour mesurer des paramètres importants comme la déformation et la température. Les avantages principaux de cette solution sont sa sensibilité élevée, sa résolution spatiale de l'ordre du mètre voire moins, la durabilité des capteurs dans le sol, leur capacité à mesurer soit des ouvrages ponctuels comme des murs ou des talus, ou de longues infrastructures de plusieurs dizaines de kilomètres comme les routes, les voies ferrées ou les digues, toutes avec la même précision.

Plusieurs dizaines d'ouvrages sont auscultés dans le monde avec cette solution depuis plus de 8 ans, démontrant ainsi sa durabilité. Par exemple, une pile de pont renforcée est auscultée avec succès depuis juillet 2004. A côté des ouvrages en terre, plusieurs ouvrages en terre, tels que bassins, barrages, digues et levées ont été auscultés pour détecter des problèmes de stabilité et de fuite.

Après avoir introduit les principes de la solution d'auscultation et les principaux résultats obtenus sur plusieurs projets anciens, cet article se concentrera sur son emploi pour ausculter les fondations de remblais sur cavités : seront décrits en premier lieu, une section de voie ferrée auscultée en continu

depuis octobre 2004, puis la fondation d'un grand bassin de stockage d'eau ausculté depuis 2011.

## 2 LA SOLUTION D'AUSCULTATION

Les capteurs à fibre optique ont été largement utilisés depuis plusieurs années dans les applications de génie civil, en particulier pour la surveillance des conduites d'hydrocarbure, dans des systèmes de surveillance de l'état de structure, ou des applications hydrauliques comme des barrages ou des digues en béton ou en terre. En associant des fibres optiques sur un géotextile (Figure 1), TenCate GeoDetect<sup>®</sup> est un capteur géotextile innovant qui améliore les performances des fibres optiques lorsqu'elles sont utilisées en contact avec le sol, du béton ou du bitume : le géotextile crée une excellente interface d'ancrage avec le milieu environnant. Grâce au très bon ancrage du géotextile dans le sol et à la bonne liaison des câbles optiques sur le géotextile, de très faibles déformations du sol peuvent être détectées. Cette interface de frottement améliore également le transfert des mouvements de géotextile vers la ligne optique. De plus, et quand cela est nécessaire, des propriétés de renforcement et raideurs en traction élevées peuvent être associées au capteur comme cela est indiqué au §3.

Différentes technologies de capteurs par fibre optique peuvent être utilisées : les réseaux de Bragg (Fiber Bragg Gratings ou FBG) employés dans le premier exemple d'application au §3, ou la mesure répartie décrite dans le deuxième exemple d'application au §4.

Les réseaux de Bragg sont des modifications locales de l'indice optique à l'intérieur de la fibre optique sous forme d'une série de petits miroirs inscrits sur une distance de quelques millimètres de long et réfléchissant une longueur d'onde donnée, proportionnelle à la température et à la déformation. A l'inverse des réseaux de Bragg qui sont des mesures ponctuelles, les technologies réparties Brillouin ou Raman mesurent tout point le long de la fibre sur des distances de plusieurs dizaines de kilomètres. Ces deux technologies permettent une mesure très précise de paramètres comme la température ou la déformation, avec des fréquences de mesure soit statiques (< 1 Hz) soit dynamiques (de 1Hz à 2 kHz).

La solution d'auscultation comprend le capteur géotextile à fibres optiques, l'instrumentation et le logiciel d'acquisition de données (Figure 1). Différentes stratégies d'auscultation peuvent être prévues lors du dimensionnement, comme une auscultation périodique ou continue à des fins d'alerte précoce.

En comparaison avec des techniques d'auscultation existantes constituées de capteurs ponctuels câblés individuellement, cette solution mesure en continu jusqu'à plusieurs dizaines de milliers de points avec une seule instrumentation sur toute la longueur de la structure. La résolution spatiale peut être dans certains cas de 0,5 m. Dès son installation, le capteur géotextile à fibre optique peut acquérir des valeurs de déformation et de température : la résolution en déformation est inférieure à 0,01% et des variations de température inférieures à 0,1°C peuvent être mesurées avec les logiciels correspondants. La technologie de mesure par fibres optiques ne nécessite aucune calibration avant mesure, seulement une compensation de la température peut être nécessaire pour des amplitudes supérieures à 10°C.

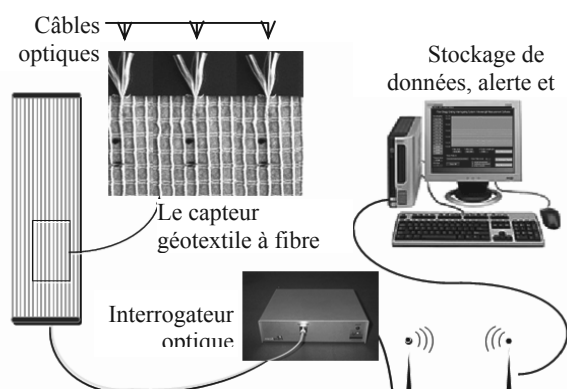


Figure 1. Composants du système d'auscultation

### 3 SYSTÈME D'ALERTE SOUS VOIE FERRÉE

A la suite de la détection de failles perpendiculaires à la voie ferrée entre Mouchard et Bourg dans la région d'Arbois (France), la SNCF a décidé de renforcer la zone suspectée active avec un système de renforcement et d'alerte par fibres optiques, à la fois pour éviter tout effondrement et rupture dommageable au niveau de la voie, et d'autre part pour détecter et éviter tout passage de train au-dessus d'une cavité de taille supérieure à 1,5 m. La surface couverte est une section à voie unique de 50 m de long et de 5 m de large. La plateforme est construite avec 25 cm de ballast sur 50 cm de sol.

Le capteur géotextile à fibre optique qui a été installé sur cette section en 2004 combine à la fois des câbles optiques et des câbles de renforcement pour augmenter la résistance et la raideur en traction, et réduire la déflexion à la surface du remblai (Figure 2). La technologie optique utilisée est celle des réseaux de Bragg (FBG) inscrits dans la fibre qui mesurent directement les modifications de déformation en renvoyant une variation de longueur d'onde. Ce sont 297 FBG qui quadrillent la zone et qui permettent de localiser des cavités de 1.2 m de diamètre avec deux FBG différents. Une armoire étanche est

placée à proximité de la zone renforcée pour protéger l'interrogateur et les systèmes de communication à distance utilisés pour ausculter la zone en continu (Briançon et al., 2006).

Malgré des conditions de mise en place difficiles (pluie, zone de travail exigüe, travail de nuit), le panneau de capteur a été installé dans les délais impartis. L'association du système de capteur avec le géotextile de renforcement améliore la facilité d'installation qui pourrait difficilement être atteinte avec des capteurs locaux conventionnels.

Les déformations mesurées lors de la construction du remblai sont inférieures à 0,5%. Le système d'alerte est installé depuis plus de 8 ans. Les mesures sont stables depuis la remise en service de la voie. La valeur seuil fixée à 2% de déformation, correspondant à une déflexion de 2 cm au niveau du rail n'a pas encore été atteinte. Aussi, le branchement d'un interrogateur dynamique permet d'acquérir des données avec une fréquence élevée (1 kHz), ce qui permet de mesurer des variations de déformation d'environ 0.3% lors du passage d'un train.

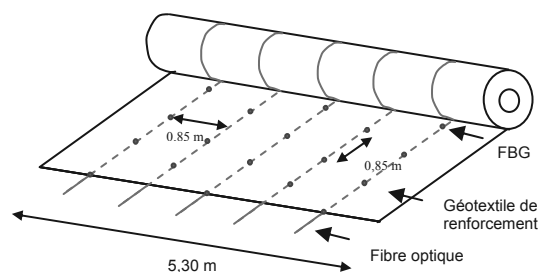


Figure 2 : Le capteur géotextile à fibres optiques renforcé



Figure 3 : Evolution des déformations sous la voie entre 2004 et 2010

## 4 L'AUSCULTATION DES FONDATIONS D'UN BASSIN

### 4.1 Description

L'objectif de ce bassin est le stockage d'eau salée industrielle pendant environ 6 mois sur 12 pour pouvoir la relarguer dans la rivière voisine lorsque celle-ci est en crue (en hiver) afin d'obtenir un taux de dilution suffisant. La surface totale du bassin est de 30 ha et a une capacité de stockage de 300 000 m<sup>3</sup> pour une hauteur d'eau maximum de 10,7 m. Il est construit à l'endroit d'une ancienne gravière à proximité d'une rivière et est délimité par une digue périphérique de 2 km fondée sur le sol naturel en dehors de la gravière. Le fond du bassin est à 4 m en-dessous du sol naturel. Il est sous le niveau de la nappe et pour cette raison étanché en fond et sur les talus par une structure d'étanchéité incluant une géomembrane PEHD de 2 mm protégée par des géotextiles et un tapis drainant granulaire en fond. Les conditions géologiques et hydrologiques, ainsi que la conception de ce bassin sont décrites en détail dans une autre publication (Artières et al. 2013).

### 4.2 Observations

Une augmentation des concentrations de produits salés correspondant au même type que ceux stockés a été détectée en 2008 dans l'eau de pompage de rabattement de nappe sous le bassin. Après vidange du bassin, des tassements ont été

observés dans les casiers E1 et D1 le long de la ligne de collecte des sources (Figure 4). Le contexte hydrogéologique de cette zone est très complexe. On a supposé une dissolution du chapeau sulfaté de la dolomie profonde par des eaux salées. Ces tassements étaient visibles sur la géomembrane sous la forme d'une déchirure de 15 cm par 3 cm et étaient dus à un fontis de 6 m<sup>2</sup> et de 3 m de profondeur. Ceci a expliqué les raisons des fuites. Sur trois autres endroits, le substratum argileux était décomprimé. A partir d'une analyse topographique, la surface totale d'effondrement a été estimée à environ 1500 m<sup>3</sup> autour des sources.

#### 4.3 Travaux de réparation

Il a été décidé une réparation du fond de la zone du bassin présentant un risque élevé de tassement en installant une structure de renforcement de la fondation par géotextile, associée à un système de détection et de localisation des fontis par capteur géotextile à fibre optique. Dans ce projet, la fonction renforcement a été dissociée de la fonction auscultation.

Le géotextile de renforcement évite à la fois que le fontis atteigne de façon soudaine la structure d'étanchéité et que la géomembrane s'allonge au-dessus d'une valeur seuil permettant de maintenir la fonction étanchéité jusqu'à ce que la cavité soit traitée. Il est dimensionné selon l'Eurocode 7 (2005). Aux états limites ultimes (ELU), les justifications sont menées en utilisant l'approche de calcul 2, avec les coefficients partiels définis dans l'Annexe Nationale [NF EN 1997-1 /NA] de l'Eurocode 7.

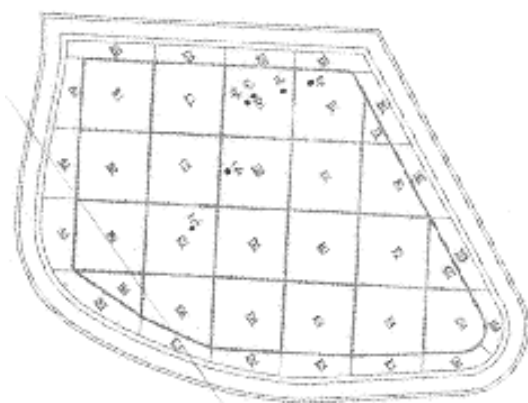


Figure 4. Numérotation des casiers et sortie des sources

La méthode de dimensionnement est une méthode simplifiée (Blivet et al. 2001) développée après le programme de recherche RAFAEL. Le dimensionnement du géotextile a été conduit en appliquant les trois états limites : un de service et deux ultimes à court et long terme (Artières et al. 2013). Le calcul aboutit à une raideur élevée ( $J=11000$  kN/m). Le géotextile mis en place est un tissu polyester TenCate Geolon PET 1600 avec une résistance en traction de 1600 kN/m selon la méthode d'essai EN ISO 10319.

Le capteur de déformation est installé sous le géotextile de renforcement pour détecter de façon précoce, localiser et suivre les mouvements du sol sur cette zone, et enfin, estimer la taille des fontis pour vérifier la compatibilité avec la taille de cavité utilisée dans les hypothèses de dimensionnement du géotextile de renforcement.

La structure reconstruite sous la structure d'étanchéité par géomembrane comprend de haut en bas : 60 cm de gravier 0/20 mm (tapis drainant), le géotextile de renforcement, 20 cm de gravier 0/16 mm et le système d'auscultation.

#### 4.4 Le capteur géotextile à fibre optique

Le capteur se présente sous forme de bandes géotextile de 76 cm de large portant 2 câbles optiques pour la mesure des déformations, la première étant la ligne principale, la deuxième

étant une ligne redondante de sécurité. La distance entre les deux câbles de déformation est de 0.6 m (Figure 4). Ces capteurs sont reliés par un câble de liaison de 200 m de long à un interrogateur optoélectronique Brillouin installé dans une cabine en tête de digue. Il n'y a donc aucun appareil électromécanique ni de source électrique dans le bassin. Cette solution est décrite plus en détail dans d'autres publications (Artières et al. 2011, Artières et Dortmund 2011).

L'interrogateur connecté à une extrémité de la fibre optique envoie un pulse laser de quelques nanosecondes qui parcourt toute la longueur de la fibre optique. En chaque point de la fibre optique, le pulse laser interfère avec la structure moléculaire de la matière en rétrodiffusant en sens inverse un spectre de lumière schématisé en figure 5. La longueur d'onde des pics secondaires Brillouin dépend notamment de l'état de déformation de la fibre optique. La résolution spatiale de la fibre est d'environ 1 m et la résolution sur la mesure de la déformation est inférieure 0,01 %.

L'interrogateur optique connecté à une extrémité de la fibre optique envoie un pulse laser que quelques nanosecondes qui est guidé tout au long de la fibre optique. A tout point de la fibre, le pulse laser interfère avec la structure moléculaire du matériau en rétrodiffusant un spectre de lumière (Figure 5). Les pics de longueur d'onde secondaires Brillouin dépendent de la déformation de la fibre et de sa température. La résolution spatiale le long de la fibre est d'environ 1, ce qui signifie que le système génère un point de mesure tous les mètres. La résolution de la mesure de la déformation est de moins de 0,01%.

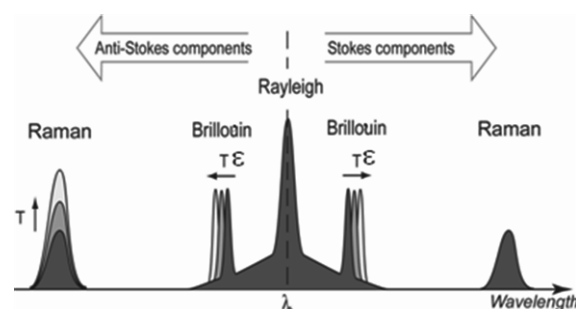


Figure 5. Spectre de lumière rétrodiffusé lors de la mesure répartie sur fibre optique ( $\lambda_0$  est la longueur d'onde de la lumière incidente)

#### 4.5 Conception et mise en œuvre de l'auscultation

Une surface d'environ 10.000 m<sup>2</sup> présente un risque de tassements liés à la remontée aléatoire de cavités souterraines. La solution d'auscultation est implantée sur une zone particulière d'environ 165 m x 20 m incurvée couvrant les casiers E1, D1 et C1 (Figure 6).

Sur cette surface, 18 bandes du capteur géotextile à fibres optiques ont été installées en 5 boucles optiques distinctes permettant de lire l'une indépendamment des autres. Les bandes sont espacées l'une de l'autre de 1,2 m correspondant à la taille minimale de cavité à détecter. Les deux câbles optiques de déformation portés par chaque bande sont raccordés séparément, ce qui constitue un total de 5 boucles principales et de 5 boucles redondantes de sécurité. Ces dix boucles sont raccordées à un câble optique de liaison de 200 m de long vers l'instrumentation. Ce sont environ 6.000 points de mesures qui couvrent la surface totale avec un pas de 0.6 m x 1 m.

Les bandes de capteur composite géotextile à fibres optiques sont déroulées sur le site selon un plan de calepinage approuvé par le Maître d'Ouvrage. Les bandes sont immédiatement lestées temporairement jusqu'à la fin de l'installation du système d'auscultation (Figure 7). La continuité des lignes optiques est contrôlée avant la pose du gravier de couverture 0/16 et du géotextile de renforcement (Figure 8).





Figure 6. Vue depuis la crête de digue du bassin et de la zone instrumentée (en clair au centre).



Figure 7. Pose de bandes capteur en fond de bassin.



Figure 8 : Installation du géotextile de renforcement.

#### 4.6 Mesures

Le bassin a été ausculté dès la fin de l'installation du système géotextile à fibre optique en mai 2011 mettant en évidence l'effet de la mise en place de la couche de remblai de 80 cm puis du remplissage en eau du bassin.

Les déformations principales ont été enregistrées lors de la mise en place du remblai qui s'explique par la rugosité importante du fond de forme et la mise sous tension des bandes capteur. Un évènement pluvieux intervenu lors de la pose des capteurs avait en effet érodé la surface du fond de forme. La moyenne des déformations est de l'ordre de 0,2% avec des pointes autour de 1% et une forte irrégularité. Un remblaiement sur support plan créé généralement des déformations initiales inférieures à 0,1%. Cette mesure a été choisie comme ligne de référence par le Maître de l'Ouvrage pour le suivi du bassin.

Le remplissage du bassin à 6 m d'eau en décembre 2011 et en novembre 2012 ne montrent pas d'accroissement sensible des déformations, en moyenne inférieures à 0,1% avec quelques points très localisés entre 0,1 et 0,4 %, ceux-ci étant encore certainement liés à la mise en place des capteurs sur le fond de forme (Figure 9).

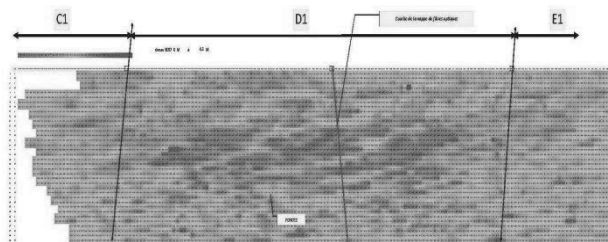


Figure 9. Evolution des déformations entre mai 2011 et novembre 2012

## 5 CONCLUSION

L'association d'une structure de renforcement par géotextile avec un système d'auscultation pour détecter les mouvements du sous-sol est une solution utilisée avec succès depuis plus de huit ans sous un remblai ferré sujet à des risques de remonté de fontis.

Cette solution a également été utilisée pour stabiliser la fondation d'un bassin industriel étanché par une géomembrane après que des tassements aient été constatés. Une structure de renforcement par géotextile a été conçue sous la structure d'étanchéité pour réduire les déformations de la géomembrane pour des tailles de cavité de 3 m. En complément, un système d'auscultation basé sur des capteurs composites géotextile à fibres optiques a été positionné en-dessous pour détecter de façon précoce et localiser les effondrements, suivre l'évolution de la taille des cavités et éventuellement planifier une opération de maintenance si leur taille dépasse les hypothèses de dimensionnement du géotextile de renforcement. La solution d'auscultation a indiqué le développement de déformations lors des réparations à cause de la rugosité élevée du fond de forme, mais aucune déformation liée à un fontis n'est apparu depuis un an et demi après son installation.

## 6 REMERCIEMENTS

L'auteur remercie Valérie Lefèbvre-Mignon, Arcadis, assistance à la Maitrise d'ouvrage, pour son aide.

## 7 REFERENCES

- Artières O., Briançon L. and Robinet A. 2011. Auscultation d'ouvrages en terre avec un système de détection et d'alerte par fibre optique. Comptes-rendus du colloque Rencontres Géosynthétiques 2011, Tours, 23 et 24 mars 2011, pp. 197-207.
- Artières O. and Dortland G. 2011. Six years earthworks monitoring with a fiber optic geotextile enabled sensor. Proceedings of the 8<sup>th</sup> International Symposium on Field Measurements in GeoMechanics, Berlin, September 12-16, 2011.
- Artières O., Lefèbvre-Mignon V. and Nancey A. 2013. Auscultation d'un fond de bassin renforcé par géotextile. Proceedings of the 9<sup>th</sup> conference on Geosynthetics, Rencontres 2013, April 9-11, Dijon, France.
- Blivet J.C., Khay M., Gourc J.P., Giraud H. 2001. Design considerations of geosynthetics for reinforced embankments subjected to localized subsidence. Proceeding of the Geosynthetics'2001. Conference, February 12-14, 2001, Portland, Oregon, USA, 741- 754.
- L. Briançon; A. Nancey; A. Robinet; M. Voet 2006. Set up of a warning system integrated inside a reinforced geotextile for the survey of railway in "Proc, IGC 8<sup>th</sup>", Sept.18-22, Yokohama, Japan 857-860; 2006.
- NF EN 1997-1 (2005) /NA. Eurocode 7 — Calcul géotechnique — Partie 1: Règles générales - Annexe Nationale à la NF EN 1997-1:2005. AFNOR

# A geoenvironmental application of an optimisation model

## Application d'un modèle d'optimisation à un problème géo-environnemental

Azimi, K., Merrifield C., Gallagher E., Smith D.  
*Coffey Geotechnics, United Kingdom*

**ABSTRACT:** A network of monitoring wells was installed in and around a refinery in mid 1990s as part of a research project aiming to investigate the impact of local groundwater on corrosion of buried foundations and underground storage facilities. Oil contaminated groundwater was evident in some of the monitoring wells. A second research project was started in 2000 to delineate the extent of the oil contamination mound(s) beneath the refinery and devise appropriate remedial measures. Of 30 initial monitoring wells, 15 were found operational inside the refinery in 2000. An optimisation technique is presented herein which assisted with augmentation of the monitoring network, thereby the cost-effective delineation of the oil mounds beneath the refinery. The Maximal Covering Location Problem (MCLP) was adapted and utilised to find the optimum number and locations of additional monitoring wells. The contamination results obtained from the augmented and optimised network of monitoring wells were analysed using a geostatistical tool and the oil contamination hot spots beneath the refinery were delineated cost-effectively.

**RÉSUMÉ :** Au milieu des années 1990, un réseau de puits de surveillance a été installé à l'intérieur et autour d'une raffinerie de pétrole pour étudier l'action des eaux souterraines sur la corrosion des fondations enterrées et des structures de stockages souterrains de la raffinerie. Une contamination par le pétrole a été détectée dans certains de ces puits. Un second projet de recherche a été lancé en 2000 pour suivre l'étendue de la contamination sous la raffinerie et concevoir des solutions appropriées pour y remédier. 15 des 30 puits fonctionnaient encore à l'intérieur de la raffinerie en 2000. Cet article présente, une technique d'optimisation du réseau de puits de surveillance afin de cartographier l'évolution de la tache de pétrole sous la raffinerie pour un coût limité. Les auteurs ont modifié le modèle d'optimisation 'Maximal Covering Location Problem' (MCLP) pour trouver le nombre optimal de puits de surveillance supplémentaires et leurs emplacements. L'analyse de ces résultats en utilisant une méthode statistique a permis de confirmer le contour de la contamination sous la raffinerie pour un coût bien défini.

**KEYWORDS:** Groundwater, contamination, monitoring, optimisation, MCLP, network augmentation

### 1 INTRODUCTION

An oil refinery constructed in the early 1970s and operated ever since caused groundwater contamination. A research project was conducted at the refinery in mid 1990s to investigate the impact of local groundwater flow on corrosion of buried foundations and underground storage facilities inside the refinery. As part of that project, a network of 30 monitoring wells was installed in and around the refinery. Oil contamination of groundwater was evident in some of the monitoring wells. A second research project was started in 2000 to delineate the extent of the oil contamination mound beneath the refinery and devise appropriate remedial solution(s). Of 30 initial monitoring wells, 15 were found to be operational inside the refinery at the beginning of the second research project. Monitoring of these wells demonstrated that free phase of oil contamination was present in groundwater at least at two separate locations inside the refinery. However, the contamination data obtained from the existing monitoring network of 15 wells were too sparse for the purpose of oil contamination delineation. Therefore, it was decided to add monitoring wells to the network within the refinery. The two major engineering challenges were identified as:

- How many monitoring wells should be added to the existing network?
- In which locations should these wells be installed?

There is substantial evidence in the literature on the application of Operations Research (OR)-based optimisation

methods in different civil and environmental engineering practices (ReVelle et al. 1997). Fields of practice such as transport engineering, urban planning and water resources management are examples where successful applications of OR methods including optimisation techniques have been demonstrated. The Maximal Covering Location Problem (MCLP) is an optimisation model proposed in the literature, primarily devised to find the optimum locations for public facilities, such as ambulance dispatch centres, on a network of demand nodes (Church and ReVelle 1974). The model was modified and applied to the groundwater contamination problem in this study to assist with the cost-effective delineation of the oil contamination mound beneath the refinery.

### 2 MAXIMAL COVERING LOCATION PROBLEM (MCLP) – CONCEPT, THEORY AND APPLICATION

An example where the MCLP can be used for the optimum usage of the resources is the requirement to add a certain number of a public facility (e.g. ambulance dispatch centres) to an existing network in a city. The city is discretized to a set of demand nodes where additional dispatch centres can be situated. Each demand node is assigned a weight representing its population with the existing dispatch centres being attributed to the nearest nodes. From the network operator's point of view, coverage of the demand nodes (i.e. population nodes in this example) on the network is the key objective with demand nodes not being located farther than a threshold distance (i.e. maximal service distance,  $S$ ) from an ambulance dispatch

centre. In other words, a node is covered if at least one facility is located within the maximal service distance of that node. Otherwise, the node is uncovered. If a network operator instinctively places all the available resources on the nodes with the greatest nodal weight (e.g. population), the outcome will not necessarily be maximum coverage of the population by the public facilities because of the likely overlaps and gaps in the coverage of the demand nodes.

In reality, the 100% coverage target is not always achievable due to limitations in the availability of supply units. If the resources are insufficient to cover all the demand nodes, the objective changes to cover as many nodes as possible within  $S$  using the limited resources. Figure 1 represents a typical discretized network of demand nodes which could be considered as the potential locations for accommodating the additional facilities. With a sufficiently large maximal service distance, for example, a single facility can cover all the demand nodes on the network; hence  $S$  is a key decision parameter.

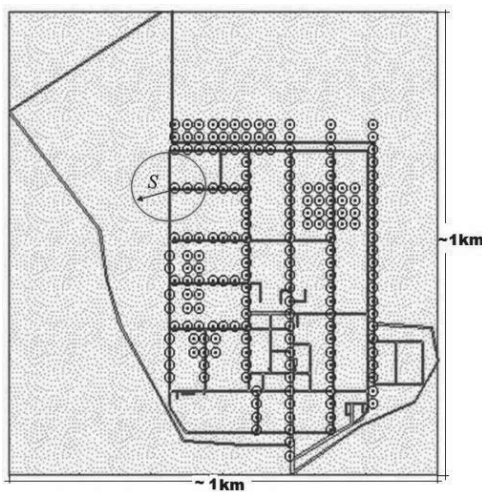


Figure 1. The concept of maximal service distance.

The MCLP is expressed as: Maximize coverage (population covered) within a desired service distance by locating a fixed number of facilities (Church and ReVelle, 1974).

The mathematical formulation of the MCLP in the context of augmentation of a groundwater monitoring network is presented in Hudak & Loaiciga (1992). Groundwater monitoring network augmentation incorporates the following stages:

- Discretize the model domain into a network of potential detection monitoring sites (nodes).
- Assign weighting to each node to quantify its relative importance for coverage by a monitoring well.
- Solve MCLP with successive values of  $S$  until target areal plume coverage is achieved.
- Determine the corresponding configuration of the added wells on the network.

### 2.1 Geometry of the grid (problem domain discretization)

An irregular grid of 188 nodes was defined within the oil refinery area taking into account the local hydrogeology as compared to similar cases where groundwater monitoring networks has been augmented, the limitations against excavation of wells on site, the spacing between the existing wells and the computational limitations for a plausible nodal weight estimation. Each of the 15 existing wells was assigned to the nearest node.

### 2.2 Nodal weight estimation

Due to the complex hydrogeological setting of the site and presence of a large number of potential sources of oil

contamination within the refinery, using physical / numerical models to calculate the nodal concentrations (weights) was considered impractical. Kriging as a stochastic interpolator was employed instead to estimate the weights. The groundwater chemical data obtained from all 22 available monitoring wells located within and around the refinery were utilised in this nodal weight estimation.

### 2.3 Results

The budget allocated for additional monitoring wells included the addition of a maximum 10 number to the existing network. Therefore, the MCLP model was solved for different values of  $P$  from 20 to 25, noting  $P$  is the total number of existing and additional wells on the network and there were 15 existing wells. There were three key decision parameters; areal plume coverage which corresponds to the vertical axis on Figure 2 and is defined as the percentage of the nodes with weight values above zero covered by one or more wells (i.e. located within distance  $S$  of one or more wells), the total number of existing and added wells ( $P$ ), and the maximal service distance  $S$  (horizontal axis on Figure 2). The marked increase in the slope of the curves on Figure 2 in two particular regions demonstrated that with a moderate increase in the value of  $S$ , the areal plume coverage would increase considerably compared to the other regions on the curves. If the values of  $S$  and the number of covered nodes (i.e. areal plume coverage) within these regions (intervals) were reasonable for decision making, then it would be possible to focus on these two regions for taking the next steps towards the final decision. The maximal service distance ( $S$ ) plays the most important role in dictating the final configuration of the added facilities. This parameter should ideally be calculated through field, laboratory and theoretical investigations. Considering the grid size of the study area, values of  $S$  in the order of 100m were justified in this study.

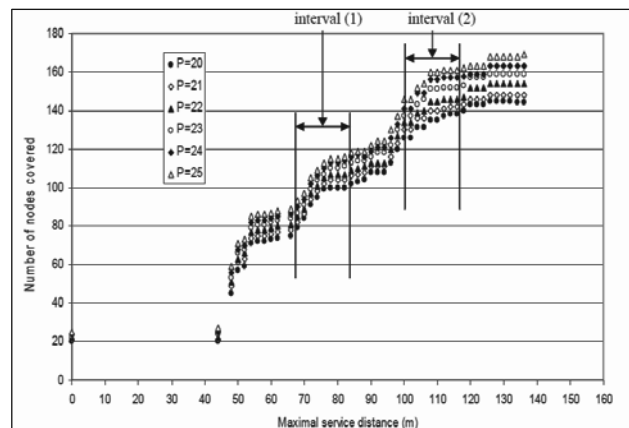


Figure 2. The coverage trend curves.

Figure 3 demonstrates that within the maximal service distance of 76m, it was possible to achieve a maximum areal plume coverage of 60% (i.e. 113 covered nodes out of total 188 nodes could be covered). This amount of coverage was not considered satisfactory. Therefore, the first interval on Figure 2 was not considered further and the second interval was selected. Figure 4 illustrates the variation of maximal service distance  $S$  versus  $P'$  (number of monitoring stations to be added). Points with unjustified values of  $S$  were not depicted on the graph. Figure 4 demonstrated that augmenting the network with 10 additional monitoring wells was somewhat insensitive to the magnitude of  $S$ , i.e. selection of 10 additional monitoring stations would result in a considerable increase in the areal plume coverage with minimum change in  $S$ . Hence, the network was augmented with 10 additional boreholes, corresponding to the areal plume coverage of 85% and  $S \sim 108$  m. The pattern of additional wells showed no clustering at the areas of high

estimated chemical concentration (weights). This model located the additional stations (i.e. monitoring wells) at regions with high concentration of contaminant and at the same time prevented clustering of the wells (See the layout in Figures 5 and 6).

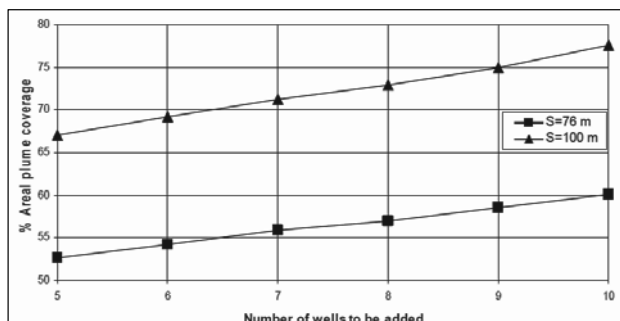


Figure 3. Cost-effectiveness curves for two distinct values of  $S$  derived from Figure 2.

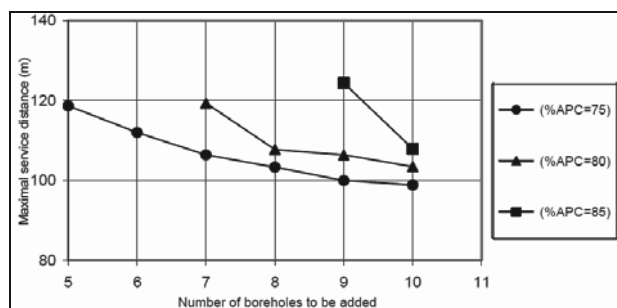


Figure 4. Variation of maximal service distance ( $S$ ) versus the number of added wells ( $P'=P-15$ ).

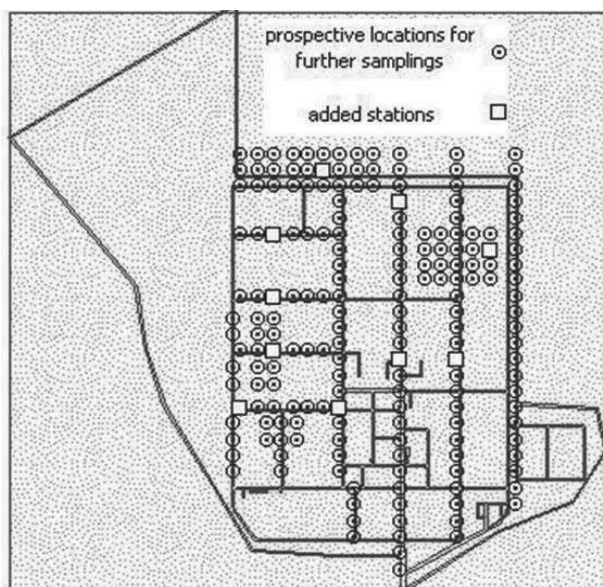


Figure 5. Added wells on the discretized network.

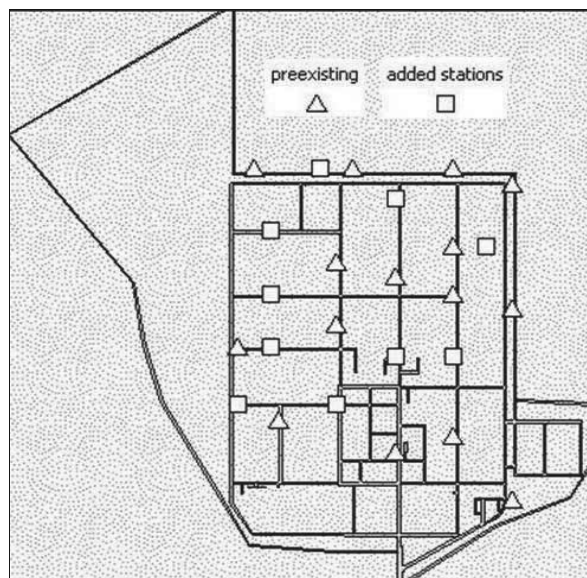


Figure 6. Added and existing wells.

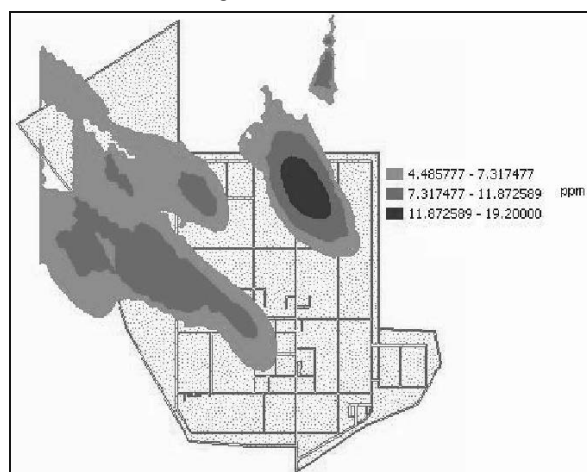


Figure 7. Hot spots of oil contamination beneath the refinery (concentrations are in terms of Total Organic Carbon).

### 3 GEOSTATISTICAL ANALYSES ON THE AUGMENTED DATA SET

A geostatistical analysis, using the same geostatistical tool which was used in nodal weight estimation (i.e. estimation of chemical concentrations at different nodes), was conducted on the extended data set to assist with delineating the locations and the extent of hot spots of oil contamination beneath the refinery. Three different hot spots were identified at three distinct areas. Figure 7 shows the location and the extent of the hot spots.

### 4 CONCLUSIONS

A geoenvironmental case history of applying an optimisation model in practice is illustrated in this paper. The Maximal Covering Location Problem (MCLP) was employed to enhance the efficiency of an existing network of monitoring wells in an oil refinery in order to assist with delineating the mounds of oil contamination beneath the refinery. After installation of the added monitoring wells at the locations predicted by the model (i.e. monitoring network augmentation), the results obtained from the augmented network demonstrated the robustness of the method. The model helped to prevent clustering of the added monitoring wells in the areas with high estimated values of the attribute (i.e. concentration) and at the same time helped to benefit the monitoring from further sampling at these areas. Using the data from the augmented network of monitoring wells

and a geostatistical tool, the oil contamination hot spots were delineated cost-effectively.

## 5 REFERENCES

- Church R. L. and ReVelle C. S. 1974. The maximal covering location problem, *Papers of the Regional Science Association* (32), 101-118
- Hudak P. F. and Loaiciga H. A. 1992. A location modeling approach for groundwater monitoring network augmentation, *Water Resources Research* 28 (3), 643-649
- ReVelle C. S., Whitlatch, E. E. and Wright J. R. 1997. *Civil and environmental systems engineering*, Prentice-Hall Inc. , US

# The role of fibre optic instrumentation in the re-use of deep foundations

## Rôle d'une instrumentation en fibre optique pour la réutilisation de fondations profondes

Bell A.  
*Cementation Skanska*

Soga K., Ouyang Y., Yan J.  
*University of Cambridge*

Wang F.  
*Tongji University*

**ABSTRACT:** The re-use of existing foundations, in particular piled foundations has increased in recent years due to the significant environmental and commercial benefits. However, there has been limited progress in assessing the condition of such piles by considering the effect of initial use and the impact from the subsequent demolition process which often requires a detailed study. This paper will provide details of a recent project in London that successfully reused all existing piles beneath the site and optical fibre sensors were instrumented to the existing foundations in order to monitor the behavior of piles during the demolition of the existing building. The use of optical fibre instrumentation is believed to be the first of such an approach in observing the behavior of reuse piles during demolition in the UK and as urban environments become more congested particularly below ground, the approach discussed in this paper will become increasingly valuable. The monitoring data is presented and discussed in detail and the role of using these sets of data in assessing the reuse strategy is also highlighted in this paper.

**RÉSUMÉ :** La réutilisation de fondations existantes, en particulier de fondations sur pieux, a augmenté ces dernières années en raison des avantages environnementaux et commerciaux significatifs. Cependant, l'état des pieux suite à leur première utilisation et le processus de démolition sont souvent négligés. Ce document présente un projet récent à Londres où les pieux ont été instrumentés avec des capteurs en fibre optique, avant la campagne de démolition. Les fibres optiques permettent de mesurer des déplacements le long des pieux lors de la démolition. L'utilisation d'une telle instrumentation est une première au Royaume-Uni. Les données de la campagne de surveillance sont présentées et discutées en détail. Une stratégie de réutilisation des fondations sur pieux est également proposée dans ce document.

**KEYWORDS:** Re-use foundations, Optical Fibre Sensors (OFS), Brillouin back-scattering

## 1 INTRODUCTION

Foundation re-use can generate significant environmental and commercial benefits, and is becoming a popular engineering option, particularly in congested urban environments. Due to the many practical constraints, most redevelopments need to be constructed on the existing foundations together with a new pile system; therefore it is crucial to understand the geotechnical behaviour of reused piles and their compatibility with the new structure. This is often difficult without removal of significant parts of the substructure. Previous researches (Leung et al., 2011; Begaj-Qerimi&McNamara, 2010) have shown that pile behavior may change with time, due to consolidation and ageing, residual stress at the pile base and increased soil stiffness; hence reused piles are often stiffer than new piles. On the other hand, the building demolition process could potentially introduce ground heaving and the physical unloading of the reused piles can also generate tension cracks. These differences in pile responses need to be properly assessed in the design of a new pile system.

A recent project in London provided the opportunity to further develop the understanding of foundation reuse by installing fibre optic sensors in both existing piles and a borehole to observe the impact of the demolition process on the changes in piles behavior and ground response. The site is located at 6 Bevis Marks and near to Liverpool Street, London, UK, and it was proposed to reuse all existing foundation piles and the majority of the basement substructure on this project.

This approach produced significant commercial and environmental benefits.

The existing piled foundations are large diameter under-ream piles, and there was a concern that these piles would be damaged during the demolition process. Such damage is usually caused either by the forces generated by the removal of significant load as the building is demolished, the tensile forces within the piles and surrounding soil, or physical damage caused by demolition of the substructure, pile caps and pile breaking down. This can lead to the reuse being questioned and ultimately being discounted.

This paper explains how optical fibre instrumentation was used to monitor pile and ground response under demolition and will present the data captured by the fibre optic instrumentation during the demolition process. It will show how the use of such sophisticated instrumentation was fundamental to the successful reuse of the existing piles on this project.

## 2 SITE DESCRIPTION

### 2.1 Existing site and proposed redevelopment

The existing building at 6 Bevis Marks was constructed in the early 1980's and comprised eight superstructure floors and two basements. The existing foundations system includes (i) piles located inside the basement, which is approximately 7.0m below pavement level, and (ii) piles constructed in the Bevis Marks pavement, which is approximately 3.5m below pavement

level as shown in Figure 1. All existing piles were designed and constructed by Cementation Skanska as under-ream piles.

The local geology comprises made ground overlying Terrace Gravels, which in turn rests on London Clay. The top of the London Clay is within 2m of the existing basement level and all piles, both existing and new, are founded within this stratum. The existing piles were designed to carry total building loads of 350,100kN and 33,900kN for those inside and outside the basement, respectively. There are a series of heavily reinforced pile caps and ground beams, and their thickness varies across the site. Typically the ground beams are around 1000mm to 1500mm deep at pile positions, and the pile caps vary from 1500mm to 4150mm deep. This complex pile foundation system practically constrains the available physical space for designing new piles.

The scheme design was developed with the existing building arrangement and existing foundation arrangement in mind. However, with the proposed building being taller (sixteen floors in lieu of eight) and the main stability systems located in slightly different areas, the existing foundations proved to be inadequate as a whole. The result of technical studies demonstrated that the existing piles were overloaded by some 85,000 kN when compared to actual load carried originally.

To enhance the existing piles where they were found to have inadequate capacity, supplementary piles needed to be installed. Figure 2 shows the significant subsurface congestion beneath the site when new piles were installed.

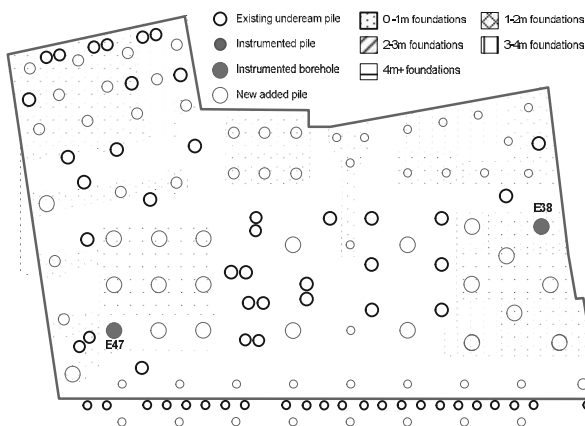


Figure 1. Pile layout and physical constraints to substructure.

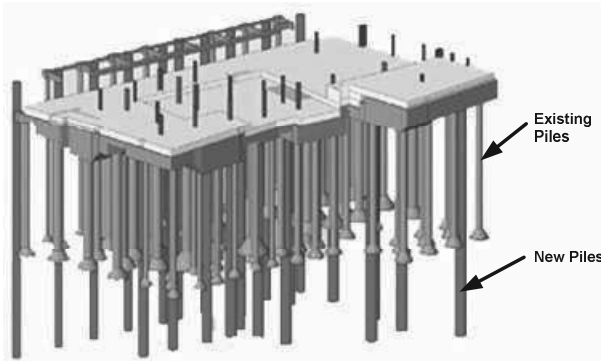


Figure 2. Foundation system including the existing and new piles.

## 2.2 BOTDR sensing principle

Brillouin Optical Time Domain Reflectometer (BOTDR) was adopted for this project. It provides sensitive strain measurement from the reflected light that travels along the standard single mode fibre optic cable. The entire fibre cable can be considered as the sensor itself. When the light travels in

the optical fibre sensor, the majority of it travels through but a small fraction is back scattered as shown in Figure 3. In the back scattered spectrum, where only Brillouin spectrums are temperature and strain dependent, the frequency shift of the Brillouin spectrum indicates the local change in the fibre properties induced by the change of strain and temperature. Hence, the change in strain and temperature along the fibre optic sensor is proportional to the frequency shift, which can be detected by the BOTDR analyzer. The analyzer used in this study is capable to sample 1 m averaged strain or temperature at every 5 cm with an accuracy of 50  $\mu\epsilon$  and up to a distance of 10km.

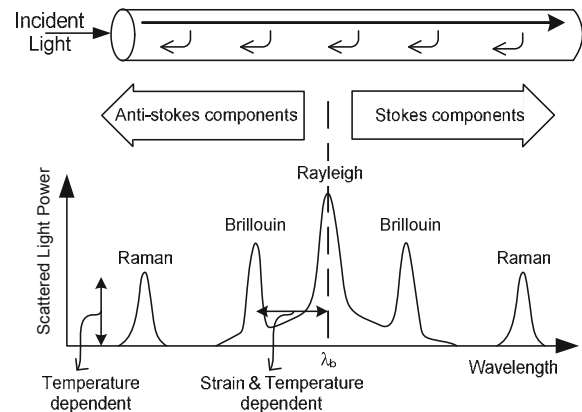


Figure 3. The spectrum of backscattered light.

Due to the principle of Brillouin backscattered sensing, the system registers strain induced by the elongation of the optical fibre itself and the strain resulted from temperature change. Therefore it is necessary to incorporate two different types of optical fibre sensing cables to compensate for temperature effect. Figure 4 shows two types of cables which have been carefully calibrated and widely used for infrastructure sensing (Klar et al., 2006; Mohammed, 2012). Figure 4a shows the strain sensing cable, which consists of four optical fibre members tightly bonded by strong nylon material. This is to ensure the strain can be fully transferred from the nylon coating to the optical fibre itself. Two steel wires at both ends reinforce the cable and make it robust enough to survive in the harsh construction environment. The temperature cable shown in Figure 4b consists of several optical fibres in a gel filled tube, so that it can contract and expand only under temperature effects, independent of mechanical strain.

The use of optical fibre technology has numerous advantages over conventional monitoring systems, it is capable of providing a continuous and full length strain profile and this makes it possible to monitor for cracking of the pile along its full depth. The continuous strain profile also provides a picture of what is happening over the full pile shaft; this would not be possible with traditional single point based system such as vibrating strain gauges or extensometers.

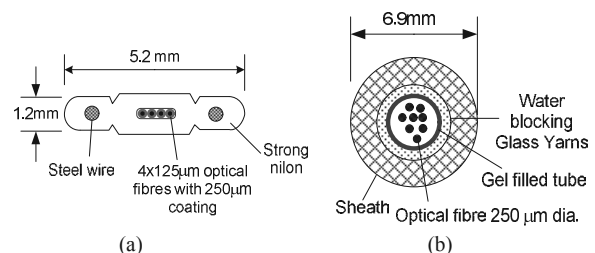


Figure 4. a) strain sensing, b) temperature sensing cable.

## 2.3 Instrumentations and field installation

Prior to demolishing the building, an under-ream pile (E47, see Fig. 1) was selected on site to be cored to full depth for



inspecting and assessing concrete quality. Fibre optic cables were attached to a flexible pipe and installed to the full depth of the cored hole. Table 1 lists the detailed level of the under ream pile. In addition, a new borehole was drilled to 35.5m adjacent to an instrumented pile in the basement and also instrumented to full depth to capture potential ground heave during the demolition process.

This paper will present the data recorded during the demolition process and summarise the results to highlighting the role of the instrumentation in the successful reuse of the deep foundations on this project. It will also include details of challenges faced in using the fibre optic sensors to instrument existing deep foundations, which is believed to be the first of such use in the UK.

Table 1. Summary of instrumented pile

	PileE47
Core length [m]	20.16
Coring length [mAOD]	7.46
Toe Level [mAOD]	-13.70
Original Design Toe Level	-13.00
Shaft Diameter [mm]	1500
Bell Diameter [mm]	3300

### 3 FIELD DATA ANALYSIS

There are ten sets of strain data that have been collected on five dates from 15/08/2011 to 05/10/2011 up to building level 3 of the demolition programme. All optical fibre strain sensing cables and optical fibre temperature sensing cables, installed in the pile and the borehole close to one of the piles, were monitored as close as possible to the removal of each floor. The data from 15/08/2011 taken when the 6th floor had been demolished and 05/10/2011 when the 3rd floor was demolished is presented in this paper to evaluate the pile and borehole performance. The original geotechnical design load on the pile was around 7,250 kN to 7,500 kN, but the structure takedown load on these piles (i.e. the load they experienced under use) is more likely to be around 65 percent of this at around 4,700 kN to 4,900 kN.

#### 3.1 Pile E47

The first set of data was taken on 15/08/2012 and has been considered as the reference for comparing with the dataset collected on 05/10/2012. The profile of strain change between the two periods is shown in Figure 5(a). In general, the axial strain is reducing from the top to the middle part of the pile (0-9m) in the range between 0 and 100 micro-strain, and the axial strain change becomes reasonably small in the base part of the pile (9-17m). After integration of the strain profile, the calculated overall vertical heave between the two periods is less than 1mm at the pile head as shown in Figure (b).

Pile E47 was initially constructed with a design concrete strength  $f_{cu}$  of 30  $N/mm^2$ , with a corresponding modulus of elasticity varying from 20 to 32  $GPa$  as suggested by BS 8110-2:1985. The concrete strength data taken from the tests on the full length cores in pile indicates that the concrete strength in-situ is between 47  $N/mm^2$  to 56  $N/mm^2$ . The modulus of elasticity of this concrete can be calculated, allowing for creep and degradation, as ranging from 26  $GPa$  to 43 $GPa$ . Figure 5(c) shows the load profile by assuming the pile Young's modulus is 26 $GPa$ . Hence, the axial force reduction at the top of pile can be estimated to be around 3,830 kN, which roughly corresponds well to the load removed between the two periods.

It is believed that nominal starter cages were installed into all of the original under-ream piles on this site and are likely to be between 9m and 12m in lengths. Reinforcement details for the existing piles were not available, as is often the case with reuse projects. The cage toes were observed in the strain

measurements at 10m to 13m as a change in the strain profile, which indicates the pile is experiencing tension forces around the base of the reinforced section. It is suspected that this is as a result of the different Young's modulus between the reinforced and unreinforced sections of the pile.

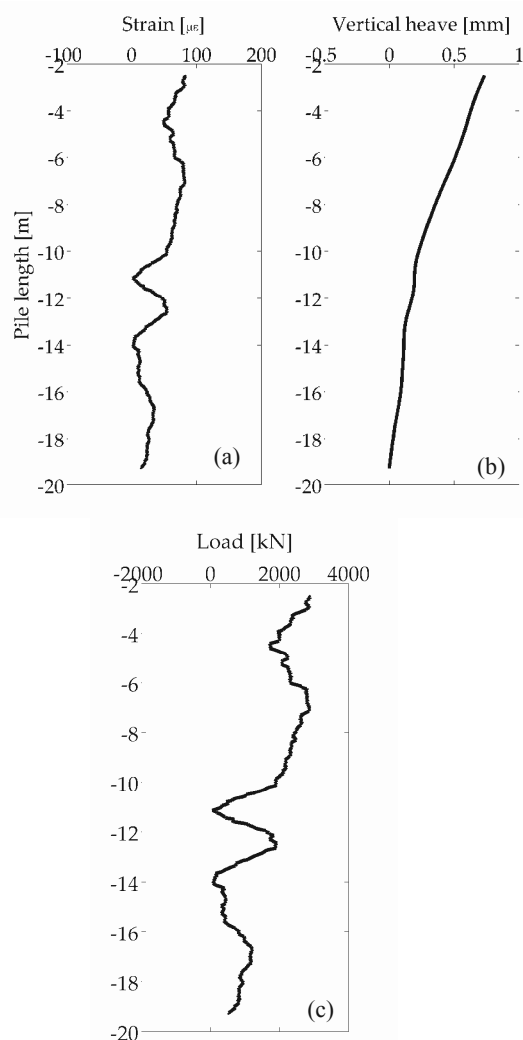


Figure 5. The calculated pile performance due to the demolition activities: a) axial strain along the pile; b) vertical heave; c) pile load.

#### 3.2 Borehole

In comparison to the pile reaction to the demolition of the substructure, the magnitude of change in strain along the borehole is less pronounced than the results observed from the pile, which ranges within 50 micro-strain and within the accuracy range of the BOTDR system. The calculated strain profiles are shown in 6 including the strain profile along the borehole and the interpreted vertical heave is about 0.4 mm at the top. Due to the limitation of the BOTDR system, it is difficult to obtain the accurate vertical displacement profile from such small strain measurement, and the data shown in Figure 6 are the best approximation of the ground movement from the borehole measurements.



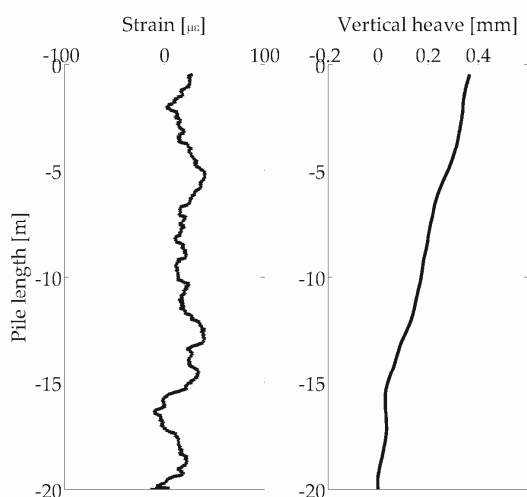


Figure 6. Strain profile along the borehole with interpreted ground heave profile.

### 3.3 Discussion

The magnitude of vertical movement measured from pile E47 during the demolition is smaller than 1mm. The resulting force generated at the top section of the pile is estimated to be around 3,800 kN by assuming the pile Young's modulus is 26GPa, and this is relatively large for a pile reinforced with only a nominal steel cage and justifies the concern towards the integrity of the pile post demolition. The significant advantage of using optical fibre instrumentation is that a continuous and full length strain profile is measured, which allows assessment of the potential for cracking of the pile as a result of the demolition induced (load removal) strains. This would be visible as localized sharp peaks within the strain profile and from such data it would even be possible to calculate potential crack thickness. There are no signs of cracking along pile E47 throughout the whole depth and as such there appears to be no visible signs of any detrimental effect of the demolition process up to the 05/10/2011.

With regard to the instrumented borehole, very small strain variation was observed during the monitored demolition process. Such small strains are indicative of small heave forces generated. This could be as a result of both the location of the borehole, which was close to the edge of the basement, and almost certainly as a result of the confining effect of the existing piles and basement slab.

There remain a large number of exiting piles that have not been instrumented and will be reused. Nevertheless, the monitored piles and borehole gave a good indication of the typical response of the existing piles beneath 6 Bevis Marks to the removal of building load during demolition. The results were an essential part of the proofing process and validated the reuse strategy.

## 4 CONCLUSIONS

Currently the primary source of information available for considering foundation reuse are limited to "as built" design and installation records. Although in the future these may be more comprehensive than what are currently available on development sites, the extent of re-use will be limited to the quality of such records. This will in turn constrain the future development options for such sites and is likely to influence the asset values of the site and the existing development, and the viability of redevelopment.

There are developments taking place continuously where more piles are being added to those installed previously, either re-using the existing piles, but more often than not, ignoring the

capacity of existing piles, further restricting the future development potential. In the UK high capacity bored piles have been widely used since the 1950s and it is not unusual for a site to be on its second or even third set of piles, all of which will obstruct and constrain further developments.

Traditionally, low strain pile integrity testing is carried out to confirm that new piles have been constructed correctly and no discontinuities exist. It is also used to assess the integrity of existing piles for reuse, usually with mixed success. Such testing is often not appropriate for pile reuse as,

- To carry out a low strain integrity test, the top of the pile needs to be exposed and structurally separated from other foundations. This is not possible where pile caps, slabs and basement substructures are to remain in place for reuse.
- Such testing only confirms if there is a crack, not how big it is or what is below it. When demolishing an existing building, the expected ground heave may crack the piles to some degree, such cracks are expected to be small and to close up upon pile reload but these tests cannot confirm this.

An alternative solution is to install fibre optic strain measuring devices into existing piles that have been cored full depth and into future piles on installation, producing a smart foundation system. Making this provision for the future will not only increase the potential for re-use and increase its asset value, but is also likely to make the asset more valuable when compared to other properties where such "future proofing" has not been incorporated. Such an approach will allow monitoring of how the piles actually perform under loading, unloading, reload and during the life cycle of the building. Results could be used to further advance our understanding of actual foundation response during the construction phase and operation of such buildings.

## 5 ACKNOWLEDGEMENTS

The authors would like to thank Waterman Structures Ltd for their initial foresight in assessing the re-use potential of the foundations on the Bevis Marks project and their considerable involvement in developing and implementing the pile reuse strategy and associated instrumentation and monitoring works.

## 6 REFERENCES

- Begaj Qerimi L. and McNamara, A. M. 2010. Physical modelling for pile foundation re-use. In *Physical Modelling in Geotechnics - Proceedings of the 7th International Conference on Physical Modelling in Geotechnics 2010, ICPMG 2010*, volume 2, pages 733-737, 2010.
- Klar, A. Bennett, P.J., Soga, K., Mair, R.J. Tester, P., Fernie, R., St John, H.D. and Torp-Peterson, G. 2006. Distributed strain measurement for pile foundations. *Proceedings of the Institution of Civil Engineers: Geotechnical Engineering*, 159(3):135-144, 2006.
- Leung, Y.F., Soga, K. and Klar, A. 2011. Multi-objective foundation optimization and its application to pile reuse. In *Geotechnical Special Publication*, pages 75-84, 2011.
- Mohamed, H 2012. Temperature and strain sensing techniques using Brillouin optical time domain reflectometry. *Proc. SPIE 8346, Smart Sensor Phenomena, Technology, Networks, and Systems Integration 2012, 83461M*, 2012.
- British Standard, 1985. Structural use of Concrete – Part 2: Code of practice for special circumstances, *Reprinted incorporating amendments Nos. 1 and 2*, BS 8110-2:1985

# Comparison of monitoring techniques for measuring deformations in an excavation

## Comparaison de techniques d'auscultation pour la mesure de déformations dans une excavation

De Vos L., Van Alboom G., Haelterman K.  
*Geotechnics Division, Flemish Government, Ghent, Belgium*

Maekelberg W.  
*TUC RAIL, Brussels, Belgium*

**ABSTRACT:** Active monitoring is often suggested as a method to decrease the required safety coefficients in the design stage of a construction. In order to apply active monitoring precise, reliable and interpretable measurements of the actual behaviour of the structure and soil-structure interaction are required. To obtain this data, accurate and robust monitoring tools should be available at an acceptable cost. An online monitoring test set-up was realized in a railway-infrastructure project site in Anderlecht (Belgium). The braced excavation consists of a nailed jet grout wall with HEB profiles, installed immediately next to a railway track. Both advanced and traditional monitoring equipment is installed to measure the deformation of the jet grout wall, deformations behind the jet grout wall (on the railway tracks) and forces in the nails. The present paper focuses on the results of the measurements in and behind the jet grout wall and on the comparison between the different techniques.

**RÉSUMÉ :** L'auscultation active est souvent suggérée comme une méthode permettant de réduire le coefficient de sécurité du dimensionnement d'un ouvrage. Afin d'appliquer une auscultation active, des mesures précises, fiables et interprétables du comportement réel des ouvrages et de l'interaction sol-structure sont requises. Afin d'obtenir ces données, des outils d'auscultation précis et robustes doivent être disponibles à un coût acceptable. Un essai de surveillance en ligne a été réalisé sur le site d'un projet d'infrastructure ferroviaire à Anderlecht (Belgique). L'excavation consiste en un mur d'étanchéité cloué, avec des profils HEB, installé à proximité immédiate de la voie ferrée. Des technologies aussi bien avancées que traditionnelles ont été utilisées pour mesurer les déformations du mur d'étanchéité, les déformations derrière le mur (sur les voies ferrées) et les forces dans les clous. Le présent article vise à comparer les résultats des mesures dans et derrière le mur et à comparer les différentes techniques de mesure.

**KEYWORDS:** active monitoring, advanced monitoring techniques, monitoring test site.

**MOTS-CLÉS:** auscultation active, outils d'auscultation avancés, site d'essai d'auscultation

## 1 INTRODUCTION.

The Geotechnics Division of the Flemish Government (GEO) realised an online monitoring test set-up to extend the experience with new monitoring techniques and to make a step forward in the application of active monitoring on construction sites. The project was partially funded by the Agency for Innovation by Science and Technology (IWT), allowing 3 firms to develop and perform online monitoring for an excavation. Verification measurements were made by several parties, using both more traditional as well as new monitoring techniques.

### 1.1 Main objective

The main goal of the project is to evaluate different monitoring results and suitability of proposed monitoring schemes for application in interactive design. This implies that accuracy, installation possibilities, reliability and cost are important aspects to be considered.

The monitoring scheme consists of measuring and logging:

- deformation of a vertical wall ( $x,y,z$ )
- maximum bending moment in a vertical wall
- deformation of the soil ( $z$ ) behind a vertical wall
- anchorage forces in nails

### 1.2 Site description and applied equipment

The monitoring site is located in Belgium, Anderlecht (Brussels), where an extra railway track will be constructed alongside the existing tracks. For the foundation of the new bridge, a nailed jet grout wall was installed next to the existing railway. By doing so, the soil could be excavated vertically and

the foundation could be realised in an open construction pit. The excavation depth is 12.5m starting from the railways. The jet grout wall starts 4m below the railway level and has a total length of 21m. HEB profiles with a length of 21m are inserted in the jet grout wall. Five rows of nails are installed over the excavated depth. Figure 1 shows pictures before excavation and after excavation. The excavation is executed in different phases. Each time 2m is excavated and consecutively, a row of nails is installed. After installation of the nails, the contractor waits at least 2 weeks before excavating the consecutive part. More information on the site can be found in Van Alboom et al. 2012 and Verstraelen et al. 2013.



Figure 1. Picture of initial situation (left) and picture of the jet grout wall after excavation (right).

### 1.2.1 Deformation of and bending moments in the jet grout wall

To measure the deformation of the jet grout wall, both advanced and traditional monitoring equipment is installed:

- Fiber Bragg Grating (fiber optics, FBGS)
- SAAF (In-place inclinometer, Inventec)

- Optical strands (fiber optics, OSMOS)
- Traditional inclinometer (GEO)
- Draw Tower Grating (fiber optics, Belgian Building Research Institute (BBRI))
- BOTDR (fiber optics, Cambridge University)

The equipment for measuring the deformation of the wall or stresses in the wall, is placed on 4 HEB profiles which are lowered over their full length in the jet grout wall. Figure 2 shows a front view of the excavation site and the location of the instrumented profiles is indicated in red. Figure 3 shows a drawing and some pictures of the FBG and BOTDR fibers which are fixed to the HEB profile. The FBG fibers are fixed in small anchor blocks which are welded to the HEB profile (size of the anchor blocks is 18mm x 18mm). Those anchors are placed every 0.5m in the upper 8m of the profile and every 2m for the lower part. The BOTDR fibers measure the strain continuously, but are locally glued to the HEB-profile (every 0.5m and 2m) for better comparison with the FBG data. To measure deformations and moments perpendicular to the wall, fibers are placed on the top and bottom flange. To measure possible deformations parallel to the wall, two extra fibers are placed at the sides of the bottom flange. Extra L-profiles, placed above all fibers, are used as a protection during installation.

The other instrumentation was similarly fixed on the HEB profiles by welding or gluing.

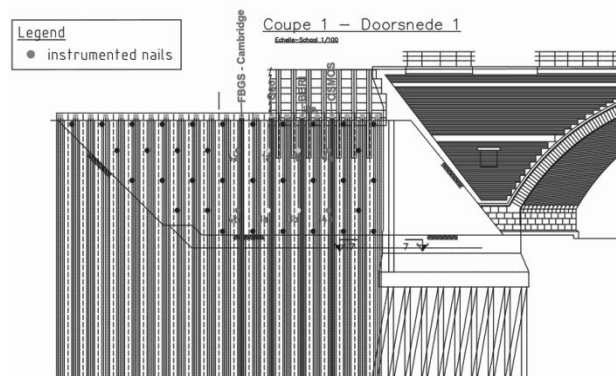


Figure 2. Front view of excavation with indication of instrumented HEB profiles.

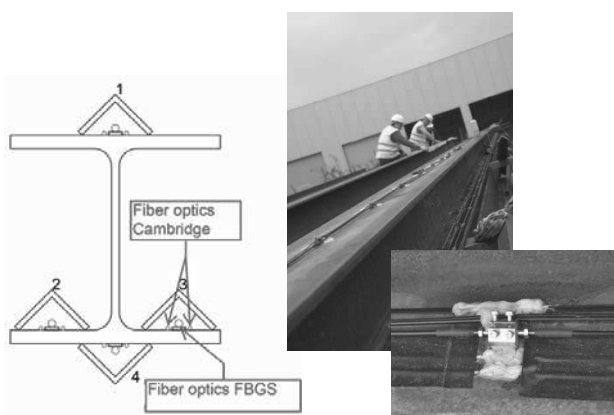


Figure 3. Sketch and pictures of a HEB profile which was instrumented with two optical fiber systems.

### 1.2.2 Settlements behind the jet grout wall

As one of the main concerns during an excavation are the settlements of the soil (and inherently the infrastructure) in the vicinity of the excavation, the vertical deformation of the soil behind the wall is one of the important parameters to be monitored. In this project specifically, deformations of the railroad track are to be avoided.

The deformations behind the wall are measured:

- with two horizontal inclinometers (a traditional one and a continuous SAAF inclinometer) which are placed perpendicular to the wall in the ballast underneath the rails. The inclinometers are attached to a Berliner wall, which is located at one side of the rails. It is assumed that this creates a fixed point;
- topographically: the rails are marked with survey nails along a length of 100m and vertical deformations are measured by topographic levelling at different stages of the project;
- with electrical beam sensors placed on the railway sleepers; the beam sensor consists of an electrolytic tilt sensor attached to a rigid metal beam. The beam, one to two meters long, is mounted on anchor bolts that are set onto the sleepers. The sensors are linked end to end, as to allow displacement values to be accumulated from anchor to anchor to provide a profile of differential movements or settlement.
- with two optical strands, placed at a certain angle with the railway on the railroad tracks .

Figure 4 gives a top view of the instrumentation which is placed on or underneath the railway tracks. It also shows the different HEB profiles which were instrumented.

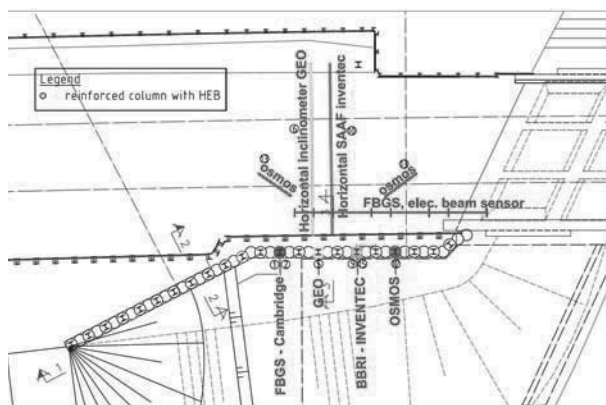


Figure 4. Top view of installed equipment.

A more detailed description of all installed equipment is given in Van Alboom et al. 2012.

### 1.3 Design of the jet grout wall

Calculations of the jet grout wall are implemented in FLAC2D by TUC Rail. They result in a maximum horizontal displacement of 21 mm, a maximum moment of 65KNm and a maximum settlement of 9mm behind the wall in the final excavation phase. A more detailed description of the calculations is given in Verstraelen et al. 2013.

### 1.4 Sequence of the execution phases

Table 1 gives the sequence of the execution phases, retrieved from photos made on site every hour. As continuous monitoring was performed, the influence of the executed works on the movement of the soil could be assessed.

Table 1. Execution phases.

Date	information
22-23/10/2011	Installation of the instrumented HEB profiles in the jet grout wall
3/11/2011	Excavation up to 1,25m below the top of the concrete beam
06-09/11/2011	Installation of the first row of nails
06-07/12/2011	Excavation up to 3m below the top of the jet grout wall
08-12/12/2011	Installation of the second row of nails

11/01/2012	Excavation up to 5m below the top of the concrete beam
17-20/01/2012	Installation of third row of nails
01-02/02/2012	Excavation up to 7m below the top of the concrete beam
14/02/2012	Putting in gravel for ground improvement
17-21/02/2012	Installation of fourth row of nails
27/02/2012	Installation load cells GEO
08-09/03/2012	Unspecified drilling activity
12-13/03/2012	Excavation up to 8,5m below the top of the concrete beam
13-14/03/2012	Installation of 5 <sup>th</sup> row of nails

## 2 MEASUREMENTS

The measurements made by the 3 tenderers are continuous and data is transferred over the internet. The verification measurements, both with traditional equipment and innovative techniques are performed at discrete moments in time.

### 2.1 Deformation of the jet grout wall

The instrumentation is placed on the HEB profiles which are lowered in the jet grout wall. The traditional inclinometer and the SAAF measure the inclination of the profile every 0.5m, allowing direct derivation of horizontal deformation of the wall.

Figure 5 shows the horizontal deformation of the HEB profiles, measured with the traditional inclinometer and the SAAF. These measurements are both made on the same date and are taken after the installation of the fourth row of nails. The excavation depth at that time is 7m. The data fit very well together. The data from the SAAF start above the reference zero level (which is the top of the grout wall), as the HEB profile did not reach full depth and protruded about 1.7m above the top of the grout wall.

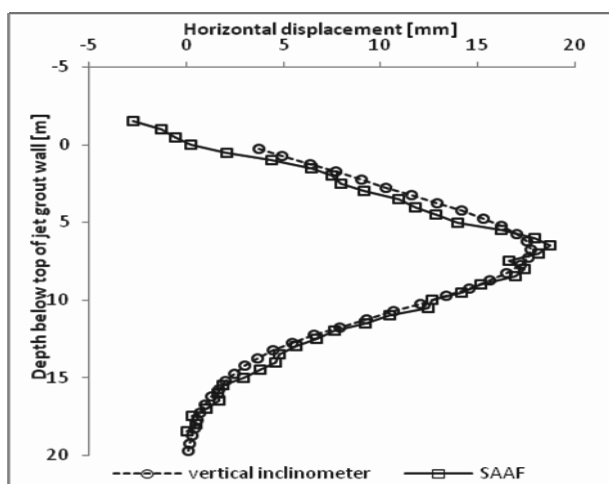


Figure 5. Horizontal deformation of the HEB profile on 07-03-2012.

The maximum horizontal displacement, measured after full excavation, amounts to 21 mm (26/04/2012) at a depth of 6.5m below the top of the grout wall for the inclinometer and 21.6mm for the SAAF. This lies very close to the calculated value of 22mm. It is found however that the direction at which the maximum deformation is found for the SAAF deviates slightly from the expected angle (perpendicular to the wall). This is probably due to a very small twist in between the different elements of the SAAF.

The other optical fiber instrumentation measures the strains in the HEB profiles and derivation of deformations can only be achieved by integration of the measured strains. This implies knowledge of the boundary conditions. Furthermore, the stiffness of the combination jet grout wall and HEB-profile needs to be estimated to obtain the deformation. It was found that there are a lot of assumptions which need to be made to obtain a reliable result. Further analysis will be attempted in the future.

### 2.2 Moments in the jet grout wall

From the inclinometers, the bending moment can be derived as:

$$M = EI \frac{d\alpha}{dx} \quad (1)$$

with E Young's modulus, I the moment of inertia of the HEB profile and  $\alpha$  the inclination.

From the fiber optics, which measure strains at regular intervals, the bending moment can be obtained as:

$$M = \epsilon EW \quad (2)$$

with  $\epsilon$  measured strain and W the section modulus. All fiber optics are mounted on the top and bottom flange of the HEB profile. Strains resulting from temperature differences or normal forces can thus be excluded and only the bending strain is withheld.

For the optical strand, measuring only 1 strain over its full length (top 10m of the HEB profile), the moment can also be derived with Eq.2, only this will result in 1 single bending moment and not in a bending moment as a function of depth.

Figure 6 shows the bending moments derived according to Eq. 1 and Eq. 2 for the different measuring techniques (except for the optical strand, as this does not result in a bending moment as a function of depth). Unfortunately, a lot of the FBG sensors placed by FBGS failed during the first weeks after installation. For this reason, they are not included in the graph. For the stiffness of the wall, the stiffness of the HEB profiles was used, as the instrumentation is placed on these profiles.

The discontinuous and continuous measurements were not always measured on the exact same dates. However, all measurements are made after the final excavation phase.

Figure 6 shows that all derived bending moments give comparable values, except for the SAAF. This can be explained by the fact that the deformation measurements of the SAAF are less "smooth". As the bending moment is a result of the derivative of the measured inclination, this results in unexpected peak values.

A maximum bending moment of about 55 kNm is derived from the measurements. This is again in the same order of magnitude as the calculations (maximum calculated bending moment of 65 kNm). For the optical strand, the derived bending moment is about 35kNm, which is considerably lower than the other measurements. Due to the smoothing which is used for the BOTDR measurements, the peak bending moment is also reduced and has a value of 39kNm, which is also less than the value obtained by the inclinometer and the FBG technique from the BBRI. The shape of the bending moment curve however, is comparable to the other results.

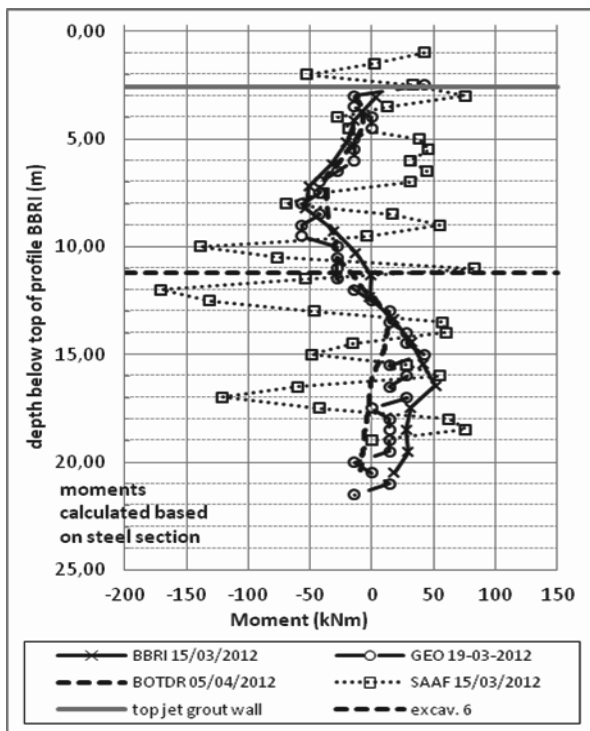


Figure 6. Bending moment HEB profile after the last excavation.

### 2.3 Settlements behind the jet grout wall

The calculated settlement prior to installation is 5mm. The measurements indicate a maximum settlement varying between 50 mm and 70mm for the different measuring techniques, which is much larger than the calculated value. Figure 7 shows the evolution in time of the maximum settlement value as measured by the SAAF. It demonstrates the great advantage of measuring continuously.

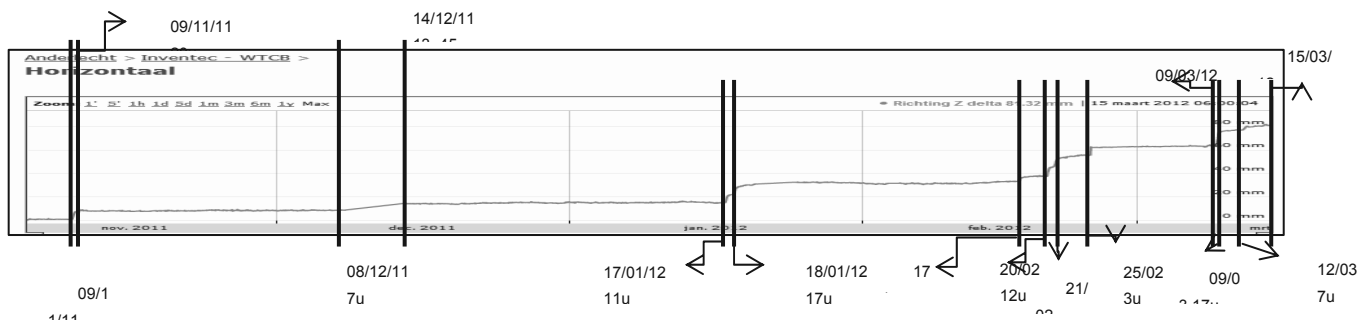


Figure 7. Maximum settlement as a function of time for the horizontal SAAF.

When comparing Table 1 with Figure 7, it can be seen that the discontinuities in the settlement curve correspond each time with the installation of the nails. In Verstraelen et al. 2013, it is explained that this is due to the execution of the jet grout nails. The settlement on 25/02/2012 is caused by lifting the tracks, due to which the inclinometer was locally displaced.

Figure 8 shows the settlement measured by the horizontal inclinometer and the SAAF on two different dates. The zero settlement point corresponds with the fixed point on the Berliner wall. A significant difference between the settlements measured with the two techniques can be observed (approx. 30%). When comparing with the topographical levelling, it can be concluded that the measurements made with the horizontal SAAF are closest to the real settlements. This can be explained by the limited length of the inclinometer tubes (8m) and the fact that the stiffness of a traditional inclinometer tube is quite high for such a short distance (and large settlements).

The “bump” in the measurements of the SAAF (circled in Figure 8) is caused by the lifting of the tracks on 25/02/2012, as explained above. This “bump” has no influence on the settlement which is measured at the end of the railway tracks.

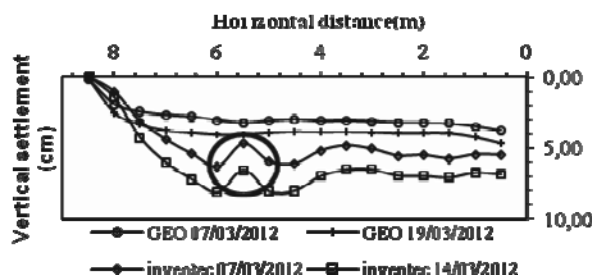


Figure 8. Settlements measured with hor. SAAF and hor. inclinometer.

The measurements made with the electrical beam sensors give comparable results to the measurement of the SAAF. The data measured with the optical strands appears to be uninterpretable. This is probably because it was in no way connected to a fixed point.

### 3 CONCLUSIONS

An extensive monitoring program was set up to compare different monitoring techniques. It appears that both new and traditional techniques can lead to the same result, when sufficient care is taken to the installation and interpretation. A significant advantage can be seen when continuous monitoring is applied, as the link with execution phases can be made.

### 4 ACKNOWLEDGEMENTS

The IWT is gratefully acknowledged for their support.

### 5 REFERENCES

Van Alboom G., De Vos L., Haelterman K., Maekelberg W. 2012. Innovative monitoring tools for on line monitoring of building excavations. A monitoring test site. *ISSMGE- TC 211 International Symposium on Ground Improvement*, Brussels, IV-327 – IV-338.

Verstraelen J., Maekelberg W., De Vos L. 2013. Design and performance of a jet grout retaining wall in a railway embankment on soft soil. *Proceedings of the 18<sup>th</sup> International Conference on Soil Mechanics and Geotechnical Engineering, Paris*

# Maintenance préventive des ouvrages hydrauliques par fibre optique

## Preventive maintenance of water retaining structures based on fiber optic systems

Fry J.-J., Courivaud J.-R.  
*EDF-CIH, Le Bourget du Lac, France*

Beck Y.-L.  
*EDF-DTG, Grenoble, France*

Pinettes P.  
*Géophyconsult, Le Bourget du Lac, France*

**RÉSUMÉ :** EDF est maître d'ouvrage de plus de 500 km de digues, dont certaines qui forment une protection d'aménagements intéressant la sécurité publique. Afin d'améliorer la sûreté de son parc, EDF travaille au concept de maintenance préventive. Il s'agit de concevoir, réaliser et gérer un système de détection précoce d'anomalies (dont les principales sont les fuites et les déformations), un modèle d'interprétation et une chaîne d'interventions précises comportant alarmes techniques, administratives et travaux de réparation adaptés. Dans ce cadre, EDF travaille depuis 1994 à développer l'utilisation de mesures réparties par fibre optique pour améliorer la surveillance des digues. En effet, la technologie fibre optique permet d'avoir une mesure de température et/ou de déformation répartie tous les mètres le long de celles-ci, mesurée en continu. Cette nouvelle technologie, placée stratégiquement dans l'ouvrage, permet de compléter la surveillance habituelle du comportement hydraulique et mécanique, assurée à ce jour avec une instrumentation classique (nivellement, piézomètre, drain), par une surveillance à la fois globale, détaillée et surtout apte à la détection des phénomènes extrêmes et des états de crise (crue, séisme, vandalisme). Cet article présente le principe de la surveillance des digues de canaux par fibre optique ainsi que les résultats de validation de cette technologie tant à l'échelle de sites test que sur sites réels du parc d'EDF.

**ABSTRACT:** EDF owns more than 500 km of dikes, some of them protecting large critical structures involving public security. In order to improve the safety of its stock of power plants, EDF develops the concept of preventive maintenance. It means design, building and operation of an early warning monitoring system (leakage and strains), plus model of interpretation and portfolio of technical or legal alarm and interventions. In that framework, EDF has been working since 1994 on the development of the use of the distributed measurements with fiber optic, to improve the monitoring of dikes and flood embankments. The fiber optic technology provides a remote control measurement of the distributed temperature and strain every meter along the embankment. This new technology strategically placed in the fill, allows to reinforce the hydraulic and mechanical behavior monitoring, which is provided to date by conventional instrumentation (leveling, piezometer, discharge rate), with simultaneously a global and detailed surveillance and an early warning system for extreme loadings and crisis (floods, earthquakes, vandalism). This paper introduces the principle of dikes monitoring using fiber optic and the validation results of this technology from both trial test sites and on EDF's real sites.

**MOTS-CLÉS :** remblai, barrage, digue, crue, séisme, sécurité, surveillance, auscultation, fibre optique, rupture, fuite

**KEYWORDS:** embankment, dam, levee, flood, earthquake, safety, surveillance, monitoring, fiber optic, failure, leakage

### 1 INTRODUCTION

En 1995, EDF est le premier gestionnaire d'ouvrages hydrauliques à tester la technologie de mesure de température répartie par fibre optique pour la surveillance des fuites d'une digue. Sur les digues, il est courant d'observer des fuites soudaines, sans que les piézomètres ne détectent une variation de la surface libre. Cette observation, souvent répétée sur des ouvrages variés, montre à quel point le phénomène d'érosion interne, à l'origine de la fuite, est local. EDF, sensibilisé à ces manifestations d'érosion interne, lors de la mise en eau des digues d'Isère Moyenne Aval en 1991, en conclut que la détection précoce de l'érosion interne ne peut pas être envisagée avec l'espacement habituel des piézomètres, mais plutôt avec un espacement de l'ordre du mètre et un système d'acquisition marchant en continu. Dans le cadre d'un groupe de travail constitué avec la CNR en 1993, il apparaît que la méthode thermométrique de GTC, détectant les anomalies thermiques provoquées par un écoulement préférentiel dans le remblai avec des mesures de température dans des forages implantés tous les 20 m, est la méthode la plus efficace pour localiser la zone de fuite. D'autre part, Johansson propose à cette époque une interprétation des mesures de thermométriques, apte à en

extraire la perméabilité et à suivre son évolution dans le temps. EDF en déduit en 1994 que la détection de l'érosion interne par l'augmentation de la perméabilité dans le temps est possible grâce aux mesures à l'interprétation de température, comme l'écrit plus tard Johansson (1997) dans sa thèse.

Cependant, la méthode n'est pas prédictive : l'intervention est curative. Il faut un nouveau saut technologique, pour détecter l'initiation de l'érosion interne, surveiller son évolution au fil du temps et décider d'une intervention ou non. Quel système a l'aptitude de mesurer la température tous les mètres et en permanence ? En discutant avec Jürgen Dornstädter en 1994, patron de GTC, EDF met en parallèle le contrôle de l'érosion interne et le contrôle des câbles électriques enterrés. Ces derniers sont mis en place avec une fibre optique, en vue de détecter à tout moment, une éventuelle coupure accidentelle du câble. L'outil existe donc à cette époque ! Il reste à l'adapter au contexte de la surveillance des ouvrages hydrauliques. Cela nécessitera plus de 15 années d'étude... Dès le premier test avec une fibre optique d'une centaine de mètres, en juillet 1995, la détection de fuites, dans le canal de drainage en pied de la digue Cusset, montre que la détection des fuites est possible, mais qu'elle est dépendante de la technologie et exige une forte précision de la mesure. D'autre part, le diagnostic est entaché de

difficultés d'interprétation, suite aux nombreux biais physiques : changement thermique de l'eau canalisé, rayonnement, pluie, perte de signal dans les soudures ou les rayons de courbure trop courts. Ce premier bilan montre l'importance de la difficulté, du temps et des moyens qu'il faudra développer, pour aboutir à une surveillance fiable. Cependant le fort enjeu de sécurité justifie les nombreux efforts pour surmonter ces difficultés. EDF veut améliorer la sûreté des aménagements les plus sensibles, en démontrant une détection précoce, un diagnostic fiable et une intervention préventive minimisant le coût la réparation. Depuis, EDF, maître d'ouvrage, développe et valide méthodiquement cette métrologie (Fry 2004).

Cet article introduit le principe de cette maintenance préventive, montre les principaux résultats de qualification et évoque le déploiement opérationnel de cette technologie.

## 2 LA MAINTENANCE PREVENTIVE

### 2.1 La mesure par fibre optique

Le principe consiste à envoyer un rayon lumineux de laser dans une fibre optique standard, dont les défauts installés à pas régulier, souvent 1 m, vont rétrodiffuser le signal, qui sera analysé par un interrogateur optoélectronique et identifié par son temps d'aller-retour et son spectre en fréquence. Les pics du spectre, dépendant de la température et de la contrainte, mesurent d'une manière indirecte et surtout répartie la température et la déformation le long de celle-ci. Les interrogateurs optoélectroniques disponibles sur le marché actuellement permettent d'obtenir une mesure tous les mètres, avec une portée allant jusqu'à 20 à 30 km. En choisissant bien l'interrogateur et en utilisant des fibres standard télécom multimodes, la précision est de 0,1°C pour une mesure de température seule avec un interrogateur Raman et une distance inférieure à 10 km. A partir d'une fibre optique monomode contrainte dans un câble, la précision des mesures de température et de déformation par un interrogateur Brillouin est de l'ordre de 1°C et de 20µm/m.

### 2.2 Surveillance active ou passive

La méthode thermométrique initiale de GTC mesure une seule fois la température. Comme ce n'est souvent pas suffisant, GTC développe un test de convection forcée, où la température est imposée par chauffé ou réfrigération (Dornstädter J. 2010). Ce mode opératoire est appelé méthode active, en opposition à la méthode passive, consistant à mesurer les températures naturelles. Le débat, autrefois vif entre les partisans de l'une ou de l'autre approche, laisse maintenant une place à chaque méthode.

Johansson (1997) n'utilise que la méthode passive associée à une modélisation numérique des échanges thermiques. EDF montre qu'une interprétation simpliste de la méthode passive dans un milieu non saturé aboutit à un diagnostic faux. Pour surmonter cette incohérence, EDF développe d'autres modèles d'interprétation, valables quelle que soit la position de la fibre optique ou celle de la nappe. Quatre modèles sont complémentaires (Beck & al. 2010), les deux premiers sont physico-statistiques, issus de la pratique de l'auscultation, tandis que les suivants sont basés sur le traitement du signal. La méthode passive a l'avantage de permettre la surveillance permanente et d'identifier les fuites à plus d'un mètre de la fibre. Son inconvénient est de nécessiter la mesure de la température de l'eau stockée ou canalisée et celle de l'air et un modèle d'interprétation complexe à plusieurs niveaux de traitement.

Perzmaier, Aufleger et Dornstadter (2007) ont été les précurseurs de la méthode active, en entourant la fibre optique d'un câble de cuivre chauffé par effet Joule sur une courte période de temps. La puissance électrique nécessaire est de 3 à

15 W/m. Cette méthode présente l'inconvénient d'être applicable uniquement à des tronçons limités de digues (< 2 km), d'avoir un faible rayon d'action (< 20 cm autour du câble), de ne pas permettre une surveillance en continu et de nécessiter quelques précautions de conception et d'utilisation afin d'assurer la sécurité du personnel.

### 2.3 Le concept de maintenance préventive

Le choix d'un système de surveillance par fibre optique n'est pas justifié sur tous les ouvrages. Une stratégie basée sur l'évaluation du risque ne montre pas de bénéfice à équiper ni les grands barrages de bonne conception, dont la sécurité est assurée par une surveillance habituelle, ni les petits barrages de risque limité, dont la rupture aurait peu de conséquences. A l'opposé, un système de détection par fibres optiques apporte un gain justifié quand l'ouvrage est de grande longueur, sur une fondation mal connue ou édifié avec une conception non conforme à l'état de l'art actuel, dont le coût de réparation est lourd pour le maître d'ouvrage, alors que des zones de faiblesse sont suspectées sans qu'elles soient localisées, laissant un doute sur la sécurité dans le temps ou en conditions extrêmes.

Le système de surveillance par fibre optique apporte dans tous les cas un complément au réseau habituel d'auscultation. C'est un outil d'aide à la gestion de crise. Que se soit après un séisme ou une crue, il a la capacité de localiser en temps réel les zones à risque et donc d'améliorer la gestion des ressources et d'accroître l'efficacité des interventions.

Le choix de la méthode et du modèle d'interprétation est lié à la stratégie du maître d'ouvrage : surveillance long terme ou court terme, pathologies à suivre, gestion du risque sismique. La mise en place de ce système de surveillance est identique à celui de la méthode observationnelle, en réunissant quatre conditions :

1. Les limites admissibles du comportement en température et/ou en déformation sont évaluées par modélisation avant d'être mesurées;

2. Le domaine des variations possibles du comportement thermique ou cinématique est jugé acceptable. Un tel système d'auscultation n'est installé que si la marge de sécurité est jugée acceptable, dans le cas contraire il s'agit de programmer en urgence la réhabilitation;

3. Le programme de suivi est établi pour vérifier si le comportement réel reste dans les limites admises. La fréquence d'acquisition est suffisamment élevée pour que le dispositif puisse détecter l'apparition de toute fuite, vérifier par la progression du phénomène s'il s'agit d'érosion interne et laisser le temps de réparer. Le choix de la méthode passive ou active doit être justifié par rapport à la cinétique des phénomènes attendus;

4. Un programme d'interventions d'urgence est défini au cas où le suivi révèle un comportement sortant des limites admissibles.

L'avantage de la maintenance prédictive est de limiter les zones endommagées par la détection précoce des pathologies menant à n'importe quel mode de rupture. Il existe 3 modes de rupture potentiels : l'érosion externe, l'érosion interne et le glissement. Chacun de ces trois modes est intercepté par le système de surveillance à base de fibres optiques de mesure de température et de déformation. Les mesures de température repèrent le risque de rupture par érosion et les mesures de déformation détectent le risque d'instabilité générale. Cela est bien démontré par les résultats du projet IJkdijk en Hollande (Koelewijn A. 2010) et (Beck & al. 2010).

## 3 VALIDATION DE LA DÉTECTION PRÉCOCE DE LA RUPTURE

L'été 2003, en pleine canicule, la digue de Wilnis se rompt, quelques heures après une inspection visuelle. La démonstration est faite que l'inspection visuelle, souvent essentielle à la

surveillance, ne garantit pas à elle seule la sûreté. Le gouvernement hollandais en prend conscience. Il décide de lancer le projet IJdijk en vue de sélectionner les meilleures technologies de détection précoce de la rupture. EDF, associé à Tencate, Géophysconsult et au projet PAREOT, voit une opportunité hors du commun de tester son approche de la sûreté.

### 3.1 Rupture par instabilité générale

Le premier test en 2008 concerne la détection du glissement d'une digue, chargée par des containers et dont le pied est excavé. 4 fibres optiques mesurent l'élongation du parement aval (Figures 1 à 3). La surface de rupture est bien détectée.

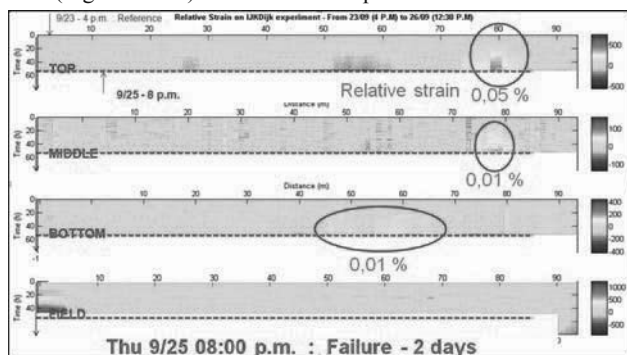


Figure 1: Elongation des 4 fibres optiques 2 jours avant la rupture

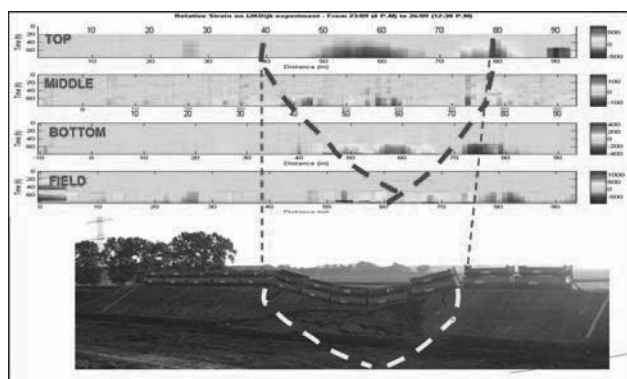


Figure 2: Détection de la surface de rupture par les 4 fibres optiques



Figure 3 : Glissement de la digue (photo Koelewijn)

### 3.2 Rupture par érosion interne

Le système de détection est de nouveau testé sur les 4 essais de détection de rupture par renard des digues expérimentales du projet IJdijk en 2009. Les remblais mesurent 3,5 m de hauteur, 15 m de longueur et ont un fruit H/V=2/1 à l'amont et aval. Les fibres optiques passives sont installées avec Tencate dans la

fondation au contact du remblai (Figure 4). La rupture est obtenue par érosion régressive en montant par palier le plan d'eau amont. La durée de l'essai varie de 4 à 6 jours. La détection visuelle et la détection par analyse de signal sont représentées respectivement sur les figures 5 et 6.

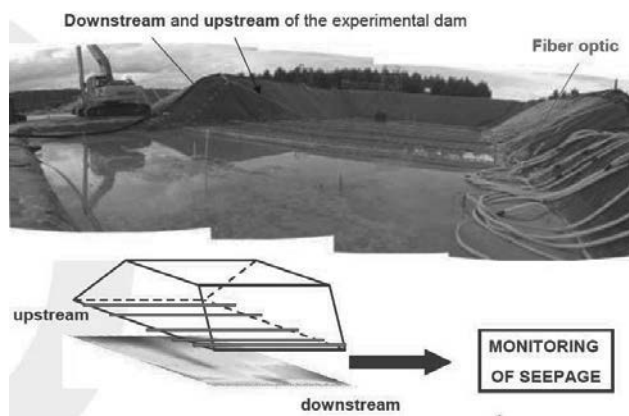


Figure 4 : Installation des fibres sous le remblai

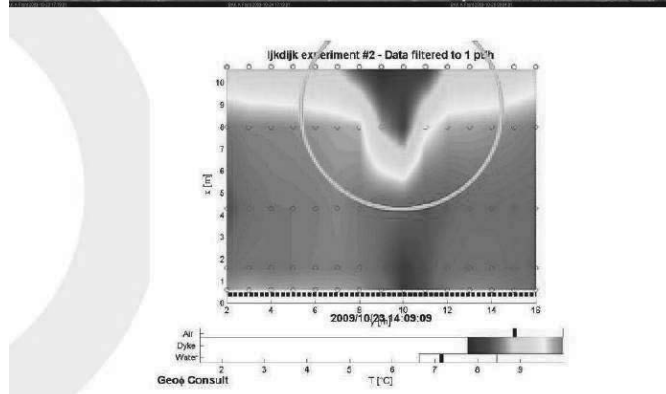


Figure 5 : Détection visuelle du renard 2 jours avant la rupture

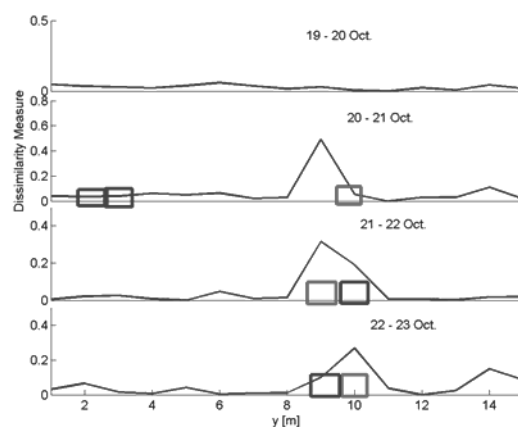


Figure 6 : détection du renard par analyse du signal

La Figure 5 montre que l'analyse visuelle détecte le renard en formation sans erreur deux jours avant la rupture dans le test N°2. La figure 6 illustre l'intérêt de l'analyse de signal sur le même test. Le réservoir est rempli le 19/10/2009 d'une charge d'eau de 1,9 m à 12h00. L'essai s'achève le 25/10/2009 à 10h00 par la rupture de la digue. Les données sont rapatriées à distance et analysées au pas journalier par géophysConsult du 19/10 à 9h18 au 25/10 à 9h10. La transformation des données de



température par analyse du signal détecte un clair précurseur de la rupture plusieurs jours avant l'analyse brute des données. Sur la Figure 6, l'absence d'anomalie au cours de la première journée d'essai (19-20/10) correspond bien à l'absence d'observation de fuite sur le terrain. Les jours suivants, des fuites sont observées et visualisées par un rectangle bleu, alors que l'entraînement et le dépôt de sable est représenté par un rectangle rouge. Le modèle d'analyse détecte bien une fuite croissante vers l'abscisse 9-10 m, là où la rupture va se produire 5 jours plus tard.

Pour chacun des quatre essais, le modèle d'analyse développé par EDF apparait plus performant que la visualisation des mesures brutes (tableau 1). Le temps de détection varie d'un test à l'autre, car les fibres n'ont pas pu être posées exactement aux endroits demandés par EDF. Cela montre l'importance de la localisation des fibres dans la conception du système de détection.

Tableau 1. Durée entre la détection et la rupture

Test	Durée (jours)	Détection visuelle	Détection analyse du signal
1	4	3 heures	3 jours
2	6	48 heures	5 jours
3	5	31 heures	3 jours
4	5	21 heures	1 jour

### 3.3 Bilan des tests de validation de IJkdijk

Que ce soit pour la détection du glissement ou de l'érosion interne, le système de fibres optiques accompagné d'un robuste modèle d'interprétation apparait la méthode la plus performante (robustesse et justesse) parmi les technologies de détection testées par la trentaine de participants du projet international.

Conforté par ces résultats d'inter-comparaison des pratiques internationales, EDF programme et déploie cette maintenance préventive en 2010 sur une série de travaux visant à réhabiliter certains biefs hydro-électriques et à optimiser leur maintenance.

## 4 APPLICATIONS

EDF dispose en 2012 de quatre ouvrages instrumentés et suivis par fibre optique. Ainsi, le canal de Curbans, de 5 km de longueur, est instrumenté par 11 km de fibre optique et est aujourd'hui suivi périodiquement par des mesures de température actives et passives. Des mesures de déformation sont faites à une fréquence plus faible. La surveillance par fibre optique de la remise en eau de l'ouvrage à la fin des travaux de réhabilitation contribue à détecter rapidement les zones de fuites (résultats de surveillance toute les 4 heures) et à diminuer les pertes d'exploitation remboursant son coût d'installation. La surveillance actuelle de l'ouvrage en exploitation montre une bonne corrélation entre les résultats d'analyse des données de température par fibre optique et les débits de drainage sous l'étanchéité rénovée, captés tous les 300 mètres. Ils mettent en évidence une décroissance due au phénomène de colmatage. Les mesures de déformation identifient trois secteurs de déformations différentielles à suivre de près.

## 5 CONCLUSION

La maintenance préventive par un système de fibres optiques permet une mesure en continue et répartie dans l'espace d'anomalies thermiques ou mécaniques, une détection précoce

des risques de rupture, une optimisation des ressources en situation de crise et une économie sur les durées d'indisponibilités ou le coût des travaux de réhabilitation. Elle est adaptée aux ouvrages de grand linéaire ou à ceux qui posent des difficultés de conception ou sont très sensibles au niveau de la sûreté.

## 6 REMERCIEMENTS

Nous remercions les nombreux partenaires (de Deltares, EDF R&D, GTC, Hydroresearch, Irex, Irstea, Tencate, Université de Grenoble) qui ont accompagné EDF et ont contribué à la qualification de la technologie à base de fibres optiques pour la surveillance des ouvrages hydrauliques.

## 7 BIBLIOGRAPHIE

- Fry, J.J. (2004) Détection de fuite sur les digues par acquisition de profils de température le long d'une fibre optique. Sécurité des digues fluviales et de navigation, Actes de colloque du CFGB, Orléans, France.
- Johansson, S. (1997) Seepage monitoring in embankment dams. PhD thesis, Royal Institute of Technology, Stockholm, Sweden
- Beck Y.L., Khan A.A., Cunat P., Guidoux C., Artières O., Mars J. and Fry J.J. (2010) Thermal Monitoring of Embankment Dams by Fiber Optics, 8th ICOLD European Club Symposium DAM SAFETY, Innsbruck, Autriche
- Perzmaier, S., Aufleger, M., Dornstädter, J. (2007) Active and passive defences against internal erosion in assessment of the risk internal erosion of water retaining structures: dams, dykes and levees. Intermediate report of the European Working Group in Internal Erosion of ICOLD 2007, pp. 194-207
- Beck Y.L., Le Clerc T., Fry J.J., Fabre J.P. and Royet P. (2010b) Leakage detection in earth dams by heated fiber optics, CDA 2010 Annual Conference, Niagara Falls, Canada
- Beck Y-L., Hénault J-M., Guidoux C. et Courivaud J-R. (2010), Surveillance des fuites dans les digues en terre par mesure de température répartie par fibre optique, Journées AGAP Qualité, 4p., St Brieuc, France
- Dornstädter J. (2010) Detection of erosion flow path during 1:1 scale experiment using fibre optic Heat Pulse Method at IJkdijk, Annual Meeting of the European Working Group on Internal Erosion, 12 avril 2010, Grenade, Espagne
- Koelwijn A. (2010) Performance of detection techniques at four full-scale seepage erosion tests, Annual Meeting of the European Working Group on Internal Erosion, 12 avril 2010, Grenade, Espagne
- Beck Y-L., Courivaud J-R., Créneau S., Delorme F. et Fry J-J., Réhabilitation de revêtement bitumineux et maintenance préventive innovante utilisant des fibres optiques : principes et application au canal de Curbans, 24ème Congrès des Grands Barrages, CIGB, Kyoto, Japon, 19p.
- Hénault J-M., Moreau G., Blairon S., Salin J., Courivaud J-R., Taillade F., Merliot E., Dubois J-P., Bertand J., Buschaert S., Mayer S. and Delphine-Lesoille S. (2010) Truly distributed optical fiber sensors for structural health monitoring: from the telecommunication optical fiber drawing tower to water leakage detection in dikes and concrete structure strain monitoring. Advances in Civil Engineering.
- Artières O., Beck Y-L., Khan A.A., Cunat P., Fry J-J., Courivaud J-R., Guidoux C. and Pinettes P. (2010), Assessment of dams and dikes behavior with a fibre optics based monitoring solution, 2nd International Congress on Dam Maintenance and Rehabilitation, 8p., Zaragoza, Spain Cao K., Wang Y., Xu Y. and Liu S. 2008. Concrete Face Rockfill Dam, *China Water Power Press*

# Evaluation of diaphragm wall as-built data to determine the risk of leakage for the Kruisplein car park excavation in Rotterdam, The Netherlands

Evaluation des données de fabrication des murs diaphragmes pour déterminer le risque de fuite dans le chantier du parking souterrain Kruisplein à Rotterdam, Pays-Bas

Hannink G.

*Engineering Consultancy Division, City of Rotterdam, The Netherlands*

Thumann V.M.

*Seaway Heavy Lifting Engineering B.V, The Netherlands, formerly Engineering Consultancy Division, City of Rotterdam, The Netherlands*

**ABSTRACT:** In the centre of Rotterdam, the Kruisplein car park is becoming the deepest underground parking facility in the country. It is being constructed since 2009, and will provide around 760 parking places on a total of five floors, of which the deepest is reaching to almost 20 m below ground surface. The retaining wall has been designed as a diaphragm wall reaching from ground surface to approximately 40 m depth. Because of some major leakage incidents in diaphragm wall type excavations in Rotterdam and elsewhere in The Netherlands, additional effort was raised to define and prepare mitigating measures to reduce the risk of leakage for the Kruisplein car park project. An extensive evaluation of as-built data of the diaphragm wall was made, including all available field records of process-parameters. Based on the outcome of the evaluation, it has been concluded that in general the diaphragm walls were of sufficient quality. No major leakage incidents have occurred to date.

**RÉSUMÉ :** Dans le centre de Rotterdam, le parking de la place Kruisplein est en train de devenir le plus profond garage souterrain du pays. Ce parking est en construction depuis 2009 et pourvoira 760 places de stationnement réparties sur cinq niveaux. Le plus profond d'entre eux atteint plus de 20 m de profondeur sous la surface du sol. Le mur de soutènement a été conçu comme une paroi moulée atteignant approximativement 40 m de profondeur. À cause de divers accidents majeurs de fuites d'eau survenus dans des excavations utilisant des parois moulées à Rotterdam et ailleurs dans les Pays-Bas, des efforts supplémentaires ont été fournis pour définir et préparer des mesures d'atténuation pour réduire le risque de fuite lors du projet du parking Kruisplein. Une évaluation étendue des données des parois moulées, incluant toutes les données de chantiers enregistrées lors de leur fabrication, est présentée. Il n'y a eu jusqu'à ce jour aucun incident majeur de fuite sur le chantier de Kruisplein.

**KEYWORDS:** diaphragm wall, deep excavation, risk of leakage, field records, as-built data, mitigating measures.

## 1 INTRODUCTION

In Rotterdam diaphragm walls are regularly applied since the construction of the Willem Railway tunnel in the nineties of the past century. For underground infrastructural projects, it is an appropriate building method, because it facilitates deep excavations under dry conditions. By connecting the diaphragm walls to the rather impermeable soil layers of the Formation of Waalre a dry building pit can easily be created. The geological conditions are favorable for this building method: in the centre of Rotterdam the rather impermeable layers of the Formation of Waalre are everywhere present between 35 and 40 m below sea level (this corresponds to the Dutch reference level NAP).

Diaphragm walls have been applied at several locations of the metropolitan light rail project RandstadRail in the beginning of this century. During the extension of metro station CS a major leak through the diaphragm walls arose when the excavation inside the building pit was at its maximum depth (14 m below sea level). As a result a huge amount of water and sand entered the building pit. With a lot of trouble, the leak was fortunately stopped within two days, and the construction of the metro station could be continued (Thumann et al. 2009).

In the same period the preparation of the underground car park Kruisplein was in full swing. The design consisted of 40 m deep diaphragm walls to make a 20 m deep excavation possible. A logical question at that moment was, how to minimize the possibility of a similar incident during the construction of the car park. This paper describes the mitigating measures taken in advance, the supervision during the construction, and the effectiveness of the precautionary measures in practice.

The construction of the Kruisplein car park is part of the overall project Rotterdam Centraal (Hannink & Thumann 2007). This major project comprises of the building of a large

Public Transport Terminal in the vicinity of the Rotterdam Central Railway Station. It is designed to facilitate passenger transfer between (inter)national trains including the high-speed train, and local public transport like trams, buses and underground trains. The excavation as required for the construction works of the Kruisplein car park covers about 5.000 m<sup>2</sup>.

Engineering of the car park Kruisplein, and supervision of the execution of the project is performed by the Engineering Consultancy Division of the City of Rotterdam.



Figure 1. Building pit of car park Kruisplein.

## 2 SOIL CONDITIONS

The ground level in the area is situated at about sea level. The geotechnical profile of the Rotterdam city area consists of anthropogenic layers (from ground level to about 5 m below sea level), and soft Holocene peat and organic clay layers (from about 5 to 17 m below sea level). Below this level Pleistocene coarse sand layers are encountered up to 35 to 40 m below sea level. These sand layers are underlain by the Formation of Waalre, consisting of over consolidated clay and sand layers. Figure 2 shows the result of a CPT. The phreatic groundwater level is about 2 m below sea level.

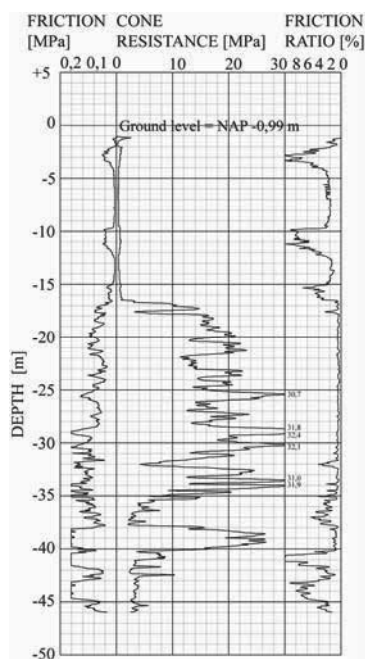


Figure 2: Results of a CPT at car park Kruisplein.

## 3 RISK ANALYSIS

In this project the principal is responsible for the design, and the contractor is responsible for the construction. The contractor is obliged to present plans about the way the risks connected to the building method are controlled, including relevant solutions and mitigating measures.

The possibility of leakage into a building pit with diaphragm walls is small, but the consequences may be very serious in case groundwater flows into the building pit. Especially in an urban environment a sand carrying leak is seen as a huge risk. Piles are founded in the sand layer with the top at 17 m below sea level. This is the same sand layer that may flow into the building pit. There are several possible causes for leakage out of this sand layer:

- the panels of the diaphragm wall are insufficiently connected;
- the base of the panel is not or insufficiently connected to the impermeable layer, for example as a result of the presence of an obstacle;
- the concrete of the panel contains intrusions of sand, peat or clay, that form weak spots in the diaphragm wall;
- the concrete of the panel contains bentonite, that forms weak spots in the diaphragm wall.

The starting point in the design stage of the car park was that the diaphragm walls would be placed at least 1.5 m into the impermeable layers of the Formation of Waalre. At the deepest point of the excavation the diaphragm wall must be able to retain a groundwater pressure difference of about 20 m.

Measures to minimize the possibility of a leaking diaphragm wall were prescribed in the contract. However, to minimize the possibility of leakage, the most was expected of measures that could facilitate the building process.

The outcome of the risk analysis indicated that to minimize the possibility of a leaking diaphragm wall:

- additional requirements should be prescribed in the contract;
- early observations of imperfections during the building process are of utmost importance;
- the execution of the project has to be monitored adequately;
- the analysis of as-built records is essential as to identify hazardous locations.

## 4 MEASURES IN THE CONTRACT

The building contract included Dutch standard RAW specifications regarding quality control of the diaphragm wall building process. The following additional contract requirements have been defined:

- the verticality of the panels shall be within 0.5% of the depth in both transverse and longitudinal directions;
- the horizontal deviations of the exposed face of a panel shall be less than 100 mm;
- 150 mm wide water-stops (rubber profiles) shall be put into every steel stop end of the diaphragm wall;
- the concrete surface of adjacent panels shall be cleaned from bentonite cake before the commencement of concreting;
- the maximum rate of concrete rising in the trench shall be 6 m/h in the Holocene clay and peat layers;
- a good connection between the floors and the diaphragm walls shall be secured. It is important not to drill unnecessary additional holes for reinforcement bars into the diaphragm walls. Zones of overlap of the reinforcement of the diaphragm wall were not allowed at the locations of the reinforcing bars;
- the maximum aggregate particle size of the concrete shall not exceed 16 mm.

Concreting records of the diaphragm wall panels had to be made to register the following possible execution imperfections:

- the time during which the trench is left open before concreting;
- the deviations of the steel stop ends;
- the deviations of the reinforcement;
- steel stop ends which are left behind;
- discontinuities in concreting.

After completing the diaphragm wall, and before starting the excavation, a check had to be made on the permeability of the building pit by means of generating a 20 m pressure difference between inside and outside of the diaphragm wall. This pumping test was meant to deliver information about the water tightness of the diaphragm wall in the sand layer with the top at 17 m below sea level, and about the water tightness of the rather impermeable layers at 40 m below sea level. A successful test however, does not exclude leakage in the execution phase, because the diaphragm wall will be excavated at one side, and will deflect. This may result into open joints between the panels.

According to the contract four boreholes for so-called sleeping wells had to be drilled around the building pit, to be able to act quickly in case of a leak. The purpose of these 'sleeping' wells was, in case of a calamity, to decrease the difference in water pressure between the inside and the outside of the building pit as soon as possible. This will make it easier to control the amount of groundwater that penetrates the building pit. The installation of pumps and mains was not required in the contract. The idea was that in case of a calamity the mobilization period would be limited.

## 5 MEASURES DURING THE EXECUTION

It was considered to be important to specify the most vulnerable processes into a number of documents that made it possible to control the processes:

- the excavation plan describes the sequence of the execution of the panels of the diaphragm wall as to minimize the possibility that a leak will occur during the night;
- the supervision plan for the construction of the diaphragm wall and for the excavation of the building pit is meant to detect imperfections in an early stage during the excavation;
- the calamity plan describes the risks connected to the construction of the diaphragm wall and the available mitigating measures at the moment of signaling a (potential) leak or a threatening calamity;
- results of monitoring activities and records give detailed information on the execution of each panel, and of possible imperfections. It is of utmost importance that the content of the documents and the point in time of handing them in are mutually agreed;

The results of the supervision by both the principal and the contractor are discussed at the building meetings, and a separate regular monitoring meeting with all persons concerned was convened.

## 6 ASSESSMENT OF DIAPHRAGM WALL QUALITY

All relevant data have been evaluated to determine potential weak-spots in the diaphragm wall along the excavation circumference.

### 6.1 Pumping test

The pumping test to check the water tightness of the diaphragm walls was executed in June 2010. The measuring results showed that the water tightness of the building pit as a whole met the requirements as formulated in the permit for water extraction. This implicated that the average quality of the diaphragm walls came up to expectations about water tightness in not excavated circumstances.

### 6.2 Field observations

Field observations by both the contractor and the supervisors of the City of Rotterdam were meant to record regular and any extraordinary circumstances during the building process of each individual panel. In practice, general data on the duration of the consecutive building stages (a.o. excavating, refreshing of bentonite suspension, lowering of steel reinforcement, concreting) and identification of excavated soil type (sand or clay) have been recorded. For some panels, underground obstacles were encountered.

### 6.3 As-built documents

Information from as-built documents has been thoroughly examined to detect any hazardous sections of the diaphragm panel. These data have been visualized as for example shown in Figures 3 to 5. Figure 3 shows amongst other things the elapsed time between:

- the start of the excavation of the trench and the start of the installation of the steel stop ends;
- the start of the installation of the steel stop ends and the end of the excavation of the trench;
- the end of the excavation of the trench and the start of the cleaning of the concrete surface;
- the start of the cleaning of the concrete surface and the start of the installation of the reinforcement cage;
- the end of the installation of the reinforcement cage and the commencement of concreting.

Long periods of elapsed time for a particular activity may indicate an increased risk of imperfections.

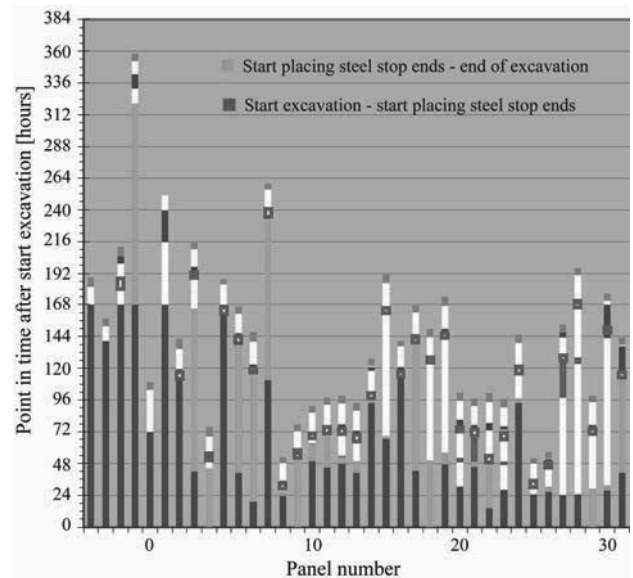


Figure 3. Continuity of the production process.

Figure 4 shows the calculated deviation of wall thickness as can be calculated from the concreting progress reports. From Figure 4 it can be identified where the panels are suspected to have a reduced thickness of more than 0.2 m. However, it is recommended to have more detailed information on the progress of the concreting process for future projects, as to increase the resolution (reliability) of this graph.

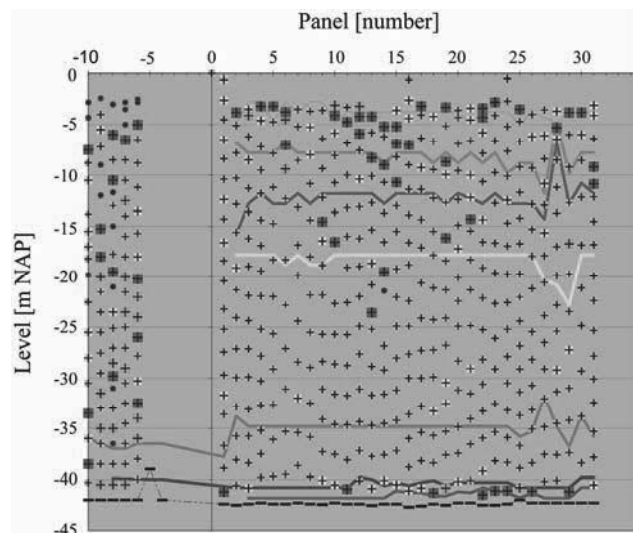


Figure 4. Deviation of panel width (data originating from leveling data and concrete consumption). The separation of the different soil layers as derived of excavation data and of geotechnical investigations is also indicated.

Figure 5 shows the position of all diaphragm wall panels at 40 m depth, as derived from crane operating monitoring equipment. Most of the panels have been excavated in two or three parts, thus giving at least two monitoring records (inclination and deviation vs. excavation depth) per panel. From Figure 5 it can be identified where the panels are suspected to have insufficient overlap. The diaphragm wall thickness as designed was 1.20 m; the allowable position with respect to overlap (zone width of 1.60 m at 40 m depth) follows from the 2% deviation of the verticality.

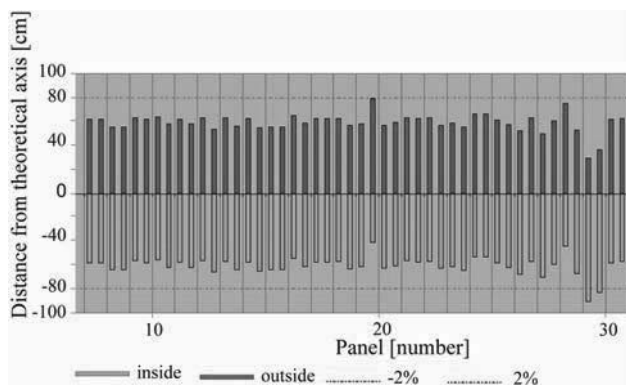


Figure 5. Relative position of the panels at 40 m depth. Dark represents the outside of the diaphragm wall; light the inside. The dotted red lines represent the 2% deviation of the verticality.

#### 6.4 Non-standard measurement techniques

Reference is made to Doornenbal et al. (2011) and Spruit et al. (2011) for more information on the experiments using non-standard measurement techniques to detect imperfections in diaphragm walls, which appeared to be quite successful.

#### 6.5 Increased risk of leakage

Combined interpretation of Figures 3 to 5 reveals areas where an increased risk of leakage has to be anticipated for, as compared to normal conditions. Following aspects have been evaluated using the outcome of the interpretation of the as-built records:

- a missing/damaged water-stop;
- no cleaning of the concrete surface;
- the elapsed time between refreshing of the bentonite and the commencement of concreting greater than 24 hours;
- encountered problems during the stop end removal works;
- concrete characteristics;
- wall thickness reduction > 0.20 m (Figure 4),
- reduced overlap < 0.80 m (Figure 5).

An overview of locations with an increased risk of leakage along the excavation circumference has been generated as shown in Figure 6.

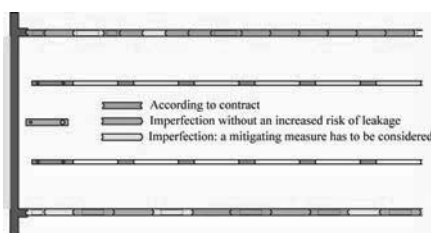


Figure 6. Increased risk of leakage.

Subsequently, a number of mitigating measures has been defined for each individual panel as to compensate the increased risk. It appeared from the overall risk analysis that careful positioning of four ‘sleeping’ wells around the excavation would provide sufficient means for acting in case of leakage at any of the identified weak spots as shown in Figure 7. Additionally, for a number of panels it has been recommended to call for an intensified inspection and repair program (when necessary) during the excavation works.

## 7 CONCLUSIONS

The realized diaphragm wall panels were in general of sufficient quality. A number of hot spots along the circumference of the building pit with an increased risk of leakage were identified. The risk profile related to leakage was considered to be at an

acceptable level if a number of mitigating measures were executed. These measures were supplementary to the required measures in the contract.

A pumping test to check the water tightness of the diaphragm walls is very valuable in case the subsoil conditions are similar to those in Rotterdam.

Supervision of the construction process appeared to be an important mitigating measure, in combination with the registration of the execution data of the diaphragm wall, and the subsequent analysis of these data.

The extensive acquisition of data as such is not new for the construction of diaphragm walls, but the systematic analysis of the data, as performed for this project, has not been noticed so far. It is recommended to do so for all future projects.

The positioning of ‘sleeping’ wells can be considered as a major mitigating measure, and is a lesson learned from the construction of the (leaking) diaphragm wall at metro station CS.



Figure 7. Positioning of the four ‘sleeping’ wells east and west of the building pit. Additional wells may be installed at the north and south side in case of a calamity in the northern or southern wall.

## ACKNOWLEDGEMENTS

The work on this subject of former colleagues Edwin Dekker and Rens Servais is gratefully acknowledged. Records of the execution of the diaphragm walls have been provided by the contractor Besix BV. Colleague Arie van de Heerik collected most of the records, and Ton de Keiser prepared the illustrations in this paper.

## REFERENCES

Doornenbal, P., Spruit, R., and Hopman, V. 2011. High resolution monitoring of temperature in diaphragm wall concrete. *Proc. FMGM2011, Berlin*.

EN 1538 2010. *Execution of special geotechnical work – Diaphragm walls*.

Hannink, G. and Thumann, V.M. 2007. Existing structures govern building methods near Rotterdam Central Station. *Geotechniek, special edition, September, 2007, 26-29*.

Spruit, R., Hopman, V., van Tol, A.F., and Broere, W. 2011. Detection of Imperfections in Diaphragm Walls, field test results. *Proc. FMGM2011, Berlin*.

Thumann, V.M., Hannink, G. and Doelder, B.R. de 2009. Ground freezing and groundwater control at underground station CS in Rotterdam. *Proc. 17<sup>th</sup> Int. Conf. On Soil Mech. and Geot. Eng., Alexandria*.

# Optimisation of bridge approach treatment via staged construction

## Optimisation du traitement de remblais d'accès à des ponts par phasage des travaux

Hsi J.P., Carson D.J., Lee C.H.  
SMEC Australia Pty Ltd, Australia

**ABSTRACT:** This paper describes an improved approach to bridge embankment transition design and construction staging that was utilised to overcome financial and programme challenges associated with the proposed initial design solution for bridge approach embankments. An alternative staged approach was developed for construction, comprising improvement of the strength and compressibility characteristics of the soft soil foundation by surcharging techniques in combination with use of prefabricated vertical drains (PVD) and high strength geotextile. Unreinforced continuous flight auger (CFA) columns were installed after surcharging to achieve smooth transition at bridge approach embankments. During construction, the behaviour of the foundation under load was closely monitored and back analysis of the performance of the improved foundation was undertaken. Construction stage design optimisations were then made to satisfy the design criteria using actual monitoring data. This approach to bridge embankment transition design provided ability for the entire subsurface profile to accommodate the applied embankment loading. As a result, major cost, programme and environmental benefits were realised during construction by avoiding the installation of approximately 88,900 lineal metres of concrete foundation piles that were specified in the initial design.

**RÉSUMÉ :** Cet article décrit une approche améliorée pour la conception et le phasage des travaux de remblais d'accès aux ponts. Cette approche a été utilisée pour répondre aux contraintes financières et de planning associées à la solution initiale proposée. Une approche alternative en termes de phasage des travaux a été développée et comprenait l'amélioration de la résistance et de la compressibilité du sol de fondation (argile molle) par l'installation de remblais de chargement, de drains verticaux préfabriqués et de géotextiles haute performance. Des colonnes en béton ont été installées après la période de chargement pour assurer une transition en douceur au niveau des remblais d'accès au pont. En phase construction, le comportement du sol de fondation sous la charge était étroitement contrôlé et une évaluation de la performance en ce qui concerne l'amélioration actuelle du sol de fondation a été réalisée. Sur la base des mesures effectuées sur chantier, certains paramètres de conception ont été optimisés en phase travaux pour satisfaire aux exigences du projet. Cette méthode de conception des remblais d'accès aux ponts a fourni à l'ensemble du sous-sol la capacité de supporter le chargement qui s'applique sur le remblai. Ainsi, de conséquents gains financiers, de temps et environnementaux ont été réalisés en phase travaux puisque cette solution a évité l'installation d'environ 88,900 mètres de pieux en béton, spécifiés dans les études initiales.

**KEYWORDS:** Ground improvement, bridge approach transition treatment, prefabricated vertical drain, CFA column, preloading.

## 1 INTRODUCTION

As a state government initiative, the AUD \$1.88B Gateway Upgrade Project in Brisbane Australia involves the design, construction, operation and 10 year maintenance (DCOM) of a new Gateway Bridge, existing Gateway Bridge refurbishment, 12km of motorway upgrade and 7km of new motorway.

Located along Brisbane's north south arterial transportation corridor, the project provides improved connectivity to infrastructure such as Brisbane's Trade Coast region, Airport and the Port of Brisbane. Construction completion for the entire project occurred during November 2010.

Delivered by Queensland Motorways Limited (QML) in partnership with Leighton Abigroup Joint Venture (LAJV) and principal designers Maunsell SMEC Joint Venture (MSJV), the project involved construction and refurbishment of 30 bridge structures. Fourteen (14) of these bridges are located within the Brisbane Airport Interchange precinct, which is characterised by soft, compressible foundation soils up to 20 m in thickness, with road embankment heights up to 13m.

Initial design for the bridge approach treatment in this area comprised use of various forms of piled embankment supported by a mixture of approximately 4,900 continuous flight auger (CFA) piles, displacement auger piles, pre-stressed concrete piles and dynamic replacement columns.

Following cost and program analysis, an alternative staged ground treatment approach was proposed and adopted for the construction of 14 of the 28 bridge approaches within the Airport precinct. This paper focuses on one such abutment (denoted as BR25A) within this area. Site based geotechnical characteristics are identified together with key aspects of the initial and alternative design approach, summary of the alternative design methodology, comparison between predicted and actual ground settlement and outcomes successfully delivered through utilisation of a staged approach to ground treatment.

## 2 GEOTECHNICAL CHARACTERISTICS

### 2.1 *Subsurface conditions*

Geotechnical investigations indicated that the Airport Interchange is underlain by up to 20m Holocene (upper and lower) and Pleistocene alluvial deposits.

Upper Holocene alluvium within the Airport Interchange area was characterised by variable deposits of clay and silt (UH-C) and sands (UH-S). Lower Holocene alluvium (LH-C) was found to be of more uniform composition, comprising compressible silty clay to up to 20m depth.

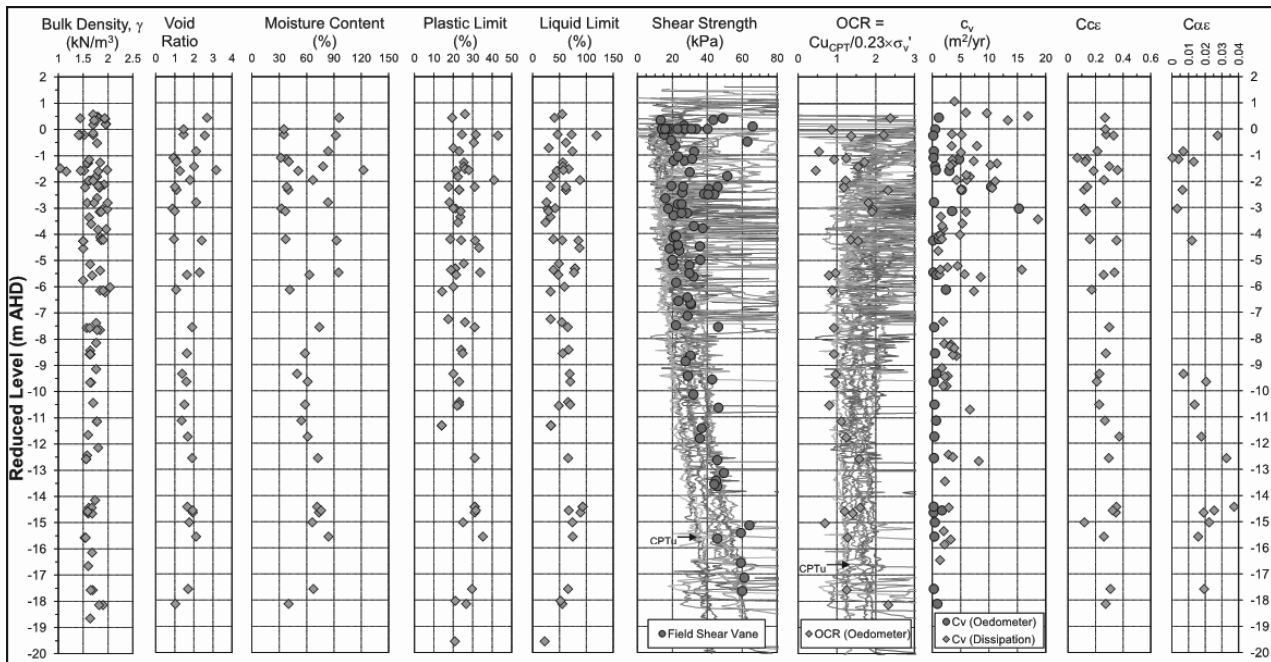


Figure 1: Soil test results - Airport Interchange precinct

Deposited during previous lower sea level, Pleistocene clay (P-C) was found to be characterised by less compressible stratum including stiff to hard clays and medium dense (or denser) sand layer. The ground water level was observed to be within 1-2m of the natural ground surface. The design ground water table was assumed at the ground surface level prior to construction (approximately RL 1.3m).

2.2 Geotechnical design parameters

The geotechnical parameters adopted for design and back-analysis of BR25A bridge approach are summarised in Table 1. Design parameters were derived taking into consideration the potential variability in the ground conditions and were calibrated against monitoring results during construction stage. The coefficient of consolidation in the horizontal direction ( $c_h$ ) was assumed to be  $2c_v$  and this ratio was found to be appropriate based on the back-analysis of field measurements.

Site investigation data indicated variation in strength, compressibility and hydraulic conductivity with depth and location within the Airport Interchange area. Field results from this vicinity indicate that the undrained shear strength ( $C_u$ ) of the compressible clay increases with depth from approximately 10kPa to 60kPa.  $C_u$  values derived from piezocone were calibrated against the shear strength determined from the field shear vane. For geotechnical design, a characteristic  $C_u$  value of  $20 + 0.6z_1$  (kPa) for UH-C and  $23.6 + 2.7z_2$  (kPa) for LH-C was selected, where  $z_1 = 0$  at RL 0 and  $z_2 = 0$  at RL -6. Over-consolidation ratios (OCR) were derived from Oedometer and piezocone data. Figure 1 shows field and laboratory test results.

3 ALTERNATIVE DESIGN DETAILS

The alternative design philosophy involved initially improving the shear strength and compressibility characteristics of the soft soil by 6 months preloading in combination with placement of 4.3m surcharge. High strength geotextile (2 layers of WX600/50) and prefabricated wick drains (1.0m triangular pattern) were utilised for stability control. Refer to Figure 2 for schematic design arrangement nominated during design stage 1.

To facilitate construction haulage, a 2m high temporary berm in the longitudinal direction was proposed and this stabilising effect was incorporated in the design. The use of temporary berm achieved a reduction in the high strength

geotextile requirement for stability control.

Following conclusion of preload, installation of final settlement transition treatment was anticipated, following review of actual performance of the embankment during preloading. The ground transition treatment for the alternative approach comprised 3 transverse rows of unreinforced concrete CFA columns (0.6m diameter on a 2.5m square grid with a UCS of 40MPa) overlain by a 20m long geotextile reinforced mattress to provide adequate pavement transition (see Figure 3). Two layers of WX1100/100 were specified in the longitudinal direction and one layer of WX200/50 in the lateral direction for the geotextile mattress. As a Stage 3 optimisation, 1m of embankment fill was excavated and replaced with lightweight fill (flyash) to increase the final over-consolidation ratio of the foundation soils and decrease preload period from 6 months to 2.4 months.

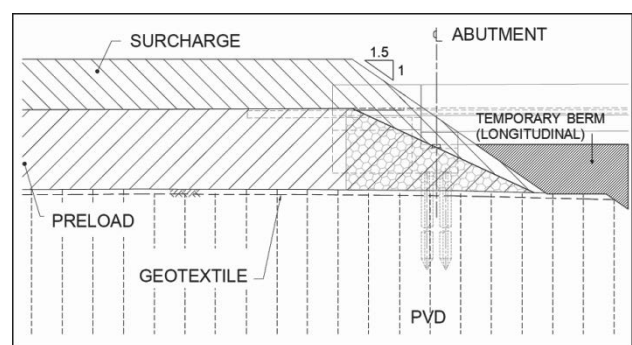


Figure 2: Typical stability and settlement control (schematic)

4 ALTERNATIVE DESIGN METHODOLOGY

The alternative design comprised a 3 staged approach to design, which occurred across the design and construction stages for the BR25A bridge approach.

4.1 Stage 1 methodology

Stage 1 involved undertaking design calculations to predict the required ground treatment to meet the settlement and stability criteria for the bridge approach transition. To meet the prescribed settlement criteria of 50mm (max) at the abutment

Table 1: Geotechnical Design Parameters

Layer	Depth (top of layer) (m)	$\gamma_t$ (kN/m <sup>3</sup> )	$c'$ (kPa)	$\Phi'$ (°)	$E'$ (MPa)	$\nu$	OCR	$C_{ce}$	$C_{re}$	$C_{ue}$	$c_v$ (m <sup>2</sup> /yr)
Fill	0.0	16.5 (16.5)	0 (0)	30 (30)	15 (15)	0.3 (0.3)	-	-	-	-	-
UH-C	0.5	17.0 (17.0)	2 (2)	27 (27)	-	-	2.5 (2.5)	0.3 (0.2)	0.03 (0.03)	0.01 (0.01)	6.0 (3.0)
UH-S	5.2	17.0 (17.0)	0 (0)	30 (30)	10 (10)	0.3 (0.3)	-	-	-	-	-
UH-C	5.5	17.0 (17.0)	2 (2)	27 (27)	-	-	2.0 (2.0)	0.3 (0.2)	0.03 (0.03)	0.01 (0.01)	6.0 (2.5)
LH-C	8.0	17.0 (17.0)	2 (2)	27 (27)	-	-	1.5 (1.5)	0.3 (0.2)	0.03 (0.03)	0.018 (0.01)	2.5 (1.5)
P-C	20.5	17.0 (17.0)	2 (2)	27 (27)	15 (15)	0.3 (0.3)	-	-	-	-	-
P-S	21.9	19.0 (19.0)	0 (0)	38 (38)	40 (40)	0.3 (0.3)	-	-	-	-	-

Note: Figures shown in brackets are values used in back analysis

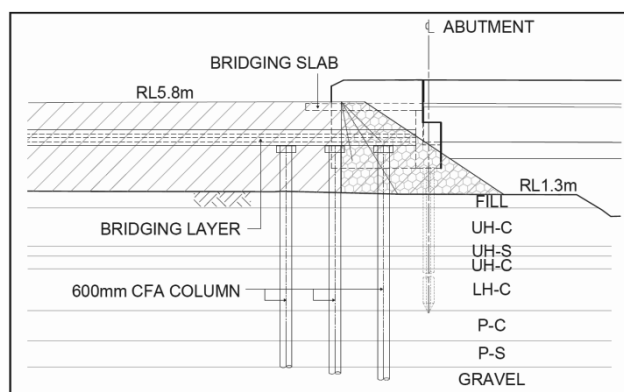


Figure 3: Typical operational stage bridge approach transition design arrangement proposed during Stage 1

location at the conclusion of the 10 years maintenance period in combination with 0.5% change in grade on the pavement surface, 6 months preloading with surcharge was proposed (refer section 3). Methodology for settlement assessment and calculation was undertaken in accordance with the method outlined by Hsi *et al.* (2008). Permeability numerical matching technique (Hird *et al.* 1992) was adopted to model the consolidation behaviour of wick drains in plain strain FEA using PLAXIS.

Suitability of the CFA column arrangement was evaluated using PLAXIS by comparing the predicted principal stresses with the allowable compression and tensile strength. Unreinforced CFA columns were modelled as non-porous elastic-perfectly plastic model with a tension cut-off at its tensile strength and plasticity parameters were obtained from compressive and tensile strengths.

In PLAXIS analysis, the two-dimensional stresses were converted into principal stresses ( $\sigma_1'$  and  $\sigma_3'$ ) in the two major and minor principal axis directions. The major principal stress value ( $\sigma_1'$ ) was compared with the factored unconfined compressive strength (UCS) and factored tensile capacity of concrete. A factor of safety of 2 was adopted for both compressive and tensile strengths. Structural adequacy was considered to be met if the principal stresses induced in the columns were less than the respective compressive and tensile capacities.

Soil structure interaction of bridge approach transition treatment was analysed in PLAXIS. The prescribed settlement method was used to analyse the differential settlement within the transition zone due to creep effect. Post construction creep settlement was firstly estimated. Subsequently, the ground behind the CFA columns was then prescribed to settle by an amount equal to the estimated post construction settlement. The embankment change in grade over any 4m length of pavement due to differential settlement was then calculated.

To meet the stability criteria (minimum safety factor of 1.2 in short term and 1.5 in long term), the embankment construction was constrained at a rate of 1m per week. Accordingly, strength gains due to consolidation of the UH-C and LH-C layers were able to be considered in the design. Time rate of consolidation of the UH-C and LH-C layers was further accelerated by use of PVD's. High strength geotextile in combination with lateral stability berms was utilised to provide additional stability control during construction. Stability analysis and design of soil reinforcement were carried out in accordance with the method outlined in Hsi and Martin (2005).

#### 4.2 Stage 2 methodology

Stage 2 involved constructing the embankment using the design arrangement in combination with monitoring of the actual embankment performance during the preload period based on an observational approach. The objective of Stage 2 was to validate the design assumptions and ensure the safe and economical construction of the embankment by controlling the filling rate. Two settlement plates and markers, one vibrating wire piezometer, three inclinometers and one extensometer were implemented at BR25A to monitor the embankment performance during filling and preloading.

#### 4.3 Stage 3 methodology

Conducted in parallel with Stage 2, Stage 3 involved back analysis during construction to validate the proposed transition design with respect to the settlement criteria. Additionally, the predicted date of preload removal was refined and investigation into opportunities to optimise the design from a cost and time perspective was undertaken. Back analysis was conducted using actual construction stage monitoring data.

To validate the magnitude of primary settlement, back analysis comprised initial modelling of the actual rate of



embankment construction in PLAXIS and then comparing the primary settlement obtained from the modelling to the settlement actually observed in the field (see Figure 4). Calibrations were then made to the soil model to achieve an acceptable match between observed and predicted behaviour. The magnitude of primary settlement inferred by the Asaoka (1978) method using a constant time step of 7 days was compared to the actual field data and numerical predictions as an additional validation check on the degree of consolidation achieved. A further validation was undertaken by comparing the actual degree of excess pore water pressure dissipation recorded by the piezometer against the degree of excess pore water pressure dissipation calculated by FEM during stage 3 back analysis (see Figure 4). The magnitude of creep settlement was estimated based on the methods described in Mesri and Feng (1991), Mesri *et al.* (1997) and Stewart *et al.* (1994) and compared with the design criteria. The recommended preload duration was then refined to ensure that the predicted post construction settlement met the design criteria.

## 5 RESULTS

As shown in Figure 4, the magnitude of primary settlement predicted in Stage 1 was significantly greater than the actual primary settlement recorded during Stage 2 field monitoring. Compressibility and consolidation parameters were calibrated (calibrated parameters shown bracketed in Table 1) to achieve a good agreement between Stage 2 actual settlement results and settlement back calculated at Stage 3. From iterations during the Stage 3 back calculation, the source of the difference between Stage 1 and Stage 3 settlement predictions was partly attributed to the higher modified compression index  $C_{ce}$  and modified recompression index  $C_{rc}$  adopted during Stage 1 design. As a result, the modified secondary compression index  $C_{ac}$  was also amended. As a further validation check, the primary settlement was also calculated using the Asaoka (1978) method. Using this method, primary settlement of approximately 1.79m was estimated, which compared reasonably well to the Stage 3 back calculated primary settlement estimate (1.80m).

The degree of excess pore pressure dissipated as measured by the piezometer during Stage 2 was compared against the degree of excess pore water dissipation from the Stage 3 back calculation. This comparison provided an additional validation check in relation to the estimated degree of consolidation of the compressible soils. A reasonable agreement between the measured (Stage 2) and back calculated degree of excess pore water dissipation (Stage 3) of the compressible soil was observed (see Figure 4).

## 6 CONCLUSIONS

An alternative staged approach to design and construction successfully achieved reductions of over 88,900 lineal metres of ground improvement piling that was specified in the initial design. BR25A approach has been presented as a ground treatment design case study; providing key geotechnical considerations, design methodology and a comparison of actual embankment performance with design predictions.

## 7 REFERENCES

- Asaoka A. 1978. Observational Procedure of Settlement Prediction, *Soils and Foundations*, Vol. 18, 4, pp 87-101.
- Hsi J.P. and Martin J. 2005. Soft Ground Treatment and Performance, Yelgun to Chinderah Freeway, NSW, Australia, *Ground Improvement – Case Histories*, Ed. Indraratna B. and Chu J., Elsevier Geo-Engineering Book Series, Volume 3, pp 563-599.

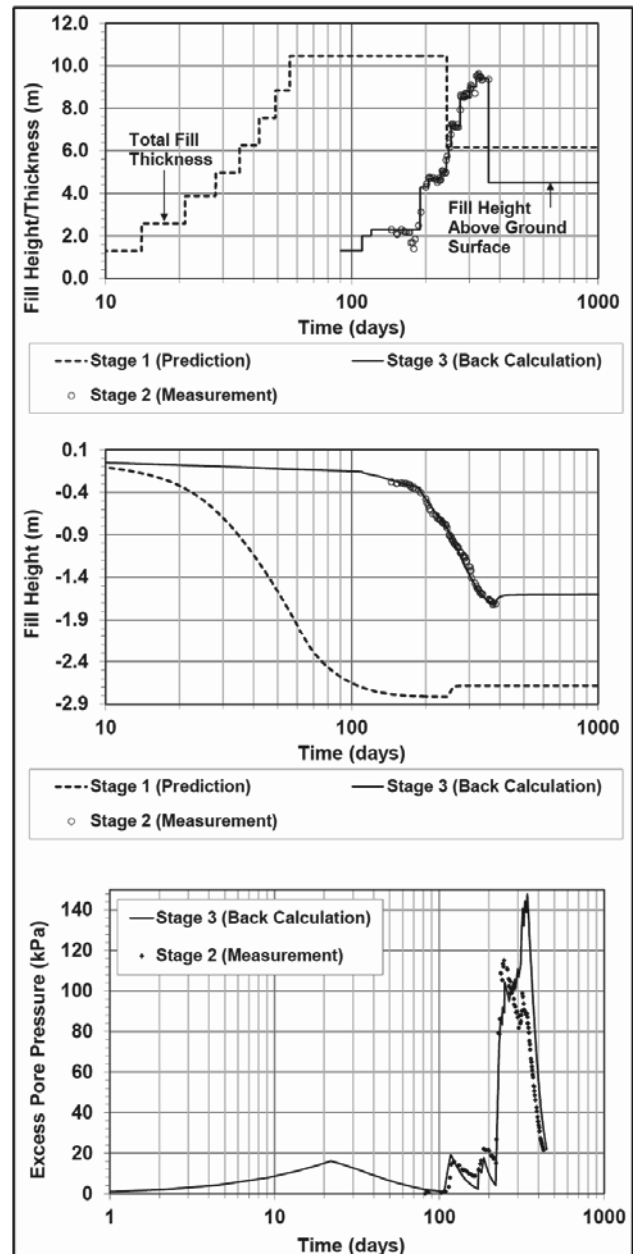


Figure 4: Predictions compared to construction monitoring

- Hsi J.P., Jones A.J. and Nguyen V. 2008. Ground Improvement Works for Brunswick Heads to Yelgun Freeway, *Australian Geomechanics Journal*, March 2008.
- Hird C.C., Pyrah I.C. and Russell D. 1992. Finite Element Modelling of Vertical Drains Beneath Embankments on Soft Ground, *Geotechnique* 42(3), pp 499-511.
- Mesri G., Stark T.D., Ajlouni M.A. and Chen C.S. 1997. Secondary Compression of Peat with or without Surcharging, *Journal of Geotechnical and Geo-environmental Engineering*, 123(5), pp 411-421.
- Mesri G. and Feng T.W. 1991. Surcharging to Reduce Secondary Settlement, Proceedings of International Conference on Geotechnical Engineering for Coastal Development – Theory to Practice, *The Japan Society of Civil Engineers, Tokyo, Japan*, 3-6 September, pp 359-364.
- Stewart J.P., Lacy H.S. and Ladd C.C. 1994. Settlement of Large Mat on Deep Compressible Soil, Vertical and Horizontal Deformations of Foundations and Embankments, *Proceedings of Settlement 94, ASCE Geotechnical Special Publication*, 40, pp 842-859.

# SWOT analysis Observational Method applications

## Analyse FFOM à l'implémentation de la méthode observationnelle

Korff M.

*Deltares and Cambridge University*

Jong de E.

*Geobest*

Bles T.J.

*Deltares*

**ABSTRACT:** The paper analyses the strengths, weaknesses, opportunities and threats (SWOT) for the application of the Observational Method in civil engineering practice. International cases, many of which are well known in literature have been analysed along the lines of the SWOT methodology. A specific number of cases has been analysed, having typical Dutch conditions, to determine country specific aspects as well. This paper describes the evaluation of the cases. This results in conditions under which the application of the Observational Method is best suitable and conditions in which it is best to avoid the observational method.

**RÉSUMÉ :** Cet article présente les résultats d'analyses Forces, Faiblesses, Opportunités, Menaces (FFOM) effectuées pour appliquer la méthode observationnelle au domaine du génie civil. L'analyse FFOM est appliquée à des réalisations internationales, bien connues dans la littérature et pour lesquelles la méthode observationnelle a été mise en œuvre. Un certain nombre de cas est analysé sous les conditions néerlandaises, afin de déterminer les éléments spécifiques pour ce pays. Cet article décrit l'évaluation des cas. Les résultats de cette évaluation sont des situations dans laquelle l'application de la méthode observationnelle est la plus appropriée et des situations dans laquelle il est préférable d'éviter la méthode observationnelle.

**KEYWORDS:** Observational Method, SWOT, cases.

## 1 INTRODUCTION

The Observational Method (OM) can produce savings in cost and programme on engineering projects, without compromising safety, and can also benefit the geotechnical community by increasing scientific knowledge. In some countries the use of OM is common practice, see for example Britain with famous papers by Powderham (1994) and Patel et al. (2007) and the CIRIA report 185 (Nicholson et al., 1999) and France with the Irex-RGCU guideline by Allagnat (2005). In many other countries, such as The Netherlands, the method is used in specific cases only and/or more reluctantly. Many papers in literature have described procedures on implementing the OM such as Powderham and Nicholson (1996) and the guidelines mentioned above, but very little attention is usually paid to the conditions in which the OM is most adequate. With use of a SWOT analysis this papers aims to provide such an overview of hurdles and conditions.

This research is performed as part of "Geoimpuls" in the Netherlands; a joint industry programme, with the ambitious goal to half the occurrence of geotechnical failure in Dutch civil engineering projects by 2015. The measures proposed were clustered into five themes by Cools (2011): geo-engineering in contracts, implementing and sharing of existing knowledge and experience, quality of design and construction processes, new knowledge for Geo-Engineering in 2015 and managing expectations. The observational method is seen as a means to obtain robust en cost-effective projects based on measurements in combination with risk-based scenarios. The method provides projects with the possibility to benefit from uncertainties in soil conditions, which results in opportunities.

## 2 ANALYSIS OF CASE HISTORIES

The paper illustrates the results of a SWOT analysis based on various projects reported in case histories. The focus of this analysis is on the conditions in the projects that make them suitable for the application of the OM. By collecting these aspects, one can check whether for a new project the application of the OM may bring benefits. If this is the case, the authors of this paper wishes to refer to the use of Eurocode 7 and specific guidelines for the correct and optimal procedures. Those procedures are not part of this paper.

Geotechnical monitoring is an essential part of the Observational Method, and if used separately mostly aims to control the construction processes and design assumptions. As part of the OM monitoring is used for design purposes as well. If the monitoring shows that a design can/must be changed with less/more conservative assumptions this is foreseen in the OM. In the SWOT analysis monitoring is also considered, as it is part of the OM. Parts of the SWOT analysis can therefor be used for geotechnical monitoring.

It must be mentioned that for a true SWOT analysis the internal (Strength, Weaknesses) and the external (Opportunities and Threats) must be clearly distinguished. In the case of the application of the OM, this may not be so evident, especially if we consider the soil conditions. In this paper, the soil is considered an internal part of the project. Furthermore, the SWOT analysis focusses on the application of the OM from the start of the project ('ab initio') and not as the 'best way out', when unwanted events already have appeared.

### **Strengths (S)**

Some project characteristics can be seen as strengths for the application of the OM. If the following characteristics exist, OM could be considered as a serious option. .

1. Multiple stages or parts in a project, Patel et al. (2007) suggest that for a good application of the OM it is necessary

to have some sort of a variation between parts or stages of the construction. This is essential to make it possible to learn from previous behaviour, which is the essence of the OM. Both projects that are multistage or that are executed according to an incremental construction process are suitable for application of the OM.

*Multistage projects* for example include a staged excavation or staged application of loads. These provide good possibilities for the OM. Subsequent stages of loading can be based on results measured in previous stages. Examples include the excavation after collapse of the Heathrow terminal described by Hitchcock (2003) and the raising of the embankment of the Betuweroute Cargo Rail on very soft soils as described in the Geotechnet report by Huybrechts (2000). Using the multi-stage construction process, reliability can be controlled by interpreting monitoring of the previous stages and by taking subsequent actions if necessary. Also excavations that progress in depth, for which the struts can be pre-stressed according to the rate of deformation, or when additional struts or soil nails can be installed depending on the deformations, may possess good characteristics for the use of the OM.

Another strength characteristic is present in projects with an *incremental construction process*. These projects are flexible in the speed with which they progress or consist of several steps. An example may be in NATM tunnelling work, or vibratory installation of (sheet) piles, where the rate of advancing can be controlled based on the monitoring results. Also projects with a long length (in similar soil conditions) for example line infrastructure projects such as roads and rail can provide a good basis for the OM, such as for example described for the Limehouse Link by Glass and Powderham (1994).

2. Short project duration in relation with beneficial short term behaviour of soil. In some cases short term soil behaviour may be a strength, such as when the undrained strength of soils is larger than the drained strength and only short term loading conditions are applicable which have diminished before drainage takes place. Here also the NATM method could be mentioned.
3. Displacements as leading design characteristic. Projects where displacements govern the design are by nature often suitable for the use of the OM. Deformations can usually be monitored accurately and extensively and provide good indication of the mechanisms that have to be controlled. When deformations of adjacent buildings are important, projects can be suitable for the OM, but it must be mentioned that the possible measures and variations might be limited to a specific and tight range of acceptable expected impact, thus giving less space for its application. It can however be considered a strength in the sense of this SWOT if a project relates to existing structures or conditions that are difficult to assess, such as the stability of an existing embankment (Lee, 2012) or old existing structures with unknown response (Chapman and Green, 2004). The application of the OM in those cases might solve otherwise unknown response of the structure. In general projects where epistemic uncertainties, which originate from insufficient knowledge of a property, can be decreased by the use of monitoring might be suitable (Nossan, 2006).
4. Integrated responsibility for both design and construction. Cases where a strong connection exists between design and construction teams and in which good communication between parties is assured, have a strong case for the use of the OM. The OM works well with an alliance contract in which risks (and opportunities) are shared between client and contractor, see section 3 of this paper.
5. Flexible and risk based culture. It can also be considered a strength if the culture of each organization involved is open to some flexibility but also very strict with regard to risk management and monitoring. If staff members are

sufficiently experienced and had proper training, preferably related to the use of the OM, this is a main benefit. A management commitment to implementing the OM approach at all levels is also an organizational strength.

6. High ground heterogeneity and or uncertainty in failure mechanism. In cases with high uncertainty a 'standard' (non OM) design approach forces the designer to make conservative design assumptions, leading to costs that possibly are not necessary and can be avoided. This leads to a potentially high cost differences between a 'standard' design and an OM design. It is the advantage of using the OM to justify a set of more favourable assumptions leading to a more cost effective design. This for instance can be the case when a decision needs to be made between a shallow foundation and a piled foundation, as has been experienced by GeoImpuls participants for a LNG terminal with high demands for dissimilar settlements, or in geological heterogeneous areas (for instance close to rivers).

Two combinations of variability are especially suitable for the OM. First, the soil strength or stiffness is not well known or has a large spread, but the load that will be presented is relatively well known (for example in NATM tunnels or deep excavations as described by Kamp (2003) or the railway example by Lee (2012). Secondly, if the opposite is the case and the load is relatively unknown but the soil strength is well known, for example in the case of deep foundations and embankments described by Peck (1969) and many others, the method could also work well. If both are known, or both are unknown, the OM is not suitable and this should be considered a threat.

#### **Weaknesses**

Opposite to the benefits are of course also weaknesses for the application of the OM. If any of the following characteristics exist, application of the OM may result in additional challenges or may not be suitable.

1. Too little time between measurements and measures. A major weakness exists if mechanisms involved in the project reveal themselves quicker than measures can be implemented. In the case of brittle failure monitoring may not provide previous warning. Brittle failure is a no go for the OM, while late appearance may make application of the OM inefficient since savings of necessary reinforcements can not be decided early enough, such as described by (Korevaar, 2012). Examples are non-ductile failures of structural members such as struts/waling connections in multi-propped basements as described by Patel (2007) or the vertical equilibrium of deep excavations.
2. Measurements that cause failure. In some mechanisms, for example related to the pull out capacity of (micro)piles or anchors, monitoring would require failure of the system, which is not acceptable.
3. Failure mechanism/parameter can not be measured. It can also be problematic if the monitoring system is not able to capture the correct mechanism or relevant parameters. This is often the case as stiffness and strength of soils are only weakly correlated, meaning that deformation measurements do not always indicate a possible failure of the strength of a material.
4. Change of failure mechanism during construction. Other weaknesses could be that during the construction process, the failure mechanisms change, for example if shallow failures become deep failures, primary consolidation becomes creep etc.
5. Costs for changes during construction are higher than profits minus costs for monitoring. The use of OM inevitably requires usually costly continuous measurements that have to be taken, interpreted and analysed during construction. During the design more scenarios need to be calculated together with analysis of other cases/experiences in order to know what to expect. These costs need to be balanced with

expected benefits. Also sometimes measures that might be needed as an outcome of OM are inefficient during construction. This for instance is described by (Schmitt and Schlosser, 2007) for the case of an excavation in Monaco where huge stays bearing on the bottom of the excavation would have caused major consequences for the completion time of the project.

Although it might seem that OM through this weakness is more beneficial in larger projects than in smaller, this not necessarily is the case. For example small embankments lend themselves often for the use of OM.

6. Communication between site and design office. Application of OM requires direct communication between site and design office, being responsible for direct analyses of the measurements. If these different cultures do not find each other easily in a project, this may cause delays in go – no go moments or even proceeding of the work on site without commitment of the design office. However, if communication is planned carefully it can even be considered a strength of OM that is brings design and construction close to each other. Projects where the culture is based on individual profit and loss opposed to mutual benefits, with extremely low bid or difficult market conditions are not suitable for the application of the OM.



Figure 1. Example project with application of OM in Amsterdam, Rokin Station

### Opportunities

Opportunities for the use of the OM are present at projects with the following characteristics:

1. Presence of risks with low, but unacceptable a priori probability of exceedance and significant consequences. For the use of OM it is necessary that the full range of possible behaviour is assessed and that it is shown that there is an acceptable probability that the actual behaviour will be within the acceptable limits (Eurocode 7). OM is suitable if the probability is higher than acceptable for a standard design, but is small enough to still have a large chance of successfully completing the project without necessary measures. This also requires the consequences to be large enough to justify the additional costs. Examples can be the impact of vibratory installation of sheet pile nearby a pipeline or possible damage by vibrations to old monumental buildings during driving of piles. The vibrations will most likely be present, but the probability of exceedance might be low enough to use the OM, in order to avoid a priori costly measures in design.
2. Stakeholders. OM lends itself perfectly for good communication with stakeholders involved in the project. For instance a critical attitude of a project's neighbours can be addressed with a proper explanation of the project risks and the way the project is organized to react pro actively if risks seem to occur. It is shown at the North South Line in Amsterdam during the application of OM in the final

excavation of Rokin Station that the stakeholders were reassured by the extensive risk based OM approach. Also the application of OM at the A2 Maastricht proved to be a very good way for communication with the stakeholder (Grote and van Dalen, 2012) The uncertainties related to the strength of the limestone and the subsequent response of the excavation wall, see Figure 2, made application of the OM suitable for a good communication strategy. However, it should also be mentioned here that miscommunication of the use of OM is a threat for the project, since it can easily be interpreted wrongly by stakeholders as a way of window-dressing a risky project.

3. Best way out. Although the authors of this paper think OM should be used 'ab initio', OM has proven many times to be a very good opportunity in case unwanted events are (nearly) happening, for instance observed from geotechnical monitoring. Because the original design already is 'in place' and can not easily be changed, an OM approach can still save the project.

### Threats

Threats for the use of the OM are present at projects with the following characteristics:

1. Quickly changing loads. One of the major and most well known threats is the possibility of quickly changing loads (causing brittle failure) such as deterioration of soils caused by intrusion of groundwater. Also external loads such as rainfall induced ground water surges or burst water mains as well as the risk for liquefaction all are potential threats for the use of the OM.
2. Unwillingness of authorities. Another type of potential threat may be the willingness for authorities to allow the method, even though according to Eurocode 7, the method is now regulated. Use of OM almost inevitable requires efforts on communication with the authorities in order to explain what OM is, why it is used, and how is ensured that a safe and sound construction will take place. This especially is the case in countries with little experience with OM, such as the Netherlands.
3. Time restrictions. Making an OM design requires more effort in the design phase. If the design capacity is not adapted this may lead to a longer design period. Projects with high planning demands can therefore be impractical for the use of OM, especially if it is expected that OM will not lead to time savings during construction.
4. Calculation methods and tools do not always allow for proper use of OM, in this case related to the necessary inverse modelling. A large amount of data becomes available during construction and needs to be processed. For instance for settlement prediction software, modules exist in which fitting between model parameters and measurements can take place in order to make better forecasts for stages to come. However, for other mechanisms such as deformations of retaining walls or designs using finite element models this is not easily done. Many calculations may need to be performed in advance in order to use OM properly during the construction. This might lead to inefficient use of OM, causing high design costs or even (if mechanisms happen outside the design expectations) the fact that OM can not be used quickly enough during construction.

It can be concluded from all of the above SWOT conditions that the observational method is best suited for projects that are governed by the serviceability limit states. It is applicable, but less suited, for designs governed by the ultimate limit states with ductile behaviour, and it is unsuitable for the ultimate limit states if brittle behaviour takes place.

### 3 CONTRACTUAL ASPECTS

When discussing the possibilities of the Observational Method in geotechnical engineering, it becomes obvious that contract requirements should facilitate or, to say the least, should not obstruct its use. In The Netherlands projects are awarded based on the so called UAV (Uniform Administrative Conditions) or the UAV-gc (Uniform Administrative Conditions for integrated contracts). In contracts where the UAV-applies, the client is responsible for the design and the contractor is responsible for the execution of the works (Traditional contract). Since it is virtually impossible to make a design with the Observational Method without expert knowledge of construction methods, there are limitations to the use of the OM in this kind of contracts. Once the contract is awarded, for instance when a contractor is selected based on general conditions and unit prices, it is possible to change the design using the expertise of the contractor.

If the UAV-gc applies the contractor is responsible for both the design and the executions of the works (Design and Construct contract). All though the possibilities for the use of the OM as a design method are significantly greater than compared to the UAV type of contract, there are still a number of challenges to overcome. One of the main challenges is that in order to get the contract awarded, the contractor first has to be selected. Since the only award criterion that is deemed truly objectively is price, a problem arises in selecting the best offer for the works. The cost price resulting from a design based on OM will vary around the cost price of the most probable way of execution of the works. By nature of the method, it is impossible to submit such a price in a bid. In the Netherlands it was concluded that in order to use the OM as a design method from the start, it is strongly advised and beneficial to execute the project in an alliance between client and contractor.

In this kind of contract client and contractor share a common objective, for example the execution of the project in a safe and cost-effective manner with a minimised risk for the surroundings. All the unknowns in a project that is designed using the OM can be a shared responsibility. Both client and contractor will be fully involved in all decision making and will have an equal part in any additional costs or benefits. Part of the Betuwelijn Cargo Rail Line (Huybrechts, 2000) has been successfully constructed in this way. The challenge of selecting the most qualified contractor remains. One of the suggestions to overcome this challenge is to have a “beauty contest” and a known budget price for the total works. In this way the client is able to select a contractor based on value (best value procurement). Contractors are asked to present themselves not only with reference to the projects they carried out in the past (track record), but also with respect to the proposed method of cooperation with the client. The staff that the contractor wants to deploy for the project will be judged not only on their technical know-how, but also on their “soft skills”, since cooperation is the key-word in an alliance type of contract.

Over the last years several projects in the Netherlands have been awarded in this manner. For the OM to be used within such contracts, all other requirements for the successful use of the OM should also be fulfilled. However, an alliance type of contract comes close to the ideal contract framework that was described as being “utopia” in CIRIA Report 185 (Nicholson et al., 1999).

### 4 PROJECT ASPECTS

Some project examples are given in this section with their relative appropriateness to the use of the OM. It must be mentioned that each project should be considered in their specific settings, both physically and organizationally. In the examples, only the most common aspects have been considered.

For deep excavations the use of the OM is usually limited to the focus on the settlements in the surrounding structures or soil. In some cases, struts can be optimized but it may not

always be possible to decide in time whether a strut layer actually can be omitted. If long cut and cover lengths are present, the subsequent sections may learn from earlier sections. Chapman describes several cases where the use of the OM was successful; whereas Karlsrud and Andresen (2008) state that the OM is not particularly suitable for deep excavations. It can be dangerous if sudden increases in water pressures may happen, accidents such as strut failure or unforeseen loads next to excavation happen. It is rather difficult to apply the OM to assure the vertical equilibrium of deep excavations, although this was actually done in Rokin station for the Amsterdam North South Line, as best way out, see Figure 1. Usually this aspect is considered as a potentially brittle behaviour, but in this specific case the behaviour was expected to be more ductile since the water carrying sand layer causing the possible uplift was very thin.

For deep foundations the method is usually difficult to apply because strength at failure often governs the design. There are however good examples that for the re-use of existing piles (Huybrechts, 2000) the OM shows some good possibilities. For TBM tunnelling the OM is often used to control the settlements, and for example not to design the tunnel lining, where standardization is always more efficient than optimization over shorter lengths. For NATM tunnelling the method is often mentioned and it should be possible if a safe base design is present. (Muir Wood, 1990) and (Kovari and Lunardi 2000) state however that the OM for NATM is actually not working in a correct way.

Embankments are usually well suited for the application of the OM. Examples are mainly related to settlement control and staged construction, but also include the control of stability (Lee, 2012). In a similar way especially suited for the OM seem projects where a surcharge is placed, a tank is filled or similar loading of soil with storage takes place. The flexible use of (pre)loading has proved very efficient in many cases.

Other types of projects suitable for the application of the OM are pipelines when deformation limits are very strict, because the allowable values are difficult to assess in design. Environmental projects (contaminated sites) have been presented by Morgenstern (1994) and drainage works by (Roberts and Preene, 1994).

Very simple structures (‘in the backyard’) are usually not suitable for the OM, because the costs of the additional monitoring are often larger than the benefits for the project.

In all types of projects where buildings are present at short distance, the method may be beneficial because they can be strictly monitored. On the other hand, much more flexibility in the system is present if no such buildings/structures are present. Usually in dealing with stringent deformation limits it is necessary to have a more robust design, which reduces the effectiveness of the use of OM.

### 5 CONCLUSIONS

Conclusions in this paper are given in the form of Go/No Go items for clients and project initiators, as well as designers in a very early stage of the project, to determine whether or not the OM could be a wise approach in their specific project, given the specific circumstances. These Go/No Go items are listed by importance, based on the opinion of the authors. Some issues form the Go/No Go list may be given facts for a project, some may be project choices that may benefit (or contradict) the use of the OM. Some items should be taken merely as reminders of how to organize the project most efficiently. These items are labelled in the third category ‘To overcome’.

Go:

- Multistage projects and/or projects with an incremental construction process.
- Presence of risks with low, but unacceptable a priori probability of exceedance and significant consequences.

- Integrated responsibility for both design and construction.
- High ground heterogeneity and/or uncertainty in failure mechanism.
- Displacements as leading design characteristic.
- Short project duration in relation with beneficial short term behaviour of soil.
- Flexible and risk based culture.
- Critical attitude of stakeholders related to the project.
- Best way out.

#### No go:

- Too little time between measurements and measures.
- Quickly changing loads.
- Failure mechanism/parameter is not measurable.
- Change of failure mechanism during construction.
- Measurements only useful after failure.
- Costs for changes during construction are higher than benefits minus costs for monitoring.

#### To be overcome:

- Communication between site and design office.
- Unwillingness of authorities.
- Time restrictions.
- Calculation methods do not always allow easy use of OM.



Figure 2. Application of OM in Maastricht for A2Maastricht tunnel (photo Reen van Beek)

## 6 ACKNOWLEDGEMENTS

This research is performed as part of “Geoimpuls” in the Netherlands; a joint industry programme, with the ambitious goal to half the occurrence of geotechnical failure in Dutch civil engineering projects by 2015. The authors wish to thank the members of the OM working group for sharing their case histories and experiences.

## 7 REFERENCES

- Allagnat, D. (editor). 2005. *La Méthode observationnelle pour le dimensionnement interactif des ouvrages*. (The observational method for the interactive design of structures). Guide Technique, Presses de l'ENPC
- Chapman, T. and Green, G. 2004. Observational method looks set to cut city building costs. *Proceedings of ICE Civil Engineering* 157, 125–133 Paper 13416
- Cools, P.M.C.B.M. 2011. The Geo-Impuls Programme reducing geotechnical failure in the Netherlands. *ISGSR 2011* in Vogt, Schuppener, Straub & Bräu eds Bundesanstalt für Wasserbau
- Glass, P.R. and Powderham, A.J. 1994. Application of the observational method at Limehouse Link. *Geotechnique* 44, No. 4, 665-679.
- Grote, B.J.H. and van Dalen, J.H. 2012. Onzeker kalksteen in grip met Observational Method, *Land + Water*, 12
- Hitchcock, A. 2003. Elimination of temporary propping using the observational method on the Heathrow airside road tunnel project. *Ground Engineering Magazine*, Vol. 36, No. 5, 30-33
- Huybrechts, N. 2000. Design Tools in Geotechnics – Observational Method and Finite Element Method. *GeoTechNet Project GTC2-2000-33033, WP3: Innovation*
- Kamp, R.A.J. van de. 2003. *Observatiemethode voor diepe bouwputten* (In Dutch). MSc. Thesis Delft University of Technology
- Karlsruh, K. and Andresen, L. 2008. Design and performance of deep excavations in soft clays. *6<sup>th</sup> international conference on case histories in geotechnical engineering*, Arlington, VA. Paper No 12.
- Korevaar, M. 2012. *De Observational Method, Onderzoek naar een veilige toepassing van deze methode voor bouwkuipen* (In Dutch). MSc. Thesis Delft University of Technology
- Kovári, K. and Lunardi, P. 2000. On the observational method in tunnelling. *Proceedings of the GeoEng 2000: an International Conference on Geotechnical & Geological Engineering*, 19-24 november, 2000. Vol. 1, 692-707, Melbourne, Australia.
- Lee, S. 2012. Application of the observational method for railway earthwork stabilisation in the UK. *Presentation DGF Geoteknisk monitoring og observationsmetoden, Copenhagen*.
- Morgenstern, N. R. 1994. The observational method in environmental geotechnics. In: *Proc. of 1st International Conference on Environmental Geotechnics*. Edmonton, 965-976.
- Muir Wood, A. 1990. The observational method revisited. In: *Proceedings of the 10th Southeast Asian Geotechnical Conference*, Taipei, 2, 37-42.
- Nicholson, D., Tse C.-M., Penny, C. 1999. *The Observational Method in ground engineering: principles and applications*. CIRIA, London, Report 185.
- Nossan, A.S. 2006. Observations on the Observational Method. *XIII. Danube-European Conference on Geotechnical Engineering*. Logar, J., Gaberc, A., Majes, B. (ed). - Ljubljana : Slovenian Geotechnical Society. 171-178
- Patel, D., Nicholson, D., Huybrechts, N. and Maertens, J. 2007. The Observational Method in Geotechnics. *Proceedings of the 14<sup>th</sup> ECSMGE*: Madrid, Spain. Vol. 2, 365-370.
- Peck, R. B. 1969. Advantages and limitations of the observational method in applied soil mechanics. *Geotechnique*, 19 2, 171-187.
- Powderham, A. J. 1994. An overview of the observational method: development in cut and cover bored tunnelling projects. *Geotechnique* 44 (4), 619-636.
- Powderham, A.J. and Nicholson, D.P. 1996. *The Observational method in geotechnical engineering*. ICE, Thomas Telford, London.
- Roberts, T.O.L. and Preene, M. 1994. The design of groundwater systems using the observational method. *Geotechnique* 44 (4), 727-734.
- Schmitt, P. and Schlosser, F. 2007. La méthode observationnelle : du suivi géotechnique au dimensionnement interactif (in French)). *Travaux* (Paris) Y. 2007, No. 844, 99-106



# Development of Method for Evaluating and Visualizing 3-dimensional Deformation of Earth Retaining Wall for Excavation

Développement des méthodes d'évaluation et de visualisation de la déformation tridimensionnelle des murs de soutènement dans les excavations

Matsumaru T., Kojima K.  
Railway Technical Research Institute

**ABSTRACT:** Monitoring of deformation of earth retaining wall for excavation is important in order to keep surrounding environment and structures safe during construction. However, there are some problems in monitoring of earth retaining walls. For example, it is difficult for the partial measurement by plum bobs to evaluate the overall behavior of the retaining walls, and the multipoint measurement using multi-element inclinometers tends to be expensive. In this paper, we developed a system to evaluate and visualize retaining wall as three-dimensional curved surface. The validity was confirmed by the simulation of the loading test on the model wall. In order to confirm the effectiveness of the proposed system to actual monitoring, we tried to apply the system to the on-site measurement. Furthermore, we proposed a method to conduct monitoring of retaining walls using this system and simple inclinometers.

**RÉSUMÉ :** Le contrôle de la déformation des murs de soutènement dans les excavations est important pour assurer la sécurité de l'environnement et des structures lors de la construction. Toutefois, le contrôle des murs de soutènement pose un certain nombre de problèmes. Il est par exemple difficile de procéder à des mesures partielles au fil à plomb pour évaluer le comportement général des murs de soutènement et les mesures multipoint à l'aide d'inclinomètres multiéléments sont plutôt onéreuses. Dans cet article, nous présentons un système d'évaluation et de visualisation des murs de soutènement sous forme d'une surface courbe tridimensionnelle. La validité du système a été confirmée par simulation d'un essai de charge sur la paroi du mur testé. Afin de vérifier l'efficacité du système proposé dans des conditions de contrôle réelles, nous avons tenté de l'appliquer lors de mesures sur le terrain. Nous proposons également une méthode de conduite du contrôle des murs de soutènement à l'aide de ce système et d'inclinomètres simples.

**KEYWORDS:** earth retaining wall, 3-dimensional deformation, cubic B-spline function, measurement, incline

## 1 INTRODUCTION

Monitoring of deformation of earth retaining wall for excavation is important in order to keep surrounding environment and structures safe during construction. However, there are some problems in monitoring of earth retaining walls. For example, it is difficult for the partial measurement by plum bobs to evaluate the overall behavior of the retaining walls, and the multipoint measurement using multi-element inclinometers tends to be expensive.

Considering these problems as backgrounds, we developed a system to evaluate and visualize retaining wall as three-dimensional curved surface. In this system, the cubic B-spline function is adopted as analytical technique, which is employed for describing shape of land as three-dimensional curved surface based on sets of data of the elevation altitude (Nonogaki et. al., 2008). We proposed a method to evaluate inclinometer data as surface without transforming incline into displacement. The validity and the adequacy was confirmed by loading test and field measurement. Furthermore, we searched the way two conduct measurement easily by using the proposed method.

## 2 EVALUATING AND VISUALIZING DEFORMATION OF RETAINING WALL IN 3-DIMENSIONAL SPACE

### 2.1 Cubic B-spline function

Figure 1 shows the 3-dimensional coordinate space for describing the deformation of the earth retaining wall. In this figure,  $x$ ,  $y$ , and  $z$  axis means the direction of the retaining wall, the depth, and the direction toward which the wall deforms. The earth retaining wall is expressed as smooth and continuous surface by the following equation.

$$f(x, y) = z \quad (1)$$

In the cubic B-spline function (Nonogaki et. al., 2008), the region for drawing the surface is divided in  $M_x$  and  $M_y$  equally-spaced areas in  $x$  and  $y$  axis. By setting the  $M_x+7$  and  $M_y+7$  equally-spaced nodes, the surface is expressed by the following equation:

$$f(x, y) = \sum_{i=1}^{M_x+3} \sum_{j=1}^{M_y+3} c_{ij} N_i(x) N_j(y) \quad (2)$$

where  $N_i(x)$  and  $N_j(y)$  is the cubic B-spline function, and  $c_{ij}$  is unknown coefficient.

In order to determine the surface, objective function  $Q$  was defined as following equation:

$$Q(f; \alpha) = J(f) + \alpha R(f) \quad (3)$$

where  $J(f)$  is the functional for evaluating the smoothness of the surface,  $R(f)$  is the function which expresses the sufficiency degree of data, and  $\alpha$  is the parameter balancing for these two functions. The surface is determined by substituting  $c_{ij}$  into equation (2) obtained from  $\partial Q(f; \alpha) / \partial c_{ij} = 0$ .  $J(f)$  is written by Shiono et al (2001).

The function which expresses the sufficiency,  $R(f)$ , is mentioned as below. The coordinate  $(x_p, y_p, z_p)$ , where a measurement equipment is placed, and the measured displacement  $u_p$  has following relationship.

$$f(x_p, y_p) = z_p + u_p \quad (4)$$

Therefore, using the error average  $\varepsilon_p$  of squares between the curved surface and the obtained displacement data,  $R(f)$  is evaluated as following equation.

$$R(f) = \sum \varepsilon_p^2 / n_p \quad (5)$$



$$\epsilon_p = \sum_{i=1}^{M_x+3} \sum_{j=1}^{M_y+3} c_{ij} N_i(x_p) N_j(y_p) - (z_p + u_p) \quad (6)$$

where  $n_h$  is the number which satisfies equation (4).

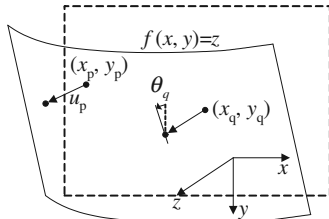


Figure 1. 3-dimensional coordinate space for drawing deformation of retaining wall

### 2.2 Use of measured inclination

In the monitoring of the retaining wall, we often measure not the displacement but the inclination because of its easiness. For this reason, it is important for developing the method to take incline data for evaluating the deformation. As follows, we show the proposed method for using the incline data.

The function  $R(f)$  is divided into two functions,  $R_h(f)$  and  $R_d(f)$ .  $R_h(f)$  expresses the sufficiency degree of displacements, and  $R_d(f)$  expresses that of inclines. Using these functions,  $R(f)$  is expressed as follow equation:

$$R(f) = R_h(f) + \gamma R_d(f) \quad (7)$$

where  $\gamma$  describes the weight of the sufficiency of inclines.  $R_h(f)$  is expressed by equation (5).

On the other hand,  $R_d(f)$  is defined as follows. At the position where an inclinometer located,  $(x_q, y_q, z_q)$ , the derivative of the function  $f$  is described by the following equation.

$$f_y(x_q, y_q) = -\tan \theta_q \quad (8)$$

Therefore, the functional  $R_d(f)$  is expressed as following equation:

$$R_d(f) = \sum_{i=1}^{n_d} \left\{ \sum_{i=1}^{M_x+3} \sum_{j=1}^{M_y+3} c_{ij} N_i(x) N_j(y) + \tan \theta_q \right\}^2 / n_d \quad (9)$$

where  $n_d$  is the number of the obtained incline data.

## 3 SIMULATION OF LOADING TEST OF MODEL WALL

### 3.1 Loading test of model wall

Figure 2 shows the photograph of loading test. The wall was 2m in height, 3m in width and 10mm in thickness. The loading was conducted for several cases, changing boundary conditions and displacement. During the loading, the displacement and the incline of the wall were measured using a lot of measurement equipments. In the following simulation, we used only the data obtained from the survey by total station (T.S.) and inclinometers.



Figure 2. Loading test of model wall.

### 3.2 Conditions of simulation

Figure 3 shows the arrangement of measurement equipments used in the simulations. (a) is the arrangement using all 128 points for the survey by T.S., (b) is using only 35 points, and (c) is using 25 inclinometers. Figure 9 shows the pattern of loading.

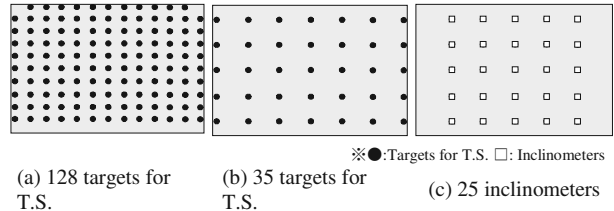


Figure 3. Arrangement of measuring points used in simulations

Figure 4 shows the arrangement of measurement equipments used in this simulation. In CASE1, 80 mm displacement was given at the top center of the wall. In CASE2, 30 mm displacement was given at the right middle part.

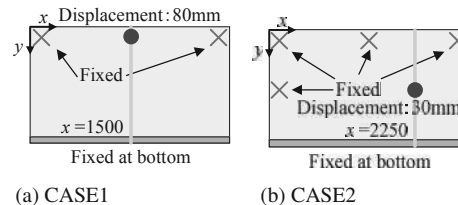


Figure 4. Loading cases used in simulation

### 3.3 Results of simulation

Figure 5 shows the simulated and visualized surface using 128 points for T.S. (arrangement (a) as shown in figure 3) in both loading cases. Figure 6 shows the distributions of displacement at the cross section shown in figure 4, in both loading cases. In figure 5, displacement obtained from the contact-type displacement gauges was also plotted. From these figures, it is seemed to be that the simulation could describe the deformed surface in 3-dimension. Furthermore, the simulated displacement for each case almost coincides with measured results using the cross-section displacement gauges, regardless of arrangements or kind of used measurement equipments.

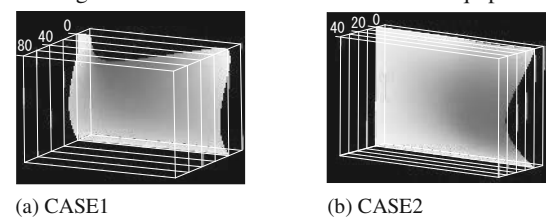


Figure 5. Evaluated and visualized deformations of wall.

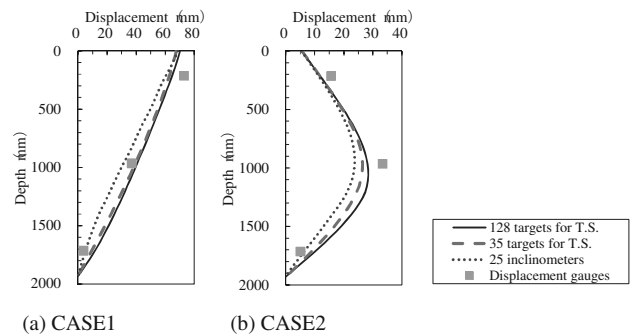


Figure 6. Distributions of displacement at cross section.

From these results, it was revealed that the developed method was suitable for the evaluation and visualization of the deformation of earth retaining wall.

#### 4 ADOPTATION OF PUROPOSED METHOD FOR FIELD MEASUREMENT

##### 4.1 Field condition of construction and measurement

Figure 7 shows the field conditions of construction and arrangement of measurement equipment. The excavating work was conducted 39 m times 16 m in area, and 9 m in depth. The surface layer of the ground was a very soft alluvial clay layer about 13m in thickness, with a small N-value of SPT, followed by a gravel layer. The type of the retaining walls was bracing method. The materials of the walls were steel sheet piles. The excavation consisted of three steps as shown in figure 7.

Monitoring the wall was conducted at the south section in order to keep safe the existing tunnel for cars. Monitoring was implemented by multi-element inclinometers. As shown in figure 7, there were four survey lines and six inclinometers were set on each line. For checking monitoring data, the survey of the displacement of the wall using the total station was also conducted at regular intervals around Line No.1 and Line No.2.

Evaluating and visualizing the deformation of the wall in 3-dimensional space was conducted in the region about 33.4m in width. Two arrangements of the measurement equipments were considered. CASE1 was the arrangement using only 24 multi-element inclinometers. CASE2 was using not only inclinometers but also the displacement obtained from the survey using T.S.

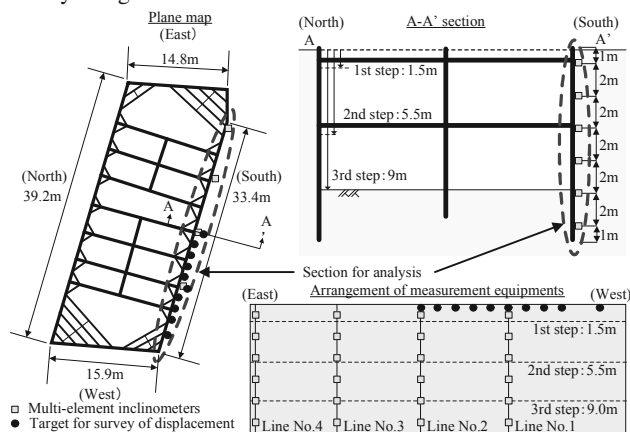


Figure 7. Conditions of field construction and measurement.

##### 4.2 3-dimensional evaluation and visualization of deformation of retaining wall

Figure 8 shows the deformed wall which was evaluated and visualized after conducted excavation at each step in CASE1. From the beginning to the end of the work, the deformation of the wall was represented satisfactorily as 3-dimensional surface. The deformation was increased as the progress of the excavating work. On the other hand, as the progress, the depth where the maximum displacement occurred at deeper depth and the deformation close to the ground level was decreased due to the influence of the reaction force by installing braces.

Figure 9 shows the distributions of deformation at the cross section No.1 and No.4 as shown in figure 7. In this figure, we also showed the displacement converted from the angle obtained from inclinometers and the distances between two inclinometers, and the displacements obtained from the survey by T.S. The distributions of displacement evaluated by proposed method coincides with the mode of directly measured deformation. The displacement obtained from the proposed method was more smoothed. Furthermore, the distributions of displacement were changed largely depending on use of results obtained from survey by T.S. In this simulation, this tendency was dramatic at section No.1, where lots of targets for survey of T.S. were located. The displacement evaluated using the targets

changed toward the displacement obtained from the survey at the top of the wall.

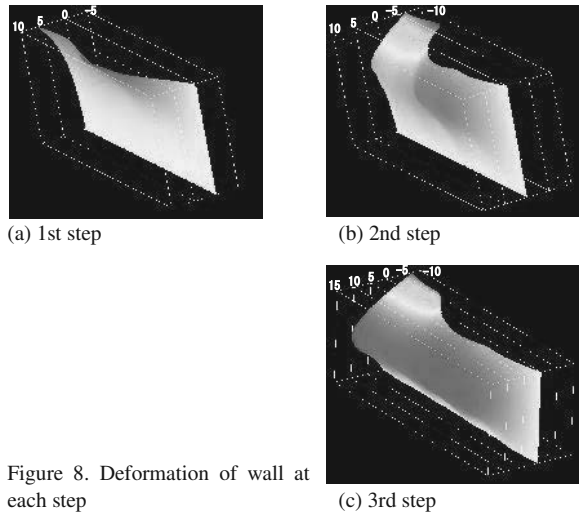


Figure 8. Deformation of wall at each step

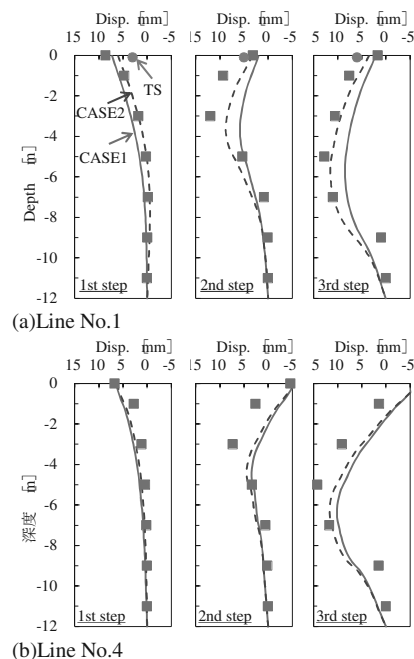


Figure 9. Distributions of displacement at cross section.

From these results, the proposed method was proved to be beneficial for field measurement.

#### 5 ADOPTATION OF PROPOSED METHOD FOR FIELD MEASUREMENT

From the study mentioned in previous sections, the validity of the proposed method was confirmed. The advantage of this method is that the data obtained from inclinometers is useful without converting to displacement. So, we can conduct the measurement using convenient inclinometers without making survey line. Therefore, by combining the proposed method and simple inclinometers, we would be able to realize precise and not expensive measurement. However, there are some problems in this method.

##### 5.1 Study of using data only upper ground

For the measurement using convenient inclinometers, it seems to be difficult to set inclinometers under the ground. The inclinometers will be set as the progress of excavating work. So, in the case only using the inclinometers located above the

ground, we studied the difference from the deformation evaluated by using all inclinometers, based on the field data mentioned in the previous section.

The number of used inclinometers in this simulation is 4 at 1st step, 12 at 2nd step and 20 at 3rd step. In this simulation, the data obtained from the survey using T.S. was also considered from 1st step.

Figure 10 shows the distributions of the displacement of the wall. The displacement at Line No.1 was quite similar with the one using all inclinometers, CASE1 in previous chapter. On the other hand, the displacement at Line No.4 was quite different because the direct measurement of displacement by T.S. was not conducted around Line No.4. So, we also simulated the monitoring case using multi-element inclinometers were added at Line No.3. The displacement almost coincided with the results using all inclinometers.

In monitoring of field excavating work, direct measurement of displacement or installation of one line for multi-inclinometers would enable the measurement using convenient inclinometers.

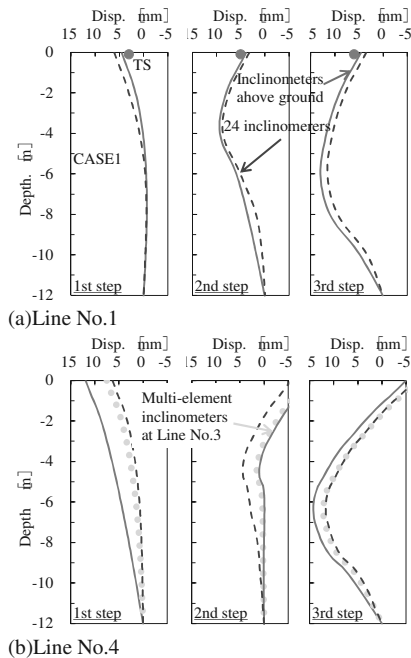


Figure 10. Distributions of displacement at cross section.

## 5.2 Study of optimal arrangement of convenient inclinometers

Finding optimal arrangement for conventional inclinometers would be executed by evaluating of degree of accuracy and choosing the most suitable surface for all considerable arrangements. Therefore, we conducted the simulation the accuracy of evaluated surface by iterative calculation.

Monte Carlo approach was adopted for iterative calculation and the number of iteration was 1000. The step of excavating work selected for calculation was 3rd step. For the simulation, the surface was evaluated by 8 inclinometers selected from 20 ones above the ground at random.

Figure 11 showed the obtained histogram. The horizontal axis is the evaluated average difference (Matsumaru et. al., 2011) from the surface simulated by using all inclinometers. It was revealed that the accuracy of evaluated deformation of the wall changed largely depending on the arrangement of inclinometers. However, the minimum of the difference was smaller than 1 mm. This mentioned that the monitoring using small number of measurement equipments had the possibility to maintain the accuracy of measurement depending on the arrangement. By conducting iterative calculation about considerable arrangement, the optimal arrangement would be realize.

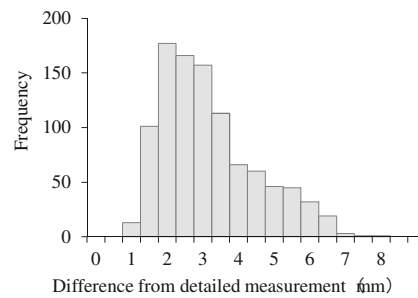


Figure 11. Histogram of average difference for considerable arrangements.

## 6 CONCLUSIONS

The purpose of this paper was system to evaluate and visualize deformation of retaining wall as three-dimensional curved surface. As the results, we achieved the following conclusions:

1. We developed a system adopting the cubic B-spline function as analytical technique and also proposed a method to evaluate inclinometer data as surface without transform inclines into displacements. The validity of the method was confirmed by the simulation of the loading tests of the model wall, because correct surfaces were droved using a small amount of data of displacement or using only inclines.
2. The adequacy of the proposed system was examined by applying this method to measurement of the field site of excavating work. From the beginning to the end of the work, the deformation of the wall was represented satisfactorily as three-dimensional surface. Furthermore, it was revealed that the evaluated deformation of the wall coincided with the surveyed displacement by the total station.
3. In order to realize easy monitoring of retaining walls, we checked the arrangement of inclinometers. By using the inclinometers installed above the excavation bottom, the deformation of the wall could be described almost in the same way as by all inclinometers. Furthermore, we checked the validity of the arrangement with smaller number of inclinometers by Monte Carlo approach. Though the evaluated deformation of the wall using smaller number of inclinometers was varied widely, the accuracy of the optimal arrangement was close to the one using all inclinometers.

## 7 ACKNOWLEDGEMENTS

The field measurement in this study was supported by Mr. Kiyoshi Kuwabara (East Japan Railway Co. Ltd) and Toshiyasu Hisashima (East Japan Railway Co. Ltd).

## 8 REFERENCES

- Matsumaru T., Tanaka Y., Suga M., Oji S. and Onishi T. 2011. Study of measurement method for constructing underground structure using three-dimensional evaluation system of measurement data, *Proceedings of the 43th Japan National Conference of Geotechnical Engineering*. (CD-ROM, in Japanese)
- Nonogaki, S., Masumoto S. and Shiono, K. 2008. Optimal determination of geology boundary surface using cubic B-spline, *Geoinformations*, Vol.19, No.12, pp.61-77.
- Shiono K., Noumi Y., Masumoto S., and Sakamoto M. 2001, Horizon2000 : revised fortran program for optimal determination of geologic surfaces based on field observation including equality-inequality constraints and slope information, *Geoinformations*, Vol.12, No.4, pp.229-249.

# Geotechnical protection of engineering infrastructure objects in large cities under intense anthropogenic impact and long term operation

Sécurité géotechnique d'ouvrages du génie civil sous influence anthropogène intense et exploitation à long terme

Perminov N.A.  
St. Petersburg University of Means of Communication, Russia

Zentsov V.N.  
"Lengiproinzhprouekt", Russia

Perminov A.N.  
NIPIC Trasspectstroy, Russia

**ABSTRACT:** This article describes more than 30-year experience of scientific and technical support, design, construction and reconstruction of water supply and sewage facilities in St. Petersburg, Sochi, etc. It describes the specific defects of long-term operation of large-size pumping stations and deep-laid tunnels that cause risks and dangers of their use. It gives the results of geotechnical and design calculations, modeling of underground and tunnel constructions taking into account risk factors determined by defects that occur during construction and operation, and also taking into account external influences, including dynamic ones. The report gives a comparative analysis of calculated and industrial experiments, provides activity and implementation experience of geotechnical support of long-term operation of engineering infrastructure.

**RÉSUMÉ :** L'article décrit l'expérience de plus 30 ans d'assistance scientifique et technique, en conception, construction et restauration d'infrastructures de distribution d'eau et d'évacuation des eaux usées à Saint-Petersbourg, Sochi, etc. L'article détaille les défauts typiques des stations de pompage de grandes dimensions et des tunnels profonds, exploités sur le long terme et amenés à des niveaux de risque et de danger au cours de leur exploitation. On donne les résultats des calculs géotechniques et de conception, en simulant le fonctionnement des tunnels profonds, compte tenu des facteurs de risque induits par les défauts apparus aux étapes de la construction et de l'exploitation, ainsi que des influences extérieures, y compris les influences dynamiques. Le rapport présente l'analyse comparative des expériences théoriques et pratiques, et fournit les mesures à mettre en œuvre pour la sécurité géotechnique des ouvrages de génie civil exploités à long terme.

**KEYWORDS:** monitoring, geotechnical analysis, objects of water disposal, deeply lying constructions, tunnels, geoecological safety.

## 1. GENERAL INFORMATION ABOUT THE OBJECTS OF DEEP ENGINEERING INFRASTRUCTURE IN LARGE CITIES

With long-term operation and intensive development of engineering infrastructure of megalopolises increase the requirements to the ecology and efficient usage of land resources. During engineering development of underground spaces of such a megalopolis, design of integrated measures for protection of town-planning environment against negative anthropogenic impact is of special actuality. Thereupon there must be introduced special safety requirements for the sewage and water treatment facilities.

Sewage (transportation) of waste waters is done through the city sewerage system and tunnel collectors. In the general drainage system these facilities account for up to 60% in large cities and up to 70% in difficult hydrogeological conditions by construction volumes and costs.

Sewerage system objects data for the most typical Russian cities with the population over 1 million people is given in table 1.

Yekaterinburg	1220	230
Novosibirsk	1150	145
Samara	1200	215
Ufa	900	180

By now around 88% of all sewage collectors are made of ferroconcrete, around 7% - of metal (steel, cast iron), around 3% - of bricks, plastic, ceramics. Tunnel sewage collectors diameter is from 1.2 to 5.6 m, they are buried from 3 to 60 m underground. For example, in St. Petersburg all sewage network is divided into three basins that serve three main pumping plants up to 70 m deep and up to 66 m in diameter, with productivity of 1.5 mln m<sup>3</sup> of sewage per day. For such conditions the main constructive solution for the tunnels are the ferroconcrete tubings with inner ferroconcrete jackets.

Transportation volumes of waste waters in some sections of the tunnels reach 20 m<sup>3</sup> per sec, and in case of decrease of their operational reliability or failure will inevitably lead to a technospheric catastrophe.

"Lengiproinzhprouekt" institute together with the St. Petersburg State Transportation University has been providing scientific and engineering maintenance, design, construction and rehabilitation of St. Petersburg sewerage system objects for more than 30 years: more than 70 pumping plants, including those with depth of 45 m, 59 m and 71 m, and with diameters of 47 m, 59 m and 66 m; more than 15 km of tunnel sewage collectors with diameters of 1.85, 2.5 and 3.4 m and with depth of 16 m, 24 and 37 m.

Table 2 shows the most typical defects of long-term operated pumping plants and deep tunnels.

Table 1. Length of sewerage networks and tunnel collectors in large cities of Russian Federation.

City	Sewerage networks length, km	Tunnel collectors length, km
Moscow	8354	550
St. Petersburg	8245	290
Volgograd	1054	52

Analysis of the materials of the investigations shows that at the moment 60% of gravity sewage tunnels and 80% of pressure sewage tunnels require repairs and sanitation. Instrumental probing (with geological radar) shows that 70-75% of inner surface of pumping plants wells and sewage tunnels have continuity violation and cracks which require strengthening of construct and renewal of waterproof shell.

Table 2. The list of defects typical for the long-term operated (more than 30-45 years) deep pumping plants and tunnel collectors.

Location of the defect	Description and photo of the defect		
Sunk wells walls	Up to -25±30m marks. On some sections of sunk well walls there's leakage through knots. In the knots area there's leakage of concrete corrosion. Defects are of repetitive nature.	-30 to -40±45m marks. On the surface of the wall there're marks of intense leakage through the cracks. Defects are of mass nature. In the knots area there's leakage of concrete corrosion.	More than -45m marks. On the surface of the wall there're marks of intense leakage through the cracks. In the knots area there's leakage of concrete corrosion. Defects are of mass nature.
Sewage tunnels lining	Tubing lining shows leakage. Underground waters go to the collector through cracks and knots in solid ferroconcrete inside lining. There's leakage of concrete corrosion and salts.	There's a water-filled space in the form of a thin gap between the tubing lining and the jacket of collector. Defects are hidden, can be found geological radar probing of collector facilities.	Solid ferroconcrete inner lining (jacket) is destroyed, there's intense leakage in welded seams.

## 2. ANALYSIS OF FACTORS INFLUENCING THE SAFETY OF DEEP ENGINEERING STRUCTURES AND MEASURES FOR THEIR ELIMINATION

### 2.1 Analysis of monitoring data for the construction of sunk large pumping plants and of the inspection results after long term operation

The slotted soil column for construction of sunk wells for main pumping plants in the conditions of St. Petersburg is characterized as follows: top part is presented by quaternary beddings to the depth of 14.0-25.0 meters (middle-density water-saturated dust sand  $E=11$  MPa,  $C=0$  MPa,  $\phi=30^\circ$ ; laminar silt sandy loam  $E=4$  MPa,  $C=0.01$  MPa,  $\phi=15^\circ$ ; laminar silt loam, very soft  $E=9$  MPa,  $C=0.025$  MPa,  $\phi=16$ ; semisolid silt loam with gravel, pebbles  $E=14$  MPa,  $C=0.028$  MPa,  $\phi=28^\circ$ ), lower part is represented by top of positioned Proterozoic bluestone ( $E=19$  MPa,  $C=0.04\pm 0.06$  MPa,  $\phi=18-21^\circ$ ).

Figure 1 shows the monitoring results for the construction of a large sunk well using the method of PSTU (Perminov N.A., Lombas S.V., 2004).

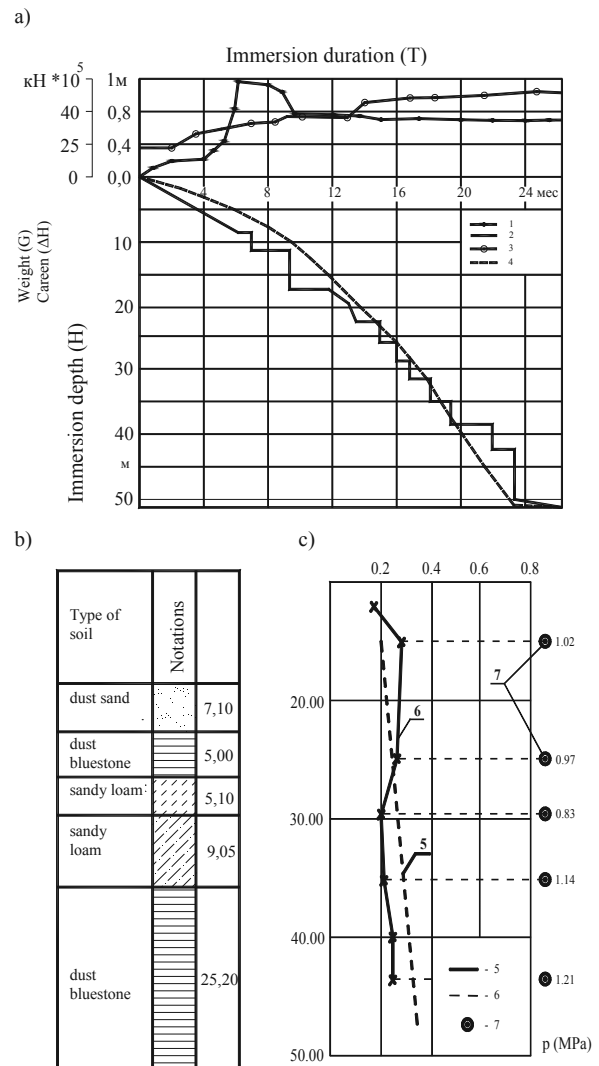


Figure 1. The monitoring results for the immersion of a large sunk well:

a) motiongram of immersion; b) engineering and geological conditions; c) monitoring data  
1 – diagram of vertical misalignment (careen); 2 – diagram of immersion; 3 – weigh of the well shell; 4 –ditch bottom; 5,6,7 – correspondingly, calculated, averaged and peak values of lateral soil pressure.

The stresses in the reinforcement and concrete were measured using primary device string type PSAS and PLDS. To determine the soil pressure membrane load cells with a range of 0 to 12MPa and measurement error of 5-7% were used. The measurement was done both in the discrete and continuous mode using the local electronic switches (LEC), and data storages (END).

Analysis of monitoring data of large sunk wells with diameters from 50 to 66m and a depth of immersion of 55 to 71m shows (see Figure 1) that in the process of immersion in the soils with different strengths and asymmetric structures deviation from the vertical axis (careen) is observed, with a shift of the center up to 1.5-1.8 m. In this case, according to an automated continuous monitoring, as a result of abrupt landings (breakdowns) stresses in the reinforcement, concrete and soil pressure may exceed the calculated and the average values (according to the discrete measurements) 12-15 times.

To estimate the stress-strain state of the well shell with a sharp landing (breakdown) numerical modeling was conducted. In the calculations the finite element method (FEM) and the software package Robot Professional 2010 were used. The calculation is carried out for spatial shell with

diameter of 66m and a height of 71m (with the number of three-dimensional finite elements equal 50828), falling under its own weight at an angle of  $15^\circ$  from a height of 140 cm on the compliant soil (average coefficient of elasticity for multilayer soil is taken  $K = 16500\text{kN/m}^3$ ). In the model because of the inclination angle the friction forces on the lateral side of the well were applied in the upper part of the shell on one side and in the bottom part on the opposite side.

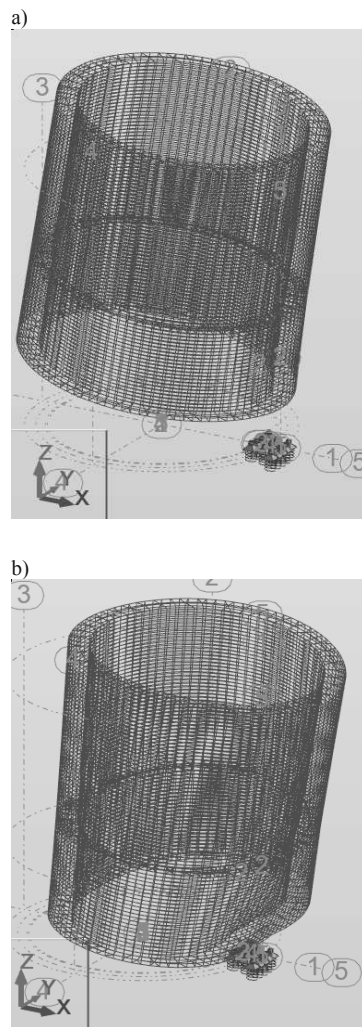


Figure 2. The results of numerical modeling of a sunk well with diameter of 66 m and a height of 71 m for the conditions of a abrupt landing (breakdown): a) the original position, and b) position after a fall from a height of 1.4 m at an angle of  $15^\circ$ .

The results of numerical modeling have shown (see Fig. 2) that in case of a dynamic blow (if the well is dropped from a height of 140 cm) equivalent von Mises stresses in the construct equal  $S_{din} = 256\text{MPa}$  at the top of the shell and  $S_{din} = 1538\text{MPa}$  in the area of the bottom rest, which respectively exceeds the limiting strength of concrete class B30 [Spred] to 14 or more times, and the changes in the geometry of the shell are observed.

Thus, already in the process of the well immersion the construction of the well is damaged and the concrete is disintegrated due to breakdowns. Later during operation micro cracks lead to leakage, seepage and corrosion of concrete. To further ensure the safety of operation of facilities of this type it is necessary to strengthen and waterproof the construct by high-pressure injection of polymer resins.

## 2.2 Geotechnical analysis of technical condition of the sewage tunnels under intensive anthropogenic impact and long term operation

Geotechnical analysis of the sewage tunnel was carried out for the most typical section located in a zone of intense dynamic impact of transport and the impact of new construction.

Figure 3 shows the diagram of the tunnel compressions for more than 35 years of service life.

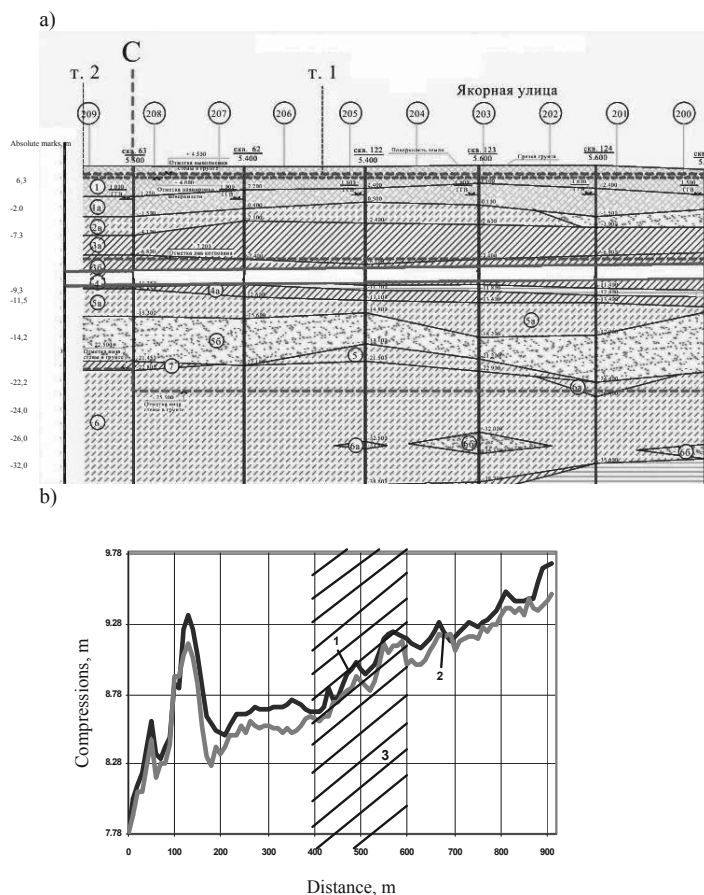


Figure 3. The diagram of comparison of the compressions on the arch axis of the collector: a) engineering and geological section, typical for laying-out sewage tunnels in St. Petersburg, b) the diagram of compressions: 1 - survey results of 2010, 2 - executive survey data of 1975, 3-area of the collector, protected from the influence of the construction by a screen of low modular material.

Uneven tunnel compressions, modified on the arch axis range from 5 to 276 mm. Comparative analysis of engineering and geological section on the tunnel route and its placement on the plan relative to the traffic junction showed that the greatest compressions up to 276 mm are located in the area of the tunnel under intense dynamic effects of the traffic, passing the layer of thixotropic quaternary deposits.

Evaluation of the dynamic impact of the transport was carried out by the study of the oscillatory process with a set of manifold gauges CM TSP installed in the arch and blocks of the recording equipment (Perminov N.A., 2011)

The frequency of the oscillations of the collector during various traffic loads from 15 to 35 Hz, and the vibration amplitude to 35-70 microns was recorded. According to the research (Goldshtein M.N., Lapidus L.S., Reznikov O.M., Storozhenko V.I., Sinaevsky N.I., 1973) for this type of ground deposits and the appropriate level of the dynamic effects the decrease of strength characteristics  $C$  and  $\phi$  is up to 35% and 17%, respectively. To ensure the operational

reliability of tunnels vibration protection measures, such as the use of spiral-wound technology for internal lining the tunnel are suggested.

For this section of the collector the numerical modeling was carried out to determine the maximum allowable axis displacement of tunnel lining. The criterion for the safety of the construct is the maximum allowable tensile stress of the concrete in the typical points of lining. Maximum allowable deformation and displacement values are presented in Figure 4.

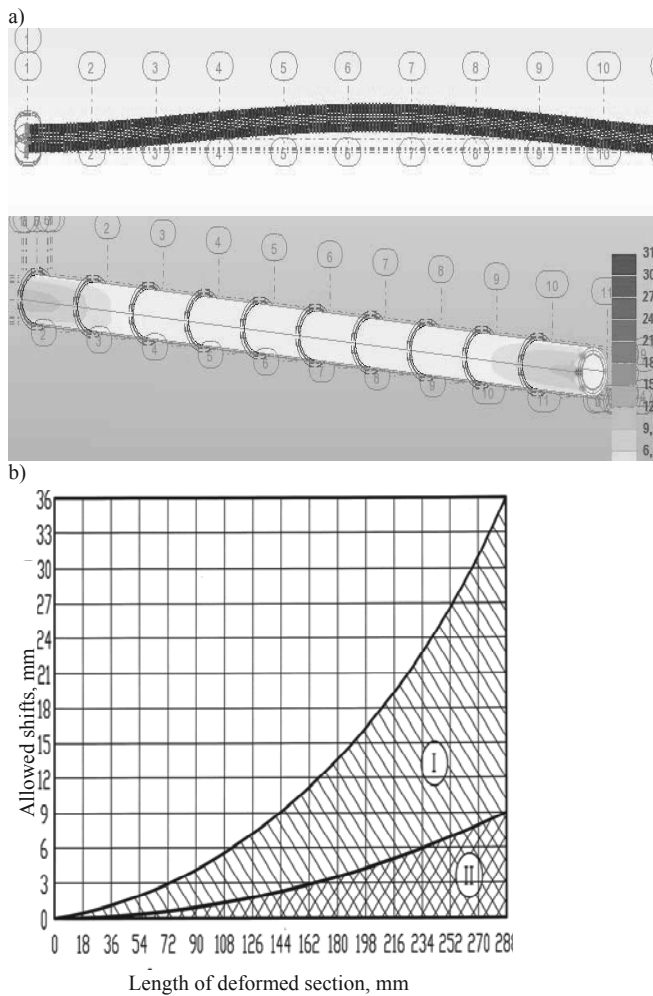


Figure 4. Calculated model of the tunnel (a), the diagram of maximum allowable tunnel lining deformation (b): 1 - Safe displacement values after the lining has been strengthened, 2 - reference value of allowed displacement

### 3. SUMMARY (CONCLUSION)

Data received from long-term field observations for continuous operated embedded constructions being a part of megapolis water discharge system as well as the results of calculation and modeling allowed to conduct geotechnical analysis of the residual bearing capacity and to develop measures to ensure the safe operation of facilities of such type under the conditions of intensive external influences.

As experience shows, the presence of geotechnical tracking of environmentally hazardous facilities of such type for the entire period of their life cycle, including design, construction and long-term operation (even under intensive man-induced impact) provides the safety of the stable functioning of the megapolis utility infrastructure.

### 4. REFERENCES

- Perminov N.A., Lombas S.V. 2004. Complete geo-technical and monitoring services for the construction of the underground structures in a megapolis. Geotechnical problems on construction of large – scale and unique projects. Proceedings Of International Geotechnical Conference dedicated to the Year of Russia in Kazakhstan 23-25 September 2004, Almaty, Kazakhstan. ISBN 9965-25-409-5 Edited by academic of NAN RK, Dr.Sc., Professor Sh.M. Aitalyev and Dr.Sc., Professor A. Zhusupbekov.
- Perminov N.A, 2011. Geotechnics of Hard Soils-Weak Rocks. Experience of tunnel collectors monitoring at engineering development of underground face of megapolis. Part 3. 1705-1712.
- Goldshtein M.N., Lapidus L.S., Reznikov O.M., Storozhenko V.I., Sinaevsky N.I. Particularities of dynamic properties of soils with pulsating load on the surface. The proceedings of an international congress on mechanics of soils and foundation engineering. – Moscow, Stroyizdat, 1973, p.329-331.

# Data assimilation strategies for parameter identification of elasto-plastic geomaterials and its application to geotechnical practice

Stratégie d'assimilation de données pour l'identification des paramètres de géomatériaux élastoplastiques et son applications à la pratique géotechnique

Shuku T., Nishimura S.

*Graduate School of Environmental and Life Science, Okayama University, Okayama 700-8530, Japan*

Murakami A., Fujisawa K.

*Graduate School of Agriculture, Kyoto University, Kyoto 606-8502, Japan*

**ABSTRACT:** The objective of this study is to demonstrate the numerical and the practical applicability of the particle filter (PF) to some geotechnical problems, i.e., the parameter identification of elasto-plastic geomaterials and the prediction of the deformation behavior of soil deposits and geotechnical structures, by applying the methodology to hypothetical experiments and an actual construction project. The results of the hypothetical experiments reveal that the parameters identified by the PF, based on the sequential importance sampling (SIS) algorithm, have converged into their true values, and that the approach presented herein can provide a highly accurate parameter identification strategy for elasto-plastic geomaterials. Moreover, the simulation results using the identified parameters are close to the actual observation data, and the ensemble-based approach produces more information about the parameters of interest than simple estimated values obtained from optimization methods. In other words, the identification comes in the form of a probability density function.

**RÉSUMÉ :** L'objet de cette étude est de démontrer l'applicabilité numérique et pratique du filtrage des particules (FP) pour certains problèmes géotechniques, à savoir, l'identification des paramètres de géomatériaux élastoplastiques et la prédiction du comportement en déformation de dépôts de sol et de structures géotechniques, en appliquant la méthodologie à des expériences hypothétiques et à des projets de construction existants. Les résultats des expériences à partir d'hypothèses montrent que les paramètres identifiés par le FP, basé sur l'algorithme d'échantillonnage d'importance séquentiel (SIS), ont convergé vers leurs valeurs réelles, et que l'approche présentée ici peut fournir une stratégie d'identification paramétrique très précise pour les géomatériaux élastoplastiques. En outre, les résultats de la simulation utilisant les paramètres identifiés sont proches des données d'observation réelles, et l'approche groupée produit plus d'informations sur les paramètres d'intérêt que de simples valeurs estimées obtenues à partir des méthodes d'optimisation. En d'autres termes, l'identification se présente sous la forme d'une fonction de densité de probabilité.

**KEYWORDS:** data assimilation, particle filter, parameter identification

## 1 INTRODUCTION

Inverse analyses have been successfully applied to linear elastic problems in which the deformation to be addressed is linear and depends only on the model parameters and the applied load; it does not depend on the loading history. However, the mechanical behavior of geomaterials is commonly described by an elasto-plastic model, and the deformation behavior displays strong nonlinearity and depends not only on the values of the parameters, but also to a great extent on the stress state and the history, whereby the identification of elasto-plastic parameters still remains a major challenge.

Data assimilation (DA) is available as a methodology to tackle the above difficulties (Nakamura *et al.* 2005). The estimation of the interest dynamic system via DA involves a combination of observation data and the underlying dynamical principles governing the system. The melding of data and dynamics is a powerful methodology, which makes efficient and realistic estimations possible. This approach has recently proven fruitful in earth science, e.g., geophysics, meteorology, and oceanography (e.g., Awaji *et al.* 2009).

Several kinds of powerful DA methods have been proposed. Among the existing strategies, this study focuses on the filtering techniques referred to as the particle filter (PF, Gordon *et al.* 1993), because it can be applied to nonlinear and non-Gaussian problems and can provide a simple conceptual formulation and ease of implementation.

Herein numerical and practical effectiveness of the DA strategies using the PF are examined for geotechnical problems through their applications to the numerical experiments and an actual construction project. For this purpose, first, we outline the concepts and methods of DA and refer to the PF. Second,

we deal with the parameter identification of elasto-plastic parameters for geomaterials applying the PF to initial and boundary value problems in geomechanics. Finally, we investigate the applicability of the PF to a practical settlement prediction of a well-documented construction project, Kobe Airport Island, comparing the obtained simulation with the observation data, and the practical effectiveness of the DA based on the PF is discussed.

## 2 DA: CONCEPTS AND METHODS

DA is a versatile methodology for estimating the state of a dynamic system of interest by merging sparse observation data into a numerical model for the system. The state of the system is usually estimated with deterministic simulation models, which are subject to the uncertainty that arises due to a lack of knowledge and a poor understanding of the physical phenomena. Meanwhile, observation data, which represent the true state, but are subject to stochastic uncertainty and randomness, may occasionally be available as a function of a subset of the system variables. Based upon a prognostic model and a limited number of observations, DA attempts to provide a more comprehensive system analysis which may lead to more accurate predictions. This approach has recently proven useful in earth science (Awaji *et al.* 2009).

Novel sequential data assimilation methods include the Ensemble Kalman Filter (EnKF, Evensen 1994) and the PF which are categorized into nonlinear Kalman filtering. Although the EnKF can be applied to nonlinear systems, it basically assumes a linear relationship between a state and the observation data in calculating a Kalman gain. Therefore, the



EnKF cannot produce satisfactory estimates if its linear approximation is invalid. This means that its application to geomaterials is difficult, because the materials display strong nonlinearity. On the other hand, as the PF does not require assumptions of linearity or Gaussianity, it is applicable to general problems. Therefore, the PF has higher potential for application to geotechnical engineering and can obtain meaningful outcomes. Brief description of the PF is summarized below.

The PF approximates probability density functions (PDFs) via a set of realizations called an ensemble that has weights, and each realization is referred to as a ‘particle’ or a ‘sample’. For example, a filtered distribution at time  $t-1$ ,  $p(x_{t-1}|y_{1:t-1})$ , where  $y_{1:t-1}$  denotes  $\{y_1, y_2, \dots, y_{t-1}\}$ , is approximated with ensemble  $\{x_{t-1}^{(1)}, x_{t-1}^{(2)}, \dots, x_{t-1}^{(N)}\}$  and weights  $\{w_{t-1}^{(1)}, w_{t-1}^{(2)}, \dots, w_{t-1}^{(N)}\}$  by the following equation:

$$p(x_{t-1}|y_{1:t-1}) \approx \frac{1}{N} \sum_{i=1}^N w_{t-1}^{(i)} \delta(x_{t-1} - x_{t-1}^{(i)}) \quad (1)$$

where  $N$  is the number of particles and  $\delta$  is the Dirac delta function.  $w_{t-1}^{(i)}$  is the weight attached to particles  $x_{t-1}^{(i)}$  and should suffice  $w_{t-1}^{(i)} \geq 1$  and  $\sum w_{t-1}^{(i)} = 1$ .

A general approach for filtering is known as sequential importance sampling (SIS) (Doucet *et al.* 2000). The SIS algorithm is based on using the importance sampling to estimate the expectations of functions of the state variables. The algorithm of SIS is summarized as follows:

1. **Initialization:**  
Generate an ensemble (set of particles)  $\{x_0^{(1)}, x_0^{(2)}, \dots, x_0^{(N)}\}$  from the initial distribution  $p(x_0)$ .
2. **Prediction:**  
Each particle  $x_{t-1}^{(i)}$  evolves according to the numerical dynamic model given by a numerical simulation method such as FEM.
3. **Filtering:**  
After obtaining measurement data  $y_t$ , calculate weight  $w_t^{(i)}$ , which expresses the ‘fitness’ of the prior particles to the observation data, and assign a weight,  $w_t^{(i)}$ , to each  $x_{t-1}^{(i)}$ .
4. **Weight update:**  
The set of weighted particles  $\{x_t^{(i)}\}$  results in an ensemble approximation of filtered distribution  $p(x_t|y_{1:t})$ .  
Set  $t = t + 1$  and go back to Step 2.

Figure 1 shows the algorithm of the PF based on the SIS.

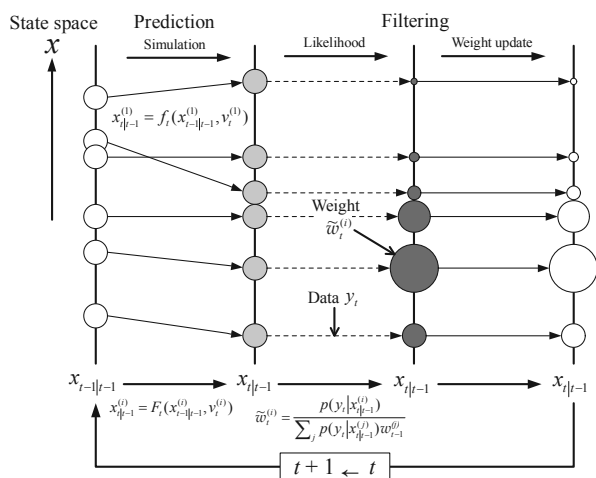


Figure 1. Algorithm of the PF based on SIS.

### 3 PARAMETER IDENTIFICATION OF CAM-CLAY MODEL USING THE PF

This chapter focuses on the soil-water coupled behavior of a clay foundation under monotonic loading, where the numerical simulation for hypothetical soil deposit under embankment is implemented to study the efficiency of the PF as a parameter identification method.

The soil-water coupled finite element analysis using the Cam-clay model were used in this example. The finite element mesh and the loading history are shown in Figures 2 and 3, respectively. Table 1 lists the parameters of the clay foundation. The placement of the observation points is also shown in Figure 2; the vertical displacements and the horizontal displacements are located at S1-S3 and at L1-L3, respectively. Some of the parameters are chosen to be identified and their values are called ‘true values’ as listed in Table 2, and we carried out 100 Monte Carlo Simulations using the sets of particles which were generated with uniform random numbers in the range shown in Table 2.

Figure 4 shows the time evolution of the identified parameters ( $\lambda$ ,  $\kappa$ , and  $M$ ). Identified parameters are computed as the weighted mean value of the particles computed by

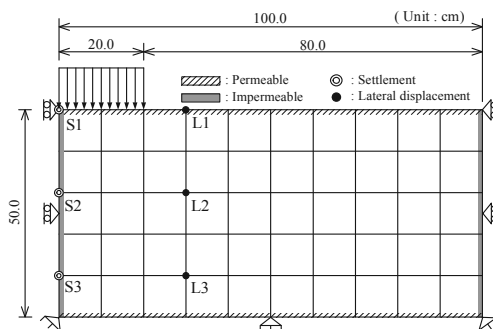


Figure 2. Finite element mesh.

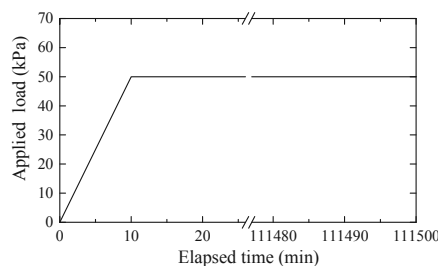


Figure 3. Loading history.

Table 1. Cam-clay parameters of the model foundation.

$\lambda$	$\kappa$	$e_0$	M
0.190	0.065	0.992	1.154

Table 2. True values of the parameters to be identified and range of particle generation.

Parameter	True value	Range
$\lambda$	0.239	0.090 ~ 0.290
$\kappa$	0.091	0.015 ~ 0.115
M	1.084	0.854 ~ 1.454

$$\bar{\phi}_t = \sum_{i=1}^N w_t^{(i)} \phi_t^{(i)} \quad (2)$$

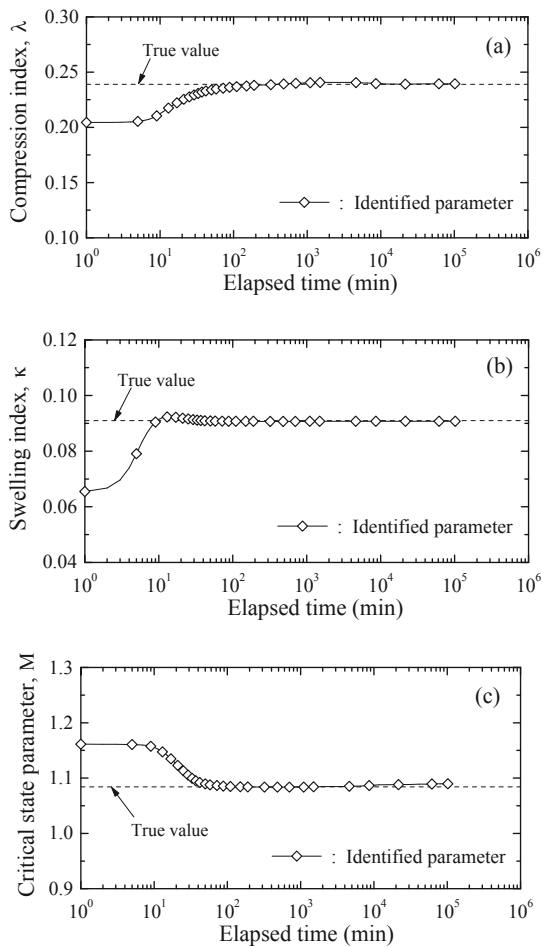


Figure 4. Time evolution of identified parameters.

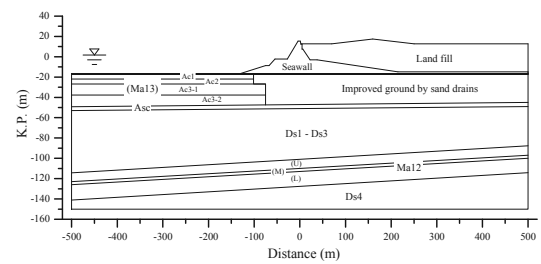
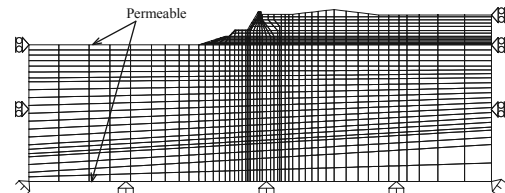
where  $\bar{\phi}_t$  and  $\phi_t^{(i)}$  indicate the identified parameter at time step  $t$  and the parameter of particle number ( $i$ ) at time step  $t$ , respectively.

The parameter identification of unknown parameters approaches the true values, although the identification starts with an incorrect  $\bar{\phi}_0$  in all cases purposefully. These results verify the effectiveness of the PF for the parameter identification of the elasto-plastic model, which presents strong nonlinear behavior.

#### 4 APPLICATION OF THE PF TO SETTLEMENT BEHAVIOR OF KOBE AIRPORT ISLAND CONSTRUCTED ON RECLAIMED LAND

The objective of this chapter is to investigate the applicability of the PF to an actual settlement prediction of a well-documented geotechnical construction project, Kobe Airport Island. To accomplish this objective, firstly, the settlements of the island are evaluated using a soil-water coupled finite element analysis with the Cam-clay model. Then, the parameters are identified using the PF. Finally, comparing the recomputed simulation using identified parameters with the observation data, the practical effectiveness of the methodology based on the PF is discussed. Some outcomes obtained from this application example were reported in Murakami *et al.* (2012).

Kobe Airport was constructed on an artificially reclaimed island just off the coast of Kobe. Figure 5 shows the cross section of the construction site. Vertical sand drains were installed in the soft clay layer in order to accelerate the settlement and increase the strength (e.g. Yamamoto *et al.* 2010).


 Figure 5. Cross section of the construction site (Yamamoto *et al.* 2010).

 Figure 6. Finite element mesh (Murakami *et al.* 2012).

The soil-water coupled finite element analysis with the Cam-clay model was adopted for analyzing the deformation behavior of the seawall and the foundation subjected to the construction and reclamation work. Figure 6 shows the finite element mesh. In the model ground, the top surface, bottom surface and the sides of sand/gravel layers were assumed to have permeable boundary conditions, whereas the sides of clay layers were assumed to have impermeable boundary conditions. The sand layers and reclaimed ground were assumed to be linear elastic, and the clay foundations were represented by the Cam-clay model.

The *mass permeability* concept, which was proposed by Asaoka *et al.* (1995), was incorporated into this analysis. Mass permeability is the permeability representative of a clay foundation, which includes the effects of inhomogeneity, partial drainage, and load intensity. We also adopted the concept in the same sense. The analysis in this chapter focuses on the settlement behavior of only the improved alluvial clay foundation, because the soil layers which are just below the improved ground, called Ds1-Ds3, are thick, have high rigidity (the N-value obtained from SPT is more than 100), and do not significantly affect the settlement of the island.

Firstly, we considered the improved ground to be homogeneous by incorporating the mass permeability concept. Then, using the PF, some parameters of the treated ground, the so-called *mass parameter* were identified to simulate settlement of the ground under the airport island. Although the some parameters affect settlement of the ground, the compression index  $\lambda$  and the permeability  $k$  were treated as the only parameters to be identified, because these two parameters directly govern consolidation behavior of clay grounds. Finally, the simulations were implemented using the identified mass parameters and observation data were compared to evaluate the practical usability of the PF.

The representative parameters of the improved grounds, referred to as mass parameter ( $P_{\text{mass}}$ ) in this study, are determined here by using equation (3) for simplicity.

$$P_{\text{mass}} = \frac{P_1 h_1 + P_2 h_2 + \dots + P_n h_n}{h_1 + h_2 + \dots + h_n} \quad (i=1,2,\dots,n) \quad (3)$$

where  $P_i$ ,  $h_i$ , and  $n$  are the parameters, the thickness of each layer, and the number of soil layers, respectively.

We conducted Monte Carlo simulations with 200 particles over the feasible space listed as follows:

$$0.30 \leq \lambda \leq 0.60, \quad 1 \times 10^{-0} \leq k \leq 1 \times 10^{-3}. \quad (4)$$

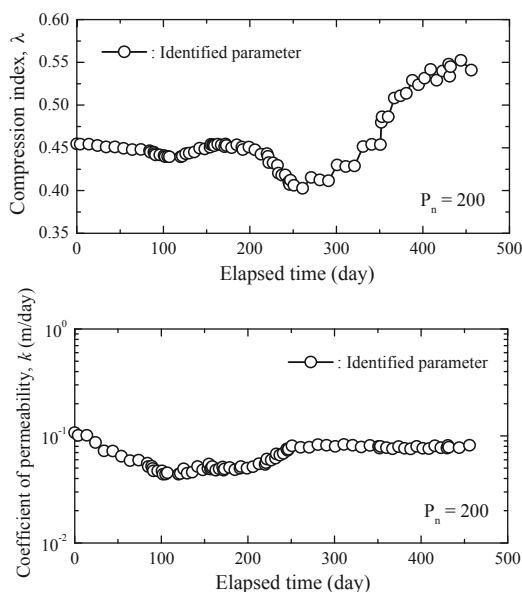


Figure 7. Time evolution of identified parameters.

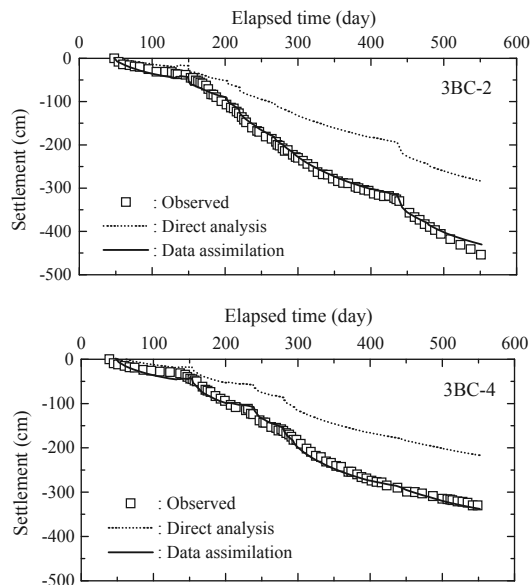


Figure 9. Simulation results using the identified parameters.

Each parameter was assumed to follow uniform randomly and was generated independently. All 200 simulations were conducted up to 676 days after the construction was started. Only the settlement values observed on the seabed were used for parameter identification.

Figure 7 shows the time evolution of the identified parameters. In the figure, the estimates for  $\lambda$  hardly change through the assimilation. In particular, after the 300<sup>th</sup> day, the path changes dramatically. On the other hand, in the result of  $k$ , the identified parameter shows almost constant value through the assimilation.

Figure 8 shows filtered PDFs of a settlement value at the 148 days after construction began. In this figure, the vertical axis represents the weight of the particle, while the horizontal axis represents settlement value. It can be seen from the Figure 8 that the distribution of the weight approximately follows the normal distribution which has sharp peak around -3.5m. From the result, we can see that the use of a large number of particles contributes to the accurate estimation of the arbitrary PDFs for settlements. This is the remarkable advantage of the PF.

The simulation results for the time-settlement relationship at observation points 3BC-2 and 3BC-4, which were placed on seabed, via the identified parameters are shown in Figure 9. The identified parameters mean the values at the end of the identification process, that is,  $t = 456$  days. In the figures, dotted line represents the result of direct analysis. Although the results of direct analysis underestimate the observation data, the simulations using the identified parameters yielded predictions with high accuracy.

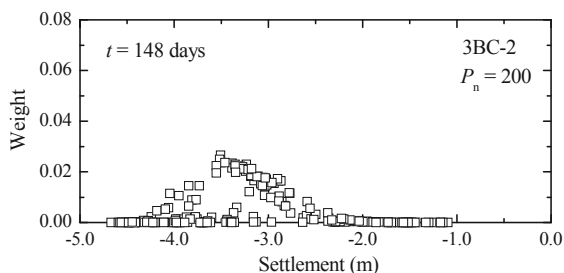


Figure 8. Filtered PDF of a settlement value.

## 5 CONCLUSIONS

In this study, we have investigated the numerical and the practical effectiveness of the DA strategies using the PF for geotechnical problems through their applications to the hypothetical experiment and the actual construction project.

The parameters identified by the PF have converged into their true values, and the presented approach has shown effective parameter-identification method for elasto-plastic geomaterials. Moreover, the simulated time-settlement behavior using the identified mass parameters has provided a good agreement with the actual observation.

In conclusion, the DA using the PF has been proven a powerful strategy for identifying elasto-plastic parameters of geomaterials and more accurate predictions of the mechanical behavior of geotechnical structures.

## 6 REFERENCES

- Asaoka A., Nakano M., Fernando G. S. K. and Nozu M. 1995. Mass permeability concept in the analysis of treated ground with sand drains, *Soils and Foundations* 35 (3), 43-53.
- Awaji T., Masafumi K., Ikeda M. and Ishikawa Y. 2009. *Data assimilation*, Kyoto University Press, 1-11 (in Japanese).
- Doucet A., Godsill S. and Andrieu C. 2000. On sequential Monte Carlo sampling methods for Bayesian filtering, *Statistics and Computing* 10, 197-208.
- Evensen G. 1994. Sequential data assimilation with a non-linear quasi-geostrophic model using Monte Carlo methods to forecast error statistics, *J. Geophys. Res.* 99, 10143-10162.
- Gordon N. J., Salmond D. J. and Smith A. F. M. 1993. Novel approach to nonlinear/non-Gaussian Bayesian state estimation, *IEE Proceedings-F* 140 (2), 107-113.
- Murakami A., Shuku T., Nishimura S., Fujisawa K. and Nakamura K. 2012. Data assimilation using the particle filter for identifying the elasto-plastic material properties of geomaterials, *Int. J. Numer. Anal. Meth. Geomech.*, DOI:10.1002/nag.2125.
- Nakamura K., Ueno G. and Higuchi T. 2005. Data assimilation: concept and algorithm, *Proc. Inst. Statist. Math.* 53 (2), 37-55 (in Japanese).
- Yamamoto T., Sakagami T., Takahashi Y., Yagiura Y., Nambu M. and Iizuka A. 2010. Establishment of soil deformation analysis method at Kobe Airport, *Doboku Gakkai Ronbunshuu C* 66 (3), 457-471 (in Japanese).

# Experimental analyses on detection of potential risk of slope failure by monitoring of shear strain in the shallow section

Analyses expérimentales sur la détection d'un risque potentiel de rupture de pente par la surveillance de la contrainte de cisaillement en pied du talus

Tamate S., Hori T.

*National Institute of Occupational Safety and Health, Tokyo, Japan*

Mikuni C., Suemasa N.

*Tokyo City University, Tokyo, Japan*

**ABSTRACT:** A large scale model test was carried out in this study to investigate the relationship between the potential risk of slope failure and an increase of the shear strain in the shallow section. A model slope made of soft deposit of Kanto-loam with 30 degrees inclination and 3.5m height was prepared. Compact shear strain meters as well as inclinometers and extensometers were installed to measure the movements of slope prior to failure. Seven steps of cuttings were carried out from the toe to make the slope unstable. The model slope did not fail soon after completion of the final cutting, and it lasted 7 minutes before it finally failed. Clear increases in the shear strain  $\theta$  had been measured as the cuttings progress. The obtained data of  $\theta$  and the displacement showed good agreement in their reactions. Accordingly, it is proven that the potential risk of slope failure was detectable by monitoring of the shear strain in the shallow section for simplicity.

**RÉSUMÉ :** Un essai sur modèle à grande échelle a été réalisé dans cette étude pour étudier la relation entre le risque potentiel de rupture de pente et une augmentation de la déformation de cisaillement dans la partie peu profonde. Une pente modèle composée de dépôts mous de Kanto-limoneux a été préparée avec une pente de 30 degrés et une hauteur de 3,5 m. Des capteurs de déformations de cisaillement compacts ont été développés et installés avec des inclinomètres et des extensomètres pour mesurer les mouvements de pente avant la rupture. Sept phases d'excavation ont été réalisées au pied pour rendre la pente instable. Le modèle de la pente ne s'est pas écroulé tout de suite après la coupe finale, et il y a eu un intervalle de 7 minutes avant la rupture. Une nette augmentation de la déformation de cisaillement  $\theta$  a été mesurée lors des excavations. Les données de  $\theta$  obtenues et le déplacement montrent un bon accord dans leurs comportements. Ainsi, il a été montré que le risque potentiel de rupture d'une pente est détectable par le suivi de la déformation de cisaillement au pied du talus pour la simplicité.

**KEYWORDS:** slope failure, monitoring, shear strain in shallow section, large scale model test.

## 1 INTRODUCTION

Slope failures frequently cause occupational accidents at construction sites. It is also known that even a small collapse can cause serious injury to workers. Therefore, slope failures must be avoided for safety reasons, and temporary retaining walls are needed to support slopes at worksite. In addition, the practice of immediate escape is also important to save human lives, and warning must be given prior to failure. Consequently, monitoring of the slopes is needed to detect increase of the potential risk of failure.

This paper will first summarize hazards that exist in the slope works. Next it will explain a large scale model test carried out to simulate the slope failure. It will also introduce a compact shear strain meter developed to measure increase of shear strain in the shallow section of slopes. Finally, its applicability will be discussed in consideration of results from the test.

## 2 HAZARDS IN WORKS ON SLOPES

Excavations and cuttings are frequently performed in many aspects of slope works. Cuttings at the toe of slopes are common in the building of retaining walls. However, cuttings may cause the slope to be unstable even though its duration is only short term. Itoh et al. (2005) reported that the volume of collapsed soil blocks in almost 60 % of all accidents was less than 50m<sup>3</sup>. Accordingly, serious damage to the workers are caused by small amount of collapsed soil blocks. In addition, safety must be maintained at the recovering operation after disasters. Collapsed soil deposited is soft and loose after seismic failure, and shear strength of remaining soil slopes was also

reduced by seismic acceleration. Therefore, slopes will become unstable after earthquakes. Meanwhile, when quick operations are also required to save refugees, sufficient time for both installation of temporary structures to support the unstable slopes and survey of the ground conditions in detail will not be given.

Hazards exist to people who work on the slopes as well as under the slopes. Moreover, the time for escape may be not given to the adjacent workers. Consequently, warning prior to the failures is important to save workers as well as an installation of temporary supports.

## 3 A LARGE SCALE MODEL TEST

### 3.1 Preparation of model ground and method of model test

A model slope of 3.5m height, 4.0m width and 30 degrees inclination was made by filling soil material as shown in Figure 1. Any compaction was not provided to simulate loose deposit of collapsed soil after seismic disasters. Several sheets of tarpaulins are placed to lubricate the friction between the retaining wall and the soil so that the plane strain condition was undertaken.

Soil material used in the test was Kanto loam that has soil properties as shown in Table 1. Figure 2 shows the relationship between the cone penetration resistance  $q_c$  and the depth from the top of slope  $d$ . Values of  $q_c$  roughly show a linear increase to  $d$  because the self-weight was loaded for consolidation.

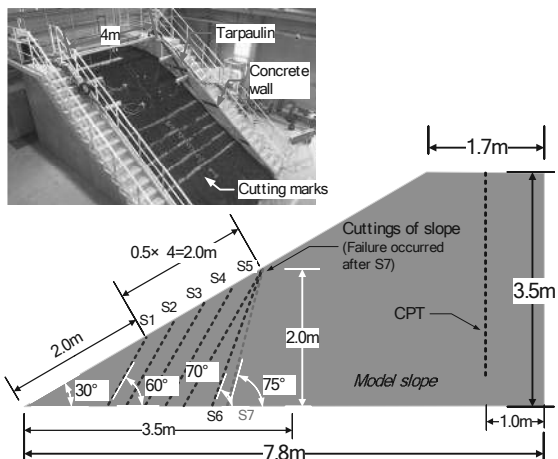


Figure 1. A profile view of model slope.

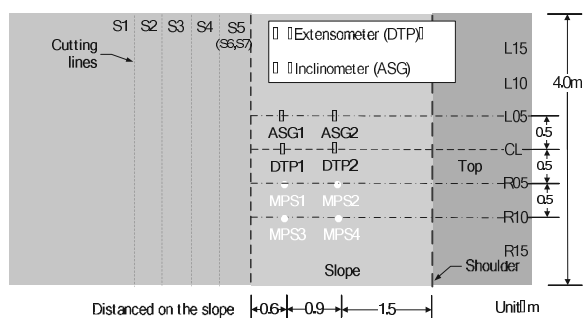


Figure 3. A plane view to show the installed position of sensors

Property	Value
Density of soil particles $\rho_s$ ( $g/cm^3$ )	2.759
Sand (0.075 ~ 2mm) %	6.2
Silt (0.005 ~ 0.075mm) %	45.3
Clay (Diameter < 0.005mm) %	48.5
Liquid limit $w_L$ (%)	158.3
Plastic limit $w_p$ (%)	97.7
Plasticity index $I_p$	60.6
Dry density $\rho_{dmax}$ ( $g/cm^3$ )	0.665
Optimum water content $w_{opt}$ (%)	102.0

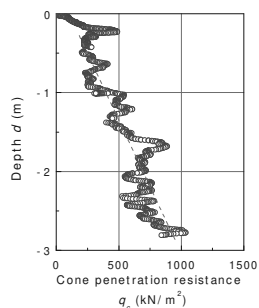


Figure 2. Relationship between cone penetration resistance and depth from the top of slope.

Seven steps of cuttings were carried out by construction machinery in the toe of slope. 60 degrees angle in the cuttings was performed from S1 to S5 that was 0.5m long from front to back as shown in Figure 1. As for S6 and S7, the cutting angle was increased to 70 degrees and 75 degrees, respectively. Thirty minutes interval time between the steps was provided to observe the movement of the slopes.

### 3.2 Installation of sensors

Three kinds of sensors, extensometers (DTP), inclinometers (ASG), and compact shear strain meters (MPS), were installed to measure the movement of the slope during the test. Figure 3 shows the installed positions of the sensors. Two sets of DTP were installed to measure increment of the displacement  $d$  by giving 0.9m interval at the center column (CL). Sensor units of DTP were set on a beam bridging over the retaining walls while extended wires were connected to pegs on the slope.

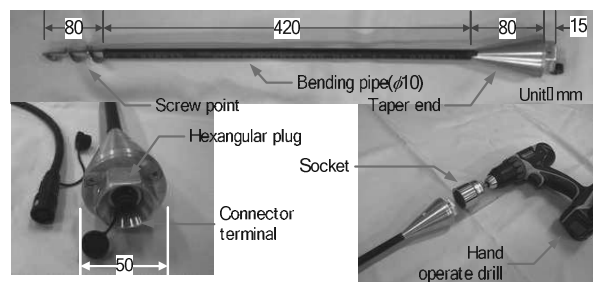


Figure 5. Shape and structure of a developed compact shear strain meter (MPS).



Photo 1. Installation of MPS

Two sets of ASG were installed to measure an increment of the angle of inclination  $\alpha$  on the surface at the column of L05 at same height as DTP. Four sets of MPS to be explained in the following section were also installed to measure increment of the interpreted shear strain  $\theta$  at the columns of both R05 and R10 in the same manner as the installation in ASG.

## 4 MEASUREMENT OF SHEAR STRAIN IN THE SHALLOW SECTION

### 4.1 Development of compact shear strain meter

A compact shear strain meter called MPS was developed to measure the shear strain in the shallow section of slopes (Tamate, 2010). MPS made of compact size rod 0.6m in length, 10mm in diameter, and 3.6N in weight is shown in Figure 4. A screw point of 80mm in length attached in the lower end enables to penetrate the unit into the ground without pre-boring. A taper end of 100mm in length is used to provide a lateral compression to the surrounding soil so that MPS reacts to the slope movement by its bending deformation. A connector terminal for data transmission composed of 7 poles is mounted at the center of a hexangular plug for rotational installation by a hand drill.

A bending pipe of 420mm in length is positioned between the screw point and the taper end. Four strain gages are pasted on both front and back of the pipe so that the electrical output increases with the bending deformation. A heat shrinkable tube covers the pipe to protect the gages from surrounding soil at installations. Since duration for the installation was less than 10 seconds, easy and quick installation is available in practice as shown in Photo 1.

### 4.2 Basic idea for the monitoring

Figure 5 shows a schematic image of distribution of displacement and shear strain in the slope. An increment of the displacements occurs near the slip plane whereas the increment converges as the distance increases. Accordingly, major shear strain develops along the slip plane. However, this study aims to monitor the shear strain in the shallow section of slopes from the easily application viewpoint (Tamate et al. 2009). MPS was developed to measure the small shear strain in the shallow sections easily.

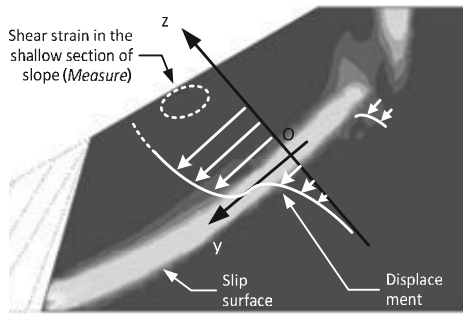
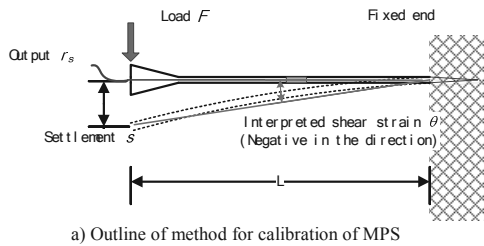
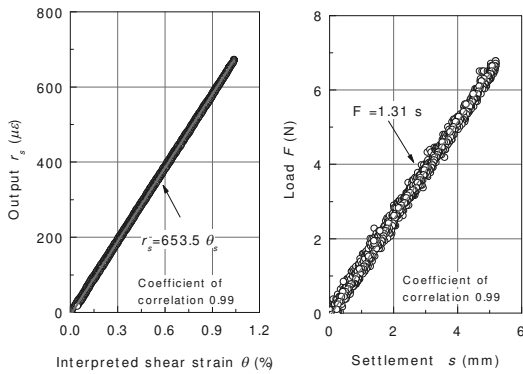


Figure 5. Schematic image of distribution of shear strain at slope failure.



a) Outline of method for calibration of MPS


 b) Electrical output  $r_s$  and interpreted shear strain  $\theta$     c) Load  $F$  and settlement  $s$   
 Figure 6. Stiffness and sensitivity of MPS

A calibration of MPS was carried out to investigate the relationship between the electrical output from MPS  $r_s$  ( $\mu\epsilon$ ) and the interpreted shear strain  $\theta$  (%).  $\theta$  was defined as the ratio of the settlement  $s$  to the effective length  $L$  of MPS as shown in Equation 1.

$$\theta(\%) = \frac{s}{L} \times 100 \quad (1)$$

A vertical load  $F$  was applied to the end of MPS that was supported by cantilever beam as shown in Figure 6. A clear linear relationship is obtained between  $r_s$  and  $\theta$  as well as between  $F$  and  $s$ . Since  $653 \mu\epsilon$  in  $r_s$  was output at 1% in  $\theta$ , a high resolution on the shear strain was confirmed.

## 5 EXPERIMENTAL ANALYSES ON MOVEMENT IN SLOPE

### 5.1 Comparison of reactions by sensors

Figure 7 shows the reactions from three kinds of the monitoring sensors. Horizontal axis means the actual time at the test. The first cutting (S1) begun at 13:00 and the final cutting (S7) was completed at 16:20. The slope collapsed twice at 16:27 and 16:36. This meant that 7 minutes remained prior to the first failure and 16 minutes existed up to the second failures after the completion of S7 as shown in Photo 2. An increase of values appeared in each curve as reactions to increase of potential risk of slope failure.

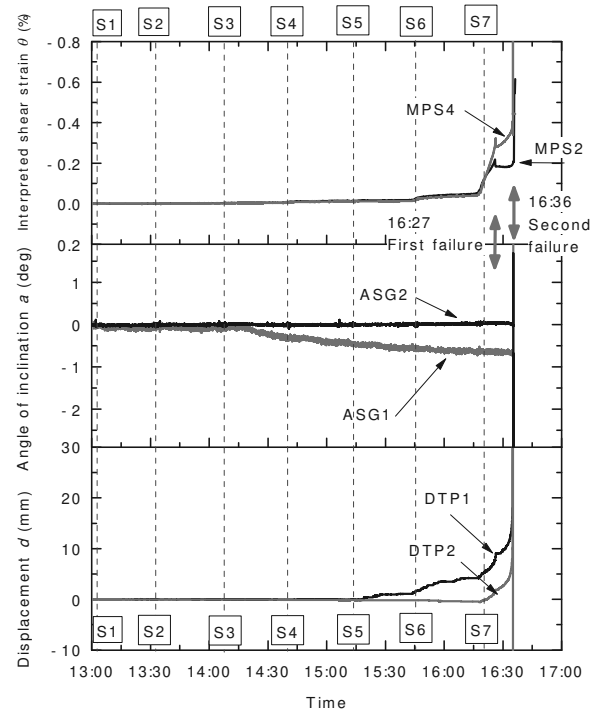


Figure 7. Comparison of reaction of sensors in the model test

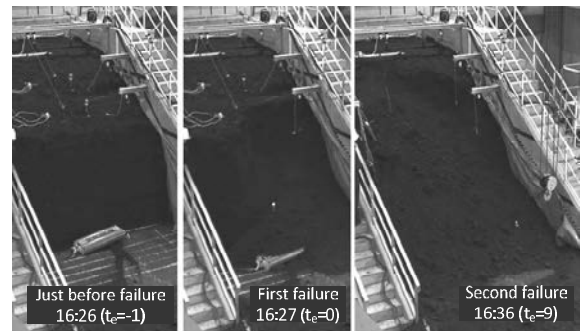
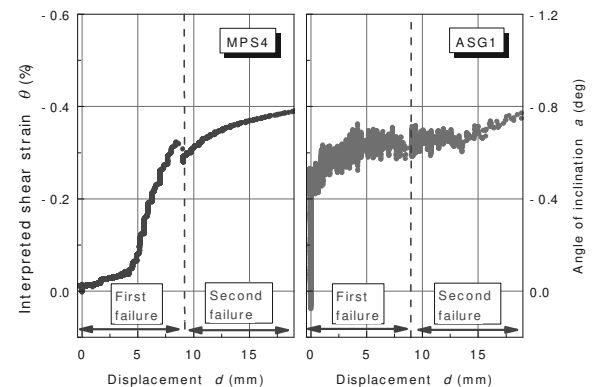


Photo 2. Process of failures in the model slope


 Figure 8. The relationship between the interpreted shear strain  $\theta$  and the displacement  $d$  (in left) and the relationship between the angles of inclination  $a$  and  $d$  (in right).

First small increase can be seen at S3 in  $\theta$  and its value shows the step increase from S3 to S7. After S7, however, values of  $\theta$  kept on increasing from 16:20 to 16:27. Both MPS2 and MPS4 installed at the upper side of the slope show the same increase. Both two curves bent at 16:27 when the first failure occurred. Moreover, values of  $\theta$  were built up again at 16:36 of the second failure.

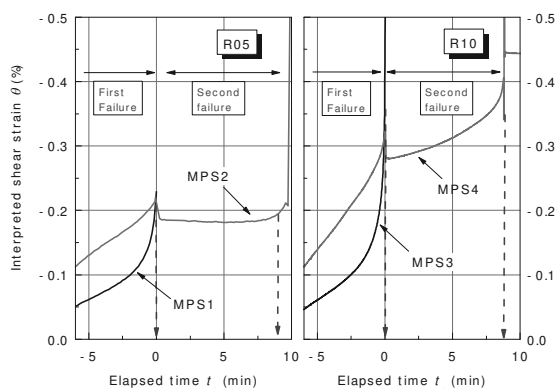


Figure 9. Increases of shear strain in the shallow section prior to the first failure and the second failure

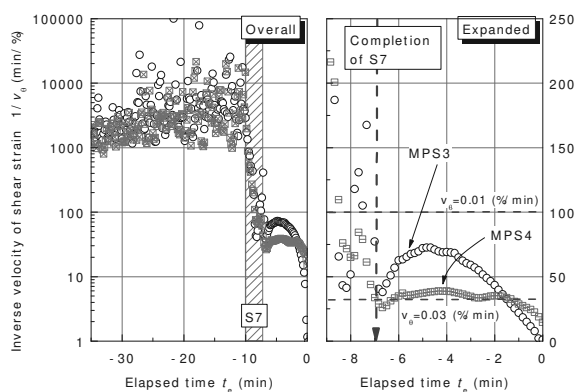


Figure 10. Decrease of the inverse velocity of shear strain prior to the first failure (Overall view in left and expanded view in right)

In addition, a displacement  $d$  increased in DTP1 installed at the lower side of slope in advance, and its value showed the step increase from S5 and S6. Same phenomena in the increase can be seen in both sets of DTP and MPS. Meanwhile, curves on angle of inclination  $a$  did not show clear reactions corresponding to the series of cuttings. A value of ASG1 was kept stable while a value of ASG2 gradual increase from S3. There was no clear reaction on  $a$  excluding those at the moment of the second failure while the slope was getting unstable.

Figure 8 shows the relationship between  $\theta$  and  $d$  in addition to the relationship between  $a$  and  $d$ .  $\theta$  shows a clear increase prior to the first failure when  $d$  hovered between 4 and 7.  $\theta$  also reacted to the second failure so that  $\theta$  still increased where  $d > 7$ . Meanwhile, values of  $a$  increased very little from -0.4 to -0.8 deg to the  $d$  though -0.4 deg of the initial drift appeared.

### 5.2 Increment of the shear strain in the shallow section prior to failure

Figure 9 shows the relationship between  $\theta$  and an elapsed time  $t_e$  recorded by 4 sets of MPS. Both MPS1 and MPS2 were installed in the column of R05 whereas MPS3 and MPS4 were installed in the R10 as shown in Figure 3.  $t_e$  is a modified value that is calculated as zero at the beginning of the first failure. Accordingly, negative values mean the remaining time until the first failure. Recorded data by both lower MPS1 and MPS3 ended at 0 of  $t_e$  because these dropped together with collapsed soil at the first failure. Upper MPS 2 and MPS4 had recorded data until the second failure. Four curves commonly show a linear increase at around -5 of  $t_e$ , and this phenomena was similar to the 2<sup>nd</sup> creep that was well known as the plastic deformation prior to failures. In addition, the value of both MPS1 and MPS3 installed inside of the failure block accelerated these increases from -3 of  $t_e$ . Same acceleration on

the increase was seen in the values of both MPS2 and MPS4 before the second failure.

The left side figure on Figure 10 shows the entire relationship between the inverse velocity of the shear strain  $1/v_\theta$  and  $t_e$  by a logarithmic scale on a vertical axis.  $v_\theta$  is defined as a value of the increment of  $\theta$  per minute.  $1/v_\theta$  of both MPS1 and MPS3 were distributed at higher values from 1,000 and 30,000, when  $t_e$  was between -35 and -10. This means at least that little  $v_\theta$  appeared 10 minutes before the first failure. However,  $1/v_\theta$  shows the drastic decrease corresponding to the beginning of the final cutting of S7. However, the slope did not fail soon. A couple minutes of time lag existed prior to both failures, and this causes people's misunderstanding of the stability.

The right side figure shows an expanded view by a linear scale on a vertical axis.  $1/v_\theta$  indicated the values between 30 and 80 min/% while 4 minutes between -7 and -3 of  $t_e$ . Accordingly, the values of  $v_\theta$  were interpreted as between 0.01 and 0.03 %/min. Consequently, the shear strain increased at mostly constant rate in the same manner as the 2<sup>nd</sup> creep. Moreover,  $1/v_\theta$  in MPS1 and MPS3 linearly decreased from -2 and -4 of  $t_e$ , respectively. This proves that values of  $\theta$  were accelerating these increases just before failures, the same as the 3<sup>rd</sup> creep. Accordingly, a clear increase of shear strain in the shallow section of the slope was confirmed in the large scale model test. In addition, it was proven that this phenomenon reflects an increase of potential risk of slope failure. Therefore, a couple of minutes could be provided for escape by identifying either the 2<sup>nd</sup> creep or the 3<sup>rd</sup> creep.

## 6 CONCLUSIONS

A large scale model test was carried out in this study to investigate relationship between the potential risk of slope failure and an increase of the shear strain in the shallow section. Developed compact shear strain meters as well as conventional sensors of inclinometers and extensometers were used in the test to measure the movement of the slope prior to failure. Seven steps of cuttings were performed in the toe to make unstable. The model slope did not fail soon after a completion of the final cutting, and around 7 minutes of the time lag existed until the beginning of failure. Clear increases in the responses of shear strains  $\theta$  in the shallow section were measured with the progress of the cuttings. The obtained data of  $\theta$  and the displacement  $d$  showed good agreement in their reactions. Accordingly, it is proven that the potential risk of slope failure was detectable by monitoring of the shear strain in the shallow section for simplicity.

## 7 ACKNOWLEDGEMENTS

The authors would like to thank Prof. Toshiyuki Kadada, Mr. Nozomu Yamamoto of Tokyo City University, Dr. Kazuya Itoh and Dr. Naotaka Kikkawa of the National Institute of Occupational Safety and Health, Japan for their cooperation in the large scale model test and analyses.

## 8 REFERENCES

- Itoh, K., Toyosawa, Y., Tamrakar, S. B. & Horii, N. 2005. Analysis of labor accidents caused by slope failure. *Landslide, Journal of the Japan Landslide Society*, 41(6), 585-597.
- Tamate, S. and Itoh, K. 2009. Monitoring of shear strain in shallow sections of slopes to detect increased risk of slope failure. *Proceedings of the 17<sup>th</sup> International Conference on Soil Mechanics and Geotechnical Engineering*, 2143-2146.
- Tamate, S. 2010. Penetration-type pipe strain gauge, *United States Patent*, No.7,762,143 B2, Jul.27.2010.

# Soutènements de grande hauteur soutenus par butons ou multi-ancrages à Monaco : de la modélisation au comportement réel

Retaining wall with struts or multi-anchored for a deep excavation in Monaco: from modeling to real behaviour

Utter N., Dervillé B.  
Soletanche-Bachy, France

Beth M.  
Soldata, France

**RÉSUMÉ :** La construction de l'immeuble Teotista comporte la réalisation d'un parking enterré de 6 sous-sols, donc d'une excavation profonde présentant toutes les particularités des projets monégasques, à savoir un environnement exigü, des ouvrages mitoyens sensibles, et la nécessité d'entailler une forte pente d'éboulis. La hauteur terrassée se trouve ainsi variable de 20 m côté aval à 30 m côté amont, nécessitant la mise en œuvre d'une paroi à contreforts prolongée par des micropieux dans le marno-calcaire rencontré en profondeur, et d'un butonnage fortement dissymétrique sur 5 niveaux, engendrant concentration d'efforts et mise en butée du terrain aval.

La complexité de la structure et du phasage, ainsi que la sensibilité de l'environnement, ont nécessité la mise en œuvre de différents types de modélisations (méthode des coefficients de réaction et méthode des éléments finis), et motivé la mise en œuvre d'une instrumentation qui a permis de confronter à la réalité ces différentes modélisations dans toutes les phases de construction.

Il a ainsi été possible de mettre en évidence la validité des calculs traditionnels dans leur domaine d'application, mais aussi de progresser dans l'appréhension correcte des frontières entre modèles de comportement et méthodes de calcul associées.

**ABSTRACT:** This paper aims at presenting the works carried out for the construction of the so-called Teotista building including a six floors underground parking requiring a deep excavation with all the specifications of the projects implemented in Monaco, i.e. a confined environment, sensitive structures in the vicinity, and the necessity to scrape a deep slope of taluses. The height thus excavated is at a range of 20 m on the downstream side to 30 m on the upstream side. This implies the implementation of buttresses with micropiles drilled in marl and limestone soil and to deal with very dissymmetrical forces transferred by five levels of inclined and pre-stresses struts.

The complexity of the structure itself, the phasing stages and the sensitive environment as well have required the implementation of several modeling systems (finite elements analysis and coefficient of subgrade reaction method), accurate monitoring system which provided a kind of reality check to ensure the assumptions made by modelling at all the stages of the construction.

By doing so, we demonstrated the validity of the traditional editing calculation notes and help advance in the right apprehension of borders between soil behaviour and associated methods for calculations.

**MOTS-CLÉS :** soutènement, butons, précontrainte, contreforts, méthode observationnelle

**KEYWORDS:** retaining wall, struts, pre-stress, buttresses, observational method

## 1 UN PROJET A FORTES CONTRAINTES

### 1.1 Une emprise limitée

Situé en Principauté de Monaco, le projet de la Tour Teotista comporte l'édification d'un immeuble de 20 étages dans un environnement particulièrement exigü. La surface au sol n'est que de 30 x 30 m et prend la forme d'un talus d'environ 25° dont la cote varie de 132 NGM à l'amont et 118 NGM à l'Aval.

### 1.2 Un voisinage dense

Le projet est situé dans un contexte urbain dense et bordé :

- au Sud par le bâtiment Garden House, immeuble R+7 fondé à 107 NGM.

- au Nord par la Villa Béatrice, habitation R+9 fondée sur semelle à 118 NGM à proximité immédiate du projet.

- à l'Ouest par l'Avenue Hector Otto Supérieure et particulièrement à proximité du Patio Palace, immeuble R+14 de 5 niveaux de sous sols.

- à l'Est par l'Avenue Hector Otto Inférieure donnant sur les Villas du Parc, bâtiment de 10 étages fondé à 108 NGM.

### 1.3 Un contexte géologique difficile

Les sondages font apparaître une stratigraphie constituée de remblais surmontant une épaisse couche d'éboulis et de colluvions à matrice argileuse. Une frange d'altération d'épaisseur variable surmonte un substratum compact constitué de formations marneuses et marno-calcaires d'âge crétacé.

La résistance élevée des couches profondes ( $E_m = 250$  à  $500$  MPa) et la géométrie étriquée du chantier ont nettement orienté la technique de soutènement utilisée. Le projet a consisté en un soutènement mixte composé d'une paroi moulée prolongée par une fiche en micropieux à partir de 1 m sous le fond de fouille.

L'utilisation d'une hydrofraise était rendue impossible par l'emprise restreinte du chantier, et l'utilisation d'une benne preneuse n'aurait pas permis d'assurer entièrement l'excavation des couches compactes.



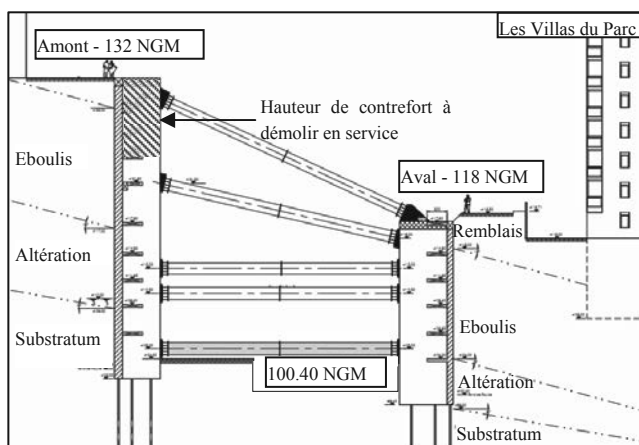


Figure 1. Coupe générale du projet

#### 1.4 Des tolérances de déplacements strictes associées à une forte contrainte architecturale

Le projet comporte 6 niveaux de sous-sols et la cote du fond de fouille est située à 103,3 NGM à l'Amont et 100,4 NGM à l'aval. Dans ce contexte urbanisé très dense et suite aux désordres observés lors de la construction du Patio Palace mitoyen, les critères de déplacements imposés par le contrat sont très sévères : les soutènements ont été dimensionnés pour que le déplacement en tête de paroi amont ne dépasse pas 2 cm, là où pour un soutènement de 30 m, il est généralement admis que les déplacements observés seront de l'ordre du 1/1000<sup>ème</sup> de la hauteur. Le tassement différentiel sous les immeubles avoisinants est limité à 0,8 pour mille.

En outre une contrainte architecturale forte qui impose dans la toute dernière phase des travaux, planchers de la tour construits, de détruire une partie des contreforts du soutènement amont afin d'obtenir une paroi en console sur 8 m de haut. La contrainte principale visait donc à réduire au maximum les déplacements de la paroi pendant les phases provisoires d'excavation pour garantir ce critère lors de la destruction des contreforts.

## 2 UN PHASAGE DE CONSTRUCTION COMPLEXE

Pour répondre à ces contraintes, il a fallu maîtriser l'espace réduit du chantier, gérer l'ensemble des techniques de travaux mis en jeu et combiner ainsi les multiples plateformes associées à chaque soutènement.



Figure 2. Vue générale du chantier en phase de forage

### 2.1 Soutènement Amont-Aval

La différence de hauteur entre le terrain naturel à l'amont et à l'aval induit une dissymétrie de poussée qu'il est nécessaire de maîtriser pour éviter tout basculement de l'ouvrage. La mise en

place de tirants longs ancrés dans le substratum étant interdite à l'amont, l'ensemble des efforts transite de l'amont vers l'aval par un système complexe de dalles, contreforts, butons et planchers.

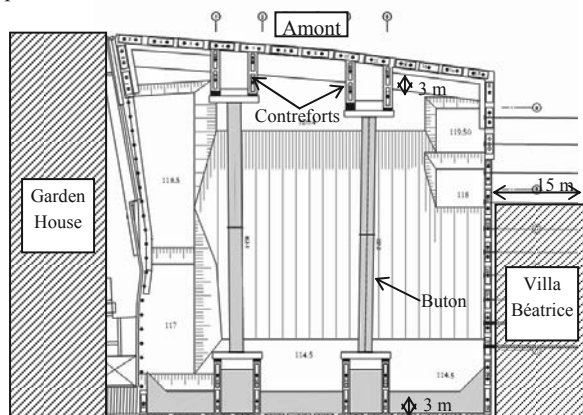


Figure 3. Vue générale des soutènements et des plateformes associées

En phase travaux, la paroi moulée amont de 0,82 m d'épaisseur s'appuie sur 9 niveaux de bandes de planchers réalisées en descendant. D'environ 3 m de large, elles permettent de transférer et concentrer les efforts au niveau des 4 contreforts de 3,75 x 0,50 m espacés tous les 12 m.

Cinq lits de butons de gros diamètre,  $\phi 1200$  mm (see Figure 10) équilibrant jusqu'à 10 000 kN chacun, retransmettent ensuite les efforts des contreforts amont aux contreforts aval. Ces butons sont précontraints afin de garantir le minimum de déplacements.

Les contreforts aval de 4,75 x 0,50 m retransmettent ensuite les efforts à la paroi moulée aval de 0,62 m d'épaisseur par l'intermédiaire des bandes de planchers. Elles transfèrent l'intégralité des efforts des contreforts aux parois puis ensuite au terrain en butée.

En phase service, la paroi moulée amont s'appuie sur les planchers et le noyau dur de la tour dont l'inertie est primordiale pour la stabilité globale de l'ouvrage. Les micropieux d'ancrage des parois sont par ailleurs sollicités pour reprendre les éventuels efforts de traction, au séisme notamment.

### 2.2 Soutènement Villa Béatrice

Le long de la Villa Béatrice, le soutènement exécuté est une paroi moulée de 0,62 m d'épaisseur maintenue en phase provisoire par 6 lits de tirants précontraints et en phase définitive par les planchers de la tour Teotista. La réalisation des tirants précontraints longs engage les tréfonds de la Villa Béatrice sur 15 m de longueur.

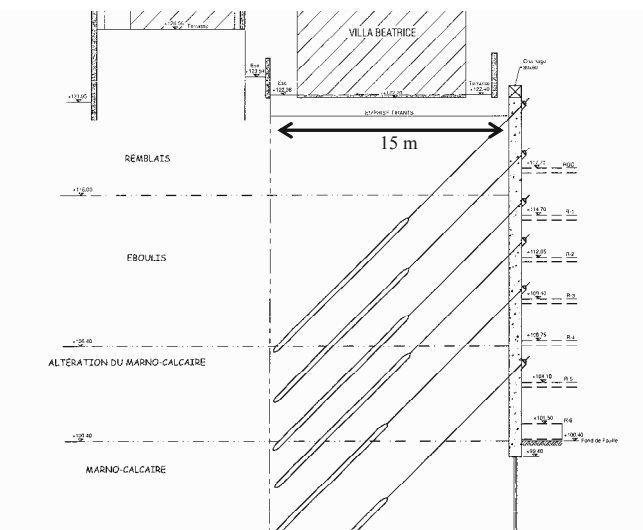


Figure 4. Coupe sur Villa Béatrice

### 2.3 Soutènement Garden House

Les fondations du Garden House se situant à 105 NGM soit environ à 4,60 m seulement du fond de fouille, il a été possible de réaliser une micro berlinoise constituée de tubes 177,8 ép 25 mm disposés tous les 1.30 m.

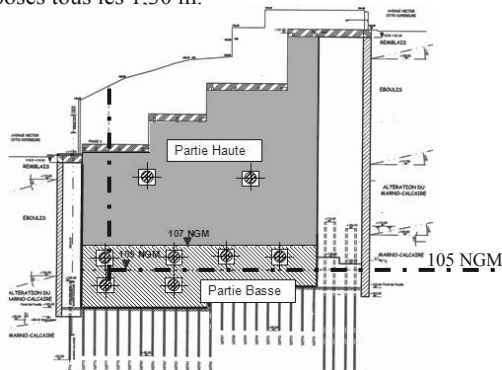


Figure 5. Elévation le long du Garden House

La partie haute du voile ne reprend aucun effort. Deux butons de principe sont cependant disposés à titre conservatoire.

## 3 DIMENSIONNEMENT

### 3.1 Modélisation et méthodes de calcul.

Afin d'estimer au mieux les déplacements du futur ouvrage, les calculs ont été effectués pour chaque soutènement au moyen du programme PARIS basé sur la méthode du coefficient de réaction (Schmitt 2009). Ce logiciel a permis de modéliser et dimensionner l'ensemble des parois, des butons, planchers et noyau central de la Tour. Le programme PLAXIS a permis, quant à lui, d'évaluer les tassements et d'appréhender le comportement global du massif.

Dans les deux modélisations, chaque paramètre a été choisi avec soin pour refléter au mieux les sollicitations réelles sur l'ouvrage. Les coefficients de poussée ont été déterminés à l'aide des tables de Kerisel Absi avec prise en compte du pendage moyen des terrains. Les coefficients de réaction sont estimés à l'aide de la formule semi-empirique de Schmitt (CNJOG 2009). Les circulations d'eau occasionnelles pouvant exister à l'interface entre les couches d'altération et du marnocalcaire compact ont été considérées sur toute la hauteur du substratum pour prendre en compte un éventuel effet barrage. Les calculs PLAXIS ont été réalisés en considérant une loi de comportement de type Hardening Soil Model (HSM), modélisant un comportement élasto-plastique des sols avec écrouissage, avec un module  $E_{50ref}$  de l'ordre de  $3Em/\alpha$ .

### 3.2 Interaction avec le Gros Œuvre

L'inertie de la tour joue un rôle essentiel dans les déplacements atteints lors de la construction, le démontage des butons et la destruction des contreforts. Les caractéristiques des éléments verticaux de l'infrastructure ont été communiquées par l'entreprise de Gros Œuvre et intégrées sous forme d'une baïonnette centrale dans l'ensemble des modélisations PARIS et PLAXIS.

En phase séisme, le Bureau d'études Structures a modélisé, l'ensemble du bâtiment en 3D à l'aide des caractéristiques d'interfaces terrain/paroi du projet, y compris les parois moulées et micro-berlinoises périmétrales. Le dimensionnement des soutènements a été effectué à l'aide des sollicitations sismiques transmises par le BET Structures. Une vérification PLAXIS a permis par ailleurs de contrôler que la butée aval obtenue était compatible avec le terrain en place.

### 3.3 Le rôle des soutènements latéraux

Les soutènements latéraux au droit de la Villa Béatrice et du Garden House ont une double fonction. Ils permettent bien évidemment de soutenir les terres mais aussi de re-transférer les efforts provenant de l'amont vers l'aval. Tout comme les butons mis en place il a été vérifié que ces soutènements étaient capables de reprendre les efforts mis en jeu.

Au droit de la Villa Béatrice, le ferrailage prévu pour les panneaux de paroi moulée a notamment été vérifié en considérant un cas de figure pénalisant où aucun frottement ne serait considéré pour la transmission des efforts entre la paroi et le sol et entre les parois au niveau des joints de panneaux.

La paroi moulée a donc été modélisée en considérant les panneaux comme indépendants et réagissant tels des « dominos » appuyés les uns sur les autres. Chaque panneau de paroi, modélisé comme un élément de poutre vertical, a ensuite été vérifié en flexion déviée.

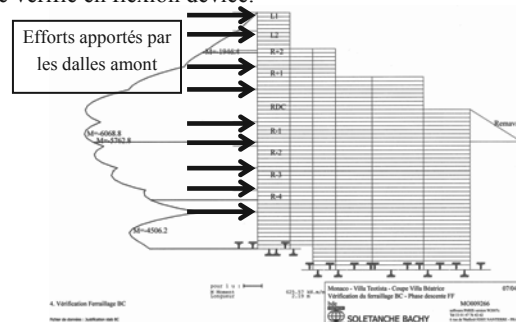


Figure 6. Modélisation PARIS – transmission des efforts Amont-Aval.

## 4 SUIVI DU COMPORTEMENT DE L'OUVRAGE

### 4.1 Dispositif de mesures

Le dispositif d'auscultation propre de la paroi comporte 7 inclinomètres et un ensemble de 20 cibles. L'instrumentation des avoisinants comprend 31 prismes, 8 capteurs de vibrations et 16 cibles réparties sur les différentes habitations jouxtant le chantier. Un ensemble de 16 extensomètres sur armatures ont été mis en place dans la paroi moulée amont. Les butons Amont-Aval sont équipés d'un système de précontrainte à perte compensée. La fréquence des mesures est continue pour l'ajustement de la précontrainte des butons et le suivi des capteurs de vibration. Le suivi topographique est hebdomadaire et bi-hebdomadaire pour les inclinomètres.

### 4.2 Suivi du soutènement Amont-Aval

La courbure des inclinomètres est globalement identique au calcul et les déplacements mis en jeu restent du même ordre de grandeur que ceux calculés. Le comportement réel de l'ouvrage est maîtrisé et aucune action corrective n'a été menée durant l'exécution des travaux.

Le déplacement maximal obtenu au fond de fouille est resté inférieur à 10 mm montrant qu'il est possible par l'application de précontrainte de garantir des déplacements exceptionnellement faibles pour une telle hauteur soutenue. Le graphique ci-dessous présente la comparaison entre déplacements mesurés et calculés. Les mesures à l'aval indiquent clairement que la transition entre l'inertie des contreforts et les micropieux se fait sur plusieurs mètres de hauteur. La modélisation du soutènement par l'association d'une part, d'un contrefort rigide, et d'autre part, de micropieux souples n'est donc pas tout à fait réaliste. Il conviendrait d'ajouter un élément intermédiaire d'inertie moyenne. Le comportement d'ensemble reste cohérent cependant.

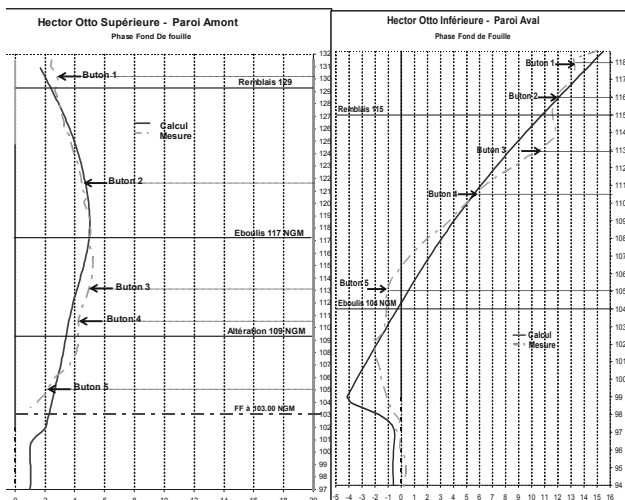


Figure 7. Comparaison des déplacements calculés et mesurés

### 4.3 Soutènement Villa Béatrice

Les mesures inclinométriques montrent que, si les déformées sont du même ordre de grandeur que celles estimées, la courbure est en revanche notablement différente de celle estimée par la méthode au coefficient de réaction, faisant apparaître un « mouvement d'ensemble ». Pourtant, la vérification de la stabilité de chaque massif d'ancrage par la méthode de Kranz fait apparaître des coefficients de sécurité largement satisfaisants (supérieurs à 1,5), voir la Figure 9. L'origine de cette déformée se trouve dans la déformation d'ensemble du massif de sol sollicité par les différents niveaux d'ancrage. La déformation théorique de ce « gabion » d'environ 15 mètres de large par 25 mètres de haut due au cisaillement induit par la poussée des terres, calculée par intégration des formules de Bresse, est en effet tout à fait comparable à celle mesurée (Bustamante et Gouvenot 1978)

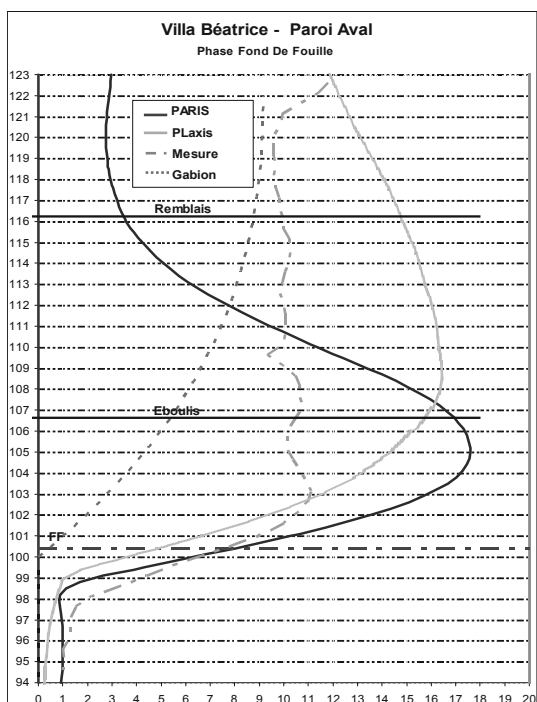


Figure 8. Comparaison des déplacements calculés et mesurés

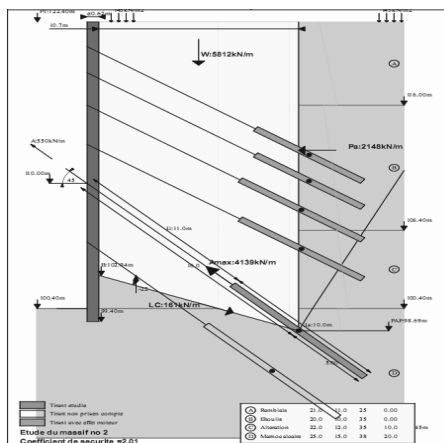


Figure 9. Vérification Kranz – Stabilité du massif d'ancrage

### 4.4 Optimisation du dimensionnement.

Après destruction des contreforts amont, les déplacements en tête de paroi moulée ont été moins prononcés que prévu. Il a donc été possible d'optimiser des places de parking en procédant au découpage des contreforts sur une hauteur supplémentaire de 2 niveaux entre le RDC et le R+2.



Figure 10. Vue du chantier – Phase réalisation du radier

## 5 CONCLUSION

L'auscultation du soutènement et des mitoyens a permis de réaliser un projet complexe en toute sécurité et de livrer au Maître d'Ouvrage un bâtiment conforme à ses spécifications. Le suivi observationnel a montré la remarquable aptitude du programme PARIS multiparois à simuler le comportement fortement interactif des parois amont et aval, et ce sans aucun recalage des paramètres géotechniques utilisés pour le projet: il faut y voir à la fois une validation du modèle de calcul lui-même, et le fruit d'une expérience antérieure du comportement des terrains monégasques et des paramètres de calcul associés.

Le suivi géotechnique a par ailleurs permis d'optimiser le soutènement d'une part, et de mettre en évidence d'autre part, la particularité des écrans avec multi-ancrage, dont l'étude ne saurait se limiter à celle de la stabilité des massifs d'ancrage, mais doit intégrer l'effet de la déformation d'ensemble.

## 6 REFERENCES :

CNJOG. 2009. Norme française NF P 94-282, Calcul géotechnique. Ouvrages de soutènement, AFNOR 2009.  
 Schmitt P. 2009. De l'importance du suivi pour maîtriser le dimensionnement des ouvrages géotechniques. Revue Française de Géotechnique. 126-127, 49-75.  
 Bustamante M., Gouvenot D. 1978. Mesure in situ sur les ouvrages maritimes de soutènement. Annales de l'ITBTP n°375.

# New Sensing Technology and New Applications in Geotechnical Engineering

## Nouvelle technologie de détection et nouvelles applications à l'ingénierie géotechnique

Wang Y.H., Ooi G.L., Gao Y.

Department of Civil and Environmental Engineering, The Hong Kong University of Science and Technology, Hong Kong

**ABSTRACT:** Soils are inherently a particulate medium, and relevant physical principles behind the macro-scale engineering properties originate from particle interactions. However, it is difficult in general to conduct measurements which can monitor soil particle movement and even characterize micromechanics behind different soil behaviour. Advancement of sensing technologies in recent years offers us the opportunity to do so. Two examples are presented in this paper. The first is on using the tactile pressure sensor (film-like sensor) to monitor the evolution of contact normal forces among particles in aged sand. The measurement reveals that the contact forces are continuously redistributed during aging. This ultimately strengthens the soil structure and therefore increases the associated small-strain shear modulus. The second is on using the miniature MEMS accelerometer to characterize the soil movement in a laboratory flow landslide. The MEMS sensors demonstrate promising results in describing the rich features of local responses of soil movement in the shear zone, e.g. liquefaction, deceleration, contraction and dilation.

**RÉSUMÉ :** Les sols sont intrinsèquement un milieu particulaire et les principes physiques pertinents derrière les propriétés mécaniques à macro-échelle proviennent d'interactions entre particules. Cependant, il est difficile en général d'effectuer des mesures qui peuvent suivre le mouvement des particules du sol et même de caractériser la micromécanique derrière différents comportements du sol. L'avancée des technologies de détection ces dernières années nous offre la possibilité de le faire. Deux exemples sont présentés dans cet article. Le premier utilise le capteur de pression tactile pour suivre l'évolution des forces de contact normales entre des particules dans du sable âgé. La mesure révèle que les forces de contact sont continuellement redistribuées au cours du vieillissement. Cela renforce finalement la structure du sol et augmente donc le module de cisaillement associé à petites déformations. Le second utilise l'accéléromètre miniature MEMS pour caractériser en laboratoire le mouvement du sol dans un glissement de terrain. Les capteurs MEMS démontrent des résultats prometteurs pour la description des caractéristiques abondantes des réponses locales du mouvement du sol dans la zone de cisaillement, par exemple, la liquéfaction, la décélération, la contraction et la dilatation.

**KEYWORDS:** tactile pressure sensor; aging mechanism; MEMS • landslide initiation mechanism.

## 1 INTRODUCTION

Measurements of micromechanical interactions among soil particles are invaluable to constitute insights into the underlying physics of different soil behavior encountered in geotechnical engineering. However, it is difficult in general to conduct measurements which can monitor soil particle movements and even characterize micromechanics involved. In recent years, manufacturing industries witness breakthroughs in both miniaturization of sensors and improvement of sensing technologies. Therefore, we have an opportunity to carry out measurement at the particulate scale. In this paper we would like to introduce two applications in laboratory testing using such new technologies: (1) tactile pressure sensor to characterize the underlying mechanisms of aging in sand, and (2) 3D Micro-Electro-Mechanical-Systems (MEMS) accelerometers to capture soil movement in the initiation process of a laboratory flow landslide.

Aging can occur in all types of soils: for instance, increases in their shear strength and shear modulus are observed as time elapses. Such aging effects in sands have been reported not only from laboratory tests but also via field observations (e.g., see review in Schmertmann 1991, Mitchell and Soga 2005, Wang and Tsui 2009; Gao et al. 2013). Nevertheless, at present, the associated underlying mechanisms remain inconclusive. In the first study, the tactile pressure sensor installed in a tailor-made oedometer was used to characterize the evolution of contact normal force among particles in dry sand during aging. The bender element sets were also utilized in parallel to monitor the associated changes in the small-strain shear modulus,  $G_{max}$ . The

ultimate goal of this experiment is to provide evidence that could account for the underlying mechanisms of aging effects.

Initiation mechanisms of flow landslides are likewise still an unsettled open discussion. There had been published studies linking the initiation process of flow landslides to pore pressure rise and presence of fines in soil (Iverson et al. 2000, Wang and Sassa 2003); however, exactly how the shear zone develops, liquefies or decelerates due to dilation prior to complete fluidization is not measured. The miniature size of 3D MEMS accelerometers (in the range of *mm*) makes the measurements of localized soil responses inside slope possible since they can move like a soil particle without any pronouncing inertial effect. Reported MEMS sensor responses shed lights on a variety of soil movement involved in the initiation process of flow landslide, which will be discussed in detail in the second study.

## 2 USING TACTILE PRESSURE SENSOR FOR THE STUDY OF AGING MECHANISMS

### 2.1 The I-scan system

Tactile pressure sensors are ultra-thin and flexible and comprise numerous individual tiny sensing elements, called sensels. These features resolve the problems associated with the conventional load cells and enable us to accurately measure stress inside soils. Fig. 1 presents the pressure mapping system used in the first study, i.e., the I-Scan® system (Tekscan Inc., MA., USA). This system consists of software, scanning electronics (called a handle), and a tactile pressure sensor. There are 1936 sensels in the sensor adopted in this study (model 5076). The sensel is a force-sensitive resistor, whose impedance

changes in response to different loading. When a force is applied to the sensor, the analog-to-digital converter assigns a digital output (DO) value between 0 and 255 (i.e., 8-bit resolution) to each sensel, depending on the corresponding impedance value. This DO can then be correlated to the pressure or other engineering units through calibration.

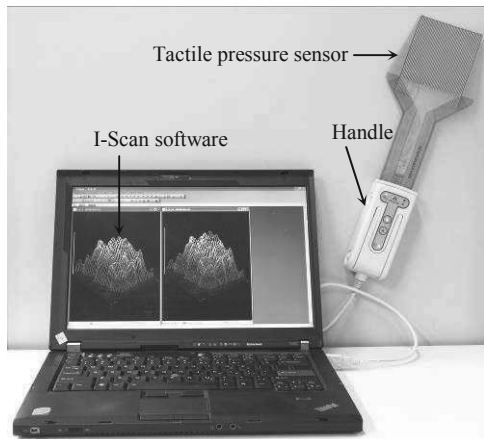


Figure 1. The I-Scan system.

2.2 Experimental setup and plan

Fig. 2 presents the experimental setup. A tailor-made oedometer with inner dimensions of  $100 \times 100 \times 40$  mm was used. Two sets of bender elements were utilized to obtain the small-strain, shear moduli  $G_{hv}$  and  $G_{hh}$ , where the first and second subscripts specify the directions of wave propagation and polarization, respectively;  $h$  means the horizontal direction and  $v$  stands for the vertical direction. Each set of bender elements consisted of one source and one receiver. The distance  $d$  between the source and the receiver is fixed at 80 mm throughout the test. The corresponding shear wave velocity  $V_s$  and shear modulus can be derived by  $G = \rho(V_s)^2 = \rho(d/t)^2$  where  $\rho$  is the soil density. The tactile pressure sensor was put between the upper and bottom box to measure the stress distribution inside soils. The calibration of tactile sensors including the creep (or drift) effect followed the procedure suggested by Gao and Wang (2012). The testing material was dry Leighton Buzzard sand (fraction E).

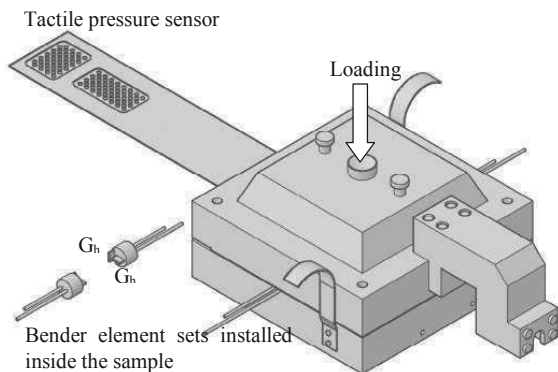


Figure 2. Experimental setup.

During the aging process, the applied vertical stress onto the sand sample was kept constant at  $\sigma_v = 197.21$  kPa for three days. The associated shear modulus changes was continuously monitored using the bender element tests and the evolution of contact normal forces among particles was constantly characterized by the tactile pressure sensor and the I-scan system.

2.3 Experimental results and discussion

Fig. 3 presents the variations in  $G_{hv}$  and  $G_{hh}$  during the aging process. The variations are presented in terms of the modulus change, i.e.,  $(G_t - G_{in})/G_{in}$  where  $G_t$  and  $G_{in}$  are the moduli at any time  $t$  and at the initial stage of  $t = 10$  min, respectively. As expected, the stiffness continues to increase, suggesting the sample is strengthened during the process of aging. In addition, the increase is greater in  $G_{hv}$  than in  $G_{hh}$ .

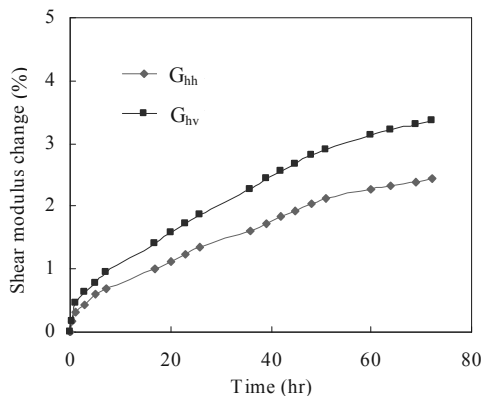


Figure 3. The experimental results of shear modulus changes versus time during three days of aging at  $\sigma_v = 197.21$  kPa.

Fig. 4 shows the probability distributions of measured, normalized contact forces (in the vertical direction,  $F_z$ ) by the tactile pressure sensor before and after three days of aging under  $\sigma_v = 197.21$  kPa. It can be readily seen that the contact forces are redistributed after three days of aging.

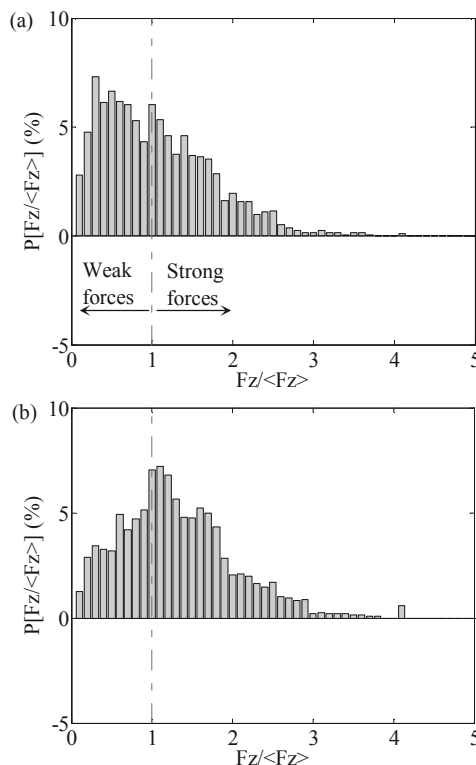


Figure 4 Experimental results of the probability distributions of normalized contact forces at  $\sigma_v = 197.21$  kPa (a) before and (b) after aging.

In order to further discuss such behavior, the contact forces are categorized into two groups, i.e., strong and weak forces. The categorization of strong and weak forces (i.e., the contact normal forces at strong and weak contacts or at strong and weak

networks) follows the suggestion of Radjai et al. (1996). When the normal contact force  $F_n$  is greater than its mean  $\langle F_n \rangle$  (i.e.,  $F_n / \langle F_n \rangle > 1$ ), it is regarded as a “strong” force; otherwise it is a “weak” force. Also found in Fig. 4 is that the probability distributions of weak forces decrease after aging. That is, the force redistribution leads to increasing contact normal forces in the weak force network such that some of the contact normal forces that originally belong to weak ones can be changed to the group of strong forces. In addition, the force distribution becomes more homogenized after aging because the associated coefficient of variation (CV) in  $F_z$  reduces from 0.726 to 0.705. Since the weak forces become fewer and the contact forces become more homogenized in the sample, the soil structure is strengthened and so is the associated  $G_{hv}$ . A comprehensive data set and more detailed explanations with the aid of DEM simulations can be found in Gao (2012) and Gao and Wang (2013).

### 3 USING THE 3D MEMS ACCELEROMETER FOR THE STUDY OF LANDSLIDE INITIATION PROCESS

Micro-Electro-Mechanical-Systems (MEMS) is a classification of devices, as well as the means of fabrication and manufacturing. In 1959, Richard Feynman took the helm of describing the “problem of manipulating and controlling things on a small scale” and thence pioneers like Analog Devices have since miniaturized conventional sensors from the size of a closed fist to that of a quarter of fingernail (Feynman 1959). The MEMS technology allows for batch-wise etching production, thereby minimizing manufacturing cost and at the same time promising standard accuracy and quality across sensors. Up until the recent 5 years only does stable 3-dimensional MEMS accelerometer become available in the market. The ADXL335 accelerometer model by Analog Devices is selected for the second study to characterize localized soil responses prior to and during landslide initiation.

The Analog Devices’ ADXL335 is a miniature accelerometer which measures  $4 \times 4 \times 1.45 \text{ mm}$  (Length  $\times$  Width  $\times$  Thickness) in size and comes at a low price, about couple US dollars per piece. It utilizes low power, typically functioning at  $3.0 \text{ V}$  and  $350 \mu\text{A}$ . The accelerometer is capable of 3-axis sensing and measures full-scale acceleration within  $\pm 3.6 \text{ g}$  with a frequency bandwidth ranging from  $0.5$  to  $1600 \text{ Hz}$  for the X and Y axes, and a range of  $0.5$  to  $550 \text{ Hz}$  for the Z axis. Fig. 5 illustrates the ADXL335 surface mounted on an in-house designed printed circuit board (PCB) since soldering by hand is impossible for the tiny pins; the PCB is  $11 \times 11 \times 2 \text{ mm}$  (Length  $\times$  Width  $\times$  Thickness) in size and the circuitry directs the corresponding pins to larger soldering points. The package was coated with several layers of air-dry polyurethane for waterproof. Also shown in Fig. 5 are the positive directions of X, Y and Z axes. The MEMS accelerometer is attractive not just because of its light-weight, miniature size, low-cost and standardized quality; it also boasts of the unique features of measuring the static acceleration of gravity in tilt-sensing applications, as well as dynamic acceleration resulting from motion, shock or vibration.

These unique features provide us with two kinds of information coming in one package. The DC bias offset in signal conditioned voltage output gives us the tilt angle in reference to the gravity. When the accelerometer is static, we can calculate the current angles of tilt in three dimensions about the accelerometer’s center of mass, known as roll, pitch and yaw; when it is in motion, we can calculate the direction of movement by finding the vector sum of the acceleration. In total 10 MEMS accelerometers were installed in both vertical and horizontal array so that dilative or contractive behavior between layers of soil could also be identified.

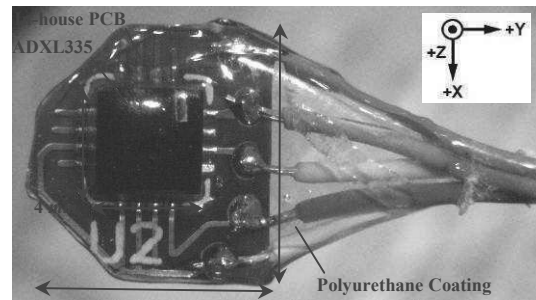


Figure 5. Analog Devices’ ADXL335 surface mounted on PCB.

#### 3.1 Calibration of 3D MEMS Accelerometer

All the MEMS accelerometers were connected to a logging computer through National Instruments’ NI-USB 6353 analog-to-digital converter with 16-bit resolution. Sampling frequency of every axis was set at  $10,000 \text{ Hz}$ . Due to batch-wise production, factory performance results of Analog Devices’ ADXL335 are compiled from 1000 pieces to determine the mean bias offset value (Analog Devices 2010); however, to further verify whether the sensors we purchased fall within the range as documented, simple calibration using an earthquake shaking table and a high-frequency vibration exciter was carried out. The mean zero bias offset value for X-axis was found to peak at  $1.51 \text{ V}$ , and for Y and Z axes the value was  $1.49 \text{ V}$ ; all sensors are functioning as detailed in the datasheet. The sensors were also left operating overnight to check for possible noise drift over time. Nothing anomalous happened and the sensors performed normally as documented in the manual. Subsequent conversions from voltage to acceleration which required parameters from the datasheet were cited directly thereafter.

#### 3.2 Laboratory Water Flume

Fig. 6 presents a side view of the well-instrumented laboratory water flume. The rectangular soil prism made of acrylic is of size  $100 \times 45.2 \times 20 \text{ cm}$  (Length  $\times$  Width  $\times$  Height). A saturation box was affixed at the back to provide standardized antecedent condition before each experiment. In addition to the MEMS accelerometer array (for the positions of accelerometer M1 to M10 see Fig. 6), basal porewater pressure transducers were also installed as indicated by the little squares; a video camera was shooting the process from the top. A layer of bottom porous stone was affixed to the flume rack to provide similar friction angle as the soil specimen at the bottom boundary.

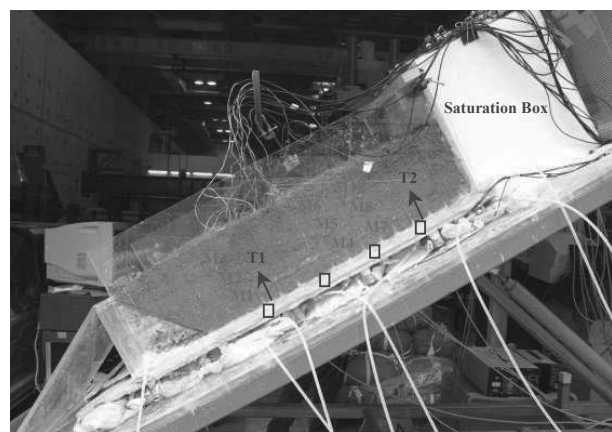


Figure 6. Laboratory water flume setup.



### 3.3 Characterization of Shear Zone Behavior with MEMS

In this section, we will demonstrate qualitative results from one of the water flume tests set out to investigate how shear zone liquefaction evolves in loose slope without any fines present. MEMS accelerometer M8 situated right within the shear zone in the rear middle of the soil mass was selected to illustrate the landslide mechanism (see Fig. 6). The loose slope was saturated by slow and little groundwater inflow at start, and a fixed interval later a sudden rise of groundwater inflow twice the original volume was first invoked at the bottom of the slope toe (indicated by T1 in Fig. 6); minutes later the rear bottom (T2 in Fig. 6). Both groundwater supply events are also indicated by vertical black lines in Fig. 7.

There are in total 3 sliding events recorded and their occurrence instances are punctuated by the vertical red lines in Fig. 7. The groundwater supply T1 at the slope bottom induced an abrupt liquefaction; inside the shear zone, Y axis of M8 registered a huge contraction and the Z-axis tracked a rotation towards the back then a forward charging jerk. However, the movement of the soil mass ceased as sudden as the initiation; the basal porewater pressure transducer tells us that the porewater pressure built up just then was dissipated. Although by now the groundwater supply T2 at the rear bottom was invoked, the soil mass did not exhibit any noticeable activity, a stark contrast to the loose slope with fines experiment in which complete fluidization occurred by the moment when T2 was invoked. Subsequently what we observed was replenishment of porewater pressure right before sliding event L2 happened and stopped almost instantaneously again; however, this time Y axis of M8 recorded a dilation instead. The porewater pressure abated after L2 then was built up again and finally the whole soil mass fluidized, initiating event L3. The movement was slow; it took 23.9 seconds in total to slide out of the flume. The activity inside shear zone as captured by M8 was a slow dilating rotation, upward and forward as the soil slowly discharged out.

In short, the MEMS accelerometers demonstrated promising results in describing the rich features of sliding events, including local responses of soil movement in the shear zone, e.g. contractions, dilations and the rolling components.

## 4 CONCLUSION

Two new sensing technologies (sensors) were successfully utilized in this paper to reveal aging mechanisms and to monitor local soil movement in a flow landslide event. Using the tactile pressure sensor allows us to measure the contact forces among soil particles and therefore is able to obtain experimental evidence that can explain the underlying mechanisms of aging effects. During aging the contact forces continue to be redistributed. This ultimately leads to increasing contact normal forces in the weak force network such that some of the contact normal forces that originally belong to weak ones can be changed to the group of strong forces. In addition, the force distribution becomes more homogenized. As a result, the soil structure is strengthened and so is the associated small-strain shear modulus.

Because of its miniature size and high sensitivity, the MEMS sensor is allowed to be buried in a laboratory slope to characterize the features of soil movement inside the shear zone during a flow landslide event, such as liquefaction, deceleration, contraction and dilation. All of these observations complement theoretical work and provides us insights into the initiation mechanisms of a flow landslide.

## 5 ACKNOWLEDGEMENTS

This research was supported by the Hong Kong Research Grants Council (GRF 621109 and 620310).

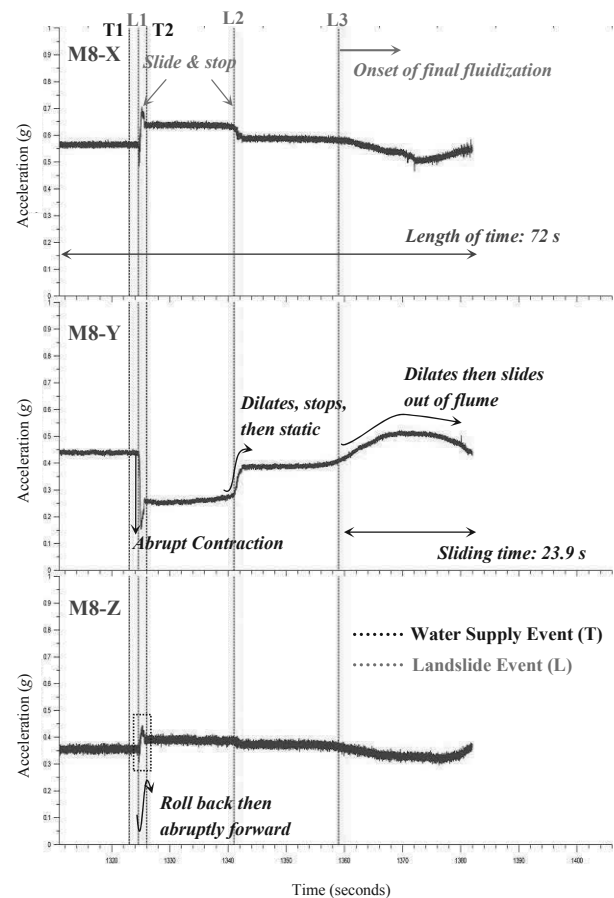


Figure 7. Characterization of sliding features within shear zone in loose slope without fines captured by MEMS accelerometer M8, demonstrating a gradual failure mode.

## 6 REFERENCES

- Feynman, R. 1959. *There's plenty of room at the bottom*. URL: <http://www.zyvex.com/nanotech/feynman.html>
- Gao Y. 2012. Experimental characterizations and DEM simulations of aging, creep and structuration in sand. Ph.D. Thesis. The Hong Kong University of Science and Technology.
- Gao Y. and Wang Y.H. 2012. Calibration of tactile pressure sensors for measuring stresses in soils. *Tentatively accepted by Geotech. Test. J. ASTM*.
- Gao Y. and Wang Y.H. 2013. The underlying mechanism of aging effects on changing sand stiffness. Submitted to Canadian Geotechnical Journal.
- Gao Y., Wang Y.H., and Su J.C.P. 2013. Mechanisms of aging-induced modulus changes in sand under isotropic and anisotropic loading. *J. Geotech. Geoenviron. Eng.* (Accepted for publication, [http://dx.doi.org/10.1061/\(ASCE\)GT.1943-5606.0000772](http://dx.doi.org/10.1061/(ASCE)GT.1943-5606.0000772)).
- Iverson, R.M., Reid, M.E., Iverson, N.R., LaHusen, R.G., Logan, M., Mann, J.E. and Brien, D.L. 2000. Acute sensitivity of landslide rates to initial soil porosity. *Science*, 290:513-516.
- Mitchell, J. K. and Soga, K. 2005. *Fundamentals of Soil Behavior*, 3rd edition, John Wiley & Sons, Inc., New York.
- Radjai, F., Jean, M., Moreau, J.J., and Roux, R. 1996. Force Distributions in Dense Two-Dimensional Granular Systems. *Phys. Rev. Lett.*, 77(2), 274-277.
- Schmertmann, J.H. (1991). The mechanical aging of soils. *J. Geotech. Engrg., ASCE*, 117(9): 1286-1330.
- Wang, G. and Sassa, K. (2003). Pore-pressure generation and movement of rainfall-induced landslides: effects of grain size and fine-particle content. *Eng. Geol.*, 69, 109-125.
- Wang, Y.H. and Tsui, K.Y. 2009. Experimental characterization of dynamic property changes in aged sands. *J. Geotech. Geoenviron. Eng., ASCE*, 135(2), 259-270.

# General Report of TC 207 Foundations and Retaining Structures

## Rapport général du TC 207 Fondations et ouvrages de soutènement

Bilfinger W.  
Vecttor Projetos, Brazil

**ABSTRACT:** Forty nine papers were included in the theme Soil Structure Interaction. These papers were divided into those related to foundations and retaining structures. The number of research papers and case histories are almost equal, showing equilibrium between academicians and practitioners. Different types of foundations are presented, as well as different types of retaining structures.

**RÉSUMÉ :** Quarante neuf articles ont été inclus dans le thème « Interaction Sol-Structure ». Ces documents ont été divisés entre ceux qui sont liés aux fondations et ceux liés aux ouvrages de soutènement. Le nombre d'articles de recherche et d'études de cas sont presque égaux, montrant l'équilibre entre les universitaires et les praticiens. Sont présentés différents types de fondations, ainsi que différents types d'ouvrages de soutènement.

**KEYWORDS:** soil-structure interaction, foundation, retaining structure, excavation.

### 1 INTRODUCTION

Foundations and retaining structures are traditional and widely used geotechnical structures in which soil-structure interaction plays a major role. For this reason, this technical session was organized by TC 207 – Soil Structure Interaction.

A total of 49 papers were included in this session, 12 focused on foundations and 37 about retaining structures. Contributions came from 28 countries, divided regionally as presented in Figure 1. Almost  $\frac{3}{4}$  of all technical papers come from Europe.

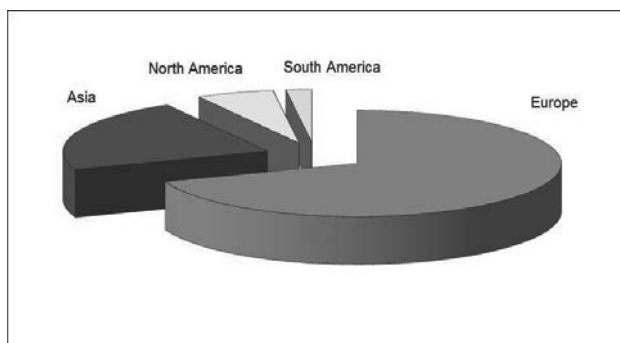


Figure 1. Origin of published papers: Europe – 39, Asia – 11, North America – 3 and 1 – South America.

23 papers present case histories and 26 research results, which show a desired equilibrium between academia and practice.

This report includes:

- A brief summary of the papers related to foundations;
- Some selected topics related to foundations;
- A brief summary of the papers related to retaining structures;
- Some selected topics related to retaining structures;
- Conclusions.

### 2 BRIEF REVIEW OF PAPERS RELATED TO FOUNDATIONS

12 papers focusing on foundations were selected for this session, 5 of them describing case histories and 7 presenting

research results. Variable topics were presented and discussed, including shallow and deep foundations, as well as soil structure interaction, specially the interaction between foundations and deep excavations.

*M. Bidasaria* presents a case history about the cofferdam for the Indira Sagar Project in India. This cofferdam was built as a gravity dam, using precast hollow concrete blocks on the upstream and downstream faces. Between the two faces, rubble was filled and later grouted by a cement-sand mixture, forming a so called stonecrete. The paper presents interesting constructive details about the construction of the cofferdam.

*E. M. Comodromos et al.* present numerical simulations to evaluate the influence of diaphragm wall construction on adjacent buildings. The 3D simulations are specific about the excavation phase, where soil is substituted by bentonite slurry, and the concrete tremied into the panel. Obtained results showed maximum settlements in the order of 5 mm, for a 6 story building founded on direct footings located closely to the wall.

*F. Cuira and B. Simon* present an analytical model to evaluate soil reinforced by vertical inclusions, considering the interaction between the reinforced and un-reinforced soil along their boundary. An analytical method is compared to 3D FE simulations and good results are obtained. Further research using centrifuges is recommended in the conclusions.

*W. Guo and J. Chu* present results of model tests of suction caissons, focusing on shallow water for near shore use. The obtained results were in good agreement with an analytical results.

*G. Hannink and O. Oung* present a case history with prediction and monitoring results of the induced movements of a 9 story high apartment building, due to excavation of a 20 m deep closely located (7m distance) excavation, retained by strutted diaphragm walls. Measured horizontal and vertical movements of the apartment building were in the order of 10 mm.

*Horn-Da Lin et al.* present numerical simulation results, where the influence of a deep excavation on nearby located buildings is evaluated. The excavation depth is around 20 m. As benchmark, results of a documented published case history are used, and good agreement was obtained. Horizontal wall



deflections were in the order of 110 mm and maximum settlements at the surface, around 80 mm.

R. Katzenbach and S. Leppla describe results of ground heave and settlement due to excavations, building construction and de-construction. The measured behavior is time dependent and occurs during years and the magnitude of the displacements is in the order of several cm. The soil responsible for this time dependent behavior is the overconsolidated Frankfurt clay. An empirical formulation that approximately describes the time dependent behavior is also proposed.

M. Korff and R. Mair present building settlement results due to deep excavations in Amsterdam. The difference between ground surface and building response as a function of foundation is highlighted and a methodology to evaluate buildings response is presented. Surface settlements in the order of 70 to 110 mm are presented, while the piled building settles only in the order of 20 to 40 mm.

T. Mizutani and Y. Kikuchi describe shaking table model tests to test seismic behavior of caisson type quay walls. The aim of the tests was to verify the possibility to increase water depth in front of the quay after soil treatment – “solidification” in the caisson foundation. It was found, that six different factors affect the caissons improved by the “solidification”. Further research will be performed to allow the development of a design methodology.

T. Pucker and J. Grabe present the structural optimization method applied to geotechnical engineering design. This use is new and, according to the authors, promising results were obtained, showing potential economy and/or improvement in performance.

V. Sesov et al. present a methodology developed for the evaluation of seismic response of historical monuments in Macedonia. 3 Case histories are presented, where this methodology was used.

A. Siemińska-Lewandowska et al. describe different uses of diaphragm walls: retaining structures and foundations. Vertical load test results are presented, with up to 7,5 mm settlement for 150% of the working load. Interesting retaining structures using T shaped diaphragm walls are also presented.

### 3 SELECTED TOPICS RELATED TO FOUNDATIONS

The papers presented related to foundations cover a wide range of issues and foundation types:

#### Direct foundations:

- Gravity “concrete” dam;
- shallow footings (influence by diaphragm wall construction; influence by nearby deep excavations);
- caissons – quay wall;
- suction caissons;

#### Soil treatment for vertical loads by rigid inclusions;

#### Deep foundations:

- Driven timber piles (influenced by nearby excavation);
- Precast concrete piles (influenced by nearby excavation);
- Barrettes and Diaphragm walls (as foundations and retaining structures);

#### Seismic design and retrofitting of different foundations;

#### Long term settlement and heave in highly overconsolidated clay;

#### Structural optimization technique – use of new technique to optimize foundations.

Two topics were selected, among this wide range presented, and are discussed in more detail.

Specifically seismic issues will not be discussed in detail in this session, as a specific session at this same conference deals with the theme.

### 3.1 Influence of Excavations on Foundations

The evaluations of E. M. Comodromos et al. showed that the construction of diaphragm walls alone lead to settlement of closely located direct foundations in the order of 5 mm. The approach presented considered complex 3D nonlinear modeling, where the excavated soil is replaced by bentonite slurry.

Additionally to this theoretical aspect, it could be added that, in the field, several times, especially in sandy soil below the groundwater level or soft clays, the operation and movements of the excavation equipment (clam shell, etc ) can generate temporary negative suction pressures, leading to “cave-ins” and additional settlements, that can be in the order of several cm.

M. Korff and R. Mair and G. Hannink and O. Oung, present monitoring results, as well as simulations of settlements induced by deep excavations.

The results presented show significant difference between measured settlements: Korff and Mair show settlements, in Amsterdam, at the ground surface of more than 100 mm and, at 10 m from a 31 m deep excavation, building settlements of almost 40 mm. G. Hannink and O. Oung, on the other hand, present settlement measurements, in Rotterdam, of less than 10 mm for a building located 7 m from a 20 m deep excavation. Both excavations are supported by braced diaphragm walls. Possible explanations for these differences are probably:

- Different soil profiles;
- Different excavation depths;
- Different diaphragm and bracing stiffnesses;

Appart from these rather obvious aspects, certainly:

- Different pile length: in the case of the excavation in Amsterdam, the piles are located well above the excavation bottom, but in the case of Rotterdam, pile toes are located almost at the same elevations;
- Location of the buildings in relation to the excavation. No specific information is available from Amsterdam, but in Rotterdam, the building is located close to the excavation, as can be seen in figure 2.

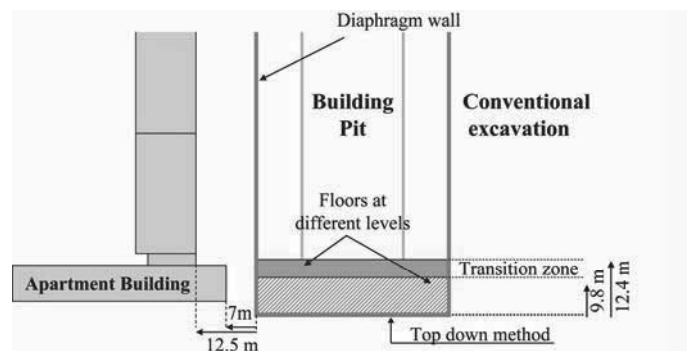


Figure 2. Position of building with relation to excavation (G. Hannink and O. Oung)

This last topic can be confirmed by the analysis of the results presented by Horn-Da Lin et al: the evaluations presented show, qualitatively, that close to the excavation borders, settlements are significantly lower than in the central part, as can be seen in figure 3. The arrows show an approximate position of the apartment building. It is clear that the settlements are significantly lower than in the central part.

Depending of the geometrical conditions, it becomes clear that 3D analyses may be necessary to adequately evaluate soil-structure interaction.

With relation to settlements induced by excavation, in the author’s opinion, the methodologies presented and discussed in Korff and Mair present tools to adequately predict building response to deep excavations, in the case of deep foundations.

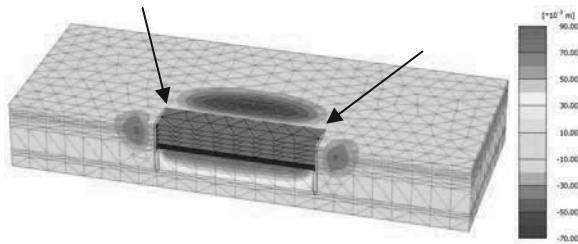


Figure 3. Settlements due to excavation (*Horn-Da Lin et al.*).

### 3.2 Loading and Unloading due to high rise buildings and excavations

The paper presented by *R. Katzenbach and S. Leppla* presents results of ground heave and settlement measurements due to excavations, building construction and de-construction. This behavior, which could be expected not only in Frankfurt, but also in other geological environments, was adequately documented during a significant time period for some buildings.

The first important issue, often neglected due to lack of reliable information, is the fact that unloading generates significant upward movement, in the order of some or even several cm.

The second issue is the time dependent behavior: a significant part of total displacements are measured at the end of construction, but between 30 and 50% of the observed behavior, occur during months or years after completion of the construction works.

*Katzenbach and Leppla* propose an empirical equation to represent this time dependent behavior. Just as an exercise, Figure 4 presents monitoring results and the equation proposed by *Katzenbach and Leppla*, and, additionally, settlements estimated using conventional consolidation theory. A consolidation coefficient at the recompression stage of  $c_v = 9 \times 10^{-2}$  cm/s was backanalyzed from the measured settlements. This value can be considered representative of overconsolidated clays.

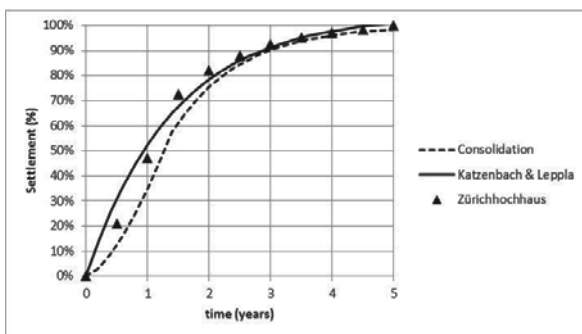


Figure 4. Settlement in % using conventional consolidation theory, the equation proposed by *Katzenbach & Leppla* and monitoring results.

From the discussion above, it becomes clear that, especially in urban environments, even for material considered relatively stiff, time dependent behavior cannot be neglected, depending of local geology.

## 4 BRIEF REVIEW OF PAPERS RELATED TO RETAINING STRUCTURES

37 papers focusing on retaining structures were selected for this session, 18 of them associated to case histories and 19 with research results. A broad range of topics related to retaining structures was presented.

*M. Abramento et al.* present a case history from Brazil, of a mixed retaining structure, reinforced earth at the top and anchored wall at the bottom, in a geotechnical environment of expansive soils. The case history includes laboratory tests of the expansive soils and anchor pull out tests, demonstrating that

injection pressures have significant impact on anchor resistance. Monitoring results of the retaining structure are also presented, showing significant horizontal displacement of the reinforced earth face, and negligible horizontal displacements of the anchored stretch.

*D. Alexiew and H. Hangen* discuss a case history from Bulgaria, where reinforced earth structures were used as retaining structures. Relatively steep, 1H:10V, and high, over 20 m, structures are presented; constructive details are included. Design considerations, including seismic actions, are also discussed.

*S. Bagheri* present the case history of the deep excavation, in marl and weather marl, associated to the construction of the “Tour Odeon” in Monaco. The excavation is more than 70 m deep and the excavation is supported by anchors.

*Ö. Bilgin and E. Mansour* discuss theoretical analysis of sheet piles in expansive soils. For a typical sheet pile wall, 10 m high and with an anchor level at 2,5 m, significant increases in anchor reactions and bending moments occur, as swelling pressure increases. Higher wall penetrations also become necessary. Swelling pressures were associated to the Plasticity Index and moisture content variations.

*C. M. Chow and Y.C. Tan.* present data related the performance of soil nails in weathered granite and fill. Several soil nail pull out tests were performed in excavations up to 20 m depth. Lateral friction measurement results varied between 50 and 140 KPa. A conservative correlation for lateral friction of 5 x SPT (in KPa) blowcount is also proposed.

*I.P. Damians et al.* discuss the influence of vertical facing stiffness on reinforced soil wall design. Numerical results showed that the loads at the base of the vertical facing and in the reinforcement are affected by the backfill and foundation material, and that the face stiffness also affects reinforcement tensile forces.

*T. Durgunoglu et al.* present a case history from Turkey, an over 20 m deep excavation close to the Bosphorus. Top down construction method was used, including excavation of rock sockets into rock with a uniaxial compressive strength varying between less than 10 MPa, up to almost 100 MPa.

*R.J. Finno et al.* discuss ground movements due to top-down construction in Chicago. For this type of construction, according to these authors, normalized horizontal movements of 0,15% to 0,2% are expected. Approximately 40% of these movements can be attributed to time dependent behavior of the concrete slabs. Significant movements can be associated to activities other than the excavation, like potholing.

*R. Frischknecht et al.* present an environmental impact evaluation, comparing a conventional concrete structure with a geosynthetic reinforced earth structure. The conclusion of the evaluation is that geosynthetic retaining structure shows a 63% to 87% lower environmental impact.

*P.P. Ganne and X. Raucroix* discuss the design of cantilever walls with a relief floor. For unsaturated, sandy, silty and alluvial clayey soils, an analytical design methodology is proposed, including pre-design recommendations.

*A. Gomes Correia et al.* present a case history of a 13 m high CSM anchored retaining wall built in Portugal. The CSM wall was built in fill, sands and weathered sandstone, reinforced by steel beams with a horizontal spacing of 1,1m. Maximum measured horizontal displacements were of 16 mm.

*A. Guilloux et al.* discuss the design, modeling and monitoring of the Tour Odeon, also presented by *Bagheri*. A 3D numerical model is presented as main design tool. The use of the observational model with a maximum horizontal displacement of 17 mm is described.

*E. Guler et al.* present the case history of a 23 m deep excavation in Istanbul. 2D and 3D numerical modeling was used to evaluate interaction between 2 tunnels, a circular shaft and a deep braced excavation. 2D and 3D models were compared and the 2D analysis showed results on the safe side. Monitoring results obtained during construction yielded reduced

horizontal displacements, in the order of 8 mm, compatible with the 3D FE analysis.

*I. Gutjahr et al.* discuss comparisons between subgrade reaction calculations, FE analysis using 2 different softwares and monitoring results of an anchored retaining structure of the Vieux Blanc-Mesnil Basin, in France.

*V.A.Ilyichev and Y.A. Gotman* present a method to optimize diaphragm wall displacements in deep excavations, by means of using soil cement mix in the active and passive parts of the soil massif. The dimensions and stiffness of the soil cement mix can be estimated using the proposed computational method. FE calculations were used to calibrate the proposed calculation method and good agreement was obtained.

*Y. S. Jang et al.* discuss two case histories from Korea of deep excavations supported by diaphragm walls. Excavations depths of 1 case is 20 m and of the other, 31 m. The retaining walls are concrete diaphragm walls, steel profiles and timber, and steel profiles and shotcrete. Horizontally, the walls are supported by anchors, in one case, and by steel struts, in the other case. Horizontal movements of 30 to almost 100 mm were measured. Forces in anchors and struts were also measured and compared to numerical simulations.

*S. Jessee and K. Rollins* present model tests to evaluate the passive pressure on skewed bridge abutments. The performed tests showed that a significant reduction was measured, as the skew angle increases. These results were compatible with numerical simulations and a simple correction factor is proposed.

*M. Long et al.* present a number of case histories of excavations in glacial tills of Ireland. 12 cases are presented, where horizontal displacements were measured. The displacements were, in most of the cases, less than 0,1% H. The conclusion of the authors are that design has been conservative and more realistic design methods and construction methods can lead to more economic design.

*D. Loukidis and R. Salgado* discuss the results of numerical simulations of earth pressure on walls supporting granular soils. The simulations, using Ottawa and Toyoura sands, with varying relative densities, showed that a minimum active pressure is obtained at 0,5% H displacement. But with higher displacements, in the order of 10% H, critical state inside the soil mass is mobilized. An equation is proposed to estimate the variation of the earth pressure coefficient as a function of the wall crest displacement.

*R. Lüftenegger et al.* present case histories of non conventional retaining structures. The structures were conceived based on the necessity to avoid the installation under neighboring buildings. 3D FE analyses were used to understand behavior. Good adherence between prediction and monitoring was not obtained, and for this reason the use of the observational method is recommended.

*T. Maeda et al.* discuss the use of inclined braceless retaining structures in sandy soil. Instead of using a vertical face, inclining it slightly, 10°, allowed the excavation of an almost 10 m deep excavation without any bracing or anchor. An analytical design method was developed and verified by centrifuge tests. Monitoring results from the site showed that the design method lead to results on the safe side.

*S. Nakajima et al.* present a methodology to inspect exiting retaining structures. The methodology includes percussion tests and vibration tests, where the natural frequency of the structures is measured to evaluate its condition.

*C.Y. Ou et al.* discuss the mechanism of settlement influence zone due to deep excavation in soft clay. The USC model is used for parametric analyses a method for predicting the settlements is proposed.

*J. Philipsen* discusses the case history of a braced excavation, built under difficult conditions, in Copenhagen. The excavation was built in quaternary clays and sands, overlaying limestone.

*A. Pinto et al.* present a case history of an anchored excavation in Lisbon. The excavation was 13 m deep and supported by vertical steel profiles associated to a CSM wall and anchors. The geotechnical profile includes superficial fill, medium sands and sandstones, and GWT 5 m below the surface. The excavation was monitored through inclinometers, with maximum horizontal displacements close to the surface of around 40 mm.

Another paper by *A. Pinto et al.* present the case history of excavations for the Leixões Terminal in Portugal. 2 different solutions are presented: CSM panels with steel profiles and CSM panels with micropiles. The excavation is around 6,5 m deep and the geotechnical profile includes hydraulic fill placed on weathered schist. CSM UCS minimum measured values were of 4 MPa.

*H. Popa et al.* discuss a case history from Bucharest. 16 m had to be excavated to accommodate a 4 to 6 m deep basement mat and 2 basements. The subsoil profile included interbedded layers of medium to compact sands and medium to stiff clays, with groundwater level 2 to 3 m above the excavation bottom. An anchored diaphragm wall was designed, built and monitored, with maximum horizontal displacements of less than 10 mm.

*C. di Prisco and F. Pisanò,* present a new anchor type. FE analyses are used to evaluate the pull out behavior of the anchor. Based on the FE analyses, an analytical method is also developed and presented.

*N. Sanvitale et al.* discuss the role of the facing on the behaviour of soil-nailed slopes under surcharge loading, using small physical models in sand. Flexional and axial stiffness influence the performance of the soil nailing system.

*T. Tanaka et al.* present results of physical and numerical models, where 3D seepage effects influence stability. Uniform sand are used for the evaluations and results show that the 3D conditions differs from those of typical 2D conditions. Correction factors from an axisymmetric simulation to no axisymmetric conditions are also presented.

*P. Turček et al.* discuss case histories of deep excavations in Bratislava. Local subsoil includes superficial quaternary sediments, mainly gravel and sand, overlaying neogene marine sediments, mainly stiff clays. Groundwater is normally at shallow depth and its control is one of the main challenges for successful construction.

*M J Turner and N A Smith* present a case history of the stabilization of a gravity quay wall in the UK. The 17 m high wall, originally built at the end of the 19<sup>th</sup> century, suffered stability problems since the mid 1980s, with horizontal displacements of around 400 mm. Evaluations showed that the difference between the high tidal variations, more than 6 m, and the groundwater level behind the wall, were leading to increasing horizontal displacements. Stabilization measures included groundwater lowering and installation of anchors.

*L. Vollmert et al.* discuss results of large scale in situ tests, as well as long term monitoring results of a reinforced earth structure. For the monitored cases, with full height panel walls as facing, the actual lateral stress measured is significantly lower than FE calculations or classic earth pressure theory, showing that current design methods are on the safe side and, possibly, a correction factor can be introduced to EBGeo design methodology.

*G. Vukotić et al.* present results of anchor bond measurements in different soils and anchor length. The influence of the fixed anchor lengths is evaluated, showing that longer anchors are less efficient than shorter anchors. A proposition or design methodology is presented, including possible use of single bore multiple anchors – “SBMA”.

*L. Warren et al.* discuss the use of drystone retaining walls, including model tests performed in the UK. Different types of walls, based on their construction methods, horizontal, vertical and random, are discussed. The type of wall is presented as a

sustainable type of structure, due to lack of mortar, use of local materials and providing habitat for animals and plants.

C. A. Wiggan *et al.* present a numerical evaluation of potential pore pressure reduction on retaining walls due to the flow between piles. Not considering a wall of secant of contiguous piles impermeable, lead pore pressure reductions that act on the wall. Results of parametric evaluations are presented, where the distance between the piles are varied, showing significant pore pressure reductions. This approach, however, leads to increased settlements at the surface.

C. Yoo and D.W. Jang discuss results of laboratory tests performed on reduced models, to evaluate the influence of rainfall on the performance of reinforced earth structures. Test results showed that wetting and drying cycles may have cause additional wall displacements, especially for structures with low safety factor.

### 5 SELECTED TOPICS RELATED TO RETAINING STRUCTURES

The technical papers related to retaining structures cover a wide range of topics, including:

- Reinforced soil – 5 papers;
- Diaphragm walls – 4 papers;
- Secant pile walls – 1 paper;
- Sheet pile walls – 3 papers;
- Soldier type walls – 3 papers;
- Mixed in place soil structures – 5 papers;
- Soil nailing and anchors – 3 papers;
- Gravity and cantilver walls – 3 papers;
- Others.

From this wide range, some topics were selected and are discussed in more detail:

- Horizontal displacements;
- Earth pressures;
- Soil nailing and anchor lateral friction;
- Soil-cement mixtures.

Unfortunately, not all papers present sufficient technical data, to allow analyses and comparisons.

#### 5.1 Horizontal displacements

The selected papers present, in some cases, monitoring results, specifically, horizontal displacements, which are summarized in Figure 5 and 6.

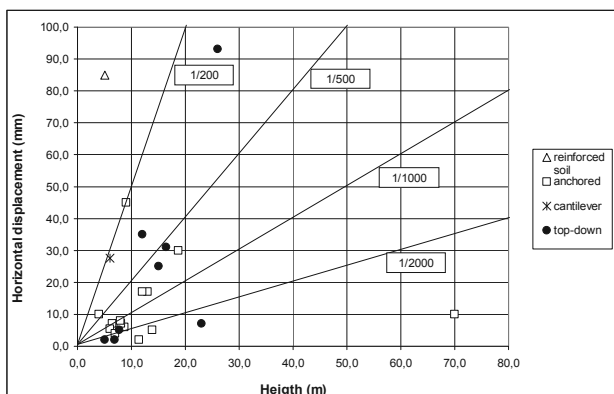


Figure 5. Horizontal displacements x excavation depths.

Very variable results can be seen; horizontal displacements / heights (H/D) from less than 1/2000 to more than 1/200 were presented.

No clear tendency can be identified in figure 5. Visually, one possible conclusion is that deeper excavations, apparently, present lower D/H values, meaning that this type of construction is, due to its complexity, designed and built with higher safety margins and possibly, more rigid. Figure 6 below presents the same data, showing normalized horizontal displacements and

excluding 1 extreme value: the 70 m high excavation (in rock) presented by S. Bagheri and A. Guilloux *et al.*

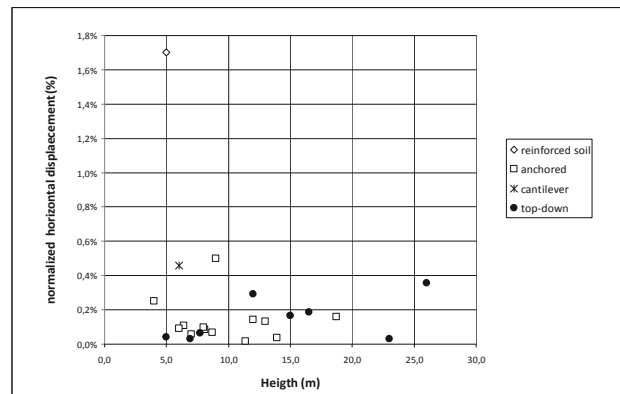


Figure 6. Normalized horizontal displacements with respect to excavation heights (depths)

In comparison to other retaining structures, relatively high horizontal displacements (85 mm =>1,7%) were measured for a reinforced earth structure (M. Abramento *et al.*). However, this magnitude of displacement, according to common practice, can be considered normal for reinforced soil structures (Sayão *et al.*, 2004).

Figure 7 shows the same results, plotted together with the data presented by Long (2001).

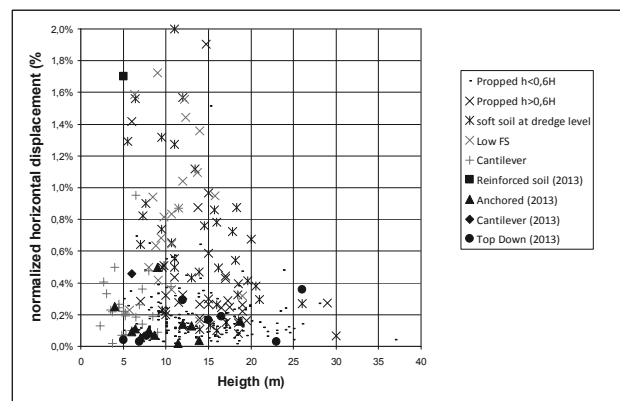


Figure 7. Normalized horizontal displacements x excavation heights, including data presented by Long (2001).

It can be seen that the published horizontal displacements are compatible with several other measurements as compiled and published in 2001.

Other published databases are also compatible with the presented data:

- Leung and Ng (2007): 0,13 %H to 0,23 % H, depending on soil stiffness;
- Wang *et al.* (2010): 0,27%H to 1,5%H, depending of retaining structure type and soil stiffness.

Common conclusion of Long (2001), Leung and Ng (2007) and Wang *et al.* (2010) are that horizontal displacements are affected mainly by safety margins, system stiffness, soil type and construction method.

Finally, the conclusions presented by R.J. Finno *et al.* are interesting: for the cases where small displacements are measured, a significant part of these displacements may be caused by time dependant behavior of concrete floor slabs.

#### 5.2 Earth Pressures

Four papers deal specifically with earth pressures: Ö. Bilgin and E. Mansour, S. Jessee and K. Rollins, D. Loukidis and R. Salgado, T. Maeda *et al.*

*Ö. Bilgin and E. Mansour* discuss theoretical analysis of sheet piles in expansive soils. The presented analyses are based on a correlation between the plasticity index (PI) and swelling potential. The analyses presented assume that swelling pressure will act in the zone where moisture varies, relatively close to the surface. Figure 8 presents results of the authors analyses, correlating anchor loads of sheet pile wall to the PI

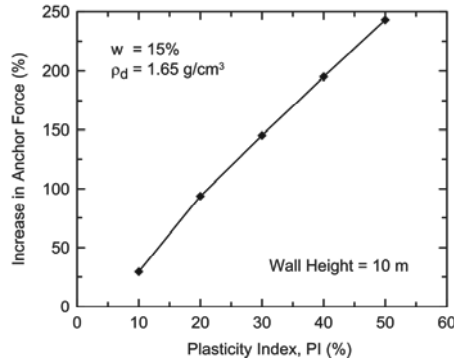


Figure 8. Effect of expansive soils on anchor force, according to *Ö. Bilgin and E. Mansour*

*S. Jessee and K. Rollins* present model tests to evaluate passive earth pressure on a “skewed” surface. Figure 9 presents a proposed reduction factor for the passive force, as a function of the skew angle.

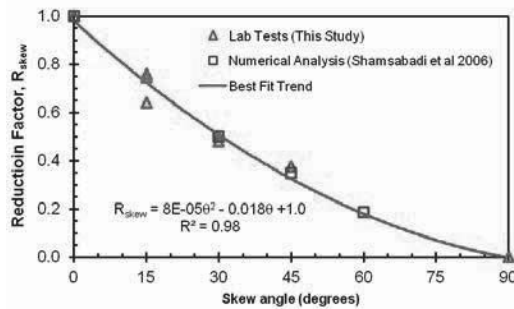


Figure 9. Test results presented by *S. Jessee and K. Rollins*.

The performed tests showed that a significant reduction was obtained as the skew angle increases. These results were compatible with numerical simulations and a simple correction factor is proposed. Peak passive pressure was developed at 2,5% to 3,5% of abutment height. Significant reductions in passive pressure were measured beyond peak (4% to 6%), with a residual stress around 40%.

Results are interesting, but direct use of results for design shall be evaluated with care.

*D. Loukidis and R. Salgado* present the results of sophisticated numerical simulations of variation of earth pressure on walls supporting granular soils. Figure 10 present one of the presented outputs and some interesting qualitative conclusions can be drawn:

For horizontal displacements of around 0,5%, minimum lateral earth pressure develops. Considering  $K_0$  around 0,5,  $K_a$  results around 0,125. As horizontal displacement increases,  $K_a$  results in the order of 0,2. The authors state that the minimum earth pressure coefficient should not be used, at least for ultimate limit state design. However, when analyzing figure 7, where a significant number of case histories showed horizontal displacements of less than 0,4 %, possibly some optimization in terms of design earth pressures can be possible.

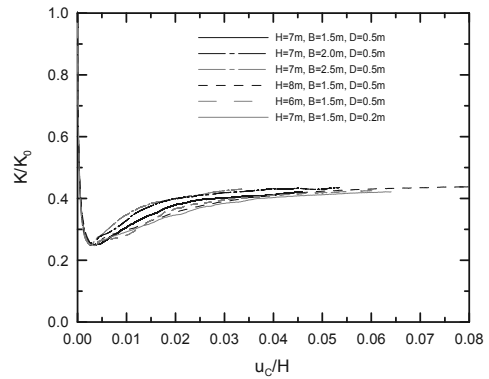


Figure 10. Results presented by *D. Loukidis and R. Salgado*: Variation of normalized lateral earth pressure coefficient with wall crest displacement from analyses with medium dense Toyoura sand ( $D_R=60\%$ )

*T. Maeda et al.* discuss the use of inclined braceless retaining structures in sandy soil. The presented evaluations showed that significant reduction in earth pressures acting on a cantilever wall can be obtained by inclining the wall facing. Figure 11 present horizontal displacements measured on model tests. It can be seen that, even for a reduced inclination of 10°, horizontal displacements reduced around 30%.

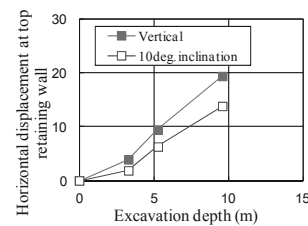


Figure 11. Relationship between excavation depth and horizontal displacement of retaining walls, considering horizontal and inclined structures, presented by *T. Maeda et al.*

Figure 12 presents earth pressures for the inclined and the vertical structure. It can be seen that, especially for deeper excavations, a significant reduction in earth pressures occurs.

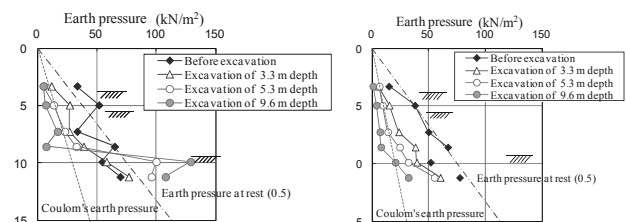


Figure 12. Earth pressures for vertical and inclined structure, presented by *T. Maeda et al.*

In the author’s opinion, the simple approach of inclining slightly a cantilever structure can bring significant saving, should be further investigated and can be used in practice.

### 5.3 Soil nailing and anchor lateral resistance

*C. M. Chow and Y.C. Tan.* present data related to the performance of soil nails in weathered granite and fill. Several soil nail pull out tests were performed in excavations of up to 20 m depth. Figure 13 presents typical pull out results, showing that maximum load is obtained between 4 and 6 mm of displacement. After a peak value, only slight increases can be seen.

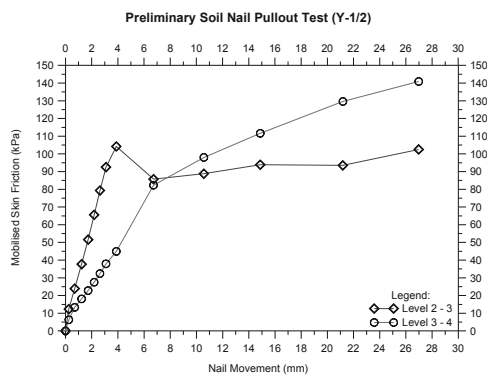


Figure 13. Pull out test results, presented by *C. M. Chow and Y.C. Tan*.

Lateral friction measurement results varied between 50 and 140 KPa. A conservative correlation for lateral friction of 5 x SPT (in KPa) blowcount is also proposed.

These results are comparable with data presented in Ortigão and Sayão (2004): for sands, approximate ratio between SPT blowcount and lateral friction is around 5, and for clays, around 3,4.

*M. Abramento et al.* presented results of pull out tests of anchors for different grouting conditions and resulting lateral friction between 80 KPa and 140 KPa. The soil where the anchors were built has an approximate SPT blowcount between 20 and 30.

Finally, just for comparison, Décourt (1982) presented a correlation between SPT blowcount and lateral friction for piles:

$$\text{Lateral friction} = 10 \times (\text{SPT} / 3 + 1).$$

Figure 14 presents graphically the lateral frictions and corresponding SPT blowcount values.

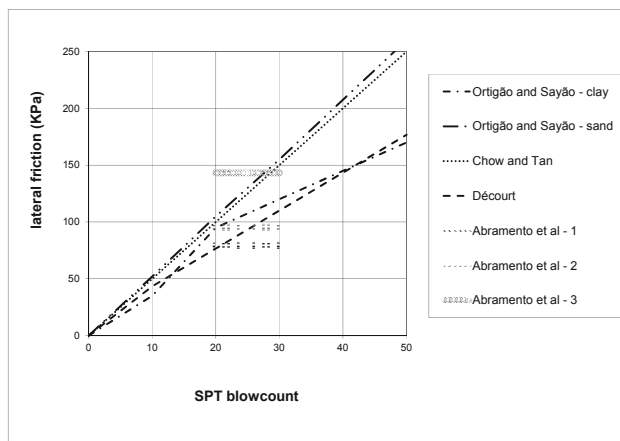


Figure 14. Lateral friction results, presented by *C. M. Chow and Y.C. Tan*, including values published by Ortigão and Sayão (2004) and Décourt (1982).

*A. Gomes Correia et al.* present results of anchor tests in medium dense sands, resulting in a lateral friction of 275 KPa. Similar results and even higher lateral frictions are presented by *G. Vukotic et al.* for tests in different soils. Unfortunately, there is no specific information available about the SPT blowcount, but probably results will be well above the graphs presented in Figure 14. Possibly, this difference occurs due the use of pressure grouting.

Even considering the limitations of the SPT blowcount as geotechnical design parameter, the correlations between the SPT and lateral friction proposed by *C. M. Chow and Y.C. Tan* seem compatible with previously published results for soil nails. Grout injection influence, in the author's opinion, shall be further investigated. Special anchor devices, like the one presented by *C. di Prisco and F. Pisanò* work completely different from cylindrical nails / anchors and further research is necessary to allow reliable comparisons.

#### 5.4 Soil mixing compressive strength

*A. Gomes Correia et al.* present a case history where CSM material, with a cement consumption of  $600 \text{ kg/m}^3$ , was tested and a minimum uniaxial compressive strength of 4 MPa was obtained. Minimum  $E_{50}$  values were 1 GPa. Unfortunately, few results with information about this important design parameter were presented. As complementary information, Figure 15 presents data published by Bilfinger et al, with results from uniaxial compressive strength tests results in soil treated with jet grouting technology.

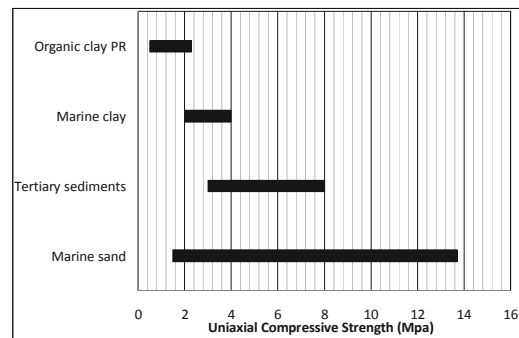


Figure 15. Uniaxial compressive strength, Bilfinger et al. (2012).

It can be seen that soil type has major influence on uniaxial compressive strength, specially the organic matter content.

## 6 CONCLUSIONS

The technical papers included in this session cover a wide range of topics. In items 3 and 5 some of these topics were discussed in more detail.

Some conclusions may be drawn with relation to three areas:

**Design:** No detailed design procedures were presented, but some interesting conclusions can be drawn from the published papers:

- Numerical modeling is a common tool to model soil and structure interaction;
- Limit equilibrium analysis and beam-spring models continue to be used in design practice;
- The observational method, meaning, the use of monitoring to control and, possibly, adjust the design, is a widespread design “philosophy”.

**Construction:** Different construction techniques and structures are discussed and presented:

- Foundations: direct footings, caissons and suction caissons, barretes and diaphragm walls, soil treatment by rigid inclusions;
- Retaining structures: diaphragm walls, secant pile walls, sheet pile walls, soldier type walls, mixed in place structures, anchored and nailed structures, reinforced soil, cantilever and gravity walls.

Most of these construction techniques and structures are already well known and the focus and innovation presented in the papers are performance, size, depth and proximity to other structures. Two exceptions are: soil treatment techniques, used in different conditions and suction caissons.

**Research:** Different research themes were presented, but one of the important investigated issues is earth pressures for different conditions. Another topic researched are mathematical models associated to techniques to optimize design procedures, and not to represent soil constitutive models.

## REFERENCES

- Bilfinger, W., da Silva, M.A.A.P., Rocha, H.C., Celestino, T.B. (2012) Tunnels in São Paulo, in Soils of the Metropolitan Regions of São Paulo and Curitiba, ABMS (in Portuguese)

- Décourt, L. (1982): "Prediction of the Bearing Capacity of Piles based exclusively on N values of the SPT", 2nd European Symposium on Penetration Testing, Amsterdam, pp. 29-34.
- Long, M. (2001) "Database for retaining wall and ground movements due to deep excavations", *J Geotech Geoenviron Eng, ASCE* 127 (3), 203–224.
- Leung, E.H.Y., Ng, C.W.W. (2007). "Wall and ground movements associated with deep excavations supported by cast in situ wall in mixed ground conditions". *J Geotech Geoenviron Eng, ASCE*, 133 (2), 129–143.
- Ortigão, J.A.R., Sayão, A.S.F.J. Handbook of Slope Stabilization. Springer, New York, 2004.
- Sayão, A.S.F.J., Azambuja, E. Ehrlich, M., Gomes, R.C. (2004) "Reinforced Walls and Slopes" in Brazilian Geosynthetic Manual, ed. Vertematti, J.C. Edgar Blücher, São Paulo (in Portuguese)
- Wang, J., Xu, Z., and Wang, W. (2010). "Wall and Ground Movements due to Deep Excavations in Shanghai Soft Soils." *J. Geotech. Geoenviron. Eng.*, 136(7), 985–994.
- APPENDIX - List of papers submitted for this session:
- FOUNDATIONS:
- Bidasaria, M. Foundation and Geotechnical Problems, Geology, Design and Construction of Cofferd Dam on Narmada River for Indira Sagar Project in Central India.
- Comodromos E. M., Papadopoulou, M.C., Konstantinidis, G.K. Effects on adjacent buildings from diaphragm wall installation.
- Cuira, F., Simon, B. Prise en compte des effets de bord dans un massif renforcé par inclusions rigides.
- Guo, W., Chu, J. Suction Caisson Installation in Shallow Water: Model Tests and Prediction.
- Hannink, G., Oung, O. Displacement of an apartment building next to a deep excavation in Rotterdam.
- Lin, H.D., Dang, H.P., Hsieh, Y.M. Assessment of Ground and Building Responses Due to Nearby Excavations Using 3D Simulation.
- Katzenbach, R., Leppla, S. Deformation behaviour of clay due to unloading and the consequences on construction problems in inner cities.
- Korff, M., Mair, R.J. Response of piled buildings to deep excavations in soft soils.
- Mizutani, T., Kikuchi, Y. Shaking table tests on caisson-type quay wall with stabilized mound.
- Pucker, T., Grabe, J. Structural Optimization in Geotechnical Engineering.
- Sesov, V., Cvetanovska, J., Edip, K. Geotechnical aspects in sustainable protection of cultural and historical monuments.
- Sieminska-Lewandowska, A., Mitew-Czajewska, M., Tomczak, U. Various use of Diaphragm walls for construction of multilevel road junction - design and monitoring of displacements.
- RETAINING STRUCTURES
- Abramento, M., Fujii, J., Cogliati, B., Assakura, V. Design, Construction and Monitoring of a Mixed Soil-Reinforced and Anchored Retaining Wall in Expansive Soil.
- Alexiew, D., Hangen, H. Design and construction of high bermless geogrid walls in a problematic mountainous seismic region in Bulgaria.
- Baghery, S. La Fouille de la Tour Odéon à Monaco : Les quatre éléments remarquables de sa conception.
- Bilgin, Ö., Mansour, E. Anchored sheet pile wall design in expansive soils.
- Chow, C.M., Tan, Y.C. Performance of Soil Nails in Weathered Granite and Fill.
- Damians, I.P., Lloret, A., Josa, A., Bathurst, R.J. Influence of facing vertical stiffness on reinforced soil wall design.
- Durgunoglu, T., Kulac, F., Ikiz, S., Akcakal, O. Top Down Construction Alongside Of Bosphorus – A Case Study.
- Finno, R.J., Arboleda, L. Kern, K., Kim, T., Sarabia, F. Computed and observed ground movements during top-down construction in Chicago.
- Frischknecht, R., Büsser-Knöpfel, S., Itten, R., Stucki, M. Comparative Life Cycle Assessment of Geosynthetics versus Concrete Retaining Wall.
- Ganne, P.P., Raucroix, X. Design of inverted T-shaped Cantilever Wall with a Relief Floor.
- Gomes Correia, A., Tinoco, J., Pinto, A., Tomásio, R. An Anchored Retaining Wall in CSM.
- Guilloux, A., Porquet, M., De Lavernée, P., Lyonnet, P., Roman, P. Conception, modélisation et auscultation d'une très grande excavation à Monaco.
- Guler, E., Osmanoglu, U., Koç, M. A Case Study of 3D FE Analysis of a Deep Excavation Adjacent to a Tunnel Construction.
- Gutjahr, I. Doucerain, M., Schmitt, P. Heumez, S., Maurel, C. Instrumentation de la paroi moulée du bassin de Blanc-Mesnil : retro-analyse et calage des modèles de calcul.
- Ilyichev, V.A., Gotman, Y.A. Calculation method of optimization the soil-cement mass dimensions to reduce the enclosure displacements in deep excavations.
- Jang, Y.S., Choi, H.C., Shin, S.M., Kim, D.Y. Case Studies of Complicate Urban Excavation from Design to Construction.
- Jessee, S., Rollins, K. Passive Pressure on Skewed Bridge Abutments.
- Long, M., O'Leary, F., Ryan, M., Looby, M. Deep excavation in Irish glacial deposits.
- Loukidis, D., Salgado, R. Active earth thrust on walls supporting granular soils: effect of wall movement.
- Lüftenegger, R., Schweiger, H.F., Marte, F. Innovative solutions for supporting excavations in slopes.
- Maeda, T., Shimada, Y., Takahashi, S., Sakahira, Y. Design and Construction of Inclined Braceless Excavation Support Applicable to Deep Excavation.
- Nakajima, S., Shinoda, M., Abe K. Inspection of structural health of existing railway retaining walls.
- Ou, C.Y., Teng, F.C., Hsieh, P.G., Chien, S.C. Mechanism of Settlement Influence due to Deep Excavation in Soft Clay.
- Philipsen, J. Establishing a high risk construction pit in a hurry.
- Pinto, A., Tomásio, R., Godinho, P. Innovative Solution of King Post Walls combined with CSM Panels.
- Pinto, A. Pita, X., Neves, M. Unusual Geotechnical Solutions at the Leixões Cruise Terminal.
- Popa, H., Manea, S., Batali, L., Olteanu, A. Aspects on designing and monitoring a deep excavation for a highly important structure.
- di Prisco, C., Pisanò, F. FEM – aided design of a novel device for soil anchoring.
- Sanvitale, N., Simonini, P., Bisson, A., Cola, S. Role of the facing on the behaviour of soil-nailed slopes under surcharge loading.
- Tanaka, T., Kusumi, S., Inoue, K. Effects of plane shapes of a cofferdam on 3D seepage failure stability and axisymmetric approximation.
- Turček, P., Frankovská, J., Súfovská, M. Stability and dewatering problems of deep excavations in Bratislava.
- Turner, M.J., Smith, N.A. Managed remediation of a large Victorian gravity quay wall using the observational method.
- Vollmert, L., Niehues, C. Concrete panel walls – Current development on interaction of earthworks, geosynthetic reinforcement and facing.
- Vukotić, G., González, J., Soriano, A. The influence of bond stress distribution on ground anchor fixed length design. Field trial results and proposal for design methodology.
- Warren, L., McCombie, P., Donohue, S. The sustainability and assessment of drystone retaining walls.
- Wiggan, C., A., Richards, D.J., Powrie, W. Numerical modelling of groundwater flow around contiguous pile retaining walls.
- Yoo, C., Jang, D.W. Geosynthetic Reinforced Soil Wall Performance under Heavy Rainfall.

# Design, Construction and Monitoring of a Mixed Soil-Reinforced and Anchored Retaining Wall in Expansive Soil

Conception, construction et surveillance d'un mur mixte de sol renforcé et ancré dans un sol gonflant

Abramento M.

*CEG Engenharia and Escola Politécnica da USP*

Fujii J.; Cogliati B., Assakura V.

*Yamamichi and CEG Engenharia*

**ABSTRACT:** Due to traffic volume increase a large stretch of a major highway linking São Paulo and Campinas City, Brazil, has recently been widened. In order to achieve the construction of additional lanes, a construction of a mixed-type retaining wall became necessary. This mixed-retaining structure consisted of a 5m high anchored wall at the bottom and a 5m high steel-reinforced retaining wall at the top, totalling a 10m high retaining wall. The bottom wall was built in a cut slope in a stiff, highly expansive, clayey soil. The steel-reinforced retaining wall was built over the lower anchored wall with both faces aligned. Anchor loads at the bottom wall were applied in stages in order to account for the increasing loads during the construction of the top wall. In order to correctly design the bottom anchored wall several undisturbed soil samples were obtained from the stiff clay. Laboratory tests included complete characterization, shear strength and expansion pressure determination. The retaining system was monitored during all construction stages. This paper presents details on the laboratory tests results, design of the retaining walls, construction steps and monitoring.

**RÉSUMÉ :** En raison du volume de trafic une portion d'une route importante reliant São Paulo et Campinas, au Brésil, a récemment été élargie. Afin de réaliser la construction de voies supplémentaires, une construction d'un mur de type mixte devenait nécessaire. Cette structure mixte consistait en un mur ancré de 5m de haut en partie basse et un mur en sol renforcé en partie haute, pour une hauteur totale de 10m de soutènement. La paroi en partie basse a été construite dans une pente en déblai dans un sol argileux raide et très expansif. Le mur en sol renforcé a été construit sur la paroi inférieure ancrée avec les deux parements alignés. Les charges d'ancrage de la paroi en partie basse ont été appliquées par paliers afin de tenir compte des charges croissantes au cours de la construction de la paroi supérieure. Afin de concevoir correctement le mur ancré plusieurs échantillons de sol intacts ont été prélevés sur l'argile raide. Les tests de laboratoire incluent la caractérisation complète, la résistance au cisaillement et à la détermination des pressions de gonflement. Le système de soutènement a été suivi pendant toutes les étapes de la construction. Cet article présente des détails des résultats des tests de laboratoire, la conception des murs de soutènement, la construction et le suivi des mesures.

**KEYWORDS:** Reinforced wall, anchored wall, expansive soil, monitoring

## 1 INTRODUCTION

Due to traffic volume increase a section of approximately 3km of a major highway linking São Paulo and Campinas city, Brazil, had to be widened. In order to achieve the construction of additional lanes, and due to geometric constraints, a mixed-type retaining wall became necessary. This mixed-retaining structure is shown in Figure 1 and consists in a 5m high anchored wall at the bottom and a 5m high steel-reinforced retaining wall at the top, totalling a 10m high retaining wall.

This paper presents details on the laboratory tests results, design of the retaining walls, construction steps and monitoring, as well as a comparison of measured and predicted displacements and loads at the top and bottom retaining walls.

## 2 SITE INVESTIGATION AND LABORATORY TESTS

SPT borings show that the local soil consists of a superficial colluvial soil characterized as a soft porous silty clay 2 to 3m thick and with blowcounts varying from 2 to 3, followed by a medium, stiff and hard clay with blowcounts larger than 15 and reaching up to 40. A picture of this last layer is shown in Figure

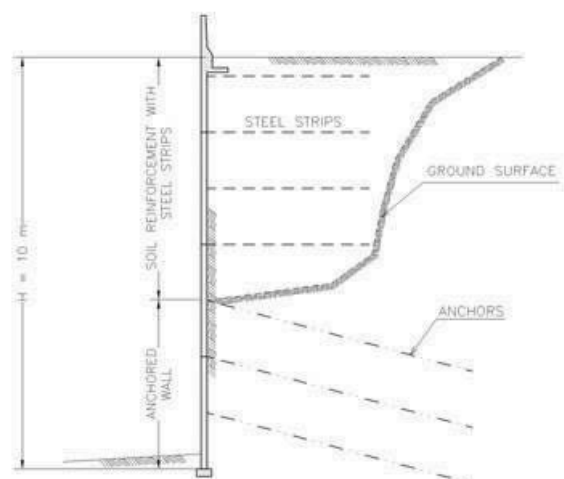


Figure 1. Typical cross-section of mixed reinforced fill-anchored wall.

2. Figures 3 and 4 show typical SPT borings results for two of the wall sections. This stiff clay layer receives the load from the



reinforced fill and had to be cut and anchored in order to widen the roadway.

Therefore, this layer was fully investigated with:

- Several SPT borings.
- Laboratory tests: direct shear and expansion tests on undisturbed samples and characterization.
- Pullout tests on anchors.

Moreover, compaction and direct shear tests were carried out on fill materials.



Figure 2. Stiff to hard silty clay layer to be cut and retained with anchored wall and surcharged with reinforced soil fill.

### 3 TEST RESULTS – STIFF TO HARD CLAY

Table 1 presents results from direct shear tests. It is worth noting the large drop in shear strength for large displacements (residual conditions). Peak strength typically occurs for very small displacements, in the range of 1mm.

Table 1. Direct shear test results.

Sample	Specimen	$\sigma$ (kPa)	$\tau_{max}$ (kPa)	$\tau_{res}$ (kPa)
Natural	CP-1	51	232	32
	CP-2	154	305	22
	CP-3	306	419	92
Saturated	CP-1	51	228	77
	CP-2	151	264	72
	CP-3	304	304	34

Table 2 presents results from expansion tests carried out on the horizontal and vertical directions. The expansion pressure is very high in the vertical direction, whereas the expansion pressure in the horizontal direction is around 6% of the vertical pressure, showing the marked influence of clay structure on its behavior (Figure 2).

Table 2. Expansion pressure for vertical and horizontal directions.

Direction	Expansion Pressure (kPa)
Vertical	440
Horizontal	30

Table 3 presents results from pullout tests on anchors 10cm in diameter and 6m long as a function of injection pressure. Anchors 202, 207 and 212 had, respectively, one, three and two functioning pressure valves. Therefore, adhesion values varied significantly from 25 to 45kN/m, demonstrating marked influence of injection pressure on adhesion.

Table 3. Pullout tests on anchors.

Segment	Adhesion (kN/m)	Injection Pressure (kgf/cm <sup>2</sup> )
202	25	$\phi/\phi/20$ (1 valve)
207	45	50/20/30 (3 valves)
212	30	$\phi/30/20$ (2 valves)

### 4 DESIGN PARAMETERS

The following design conditions and strength parameters were considered for design:

- End-of-Construction (EOC): peak shear strength parameters and natural water content, with and without expansion pressure.
- Long-Term and Peak Condition (LTP): saturated peak shear strength parameters, with and without expansion pressure.
- Long-Term and Residual Condition (LTR): saturated residual shear strength parameters, with expansion pressure.

A possible decrease in adhesion due to soil saturation was also considered in adhesion. Increase in anchor loads due to expansion pressure was taken into account for anchor design.

With basis on the laboratory and field tests, and following the procedures outlined in ABNT NBR 11.682 – Slope Stability, the parameters presented in Table 5 were used in wall design.

Table 5 – Design parameters.

Parameter	Condition/			
	EOC	LTP	LTR	MSE*
Soil unit weight (kN/m <sup>3</sup> )	20	20	20	20
Cohesion intercept (kPa)	60	40	0	30
Friction angle (°)	30	18	18	25
Anchor adhesion (kPa)	Average	100	90	125
	Maximum	140	125	
Same with expansion (kPa)	Average	70	65	-
	Maximum	100	90	
Puncture anchor head (kN)		430		

\*MSE :Soil Parameters for Mechanically Stabilized Earth Wall

## 5 DESIGN AND CONSTRUCTION OF ANCHORED WALL

A limit equilibrium program was used to design the anchored wall, considering the reinforced wall on the top and a traffic surcharge of 25kPa. Potential failure surfaces were always very close to the anchored wall face. As a result, the free section of the anchors were short, in the order of 3.0m. This is the minimum length accepted by ABNT NBR 5629 – Anchored Walls. Anchor length was varied in order to achieve minimum Safety Factor of 1.8 for EOC, 1.5 for LTP, and 1.2 for LTR conditions, resulting the following anchor distribution:

- Cable anchors, 5x12,7mm 190RB, yield stress= 1708MPa
- Working load = 430kN
- Testing load = 760kN
- Minimum spacing = 1,6m
- Maximum spacing = 2,0m
- Inclination with horizontal = 20 degrees
- Free length = 3,0m
- Anchored length = varying from 6.0 to 9.0m
- Anchor diameter = 100mm

Water table close to the base of the anchored wall was found in several SPT bores. Therefore, horizontal drains 15m long were installed every 2.4m along the wall base. The stiff clay layer was carefully excavated to install the anchors and build the reinforced concrete face 30cm thick. For each anchor level the anchors were loaded to 50% of the working load. Construction of the reinforced fill started after the completion of the anchored wall. When the reinforced fill height reached around 70% of the final fill height the anchors were re-loaded with 100% of the final working load.

## 6 WALL MONITORING

In order to monitor wall behavior a monitoring system was installed along the wall. It consisted of:

- 3 inclinometers 15m deep installed
- 3 load cells installed at selected anchor heads
- 20 displacement pins

Inclinometers were installed in boreholes along the front face of the anchored wall, and extended upwards during placement of the reinforced fill.

Several readings were obtained during construction of the lower anchored section and continued during construction of the upper reinforced fill section.

## 7 MONITORING RESULTS

Figures 3 and 4 show inclinometers results for 2 of the instrumented sections: Section I-200 and Section I-205. The results show that:

- The displacements increase continuously with construction of the lower anchored wall and the upper reinforced soil wall.
- Displacements of the lower anchored wall were generally small, in the range of 5 to 10mm.
- Small face displacements were expected for the stiff clay layer. However, for these displacements level it is possible that residual conditions may be attained by the clay layer during wall construction.
- For the upper reinforced fill, however, face displacements were relatively high. Measured displacements varied from around 10mm at the bottom up to 70 to 80mm for the upper part of the fill.

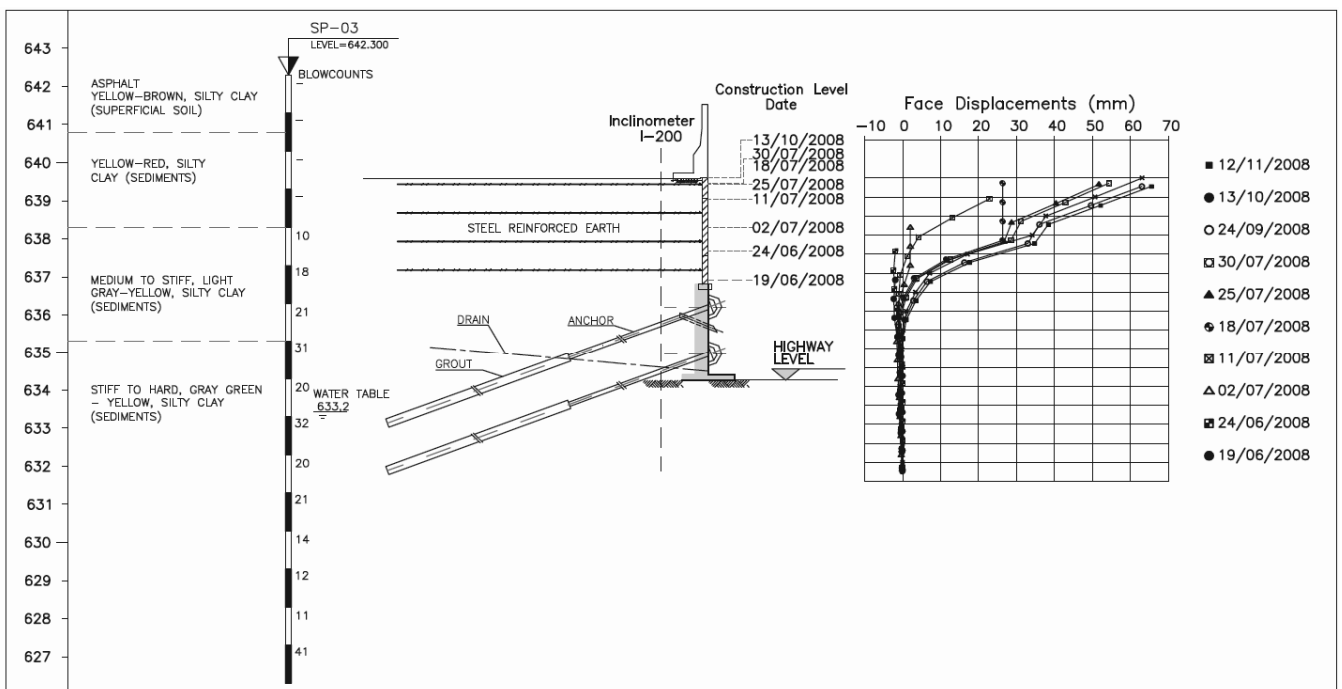


Figure 3. Inclinometer results in Section I-200.

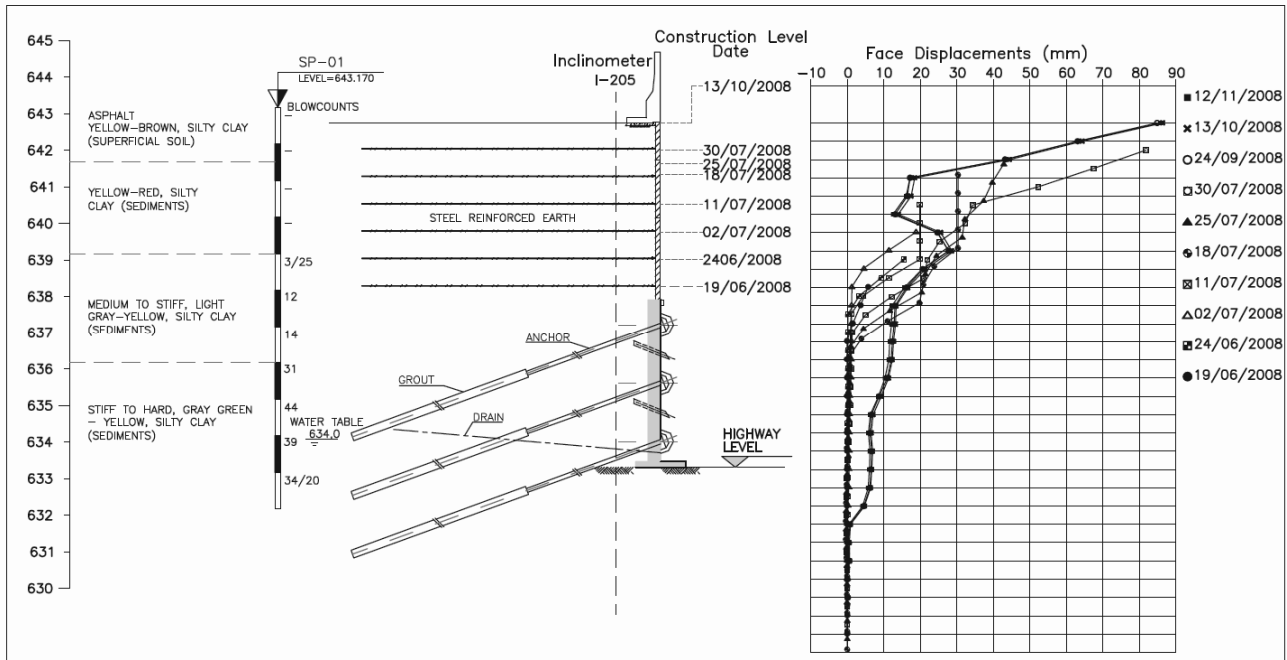


Figure 4. Inclinometer results in Section I-205.

## 8 CONSTRUCTION CONDITIONS

Figures 5 and 6 show construction conditions, especially the upper part of the reinforced soil fill with the reinforcing steel strips and the face of the anchored wall face at the bottom.



Figure 5. General view of the top part of the reinforced soil fill.



Figure 6. General view of the highest section of wall.

## 9 CONCLUSIONS

The following conclusions can be summarized:

- The stiff clay layer has relatively high strength parameters for peak conditions.
- Residual conditions are achieved for relatively low displacements, around 1mm.
- Due to structural conditions the stiff clay has relatively high vertical expansion pressures, around 440kPa, whereas horizontal pressures are relatively low, around 30kPa.
- Displacements of the lower anchored wall were generally small, in the range of 5 to 10mm.
- These small face displacements were expected for the stiff clay layer. However, for these displacements level it is possible that residual conditions may be attained by the clay layer during wall construction.
- For the upper reinforced fill, however, face displacements were relatively high. Measured displacements varied from around 10mm at the bottom up to 70 to 80mm for the upper part of the fill.

## 10 ACKNOWLEDGEMENTS

The authors are grateful to Ms. Karina Tomoko Hentona for helping in preparing the figures.

## 11 REFERENCES

- ABNT NBR 61822 – 2007. Slope Stability.  
 ABNT NBR 5629 – 2006. Anchored Walls.

# Design and construction of high bermless geogrid walls in a problematic mountainous seismic region in Bulgaria

Conception et construction de murs renforcés par des géogrilles de grande hauteur et sans risberme dans une région montagneuse sismique problématique en Bulgarie

Alexiew D., Hangen H.  
HUESKER Synthetic GmbH, Gescher, Germany

Geogrids made of geosynthetics can replace conventional building materials like concrete. In this article, goal and scope, basic data and the results of a comparative life cycle assessment of concrete reinforced retaining walls (CRRW) and geosynthetics reinforced retaining walls (GRRW) are described. One running meter of a three meters high retaining wall forms the basis for comparison. The two walls have the same technical performance and an equal life time of 100 years. The GRRW has a lower demand of steel and concrete compared to the CRRW. The product system includes the supply of the raw materials, the manufacture of the geotextiles and the concrete, the construction of the wall, its use and its end of life. The life cycle assessment reveals that the GRRW causes lower environmental impacts. The cumulative greenhouse gas emissions of 300 m CRRW are 400 t and 70 t in case of GRRW. The use of an environmentally friendlier lorry in a sensitivity analysis and monte carlo simulation confirm the lower environmental impacts caused by the construction of a GRRW compared to a CRRW. More than 70 % of the environmental impacts of the geogrids production are caused by the raw material provision (plastic granulate) and the electricity demand in manufacturing.

**RÉSUMÉ :** Les Géogrilles peuvent remplacer les matériaux conventionnels comme le béton. Cet article contient une description de l'objectif et du champ d'étude, l'inventaire et les résultats d'une analyse comparative du cycle de vie d'un épaulement géotextile et d'un soutènement conventionnel. La comparaison est faite sur un mètre courant d'un épaulement de trois mètres de hauteur. Les deux alternatives ont les mêmes propriétés techniques et la même durée de vie de 100 ans. Les systèmes contiennent la provision des matériaux, la fabrication des géotextiles et du béton, la construction, l'utilisation et l'évacuation de l'épaulement. L'analyse de cycle de vie démontre qu'un mètre courant d'un épaulement géotextile cause moins d'impacts environnementaux qu'un mètre courant d'un épaulement de béton. 300 mètres d'un épaulement de béton entraînent 400 t CO<sub>2</sub>-eq, celui de géotextile 70 t CO<sub>2</sub>-eq des émissions des gaz à effet de serre. L'utilisation de camions avec des émissions réduites ne change pas les résultats. Une simulation « monte carlo » confirme la stabilité des résultats. La provision des matériaux et l'électricité utilisé dans la fabrication de la couche de filtre géotextile sont des facteurs primordiaux (plus de 70 %) en ce qui concerne les impacts environnementaux du géogrille utilisé dans l'épaulement géotextile.

**KEYWORDS:** geogrid-reinforced walls, facing, seismicity, slope instability, steep slopes  
**MOTS-CLÉS:** épaulement, géotextile, géogrillé, béton, analyse de cycle de vie, ACV

## 1. INTRODUCTION

In the Rhodope Mountains in the south of Bulgaria the route of the important Road III-868 from Devin to Mihalkovo being part of the National Road Network had to be completely changed due to the erection of a new dam on the River Vacha. The old road along the river had to be moved from the river valley to the hills by up to some hundred meters. The new route has a length of 11 km (Figure 1). Figure 2 provides an overview of the mountainous terrain, of the position of the old road in the valley and of the new road uphill. The mountainous terrain is characterized by sophisticated topography (very steep irregular slopes, Figure 2), varying geological and hydro logical conditions, instability tendencies in some places and non-availability of easy access for construction. Additionally, the region has a significant seismic activity.



Figure 1. Old route of Road III-868 in the valley and new one uphill through the mountains.



Figure 2. Overview of the mountainous terrain and exemplary positions of the old and new road.

The solution had to meet a wide range of criteria and goals: low costs, quick and easy construction, soil-mass balance (say minimum export / import of soil, say maximum re-use of excavated local soils), minimal environmental impact, as light as possible additional construction materials to ensure easy transportation and low energy consumption ("carbon finger print"), minimum use of heavy equipment, narrow base for retaining walls for an easy into-slope-adaptation, seismic resistance, and last but not least a tight time schedule of less than three years for the 11 km of new road incl. of a tunnel.

The final optimized solution meeting the criteria mentioned above in a balanced way included twenty walls from geogrid-reinforced soil (GRS) with a total length of 2 km, heights of up to 20+ m and a face inclination of 10v:1h (say nearly vertical) without any berms, what is quite unique (see below).

The GRS-walls were chosen (besides other advantages, e.g. more than 30% costs savings versus “common” concrete solutions) due to their excellent adaptation to the environment and their high ductility resulting in high robustness against seismic impact and slope movements. Flexible geogrids were used as reinforcement.

A special type of thin stone-filled wall facing was adapted to fit the landscape, to use local rocky material and to speed up construction. The facing is very flexible and thus of higher resistance against earthquakes and possible slope movements.

## 2. GENERAL CONCEPTS AND PHILOSOPHY

The project was developed by the General Consultant “Energoprojekt - Hydropower” (Sweco Group) Bulgaria and by the Road Designer “Burda Engineering” Bulgaria with consultancy from the company of the authors. Some specific points have to be mentioned:

A. Because of the very steep natural slopes (sometimes steeper than 1v:1h) the optimal positioning and foundation of all walls asked for almost vertical front inclinations of 10v:1h to achieve a better adaptation to the slope geometry. The base width of the cross-sections had to be minimized thus minimizing excavation (Figure 3c) and expansion down the slope as well (Figure 3a).

B. To optimize the soil mass balance but also based on common practice and conservatism three types of cross-sections were foreseen: without berms (typically up to 6-8 m), with one berm (typically up to 14 m) and with two berms (up to 22 m) (Figure 3).

C. The final stability analyses and design of the GRS-walls were to be completed after beginning of construction (due to site logistics few of the structures could be started at the same time, in reality a progressive construction was carried out along sections of the route). The specifications put to tender were founded on the basic concept and on the typical cross-sections in Figure 3 a, b, c (these were

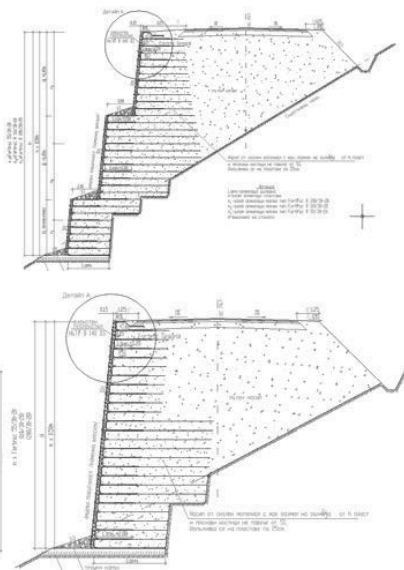


Figure 3. Basic concepts for typical cross-sections: front (facing) inclination always 10v:1h, but different number of berms; from top to bottom: a, b, c.

indicative only, being based on preliminary stability analyses); it was assumed that these will be not the final solutions. The reason for this philosophy was the uncertainty in the real geotechnical and topographical conditions along the 11 km of road, because due to the extremely difficult access the survey and site investigation had been relatively modest.

D. The facing was an important issue. After checking different options the so called “Muralex® Stone” facing system was chosen. Its

concept is based on the idea of a “hanging facade” added and connected in a later construction stage to the “real” bearing geogrid structure (Figure 4).

The system leads to important advantages:

- the geogrids are hidden and protected against UV, impact, fire and vandalism;
- possible wall deformations during construction occur before facing installation - the facing starts its design life deformation-free;
- ductile behavior of the facing under seismic impact and generally under wall deformations of any type in the post-construction stage, because it is quite flexible, say there is no rigid connection to the “real” GRS (Figure 4);
- no special facing foundation is needed;
- a wide range of rocky material available from the excavations on site can be used etc.

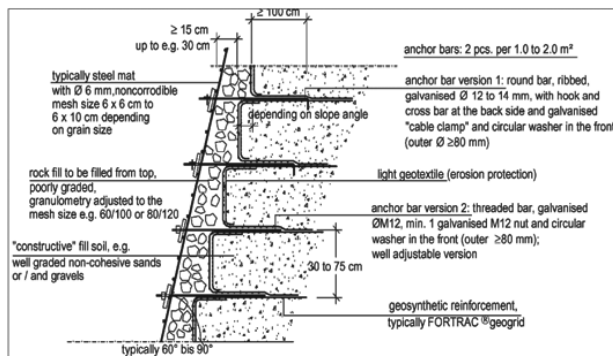


Figure 4. A typical version of the facing system Muralex®.

## 3. GEOLOGICAL AND HYDROLOGICAL CONDITIONS

The geology along the new route varies significantly (Figure 5). The GRS-walls and their foundations can contact at the back resp. be embedded in (Figure 3) any local soil from silty or sandy clays with stone inclusions (slope talus) to more or less monolithic rock. This enormous inhomogeneity resulted in a low level of predictability not only regarding the local slope soils, but also regarding the parameters of the fill soil; the latter consists (although after pre-selection) from excavated local materials from different cuts along the new route.

The geotechnical survey before beginning of construction was not very detailed. It was decided together with the General Investor “National Electricity Company”, Bulgaria, the General Contractor “Alpine Bau”, Austria, the Consultants (see above) and the Bulgarian Subcontractors for the road construction to assume in all final stability analyses relatively conservative average local soils and fill parameters. Many of the walls cross small valleys; in such cases standard culverts were planned being integrated into the GRS-walls. No water veins were known before beginning of execution. Nevertheless for all walls drainage blankets were implemented at the wall base.

## 4. SOME STABILITY ANALYSIS ISSUES

For all stability analyses the well known method of circles according to Bishop was used together with additional analyses of polygonal failure planes using the so called Sliding Blocks Method. All analyses were performed in the Engineering Department of the company of the authors. The concept of global factor of safety (FOS) acc. to the German Codes (e.g. DIN 4084) was applied throughout the project from the same beginning (preliminary designs in 2004) until the last adaptations and changes under running execution in 2009, although in the meantime the Codes had changed to partial factors of safety.

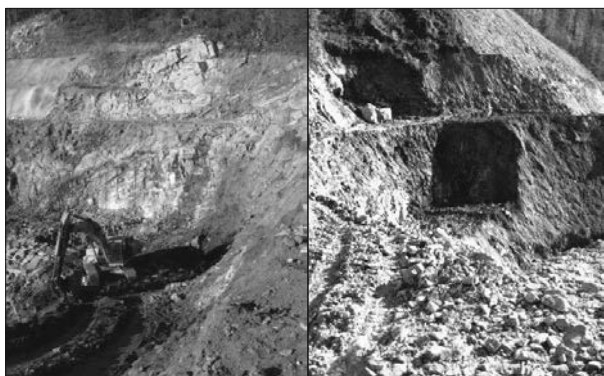


Figure 5. Examples of the enormous inhomogeneity of the local soils and rocks.

“Internal”, “external” and “compound” stability modes were separately checked to keep conformity with the preliminary designs in 2004, although this differentiation is questionable; for more details see Alexiew (2004 & 2005).

Note that in the meantime in the new issue of the German recommendations EBGeo (2010) the distinction internal-external-compound was eliminated, as well as e.g. the formal distinction between “slopes” and “walls”.

Geogrids from the “FORTRAC® T”-family were chosen as reinforcement due to their high specific short- and long-term strength, low short- and long-term strain, low creep, high coefficient of bond to a wide range of soils and flexibility resulting into an easy installation. The range of geogrids for this project was from FORTRAC® T 55 to FORTRAC® T 200.

The required factors of safety (FOS) were chosen according to the Bulgarian Standards with  $FOS > 1.3$  for normal (static) conditions. In Figure 6 a typical Bishop circle analysis is shown (for the internal stability only, say the failure surface crosses exclusively the reinforced zone).

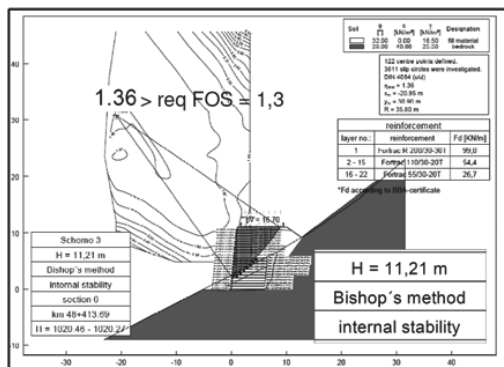


Figure 6. Typical example of stability analysis according to Bishop (only “internal” shown).

A specific issue was the seismic analysis; the region is of significant seismic activity with a magnitude of VII acc. to Richter.

The Bulgarian concepts for seismic design from 1980 being still valid with small modifications during the period of analysis were adopted throughout the project (CDBSSR 1987, CDRW 1986, SGDSR 1987).

Figure 7 shows an overview of the seismic activity in Bulgaria together with the position of the Devin-Mihalkovo project and the zone with VII acc. to Richter with a coefficient of horizontal acceleration  $k_h = 0.15$ . A vertical acceleration is not being taken into account.

For the acting seismic forces  $F_{seismic}$  the Equation 1 can be used (CDBSSR 1987, CDRW 1986, SGDSR 1987):

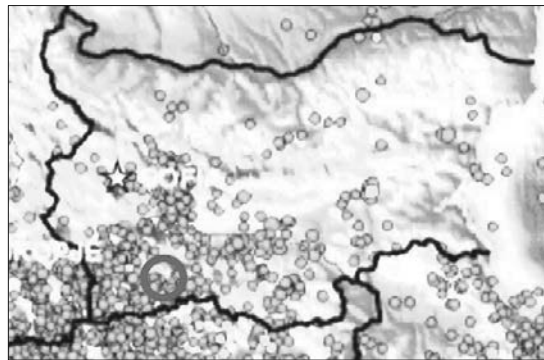


Figure 7. Seismic activities in Bulgaria, the project position is marked.

$$F_{seismic} = 1.30 \cdot R_{response} \cdot k_h \cdot (\text{permanent loads} + 0.50 \cdot \text{traffic loads}) \quad (1)$$

where  $R_{response}$  = coefficient of response of the structure to seismic impact;  $k_h$  = coefficient of horizontal acceleration; 1.30 and 0.50 = partial safety factors on the side of action for seismic design cases.

$R_{response}$  has higher values e.g. up to 0.40 for rigid (brittle, e.g. masonry, concrete) structures and lower values e.g. 0.25 for ductile structures like earth dams and embankments. It seems logic and conclusive that earth systems reinforced by flexible geogrids should be at least so ductile and able to dissipate seismic energy remaining intact as non-reinforced earth dams.

This concept and the corresponding calculation results seem to be coherent with the experience, conclusions and recommendations in e.g. Tatsuoka et al (1998) and other publications confirming the very advantageous behavior of GRS-walls under seismic impact.

Note that for seismic analyses the Bulgarian codes (CDBSSR 1987, CDRW 1986, SGDSR 1987) ask for a  $FOS > 1.1$ , for more details and previous “seismic” projects see e.g. Jossifowa & Alexiew (2002).

One specific issue more in the Bulgarian codes is the reduction of the angle of internal friction acc. to Equations 2 & 3 depending on the intensity of earthquake:

$$\varphi_{characteristic, seismic} = \varphi_{characteristic, static} - \Delta\varphi \quad (2)$$

where

$$\Delta\varphi = \Delta\varphi(\text{magnitude acc. to Richter}) \quad (3)$$

For the project under discussion with a magnitude of VII acc. to Richter  $\Delta\varphi = 3.5^\circ$ .

Because the software used (GGU Stability by Civil Serve) does not include a calculation conform to Equation 1 and considers only directly  $k_h$ , the latter had to be modified “by hand” before the input.

## 5. EXECUTION, PROBLEMS, SOLUTIONS, EXPERIENCE

Execution started in summer 2007. First problems arose soon: the topography deviated sometimes significantly from the expected one, the real terrain was sometimes higher or lower than it should be, the real slope inclination often steeper. Step by step many of the cross-sections had to be re-designed. At the end of the day all GRS-walls, even the highest with over 20 m height, became “bermless”, what is quite unique.

The “bermless” solution offers significant advantages: the base width of the cross-sections becomes minimal (Figure 3). This helped to avoid deep cuts into the hillside and/or an expansion of the trapezoid beyond the steep slope line (to the left in Figure 3). Additionally, in some cases the geology deviated significantly from the assumptions; this resulted in re-design as well.

Often surprising water veins in the natural slopes had to be drained promptly. For this purpose thick wicks from rolled non-woven geotextiles were installed ending on the front side of wall as a quick ad hoc solution.

In Figure 8 typical construction stages and details are depicted. Figure 9 shows one of the completed walls just before handing the route over for operation.



Figure 8. Left: construction stages (formwork, geogrids, anchor bars, facing), right: top view of the stone-filled facing used.



Figure 9. Top view of a completed GRS-wall.

## 6. FINAL REMARKS

The new Road III-868 from Devin to Mihalkovo in the Rhodope Mountains in southern Bulgaria was a challenge in terms of optimal concept, design, execution, re-design during execution, time schedule and costs. It crosses a terrain with sophisticated topography and geology in a seismic region. Its length amounts to 11 km comprising one tunnel and twenty geogrid-reinforced almost vertical soil walls of totally 2 km length and up to 20+ m height.

A specific type of facing was adopted to fulfil a wide range of requirements.

Almost all GRS-walls had to be re-designed and adopted under running route execution, resulting throughout in non-common high bermless solutions.

Nevertheless, it was possible to meet all project goals regarding time schedule and costs (among others; see the description of criteria, goals and optimized solution in Chapter 1). The success is based on the one hand on the advantages and flexibility of geosynthetic solutions in geotechnical engineering in terms of easy and quick construction process and adaptation and on the other hand on the excellent co-operation of all participants: Investor, Owner, Consultants, Contractors and Geosynthetic Company.

The road is since summer 2010 under traffic, the GRS-walls demonstrate until now an excellent behavior both in terms of stability and low deformability.

This transportation project is may be the most distinctive in the Balkan region during the last years.

## 7. ACKNOWLEDGEMENTS

The authors would like to express their gratitude to all colleagues with the Investor, Consultants and Contractors for the excellent and competent collaboration during all project stages and even (and particularly) in some difficult phases.

## 8. REFERENCES

- Alexiew, D. (2004): Geosynthetic Reinforced Slopes: Basics of Design and some Projects. *Proc. of the Indian Conference Geosynthetics – New Horizons*, New Delhi, India: 73 – 85.
- Alexiew, D. (2005). Zur Berechnung und Ausführung geokunststoffbewehrter "Böschungen" und "Wände": aktuelle Kommentare und Projektbeispiele. *Proc. 5. Österreichische Geotechniktagung*, ÖIAV, Wien, Austria: 87 – 105.
- CDBSSR Code for the design of buildings and structures in seismic regions (1987). *KTSU & BAN*, Sofia, Bulgaria. (in Bulgarian)
- CDRW Code for the design of retaining walls (1986). *MBI Ministry for building industry*, Bulletin BSA, Vol. XXX/10, Sofia, Bulgaria. (in Bulgarian).
- DIN 1054. Baugrund - Sicherheitsnachweise im Erd- und Grundbau (Ground - Verification of the safety of earthworks and foundations), *Deutsches Institut für Normung*, Berlin, Deutschland.
- DIN 4084. Baugrund - Geländebruchberechnungen (Soil - Calculation of embankment failure and overall stability of retaining structures), *Deutsches Institut für Normung*, Berlin, Deutschland.
- EBGEO 2010 Recommendations for Design and Analysis of Earth Structures using Geosynthetic Reinforcement, *DGGT / Ernst & Sohn*, Essen/Berlin, Deutschland.
- Jossifova, S. and Alexiew, D. (2002). Geogitterbewehrte Stützbauwerke an Autobahnen und Nationalstrassen in Bulgarien, *Proc. 12. Donau-Europäische Konferenz „Geotechnisches Ingenieurwesen“*, DGGT, Passau, Deutschland: 389-396.
- SGDSR Specialties in the geotechnical design in seismic regions (1987). *MBI Ministry for building industry*, Bulletin BSA, Vol. XXXII/11, Sofia, Bulgaria. (in Bulgarian).
- Tatsuoka, F., Koseki, J., Tateyama, M., Munaf, Y. and Horii, N. (1998): Seismic stability against high seismic loads of geosynthetic-reinforced soil retaining structures. Keynote Lecture. *Proc. 6<sup>th</sup> International Conference on Geosynthetics*, Atlanta, USA, 1: 103 - 142.

# La fouille de la tour Odéon à Monaco : les quatre éléments remarquables de sa conception

The Deep Excavation of the Odéon Tower in Monaco: The four outstanding elements in its design

Baghery S.

Tractebel Engineering (France)/Coyne et Bellier, Gennevilliers (92), France

**RÉSUMÉ :** La construction de la tour Odéon à Monaco nécessite la réalisation d'une fouille profonde au sein d'un versant très pentu, dans des terrains de caractéristiques médiocres. Le soutènement en a été rendu possible par quatre options remarquables prises par le concepteur, à savoir (1) une construction « top-down » à l'aide d'appuis pré-fondés, (2) la constitution d'une voûte élastique dans le sol côté montagne, ceci par modulation de l'effort de pré-charge par tirants d'ancrage, (3) le fretage du sol au pied des parois à l'aide de clous verticaux en fibre de verre et (4) la prise en compte des effets du déchargement du sol sur les appuis pré-fondés.

**ABSTRACT:** The construction of the 180-meters-tall Odéon skyscraper building in Monaco calls for a 72-meters-deep excavation to be dug in a steep hillside. The design of the retaining system for this excavation was made possible by Tractebel Engineering (France)/Coyne et Bellier making four unique design choices, namely (1) a "top-down" construction method, (2) the mobilization of an elastic arch in the foundation soil on the upstream side of the works, (3) reinforcing by fibre glass nails the soil below the deepest elements of the foundation, and (4) taking into account the effects, on the supports, of the sequence of construction.

**KEYWORDS:** Retaining walls, top-and-down construction, vault effect, soil reinforcement, heaving

**MOTS-CLÉS:** Soutènement, Construction en taupe, Top-Down, Effet de voûte, renforcement de sol, gonflement de sol.

## 1 INTRODUCTION

Avec une hauteur totale de 180 mètres, la tour Odéon, actuellement construite à Monaco sous la maîtrise d'ouvrage de la SCI-Odéon, restera pour un certain temps la plus haute tour de la Principauté. Alexandre Giraldi en est l'architecte. Elle est construite par l'entreprise Vinci, avec la contribution de Soletanche-Bachy pour les travaux de la fouille.

La réalisation de cet ouvrage nécessite l'excavation d'une fouille atteignant 72 mètres dans la partie la plus profonde (Figure 1). Alors que de nombreuses constructions sensibles situées au voisinage doivent être maintenues intactes, les travaux d'excavation exigent la conception de solutions originales, à la hauteur de ce projet audacieux.

tour, en tant qu'éléments de contreventement et raidisseurs parasismiques. Tractebel Engineering (France)/Coyne et Bellier a assuré la conception de ces deux parties du projet.

Lorsque les profondeurs d'une excavation dépassent les valeurs critiques eu égard aux caractéristiques du sol, le concepteur est confronté à un déficit intrinsèque de butée dans le sol. Il doit alors adopter des mesures innovantes. C'est grâce à de telles mesures que la réalisation d'une fouille avec une profondeur rarement atteinte dans des terrains de telles caractéristiques a été possible. Des études et investigations très poussées ont été nécessaires en amont des phases de contractualisation. Elles ont notamment comporté des modélisations tridimensionnelles des travaux, du massif et des constructions environnantes.

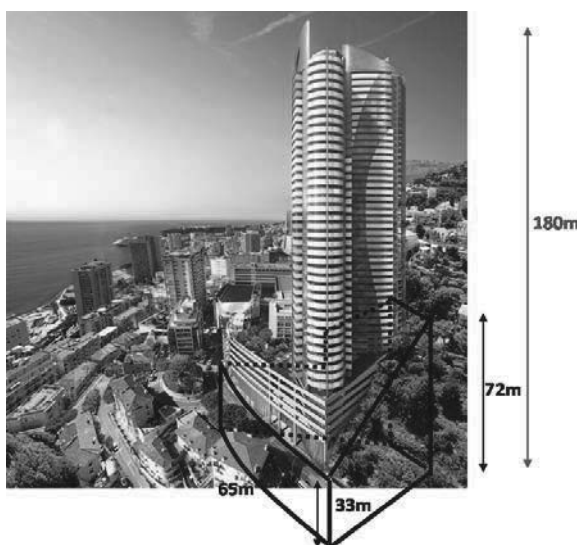


Figure 1: Le site, la tour et sa fouille

La conception du soutènement a été étroitement associée à la méthode et au phasage de construction de la tour, à la géométrie de la fouille et à la topographie du site. Les ouvrages de soutènement remplissent eux-mêmes un rôle structurel pour la

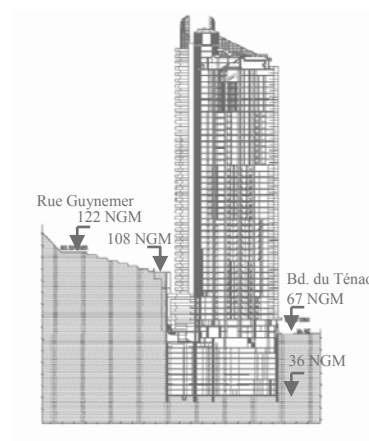


Figure 2: Versant en terrasse, le dénivelé, nivellement

## 2 LE SITE

Il s'agit d'un site très exigu, sur un versant en terrasses. Le dénivelé du terrain naturel entre l'amont et l'aval de la tour est de l'ordre de 40 mètres (Figure 2).

Les profils géotechniques indiquent une couche supérieure de remblai et d'éboulis sur une épaisseur qui atteint 25 mètres en amont, tandis qu'en aval, cette épaisseur varie fortement du fait des constructions récentes. Sous cette couche superficielle, on rencontre une couche marno-calcaire avec des poches plus



ou moins altérées vers les profondeurs 35-50 NGM. La couche marno-calcaire repose sur un substratum calcaire profond. Le toit du calcaire dessine une surface chaotique et variable. Il se situe en général sous la cote 30 NGM (Figure 3).

Le pendage général de la couche marno-calcaire (non représenté ci-dessous) est dirigé de l'amont vers l'aval. Il est donc favorable, lors de l'ouverture de la fouille, à la stabilité au glissement du massif soutenu côté montagne.

Une grande partie des niveaux piézométriques varie entre 10 et 20 mètres sous le niveau du terrain naturel, avec des fluctuations importantes qui atteignent fréquemment 4 à 5 mètres. Il s'agit d'une nappe superficielle qui coule à la surface de la couche marno-calcaire. A cause de sa faible perméabilité, cette dernière sépare la nappe superficielle d'une nappe plus profonde qui baigne dans le calcaire avec un niveau piézométrique situé environ 40 mètres plus bas que celui de la nappe superficielle.

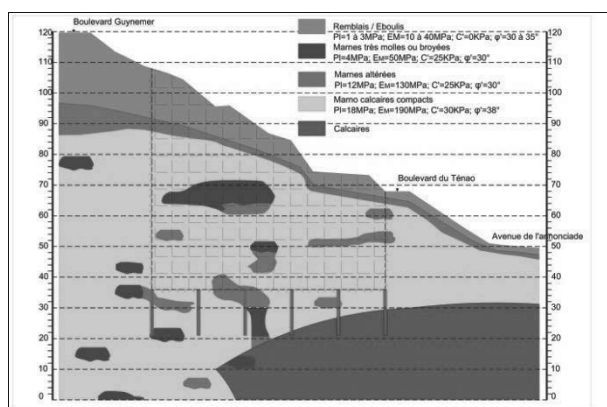


Figure 3: Coupe géologique, caractéristiques géotechniques

La bordure de la fouille est occupée par des bâtiments publics ou privés à des distances plus ou moins proches de la fouille. Compte tenu de la profondeur des excavations, un certain nombre d'entre eux se situe dans les zones d'influence des déplacements engendrés par les travaux d'excavation. Ce voisinage impose des contraintes d'exécution, notamment en termes du respect de déplacements admissibles.

### 3 OUVRAGES DE SOUTÈNEMENT: LES QUATRE ÉLÉMENTS REMARQUABLES

Les dix niveaux d'infrastructure comportent des planchers « butonnants » confinés entre les parois de la fouille. Ces planchers n'ont pas de joints et peuvent donc transmettre entre parois opposées les efforts de poussée ou de butée. La superstructure se développe au-dessus du boulevard du Ténac sur environ cinquante niveaux supplémentaires.

Si la stabilisation des parois de soutènement sous le boulevard du Ténac peut être assurée au moyen d'un système de planchers butonnants, ce n'est pas le cas pour les parois situées au-dessus de ce boulevard, à cause de l'absence de terrain offrant butée en vis-à-vis. C'est pourquoi les parois poussant au vide ont été stabilisées à l'aide de tirants d'ancrage.

Par ailleurs, l'exiguïté et les contraintes d'accès au site ont donné lieu à une solution de soutènement étagé des parois. En effet, la configuration des lieux avant les premiers travaux n'était pas défavorable à l'utilisation d'engins lourds. Ainsi, la réalisation des premiers écrans de soutènement à l'aide d'engins de taille réduite permet la réalisation de plateformes pouvant recevoir des engins plus encombrants. C'est pourquoi les premiers écrans de soutènement sont de type « mini-berlinoise », passant ensuite à des écrans de type berlinoise, avant de voir apparaître des écrans en paroi-moulée.

#### 3.1 Une construction "Top-Down"

Deux objectifs principaux nous ont conduit à adopter cette méthode de construction : a) Avantages offerts par des planchers butonnants (Figure 4) comme solution plus sûre d'équilibre des poussées en profondeur et dispositifs plus rigide pour limiter les déplacements des parois, et, b) Gain de temps dans la réalisation de la tour. En ce qui concerne ce dernier point, il a été considéré que dans le délai nécessaire à l'extraction des quelques 65 000 m<sup>3</sup> de terre des niveaux de sous-sol et à la réalisation en « taupe » des 10 niveaux de plancher correspondants, on pourrait construire simultanément les 50 niveaux de superstructure. Pour atteindre cet objectif, il a fallu réaliser des appuis profonds de la tour avant le démarrage de sa construction. Il s'agit des barrettes de fondation d'épaisseur 1m, forées aux environs de la cote 70 NGM, après les travaux d'excavation et de soutènement de la partie tirantée des parois. Il est à noter que la contrainte de compression moyenne développée dans ces barrettes par la tour en phase d'exploitation s'approchera de la valeur de 10 MPa. Ce niveau de sollicitation aurait pu rendre la solution non-faisable sans l'évolution des textes réglementaires, évolution apparue avec la mise en vigueur de la norme NF94-282 en février 2010, au moment de l'élaboration de la conception.

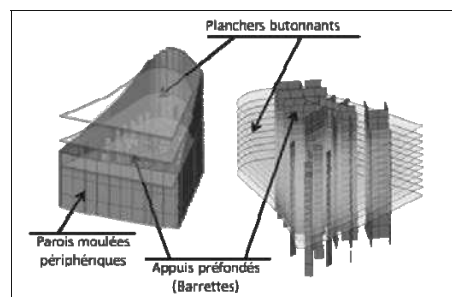


Figure 4 : Parois périphériques, barrettes et planchers butonnants

Au fur et à mesure de la construction des structures, les barrettes profondées reçoivent des charges gravitaires alors que les planchers de sous-sol, portés par les barrettes assurent le rôle simultané de diaphragmes dans la transmission des efforts horizontaux.

#### 3.2 Une voûte en sol

La topographie et la géométrie de l'excavation ont été mises au service de la conception du soutènement de la paroi la plus profonde de la fouille, dans la zone où les poussées sont les plus importantes du fait de la profondeur et de la pente du versant. Mais la portée de la paroi dans cette même zone est plus courte, ce qui nous a encouragé à en profiter pour inscrire dans le terrain le funiculaire des poussées, évitant notamment de solliciter la paroi profonde et limitant ainsi les déplacements. On aurait pu penser, a priori, que ce funiculaire existait en soi par le fait de la géométrie ("effet de voûte"). Mais cette affirmation ne tient pas compte du trop grand déviateur des contraintes (tangentielle et radiale), qui amène le sol de la "voûte" à se déformer à l'état plastique. Pour profiter de l'effet bénéfique de la voûte il a fallu ramener le sol qui la constitue à l'état élastique.

Si la limite élastique dans le sol à l'arrière de la paroi n'est pas dépassée à l'état initial, ce n'est pas forcément le cas avec l'excavation des sols devant la paroi, qui augmente progressivement la contrainte tangentielle dans le sol arrière. Dans le cas où la contrainte radiale reste trop faible, le déviateur s'agrandit et "pousse" le sol dans la plasticité qui engendre à son tour des déplacements importants (Figure 5).

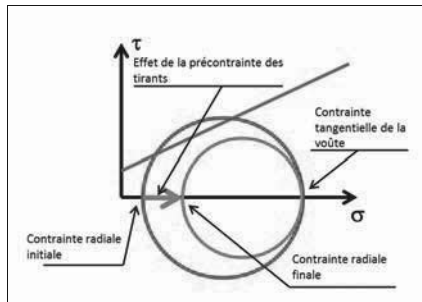


Figure 5 : État de contraintes de la voûte en sol

La solution réside donc dans l'augmentation de la précontrainte radiale à l'aide des tirants d'ancrage qui sont disposés dans la même direction en amont de la fouille.

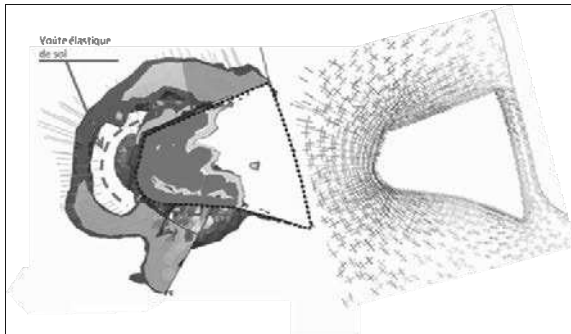


Figure 6: Voûte élastique dans le sol amont (gauche), cheminement des contraintes de la voûte vers les côtés latéraux de la fouille (droite)

La figure 6 (à gauche) montre une voûte en sol créée à l'arrière de la paroi amont, voûte qui redirige les poussées vers les côtés latéraux de la fouille (à droite), soulageant ainsi la paroi la plus profonde exposée à soutenir les charges les plus importantes.


 Figure 7: Etat d'avancement du chantier à  $\approx 40\%$  des excavations

En revanche, on peut y remarquer les zones plastiques formées dans la zone des bulbes d'ancrage et à l'arrière des parois plus ou moins rectilignes. Elle illustre également le cheminement des contraintes dans le sol et l'efficacité de la voûte élastique inscrite dans le sol. La figure 7 montre l'état d'avancement du chantier (à environ 40%) de soutènement et des excavations.

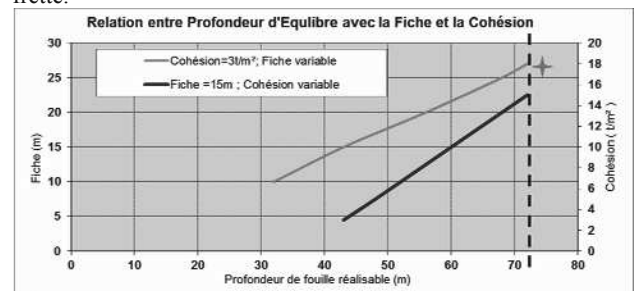
### 3.3 Frettage du sol

Lorsqu'une fouille dépasse 40 ou 50 mètres de profondeur dans des sols de cohésion faible à moyenne, deux solutions se présentent. La première consiste à mobiliser une masse très importante de sol en butée, ce qui nécessite une fiche de paroi très rigide et surtout très profonde. La seconde fait appel à une amélioration de la cohésion apparente du sol (Figure 8). Nous avons opté pour cette deuxième solution en frettant le sol au

pied des parois de grande profondeur à l'aide de clous verticaux en fibre de verre.

Notons que les barrettes de fondation réalisées par anticipation (appuis préfondés) contribuent, pour leur part, au frettage du sol. Néanmoins, il faudra tenir compte des sollicitations qu'elles encaissent par ailleurs. On vérifiera donc que l'accumulation des contraintes suivant les différents modes de fonctionnement (fondation, frette, inclusion soumise aux effets dus à l'expansion du sol –voir §3.4-) ne dépasse pas la résistance admissible de ces éléments.

L'évaluation de la cohésion apparente apportée par des frettes se fait en comparant la résistance (au glissement par exemple) du sol non-fretté, mais augmenté en cohésion, avec sa configuration frettée munie de la cohésion d'origine. Une analyse itérative des deux schémas aboutira à la valeur de la cohésion apparente qu'il faudra attribuer au sol d'origine pour être équivalent, en termes du critère de résistance choisie, avec le sol fretté.



✦ Dans ce terrain, l'équilibre des poussées exige, soit 28 mètres de fiche rigide avec la cohésion de base ( $3 \text{ t/m}^2$ ), soit une cohésion améliorée de  $18 \text{ t/m}^2$  avec 15 mètres de fiche.

Figure 8: Profondeur d'équilibre poussées-butées en fonction de la profondeur de la fiche ou de la valeur de la cohésion

### 3.4 Effets du déchargement du sol sur les préfondés

Comme il a été rappelé plus haut (§3.1), des barrettes de fondation ont été conçues pour être réalisées à un stade où il reste encore à excaver 35 mètres de terrain. Comme fondations, elles supportent les charges de la tour au fur et à mesure de sa construction. De ce fait, elles sont soumises à des contraintes de cisaillement puisqu'elles s'enfoncent dans le sol encaissant. Dans ce schéma, la contrainte de cisaillement développée le long du fût d'une barrette est dans la même direction que le mouvement du sol par rapport au fût, du bas vers le haut. Autrement dit, l'action du sol sur le fût est une contrainte tangentielle (frottement) dans le sens ascendant. Nous lui attribuons le signe « + ». Ces contraintes de cisaillement varient d'une valeur minimale à la base du fût vers une valeur maximale à sa tête (figure 9-a). Si la limite de plasticité devait être atteinte, elle le serait d'abord dans la partie supérieure où la courbe des valeurs serait plafonnée à la valeur plastique.

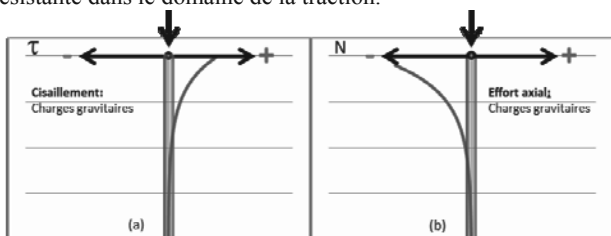
Par ailleurs, sous l'action des charges gravitaires, la valeur de l'effort de compression dans le fût diminue en profondeur, puisqu'une partie de cet effort est absorbée par le sol avec la mobilisation du cisaillement autour du fût (figure 9-b).

Avec l'excavation en présence des appuis préfondés, le sol encaissant autour de ces appuis (barrettes) se décharge et subit de ce fait une extension (gonflement), à l'opposé du phénomène de tassement, développant ainsi autour du fût des barrettes une deuxième catégorie de contraintes de cisaillement. Dans ce type de schéma (gonflement ou tassement du sol encaissant), et dans l'hypothèse d'un sol homogène doté d'un comportement linéaire, le bilan du cisaillement développé autour du fût est nul si l'effet sur le terme de pointe est négligé. La courbe de cisaillement à l'interface sol-fût, sous l'effet du gonflement du sol, possède un point d'inflexion (figure 10-a). Les contraintes de cisaillement changent de signe de part et d'autre de ce point. Dans le cas de gonflement du sol, les contraintes de cisaillement

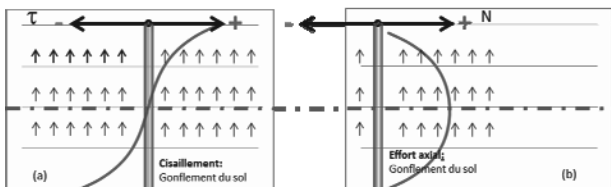
sur la partie située au-dessus du point d'inflexion sont du même signe que les cisaillements provoqués par les charges gravitaires. Dans cette partie, les cisaillements dus à ces deux phénomènes se cumulent (figure 11-a). Nous sommes donc, en cas de gonflement du sol encaissant, face à des contraintes majorées de cisaillement dans la partie supérieure du fût. Sur la partie située sous le point d'inflexion, le signe de la contrainte de cisaillement à l'interface sol-fût provoquée par le gonflement du sol est à l'opposé du signe des cisaillements dus aux charges gravitaires. Sur cette partie, les deux catégories de cisaillements se retranchent et les contraintes de cisaillement résultantes sont minorées.

L'effort axial dû au seul phénomène de gonflement du sol est une traction (figure 10-b) et sa courbe de variation le long du fût est une courbe pseudo-parabolique. Sa valeur maximale se situe au droit du point d'inflexion de la courbe de cisaillement provoqué par le gonflement. En l'absence d'effet sur le terme de pointe, c'est une force interne et elle se retranche de l'effort de compression engendré par les charges gravitaires (figure 11-b). C'est précisément cette valeur résultante qu'il convient de contrôler à chaque phase en mettant en parallèle la vitesse de la construction des structures (« Top » - compression des barrettes) avec la vitesse des excavations (« Down » - traction des barrettes). Le risque est bien l'apparition d'une traction excessive à une phase donnée des travaux, traction qui serait incompatible avec la résistance admissible de la section des barrettes. Ce risque est d'autant plus grand que l'effort de compression axial dû aux charges gravitaires n'est pas grand, le module du sol au déchargement est faible, la raideur axiale des appuis profonds est forte et la raideur au cisaillement du sol est élevée.

On peut conclure, ici, que le gonflement du sol réduit l'effort de compression dû aux charges gravitaires dans le fût. Sous certaines conditions il peut même l'annuler et pousser la section résistante dans le domaine de la traction.

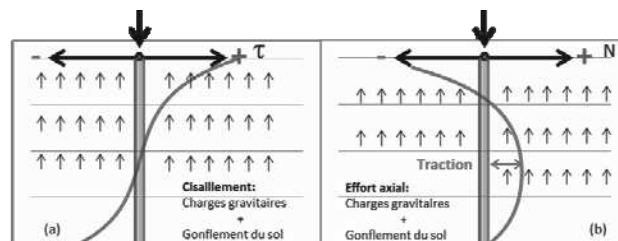


Figures 9(a,b): Cisaillement et effort axial dans les appuis profonds dus aux charges gravitaires (sans terme de pointe)

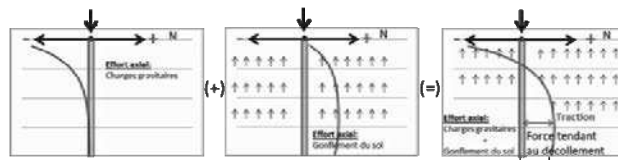


Figures 10(a,b): Cisaillement et effort axial dans appuis profonds dus au gonflement du sol encaissant (sans terme de pointe)

Il est à noter qu'en présence d'un terme de pointe à la base des appuis profonds, les contraintes de cisaillement et les efforts axiaux dus aux charges gravitaires ne se cumulent pas toujours linéairement. En effet, lorsqu'il devient prépondérant, le phénomène de gonflement peut totalement annuler le terme de pointe (effort de compression) dû aux charges gravitaires et créer ainsi une tendance au décollement de la pointe (figure 12). Dans ce cas, une analyse non-linéaire à chacune des phases de chargement où ce phénomène apparaît devient nécessaire.



Figures 11(a,b): Cisaillement et effort axial dans appuis profonds dus aux charges gravitaires + gonflement du sol encaissant (sans terme de pointe)



Figures 12: Cisaillement et effort axial dans appuis profonds dus aux charges gravitaires + gonflement du sol encaissant (avec terme de pointe) – Risque de décollement en pointe

Ce type d'analyse a été conduit sur l'ensemble des profonds (barrettes) de la tour Odéon. L'appréciation de l'amplitude du gonflement du sol dû aux excavations (déchargement) est un préalable à ce type d'analyse. Cela a été possible grâce aux études tridimensionnelles tenant compte du comportement non-linéaire du sol, englobant une large partie du massif et simulant les différentes phases de la construction. Toutes ces études complexes ont été conduites au stade de la conception, avant la contractualisation du marché d'entreprise.

#### 4 CONCLUSIONS

La construction de la tour Odéon nécessite la réalisation d'une fouille de 72 mètres de profondeur au sein d'un versant très pentu, dans des terrains de caractéristiques médiocres et sur un site urbain majeur. Les travaux et leurs séquences de réalisation devaient être conçus de telle sorte que les mouvements de nombreuses constructions sensibles situées en bordure immédiate de la fouille restent dans des limites restreintes. Quatre éléments remarquables et innovants de la conception ont été développés dans cet article :

- a) : une construction « top-down » à l'aide d'appuis pré-fondés,
- b) : la constitution d'une voûte élastique dans le sol côté montage,
- c) : le fretage du sol en pied des parois les plus hautes,
- d) : la prise en compte des effets du déchargement du sol sur les appuis pré-fondés.

Le premier élément (a) permet de réduire d'un an le délai global de la construction, qui est de quatre ans. Le deuxième élément (b) transforme le sol en une structure en voûte pour réorienter les poussées qu'il génère. Les deux derniers éléments (c et d) rendent possible le choix technique indiqué en (a).

#### 5 REFERENCES

- Baghery S., Bouvard A., Miszlai I. (2012). Conception et dimensionnement des ouvrages de soutènement de la fouille de la Tour Odéon à Monaco. *Journées Nationales de Géotechnique et de Géologie de l'Ingénieur JNGG2012*—Bordeaux 4-6 juillet 2012.
- Gastbled O.J., Baghery S. (2010). 3D modeling of a deep excavation in a sloping site for the assessment of induced ground movements. *7th European Conference on Numerical Methods in Geotechnical Engineering (NUMGE)*, Trondheim, Norvège.

# 3D Finite Element Analyses for a Laterally Loaded Pile Wall in Marine Environment– Case History

## Analyses 3D par éléments finis pour un mur de quai chargés latéralement dans un port – Etude de cas

Bahr M.A., Tarek M.F., El-Ghamrawy M.K., Abouzaid K.S.  
*Al-Azhar University, Egypt*

Shaarawi E.M.  
*Fayum University, Egypt.*

**ABSTRACT:** This paper presents a 3D finite element study on a model to simulate an horizontal load test on a retaining pile wall. The piles wall was constructed at the site of Port Ghalib marina on the Red-Sea coast of Egypt which is considered as an active seismic area. The subsoil layers consist of 2 m to 3 m gravelly sand followed by a deep clayey silt layer. The ground water was observed at a depth of about 1.10 m below ground surface. The purpose of the test is to evaluate the pile displacement characteristics under exposed loads. Numerically a 10 m – length pile was modelled to simulate the actual case. Effect of surcharge, earth pressure and earthquake loads were taken into consideration. The numerical analysis was performed and the results have been found to be in good agreement with the measured field test results. In addition the finite element method make an ability to predict the deflection along the pile length.

**RÉSUMÉ :** Cet article présente un modèle 3D éléments de dimension par élément finie pour' simuler un chargement horizontal d'un mur de quai du port de plaisance de Port Ghalib sur les côtes égyptienne de la mer Rouge qui est une zone sismique. La stratigraphie est constitué d'une couche de 2 à 3 m de sable graveleux, en surface, suivie d'une couche de limon argileux, en profondeur. La nappe phréatique est située à 1,1 m de la surface. L'objectif de l'analyse est de caractériser le déplacement latéral du mur en fonction du chargement. Le modèle numérique a été construit pour simuler le cas réel. Les effets de la surcharge, pression des terres et effets des seismes, ont été pris en compte dans le modèle. L'analyse numérique et les résultats sont en accord avec les résultats des expérimentaux de terrain. En outre, la méthode des éléments finis donne une prédiction de la déviation le long du mur.

**KEYWORDS:** 3-D FEE model, analysis, earthquake load, lateral loading, pile wall, Red sea.

**MOTS-CLÉS :** modèle FEE 3-D, analyse, la charge tremblement de terre, chargement latéral, palplanches, Mer Rouge.

### 1. SUBSOIL PROFILE CONDITIONS AND PILE GEOMETRY

Soil investigation showed that the soil profile at the site is as follows:

Top layer (yellowish brown, gravel and sand) from ground surface with depth ranging from 2 to 3 m, followed by a layer of grey clayey silt, some fine sand, traces of broken shells, extended to the end of executed boreholes (at depth of about 20 m).

The Standard penetration test (SPT) shows the N values as follows:

- From depth of 2 m to 7 m level N has values between 2 and 13
- From depth of 7 m to 11 m level N = 3
- From depth 11m to the end of boring N has values between 7 and 11

Ground water was observed e at 1.10 m below ground surface. The pile wall consists of contiguous bored piles of 1.0m diameter and 10m length.

### 2. FINITE ELEMENT MODELLING

The finite element mesh considered in three dimensional nonlinear finite element analysis as discussed in Abouzaid et. Al. (2010) is shown in Figure (1-a). Based on symmetry, only one pile of the model is meshed. 20 nodes brick element Solid 95 were used to simulate both soil, and pile with cap. It should be noted that these quadratic elements exhibit high accuracy even for high aspect ratios and can model accurately bending of solid piles. During mesh design stage, a study was performed to

decide on appropriate (balanced) mesh size. The study showed that a much larger mesh, with more elements (of lower aspect ratios) would account for a fairly small change in results, so the current mesh is sufficient for analysis.

The concrete pile section, with a diameter of 1.0 m and pile cap beam have been meshed by Twenty node brick elements as shown in figure (1a-1b) with the elastic property of concrete. The soil domain has been simulated by strip of 1 m width with symmetry conditions on both sides. The depth of soil considered below the pile tip 10 times the pile diameter. The domain of soil considered has been found very much suitable for the analysis of the laterally loaded pile as when loaded till failure the soil elements at and near boundary do not experience any deflection. Also the soil elements at and near to the bottom boundary do not experience any deflection. The soil has been modeled as elastoplastic medium following Drucker-Prager (1952) .

Soil domain has vertically been divided to 20 layers, each of thickness 1/20 of the pile embedded length to allow the soil variation with depth. The elastic modulus is taken proportional to strength parameter (c).

The boundary conditions considered are shown in Figure (6-8a), the translations UX have been constrained in outer YZ plans, and only UZ and UY have been permitted whereas UY have been constrained in outer XZ plans, and only UZ, and UX have been permitted, also the translation UZ have been constrained over the area the soil block bottom and the translations UX, and UY have been permitted, this have been done to overcome the singularity of matrices and to help to get convergence. All nodes

of the symmetry plane have been constrained in direction perpendicular to the plane of symmetry.

The interface between the pile and soil have been represented by a couple of 8 node contact element named CONTACT 170 and 8 node target elements named TARGET 174, that was described in the chapter 3. The purpose of this couple is to mimic the installation effects on piles (drilled or driven). It also serves a purpose of a simplified interface which allows for tension cut-off (gaping) and controlled, coupled horizontal and vertical stiffness. The contact between pile and soil was supposed to be rough and were simulated by Drucker–Prager model with a friction angle of value corresponding to each layer.

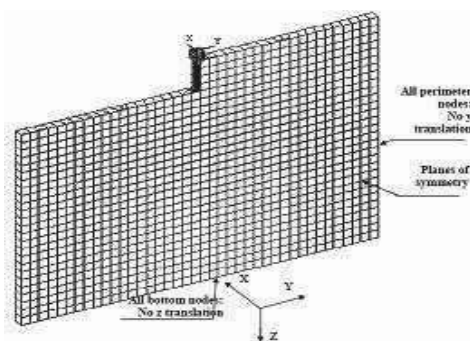


Figure (1-a): 3D Finite Element Model for Contiguous Piles Wall.

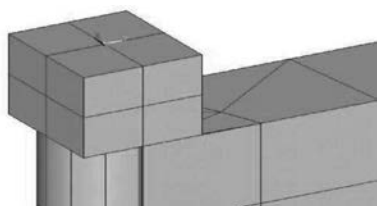


Figure (1-b): Pile Cap Mesh.

### 3. LOADING CONDITIONS

Loading for this case is presented in Table (1). The pile cap has been proposed to laterally load  $P$  at the pile head in the negative direction of  $y$  axis, in addition to surcharge load, with excavation at various stages. Ten load cases were performed to simulate the lateral load test loads and study the pile behaviour under different load cases and compare with measured results

Table (1) Applied Load in Each loading Case for Contiguous Piles Wall.

Load case No.	Applied load ( $P$ ) (kN)
1	Before Applying surcharge load of 20 kN/m
2	Applying surcharge load of 20 kN/m
3	After excavation to -2.5 m from ground level
4	After excavation to -5 m from ground level
5	24 hrs after excavation to -5 m from ground level
6	Applying 21 ton horizontal load
7	After releasing 21 ton horizontal load

8	Just after Applying 300 kN horizontal load
9	24 hrs after Applying 300 kN horizontal load
10	After releasing 300 kN horizontal load

## 4. RESULTS AND DISCUSSION

### 4.1 Pile-Soil Deformation

Figures (2-a, b, c, d, and e) show the contour of pile and soil movement in direction  $Y$  axis, the deflection along the pile for the load cases no 2, 3, 4, 6, and 8.

In figure (2-a), after applying a vertical surcharge It is interesting to note that the plastic zone propagates deeply with a high densification in top layers till reaches the minimum values at the end of the model and extended below, this means that the settlement under the surcharge induced a lateral movement to the pile towards the settled side (right side), but the pile was rigid enough to retain the other side without movement especially the movements was very low so it does not extend far from the pile. Moreover, the instrumented side (right side) features much larger plastic zone while the plastic zone for the extension side (left side) is confined to the interface layer.

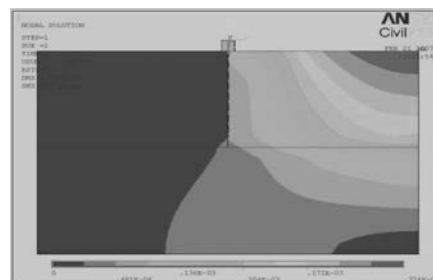


Figure (2-a) Contour of Deflections along the Pile under Surcharge Load .

In figure (2-b), after excavation to -2.5 m from ground level, It is noted that the excavation process resulted in a lateral movement of pile towards the excavation, and a small wedge of soil in front of the pile (left side) exhibits a small movement mobilizing a passive resistance in the front of the pile, but the right side is still affected by the surcharge load settlement which moves the soil very slightly in opposite direction

In figure (2-c), after excavation to -5.0 m from ground level, It is noted that the increase of excavation process resulted in increasing the lateral movement of pile towards the excavation, increasing the wedge of soil in front of the pile (left side) exhibits a bigger movement mobilizing a passive resistance in the front of the pile than the previous case, but the right side is still affected by the surcharge load settlement which moves the soil very slightly in opposite direction but less than the previous case.

In figure (2-d), Applying 21 ton horizontal load, It is noted that applying lateral load in increasing the lateral movement of pile towards the excavation, resulted increasing the wedge of soil in front of the pile (left side) exhibits a bigger movement mobilizing a passive resistance in the front of the pile the movement propagates deeper than the previous case and, but the right side is still affected by the surcharge load settlement which moves the soil very slightly in opposite direction but less than the previous case .



pressure was also performed to check results and it was found that soil pressure were within 97% accuracy.

$$MX = \frac{d(ROTX)}{dz} \tag{2}$$

$$QX = \frac{d(ROTX)}{dz} \tag{3}$$

$$PX = \frac{d(ROTX)}{dz} \tag{4}$$

4.2 Pile Head Displacement.

Figure (4) shows a comparison for the measured pile head displacement and that estimated from the present study. It is noted that a very well agreement between the two curves is existing where the R- squared value is 94%. The pile was just instrumented on the top, thus diagram column represent one case of loading.

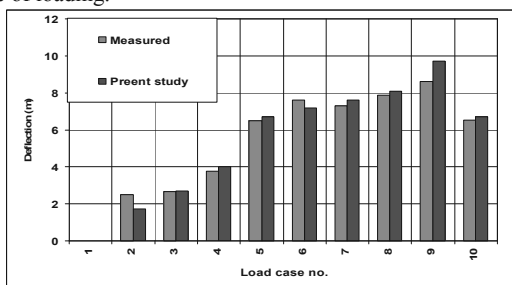
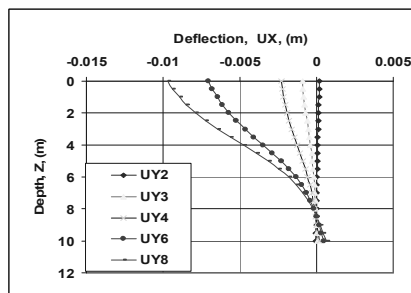


Figure (4) Predicted, and Measured Pile Head Deflection .

4.3 Pile Straining Characteristics

Figures (5- a) to (5- c ), show the lateral deflection (UYn), bending moment (MYn), and soil reaction (pressure) (PYn) respectively along Pile Shaft due to the decided loading conditions illustrated in table (1). It is interesting to note that the change in location of maximum bending moment, peak zones of soil reactions, and points of hinges induced in different case of loading, where the point of maximum moment changed from -3 m to -5 m in case of excavation to -2.5m and -4 m , respectively. The beak of soil resistance is observed at -3.0 m in case of excavation to -2.5m and at -5.2 m in case of excavation to -5m. Also, the point of reversing soil reaction was observed at -7.75m.



Figure(5-a): Lateral Deflection along Pile Shaft .

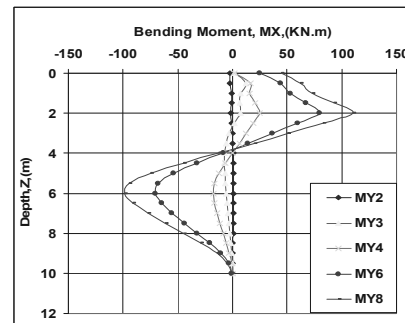


Figure (5-b): Bending Moment along Pile Shaft

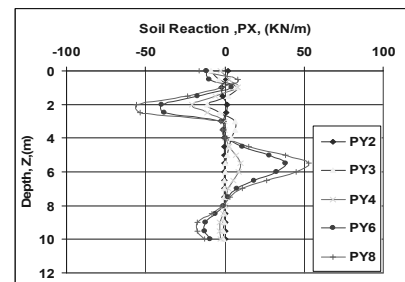


Figure (5-c): Soil Reaction along Pile Shaft.

5. CONCLUSIONS

The main findings can be summarized as follows:

- 3D finite element model gives the possibility of reaching high levels of loading until failure which is not available in full scale load tests.
- 3D finite elements can compensate for performing full scale lateral load tests with a good degree of trust to get reliable behavior of pile under loads saving time, effort , and cost.
- It is noted that good agreement between the measured and estimated from results of the finite element model. It is very important to obtain soil properties from high quality field or laboratory tests, as these will have direct effect on the analysis results.
- Pile and soil geometries must also be determined to a high degree of accuracy as these will also affect analysis outcome. Remembering the adage in computer modelling.

6. REFERENCES

Abouzaid, K.S., Shaarawi, E., El-Ghamrawy, M., Tarek, M.F., and Bahr, M.A. ,(2010), " Three Dimensional Finite Element Model for a Laterally Loaded Pile in Stiff Clay" Proc. 11th Int Conf., Cairo, Egypt Vol.3, pp. c34.

Alizadeh, M. and Lalvani, L. (2000), Lateral Load-Deflection Response of Single Piles in Sand, Electronic Journal of Geotechnical Engineering. Vol. 5.

Clark, J. I., Mckeown, S., Lester, W. B., and Eibner, L. J. (1985). "The lateral load capacity of large diameter concrete piles." 38th Canadian Geotechnical Conference, Theory and Practice in Foundation Engineering, Bolton, England.

Drucker, D.C. and Prager, W (1952), Soil Mechanics and Plastic Analysis of Limit Design, Quart. Applied Mathematics, Vol. 10, No.2, pp.157-165.

Jeremic, B., and Yang, Z (2002).Numerical analysis of pile behaviour under lateral loads in layered elastic-plastic soils. International Journal for Numerical and Analytical Methods in Geomechanics; 26:1385-1406

Maharaj, D. K. (2003), Load-Deflection Response of Laterally Loaded Single Pile by Nonlinear Finite Element Analysis, Electronic Journal of Geotechnical Engineering. Vol. 8, Bundle C, Paper 0342.

# Design and construction of a coffer dam on Narmada River for Indira Sagar project in central India: a case study of innovative foundation

## Conception innovante et construction d'un batardeau provisoire pour le barrage sur la rivière Narmada dans le cadre du projet Sagara en Inde centrale

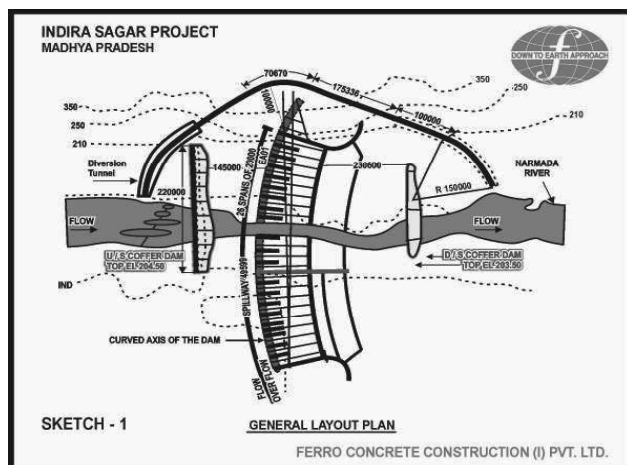
Bidasaria M.  
*Ferro Concrete Const. (India)*

**ABSTRACT:** Indira Sagar Project in M.P., a multipurpose project, a 92 m high dam on Narmada river was required to be constructed but during off monsoon period flow of 300 cumecs of river Narmada was to be diverted so that dam can be constructed. For this, it was necessary to construct a 24 m high coffer dam to divert the off monsoon flow through a diversion tunnel from left abutment. This coffer dam was to be founded on a complex geological strata. To construct this 24 m high coffer dam, a new concept of innovative design used for first time in any country to construct a coffer dam, using 5 tons pre-cast blocks as shuttering on both faces of a coffer dam and filling the enclosure with boulders and stonecrete them under water. The work of 24 m high coffer dam has been done underground and under water for 12 m height using stonecrete and balance 12 m by conventional stone masonry.

**RÉSUMÉ :** Pour la construction du projet de barrage principal de 92m de hauteur sur la rivière Narmada des ouvrages provisoires de détournement de la rivière étaient nécessaires dans un contexte géologique difficile. L'article présente la conception innovante de batardeaux utilisant des blocs creux préfabriqués en béton avec bétonnage sous eau après mise en place d'encrochements.

### 1 INTRODUCTION

Indira Sagar Project is situated near Punasa about 60 Km. from Khandwa Town in Madhya Pradesh. To construct this dam, it was essential to divert Narmada river during off monsoon period from the original flow route, so that dam can be constructed without any hindrances. For this, conceptually it was necessary to have two important Component i.e. one u/s and d/s coffer dam to stop and divert Narmada river flowing from the original flow route, where proposed main dam was to be constructed and another a diversion tunnel through which Narmada post monsoon flow of 300 cumecs can be diverted during working period. That is how the construction of u/s and d/s coffer dam was necessitated. A sketch showing the various component like, u/s and d/s coffer dam diversion tunnel, proposed main dam etc. is shown in sketch – 1.



### 2. FOUNDATION AND GEOTECHNICAL PROBLEMS AND GEOLOGY

The Geological survey of India had carried out elaborate geological studies at the Indira Sagar Project dam site. It has been indicated that the dam site is located in the upper vindhyan inter bedded sequence of tough quartz arenites (quartzite), sand stones with minor silt stones. The bed in

general has an ENE-WSW strike and dip by 15-25 towards NNW with exceptional steep dips of 40-45 due to local warping. Bedding shears of 10-25 cm thickness confined to the silt stone beds are common features. The dam area in the river bed is occupied by a number of ENE-WSW trending vertical fault/shear zone, indicating horst/graben structure showing relative vertical displacement of blocks. It is WSW continuation of the Sone-Narmada fault. Mapping of the area has identified about five shear zones ranging steep dipping to vertical. These zones are braided with clayey gouge shear seams of 0.10-0.75 m thickness enveloping competent fractured lenses of quartzites and sand stone of 0.50 m to 2.5 m width sketch-2 shows geological L-section along main dam axis.

The fault zone includes the shearing (Sz-5), by virtue of its disposition and continuity, extends beyond the coffer dam located about 80 m upstream of the exposed section and opens in to the water pool, created by the upstream coffer dam inspite of being directly connected to this water pool, created by the upstream coffer dam. In spite of being directly connected to this water pool with a head difference of about 18-20 m the exposed section is completely dry and points to the near impervious nature of the fault zone material. Permeability test carried out in the new test holes in the fault zone confirm this observation (< 1 lugeon).

Except in the highly crushed zone/intrusion dyke, the fault zone material looks well compacted and was expected to have a high in situ density in the range of 2.2-2.3. The shear strength parameters were high and grain porosity may not exceed 20 %. The material did not show any significant deterioration notwithstanding the fact that there has been water to a depth of 1-2 m standing on it for a considerable time.

Even though the strata for foundation of coffer dam looked positive, for further dam design and stability of coffer dam foundation, detailed geotechnical investigation were necessary to eliminate geological surprises. Due to lukewarm report about highly Crushed zone/Intrusion dyke the foundations of coffer dam needed additional treatment to make it water tight. Further site investigation were carried out as given in the table below.

It may be observed that during pre-construction stages, to determine the detailed design parameters, following method of site investigations were performed :-



1	Geological mapping.	Over 0.75 Sq.Km on 1:1000 scale.
2	Core drilling	Double tube barrel – over 3000 m Triple tube barrel – over 500 m
3	Trenches	Three parallel trenches of +30 m. Six cross trenches of + 15 m
4	Shafts	Six shafts of 9.5 to 18m depth, 3.5 m dia.
5	Drifts	Four drifts of +16 – 23 m.
6	Bore hole camera studies	In 2 drill holes to study cavitations in silt stone/bedding shear zones.

This Data indicated that the sheared /crusted rock mass shall get consolidated if consolidation grouting is carried out and after completion of coffer dam, curtain grouting is also recommended, 1 m from the u/s face of coffer dam. Both these treatments were absolutely necessary in view of typical geotechnical problem faced. These treatments were carried out.

3. COFFER DAM - UPSTREAM AND DOWNSTREAM

The u/s coffer dam was necessitated to stop and divert the post monsoon river flow, to facilitate construction of main dam. This post monsoon flow ranging from 300 cumecs to 100 cumecs was required to be diverted from a diversion tunnel which was under construction through the left abutment.

As the construction of diversion tunnel was getting delayed considerably, provision of six sluices in the body of u/s coffer dam was envisaged to pass the post monsoon flow.

3.1 Concept.

The work consists of design and construction of upstream and downstream coffer dam of Indira Sagar Project. This was the new concept of design used for first time in any country to construct a coffer dam using 5 tons pre-cast blocks as shuttering on both faces u/s and d/s side of a dam, and filling the enclosure with boulders and stonecrete them under water. All work of coffer dam has been done underground and under water upto RL 193.5 m.

The maximum height of u/s coffer dam was 24 meter, 12 m under water and 12 m above water. The lowest foundation level in river bed was ± 180.60 m. For under water portion 5 ton hollow pre-cast c.c. blocks were casted and placed on the u/s and d/s face of dam, as a shuttering in a cell of 15 m length with the help of divers. Before placing the blocks, river bed was leveled by using blasting under water and with special technique, PC blocks were placed. Boulders were filled in the enclosure of a 15 m long cell and grout pipe with safety reinforcement were placed. The cell of 15 m was thoroughly caulked from outside, so that river flow does not have any effect in the cell. A colloidal grout, made out of sand, cement water and super plasticiser was pumped through the grout pipe at bottom and level of grout slowly built up from down upward. Thus colloidal grout (colcrete) replacing the water in the voids of the boulder and converting the boulder mass into concrete. This under water work was carried out upto 193.50 m level. About six pre-fabricated construction sluices of 2 m x 3 m were placed to take care of post monsoon discharges upto 300 cumecs as the diversion tunnel was under construction and was not ready.

Stone masonry was constructed above water level over the underwater works from RL 193.5 m and raised upto RL 204.50 m.

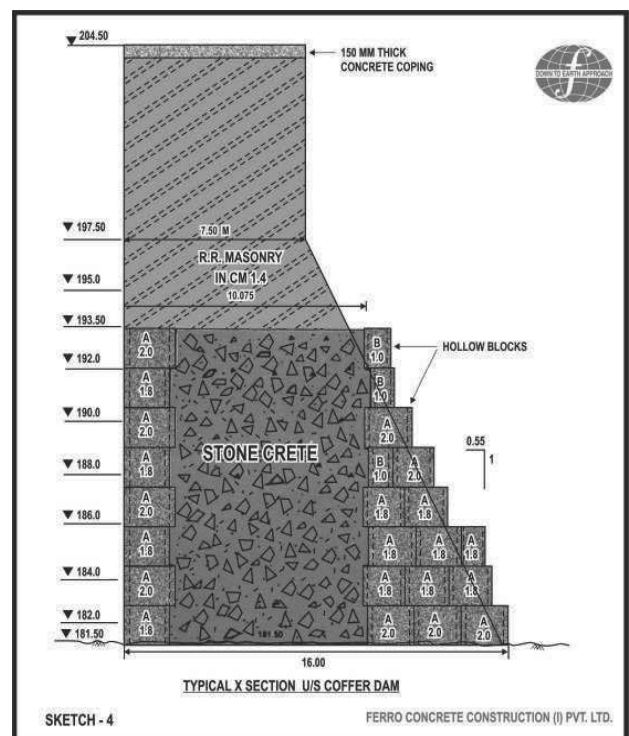
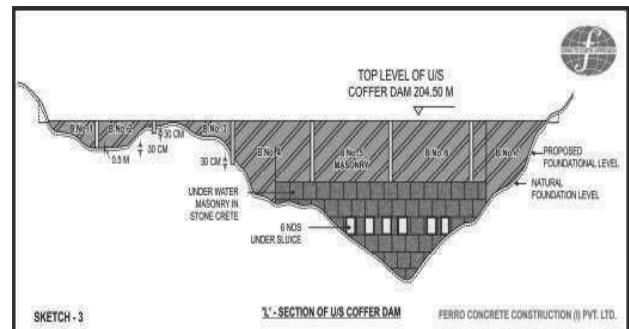
3.2 Design.

Height of u/s coffer dam was 24 m with the lowest foundation level kept at 180.6 and top of coffer dam as RL 204.5m. It has been designed on the principle of gravity dam, duly checked, for stability in various condition like Reservoir empty and Reservoir full etc. with following parameters :-

3.2.1 Cofferdam:

- a) Above water level, Random rubble masonry with a compressive strength of 10.5 N/mm<sup>2</sup> (cement mortar 1:4 approximate) with selected stone placed in u/s and d/s face.
- b) Under water stonecrete masonry in 1:2 and 1:3 concrete with P.C.C. Blocks on u/s & d/s faces.
- c) PCC blocks in M-15 grade Concrete.
- d) Coping : Concrete of M20 grade (c.c. 1:1.5:3) with 20 mm graded metal.

It may be observed that for underwater work, PCC blocks were kept on u/s and d/s section of the coffer dam and they were considered as a homogenous part of the full section. Dam cross section and L-section can be seen vide sketch – 3 and 4.



#### 4 CONSTRUCTION SEQUENCE OF COFFER DAM U/S.

Following is the Construction sequence.

##### 4.1 Casting yard for Pre-cast hollow blocks.

A casting yard having all facilities to cast hollow blocks under controlled conditions was made on left bank. The pre-cast/hollow blocks of size of 1.5 m x 1.5 m x 1.5 were casted in this yard. Suitable storage for form work and construction materials like stone grit, sand, water curing tank etc. were arranged on this platform to keep adequate stocks at site. The yard was equipped with form vibrators etc. and the traveling gantry with 10 T capacity. One electric hoist was fitted at this platform. The blocks were handled and loaded in flat bottom trucks by said gantry to carry it upto working platform on left flank from where, finally they were taken for construction using crawler mounted cranes at site.

##### 4.2 Precast Hollow Blocks :-

It was proposed to use hollow-precast blocks in the u/s and d/s of the dam profile under water. This enclosure were termed as stonecrete cell. At a time, 15 m length of coffer dam was undertaken in hand. Selected rubbles were filled within this enclosure along with colgrout pipes to carry out under water work. These colgrout pipe of 80 mm  $\phi$  were kept in a grid of 3 m and individual pipes were surrounded with a circular coil made of 6 mm, Tor to protect them during boulder filling. These blocks in addition to forming the enclosure have helped to stop flow of water within the enclosure as well as in voids of the rubbles.

The shape of the blocks on upstream and down streams faces of the coffer dam were nearly confirming to the designed profile.

To provide necessary interlocking amongst the blocks, male and female grooves were provided in each block. The blocks of special dimensions for maintaining uniform level of courses were casted as per requirement. The necessary shear keys and lifting hooks were provided in each block. The blocks were casted in the rigid steel forms so as to ensure uniform dimensions and minimum tolerances. The blocks were cast in advance and stacked in the casting yard.

##### 4.3 Preparation of Foundation.-

The left and right flanks which were much above water level of river were excavated to reach sound rock level to accommodate the length of coffer dam. Right flank in particular, was braided with clayey gougey shear seam of varying thickness from 2m to 6m. On the left flank excavation bedding shears of 16 to 25 cm thickness confined to the silt stones were commonly seen. Few photographs of the excavation and shear seam are exhibited below.

Foundation preparation in the river portion comprised of removal of silt, debris, loose rock and leveling of bed rock by underwater blasting wherever necessary. This was done using expert divers.

In order that the precast blocks from the pattern masonry walls required to be raised in uniform courses, the precise soundings were taken and loose materials were removed from its underneath. The area was leveled using special sizes of the blocks, or executing under water concreting for leveling course. It was observed that foundation rock was undulated at places. Hence levels were taken at a grid of 2 m and drawn on graph sheet. The gap between the leveled foundation and underneath of the blocks were caulked to achieve reasonable water tight joint.

##### 4.4 Launching of Blocks.

After the river bed is cleared of loose materials and leveled to receive the first course of the blocks as described under preparation of foundation para (III) above, the pre-cast hollow blocks were lifted from the working platform and carried by crane and lowered in position in the cell. Before lowering the PCC blocks, a steel frame made of 100 mm M.S. angle, is first lowered in place on 40 mm bed of stone chips and this frame is leveled horizontally on this bed. Expert divers had positioned the blocks at proper places either on the u/s or d/s of the enclosure as required, but within these steel frames which were leveled horizontally on the bed of 40 mm stone chips.



Each operation of block launching consisted of placement of blocks in the bottom course, to be followed by blocks in upper course. Till they were placed upto the level of 193.50 M. The launching of blocks is shown in photograph above.

Normally the blocks will be placed in required courses on up-stream and downstream sides of the u/s and d/s coffer dams. As the blocks are required to be in course it will be imperative to break the joints between the courses. Proper care was taken to break these joints in subsequent courses. As a matter of abundant precaution, the space in between the rows of blocks, will be filled with selected rubble near the blocks and around the pipes placed for colgrouting, so that the same does not get disturbed while filling up of rubble/stones in the cell

##### 4.5 Packing of Rubbles.

After the blocks are carefully launched and erected on either side in courses and the space in between interspersed with colcrete pipes, as stated above, rubble will be placed to fill-up the entire space between the rows of blocks in a 15 m cell. This rubble filling shall be done layer by layer in a systematic way using the large buckets with drop bottoms, handled by cranes.

##### 4.6 Stonecreting Operations.

The stonecrete process consists of making a grout of cement, sand and water in which cement has been so completely hydrated by high speed mechanical mixing, that the grout attains a colloidal form. This grout is stable and particularly fluent. It contains no chemical admixtures which might ultimately be harmful. When colloidal grout is poured in rubble aggregate the voids in the rubble filling are completely filled by penetration and the whole mass sets as a dense, solid concrete which is termed as "STONECRETE".

##### 4.7 Preparation of Colloidal Grout.

The Colloidal grout was prepared in double drum colcrete mixer consisting of sand, cement and water in desired proportions to obtain colloidal grout. In colloidal mixer, the

wetting of solid ingredients results from the shearing action which takes place in the specially designed impellers and matching casings of the colloidal mixers. The colloidal grout of specific gravity upto 1.8 to 2 is obtained using these high velocity mixers. Colloidal grout has enough fluidity to flow like grout and does not get separated when it comes in contact with water. It displaces water from the voids of stone/rubbles due to high specific gravity.

The double drum stonecrete mixer produces colloidal grout at the rate of 5 to 10 M<sup>3</sup>/hr. of 1:2 mix or 6 to 12 M<sup>3</sup>/hr. of 1:3 mix. When colloidal grout is stored without agitation in tanks after mixing, a little settlement is to be expected because sand invariably contains some oversize particles. When it is pumped direct by the mixer to the work in normal practice, the oversize particles do not have time to settle out.

#### 4.8 Placement of Colloidal Grout.

Colloidal grout does not mix with water unless agitated with it.

The colloidal grout so prepared is pumped, through 80 mm  $\Phi$  pipes placed in the rubbles using special roto or colmono pumps. The grout will be pumped at the bottom of pre-packed stones under pressure and will be allowed to rise uniformly in the cell displacing all the water from the voids due to its gravity. Once the grout travels upto the top of the course, the colgrouting is stopped when it emerges out of boulders at a level of 193.50 m of working platform level. After which the crawler mounted cranes will be advanced to tackle the next cell of the coffer dam till entire length 220 m length of u/s coffer dam is completed from one end. Construction sluices were left in the u/s coffer dam for diverting the water in final stages of closure of the coffer dam.

#### 4.9 Construction Sluices.

Pre fabricated M.S. sluice barrel were lowered in the central portion of u/s coffer dam keeping invert level at RL 186. In all, six sluices of 2 m x 3 m were installed. Rigid steel boxes were provided in the blocks for forming the approach tunnel for sluices. The construction sluices were installed under water with the help of the expert divers and is shown in photograph below.



4.10 Masonry Works above water level.

Construction of masonry in the flank blocks and above water level on stonecrete platform, upto top of coffer dam was done using conventional method of construction. The coffer dam above RL 193.5 was constructed in masonry upto RL 204.5 M and is shown in photograph. This was taken up immediately after the construction upto RL 193.5 under water using stonecrete. A coping 150 mm thick was laid at RL 204.5 m on the masonry using M-20 grade concrete.

## 5. DRILLING AND GROUTING.

### 5.1 Consolidation Grouting.

Looking to the geology, it was recommended to adopt a grid of drill holes at 3 m c/c on both side, besides about 82 Nos. of special grout holes were identified keeping in mind the location of various fault zones.

Depth of consolidation grout holes was 6 m in foundation rock.

## 6. CURTAIN GROUTING.

It was recommended to provide a single row of grout curtain, 1 m from the u/s face of the coffer dam, spacing of holes were kept as 3 m c/c. Depth of grout curtain holes in foundation rock was kept as 15 m.

This grout curtain was provided in stages of 5 m of drilling and grouting in descending order method.

It was observed that in consolidation grouting, intake of cement was 45 kg/meter and in curtain grouting it was 26 kg./meter.

## 7. D/S. COFFER DAM:

The construction of d/s coffer dam was done using the same methodology as explain under para 3 sub para I to IX. The top of d/s coffer dam was kept as 203.50 m i.e. 1 m below the u/s coffer dam. The main purpose of this coffer dam was, not to allow the river water which was diverted through the diversion tunnel (back water) in the d/s of the river.

### Closure of Sluices 6 Nos. in coffer dam:

It was essential to ensure following works completed before closure of sluices were taken in hand :-

## 8 CONCLUSION

Coffer Dam u/s and d/s, for the Indira Sagar Project had been successfully constructed and performed well, as a result the work of 92 m high I.S.P. main dam could be expeditiously carried out on mighty Narmada River.

The unique and innovative design, using 5 Tons Pre-cast hollow blocks with underwater stonecrete technique for the first time in the country, has successfully been used in Indira Sagar Project.

## 9 REFERENCES

- Ahmed M.J. - Assessment of Geological and Technical inputs for optimization of Designs of Indira Sagar Project, M.P. India.
- Billore M.S., Geed V.K., - Photographs.
- M. Krishnamoorthy, G.C. Vyas, Rajeev Sachedeva – Civil design aspects of Indira Sagar Project.
- Tripathi D.C. Amitabh Sharan, - Shearzone treatment : A case study of Indira Sagar Project on Narmada River, M.P. India.

# Anchored sheet pile wall design in expansive soils

## Conception d'un mur de palplanches ancré dans les sols expansifs

Bilgin Ö., Mansour E.  
University of Dayton, Dayton, Ohio, U.S.A.

**ABSTRACT:** Expansive soils cause damage to civil engineering structures in various parts of the world, because they swell when absorb water and shrink when dry out. Due to swelling pressures, retaining walls can be subjected to additional lateral pressures causing increased wall deformations and bending moments. Anchor forces can also increase, if the walls are anchored. When expansive soils are present behind retaining walls, swell pressures should also be considered during design in addition to the traditional lateral earth pressures. This study proposes a method to predict potential swell pressures acting on retaining walls for use in design of these walls. A parametric study using the limit equilibrium approach was performed to investigate the effect of swell pressures on the design of anchored sheet pile walls in expansive soils. The results of the study show that the presence of expansive soils can significantly affect earth retaining structures and swell pressures should be considered in the design of retaining walls when the expansive soils are present at the site.

**RÉSUMÉ :** Les sols expansifs causent des dommages à des structures de génie civil dans diverses parties du monde, ils gonflent quand ils absorbent de l'eau et se contractent quand ils se dessèchent. En raison des pressions de gonflement, les murs de soutènement peuvent être soumis à des pressions latérales supplémentaires augmentant les déformations et les moments fléchissant. Les forces d'ancrage peuvent également augmenter, si les murs sont ancrés. Lorsque les sols expansifs sont présents derrière les murs de soutènement, les pressions de gonflement devraient également être envisagées, en plus des pressions latérales des terres traditionnelles. Dans cette étude, une méthode a été proposée pour prédire d'éventuelles pressions de gonflement agissant sur les murs de soutènement, à utiliser dans la conception de murs de soutènement. Une étude paramétrique en utilisant l'approche d'équilibre limite a été réalisée pour étudier l'effet des pressions de gonflement sur la conception de rideaux de palplanches ancrées dans les sols expansifs. Les résultats de l'étude montrent que la présence de sols expansifs, peut influencer considérablement la conception de structures de soutènement et doit être pris en compte dans la conception des murs lorsque les sols expansifs sont présents sur le site.

**KEYWORDS:** Retaining wall, anchored sheet pile wall, expansive soil, swell pressure, wall design.

## 1 INTRODUCTION AND OVERVIEW

The sidewalls of structures and retaining walls may experience additional lateral pressures when they are located within expansive soils. When the expansive soils absorb water the moisture content increases and the soil tends to expand. If the free swelling or expansion of the clay is restricted, then swell pressures develop and this cause an increase in the lateral pressures acting on the structures. The design of retaining walls usually specifies cohesionless soils as a backfill material behind the wall mainly to avoid hydrostatic pressures by providing easy drainage. These cohesionless materials also help to prevent swell pressures that may develop if cohesive soils are used.

Due to economical reasons, local soils which may be expansive are sometimes used as a backfill material (Thomas et al. 2009). However, use of these soils as backfill may result in wall failures (Marsh and Walsh 1996) not only because of the hydrostatic pressures but also due to the additional lateral earth pressures caused by the swelling of expansive soils.

The selection of soils behind the wall is not even optional for in-situ retaining walls, such as cantilever and anchored sheet pile walls, slurry walls, secant and tangent pile walls. These walls are installed in existing soils and front of the wall is usually excavated. When these walls are installed at locations where expansive soils are present, the walls would experience not only the traditional lateral earth pressures but also the swell pressures when soil's moisture content increases.

The objective of this study is to investigate the behavior of anchored sheet pile walls when they are installed in expansive soils and exposed to additional stresses due to the swelling of

these soils.

### 1.1 Expansive soils

The best way to deal with the shrinkage and swelling of expansive soils is to maintain constant soil moisture. If the soil moisture content does not change, there can be no shrinkage or swelling. However, it is usually not possible to maintain constant soil moisture. Moisture content fluctuates due to several factors, such as precipitation and evaporation. The seasonal variation of soil moisture is much higher at shallower depths and it decreases as the depth below the ground surface increases (Figure 1).

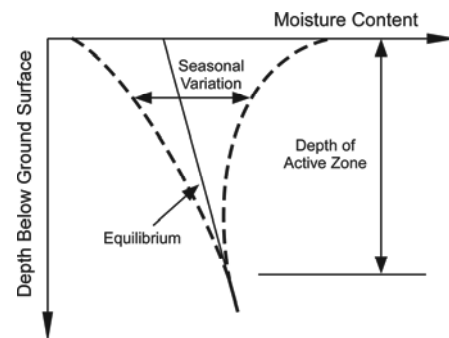


Figure 1. Moisture content fluctuations with depth.

Table 1. Classification of swell potential (after USACE 1983).

Classification of swell potential	Plasticity index, PI (%)
Low	< 25
Marginal	25 – 35
High	> 35

The depth where the seasonal soil moisture variations occur below the ground surface is called the active zone as shown in Figure 1. The depth of active zone is influenced by soil permeability, precipitation and evaporation amounts, seasonal temperature fluctuations, and presence of tree roots. Active zone depths in several U.S. cities were reported by O'Neill and Poormoayed (1980) as: 1.5 to 3.0 m in Houston, Texas; 2.1 to 4.2 m in Dallas, Texas; 3.0 to 4.6 m in Denver, Colorado; and 3.0 to 9.0 m in San Antonio, Texas.

The degree of swell potential of expansive soils can be classified by the soil's liquid limit,  $LL$ , or plasticity index,  $PI$ . As the liquid limit or plasticity index increases, the swell potential of the soil increases. The classification used by the U.S. Army Corps of Engineers (USACE) (1983) based on the plasticity index is given in Table 1.

### 1.2 Conventional sheet pile wall design

The design of sheet pile walls is based on active and passive earth pressures which are concerned with the failure condition using the Mohr-Coulomb failure criterion. For a typical wall section, the lateral earth pressures and the resulting forces acting on the wall are shown in Figure 2, where  $P'_A$  and  $P'_P$  are resultant effective active and passive earth forces, respectively;  $d_A$  and  $d_P$  are moment arms with respect to the anchor elevation; and  $FS$  is factor of safety. The factor of safety is applied to the passive loads during wall design (NAVFAC 1986; USACE 1994). The safety factors are used to take into account the uncertainties in soil conditions, method of stability analysis, loading conditions, as well as to restraint soil movements at an acceptable level (Potts and Fourie 1984).

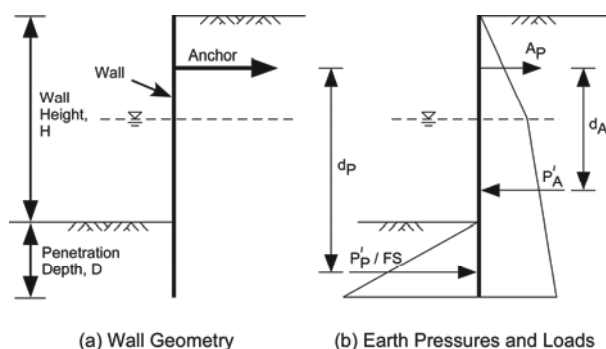


Figure 2. Typical sheet pile wall section and forces acting on the wall.

Wall penetration depth required below the bottom of the excavation is determined by considering the moment equilibrium about the anchor elevation. Because the water level is assumed to be at the same elevation behind and in front of the wall during this study, hydrostatic forces cancel each other. Once the wall penetration depth is determined, the anchor force,  $A_p$ , is calculated from horizontal force equilibrium. Based on the active and passive pressure distributions and the calculated anchor force, maximum wall bending moment is determined. The design moment is calculated by applying the moment reduction factor (Rowe 1952) to the calculated maximum bending moment. The steel sheet pile section is then selected based on the design moment, and the wall design is completed by selection and design of an anchorage system. This conventional design approach does not take into account any

swell pressures that may affect walls when they are installed at locations where expansive soils are present.

## 2 METHOD OF APPROACH

The effect of swelling pressures on anchored sheet pile wall behavior has been investigated through a range of expansive soil activity. The swell pressures were calculated for a range of plasticity index values covering soils from low to high swell potential based on a study performed by Erzin and Erol (2007). Using these swell pressure potentials and moisture change profile in the ground within the active zone, the swell pressure distribution was developed. The swell pressure distribution developed was then applied on the anchored sheet pile wall as potential swell pressure, additional to the lateral earth pressures presented in Figure 2.

A parametric study for a range of plasticity index values, i.e. expansive soil activity and swell potentials, have been performed using the free earth support design method to investigate the effect of swell pressures on anchored sheet pile walls. Design of the wall was first performed for non-expansive soils, i.e. using only the traditional lateral earth pressure distributions, as a baseline case. Then the swell pressures, based on the varying plasticity index values, have been applied and the wall was re-analyzed.

## 3 SWELL PRESSURES

There are many factors that govern expansive behavior of soils. The primary factors are availability of moisture, amount and type of clay particles, and initial condition of soil in terms of dry density and moisture content (Day 1994). Several earlier studies (e.g., Snethen 1980, Erzin and Erol 2007) indicate that soil suction is the most relevant soil parameter for the characterization of swell behavior of expansive soils.

Multiple regression analyses carried out by Erzin and Erol (2007) revealed that the soil suction relates to the plasticity index and water content as

$$\log s = 2.02 + 0.00603 PI - 0.0769 w \quad (1)$$

where  $s$ =soil suction (in bar),  $PI$ =plasticity index (in percent), and  $w$ =water content (in percent). The study performed by Erzin and Erol (2007) also showed that the swell pressure, for pressures between 0 and 100 kPa, can be given as

$$\sigma_s = -3.72 + 0.0111 PI + 2.077 \rho_{dry} + 0.244 \log s \quad (2)$$

where  $\sigma_s$ =swell pressure ( $\text{kg}/\text{cm}^2$ ),  $PI$ =plasticity index (in percent),  $\rho_{dry}$ =dry density ( $\text{g}/\text{cm}^3$ ), and  $s$ =soil suction (in bar).

For this study, the plasticity index was used as the only variable to determine swell pressures. The plasticity index values considered ranged from 10% to 50%, which covers low to highly expansive soils as presented in Table 1. A constant value of 15% for the moisture content and a constant value of  $1.65 \text{ g}/\text{cm}^3$  for the dry density were used. These selected values represent average values of the ranges considered by Erzin and Erol (2007) in their study. The swell pressures calculated using Eq. 2 for the range of plasticity index values studied, with the moisture content of 15% and dry density of  $1.65 \text{ g}/\text{cm}^3$ , are shown in Figure 3.

### 3.1 Distribution of lateral swell pressures behind the wall

As shown in Figure 1, seasonal variation of soil moisture content is the highest at the ground surface and it diminishes as the depth from the ground surface increases. The change in the moisture content with increasing depth is not linear. However, the variation is assumed to be linear in this study. This

assumption is conservative, since the predicted swell pressures will be larger than the actual ones. The simplified linear model is shown in Figure 4.

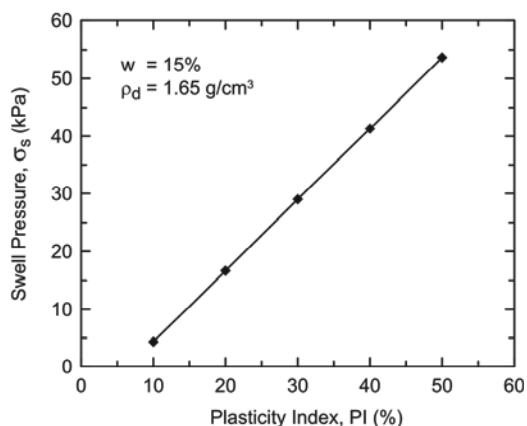


Figure 3. Swell pressure versus plasticity index.

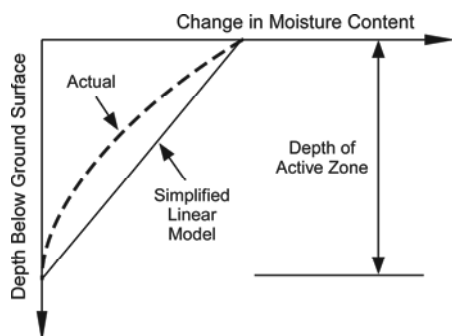


Figure 4. Change in moisture content with depth.

Because the change in moisture content causes the swelling of expansive soils, swell pressure will be maximum at the ground surface and will decrease as the depth increases. These maximum pressures, i.e. potential swell pressures, can be determined using Eq. 2. However, swell pressures close to the ground surface will not reach their potential due to shallow depths where soil confinement pressures are relatively lower. Soils closer to the ground surface will be able to expand, and full swell pressures determined by Eq. 2 will not be able to develop. When swelling occurs, passive lateral earth pressure conditions develop near the ground surface. Therefore, the passive earth pressures can be used as an upper limit for swell pressures near the ground surface. A schematic of the additional lateral pressure developed behind the wall due to the swelling of expansive soil is shown in Figure 5, where the potential swell pressure,  $\sigma_s$ , is determined by Eq. 2. When the swell pressures exceed the passive earth pressures near the ground surface (i.e., within the critical depth,  $z_c$ , shown in Figure 5), the additional lateral pressures due to the swelling of soil are capped by the passive earth pressures.

#### 4 ANALYSIS AND RESULTS

The analyses were performed for a fixed wall height of 10 m with anchor level located at 2.5 m below the top of the wall. The anchor level was selected based on a study performed by Bilgin and Erten (2009) which showed that the best anchor location to have minimum wall deformations was  $0.25 \times H$  below from the top of wall, where  $H$  is the wall height. The active zone depth used in the study was 5.0 m, selected based on the values given by O'Neill and Poormoayed (1980) as mentioned previously. The groundwater table is also assumed to be 5.0 m

below the top of wall and at the same elevation on both sides of the wall. A schematic of the pressure diagrams used to perform parametric study are shown in Figure 6.

The analysis results are shown in Figure 7 through Figure 9, as a percent increase in the wall penetration depth, maximum wall bending moment, and anchor force versus soil plasticity index. The percent increase is given with respect to the baseline case in which the anchored sheet pile wall was installed in non-expansive soil. The results show that as the plasticity index increases the wall penetration depth, maximum wall bending moment, and anchor force can increase significantly.

##### 4.1 Wall penetration depth

The effect of expansive soils and potential swell pressure, calculated based on the soil plasticity index, on anchored sheet pile wall penetration depth is presented in Figure 7. As shown in Figure 7, an increase in the plasticity index, i.e. increase in the activity of expansive soils, can result in significant increase in wall penetration depth. Compared with the wall installed in non-expansive soil, the wall penetration depth can increase more than 85% and 125% for low and marginally expansive soils, respectively. Within the plasticity index range considered during this study, the wall penetration depth can increase as much as 190% which is for the plasticity index of 50%.

##### 4.2 Wall bending moment

The effect of expansive soils and potential swell pressures on wall maximum bending moment is shown in Figure 8. The results show that wall bending moment increases as the plasticity index of soil increases. While the presence of marginally expansive soils with fully reached swell potential can result in approximately 105% increase in wall bending moment, an increase of up to 170% can occur for soils with plastic index values of 50%, i.e. highly expansive soils.

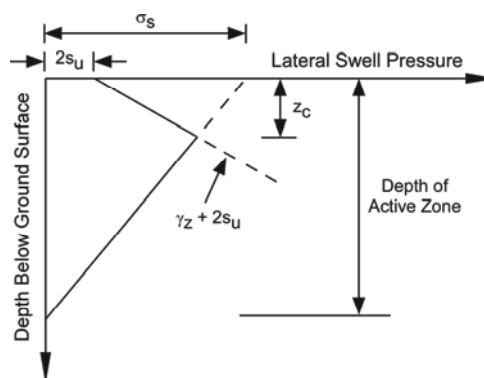


Figure 5. Lateral pressure distribution due to swelling of expansive soil.

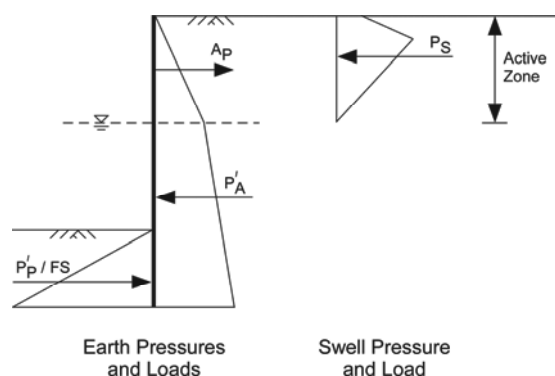


Figure 6. Soil and swell pressures acting on the wall.

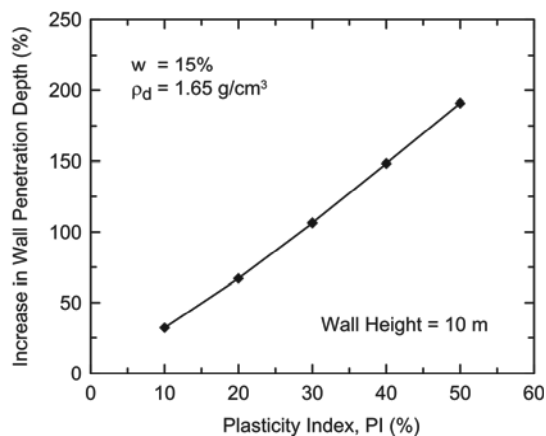


Figure 7. Effect of expansive soils on wall penetration depth.

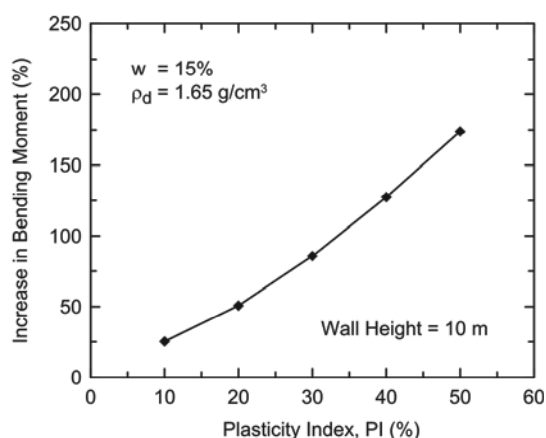


Figure 8. Effect of expansive soils on wall bending moment.

### 4.3 Anchor force

The effect of expansive soils and potential swell pressure on anchor force is presented in Figure 9. The results show that the anchor force increases as the plasticity index of soil increases, similar to the wall penetration depth and bending moments. However, the presence of expansive soils has the most significant effect on the anchor forces. This is because of the fact that the anchor is located closer to the top of sheet pile wall and the swell pressures are higher closer to the ground surface due to more fluctuations in soil moisture content in this zone. Within the range of parameters considered, an increase in the anchor force can be as much as 240% (when plasticity index is 50%) compared to the condition where the wall is installed in non-expansive soil.

## 5 SUMMARY AND CONCLUSIONS

The design of retaining walls usually specifies cohesionless soils as a backfill material behind the wall, however, in-situ retaining walls, such as anchored sheet pile walls, are installed in existing soils. Expansive soils exist in many locations around the world, and the design of anchored sheet pile walls needs to consider the effect of soil swell pressures when these walls are installed in these soils.

In this paper the effect of expansive soils and swell pressures on anchored sheet pile walls, in terms of wall penetration depth, wall bending moment, and anchor force were investigated. The swell pressures were determined using the soil plasticity index, based on earlier studies. For the cases studied and range of soil properties considered, the analysis results show that the effect of expansive soils on anchored sheet pile walls can be significant,

even if the soils at the site are low to marginally expansive. For soils with the plasticity index of 50%, indicative of highly expansive soils, and for wall geometry and soil conditions considered during this study, the analysis results show that the wall penetration depth increased 190%, wall bending moments increased 170%, and anchor force increased 240%, compared with the wall design when soils at the site are non-expansive. The maximum increase was observed in the anchor force, because higher swell pressures develop closer to the ground surface due to the seasonal changes in moisture content. It should be noted that the swell pressures determined using the plasticity index values represent the maximum potential swell pressures, i.e. upper limit, and these pressures may not develop during each seasonal changes.

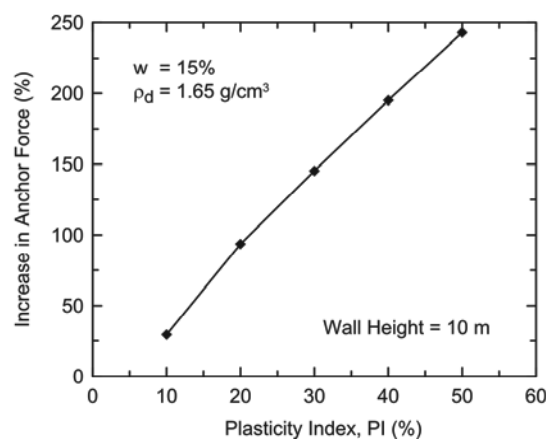


Figure 9. Effect of expansive soils on anchor force.

## 6 REFERENCES

- Bilgin Ö. and Erten M.B. 2009. Analysis of anchored sheet pile wall deformations. *Contemporary topics in ground modification, problem soils, and geo-support (GSP 187)*. Proceedings, International Foundation Congress & Equipment Expo 2009, Orlando, Florida, 137-144.
- Day R.W. 1994. Performance of slab-on-grade foundations on expansive soils. *Journal of Performance of Constructed Facilities* 8 (2), 129-138.
- Erzin Y. and Erol O. 2007. Swell pressure prediction by suction methods. *Engineering Geology* 92 (3-4), 133-145.
- Marsh E.T. and Walsh R.K. 1996. Common causes of retaining-wall distress: case study. *Journal of Performance of Constructed Facilities* 10 (1), 35-38.
- Naval Facilities Engineering Command (NAVFAC) 1986. *Foundations and earth structures, NAVFAC DM 7.02*, Alexandria, VA.
- O'Neill M.W. and Poormoayed, N. 1980. Methodology for foundations on expansive clays. *Journal of the Geotechnical Engineering Division* 106 (GT12), 1345-1367.
- Potts D.M. and Fourie A.B. 1984. The behavior of a propped retaining wall: Results of a numerical experiment. *Geotechnique* 34 (3), 383-404.
- Rowe P.W. 1952. Anchored sheet-pile walls. *Proc.- Inst. Civ. Eng.* 1 (1), 27-70.
- Sneath D.R. 1980. Characterization of expansive soils using soil suction data. *Proceedings of the 4th International Conference on Expansive Soils*, Denver, Colorado, 54-75.
- Thomas M.G., Puppala A.J., and Hoyos L.R. 2009. Influence of swell pressure from expansive fill on retaining wall stability. *Contemporary topics in ground modification, problem soils, and geo-support (GSP 187)*. Proceedings, International Foundation Congress & Equipment Expo 2009, Orlando, Florida, 590-597.
- U.S. Army Corps of Engineers (USACE) 1983. *Foundations in expansive soils, TM 5-818-7*, Washington, DC.
- U.S. Army Corps of Engineers (USACE) 1994. *Design of sheet pile walls, EM 1110-2-2504*, Washington, DC.

# Performance of Soil Nails in Weathered Granite and Fill

## Performance de renforcement par clouage du granite altéré et du remblai

Chow C.-M., Chee-Meng, Tan Y.-C.

G&P Geotechnics Sdn Bhd, Kuala Lumpur, Malaysia ([www.gnpgeo.com.my](http://www.gnpgeo.com.my))

**ABSTRACT:** Soil nail is increasingly common in Malaysia for infrastructure works where high cut slope is often formed to accommodate road alignment, facilities, etc. In recent years, soil nailing has also proven to be a viable, cost-effective and environmental friendly alternative solution for deep excavation of basement to replace conventional solutions using vertical retaining wall such as contiguous bored pile, secant pile or diaphragm wall. Applications of soil nail for basement construction of up to 30m deep have been successfully designed and constructed where performance of the soil nailing works have been verified based on monitoring results. Design assumptions for the skin friction between the soil and grouted body of soil nail were also verified using instrumented preliminary and working pull-out tests on the soil nails. This paper discusses results of the pull-out tests on the soil nails and based on analysis of the test results, recommendations on the skin friction applicable for soil nail design are presented.

**RÉSUMÉ :** Les clous de sols sont de plus en plus communs en Malaisie pour les travaux d'infrastructure où une forte pente de talus est souvent créée pour le tracé de la route, pour accueillir les installations, etc. Ces dernières années, le clouage de sol s'est également avéré être une solution alternative viable, rentable et écologique pour remplacer les solutions classiques utilisant un mur de soutènement vertical tels que les pieux forés contigus, les pieux sécants ou les parois moulées pour les excavations profondes des travaux de fondations. Les applications du clouage de sol dans la construction d'excavations de plus de 30m de profondeur ont été correctement conçues et mises en œuvre et leurs performances ont également été vérifiées sur la base de mesures répétées. Les hypothèses de calcul des efforts d'adhérence entre le sol et les clous de sols avec injection ont également été vérifiées par des tests d'arrachement. Cet article présente les résultats des tests d'arrachement sur des clous de sol et sur la base de l'analyse de ces résultats, propose des recommandations sur la capacité en de scellement à prendre en compte lors de la conception des clous de sol.

**KEYWORDS:** Soil nail, skin friction, pull-out tests, deep excavation.

### 1 INTRODUCTION

Soil nails are increasingly common in Malaysia for infrastructure works where high cut slope is often formed to accommodate road alignment, facilities, etc. Soil nail is advantageous compared to other retaining wall system as the soil nails are installed directly onto the final slope/wall profile and as such, minimises earthworks compared to conventional retaining wall. Furthermore, soil nails installation also does not require heavy machineries compared to system such as contiguous bored pile (CBP), diaphragm wall/secant pile. Malaysia's experiences in soil nail design and construction have been discussed by Chow & Tan 2006 and Chow & Tan 2011.

In recent years, the use of soil nails as alternative solution to vertical retaining wall for basement excavation is also gaining popularity and has been successfully designed and constructed for basement excavation of up to 30m deep. This paper discusses the design and construction of a soil nailed slope for basement excavation of a commercial development in Mont' Kiara, Kuala Lumpur, Malaysia with excavation depth of up to 20m.

### 2 GENERAL GEOLOGY AND SUBSURFACE INFORMATION

The site is underlain by the Kuala Lumpur Granite formation. The granite rocks are generally whitish grey and dark grey in colour except certain parts with iron stained markings that gives orange and dark red colours to the rocks. The texture and composition of the granitic rock generally ranges from coarse to very coarse-grained.

A total of twenty nine boreholes were carried out at the site to facilitate retrieval of undisturbed soil samples for laboratory testing (e.g. Atterberg limits tests, Isotropically Consolidated Undrained Triaxial – CIU tests, etc.) and also in-situ tests such as Standard Penetration Tests (SPT). The interpreted borehole profiles relevant to the soil nail slope showing the SPT-N values, major/minor components of soil and Rock Quality Designation (RQD) for rock are shown in Figure 1. Some of the materials near to the surface, especially for materials with low SPT 'N' values (< 5) are filled materials.

Generally, the subsoil consists mainly silty SAND and sandy SILT with Liquid Limit (LL) ranging from 25% to 71% and Plastic Limit (PL) ranging from 15% to 42% and can be classified as low to high plasticity silty/clayey materials.

A total of eleven Isotropically Consolidated Undrained Triaxial (CIU) tests and four Direct Shear Box tests were carried out to determine the shear strength of the soil. The shear strength parameters of the subsoil adopted for design are  $c'=3.5\text{kPa}$ ,  $\phi'=30^\circ$ .

### 3 DESIGN OF SOIL NAIL SLOPE FOR BASEMENT EXCAVATION

The soil nail slope with retained height of up to 20m is designed to ensure minimum long-term factor of safety of 1.4 as the soil nail slope will be permanent.



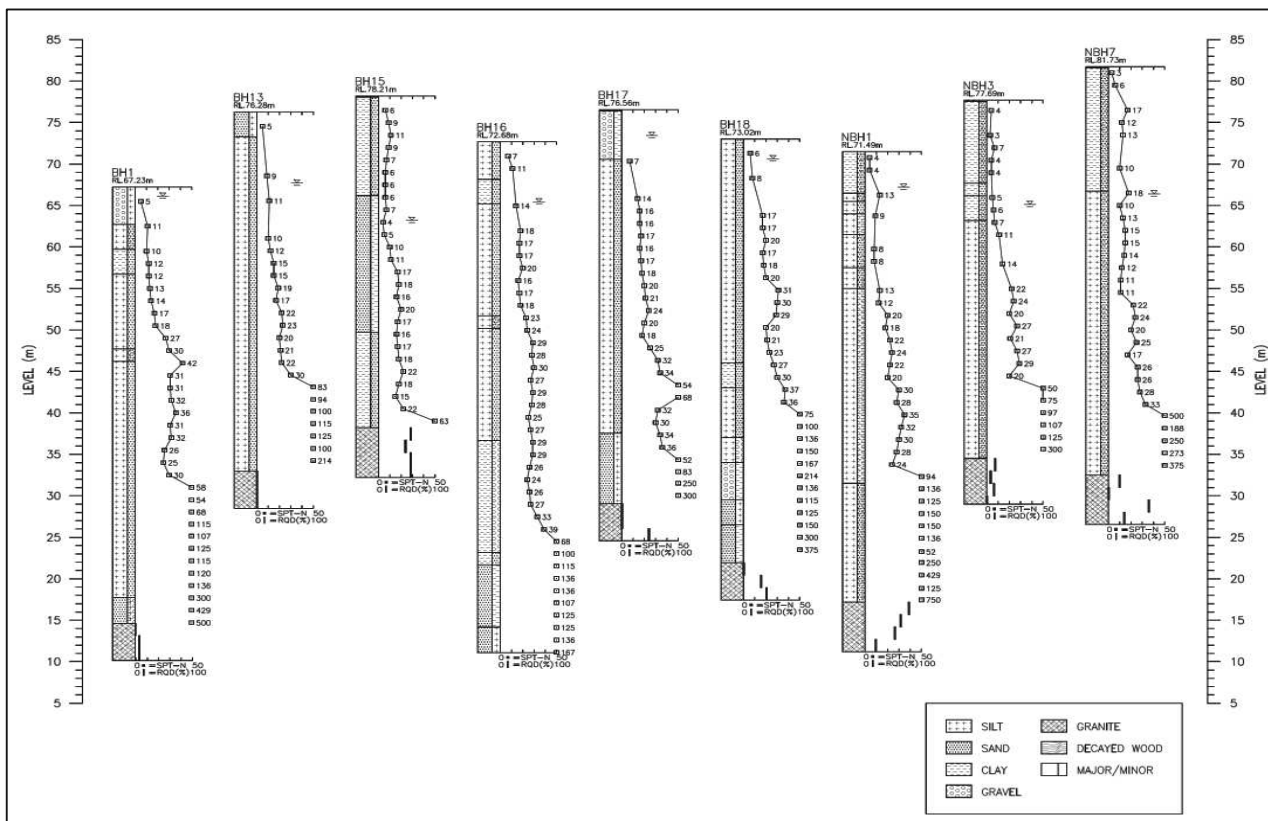


Figure 1. Borehole profiles relevant to soil nail slope.

Critical to the design of the soil nail slope is the assumptions on the skin friction between the ground and the grouted body of soil nail and as such, a series of instrumented pull-out tests on preliminary soil nails (non-working soil nails) were carried out at site to verify the design assumptions. The soil nails adopted at site generally consists of 4m to 18m length soil nails with 16mm to 32mm diameter galvanized high yield reinforcement (yield strength = 460N/mm<sup>2</sup>) slotted inside a 150mm diameter hole formed by open hole construction (without temporary casing) and filled with Grade 30 non-shrink grout.

### 3.1 Soil nail pull-out tests

A total of six numbers of instrumented pull-out tests on preliminary soil nails (non-working soil nails) were completed at the time this paper is prepared and the details of the pull-out tests are summarized in Table 1. All the soil nails are 6m length with 5m grouted length and 1m ungrouted length (free length) at the top. Typical set-up for the pull-out tests is shown in Figure 2 while details of the instrumented preliminary soil nails are shown in Figure 3.



Figure 2. Typical set-up for pull-out tests.

tests on preliminary soil nails (non-working soil nails).

Nail No.	Bar Diameter (mm)	Maximum test load achieved (kN)	Nearest borehole
Y-7 (RL 75.19)	25	175.0	BH-15
W/X-16 (RL 71.40)	25	140.0	BH-13
Y-10* (RL 73.24)	25	131.2	BH-15, NBH-3
Y-13* (RL 74.50)	25	148.8	NBH-3
Y-7* (RL 73.24)	25	78.8	BH-15
Y-1/2 (RL 74.00)	32	286.0	NBH-7

Note:

1. Different maximum test load is achieved primarily due to various site issues such as improper test set-up where the dial gauge has reached its maximum travel distance, malfunctioning of the load cell, etc. and not due to inadequate bond strength of the soil.
2. \* - Results ignored due to improper preparation of free length at the soil nail head which interferes with instrumentation results.

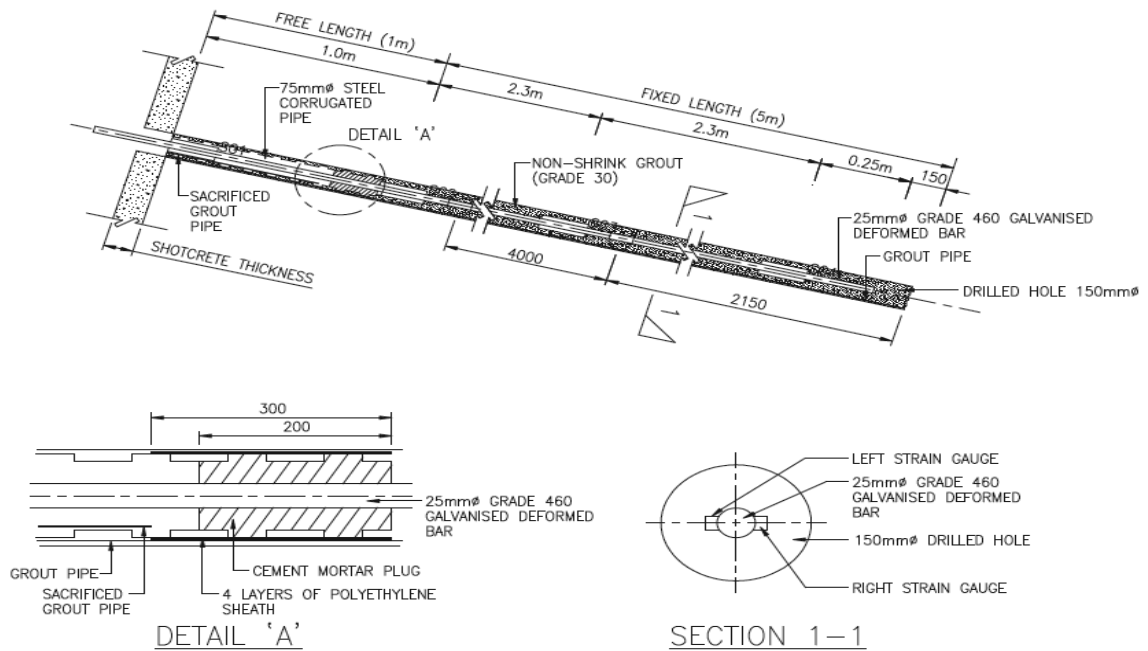


Figure 3. Typical details of instrumented preliminary soil nail.

#### 4 RESULTS OF INSTRUMENTED PULL-OUT TESTS

The test procedures and testing sequence of the soil nails are in accordance with FHWA 1998 and the loading schedule is summarised in Table 2. The pull-out test results showing the mobilised skin friction vs nail movement are shown in Figures 4 to 6.

Table 2. Pull-out tests loading schedule (FHWA 1998).

Load	Hold Time (minutes)
0.25 DTL	10
0.50 DTL	10
0.75 DTL	10
1.00 DTL	10
1.25 DTL	10
1.50 DTL (Creep Test)	60
1.75 DTL	10
2.00 DTL	60
Repeat cycle if test load increased to 3.00 DTL	

Note:

1. DTL – Design test load
2. Test load limited to maximum 80% yield strength of nail reinforcement

The longer holding time of 60 minutes at 1.50 DTL and 2.00 DTL is to monitor creep movement. The acceptance criteria is total creep movement of less than 2mm per log cycle of time between the 6 and 60 minute readings and the creep rate is linear or decreasing throughout the creep test load hold period.

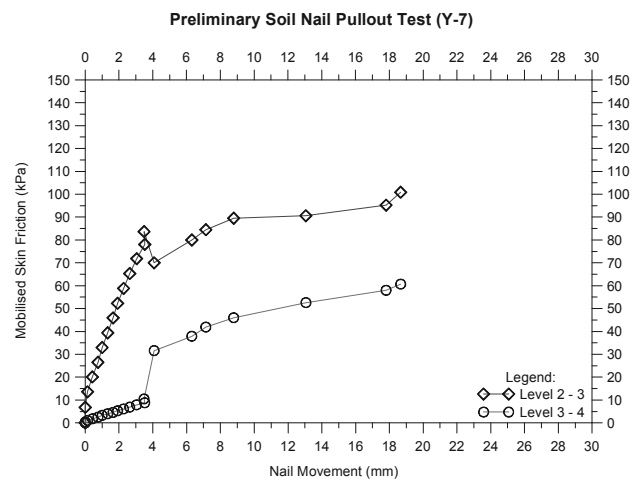


Figure 4. Pull-out test results for nail Y-7.

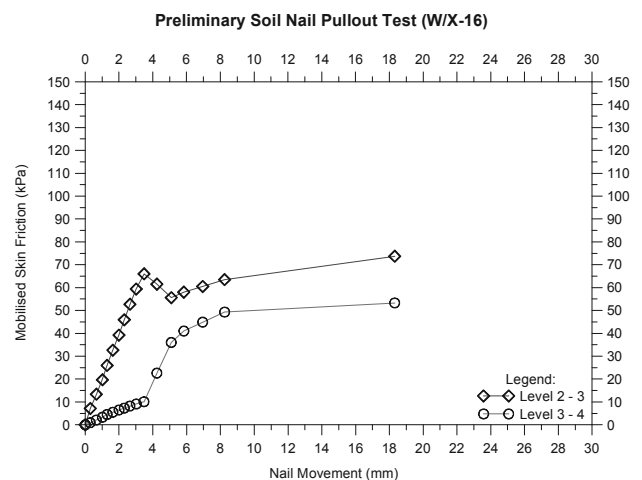


Figure 5. Pull-out test results for nail W/X-16.

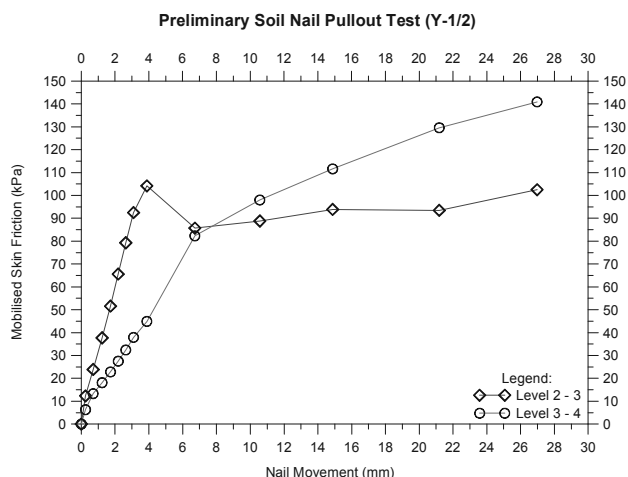


Figure 6. Pull-out test results for nail Y-1/2.

From the pull-out tests, the following observations could be made:

- The ultimate skin friction is mobilised at relatively small nail movement of approximately 4 to 6mm which is about 3-4% of the diameter of the drilled hole.
- Only nail Y-1/2 demonstrates the expected behaviour where initially, more load is transferred to the upper part of the nail until the upper part reaches the ultimate skin friction and thereafter, more load is transferred to the lower part of the nail.
- Other nails (Y-7 and W/X-16) also demonstrated behaviour where initially, more load is transferred to the upper part of the nail. However, the mobilised skin friction for the upper part of the nail has rather unexpectedly continued to increase after the initial drop. This is unexpected and is possibly due to interference from the shotcreted slope surface where the pull-out tests were conducted. It is possible that the shotcreted slope surface restricts the expansion of the soil particles during testing and contributed to the increase in mobilised skin friction for the upper part of the nail.
- The SPT-N values at the level of the tested soil nails typically range from 5 to 13 (average about 10) and the mobilised skin friction recorded range from 50 to 140kPa. This indicate a conservative correlation of skin friction can be 5x SPT-N for soil nail design in weathered granite or fill.
- Results of the pull-out tests also indicate the equation proposed by HA 68/94 (see Eq. 1) underpredicts the mobilised skin friction considerably.

$$Q = \sigma'_n \tan \phi' + c' \text{ (kN/m}^2\text{)} \quad (1)$$

where

$\sigma'_n$  = average radial effective stress  
 $\phi', c'$  = soil shear strength parameters

## 5 CONCLUSIONS

A series of instrumented pull-out tests were carried out for a proposed basement with excavation up to 20m deep supported using soil nailed slope. The pull-out test results indicate a conservative preliminary correlation for skin friction between the ground and the grouted soil nail of 5x SPT-N can be adopted for soil nail design in weathered granite or fill.

Further pull-out tests at deeper layers of the subsoil are currently being carried out at site and the results will be presented in the future. Some improvement to the current test procedures will also be carried out such as hacking a larger area of the shotcreted surface surrounding the test nail in order to ensure the results are not affected by the shotcreted slope surface.

## 6 ACKNOWLEDGEMENTS

The Authors acknowledge the contributions of Mr. Lim Fang Liang and Mr. Tong Han Seng for their hard work and dedication as part of the geotechnical design team of the project.

## 7 REFERENCES

- Chow Chee-Meng and Tan Yean-Chin. 2006. Soil nail design: A Malaysian Perspective. *International Conference on Slopes*, 379-400.
- Chow Chee-Meng and Tan Yean-Chin. 2011. Deep excavation for basement via soil nailing method. *APEC Seminar on the State-of-the-practice of Deep Excavation Works from Malaysia, Taiwan and Hong Kong*, 75-94.
- FHWA. 1998. *Manual for design & construction monitoring of soil nail walls*. USA.
- HA 68/94. 1994. *Design Methods for the Reinforcement of Highway Slopes by Reinforced Soil and Soil Nailing Techniques*. UK.

# Effects on adjacent buildings from diaphragm wall installation

## Effets sur des bâtiments adjacents liés à l'installation de parois moulées

Comodromos E.M., Papadopoulou M.C.  
*Dept. of Civil Engineering, University of Thessaly, Greece*

Konstantinidis G.K.  
*Manager, Attiko Metro S.A., Greece*

**ABSTRACT:** A new approach for simulating the excavation and construction of subsequent panels is proposed to investigate the effects from the installation of diaphragm walls on the surrounding soil and adjacent buildings. The method has been combined with a 3-D nonlinear analysis and a constitutive law providing bulk and shear modulus variation, depending on the stress path (loading, unloading, reloading). The effects on an adjacent building have been investigated by applying a full soil-structure interaction analysis including the whole building. Contrary to lateral movements, which mostly take place at the panel under construction, it was found that the effect of settlements covers a larger area leading to a progressive settlement increase. The effect highly depends on the distance from the panel under construction. Settlement profiles and settlements at specific points as increasing with subsequent panels installation are given providing the ability of specific monitoring guidelines for the upcoming construction of the diaphragm wall in front of the building.

**RÉSUMÉ :** Une nouvelle approche pour simuler l'excavation et la construction des panneaux subséquents est proposée pour étudier les effets liés à l'installation de parois moulées adjacents sur les bâtiments et le sol adjacents. La méthode a été associée à une analyse 3-D non linéaire et une loi de comportement qui permet la variation des modules de déformations en fonction des chemins des contraintes. Les effets sur un bâtiment adjacent ont été étudiés en appliquant une analyse d'interaction sol-structures pleine, qui inclut l'ensemble du bâtiment voisin. Contrairement aux mouvements latéraux, qui principalement prennent lieu à partir du panneau en cours de construction, il a été constaté que l'effet des tassements couvre une plus grande région, conduisant à une augmentation progressive de tassements. Les effets dépendent fortement de la distance au panneau en cours de construction. Les profils des tassements et tassements aux points spécifiques augmentant progressivement avec l'installation des panneaux sont donnés en face de l'immeuble où la paroi moulée est en cours de construction.

**KEYWORDS:** diaphragm walls, soil-structure interaction, multi-stage analysis, buildings settlements.

### 1 INTRODUCTION

It is widely accepted that the process of installing diaphragm walls can result in potentially significant soil displacements and cause substantial reductions in horizontal stress. Depending on the soil profile, the diaphragm wall configuration (length and construction sequence) and the close existence of adjacent buildings with poor foundations may render the effects of diaphragm wall installation considerable. Field monitoring confirms that ground movements resulting from diaphragm wall installation could be a significant component of the overall displacement (Burland and Hancock 1977, Tedd et al. 1984, Symons and Carder 1993), while centrifuge tests verified the development of the effect as well (Powrie and Kantartzi 1996). Recent field evidences recorded during the on going construction of subway stations in Thessaloniki demonstrated that the component of ground movements resulting from the diaphragm wall installation may be higher than 50% of the overall displacements. It is therefore evident that the simplistic assumption of a 'wished-in-place' wall (installation without any change in stress and cinematic field) commonly applied for design purposes is rather questionable.

The aim of the present paper is to investigate the effect of a diaphragm wall installation to adjacent buildings with relatively poor foundations. The sequential installation of each individual diaphragm wall panel installation was simulated by a substitution of the parameters of excavated elements with those corresponding to the bentonite slurry and later on by the

concrete tremied into the panel. Valuable qualitative and quantitative conclusions regarding the variation of the effects to the adjacent building have been drawn.

### 1 INSTALLATION PROCEDURE MODELLING

With the aim of minimising disturbance and increase stability during the excavation process, rotary drilling machines for slot excavation have been used in Thessaloniki's underground stations with poor soil conditions. Figure 1, on the left side, shows a rotary drilling machine equipped with cutting wheels and a reverse circulation system. On the right side of Figure 1 the numerical simulation of the excavation process is illustrated. The soil from the surface level down to the upper limit of the rotary wheels (line A), is replaced by a material simulating the bentonite slurry. Appropriate, very small values are attributed to the bulk and the shear modulus of the material. Within that zone the stresses are initialised to the values hydrostatically defined from the weight of bentonite slurry. This simulation process ensures that stresses within this zone remain always equal to the hydrostatic conditions no matter the deformation level. However, in the area occupied by the rotary cutters (area between line A and line B) the development of static hydrostatic pressure is not evident. For this reason, in that zone the stresses are not initialised hydrostatically and only internal gravitational stresses are considered. Within this zone the material (cuttings with bentonite slurry) has higher unit weight and is stiffer than bentonite slurry. The zone undertakes the pressure from the

surrounding elements depending on the internal gravitational stresses, the stiffness and the shear resistance of the surrounding soil elements, and the arching developed around the trench. This complicated mechanism provokes a redistribution of stresses and the surrounding soil elements undergo some deformation. As a result horizontal displacements at the wall/soil interface are governed by the ability of the soil to move in response to the reduction in lateral stresses during the wall installation. The above mechanism leads to a temporary reduction of the horizontal stresses in the surrounding excavation faces, which however increase to the hydrostatic bentonite slurry pressure in the next stage of excavation. When the excavation of a panel is accomplished concrete is cast in place using tremie pipes. The same numerical process is applied to simulate the panel completion, i.e. appropriate values are attributed to the bulk and the shear modulus of the material simulating wet concrete, while, stresses are initialised to the values hydrostatically defined from the weight of wet concrete. When equilibrium is attained, regular concrete values are attributed to bulk and the shear modulus to the panel. The above simulation process is repeated over the entire depth of the panel.

The aforementioned simulation process reflects the construction of a single panel and is applied to all panels in a diaphragm wall. However, the response of each particular panel is greatly influenced by the construction sequence. Obviously when constructing a subsequent panel, with already completed adjacent panels, the effect of arching is strengthened due the high resistance of these elements. As a result a stress increase is observed not only at the adjacent soil, but also on neighbouring panels that have already been casted. Thus over the period of wall construction there will be a progressive transferring of load back and forth laterally, either from a primary panel to the adjacent soil or, as the wall progresses, from new panels to panels previously casted. It can be realised that when accurate prediction of displacements and stresses redistribution are demanded, a profound 3-D nonlinear multi-stage numerical analysis is required.

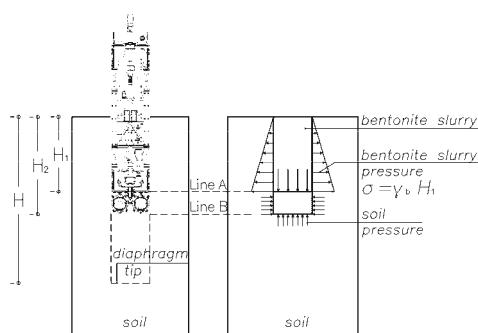


Figure 1. Schematic illustration of the proposed approach for simulating a single panel excavation

## 2 NUMERICAL SIMULATION

### 2.1 Project description

The station of Analipsis, 210 m long and 16.4 m wide, is considered as one of the most critical of the underground of Thessaloniki. With the exception of the surficial layer the soil conditions are relatively good. However, the fact that the diaphragm wall is located very close to adjacent buildings with poor foundations, in many cases, renders the construction of the diaphragm wall extremely demanding. According to the guidelines of the German code DIN 4126, the critical zone around the trench excavation extends up to a distance of 70% of the pile length. For this reason a relatively small typical panel length  $L = 2.8$  m was applied and a rotary cutting machine was selected to perform the ongoing excavation of the panels. The

thickness of the panels is  $t = 1.20$  m, its depth is  $H = 44.0$  m and the basement of the station is 28.0 m below the ground surface.

### 2.2 Soil model and material properties

The ground conditions at the site together with the soil properties of each soil layer, derived from the carried out geotechnical investigation and the evaluation of in-situ and laboratory tests are presented in Table 1. The groundwater level was encountered at 5.0 m below the ground level. Pressuremeter tests were carried out at the area to assess the in situ horizontal stresses and, according to the evaluation of the results, a constant value of  $K_0 = 0.54$  has been adopted.

Bearing in mind the crucial effect and the necessity for settlements predictions to the adjacent buildings, a constitutive law with double yielding (FLAC 3D) has been applied in the present study. The model includes a volumetric yield cap surface in addition to Mohr-Coulomb shear and tensile failure envelopes. The cap surface is independent of the shear strength and it consists of a vertical line on a plot of shear stress vs mean stress with a trace on the mean stress axis defined as cap pressure  $p_c$ . Any violation of the cap surface produces volumetric plastic strain following a piecewise-linear law prescribed in a user-supplied table. The tangential bulk and shear moduli evolve as plastic volumetric strain takes place according to a special law defined in terms of a constant factor,  $R$ , which is the ratio of elastic bulk modulus,  $K_e$ , to plastic bulk modulus,  $K_t$ . The relevant values adopted are given in Table 1.

The concrete diaphragm wall behaviour was considered as an isotropic linear elastic. Linear elastic behaviour was attributed to the bentonite slurry with infinitesimal deformation values. The shear strength of bentonite slurry with unit weight of  $11 \text{ kN/m}^3$  is of the order 50 Pa (DIN4126). A reasonable value for the slurry shear modulus is three hundred times the shear strength,  $G_{sl} = 15 \text{ kPa}$ , while the Poisson's ratio was taken equal to 0.49. The application of these values to the analysis produced stresses within the bentonite computational domain equal to hydrostatic gravitational state, ensuring that appropriate hydrostatic pressures were developed at the trench faces. A higher value of unit weight ( $12.5 \text{ kN/m}^3$ ) has been attributed to cutting products mixed with bentonite slurry and similarly the shear modulus has been taken equal to 25 kPa. Taking into account that the construction schedule, the time period between adjacent panels installation, particularly the primary panels, is quite enough for any excess pore dissipation an effective stress analysis was applied.

Table 1. Geotechnical properties of soil layers.

Layer	Fill	A1a	A1b	A1c	B
Depth (m)	0 - 3	3 - 10	10 - 35	35 - 40	40 - 60
Effective cohesion, $c'$ (kPa)	3	3	5	40	50
Effective angle of friction, $\phi'$ (deg)	30	25	25	25	25
Poisson's ration, $\nu$	0.3	0.3	0.3	0.3	0.3
Plastic bulk modulus, $K_t$ (kPa)	4,000	5,000	8,500	10,000	10,000
Ratio of elastic to plastic bulk modulus, $R$	5	6.5	10.5	12	12
Cap pressure, $p_c$ (kPa)	100	100	NC*	NC*	NC*

Remark: NC means that cap pressure is equal to the in-situ mean stress

### 2.3 Simulation procedure

The effective numerical simulation of typical construction procedure for a cast in situ diaphragm wall must reflect the stages and the mechanisms developed during the excavation and throughout the completion of the wall. The first step was to establish the in-situ state of stresses. The construction of a single panel was simulated in 22 stages during which the excavation was advanced in 2.0 m. Within each stage the soil in

the excavation zone was replaced by cutting-bentonite, while the area above the zone being excavated was replaced by bentonite. The end of the excavation was followed by wet concrete placing and the value of  $E_{wc} = 1,000$  MPa was attributed to Young's modulus and  $\nu_{wc} = 0.49$  to Poisson's ratio. The last stage of analysis corresponded to concrete hardening. The same process was applied to all panels under consideration. The most critical location in the area of the station corresponds to poor building foundation conditions very close to the diaphragm wall. The analysis is therefore focused on that. Prior to the currently presented full soil-structure interaction analysis including a 6-storey building, numerical analyses of a single panel construction and of a wall and an adjacent foundation verified the proposed simulation process as well as the constitutive law and the values for the parameters. Figure 2 shows the foundation plan of the adjacent building together with the location of the diaphragm wall and a curtain of micropiles used to minimize the effect of panels' installation. Further to the bay number of each panel the figure shows the panel type (primary, P, or secondary, S) and the order of installation in the circles on the right side of each panel. The foundation consists of individual footings connected with  $0.20 \text{ m} \times 0.50 \text{ m}$  reinforced concrete beams. The foundation level is at 3.0 m from the ground surface. The F.D. mesh included 89,000 3-D elements, 4,272 shell elements and 225 beam elements. The dead weight of the building has been explicitly introduced by the gravity of each element while a uniform load of 5 kPa has been applied to each slab to simulate all other permanent and variable loads. After the establishment of the initial stresses, the installation of the micropiles was introduced followed by the installation of the 9 panels according to the previously described approach. The sequence of installation is presented in Figure 3.

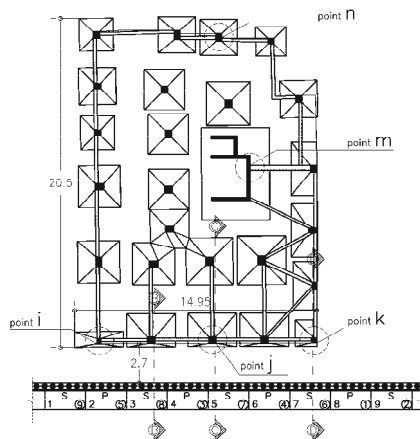


Figure 2. Individual footings of a 6-storey building together with the diaphragm wall and the micropiles

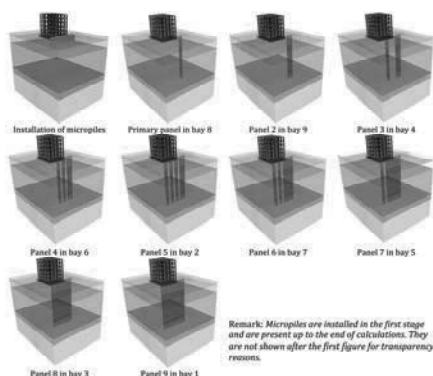


Figure 3. Sequence of panel installation

### 3 NUMERICAL RESULTS

The contour values for soil settlements, the building floors' settlements and the axial forces of the building columns developed after the completion of the first element (element no 8) are illustrated in Figure 4. For visibility reasons the figure is given in a section at the building face and a cross section at the middle of the building. It can be seen that the maximum soil settlement is located around the excavated panel and is of the order of 2.4 mm. The maximum settlement of the building is located at its corner nearby the excavated panel and the contours show a uniform reduction with distance from that point.

The sequential construction of the next panels provokes the maximum effect in front of each panel, as it has been expected, but at the same time contributes to a progressive increase of settlements in a widespread zone. When the primary panels are installed, an increase of settlements to the value of 4.2 mm is occurred. The soil settlements progressively decrease with the distance from the diaphragm wall and are almost zero at the backside of the building. The completion of the wall with the rest 4 secondary panels does not encounter significant increase to the maximum value of the soil settlements. The final value of maximum settlement is 5.3 mm and the same value is developed at the external side of the building close to the diaphragm wall. From the comparison of the axial forces variation throughout the construction of the panel arises that the panels' installation does not practically affect them.

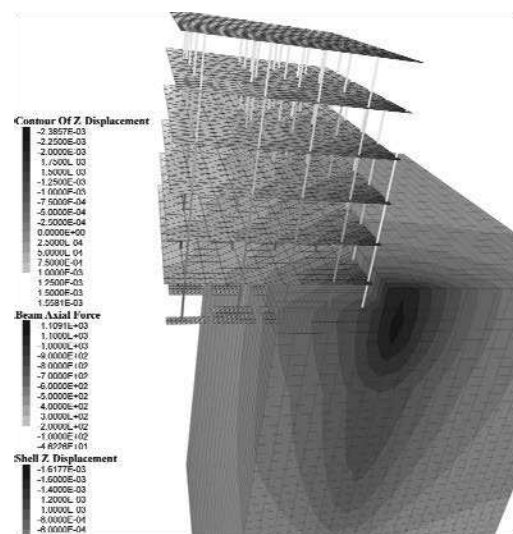


Figure 4. Soil and building settlement contours together with column axial forces after the completion of the first panel (bay no 8)

Figure 5a illustrates the variation of the horizontal displacements with depth below the external boundary of a footing at the front side of the building (cross section 'C-C'). The values are not exceeding the order of 1.0 mm and this is mainly due to the existence of the micropiles. The construction of the panels with bay no 8 and 9 (first and second in construction sequence) are relatively too far from that point and they do not provoke any horizontal displacement at the point under consideration. The panel with bay no 5 is just in front of the point and this explains the important movement of the displacement field during the construction of this panel. Similar are the results in the case of the point below the footing at the edge of the external footing at section 'D-D', Figure 5b.

The most important effect to the adjacent building is the anticipated settlements, the angular distortion that will develop to the foundation and if that last could be capable of provoking any notable bending moment to the foundation elements. Figure 6 illustrates the progressive increase of the settlements across the section 'C-C'. On the same figure the location of the diaphragm wall and the foundation of the building are shown.

The construction of every panel contributes to a progressive increase of settlements, with the maximum influence experienced when the primary panel close to the cross section is installed. This explains the maximum difference observed when panel no 4 is installed. The maximum settlement is developed at the end of the construction of all panels, its value is of the order of 5.5 mm and occurs at the front side of the building.

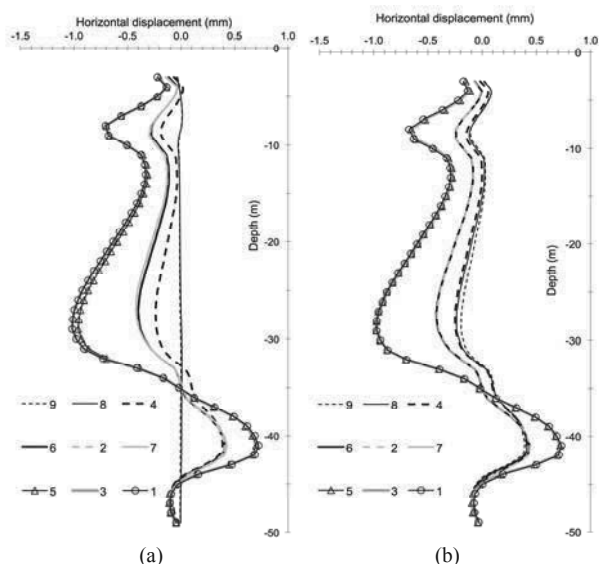


Figure 5. Profile of horizontal displacements below the external footing at (a) the mid-face, point j, and (b) the end-face of the building, point k

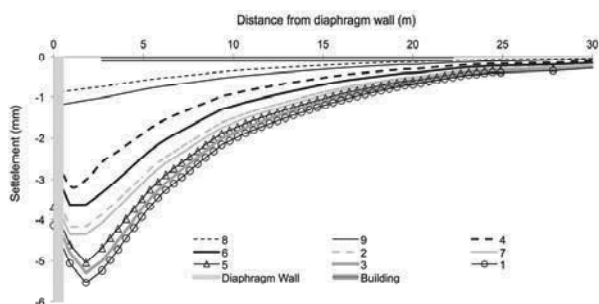


Figure 6. Development of settlement profile with panel sequence construction at cross section 'C-C'

It is worth noticing that the settlement values estimated from the 3-D analysis are leading to an angular distortion of 1:5,000. This value is considerably lower than the limits provided by CIRIA and the CFEM.

An effective design of complex retaining structures, with closely adjacent buildings, includes instrumentation and monitoring to ensure the safety of the construction and control the effect on the adjacent buildings. These data will be available when the diaphragm wall at this area will commence and histograms giving the contribution to cumulative settlements of each particular panel can be drawn. It is therefore extremely helpful to give these histograms resulting from the 3-D analysis and follow up the values as the wall is constructed. Figure 7 illustrates the numerically established cumulative settlements after the completion of each panel, at the characteristic points, i, j, k, m and n. The location of each panel corresponds to relative position from left to right, while the installation sequence is given on the top of the histograms.

It can be seen that the final settlements at the front face of the building (points i, j and k) are of the same magnitude and that the values provided for the points far from the diaphragm wall (points m and n) are drastically lower and with no practical effect on the building. It is clearly evident that Figure 7 can be efficiently used to compare settlements during the up coming

construction and provide alarm signal in case of significantly higher settlements values.

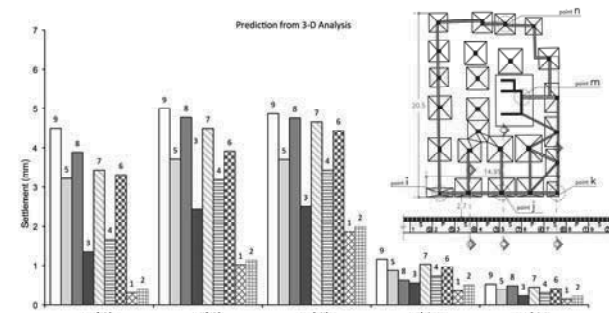


Figure 7. Predicted development of cumulative settlements at points i, j, k, m and n at the end of each panel construction

#### 4 CONCLUSION

In this paper the effects from the installation of diaphragm walls have been investigated using a new approach for simulating the excavation and construction of subsequent panels. The method has been combined with a 3-D nonlinear analysis and a constitutive law providing bulk and shear modulus variation, depending on the stress path (loading, unloading, reloading). It has been observed that the most significant effect in front of a given panel occurs during the installation of that panel and that the effect on stress reduction and lateral movements in front of the subsequent panels is rather limited. The method has been used to estimate the effects on an adjacent 6-storey building by applying a full soil-structure interaction including the whole building. Progressively increased with subsequent panels installation settlement profiles are given along the building foundation. Moreover, settlements at specific points where leveling captures have been installed are given in cumulative form. The predictions indicate that the angular distortion of the building remains under the required limits of serviceability and at the same time provide the guidelines for the monitoring of the upcoming construction of the diaphragm wall in front of the building.

#### 5 REFERENCES

Burland J.B. and Hancock R.J.R. 1977. Underground car park at the House of Commons, London: geo- technical aspects. *Struct Engr* 55 (2), 87-100.  
 Tedd P., Chard B.M., Charles J.A. and Symons I.F. 1984. Behaviour of a propped embedded retaining wall in stiff clay at Bell Common Tunnel. *Geotechnique* 34 (4), 513-32.  
 Symons I.F. and Carder D.R. 1993. Stress changes in stiff clay caused by the installation of embedded retaining walls. *Retaining structures*. Thomas Telford, London.  
 Powrie W. and Kantartzi C. 1996. Ground response during diaphragm wall installation in clay: centrifuge model tests. *Geotechnique* 46 (4), 725-39.  
 DIN 4126. 1986. *Cast-in-situ concrete diaphragm walls*. Berlin.  
 Itasca. 2009. *FLAC3D, Fast Lagrangian analysis of continua*, version 4.0: User's and theory manuals. Itasca Consulting Group, Inc. Minneapolis.  
 CIRIA. 1983. *Settlement of structures on clay soils. Report 113*, London.  
 Canadian Geotechnical Society. 1992. *Canadian foundation engineering manual*. British Publishers Ktd, Vancouver.

# Prise en compte des effets de bord dans un massif renforcé par inclusions rigides

## Modeling edge effects at the periphery of a rigid inclusion reinforced soil volume

Cuira F., Simon B.  
TERRASOL, Paris, France

**RÉSUMÉ :** En périphérie d'un massif de sol renforcé par inclusions rigides il se développe une interaction entre la zone renforcée et la zone non renforcée. Ces effets de bord rendent inapplicables les modèles limités à l'étude d'une cellule élémentaire au sein d'un réseau infini d'inclusions qui adoptent l'hypothèse d'un cisaillement nul sur la frontière de la maille étudiée. Le modèle exposé de type biphasique exprime les équations d'équilibre dans deux domaines apposés, « inclusion » et « sol », en introduisant à la fois le cisaillement interne qui se développe entre l'inclusion et le sol tributaire et le cisaillement externe qui se développe sur tout ou partie de la frontière de la maille, lorsque celle-ci est située en périphérie de la zone renforcée par inclusions. Les cisaillements sont pris en compte en exploitant la notion de loi de transfert t-z appliquée au déplacement relatif entre les domaines considérés. La résolution s'appuie sur une discrétisation 1D des deux domaines et une formulation éléments finis. Différents exemples de semelles sur inclusions sont présentés dont les résultats s'avèrent en bon accord avec ceux de modèles numériques 3D, beaucoup plus complexes à mettre en œuvre. L'évaluation de la méthode se poursuit en exploitant les résultats de modèles physiques en centrifugeuse.

**ABSTRACT:** At the periphery of a soil volume reinforced by rigid inclusions, interaction between the reinforced soil and the unreinforced soil cannot be neglected. Such edge effects prevent use of the commonly used unit cell model which assumes no shear at the model outer boundary. The proposed model, a simplified form of a two-phase model, expresses equilibrium within two side by side domains « inclusion » and « soil » by introducing shear between inclusion and the tributary soil volume within the cell on the one hand and shear along all or part of the outer “soil” domain boundary, on the other hand, when cell under study is at periphery of the reinforced volume. Shear is taken into account through use of t-z transfer curves based on the domain relative displacements. A 1D discrete model of both domains is used together with a finite element formulation. This is applied to different cases of footings over soil reinforced by rigid inclusions. Results agree well with those obtained by other 3D numerical models, which remain a far more difficult task. Further evaluation is planned using the results of centrifuge test models.

**MOTS-CLÉS:** renforcement du sol, inclusions rigides, semelle sur inclusions, modèle analytique, effets de bord.

**KEYWORDS:** soil reinforcement, rigid inclusions, shallow foundations, analytical modelling, edge effects.

## 1 INTRODUCTION

Le renforcement par inclusions rigides a vu son intérêt largement reconnu pour les ouvrages étendus de type remblais ou dallages (locaux industriels). Le dimensionnement s'appuie généralement sur des modèles de calcul réduits à l'étude d'une cellule élémentaire représentant le comportement d'une maille courante centrée sur une inclusion et incluant le volume de sol et la fondation d'ouvrage afférents (Cuira et Simon, 2009, Simon, 2012). Le caractère répété du motif permet de considérer que le cisaillement est nul au bord du modèle, ce qui en simplifie considérablement la construction. Ces modèles apportent tous les éléments nécessaires au dimensionnement des ouvrages en partie courante ; leur validité a été largement éprouvée dans le cadre du projet national ASIRI (2012) par la confrontation des résultats obtenus avec ceux d'expérimentations en vraie grandeur, de modèles physiques ainsi que de modélisations numériques avancées. Ils sont en revanche insuffisants pour traiter des zones périphériques où les cellules placées au bord sont en interaction avec des cellules intérieures mais aussi avec le massif extérieur non renforcé : l'hypothèse de symétrie permettant de considérer un cisaillement nul aux bords du modèle n'est plus applicable. La validité de ces modèles se heurte également au cas des ouvrages d'emprise limitée tels des semelles sous poteaux ou voiles porteurs, pour lesquels la prise en compte des phénomènes de bord devient là encore une nécessité absolue.

La modélisation de ces configurations particulières (bord d'ouvrage étendu ou ouvrage d'emprise limitée) nécessite en toute rigueur des modèles en trois dimensions dont les limites doivent être étendues largement au-delà du volume de sol renforcé, à la différence des modèles de cellule élémentaire. Une telle modélisation est incontestablement mal adaptée à des études courantes, appelées de surcroît et en dépit du caractère

non exceptionnel des fondations concernées, à examiner un grand nombre de cas de charges. Les Recommandations ASIRI (2012) ont ainsi détaillé plusieurs méthodes simplifiées pour traiter ces configurations dans le cas d'un chargement vertical avec des outils classiques du calcul des fondations. Toutes ces méthodes nécessitent cependant une procédure par étapes.

Cette communication présente la généralisation d'une de ces méthodes qui permet de s'affranchir d'un calcul par étapes, en traitant simultanément les interactions internes se développant au sein du massif renforcé et externes se développant aux bords de celui-ci avec le sol environnant non renforcé. L'équilibre mécanique du volume renforcé est ainsi exprimé en combinant des lois d'interface sol/inclusions (internes) et sol/sol (externes), toutes basées sur les déplacements relatifs afférents.

## 2 ASPECTS THEORIQUES

### 2.1 Principe

On considère le cas d'une cellule élémentaire représentant une maille quelconque (courante ou périphérique) centrée sur une inclusion. La cellule est soumise à un chargement vertical et est décomposée en deux domaines complémentaires : le domaine « inclusion » constitué par l'inclusion elle-même et les volumes de sol qui la prolongent jusqu'aux limites inférieure et supérieure du modèle, et le domaine « sol » constitué par le volume de sol complémentaire au domaine « inclusion ». L'interaction entre les deux volumes est supposée entièrement décrite par le cisaillement vertical  $\tau_{int}$  qui se développe sur leur frontière verticale définie par le périmètre de l'inclusion noté  $P_{int}$ . En périphérie de la cellule, l'interaction éventuelle avec le sol environnant non renforcé est supposée entièrement décrite



par un cisaillement vertical extérieur  $\tau_{ext}$  comme le schématise la figure ci-dessous.

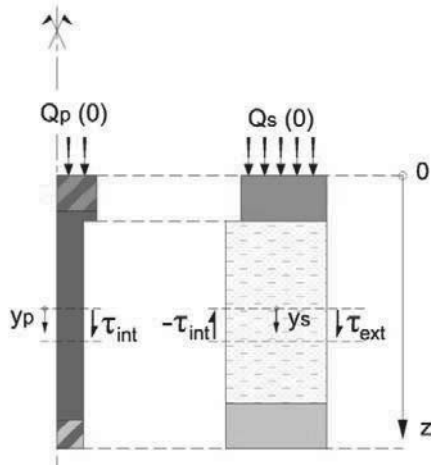


Figure 1. Modèle généralisé de la cellule élémentaire – vue en coupe.

Le cisaillement extérieur  $\tau_{ext}$  est supposé se développer sur une fraction  $\beta \times P_{ext}$  ( $0 \leq \beta \leq 1$ ) du périmètre extérieur total  $P_{ext}$  de la cellule comme le schématise la figure ci-dessous.

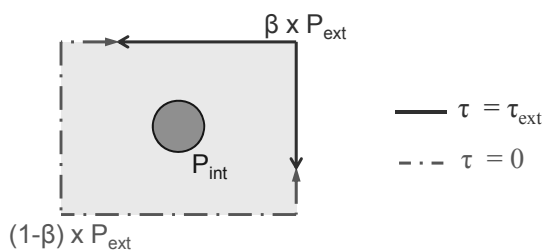


Figure 2. Modèle généralisé de la cellule élémentaire – vue en plan.

Les deux domaines sont assimilés à deux cylindres concentriques de sections équivalentes. On désigne par  $S_p(z)$  la section du domaine « inclusion » à la profondeur  $z$ . La section du domaine « sol » s'en déduit à l'aide de la relation :  $S_s(z) = S_{maille} - S_p(z)$  où  $S_{maille}$  désigne l'aire totale de la maille.

## 2.2 Mise en équation

On désigne par  $y_p(z)$  et  $y_s(z)$  les tassements respectifs des domaines « inclusion » et « sol ». La combinaison des équations d'équilibre et de comportement des cylindres équivalents aux deux domaines conduit au système d'équations (1), où  $E_p(z)$  et  $E_s(z)$  représentent respectivement les modules de déformation verticale des domaines « inclusion » et « sol ». Pour le domaine « sol », le tassement  $y_s(z)$  est supposé uniforme à toute profondeur  $z$  et  $E_s(z)$  est assimilé au module équivalent pour l'amplitude de chargement calculée.

$$\text{Domaine inclusion} \quad E_p S_p \frac{d^2 y_p}{dz^2} = \tau_{int} P_{int} \quad (1)$$

$$\text{Domaine sol} \quad E_s S_s \frac{d^2 y_s}{dz^2} = -\tau_{int} P_{int} + \beta \tau_{ext} P_{ext}$$

L'interaction entre les deux domaines est décrite au niveau de chaque couche par une fonction de transfert exprimant la dépendance du cisaillement  $\tau_{int}$  avec le déplacement relatif entre les deux domaines :

$$\tau_{int} = f(y_p - y_s) \quad (2)$$

L'interaction éventuelle entre la cellule et le sol environnant non renforcé est décrite par une fonction de transfert reliant le

cisaillement extérieur  $\tau_{ext}$  au déplacement absolu du domaine sol :

$$\tau_{ext} = f(y_s) \quad (3)$$

La combinaison des équations (1), (2) et (3) conduit à un système global à 4 équations et 4 inconnues :  $y_p$ ,  $y_s$ ,  $\tau_{int}$  et  $\tau_{ext}$ .

## 2.3 Résolution

Le système précédent est complété par les conditions aux limites suivantes :

- charge totale appliquée en tête du modèle  $Q_p(0)+Q_s(0)$ ;
- fraction de charge transmise en tête du domaine inclusion  $E_{QP} = Q_p(0)/[Q_p(0)+Q_s(0)]$  ;
- loi de mobilisation de l'effort de pointe avec le déplacement relatif.

En présence d'un élément de fondation rigide en surface (radier ou semelle), la valeur de  $E_{QP}$  est établie en recherchant l'égalité des tassements en surface  $y_p(0)$  et  $y_s(0)$ , ce qui est justifié par le fait que les déformations de l'élément structurel de surface sont négligeables devant celles du sol.

La résolution numérique du système est menée à l'aide d'une formulation en éléments finis. Chacun des deux domaines est discrétisé selon un maillage unidimensionnel avec des éléments à deux nœuds et un degré de liberté par nœud. Dans le cadre de cette discrétisation, le système d'équations précédent s'écrit sous la forme d'un système matriciel équivalent, ce qui simplifie la résolution. La non-linéarité des courbes de transfert implique une procédure itérative visant à assurer la compatibilité en tout point entre cisaillement et déplacement.

## 2.4 Mise en œuvre pratique

### 2.4.1 Choix du paramètre $\beta$

L'introduction du paramètre  $\beta$  dans le modèle de la cellule élémentaire permet d'aller au-delà de la configuration particulière d'une maille courante où les conditions de symétries justifient l'hypothèse d'un cisaillement nul en périphérie du modèle ( $\beta = 0$ ). Le choix d'un  $\beta \neq 0$  implique la prise en compte d'un cisaillement extérieur entre la cellule et le sol environnant non renforcé, sur une partie du périmètre extérieur de la cellule. Dans le cas d'une maille carrée (figure ci-dessous), cela peut être par exemple représentatif d'une cellule située au bord du massif renforcé ( $\beta = 0,25$ ), le cas d'une cellule située à l'angle ( $\beta = 0,5$ ), le cas d'une semelle sur deux inclusions ( $\beta = 0,75$ ) ou une inclusion unique ( $\beta = 1$ ).

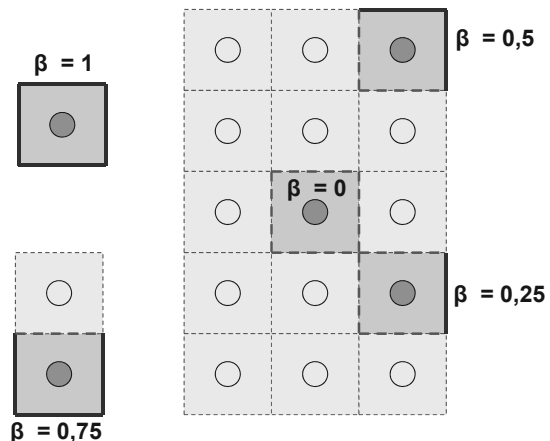


Figure 3. Choix du paramètre  $\beta$  pour le cas d'une maille carrée.

## 2.4.2 Fonctions de transfert

Ces fonctions de transfert sont utilisées pour caractériser la mobilisation des cisaillements interne ( $\tau_{int}$ ) et externe ( $\tau_{ext}$ ) ainsi que les réactions en pointe. On utilise pour cela les lois bilinéaires du type proposé par Frank et Zhao (1982) caractérisées par deux paramètres : un paramètre de pente ( $K_i$  ou  $K_p$ ) et une valeur de contrainte limite ( $q_s$  ou  $q_p$ ).

Pour le cisaillement interne et la mobilisation des réactions en pointe, ces lois sont construites directement à partir des paramètres pressiométriques.

Pour le cisaillement extérieur  $\tau_{ext}$ , la valeur de contrainte limite  $q_s$  peut être reliée à la contrainte verticale dans le sol non renforcé  $\sigma_{v0}$  par une relation du type  $q_s = k \tan \delta \cdot \sigma_{v0}$ . Les valeurs choisies pour  $q_s$  et le paramètre de pente peuvent être ajustés de manière à retrouver par le modèle du type exposé, appliqué au cas d'une inclusion de section nulle, un tassement identique à celui de la semelle superficielle rigide sur sol non renforcé calculé par la méthode pressiométrique (Frank, 1999).

## 3 APPLICATION SIMPLE : CAS D'UNE SEMELLE SUR UNE SEULE INCLUSION

### 3.1 Paramètres d'entrée

L'exemple étudié est celui d'une semelle carrée de 1,33 m de côté, renforcée par une seule inclusion de diamètre 40 cm placée dans l'axe. Deux situations sont étudiées : le cas d'une semelle en contact direct avec l'inclusion (mode « fondation mixte »), et le cas d'une couche de forme intercalaire de 50 cm d'épaisseur (mode « inclusion rigide »). La figure ci-dessous présente la coupe du calcul et les données géotechniques utiles.

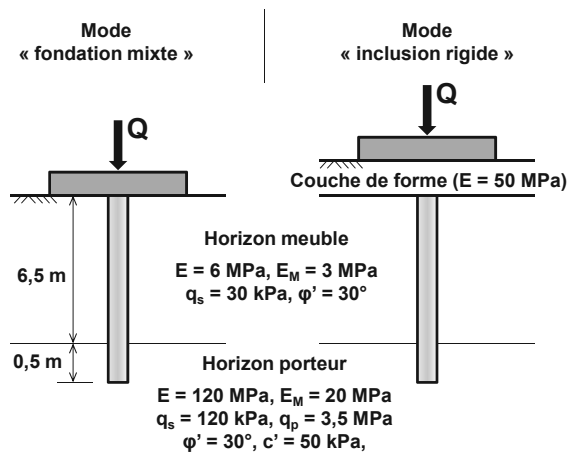


Figure 4. Cas d'une semelle sur une seule inclusion - Coupe de calcul.

Dans le cas d'une maille unique, le paramètre  $\beta$  est pris égal à 1,00 : le cisaillement extérieur avec le massif de sol non renforcé se développe sur tout le périmètre. Les fonctions de transfert sont constituées selon la démarche décrite en §2.4.2 : en particulier, pour le cisaillement extérieur, le calage du paramètre de pente  $K_i$  conduit à une valeur équivalente de  $K_i = 2,7$  MPa/m. Pour le mode « inclusion rigide », le domaine inclusion est prolongé dans le matelas : la loi d'interface entre les domaines inclusion et sol sur la hauteur du matelas est construite en considérant un module pressiométrique  $E_M = 10$  MPa et un frottement unitaire limite égal à  $k \tan \delta \cdot \sigma_s$  avec  $k \tan \delta = 1$  -et  $\sigma_s$  la contrainte verticale moyenne dans le domaine sol, sur la hauteur du matelas.

Les résultats du calcul sont comparés à ceux d'un traitement en éléments finis sous PLAXIS (modèle axisymétrique équivalent). Dans ce modèle, tous les sols ont un comportement élasto-plastique parfait avec un critère de rupture de Mohr Coulomb : les paramètres d'entrée sont ceux de la Figure 4. Le

choix des paramètres, et notamment ceux décrivant le comportement en pointe (module de déformation et paramètres de cisaillement), a été validé au préalable par calage des courbes de chargement axial d'une inclusion isolée chargée directement en tête (sans semelle), calculées respectivement par un modèle PLAXIS ou un modèle analytique à l'aide des lois de Frank et Zhao.

### 3.2 Sans matelas de répartition : mode « fondation mixte »

La première situation étudiée est celle d'un contact direct entre la semelle et l'inclusion (fondation mixte). Une partie de la charge totale  $Q$  appliquée sur la semelle est reprise par le sol, mais le frottement mobilisé sur la hauteur de l'inclusion demeure positif : la charge maximale dans l'inclusion est obtenue en tête. La figure ci-dessous présente les résultats obtenus selon un diagramme Effort – Tassement. Deux courbes sont représentées : celle du tassement de la semelle en fonction de la charge appliquée (Courbe 1), et celle du tassement de la semelle (= tassement en tête de l'inclusion) en fonction de l'effort maximal dans l'inclusion (Courbe 2). Les résultats se révèlent en bon accord avec ceux de PLAXIS.

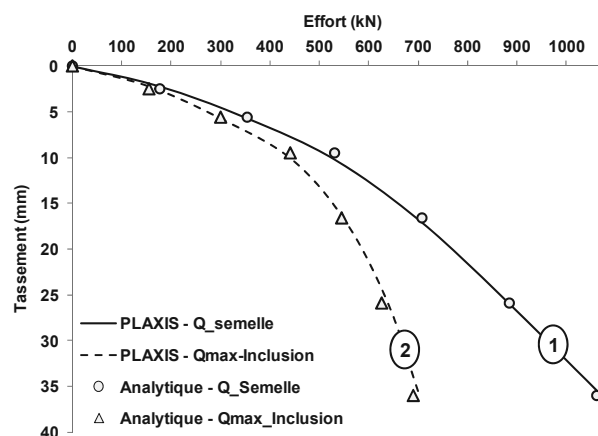


Figure 5. Effort sur la semelle et effort maximal dans l'inclusion en fonction du tassement en tête - cas d'une fondation mixte.

### 3.3 Avec matelas de répartition : mode « inclusion rigide »

Dans cette situation, une couche de forme sépare la semelle de l'inclusion. La principale différence avec le cas précédent est l'apparition d'un frottement négatif : l'effort maximal dans l'inclusion n'est pas obtenu en tête mais au niveau du plan neutre identifié ici vers 1,0 m de profondeur. La même concordance peut être observée avec PLAXIS.

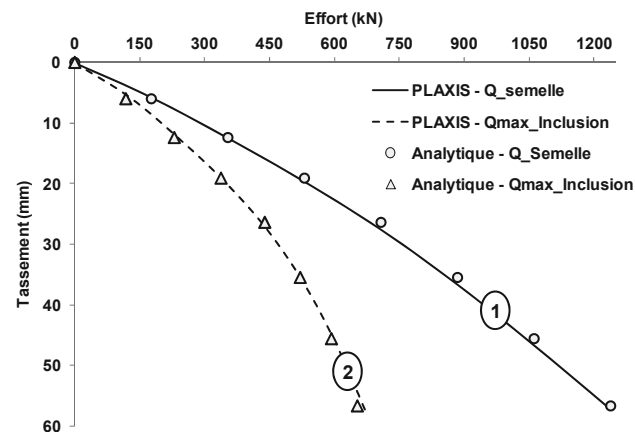


Figure 6. Effort sur la semelle et effort maximal dans l'inclusion en fonction du tassement en tête du modèle - cas d'une inclusion rigide.

#### 4 CAS D'UNE SEMELLE SUR QUATRE INCLUSIONS RIGIDES

La situation choisie correspond à une étude numérique conduite dans le cadre du projet ASIRI. Une semelle carrée de côté 2,8 m repose par l'intermédiaire d'un matelas de répartition d'épaisseur 0,5 m sur un sol compressible renforcé par 4 inclusions de diamètre 0,34 m. Le sol compressible repose sur un substratum rigide et est légèrement surconsolidé (surconsolidation de 10 kPa).

Cette configuration a fait l'objet d'une étude paramétrique détaillée à l'aide du logiciel Flac 3D, couvrant un large éventail de cas de charge appliqués à la semelle (Dias et Simon, 2012). La comparaison concerne le cas d'un chargement de la semelle par un effort vertical centré  $Q = 1568$  kN.

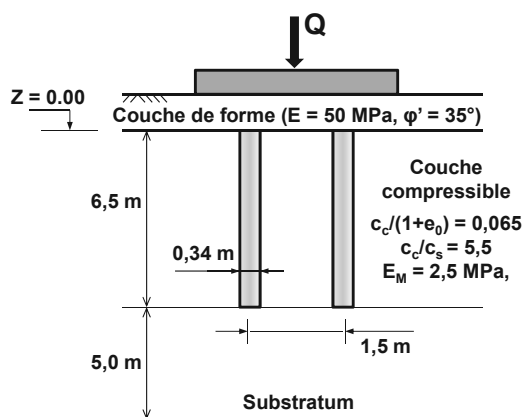


Figure 7. Cas d'une semelle sur quatre inclusions - Coupe de calcul.

La méthode exposée a été appliquée à un modèle représentant un quart de la semelle en adoptant pour le paramètre  $\beta$  la valeur 0,5. Les lois d'interaction sont construites selon la formulation de Frank et Zhao en adoptant les valeurs  $K_t$  et  $K_p$  calculées avec  $E_M = 2,5$  MPa et en ajustant les valeurs limites relatives au cisaillement  $\tau_{int}$  pour respecter la relation  $q_s(z) = K \tan \delta \cdot \sigma_s(z)$  où  $\sigma_s(z)$  désigne la contrainte verticale dans le domaine sol à la cote  $z$  et celles concernant le cisaillement  $\tau_{ext}$  pour respecter la relation  $q_s(z) = K \tan \delta \cdot \sigma_{v,0}'(z)$  où  $\sigma_{v,0}'(z)$  désigne la contrainte verticale initiale dans le massif non renforcé à la cote  $z$ . Le facteur  $K \tan \delta$  a été pris égal à 0,3 pour le cisaillement intérieur comme celui extérieur.

La Figure 8 présente les tassements calculés dans les domaines « inclusion » et « sol » en fonction de la profondeur.

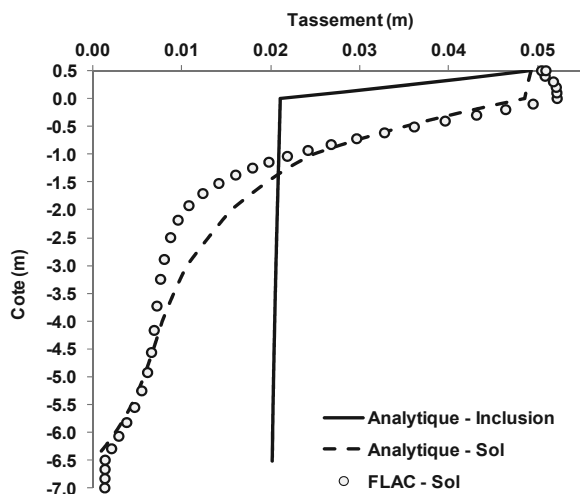


Figure 8. Profils de tassement des domaines « inclusion » et « sol » et comparaison à celui calculé dans l'axe du modèle Flac3D.

Le plan neutre s'établit 1,5 m sous la base du matelas. Le tassement dans le domaine « sol » se révèle proche de celui obtenu dans l'axe de la semelle par le modèle Flac3D.

La Figure 9 présente la distribution des efforts  $Q_s(z)$  et  $Q_p(z)$  avec la profondeur sous le sommet de la semelle ; l'effort  $Q_p(z)$  dans l'inclusion est maximal au niveau du plan neutre. La valeur atteinte se révèle d'un ordre de grandeur comparable à celle du modèle Flac3D, même si celui-ci révèle le plan neutre à une profondeur supérieure.

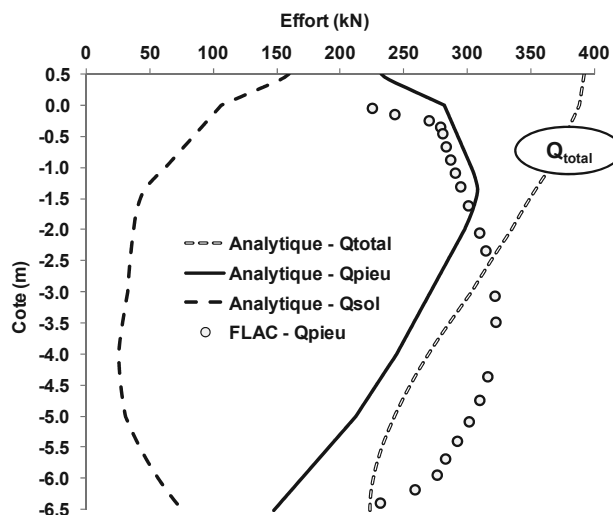


Figure 9. Effort axial dans les domaines « inclusion » et « sol » et comparaison à celui calculé dans une inclusion du modèle Flac3D.

La figure ci-dessus présente également l'évolution de l'effort total [ $Q_s(z) + Q_p(z)$ ] avec la profondeur : celui-ci varie de 392 kN en tête du modèle (seul un quart de la semelle a été modélisé) à 224 kN à la base. La dissipation observée ( $392 - 224 = 168$  kN) est liée au cisaillement extérieur représentant les interactions avec le sol environnant non renforcé.

#### 5 CONCLUSION

La méthode analytique exposée permet de prendre en compte les effets de bord qui sont à considérer autour d'un massif de sol renforcé par inclusions rigides. La comparaison des résultats ainsi obtenus à ceux issus de modèles 3D éléments finis ou différences finies, beaucoup plus complexes à mettre en œuvre s'avère tout à fait encourageante. L'évaluation de la méthode se poursuit sur des résultats de modèles physiques en centrifugeuse.

#### 6 REFERENCES BIBLIOGRAPHIQUES

ASIRI 2012, *Recommendations for the design, construction and control of rigid inclusion ground improvements*, IREX – Presses des Ponts, Paris.

Cuir F. & Simon B. 2009, Deux outils simples pour traiter des interactions complexes d'un massif renforcé par inclusions rigides, 17th ICSMGE, Alexandria, 1163-1166.

Dias D. & Simon B. 2012, Spread foundations on rigid inclusions subjected to complex loading: comparison of 3D numerical and simplified analytical modelling, TC211, IS-GI Brussels.

Frank R. & Zhao S.R. 1982, Estimation par les paramètres pressiométriques de l'enfoncement sous charge axiale des pieux forés dans les sols fins. *Bull. Liaison P. et Ch.*, 119, 17-24.

Frank R. 1999, *Calcul des fondations superficielles et profondes*, Techniques de l'Ingénieur – Presses des Ponts, Paris.

Simon B., 2012, General report S5, Rigid inclusions and stone columns, TC211, IS-GI Brussels.

# Influence of facing vertical stiffness on reinforced soil wall design

## Influence de la rigidité verticale du parement dans la conception des murs en sols renforcés

Damians I.P., Lloret A., Josa A.  
*Universitat Politècnica de Catalunya (UPC) – BarcelonaTech*

Bathurst R.J.  
*Royal Military College of Canada*

**ABSTRACT:** Current design practices for reinforced soil walls typically ignore the influence of facing type and foundation compressibility on the magnitude and distribution of reinforcement loads in steel reinforced soil walls under operational conditions. In this paper, the effect of the facing vertical stiffness (due to elastomeric bearing pads placed in the horizontal joints between panels) on load capacity of steel reinforced soil walls is examined in a systematic manner using a numerical modelling approach. Numerical modelling was carried out using the commercial finite element program PLAXIS. The numerical model was verified against measurements recorded for an instrumented 6 m-high wall reinforced with steel strips. The influence of the facing stiffness and backfill-foundation stiffness combinations on the vertical load through the facing and on the magnitude and distribution of the reinforcement loads was examined. For walls subjected to operational (working stress) conditions at end of construction, the numerical results confirm that the vertical stiffness of the facing and soil-stiffness combinations can have a great effect on the vertical facing loads and on the magnitude and distribution of the load mobilized in the soil reinforcement layers.

**RÉSUMÉ:** Les pratiques actuelles de conception des murs en sol renforcé ignorent généralement l'influence du type du parement et de la rigidité de la fondation sur l'ampleur et la répartition des charges de renforcement. Dans cet article, on utilise une approche par modélisation numérique pour examiner systématiquement l'effet de la rigidité du parement vertical (due à la présence de cales en élastomère placées dans les joints horizontaux entre panneaux) sur la capacité de charge des murs renforcés sol/acier. La modélisation numérique a été réalisée à l'aide du code commercial Éléments Finis PLAXIS. Le modèle numérique a été validé sur des mesures enregistrées lors de l'expérimentation d'un mur d'une hauteur de 6 m et renforcé par des bandes d'acier. Le modèle permet de tester l'influence de différentes combinaisons entre la rigidité du parement et celle du remblai-fondation sur les valeurs des charges verticales dans le parement et les efforts dans les éléments de renforcement. Pour les murs travaillant en conditions opérationnelles (sous efforts de service) à la fin de leur construction, les résultats numériques confirment que ces combinaisons ont un grand effet sur les charges verticales et la distribution des efforts mobilisés dans les couches de renforcement.

**KEYWORDS:** reinforced soil retaining walls, steel strips, facing panels, finite element modelling.

### 1 INTRODUCTION AND GENERAL APPROACH

The mechanical behaviour of reinforced soil walls is complicated due to the mechanical complexity of the component materials (including soil type/arrangement), their interactions, wall geometry, and the influence of method of construction. Most reinforced soil walls are designed assuming that the wall foundation is rigid and/or does not influence the magnitude and distribution of reinforcement loads under operational conditions. This assumption may not apply to walls constructed over compressible foundations. This paper describes the results of a series of numerical simulations that were carried out on a 6-m high wall with precast concrete panels with metallically reinforced soil and constructed with backfill (reinforced soil and retained fill) and foundation soils having different stiffness, and different number of horizontal joints (i.e. different height of the panel units) along the facing elevation.

The program PLAXIS (PLAXIS 2008) was used to carry out the numerical simulations. The reference case for model calibration is the instrumented 6 m-high precast panel facing wall reinforced with steel strips reported by Chida and Nakagaki (1979). All the results in the present study correspond to operational (working stress) conditions at the end of the construction.

### 2 NUMERICAL MODEL

#### 2.1 General

The PLAXIS global geometry, structural components, and the numerical mesh to simulate the performance of the reference instrumented case are illustrated in Figure 1.

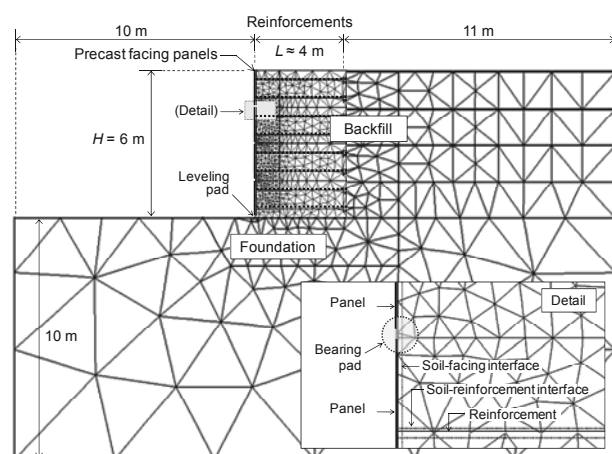


Figure 1. PLAXIS numerical model

## 2.2 Materials properties

### 2.3.1 Soil

Material properties for the soil zones (backfill and foundation) are summarized in Table 1. Two different stiffness of the backfill were considered to represent different scenarios due to the effects of compaction. The more compressible soil case (with assumed  $E_{backfill} = 10$  MPa) does not imply that poorly compacted soils should be used in the construction of these types of structures, but was used to ensure detectable differences between simulation outcomes. Moreover, the first meter of reinforced soil in contact with the facing is commonly constructed with less compaction energy and hence was assumed to have one half the stiffness of the fully compacted soil. Two other cases were assumed for the foundation soil; nevertheless, the actual foundation stiffness for the reference wall case was not reported by Chida and Nakagaki. The stiffness combinations in Table 1 result in four boundary cases to be examined.

Plane-strain boundary conditions were considered for the selection of the internal friction angle of the soils. The soil material properties also define the strength and stiffness of the interfaces between the soil and the structural elements (panels and reinforcement) using a reduction factor ( $R_i$ ), which is the ratio of interface shear strength to shear strength of the surrounding soil. The values chosen for this factor in each case (soil-facing and soil-reinforcement) are based on reported data and actual mechanical behavior of these interactions.

Table 1. Model properties of the soil materials

Parameters	Foundation	Backfill	
		> 1.0 m from face	< 1.0 m from face
Unit weight (kN/m <sup>3</sup> )	20	18	18
Cohesion (kPa)	1	1	1
Friction angle (°)	36	44	44
Dilatancy angle (°)	6	14	14
Elastic modulus (MPa)	10 – 1000	10 & 100	5 & 50
Poisson's ratio	0.3	0.3	0.3
Interface reduction factor	1	1	0.3 & 0.6

### 2.3.2 Reinforcement

Reinforcement elements were modelled using the “geogrid” PLAXIS elements as continuous sheets that have only axial stiffness and can transmit load to the surrounding soil through interface shear ( $R_i$  parameter). The equivalent linear-elastic axial stiffness of the geogrid element for each layer of reinforcement elements is computed as follows:

$$(EA)_{geogrid} = E_{reinforcement} A_{reinforcement} \frac{n_{reinforcements}}{L_{panel}} \quad (1)$$

Where:  $E_{reinforcement}$  is the stiffness modulus of the reinforcement layers (200 GPa for steel);  $A_{strip}$  is the cross-sectional area of one strip (100 × 2.3 mm);  $n_{strips}$  is the number of strips along one panel (two strip-units), and  $L_{panel}$  is the panel width assumed as 1.5 m. The resulting axial stiffness of the geogrid element is about 60 MPa/m. Other analyses considering different axial stiffness modulus equivalent to other steel reinforced types (e.g. bar mats with axial stiffness about 40 MPa/m) do not generate significant variations from the results presented in this study.

### 2.3.3 Facing-beam elements

The facing was defined by PLAXIS “beam” elements, and is comprised of the panels and the elastomeric bearing pads. The bearing pads are installed in the horizontal joints between contiguous vertical panels and are used in practice to prevent concrete-to-concrete panel contact.

Material properties for the concrete facing panels and horizontal joints are summarized in Table 2. The material type, dimensions and number of bearing pads can vary between projects (Neely and Tan 2010). The same Equation 1 can be used to obtain the parametrical values of the bearing pad elements (Damians et al 2013). In the present analyses, two EPDM (ethylene propylene diene monomer (M-class) rubber) bearing pads were assumed in each horizontal joint between per panel width.

Table 2. Model properties of the beam elements

Parameters	Panels	Bearing pads (EPDM)
Axial stiffness (MN/m)	6.0	0.1
Bending stiffness (kN/m <sup>2</sup> /m)	11	0.3
Weight (kN/m/m)	4.5	0.2
Poisson's ratio	0.15	0.49

## 3 RESULTS

### 3.1 Numerical and reported physical data comparison

Numerical predicted vertical loads at the base of the facing panels and the reinforcement loads were compared to values reported by Chida and Nakagaki (1979) during calibration of the numerical model.

#### 3.1.1 Vertical loads under facing

Damians et al. (2013) have shown from a review of instrumented case studies that the vertical load at the base of a precast facing wall with steel reinforced soil elements is greater than the self-weight of the panels. The vertical load under facing is a combination of facing self-weight, soil-panel shear and reinforcement down-drag loads, which generate reported load factors from 1.8 to 4.7 times the self-weight of the panels in steel reinforced soil walls (a value of 2.1 is computed for the reference wall reported by Chida and Nakagaki). It should be noted that the studied cases are restricted to steel reinforced soil walls. However, there are similar data for an instrumented full-scale 6-m high geosynthetic-reinforced soil wall with incremental concrete panels constructed in the laboratory (Tariji et al. 1996); the computed vertical load factor is 2.2 for this structure.

Figures 2a and 2b summarize results that take into account the effect of the backfill and foundation stiffness scenarios and the backfill-facing interface shear strength ( $R_i$  value of 0.3 and 0.6).

The data show that the larger  $R_i$ -value assumed results in a range of total vertical facing loads that vary from the reported value of 53.3 kN/m for the reference case. Assuming a value of  $R_i = 0.3$  generates four stiffness scenarios that include the measured case study value more accurately (modifying the  $E_{backfill}$  from 100 to 10 MPa when  $E_{foundation}$  is 1000 MPa, or modifying  $E_{foundation}$  from 1000 to 10 MPa when  $E_{backfill}$  is constant at 100 MPa).

Typically, the recommended interface shear strength factor values are about 0.6 times the shear strength of the surrounding soil. However, analysis of a wall reported by Runser et al. (2001) showed that a value of  $R_i = 0.3$  was gave more accurate

predictions (Damians et al. 2013). This value was adopted in the current study.

### 3.1.2 Reinforcement loads

In Figure 3 are shown the results of the reinforcement tensile loads obtained from numerical modelling and comparison with measured data for selected strips at different elevations. The reinforcement length considered in this study is 0.6 – 0.7 times the total wall height. Steel strips with lengths from 4.0 to 5.0 m were used in the reference case study, so all locations along any reinforcement layer are normalized with the respect to the layer length.

The presented results show good agreement between the numerical model results and measured data. The backfill-foundation stiffness combination results give different tensile-load distributions in the reinforcement layers. The effect of the less-compacted soil near the facing can be clearly detected with the discontinuity at a normalized distance from 0 to 0.25.

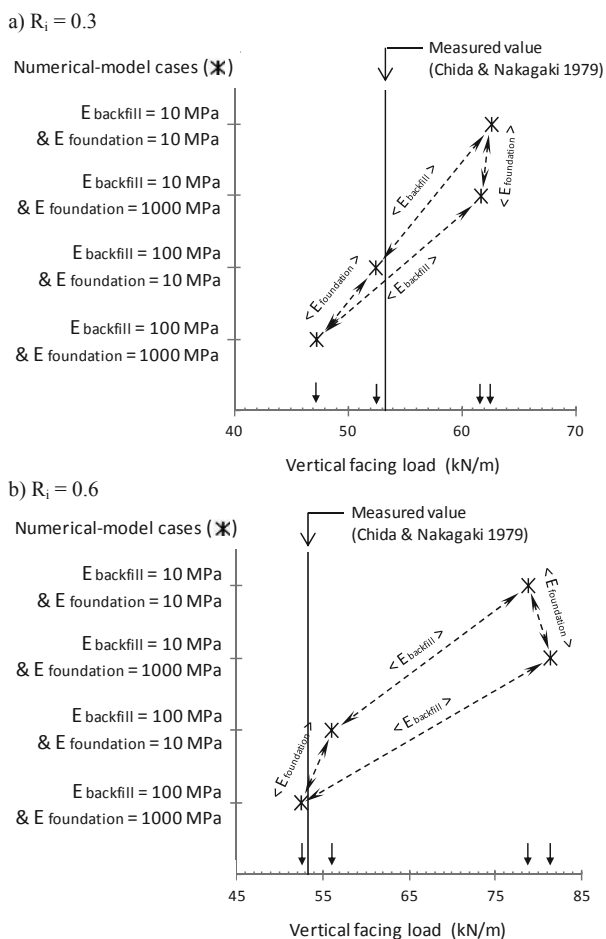


Figure 2. Total vertical loads under the facing assuming soil-facing interface reduction factor  $R_i = 0.3$  (a), and  $R_i = 0.6$  (b)

### 3.2 Influence of vertical facing stiffness

As noted earlier, the vertical facing stiffness was modified by changing the number of horizontal joints along the facing height of the wall. The reported case (base-case) had three horizontal joints (four panels of 1.5 m-height). Three other cases were considered to investigate the effect of the vertical facing stiffness (see Figure 4).

Figure 5 shows the numerical model reinforcement tensile-loads with respect to the number of horizontal joints. The values correspond to the maximum load ( $T_{maximum}$ ) of all the reinforcement strips, its related strip, and the normalized

distance of  $T_{max}$  to the facing in the strip. Reported values obtained from Chida and Nakagaki (1979) are also shown.

First, it can be noted that there is little difference in the predicted  $T_{max}$  value with respect to the backfill and foundation stiffness combinations (less than 4 kN/m in the case with more divergence, i.e.  $E_{backfill} = 100$  MPa and  $E_{foundation} = 10$  MPa combination). All the  $T_{max}$  values (numerical and measured) are located at the bottom zone of the wall (all at the layer located at 1.13 m, except the numerical case with  $E_{backfill} = 100$  MPa and  $E_{foundation} = 10$  MPa). With respect to their location in the reinforcement (normalized distance from the facing), all the  $T_{max}$  values are located between 0.3 and 0.5.

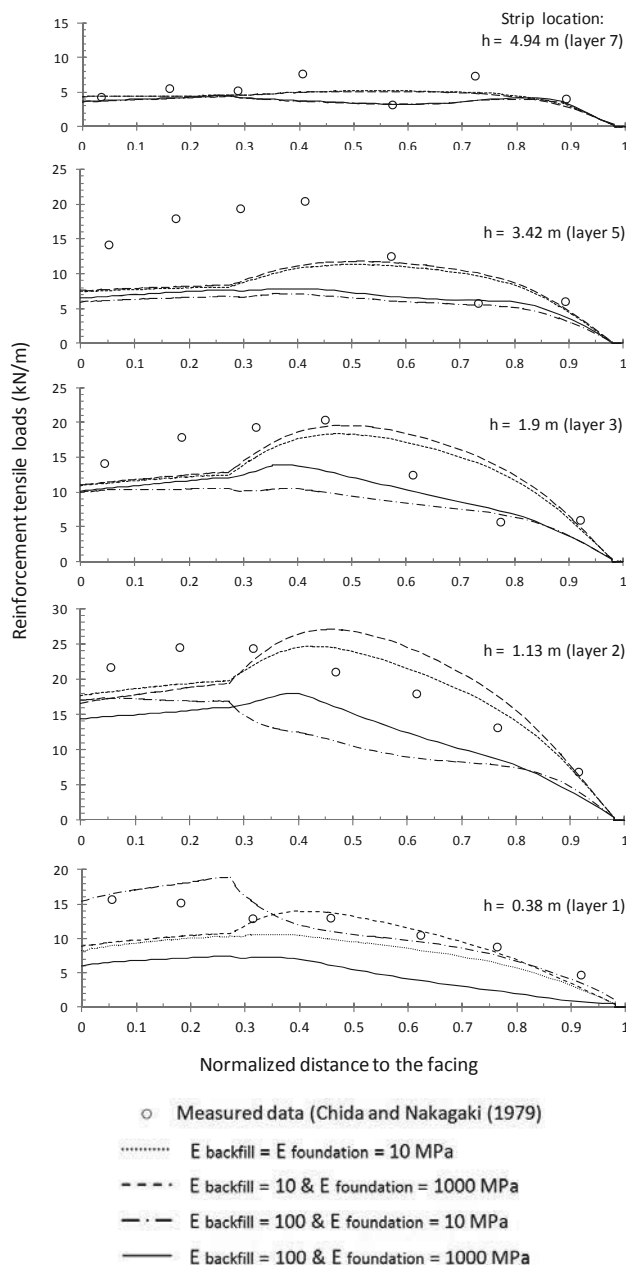


Figure 3. Tensile-load distribution of the wall reinforcements at the end of construction. (Normalized distance = distance to the facing of a stress i-point / total length of the reinforcement)

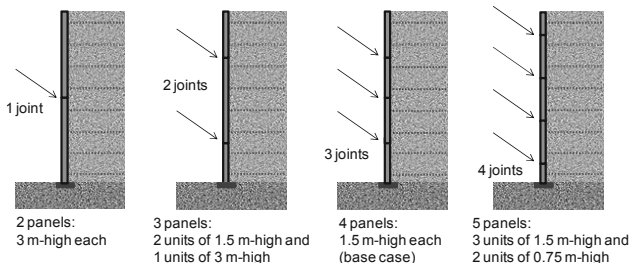


Figure 4. Schema about the horizontal joint options considered

Figure 6 shows the effect of the foundation stiffness and the vertical facing stiffness on the total vertical loads at base of the facing. Three additional foundation stiffness cases are considered here in order to obtain more data points. It can be observed that higher values of the foundation stiffness (elastic modulus) generate lower values of the total vertical load under the facing. If the total vertical load under the facing with respect to the number horizontal joints is analyzed (Figure 6), a significant influence of the vertical facing stiffness on the results can be noted. This influence is less relevant if the lowest modulus of the backfill soil is assumed (i.e.  $E_{backfill} = 10$  MPa, which generates a range of about 3 kN/m between boundary cases). If the backfill soil is assumed with higher stiffness value ( $E_{backfill} = 100$  MPa), the variation of the vertical load is more significant with a range of 15 kN/m for the single joint case, and 20 kN/m for the four joint case.

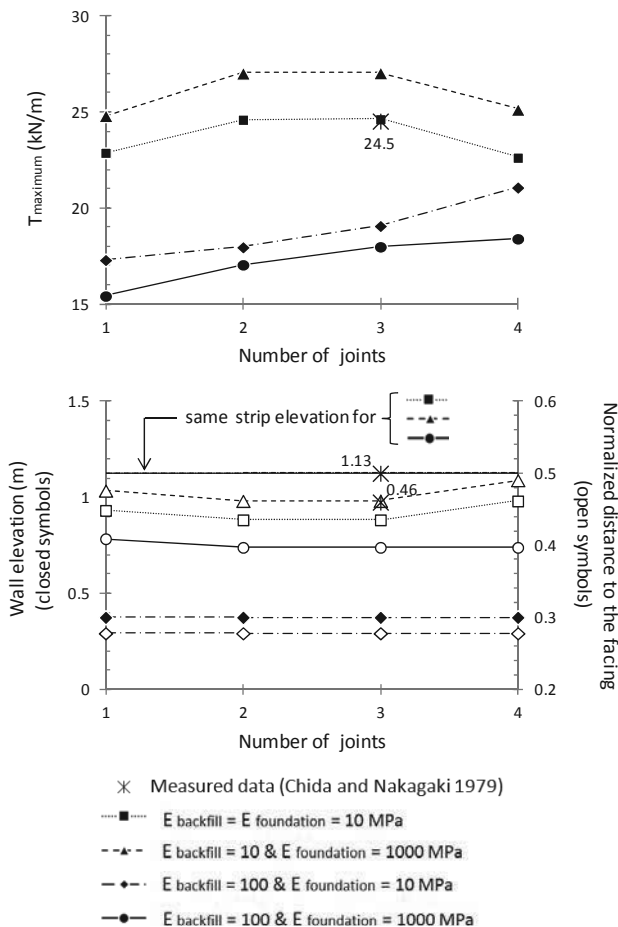


Figure 5. Maximum reinforcement loads ( $T_{max}$ ) with respect to the number of horizontal joints and backfill-foundation stiffness combination (upper figure), and the  $T_{max}$  location in the backfill (reinforcement layer and distance to the facing; bottom figure)

4 CONCLUSIONS

The mechanical behaviour of reinforced soil walls is complicated due to the mechanical complexity of the component materials, their interactions, wall geometry and soil type/arrangement, in addition to the unquantifiable effects of construction method and quality. Nevertheless, current design methods are typically based on classical notions of soil and reinforcement ultimate strength. Furthermore, internal stability design using conventional analytical solutions assumes that the compressibility of the foundation soil does not influence reinforcement loads.

The numerical simulation results in the current study demonstrate, first, that vertical loads at the base of the facing are affected directly by the backfill and foundation stiffness scenario and the soil-facing interface shear strength; second, there is a significant variation of reinforcement tensile load results depending on the combination of the backfill and foundation stiffness values; and third, the vertical stiffness of the facing (represented by the number of horizontal joints along the facing, that can be also be understood as different thicknesses of the bearing pad elements) produce significantly different effects on the vertical facing load and the reinforcement tensile loads. These three outcomes cannot be predicted for walls under operational (working stress) conditions using current strength-based design methods for the calculation of reinforcement loads.

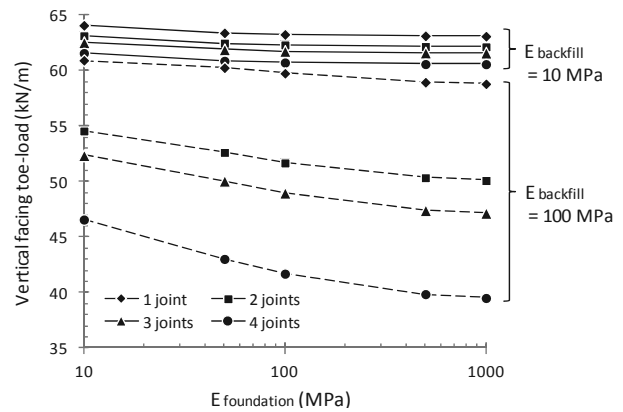


Figure 6. Vertical facing toe-load comparison with facing, foundation and backfill stiffness

5 REFERENCES

Chida, S. and Nakagaki, M. 1979. Test and experiment on a full-scale model of reinforced earth wall. *Proceedings of the International Conference on Soil Reinforcement*, Paris, France, Vol. 2, pp. 533-538.

Damians, I.P., Bathurst, R.J., Josa, A., Lloret, A. and Albuquerque, P.J.R. 2013. Vertical facing loads in steel reinforced soil walls. *ASCE Journal of Geotechnical & Geoenvironmental Engineering* (in press).

Neely, W.J. and Tan, S.L. 2010. Effects of second order design factors on the behaviour of MSE walls. Earth Retention Conference 3. Earth Retaining Structures Committee of the Geo-Institute of ASCE. Geotechnical Special Publications (GSP) n. 208. *Proceedings of the 2010 Earth Retention Conference*, Bellevue, Washington, August 1-4, 2010, pp. 522-530.

PLAXIS. 2008. Reference Manual, 2D - Version 9.0. PLAXIS B.V., Delft University of Technology, The Netherlands.

Runser, D.J., Fox, P.J. and Bourdeau, P.L. 2001. Field performance of a 17 m-high reinforced soil retaining wall. *Geosynthetics International*, 8(5): 367-391.

Tajiri, N., Sasaki, H., Nishimura, J., Ochiai, Y. and Dobashi, K. 1996. Full-scale failure experiments of geotextile-reinforced soil walls with different facings. *IS-Kyushu 96, 3rd International Symposium on Earth Reinforcement*, Fukuoka, Japan, pp. 525-530.

# Earth Pressure from Strip Footings on an Anchored Sheet Pile Wall

## Poussée des terres provenant de semelles filantes sur un mur de palplanches ancré

Denver H., Kellezi L.

*GEO-Danish Geotechnical Institute, Lyngby, Denmark*

**ABSTRACT :** A strip footing is frequently situated near a sheet pile wall. Assessment of the extra pressure on the wall generated by a footing causes theoretical problems for the designer. The distribution of this pressure depends in fact on many parameters. Besides the location and magnitude of the load a characterization of the soil and the wall is necessary for a rational design. Furthermore, the movement of the wall has a significant impact on the pressure. In this paper an anchored wall is investigated where the movement in failure is a rotation about the anchor point. The problem is solved by means of different analytical methods compared with solutions by finite element modeling applied to a number of representative examples. These comprise different strengths for the cohesion-less soil and different load scenarios. After a discussion of the results a simple calculation procedure is proposed.

**RÉSUMÉ :** Une semelle filante est souvent située à proximité d'un mur de palplanches. L'évaluation de la pression supplémentaire sur la paroi générée par la semelle provoque des problèmes théoriques pour le concepteur. La répartition de cette pression dépend en fait de nombreux paramètres. Outre l'emplacement et l'ampleur de la charge, une caractérisation du sol et du mur est nécessaire pour une conception rationnelle. De plus, tout déplacement de la paroi a un impact significatif sur la pression. Dans cet article, une paroi ancrée est étudiée lorsque le déplacement amenant à une défaillance consiste en une inclinaison autour du point d'ancrage. Le problème est résolu par le biais de différentes méthodes d'analyse que l'on compare aux solutions de modélisation d'éléments finis, appliquées à de nombreux exemples représentatifs. Celles-ci comprennent différentes forces pour un sol sans cohésion ainsi que différentes configurations de charge. Une simple procédure de calcul est proposée après la discussion des résultats.

**KEYWORDS:** Sheet pile wall, continuous footing, earth pressure, finite element method, sand, stress distribution.

### 1 INTRODUCTION

Sheet pile wall design methods in Europe generally rely on simplified earth pressure theories where the failure mechanism of the soil is in fact not compatible with the wall deflections. The Danish design method of sheet pile walls is based on Brinch Hansen's earth pressure theory, which assumes plastic behaviour for the wall and the soil. The computer program SPOOKS, which is a product from GEO-Danish Geotechnical Institute, is successfully used for sheet pile wall design in Denmark and abroad. The program calculates the required driving depth, the maximum bending moment and the anchor force for a user defined failure mode of the wall and the adjacent soil. The wall may be either anchored or free and either hinged or fixed in an anchor point. In the limit state a yield hinge in the wall with an ultimate positive moment may develop below the anchor level.

When excavating close to an existing building the effect of the partial distributed loads, from for example strip foundations (two dimensional (2D) conditions), or plate foundations (three dimensional (3D) conditions), are usually implemented in the sheet pile wall plastic design by means of the elasticity theory and the principle of superposition, where the extra earth pressure simply is added to the plastic solution. It is however not correct in the plastic design to separately calculate the active earth pressures from partial distributed loads without taking into account the active pressure from the unit weight of the soil.

The objective of the present paper is to supplement an earlier investigation for a free wall, Denver & Kellezi (2011), with establishment of an empirical relationship to estimate the extra earth pressure on an anchored sheet pile wall from a strip load behind the wall. This relationship is compared with solutions from finite elements (FE) results. The additional pressure is found as the difference between the combined pressure from self weight of the soil and the strip footing and the pressure

from only the self weight. In an attempt to assess the additional pressure on the wall, different approaches are investigated:

- Analytical calculations by the theory of plasticity on a suitable rupture figure.
- Empirical solutions inspired by Coulomb's theory.
- Numerical modelling by the FE method.

### 2 GENERAL

The earth pressure calculation on a wall is here illustrated by the Danish method denoted as Earth Pressure Calculation. This method has been proposed by J. B. Hansen (1953) and is extensively used in Denmark. The pressure on the wall ( $e$ ) is calculated as a sum of three terms as given in equation (1).

$$e = \gamma' d K_\gamma + q K_p + (c K_c) \quad (1)$$

These terms and the other parameters used in the calculation are:  $\gamma'$  the effective unit weight of the soil;  $K$  the earth pressure coefficient (different for the three terms);  $c$  the cohesion of the soil;  $p$  the surface load behind the wall, and  $d$  the depth along the wall from the soil surface. The last term is enclosed in parenthesis as this paper deals only with frictional soil.

In the Danish method the wall is considered composed of several rigid parts interconnected by yield hinges. Each part is assumed to rotate about a point and the earth pressure coefficients are functions of the position of this point and the direction of rotation (besides the friction angle of the soil,  $\varphi$ ). Examples of anchored walls with yield hinges are shown in Figure 1, and examples of rupture figures used for calculation of  $K$  are shown in Figure 3. The result of each calculation is the total force on the wall and the point of application. The normal component of this force ( $E$ ) is distributed along the wall. A part of  $E$  is applied near the top as a Prandtl rupture zone.



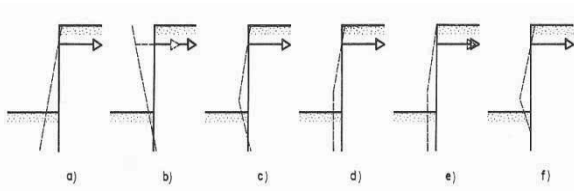


Figure 1, Anchored wall in failure composed of one or more rigid segments connected by yield hinges in failure. This paper deals with failure mode a) marked with rectangular.

A pressure jump near the top is then applied to ensure that the effect of the distribution (in terms of total force and moment) corresponds with the rupture figure. The method has been described in detail by Mortensen & Steinfeldt (2001) and results of calculated examples are compared with FE calculations.

### 3 COMPUTER PROGRAM ‘SPOOKS’

Although J. B. Hansen has developed a complete set of diagrams to find the values of  $K$ , the earth pressure calculation for a specific design situation is rather time consuming. To this end GEO-Danish Geotechnical Institute has made a commercially available computer program named ‘SPOOKS’.

Here, apart from the geometry of the excavation, the soil conditions and water tables, only a selection of the total wall movements (as shown in Figure 1) is necessary as input. The results are a distribution of both earth and water pressures, curve of bending moments along the wall, tip level, and anchor force. All together ready for the final design of the sheet pile wall profile and anchor. However, this program has no facility to include a partial surface load.

### 4 THEORY OF PLASTICITY

A method to assess the extra soil pressure caused by a partial load has been introduced by J.S. Steinfeldt and B. Hansen (1984). The Danish method to calculate the earth pressure coefficient from a relevant rupture line has been adopted. A circular rupture line is used as an appropriate choice for a rotation about a point at the anchor level. The stresses from the rupture line are determined by the Kötter’s differential equation. The total force is found by integration of this equation presented by Brinch Hansen (1953) and shown as the resulting force ( $F_o$ ) and moment ( $M_o$ ) about the centre of the circle as shown in Figure 2 where the significance of the variables is indicated.

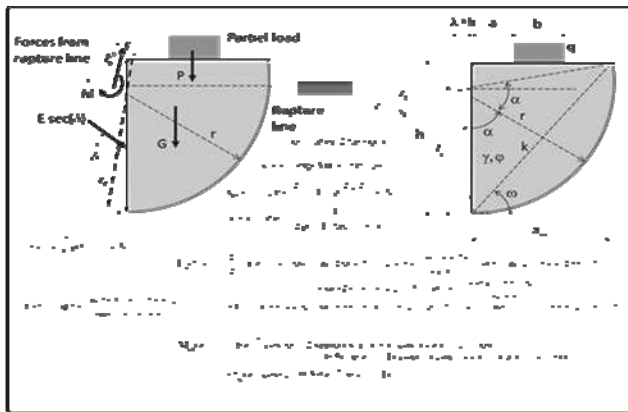


Figure 2, Analytical method where circular rupture figure is applied. Negative values of  $\phi$  and  $\delta$  shall be applied as the rupture is active.

It should be mentioned that  $t_c = \sqrt{q^2 + \tau^2}$  where  $t_c$  refers to the starting point of the integration where the rupture circle meets the soil surface and  $\sigma$  and  $\tau$  are coordinates to the yield point in the Mohr’s circle. The function  $q(\lambda)$  refers to the value of  $q$  in the point where the circle meets the surface. ( $q$  beneath the load

and 0 otherwise). The three unknowns ( $\lambda$ ,  $E$ , and  $z_p$ ) are finally found by the three equilibrium equations.

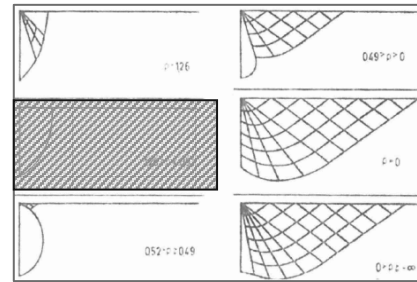


Figure 3, Rupture figures with different rotation points ( $\rho$ : relative height from the bottom of the wall). The figures are drawn for  $\phi = 30^\circ$ ,  $c = 0$  and rough wall rotating clockwise. The pure line rupture is investigated analytically in this paper (shaded in the figure).

This method (Figure 3 shaded) is in detail introduced and discussed by the authors and the results of a large number of load scenarios are presented in their paper.

### 5 EMPIRICAL METHOD

It is usual practice to apply a soil pressure derived from the distribution for the uniformly loaded surface. A minor part of this distribution is then used situated to a depth interval defined by inclined lines through the soil.

In Figure 4 a method of this kind often used in Denmark is shown. However, a tail below the lower line has been in this method proposed by K. Mortensen (1973) who has pointed out the complexity of the problem assuming a smooth wall that rotates anti-clockwise about a point below the tip of the wall. Consequently, the upper part with the even distribution is given by an active Rankine rupture figure. The tail is probably inspired by calculations by Coulomb’s method where the lower part is more dependent of other parameters than  $a$  and  $b$ .

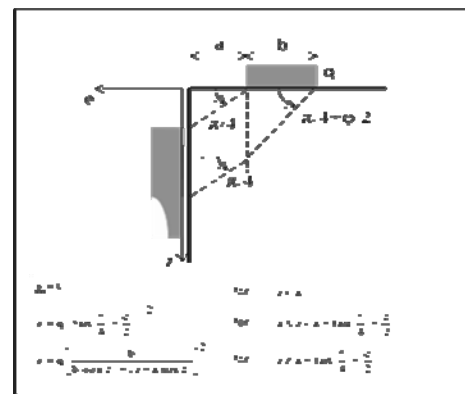


Figure 4, Empirical method based partly on the Coulomb’s earth pressure theory.

As this method is often used also for other movements, en lieu of other procedures it is adopted here as an example of an empirical solution.

### 6 ELASTIC SOLUTION

An elastic solution developed by Boussinesq (1885) is often used because of its simplicity as shown in Figure 5. Besides the theory of elasticity a smooth vertical wall without any movement is assumed. This method is often questioned as the resulting distribution is too large and situated much too high on the wall with respect to results from model tests and calculations based on the Coulomb’s method.

This is also the authors experience when the movement of the wall is anti clockwise about a low point in the wall. However, if the movement is a clockwise rotation about the anchor (as in this paper) the assumptions for an elastic solution are more justified.

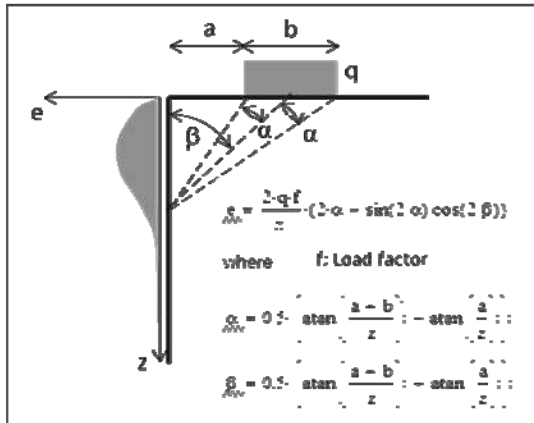


Figure 5, Elastic solution by Boussinesq (1885)

7 FINITE ELEMENT METHOD

In order to validate the method a number of load scenarios have been calculated by the FE program Plaxis 2011.

A 2D mesh pattern has been generated using triangular finite elements (15-noded). Sand is modeled in drained conditions using the Mohr-Coulomb constitutive model. The sheet pile wall is assumed weightless and with a large stiffness to prevent any interaction of stresses caused by deformation of the wall. The initial geostatic conditions are calculated first. Mesh sensitivity analyses have been carried out and an optimal mesh pattern with respect to element size and obtained accuracy has been chosen for the final analyses.

Plaxis plastic analyses (small deformation theory) and Updated Mesh (large deformation theory) have been applied to estimate the effect of the wall movement on the results. The calculations are carried out in different ways considering the impact the staged construction (excavating after, before or at the same time with the load application) has on the results.

Some different load scenarios are modeled and calculated to illustrate the problem. The loads / pressures applied over the foundations are chosen in such a way that the foundation bearing capacity is satisfied. The load scenarios are shown in Table 1.

Table 1, Load scenarios calculated

No	φ	a	b	q	No	φ	a	b	q
	(deg)	(m)	(m)	(kPa)		(deg)	(m)	(m)	(kPa)
1	30	1	2.5	125	6	40	1	2.5	713
2	30	1	1	50	7	40	1	1	285
3	30	2.5	1	50	8	40	2.5	1	285
4	30	5	1	50	9	40	5	1	285
5	30	0	∞	50	10	40	0	∞	285
h = 12 m    γ = 14 kN/m <sup>3</sup> c = 0 kPa    rough wall									
Height to rotation point:    h <sub>p</sub> = 9.6 m									

A unit weight has been applied to the soil to provide a realistic stress distribution near the top of the wall. Interface elements are applied along the wall. However, the soil strength at the interface has not been reduced as a rough wall is considered. The influence of the load on the wall has thus been derived as the difference between results of calculations of the wall with load and unit weight and with unit weight alone.

A rigid anchor is applied at a depth corresponding to 0.8\*h referring to the bottom of excavation or the height of the wall h.

The anchor point ensures a rotation around this point during failure (Figure 6).

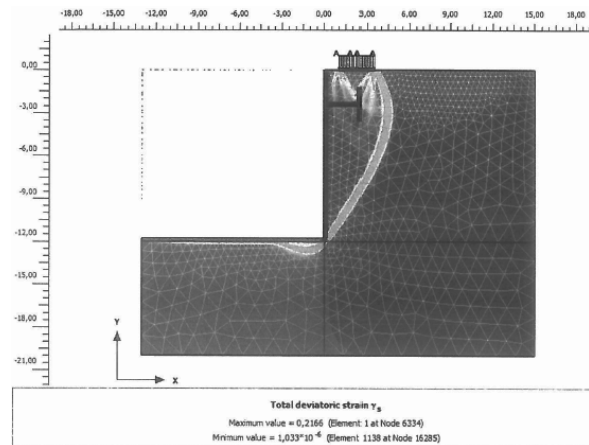


Figure 6 FE model example, (φ=30° a=1.0 m b=2.5 m or a/b=0.4 p=125 kPa).

A complete presentation of the results is not included due to lack of space. The normal pressure (e) on wall from the soil, and the soil plus load, and the additional pressure from the load derived as their difference (Delta e) are derived from the interface zone as given in Figure 7 and 8 for both soil types considered. The FE results are used as benchmarks for the accuracy of the other methods and shown relative to those in the discussion.

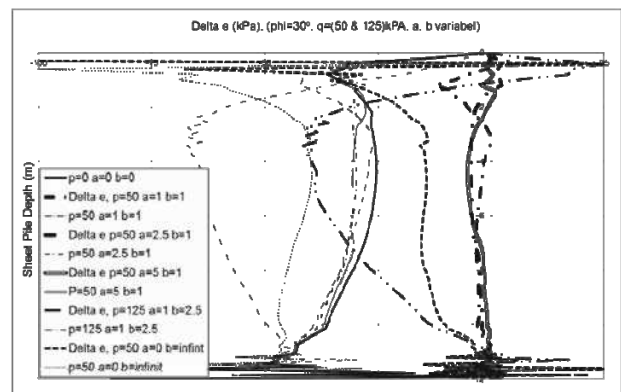


Figure 7 FE models results (φ=30°)

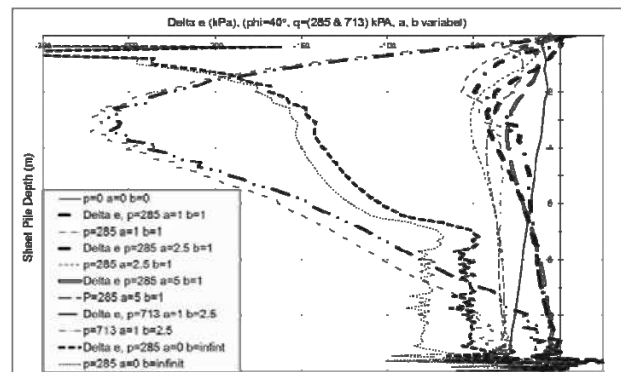


Figure 8 FE models results (φ=40°)

8 DISCUSSION OF CALCULATIONS

It was expected that a study of the theory of plasticity would yield a deeper insight into the problem and provide useful results. However, our calculations have produced rather scattered results. The calculations presented by Steinfeldt & Hansen do by no means suggest simple relations to the input

parameters. Their recommendation is also to make a computer code using the detailed described procedure and solve the problem in question explicitly. The resulting force from the integration along a rupture line consists together with simple zone ruptures the backbone of the Danish earth pressure theory, and should by no means be questioned here.

It should be mentioned that the procedure involves two calculations: (i) a calculation with both  $P$  and  $G$  (Figure 2), and (ii) a calculation with  $G$  alone. The influence of  $P$  is found by a subtraction of the two vectors. As  $G$  is great compared to  $P$  the latter is poorly determined and also problems with the validity of supposition as assumed here will distort the result.

Another problem is connected with the integration of the Kötter's equation. The only contribution to a change of the ambient stress condition is caused by the unit weight. However, the rupture line will pass through domains in the soil much differently affected by the partial loaded surface.

In every case the method will not provide the distribution of the pressure which is imperative especially to determine the moment in the wall in the anchor level.

### 9 PROPOSED PROCEDURE

When a procedure to assess the influence of a partial loaded surface it should be taken into consideration that the proposed distribution should converge to the distribution usually applied for a fully loaded surface.

The procedure proposed is:

- Calculate the elastic distribution ( $e_e(z)$ ) using the equations in Figure 5.
- Calculate the distribution usually used for a fully loaded soil surface. Use only the part of this distribution corresponding to the uniform part of the distribution ( $e_p(z)$ ) shown in Figure 4.
- The final distribution is:  $e(z) = W * e_p + (1-W) * e_e(z)$ , where  $W$  is a weight function  $W = 1.5 * (F - 0.167) - 2 * (F - 0.5)^3$  and  $F = 0.8 * b/h$ .

### 10 VERIFICATION

The benchmark for the verification is chosen as the results of the FE calculations. As before mentioned it is difficult to characterize the distributions by simple means. We have here focused on the usage of the distribution: (i) to calculate the anchor force ( $A$ ), and (ii) to calculate the moment in the wall in the anchor level ( $M$ ).

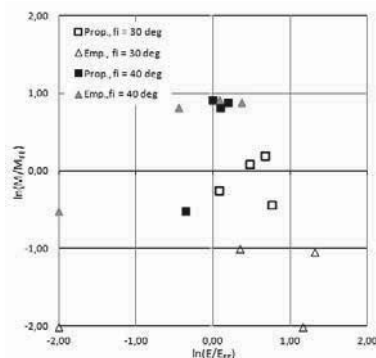


Figure 9, Accuracy of the methods (Empirical, Proposed vs. FE).

The anchor force is estimated as the part of the distribution above the depth  $z$  equal to double the height of the wall above the anchor. This procedure excludes the results found by the theory of plasticity to be represented. The quantities  $\ln(A/A_{FE})$  and  $\ln(M/M_{FE})$  are made where the denominators are the results from the FE calculations. These quantities are plotted against each other in Figure 9 for load cases (1-4) and (6-9).

When a quantity is greater than zero, the predicted value is on the safe side. When a quantity is 1 the corresponding ratio is 2.7. If  $A$ , or  $M$  is zero the quantity is minus infinity but plotted on the frame of the diagram.

A study of Figure 9 shows that the proposed procedure is superior to the empirical procedure and the fit is surprisingly accurate taking into account the complexity of the problem.

In order to offer a qualitative impression of the results a single distribution from the FE calculations is shown in Figure 10. This distribution is supplemented with distributions from two other methods (Empirical and Proposed).

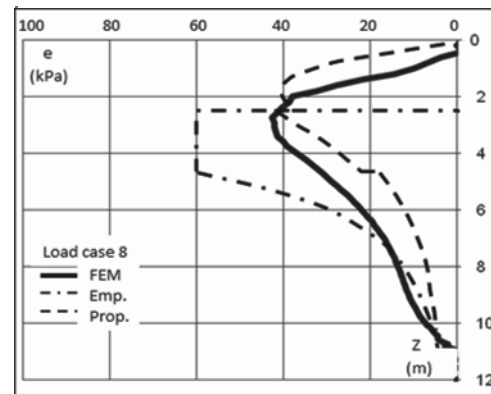


Figure 10, Normal pressure distribution ( $e$ ) from FE calculations compared with other methods (Empirical, Proposed) for a single load, (Load Case 8).

### 11 CONCLUSION

A procedure to calculate the pressure distribution has been proposed and has proved an excellent fit with results from FE calculations. The procedure is based on the theory of elasticity where the assumption of an immobile wall is justified by the high rotation point. The result converges to the usually applied when the entire surface is loaded.

### 12 ACKNOWLEDGEMENT

The authors acknowledge GEO-Danish Geotechnical Institute for the financial support of the project.

### 13 REFERENCES

Boussinesq, J. 1885, *Application des potentiels a l'etude de l'equilibre et du mouvement des solides elastiques*. Gauthier-Villars, Paris.

Brinch Hansen J. 1953, *Earth Pressure Calculation*, Danish Technical Press, Copenhagen.

Coulomb CA. 1776, *Essai sur une application des r les des maximis et minimis a quelques problems de statique*. *Memoires Acad. Royale des Sciences*, Vol. 7. Paris.

Denver H., Kellezi L. 2011, Earth pressure from a nearby building on sheet pile walls. *Proc. 17<sup>th</sup> European Conf. Soil Mechanics and Geotechnical Engineering*. Athens.

Mortensen N., Steenfelt J.S. 2001, Danish plastic design of sheet pile walls revisited in the light of FEM, *Proc. 15<sup>th</sup> Int. Conf. Soil Mechanics and Geotechnical Engineering*. Istanbul.

Plaxis, 2011, *FE Code for Soil and Rock Analyses*, User's Manual, A.A. Balkema, Rotterdam.

Steenfelt J.S., Hansen B. 1984, Sheet pile design earth pressure for strip load, *J. Geotecn. Engrg. ASCE* Vol. 110, No. 7.

# Top-Down Construction Alongside Of Bosphorus – A Case Study

## Construction en « Top-Down » le long du Bosphore – Une étude de cas

Durgunoglu T., Kulac F., Ikiz S., Akcakal O.  
*Zetas Zemin Teknolojisi A.S., Istanbul, Turkey*

**ABSTRACT:** Hatice Sultan and Fehime Sultan Residences are two historical Ottoman waterfront mansions placed on the European shore of Bosphorus in Istanbul. Within the restoration campaign of these mansions, it is planned to add four basement levels under the complete plot with the exception of preserved two corners where Hatice Sultan Residence and an old and large tree exist. The depth of the excavation needed for the basements is about 24 m below ground surface of which 21.20 m will be below groundwater level. The excavation should take place just 75 m far from the southwest pylon of the Bosphorus Suspension Bridge. Soil profile consists of uncontrolled fill, marine alluvium layer and bedrock which is sloped towards the seaside with a varying inclination. Steel propping system was set forth by the geotechnical design group of the Client, though this method was eliminated later during the bidding stage, because it was found impractical due to their obstacle in basement construction. The method of top-down construction of the basement levels with permanent diaphragm wall and bored piles socketed into bedrock was agreed to be realized by the Client based on the alternative proposal given by the foundation subcontractor during the bidding stage. THY -Do&Co JV Ortakoy Hotel Project is an interesting case-study where a challenging supporting system is being implemented near the Bosphorus in very poor soil conditions, under high seismicity.

**RÉSUMÉ :** Les Résidences de Hatice Sultan et de Fehime Sultan sont deux yalis Ottomanes historiques situées sur la côte Européenne du Bosphore, à Istanbul. Le projet de rénovation de ces yalis prévoit d'ajouter quatre étages en sous-sol sous l'ensemble du terrain, à l'exception de deux zones préservées où sont situés la Résidence de Hatice Sultan et un arbre centenaire. Une excavation de 24m sous le niveau du terrain naturel est requise pour la réalisation des sous-sols dont environ 21,20 m sous le niveau de la nappe phréatique. L'excavation aura lieu à tout juste 75 m du pylône sud-ouest du Pont sur le Bosphore. Le profil du sol est constitué de remblais non contrôlés, de couches d'alluvions marins reposant sur un substratum rocheux s'enfonçant avec une inclinaison variable en allant vers le Bosphore. Cependant, le design initial du client basé sur la mise en œuvre d'un système de soutènement en acier a été plus tard écarté car ne permettant pas la réalisation ultérieure des niveaux de sous-sol. La méthode de construction en « top-down » utilisant une paroi moulée et des pieux forés ancrés dans le substratum rocheux a finalement été sélectionnée par le Client, sur la base de la proposition alternative remise par le sous-traitant lors de l'appel d'offres. Le Projet de THY - Do&Co JV Ortakoy Hôtel est une étude de cas intéressante pour lequel un soutènement a dû être mis en œuvre à proximité du Bosphore, avec des conditions de sol très difficiles et en prenant en compte de forts risques sismiques.

**KEYWORDS:** Top-Down Construction

## 1 INTRODUCTION

Fehime Sultan and Hatice Sultan Residences are one of the historical Ottoman waterfront mansions constructed alongside the Bosphorus. These residences were constructed in the second half of the 19th the Century by Sultan Abdulhamid II as a wedding present for two daughters of Sultan Murat V. Later on, Fehime Sultan Residence was given as a gift to Gazi Osman Pasha for his success in Plevne Defense against Russian Army. During the Turkish Republic period this mansion served as a primary school and unfortunately was seriously damaged in a recent fire in 2002. On the other hand Hatice Sultan Residence served as an orphanage and then as private swimmers club in the later periods. The plot has been recently purchased by Turkish Airlines - Do&Co JV on BOT basis and is planned to be restored and developed to serve as a boutique hotel. Ruins of the Fehime Sultan Residence have been transferred to the restoration workshop. This beautiful and historical mansion is planned to be re-constructed using its original fragments. Within this restoration campaign, it is also planned to add four basement levels under the complete plot with the exception of two corners where Hatice Sultan Residence and an old and large tree exist. This deep excavation is agreed to be implemented with the Top-Down construction method because of the poor soil conditions, high ground water table and important

neighboring infrastructures. On the date of the paper submission, the diaphragm wall construction was just finalized. Therefore, only findings and implications of design and methodology together with diaphragm wall construction are presented within this paper.

## 2 PROJECT DESCRIPTION

Fehime Sultan and Hatice Sultan residences are located in district of Ortakoy alongside of Bosphorus and approximately 75 m away the southwest pylon of the Bosphorus Suspension Bridge in Istanbul (Figures 1a and 1b). Within the restoration campaign of these residences four basement floors are planned to be constructed in the entire plot. The periphery of the basement floors encloses the plot limit, except two corners on where Hatice Sultan residence and a historical tree exist (Figure 2). Basement excavation will be realized under Fehime Sultan residence location at the left in Figure 2 because ruins of this residence as a result of fire have been removed to restoration workshop area before the commencement of the works. The perimeter of the excavation plot is about 372 m and the area of the plot is approx. 6064 m<sup>2</sup>. Site elevations are varying between +1.00 m to +3.00 m. Excavation elevation is 21.20 m below the

sea level and maximum excavation depth is approximately 24 m.



Figure 1a and 1b. General View of the Site Figure and Location of the Site in Istanbul



Figure 2. Periphery of the Excavation (photo after the fire of 2002 and before the start of the restoration campaign)

During the bidding stage, top-down construction proposed by the foundation subcontractor was considered as a suitable method under the existing conditions. Typical cross section of the basement structures through the perpendicular direction to the seashore is given in Figure 3. It is planned to use the diaphragm walls as permanent periphery walls of the basement floors, construct the bored piles as permanent columns of the underground structure and integrate the foundation and slabs with the permanent wall and columns during the top-down construction method. This choice resulted in the necessity to develop special details for ground water isolation and continuity of the structural elements.

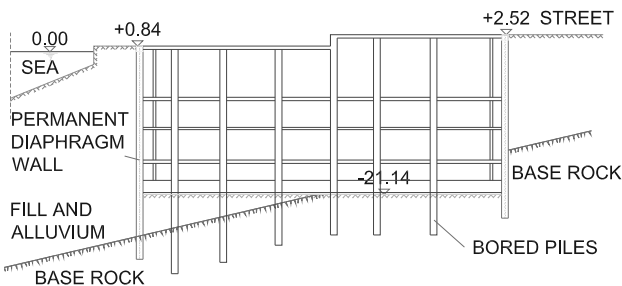


Figure 3. Section of the Basement Structure in Perpendicular to the Seashore

### 3 GEOTECHNICAL MODELLING

Within the soil investigations ten boreholes were implemented with a maximum length of 50 m. Two of the boreholes adjacent to the seaside were implemented with 45° inclination and length of these boreholes was 100 m. Also within the geophysical measurements, MASW and microtremor studies are implemented in the site to obtain the geodynamic modeling of subsoils.

Soil profile consists in sequence from top to down as of uncontrolled fill, marine alluvium and bedrock. Dyke, sandstone and shale are the commonly encountered rock types at the site. According to the results of vertical boreholes at the site bedrock is located between 13.50 m and 27.20 m under the sea level. Therefore length of the diaphragm wall and bored piles are chosen variable from one location to another in accordance to

encountered bedrock elevations. Typical soil profile is given in Figure 4.

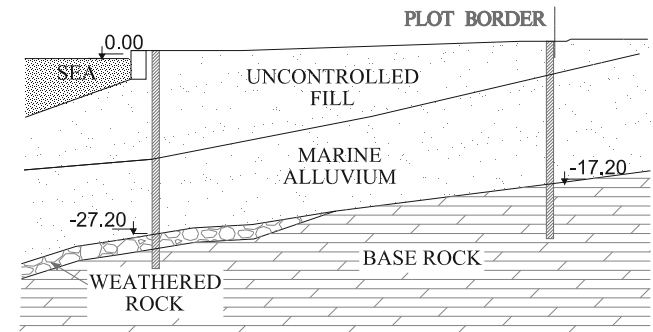


Figure 4. Typical Soil Profile

Simplified average drained shear parameters of the alluvial soil layers based on the field and laboratory testings are given in Table 1. Ground water table is located within 1.0m to 3.0m below the ground surface.

Table 1. Soil Properties

Layer	$\gamma$ (kN/m <sup>3</sup> )	$\phi'$ (°)	$c'$ (kN/m <sup>2</sup> )
Uncontrolled Fill and Marine Alluvium	18	28	1
Weathered Rock	22	33	20
Bedrock	24	33	50

### 4 PRELIMINARY DESIGN

The preliminary retaining system has been proposed by a geotechnical design group employed by the Client prior to the tender, which consisting a peripheral diaphragm wall and tubular steel struts. Diaphragm wall thickness was considered as 800 mm and planned to be used only temporarily during the excavation. To support the diaphragm wall, four rows of steel struts are proposed to be implemented. The spacing between the struts was 5.0 m in vertical and 8.20 m in horizontal directions. Typical cross section of the tender design is given in Figure 5.

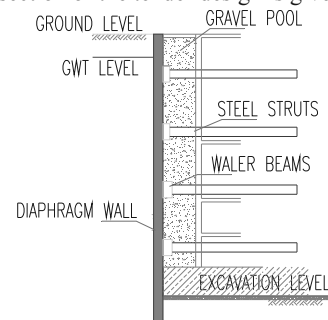


Figure 5. Tender Design Typical Cross Section

Complete underground structure were planned to be constructed 21.20 m below the water table. As a result, the uplift of the underground structure is one of the critical issues for the design.

### 5 PROPOSED ALTERNATIVE DESIGN

During the bidding stage the applicability towards the construction of underground structure and the cost of the tender design was examined. One of the drawbacks realized was that the space between the steel tubular struts was very limited to implement the excavation works in a safe and efficient manner. As a result, alternative top-down construction method was proposed to eliminate the implications of steel struts. Further, in order to eliminate the gravel filled between the walls; namely

gravel pool, proposed in the preliminary design, uplift loads are proposed to be taken by tension piles under the foundation.

As described in the previous sections, the site is located in a densely populated urban zone and there are important neighboring infrastructures around the plot. In order to minimize the lateral displacements to be realized during excavation implication of the proposed top down procedure was very effective and superior compare to strutted excavation.

In the proposed top down method permanent diaphragm walls and piles are to be constructed prior to excavation works. Later ground level r. c. floor will be constructed except the part behind the Hatice Sultan residence (Figure 6).

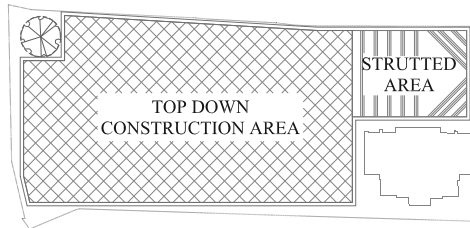


Figure 6. Top Down Construction Area

Soil under the ground level floor will be excavated phase by phase until the bottom elevation of foundation. In parallel to excavation works 1st basement r. c. floor will be constructed. The part of limited excavation plot behind the Hatice Sultan Residence will be supported with steel struts to provide space for ramps which will be used for the transportation of the excavated material. Top down construction steps will continue similarly as 2nd basement floor 3rd basement floor and foundation respectively (Figure 7).

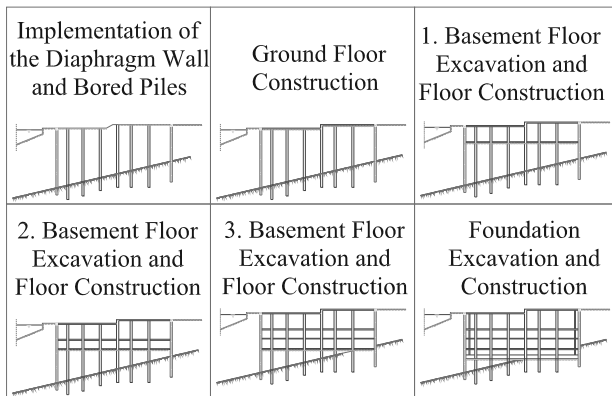


Figure 7. Top Down Construction Steps

Groundwater seepage into the excavation site is evaluated by seepage analysis and optimum socket length in to the bedrock is determined as 5.0 m. Also settlements due to the lowering groundwater table are estimated and found to be less than 18 mm which is considered as tolerable for the existing structures.

Bored piles are designed to be used as compression and tension members depending on the loading conditions. Therefore, piles which will act as permanent columns of the underground structure are extended into the bedrock having minimum socket length of 6.0 m based on the result of pile tension test conducted at the site in order to satisfy the most critical tension loading condition under the uplift forces. Tension capacity of the piles are estimated and taken into account against uplift forces.

In the top down construction, floor and foundation reinforcements will be integrated into the permanent diaphragm wall and piles with the aid of additional link reinforcements

which are already placed in these elements. Details of these link reinforcements are given in the next section.

After the top down construction steps the limited area behind the Hatice Sultan Residence will be constructed with conventional method from bottom to top in parallel to dissembling the steel struts. Special water-proofing works will also be implemented under the foundation and on the constructive inner wall during the down to top construction steps.

## 6 CONSTRUCTION STAGE OF DIAPHRAGM WALLS

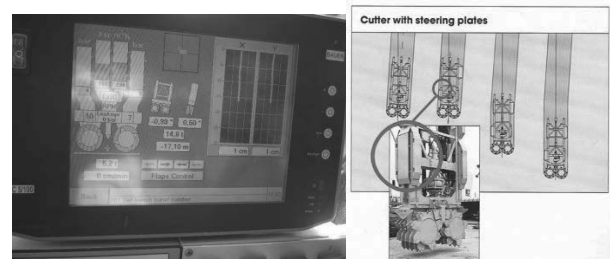
At the time of paper submission, diaphragm wall construction was just completed and preparations have been realized to initiate the piling works. Therefore only diaphragm wall construction stage would be covered within the paper.

To implement the diaphragm wall in required socket lengths in the bedrock formation, hydrofraise machine was mobilized for this project having 81 kNm max. torque per gear box, and 25 rpm max. revolution, with a max cutting depth capacity of 70m (Figure 8).



Figure 8. Diaphragm Wall Machine, Hydrofraise-Cutter

Another reason of implementing the hydrofraise-cutter machine was to provide a better verticality control during the construction of the permanent diaphragm walls. The verticality was monitored parallel to diaphragm wall excavation and direction of the cutter controlled with the help of the flaps on the edges (Figures 9a and 9b).



Figures 9a and 9b. Verticality Control System

During the soil investigations encountered maximum UCS values of the bedrock are given at the Table 2 below.

Table 2. Unconfined Compression Strength (UCS) values- Mpa

UCS Value	Intrusive Dyke		Sandstone		Shale Sandstone	
	Min.	Max.	Min.	Max.	Min.	Max.
	0.7	65	3.6	160	1.0	67

The distribution of the UCS values with the depth is given in Figure 10.

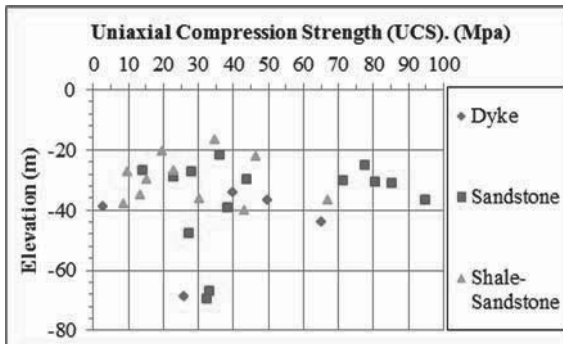


Figure 10. Unconfined Compression Strength (UCS) Values with Depth

The socket length of the diaphragm wall is variable due to the variability of the lithology of bedrock. It is estimated that the minimum 5.0 m socket length in the rock formation will be required. With the utilized hydrofraise cutter diaphragm wall machine, it was possible to construct approximately 2.65 m/day on plan (equals to 60 m<sup>2</sup> diaphragm wall per day) in average.

To integrate the slabs and foundation with the diaphragm walls additional link reinforcements are placed in the reinforcement cage (Figure 11). It is planned to chip the concrete on these elevations to bend the additional reinforcement into the slab and foundation elements.

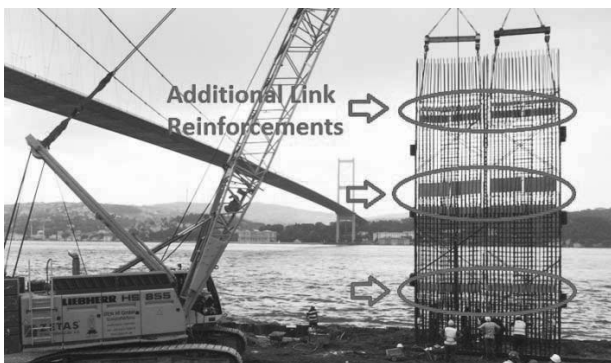


Figure 11. Additional Link Reinforcements on the Slab Elevations

Prior to diaphragm wall construction on the seaside, it was planned to implement sheet piles at the shore to remove the large quay stones at the back side and to prevent the negative fluctuation effect of the sea during the diaphragm wall construction. Sheet piles also contribute to the overall stability of the quay under the weight of heavy diaphragm wall machine. Sheet piling application is presented in the Figures 12a and 12b.



Figures 12a and 12b Sheet Piling

## 7 CONCLUSIONS

Within the restoration campaign of two beautiful historical mansions from Ottomans alongside the Bosphorus namely Hatice Sultan and Fehime Sultan, four basement floors was planned to be constructed with a maximum excavation depth of 24 m. Tender design for the retaining system of this excavation was temporary diaphragm walls supported with steel tubular struts. Due to the lack of enough spacing between the struts, applicability of the excavation works to achieve the desired speed was found to be questionable. Therefore an alternative system of top down construction method was proposed during the bidding stage. Prior to the excavation, it is proposed to construct the diaphragm wall and bored piles which will be also part of permanent structure of the basement so a remarkable saving and speed together with additional safety could be provided to the project. Another benefit of this system was also allowing extension of bored piles which are also columns of the basement into the bedrock to have desired tension resistance against uplift. This design gave a chance to eliminate the gravel pool proposed in preliminary design and provided additional space in basement floors. Integration of diaphragm wall, slabs and foundation is realized with additional link reinforcements and these reinforcements are placed in their for seen locations during the cage preparation. Sheet piles implemented also successfully prior to the seaside diaphragm wall construction in order to eliminate the negative effect of sea. In spite of the high UCS values it was possible to construct the diaphragm walls socketing 5.0 m deep into the bedrock with high capacity hydrofraise – cutter diaphragm wall machine at a reasonable rate. It is concluded that with the implication of top down construction method, part of this challenging project is completed successfully in economical, safe and timely manner.

## 8 ACKNOWLEDGMENT

We would like to extend our great appreciation to Mr. Hamdi Topcu, Chairman of Executive committee of Turkish Airlines and Mr. Atilla Dogudan, Chairman of Do-Co Corporation. The coordination and cooperation of Guryapi Construction Company are also gratefully acknowledged.

# Experiences with SBMA ground anchors in spanish soils

## Etude expérimentale avec les tirants d'ancrage SBMA dans le sol espagnol

Fernandez Vincent J.M.

Universidad de Buenos Aires, Universidad Catolica Argentina, Geotecnika SRL

**ABSTRACT:** The load transfer mechanism of steel, subjected to axial tension, adhered to a soil or rock through a cement grout is not through a uniform stress distribution. This results from the general incompatibility between the modulus of elasticity of steel, grout and soil, causing the phenomenon known as progressive debonding, as it causes the increase of the load of the anchor. The investigation of this phenomenon, the development of this knowledge and its application to industry has resulted in the SBMA System. This system applies much more efficiently the bond stresses available in the field through the use of various units within a single anchor borehole. We present brief guidelines for their design, and case histories within different geotechnical units in Spain.

**RÉSUMÉ :** Le mécanisme de transfert de charge d'un tirant en acier, soumis à une traction axiale, scellé dans le sol ou le rocher par un coulis de ciment ne se fait pas avec une répartition uniforme des contraintes. Ceci résulte de l'incompatibilité générale entre le module d'élasticité de l'acier, le coulis et le sol, provoquant un phénomène de décollement progressif et d'augmentation de la charge de l'ancrage. L'étude de ce phénomène, le développement d'un savoir et son application à l'industrie sont synthétisés dans le système SBMA. L'utilisation de plusieurs éléments dans un seul forage permet d'augmenter l'efficacité de l'ancrage. La communication présente des directives de conception, et des cas historiques dans différentes unités géotechniques en Espagne.

**KEYWORDS:** design – ground anchor – multiple anchor - load transfer – efficiency factor – fixed length

**MOTS CLES:** Conception, tirants, ancrage multiples, charge de transfert, facteur d'efficacité, longueur de scellement

### 1 INTRODUCTION.

Anchor design codes allow engineers to assume load is distributed uniformly through the length of an anchor, but experts acknowledge that the ultimate load is not proportional to the anchor's fixed length.

Anthony D. Barley's (1995, 1997, 2003) research and development for over a decade confirmed and extended existing independently works coming to the same conclusion of the non-uniformity of the distribution of adhesion in the fixed length anchor, but finally introducing the efficiency factor for calculating the length of the fixed length of an anchor considering this phenomenon. This research was then applied to the development of a new technology for ground and rock posttensioned anchors called Single Bore Multiple Anchor (SBMA).

In 2004 this technology was introduced in Spain, in which the author was responsible. This was done with the technical support of A. Barley.

### 2. DESCRIPTION

The system involves the installation of multiple units in a single anchor borehole. Each unit has its own single tendon, his own free length, length of bulb and is loaded using its own tensioning unit. The tensioning of all anchor units is performed simultaneously by a hydraulic jacks synchronized equipment that ensure that the load applied to the various units is always the same. The sum of the loads of the various units loads totaled the anchor total of the SBMA. With the design conception, there is no theoretical limitation on the overall bond length used (the sum of the fixed lengths of the various units), while for the conventional anchors little increase is expected load over fixed lengths of 8 to 10 meters.

Another advantage of the system is the opportunity to take account of the varying strata within the ground, as each anchor

within a bore can be designed for different ground conditions. Experts agree that the SBMA system is most effective in weak soils either to enhance capacity or to reduce the total number of anchors. However, they are not economically viable where the structural loading requires only low load anchors at wide spacings.

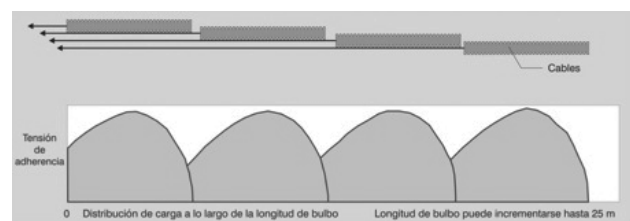


Figure 1. Adhesion stress distribution in several efficient units

### 3. DESIGN

#### 3.1 Efficiency factor

The relationship between the stiffness of the fixed anchor (controlled by the steel tendon) and the stiffness of the ground governs the rate of progressive debonding as an anchor is loaded and hence affects fixed length efficiency.

The nonlinearity of the mobilization of the value of the grout/ground bond stress ( $\tau_{ult}$  vs.  $\tau_{res}$ ) along the fixed length could be accounted by the efficiency factor for ground anchors.

$$f_{eff} = 1.6 \cdot L^{-0.57} \quad (1)$$



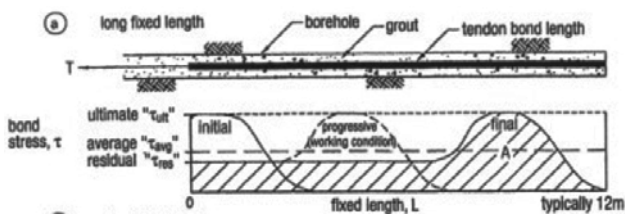


Figure 2. Bond stress distribution in the fixed length for different stages of a load test until failure. The area A is the failure load of the fixed length of the anchor. (Barley and Ostermayer, 2003).

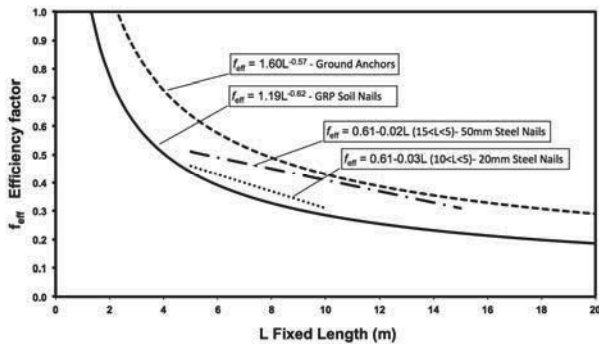


Figure 3. Efficiency factor for Ground Anchors, Steel and GRP Soil Nails (Barley, 1997)

The ultimate geotechnical capacity of the anchor ( $T_{ult}$ ) is:

$$T_{ult} = (\pi \cdot d \cdot \tau_{ult}) \cdot f_{eff} \cdot L \quad (2)$$

This formula does not apply to granular soils where the capacity to borehole diameter ( $d$ ) it is not linear and has to be established by meter of fixed length.

All load transfer mechanisms from tendon to grout induce bursting forces in the grout of one degree or another. Generally, the greater the mechanical locking effect (end plate or major deformations) the greater the bursting forces. It follows that the shorter the tendon bond length the greater the mechanical locking to allow the potential transfer of full tendon load capacity. However, this can only be effected where the ground or strong rock will provide adequate confinement of the grout column to prevent bursting failure. So to reduce the inefficiency in load transfer (entire fixed length in shear and tension) it is appropriate to utilize tendon bond lengths long enough to eliminate the risk of bursting failure yet as short as possible to gain maximum efficiency from grout/ground bond (Figure 4).

The high values of bond stress at the grout/ground interface results from the dilatancy effects of the soil in the shear zone, and interlocking at the rough interface, all as a consequence of an increase in radial normal stress.

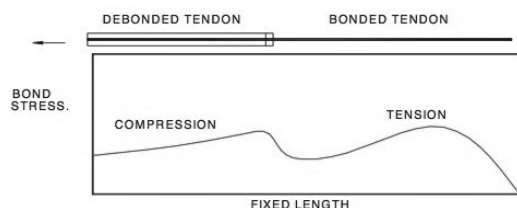


Figure 4. Probable bond stress distribution in compression and combined shear and tension.

### 3.2 Preliminary tests

Where preliminary trial anchors are tested to failure, each unit anchor yields its own value of ultimate bond capacity and hence more intensive data than conventional test anchors. The in situ testing of many of these multiple anchors with variable unit lengths has therefore recently extended the knowledge and

understanding of the tendon/grout/ground bond mechanism. The SBMA system has been utilized in permanent anchors and temporary anchors (including those with removable tendons).

Test anchors of length 2.5 to 5 metres may easily be taken to failure to establish the ultimate bond stress of that length and then the fixed length of production anchors accurately, designed to provide the required factor of safety. In the trials it is important to control the grouted length tested.



Figure 5. Trial research test with multiple synchronized hydraulic jacks in Parking La Vega, Murcia, 2005.

## 4. CASE HISTORIES

### 4.1 La China Stormwater management pond (Madrid)

In carrying out the excavation depth of 15.0 meters, were implemented temporary SBMA anchors of 2000 kN design load, using four units in the soil strata called "Peñuela" (gypsum with interbedded clays). The system was used always in combination with an injection unit located in each bulb known in spanish specification as IR that involves a postgrouting procedure and each units had 3x0,6" steel strand.

Research trials conducted according to the standard UNE 1537, allowed to change the original traditional ground anchors design, for less multiple anchors with increased load and efficiency.

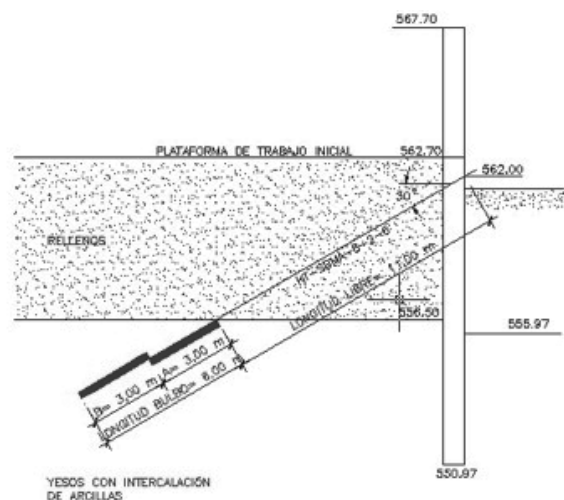


Figure 6. Section of diaphragm wall with trial anchor test TA2.

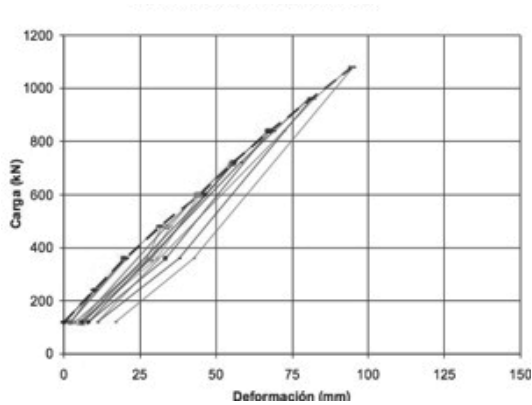


Figure 7. Load-deformation curve of trial test unit TA2-A.

#### 4.2 Parking La Vega (Murcia)

For the excavation of a parking 16.0 meters deep, with 9.0 meters of water thrust, one row of temporary SBMA anchors of 1900 kN were executed using four units in a dense gravel. This bearing layer was underlying clays and silts with medium consistency supported by a diaphragm wall thickness of 0.80 m. This solution as an alternative to a 0.60 m thick wall and two levels of traditional anchors.

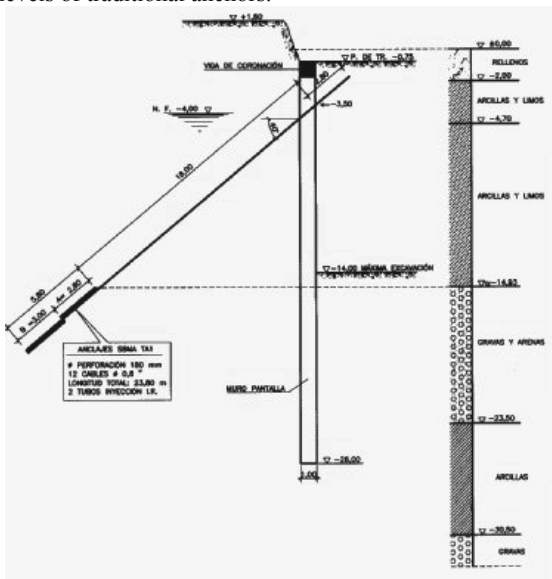


Figure 8. Section of diaphragm wall with trial anchor test TA1.

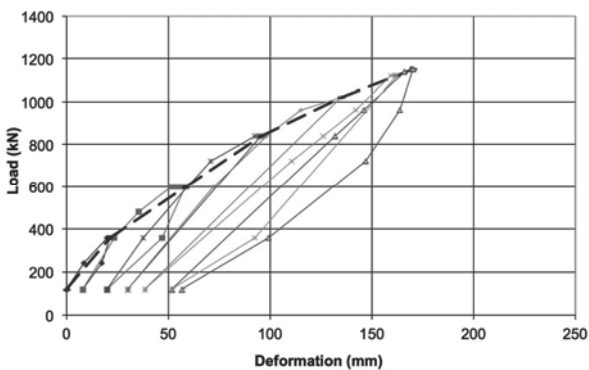


Figure 9. Load-deformation curve of trial test unit TA1-B.

#### 4.3 Palacio de los Congresos (Cartagena)

The Cartagena Convention Centre, located next to the port, run an excavation depth of 13.0 meters, with 10.0 meters of water

pressure. The containment wall was formed by a diaphragm wall 1.00 m thick and 2000 kN temporary anchors, bulb units in both compact red clays, and gravelly dense sands according to the geotechnical profile of each sector, and combinations of both soils in the same anchor. The inclination of the anchors was 30 to 40 degrees to the vertical, in order to avoid obstacles and achieve the desired geotechnical units.



Figure 10. Investigation test in trial SBMA anchor in the port zone.

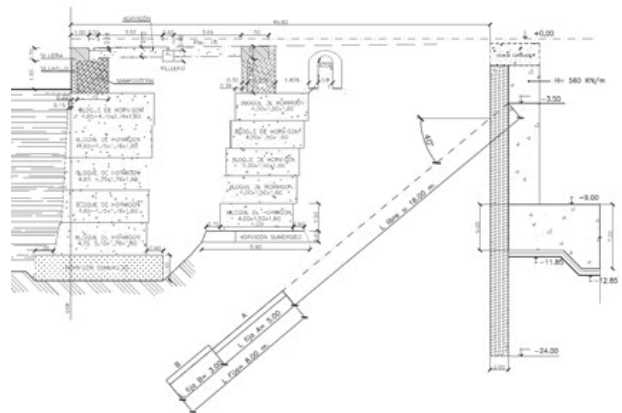


Figure 11. Section of port zone. Diaphragm wall with trial anchor.

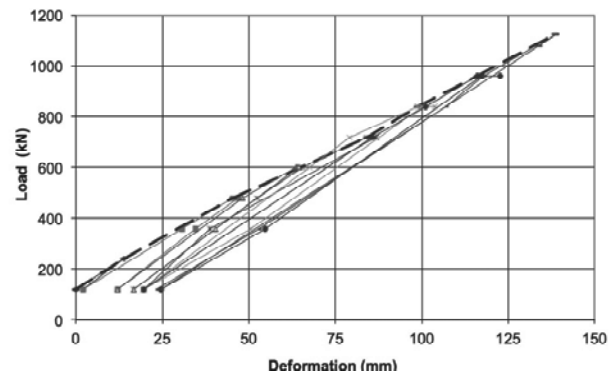


Figure 12. Load-deformation curve of trial test unit 55-B.

#### 4.4 El Corte Ingles (Albacete)

In the execution of the excavation depth of 14.0 meters, were implemented temporary anchors SBMA of 1200-1800 kN

design load, using three and four units in clays and silts of medium consistency, supporting a diaphragm wall of 0,80 m thickness with a water head of 10 meters. They were employed four rows of anchors, the first line with traditional anchors and the other three with SBMA.

In the preliminary research trials, within the present cohesive soils ( $N_{SPT} < 8$ ), the distribution of the adhesion along the fixed lengths tested was close to linear. The same is known of loose granular soils.



Figure 13. General view of the jobsite at design excavation level.



Figure 14. Execution of acceptance tests in El Corte Ingles

Within the reference work, we tested the use of multiple removable anchors as a modern solution to urban problems of public land use. This anchor also employs several units, each consisting of a single tendon lubricated and encapsulated in its entire length, which is bent in a special chair 180 degrees. The chair has a steel bar and the whole performs as a compression anchor, which transfers the load to the cement grout and ground. Thereof the anchorage capacity determines the number of units. The cable of each unit is then removed by pulling one of its ends. The complete withdrawal of steel anchors once their useful life is due, freeing of "pollution" of the ground for future use (subway/metro, underground pipes, buildings with deep foundations or basements, etc.)

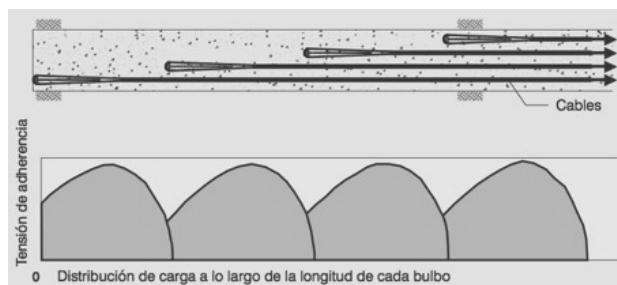


Figure 15. Removable SBMA units, schematic arrangement.



Figure 16. Removing an anchor unit with a force of 50-150 kN.

## 5. CONCLUSIONS

SBMA ground anchors are currently the most advanced technology for greater efficiency in the use of high adhesion capacity of the ground by the technologies currently employed in the execution of post-tensioned anchors. This system increases the limit loads traditional anchors used in soils, and innovation in paradigms hitherto employed in reference to the design and implementation of the fixed length of an anchor.

The efficiency factor should be complemented with more test data from different soil units with different consistency or relative density; so further detailed test trials research for the better understanding of each geotechnical unit is to be done. Meanwhile, there is experience accumulated in the countries where this technique has been being used the last 20 years.

## 6. ACKNOWLEDGEMENTS

The author thanks Kellerterra S.L. for the information herein presented, acquired during his service as its Technical Director. Also I am grateful of having met Tony Barley, and having shared professionally and personally these presented works.

## 7. REFERENCES

- Barley, A.D. 1995. Theory and practice of the Single Bore Multiple Anchor System. Anker in Theorie and Praxis. *Proc. Int. Symposium Salzburg Okt.* Balkema Rotterdam, 293-301
- Barley A.D. and C.R. Windsor. (2000). Recent advances in ground anchor and ground reinforcement technology with reference to the development of the art. *GeoEng 2000 International Conference*, November 19-21, Melbourne, Australia.
- Barley, A.D., Ostermayer, H. 2003. Ground Anchors. *Geotechnical Engineering Handbook*, Ernst & Sohn, 169-215.
- Fernández Vincent, J.M., 2005. Anclajes de Bulbo Múltiple. 5<sup>a</sup> Sesión, *Jornadas Técnicas SEMSIG-AETESS - Madrid*.
- Fernández Vincent, J.M., 2010. Teoría y práctica del anclaje de bulbo múltiple. *XX Congreso argentino de Mecánica de Suelos e Ingeniería Geotécnica*, Mendoza, Argentina. 457- 464.
- Fernández Vincent, J.M., 2011. Casos de aplicación del anclaje de bulbo múltiple. *14th Pan-American Conference on Soil Mechanics and Geotechnical Engineering*. Toronto, Canada.
- Ostermayer, H. (1974). Construction carrying behaviour and creep characteristics of Ground Anchors. *ICE Conference on Diaphragm Walls and Anchorages*, London, pp. 141-151.
- UNE 1537 - Execution of special geotechnical works - Ground anchors.

# Computed and observed ground movements during top-down construction in Chicago

## Mouvements de terrains calculés et observés en construction descendante à Chicago

Finno R.J., Arboleda L., Kern K.

*Department of Civil and Environmental Engineering, Northwestern University, Evanston, IL, USA*

Kim T.

*Korea Railroad Research Institute, Uiwang, Korea*

Sarabia F.

*AECOM, Vernon Hills, IL, USA*

**ABSTRACT:** Two detailed case studies of deep excavations in Chicago made with top down techniques are presented. The importance of considering all aspects of the construction process when estimating ground movements is emphasized. Detailed construction records were maintained at both sites. Inclinometers located within the walls, close to the walls and 7 m from the wall provided lateral movements throughout construction. Ground surface settlements were obtained by optical survey of several hundred observation points at each project. In addition, one of the projects included 88 strain gages installed in the floor slabs to measure time dependent responses of the concrete slabs used as lateral support for more than four years. The movements are presented in relation to construction activities and causes of incremental movements are identified. The lateral movements that arose from cycles of excavation and bracing accounted for approximately one-quarter and one-half the total movements at the two sites. Of these, field performance data and results of numerical simulations showed that approximately 40% of the movements arose from the time-dependent responses of the concrete floor slabs.

**RÉSUMÉ :** Deux études de cas détaillées d'excavation profondes réalisées à Chicago en construction descendante sont présentées. L'accent est mis sur l'importance de prendre en considération tous les aspects du procédé de construction. Des registres de construction détaillés ont été maintenus sur les deux projets. Des inclinomètres situés dans les murs, à proximité des murs et à 7m du mur ont mesuré les déplacements horizontaux tout au long de la construction. Les affaissements de surface ont été observés à l'aide d'un relevé topographique optique comprenant plusieurs centaines de points pour chaque projet. De plus, l'un des projets comprenait 88 jauges de déformations installées dans les dalles de plancher pour mesurer les réponses dans le temps des dalles de béton utilisées comme supports latéraux pendant plus de quatre ans. Les mouvements sont mis en relation avec les activités de construction et les causes des mouvements progressifs sont identifiées. Les mouvements latéraux causés par les cycles d'excavation et de contreventement ont représenté environ la moitié et le quart des mouvements totaux sur les deux projets. Pour ceux-ci, les résultats des tests sur le terrain et des simulations numériques ont montré qu'environ un tiers des mouvements était causé par les réponses dans le temps des dalles de planchers en béton.

**KEYWORDS:** Excavation, top-down support, ground movements, clays, time-dependent concrete response

## 1 INTRODUCTION

Use of top down construction has increased as more developers have seen the benefit of taking the excavation portion of a project off the critical path. Top down methods use permanent walls and flooring systems as temporary support and thus the support systems are very stiff. Yet, there are conflicting data concerning whether resulting movements are smaller than those associated with bottom-up methods. For example, Long (2001) observed no discernible difference in the performance of internally supported, anchored, or top-down systems based on examination of 296 excavation case studies. Kung (2009) reported results of 26 excavations made through Taipei silty clay which showed the maximum lateral wall deflection induced by the top-down methods were 1.3 times larger than that induced by bottom up methods. These observations are surprising given that the floor slabs are in theory much stiffer than either cross-lot braces or ground anchors, and that it is not possible to overexcavate the soil – i.e., make a deeper cut than planned so that the support system is essentially more flexible than planned in design - during construction since one must cast each floor on the ground.

This paper summarizes two case studies of deep excavations in Chicago made with top down techniques. Detailed construction records were maintained at both the Block 37 and One Museum Park West (OMPW) projects. Performance during construction is illustrated with results of inclinometers

located close to the walls and optical surveys of points on the ground adjacent to the excavations. In addition, one of the projects included 88 strain gages installed in the floor slabs to measure for four years the time-dependent responses of the concrete slabs used as lateral support. The movements are presented in relation to construction activities at both sites and causes of incremental movements are identified. It is shown that the movements that occurred during cycles of excavation and bracing are small, and about 40% of these movements are attributable to the time-dependent responses of the concrete slabs. The importance of considering all aspects of the construction process when evaluating movements is emphasized.

## 2 SUBSURFACE CONDITIONS

The subsurface conditions at the two sites are summarized in Figure 1 which shows the natural water contents and undrained shear strengths found from results of site investigations at each location. The surficial layer is an urban fill material consisting of sandy soils and construction debris. Underlying the fill material is a sequence of glacially deposited clays. The first two layers are soft to medium stiff clays which are very similar mineralogically, but exhibit different geotechnical characteristics due to the type of glacial deposition. The Blodgett stratum underlies the urban fill and was deposited in a

supra-glacial environment, which include glaciolucustrine clays and melt-out and flow tills (Chung and Finno, 1992). Because of this complicated depositional environment, the Blodgett generally has variable geotechnical characteristics, including water content, strength and stiffness. A desiccated crust is often present on top of the Blodgett stratum. At these sites, the crust is relatively thin, and in some cases is not present at all. Underlying the Blodgett stratum is a medium stiff clay, called the Deerfield stratum. This stratum exhibits much more uniform geotechnical characteristics than the Blodgett because the Deerfield was deposited as a basal melt-out till or a waterlain paratill. The stiff Park Ridge clay underlies the Deerfield layer. It is generally a little more overconsolidated than the upper clays, with an OCR of about 1.5. A deposit locally known as “hardpan” is found beneath the Park Ridge stratum. The soils in the hardpan are very stiff to hard and consist of silty clays to clayey silts and contain occasional lenses of sandy soils. These soils are basal tills and overconsolidated.

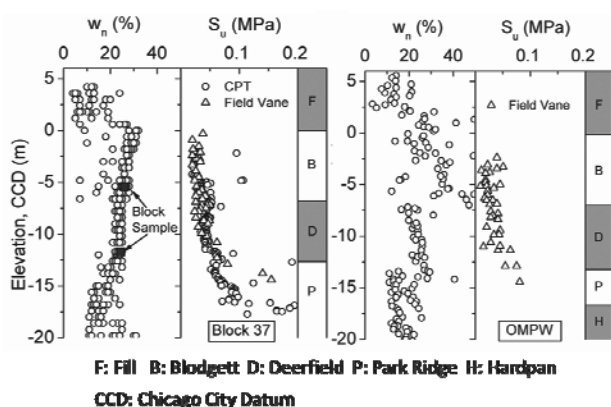


Figure 1. Subsurface conditions

### 3 BLOCK 37 PROJECT

Lateral support for the Block 37 excavation consisted of a 0.9 m thick reinforced concrete slurry wall and four levels of reinforced concrete floor slabs. After installation of the slurry wall, existing foundations from previous buildings were removed. These potholing activities were extensive near the north end of the excavation, and excavations reached as deep as 6 m. After the abandoned foundations and walls were removed, the excavations were backfilled.

Thereafter the excavation progressed in stages to the levels of the four basement floors (B1, B2, B3 and B4). Because the “ground” slab was placed after slab B1, the slurry wall was cantilevered with an unsupported length of about 7 m before any lateral support was placed. Thus this excavation deviated from an ideal top-down construction system because the lateral support was not installed prior to any significant excavation. The contractor made the decision to delay placement of the ground surface slab on the basis of construction expediency. A complete description of the activities at the site and performance of the excavation is found in Kern (2011).

#### 3.1 Ground movements during construction

The development of ground movements during construction is summarized in Figure 2. The optical survey points and inclinometer were located adjacent to the north wall of the excavation. The settlements are typical of the maximum values measured along this side of the excavation. The horizontal movements were taken from an inclinometer located 1 m behind the slurry wall near its center and were taken from elevation – 9 m CCD. Lateral movements versus depth will be discussed in the next section. Also shown on the figure is a record of the

construction activities so the causes of the movements are apparent.

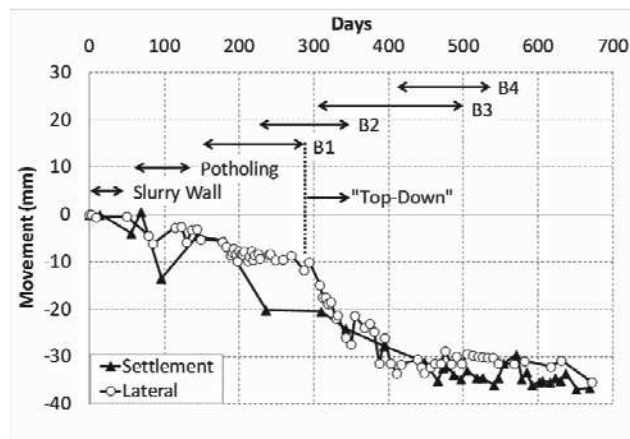


Figure 2. Settlements and lateral movements at Block 37

The maximum settlement and lateral movement observed at this section was 36 mm. As is apparent from the figure, significant ground movements developed during both the potholing activities and the first portion of the excavation when the large cantilever stage existed as the contractor excavated to the B1 slab level. These activities caused about 60% of the settlements that developed throughout the entire construction process. This large percentage was caused by the contractor’s decision to start the top-down process after the first level basement was constructed. The removal of the old foundations and slabs also contributed to the relatively large movements observed along this wall.

#### 3.2 Lateral movements adjacent to wall

Typical distributions of lateral ground movements with depth are shown in Figure 3 for inclinometers located 1 m and 7 m from the wall. These inclinometers were installed prior to any construction at the site and thus indicate the complete lateral response. The large influence of the potholing and initial cantilever stage of the excavation is seen clearly in the results.

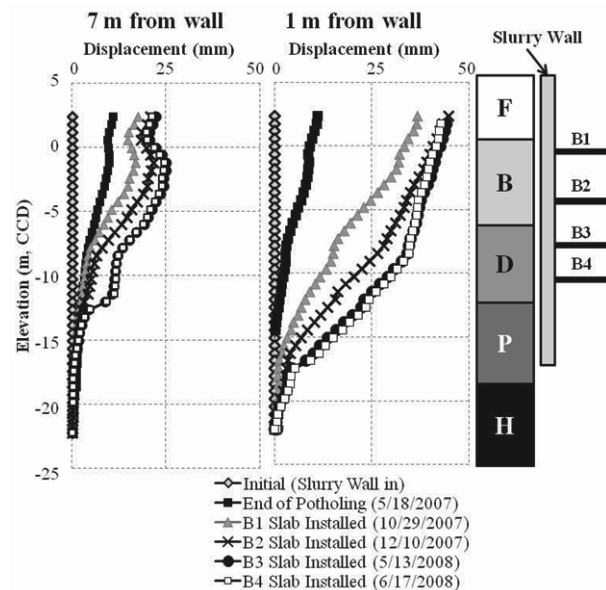


Figure 3. Lateral ground movements at Block 37

### 4 ONE MUSEUM PARK WEST PROJECT.

The One Museum Park West project involved constructing a 53-story reinforced concrete tower with a central core and four or five basement levels that extended approximately 15.3 m

below grade. The central core was excavated using a circular cofferdam, consisting of a sheet-pile wall and horizontal ring beams for internal bracing. The construction of the tower core was performed in a conventional “bottom-up” manner. The basement was constructed with steel beam reinforced concrete secant pile walls using top-down construction procedures. After leveling the site, the perimeter wall was installed and caisson foundations constructed. After the central core cofferdam was built, the excavation of the remainder of the site is being made with “top-down” construction methods. The perimeter secant pile wall is utilized as a permanent load bearing wall. Lateral bracing is provided by 4 or 5 levels of permanent floor slabs, depending on the location within the structure. After the ground level slab was cast integrally with the slurry wall, excavation proceed top-down by excavating to the bottom of the second level floor slab, casting that slab integrally to the slurry wall, and repeating the process until the final excavation depth was reached. Detailed descriptions of the construction and performance of this project are found in Sarabia (2012) and Arboleda (2013).

The development of ground movements during construction is summarized in Figure 4. Again, both settlements and lateral movements are represented in the figure. In this case, only the settlements provide a complete record of the ground response during construction. The inclinometers were located within 1 m of the secant pile wall at all locations, and were damaged as the wall was installed. Replacement inclinometers were initialized prior to the start of top-down excavation, so these data do not reflect deformations that developed as the wall and caissons were installed, or as the central core cofferdam was constructed. The data for the lateral movements were taken from the location of the maximum lateral movement recorded by the inclinometer, in this case, from elevation -8 m CCD. The settlements are typical of the maximum values measured along the west side of the excavation. Also shown on the figure is a record of the construction activities so the causes of the movements are apparent.

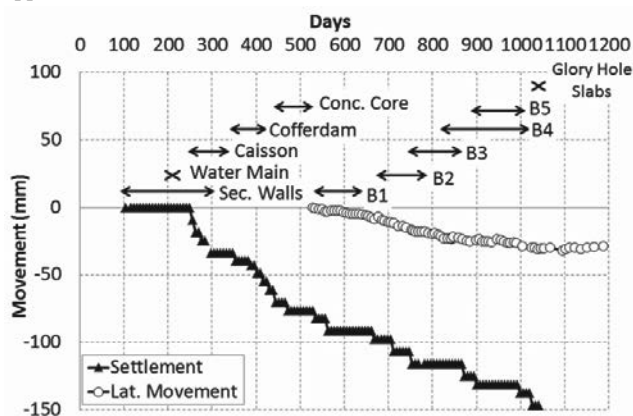


Figure 4. Settlements and lateral movements at OMPW

The maximum settlement observed at this section was 150 mm and the maximum lateral movement was 30 mm. As is apparent from the figure, significant ground movements developed throughout construction. The portions of the settlements that occurred during different phases of construction are summarized in Table 1. The activities before the top down portion of the project started resulted in 75% of the total settlements observed during construction.

Table 1. Settlements during construction activities

Construction activity	Settlement (mm)
Secant pile wall installation	11
Caisson installation	12
Water main relocation	5
Central cofferdam construction	12
Top-down construction	13

## 5 WALL MOVEMENTS DURING EXCAVATION

The lateral deformations that were recorded at OMPW only reflect those that occurred during top-down construction. Data from an inclinometer located in the middle of the west wall are shown on Figure 5. Also shown on the figure are the lateral movements that developed at Block 37 during the top-down phase of that construction, i.e., those after slab B1 was cast.

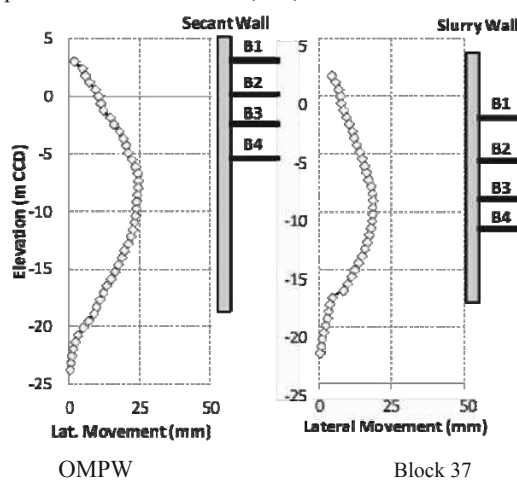


Figure 5. Lateral movements during top-down excavation only

The trends in these data reflect expected responses for an excavation made using top-down methods with very stiff walls and supports. Very little lateral movement is observed at the uppermost slab which was cast at the ground surface. The normalized maximum horizontal movements (movement/depth of excavation) were 0.14% and 0.2% at the Block 37 and OMPW sections, respectively. These values are more in line with what one would expect from a very stiff excavation with no overexcavation. However, it is clear that movements developed at both sites as a result of other construction activities or procedures that were not employed with the goal of minimizing ground movements. When using precedent for a first order estimate of expected ground movements for a top-down procedure, these data provide useful estimates. One should not indiscriminately use performance data without considering all activities that occurred during construction.

## 6 TIME-DEPENDENT RESPONSES OF FLOOR SLABS

The concrete floor slabs that serve as lateral bracing for these two projects were cast integrally with the support walls. As such, the floor slabs contracted as the concrete cured and crept under load. This time-dependent component of movement contributed to the wall deformations and analyses were conducted to evaluate the magnitude of this effect. Eighty-eight vibrating wire strain gages were cast into the OMPW slabs at four levels and at five sections so as to directly measure the strains in the slab that developed over time. Detailed descriptions of the instrumentation and results of analyses are given in Arboleda (2013).

To illustrate the influence of the time-dependent properties of concrete on the lateral movements of the secant walls, 3D

finite element simulations of the top-down construction process were conducted using SAP2000. The nonlinear time-dependent concrete effects of shrinkage, creep and variation of the modulus of elasticity with time were considered in the analysis. The analysis was performed in a step-by-step basis for the entire construction sequence using nonlinear stage construction without geometric nonlinearity.

Figure 6 shows the model after the first basement level was placed. The reinforced concrete columns and caissons were modeled as frame elements whereas the basement slabs, secant walls, foundation mat, corewalls, and interior shear walls were modeled as thin shell elements. The cross section of the secant walls consisted of concrete elements with embedded wide flange sections (W24, W33) and was modeled using an equivalent thickness based on the transformed section. Structural loads were applied, but lateral earth loads were not.

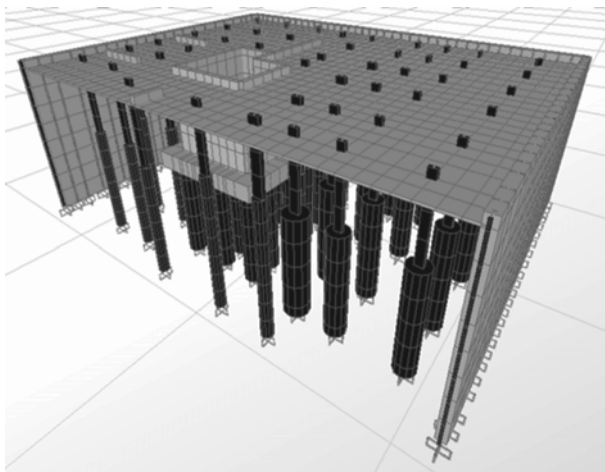


Figure 6. Model for time-dependent slab response at OMPW

The concrete was assumed isotropic with compressive strength taken from the as-built structural drawings and verified with the concrete reports provided by the contractor. The time-dependent behavior of concrete was included only for the basement slabs. The concrete properties were calculated based on standard concrete practice methods defined in ACI (2011) for a Poisson ratio of 0.2. The nonlinear variation of shrinkage with time was based on average values of the standard concrete practice codes: ACI 209, CEB-FIP 1990, AASHTO LRFD 2010, AS3600-2009, and NEN 6720.

The results of the analyses are given in Figure 7, where both the computed time-dependent movements of the walls at the end of each slab placement stage are compared to the total lateral movements of an inclinometer 1 m behind the wall. The lateral movements shown correspond to those that developed after the excavation to the first slab level was made, so that one can directly see the contributions of the time-dependent movements to the lateral deformations. About 40% of the lateral movements can be attributed to the time dependent effects of the concrete slabs.

## 7 CONCLUSION

Based on the results of the data and analyses summarized herein, the following conclusions can be drawn regarding these two excavations:

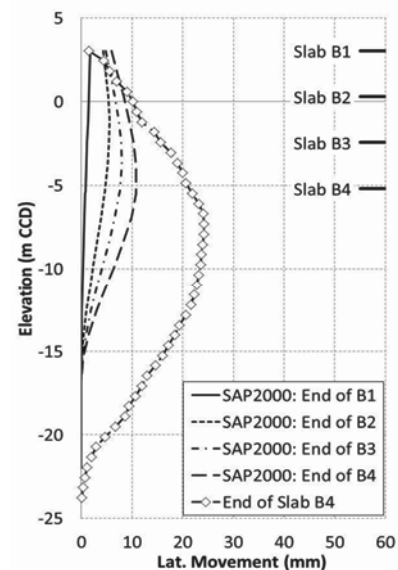


Figure 7. Computed time-dependent and observed lateral movements after slab B4 placed at OMPW

1. Top-down excavations in clays can be expected to result in normalized horizontal movements of approximately 0.15 to .2% when the uppermost slab is placed close to the ground surface so as to minimize the cantilever movements associated with the excavation process.
2. Of these “top-down” movements, approximately 40 % could be attributed to the time-dependent response of the concrete floor slabs.
3. Other construction activities or expedient excavation procedures led to movements that constituted 60 to 75% of the total movements that developed during construction. Use of precedence in estimating ground movements must be tempered by a realization of other site activities that can lead to ground movements.

## 6 ACKNOWLEDGEMENTS

Financial support for this work was provided by National Science Foundation grant CMMI-0928184 and the Infrastructure Technology Institute of Northwestern University.

## 7 REFERENCES

- American Concrete Institute (2011), "Building Code Requirements for Structural Concrete (ACI 318-11) and Commentary," Farmington Hills, MI.
- Arboleda, L. (2013). "Influence of time-dependent effects on movements associated with top-down excavations," PhD dissertation, Northwestern University, Evanston, IL
- Chung, C.-K. and Finno, R.J., "Influence of depositional processes on the geotechnical parameters of Chicago glacial clays," *Engineering Geology*, 32, 1992, 225-242.
- Kern, K. (2011). "Analysis of top-down construction at the Block 37 project in Chicago II," MS thesis, Northwestern University, Evanston, IL
- Kung, G. T.-C. ( 2009). "Comparison of excavation-induced wall deflection using top-down and bottom-up construction methods in Taipei silty clay," *Computers and Geotechnics*, Volume 36, Issue 3, April, 373-385.
- Long, M. (2001) "Database for retaining wall and ground movements due to deep excavations," *J Geotech Geoenviron Eng, ASCE*, 127 (3), 203-224.
- Sarabia, F. (2012). "Hypoplastic constitutive law adapted to simulate excavations in Chicago glacial clays," PhD thesis, Northwestern University, Evanston, IL



# Comparative Life Cycle Assessment of Geosynthetics versus Concrete Retaining Wall

Analyse de cycle de vie comparative d'un épaulement géotextile et conventionnel

Frischknecht R., Büsser-Knöpfel S., Itten R.  
*treeze Ltd., Kanzleistrasse 4, 8610 Uster, Switzerland*

Stucki M.  
*Zurich University of Applied Sciences, Institute of Natural Resource Sciences, Campus Grüental, 8820 Wädenswil Switzerland*

Wallbaum H.  
*Chalmers University of Technology, Civil and Environmental Engineering, 412 96 Göteborg, Sweden*

**ABSTRACT:** Geogrids made of geosynthetics can replace conventional building materials like concrete. In this article, goal and scope, basic data and the results of a comparative life cycle assessment of concrete reinforced retaining walls (CRRW) and geosynthetics reinforced retaining walls (GRRW) are described. One running meter of a three meters high retaining wall forms the basis for comparison. The two walls have the same technical performance and an equal life time of 100 years. The GRRW has a lower demand of steel and concrete compared to the CRRW. The product system includes the supply of the raw materials, the manufacture of the geotextiles and the concrete, the construction of the wall, its use and its end of life. The life cycle assessment reveals that the GRRW causes lower environmental impacts. The cumulative greenhouse gas emissions of 300 m CRRW are 400 t and 70 t in case of GRRW. The use of an environmentally friendlier lorry in a sensitivity analysis and monte carlo simulation confirm the lower environmental impacts caused by the construction of a GRRW compared to a CRRW. More than 70 % of the environmental impacts of the geogrids production are caused by the raw material provision (plastic granulate) and the electricity demand in manufacturing.

**RÉSUMÉ :** Géogrids peuvent remplacer les matériaux conventionnels comme le béton. Cet article contient une description de la définition de l'objectif et du champ d'étude, de l'analyse de l'inventaire et des résultats d'un analyse de cycle de vie comparative d'un épaulement géotextile et conventionnel. La comparaison est faite sur un mètre courant d'un épaulement de trois mètre d'hauteur. Les deux alternatives ont les mêmes propriétés techniques et la même durée de vie de 100 ans. Les systèmes contiennent la provision des matériaux, la fabrication des géotextiles et du béton, la construction, l'utilisation et l'évacuation de l'épaulement. L'analyse de cycle de vie démontre qu'un mètre courant d'un épaulement géotextile cause moins d'impacts environnementaux qu'un mètre courant d'un épaulement de béton. 300 mètres d'un épaulement de béton entraîne 400 t CO<sub>2</sub>-eq, celui de géotextile 70 t CO<sub>2</sub>-eq des émissions des gaz à effet de serre. L'utilisation des camions avec les émissions réduites ne change pas les résultats. Une simulation « monte carlo » confirme la stabilité des résultats. La provision des matériaux et l'électricité utilisé dans la fabrication de la couche de filtre géotextile sont des facteurs primordiaux (plus que 70 %) en ce qui concerne les impacts environnementaux du géogrid utilisé dans l'épaulement géotextile.

**KEYWORDS:** retaining wall, slope retention, geosynthetics, concrete, geogrid, life cycle assessment, LCA

**MOTS CLÉS :** épaulement, géotextile, géogrid, béton, analyse de cycle de vie, ACV

## 1 INTRODUCTION

Geosynthetic materials are used in many different applications in civil and underground engineering, such as in road construction, in foundation stabilisation, in landfill construction and in slope retention. In most cases they are used instead of minerals based materials such as concrete, gravel or lime.

Environmental aspects get more and more relevant in the construction sector. That is why the environmental performance of technical solutions in the civil and underground engineering sector gets more and more attention.

The European Association for Geosynthetic Manufacturers (E.A.G.M.) commissioned ETH Zürich and Rolf Frischknecht (formerly working at ESU-services Ltd.) to quantify the environmental performance of commonly applied construction materials (such as concrete, cement, lime or gravel) versus geosynthetics (Stucki et al. 2011).

In this article, the results of a comparative Life Cycle Assessment (LCA) of slope retention are described. The slope retention is either provided by a concrete reinforced retaining

wall (CRRW) or a geosynthetics reinforced retaining wall (GRRW).

The environmental performance is assessed with eight impact category indicators. These are Cumulative Energy Demand (CED, Frischknecht et al. 2007), Climate Change (Global Warming Potential, GWP100, Solomon et al. 2007), Photochemical Ozone Formation (Guinée et al. 2001a; b), Particulate Formation (Goedkoop et al. 2009), Acidification (Guinée et al. 2001a; b), Eutrophication (effects of nitrate and phosphate accumulation on aquatic systems, Guinée et al. 2001a; b), Land competition (Guinée et al. 2001a; b), and Water use (indicator developed by the authors). The calculations are performed with the software SimaPro (PRé Consultants 2012).

## 2 GEOSYNTHETIC VERSUS CONCRETE RETAINING WALL

It may be necessary in some cases, especially in the construction of traffic infrastructure, to build-up very steep walls. For such walls, supporting structures are necessary. The retaining walls need to meet defined tensile and shear



strengths. Retaining walls can be reinforced with concrete or geogrid made of geosynthetics.

The functional unit is defined as the construction and disposal of 1 m slope retention with a 3 meters high wall, referring to a standard cross-section. Thus, the functional unit is independent of the length of the wall.

Polyethylene and PET granules are used as basic material of the geogrid. The geogrid has to achieve a long-term strength of 14 kN/m. A scheme of both types of retaining walls are shown in Fig. 1.

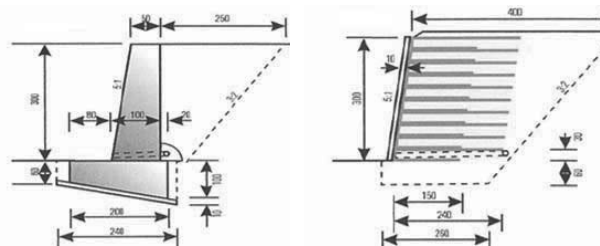


Figure 1. Scheme of the concrete reinforced retaining wall (CRRW, left) and the geosynthetics reinforced retaining wall (GRRW, right)

Some important key figures of the construction of a reinforced retaining wall are summarized in Tab. 1. The information refers to one meter of slope retention infrastructure and a time period of 100 years. Diesel is used in building machines for the excavation of the foundation and the compaction of the ground. The NMVOC emissions shown are released from the bitumen used to seal the concrete wall. The use of recycled gravel is not considered, since usually no onsite recycled gravel with specific properties is available when building reinforced retaining wall for the first time.

Tab. 1 shows specific values of the retaining walls for both alternatives. The material on site is used as fill material, wall embankments and cover material in case of a GRRW. A drainage layer made of gravel with a thickness of at least 30 cm behind the concrete lining is necessary. To be consistent with the CRRW, a gravel layer thickness of 80 cm is assumed in both cases. Round gravel is used for drainage purposes.

Table 1. Selected key figures describing the two constructions of one meter reinforced retaining wall

	Unit	CRRW	GRRW
Concrete	m <sup>3</sup> /m	1.60	-
Lean mix concrete	m <sup>3</sup> /m	0.24	-
Structural concrete	m <sup>3</sup> /m	2.10	0.31
Reinforcing steel	kg/m	153	-
Gravel	t/m	4.3	4.3
Bitumen	kg/m	2.84	-
Three layered laminated board	m <sup>3</sup> /m	0.01	-
Geosynthetic	m <sup>2</sup> /m	-	39.2
Polystyrene foam slab	kg/m	0.25	-
Polyethylene	kg/m	1.74	2.02
Diesel in building machine	MJ/m	11.6	53.9
Transport, lorry	tkm/m	701	265
Transport, freight, rail	tkm/m	33.2	6.9
Land use	m <sup>2</sup> /m	1.0	0.6
NMVOC	g/m	20	-

The difference between the CRRW and GRRW lies in the amount of concrete, steel and bitumen used, the energy con-

sumption that is related to the slope retention used (material transportation, excavation etc.), and the use of geosynthetics.

In a sensitivity analysis, it is analysed how the results of the slope retention change, when a low emission Euro5 lorry (>32 t) is used for the transportation of the materials to the construction site instead of an average European lorry (>16 t).

### 3 MANUFACTURING OF THE GEOGRID

Data about geosynthetic material production are gathered at the numerous companies participating in the project using pre-designed questionnaires. The company specific life cycle inventories are used to establish average life cycle inventories of geosynthetic material.

The data collected include qualitative information of system relevant products and processes from the producer, information from suppliers of the producer (where possible) as well as data from technical reference documents (e.g. related studies, product declarations, etc.). Average LCI are established on the basis of equally weighted averages of the environmental performance of the products manufactured by the participating companies.

The primary source of background inventory data used in this study is the ecoinvent data v2.2 (ecoinvent Centre 2010), which contain inventory data of many basic materials and services. In total, data from 5 questionnaires concerning the production of geosynthetic geogrids used in slope retention applications are included. The quality of the data received is considered to be accurate. The level of detail is balanced in a few cases before modelling an average geosynthetic layer.

Tab. 2 shows important key figures of the production of an average geosynthetic geogrid

Table 2. Selected key figures referring to the production of 1 kg geosynthetic layer used in slope retention

	Unit	Value
Raw materials	kg/kg	1.02
Water	kg/kg	0.86
Lubricating oil	kg/kg	7.30*10 <sup>-5</sup>
Electricity	kWh/kg	0.73
Thermal energy	MJ/kg	1.24
Fuel for forklifts	MJ/kg	0.13
Building hall	m <sup>2</sup> /kg	6.32*10 <sup>-6</sup>

### 4 LIFE CYCLE IMPACT ASSESSMENT

In this section the environmental impacts of 1 m slope retention with a height of 3 m over the full life cycle are evaluated. The life cycle includes the provision of raw materials as well as the construction and disposal phases.

In Fig. 2 the environmental impacts over the full life cycle of the slope retention are shown. The environmental impacts of the case with the highest environmental impacts are scaled to 100%. The total impacts are divided into the sections wall, raw materials (concrete, gravel, geosynthetic layers, reinforcing steel, bitumen, wooden board), building machine (construction requirements), transports (of raw materials to construction site) and disposal of the wall (includes transports from the construction site to the disposal site and impacts of the disposal of the different materials).

The GRRW (4B) causes lower environmental impacts compared to the CRRW (4A) in all impact categories considered. The non-renewable cumulative energy demand of the construction and disposal of 1 meter CRRW (4A) with a height of 3 meters is 12'700 MJ-eq and 3'100 MJ-eq in case

of GRRW (4B). The cumulative greenhouse gas emissions amount to 1.3 t CO<sub>2</sub>-eq in case of the CRRW (4A) and 0.2 t CO<sub>2</sub>-eq in case of the GRRW (4B). Correspondingly, the cumulative greenhouse gas emissions of 300 m CRRW (4A) are 400 t and 70 t in case of GRRW (4B).

The most relevant aspects concerning the environmental impacts of the life cycle of the CRRW (4A) are concrete, reinforcing steel, transportation and disposal. This order of relevance changes depending on the impact category indicators. The high share of concrete in the global warming indicator can be explained by the production process of clinker. During its calcination process geogenic CO<sub>2</sub> emissions arise. Reinforcing steel consists of 63 % primary steel and 37 % recycled steel. Most environmental impacts of the reinforcing steel arise from the fuel consumption and the emissions during the sinter and pig iron production in the supply chain of the primary steel. Disposal includes the disposal as well as transports from the construction site to the disposal site in case the material is not recycled. Impacts of disposal are dominated by the high amount of concrete which is landfilled. While direct emissions of landfilling concrete are negligible, the construction of the landfill and the transport of concrete to the landfill site are important. The land competition indicator is strongly influenced by the direct land use of the slope retention as well as by the wooden board used in the formworks. Gravel is responsible for a considerable share of the total amount of water used because substantial amounts of water are needed in gravel production.

Concrete, the geosynthetic and transportation mostly cause the highest burdens of the life cycle of the GRRW (4B). The share of the geogrid to the overall impacts is relatively high because on one hand several layers, and thus a considerable amount of geogrid, are required. On the other hand most materials used in the construction of the slope retention are available on-site and thus do not cause substantial environmental impacts (compare Tab. 1). The disposal gains importance in the categories eutrophication and global warming. The global warming impacts of disposal are caused by burning geogrids in waste incineration plants, which leads to fossil CO<sub>2</sub> emissions. Gravel dominates the water use indicator and the direct land use of the slope retention wall during its use is dominating land competition.

The main driving forces for the difference between CRRW (4A) and GRRW (4B) are the higher amount of concrete used in CRRW (4A) as well as the use of reinforcing steel, which additionally leads to higher transport expenditures. With regard to CED renewable and land competition the wooden board additionally increases the difference in total impacts because wood is a renewable resource with a high direct land occupation. Direct land competition is lower for the GRRW (4B) because the sprayed concrete lining is thinner than the CRRW (4A) and the embankment and backfilling area is not considered as occupied land.

The share of the geosynthetic material on the overall environmental impacts is between 3 % and 44 % (water use and CED non-renewable, respectively).

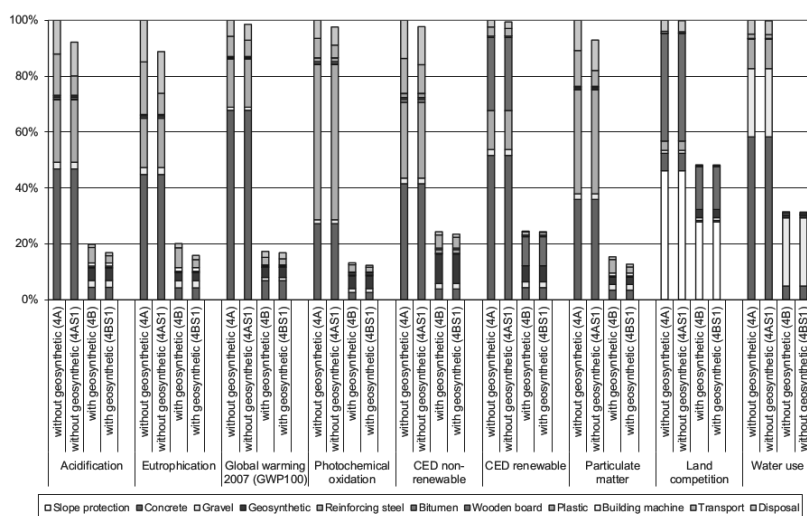


Figure 2. Sensitivity analysis: Environmental impacts of the life cycle of 1 m conventional (4A) and geosynthetic retaining wall (4B). 4AS1 and 4BS1 refer to the sensitivity analysis with a Euro5 lorry transportation. For each indicator, the case with highest environmental impacts is scaled to 100%.

#### 4.1 Sensitivity analysis

In a sensitivity analysis, it is analysed how the results of the slope retention change, when a Euro5 lorry (>32 t) is used for the transportation of the materials to the construction site instead of an average European lorry (>16 t).

Fig. 2 reveals that if a Euro5 lorry with lower exhaust emissions is used for the transportation, the environmental impacts of the GRRW (4BS1) are reduced between 0.1 % and 22.8 % (land competition and eutrophication respectively), whereas the environmental impacts of the CRRW (4AS1) are decreased between 0.2 % and 13.2 % (land competition and eutrophication respectively). The use of a Euro5 lorry leads among others to lower NO<sub>x</sub> emissions, which influences eutrophication. Land competition is obviously not influenced much by using another type of lorry.

#### 4.2 Contribution Analysis Geosynthetic Production

In this section the environmental impacts of 1 kg geogrid are evaluated. The life cycle includes the provision and use of raw materials, working materials, energy carriers, infrastructure and disposal processes. The category geosynthetic in Fig. 3 comprises the direct burdens of the geosynthetic production. This includes land occupied to produce the geosynthetic as well as process emissions (e.g. NMVOC, particulate and COD emissions) from the production process but not emissions from electricity and fuel combustion which are displayed separately. The environmental impacts of the geogrid are shown in Fig. 3. The cumulative greenhouse gas emissions amount to 3.4 kg CO<sub>2</sub>-eq per kg.

Environmental impacts are mostly dominated by the raw material provision and electricity consumption. Raw material

includes different types of plastics. Country-specific electricity mixes are modelled for each company and thus impacts of electricity consumption depend not only on the amount of electricity needed but also on its mix. The higher share of electricity in CED renewable can be explained by the use of hydroelectric power plants in the electricity mixes of several factories. And the relatively high share in eutrophication is mainly due to electricity from lignite. The share of heating energy and fuel consumption for forklifts is between 0.01 % (land competition) and 2.8 % (global warming) and is thus not considered to be of primary

importance. With regard to land competition the geosynthetic production plays an important role. The impacts are dominated by the direct land use, i.e. land which is occupied by the manufacturer plant in which the geosynthetic is produced. Indirect land uses, i.e. land occupation stemming from upstream processes, are significantly lower because no land occupation is reported in the inventories of plastic feedstock and no land intensive products such as wood are used in considerable amounts. Water consumption is included in the working materials. As a consequence, this category bears about 5 % of the total amount of water used.

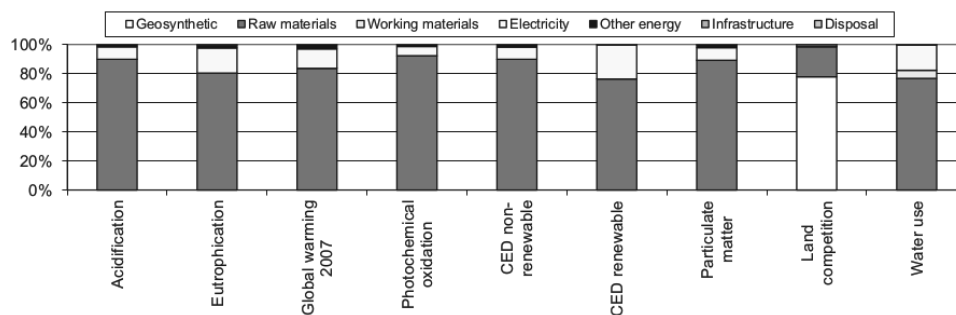


Figure 3. Environmental impacts of the life cycle of 1 kg geogrid. Geosynthetic includes direct burdens of the geosynthetic production. Raw materials include plastic, extrusion if necessary and additives, working materials include water (tap and deionised) and lubricating oil, other energy includes thermal energy and fuels, infrastructure covers the production plant and disposal comprises wastewater treatment and disposal of different types of waste.

## 5 DISCUSSION AND CONCLUSION

The use of geosynthetics leads to lower environmental impacts of slope retention in all indicators investigated. The specific climate change impact of the construction of the slope retention (1 m slope retention with a 3 meters high wall) using geosynthetics is about 1 ton CO<sub>2</sub>-eq per meter lower compared to a conventional alternative. This difference is equal to about 84 % of the overall climate change impact of the construction and disposal efforts of an entire conventional slope retention system during its 100 years lifetime.

If a Euro5 lorry with lower exhaust emissions than an average fleet lorry is used for the transportation of materials, the environmental impacts of both cases are somewhat reduced regarding some indicators. However, this does not affect the overall conclusions of the comparison.

Slope retentions are individual solutions in a particular situation. The height of slope retention walls and the horizontal loads on it may differ, which may lead to differences in thickness and reinforcement. Thus, generalising assumptions were necessary to model a typical slope retention. Data about on-site material used, gravel extraction, concrete and the use of building machines are based on generic data and knowledge of individual civil engineering experts.

Based on the uncertainty assessment it can be safely stated that the geosynthetics reinforced slope retention shows lower environmental impacts than the concrete wall. Despite the necessary simplifications and assumptions, the results of the comparison are considered to be significant and reliable.

A geosynthetic reinforced wall used for slope retention constitutes a different system compared to a concrete reinforced wall. Nevertheless, both systems provide the same function by enabling the build-up of steep walls. Compared to the conventional slope retention, the geosynthetic reinforced wall substitutes the use of concrete and reinforcing steel, which results between 63 % and 87 % lower environmental impacts.

## 6 REFERENCES

ecoinvent Centre (2010) ecoinvent data v2.2, ecoinvent reports No. 1-25. Swiss Centre for Life Cycle Inventories, Dübendorf, Switzerland, retrieved from: [www.ecoinvent.org](http://www.ecoinvent.org).

Frischknecht R., Jungbluth N., Althaus H.-J., Bauer C., Doka G., Dones R., Hellweg S., Hischier R., Humbert S., Margni M. and Nemecek T. (2007) Implementation of Life Cycle Impact Assessment Methods. ecoinvent report No. 3, v2.0. Swiss Centre for Life Cycle Inventories, Dübendorf, CH, retrieved from: [www.ecoinvent.org](http://www.ecoinvent.org).

Goedkoop M., Heijungs R., Huijbregts M. A. J., De Schryver A., Struijs J. and van Zelm R. (2009) ReCiPe 2008 - A life cycle impact assessment method which comprises harmonised category indicators at the midpoint and the endpoint level. First edition. Report I: Characterisation, NL, retrieved from: [lcia-recipe.net/](http://lcia-recipe.net/).

Guinée J. B., (final editor), Gorrée M., Heijungs R., Huppes G., Kleijn R., de Koning A., van Oers L., Wegener Sleswijk A., Suh S., Udo de Haes H. A., de Bruijn H., van Duin R., Huijbregts M. A. J., Lindeijer E., Roorda A. A. H. and Weidema B. P. (2001a) Life cycle assessment; An operational guide to the ISO standards; Part 3: Scientific Background. Ministry of Housing, Spatial Planning and Environment (VROM) and Centre of Environmental Science (CML), Den Haag and Leiden, The Netherlands, retrieved from: [www.leidenuniv.nl/cml/ssp/projects/lca2/lca2.html](http://www.leidenuniv.nl/cml/ssp/projects/lca2/lca2.html).

Guinée J. B., (final editor), Gorrée M., Heijungs R., Huppes G., Kleijn R., de Koning A., van Oers L., Wegener Sleswijk A., Suh S., Udo de Haes H. A., de Bruijn H., van Duin R., Huijbregts M. A. J., Lindeijer E., Roorda A. A. H. and Weidema B. P. (2001b) Life cycle assessment; An operational guide to the ISO standards; Parts 1 and 2. Ministry of Housing, Spatial Planning and Environment (VROM) and Centre of Environmental Science (CML), Den Haag and Leiden, The Netherlands, retrieved from: [www.leidenuniv.nl/cml/ssp/projects/lca2/lca2.html](http://www.leidenuniv.nl/cml/ssp/projects/lca2/lca2.html).

PRÉ Consultants (2012) SimaPro 7.3.3, Amersfoort, NL, retrieved from: [www.esu-services.ch/simapro/](http://www.esu-services.ch/simapro/).

Solomon S., Qin D., Manning M., Alley R. B., Berntsen T., Bindoff N. L., Chen Z., Chidthaisong A., Gregory J. M., Hegerl G. C., Heimann M., Hewitson B., Hoskins B. J., Joos F., Jouzel J., Kattsov V., Lohmann U., Matsuno T., Molina M., Nicholls N., Overpeck J., Raga G., Ramaswamy V., Ren J., Rusticucci M., Somerville R., Stocker T. F., Whetton P., Wood R. A. and Wratt D. (2007) Technical Summary. In: Climate Change 2007: The Physical Science Basis. Contribution of Working Group I to the Fourth Assessment Report of the Intergovernmental Panel on Climate Change (IPCC), Cambridge University Press, Cambridge, United Kingdom and New York, NY, USA.

Stucki M., Büsser S., Itten R., Frischknecht R. and Wallbaum H. (2011) Comparative Life Cycle Assessment of Geosynthetics versus Conventional Construction Material. ESU-services Ltd. commissioned by European Association for Geosynthetic Manufacturers (EAGM), Uster and Zürich, CH.

# Design of inverted T-shaped Cantilever Wall with a Relief Floor

## Conception d'un mur équerre avec dalle de délestage

Ganne P.P., Raucroix X.

Engineering department, BESIX, Gemeenschappenlaan 100, 1200 Brussels, Belgium

**ABSTRACT:** Cantilever walls are widely used as ground retaining structures. The analytical approach of L-shaped and inverted T-shaped cantilever walls results in reliable designs. This paper proposes and discusses an analytical approach for the geotechnical design of inverted T-shaped cantilever walls with relief floor. This approach combines the analytical approaches of inverted T-shaped walls and of relief floors. The resulting analytical approach is verified by numerical simulations of inverted T-shaped cantilever walls with relief floor for 5m till 10m high retaining structures in unsaturated sandy soils, silty soils and alluvial clayey soils. Finally, rules of thumbs for typical dimensions of the inverted T-shaped cantilever wall with relief floor are given, based on experience, analytical calculations and numerical simulations.

**RÉSUMÉ :** Les murs équerres sont communément répandus comme structure de soutènement. D'un point de vue de la conception géotechnique, les méthodes analytiques sont éprouvées. Cet article propose et discute une approche analytique pour la conception géotechnique des murs équerres avec dalle de délestage. Cette approche combine l'approche de dimensionnement analytique des murs équerres avec l'effet d'ombre des dalles de délestage. L'approche analytique proposée est justifiée à l'aide de simulations numériques modélisant des murs équerres avec dalle de délestage reprenant des différences de niveau allant de 5m à 10m et ce, dans des sols non-saturés de nature sableuse, silteuse et alluvio-argileuse. En conclusion, des dimensions typiques de murs équerres avec dalle de délestage sont données, basées sur l'expérience, des calculs analytiques et des simulations numériques.

**KEYWORDS:** inverted T-shaped cantilever wall, relief floor, soil retaining structure, finite element code

### 1 INTRODUCTION

In recent decades, the number of installations of permanent ground retaining structures is drastically increasing. One of the oldest ground retaining structures are the gravity walls. They have a very easy way of realization and are particularly suitable for retained heights of less than 3m. While they can be designed for greater heights, other types of retaining walls such as L-shaped cantilever walls are usually more economical as the height increases.

L-shaped cantilever walls uses the soil upon the heel to stabilize the horizontal soil pressures. One of the disadvantages of the L-shaped cantilever walls is the high ratio between the horizontal loads due to soil pressures and the vertical soil weight, causing a disadvantageous eccentricity of the forces at the base slab. Therefore, the length of the base slab can amount up to 70% (sandy soils) and up to 120% (alluvial clay) of the retaining height. In most projects, the realization of L-shape structure is not possible due to the lack of required space to excavate up to the rear edge of the base slab level with a reasonable slope.

It is usually more economical to design the L-shaped cantilever wall with a toe at its front side: the inverted T-shaped cantilever wall. This increases the moment arm and reduces the disadvantageous eccentricity of the forces in the base slab. The distance between the front of the stem and the back of the heel of the cantilever wall amounts to 50% (sandy soils) or to 60% (alluvial clay) of the retaining height.

In some cases, it is more economical to further reduce the required space between the front wall face and the temporary slope at the back of the structure. In these cases, a relief floor

could be added : the inverted T-shaped cantilever wall with relief floor. In this way, (1) the disadvantageous horizontal soil forces are reduced and (2) the disadvantageous eccentricity of the forces at the base slab could be reduced, generally down to a negligible low value. The distance between the front of the stem and the back of the heel of the cantilever wall amounts only 20% (sandy soils) or to 40% (alluvial clay) of the retaining height.

The construction of the inverted T-shaped cantilever wall with a relief floor itself is in most of the cases of lower economical interest than the inverted T-shaped cantilever wall. Nevertheless, reducing the space between the front of the stem and the heel, increases the available space for the excavation, necessary to reach the level of the base slab. The possible economic benefit may be found in the less expensive temporary excavation method.

The geometry of an inverted T-shaped cantilever wall with a relief floor depends on the conditions of the specific project. Therefore, each realization must be based on thorough geotechnical evaluation of its design, a hydrogeological evaluation, a detailed structural design, an analyses of the construction methodology and a general risk evaluation.

This paper proposes a simplified analytical approach for the geotechnical design of the inverted T-shaped cantilever wall with a relief floor. This simplified analytical approach is checked by numerical simulations for unsaturated sandy soils, silty soils and alluvial clays. Finally, typical dimensions which can be used for predesign estimations are given, based on experience, analytical and numerical calculations.

### 1 ANALYTICAL APPROACH OF A L-SHAPED WALL WITH A RELIEF FLOOR

The envisaged geotechnical structure is an inverted T-shaped cantilever wall with a relief floor. Figure 1 shows a typical section of this construction with a retaining soil height of 8.6m. The foundation level is 0.8m below ground surface, in order to place it under the frost line. In order to study the behavior of this structure, a brief review of the behavior of L-shaped cantilever walls and the influence of a relief floor is given, before the global analytical approach is proposed.

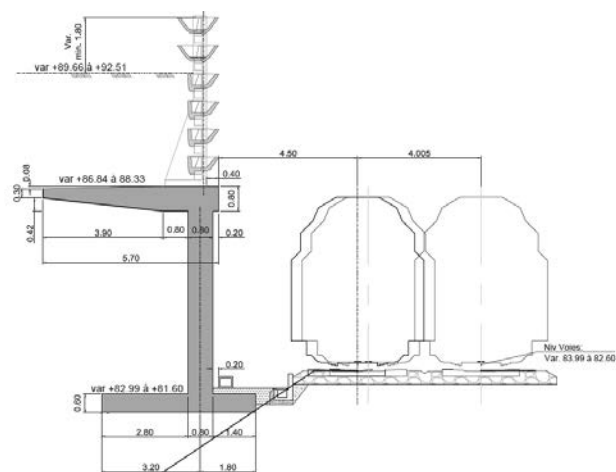


Figure 1. View of the inverted T-shaped cantilever wall with a relief floor of 3.9 m.

#### 1.1 Geotechnical principle of L-shaped cantilever wall

The geotechnical behavior of a L-shaped or an inverted T-shaped cantilever wall is quite complex (Figure 2). When the L-shaped wall fails geotechnically, the failure surfaces E-F, A-D and A-C occur. All these failure surfaces have an inclination of  $\pi/4 - \varphi/2$  from the vertical A-B (further called 'virtual back'). All the soil in the block A-C-D can be described as active Rankine soil. The block A-C-F-E deforms and slides downwards simultaneously. The soil pressure distribution in the block A-C-D is symmetrical about the vertical A-B, on which horizontal soil pressures are present. This theory is confirmed by numerical modeling (e.g. Arnold, 2010).

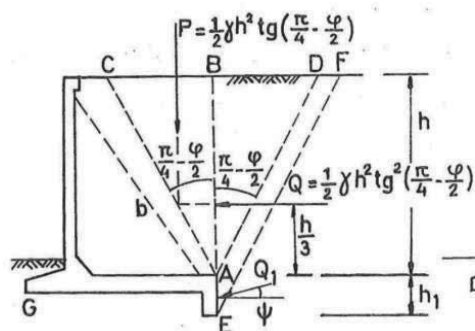


Figure 2. Soil rupture surface (wing shape : C-A and E-F) of a L-shaped cantilever wall (after Vandepitte, 1979).

It is shown that this complex geotechnical behavior of the L-shaped or an inverted T-shaped cantilever wall is equivalent to the following simplified structure (Rouili et al. 2005; Vandepitte 1979). The wall together with the backfill up to a vertical plane above its heel (A-B i.e. 'virtual back') is treated as a monolithic block. Gravity forces, surface loads and horizontal active soil pressures acting at the virtual back may be assumed. This block is checked against sliding, overturning and

bearing capacity failures in the ultimate limit state (GEO 2000; Frank et al. 2004).

This approach is mathematically equivalent to the consideration of the wall together with the backfill up to the plane A-C (Figure 3).

It has to be stressed that though the two above approaches are equivalent for the design of the L-shaped or an inverted T-shaped cantilever wall, the wing-shaped soil rupture surface is the only physical failure mode.

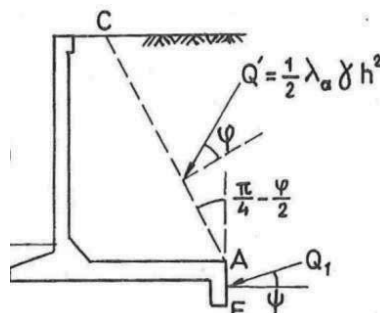


Figure 3. Alternative design rupture surface C-A-E of a L-shaped cantilever wall (after Vandepitte, 1979).

#### 1.2 Geotechnical principle of a relief floor

Geotechnical constructions sometimes uses a relief floor. If the relief floor is rigidly build-in in the geotechnical construction, it implies three stabilizing effects (Figure 4):

1. the backfill in the area A'-A-B engenders a stabilizing moment against overturning,
2. a reduction of the total horizontal soil pressure, increasing the safety to sliding,
3. a reduced eccentricity of the global force at the base, increasing the bearing capacity.

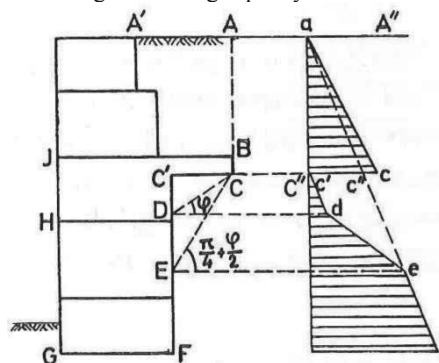


Figure 4. Four zones of soil pressure distribution A-C, C'-D, D-E and E-F. (after Vandepitte, 1979).

Four zones of horizontal soil pressure can be distinguished:

- Zone 1 : A-C is not influenced by the relief floor.
- Zone 2 : C'-D is totally influenced by the relief floor. The horizontal soil pressure is 0 in C'.
- Zone 3 : D-E is partly influenced by the relief floor. The horizontal soil pressures increases linearly from d to e.
- Zone 4 : E-F is not influenced by the relief floor. The horizontal soil pressure correspond to the active soil pressure, taking into account the surface level A'A and the present surface load.

#### 1.3 Simplified analytical approach of an inverted T-shaped cantilever wall with a relief floor.

The proposed simplified analytical approach combines the theory of the L-shaped cantilever wall and the theory of the relief floor. Two virtual backs are defined : upper virtual back A-B and lower virtual back C'-F (Figure 5).

The wall together with the backfill up to the virtual backs (A-B and C'-F) is treated as a monolithic block. Surcharges and horizontal active soil pressures acting on the virtual backs and gravity forces may be taken into account. On the lower virtual back (under the relief floor level), horizontal soil pressures as described in §1.2 are assumed. This monolithic block is checked against sliding, overturning and bearing capacity failures in the ultimate limit state.

It has to be stressed that the above approach is a simplification of the physical behavior. The physical soil rupture surface does not follow the two virtual backs, but corresponds more with wing-shapes.

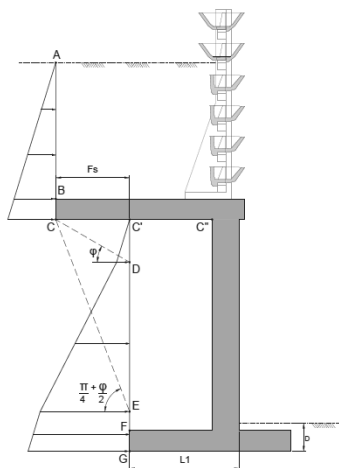


Figure 5. Virtual backs as in the analytical approach of an inverted T-shaped cantilever wall with a relief floor.

## 2 NUMERICAL SIMULATION OF INVERTED T-SHAPED CANTILEVER WALL WITH RELIEF FLOOR

For the numerical validation of the inverted T-shaped cantilever wall with a relief floor, two-dimensional finite element code PLAXIS is used. The Hardening soil model in plane strain is used to model the soil (Brinkgreve et al. 2002).

### 2.1 Simulation of excavation stages

Accomplishment of physical modeling, including simulation for gravity stresses is followed with the calculation program. Simulation of the entire inverted T-shaped cantilever wall with relief floor is carried out in a sequence of construction stages. In each construction stage a sufficient number of calculation steps are used to obtain an equilibrium-state:

- Stage 1 : initial situation (gravity loading, soil with temporary cohesion)
- Stage 2 : excavation till bottom level of the cantilever wall (soil with temporary cohesion)

Table 1. Soil parameters of sandy soil, silty soil and clayey soil, as used in the numerical simulations (the stiffness is expressed at a reference pressure of 100 kPa).

	Sandy soil	Silty soil	Clayey soil
$\gamma_{\text{unsat}}$	17kN/m <sup>3</sup>	18kN/m <sup>3</sup>	17kN/m <sup>3</sup>
$E^{\text{ref}}_{\text{oad}}$	22,30.10 <sup>3</sup> kN/m <sup>2</sup>	6.10 <sup>3</sup> kN/m <sup>2</sup>	4.10 <sup>3</sup> kN/m <sup>2</sup>
$E^{\text{ref}}_{50}$	22,30.10 <sup>3</sup> kN/m <sup>2</sup>	9.10 <sup>3</sup> kN/m <sup>2</sup>	8.10 <sup>3</sup> kN/m <sup>2</sup>
$E^{\text{ref}}_{\text{ur}}$	66,90.10 <sup>3</sup> kN/m <sup>2</sup>	36.10 <sup>3</sup> kN/m <sup>2</sup>	40.10 <sup>3</sup> kN/m <sup>2</sup>
$m$	0,50	0,75	1,00
$c^{\text{temp}}$	4kPa	4kPa	4kPa
$c^{\text{perm}}$	0,1kPa	2kPa	4kPa
$\phi^{\text{p}}$	30°	25°	22°

- Stage 3 : construction and back fill of the cantilever wall till level of relief floor (soil with temporary cohesion)
- Stage 4 : Construction and back fill of the relief floor till final level (final situation, permanent soil parameters, SLS)
- Stage 5 : Determination of factor of safety using c-phi reduction (ULS).

The model simulates 100m (length) by 50m (depth) using 4825 elements (15-noded). The elements around the inverted T-shaped cantilever with relief floor are highly refined. The geotechnical behavior is simulated in unsaturated sandy soils, silty soils and alluvial clayey soils (Table 1).

### 2.2 Numerical simulation of an inverted T-shaped cantilever wall in sandy soil

A typical section of inverted T-shaped cantilever wall is simulated (Figure 1), retaining the soil over 8,6 m of height. The used geometry implies a L1 = 3,6m and a Fs = 1,9m (Figure 5). The buried depth of the base slab D is in this case 0,6m. The used type of in situ soil and the backfill soil are in this example the above described 'Sandy soil'.

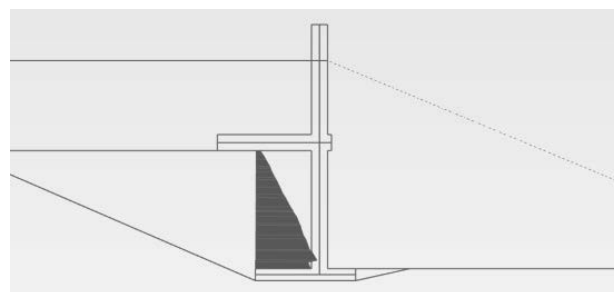


Figure 6. Horizontal effective soil pressures at the lower virtual back up to 61,3kPa at stage 4 (c-phi reduction of 1,20).

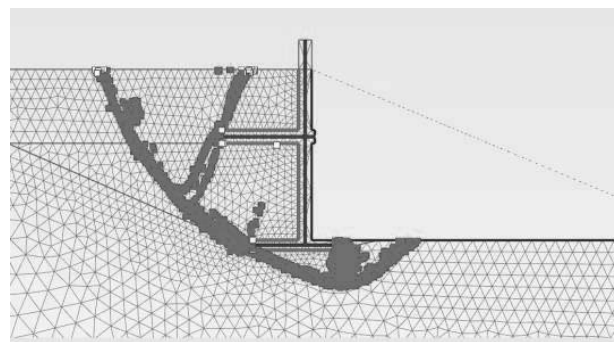


Figure 7. Positions of elements with a Mohr-Coulomb plastic behavior in stage 4 (c-phi reduction of 1,20).

The global geotechnical safety, calculated by the c-phi reduction is 1,20. Figure 7 shows the positions of the elements which are in the plastic zone of the Mohr-Coulomb law. The failure surface underneath the foundation level suggests a failure mode of bearing capacity. As the inverted T-shaped cantilever wall deforms, failure surfaces, inclined at  $\pi/4 - \phi/2$  from the vertical, at the upper and lower virtual backs occur. This corresponds with the described failure 'wings' in § 1.1.

The effective horizontal stresses at the upper virtual back increases from 0kPa up to 29kPa. At the lower virtual back, the effective horizontal stresses increases from 2kPa up to 70kPa. Figure 6 shows that the influence of the relief floor isn't total : the relief floor deforms 3cm downwards, causing a small horizontal effective stress (2kPa) at the top of the lower virtual back. The mean effective vertical stress at the base slab amounts to 228kPa.

### 2.3 Comparison of the numerical simulation with the proposed analytical approach

The inverted T-shaped cantilever wall with a relief floor in § 3.2 is compared with the analytical calculation as described in § 2.3. The geometry and the soil parameters are similar inputs in both approaches.

Remember that the analytical calculations consider active soil pressures. Therefore, the analytical approach assumes a displacement of the structure. In the numerical simulations, this displacement of the structure occurs only in stage 5 ‘c-phi-reduction’. When forces in the analytical calculations are compared to those in the c-phi reduction stage of the numerical simulations, it is important to notify that the actual cohesion  $c'$  and angle of internal friction of the soil  $\phi'$  are reduced.

In the analytical approach, the factor of safety is 3,39 for the overturning failure mode, 1,98 for the sliding and 2,14 for the bearing failure mode. Figure 7 suggests that the failure mode of the numerical model is the bearing capacity (c-phi reduction safety factor = 1,20).

Table 2 shows that the difference of the horizontal forces at the virtual backs in the analytical approach and in the numerical simulations is below 8%. The difference of the vertical force at the foundation amounts to 15%.

Table 2. Comparison of the horizontal and vertical forces at the virtual backs and the foundation in the analytical approach and the numerical simulations.

	Anal. approach	Num. simulation
Horizontal force at upper virtual back	57kN/m <sup>2</sup>	62kN/m <sup>2</sup>
Horizontal force at lower virtual back	230kN/m <sup>2</sup>	211kN/m <sup>2</sup>
Vertical force at foundation	951kN/m <sup>2</sup>	1117kN/m <sup>2</sup>

### 3 PREDESIGN OF L-SHAPED CANTILEVER WITH RELIEF FLOOR

Based on experience, numerical modeling and hand calculations, typical dimensions of reliable inverted T-shaped cantilever walls with a relief floor could be estimated. For sandy soil and a buried depth of 0,8m and 1,3m; the L1 is about 20% to 40% of the retained soil height H; the Fs (as defined in Figure 5) is about 1,5 to 2,5 m (Figure 8).

The level of the relief floor is of less importance for the geotechnical design, as long as the full stress relief is applied on the virtual back of the inverted T-shaped wall. Furthermore, it is good practice to design the level of the relief floor at about the half of the retained soil height.

The type of soil in situ is an important geotechnical parameter, specially for the bearing capacity and sliding failure mode. For inverted T-shaped walls with relief floor, retaining a soil height of 5 m, a buried depth  $D = 1,3m$ ; the length L1 varies from 1m (sandy soil) to 2m (clayey soil) (Figure 9).

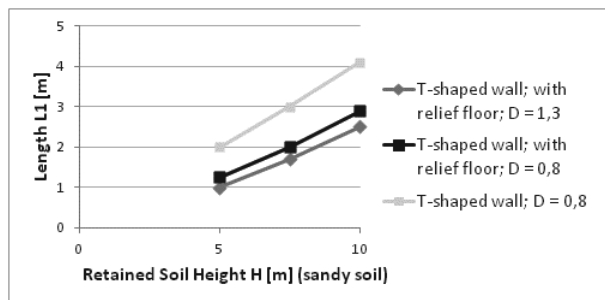


Figure 8. Typical distance between the front of the stem and the back of the heel (L1 [m]) of inverted T-shaped cantilever walls with and without relief floor in sandy soils.

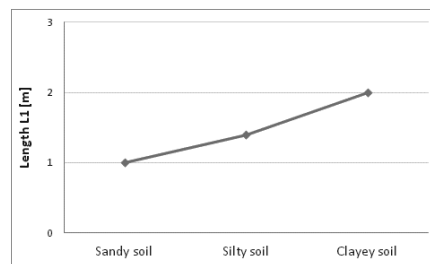


Figure 9. Typical distance between the front of the stem and the back of the heel (L1 [m]) of inverted T-shaped cantilever walls with a relief floor in sandy, silty and clayey soils (retained soil height of 5,0m; buried depth of base slab  $D = 1,3$ ).

### 4 CONCLUSIONS

The geometry of an inverted T-shaped cantilever wall with a relief floor depends on the height of the retaining soil, the surcharges, the depth of the foundation base slab, the geotechnical parameters of the soil in situ and of the backfill, the possible length of the toe and so forth.

In the case of unsaturated sandy soils, silty soils and alluvial clayey soils, an analytical approach is proposed and confirmed by numerical simulations. The analytical approach is based on an upper and a lower vertical virtual back. The wall together with the backfill up to the virtual backs are treated as a monolithic block. At the lower virtual back, the horizontal soil pressures are reduced, due to the presence of the relief floor. This monolithic block is checked against sliding, overturning and bearing capacity failures in the ultimate limit state.

For predesign estimations, a typical inverted T-shaped cantilever wall with a relief floor may be considered:

- the distance between the front of the stem and the back of the heel is about 20% to 40% of the retained soil height,
- the length of the toe is similar to the length of the heel,
- the base slab is buried deeper than the frost line,
- the difference between the length of the relief floor and the length of the heel is about 1,5m to 2,5m,
- the level of the relief floor is about the half of the retained soil height.

Though some general rules of thumbs for the dimensions of an inverted T-shaped cantilever wall with relief floor are given, each realization must be based on thorough geotechnical evaluation of its design, a hydrogeological evaluation, a detailed structural design, an analyses of the construction methodology and a general risk evaluation.

### 5 REFERENCES

Arnold M. 2010. Physical modeling of L-shaped retaining walls. *Physical Modeling in Geotechnics*, Proceedings of the 7<sup>th</sup> International Conference on Physical Modelling in Geotechnics (ICPMG 2010) 425-430 Zurich.

Brinkgreve R., Al-Khoury R., Bakker K., Bonnier P., Brand P., Broere W., Burd H., Sotys G., Vermeer P. and Haag D. 2002. *Plaxis - finite element code for soil and rock analyses. User's manual Ver. 8.0*. A.A. Balkema, Rotterdam.

Frank R., Bauduin C., Driscoll R., Kavvas M., Krebs Ovesen N., Orr T. and Schuppener B. 2004. *Designers' Guide to EN 1997-1 Eurocode 7 : Geotechnical design - General rules*. Thomas Telford, London.

GEO - geotechnical engineering office. 2000. *Guide to retaining wall design*. Hong Kong.

Rouili A., Djerbib Y. and Touahmia M. 2005. Numerical modeling of an L-shaped very stiff concrete retaining wall. *Sciences & Technique* 24 (B) 69-74.

Vandepitte D., 1979. *Berekening van constructies*. Scientia, Genth. (in Dutch).

# An Anchored Retaining Wall in CSM

## Un soutènement ancré en CSM

Gomes Correia A., Tinoco J.  
*C-TAC - University of Minho, Guimarães, Portugal*

Pinto A., Tomásio R.  
*JetSJ Geotecnia, Lisboa, Portugal*

**ABSTRACT:** Cutter soil mixing (CSM) is being recently used in Portugal in several applications. This paper describes a solution in cutter soil mixing reinforced with vertical steel profiles IPE270 for a retaining wall with 66 m long and 13 m high constructed in geological formations of landfill materials, Miocene sandy soils and sandstones, with a phreatic level around 8 m depth. This construction is done nearby commercial buildings. The solution is justified against more classical solutions for anchored retaining walls considering the following aspects: feasibility of CSM in the geological and environment conditions, predict behaviour during and post construction, simplicity of construction process, time of construction, economy and quality assurance. Numerical modelling using a commercial program is carried out, based in geotechnical parameters established at the project level, showing a good agreement of the observed data, in terms of horizontal displacements of the wall and also of the safety levels against bending, shear and compression.

**RÉSUMÉ :** La technique « cutter soil mixing » (CSM) a été récemment utilisée au Portugal dans plusieurs applications. Cet article décrit une solution CSM renforcé avec des profilés verticaux IPE270 pour un mur de soutènement avec 66 m de long et 13 m de haut construit dans des formations géologiques de matériaux de remblai, des formations du Miocène de sols sablonneux et des grès, avec un niveau de nappe phréatique autour de 8 m de profondeur. Cette construction se fait à proximité de bâtiments commerciaux. La solution est justifiée par rapport aux solutions plus classiques des murs de soutènement ancrés tenant compte des aspects suivants: faisabilité du CSM dans une vaste gamme des conditions géologiques et de l'environnement, prévoir le comportement durant et après construction, simplicité du processus de construction, le temps de construction, l'économie et l'assurance-qualité. Une modélisation numérique au moyen d'un programme commercial est effectuée avec l'utilisation des paramètres géotechniques établis au niveau du projet, montrant une bonne concordance des données observées, en termes de déplacements horizontaux de la paroi, autant que des niveaux de sécurité contre la flexion, le cisaillement et la compression.

**KEYWORDS:** soil treatment, deep soil mixing, cutter soil mixing, retaining wall.

### 1 INTRODUCTION

Deep Mixing is an in situ soil treatment method that makes use of a technology in which the soil is mechanically mixed with other materials, mainly binders. The composite material will have improved benefits in terms of resistance, compressibility and permeability (Larsson 2003, Bruce 2000). One of the variants of Deep Mixing is the Cutter Soil Mixing (CSM) technique, which produces panel elements with an accurate geometry, vertically and direction. Additionally, low disturbance is induced on the soil and nearby structures, making their use appropriate in urban areas. Furthermore, this technique has shown a great technical versatility and efficiency, as well as economical advantages, including the optimization of the construction schedule (Ameratunga et al., 2009, Capelo et al. 2012, Marzano et al., 2009, Pinto et al. 2011).

This paper describes an innovative solution involving CSM panels combined with a reinforced concrete wall, for a permanent ground anchored retained structure, with about 66 m long and 13 m high constructed in geological formations of heterogeneous landfill materials, Miocene sandy soils and medium weathered sandstones, with a phreatic level around 8 m depth. This construction is done nearby industrial buildings. Consequently their main purpose was to act as a support system maintaining the stability of the excavation against lateral earth pressures, while controlling the deformation and settlement of the surrounding structures (Porbaha, 2000).

The retaining wall uses soil-cement panels with a minimum depth above the excavation level of 4 m and cross-section of 2.4 x 0.5 m<sup>2</sup>, including 0.20 m of overlapping, were built using the

CSM technology. The panels were reinforced with vertical IPE270 (S275JR) hot rolled steel profiles (Euronorm 19-57), spaced in average 1,1m, in order to resist both to the earth and water pressures, as well as to ensure a better control of deformations. The steel profiles were placed inside the panels, before the cement started the curing process. The wall was braced by four (case study) or three levels of permanent ground anchors, applied at the capping beam as well as at the distribution beams, integrated on the reinforced concrete lining wall (Figure 1). As already stated, the soil-cement panels were lined with a reinforced concrete 0.20m thickness wall, connected to the vertical IPE270 profiles with steel cantilevers, allowing the mobilization of the global resistance of both the steel profiles and the lining reinforced concrete wall, acting a Berlin wall combined with CSM panels. The design criteria, verifying Ultimate Limit State and the Serviceability Limit State, as well as the limitation of the water inflow, were established by the support of 2D FEM analysis using commercial PLAXIS<sup>®</sup> software. In this paper a comparison between the control and monitoring parameters with design parameters is done in order to support the discussion about the reliability of both the solution and the construction method.



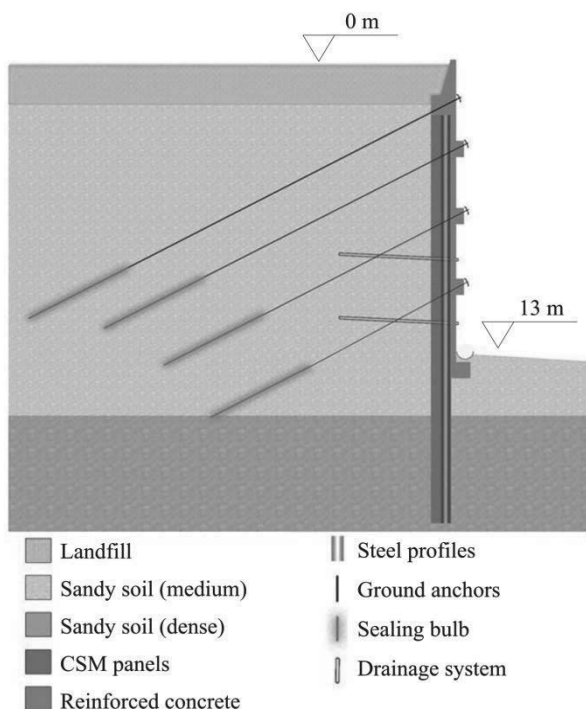


Figure 1. Representative schema of the solution proposed for the retained wall.

## 2 SITE AND SUBSURFACE CONDITIONS

The local geological conditions were heterogeneous. The excavation works intersected, from the surface, heterogeneous landfills and Miocene medium dense to dense sands and medium weathered sandstones. The ground water table was located about 5m above the final excavation level. Taking into account this scenario, an initial solution of Berlin walls was considered. A more detailed information about the site and subsurface conditions can be consulted in Pinto et al (2013).

## 3 CSM WALL MODELLING AND DESIGN CRITERIA

The modelling work was carried out using the commercial PLAXIS<sup>®</sup> software. The *Hardening-Soil* model was adopted for the different soil layers based in the available geotechnical laboratory and field data and taking into account all the excavation phases. Table 1 summarizes the main soil parameters.

Table 1. Main soil properties for modeling.

Constitutive model: Hardening-Soil	Landfill	Sandy soil (medium)	Sandy soil (dense)
$\gamma_t$ (kN/m <sup>3</sup> )	16	17	19
$E_{50}^{ref}$ (kN/m <sup>2</sup> )	10,000	20,000	35,000
$E_{oed}^{ref}$ (kN/m <sup>2</sup> )	10,000	20,000	35,000
$E_{ur}^{ref}$ (kN/m <sup>2</sup> )	30,000	60,000	105,000
Parameter m	0.5	0.5	0.6
$c'$	0	0	0
$\phi'$ (°)	22	33	35

For the soil-cement material produced by the CSM technology, using a cement consumption ratio of about 600kg/m<sup>3</sup>, the Mohr-Coulomb constitutive model was adopted and the parameters summarized in Table 2 were used.

Table 2. Main CSM panels parameters used in the modeling.

Constitutive model: Mohr-Coulomb	CSM panels
$\gamma_t$ (kN/m <sup>3</sup> )	22
$E_{ref}$ (kN/m <sup>2</sup> )	1000000
$\nu$	0.3
$c'$ (kN/m <sup>2</sup> )	600
$\phi'$ (°)	35

With the purpose to approximate the behavior of the structure to the real behavior, the three configurations shown in Figure 2 were considered: a) two half vertical IPE270 spaced in 1.1 m, b) two half vertical IPE270 spaced in 1.1 m plus lining wall and c) two half vertical IPE270 spaced in 1.1 m plus lining wall and CSM panels.

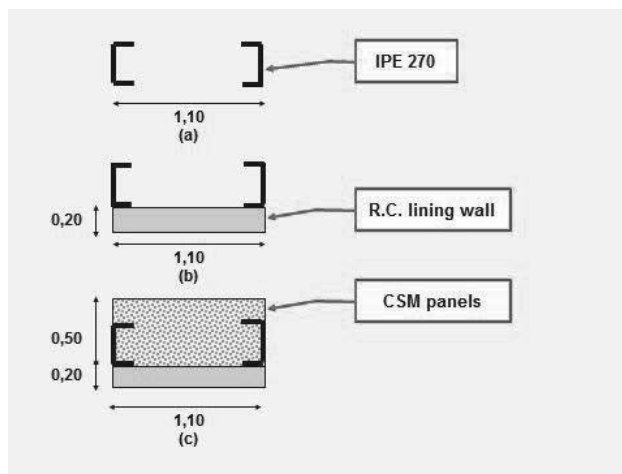


Figure 2. Configurations adopted in the modeling: a) two half vertical IPE270 spaced in 1.1 m, b) two half vertical IPE270 spaced in 1.1 m plus lining wall and c) two half vertical IPE270 spaced in 1.1 m plus lining wall and CSM panels.

For the structural analysis, load combinations for the Ultimate Limit State and for the Serviceability Limit State were defined according to Pereira (2011). The obtained results of 2D FEM analysis (mesh consisted of plane strain, 15-node elements) in terms of efforts and displacements are illustrated in Figure 3 and Figure 4 respectively.

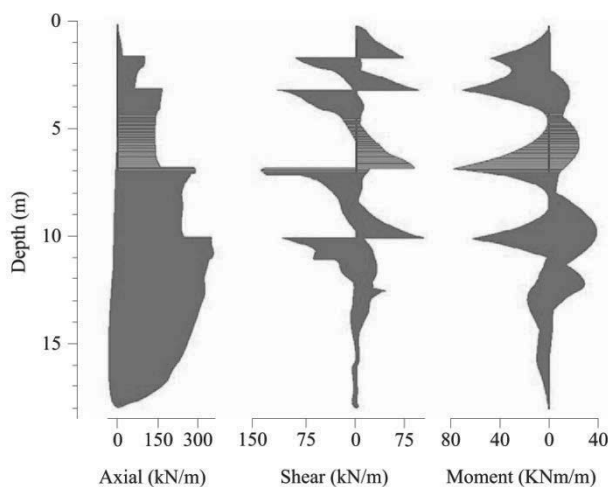


Figure 3. Efforts diagrams.

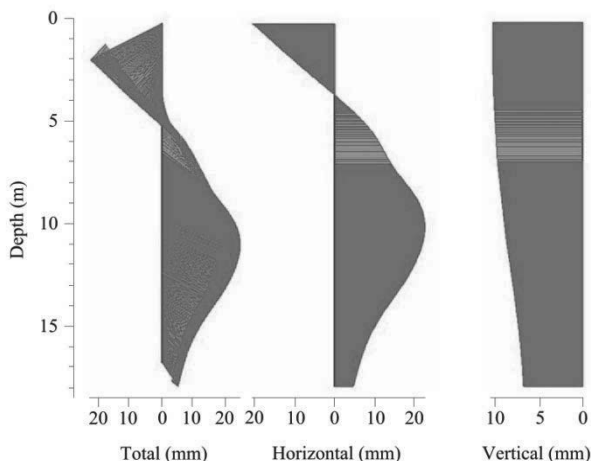


Figure 4. Displacement diagrams.

For the verification of the ultimate limit states was assumed a simplified approach. Thus, it was considered that the strength capacity is the individual combination of the strength resistance of the CSM panels, the IPE270 profiles and the reinforced concrete lining wall.

Summarising the main results obtained are the following:

- $M_{Rd}$  (resistant bending moment) = 167 kNm/m > 1.5  $M_{Ed}$  (maximum acting bending moment) = 119 kNm/m;
- $V_{Rd}$  (resistant shear force) = 251 kN/m > 1.5  $V_{Ed}$  (maximum acting shear force) = 207 kN/m;
- $\sigma_{Rd}$  (resistant compression stress of CSM) = 2 MPa (with FS=2) > 1.5  $\sigma_{Ed}$  (maximum acting normal stress) = 1.1 MPa;
- $S_H$  (maximum horizontal displacement) = 22.7 mm at about 10m depth.

Based in these results the following design criteria were established: take into account the resistance and stiffness of both the steel profiles and the reinforced concrete lining wall. The contribution of the CSM panels was considered in order to protect and confine the steel profiles (exploration phase) and to perform as preliminary ground improvement, allowing the execution of the excavation works without any restriction, in each level.

#### 4 QUALITY CONTROL / QUALITY ASSURANCE

##### 4.1 Control of production parameters

One of the major issues of the CSM technology is the high quality control and quality assurance (QC/QA), allowing on real time the monitoring and correction of important parameters, such as: depth, inclination, speed of mixing tools, pressure (ground and binder slurry) on cutter wheels, rate and total volume of pumped slurry (Figure 5).

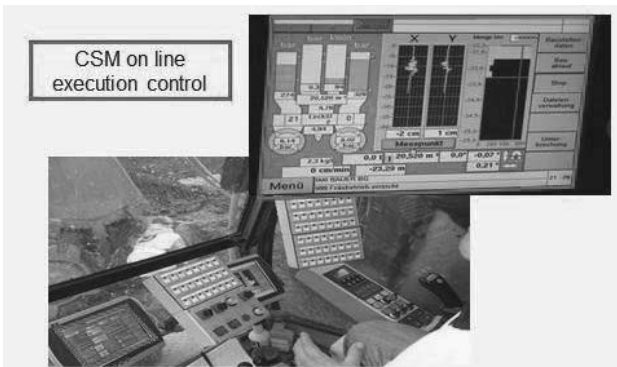


Figure 5. CSM on line execution control.

##### 4.2 Control of mechanical soil-cement properties

The execution control is complemented by a tight quality control and quality assurance, allowing the confirmation of both the main resistance, homogeneity and deformability of the soil-cement (soil-binder) parameters. For this purpose, samples from fresh material (before on suitability tested panels and during construction) and cores from the executed panels (after a certain curing age ranging from 7 to 28 days) were collected in order to access the material homogeneity, as well as to perform laboratorial tests with different ages, mainly unconfined compression strength (UCS) and Modulus ( $E_{s50}$  – secant modulus at 50% of maximum stress of UCS). The results obtained confirm an UCS minimal of 4MPa and a  $E_{s50}$  not lesser than 1GPa, satisfying the design criteria (Figure 6).

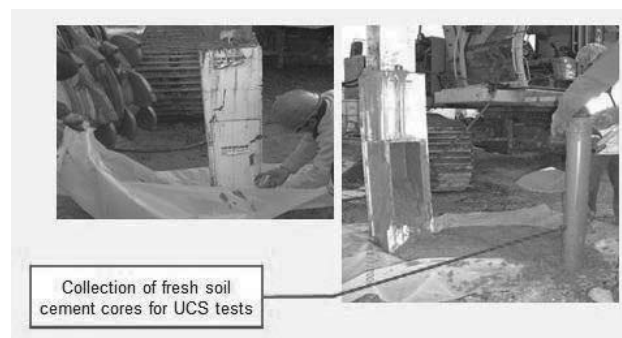


Figure 6. Collection of soil - cement fresh cores.

Taking into account the results of the UCS load tests, mainly on the suitability test panels, the following parameters were adopted for the execution of the CSM panels are presented on Figure 7.

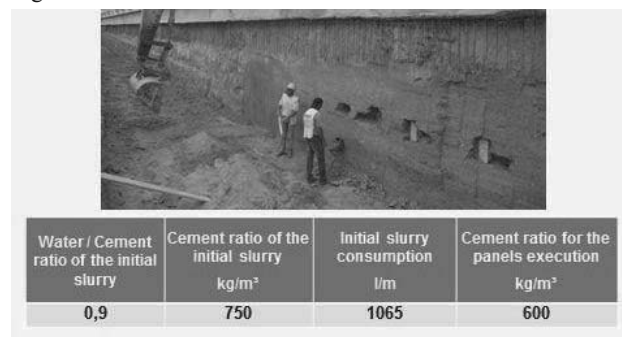


Figure 7. Adopted values for the CSM panels execution parameters.

Regarding the QC/QA of the solution, it should also be pointed out the execution of suitability and reception tests for all the permanent ground anchors, allowing the optimization of the anchors grout body length (Figures 8 and 9).

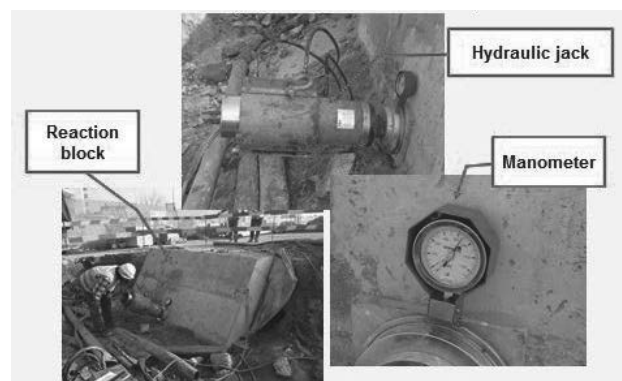


Figure 8. Permanent ground anchor suitability test.

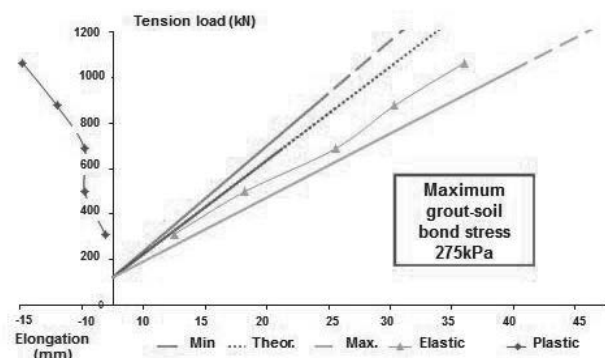


Figure 9. Main results of the ground anchor suitability test.

### 5 CSM WALL PERFORMANCE

The implemented monitoring and observation plan, is shown on Figure 10, including 2 inclinometers and 7 topographic targets.

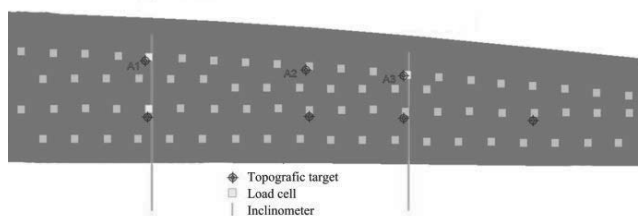


Figure 10. Monitoring and observation plan.

Figure 11 shows that the maximum displacement was observed at 10 m depth, corresponding to 15 mm (inclinometer I8).

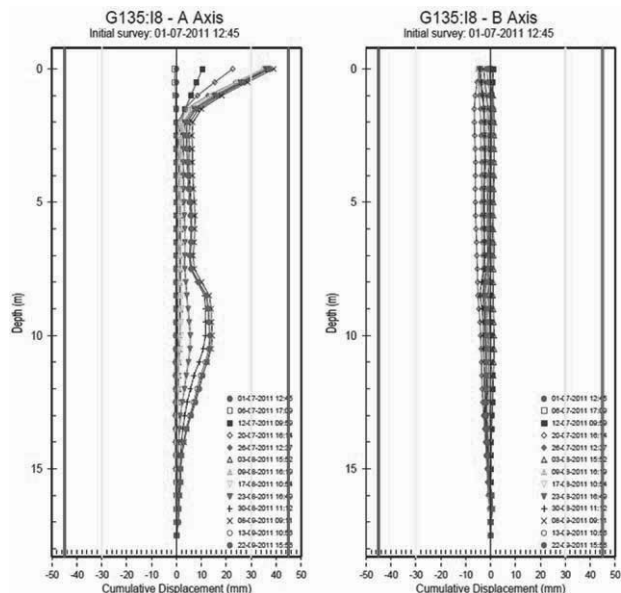


Figure 11. Displacement recorded at the inclinometer I8.

In Figure 12 it is observed that the maximum vertical displacement is 4 mm and that the maximum horizontal displacement is 17 mm.

These results show that the FEM analysis, with the presented input data, has given a good analytical prediction of the observed horizontal displacement, mainly confirming the depth where the maximum horizontal displacement occurred.

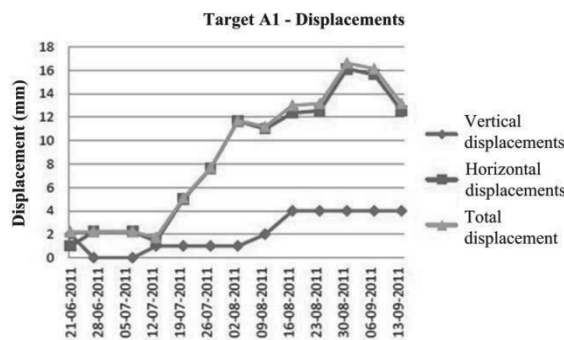


Figure 12. Displacement recorded at the topographic target A1.

### 6 MAIN CONCLUSIONS

The case study presented in this paper shows the good performance, mainly low deformations, of an anchored retaining structure, combining CSM panels with a reinforced concrete lining wall, leading to the optimization of both the construction overall schedule and budget in a complex geotechnical and site conditions. It was also shown that the use of commercial FEM software with appropriated input data gives a reasonable prediction of the main displacements, which are critical for the verification of both the ultimate and serviceability limit states, for all the excavation phases.

### 7 ACKNOWLEDGEMENTS

The authors wish to thank to “Fundação para a Ciência e a Tecnologia” (FCT) for the financial support under the strategic project PEst-OE/ ECI/UI4047/2011. In addition, the authors would like to thank the contribution of Ângelo Pereira.

### 8 REFERENCES

Ameratunga J.; Brown D.; Ramachadran R.; Denny R. (2009). “Ground improvement for a large above ground storage tank using cutter soil mixing columns.” *Proc. 17th International Conference on Soil Mechanics and Geotechnical Engineering*, Alexandria, Egypt, pp. 2280-2283.

Bruce D.A. 2000. An introduction to the deep soil mixing methods as used in geotechnical applications. *Federal Highway Administration*, Georgetown.

Capelo A., Gomes Correia A., Ramos L.R., Pinto A. And Tomásio R. 2012. Modeling and monitoring of an excavation support using CSM. *4th International Conference on Grouting and Deep Mixing*, New Orleans, Louisiana, USA, ASCE, GSP (in printing).

Larsson S. 2003. Mixing processes for ground improvement by deep mixing. *Department of Civil and Environmental Engineering, Royal Institute of Technology in Stockholm*.

Marzano I.P., Osman A.A-M., Grisolia M., Al-Tabbaa A. 2009. Mechanical performance of different stabilised soils for application in stratified ground. *17th International Conference on Soil Mechanics and Geotechnical Engineering*, Alexandria, Egypt, pp. 2276-2279.

Pereira A. 2011. *Application of Cutter Soil Mixing Technology in containment of a retaining wall anchored linear*. MSc dissertation, Guimarães (in Portuguese).

Pinto A., Tomásio R., Pita X., Pereira A. and Peixoto A. 2011. Cutter Soil Mixing Solutions in Portugal on Hard Soils and Weak Rocks. *Proc. 15th European Conference on Soil Mechanics and Geotechnical Engineering*, September 2011, Athens, Greece, Part 2 – 3.3 – Ground Reinforcement, pp. 1037-1042.

Pinto A., Tomásio R., Godinho P., 2013. Innovative Solution of King Post Walls combined with CSM. *Proc. 18th European Conference on Soil Mechanics and Geotechnical Engineering*, Paris, France.

Porbaha, A. (2000). State of the Art in Deep Mixing Technology. Part IV: Design Considerations. *Ground Improvement*, 4(3), 111-125.

# Conception, modélisation et auscultation d'une très grande excavation à Monaco

## Design, modelization and monitoring for a very large excavation in Monaco

Guilloux A., Porquet M.  
Terrasol, Paris France

De Lavernée P., Lyonnet P.  
Soletanche-Bachy, Rueil Malmaison, France

Roman P.  
Vinci Construction, Monaco

**RÉSUMÉ :** la construction d'une grande tour à Monaco, de 160 m de hauteur avec 10 niveaux de sous-sols et sur un terrain en forte pente, conduit à réaliser une excavation de 70 m de profondeur, dans un environnement très urbanisé. La communication présente les principes de conception de cet ouvrage exceptionnel, et notamment les modélisations numériques 3D mises en œuvre pour prédire les déformations de l'ouvrage et des avoisinants. On décrit ensuite le comportement de l'ouvrage pendant l'excavation, suivi selon les principes de la méthode observationnelle, ainsi que quelques adaptations rendues nécessaires au cours des travaux dans certaines parties d'ouvrage dont le comportement s'écartait des prévisions.

**ABSTRACT:** the construction of a high rise building in Monaco, of 160 m high with 10 basements levels and over a steep slope, required a 70 m deep excavation in an urbanized environment. The paper describes the main features of the design for this outstanding geotechnical structure, together with the 3D FE models developed for prediction of deformations of the retaining structures and the existing surrounding buildings. The actual behavior during the excavation, analyzed according to the principle of the observational method, will be described, as well as some changes in the work progress required in some areas due to a behavior somewhat different from the predictions.

**MOTS-CLES :** grande excavation, modélisation, auscultation, méthode observationnelle –

**KEYWORDS:** deep excavation, modelization, monitoring, observational method.

## 1 PRESENTATION

Le projet Odéon à Monaco consiste en la construction d'une tour de 160 m de hauteur sur un versant en forte pente et dans un contexte déjà fortement urbanisé. L'emprise du projet, la topographie, et la construction de 10 niveaux de sous-sol en infrastructures de la tour conduisent à réaliser un ouvrage de soutènement de très grande hauteur, environ 70 m, dont 35 m en parois berlinoises ancrées par tirants actifs et près de 40 m en paroi moulées butonnées par les planchers de sous-sols.

La géologie du site est constituée d'éboulis surmontant des marnes noires de qualité médiocre et des calcaires profonds. La tour elle-même repose sur des barrettes préfondées, permettant la construction selon la méthode « up and down », ancrées en moyenne à 50 m de profondeur sous le niveau du rez de chaussée.

Outre les dimensions tout à fait exceptionnelles de l'excavation, l'enjeu géotechnique majeur consistait à garantir des déplacements des ouvrages avoisinants existants inférieurs à 5 mm, et la méthode observationnelle était imposée pour garantir le succès de l'opération.

La communication présente :

- La conception globale du projet et le dimensionnement des divers éléments de soutènement et fondation ;
- Les modélisations numériques géotechniques 3D qui ont été élaborés à différents stades du projet, intégrant l'ensemble des fondations (parois moulées périmétriques et barrettes, planchers des sous sols) et des soutènements, y compris tirants et pieux des berlinoises, et reproduisant les phases de construction. Ces modèles ont globalement permis de valider les méthodes et phasages de construction ;
- Les performances réellement observées, notamment en termes de déplacements sur les avoisinants, qui ont dans l'ensemble confirmé les ordres de grandeur attendus.

Elle décrit également quelques adaptations du projet qui ont été mises en œuvre dans le cadre de la méthode observationnelle, et qui ont permis de gérer les situations où les déplacements observés sur des bâtiments avoisinants ont dépassés les seuils.

## 2 DESCRIPTION DU PROJET

### 2.1 L'ouvrage et son phasage de réalisation

La tour s'inscrit dans un talus naturel de pente moyenne 25°, qui doit être en conséquence rogné sur un dénivelé de plus de 40 m, entre la cote 110.0 NGM en amont et le niveau de la rue en aval à 67.0 NGM. Elle se compose de 2 parties en forme de pétales ayant respectivement 44 et 48 étages au-dessus d'un parking de 10 niveaux en sous-sol. L'ensemble est fondé sur une paroi moulée périphérique en forme d'auge vue en plan, et sur un réseau de barrettes intérieures. La paroi moulée est prolongée verticalement en superstructure par un voile pour épouser le versant sculpté en amphithéâtre, constituant un socle rigide dont le rôle est capital vis-à-vis de la reprise des efforts liés à la dissymétrie du site.

L'ouverture de la fouille se fait à l'abri de 3 soutènements étagés successifs (Figure 1) :

- Une microberloise de 15 m, avec micropieux  $\phi$  219 ayant une fiche de 8 m et espacés d'environ 1 m ;
- Une berlinoise de 20 m, avec pieux  $\phi$  1000 espacés de 2 m et ancrés d'en moyenne 12 m ;
- Et enfin la paroi moulée de 30 à 40 m de haut renforcée dans certaines zones par des contreforts.

Ces dispositions visent, au fur et à mesure du terrassement, à la constitution de plates-formes de travail de plus en plus larges pour l'utilisation d'un matériel de plus forte capacité permettant la mise en œuvre de soutènements de plus forte inertie.

Ente les cotes 110.0 NGM et 64.0 NGM, les berlinoises et la partie supérieure de la paroi moulée sont ancrées par 18 lignes de tirants de longueur maximum 42 m.

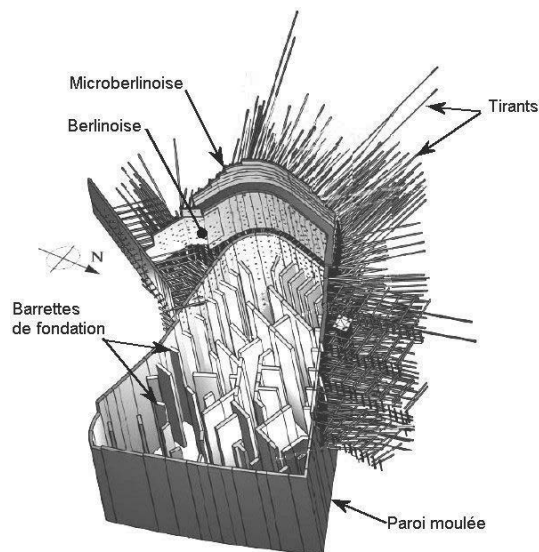


Figure 1 : Vue 3D des soutènements et fondations

A la cote 64.0/67.0 NGM, la dalle de couverture du parking est coulée, après quoi la construction de la tour en up & down peut débuter : il s'agit de construire simultanément la superstructure et l'infrastructure, à raison de trois étages de superstructure pour un niveau d'infrastructure en taube, la paroi moulée et ses contreforts prenant appui sur les dalles de sous-sols coulées à l'avancement et portées par les barrettes de fondations profondées.

## 2.2 Le contexte géotechnique

Géologiquement la structure tectonique régionale est complexe : l'ensemble du versant est constitué d'un système d'écaillés, et au droit du site on rencontre des marnes Cénomaniennes. Ces dernières, qui ont déjà été à l'origine de difficultés lors de la réalisation de grandes excavations à Monaco, constituent l'essentiel des terrains à excaver, avec localement un substratum calcaire, qui remonte à la faveur d'une faille. Notons que la faille du Larvotto se situe légèrement en aval du site.

Le site a fait l'objet d'une importante reconnaissance, avec environ 35 sondages, carottés, destructifs et pressiométriques, sur des profondeurs atteignant couramment 90 m, et jusqu'à 120 m. La Figure 2 montre une coupe transversale, mettant en évidence la couche de colluvions épaisse de 25 m en amont du site, puis les marnes du Cénomaniens, plus ou moins déstructurées, et localement les calcaires profonds.

On notera tout particulièrement la présence de niveaux décomprimés dans les marnes, mis en évidence par leur description sur carottes et par des modules pressiométriques très faibles (< 50 MPa), alors qu'ils sont de l'ordre de 200 à 300 MPa dans les marnes saines. Cette conséquence probable de la tectonique du site a été l'un des enjeux importants du projet de soutènement.

L'hydrogéologie montre une nappe de surface dans les éboulis, suivant la pente à 15-20 m sous le TN et une nappe captive en charge dans les calcaires profonds. Mais les capteurs de pression interstitielle dans les marnes montrent également des valeurs de pression correspondant à la nappe de surface, et ce au moins localement et temporairement : la conception du projet a du également tenir compte de ces fortes charges piézométriques.

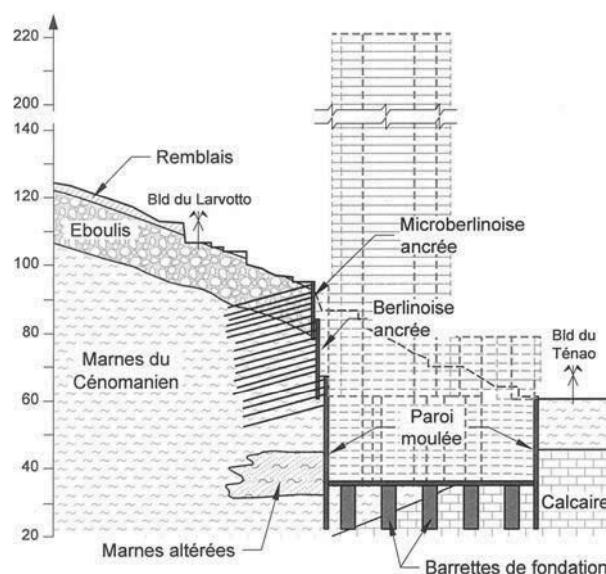


Figure 2 : Profil géologique et projet

## 2.3 La conception des soutènements et fondations

La hauteur importante de la tour, et les actions qui en résultent sur les fondations sous l'effet du vent et du séisme, ont nécessité une étroite liaison entre les études de la structure et des soutènements. En effet, la paroi moulée périphérique fonctionne à la fois comme soutènement des terres et comme fondation de la tour. Les effets de renversement sur la tour, notamment sous séisme, mettent en traction la paroi moulée amont. Par ailleurs, en phase de service, la tour doit être calculée sous l'hypothèse d'une détente des tirants des berlinoises, les massifs de terre s'appuyant directement sur le socle de la superstructure.

Pour ces diverses raisons, les soutènements ont fait l'objet de plusieurs vérifications. En phase d'excavation, ils ont été dimensionnés par la méthode classique des calculs au coefficient de réaction, complétée par des calculs de stabilité générale faisant intervenir la longueur des tirants. L'ensemble a été conduit selon des profils transversaux bidimensionnels, malgré le caractère fortement tridimensionnel du projet, conduisant à une approche a priori sécuritaire.

En phase de service, pour vérifier le comportement de la paroi moulée associée à la tour, un modèle 3D structurel des infrastructures a été élaboré, sur lequel ont été appliquées les poussées issues des calculs de soutènement au coefficient de réaction, et les actions propres à la tour (vent, séisme, charges verticales). Afin de prendre en compte l'effet des phases de terrassement sur les sollicitations finales dans la paroi moulée, il a été également introduit un cas de charge élémentaire représentant le décalage de moment et d'effort tranchant dans la paroi entre un calcul phasé et un calcul non phasé négligeant les terrassements. Le modèle de l'infrastructure ainsi étudiée fournit les cartographies d'armatures à prendre en compte dans le dessin des cages de paroi moulée et conduit à un dimensionnement rigoureux et optimum.

La méthodologie de construction de la tour en up & down permet d'assurer la stabilité générale et de maîtriser au mieux les modifications de contraintes dans le massif. En effet :

- En phase de terrassement, le poids de la tour compense partiellement le poids des terres excavées qui sont stabilisatrices vis-à-vis des cercles de grand glissement ;
- Les tassements se produisent au fur et à mesure de la construction et sont compensés par le soulèvement du fond de fouille.

Enfin, malgré le caractère de roche tendre des terrains, un clouage vertical en fibres de verre a été nécessaire devant la paroi moulée amont, afin d'améliorer la butée mobilisable lors des dernières passes de terrassement où la paroi est soumise à

une poussée approchant les 1000 kPa dans les zones de marnes altérées.

### 3 LES MODÉLISATIONS NUMÉRIQUES

#### 3.1 Modélisation 3D globale sous CESAR 3D

Après un premier modèle géotechnique tridimensionnel réalisé par Coyne et Bellier dans le cadre des études de conception, nous avons conduit, dès le démarrage des études d'exécution, une nouvelle modélisation géotechnique 3D de l'ensemble du projet, intégrant les interfaces géologiques, les avoisinants existants et les nouvelles infrastructures, réalisée avec CESAR 3D v5. Le modèle (Figure 5) comporte 57 phases de calcul reproduisant toutes les étapes des travaux depuis l'excavation des premières plateformes jusqu'à l'application des charges de superstructures sur les barrettes de fondations.

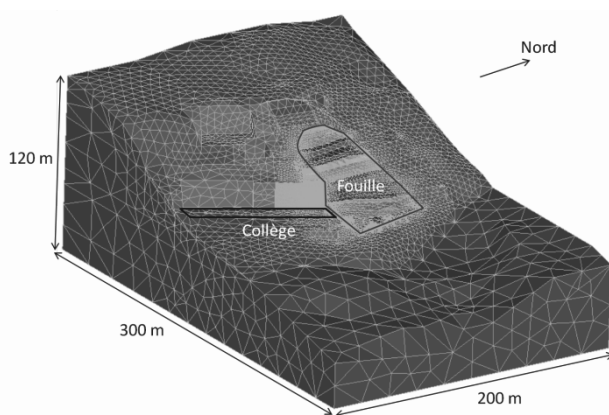


Figure 3 : Vue du modèle 3D général

Les résultats mettent en évidence l'effet de voûte lié à la forme de l'excavation et conduisent à des déplacements des avoisinants de l'ordre de 5 mm en déplacement horizontal, et presque toujours inférieurs à 5 mm en soulèvement. Les déplacements calculés les plus importants sont situés près du collège Charles III.

#### 3.2 Modélisation 3D locale sous Plaxis 3D

Suite à un changement de méthode pour réaliser les soutènements au niveau du collège, un autre calcul centré sur ce bâtiment a été réalisé avec Plaxis 3D. Ce modèle « simplifié » (Figure 4) ne comprend que les structures existantes du collège, la variante de soutènement, et une moitié de l'excavation principale. La stabilité de l'ensemble est assurée par les conditions aux limites, et l'effet de voûte est reproduit par une surcharge à l'arrière du modèle.

Les déplacements calculés restent comparables à ceux obtenus précédemment et montrent que la nouvelle solution de soutènement garantit bien la stabilité de l'ensemble.

#### 3.3 Apport des modélisations

Ces modélisations 3D ont permis la prise en compte des effets 3D tels que l'effet de voûte et la validation de systèmes de soutènement complexes, notamment vis-à-vis des déplacements des structures et des avoisinants. Le comportement fortement 3D de l'ouvrage est bien mis en évidence, avec notamment des déplacements des soutènements de l'ordre de 10 mm au maximum, très inférieurs aux 30 mm évalués par les calculs 2D au modules de réaction.

En outre, une approche de la stabilité générale a pu être conduite sur la base du modèle global, en affectant les paramètres de résistance au cisaillement des terrains de coefficients réducteurs partiels, et en vérifiant l'équilibre numérique du modèle avec ses caractéristiques réduites.

## 4 L'APPLICATION DE LA MÉTHODE OBSERVATIONNELLE

### 4.1 Auscultation mise en œuvre

L'auscultation de l'ouvrage et de ses avoisinants est organisée selon 10 profils verticaux (3 à l'amont côté ouest, 3 côté collège au sud, 2 côté Nord et 2 à l'aval côté Est) tel qu'illustré sur Figure 4. Sur chacun de ces profils, les différents instruments de mesures permettent de recouper les informations.



Figure 4 : Vue en plan du projet et des profils d'auscultation

La mise en place du dispositif d'auscultation de l'ouvrage et de ses avoisinants s'est faite de manière progressive :

- En premier lieu, dès le début des travaux, les avoisinants (villas et immeubles aux alentours, collège Charles III, paroi moulée amont du collège) ont été équipés de cibles topographiques ; des inclinomètres profonds ont été réalisés dans le terrain (jusqu'à 80 m de profondeur) à l'amont et autour de l'emprise de la future fouille, et une dizaine de piézomètres a également été réalisée tout autour de la fouille ;
- Puis les ouvrages ont été équipés au fur et à mesure de la réalisation : mise en place d'inclinomètres noyés dans les micropieux, pieux et paroi moulée, de cibles topographiques, d'extensomètres de forages, de cellules dynamométriques en tête de tirants, ainsi que de jauges de contraintes dans les barrettes et certaines dalles. L'auscultation des avoisinants a également été renforcée tout au long du chantier avec l'ajout de cibles complémentaires et de fissuromètres dans les zones ayant subi des déplacements au cours de travaux.

Pour les profils les plus hauts côté amont, 3 séries d'inclinomètres sont placées en recouvrement relatif sur la microberlinoise, la berlinoise et la paroi-moulée, de façon à reconstituer un profil inclinométrique complet intéressant les divers soutènements. Ils sont également équipés d'environ 7 cellules de charges sur les têtes de tirants, réparties sur les 18 lits.

Les cibles topographiques sont elles aussi disposées le long des profils à raison d'une cible toutes les 2 passes de terrassement soit environ une cible tous les 5 mètres, avec une cible en tête de chaque ouvrage.

Les extensomètres de forage sont pour certains ancrés à une profondeur de 60 m à l'arrière du soutènement, au-delà des tirants les plus longs, avec une ancre tous les 10 m.

Inévitablement un certain nombre d'instruments situés dans le terrain à l'amont du projet a été détruit au moment de la réalisation des tirants de la berlinoise, et a dû être remplacé. C'est notamment le cas des piézomètres, qui ont été remplacés le plus souvent par des capteurs de pression interstitielle.

#### 4.2 Choix des seuils

La limite admissible de déplacements des immeubles mitoyens a été fixée contractuellement à 5 mm, avec un seuil d’alerte à 3 mm.

Vis-à-vis des soutènements eux-mêmes, le contrat spécifiait uniquement des critères de déplacements pour le dimensionnement selon la méthode de calcul au coefficient de réaction (calcul 2D) :

- 30 mm pour les parois non joutées par des immeubles ;
- 15 mm pour les points situés à plus de 10 m des fondations des immeubles ;
- 3 à 10 mm pour les points entre 5 et 10 m de ces fondations ;
- 3 mm pour les points situés à moins de 5 m des fondations.

Il faut souligner que les déplacements calculés par les méthodes aux éléments finis (3D) sont largement inférieurs à ceux obtenus par les méthodes 2D.

### 5 LE COMPORTEMENT EN COURS DE TRAVAUX

#### 5.1 En zone courante

On notera tout d’abord que la précision du théodolite automatique est tout à fait remarquable : avec une mesure toutes les trois heures, la précision obtenue est de l’ordre de +/- 0,5 mm, comme cela apparait sur les courbes de suivi topographique. De même la précision des extensomètres de forage est tout aussi remarquable : +/- 0,1 mm. Seule la précision des inclinomètres est plus aléatoire : il apparait que celle-ci dépend fortement de la qualité du scellement, en relation avec la qualité des terrains trouvés et bien sûr de la hauteur de l’inclinomètre. Un post-traitement de type correction de pied, ou autre, améliore nettement la fiabilité des résultats.

En vue de l’analyse des mesures, le Bureau d’Etudes avait transmis, pour les profils types, les courbes de déplacements calculés phase par phase, pour comparaison avec les mesures inclinométriques.

Les mesures montrent, notamment en zone amont, des déplacements inclinométriques de la paroi moulée de quelques millimètres, nettement plus faibles que ceux calculés avec la méthode au coefficient de réaction en 2D, qui atteignaient 10 à 15 mm dans cette zone (Figure 5).

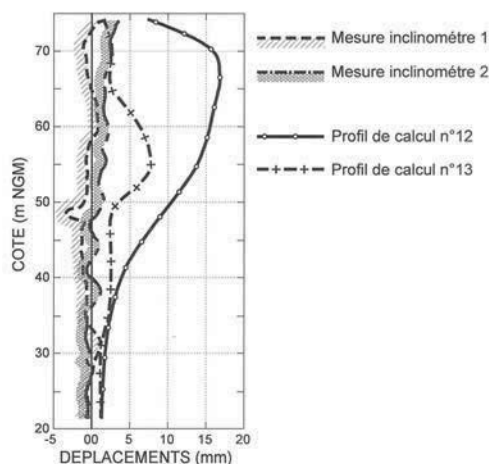


Figure 5 : déplacements calculés et mesurés des parois

Ceci était prévisible, comme le montraient les résultats des calculs numériques 3D, du fait de la géométrie de la fouille beaucoup plus haute que large, qui favorise la formation de voûtes de décharge horizontales, réduisant ainsi la poussée effective sur le soutènement.

D’une façon générale, on peut souligner que les déplacements maximaux  $\delta$  des parois de soutènement restent de l’ordre de 10 mm au maximum, ce qui est remarquable pour un soutènement de hauteur totale  $H = 70$  m :  $\delta/H \approx 0.15/1000^\circ$ .

#### 5.2 Exemple d’écarts par rapport au modèle et adaptations du projet

D’une façon générale, il n’a été constaté que peu d’écarts significatifs entre le comportement observé et les prévisions de déplacements fournies par les calculs.

Les premiers écarts l’ont été dès le début du chantier, lors de la foration des premiers tirants dans les éboulis qui ont conduit à des déplacements centimétriques, dépassant les seuils, sur certains avoisinants. Ces premiers mouvements, attribués à l’effet de la foration et du scellement des tirants dans les éboulis, nous ont conduits à adapter la méthode de forage : abandon des forages à l’air en faveur de méthodes au tricône sous coulis, et forage « Sonic ».

Ainsi, pour la villa Bataglia, située au nord-ouest du projet et qui avait subi des déplacements allant jusqu’à 14 mm, nous avons été conduits à réaliser un soutènement spécifique en aval de la villa : longrines en béton armé de 1 m de haut sur deux niveaux, ancrées par 8 tirants de 15 m de long scellés dans les éboulis, et 3 tirants de 21 m dans les marnes. Ce soutènement a permis d’éviter l’évolution des mouvements jusqu’à la fin des travaux de perforation et d’injection de coulis dans cette zone. A ce jour, soit environ un an et demi après ces travaux, plus aucun déplacement complémentaire n’a été observé.

Un autre écart de comportement structurel a pu être constaté, cette fois-ci sur l’ouvrage en construction : dans la zone située au droit du collège, la paroi moulée se trouvait localement en console maintenue par trois lits de tirants, après un terrassement de 7 m pour le coulage de la dalle RDC. Les déplacements mesurés en tête de la paroi moulée ont atteint 13 mm, supérieurs aux déplacements calculés. Le bureau d’études a alors lancé une rétro-analyse, qui a montré que ces mouvements pouvaient être attribués à une « surcharge » résultant de l’accumulation d’eau derrière la paroi, en relation avec les venues d’eau rencontrées lors de la foration de certains tirants.

Nous avons donc réalisé des drains complémentaires et trois tirants d’ancrages supplémentaires. Lors de la foration des drains complémentaires, il a été constaté un fort débit pendant les premiers jours et une atténuation par la suite. Ce dispositif a permis de stopper les déplacements, en attendant le butonnage par la réalisation des planchers correspondants.

### 6 CONCLUSION

Cet ouvrage, exceptionnel par sa hauteur (70 m de soutènement) et par son environnement imposant des contraintes très strictes de déplacements, a pu être mené à bien grâce à une conception d’origine adaptée, notamment par sa géométrie en voûte et par la méthode de construction en « Top & Down », et par des études alliant des approches traditionnelles négligeant tout effet tridimensionnel, et des modélisations numériques 3D permettant d’évaluer les effets bénéfiques de cette géométrie en reproduisant tous les éléments de soutènement et d’infrastructure et le phasage détaillé de l’opération.

Mais tout autant que la conception, c’est le suivi rigoureux du chantier, conduit selon les principes de la méthode observationnelle, qui a permis d’atteindre les performances attendues (déplacement horizontal en tête de l’ordre de  $0.15/1000^\circ$  de la hauteur), et de traiter à temps les rares, mais inévitables, anomalies de comportement local.

### 7 REMERCIEMENTS

Les auteurs remercient : le Maître d’Ouvrage : Groupe Marzocco, la Maîtrise d’œuvre générale : Cabinet d’Architecte GIRALDI, le Bureau d’Etudes Structure : Coyne et Bellier, le Bureau de contrôle : SOCOTEC, et le Bureau d’Etudes Géotechnique : E&G.

# A Case Study of 3D FE Analysis of a Deep Excavation Adjacent to a Tunnel Construction

Une étude de cas d'une simulation tridimensionnelle d'analyse par éléments finis d'une excavation profonde adjacente à une construction d'un tunnel

Guler E.

*Bosphorus University, Istanbul, Turkey*

Osmanoglu U., Koç M.

*ELC Group Inc. (Royal HaskoningDHV Turkey), Istanbul, Turkey*

**ABSTRACT:** This paper describes the 3D geotechnical FE analysis and design of a deep excavation bracing system. The location is situated in a very dense business area in Istanbul. The maximum height of the excavation is ~23 m to accommodate 7 basement floors. The layout has a non-uniform shape, surrounded with existing high rise structures with multi-basement floors, and an underpass connection to E-5 Motorway. In addition to these, the most outstanding characteristic of this design is the pedestrian tunnel and the shaft that is very close to the excavation pit. Both of these underground structures were being constructed throughout the same construction period as the deep excavation. At the non-anchoring zones adjacent to the tunnel and shaft, steel struts have been used. As a compound engineering service, soil investigation – design – site supervision – geotechnical instrumentation works was carried out. Therefore a comprehensive data for comparison between design results and in-situ performance could be gathered. This paper focuses on the details of the sophisticated 3D FE analysis and the comparison with the in-situ performance of the shoring system.

**RÉSUMÉ :** Ce document décrit l'analyse géotechnique 3D par éléments finis et la conception d'un système de contreventement utilisé dans l'excavation profonde. L'emplacement est situé dans un quartier très dense à Istanbul. La hauteur maximale de l'excavation est de 23 m pour 7 sous-sols. Le site a une forme non uniforme, entouré de structures existantes de grande hauteur avec multi-sous-sols, une connexion souterraine de l'autoroute E-5. En plus de cela, la caractéristique la plus remarquable de cette conception est le tunnel pour piétons et l'arbre qui est très proche de l'excavation. Ces deux structures souterraines ont été construites pendant la même période que la construction de l'excavation profonde. Au niveau des zones de non-ancrage adjacentes au tunnel et à l'arbre, des entretoises en acier sont utilisées. En tant que service d'ingénierie l'étude du sol, - la conception - la supervision de chantier - les travaux en instrumentation géotechnique ont été réalisées. Par conséquent un ensemble de données complètes pour la comparaison entre les résultats de la conception et de la performance in-situ aurait pu être recueillie. Ce document se concentre sur les détails d'une simulation 3D sophistiquée d'Analyse par éléments finis et la comparaison des performances in-situ du système d'étaie.

**KEYWORDS:** 3D FE Analysis, Deep Excavation, Case Study, Excavation-Tunnel-Shaft interaction.

## 1 INTRODUCTION

The deep excavation retaining system project is located at the European side of Istanbul. The plan view of the site is presented in Figure 1. The depth of the excavation is 23 m. The ongoing construction of a pedestrian tunnel and entrance shaft adjacent to this excavation makes the design of the retaining system complicated. Interaction with this deep excavation work was not considered in the design of the tunnel and shaft. Hence, the shoring design for the deep excavation had to consider the very close tunnel and shaft which were still being constructed and standing with their temporary support systems during the excavation works. Since the interaction between the deep excavation and the simultaneously constructed shaft and tunnel cannot be modeled with only a 2D analysis (plain-strain model), a 3D Geotechnical FE analysis (especially for the shaft location) had to be conducted.

The pedestrian tunnel has a span of 7 m at a distance of 7 m to the piles of the shoring system. The shaft has a diameter of 6 m at 2.5 m distance to the piles of the shoring system. The tunnel and shaft's temporary support system was composing of ~20 cm shotcrete facing and rock bolts. In the tunnel 4 m long rock bolts were used only at the top heading. In the shaft 2 m long radial rock bolts were used. The temporary excavation system of the building is designed with micro piles, pre-stressed anchors and steel struts at non-anchoring zones due to tunnel and shaft. The elevation corresponds roughly to the foundation level of the excavation pit.

The software used in this project were TNO DIANA for 3D modeling and Plaxis V.11 for 2D modeling (for the analysis at the tunnel side).

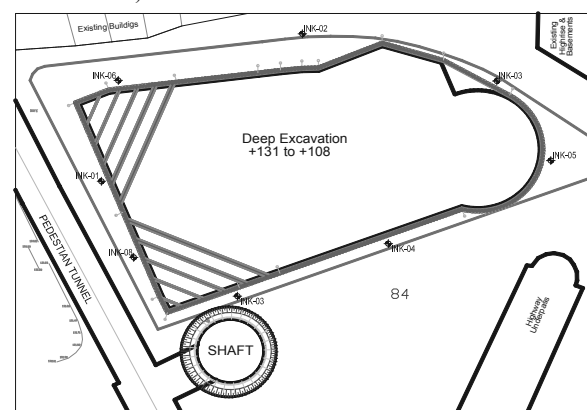


Figure 1. Site layout with surrounding structures

## 2 DESIGN PHASE

The design works were carried out based on the geological & geotechnical data obtained from the site investigations. Surcharge loads were considered wherever necessary.



### 2.1 Geological & Geotechnical Conditions

The geology of the site mainly consists of Carboniferous aged Trace Formation’s intercalation of sandstone – siltstone layers. The bedrock is overlain by weathered particles of the Trace Formation in clay matrix with thicknesses varying between 3 ~ 4 m. Finally the site is covered with artificial fill with a thickness of ~2 m. The bedrock is divided in to two fictitious layers at a depth of 14 m according to the increasing rock mass quality. Except leakage water from the discontinuities and fractures, no groundwater table was encountered at the site. The proposed stratigraphy and the engineering parameters used in modeling are presented in Table 1.

Table 1. Proposed stratigraphy and engineering parameters

Layer	Fill	Residual Zone	Bedrock-1	Bedrock-2
Thickness (m)	2	5	7	-
c (kPa)	0	1	5	10
$\phi$ (°)	25	30	35	38
$\gamma$ (kN/m <sup>3</sup> )	18	20	22.5	23
E (kN/m <sup>2</sup> )	5,000	25,000	100,000	150,000
$\nu$	0.35	0.30	0.28	0.25

### 2.2 Design Philosophy

Since the construction of the pedestrian tunnel and shaft were ongoing at the time, the initiation of the phased construction model had to be started with simulation of these structures. The design work was aiming to find out the effects of the deep excavation on the tunnel and shaft structures. In order to detect the magnitude (after initial phase) and variations of the section forces together with the deformations of the tunnel and shafts’ temporary support system throughout the deep excavation, dewatering and basement construction stages, the shotcrete facing was modeled with shell elements.

The deep excavation support system was designed contiguous (without a gap) to the basement walls that will be constructed after the completion of the deep excavation. This is mainly due to the clients’ demand for minimum space loss. This philosophy turned in to an advantage for the adjacent tunnel and shaft, since every constructed basement floor constituted a rigid support to the shoring system, hence the effects of dewatering stages could be minimized on tunnel and shaft.

Both the 2D and 3D finite elements models were constituted in compliance with in-situ construction steps (tunnel & shaft construction, staged deep excavation procedure, staged basement construction and dewatering of the steel struts).

The steel struts, piles of shoring system, shotcrete facing and the rockbolts were modeled as linear elastic materials. The properties of these linear elastic materials are given in Table 2. All struts used were tubular steel with a thickness of 10.3 mm.

Table 2. Elastic and rigidity variables

Material	E (kN/m <sup>2</sup> )	D Spacing (m)	d Diameter	$\nu$
Micropiles	2.5E7	0.60	30 cm	0.20
Shotcrete	2.0E7	cont.	20 cm	0.20
Steel struts	2.1E8	3	16” ~ 32”	0.28
Rockbolts	1E7	1.5	51 mm	0.28

### 2.3 2D FE Analysis

General approach to model a deep excavation in geotechnical engineering is to execute Limit Equilibrium stability analysis to get the satisfactory factor of safety and a FEA to check the

compliance of deformation criteria. Since 2D FEA is a fast and effective design tool, the same methodology was used for the subjected project.

The 2D FE model at the adjacent tunnel location is given in Figure 2.

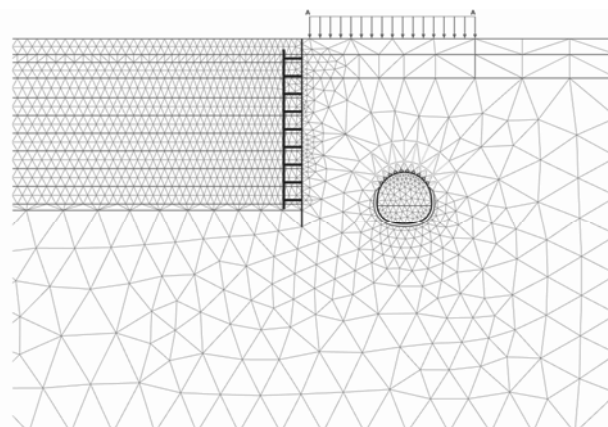


Figure 2. 2D FE model from tunnel section

Deformation analyses were carried out with commercial software package of PLAXIS. Mohr Coulomb material model was used for the design based on the expertise of deep excavation designs and their feedback from in-situ performance, in similar geological circumstances which is very widespread in Istanbul.

### 2.4 3D FE Analysis

A 3D FE Analysis had to be conducted in order to simulate the interaction between the deep excavation works and tunnel&shaft. The main goal of the 3D modeling study was to establish an appropriate excavation system and sequence, hence only the related part of the system was focused in the analysis. By this means, the processing time in such a complex model could be reduced to a reasonable level. As it is in 2D FEA, also Mohr-Coulomb material model was used in the 3D FEA. All engineering parameters were kept same.

The 3D FE model is given in Figure 3.

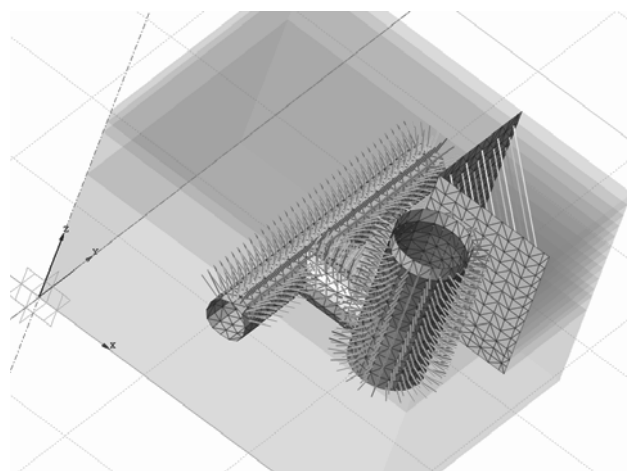


Figure 3. 3D FE model from with nearby tunnel and shaft

## 3 RESULTS FROM THE ANALYSES

The main purpose of this modeling study was to find out the interaction between the tunnel&shaft structures with (and during) the deep excavation works. Therefore, the specific values (bending moments, shear forces, normal forces, and

displacements) are presented in this paper (both from 2D FEA and 3D FEA) in Table 3. The given results for the tunnel and shaft structures are values prior to excavation and final values after completion of deep excavation work.

Table 3. Results of FEA

Result	2D FEA	3D FEA
Deformation of shoring (mm)	7.8	4.2
Deformation of Tunnel (mm)	9 / 3	2.0
Deformation of Shaft (mm)	NA	3.2
Bnd.Moment on Shoring (kNm/m)	97.3	31
Bnd.Moment on Tunnel (kNm/m)	9 / 16.4	8.4 / 8.7
Bnd.Moment on Shaft (kNm/m)	NA	13.9 / 16.1
Shear Force on Shoring (kN/m)	132.4	83
Shear Force on Tunnel (kN/m)	20.2 / 22.5	26.8 / 25.3
Shear Force on Shaft (kN/m)	NA	20.0 / 19.6
Normal Force on Shoring (kN/m)	416.8	366
Normal Force on Tunnel (kN/m)	470.7 / 633.4	545 / 532
Normal Force on Shaft (kN/m)	NA	800 / 666

The result for total deformation from the 3D FEA is presented in Figure 4. The result for total deformation from the 2D FEA is presented in Figure 5.

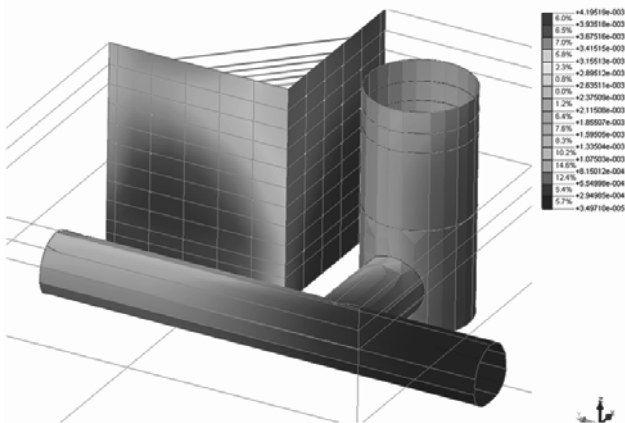


Figure 4. Total displacement from 3D FEA (max. 4.2 mm)

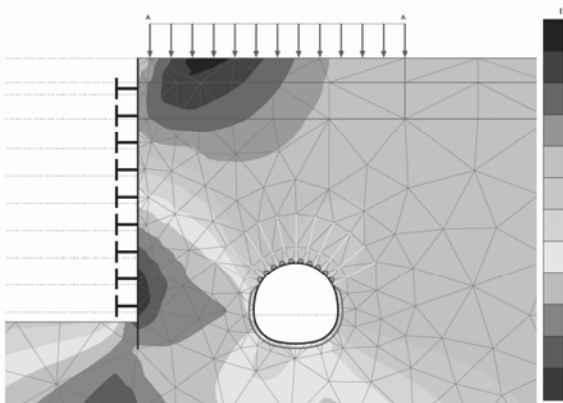


Figure 5. Total displacement from 2D FEA (max. 7.8 mm)

The result for bending moments (on all shell elements) is presented in Figure 6.

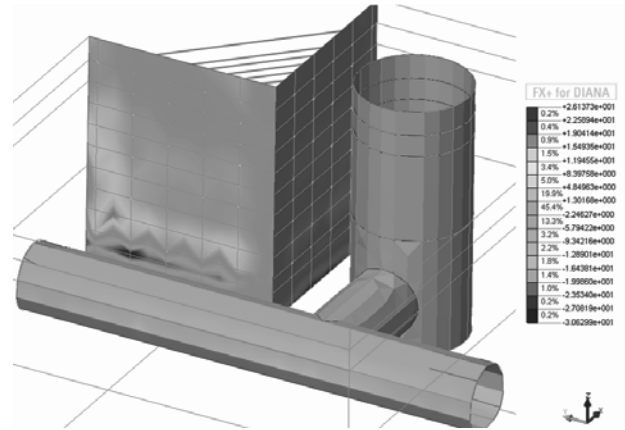


Figure 6. Bending moments from 3D FEA (max. 31 kNm/m shoring, max. 8.7 kNm/m tunnel, max. 16.1 kNm/m shaft).

In addition to deformations and section forces, the axial forces on the steel struts are also calculated and compared with both 2D and 3D FEA. The values are presented (as the envelope values for all construction and demounting stages) in Table 4.

Table 4. Results of Axial Forces in struts

Result	2D FEA	3D FEA
Axial Forces (kN)	263 kN/m	627-765 kN*

\*The assumed length of struts in 2D is 20 m hence the results of 17-23 m struts in 3D model are given. The spacing of the struts in 2D model is 4.0 m, so that the value of 263 kN/m (perpendicular to the surface) shall be multiplied by 3 in order to get the axial perpendicular force of an individual strut.

The results for steel strut axial forces from 3D FEA are presented in Figure 7.

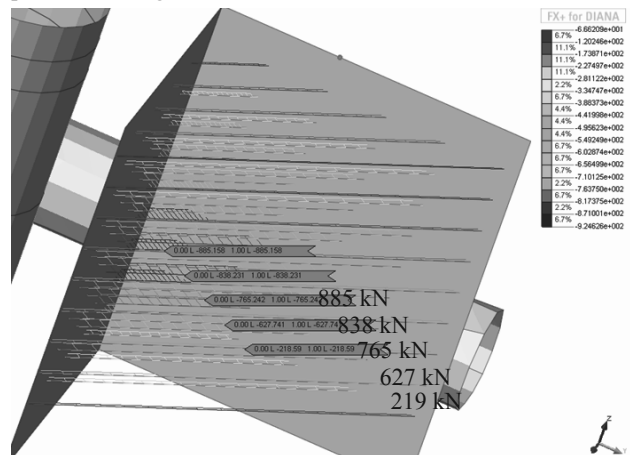


Figure 7. Total strut forces from 3D FEA (max. 885 kN)

#### 4 CONSTRUCTION AND MONITORING PHASE

During construction period, a geotechnical instrumentation program, consisting of inclinometers, optic survey points (for deformation monitoring) and strain-gauges (for axial force and dependently stresses on steel struts), has been carried out. This monitoring program gave reliable data and so it was possible to verify the design results with in-situ performance that has been gathered.

The maximum deformation on the inclinometer at shaft location (INK-07) was measured as ~7 mm. The maximum deformation values received from optical surveys are also ~7 mm at shaft location and ~8 mm at the tunnel location. Inclinometer and optic survey results are presented in Figure 8.



# Suction Caisson Installation in Shallow Water: Model Tests and Prediction

## Installation de caissons à succion en eau peu profonde: essais et prédiction

Guo W.

*School of Civil & Environmental Engineering, Nanyang Technological University, Singapore*

Chu J.

*Department Civil, Construction & Environmental Engineering, Iowa State University, USA*

**ABSTRACT:** Suction caissons have been used as foundations to support mainly offshore structures such as offshore oil rigs in deep water where a large suction pressure can be generated. Studies have been made recently to use this method for near shore foundations in shallow water where the suction that can be applied is much smaller. In this paper, a study on the installation of suction caissons in clay in shallow water using large scale model tests is presented. The model test setup and test results are discussed. The effects of soil plug and side friction are evaluated. An analytical method proposed by Houlsby and Byrne is adopted to predict the penetration versus time relationship. The analytical solutions agree well with the model test results.

**RÉSUMÉ:** Les caissons à succion ont été utilisés principalement pour les fondations de structures offshore en eau profonde permettant de générer de fortes pressions de succion. Cet article présente une étude sur une installation de caisson dans de l'argile à faible profondeur en utilisant un modèle à grande échelle. Les résistances d'arrachement et frottements latéraux sont évalués. La méthode analytique proposée par Houlsby et Byrne est adoptée pour prédire la relation pénétration-temps et donne de bons résultats

**KEYWORDS:** Caisson; Clay; Model Test.

## 1 INTRODUCTION

A research project to use super-size cylindrical structures to form underwater space and at the same time create land on top is being carried out in Singapore. As the seabed soil is mainly soft clay, suction caissons were considered on possible form of foundations to support part of the reclaimed land for buildings or other types of structures to be built on top of it, the foundation types for the offshore structures have to be developed using innovative solutions. The most difficult design condition is when the seabed soil is soft. It would be too costly to treat the soft soil offshore. One innovative solution is to use suction caissons.

Normally suction caissons are large, hollow, cylindrical steel or concrete structures in form of upturned bucket shape, and are penetrated into the seafloor bottom sediments by self-weight and suction pressure. The principle of the suction caisson technique is to apply suction inside a sealed cylindrical caisson to create a downward net force to sink the caisson into the seabed soil. After the suction is removed, the foundation is constructed without treating the soft soil. The suction caisson have been successfully employed in recent years in many projects including mooring anchors (Andersen and Jostad, 1999; Andresen et al., 2011; Randolph et al., 2011; Wang et al., 1975), beak water or sea walls (Chu et al., 2012), offshore platforms (Zhang et al., 2007; Zhang and Ding, 2011) and foundation for wind turbine in deep waters (Byrne et al., 2002; Gavin et al., 2011; Houlsby et al., 2005c).

For caissons used in deep water, the hydrostatic water pressure as provided by the water depth can contribute to suction pressure to compress the caisson into seabed. However, in relatively shallow water, there may not be sufficient suction to allow the caisson to penetrate to the required depth. Another factor affecting the penetration of a suction caisson is the soil plug formed inside the caisson. When a caisson is penetrated into clay, soil will go inside the open ended hollow caisson and form soil plug. The soil plug resists the penetration of the caisson. For this purpose and for the development of suitable design methods, model tests and numerical studies were carried out.

Analytical methods for analyzing the installation process of suction caisson have also been proposed (Andersen et al., 2005;

Chen et al., 2009; Houlsby and Byrne, 2005a, 2005b; House and Randolph, 2001; House et al., 1999; Tran and Randolph, 2008). In the method by Houlsby and Byrne (2005a, 2005b), a constant penetration velocity was assumed. The driving forces and soil resistance were also assumed to be balanced during the whole installation process. This method was adopted to calculate the amount of penetration of suction caisson subjected to a constant driving force. The solution of this method was compared with those from the model tests and good agreement was achieved. Some of the key design parameters were also evaluated based on the model test results.

## 2 MODEL TESTS

### 2.1 Soil Preparation

The soil used for the model tests was consolidated from kaolin slurry. Factory made kaolin powder was used because of its high coefficient of consolidation, low compressibility and commercial availability. The kaolin used was supplied by Kaolin Malaysia Sdn. Bhd. It has a specific gravity of 2.61, a liquid limit of 61% and a plastic limit of 38%.

The kaolin powder was mixed with tap water into a slurry form with water content of 81.3%. After mixing, the desired slurry was transferred to the consolidation tank as shown in Figure 1. Then the top cap and piston were mounted onto the cylindrical tank. A compressed air pressure of 60kPa was applied on top of the piston to consolidate the kaolin slurry for about 10 days. The friction between the piston and the tank wall was 17.35 kN measured by a calibration test before the test. Therefore, the effective consolidation pressure was 37.9 kPa only.

The consolidated water was allowed to drain freely through a drainage valve at the bottom of base plate. In order to consolidate the kaolin slurry faster, a filter layer were designed on the bottom of the tank including two layers of geotextile, fine sand and gravel. The movement of piston was monitored by a laser sensor (Keyence®IL-600). After the consolidation was completed, the air pressure was reduced to zero and the top cap was removed to allow soil samples to be taken for undrained shear strength and water content tests. The water content of the tested soil was 42.7%. The average undrained shear strength

( $S_u$ ) was 13 kPa as measured by lab shear vane method along the tank depth.

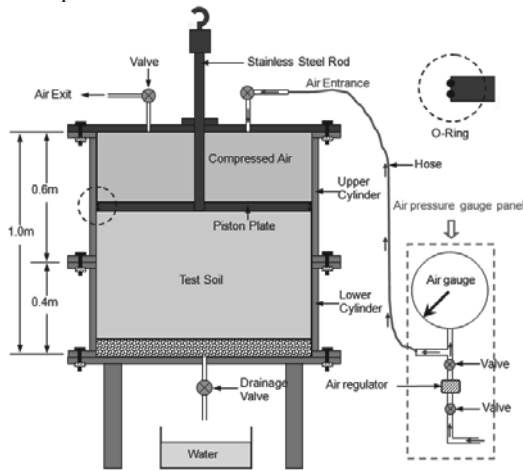


Figure 1 Consolidation procedure of kaolin

### 2.2 Caisson Installation

The caisson was made by an inner steel skirt and covered by a layer of concrete with its total height of 400mm, diameter of 205mm and wall thickness of 22.5mm. The Caisson was assembled with a designed piston which made it possible to monitor the process of soil plug during installation tests. The piston consisted of a ‘Teflon’ plate and a steel rod. The plate was 25 mm thick and 150 mm in diameter with steel rod mounted in the middle. A crew with a height of 20 mm was used to strengthen the connection of the rod and the plate. Thus the clear internal skirt length of the caisson reduced from 400mm to 335 mm. The total weight of caisson and piston was 27.2kg.

The vacuum loading system was composed by a vacuum pump (EVISA E25), a vacuum gauge, two bowl vacuum filters, a vacuum tank, and a hose, as illustrate in Figure 2. Note that during suction installation tests, one more absolute pressure transducer was mounted in the caisson cavity to test the vacuum pressure.

The miniature pore water pressure transducers (PPTs) were used in this model test to measure the pore water pressure changes. Such a miniature size was necessary to minimize the influence of the measuring device to the overall soil behavior during model test. Before a model test, all PPTs were calibrated by using water pressure generated in a triaxial cell. The preinstalled positions of the PPTs on the top cap are shown in Figure 2.

The displacement of the piston in the consolidation tank or that of the suction caisson during the model test was measured by laser sensor (KEYENCE IL series) which had an effective measurement range from 20cm to 1.0m. The displacement of piston rod in caisson was also measure by another laser sensor by mounting an aluminum plate on to the rod. The third laser sensor was mounted on the frame to measure the displacement of suction caisson. Two other laser sensors were used to measure the soil movement on caisson sides as shown in Figure 2. This contact-free displacement measuring method offered both reliability and convenience.

### 2.3 Model Test Results

The model test results of caisson penetrated into the soil bed assisted by vacuum pressure was discussed in this section. Since the self-weight was not able to provide enough penetration force for caisson insertion, the caisson was manually penetrated into soil in a short distance to ensure that the applied suction would not leakage. The applied vacuum pressures in Model Test No. 1 and No. 2 during the suction installation are shown in Figure 3. It can be seen that the vacuum pressure increased very slowly

till to the largest magnitude of -80kPa. The displacements of the caisson and soil plug are shown in Figure 4 and Figure 5, respectively. It can be seen that the soil plug was moving upward throughout the installation procedure. At the beginning, the soil plugs increased nearly linearly with the time. At the time of 81s for test No. 1 and 96s for test No. 2, there was a sudden jump in the displacement. This happened because the soil plug was broken suddenly. During this period, the caisson had no penetration.

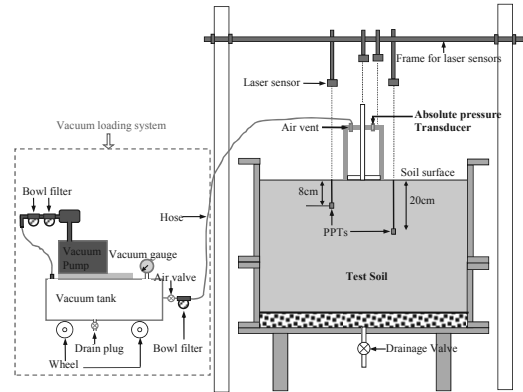


Figure 2 Installation of suction caisson

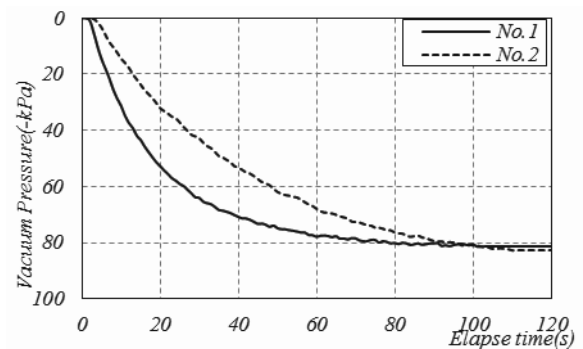


Figure 3 Vacuum pressure vs. time curve

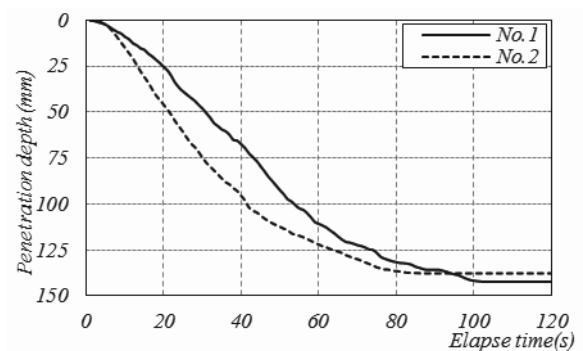


Figure 4 Penetration depth vs. time curve

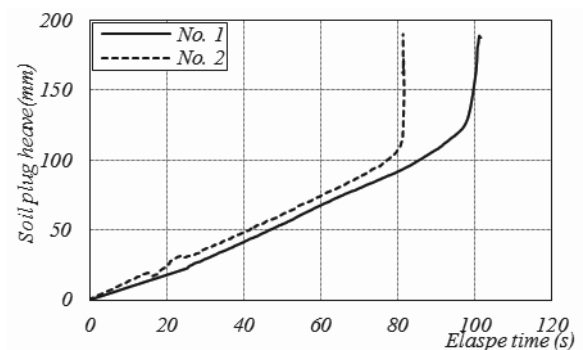


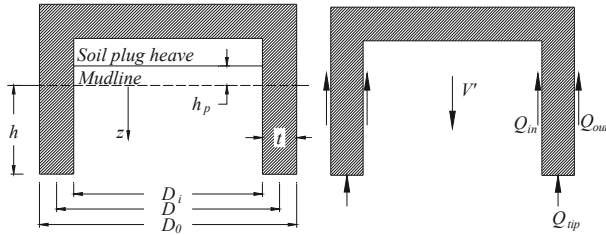
Figure 5 Penetration depth vs. soil plug heave curve

### 3 ANALYTICAL SOLUTIONS

An analytical method to simulate the penetration procedure for suction caisson in clay has been proposed by Houlsby and Byne (2005b). The friction between internal caisson wall and internal clay and that between external wall and external clay were considered separately by using different friction coefficient (different  $\alpha$  value). The self-weight penetration and suction assistant penetration have been made a clear distinction. As the self-weight penetration is very small in our 1-g model tests, only the suction assistant penetration process is discussed in this paper.

A simplified cross-section of the suction caisson is shown in Figure 6. The vertical coordinates, measured at a depth below the mud line, is set up with  $z$ . The inside, outside and average diameters of the caisson are represented by  $D_i$ ,  $D_o$ ,  $D$  respectively. Therefore,  $D_i = D_o - 2t$  and  $D = (D_i + D_o)/2$  where  $t$  is the thickness of the caisson wall. The total height of the caisson is  $L$  and height embedment into the seabed is  $h$ . The soil plug higher than the mud line inside of the caisson is denoted as  $h_p$ . The unit weight of water is  $\gamma_w$  and that of soil is  $\gamma$ .

As illustrated in Figure 6(b), the total effective weight of suction caisson is presented as  $V'$ . The side frictions between soil with outside and inside of the caisson are written as  $Q_{in}$  and  $Q_{out}$ , respectively. The end bearing capacity on the tip of suction caisson is defined as  $Q_{tip}$ .



(a) Parameters definition (b) Free body diagram  
Figure 6 Cross section of suction caisson (Modified after Houlsby and Byne, 2005b)

When the caisson penetrates into the soil, a bearing capacity failure will occur around the wall tip. It is assumed that the soil plug is mainly due to these displaced soil flow into the caisson. We make the simplifying assumptions that: (a) there is a volume of clay,  $V_s$ , flows into the caisson because of the replacement of caisson walls,  $V_c$ , and  $V_s = mV_c$ ; (b) the flowed clay does not change the original unit weight of clay within the caisson; and (c) the flowed clay forms the soil plug with its height shown in Eq. (1). These assumptions were especially valid for the suction caisson installed in clay which have already been verified by model test results (Whittle et al., 1998), prototype behavior (Colliat et al., 1996), and finite element analyses (Andersen and Jostad, 2002; Andersen and Jostad, 2004). The values of  $m$  will be calculated using the model test results.

$$h_p = m(D_o^2 / D_i^2 - 1)h \quad (1)$$

For the case of suction caisson installation in clay, the calculation neglects the effect of the applied suction pressure and the side frictions along the caisson walls. Then this procedure can be treated as undrained conditions. Therefore, the side frictions are calculated by applying a factor  $\alpha$  to the value of the undrained strength ( $\alpha$ -method), i.e.  $Q_{in} = \alpha s_{u0}(\pi D_i)$  and  $Q_{out} = \alpha s_{u0}(\pi D_o)$  where  $s_{u0}$  is average undrained strength between mud line and depth  $h$ . If the undrained strength of clay increased along depth linearly, i.e.  $s_u = s_{u1} + \rho z$ , the average undrained strength of soil,  $s_{u0}$ , can be calculated as  $s_{u0} = s_{u1} + \rho h/2$  where  $\rho$  is the coefficient of undrained strength increasing. Similar calculation method can also be applied to the internal

undrained strength,  $s_{ui}$ . The bearing capacity on the tip is calculated according to the standard bearing capacity calculation, i.e.  $\sigma'_{tip} = \gamma' h N_q + s_{u2} N_c$  and  $s_{u2} = s_{u0} + \rho h$ , where  $N_c$  is the capacity factor for a deep strip footing in clay (a typical value of 9 may be adopted) and  $N_q = 1$  for undrained analysis. During the suction assisted penetrations, the driving force is the weight of suction caisson and applied suction pressure. The resistance to the caisson is calculated as the sum of the side frictions ( $Q_{in} + Q_{out}$ ) and the end bearing capacity on the tip ( $Q_{tip}$ ). The force equilibrium along the vertical direction yields the following equation:

$$V' + s \left( \frac{\pi D_o^2}{4} \right) = h \alpha_0 s_{u0} (\pi D_o) + (h + h_p) \alpha_i s_{ui} (\pi D_i) + (\gamma' h + s_{u2} N_c) (\pi D t) \quad (2)$$

The internal and external side frictions calculated by  $(h + h_p) \alpha_i s_{ui}$  and  $h \alpha_0 s_{u0}$  may be assumed to have the same magnitude. This is reasonable as the internally remold clay will have a lower undrained shear strength and a lower coefficient of side friction (Andersen and Jostad, 2004). Then Eq. (2) can be further simplified as follows:

$$V' + s \left( \frac{\pi D_o^2}{4} \right) = 2 h \alpha_0 s_{u0} \pi D + (\gamma' h + s_{u2} N_c) (\pi D t) \quad (3)$$

The penetration depth  $h$  can be derived from Eq. (3) and shown as follows:

$$h = \frac{V' + s \left( \frac{\pi D_o^2}{4} \right) - s_{u2} N_c (\pi D t)}{2 \alpha_0 s_{u0} \pi D + \gamma' (\pi D t)} \quad (4)$$

### 4 COMPARISON BETWEEN THE TWO METHODS

It should be point out that the analytical method for caisson penetration is only applicable when the caisson is penetrating into clay with a constant velocity. Then the driving forces and resistance forces can be treated as balanced during each calculation step. The results shown in Figure 4, the penetration depth versus time curve is almost in a linear relationship. The comparisons between these two sets of results were made by assuming the caisson was penetrated into the clay in a constant speed or the forces in each calculation step were balanced.

In the following calculation, the tested vacuum pressures were taken as inputs. This procedure maybe not the way for engineering designing but could be used to verify the accuracy of this theoretical method. The comparison could also give a way to evaluate the key design parameters for caisson designing. The average undrained shear strength of soil bed used for calculation was  $13 \text{ kPa}$  as discussed in section 2.1. The values of  $N_c$  and  $N_q$  for undrained analysis were adopted as 9.0 and 1.0, respectively. The average unit weight of soil bed is  $12.3 \text{ kN/m}^3$  which can easily be derived from  $w\%$  (42.7%) and  $G_s$  (2.61). The total weight of concrete caisson is  $0.272 \text{ kN}$  ( $27.2 \times 10 \text{ kN}$ ).

The model test results and the analytical results for the displacement of suction caisson are compared in Figure 7. It can be seen that when  $\alpha = 0.72$ , the two sets of results agree well with each other. The analytical results show that the penetration of suction caisson needs a minimum driving suction pressure. However, the model tests show a much smaller value. Furthermore, the penetration procedure for model No. 2 was delayed (start time of  $t = 25 \text{ s}$ ) comparing to model No. 1 (starting time of  $t = 13 \text{ s}$ ) because the applying speed of vacuum pressure for model No. 2 is lower than that for model No. 1.

The comparison between the theoretical and the model test results regarding the heave of soil plug is shown in Figure 8. The analytical model indicates that a minimum vacuum pressure is required for the soil plug to start to heave as there is no plug

movement at the beginning. This is related to the assumption that the heave of soil plug is caused by the penetration of caisson walls. A fitting of the experimental curves using a value of  $m=1.4$  was also made.  $m=1.4$  implies that the volume of the soil going into the caisson cavity was 140% of the volume of the soil replaced. This is possible as the additional 40% could come from the expansion of the remolded soil or flow of soil beneath the caisson. As discussed before, the soil plug was broken at the end of the experiments. This aspect could not be modeled by the analytical method.

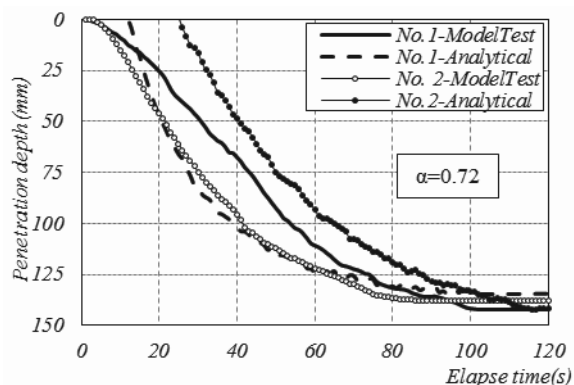


Figure 7 Predicted and measured penetration depth vs. time curves

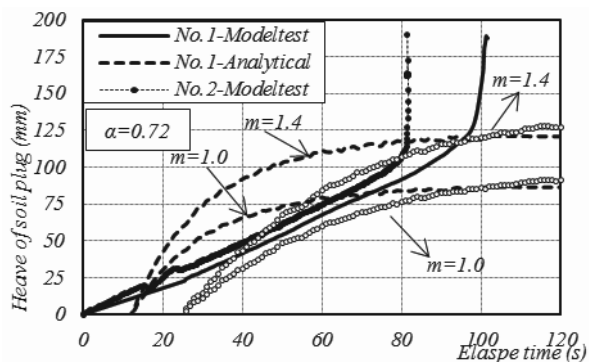


Figure 8 Predicted and measured heave vs. time curves

## 5 CONCLUSIONS

Suction caissons have been used mainly as foundations to support offshore structures in deep water. Their applications in shallow water are more challenging as the amount of suction that can be applied to install the caissons is much less. Several model tests on the use of suction caisson in clay in shallow water were carried out. The height of soil plug, displacement of the suction caisson and applied vacuum pressure were measured during the model tests. An analytical method proposed by Housby and Byrne (2005b) were adopted to simulate the model test results. The analytical results agree well with the model test results with the selection of appropriate parameters.

## 6 ACKNOWLEDGEMENT

The authors would like to thank Dr. LIU Kejin, WU Shifan and LI Mangyuan for their contribution to the research program and Prof YAN Shuwang for useful discussions with him.

## 7 REFERENCES

Andersen, K.H., Jeanjean, P., Luger, D., Jostad, H.P., 2005. Centrifuge tests on installation of suction anchors in soft clay. *Ocean Engineering* 32, 845-863.

- Andersen, K.H., Jostad, H.P., 1999. Foundation Design of Skirted Foundations and Anchors in Clay, *Offshore Technology Conference*, Houston, Texas.
- Andersen, K.H., Jostad, H.P., 2002. Shear Strength Along Outside Wall of Suction Anchors in Clay after Installation, *Proceedings of The Twelfth (2002) International Offshore and Polar Engineering Conference*. Kitakyushu, Japan.
- Andersen, K.H., Jostad, H.P., 2004. Shear Strength Along Inside of Suction Anchor Skirt Wall in Clay, *Offshore Technology Conference*, Houston, Texas.
- Andresen, L., Jostad, H.P., Andersen, K.H., 2011. Finite Element Analyses Applied in Design of Foundations and Anchors for Offshore Structures. *International Journal of Geomechanics* 11, 417-430.
- Byrne, B.W., Housby, G.T., Martin, C.M., Fish, P., 2002. Suction caisson foundation for offshore wind turbines. *Wind Engineering* 26, 145-155.
- Chen, W., Zhou, H., Randolph, M.F., 2009. Effect of Installation Method on External Shaft Friction of Caissons in Soft Clay. *Journal of Geotechnical and Geoenvironmental Engineering* 135, 605-615.
- Chu, J., Yan, S.W., Li, W., 2012. Innovative methods for dike construction – An overview. *Geotextiles and Geomembranes* 30, 35-42.
- Colliat, J.-L., Boisard, P., Gramet, J.-C., Sparrevik, P., 1996. Design and installation of suction anchor piles at a soft clay site in the Gulf of Guinea. *Paper OTC 8150, Offshore Technology Conference*, Houston, Texas.
- Gavin, K., Igoe, D., Doherty, P., 2011. Piles for offshore wind turbines: A state of the art review. *Ice Geotechnical Engineering Journal* 164 245-256.
- Housby, G.T., Byrne, B.W., 2000. Suction Caisson Foundations for Offshore Wind Turbines and Anemometer Masts. *Wind Engineering* 24, 249-255.
- Housby, G.T., Byrne, B.W., 2005a. Design procedures for installation of suction caissons in sand. *Proceedings of the ICE - Geotechnical Engineering* 158, 135 -144.
- Housby, G.T., Byrne, B.W., 2005b. Design procedures for installation of suction caissons in clay and other materials. *Proceedings of the ICE - Geotechnical Engineering* 158, 75 -82.
- Housby, G.T., Kelly, R.B., Huxtable, J., Byrne, B.W., 2005c. Field trials of suction caissons in clay for offshore wind turbine foundations. *Géotechnique* 55, 287-296.
- House, A.R., Randolph, M.F., 2001. Installation and Pull-Out Capacity of Stiffened Suction Caissons in Cohesive Sediments, *Proceedings of the Eleventh (2001) International Offshore and Polar Engineering Conference*, Stavanger, Norway, pp. 17-22.
- House, A.R., Randolph, M.F., Borbas, M.E., 1999. Limiting Aspect Ratio for Suction Caisson Installation in Clay, *Proceedings of the Ninth (1999) International Offshore and Polar Engineering Conference*. Brest, France.
- Randolph, M.F., Gaudin, C., Gourvenec, S.M., White, D.J., Boylan, N., Cassidy, M.J., 2011. Recent advances in offshore geotechnics for deep water oil and gas developments. *Ocean Engineering* 38, 818-834.
- Tran, M.N., Randolph, M.F., 2008. Variation of suction pressure during caisson installation in sand. *Géotechnique* 58, 1-11.
- Wang, M.C., Nacci, V.A., Demars, K.R., 1975. Behavior of underwater suction anchor in soil. *Ocean Engineering* 3, 47-62.
- Whittle, A.J., Germaine, J.T., Cauble, D.F., 1998. Behavior of Miniature Suction Caissons in Clay, *Proc., Offshore Site Inv. Found. Behavior '98*. London, UK, pp. 279-300.
- Zhang, J.H., Zhang, L.M., Lu, X.B., 2007. Centrifuge modeling of suction bucket foundations for platforms under ice-sheet-induced cyclic lateral loadings. *Ocean Engineering* 34, 1069-1079.
- Zhang, P., Ding, H., 2011. Bearing capacity of the bucket spudcan foundation for offshore jack-up drilling platforms. *Petroleum Exploration and Development* 38, 237-242.

# Instrumentation de la paroi moulée du bassin de Blanc-Mesnil : retro-analyse et calage des modèles de calcul

## Instrumentation of the diaphragm wall of the Blanc-Mesnil Basin : retro-analysis and calibration of calculation models

Gutjahr I., Doucerain M., Schmitt P.  
SOLETANCHE-BACHY, Paris, France

Heumez S., Maurel C.  
CETE-IF, Le Bourget, France

**RÉSUMÉ :** Le chantier du bassin du Vieux Blanc-Mesnil a fait l'objet d'une instrumentation afin de confronter le comportement réel de l'ouvrage aux calculs aux coefficients de réaction menés lors des études d'exécution, puis en complément aux calculs aux éléments finis. Une particularité de ce projet réside dans le fait que le soutènement est surmonté d'un talus de grande hauteur, le suivi du comportement du soutènement permet donc également de comparer les différentes modélisations d'un talus à la réalité. Suite aux différences constatées entre les courbes de déformée réelle et calculée lors des études d'exécution, il a été procédé à un affinage du modèle géotechnique consistant à ne tenir compte que des sondages les plus proches des sections instrumentées. Il a ainsi été possible de valider les résultats obtenus par les différentes méthodes (coefficient de réaction et éléments finis), moyennant la prise en compte d'une modélisation réaliste du talus et l'utilisation de paramètres de sols équivalents et représentatifs.

**ABSTRACT:** The diaphragm wall of the Blanc-Mesnil Basin was subject to instrumentation in order to compare the structure's actual behaviour to calculations based on the coefficient of subgrade reaction, as used in the execution studies, as well as to calculations based on the finite element model. A peculiarity of this project lies in the fact that the retaining wall is surmounted by a high slope, thus the monitoring also permits to compare different slope calculation models to reality. Following the differences observed between the measured and calculated displacement curves, the geotechnical model was refined considering the boreholes closest to the surveyed sections. Thus it has been possible to validate the results obtained by different calculation models (finite element and coefficient of subgrade reaction).

**Mots-Clés :** suivi inclinométrique, modélisation d'un talus, calcul aux coefficients de réaction, calcul aux éléments finis

**Keywords:** inclinometer survey, slope calculation model, coefficient of subgrade reaction calculation, finite elements calculation

### 1 INTRODUCTION

Le soutènement périphérique du bassin de retenue du Vieux Blanc-Mesnil est constitué d'une paroi moulée d'épaisseur 0.80m ancrée par un niveau de tirants précontraints à caractère permanent.

Deux sections distinctes ont fait l'objet d'une instrumentation et d'un suivi complets dans le cadre de l'action de recherche FONDAMS pilotée par l'IFSTTAR afin de permettre une analyse du comportement réel de l'ouvrage puis ensuite le comparer non seulement aux calculs aux coefficients de réaction utilisés pour le dimensionnement, mais encore aux calculs aux éléments finis réalisés *a posteriori*.

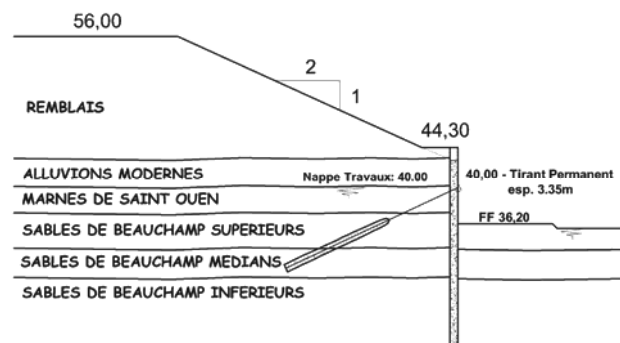


Figure 1. Profil de mesure « Coupe 1 B ».

Un intérêt particulier du projet est la présence d'un talus surmontant la paroi moulée sur une forte hauteur, variable de 7

à 12 m au droit des deux profils de mesure. La comparaison entre le comportement réel de l'ouvrage et les calculs permettra ainsi de confronter les différentes modélisations d'un talus utilisées dans la pratique courante à la réalité des mesures.

On a utilisé le logiciel PARIS (logiciel de calcul interne Solétanche-Bachy) pour les calculs aux coefficients de réaction et le logiciel PLAXIS 2D pour les calculs aux éléments finis.

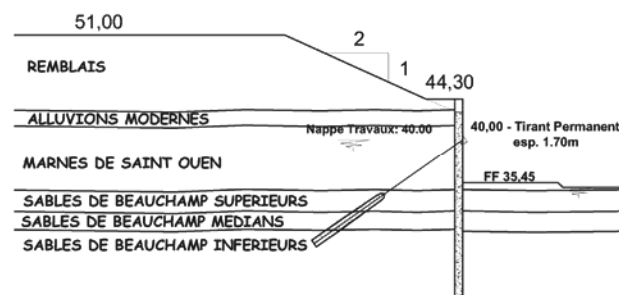


Figure 2. Profil de mesure « Coupe 2 B ».

### 2 PRÉSENTATION DES MESURES

L'instrumentation de la paroi a consisté en la mise en place de deux inclinomètres scellés dans des tubes de réservation liés aux cages d'armatures de deux panneaux distincts. Plusieurs relevés inclinométriques ont donc été possibles au cours de la réalisation du bassin (un point zéro avant le début des excavations, une mesure lors de la phase en console avant la



mise en tension des tirants, et une mesure en phase fond de fouille). La précision des mesures inclinométriques est de l'ordre de 0,1 mm/m.

Afin de suivre l'évolution des efforts dans les tirants, des cales dynamométriques ont également été installées.

### 3 MODÉLISATION D'UN TALUS POUR LES CALCULS AUX COEFFICIENTS DE REACTION

Avant de procéder aux calculs de recalage, nous avons d'abord tenté d'établir quelle modélisation du talus est la mieux adaptée à la géométrie et au phasage du projet.

Pour cela nous avons mené une étude comparative portant sur la géométrie de la Coupe 1 B.

#### 3.1 Modélisations étudiées

Nous avons comparé la modélisation du talus fini par différentes méthodes :

- approches en plasticité avec hypothèse sur le schéma de rupture : méthodes de Graux (Graux, 1967) ou Houy par bandes horizontales
- approches en élasticité : méthode de Boussinesq par bandes horizontales ou verticales
- approche en plasticité avec recherche du schéma de rupture critique : module de calcul « talus-risberme » de PARIS par recherche automatique de lignes de rupture critiques (voir figure 3) (Schmitt et al, 2002)

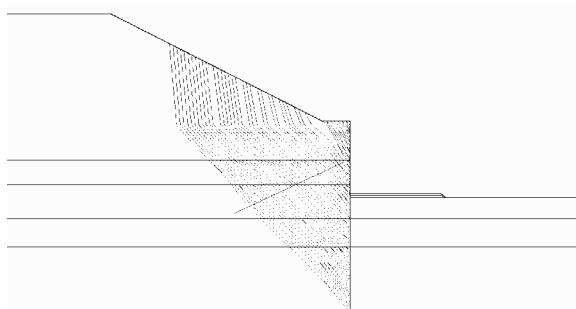


Figure 3. Lignes de rupture – modèle « Talus-Risberme ».

Nous avons complété ces approches par le calcul des talus infinis par les coefficients de Caquot-Kérisel (1990), constituant dans le cadre de notre projet une méthode de référence car :

- l'angle du talus (27°) est inférieur à l'angle de frottement interne des remblais (30°).
- le talus peut être considéré infini par rapport à la hauteur excavée.

Afin de prendre en compte le retrait du talus par rapport à la paroi, nous avons réalisé 2 calculs de talus infini avec 2 cotes de pied de talus correspondant pour l'un à l'impact du prolongement du talus réel avec la paroi (42.90 NGF) et pour l'autre au sommet de la paroi (44.30 NGF) duquel on fait partir un talus fictif parallèle au talus réel, constituant ainsi les 2 bornes de référence pour la comparaison des différentes modélisations.

#### 3.2 Analyse des résultats et conclusion

Les calculs ont été menés avec le logiciel PARIS. Nous avons analysé l'influence des différentes modélisations sur les poussées actives et réelles ainsi que sur les déformées du soutènement par rapport aux bornes de référence données par les calculs des talus infinis.

Les conclusions sont les mêmes pour l'ensemble des paramètres comparés.

On constate notamment que les approches en élasticité donnent des poussées et déformées largement supérieures aux

autres modèles et aux bornes de référence, comme il fallait s'y attendre.

Les approches en plasticité avec hypothèse sur le schéma de rupture donnent des poussées et déformées supérieures aux bornes de référence et au modèle « talus risberme ».

Enfin la modélisation « talus risberme » donne les résultats les plus proches des bornes de référence. De plus, on constate que cette modélisation donne des courbes de poussée lissées, ne présentant pas les sauts observés dans les calculs « talus infini », ce qui devrait se rapprocher le plus des poussées réelles dans le terrain.

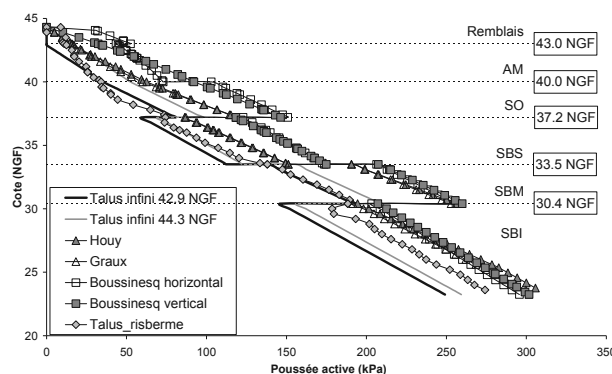


Figure 4. Comparaison des poussées actives selon modèle.

Notons que la modélisation « talus risberme » permet de modéliser l'aménagement d'une plateforme de circulation à l'arrière du soutènement, subtilité ne pouvant pas être prise en compte par les modèles « talus infini » ce qui explique que la poussée calculée par PARIS soit localement inférieure à la borne minimale : ceci traduit simplement le fait que la ligne d'influence du talus intercepte l'écran à une cote inférieure à 42.90, comme on le voit sur la figure 3.

Nous avons donc retenu la modélisation « talus risberme » pour les calculs aux coefficients de réaction.

### 4 COMPARAISON DES COURBES INCLINOMÉTRIQUES AVEC COURBES DE CALCUL CORRESPONDANT AUX CALCULS D'EXÉCUTION

Après avoir adapté les stratigraphies en fonction des sondages situés à proximité des inclinomètres, nous avons estimé les courbes de déformées théoriques à l'aide de calculs aux coefficients de réaction, en considérant les caractéristiques géotechniques des terrains tels que considérés lors des études d'exécution.

Tableau 1. Caractéristiques des terrains « Etudes d'exécution »

Terrain	EM / pl (MPa)	$\gamma / \gamma'$ (kN/m <sup>3</sup> )	$\phi$ (°)	c (kPa)	k (MN/m <sup>3</sup> )
Remblais	8.3 / 1.1	20 / 10	30	0	8.1
Alluvions Modernes	6.2 / 0.7	20 / 10	30	0	8.1
Marnes de St. Ouen	8.3 / 1.1	20 / 10	30	0	11.2
Beauchamp Supérieurs	23 / 2.3	22 / 12	35	0	36.5
Beauchamp médians	16 / 2.2	22 / 12	30	5	22.5
Beauchamp Inférieurs	37 / 3.8	22 / 12	35	10	67.5

EM / pl : module pressiométrique / pression limite

$\gamma / \gamma'$  : poids volumique / poids volumique déjaugé

$\phi$  : angle de frottement interne

c : cohésion

k : coefficient de réaction estimé selon la formule de Schmitt(1998)

#### 4.1 Coupe 1 B

On constate que les courbes obtenues pour la phase console divergent tandis qu'elles sont proches pour la phase fond de fouille. Nous en déduisons que pour la phase console les caractéristiques et modèles de calcul initialement retenus sont globalement réalistes, mais les propriétés mécaniques des terrains supérieurs semblent sous-évaluées.

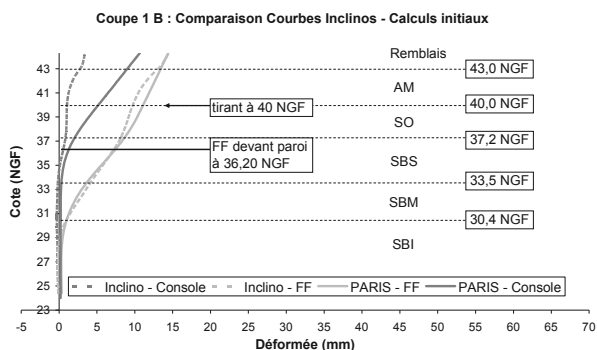


Figure 5. Coupe 1 B : Comparaison des Courbes de Déformées.

#### 4.2 Coupe 2 B

Nous observons que les déplacements calculés sont supérieurs aux déplacements mesurés. Bien que l'influence du talus soit moindre en raison de sa plus faible hauteur, l'écart entre les déplacements calculés et mesurés est systématiquement plus important que dans la coupe 1B, ce qui tend à montrer que les caractéristiques réelles des terrains sont globalement meilleures.

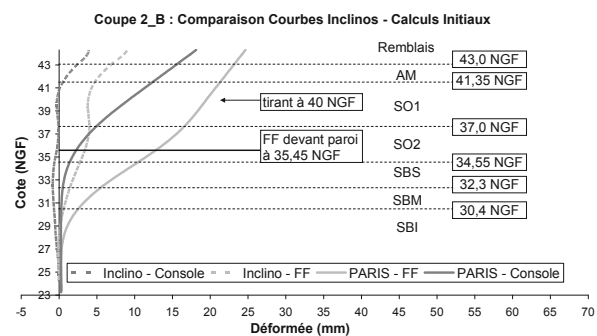


Figure 6. Coupe 2 B : Comparaison des Courbes de Déformées.

L'amplitude des déformations mesurée est parfois très faible, ce qui rend illusoire toute interprétation précise de l'allure des déformées. Par ailleurs des paramètres ne pouvant pas être pris en compte dans les calculs peuvent avoir une influence : la qualité du scellement des tubes inclinométriques, la poutre de couronnement (poids important et discontinuité du bétonnage), la température...

Afin de permettre une bonne interprétation des courbes de déformées obtenues par les mesures inclinométriques, il est toujours utile de disposer de plusieurs relevés concomitants (cibles topographiques, cales des tirants, niveaux piézométriques).

## 5 CALCULS DE RECALAGE

Suite aux divergences entre les courbes de déformées réelles et théoriques, nous avons recalé le modèle géotechnique en ne tenant compte que des sondages proches des sections étudiées.

En l'absence de mesures du niveau de la nappe phréatique nous avons gardé le niveau de calcul.

#### 5.1 Calculs aux coefficients de réaction

Nous avons introduit deux couches de St.Ouen suite à l'analyse du sondage PR107 situé au droit du profil 2B et qui montre des caractéristiques pressiométriques nettement meilleures dans la partie basse de cette couche. Etant donné que l'épaisseur de la couche de St.Ouen est plus importante au droit du profil 2B (7m) qu'au droit du profil 1B (3m), nous avons considéré cette deuxième partie du St.Ouen uniquement pour les calculs de recalage du profil 2B.

Nous avons également introduit une cohésion à court-terme dans les Alluvions Modernes ainsi que dans les deux couches du St.Ouen, justifiée par la faible durée entre la mesure 0 des inclinomètres et la mesure de la phase console (1 mois).

De plus nous avons revu les valeurs des coefficients de réaction des terrains suite à l'analyse du sondage PR107 montrant des valeurs pressiométriques plus élevées que celles considérées lors des études d'exécution.

Tableau 2. Caractéristiques des terrains obtenus après recalage.

Terrain	$E_M / pl$ (MPa)	$\gamma / \gamma'$ (kN/m <sup>3</sup> )	$\phi$ (°)	$c - ct$ (kPa)	$c - lt$ (kPa)	$k$ (MN/m <sup>3</sup> )
Remblais	8.3 / 1.1	20 / 10	30	0	0	8.1
Alluvions Modernes	6.2 / 0.7	20 / 10	30	5	0	8.1
Marnes de St. Ouen 1	6.4 / 0.9	20 / 10	30	15	0	20
<b>Marnes de St. Ouen 2</b>	<b>30 / 3.0</b>	<b>20 / 10</b>	<b>30</b>	<b>40</b>	<b>15</b>	<b>75</b>
Beauchamp Supérieurs	40 / 3.2	22 / 12	35	0	0	65
Beauchamp médians	29 / 2.6	22 / 12	30	5	5	35
Beauchamp Inférieurs	55 / 3.5	22 / 12	35	10	10	80

Modifications par rapport aux paramètres initiaux en gras.

Nous obtenons les courbes suivantes :

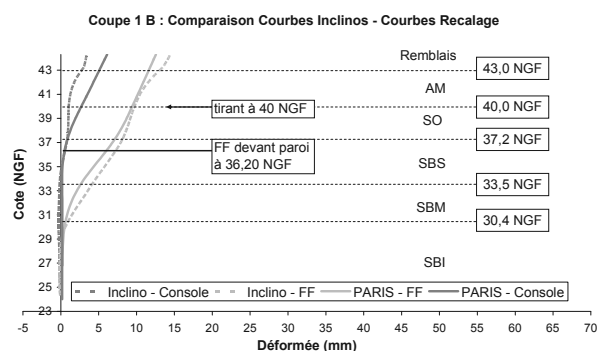


Figure 7. Coupe 1 B : Comparaison des Courbes de Déformées après recalage.

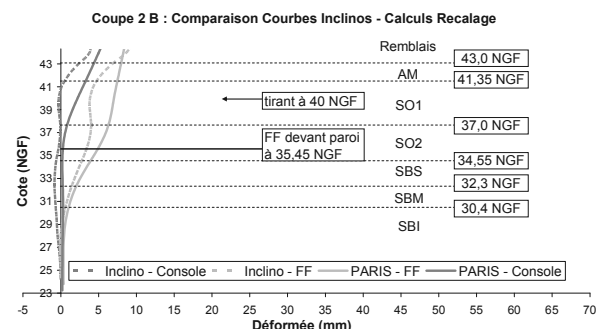


Figure 8. Coupe 2 B : Comparaison des déformées après recalage.

Concernant les efforts dans les tirants, nous observons que les efforts trouvés par le calcul de recalage sont environ 10%

plus importants que les efforts mesurés après le terrassement au fond de fouille.

### 5.2 Calculs aux éléments finis

Parallèlement aux calculs aux coefficients de réaction, des calculs par la méthode des éléments finis ont été menés à l'aide du logiciel Plaxis2D. Afin de permettre la comparaison entre les deux méthodes de calcul, nous avons repris les mêmes caractéristiques des sols (issues du recalage).

La loi de comportement considérée est élasto-plastique avec critère de plasticité de Mohr-Coulomb. Les modules d'Young ont été fixés grâce à la relation  $E_Y=4E_M/\alpha$  (avec  $E_M$  module pressiométrique, et  $\alpha$  coefficient rhéologique des sols).

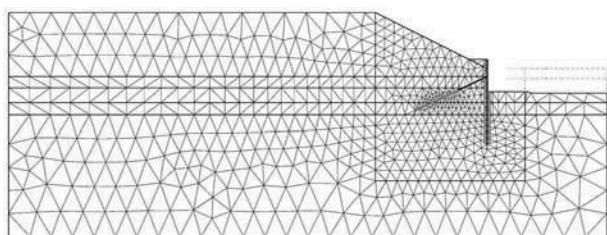


Figure 9. Vue du maillage de la coupe 1B.

La présence de la pente oblige à éloigner assez fortement la limite gauche du modèle pour minimiser l'influence des conditions limites (tout en ne l'éloignant pas trop car cela a une incidence sur la propagation des déformations). La limite droite a été choisie sur l'axe de symétrie du bassin.

Afin de prendre en compte l'inclinaison des contraintes dans la pente, la première phase de calcul a été une phase fictive d'application de la gravité.

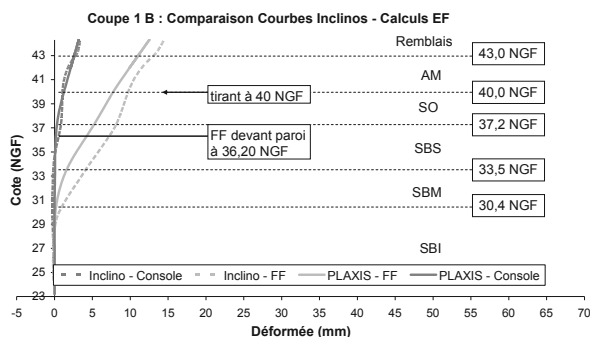


Figure 10. Coupe 1 B : Comparaison des Courbes de Déformées mesurées et calculées par EF.

On constate qu'il existe une bonne concordance entre les déformées mesurées et calculées. Certains phénomènes ne sont cependant pas retrouvés par le calcul, comme la déformation vers 41 m NGF de la coupe 2B (cette déformation est présente dès la phase console, et pourrait être due à la réalisation de la poutre de couronnement).

On notera également qu'il existe un déplacement d'ensemble de la paroi (translation horizontale vers la fouille de 3,2 mm pour 1B et de 1,5 mm pour 2B), non représenté sur les courbes de déformées. Ce déplacement d'ensemble est peu réaliste et est certainement lié à la modélisation numérique, mais en l'absence de suivi topométrique, et avec des mesures inclinométriques ne descendant pas sous la base de la paroi, il n'est pas possible de certifier que ce mouvement d'ensemble n'existe pas.

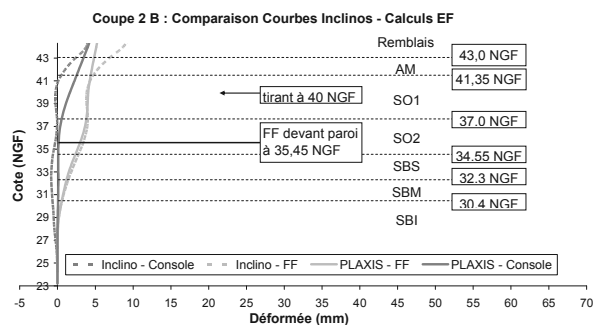


Figure 11. Coupe 2 B : Comparaison des déformées mesurées et calculées par EF.

Quant aux efforts calculés dans les tirants, on constate qu'ils sont sous-estimés de 15% pour la coupe 1B, et surestimés de 20% pour la coupe 2B.

## 6 CONCLUSIONS

On observe que les résultats des calculs de recalage obtenus avec PARIS et PLAXIS avec les mêmes caractéristiques de terrain, sont très similaires, tant en valeur qu'en allure de déformée et relativement proches des mesures inclinométriques.

L'ensemble des calculs menés, et notamment la similarité des résultats obtenus par PARIS et PLAXIS 2D, montre la validité du modèle « talus risberme » avec recherche automatique des lignes de rupture critiques dans le cadre de cette étude, ainsi que la bonne concordance du calcul aux éléments finis en modèle Mohr-Coulomb ( $E_Y=4E_M/\alpha$ ) avec le calcul aux coefficients de réaction estimés selon Schmitt, ce qui confirme les résultats obtenus sur des chantiers antérieurs (Schmitt 2009)

## 7 REMERCIEMENTS

Remerciements à l'IFSTTAR qui a permis la mise en place de l'instrumentation et une partie de cette étude dans le cadre de l'opération de recherche FONDAMS.

## 8 RÉFÉRENCES

Mestat P., Prat M. 1999. *Ouvrages en interaction*. Hermès.  
 Marten S., Delattre L., Magnan J-P. 2005. *Etude expérimentale et méthodologique sur le comportement des écrans de soutènement*. LCPC.  
 Schmitt P., 1998. *De l'élasticité linéaire au coefficient de réaction*. Revue Française de Géotechnique n°85.  
 Caquot A., Kérisel J. 1990. *Tables de Poussée et Butée 3<sup>ème</sup> édition*. Presse de l'Ecole Nationale des Ponts et Chaussées.  
 Graux D, 1967. *Fondations et Excavations Profondes – Tome 1 : Géotechnique Appliquée*. Editions Eyrolles.  
 Schmitt P., Dodel E. 2002. *Méthodes Numériques en Géotechnique*. 5<sup>ème</sup> conférence européenne. NUMGE 2002.  
 Schmitt P., 2009. *De l'importance du suivi pour maîtriser le dimensionnement des ouvrages géotechniques*. Revue Française de Géotechnique n°126-127.

# Displacement of an apartment building next to a deep excavation in Rotterdam

## Déplacements d'un bâtiment d'habitation adjacent à un chantier profond d'excavation à Rotterdam

Hannink G., Oung O.

*Engineering Consultancy Division, City of Rotterdam, The Netherlands*

**ABSTRACT:** A new underground car park is being realized near the Rotterdam Central Railway Station. The car park will contain five stories and will be about 150 m long and 35 m wide. The depth of the underground car park is about 20 m. Tall office buildings are present at both sides. A 30 m high apartment building is situated perpendicular to the car park, and the distance of this building to the car park is only 7 m. This building is founded on prefabricated concrete piles with a base level that equals the excavation depth of the car park. The underground car park is being realized inside a dry building pit surrounded by 40 m deep diaphragm walls. Predictions, based on calculations with analytical as well as 2D and 3D finite element models, showed that the expected settlements of the apartment building were acceptable. The measured displacements remained well within the limits that were predicted.

**RÉSUMÉ :** Près de la gare ferroviaire centrale de Rotterdam, un parking souterrain est encore en construction. Ce parking sera pourvu de cinq niveaux et aura les dimensions de 150 m de long en 35 m de large. La profondeur de ce parking sera de 20 m. Le long des côtés du parking en construction se trouve de hauts bâtiments. En particulier, un bâtiment d'environ 30 m de haut est situé à peine à une distance de 7 m de ce parking et se tient perpendiculairement à celui-ci. Ce bâtiment est fondé sur des pieux en béton préfabriqués dont la base est au même niveau que celui de l'excavation réalisée pour la construction du parking. Cette excavation est délimitée par des parois moulées dont la base se trouve à 40 m de profondeur. Les prédictions, basées sur des calculs pour lesquelles des modèles d'éléments finis bi- et tridimensionnels ont été montés, ont montré que les tassements de ce bâtiment prédits étaient acceptables. Les déplacements mesurés durant la réalisation de l'excavation sont restés dans les limites des calculs de prédiction.

**KEYWORDS:** deep excavation, settlement of structures, finite element models, prediction, monitoring.

### 1 INTRODUCTION

In the centre of Rotterdam, extensive reconstruction works are executed as part of the overall project Rotterdam Centraal. The reconstruction comprises of the building of a large Public Transport Terminal to facilitate passenger transfer between (inter)national trains including the high-speed train, and local public transport like trams, buses and underground trains. The project also includes a new underground metro station, a new underground parking facility for bicycles, a new traffic tunnel below a newly created square, and a new underground car park.

The car park will contain five stories and will be about 150 m long and 35 m wide. The depth of the underground car park is about 20 m. Tall office buildings are present at both sides. A 30 m high apartment building is situated perpendicular to the car park and the distance of this building to the car park is only 7 m (see Figure 1).

The apartment building is founded on prefabricated concrete piles with a base level that equals the excavation depth of the car park. The underground car park is being realized inside a dry building pit surrounded by 40 m deep diaphragm walls.

Calculations of the expected settlement of the apartment building were made in the design stage of the project, and a fall-back option was thought out in case the settlement would exceed the criteria.

The apartment building was continuously monitored during the construction of the parking facility. This paper describes the expected impact of the construction of the underground car park on the apartment building, and the results of the monitoring. The car park is presently in the final stage of construction.

Engineering of the car park Kruisplein, and supervision of the execution of the project is performed by the Engineering Consultancy Division of the City of Rotterdam.



Figure 1. The construction of the underground car park Kruisplein (February 2012). The apartment building is situated in front, at the left (perpendicular to the car park). Photograph Nick de Jonge – Skeyes fotografie.

### 1.1 Subsoil

The ground level in the area is situated at about sea level (this corresponds to the Dutch reference level NAP). The subsurface conditions at the building site are presented in Table 1. The hydraulic head in the fill is about 1.5 m below sea level, and in the Pleistocene sand layers about 2 m below sea level.

Table 1. Soil conditions

Elevation (m NAP)		Origin – Type of soil
from	to	
-0.3	-4.5	Fill - sand
-4.5	-5.5	Holocene - soft clay
-5.5	-8.0	Holocene - peat
-8.0	-17.0	Holocene - soft clay
-17.0	-35.0	Pleistocene - sand
-35.0	-37.0	Pleistocene - stiff clay
-37.0	-40.0	Pleistocene - sand

### 1.2 Challenge

The horizontal as well as the vertical equilibrium of the foundation of the apartment building may be influenced by the building activities (see Figure 2). The foundation piles of the apartment building:

- will be horizontally loaded by the soil that displaces into the direction of the diaphragm wall, because of its deflection;
- will displace vertically, because the soil that displaces into the direction of the diaphragm walls also displaces slightly into the vertical direction;
- will displace vertically, because the deflection of the diaphragm wall causes some relaxation of the sand layer, and therefore results in a decrease of the bearing capacity.

The effects of these phenomena had to be assessed, and taken into account during the design stage of the construction of the underground car park.

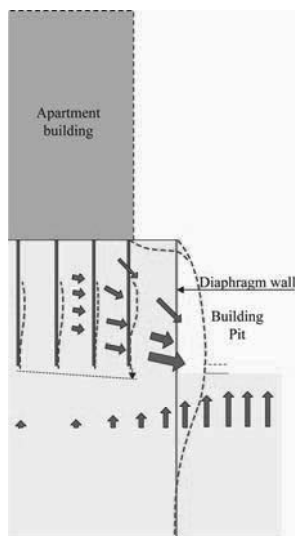


Figure 2. The consequences of the deflection of the diaphragm wall to the apartment building.

## 2 APARTMENT BUILDING

The length of the apartment building is 50 m, the width is 10 m. Prefabricated concrete piles 380 mm square and 450 mm square support the building. The foundation piles are connected by beams in north-south direction. The pile rows in the vicinity of the building pit support via columns bearing walls (see Figure 3). These walls distribute the load to the piles. The apartment

building can therefore be considered as stiff in the north-south direction. In the east-west direction pile rows are not able to redistribute the loads. In that direction the apartment building is considered as flexible.



Figure 3. The apartment building.

Before analyzing the expected settlement behavior of the apartment building, the building regulations of the period in which the apartment building was constructed had to be translated, and compared with the current building regulations. Therefore calculations of the vertical bearing capacity of the foundation piles were made, based on the Dutch standard NEN 6743-1. The original building documents of the apartment building mentioned the design loads on the piles. These had to be converted first into representative and design values. This resulted in a ratio of 1.9 between the average bearing capacity of the pile foundation and the representative value of the load. This fits reasonably well with the overall safety factor of 2.0 that was used for this type of piles in the period the apartment building was constructed. Because of this small difference in safety level NEN 6743-1 was used to analyze the settlement behavior of the apartment building.

## 3 ANALYSIS

### 3.1 Settlement due to the relaxation of the subsoil

The analysis was directed to the first five rows of piles of the apartment building. The first row is situated at about 7 m distance of the diaphragm wall; the fifth at about 23 m. The distance between the pile rows is 3.9 m. Load-settlement diagrams have been derived for a single prefabricated concrete pile based on general curves presented in NEN 6743-1. Both a pile 380 mm square and a pile 450 mm square were considered.

The calculations with the computer code MFoundation 5.3.1.4 were based on data of six CPT's. The maximum bearing capacity for each CPT, the representative value of the average bearing capacity and the design value of the bearing capacity were determined for both pile sizes. The magnitude of the negative skin friction was also calculated.

The subsoil, in particularly the sand layer with the top at 17 m below sea level, will relax as a result of the excavation of the

building pit. Based on CPT-measurements of the cone resistance at a comparable building pit, it was assumed that the relaxation amounts to 20% up to a distance of 12 m of the building pit, and that the relaxation from this distance decreases with 2.5% every 5 m. The decrease of the vertical bearing capacity was assumed to be proportional to the relaxation of the sand layer.

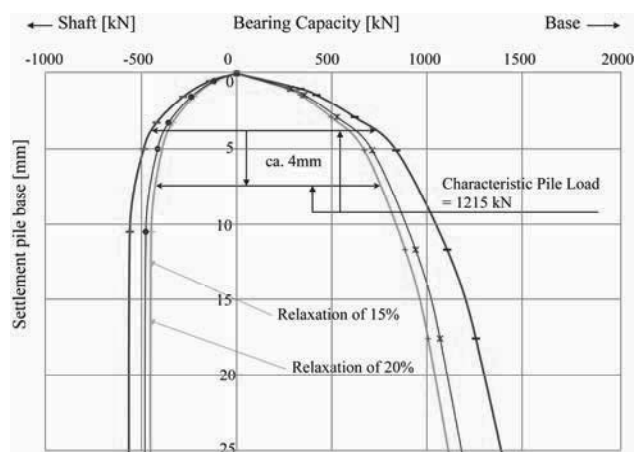


Figure 4. Graphical determination of the pile base settlement.

Load-settlement diagrams have been composed for the serviceability limit state, based on NEN 6743-1 (see Figure 4). For example, a pile base settlement of 4 mm is expected for the original situation. Due to a relaxation of the sand layer of 20% a pile base settlement of 8 mm is calculated, thus an additional settlement of 4 mm as a consequence of the relaxation.

It was concluded that the piles 380 mm square could settle 2 to 4 mm as a result of a relaxation of the sand layer of 12.5 to 20%. For piles 450 mm square these values varied between 3.5 and 5 mm.

### 3.2 Horizontal soil displacement due to the deflection of the diaphragm wall

The greenfield horizontal soil displacement at the position of the relevant foundation piles of the apartment building has been calculated by using the Hardening Soil (HS) model with the Small Strain Stiffness (HSS), of the computer code Plaxis 2D 8.5. Three cross-sections were considered (see Figure 5):

- at the middle section of the building pit where the excavation took place according to the conventional method;
- next to the apartment building, where the car park was built according to the top down method: after the construction of the diaphragm wall the roof is built, and after that the soil is excavated below the roof and the successive floors are made;
- in the transition zone between the two building methods.

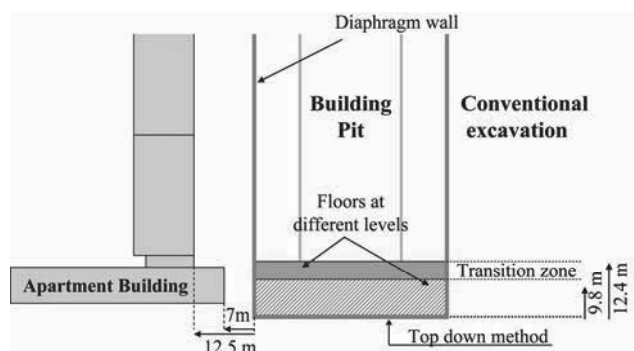


Figure 5. The cross-sections of the building pit that were considered with the Plaxis 2D computer code.

The different stages of the excavation with the corresponding lowering of the groundwater pressures in the building pit, and the installation of the successive layers of struts have been

considered, and the displacements have been calculated. The stiffness of the diaphragm wall was based on cracked concrete.

The calculated deflection of the diaphragm wall was about 70 mm in the middle section of the building pit, at a depth of 18 m. Next to the apartment building, the deflection was about 40 mm, at a depth of 20 m. The expected deflection of the diaphragm wall was about 55 mm in the transition zone.

At the location of the first pile row of the apartment building, the calculated greenfield horizontal soil displacement was 20 mm. At the following pile rows this displacement was according to the calculations 10 to 15 mm.

From additional calculations with the elastoplastic spring model of the computer code MSheet 7.7, it was concluded that the expected moments and shear forces in the foundation piles would remain smaller than the acceptable values.

### 3.3 Consequences of the soil displacement to the pile foundation

The computer code Plaxis 3D Foundation 2.1 has been used to determine the combined effect of the horizontal and vertical ground displacements. With the computer code MFoundation 5.3.1.4 the vertical displacement was considered, and with the computer code Plaxis 2D 8.5 the greenfield horizontal soil displacement.

The diaphragm wall has been modeled from the southern wall up to the middle of the conventionally built section. The floors that are part of the section that was built according to the top down method form part of the model. Only the five pile rows next to the building pit, and the complete ground floor were part of the model.

The piles were modeled as embedded piles. This made it possible to determine the moments and shear forces as well as the displacement of the foundation piles directly from the calculations. The calculated settlements of the pile base may be exaggerated, because the model does not take into account the densification of the soil as a result of the installation of the piles.

The with the computer code Plaxis 2D calculated deflection of the different parts of the diaphragm wall was used to calibrate the Plaxis 3D model. For the greater part of the building pit the calculated maximum horizontal displacement of the diaphragm wall was about 70 mm, in accordance with the results of the calculations with the Plaxis 2D computer code. Near the southern part of the diaphragm wall the calculated displacement varied between 15 and 40 mm.

According to the calculations, the pile base of both the 380 mm pile, and the 450 mm piles will settle 8 to 12 mm as a consequence of the soil displacement. The calculated horizontal deflection of the foundation piles was 25 mm as a maximum. The calculated moments and shear forces are relatively small.

## 4 PREDICTION

Based on the calculations the predicted settlement of the apartment building was 2 to 5 mm due to relaxation and 8 to 12 mm due to the soil displacement. This means in total 10 to 15 mm as a consequence of the building activities for the underground car park. Damage was not expected, because of the decrease of settlement with distance from the building pit. The settlement difference of the piles was expected to be small.

Horizontal displacements of the pile foundation, varying between 10 and 25 mm, were also expected. Also no damage was expected in this case, because the displacement would manifest itself underground, with only a limited effect on the foundation piles and the superstructure.

## 5 MONITORING

### 5.1 Set-up

Measuring points at 4 m above ground level were installed on the columns that were supported by the first four rows of piles of the apartment building (see Figure 6).

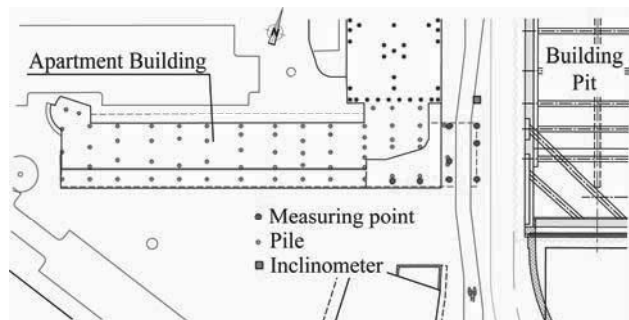


Figure 6. Measuring points on the apartment building.

Vertical and horizontal displacements were continuously monitored by a measuring device on top of a building at a distance of more than 50 m. The results of these measurements were periodically checked by measurements that were discontinuously executed as part of an extensive measuring program around the building pit.

The results of periodically executed inclinometer measurements offered another way to check the actual displacements. The inclinometers were situated next to the apartment building at a distance of 7 m from the diaphragm wall. This corresponds to the distance of the first pile row of the apartment building from the diaphragm wall.

The owner of the apartment building was fortnightly informed about the monitoring results.

### 5.2 Criteria

A relative rotation of the apartment building of 1:600 was used as the value to intervene, and a relative rotation of 1:750 served as the value to prepare mitigating measures. Because of practical reasons these values have been converted to settlement values of 15 and 12 mm respectively at any specific point.

### 5.3 Results

The continuous measurements started in January 2010. The measured displacements appear to be according to the prediction (see Figure 7). Meanwhile the apartment building is stable, and only a limited settlement has occurred.

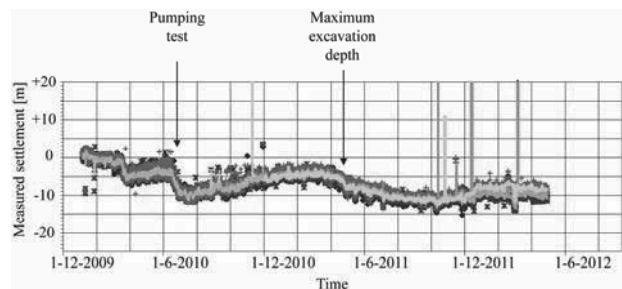


Figure 7. Measured vertical displacements in the period from January 2010 till May 2012.

The in June 2010 measured vertical displacement of the east front of the apartment building was the reason that the fall-back option was prepared. However, the further development of the settlement did not give rise to the actual installment of additional foundation piles below the east front.

The measurement results show that the apartment building rose again some 5 mm after the execution of the water tightness test. During the excavation of the deepest part of the building pit the apartment building settled some 8 mm. The maximum settlement of the east front appeared to be 10 to 15 mm, in accordance with the prediction.

The measured horizontal displacement of the apartment building varied between +10 and -10 mm (see Figure 8).

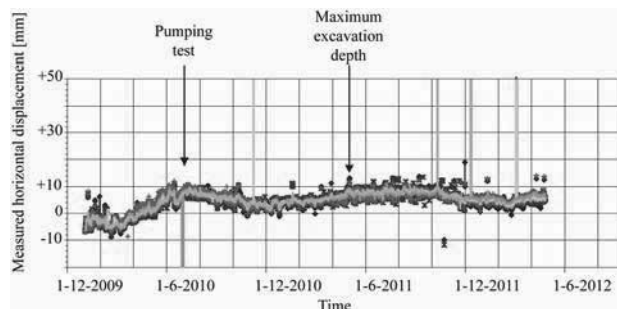


Figure 8. Measured horizontal displacements in the period from January 2010 till May 2012.

Inclinometer measurements started in July 2010, after the execution of the water tightness test. Next to the apartment building the maximum measured deflection of the diaphragm wall was about 35 mm at 15 m depth. At a distance of 7 m from the diaphragm wall the maximum horizontal soil displacement was about 40 mm at a depth between 5 and 10 m. From additional calculations with the elastoplastic spring model, it was concluded that the moments and shear forces in the foundation piles were smaller than the acceptable values.

## 6 CONCLUSIONS

Diaphragm walls are an appropriate type of retaining wall in an urban environment, but will also deflect as a result of a deep excavation. The consequences for adjacent structures must therefore be studied in the design stage.

A risk analysis helped to find the optimal design for the building pit as to restrict the uncertainties for adjacent structures to a minimum. It also helped to create fall-back options.

The results of the test of the water tightness of the building pit showed in an early stage that the apartment building was vulnerable to deformations of the subsoil. This resulted in a great attention for monitoring results during the whole construction period by all persons concerned.

Accurate predictions about the expected vertical and horizontal displacements appeared to be possible with the help of the available computer codes.

The case of the apartment building next to a deep building pit showed for all that a systematic approach is needed to overcome the presented challenges.

## 7 REFERENCES

- NEN 6743-1 2006. *Geotechnics – Calculation method for bearing capacity of pile foundation – Compression piles*. Nederlands Normalisatie-instituut, Delft (in Dutch).

# Calculation method of optimization the soil-cement mass dimensions to reduce the enclosure displacements in deep excavation

Calcul des dimensions optimales du massif du sol-ciment pour réduire les déplacements de fouilles profondes

Ilyichev V.A.  
Russian Academy of Architecture and Construction Sciences, Moscow, Russia

Gotman Y.A.  
Company Ltd 'Podzemproekt', Moscow, Russia

**ABSTRACT:** In the article basic condition to the calculation the soil-cement massif optimum dimensions, which ensure the assigned value of deep excavation wall displacement are presented. Problem statement and it's solution with the application of a Winkler-bed model, standard procedures for analysis of massive retaining walls and theory of optimum design are described. Some results of calculations and benchmark of these results with the use of PLAXIS 2D software package are given.

**RÉSUMÉ :** Le procédé de calcul est décrit pour la détermination des dimensions d'une masse de sol-ciment en utilisant un modèle de "Winkler-bed", des procédures standard pour l'analyse des murs de soutènement poids, et la théorie de la conception optimale. Les résultats des calculs et leur évaluation à l'aide du logiciel PLAXIS 2D sont présentés.

**KEYWORDS:** diaphragm wall, optimal design, Winkler-bed model, coefficient of stiffness.

## 1 INTRODUCTION

Acceleration of work execution for underground space constructing in dense urban conditions with the minimum influence upon surrounding buildings is one of the main problems of underground structures design today. The given paper presents the design method of optimization of the raised problem design decision. The method of excavation "top-down" is used as technological scheme only with upper floor installation and as optimized (variable) parameter, the dimensions of soil-cement mass (SCM) combined with enclosure (diaphragm wall) that provides the excavation without intermediate strutting system and minimization of wall displacement (Fig. 1).

So the main task is to determine the minimum volume of the SCM with the condition that the horizontal displacements of the enclosure during excavation of the pit do not exceed the assigned value  $S^h_{max} \leq S^{pred}$ .

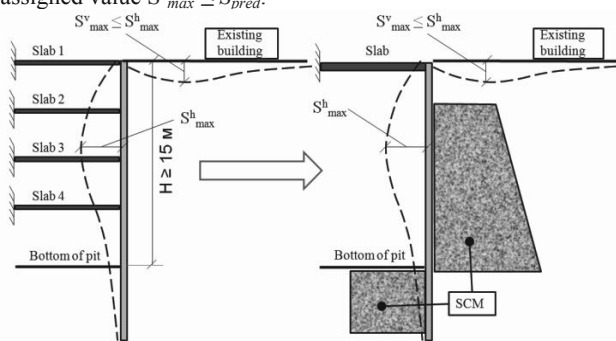


Figure 1. Problem condition

## 1 PROBLEM STATEMENT

The computational model of the optimized "wall-SCM-soil" system can be represented as a beam on an elastic Winkler bed, where the beam simulates the pit enclosure, and the SCM working in consort with the soil of the elastic bed. The stiffness coefficient of the bed, which varies over the height of the enclosure, is the only parameter of the model used to

determine the dimensions of the SCM. The stiffness coefficient of the elastic bed, and the development of a procedure to determine the SCM dimensions corresponding to the optimal solution will therefore be the subject of optimization problem.

In its initial state of rest, the enclosure is treated as a beam affixed on two sides by prestressed springs that describe the "SCM-soil" system (Fig. 2, a, b), whereupon the prestress corresponds to the lateral pressure of the soil  $q_{01}$  in a state of rest (Fig. 2, c, d). As the pit is excavated, the prestressed springs (soil) then disappears on one side together with the pressure, which they have created, and the system is taken out of equilibrium. To attain equilibrium, the enclosure is displaced within the pit (Fig. 2, e). Here, the springs below the bottom of the pit are mutually disturbed on the inside, but are undisturbed on the outside, altering the pressure of the springs against the enclosure (Fig. 2, f). During compression, this pressure is increased, and is

$$q_2 = q_{02} + kz, \quad (1)$$

but is diminished on release

$$q_1 = q_{01} - kz, \quad (2)$$

whereupon the change in pressure will depend on the coefficient of stiffness  $k$  of each spring, and the displacement  $z$  of the enclosure at the corresponding point.

During excavation, therefore, the SCM as a component part of the soil, which is simulated by the springs (Fig. 2, g) is displaced inside the pit, and the pressure against the enclosure is changed in conformity with (1) and (2), and the pressure against the SCM remains as before  $q_{02}$  and  $q_{01}$  on the side of the soil, when no Coulomb active or passive pressure is formed.

Considering that the displacement of the soil and beam below the bottom of the pit is less than that within the bounds of the pit over its height, let us simplify the computational diagram. The work of the springs on the outside of the pit below its bottom can be neglected (Fig. 2, h), and replaced by a constant pressure of the soil in a state of rest. If these springs are eliminated from the computational diagram of the beam on the outside of the pit, the pressure of the soil against the enclosure below the bottom of pit will be  $q_0 = q_{01} - q_{02}$ , and the springs on the inside beneath its bottom will be under no prestress.



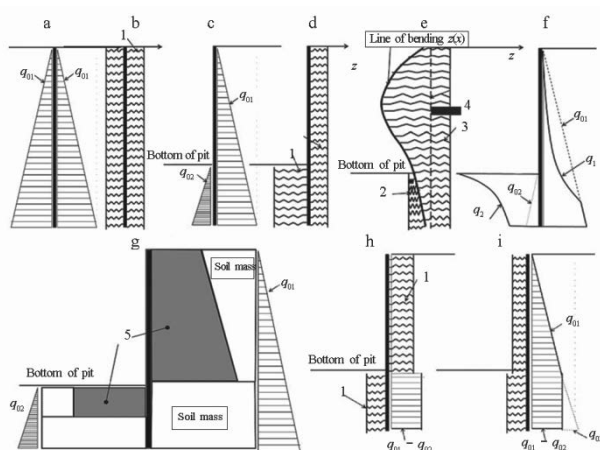


Figure 2. Steps in formulation of computational diagram: 1) elastic prestressed springs; 2) and 3) compression and release of springs; 4) position of enclosure prior to excavation of pit; 5) SCM.

Considering that the displacement of the soil and beam below the bottom of the pit is less than that within the bounds of the pit over its height, let us simplify the computational diagram. The work of the springs on the outside of the pit below its bottom can be neglected (Fig. 2, h), and replaced by a constant pressure of the soil in a state of rest. If these springs are eliminated from the computational diagram of the beam on the outside of the pit, the pressure of the soil against the enclosure below the bottom of pit will be  $q_0 = q_{01} - q_{02}$ , and the springs on the inside beneath its bottom will be under no prestress.

To convert to the standard diagram of a beam on an elastic bed, let us point out that the amount  $k \cdot z$  by which the pressure of the springs is reduced against the enclosure during release in (2) is the reaction of ordinary springs with no prestress, which are positioned on the opposite side when acted upon by force  $q_{01}$ . The work of the prestressed springs is then equivalent to the work of stress-free springs under a load equal to the prestress.

Consequently, the problem reduces to one of a beam on an elastic bed (Fig. 2, i), where the beam represents the pit enclosure, the external load is the lateral pressure of the soil in a state of rest  $q_0 = q_{01} - q_{02}$ , and the coefficients of the elastic bed are the stiffness coefficients  $k$  of the "SCM-soil" system, which depend on the dimensions and shape of the SCM, as well on the strength and deformation characteristics of the soil. Considering the above, let us determine the following for further analysis:

1) the active pressure against the "enclosure-SCM-soil" system – the pressure  $q_0$  of the soil at rest;

2) the contact pressure on the enclosure, which can be transmitted through the SCM

$$q = q_0 - kz; \quad (3)$$

3) the reactive pressure of the SCM – that portion of the active pressure against the system, which can be taken up by the SCM as the system transitions to a new equilibrium position after excavation of the pit

$$r = kz. \quad (4)$$

Depending on the displacements of the enclosure, the soil mass may function in an elastic stage, which can be described by the work of elastic springs, or a plastic stage when the contact pressure against the enclosure attains the active or passive pressure of the soil. Since the basic purpose of SCM use is to ensure preservation of surrounding development, the stress-strain state (SSS) of the surrounding soil mass should not go over into a plastic state, and the displacements of the enclosure during excavation should be so small that Coulomb's limiting equilibrium will not be realized. In the analyses, therefore, only the elastic work of the system, where the SCM ensures that the soil, and, accordingly, the "SCM-soil"

system, will function elastically, is ensured. This enables us to perform the calculations in a linear statement, appreciably simplifying solution of the problem of the optimal design of the system under consideration.

In conformity with the physical essence of the problem, the contact pressure against the enclosure above the bottom of the pit cannot be less than zero (cannot act in the opposite direction due to excavation of the pit). For stiffness coefficients above the bottom of the pit should be satisfied the condition

$$q = q_0 - kz \geq 0. \quad (5)$$

Using (5) the "enclosure-SCM-soil" system, therefore, it is possible to use a finite-element formulation of a beam on an elastic bed, where the lateral pressure of the soil in a state of rest is the load.

Let us borrow terminology from (Hogg and Arora 1983) to construct the mathematical optimal-design model. Terms of the theory of matrix calculus can also be used when necessary.

In the computational model selected:

– the *equation of state* is the matrix equation of the finite-element method (FEM)

$$K(k)Z - Q = 0, \quad (6)$$

where  $K(k)$  is the global stiffness matrix of the system, the elements of which will depend on  $k$ , and  $Q$  and  $Z$  are the vectors of the nodal loads and displacements, respectively;

– the *state variables* are the displacements  $Z$  at the nodes of the finite-element diagram, which describe the behavior of the system in question under load. The transposed form of the vector

$$Z = [Z_1, Z_2, Z_3, \dots, Z_m], \quad (7)$$

where  $m$  is the number of degrees of freedom and state variables  $m = 2n + 2$ , and  $n$  is the number of finite elements. After exclusion the angle of rotation from vector  $Z$  the vector  $z$  of horizontal displacements expressed as follows

$$z = [Z_1, Z_3, \dots, Z_{m-1}] = [z_1, z_2, z_3, \dots, z_{n+1}]; \quad (7a)$$

– the *design variables* are contained in the set of coefficients  $k$ , which describes the system itself, but not its behavior.

$$k = [k_1, k_2, k_3, \dots, k_n]. \quad (8)$$

For the computational diagram under consideration, let us write in the terms of the problem statement of an optimal finite-dimensional design in state space.

It is required to determine the set of design variables  $k$ , which will minimize the efficiency function, as determined by the total stiffness coefficient with respect to all finite elements of the model

$$\psi_0 = \psi_0(k) = \sum k_i \rightarrow \min, i = 1 \dots n \quad (9)$$

$$\text{when state equations} \quad h(k, z) = K(k)Z - Q = 0 \quad (10)$$

$$\text{and constraints} \quad \psi(k, z) = [\psi_1(Z), \psi_2(k), \psi_3(k), \psi_4(k, Z)]^T \leq 0 \quad (11)$$

exist, where  $\psi(k, Z)$  is the set of its type of constraints,  $i = 1-4$ .

Let us define the types of bounded functions.

1. Bounded-function vector  $\psi_1(Z)$  is determined from the conditions of the problem for which limits should be placed on horizontal displacements  $z$  (7, a) at all  $n + 1$  nodes of the enclosure, which is broken down into  $n$  elements. The expressions  $\psi_1(Z)$  are derived proceeding from the inequalities

$$z_1 \leq S_{\max}, i = 1 \dots n + 1 \quad (12)$$

2. The vector function  $\psi_2(k)$  reflects the limits placed on the design variables  $k$ . Expressions for

$$\psi_2(k) \text{ are derived, proceeding from the inequalities} \quad k_i \leq k_{\max}, k_i \geq k_{\min}; i = 1 \dots e, \quad (13)$$

where  $e$  is the number of the last element situated above the base of the pit,  $k_{\max}$  is the value defining the upper limit of the variation of a variable, and  $k_{\min} = 0$  is the lower limit of variation in the absence of an SCM.

3. The vector function  $\psi_3(k)$  reflects the limits placed on the design variables  $k$  below the bottom of the pit. The expressions for  $\psi_3(k)$  are derived from the inequalities

$$k_i < k_{max}; k_i > k_{min}; i = e + 1 \dots n, \quad (14)$$

where  $k_{min}$  is the lower limit of variation, and  $k_{min} = k_{so}$  corresponds to the stiffness coefficient of the soil when functioning elastically.

4. The vector function  $\psi_4(k, Z)$  reflects the constraint that ensures fulfillment of (5) – a reduction in pressure on the elements residing above the base of the pit, and cannot exceed the active horizontal load of the soil at rest on the corresponding element. The expressions for  $\psi_4(k, Z)$  are derived from the inequalities

$$r_i = k_i \cdot z_i < q; i = 1 \dots e + 1 \quad (15)$$

where  $r_i$  is the reduction in pressure, or the reaction of the elastic bed at the  $i$ th node,  $k_i$  is the coefficient of the elastic bed at the  $i$ th node, and  $z_i$  is the horizontal displacement  $z$  (7, a) at the  $i$ th node.

In the problem under consideration, the limits are represented by the following type of set:

$$\psi(k, z) = [\psi_1(Z), \psi_2(k), \psi_3(k), \psi_4(k, z)] \quad (16)$$

Using (9), (10), and (16), the structure and analytical form of the components of the mathematical optimal-design model are entirely defined and ready for the solution.

## 2 PROBLEM SOLUTION

The search algorithm for optimization based on the method of gradient projection, where that variation in design variables, for which the efficiency function is decreased, and the limits are not violated, is determined in each interval, is compiled for the problem's solution, and is implemented in the software package MATLAB v.7.9.0. The gradients of the efficiency and bounded functions with respect to design variables are required for construction of the algorithm are determined from analysis of the sensitivity of the design in state space (Hogg and Arora 1983).

The search strategies consist in the plotting of a succession of  $k^p$  points calculated in accordance with the rule

$$k^{p+1} = k^p + \delta k^p, p = 0, 1, \dots, \quad (17)$$

where  $p$  is the number of iterations,  $k^p$  is a vector in the form of (8), and  $\delta k^p$  is the vector of variation in the design variables, which decreases the efficiency function as determined for each  $p$  using the gradients obtained from sensitivity analysis of the design.

Figure 3 shows a geometric interpretation of the performance of the algorithm for a two-dimensional space. The resultant vector of the variation in the design  $\delta k^p$  is obtained as a result and the iteration process of the search for the conditional extremum acquires the form shown in Fig. 3

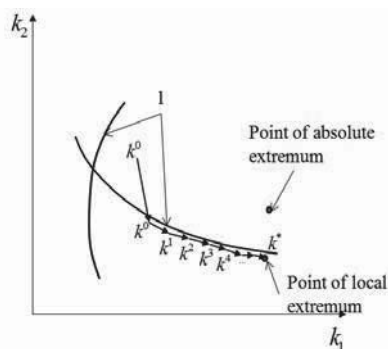


Figure 3. Geometric interpretation of algorithm performance:

1) curve of bounded function;

After running the algorithm, the succession of points converges on the optimal value of the efficiency function, i.e., the optimal distribution of  $k^*$ . As a result of running the

algorithm, the sequence of points converges to the optimal value of the efficiency function, i.e., to the optimal distribution of the coefficient  $k^*$  of the bed's stiffness.

The dimensions of the SCM corresponding to this stiffness are required for determination of the optimal distribution of the coefficient  $k$ . The following are basic initial data for determination of the optimal dimensions of the SCM:

- the minimum height  $h$  of the SCM, as determined above and below the bottom of the pit based on the distribution curves of  $k$  and the reactive pressure  $R$ ;

- the total reactive pressure of the SCM over the height  $h$ , which should be taken up by the SCM as a component part of the soil in order that the "SCM-soil" system correspond to the elastic behavior

$$R = \sum r_i, \quad (18)$$

where  $i$  is the number of nodes over the height  $h$ , and the point of application of the force  $R$  resides at the level of the center of gravity  $r$  of the plot; and,

- the average displacement  $z_{avg}$  of the enclosure over height  $h$ , which corresponds to the displacement of the SCM under the action of  $R$

$$z_{avg} = \sum z_i / v, \quad (19)$$

where  $v$  and  $i$  are the number of nodes, and the numbers of the nodes over height  $h$ .

Use of  $R$  and  $z_{avg}$  enable us to convert to the assumption that as a component part of the soil, the SCM functions as a solid body, and is not calculated for individual elements over the height.

It is therefore required to determine the minimum dimensions of the SCM for which it will experience a horizontal displacement  $z_{avg}$  under the horizontal force  $R$ .

Let us examine the application of the above-indicated computational principles in an example of the calculation of optimal SCM dimensions for the excavation of a pit in sand with the following initial data: specific weight  $\gamma = 20 \text{ kN/m}^3$ , overall compression modulus  $E = 25,000 \text{ kPa}$ , angle of internal friction in shear  $\varphi = 30^\circ$ , cohesion  $c = 1.0 \text{ kPa}$ , pit depth of 20 m, enclosure depth of 30 m, a "diaphragm wall" enclosure with a thickness of 800 mm, and an upper thrust bracing consisting of a reinforced concrete span with a thickness of 500 mm.

Solution of the optimal-design problem (Fig. 4) includes curves of enclosure displacements (Fig. 4, a), distributions of the optimal stiffness coefficient over the height of the enclosure (Fig. 4, b), the reactive pressure (Fig. 4, c), and the contact pressure (Fig. 4, d).

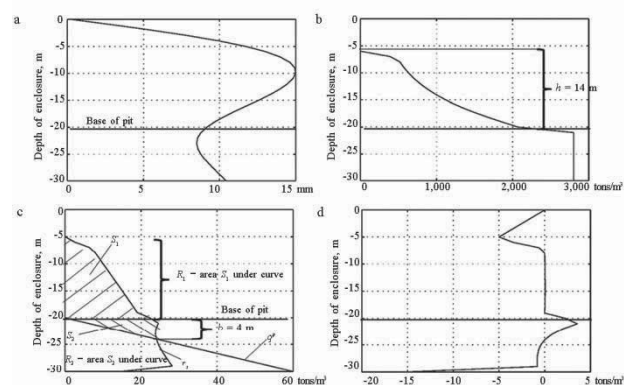


Figure 4. Results of calculation for  $S_{max} = 15 \text{ mm}$ : a) displacement; b) stiffness coefficient diagram; c) reactive pressure; d) contact pressure

To determine the optimal dimensions, let us examine the SCM above and below the bottom of the pit.

According to the plot (Fig. 4, b), the SCM above the bottom of the pit extends to the point along the height where  $k = 0$  and  $h = 14 \text{ m}$ . For the enclosure above the bottom of the pit where  $k = 0$ , no soil cement is required. Let us consider the SCM a massive retaining wall 14 m high, the upper and lower bases  $a$  and  $b$  of which should be determined from calculation of (18) for a

horizontal load  $R_1$  corresponding to area  $S_1$  under the reactive-pressure curve in Fig. 4, c and the displacements  $z_{av/2}$  (19).

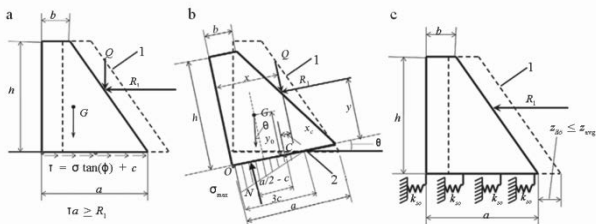


Figure 5. Computational diagrams for SCM above bottom of pit: 1) initial position; 2) turning point.

The optimal dimensions of the SCM on the outside of the pit were found by solving the other optimization problem which minimize cross sectional area of the massive retaining wall (trapezoid)

$$\Psi_0(a, b) = (a+b)h/2 \rightarrow \min \quad (20)$$

for limits ensuring observance of the following conditions:

1) stability against shear (Fig. 5, a)

$$(Q(a, b) + G(a, b))\tan(\varphi) + ca \geq R_1, \quad (21)$$

where  $Q$  is the weight of the soil in the SCM benches;

2) stability against overturning about a certain point (Fig. 5, b) with consideration of the deforming bed in accordance with Klein's procedure (Klein 1964)

$$M_{re}(a, b) = N(a/2 - c) \geq M_d(a, b) = R_1y + G(a/2 - x) - Qx_c; \quad (22)$$

3) the displacement  $z_{sc}$  of the SCM under the action of  $R_1$  should not exceed the displacement

$z_{avg}$  averaged over the height  $h$  (Fig. 5, c).

$$z_{sc} = \frac{R_1}{k_{sp} a \cdot tg\varphi} \leq z_{cp};$$

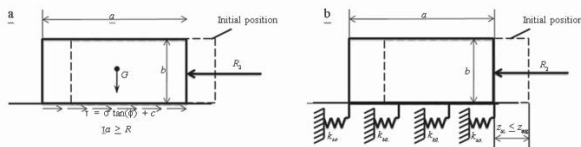


Figure 6. Computational diagram for SCM below bottom of pit

If the first two stability conditions are observed, the displacement of the SCM is determined only by the horizontal deformation of the soil in the bed, which is described by the stiffness coefficient  $k_{so}$  of the soil when the rotation of the mass is disregarded.

In order for the system to function in the elastic stage, the dimensions of the SCM below the bottom of the pit are determined with consideration of the fact the soil takes up the reactive pressure, and the SCM the remaining portion. Above the point of intersection, the reactive pressure exceeds the passive pressure of the soil  $q_p$  (see Fig. 4, c), but is lower than the passive pressure below the point; the minimal height of the SCM will therefore correspond to the distance from the bottom of the pit to the point of intersection of the  $r$  and  $q_p$  curves. Here, the design load on the SCM is calculated based on area  $S_2$  (see Fig. 4, c)

The optimal dimensions of the SCM under the bottom of the pit are determined by solving the optimization problem which minimize the value of the efficiency function corresponding to the cross-sectional area of the mass

$$\Psi_0(a, b) = ab \rightarrow \min \quad (25)$$

with limits ensuring observance of the following conditions:

- the stability of the SCM against shear (Fig. 6, a)

$$R_2 \leq F_n = G \tan(\varphi) + ca; \quad (26)$$

- the displacement  $z_{sc}$  of the SCM under load  $R_2$  is no greater than the displacement  $z_{avg}$  averaged over height  $h$  (Fig. 6, b)

$$z_{sc} = \frac{R_2}{k_{so} a \cdot tg\varphi} \leq z_{avg} \quad (27)$$

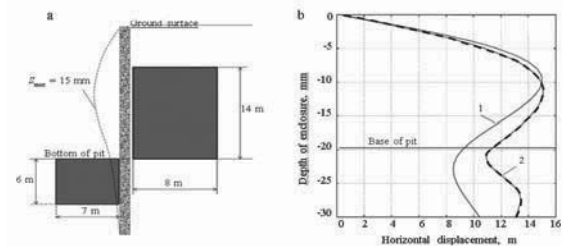


Figure 7. Results of problem solution: a) optimal SCM dimensions when  $S_{max} = 15$  mm; b) results of comparison: 1) elastic bed; 2) PLAXIS 2D.

The optimal dimensions are determined for the allowable displacement of the enclosure  $S_{max} = 15$  mm as a result of solution of the problems described (Fig. 7, a).

The numerical modeling was performed in the software package PLAXIS 2D with consideration of the SCM dimensions obtained, and plots of the horizontal displacements were compared (Fig. 7, b). The discrepancy between the maximum horizontal displacements was insignificant, although the pattern of the curves differed somewhat. Similar calculations and comparison with PLAXIS were conducted for the same initial data, but with limits placed on the displacements  $S_{max} = 30$  and 60 mm. It was established that the SCM dimensions obtained with use of the proposed method yielded a high safety factor with respect to displacements with increasing tolerances. Application of the method in question is therefore restricted to the region of small enclosure displacements; this does not contradict the goals of the stated problem.

### 3 CONCLUSIONS

A computational method is developed for determination of the optimal dimensions of a soil-cement mass (SCM) that reduces the displacements of an enclosure to required values. The method includes:

- a computerized-search algorithm for optimal engineering of the coefficient of stiffness of an elastic bed; and,
- calculation of optimal SCM dimensions corresponding to the optimal stiffness using standard procedures for analysis of massive retaining walls.

The computational method makes it possible to determine optimal SCM dimensions for the excavation of deep pits in a dense urban setting, when it is necessary to shorten considerably the construction time, and ensure a minimal effect of excavation on surrounding development.

### 4 REFERENCES

- Gotman Yu.A. 2010. Variant design of using the jet-grouting technology for reduction of the settlements of existing buildings during construction of an underground complex in Moscow., *Geotechnical Engineering 20. View of Young European Geotechnical Engineers*, Brno, 134-139.
- Hogg E. and Arora Ya. 1983. Applied Optimal Design. *Mechanical Systems and Structures* [Russian translation], Mir, Moscow.
- Klein G.K. 1964. *Analysis of Retaining Walls* [in Russian], Vysshaya Shkola, Moscow.

# Case Studies of Complicate Urban Excavation from Design to Construction

## Études de cas d'excavations complexes en site urbain: de la conception à la construction

Jang Y.S.

*Dept. of Civil & Env. Eng., Dongguk Univ., Seoul, Korea*

Choi H.C.

*Architectural Structure Team. SK E&C*

Shin S.M., Kim D.Y.

*Saegil Engineering & Consulting. Co. Ltd., Seoul, Korea*

**ABSTRACT:** Various types of retaining walls, e.g. H-Pile with Timber, C.I.P (cast in place pile) and subsurface continuous walls, are domestically used for excavation sites in Korea depending on the site conditions, architectural structure and geotechnical conditions. Ground Anchor, strut and permanent slab are used as support methods. The wall displacements and axial forces of the struts are variable depending on the excavation depth, groundwater level and construction methods, etc. In this study, case studies are performed for the excavation sites, where the modified slab methods, e.g S.P.S, and S.T.D are used and the ground anchors as temporary supports. The wall displacements and the axial forces predicted at the design stage and monitored in the actual excavation stage are analyzed. The advantage of construction time using the permanent slab method is discussed.

**RÉSUMÉ :** Différents types de murs de soutènement, par exemple pieu en H avec du bois, CIP (Pieu en béton coulé en place) et des parois continues ancrées dans le sol, sont à usage domestique pour les sites d'excavation en Corée suivant les conditions du site, la structure architecturale et les conditions géotechniques. Ancrage au sol, entretoise et dalle fixe sont utilisés comme méthodes d'étalement. Les déplacements du mur et les forces axiales des entretoises sont variables en fonction de la profondeur de l'excavation, du niveau des eaux souterraines et des méthodes de construction, etc. Dans cet article, des études de cas sont réalisées pour les sites d'excavation, où les méthodes de dalle modifiées (SPS, MST) sont utilisées et aussi les ancrages au sol comme des appuis temporaires. Les déplacements du mur et les forces axiales prévus au stade de la conception sont examinés et analysés dans la phase réelle d'excavation. L'avantage de la durée de construction en utilisant la méthode de dalle permanente est discuté dans cet article.

**KEYWORDS:** S.P.S, S.T.D, C.I.P, Ground Anchor, Strut, Slab, Displacement, Axial force, Construction time

**MOTS-CLÉS :** S.P.S, S.T.D, C.I.P, Ancrage au sol, entretoise, dalle, déplacement, force axiale, durée de construction

### 1 INTRODUCTION

Recent urban building construction has trends of deep excavation and the methods of excavation are diversified. In addition, various types of structures, e.g. the subway tunnels and utility lines and pre-existing buildings are located around the excavation sites. Therefore, when the excavation is done in the metropolitan area, the excavation plans must be made considering the safety, constructability and cost effectiveness synthetically.

In this paper, the retaining wall displacements and the axial forces of the excavation sites which are constructed using the various supports, e.g. C.I.P. with ground anchor, and the permanent slab methods, i.e. S.P.S and S.T.D., are monitored and analyzed using the related case histories.

### 2 EXCAVATION METHODS

In the case studies, two new excavation methods, i.e. S.P.S and S.T.D, are used and the concepts of each methods are introduced. In the S.P.S(Strut as Permanent system) method, the subsurface steel frame and beams are designed strong enough to endure the temporary and permanent external pressures. They are used as temporary retaining walls while the excavation is going on. They can also be used as the walls of main structures without dismantling of strut after the excavation is finished. Fig. 1 shows the conceptual diagram and the field example.

S.T.D (Strut Top Down) method can use the struts which increase the resistance to horizontal pressures. It can also use various types of basement slabs such as beam & girder as well

as one or two way wide beams (Sho et al. 2004). Fig. 2 shows the conceptual view of S.T.D construction and the field example.

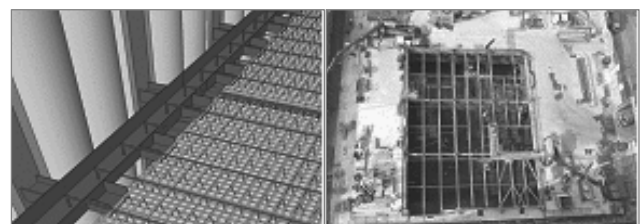


Figure 1. Conceptual diagram and field example of S.P.S

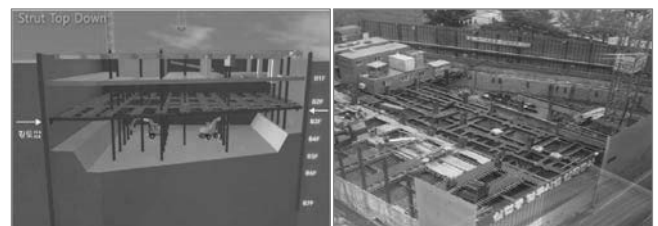


Figure 2. Conceptual diagram and field example of S.T.D

### 3 SITE CONDITIONS

#### 3.1 Site 1: S.P.S and ground anchor on C.I.P wall

Site 1 is the office facility of 7th floor on the ground and 3rd floor in the basement. The building is located at Chung Ju in the central region of Korea (Saegil E&C, 2011a). The excavation depth is in the range of of GL.-14.0m~GL.-20.0m. High apartments with deep parking lot are in the southern part of the site. A building with basement is located 20m apart from the site in the west. Roads of 35m and 23m are located at the north and the east part of the site.

Two types of retaining walls are used, i.e. rigid C.I.P wall and H-Pile & Timber. Ground anchor is used as the support of both walls. Considering the tall buildings with basements, S.P.S method is used at the southern part (Fig. 3).

The soil profile of the excavated site is composed of buried soil layer, alluvial layer, weathered soil and rock layers from the surface. Most of the excavated parts are composed of soils (Fig.4). Two sections, i.e. S.P.S and ground anchor, are selected as the analysis section in this paper (Fig. 5).

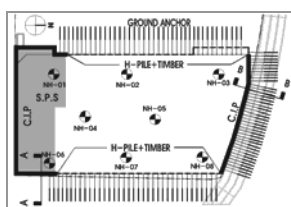


Figure 3. Plan view of site 1

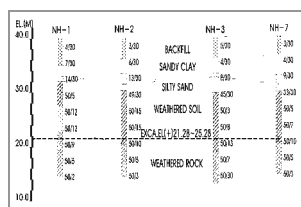


Figure 4. Soil profile of site 1

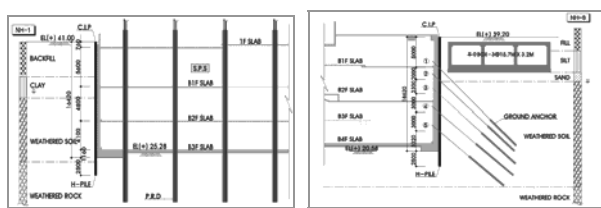


Figure 5. Section view of Site 1

#### 3.2 Site 2: S.T.D and C.I.P

Site 2 is the office facility of 23rd floor on the ground and 7th floor in the basement. The building is located at Sang Am dong, Seoul, Korea (Saegil E&C, 2011b). The excavation depth is in the range of GL.-25.0m~GL.-31.0m. A building of 20th floor on the ground and 5th floor in the basements is located to the north of the site. In the east, the road of 30m wide and the building with 21st floor on the ground and 7th floor in the basements is located. The roads of 30m wide are located to the south and the west directions.

The retaining wall is composed of C.I.P in the soil layer and H-Pile & shotcrete in the rock layer. S.T.D method is used as the support of the excavation site (Fig. 6).

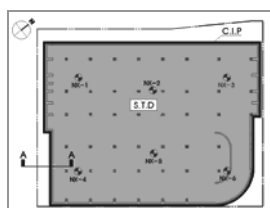


Figure 6. Plan view of site 2

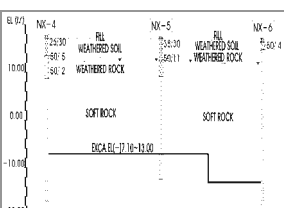


Figure 7. Soil profile of site 2

The soil profile of the excavated site is composed of buried soil layer, weathered soil and rock layers, and soft rock layer from the surface. The geotechnical investigation shows that the

soft rock appears at the shallow depth of GL.-2.4m and GL.-9.2m (Fig. 7).

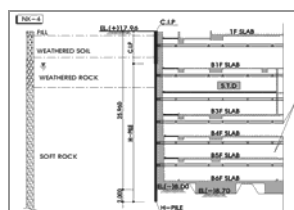


Figure 8. S.T.D Section A-A'

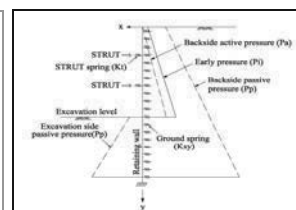


Figure 9. Schematic section for Analysis Program

The sections of retaining walls, i.e. C.I.P in the soil layer and H-Pile & shotcrete in the rock layer are selected for analysis. S.T.D method is used as the supports of the excavated site (Fig. 8).

### 4 ANALYSIS PROGRAM FOR DESIGN

The program used in the design stage is SUNEX(Step Under ground EXcavation), which is a stress-strain analysis program commonly used for the design of the deep excavation site in Korea (Geogroup Eng., 2010). This program calculates earth pressure on the braced earth retaining system, horizontal displacement, shear force and bending moment of vertical wall and axial force of supports and tieback anchors for step by step excavation.

The program adopts elasto-plastic behavior of soil to calculate earth pressure on the retaining wall. Calculation model includes elastic beam for vertical wall (elastic-plastic beam optional), elastic spring for strut and tieback anchor, elasto-plastic spring for active and passive soil (Fig. 9).

### 5 COMPARISON OF DESIGN AND MONITORED VALUES

Both the wall displacement and the axial stress of the struts obtained either from the design stage using the SUNEX or from the field monitoring using the field installed instruments. In this section, The two values are compared by separating to the mid and the final stage of the excavation.

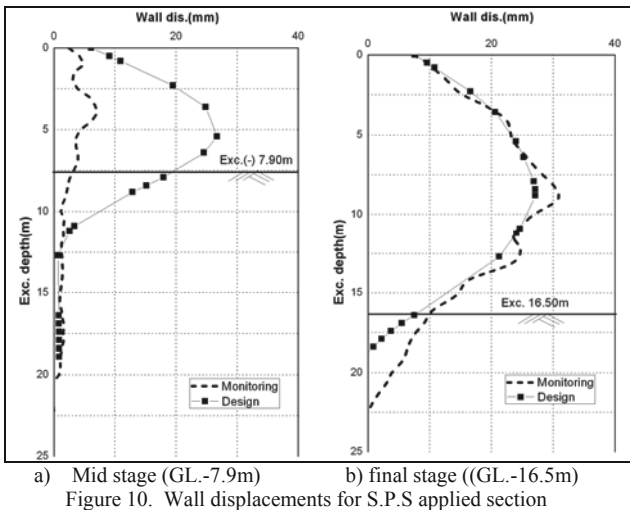
#### 5.1 Wall displacements

##### 5.1.1 Site 1 : S.P.S and ground anchor on C.I.P wall

The displacements of wall in which S.P.S method is applied are shown in Fig. 10 for the mid and final stages of excavation, i.e. GL.-7.9m and GL.-16.5 m.

In the mid stage of excavation, the predicted design displacement was 26.7mm and was greater about 20mm than the monitored displacement of 7.0 mm. This discrepancy seemed to come from the fact that the influence factors, e.g. the loads behind the wall, the excavation height for installation of supports, and weak soil profiles near the ground surface, were selected conservatively compared with the real field conditions.

However, in the final stage the two values were come out quite close. The reasons for this consistency are: (1) The construction conditions was very similar to the one adopted in the design stage, according to the construction process identified at the site; (2) In S.P.S method, it is able to install the steel supports immediately after the excavation. This gives an advantage of reducing the time delayed displacement of the wall, which developed the quite consistent displacements between the design stage and the actual excavation.

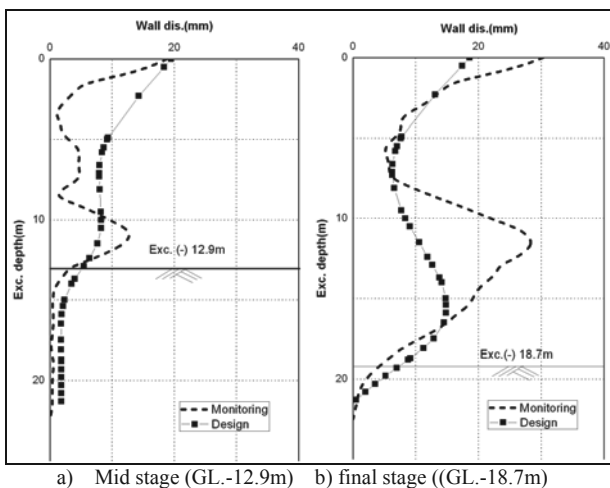


a) Mid stage (GL.-7.9m) b) final stage (GL.-16.5m)  
Figure 10. Wall displacements for S.P.S applied section

The displacements of the wall where the ground anchors are applied are shown in Fig. 11. As can be recognized in the figure, the predicted displacement in the mid stage was larger than the monitored value. In the final stage, the two displacements are consistent partly but larger displacements of 10mm are monitored at the upper and central positions of the wall.

This large displacement seems to come from the initial over-excavation length of more than 5m due to the sewage culvert box near the ground surface in Fig. 5b. As the excavation went on the final stage, the spacing of the ground anchors was about 3m and the over-excavation which was greater than the designed strut spacing was made in the field.

Therefore, it is judged that a particular sites like this one which has large sewage culvert box near the ground surface and the over excavation is made near the final stage needs the detailed design and construction considering all the factors related to spacing of the ground anchor and strut, initial displacement of the wall near the ground surface and the geotechnical conditions included.



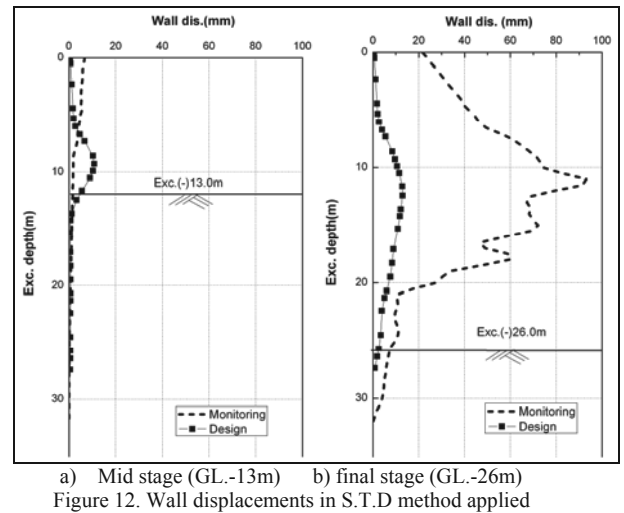
a) Mid stage (GL.-12.9m) b) final stage (GL.-18.7m)  
Figure 11. Wall displacements for ground anchor applied section

5.1.2 Site 2: S.T.D and C.I.P

Fig. 12 shows the wall displacements for mid and final stages of excavation in the site 2 where S.T.D method is applied. The excavation depths of mid and final excavation stages were GL.-13.0m and GL.-26.0m, respectively. In the mid stage, the predicted and monitored displacements came out very similar. In the final stage, large discrepancy was recognized for the

predicted and the monitored displacements, i.e. 13mm and 93.1mm, respectively.

Proper construction process and the favorable soil conditions near ground surface seemed to create the consistent wall displacements in the mid stage. Large monitored wall displacements may come from the fact that (1) The design condition would not include the time effect of concrete curing in the slab; (2) over excavation was made since the weathered and soft rocks appeared in the initial stages of excavation. The large discrepancy of the wall displacement about 80mm was the accumulated displacement of the 26m deep excavation.



a) Mid stage (GL.-13m) b) final stage (GL.-26m)  
Figure 12. Wall displacements in S.T.D method applied

6 AXIAL FORCES OF RESISTANT BODIES

6.1 Site 1 : S.P.S and ground anchor on C.I.P wall

Fig. 13a shows the predicted and monitored axial forces acting the struts of S.P.S. The two axial forces in the initial stage showed large difference, because the construction conditions, e.g. ambient temperature and impacts, etc, create large changes in the strain gages measuring the axial forces. However, this discrepancy was reduced as the predicted and monitored displacements became similar (see Fig. 10b).

It is necessary to identify the wall displacements together when the axial forces in the supports of S.P.S are analyzed.

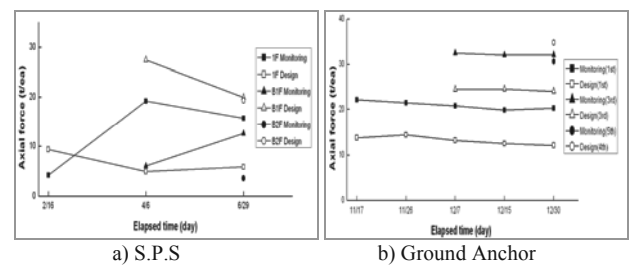


Figure 13 Axial forces for site 1

Fig 13b shows the axial forces of ground anchors in the locations where the ground anchors were applied. In general, the pre-stress considered in the design stage is sufficiently reflected on the ground anchors constructed in the field. However, the monitored axial forces tend to be larger than the predicted values in the design stage in site 1, although the pre-stresses are fully reflected at the excavation.

According to Fig. 11b, the axial forces were large at the locations in which the large wall displacements are detected. At the location of 5th floor in which the design and monitored

displacements are closer to each other, the two axial forces were also close to the values of 35tons.

High correlation is recognized between the wall displacements and the axial forces in the struts. In addition, the changes of axial forces were negligible as the time elapses at the locations where the large wall displacements are detected. This means that the ground anchors are working quite well at such locations (Jang et al., 2012).

6.2 Site 2: S.T.D and C.I.P

Fig. 14 shows the axial forces which act on the slab of S.T.D method by comparing design and monitored values. The monitored axial forces are mostly larger than the predicted values set in the design stage. This result came from the increased wall displacement due to over-excavation and the characteristics of S.T.D. method.

Contrary to the direction of the soil pressures, tensile forces are developed on the 1st anchor from the top. This may come from the large displacement in the central part of the wall, i.e. B2F and B3F, which gave reverse stresses on the upper part of the wall.

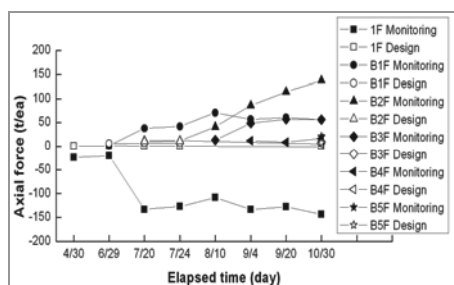


Figure 14. Section A-A' Slab axial forces

7 COMPARISON OF CONSTRUCTION TIME

The current retaining wall design, which uses slab as the support of the wall, applies S.P.S and S.T.D methods. These methods can save the construction time because they can support the retaining walls as well as can use the slabs as the permanent basement structure of the building. The two sites have different excavation area and depth. Hence a direct comparison of the construction period was difficult. In this study, construction period was calculated and relative comparison was made based on the Site 1, which was quantified by area (15,000 m<sup>2</sup>) and the excavation depth (GL.-19m).

Table 1 shows the comparison of the construction time of the basement for different support methods. In Site 1 where the ground anchors are partly used, the construction time was 9 months. However, in Site 2 where the slab support S.T.D is used, the slabs are installed simultaneously with the excavation and the time taken to finish the basement structure was 7 months.

Table 1. Comparison of construction time for two sites

Construction Method		Site 1: Chung Ju	Site 2 : Sang Am
		S.P.S & Anchor	S.T.D
Excavation Depth		GL.-19m	GL.-26m
Excavation And Sub- structure	Start	2010.10	2012.04
	End	2011.06	2012.11
	Period	9 month	7 month

8 CONCLUSIONS

In this study the displacement on the C.I.P. walls and the axial forces on the slabs are monitored in the two excavation sites. In the sites, two new top down methods, S.P.S & S.T.D, are applied with the traditional support method, i.e. ground anchor. The monitored values are analyzed and compared with those predicted at the design stage. The conclusions obtained are the following:

- 1) The monitored displacements of C.I.P rigid walls with S.P.S support were similar to the predicted values. The displacement of the S.P.S support wall came from the characteristics of the support which does not applies the pre-stresses to the wall. The displacement of the wall is allowed by the slab without restriction.
- 2) Even though the rock layer is appeared in the shallow depth, large displacements and axial forces are monitored compared to the values predicted at the design stage in the site where S.T.D. method is applied. This is because the excavation depth is deep and the over-excavation was made at the final stage of construction to reduce the construction time.
- 3) It is necessary to reflect the characteristics of the excavation method and the soil conditions when the retaining walls are planned for excavation site. At the site of excavation, the monitored value in each stage should be reviewed and compared with the designed values. Feedback analysis is sometimes needed when some field problems are anticipated.
- 4) Quantitative inspection of the construction time of the selected sites identifies the significant reduction of the construction time when the slab support methods are applied compared with the traditional ground anchor supports.

9 ACKNOWLEDGEMENTS

This research was supported by the Basic Science Research Program through the National Research Foundation of Korea (NRF), funded by the Ministry of Education, Science and Technology (No.2012-0002408). This paper is also a part of the result from the "Maintenance of Foundation Design Criteria under the Construction Facilities for Standardization", the "Construction & Transportation R&D Policy and Infrastructure Project".

10 REFERENCES

Geogroup Eng.(2010),"SUNEX Manual, 13th Ver. 6.01. SI Version", P1-3.  
 Jang ,Y. S., S.M Shin and J.H. Hoe (2012), "A Study on Design and Construction of Earth Retaining Wall Using Multi-Supporting System", KGS-IGS Geotechnical Workshop, I.I.T., New Delhi, December 12.  
 Saegil E&C (2011a), "Hyundai Department Chung Ju Excavation Design and Field Monitoring Report"  
 Saegil E&C (2011b), "SANG-AM DMC E2-3BL Excavation Design and Field Monitoring Report"  
 Sho, Kwang-Ho (2011) "Study on the Application of Semi-open cut Top-Down Construction for Framework" Journal of the Korean Association for Spatial Structures, Vol.11, No.2, pp.129~138.

# Passive Pressure on Skewed Bridge Abutments

## Pression passive sur des culées de pont asymétriques

Jessee S.

*Terracon Consultants, Oklahoma City, Oklahoma, USA*

Rollins K.

*Brigham Young University, Provo, Utah, USA*

**ABSTRACT:** The passive force-deflection relationship for abutment walls is important for bridges subjected to thermal expansion and seismic forces. Although a number of tests have been performed to investigate these relationships for non-skewed abutments, no tests have been performed for skewed abutments. To determine the influence of skew angle on the development of passive force, lab tests were performed on a wall with skew angles of 0°, 15°, 30°, and 45°. The wall was 1.26 m wide and 0.61 m high and the backfill consisted of dense compacted sand. As the skew angle increased, the passive force decreased substantially with a reduction of 50% at a skew of 30°. An adjustment factor was developed to account for the reduced capacity as a function of skew angle. The horizontal displacement necessary to develop the peak passive force was typically about 2.5 to 3.5% of the wall height, H, and the residual passive force typically dropped by 40% at a deflection of 4 to 6% of H. For the no-skew case, the shape of the failure plane closely resembled that predicted by the Rankine theory but was much shorter than that predicted by the log-spiral approach. Nevertheless, the log-spiral method accurately predicted the measured force while the Rankine method grossly under predicted the force.

**RÉSUMÉ:** La relation force- déformation passive des murs en retour est importante pour les ponts soumis à la dilatation thermique et des forces sismiques. Bien qu'un certain nombre de tests aient été réalisés afin d'étudier ces relations pour les murs non-biais, aucun test n'a été effectué pour les murs biais. Pour déterminer l'influence de l'angle du biais sur le développement de la force passive, des tests de laboratoire ont été effectués sur un mur ayant des angles de 0°, 15°, 30° et 45°. Le mur a une largeur de 1.26 m et 0.61 m de hauteur, le remblai se compose de sable compacté. Lorsque l'angle du biais augmente, la force passive diminue considérablement avec une réduction de 50% pour un biais de 30°. Un facteur d'ajustement a été mis au point pour tenir compte de la réduction de capacité en fonction de l'angle du biais. Le déplacement horizontal nécessaire pour développer la force maximale passive est généralement d'environ de 2.5 à 3.5% de la hauteur du mur H, et la force résiduelle passive chute généralement de 40% pour un biais de 4 à 6% de H. Pour les cas non-biais, la forme du plan de rupture est proche de celle prévue par la théorie de Rankine, mais beaucoup plus courte que celle prédite par la méthode de la spirale logarithmique. Néanmoins, la méthode de la spirale logarithmique prédit avec précision la force mesurée alors que la méthode de Rankine sous-évalue largement la force.

**KEYWORDS:** Passive force, Passive Pressure, Skewed abutments, Earth pressure, Dense sand, Plane Strain, Log-Spiral.

## 1 INTRODUCTION

The passive force-deflection relationship for abutment walls is important for bridges subjected to thermal expansion and seismic forces. Although a number of tests have been performed to investigate these relationships for non-skewed abutments (Maroney 1995, Duncan and Mokwa 2001, Rollins and Cole 2006, Rollins and Sparks 2002, Lemnitzer et al 2009), no tests have been performed to investigate these relationships for skewed abutments. Performance of skewed bridges during the 2010 M8.8 Chilean earthquake suggests that this may be an issue of concern as several such bridges were observed to have rotated about a vertical axis, becoming unseated in their acute corners (EERI, 2010).

While current design codes (AASHTO 2011) consider that the ultimate passive force will be the same for a skewed abutment as for a non-skewed abutment, numerical analyses performed by Shamsabadi et al. (2006) indicate that the passive force will decrease substantially as the skew angle increases. Reduced passive force on skewed abutments would be particularly important for bridges subject to seismic forces or integral abutments subject to thermal expansion. To better determine the influence of skew angle on the development of passive force, a series of large size laboratory tests were performed on a wall that was 1.26 m (4.1 ft) wide and 0.61 m (2 ft) high. A dense sand was compacted behind the wall to simulate a bridge approach fill. Passive force-deflection curves were measured for skew angles of 0°, 15°, 30°, and 45°. Vertical

columns of red soil were embedded into the backfill sand so that the failure surface could be located at the completion of the testing. This paper describes the test program, the test results, and the implications for design practice based on analysis of the test results.

## 1 BACKGROUND

The distribution of forces at the interface between a skewed bridge and the adjacent backfill soil is illustrated in Fig. 1 as originally outlined by Burke (1994). The longitudinal force ( $P_L$ ) can be induced by thermal expansion or seismic forces. For static or simplified pseudo-static analyses, the components of the longitudinal force normal and transverse to the abutment must be resisted by the passive force ( $P_p$ ) normal to the abutment backwall and the shear resistance ( $P_R$ ) on the backwall. Summing forces normal to the abutment produces the equation

$$P_p = P_L \cos \theta \quad (1)$$

where  $\theta$  is the skew angle of the backwall.



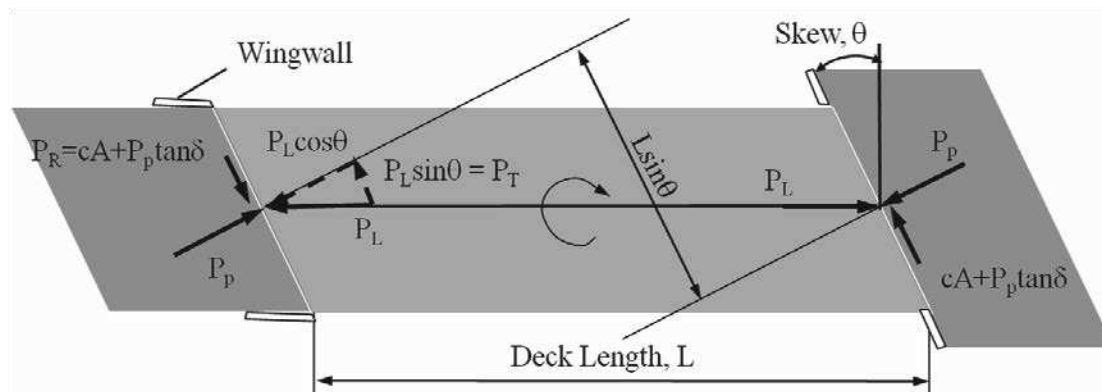


Figure 1. Illustration of forces acting on a skewed bridge at the soil-abutment interface

The transverse applied shear force ( $P_T$ ) can be computed using the equation

$$P_T = P_L \sin \theta \quad (2)$$

while the transverse shear resistance ( $P_R$ ) can be given by the equation

$$P_R = cA + P_p \tan \delta \quad (3)$$

Summing forces transverse to the backwall produces the equation

$$(cA + P_p \tan \delta) / F_s \geq P_L \sin \theta \quad (4)$$

where  $c$  is the soil cohesion,  $A$  is the area of the backwall,  $\delta$  is the angle of wall friction between the backfill soil and the concrete abutment backwall, and  $F_s$  is a factor of safety. If the applied transverse shear resistance exceeds the ultimate shear resistance, the abutment could slide against the soil leading to an unstable condition.

In addition, the offset in passive force on the abutments produce a force couple which must be resisted by the force couple produced by the shear resistances on each abutment. Summing moments about a vertical axis leads to the equation

$$(cA + P_p \tan \delta) L \cos \theta / F_s \geq P_p L \sin \theta \quad (5)$$

Again, if the shear resistance is insufficient, the bridge will tend to rotate, which would likely change the distribution of passive force on the abutments. Based on Eq 5, Burke (1994) suggested that rotation would be expected for skew angles greater than  $15^\circ$  with smooth abutment-soil interfaces and no cohesion as the factor of safety dropped from 1.5 to 1.0. If cohesion is ignored, the potential for rotation is independent of both  $P_p$  and the length of the bridge,  $L$ .

## 2 TEST LAYOUT

The test layout is illustrated in Fig. 2. A concrete wall 1.26 m (4.13 ft) wide and 0.61 m (2 ft) high was used to model the backwall of an abutment. Passive force-deflection tests were performed with skew angles ( $\theta$ ) of  $0^\circ$ ,  $15^\circ$ ,  $30^\circ$ , and  $45^\circ$ . Two tests were performed for each skew angle to evaluate repeatability. A dense sand was compacted behind the wall to simulate the backfill in a typical approach fill. The sand backfill was 0.9 m (3 ft) thick and extended 0.3 m (1 ft) below the base of the wall. The backfill was 3 to 4 m (10 to 13 ft) long to completely contain the failure surface and was slightly wider than the wall 1.28 m (4.21 ft) to allow the backwall to move into the sand backfill without any friction on the concrete sidewall. To support the sand backfill during compaction, two

1.5 m concrete blocks were bolted to the structural floor of the laboratory on either side of the fill near the wall. Beyond the concrete blocks, plywood walls were braced into a vertical position. Two plastic sheets were placed along the sidewalls to create a low friction surface and produce a 2D or approximately plane strain geometry. A base was constructed below the concrete backwall and rollers were placed at the interface between the backwall and the base to provide a normal force but minimize base friction.

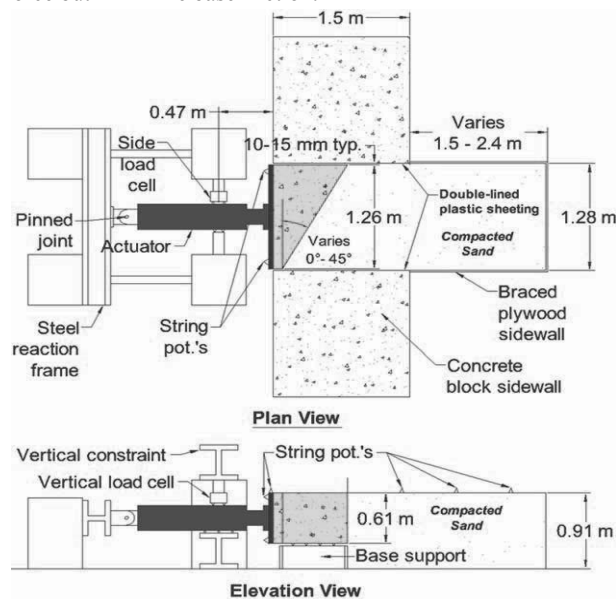


Figure 2. Plan and elevation views of the test layout.

Tests were performed by pushing the backwall longitudinally into the backfill sand using a 490 kN (110 kip) hydraulic actuator which was bolted to the backwall. Load was applied at a rate of 0.25 mm/min (0.1 inch/min); but sand is not very rate sensitive. Vertical and horizontal load cells were mounted between the reaction frame and the actuator so that the loads necessary to hold the wall in place could be measured.

### 2.1 Instrumentation

Load was measured by pressure transducers in the actuator. To measure the movement of the backwall, four longitudinal string potentiometers were positioned at the corners of the wall and two transverse string pots were positioned at the top and bottom of one side. In addition, a final string pot was used to monitor the vertical movement.

The position of the failure surface was monitored by marking 0.3 m (1 ft) square grids at the backfill surface. The subsurface failure plane position was located by placing vertical

columns of red sand spaced along the longitudinal axis behind the wall.

## 2.2 Backfill soil properties

The sand backfill is clean poorly-graded sand classifying as SP according to the Unified Soil Classification System and A-1-b according to the AASHTO system. The particle size distribution curve falls within the gradation limits for washed concrete sand (ASTM C33) with  $C_u$  of 3.7 and  $C_c$  of 0.7. A modified Proctor test was performed on the sand and indicated a maximum dry unit weight of 17.8 kN/m<sup>3</sup> (113.5 lbs/ft<sup>3</sup>). The sand was placed in 150 mm (6 in) lifts and the average relative compaction achieved was typically about 98%.

Load testing was generally performed two days after compaction and moisture content measurements at various depths were made immediately after testing. These measurements indicated good consistency between tests, with the moisture content typically falling within 7 to 9%.

Based on a direct shear test the drained friction angle ( $\phi'$ ) was found to be 46° with a cohesion of 7 kPa (140 psf). Interface friction tests were also performed between the sand and the concrete and a wall friction angle ( $\phi$ ) of 33° was measured.

Because the compacted sand in a partially saturated state could be excavated with a vertical face and remained stable for long periods, the potential for apparent cohesion owing to matric suction was also investigated. Suction measurements indicated that the sand at the moisture content during testing had a matric suction ( $\psi$ ) (negative pressure relative to atmospheric pressure) of approximately 4 to 5 kPa (80 to 100 psf). Based on recommendations of Likos et al (2010), this magnitude of suction produces an apparent cohesion ( $c_a$ ) of approximately 4 to 5 kPa (80 to 100 psf).

## 3 TEST RESULTS

### 3.1 Passive force-deflection curves

The passive force versus longitudinal deflection curves for the tests at each of the skew angles are plotted in Fig. 3. Although the initial stiffness for each curve is remarkably similar, the peak passive force clearly decreases as the skew angle increases. In addition, there appear to be some differences in the shape of the passive force displacement curves as skew angle increases.

The passive force-deflection curve appears to exhibit a typical hyperbolic curve shape for the no skew case however, it transitions to a different shape as the skew angle increases. As the skew angle increases, the passive force exhibits a longer plateau where the force remains relatively constant or increases gradually with deflection before reaching a peak and abruptly decreasing to a residual value. The peak passive force typically developed at a normalized deflection of 2.5% to 3.5% of the wall height (H), and did not change consistently with skew angle. The tests typically showed a reduction in the passive force to a residual value at a normalized displacement of 0.04H to 0.06H. The post-peak residual strength ranged from 53 to 72% of the peak value with an average of 60%. This decrease in post peak resistance is consistent with results from the direct shear tests.

The peak passive force for each test at a given skew angle has been divided by the peak passive force at zero skew and the results are plotted as a function of skew angle in Fig. 4. Normalized data from numerical analyses of skew abutments reported by Shamsabadi et al (2006) are also shown in Fig. 4 and the results follow the same trend line. The curve has been extrapolated to zero at a skew angle of 90°. The no skew case involves pure passive resistance and zero shear force. A skewed wall is subject to a combination of both passive resistance and side shear force. At the largest possible skew angle, 90°, the

forces acting on the wall transition to pure side shear force with zero passive resistance.

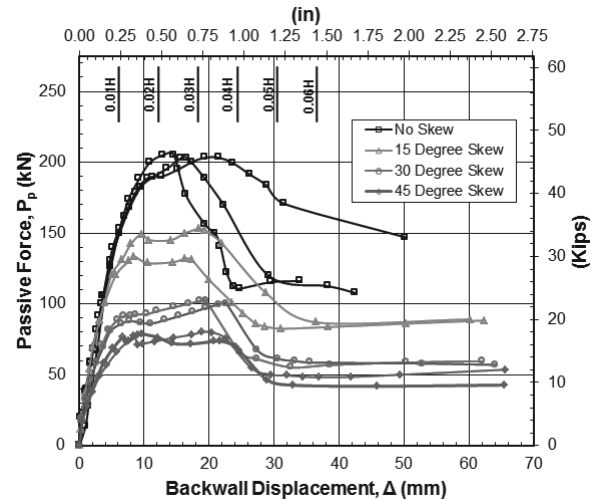


Figure 3. Passive force versus longitudinal backwall displacement for the tests at each skew angle.

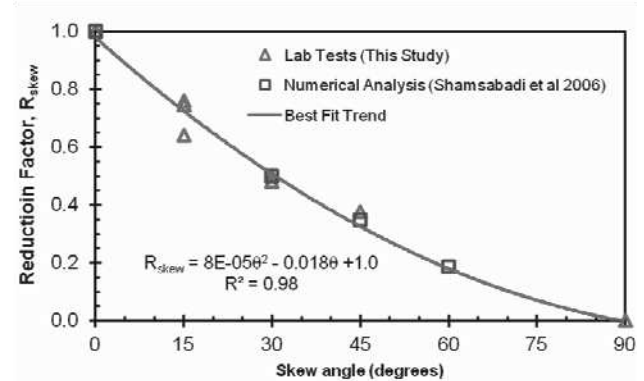


Figure 4. Normalized peak passive force versus skew angle from lab tests and numerical model results.

As indicated previously, vertical and horizontal displacements of the wall during the tests were minimal. Wall displacement was less than 4.4 mm for vertical movement and less than 2.3 mm for transverse movement for the skew angles tested.

### 3.2 Failure surface geometry

The failure surface for the no skew case was approximately the same length across the width of the sand box; however, when a skew angle was involved, the failure surface also exhibited a skew across the width of the sand box. The failure surface did not manifest itself at the ground surface until after the peak force had been reached.

The failure surface within the sand was clearly identifiable from the offset in the red sand columns. The failure surface geometry is shown as a function of distance behind the middle of the wall for the various skew angles in Fig. 5. In addition, the ground surface heave is also plotted for each test. The average length of the failure surface behind the middle of the wall was 2.1 m (7.0 ft) with a standard deviation of 0.3 m (1.0 ft). The length of the failure surface ranged from 1.8 to 2.6 m (5.9 to 8.6 ft). The failure surface typically extended 75 mm to 300 mm horizontally from the bottom of the wall then exhibited a relatively linear trend line upward to the surface. The angle of inclination of the trend line was between 19° and 21.5° with an average of 20°. Assuming that the angle of inclination ( $\alpha$ ) of the straight line segment of the log-spiral failure wedge is given by the equation:

$$\alpha = 45 - \phi'/2 \quad (8)$$

as suggested by Terzaghi and Peck (1948), then the interpreted drained friction angle would be between 47° and 52° with an average of 50°. The inferred friction angle value is higher than the measured friction angle from the direct shear test, but is close to the value that would be expected for the plane strain friction angle. The conditions and geometry of the sand box simulated a plane strain condition as well. Based on a number of studies, Kulhawy and Mayne (1990) determined that the plane strain friction angle for dense sand was 11% higher than the triaxial value on average. Thus, the plane strain friction angle for the sand used in the tests would be about 51°, which is approximately the same value as that of the inferred friction angle from the inclination of the failure wedge.

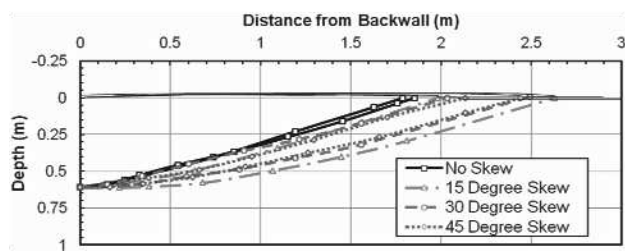


Figure 5. Measured failure surface depth versus distance from the backwall for each test.

#### 4 ANALYSIS OF RESULTS

Test results were analyzed using the Rankine (1857) and log-spiral (Terzaghi, 1948) passive pressure theories. Table 1 shows comparisons of the test results with computed passive force and failure surface orientation for the no-skew case. The measured and theoretical failure surface geometries for the no-skew case relative to the top of the wall are shown in Fig. 6. For the analysis, the soil friction angle was taken as 50°, consistent with the plane strain value, with a cohesion of 4.5 kPa (90 psf), and the wall friction angle was taken as 33° based on interface tests. While the failure plane according to the log-spiral method generally exceeded the length of the failure surface by 45 to 50%, this method was most effective in computing passive force. In contrast, the Rankine method grossly underestimated the measured force, but gave a reasonable approximation of the failure surface geometry. Although the Coulomb theory is widely used, it is limited to cases where  $\delta/\phi$  is less than about 0.5. For these tests,  $\delta/\phi$  is equal to 0.66. Thus, analyses using the Coulomb method predict an unreasonably high value for the passive force, and the failure surface extent is likewise unreasonably over-predicted (see Table 1).

#### 5 CONCLUSIONS

1. Large scale laboratory tests and numerical analyses indicate that the peak passive force for a skewed abutment significantly decreases as the skew angle increases. Based on available results, this reduction can be accounted for by using a simple reduction factor. This reduction may be dependent on abutment geometry and other unknown factors and should thus be used with caution until further research is performed.
2. For the dense sand typical of approach fills, the peak passive force for all tests typically developed at longitudinal deflections between 0.025H and 0.035H. However, the shape of the passive force-deflection curve up to the peak value transitioned from a typical hyperbolic shape for the no skew case to a bilinear shape for the skewed walls.
3. At wall displacements beyond the peak (0.04 to 0.06H) the passive force decreased substantially and the residual force was typically about 40% below the peak force, which is in agreement with the behavior in the direct shear tests.
4. Based on the measured soil parameters the log spiral method provided the best agreement with the measured passive force,

while the Rankine method grossly underestimated the force. However, the failure surface geometry was closer to that predicted by the Rankine method than the log spiral shape.

Table 1. Summary of measured tests results in comparison with computed values using different passive pressure theories.

	Passive Force		Failure Surface Geometry	
	(kN)	% of measured	Orientation (degrees)	Extent (m)
Avg. Measured	205 (46 kips)	100	20	1.8 (6.0 ft)
Coulomb Theory	1115 (251 kips)	545	3.4	10 (33 ft)
Rankine Theory	51 (12 kips)	25	20	1.8 (5.8 ft)
Log-Spiral Theory	205 (46 kips)	100	-	3.1 (10 ft)

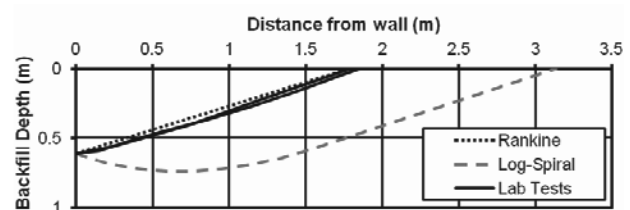


Figure 6. Measured and theoretical failure surface geometries for the no-skew case.

#### 6 REFERENCES

- AASHTO (2011), Guide Specifications for LRFD Seismic Bridge Design, 2<sup>nd</sup> Edition. 286 p.
- Burke, M.P. Jr. (1994). "Semi-Integral bridges: movements and forces". Transportation Research Record 1460, Transportation Research Board, Washington, D.C., p. 1-7.
- Cole, R.T and Rollins, K.M. (2006). "Passive Earth Pressure Mobilization During Cyclic Loading." *J. Geotech. & Geoenviron. Eng.*, ASCE, 132(9), 1154-1164.
- Duncan, J. M., and Mokwa, R. M. (2001). "Passive earth pressures: theories and tests." *J. Geotech. & Geoenviron. Eng.*, ASCE Vol. 127, No. 3, pp. 248-257.
- EERI (2010). "The M<sub>w</sub> 8.8 Chile Earthquake of February 27, 2010". EERI Special Earthquake Report. June, 2010.
- Kulhawy, F. H., and Mayne, P. W. (1990). "Manual on estimating soil properties for foundation design." Research Project 1493-6, EL-6800, Electric Power Research Institute. Palo Alto, California.
- Lemnitzer, A., Ahlberg, E.R., Nigbor, R.L., Shamsabadi, A., Wallace, J.W., and Stewart, J.P. (2009). "Lateral performance of full-scale bridge abutment wall with granular backfill," *J. Geotech. & Geoenviron. Eng.*, ASCE, 135 (4), 506-514.
- Likos, W.J. Wayllace, A., Godt, J., and Ning, L. (2010). "Direct shear apparatus for unsaturated sands at low suction and stress". *Geotech. Testing J.*, ASTM, 33(5)
- Maroney, B.H. (1995) "Large scale abutment tests to determine stiffness and ultimate strength under seismic loading" Ph.D. Dissertation, Civil Engineering Dept., University of California, Davis.
- Rankine, W. J. (1857). On the stability of loose earth. *Philosophical Transactions of the Royal Society of London*, 147.
- Rollins, K.M. and Cole, R.T. (2006). "Cyclic Lateral Load Behavior of a Pile Cap and Backfill." *J. Geotech. & Geoenviron. Eng.*, ASCE, 132(9), 1143-1153.
- Rollins, K.M. and Sparks, A.E. (2002) "Lateral Load Capacity of a Full-Scale Fixed-Head Pile Group." *J. Geotech. & Geoenviron. Eng.*, ASCE, Vol. 128, No. 9, p. 711-723.
- Shamsabadi, A. Kapuskar, M. and Zand, A. (2006). "Three-dimensional nonlinear finite-element soil-Abutment structure interaction model for skewed bridges". 5th National Seismic Conf. on Bridges and Highways, FHWA, p.
- Terzaghi K. and Peck, R. B. (1948). *Soil Mechanics in Engineering Practice*, John Wiley and Sons, New York, p.

# Deformation behaviour of clay due to unloading and the consequences on construction projects in inner cities

## Étude du comportement en déformations de l'argile suite à un retrait de charge et conséquences lors de projets de constructions en zone urbaine

Katzenbach R., Leppla S.

Technische Universität Darmstadt, Institute and Laboratory of Geotechnics, Germany

**ABSTRACT:** In the course of construction projects in many cases the soil is unloaded. For example at the construction of excavations or the deconstruction of existing buildings the soil relaxes due to the reduced stress level. Cohesive soil materials like clay react strongly time dependent. At all construction projects in the city of Frankfurt am Main, Germany, which belong to the Geotechnical Category 3 regarding Eurocode EC 7 the deformation of the soil was measured during and after the construction works. It has to be determined that the settlement relevant soil layer, the tertiary Frankfurt Clay, relaxes time-delayed due to the unloading in the dimension of centimetres. The new acknowledgement of the deformation behaviour of the Frankfurt Clay due to unloading the subsoil is presented in detail by typical projects for the development of the city.

**RÉSUMÉ :** Il arrive régulièrement dans le cadre de projets de construction en zone urbaine que le sol subisse un déchargement. Dans le cas d'excavations par exemple, le sol se détend suite à une baisse des contraintes appliquées. Le comportement des sols cohésifs tels que l'argile dépend fortement du temps. Pour l'ensemble des projets de construction à Francfort en Allemagne, ces projets étant classés en Catégorie Géotechnique 3 selon l'Eurocode 7, les déformations du sol ont été mesurées pendant et après les travaux. Il est à mettre en avant que le sol de la couche pertinente en terme de tassements, l'argile tertiaire de Francfort (Frankfurt Clay), subit un relâchement différé dans le temps suite au retrait de charge de l'ordre du centimètre. Les nouvelles reconnaissances sur le comportement de l'argile de Francfort suite à un déchargement du sol sont présentées ici en détail pour des projets typiques dans le cadre du développement de la ville.

**KEYWORDS:** Soil-structure-interaction, Frankfurt Clay, time dependent deformation behaviour, observational method.

### 1 INTRODUCTION

Since the beginning of the large infrastructure and high-rise building constructions in Frankfurt am Main the bearing and deformation behaviour of the Frankfurt Clay has been scientifically researched intensely (Chambosse 1972, Breth and Stroh 1974, Amman et al. 1975, Sommer et al. 1990, König 1994, Katzenbach and Moormann 1999, Breth and Katzenbach 2000, Katzenbach et al. 2001, Moormann 2002, Katzenbach et al. 2002, Dürrwang et al. 2007, Janke et al. 2010, Vogler 2010, Katzenbach et al. 2011). The first research and experiences made with the Frankfurt Clay result from new constructions, i.e. from high-rise buildings and tunnel constructions.

Due to the development of the city a lot of deconstruction activities occur in advance of new construction projects. In the course of these projects new knowledge about the time dependent bearing and deformation behaviour of the Frankfurt Clay is obtained, especially if there is a larger timeframe between the deconstruction (unloading) and the new construction activity (reloading). In such cases the uplifting is not overlapped or compensated by an early reloading. For example a deep excavation base usually heaves up to several centimetres as shown in Figure 1 (Amman et al. 1974).

The time dependent deformation behaviour of the over-consolidated tertiary Frankfurt Clay is presented in detail by 2 large deconstruction projects. The first project is the deconstruction of the building complex of the Zürich Insurance consisting of 2 high-rise buildings (Zürichhochhaus I and II) and the construction of the new high-rise building Opernturm at the same location. The project is located very close to a tunnel of the metro system. The second project is the deconstruction of an up to 14 storeys high-rise building in the historic centre of Frankfurt am Main. The project is located directly over 2 tunnels and an underground station of the metro system.

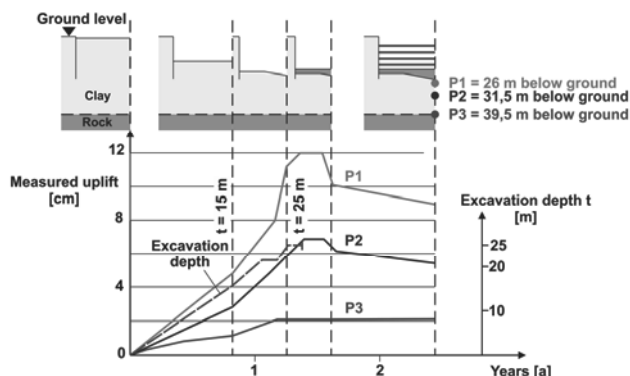


Figure 1. Measured uplift of the surface of the excavation pit at BfG high-rise building (now: European Central Bank ECB).

### 2 DECONSTRUCTION OF THE ZÜRICH INSURANCE HIGH-RISE BUILDINGS

The Zürich Insurance building complex was built between 1959 and 1963. It consisted of 2 high-rise buildings (Zürichhochhaus I and II) with heights of 70 m and 63 m and annexe to the high-rise buildings with up to 8 storeys. The complex was founded on a raft in a depth of 7 m below the surface. In the years 2001 and 2002 the complex was deconstructed down to the ground

level. The sublevels remained. A cross section through the project area is shown in Figure 2.

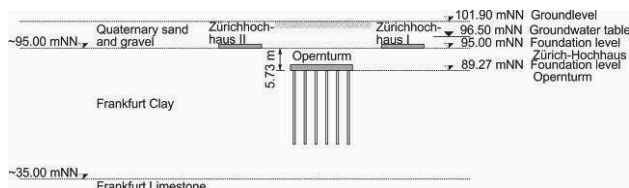


Figure 2. Soil, groundwater and foundation conditions.

5 years after the deconstruction the 177 m high-rise building Opernturm was built. The annexe of the high-rise building is up to 7 storeys high (Fig. 3) and was founded on the existing raft foundation. Under the Opernturm the existing raft was deconstructed and a new sublevel was built.



Figure 3. New high-rise building Opernturm.

The Opernturm is founded on a Combined Pile-Raft-Foundation (CPRF) consisting of a 3 m thick raft and 57 piles with a diameter of 1.5 m and a length of 40 m. For design of the CPRF a whole characteristic load of 1,500 MN was calculated. The bearing behaviour of the CPRF is described by the CPRF-coefficient  $\alpha_{CPRF}$ , explained in Equation (1) (Viggiane 1998, Hanisch et al. 2002). The Opernturm has a  $\alpha_{CPRF} = 0.9$ .

$$\alpha_{CPRF} = \frac{\sum_{j=1}^n R_{pile,k,j}}{R_{tot,k}} \quad (1)$$

The soil and groundwater conditions are typical for the inner city of Frankfurt am Main:

- 0 m to 7 m: quaternary sands and gravel
- 7 m to 67 m: Frankfurt Clay
- below 67 m: Frankfurt Limestone
- groundwater level in a depth of 5.5 m

The measured settlements during the construction of the Zürichhochhaus I and II as well as the uplift during their deconstruction are depicted in Figure 4. The measured settlements increase continuously up to 60 % of the final settlement during the construction time of the superstructure. Due to the consolidation process the deformation rate decreases continuously. About 5 years after the construction the settlement stopped at 9.5 cm at Zürichhochhaus I and 8.5 cm at Zürichhochhaus II. The deconstruction started in the middle of 2001. In March 2002 the deconstruction was completed. Only

the sublevels were kept. After 5 years the measured uplift is in the same magnitude as the settlements before.

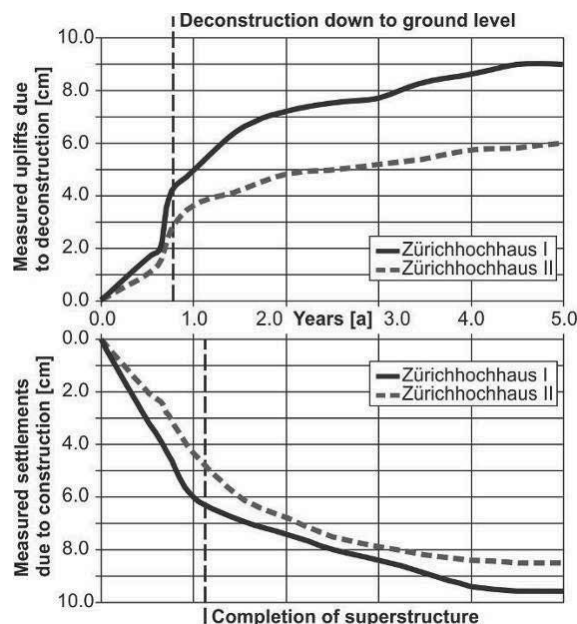


Figure 4. Measured settlements and uplifts of the soil in the area of the high-rise buildings.

The measured time dependent settlement and uplift evolution with reference to the maximum value can be approximately mathematically described by Equation 2. Figure 5 shows the application of Equation 2 to the presented project.

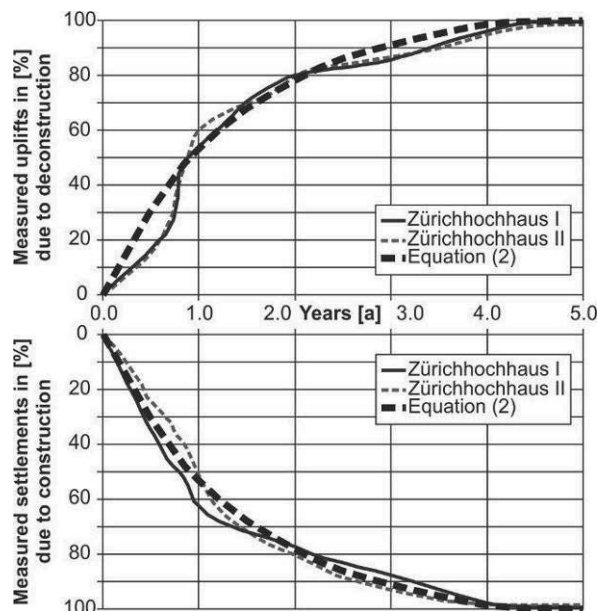


Figure 5. Measured settlement and uplift and correlation to Equation 2.

$$\frac{s(t)}{s_{max}} = k \cdot (1 - e^{-(n \cdot t)}) \quad (2)$$

where:  $k$  = Consolidation factor  
 here:  $k = 0,104 [-]$   
 $n$  = Time factor  
 here:  $n = 0,7 [-]$   
 $t$  = Time in years ( $t \leq 5$  years)

(3)

$$\frac{s(t)}{s_{\max}} = k \cdot (1 - e^{-(n \cdot t)})$$

where:  $k$  = Consolidation factor  
 here:  $k = 0,104 [-]$   
 $n$  = Time factor  
 here:  $n = 0,7 [-]$   
 $t$  = Time in years ( $t \leq 5$  years)

To verify Equation 2 the measured time dependent settlement behaviour during the construction of the high-rise building Mainzer Landstraße in Frankfurt am Main is used (Fig. 6). The construction of the 155 m high-rise building began in 1973 and the settlements were measured for 5 years. After this time a settlement of 25.4 cm was measured in the core area of the high-rise building. At the completion of the superstructure after 1.5 years the measured settlement was about 70% of the total settlement. The estimation of the time dependent deformation behaviour can also be described by Equation 2.

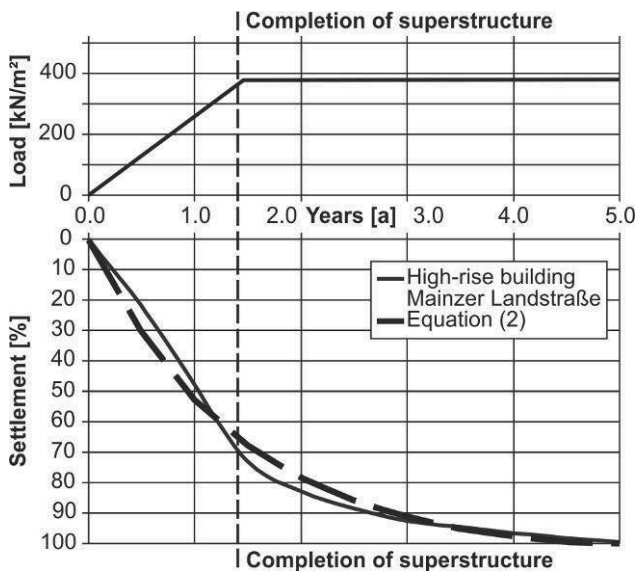


Figure 6. Measured settlement of the high-rise building Mainzer Landstraße.

### 3 DECONSTRUCTION OF A HIGH-RISE BUILDING FOUNDED ON AN UNDERGROUND STATION

In the context of the urban development the city of Frankfurt am Main plans to redesign the historic centre. Historic façades and buildings will be reconstructed. To create the necessary space on the surface an up to 14 storeys high-rise building was deconstructed. According to the present state of planning the deconstruction was carried out down to the sublevels.

The high-rise building and its underground parking overlay 2 tunnels and an underground station of the urban metro system. The loads of the superstructures are directly transferred onto the tunnels and underground station. Figures 7 and 8 give an overview on the primary situation prior to the deconstruction. The sealing of the structures was made of outside layers of bitumen-based materials. It must be guaranteed that during the deconstruction of the existing high-rise building and the construction of the new buildings the sealing of the underground structures and the sublevels remained intact. For this purpose especially the uplifts due to the deconstruction and the deformations of the underground structures and the sublevels had to be monitored during the execution of the project according to the observational method.

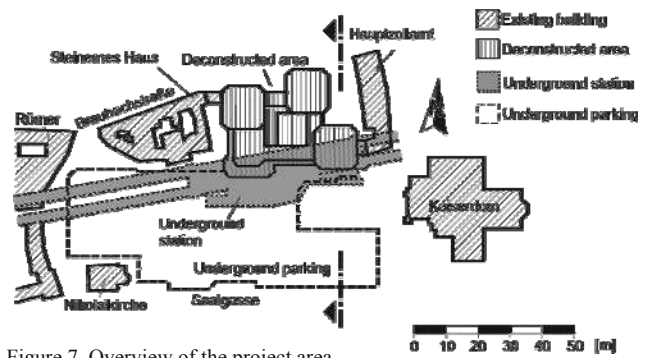


Figure 7. Overview of the project area.

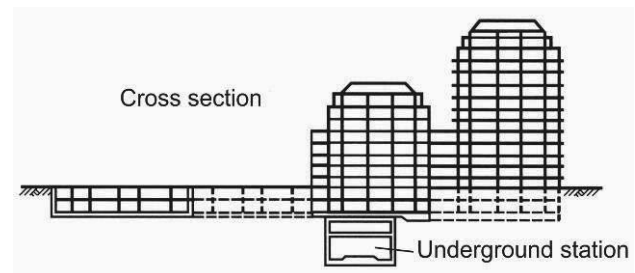


Figure 8. Cross section of Figure 6.

The soil and groundwater conditions are as follows:

- 0 m to 7 m: quaternary sands and gravel
- 7 m to 30 m: Frankfurt Clay
- below 30 m: Frankfurt Limestone
- groundwater level in a depth of 6 m

The groundwater level is influenced by the river Main which is 180 m far away. In the course of the geotechnical survey two aquifers have been encountered. The top aquifer is located in the non-cohesive soil. The lower confined groundwater layer is located in the Frankfurt Clay and in the Frankfurt Limestone.

According to the classification of the project into the Geotechnical Category 3, that is the Category for very difficult projects in EC 7, an extensive geodetic monitoring program with 580 measuring points was installed. 220 measuring points are located around the deconstructed building, 110 are located in the underground parking and in the sublevels of the deconstructed building, 30 are in the underground station and the remaining 220 are located in the tunnels.

The existing buildings were deconstructed down to the 2 sublevels. The uplift that occurred due to the unloaded of the soil is shown on selected points (Figures 9 and 10).

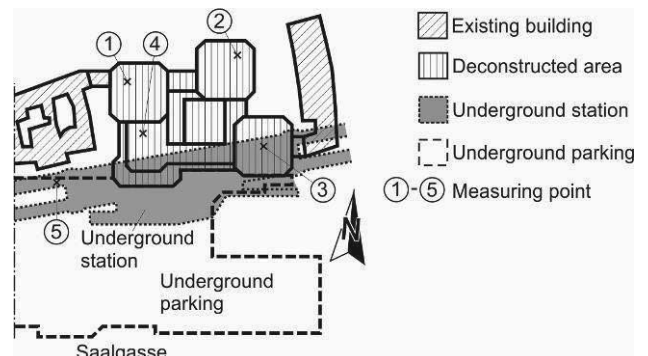


Figure 9. Selected measuring points.

The selected measuring points 1 to 4 are in the sublevel of the former high-rise building. Measuring point 5 is at the transition of the underground station to the tunnel. At the

measuring points 1 to 4 uplift between 1 cm and 5 cm was detected in the deconstruction time (March to December 2010). The measured uplift of measuring point 5 is less than 0.5 cm.

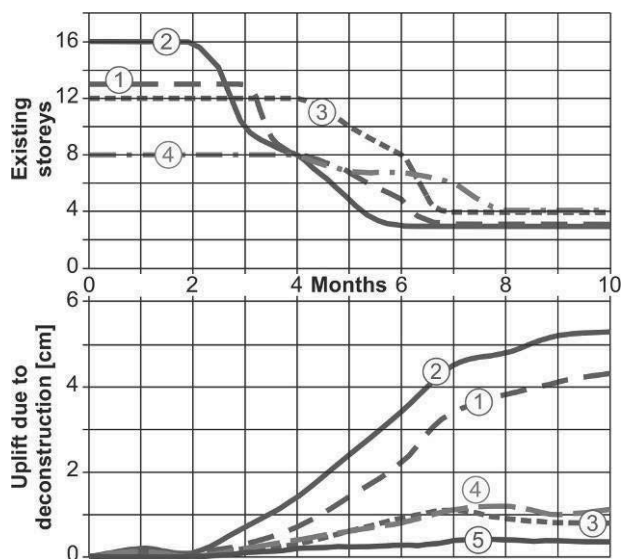


Figure 10. Measured uplift at selected measuring points.

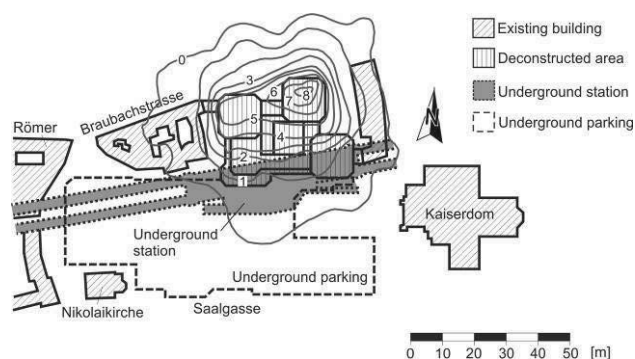


Figure 11. Measured uplift of the whole project area [cm].

After the deconstruction down to the sublevels in December 2010, the modification of the sublevels began. In that phase the loads only were changed insignificantly. The uplift of the whole project area and the neighbourhood in October 2012 is drawn in Figure 11. The uplift due to the reduced stress level of the stress and time related deformation behaviour of the Frankfurt Clay is continuously raising due to the consolidation processes. A maximum uplift of 8.5 cm was measured in the area where the most storeys were deconstructed. The uplifts fade down related to the distance very quickly. So no dangerous deformations of the neighbourhood were measured.

#### 4 CONCLUSIONS

At the construction of excavations or the deconstruction of existing buildings the soil is unloaded and relaxes due to the reduced stress level. Cohesive soil materials like clay react strongly time dependent. For example the tertiary Frankfurt Clay relaxes time-delayed due to the unloading in the dimension of centimetres. Regarding the guarantee of the stability and the serviceability of structures in the neighbourhood the influence of the arising deformation of the soil has to be taken into

account during an early planning stage and has to be considered during analyses and design.

For verification of the analyses and to proof the design all projects with large soil deformations have to be monitored by means of the observational method. Only high-level analyses compared with the observational method are the guarantee for a safe construction phase for the project itself and the influenced structures.

#### 5 REFERENCES

Amman, P., Breth, H., Stroh, D. 1975. Verformungsverhalten des Baugrundes beim Baugrubenaushub und anschließendem Hochhausbau am Beispiel des Frankfurter Tons. *Mitteilungen des Institutes und der Versuchsanstalt für Geotechnik der Technischen Universität Darmstadt*, Heft 15.

Breth, H., Stroh, D. 1974. Das Verformungsverhalten des Frankfurter Tons beim Aushub einer tiefen Baugrube und bei anschließender Belastung durch ein Hochhaus. *13. Baugrundtagung der Deutschen Gesellschaft für Geotechnik in Frankfurt am Main*, 51-70

Breth, H., Katzenbach, R., 2000. Entwicklungen in der Geotechnik, gespiegelt in 75 Bänden des Bauingenieur. *Bauingenieur 75*, Heft 7/8, 365-371.

Chambosse, G. 1972. Das Verformungsverhalten des Frankfurter Tons beim Tunnelvortrieb. *Mitteilungen des Institutes und der Versuchsanstalt für Geotechnik der Technischen Universität Darmstadt*, Heft 10.

CEN European Committee of Standardization 2008. Eurocode 7: Geotechnical design – Part 1: General rules.

Dürwang, R., El-Mossallamy, Y., Reininger-Behrenroth, M. 2007. Neue Erkenntnisse zum Verformungsverhalten des Frankfurter Tons. *Bautechnik 84*, Heft 3, 190-192.

Hanisch, J., Katzenbach, R., König, G. *Kombinierte Pfahl-Plattengründungen*. Wilhelm Ernst & Sohn, Berlin.

Katzenbach, R., Moormann, C. 1999. Geotechnical field measurements applied to a 240 m high office tower constructed by top/down methods in Frankfurt Clay. *5th International Symposium on Field Measurements in Geomechanics in Singapore*, 325-330.

Katzenbach, R., Hoffmann, H., Moormann, C., Vogler, M. 2001. Neue geotechnische Konzepte für den technisch und wirtschaftlich optimierten Hochhausbau. *Bauingenieur 76*, Heft 7/8, 314-325.

Katzenbach, R., Turek, J., Vogler, M. 2002. Entwicklung einer horizontal belasteten KPP am Beispiel der neuen Messehalle 3 in Frankfurt am Main. *Bauingenieur 77*, Heft 9, 393-398.

Katzenbach, R., Leppla, S., Seip, M. 2011. Das Verformungsverhalten des Frankfurter Tons infolge Baugrundentlastung. *Bauingenieur 86*, Heft 5, 233-240.

König, G. 1994. Innovationen im Bauwesen durch Forschung und Entwicklung an den Hochschulen. *Mitteilungen des Institutes und der Versuchsanstalt für Geotechnik der Technischen Universität Darmstadt*, Heft 32, 87-112.

Janke, O., Zoll, V., Sommer, F., Waberseck, T. 2010. Palais Quartier (Frankfurt HochVier) – Herausfordernde Deckelbauweise im Herzen der City. *Mitteilungen des Institutes und der Versuchsanstalt für Geotechnik der Technischen Universität Darmstadt*, Heft 86, 113-124.

Moormann, C. 2002. Trag- und Verformungsverhalten tiefer Baugruben in bindigen Böden unter besonderer Berücksichtigung der Baugrund-Tragwerk- und der Baugrund-Grundwasser-Interaktion. *Mitteilungen des Institutes und der Versuchsanstalt für Geotechnik der Technischen Universität Darmstadt*, Heft 59.

Sommer, H., Katzenbach, R., DeBenedittis, C. 1990. Last-Verformungsverhalten des Messeturms in Frankfurt am Main. *28. Baugrundtagung der Deutschen Gesellschaft für Geotechnik in Karlsruhe*, 371-380.

Viggiane, C. 1998. Pile groups and piled raft behaviour. *3rd International Geotechnical Seminar on Deep Foundations and Bored and Auger Piles*, Ghent, 77-91.

Vogler, M. 2010. Berücksichtigung innerstädtischer Randbedingungen beim Entwurf tiefer Baugruben und Hochhausgründungen am Beispiel des Palais Quartier in Frankfurt am Main. *Bauingenieur 85*, Heft 6, 273-281.

# Large tailings heaps and the influence on infrastructures due to the resulting soil deformation

Les grands terrils miniers et leur influence sur les infrastructures voisines à travers la déformation des sols

Katzenbach R., Leppla S.

*Technische Universität Darmstadt, Institute and Laboratory of Geotechnics, Germany*

Seip M.

*Ingenieursozietät Professor Dr.-Ing. Katzenbach GmbH, Frankfurt am Main, Germany*

Schleinig J.-P.

*K+S Aktiengesellschaft, Kassel, Germany*

Schnürer F.

*K+S KALI GmbH, Kassel, Germany*

**ABSTRACT:** In the context of potassium fertilizer production the residua, mostly consisting of granular rock salt, is stored on large tailings heaps. The salt residue has a strongly visco-plastic material behaviour with a rate-dependant strength. The heaps have a base area up to a square kilometre and heights up to 120 m. Using the Finite-Element-Method (FEM) and a numerical constitutive law for the salt residue, developed at the Technische Universität Darmstadt (TU Darmstadt), the influence of the heaps on infrastructures like buildings, streets, railway tracks and pipelines can be estimated. In the context of the approval procedures of the extension of existing heaps comprehensive numerical investigations regarding stresses and deformations are necessary to guarantee the stability and the serviceability of the heaps and influenced infrastructures. For verification of the numerical investigations according to the observational method monitoring programs have to be installed.

**RÉSUMÉ :** Dans le contexte actuel de production d'engrais riches en potassium, les résidus, principalement constitués de sel gemme granulaire, sont stockés sous forme de larges terrils. Les résidus salins présentent un important comportement visco-plastique, et une résistance à la rupture fortement dépendante du temps. La surface occupée par ces terrils peut atteindre un kilomètre carré et une hauteur de 120m. L'influence de ces terrils sur les infrastructures du type bâtiments, routes, rails et pipelines peut être estimée en combinant la Méthode des Eléments Finis (MEF) et l'utilisation d'une loi constitutive numérique pour le matériau salin, développée à la Technische Universität Darmstadt (TU Darmstadt). Dans le contexte actuel qui encourage l'extension des terrils existants, il devient nécessaire de mener des études numériques poussées évaluant les contraintes et déformations, afin de garantir la stabilité et le bon fonctionnement des terrils et des infrastructures avoisinantes. Des programmes de contrôle doivent être mis en place afin d'effectuer la vérification des études numériques, obtenues grâce aux méthodes observationnelles.

**KEYWORDS:** Tailings heap, visco-plastic material behaviour, observational method.

**MOTS-CLES :** Terrils miniers, comportement visco-plastique, méthode observationnelle

## 1 INTRODUCTION

During the production of potash and the converting into fertilizer for agriculture and into specialty products for the chemical industry a large amount of residua, mostly consisting of granular rock salt, is deposited on large heaps. The resulting tailings heaps with a ground view up to 1 km<sup>2</sup> and a height up to 120 m cause normal stresses of 2,200 kN/m<sup>2</sup> and shear stresses of 550 kN/m<sup>2</sup> on the contact surface. An impression of the dimensions of such tailings heaps is given in Figure 1.



Figure 1. Rock salt heaps.

For analyses of the load and deformation behaviour of the heaps the Finite-Element-Method (FEM) in combination with elastoplastic constitutive laws for the soil and a viscoplastic constitutive law for the granular rock salt, developed at the Institute and Laboratory of Geotechnics of the TU Darmstadt, are used.

The verification of the developed constitutive law for the granular rock salt was done by back-analyses of laboratory tests and the monitoring data of specific projects. The paper focuses on the challenges of an extension of a tailings heap and the influence on a railway track as only 1 example from engineering practice (Katzenbach et al. 2004, Katzenbach et al. 2006).

## 2 PROJECT DESCRIPTION

In order to ensure the further production an existing 120 m high tailings heap needs to be extended (Figure 2).

The planned extension of the tailings heap approaches the railway track to the south. The existing heap was stored in blocks with a lower and an upper layer (Figures 3 and 4). The slope ratio is up to 40°. Since 2008 the extension is stored with layers on the slope (Figure 5).



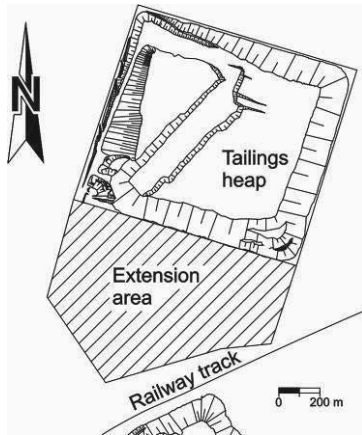


Figure 2. Site plan of the project.



Figure 3. Spreader on a heap.

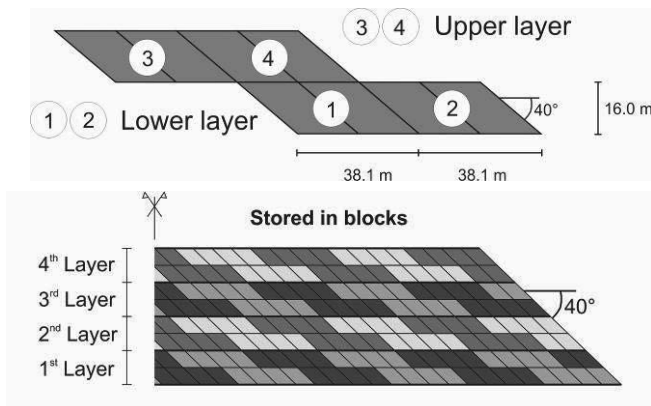


Figure 4. Schematic procedure of the block storing method.

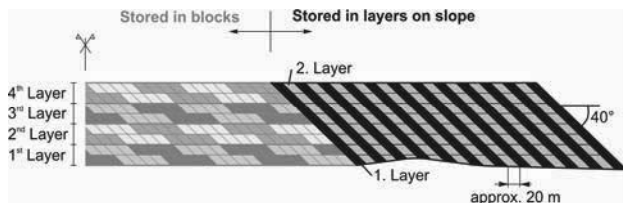


Figure 5. Schematic storing with layers on the slope.

The project area is situated in a glacial plain with a rather flat ground surface. The soil is horizontally stratified. At the surface a 5 m to 10 m thick layer of sand and marl glacial deposits was investigated. Below the sand and marl deposits a 50 m thick layer of quaternary sand with loose density was found, followed by a 130 m to 150 m thick layer of Rupel Clay and dense sand with varying layers of silt. At a depth of approximately 200 m

below the surface the new red sandstone begins. The groundwater level is about 5 m below the surface.

### 3 MATERIAL BEHAVIOUR OF GRANULAR ROCK SALT

The material behaviour of granular rock salt is characterized by a distinctive time and stress dependence. Initially fresh granular rock salt has a non-cohesive texture. After a short period the loose, granular rock salt converts into a cohesive texture with a high strength (Ankes 1972). The salt material attains a shear strength with a friction angle of  $\phi' = 50^\circ$  and a cohesion of  $c' = 850 \text{ kN/m}^2$ , as well as a stiffness of  $E_s = 2,500 \text{ MN/m}^2$ . The material behaviour of the granular rock salt is strongly dependent to the deformation rate. High, overcritical deformation rates lead to high strength and stiffness of the rock salt and to brittle fracture. Small, undercritical deformation rates lead to minor strength and stiffness and to a plastic creep without fracture.

Directly after storing the granular stockpiled material has a density of  $\rho = 1.4 \text{ to } 1.5 \text{ t/m}^3$ . Due to the atmosphere, chemical processes and the pressure because of the increasing covering the granular stockpiled material in the core of the heap transforms nearly into solid body.

Under constant deviatoric stress the stockpiled material presents a constant creep behaviour despite a huge strength. The material behaviour of stockpiled material is strongly dependent on the state of stress and of the deformation rate. Figure 6 shows the results of two strain controlled triaxial tests on specimen of stockpiled material, obtained from core drillings from the top of a heap. For both tests a cell pressure of  $\sigma_3 = 0.5 \text{ MN/m}^2$  was specified. Both deformation rates vary by the factor 1,000.

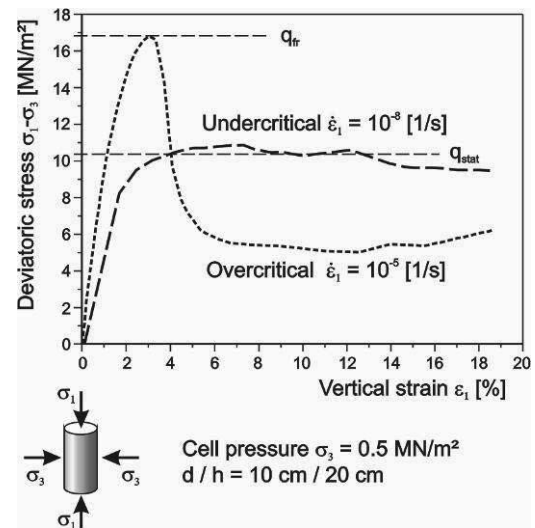


Figure 6. Typical results of strain controlled triaxial tests on stockpiled material samples.

The sample with the higher, overcritical deformation rate of  $d\epsilon/dt = 10^{-5} \text{ 1/s}$  presents the usual material behaviour on high deformation rates. After the peak stress  $q_{fr}$  follows a deep drop of the deviatoric stress (brittle fracture). The sample with the lower (undercritical) deformation rate of  $d\epsilon/dt = 10^{-8} \text{ 1/s}$  does not collapse. The sample creeps under a constant deviatoric stress  $q_{stat}$ .

On the left in Figure 7 is shown the specimen after the test with undercritical deformation rate. On the right is shown the specimen after the test with overcritical deformation rate.

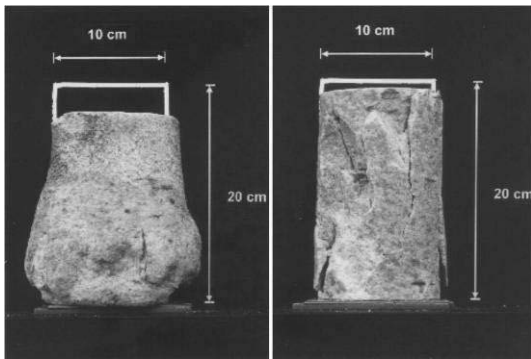


Figure 7. Specimens of triaxial tests with undercritical (left) and overcritical (right) deformation rates.

Due to deviatoric stress levels the stockpiled material creeps with high deformation rates at the beginning. The deformation rate decreases under constant deviatoric stress dependent on the time and approaches asymptotic the stationary creep rate (Figure 8).

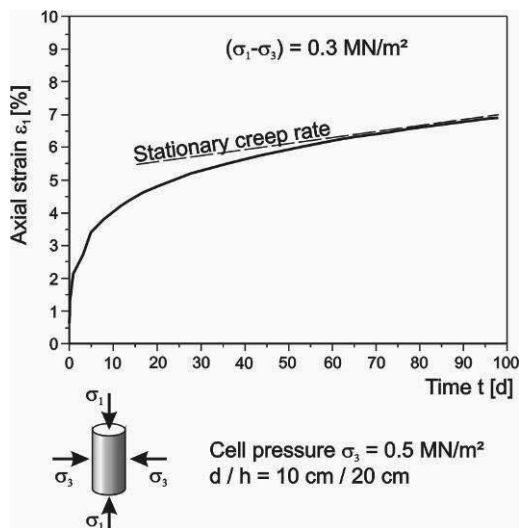


Figure 8. Typical creep curve of granular stockpiled material.

For further information of the material behaviour of granular rock salt see *Fordham 1988, Munsan and Wawersik 1991, Chumbe et al. 1996 and Boley 1999.*

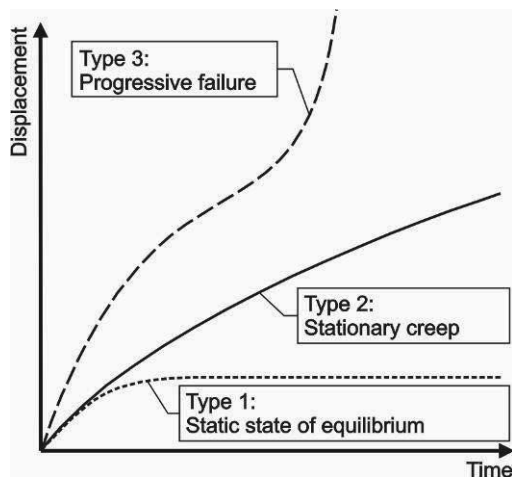


Figure 9. Deformation rate dependent system behaviour.

Although the heaps have a slow creep deformation and the soil has a continuously, slow changing load the heaps do not collapse due to the viscoplastic material behaviour of the granular rock salt as long as the deformation rate is undercritical. The collapse of the slope of a heap only results from a progressive failure (Figure 9) due to an increasing overcritical deformation rate. The system behaviour of a heap consisting of granular rock salt normally is like type 2 in Figure 9, if there is no weakening in the contact area.

On the basis of more than 150 triaxial tests a constitutive law for the material behaviour of granular stockpiled material was developed at the Institute and Laboratory of Geotechnics of TU Darmstadt (Boley 1999, Wachter 2009, Wachter and Katzenbach 2009). This constitutive law was implemented in a Finite-Element-Software for analyses of the ultimate limit state (ULS) and serviceability limit state (SLS) of granular rock salt heaps and infrastructures and buildings in the influenced area around the heaps.

#### 4 ANALYSES OF THE EXTENSION OF THE HEAP

For analyses of the extension of a tailings heap and the influence on the railway track numerical simulations using the FEM were carried out. The model has a length of 1,800 m. The heap is 120 m high. Regarding the analyses of an extreme situation the groundwater level was set to the surface. The soil is modelled with an elastoplastic constitutive law based on a modified Drucker-Prager-Modell, the new red sandstone was modelled with an elastic constitutive law. The FE-Model is shown in Figure 10.

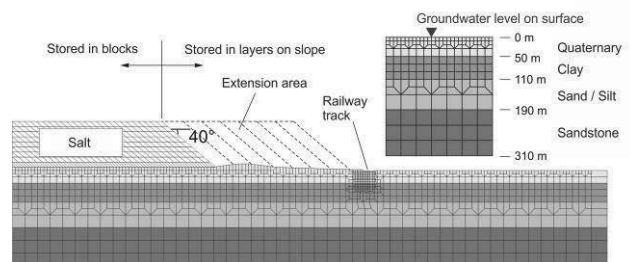


Figure 10. FE-Model of the soil and the heap before and after the extension.

The interaction between the tailings heap and the soil is modelled by a contact surface. The shear strength is defined by the friction law of *Coulomb*. The shear stress is proportional to the vertical stress. The time dependent material behaviour and the changing geometry of the heap are considered by a step-by-step analysis.

Figure 11 shows the analysed cross sections. The horizontal distance  $s_t$  of the toe of the slope to the railway track is varying along the track.

The relative deformations and the deformation rates have been calculated. The deformation rates increase when the extension approaches the railway track and decrease to a low rate when the extension area is totally filled up.

Due to the complexity of the project and the interaction between soil, heap and the infrastructure an extensive monitoring program according to the observational method was installed. The main part of the monitoring program consists of geodetic and geotechnical measurements (Figure 12).

For example the measured, absolute, horizontal displacements orthogonal to the toe of the slope of 2 measurement points are presented. The measurement point MR 54 is at the toe of the slope before the extension started. The measurement point MR 51 had a distance of 150 m to the toe of the slope before the extension started.

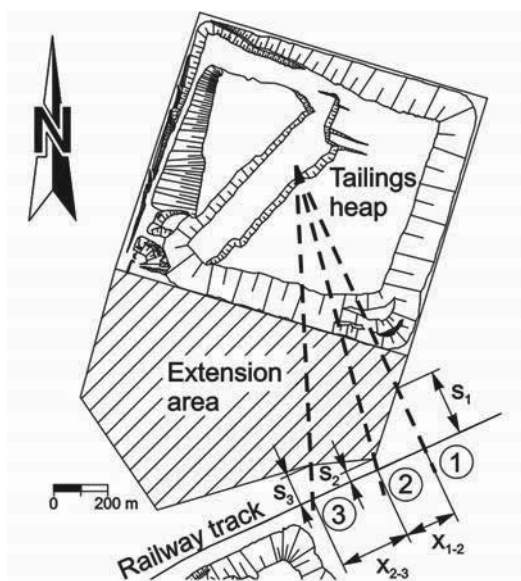


Figure 11. Cross sections for the analyses of the deformation of the railway track.

The measurement point MR 54 had a horizontal displacement of 0.30 m before it was covered with salt. After the covering no further measurement data for this point existed. The measurement point MR 51 had a horizontal displacement of 0.45 m before it was covered with salt.

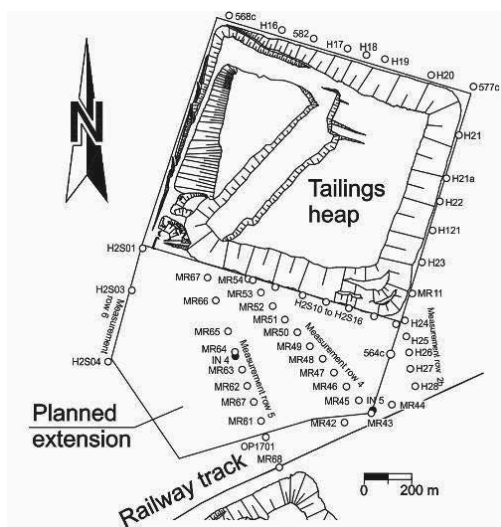


Figure 12. Geodetic and geotechnical monitoring program.

For calibration of the numerical simulations the calculated displacements are compared to the measurement data. In result numerical simulations supply horizontal displacements in a comparable range.

## 5 CONCLUSIONS

Due to the storing of granular residues of potash production on large tailings heaps enormous loads are transferred into the soil. In this context vertical and horizontal deformation occur even in a distance of hundreds of metres. For analyses of the ultimate limit state and the serviceability limit state of the heaps and infrastructures and buildings in the area of influence realistic simulations are necessary.

Using a complex constitutive law for the viscoplastic stockpiled material, developed at the Institute and the Laboratory of Geotechnics of TU Darmstadt, the numerical simulations of an extension of a heap and the influence on a railway track were investigated. The comparison of the results of the numerical simulations and the monitoring program shows a good accordance.

The developed constitutive law can be judged as a robust, efficient and purposeful material routine which offers an instrument for the simulation and investigation of complicated, time variant systems using numerical simulations.

## 6 REFERENCES

Ankes, A. 1972. Untersuchung bodenphysikalischer Eigenschaften von Rückstand. *Dissertation an der Fakultät für Technische Wissenschaften der Bergakademie Freiberg.*

Boley, C. 1999. Untersuchungen zur Viskoplastizität und Festigkeit von Steinsalz. *Mitteilungen des Institutes und der Versuchsanstalt für Geotechnik der Technischen Universität Darmstadt, Heft 48.*

Chumbe, D., Lloret, A., Alonso, E. 1996. Creep and permeability tests on compacted granular salt. *4<sup>th</sup> Conference on the Mechanical Behaviour of Salt*, Montreal, Canada, 331-339.

Fordham, C.J. 1988. Behaviour of granular halite for use as a backfill in potash mines. *Dissertation at University of Waterloo, Canada.*

Katzenbach, R., Giere, J., Seip, M. 2004. Stability and serviceability of a railway track and a gas pipeline at the base of steep creeping slopes. *1st European Regional International Association for Engineering Geology Conference*, Liège, Belgium, 11 p.

Katzenbach, R., Giere, J., Seip, M. 2006. Aspects of safety and serviceability of heaps with viscoplastic materials due to man-made liners or natural slip-surfaces. *Geo Environmental Engineering Conference*, Kyoto, Japan, 237-244.

Munson, D.E., Wawersik, W.R. 1991. Constitutive modelling of salt behaviour – state of the technology. *7<sup>th</sup> International Conference on rock mechanics, Workshop on Rock Salt Mechanics*, 1797-1810.

Wachter, S. 2009. Dreidimensionale, zeitvariante stoffliche Modellierung von granularem Steinsalz. *Mitteilungen des Institutes und der Versuchsanstalt für Geotechnik der Technischen Universität Darmstadt, Heft 82.*

Wachter, S., Katzenbach, R. 2009. CAPCREEP – Ein benutzerdefiniertes Stoffmodell zur Untersuchung von Rückstandshalden. *Bauingenieur 84, Heft 9*, 368-373.

# In-situ tests of permanent prestressed ground anchors with alternative designs of anchor bond length

## Essais in situ des tirants d'ancrage précontraints permanents avec des conceptions alternatives de la longueur de scellement

Klemenc I.  
Slovenian National Building and Civil Engineering Institute

Logar J.  
University of Ljubljana, Faculty of Civil and Geodetic Engineering

**ABSTRACT:** Some concepts of cost efficient ground anchors with enhanced pull-out resistance from single borehole already exist: single bore multiple anchors (Barley, 1990) and prestressed ground anchors of variable stiffness (Škrabl, 2004). A third alternative with anchor bond length of increased stiffness has been proposed. All three concepts have been combined with the concept of comprehensive corrosion protection. Five anchors of all three design alternatives as well as ten investigation tests on standard permanent prestressed ground anchors were tested in-situ on a large retaining wall in N-E Slovenia. The paper presents the design of each type of anchor bond length, test procedure and test results. The test results of our in-situ research on the specific location show that the highest anchor pull-out resistance was obtained for the anchor bond length of increased stiffness.

**RÉSUMÉ:** En plus des conceptions existantes d'augmentation de la résistance des tirants d'ancrage dans un même forage avec un bon rapport coûts-efficacité, tels les tirants à torons multiples (technologie SBMA – Barley, 1990) et les tirants précontraints de rigidité variable (Škrabl, 2004), nous proposons une troisième alternative: les tirants d'ancrage à rigidité renforcée. Les trois types étudiés ont été combinés parallèlement avec une conception de protection anti-corrosion. Nous avons testé in situ des ensembles de cinq groupes de chacun des trois types proposés et de dix tirants d'ancrage standard, sur une construction de soutènement importante réalisée dans la partie nord-est de la Slovénie. Dans cet article nous présentons le dimensionnement de la longueur de scellement de tous les types de tirants d'ancrage ainsi que le déroulement et les résultats des essais effectués. Les résultats des essais in situ démontrent que la résistance maximale est obtenue avec la longueur de scellement du tirant à rigidité renforcée.

**KEYWORDS:** ground anchor, design of bond length, pull-out resistance, in-situ test, comprehensive corrosion protection.

## 1 INTRODUCTION

In 1934 the first prestressed ground anchors were built during the raising of the Cheurfas Dam (Algeria). Such anchors have been increasingly used since then, in cases, where the execution of other geotechnical measures is significantly more difficult, more expensive or even impossible. The most widespread is the use of the friction tensile type of ground anchors (Limelette, 2008), with which the technological design and implementation of the corrosion protection has reached a level that promises a long-term operation (provided that adequate maintenance is ensured). This especially applies to anchors with a comprehensive corrosion protection, which was two decades ago developed in Switzerland: the steel parts of these anchors are encapsulated by a waterproof polyethylene (PE) cover, which also provides electrical isolation of steel parts against the environment. In parallel with technological improvements, the price of anchors has also grown. Therefore, increasing tendencies to rationalize anchors have appeared.

Three different simple modifications of a permanent prestressed anchor bond length were designed and investigated in order to achieve higher values of pull-out resistances and better efficiencies of anchors. The prototypes of such alternative anchors were installed and tested in a testing field. The obtained results were compared with those of reference anchors.

## 2 ALTERNATIVE DESIGNS OF BOND LENGTHS

The starting-point in the task of searching for the most effective concept of permanent prestressed ground anchors with the tendon contained within joint PE cover were reference (standard) anchors **RCP/D**. These anchors were used in a retaining wall that served as a test site. The total length of each

individual anchor is  $l = 35$  m with the tendon bond length of  $l_v = 7$  m, consisting of six low-relaxation strands  $\varnothing 15.2$  mm ( $f_{p0.1k}/f_{pk} = 1670/1860$  MPa).

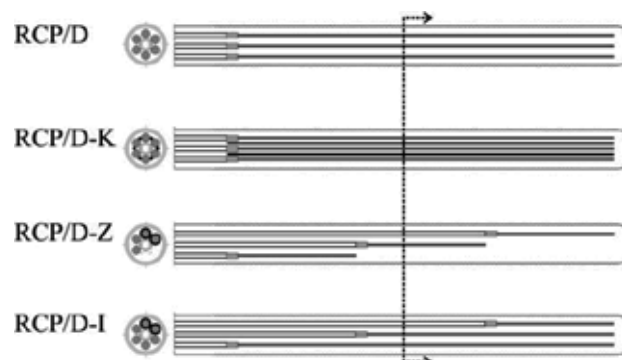


Figure 1. Conceptual designs of bond lengths of permanent prestressed strand anchors with joint PE encapsulation: reference anchor RCP/D, alternative types of anchors RCP/D-K (increased stiffness of bond length), RCP/D-Z (multiple anchor) and RCP/D-I (anchor of variable stiffness).

Three different conceptual designs of anchor bond lengths (Fig. 1) were conceived and implemented with the intention to improve stress distribution along the tendon bond length and to consequently increase the pull-out capacity of anchors:

- anchors with increased stiffness of bond length, with which six additional steel wires  $\varnothing 5$  mm were placed in empty spaces among bond lengths of strands (type **RCP/D-K** with strand free lengths of 28 m and strand bond lengths of 7 m),
- multiple anchors with staggered anchor units based on the idea of Barley's anchors SBMA, only that three anchor units

(two strands each) of 2.2 m bond length were not installed into a borehole as independent elements but were placed into the joint corrugated PE duct (type **RCP/D-Z** with strand free lengths of 28 m, 30.4 m and 32.8 m),

- *anchors with variable stiffness of bond length* after the patent of Škrabl, 2004, with the tendon combined of three anchor units (2 strands each), with strand free lengths of 28.0 m, 30.4 m and 32.8 m, and with strand bond lengths of 7.0 m, 4.6 m and 2.2 m (type **RCP/D-I**).

### 3 IN-SITU TESTING

The test field has been located at the level of the middle berm of a larger retaining wall, where load-bearing stratum consists of marl and silty marls with thin lenses of siltstone and sandstone. A total of 18 anchors were installed: three reference RCP/D anchors and five anchors of each alternative type (RCP/D-K, RCP/D-Z and RCP/D-I). Boreholes, deflected 15° downwards, were drilled with a chisel (Ø 140 mm) using air-flushing for the removal of drill spoil. The ratio of 6-strand anchor steel cross-sectional area to cross-sectional area of the borehole equaled 5.5% of the theoretical cross-sectional area of the borehole. The appearance of moist in the ground was repeatedly detected in the region of the anchor bond lengths. Cement grout with w/c ratio of 0.42 was used for grouting within the PE encapsulation as well as for the collar of the borehole with an average grout consumption of about 17 dm<sup>3</sup>/m<sup>1</sup>.

At in-situ testing individual strands were tensioned with monostrand jacks, connected to a joint hydraulically synchronized system (Fig. 2). An electrical load cell was used for the precise adjustment of stressing forces. Extensions and creep behavior of strands were measured with digital displacement transducers, attached on the monostrand jacks.



Figure 2. Test setup for simultaneous stressing of all strands of prestressed ground anchors using monostrand jacks.

As a measure for the assessment of load-bearing characteristics of anchor bond lengths creep displacement rate  $k$  was used (Ostermayer, 1975):

$$k = \frac{s_2 - s_1}{\log t_2 / t_1} \quad (1)$$

where  $s_1$  and  $s_2$  are head displacements at times  $t_1$  and  $t_2$ , respectively. For the failure of anchor bond length the critical creep displacement rate  $k_{crit} = 2$  mm was used.

All reference anchors and one anchor of each alternative type were tested up to the maximum test load  $P_{pv} = 1254$  kN (80 % steel tensile strength  $R_m$ ) or until failure of anchor bond length was reached (*investigation test* - IT). Other alternative anchors were tested using the same procedure, except that the

test was stopped at the first sign of anchor bond length failure, i.e. as soon as  $k_{crit}$  appeared (*comprehensive suitability test* - CST). All test field anchors were tested according to the loading procedure and methodology for IT as described in Swiss standard SIA 267/1, which is very similar to test Method 1 of standard EN 1537: each anchor was loaded in eight incremental cycles from a datum load  $P_a = 150$  kN (10 %  $R_m$ ) to the maximum test load  $P_{pv}$ . The increments of strand extensions were measured at the end of specified time intervals, which were used for the evaluation of  $k$  values. Individual strand extensions as well as average extensions for all strands of the RCP/D-I anchor SBZ-33 at load level  $P_6 = 978$  kN of CST are presented on the left diagram of Fig. 3. The right diagram shows the development of apparent free lengths  $l_f$  of individual strands during the same CST, which is based on the measured elastic displacement  $\Delta s_{el}$  at load decreasing from current level  $P_i$  to the initial level  $P_a$ , knowing the characteristics of the tendon (cross-section area  $A_p$  and modulus of elasticity  $E_p$ ):

$$l_f(P_i) = \frac{\Delta s_{el}}{P_i - P_a} A_p E_p \quad (2)$$

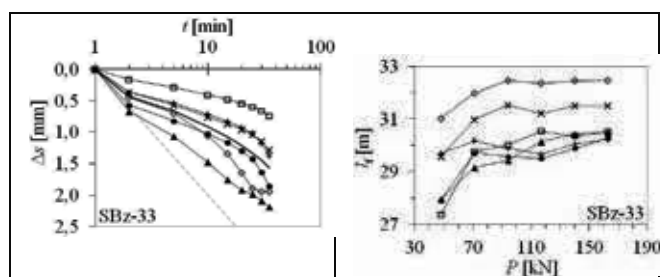


Figure 3. Measured increments of displacements of the anchor SBZ-33 (type RCP/D-I) at load level  $P_6$  of CST (left), apparent free lengths of individual strands  $l_f$  during CST (right).

The behaviour characteristics of anchor bond length could be recognized only on the basis of strand extensions, measured on displacement transducers, fixed on the monostrand jacks. The problem is that due to the limited amount of data and the inability of physical insight into the bond lengths deep in the load bearing stratum, we cannot always directly link measured extensions with creep displacement rate  $k$  of the bond length (i.e. it is not necessary that each measured strand extension actually originates from the bond length deterioration). Therefore, in the analysis of the in-situ test results it is recommendable to compare the  $k$  values of individual strand with the  $k$  values of other individual strands of the same tendon, with  $k$  values of anchor units (average of two strands, only at types RCP/D-Z and RCP/D-I), with the average  $k$  values of all strands, as well as with the permanent displacements  $\Delta s_{bl}$  and apparent free lengths  $l_f$ , obtained after each loading stage. In order to prevent sudden failures of bond lengths at CST, an appropriate software tool was prepared to enable simultaneous recording and evaluation of the most important behaviour parameters of an anchor during in-situ test.

### 4 ANALYSIS OF RESULTS OF THE IN-SITU TESTING

There are several possible failure mechanisms at the anchor bond length, which occur at the IT of prestressed ground anchor with a comprehensive corrosion protection: inside or outside the PE corrugated duct, under some circumstances it may also come to the rupture of PE duct. The types and incidences of individual mechanisms depend on the design of bond length and packing connections at the transition between strand free and bond lengths, possible surface contamination of the bare strand bond length, the design, dimensions and distribution of the constituent components of anchors, local conditions in the ground, configuration of strands in the bond length, drilling and flushing techniques as well as specifics of grouting. According to the

principle of the weakest link in the chain, there starts a mechanism that occurs at the lowest load level, although in the following load steps some additional mechanisms may also occur.

The bond lengths (2.2 m) of the shortest anchor units (RCP/D-Z and RCP/D-I anchors) were determined according to the available anchor bond length 7 m and previous experience (Barley and Windsor, 2000, Bruce et al., 2007). The bare strands of the bond length of RCP/D and RCP/D-K anchors were spirally rotated along the longitudinal axis, while the strands of the short bond length of RCP/D-Z and RCP/D-I anchors were straight. The bare strands of the bond length of RCP/D anchors (and to a certain extent of RCP/D-K anchors) were additionally arranged in a pattern of alternating spatial extension and compression of strands. Although the lengths of strand bond lengths were selected in accordance with the aforementioned recommendations, the analysis of the in-situ test results of RCP/D-Z and RCP/D-I anchors showed predominant mechanism of pull-out of strands bond length from cement grout inside the corrugated PE duct. Such behavior can be associated with the greasing technology of strand free length, in which some strands in bond lengths can be locally stained with vaseline, although most of the stains were later on removed. Contrary to expectations, only in individual cases of RCP/D and RCP/D-K anchors, there appeared the pull-out mechanism of the whole tendon from the cement grout inside corrugated PE duct. Such behaviour can be partly ascribed to the local contamination of bare strands with vaseline stains, and partly to the direct contact of strand bond lengths with the bottom part of the corrugated PE duct (no minimum grout cover was provided).

The behaviour of anchor bond length is reflected in the most important outcome of the IT: pull-out resistance  $R_a$ , which is determined as the intersection of experimentally obtained curve of interval creep displacement rate  $k_{int}$  to the assumed margin that denotes the failure of an anchor  $k_{crit} = 2$  mm. In cases where such intersection does not exist, the failure of anchor bond length is not reached – in these cases the standard SIA 267/1 allows for an extrapolation of  $R_a$  as a proof load extrapolated up to 10%. The problem with this assessment remains when the anchor bond length can be assessed as failed, or in other words, in those cases when it is a reasonable to expect that the anchor bond length would be able to sustain a load of 1.10  $P_{pv}$ . The analysis of in-situ obtained test results for the considered type of anchors showed: if the following criteria are satisfied, this could be a suitable basis for 10 % extrapolation of  $P_{pv}$ , provided that the estimate is made by an experienced specialist:

- linear trend approximation of the creep displacement rates at the proof load  $P_{pv}$  (considering all strands and the anchor as a whole) should not exhibit any noticeable increase in creep rate,
- maximum creep displacement rate in each time interval after the second minute of observation (for each strand and the anchor as a whole) must not exceed the criterion of failure  $k_{crit}$ ,
- the interval creep displacement rate  $k_{int}(P_{pv})$ , of each strand and the anchor as a whole should not be greater than 1.35.

Results of all performed in-situ tests are presented as values of pull-out resistances  $R_a$  [kN] (Table 1) as well as in the diagrams of interval creep displacement rates  $k_{int}$  obtained at all stages of IT and CST (Fig. 4).

The general impression in the ratio of pull-out resistances among various types of tested anchors can already be obtained on the basis of visual assessment of the curves in the diagrams: the highest values of anchor bond length resistance (i.e. high loads  $P$  reached at low values of  $k_{int}$ ) were achieved at RCP/D-K anchors with increased stiffness of bond length, which slightly exceeded the bond length resistance of reference RCP/D anchors. An unexpectedly rapid failure of two reference RCP/D anchors was a result of problems at grouting (anchor SBz-23) and distinctive slip of two strands, probably due to bare strand contamination with vaseline (anchor SBz-59). On the other hand, multiple anchors with staggered bond lengths (RCP/D-Z

type) demonstrated the poorest performance of all tested anchors due to early failure of bond lengths at low load stages of IT or CST (deterioration of bond between strands and cement grout resulted in the pull-out of the strands). The behaviour of RCP/D-Z and RCP/D-I anchors was probably influenced by the surface contamination with vaseline as well as configuration of strands in the bond length. Additional impairment of the conditions within the corrugated PE duct was caused by the use of soft and relatively spacious packing connections in the transition between anchor unit bond and free length.

Table 1. Results of in-situ tests: pull-out resistances  $R_a$  [kN] of all tested anchors of reference and alternative types.

RCP/D	RCP-D/K	RCP-D/Z	RCP-D/I
Anchor $R_a$ [kN]	Anchor $R_a$ [kN]	Anchor $R_a$ [kN]	Anchor $R_a$ [kN]
TS-01* 800	SBz-89* 1254	SBz-56* 702	SBz-86* 1144
TS-02* 979	SBz-18# 978	SBz-36# 694	SBz-12# 604
TS-03* 981	SBz-39# 1231	SBz-63# 469	SBz-33# 1248
TS-04* 1015	SBz-66# 1220	SBz-81# 837	SBz-60# 789
TS-05* 1095	SBz-84# 978	SBz-15# 400	SBz-78# 840
TS-06* 1195			
TS-07* 1227	*... Result of IT.		
SBz-23* 651	#... Result of CST.		
SBz-56* 1211			
SBz-59* 642			

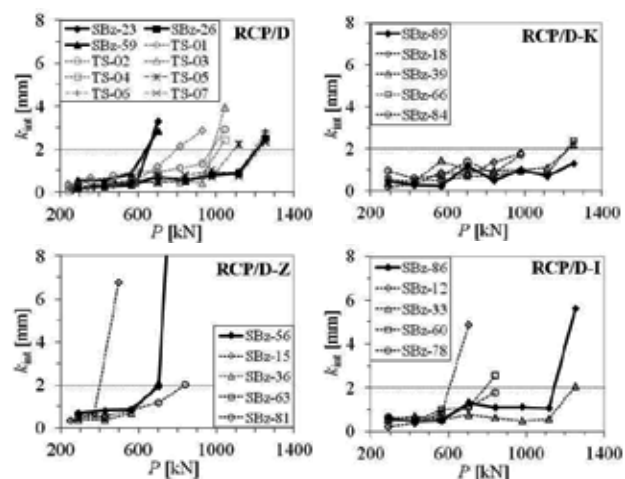


Figure 4. Interval creep displacement rates  $k_{int}$  for reference testing anchors as well as for all types of alternative anchors.

To confirm the relationships among pull-out resistances  $R_a$  (Table 1) a one-sided Student's T-test with unequal variance was used to check whether the average values of different types of anchors differ significantly from each other.

Results of testing the hypothesis of the equality of the means of two normal populations at the 5 % significance level showed that the mean value of RCP/D-Z anchor pull-out resistance was statistically typically lower than the mean values of pull-out resistance of reference RCP/D and alternative RCP/D-K anchors (Table 2). Somewhat unexpectedly, using statistical methods we could not confirm that the mean value of RCP/D-Z anchor pull-out resistance was statistically typically lower than the mean value of pull-out resistance of RCP/D-I anchors, as it could be inferred only on the basis of visual comparison of the curves in the graphs in Fig. 4.

Table 2. Results of one-sided Student's T-test with unequal variance of mean pull-out resistances  $R_a$  for reference and alternative anchors.

	RCP/D	RCP/D-K	RCP/D-Z	RCP/D-I
Mean	980	1132	620	925
Variance	47770	19965	32622	70263
Standard deviation	218,6	141,3	180,6	265,1
Coef. of variation	0,223	0,125	0,291	0,287
RCP/D	-			
RCP/D-K	13,0 %	-		
RCP/D-Z	<b>0,7 %</b>	<b>0,1 %</b>	-	
RCP/D-I	70,3 %	17,3 %	7,1 %	-

## 5 CONCLUSIONS

Based on the theoretical background of bond length behaviour of a prestressed ground anchor and the patents of Barley and Škrabl, three types of anchors with alternative concepts of bond lengths inside PE encapsulation (RCP/D-K, RCP/D-Z and RCP/D-I types) were designed, installed and tested at a test field. The behaviour of alternative types of anchors was compared with the behaviour of the reference RCP/D anchors. Different aspects of design (especially limited anchor bond length of 7 m, the diameter of available type of corrugated PE duct), formation, manufacturing details and installation of testing field anchors resulted in different pull-out resistances  $R_a$  and they indicate the relations among bond length capacities of different anchor types.

Test results of 25 anchors showed that the maximum values of pull-out resistance  $R_a$  were reached at the modified RCP/D-K anchors with increased stiffness of bond length - the mean values of  $R_a$  of RCP/D-K anchors exceeded the mean values of  $R_a$  of RCP/D anchors by 16 %. Although the free space within the corrugated PE duct of bond length of the RCP/D-K anchors was very restricted, allowing only  $\varnothing$  5 mm additional steel wires to be installed (instead of originally planned  $\varnothing$  12.5 mm steel strands), high values of pull-out resistances of RCP/D-K anchors were obtained. The behaviour of RCP/D-Z and RCP/D-I anchors was probably influenced by the surface contamination with vaseline as well as the configuration of strands in the bond length. Additional impairment of the conditions within the corrugated PE duct was caused by the use of soft and relatively spacious packing connections in the transition between anchor units bond and free length. The RCP/D-Z anchors demonstrated the poorest performance of all tested anchors (the bond length of RCP/D-Z anchors failed at low force levels of IT and CST). In all cases local debonding at the strand/grout interface resulted in the pull-out of strands. With improvement of particular technological details of alternative anchors, higher values of pull-out resistances can be expected. According to the experiences of Barley with multiple anchors, the pull-out resistances of RCP/D-Z anchors should attain (and probably exceed) the pull-out resistances of reference RCP/D anchors, provided that the pull-out of strands from cement grout, placed within the corrugated PE duct, is prevented. At least it is necessary to provide the immaculate condition of bare strands in the bond length within the PE encapsulation. Moreover, it is also possible that instead of RCP/D-K anchors the highest values of pull-out resistance could be achieved at one of the other alternative types (RCP/D-I or RCP/D-Z).

With the intention to increase the efficiency of alternative types of permanent prestressed anchors (RCP/D-K, RCP/D-Z and RCP/D-I) the following improvements are suggested:

- Results of field testing confirm the already known fact (Littlejohn, 1993, Hanna, 1982) that for effective performance

of bond length the bare strands should be covered with sufficiently thick layer of cement grout, irrespective of the anchor bond length design.

- The efficiency of anchor bond length could be improved with the increase of corrugated PE duct diameter. In that case the region around bare strands within corrugated PE duct could be reinforced (spiral micro reinforcement, cement grout with admixed fibres, etc.). Simultaneously, extra space would be gained for nodding or local deforming of strands.
- The efficiency of RCP/D-Z and RCP/D-I anchors could also be improved by upgrading the technological detail of anchor unit packing connections at the transition between strand bond and free lengths. Performance of RCP/D-z and RCP/D-I anchors could also be improved if the greased and sheathed strands in the free length would possibly be replaced with some other solution that offers higher stiffness in radial direction.
- For specific design of RCP/D-Z and RCP/D-I anchors the combination of strand and anchor unit nodding is suggested, whereat the minimal anchor unit strands bond length should be 2.5 m (in case of the increased diameter of corrugated PE duct) and 3.0 m (in case of the unchanged diameter of corrugated PE duct).

## 6 ACKNOWLEDGEMENTS

The authors are grateful to the Slovenian motorway agency DARS, for their financing of the research project. We are also much obliged to the manufacturer CA.TI. Carnica Tiranti, Srl, Italy for their donation of the anchors, and to the contractor GEOT for successful installation and in-situ testing of anchors.

## 7 REFERENCES

- Barley A.D. 1990. Ground anchorage containing a multiple of ground anchorages : patent number EP 0 356 215 A2. European Patent Office.
- Barley A.D. and Windsor C.R. 2000. Recent advances in ground anchor and reinforcement technology with reference to the development of the art. International conference on geotechnics and geotechnical engineering, vol. 1. 19th - 24th November 2000, Melbourne, Australia. Basel, Lancaster: 1157-1252.
- Bruce M.E.C., Gómez J., Traylor R.P. 2007. Repeated lift-off testing of single bore multiple anchors for dam retaining wall over a 5-year period. V: Littlejohn, G.S. (ed.). International conference on ground anchorages and anchored structures in service. ICE London, November 2007. London, Thomas Telford: str. 111-119.
- Hanna T.H. 1982. Foundations in tension : ground anchors. Trans Tech Publications. New York, McGraw Hill Book Co.
- Hutchinson D. and Diederichs M. 1996. Cablebolting in underground mines. Richmond, Canada, BiTech Publisher Ltd.
- Klemenc I. 2011. Investigation tests of permanent prestressed strand ground anchors with various designs of tendon bond length : doctoral thesis (in Slovene). Ljubljana.
- Limelette test fields results. 2008. Proceedings of the international symposium ground anchors. 14 May 2008, Brussels, Belgium.
- Littlejohn S. 1993. Overview of rock anchorages. Hudson, J.A. (ed.). Comprehensive rock engineering : excavation, support and monitoring, vol. 4. Oxford, Pergamon Press.
- Ostermayer H. 1975. Construction, carrying behaviour and creep characteristics of ground anchors. Conference on Diaphragm Walls and Anchorages. ICE London, September 1974, 141-151.
- Škrabl S. 2004. Prestressed ground anchors of variable stiffness : patent number 21320 (in Slovene). Ljubljana : SIPO.

# Response of piled buildings to deep excavations in soft soils

## Déformations des bâtiments liés aux excavations profondes situés dans les sols mous

Korff M.  
Delft and Cambridge University

Mair R.J.  
Cambridge University

**ABSTRACT:** This paper explores the building displacements related to deep excavations for a case study from the Netherlands: the construction of the North South Metro Line in Amsterdam. The overall goal of the analysis of the displacement is to study the interaction of deep excavations with piled buildings. The response of buildings is governed by the soil displacements resulting from the excavation. These displacements are described in a second, related paper in this conference. In this paper, the response of the piled buildings is described.

**RÉSUMÉ :** Les auteurs ont analysé déformations des bâtiments liés aux excavations profondes à Amsterdam pour la Ligne nord/sud. L'objectif général de l'analyse des déformations est d'étudier l'interaction des excavations profondes avec des bâtiments sur pieux. La réponse des bâtiments est régie par les déformations du sol résultant de l'excavation. Ces déformations, du niveau de la surface et de niveaux plus profonds, sont décrites dans un article connexe à cette conférence. Dans le document présent, la réponse des bâtiments sur pieux est décrite.

**KEYWORDS:** deep excavation, ground displacement, piles.

### 1 INTRODUCTION

The North-South Line in Amsterdam passes under the historical centre of the city in twin tunnels. Five underground stations are currently under construction. Rokin, Vijzelgracht and Ceintuurbaan Station are three of the deep stations in the historic city centre. They are built using the top down method, see Figure 1. In a related paper for this conference by the same authors, the construction method and ground displacements related to the deep excavations have been described. The settlement measurements for the Amsterdam deep excavations have been compared to several, mostly empirical, relationships to determine the green field surface displacements and displacements at depth. In summary, the surface displacement behind the wall is 0.3 – 1.0% of the excavation depth, if all construction works are included. Surface displacements behind the wall can be much larger than the wall deflections and become negligible at 2-3 times the excavated depth away from the wall. The shape of the displacement fits the proposed profile by (Hsieh and Ou 1998) best. In all three of the Amsterdam cases, the largest effect on the ground surface displacement can be attributed to the preliminary activities, which include amongst others the diaphragm wall construction, jet grout strut installation and construction of the roof, and took in total about 4 years. See Table 1 for details.

Table 1 Construction activities and dates for Ceintuurbaan

Construction activity	End date
Base monitoring start 2001	2003-11-01
Preliminary activities	2007-04-01
Excavation to NAP -6.2m	2007-09-13
Excavation to NAP -15.3 m	2007-12-10
Excavation to NAP -19.4 m	2008-03-01
Excavation to NAP -24 m	2008-08-01
Excavation to NAP -25.6 m	2009-06-24
Floor construction, pumping test	

The actual excavation stage caused only about 25-45% of the surface displacements, with 55-75% attributed to the

preliminary activities. At larger excavation depths the influence zone is significantly smaller than 2 times the excavation depth.

This paper describes the building displacements related to the excavation works in more detail.

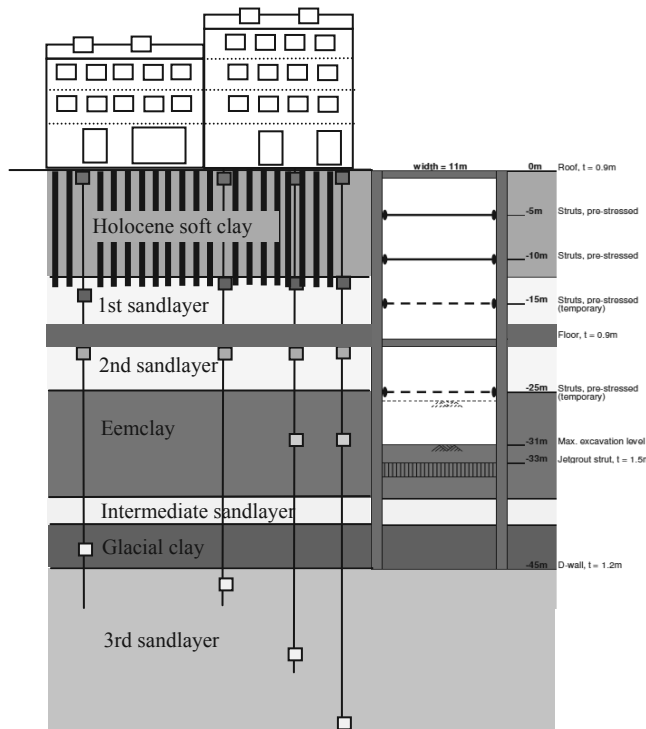


Figure 1 Cross section of Ceintuurbaan Station with soil profile and extensometer locations.



## 2 SOIL-STRUCTURE INTERACTION

The excavation-induced displacements described in the related paper can be considered as green field displacements. To assess the potential impact of these ground displacements on buildings, these displacements are usually directly projected onto the building, leading to bending and shear strains in the structure. It is however known that the presence of the building and the interface between building and soil also influences the settlement trough and transfer of deformations to the building. (Potts and Addenbrooke 1996, Franzius et al. 2006 and Farrell 2010) have shown this for displacements related to tunnels and (Goh and Mair 2011) for buildings influenced by deep excavations. (Goh and Mair 2011) modified the relative stiffness proposed by Potts and Addenbrooke for tunnelling to the following for deep excavations:

$$\rho_{exc}^* = \frac{EI}{E_s L^3} \quad (1)$$

$$\alpha_{exc}^* = \frac{EA}{E_s B} \quad (2)$$

where EI is the building stiffness, Es a representative soil stiffness and L the length of the building in either hogging or sagging. EA is the axial stiffness of the building and B is the total length of the building.

Furthermore (Jacobsz et al. 2005) described the soil-structure interaction in more detail for piled buildings related to tunnelling. In Amsterdam the piled buildings were influenced by deep excavations, which requires a combined approach influenced by the presence of pile foundations: the initial stresses in the foundation and the ground, and possible load transfer within the building. If these effects are not considered, the current assessment methods may be too conservative or too optimistic, leading to costly measures either being taken unnecessarily or having to be applied at a late stage in the project.

## 3 BUILDING AND FOUNDATION CHARACTERISTICS

Most buildings in the historic centre of Amsterdam are built with masonry walls, wooden floors and timber pile foundations, the piles being founded in the First Sand Layer at about 12m below the surface level (see Figure 1). More recent buildings with 1-4 storeys are built with concrete walls and floors and prefabricated concrete or steel piles. Foundations for some recent buildings are in deeper layers such as the second sand layer. The buildings considered in this paper are from the older type, see Figure 2.



Figure 2 Historic buildings at Vijzelgracht (left) and Ceintuurbaan Station (right), dated 1880-1920

The wooden piles are installed in pairs, see Figure 3, with 0.8m between the pairs. Pile diameters for the timber piles vary from

160 - 300 mm (typical 180-200 mm) at the head and usually diminish by 8 mm/m to about 70-200 mm (typical 120-140 mm) at the toe. Based on several pile load tests in the historic centre it is known that the wooden pile foundations have low factors of safety. Up to 15% of the buildings of this age in Amsterdam are not up to current standards, according to (van Tol 1994). A large number of timber piles deteriorate due to decay of the wood, which may lead to a different kind of building response; this effect is not described here.

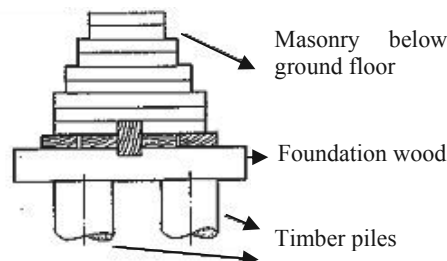


Figure 3 Typical cross section of base of the wall in masonry buildings (Zantkuyl 1993)

Two typical load-displacement curves are shown in Figure 4. The timber piles in failure generally find 60% of their capacity at the toe, 10% as friction in the sand layer and 30% as friction in the Holocene clay the maximum shaft friction develops at a relative displacement of about 25 mm and in the base sand layer at about 15 mm. The maximum base capacity for piles with average diameter at the base of 130 mm is reached at about 10% of the diameter, which is consistent with common design methods. The high horizontal flexibility assures that the piles can move rather easily with the soil in horizontal direction, compared to concrete piles.

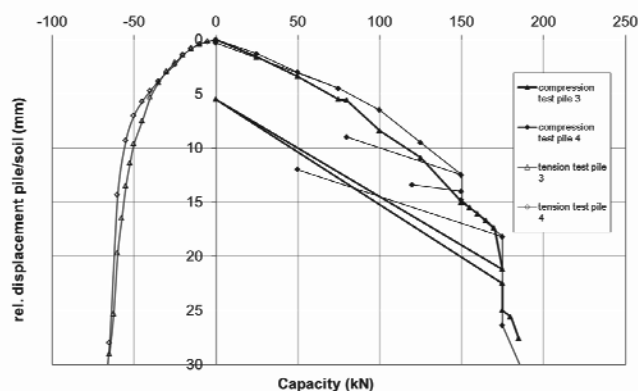


Figure 4 Representative load-settlement curves for timber piles in Amsterdam (Hoekstra 1974)

To determine the response of piled buildings to excavations knowledge of the current state of the piles is essential. Most piles in the historic centre of Amsterdam will already have experienced the maximum negative skin friction possible over time. The presence of soft soil layers combined with earlier city developments which included raising of the ground level causes on-going subsidence due to consolidation and creep. Negative skin friction develops as a result along the shaft of a pile when the soil surrounding the pile settles more than the pile itself. Positive skin friction occurs in opposite circumstances when the pile settles more than the surrounding soil. Both forces are likely to act on the timber piles in Amsterdam, see Figure 5.

#### 4 RESPONSE OF PILED BUILDINGS

For end bearing piles with sufficient factor of safety the neutral level is found close to the location of the bearing layer. For the most historic Amsterdam foundations, the reserve capacity is smaller, and positive skin friction is also found in the soft or settling layers. The maximum force in the pile is found at the neutral level (the level at which the soil and pile settlements are the same and the shear stresses acting on the pile change direction). Usually in Amsterdam, it is considered that the negative skin friction is already fully mobilized before the excavation takes place.

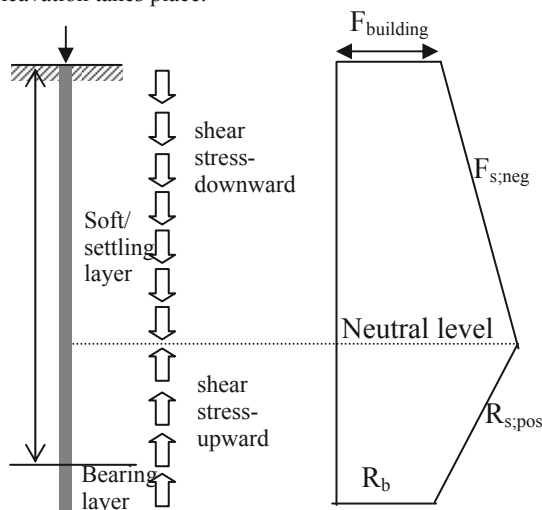


Figure 5 Development of negative and positive skin friction along a pile with low factor of safety

Buildings in the influence zone of the excavation may experience several phenomena:

1. reduction of pile capacity due to lower stress levels ( $s_1$ )
2. settlement of soil below the pile base ( $s_2$ )
3. development of negative (or positive) skin friction due to relative movements of the soil and the pile shaft ( $s_3$ )
4. redistribution of pile load between the piles ( $s_4$ )
5. horizontal deformations of the piles.

The settlement of the pile head is determined by the combination of the first four effects described above:

$$s = s_1 + s_2 + s_3 + s_4 \quad (3)$$

Settlement  $s_1$  for end bearing piles is significant if the pile tips are very close to the excavation and stress relief takes place around the pile tip. Settlement  $s_2$  does not involve interaction with the piles, whereas  $s_3$  is a true interaction component. For end bearing piles complying with current standards negative skin friction, if already fully developed, will not cause additional settlements, which means  $s_3 = 0$ . For all other piles  $s_3$  depends on the amount of negative skin friction mobilized in the initial state. If the shaft friction is already fully mobilized, the neutral level will remain at about the same level and the pile follows the settlement of the soil at this level. If the shaft friction initially is not developed completely, the neutral level will change if soil displacements take place. For piles close to failure, the neutral level is found close to the surface and  $s_3$  is about equal to the surface settlement.

An important issue is to determine the initial neutral level. This could be done theoretically based on CPT data or from historic data of relative building settlements to surface settlements. Based on the average pile capacity, the neutral level for an old pile in Amsterdam is found to be between NAP -7 and NAP -12 m, depending on the load on the pile, see (Korff 2012). Assuming a linear relationship between the ground settlement at surface and pile tip level, the pile-soil interaction

can be determined from the relative position of the neutral level to the surface and the tip level, see Figure 6.

If the negative skin friction is not fully mobilized at the initial state or if the tip resistance reduces, the skin friction will further mobilize, which will raise the neutral level. Settlement  $s_3$  might also include an elastic component of the shortening of the pile if the total stress in the pile increases with increasing negative skin friction. If the pile redistributes its load,  $s_4$  needs to be determined together with  $s_3$ . This could occur if the piles closest to the excavation settle more than the piles further away. The building stiffness will prevent the building from following the different pile movements and the pile load will redistribute accordingly. If this happens, the external load on the pile changes, leading to a new equilibrium. This effect should be determined by a coupled analysis for a pile group, such as with a boundary element method as described by (Xu and Poulos 2000).

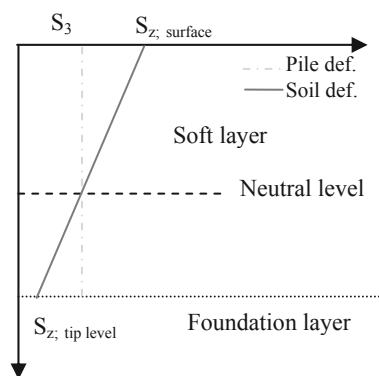


Figure 6 Settlement profile and neutral level, assuming linear relationship

#### 5 BUILDING DISPLACEMENTS

The effects that cause the piles and hence the buildings to settle have been evaluated by analysing substantial amounts of monitoring data available from the Amsterdam cases. The settlement of the building is compared to the greenfield soil deformations at surface and pile tip level. It is not possible to distinguish between the contributions of  $s_1$ ,  $s_3$  and  $s_4$ . Settlement  $s_2$  however can be directly evaluated against the results of the extensometer measurements at pile tip level. Figure 7 shows the building displacements (LevelingS) compared to the soil displacements at surface (GroundSurface) and pile tip level (ExtensioNAP-12m) for a series of buildings with old timber piles. The settlement of these buildings is equal to the soil settlement at approximately 0.3 to 0.5 times the pile length if a linear soil settlement profile between the surface settlement and the settlement at the first sand layer is assumed.

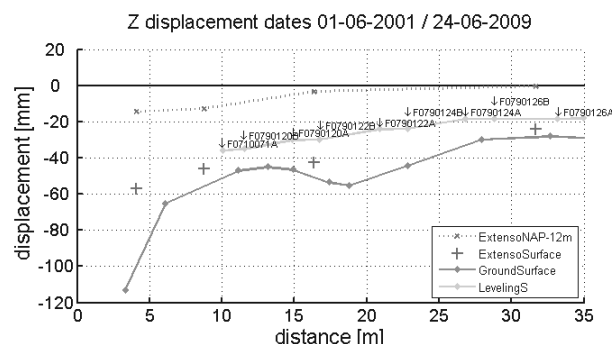


Figure 7 Ground and building displacements for CS13044 (at Ceintuurbaan).

In most cases in practice, no detailed information is present about the foundation and the soil-pile interaction has to be estimated or measured during construction.

For a second series of buildings with more modern foundations (old timber piles combined with renovation steel piles), the depth at which the pile and soil settlement are equal is found at approximately 0.8 – 1.0 times the pile length, see Figure 8.

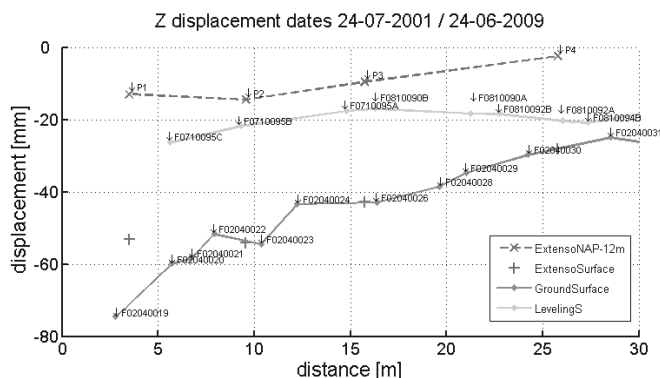


Figure 8 Ground and building displacements for CS13110 (at Ceintuurbaan) in the period 2001-2009

Based on the soil and building displacements as presented in more detail in (Korff 2012), the average interaction between pile and soil is found at 0.3 – 0.8 times the pile length for most original timber pile foundations and 0.8-1.0 times the pile length for most renewed foundations in the first sand layer. Some modern buildings settle very little and the pile settles the same as the pile tip level (1.0).

The settlement of the piles is shown to be between the settlement of the surface and the foundation layer. The deflection of the building is smaller than the deflection of either of the surface or base level soil deflections due to the stiffness of the building. The (Goh and Mair 2011) method to compare building settlement with greenfield settlement was used to determine the modification factors. In this case this was done comparing with greenfield surface settlement and with greenfield settlement of the foundation layer (first sand). For the deflection of buildings next to excavations, deforming in hogging shape, the modification factor is based on (Potts and Addenbrooke 1996):

$$M_{hog}^{DR} = \frac{\Delta/L \text{ hog, building}}{\Delta/L \text{ hog, greenfield}} \quad (4)$$

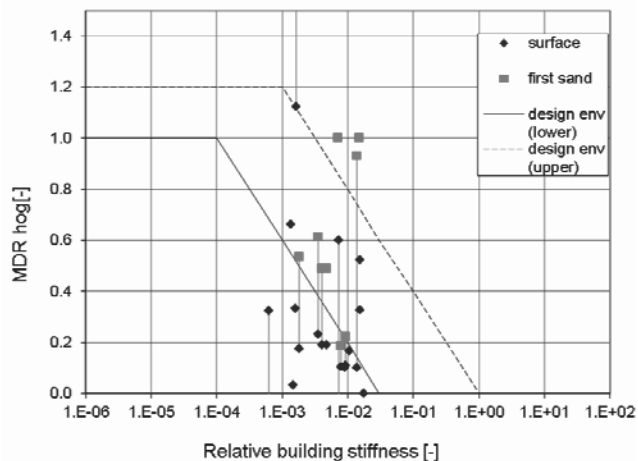


Figure 9 Modification factors from Amsterdam deep excavation for surface level and foundation level, compared with the design envelope presented by (Mair 2011)

The deflection of the buildings is clearly less than the deflected shape of the surface (70% reduction). A reduction of the deflection of 45% is found compared to the foundation level. The variation in these factors can to a certain degree be explained by the relative stiffness of the buildings compared to the soil as shown in Figure 9.

## 6 CONCLUSIONS

Piled buildings adjacent to deep excavations have to be assessed differently from buildings with shallow foundations. Piled buildings settle an amount between the surface settlement (for friction piles in failure) and tip level settlement (for end bearing piles with sufficient capacity to take full negative skin friction). The precise soil-pile interaction can be estimated based on the pile load, the pile capacity and the shaft friction development based on a method described in (Korff 2012). Based on measurements of Amsterdam timber pile foundations, the pile settlement is equal to the soil settlement at a depth of 0.3 – 0.8 times the pile length for most original timber pile foundations and 0.8-1.0 times the pile length for most renewed foundations in the first sand layer. Most of the modern buildings settle not more than the pile tip level.

The method proposed by (Goh and Mair 2011) provides a realistic, although rather large, range of possible modification factors to estimate the building deflection compared to the deflected shape of the soil surface and foundation level.

## ACKNOWLEDGEMENTS

This research was performed in cooperation with the Dutch Centre for Underground Construction (COB). The authors wish to thank the city of Amsterdam for permission to use the data.

## REFERENCES

Franzius J. N. Potts D. M. and Burland J. B. 2006. The response of surface structures to tunnel construction. *Proc. Institution of the Civil Engineers Geotechnical Engineering* 1591, 3–17

Farrell R.P. 2010. *Tunnelling in sands and the response of buildings*. Ph.D thesis Cambridge University UK.

Goh K.H. and Mair R.J. 2011. The response of buildings to movements induced by deep excavations. *Geotechnical Aspects of Underground Construction in Soft Ground - Proceedings of the 7th International Symposium on Geotechnical Aspects of Underground Construction in Soft Ground* Rome, 903-910.

Hoekstra J. and Bokhoven W. 1974. *Systematisch funderingsonderzoek van de Dapperbuurt* "Systematic foundation research in the Dapperbuurt area". Laboratorium voor Grondmechnica Delft reference CO-21606/503 In Dutch.

Hsieh P. G. and Ou C. Y. 1998.. Shape of ground surface settlement profiles caused by excavation. *Canadian Geotechnical Journal* 35, 1004–1017.

Jacobsz S. W.; Bowers K.H.; Moss N.A.; Zanardo G. 2005. The effects of tunnelling on piled structures on the CTRL. *Geotechnical Aspects of Underground Construction in Soft Ground* Amsterdam Taylor&Francis Group London.

Korff M. 2012. *Response of piled buildings to the construction of deep excavations*. Ph.D thesis Cambridge University

Mair R.J. 2011. Tunnelling and deep excavations - Ground movements and their effects. Keynote Lecture. *Proceedings of the XV European Conference in Soil Mechanics and Geotechnical Engineering ECSMGE-Athens*.

Potts D. M. and Addenbrooke T. I. 1996. The influence of an existing structure on the ground movements due to tunnelling. *Geotechnical Aspects of Underground Construction in Soft Ground* London.

van Tol A.F. 1994. *Hoe betrouwbaar is de paalfundering?* Lecture at installation as professor at Delft University of Technology

Xu K.J. and Poulos H.G. 2000. Theoretical Study of Pile Behaviour Induced by a Soil Cut. *Proceedings GeoEng 2000*, CD volume.

Zantkuijl H. J. 1993. *Bouwen in Amsterdam - Het woonhuis in de stad Building in Amsterdam*. Amsterdam Architectura & Natura.

# Deep excavation in Irish glacial deposits

## Excavation profonde des dépôts glaciaires Irlandais

Long M., O'Leary F.

*Department of Civil, Structural and Environmental Engineering, University College Dublin (UCD), Ireland*

Ryan M., Looby M.

*Byrne Looby Partners, Dublin, Ireland*

**ABSTRACT:** A good number of deep excavations have been recently completed in Irish glacial deposits. These have included propped walls up to 12 m deep. Experience elsewhere in the world was used to design and construct these walls. However case history data has shown that the behaviour of these walls is very rigid and much stiffer than comparable systems worldwide. It appears this behaviour is due to the inherent natural strength and stiffness of the soil and the slow dissipation of excavation induced depressed pore pressures or suctions. There appears to be scope for developing more efficient designs and in particular for greater use of cantilever walls and less stiff systems with smaller piles and reducing propping requirements. For temporary works, the use of undrained parameters in serviceability limit state calculations together with implementation of the observational approach on site could be considered for future schemes.

**RÉSUMÉ :** Un bon nombre d'excavations profondes ont été récemment réalisées dans les dépôts glaciaires Irlandais. Elles ont inclus des murs de soutènement jusqu'à 12 mètre de profondeur. La conception de ces murs a été réalisée grâce aux méthodes utilisées dans les autres pays du monde. Toutefois, les analyses a posteriori ont montré que les caractéristiques de ces murs étaient extrêmement rigides et bien plus rigide que d'autres systèmes comparables dans le monde. Il semble que ces caractéristiques sont dues à la résistance naturelle et à la rigidité du sol ainsi qu'à la lente dissipation des pressions interstitielles déprimées ou aux suctions induites par la réalisation des excavations. Il semble y avoir des possibilités de développer des méthodes de conceptions plus réalistes et moins conservatives permettant en particulier une utilisation accrue des murs cantilevers et des systèmes moins rigides avec de petits pieux de fondation et en réduisant les besoins de butonnage ou d'ancrage. Pour les travaux temporaires, l'utilisation de paramètres non drainés dans les calculs des états limite de service ainsi que la mise en œuvre de l'approche observationnelle sur le chantier, pourraient être envisagées pour de futurs projets.

**KEYWORDS:** deep excavations; retaining walls; glacial deposits; ground movements

### 1 INTRODUCTION.

Over the previous 15 years, economic growth in Ireland has led to an increase in the use of underground space, with some development now including four underground levels. Valuable full scale data has been obtained from a good number of these projects. The purpose of this paper is to provide an overview of aspects relating to the design, construction and behaviour of retaining walls in Irish glacial deposits.

This paper will exclude projects located in the two main cities of Dublin and Cork. Case histories from these two locations have already been well documented (Long et al., 2012a; Long et al., 2012b; Long et al., 2012c; Long et al., 2013).

Specifically the paper will:

- Briefly review the background geology and ground conditions,
- Outline the presently used design approach,
- Review in detail the general behavior of walls in Irish glacial deposits by reference to two case histories namely:
  - lightly supported "regular" wall for 6 m excavation in Limerick,
  - 6 m excavation in Middleton, Co. Cork where a cantilever solution was used,
- Present an overall summary of the behavior of retaining walls in Irish glacial deposits compared to similar support systems worldwide,
- Provide some overall conclusions and recommendations for the design and construction of future similar schemes.

### 2 BACKGROUND GEOLOGY

Broadly speaking the coastline of Ireland is formed of strong older igneous and metamorphic rocks such as sandstones, granites and quartzite. The central basin of Ireland is formed of Carboniferous limestone. However the engineering geology of Ireland is dominated by the mantle of 10,000 to 15,000 year old glacial tills and glacial sands and gravels which cover much of the country. These deposits generally have a high gravel, cobble and boulder content and are usually medium dense to dense or stiff to very stiff in consistency. They form a thin layer (but usually greater than 3 m in thickness) draped over and conforming to the underlying bedrock topography. Later alluvial activity has covered the glacial deposits with soft clays, silts and peats in some low lying areas, in estuaries and along river flood plains (Edwards and Warren, 1985).

### 3 THE SITES

The location of the study sites is shown on Figure 1 and some details of the projects under consideration are given on Table 1. The sites are located throughout Ireland but mostly in the most populated areas to the east and south-east.

At each of the chosen sites inclinometers had been used to measure the lateral pile retaining wall movements. Details given on Table 1 include the depth of excavation (H), the support details including the spacing of the structural piles and the maximum measured pile deflection ( $\delta_h$  max).

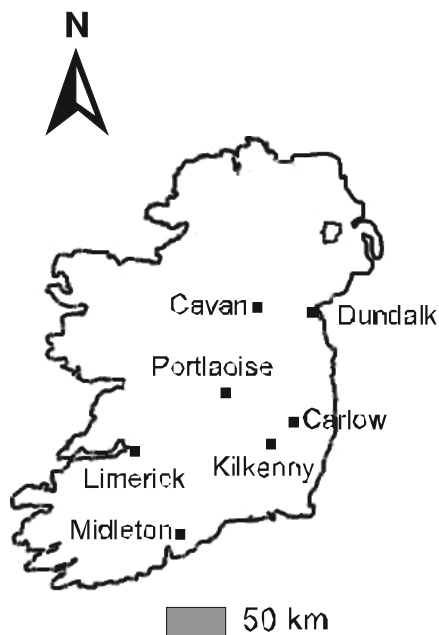


Figure 1. Location of study sites

Table 1. Details of study sites

Site No.	Location	H (m)	Support Configuration	Wall type
1	Savoy Limerick 1	6.4	Single anchor	Secant
2	Savoy Limerick 2	5.8	Single anchor	Secant
3	Main St. Cavan	9.0	Two anchors	Contiguous
4	Dundalk Cellar	8.7	Single anchor	Secant
5	Dundalk Bunker	8.1	Single anchor	Secant
6	Midleton Cantilever	6.0	Cantilever	Secant
7	Midleton Anchored	6.0	Single anchor	Secant
8	Kilkenny	7.7	Single prop	Contiguous
9	Kilkenny	6.9	Single prop	Contiguous
10	Shaws Carlow	5.0	Single prop	
11	Portlaoise SC Phase 1	12.0	Two anchors	Secant
12	Portlaoise SC Phase 2	7.0	Single anchor	Secant

Table 1 continued

Site No	Pile dia. (mm) / spacing (m) / length (m)	$\delta_h$ max (mm)	Reference
1	600 / 1 / 8.4	7	BLP files
2	600 / 1 / 7.8	2	BLP files
3	192 / 0.25 / 14	45	BLP files
4	640 / 1.4 / 10	6	BLP files
5	640 / 1.4 / 12	7	BLP files
6	640 / 1.2 / 16.5	27.5	BLP files
7	640 / 1.2 / 14	5.5	BLP files
8	600 / 0.75	5	Arup files
9	600 / 0.75	2	Arup files
10	n/a	2	NVM files
11	640 / 1.0 / 14	17	BLP files
12	640 / 1.0 / 7	4	BLP files

#### 4 DESIGN

Current geotechnical design procedures for retaining walls in Irish glacial deposits often involves the following steps:

- Following the general guidelines of Gaba et al. (2003) or BS8002 (BSI, 1994), for ultimate limit state, determine the required retaining wall toe penetration. Calculations use effective stresses and are often performed by hand, using conventional Rankine active and passive earth pressure theory, or with a relatively simple piece of software,
- Check that this toe penetration is adequate to support any vertical loads and also to prevent significant water seepage,
- Determine wall bending moments, shears, prop / waler forces and lateral wall movements (serviceability limit state) by means of a beam – spring computer program such as OASYS – FREW<sup>®</sup>,
- Determine the associated ground movements using empirical based methods, such as those developed by Clough and O'Rourke (1990). Possible adjacent building damage is then assessed by comparing parameters such as differential settlement with empirically based tolerable limits, e.g. those of Burland et al. (1977)

#### 5 OVERVIEW ALL SITES

Data for the 12 available case histories are presented in Table 1. A plot of maximum measured lateral movement ( $\delta_h$ ) versus retained height (H) is shown on Figure 2. Except for the Main St. Cavan, Portlaoise Phase 1 and the Midleton cantilever excavations,  $\delta_h$  values are less than 7 mm. There does appear to be some weak tendency for an increase in  $\delta_h$  with H.

Also shown on Figure 2 are lines representing normalised movement ( $\delta_h/H$ ) of 0.08% and 0.4%. The former relationship was obtained by Long et al. (2012a) for projects in Dublin boulder clay – a very stiff glacial lodgement till. The behaviour of the projects presented here is similar if not better than the Dublin sites. The 0.4% line represents a typical design value as recommended by Gaba et al. (2003) in CIRIA Report C580 and clearly this relationship is very conservative for most of the cases presented but is consistent with the data from the Cavan and Midleton cantilever sites.

The data shown on Figure 2 takes no account of the retaining wall type, its stiffness or the prop / anchor configuration. In order to attempt to include these factors, the data are replotted on Figure 3 in the normalised form of  $\delta_h/H$  against Clough et al. (1989) system stiffness. This is defined on Figure 3 where  $EI$  = wall stiffness,  $\gamma_w$  = unit weight of water (so as to make expression unitless) and  $s$  = support spacing.

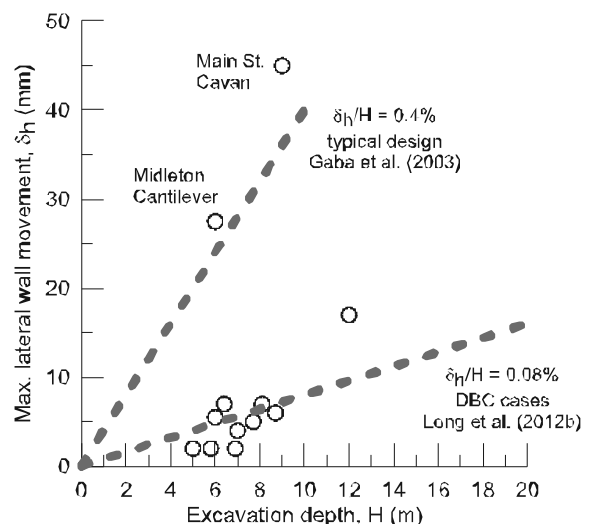


Figure 2. Maximum lateral wall movement versus excavation depth

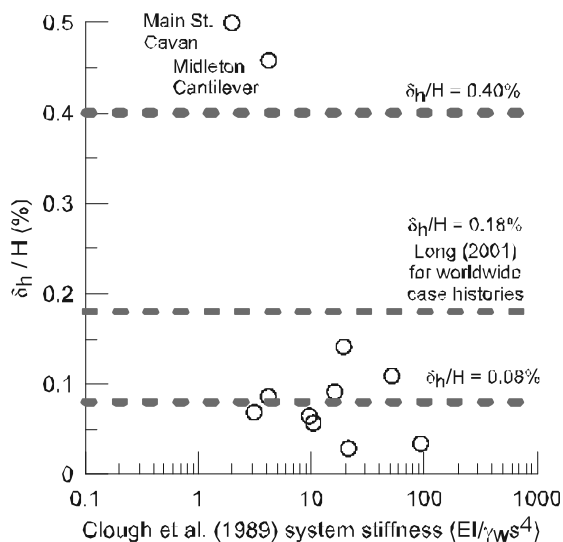


Figure 3. Normalised maximum lateral wall movement versus Clough et al. (1989) system stiffness

The two relationships included in Figure 2 are also shown here. In addition the relationship  $\delta_h/H = 0.18$ , which was obtained by Long (2001) for an average of 169 case histories worldwide where there was stiff soil at dredge level, is also shown. Lateral movement is clearly a function of system stiffness with the two walls with low system stiffness showing relatively high movements. The Cavan wall had very slender piles and the Midleton wall had no props or anchors. However the remaining data plot well below the worldwide trend suggesting that a more flexible (and hence a more economic) wall may perform adequately in many cases.

Some of the trends shown on Figure 2 and 3 are explored further by examining two detailed case histories as follows

### 6 CASE HISTORY OF A LIGHTLY SUPPORTED “REGULAR” WALL – SAVOY, LIMERICK

Details of this site are shown on Figure 4. The approach and techniques used at the Savoy Site are typical of those used at many sites in Ireland. The site is underlain by about 2 m of made ground over about 5 m of glacial deposits over limestone bedrock. The glacial deposits have standard penetration test (SPT) N values increasing from about 20 blows / 300 mm near the top of the stratum to an average of 60 blows / 300 mm with depth.

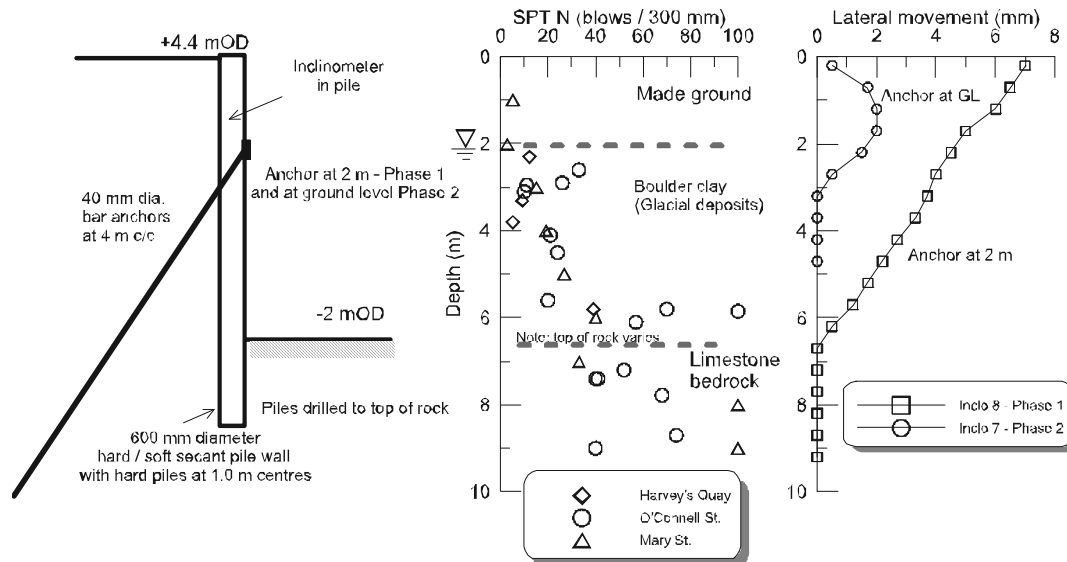


Figure 4. Savoy, Limerick

The retaining wall was required for temporary works purposes only and comprised a 600 mm diameter “hard / soft” secant wall with a single anchor. For the Phase 1 excavation the anchor was located at about 2 m depth. Much of the 7 mm or so movement recorded occurred while the wall was acting in a cantilever mode during the installation of the anchors. This is consistent with the findings of Long (2001) for a good number of world wide projects. Thus for Phase 2 the anchor was relocated to ground level and the measured movements were much smaller.

It would seem that a less stiff system, e.g. smaller diameter / more widely spaced piles or a cantilever wall would have performed perfectly adequately in this case.

### 7 CASE HISTORY OF CANTILEVER WALL

Details for the Midleton site are shown on Figure 5. This project was carried out in 2012 and thus many of the lessons learned over the previous 10 to 15 years could be used. Again the wall was required for temporary works purposes. It comprised a “hard / firm” secant pile wall with 640 mm diameter structural “male” piles and 900 mm diameter “female”. A single anchor was used at locations where sensitive adjacent buildings were present. However for non sensitive areas of the site and based on the experiences listed above a cantilever solution was used.

Ground conditions are more complex than those at Limerick and comprised a variable sequence of glacial clays, silts, sands and gravels. SPT N values increase from about 10 blows / 300 mm at the surface to an average of 25 blows / 300 mm at 7 m depth and thereafter remain approximately constant.

As would have been expected from previous experience measured movements for anchored section were very small. For the cantilever sections the wall also behaved very well and maximum lateral movements were of the order of 20 mm

Predicted wall deflections, using *FREW*<sup>®</sup> for the anchored wall are also shown on Figure 5. The key input parameters are the effective friction angle ( $\phi'$ ), the undrained shear strength ( $s_u$ ) and the Young's modulus ( $E_u$  or  $E'$ ). These were determined from correlations with SPT N. For the clay layers it was assumed  $s_u = 5N$  and  $E_u = 750N$  (Gaba et al., 2003; Stroud, 1988). For the granular soils  $E'$  was assumed = 2500N and  $\phi'$  was found from the relationships of Peck et al. (1974).

It can be seen that the predicted values considerably overestimate the measured ones. A similar finding was made for the cantilever wall at Midleton.

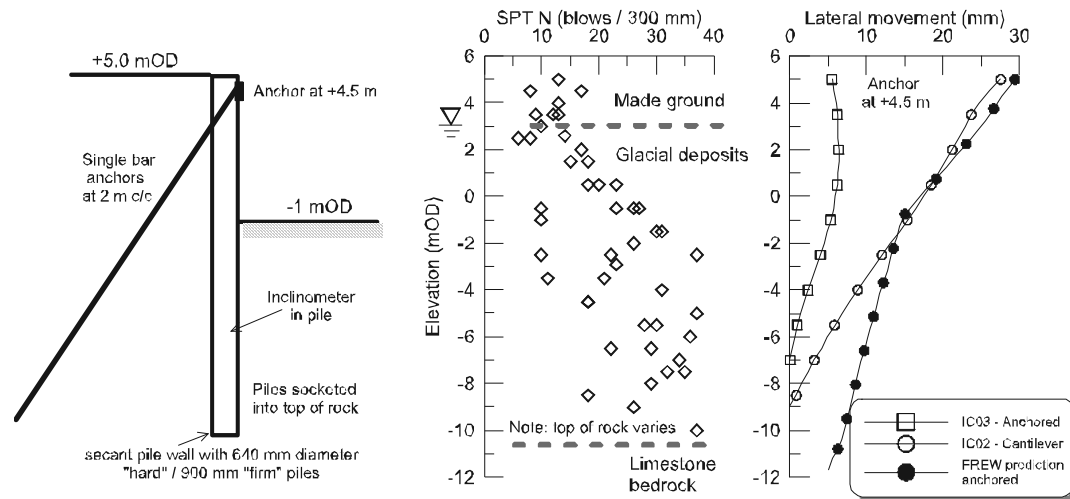


Figure 5. Midleton

## 8 DISCUSSION

The reasons for the very stiff behaviour of the retaining walls in Irish glacial deposits are complex but are due to a combination of the following factors:

- Excavation induced depressed pore pressures (or even suctions) in the material. These result in increased effective stress and hence stability (Long et al., 2012a).
- The low permeability of the clay fraction of the material ( $10^{-10}$  m/s or less) meaning that the dissipation of the depressed pore pressures takes a long time.
- The material has extremely high strength and stiffness.

A possible approach for the design of temporary retaining structures in the clay fraction of the material may be in the use of undrained parameters in conjunction with the observational approach. This approach should only be considered where the predicted deflections using an effective stress approach would be within defect limits to prevent the possibility of damage, economic loss or unsafe situations. The risk associated with the decision should be clearly assessed in terms of understanding of the site geology, type and condition of structures to the rear of the pile wall and the quality of monitoring procedures and contingency measures put in place.

It seems there is scope for the greater use of cantilever walls, less stiff walls (e.g. smaller diameter piles) and also greater retained heights at least for temporary works purposes. It must also be emphasised that an effective stress design approach is always needed for the ultimate limit state analysis in permanent works as the suctions will eventually dissipate.

## 9 CONCLUSIONS

Case history data confirms that retaining wall behaviour in Irish glacial deposits is extremely stiff.

The reasons for this stiff behaviour lie in the low permeability and high strength and stiffness of the material and the resulting very slow dissipation of depressed excavation induced pore pressures.

It appears that the current approach, for serviceability limit state calculations, which usually involves beam – spring type computer programs is clearly conservative.

For temporary works, the use of undrained parameters in conjunction with the observational approach may be considered for reducing predicted deflections to simplify the construction sequence and reduce costs.

There is scope for greater use of cantilever walls and walls and systems with lower stiffness.

## 10 ACKNOWLEDGEMENTS

Some of the data used in this paper was kindly provided by Mr. Tony O'Dowd of PJ Edwards & Co., Mr. Pat Fox of Murphy International Ltd., Mr. Patrick Casey of Arup Consulting Engineers and Mr. Eddie Meade of NVM Ltd. and their co-operation is gratefully acknowledged.

## 11 REFERENCES

- BSI, 1994. *Code of practice for earth retaining structures*
- Burland, J.B., Broms, B.B. and De Mello, V., 1977. Behaviour of foundations and structures, *Proceedings IX<sup>th</sup> International Conference on Soil Mechanics and Foundation Engineering*, Tokyo, pp. 495 - 546.
- Clough, G.W. and O'Rourke, T.D., 1990. Construction induced movements of in situ walls, *Proceedings ASCE Conf. on Design and Performance of Earth Retaining Structures*, ASCE Pub. No. 25, Cornell, pp. 439 - 470.
- Clough, G.W., Smith, E.M. and Sweeney, B.P., 1989. Movement control of excavation support systems by iterative design, *Proceedings ASCE Foundation Eng: Current Principles and Practices*. ASCE, pp. 869 - 884.
- Edwards, K.J. and Warren, W.P., 1985. The Quaternary studies in Ireland. In: K.J. Edwards and W.P. Warren (Editors), *The Quaternary History of Ireland*. Academic Press, London, pp. 1 - 16.
- Gaba, A.R., Simpson, B., Powrie, W. and Beadman, D.R., 2003. Embedded retaining walls - Guidance for economic design, *CIRIA Report No. C580*.
- Long, M., 2001. A database for retaining wall and ground movements due to deep excavations. *Journal of Geotechnical and Geoenvironmental Engineering*, ASCE, 127(3): 203 - 224.
- Long, M., Brangan, C., Menkiti, C., Looby, M. and Casey, P., 2012a. Retaining walls in Dublin Boulder Clay, Ireland. *Institution of Civil Engineers Journal of Geotechnical Engineering*, 165(GE4, August): 247 - 266.
- Long, M., Daynes, P.J., Donohue, S. and Looby, M., 2012b. Retaining wall behaviour in Dublin's fluvio-glacial gravel, Ireland. *Institution of Civil Engineers Journal of Geotechnical Engineering*, 165(GE5, October): 289 - 307.
- Long, M., Menkiti, C., Skipper, J., Brangan, C. and Looby, M., 2012c. Retaining wall behaviour in Dublin's estuarine deposits, Ireland. *Institution of Civil Engineers Journal of Geotechnical Engineering*, 165(GE6, December): 351 - 365.
- Long, M., Murphy, M., Roberts, T., Clancy, N. and Murphy, P., 2013. Deep excavations in water bearing gravels in Cork. *Quarterly Journal of Engineering Geology (QJEGH)* Paper submitted November 2012.
- Peck, R.B., Hanson, W.E. and Thorburn, T.H., 1974. *Foundation Engineering* 2nd Ed. John Wiley and Sons, New York.
- Stroud, M.A., 1988. The standard penetration test: its application and interpretation, *Proceedings ICE Conference on Penetration Testing in the UK*. Thomas Telford, London, University of Birmingham, pp. 29 - 51.

# Active earth thrust on walls supporting granular soils: effect of wall movement

Pression active des terres sur des murs soutenant des sols granulaires: l'effet du mouvement du mur

Loukidis D.  
University of Cyprus, Cyprus

Salgado R.  
Purdue University, USA

**ABSTRACT:** The methods currently used in the design practice of retaining walls supporting granular soils (sand, gravel, silt, and their mixtures) assume that the soil friction angle and, consequently, the active earth pressure coefficient  $K_A$  are independent of wall movement. However, the mobilized friction angle inside the retained soil in reality first reaches a peak value and then decreases towards the critical state value as shear strain increases with wall movement. This study aims to investigate the development and evolution of the active earth pressure by modeling the soil mechanical behavior in a realistic way in a series of finite element analyses. Based on the numerical results, an equation is proposed for the estimation of  $K_A$  as a function of the initial relative density and the wall crest displacement.

**RÉSUMÉ :** Les méthodes actuellement utilisées dans la pratique de la conception des murs de soutènement supportant des sols granulaires (sable, gravier, limon et leurs mélanges) supposent que l'angle de frottement du sol et, par conséquent, le coefficient de pression active des terres  $K_A$  sont indépendantes du mouvement du mur. Toutefois, l'angle de frottement mobilisé à l'intérieur du sol retenu atteint en réalité d'abord une valeur de pic, puis diminue vers la valeur d'état critique à mesure que la déformation en cisaillement augmente avec le mouvement du mur. Cette étude vise à étudier le développement et l'évolution de la pression active des terres par la modélisation du comportement mécanique des sols de manière réaliste dans une série d'analyses par éléments finis. Sur la base des résultats numériques, une équation est proposée pour l'estimation de  $K_A$  en fonction de la densité relative initiale et le déplacement en crête du mur.

**KEYWORDS:** retaining wall, active earth pressure, sands, finite element analysis.

## 1 INTRODUCTION

The active earth pressure is expressed as the product of the vertical effective stress  $\sigma'_v$ , in the retained soil mass or backfill and the active earth pressure coefficient  $K_A$ . The earliest and simplest methods for the calculation of the active earth pressure for purely frictional soils are those based on the Coulomb and Rankine theories. For a retained soil with horizontal free surface and a vertical wall backface, Coulomb's solution yields

$$K_A = \frac{\cos^2 \phi}{\cos \delta \left[ 1 + \sqrt{\frac{\sin(\phi + \delta) \sin \phi}{\cos \delta}} \right]^2} \quad (1)$$

The Coulomb solution can be proven to be equivalent to a rigorous limit analysis upper bound solution. It is also in good agreement with other upper bound solutions (Chen 1975, Soubra and Macuh 2002), as well as the lower bound solution by Lancellotta (2002), with the differences not exceeding 7%.

Furthermore, these methods, which are currently used in design practice, assume that  $\phi$  and, consequently, the active earth pressure coefficient  $K_A$  are constant, i.e. their values do not change as the wall moves. However, the value of the mobilized friction angle in reality depends on a number of factors, such as the current mean effective stress, and, most importantly, the shear strain. Granular soils, unless in a very loose state, are strain-softening materials, meaning that the mobilized friction angle first reaches a peak value  $\phi_p$  and then decreases towards the critical state value  $\phi_c$ . Hence, the active state developing inside the mass of the supported soil is a function of the wall movement.

The goal of this study is to investigate the development and evolution of the active earth pressure as the wall moves away from the retained soil using finite element (FE) analysis. The study focuses on retaining wall that are free to translate and rotate, such as gravity walls, cantilever walls and self-supported (cantilevered) sheet pile, secant pile or slurry walls. The mechanical behavior of the soil is captured realistically using a two-surface constitutive model based on critical state soil mechanics.

## 2 FINITE ELEMENT METHODOLOGY

The FE analyses were performed using the code SNAC (Abbo and Sloan 2000). A typical finite element mesh is shown in Fig. 1. The mesh consists of 8-noded, plane-strain quadrilateral elements and includes the wall, the supported soil and the foundation soil. The free surface of the supported soil is horizontal and without surcharge. The wall has a rectangular cross-section with width  $B$  and height  $H$ , and is modeled as a linear elastic material with very large Young's modulus so that it can be considered rigid. The retaining wall is also embedded a small distance  $D$  into the foundation soil. The analyses start with the supported soil at rest ( $K_0$  state). No interface elements are placed between the soil and the wall. As a consequence, slippage between the wall and retained soil occurs due to the formation inside the soil mass of a shear band parallel to the wall backface. This roughness condition is realistic for walls made out of concrete; however, this may not be the case for sheet pile walls.



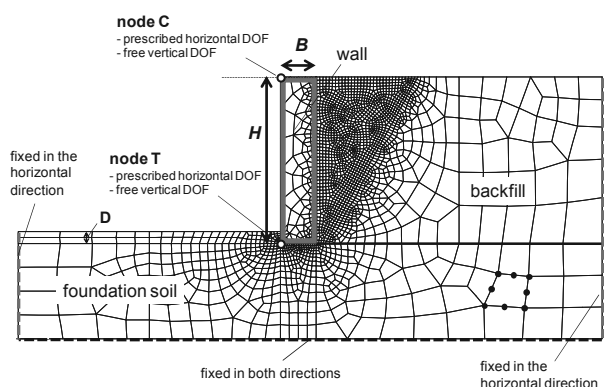


Figure 1. Typical mesh and boundary conditions used in the FE analyses.

The constitutive model used in this study is the two-surface plasticity model based on critical state soil mechanics developed originally by Manzari and Dafalias (1997) and subsequently modified by Dafalias et al. (2004) and Loukidis and Salgado (2009). The model parameters were determined by Loukidis and Salgado (2009) for two sands: air-pluviated/dry-deposited Toyoura sand and Ottawa sand. The model takes into account inherent and stress-induced anisotropy, and predicts accurately the soil response at both small and large strain regimes.

Because the problem under investigation involves material softening, the numerical simulations were inherently unstable. For this reason, the analyses were performed under displacement control. In the beginning of the analysis, the wall is fully supported at two points, namely the crest (node C) and the toe (node T), shown in Fig. 1, where the corresponding horizontal reactions are  $R_{C,0}$  and  $R_{T,0}$ , respectively. Equivalently, the wall is initially prevented to move horizontally or rotate because of the external application of a horizontal force  $F_{ext,0} = R_{C,0} + R_{T,0}$  and a moment  $M_{ext,0} = R_{C,0}/H$ . The analysis proceeds by the application of horizontal displacement increments  $\Delta u_C$  and  $\Delta u_T$  pointing away from the retained soil. As a result, the reactions  $F_{ext}$  ( $=R_C + R_T$ ) and  $M_{ext} = R_C/H$  begin to decrease. These displacement increments are applied in such way that the ratio  $F_{ext}/F_{ext,0}$  is maintained equal to the ratio  $M_{ext}/M_{ext,0}$ . As a consequence, the prescribed displacements  $u_C$  and  $u_T$  are not equal to each other, leading to an overall wall motion that includes both translation and rotation. The wall is allowed to move vertically as no restraints are imposed on its nodes in the vertical direction.

### 3 SIMULATION RESULTS

Finite element analyses were performed for  $B$  ranging from 1.5m to 2.5m and  $H$  ranging from 6m to 8m. The sand unit weight  $\gamma$  was set equal to  $18\text{kN/m}^3$ , while the coefficient  $K_0$  was set equal to 0.5. For the sake of simplicity, the foundation soil is assumed to be of the same type and density as the retained soil.

#### 3.1 Failure mechanism

Fig. 2 shows contours of the incremental maximum shear strain  $\gamma_{max}$  at the final stages of the simulations. The failure mechanism inside the supported soil consists of a wedge shaped sliding mass delimited by the wall backface and an oblique shear band originating from the heel of the wall. It can be seen also that families of secondary shear bands develop inside the sliding wedge. This is consistent with experimental observations by Leśniewska and Mróz (2001), as well as with FE analysis results by Gudehus and Nubel (2004). As shown in Fig. 2, the inclination angle of the shear bands in the retained

soil mass with respect to the horizontal is larger in the case of dense than loose sand. A shear band running parallel to the wall back face also forms in all analyses, representing sliding between the sliding soil mass (wedge) and the wall.

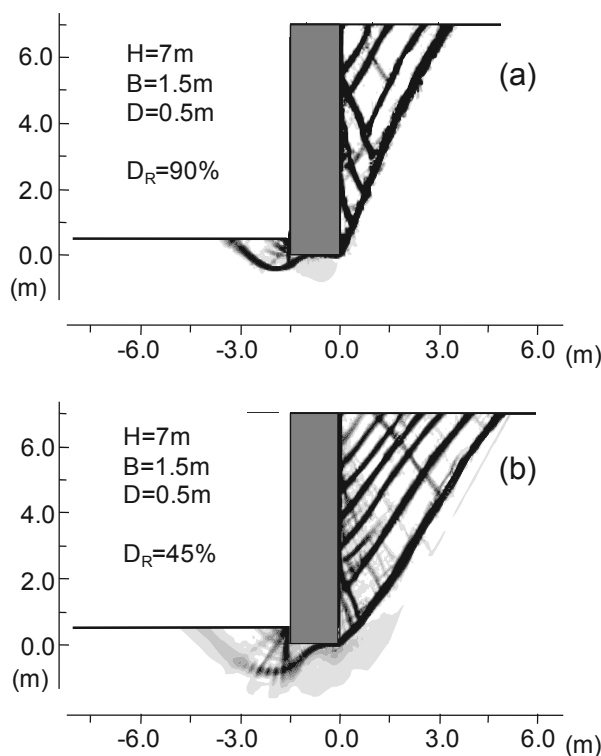


Figure 2. Contours of incremental  $\gamma_{max}$  from analyses with dense and loose Ottawa sand.

Below the wall base, a bearing capacity mechanism forms, the shape of which resembles that of mechanisms presented by Loukidis et al. (2008) for the case of strip footings on purely frictional material and subjected to eccentric and inclined loading.

#### 3.2 Active earth pressure evolution

Fig. 3 illustrates how the normal (horizontal) stress distribution along the back of the wall changes during an analysis. At the beginning, there is the triangular stress distribution corresponding to geostatic stress conditions ( $K=K_0$ ). With increasing wall displacement, the horizontal stress decreases progressively until a minimum active pressure state (MPS) is reached. From that point on, the average horizontal stress increases, but at a much lower rate than the rate at which it decreased earlier. Although before the MPS the stress distribution is smooth, afterwards, local peaks and valleys develop as consequence of bifurcation and the shear banding inside the sliding mass.

The evolution of the lateral earth pressure coefficient  $K$  with crest displacement  $u_C$  is shown in Fig. 4 for analyses with Toyoura sand with 60% relative density but different values of  $H$ ,  $B$ , and  $D$ . It can be seen that  $K$  drops sharply towards a minimum value ( $K_{A,min}$ ) corresponding to MPS at  $u_C$  approximately equal to  $0.003H$  and, subsequently, rises smoothly, approaching a residual value ( $K_{A,cr}$ ) related to the full development of critical state inside the sliding wedge. The results in Fig. 4 suggest that  $K_{A,min}$  and  $K_{A,cr}$  are practically independent of the wall dimensions and the embedment.

Fig. 5 shows the  $K/K_0$  evolution for Toyoura and Ottawa sands with different values of relative density. The figure also

shows the  $K_A$  value resulting from finite element analyses for an elastic-perfectly plastic soil following the Mohr-Coulomb failure criterion (M-C analyses) with friction angle  $\phi$  equal to the critical state friction angle value  $\phi_c$  of each sand for plane strain conditions and dilatancy angle  $\psi$  equal to zero (consistent with the constant volume response at critical state).

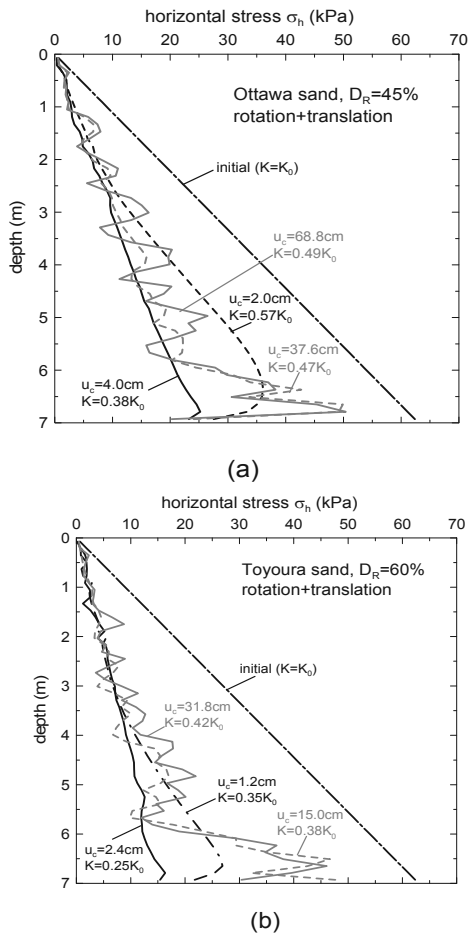


Figure 3. Examples of horizontal stress distribution acting on the wall backface at different stages during the analysis.

As expected,  $K_{A,min}$  decreases with increasing relative density and, consequently, peak friction angle. The crest displacement required for reaching the MPS is in the  $0.003H$  to  $0.006H$  range, regardless the  $D_R$  value. On the other hand, attainment of  $K_{A,cr}$  requires  $u_c$  larger than  $0.10H$ .

Interestingly,  $K_{A,cr}$  seems also to depend on the relative density despite the fact that  $\phi_c$  is independent of  $D_R$ . Only the curves for loose sand appear to attain  $K_{A,cr}$  values that are in agreement with the  $K_A$  from the analyses with a perfectly plastic soil with material parameters consistent with critical state. This is because the inclination of the sliding plane delimiting the wedge depends on the dilatancy that the soil exhibits during the early stages of the wall movement, since the theoretical value of the shear band inclination with respect to the minor stress (i.e. horizontal) axis is equal to  $45^\circ + (\phi + \psi)/4$  (Vardoulakis 1980). The sliding wedge forms at MPS, when the soil mass close to the wall is strongly dilative for all except very loose sand. Once the main inclined shear band forms, it tends to stay more or less at that location because of strain localization.

In most of the analyses, the  $u_c$  values required to cause bearing capacity failure of the wall foundation is in the  $0.01H$  to  $0.09H$  range, corresponding to toe displacement of  $0.01B$  to  $0.065B$ . Hence, the foundation is expected to fail before full development of the residual active earth pressure state.

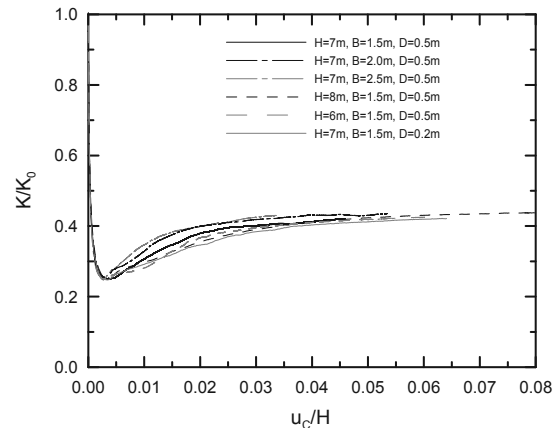


Figure 4. Variation of normalized lateral earth pressure coefficient with wall crest displacement from analyses with medium dense Toyoura sand ( $D_R=60\%$ ).

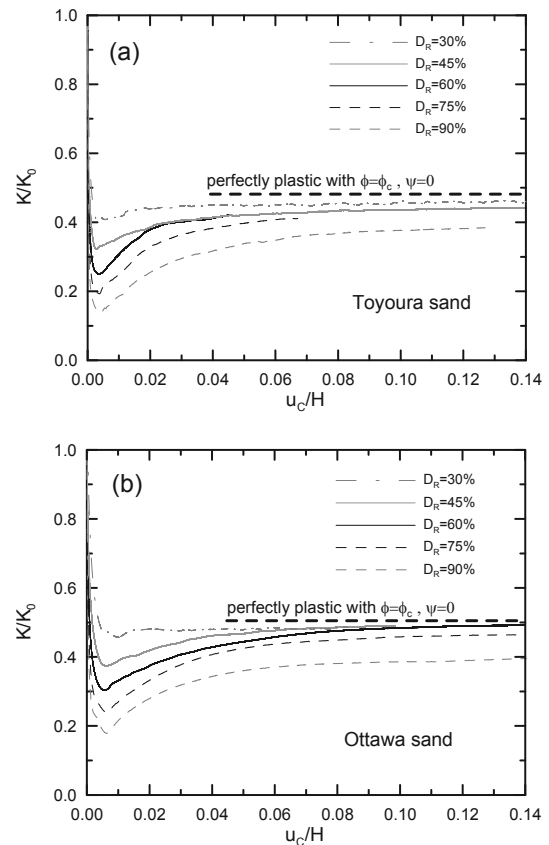


Figure 5. Variation of normalized lateral earth pressure coefficient with wall crest displacement from analyses of a wall with  $H=7m$ ,  $B=1.5m$  and  $D=0.5m$ .

### 3.3 Mobilized resistance along the wall-soil interface

The mobilized friction coefficient  $\mu$  ( $=\tan\delta$ ) on the wall backface reaches a peak value at very early stages of the analyses, before the attainment of the MPS. After the peak,  $\delta$  decreases quickly towards a residual value  $\delta_c$  that is consistent with development of critical state inside the thin shear band that runs parallel to the wall backface. Despite this, it can be seen that the mobilized friction angle  $\delta_{mob}$  at MPS ranges from 1.0 to 1.25 times the  $\delta_c$  (Fig. 6). The  $\delta_c$  values are  $30.8^\circ$  and  $29.6^\circ$  for Toyoura sand and Ottawa sand, respectively. These are consistent with the theoretical  $\delta_c$  values calculated as  $\arctan(\sin\phi_{c,ps})$ , where  $\phi_{c,ps}$  is the critical state friction angle for plane strain conditions. For Toyoura and Ottawa sands, this takes the values of  $36.6^\circ$  and  $34.6^\circ$ , respectively, which are

roughly 4° to 5° larger than the values corresponding to triaxial compression conditions  $\phi_{c, TX}$  (=31.6° and 30.2°, respectively).

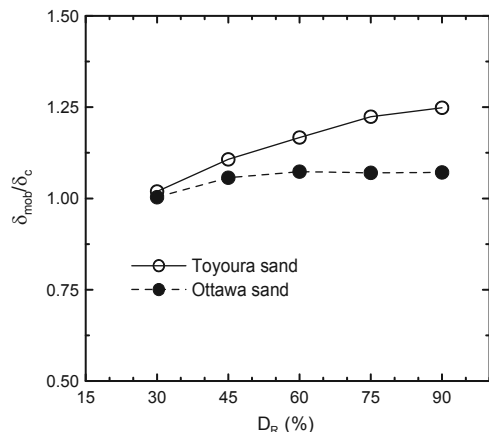


Figure 6. Ratio of the  $\delta$  mobilized along the wall-soil interface at MPS to the  $\delta$  corresponding to critical state conditions.

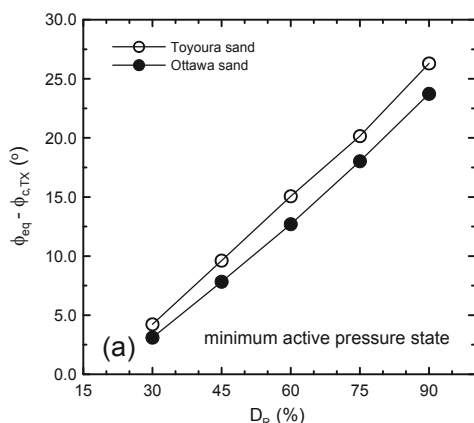


Figure 7. Equivalent value of the friction angle to be used in the calculation of  $K_{A,min}$ .

### 3.4 Expression for the estimation of $K_A$

The variation of the earth pressure coefficient  $K$  with crest displacement  $u_C$  observed in Figs. 4 and 5 can be described mathematically by the following equation:

$$K = \left[ \frac{\frac{(K_0 - K_{A,cr})}{(K_0 - K_{A,min})} u_{Cp} - 2u_C}{\frac{u_{Cp}}{(K_0 - K_{A,min})} + \frac{u_C^2}{(K_{A,cr} - K_{A,min}) u_{Cp}}} \right] + K_{A,cr} \quad (2)$$

where  $u_{Cp}$  is the crest displacement needed to reach MPS. Based on the previous discussion,  $u_{Cp}$  can be taken equal to  $0.005H$ .

The characteristic values of the active earth pressure coefficient,  $K_{A,min}$  and  $K_{A,cr}$ , can be calculated using the Coulomb's equation (Eq. 1) with suitable (equivalent) values  $\phi_{eq}$  for the mobilized friction angle inside the sliding wedge. In Fig. 7, we see that there is a linear dependence between  $\phi_{eq}$  for MPS and  $\phi_{c, TX}$ , which can be expressed by

$$\phi_{eq}^{(MPS)} = \phi_{c, TX} + \left( 35 \frac{D_R}{100\%} - 7^\circ \right) \quad (3)$$

We consider  $\phi_{c, TX}$  instead the more physically suitable  $\phi_{c, PS}$  because it is easier to estimate through empirical relationships, measurements of the angle of repose on a conical soil heap, or a few triaxial compression tests. On the other hand, to calculate  $K_{A,cr}$ , the friction angle can be estimated using

$$\phi_{eq}^{(cr)} = \phi_{c, TX} + \left( 9 \frac{D_R}{100\%} - 2^\circ \right) \quad (4)$$

For the calculation of both  $K_{A,min}$  and  $K_{A,cr}$  using Eq. (1), the wall-soil interface friction angle  $\delta$  can be conservatively set equal to  $\delta_c$  estimated as  $\arctan[\sin(\phi_{c, TX} + 4^\circ)]$ . Finally, it should be pointed out that, according to the numerical results, the point of application of the active earth thrust at MPS is at a distance roughly  $H/3$  from the wall base, while for the residual state is slightly smaller (roughly  $0.3H$ ).

## 4 CONCLUSIONS

This paper presented the results of a set of finite element analyses of a retaining wall supporting sand. Based on numerical results, the active earth pressure coefficient attains a minimum value  $K_{A,min}$  at wall crest displacements of the order of  $0.005H$ . Hence, from a practical standpoint, this state is of limited relevance to ultimate limit state (ULS) design; it is possibly representative of a serviceability limit state (SLS) design. A residual (maximum) value  $K_{A,cr}$  associated to full mobilization of critical state inside the soil mass is practically reached at crest displacements of the order of  $0.1H$ .

The  $K_A$  to be used in ULS calculations can be estimated using the proposed Eq. (2), provided that the designer knows *a priori* the wall crest displacement  $u_C$  corresponding to ULS. In case there is a structure founded on the supported soil, the  $u_C$  can be set equal to the allowable foundation displacement value compatible with the ULS for the structure, established according to design code provisions. In the opposite case, the  $u_C$  could be set equal to 7 times the horizontal base displacement required for wall foundation failure. In the case of granular foundation soils, this base displacement can be conservatively taken as 0.05 times the base width.

## 5 REFERENCES

- Abbo, A.J. and Sloan, S.W. 2000. *SNAC, User manual, Version 2.0*. Department of Civil, Surveying and Environmental Engineering, University of Newcastle, Callaghan, Australia.
- Dafalias, Y.F., Papadimitriou, A. G. and Li, X. S. 2004. Sand plasticity model accounting for inherent fabric anisotropy. *Journal of Engineering Mechanics*, ASCE, 130(11), 1319-1333.
- Gudehus, G. and Nübel, K. 2004. Evolution of shear bands in sand. *Géotechnique*, 54(3), 187-201.
- Lancellotta, R. 2002. Analytical solution of passive earth pressure. *Géotechnique*, 52(8), 617-619.
- Leśniewska, D. & Mróz, Z. 2001. Study of evolution of shear band systems in sand retained by flexible wall. *International Journal for Numerical and Analytical Methods in Geomechanics*, 25, 909-932.
- Loukidis, D. and Salgado, R. 2009. Modeling sand response using two-surface plasticity. *Computers and Geotechnics*, 36(1-2), 166-186.
- Loukidis, D., Chakraborty, T. and Salgado, R. 2008. Bearing capacity of strip footings on purely frictional soil under eccentric and inclined loads. *Canadian Geotechnical Journal*, 45(6), 768-787.
- Manzari, M.T. and Dafalias, Y.F. 1997. A critical state two-surface plasticity model for sands. *Géotechnique*, 47(2), 255-272.
- Soubra, A-H and Macuh, B. 2002. Active and passive earth pressure coefficients by a kinematical approach. *Proceedings of the Institution of Civil Engineers – Geotechnical Engineering*, 155(2), 119-131.
- Vardoulakis, I. 1980. Shear band inclination and shear modulus of sand in biaxial tests. *International Journal for Numerical and Analytical Methods in Geomechanics*, 4(2), 103-119.

# Innovative solutions for supporting excavations in slopes

## Solutions innovantes pour le soutien d'excavations situées dans des terrains en pente

Lüftenegger R.  
GDP ZT-OG, Austria

Schweiger H.F., Marte R.  
Institute for Soil Mechanics and Foundation Engineering, Graz University of Technology, Austria

**ABSTRACT:** The design of support measures for deep excavations is one of the key tasks in geotechnical engineering. The choice of the most appropriate support system depends on various obvious factors such as ground conditions and excavation depth but sometimes also on less obvious boundary conditions, for example when construction of ground anchors is not possible because permission of placing them in neighbouring property is not given. In these cases other options have to be pursued, resulting sometimes in non-conventional solutions. Examples for such innovative support systems are presented in this paper. In the first case the arching effect of the retaining structure was used to design an excavation pit without any anchors reaching on the neighbouring ground, because there was no permission for construction elements there. The 6 meter spanned arches consist of mixed in place columns (MIP), which rest on supporting walls (also mixed in place columns) oriented in the direction of the slope. In the second example the behaviour of a serrated sheet pile has been investigated. Comprehensive 3D finite element analyses have been performed in order to prove that the suggested retaining structures are feasible solutions.

**RÉSUMÉ :** La conception des mesures de soutènement pour les excavations profondes est une des tâches fondamentales dans la géotechnique. Le choix du système le plus approprié dépend de plusieurs facteurs évidents comme les conditions de sol ou la profondeur de l'excavation, mais parfois aussi de contraintes moins évidentes comme par exemple le cas où des ancrages ne sont pas possibles parce qu'il n'y a pas d'autorisation pour l'installation dans la propriété voisine. Dans ces cas, d'autres options doivent être envisagées, qui résultent parfois dans des solutions non-conventionnelles. Quelques exemples de telles solutions sont présentés. Dans le premier cas, l'effet de voûte de la structure de soutènement a été utilisé pour la conception d'une excavation qui bordait une propriété pour laquelle il n'y avait pas d'autorisation pour l'installation des éléments d'ancrage. Les voûtes avec une portée de 6 mètres ont été réalisées avec des colonnes « Mixed in Place » (MIP) qui prenaient appui sur des parois orientées dans la direction de la pente. Dans le deuxième exemple, le comportement d'une palplanche dentelée a été examiné. Des analyses par la méthode des éléments finis 3D complètes ont été effectuées afin de prouver que la structure de soutien proposée était une solution réalisable.

**KEYWORDS:** deep excavation, finite element method, three-dimensional analysis.

## 1 INTRODUCTION

The design of support measures for deep excavations is one of the key tasks in geotechnical engineering and, depending on soil conditions and adjacent infrastructure, many different options exist. One of the most difficult situations to overcome is when space for support measures is limited and due to legal reasons support elements such as ground anchors cannot be built on neighbouring ground. The obvious solution in these cases, namely putting struts, is often not very convenient for the excavation process and sometimes even not possible, e.g. if the excavation is situated in a slope. These cases require special attention and two case histories where innovative solutions have been found are presented in this paper.

## 2 NUMERICAL ANALYSIS

In order to demonstrate the feasibility of the proposed design and to assess expected deformations a number of three-dimensional finite element analyses have been carried out. These analyses also served as basis for the design of the structural elements. The finite element code Plaxis 3D Foundation has been used for all analyses presented in this paper (Brinkgreve and Swolfs 2007).

It is well established that for this type of analysis simple linear elastic-perfectly plastic constitutive models are not very well suited and therefore a more advanced model, namely the

Hardening Soil model, has been employed. This model is a so-called double hardening model and allows for plastic compaction (cap hardening) as well as plastic shearing due to deviatoric loading (friction hardening). The main features of this model, as implemented in Plaxis, can be summarized as following.

- Stress dependent stiffness according to a power law.
- Plastic straining due to primary deviatoric loading.
- Plastic straining due to primary compression.
- Elastic unloading / reloading.
- Failure according to the Mohr-Coulomb criterion.

A more detailed description of the Hardening Soil model can be found e.g. in Schanz et al. 1999.

## 3 CASE HISTORY 1 – MIXED IN PLACE COLUMNS

The first example is concerned with an excavation situated in a slope, just below existing buildings. The owner of one of the buildings was particularly alerted because he experienced significant damage to his building in the past due to nearby construction activities. He did not allow ground anchors to reach his property. Thus the task was to stabilize the excavation without ground anchors and at the same time provide sufficient support to keep deformations, which could lead to damage of the building located above the excavation, to an absolute minimum. This could be achieved by arches of 6 meter span

constructed by mixed in place columns (MIP), which rest on supporting walls (also mixed in place columns) oriented in the direction of the slope. The earth pressure exerted from the slope was transferred to 5 meter deep mixed in place walls underneath the planned building at the base of the slope. Figure 1 shows the slope with the supporting structure and Figure 2 a detail of the MIP columns.

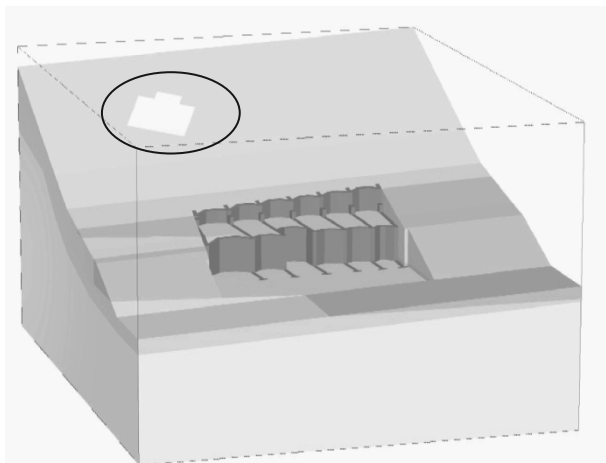


Figure 1. Overview of slope and support structure including critical building.

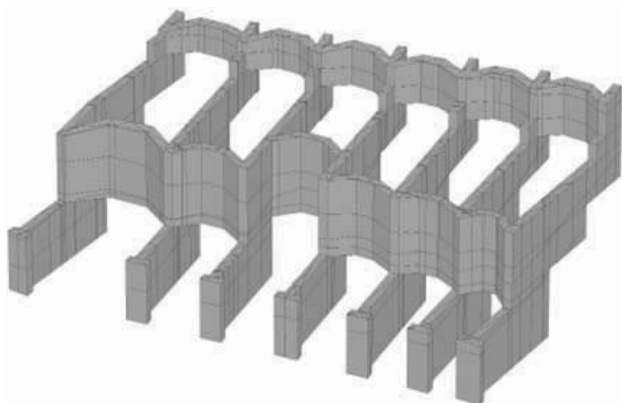


Figure 2. Layout of support structure (MIP columns).

Based on the results from site investigations a representative underground model consisting of three layers was established for the 3D finite element analysis, namely soft sandy silt (0-4 m below surface), stiff laminated sand-silt (4-8 m below surface) and semi-solid sand-silt (below 8 m from surface). The most important parameters for these layers are summarized in Table 1.  $E_{oed}^{ref}$  is the stiffness from an oedometer test for the reference vertical effective stress of 100 kPa,  $E_{50}^{ref}$  is a secant stiffness at 50% of maximum deviatoric stress in a triaxial compression test at a reference cell pressure  $\sigma_3' = 100$  kPa,  $E_{ur}^{ref}$  is the unloading/reloading stiffness, again at a reference cell pressure of 100 kPa from a triaxial test, and  $m$  is a parameter determining the stress dependency of above stiffness parameters.  $\phi'$ ,  $c'$  and  $\psi$  are the conventional Mohr-Coulomb strength parameters which define ultimate strength in the Hardening Soil model.

The MIP-method improves the mechanical properties of a soil by mechanically mixing and adding binder slurry. The result is a "soil-concrete-mixture" in which the soil is used as aggregate. For the MIP-columns a constitutive model based on the Mohr-Coulomb failure criterion was applied. Based on an unconfined compressive strength of 5 MN/m<sup>2</sup>, whereas this value includes a partial factor of safety on material strength, the material parameters listed in Table 2 have been adopted.

Table 1. Material parameters for Hardening Soil model for soil layers.

Parameter	Layer 1	Layer 2	Layer 3
Friction angle, $\phi'$ (°)	25	27.5	30
Cohesion, $c'$ (kPa)	0	1	5
Dilatancy angle, $\psi$ (°)	0	0	0
Unit weight, $\gamma$ (kN/m <sup>3</sup> )	20	20.5	21
$E_{oed}^{ref} = E_{50}^{ref}$ (kPa)	10000	25000	45000
$E_{ur}^{ref}$ (kPa)	30000	75000	135000
$m$ (-)	0.5	0.5	0.5

Table 2. Material parameters for MIP-columns.

Parameter	MIP
Friction angle, $\phi'$ (°)	30
Cohesion, $c'$ (kPa)	250
Unit weight, $\gamma$ (kN/m <sup>3</sup> )	22
Elasticity modulus (kPa)	300000
Tension cut off* $\sigma_t$ (kPa)	125

\* based on reinforcement by steel rods and nails

The results of the calculation show the expected stiff behaviour of the chosen support system. The maximum calculated horizontal deformation of about 15 mm occurs at the front upper corner of the lower excavation step (Figure 3). At the back of the wall (near the border of the neighbouring property) deformations are in the order of millimetres and thus the expected settlements in this area can be considered to be not significant and will not cause any damage to the building (Figure 4). However, the finite element analysis could not model the construction process of the MIP-columns, i.e. the columns were assumed "wished-in-place" before excavation starts and therefore displacements due to the construction process have to be added to these values.

The 3D-model was also used to check the tension zones in the MIP-body. The main tension stresses were located at the connections of the arches and the wall elements. In this area the MIP-wall was reinforced with steel beams (HE-B profiles).

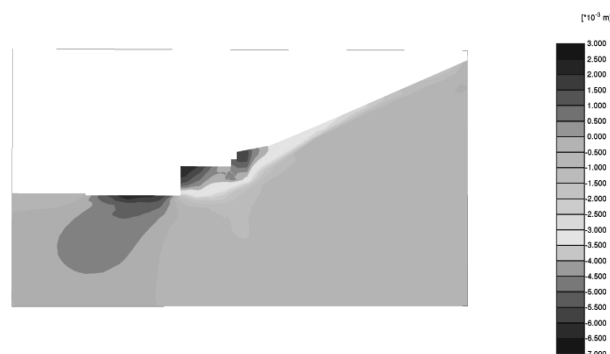


Figure 3. Calculated horizontal displacements, cross section

The measurements during construction on one hand confirmed the results for the numerical analysis but on the other hand showed that significant deformations occurred during construction of the MIP-columns itself (Figure 5). After construction of the columns (panels) deformation measured were less than 15 mm, comparing well with the finite element

predictions. Figure 5 shows the deformations of different points on the top of the MIP-wall. At the neighbouring buildings no movements were recorded. Figure 6 presents a view of excavated MIP-walls.

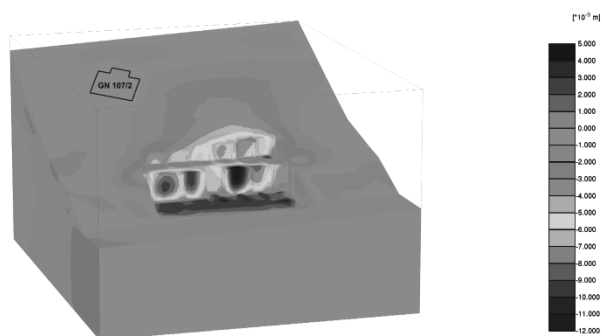


Figure 4. Calculated horizontal displacements with critical building

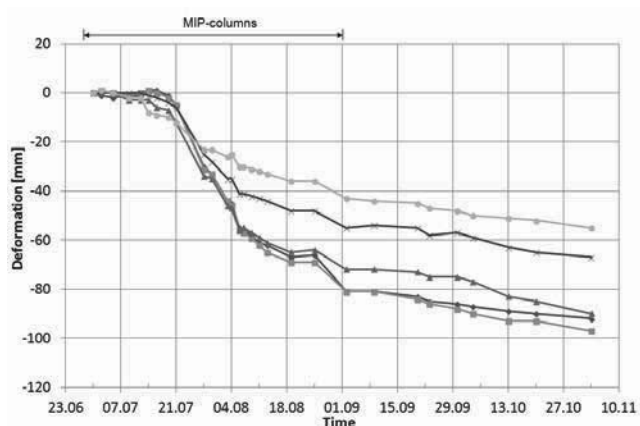


Figure 5. Measured horizontal displacements at several points at the top of the MIP-wall



Figure 6. View of excavated MIP-walls

The large deformations during the production of the columns had two main reasons. In the first part of the production too many MIP columns were produced within a small area. The MIP columns, which take some time to gain strength, weakened the slope during construction, which was already close to critical state. Furthermore, to reduce the length of the MIP columns (in order to save money), deeper working planes than planned were excavated.

This presented case study clearly shows that it is possible to support the earth pressure exerted from a slope by arches constructed by means of soil improvement techniques without

any anchors reaching on neighbouring ground. The numerical analysis was able to prove that the design concept is feasible, however, it is important to observe the deformation during the construction stages because not all aspects of the construction process, in this case of the MIP-columns, can be taken into account in the numerical model.

#### 4 EXAMPLE 2 - SERRATED SHEET PILE WALL

The second example is concerned with the same problem, namely limited space for support measures, but this time it is in an urban environment, namely in the city of Salzburg, Austria. Again the excavation was very close to the adjacent property and it was not allowed to put any construction elements, such as ground anchors, there. In this case the solution chosen was a serrated sheet pile wall. Generally, the subsoil conditions in Salzburg consist of a top layer with backfill and gravel, and soft silty sand and clayey silt layers underneath. The layout of the sheet pile wall follows from Figure 7 (3D finite element model). Every 6 to 8 m there is a 3 m deep indentation in the sheet pile wall. The construction of diagonal compression and tension bars at the top transfers the earth pressure to the right-angled parts of the sheet pile walls. A steel construction, similar to a whaler beam, on top prevents non-homogeneous deformations of the wall. After excavation a drainage layer and a concrete slab is installed to prevent long term movements of the wall and to reduce the influence of the soft layers below excavation level.

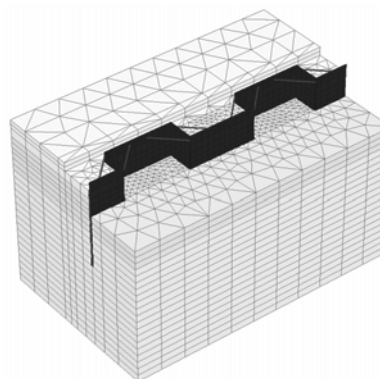


Figure 7. 3D finite element model

The key material parameters for the soil layers considered in the analysis are listed in Table 3. Again the Hardening Soil model has been employed.

Table 3. Material parameters for Hardening Soil model for soil layers.

Parameter	<i>backfill</i>	<i>silty sand</i>	<i>clayey silt</i>
Friction angle, $\varphi'$ (°)	35	27.5	25
Cohesion, $c'$ (kPa)	0,1	3	5
Dilatancy angle, $\psi$ (°)	0	0	0
Unit weight, (kN/m <sup>3</sup> )	19/21	20/21	18/20
$E_{oed}^{ref} = E_{50}^{ref}$ (kPa)	52000	30000	15000
$E_{ur}^{ref}$ (kPa)	208000	120000	60000
$m$ (-)	0	0.5	0.5

The 3D model showed that deformations can be kept to a minimum with maximum values below 10 mm (Figure 8), which was also confirmed by observations during construction. Deformations due to driving and removing of the sheet pile wall are not considered in the analysis. Experience has shown that in this type of soils settlements can reach 20 to 30 mm, and in this particular case observed values were within the lower range.

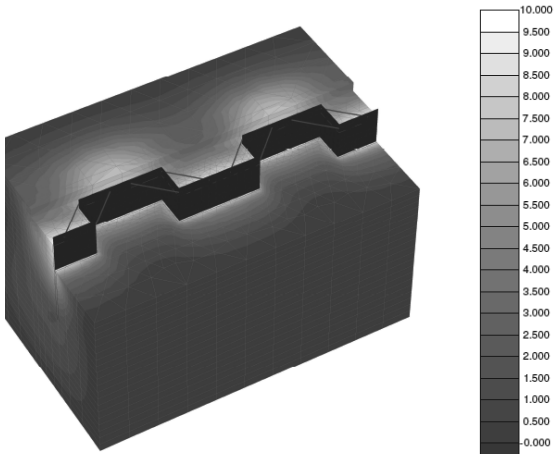


Figure 8. Calculated horizontal displacements

The bending moments of a sheet pile wall with this particular shape and the strengthening construction on top of the wall is not the same as for a cantilever wall, which one would obtain from a 2D analysis and therefore the 3D analysis was essential and helped to estimate the influence of the special support measures. However, 3D finite element analyses are quite time consuming if many different scenarios have to be investigated.

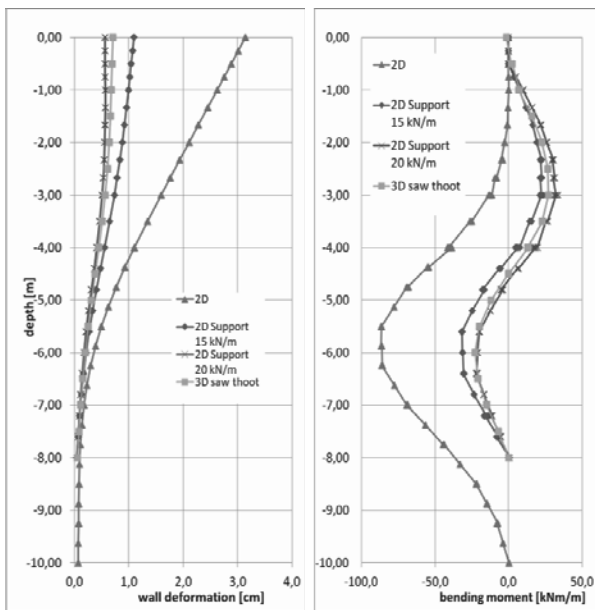


Figure 9. Comparison of 2D and 3D analysis of wall deformation and bending moments

An attempt was therefore made to develop an equivalent 2D analysis for performing parametric studies for a preliminary design. For that reason a 2D model of the sheet pile wall with a supporting force on top of the wall was created. It turned out that for the case of a 8 m deep sheet pile wall and a 4 m deep excavation (groundwater is also at 4 m depth) a supporting force between 15 kN/m und 20 kN/m lead to similar wall deformations und bending moments (Figure 9). This supporting force has to be carried from the additional wall elements spanning across the edges of the two lines of the serrated sheet pile wall (see also Figure 8). The calculations revealed that the earth pressure distribution of the rectangular part of the serrated sheet pile wall is between the active and the at-rest earth pressure (see Figure 10).

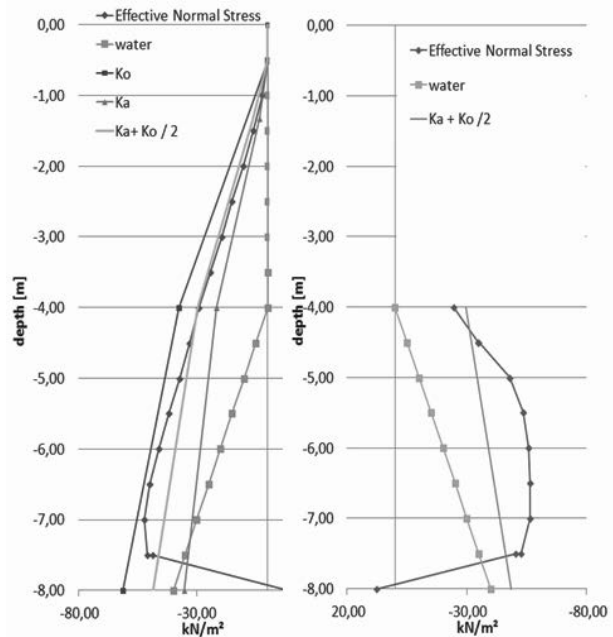


Figure 10. Earth pressure distribution on active and passive side

For the given geometry (distance of 8 m between the rectangular walls) this earth pressure distribution leads to a maximum resistance by wall friction of about 20 kN/m. This shows a good correlation with the presented calculations.

## 5 CONCLUSIONS

3D finite element modelling allows complex geotechnical structures to be analysed. In the two presented case histories the calculations helped to estimate the arching effect of a curved retaining structure in order to design an excavation pit without any anchors reaching on the neighbouring ground. In the second example the behaviour of a serrated sheet pile has been investigated. In both case the numerical analyses proved the feasibility of the chosen design and improved the understanding how these complex structures behave.

However, even with 3D models it is usually not possible to include all excavation stages in great detail and, more importantly, installation effects are beyond the capabilities of standard numerical tools and this has to be kept in mind when assessing numerical results. Therefore it is essential to monitor the behaviour of the structure during construction and have appropriate counter measures in mind when deformations due to installation effects or unforeseen ground conditions reach critical limits.

## 6 REFERENCES

Brinkgreve R.B.J. and Swolfs W.M. 2007. Plaxis 3D Foundation, Users Manual, Plaxis bv, Delft, The Netherlands  
 Schanz T., Vermeer P.A. and Bonnier P. 1999. The Hardening-Soil model: Formulation and verification. *Beyond 2000 in Computational Geotechnics*, R.J.B. Brinkgreve (ed.), Balkema, Rotterdam, 281-290.

# Design and Construction of Inclined-Braceless Excavation Support Applicable to Deep Excavation

## Dimensionnement et Construction du Support d'Excavation Incliné Sans Butons Applicable à une Excavation Profonde

Maeda T., Shimada Y., Takahashi S., Sakahira Y.  
*Obayashi Corporation*

**ABSTRACT:** The inclined-braceless excavation support (IBES) construction method is characterized by allowing the reduction of retaining wall rigidity and omission of shoring because it reduces the earth pressure acting on the wall, compared with construction using vertical retaining walls. Thus, there are cases where inclined retaining walls are more beneficial in terms of workability and economy than vertical retaining walls, depending on the excavation depth or ground conditions. For the inclined-braceless excavation support construction method applied at open-cut (excavation depth of 9.6m) construction site, this paper presents results of centrifugal model experiments that reflected the actual excavation cross section, the design of the retaining walls in consideration of the inclination of the wall, applied construction method, and measurement results at the site.

**RÉSUMÉ:** On peut s'attendre à ce qu'une paroi de soutènement inclinée subisse une pression du sol moindre qu'une paroi verticale classique. Le Support d'Excavation Incliné Sans Butons (SEISB) pourrait donc offrir des avantages: un besoin de rigidité réduit et la disparation des étrépillons ou des ancrages. Selon la profondeur d'excavation et les conditions de sol, il peut aussi être plus efficace qu'un système vertical en termes de coût et de durée des travaux. Le présent document rapporte le cas d'un chantier où la méthode SEISB a été utilisée pour une excavation de 9,6m de profondeur: test en centrifugeuse sur un modèle de la coupe d'excavation du chantier, dimensionnement prenant en compte la pression du sol sur un support incliné, méthode de construction adaptée et réalisation des travaux.

**KEYWORDS:** Inclined-braceless excavation support, steel sheet pile, centrifuge model experiment, earth pressure

### 1 INTRODUCTION

According to earth pressure theory, the earth pressure acting on temporary earth retaining walls set up during excavation work is reduced when the earth retaining wall is reclined. However, earth retaining walls are generally installed vertically in consideration of workability and construction site limitations, and no earth retaining walls which utilized effect of reduced earth pressure for inclined retaining wall were implemented. Furthermore, deep excavation work requires shoring such as bracing or ground anchors for vertical earth retaining walls with high rigidity (Figure 1).

The inclined-braceless excavation support (IBES) construction method is characterized by allowing the reduction of wall rigidity and omission of shoring because it reduces the earth pressure acting on the wall, compared with construction using vertical retaining walls (Figure 2). Thus, there are cases where inclined retaining walls are more beneficial in terms of workability and economy than vertical retaining walls, depending on the excavation depth or ground conditions.

The authors have previously conducted centrifugal model experiments on inclined-braceless retaining walls using sand ground to examine earth pressure distributions and deformation behavior (Shimada et al. 2010, 2011) and quantitatively confirmed that the earth pressure acting on the retaining walls and deformation arising from excavation can be reduced by inclining the retaining walls.

This paper reports on centrifugal model experiments that reflected the excavation cross section at an actual scale construction site for the inclined-braceless retaining wall construction method to determine its suitability, the design of inclined-braceless retaining walls using reduced earth pressure by inclination of the wall, applied construction method, and measurement results at the site.

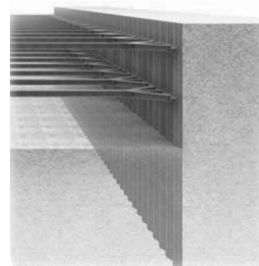


Figure 1 Vertical retaining wall

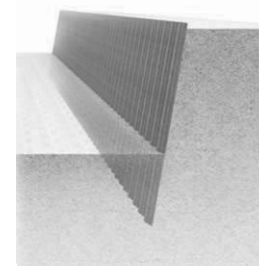


Figure 2. Inclined-braceless retaining wall

### 2 SUMMARY AND ISSUES OF CONSTRUCTION METHOD FOR INCLINED-BRACELESS RETAINING WALL

Cantilever retaining walls have been widely adopted to retain earth at relatively shallow excavation depths (3–4 m). Inclined-braceless retaining walls are an attempt to switch from the conventional concept of vertical retaining walls in order to reduce earth pressure and make it possible to apply cantilever retaining walls even at deeper excavation depths.

There are no application examples of temporary inclined retaining walls; design issues for the inclined-braceless retaining wall construction method include calculation of the earth pressure while considering the inclination of the retaining wall, and consideration of rollover not only to the excavation side but also to the back side in calculation of embedding of walls. Construction issues include the accuracy of the inclination angle set during retaining wall installation and the construction work cycle time. Centrifuge model experiments conducted to examine these design issues, the applied design



methods, and actual performance at construction sites where the design methods were implemented are described below.

### 3 CENTRIFUGE MODEL EXPERIMENT OF INCLINED-BRACELESS RETAINING WALL

#### 3.1 Experiment method

A 1/33-scale model ground was prepared to develop excavation cross sections of applicable construction sites (Figure 3) for this experiment. A maximum centrifugal acceleration of 33g was loaded to examine deformation of the retaining wall and distribution of the earth pressure. Figure 4 shows an outline of the model ground. The dimensions of the soil container were 80 cm width × 50 cm height × 20 cm depth. The front side of the container was fabricated from an acrylic plate so that ground displacements could be measured. A Teflon sheet was attached between the soil container, including the acrylic plate, and the model ground to reduce friction. The depth of the model ground was developed with berm to a maximum of 29 cm, and the height of the retaining wall was 36 cm. The model ground is shown in Photo 1. The retaining wall was created assuming that the retaining walls would be made of steel sheet piles. A compact earth pressure gauge (6 mm dia., capacity of 1 MN/m<sup>2</sup>) was embedded at seven locations on the active side and at four locations on the passive side to measure the earth pressure acting on the wall surface. The retaining wall model was installed and then filled with dry Toyoura standard sand by the airdrop method to prepare the model ground. Excavation steps were simulated during the experiment by repeating the method of loading centrifugal acceleration after the prescribed excavation work was performed at a 1g site. Table 1 shows the experimental cases.

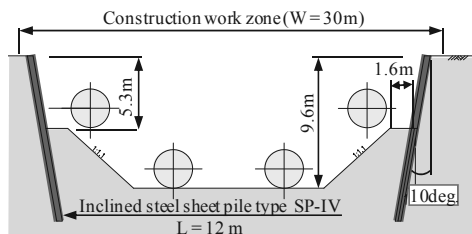


Figure 3. Cross-section of inclined-braceless retaining wall applied at site

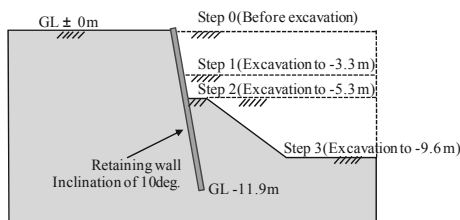


Figure 4. Outline of model ground.

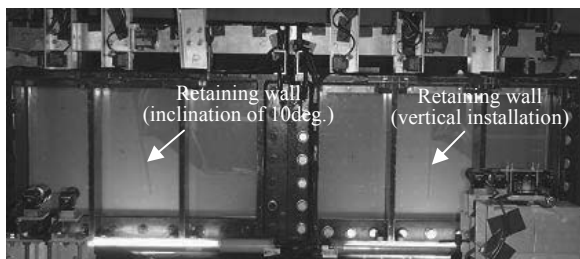


Photo 1. Model ground

Table 1: Experiment Cases

No.	Case 1	Case 2
Retaining wall conditions	Vertical	Inclined (inclination of 10 degree)
Retaining wall model	Made of aluminum, thickness of 7 mm	
Ground	Material: Toyoura standard sand (dry) Density: $\rho_d = 1.55 \text{ g/cm}^3$ Preparation method: Airdrop method	
Excavation steps	Step 0: Before excavation Step 1: Excavation depth of 3.3 m Step 2: Excavation depth of 5.3 m Step 3: Excavation depth of 9.6 m	

#### 3.2 Experiment results

Figures 5 and 6 show the deformation behavior of the retaining wall due to excavation work. The displacements shown below were converted to actual-scale displacements by multiplying the experimental measurement results by 33. Figure 5 shows the displacement distribution of the retaining wall for each excavation stage. The horizontal displacement was larger at higher sections of the wall, and deformation occurred in the frontal incline with the lower section of the wall as the axis. Regardless of the excavation depth, the amount of horizontal displacement of the inclined walls was smaller than that of the vertically installed walls. Figure 6 shows the relationship between the excavation depth and horizontal displacement at top of the wall. The deformation increased in correlation to the depth; the displacement of the vertically installed wall was measured at the maximum excavation depth as 20 cm, whereas that of the inclined wall was about 14 cm. Thus, the experimental results confirmed that the amount of deformation was about 30% smaller with inclined walls.

Strain gauges were attached to the front and back surfaces of the wall in the direction of the depth at three locations in order to obtain the bending status of the wall. Figure 7 shows the depth distribution of the bending strain: the maximum value was obtained in the vicinity of the center of the wall regardless of whether the wall was inclined. The maximum bending strain was smaller with inclined walls than with vertically installed walls regardless of the excavation depth. The gap between the two was larger when the excavation depth was 9.6 m than when it was 3.3 m; the effects of inclining the wall were significant and evident.

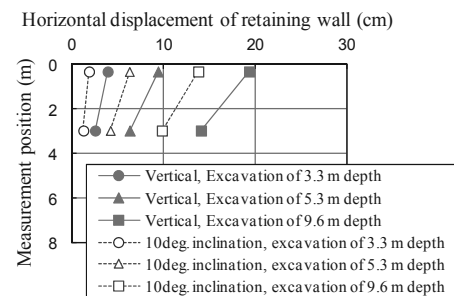


Figure 5. Horizontal displacement distribution of retaining walls

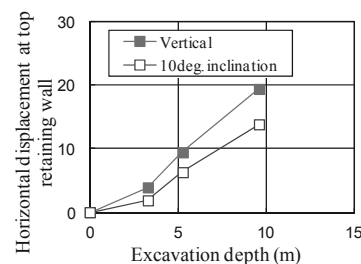


Figure 6. Relationship between excavation depth and horizontal displacement of retaining walls

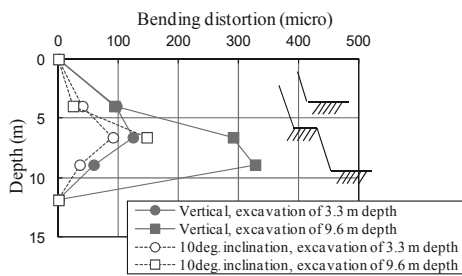


Figure 7. Bending strain distribution of retaining

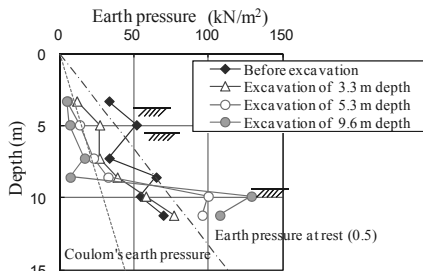


Figure 8. Earth pressure acting on wall surfaces - vertical retaining walls

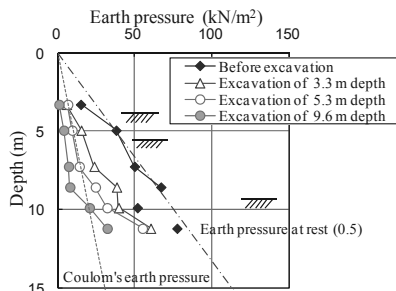


Figure 9. Earth pressure acting on wall surfaces - inclined retaining walls

Figures 8 and 9 show the depth distribution of the active earth pressure that acted on the wall. Although the measurement results for the vertically installed wall showed dispersions prior to excavation, the validity of the earth pressure measurements taken by this equipment were confirmed because they were approximately equal to the earth pressure at rest assuming  $K_0 = 0.5$ , as noted in the figure. The earth pressure decreased in the excavated sections and increased more than the earth pressure at rest in the embedded sections. The figure shows the Coulomb's earth pressure, where the friction angle of the retaining wall was considered to be  $\phi/3$ . The active earth pressure measured at the excavated sections was slightly smaller in distribution than the Coulomb's earth pressure. The earth pressure acting on the inclined wall decreased more than the earth pressure at rest regardless of depth. Thus, the acting pressure was smaller than that of the vertically installed wall, which confirmed that inclination of the wall contributed to the stability of the wall in terms of earth pressure as well.

## 4 DESIGN OF INCLINED-BRACELESS RETAINING WALL

### 4.1 Calculation method for earth pressure

Ground of the site (Figure 3) was a landfill comprised primarily of loose fine sand (layer thickness: 12 m, N-value: 3–5, and  $\phi$ :  $33^\circ$ ). The inclination of the retaining wall could not be considered in the conventional design of the temporary retaining walls, because the Rankine–Resal formula is generally applied to the active earth pressure used. The earth pressure calculation method with Coulomb's formula (Figure 10) used in the design of permanent retaining walls, which considers the inclination of the wall, was therefore applied. Its use was determined safe for design purposes because the earth pressure reduction effect was confirmed in the centrifugal model

experiments with inclined walls. Similarly, the Coulomb's earth pressure was adopted for the passive earth pressure.

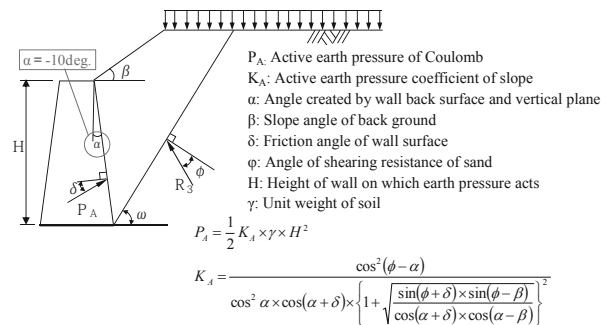


Figure 10. Active earth pressure calculation

### 4.2 Calculation method for embedding lengths

The embedding length was calculated using not only the “method for determining embedding length to maintain balance based on earth pressure” but also the “overall slippage including the retaining wall.” The circular slipping calculation (Figure 11) was performed to determine the embedding length so that both of the above methods were satisfied. The safety factor for the arc slipping calculation was set to 1.2.

### 4.3 Calculation of retaining wall displacements and stresses

The displacements and stresses that occurred with the retaining wall were calculated based on elasto-plasticity analysis, which evaluated the earth pressure and wall embedding length given in subsections 4.1 and 4.2 above, by considering the retaining wall as a finite length elastic beam and ground as an elasto-plastic spring (figure 12).

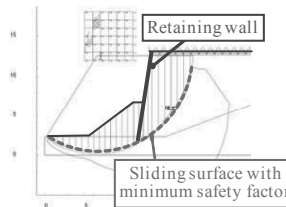


Figure 11. Verification on slipping stability

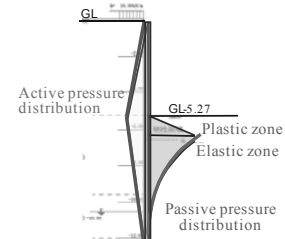


Figure 12. Elasto-plastic analysis

## 5 CONSTRUCTION WORK IMPLEMENTATION RECORD FOR INCLINED-BRACELESS RETAINING WALLS

### 5.1 Summary of applied construction sites

The construction sites where the inclined-braceless retaining walls were applied were located within premises used by existing electric power plant and new plant construction. Excavation work had to be performed to install two sets of water intake and water discharge steel pipes (each pipe with a diameter of 2800 mm) in a restricted construction work zone with a width of 30 m (Figures 3 and 13). The period of construction work, which included piping work, needed to be less than six months owing to adjustments that had to be made to accommodate the progress of the main unit construction work being performed at new electric power plant.

In order to satisfy the above conditions, the inclined-braceless excavation retaining wall construction method which reduces earth pressure by inclining the wall, was adopted as it requires no shoring, even when the excavation depth is deep. The retaining wall was fabricated from steel sheet pile type SP-IV, and the inclination of the retaining wall was set to 10 degree owing to restrictions imposed within the construction work zone and the excavation cross section necessary for piping work.

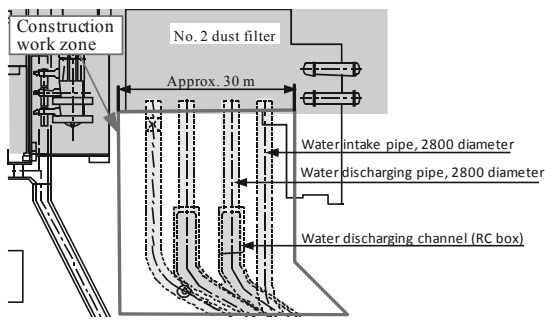


Figure 13. Construction work zone plan

5.2 Inclined-braceless retaining wall construction method

The steel sheet piles driven in at an inclination angle were installed in a manner similar to ordinary vertical installation: a silent piler was used combined with a water jet to reduce the insertion resistance. Because the piler was tilted according to the inclination of the piles being installed, an auxiliary cylinder was installed on the piler main unit to control the angle (Photo 2 and 3). The initial insertion until the piler was set on the piles used a blocking base (110 kN), similar to ordinary vertical installation. The top plate of the blocking base was inclined by 10 degree to accommodate the inclined installation of the piles (Photo 4). The inclination angle was monitored by infrared laser units installed at two locations aside from inclined finishing stake.

5.3 Comparison of onsite measurement results and design values

5.3.1 Earth pressure

The distribution of actual measurements for the earth pressure, which was taken by wall-surface-mounted earth pressure gauges at the time of the final excavation, indicated 20%–50% of the design values on the back side (active side) and 5% of the ultimate value on the excavation side (passive side) (figure 14). The setting method for coefficient of earth pressure (applying the Coulomb’s formula) was considered to be valid because the gradient (equivalent to the earth pressure coefficient) up to GL-3m was roughly equal for the active earth pressure distribution. With regard to the passive earth pressure, the displacement of the retaining wall was small and the ground had a sufficient margin for resistance on the passive side.

5.3.2 Displacements and stresses of steel sheet piles

The maximum displacement during final excavation was 24.1mm, which was about 20% of the design value of 119.2mm (Figure 15). The maximum stress level of the steel sheet piles according to strain gauges was a tensile stress of 8.4N/mm<sup>2</sup>, which is extremely small and about 8% of the design value of 103N/mm<sup>2</sup>. Furthermore, the bending moment distribution obtained by converting the measurement data from the inclinometers was roughly the same as the bending moment distribution obtained from strain gauges.



Photo 2. Overall view of installation work



Photo 3. Auxiliary cylinder



Photo 4. Blocking base

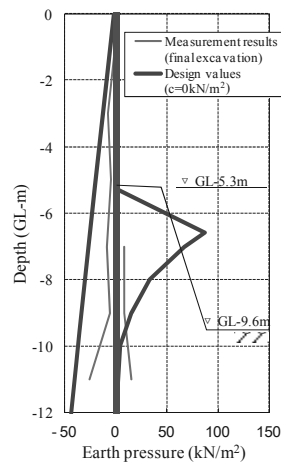


Figure 14. Earth pressure distribution comparison

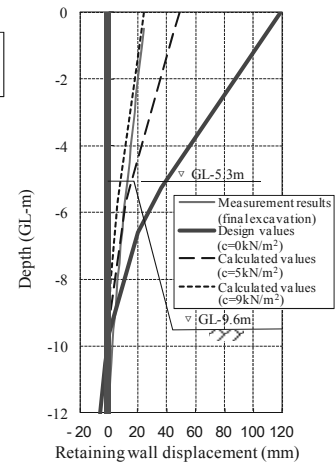


Figure 15. Retaining wall displacement

6 CONCLUSIONS

For the inclined-braceless retaining walls (inclination of 10 degree) with an excavation depth of 9.6 m in sand ground, the effects of earth pressure reduction and stability of retaining wall were verified by a centrifugal model experiment. A design method was developed that considers inclination of the wall by using the Coulomb’s formula in elasto-plastic analysis so that inclined-braceless retaining walls can be adopted at actual construction sites. The actual measurement values taken onsite for the earth pressure acting on the retaining wall and the displacement and stress of the retaining wall both agreed with the design values. Thus, the safety of the retaining wall can be secured using the proposed design method. The inclined retaining wall construction method was used to realize a cantilever retaining wall without shoring despite a deep excavation depth of 9.6 m. Thus, excavation, piping, and building work can be completed in a short term and safely.

We will collect design and construction work track records for the inclined retaining walls under a variety of ground conditions for verification of evaluation methods for analysis models, soil parameters, and earth pressure, and cycle time of construction work, in order to establish more practical design and construction methods.

7 REFERENCES

Shimada Y., Matsumoto S., Takahashi S. and Sugie S. 2010. Centrifugal model experiments pertaining to earth pressure of sand ground acting on cantilever retaining walls. *Proceedings of the 65<sup>th</sup> Annual Conference of the Japan Society of Civil Engineers*, III-456.  
 Shimada Y., Idemitsu M., Takahashi S. and Maeda T. 2011. Centrifugal model experiments pertaining to earth pressure of sand ground acting on steel sheet pile cantilever retaining walls. *46<sup>th</sup> Japan National Conference on Geotechnical Engineering*, 682.

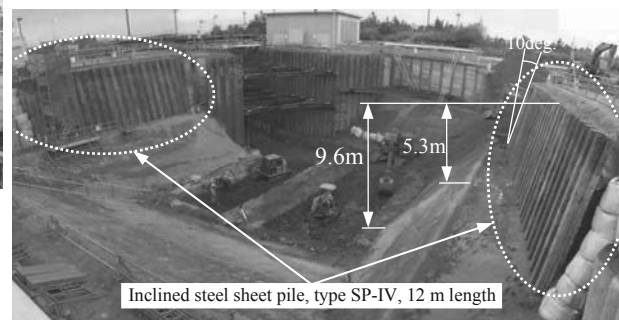


Photo 5. Overall view of excavation completed site

# Shaking table tests on caisson-type quay wall with stabilized mound

## Essais à table vibrante sur les murs de quai de type caisson avec butte stabilisée

Mizutani T.

*Geotechnical Engineering Field, Port and Airport Research Institute*

Kikuchi Y.

*Professor, Department of Civil Engineering, Tokyo University of Science*

**ABSTRACT:** Caisson-type quay walls were one of the major types of quay walls in Japan. It was desired to increase the front-water depth of them, because vessels coming alongside them become larger and larger. The authors have been studying on a new construction method for the improvement. The method consisted of two steps. Step 1 was to solidify a part of rubble mound beneath a caisson and step 2 was to cut it to increase the front-water depth of the caisson. A series of shaking table tests were conducted to study the seismic behavior of caisson-type quay walls improved by the new method. This paper will introduce the test results and discuss the factors which affected the seismic behavior of the caisson-type quay walls with stabilized mound.

**RÉSUMÉ :** Les murs de quai de type caisson constituent l'un des types majeurs de murs de quai au Japon. On a désiré augmenter la profondeur frontale face à la mer car les navires venant accoster le long des quais deviennent de plus en plus gros. Les auteurs ont étudié une nouvelle méthode de construction afin d'apporter des améliorations. Cette méthode est constituée de 2 étapes. La 1ère étape consiste à solidifier une partie de la butte de gravats sous le caisson et la 2ème étape à le découper afin d'augmenter la profondeur frontale du caisson. Une série d'essais à table vibrante a été menée afin d'étudier le comportement sismique des murs de quai de type caisson qui ont été améliorés grâce à cette nouvelle méthode. Cette étude présente les résultats des essais et analyse les facteurs qui affectent le comportement sismique des murs de quai de type caisson avec butte stabilisée.

**KEYWORDS:** caisson-type quay wall, front-water-depth enlargement, shaking table test

## 1. INTRODUCTION

In recent years, there has been increasing demand to reduce costs for public works in Japan. Correspondingly, great efforts have been directed toward using and upgrading existing infrastructures efficiently. In this context, the authors have been studying methods for enhancement and improvement of existing port facilities.

Because the caisson-type quay wall (see Figure 1) is one of the major types used in Japan (OCDI 2009), it is desirable that this type quay wall have more front-water depth to better accommodate the larger and larger vessels coming alongside. A method often employed for this improvement is to construct a new pier front onto the caisson quay wall as shown in Figure 2. It is impossible, however, to adopt this method for a caisson quay wall when there is not enough frontal space: thus, a new improvement method applicable to such situations is being developed. In the new method, a rubble mound beneath a caisson is solidified then cut to increase the front-water depth of the caisson as shown in Figure 3.

The authors conducted a series of shaking table tests to study the seismic behavior of caisson-type quay walls improved by the new method.

## 2. TEST METHOD

A model of a caisson quay wall was built in a sand box whose inside dimensions were 85cm in length, 35.4cm in width and 65cm in height. Figure 4 shows a schematic view of the model. The gravel layer at the bottom of the sand box was part of the box (for drainage). It was compacted sufficiently and it was assumed that the deformation of the gravel layer would not affect test results. A non-woven fabric was put on the surface of the gravel layer for sand prevention. The tests focused on the vibrational property and deformation mode of the quay walls

with a stabilized mound; the model ground was dry for simplicity.

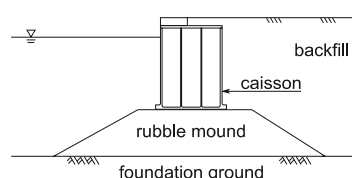


Figure 1. Typical cross-section of the caisson-type quay wall.

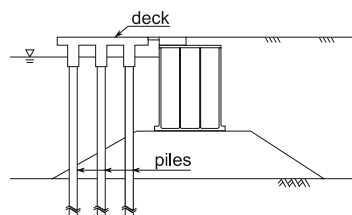


Figure 2. Construction of a new pier to enlarge the front-water depth of the caisson-type quay wall.

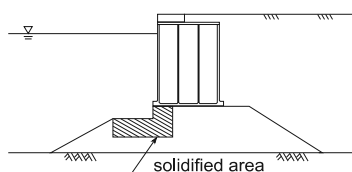


Figure 3. The new method to enlarge the front-water depth of the caisson-type quay wall without change in the face line of the quay wall.



tilted; the data were not processed because the accuracy of the measurement of acceleration would be less.

For the test results with 100Gal (gray marks in figures), it could be said that the amplification was small and that there was no large difference among the tests. The amplitude of seaward acceleration was slightly larger than that landward.

In the case of the test with 300Gal (black marks in figures), the amplification tendency differed among the test cases. In the case of quay walls with Type 1 and Type 2 blocks, the acceleration amplitudes at the crown of the caisson were smaller than in the test without blocks both seaward and landward; the stability of the caisson was improved by the blocks. In the case of Type 3 blocks, the amplitude seaward was larger than in the test without blocks at the crown of the caisson, while the amplitude landward was smaller. It was remarkable that the amplitude at the head of the Type 3 block (a5) was much larger in both directions.

Figures 8 and 9 show the phase delay of the acceleration observed in the tests. The phase delay was calculated in the same way as acceleration amplitude. Figure 8 and 9 show that there was no large delay in the case of the tests with 100Gal. Large delay was detected in the landward acceleration observed in the tests with 300Gal acceleration as shown in Figure 9. In the tests with Type 1 and Type 2 blocks, the delay was the same as in the test without any blocks. On the other hand, delay of acceleration landward in the case of the test with Type 3 blocks was much larger than in the case without blocks.

One of the causes of the large acceleration amplitude and delay observed in the test with Type 3 blocks could be the instability of the blocks because the shape was vertically long.

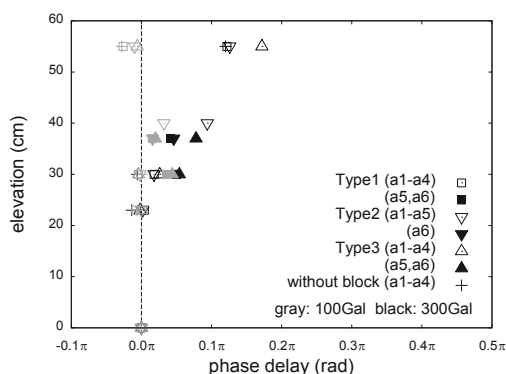


Figure 8. Phase delay of acceleration seaward.

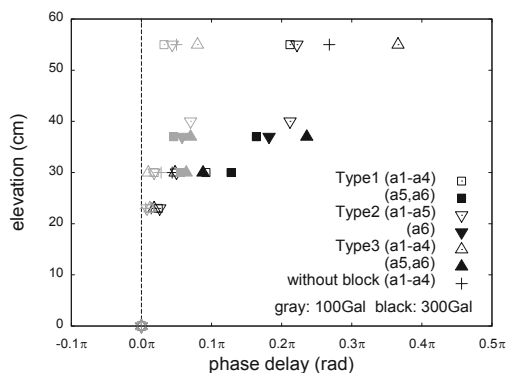


Figure 9. Phase delay of acceleration landward.

#### 4. DISPLACEMENT OF QUAY WALL

The trace of the top-left corner of the caisson in Figure 4 was calculated from displacement measured by d1-d3 for each case. Figure 10 shows the trace observed during the final step of

shaking. The maximum acceleration of the input wave for the final shaking was different among the tests as mentioned before. Tilt angle of the caissons was also calculated from the data of displacement meter; Figure 11 shows the tilt angle observed during the final step.

Figure 12 shows the deformation of the quay wall models observed after the tests. A few millimeters of settlement of the foundation ground were observed in all cases. Sand dropped into clearance gap between the rubble mound and the sand box; the boundary between the mound and the backfill ground was not clear. Figure 12 shows the boundary in outline.

In the case of the model without blocks, the caisson moved seaward with forward inclining as shown in Figures 11 and 12; the large deformation observed with the input wave whose maximum acceleration was 500Gal and the test was aborted (see Figure 12). The caisson in the test with Type 4 blocks showed similar behavior as in the test without blocks. Thus the improved quay wall with Type 4 blocks was comparable in seismic resistance to the quay wall before improvement in spite of the front-water-depth enlargement. Figure 11 shows the tilting of the caisson with Type 4 blocks smaller than the caisson without blocks. The caisson with Type 4 blocks was displaced with small rotation as shown in Figure 12. It could be said that even small blocks like Type 4 had a certain degree of effect on caisson stability.

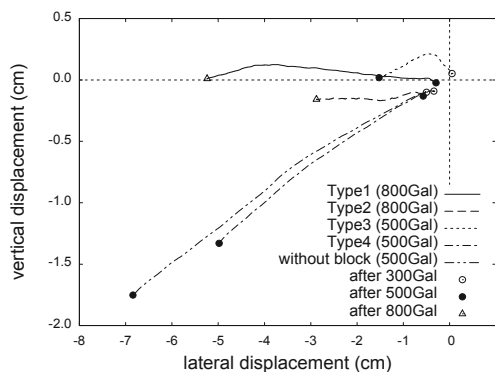


Figure 10. Trace of the top-left corner of the caisson.

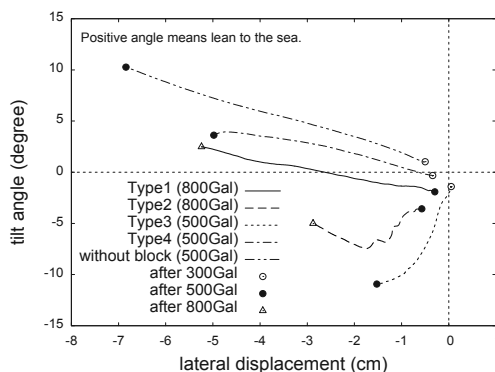


Figure 11. Relationship between tilt angle and lateral displacement of the caisson.

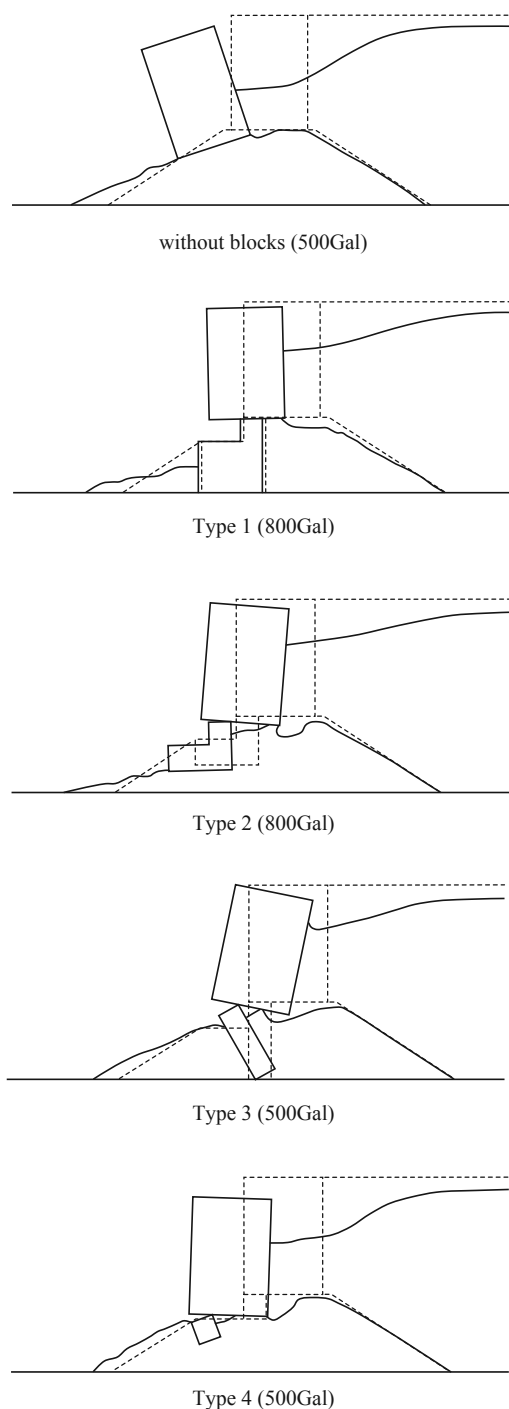


Figure 12. Deformation of the quay wall models after the tests.

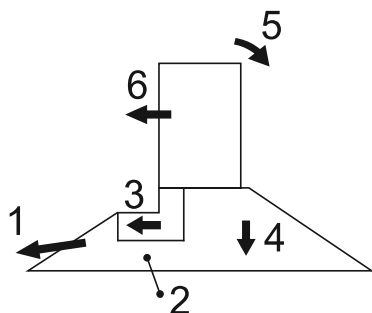


Figure 13. Factors affected the behavior of the improved quay walls.

The caisson with Type 1 blocks had small backward inclining after 500Gal shaking as shown in Figure 11, and was displaced seaward over the block by 800Gal shaking (see Figure 10). After the tests, the tilt angle of the caisson returned to about zero degree. The caisson with Type 2 blocks had backward inclining after 500Gal, the same as the caisson with Type 1 blocks; however, during 800Gal shaking, the blocks moved seaward together with the caisson and the backward inclination of the caisson remained (see Figure 12).

In the case of the model with Type 3 blocks, the blocks leaned seaward, and the caisson had significantly large backward inclining after 500Gal shaking. One of the causes of this result could be the lack of stability of the blocks. The inherent stability of the blocks would be an important factor of the new improvement method.

Based on the final deformation shown in Figure 12 and the results of measurement mentioned above (especially from the observed displacement), it could be said that six factors affected the behavior of the improved quay wall: (1) collapse of foreside slope rubble mound, (2) dimensions of solidified area and ground condition beneath solidified area, (3) displacement of solidified area, (4) settlement of rubble mound and differential settlement between solidified area and rubble mound, (5) leaning of caisson, and (6) displacement of caisson. The numbers correspond to those indicated in Figure 13. These factors correlated strongly with each other, making it was difficult to clarify which was the dominant factor on the behavior of quay walls.

## 5. CONCLUSION

A series of shaking table tests were conducted to study the seismic behavior of caisson-type quay walls improved by the new method. It was derived from the results of the model tests that six factors affected the behavior of the caisson-type quay walls improved by the new method. Further study will be continued to evaluate the effect of each factor, and the design methodology of the new-type quay walls will be discussed base on the results.

## 6. ACKNOWLEDGEMENTS

This work was supported by the Kanto Regional Development Bureau, Ministry of Land, Infrastructure, Transport and Tourism in Japan, and was a part of cooperative research between the Port and Airport Research Institute and the Japan Dredging and Reclamation Engineering Association. The authors greatly appreciate their contribution.

## 7. REFERENCES

The Overseas Coastal Area Development Institute of Japan. 2009. *Technical standards and commentaries for port and harbour facilities in Japan*. OCDE, Tokyo.

# Inspection of structural health of existing railway retaining walls

Inspection de l'état structurel des murs de soutènement des voies de chemin de fer existantes

Nakajima S., Shinoda M., Abe K.

Railway Technical Research Institute, Japan

**ABSTRACT:** This study aims to develop an inspection method of a structural health of the existing retaining walls. This paper begins with the brief introduction of the current state of the existing retaining structures. Second, applicability of the percussion test for the evaluation of structural health of existing retaining wall is examined by conducting a large numbers of the percussion test on retaining walls at the site. It was found from the percussion test that structural health of the ashlar wall could be quantitatively evaluated by the percussion test while it was found to be difficult to apply the percussion test for the quantitative evaluation of the leaning type retaining wall. Third, applicability of the small scale vibrator, which was newly developed to improve the disadvantage of the percussion test as the inspection method of the retaining wall, was examined through the prototype scale model test on the existing leaning type retaining wall. It was found from the series of model test that the vibration tests were effective in evaluating the characteristics of dynamic properties of the retaining walls, which were affected by structural health of the retaining walls. This result indicated that the small scale vibration tests could be applicable to evaluate the structural health of the existing retaining structures.

**RÉSUMÉ :** Cette étude vise au développement d'une méthode d'inspection de l'état structurel des murs de soutènement existants. L'article commence par une brève présentation de l'état actuel des structures de soutènement existantes. Il se poursuit par l'exposition de l'analyse de l'applicabilité des essais aux chocs à l'évaluation de l'état structurel des murs de soutènement existants conduits sur des murs de soutènement sur le terrain. Ces essais aux chocs ont montré qu'ils permettaient une évaluation quantitative des murs de soutènement de type en béton mais qu'ils ne se prêtaient guère à l'évaluation des murs de soutènement de type incliné. Une troisième partie est consacrée à l'applicabilité d'un vibreur à faible échelle nouvellement mis au point qui permet de palier les inconvénients des essais aux chocs comme méthode d'inspection des murs de soutènement. Un appareil prototype a été utilisé pour l'inspection des murs de soutènement de type incliné. La série d'essais modèles conduite a mis en évidence que les essais aux vibrations permettaient de bien évaluer les caractéristiques des propriétés dynamiques des murs de soutènement affectés par leur état structurel. Les auteurs concluent que les essais aux vibrations à petite échelle peuvent être appliqués dans l'évaluation de l'état structurel des murs de soutènement existants.

**KEYWORDS:** Retaining walls, condition rating, small scale exciter, vibration testing

## 1 BACKGROUND

In Japan, there are many old existing railway structures and it enhances the importance of the proper maintenance methodology. For the proper management of the railway structures, it is important to detect deformations of the structures in early stage. Once deformations are observed, continuous observations and retrofitting works are also important. As for the Japanese railway structures, it has already developed to evaluate a structural health of bridge piers quantitatively, which makes it possible to maintain structures efficiently. On the other hand, a visual inspection is still conducted to evaluate a structural health of the existing retaining walls because quantitative inspection method for the existing retaining wall has not yet developed. It is required to evaluate a structural health of the existing retaining walls quantitatively because a result of the visual inspection is highly dependent on the subjective judgment of an inspector.

Based on the background above, this study aims to develop an inspection method for the condition rating of the existing retaining walls.

## 2 CURRENT STATE OF THE RAILWAY RETAINING STRUCTURE

### 2.1 Maintenance standards in Japan

There are approximately 30 thousand kilometers of the railway lines in Japan, which are operated by many railway organizations (seven Japan Railway companies, over 100 private railway companies and several local governments).

Japanese railway organizations maintain their structures safety conditions by referring to the Japanese maintenance code of Maintenance Standards in Japan (RTRI, 2007). General procedure for structural maintenance in the Management standards and relationships between the soundness and the structure state are shown in Figure 1 and Table 1.

As indicated in Figure 1, "General Inspection" is conducted to all of the railway structures within the intervals of two years mainly by visual inspection. On the other hand, "Individual

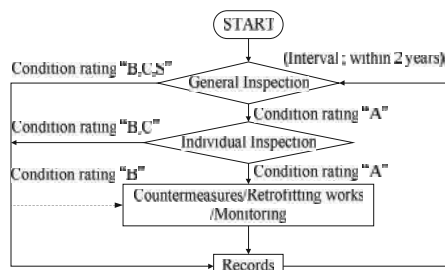


Figure 1. Maintenance procedure according to the Maintenance standards in Japan

Table 1. Relationships between rated condition and structure state

Condition rating	Structure state
A	State that threatens operational safety, safety of passengers, public safety, guarantee of regular train operation, or deterioration that might cause this state
B	Deterioration that might result in a future soundness rank of A
C	Slight deterioration
S	Good condition



Inspection” is performed to the specific structures in which severe deterioration are detected at the time of the General Inspection by means of detailed visual survey or using measuring equipments. As discussed in BACKGROUND, this study aims to develop a methodology which can be used for the condition rating of the retaining walls quantitatively as an alternative method of detailed visual survey.

### 2.2 Survey on current state of Japanese railway retaining walls

A preliminary survey on current state of Japanese railway retaining structures was conducted. In the preliminary survey, information of typical types of retaining walls in Japan was extracted from the database of the “Structural Management Supporting system (SMS)” (Oyado et al. 2010). In total, the data of 7,989 sites could be extracted. Figure 2 shows the relationships between the type of retaining wall and construction length, which could be obtained using the efficient 1,657 sites data. Construction length of the leaning type retaining wall stands first among all the types of the retaining walls and it accounted for 38.3 % of the efficient data. The percentage of the masonry and ashlar block retaining wall reaches to 37.8 % as well. It was found from the above survey that the leaning type and masonry or ashlar block retaining wall occupies 76.1 % of the total construction length and it indicated the importance of the management of these structures.

### 2.3 Deformation of retaining walls

Deformation of the railway retaining structures can be divided into two groups; one is the deformation due to destabilization, the other one is the deformation due to deterioration. Typical deformation of the railway retaining structures is schematically illustrated in Figure 3.

Settlement, inclination, swelling, difference in level and difference at construction joint due to external thrusts can be categorized to the deformation due to the destabilization. Exfoliation of concrete, clogging of the drainage facilities is categorized to the deformation due to the deterioration. Cyclic load due to the train passing, increase of earth pressure due to the additional construction of the embankment, increase of dynamic earth pressure due to the earthquake, increase of water

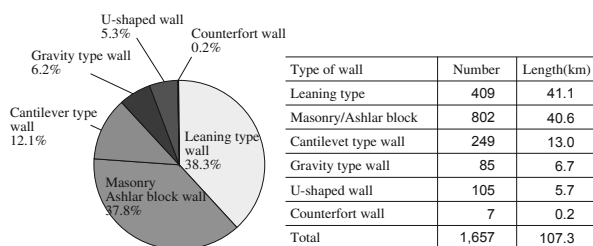


Figure 2. Relationships between construction length and types of retaining wall

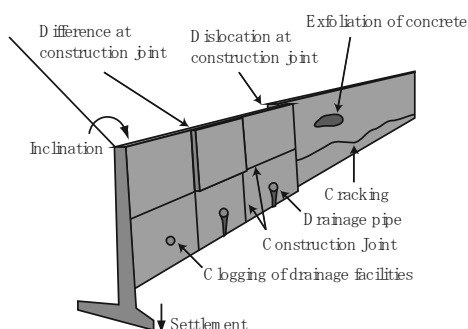


Figure 3. Typical deformation of retaining wall

pressure due to the change of the water level in backfill soil are thought to be the source of the external thrusts, which could cause the deformation due to the destabilization.

On the other hand, deterioration is thought to be caused by the cyclic change of the thermal or humid condition during the long period of its use. Deformation due to the destabilization could be secondary source of the deformation like backfill loosening, bearing capacity failure. Therefore, early detection and retrofitting work against the deformation due to the destabilization are highly important, while it has not yet been developed a methodology to detect such phenomenon by the nondestructive tests. Based on the discussion above, development of a nondestructive evaluation method of the existing retaining wall is attempted in this study.

## 3 APPLICATION OF PERCUSSION TEST FOR CONDITION RATING OF RETAINING STRUCTURES

### 3.1 Percussion test

In Japanese railway field works, nondestructive evaluation of the bridge substructure has been carried out by conducting a percussion test (Nishimura et al. 1989) . In the percussion test, the natural frequency of the bridge pier is measured with high accuracy and it is used for the evaluation of the structural health of the pier. This method was based on the knowledge that the natural frequency of the bridge substructure decreased with the damage of the structures and increased with the reinforcement.

Natural frequency of the bridge piers is evaluated by carrying out a spectrum analysis using measured free vibration, which is recorded by velocity sensors. Free vibration is induced by hitting the top of the piers using an iron ball. In practice, current performance of bridge pier can be evaluated by comparing the measured natural frequency with the one of immediately after the construction or the criterion of the potential natural frequency. Potential natural frequency is the experimentally-based proposed value by Railway Technical Research Institute so as to be used for the site where the natural frequency immediately after the construction was not recorded.

### 3.2 Site test results

A series of site test was carried out so as to examine the applicability of percussion test for the condition rating of retaining wall. In the series of site tests, leaning type and ashlar wall are highlighted because construction length of these types of retaining wall was much longer than the other types of walls. As summarized in Table 2, 52 site tests were carried out by selecting the deformed and sound retaining walls so as to investigate into the difference of the vibration characteristics of retaining wall. Percussion test was conducted by hitting the iron ball at the top of the retaining wall and vibration was measured by the velocity sensors attached at the top, middle and bottom of the retaining wall.

Figure 4 shows an example of test result obtained from test No. 3. Predominant frequency of 26.6 Hz could be evaluated based on the changes of phase angle, while the peak amplitude was not clearly observed. This behavior indicates that natural frequency based condition rating, which has been adopted in the condition rating of the bridge substructure, was difficult possibly because the mode of vibration of retaining walls are generally more complicated than the originally bridge substructures. As an alternative index for the condition rating of the retaining wall, the authors proposed the value of spectrum area  $S_a$ , which could be evaluated by integrating the Fourier's spectrum of the amplitude as schematically illustrated in Figure 4b), while frequency range of 3 to 40 Hz was selected in this study. Figures 5 and 6 show the relationships between results of condition rating based on visual inspection and the values of

Table 2 Summary of test sites in this study

No.	Company	Type	Height(m)	Deformation	No.	Company	Type	Height(m)	Deformation
1	A	Leaning	7.2	None	26	F	Leaning	3	None
2			7.2	None	27			2.64	None
3			7.2	Cracking	28			3.95	None
4			7.2	None	29	H	Leaning	5.48	Cracking
5			7.2	None	30			5.48	Cracking
6			7.2	None	31			5.48	Cracking
7			7.2	None	32			5.4	Cracking
8	B	Leaning	6.3	Cracking	33	I	Ashlars wall	6.4	None
9			6.3	Cracking	34			2.4	Cracking
10			6.3	Cracking	35	4.2	None		
11			6.3	None	36	4.1	None		
12			3.9	Cracking	37	4.1	None		
13			3.35	None	38	4.1	None		
14			3.6	None	39	4	Inclination		
15	C	Leaning	3.6	None	40	K	Ashlars wall	4	Inclination
16			3.6	None	41			4	Inclination
17			3.6	None	42			4	Inclination
18	D	Gravity	4.8	None	43	L	Ashlars wall	5.7	Cracking
19			4.3	None	44			5.4	None
20			3.3	None	45	2.6	None		
21			3.7	Cracking	46	M	Ashlars wall	3	None
22			2.9	Cracking	47			3.4	None
23			3.2	None	48	3.3	None		
24			E	Leaning	4.15	None	49	N	Ashlars wall
25	4.15	None			50	3.3	None		
	4.15	None			51	3.3	None		
					52		3.3	None	

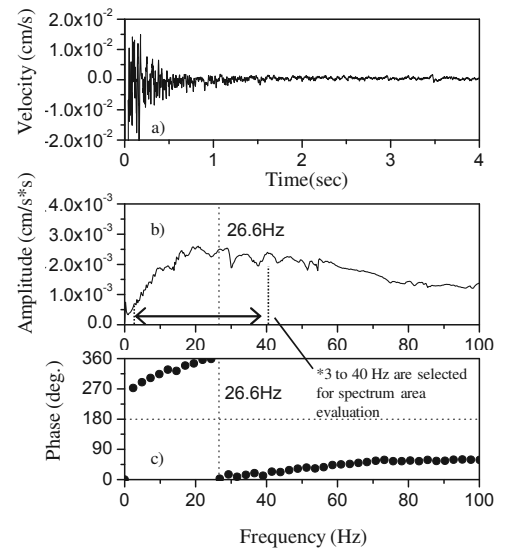


Figure 4. Example of test result obtained from site No.3

spectrum area. In the cases of ashlars wall shown in Figure 5, the values of spectrum area Sa of retaining walls rated as “A(deformed)” were generally larger than the ones of retaining walls rated as “B(no deformation)”, which shows the validity of spectrum area for the condition rating of retaining walls.

In the cases of the leaning type retaining wall shown in Figure 6, a good correlation between the result of visually inspected condition rating and the values of spectrum area could not be found. In the sites No. 6, 20, 21 and 24, the values of spectrum area was much larger than the other sites although they were rated as “B (no deformation)”, which might imply that the progress of the deformation at the part in which is difficult to detect by visual inspection (e.g. subsoil, backfill, etc.). On the other hand, at the sites 27, 26, 25 and 3, the values of spectrum area were not necessarily larger than the other sites although they were categorized as “A(deformed)”.

Percussion test has some problems (Nakajima et al., 2012) ; 1) heavy weight of iron ball (safety, portability) , 2) scattering of impact force depending on inspectors (repeatability) and 3) attenuation of impact force especially in high frequency range(limited range of input frequency). In applying to the condition rating of retaining wall, second and third problems would make it difficult to rate the condition of the retaining wall properly especially in the case of the leaning type retaining wall. Therefore, the authors developed a small scale exciter (Shinoda et al., 2012), which could apply constant sweep sinusoidal excitation under mechanically manipulation, which could solve second and third problems. A prototype scale loading test on leaning type retaining wall model was conducted so as to examine the applicability of the newly developed small scale exciter.

#### 4 PROTOTYPE SCALE LOADING TEST

Cross section of constructed leaning type retaining wall with height of 4.3 m and width of 1.5 m is shown in Figure 7. In Figure 7, the outline of the developed small scale exciter is also summarized. Retaining wall was constructed on the stiff base layer while its backfill consisted of the cobbles, sand backfill with degree of compaction  $D_c$  of 90 % and densely compacted gravelly sand. In the loading test, the retaining wall was subjected to the cyclic loading and unloading processes by applying the vertical load at the surface of the backfill using the hydraulic jack while their amplitude were gradually increased as shown in Figure 8. Gravelly sand layer inclined 30 degrees

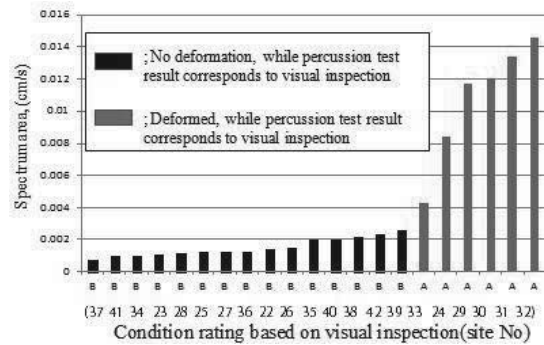


Figure 5. Relationships between condition rating by visual inspection and value of spectrum area (Ashlars wall)

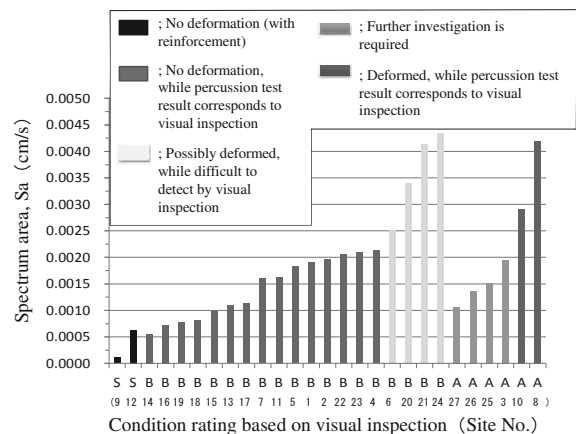


Figure 6. Relationships between condition rating by visual inspection and value of spectrum area (Leaning type retaining wall)

from the horizontal direction so as to apply horizontal load to the retaining wall efficiently.

In the loading test, cyclic loading and unloading processes were applied to the leaning type retaining wall model (Case 1). A soil nailing reinforcement with diameter of 60 mm and length of 4000 mm was installed after horizontal displacement at the wall top exceeded 50 mm. As the second case (Case 2), the model wall reinforced with the top nailing was subjected same loading and unloading processes with Case 1. Lastly, the model wall with top and bottom nailing, which was installed after Case 2, was subjected to the same loading processes while the maximum amplitude of load was applied to the wall in the end

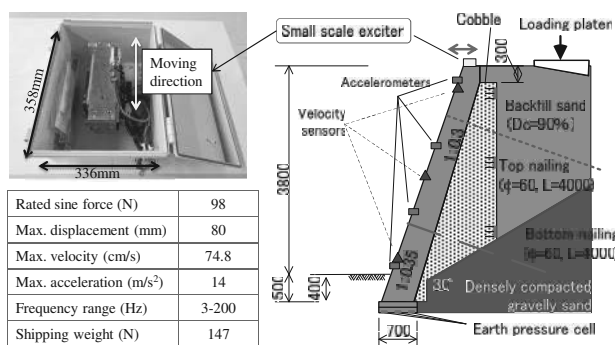


Figure 7. Cross section of model and outline of developed exciter (unit in mm)

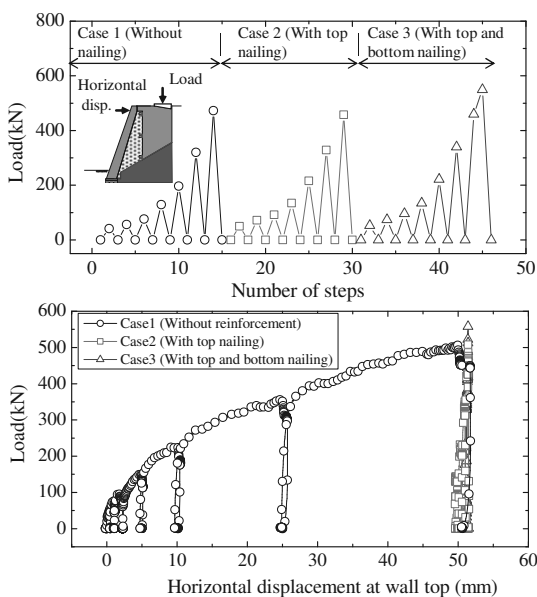


Figure 8. Loading process and load-displacement relationships

of loading process (Case 3). The loading and unloading processes in each case were summarized in Figure 8.

At every loading and unloading process, sets of percussion test with a set of velocity sensors and vibration tests using the developed small scale exciter with a set of accelerometers were conducted so as to investigate into the difference of vibration characteristics obtained from each test. Vibration test was conducted by applying the sinusoidal sweep excitation to the retaining wall model by the small scale exciter fixed at the top of the retaining wall, while the constant amplitude of 1000 gals with frequency range of 3 to 100 Hz and sweeping rate of 3 Hz/sec were adopted as the test condition.

Figure 8 also shows load-displacement relationships obtained from the loadcell installed at the hydraulic jack and displacement transducer at the top of the retaining wall. As clearly shown in Figure 8, the increment of the wall top displacement was drastically reduced by adding the soil nailing although the same amplitude of loading processes were applied to the wall. Displacement increment during a set of loading and unloading processes in Cases 1, 2 and 3 were 50mm, 1.0mm and 0.5 mm respectively.

Figure 9 shows relationships between the number of step and the results from the percussion test and vibration test, while the values of spectrum area of frequency range of 3 to 40 Hz were plotted in the vertical axes. It should be emphasized that the spectrum area evaluated from the percussion test results Sa[p] has the dimension of velocity (cm/sec) because it was evaluated from the integration of the relationships between the Fourier's amplitude of velocity (cm/sec\*sec) computed from records of the velocity sensor at the top of the wall and the frequency

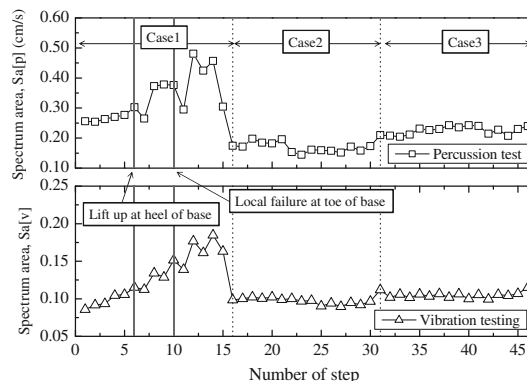


Figure 9. Cross section of model (unit in mm)

(1/sec). On the other hand, the spectrum area calculated from the vibration testing Sa[v] did not have any dimensions because it was evaluated from the transfer function of the top accelerometer against the input acceleration.

It was found from Figure 9 that the values of Sa[p] and Sa[v] increased with the number of step. Moreover, the effect of the nailing could be also detected as the reduction of the values of Sa[p] and Sa[v] in Cases 2 and 3 as compared with Case 1. The difference between Sa[p] and Sa[v] could be found especially in loading and unloading process. The values of Sa[v] increased in the loading process and reduced in the unloading process, which indicated that the spectrum area Sa[v] based condition rating using the vibration testing with the small scale exciter could detect a minor change of the stability of the retaining wall. The value of Sa[p], however, could not detect a minor change during single loading and unloading process, which was possibly because the input force could not be kept constant. It was found from the results of the site tests and prototype scale loading test that the percussion test and the vibration testing could be applicable, while vibration testing could detect a minor change of the stability of the retaining wall.

## 5 SUMMARY

It was attempted in this study to develop a inspection method of the existing retaining wall. It was found from the preliminary survey on the current state of Japanese railway retaining wall that condition rating of the leaning and the ashlar wall are important because of their huge amount of existing structures. Based on the site test and prototype scale loading test, it was found that the percussion test and vibration test using the spectrum as an index could be applicable for the condition rating of existing retaining walls.

## 6 REFERENCES

Oyado, M., Miyashita, M., Ueda, S. and Sakairi, A., An at-tempt of rationalization for maintenance of railway structure using supporting system, *Proc. of 5th International conference for bridge maintenance, Safety and Management*, pp.3459-3466, 2010.  
 Railway Technical Research Institute, *Maintenance Standards for Railway structures*, 2007.  
 Nishimura A., Okumura, F. and Tanamura S., Integrity Judgment of Railway Bridges by Percussion Tests for Structure Response, *Quarterly Report of RTRI*, Vol. 29, No.4, pp.184-189., 1988.  
 S. Nakajima, M. Shinoda, K. Abe, T. Mai and T. Ehara: Study on inspection method for railway existing retaining walls using vibration testing, *IS-Hokkaido 2012: 2nd international conference on transportation geotechnics*, 2012.  
 Shinoda, M., Nakajima, S., Abe, K., Tetsuo M. and Ehara, T.: Development of nondestructive inspection method of railway bridge substructures with small vibration exciter, *Proc of the International workshop on ICT in Geo-Engineering (ICTGE2012)*, 17-18 May 2012.

# Mechanism of Settlement Influence Zone due to Deep Excavation in Soft Clay

## Mécanisme de la zone d'influence de tassement dû à une excavation profonde dans l'argile molle

Ou C.-Y., Teng F.-C.

National Taiwan University of Science and Technology, Taipei, Taiwan

Hsieh P.-G.

Hwa Hsia Institute of Technology, New Taipei, Taiwan

Chien S.-C.

Aletheia University, New Taipei, Taiwan

**ABSTRACT:** The objective of this study is to examine the mechanism of settlement induced by deep excavation through finite element analysis. The USC model was selected for this purpose through the calibration of different soil constitutive models. A series of parametric studies were then performed. It was found that in addition to the excavation depth, excavation width, the soft clay thickness and depth to the hard soil are also related to the settlement influence zone. A simple method derived from the basal heave failure mechanism is proposed to predict the settlement influence zone. One case history and one hypothetical excavation with the 80 m thick soft clay were used to verify the proposed method. For comparison, the existing empirical formulae were also used for prediction.

**RÉSUMÉ :** L'objectif de cette étude est d'examiner le mécanisme de tassement induit par une excavation profonde à travers l'analyse d'éléments finis. Le modèle USC a été choisi à cet effet par le calibrage de différents modèles de sol. Une série d'études paramétriques a ensuite été réalisée. Il a été constaté qu'en plus de la profondeur et de la largeur de l'excavation, l'épaisseur et la profondeur de l'argile molle sur le sol dur sont également liées à la zone d'influence du tassement. Une méthode simple dérivée du mécanisme de rupture par soulèvement basal est proposée pour prédire la zone d'influence du tassement. Une étude de cas et un travail d'excavation hypothétique de l'argile molle sur 80 m d'épaisseur ont été utilisés pour vérifier la méthode proposée. À titre de comparaison, les formules empiriques existantes ont également été utilisées pour la prédiction.

**KEYWORDS:** Deep Excavation, Soft Clay, Settlement, Constitutive Model, Settlement Mechanism

### 1 INTRODUCTION

The finite element method and empirical methods are often used to predict the ground settlement induced by deep excavation. The finite element method usually gives better predictions for wall deflection than for ground settlements unless small strain characteristics of soil are taken into account. Ideally, empirical methods should be able to predict ground settlements well because they are mainly derived from field observations of case histories. However, most of them yield poor prediction in ground settlement because settlement mechanism is unclear, case histories adopted is limited, and the excavation depth is the only parameter used in formulas.

The objective of this paper is to investigate the mechanism of ground settlement induced by deep excavation under the plane strain condition through finite element analysis. The study focuses on the settlement under the normal excavation condition, that is, no dewatering induced settlement, no excessively long construction duration causing the occurrence of creep, and no serious construction defects. A suitable soil constitutive model was selected through calibration process. Then a series of parametric studies were performed and the settlement mechanism is proposed.

### 2 CALIBRATION OF SOIL CONSTITUTIVE MODELS

Since "settlement influence zone" is not rigorously defined, the authors proposed the conception of the primary influence zone (*PIZ*) and the secondary influence zone (*SIZ*) on the basis of the principles of mechanics and regression analysis of excavation case histories (Hsieh and Ou 1998). The settlement curve is steep in the *PIZ* where buildings receive more influence and in the *SIZ* the slope of the curve is gentle and its influence on buildings is insignificant. Finite element analyses are used to capture the characteristics of *PIZ*.

Four soil constitutive models including the Hardening Soil (HS) model, Hardening Soil with Small Strain (HSS) model,  $\phi=0$  Mohr-Coulomb (MC) model, and Undrained Soft Clay (USC) model, were adopted. Of these, the HS and HSS model are the effective stress model and the  $\phi=0$  MC model and USC model are the total stress model. Both the HSS model and USC model take into account that the soil exhibits high stiffness at small strain.

Though the USC model is a total stress model, it considers the variation of undrained shear strength with principal stress rotation, variation of Young's modulus with the increase of stress level, high stiffness of soil at small strain, and rational way to determine the undrained shear strength (Hsieh and Ou 2011). Similar to Duncan and Chang's model, the tangent Young's modulus ( $E_t$ ) in the primary loading is derived as

$$E_t = E_{ur}(1 - R_f SL)^2 \quad (1)$$

where  $R_f$  is the failure ratio,  $SL$  is the stress level,  $E_{ur}$  is the unloading/reloading Young's modulus.

The  $E_{ur}$  should degrade with the increase of strain or stress level. The degraded Young's modulus is assumed to follow a hyperbolic function as

$$\frac{E_{ur}}{E_i} = 1 - \frac{SL - SL_i}{m + n(SL - SL_i)} \quad (2)$$

where  $m$  and  $n$  are the degradation parameters relative to the stress level,  $E_i$  is the Young's modulus at small strain,  $SL_i$  is the stress level corresponding to the threshold value of the small strain or the initial yield strain.

An elastic surface, ES, is defined to represent the small strain characteristics for the state of stress inside the elastic surface. Figure 1 shows the relationships of stress and strain and of

elastic, yield and failure surfaces. Thus, A total of seven parameters are required for the USC model, i.e.,  $s_{uc}$  (undrained shear strength from  $K_0$ -consolidated undrained compression test),  $E_i$  (Young's modulus at small strain)  $\epsilon_s$  (threshold of small strain)  $R_f$  (failure ratio)  $K_{ss}$  (ratio of the undrained shear strength from undrained shear strength from  $K_0$ -consolidated undrained compression test to that from undrained shear strength from  $K_0$ -consolidated undrained extension test) as well as  $m$  and  $n$  (degradation parameters).

The TNEC case history was used for calibration (Ou et al. 1998). Figure 2 shows the comparison of wall deflections and ground movements obtained from field observation and those from finite element analysis using different models. Except for the  $\phi=0$  MC model where  $E_u/s_u$  was assumed to be 400 according to the local experiences, other soil parameters such as undrained shear strength,  $E_{50}^{ref}$ ,  $E_{ur}^{ref}$ ,  $E_{oed}^{ref}$ ,  $G_0^{ref}$  were determined from laboratory tests.  $\gamma_{0.7}$  were calibrated to be  $5 \times 10^{-5}$ . Details of the soil parameter evaluation can be found in Lim et al. (2010). Though wall deflections can be predicted well for all models, only the USC model can yield ground settlements close to field observations (Figure 2). Moreover, a hypothetical excavation with an 80 m thick soft clay where its properties were assumed to be the same as the third soil layer of the TNEC case was used for further calibration. The USC model gives a more reasonable prediction in wall deflection and ground settlements than other three soil models (Figure 3). The USC model is thus adopted for parametric studies.

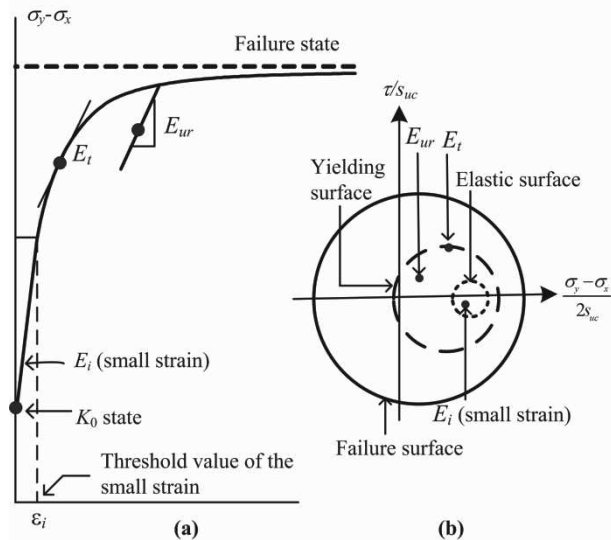


Figure 1. Concept of the USC model (a) Stress-strain behavior (b) Relationship of failure, yield and elastic surfaces.

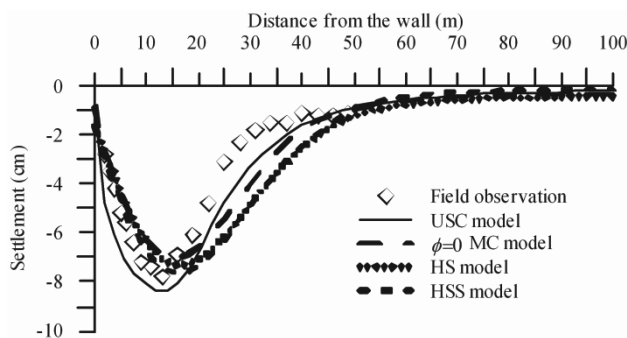


Figure 2. Comparison of settlements from field observation with those from analyses for TNEC

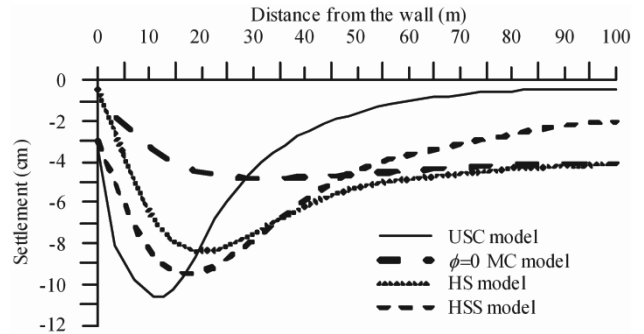


Figure 3. Comparison of settlements from various soil models for a hypothetical excavation with 80 m thick soft clay

### 3 PARAMETRIC STUDIES AND MECHANISM OF SETTLEMENT

A wide range of assumed excavation cases including excavation depth of 9 to 20 m, excavation width of 20 to 60 m, normalized undrained shear strength ( $CK_0UC$ ) of 0.28 to 0.34, depth to hard rock of 25 to 50 m was analyzed using the USC model. A typical parametric result, variation of movements with the excavation width, is shown in Figure 4, indicating that the  $PIZ$  changes with the excavation width. The excavation depth, excavation depth, thickness of soil clay and depth to hard rock are all affecting the  $PIZ$ . Based on the parametric results, we have found the following relationship

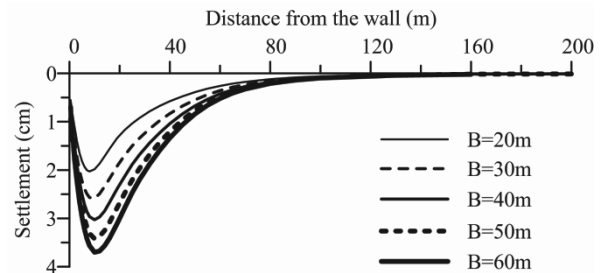


Figure 4. Variation of ground settlement with excavation width (B) for  $s_{uc}/\sigma'_v=0.3$ .

When the rock-like soil is very deep, i.e.,  $H_g$  is very large

$$\text{If } \sqrt{B^2 + H_e^2} \leq 2 H_e, PIZ \approx 2 H_e$$

$$\text{If } \sqrt{B^2 + H_e^2} > 2 H_e, PIZ \approx \sqrt{B^2 + H_e^2}$$

When the rock-like soil is of the limited depth, i.e.,  $H_g$  is relatively small

$$\text{If } \sqrt{B^2 + H_e^2} \leq 2 H_e,$$

$$2 H_e \leq H_g, PIZ \approx 2 H_e; 2 H_e > H_g, PIZ \approx H_g$$

$$\text{If } \sqrt{B^2 + H_e^2} > 2 H_e,$$

$$\sqrt{B^2 + H_e^2} \leq H_g, PIZ \approx \sqrt{B^2 + H_e^2};$$

$$\sqrt{B^2 + H_e^2} > H_g, PIZ \approx H_g.$$

The above results are summarized below:

$$\text{When } \sqrt{B^2 + H_e^2} > 2 H_e \text{ (wide), } PIZ = \min(\sqrt{B^2 + H_e^2}, H_g) \quad (3)$$

$$\text{When } \sqrt{B^2 + H_e^2} \leq 2 H_e \text{ (narrow), } PIZ = \min(2 H_e, H_g) \quad (4)$$

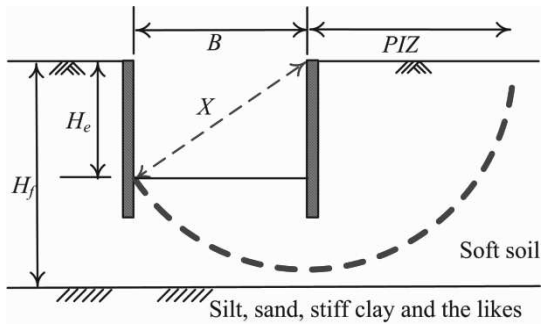


Figure 5. Basal heave failure mode and PIZ.

Comparing Eq. 3 and Figure 5 may show that the  $PIZ$  matches the failure zone or potential failure zone. The  $PIZ$  also matches the strain contours from the analysis of the TNEC excavation at stage 7 ( $H_e=11.8$  m) and that of the plastic-points when the strength is reduced to induce basal heave (Figure 6). This is because the strain in the  $PIZ$  should be very large, which in turn induces a relatively large settlement. Therefore, for excavation in soft clay, the  $PIZ$  is assumed to be the potential basal heave zone but limited by the non-soft clay, such as silt, sand etc (Figure 5). For simplification,  $(B^2+H^2)^{1/2}$  in Eq. 3 is replaced with the excavation width,  $B$ . Eq. 3 is thus rewritten as

$$PIZ_1 = \min(H_f, B) \quad (5)$$

where  $H_f$  is the thickness of the soft clay.

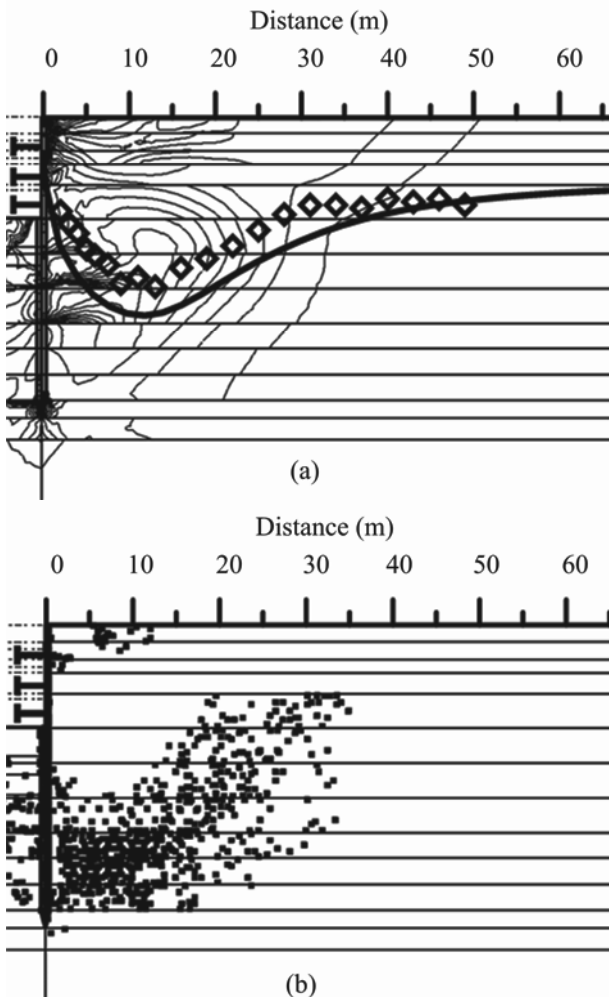


Figure 6. Excavation at Stage 7 for TNEC (a) Strain contours (b) Plastic points when the strength is reduced to cause basal heave.

The relationship in Eq. 4 indicates that the  $PIZ$  matches the active zone based on two times the excavation depth. This is because when excavation begins, the wall moves toward the excavation zone and the active zone also occurs behind the wall. Based on the stability analysis, the embedment depth of the wall is usually equal to the excavation depth. The  $PIZ$  is coincident with the active failure zone but limited by the rock-like soil. The above equation can be rewritten as

$$PIZ_2 = \min(2H_e, H_g) \quad (6)$$

where  $H_g$  is the depth of rock-like soil.

Both  $PIZ_1$  and  $PIZ_2$  are the failure zone or potential failure zones. Therefore, the  $PIZ$  is the maximum of the potential failure zones. The method for predicting concave and spandrel types of ground settlement by Hsieh and Ou (1998) is then modified, in which the  $PIZ$  derived in this study replaces the  $2H_e$ , as shown in Figure 7. Details of the derivation can be found in Ou and Hsieh (2011).

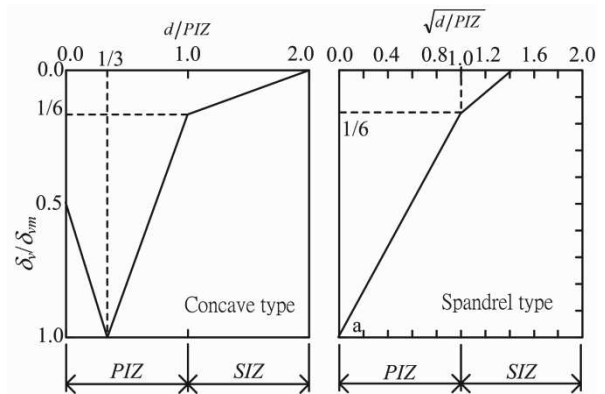


Figure 7. The proposed method for predicting the ground surface settlement.

#### 4 VERIFICATION

The TNEC case history and the ground settlement obtained from finite element analysis of the hypothetical excavation with the 80 thick are used for verification. In the TNEC case history, at stage 5,  $2H_e=17.2$  m. If the cobble-gravel soil is regarded as a rock-like soil,  $H_g=46$  m. Concerning the active failure zone,  $PIZ_2=17.2$  m. With the depth of the bottom of the soft clay ( $H_f$ ) being 37.5 m, for the potential basal heave failure mode,  $PIZ_1=37.5$  m. Thus, the  $PIZ$  is 37.5 m. At stage 7,  $2H_e=23.6$  m,  $H_g=46$  m,  $PIZ_2=23.6$  m;  $B=40$  m,  $H_f=37.5$  m,  $PIZ_1=37.5$  m. Thus, the  $PIZ$  is 37.5 m. Similarly, the  $PIZ$  at the final stage ( $2H_e=39.4$  m), is inferred to be 39.4 m. Figure 8 show the comparison between the proposed method (Ou and Hsieh 2011), Hsieh and Ou (1998) and Clough and O'Rourke (1990). The proposed method satisfactorily conforms to the field measurements, while those from other two methods are not.

In the hypothetical excavation with the 80 m thick soft clay, the excavation depths at stages 5, 7 and final are also 8.6, 11.8 and 19.7 m, respectively. The excavation width=40m. The hard soil is located at 80 m. Using the method similar to those in the TNEC case, the estimated  $PIZ$  for stages 5, 7 and final are all equal to 40m. Figure 9 shows the comparison of settlement obtained from the USC analysis with those from the three methods. The proposed method is able to give a more reasonable prediction in the settlement of  $PIZ$  than the other two methods.

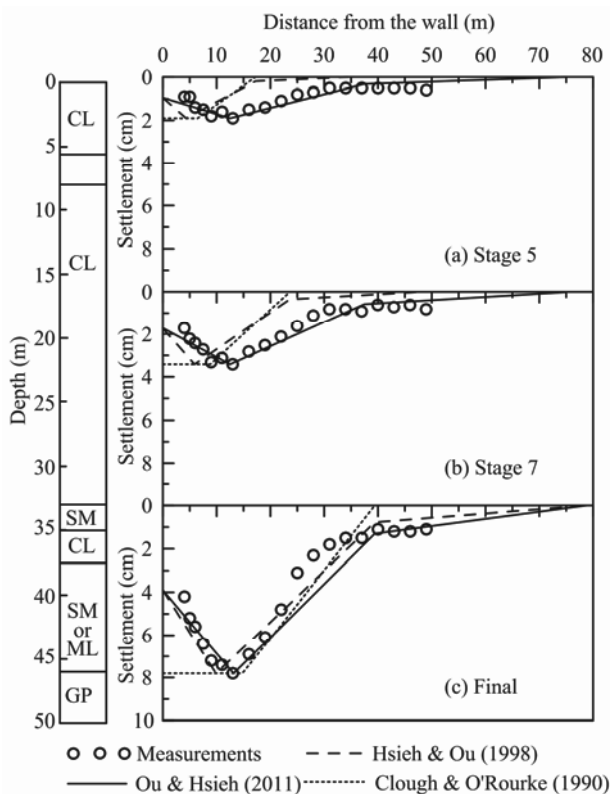


Figure 8. Verification of the proposed method for TNEC excavation.

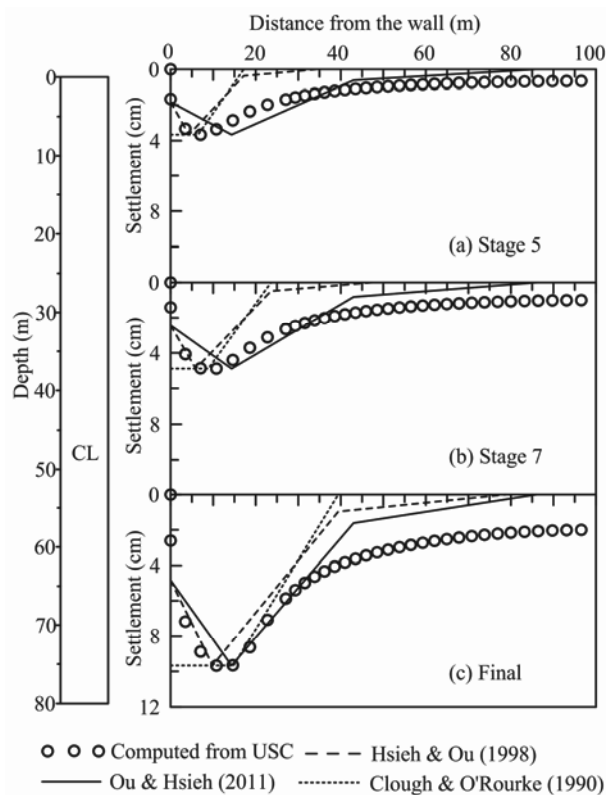


Figure 9. Verification of the proposed method for the hypothetical excavation with the 80 m thick soft clay.

## 5 CONCLUSION

The objective of this paper is to investigate the mechanism of ground settlement induced by deep excavation under the plane strain condition through finite element analysis. The study

focuses on the settlement under the normal excavation condition, that is, no dewatering induced settlement, no excessively long construction duration causing the occurrence of creep, and no serious construction defects. The USC model was selected to perform parametric studies to find the dominating factors affecting settlement influence zone based on the calibration of a well-documented case history and a hypothetical excavation with 80 m thick soft clay using various soil models. It is found that the primary influence zone is mainly the active failure zone or the potential failure zone due to basal heave. A method is then proposed to estimate the primary influence zone from the relevant parameters such as two times excavation depth, excavation width, depth to rock-like soil layer and depth of the bottom of the soft clay. Case studies reveals that the proposed method improves the prediction of settlement for excavations whose twice the excavation depth are very different than excavation width, depth to rock-like soil layer and depth of the bottom of the soft clay. The methods of Clough and O'Rourke and Hsieh and Ou only yield moderately good prediction results for the settlement at the final stage for most of the cases and largely poor predictions at the intermediate stages, which can be treated as single case histories because the excavation depth is the only parameter used in the formula.

## 6 REFERENCES

- Clough G.W. and O'Rourke T.D. 1990. Construction-induced movements of in situ walls. Proceedings of the Design and Performance of Earth Retaining Structures, ASCE Special Publication, 439-470.
- Hsieh P.G. and Ou C.Y. 1998. Shape of ground surface settlement profiles caused by excavation. Canadian Geotechnical Journal 35(6), 1004-1017.
- Hsieh, P.G. and Ou, C.Y. 2011, Analysis of nonlinear stress and strain in clay under the undrained condition, Journal of Mechanics, 27 (2), 201-213.
- Lim, A., Ou, C.Y. and Hsieh, P.G. 2010. Evaluation of clay constitutive models for analysis of deep excavation under undrained conditions, Journal of GeoEngineering, 5(1), 9-20.
- Ou, C.Y. and Hsieh, P.G. 2011. A simplified method for predicting ground settlement profiles induced by excavation in soft clay, Computers and Geotechnics 38(12), 987-997.
- Ou, C.Y., Liao, J.T. and Lin, H.D. 1998. Performance of diaphragm wall constructed using top-down method, Journal of Geotechnical and Geoenvironmental Engineering, ASCE, 124(9), 798-808.

# Establishing a high risk construction pit in a hurry

## L'établissement d'une excavation profonde à risque élevé en court temps

Philipsen J.  
Ramboll, Denmark

**ABSTRACT:** In order to establish a cut & cover road tunnel in Copenhagen, a deep construction pit is established. The future tunnel will run below four railway lines and alongside a fifth, the latter being in poor condition. Since all five railway tracks are vital for the infrastructure in the region, it was not possible to close down all lines during the construction period simultaneously. In fact only two fixed and extremely short closures were allowed for in the construction schedule. This paper presents the thought processes and considerations of the parties involved during the design and planning phase and contains a description of the outcome, that is, the chosen solutions and structural elements.

**RÉSUMÉ :** Afin de construire un « cut & cover » tunnel routier à Copenhague, une excavation profonde est réalisée. Le futur tunnel est construit sous quatre lignes de chemin de fer et à côté d'une cinquième, cette dernière étant en mauvais état. Étant donné que les cinq voies ferrées sont vitales pour l'infrastructure de la région, il n'était pas possible de fermer toutes les lignes au cours de la période de construction en même temps. En fait, seulement deux fermetures fixes et extrêmement courtes ont été accordées par les autorités. L'article présente les considérations faites par les acteurs concernées lors de la conception et la phase de planification du projet et une description des résultats et les solutions choisies.

**KEYWORDS:** Construction pit, Temporary retaining structures

### 1 INTRODUCTION

In Copenhagen a cut & cover tunnel is being established as a part of the new road Nordhavnsvej connecting an existing motorway with the city center of Copenhagen. The construction period is 2011-2015.

The tunnel is a traditional concrete twin tube box tunnel with two road lanes in each tube, build bottom up in a dry construction pit. The length of the tunnel is about 650m.

The alignment of the future tunnel runs below four railway lines at ground level, along a fifth railway line in an old fragile tunnel, below a busy main road and into a narrow path between existing buildings. Figure 1 shows the horizontal alignment and some of the key structures



Figure 1. Horizontal alignment and key structures.

The existing railway lines connect a large part of northern Copenhagen and Zealand to the City centre of Copenhagen, the capital's airport and subsequently to Sweden via the fixed link across the Øresund, which means that they are vital for the infrastructure in the region. Consequently it was not possible to close down all lines during the construction period simultaneously. Only two extremely short main closures were allowed for at each end of the construction schedule.

Figure 2 shows a photo of the 5 railway lines taken from east towards west.



Figure 2. Picture taken prior to project start up showing the 5 railway lines.

The client (the Municipality of Copenhagen) chose Ramboll to be the client's consultants, preparing the detailed design of all permanent works, while the design of the temporary structures was chosen to be split in two parts with different premises and responsibilities.

In the central and most complex part of tunnel alignment - which means at the railway crossing - the client chose a contract form whereby the contractor (Pihl-Zueblin JV) and Rambøll should sit together and optimize the temporary structures at the railway crossing with due consideration, of course, to economy and safety, but most of all with reference to the time schedule.

In the remaining parts of the alignment (the ends) the contractor designed the temporary structures, which e.g. included retaining walls and temporary bridges across the construction pit to facilitate the main road to be open during the complete construction period.



This present paper focuses solely on the temporary retaining structures in the railway crossing which the parties - in close corporation - identified as the optimal.

## 2 OVERALL GEOMETRY

The vertical alignment of the tunnel is governed by the alignment of the existing rails which are not allowed to be changed. This means that the depth of the construction pit is determined from the height of the future permanent tunnel structure and a required soil cover between the railway tracks and the tunnel roof. The width of the construction pit is about 20m

Figure 3 shows a plan and a longitudinal section at the railway crossing (from St. 5075 to St. 5230).

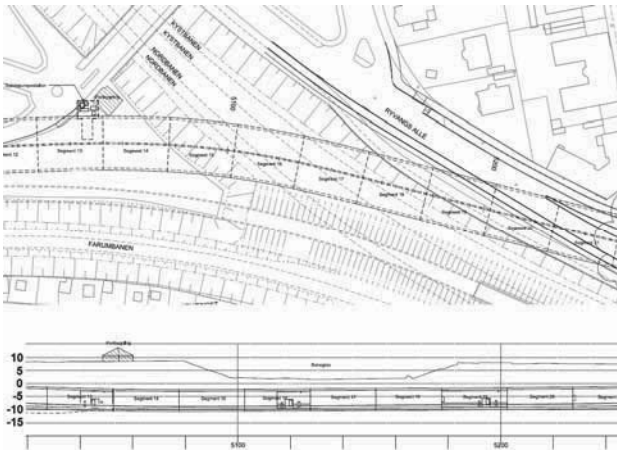


Figure 3. Plan and longitudinal section at the railway crossing.

As shown in Figure 3 the existing railway lines lies in a dell in the terrain. This dell is dug out in the glacial deposits when the railway lines were established.

## 3 GROUND CONDITIONS

The ground conditions at the railway crossing – and for the Nordhavnsvej project in general - are characteristic for the Copenhagen area.

### 3.1 Soil

Below a thin layer of fill, the intact soil generally consists of a 10-20m thick quaternary layer of firm clay till with encapsulated layers of melt water sand and gravel. Underneath the quaternary soils limestone is met where the upper 3m is assumed to be glacially disturbed.

As shown in Figure 4 the number of geotechnical investigations in the railway crossing is significant.

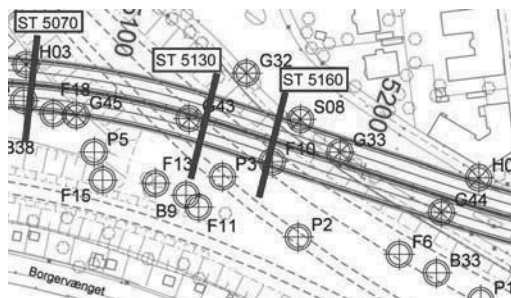


Figure 4. Plan of geotechnical investigations.

The soil parameters are determined from shear vane tests and SPTs carried out in the boreholes, triaxial and oedometer tests

performed in the laboratory on the clay till, VSPs and a priori knowledge of the soil conditions in general.

The sections in St. 5075, St. 5130 and St.5160 shown in Figure 4 indicates the three cross sections being design profiles/representatives for the railway crossing. Figure 5-6 show the assumed geological strata at these three sections

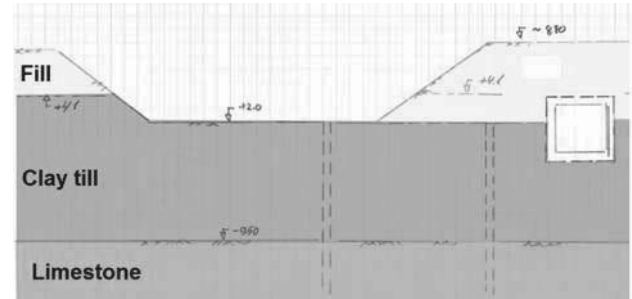


Figure 5. Geological stratum at St. 5075.

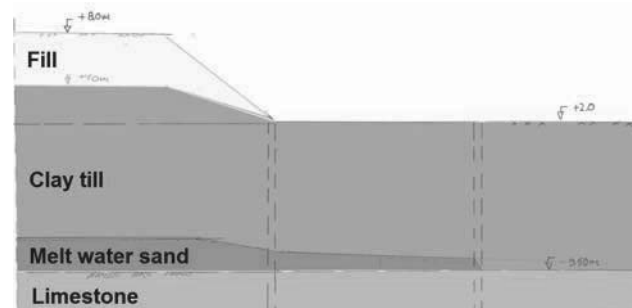


Figure 6. Geological stratum at St. 5130.

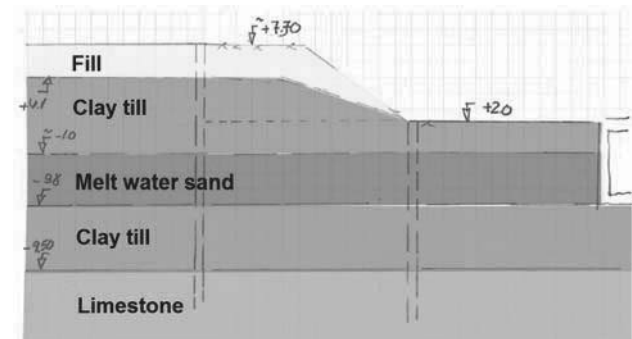


Figure 7. Geological stratum at St. 5160.

### 3.2 Ground water

At Nordhavnsvej the primary and secondary aquifers are separated. The primary aquifer is the limestone and the secondary aquifer is in the quaternary soils. The water levels are more or less coincident situated a few meters below original glacial ground level except at the railway crossing where the dell in the ground level causes the ground water level down to the terrain.

For the construction of the Nordhavnsvej tunnel it is necessary to lower the ground water level in the limestone temporarily to be able to build the permanent structures. Due to limitations on the allowance of lowering the ground water level in the secondary aquifer, a significant lowering and re-infiltration management system was established.

## 4 STRUCTURAL SOLUTION

Because of the requirement, that all four crossing railway lines must be in service in the complete construction period except for a few short closures, a number of different solutions to

respect that were considered during the early stages of the project, including pipe arching, top down and the chosen solution, being construction of four temporary steel bridges carrying each a railway line across an open construction pit, facilitating the tunnel to be build bottom up.

Since the railway lines cross the construction pit with rather small angles, the bridge spans are between approx. 40m and 70m. The bridges are prefabricated steel bridges founded on 2-5 bored piles below each bridge placed inside the pit, the retaining walls and concrete foundations with transition slabs at each end.

For safety reasons the bridges are connected in pairs to provide footpaths. Figure 8 shows a cross section in the bridges.

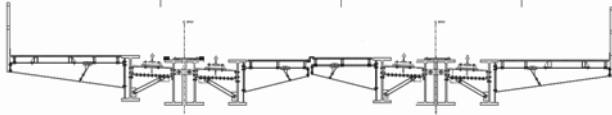


Figure 8. Cross section in temporary bridges.

The type of retaining wall is determined by the constructability in the very hard clay till and the limestone, containing significant amounts of boulders and flint respectively.

In the tender material a solution with steel sheet piles placed in a cement-bentonit slurry trench was prescribed, but during the optimization phase the contractor suggested to use secant pile walls, type hard-firm, since this method is already used outside the railway crossing and consequently well tested before constructing the retaining walls during the railway closure.

The secant piles are established with the Kelly method, cased until 0.5m below excavation level (diameter 1180mm) and below that uncased to the bottom (diameter 1080mm). The walls are staggered so that the firm piles are stopped 1.5m below excavation level. Hard piles are reinforced with 14 or 18pcs. K40 longitudinal reinforcement and K14 spiral shear reinforcement.

To avoid significant crushing works on the secant piles after establishing the tunnel, HEB profiles are casted into the top of the reinforced secant piles or the capping beam and timber lagging is used as infill, forming fixed soldier pile walls, which can easily be cut down and removed respectively. Figure 9 shows one of the encastered soldier pile walls.



Figure 9. Encastered soldier pile wall.

The support system in the railway crossing consist of two levels of walings and steel tube props, supplemented by ground anchors to balance the system where the ground level is significantly different on the two sides of the construction pit.

Where the terrain is at railway level, the upper waling is a concrete capping beam placed on top of the secant piles and attached to the piles by 5 threadbars per reinforced pile as shown in Figure 10. The solution is chosen because it is fast to wash away the upper (poor) concrete in the secant piles, place the prefabricated reinforcement cages for the capping beam and get it all casted together.

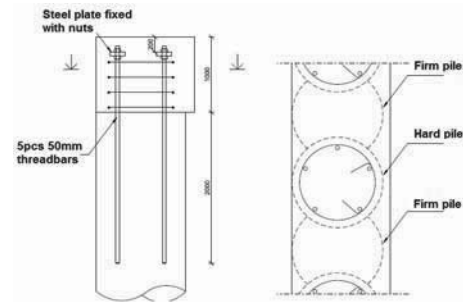


Figure 10. Connection between reinforced secant piles and upper capping beam.

The props in the upper support system are all steel types with 25mm thickness and diameters ranging from 610mm to 820mm and placed unevenly with distances of about 6-8m. The location of the props are of course governed by the capacities of the capping beams and props, but also by the location of the concrete beams spanning from the capping beam to the foundation piles supporting the rail bridges. Figure 11 shows the upper support system and support beams for the bridges and Figure 12 shows a picture of one of the support beams.

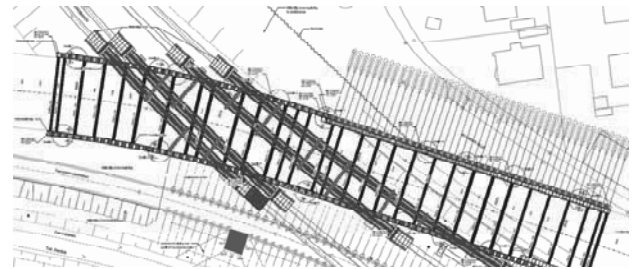


Figure 11. Upper support system and support beams.



Figure 12. Picture of support beam.

The props and walings in the lower support system are very temporary. As soon as the bottom slab of the tunnel is established, the props and walings are removed. Consequently a steel solution with double HEB-profiles and steel tube props is chosen, since the establishing and removing of this system is less time consuming than any concrete solution.

## 5 DESIGN

The design of the retaining walls and the support systems have been carried out using 2D numerical approaches since the effect of asymmetric loading is considerable; different terrain levels, different ground water levels and different loads on each side of the construction pit leading to props pushing excess force from one side to the other. For ULS analyses FEM have been used and cross checked with subgrade reaction models. In SLS small strain stiffness has been considered in FEM analyses.

To ensure that any 3D effects – like the partial loads from trains - were considered realistically in the 2D models, small 3D

FEM models were established and the results were incorporated in the 2D models.

Like for the geological strata, three representative structural cross sections were developed. The sections appear in Figure 13.

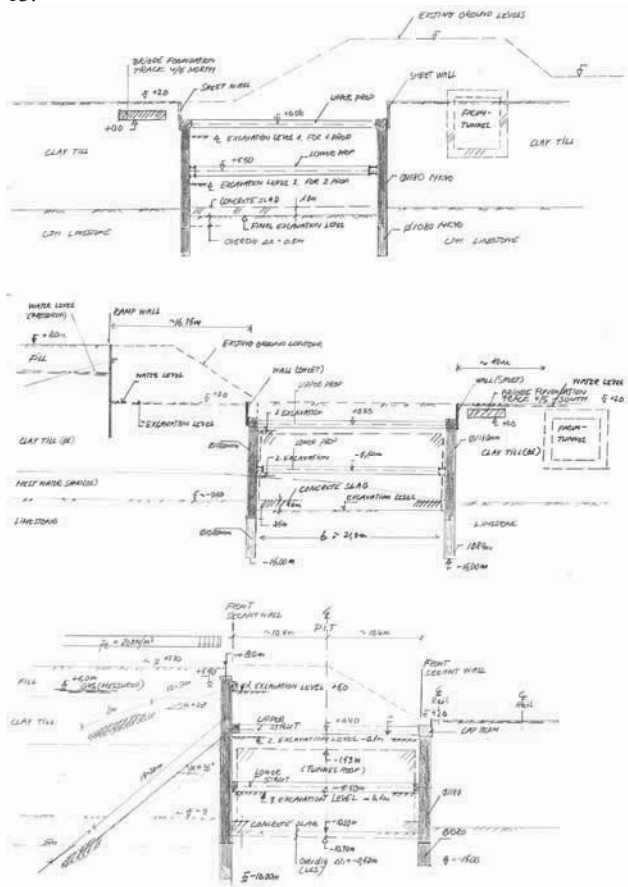


Figure 13. Representative structural cross sections.

The longitudinal reinforcement in the secant piles is checked to behave elastically in SLS, while in ULS and ALS plastic behavior is accepted. The shear reinforcement in the piles are designed using the crack sliding model for a circular cross sections, which is a further development of the plasticity-based crack sliding model originally developed for rectangular beams.

The distribution of sectional forces in props and walings are like the retaining wall design based on numerical methods, in this case spring models taking the stiffness of both the soil and the structural elements into account.

In addition to the load cases considered in the design of the secant pile walls the support systems are designed to withstand temperature loads on the props and the two ALS situations; unintended impacts from a single load and failure of a prop or anchor.

## 6 MONITORING

Due to strict requirements for deformations of the railway tracks and the aim to avoid structural damage to existing structures, a rather comprehensive monitoring program with accompanying action lists were developed. The monitoring includes; monitoring of rotations and deflections of the secant pile walls via measuring points and inclinometers installed on and in singled out piles, monitoring of forces in certain struts and ground anchors and monitoring of movements of foundations, railway sleepers and terrain in general. Furthermore of course the ground water heads in both the primary and secondary

aquifers are monitored. All monitoring data are stored in a database.

The measured deformations and forces are continuously compared to the expected magnitudes determined in the SLS analyses. In the analyses a number of combinations of different ground water and load conditions are investigated, leading to so called trigger levels for each measuring item in each construction stage. The trigger levels are threshold values of when certain actions must be taken or measures must be done. The trigger levels are presented on a number of drawings, so that they can easily be compared to the monitored conditions on site. Figure 14 shows an example of how the trigger levels are displayed (wall deflections when excavating for establishing of the lower support system at St. 5200).

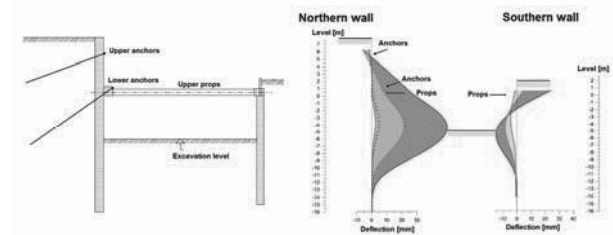


Figure 14. Example of trigger level display.

The monitoring is as a starting point performed with measurements on daily basis, but since most the measurements are performed automatically the frequency can easily be raised if any unexpected development in deformations and/or forces is recorded or lowered if no critical development is recorded.

## 7 CONCLUSIONS

To be able to construct the future Nordhavnsvej tunnel in Copenhagen, a construction pit with crossing railway lines and a tight construction schedule has been established.

Through corporation between Client, contractor and consultant the mission of not violating short and fixed closures was accomplished. Figure 15 shows a picture of the project stage in December 2012, where installation of the lower support system was ongoing.



Figure 15. Picture of the railway crossing, December 2012.

# Innovative Solution of King Post Walls combined with CSM Panels

## Solution Innovante de Parois Berlinoise combinée avec des Panneaux de CSM

Pinto A., Tomásio R., Godinho P.  
JetSJ Geotecnia Lda

**ABSTRACT:** The aim of this paper is to present the main design and execution criteria related with the innovative solution of earth retaining walls combining the King Post Walls (Berlin) with the CSM (Cutter Soil Mixing) panel's technology. A case study where the solution was applied is presented, confirming the solution excellent overall performance.

**RÉSUMÉ :** Dans cet article sont présentés les critères principaux de conception et d'exécution de la solution innovante qui combine des parois de soutènement (Berloinoise) avec de panneaux de CSM (Cutter Soil Mixing). Un cas d'étude avec ce type de solution est présenté, confirmant l'excellente performance globale de la solution.

**KEYWORDS:** cutter soil mixing, Berlin wall

## 1 INTRODUCTION

The traditional and widespread King Post Walls (Berlin) technology has some disadvantages, mainly the excavation schedule as well as the confinement reduction of the supported soil during the excavations works, mainly in cohesionless soils (Figure 1). In order to overcome this disadvantage, the Berlin solution can be combined with the CSM technology, which acts as a preliminary treatment of the supported soil.

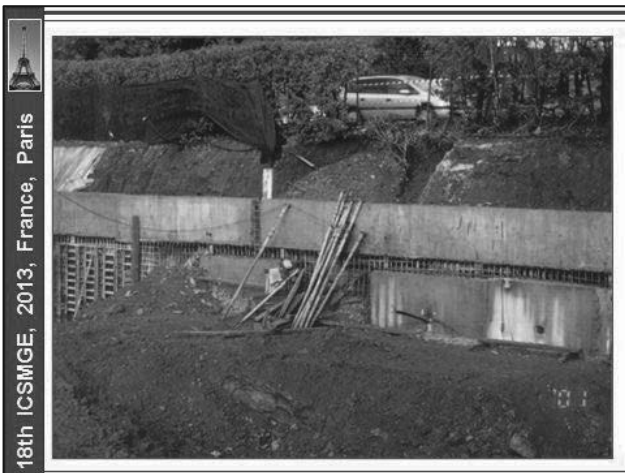


Figure 1. View of the confinement reduction of the supported soil during the excavation works using the Berlin Wall technology.

As an example of this combined solution the case of the enlargement of a railway platform, in order to accommodate the new infrastructures at the connection between two main railway lines in Lisbon, Portugal, is presented (Gomes Correia et al., 2013), following previous works using the CSM technology (Pinto A. et al., 2011). For this purpose it was necessary to perform several excavations with 13m of maximum depth. Due to neighbourhood conditions, three retaining structures (M1, M2 and M3) were built using the combination of Berlin wall with the CSM technology. In this paper the case of the M3 wall is presented, with 13m height and about 66m wide (Figure 2).

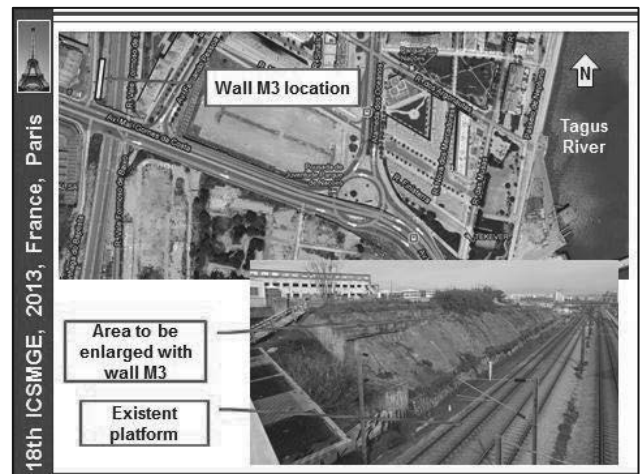


Figure 2. Wall M3 location.

## 2 MAIN CONDITIONS

### 2.1 Geological and geotechnical conditions

The local geological conditions were heterogeneous. The excavation works intersected, from the surface, heterogeneous landfills and Miocene medium dense to dense sands and sandstones. The ground water table was located about 5m above the final excavation level (Figures 3 and 6).

### 2.2 Other conditions

The main neighbourhood conditions included the existent railway lines (under operation and connecting the two Portuguese main cities), several industrial and sensitive buildings, located behind the walls, as well as the important viaduct of the Marechal Gomes da Costa Avenue, over the railway lines, pointing out the importance to control the walls deformation during and after the excavation works (Figure 4).

Geotechnical Conditions						
Geotechnical zone	Ground	SPT n	$\gamma$ kN/m <sup>3</sup>	E kPa	$\phi$	$c'$ kPa
ZG1	Fills	-	19	10.000	22	0
ZG2	Medium compacted sands	20	20	20.000	33	0
ZG3	Dense sands and sandstones	60	21	35.000	35	0
CSM panels			22	1.000.000	600	35

Ground water table was observed at a depth of about 10m, some times above the final excavation level

Figure 3. Main geotechnical conditions.

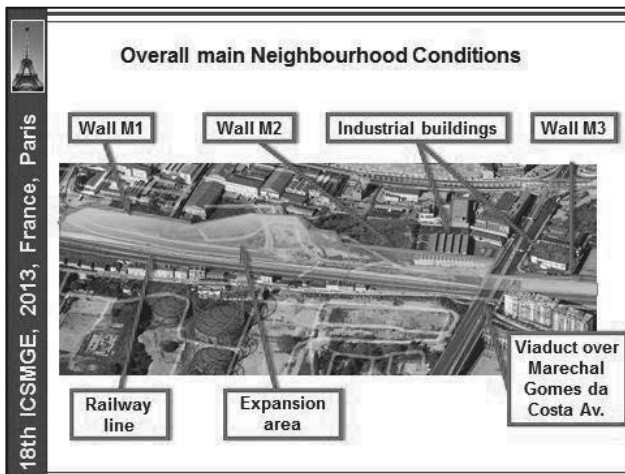


Figure 4. Overall main neighbourhood conditions.

### 3 ADOPTED SOLUTION

In order to allow the excavation works minimizing the ground loss of confinement effect, soil - cement panels with a maximum depth of about 18m and a cross section of 2,4 x 0,5m<sup>2</sup>, including 0,20m of overlapping, were preliminarily built using the CSM technology. The panels were reinforced with vertical IPE240 hot rolled steel profiles (Euronorm 19-57), spaced in average 1,1m, in order to resist to the earth and ground water pressures, as well as to assure a better control of the retaining structure deformations (Figure 5).

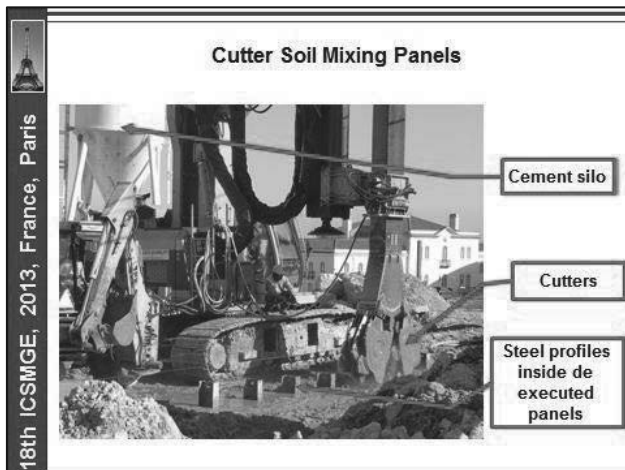


Figure 5. Execution of the soil - cement panels using CSM technology.

The steel profiles were placed inside the soil - cement panels, before the cement started the curing process, and were braced by four or three levels of permanent ground anchors, applied at the reinforced concrete capping beam, as well as at the distribution beams (Figures 6, 7 and 8).

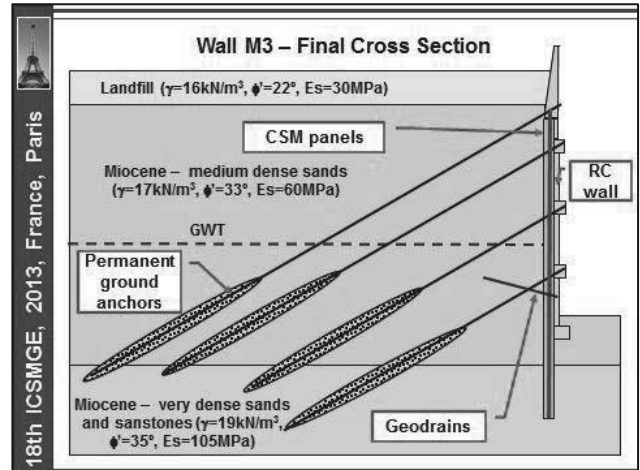


Figure 6. Final cross section of the wall M3.

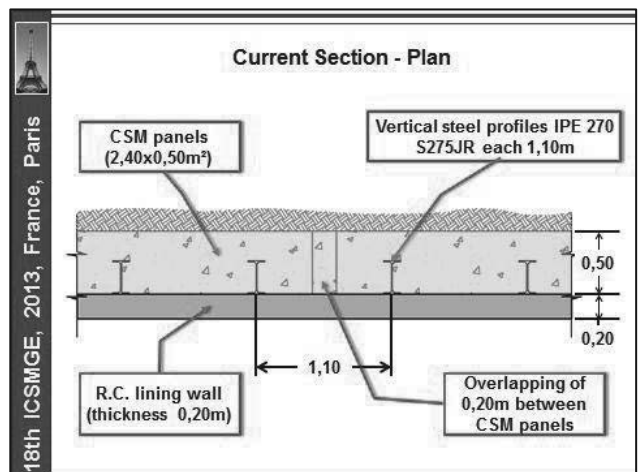


Figure 7. Plan of the wall M3 current section.

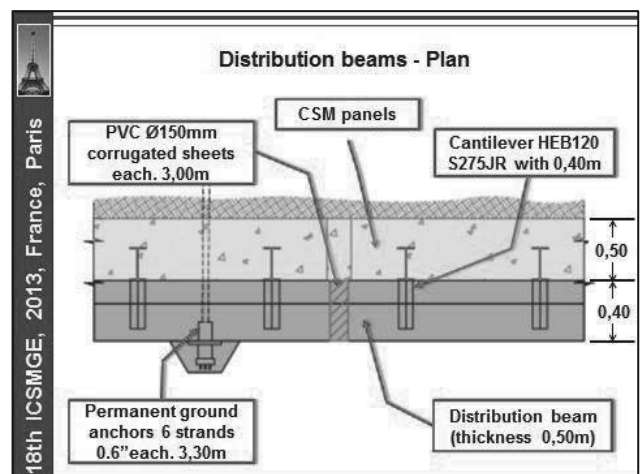


Figure 8. Plan of the wall M3 at the distribution beams section.

As already stated, according to the innovative solution combining the Berlin wall with the CSM technology, the soil - cement panels were designed in order to be integrated on the final earth retaining solution, including the 0,2m thickness lining reinforced concrete (RC) wall and beams (capping and distribution), and also to minimize the water inflow to the

excavation platform (Figure 7, 8 and 9). The preliminary ground improvement effect due to the soil - cement panels allowed the execution of the excavation works without any restrictions, with big advantages on the excavation works schedule, as well as on the RC wall finishing face (Figure 9).

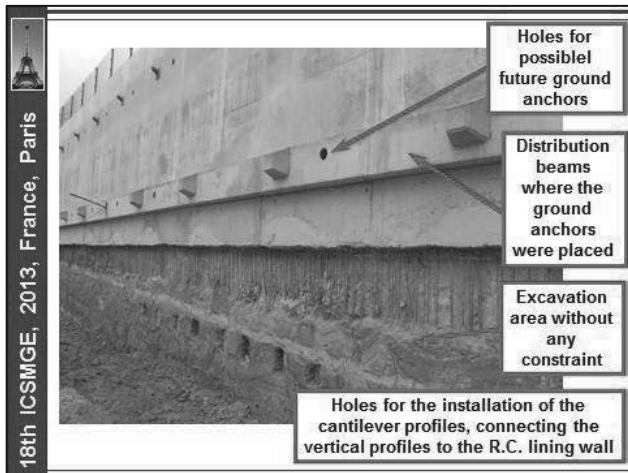


Figure 9. Plan of the wall M3 at the distribution beams section.

The combination of the soil - cement panels with the lining RC wall allowed the construction of a safe and economical solution, overcoming the main disadvantages of the Berlin wall solution (initial solution proposed for the same Project) and spreading the solution application field to almost every kind of geological and geotechnical scenarios, as well as to complex and sensitive neighbourhood conditions.

#### 4 MAIN CONSTRUCTION PHASES

One of the main advantages of the adopted solution was the possibility to reduce the excavation works overall schedule and also to decrease the loss of confinement of the excavated soil and, consequently, to decrease the wall and the neighborhood structures and infrastructures deformations.

The main construction phases are presented on the Figures 10 to 15. As already stated, it should be pointed out the big advantage of the full width excavation, in each level, only possible due to the soil - cement panels ground improvement effect, leading to a big optimization of the construction overall schedule. Due to the versatility of the CSM technology, it should also be pointed out the possibility to apply this solution to almost every kind of geological and geotechnical scenarios, ranging from heterogeneous landfills and soft soils to medium weathered rocks, like the sandstones intersected on present site.

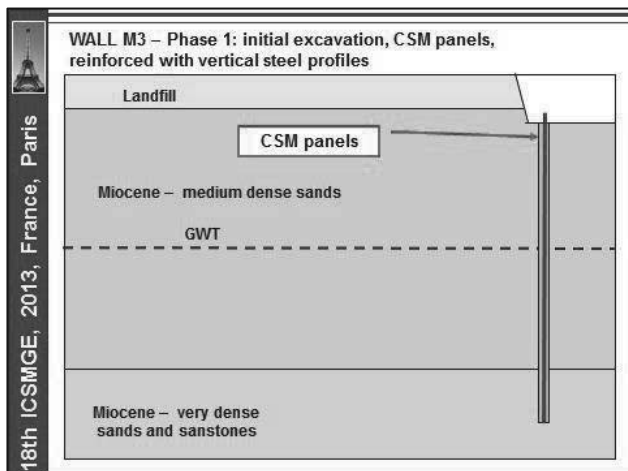


Figure 10. Phase 1.

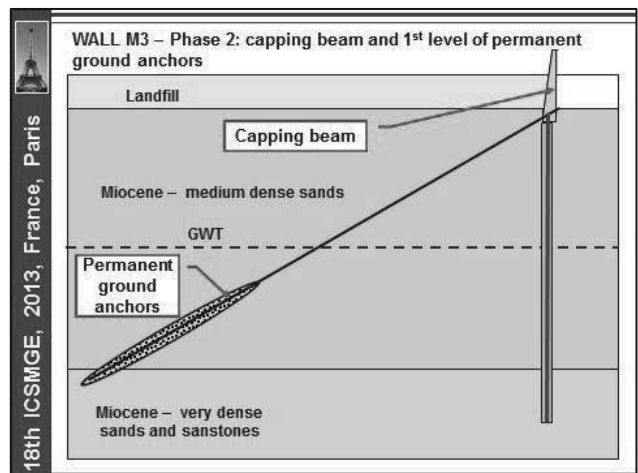


Figure 11. Phase 2.

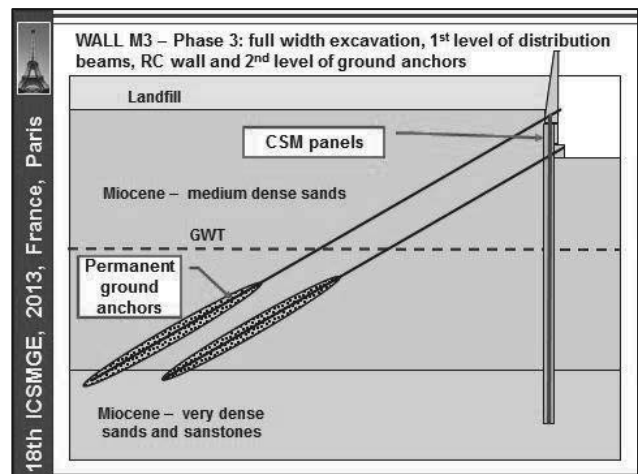


Figure 12. Phase 3.

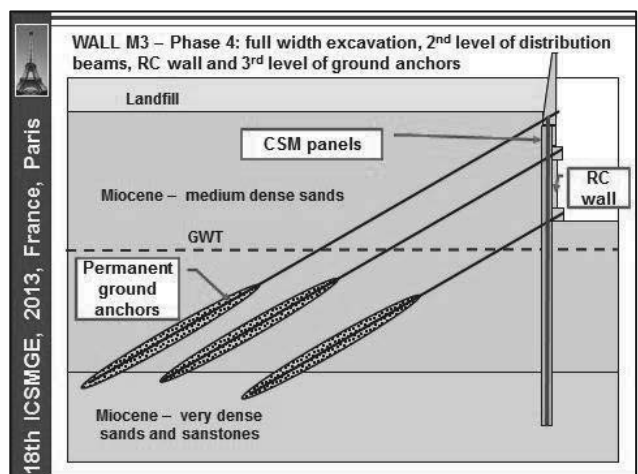


Figure 13. Phase 4.

A tight quality control and quality assurance of the main geotechnical works: soil - cement panels using CSM technology and permanent ground anchors, was implemented, including UCS tests on soil - cement cores and suitability and reception tests on permanent ground anchors (Gomes Correia et al., 2013).



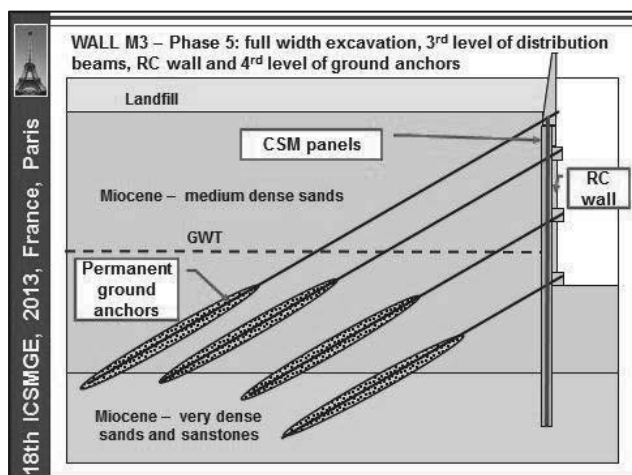


Figure 14. Phase 5.

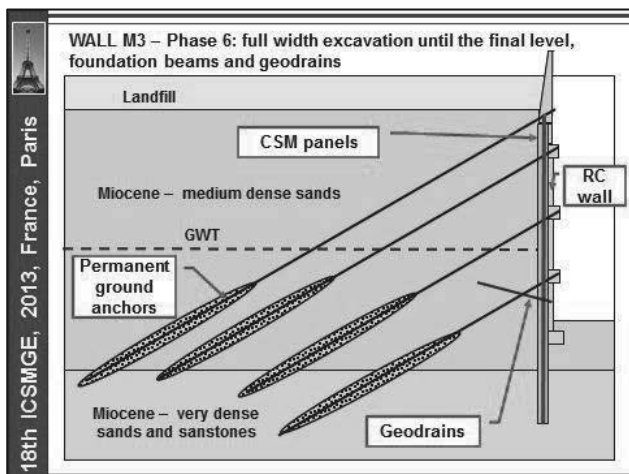


Figure 15. Phase 6.

## 5 DESIGN

All the soil - cement panels were design in order to achieve an unconfined compression resistance of at least 4,0MPa and a Young Modulus of 1GPa. Due to the soil and water chemical properties, pozolanic cement was adopted. For the design of the adopted solution FEM analysis was carried out, using Plaxis 2D software. The maximum estimated horizontal displacement was about 64mm due to the most critical seismic action (Figure 16).

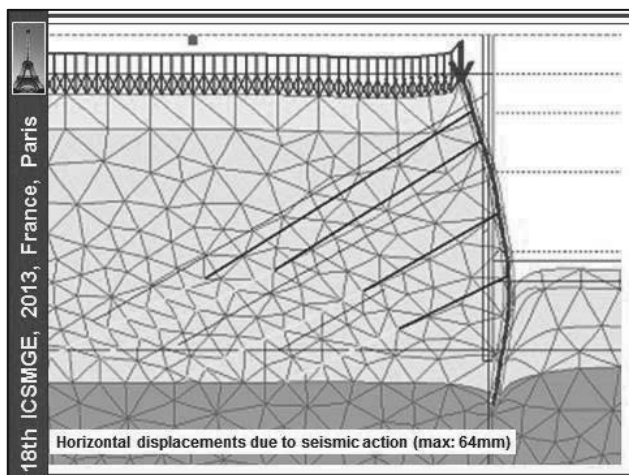


Figure 16. Horizontal displacements according to the FEM model.

## 6 MONITORING AND SURVEY PLAN

Considering the innovative aspects of the described solutions, a tight monitoring and survey plan was applied, taking into account the need to perform the construction in safe and economic conditions, for both the site and the neighbourhood conditions. In order to accomplish this goal the following equipment's /devices were installed: inclinometers (11un.), topographic targets (65un.) and ground anchors load cells (22un.). Measurements confirmed the excellent overall behavior of the adopted solution, confirming the importance of the previous confinement on the supported soil due to the soil - cement panels, leading, in general, to lower deformations than the ones predicted at the design stage, in spite of some anomalous movements, as presented on Figure 17.

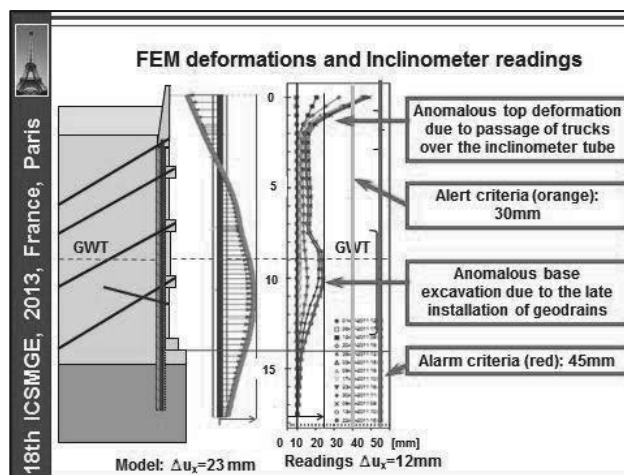


Figure 17. Comparison between predicted FEM deformations and inclinometer readings for static actions.

## 7 MAIN CONCLUSIONS

As main conclusions it is possible to point out the following advantages of the adopted solution:

- Good confinement of the excavated soils, due to the preliminary ground improvement effect of the soil - cement panels, allowing a very high and safe construction rate;
- Low deformations as confirmed by the monitoring.
- Good wall finishing face and water tightness.
- Environmental advantages associated to the CSM technology, minimizing the excavated ground volume.
- Application field to almost every kind of geological and geotechnical scenarios, as well as to complex and sensitive neighbourhood conditions.

## 8 ACKNOWLEDGEMENTS

The authors are grateful to the owner of the walls, REFER, for his permission to the presentation of this paper. The construction works were performed by OBRECOL (general contractor) and GEORUMO (geotechnical contractor).

## 9 REFERENCES

- Gomes Correia A., Tinoco J., Pinto A. and Tomásio R., 2013. An Anchored Retaining Wall in CSM. *Proc. 18th European Conference on Soil Mechanics and Geotechnical Engineering*, Paris, France.
- Pinto A., Tomásio R., Pita X., Pereira A. and Peixoto A. 2011. Cutter Soil Mixing Solutions in Portugal on Hard Soils and Weak Rocks. *Proc. 15th European Conference on Soil Mechanics and Geotechnical Engineering*, September 2011, Athens, Greece, Part 2 - 3.3 - Ground Reinforcement, pp. 1037-1042.

# Unusual Geotechnical Solutions at the Leixões Cruise Terminal

## Solutions géotechniques inhabituelles au terminal de croisières de Leixões

Pinto A., Pita X., Neves M.

JetSJ Geotecnia Lda

Vaz J.

Dimstrut – Engenharia de Estruturas Lda

**ABSTRACT:** The aim of this paper is to present the main design and execution criteria related with both cofferdam and foundations solutions, using soil-cement panels, micropiles and bored piles in several applications, at the new Leixões Cruise Terminal, located at the Leixões Port, in Portugal. The Terminal building is being built with one basement on a marine environment, over very difficult geological and geotechnical conditions, which demanded the use of some unusual and integrated geotechnical solutions.

**RÉSUMÉ :** Dans cet article sont présentés les principaux critères de conception et d'exécution associés aux solutions des parois de soutènement et des fondations, utilisant panneaux de sol - ciment, micropieux et pieux forés, pour le nouveau Terminal de Croisières du Port de Leixões, au Portugal. Le bâtiment, avec un plancher au-dessous du niveau de l'eau est placé dans une ambiance maritime. Ce scénario complexe a demandé l'utilisation de quelques solutions géotechniques peu communes et intégrées.

**KEYWORDS:** cutter soil mixing, piles, micropiles.

### 1 INTRODUCTION

The construction of the new Cruise Terminal at Leixões, at the North of Portugal, as a consequence to the constant increase of the cruise traffic, was a challenge from both the geotechnical and structural point of views, mainly due to very difficult and unusual conditions, ranging from the geological and geotechnical scenario to the existent and under operation Leixões Port infrastructures, mainly the South break water, as well as the existent boarding deck (Figures 1 and 2).

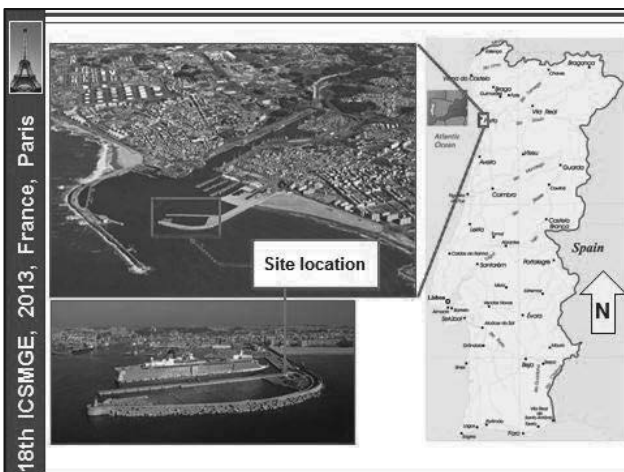


Figure 1. Site location.

According to the Terminal Project it was necessary to build one basement bellow the water table, including several earth retaining structures in order to allow the excavation works on dry conditions leading to a global cofferdam effect. For this purpose soil - cement panels, using CSM technology, reinforced with steel profiles, micropiles (both for foundation and cut off effect) and the existent sheet piles were used. Also pointed out are the adopted special foundations of a very complex structure, including bored piles and micropiles (Figure 3).

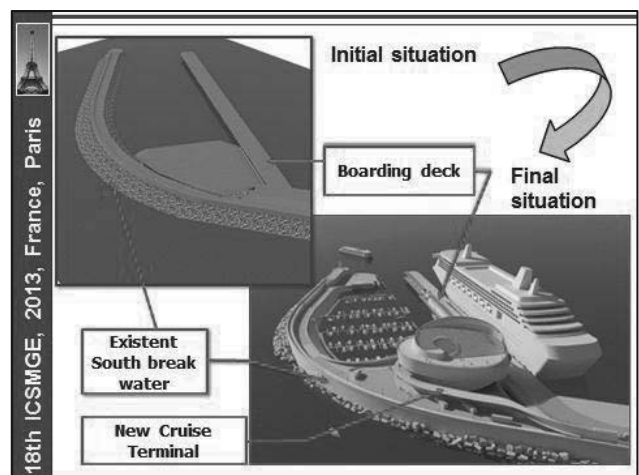


Figure 2. Existent and final situations.

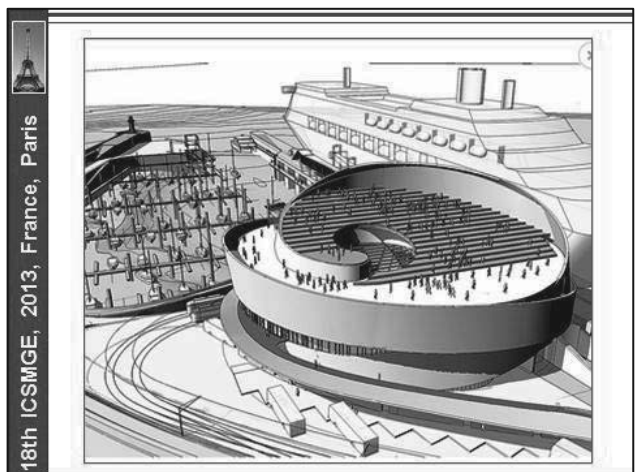


Figure 3. Perspective of the Cruise Terminal building.



2 MAIN CONDITIONS

2.1 Geological and geotechnical conditions

The local geological conditions were homogeneous, but very complex. The excavation works intersected, from the surface, level +5,0m, sandy and silty materials, correspondent to the hydraulic embankment created for working platform purpose. The embankment fill is resting over the bed rock, weathered schist, as previously to the construction of the embankment the existent alluvial material was dredged (Figures 4 and 5).

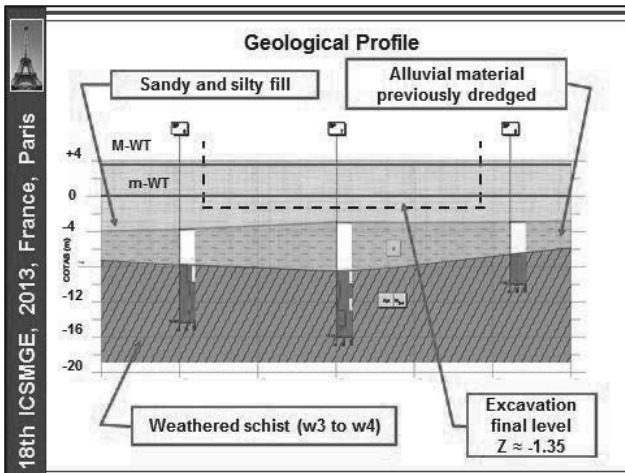


Figure 4. Geological profile.

The water table level ranged from +4,0m to -0,25m according to the Atlantic Ocean tide (Figure 5).

Main Geotechnical Parameters					
Geotechnical Zone	Ground	$\gamma$ [kN/m <sup>3</sup> ]	E [kPa]	$\phi$ [°]	c' [kPa]
ZG1	Sandy and silty fill	16	15.000	20	5
ZG2	Break water stones (rip rap)	22	60.000	25	10
ZG3	Schist	20	120.000	50	100

Water level ranged from +4,0m (high tide) to -0,25m (low tide)

Figure 5. Adopted geotechnical parameters.

2.2. Other conditions

The main neighbourhood conditions included the existent infrastructures, under operation, mainly: the South side break water, accommodating several infrastructures, and the East side cruises boarding deck, a reinforced concrete slab supported by reinforced concrete bored piles. When the embankment was constructed, a sheet pile wall was installed at the boarding border face, in order to improve the hydraulic embankment confinement (Figure 6).

The South side cofferdam walls, as well as of the South side special foundations had to intersect the break water rip rap (8kN to 130kN). This situation was confirmed as an important issue mainly for the execution of the cofferdam walls, as well as for the construction of the bored piles.

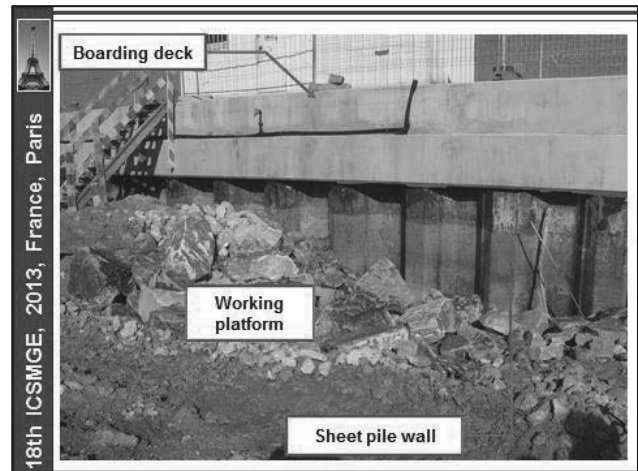


Figure 6. Main neighbourhood conditions: boarding deck.

3 ADOPTED SOLUTIONS

3.1 Global cofferdam

In order to allow the excavation works on dry conditions, three main retaining structures solutions were adopted (Figure 7).

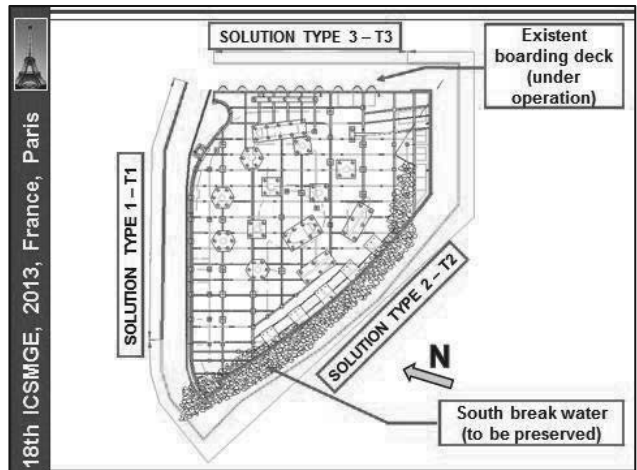


Figure 7. Adopted solutions for the global cofferdam.

Solution type 1 (T1): soil - cement panels with a cross section of 2,4 x 0,5m<sup>2</sup>, including 0,20m of overlapping and 1m of embedment at the bed rock, performed using the CSM technology (Figures 8 to 11), taking into account the experience obtained on previous works (Pinto et al., 2011).

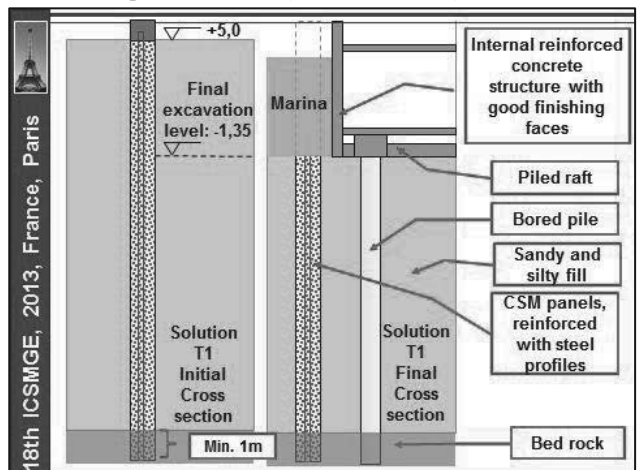


Figure 8. Solution T1 – initial and final cross section.

The soil - cement panels, with UCS resistance not lesser than 4MPa, were reinforced with vertical IPE330 steel profiles (Euronorm 19-57), spaced 0,55m in average, in order to resist to the earth and water pressures, as well as to ensure a better control of the deformations. The steel profiles were placed inside the panels, before the cement started the curing process and capped by a reinforced concrete beam (Figure 8 to 11).

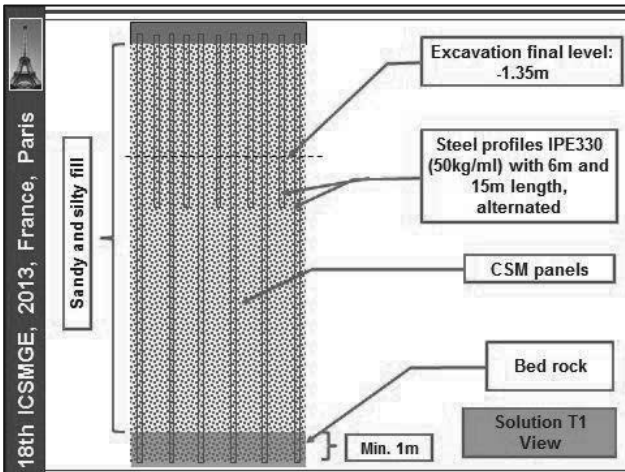


Figure 9. Solution T1 – view.

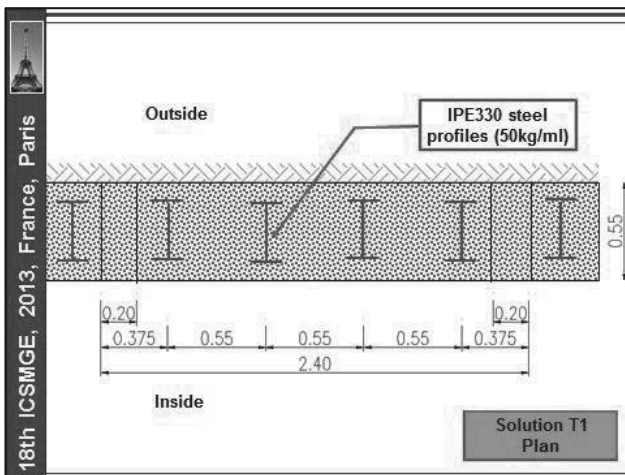


Figure 10. Solution T1 – plan.

The soil - cement panels will be demolished from the internal structure foundation level to the top, in order to allow the reinforced concrete (r.c.) wall with a very good finishing face, being visible from the adjacent marina, (Figure 12).

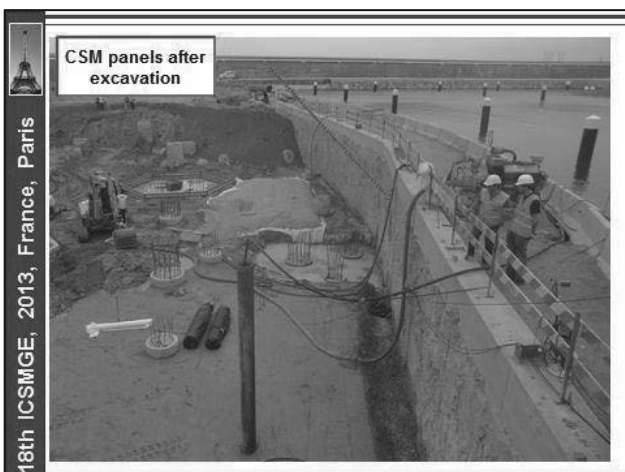


Figure 11. Solution T1 – view of soil-cement panels after excavation.

**Solution type 2 (T2):** soil - cement panels with a cross section of 2,4 x 0,5m<sup>2</sup>, including 0,20m of overlapping on a height of approximately 6.5m, correspondent to the previous excavation depth, performed in order to replace the break water rip rap by a sandy fill. The panels were built using the CSM technology. Below the soil - cement panels the cofferdam cut off effect was assured through a curtain, performed using alternated slurry cement injections through steel tubes and micropiles N80  $\phi$ 114,3x12mm, those also with foundation purposes and sealed 4m on the bed rock (Figures 12 to 15).

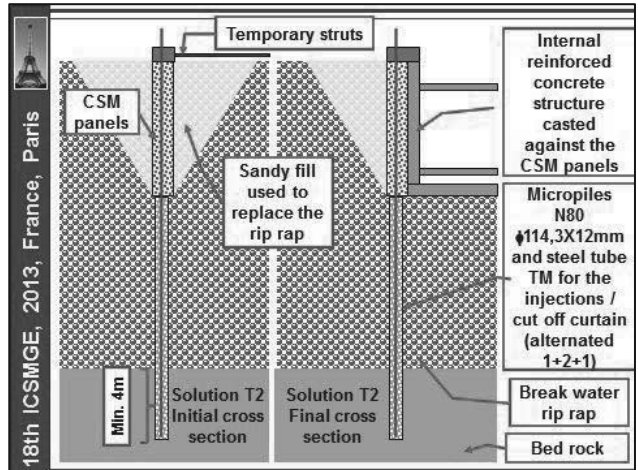


Figure 12. Solution T2 – initial and final cross section.

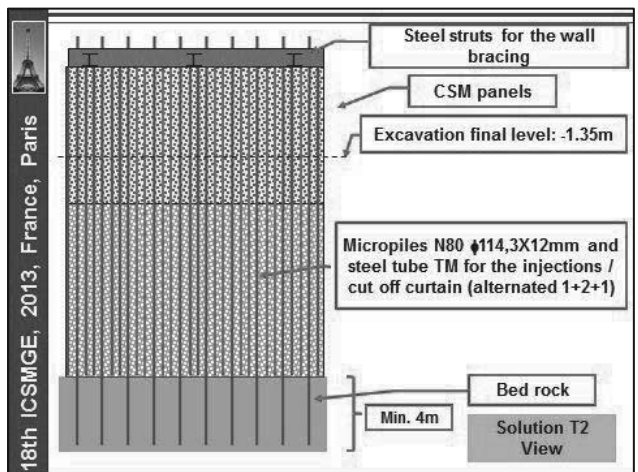


Figure 13. Solution T2 – view.

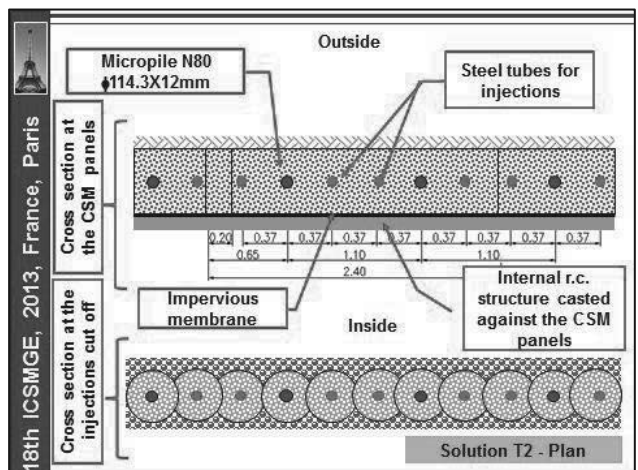


Figure 14. Solution T2 – plan.

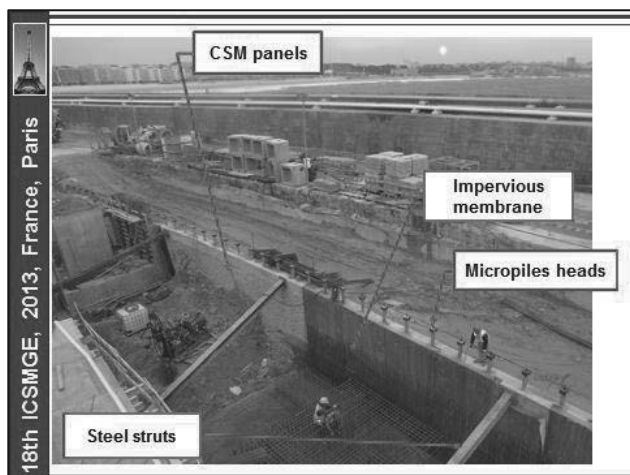


Figure 15. Solution T2 – soil - cement panels after excavation.

Solution type 3 (T3): the existent sheet pile wall was integrated on the global cofferdam, using a bracing system, steel ties, connected to the head of the boarding deck foundation piles (Figure 16).

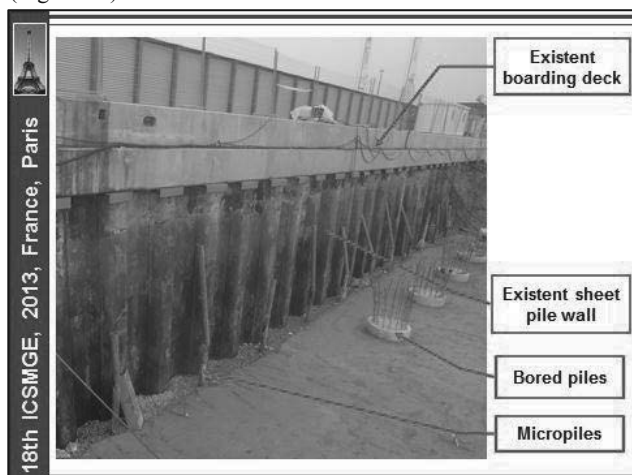


Figure 16. Solution T3 – view of the sheet pile wall after excavation.

### 3.2 Foundations

For the foundations of the Terminal building reinforced concrete bored piles ( $\phi 800\text{mm}$  and  $\phi 1200\text{mm}$ ) and steel micropiles N80  $\phi 139,7 \times 12\text{mm}$  were adopted. Micropiles were used also to resist to both light compression and tension loads, when the structure self-weight was not enough to equilibrate the hydrostatic pressures. Micropiles were designed against corrosion taking into account a sacrificial thickness. All the piles and micropiles were capped by a reinforced concrete raft, cast against an impervious membrane.

## 4 DESIGN

For the design of the adopted solutions, earth retaining structures and foundations, 2D, including axisymmetric, FEM analysis was carried out, using Plaxis software (Figure 17).

## 5 MONITORING AND SURVEY PLAN

A monitoring and survey plan was applied taking into account the need to perform the construction in safe and economic conditions, including inclinometers and topographic marks. Measurements confirmed the excellent overall behavior of the adopted solution, with the exception of a local area at solution T1, demanding the implementation of strengthening measures:

inclined steel struts connecting the capping beams to the foundations piles (Figure 18).

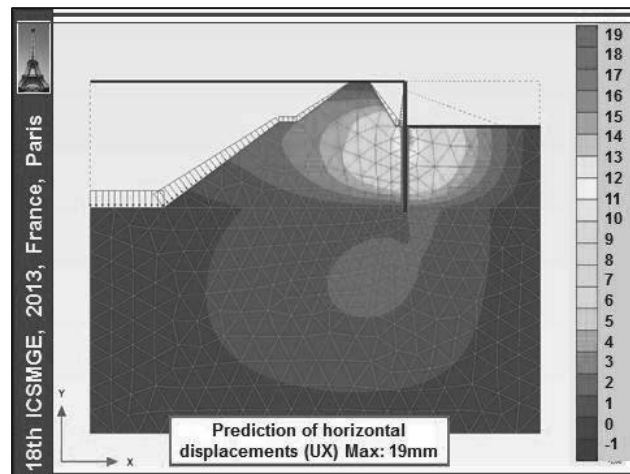


Figure 17. 2D FEM analysis for section T1.

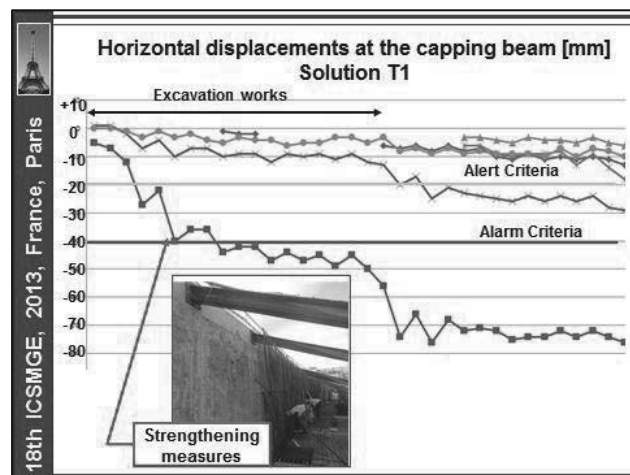


Figure 18. Horizontal displacements at topographic marks - solution T1.

## 6 MAIN CONCLUSIONS

Taking into account the complex scenario of the presented work, it is possible to point out the following points:

- Good water tightness, mainly due to the cofferdam effect assured by the embedment of the soil - cement panels at the bed rock, as well as due to the injections cut off curtain.
- Low deformations, confirmed by the monitoring results.
- Peripheral r.c. walls with very good finishing faces.

Also very important was the control of both costs and construction schedule.

## 7 ACKNOWLEDGEMENTS

The authors are grateful to the owner of the Terminal building, APDL (Administração do Porto de Leixões), for his permission to the presentation of this paper. The construction works were performed by OPWAY and FERREIRAS (general contractors) and GEORUMO and HAGEN (geotechnical contractors).

## 8 REFERENCES

Pinto A., Tomásio R., Pita X., Pereira A. and Peixoto A. 2011. Cutter Soil Mixing Solutions in Portugal on Hard Soils and Weak Rocks. *Proc. 15th European Conference on Soil Mechanics and Geotechnical Engineering*, September 2011, Athens, Greece, Part 2 – 3.3 – Ground Reinforcement, pp. 1037–1042.

# Aspects on designing and monitoring a deep excavation for a highly important structure

Aspects de conception et de suivi d'une excavation profonde d'une très importante structure

Popa H., Manea S., Batali L., Olteanu A.

*Technical University of Civil Engineering of Bucharest, Geotechnical and Foundations Department, Romania*

**ABSTRACT:** Building large and deep excavations in urban areas is always a complex problem. The geotechnical investigation should be very detailed and the design rigorous. As well, the monitoring of such a work is mandatory. The paper presents a retaining structure from Bucharest, Romania for a deep excavation of 66 x 127 m size in plan and a maximum depth of over 16 m. This open pit was required for building the infrastructure of the largest Cathedral in Romania, the National Redemption Cathedral. The paper presents aspects regarding the geotechnical investigations and interpretation, soil parameters, calculation of the diaphragm wall, anchors and dewatering system, as well as displacement monitoring.

**RÉSUMÉ :** Les excavations profondes et de grandes dimensions réalisées en milieu urbain représentent toujours un problème complexe. L'investigation géotechnique doit être très détaillée et la conception rigoureuse. De même, le suivi d'un tel ouvrage est obligatoire. L'article présente une structure de soutènement de Bucarest, Roumanie pour une fouille de plus de 16 m de profondeur et ayant 66 x 127 m dimension en plan. Cette excavation a été nécessaire pour construire l'infrastructure de la plus grande Cathédrale de Roumanie, la Cathédrale de la Rédemption du Peuple. L'article présente des aspects concernant l'investigation géotechnique et son interprétation, les paramètres du sol, le calcul de la paroi de soutènement, des ancrages et du système de rabattement de nappe, ainsi que le suivi des déplacements.

**KEYWORDS:** retaining structure, diaphragm wall, deep excavation.

## 1 INTRODUCTION

At the present, in Bucharest is under construction the larger orthodox cathedral in Romania, the National Redemption Cathedral. The location of the Cathedral is in the city centre, next to another very large building, the People's House, on a high area called the Arsenal Hill.

The size of the future Cathedral is: length and height of more than 120 m and a width of over 60 m. The Cathedral basement has 2 stories and the total surface of the future cathedral plus the adjacent buildings is of about 11 000 sqm. Figure 1 presents the photo of the concept design of the future cathedral.



Figure 1. Concept design of the future National Redemption Cathedral.

Based on previous analyses of various foundation solutions it was chosen as final solution a cellular raft (basement walls as part of mat) of 4 – 6 m thickness. The raft thickness plus the basement height led to the necessity of excavating a pit of up to

16 m depth. Taking into account the pit depth, as well as its large size (~ 127 m x 66 m) it was chosen as retaining structure a diaphragm wall supported by anchors.

The Cathedral project, including also the deep excavation retaining structure has been submitted to a national contest for choosing the best option.

Paper presents aspects regarding the geotechnical investigation of the site, the design of the diaphragm walls, construction and monitoring the deep excavation.

## 2 SITE INVESTIGATION

Geotechnical investigation was performed in two stages:

- a preliminary geotechnical study (2008) based on which several preliminary projects were drawn in order to participate to the national contest;
- after selecting the best project, a new detailed geotechnical study was performed by the Technical University of Civil Engineering of Bucharest for the final design of the Cathedral foundations and open pit diaphragm walls.

This geotechnical study comprised the following site investigations: 8 boreholes 25 – 70 m deep, SPT tests, hydro-geological measurements (permeability, analysis of the groundwater flow regime).

Laboratory tests comprised static and cyclic triaxial tests, for determining both shear strength and dynamic parameters of soils. As well, were carried out tests with various stress paths, with unloading – reloading cycles for determining the calculation parameters for the retaining wall. Table 1 presents the main soil parameters obtained from the site and laboratory investigations.

Table 1. Geotechnical parameters

layer	thickness, m	$E_{oed}$ , MPa	$\frac{E_d}{G_d}$ , MPa	$k_o$	$\phi'$ , °	$c'$ , kPa	$N_{SPT}$
1 man-made fill	0.6-2.8	-	-	-	-	-	-
2 silty clay	11.4-16.2	7-16	$\frac{56.5}{19.5}$	0.6-0.7	16-23	51-92	10-34
3 sand, gravel	0.9-6.9	30*	-	0.4	35*	-	16-33
4 clay	10.5-16	8.3-11.7	$\frac{54.5}{18.9}$	0.7	9-20	61-113	11-39
5 sand	6.7-7	40*	$\frac{57.8}{20.2}$	0.5	30*	-	23-59
6 clay	21.7-27.8	-	$\frac{71.2}{-}$	-	14	141	-

\* - values estimated from SPT tests.

where:

- $E_{oed}$  – oedometric modulus, corresponding to 0.2-0.3 MPa stress interval;
- $E_d, G_d$  – linear deformation modulus and shear modulus for 300 kPa stress;
- $k_o$  – at rest earth coefficient;
- $\phi', c'$  - drained shear strength parameters;
- $N_{SPT}$  – number of blows from SPT test.

Hydro-geological study emphasized two aquifers: a free level aquifer (layer 3) and a second confined aquifer (layer 5). The excavation will be 2 – 3 m below the groundwater level.

### 3 RETAINING STRUCTURE

#### 3.1 Geometrical and technological characteristics

The deep excavation was retained using diaphragm walls 80 cm thick, with variable length, from 20 m to 24 m. The lower level of the wall remained constant (+60.50 m), while the upper level varied according to the architectural details of the basement and adjacent buildings (+84.50 m along the long sides and +80.50 m along the short sides of the pit).

Figure 2 presents a layout of the diaphragm wall enclosure and the final excavation levels.

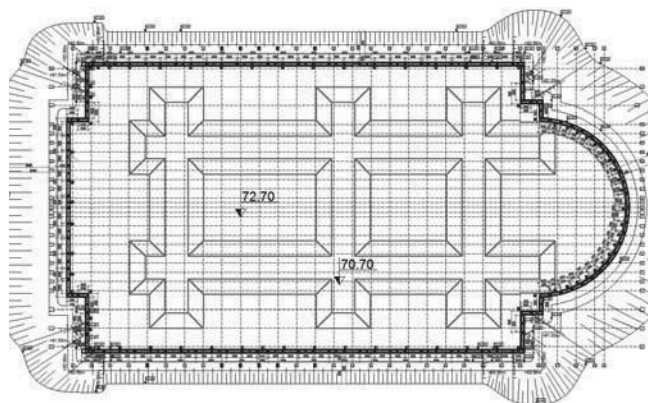


Figure 2. General layout of the diaphragm wall enclosure

The natural ground level varies on the site around +87.0 m, so for the working platforms required for the diaphragm walls execution, a sloped excavation was realized. The final

excavation levels are +72.7 m and +70.7 m (for the 6 m thick raft area), respectively, which led to a maximum excavation level of approx. 16.3 m below the ground level.

It can be seen that the foundation level of the raft is in the sand and gravel layer (layer 2).

The temporary support of the diaphragm wall was ensured using 2 or 3 levels of anchors. The total length of the anchors was comprised between 20 m and 25 m. In the corners were used metallic struts and wale beams.

Figure 3 presents a cross section through the diaphragm wall for the sides with 3 anchor levels.

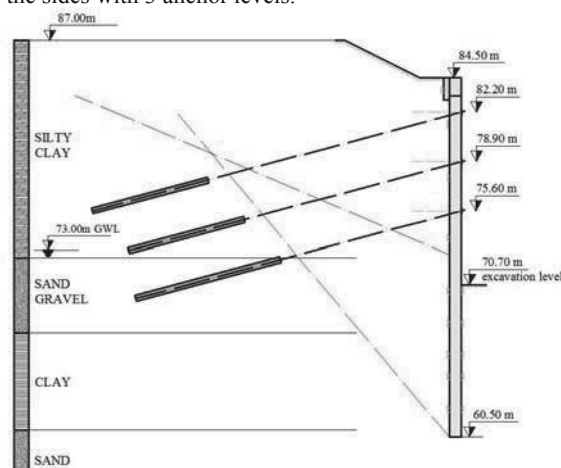


Figure 3. Cross section through the diaphragm wall

For the anchors on 3 levels the characteristics are the following:

- Anchors level 1: +82.20 m
  - inter-axis distance: ~ 1.75 m
  - number of strands in each anchor: 4
  - maximum pull-put force / anchor estimated by calculation (ULS) = 200 kN
- Anchors level 2: +78.90 m
  - inter-axis distance: ~ 1.75 m
  - number of strands in each anchor: 4
  - maximum pull-put force / anchor estimated by calculation (ULS) = 250 kN
- Anchors level 3: +75.60 m
  - inter-axis distance: ~ 1.20 m
  - number of strands in each anchor: 6
  - maximum pull-put force / anchor estimated by calculation (ULS) = 320 kN.

As it can be seen on figure 3, the lowest level of the pit base is 3.0 m below the groundwater level. The soil permeability and the ground level differences led to a water flux in the enclosure of about 90 l/s, unevenly distributed, being higher on the Southern side. Considering these conditions, a dewatering system was designed, comprising 12 wells disposed along the enclosure sides.

#### 3.2 Diaphragm wall calculation

Diaphragm wall calculation was done based on Eurocode 7 (SR EN 1997-1:2004 and the Romanian National Annex SR EN 1997-1/NB). According to the National Annex in Romania, the calculations were performed for design approaches 1 and 3, approach 2 not being recommended by this document.

As well, according to the Romanian technical norm for retaining structures (NP 124-2010), the seismic action was considered on the wall. The seismic coefficient was decreased considering the temporary character of the retaining structure, according to the same technical norm.

Figure 4 shows some of the results obtained for the stresses in the diaphragm wall, corresponding to the side with 3 levels of anchors, for ULS calculation. Calculations were performed

according to technological stages (excavation and installation, anchors pretension) up to the final excavation level.

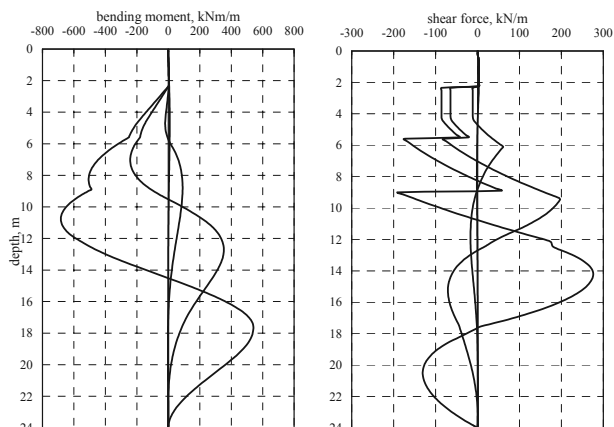


Figure 4. Bending moment and shear force in the diaphragm wall

Figure 5 shows the horizontal displacements of the wall corresponding to the same calculation stages (SLS calculation). It can be seen that the maximum displacements are less than 10 mm, which was confirmed by the inclinometer measurements, presented figure 11.

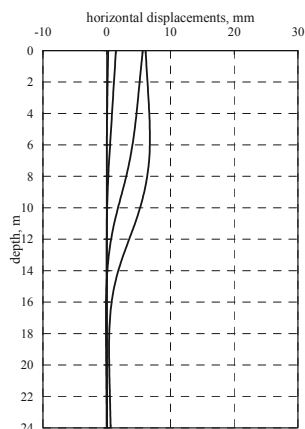


Figure 5. Horizontal displacements of the diaphragm wall

### 3.3 Aspects during the diaphragm wall execution

Figures 6...9 present some photos taken during the execution of the deep excavation.



Figure 6. Installing the reinforcement cage of the diaphragm wall



Figure 7. Installation of the first level of anchors



Figure 8. Final stage of excavation



Figure 9. Lead waterproofing

As it can be seen in photo figure 9, prior to build the raft a waterproofing layer has been laid on the excavation base. Considering the life time of the cathedral of minimum 500 years, the waterproofing was done with lead, being the only solution guaranteed on such long time. From this point of view, this solution is new for Romanian civil engineering.

### 3.4 Monitoring the diaphragm wall

The enclosure monitoring was performed by measuring:

- vertical displacements of the wall - measured at the linking beam level using geodetic methods;
- horizontal displacements of the wall - measured at the linking beam level and along the wall depth using inclinometer measurements;
- outflow from the dewatering wells;
- groundwater level inside and outside the enclosure.



Regarding the inclinometer measurements, these were carried out using 6 tubes located in various areas and along different sides of the diaphragm wall (4 on the sides with 3 anchors level and 2 along the sides with 2 anchor levels). A cross section showing the position of the inclinometer tube inside the diaphragm wall is presented in figure 10.

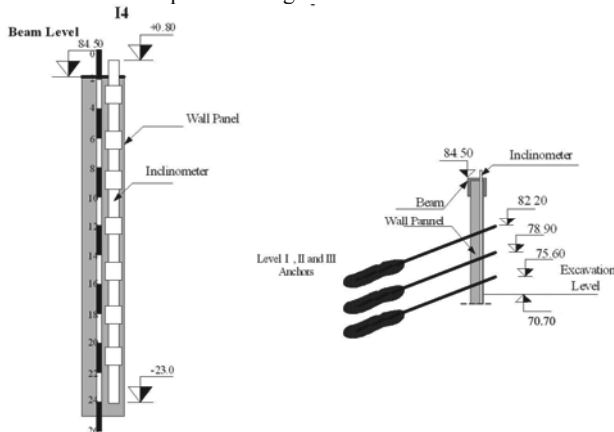


Figure 10. Inclinometer location inside the diaphragm wall

The monitoring of the anchored structure was carried out from April 15 2011 until January 12 2012. The activity during the 9 months of monitoring was according to the technological stages of the excavation works and retaining structure.

The frequency of monitoring activity was established according to preliminary stages of infrastructure works. Due to the construction progress, changes in construction technology flow on site (adjacent traffic infrastructure, frequency and tensioning of anchors system, etc.), weather changes (temperatures on 2012 winter) the frequency of the measurements was increased.

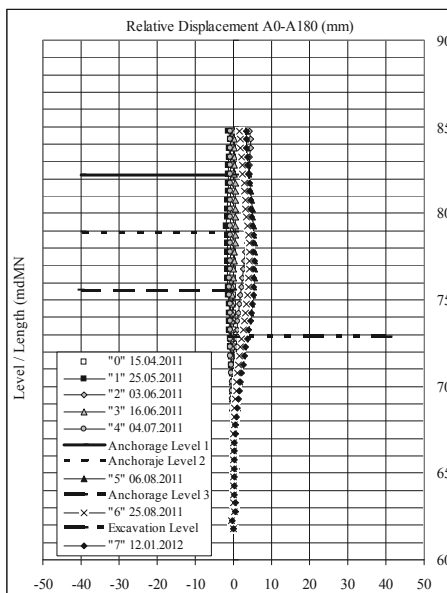


Figure 11. Inclinometer measurements for the diaphragm wall

The main purpose of monitoring activity was to verify design assumptions regarding the deformations of the structure, but also to provide detailed information on the effect induced by the anchors on the retaining wall.

Figure 11 presents a graph of the measured lateral displacement of the wall for the side with 3 anchor levels.

According to measurements, the maximum horizontal displacement of the diaphragm wall didn't exceed, on all sides, 10 mm, confirming the estimation by calculation.

#### 4 CONCLUSIONS

Designing and building a retaining structure for a deep excavation in urban area is always a challenge, taking into account the associated risks. The characteristic parameters of interaction are numerous and their control difficult. For this reason the approach of such works should be done carefully during all stages: geotechnical investigation, design, execution and service.

Paper presents a case study for a deep excavation in centre Bucharest required for the construction of the Redemption Cathedral, which was approached according to Eurocode 7. Considering its size and the supporting system using anchors, this excavation is among the largest in Romania. The anchor supporting system allowed a space-free enclosure and the infrastructure works took place very rapidly.

The work was classified as in geotechnical category no. 3, which imposed a complex approach also from geotechnical investigation, as from design point of view. The execution was permanently monitored and the measurements were compared with the calculations, allowing a rapid intervention if the real behavior would be different from the estimated one.

#### 5 ACKNOWLEDGEMENTS

Authors acknowledge The Romanian Patriarchy and to SC Alfel Construct SRL (general designer) for allowing this paper to be published and for providing some of the data used in this paper.

#### 6 REFERENCES

- SR EN 1997-1:2004 Eurocod 7: Proiectarea geotehnică. Partea 1: Reguli generale.
- SR EN 1997-2:2007 Eurocod 7: Proiectarea geotehnică. Partea 2: Investigarea și încercarea terenului.
- SR EN 1997-1:2004/NB:2007 Eurocod 7: Proiectarea geotehnică. Partea 1: Reguli generale. Anexa națională.
- NP 124-2010 Normativ privind proiectarea geotehnică a lucrărilor de susținere.

# FEM-aided design of a novel device for soil anchoring

## Conception assistée par éléments finis d'un nouveau système pour l'ancrage des sols

Prisco di C., Pisanò F.  
*Politecnico di Milano*

**ABSTRACT:** In this paper the pull-out performance of an innovative system for soil anchoring is mechanically interpreted on the basis of a preliminary finite element investigation. The system consists of a tie rod equipped with thick steel sockets, extruding into the soil to increase the overall pull-out bearing capacity. The effectiveness of the anchorage comes from two correlated strength mechanisms: a direct one, associated with the shear/flexural strength of the sockets themselves; and an indirect one, in the form of a remarkable increase in the normal confinement on the tie rod and hence in the available shear strength. Finally, the numerical results are exploited to conceive a design-oriented analytical model for the prediction of the pull-out bearing capacity.

**RÉSUMÉ:** Dans cette article, le comportement en tension de un nouveau système pour l' ancrage dans les sols est interprété sur la base de une analyse préliminaire avec les éléments finis. Dans le système il y a une bar en métal avec des puntons qui s'extrudent dans le sol pour augmenter la capacité totale de l'instrument. L'efficience de l' ancrage dérive de deux mécanismes résistants: un qui peut être définis direct, associe a la résistance des puntons, et un indirect, associe à l'incrément du confinement sur la bar. Les résultats numériques ont été utilisés pour définir un model interprétatif du fonctionnement du system d' ancrage.

**KEYWORDS:** soil anchoring, pull-out, soil–structure interaction, finite element analyses, plasticity

## 1 INTRODUCTION

The analysis and the design of soil anchors are of major interest to geotechnical engineers in many practical applications, including retaining structures, transmission towers, marine pipelines, etc. For these purposes, the employment of the Finite Element Method (FEM) is progressively increasing, as it overcomes the limitations of most empirical/analytical approaches (Das 1990) in dealing with complex geometries and material non-linearities. On the research side, only a few papers present numerical results about soil anchoring systems, compared to the available experimental data and analytical predictions (see for instance Rowe and Davis (1982a,b), Merifield and Sloan (2006)).

This paper summarizes a recent research activity (di Prisco and Pisanò 2012) concerning the study of a novel device for soil anchoring. This latter is formed by a tie rod equipped with thick steel sockets, which are extruded into the soil to ensure a remarkable pull-out capacity.

To investigate the soil–structure interaction (SSI) mechanisms determining the effectiveness of the system, FEM simulations of pull-out tests have been performed. Then, based on the critical analysis of the numerical outcomes, an analytical model for the estimation of the pull-out capacity has been set up. Despite the approximations introduced, the good agreement between analytical and FEM results is believed to represent the starting point for the conception of a reliable design procedure.

## 2 FEM SIMULATION OF PULL-OUT TESTS

The novel setup of the anchoring device under consideration is characterized by the presence of internal steel sockets along the tie rod shaft, to be extruded - after the rod installation - into the soil by means of a hydraulic system. Recent in situ pull-out tests have highlighted how socket extrusion ensures a very large bearing capacity (Santoro 2009), much larger than in the usual case of grouted anchorages.

Figure 1 sketches the installation of the anchoring system, composed of the tie rod and the extruded steel sockets, while Figure 2 illustrates the telescopic structure of the sockets. The system is rather flexible in terms of geometrical configuration as the number, the location, and the orientation of the sockets can be freely designed; its installation is extremely fast and inexpensive.

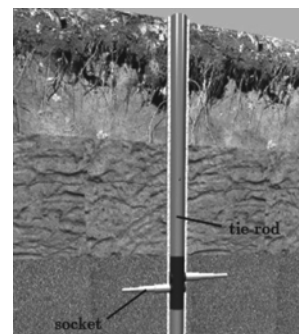


Figure 1. The anchoring system.



Figure 2. The steel sockets.

### 2.1 FEM model

The geometrical configuration for numerical analyses has been kept as simple as possible, but sufficiently accurate to reproduce the most relevant structural details. If the four sockets



were located at the same vertical level (they are not to allow room for the extruding hydraulic circuits), the anchor would be characterized by four (vertical) symmetry planes. Although this is not exactly true, it has been here assumed for computational convenience that the different socket elevations only slightly violate such symmetries: accordingly, only a quarter of the whole geometry has been considered and discretized.

The FEM mesh employed is shown in Figure 3. The discretization – performed by adopting quadratic tetrahedral elements - is finer around the sockets and the tie rod, i.e. where the solution is expected to exhibit the largest gradients. The external soil boundaries have been placed sufficiently far from the anchor, so as to not affect the global pull-out response.

Since the main purpose of this preliminary study was the highlighting of SSI mechanisms, for the sake of simplicity no sophisticated material models have been considered. In particular, the soil mechanical behaviour has been modelled by means of a simple Mohr-Coulomb perfectly-plastic constitutive relationship with non-associated flow rule (i.e. with different friction and dilatancy angles), while a von Mises perfectly-plastic associated model has been adopted for the anchor structural members. A linear variation along the depth has been introduced for the soil Young modulus, to account for the stiffening induced by the increase in normal confinement. Moreover, as is commonly done in SSI analyses, a widthless perfectly-plastic interface layer has been interposed between the anchor and the surrounding soil to allow both shear and tension detachments.

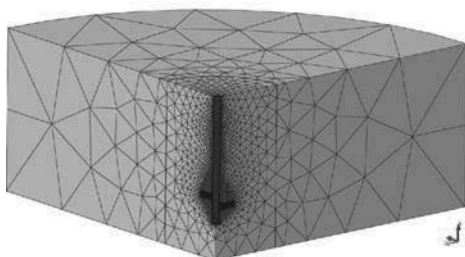


Figure 3. FEM model.

Apparently, the length of the tie rod, i.e., the socket extrusion depth, greatly influences the pull-out capacity of the anchor: as deeper anchors are considered, larger discrete models should be defined, implying an increase in computational costs. Conversely, in order to investigate how the strength contribution coming from the steel sockets is affected by the initial stress state, an approximate approach has been here adopted for the first preliminary analyses. In particular, to simulate a real higher embedment, the same model in Figure 3 has been used for different physical depths, by using an equivalent “embedment surcharge”  $q_{emb}$  on the top of the reduced model (obviously, this assumption neglects the frictional pull-out resistance provided by the missing upper soil).

### 2.2 Main inferences from FEM analyses

In what follows, the main observations derived from the analysis of the preliminary FEM results (with embedment surcharge) are qualitatively summarized.

All the pull-out tests have been performed by imposing a prescribed upward displacement  $\delta$  at the top of the tie rod, recording the corresponding reaction forces to quantify the global resistance provided by the neighboring soil. While the total pull-out force readily results from the top reaction forces, two distinct contributions can be recognized and estimated on the basis of the FEM outputs. In particular, the global capacity has been split into a first frictional component mobilized along the tie rod, and a second contribution directly carried by the steel sockets.

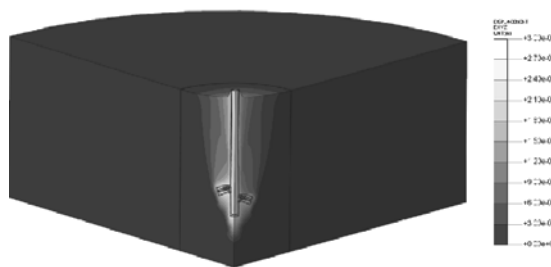


Figure 4. Total displacement contour plot at the onset of failure.

As an example, Figure 4 illustrates the contour plot of the total displacement (absolute value) at the onset of the collapse. The global failure mechanism takes place in the form of a soil wedge surrounding the anchor and moving upward as the anchor itself is pulled-out. Such a failure mechanism is further illustrated in terms of the plastic shear strain in Figure 5: the shear strain concentrations take place along the tie rod and close to the sockets, so that the formation of a failure wedge is apparent.



Figure 5. Plastic shear strain contour plot at the onset of failure.

Figure 6 shows, for four different  $q_{emb}$  values, the pull-out curves (force vs. displacement) estimated for the whole anchorage, i.e. four times the force computed for the quarter anchor (this would rigorously hold if the steel sockets were at the same elevation). In all the cases considered, the mechanical response of the anchorage is overall ductile and the limit pull-out load (horizontal plateau) is achieved after quite large displacements. Besides the expected increase in the bearing capacity at larger  $q_{emb}$ , it is also worth noting that, owing to the aforementioned spatial variation of the soil Young modulus, the limit load is achieved at about the same displacement level  $\delta$ .

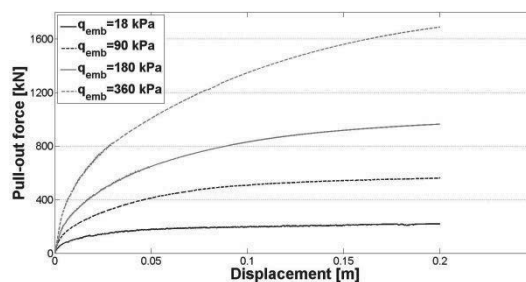


Figure 6. Pull-out responses at increasing embedment surcharge.

Both the above frictional and socket strength contributions have been separately evaluated for all the FEM analyses performed. The obtained values – not reported here for the sake of brevity – show that the lateral frictional forces and the contribution provided by the steel sockets are quantitatively comparable. Such large lateral forces could not be explained by assuming a standard  $k_0$  distribution for the confining stress ( $k_0$  stands for the at rest earth pressure coefficient) all around the tie rod. In contrast, the numerical simulation shows a significant increase in confining stresses as the anchor is pulled-out, up to values much larger than the at rest ones. Figure 7 illustrates the final contour plot of the radial stress, in which the severe perturbation of the initial (linear) at rest distribution is evident.

In the light of these considerations, the influence of the steel sockets on the global pull-out capacity can be said to be twofold. First, the sockets directly sustain a portion  $F_{socket}$  of the external load owing to their shear/flexural strength: henceforth, this will be referred to as the “direct effect”. Besides this, an “indirect effect” stems from the formation of a global failure mechanism with a remarkable increase in the radial stress around the tie rod and, therefore, in the mobilizable shear force  $F_{lateral}$ . For any future design purpose, the necessity of a reliable estimation of both  $F_{socket}$  and  $F_{lateral}$  is self-evident.



7. Radial stress contour plot at the onset of failure.

### 3 A DESIGN-ORIENTED ANALYTICAL MODEL

In this section a design-oriented analytical model is defined to estimate each resisting component contributing to the total pull-out capacity of the anchor. The accuracy of the model has been also assessed by comparing the analytical results with the outcomes from full-size FEM analyses, i.e. with no embedment surcharge.

Apparently, the near presence of the tie rod prevents the sockets from being interpreted as isolated deeply buried pipes, so that the force exerted by the soil on each socket (and viceversa) cannot be evaluated via the well-known concept of “uplift coefficient” (or even “break-out coefficient” - see for instance, Rowe and Davis (1982a,b), Merifield and Sloan (2006), White *et al.* (2008)). In contrast, it has been numerically observed that the soil between a single socket and the tie rod behaves as if it was rigidly connected to the anchor, giving rise to a sort of “corkscrew mechanism”.

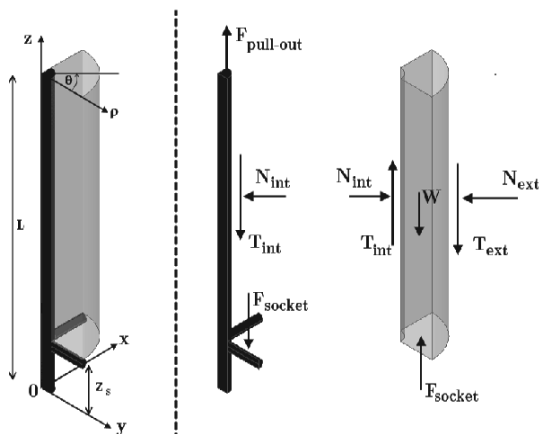


Figure 8. Simplified static scheme for the anchoring system.

To evaluate at the same time both  $F_{socket}$  and  $F_{lateral}$ , the simplified vertical wedge mechanism in Figure 7 (left picture) is considered (the shear force  $T_{int}$  coincides with  $F_{lateral}$ ). For the sake of simplicity, the two half-sockets are assumed to be positioned at the same elevation, so that a cylindrical reference frame  $(\rho, \theta, z)$  can be setup to describe an axisymmetric stress/strain state within the soil wedge (axisymmetric conditions are indeed expected beyond a given distance over the sockets). The right picture in Figure 8 illustrates the reference static scheme, i.e. the forces acting both on the tie rod and the

soil wedge (the rod weight is neglected and boundary reaction forces are not visualized).

From the analysis of all numerical results the following conclusions have been drawn:

1. except for local disturbances next to the sockets, all the stress components are almost linearly distributed along the vertical  $z$ -axis;
2. the vertical direct strain component  $\varepsilon_z$  is much less than the other two ( $\varepsilon_\rho$  and  $\varepsilon_\theta$ ), so that  $\varepsilon_z = 0$  can be assumed;
3. the normal force  $N_{ext}$  in Figure 8 can be approximately evaluated by assuming a  $k_p$  linear distribution for the radial stress  $\sigma_r$  along the outer side of the soil wedge ( $k_p$  stands for the passive earth pressure coefficient);
4. the inner and the outer  $\sigma_r$  distributions can be linearly related through a dimensionless constant  $\lambda$ ;
5. the failure distributions of the mobilized friction angle  $\phi_{mob} = \arctan(\tau_{z\rho} / \sigma_\rho)$  along the inner and outer sides of the soil wedge exhibit a mean value less than the soil friction angle  $\phi$  and approximately equal to:

$$\tan \phi_{mob}^{lim} = \frac{\cos \phi \cos \psi}{1 - \sin \phi \sin \psi} \quad (1)$$

where  $\psi$  is the soil dilatancy angle.

Relationship (1) stems from the fact that, during the pull-out process, the aforementioned soil wedge undergoes a sort of “axisymmetric simple shear loading”. In other words, the loading conditions of the soil elements around the tie rod are highly constrained and similar to those a soil specimen experiences within a so-called simple shear apparatus: as was recently discussed by di Prisco and Pisanò (2011), this implies the material dilatancy to significantly affect the limit shear stress.

The above considerations lead to the formulation of the following system of equations:

$$\begin{cases} T_{int} + F_{socket} = T_{ext} \\ T_{int} = N_{int} \tan \phi_{mob} \\ T_{ext} = N_{ext} \tan \phi_{mob} \\ N_{int} = \lambda N_{ext} \end{cases} \quad (2)$$

with the unknowns  $N_{int}$ ,  $T_{int}$  ( $= F_{lateral}$ ),  $T_{ext}$  and  $F_{socket}$  ( $N_{ext}$  is simply obtained by integrating the  $k_p$ - $\sigma_r$  distribution along the outer surface of the soil wedge). While the equations in system (2) hold at any stage of the loading process,  $\phi_{mob} = \phi_{mob}^{lim}$  is to be set at failure – i.e. when the limit frictional capacity is attained along the sides of the soil wedge.

For system (2) to be solved, the determination of the coefficient  $\lambda$  introduced in the previous assumption 4 is required. For this purpose, an original procedure has then been conceived: this is based on the solution of a classical rock engineering problem, concerning the determination of the elastic stress state around a circular cavity (Jaeger *et al.* 2007). For this purpose, an axisymmetric boundary value problem has been posed by assuming that: (i) the soil wedge in Figure 8 is internally elastic; (ii) the direct strain  $\varepsilon_z$  is nil; and (iii) the vertical stress gradients are much lower than those along the radial direction. While the problem formulation and the solution strategy can be found in di Prisco and Pisanò (2012), the obtained  $\lambda$  expression is reported here:

$$\lambda = \frac{\pi}{4} R(L - z_s) \left( \frac{c_1}{2} - \frac{c_2}{2R^2} \right) \quad (3)$$

where:

$$\left\{ \begin{array}{l} c_1 = \frac{8(R+l)}{\pi(L-z_s)[l^2 + 2lR + 2(1-\nu)R^2]} \\ c_2 = \frac{8R^2(R+l)(2\nu-1)}{\pi(L-z_s)[l^2 + 2lR + 2(1-\nu)R^2]} \end{array} \right. \quad (4)$$

In expressions (3) and (4),  $R$  and  $L$  are the radius and the length of the tie rod, while  $l$  and  $z_s$  stand for the length and the elevation (with respect to the bottom of the tie rod) of the steel sockets.

The straightforward solution of system (2) allows of estimating both  $F_{socket}$  and  $T_{int}$  ( $=F_{lateral}$ ). The soundness of the above assumptions has been verified for all the performed simulations and, in particular, for the full-size analyses (3 m and 7 m embedment) a satisfactory agreement in terms not only of total pull-out force (errors less than 10%) but also of the single contributions has been found. Further confirmation is given in Figures 9 and 10, where the analytical predictions for the radial (a, circular marked line) and shear (b, square marked line) stresses along the inner side of the soil wedge are compared with the FEM results (black solid line).

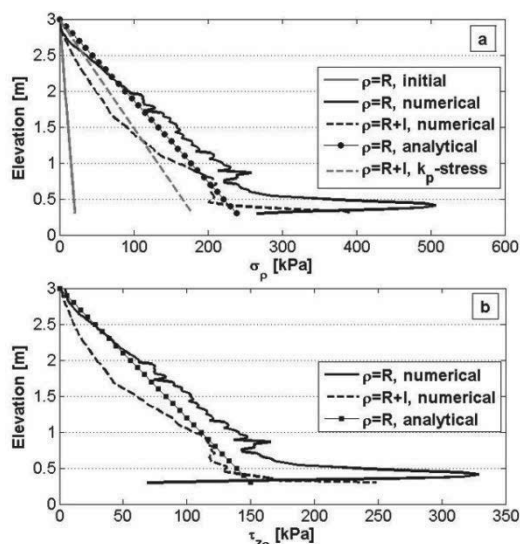


Figure 9. FEM and analytical stress distributions for the full-size model with 3m-embedded sockets.

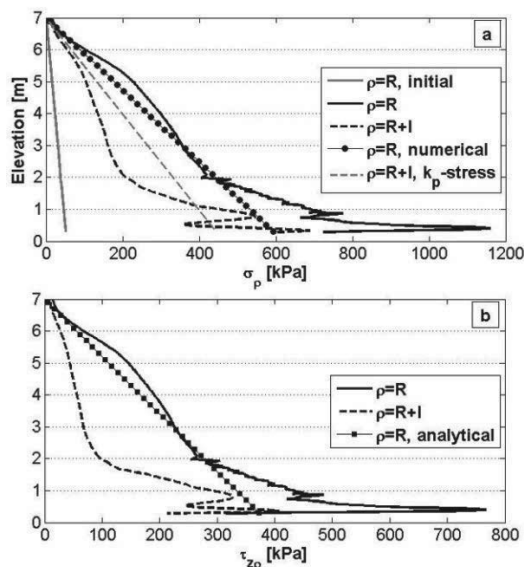


Figure 10. FEM and analytical stress distributions for the full-size model with 7m-embedded sockets.

#### 4 CONCLUSIONS

The pull-out performance of an innovative soil anchoring system has been numerically investigated through FEM analyses. The anchoring device is composed of a tie rod and a set of steel sockets, the latter to be extruded into the soil; former in situ tests have shown the steel sockets largely improve the pull-out performance of the anchorage. The device installation is fast, flexible and inexpensive, while in most cases additional soil grouting becomes optional.

In this work, vertical pull-out tests have been first simulated to explore the SSI mechanisms determining the pull-out capacity of the device, whence the following conclusions have been drawn:

- the steel sockets contribute to the global pull-out capacity in a twofold manner. In a direct way, they sustain a significant part of the total load owing to their shear/flexural strength; they also provide an indirect contribution, by increasing the lateral confinement and the mobilizable friction along the tie rod;
- in all the cases considered, failure develops up to the free surface through a global mechanism involving a cylindrical vertical soil wedge;
- the pull-out strength increases for deeper anchors. Its dependence on socket depth has been found to be, within the investigated range, almost linear;

A simplified analytical model was then proposed to simultaneously estimate the strength contributions – both direct and indirect – given by the sockets. This relies on a set of simplifying hypotheses suggested from the results of FEM simulations, and provides results in good agreement with the numerical outcomes. Although only vertical pull-out tests were considered, the above inferences are believed to apply for inclined anchors as well, since only a slight influence of the initial in situ stresses was found.

The proposed model clarifies the mechanical working conditions of the anchoring system and provides practitioners with a preliminary design framework. In the near future, further efforts will be devoted to analyse the device in the case of more complex geological conditions and, as more experimental results become available, to validate numerical/analytical predictions with respect to in situ measurements.

#### 5 ACKNOWLEDGEMENTS

JOBSSOIL s.r.l and MIDAS/GTS are gratefully acknowledged for the financial support.

#### 6 REFERENCES

- Das B.M. 1990. *Earth anchors*. Elsevier.
- di Prisco C.G. and Pisanò F. 2011. An exercise on slope stability and perfect elasto-plasticity. *Geotechnique* 61 (11), 923-934.
- di Prisco G.C. and Pisanò F. 2012. Numerical modelling and mechanical analysis of an innovative soil anchoring system. Submitted to *Acta Geotechnica*.
- Jaeger J., Cook N.G. and Zimmermann R. 2007. *Fundamentals of rock mechanics*. Wiley-Blackwell
- Merifield R.S. and Sloan S.W. 2006. The ultimate pull-out capacity in frictional soils. *Canadian Geotechnical Journal* 43 (8), 852-868.
- Rowe R.K. and Davis E.H. 1982a. The behaviour of anchor plates in clay. *Geotechnique* 32 (1), 9-23.
- Rowe R.K. and Davis E.H. 1982b. The behaviour of anchor plates in sand. *Geotechnique* 32 (1), 25-41.
- Santoro V.M. 2009. TFEG tensioned elements: from design to implementation. <http://www.jobsoil.it/iltfeg.html> 4 (Feb 24 2009).
- White D.J. Cheuk C.Y. and Bolton D. 2008. The uplift resistance of pipes and plate anchors buried in sand. *Geotechnique* 58 (10), 771-779.

# Structural Optimization in Geotechnical Engineering

## Optimisation de la structure dans la géotechnique

Pucker T., Grabe J.

Hamburg University of Technology, Institute of Geotechnical Engineering and Construction Management

**ABSTRACT:** Structural optimization methods are used for a wide range of engineering problems. In geotechnical engineering however, only limited experience exists with these methods. The possibilities and difficulties in applying such techniques to geotechnical problems are discussed in this paper and the adaption of the commonly known SIMP-method (Solid Isotropic Material with Penalization) to geotechnical problems is introduced. An application example is used to demonstrate the potential of structural optimization in geotechnical engineering.

**RÉSUMÉ :** Des méthodes de l'optimisation de la structure sont employés dans beaucoup de disciplines d'ingénieurs. Mais il y a quand-même peu d'expériences dans le domaine de la géotechnique. Les possibilités et les difficultés de l'application de ces procédures d'optimisation dans la géotechnique sont discutées dans cet article. L'application de la méthode SIMP est présenté. Un exemple est présenté pour montrer le potentiel de l'application de cette méthode.

**KEYWORDS:** topology, optimization, optimisation

### 1 INTRODUCTION

Structural optimization methods are used for a wide range of engineering problems, for instance in aviation and automotive engineering. In geotechnical engineering however, only limited experience exists with such methods. The possibilities and difficulties in applying these techniques to geotechnical problems are discussed in this paper and the adaption of the commonly known SIMP-method to geotechnical problems is introduced.

#### 1.1 Structural Optimization

Structural Optimization can be classified in three categories. The first category is called topology optimization and describes the main geometry of a design. Topology is a mathematical field used to describe geometrical structures. A geotechnical example of different topologies to stabilize a slope is shown in Figure 1.

Figure 1a) shows the design problem. Different constructions can be used to solve this task, for example a gravity wall (Figure 1b), a single anchored wall (Figure 1c) or a grouted anchored wall (Figure 1d). These three constructions differ in their topology. Some topology optimization algorithms can be found in Bendsøe (1995) or Allaire (2005).

Once a topology is chosen, the shape of the topology can be optimized with regard to the design problem. Concerning the design problem in Figure 1, the topology in Figure 1d is chosen. Figure 2 shows different possibilities to optimize the shape of the topology in Figure 1d during the category shape optimization, for example the variation of the anchor positions (b), of the anchor inclination (c) or the anchor length (d). The variations in Figure 2 b)-d) can be varied regarding an optimization task, for instance the minimization of the bending of the wall or minimization of the installation costs. The application of shape optimization algorithms in geotechnical application has been shown in Kinzler (2007) and Grabe et al. (2010, 2011).

The third category is the dimension optimization of each construction part. Within this category every cross section and dimension is determined. Neither the topology nor the shape can be changed by the dimension optimization. The dimension optimization is the most widely applied category of structural optimization in geotechnical engineering. The shape optimization of Figure 2 results in the shape shown in Figure 3. For this example, possible parameters for the dimension optimization are given in Figure 3.

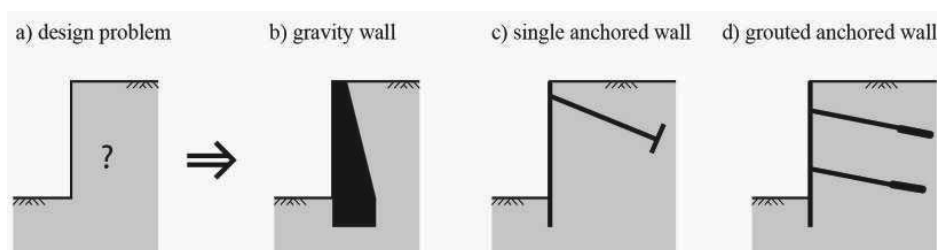


Figure 1. Different topologies for a design problem a): b) gravity wall, c) single anchored wall, d) grouted anchored wall

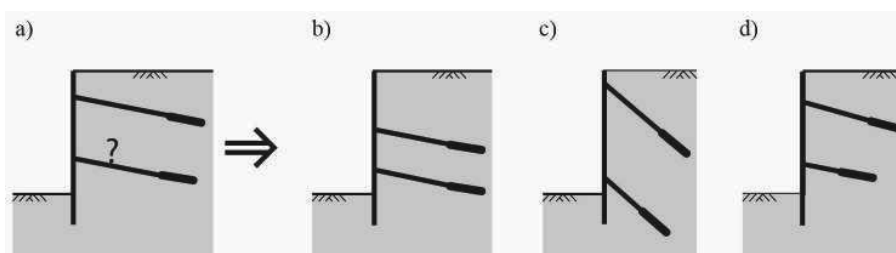


Figure 2. Shape optimization: a) main topology, b) variation 1: anchor position, c) variation 2: anchor inclination, d) variation 3: anchor length

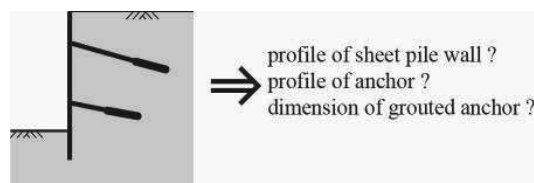


Figure 3. Dimension optimization

## 2 NUMERICAL OPTIMIZATION ALGORITHM

An iterative algorithm is used to solve the optimization problem numerically. First a topology is created and second its load-displacement behavior is determined using a finite-element analysis. In the next step, the results of the finite-element analysis are interpreted and transmitted to a topology optimization algorithm, which creates a new improved topology. Afterwards step two is performed again.

The SIMP-Method (Solid Isotropic Material with Penalization) after Sigmund (2001) is used as topology optimization algorithm. The algorithm is based on the idea, that the material of the optimized structure already exists in the design domain  $\Omega$ , but is not optimally distributed. Therefore, the material is equally distributed in the design domain  $\Omega$  at the beginning of the optimization process. The material distribution changes during the optimization process and the material compacts in areas where it is needed to achieve the optimization task.

The design domain  $\Omega$  is discretized with finite elements. The material parameters are specified individually for each element depending on the material distribution. The virtual density  $\rho$  at a point  $a$  has to be between 0 and 1, see Equation 1.

$$\rho(a) = \begin{cases} 0 \rightarrow \text{no material} \\ 1 \rightarrow \text{material} \end{cases} \quad (1)$$

Regarding a geotechnical application, for example a foundation made of concrete, a finite-element with  $\rho(a) = 0$  is a soil element and with  $\rho(a) = 1$  is a concrete element.

Using the SIMP-Method, the objective function is the minimization of the compliance of the structure in the design domain  $\Omega$ . Thus, the stiffness of the structure is maximized. The compliance of the structure can be expressed using the internal energy of the system. The internal energy  $c$  of an elastic material is defined by Equation 2.

$$c(\mathbf{x}) = U^T K U \quad (2)$$

In Equation 2  $U$  is the global deformation tensor,  $K$  the global stiffness matrix and  $\mathbf{x}$  the tensor of design parameters. The virtual density  $\rho(a)$  matches the design parameters of  $x_i$  of the tensor  $\mathbf{x}$  at point  $a$ .

The minimization of the compliance is restricted by two constraints. The first constraint ensures that the observed system is in equilibrium an every step of the optimization process. Using the finite-element method, this constraint is ensured by Equation 3.  $F$  is the global tensor of the external forces.

$$K U = F \quad (3)$$

The second constraint ensures that the volume of the material distributed in the design domain remains constant during the optimization process, see Equation 4.  $V_\delta$  is the volume of the structure.

$$\int_{\Omega^{mat}} 1 d\Omega = V_\delta \quad (4)$$

Additionally, the design parameters  $x_i$  are limited by an upper and an lower bound, such that the optimized material parameters lie within to the physically possible range.

The optimization task for minimal compliance design can be written using Equation 5.  $U_e$  is the element deformation tensor,  $K_e$  the element stiffness matrix,  $\rho_e$  the element virtual density,  $\delta$  the volume fraction,  $V_\delta$  the structure volume and  $V_0$  is the volume of the design domain. The values of the material distribution are limited by  $x_{min}$  to avoid singularities during the finite-element analysis. Using the algorithm for geotechnical application, this limit is not necessary because the stiffness of an element belongs to the soils stiffness at  $x_i = 0$  and cannot tend to zero.

$$\left. \begin{array}{l} \min : \quad c(x) = U^T K U = \sum_e^N (\rho_e)^p U_e^T K_e U_e \\ \text{subject to:} \quad \left. \begin{array}{l} K U = F \\ V_\delta = V_0 \cdot \delta \\ 0 < x_{min} \leq x \leq 1 \end{array} \right\} \end{array} \right\} \quad (5)$$

The penalty  $p$  controls the material change-over to ensure complete material change for example from soil to concrete, see Figure 4.

The improved topology in every iteration step is determined using the method of optimal criteria, see Equation 6 (Bendsøe 1995). A positive move-limit  $m$  and a numerical damping coefficient  $\eta = 0.50$  are introduced, see Bendsøe (1995). The move-limit  $m$  limits the change of the topology in each iteration step. The sensitivity of the objective function is expressed in Equation 7. Using the Lagrangian multiplier  $\lambda$ ,  $B_e$  is defined in Equation 8.

$$\rho_e^{new} \begin{cases} \max(\rho_{min}, \rho_e - m), & \text{if } \rho_e B_e^\eta \leq \max(\rho_{min}, \rho_e - m) \\ \rho_e B_e^\eta, & \text{if } \max(\rho_{min}, \rho_e - m) < \rho_e B_e^\eta < \max(1, \rho_e + m) \\ \min(1, \rho_e + m), & \text{if } \min(1, \rho_e + m) \leq \rho_e B_e^\eta \end{cases} \quad (6)$$

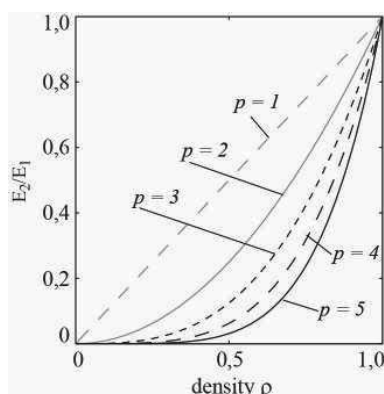


Figure 4: Change-over of the Young's modulus  $E$  of two different materials depending on different values of the penalty term  $p$

### 3 APPLICATION

#### 1.2 Numerical model

The presented topology optimization algorithm is applied to a vertically loaded strip footing foundation. The topology underneath the foundation is to be optimized. The initial width of the foundation is 2 m and the height is 1 m. The load-settlement behavior is simulated in a 2D finite-element analysis. The discretization of the model is shown in Figure 5.

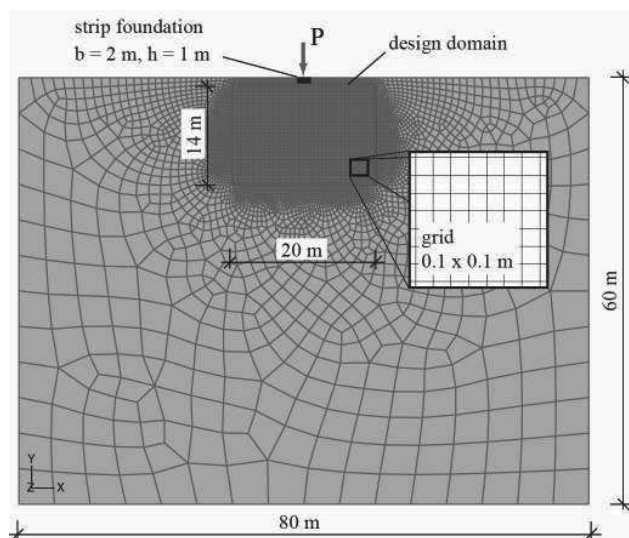


Figure 5. Discretization of the FE-model of a strip foundation with a width of 2 m and a height of 1 m, vertically loaded with 500 kN at the loading point P

The foundation is vertically loaded with 500 kN. The soil and the improved material underneath the strip foundation is modeled using the hypoplastic constitutive model after von Wolffersdorff (1996) with the extension of intergranular strain after Niemunis and Herle (1997). Detailed information can be found in Pucker and Grabe (2011).

$$\frac{\partial c}{\partial \rho_e} = -\frac{\partial c}{\partial \rho_e} p(\rho_e)^{p-1} U_e^T K_e U_e \quad (7)$$

$$\frac{\partial \rho_e}{\partial V} = \frac{\lambda}{\partial V} \frac{\partial V}{\partial \rho_e} \quad (8)$$

#### 1.3 Optimization

Three optimizations are performed at different material volumes. The material volume is 2%, 5% and 10% of the design domain. The design domain is 20 m of width and 14 m of height, see Figure 5.

#### 1.4 Results

In Figure 7 the optimized topologies with 2%, 5% and 10% material volume are illustrated. Regarding the 2% material volume, mainly the area at the foundation edges are compacted. Since the foundation can be considered to be rigid, the optimization results can be explained with the theory of a rigid foundation on an elastic half-space, according to which high stresses will occur at the edges of the foundation. The optimization algorithm compacts the material mainly in these areas.

Figure 6 shows the displacement of the soil underneath the foundation with the unoptimized (Figure 6 a) and the optimized (Figure 6 b) structure with a volume of 5%. The settlements can be reduced up to 50%.

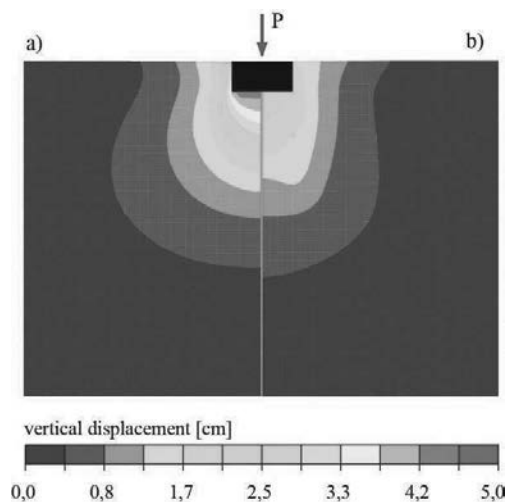


Figure 6. Vertical displacement before (left) and after (right) the topology optimization with 5% material volume

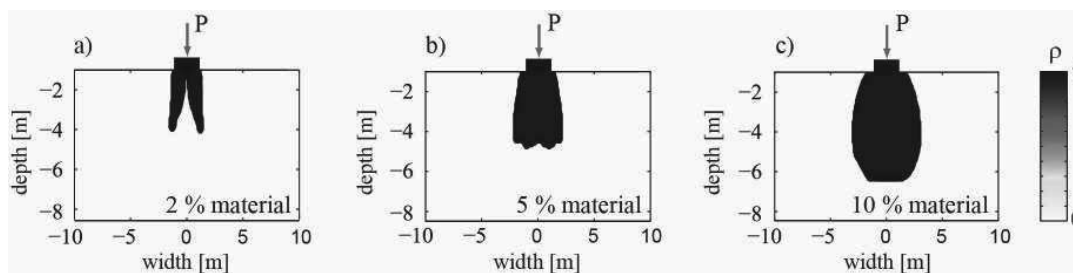


Figure 7. Optimized foundations with a) 2% material volume, b) 5% material volume, c) 10% material volume

The influence of the material volume on the improvement is shown in Figure 8. Figure 8 top shows the material volume over the vertical load  $P$  at different settlements. The applicable load at a settlement restriction about 1 cm cannot be significantly improved using more than 2% material volume. Regarding higher settlement restrictions, the increase of the material volume also increases the applicable load  $P$ .

The same results can be obtained from the load settlement curves of the improved foundations in Figure 8 bottom. The main improvement is reached with a material volume about 2%.

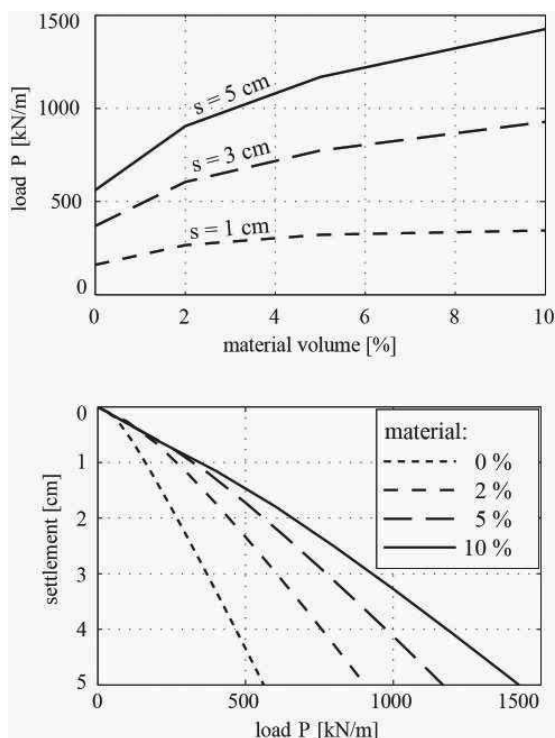


Figure 8. top: load  $P$  over material volume at different settlement restrictions; bottom: load-settlement curves of the optimized foundation topologies

### 1.5 Practical realization

The practical realization of the optimized topologies can be quite difficult. The optimized topologies of the presented example can be realized using the jet grouting method. This method allows the realization of every possible topology restricted by the minimum diameter of a jet grouting body.

Another possibility to realize such topologies is the interpretation of the topologies and the conversion of the topology into standard geotechnical construction parts. The realization of the topology with 2% material can be done using a classical strip foundation topology in combination with micro piles, see Figure 9.

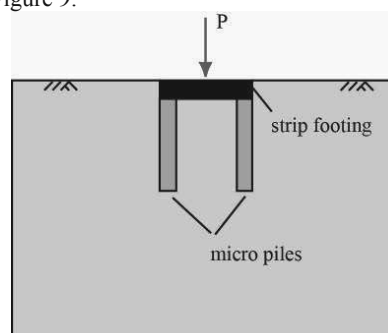


Figure 9. Possible practical realization of the topology with 2% material volume

## 2 CONCLUSION

The application of topology optimization in geotechnical engineering was presented. The applied SIMP-Method is suitable for geotechnical problems. In the presented example, the settlements of a strip foundation could be reduced up 66%.

Topology optimization in geotechnical engineering has a great potential and can lead to innovative and efficient designs.

## 3 REFERENCES (TNR 8)

Allaire G., De Gournay F., Jouve F. And Toader A.-M. 2005. A level-set method for shape optimization. *Control and Cybernetics* 34.

Bendsøe M.P. 1995. Optimization of structural topology, shape and material. Berlin, Heidelberg, New York

Grabe J., Kinzler S., Pucker T. And Mardfeldt B. 2010. Untersuchung des Tragverhaltens und der Anwendbarkeit numerischer Optimierungsverfahren für Kaikonstruktionen. *Tagungsband der 31. Baugrundtagung 2010 in München*, 123-129

Grabe J., Pucker T., Busch P. 2012. Non-linear numerical model for the design process of deep foundations with regard to effects of pile installation. *Proceedings of 9th International Conference on Testing and Design Methods for Deep Foundations 2012 in Kanazawa/Japan*, edited by T. Matsumoto, 55-64

Kinzler S. 2007. Entwurf einer Pfahlgründung unter Anwendung der Mehrkriterien-Optimierung. *Der Bauingenieur* 82, 367-379.

Sigmund O. 2001. A 99 line topology optimization code written in Matlab. *Structural and Multidisciplinary Optimization*, 21, 120-127

Niemunis A. and Herle I. 1997. Hypoplastic model for cohesionless soils with elastic strain range. *Mechanics of Frictional and Cohesive Material*, 2, 279-299

Pucker T. and Grabe J. 2011. Structural optimization in geotechnical engineering - basics and application. *Acta Geotechnica*, 6, 41-49, DOI: 10.1007/s11440-011-0134-7

Von Wolffersdorff P.-A.. 1996. A hypoplastic relation for granular materials with predefined limit state surface. *Mechanics of Frictional and Cohesive Material*, 1, 251-271

# Role of the facing on the behaviour of soil-nailed slopes under surcharge loading

## Rôle du parement sur le comportement des pentes de sol cloué sous surcharge

Sanvitale N., Simonini P., Bisson A., Cola S.

Department of Civil, Environmental and Architectural Engineering - University of Padova - Italy

**ABSTRACT:** Soil nailing is an economic and efficient method to reinforce soils, involving the insertion of threaded bars into natural unstable slope for increasing the overall stability or into cut slopes during the top-down process of excavation. The retained soil, the resisting reinforcements and the external facing are the main components of a soil-nailed structure. Their composite interactions determine the performance of soil-nail construction in terms of deformations and stability. Even if the international codes deal about the possibility of use rigid or flexible external facing, the role of facing stiffness is not sufficiently studied and evaluated. To this aim, some tests with various facing types, differing in stiffness and continuity, were carried out so far in 1g small scale physical model. The experimental results show the importance of both flexional and axial stiffness of facing in controlling the deformation of the wall during excavation and the maximum surcharge applicable at the rear of wall.

**RÉSUMÉ:** Le clouage du sol est une méthode économique et efficace pour renforcer le sol en place: il consiste en l'insertion de barres d'acier filetées ou d'autres barres dans les pentes naturelles instables ou dans des talus au cours du processus de l'excavation pour augmenter la stabilité globale. Le sol soutenu, les barres résistantes et le parement extérieur sont les principales composantes d'une structure du sol cloué. Leurs interactions mutuelles déterminent la performance du *soil nailing* en termes de déformations et de stabilité. Même si les codes internationaux considèrent la possibilité d'utiliser des parements extérieurs rigides ou flexibles, le rôle de la raideur du parement n'a pas été suffisamment étudié et évalué. Avec ce but ont été réalisées des épreuves dans un modèle physique avec des parements différents en rigidité et continuité. Les résultats expérimentaux soulignent l'importance de la raideur en flexion et en traction-compression du parement extérieur dans le contrôle de la déformation de la paroi pendant l'excavation, et la valeur maximale de la charge applicable à l'arrière du mur.

**KEYWORDS:** soil nailing, facing, retaining wall, soil reinforcement, physical model.

## 1 INTRODUCTION

Soil nailing is an economical and efficient reinforcement technique used as a remedial measure in unstable natural slopes or as retaining structure for excavated slopes. In comparison with other retaining structures, soil nailing permits to reduce the excavated soil volume, saving construction materials and realization time. Its first applications were proposed in France for the Couterre project (Plumelle et al. 1990) and in Germany (Stocker 1976). Even if many studies and researches have been already performed and several national codes or guide lines exist, the role of facing in controlling the deformation of excavated front or the slope overall stability is not completely understood yet.

On this matter, the new code EN 14490:2010 indicates the possible use of three types of facing which are:

- *hard facing* which has to fulfil the function of stabilizing the slope between the nails and shell therefore be dimensioned to sustain the maximum expected destabilizing forces;
- *flexible facing* designed to provide the necessary restrains to the areas of slope face between the bearing plates as well as the erosion control;
- *soft facing* with the primary function of controlling slope erosion in conjunction of vegetation.

Even if the EN 14490:2010 reports some examples for the three types of facing, it does not give precise indications on how to evaluate the forces applied by soil on facing or the stiffness of facing.

In order to improve the understanding of the role of facing on the resistant mechanisms of soil nailing, this paper presents

the results of an experimental program carried out on a 1g small scale physical model of sandy slope reinforced with soil nailing and brought to collapse by surcharge loading: in the tests six facings, differing for continuity and stiffness, were utilized to restrain the soil between nails.

## 2 PHYSICAL MODEL

The model face is 39.5 cm wide and 40 cm high, with a wall dip angle of 80° (Figure 1). The soil is medium-fine sand from Adige river with the following characteristics (Gottardi and Simonini 2003): mean particle diameter  $D_{50} = 0.42$  mm, non-uniformity coefficient  $C_u = D_{60}/D_{10} = 2.0$ , specific bulk weight  $G_s = 2.71$ , minimum and maximum dry specific weight  $\gamma_{d,min} = 13.6$  kN/m<sup>3</sup> and  $\gamma_{d,max} = 16.5$  kN/m<sup>3</sup>, peak friction angle  $\phi_{peak} = 42-43^\circ$  and critical friction angle  $\phi_{crit} = 35^\circ$ .

The sand is prepared in homogeneous layers into a caisson with pluvial deposition method reaching a relative density of about 85%. During deposition the caisson is maintained inclined at 20° to deposit homogeneously the sand also at rear of facing and to simplify the nail installation. In the meanwhile, the cover is fixedly bonded in vertical position, using four wooden blocks behind which will be subsequently removed to simulate the excavation.

The deposition is temporarily stopped to install the nails in 4 horizontal lines and 3 vertical lines, with spacing  $s_v = 10.2$  cm and  $s_h = 13.2$  cm respectively.

The nails are 32.5 cm long aluminium tubes, with an external diameter of 6 mm and covered with 1 mm thick layer of glued Adige sand. They are perpendicularly connected to the



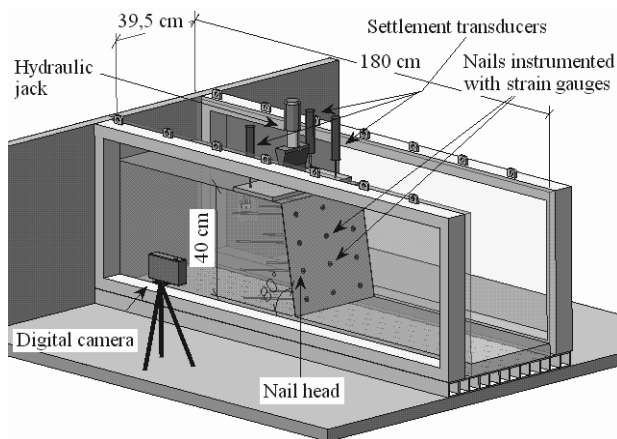


Figure 1 Perspective view of 1g physical model.

facing with a 1.2 cm annular rod and a small steel pin.

The monitoring system includes:

- A load cell between to the vertical jack and the plate to measure the load;
- Three vertical displacement transducers recording the plate settlements;
- A digital camera taking lateral images of the model during the entire test. By applying the Particle Image Velocimetry (PIV) technique (White et al. 2003) to the image sequences it is possible to reconstruct the evolution of displacement during the test;
- A laser scanner for monitoring the frontal displacement of the face at some significant load steps. Since the scanner takes about 1 min to complete the scansion, the loading sequence must be temporarily stopped. A small load reduction, due to the occurrence of the soil viscous strains, was observed in this short time interval;
- Eight strain gauges, glued pair by pair, at 2.3, 10.4, 18.5 and 26.7 cm from the face, on the nails located along the central vertical section at 15.3 and 25.4 cm from the top (the central ones). They permit to reconstruct the distribution of axial strain and, consequently, of axial stress along nails.

In order to evaluate which stiffness – i.e. the axial or the flexional ones - mostly influences the soil nailing behaviour during excavation and subsequent plate loading, six tests were performed with different facing types (Table 1 summarises the geometrical and mechanical properties of the various coverings). Four facings, covering the entire excavated front, were: *a*) 4 mm-thick plate of Polymethyl methacrylate (PMMA); *b*) a 0.25 mm-thick sheet of brass (BRASS); *c*) a steel mesh formed by 1-mm wires, perpendicularly welded at 6 mm spacing (MESH); *d*) a steel net formed by 0.24 mm-diameter wires, perpendicularly woven (NET). Three of these continuous coverings have an axial stiffness with the same order of

magnitude but a flexional stiffness decreasing about one order from one to another facing, while the fourth is very deformable both in axial and flexional sense.

The other ones are two discontinuous facing constituted by rectangular tiles in PMMA (obtained by cutting a PMMA cover like that used in test *a*): in these cases the covering ratio, defined as the ratio between the total covered area and the total extension of facing, are respectively equal to 95% (PMMA95) and 25% (PMMA25). Due to this discontinuity the axial stiffness vanishes, so these covers are flexional stiff (like the test *a*) but without any axial stiffness.

Since the soil forming the model is dry sand without cohesion, to avoid the collapse of sand among the tiles or across the mesh holes, a very light and low-resistant geo-synthetic behind them was set up. The same geo-synthetic was also inserted at the rear of the other facings to reach homogeneous test conditions.

After the models being completely set up, they were driven to failure in three steps: 1) application of a uniform load  $q$  of 24 kPa on the plate; 2) removing one by one of four wooden blocks, simulating the front excavation; 3) application of an increasing uniform load on the plate up to failure.

### 3 MODEL RESPONSE DURING EXCAVATION

Figure 2 depicts the vertical displacements of the plate,  $\Delta y_p$ , during the 4 steps of excavations in the all the tests. Even if the plate horizontal displacements,  $\Delta x_p$ , (obtained from the PIV analysis of digital images) are not reported here for brevity, they show a similar trend with the same magnitude order of vertical settlements – i.e.  $\Delta y_p/\Delta x_p \approx 1$ . Moreover, since the plate is located just at the rear of facing, the horizontal plate displacement may be considered equal to the horizontal displacement of the front tip.

Note that the vertical displacement does not exceed 0.5 mm (equivalent to 0.13% of the slope height) in tests *a* and *b* with very rigid facings (PMMA and MESH), while the maximum displacement, equal to about 2 mm and equivalent to 0.5% of the height, is observed in the tests *d* and *e* with very deformable facing (NET and PMMA25).

It is also interesting to observe that in the test with PMMA95, with discontinuous covering, the displacement does not exceed the 0.27% of the height: this means that the high flexional stiffness of PMMA tiles prevents the soil near to the face to move laterally.

Figure 3 reports the tensile force distribution along the monitored nails at the end of the excavation. Even if the tensile force is determined in few points, it is possible to recognize the typical bell-shaped distribution observed in many applications and described in the international practical guides (i.e. FWHA 2003, Geoguide7 2008). As known, the slope of the lateral segments depends on the shear stresses mobilized at the interface soil-nail in the active and passive zone respectively.

Table 1. Mechanical characteristics of facings adopted in the physical model.

Model	Facing	Covering ratio (%)	Thickness/ Wire Diam. (mm)	Wire spacing (mm)	Young modulus E (GPa)	Axial stiffness EA/m (N/mm)	Flexional stiffness EJ/m (Nmm <sup>2</sup> /mm)
a	PMMA	100	4	-	3.2	12800	17066.67
b	MESH	100	1	6	210	26180	3318.06
c	BRASS	100	0.25	-	126	31500	236.25
d	NET	100	0.24	1.02	70	3105*	22.66
e	PMMA95	95	4	-	3.2	-	-
f	PMMA25	25	4	-	3.2	-	-

\* The axial stiffness of canvas is the mean values obtained from to traction tests performed on two 178mm x 25mm samples.

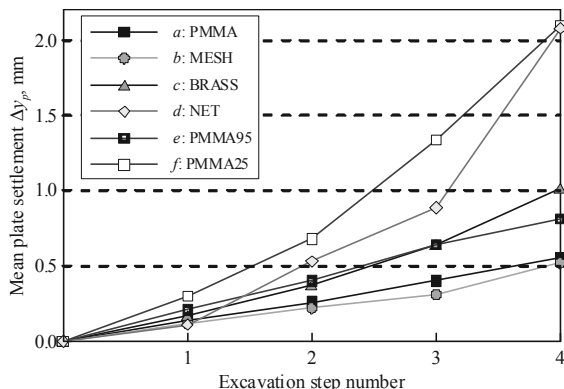


Figure 2. Average plate vertical displacement during four excavation steps in all the tests.

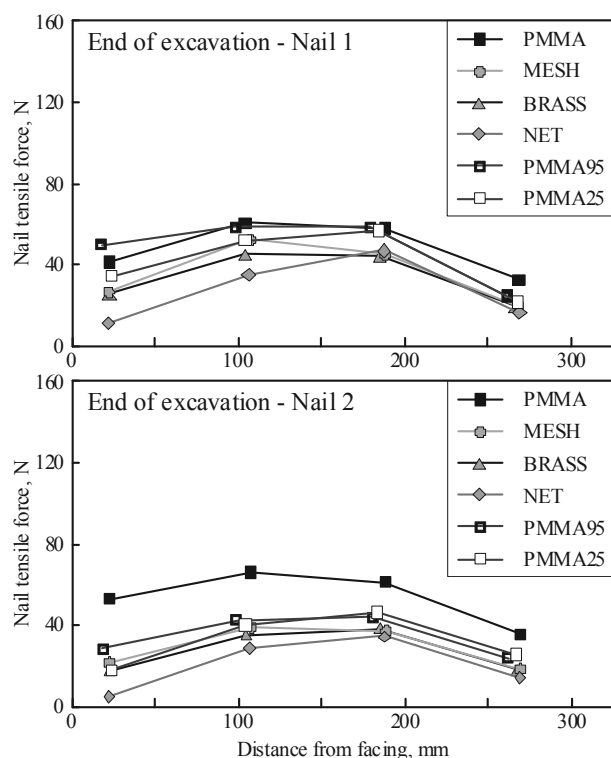


Figure 3. Distribution of tensile force along the monitored nails at the end of excavation: (a) upper nail; (b) lower nail.

The stiffness of facing strongly influences the characteristics of tensile force distribution, such as the slope of two lateral segments, the tensile force at the connection with facing,  $N_{head}$ , and the location  $X_{max}$  of maximum traction,  $N_{max}$ .

The highest  $N_{head}$  is reached in tests *a* and *e* (PMMA and PMMA95), with  $N_{head}$  gradually decreasing according to the facing deformability: the lowest values are due to tests with NET and PMMA25. On other hand, the difference  $N_{max} - N_{head}$  and consequently the slope of segment in the active zone, is less for tests with PMMA and PMMA95, gradually increasing with facing deformability. Finally,  $X_{max}$  is located closer to the face in tests with PMMA and PMMA95, while it moves itself from face using deformable covering (NET and PMMA25).

This means that if a rigid facing prevents the soil behind the face to dilate, limiting, as previously explained, the face horizontal displacements. In addition it also reduces the relative soil-nail displacement in the active zone and the increase of shear stress mobilized at this interface. On the contrary, to reduce the face deformation, the nails have to be more stressed by higher soil pressure acting at the rear of facing, because the

soil could not reach the active state condition with the mobilization of the minimum horizontal stress.

#### 4 MODEL RESPONSE DURING PLATE LOADING

Figure 4 plots the load applied to the plate during the phase *c* vs. the mean vertical displacements of the plate. Temporary reductions of the load are evident in the graph and they are due to the temporary stops of loading piston for performing the laser scanner of the front.

Figure 5 compares the spatial distribution of the cumulated shear strains at collapse in tests with PMMA, NET and PMMA25 (for brevity we choose only the most meaningful images): the shear strain distribution is determined by applying the PIV analysis to the lateral images of models.

In all the model tests, failure appears to be combined with localization of shear strain along one or more narrow bands. The mostly well-defined band moves from the plate edge (the one opposite to the face) towards the face base intercepting all the nails and delimiting the wedge pushing on facing: the wedge is characterized by a size related with the maximum load reached in the test: the greater is the maximum load, the larger is the wedge. Other bands, less clear, individuate a wedge like those that typically form below shallow foundations.

Figure 6 plots the distribution of tensile force along the monitored nails when a load of 5,45 kN is applied on the plate: note that at this load level the model *d* is approaching the collapse, and some problems affect the strain-gauge readings (localization of plastic strain in nail n.1 and detachment of one strain-gauge in nail n.2) and the correct evaluation of tension value. Moreover, data from test PMMA95 are not reported in Figure 6, because some problems occurred in the electrical connections induce to consider them not reliable.

These results permit to point out the important role played by the facing. The maximum load supported by the retaining system with rigid facing PMMA,  $P_{max,a}$ , is about five times greater than the load supported in test with NET,  $P_{max,d}$ , that represents the minimum load measured in all the tests. Other models support loads in the range  $0.83-0.97P_{max,a}$  with higher values in tests with MESH and PMMA95, the most rigid covers.

From the comparison suggested in Figure 6 it is evident that the collapse of model *d* is due to the overcoming of the pull-out resistance in the passive zone of soils. The relative soil-nail displacements, cumulated in the active zone as consequence of facing buckling, induced the increase of tensile gradient in the section of nails close to the face. Consequently, also the maximum traction increases significantly:  $N_{max}$  in test *d* is 3-4 times greater than that determined in all other tests. This high tensile force has to be compensated by the frictional resistance along the nails in the passive zone. This is evident from Figure 6, because the slopes of the tensile profile in the most internal part of the nails are greater than those characterizing the results

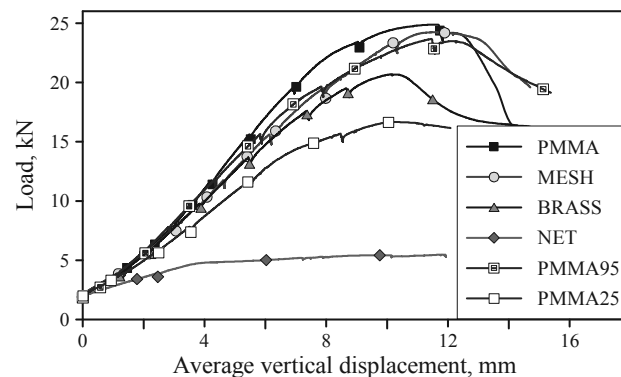


Figure 4. Load on the plate vs. mean settlements during loading phase up to collapse.

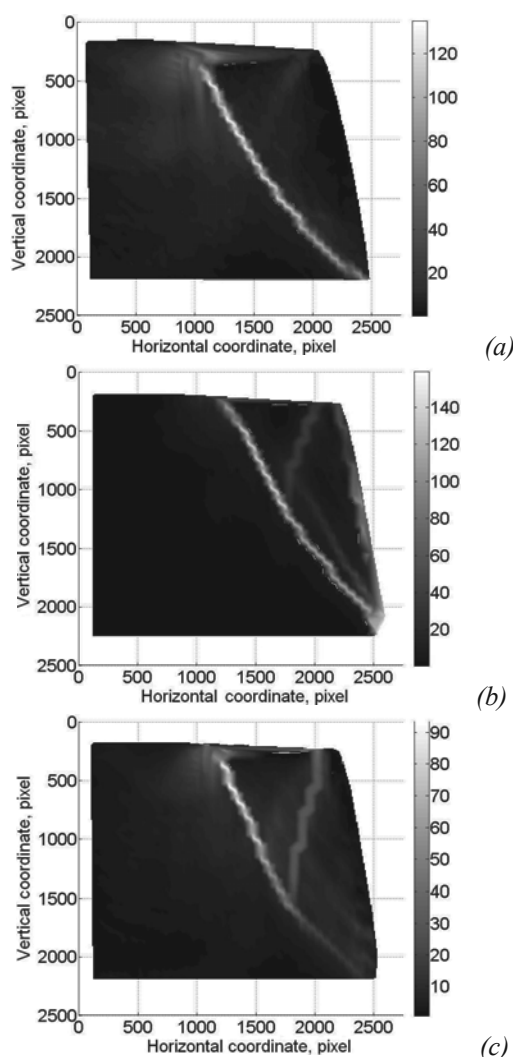


Figure 5. Total shear strain distribution at the face collapse, determined by mean of PIV in tests with PMMA (a), NET (b) and PMMA25 (c).

of other tests. It is important to note that the points marked by an asterisk in Figure 6 are largely overestimated, because approaching the failure the nails underwent to large and concentrated flexional plastic strains, also for the presence of rupture wedge of shallow foundation, and, in this strain state the relationship strain-stress is not linear yet.

Of course the tensile force distributions along nails for all the tests at failure are similar to those recorded for model *d*, even if they are not here reported for sake of brevity.

## 5 FINAL REMARKS

From the experimental results discussed above it is possible to observe that both flexional and axial stiffness influence the performance of a soil nailing system in excavation and at collapse. If the facing has no continuity, its flexional stiffness can hinder the front deformation during excavation, thus limiting the mobilization of shear stress along nails. In addition, if the facing is flexionally deformable but characterized by low axial deformability, horizontal displacements of the front too can be controlled. In both of the cases, at the end of excavation, the system has still a high level of safety in relation to the global stability problem. On the contrary, the largest deformations accumulated with excavation can reduce the safety margin.

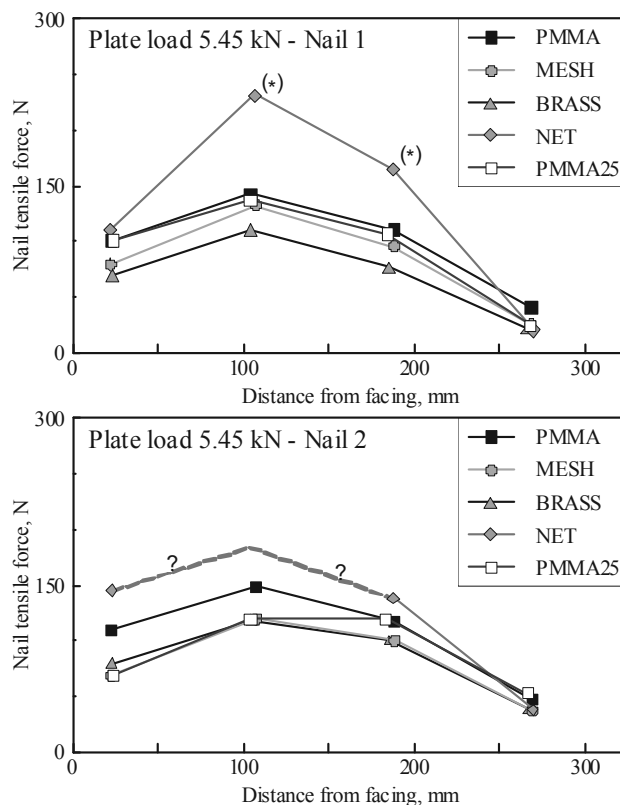


Figure 6. Distribution of tensile force along the monitored nails when the load on plate is equal to 5.45 kN (collapse load of test with NET): (a) upper nail; (b) lower nail. Notes: 1) the tensile data indicated with asterisk (\*) are determined from strain-gauge readings at a load of 5.30 kN because at greater loads the nails experimented plastic strains in these positions; 2) The trends indicated with (?) are only presumed, not measured, due to the detachment of the 2<sup>nd</sup> strain-gauge.

## 6 ACKNOWLEDGEMENTS

We want to thank the Dalla Gassa s.r.l. (Cornedo Vicentino, Italy), which sponsor this research, and Dr. D.Pilotto and M.Miuzzi for the valuable help given in the experimental tests.

## 7 REFERENCES

- Geoguide7, 2008. *Guide to Soil Nail design and construction*. Geotechnical Engineering Office, Hong Kong.
- Gottardi G., Simonini P., 2003. The viscoplastic behaviour of a geogrid-reinforced model wall. *Geosynthetics International*, 10: 34-46. ISSN: 1072-6349, doi: 10.1680/gein.2003.10.1.34.
- EN 14490:2010: *Execution of special geotechnical works — Soil nailing*.
- FHWA-IF-03-017, 2003. *Geotechnical Engineering circular No. 7 – Soil Nail Walls*.
- Plumelle C., Schlosser F., Oclage P. and Knochenmus G., 1990. French national research project on Soil Nailing: CLOUTERRE, *Geotechnical Special Publication ASCE*, 25, 660-675.
- Stocker M., 1976. Bodenvernagelung, Vorträge der Baugrundtagung, Nürnberg, *Deutsche Gesellschaft für Erd- und Grundbau e.v.*, Essen.
- White, D.J., Take, W.A. & Bolton, M.D. 2003. Soil deformation measurement using particle image velocimetry (PIV) and photogrammetry, *Géotechnique* 53(7): 619-631.

# Comparative study of different deep excavation retaining systems

## Etude comparative de différents systèmes de soutènement de fouilles profondes

Josifovski J., Gjorgjevski S.

Department for Geotechnics, Faculty of Civil Engineering-Skopje, University Ss. Cyril and Methodius - R. Macedonia

**ABSTRACT:** In the past period a building expansion and rapid construction in highly urbanized city centre of Skopje (capital of the R. Macedonia) has been witnessed. In most cases the structures are small administrative buildings which do not exceed 800m<sup>2</sup> with underground often used for offices or parking. This has been an inspiration to investigate the comparative advantages of different deep excavation retaining systems. In fact three designer tasks, very similar by many parameters, had been used to draw the general conclusions. The selected construction sites are located closely to each other, thus share similar ground conditions. The following retaining systems were considered: (1) system of soldier H piles with lagging, (2) reinforced concrete diaphragm wall, (3) secant pile wall with primary (reinforced concrete) and secondary (concrete) piles. Although systems are different in general they can still be compared, especially from the economic point of view. All retaining systems had been calculated numerically and controlled according to the Eurocode provisions. The concluding remarks offer a preferred solution for underground construction on narrow and build-up sites.

**RÉSUMÉ:** Le centre-ville très urbanisée de Skopje (capitale de la république de Macédoine) a été témoin ces derniers temps de nombreuses constructions de bâtiments neufs. Dans la plupart des cas, ce sont de petits bâtiments administratifs qui ne dépassent pas 800m<sup>2</sup> avec des sous-sols souvent utilisé pour des bureaux ou le parking. Cela a été l'occasion d'enquêter sur les avantages comparatifs des différents systèmes de soutènement de fouilles profondes. En fait, trois principes de soutènement, très semblables par de nombreux paramètres, ont été utilisés pour tirer des conclusions générales. Les chantiers de construction sélectionnés sont très proches les uns des autres avec des conditions de sol similaires. Les systèmes de soutènement suivants ont été considérés: (1) Système de poutres en H soudée après-coup, (2) paroi moulée en béton armé, (3) pieux sécants avec pieux primaire (béton armé) et secondaire (béton). Bien que les systèmes soient différents, en général, ils peuvent encore être comparés, en particulier du point de vue économique. Tous les systèmes de soutènement ont été calculés numériquement et contrôlés selon les dispositions Eurocode. Les conclusions offrent une solution pratique pour la construction souterraine en zone densément construite.

**KEYWORDS:** deep excavation, retaining system, supporting elements, finite element analysis.

## 1 INTRODUCTION

The problem of deep excavation in highly urbanized area such as the city centre of Skopje has proved to be quite formidable engineering task. In particular the greater depth and the built-up surrounding make it especially difficult. The ever growing prize of a square meter has led to extensive utilization of the underground. Such an idea has been very attractive for the investors which always look for the most economic solution of the underground works, generally constrained by the excavation depth and retaining system.

The tendency to optimize the structures has been an inspiration for the authors to investigate the comparative advantages of different deep excavation retaining systems and their supporting elements. The objective has been to offer a qualitative study which considers all relevant aspects of the underground construction in urban areas.

The paper presents case studies of three different retaining systems used to secure the excavation pits which do not exceed 800m<sup>2</sup> in base. All of them are located in the area of around 2km, thus share similar ground conditions. There are different limitations and/or specifics on every site, as to the surrounding e.g. existing structures or very frequent streets. The depth of the excavation pit varies from 6.5 to 18m. All retaining systems had been calculated numerically and controlled according to the Eurocode provisions.

### 1.1 System of soldier H piles with lagging

In the first case example a 7m deep pit should be excavated for the construction of the new National theatre. Larger part of the structure has been already finished, only the part adjacent to the street is left to be erected. The excavation pit is rather narrow only 3.05m in width (enlarging to 6.1m) and 36.65m long, see Figure 1.



Figure 1. Site location No.1 in front of the new National theatre.

The task has been to secure the pit from only one side (namely from the frequent street which connects the main city square) allowing undisturbed traffic and pedestrian communication. As solution a temporary structure of soldier H piles with lagging has been proposed. The supporting system uses rickers and struts (positioned on -2.0m and -4.65m from the top) acting upon the foundation of the existing structure. There were several arguments in favour of this solution, foremost it is light and suitable for a temporary structure, does not take a lot of space and last but not least it is relatively cheap.

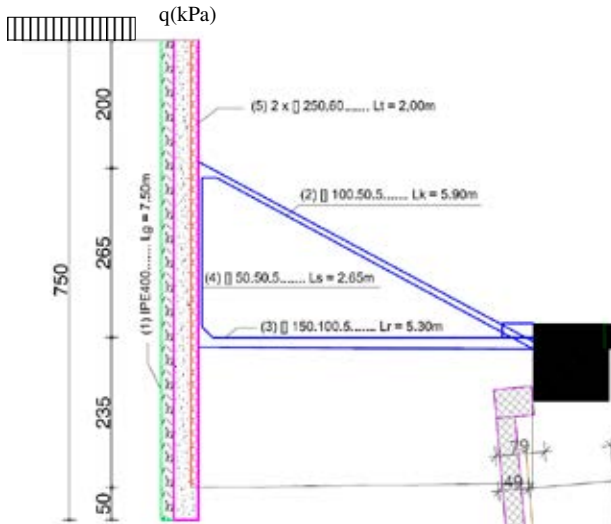


Figure 2. Site location No.1 with RW as soldier H piles with lagging.

The structure is modular consisted of eighteen soldier H piles placed on every 2m with total length of 7.5m. The piles are embedded with depth 0.5m. A steel IPE 40 profile has been chosen according to DIN 1025 B1.5 and DIN 17100 specifications.

The ground profile from 0 to 3m is defined by a layer of fill with pieces of construction material such as bricks and mortar. From 3 to 7.5m there is clayly silt with smaller pieces of construction debris with the following material properties: unit density as  $\gamma=19\text{kN/m}^3$ , cohesion as  $c=5\text{kPa}$ , angle of internal friction as  $\phi=28^\circ$  and Compressibility modulus as  $M_v=8000\text{kPa}$ . A standard traffic load with  $q=16.67\text{kPa}$  acting on the far away and  $p=5\text{kPa}$  on the nearby strip has been assumed.

The problem is calculated using the finite element method using plane and beam element. The structural elements of the wall are assumed to be linear with smeared stiffness as in equivalent plane-strain model. The soil is discretized by Mohr-Coulomb material behaviour. A plot of the total displacements is shown in the Figure 3.

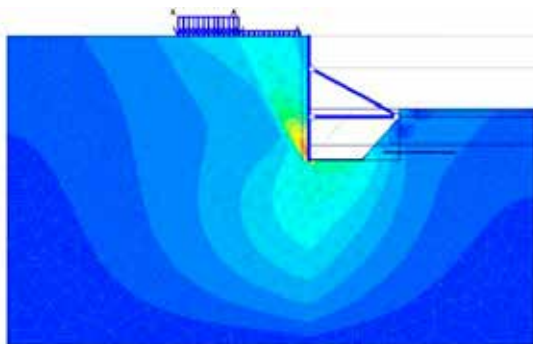


Figure 3. Shading plot of the total displacements.

The maximal total displacement is 64mm registered in the toe of the wall while on the top(-surface) it is around 10 times smaller.

The results of the analysis of soldier H pile wall are presented in the Figure 4.

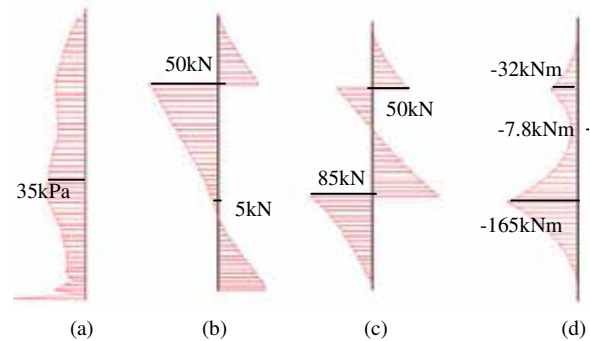


Figure 4. Diagram of (a) Active earth pressure, (b) Axial force, (c) Shear force and (d) Bending moment.

The steel cross sections are calculated according to the provisions in EC3 with  $\gamma_s=1.15$ . A steel type „Fe235“ with allowable stress of 204MPa has been used.

The rickers prop the wall at -2.0m and are positioned at angle of 23.5 degrees with length of  $L_k=6.65\text{m}$ . They are designed as a rectangular hollow section [100.50.5. The struts prop the wall at -4.65m with length of  $L_s=6.1\text{m}$ . They are designed to accept compression force using rectangular hollow section [150.100.5. Last but not least, the wooden lagging ( $b=25\text{cm}$ ,  $l=182\text{cm}$  and  $t=12\text{cm}$ ) are positioned over the height of 7m between the soldier piles.

Finally, the global stability is controlled using the so-called *phi-c* reduction procedure. A global factor of safety  $F_s=1.37$  has been obtained which is larger than 1.1 as recommended value for temporary structure.

### 1.2 Top to down construction of system with diaphragm wall

Following the site conditions (see Figure 5) a building with five underground floors with depth of -15.86m should be constructed. From two sides there are existing buildings, one of which is adjacent on six floors and one basement while the other one is 3m away with only two floors and shallow basement. From the third side there is very frequent boulevard which leads to the centre and main city square.



Figure 5. Site location No.2 on M.T. Gologanov boulevard.

The base dimension of the excavated pit are 27.65x11.55m not very large around 320m<sup>2</sup>, but due to the difficult surrounding conditions and the great depth it has been decided to use the top to down approach of construction. The diaphragm wall is considered to be a permanent structural element, which in the first phase carries the horizontal (earth) pressure loads while in exploitation it will be responsible also for the loads from the superstructure. Following the top-down procedure the diaphragm will be supported by the previously constructed RC



slabs, thus enabling the further excavation of the pit. The excavation process and slab support construction is described in Table 1 with respect to the depth  $h$ .

Table 1. Excavation phases

Phase	1	2	3	4	5	6	7
$h$ (m)	0.0	-3.5	-6.11	-8.5	-10.9	-13.9	-15.8

The diaphragm RC segments are 2.5m long and 0.4m width organized as primary and secondary. The base plan with depth and sequence of construction is presented in Figure 6.

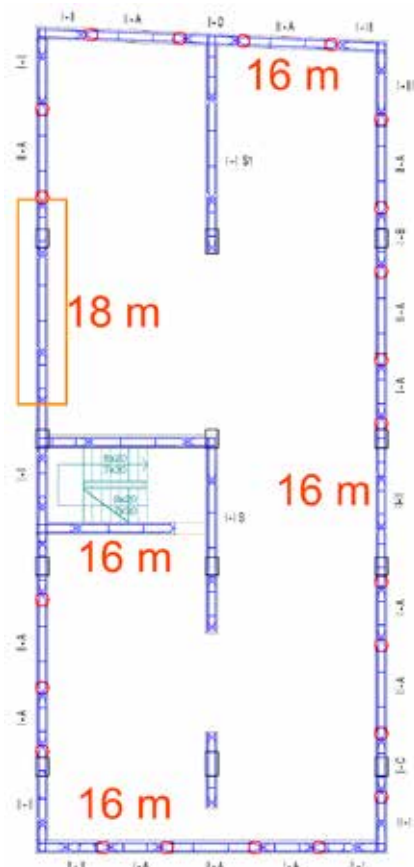


Figure 6. Base plan of primary and secondary diaphragm segments.

The depth is 16m only in one section its 18m due to the requirement necessary for elevator equipment. The soil profile is established through set of field and laboratory investigations which were used to define the material properties given Table 2.

Table 2. Soil properties

Type	$h$ (m)	$\gamma$ (kN/m <sup>3</sup> )	$\nu$ (/)	$M_c$ (MPa)	$c$ (kPa)	$\phi$ ( $^\circ$ )
N	-1.0	17.0	0.30	3	5	18
GW	-3.5	19.0	0.32	30	0	32
M	-4.0	22.0	0.27	35	100	30
M	-10.0	24.0	0.26	45	150	32
M	-20.0	24.0	0.26	55	200	34

where  $\gamma$  is a unit weight,  $\nu$  is a Poisson's ratio,  $M_c$  is Compression modulus,  $c$  is cohesion and  $\phi$  is angle of internal friction. They are given for every lithological unit: top layer (N) is a man-made embankment brownish silty clay containing pieces of bricks and roots with a thickness of 1m, followed by layer (GW) is sandy gravel with thickness of 2.5m to 3.7m; continuing as a layers (M) which are Neogene's deposits composed by claylike Marls to highly weathered alveoli. The

underground water is detected at -3.2m below ground surface in layers (GW) while the bottom layers are with low permeability and relatively dry.

In order to obtain more realistic behaviour of the deep excavation process secured by diaphragm wall, the problem has been analyzed using the finite element method. The ground stress-strain state during excavation is determined through a plane-strain finite element model. The soil is discretized as elasto-plastic material using a Mohr-Coulomb definition vis-avis the reinforced concrete wall as a linear material. The spatial discretization had been varied depending on the situation and detailing level but in general triangular plane elements with 15 nodes had been used. Two cross sections both in X-X and Y-Y direction had been discretized and calculated. The structural elements were modelled using three node beam elements, see Figure 7.

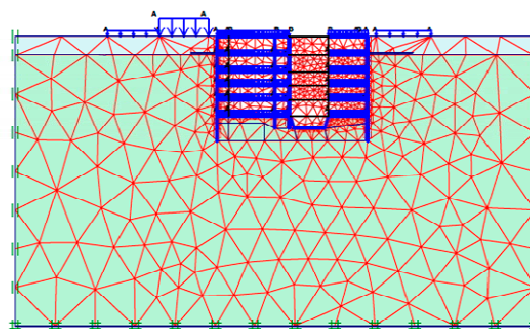


Figure 7. Finite element model of X1-X1 section.

The underground structure has been calculated for two loading combinations, namely the construction loading situation with pit excavation (in 6 phases = 1-diaphragm wall + 5-floor slabs) and exploitation situation (with permanent + temporary + seismic loads). In Figure 8 the total displacements of underground structure is presented for the second loading combination.

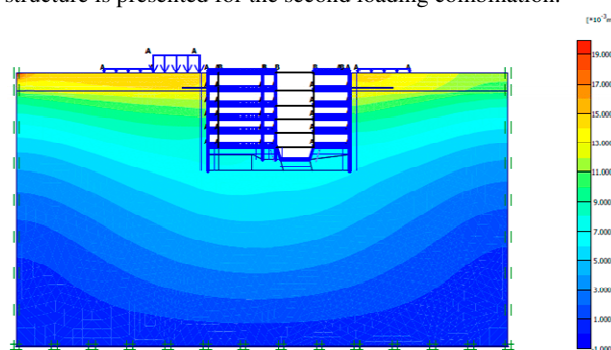


Figure 8. Total displacement of the soil-structure system in X1-X1 section.

The maximal registered displacement is 14mm with predominantly horizontal component (stiff rocking response) due to the seismic loading. According to the stress-strain distribution the internal quantities of the structural elements had been determined. They were used for structural design of elements such as, diaphragm wall, floor slabs and foundation plate. The reinforcement is determined according to the EC2 for C35/45 and S500 (with  $\gamma_c=1.5$  and  $\gamma_s=1.15$ ). The reinforcement of the diaphragm wall is around  $0.8\%A_c$  (area of concrete section). The 47% of the total reinforcement will be used for the diaphragm wall, 18% for the foundation plate and 35% for the floor slabs.

### 1.3 System of secant pile wall

For the same site (see Figure 5) an alternative solution has been analysed with secant pile retaining wall to secure the excavation pit (27.65x11.55m) but this time with depth of 6.5m. In this scenario only two floors are planned to be constructed using a temporary retaining structure. In the first phase the primary, (reinforced concrete) piles with diameter of 0.6m and length of 7.5m spaced exactly 1.2m should be executed. In the next phase the secondary (concrete) piles with the same diameter but shorter depth of 5.5m are constructed. On the top they are connected by a beam with dimensions 0.6x0.4m as shown in Figure 9.

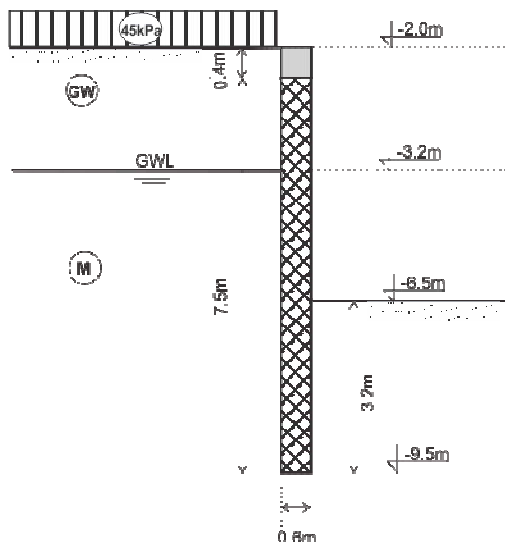


Figure 9. A plan of the secant pile wall in X1-X1 section.

The problem is discretized using three-dimensional finite element model where the soil profile is identical to the one described in Table 2. For the spatial discretization volume elements are used in combination with nonlinear-plastic material definition for the soil and linear-elastic for the concrete. The calculation is used to determine the stress-strain behaviour of the soil-structure interaction system, hence presented through the total displacement in Figure 10.

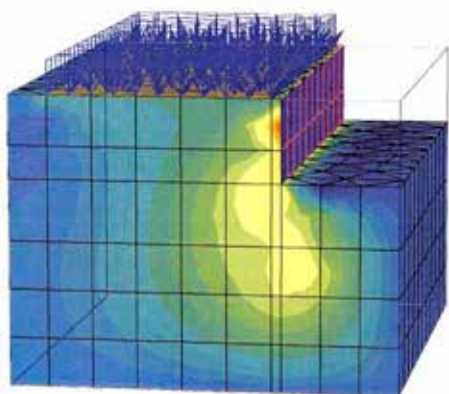


Figure 10. Total displacement of the soil-structure system in X1-X1 section.

A maximal earth pressure of 33.7kN/m<sup>2</sup> causes horizontal displacement of 9.8mm, which have been considered as acceptable. Furthermore, the diagrams of internal pile quantities are presented in Figure 11.

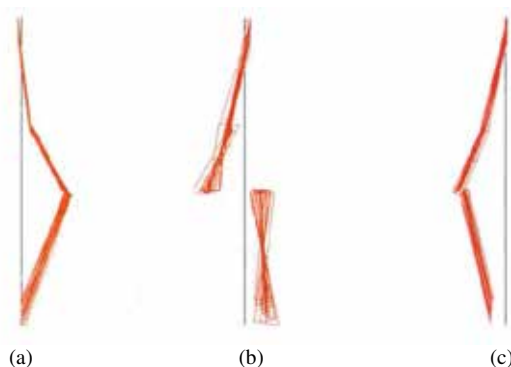


Figure 11. Diagram of (a) Axial force, (b) Shear force and (c) Bending moments in the pile.

The values of the maximal internal quantities: bending moment  $M=56.81\text{kNm}$ , shear force  $Q=43.64\text{kN}$  and axial force is  $N=-114.8\text{kN}$ . The pile design has been made using interaction (M-N) diagrams for C30/37 providing the following reinforcement: longitudinal  $14\phi 16$  ( $28.2\text{cm}^2$ ) and stirrups  $\phi 8/20\text{cm}$ . Finally, the global stability is controlled where a safety factor  $F_s=1.55$  is obtained.

## 2 CONCLUSION

The solder H pile wall with lagging is rarely used in our practice, although it is highly efficient and cost effective for situations where there is no ground water. Also a greater depth can be reached when combined with adequate supporting system e.g. tieback. Nevertheless, in Skopje there are few locations with low GWL. Although very formidable the systems with diaphragm wall are seldom used, partially because there is almost no experience nor there has been clear cost-benefit analysis. For a long period of time it has been thought that the costs are very height, which with the present study had proven not to be the case. Combined with the top-down method of construction where the wall is permanent structure according to our analyses remains very cost effective solution. The secant pile wall technique, in contrast, is very often used in our practice, sometimes in combination with anchors when greater depth is needed. It represents formidable solution but usually takes a lot of the available space and construction time, also brings high expenses since it is often a temporary structure.

Finally, when comparing all retaining structures we had come to conclusion that the diaphragm wall represents a preferred solution for underground construction in highly urbanized (build-up) areas and situations with high ground water level as it is usually the case in Skopje.

## 3 REFERENCES

German Society for Geotechnics (Deutsche Gesellschaft für Geotechnik.V.) 2003. Recommendations on Excavations, Ernst & Sohn Verlag für Architektur und technische Wissenschaften GmbH & Co. KG, Berlin, ISBN 3-433-01712-3.

Kempfert, H.G. and Gebreselassie, B. 2006. Excavations and Foundations in Soft Soils, Springer-Verlag Berlin Heidelberg, ISBN 540-32894-7.

Potts, D.M. and Zdravkovic, L. 2001. Finite element analysis in geotechnical engineering: application. Imperial College of Science, Technology and Medicine, Thomas Telford Publishing, Thomas Telford Ltd, ISBN 0-7277 2753-2.

Moeller G. 2012. Geotechnik. Grunbau, Bauingenieur-Praxis, 2 Ed. Ernst & Sons, A Wiley Company ISBN: 978-3-433-02976-3.

EN 1997-1:1994 Eurocode 7: Geotechnical design - General rules

EN 1538:2000 Execution of special geotechnical works – Diaphragm walls

# Various use of diaphragm walls for construction of multilevel road junction – Design and monitoring of displacements

Diverses utilisations de parois moulées pour la construction de l'intersection des routes à plusieurs niveaux – Conception et le suivi des déplacements

Siemińska-Lewandowska A., Mitew-Czajewska M.  
Warsaw University of Technology, Warsaw, Poland

Tomczak U.  
Soletanche Polska Sp. z o.o., Warsaw, Poland

**ABSTRACT:** The paper presents various use of diaphragm walls for the construction of four-level junction in Warsaw. Diaphragm walls were chosen as a best solution for abutments of 2 viaducts and 1 flyover, foundations (barrettes) under 7 pillars, 60 to 100cm thick retaining walls with total length of over 570 running meters. In the paper detailed technical descriptions, geotechnical conditions, predicted theoretical horizontal and vertical displacements of walls for all mentioned diaphragm wall applications are presented. Finally, the comparison of the results of theoretical analysis and real scale monitoring results (displacements measurements and load tests) in accordance with construction stages is presented and discussed.

**RÉSUMÉ :** Cet article présente différentes utilisations de parois moulées pour la construction d'une jonction de quatre niveaux à Varsovie. Les parois moulées ont été choisies comme une meilleure solution pour les butées de 2 viaducs et 1 voie surélevée, les fondations (barrettes) sous 7 piliers, des murs de soutènement épais de 60 à 100 cm avec une longueur totale de plus de 570 mètres. Dans le document des descriptions techniques détaillées, des conditions géotechniques, les prévisions de déplacements horizontaux et verticaux théoriques des murs pour toutes les applications de parois moulées mentionnées sont présentés. Enfin, la comparaison des résultats de l'analyse théorique et les résultats en vraie grandeur (mesures de déplacements et de tests de charge) de la surveillance conformément aux étapes de la construction est présentée et discutée.

**KEYWORDS:** diaphragm wall, deep excavation, foundation, barrettes

## 1 INTRODUCTION

In Poland nowadays, especially before euro 2012, road network and new motorways connecting Poland and Ukraine with Western Europe are being built. Construction of Warsaw bypass is the place where huge multilevel road junctions are built.

The case discussed in the paper is 3 level road junction consisting of 2 flyovers (indicated as E1, E2 at fig. 1) and 2 viaducts (indicated as W1, W2 at fig. 1). The original building permit design assumed that the abutments and columns were to be founded on large-diameter piles with the diameter 120 and 150 cm. The accompanying RC retaining walls and viaduct abutments were to be erected in traditional formwork. The original design assumed that the embedded part of the junction was to be built with a temporary casing in the form of sheet piling with an RC capping beam at the top. The walls were to be anchored with 1 level of soil nails. Permanent structure was

designed as retaining walls connected with water tight foundation plate. During the execution design stage, due to economical and technological reasons, the solution was much simplified - only diaphragm walls were used for all parts of the structure, i.e. for:

- excavation walls – retaining structures,
- foundations – barrettes of viaduct columns as well as barrettes of columns and abutments of flyovers,
- viaduct abutments – T-shaped diaphragm walls.

The new solution allowed the significant shortening of construction works through the use of diaphragm walls as temporary and permanent structure. Figure 1 presents the general arrangement of the discussed road junction and indicates parts of the structure described in the paper.

In the design stage theoretical displacements and bearing capacities of these structures were calculated. During construction, at each of discussed structure parts, the real

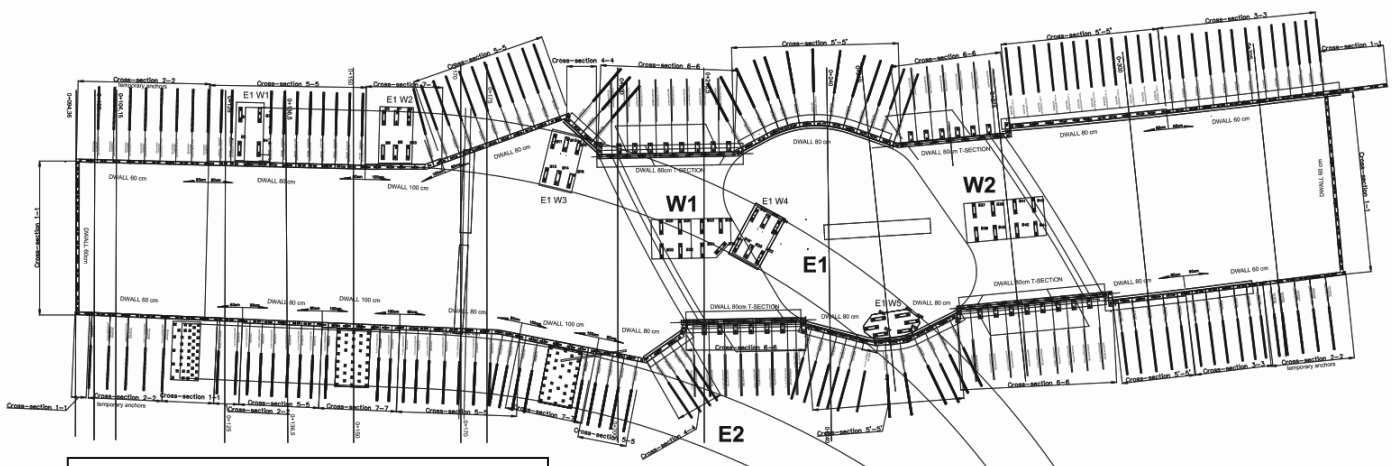


Fig. 1 General arrangement



horizontal displacements and settlements were measured and compared to theoretical values calculated in the design stage. It has allowed an assessment of the correctness of the solution.

## 2 GEOTECHNICAL AND HYDROLOGICAL CONDITIONS

The ground in the land plot consists mainly of Quaternary formations: river sediments and glaciofluvial deposits as well as glacial deposits. In the entire area involved in the investment, the near-surface layers below man-made fills consist of medium-dense and dense sands and gravels reaching down to the max. depth of 18.8 m. Below (the layer roof from 10.6 to -18.8 m), there are glacial clays, deposited in the form of stiff sandy clays, clayey sands and, locally, silty clays. The layer of anthropogenic soils is not very thick: maximum thickness: 2.2m, average thickness: about 0.5-1.00 m.

Within the entire area, a continuous ground water table was found in the layer of glaciofluvial sands. The ground water table was located at about -4.5 m below the ground level. Occasionally, the water table was confined by lenses of cohesive soils.

## 3 DIAPHRAGM WALLS AS A RETAINING WALL

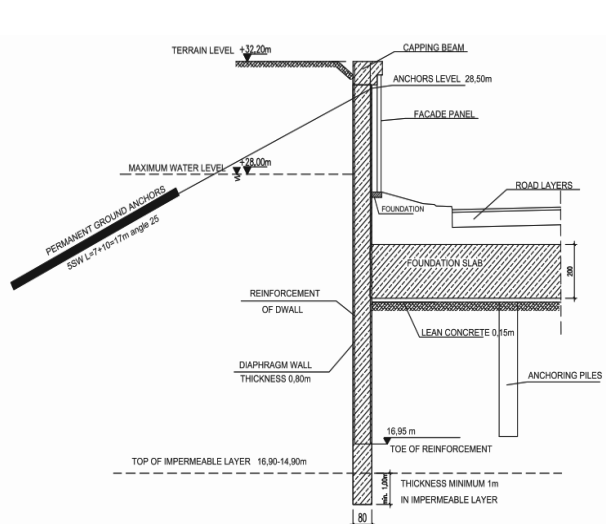


Fig. 2 Typical cross-section of the excavation wall; 80cm thick diaphragm walls, anchored using permanent anchors.

Due to variable embedding of the excavation below the ground level, down to the maximum depth of 10 m below the ground level, diaphragm walls with 3 different thickness values were implemented, namely 60 cm, 80 cm and 100 cm. Moreover, different types of protective measures were implemented to ensure stability of casing walls, i.e:

- temporary ground anchors, 600 kN capacity (cross – section 2-2),
- permanent ground anchors, 600 - 700 kN capacity (cross-sections 3-3, 4-4, 5-5),
- permanent ground anchors in the area of T-shaped D-walls, 700 kN capacity (cross section 6-6).

Some parts of walls remained not supported (cantilever walls) due to the small height of excavation (cross-section 1-1) or possible collisions with pile foundations outside the wall (cross-section 7-7).

In total 148 ground anchors were executed (18 temporary and 130 permanent) and 31 permanent ground anchors for abutments.

Diaphragm walls along the entire perimeter of the facility (including the transversal walls) were embedded at least 1 m down into the impermeable layer, in order to minimise the inflow of water into the excavation (fig 2). Due to unbalanced hydrostatic pressure, the ground slab was anchored with

displacement piles in its central part in the deepest excavation (fig 2).

Diaphragm walls were designed to resist loads resulting from soil pressures and from service loads at the ground surface generated by vehicles and stored materials, amounting to  $q=12,0$  kPa in the zone removed by at least 1.5 m from the wall face, and loads generated by heavy traffic, amounting to  $q=30$  kPa. Additionally, the design considered a load generated with vehicle K located on the roadway located in close vicinity of the diaphragm wall, in compliance with standard PN-85/S-10030 Bridges. Loads.

Static analysis of diaphragm walls were made using dependent pressures method (PAROI). 7 typical calculation cross-sections were verified. Typical results of calculations – bending moments and displacements – are shown at fig. 3. Maximum theoretical values of horizontal wall displacements are as follows:

- cantilever D-wall - 6 mm;
- D-wall and temporary ground anchors - 15 mm;
- D-wall and permanent ground anchors - 12mm;
- T-shaped D-walls - 8mm.

Corresponding bending moments amount to 180 kNm/m up to 700 kNm/m.

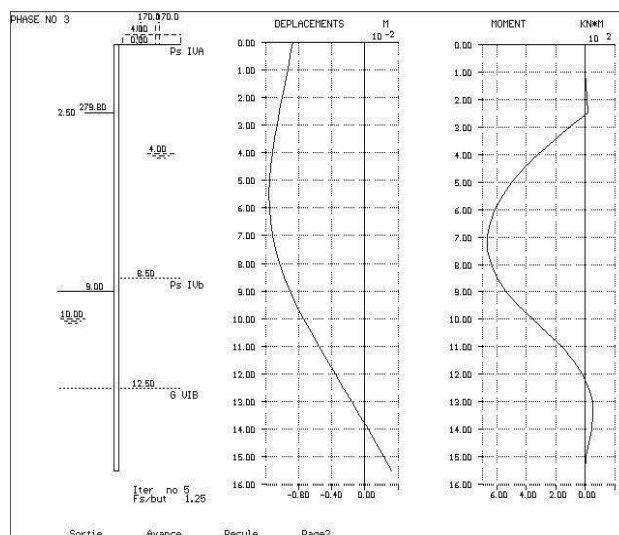


Fig. 3 Theoretical values of bending moments and horizontal displacements for 80cm thick D-wall with permanent ground anchors (cross-section 5-5) in the final construction stage.

Benchmarks for geodesic measurements were located on the capping beam of diaphragm walls, spaced every 50 m at the maximum. Measurements were carried out for particular stages of execution of works on site, at least once every month or more frequently.

Construction stages were as follows:

- site preparation, sub-base preparation, construction of guide walls and D-walls with RC capping beam – reference measurement,
- excavation 0,5m below the anchoring level – measurement 1,
- execution and stressing of ground anchors – measurement 2,
- final excavation – measurement 3,
- verification of displacements during the execution of driven piles – subsequent measurements.

Particular attention was paid to measurements of wall displacements in the vicinity of works consisting in driving displacement piles in, in order to anchor the ground slab. In the view of the presence of a layer of silty sands, designers were concerned about the impact of dynamic pile driving on the load-carrying capacity of ground anchors, whose bearing plates are

embedded in these sands. The monitoring of displacements of the capping beams of diaphragm walls showed that their maximum value reached 10 mm for an 80 cm thick wall, anchored with permanent anchors. In the case of other cross-sections, displacements were smaller and reached up to 8 mm. No increased displacements of the diaphragm wall were observed during the process of pile driving.

Design works had to face additional difficulties resulting from the very complex shape of the facility, involving 4 abutments (T-shaped D-walls, cross-section 6-6) and curved walls that encased the roundabout (cross-section 5'-5'). Both the excavation bottom and the top of the walls and the capping beam were located in slopes. Due to this fact combined with variable thickness and varied strut methods, almost every single reinforcing cage of a diaphragm wall was of different type. Therefore, the contractor who constructed diaphragm walls was forced to stick strictly to the schedule of execution of particular sections, without any possibility of introducing changes during the works.

#### 4 DIAPHRAGM WALLS AS FOUNDATIONS FOR PILLARS AND COLUMNS

A foundation on barrettes (parts of diaphragm walls) – instead of large-diameter piles ( $\varnothing$  120/150) implemented in the construction design – was designed for 5 supports of the flyover E1 (4 pillars and 1 abutment) and viaducts pillars – viaducts: W1 and W2 (fig.1). The barrettes – as fragments of diaphragm walls – have a very large base. Therefore, they can transmit very high loads. For this reason, they are very useful for structures subjected to very high loads, as in this particular case of bridge structures.

The replacement, for instance, of the support consisting of 11 piles that were 150 cm in diameter with 6 barrettes resulted in a considerable acceleration of works, which brought about a measurable financial result in this particular case. Typical arrangement of the pillar foundation is shown at fig. 4.

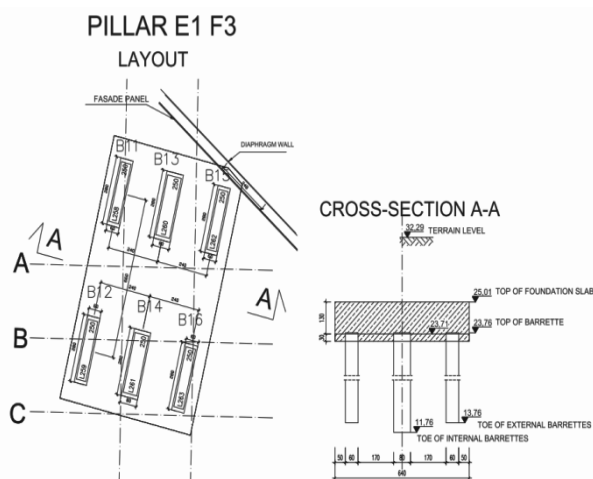


Fig.4 Typical pillar foundation arrangement

Barrettes implemented as foundations for pillars had the following dimensions: 0.6x2.80 m and 0.8x2.8m. They were from 10.0 to 15.0 m long. They transmitted vertical forces reaching the max. value of 7600 kN and the bending moment reaching the max. value of 4996 kNm. In total 44 barrettes were erected.

Internal forces and moments for each barrette were calculated using ROBOT software, modelling supports loaded by a possible most unfavourable load combination. Due to unsymmetrical loading of supports each barrette had different loading (both - compression as well as tension) and different bending moments in both directions.

For each of barrettes additional boreholes were made in order to verify geotechnical conditions. Only then the design of lengths and calculation of bearing capacities of barrettes were made. It was considered that barrettes were founded in the stiff sandy clay layer and the shaft friction was calculated considering 2 geotechnical layers along barrettes, i.e. stiff sandy clays and medium dense to dense fine and silty sands.

Base bearing capacities and shaft frictions were calculated basing on the regulations of PN-83-B-02482 Foundations. Bearing capacity of piles and piles foundations.

A base injection system was designed for all barrettes, in order to ensure as high load-carrying capacity of a barrette as possible, while ensuring minimum settlements. In each support, one barrette was selected to be subjected test vertical loads, supposed to confirm the adapted geotechnical parameters were correct. The results of test loading showed that the load-carrying capacity of barrettes was higher than necessary, while the settlements were smaller than admissible.

Vertical loading tests of barrettes was carried out for 6 barrettes that were gradually loaded up to the maximum of 150% of the calculation force. After reaching 100% of design load the barrettes were unloaded in order to measure the resulting permanent settlement. Analogical procedure was used after reaching 150% calculation force. Permanent settlements at the 150% force (i.e. 5286 - 10397 kN) did not exceed 4 mm, while they reached 2 mm for 100% of the calculation force (i.e. 3524 - 6931 kN). The barrette (dimensions: 0.6x2.8m, length: 13.1m) subjected to the greatest load experienced maximum settlement of 4.35 mm at the load of 10397 kN, where permanent settlement reached 2.91 mm. The results of settlement measurements during test loading of barrettes are compiled in table 1.

Table 1. The results of vertical loading tests of barrettes – settlements.

No.	Dimensions	Settlements for 100%Q		Settlements for 150%Q	
		temporary	permanent	temporary	permanent
B8	2,8x0,8 x10,0m	6001 kN		9002 kN	
		3,96mm	1,61mm	7,54 mm	3,53 mm
B12	2,8x0,6 x10,0m	3524 kN		5286 kN	
		1,33mm	0,75mm	2,82mm	1,71mm
B18	2,8x0,6 x10,0m	5889 kN		8834 kN	
		2,36mm	1,32mm	4,56mm	2,69mm
B31	2,8x0,6 x12,0m	5989 kN		8984 kN	
		2,53mm	1,32mm	5,29mm	3,09mm
B24	2,8x0,6 x13,1m	6931 kN		10397 kN	
		1,99mm	1,08mm	4,35mm	2,91mm
B41	2,8x0,6 x14,0m	4594 kN		6891 kN	
		1,80mm	1,14mm	4,17mm	2,84mm

As a part of interpretation of the test loading results auxiliary graphs were plotted as shown at fig. 5, in order to help calculate the bearing capacity of barrettes.

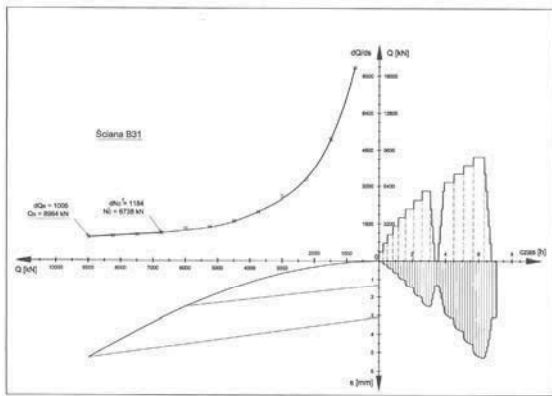


Fig. 5 Static load test result

### 5 DIAPHRAGM WALLS AS VIADUCT ABUTMENTS

The contour of the casing of the lowest level of the junction contained 4 viaduct abutments (viaduct W1 and W2). They were designed as 80 cm thick T-shaped diaphragm walls. Additional limitations were imposed for these fragments of diaphragm walls with respect to both horizontal and vertical displacements, caused by the selection of appropriate bearings. Additional permanent anchors were implemented – fig. 6, in order to minimize horizontal displacements of walls. In total, in the area of viaduct abutments, 31 permanent ground anchors of the 700kN capacity, were erected.

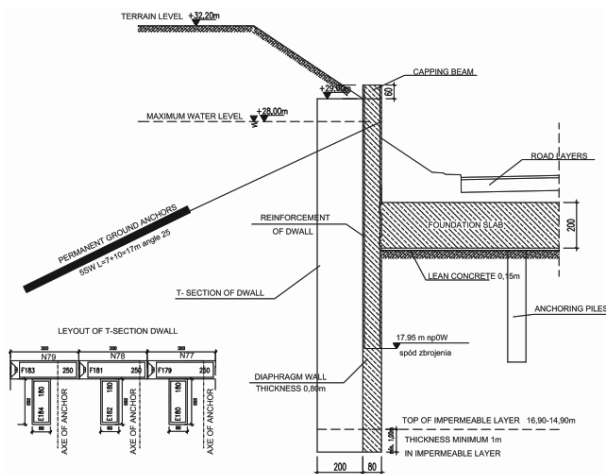


Fig. 6 Typical T-shaped D-wall cross-section for the W2 viaduct abutment.

Due to the fact that abutments were founded in the same stiff sandy clay layer as remaining barrettes made for the foundations of pillars, additional, special loading tests were not carried out for the T-shaped diaphragm walls. Bearing capacities of T-shaped barrettes were calculated by interpolation of the results of tests loadings of individual barrettes executed in the near vicinity of abutments. Additional limitations were imposed for T-shaped diaphragm walls with respect to horizontal displacements. In order to comply with limitations and minimize horizontal displacements of walls additional permanent anchors were implemented. The design load of permanent anchors was verified during acceptance tests. Each anchor was stressed up to 125% of its design load and after stabilization of creeping it was blocked at 80% of its design load. There were no excess permanent or elastic strains of anchor tendons measured, in accordance with regulations of

the code: PN-EN 1537 Execution of special geotechnical works. Ground anchors.

### 6 SUMMARY AND CONCLUSIONS

The results of diaphragm walls (as retaining walls) horizontal displacements measurements confirmed the correctness of static analysis of walls and prediction of their displacements, both made during design stage. Maximum value of horizontal displacement reached 10 mm for an 80 cm thick wall, anchored with permanent anchors and it didn't exceed neither theoretical nor permissible values. In the case of all other cross-sections, displacements were smaller and reached up only to 8 mm.

The results of vertical loading tests made for the barrettes confirmed the value of calculated theoretical bearing capacity being 7600 kN to be correct.

There were no significant horizontal displacements of T-shaped diaphragm walls noted (measured).

The new solution applied in the execution design (replacing the original one from the building permit design) was correct and resulted in significant savings due to the use of only one technology for the foundation and the retaining system (diaphragm walls) of the entire 3 level road junction construction. Most of the savings were obtained as a result of significant shortening of construction works.

### 7 REFERENCES (TNR 8)

- Soletanche Polska Sp. z o.o. 2010 Design of diaphragm walls for Łopuszańska-Kleszczowa junction, Warsaw
- Soletanche Polska Sp. z o.o. 2010 Design of anchors for Łopuszańska-Kleszczowa junction, Warsaw
- Soletanche Polska Sp. z o.o. 2008 Design of barrettes for Łopuszańska-Kleszczowa junction, Bydgoszcz
- GEOTECH Sp. z o.o. 2010 Geotechnical documentation for Łopuszańska-Kleszczowa junction, Warsaw
- PN-EN 1538 Execution of special geotechnical works – Diaphragm walls.
- PN-EN 1537 Execution of special geotechnical works – Ground anchors.
- PN-83/B-02482 Foundations. Bearing capacity of piles and piles foundations.

# Effects of plane shapes of a cofferdam on 3D seepage failure stability and axisymmetric approximation

Effets des formes planes d'un batardeau sur la stabilité après une rupture par infiltration tridimensionnelle et sur l'approximation axisymétrique

Tanaka T., Kusumi S., Inoue K.

*Department of Agricultural and Environmental Engineering, Kobe University, JAPAN*

**ABSTRACT:** In the excavation of soil with a high ground water level, seepage failure is often a problem. For excavations over a large area, seepage failure is a problem in two dimensions. In contrast, the more the region of a cofferdam is restricted, the greater the seepage flow concentrates three-dimensionally. This three-dimensionally concentrated flow lowers the safety factor for seepage failure more than under the two-dimensional condition. In this paper, seepage failure experiments were conducted under three-dimensional flow conditions for various cases of penetration ratios of sheet piles and analyses of FEM seepage flow and stability against the seepage failure of soil were carried out using the Prismatic failure concept 3D. The critical hydraulic head differences obtained by experiments and the theoretical values are examined for several cases. Effects of plane shapes of a cofferdam on the theoretical critical hydraulic head differences and axisymmetric modeling of three-dimensional seepage failure are also discussed.

**RÉSUMÉ :** Dans le cas de l'excavation d'un sol où le niveau des eaux souterraines est élevé, la rupture par infiltration constitue souvent un problème. Lorsque l'excavation est effectuée sur une grande surface, la rupture par infiltration devient alors un problème en deux dimensions. En revanche, plus la zone du batardeau est limitée, plus le flux d'infiltration se concentre en trois dimensions. Or, comparé à ce qui se passe dans un contexte bidimensionnel, ce flux concentré de manière tridimensionnelle réduit davantage le facteur sécurité lié à une rupture par infiltration. Dans cet article, nous décrivons les expériences sur la rupture par infiltration menées dans les conditions d'un flux tridimensionnel pour divers ratios de pénétration dans des palplanches. Nous y rapportons aussi les analyses du flux d'infiltration et de la stabilité suivant le modèle FEM par rapport à la rupture par infiltration du sol, menées à l'aide d'un concept prismatique de rupture en trois dimensions. Nous avons examiné, pour plusieurs cas, les rapports de niveau hydraulique obtenus dans les expériences et la théorie. Les effets des formes planes d'un batardeau sur les rapports de niveau hydraulique critiques d'ordre théorique et la modélisation axisymétrique de la rupture par infiltration tridimensionnelle y sont également évoqués.

**KEYWORDS:** three dimensional seepage failure (3DSF), surface shape of a cofferdam, axisymmetric modeling of 3DSF

## 1 INTRODUCTION

In the excavation of soil with a high ground water level, sheet piles or diaphragm walls are often used to retain soil and water. Under such conditions, seepage flow occurs through the soil, and seepage failure is often a problem. For excavations over a large area, seepage failure is a problem in two dimensions. In contrast, the more the region of a cofferdam is restricted and the deeper the penetration of the sheet piles, the greater the seepage flow concentrates three-dimensionally within it. The three-dimensionally concentrated flow lowers the safety factor for seepage failure more than under the two-dimensional condition (Nikkei construction, 2001). Such a case must be treated in three dimensions.

In this paper, seepage failure experiments were conducted under three-dimensional flow conditions for various cases of total depths of soil,  $T$ , and penetrated depths of sheet piles,  $D$ , with a plane shape of a cofferdam of 1:2. Analyses of FEM seepage flow and stability against the seepage failure of soil were carried out using the Prismatic failure concept 3D. The hydraulic head differences at deformation in the experiment,  $H_p$ , and theoretical critical hydraulic head differences based on the Prismatic failure concept 3D,  $H_c$ , are examined for the same cases. The theoretical critical hydraulic head differences for various plane shapes of a cofferdam, e.g., short to long length of 1:1, 1:2, 1:3, and 1:4, were calculated, and the effects of plane shapes of a cofferdam on the theoretical critical hydraulic head differences are discussed. The axisymmetric modeling of three-dimensional seepage failure is also discussed.

## 2 THREE DIMENSIONAL EXPERIMENTS

### 2.1 Test apparatus

A test apparatus was designed to study 3D seepage failure of soil within a cofferdam as shown in Figure 1. In the experiment, one quarter of the three dimensional region is examined. The seepage tank is made of stainless steel, 1,000mm wide, 1,300mm high and 1,000mm deep. The front of the tank is made of transparent glass for observation of the behavior of soil particles inside and the right side of the tank is equipped with 283 piezometer holes for the measurement of pore water pressures. A cofferdam is mounted on the right/front side with surface size 200mm×400mm. Seepage water flows through a sand model under the difference in water head  $H$  between the downstream water level at the top of the right-hand-side drainage hole and the upstream water level kept constant by the constant-head device.

### 2.2 Test material and test cases

In seepage failure experiments, uniform fine sand (Lake Biwa Sand 3: under 850 $\mu$ m mesh, 50% grain size  $D_{50}$ =0.283 mm, specific gravity  $G_s$ =2.67 and uniformity coefficient  $U_c$ =1.40) was used. Seventeen tests E0301 to E0317 were conducted. The following notation is used:  $T_1$  and  $D_1$  are the total depth of soil and penetration depth of sheet piles on the upstream side,  $T$  and  $D$  are those on the downstream side,  $d$  ( $=D_1-D$ ) is the excavation depth for the excavation model, and  $D_r$  is the relative density of soil. For a no-excavation model,  $T_1=T$ ,  $D_1=D$  and  $d=0$  are applied.

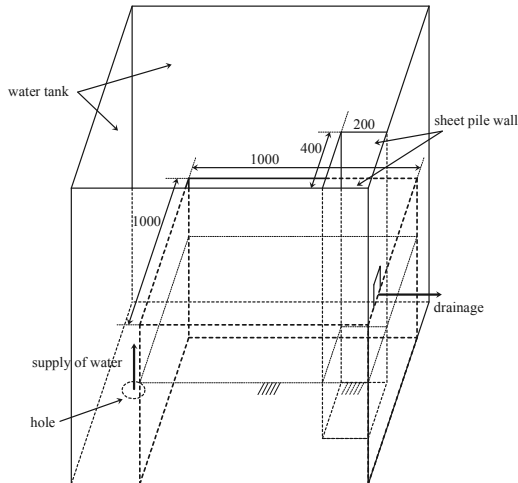


Figure 1. Schematic sketch showing test apparatus

### 3 EXPERIMENTAL RESULTS

#### 3.1 $H-Q_{15}$ curve and change in shapes of soil surface

Figure 2 shows the  $H-Q_{15}$  curve for test E0317, where  $Q_{15}$  is the discharge at 15 degrees Centigrade. It is observed from Figure 2 that  $Q_{15}$  increases linearly with increasing  $H$  until a certain value  $H_d$ .  $H_d$  value is referred to as the hydraulic head difference at which the  $H-Q_{15}$  curve diverts from linearity. As stated below, at almost the same point as  $H_d$ , the soil surface begins to settle on the upstream side and rise on the downstream side. This is because, just at this point, the soil loosens on the downstream side, the void space enlarges, permeability of the soil grows larger, and discharge increases non-linearly with  $H$ . As  $H$  increases beyond  $H_d$ ,  $Q_{15}$  becomes larger with increasing  $H$  more steeply than before, and the ground finally collapses at the hydraulic head difference at failure  $H_f$ .

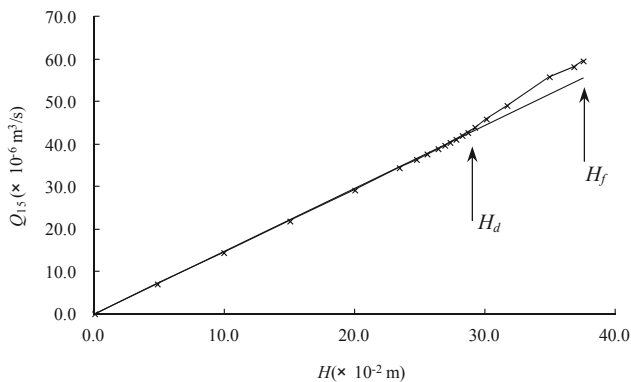


Figure 2.  $H-Q_{15}$  curves for test E0317

The heights of the soil surface are measured at several chosen points along the measurement line shown in Figure 3. The measurement line is a bisector of the right angle of the inside corner of the rectangular diaphragm wall. Figures 4 (a)-(c) show the changes in shape of the surface of the sand model along the surface height measurement line with increase in  $H$ , from  $H=4.81$ cm at the first step to  $H=36.78$ cm at one step before failure. The model sand is in a stable state at early steps of  $H$  (Figure 4(a)). When  $H$  increases beyond a certain value  $H_y$ , the model sand changes in shape near the sheet pile wall. The surface of the soil in the vicinity of the sheet pile wall subsides on the upstream side and rises on the downstream side (Figure 4(b)). The value of  $H_y$  is referred to as the hydraulic head difference at onset of deformation. It was found from a series of

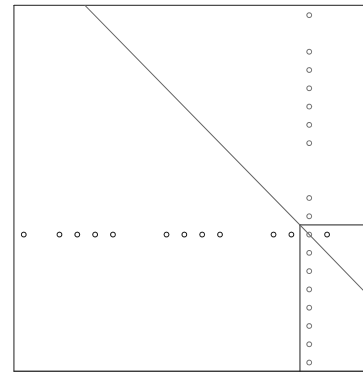
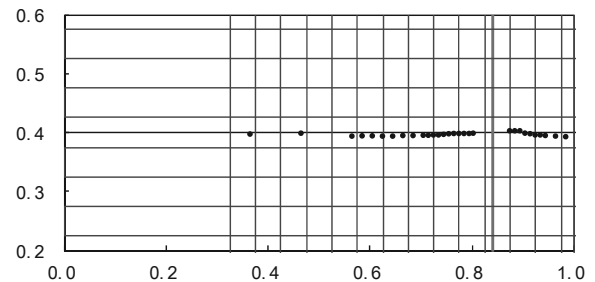
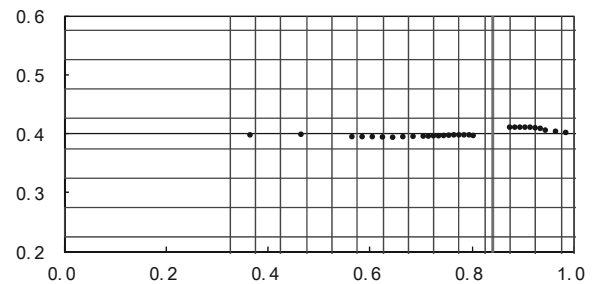


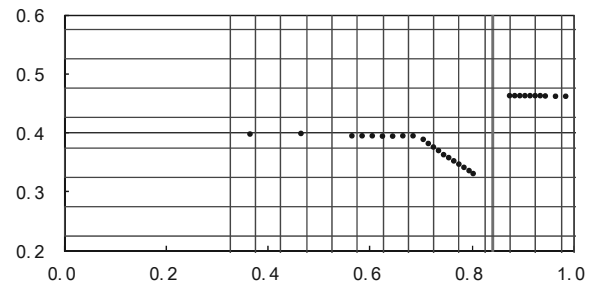
Figure 3. Measurement line of the height of soil surface



(a) At the early step of  $H$  ( $H=4.81$ cm)



(b) At the  $H$  value just beyond  $H_y$  ( $H=30.06$ cm)



(c) At the one step before failure ( $H=36.78$ cm)

Figure 4. Changes in shape of surface of sand model along the surface height measurement line with increase in  $H$



Figure 5. A close-up photo of the upstream inverse conical shape at  $H=36.78$ cm (E0317)

tests that the experimental results lead to the interesting conclusion  $H_y = H_d$ .

Subsidence of the upstream soil surface and rising of the downstream soil surface proceed with steps of increasing  $H$ . The upstream soil surface is an inverse conical shape centered at the outer corner of the rectangular diaphragm wall. A close-up photo of the upstream inverse conical shape is shown in Figure 5 at  $H=36.78\text{cm}$  (E0317). The rise in the downstream soil surface occurs uniformly within a certain width from the sheet pile wall. As  $H$  increases and approaches  $H_f$ , the upstream subsidence shows a clear inverse conical shape, and sand particles are observed to roll down the slope of the upstream soil surface (Figure 4 (c)).

#### 4 STABILITY ANALYSES –RESULTS AND DISCUSSIONS–

##### 4.1 Prismatic failure concept 3D

The Prismatic failure concept 3D presented by Tanaka et al. (2012) is used for estimating the stability against seepage failure of soil. In the Prismatic failure concept 3D, we assume that the body of soil lifted by seepage water has the shape of a prism with a certain height and width adjoining the sheet pile wall. The rise of the prism is resisted by the submerged weight,  $W'$ , and frictions  $F_{RL}$  and  $F_{RCR}$  on the left and right sides and  $F_{RF}$  and  $F_{RCB}$ , on the front and back sides. The safety factor  $F_s$  with respect to the rise of the prism, which is subjected to the excess pore water pressure on its base,  $U_e$ , is given as:

$$F_s = \frac{W' + F_{RL} + F_{RCR} + F_{RF} + F_{RCB}}{U_e} \quad (1)$$

For the hydraulic head difference  $H$  between up- and downstream sides, safety factors,  $F_s$ , are calculated for all of the prisms within a cofferdam. The safety factor  $F_s$  takes the minimum  $F_{s\min}$  for a certain prism among all of the prisms. The calculation is iterated for another hydraulic head difference,  $H$ , until the condition whereby  $F_{s\min}$  becomes nearly equal to 1.0 is found.  $H=H_c$  at which the condition  $F_{s\min}=1.0$  is applied is defined as the critical hydraulic head difference. The prism with a value of  $F_{s\min}=1.0$  among all of the prisms for  $H=H_c$  is defined as the critical prism. We could say that the critical prism is separated from the underlying soil at its base when  $H$  exceeds  $H_c$ . Safety factors using the Prismatic failure concept 3D when considering frictions are discussed below.

##### 4.2 Relationship between hydraulic head differences $H_c$ (by theory) and $H_y$ (by experiment)

For Lake Biwa sand 3 of  $D_r=50\%$ , the theoretical hydraulic head difference by the Prismatic failure concept 3D,  $H_{PF}$  [Tanaka et al. 2012] is analyzed taking the anisotropy of the test sand to be  $k_{xy}/k_{zz}=1.20$  [Tanaka et al. 2011]. Figure 6 shows the relationship between  $D/T$  and  $H_c\gamma_w/T\gamma'$  for a no-excavation model. The experimental results are also plotted in Figure 6. It is observed from Figure 6 that the calculated critical hydraulic head differences  $H_{PF}$  are very close to the measured  $H_y$ . The Prismatic failure concept 3D thus proved to be a useful method for calculating critical hydraulic head difference at the onset of deformation of soil within a cofferdam. The same is true of the excavation model.

##### 4.3 Effects of surface shape of a cofferdam on $H_c$

Let us consider a cofferdam whose surface shape is rectangular with the shorter length at  $B$  and longer length at  $L$  (see Figure 7). Four cases of  $B:L=1:1, 1:2, 1:3$  and  $1:4$  are analyzed for constant values of  $B=0.2\text{m}$  and  $W=0.8\text{m}$ . Figure 8 shows the relationship between  $D/T$  and  $H_c\gamma_w/T\gamma'$ . It follows from Figure 8 that:

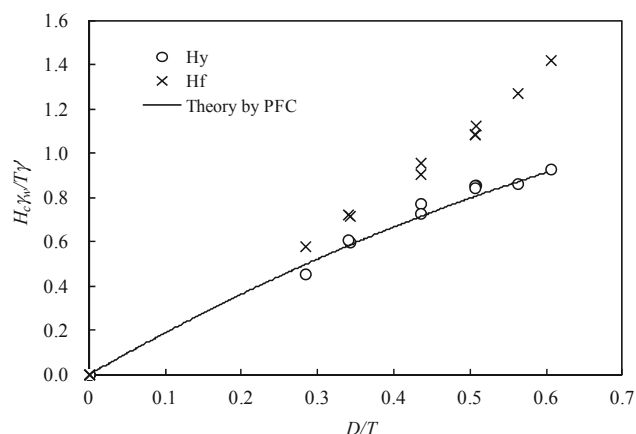


Figure 6. Relationship between  $D/T$  and  $H_c\gamma_w/T\gamma'$  for no excavation model

- (1)  $H_c$  gives the lowest value in the case of 1:1.
- (2) For the same value of penetration ratio of sheet piles,  $D/T$ , the critical hydraulic head differences,  $H_c$ , are given as follows in order of increasing magnitude:  $1:1 < 1:2 < 1:3 < 1:4$ .
- (3) For the same value of a short length, the more the longer length increases, the smaller the effect of the longer length on  $H_c$  becomes.  $H_c$  in the case of 1:3 almost equals the  $H_c$  in the case of 1:4 for the same value of  $D/T$ .
- (4) For a small value of  $D/T$ , all of the  $H_c$  values are nearly equal in cases of 1:1, 1:2, 1:3, and 1:4.

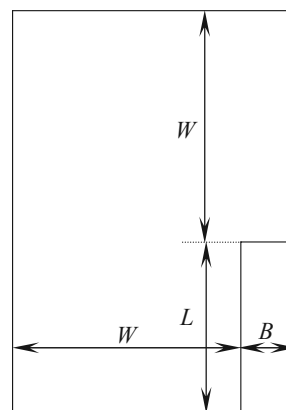


Figure 7. Plane shape of a cofferdam

#### 5 AXISYMMETRIC MODELING OF THREE-DIMENSIONAL SEEPAGE FLOW

In the experiment, one quarter of the three dimensional region is examined as stated earlier. The surface shape of the cofferdam is rectangular with the shorter length at 1 and longer length at 2. Considering an inscribed circle in the shorter side of the rectangle as shown in Figure 9, an axisymmetric seepage flow through the soil is used to model such a three-dimensional flow.

Let us consider the three dimensional and approximate axisymmetric conditions:  $T=40\text{cm}$ ,  $D=20\text{cm}$  and  $R=20\text{cm}$  for the non-excavation sand models, where  $R$  is the radius of the circular wall in the axisymmetric condition. Figure 10 shows the relationship between the penetration ratio of sheet piles  $D/T$  and the non-dimensional value of  $H_c$ ,  $H_c\gamma_w/T\gamma'$ . It is found from Figure 10 that the three dimensional seepage failure phenomena are well approximated using axisymmetric seepage failure. For further details, the following points may be made:

- (1)  $D/T \leq 0.40$   $H_c$  values are larger in the AXS flow than in the 3D flow; in particular the approximate accuracy with respect to  $H_c$ ,  $(H_{c\text{AXS}} - H_{c\text{3D}})/H_{c\text{3D}}$ , is about +17% for  $D/T = 0.27$ . This

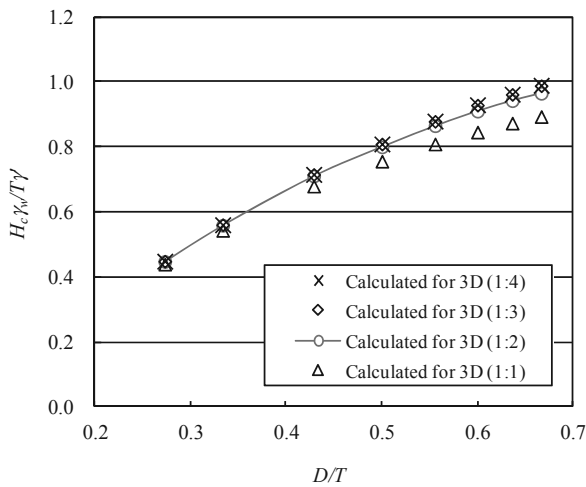


Figure 8. Relationships between  $D/T$  and  $H_c \gamma_w / T \gamma'$  for various plane shapes

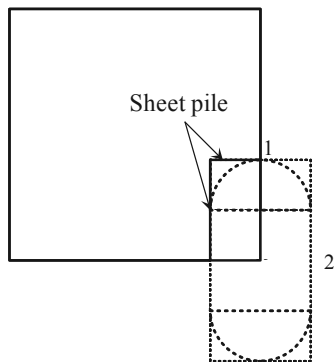


Figure 9. Plane figure of the 3D test apparatus (axisymmetric modeling)

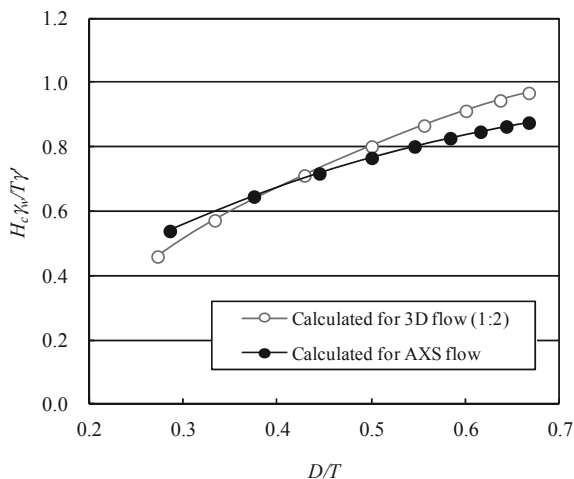


Figure 10. Relationship between  $D/T$  and  $H_c \gamma_w / T \gamma'$  (Axisymmetric modeling of 3D flow)

means that assuming that the 3D flow is the same as AXS flow leads to an overestimation of  $H_c$ , and generates unreasonable results with respect to seepage failure.

(2)  $D/T > 0.40$   $H_c$  values are smaller in the axisymmetric case than in the three-dimensional case; the approximate accuracy,  $(H_{c, \text{AXS}} - H_{c, \text{3D}}) / H_{c, \text{3D}}$ , is about  $-9\%$  for  $D/T = 0.67$ . This means that assuming that the 3D flow is the same as AXS flow leads to an underestimation of  $H_c$ , and generates uneconomical designs with respect to the  $H_c$  value.

For the same value of  $D/T$ , the  $H_c$  values are given as follows in order of increasing magnitude:  $B:L = 1:1 < 1:2 < 1:3 < 1:4$  as stated in Section 4.3. The same axisymmetric approximation is

applied in these four cases. So, the difference in  $H_c$  between 3D and AXS flows changes, and the approximate accuracies,  $(H_{c, \text{AXS}} - H_{c, \text{3D}}) / H_{c, \text{3D}}$ , are given as  $-2\%$  (1 : 1),  $-9\%$  (1 : 2),  $-11\%$  (1 : 3) and  $-12\%$  (1 : 4) for  $D/T = 0.67$ .

## 6 CONCLUSIONS

Seepage failure experiments were conducted under three-dimensional flow conditions for various cases of total depths of soil,  $T$ , and penetrated depths of sheet piles,  $D$ , and analyses of FEM seepage flow and stability against the seepage failure of soil were carried out using the Prismatic failure concept 3D (pfc 3D). From discussions, the following results were obtained:

(1) With an increase in the hydraulic head difference between up- and downstream,  $H$ , the discharge at  $15^\circ\text{C}$ ,  $Q_{15}$ , increases linearly for a smaller value of  $H$ , but changes abruptly and non-linearly beyond the point  $H=H_d$ .  $H_d$  is referred to as the hydraulic head difference at an abrupt change of the  $H-Q_{15}$  curve.

(2) In correlation with the above phenomenon regarding the  $H$  and  $Q_{15}$  relationship, the height of the soil surface changes at the front (downstream) and rear (upstream) of the sheet piles. When  $H$  increases beyond  $H_y$ , a downstream rise and upstream drop of the soil surface occur.  $H_y$  is referred to as the hydraulic head difference at the onset of soil deformation.

(3) Sand particles move from up- to downstream sides under the bottom edges of the sheet piles. The upstream soil surface is an inverse conical shape centered at the outer corner of the rectangular diaphragm wall.

(4) The experimental results led to the interesting conclusion that  $H_y=H_d$ .

(5) The hydraulic head differences at deformation in the experiment,  $H_y (=H_d)$ , are nearly equal to the theoretical critical hydraulic head differences based on the pfc 3D,  $H_c$ .

The theoretical critical hydraulic head differences for various plane shapes of a cofferdam, e.g., a short to long length of 1:1, 1:2, 1:3, and 1:4, were calculated, and the following results were obtained:

(6)  $H_c$  gives the lowest value in the case of 1:1.

(7) For the same value of the penetration ratio of sheet piles,  $D/T$ , the critical hydraulic head differences,  $H_c$ , are given as follows in order of increasing magnitude:  $1:1 < 1:2 < 1:3 < 1:4$ .

(8) For the same value of a short length, the more the longer length increases, the smaller the effect of the longer length on  $H_c$  becomes.  $H_c$  in the case of 1:3 almost equals the  $H_c$  in the case of 1:4 for the same value of  $D/T$ .

(9) For a small value of  $D/T$ , all of the  $H_c$  values are nearly equal in cases of 1:1, 1:2, 1:3, and 1:4.

The axisymmetric modeling of three-dimensional seepage failure was discussed, concluding as follows:

(10) With respect to the seepage failure problem, axisymmetric seepage flow through soil within a cylindrical wall can be used to model such a three-dimensional flow. The magnitudes of the critical hydraulic head differences  $H_{c, \text{3D}}$  (in three dimensions) and  $H_{c, \text{AXS}}$  (axisymmetric model) are given as follows for the 3D case of 1:2 and its axisymmetric model:  $H_{c, \text{3D}} < H_{c, \text{AXS}}$  for  $D/T \leq 0.40$ , and  $H_{c, \text{3D}} > H_{c, \text{AXS}}$  for  $D/T > 0.40$ .

## 7 REFERENCES

- Nikkei Construction. 2001. Shortage of penetration depth of sheet piles, Nikkei Business Publications, 37-38, 2001.9.28.
- Tanaka T., Naganuma H., Shinha M., Kusumi S. and Inoue K. 2011. Anisotropic permeability of soil on 3D seepage failure experiments, *Procs. of the 68th annual meeting of the Kyoto Branch of Japanese Society of Irrigation, Drainage and Rural Engineering*, 3-5 - 3-6.
- Tanaka T., Hirose D. and Kusumi S. 2012. Seepage failure of sand within a cofferdam in three dimensions -Prismatic failure concept 3D and analytical consideration-, *Report of Research Center for Urban Safety and Security*, Kobe University, No.12, 285-299.

# Stability and dewatering problems of deep excavations in Bratislava

Les problèmes de stabilité et d'assèchement des excavations profondes dans la ville de Bratislava

Turček P., Frankovská J., Súľovská M.

Faculty of Civil Engineering, Slovak University of Technology in Bratislava, Slovakia

**ABSTRACT:** Geotechnical design and execution of deep excavations of high-rise buildings in urban areas are presented in the paper. Design of retaining structure and subsoil behaviour based on the results of in situ measurement during execution with the aim to minimise the settlement of high-rise building are discussed. Limited space on the surface and ground conditions in Bratislava are important factors for design of foundations. Quaternary sediments, coarse grained soils, mainly sands and gravels reach down to the depths of 12 to 20 m, Neogene sediments, mainly clays and silty sands with confined ground water level occur deeper. Ground water level occurs from 2 to 6 m below the surface level. Several examples of excavations where the risks of local hydraulic failure were present are analysed. The paper summarizes stability and dewatering problems associated with design and execution of deep excavations in the city of Bratislava.

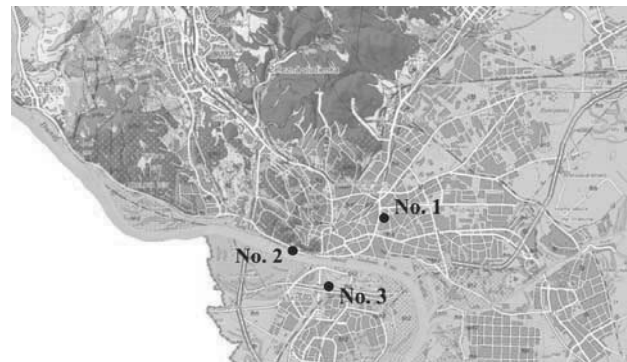
**RÉSUMÉ :** La conception géotechnique et l'exécution des fouilles profondes de bâtiments de grande hauteur dans les zones urbaines sont présentées dans le document. La conception de structure de soutènement et le comportement du sous-sol sur la base des résultats des mesures in situ lors de l'exécution dans le but de minimiser le tassement des bâtiments de grande hauteur sont discutés. L'espace limité sur la surface et les conditions du sol à Bratislava sont des facteurs importants pour la conception des fondations. Les sols à gros grains du Quaternaire, principalement les sables et graves descendent jusqu'aux profondeurs de 12 à 20 m, les argiles du Néogène et les sables silteux avec une nappe en charge se trouvent plus profonds. Le niveau de la nappe se trouve de 2 à 6 m en dessous du niveau de la surface. Plusieurs exemples de fouilles sont présentés où les risques d'une défaillance hydraulique locale ont été analysés. Le document résume les problèmes de stabilité et d'assèchement associés à la conception et à l'exécution des excavations profondes dans la ville de Bratislava.

**KEYWORDS:** retaining structure, deep excavations, geotechnical design, subsoil behavior

## 1 INTRODUCTION

Geological conditions in Bratislava are determined mostly by Quaternary sediments of the Danube river, Neogene sediments and Cenozoic crystalline rocks (biotite granites to granodiorites, diorite and gneisses) of Carpathians. The most important construction activities in last 20 years have been concentrated in the Danube area, with the Quaternary sediments (coarse grained soils, mainly sands and gravels) with thickness of 12 to 15 m, in the city of and in near vicinity of Bratislava. South and southeastward the depth is increasing, up to 400 m under Gabčíkovo (27 km from Bratislava). The Quaternary sediments are underlayed by fine-grained Neogene marine sediments with typical altering of fine grained and coarse grained sediments. Fine grained sediments are classified as clays from firm to very stiff consistency. Coarse grained sediments are classified as dense sands, silty fine sands and clayey sands. Under the Neogene deposits there are the same crystalline rocks as on the northern side of Bratislava (Kopecký, Černý, 2008). Underground water has two main horizons. One is underground water in Quaternary deposits with free water table donated by water from precipitation and from Danube river. The second horizon is groundwater confined in the Neogene deposits. The water is pressurized and recharged by underground water flowing from nearby Male Karpaty Mts.

Limited space on the surface and ground conditions in Bratislava are the important factors for design of foundations. Three examples of deep excavation where the risk of local hydraulic failure was present are analysed.





Legend:  
Cenozoic crystalline rocks:  biotite granites, granodiorites, diorites,  
Quaternary deposits:  slope deposits,  river deposits

Figure 1. Geological map of Bratislava region and location of case studies.

## 2 EXCAVATION FOR BUSINESS CENTER ON KARADZICOVA STREET

The first case study is excavation situated on the left side of Danube River in the city centre on Karadzicova street. Foundation pit was constructed for the high-rise building with 30 floors and 3 underground floors. The longer side of the foundation pit with the dimensions of 200x39 m and depth of 11.4 m was adjacent to existing buildings, two sides were



adjacent to streets and only one short site was open to free space. This layout requires minimisation of horizontal deformation of the retaining structure. Furthermore, there was interest to use all space available on the construction lot, i.e. to exclude technologies that would interfere with the ground plan and decrease the usable volume of the underground floors.

In the first section of the foundation pit up to the depth 4.5 m, where dry conditions were expected, the soil nailing was used as support. The jet grouted wall in deeper section was anchored by one level of ground anchors 15 m long, with 25° inclination, the anchor force was 670 kN and spacing of the anchors 1.6 m. The retaining wall was prestressed in vertical direction due to the necessity to carry large bending moments (bending moment of 1332 kNm per meter of wall was expected by full excavation of the pit); this pre-stressing was supposed to limit the horizontal deformation (see fig. 2 and 3).

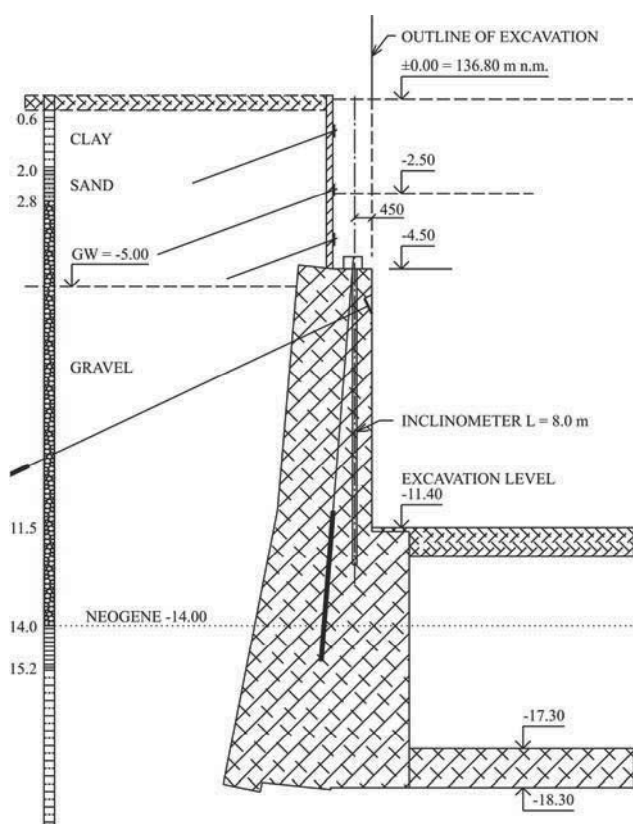


Figure 2. Cross section of retaining structure made by soil nailing and jet grouting.

According to geotechnical investigation the Neogene soils with high permeability are expected at the excavation base. Therefore a sealed bottom of the foundation pit was proposed by overlapping short columns constructed by jet grouting. This solution proved to positively influence the settlement of the building. Horizontal deformation in the level of the retaining wall 3.3 mm and 19.15 mm in the lower embedded part under the bottom of the excavation (in the direction of the excavation) were expected in geotechnical design. By full excavation the toe of retaining wall was expected to move into the foundation pit by 52.56 mm. Nine inclinometers were installed around the foundation pit in the wall constructed by jet grouting. The example of measurements from inclinometer no. 3, where the highest deformations (not higher than 2 mm in the direction into the pit) were indicated, is on figure 4.

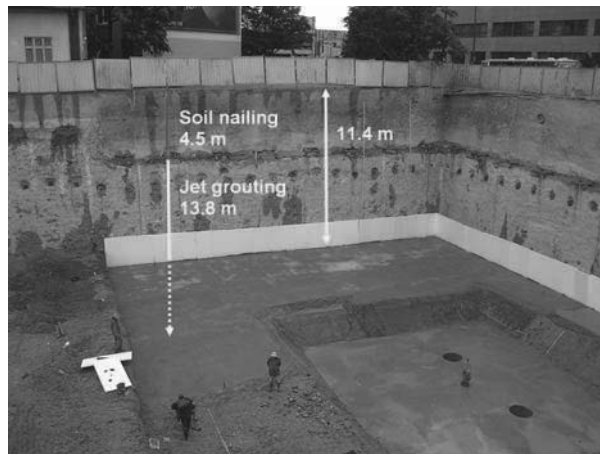


Figure 3. View into the excavation. Retaining structure made by soil nailing and jet grouting.

Similar results with even lower deformations were measured by other inclinometers. This favourable outcome was achieved thanks to high stiffness of the retaining wall prestressed in vertical direction. The stiffness of weak sandy clays under the bottom of excavation has been increased by constructing a horizontal barrier by jet grouting.

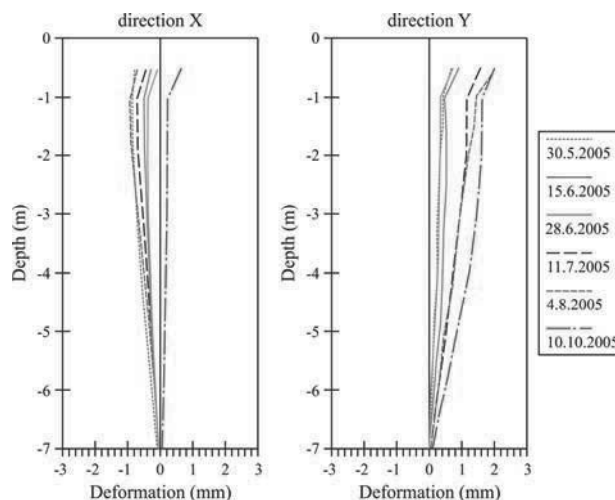


Figure 4. Horizontal deformations of retaining structure during construction.

### 3 EXCAVATION FOR RIVER PARK

The second case study is the foundation pit with dimensions of 265x53.5 m and depth of 9.0 m (fig. 5) situated directly at Danube riverside (in the distance of 12 m to Danube river). Retaining walls for foundation pit were designed as a secant pile wall embedded 1m into the weathered rock base. Danube coarse grained soils are well-known by their susceptibility to piping. The analysis of the risk of filtration failures is important in geotechnical design. Risk of the internal erosion (structural erosion) is affected by granularity of gravel or sand soils, situated in this region. Therefore the analysis of seepages effect on safety of construction and its subsoil it is necessary to carefully observe mainly development of filtration velocities or hydraulic gradients, which are decisive from the viewpoint of reviewing filtration stability of soils (Bednárová et al., 2010). According to geotechnical investigation the value of permeability coefficient (hydraulic conductivity) of gravel  $k$  is in the range from  $1.5 \times 10^{-2}$  to  $6.5 \times 10^{-3}$  m/s. The characteristic value of  $k$  equal to  $1 \times 10^{-5}$  m/s was evaluated from the results of water pressure tests. The permeability coefficient  $k = 1 \times 10^{-7}$

m/s was used in pile walls design (representing mainly leakages between the piles). Seepage in the foundation pit consists of wall and bottom rate of seepage. The seepage through the pile wall on section 1 was 0.008 l/s and can be obtained from equation

$$q_{wl} = \frac{k_s}{2 t_s} (H^2 - d^2) = 7.7 \times 10^{-6} \text{ m}^3 \text{ s}^{-1} \quad (1)$$

where  $H$  is the height of the water column,  
 $d$  embedding of the wall under the bottom of the foundation pit.

The predicted flow rate at the pit through walls was 2.12 l/s in the section farther from Danube and 2.23 l/s in the section closer to Danube.

Flow rate through the bottom was determined by the relation

$$Q_b = k i A_d = 0.0567 \text{ m}^3/\text{s} = 56.7 \text{ l/s} \quad (2)$$

The total rate of seepage can be given as

$$Q = Q_{wl} + Q_{w2} + Q_b = 61.55 \text{ l/s} \approx 62 \text{ l/s} \approx 223 \text{ m}^3/\text{h} \quad (3)$$

In case the groundwater level reaches 138.0 m above sea level (i.e. level of the pile heads), the rate of seepage in the pit increases to 266 m<sup>3</sup>/h.

At the beginning of water pumping, static reserve of groundwater from closed space was pumped from the foundation pit besides the inflow. The volume of saturated gravels is 92170 m<sup>3</sup>, of which volume of water by the assumption of 25 % active porosity is 23043 m<sup>3</sup>. This amount of water is presumed to be pumped in 9 days (during excavation works) when pumping more water than 30 l/s over pumped water flow into the foundation pit.

In order to secure dry foundation pit it was recommended to modify the length of the piles according to the actual conditions even though it might result in longer piles in certain sections compared to the design. Seven pumping wells with diameter 600 mm were proposed with recommendation to verify the actual pumped amounts. Contractor did not trust the assumption of the calculation and constructed 10 wells.

During the excavation of the foundation pit, a measuring of the groundwater movement was performed at all 10 pumping wells (water was permanently pumped only from 2 wells).

Parameters of groundwater movement were determined by the single borehole indicator method, based on the principle of diluting the indicator. NaCl was used as the indicator. Evaluating NaCl concentration was performed by the Radelkis OK 104 tool/instrument on battery source, which recorded the conductivity of the saline solution. Sensors of the Radelkis set with prolonged cable were used as detectors. The value of filter speed ( $v_f$ ) in each depth level, as well as the average value for the whole measured wall, was calculated according to the relation

$$v_f = \frac{\pi d \beta}{4 \alpha \delta t} \ln \frac{c_0 - c_p}{c - c_p} \quad (4)$$

where  $d$  is the inner diameter of the borehole ( $d = 0.8$  m);

$\alpha$  - coefficient of drainage impact of the borehole; base on comparable experience the value  $\alpha = 2$  was used;

$\beta$  - ratio used for volume decreasing ( $\beta = 1$ );

$\delta$  - coefficient considering the sealing impact on the ratio of flow concentration ( $\delta = 1$ );

$t$  - time equal to the difference between  $c_0$  and  $c$ ;

$c_0$  - initial concentration of the indicator;

$c$  - concentration in time  $t$ ;

$c_p$  - background of the indication substance before indicating the environment.

Average value of filter speed for the test section can be determined by the relation

$$\bar{v}_f = \frac{\sum v_{fi} \Delta h_i}{\sum \Delta h_i} \quad (5)$$

Evaluated filter speed in all measured objects depend on the location and ground conditions (gravel). No well showed an anomaly of permeability of depth that would indicate increased inflows from certain depth level or from the bottom of the foundation pit. In 2 wells where the water was pumped, filter speed in the range of 1.4 to 4.7 x 10<sup>-3</sup> m/s was measured, while in other cases it was  $v_f = 2.2 \times 10^{-4}$  to 6.7 x 10<sup>-5</sup> m/s. Very low seepage ratio was measured in line where jet grouting by the pile wall was performed, which proves reliability of the sealing system. Depth division of the filter speeds confirmed non-homogeneity of the gravel location (in some depth the sand fraction was missing).



Figure 5. Foundation pit with dimensions of 265 x 53,5 m and depth of 12 m next to Danube river.

Stable pumping at 20 l/s decreased the groundwater head under the level of excavation base. Decreasing the groundwater head in the area of the foundation pit and evaluation of the movement tests by diluting method indicated that lesser amount of water is required to be pumped from the foundation pit than expected amount of water in the project design (62 l/s). In conclusion it was stated that the retaining structure created a foundation pit with required sealing function.

When preparing the base foundation for placing the underlying concrete, the excavation in the north-western corner of the foundation pit deepened for 0.3 m more than was necessary and minor water seepage occurred along the pile wall that held at the same level for several days. It was confirmed by leveling that the groundwater head in the wet area by the pile wall was 0.48 m below the upper edge of the base concrete and held at the same level. Performed test of natural conductivity of the water seepage helped in identifying its origin. Two locations of leakage were confirmed in the wet area along the pile wall. It was evaluated as the water seepage into the foundation pit area through the contact of the piles connection in the wall where the discontinuities in the rock massive were collectors of the water. Drainage to the nearest active pumping well had to be installed in order to solve the problem. At the same time it was necessary to replace existing soil by gravel without the sand fraction in the foundation pit area and thoroughly compact the layers of this soil replacement, in order to eliminate the risk of higher deformations of the future base structure.

#### 4 DEEP EXCAVATION IN PETRZALKA

Quaternary gravel sediments on the right side of Danube were characterized as loose to medium dense coarse grained soils with the values of density index  $I_D$  varying from 0.25 to 0.63

and deformation modulus  $E_{def} = 30$  up to 112 MPa according to geological investigation by dynamic penetration testing up to the depth 40m. Locally in layers with fine-grained gravel with minimal sand filling the value if  $I_D$  was 0.15 and deformation modulus  $E_{def} = 16$  MPa. Average thickness of the quaternary gravels was 13 m. Neogene sediments were represented mostly by sandy clays (*saCl*) with firm filling of clay, with sand locations with addition of fine-grained soil (less than 15 %), to a small extent also with silts of middle plasticity to clays of high plasticity in depths of 19.8 to 20.6 m and 25.3 to 26.4 m. The value  $E_{def}$  determined by dynamic penetration tests was 20 to 28 MPa in Neogene soils.

Contact stress in base foundation of the high building was 500 to 800 kPa. Limit settlement determined the type of foundation (rafts or piles). Based on the information about disproportionately high compressibility of the subsoil, ground treatment by deep vibratory compaction was performed. Base foundation was located in the depth of 4.0 m under the surface. The raft is 1.4 m thick, in deepened parts 2.0 m. Density of compaction points was in raster of 2.2 x 2.4 m for stress of 800 kPa, under pad footings and strip footings in raster 2.5x 2.5 m to 1.75 x 3.5 m for stress of 500 kPa and under pads and strips in raster 1.8 x 1.8 m for stress of 800 kPa. The length of the piles for stress of 800 kPa was in depth of 3.0 m from the working base under the surface 10,0 m (i.e. till the Neogene in the depth of 13.0 m), shortened to 7 m in area with load of 500 kPa.

This arrangement was based on previous comparable experience in Quaternary gravel sediments of Bratislava where the verified deformation modulus of the vibrated gravel columns reached the average value of  $E_{def}$  equal to 500 MPa and increasing of the deformation modulus of average environment was proved by the values  $E_{def}$  from 250 to 300 MPa. The calculation of the average deformation modulus of improved subsoil in the area A in question is according to the relation

$$E_{def} = \frac{A_g E_g + A_s E_s}{A} \quad (6)$$

where  $A_g$  is the area of vibrated stone columns  
 $E_g$  – deformation modulus of the vibrated stone columns  
 $A_s$  – area of the unimproved soil  
 $E_s$  – deformation modulus of the unimproved soil

After constructing the vibrated stone columns, dynamic penetration tests were performed, located in the middle of the vibrated stone columns. Increase in the deformation modulus with depth was also proved, which was taken into account in the calculation of predicted settlement based on the monitored data. Average value of  $E_{def} = 284$  MPa was measured under the base foundation up to depth of 2 m. The predicted final settlements are summarized in the table 1.

Table 1. The values of settlement calculated for different foundations.

Foundation	Settlement s (mm)
Spread foundation without soil improvement	104.46
Spread foundation with soil treatment by stone columns ( $E_{def}$ based on comparable experience)	67.01
Spread foundation with soil treatment by stone columns ( $E_{def}$ based on site testing)	64.55
Pile foundation	73.97

During the construction of the high building the vertical and horizontal deformations were monitored. The measured value of settlement after consolidation process reached 52.2 mm.

## 5 CONCLUSIONS

The key value in the design of high building foundation in deep excavation pits is the limit usability state. Most questions are raised by the simulation of soil deformation characteristics and expected groundwater inflows. Good prognosis of deformations is based on combination of determining correct soil deformation characteristics verified by laboratory and field tests in the whole deformation zone and selecting the right calculation method. The project must respond to the architect's requirements by suitable design, its monitoring and potential modification of stiffness of the retaining structure, subsoil and additional sealing elements.

Geotechnical design and execution of deep excavations of high-rise buildings in urban areas are presented in the paper. Design of the retaining structure and subsoil behaviour based on the results of in situ measurement during execution with the aim of minimising the settlement of high-rise building are discussed. The paper summarizes stability and dewatering problems associated with design and execution of deep excavations in the city of Bratislava. The results of geotechnical calculations have been compared to the results of in-situ measurements.

## 6 ACKNOWLEDGEMENTS

The present work has been supported by the project of the Slovak Science Agency VEGA No. 1/0241/13 and by the Ministry of Education, Science, Research and Sport of the Slovak Republic within the bounds of OPVaV project No. 26220220140.

## 7 REFERENCES

- Bednárová, E. Minárik, M. Grambličková, D. Sabo, J. 2010. Flood Protection of Bratislava and its Specifics from the Viewpoint of Geological Composition of Surrounding Environment. In: *XIV<sup>th</sup> Danube-European Conference on Geotechnical Engineering: Proceedings*. Slovak University of Technology in Bratislava, Slovakia, 7 p.
- Kopecký M. Černý M. 2008. Landslides remediation of railway cut in Bratislava. *Czech Journal Silnice a železnice*. 3/2008. Part Foundation
- Ťavoda O. and Šabo A. *Foundation below groundwater*. ALFA, Bratislava, 1986, 272 pp.
- Turček P. and Hulla, J. *Foundation engineering*. JAGA, Bratislava, 2004, 360 pp.
- Turček, P. and Súľovská M. Using the observation method for foundation of high-rise buildings. In: *Proceedings of the 14<sup>th</sup> European Conference on Soil Mechanics and Geotechnical Engineering*. Vol. 2. Madrid, 2007, Millpress Rotterdam. p. 419 – 422.

# Managed remediation of a large Victorian gravity quay wall using the observational method

Stabilisation d'un grand mur de quai de l'époque Victorienne gérée en utilisant la méthode observationnelle

Turner M J, Smith N A  
*Applied Geotechnical Engineering, UK*

**ABSTRACT:** The paper describes on-going work to control the stability of a large gravity quay wall at a port on the western seaboard of the UK, which has had a history of instability dating back over several decades. In 1999 further ground movements of the wall were triggered by leakage from a fractured water main in the quayside behind the wall. This caused severe settlement damage to the quay and associated storage warehouses on the quayside. Monitoring of the affected area of the wall was established in early 2000, with additional ground investigations and instrumentation to supplement existing data. By the end of September 2000 the worst affected parts of the wall were moving outwards at a rate of 10mm/day. The movements were initially arrested by groundwater lowering. Subsequently additional remedial measures consisting of anchors and shear keys were designed and installed to provide physical restraint. The Owner wished to minimise capital expenditure and instead to use an observational approach (Peck 1969) and to respond to the information obtained. The work had therefore attained what was regarded as an acceptable steady state, with continued managed remediation to ensure that the wall's stability is maintained and the Owner can continue to use the berthing facilities.

**RÉSUMÉ:** Le document décrit les travaux en cours pour contrôler la stabilité d'un grand mur de quai dans un port de la côte ouest du Royaume-Uni, qui avait un historique d'instabilité datant de plusieurs décennies. En 1999, de nouveaux mouvements de terrain et du mur furent déclenchés par une fuite d'eau due à une rupture de tuyaux d'alimentation en eau du quai qui étaient derrière le mur. Ceci causa des dommages graves au quai et aux entrepôts de stockage sur le quai. La surveillance de la zone affectée du mur commença au début de 2000, avec addition d'instruments de mesure supplémentaires et investigations complémentaires du sol pour compléter les données existantes. À la fin de Septembre 2000, les zones les plus touchées du mur se déplaçaient vers l'extérieur à une vitesse de 10mm/jour. Les mouvements furent arrêtés par l'abaissement des eaux souterraines. Par la suite d'autres mesures correctives constituées de tirants d'ancrage et de piles pour éviter les glissements furent conçues et installées pour assurer la contention physique du mur. Le propriétaire souhaitait minimiser l'investissement initial et préférerait utiliser une approche observationnelle (Peck 1969) en réponse aux informations obtenues. Le mur était assez stable pour utiliser le quai en continuant l'application opportune des mesures correctives pour assurer la contention du mur, et le propriétaire peut continuer à utiliser les installations d'accostage.

**KEYWORDS:** gravity walls; long-term monitoring; long-term displacements; ground anchors; water pressures; effects of dewatering.

## 1 INTRODUCTION

A section of harbour wall at a port on the western seaboard of the UK has a history of instability dating back over more than thirty years. Measurements taken in the 1980s had indicated that the maximum total horizontal movement of the wall up to that date had been more than 400mm. In 1999 further ground movements of the wall were triggered by leakage from a fractured water main in the quayside behind the wall. This caused outward movements along a length of over 80 metres, and severe settlement damage to the quay and associated storage warehouses on the quayside.

The harbour works were constructed at the end of the 19<sup>th</sup> Century. The wall is a gravity structure of mass concrete and masonry with sandstone "plums". At its top, it is some 17 metres above the harbour bed level; it is about 2 metres wide at its crest, increasing to almost 9 metres at its base. There is a large tidal range at the site.

After the 1999 movements, monitoring of the affected area of the quay wall was established in early 2000, with additional ground investigations to supplement existing data and to confirm the wall dimensions and the ground/groundwater conditions behind the wall. Inclined meters and piezometers were also installed to monitor water levels and the wall behaviour. Survey lines were established perpendicular to the wall and extending back to stable reference markers remote from the wall, with intermediate reference points to measure lateral and vertical movements in the ground behind the wall.

By mid-2000 the monitoring data showed a deteriorating situation, with outward movements of the wall accelerating from an initial value of around 15 to 20mm per month to as much as 100mm/month, and increasing. By the end of

September of that year the worst affected parts of the wall were moving outwards at a rate of 10mm/day, and measures were put in place to stabilise the wall immediately in the short term, together with further works to ensure the stability of the quay wall in the medium term.

This current paper describes these measures and the long term monitoring of the wall over the past decade.

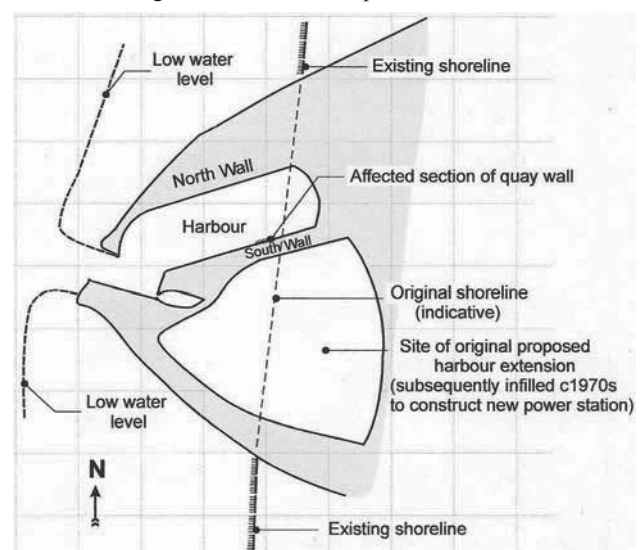


Figure 1. Outline plan of the site.

## 2 BRIEF HISTORY OF THE SITE

The harbour walls were constructed in the dry within a large embayment formed by advancing two curved embankments from the shore to meet at a central point, which would form the entrance to the harbour, as illustrated on Figure 1. This entrance point was closed by a temporary dam for the construction works and the site was drained by pumping. The harbour was then excavated in the dry.

A typical section through the quay wall is shown on Figure 2. The walls were constructed of mass concrete and, in the larger sections, large sandstone “plums” were incorporated into the concrete. The quay was intended for both passenger and livestock traffic. In view of the large tidal range provision was made for loading and off-loading at any state of the tide. This was achieved by constructing access-ways through the wall at two levels. These were connected to subways and stairways on the landward side of the wall. On the seaward side the quay wall was fronted by a heavy timber staging with continuous landings at the necessary levels to give access from the steamers into the subways.

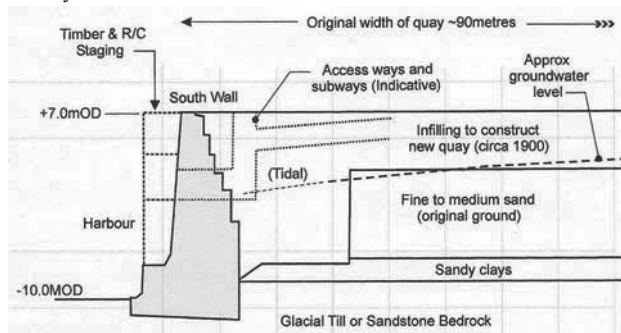


Figure 2. Typical cross-section through quay wall.

As illustrated on Figure 1, the affected quay, known as the ‘South Quay’ was constructed on the harbour side of a central spine embankment within the construction site. To the south of this, the remaining area was planned as a future extension to the harbour, but this extension was never constructed. In the 1970s this area was infilled and a large power station constructed on the site

In the early 1980s surface settlement was noted behind a 40m long section of the quay wall. This was repaired by infilling and releveling to grade. Further repairs were undertaken in 1988, when a maximum settlement of 400mm was reported on the quay surface prior to reconstruction. Following these repair works the quay surface settled a further 30mm of settlement within a year, and the worst-affected area was reported as extending over an 85 metre length of the wall, although the effect was also discernible beyond this. Crane rails which had been relaid along the quayside in 1972 were found to have deviated by up to 100mm towards the harbour over a 100m length of the quay wall.

Detailed surveys taken in 1991 indicated that the South Quay was showing a distinct bulge of as much as 430mm towards the harbour, and the zone of movement extended for some 200m along the wall. Shortly after these measurements were taken, a break occurred in a water main some 13m behind the crest of the wall, due to the continuing outward displacement of the quay wall. At this time a remedial works solution using high capacity ground anchors was proposed, but not proceeded with.

In late 1999 a further major leak occurred from a fractured water main near the centre of the previous movements, causing accelerated wall movements and severe ground settlements beneath the quay itself. The next sections describe subsequent evaluation and remedial works following this particular incident.

## 3 GROUND INVESTIGATIONS AND OBSERVATIONS (2000-2001)

In early 2000 Applied Geotechnical Engineering was requested by the port owner to undertake investigations as to the cause of the movements and to advise on the measures required to stabilise the South Quay wall.

A targeted ground investigation was commissioned, to supplement information available from previous investigations undertaken in 1990/1992. In addition, inclinometers were installed at five locations along the crest of the affected length of wall and were continued through the base of the wall and any superficial soils into bedrock at depth. A further three inclinometers were installed behind the wall to monitor the behaviour of the retained soils. Water observation boreholes were also installed behind the quay wall to monitor groundwater conditions.

In addition a series of “traverse lines” was established perpendicular to the wall and extending back to stable ground well beyond any zone of influence of the wall movements. These were monitored by conventional surveying techniques to determine horizontal and vertical displacements.

### 3.1 Geology and Ground Conditions at the Site

The ground was raised behind the masonry quay walls using the material excavated to form the harbour. Beneath these surface construction materials, the South Quay is underlain by fine to medium grained sands of Quaternary age. In some places these are underlain by soft sandy silty clays. These materials rest upon either Glacial Till (typified as reddish brown, stony, clayey silts), or, more commonly, directly onto bedrock. At the western end of the quay, bedrock consists of sandstones with subordinate marls of Permo-Triassic age. Over the eastern end older sandstones and siltstones of Upper Carboniferous Namurian (Millstone Grit) age are present. The boundary between the two rock formations is formed by a large fault, trending in a NNW – SSE direction, which cuts at right angles across the line of the South Quay, slightly west of its central point, and close to the centre point of the historic movement of the wall. The fault zone was also identified during the construction of the power station to the south.

This fault zone is associated with heavy flows of groundwater under artesian or sub-artesian pressures. Before the power station was constructed a freshwater lake formed in the area of the old proposed harbour extension.

The investigations led to the conclusion that groundwater flows from this source to the south of the South Quay were the root cause of the wall instability, as described below.

### 3.2 Groundwater observations

It was soon apparent from the monitoring data that the movement of the wall was driven by the groundwater held behind it. The rate of drainage of the water below the wall was relatively slow, so that the difference in water levels between the front and the back of the wall was highest at low tide, as shown in Figure 3. At these points the wall would ratchet forward, and not quite recover its original location as the tide level rose. By inference, the effect was greatest at times of high tidal difference (Spring tides).

The water observation standpipes confirmed that close to the quay wall, water levels varied tidally between about +4m OD and +1.4mOD. Some fifty metres south of the face of the quay wall, water levels varied between +2.9 and +2.7m OD with the tide. At a distance of 100 metres groundwater levels were almost static, with very little discernible tidal variation, and were around +3.7m OD.

It was also noted that the salinity of the groundwater changed from south to north. In the south the groundwater was fresh or brackish. Close to the quay wall the salinity altered with the tide. At low tide it was brackish or fresh. At high tide, as

seawater clearly flooded behind the wall, the groundwater became salty.

There was therefore a discernible hydraulic gradient from the power station site in the south, northwards towards the quay wall. It was also clear that the bulk of the groundwater was fresh water, flowing from the power station site towards the South Quay. In addition it was quite possible that concentrated groundwater flow was occurring in the fault zone in the vicinity of the harbour, although in the location of the South Quay the zone was buried beneath a cover of Glacial Till.

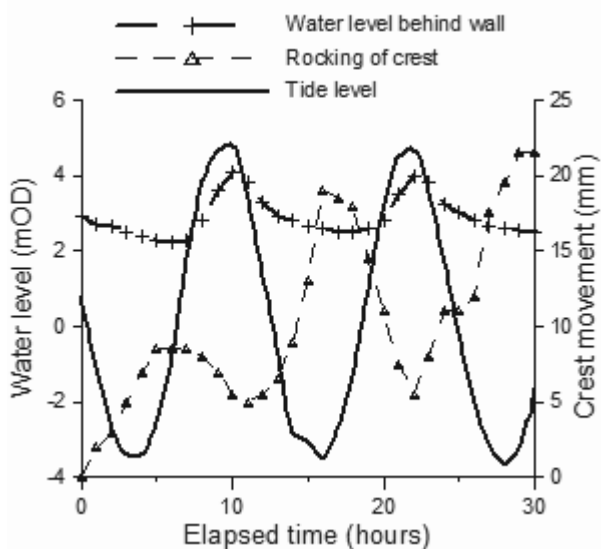


Figure 3 Water levels and crest movements, 13-14 Oct 2000.

The analyses showed that the high groundwater level behind the quay wall was the predominant driver of the instability and the observed wall movements.

### 3.3 Wall Movements (2000)

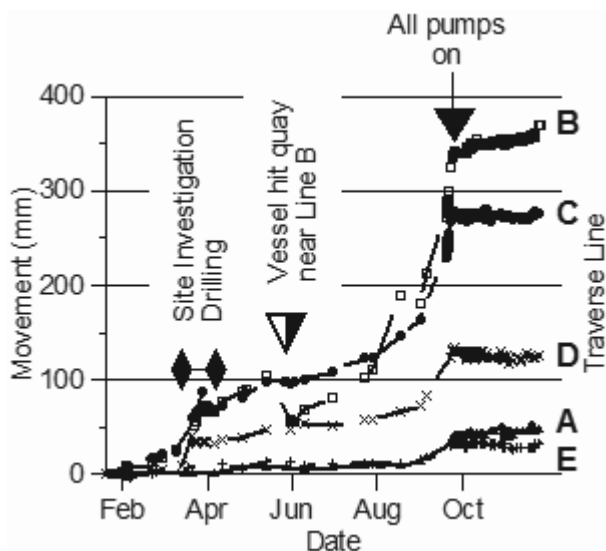


Figure 4. Crest movements during 2000.

The displacements of the quay wall measured at the traverse lines are illustrated on Figure 4. It can be seen that there was a noticeable effect upon outward wall displacements while the site investigation works were being undertaken in April 2000. Figure 4 also shows that the rate of outward movement also began to increase markedly in September of that year, and was accelerating. By September 2000 the worst affected area of the quay wall (Traverse Lines B and C on Figure 4) had recorded between 270 and 350mm of outward movement, relative to their

values in January of that year. At this time the analysis, design and procurement of the remedial works was still being progressed, but, based upon the evidence of the increased wall movements during the investigation work, contingency plans had already been put in place to deal with such a situation. Eleven dewatering wells were installed in a line behind the quay wall at approximately 10m centres, to lower the ground water level behind the wall. At that time the wall was moving forward by more than 10mm per day at the worst affected part, and was rocking measurably with the tide. The pumps were started as soon as the wells were connected, over a three day period, the first three being commissioned on 17 October and the balance by 19 October 2000.

As soon as the first pumps were started, the wall movement virtually ceased, as can be seen from Figure 4. Measurements eight days later showed that the amplitude of the rocking motion was less than half its magnitude prior to pumping. With the wall stabilised, work on installing permanent drainage and ground anchors could begin. The effects of the dewatering upon the groundwater levels behind the wall are illustrated on Figure 5.

A feature of Figure 5 is that a distinct 'plateau' can be seen in the levels recorded for the water immediately behind the quay wall. The level of the retained water is drawn down to 0.0mOD by the pumping wells as the tide falls. It does not fall below this level, however, giving the step-like feature in the graph. The 0.0mOD level coincides with the invert level of the lower access-ways through the quay wall, which were open to the sea. When the tide was above 0.0m, on a falling tide, the retained water was clearly draining through these accessways, as well as being removed by the pumping wells. Once the tide fell below this level, then the pumping wells alone were removing the retained water, and, on the evidence of these readings, could only maintain the retained water at about the 0.0mOD level against the fresh water flowing from the landward side of the quay wall.

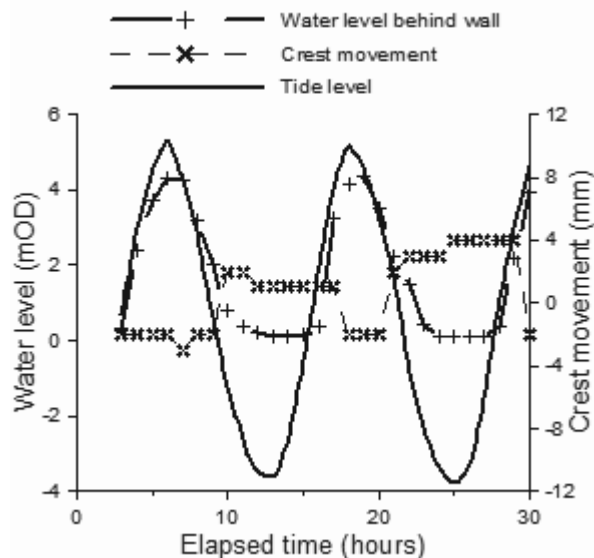


Figure 5. Water levels and crest movements 27-28 Oct 2000.

## 4 OUTLINE OF INTERIM REMEDIAL MEASURES (2001 – 2002)

It was recognised from the outset that the efficiency of the wells was likely to deteriorate in the medium term due to bio-fouling. Hence, additional measures were designed to provide physical restraint to the worst affected section of the wall. These consisted of seventeen 1050kN permanent rock anchors installed through the face of the wall at an inclination of 43° to the vertical; twenty-four 525 or 626kN permanent anchors through the crest of the wall inclined to landward at 10° to the

vertical and approximately thirty near-vertical 63.5mm diameter shear keys into rock beneath the base of the wall.

In addition, a series of sub-horizontal drainage wells were installed through the quay wall at a level of +0.0m OD, to speed the drainage of the retained soils.

These works were completed in early 2002.

#### 5 WALL BEHAVIOUR 2002 – 2012

The dewatering wells were shut off in April 2002 and the wall behaviour was monitored.

The response of the wall in terms of its outward movement as measured by the inclinometers and the traverse line surveys is illustrated in Figure 6.

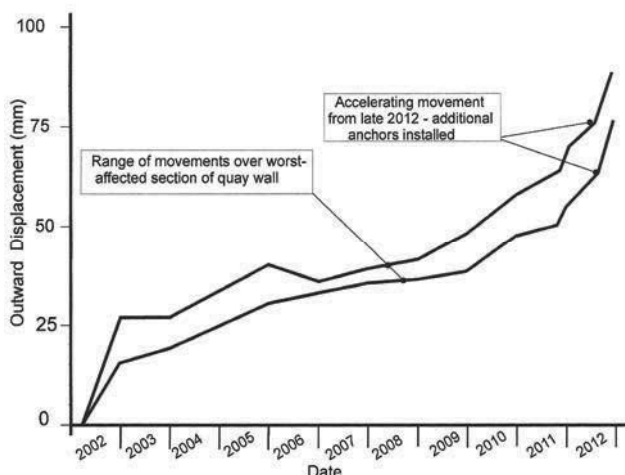


Figure 6. Wall displacements at crest level 2002 to 2012. (Toe displacements similar but generally smaller.)

Initial wall movements over the first 5-6 months were between 5 and 10mm at the crest and toe of the wall as the anchors took up further load. Load increases in the 43° anchors were typically between 50 and 200kN over this period.

By the end of 2002 the movements had stabilised at around 16 to 26mm at the crest, and 15 to 20mm at the toe. These data confirmed that the predominant mode of movement of the quay wall in the most active area was by sliding along a plane coincident with or close to the interface between the base of the wall and the underlying strata.

Over the next 3 years outward crest movements over the anchored section had increased to 30 to 40mm relative to the April 2002 readings and toe movements were between 35 and 40mm. Loads in the 43° anchors had increased by between 200 and 250kN. It had been planned to complete the main remediation works within this 3-year timeframe, but the monitoring works had demonstrated that movements were remaining controllable. The main works were put on hold, therefore and a watching brief was maintained on the wall. Based upon the previous readings, a movement criterion of 10mm/year had been adopted as a signal that further support works needed to be put in place.

By 2009 the loads in some 43° anchors were approaching or exceeding 1200kN – 15% above their design loads. Any anchors found to be in excess of this load level were being relaxed to avoid overstressing.

Outward wall movements over the anchored section generally continued at a rate of around 3 to 5mm per year.

By 2012, however, inclinometer and traverse line readings were indicating that outward wall movements were reaching 10 to 12mm per year, and the loads in the 43° anchors were increasing at an average of around 150 to 300kN per year. Additional interim measures were undertaken at the end of 2012, when a further six 1800kN capacity 43° anchors were installed through the face of the wall over the anchored section.

The aim of these works is to reduce outward movements back to acceptable levels.

These additional limited-scope works are intended to allow the continued limited working of the quay, consistent with the current requirements of the Port. As demand rises or operational needs change at the Port, then full remediation works will be implemented to upgrade the South Quay facilities to meet this demand.

For reference, the data from Figures 4 and 6 have been combined on Figure 7 to illustrate the relative degrees of movement measured at the crest of the quay wall over the worst affected section from 2000 to the present day. The figure clearly shows the rapid, and probably catastrophic, accelerating rates of movement in 2000, before the dewatering was switched on, followed by the relatively slow but continuing movements over the next 9-10 years, but increasing latterly.

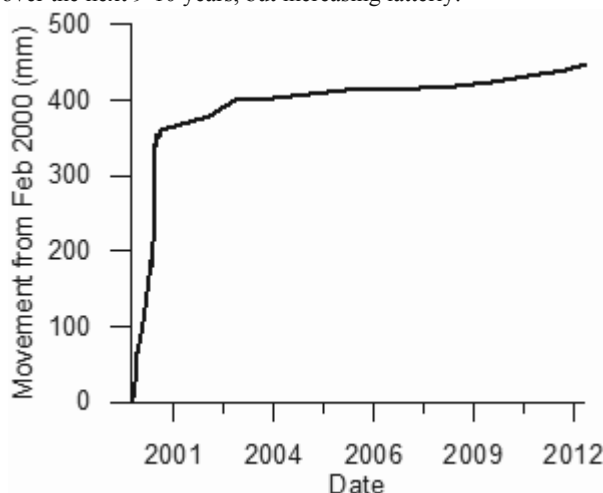


Figure 7 Wall crest movements between February 2000 and June 2012

## 6 SUMMARY AND CONCLUSIONS

The long-term monitoring of this 19<sup>th</sup> Century harbour wall over the last twelve years in particular, (but with records extending back over thirty years) has given a unique opportunity to gain an insight into the behaviour and relative ‘flexibility’ of such structures. The data gained from this work highlight the importance of monitoring such structures once they are perceived to be ‘at risk’, and the need to establish ‘trigger values’ related not just to overall movements but to rates of movement, and, in particular where rates of movement are seen to be accelerating over time.

## 7 ACKNOWLEDGEMENTS

The authors acknowledge with thanks the permission and co-operation of the port owners and their engineers in gathering and collating the data obtained from these monitoring works and allowing their publication in this paper.

## 8 REFERENCE

Peck R. B. 1969. Avantages and limitations of the observational method in applied soil mechanics. *Géotechnique* 19 (2), 171-187.

# Concrete panel walls – Current development on interaction of earthworks, geosynthetic reinforcement and facing

Comportement des parements béton de murs de soutènement en sols renforcés – interaction entre les sols remblayés, le renforcement et le parement

Vollmert L., Niehues C.

*BBG Bauberatung Geokunststoffe GmbH & Co. KG, Espelkamp, Germany*

Pachomow D.

*Technische Universität Cottbus, Cottbus, Germany*

Herold A.

*IBH – Herold & Partner Ingenieure, Weimar, Germany*

Verstraaten W.

*KWS Infra b.v., De Meern, The Netherlands*

**ABSTRACT:** Reinforced soil structures have become an appropriate construction method for infrastructural buildings. Several types of facing are commonly used. Full height panels or segmental panels with a certain height are mainly used for flyover constructions and bridge abutments. The design of the constructions depends on the stiffness of the facing element. Large scale test with loads up to 450 kPa at laboratory conditions as well as on site test with one year of continuous measurement under weathering conditions are presented and compared to analytical design and calculations using commercial finite element software. The results indicate that this type of structure can be designed on the safe side using current design standards and benefits given by the interaction of stiff geogrid reinforcement and soil.

**RÉSUMÉ :** Les ouvrages en remblai renforcé sont devenus une méthode de construction adaptée aux projets d'infrastructures. Plusieurs types de parement sont couramment utilisés. Des panneaux de pleine hauteur, ou panneaux segmentaires avec une certaine hauteur, sont principalement utilisés pour les constructions surélevées et les culées de pont. La conception de ces ouvrages dépend de la rigidité de l'élément de parement. Cet article présente des essais réalisés à grande échelle avec des charges allant jusqu'à 450 kPa, en condition de laboratoire ainsi que sur site, avec une année de mesure en continu en condition de vieillissement. Les résultats sont comparés à la conception analytique et aux calculs réalisés à l'aide d'un logiciel commercial d'éléments finis. Les résultats montrent que ce type d'ouvrage peut être conçu de façon sécuritaire suivant les normes de conceptions actuelles et les avantages apportés par l'interaction d'une géogridde rigide avec le sol.

**KEYWORDS:** geosynthetic reinforced walls, concrete, design, testing, execution, DIN EN 14475, EBGEO, BS8006

## 1 INTRODUCTION

Creating robust and sustainable constructions in geotechnical engineering has become an upcoming topic in terms of reduction of carbon footprint as well as on cost reduction on PPP projects. Combining technologies for slim precast concrete panels with stiff geosynthetic reinforced walls allows for the use of local and in some cases even treated soils.

In the last years recent research has led to further understanding of reinforcing interaction, leading to design approaches published in EBGEO and allowing for a reduction of lateral stress on the facing constructions.

Design of precast panels in practice requires attention to the transport phase as well as on the construction steps during execution and serviceability limit state.

## 2 DESIGN OF REINFORCED STRUCTURES

DIN EN 14475, the British design code BS8006 as well as the German design recommendations EBGEO are state-of-the-art standards in order to safeguard the constructions.

Special attention has to be paid to the design of the facing, as these elements are directly exposed to the environment and deformations of the construction can be seen immediately. The mentioned design codes do not give a unique calculation of lateral stress acting on the facing elements. DIN EN 14475 already differentiates between several types of facing elements, depending on the stiffness:

- Rigid facings, e.g. full height panels

- Semi-flexible facings, e.g. concrete blocks without rigid connections, gabion baskets
- Flexible facings, e.g. wrap-around method

The lateral stress has to be different from the active earth pressure calculated according to Rankine's theory due to the geosynthetic reinforcing elements, "nailing" the fictive failure zone. As this becomes a hyper static system, the earth pressure distribution on the facing is indifferent.

Nevertheless, the design has to be proper and worked out on the safe side, so additional information has to be gained from sites and large scale tests, especially taking influence of water, subsoil settlements and installation conditions (compaction, construction steps, etc.) into consideration.

## 3 CURRENT DEVELOPMENT

### 3.1 *Lateral stress on facing*

Pachomow et al. (2007) collected several test-field data of executed walls in heights between 2.0 m and up to 30 m, with information concerning the lateral pressure on the facing given. It is interesting that the lateral stress gained by self-weight of the construction remained within a range of up to 50 kPa, although significant higher values would have been expected especially for high walls.

Normalising the height of all test field data, and recognising that nearly all data are linked to non-cohesive soils as well as to slope inclinations between 70° and 90°, the relationship between the vertical and lateral stress can be compared to the



active earth pressure coefficient, being expected in the range of 0.2 and 0.35, depending on the theory and boundary conditions. Figure 1 indicates that the normalised lateral stress on the facing is significantly less for reinforced structures. Furthermore, the data indicate that the absolute height might not have a decisive influence at all, but the normalised one.

Ruiken et al. (2010) have demonstrated the arching effects close to the facing of a geogrid-reinforced soil sample, using biaxial tests at plane strain conditions. The degree of arching and the absolute value of stress reduction depends on the lateral movement of the facing as well as on the degree of reinforcement, see also Bussert (2006).

Based on full scale tests using several commonly known reinforcing products varying in a small range of nominal strength from 40 kN/m up to 55 kN/m a clear tendency can be obtained concerning the stiffness, described by the secant modulus J of the products:

$$J \text{ [kN/m]} = \text{strength } F \text{ [kN/m]} / \text{strain } \varepsilon \text{ [%]} \quad (\text{eq. 1})$$

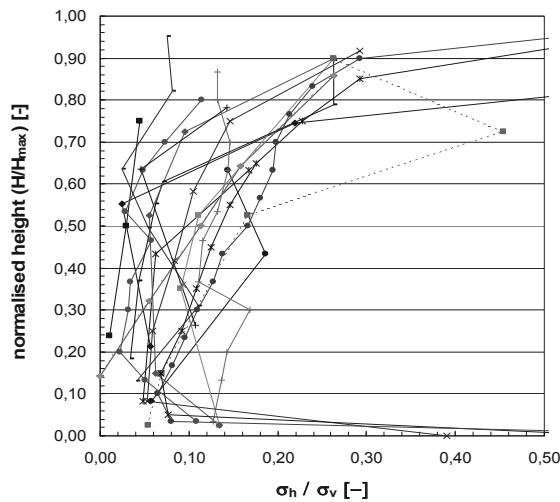


Figure 1. Compiled data of lateral stress to facing, presented at normalized height and relationship between normal load  $\sigma_h$  and lateral pressure  $\sigma_v$ .

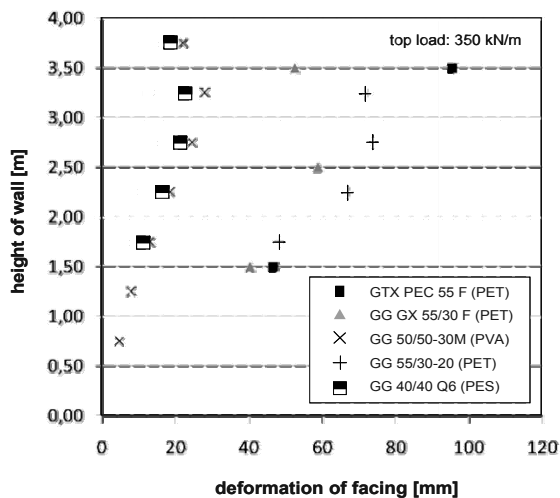


Figure 2. Deformation of full scale walls with semi-flexible facing, depending on the product (Pachomow & Herold, 2009).

Figure 2 shows preliminary results of a 4.0 m high construction using a weak facing system and a load beam 1.0 m behind the wall surface, applying a top load of up to 350 kPa. The deformation varies significantly depending on the type of product. All products performed satisfactory in an acceptable

range, while some products allow for higher loads and show an enhanced performance in terms of serviceability.

#### 4 EUROPEAN DESIGN CODES

Exemplarily the mostly used design codes in Europe, BS 8006 and EBGEO 2010, dealing with reinforced earth will be discussed in the following.

Following the basic principles of designing reinforced soil, based on the results shown in Chapter 3, EBGEO allows further for a reduction of the lateral stress as compared to the Rankine's active earth pressure. The well-known coefficient for the lateral active earth pressure  $k_{ak}$  is just used as basic parameter (eq. 2), taking the inclination of the wall as well as the soil parameters (e.g. angle of internal friction  $\phi'$ ) into consideration. The correction factor  $\eta_G$  as per Figure 3 is then applied, knowing well that using the lateral active earth pressure  $k_{ak}$  as basic parameter is just an interim solution up to full understanding and modeling of reinforced earth. In the upper part of the construction respectively on the actual construction level, the earth pressure due to compaction (not shown in Figure 3, typically up to 25 kPa) becomes decisive, but is going to be superimposed by the earth pressure resulting from the self-weight of the construction.

$$E_{\text{Facing}} = (\eta_g * k_{a_{gh,k}} * \gamma_k * H_i * \gamma_G + \eta_q * k_{a_{qh,k}} * q * \gamma_Q) * l_v \quad (\text{eq. 2})$$

- with
- $E_{\text{Facing}}$  Earth pressure on facing [kN/m]
- $\eta_g, \eta_q$  Matching coefficient [-]
- $k_{a_{gh,k}}, k_{a_{qh,k}}$  Coefficient active earth pressure [-]
- $\gamma_k$  Weight of the soil [kN/m<sup>3</sup>]
- $H_i$  Covering [m]
- $q$  Traffic load [kN/m<sup>2</sup>]
- $\gamma_G, \gamma_Q$  Partial safety factor DIN 1054 [-]
- $l_v$  Vertical space between layers [m]

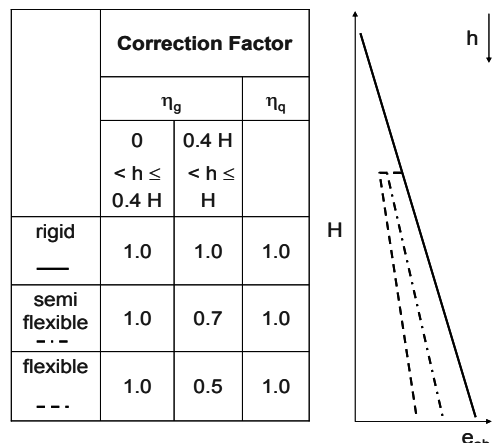


Figure 3. Correction factors applied to  $k_{ah}$  according to EBGEO, 2010.

In opposition to EBGEO, the earth pressure following BS 8006 is calculated using the active earth pressure coefficient  $k_{ah}$  for the structure, superimposed by  $k_0$  in the upper part. The reduced stress acting on the front of the construction depending on the stiffness of the wall-facings is considered by a reduction of the connection stress, e.g. by 25 % in the upper 60 % of wall height using wrap-around method.

The BS 8006 concept results in having the highest connection stress requirements at the footing of the construction, while research and lessons learned from failures indicate to have the highest stress levels at approx. 1/3 height starting from the bottom of the walls.

Nevertheless, the reduction of the lateral earth pressure of both concepts has a direct influence on the design of reinforced walls and allows for steep walls with a friction connection between e.g. blocks and reinforcement.

## 5 LARGE-SCALE TEST IN SITU

### 5.1 Design and set-up

In addition to the large scale tests on full height panel walls performed by Pachomow, a full scale trial has been performed by KWS Utrecht, Netherlands, supported by NAUE, Germany. While under laboratory conditions high loads up to 450 kPa could have been applied to the structure, in situ the influence on installation procedure, weathering (changes of moisture-content and temperature) and long term effects caused by the thermoplastic characteristics of the used high strength Polyester geogrid could be investigated. Figure 4 gives the cross section of the test set-up for the in-situ test with geometry comparable to the laboratory test.

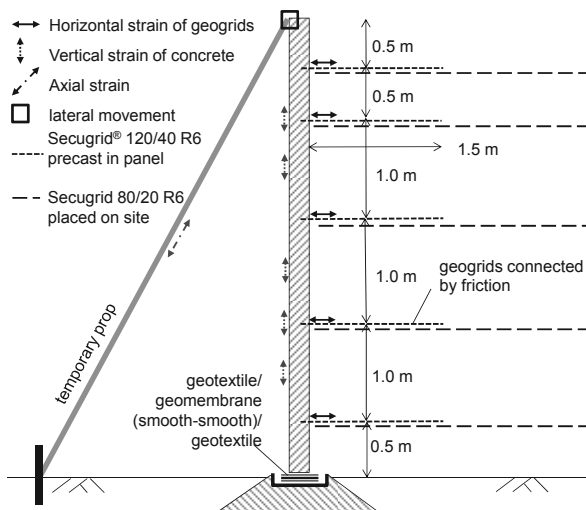


Figure 4. Test setup full height panel wall, KWS Utrecht

To reduce the required amount of structural steel for the construction, the panel has not been designed using conventional design methods, but taking the results from laboratory test explained in Chapter 4 into consideration. Therefore, the design configuration has been optimized, assuming the load distribution given in EBGEO, applying an overall safety to the earth pressure distribution of 1.5 (assumption).

The load distribution has been applied to the panel design, testing several static systems and designs to optimize the amount of required structural steel. At the end, the system could be optimized for transport steel only.

To make the system as easy as possible, only 1.5 m long strips of the reinforcement have been precast to the concrete (Figures 4, 5a). The required length of the reinforcement to fit the overall safety according to EBGEO has been placed on site, just overlapped by friction. For the earth pressure distribution, satisfactory pull-out resistance of the strips from the reinforced backfill has to be ensured.

Several types of instrumentation have been used, taking the static principle of  $\Sigma H = 0$  into consideration. The sum of forces acting on the backside of the panel shall be equal to the forces

acting on the geogrids, the temporary prop, added by the friction on the toe of the panel.

Therefore, the toe of the panel has been designed as plain bearing, using geosynthetic components for sliding purposes with tested and well-known friction parameters for back-analysis of the forces acting at the toe. Temporary wooden wedges, applied during placing the panel, have been removed after the installation of the first 1.5 m of backfill material, so lateral movement of the panel toe was possible but has not been observed.

Further on, it had to be ensured that the material used is applicable to the use in concrete, as it is given here by independent testing and applying a partial reduction factor for environmental influences to the polyester material of 1.18 [-].

To predict stress, strain and lateral movement of the stage construction, finite element (FE) analysis have been worked out using PLAXIS 2D, 2011. These calculations are also usable for comparing the measurements and predictions for the reference times  $t_0 \dots t_5$  charged as indicator for significant changes in the static system with construction stage and time, Figure 5.

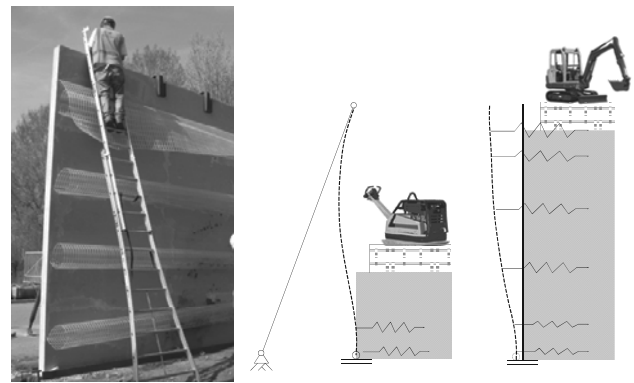


Figure 5a. Installation procedure and expected deformations of wall.

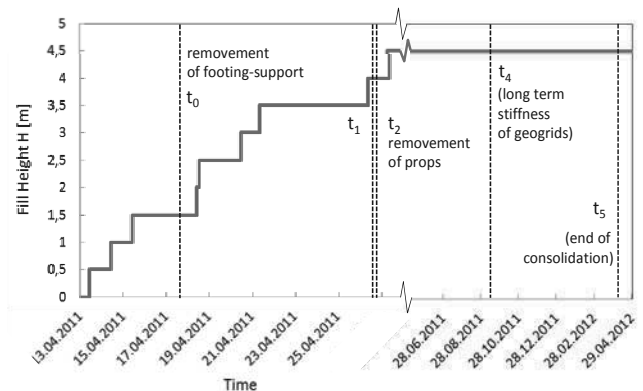


Figure 5b. Time schedule of construction.

### 5.2 Measuring strain and back-calculation of stress

For the back-analysis of horizontal forces from strain recordings, the corresponding stress has to be known. This can be read from isochronous stress-strain curves, as far as they are available. For the used material here, Secugrid<sup>®</sup> made from polyethylenterephthalat (PET), the curves are given. The back-analysis for representative times  $t_0$ ,  $t_1$  and  $t_2$  (see Figure 7) has been worked out using the isochronous curve for 1 hour, representative for the situation immediately after compaction of soil. As this gives conservative values of stress, no further differentiation is required.

For the time  $t_4$  and  $t_5$ , long term stiffness has been calculated using the isochronous curve for 1000 h, also giving

conservative values for stress, as  $t_4$  is approx. at 2880 h and  $t_5$  at 6500 h.

### 5.3 Main findings

Up to the date of printing, the construction is approximately one year in service. Data recording is available continuously during installation and in sequences during the service period. Within the service period, also 24h-measurements have been done to get an impression of temperature changes within the wall. Figure 6 gives the strain recording for the total time, indicating a very low level of strain of less than 1%, as it has to be expected. Nevertheless, only the three layers on the bottom get a significant loading. Two layers of geogrids on the top are up to now not taking any load. As these layers are mainly designed for a top-load of the construction not performed yet, the results fit with the expectations.

Removing the prop ( $t_1$  to  $t_2$ ) has been expected to increase the strain in the upper layers of the geogrids. Actually, this could not be found on site. The absolute values of strain (and therefore stress) at each layer remained stable.

For the sum of horizontal loads, compiled for the representative time  $t_0$  to  $t_5$ , measured forces as well as forces from FE-calculation and analytical approach by classical earth pressure theory can be compared. Friction at the toe of the wall, forces on the temporary prop as well as forces at the geogrids, measured right behind the wall, have to be compiled.

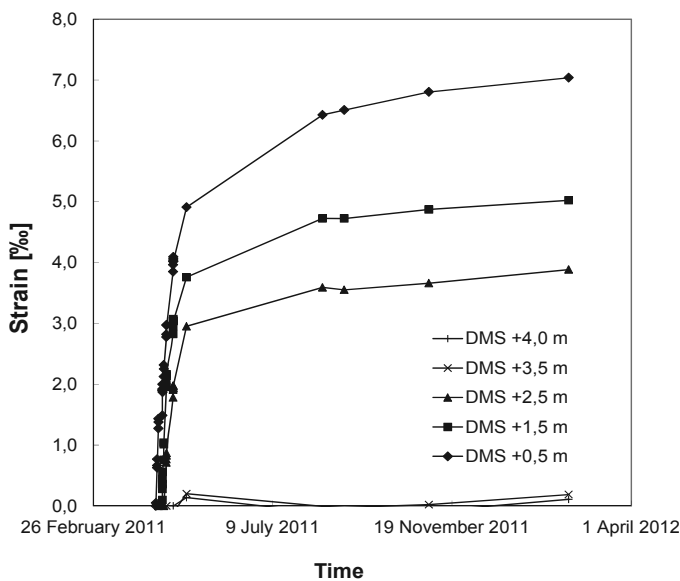


Figure 6. Entire strain recordings of the geogrids (DMS: strain gauge applied to geogrid).

For time  $t_0$  to  $t_4$ , the results gained by PLAXIS come quite close to the results gained from measurements in situ, Figure 7. Taking the rotation backwards due to settlements into consideration (time  $t_5$ ), PLAXIS gives a significant increase in stress, not be found on site.

In comparison to the measurements, results given by classical earth pressure have not been found to represent the reality for this combination of reinforcement and facing, neither the laboratory one nor the in-situ one. The difference is at least between 30% and 40% and therefore in line with the current status of research on reinforced soils. Compared to the design situation according to EBGEO, a reduction of lateral stress for the load case “unit weight of structure” and therefore a correction factor  $\eta_g \geq 0.7$  would be acceptable from the author’s point of view.

## 6 SUMMARY

Full scale laboratory tests have been performed for a full height panel wall, combined with a geogrid-reinforced soil structure. Tests are performed at loads up to 450 kPa according to bridge abutments as well as at dynamic loadings.

A comparable setup of a full scale panel wall has also been tested in situ. Monitoring of the reinforced wall allows for satisfactory back-analysis of the constructions steps.

The measured stress conditions fit with the expected low stress approach for the combined structure, given by FE-analysis. The findings combine the current results of international research and updated design approaches (EBGEO) also for full height panel walls. They allow for the consideration of a reduced earth pressure distribution in design as well as for simplified construction.

Due to limitations, the setup and results cannot be transferred to all combinations of reinforcement, soil and panel-systems, but allow for further analysis by FE calculations.

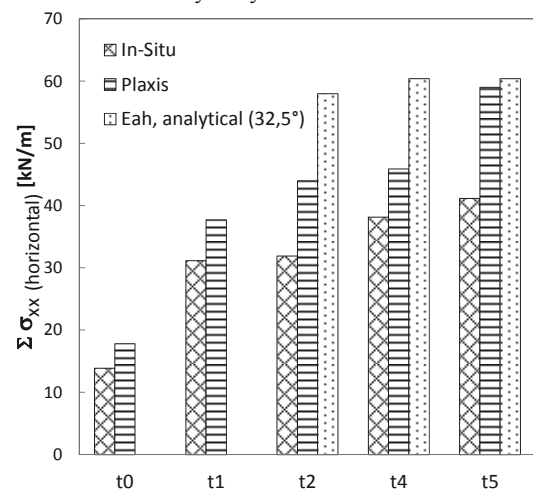


Figure 7. Comparison of measured lateral stress in situ, prediction by FE-analysis and prediction by classical earth pressure theory

## 7 REFERENCES

- EBGEO - Recommendations for Design and Analysis of Earth Structures using Geosynthetic Reinforcements. 2nd Edition. Published by German Geotechnical Society (DGGT). Ernst & Sohn, Berlin, 2011.
- DIN EN 14475, 2006-04: Execution of special geotechnical works - Reinforced fill.
- BS 8006-1, 2010-10: Code of practice for strengthened/reinforced soils and other fills.
- Pachomow, D., Vollmert, L. & Herold, A. (2007): „Der Ansatz des horizontalen Erddrucks auf die Front von KBE-Systemen“. Tagungsband zur 10. FS-KGEO 2007.
- Ruiken, A., Ziegler, M., Vollmert, L. & Duzic, I. (2010): “Recent findings about the confining effects of geogrids from large scale laboratory testing”. 9th International Conference on Geosynthetics, Brazil, 2010.
- Bussert, F. (2006): „Verformungsverhalten geokunststoffbewehrter Erdstützkörper – Einflussgrößen zur Ermittlung der Gebrauchstauglichkeit“. Dissertation. TU Clausthal, Schriftenreihe des Instituts für Geotechnik und Markscheidewesen, Heft 13/2006.
- Pachomow, D. & Herold, A. (2009): „Zum Last-Verformungsverhalten von KBE-Konstruktionen im Frontbereich“. Vortrag zum VI. Geokunststoff-Kolloquium in Bad Wildungen der NAUE GmbH & Co. KG, Espelkamp.

# The influence of bond stress distribution on ground anchor fixed length design. Field trial results and proposal for design methodology

L'influence de la répartition des contraintes sur les tirants d'ancrage de longueur fixe. Résultats de planche d'essais et proposition de méthodologie de conception

Vukotić G.  
Kellerterra, S.L.

González Galindo J., Soriano A.  
Universidad Politécnica de Madrid

**ABSTRACT:** This paper presents a brief analysis and comparison of different recommendations for a ground anchor fixed length design and a load transfer capacity at grout-ground interface, comparing it with the full scale test results recently carried out in Spain. Simple methodology for ground anchor routine design is proposed, incorporating efficiency factor as a conceptual control of anchor capacity, and fixed length criteria to determine range of application of conventional anchors, with single fixed length unit, or Single Bore Multiple Anchors (SBMA). Ground anchors discussed in this paper are cement pressure grouted, formed by pre-stressed strand tendons that are installed in soil or rock.

**RÉSUMÉ:** Cet article présente une brève analyse et la comparaison des différentes recommandations pour la conception de tirant d'ancrage de longueur fixe et la capacité de transfert de charge à l'interface coulis-sol, en le comparant avec les résultats d'essais à échelle réelle obtenus en Espagne au cours des dernières années. Une méthodologie simple pour la conception de tirant d'ancrage est proposée; elle intègre le facteur d'efficacité comme un contrôle conceptuel de la capacité de l'ancrage et les critères de longueur fixe pour déterminer le champ d'application des tirants d'ancrage conventionnels, d'unique longueur fixe, ou d'ancrages multiples en un unique forage (SBMA pour ses sigles en anglais). Les tirants d'ancrage décrits dans ce document sont injectés à pression au moyen d'un coulis de ciment et sont formés par un faisceau de câbles d'acier précontraints qui sont installés dans le sol ou la roche.

**KEYWORDS:** anchor, fixed length, bond stress, efficiency factor.

## 1 INTRODUCTION

Nowadays anchors represent a key medium to sustain and strengthen slopes formed by instable soils and fractured rocks, and to ensure the stability of various types of gravity structures.

Regarding bond stress and load transfer capacity at the grout-ground interface, most procedures for anchor design are empirical values or formulas derived by local experiences, very difficult to extrapolate for different locations or execution systems. The design procedure is often simplified, considering direct proportionality between fixed anchor length and its load capacity, as it is prevailing practice in Spain and South America.

However, since late 1960s numerous authors demonstrate bond stress or skin friction distribution to be highly non-uniform at all stages of loading, with high bond stress mobilization along reduced fixed length. In the following chapters, based on presented references and analysis of the field trial results recently performed in Spain, the methodology for anchor fixed length design is proposed.

## 2 DESIGN OF THE FIXED ANCHOR LENGTH

### 2.1 Current practice

Design assumption of uniform load distribution along the fixed anchor length is not only limited to usual methodology and standards in Spain and South America but is internationally generally adopted. Considering this hypothesis the ultimate or capacity of the anchor is commonly expressed as follows:

$$T_{ult} = \pi \cdot d \cdot L_{fix} \cdot \tau_{ult} \quad (1)$$

where:  $d$  = anchor diameter,  $L_{fix}$  = anchor fixed length and  $\tau_{ult}$  = ultimate bond stress.

This formula differs from experimental and theoretical evidence that corroborate that there is no linear dependency of ultimate capacity on fixed anchor length.

### 2.2 Non-uniform bond stress distribution

It is fully acknowledged by numerous researchers that the distribution of stress along the fixed anchor length is non-uniform, both at low stress levels and at failure. This phenomenon results from the general incompatibility between elastic modulus and corresponding deformation of the anchor strands, cement grout and ground.

Field tests on instrumented conventional anchors, reported by Muller (1966), Berrardi (1967), Ostermayer (1974), Ostermayer and Scheele (1977), Mastrantuono and Tomillo (1977), Barley (1995) and Briaud et al. (1998), showed that when applying the initial load the bond stress is concentrated over the proximal length of the fixed anchor, leaving a significant part of the fixed length towards distal end unstressed. By the evolution of the load the bond stress concentration zone is transferred along the fixed anchor as the bond stress along either the tendon/grout or grout/ground interface is exceeded.

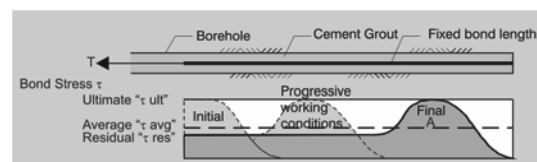


Figure 1. Development of bond stress distribution along a fully bonded fixed anchor length (Barley 1995).

Simultaneously, due to progressive debonding, stress at the proximal end reduces to residual values. The bond stress concentration zone reaches distal end of the anchor just before the failure, as it can be seen in Figure 1.

The same mechanism of a non-linear load and bond distribution was confirmed by laboratory full-scale test accomplished by Weerasinghe (1993). It is also important to mention investigation done by Coates and Yu (1970), which studied stress distribution around a cylindrical anchorage in triaxial stress field using finite element methods. The results emphasize the non-uniform bond stress distribution for the ratio of the elastic modulus of the anchor material ( $E_A$ ) and the rock ( $E_R$ ) less than 10 ( $E_A/E_R < 10$ ), which is very common for wide range of rocks and soils in which anchors are usually constructed.

### 2.3 Efficiency factor

There have been a number of attempts to quantify the non-uniform load distribution and to introduce effects of progressive debonding into Formula 1. Casanovas (1989) recommended design based on definition of apparent fixed length ( $L_{ve}$ ) over which the ultimate bond stress can be mobilized:

$$L_{ve} = \left( \frac{L_{fix}}{L_0} \right)^{\frac{1}{\log(0.1 \cdot \frac{\tau_{ult}}{\tau_0})}} \cdot L_0 \quad (2)$$

where:  $L_{ve}$  = apparent fixed length over which  $\tau_{ult}$  (kN/m<sup>2</sup>) operates,  $L_0$  = reference length of 1 m,  $\tau_0$  = reference value of 1 kN/m<sup>2</sup>.

To understand better efficiency factor concept it is possible to analyze Figure 1 and to compare area  $A$ , that corresponds to the final and maximum load stage, with the total area below  $\tau_{ult}$ .

$$f_{eff} = \frac{Area.A}{Area.below.\tau_{ult}} \quad (3)$$

Then, ultimate anchor capacity can be expressed as follows:

$$T_{ult} = \pi \cdot d \cdot L_{fix} \cdot \tau_{fix} \cdot f_{eff} \quad (4)$$

Research based on over 60 full scale tests performed on different anchor fixed lengths, installed in wide range of soil (clays, silty clays, sandy clays, boulder clay and glacial till), permitted development of the concept of the efficiency factor (Barley 1995 and 1997, Barley and Windsor 2000). Figure 2 presents the distribution of the values of the efficiency factor ( $f_{eff}$ ) against anchor fixed length, and the best fit curve can be expressed by following expression:

$$f_{eff} = 1,6 \cdot \left( \frac{L_{fix}}{L_0} \right)^{-0,57} \quad (5)$$

It is important to emphasize that Barley's efficiency factor is quite consistent with Ostermayer (1974) diagrammatic presentation of the ultimate medium skin friction against fixed length for similar soil characteristics and anchor construction process, as it can be seen in Figure 2.

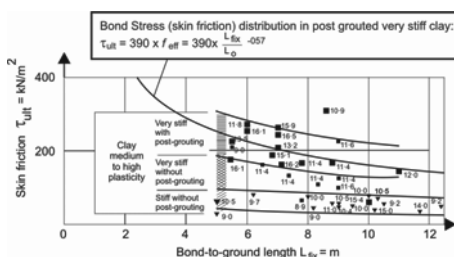


Figure 2. Ostermayer's (1974) boundary lines vs. Barley's (1995) efficiency factor.

Barley (1995) also suggested the efficiency factor for sands, correlating efficiency with the fixed length and the friction angle:

$$f_{eff} = (0,91) \frac{L_{fix} \cdot \tan \varphi}{L_0} \quad (6)$$

One of the most extensive attempts to model construction technique, characteristics and behaviour of anchors have been accomplished by Mecsi (1995), based on analysis of results from numerous installed and monitored anchors.

Analytical solution and simple graphical method based on the theory of expanded cylindrical cavity provide the possibility to define the approximate pull-out capacity. The Analysis of load distribution for the known anchor geometry and rigidity permits determination of the specific pull-out resistance of a 1 m anchor length ( $t_{ult}$ ) and the length of the fully mobilised bond stress ( $L_b$ ). Considering that only reduced percentage of maximum bond stress can be mobilised over the remaining fixed anchor length ( $L_{fix} - L_b$ ), the ultimate anchor capacity can be expressed by the following expression:

$$T_{ult} = \tau_{ult} \left[ L_0 + \frac{1}{k} \cdot \text{th} [k \cdot (L_{fix} - L_0)] \right] \quad (7)$$

$$k = \sqrt{\frac{\tau_{ult}}{E_{steel} \cdot A_{steel} \cdot \Delta_{ult}}} \quad (8)$$

where:  $k$  = rigidity index,  $E_{steel}$  = steel deformation modulus,  $A_{steel}$  = steel tendon area,  $\Delta_{ult}$  = elongation of the shear strength length ( $L_{fix} - L_0$ ).

Based on data from Ostermayer and Scheele (1997), Woods and Barkhordari (1997) proposed efficiency factor for its incorporation in the expression for ultimate capacity of low-pressured anchors in sand (Formula 10), recommended in BS 8081 (1989), which is a function both of fixed anchor length and friction angle:

$$f_{eff} = \exp(-0,05 \cdot \frac{L_{fix}}{L_0} \cdot \tan \varphi) \quad (9)$$

where:  $L_0$  = reference length of 1 m.

$$T_{ult} = f_{eff} \cdot L_{fix} \cdot n \cdot \tan(\varphi) \quad (10)$$

### 2.4 Single Bore Multiple Anchors - SBMA

This system involves the installation of a multiple unit anchors into a single borehole, with enough short unit lengths to reduce or even to avoid the progressive debonding. Each unit is formed by individual tendon and is loaded with the corresponding unit stressing jack, mobilizing its own capacity independently of other unit anchors.

Application of this system permits the unlimited theoretical total fixed length, while conventional anchors formed by only one unit do not provide beneficial effects in load capacity for fixed length superior to 10 m as is stated by numerous authors and design guidelines or codes.

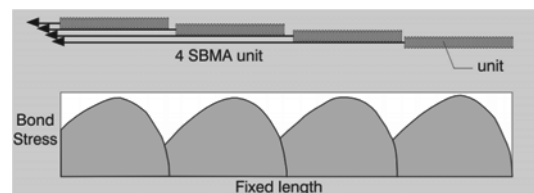


Figure 3. Development of bond stress along a four unit single bore multiple anchor (Barley, 1997).

Total fixed lengths of 10 to 20 m are frequently used in all types of soils, achieving high anchor capacities (2000 to 5000 kN) that are almost three times greater than the normal conventional anchors capacity values (Barley 1997, Barley and Windsor 2000). A comparison of load distribution between conventional and SBMA anchor is presented in Figure 3.



N°/Type of Anc.	$L_{fix}$ m	$T_{ult}$ kN	$\tau_{ult}$ kN/m <sup>2</sup>	$f_{eff}$
8 SBMA (18 units)	2.5	450-540	322-386	1
2 Conventional	7.5	960-1080	230-254	0.59-0.79

### 3.4 Summary

An extensive series of field anchor tests performed in different soils showed that:

- there is no direct proportionality between fixed anchor length and its ultimate load capacity;
- obtained values of the average ultimate bond stresses in cohesive soils fit well with Ostermayer's (1974) diagrammatic presentation of skin friction against fixed length, while results obtained in gravelly sands fit well with Ostermayer and Scheele (1978) presentation of ultimate load capacity vs. anchor length;
- ranges of obtained efficiency factors are consistent with tendency of values proposed by Barley (1995);
- efficiency factor can be considered as a conceptual control of anchor ultimate capacity;
- fixed anchor lengths longer than 10 m do not contribute significant beneficial effects on capacity.
- SBMA anchors permits construction of high anchor capacities that approach more than two times that of the conventional anchors which utilize long inefficient fixed length.

## 4 PROPOSAL FOR DESIGN METHODOLOGY

Based on the information presented in previous chapters, proposal for design methodology for cement grouted anchors formed by steel tendons is presented below, considering most important parameters that define its capacity, like: soil characteristics, execution process, ultimate and average bond capacity, fixed length, type of anchors (conventional or SBMA), stress distribution and efficiency factor.

Emphasis is placed on the effects of progressive debonding that cause the non-uniform stress distribution along the fixed length, with efficiency factor as a conceptual control of anchor capacity. Due to the number of parameters that enter the analysis, recommended methodology has an iterative character, as it can be seen in Figure 6. Some of the most important steps of the flow chart are commented below.

Phase I: Evaluation of the site subsoil conditions and relevant properties of in situ soil and rock, as a factor that directly influence steps in the Phase II (construction system and skin friction estimation).

Phase II: For the skin friction estimation it is recommended to use at least two sources, taking into account the concept or formula that will be applied for the anchor design. If pre-design load tests are performed to evaluate ultimate anchor load capacity, construction process has to be exactly the same as planned for production anchors, and fixed lengths should be similar with test anchors. For the first iteration anchor length is calculated considering uniform bond stress distribution (Equation 1). If calculated fixed length is larger than 5 m, construction process can be reconsidered (Alternative A), varying anchor diameter or type of grouting, with objective to reduce fixed length up to 5 m. Other option (Alternative B) is to introduce directly the efficiency factor.

Phase III: If the fixed length obtained considering non-uniformity is in the range between 5 and 10 m, two alternatives are proposed. First alternative considers conventional type of anchor, with unique fixed length unit calculated taking into account efficiency factor ( $f_{eff}$ ) – Equation 2. Another alternative

is the application of SBMA. In this case fixed length of each unit that forms SBMA is calculated considering corresponding efficiency factor ( $f_{eff}$ ) – Equation 3.

If the fixed length, obtained considering non-uniformity is greater than 10 m it is recommended to apply SBMA anchors.

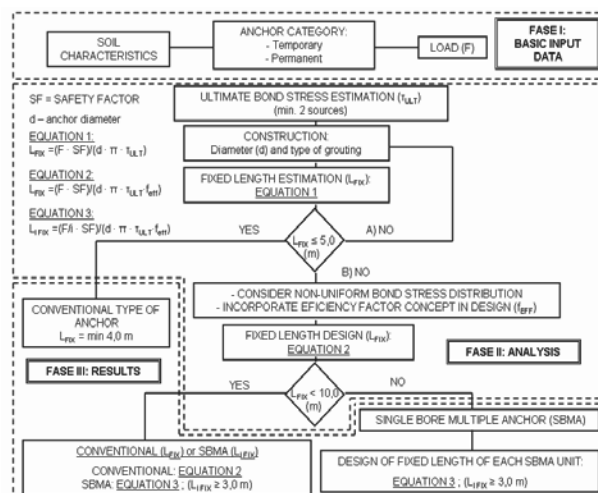


Figure 6. Flow chart for design of fixed anchor length.

## 5 REFERENCES

- Barley A.D. (1995). Theory and Practice of the Single Bore Multiple Anchor System. *Proc. Int. Symposium Salzburg*, Balkema Rotterdam, pp 293-301.
- Barley A.D. (1997). The Single Bore Multiple Anchor System. *Proc. Int. Conf.: Ground anchorages and anchored structures*. London, pp. 65-75.
- Barley A.D. and Windsor, C.R. (2000). Recent advances in ground anchor and grout reinforcement technology with reference to the development of the art. *GeoEng 2000, Int. Conf. on Geotechnical and Geological Engineering*. Melbourne, pp. 1083-1094.
- Berardi G. (1967). Sul Comportamento Deglie Ancoraggi Immersi in Terreni Diversi. *Università Genova, Inst. Contr. Sc. Serie III* (60), pp 18-19.
- Briaud J.L., Powers W.F. and Weatherby D.E. (1998). Should Grouted Anchors Have Short Tendon Bond Length?. *Journal of Geotechnical and Geoenvironmental Engineering ASCE*, pp. 110-119.
- BrS 8081 (1989). British Standard Code of Practice for Ground Anchorages. BSI, London.
- Casanovas (1989). Anchoring in rock. Elsevier Scientific Publishing Company, pp 0-33.
- Coates D.F. and Yu Y.S. (1970). Three dimensional stress distribution around a cylindrical hole and anchor. *Proc. of 2 Int. Conf. on Rock Mechanics*. Belgrade, pp. 175-182.
- EN 1537 European Standard (2010). Execution of special geotechnical work – Ground Anchors.
- Mesci J. (1997). Some Practical and Theoretical Aspects of Grouted Soil Anchors. *Proc. of Int. Conf. Ground Anchorages and Anchorages Structures*. London, pp. 119-130.
- Muller H. (1966). Erfnungenmit Verakurungen System BBRV in Fels- und Lock-ergensteinen. *Schweizerische Bauzeitung*, 84 (4), pp. 77-82.
- Ostermayer H. (1974). Construction carrying behavior and creep characteristics of ground anchors. *Int. Conf. On Diaphragm Walls and Anchorages. I.C.E. London*, Septiembre 18-20, pp. 141-151.
- Ostermayer H. and Scheele F. (1977). Research and Ground Anchors in Non-Cohesive Soils. *Géotechnique 3*, pp. 92-97.
- Weerasinghe R.B. (1993). The Behaviour of Anchorages in Weak Mudstone. PhD Tesis, University of Bradford.
- Woods R.I. and Barkhordari K. (1997). The Influence of Bond Stress Distribution on Ground Anchor Design. *Proc. of Int. Conf. Ground Anchorages and Anchorages Structures*. London, pp. 55-64.

# The sustainability and assessment of drystone retaining walls

## Le développement durable et l'évaluation des murs de soutènement en pierres sèches

Warren L., McCombie P.  
*University of Bath*

Donohue S.  
*Queens University Belfast*

**ABSTRACT:** The art of drystone walling is a highly sustainable traditional practise which uses local materials and craftsmen. As no mortar is used they have low embodied carbon, and much repair work or rebuilding can be carried out using very little if any new materials. However local practices developed to suit local materials, leading to a range of construction styles, making them difficult to assess. This paper examines a range of construction styles of drystone retaining walls in use across the United Kingdom. Understanding of the substantial variations of construction style is essential to enable proper assessment of these structures. Different frictional and weathering characteristics, and the naturally occurring shapes of stone found in an area, all affect the ways in which the stones have traditionally been assembled into walls. Ease of construction also plays a part, as the craftsman will naturally wish to achieve a robust construction in a way that is economical of time and effort. Aesthetics may be very important, for both client and craftsman. It is also shown that construction style is influenced by the location and function of the structures, with harbour walls particularly likely to have unique characteristics, and the reasons for this are explored.

**RÉSUMÉ :** L'art de la pierre sèche est une pratique hautement durable traditionnelle qui utilise des matériaux et des artisans locaux. En l'absence de mortier, elles ont une faible carbone incorporé, et les travaux de réparation ou de reconstruction bien peut exiger très peu ou pas de nouveaux matériaux. Cependant les pratiques locales développées pour répondre à des matériaux locaux, conduisant à une gamme de styles de construction, ce qui les rend difficiles à évaluer. Cet article examine une gamme de styles de construction de murs de soutènement en pierres sèches utilisées dans l'ensemble du Royaume-Uni. Compréhension des variations importantes du style de construction est essentielle pour permettre une évaluation adéquate de ces structures. Différentes caractéristiques de frottement et aux intempéries, et les formes naturelles de pierre trouvés, affectent la façon dont les pierres ont traditionnellement été assemblés. Facilité de construction joue également un rôle. L'esthétique peut être très important, à la fois pour le client et l'artisan. Il est également démontré que le style de construction est influencée par l'emplacement et la fonction des structures, avec des murs du port particulièrement susceptibles d'avoir des caractéristiques uniques, et les raisons de cette situation sont explorées.

**KEYWORDS:** Drystone, Construction styles, Assessment

## 1 INTRODUCTION.

Throughout the UK there are many different styles and types of walling to be found. Most styles can be categorised as horizontal construction, vertical construction or random construction (Figure 1). Each has its own unique features and is often associated with certain areas of the country and corresponding rock types. Horizontal construction is often found with more blocky types of stone such as limestones, which can be stacked in a more conventional fashion; the stones are also sometimes worked to give a better fit. Horizontal construction is probably the most common type of construction within the UK. Vertical construction is mainly associated with slate type stones that can be tightly packed and may be less successful in a horizontal configuration. Random construction is mainly associated with more granitic type rocks which are hard to work and are often irregular in shape. These styles are sometimes found in combination in a single wall with a single type of stone, and there are variations such as the herringbone construction, found in parts of Cornwall.

It could be argued that every drystone retaining wall works in essentially the same way, as every wall is essentially a gravity retaining wall that relies on the frictional forces between the stone for stability. However, each style is likely to use the mechanical properties of the stones in different ways to achieve the required coherence. The failure and movement of horizontally constructed walls is comparatively well documented and understood (Mundell, 2009) when compared to

the other construction styles. The mechanical differences between the styles are explored below.

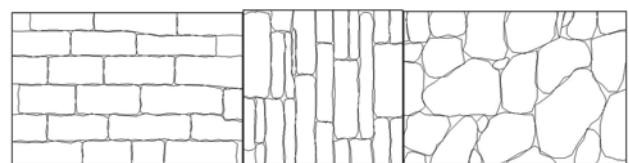


Figure 1. Different wall styles found in the United Kingdom: horizontal construction, vertical construction, random construction.

### 1.1 Horizontal Construction

Experimental testing and numerical modelling (McCombie et al. 2012, Mundell et al. 2009, Colas et al. 2010, Villemus et al. 2007) have shown that the overturning moment due to the horizontal component of earth pressure is resisted in part by the vertical component acting in downwards shear on the back of the wall, with very small deformations for well-constructed walls in a normal condition. As walls become overloaded the deformations can become considerable, often showing the classic bulged profile as the walls adapt their shape to the higher applied load (Figure 2). Ultimately, the walls will typically overturn, though if a smooth stone is used the wall or a part of it may slide forwards first. If the wall is constructed in a well-bonded manner, with stones overlapping, then a tensile strength can develop along the length of the wall which greatly assists in



the redistribution of load, and helps give the wall substantial ductility. This behaviour is dependent upon a horizontal construction. A less beneficial consequence of horizontal construction is the reliance on through stones to connect coursed layers of stone at the front and back of the wall across an infill of rubble. These stones are necessarily larger than those used for the rest of the construction, and there may not be sufficient to ensure that the wall behaves monolithically, giving a greater chance of movement and hence failure.



Figure 2. 2.4m high test wall at the University of Bath showing a classic bulged profile in a limestone wall of horizontal construction.

### 1.2 Vertical Construction

There has been no notable published research into vertical or random forms of construction, but some indications of how they perform may be inferred from observations, in relation to the behaviour of horizontal constructions.



Figure 3. Model test showing concrete blocks partially rotated and wedged in against the sides of the test box.

Discussions with wallers who use the vertical form of construction, and detailed observations carried out in Somerset and Cornwall, suggest that vertical construction is reliant on compressional pre-stressing forces. In the majority of vertically constructed walls all stones either penetrate the full width of the wall, or are tightly packed throughout the wall depth creating an effectively continuous cross section. During construction pre-stressing is induced through the wedging of stones at regular

intervals which when combined with the overall confinement from the rest of the wall produces a compressional force. As the walls are backfilled, material will fill any remaining gaps at the back of the wall further strengthening the wedging. Evidence of this is shown in work carried out by Bailey (2008) in conjunction with Mundell (2009) (Figure 3). In Bailey's work during initial experiments using smaller individual blocks it was found that the backfill became wedged between the blocks making them virtually impossible to remove from the testing box. This was a nuisance for these tests, but gives useful information about the mechanical wedging of other wall types.

### 1.3 Random Construction

Random construction is likely to have features common to both the horizontal and vertical construction methods, however the variable morphology of the stones in random construction make it difficult to make generalised assumptions regarding any further mechanisms involved. However, it can be seen that an absence of bonding prevents the development of tensile strength along the wall face, whilst the lack of alignment of vertical stones prevents useful pre-stressing. Randomly constructed walls must rely much more on the size and weight of individual stones.

Table 1. Locations, principal stone types, and principal construction styles in this study.

Location	Geology	Wall Construction
Boscastle, Cornwall, UK	Slate	Vertical Herringbone
Mousehole, Cornwall, UK	Granite	Random
Dartmoor, Devon, UK	Igneous Intrusion	Random
Brompton Regis, Somerset, UK	Morte Slate	Vertical
Northleach, Gloucestershire, UK	Limestone Formations	Horizontal
Bath, Somerset, UK	Interbedded Limestone	Horizontal

The use of these different styles is often found to relate to the types of stone available in a given area. Horizontal construction is often found where stones are more block like in their nature, either naturally or by easy working to desired shapes. The stones used in horizontal construction are often stone types with more frictional surfaces, such as limestones, which help the stones to transfer loading more than any other mechanisms which might occur within the wall. Vertical construction seems more likely to be used with more slaty type materials. Due to its laminated nature slate is often found with a comparatively thin cross section that lends itself more to this style. This form of construction is likely to be beneficial for stones such as slate which have comparatively low surface friction because shear load from earth pressure is transmitted through contact between the rough edges of the stones rather than the smooth surfaces. Random construction is often found where stone is difficult to work e.g. granitic areas or where there is a variety of local stone types, which may all be used in conjunction within a wall. The geology of an area therefore has considerable influence on the locally dominant forms of construction, but it is still possible to see different styles within the same wall (Table 1).

## 2 SPECIFIC CONSTRUCTION STYLES – HARBOUR WALLS

Although wall construction style is often a reflection of locally available stone, sometimes the construction style reflects the purpose of the wall. Probably the best examples of this are the harbour walls found around the United Kingdom. Many of these walls are of significant age - parts of the quay in Mousehole are reported to date back to 1390 (Cornwall-online.co.uk) suggesting that they are well suited to their usage. Mousehole is also unusual when looking at harbour walls as much of it is uncut random rubble.



Figure 4. Wall at Mousehole, Cornwall, containing of large blocks.

It is typical when looking at harbour walls to find vertical construction as you would find with slate type materials, but they can be on a far larger scale to that found in a typical wall. Stones may also be shaped to suit vertical construction even if they are not usually built in the fashion, or are constructed from slate sheets far larger than you may expect to find in a typical vertically constructed wall. This is likely to be linked to the convenience of transport material by water, allowing larger stones to be transported. The vertical construction and larger stone sizes are both advantages in harbour construction. The verticality of the stone helps to prevent uplift by presenting a small bottom face for waves to act on, and provides better drainage for sea water, both during the changing tides and under wave penetration. Being drystone and hence free draining is better suited to harbour construction than most other wall types, in which any water which penetrated the wall under wave pressure may not flow out quickly under gravity alone, inducing extra pressures on the rear of the wall. Having a more massive construction provides better protection from wave action as a greater force is needed to move individual stones within the wall. The voided nature of drystone is also likely to help with wave energy dissipation as waves will break up into the wall on impact, as opposed to being reflected or running up and over an impermeable concrete wall.

Research has been carried out into the construction and tradition of drystone harbours by Richard Tufnell (2012) which he presented at the 13th International Dry Stone Walling Congress in September 2012

## 3 UNDERSTANDING CONSTRUCTION AND ASSESSMENT

Many of the current drystone retaining structures were constructed around 100 years ago with no records of how or exactly when they were constructed. Even many of the modern walls are constructed based on rules of thumb, with little or no input from engineers. Many of these walls have remained stable for a number of years and still continue to do so, retaining a significant proportion of various transport infrastructures throughout the United Kingdom, as well as being used in other applications such as harbour walls and domestic use.

Since the majority of these structures have been built, the loadings that they are subjected to have increased, particularly on the road networks. This combined with the increasing age of the walls and the need to be able to replace or repair walls before collapse means that improved assessment drystone retaining wall stability is increased. The assessment of these structures by engineers is often tricky due to the lack of formal engineering input during their design, as well as a lack of knowledge of failure mechanisms, unlike with more modern retaining structures. Assessing these structures in the same way as modern structures is inappropriate due to their un-mortared nature and inherent flexibility, which means that obvious deformation within the wall does not automatically mean that the wall is unsafe. Guidance on assessment can be found in work by O'Reilly and Perry (2009) and through the various publications by the dry stone walling association. However much of the guidance given is qualitative and relies on the judgement of the engineer assessing the wall as to whether it is safe or not. Where an engineer is familiar with drystone walls in general and the walls he is looking at in particular, then a reasonable assessment is likely to be made. However if an engineer has little to no experience of drystone walls they may take the walls' natural deformations and oddities to be signs of failure, and hence make an inaccurate or insecure judgement. This in turn may lead to walls unnecessarily being taken down and replaced with less sustainable modern alternatives which are out of keeping with their surroundings. It could also lead to a failure which should have been prevented

In order to improve assessment of these structures further engineering knowledge of them is required, both in terms of overall structural behaviour and the effects of properties of individual elements. This should include consideration of how these factors might change with time, such as the weathering of the stone. By understanding generic wall behaviour and how different factors affect this new assessment techniques can be developed that can enable the engineering judgement to be better informed.

It is also important to note the modifications that are often made to drystone retaining walls, often in good faith, which can be detrimental to the wall's health. For example, it is common practise for dry stone walls to be grouted or pointed either in an effort to prevent further movement, or to protect the base of a wall from salt spray, particularly in limestone areas. However in doing so the drainage paths through the wall are often blocked, thus taking away one of the main advantages of drystone retaining walls, which is that due to their un-mortared nature they are free draining. This can cause a build-up of water pressures behind the wall which did not exist before, and ultimately lead to collapse. The grouting of a wall will probably reduce its flexibility, which can be detrimental in two ways. If the wall is less ductile then it is unable to redistribute load concentrations, or distribute load away from weak areas, which could result in a local failure leading to a general collapse. On the other hand, a local crack which might allow a safe redistribution of load might give serious concern.

Unfortunately as with most retaining type walls a number of harbour walls are also being grouted. This is potentially understandable in harbour walls as over time wave action is likely to have caused some visible damage to the wall, and it

may be deemed necessary to protect the wall. However due to their voided nature these walls often need more grout than initially estimated and there is no guarantee that the grouting has been done sufficiently to fill all the voids in a wall. It is also difficult to know where the injected grout ends up. Grouting not only stops the draining of water that enters the wall through wave and sea action, but also most harbour walls retain land behind them so that the grouting will also prevent the drainage of groundwater, which as before exerts extra pressures on the wall and potentially causes failure.

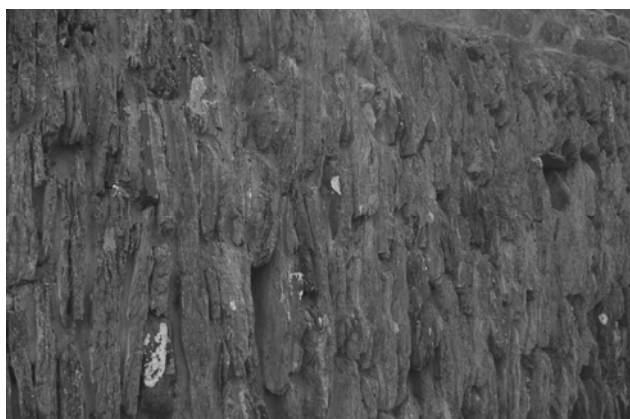


Figure 5. Grouted wall of vertical construction at Port Gavern, Cornwall

A general difficulty of assessing walls which have failed is that due to their un-mortared nature, all that is usually left of a failed section of wall is a pile of rubble that is almost impossible to analyse, and it cannot be assumed that adjacent standing sections give a true indication of the form of a failed section. Some judgement may be able to be made about the foundations or conditions of the backfill but little can be said about the wall. Increasing the understanding of how these walls work as well as improving assessment it may make it easier for engineers to use drystone walling in new build projects or to replace existing damaged walls, rather than their more modern and less sustainable counterparts.

### 3.1 Appearance Vs. Wall Quality

When assessing a drystone wall much weight might be given to the appearance of the wall at its face. This can be deceiving, especially as the way in which walls are finished is likely to have changed over the years. It is likely that the majority of walls built a hundred years or more ago had greater emphasis on function, whereas aesthetics are likely to be an important factor in choice of drystone walling today. This means that quality of the aesthetics is easily taken as a proxy for quality of construction, but just because the wall face looks even and is cleanly finished does not mean that the wall behind will be to the same standard - and vice versa. For example, wallers cite cases where freestanding walls have appeared to be well constructed and have a good finish but have failed within months of being built, because instead of being constructed with properly packed filling they have been filled with pea shingle with no through stones, preventing the wall from performing as a monolith. In another case a waller was asked by a client to build a small retaining wall which was to have a hedge planted in front of it, so ultimately was not worried about the finished appearance of the wall. He also did not want any wastage of the stone, whereas normally a certain amount of stone is left at the end where stones have been shaped or just not used in the wall. However this wall was built to no less a standard than other walls he had built for the same client which had a very high quality of finish to them.

## 4 THE SUSTAINABILITY OF DRYSTONE WALLS

As with most constructions the sustainability of drystone walls must also be considered. When considering drystone structures this will also include the ecology impacts of the walls providing habitat and shelter for both animals and plants.

Drystone walls are naturally very sustainable structures and with the current imperative of low carbon structures are an almost ideal solution. Their main advantage is a lack of mortar, this not only means that the walls lack the embodied carbon associated with the mortar, but that when repair or rebuild is required very little if any new material is required. This does however depend on the stone type; for example a limestone wall is more likely to need some new material as limestone is prone to decay from water and frost. Traditionally walls have been built with materials local to where the wall was built, as with most vernacular structures, and this has continued through the generations of wall builders so that even today new materials are usually obtained from local quarries or sources well known to the waller. This means that there is minimal transport of materials, thus reducing the embodied carbon within a drystone wall. Drystone walls also provide an excellent habitat for a variety of animals and plants and various research has been carried out where drystone walls have been highlighted. (Hynes and Fairley 1978, Cody and Cody 1972,)

## 5 CONCLUSIONS

Drystone retaining walls of horizontal construction have dominated scientific work to date, but regional construction styles which have developed in response to the type of stone available or particular requirements may behave in significantly different ways. It is important that these differences are understood if the stability of walls is to be assessed correctly.

## 6 REFERENCES

- Bailey, C. 2008. Model Tests of Dry Stone Retaining Walls. *MEng Dissertation: University of Bath: Dept. Architecture and Civil Engineering*.
- Cody, M.L., Cody, C.B.J. 1972. Territory Size, Clutch Size and Food in Populations of Wrens. *The Condor*. Vol.74. pp. 473-477.
- Colas, A.S., Morel, J.C., Garnier, D. 2010. Full-scale Field Trials to Assess Dry-Stone Retaining Wall Stability, *Engineering Structures*, Vol. 32, pp. 1215-1222.
- Cornwall-Online, Mousehole-West Cornwall, Available from: <http://www.cornwall-online.co.uk/westcornwall/mousehole.htm> [Accessed 5th November 2012]
- Hynes, J.A., Fairley J.S. 1978. A Population Study of Fieldmice in Dry-Stone Walls. *The Irish Naturalists Journal*, Vol. 19. pp. 180-184.
- McCombie, P., Mundell, C., Heath, A., and Walker, P. 2012. Drystone Retaining Walls: Ductile Engineering Structures with Tensile Strength. *Engineering Structures*, 45.
- Mundell, C. 2009. Large Scale Testing of Drystone Retaining Structures. *PhD Thesis: University of Bath: Dept. Architecture and Civil Engineering*
- Mundell, C., McCombie, P., Bailey, C., Heath, A., and Walker, P. 2009. Limit-equilibrium assessment of Drystone Retaining Structure. *Proceedings of the Institution of Civil Engineers-Geotechnical Engineering*, 162 (4), pp. 203-212
- O'Reilly, M.P., Perry, J., 2009. Drystone Retaining Walls and their Modifications – Condition Appraisal and Remedial Treatment. *CIRIA, London*.
- Tufnell, R., 2012. Dry Stone and the Sea: Techniques and Traditions of Dry Stone Harbours and Jetties in the British Isles. *13<sup>th</sup> International Dry Stone Walling Congress* (Unpublished at time of writing)
- Villemus, B., Morel, J.C., Boutin, C. 2007. Experimental Assessment of Dry Stone Retaining Wall Stability on a Rigid Foundation. *Engineering Structures*. Vol.29, pp. 2124-2132.

# Numerical modelling of groundwater flow around contiguous pile retaining walls

Modélisation numérique des écoulements des eaux souterraines autour d'écrans de soutènement de pieux contigus

Wiggan C. A., Richards D.J., Powrie W.

University of Southampton, Southampton SO17 1BJ, United Kingdom

**ABSTRACT:** Pore water pressure constitutes a significant proportion of the lateral load acting on a retaining wall. Consequently, guidelines often mandate that the worst case hydraulic conditions are applied in the design of retaining walls. This invariably dictates that retaining walls are treated as impermeable unless special consideration is given to the maintenance of drainage systems or to the prevention of infiltration. Contiguous pile retaining walls are, however, by their nature permeable unless considerable effort is expended to prevent seepage through gaps. If allowed, this seepage can result in reduced active side pore water pressures. Numerical simulations were conducted to determine the impact on pore water pressures of varying the pile gap ( $x$ ) to diameter ( $d$ ) ratio,  $x/d$ , in a contiguous pile retaining wall. A relationship between  $x/d$  and the effective bulk wall permeability,  $k_p$  was derived, and applied to two-dimensional simulations representing a contiguous pile wall. The results show that pore pressures behind the retaining wall reduced significantly with increased  $x/d$ .

**RÉSUMÉ:** La pression de l'eau interstitielle constitue une part importante des charges latérales agissant sur les parois d'un mur de soutènement. Par conséquent, les règles de l'art imposent que les pires conditions hydrauliques soient considérées dans la conception d'un mur de soutènement. Cela impose invariablement que les murs de soutènement soient considérés comme imperméables à moins que des considérations particulières soient données à l'entretien des systèmes de drainage ou à la prévention des infiltrations. Les murs de soutènement constitués de pieux contigus, sont cependant perméables (de par leur structure), à moins que des efforts considérables soient déployés pour empêcher les infiltrations à travers les intervalles. Ces infiltrations peuvent entraîner une réduction des pressions interstitielles effectives. Des simulations numériques ont été réalisées afin de déterminer l'impact des variations de l'espace entre palplanches ( $x$ ), de diamètre ( $d$ ), de ratio,  $x/d$ , sur les pressions interstitielles d'un mur de soutènement constitué de pieux contigus. Une relation entre le ratio  $x/d$  et la réelle perméabilité du mur,  $k_p$  a été déduite et appliquée à un modèle à deux dimensions représentant un mur en pieux contigus. Les résultats montrent que les pressions interstitielles derrière le mur de soutènement diminuent significativement lorsque le ratio  $x/d$  augmente.

**KEYWORDS:** Pore water pressure, numerical modelling, retaining wall, seepage forces, surface settlement

## 1 INTRODUCTION

Guidelines generally require that the most onerous tenable pore water pressure distribution is adopted for the design of subsurface retaining structures. For example, Eurocode 7 recommends that, unless reliable drainage can be provided or infiltration prevented, retaining walls should be designed with the water table at the ground surface (BSI, 2004). This can however cause over-conservative and unnecessarily expensive engineering solutions which go against the ethos of sustainable development. It would be advantageous if, based on the bulk permeability of the structure, the hydraulic loads on retaining walls could be treated as reduced.

There is however limited research into how the geometry influences hydraulic loads on retaining walls although, according to CIRIA 580, 'economic advantages' might be derived if through-wall seepage is allowed (Gaba et al. 2003). This is due mainly to the reduction in pore pressures because of through-wall seepage. Research into ways of facilitating through-wall seepage and quantifying its effect is necessary.

### 1.1 Research in hydraulic loads around retaining structures

Previous research has not generally sought to distinguish between the long-term pore water pressure distributions around different types of retaining walls. For example, Potts and Burland (1983) and Hubbard et al. (1984) showed that the long-term pore pressures behind a secant pile retaining wall recovered to near their pre-construction values as might be

expected of an impermeable wall in fine soils. Powrie et al. (1999) and Carder et al. (1999) observed a reduction in pore pressures following construction of a contiguous pile retaining wall at Woodford. The pore pressures at Woodford however, did not return to their pre-construction values in the long-term. This reduction was attributed at the time to under-drainage to the more permeable chalk layer and therefore no consideration was given to the possible contribution of through-wall seepage. However Clark (2006) and Richards et al. (2007) have shown that there was a reduction in long-term pore pressures measured at a contiguous pile retaining wall in over-consolidated clay at Ashford. The pore pressures have not returned to their pre-construction values. Although there is underdrainage to the more permeable Weald Clay at Ashford, there is evidence that the long-term reduction in pore pressure can be attributed to through-wall seepage.

In contrast to retaining walls, there has been significant research into methods of reducing pore water pressures acting on shallow tunnels and on tunnels acting as drains. Despite an earlier assumption by Atkinson and Mair (1983) that groundwater loadings do not change significantly in the presence of varying hydraulic conditions, it has been shown by numerical analyses that segmented tunnel linings do in fact allow seepage of groundwater which contributes to reduced pore water pressures around tunnels in fine grained soils. Pore pressures at segmented lined tunnels approach atmospheric values and increase with distance away from the tunnel (Shin et

al. (2002), Lee and Nam (2006), Bobet and Nam (2007) and Arjnoi et al. (2009)).

The corresponding reductions in axial forces and stresses on segmented tunnel linings in comparison with fully waterproofed linings are significant, although inconsistent. For example Arjnoi et al (2009) observed a 20% reduction, Lee and Nam (2001) 25%, Potts et al. (2002) up to 30% and Lee and Nam (2006) up to a 70% reduction.

1.1.1 Surface settlement

Notwithstanding the potential advantages of allowing through-structure seepage, some detrimental effects have been noted in the analyses of shallow tunnels which might be relevant to through-wall seepage. Significant settlements have been observed associated with segmented lined tunnels acting as drains in fine grained soils. For example, Yoo (2005) noted that settlement was proportional to the amount of drawdown in the groundwater levels around the tunnel. Consolidation settlement,  $\rho$  due to the drawdown of groundwater level may be estimated in a similar manner by considering the one dimensional stiffness modulus,  $E'_0$  of the soil as shown in equations 1 and 2 (Roberts et al. 2007).

$$E'_0 = 400 \sigma'_{v} \tag{1}$$

$$\rho = \frac{D_w \gamma_w S_{av}}{E'_{0av}} \tag{2}$$

where  $\sigma'_{v}$ ,  $D_w$ ,  $\gamma_w$  and  $S_{av}$  are the vertical effective stress, thickness of the soil layer, unit weight of water and average drawdown respectively.

In this paper, pore water pressure variations around contiguous pile retaining walls are investigated numerically. An expression for the resulting effective bulk wall permeability  $k_p$ , is derived. This is then applied to two dimensional analyses of contiguous and secant pile retaining walls to highlight the advantages of a semi-permeable structure.

2 NUMERICAL ANALYSES

Numerical simulations were conducted using the finite difference geotechnical application FLAC2D (ITASCA, 2012). The investigations were undertaken in two phases. Horizontal flow was simulated in phase 1 to determine how pore pressures and steady state flow vary with  $x/d$  in order to derive an expression for  $k_p/k_s$ . This relationship was then applied to a vertical plane flow in phase 2 and the pore pressures calculated.

Preliminary analysis, not included in this report, were carried out to establish i) suitable boundary locations, ii) the size of the numerical grid and iii) the limiting value of  $x/d$ . Grid boundaries were selected such that  $x/d$  did not influence the far-field conditions. It was determined that increasing  $x/d$  above 2 did not significantly impact the results.

2.1 Model soil and wall properties

An elastic constitutive soil model was used in all analyses. Elastic properties of bulk and shear moduli were used instead of Young's modulus and Poisson's ratios. The soil and model pile section and the model wall in phases 1 and 2 respectively were represented by grid elements attached directly to the soil grid without the use of interface elements so as to allow cross-boundary flow. Uncoupled groundwater flow analyses which ignored the impact of mechanically induced pore pressures were performed.

2.2 Derivation of bulk wall permeability,  $k_p$

The simulations started with a 'wished into place' model pile section and the water level at the surface. Pore pressures at the

discharge surface shown in figure 1 were lowered incrementally corresponding to pressure drops  $U_i$  for each step. Steady state discharge and pore pressures were measured and fluid flow-paths tracked for different pile gap to diameter ratios  $x/d$ .

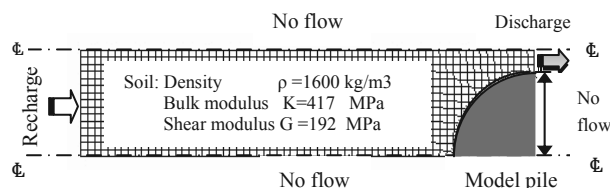


Figure 1. Plan of typical numerical grid showing boundary conditions for phase 1 analyses.

2.2.1 Results and discussion

Darcy's equation for steady state flow (Eq. 3) was applied using the parameters  $\Delta l$ ,  $h_1$ , and  $h_2$  indicated in figure 2 and the values compared with the numerically derived flow rates ( $Q_i$ ) in figure 3 at pressure differences,  $U_i$ .

$$Q = A_p k_p \frac{h_1 - h_2}{\Delta l} \tag{3}$$

where  $(h_1 - h_2)/\Delta l$  is the hydraulic gradient between the distance of influence and the discharge surface (see Figure 2). (The distance of influence was selected as the point beyond which the hydraulic gradient was uniform).

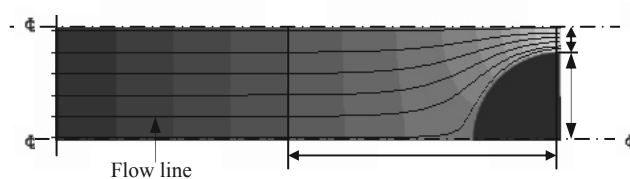


Figure 2. Calculating bulk wall permeability,  $k_p$  and flow-paths.

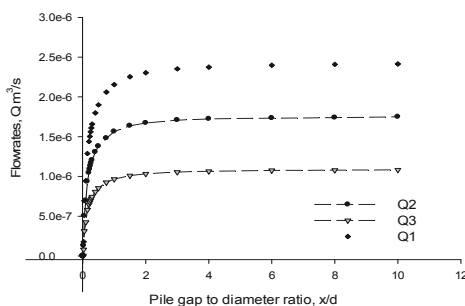


Figure 3. Steady state flow-rates,  $Q_i$  at various pressure drops  $U_i$ .

The resulting bulk wall permeability was calculated for a soil permeability  $k_s = 2 \times 10^{-5}$  m/s and plotted for three values of  $U_i$  (see Figure 4). The empirical hyperbolic relationship between the pile gap to diameter ratios  $x/d$  and permeability ratios  $k_p/k_s$  derived in the phase 1 simulation is given in equation 4.

$$\frac{k_p}{k_s} = \frac{4 \frac{x}{d}}{1 + 4 \frac{x}{d}} \tag{4}$$

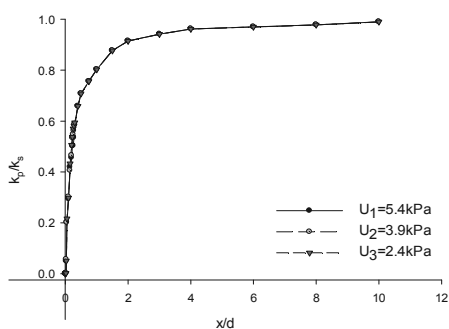


Figure 4. Calculated permeability from FLAC2D simulations.

2.3 Application of derived expression to 2D analyses

The aim of phase 2 simulations was to test the application of the permeability expression derived in phase 1.

2.3.1 Procedure

A continuous wall was used to represent the contiguous pile retaining wall. The model wall thickness (t) was calculated by equating the second moments of area (I) of the different cross-sections (A) as outlined by Powrie et al (1999) (Eq. 5). This gave a result similar to the stiffness approach adopted by Day and Potts (1993) (see Eq. 6 and 7).

$$I_p = I_m \tag{5}$$

$$tE_{eq} = EA \tag{6}$$

$$E_{eq} = EI \tag{7}$$

where  $E_{eq}$  and  $E$  are the equivalent model wall stiffness and material Young's modulus respectively.

The simulations commenced as before with a 'wished into place' model wall. Pore pressures were varied corresponding to  $U_i$  as before for different pile gap to diameter ratios,  $x/d$ .

2.3.2 Results and discussion

It was observed that flow patterns for the 'permeable' walls deviated from the classically accepted flow around an impermeable retaining wall especially at higher values of  $x/d$ . This seems to suggest that through-wall flow is taking place for  $x/d > 0.0$  as shown in figure 5.

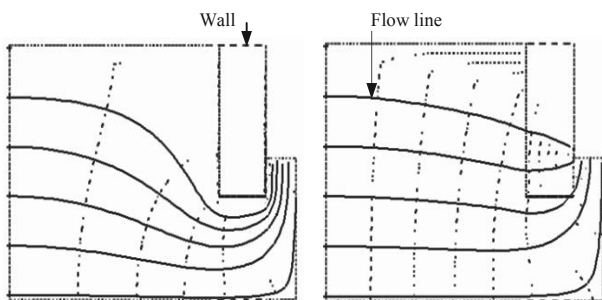


Figure 5. Tracked flow-paths for  $x/d=0$  and  $x/d=0.1$ . Note these are not intended to be flownets, hence the flow elements are not "square".

2.3.3 Pore pressure distribution

Pore pressures ratios  $P_i/P_0$  are plotted against normalized distance (L/d) from the model wall in figure 6 for various values of  $x/d$ .

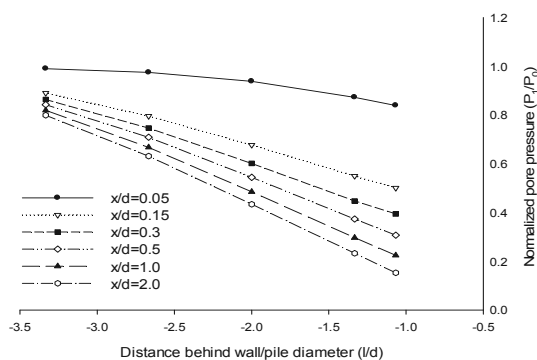


Figure 6. Normalised pore pressures for different  $x/d$  against distance (L/d) from the wall.

It was observed that pore pressures at each position behind the wall decreased with  $x/d$  as the equivalent permeability increased. Further analyses have shown that the pore pressures and hence hydraulic head reduce towards the wall (Figure 7).

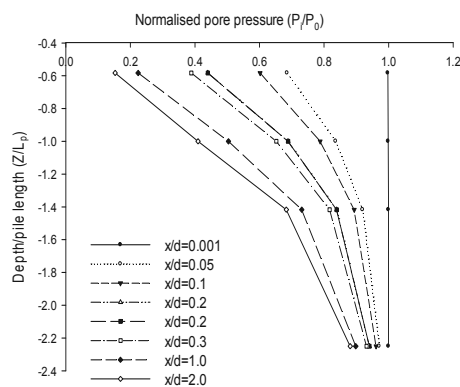


Figure 7. Normalised pore pressure versus normalized depth below soil surface for different values of  $x/d$ .

2.3.4 The effect of seepage on surface settlement

Surface settlements increased as the bulk permeability of the wall increased (see Figure 8). The calculated settlement values were compared with an estimated solution which uses the one dimensional stiffness modulus (Roberts et al 2007). It was noted that the 1D stiffness modulus method over-predicted surface settlement at higher  $x/d$  as shown in Figure 9. This is unsurprising as in this approach all volume change is assumed to manifest as vertical settlement.

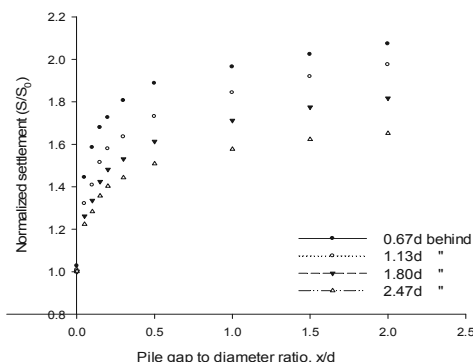


Figure 8. Normalised settlement increases with soil/structure permeability.

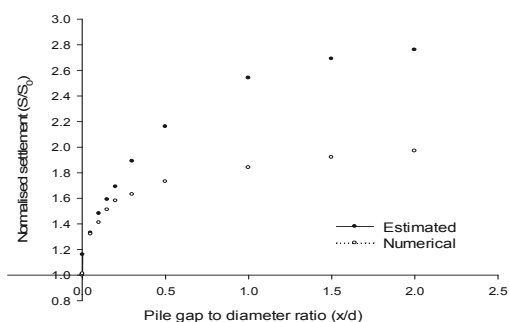


Figure 9. Comparison of analytical and numerical solutions for surface settlement variation with  $x/d$ .

### 2.5 Secant versus Contiguous Pile Retaining Walls

Comparisons were made between retaining walls formed of contiguous and secant piles 20m long with 10m excavation depth in homogeneous soil. Figure 10 shows that the pore pressure profiles are slightly less than hydrostatic for the secant and significantly less than hydrostatic for the contiguous pile wall.

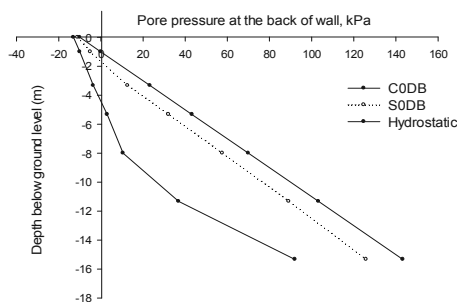


Figure 10. Comparison of pore pressure profiles for secant and contiguous pile walls against hydrostatic pressure.

## 3 CONCLUSIONS

Limited research has previously been carried out on the influence of retaining wall geometry on the development of hydraulic loads on the active side. Numerical simulations presented in this paper have shown that the pore pressure magnitude behind bored pile retaining walls reduces with increasing pile gap to diameter ratio,  $x/d$ . This reduction in lateral loads however is accompanied by an increase surface settlement. However, the potential benefits of allowing through-wall seepage are likely to be greater than the drawbacks.

## 4 ACKNOWLEDGEMENTS

Funding for this research was provided by the Engineering and Physical Sciences Research Council, (EPSRC) grant number EP/F063482.

## 5 REFERENCES

Arjinoi, P., Jeong, J.H., Kim, C.Y., & Park, K.H. 2009. Effect of drainage conditions on porewater pressure distributions and lining stresses in drained tunnels. *Tunnelling and Underground Space Technology*, 24, (4) 376-389.

Atkinson, J.H. & Mair, R.J. 1983. Loads on Leaking and Watertight Tunnel Linings, Sewers and Buried Pipes due to Groundwater. *Geotechnique*, 33, (3) 341-344

Bobet, A. & Nam, S.W. 2007. Stresses around pressure tunnels with semi-permeable liners. *Rock Mechanics and Rock Engineering*, 40, (3) 287-315.

BSI 2004, Eurocode 7: Geotechnical design Part 1, General Rules. EN1997-1:2004, British Standard Institution.

Carder, D.R., Watson, G.V.R., Chandler, R.J., & Powrie, W. 1999. Long-term performance of an embedded retaining wall with a stabilizing base slab. *Proceedings of the Institution of Civil Engineers-Geotechnical Engineering*, 137, (2) 63-74.

Clark, J. 2006. Performance of a propped retaining wall at the Channel Tunnel Rail Link, Ashford. PhD University of Southampton.

Day, R.A. & Potts, D.M. 1993. Modeling Sheet Pile Retaining Walls. *Computers and Geotechnics*, 15, (3) 125-143

Gaba, A.R., Simpson, B., Beadman, D.R., & Powrie, W. 2003. Embedded retaining walls: guidance for economic design. *Proceedings of the Institution of Civil Engineers-Geotechnical Engineering*, 156, (1) 13-15.

Hubbard, H.W., Potts, D.M., & Miller, D. 1984. Design of the retaining walls for the M25 cut and cover tunnel at Bell Common. *Geotechnique*, 34, (4) 495-512

ITASCA. Fast Lagrangian Analysis of Continua in 2 Dimensions. User Manual. Itasca Consulting Group[7.0]. 2012. Minneapolis, USA. Ref Type: Computer Program

Kolymbas, D. & Wagner, P. 2007. Groundwater ingress to tunnels - The exact analytical solution. *Tunnelling and Underground Space Technology*, 22, (1) 23-27.

Lee, I. M. & Nam, S. W. 2001, The study of seepage forces acting on tunnel lining and tunnel face in shallow tunnels. *Tunnelling and Underground Space Technology*, 16, (1) 31-40.

Lee, I. M. & Nam, S. W. 2006, Seepage Force Considerations in Tunnelling, In *International Symposium on Underground Excavation and Tunnelling*.

Potts, D. M., Axelsson, K., Grande, L., Schweiger, H., & Long, M. Guidelines for the use of advanced numerical analysis. 2002. Thomas Telford Publishing. Ref Type: Edited Book

Potts, D. M. & Burland, J. B. 1983, Numerical investigation of retaining wall at Bell Common Tunnel.

Powrie, W., Chandler, R.J., Carder, D.R., & Watson, G.V.R. 1999. Back-analysis of an embedded retaining wall with a stabilizing base slab. *Proceedings of the Institution of Civil Engineers-Geotechnical Engineering*, 137, (2) 75-86.

Richards, D.J., Powrie, W., Roscoe, H., & Clark, J. 2007. Pore water pressure and horizontal stress changes measured during construction of a contiguous bored pile multi-propped retaining wall in Lower Cretaceous clays. *Geotechnique*, 57, (2) 197-205.

Roberts, T.O.L., Roscoe, H., Powrie, W., & Butcher, D.J.E. 2007. Controlling clay pore pressures for cut-and-cover tunnelling. *Proceedings of the Institution of Civil Engineers-Geotechnical Engineering*, 160, (4) 227-236.

Shin, J.H. 2010. Analytical and combined numerical methods evaluating pore water pressure on tunnels. *Geotechnique*, 60, (2) 141-145.

Shin, J.H., Addenbrooke, T.I., & Potts, D.M. 2002. A numerical study of the effect of groundwater movement on long-term tunnel behaviour. *Geotechnique*, 52, (6) 391-403.

Yoo, C.S. 2005. Interaction between tunnelling and groundwater, Numerical investigation using three dimensional stress pore pressure coupled analysis. *Journal of Geotechnical and Geoenvironmental Engineering*, 131, )2= 497β513.

# Geosynthetic Reinforced Soil Wall Performance under Heavy Rainfall

## La performance du mur en sol renforcé par géosynthétiques sous de fortes pluies

Yoo C., Jang D.W.

*Dept. of Civil and Environmental Engineering, Sungkyunkwan University, Suwon, Korea*

**ABSTRACT:** Global warming is now considered to be one of the greatest threats to earth. The direct consequence of the temperature increase due to the global warming include a rise in sea levels and a change in the amount and pattern of precipitation. Since the amount pattern of precipitation have of paramount implications to short and long-term performance of geo-structures, geo-engineers should pay attention to the issue of global warming. In this paper, the results of laboratory investigation into the effect of rainfall on the performance of geosynthetic reinforced soil wall (GRSW) are presented. A series of model tests were performed using reduced scale model walls, which were reduced from a full-scale GRS wall according to the similitude law. The model GRSWs were subjected to cycles of wetting and drying process with different rainfall intensities but with a same amount. The results show that the cycles of wetting and drying associated with a heavy rainfall may induce additional wall displacement and reinforcement strains in GRSWs, and that such trends have significant implications to GRSW stability, especially for walls designed with marginal factor of safety in terms of long-term performance.

**RÉSUMÉ :** Le réchauffement climatique est aujourd'hui considéré comme l'une des plus grandes menaces pour la terre. Les conséquences directes de l'augmentation de température due au réchauffement climatique incluent notamment l'élévation du niveau des mers et un changement dans la quantité et le régime des précipitations. Ces paramètres ayant des implications primordiales sur les performances à court et à long terme de géo-structures, les géo-ingénieurs devraient prêter attention à la question du réchauffement climatique. Dans cet article, les résultats des études en laboratoire sur les effets de fortes précipitations pour la performance des murs en sol renforcé par géosynthétiques (GRSW) sont présentés. Une série d'essais sur modèles réduits a été réalisée avec des modèles réduits d'un mur à pleine échelle GRS suivant la loi de similitude. Les modèles GRSW ont été soumis à des cycles de mouillage et de séchage avec des intensités pluviométriques différentes. Les résultats montrent que les cycles de mouillage et de séchage associés à une forte pluie peuvent provoquer un déplacement supplémentaire du mur et les tensions dans le renforcement, et que ces tendances ont des implications importantes pour les GRSW conçus avec un faible facteur de sécurité en termes de performance à long terme

**KEYWORDS:** Climate change, Rainfall, Reduced-scale model test, Matric suction, Pore water pressure

## 1 INTRODUCTION

Since the early 20<sup>th</sup> century, Earth's mean surface temperature has increased by about 0.8°C with about two-thirds of the increase occurring since 1980. A climate model projects that the global surface temperature will probably rise further 1.1 to 6.4°C during the twenty-first century (IPCC 2007). An increase in global temperature will cause sea levels to rise and will change amount and pattern of precipitation as well. Korea is no exception from the issue of global warming. The Korean Meteorological Administration (KMA) has made a report on climate change characteristics during the period of 1996–2005 that the mean temperature has increased by 0.6°C from the last 30 year mean temperature during the period between 1971 to 2000 (KMA 2008). The annual precipitation has also increased by 11%. It is projected that the temperature increase will be as great as 4°C with an annual precipitation increase of 17% by the end of 21<sup>st</sup> century. Since the increase in precipitation has of paramount implications to short and long-term performance of geo-structures, geo-engineers should pay attention to the issue of global warming.

In response to the need for addressing the effect of rainfall on geo-structures for design and construction, a number of studies have been undertaken. Most of the available studies are, however, focused more or less on the effect of rainfall on natural slopes (Gasmo et al. 2000, Tsaparas et al. 2002, Zhan and Ng 2004, Cai and Ugai 2004, Cheuk et al. 2005, Garcia et al. 2006, Rahardio et al. 2007, Rahimi et al. 2011) except Blake et al. (2003) and Yoo et al. (2008a, 2008b) in which the effect

of rainfall on retaining structures was investigated. More specifically, Yoo et al. (2008a, 2008b) investigated the effect of rainfall on GRSWs using a series of limit equilibrium analyses within the framework of unsaturated shear strength, coupled with transient infiltration analyses. Much still need to be studied on the subject of the effect of rainfall on geo-structures.

In this paper, the results of a laboratory investigation into the effect of rainfall on the performance of geosynthetic reinforced soil wall (GRSW) are presented. A series of model tests were performed using reduced scale model walls, which were reduced from a full-scale GRS wall according to the similitude law. The model GRSWs were subjected to cycles of wetting and drying process with different rainfall intensities but with the same total rainfall.

## 2 REDUCED SCALE MODEL TEST

A series of reduced scale model tests were performed with due consideration of the wetting and drying process. Details of the model tests and the results are given in the subsequent sections.

### 2.1 Model wall and backfill soil

The reduced scale model tests were performed using 0.5 m high reduced scale model GRSWs constructed in a test box, having dimensions of 0.9 m x 0.4 m in plan and 0.6 m in height, made of 2 cm thick Plexiglas as shown in Figure 1. The test box was made sufficiently rigid to maintain the plane-strain condition during test. The wall facing, made of 0.5 cm thick Plexiglas,



was hinged at the bottom of the test box so as to allow lateral displacement to occur during the wetting and drying process.

The backfill soil was a non-plastic poorly-graded sand, commonly known as decomposed granite soils (DCG) in Korea, classified as SP as per ASTM 2487 (ASTM 1992) with the effective size ( $D_{10}$ ), uniformity coefficient ( $C_u$ ), and coefficient of curvature ( $C_c$ ) of 0.36 mm, 5.3 and 1.1, respectively. The soil was compacted to 70% of its maximum unit weight ( $19kN/m^3$ ) to create reinforced as well as retained zones. The estimated effective internal friction angle ( $\phi'$ ) using a series of consolidated-undrained (CU) triaxial compression tests with pore pressure measurements at a density corresponding to the as-compacted state was determined as approximately  $35^\circ$  with a shear stress intercept of 8 kPa.

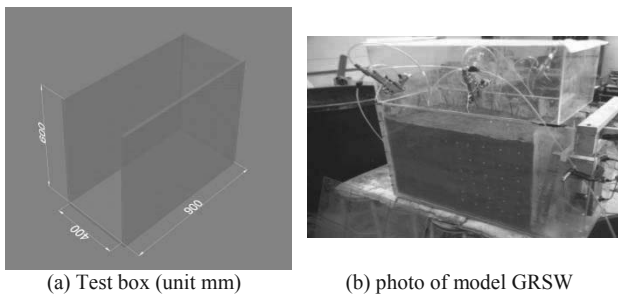


Figure 1. Test box and model GRSW

A non-woven geotextile was used as reinforcement. Note however that the tensile strength of the non-woven geotextile was intentionally reduced by creating 5 mm x 5 mm square holes (Figure 2) to have an ultimate tensile strength of  $3.8 \times 10^{-2} kN/m$ . Six layers of reinforcement, 35 cm in length each, were placed at a vertical spacing of 6 cm (Figure 3). The reinforcement layers were firmly connected to the wall facing by bolting.

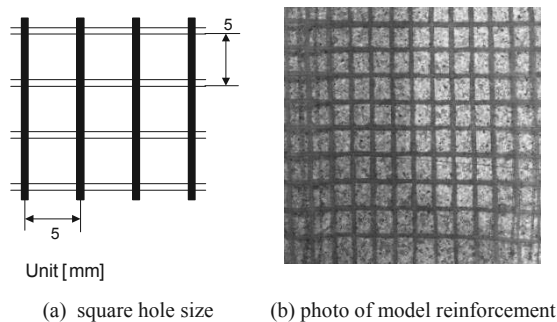


Figure 2. Model geotextile reinforcement

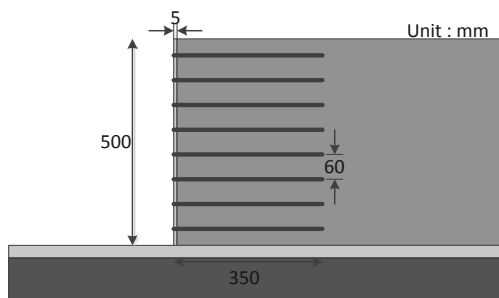


Figure 3. Schematic sectional view of model GRSW

### 2.2 Rainfall simulation

Three cycles of wetting and drying were applied to the model walls to simulate the natural weather condition. Two rainfall intensities ( $I_r$ ) were considered, i.e., 18.7 mm/h and 56.2 mm/h

for a given total precipitation of 450 mm. The duration of the rainfall for the case with  $I_r = 18.7 mm/h$  was therefore 24 hours while 8 hour duration was used for the case with  $I_r = 56.2 mm/h$ . Note that these rainfall conditions were based on the actual rainfall occurred in 2011 in Kyoung-Gi province, Korea. Followed after each wetting process was a 24 hour drying period prior to the ensuing wetting to observe the wall behavior during the repeated wetting and drying.

The rainfall was simulated by spraying water at the top of the backfill using spray guns with 15HP compressor and a 20W water motor (Figure 4).

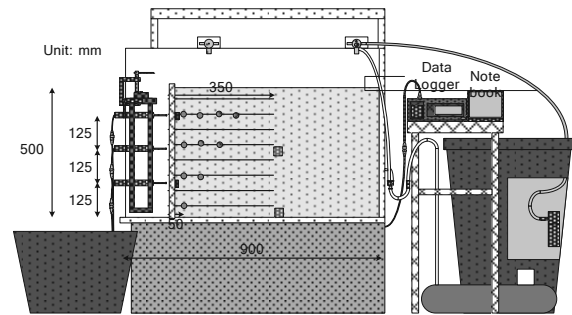


Figure 4. Schematic diagram of rainfall simulator

### 2.3 Instrumentation

The performance of the model GRSW under a series of wetting and drying cycles was evaluated in terms of wall facing displacements, pore water pressures, and reinforcement strains. The layout of instrumentation program is shown in Figure 5.

As shown, the horizontal displacements of the wall facing were measured by using three LVDTs having gauge length of 100 mm, placed at locations along a vertical row. In addition, the wetting and drying cycle induced reinforcement strains were measured using high-elongation strain gauges, manufactured by Tokyo Sokki Kenyujo Company (Model YFLA-5-5L) which were mounted directly onto the selected reinforcement layers in one array. Also installed at the back of the reinforced zone were two pore pressure cells (Model BPR-A-200 kPa) at the bottom (0 mm) and 250 mm above the wall base. The volumetric water content of the backfill soil during the wetting and the drying process was also measured using a tensiometer (Model EC-5).

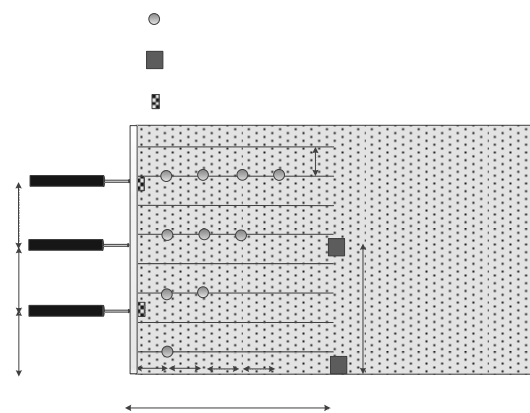


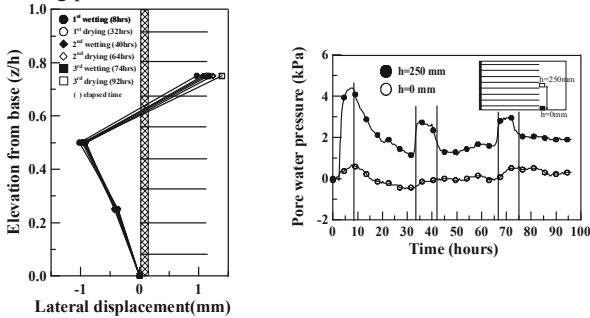
Figure 5. Instrumentation layout

## 3 RESULTS AND DISCUSSION

### 3.1 General behavior

Figure 6 show the measured data for the rainfall intensity of  $I_r = 56.2 mm/h$ . As mentioned, the 56.2 mm/h intensity rainfall

lasted for 8 hours for wetting. As shown in Figure 6(a), the wall displacement increased about 1 mm during the 1<sup>st</sup> cycle of wetting after which no significant increase was recorded. The pore water pressures measured at the bottom and the mid-height at the back of reinforced zone tended to increase during the first wetting period as great as 4 kPa, followed by gradual decreases during the ensuing 24 hour drying period as shown in Figure 6(b). As observed in the wall displacement, the largest increase in the pore water pressure was measured during in the first wetting period.



(a) wall displacement (b) pore pressure  
Figure 6. Wall displacement and pore pressure ( $I_r = 56.2 \text{ mm/h}$ )

Shown in Figure 7 are the measured reinforcement strains in the selected reinforcement layers. Of salient features are twofold. First, the reinforcement strains tended to steadily increase over the repeated wetting and drying cycles unlike the wall displacements and the pore water pressures which showed cycles of fluctuation during the wetting and drying process. Second, larger strains, as great as 0.015%, are measured in the upper reinforcement layers than in the lower layers due possibly to the downward movement of wetting front caused by the rainfall infiltration.

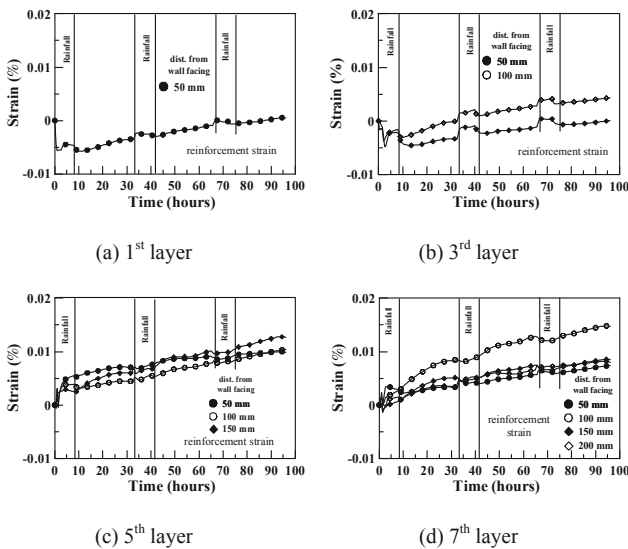


Figure 7. Reinforcement strains ( $I_r = 56.2 \text{ mm/h}$ )

Figure 8 shows the time variation of volumetric water content ( $\theta$ ) measured at 160 mm above the wall base at the back of the reinforced zone. As shown, the initial volumetric water content of 0.05 at the measuring point sharply increased to 0.35 after which it remained constant over the remaining wetting period. During the drying period,  $\theta$  then sharply decreased to 0.2 and remained constant during the entire drying period. A similar trend can be observed in the following cycles suggesting that the cycles of the wetting and drying with the rainfall intensity and duration considered in this study may increase the water content of the backfill soil.

The results shown here indicate that the repeated cycles of wetting and drying associated with a heavy rainfall may induce additional wall displacement and reinforcement strains in GRSWs. Such results suggest that the weather induced wetting drying has significant implications to GRSWs designed with marginal factor of safety in terms of long-term stability.

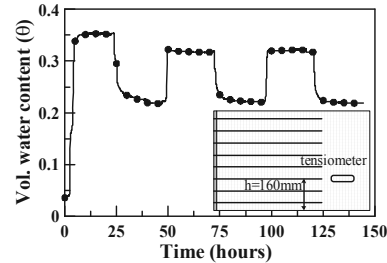


Figure 8. Time variation of volumetric water content ( $\theta$ )

### 3.2 Effect of rainfall intensity

Figures 9 and 10 show the measured wall displacements and the reinforcement strains for the case with a rainfall intensity of 18.7 mm/h. Note that the total rainfall was kept same at 450 mm as in the case of  $I_r = 56.2 \text{ mm/h}$  but with a longer wetting period of 24 hours. The discrepancies in the wall performance between the two cases can therefore be thought to stem from the rainfall intensity.

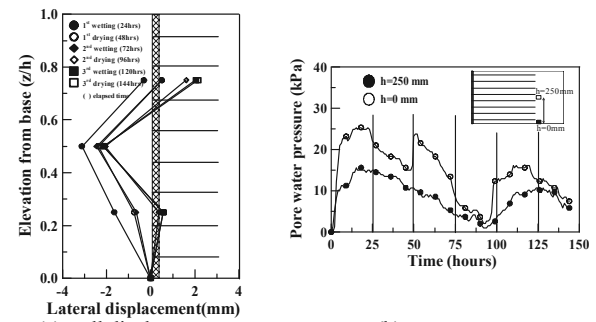


Figure 9. Wall displacement and pore pressure ( $I_r = 18.7 \text{ mm/h}$ )

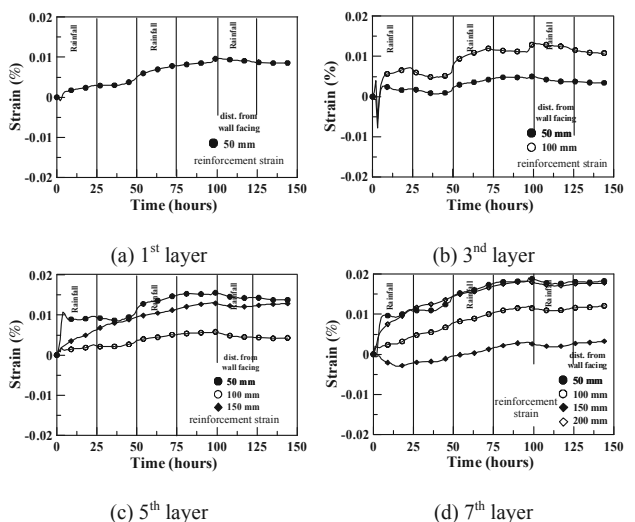


Figure 10. Reinforcement strains ( $I_r = 18.7 \text{ mm/h}$ )

The direct comparison between the two cases reveals that the case with the smaller rainfall intensity but with the longer duration generally induces larger wall displacements and reinforcement strains except for the pore water pressure measured at the back of reinforced zone. Considering the backfill soil being a high permeability soil, these results

contradict those reported by Cai and Ugai (2005) as well as Rahardjo et al. (2007) which were based on a numerical study. A further study is therefore warranted to confirm the effect of rainfall intensity. It can however be stated that the rainfall intensity is a controlling factor for the performance of a GRSW during rainfall infiltration as reported by Rahardjo et al. (2007) in their study concerning natural slopes.

#### 4 CONCLUSIONS

In this study, the results of laboratory investigation into the effect of rainfall on the performance of a geosynthetic reinforced soil wall (GRSW) using reduced scale model tests are presented. The model GRSWs were subjected to cycles of wetting and drying process with different rainfall intensities but with the same total rainfall. The results show that the cycles of wetting and drying associated with a heavy rainfall may induce additional wall displacement and reinforcement strains in GRSWs, and that such trends have significant implications to GRSWs with marginal factor of safety in terms of long-term performance. The effect of rainfall intensity for a given total rainfall is such that the case with a smaller rainfall intensity but with a longer duration generally induces larger wall displacements and reinforcement strains except for the pore water pressure measured at the back of reinforced zone. Although a further study is required to confirm the effect of rainfall intensity, it can be concluded that the rainfall intensity is a governing factor for the performance of a GRSW during rainfall infiltration.

#### 5 ACKNOWLEDGEMENT

This research is supported by Grant No. 20100008227 from the Basic Research Program of the Korea Science & Engineering Foundation. The financial support is gratefully acknowledged.

#### 6 REFERENCES

- ASTM 1992. Standard test method for classification of soils for engineering purposes. ASTM D2487-90, Annual Books of ASTM Standards, West Conshohocken, PA., 4.08, 326-336.
- Cai, F. and Ugai, K. 2005. Numerical Analysis of Rainfall Effects on Slope Stability. *International Journal of Geomechanics*, 4(2), 69-78.
- Cheuk, C.Y., Ng, C.W.W., and Sun, H.W. 2005. Numerical experiments of soil nails in loose fill slopes subjected to rainfall infiltration effects. *Computers and Geotechnics*, 32(4), 290-303.
- Garcia, E.F., Gallage, C.P.K., and Uchimura, T. 2006. Unsaturated infiltration on artificial embankments reinforced with geosynthetics. *Prof. of 8<sup>th</sup> International Symposium on Geosynthetics*, Kuwano and Koseki (eds). 1417-1420.
- Gasmo, J.M., Rahardjo, H., and Leong, E.C. 2000. Infiltration effects on stability of a residual soil slope. *Computers and Geotechnics*, 26, 145-165.
- IPCC 2007. Summary for Policymakers" (PDF). *Climate Change 2007: The Physical Science Basis. Contribution of Working Group I to the Fourth Assessment Report of the Intergovernmental Panel on Climate Change*. [http://ipcc-wg1.ucar.edu/wg1/Report/AR4WG1\\_Print\\_SPM.pdf](http://ipcc-wg1.ucar.edu/wg1/Report/AR4WG1_Print_SPM.pdf).
- Korean Meteorological Administration 2008. Report on Climate Change and Mitigation: Dept. of Climate Change Response: Climate Change Information Center, (in Korean).
- Rahardjo, H., Ong, T.H., Rezaei, R.B., and Leong, E.C. 2007. Factors controlling Instability of Hogeneous Soil Slopes under Rainfall. *Journal of Geotechnical and Geoenvironmental Engineering*, ASCE, 133(12), 1532-1543.
- Rahimi, A., Rahardjo, H., Leong, E. C. 2011. Effect of Antecedent Rainfall Patterns on Rainfall-Induced Slope Failure, *Journal of Geotechnical and Geoenvironmental Engineering*, ASCE, 137(5), 483-491
- Tsaras, I., Rahardjo, H., Toll, D.G., and Leong, E.C. 2002. Controlling parameters for rainfall-induced landslides. *Computers and Geotechnics*, 29(1), 1-27.
- Yoo, C., Kim, S.B., and Jung, H.S. 2008a. A numerical investigation on effect of vertical drainage system on geosynthetic reinforced soil wall during rainfall. *Journal of Korean Geotechnical Engineering*, 24(5), 99-106.
- Yoo, C., Kim, S.B., and Han, J.Y. 2008b. A numerical investigation on stability of geosynthetic reinforced soil wall during rainfall. *Journal of Korean Geotechnical Engineering*, 24(12), 1-12.
- Zhan, L.T. and Ng, C.W.W. 2004. Analytical Analysis of Rainfall Infiltration Mechanism in Unsaturated Soils. *International Journal of Geomechanics*, 4(4), 273-284.

# General Report of TC 208 Slope Stability in Engineering Practice

Rapport général du TC 208  
La stabilité des talus dans la pratique de l'ingénieur

Bowman E.T.  
University of Sheffield

Fannin R.J.  
University of British Columbia

**ABSTRACT:** This General Report reviews 37 papers from 21 countries or provinces that were submitted to the conference on the topic of slope stability in engineering practice. These papers serve either to advance the state-of-the-art, else to inform the state-of-practice. Further, by developing new knowledge, else refining existing knowledge, the observations reported in the papers and the conclusions that are drawn from them provide for improved decision-making in the face of risk and uncertainty.

**RÉSUMÉ :** Le présent rapport général passe en revue les 37 communications provenant de 21 pays et provinces qui ont été soumis au Congrès sur le sujet traitant de la stabilité des talus dans la pratique de l'ingénieur. Les communications ont comme objectif soit de faire évoluer l'état des connaissances, soit de rendre compte de la pratique actuelle. Par le développement de nouvelles connaissances ou par l'affinement de connaissances existantes, les observations relatées dans ces communications et les conclusions qui en sont tirées permettent d'améliorer les processus décisionnels face aux risques et aux incertitudes.

**KEYWORDS:** Slope stability, landslide, debris flow

## 1 INTRODUCTION

Slope stability in engineering practice is considered by many to be a broad-ranging subject, and this viewpoint is perhaps supported by the diversity of papers submitted to the conference. Yet, in reality, studies of slope stability in engineering practice are unified by the common objective of a better understanding of (i) the spatial and temporal variation of demand and capacity at the point of origin and (ii) the magnitude and travel distance of the event along its path of movement downslope. All of the papers submitted to the conference address these objectives in one form or another. In this regard, the findings of the papers serve either to advance the state-of-the-art, else to inform the state-of-practice. More importantly, by developing new knowledge, else refining existing knowledge, the observations reported in the papers and the conclusions that are drawn from them provide for improved decision-making in the face of risk and uncertainty.

This General Report reviews 37 papers from 21 countries or provinces that were submitted to the conference on the topic of slope stability in engineering practice.

### 1.1 Focus / approach of papers

Table 1 indicates that there is overlap in the focus of many of the papers, with 24 of them sharing two or more approaches or topics. This is particularly evident for papers that have a case study element with 14 of these linking to a numerical model, detailed field study and/or risk assessment. It is encouraging to see that such case studies are being increasingly presented with a critical and quantitative assessment of the factors that may have contributed to a slope failure occurring. A further 4 of the case study papers directly link to implementation of mitigation measures (*Şengör et al.*; *Coutinho and da Silva*; *Bozo and Allkja*; *Chang and Huang*), although with the exception of the paper by *Şengör et al.*, other than qualitatively showing the utility of such measures, the outcomes are neither analysed nor presented in detail.

Table 1. Number of papers by approach or focus.

Approach / focus	Papers
Case study	21
Numerical - deterministic	9
Numerical - probabilistic	6
Field study / instrumentation	6
Experimental / physical model	6
Risk assessment	6
Mitigation measures	6

In contrast, it is interesting to note that 4 of the 9 papers that use deterministic numerical models do not attempt to validate against any particular field situation. In these cases, the models in question may be still at the development stage (*Saha*; *Nonoyama et al.*; *Law et al.*) else the authors intend to illustrate a potentially general mechanism of failure (*Dey et al.*).

A total of 6 papers present a detailed study of a particular area via field instrumentation or discuss the development of instrumentation for monitoring of slope instability, while a further 6 papers present an experimental analysis of soil behavior or a detailed physical model of a particular scenario. These approaches are important to enable an understanding of fundamental mechanisms of slope instability and can be very important to determining the details of complex interactions between, for example, groundwater and precipitation on rainfall-induced landslides, or sediment supply and frequency of debris flows.

Six papers take a risk assessment approach – either for a defined area for site-specific purposes related to risk assessment or for a more regional approach that is more appropriate to concern of risk management.

### 1.2 Type of instability investigated

Table 2 shows the types of landslide failures that are discussed in the papers. Approximately 30% of the papers are on rainfall-induced landslides, 8% on earthquake-induced landslides (solely) and nearly 30% on debris flows or flow-

slides, with multi-hazard landslides (mostly earthquake coupled with debris flow) accounting for 10%. The remaining papers address progressive slides (4%) or the triggering / landslide type is unspecified (19%).

The fact that there are 10 papers on debris flows or flow slides is a marked increase on previous years. For the 16<sup>th</sup> International Conference on Soil Mechanics and Geotechnical Engineering, Chau (2005) noted that only two papers dealt with debris flows. While as Chau (2005) has pointed out, there are dedicated conferences on debris flows elsewhere, the inclusion of these papers in a broader geotechnical forum is promising in terms of applying geotechnical rigor to a problematic subject of global concern.

The recognition of landslides within a multi-hazard causal framework is also extremely important, although the number of papers presented is still relatively small. As determined by Lin et al. (2004), amongst others, earthquakes can lead to worsening conditions for landslides and debris flows, while landslides can be the precursor of debris flows particularly where the landslide meets a body of water or ice. A thorough understanding of the complexity of such scenarios is believed warranted, because the state-of-the-art must continue to inform the state-of-practice and, on occasion, the cutting-edge of practice is challenged to address some very challenging realities of risk management.

Table 2. Number of papers by instability type

Type of failure	Papers
Rainfall / pore pressure induced	11 (14)
Earthquake induced	3 (7)
Debris flow / flow slide	10 (11)
Multi-hazard	4
Progressive	2
Unspecified	7

(Parentheses indicate numbers that include multi-hazard papers)

### 1.3 Breakdown of research papers by country

Table 3 presents the number of papers from different countries and indicates an important reality with respect to where research activity is currently concentrated by region. As has been previously noted by Petley (2012), much of the work on landslides is carried out by researchers in developed economies, where the focus has moved from life impacts (which have been reduced over time due to the development of a relatively good understanding of catastrophic landslide behavior in these countries) to economic impacts (which may be more influenced by slower movements and low-magnitude, albeit high- frequency events). However, in emerging and developing economies, which have large numbers of landslides per annum, there is relatively little research on-going, the threat to life remains unacceptably large.

Table 1. Number of papers in session by country / province

Country	Papers	Country	Papers
Norway	6	India	1
Japan	4	Korea	1
Taiwan / Chinese Taipei	4	Lebanon	1
USA	4	New Zealand	1
Hong Kong, China	3	Russia	1
Albania	2	Sweden	1
Brazil	1	Turkey	1
Canada	1	United Kingdom	1
Mainland China	1	Vietnam	1
Greece	1		

To illustrate this, Figure 1 after Petley (2012) presents the total number of publications on landslides found in ISI journals for each country (taken from provenience of the lead author's

institution) against the recorded number of fatalities in those countries in the period from 2004 to 2010. He has divided the figure into three zones – termed research intensive, research active, and research inactive. The results clearly show that many countries which are least research active have some of the highest incidences of landslide fatalities.

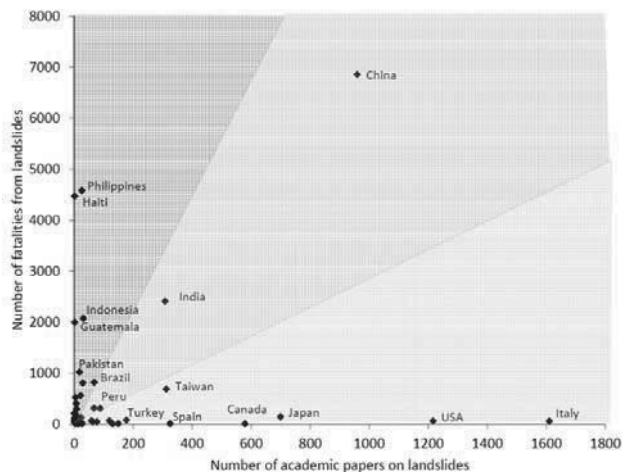


Figure 1. Total number of publications on landslides / slope stability by country in ISI journals from 2006-2010, reproduced from Petley (2012).

Using China as an example, Petley (2012) also showed that increasing the research intensity within a country prone to landslide activity can reduce the rate of fatalities experienced. Two decades of data from 1990 to 2013 are reproduced in Figure 2.

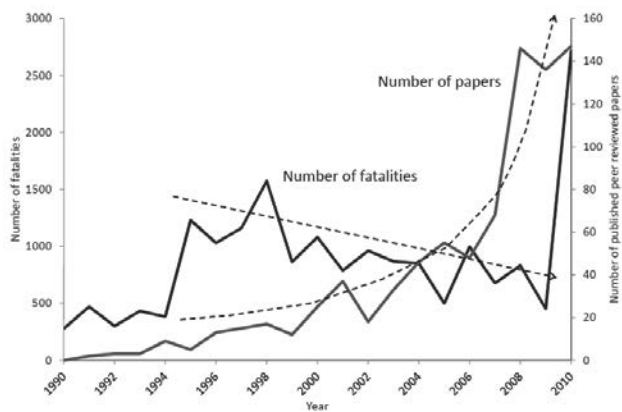


Figure 2. Example of the effect of increasing annual research on landslides on the rate of fatalities in China over 20 years, after Petley (2012). Note that a single landslide that occurred in 2010 in Gansu province killed over 1700 people, which distorts the overall dataset.

In the following section, papers are grouped by type of instability (Table 2).

## 2 RAINFALL / PORE PRESSURE INDUCED SLOPE INSTABILITY

3 This section discusses the major findings of the 11 papers on rainfall or elevated pore pressure induced landslides.

Two papers by Wang et al. and Uchimura et al. discuss the use of a tilt-sensor to detect the onset of instability in slopes that are experiencing creep movements. Wang et al. covers details of innovative sensor development and field installation. Uchimura et al. elaborates further on the use of the device coupled with volumetric water sensors within an experimental arrangement of artificial rainfall on natural ground. The experiments show that instability can be detected by an increase in the rate of change of the tilt angle, while the volumetric water content is related to

the deformation, and is independent of the rainfall period. Some interesting observations are made regarding the influence of the soil water characteristic curve (SWCC) on the deformation behavior of an unsaturated slope undergoing infiltration – in particular, that a temporary reduction in deformation rate may not be indicative of increased stabilization, but rather an effect of the reduced rate of change of suction loss with infiltration. The finding is an excellent illustration of the potential for the state-of-the-art to influence the state-of-the-practice.

*Nakata et al.* examines the influence of pore pressure cycles on the collapse behavior of a slope in a study combining element testing of a standard sand with field monitoring of a natural slope. Plane strain compression tests carried out on Toyoura sand showed that cycles of pore pressure always led to soil hardening rather than increasing the likelihood of failure. In the field, it was found that the slope's behavior was a function of both the recent and antecedent rainfall, yielding a recommendation to monitor the groundwater level as well as the use of rainfall data to understand the fundamentals of collapse behavior.

*Rahhal et al.* presents a study on two landslides that occurred in Lebanon for which geotechnical parameters were obtained via laboratory testing. Slope stability analysis of one slide showed that a loss of cohesion in the clay, at the interface of the clay and underlying stiffer material, due to seasonal moisture infiltration, resulted in the instabilities that were reported. For the second study area, weakening and loss of cohesion in clay schist due to prolonged water contact was thought to be largely responsible for the instabilities recorded, with a minor contribution from cracks that were opened allowing water infiltration.

*Jeng et al.* present a study on the effects of heavy rainfall on a slope in northeastern Taiwan that is covered with a 10-20m depth of colluvium and instrumented with a surface monitoring system. The results from 295 locations of settlement and displacement monitoring locations are evaluated, together with the significance of rainfall on initiating ground movements. Figure 3 shows annual surface settlements of up to 20mm in the study area. From the analysis of the influence of typhoon rainfall on the ground displacements in different parts of the site, a threshold value curve of risk for rainfall was proposed for the area and a slope stabilization programme subsequently recommended by the authors. Once again, a careful series of field observations serve to influence the state-of-the-practice.

*Kavvadas et al.* presents the management of a mine site in Greece in which significant ground displacements are seen to occur with rainfall. Figure 4 shows a generally good correlation between surface velocities as determined at monitoring prisms (top) and rainfall records taken approximately 6km away (bottom). The data indicates a stick – slip mechanism and a regressive movement in which the velocity does not increase or decrease at a constant rate but undergoes abrupt changes. The authors posit that, during and after heavy precipitation, the water-filled tension cracks provide an increasing driving force. As displacement continues, the width of the cracks increases and the water level drops with a resulting dissipation of water pressure. This is a different mechanism to that of tertiary creep in which an increase in velocity of slope movement may be the precursor to imminent failure (Rose and Hungr, 2007).

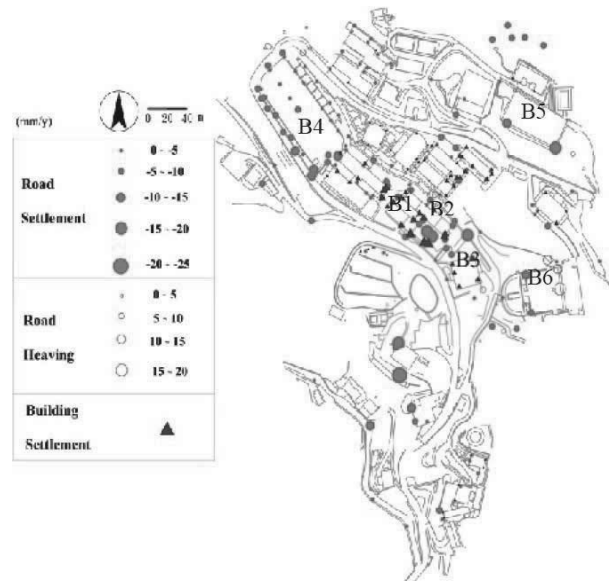


Figure 3. Jeng et al. Annual surface settlement distribution

*Kavvadas et al.* highlights the importance of understanding the underlying mechanism of slope deformation and, in doing so, shows that high mine slopes can operate under large rates of displacement, as long as the type of sliding mechanism is identified and continuously monitored. Finally, the paper shows that remedial measures can be incorporated in a mine plan in order to reduce movements, if not to arrest them entirely.

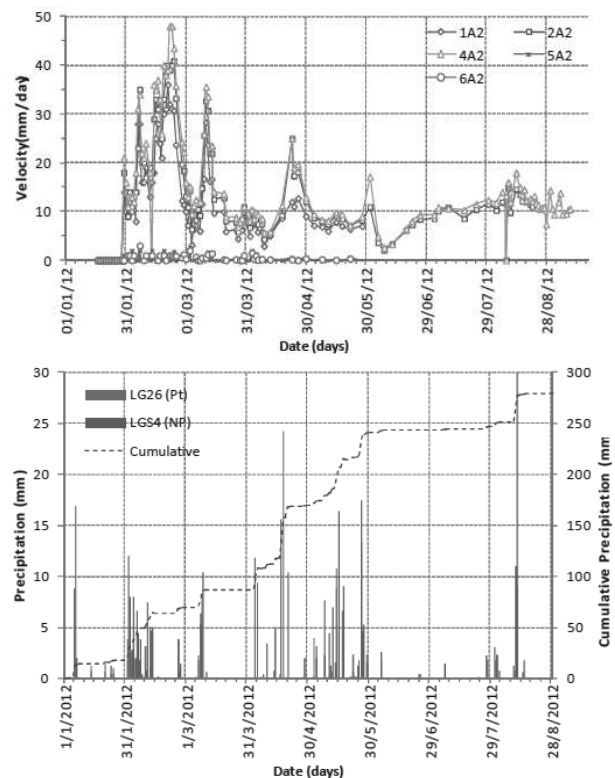


Figure 4. Kavvadas et al. Correspondence of slope velocity change with precipitation.

*Coutinho and da Silva* present a paper on the characterization, analysis and stabilization of a landslide located in a township in Brazil. The soil formation is characterised as sandy clay to silty sand (Barreiras formation) and residual granitic soil. The landslide was analysed as a two-part process during a precipitation event (Figure 5). The analysis suggested that the upper part of the slide zone failed first, due to a lower

permeability zone, leading to elevated pore pressures in that zone during heavy rainfall. The upper slope failure then resulted in an additional surcharge loading and failure in the lower slide mass. This paper highlights the importance of local geological conditions on the triggering of slope instability and that localized heterogeneity can play a major role in the distribution of groundwater flow.

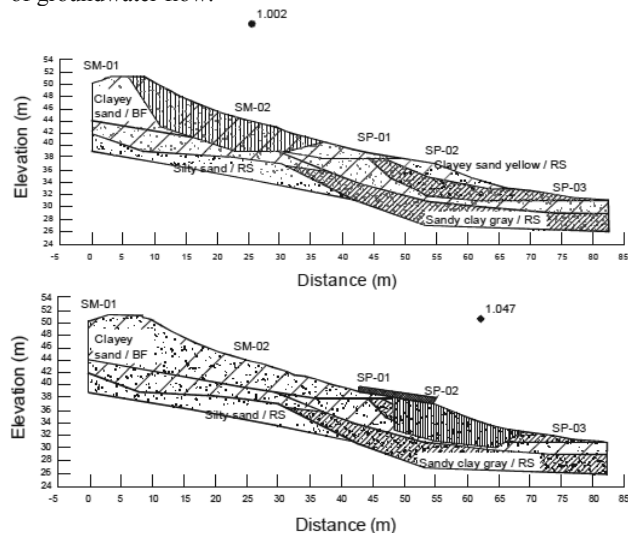


Figure 5. Coutinho and da Silva. Upper and lower slope failure models.

*Son et al.* present a study on landslide susceptibility zonation for an area in the south central coast of Vietnam developed using a Bayesian conditional probability model. Surveyed landslides from one year's rainy season were used as inputs to the model which was examined to develop suitable weighting factors on elements such as elevation, slope angle, drainage distance, geology etc. and was integrated with GIS analytical tools to produce the map. The reliability of the model can be improved as new landslide occurrences are updated annually in the landslide inventory.

*Tremblay et al.* discuss the influence of climate change on the risk of landslides and its assessment for a valley in Sweden. Notable effects of climate change are increases in annual precipitation and temperature and potential reduction in water levels in the river through dry summer periods (although controlled by the authorities) and increased river flows in winter (Figure 6). Each of these scenarios may lead to a decrease in slope stability around the river valley. Readers are referred to detailed risk assessment and reports available from SGI.

*Li et al.* discusses the detailed instrumentation and full-scale field monitoring programme for a study on the mechanisms of rainfall-induced sliding slope, through a study conducted for a new development in Hainan, China. Large variations of volumetric water content and matric suction at shallow depth in decomposed granitic soils, during the rainy season, may explain why so many slope failures have occurred in this region at times of heavy rainstorm activity. The paper also highlights the inherent difficulties associated with the protection of delicate monitoring instruments on an active construction site.

*Harris et al.* describes the implementation of an early warning system (EWS) for a highway embankment subject to rainfall induced landsliding. Volumetric water content sensors were installed at a cross section of the site. A 2D finite element model was then used to replicate the response of the sensors to rainfall, using monitored rainfall events as an input. Next, a limit equilibrium analysis was carried out and an artificial neural network was trained to predict the factor of safety obtained using the sensor readings as inputs. Data from rainfall forecasts are then used to establish a predicted factor of safety for the slope in real time, allowing road-users to be advised accordingly.

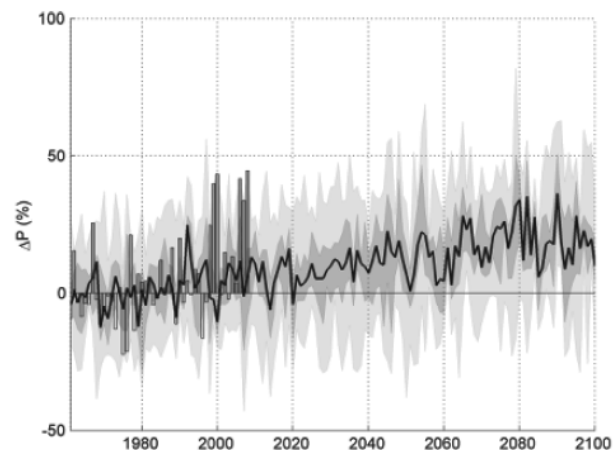


Figure 6. Tremblay et al. Percentage increase in precipitation with year from 16 climate scenarios after Bergstrom et al. (2011)

### 3 DEBRIS FLOWS AND FLOW SLIDES

In total 10 papers are presented on debris flow or flow slide initiation, and aspects of runout or travel distance if the specifics of entrainment of debris along the path of movement as taken into account (see Fannin and Bowman, 2010)

Several studies are presented that use statistical data to derive debris flow hazard potential in particular areas based on local topography and associated hydro-geological behavior. Some of these studies follow statistical-empirical methodologies that do not require precipitation inputs, and may be used for a general assessment of debris flow potential, while other studies include a temporal element by taking account of precipitation records. *Yune et al.* present a paper on debris flows that occurred in the Umyeon Mountain area of Seoul, Korea during the rainy season of 2011, determining that most were initiated from small slope failures induced by high-intensity rainfall. The paper discusses the application of a statistical landslide hazard map which has been developed on parameters such as slope angle and direction, strength of soil, hazard record, rainfall condition and plantation type. This map has demonstrated the ability to highlight areas that are vulnerable to heavy-rainfall-induced slope failure and resulting debris flow disasters.

*Lin and Lin* present a study on the analysis of debris flow torrents in Nantou County, Taiwan, using discriminant analysis based on 199 known debris flow torrents and 175 non-debris flow torrents. The influence factors included: watershed area, stream length, form factor, hypsometric integral, stream mean slope, slope distribution, slope aspect, and geological formation. In order to examine the feasibility of the model, the data sets of debris flow torrents and non-debris flow torrents not used in developing the estimation models were used for validation and prediction.

*Cepeda et al.* presents a probabilistic procedure based on a Monte Carlo simulation for run-out modeling of debris flows, in order to analyse the effect of uncertainties in the input parameters. The framework is based on a dynamic model, which is combined with an explicit representation of the different parameter uncertainties. The main goal is to present a framework to obtain potentially expected run-outs and intensities in areas where it is not possible to determine the rheological parameters on the basis of back analyses.

Two papers are presented that use experimental techniques to examine debris flow behavior. *Katzenbach and Bergmann* present a paper to understand some fundamental flow properties of saturated soil in a large-scale experimental apparatus. The study is designed to examine the influence of parameters such as grain size, grain shape and grain size distribution, water content and pressures on the flow behaviour. This paper focuses on coarse grained water-saturated soils, which excludes the

complexities of cohesive internal forces. Initial results indicate the importance of particle size on the flow velocity of the granular mixture. Results are intended to supplement numerical work that is on-going.

*Choi et al.* present a paper on a series of flume tests that examine the influence of baffle row number on reduction of debris frontal velocity. The average frontal velocity of the debris flow downstream of the array of baffles was measured. Results show one row to be ineffective in reducing the debris frontal velocity, however, two to three rows of baffles exhibit notable frontal velocity reduction.

*Law et al.* present a related paper to that of *Choi et al.* on the dynamic interaction between a granular surge flow and baffles. In contrast however, *Law et al.* use the three-dimensional discrete element method with the granular flow medium modeled as spherical discrete elements and the baffles as rigid square objects. The location, velocity and forces acting on the individual elements during the impact and interaction process are presented. Assessment of the numerical results indicates that a single row of baffles is effective in reducing the kinetic energy and discharge of the granular flow. Interestingly, this actually runs counter to the findings of *Choi et al.* One possibility for this may be a difference in the relative size of largest particles to the baffle spacing used in the experiments by *Law et al.* and *Choi et al.* although data on this are not available from *Choi et al.*

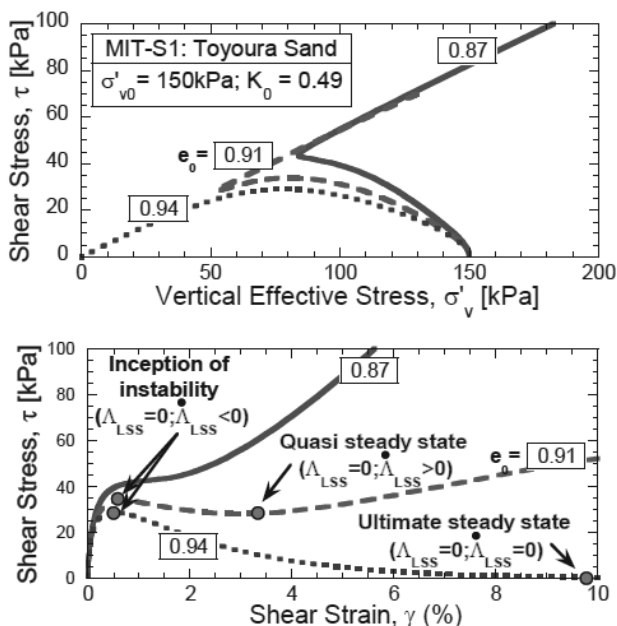


Figure 7. Buscarnera and Whittle. MIT-S1 constitutive model predictions for a sand in undrained shear at different initial void ratios.

*Buscarnera and Whittle* present a framework for evaluating the triggering of flow slides in infinite slopes using the anisotropic MIT-S1 model. The selected soil model is able to simulate realistic transitions in the contractive/dilatative response of sands and enables the prediction of the shear perturbations able to induce instability (Figure 7), as well as the location of potentially unstable zones within the soil mass. In order to show the capabilities of the proposed approach, the methodology has been applied to the well-known case of slope failures in the Nerlerk berm: results suggest that static liquefaction is likely to have contributed to the failures. The analyses illustrate a unified methodology that combines the theory of material stability, the critical state framework for sands and data from in situ tests. The authors state that the methodology offers a simple, consistent and complete geomechanical framework for interpreting and predicting the triggering of flow slides that can be easily applied to other similar engineering cases.

*Thakur et al.* propose a new approach to assess the potential for flow slides via a new laboratory test procedure referred to as the quickness test. The test focuses on remoulded behaviour of sensitive clays in terms of a numerical value referred as quickness ( $Q$ ). Based on their study, it is found that a  $Q < 15\%$  or remoulded undrained shear strength  $c_{ur} > 1$  kPa seems to be the threshold limit above which the extent of retrogression of a landslide is limited to the initial slide. This criterion has been supported using data available from several Norwegian landslides in sensitive clays.

*Winter et al.* present fragility curves as a means of describing the vulnerability of elements at risk to impact by a debris flow. The specific category of element considered in the paper is a road. Expert engineering judgment was used to develop preliminary fragility curves, from a compilation of responses to a questionnaire. Analysis and interpretation of the collected data is made with reference to two events, in an attempt to relate event volume to the probability of a state of damage.

#### 4 EARTHQUAKE INDUCED SLOPE INSTABILITY

Consideration of seismic slope stability occurs in several papers, two of which are considered here and five of which are more rationally addressed within the context of multi-hazard considerations in the section that follows this one.

*Strenk and Wartmen* present the findings of a sensitivity analysis conducted on an idealized slope, to examine uncertainty in seismic deformations established using the Newmark rigid-block method, given variability in ground motion. The effect was found to be most pronounced at low acceleration ratios, and little influence of frequency content and waveform was observed. The findings suggest that use of spectral matching to create variability in both intensity and frequency may be “of limited utility”.

*Paçi et al.* presents a study on the stability of a new road located in a very disturbed tectonic zone where the rock quality is extremely poor. Active surface slides are very unstable due to water ingress especially during seismic events. Geotechnical parameters of the intact flysch / clay and limestone rock are determined from laboratory tests and empirical methods, while for residual parameters, a back-analysis is carried out using Plaxis 2D software. Hence, slope stability problems resulting from seismic loading are examined in two stages. The first model determines a critical sliding plane (if any) under an artificial accelerogram that takes account of near-source effects and then the second uses residual parameters for the soil strength mobilized within the sliding plane. The second model is used to define and design the engineering measures (walls, piles, anchored wires, nails, etc.). This two-step process, is a pragmatic approach for designing mitigation measures for prefailed slopes, and may also be used for pore-pressure induced instabilities (e.g. Tatarniuk and Bowman, 2012).

#### 5 MULTI-HAZARD INSTABILITY OF SLOPES

*Nadim and Liu* present on the use of Bayesian networks to inform reasoning when there is uncertainty and reliance on expert judgment, such as is done in many branches of civil engineering (for example, avalanche risk assessment, dam risk analysis etc.). They built a network for consideration of earthquake-triggered landslides using the open-source MATLAB package BNT, and used it to conduct a sensitivity analysis. The method is believed to have merit in deciding where to take no action, versus installing a warning system, else opting for active countermeasures.

*Chang and Huang* present an interesting case study on the influence of the Chi-Chi earthquake in 1999 on a road above slope that had been stable. Although no obvious damages to the road were observed at the time of shaking, during Typhoon Nari in 2001, several parallel cracks developed along the road alignment – suggestive of underlying instability. Remedial work



was initiated. Nonetheless, a loss of road base during the monsoon season the next year imposed a stop on the work. The remedial plan was revised and implemented, but failed again due to typhoons in 2005. The current repair works have been completed and generally show no major signs of slope distress. However, data from subsurface exploration and in-situ monitoring have shown signs of slope instability.

Figure 8 indicates potential slip surfaces in the upslope that would have impact on the road section. The downhill side slope also was not improved during the remedial works and its surface was bared with remains of previous slides. The upslope mitigation works are not useful for the stability of the downslope area and do not remove the concerns regarding the long-term stability of the road section and slopes at the site. Discussion addresses the potential for further remedial works, but it is pointed out that the cost of these may make a rerouting of the road desirable in the long term.

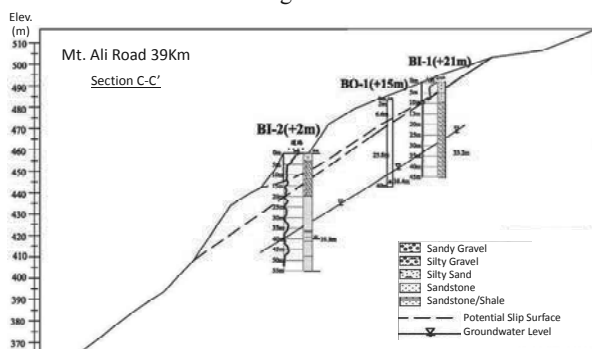


Figure 8. Chang and Huang. Instabilities detected by borehole investigation

*Long and Tjok* present a paper on submarine slope instability due to earthquake excitation leading to mass gravity flow which may pose risk for the integrity of offshore structures along the flow path. This paper demonstrates the ability of using a fully coupled nonlinear effective stress analysis to simulate the development of liquefaction and the instability of a liquefied slope. A prediction of run-out distance of subsequent debris flows is also made. The authors use a 1D model and parameters correlated with liquidity index in the absence of other data, although they also point out that estimation of run-out distance should be tested and calibrated to the case in question.

*Quan Luna et al.* present a study on the effects of earthquakes on subsequent slope stability, undertaken in an explicitly multi-hazard framework. The developed model is designed to give a rough spatial and temporal prediction of expected change in landslide hazard in an area following an earthquake. The model is able to describe the reduced impact of earthquakes with distance from the epicenter as well as how the soil loses strength due to shaking and gradually regains it with time. These reductions are then applied to an equilibrium stability analysis in order to compute new factors of safety on stability. The model is demonstrated by using a virtual region, and while further work is required to calibrate and validate the model with respect to real situations, it provides a mechanism whereby prospective outcomes from future hazards can be investigated in a conceptual manner.

*Cohen-Waeber et al.* presents data from a project combining GPS and InSAR time series analyses for the detailed characterization of spatial and temporal landslide deformation as a result of static and dynamic forces. A review of three independent InSAR time series analyses of the Berkeley Hills from 1992-2011 shows remarkable consistency. They reveal accelerated landslide surface deformation as a consequence of precipitation, though not in relation to seismic activity. Further, after a mild wet season in early 2012, the GPS instrumentation of several landslides in the Berkeley Hills has recorded well-defined precipitation triggered slope movement. In contrast, the occurrence of a nearby Mw = 4 earthquake did not appear to

have produced a measurable effect (Figure 9). Both InSAR and GPS studies confirm strong correlation and sensitivity to periods of precipitation, and downslope sliding velocities of around 30 mm/year. These observations, taken over longer time periods will enable important insight on the triggering mechanisms and internal landslide behavior of this area.

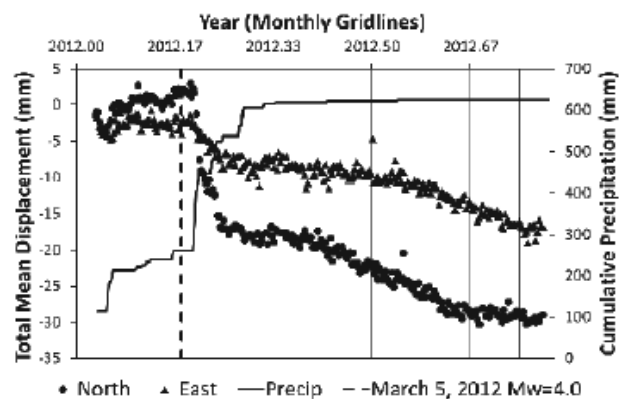


Figure 9. Cohen-Waeber et al. North (circles) and east (triangles) components of relative displacement with respect to reference site P224 shown together with cumulative precipitation (solid line) and time of Mw = 4 earthquake (dashed line).

## 6 PROGRESSIVE FAILURE OF SLOPES

Two contrasting papers on progressive failure are included – the first presents retrogressive failures in tuff over an existing landslide area, and the second investigates the strain softening behavior of sensitive clays leading to river bank erosion.

*Sengör et al.* present a paper on a landslide that occurred during foundation excavation of an industrial plant in Turkey. The instability occurred in a natural slope with a slope angle of 9°-13°. The sliding mass grew progressively backward into the slope as multistage rupture surfaces from the toe of the landslide developed. Back-analyses and laboratory tests were performed for the determination of shear strength parameters at the sliding surface. Mitigation measures included: two rows of stabilizing piles which were analyzed by FE independently for geotechnical and structural performance, permanent ground anchors, and surface drainage. The deformations of the system were measured by 12 inclinometers (8 in the soil, 4 in the piles) at each stage of the construction works and there have been no displacements in three years since completion.

*Dey et al.* present a study on upward progressive failure due to river bank erosion in sensitive Canadian clay which is numerically modeled using nonlinear post-peak strain softening behavior. Three cases are analyzed. In Case-I, the ground surface is horizontal and there is a 15m thick layer of sensitive clay below a 5m crust. The Case-II is same as Case-I but the ground surface is inclined upward at 4°. In Case-III only a 1.0 m thick sensitive clay layer parallel to the horizontal ground surface from the toe of the slope is assumed, with the crust the same as for Case I. In Cases I and II global failure was found to occur. However, for Case-III, although global failure did not occur, the shear band propagation reduced the shear strength in the potential failure plane significantly over a large distance and the slope might be marginally stable for further loading. Hence it is shown that the pattern of propagation of shear band varies with soil type and slope geometry.

## 7 UNCLASSIFIED

This last group of papers includes some highly theoretical contributions and some highly pragmatic ones – both ends of which help to advance the state of knowledge or practice within the profession.

Saha develops a global population-based search procedure (APMA) and applies this to a classic slope-stability problem as originally defined by Spencer (1967). It does not require problem-specific knowledge in searching the critical slip-surface of a soil slope but rather is a heuristic technique based on the 'generate-and-test' strategy. The results show that a lower factor of safety may be obtained with this technique than is found by Methods-of-Slices that are commonly used.

Bogomolov *et al.* suggest a method for calculating the stability of a loaded slope, based on the combined use of the finite element method, complex function theory and the principle of virtual displacements, as formalized in a computer program by the authors. The method ensures that a minimal condition of the factor of safety  $K$  value at each point is obtained without simplifying assumptions.

Nonoyama *et al.* apply the SPH (Smoothed Particle Hydrodynamics) method to a series of slope stability problems. This numerical method, in which continuum-based constitutive relations are input, can handle large deformation problems because it is based on a free mesh system. This means it has the potential to describe the deformation of geomaterials from the initial state to subsequent large deformation and can be used to estimate deformation and failure conditions simultaneously. Using two example constitutive models, the authors present analysis of both simple slopes and those with countermeasures (piles) included and compare results to those obtained by the Fellenius method.

In their extremely practical contribution, Yeh *et al.* introduce the currently most adopted ground anchoring inspection system used in Taiwan for anchoring slopes. The paper also proposes a new method of ground anchoring assessment, in order to establish a standardized quantitative analysis procedure for professional reference. They find that four categories of assessment should be made: inspecting the exterior of the anchor, the anchor head, an endoscopy inspection and conducting lift-off tests. They also examine the most common shortcomings of anchor installation and suggest remedies.

Bozo and Allkja present a study on the cuttings constructed for the Vlora road in Albania. A description of the geological setting of the site and of the rock and soil profiles is provided. Using in situ and laboratory tests they have determined the type of cuts and their geometrical forms in a manner designed to protect both the environment and the stability of slopes. Correlations between in situ test results and soil types are given as well as classification data and strength data for the soils encountered. They have also carried out some classifications of cuts for the road taking into account the conditions of the terrain.

The paper by Lo and Lam highlights some key lessons learnt and observations made from selected landslide investigations by the Geotechnical Engineering Office (GEO) of the of the Civil Engineering and Development Department (CEDD) of Hong Kong. On average, about 300 landslides are reported to GEO in Hong Kong each year. The paper discusses the use of robust stabilization measures for cut slopes, improved rock slope engineering practices, enhanced practices in the monitoring and maintenance of water-carrying services affecting slopes and improvement to drainage detailing.

Du *et al.* propose a quantitative model for estimating the vulnerability of elements at risk from impact by a slope failure, where vulnerability is defined as a function of landslide intensity and of susceptibility of the element. A conceptual framework is described for the model, and commentary provided on parametric inputs to it, together with suggested values for those parameters. The authors acknowledge the limitations of the model in its current form, which arise from a need to calibrate some of the input parameters.

Lacasse *et al.* summarize the findings of a European Commission project, SafeLand and its related 'toolbox' that is web-based, which includes nearly 75 mitigation measures for different types of landslide. Features of the toolbox are

described, which extend to estimates of cost-benefit factors and likely effectiveness, all of which are predicated on a ranking of the most appropriate mitigation measures. In this regard, the toolbox takes the form of a decision-support tool.

## 8 SUMMARY REMARKS

In engineering, like many other subjects of professional practice, it is important that the state-of-the-art continue to inform the state-of-the-practice. In reality, the state-of-the-practice involves risk management, whether it is done implicitly or explicitly. It is by developing new knowledge, else refining existing knowledge, that the findings of research enable improved decision-making in the face of risk and uncertainty. A total of 37 papers were submitted to the conference on the topic of slope stability in engineering practice.

Although they are broad-ranging in subject matter, they are unified by a common thematic objective of better understanding the spatial and temporal variation of demand and capacity at the point of slope instability, together with the magnitude and likely run-out or travel distance of the ensuing event. In many respects the findings of these studies are a timely reminder of the observations of Karl Terzaghi that "In soil mechanics the accuracy of computed results never exceeds that of a crude estimate, and the principal function of theory consists in teaching us what and how to observe in the field" (Goodman, 1999).

## 9 REFERENCES (TNR 8)

- Chau K.T. 2005. General Report for Technical Session 4a: Slope stability and landslides. *Proceedings of 16<sup>th</sup> International Conference on Soil Mechanics and Geotechnical Engineering*, Osaka, Japan.
- Fannin R.J. and Bowman E.T. 2010. Debris flows—entrainment, deposition and travel distance. *Proceedings of 11<sup>th</sup> IAEG Congress: Geologically Active*, 5-8 Sept 2010, Auckland, New Zealand
- Goodman, R.E. (1999). Karl Terzaghi: the engineer as artist. ASCE Press, Reston, VA, USA, 340p.
- Lin C.W., Shieh C. L., Yuan B. D., Shieh Y. C., Liu S. H. and Lee S. Y. 2004. Impact of Chi-Chi earthquake on the occurrence of landslides and debris flows: example from the Chenyulan River watershed, Nantou, Taiwan. *Engineering Geology*, 71, 49-61
- Petley D. 2012. Landslides and engineered slopes: Protecting society through improved understanding. *Proceedings of 11th International & 2nd North American Symposium on Landslides*, 3-8 June 2012, Banff, Canada.
- Rose N.D and Hungr O. 2007. Forecasting potential rock slope failure in open pit mines using the inverse-velocity method. *International Journal of Rock Mechanics & Mining Sciences*, Vol. 44, 308-320.
- Tatarniuk, C.M. and Bowman, E.T. (2012) Case Study of a Road Embankment Failure Mitigated Using Deep Soil Mixing. *4th International Conference on Grouting and Deep Mixing (ICOG)*, 16-18 Feb 2012. New Orleans, LA, USA:

## 10 PAPERS IN THE TECHNICAL SESSION

- .Bogomolov A.N., Ushakov A.N. and Bogomolova O.A. Calculation of slopes stability based on the energy approach.
- Bozo L. and Allkja S. Preservation of slope stability along the bypass Vlora.
- Buscarnera G. and Whittle A.J. Model prediction of flow slide triggering in shallow sandy slopes.
- Cepeda J., Quan Luna B. and Nadim F. Assessment of landslide run-out by Monte Carlo simulations.
- Chang M. and Huang R. The challenge of the slope failure problem and its remedial considerations at Mileage 39Km, Mt. Ali Road, Taiwan.
- Choi C.E., Ng C.W.W., Kwan J.S.H., Shiu H.Y.K., Ho K.K.S. and Koo R.C.H. Downstream frontal velocity reduction resulting from baffles.
- Cohen-Waeber J., Sitar N. and Bürgmann R. GPS instrumentation and remote sensing study of slow moving landslides in the eastern San Francisco Bay hills, California, USA.

- Coutinho R.Q. and da Silva M.M. Geotechnical characterization, stability analysis, and the stabilization process for a landslide in a area of Barreiras Formation and granite residual soils, Pernambuco.
- Dey R., Hawlader B., Philips R. and Soga K. Progressive Failure of Slopes with Sensitive Clay Layers.
- Du Y, Yin K., Nadim F. and Lacasse S. Quantitative vulnerability estimation for landslides.
- Harris S., Orense R. and Itoh K. A site specific early warning system for rainfall induced landslides.
- Jeng C.J. and Sue D.Z. Characteristics of ground motion on colluviums slope induced by natural disasters.
- Katzenbach R. and Bergmann C. Investigation on mass flow of saturated soil by large scale experiments.
- Kavvas M., Agioutantis Z., Schilizzi P. and Steiakakis C. Stability of open-pit lignite mines in Northern Greece.
- Lacasse S., Kalsnes B., Vaciago G., Choi Y.G. and Lam A. A web-based tool for ranking landslide mitigation measures.
- Law R.P.H., Lam A.Y.T. and Choi K.Y. A numerical study of granular surge flow through a row of baffles.
- Li A.G., Qiu, J.J., Mo J.F., Gao W., Tham L.G. and Yan R.W.M. Full-scale field monitoring of a rainfall-induced sliding slope in Hainan, China.
- Lin M.L. and Lin Y.S. Estimation and prediction of debris flow potential using discrimination analysis.
- Lo D.O.K. and Lam H.W.K. Value of landslide investigation to geotechnical engineering practice in Hong Kong.
- Long X. and Tjok K-M. Analyses of seismic slope stability and subsequent debris flow modeling.
- Nadim F. and Liu Z.Q. Quantitative risk assessment for earthquake-triggered landslides using Bayesian network.
- Nakata Y., Kajiwara T. and Yoshimoto N. Collapse behavior of slope due to change in pore water pressure.
- Nonoyama H., Yashima A. and Moriguchi S. Future evolution of slope stability analysis created by SPH method.
- Paçi E., Cullufi H. and Dervishaj A. Slope stability along a new road “Drisht-Drisht castle”.
- Quan Luna B., Vangelsten B.V., Liu Z.Q., Eidsvig U. and Nadim F. Landslides induced by the interaction of an earthquake and subsequent rainfall. A spatial and temporal model.
- Rahhal M.E., Hajal M., Seoud J.P. and Rafie E. Analyse des glissements de terrains en région urbanisée.
- Saha A. A smart adaptive multivariable search algorithm applied to slope stability in locating the global optima.
- Şengör M.Y., Ergun M.U. and Huvaj N. Landslide stabilization by piles: A case history.
- Son N.T., Ha P.T.S. and Son L.M. Landslide susceptibility mapping using Bayesian conditional probability model at An Linh Commune, Tuy An District, Phu Yen Province, Vietnam.
- Strenk P.M. and Wartman J. Influence of ground motion variability on seismic displacement uncertainty.
- Thakur V., Degago S.A., Oset F., Dolva B.K. and Aabøe R. A new approach to assess the potential for flow slide in sensitive clays.
- Tremblay M., Svahn V. and Lundström K. Landslide risk assessment in the Göta river valley: effect of climate changes.
- Uchimura T., Gizachew G., Wang L., Nishi S. and Seko, I. Deformation and water seepage observed in a natural slope during failure process by artificial heavy rainfall.
- Wang L., Nishie S., Seko I. and Uchimura, T. Study on field detection and monitoring of slope instability by measuring tilting motion on the slope surface.
- Winter M.G., Smith J.T., Fotopoulou S. & Pitilakis K., Mavrouli O. and Corominas J. The physical vulnerability of roads to debris flow.
- Yeh H-S., Wang C-S., Wei C-Y., Lee S-M., Ho T-Y., Hsiao C-A. and Tsai L-S. Inspection and capacity assessment of anchored slopes.
- Yune C-Y., Kim G., Lee S.W. and Paik J. 2011 Seoul debris flow and risk analysis.

# Calculation of slopes stability based on the energy approach

## Calcul de la stabilité des pentes sur la base de l'approche énergétique

Bogomolov A.N., Ushakov A.N., Bogomolova O.A.

*Volgograd State University of Architecture and Civil Engineering, Volgograd, Russia*

**ABSTRACT:** For quantitative evaluation of slope's stability value safety factor coefficient  $K$  is used, defined by various known methods. However, the results ensued in this way for identical objects may substantially differ. The reason for this are numerous assumptions and simplifications adopted in the calculations. Approach based on the analysis of the stress fields and displacement of soil mass points and principle of virtual displacements allows to get adequate results while solving the corresponding task. The used method of sliding surface constructing ensures realization of minimal condition of  $K$  value at each point. Analysis of the stress-strain state of homogeneous and heterogeneous slopes is accomplished by using finite element method (FEM), and the boundary conditions imposed on the design scheme FEM are processed based on the analytical solutions of the first basic boundary value problem of elasticity theory for homogeneous weight simply connected domain, get by the authors.

**RÉSUMÉ :** Pour l'évaluation quantitative de la stabilité des pentes on utilise la valeur du facteur de sécurité  $K$ , définie par diverses méthodes connues. Cependant, les résultats obtenus de cette manière pour des objets identiques peuvent différer substantiellement. Les raisons de cette situation sont de nombreuses hypothèses et simplifications adoptées dans les calculs. Obtenir des résultats satisfaisants lors de la résolution du problème correspondant devient possible grâce à l'approche basée sur l'analyse des champs de tensions et de déplacements des points du massif de sol et aussi sur le principe des déplacements virtuels. La méthode utilisée de la construction de la surface de glissement assure l'accomplissement d'une condition de minimalité pour la valeur  $K$  dans chaque son point. L'analyse de l'état précontraint et déformé des pentes homogènes et hétérogènes est réalisée en utilisant la méthode des éléments finis (FEM), tandis que les conditions aux limites, imposées au schéma de calcul FEM, sont traitées sur la base des solutions analytiques du premier problème aux limites faisant partie de la théorie de l'élasticité pour une domaine homogène simplement connexe, obtenues par les auteurs.

**KEYWORDS:** slope, safety factor, stresses, displacements, work, restraining and moving forces

### 1. QUESTION STATUS

Principle of virtual displacements - one of the basic principles of mechanics, evaluating general condition of equilibrium of the mechanical system. It is widely used in static studies of material systems, with the effect imposed on the system connections, considered by adding appropriate reactions. This principle has been used previously in the stability of slopes calculation (Goldstein 1969, Dorfman 1975, Magdeev 1973, etc.), however, movements of the points lied on the most probable slip surface, are not appointed on the basis of the stress-strain state analysis of near the slope area and arbitrarily vary in magnitude until the condition  $K=K_{min}$  is achieved.

In addition the following quite not correct assumptions can be provided:

- sliding prism splits into separate blocks, the interaction force and the friction between them is rarely taken into account; orientation of this forces and the position of the points of their application does not settle, and set arbitrarily to make a statically indeterminate task about equilibrium of blocks, statically determinate;

- the form and position of the fracture surface are taken in advance, in the process of problem solving their direct link with physical and mechanical properties of soils, slope geometry, surface loads is not established;

- almost always only one (and approximately in the form of bay weight) vertical  $\sigma_z$  component of the stress at near the slope area is taken into account;

- semi-infinite slope is considered (the fact of stress concentration in the transition region of the slope into the base is left out of the account); well-known calculation methods

doesn't allow to take into account mutual influence of embankment's slopes and excavations on their stability, as in the design scheme base of the slope is not considered, and the daily surface of the slope is infinite, etc. and so on;

- in stability calculation such important value as the coefficient of lateral earth pressure  $\xi_0$  is not considered and etc.

All this makes it necessary to look for new solutions of the slope's stability problem, in particular, based on the analysis of the stress-strain state.

Known method (Potapova 2001), when the value of  $K$  is defined as algebraic sum of work of restraining and shearing forces acting at the points of most likely slip line

$$K = \frac{\sum A_i y_{\partial}}{\sum A_i c_{\partial}} = \frac{\sum (F_i y_{\partial} \delta_i \cos \alpha_i y_{\partial})}{\sum (F_i c_{\partial} \delta_i \cos \alpha_i c_{\partial})}, \quad (1)$$

where  $F_i y_{\partial}; F_i c_{\partial}$  - restraining and shearing forces agreeably;

$\delta_i$  - complete movement;  $\alpha_i y_{\partial}; \alpha_i c_{\partial}$  - angles between positive directions of the restraining and shearing forces and direction of the total displacement vector, respectively, in the  $i$ -th point of the sliding surface. Equation (1), in our opinion, is not quite correct, because in this equation full displacements of the points made of movements of the external load and dead weight of the soil are taken into account. Movements from dead weight of soil are formed during all period of the soil mass existence, and therefore their true values cannot be reliably

determined using the theory of elasticity, which may affect the validity of the getting result. Ignoring of this fact can lead to getting while calculation overstated or, conversely, understated safety factors that may result in additional costs of material resources, or emergency initiation.

2. PROPOSED APPROACH

The following algorithm for calculating the value of the slope safety factor K of loaded soil slope, based on the joint application of the finite element method (FEM) and methods of complex function theory (Kolosoov 1934, Muskhelishvili, 1966):

a) design scheme of FEM is made up provided with maximum possible degree of homogeneity of the finite element mesh observance, which provides the minimum width of the stiffness matrix of the system;

b) based on an analytical solution of the first fundamental boundary value problem of elasticity theory for a homogeneous isotropic half-plane with a curvilinear boundary (Bogomolov 1996) data handling of boundary conditions applied to uniform FEM scheme so that the stress values  $\sigma_x; \sigma_z; \tau_{zx}$  at the corresponding points of the investigating region, found by FEM and analytical solution, coincided with the maximum degree of accuracy;

c) in the case of heterogeneous geological structure of the slope, therein geological elements endowing with corresponding physical and mechanical properties (solid weight  $\gamma$ , specific cohesion C; angle of internal friction  $\varphi$ , coefficient of elasticity E; coefficient of lateral pressure  $\xi_0$  (Poisson's ratio  $\mu$ )) are extracted;

d) to the study area  $n$  external loads are applied, which according to all parameters coincide with loads specified in problem specification, but the values of their intensities  $q_n \rightarrow 0$ . If in the near the slope area plastic deformation regions are absent, the construction of most likely slip surface is performed by the method (Tsvetkov 1979), ensuring fulfillment of the condition of minimum value of K at each point. At the same time the safety factor value  $K_i$  in the  $i$ -th point of the soil mass is determined by the following expression

$$K_i = \frac{[0,5(\sigma_{iz} - \sigma_{ix}) \cos 2\alpha_i + 0,5(\sigma_{ix} - \sigma_{iz})]tg\varphi}{0,5(\sigma_{ix} - \sigma_{iz}) \sin \alpha_i + \tau_{ixz} \cos 2\alpha_i} + \rightarrow$$

$$\rightarrow + \frac{[\tau_{ixz} \sin 2\alpha_i + 2\sigma_{cb}]tg\varphi}{0,5(\sigma_{ix} - \sigma_{iz}) \sin \alpha_i + \tau_{ixz} \cos 2\alpha_i} \quad (2)$$

where:  $\sigma_{cb}=C/tg\varphi$  - cohesion pressure, numerator and denominator of the formula (2) determine, respectively, the numerical values of restraining  $F_{\text{voi}}$  and shearing  $F_{\text{coi}}$  forces acting in the  $i$ -th point of the slip surface along the most likely site of shift. Analysis of formula (2) shows that the value of  $K_i$  depends on the components of the stress and angle  $\alpha_i$  most likely site shift at each point of sliding surface, as well as physical properties of soil.

The value of  $\alpha_i$  is defined by formulas (4), which arise from the boundary condition (3)

$$\left. \begin{aligned} \frac{\partial K}{\partial \alpha} &= 0; \\ \frac{\partial^2 K}{\partial \alpha^2} &> 0. \end{aligned} \right\} \quad (3)$$

$$\sin 2\alpha_i = 2N\tau_{ixy} + (\sigma_{iy} - \sigma_{ix}) \sqrt{\frac{1}{L} - N^2} \quad (4)$$

where:

$$L = (\sigma_{ix} - \sigma_{iy})^2 + 4\tau_{ixy}^2; N = (\sigma_{iy} + \sigma_{ix} + 2\sigma_{cb})^{-1}$$

If the plastic deformation regions have been developed, but their sizes are small, then the construction of the most probable slip surface is carried out by a method built on the basis of approximate solutions of the mixed problem of elasticity theory and plasticity theory of soil (Bogomolov 1996). In this case, the stress at the plastic region (marked by a prime) are given by

$$\left. \begin{aligned} \sigma'_{iz} &= \sigma_{iz}; \\ \sigma'_{ix} &= \frac{\sigma_{iz}(l - \sin \varphi) - 2\sigma_{cb} \sin \varphi}{l + \sin \varphi}; \\ \tau'_{ixz} &= \frac{(\sigma_{iz} + \sigma_{cb})b \sin \varphi}{l + \sin \varphi}, \end{aligned} \right\} \quad (5)$$

where  $b = tg 2\alpha_i^*; l = (1 + b^2)^{0,5}; \alpha_i^* = \alpha_i - (\pi/4 + \varphi/2)$ .

The value of the safety factor coefficient  $K_i'$  at the point of the slope, which is in the plastic area (obviously  $K_i' = 1$ ) is given by

$$K_i' = \frac{(\sigma_{iz} + \sigma_{cb}) \sin \varphi (\cos 2\alpha_i^* + b \sin 2\alpha_i^*) + \sigma_{iz} l + \sigma_{cb} b}{(\sigma_{iz} + \sigma_{cb})(b \cos 2\alpha_i^* - 2) \cos \varphi} \quad (6)$$

The numerator and denominator of formula (6) determine values of appropriate restraining and shearing forces. In  $m$  points of sliding surface with the help of FEM total displacements from the gravity forces and the external load are calculated. Note that construction of the most probable slip surface is carried out with such a step, that the difference between the horizontal coordinates of neighboring points on it is  $x_{k+1} - x_k = \dots \dots x_{m+1} - x_m = 0,01H$  (where  $H$  - the height of the slope).

e) the value of the intensity of the external load is increased to the calculated value. Once again we construct the most probable slip surface and the calculation of the total displacements in its  $m$  points.

f) the principle of virtual displacements is used, at the same time the role of the possible movements is carried out by differences of movements in corresponding  $m$  points of the sliding surface, obtained under the use of two previous steps of the algorithm. The role of active forces is played by restraining and shearing forces acting at the same  $m$  points of slip surface. The formula for calculating the safety factor value of the slope, provided that the plastic deformation is absent, has the form

$$K = \frac{\sum A_i y \delta}{\sum A_i c \delta} = \frac{\sum (F_i y \delta (\Delta_i - \delta_i) \cos \alpha_i y \delta)}{\sum (F_i c \delta (\Delta_i - \delta_i) \cos \alpha_i c \delta)} \quad (7)$$

where:  $\delta_i$  and  $\Delta_i$  - respectively the total displacement of  $i$ -th point of the most probable slip surface, calculated from the action of its own weight of soil, provided that  $q_n \rightarrow 0$ , and taking into account dead weight of soil, provided that the value of the intensity of the external loads are equal to calculated values, i.e.  $q_n = q_p$ .

The value of the safety factor coefficient of the slope in the case of plastic regions in the near the slope area is determined by the formula

$$K = \frac{S'_{y\partial} + S_{y\partial}}{S'_{c\partial} + S_{c\partial}} \quad (8)$$

where:  $S'_{y\partial}$  and  $S'_{c\partial}$  - squares of restraining and shearing force's diagrams, built along a section of the most probable slip surface that is in the region of plastic deformation,  $S_{y\partial}$  and

$S_{c\partial}$  - squares of restraining and shearing force's diagrams, built for the area most likely slip surface, which is outside the boundaries of the plastic deformation regions. In that way, if in a soil mass there are no plastic deformation regions or their sizes are small, then the proposed procedure excludes from examination of displacement from dead weight of the soil, which, as noted above, it is impossible to determine exactly what increases the reliability of the getting results.

### 3. PROCEDURE FORMALIZATION

Described above procedure is formalized in a computer program (Bogomolov and others, 2010), which allows to calculate stability of homogeneous slopes and slopes of complex geological structure with any configuration of the outer boundary. At the same time all strength and deformation characteristics of the soil are taken into account, to the surface of the slope can be applied almost any number of point and distributed loads of any orientation, length and intensity. It is possible inside the design schemes automatically generate fields of various shapes, endowed with certain properties, including the voids. Figures 1 and 2 show the most probable slip surfaces in the absence of the plastic deformation areas and while their development. Here

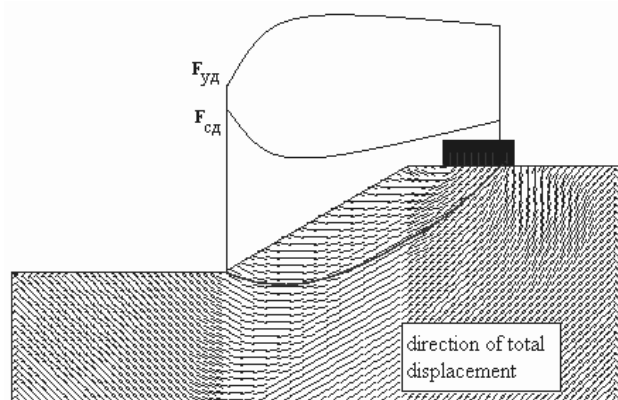


Figure 1. Fragment of a design scheme and work diagrams of restraining and shearing forces (plastic deformation areas are not presented)

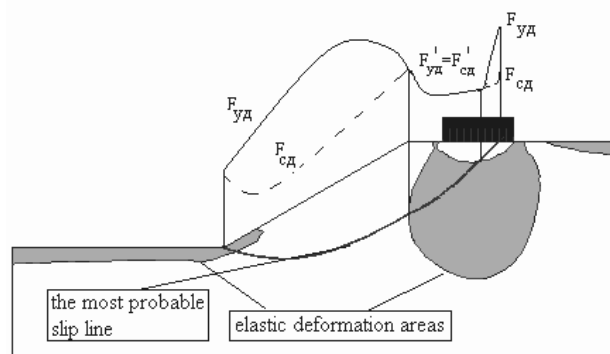


Figure 2. Work diagrams of restraining and shearing forces provided formation of plastic deformation areas

built in the computer program shell developed by the authors work diagrams of restraining and shearing forces acting at the points of the sliding surfaces are shown. Areas of diagrams are calculated automatically and are used in calculations of the safety factor value (see equation (8)).

Note one more circumstance. If the slope is uniform, then safety factor value calculated by the proposed method is independent from the value of deformation modulus of soil  $E_o$ , as in this case, displacements linearly depend on the numerical value. If the slope is not uniform, then the stresses at the points of soil mass will depend on size of the deformation modules and coefficient of lateral earth pressure of the nearby geological engineering elements. Consequently, the safety factor value will also be a function of these variables. This fact cannot be accounted by any of these methods, during the implementation of which analysis of the stress-strain state of the soil mass is not conducted.

### 4. COMPARISON OF NUMERICAL RESULTS WITH EXPERIMENTAL DATA AND FIELD OBSERVATIONS

We (Bogomolov & Vereshchagin, 1990) conducted experiments on the destruction of loaded slopes, made on the models from equivalent materials, as a basis for which were used: a) a mixture of river sand (97%) and motor oil (3%) having the following physical properties:  $\gamma=1,55 \text{ t/m}^3$ ;  $C=0,49 \text{ MPa}$ ;  $\varphi=24^\circ$ ; b) gelatinegel XC having the following characteristics: mass concentration of gelatine 30% -  $\gamma=1,15 \text{ t/m}^3$ ;  $C=72 \text{ MPa}$ ;  $\varphi=25,5^\circ$ , and at 15% -  $\gamma=1,078 \text{ t/m}^3$ ;  $C=34,8 \text{ MPa}$ ;  $\varphi=13,5^\circ$ . Value  $\xi_o$  for sand-oil mixture is set by pulling steel strips in a tray filled with the material which is under study (Terzaghi 1961), equal  $\xi_o=0,75$ .

Models from sand and oil mixture have height  $H=0,3 \text{ m}$ , width  $L=0,6 \text{ m}$ ,  $\beta=75^\circ$ . They were loaded with uniformly distributed load over the stamp which has the following dimensions in plan  $0,6 \times 0,5 \text{ m}$ , consistently placed at a distance  $b=0,25H; 0,5H$  from the edge of the escarpment. When  $b=0$  the average value (based on 10 experiments) of the intensity of the breaking load  $q_p=1,84 \text{ kPa}$ , when  $b=0,25H$  -  $q_p=0,78 \text{ kPa}$ , and when  $b=0,5H$  -  $q_p=1,39 \text{ kPa}$ . Calculated safety factor values for each of the three variants were found to be  $K_1=1,11$ ;  $K_2=0,99$ ;  $K_3=1,02$ . Evidently these values differs from limit value  $K=1$  for no more than 11%.

Models from gelatinegel XC formed in dismountable container made of organic glass, in the same forms loading of models up to failure was conducted, and at this moment loading size was fixed. Safety factor values, calculated on the basis of our proposals for the moment of destruction, were found to be  $K_{30\%}=1,08$  and  $K_{15\%}=1,1$ , i.e. differ from the limiting value of  $K=1$ , on 8% and 10%.

Figure 3 show the most probable surface of failure obtained theoretically (1 and 2) and in experiments (1' and 2'), which are almost identical to the corresponding models.

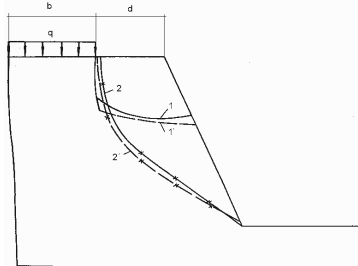


Figure 3. Theoretical and experimental slip lines in model made of equivalent materials

A case (Mochak 1964) of landslides formation in the quarry in Tsinzendorf (Germany) in the excavator ledge with the angle  $\beta=36^\circ$  was described. Soils - ribbon clay with the following content 42,9-58,5 of silt and 30,6-43,5% of clay, consistency – flexibly soft, with  $\varphi=21^\circ$ ,  $C=17,2$  kPa. The intensity of the load created by the excavator, which was at the edge of the slope ( $d=0$ ),  $q=4,4$  kPa, its width  $b=7$  m.

Author (Mochak 1964) calculated the slope stability by the method of K. Tercagi, resulting in safety factor value determined to be  $KT=1,19$ . The calculation by the proposed method results in  $K=0,97$ , which is only 3% different from the limit.

## 5 CONCLUSIONS

Method for calculating of loaded slope's stability, based on the combined use of the finite element method, complex function theory and the principle of virtual displacements, which is formalized in a computer program was suggested. The results of calculations with the help of the program that was announced with sufficient accuracy for engineering practice with the experimental data and behavior of landslide danger objects specifically.

## 6 REFERENCES

- Goldstein M.N. 1969. About calculus of variations application to the stability of foundations and slopes. Bases, foundations and soil mechanics 1, 2-6.
- Dorfman A.G. 1977. The exact analytical solution of new problems in the stability of slopes theory. Geotechnical issues, 26, 53-57.
- Magdeev U.H 1972. Investigation of slopes stability by variational method in conditions of the spatial task. Geotechnics questions, 20, 120-129.
- Potapova, N.N. 2001. Evaluation of slopes stability and soil bearing capacity of foundations on the basis of distribution of stresses and displacements analysis. Dissertation, 205.
- Kolosov G.V. 1934. Application of complex diagrams and complex function theory to the elasticity theory. Scientific and technical information department, Moscow.
- Muskhelishvili N.I. 1966. Some basic problems of the mathematical elasticity theory. Science, Moscow.
- Bogomolov A.N. 1996. Calculation of carrying capacity of the facility foundations and stability of soil masses in elastoplastic formulation. Perm State Technical University, Perm.
- Cvetkov V.K. 1979. Calculation of slopes and scarps stability. Lower Volga Book Publishers, Volgograd.
- Bogomolov A.N., Bogomolova O.A., Redin A.V., Nestratov M. Ju., Potapova N.N., Stepanov M.M., Ushakov A.N. Stability. Stress-strain state. Certificate of state registration of computer programs № 2009613499 from 30.06.2009.
- Bogomolov A.N. & Vereshchagin V.P. 1990. Modelling of the loaded slopes destruction. Foundations in the geological conditions of Urals. PPI, Perm, 112-114.
- Tercagi K. 1961. Theory of soil mechanics. Gosstroyizdat, Moscow, 507.
- Mochak G. 1964. Landslides as a result of the existing sliding surfaces and contact layers in glacial deposits. Meeting materials of studying landslides and strife with them measures. Kiev, 53-57.

# Preservation of slope stability along the by-pass Vlora

Maintien de la stabilité des pentes dans le contournement de « vlora »

Bozo L.  
POLIS University

Allkja S.  
ALTEA& GEOSTODIO 2000 Shpk

**ABSTRACT:**The development of the tourism in Albania is a very profitable branch of the economy. For this reason we have request to construct much new roads. One of them is the road to Jonian sea side which is with rarely beautiful nature. In this zone has constructed much restaurants, hotels, touristic resorts, but the access to them is difficult because the low quality of the existing roads. In these conditions is decided construction of the by-pass Vlora, and we have accomplished the geological and geotechnical study along the track of the new road. By this study we have in evidence : a) all dangerous phenomena's which can appear during the construction of the road, b) the sites where the road will passes by viaducts and bridges, c) the zones where the road will passes by cuts, d) the zones where the road will passes by embankments. In this paper we would like to present our study about the road's section which passes by cuts in hills terrain. By in situ tests and laboratory tests we have determined the kind of cuts, their geometrical forms in manner to protect environment and stability of slopes. Also we have take some classifications of cuts in this road regarding real conditions of the terrain.

**RESUME:** Le tourisme en Albanie est l'une des activités les plus profitable pour l'économie du pays. Afin d'en accélérer le développement, le pays à souhaiter construire un grand nombre de nouvelles routes. L'une d'entre elle est la route qui conduit au littoral de Jonian, site naturel d'une grande beauté. Dans cette zone ont été construits beaucoup d'hôtels, de restaurants et des stations touristiques. Malheureusement, l'accès au site de Jonian est difficile à cause des routes de qualité médiocres. Aussi, a été décidé la construction du contournement de "Vlora" et à cette occasion, de nombreuses études géologique et géotechnique ont été effectué. Grace à ces études in-situ, nous avons pu a) détecter les phénomènes dangereux qui sont susceptibles d'apparaître pendant de la construction de la route, b) identifier les sites où la construction de la route Allait induire la construction de viaducs et de ponts, c) les zones des excavations seraient nécessaires, d) les zones où des remblais devraient être édifier. Dans cet article, nous souhaitons présenter notre étude sur la portion de route pour laquelle des excavations ont été réalisées. Par le biais d'essais in-situ et d'essais de laboratoire, nous avons pu dimensionner les excavations à effectuer en tenant compte de la problématique de la stabilité des talus.

**KEYWORDS:** cutting, slope, stability, geological study, geotechnical study, environment, classification.

## 1. INTRODUCTION

The new road "By-pass Vlora" passes in the hill's and mountain's zones, which intersects several small streams and rivers. In the 29 km of their length 80% of the road passes in cutting and 20% in embankment. The hills of east part of the city Vlora are longitudinal of the direction of the Vlora By-pass. These hills are built from sedimentary rocks and they form steep rocky slopes. The soft slopes of these hills are transformed into agricultural lands, while the deep slopes are covertures with small trees. The intention of the study is the determination of the physical and mechanical properties of the soils and rocks encountered in the area where will passes the new road. The data taken from field and laboratory works will be useful to made the detailed road project for embankments, cutting, new bridges, or viaducts etc. Also from geological and geotechnical study can judge for the dangerous phenomena's which can appear during the construction and exploitation of road and for the selection of the construction material. These properties are determined by specimens from bore-holes, trial pits, refraction seismic tests, field tests, and laboratory tests. We want to present in our study the following problems: The evidence of the dangerous phenomena's for the road and environment. Determination of the physical and mechanical properties of the soils and rocks in this zone.

The evidence of the zones where the road passes in cutting and their calculation.

Classification of the different cutting's types.

Engineering measures for the protection of the equilibrium of the slopes and environment in the zone of the new road.

## 2. PHYSICAL GEOLOGICAL AND GEODYNAMICAL PHENOMENA'S

By Albanian geological map, existing investigations and new information from our study, in the zone where will passes the new road, we have evidenced or observed the following geological phenomena's:[1]

### 2.1. Erosion Phenomenon

This phenomenon is visible in all hilly part of the road's axis. The heavy rainfall, the current of the surface water, the inclination of the slopes, the type of the soils and weathered part of core formation are causes of this phenomenon. The body of road is at the middle part of the valley and it is exposed to this phenomenon and negative action of the erosion. For this we recommended not only remove the water by means of ditches, but during excavation, the road must protected in the upper and bottom part, to not allow erode of the slope's material, small surface slides and detaching of the mass rock.



2.2. Weathering Phenomenon

This phenomenon is visible at the rock formation that are composed by sedimentary rocks( mudstone, sandstone, conglomerates), which are new deposits with weak clay cementation. Under the action of the atmospheric agents they are transformed from weak rock to soils. When the road passes in cutting in the zone with clay rocks we will be attention and we will take the engineering measures to protect the stability of the environment.

2.3. The movement and sliding of the weathered mass rocks

From the beginning of the new road we have identified some zones with limited area landslide. The kind of the instability are:

- Slide of the colluviums
- Slide of the upper part of the weathered rocks
- Rock landslides
- Debris flow

We thing that , the design of this road to show maximal care for the stability of the slopes during and after the construction of the road and a special attention must to paid for the protection of the foundations of the bridges that are on the slopes prone to slide.

2.4. Activity of the tectonic movements(tectonic faults )

In Albania there are a developed regional tectonics, which is mainly horizontal with a ,low angle over thrust and others secondary tectonic movement.[5] The eastern areas have moved with a low angle over thrust towards west. This phenomenon has caused a total destruction of the rock mass in 7 km length of the road, and it is associated with a lot of other local tectonics. These zones are founded in the contact between different rocks, or inside the same rock. As result of this phenomenon in the hills side many rocky mass have moved toward the relieve fall and have created a rocky bent relieve. We must be very attention to not destruct the existing brittle, or frail equilibrium.

2.5 Seismic Hazard

After Albanian Seismic Code [4] the zone to be studied is classify ( by MKS-64) with intensity 8 ball and the soils in the second category [ ]. For calculation of the slope stability, by [ 2 ] we can use  $a_{max} = 0,2g$ , and the deep of epicentrum 25-30 km. For these conditions some of the observed slides can to reactivate caused the destruction of the road.

3. GEOLOGY AND HYDROGEOLOGY

The geological structure of the studied area[1] is composed by sedimentary deposits, limestone rocks, and granular rocks as below:

3.1 Limestone rock (Pg<sub>2</sub>, Cr<sub>2</sub>, Cr<sub>1</sub>, J<sub>1</sub>, J<sub>2-3</sub> up T<sub>3</sub>).

They have white to grey color, little cracks, in some part karst phenomenon, very resistible against atmospheric agents, very good characteristics for the foundations of the bridges, stabilized slopes and for the embankment.

3.2 Paleogene's deposits (Pg<sub>1</sub>, Pg<sub>3</sub><sup>1</sup>).

They are flysch deposits, brown to beige color, medium to weak cementation, in superficial part weathered, they form unstable slopes and at Radhima is very active sliding zone.

3.3. Neogene's deposits ( N<sub>1</sub><sup>2h</sup>, N<sub>1</sub><sup>2t</sup>, N<sub>1</sub><sup>3</sup> ).

They are composed by mudstone, sandstone and rare conglomerates, conglobreccias, brown to beige color, good to weak cementation with superficial part weathered. In the mudstone layer and colluviums dposites can observed landslide.

3.4. Quaternary deposits ( Q<sub>4</sub> ),

Are alluvial, torrent and colluviums deposits. Alluviums of the Dukati and Shushica rivers are consolidated gravel, sands, silty- sands, silty- clay, with 20-25m thickness. Elluviums or torrent deposits are moderate consolidate silty- clay, silty- sands with 8-15 m thickness. Colluviums are presented by silty- clays and gravely-silty-clays, moderate consolidated, unstable and with 2-4,5m thickness.

The level of the underground water is deep and the water is not aggressive to concrete and steel.

4. FIELD AND LABORATORY INVESTIGATIONS

For the part of the road that passes in cutting or over embankments, we have made trial pits which passes by viaducts and bridges, we have made bore-holes until 10-40m depth. At the same time we have realized SPT-tests and laboratory tests in ALTEA laboratory from samples taken by BH. From laboratory test[1] we have determined physical and mechanical properties for the soils, some characteristics for the rocks, and LA, soundnes, Proctor, CBR etc for the disturbed soils and rocks which will be serve as building material for the road and embankment.

4.1. Results of the site investigations.

From BH we have discover some different layers and we have compile the geological profile.

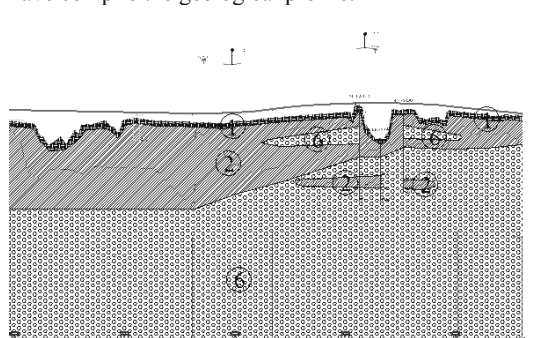


Fig. 1 Geological Profile

4.1.1 By description of layers and SPT-tests we have evidence six layers (Table 1)

Table 1. Description of the different layers

Nr.of layer	Description	Thickness(m)	Classification	N <sub>SP</sub>
1	soft brown	silty-clay	3-4	CL 9-12
2	medium dense	silty-clay-gravel	3,5-4	GC 24-28
3	clayey's elluvium	6-8	ML-CL	60-80
4	sand's elluvium	4-6	SM	50-60
5	gravel and sandy-silty-gravel	7-14	GM	35-50
6	moderately weak mudstone	7-30	- 80-12	and sandston

4.2. Results of laboratory investigations

From laboratory tests we have determined the following parameters :

Grain size distribution

Moisture content  $W = (5-29)\%$  mean 15%  
 Specific gravity  $\gamma_0 = (26-27,2) \text{ kN/m}^3$  mean 26,5  $\text{kN/m}^3$   
 Bulk density  $\gamma = (18,8-23) \text{ kN/m}^3$  mean 19,5  $\text{kN/m}^3$   
 Limits of plasticity ( liquid)  $LL = (18-50)\%$  ( plastic)  
 $PL = (13-28)\%$  mean 34% and 25%  
 Void ratio  $e = 0,355-0,743$  mean 0,62  
 Resistive parameters of soils by direct shear test :  
 $C = 22-25 \text{ kPa}$  mean 23  $\text{kPa}$   $\phi = 22^\circ-24^\circ$   
 mean  $23^\circ$   
 Bearing capacity  $R = 150-300 \text{ Kpa}$  mean 200kpa  
 Modulus of deformation  $E = (0,4-0,7) \cdot 10^4 \text{ kPa}$  mean  $0,55 \cdot 10^4 \text{ kPa}$  etc.

4.3. Correlation between different soil parameters.

After elaboration of the results from laboratory tests and in situ tests we have take the following correlations :  
 Correlation between bearing capacity of each layer “R” and percentage of gravel.

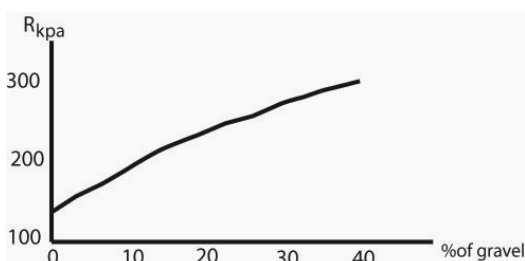


Fig.2 Correlation between R and percentage of gravel

Correlation between bearing capacity “R” and percentage of silty grains

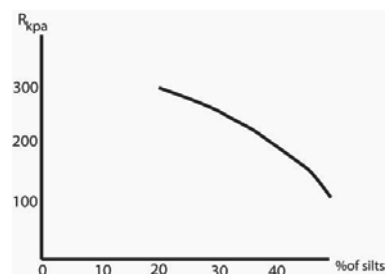


Fig.3 Correlation between R and percentage of silty grains

Correlation between bearing capacity “R” and modulus of deformation “E”( fig.4)

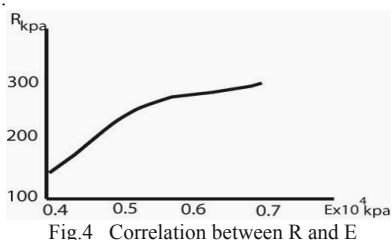


Fig.4 Correlation between R and E

Correlation between  $N_{SPT}$  and void ratio “e”

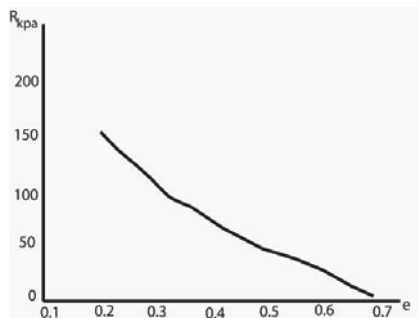


Fig.5 Correlation  $N_{SPT}$ -e

Correlation between  $N_{SPT}$  and percentage of gravel grains

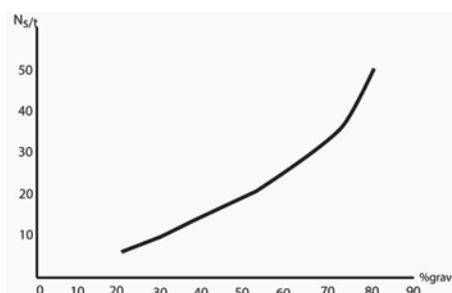


Fig.6 Correlation  $N_{SPT}$  and percentage of gravel grains

By the results of the test in direct shear apparatus we have the following values :

In the upper layers ( 3-5 m depth), which are “UCS” classification are silty-clay, maximum shear strength is 0,88, that to say the soils are with low sensibility.

The “pic” value and the “residual” value of the resistive parameters of this layer are :  $\phi_p = 23^\circ-24^\circ$   
 $\phi_{res} = 20^\circ$ ;  $C_p = 20-25 \text{ KPa}$ ,  $C_{res} = 10 \text{ KPa}$

From static loading test, for the upper layer ( 3m depth) they are suitable for the construction of the road because they have  $R > 150 \text{ KPa}$  and  $E > 40 \text{ MPa}$ .

5. THE CHOICE OF THE CUTTING’S TYPE

The choice we base in our calculations about the stability of the cohesive slopes that have :

$\gamma = 19-20 \text{ KN/m}^3$ ,  $\phi = 23^\circ-24^\circ$ ,  $C = 20-25 \text{ KPa}$ . In the zones where are visible slides we have determined the depth of the sliding surface ( 4-5 )m and residual resistive parameters of the soil  $\phi = 20^\circ$ ,  $C = 10 \text{ Kpa}$ . For the seismic zone with magnitude  $M = 5,5$ , depth of epicentrum of the earthquake 25- 30 km, second category of soils and  $a_{max} = 0,2g$ , by [ 3 ] we have take the coefficient  $K_s = 0,07$  for the calculation of the supplement earth inertial force. The factor of safety “FS”, in general, is  $FS = 1,5-1,8$  but we have the cases when  $FS, 1,3$ . The types of cutting choice by us satisfied three conditions:

- Preservation of existing equilibrium of natural slopes
- Unloading of the part of the slopes when they are in limit state (  $FS, 1,3$ ).
- Harmonization of the cuttings with environment to create beautiful landscape.

5.1 Classification of the cuttings

For the road with length 29 km, where 80% passes in cutting, by our study we have made some classification:

5.1.1 Classification by relief

The hills when passes the new road have the slopes with inclination 10°-35° and more.

Regarding this relief we have use four categories of cuttings

Table 2 Classification by relief

Category	Slope inclination	Nr.of escalations	Schema H <sub>1</sub> H <sub>2</sub>
1	(8-14)°	1 and 2	3-8 2-4
2	(15-22)°	2 and 3	8-15 1,5-3
3	(23-30)°	2 and 3 in	8-14 3-14
4	(31-35)°	5 and 6	18-24 10-28

5.1.2 Classification by geological conditions

In the unstable slopes we have choice two categories of cuttings:

Construction of the cuttings by excavation of the part of the sliding mass

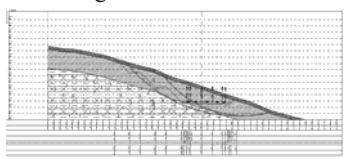
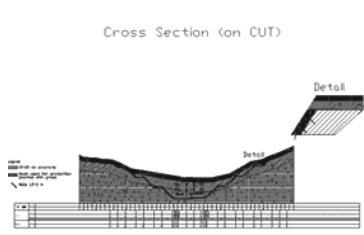


Fig7 Cutting by excavation in the sliding mass

Construction of the cuttings based in the stable rock mass and preservation of slopes by nails protection mesh and concrete slab.



5.1.3 Classification by geotechnical properties of the slope's soils

Regarding the resistive soils parameters of the slopes and characteristics of the rock mass of the slopes also the inclination and fault direction of the layers in slopes, we have design three categories of slopes ( Table 3 )

5.1.4. Classification by geotechnical properties

Table 3

Geotechnical characteristics)	High(H),width(b),inclination( $\alpha$ )
Rock mas $R_c = (50- 60)Mpa$	$H = ( 3-6 ) m$ $b = ( 2-3 ) m$ $\alpha = 60^{\circ}-65^{\circ} m = 2:1$
Medium cemented soils $\phi = 25^{\circ} C = 50KPa$	$\alpha = ( 60-65 )^{\circ} m = 2:1$ $H = ( 3-5 ) m b = ( 2-3 ) m \alpha = 45^{\circ}$ $m = 1:1$
Silty-clay soils $\phi = (20-23)^{\circ}$ $C = 20KPa$	$H = ( 3-5 ) m$ $b = ( 2-3 ) m \alpha = (33-35)^{\circ}$ $m = 1:1,5$

5.1.5. Classification by dangerous phenomena's.

Regarding the more dangerous phenomena's which can appear during the construction and exploitation period of the new road, we have made the following classification. In the colluviums zones ,which are in limit state of equilibrium, we can predict the protective geotechnical structures as piles, sheet piles and retaining walls

In more weathering zones we have predict protective geo-synthetic covertures combined with different vegetable

In the rock zones with intensive erosion phenomena's or weathering phenomena's we can use protective metallic mesh combined with metallic construction

6. CONCLUSIONS

For the new road "By-pass Vlora" that passes in cutting we have take the following conclusions:

By geometry we have classify three types of cuttings:

With big cut in left side

With big cut in right side

With two big cuts in both sides

By cutting's height we have three classifications:

Shallow cutting  $H = 5m - 6m$

Middle cutting  $H = 6m - 15m$

Deep cutting  $H > 15m$

By intersect layers the cuttings are classify:

Cutting which intersects 1 layer

Cutting which intersects two or more layers

Regarding the dangerous zones we have classify:

Cutting without the sliding plane

Cutting with presence of the sliding plane

Regarding the base of the road in cutting we have classify:

Cutting based completely in the same layer

Cutting based in two layers

Cutting based in core formation

partially in embankment

Escalations we have made regarding the inclination of the terrain to secure esthetical harmonization with environment, not damage of the environment and security for the road.

In the sliding zones we must undertake ( predict) the following engineering measures:

Excavation of the soils over sliding surface to unload the slope

Construction of the retaining walls, anchorage walls etc

Enforcement of the slopes by piles, micro-piles etc

In the zones that have evidence the rolling rock mass must take the following engineering measures:

Horizontal drainage

Enforcement by metallic nyle mesh combined with metallic profiles

Use vegetable revetment

Enforcement by geo-synthetics, concrete revetment etc

7. REFERENCES

Altea & Geostudio 2000 Shpk 2011 Report on the geological and geotechnical conditions of "Vlora by-pass" Tirana  
 Bozo L. 1989 Behaviour of the basements and foundations under seismic action- Ph.D. Thesis Tirana  
 Bozo L. 2004 Soil Dynamics – Vol. 1,2,3 Press "Natyra" Tirana  
 KTP-Antisizmic (Albanian Seismic Code for construction design) 1989 Tirana  
 Landslide and Geo-environment 2011 Proceedings of the International Symposium Press "Natyra" Tirana

# A Methodology for Evaluating Liquefaction Susceptibility in Shallow Sandy Slopes

Une méthodologie pour l'évaluation de susceptibilité à la liquéfaction dans les pentes sableuses

Buscarnera G.  
Northwestern University

Whittle A.J.  
Massachusetts Institute of Technology

**ABSTRACT:** The paper illustrates a modeling approach for evaluating the liquefaction susceptibility of shallow sandy slopes. The proposed methodology consists of two main components: (i) a theoretical framework for undrained stability and (ii) the MIT-S1 constitutive model for simulating the response of sands. In the first part of the paper, the use of a stability index able to capture the onset of undrained failure in infinite slopes is illustrated. In the second part, the practical significance of the method is discussed by back-analyzing the series of flow failures in an underwater berm at the Nerlerk site. The reinterpretation of these events in the light of the theory of material stability confirmed that liquefaction was a plausible mechanism for the failures. In addition, the analyses have provided a prediction of the spatial distribution of the unstable masses which is compatible with what was observed through bathimetric surveys conducted after the events. This particular application of the theory supports the idea that realistic constitutive modeling is crucial for achieving consistent predictions of liquefaction potential under field conditions.

**RÉSUMÉ:** L'article illustre une approche de modélisation pour évaluer la susceptibilité à la liquéfaction des pentes sablonneuses peu profondes. La méthodologie proposée se compose de deux éléments principaux: (i) un cadre théorique pour la stabilité non drainée et (ii) MIT-S1, le modèle de comportement pour la simulation de la réponse des sables. La première partie du document illustre l'utilisation d'un indice de stabilité capable de saisir le début de la rupture dans des pentes infinies dans des conditions non drainées. Dans la deuxième partie, les implications pratiques de la méthode sont évaluées par rétro-analyse d'une série de ruptures par écoulement dans une risberme sous-marine sur le site de Nerlerk. La réinterprétation de ces événements, à la lumière de la théorie de la stabilité des matériaux, a confirmé que la liquéfaction est un mécanisme plausible pour expliquer ces défaillances. En outre, les analyses ont fourni une prédiction de la distribution spatiale des masses instables, qui est compatible avec ce qui a été observé par des mesures bathimétriques menées après les défaillances. Cette application de la théorie soutient l'idée qu'une modélisation réaliste du comportement est essentielle pour faire des prédictions cohérentes de potentiel de liquéfaction dans des conditions de terrain réalistes.

**KEYWORDS:** sands, static liquefaction, flow slides, material stability, theoretical analyses, constitutive modeling.

## 1 INTRODUCTION.

Landslides and slope failures are widely recognized as one of the major natural hazards affecting both the development of densely populated areas in rugged terrain and the design of artificial earthworks [Terzaghi 1957, Sladen et al. 1985b]. Within the general class of slope failures, runaway instabilities or flow slides represent impressive phenomena that still raise several open questions.

Even though various studies have been carried out on the subject [Sladen et al. 1985a, Lade 1993], there is still need for advanced tools of analysis that can explain catastrophic failures, evaluate hazard levels in landslide prone areas and define geotechnical design criteria. The purpose of this work is to propose a predictive modeling methodology to study flow slide phenomena. The proposed methodology aims to evaluate (i) the shear perturbations that can trigger a flow slide, (ii) the spatial distribution of soil masses prone to liquefaction and (iii) the characteristics of the post-failure response of the slope.

## 2 MODELING FLOW SLIDE TRIGGERING.

The evaluation of liquefaction conditions based on geotechnical criteria typically relies on the combined use of the critical state theory and empirical observations from laboratory experiments and in situ tests [Poulos et al. 1985]. Although these methods provide guidance to assist engineering judgement, they lack appropriate geomechanical foundations that can be applied to general cases.

Indeed, the application of stability criteria to field conditions requires accurate consideration of the realistic static-kinematic characteristics of the problem at stake. An important example is represented by shallow slopes, in which initial stress conditions and kinematics are highly anisotropic and cannot be appropriately represented through classical triaxial testing. One of the first approaches to consider the role of soil behavior through a comprehensive constitutive model was suggested by di Prisco et al. (1995). In order to study the onset of a flow slide, these authors considered the geometry of an infinite slope (Figure 1) and modeled sand behavior through simple shear simulations.

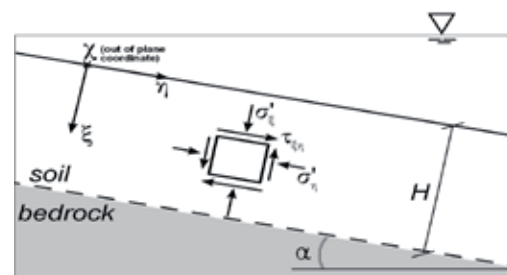


Figure 1. Reference system for a submerged infinite slope and initial stress conditions.

The present paper discusses a methodology which is inspired by this original idea, but tries to link it directly to the critical

state of sands and in situ observations. The key contribution is the incorporation of a constitutive model with predictive capabilities for describing transitions from contractive to dilative volumetric behavior upon shearing. As a result, the approach is able to distinguish among different types of sand response induced by an undrained perturbation (e.g., complete liquefaction, partial liquefaction, etc.), which is an essential aspect to define the expected post-failure behavior of a sliding mass.

In order to define in appropriate mathematical terms the onset of failure in a shallow infinite slope, our methodology frames static liquefaction within the theory of material stability [Hill, 1958, Buscarnera et al. 2011, Buscarnera and Whittle 2013]. In particular, we introduce an index for undrained simple shear failure:

$$\Lambda_{LSS} = H - H_{LSS} \quad (1)$$

where  $H$  is the hardening modulus of the sand considered as an elastoplastic medium, while  $H_{LSS}$  is a kinematic correction factor that depends on the mode of deformation. Vanishing values of (1) indicate the onset of unstable conditions. In other words,  $H_{LSS}$  represents a critical value of the hardening modulus at which undrained simple shear perturbations are no longer admissible. More details about the derivation of the index (1) are given by Buscarnera and Whittle (2012). For the purpose of the current paper, it is sufficient to note that positive values of (1) at a given state of stress and density reflect a stable undrained response of the infinite slope, while vanishing/negative values indicate the loss of undrained strength capacity. In this way, the values of  $\Lambda_{LSS}$  (as well as its increment,  $\Delta\Lambda_{LSS}$ ) can be used to assess both the initial stability conditions prior to shearing and the critical triggering perturbations. More specifically, the simple shear response predicted by a constitutive model can be interpreted by means of (1), identifying the stresses at the initiation of a flow failure and the residual margin of safety. For example, Figure 2 illustrates two MIT-S1 simulations of undrained simple shear response at the same level of initial vertical effective stress but with different values of initial shear stresses (representing different slope angles).

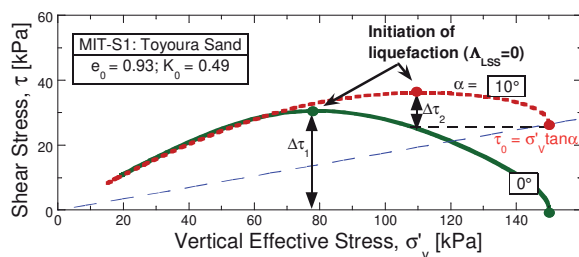


Figure 2. Example of simple shear simulations (loose Toyoura Sand simulated with the MIT-S1 model).

The results illustrate that the initial state of stress affects the magnitude of the shear perturbation required to induce instability ( $\Delta\tau_1$  vs  $\Delta\tau_2$ ). The onset of an instability coincides with the peak in the shear stress, and can be readily interpreted through the stability index (1).

As is well known, the undrained behavior of sands is also influenced by changes in the effective stress and density. For example, even very loose sands can exhibit a tendency to dilate at low effective stress levels, but will collapse for undrained shearing at high levels of effective stress. Hence, the prediction of liquefaction potential requires a constitutive framework that can simulate realistically the stress-strain properties as functions of stress level and density. To illustrate this aspect, Figure 3 shows MIT-S1 simulations for a pre-shear void ratio ranging from 0.87 to 0.94, with the model predicting a sharp transition from a stable behavior to complete collapse.

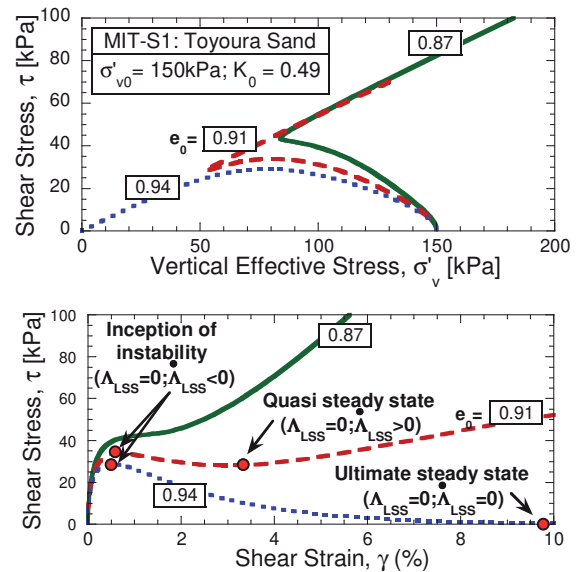


Figure 3. MIT-S1 predictions: effect of void ratio on undrained simple shear response of Toyoura Sand: a) stress path; b) stress-strain behavior.

The effect of confining pressure and density on the undrained response of sands implies that the perturbation shear stress ratio,  $\Delta\tau/\sigma'_{v0}$ , associated with the initiation of liquefaction is not only a function of the slope angle, but must be evaluated at the depth of interest. This information can be encapsulated in appropriate stability charts of the triggering perturbations. Figure 4 gives an example of such charts, and uses MIT-S1 simulations for a constant value of the initial void ratio to show the effect of the stress level on the predicted triggering perturbations.

In general, such charts should be evaluated at any depth of interest, being they a function of the values of density and stress state at that specific location. Once the stability charts expressing the shear resistance potential have been obtained, it is possible to define the variation of the triggering perturbation at any depth. These capabilities are illustrated in the next section by applying the theory for a case study involving flow failures in a sandy deposit.

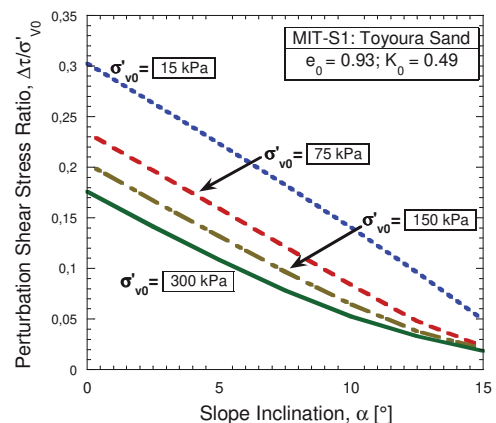


Figure 4. Effect of effective stress level on the stability charts (all points in the chart are characterized by  $\Lambda_{LSS}=0$ ).

### 3 EXAMPLE OF APPLICATION: THE NERLERK CASE.

The Nerlerk berm case history refers to an impressive series of slope failures that took place in 1983 during construction of an artificial island in the Canadian Beaufort Sea (Sladen et al., 1985b). We have used the MIT-S1 model to investigate potential static liquefaction mechanisms in the Nerlerk berm. In order to apply the theory to the Nerlerk case, it is assumed that the local behavior of the sides of the berm can be approximated

by considering stress conditions in an infinite slope. Although this choice represents an important simplification of the real geometry, this assumption allows an immediate mechanical evaluation of possible incipient instabilities within the fill and provides an insight on the type of expected undrained phenomena.

The application of the methodology is based on the calibration of the MIT-S1 model parameters for the site-specific properties of the Nerlerk sands. Given the lack of data, the calibration procedure required a number of approximations. Here only some key aspects of the calibration process are described, while more details are available in Buscarnera and Whittle (2012). First, the parameters governing the critical state of the Nerlerk sands have been evaluated on the basis of the available literature data (Sladen et al., 1985a). Then, the critical state properties of the Nerlerk sands have been compared with those of similar Arctic sands (Figure 5), for which one-dimensional compression data were available.

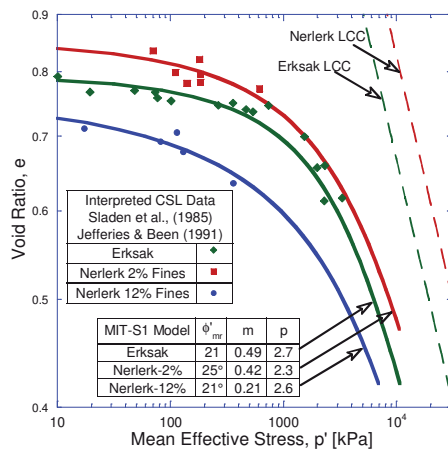


Figure 5. Comparison of Critical State Lines (CSL) and Limit Compression Curves (LCC; dotted lines) for Erksak and Nerlerk sands (while fines content affects the CSL of Nerlerk sand, no influence on the LCC is assumed given the lack of data).

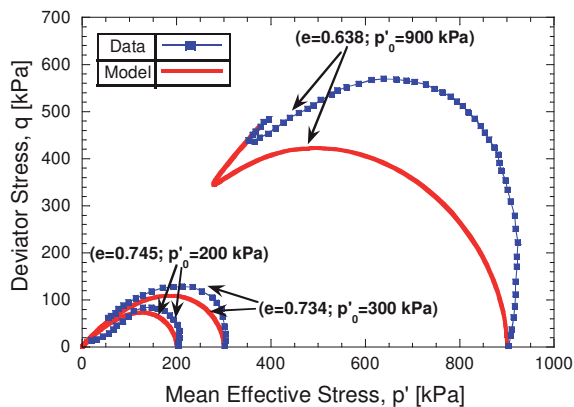


Figure 6. Comparison of computed and measured undrained shear behavior for Nerlerk Sand with 12% fines.

Such comparisons, together with empirical considerations compiled for a broad set of sands (Pestana and Whittle, 1995), allowed the definition of a set of parameters for the compression response of Nerlerk sands. The remaining model constants were calibrated using data on the undrained response (Figure 6).

In order to use the calibrated MIT-S1 model for the Nerlerk berms it is finally necessary to define the in situ void ratios along the slope profile and evaluate the stability charts of the Nerlerk berm for several depths within the slope. The first step is largely dependent on a reliable interpretation of the available in situ tests. Several CPT tests were performed on the hydraulic

fills at Nerlerk, with the aim of estimating the in situ density. For consistency with prior studies (Sladen et al. 1985b; Lade 1993), the current analyses assume that relative density ( $D_r$ ) can be estimated using the CPT correlation proposed by Baldi et al. (1982). It is clear that the choice of a specific interpretation method for CPT test results will affect the estimation of relative density (and, in turn, the model predictions). This uncertainty, however, is probably unavoidable in any method of interpretation. Figure 7 shows that the estimated values for  $D_r$  range from 30 to 55 %, while Figure 8 illustrates the distribution of these initial states relative to the CSL of Nerlerk sands with 12% fines content.

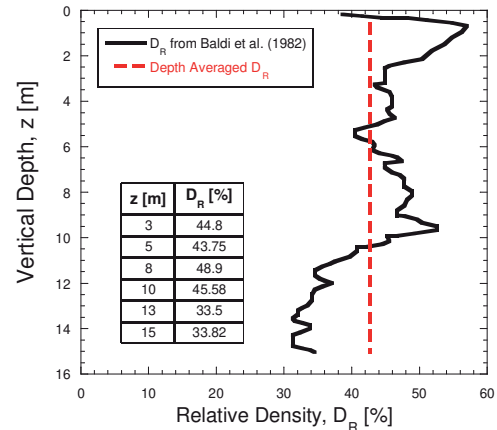


Figure 7. In situ relative density from CPT tests (Baldi et al. 1982)

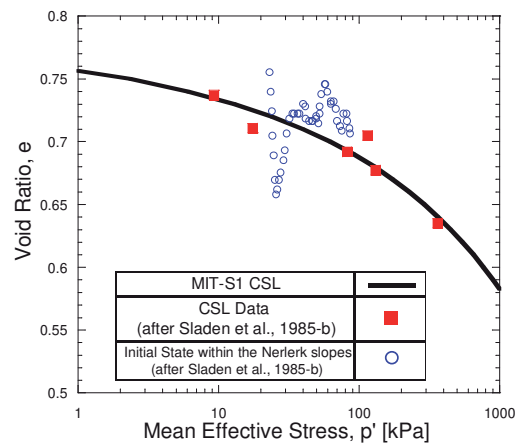


Figure 8. Relative location of in situ and critical states for Nerlerk sands

Figure 9 shows the computed stability charts at selected depths for infinite slopes in Nerlerk sand, while Figure 10 illustrates the undrained response predicted by the MIT-S1 model at various depths for a slope made of the same material and characterized by a slope angle  $\alpha=13^\circ$ .

The results show that the magnitude of the shear perturbation needed to cause instability can be significantly affected by the selected depth within the slope profile. More specifically, the analyses define the initial state of stability within the Nerlerk berm slopes in a proper mechanical sense, allowing a prediction of the critical inclination for incipient instability. Since the Nerlerk berm was constructed at slope angles in the range  $\alpha=10^\circ-13^\circ$ , these results suggest that the Nerlerk slopes were likely not in an incipient state of instability, and additional shear stresses were required to trigger flow failures. In other locations where steeper slopes were recorded, however, only very small perturbations in shear stress could have triggered failure. This result suggests that an undrained collapse triggered by rapid deposition can be considered as a mechanically feasible failure mechanism for the berm.



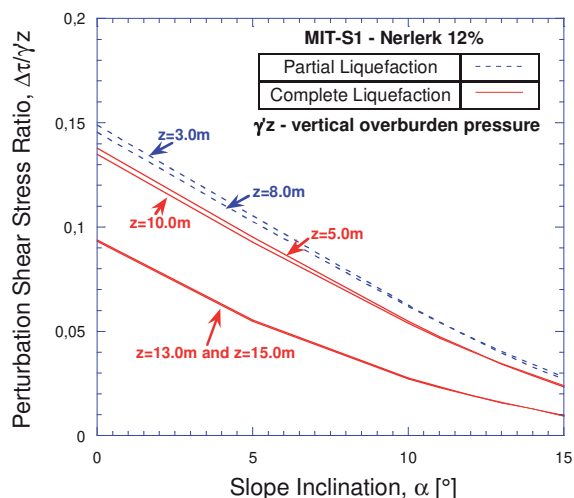


Figure 9. Stability charts for the Nerlerk berm.

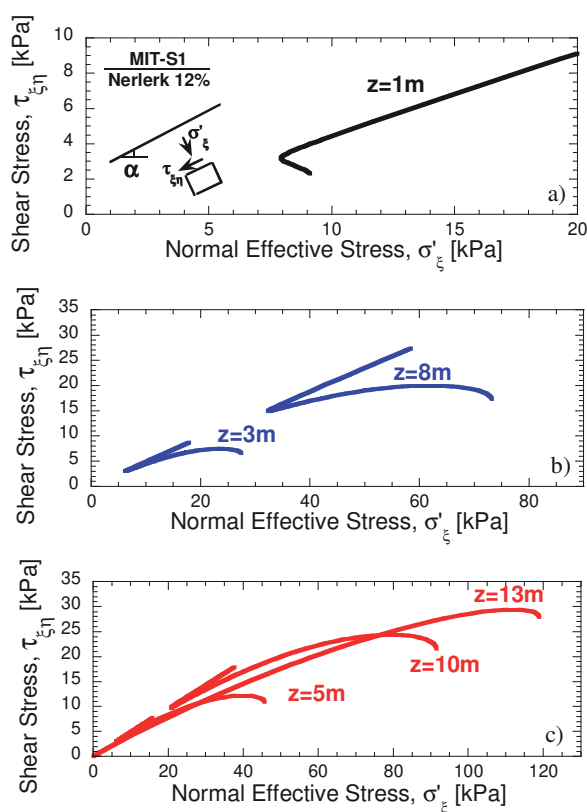


Figure 10. Predictions of undrained response across the Nerlerk berm section ( $\alpha=13^\circ$ ): a) no potential for liquefaction; b) limited potential for liquefaction; c) high potential for liquefaction.

#### 4 CONCLUSIONS

This paper has presented a framework for evaluating the triggering of flow slides in infinite slopes by modeling the undrained shear behavior using the anisotropic MIT-S1 model. The selected soil model is able to simulate realistic transitions in the contractive/dilatative response of sands and enables the prediction of the shear perturbations able to induce instability, as well as the location of potentially unstable zones within the soil mass. In this paper, these features have been used to derive stability charts of triggering perturbations for different combinations of initial density and stress state.

In practice the model needs to be calibrated for the site specific properties of the soil, and requires reliable data on in situ density in order to make predictions of liquefaction

potential. In order to show the capabilities of the proposed approach, the methodology has been applied to the well-known case of slope failures in the Nerlerk berm. A general picture of the distribution of liquefaction susceptibility on the Nerlerk slope profile has been obtained. The analyses have been based on the calibration of model input parameters against published laboratory test results, while empirical correlations for CPT data have been used to define the initial density conditions prior to shearing. The results show that there were two zones within the slope that were vulnerable to flow failure. Although some sections of the berm were oversteepened, most were deposited with a slope angle  $\alpha=10^\circ-13^\circ$ . For these slope angles, the current analyses show that instability could have been triggered by the undrained perturbations possibly induced by the rapid deposition of hydraulic fill. Thus, static liquefaction is likely to have contributed to the observed failures, confirming earlier hypotheses by Sladen et al. (1985b).

The analyses presented in this work illustrate a unified methodology that combines the theory of material stability, the critical state framework for sands and data from in situ tests. As a result, the proposed methodology offers a simple, consistent and complete geomechanical framework for interpreting and predicting the triggering of flow slides that can be easily applied to other similar engineering cases.

#### 5 REFERENCES

- Baldi G., Bellotti R., Ghionna V., Jamiolkowski M., Pasqualini E. (1982). Design parameters for sands from CPT. Proceedings of the Second European Symposium on Penetration Testing, ESOPT 11, Amsterdam, Holland, pp. 425-432.
- Buscarnera, G., Whittle, A.J. (2012). "Constitutive modeling approach for evaluating the triggering of flow slides". *Can. Geotech. J.* 49(5): 499-511.
- Buscarnera, G., Whittle, A.J. (2013). Model prediction of static liquefaction: the influence of the initial state on potential instabilities. To appear on *J. Geotech. Geoenviron. Eng. ASCE*.
- Buscarnera G., Dattola G., di Prisco, C. (2011). Controllability, uniqueness and existence of the incremental response: a mathematical criterion for elastoplastic constitutive laws. *Int. J. Solids Struct.*, 48 (13), 1867-1878.
- di Prisco C, Matiotti R, Nova R. (1995). Theoretical investigation of the undrained stability of shallow submerged slopes, *Géotechnique*, 45, 479-496.
- Hicks M. A., Boughrarou R. (1998). Finite element analysis of the Nerlerk underwater berm failures. *Géotechnique* 48, No. 2, 169-185.
- Jefferies M.G., Been K. (1991). Implications for critical state theory from isotropic compression of sand. *Géotechnique* 50:44, 419-429.
- Hill, R. (1958). A general theory of uniqueness and stability in elastic-plastic solids. *J. of the Mech. and Phys. of Solids* 6, pp. 239-249.
- Lade P. V. (1993). Initiation of static instability in the submarine Nerlerk berm. *Can. Geotech. J.* 30, 895-904.
- Pestana J.M., Whittle A.J. (1995). Compression model for cohesionless soils, *Géotechnique*, 45 (4), 611-631.
- Pestana J.M., Whittle, A.J. (1999). Formulation of a unified constitutive model for clays and sands, *Int. J. Numer. Anal. Meth. Geomech.*, 23, 1215-1243.
- Poulos, S.J., Castro, G. and France, J. (1985). Liquefaction evaluation procedure. *Journal of the Geotechnical Engineering Division, ASCE*. 111(6): 772-792
- Sladen, J. A., D'Hollander, R. D. & Krahn, J. (1985a). The liquefaction of sands, a collapse surface approach. *Can. Geotech. J.* 22, 564-578.
- Sladen, J. A., D'Hollander, R. D., Krahn, J. & Mitchell D. E. (1985b). Back analysis of the Nerlerk berm Liquefaction slides. *Can. Geotech. J.* 22, 579-588.
- Terzaghi K. (1957). Varieties of submarine slope failures. *NGI Publication N. 25*, 1-16.

# Assessment of landslide run-out by Monte Carlo simulations

## Évaluation de la dynamique des glissements de terrain par des simulations de Monte-Carlo

Cepeda J., Quan Luna B., Nadim F.

*Norwegian Geotechnical Institute – NGI and International Centre for Geohazards - ICG, Oslo, Norway.*

**ABSTRACT:** Landslides run-out models are based on theoretical descriptions of mass motion which attempt to model the complex behaviour of the actual flow phenomenon. To reproduce the general features of the mass motion, these models simplify the problem by using parameters that account for complex aspects, which are not explicitly included. This simplification results in model parameters that cannot be related to a specific physical process, and therefore cannot be directly measured. In order to analyse the effect of uncertainties in the input parameters, a probabilistic procedure based on a Monte Carlo simulation for run-out modelling was considered. The framework is based on a dynamic model (MassMov2D), which is combined with an explicit representation of the different parameter uncertainties. The main goal with the proposed methodology is to present a framework to obtain potentially expected run-out extents and intensities in areas where it is not possible to determine the rheological parameters on the basis of back-analyses. The outlined procedure provides a useful approach for experts to produce hazard or risk maps in cases where historical records are either poorly documented or completely lacking, as well as to derive confidence limits on the proposed zoning.

**RÉSUMÉ :** Les modèles de la dynamique des glissements de terrain sont basés sur des formulations mathématiques qui tentent de théorétiser les phénomènes d'écoulement réels, par nature très complexes. Afin de simuler les caractéristiques générales du mouvement, ces modèles utilisent des paramètres qui représentent et simplifient les aspects complexes du problème, sans pour autant les prendre en compte explicitement. Il en résulte une simplification des paramètres du modèle: ceux-ci ne sont donc plus liés à un processus physique réel, et ne peuvent par conséquent pas être mesurés directement. Afin d'analyser l'effet des incertitudes entourant ces paramètres, une approche probabiliste, basée sur la méthode de Monte Carlo, a été employée. Celle-ci se base sur un modèle dynamique (MassMov2D) ainsi que sur une représentation explicite des incertitudes des différents paramètres. L'objectif principal de cette méthode est de proposer une approche générale dans le but de prédire la taille et l'amplitude des glissements de terrain dans des zones où il n'est normalement pas possible de déterminer les paramètres rhéologiques par méthode arrière. La méthode décrite ici propose une approche pratique afin d'établir des cartes de risque dans les cas où la documentation est limitée, voire inexistante, ainsi que pour estimer les limites de confiance des zonages proposés.

**KEYWORDS:** Landslides, run-out, Monte Carlo, Bingham rheology, Voellmy rheology, quantitative risk assessment.

## 1 INTRODUCTION

Dynamic run-out models for landslides are able to simulate the spatial distribution of depth and velocity of the moving mass, which is essential for a quantitative evaluation of hazard and risk at a specific site. Another advantage of the application of dynamic models is that they can simulate the effect of variations in the release volume as well as in the rheological parameters for different scenarios including ones that have no historical evidences.

In practice, a substantial degree of uncertainty characterizes the definition of the deterministic model parameters. This is due to the lack of experimental data and the poor knowledge of the mechanical behaviour of the moving flows. Consequently all models, either those widely used in practical applications or those more recently developed, are based on simplified theoretical descriptions of mass motion which try to capture the complex rheology of the flow phenomenon. This results in a generalization of all models to attempt to reproduce the general features of the moving mass through the use of parameters (mostly for evaluating base shear) which account for aspects not explicitly described or oversimplified. The outcome is that the model parameters cannot be related to a specific physical process, and therefore directly measured, but need to be calibrated. At the moment, a relatively complete and well-established calibration for most of the run-out models is still lacking or not reliable enough to be applied in practical applications. This is connected with one of the basic limitations with the use of dynamic run-out models, which are significantly sensitive to the parameters controlling the base shear (Revellino et al. 2004, Hurlimann et al. 2007, Hungr & McDougall 2009). Inherent uncertainties in the specification of the input data for models are well acknowledged but usually not explicitly

incorporated into the analyses. Such uncertainties are normally addressed through conservative estimate of parameters, or in some cases, by a sensitivity analysis. These approaches do not integrate objectively the estimation of uncertainties, and thus may be impractical and lead to either conservative or underestimated hazard levels.

In order to analyze the effect of the uncertainty of input parameters, a probabilistic framework based on a Monte Carlo simulation for run-out modelling is considered as an alternative approach. Monte Carlo analysis is a method that uses statistical sampling techniques of input parameters to derive the probability distributions of solutions for mathematical equations or models. The Monte Carlo analysis was initially developed in the 1940's and it has been applied to a wide variety of problems for addressing the uncertainty of data and models (Metropolis 1987).

## 2 METHODOLOGY

The dynamic model used in this study was MassMov2D (Beguiria et al. 2009), which solves the equations of conservation of mass and momentum averaged over the depth of the landslide mass using an Eulerian scheme scripted in PCRaster, a GIS modelling environment (Karszenberg et al. 2001). In the equation of conservation of momentum, the shear stress at the bed contact (base of the analysed differential column) is calculated using a rheological model (a relation coupling stresses and strain rates) that should be physically consistent with the overall behaviour of the landslide. In this particular case, two models are used for describing frictional and cohesive-like dominated behaviours, namely the Voellmy and the Bingham models. Simplified formulations of these models are presented in Equations (1) and (2), respectively:



$$\tau = \sigma \tan \phi_{app} + \frac{\rho g v^2}{\xi} \quad (1)$$

$$\tau = \tau_y + \mu \dot{\gamma} \quad (2)$$

where,  $\tau$  is the shear stress at the base of a differential column of landslide mass,  $\sigma$  is the normal stress at the base,  $\phi_{app}$  is an apparent friction angle,  $\rho$  is the bulk density of the landslide mass,  $g$  is the acceleration of gravity,  $v$  is the velocity,  $\xi$  is the turbulent coefficient,  $\tau_y$  is the yield strength,  $\mu$  is the viscosity, and  $\dot{\gamma}$  is the shear strain rate. The apparent friction angle and the turbulent coefficient are material parameters of the Voellmy rheology. The yield strength and the viscosity are the corresponding parameters for the Bingham model.

The main objective of the present application of the Monte Carlo analysis is to examine the effect of uncertainty associated to the variability of the rheological parameters of the Voellmy and Bingham models on the estimation of debris flow run-out. This method allows evaluating the probability distribution of the relevant output parameters (intensity parameters) for a hazard assessment once the proper probability distributions for the parameters of both rheologies have been defined. In other words, it is possible to account explicitly and objectively for the effect of uncertainties in the model. For the application of the Monte Carlo analysis, each of the input parameters was assigned a distribution. The output from the model is calculated several times for a set of randomly selected input parameters. This produces a probability distribution for the output values, such that the uncertainty for the exceedance of any particular value can be estimated. Figure 1 presents a simplified flowchart of this procedure.

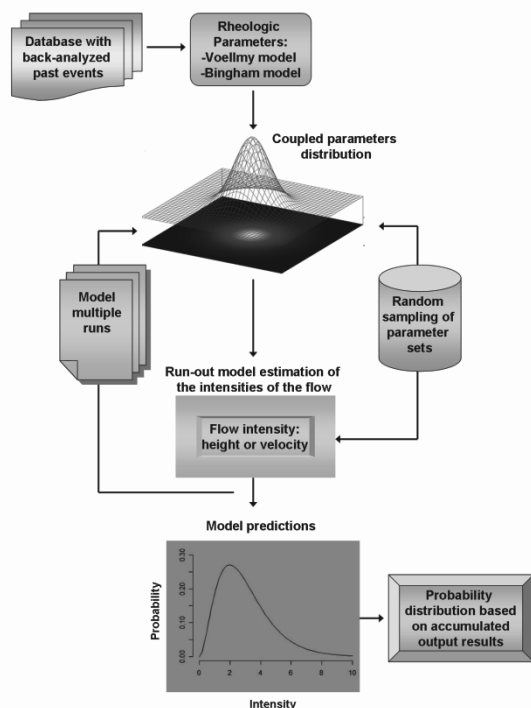


Figure 1. Flow chart of the application of a Monte Carlo method for a probabilistic assessment of landslide run-out.

The uncertainty resulting from the physical process (variability inherent to the phenomenon) is expressed inside the probability density functions of the parameters characterizing the base shear. An extensive literature study was carried out for collecting a database of past back-analyzed landslides, including the calibrated rheological parameters for each event. The

relationships between the parameters of the Voellmy and Bingham rheologies were modelled as a “Gaussian Copula” to define the probability density function for both rheological models (Fig. 2)

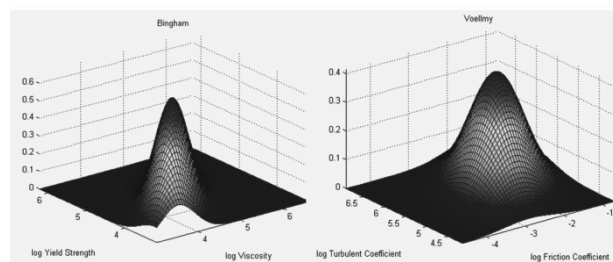


Figure 2. Fitted “Gaussian copula” distribution function to the Bingham rheology (left) and Voellmy rheology (right).

Each distribution was randomly sampled to obtain a set of 5000 pairs of rheological parameters. In the next step, a routine was coded to repeatedly run the simulations for each pair of parameters. At the end of each simulation, the output values of peak intensity parameters (maximum depth and velocity) were saved for selected points on the area of interest. Finally, the output values were fitted to a theoretical probability density function. The parameters for each probability distribution were reported. In addition, the probability that the output exceeds a particular value or will fall within a certain range was calculated.

The dynamic run-out model MassMov2D (Beguiria et al. 2009) was selected because it allows the use of scripts which can be modified to include output reports in the form of maps or text files. A batch file was built-in and incorporated inside MassMov2D which selects the randomly generated sets of parameters to produce multiple simulations. The results of each simulation regarding the maximum flow depth and maximum velocity at each control point were reported in a text file form for being fitted to a theoretical probability density function.

### 3 STUDY CASES

#### 3.1 The Faucon catchment in the Barcelonnette Basin

Inside the Barcelonnette Basin, the Faucon torrent was selected as a test site. The Faucon catchment is a steep forested watershed with an area of approximately 10.5 km<sup>2</sup> which rises to 2984 m a.s.l. Most slopes are steeper than 25°, reaching 80° at the highest elevations. Many of the slopes in the Faucon catchment are covered by various types of Quaternary deposits: thick taluses of poorly sorted debris; moraine deposits; screes and landslide debris. These deposits have a sandy-silty matrix, may include boulders up to 1–2 m in size and are between 3 and 15 m thick (Remaître 2006). The main incised channel has an average slope of about 20°, ranging from 80° in the headwater basin to 4° on the alluvial fan, and is approximately 5500 m in length. Channel morphology is characterized by a V-shaped profile with a steep channel in the upper part, and a flat-floored cross-profile between steep slopes. The Faucon torrent has formed a 2 km<sup>2</sup> debris-fan that spreads across the Ubaye valley floor. It has a slope gradient ranging from 4 to 9°. The fan consists mostly of cohesionless and highly permeable debris (debris-flows strata and/or torrent deposits) (Remaître et al 2005). Two points within the area of interest (in terms of exposed elements) were selected on the accumulation area to calculate the maximum flow height and the maximum velocity (Fig. 3).

### 3.2 Tresenda village in the Valtellina Valley

Valtellina is an important Italian alpine valley located in Central Italian Alps (Northern Italy, Sondrio Province). The valley starts near Bormio (1,225 m a.s.l.) and it runs for about 100 km to Colico (218 m a.s.l.) near Como Lake. The axis of the valley is formed by the Adda River, originating from small lakes in the Rhaetian Alps at 2,335 m a.s.l. The Adda River flows through the entire valley in a flat alluvial plain up to 3 km wide and it joins the Po River in the Lombardy Plain. Valtellina has a U-shaped valley profile derived from Quaternary glacial activity. The lower part of the valley flanks are covered with glacial, fluvio-glacial, and colluvial deposits of variable thickness (Crosta et al. 2003) The Tresenda village is located in the Valtellina area and is located in the municipality of Teglio in the Valtellina Valley. Spatial information of past damage derived from historical records, local chronicles, and interviews with local people confirmed that the village of Tresenda was affected by debris flows events which caused significant losses in 1983, 2000 and 2002. Soil slips, resulting in debris flows were triggered on the steep slopes above Tresenda, where the soil thickness varies from 0.7 to 2.5 m.

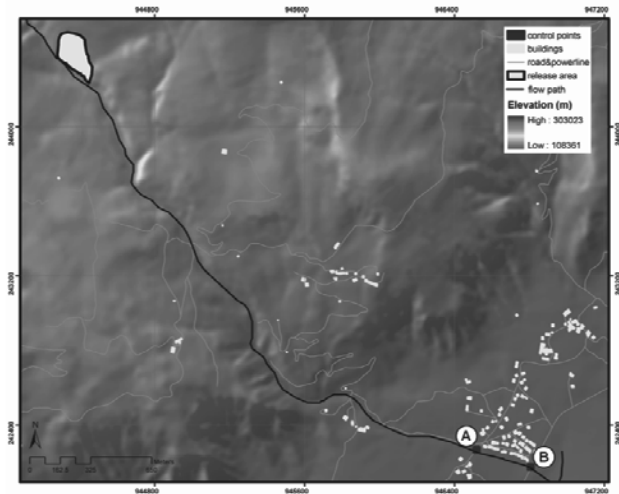


Figure 3. Digital elevation model of the Faucon catchment with the location of the two points used for reporting the results (A and B).

The documented past events crossed minor roads and impacted buildings in the Tresenda village, while running along main drainage lines (Cancelli & Nova 1985, Guzzetti et al. 1992). Major events in future may produce casualties and serious property damages as well as the obstruction of a main road. In the Tresenda case study two location points were also located within the area having the highest concentration of exposed elements.

## 4 RESULTS

### 4.1 Application of the methodology to the Faucon catchment

The release volume chosen in the Faucon study was 50,000 m<sup>3</sup> and was set as constant in the simulations. Past events in the Faucon area have had final volumes between 55,000 m<sup>3</sup> – 80,000 m<sup>3</sup>. The unit weight of the debris flow was set to a constant value of 19 kN/m<sup>3</sup>. The time step was set at 1 s and the total duration of each simulation was 500 s. The Monte Carlo method applied in the Faucon catchment was modelled with the Bingham model. This model was selected because of the geo-environmental setting of the area where past events are described to have viscoplastic behaviour (Remaître et al. 2005). In total, 5,000 runs were completed corresponding to the input parameters obtained from randomly sampling the fitted Gaussian copula. For each of the 5,000 runs, the maximum flow

heights and maximum velocities were reported for each of the two points. The results of each point were used to populate a probability density function of each intensity parameter. A Gamma distribution was the distribution that best fitted the maximum flow height and velocities measured in points A and B (Fig. 5 & 6).

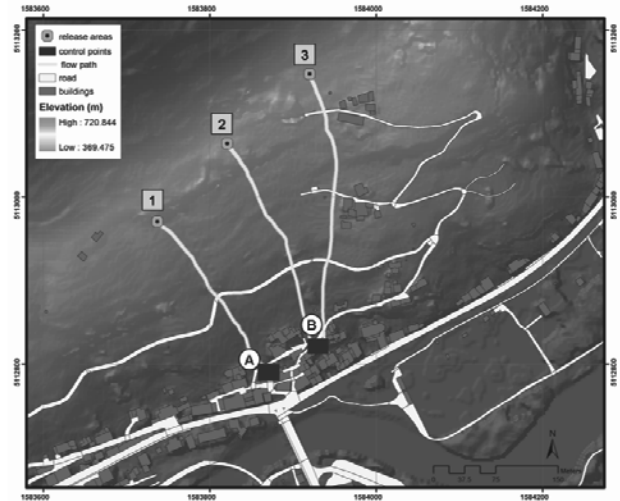


Figure 4. Digital elevation model of the Tresenda village with the location of the two points used for reporting the results (A and B) and three different release areas (1, 2 and 3).

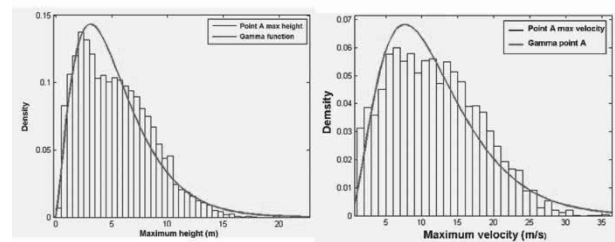


Figure 5. Gamma distribution fitted to the maximum height (left) and velocities (right) values obtained in point A.

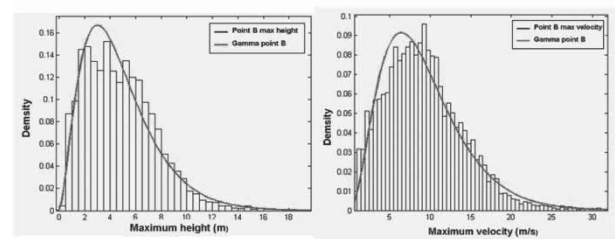


Figure 6. Gamma distribution fitted to the maximum height (left) and velocities (right) values obtained in point B

The obtained results of the mean values of height and velocity computed with the Monte Carlo method were compared with the events that took place in 1996 and 2003 (Remaître et al. 2008, Remaître et al. 2009). In both cases, the mean value of the distribution overestimates the flow height and the flow velocities. In the results, point A which is located higher up in the catchment than point B (apex of the fan) reports higher values for both intensity parameters (height and velocity).

### 4.2 Application of the methodology to the Tresenda village

In the Tresenda case, the main purpose of the study was to observe the response of the model when using more than one release area. In the Tresenda case, three simultaneous release

areas with different volumes were considered (Table 1). The initiation of the debris flow is assumed to be caused by soil slips and the flows are unchanneled along most of the path. The unit weight of debris flow was set to the same value as in the case of Faucon. The total duration for each simulation was 500 s. The Voellmy model was used in the run-out analysis.

In total, 5,000 simulations were carried out associated to the corresponding set of input parameters sampled from the Gaussian copula. For each simulation

Table 1 Release volume used for the Monte Carlo simulation for the three different release areas in the Tresenda village

Release Volume (m <sup>3</sup> )	
Release area 1	1424
Release area 2	1410
Release area 3	1518
Total released volume	4352

the maximum flow heights and maximum velocities were reported for each point. Also in the Tresenda case, a Gamma distribution had the best fit to the output parameters. Figures 7 and 8 show the results for the maximum flow height and velocities calculated in points A and B.

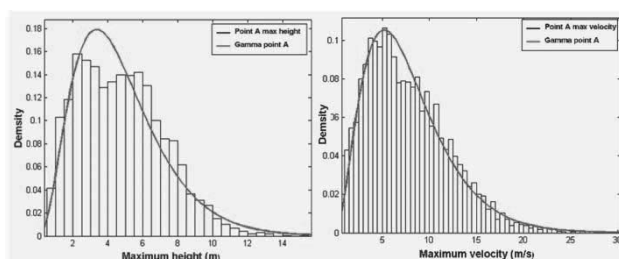


Figure 7. Gamma distribution fitted to the maximum height (left) and velocities (right) values obtained in point A.

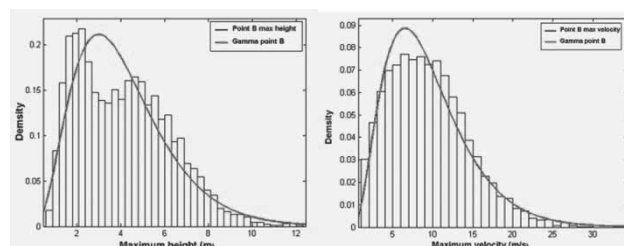


Figure 8. Gamma distribution fitted to the maximum height (left) and velocities (right) values obtained in point B.

The results for the Tresenda case study were compared with events in 1983 and 2002. In these incidents, only information regarding the flow heights was available (no velocities were estimated for these events). In the Tresenda case, the mean value of the flow height in point A is overestimated compared to the actual event while point B has a lower mean value than the observed event. In the Tresenda case the simulated values are closer to the actual events than in the Faucon case. This can be possibly attributed to the potential of the Voellmy rheology to model consistently these types of events.

## 5 CONCLUSIONS

The Monte Carlo method offers the advantage of modelling the probability distributions of the intensity parameters from run-out simulations. Of course, the reliability of the fitted probability density functions for the input parameters strongly depends on the completeness and accuracy of the original back-analyses included in the collected database. Another limitation of this study is that the estimated probabilities do not explicitly

account for the temporality of the phenomena. For future assessments it is recommended that run-out simulations using a stochastic approach become a routine practice in order to produce adequate future hazard scenarios and quantify the uncertainty due to the input parameters. This will result in intensity maps that are easier to interpret for end users, especially within a probabilistic framework for landslide mitigation.

## 6 ACKNOWLEDGEMENTS

The authors would like to thank Jean Philippe Malet and Alexandre Remaître from the University of Strasbourg for the data of the Faucon catchment.

## 7 REFERENCES

- Begueria S., van Asch Th.W.J., Malet J.-P., Grondahl S. 2009. A GIS-based numerical model for simulating the kinematics of mud and debris flows over complex terrain. *Nat. Hazards and Earth Syst. Sci.*, 9, pp. 1897-1909.
- Cancelli A. and Nova R. 1985. Landslides in soil debris cover triggered by rainstorms in Valtellina (Central Alps – Italy). In: Proceedings of 4th International Conference and Field Workshop on Landslides. The Japan Geological Society, Tokyo, pp. 267–272.
- Crosta G.B., Dal Negro P., Fratini P. 2003. Soil slips and debris flows on terraced slopes. *Nat. Hazards and Earth Syst. Sci.*, 3, 31- 42.
- Guzzetti F., Crosta G., Marchetti M., Reichenbach P. 1992. Debris flows triggered by the July, 17–19, 1987 storm in the Valtellina area (Northern Italy). International Symposium Interpraevent 1992, Bern, Switzerland, pp. 193-203
- Hungr O. and McDougall S. 2009. Two numerical models for landslide dynamic analysis. *Computers & Geosciences* 35, pp. 978–992.
- Hürlimann M., Medina V., Bateman A., Copons R., Altimir J. 2007. Comparison of different techniques to analyse the mobility of debris flows during hazard assessment-Case study in La Comella catchment, Andorra. In Chen & Majors (eds.) Debris-Flow Hazard Mitigation :Mechanics, Prediction and Assessment. Millpress, Netherlands, pp. 411-422.
- Karssenber, D., Burrough, P. A., Sluiter, R., De Jong, K. 2001. The PCRaster software and course materials for teaching numerical modelling in the environmental sciences. *Transactions in GIS*, 5(2), pp. 99-110.
- Metropolis N. 1987. "The beginning of the Monte Carlo method". Los Alamos Science (1987 Special Issue dedicated to Stanislaw Ulam): 125–130.
- Remaître A., Malet J.-P., Maquaire O. 2005. Morphology and sedimentology of a complex debris flow in a clay-shale basin. *Earth Surf. Process. Landforms* 30 pp.339-348.
- Remaître A. 2006. Morphologie et dynamique des laves torrentielles: Applications aux torrents des Terres Noires du bassin de Barcelonnette (Alpes du Sud). Ph.D. thesis.
- Remaître A., van Asch Th.W.J., Malet J.-P., Maquaire O. 2008. Influence of check dams on debris flow run-out intensity. *Nat. Hazards Earth Syst. Sci.* 8, pp. 1403-1416.
- Remaître A., Malet J.-P., Maquaire O. 2009. Sediment budget and morphology of the 2003 Faucon debris flow (South French Alps): scouring and channel-shaping processes. Proc. Landslide Processes: from geomorphological mapping to dynamic modelling, pp. 75-80.

# The Challenge of the Slope Failure Problem and Its Remedial Considerations at Mileage 39km, Mt. Ali Road, Taiwan

Le défi du problème du glissement de pente et des dispositions correctives apportées, au kilomètre 39, de la route Mt. Ali Road, à Taïwan

Chang M., Huang R.  
*National Yunlin University of Sci. & Tech., Taiwan*

**ABSTRACT:** Mt. Ali Road is a main scenic route to Alishan National Scenic Area and Yushan National Park in the middle of Taiwan. At Mileage 39Km, the downslope side of the road consists of a 200m deep 60° angle bare cliff with a creek passing around the slope's toe. Despite complex geologic conditions, the underlying slope materials appeared competent for about 20 years after the road opening. In 1999, however, a severe earthquake (Chi-Chi,  $M_w = 7.6$ ) hit central Taiwan and caused numerous landslips in the mountain range of the island. Although no obvious damages to the road were observed after the time of shaking, the geologic setting of the site was deteriorating. During the attack of Typhoon Nari in 2001, the first serious effect on the road appeared and caused several parallel cracks along the alignment. Remedial work was initiated. Nonetheless, a loss of road base during the monsoon season next year had called for a stop of the work. The remedial plan was revised and implemented, but failed again due to Typhoons Talim and Longwang in 2005. The current repair works have been completed and generally show no major signs of slope distress. In view of repair histories and the geologic setting, this paper discusses the concerns and challenges for long-term stability of slopes at the site.

**RÉSUMÉ :** Mt. Ali Road est une route principale pittoresque qui mène à l'Alishan National Scenic Area et au parc national de Yushan, au centre de Taïwan. Au kilomètre 39, le côté aval de la route est formé d'une falaise nue de 200m de haut, inclinée à 60° avec un ruisseau la bordant en pied de pente. En dépit des conditions géologiques complexes, les matériaux de la pente se sont bien comportés au cours des 20 années l'ouverture de la route. Cependant, un violent tremblement de terre (Chi-Chi,  $M_w = 7,6$ ) a frappé le centre de Taïwan en 1999, et a causé de nombreux glissements de terrain dans la partie montagneuse de l'île. Bien qu'aucun dommage apparent n'ait été détecté après la secousse, la situation géologique du site s'est détériorée. Les premiers effets conséquents ont pu être observés lors du typhon Nari en 2001, plusieurs fissures parallèles étant apparues le long du tracé. Un projet de confortement fut entrepris. Malgré cela, une rupture de la couche de fondation, de la route l'année suivante pendant la saison des moussons a nécessité un arrêt temporaire des travaux. Le projet fut révisé et remis en œuvre, mais a dû être à nouveau arrêté en raison des typhons Talim et Longwang en 2005. Les réparations sont aujourd'hui terminées, et la pente ne montre en général aucun signe de désordre. Compte tenu de l'historique des réparations et de la situation géologique, ce document aborde les préoccupations et les défis concernant la stabilité à long terme des pentes du site.

**KEYWORDS:** slope failure, repair works, landslide prevention and mitigation, slope stability, case histories, Mt. Ali Road.

## 1 GENERAL

Mt. Ali Road is a main scenic route to Alishan National Scenic Area and Yushan National Park in the middle of Taiwan. As entering into the hilly terrain of central mountain range of the island, the road starts climbing up along the side of slopes for a distance of about 5Km until it reaches a hill top with an elevation of 460m MSL at the mileage of 39Km, where the road levels off and makes a loop around the hill. The downslope side of the road at this location consists of a 200m deep 60° angle bare cliff with a creek passing around the slope's toe.

Although both regional and local geology generally show a complex geologic structure at the site, the subgrade materials and underlying rock appeared competent for about 20 years since the road's opening. Figure 1 shows the regional geology of the area, and Figure 2 illustrates the geologic profile of the road section and its adjacent slopes.

On September 21, 1999, a severe earthquake (Chi-Chi,  $M_w = 7.6$ ) hit central Taiwan and caused numerous landslips or slope failures in the mountain range of the island, as indicated in Figure 3. Based on studies by National Center for Researches on Earthquake Engineering (NCREE 2000), approximately 1500-2000 landslides were directly induced by the earthquake. Although the shaking did not have immediate impacts at the site, the condition of the road and its adjacent side slopes appears to be deteriorating.

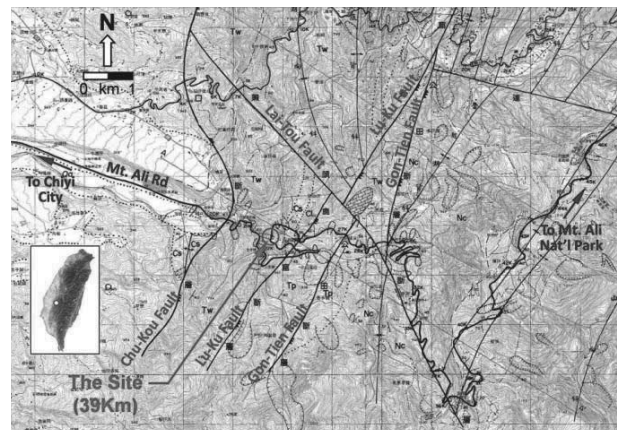


Figure 1. Regional geology of the area (Liu & Tseng 2000).

The monsoon season normally starts from early April to the end of September in the island. Annual precipitation is around 2150mm (Sinica 1999). Figure 4 shows accumulated rainfalls of the site in 2001 & 2005 were 4700mm & 4600mm, respectively. As will be discussed later, the abundance of rainfalls appeared to have contributed to the failures of slopes along the Mileage 39Km in 2001 & 2005.

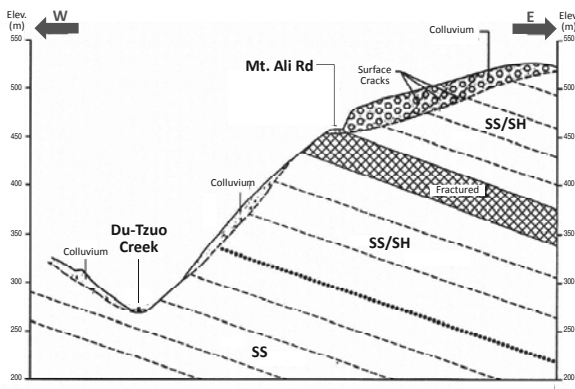


Figure 2. Geologic cross-section at the 39Km project site (CECI 2005).

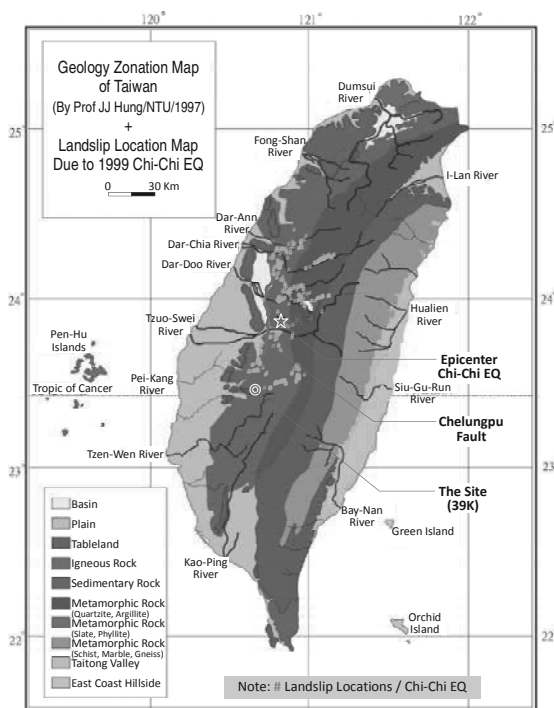


Figure 3. Locations of landslides due to Chi-Chi EQ (NCKU 2000).

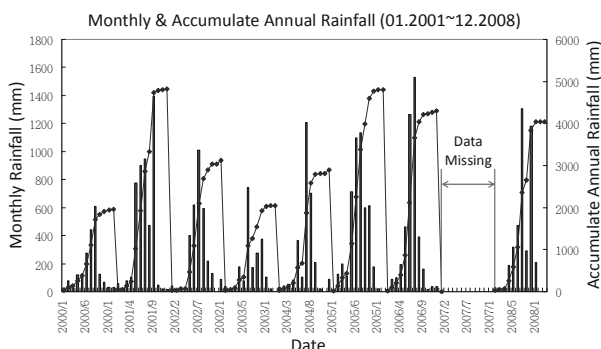


Figure 4. Monthly and accumulated rainfalls at the site (Peng 2009).

## 2 SLOPE FAILURE & ROAD REPAIR HISTORIES

Prior to failures of the subject slopes, a severe typhoon (Herb) with a rainfall of about 2000mm attacked Taiwan in 1996 and resulted in significant damages in central region of the island. Based on an official investigation report, the event had caused 91 landslides and 57 losses of road base along the entire length of

Mt. Ali Road (DOT 1996). However, the subject road and its slopes were only experienced very minor effects due to this typhoon and had no influence on the slope stability. Three years after the severe typhoon incident, a damaging earthquake (Chi-Chi, 1999) occurred. As mentioned previously, the earthquake had resulted in numerous landslips in central Taiwan. Although the site and its adjacent slopes appeared to be competent during the shaking, the in-situ earthen materials were apparently weakened and deteriorating due to the earthquake. In subsequent years, signs of slope distress and movement became obvious, and some key events and associated repair histories are discussed in the following sections.

### 2.1 2001 Typhoon Nari

Typhoon Nari swiped Taiwan in September, 2001, and brought about 1400mm precipitation to the site, 4700mm for the entire year. This had been the largest rainfall event since the attack of Typhoon Herb in 1996. The site had experienced a series of parallel cracks of 10~80cm in width along the road alignment which called for a temporary shutdown for one lane of the road. A remedial action was subsequently taken by District V of Directorate General of Highways (DGH), Taiwan, that included the repair of surface cracks by a new AC paving and a planning on reconstruction of the road section by conventional retaining structure on the downhill side of the road.

### 2.2 2002 monsoon rainfalls

As the reconstruction work for the retaining structure was about to start in 8 months after Typhoon Nari, a failure in downslope of the road occurred (Figure 5). The failure was apparently due to the intense rainfall during the monsoon season. Recorded accumulated precipitation was greater than 1000mm within the two months prior to the failure.



Figure 5. Slope failure at Mileage 39Km due to 2002 monsoon rainfalls.

The original construction work had to be terminated and re-planned. In view of steep downslope and insufficient road width, DGH had once considered remedying the problem by cutting back and flattening the upslope. However, the plan was turned down due to unsuccessful negotiations with local ownerships of lands adjacent to the road.

The remedial plan was finally decided to limit within the extent of the road owned by DGH. Considerations of the road redesign had included a section of box-type concrete structure, as shown in Figure 6, which would provide a design with enough road width, structure rigidity, and relatively light-weight. The box structure was secured to the native ground by two rows of ground anchors, each of which with a total length of 35m, a horizontal spacing of 20m, and an anchor force of 45T. The

base of the box structure was also fixed to the ground by a series of mini piles of 16m in length.  
Figure 7 shows the rebuilt road section after completion of the remedial works.

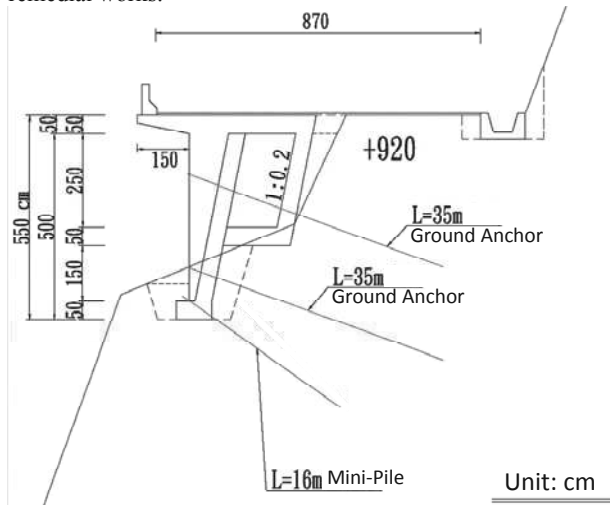


Figure 6. Box-type structure design for road section at Mileage 39Km.

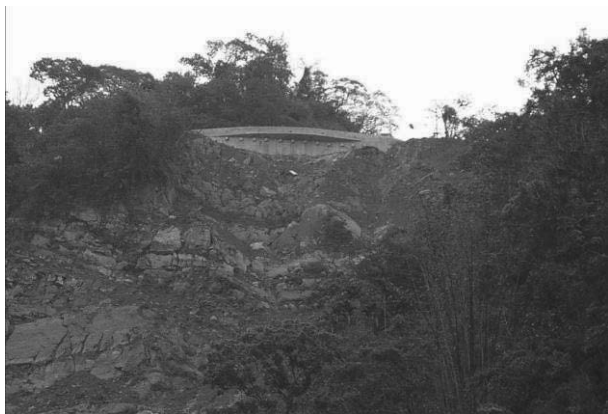


Figure 7. Completion of box-type structure at Mileage 39Km.

### 2.3 2005 Typhoons Talim & Longwang

The new road section appeared to be in good shape for the next 1-1/2 years until mid of 2005 when the precipitation started to reach another historic peak.



Figure 8. Failure of box-structure road section due to Typhoon Talim.

In late August of 2005, a severe Typhoon Talim slammed Taiwan. By considering a series of heavy rainfalls in the previous two months, the accumulated precipitation of the year at the site had exceeded 4000mm. As a result, the box-type structure finally gave up and the entire road section of about 100m in length fell into the valley (Figure 8).

Post-failure investigation had revealed that the loss of entire road section was due to the downslope movement of the uphill slope mass which pushed the box-type structure, tore down the ground anchor tendons, and sheared off the mini piles.

Emergency action was implemented right after the failure by constructing a temporary road to the uphill side and installing I-beams for the downhill support (Figure 9) in order to maintain the local traffic (DGH 2005).



Figure 9. Emergency repair of the road section due to Typhoon Talim.

In late September, 2005, the emergency measure failed again one month after the attack of Typhoon Longwang. The temporary road lost 5m of its road width. Site reconnaissance showed significant tension cracks at the crest of uphill slope.

District V of DGH had to launch another remedial measure to mitigate potential impacts on the road section in the future. The plan had considered mostly the upslope protections that included filling of tension cracks, rechanneling surface drainage, installing subsurface horizontal drains, and surface vegetation, etc. Figure 10 shows the completion of upslope remedial works after Typhoon Longwang.



Figure 10. Completion of upslope remedial works at Mileage 39Km.

### 3 FIELD MONITORING & STABILITY ANALYSIS

In the following few years after Typhoon Longwang, the annual precipitation of the site was decreasing. To date the road section and its adjacent slopes appear competent for maintaining local traffic. However, data from subsurface exploration and in-situ monitoring during the previous remedial works showed signs of slope instability at the site (LEC 2006). Figure 11 indicates potential sliding masses (slip surfaces) in the upslope that would have impact on the Mileage 39Km road section. The downhill side slope was not improved during the remedial works and its surface was bared with remains of previous slides, as shown in Figure 12.

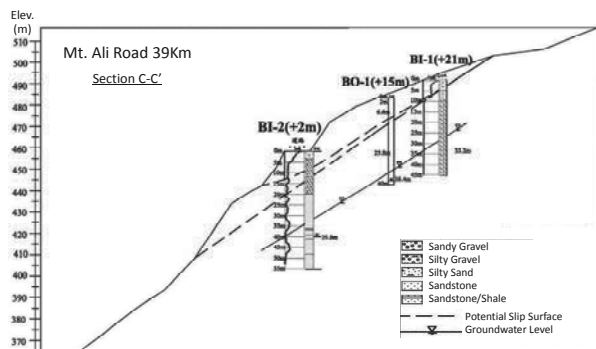


Figure 11. Material strata and potential slip surfaces at Mileage 39Km.



Figure 12. Downhill slope of Mt. Ali road section at Mileage 39Km.

### 4 CONCLUSIONS

In view of past failure incidents and associated remedial works, the road section at Mileage 39Km and the alongside slopes are still at perceivable risks of a potential slide. The signs of slope instability appeared to be pronounced since the attack of 1999 Chi-Chi Earthquake, which was believed that the shaking had weakened the underlying geologic units and thus accelerated the weathering process of materials at the site.

Conclusions on causes of slope instability and measures of slope mitigation for this site can be drawn and discussed below.

#### 4.1 Potential & triggering factors

From a retrospective stand point, the factors that had caused instabilities of slopes at Mileage 39Km road section could be attributed to the following:

- A complex geologic structure at the site (Figure 1) where the underlying geologic units are generally fractured.
- The 1999 earthquake shaking that had weakened underlying geologic structure and enhanced deterioration process of the materials.
- The steep downhill slope geometry (60° angle & 200m deep).

- The potential uphill sliding masses (Figure 11).
- The unprotected downhill slope surface that enhanced rainfall infiltration and surface runoff erosion.
- A long-term erosion of slope toe by Do-Tzuo Creek (Figure 12).
- The abundance of groundwater that was observed seeping out of the surface of downhill slope.
- The prolonged and intense rainfalls that infiltrated, saturated and softened the slope materials, increased the perched water level, and directly triggered the slips.

#### 4.2 Long-term stability considerations

The previous remedial works at site after Typhoon Longwang has been successful to date. However, the work details were mainly for improvements on surface protection of the upslope. From the analysis above on causes of slope failure, the current remedial activities would be helpful to mitigate the infiltration of rainfall and possibly prevent the triggering of a slide in the upslope. It would not be useful, however, for the stability of downslope, and would not either remove the concerns (i.e., potential factors) above that could be detrimental to the long-term stability of the road section and slopes at the site.

In accordance, more stability considerations and measures need to be taken to ensure the safety of the road section, and to maintain the transportation function of Mt. Ali Road as well. The considerations might include:

- Removal of potential sliding masses or reducing slope angle in the uphill.
  - Downhill slope protection including vegetation and drainage installations.
  - Road base and adjacent slopes strengthening by piling and anchoring.
  - Subsurface drainage installations in uphill & downhill slopes.
  - In-situ monitoring and warning system installation.
- The above measures appear to be sound from an engineering standpoint. However, the total cost and time for all of the above works would be extremely high, in view of difficulties in access for construction and generally incompetent subsurface materials at the site. Another option would appear more favorable as to reroute the Mt. Ali Road away from this difficult section.

### 5 ACKNOWLEDGEMENTS

The authors would like to thank District V, Directorate General of Highways, Taiwan, for providing documents for this study.

### 6 REFERENCES

- China Engineering Consultants, Inc. (CECI). 2005. *Engineering planning and budget estimate for slope mitigation at Mileage 39Km, Mt. Ali Road, Taiwan*. The 5<sup>th</sup> District, DGH/DOT, Taiwan.
- Department of Transportation (DOC). 1996. *Taiwan Province Government. 1996. Documentary of Typhoon Herb*.
- Directorate General of Highway (DGH). Taiwan. 2005. *Emergency plan for mitigation of slope failure at Mileage 39Km, Mt. Ali Road due to Typhoon Talim*.
- Land Engineering Consultants, Co. (LEC). 2006. *Report on land survey, subsurface exploration, and in-situ monitoring for slope failure at Mileage 39Km, Mt. Ali Road, Taiwan*.
- Liu S.D. and Tseng J.J. 2000. *Investigation report on geology and landslides along Mt. Ali Road, Taiwan*. Central Geology Survey, MOE, Taiwan.
- National Center for Researches on Earthquake Engineering (NCREE). 2000. *Investigation report on geotechnical engineering damages due to September 21, 1999, Chi-Chi Earthquake*. Taipei, Taiwan.
- Peng K.Y. 2009. *A study on groundwater fluctuation and geology structure through rainfall and well pumping*. MS thesis, NYUST, Taiwan.
- Sinica, Taiwan, ROC. 1999. <http://webgis.sinica.edu.tw/epa/epa.html>.



# Downstream Frontal Velocity Reduction Resulting from Baffles

Effets des déflecteurs dans la réduction des vitesses frontales dans un écoulement descendant.

Choi C.E., Ng C.W.W.

*Department of Civil and Environmental Engineering, Hong Kong University of Science and Technology*

Kwan J.S.H., Shiu H.Y.K., Ho K.K.S., Koo R.C.H.

*Geotechnical Engineering Office, Civil Engineering and Development Department, HKSAR*

**ABSTRACT:** Debris flows occur in mountainous regions during rainfall and can result in disastrous consequences to downstream facilities if appropriate mitigation measures are not taken. Common mitigation measures include flow impeding structures within the flow path. An array of baffles is a type of flow impeding structure used primarily to reduce the mobility of landslide debris. However, they are usually designed on an empirical and prescriptive basis and the degree of impedance resulting from an array of debris flow baffles is not well understood. This paper presents a series of systematic flume tests examining the influence of baffle row number on reduction of debris frontal velocity. Photoconductive sensors installed at the base of the flume channel have been used to measure the average frontal velocity of the debris flow downstream of the array of baffles. Results show that one row is ineffective in reducing the debris frontal velocity. Two to three rows of baffles exhibit notable frontal velocity reduction.

**RÉSUMÉ :** Les coulées de granulaires représentent un risque majeur en régions montagneuses en période de fortes pluies et peuvent avoir des conséquences désastreuses pour les installations en aval si des mesures appropriées ne sont prises. De telles mesures comprennent la construction de déflecteurs à matériaux sur le parcours des coulées avec pour objectif principal est de réduire la mobilité de la masse granulaire en mouvement. Cependant, la construction de ces déflecteurs repose sur des hypothèses empiriques. La contribution exacte des déflecteur est mal comprise à l'heure actuelle et elle est difficile à évaluer précisément. Cet article présente une série de tests expérimentaux ayant pour objectif d'évaluer l'influence de l'augmentation du nombre de déflecteurs sur la réduction de la vitesse frontale de la coulée granulaire. Des capteurs photoconducteurs placés dans le fond du canal de test ont été utilisés pour mesurer la vitesse frontale moyenne des grains en aval des déflecteurs installées. Les résultats révèlent qu'au moins deux à trois rangées de déflecteurs sont nécessaires pour avoir une réduction significative de la vitesse frontale de l'écoulement.

**KEYWORDS:** physical modelling; flume; debris flow; baffles; landslide mitigation measures

## 1 INTRODUCTION

Ground mass detached from landslide source travels down hillside under gravitational actions. Landslide debris can have high mobility and can result in serious consequences to downstream facilities. Velocity of debris fronts can reach up to 30 m/s (Costa 1984; Rickenmann 1999) with peak discharges several times greater than floods occurring in the same catchment (Hung et al. 1984). In order to mitigate this hazardous phenomenon, debris-resisting structures are often used as defence measures to retain landslide debris and impede debris mobility (Mizuyama 2008). Defence measures may include the rigid and flexible barriers (Wendeler et al. 2007), levees, slit dams (Watanabe et al. 1980), and arrays of baffles.

The primary function of baffles is to impede the flow pattern such that flow slows down after it passes through the baffles (USFHA 2006). Baffles can be installed upstream of barriers to reduce the impact resistance required by the barriers and to promote lateral dispersion of flow in deposition basins (Cosenza et al. 2006). Figure 1 shows rectangular gabion baffles installed in front of a rigid barrier in Lantau Island, Hong Kong. Baffles are usually designed by empirical and prescriptive methods and their fundamental impedance capacity is not well understood.

Similar studies on snow avalanche impeding obstacles report that an individual row of obstacles can dissipate energy by 20% and an additional row contributes to 10% extra energy dissipation (Hakanordottir et al. 2001). Salm (1987) reports that the degree of impedance can be estimated based on the consideration of the cross-sectional blockage over the channel area. However, the above criteria are applicable only for snow avalanches because the flow regimes characterising avalanche and debris flow are quite different (see Sect. 2.1 for further

details). This study aims to examine the reduction of downstream debris frontal velocity resulting from an array of baffles. The influence of the number of staggered rows of baffles on downstream debris frontal velocity is investigated.



Figure 1. Array of baffles installed in front of a rigid barrier in Lantau Island, Hong Kong

## 2 METHODOLOGY

### 2.1 Scaling

Three types of similitude are required for modelling debris flow-baffle interaction; they are (i) geometric similarity, (ii) kinematic similarity, and (iii) dynamic similarity. For simplicity, geometric similarity is achieved by normalising



model dimension by the flume channel width and debris flow depth (more details presented in Sect. 3). Kinematic similarity describes the impedance resulting from baffle interaction which is unknown and constitutes the objective of this study. Dynamic similarity is attained by adopting the Froude number,  $F_r$ , which governs the behaviour of gravity-driven flows in open channels. The  $F_r$  number is the ratio of inertial forces to the gravitational forces and is given as follows:

$$F_r = \frac{v}{\sqrt{gh}} \quad (1)$$

where  $v$  = frontal velocity (m/s),  $g$  = gravitational acceleration ( $\text{m/s}^2$ ), and  $h$  = debris flow depth (m).

Debris flow can be characterised with approaching  $F_r$  which ranges from 0 to 4.5 (Arrattano et al. 1997, Hubl et al. 2009) based on field observations. An  $F_r \approx 3$  is adopted for characterising the approaching flow in this study. This corresponds to debris flow event with an approaching velocity of about 10 m/s and flow depth of about 1 m. Details of the scaling process and control test are discussed by Ng et al. (2012).

## 2.2 Flume model

Further to flume experimental studies of debris flow mechanisms (Law et al. 2008, Zhou et al. 2009) at the Hong Kong University of Science and Technology (HKUST), a new five metre long rectangular flume (see Figure 2) with a channel base width of 0.2 m and height of side walls of 0.5 m was developed for this study. Based on calibration exercises, an inclination angle of  $26^\circ$  is used (Ng et al. 2012) to match an  $F_r \approx 3$ . Instrumentation and lighting are mounted on the external frame surrounding the flume. Debris material is contained in a storage container located at the most upstream end of the flume. The storage container has a maximum storage volume of  $0.08 \text{ m}^3$  and is equipped with a spring-loaded door secured by a magnetic lock. At the most downstream end of the flume is a deposition container for collecting debris materials.

## 2.3 Instrumentation

Ten photoconductive sensors are installed throughout the base of the flume at intervals of 0.5 m. When debris passes over the sensor, a signal is sent to the data logger at that particular instant. With the known spacing and difference in time at which signals are received between two sensors, the average debris frontal velocity can be deduced along the entire transportation zone. The uncertainty of photoconductive sensors is estimated to be  $\pm 0.05 \text{ m/s}$ .

Laser sensors are mounted over the top of the channel to capture centreline flow depths at specific locations along the flume. Furthermore, high speed cameras are installed above and at the side of the flume to capture the flow dynamics during interaction with the array of baffles. The full resolution capacity of the cameras is  $1024 \times 1024$  pixels and with a potential frequency of 759 frames per second.

## 3 TEST PROGRAMME

A series of four flume experiments are presented in this paper. The details of experiments are given in Table 1. The four experiments consist of one control experiment without baffles in the channel to serve as reference and the three baffle configurations which vary in number of staggered rows (one to three rows). All experiments have been repeated to ensure repeatability. For simplicity, a single baffle height of 0.75 times the approach debris flow depth ( $h = 80 \text{ mm}$ ) is adopted for all configurations. Details on the approach debris flow depth are discussed by Ng et al. (2012). The degree of transverse

blockage is selected as 30% in this study. The degree of transverse blockage is defined as the sum of obstruction in the transverse direction divided by the width of the flume channel. According to Ikeya and Uehara (1980) and Watanabe et al. (1980), slit dams function primarily to retain flow material through the mechanism of arching, while baffles primarily impeded the flow mobility. Slit dams entail an equivalent degree of transverse blockage of greater than 40%, therefore the degree of transverse blockage selected in this study (i.e. 30%) is appropriate for modelling debris flow baffles.

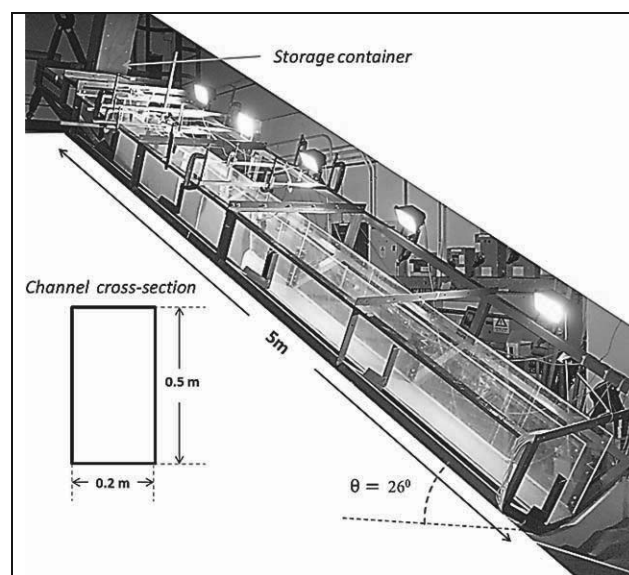


Figure 2. Flume model setup

Table 1. Test programme

Test ID	Baffle height (h)	Transverse blockage (%)	Number of rows
H0 R1	0	0	0
H075 R1	0.75h	30	1
H075 R2	0.75h	30	2
H075 R3	0.75h	30	3

$h$ : approach flow depth (80 mm)

The arrangement of full and half sized baffles used to create a staggered formation as shown in Fig. 3. The dimensions of full baffles are  $20 \text{ mm} \times 20 \text{ mm} \times 60 \text{ mm}$ , and the dimensions of half baffles are  $20 \text{ mm} \times 10 \text{ mm} \times 60 \text{ mm}$ . The spacing between successive rows is selected to be 50 mm or 0.25 times the width of the flume channel. This spacing is selected based on recommendations by Hakonardottir et al. (2001) that baffles should be placed as close together as possible to promote the deflection and interception of discharge from the slits of the previous row.

## 4 EXPERIMENTAL RESULTS

### 5.1 Flow dynamics

As a flow front impacts an array of baffles, streams of debris material discharge through the slits and part of debris also runs up along the upstream vertical face of the baffles simultaneously. The debris run up eventually exceeds the baffle height and some materials become airborne. Synchronously, material is deposited upstream of the baffles. The upstream flow eventually rides over the deposited material and cascades over the array of baffles. There are essentially two components of downstream discharge, namely discharge through and overtop of the baffles, both of which combine and propagate downslope after the landing of overflow trajectory.

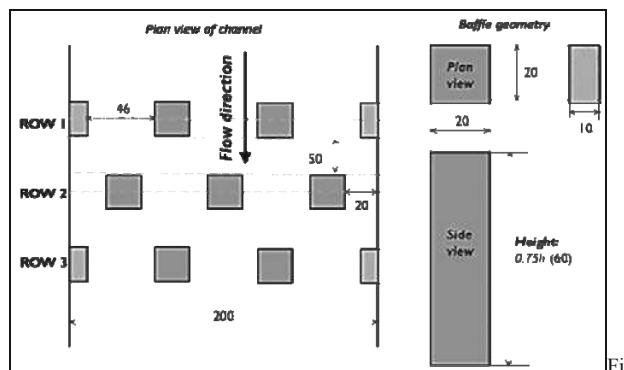


Figure 3. Baffle arrangement and dimensions (all dimensions in mm)

### 5.2 Frontal velocity

The measured debris frontal velocity profiles of different tests are compared and shown in Fig. 4. The measured debris frontal velocity is plotted against normalised distance travelled along the transportation zone ( $N_d$ ), which is the ratio of distance travelled by the debris front along the 5 meter flume. The debris flow direction is from left to right on x-axis and the location of the baffles along the transportation zone is shown as a vertical dashed line.

The frontal debris velocity profile of the control test (H0\_R0) is shown as a reference for comparison purposes. The debris frontal velocity of the control test rapidly increases upon release from the storage container. At  $N_d = 0.2$ , a steady debris flow profile develops, beyond  $N_d = 0.6$ , the debris frontal velocity begins to decrease. A similar debris velocity profile is observed in the experiment of one-row baffle test (H075\_R1). However, for the two-row and three-row baffle tests, a prominent debris velocity reduction at the immediate downstream of the baffle groups was observed. The velocity profile rapidly decreases to less than 2 m/s after which it gradually increases beyond  $N_d = 0.3$ .

Results show that one row of baffles (H075\_R1) exhibits negligible reduction in frontal debris velocity and the propagation of the front is similar to unobstructed flow (H0\_R0). Obvious reduction in debris frontal velocity is observed in the test with two rows of baffles (H075\_R2) at the location immediately downstream of the baffle group. This may be attributed to the second row of staggered baffles intercepting the discharge from the slits of the first row which dissipates energy by disrupting streamlines of the flow (USFHA 2006). The provision of an additional row of baffles (i.e. the third row; test H075\_R3 refers) exhibits a frontal debris velocity reduction of 47% at  $N_d = 0.3$  relative to the control experiment, whereas two rows of baffles (H075\_R2) only exhibits 30% reduction of frontal debris velocity relative to the control experiment at  $N_d = 0.3$ . Moreover, the higher frontal velocity reduction may be attributed to an additional third row of baffles which intercepts discharge from the second row and disrupts streamlines. Beyond  $N_d = 0.4$ , two rows (H075\_R2) and three rows (H075\_R3) baffle groups exhibit a similar gradual increase in frontal debris velocities. An increase in frontal debris velocities may be attributed to subsequent excessive overflow of material due to the use of shorter baffles (0.75 times the approach flow depth) in this study. Overflow of debris in test H075\_R1 is captured from high speed imagery at the side of the flume model and is shown in Fig. 5. Overflow does not experience impedance and launches downstream (Barbolini et al. 2009) to increase the momentum and thus the frontal velocity of the flow. Overflow is hazardous particularly in situations where its trajectory is not easily predicted. Johannesson (2001) surveyed a torrent which had been deflected by a dam at Flateyri in north-western Iceland and observed that the deflected stream came to rest 100 m further downslope than the un-deflected part. The mechanism of overflow appears to be significant and results from this study require further interpretation.

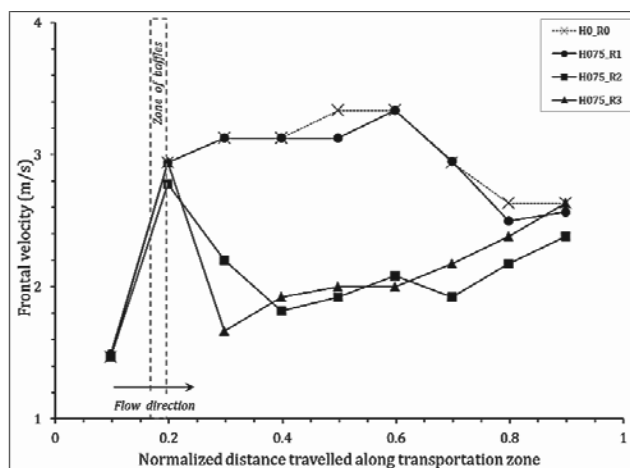


Figure 4. Comparison of measured frontal velocity

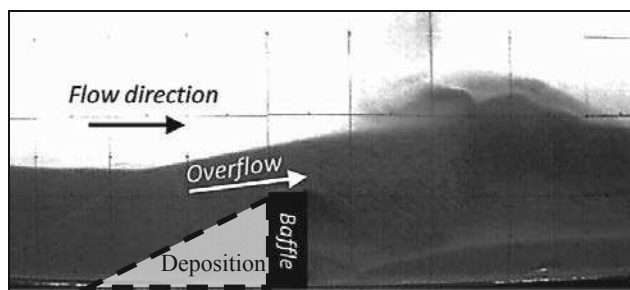


Figure 5. Observed overflow dynamics (test H075\_R1)

### 5.3 Preliminary Particle Image Velocimetry (PIV) analysis

A preliminary Particle Image Velocimetry (PIV) analysis has been carried out to investigate the flow dynamics and quantify the flow velocity by interpreting the results of the flume test using the Particle Image Velocimetry package (geoPIV) developed by White et al (2003). This package is developed based on close-range photogrammetry techniques capable of tracing movements of soil grains captured in high-resolution images. It produces displacement and velocity vectors of the soil grains.

Typical flume test results for three rows of baffles produced by geoPIV are presented in Figure 6. It shows the flow dynamics of the debris upon hitting the baffles. Details of debris run-up against baffles, deposition behind baffles and filling up of the baffle zone and the subsequent overflowing from the crest of baffles were captured. In general, the preliminary results of the calculated velocity vectors by PIV method are consistent with the measured debris frontal velocity by the instrumented photo-sensors. Further PIV analysis will be carried out in the next stage of interpretation of the experimental study.

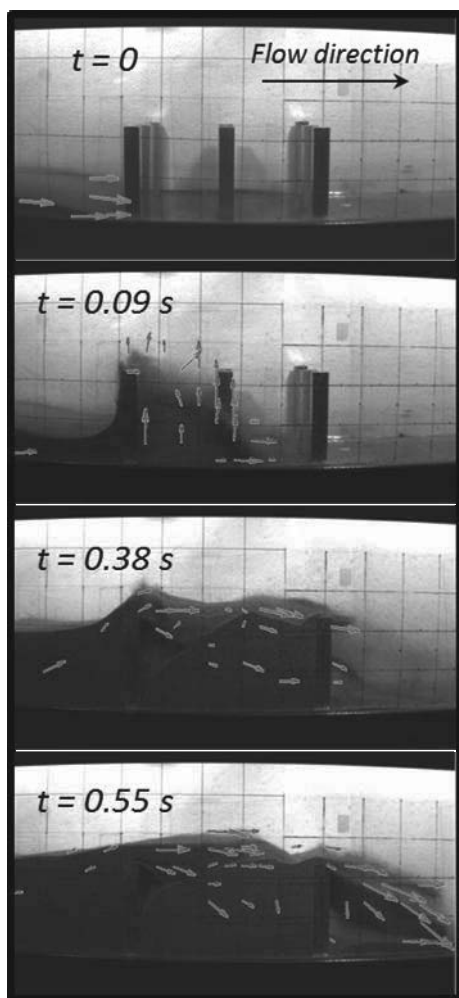


Figure 6. Preliminary results using PIV method

## 5 CONCLUSIONS

A series of systematic flume experiments modelling debris-baffle interaction has been conducted. The influence of increasing the row number on frontal debris velocity is presented and some preliminary conclusions are drawn as follows:

1. One row of baffles exhibits negligible reduction of frontal debris velocity compared to unobstructed channelised flow.
2. Two and three rows of baffles result in reduction of frontal debris velocities immediately at the downstream from the array of baffles. Increasing the number of staggered rows of baffles disrupts streamlines and intercepts discharge from slits of the previous row of baffles which dissipates energy and reduces the frontal debris velocity.
3. Overflow resulting from the use of baffles may result in subsequent increase in frontal velocity downstream and warrants further studies.

## 6 ACKNOWLEDGEMENTS

This paper is published with the permission of the Head of the Geotechnical Engineering Office (GEO) and the Director of Civil Engineering and Development, Government of the Hong Kong SAR, China. Also the financial supports from GEO and HKUST9/CRF/09 are acknowledged.

## 7 REFERENCES

- Arattano, M., Deganutti, A. M. and Marchi, L. 1997. Debris flow monitoring activities in an instrumented watershed on the Italian Alps. *Proceedings of the 1st ASCE International Conference on Debris-Flow Hazards Mitigation: Mechanics, Prediction and Assessment*, San Francisco, California, 506-515.
- Barbolini, M., Domaas, U., Faug, T., Gauer, P., Hakonardottir, K.M., Harbitz, C.B., Issler, D., Johannesson, T., Lied, K., Naaim, M., Naaim Bouvet, F. and Rammer, L. 2009. *The design of avalanche protection dams recent practical and theoretical developments*. European Commission, Luxembourg, 212 p.
- Cosenza, E., Cozzolino, L., Pianese, D., Fabbrocino, G., and Acanfora, M. 2006. Concrete structures for mitigation of debris-flow hazard in the Montoro Inferiore Area, Southern Italy. *Proceedings of 2<sup>nd</sup> International Congress*, Naples, Italy, 12 p.
- Costa, J.E., 1984. Physical geomorphology of debris flows. *Costa, J.E.; Fleischer, P.J. (eds.): Developments and Applications of Geomorphology*. Berlin: Springer, 268-317.
- Hákonardóttir, K. M., Jóhannesson, T., Tiefenbacher, F. and Kern, M. 2001. *A laboratory Study of the Retarding Effect of Braking Mounds in 3, 6 and 9m Long Chutes*, Reykjavik, Veðurstofa Íslands, Report No. 01007.
- Hubl, J., Suda, J., Proske, D., Kaitna, R. and Scheidl, C. 2009. Debris flow impact estimation. *Proceedings of International Symposium on Water Management and Hydraulic Engineering*, Ohrid, Macedonia, 137-148.
- Hungr, O., Morgan, G.C. and Kellerhals, R. 1984. Quantitative analysis of debris flow torrent hazards for design of remedial measures. *Can. Geotechnical Journal*, 21, 663-677.
- Ikeya, H. and Uehara, S. 1980. Experimental study about the sediment control of slit sabo dams. *Journal of the Japan Erosion Control Engineering Society*, 114, 37-44 (in Japanese).
- Jóhannesson, T. 2001. Run-up of two avalanches on the deflecting dams at Flateyri, northwestern Iceland. *Annals of Glaciology*, 32(1), 350-354.
- Law, R.P.H., Zhou, G.D., Chan, Y.M. and Ng, C.W.W. 2007. Investigations of fundamental mechanisms of dry granular debris flow. *Proceedings of the 16<sup>th</sup> Southeast Asia Geotechnical Conference*, Malaysia.
- Law, P.H. 2008. *Investigations of Mobility and Impact Behaviour of Granular Flows*. MPhil Thesis, The Hong Kong University of Science and Technology, Hong Kong.
- Mizuyama, T. 2008. Structural countermeasures for debris flow disasters. *International Journal of Erosion Control Engineering* 1(2), 38-43.
- Ng, C.W.W., Choi, C.E., Kwan, J.H.S., Ho, K.S.S and Koo, R.C.H. 2012. Flume modelling of debris resisting baffles. *Proceedings of AGS Seminar on Natural Terrain Hazard Mitigation Measures 2012*, Hong Kong, 16-21.
- Rickenmann, D. 1999. Empirical relationships for debris flows. *Natural Hazards*, 19(1), 47-77.
- Salm, B. 1987. *Schnee, Lawinen und Lawinenschutz*. Vorlesungsskript, 273 p. ETH Zurich
- Teufelsbauer, H., Wang, Y., Pudasaini, S.P., Borja, R.I. and Wu, W. 2011. DEM simulation of impact force exerted by granular flow on rigid structures. *Acta Geotechnica*: 10.1007/s11440-011-0140-9.
- United States Federal Highway Administration. 2006. *Hydraulic Design of Energy Dissipaters for Culverts and Channels*, Hydraulic Engineering Circular No. 14. Publication No. FHWA-NHI-06-086, 286 p.
- Watanabe, M., Mizuyama, T., and Uehara, S. 1980. Review of debris flow countermeasure facilities. *Journal of the Japan Erosion Control Engineering Society*, 115, 40-45 (in Japanese).
- Wendeler, C., Volkwein, A., Denk, M., Roth A. and Wartmann S. 2007. Field measurements used for numerical modeling of flexible debris flow barriers. *4th DFHM Conference*. Chengdu.
- White, D.J., Take, W.A. & Bolton, M.D. (2003). Soil Deformation Measurement using Particle Image Velocimetry (PIV) and Photogrammetry. *Geotechnique*, 53, 619-631.
- Zhou, G.D., Law, R.P.H. and Ng, C.W.W. 2009. The mechanisms of debris flow: a preliminary study. *Proceedings of the 17<sup>th</sup> ICSMGE*, Alexandria, Egypt, 2, 1570-1573.

# GPS instrumentation and remote sensing study of slow moving landslides in the eastern San Francisco Bay hills, California, USA

Instrumentation GPS et télédétection de glissements de terrains lents dans les collines est de la Baie de San Francisco, Californie, USA

Cohen-Waeber J., Sitar N.  
*University of California Berkeley, Civil and Environmental Engineering*

Bürgmann R.  
*University of California Berkeley, Earth and Planetary Science*

**ABSTRACT:** Active slow moving landslides in the East Bay Hills, San Francisco, California, have been the object of many investigations over recent decades, though their mechanisms are still poorly understood. Contemporary geodetic technologies, such as continuous Global Positioning Systems (GPS) and Interferometric Synthetic Aperture Radar (InSAR), allow for remote detection and characterization of ground surface displacements with sub-centimeter precision and accuracy. This project combines GPS and InSAR time series analyses for the characterization of spatial and temporal landslide deformation as a result of static and dynamic forces. Several independent InSAR time series analyses show accelerated landslide surface deformation as an effect of precipitation, though not in relation to recent seismic activity. Additionally, recent advances in InSAR analysis methods allow the observation of intra-slide deformation patterns. Since the implementation of a comprehensive continuous GPS network in January 2012, landslide related surface displacements have also been recorded in response to precipitation. Both InSAR and GPS studies not only confirm strong correlation and sensitivity to periods of precipitation but downslope sliding velocities of around 30 mm/year as well.

**RÉSUMÉ :** Bien que leurs mécanismes soient encore mal compris, des glissements de terrains lents dans les collines Est de la baie de San Francisco, Californie, font depuis plusieurs décennies l'objet de nombreuses recherches. Les technologies géodésiques d'aujourd'hui comme le GPS continu et l'InSAR, permettent la télédétection et la caractérisation de déplacements de la surface terrestre avec précision et exactitude millimétrique. Ce projet a donc pour but de caractériser les déformations spatio-temporelles de la surface terrestre, liés aux glissements de terrains sous effets statiques et dynamiques, par l'application de ces outils géodésiques. Plusieurs analyses indépendantes de séries chronologiques InSAR montrent une accélération superficielle de ces glissements sous l'effet de précipitation mais pas sous l'effet d'activité sismique. D'avantage, de récents progrès des méthodes analytiques d'InSAR permettent l'étude des modes de déformation intra-glissements. La mise en place d'un réseau GPS en Janvier 2012, montre aussi une accélération des glissements sous l'effet de précipitation. Ces deux méthodes confirment non seulement une sensibilité aux périodes de précipitation, mais aussi une vitesse approximative de 30 mm/an.

**KEYWORDS:** Landslides, creep, GPS, InSAR.

## 1 INTRODUCTION

Recent advances in geodetic technologies allow for remote data collection and the analysis of spatial and temporal ground surface deformation at a scale that was previously not possible. Technologies such as continuous GPS and Interferometric Synthetic Aperture Radar (InSAR) are capable of measuring active surface displacement with as much as sub-centimeter precision and accuracy. This clearly lends itself to the characterization of active slow moving landslides. Furthermore, the urgency for improved efficiency of primary geologic and geotechnical site investigations stresses that these methods be incorporated in the current state of practice.

Active landsliding across the Lawrence Berkeley National Laboratory (LBNL) site and the East Bay Hills, California, has been the object of many investigations over recent decades. Though studies suggest a trend in landslide mobility is associated with regional climate and active tectonic conditions in addition to the local geologic setting, the mechanisms of these currently slow moving slides are still poorly understood. Thus, the objective of this study is to characterize slope deformation as a result of static and dynamic forces by a careful observational program using the most current geodetic technologies. The intent is to help develop a method for the remote determination and evaluation of landslide hazards and their eventual risk assessment.

This monitoring program includes the instrumentation of individual landslides with a comprehensive network of permanent, continuously streaming GPS stations, and regional

monitoring of slope surface deformation by InSAR time series analysis. To date, historical InSAR and recent GPS observations confirm similar downslope sliding velocities as an effect of precipitation, though not in relation to seismic activity. A closer review of InSAR time series also reveals a pattern of intra-slide surface deformation and important insight on internal slide mechanisms. This is a presentation of preliminary GPS findings and an observation of InSAR time series analyses.

## 2 GEOLOGIC SETTING

The study area for this project is located along the western flank of the Berkeley Hills, east of the San Francisco Bay, California. The local geology is the product of an approximately 360 million year old accretionary process during which the North American Plate margin transitioned from subduction of the Farallon Plate to a transform boundary against the Pacific Plate. Hence, several orogenies and accreted terranes are responsible for a wide variety of metamorphic, volcanic and sedimentary formations in this relatively small area known as the California Coast Range geomorphic province, characterized by a northwest trending and low lying mountain range.

As part of the California Coast Range geomorphic province, the Berkeley Hills are an uplifted block of Jurassic to Tertiary sedimentary, volcanic and metamorphic rocks bound by the Hayward and Calaveras faults and folded in a northwest trending synclinal form during regional transpression related to the active plate margin 1-2 million years ago. Now largely

overlain by Quaternary colluvial and alluvial deposits, this highly fractured, intensely weathered, moderately soft rock is prone to landsliding.

In addition to the geologic setting, studies suggest that Berkeley Hills landslide mobility is driven by precipitation and regional active tectonic conditions (Alan Kropp and Associates 2002, Hilley et al. 2004, Quigley et al. 2010). Local orographic precipitation forms a wet microclimate and the close proximity to active fault traces within the San Andreas Fault zone brings strong seismicity. Today, several hundred landslide-related geologic and geotechnical investigation reports are available for LBNL and the Berkeley Hills alone, and form a solid background to this project.

### 3 METHODOLOGY

Two state of the art geodetic sensing technologies form the primary modes of data acquisition in this project: high rate, continuously streaming, GPS and InSAR. While these methods have individually been shown capable of measuring active ground surface displacement at scales that were previously not possible; the appropriate characterization of landslide related slope movement benefits from the application of both.

Where continuous GPS provides three dimensional ground surface displacement measurements with millimeter scale accuracy and precision at full temporal resolution, the spatial distribution of measurement points is sparse. On the other hand, InSAR time series analysis produces improved spatial averages at decameter resolution with sub-centimeter precision, and the inclusion of datasets spanning several decades of observations. These methods are complimentary using deformation detected across a GPS network to calibrate that measured using InSAR.

The objective is thus to accurately measure landslide slope deformation over time. Combining these methods allows for spatial and temporal analysis of ground surface displacements due to landsliding in relation to local precipitation and ground shaking events. By incorporating these surface observations with previous investigations and monitoring, the landslide mechanisms can then be modeled.

#### 3.1 GPS Data Acquisition

The first phase of this project has been to establish a network of continuously streaming GPS stations to track landslide related ground surface displacement over time. This involves the instrumentation of individual landslides with autonomous, continuously streaming GPS stations, as well as several permanent reference stations. Each landslide station has been specifically designed for permanent, stand-alone installation and built to capture landslide displacement at depth. Anchored on a deep seated reinforced concrete foundation to limit the effects of surficial disturbance, the stations are solar powered and equipped with a wireless antenna for remote access. Reference station locations are chosen on the basis of proximity to the "mobile" devices and being seated on immobile ground.

Since January 2012, 5 such "mobile" stations have been successfully installed at LBNL and one at the University of California Blake Garden on the Blakemont Landslide. One reference station has been established at the Lawrence Hall of Science above LBNL. Average daily solutions are being obtained for each station based on a 1Hz data set, and a 25Hz buffer is held for displacement-time histories in the case of seismic activity. Three additional sites are in the process of being developed.

#### 3.2 InSAR Time Series

InSAR time series are a record of change in radar signal return phase over time, reflecting the change in distance between the ground surface and a satellite based radar platform (or range-

change). The strength of the return signal for each radar pulse is dependent of the physical properties of the target (or scatterer). Where distinct structures will return a persistent strong signal, less prominent surfaces will return lower intensity distributed signals and noise. Among others, two types of InSAR time series analyses are thus known as Permanent or Distributed Scatterer methods (respectively).

With the concurrent development of the GPS network, analysis of InSAR time series has also begun, though is not presented here in detail. Rather, a brief review of prior results is described with observations based on TerraSAR-X satellite data processed with the Tele-Rilevamento Europa (TRE) SqueeSAR™ algorithm (Ferretti et al. 2011, Giannico et al. 2011).

### 4 PRIOR GEODETIC RESULTS

The use of InSAR time series analysis has been shown to successfully track landslide related ground surface displacement in the Berkeley Hills area using data sets from different satellites over several time periods between 1992 and 2011 (Hilley et al. 2004, Quigley et al. 2010, Giannico et al. 2011). In each case, analysis of Permanent and/or Distributed Scatterers over the period of interest clearly exhibit accelerated rates of displacement related to periods of high precipitation. Though no such relationship could be established with local seismicity, it is considered to be likely that large earthquakes can accelerate landslide motion. Furthermore, one attempt at the use of Continuous GPS to track landslide motion was also of no avail (Quigley et al. 2010).

#### 4.1 1992-2007 Time Series of ERS and RADARSAT

In the InSAR time series analysis of Permanent Scatterers performed by Hilley et al. (2004), known landslides across the Berkeley Hills were successfully detected and tracked from 1992 to 2001 using ERS-1 and ERS-2 data acquisitions. Over this period, these data indicate landslide related surface displacement rates varied between 5 to 7 mm/year range-change in the radar line of sight direction. Based on local average slope inclinations, this implies equivalent downslope velocities of 27 to 38 mm/year and has been verified in the field by subsurface inclinometer displacement measurements of approximately 33 mm/year (Allan Kropp and Associates 2002). Hilley et al. (2004) also observed that periods of landslide acceleration were closely related to seasonal precipitation, though non-linear in that precipitation related displacement did not occur immediately, with lag times of up to 3 months, and did not predictably increase with larger events. Additionally, Hilley et al. (2004) suggest the potential for seismic related landslide displacement given a  $M_w \approx 3.9$  Hayward fault event on December 4, 1998. Though the temporal resolution of the time series could not directly document seismically triggered deformation, unexpectedly high InSAR displacement measurements were observed relative to the amount of precipitation during the same period.

Similarly, Quigley et al. (2010) examine seasonal precipitation-related displacement, supplementing the same ERS data set with RADARSAT-1 acquisitions from 2001 to 2006. Landslide displacement was shown not only to be of same magnitude, but clearly seasonal and sensitive to variations in rainfall patterns. Detrended and stacked (by month) observations plotted against average monthly precipitation exhibited a clear 1 to 3 month displacement response lag time and a positive correlation to the intensity of precipitation.

#### 4.2 2007-2009 Continuous GPS Tracking.

Quigley et al. (2010) used Continuous GPS at one known active landslide location to track surficial displacements between 2007 and 2009. Though InSAR time series (Hilley et

al. 2004) and local inclinometer data (Quigley et al. 2010) clearly illustrated slide activity in the years before the station's installation, the GPS monitoring did not. This was likely due to a particularly dry period and the station was disassembled before an adequate data set could be collected to observe long term landslide behaviors.

## 5 RECENT INSAR TIME SERIES OBSERVATIONS

While the Permanent Scatterer InSAR method uses stable coherent targets as shown in the examples above, it is also limited by their presence. To increase the number of observed scatterers and improve time series resolution, the new proprietary algorithm (SqueeSAR™) developed by TRE (Ferreti et al. 2011), utilizes both the Permanent and Distributed Scatterer methods. Thus, a third InSAR time series analysis was performed over the Berkeley Hills by Giannico et al. (2011) applying the SqueeSAR™ method to TerraSAR-X data acquisitions from 2009-2011.

As observed in the 1992-2007 InSAR time series analyses (Hilley et al. 2004, Quigley et al. 2010), landslide related displacements were clearly identifiable with velocities averaging between 6 and 8 mm/year range-change and with periods of precipitation-related acceleration. Figures 1 and 2 show the location and average displacement time histories for different areas (top, middle and bottom) within the Blakemont Landslide (respectively), plotted against cumulative precipitation over the period of observation.

Located at the northern-most end of the study area, field investigations have described the Blakemont Landslide as an approximately 915-m-long, 215-m-wide translational soil and rock landslide with nested rotational failures, and an active sliding depth of 8 to 20 m (Alan Kropp and Associates 2002). While the entire slide appears to be moving coherently downslope (increasing range-change displacement from the descending orbit acquisition), clear accelerations occur in early 2010 and early 2011, some 3 months after the onset of each wet season. Furthermore, the landslide exhibits a positive correlation between displacement and intensity of precipitation with smooth variations during a more gradual 2009-2010 wet season, in comparison to abrupt accelerations during a higher intensity 2010-2011 season.

An important advantage of the higher spatial resolution afforded by the TRE SqueeSAR™ method is a better understanding of landslide mechanisms as expressed at the ground surface. A closer look at the downslope displacements of different areas within the Blakemont Landslide (Figure 2) reveals that it is in fact not moving as one coherent mass, rather with what physicists would call an "accordion effect". Differencing the average downslope displacements of each of the highlighted areas from top to bottom of the landslide, a pattern of apparent landslide shortening (positive) and extension (negative) becomes evident (Figure 3). Here the largest differential displacement variations are observed between the top and bottom areas of the landslide. During wet seasons, the difference in displacement between top and bottom of the landslide increases as the lower portions of the slide accelerate earlier than the upper portions. The same can be said for the opposite case during dry periods, when the difference in displacement between the top and bottom of the landslide decreases as the lower portions of the landslide slow and the upper portions catch up. Naturally, as this currently short dataset is augmented, it is the authors' hope to observe similar trends over longer time periods.

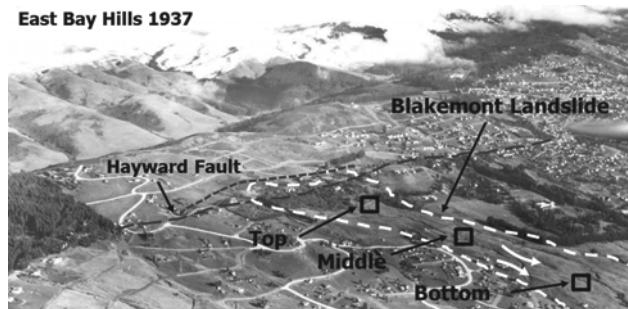


Figure 1. 1937 Oblique view of Blakemont landslide showing location of approximate highlighted areas in TerraSAR-X InSAR study.

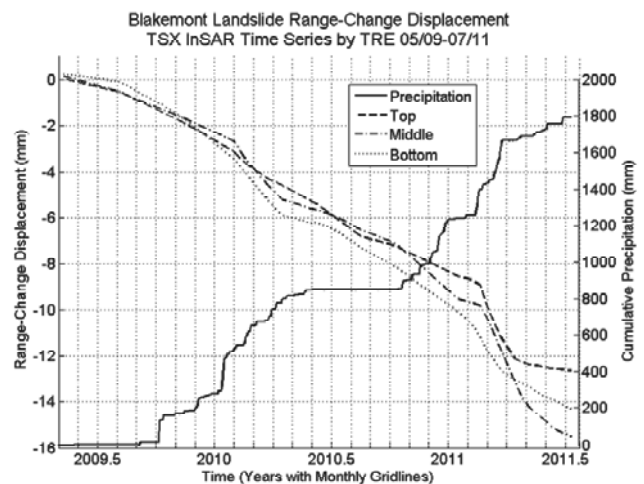


Figure 2. TRE SqueeSAR™ analysis of TerraSAR-X data acquisitions (2009-2011), illustrating average downslope (negative) range-change displacement (left axis) in top, middle and bottom areas of Blakemont Landslide versus cumulative precipitation (right axis).

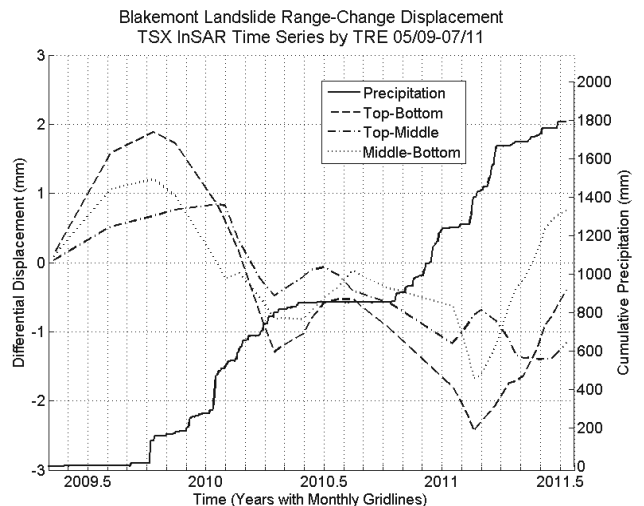


Figure 3. Differential of average downslope displacements (left axis) from TRE SqueeSAR™ analysis of TerraSAR-X acquisitions (2009-2011) between highlighted areas of the Blakemont Landslide, from top to bottom, plotted against cumulative precipitation (right axis).

## 6 PRELIMINARY GPS RESULTS

Daily solutions from the first 6 continuously streaming GPS stations have been recorded since their installation in January 2012. Highlighted here are stations "LRA 1-3" located on the same landslide in Chicken Canyon at LBNL, as depicted in the 1935 air photo (Figure 4). While historical ground surface displacement related to this landslide has yet to be characterized and quantified, extensive field investigations have described it



as an approximately 230-m-long, 75-m-wide and 24-m-deep translational soil and rock landslide with nested rotational failures (Alan Kropp and Associates 2009).

Already, a clear signal at each of these 3 stations is apparent, showing down-slope displacements of up to 3 cm which occurred directly related to local precipitation. As an example, Figure 5 illustrates the time history of daily solutions for station LRA 2 from January through October 2012, plotted against cumulative rainfall. To remove tectonic related displacements and measure actual displacement of the station, daily solutions for the station's North and East baselines are taken with respect to a fixed station (P224) several kilometers to the South. As such, LRA-2 clearly exhibits long term down-slope displacement to the southwest, accelerating during large rainfall events. Also indicated in Figure 5 is the time of the March 5, 2012  $M_w = 4.0$  Hayward fault earthquake with epicenter in El Cerrito, CA, approximately 10 km north of the site. While no clear seismically driven permanent slope displacements can be discerned, this may be due to the "dry" state of the landslide as well as the event's size and distance.

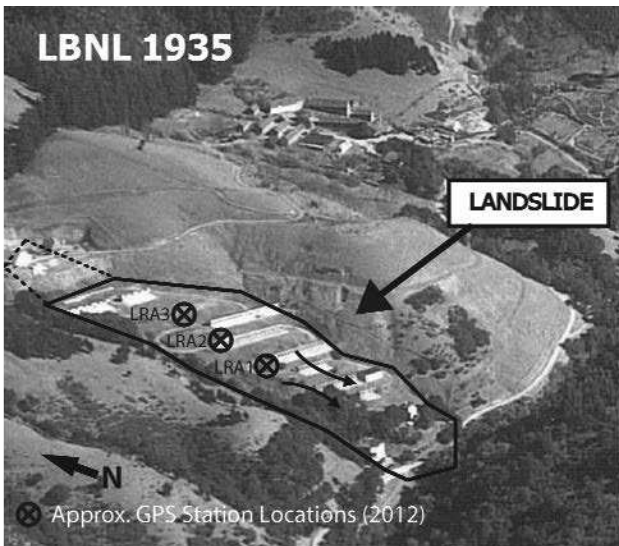


Figure 4. 1935 Oblique view of LBNL landslide with current GPS station locations.

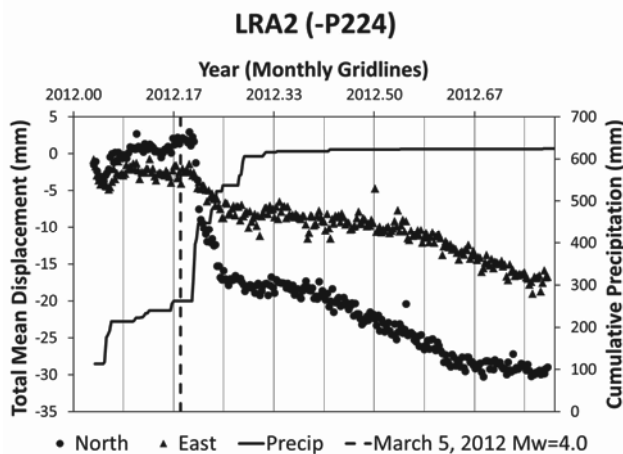


Figure 5. GPS position time series of station LRA 2 with respect to reference station P224. North (circles) and east (triangles) components of relative displacement with respect to reference site P224 are show together with cumulative precipitation (solid line) and time of  $M_w = 4$  earthquake (dashed line).

## 7 CONCLUSION

A review of three independent InSAR time series analyses of the Berkeley Hills, from separate satellite acquisitions and over different time intervals from 1992-2011 shows remarkable consistency. In each case, similar mean landslide velocities were estimated, and precipitation dependent displacement behavior was observed. Though we were not able to document any motions induced by recent moderate earthquakes in the region, improved spatial resolution has allowed us to draw preliminary conclusions on the mechanics of displacement within one landslide. Further insight is expected as the quality of analysis improves and larger datasets are acquired.

After a mild wet season, the GPS instrumentation of several landslides in the Berkeley Hills, has recorded well-defined precipitation triggered slope movement. In contrast, the occurrence of a nearby  $M_w = 4$  earthquake did not appear to have produced a measurable effect. Overall, the system has already demonstrated its capability to record landslide motions that otherwise would not have been observed with such level of detail and it continues to function and collect new data.

While both methods of observation presented here have not yet been directly compared, they do exhibit similar trends. In both cases, records of landslide related surface displacement have comparable down-slope velocities, increased with periods of precipitation and varied with its intensity. Observations over longer periods will provide important insight on the triggering mechanisms and internal landslide behavior we have described.

## 8 ACKNOWLEDGEMENTS

We gratefully acknowledge our financial support from the Lawrence Berkeley National Laboratory, Earth Science Division Director's Fund.

## 9 REFERENCES

- Alan Kropp and Associates 2002. Blakemont Area Geologic Study, El Cerrito and Kensington CA. Report. Berkeley. CA.
- Alan Kropp and Associates 2009. Geologic and Geotechnical Investigation Report, Helios Energy Research Facility, University of California Berkeley, Berkeley CA. Report. Berkeley. CA.
- Ferretti A., Fumagalli A., Novali F., Prati C., Rocca F., Rucci A. 2011. A New Algorithm for Processing Interferometric Data-Stacks: SqueeSAR. *IEEE Geoscience and Remote Sensing* 49(9), 3460-3470.
- Giannico C. and Ferretti A. 2011. SqueeSAR<sup>TM</sup> Analysis Area: Berkeley. *Processing Report*. Tele-Rilevamento Europa, Milano, IT.
- Hilley G.E., Bürgmann R., Ferretti A., Novali F. and Rocca F. 2004. Dynamics of Slow Moving Landslides From Permanent Scatterer Analysis. *Science* 304, 1952-1955.
- Quigley K. C., Bürgmann R., Giannico C. and Novali F. 2010. Seasonal Acceleration and Structure of Slow Moving Landslides in the Berkeley Hills. Proceedings of the Third Conference on Earthquake Hazards in the Eastern San Francisco Bay Area; edited by Keith Knudsen. *California Geological Survey Special Report 219*, 169-178.

# Geotechnical Characterization, Stability Analysis, and the Stabilization Process for a Landslide in a area of Barreiras Formation and Granite Residual Soils, Pernambuco

Caractérisation géotechnique, analyse de la stabilité et procédés de stabilisation pour un glissement de terrain dans des matériaux du type « Barreiras Formation » et sols de granite résiduel, Pernambuco

Coutinho R.Q.

*Federal University of Pernambuco, Brazil*

Silva da M.M.

*Federal Educational Institute of Pernambuco, Brazil*

**ABSTRACT:** A large number of Brazilians live in conditions that involve elevated risk for landslides. Both technical and social problems are involved. This study presents results of a research project involving technical support for the Municipal administration of the City of Camaragibe - PE. An important landslide occurred in an occupied area after a period of intense rainfall, causing considerable losses for the local population. Three years later, another period of intense rainfall exacerbated the problem, causing cracks to develop in the walls and foundations of many houses, and broadening the area initially affected. An important program involving investigation that included field and laboratory activities, instrumentation, and stability and flow analysis was carried out. The results produced were considered to be very satisfactory, and they were able to point out the main causal factors, along with the mechanisms involving the landslide, which could then be better understood, and thoroughly studied. Afterwards, a proposal for stabilization for the entire area was elaborated, aiming to significantly reduce the risk levels by means of superficial and sub-superficial drainage, geometric modifications, placement of structures for stabilization of the land, and other activities.

**RÉSUMÉ :** Un grand nombre de brésiliens vivent dans des zones à risque d'un point de vue des glissements de terrain. Cela engendre des problèmes aussi bien techniques que sociétaux. Les travaux présentés dans cet article découlent d'un projet de recherche financé par l'administration municipale de la ville de Camaragibe – PE. Suite à un épisode pluvieux très important, un glissement de terrain s'est produit et a causé des dégâts considérables pour la population locale. Trois années plus tard, un nouvel épisode pluvieux a aggravé la situation et de nombreux ouvrages furent endommagés (murs de soutènement, fondations de maisons, ...). Un programme d'investigation important fût alors mis en place : instrumentation sur site, analyses de stabilité et d'écoulement. On présente dans cet article une synthèse des résultats obtenus ainsi que les mécanismes aux origines des instabilités. Pour finir, une solution de stabilisation du site est proposée, avec pour but de réduire significativement le niveau de risque (drainage, modification géométrique de la pente et mise en œuvre d'ouvrages de stabilisation).

**KEYWORDS:** geotechnical characterization, slope stability, stabilization process.

## 1 INTRODUCTION

This paper presents study results from a research project, including details involving technical support supplied to the Municipal administration of the City of Camaragibe – PE, Brazil. The area investigated is located in the Township of Camaragibe, belonging to the western portion of the Recife Metropolitan Region. The landslide that occurred was classified as a multiple rotational landslide, characterized by the appearance of various steps along its slope. Geological characteristics of the area studied define an unsaturated granite residual soil that is partially covered by the Barreiras Formation. The residual soil of granite is found throughout the entire city. In some places, the granite rock mass is exposed.

In the Recife Metropolitan Region, it is common to find crystalline based rocks (Granite-Gneissic complex) covered by granite residual soils that originate from a crystalline structure; and by sediments from the Barreiras Formation. The crystalline base is formed by ancient intrusive rocks (1.5 to 21 billion years) belonging to the Pernambuco – Alagoas Massif. It presents at least four phases of deformation, the latter of which, associated to the faults deformed, resulted in the formation of the “Pernambuco Lineamento”.

The results presented here refer to a synthesis of the program of geotechnical characterization (field and laboratory testing, along with instrumentation), flow and stability analysis, and proposals for stabilization of the area in an attempt to significantly reduce the level of risk. This study aims to give

continuity to a research project by the GEGEP – DEC / UFPE, with support from the CNPq/FACEPE, designed to comprehend and elaborate mechanisms involving instability of slopes, and providing manners in which stabilization can be achieved.

## 2 GEOTECHNICAL CHARACTERIZATION

In the studies, an extensive effort involving *in situ* and laboratory investigation was carried out. For basic geotechnical characterization, laboratory analysis consisted of physical, chemical, and mineralogical characterization tests, strength tests (including direct shear tests, and direct shear tests utilizing controlled suction), and oedometer tests.

The *in situ* investigation carried out in the area was performed by using topographic profiles of the region, cross sections, geological engineering mapping, subsurface exploration (soil / rock mass – SPT / RQD measurements), soil moisture content profiles, sampling of soils (Block and Denison), and field permeability tests (Guelf). Field instrumentation utilized piezometer, water table level, inclinometer, and rainfall measurement equipment. More information can be found in Silva (2007) and Silva *et al.* (2009).

### 2.1 Field Investigation Results

For the subsurface exploration, twelve boreholes were utilized in the area investigated. Ten were carried out in soil (SPT), and



two more in soil and rocky mass (SPT / Core boring–RQD). All boreholes the SPT was measured for each 0.5 m, in general with a depth of 10 to 15 m, but some went down to 20 m (SM-01, SM-02 and SP-02). Geological characteristics were identified together with soil / material descriptions.

In general, for all borehole tests performed, the SPT values ranged from 2 to 17 down to a depth of 7 m from the level of the natural ground surface, within the limits of the two geological formations. From this point on, the SPT values increase markedly, up to an order of 30, until becoming impenetrable to the SPT borehole. In the vertical profile, soil types vary from clayey sand, to sandy clay, silty sand, and sandy silt, with the layers varying in thickness, and showing the presence of increased amounts of sandy materials. The greatest alterations in SPT values were found very close to the Barreiras Formation contact with the granite residual soil. An exception involved the SP-02 borehole, found to be basically granite residual soil (Figure 1). Due to high sand content, the Barreiras Formation in the area is identified as an alluvial plain facie. Based on technical interpretation, the failure surface was shown to be near to the geological formation contact point, later confirmed by instrumentation (inclinometer results).

The presence of granite residual soil from the ground level in the SP-02 region demonstrated a profound influence on the landslide process, as evidenced later on in the study.

Soil profile cross-sections were detailed from the subsurface exploration, along with results from geological engineering mapping. Typical soil profile information is shown in Figure 1.

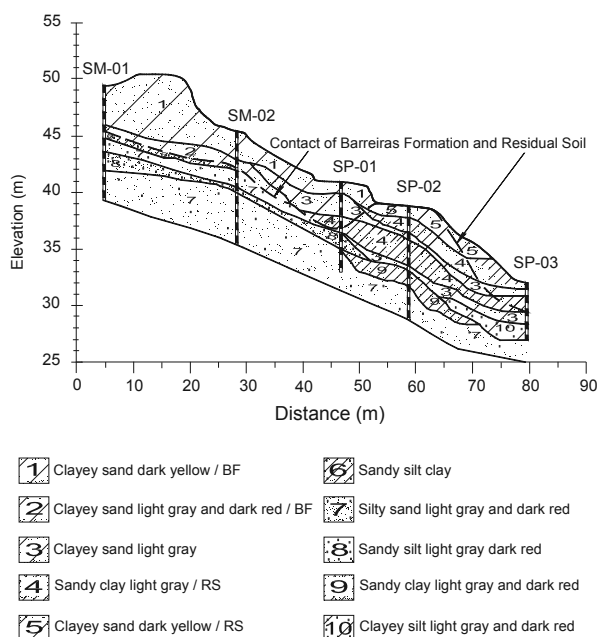


Figure 1. Typical Soil profile-cross section – post failure.

The climate in the area is classified by Koppen, as ‘As’, described as humid tropical, with rainy periods during the autumn – winter seasons, and a dry period during the summer.

Rainfall precipitation in the Camaragibe township region was measured by instruments installed in two places, initially in a location within the city (during 2000 to 2004), and then later via instrumentation installed in the landslide area (2004 to 2006).

The rainy season is concentrated in the months from March to August, with the precipitation approximating average monthly maximum levels ranging from 150 mm to 600 mm. From January to March the average maximum monthly precipitation is around 150 mm, with April, May, July and August showing 250 mm. The month of June presented

precipitation above 500 mm, being considered the critical period for landslides. During the period from September to December, precipitation levels were lower, averaging around 50 mm. The period from September to February normally presents less precipitation; however, in some years (examples being 2000, 2002, 2004 and 2010) significant rainfall occurs in the months of January and February. During 2000, the annual rainfall level was above the general average, with increased precipitation during most of the calendar months. This occurrence coincided with the first appearance of signals of a non-stabilization condition in the area. Landslides occurred in June of 2002, after a period of intense rainfall.

Hydraulic conductivity of the soils was determined through field testing using a Guelph permeameter, an in-hole constant head permeameter employing the Mariotte Principle. It delivers essentially a “point” measurement. The tests were made along of the slide, close for the SPT boreholes, and was performed for each 0.5 m to a depth of 2.5 m. In the Barreiras Formation soils, permeability results varied from 2 to 6 x 10<sup>-6</sup> m/s, with higher values from the materials containing a higher percentage of sand. In the SP-02 region (Figure 1), granite residual soils are present in the surface levels, presenting permeability results in the order of 2 x 10<sup>-7</sup> m/s, and demonstrating values 10 times lower than the corresponding Barreiras Formation. This difference influenced flow conditions in the slide area.

The field instrumentation program in the landslide area was based on 25 Casagrande type piezometers (with 18 Casagrande piezometers having the ability to register maximum levels during a rainy period), 6 water level instruments, 5 vertical inclinometers, and 1 rainfall registration instrument.

In general the period of highest elevation of the piezometric level coincides with the period of high rainfall, in the months from March to August (with water managing to emerge from the surface level of the ground near borehole SP-01). Starting during the month of September, piezometric levels show a reduction, tending to remain constant until March, coinciding with the dry season. Similar behavior can be observed regarding the water levels encountered. Even in periods of low rainfall intensity, piezometric levels are observed to be quite high, demonstrating hydraulic influence on slope stability.

Results obtained in the vertical inclinometer analysis relating to borehole SP-02 showed maximum horizontal displacement of 130 mm as a block mass. It should be noted that horizontal displacements measured refer to the stage of reactivation, featuring movements along the existing failure surface, given that instrumentation was implemented in November 2004, after the occurrence of the failure. The influence rainwater had in the acceleration of horizontal movements was clear in observations regarding the slope studied. It appears that during a period of reduced rainfall (November 2004 to March 2005) the displacements observed were virtually nil, without significance.

Results of the vertical readings from inclinometers confirmed the information obtained from the SPTs boreholes, showing that the failure surface seems to be very close to the contact between the Barreiras Formation, and the granite residual soils, measured to be located at a depth just over 7 m from the surface of the ground, the exception being the region around SP-02, where only residual soils are found.

## 2.2 Laboratory Investigation Results

The mature residual granite soil studied presents a fine texture, with a liquid limit of 54%, plasticity limit of 32% (PI=22%), grain size distribution of 39% clay, 26% silt, 23% fine sand, and 12% a mixture of medium and thick sand. The soil is classified as CL in the Unified Classification System.

Grain-size distribution test without the use of deflocculates was also performed. Grain size distribution was designated as

5% clay; 33% silt; 50% fine sand, and 12% medium and thick sand; showing a strong reduction in the portions of clay, and increases in the fine sand portions. Results indicate that the particles of clay in this soil are aggregated in their natural state.

The soil-water characteristic curve obtained through the paper filter method, Haines funnel and Richard's chamber, is presented in Figure 2. The format of the curve displays a saddle aspect, allowing it to be divided into three distinct stretches. The curves indicate an initial air entry suction of 1 kPa, where desaturation begins. After that, a region approximating horizontal is observed, where suction varies from 20 to 200 kPa. In the last stretch, a second air entry value is depicted, where the water content starts to diminish with the increase in suction due to the removal of water from the soil micro pores (see more information in Silva and Coutinho, 2009).

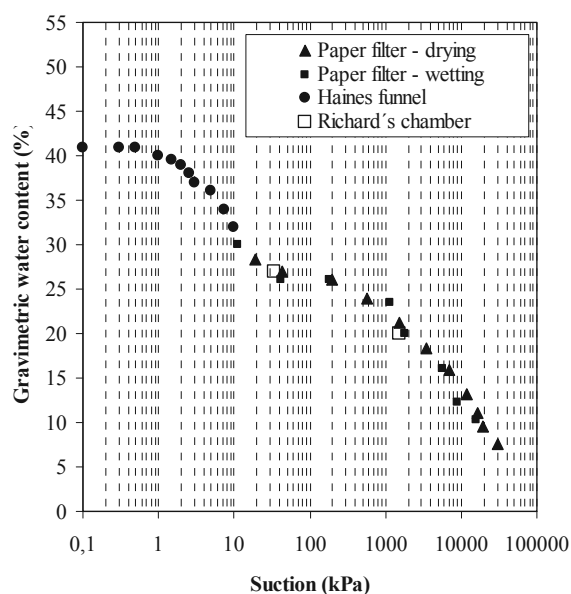
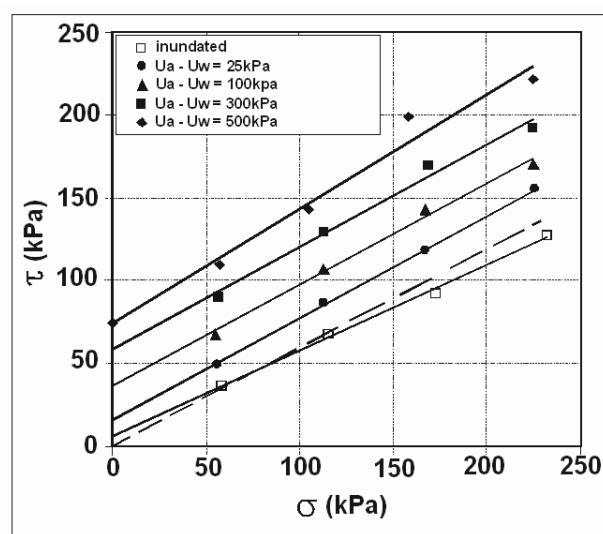


Figure 2. Soil-water characteristic curve from mature residual soil from Camaragibe-PE - Silva and Coutinho (2009)

The shear strength was determined using conventional and controlled suction direct shear tests. The equipment used consisted of a conventional press, adapted for use with a cell that allowed the imposition and control of suction through the principle of translation of axes.

The suction is imposed on the soil by the difference between air pressure supplied by hydrogen applied through an air valve, and the water column maintained in the reservoir fixed on top of the press. The tension is applied through a system of hanging weights, identical to the conventional direct shear tests. The air pressure was applied only under the weight of a charge transference plate, and it was maintained during 10 days. The horizontal force was determined through a load ring. The suctions employed were 25, 100, 300 and 500 kPa. After this period (of suction equilibrium), specific normal stress values were applied, accompanying the deformations up to stabilization. The normal stresses adopted were 50, 100, 150 and 200 kPa, and they were maintained for a minimum of 24 hours. Square samples were used that measured 50 mm or 100 mm the side, and 22 mm or 44 mm in height.

The shear strength envelopes in the plain ( $\sigma_v$ ,  $\tau$ ) for the suction values of 25, 100, 300 and 500 kPa are represented in Figure 3. Envelopes considering suction of 0 kPa, obtained through conventional direct shear tests in the submerged condition, are also presented in this figure. It can be observed that the friction angle, in general, is close to 31°. The results indicate that the envelopes are near to linear in the stress range.



( $U_a - U_w$ )= 0kPa	$c = 9,7\text{kPa}$	$\phi = 26,3^\circ$	$R^2 = 0,996$
( $U_a - U_w$ )= 0kPa	$c = 0,0\text{kPa}$	$\phi = 31,0^\circ$	estimated
( $U_a - U_w$ )= 25kPa	$c = 15,4\text{kPa}$	$\phi = 31,6^\circ$	$R^2 = 0,999$
( $U_a - U_w$ )= 100kPa	$c = 36,5\text{kPa}$	$\phi = 31,3^\circ$	$R^2 = 0,991$
( $U_a - U_w$ )= 300kPa	$c = 58,7\text{kPa}$	$\phi = 31,5^\circ$	$R^2 = 0,987$
( $U_a - U_w$ )= 500kPa	$c = 74,7\text{kPa}$	$\phi = 34,4^\circ$	$R^2 = 0,956$

Figure 3. Shear strength envelopes for different values of suction - mature residual soil from Camaragibe.

### 3 STABILITY ANALYSIS

Through the field investigation, together with flow and stability studies (failure and post failure conditions), a clear perception and understanding of the landslide mechanism was made possible. In this paper, only results corresponding to the failure state are presented. The slope stability evaluation was performed using Spencer method with consideration given to the original topography for the main cross section, as a two-dimensional saturated stability analysis, and considering the "actual" failure surface, along with the pore pressure distribution obtained from the flow analysis, and the geotechnical parameters obtained from laboratory testing (conventional direct shear tests in the submerged condition). Due to the intense rainfall during the failure period, the water level was considered at the surface position from the results produced through instrumentation and field observation, with the materials being in a saturated condition (Silva et al. 2009).

Flow analysis was performed for the failure condition, considering all the information from the studies, including the geotechnical profile, the geotechnical parameters of hydraulic conductivity for the materials composing the Barreiras Formation and residual soils, along with the rainfall and water level conditions. A summary of pore pressure distribution results is shown in Figure 4. Higher positive pore pressure values in the SP-01 and SP-02 regions were obtained showing ascends flow. These results are due to the variability of the soil profile and differences among the hydraulic conductivity values occurring for the materials. This condition is in conformity with water flow observed in this area during the period of intense rainfall.

With the flow analysis results that were provided, stability evaluation for global failure was initially performed (one-step failure) for the complete slope cross-section. The safety factor result was 1.278, showed not to be a condition for failure. Stability analysis was then performed considering the possibility of two-step failure, taking into account the concentrated high pore pressure values around the SP-01 region.

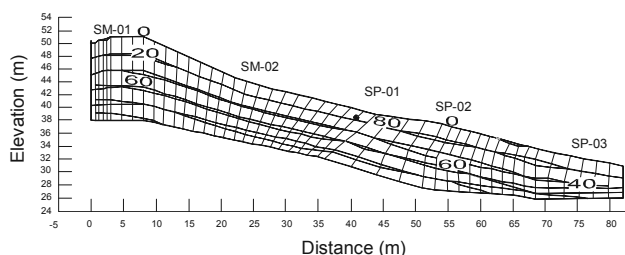


Figure 4. Flow Analysis – Pore Pressure Distribution.

The first landslide occurred between the positions SM 02 and SP-01. For this case, the safety factor value was 1.002, for practical purposes, considered to be a condition of failure, and initiating the landslide mechanism in the area (Figure 5).

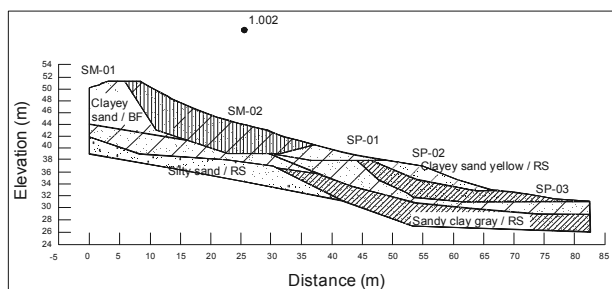


Figure 5. Back-analysis of the first slope failure – from SM-01 to SP01

The mass that moved in this area (from the first failure) caused a surcharge estimated at 30KN/m between positions SP-01 and SP-02, which associated with pore pressure conditions, provoked the second step of the landslide. With this understanding, stability analysis was performed (back-analysis) using geotechnical information from the field and laboratory investigations. Figure 6 presents the minimum safety factor value obtained (1.047), confirming the displacements, and the failure mechanism considered to be the cause of the landslide that occurred in the area.

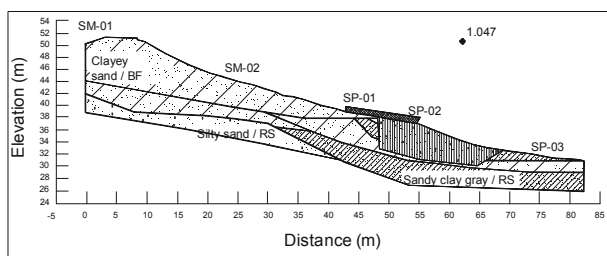


Figure 6. Back-analysis of the second slope failure – SP-01 to SP-03

After three years, another intense rainfall period amplified the problem, with cracks forming in many other houses, and extending the area initially showing damage. See the right side of the two upper-center squares of Figure 7.

#### 4 MITIGATION AND REHABILITATION MEASURES

The mitigation and rehabilitation measures consisted of reducing damage and losses through control of the processes, and protection of the exposed elements in order to reduce their vulnerability. During the investigation and studies, it became possible to understand the processes involved, and to identify the causal factors and triggering mechanisms in the area. The general plan was to propose a risk management program that included both structural and non-structural mitigating actions, considering the social conditions of the area (Coutinho, 2011).

The stabilization measures proposed for all damaged areas (initial and extended areas) included: surface and subsurface drainage (sub-horizontal drains), surface protection, placement of access stairs with surface drainage, modification of slope shape, installation of retaining walls, definition of areas where occupation was to be prohibited, definition of houses to be relocated, dissemination of information to the public, and raising overall awareness of the conditions, along with community consciousness. Figure 7 shows some of the mitigation and control measures proposed.

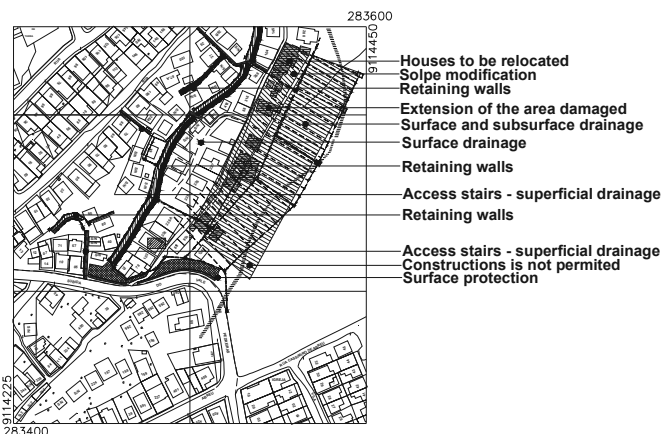


Figure 7. Measures Proposed for Mitigation and Control

#### 5 CONCLUSION

The geotechnical characterization, along with flow and stability analyses / back-analysis results, were considered to be very satisfactory, and in accordance with the literature, permitting that the principal causal factors, and the mechanisms of the landslide could be comprehended and studied. It was understood that due to the heavy rainfall, the water level became elevated, saturating the soil, and producing a concentrated flow. The strength parameters used in the analysis were derived from direct shear laboratory tests in the corresponding condition. Considering all of the information available, mitigation and rehabilitation measures were then proposed, generating a risk management program that included structural and non-structural stabilization actions, considering the social conditions of the area.

#### 6 ACKNOWLEDGEMENTS

The authors are grateful to the CNPq, FACEPE, and Camaragibe City Administration for research support, and all members of the GEGEP/UFPE who participated in the projects.

#### 7 REFERENCES

Coutinho, R. Q.; Silva, M. M. and Lafayeete, K. P. V. 2011. Geotechnical characterization of two unsaturated mature granite residual soils from Pernambuco, Brazil. *PCSMGE*. CD-ROM Proceedings, p.7. Toronto, Canada.

Coutinho, R. Q. 2011. Projeto de Estabilização de Encostas no Município de Camaragibe – PE. Relatório Técnico (“Technical Report”). Prefeitura de Camaragibe – PE, Brazil.

Silva, M. M.; Coutinho, R. Q. and Lacerda, W. A. 2009. Estudo de um movimento de massa ocorrido numa encosta em Camaragibe, Pernambuco. *COBRAE*. CD-ROM, p. 10. São Paulo, Brazil.

Silva, M. M. and Coutinho, R. Q. 2009. Geotechnical characterization of an unsaturated residual soil of granite from Pernambuco, Brazil. *17<sup>th</sup>. ICSMGE*. v. 5, 3417-3420. Alexandria, Egypt.

Silva, M. M. 2007. Estudo geológico – geotécnico de uma encosta com problemas de instabilidade no Município de Camaragibe – PE. Tese de Doutorado (DSc.). UFPE. Engenharia Civil, Recife-PE, Brazil.

# Progressive failure of slopes with sensitive clay layers

## Rupture progressive de pentes comportant des couches d'argile sensible

Dey R., Hawlader B.

*Memorial University of Newfoundland, St. John's, Canada.*

Phillips R.

*C-CORE, St. John's, Canada.*

Soga K.

*University of Cambridge, Cambridge, UK.*

**ABSTRACT:** Progressive failure of slopes can trigger large scale landslides. The presence of sensitive clay layers is one of the main reasons for progressive failure of a slope. The whole soil mass involved in a potential landslide might be of sensitive clay, while in some cases there exist only thin layers of sensitive clay interbedded with relatively strong soils. The movement of a slope might be initiated due to the presence of a weak soil layer, where the shear stress is increased or soil strength is reduced by various triggering factors. Once the failure/movement is initiated in a small zone, the imbalanced force is transferred to the surrounding soil in which slip surface might propagate in the form of a shear band through the sensitive clay layer even though the sensitive clay layer is relatively thin. The propagation of shear band in sensitive clay is also associated with post-peak strain softening behaviour of soil. In this study, upward progressive failure due to river bank erosion has been modelled using nonlinear post-peak strain softening behaviour. It is shown that the pattern of propagation of shear band varies with soil type and slope geometry.

**RÉSUMÉ :** La rupture progressive de pentes peut déclencher des glissements de terrain de grande envergure. La présence de couches d'argile sensible est l'une des principales raisons de la rupture progressive d'une pente. La masse de sol impliquée dans un glissement de terrain potentiel pourrait être totalement constituée d'argile sensible, alors que dans certains cas, il existe seulement des couches minces d'argile sensible intercalées entre des sols relativement résistants. Le mouvement d'une pente peut être initié en raison de la présence d'une couche de sol peu résistant, dans laquelle le taux de cisaillement augmente ou sa résistance diminue en raison de divers facteurs de déclenchement. Lorsque la rupture / le mouvement sont initiés dans une petite zone, le déséquilibre de force se développe vers le sol environnant, dans lequel la surface de glissement peut se propager sous forme d'une bande de cisaillement à travers la couche d'argile sensible, même si la couche d'argile sensible est relativement mince. La propagation des bandes de cisaillement dans l'argile sensible est également associée au ramollissement post-pic du comportement du sol. Dans cette étude, la rupture progressive amont due à l'érosion des berges a été modélisée par le ramollissement non-linéaire post-pic du comportement. Il est montré que le faciès de propagation des bandes de cisaillement varie en fonction du type de sol et de la géométrie de la pente.

**KEYWORDS:** Sensitive clay, progressive failure, spread, shear band propagation, strain softening.

### 1. INTRODUCTION

Large landslides in soft sensitive clays are common in Eastern Canada and Scandinavia. Most of the onshore slides which occurred in soft sensitive clay have been reported as progressive in nature (Bernander 2000, Locat et al. 2008, Quinn 2009, Locat et al. 2011). The presence of strain-softening clay layers is one of the main reasons for progressive failure of a slope. These slides could be in the form of multiple retrogressive, translational progressive or spreads (Tavenas 1984, Karlsrud et al. 1984). Failure might be initiated in a fully stable and/or marginally stable slope depending on the nature of triggering factors. Failure could propagate either in upward or downward direction and the movement of the slope might be initiated due to the presence of a weak soil layer, where the shear stress is increased or soil strength is reduced by various triggering factors. Large landslides in sensitive clays classified as spread (Cruden and Varnes 1996) might be triggered by erosion near the toe of the river bank slope (Quinn et al. 2007, Locat et al. 2008). Numerous spread failures such as Sköttorp landslide in Sweden (Odenstad 1951) and the landslides occurred in Quebec including 1989 Saint-Liguori landslide (Grondin and Demers 1996), Saint-Ambroise-de-Kildare landslide (Carson 1979), Saint-Barnabé-Nord slide (Locat et al. 2008) have been reported to be triggered by erosion at the toe of the slope (Bernander 2000, Locat et al. 2008, Quinn et al. 2007, Locat et al. 2011), although it is very difficult to identify the true disturbing agents which caused these spread failures.

Progressive failure might occur in drained as well as undrained conditions. Bjerrum (1967) explained upward

progressive failure initiation in an intact slope containing overconsolidated plastic clays and clay shales and considered the failure as drained. Sensitive clays from Eastern Canada and Scandinavia show strain softening behavior under undrained loading which has been considered as one of the main reasons for developing progressive failure (Bernander 2000, Locat et al. 2008, Quinn 2009, Locat et al. 2011). Hence undrained condition is considered in this study for analyzing spread failure.

During Ormen Lange field development, numerical simulations have been carried out by Norwegian Geotechnical Institute (NGI) using PLAXIS software to analyze the potential of retrogressive sliding due to strain softening effect in mild clay slopes (NGI 2001). Anderson and Jostad (2007) conducted numerical analyses of progressive failure of slope by modeling the shear band as an interface element using the NGI finite element (FE) code BIFURC. Quinn (2009) also demonstrates the use of linear elastic fracture mechanics concept in progressive failure of slopes.

This paper describes a numerical technique which can be used to analyze the spread or upward progressive failure of a slope typically occurs in river banks due to toe erosion.

### 2. PROBLEM DEFINITION

The geometry of the slope modeled in this study is shown in Fig. 1. The river bank has a slope of 30° to the horizontal. A thick crust of overconsolidated clay near the face of the slope and below the ground surface is assumed. For simplicity the

groundwater table is assumed at the crest of the slope and the river is full. A block of soil near the toe of the slope shown by the hatched zone is removed, which could be caused by erosion or by excavation in the field. This block will be referred as “excavated/eroded soil block.” It is also assumed that the erosion or excavation is occurred relatively fast such that the deformation/failure of remaining soil is in undrained condition.

Three cases are simulated in this study. In Case-I, the ground surface is horizontal and there is a 15 m thick layer of sensitive clay below the 5 m crust. The Case-II is same as Case-I but the ground surface is inclined upward at 4°. Sometimes in the field there may not be a thick sensitive clay layer. To investigate the effect of thickness of the sensitive clay layer, in Case-III only 1.0 m thick sensitive clay layer parallel to the horizontal ground surface from the toe of the slope is assumed. The soil above this layer has the same geotechnical properties of the crust used in Cases I & II. In all three cases, the base layer below the toe of the slope is very stiff and therefore the failure is occurred in the soil above the base layer. The length of the soil domain in the present FE model is 500 m and therefore no significant effects on the results are expected from the right boundary.

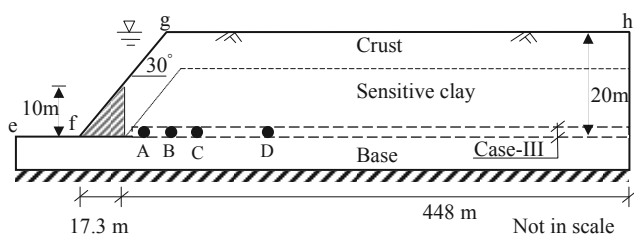


Figure 1. Geometry of the slope used in numerical analysis

### 3. FINITE ELEMENT MODELING

#### 3.1 Numerical technique

ABAQUS 6.10 EF-1 is used in this study. The progressive slope failure is fundamentally a large deformation problem as very large plastic shear strain is developed in a thin layer of soil through which the failure of the slope is occurred. Conventional finite element techniques developed in Lagrangian framework cannot model such large strain problems because significant mesh distortion occurs. In order to overcome these issues, Coupled Eulerian-Lagrangian (CEL) technique currently available in ABAQUS FE software is used. The finite element model consists of three parts: (i) soil, (ii) excavated/eroded soil block, and (iii) void space to accommodate displaced soil mass. The soil is modeled as Eulerian material using EC3D8R elements, which are 8-noded linear brick, multi-material, reduced integration with hourglass control elements. In ABAQUS CEL, the Eulerian material (soil) can flow through the fixed mesh. Therefore, there is no numerical issue of mesh distortion or mesh tangling even at large strain in the zone around the failure plane.

The excavated/eroded soil block is modeled in Lagrangian framework as a rigid body, which makes the model computationally efficient. A void space is created above the model shown in Fig. 1 using the “volume fraction” tool. Soil and void spaces are created in Eulerian domain using Eulerian Volume Fraction (EVF). For void space EVF is zero (i.e. no soil). On the other hand, EVF is unity in clay layers shown in Fig. 1, which means these elements are filled with Eulerian material (soil).

Zero velocity boundary conditions are applied at all faces of the Eulerian domain (Fig.1) to make sure that Eulerian materials are within the domain and cannot move outside. That means, the bottom of the model shown in Fig. 1 is restrained from any movement, while all the vertical faces are restrained from any lateral movement. No boundary condition is applied at the soil-

void interface (efgh in Fig. 1) so that the soil can move into the void space when displaced.

Only a three-dimensional model can be generated in ABAQUS CEL. In the present study the model is only one element thick, which represents the plane strain condition.

The numerical analysis consists of two steps of loading. In the first step geostatic load is applied to bring the soil in in-situ condition. Note that under geostatic step the slope is stable with some shear stress especially near the river bank. In the second step, the rigid block of excavated/eroded soil is moved horizontally 2 m to the left using displacement boundary condition.

#### 3.2 Soil parameters

Table 1 shows the geotechnical parameters used in this study. The crust has an average undrained shear strength of 60 kPa, and a modulus of elasticity of 10 MPa (=167s<sub>u</sub>). The soil in the base layer is assumed to be very strong and s<sub>u</sub>=250 kPa and E<sub>u</sub>=100 MPa is used.

Table 1. Parameters for finite element modelling.

Crust	
Undrained modulus of elasticity, E <sub>u</sub> (kPa)	10,000
Undrained shear strength, s <sub>u</sub> (kPa)	60
Submerged unit weight of soil, γ <sub>2</sub> (kN/m <sup>3</sup> )	9.0
Poisson's ratio, ν <sub>u</sub>	0.495
Sensitive clay	
Undrained modulus of elasticity, E <sub>u</sub> (kPa)	7,500
Poisson's ratio, ν <sub>u</sub>	0.495
Peak undrained shear strength, s <sub>up</sub> (kPa)	50
Residual undrained shear strength, s <sub>ur</sub> (kPa)	10
Submerged unit weight of soil, γ <sub>2</sub> (kN/m <sup>3</sup> )	8.0
Plastic shear strain for 95% degradation of soil strength, γ <sup>p</sup> <sub>95</sub> (%)	33

Proper modeling of stress-strain behavior of sensitive clay layer is the key component of progressive failure analyses in sensitive clays. When sensitive clay is subjected to undrained loading it shows post-peak softening behavior. Various authors (e.g. Tavenas et al. 1983, Quinn 2009) showed that the post-peak softening behavior is related to post-peak displacement or plastic shear strain. The following exponential relationship of shear strength degradation as a function of plastic shear strain is used in the present study.

$$s_u = [1 + (S_t - 1) \exp(-3\delta/\delta_{95})] s_{ur} \quad (1)$$

where s<sub>u</sub> is the strain-softened undrained shear strength at δ; S<sub>t</sub> is sensitivity of the soil;  $^{TM} = ^{TM}_{total} - ^{TM}_p$  where  $^{TM}_p$  is the displacement required to attain the peak undrained shear strength (s<sub>up</sub>); and δ<sub>95</sub> is the value of δ at which the undrained shear strength of the soil is reduced by 95% of (s<sub>up</sub>-s<sub>ur</sub>). Equation 1 is a modified form of strength degradation equation proposed by Einav and Randolph (2005) and was used by the authors (Dey et al. 2012) to model submarine landslides. If the thickness of shear band (t) is known, the corresponding plastic shear strain (γ<sup>p</sup>) can be calculated as, γ<sup>p</sup>=δ/t assuming simple shear condition. Therefore, Eq.1 in terms of γ<sup>p</sup> can be written as

$$s_u = [1 + (S_t - 1) \exp(-3\gamma^p/\gamma^p_{95})] s_{ur} \quad (2)$$

where γ<sup>p</sup><sub>95</sub> is the value of γ<sup>p</sup> at 95% strength reduction (i.e. γ<sup>p</sup><sub>95</sub>=δ<sub>95</sub>/t). Note that, it is very difficult to determine the thickness of the shear band in the field. Similar to some previous studies (e.g. Quinn 2009) t=0.375 m is used which is same as the mesh height used in the present FE analysis. In ABAQUS the degradation of shear strength of sensitive clay is varied as a function of plastic strain. The parameters used to

model the sensitive clay using Eq. 2 are also shown in Table 1. These parameters are estimated based on the laboratory tests conducted on sensitive clays (e.g. Tavenas et al., 1983) and the interpretation of test data and constitutive model development by other researchers (e.g. Bernander 2000, Leroueil 2001, Locat et al. 2008, Quinn 2009, Locat et al. 2011).

#### 4. FINITE ELEMENT RESULTS

##### 4.1 Propagation of shear band

Figure 2 shows the variation of equivalent plastic shear strain for three cases. In Cases-I & II the shear band initially propagates horizontally and then curved upward resulting in global failure. The failed soil mass follows the excavated/eroded soil block. Figures 2(a) & 2(b) show the equivalent plastic shear strain when the plastic shear strain in the entire failure plane is greater than  $\gamma_{95}^p$ . Global failure does not occur in Case-III (Fig. 2c). There is an approximately 1.4 m gap between the vertical face of the block and soil mass at the right. The shear band propagates horizontally and finally ended at certain length. Figure 2(c) also shows the plastic shear strain when the shear band propagation is ended. Whether the shear

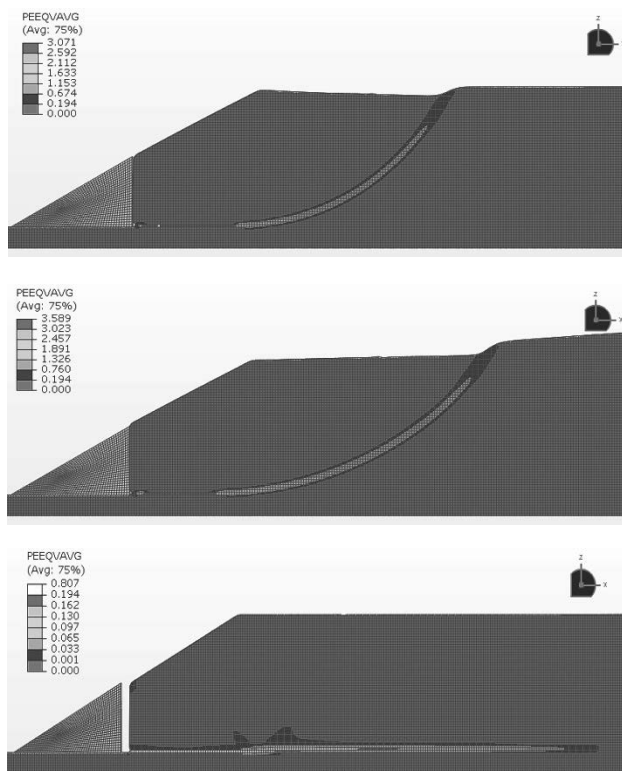


Figure 2. Developed equivalent plastic strain in the softening layer in case I, II and III respectively

band will propagate upward and cause the global failure or not, depends on the shear strength of the upper soil layer and mobilized shear strength along the shear band. For the soil properties and geometry used in the present study the failure pattern is almost same for Cases-I and II. However, the released energy from the excavated/eroded soil block is not sufficient to move the shear band upward in Case-III to cause the failure of the slope.

The equivalent plastic shear strain, denoted by the symbol PEEQVAVG in Fig. 2, is related to  $\gamma^p$  as  $PEEQVAVG = \gamma^p / \epsilon_{95}^p$ . According to Eq. (2), when  $\gamma^p \epsilon_{95}^p (=33\%)$ , that means  $PEEQVAVG=0.194$ , the undrained shear strength is less than

12 kPa ( $=50 \cdot 0.95(50-10)$ ). Figure 2(c) shows that the equivalent plastic shear strain greater than 0.194 is developed in the shear band only near the vertical face of excavated/eroded block in Case-III. However, the equivalent plastic shear strain greater than 0.194 is developed in the entire length of the failure plane in Case-I & Case-II. Therefore, the failure of the slope is occurred in both cases at residual shear strength on the failure plane as large strain is developed.

##### 4.2 Shear stress and mobilized shear strength

The Case-III is considered for further examination of the development of shear stress and mobilized shear strength along the potential failure plane. Figure 3 shows the variation of shear stress along the failure plane with movement of excavated/eroded block. Shear stress for four displacements (115 mm, 245 mm, 380 mm and 500 mm) are shown. In order to explain the process, consider the shear stress on the potential failure plane for the block displacement of 115 mm. The maximum shear stress (50 kPa) is developed at 12.5 m from the vertical face of the cut. The shear stress between 0 to 12.5 m is less than 50 kPa (i.e.  $s_{up}$ ) and greater than 10 kPa (i.e.  $s_{ur}$ ). That means, 0-12.5 m of the shear band represents the post-peak softening zone where the reduction of shear strength is occurred because of plastic strain as Eq. 2, and the mobilized shear strength is in between the peak and residual shear strength of the soil. In the right side of the peak (i.e. distance greater than 12.5 m) the shear stress is again reduced with distance. For this displacement of the block (115 mm), the shear stress in the

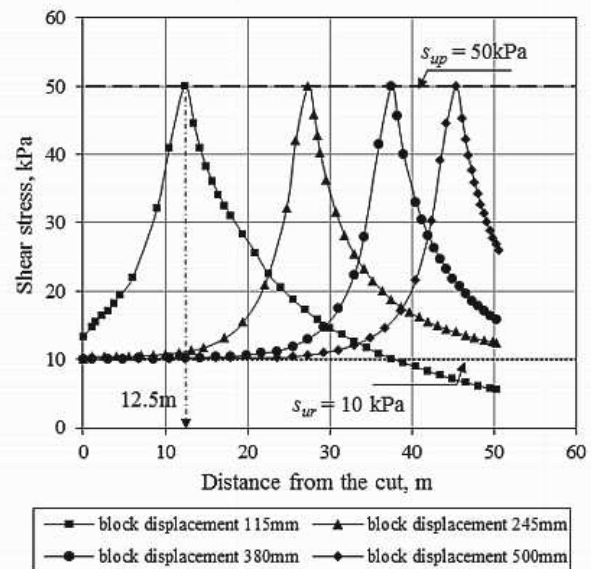


Figure 3. Shear stress along the potential failure plane

potential failure plane at a distance greater than 12.5 m is not increased to the peak, and therefore it represents the pre-peak behavior. At a very large distance, the shear stress is reduced to zero in Case-III as the ground surface is horizontal. The pattern of shear stress development for any other displacement of the block is similar as shown in Fig. 3. The location of the peak shear stress shifts to the right with increase in block displacement; that means a greater length of the potential failure plane is in post-peak stress-strain condition. For example, for 500 mm block movement the peak is occurred at 45.5 m and therefore 0-45.5 m is in post-peak condition with approximately 30 m in residual shear strength level. This process will be continued until the shear band propagation is ended for stable slopes as in Case-III. However, if the failure is occurred, as in Case-I and II, the large plastic shear strain will reduce the shear

strength of soil in the entire failure plane to the residual shear strength and global failure will occur.

Figure 4 shows the variation of shear stress at 4 different locations A, B, C and D (Fig. 1) which are located from the vertical face of the excavated/eroded block at horizontal distance of 3 m, 12.5 m, 25 m and 35 m, respectively. Consider the soil element B at 12.5 m distance. The shear stress in this element is increasing with movement of the excavated/eroded soil block. When the block is displaced by an amount of 115 mm, the shear stress in this element is reached to the peak shear strength of the soil (50 kPa). However, at this displacement of the block, the element A is almost at the residual shear strength. On the other hand, the elements C and D are still in the pre-peak state. That means the shear stress is gradually transferred to the soil elements in the right with displacement of the excavated/eroded soil block. For the soil element under the slope of the river bank there is an initial shear stress. With movement of the block the shear stress is increased from that initial value. However, the initial shear stress is less in the elements far from the river bank. Similar variation in shear stress and mobilized shear strength are obtained for Case-I and II.

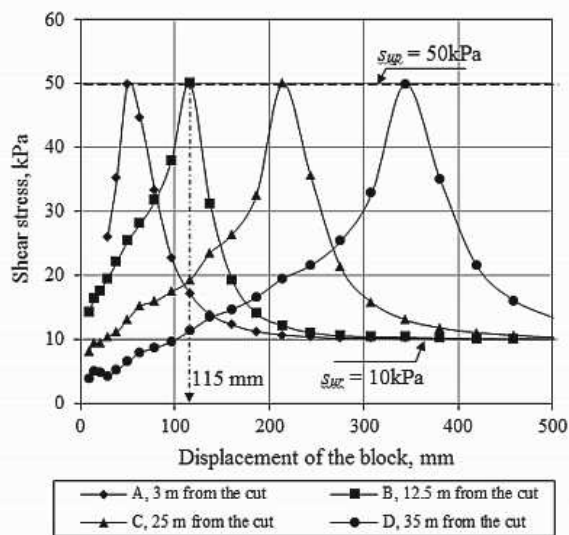


Figure 4. Variation of shear stress at four different locations from the cut

## 5. CONCLUSION

This paper presents a new numerical approach to model the initiation and propagation of shear band in upward progressive failure as encountered near the river banks. Toe erosion is considered as the triggering factor. Coupled Eulerian-Lagrangian (CEL) approach currently available in ABAQUS FE software is used for numerical analysis. Nonlinear strain softening behavior of sensitive clay is incorporated in this large deformation finite element analysis. Three cases are analyzed in this study. In Cases I and II global failure is occurred. However, in Case-III, although global failure is not occurred, the shear band propagation reduced the shear strength in the potential failure plane significantly over a large distance and the slope might be marginally stable for further loading.

## 6. ACKNOWLEDGEMENTS

The writers would like to acknowledge the financial support from Research & Development Corporation of Newfoundland and Labrador and C-CORE.

## 7. REFERENCES

- Anderson L. and Jostad H.P. 2007. Numerical modeling of failure mechanisms in sensitive soft clays — application to offshore geohazards. Offshore Tech. Conf., Texas. Paper OTC 18650.
- Bernander S. 2000. Progressive failure in long natural slopes: formation, potential extension and configuration of finished slides in strain-softening soils. Licentiate Thesis, Luleå University of Technology.
- Bjerrum L. 1967. Progressive failure in slopes in overconsolidated plastic clay and clay shales. Terzaghi Lecture. J. of the Soil Mech. and Found. Div., ASCE 93(5), 3-49.
- Carson M.A. 1979. On the retrogression of landslides in sensitive muddy sediments: Reply. Can. Geotech. J. 16(2), 431-444.
- Cruden D.M. and Varnes D.J. 1996. Landslides types and processes. In Landslides investigation and mitigation. Special Report 247. Transportation Research Board, NRC. Edited by A.K. Turner and R.L. Schuster. National Academy Press, Washington, D.C., 37-75.
- Dey R., Hawlader B., Phillips R. and Soga K. 2012. Effects of shear band propagation on submarine landslide. Proc. of the 22<sup>nd</sup> Int. Offshore and Polar Engineering Conf., Rhodes, Greece, 766-773.
- Einav I. and Randolph M.F. 2005. Combining upper bound and strain path methods for evaluating penetration resistance. Int. J. Num. Methods Engineering 63(14), 1991-2016.
- Grondin G. and Demers D. 1996. The Saint-Liguori flakeslide: Characterization and remedial works. In Proc. of the 7th Int. Symposium on Landslides, Trondheim, Norway, 2, 743-748.
- Gregersen O. 1981. The quick clay landslide in Rissa, Norway. In Proc. of the 10th Int. Conf. on Soil Mech. and Foundation Engineering, Stockholm, Sweden. NGI, Publication No. 135, 421-426.
- Karlsrud K., Aas G. and Gregersen O. 1984. Can we predict landslide hazards in soft sensitive clays? Summary of Norwegian practice and experiences. In Proc. of the 4th Int. Symposium on Landslides, Toronto, Ont., 1, 107-130.
- Leroueil S. 2001. Natural slopes and cuts: movement and failure mechanisms. Géotechnique 51 (3), 197-243.
- Locat A., Leroueil S., Bernander S., Demers D., Locat J. and Ouehb L. 2008. Study of a lateral spread failure in an eastern Canada clay deposit in relation with progressive failure: the Saint-Barnabé-Nord slide. In Proc. of the 4th Canadian Conf. on Geohazards: From Causes to Management, Québec, Que., 89-96.
- Locat A., Leroueil S., Bernander S., Demers D., Jostad H.P. and Ouehb L. 2011. Progressive failures in eastern Canadian and Scandinavian sensitive clays. Can. Geotech. J. 48 (11), 1696-1712.
- NGI Report 2001. Effect of strain softening on stability analysis. Analysis of retrogressive sliding due to strain softening-Ormen Lange case study, Report No 521001 (10).
- Odenstad S. 1951. The landslide at Sköttorp on the Lidan River, February 2, 1946. Royal Swedish Institute Proceedings 4, 1-38.
- Quinn P., Diederichs M.S., Hutchinson D.J. and Rowe R.K. 2007. An exploration of the mechanics of retrogressive landslides in sensitive clay. In Proc. of the 60th Canadian Geotechnical Conf., Ottawa, Ontario, 721-727.
- Quinn P. 2009. Large Landslides in Sensitive Clay in Eastern Canada and the Associated Hazard and Risk to Linear Infrastructure. Doctoral thesis, Queen's University.
- Tavenas F., Flon P., Leroueil S. and Lebeus J. 1983. Remolding energy and risk of slide retrogression in sensitive clays. Proc. of the Symposium on Slopes on Soft Clays, Linköping, Sweden, SGI Report No. 17, 423-454.
- Tavenas F. 1984. Landslides in Canadian sensitive clays — a state-of-the-art. In Proc. of the 4th Int. Symposium on Landslides, Toronto, Ont., 1, 141-153.

# Quantitative vulnerability estimation for individual landslides

## Estimation quantitative de la vulnérabilité aux glissements de terrain

Du J., Yin K.

China University of Geosciences (Wuhan), China

Nadim F., Lacasse S.

International Centre for Geohazards / Norwegian Geotechnical Institute (NGI), Norway

**ABSTRACT:** Vulnerability has not been systematically considered for landslides until recently, but is a fundamental component in the evaluation of risk. Vulnerability depends on the landslide intensity, the characteristics of the elements at risk, and the impact of landslide. A quantitative model is proposed to estimate the vulnerability of the exposed structures and individuals. The model accounts for landslide intensity, different classes of vulnerable elements and the impact of both slow and rapid moving slides.

**RÉSUMÉ :** La vulnérabilité est un facteur important du risque associé aux glissements et n'a pas été considérée jusqu'à tout récemment. Elle dépend de l'intensité et de l'impact du glissement et des propriétés des éléments exposés. L'article propose un modèle calculant la vulnérabilité de structures et d'individus. Ses paramètres caractérisent l'intensité du glissement, tiennent compte de différentes classes de vulnérabilité et distinguent l'impact de glissements évoluant lentement et rapidement.

**KEYWORDS:** Landslide, Quantitative vulnerability evaluation, Intensity, Susceptibility

## 1 INTRODUCTION

The ISSMGE glossary of risk assessment terms defines vulnerability as the degree of loss to an element within the area affected by the landslide hazard. It is expressed on a scale of 0 (no loss) to 1 (total loss). In contrast to flooding and earthquakes, it is not straightforward to define or assess, the vulnerability to landslides, due to the complexity and range of the landslide process (Leroi 1996). However vulnerability can influence the losses to a greater degree than the hazard (Einstein 1988; Alexander 2004). Despite this, it is an economic and political necessity to quantify vulnerability (Varnes 1984; Alexander 1984).

Two different perspectives exist for the vulnerability estimation: that based on the natural sciences and that based on the social sciences (Crozier 2004). Most often, the assessments of landslide risk are based on the natural science approaches. Some apply damage matrices (Leone 1996) based on qualitative (Cardinali 2002) and quantitative approaches (Fell, 1994). Conceptual frameworks for quantitative vulnerability estimation have been presented (Düzgün and Lacasse 2005, Uzielli *et al* 2008).

## 2 PROPOSED MODEL

Following Uzielli *et al* (2008) and Li (2010), the proposed model defines vulnerability as a function of landslide intensity and susceptibility of element at risk. The parameters are established on the basis of the landslide impact mechanism and categories of vulnerable elements. The proposed vulnerability model is defined by Eq. 1 and represented graphically in Fig. 1:

$$\begin{aligned} \text{For } I \leq 1-S & \quad V = \frac{1}{2}[I/(1-S)]^2 \\ \text{For } I > 1-S & \quad V = 1 - \frac{1}{2}[(1-I)/S]^2 \end{aligned} \quad (1)$$

$V \in [0, 1]$  is the vulnerability of elements exposed to the threat. For structures, 1 means that the structure is completely destroyed, while values less than one represent the degree of damage and 0 describing no damage. For individuals, 1 means loss of life, while a value  $< 1$  is the probability of loss of life.  $I \in [0, 1]$  is the intensity of landslide. An intensity of 1 means that the landslide has the potential of destroying all elements in its path.

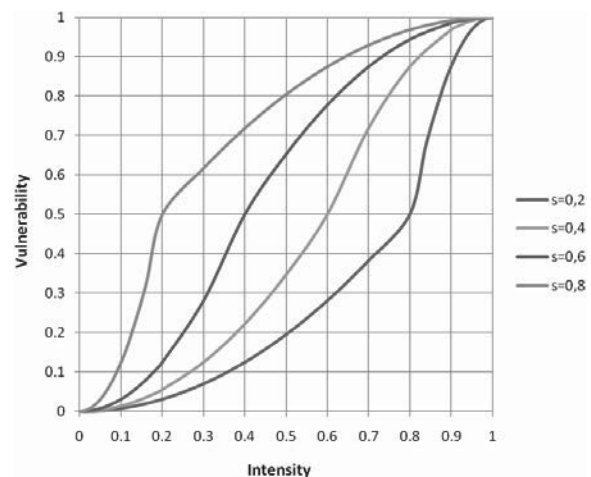


Fig. 1 Vulnerability ( $V$ ) from susceptibility ( $S$ ) and landslide intensity ( $I$ ).

$S \in [0, 1]$  is the element susceptibility:  $S=0$  means that the vulnerable element has high inherent resistance under impact. The terms  $V$ ,  $I$  and  $S$  are non-dimensional and the values of 1 and 0 indicate the highest and lowest boundaries for the three parameters. To account for the landslide impact in the vulnerability estimation, two stages of deformation are considered: 1) a slow deformation stage and 2) the failure (rapid movement) stage.

## 3 LANDSLIDE INTENSITY

The definition of vulnerability requires information on landslide intensity (Guzzetti *et al* 1996), which should include information on the landslide severity degree and spatial dimensions.

### 3.1 Slow deformation stage

Under slow deformation, cracks and tilting may occur in structures located on the landslide, due to displacement and velocity of the ground surface and foundation substrata. The intensity parameters include landslide velocity and local deformation,



which describe the severity degree, and landslide depth, which reflects the spatial dimensions. The model is defined as:

$$I_{def} = 1 - (1 - I_{d-def})(1 - I_{d-vel})(1 - I_{d-dep}) \quad (2)$$

where  $I_{d-def}$ ,  $I_{d-vel}$  and  $I_{d-dep}$  are the parameters for deformation, velocity and landslide depth at the location of the structure. The deformations include settlement, horizontal movement and inclination (Bell 1978; Peng 1992; Zheng 2007). A basic relationship (Eq. 3) seems to provide a good approximation:

$$W_s = aW_g + bW_s \quad (3)$$

where  $W_s$  and  $W_g$  are the deformations of structure and ground,  $a$  is the slope and  $b$  is the intercept. Table 1 gives the range of  $a$  and  $b$  vs movement and structure types (Peng 1992; Zheng 2007). The deformation intensity depends on the ratio of deformation to allowable threshold value as shown in Table 2.

Table 1.  $a$  and  $b$  as function of ground deformation and structure type

Structure	Brick masonry, concrete structures		Reinforced (RC) concrete structures	
	$a$	$b$	$a$	$b$
Settlement (mm)	0.87-0.99	0.50-1.27	0.96-1.03	1.19-3.57
Tension (mm/m)	0.74-0.89	—	0.68-0.71	—
Compression (mm/m)	0.28-0.32	—	0.24-0.27	—
Inclination (mm/m)	0.99-1.06	0.80-0.90	0.69-0.97	0.03-0.2

Table 2. Proposed value of intensity parameters for deformation

Ratio of deformation to allowable threshold	$I_{d-def}$
<0.2	0.1
0.2-0.4	0.2
0.4-0.6	0.4
0.6-0.8	0.6
0.8-1.0	0.8
1.0-1.2	0.9
≥1.2	1.0

According to the landslide movement scale and response of structures (Cruden and Varnes 1996), the intensity of the landslide velocity can be obtained by the model described in Eq. 4 (Li 2010).  $V$  is the velocity of landslide (mm/s).

$$\begin{aligned} \text{For } v \leq 5 \times 10^{-7} & \quad I_{d-vel} = 0 \\ \text{For } 5 \times 10^{-7} < v \leq 5 \times 10^{-1} & \quad I_{d-vel} = 1/36[\log_{10} v + 6.30]^2 \\ \text{For } v \geq 5 \times 10^{-1} & \quad I_{d-vel} = 1 \end{aligned} \quad (4)$$

For structures on a moving landslide, the degree of damage depends mainly on the relative depth of the structure foundation to the sliding surface. Ragozin (2000) quantified the vulnerability of structures as a function of the foundation depth  $h$  (m) depending on the depth of predicted landslide  $d$  (m). The model described by Eq. 5 is proposed used.

$$\begin{aligned} \text{For } d/h < 0.8 & \quad I_{d-dep} = (1.25 \cdot d/h)^{1/3} \\ \text{For } 0.8 < d/h \leq 1.2 & \quad I_{d-dep} = 1 \\ \text{For } d/h > 1.2 & \quad I_{d-dep} = 1.44 \cdot (d/h)^{-2} \end{aligned} \quad (5)$$

### 3.2 Failure stage

#### 3.2.1 Landslide intensity for structures

The structures located within the release zone of a rapidly moving landslide are completely destroyed and have a vulnerability of 1.0. For the structures within the run-out distance, the impact mechanisms can be divided into two main categories: burial and impact pressure. For structures, the intensity of the landslide is defined as a function of its depth and impact pressure, where  $I_{pre}$  and  $I_{f-dep}$  are impact pressure and landslide depth parameters:

$$I_{fai-s} = 1 - (1 - I_{pre})(1 - I_{f-dep}) \quad (6)$$

#### (1) Impact pressure

After the landslide fails, the horizontal impact pressure is the main cause of damage to structures (Glade 2004; Ulusay 2007). Petrazzuoli (2004) analyzed the collapse limit load of regular and irregular RC structures to horizontal pressure with the strong beams and weak columns structural models. The proposed vulnerability model uses the average value of each typology to estimate the horizontal pressure limit  $P$  vs the number of

stories  $n$ , in which the values of coefficient  $\alpha$  and  $\beta$  for each structure type are listed in Table 3.

$$P = \alpha n(n) + \beta \quad (7)$$

Table 3. Coefficients  $\alpha$  and  $\beta$  in Eq. 7 for different structure types.

Structure	Strongly aseismic	Weakly aseismic	Strongly non-aseismic	Weakly non-aseismic
Regular structure				
A	-4.384	-2.717	-2.157	-1.276
B	19.125	13.164	10.568	7.693
Irregular structure				
A	-3.779	-2.467	-1.821	-1.343
B	14.553	10.288	8.068	6.066

The ratio of landslide impact pressure on the building to horizontal pressure limit is defined as the intensity parameter  $I_{pre}$  (Table 4). The horizontal pressure limit of RC frame can be obtained according to Eq. 7, while the limit pressure of terracotta panels in Table 5 can be used for masonry structure.

Table 4. Proposed values of impact pressure intensity parameter.

Landslide impact pressure/Structure horizontal pressure limit	$I_{pre}$
<0.1	0.05
0.1-0.2	0.20
0.2-0.4	0.40
0.4-0.7	0.70
0.7-1.0	0.90
≥1.0	1.00

Table 5. Estimated resistances of buildings and elements (Spence 2004)

Building elements	Failure pressure(kPa)
Terracotta tile infill panel with openings	7.6-8.9
Terracotta tile infill panel without openings	5.5
Tuff infill panel (length 4 m, thickness 40 cm)	6.8-9
Tuff infill panel (length 4 m, thickness 60 cm)	10-13
Weak non-aseismic RC buildings (1 to 3 storeys)	4.5-8
Strong non-aseismic RC buildings (4 to 7 storeys)	5-9
Weak aseismic RC buildings (multi-storeys)	5-10
Strong aseismic RC buildings (multi-storeys)	6-14

#### (2) Landslide depth

As inferred from the structural damage, the intensity parameter for landslide depth should be defined as the ratio of landslide depth to height of structure. When landslide depth is equal to or greater than the structure, the structure loses completely lose its functionality. The proposed values of  $I_{f-dep}$  are found in Table 6.

Table 6. Proposed values of landslide depth intensity parameter

Ratio of landslide depth to height of structure	$I_{f-dep}$
<0.2	0.10
0.2-0.4	0.30
0.4-0.6	0.50
0.6-0.8	0.70
0.8-1.0	0.90
≥1.0	1.00

Depending on location, the persons within the affected area can be divided into two categories: indoors and outdoors. Landslide velocity, depth and width become the intensity parameters:

$$I_{fai-p} = 1 - (1 - I_{f-vel})(1 - I'_{f-dep})(1 - I_{wid}) \quad (8)$$

where  $I_{f-vel}$ ,  $I'_{f-dep}$  and  $I_{wid}$  are the parameters of landslide velocity, depth and width, respectively. A moving slide depth greater than knee-height makes it difficult to escape. Using 1.6 m and 0.482 (Swami 2006) as average height and leg ratio, a threshold value of 0.8m for critical landslide depth is obtained. The values of  $I'_{f-dep}$  in Table 7 are proposed:

For landslide width, five degrees are identified to allow for change in landslide activity conditions (Table 8). The landslide velocity scale defined by Eq. 9 is identical to that proposed by Li (2010). The value  $v$  is the velocity of the landslide (mm/s).

$$\begin{aligned} \text{For } v \leq 5 \times 10^{-1} & \quad I_{d-vel} = 0 \\ \text{For } 5 \times 10^{-1} < v \leq 5 \times 10^3 & \quad I_{d-vel} = 1/16[\log_{10} v + 0.3]^2 \\ \text{For } v \geq 5 \times 10^3 & \quad I_{d-vel} = 1 \end{aligned} \quad (9)$$

Table 7. Proposed values of landslide depth intensity parameter

Landslide depth (m)	$I'_{f-dep}$
<0.1	0.10
0.1-0.3	0.30
0.3-0.6	0.70
0.6-0.8	0.90
≥0.8	1.00

Table 8. Proposed values of landslide width intensity parameter

Landslide width (m)	$I_{wid}$
< 50	0.10
50-200	0.30
200-400	0.50
400-700	0.80
≥ 700	1.00

## 4 SUSCEPTIBILITY

### 4.1 Susceptibility of structures

The capacity of a structure to withstand the landslide hazard depends on the morphological characteristics and utilization conditions (Amatruda 2004; Coburn 2002). Four parameters were considered, including structure type  $s_{str}$ , maintenance state  $s_{mai}$ , ratio of service years to design service life  $s_{ser}$  and the difference in the directionality of landslide movement and the principal longitudinal direction of the structure  $s_{dir}$ , with the model given in Eq. 10. Together, these parameters describe the susceptibility of the structures to be damaged by a landslide (Table 9 for  $s_{str}$ , Table 10 for  $s_{mai}$ , Table 11 for  $s_{ser}$ , Table 12 for  $s_{dir}$ ).

$$S_s = 1 - (1 - s_{str})(1 - s_{mai})(1 - s_{ser})(1 - s_{dir}) \quad (10)$$

Table 9 Structure susceptibility parameter (Heinimann 1999)

Structural typology	Resistance	$S_{str}$
Lightest, simple structures	Very high	1.00
Light structures	High	0.90
Rock masonry and concrete	Medium	0.70
Brick masonry, concrete structures	Low	0.50
Reinforced concrete structures	Very low	0.30
Reinforced structures	Extremely low	0.10

Table 10 Proposed values of maintenance state susceptibility parameter

State of maintenance	$S_{mai}$
Extremely good	0.00
Good	0.05
Slight deformation	0.25
Medium deformation	0.50
Serious deformation	0.75
Extremely Serious deformation	1.00

The damage would be most serious when the angle between the two directions is 0° and be lightest when the angle gets close to 45° (Table 12).

Table 11 Proposed values of service year susceptibility parameter

Ratio of service year to design service life	$S_{ser}$
≤ 0.1	0.05
0.1 - 0.4	0.10

Table 14. Proposed values of “generic” early warning system susceptibility parameter

Completeness level	$S_{war}$	Description of risk reduction or risk avoidance measure
None	1.0	Investigate the geological background and deformation of the landslide, without any monitoring measures.
Simple	0.6-1.0	Simple manual monitoring measurements with low precision and measurements at long interval (one month), e.g. manual measurement of extension velocity of crack and subsidence velocity of head of landslide.
Moderate	0.2-0.6	Accurate monitoring equipment with moderate precision, long interval readings (one month) and low distribution density of monitoring points; monitoring involves only geological parameters; investigation of population exposed to landslide risk; simple emergency plan includes warning transmission and evacuation paths.
Comprehensive	0.0-0.2	Accurate monitoring equipment with high precision and close interval readings (one day/one week); density of monitoring points high enough to sense deformation of entire landslide; monitoring involves geophysical, atmospheric, hydrodynamic and soil quantities; decision procedures in place based on experience with time prediction, triggering threshold and evacuation successes/failures with landslide; overview of population and public facilities exposed; overall emergency plan includes warning transmission, evacuation paths, logistics, medical assistance and so on.

0.4 - 0.6	0.30
0.6 - 0.8	0.50
0.8 - 1.0	0.70
1.0 - 1.2	0.80
> 1.2	1.00

Table 12. Values of directionality difference susceptibility parameter.

Directionality of landslide movement (°)	$S_{dir}$
0-5	1.0-0.6
5-15	0.6-0.4
15-30	0.4-0.2
30-45	0.2-0.0

### 4.2 Human susceptibility

The susceptibility of persons to be hurt or killed by the landslide depends strongly on the cognitive and reaction capacity upon the occurrence of a landslide and the protection measures at the site, e.g. escape routes or early warning system. The following model was proposed to describe the landslide susceptibility for persons:

$$S_p = 1 - (1 - s_{hel})(1 - s_{age})(1 - s_{war}) \quad (11)$$

where  $s_{hel}$ ,  $s_{age}$  and  $s_{war}$  are the susceptibility parameters, health condition, age and existence of a warning system, respectively.

A person's health condition, i.e. evacuation capacity, can be divided into three classes: 1) healthy, 2) weak physical condition, e.g. chronic disease slowing down movement, and 3) complete incapacitation with inability to evacuate. The susceptibility parameter values listed in Table 13 are proposed.

On the basis of fatality rate-age distribution data from earthquakes, Li (2010) proposed a quadratic polynomial function (Eq. 12) in terms of age  $a$ , which was adopted in this paper:

$$s_{age} = 0.95 - 0.00486 [\text{INT}(a/5) - 5]^2 \quad (12)$$

where INT() is the downward rounded integer function.

Table 13. Proposed values of health condition susceptibility parameter.

Health condition	$S_{hel}$
Healthy	0-0.1
Weak physical condition	0.1-0.8
Complete incapacitation	0.8-1.0

“Early warning” refers to all the measures that can be taken before the occurrence of a catastrophic event reducing the risk or contributing to avoid it (Table 14). Completeness level in the table refers to the efficiency of early warning or other mitigation measures in place to reduce or avoid risk.

## 5 VULNERABILITY OF PERSONS IN STRUCTURES

When a landslide occurs, the vulnerability of persons in the structures is directly correlated with the structure damage.

To estimate the casualty level in a building, one needs to assess the proportion of people trapped in the debris of a collapsed building and the casualty level for different degrees of damage.

When buildings collapse, not all the occupants are trapped inside. The number of people trapped in a collapsed building depends on the size and type of building, the collapse itself, the time of collapse and the escape options during and after the col-

lapse. Masonry and reinforced concrete, have different collapse mechanisms and rubble characteristics. The total collapse of masonry buildings provides smaller cavities than the collapse of frame structures. Li (2010) proposed an exponential description of the vulnerability of persons inside structures. Coburn (2002) estimated the average percentage of occupants trapped in a collapsed building to range between 30% and 70%, and estimated the injured proportion of occupants at collapse (Table 15).

The four levels of casualty, i.e. fatalities, seriously injured, moderately injured and lightly injured or uninjured, were denoted by vulnerability values of 1, 0.8, 0.5 and 0.2. The vulnerability of persons ( $V_p$ ) in different structures is listed in Table 16 ( $V_s = 1$  or collapse). Equation 13 quantifies the vulnerability of persons  $V_p$  (index  $\alpha$  for different structures is listed in Table 16).

$$V_p = 0.001 \exp(\alpha V_s) \quad (13)$$

Table 15. Casualty distribution, collapsed buildings (Coburn 2002)

Class	Fatalities	Seriously injured	Moderately injured	Lightly injured or uninjured
Masonry	17.5	10	17.5	55
RC frame	21	0.8	9.2	70
RC shear wall	10	0.7	9.3	80
Steel	16	0.6	9.4	75
Timber	0.6	0.2	10.2	89

Table 16. Vulnerability of persons and value of index  $\alpha$

Structure type	Masonry	RC frame	Steel	RC shear wall	Timber
$V_p$ (when $V_s = 1$ )	0.45	0.40	0.36	0.31	0.24
$\alpha$	6.1	6	5.9	5.75	5.5

## 6 CONCLUSIONS

A model for the quantitative estimate of landslide vulnerability is proposed with two parameters: landslide intensity and susceptibility of the elements at risk. A reliable estimate of landslide intensity should consider the relationship between landslide severity and spatial dimensions. For the slow-moving landslides, the quantitative relationships for three categories of ground deformation and structure response are considered in the assessment of the landslide intensity. Based on empirical data, a function describing the ratio of landslide depth to foundation depth can be used to estimate the effect of geometric intensity.

In the landslide failing stage, intensity models were established for stationary and non-stationary vulnerable elements. Impact pressure and landslide depth were included in the vulnerability assessment of structures. For persons in open space, the parameters include landslide velocity, depth and width.

Functions of horizontal limit pressure versus the number of storeys of different structures were proposed to quantify the landslide impact intensity parameter of the moving mass. For the human susceptibility, generic mitigation measures were proposed to include a component of risk prevention and emergency awareness. Further, collapse mechanisms and construction characteristics of different construction types, the vulnerability functions for persons in different structure categories were proposed.

The model has limitations and needs further research. Some of the subjective and empirical parameters in the model should be calibrated and gradually documented with the addition of objective data, experience, observations and expert judgment.

## 7 ACKNOWLEDGEMENTS

This research was funded by The National Natural Sciences Foundation of China (40872176). The work described was done while the first author was a guest researcher at the International Centre for Geohazards (ICG) at NGI. The first author thanks the China Scholarship Council, NGI and the Research Council of Norway for funding her stay at ICG/NGI. The authors thank also Prof. O. Hungr (University of British Columbia), who kindly provided a beta version of DAN3D to NGI, and Drs. J.M. Cepeda and D. Issler of NGI for their help and guidance.

## 8 REFERENCES

- Alexander, D.E. 1984. Building damage by landslide: the case of Ancona, Italy. *Ekistics-The Problems and Science of Human Settlements*, 51:452-462.
- Alexander, D.E. 2004. *Vulnerability to landslide. Landslide Hazard and Risk*. John Wiley & Sons, Ltd. pp. 175-198.
- Amatruda, G., Bonnard, C., Castelli, M. et al. 2004. A key approach: the IMIRILAND project method. Identification and mitigation of large landslide risks in Europe - advances in risk assessment. In: Bonnard et al (Eds.), *European Commission, Fifth Framework Program*. Balkema. 13-44.
- Bell, S.E. 1978. *Successful design for mining subsidence. Large movements and structures*. New York: Acad. Press 562-578.
- Crozier, M.J., Glade, T. 2004. Landslide hazard and risk: issues, concepts and approach. *Landslide hazard and Risk*. John Wiley & Sons, Ltd. 1-40.
- Coburn, A., Spence, R. 2002. *Earthquake protection*. John Wiley & Sons Ltd, The Atrium, Southern Gate, Chichester, West Sussex PO19 8SQ, England.
- Cruden, D.M., Varnes, D.J. 1996. Landslide types and processes. In: *Landslide investigation and mitigation*. National Academy Press, Washington 36-75.
- Cardinali, M., Reichenbach, P., Guzzetti, F. et al. 2002. A geomorphological approach to the estimation of landslide hazards and risks in Umbria, Central Italy. *Natural Hazards and Earth System Sciences* 2:57-72
- Düzgün, HSB, Lacasse, S. 2005. Vulnerability and acceptable risk in integrated risk assessment framework. Hungr et al (eds) *Landslide risk management*. Balkema, NL. 505-515.
- Einstein, H.H. 1988. Special lecture - landslide risk assessment procedure. In: *5<sup>th</sup> International Symposium on Landslides*. Landslides 2:1075-1090.
- Fell, R. 1994. Landslide risk assessment and acceptable risk. *Canadian Geotechnical Journal* 31:261-272
- Glade, T. 2003. Vulnerability assessment in landslide risk analysis. *Erde* 134(2):123-146.
- Glade, T., Crozier, M.J. 2004. The Natural of Landslide Hazard Impact. *Landslide Hazard and Risk*. England: John Wiley & Sons, Ltd, 44-74.
- Guzzetti, F., Carrara, A., Cardinali, M., Reichenbach, P. 1996. Landslide hazard evaluation: an aid to a sustainable development. *Geomorphol* 31:181-216
- Heinimann, H.R. 1999. Risikoanalyse bei gravitativen Naturgefahren-Fallbeispiele & Daten. *Umwelt-Materialien* 107/1, Bern.
- Leroi, E. 1996. Landslide hazard-risk maps at different scales: objectives, tools and development. *Proc. of 7<sup>th</sup> international symposium on landslides*, June 17-21, Trondheim, 35-51.
- Leone, F., Ast'è, J.P., Leroi, E. 1996. Vulnerability assessment of elements exposed to mass moving: working towards a better risk perception. In: Senneset K (ed) *Landslides*. Balkema, Rotterdam, 263-269.
- Li, Z, Nadim, F, Huang, HW, Uzielli, M, Lacasse, S. 2010. Quantitative vulnerability estimation for scenario-based landslide hazards, *Landslides* 7:125-134.
- Peng, S.S. 1992. *Surface subsidence engineering*. Colorado: Society for Mining, Metallurgy and Exploration 77-90.
- Swami, V., Einon, D., Furnham, A. 2006. The leg-to-body ratio as a human aesthetic criterion, *Body Image* 3:317-323.
- Ulusay, R., Aydan, Ö., Kılıç, R. 2007. Geotechnical assessment of the 2005 Kuzulu landslide *Engin. Geology* 89:112-128.
- Uzielli, M., Nadim, F., Lacasse, S., Kaynia, A.M. 2008. A conceptual framework for quantitative estimation of physical vulnerability to landslides. *Engin. Geology* 102:251-256.
- Varnes, D.J. 1984. *Landslide hazard zonation: a review of principles and practice*. UNESCO, France, 1-63.
- Zheng, K.Z., Guo, G.L., Tan, Z.X. 2001. Analysis of Movement and Deformation Characteristics of Buildings Above Mining Subsidence Areas. *Journal of China University of Mining & Technology* 30(4):354-358.

# A site specific early warning system for rainfall induced landslides

Utilisation d'un site spécifique pour l'élaboration d'un système d'alerte rapide pour les instabilités de pente induites par les pluies.

Harris S., Orense R.

*Department of Civil and Environmental Engineering, The University of Auckland, Auckland, New Zealand*

Itoh K.

*National Institute of Occupational Safety and Health, Tokyo, Japan*

**ABSTRACT:** An early warning system (EWS) to warn users of imminent landsliding caused by rainfall has been developed. The EWS is deterministic, based on a pre-determined failure mechanism present at a specific site. A prototype of the EWS was developed for a roadway embankment located in Silverdale, New Zealand. Prolonged rainfall caused a landslide at the site in 2008. Soil debris from this landslide event almost obstructed a major highway, which could have been potentially dangerous to motorists as well as causing major delays to the Auckland roading network. Volumetric water content sensors were installed at various depths and locations along the same cross section of the site. A 2D finite element model was used to replicate the response of the sensors to rainfall, using monitored rainfall events as an influx in the model. Next, a limit equilibrium analysis was used to obtain the factor of safety against slope failure for each time step in the finite element model. An artificial neural network was then trained to predict this factor of safety using the sensor readings as inputs. Thus, the factor of safety of the slope can be predicted in real time. This predicted factor of safety forms the basis of the EWS.

**RÉSUMÉ :** Un système d'alerte précoce (SAP) pour avertir les utilisateurs de glissements de terrain provoqués par des pluies imminentes a été développé. Le SAP est déterministe, basée sur les mécanismes de rupture pré-déterminés présents sur un site spécifique. Un prototype du SAP a été développé pour un remblai de la chaussée située à Silverdale en Nouvelle-Zélande. Des pluies prolongées ont causé un glissement de terrain sur le site en 2008. Les coulées de sol engendrées par ce glissement de terrain ont presque obstrué une route importante, ce qui aurait pu être potentiellement dangereux pour les automobilistes ainsi qu'être à l'origine de retards importants sur le réseau routiers d'Auckland. Des capteurs volumétriques de teneur en eau ont été installés à des profondeurs différentes et à des emplacements variés le long de la section transversale du site. Un modèle par éléments finis 2D a été utilisé pour reproduire la réponse des capteurs aux précipitations, en utilisant les données expérimentales de comme données d'entrée. Ensuite, une analyse d'équilibre limite a été utilisée pour obtenir le facteur de sécurité pour la stabilité de la pente pour chaque pas de temps. Un réseau neuronal artificiel a ensuite été formé pour prédire ce facteur de sécurité en utilisant les relevés du capteur comme modèle. Ainsi, le facteur de sécurité de la pente peut être prédite en temps réel. Ce facteur de sécurité prévu est à la base du SAP.

**KEYWORDS:** rainfall, landslide, artificial neural network, early warning system

## 1 INTRODUCTION

As a means to mitigate the risk of rainfall induced landslides which cause millions of dollars' worth of damage each year in New Zealand (NIWA & GNS Science, 2010), an early warning system (EWS) has been developed. A prototype of this EWS was installed at a site in Silverdale, Northland, New Zealand. Much of the damage which incurs from rainfall induced landslides occurs in this region of New Zealand (NIWA & GNS Science, 2009).

EWSs for rainfall induced landslides started as empirical relationships which related the number of landslides in a given region to the intensity and duration of rainfall events. Examples can be seen in Dhakal & Sidle (2004), Keefer et al (1987) and Caine (1980). As technologies have developed, focus on EWSs has become more site specific. Current EWSs rely on measuring parameters such as pore pressure and displacement at a given site. Such EWSs are based on issuing an alarm when a predetermined level of these parameters has been reached (Chae & Kim, 2012; Intrieri et al., 2012). The EWS developed in this research was required to return to the user a number related to the possibility of failure, and also a timeframe for failure to occur. To achieve this, volumetric water content (VWC) sensors were installed at a variety of depths at the toe, mid-point and top of the slope. A tipping bucket rain gauge was used to monitor the intensity and duration of rainfall events. The fluctuations in VWC recorded by the sensors were replicated in a finite

element model (FEM), using the recorded rainfall events as an influx into the slope. Next, a limit equilibrium analysis was used to determine the factor of safety (FOS) at each time step in the FEM. Thus, a database was created which contained values of the VWC as measured by the sensors at the site, and the corresponding FOS. This database was then used to train an artificial neural network (ANN). The ANN can thus predict the FOS of the slope in real time, using sensor readings as an input. The ANN can also predict the future FOS of the slope, using rainfall forecasts for the site as an input. The trend of the predicted FOS using the sensor data, and the future FOS obtained according to the rainfall forecast, form the basis of the EWS. Based on this information the user of the EWS can take the required action; in this case, lowering speed limits and putting detours in place.

### 1.1 Site and Soil Description

The site consists of a roadway embankment created from a cut operation during the construction of State Highway One, which runs parallel to the toe of the embankment. State Highway One is a major arterial which services Auckland city. The slope angle of the embankment is approximately 15°. A concrete dish drain is located on a bench at mid-height of the slope. The site is grassed, with some low height trees present. Debris from a landslide which occurred at the site in 2008 following prolonged rainfall almost crossed into the traffic lanes of State

Highway One, which could be potentially dangerous to motorists and cause significant disruption to the Auckland road network.

The soil at the site consists of weathered soil from the Northland Allochthon formation, which is renowned for its montmorillonite content (Power, 2005). This formation is susceptible to landsliding due to seasonal pore-pressure changes (Lentfer, 2007; O'Sullivan, 2009). The site consists of 3 strata; the underlying parent rock, a transition zone and a completely weathered residual soil. The transition zone consists of unweathered rock fragments in a silty clayey matrix. This transition zone has many slickensided shear surfaces present, and is thought to be one of the underlying factors that give rise to the susceptibility of the formation to landslides. The residual soil is a silty clay, susceptible to shrink swell movement. In general, sites in the Northland Allochthon have high ground water tables even in dry periods (O'Sullivan, 2009).

For a more detailed description of the site and soil properties, the reader is referred to Harris et al. (2012).

## 2 METHODOLOGY

A total of 13 VWC sensors were installed along the same cross section of the slope; at the toe, mid-height and crest. The sensors consisted of MP406s and ECH<sub>2</sub>O probes (ICT International Pty Ltd, 2012), which were installed at approximately 0.25m depth intervals. A tipping bucket rain-gauge was used to record rainfall events. Recordings were made via a data logger at an hourly interval.

*SEEP/W* (GEO-SLOPE International Ltd, 2009a) was used for the FEM. The hourly rainfall captured at the site was input as an influx into the slope. A general evaporation pattern was applied to the model as a negative influx between rainfall events. This generalised evaporation pattern was based on a trial and error method to get the best agreement between the FEM results and the field monitoring results. The level of evaporation applied following a rainfall event was determined by the cumulative rainfall amount of the event. This FEM was coupled with the limit equilibrium analysis (LEA) program *SLOPE/W* (GEO-SLOPE International Ltd, 2009b). Thus at each hourly time step in the FEM, the FOS was obtained.

The soil properties used in these models are given in Table 1. The soil water characteristic curve was described using the Van Genuchten (1980) method, the parameters of which were obtained using the pressure plate apparatus. The permeability was determined using the falling head method. A variety of triaxial tests, including constant shear drained tests, were used to determine the shear strength parameters. The shear strength values used for the top soil layer were reasonably high to force the slip surface obtained in the LEA to a reasonable depth.  $\phi^b$  represents the angle of shearing resistance due to matric suctions, as described by Fredlund et al. (1978)

Table 1. Soil parameters used in the models.

	Van Genuchten (1980) Parameter					Shear Strength		
	k	a	n	m	$\theta_r$	$\phi^a$	$\phi^b$	c
	m/hr $10^{-3}$	kPa <sup>-1</sup>			%	°	°	kPa
Top Soil	36	608	3.27	0.69	38.5	40	20	10
Residual Soil	0.36	608	3.27	0.69	38.5	36	20	0
Transition Zone	0.036	297	5.23	0.81	37.2	21	20	3
Underlying Rock	0.0036	29	5.23	0.81	37.2	35	20	5

The ANN was developed using the software *Matlab* (The MathWorks Inc, 2012). For more information regarding ANNs and their use in geotechnical engineering, the reader is referred to Khanlari et al. (2012). The ANN was trained to predict the LEA-obtained FOS using the sensor readings from the field monitoring as inputs. The ANN was developed as a closed-loop

recurrent dynamic network, where the FOS predicted by the ANN for the previous time-step was used as an input for the prediction of the FOS for the current time-step. The Levenberg-Marquardt method (Mathworks, 2010) was used to optimize the ANN, which had 10 hidden layers. The accuracy of the ANN improved when cumulative rainfall amounts were included as inputs into the ANN. Thus, cumulative rainfall amounts ranging from 2 to 200 hours were included as inputs into the ANN.

A second ANN was developed which predicts the LEA obtained FOS based solely on rainfall data. Thus the future FOS could be predicted at the site using rainfall forecasts obtained from the Meteorological Service of New Zealand (2012).

## 3 RESULTS

A reasonable agreement was obtained between the field measured and FEM obtained VWC. The permeability of the top soil layer had to be increased in the FEM in comparison to the underlying soil layers to obtain the required infiltration amount. Presumably this reflects the discontinuities such as surface cracks and vegetation of the soil. In some locations the agreement was very good, in others the agreement quite poor. The reason for this is thought to be due to natural variability within the soil, as described by Dai et al. (2002).

To confirm this modelling process, the rainfall record obtained from the Meteorological Service of New Zealand (2012) leading up to the 2008 landslide was input into the models. As a FOS of just above unity was obtained at approximately the same time as the landslide occurred, it is assumed that the models used in the development of this EWS were reasonably accurate.

Because few extreme rainfall events occurred during the field monitoring period, artificial rainfall events were input into the rainfall record. Such artificial rainfall events can be seen in the upper graph of Figure 1, at an elapsed time of 1500 hours and 2200 hours. The comparison between the FOS obtained from the LEA, that obtained from the ANN using sensor data, and that obtained from the ANN using just rainfall data is shown in the lower graph of Figure 1. As observed, at each significant rainfall event there is a large decrease in the FOS. This FOS recovers rapidly following the rainfall event.

The ANNs are reasonably accurate at predicting the LEA obtained FOS. The mean squared error of the ANN using sensor was 0.41. Using just rainfall data, the mean squared error increased to 1.16. The FOS predicted by the ANNs is susceptible to large fluctuations, particularly during times of evaporation. This is seen at elapsed times of approximately 1600 hours and 2600 hours. Because these fluctuations occur during times of evaporation, they are not critical to the accuracy of the EWS; however they do indicate that some discrepancies occur due to the generalised evaporation pattern which was used. If a deterministic approach was used to measure evaporation, such as that described by Penman (1948), it is thought that such discrepancies will be minimised. The improvement in accuracy from the ANN which uses just rainfall data as an input, compared to the ANN which uses sensor data also, indicates that the use of the sensors provides an indication as to the actual amount of rainfall infiltration in the slope.

To provide an example of the EWS in use, the data corresponding to the point shown in Figure 1 was input into the EWS. The resulting plot is shown in Figure 2. Elapsed time = 0 corresponds to the point in time when the data was obtained from the site. The upper graph in Figure 2 shows the rainfall record obtained from the site (from an elapsed time of -24 to an elapsed time of 0). The rainfall is constant as it is obtained during an artificial rainfall event, as shown in Figure 1 (a). The rainfall record in Figure 2 from an elapsed time of 0 to and elapsed time of 5 hours is that obtained from the forecast.

The solid line in the lower graph of Figure 2 is the ANN – predicted FOS of the last 24 hours, using the sensor data as inputs. The dotted line is the predicted FOS over the next 5

hours, using the rainfall forecast data as an input. Because the ANN using the sensor data is more accurate than that using just rainfall data, this predicted FOS using rainfall forecasts loses

accuracy over time. Thus, the predicted future FOS using rainfall forecast data is set to equal the FOS predicted using sensor data each time the sensor data is downloaded.

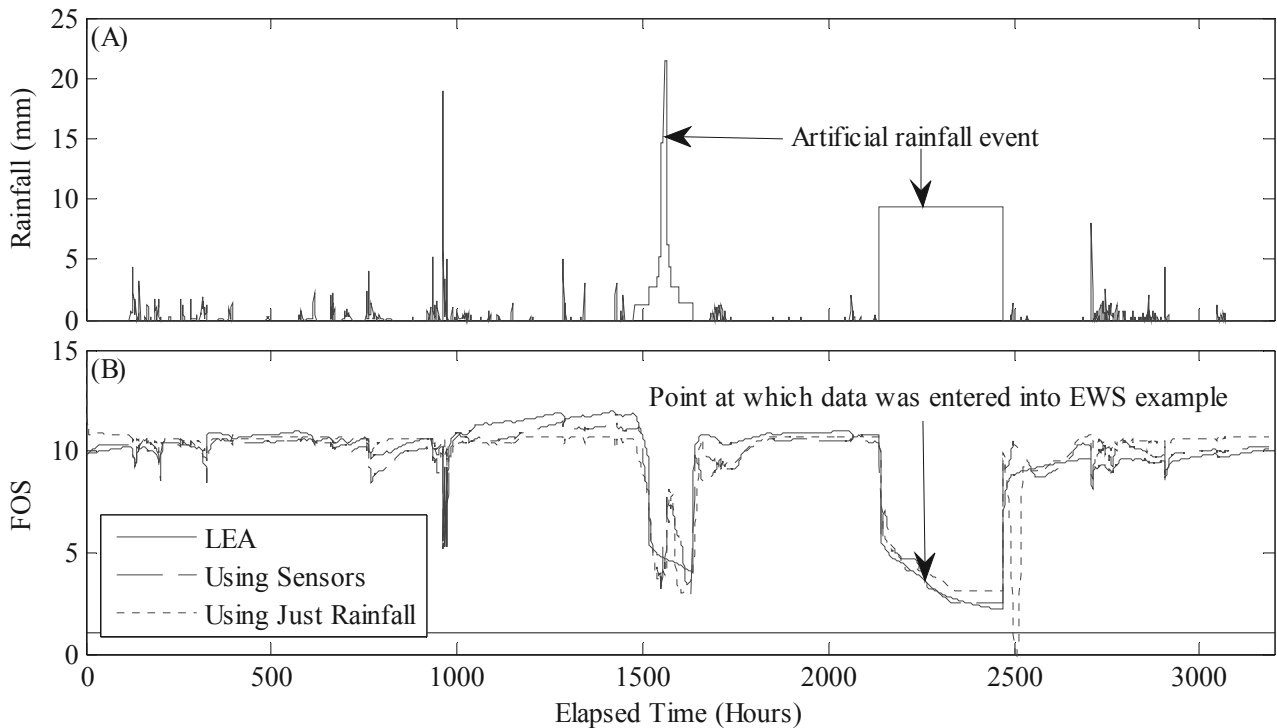


Figure 1. (A) Rainfall events input into the FEM and (B) corresponding FOS obtained from LEA, the ANN using field measured data, and the ANN using only rainfall events. The black line shows a FOS of unity (i.e. when failure will occur).

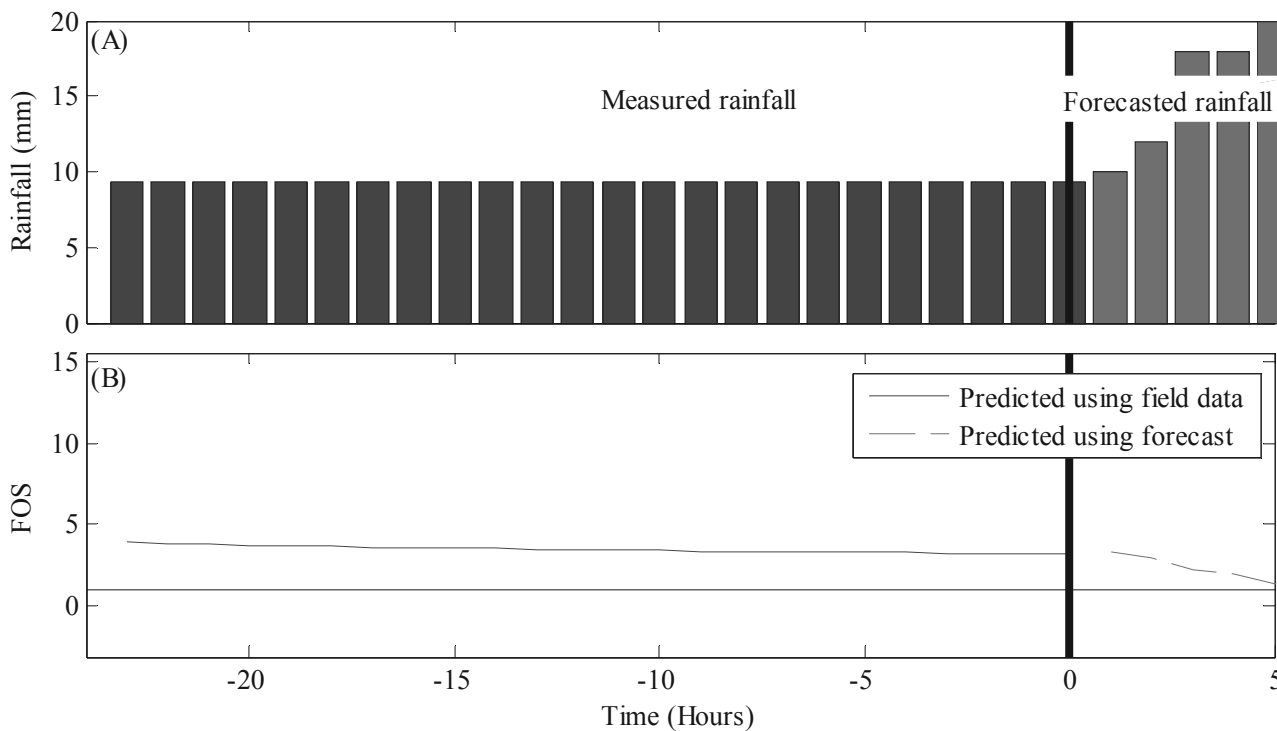


Figure 2. Example of the EWS in use. Elapsed time = 0 corresponds to the point in time at which the data was downloaded from the site (shown in Figure 1). The upper graph (A) shows the rainfall recorded at the site, and the forecasted rainfall at the site. The lower graph (B) shows the predicted FOS using the field data, and the predicted future FOS using the rainfall forecast. A FOS of unity is shown by a black line.

#### 4 APPLICATION OF THE EWS

The use of the EWS is summarised as follows. During a heavy rainfall event the field data is downloaded from the site in real time via the internet. This field data is then uploaded into the EWS. The FOS of the previous 24 hours, using the field data, is then obtained using the ANN. Based on the rate of change of this predicted FOS, the time until the FOS will reach a FOS of unity is returned to the user.

Next, the rainfall forecast for the next 5 hours for the site is obtained from the Meteorological Service of New Zealand (2012) via the internet. This forecast can be freely obtained by the public. This forecast is based on the Weather Research and Forecasting model, using data obtained from automatic weather stations, weather radar facilities, upper air sites and marine observation stations (Bridges, 2011). The predicted FOS over the next 5 hours is obtained using this rainfall forecast as an input into the ANN. The starting FOS for this predicted FOS is the last FOS obtained using the actual sensor data. Because of the difficulty in verifying forecasts at a local scale (Hodson, 2009), both the predicted FOS according to this forecast, and the rate of change of the FOS obtained from the field monitoring data, are used to estimate when failure may occur.

If failure is predicted to occur within five hours, then a stage one warning is issued. This involves warning motorists to lower speed limits around the landslide site. If failure is to occur within one hour, then a stage two warning is issued. This puts a detour in place, so motorists avoid the site altogether. Two warnings were used because the detour route adds approximately 25 minutes to the journey. Thus this detour route is put in place as late as possible to avoid frustration with the EWS due to false alarms. Warning motorists to lower speeds around the possible landslide site in advance is intended provide a balance between minimising the cost should the landslide occur, and avoiding frustration at the delay to motorists. During periods of heavy rainfall, the EWS should be updated on an hourly basis.

#### 5 CONCLUSIONS

A site specific EWS for rainfall induced landslides has been developed. The EWS is based on the ability to predict the current FOS of the site using ANNs, rainfall forecast data and real time field measurements. The EWS proves to be useful at predicting when failure might occur, and also returns to the user a parameter related to the possibility of failure (the current FOS).

A FEM was used to replicate the field response of the site to rainfall events. This FEM was coupled with a LEA to predict the FOS at each time-step. The results of this modelling process were reasonably accurate, considering discrepancies caused by natural variation within the soil and the generalised evaporation pattern which was applied within the model.

The ANN which uses field measured data could predict the LEA obtained FOS with good accuracy; a mean squared error of 0.41 was obtained. To predict the future FOS, an ANN using just rainfall forecast data was developed. This ANN was less accurate, with a mean squared error of 1.16 obtained.

It is envisioned that the methodology used to develop this EWS can be replicated at a variety of sites as a means of risk reduction for rainfall induced landslides.

#### 6 ACKNOWLEDGEMENTS

The Authors would like to thank the Auckland Motorways Alliance, Babbage Consultants, Beca Consultants and Hiway Geotechnical for their assistance throughout the project.

#### 7 REFERENCES

- Bridges, J. (2011). MetService's Investment in Forecasting. Retrieved 10 December, 2012, from <http://blog.metservice.com/2011/04/metservice%E2%80%99s-investment-in-forecasting/>
- Caine, N. (1980). The rainfall intensity-duration control of shallow landslides and debris flows. *Geografiska Annaler Series A*, 62(1-2), 23-27.
- Chae, B.-G., & Kim, M.-I. (2012). Suggestion of a method for landslide early warning using the change in the volumetric water content gradient due to rainfall infiltration. *Environmental Earth Sciences*, 66(7), 1973-1986.
- Dai, F. C., Lee, C. F., & Ngai, Y. Y. (2002). Landslide risk assessment and management: an overview. *Engineering Geology*, 64, 65-87.
- Dhokal, A. S., & Sidle, R. C. (2004). Distributed simulations of landslides for different rainfall conditions. *Hydrological Processes*, 18(4), 757-776.
- Fredlund, D. G., Morgenstern, N. R., & Widger, R. A. (1978). The shear strength of unsaturated soils. *Canadian Geotechnical Journal*, 15(3), 313-321.
- GEO-SLOPE International Ltd. (2009a). *Seepage Modeling with SEEP/W 2007, An Engineering Methodology, Fourth Edition* (4 ed.). Calgary, Alberta, Canada: GEO-SLOPE International Ltd.
- GEO-SLOPE International Ltd. (2009b). *Stability Modeling with SLOPE/W 2007 Version, An Engineering Methodology, Fourth Edition* (4 ed.). Calgary, Alberta, Canada: GEO-SLOPE International Ltd.
- Harris, S. J., Orense, R. P., & Itoh, K. (2012). Back analyses of rainfall-induced slope failure in Northland Allochthon formation. *Landslides*, 9(3), 349-356.
- Hodson, A. (2009). Weather Forecast Accuracy: Part 1 Rainfall. Retrieved 17 December, 2012, from <http://www.hortplus.com/main/article/weathersense/ws0903.pdf>
- ICT International Pty Ltd. (2012). Solutions for Soil, Plant and Environmental monitoring. Retrieved 31 August, 2012, from <http://www.ictinternational.com.au/>
- Intrieri, E., Gigli, G., Mugnai, F., Fanti, R., & Casagli, N. (2012). Design and implementation of a landslide early warning system. *Engineering Geology*, 147-148, 124-136.
- Keefer, D. K., Wilson, R. C., Mark, R. K., Brabb, E. E., Brown, W. M., Ellen, S. D., et al. (1987). Real-time landslide warning during heavy rainfall. *Science*, 238(4829), 921-925.
- Khanlari, G. R., Heidari, M., Momeni, A. A., & Abdilor, Y. (2012). Prediction of shear strength parameters of soils using artificial neural networks and multivariate regression methods. *Engineering Geology*, 131-132, 11-18.
- Lentfer, K. (2007). *Engineering geology of the Northland Allochthon, Silverdale, North Auckland, New Zealand*. Unpublished Master Thesis, The University Of Auckland, Auckland.
- Mathworks. (2010). NARX Network (narxnet, closeloop), *Matlab Users Guide*.
- Meteorological Service of New Zealand Ltd. (2012). MetService.com - your website for New Zealand Weather Forecasts. Retrieved 20 September, 2012, from <http://www.metservice.com/national/index>
- NIWA, & GNS Science. (2009). *Natural Hazards 2008*.
- NIWA, & GNS Science. (2010). *Natural Hazards 2009*.
- O'Sullivan, A. S. (2009). *Suitability of Advanced Soil Models for Stability Analysis of Slopes in Northland Soils*. Masters Thesis, The University of Auckland, Auckland.
- Penman, H. L. (1948). Natural Evaporation from Open Water, Bare Soil and Grass. *Proceedings of the Royal Society of London. Series A, Mathematical and Physical Sciences*, 193(1032), 120-145.
- Power, J. (2005). *Engineering Geological Properties and Slope Movements in the Pakiri Formation and Northland Allochthon, Mahunrangi, North Auckland, New Zealand*. The University of Auckland, Auckland.
- The MathWorks Inc. (2012). *Matlab The Language of Technical Computing*. Retrieved 4 September, 2012, from <http://www.mathworks.nl/products/matlab/>
- Van Genuchten, M. T. (1980). A closed-form equation for predicting the hydraulic conductivity of unsaturated soils *Soil Science Society of America Journal*, 44(5), 892-898.

# Characteristics of Ground Motion on Colluviums Slope Induced by Heavy Rainfall

## Caractéristiques du déplacement du sol sur la pente de colluvions induit par la pluie violente

Jeng C.J., Sue D.Z.  
Huafan University, Taiwan

**ABSTRACT:** In this study, a slope covered with various depths of colluvium soil and set up with monitoring system has been studied. The results from hundreds of settlement and displacement observation marks were taken into account. It was found that the maximum settlement and displacement were concentrated around the buildings of Hui-tsui, Zhian and Wu-Ming, and coincided with rainfall records for the area. The direction and distribution of displacement and surface cracks supports previous findings of a sliding block. The slope stability analysis for this study was carried out with the STABL program. A drainage system with additional stability measures was proposed to prevent an unstable slope caused by the rising up of the ground water table during rainfall. Finally, a curve showing the relationship between rainfall and slope stability is established and presented.

**RÉSUMÉ :** Dans cette étude, une pente couverte de colluvions de différentes profondeurs et équipée d'un système de surveillance a été étudiée, ayant recours aux remarques tirées des observations sur les affaissements et les déplacements de la pente. Nous avons découvert que les plus grands affaissements et déplacements de pente, coïncidant avec les précipitations dans la région, avaient lieu autour des bâtiments Hui-tsui, Zhian et Wu-Ming. La direction et la répartition des déplacements de pente ont confirmés nos recherches précédentes sur un bloc coulissant. Cette recherche a été faite avec le programme STABL. Un système d'évacuation des eaux avec des mesures de stabilité a été proposé pour protéger une pente instable contre les eaux souterraines qui montaient lors des averses. À la fin de cette étude, une courbe a été présentée pour expliciter la relation entre les précipitations et la stabilité de pente.

**KEYWORDS:** colluviums slope, ground monitoring, settlement and displacement, slope stability analysis, threshold value of rainfall.

### 1 INTRODUCTION

Rainstorms frequently trigger colluvium landslides. For example, in November 1993, more than 800 landslides were triggered by rainstorms on Lantau Island, Hong Kong (Dai & Lee 2002). In Taiwan, colluvium slope disasters related to rainfall are very common (Jeng et al, 2007; Jeng and Lin, 2011; Pan et al, 2008). The threshold values of typhoon disasters were studied extensively by Wang and Yeh(2011) and Hu and Liao (2010). This paper focuses on the effects of heavy rainfall on the colluvium slopes in northeastern Taiwan. The results from 295 points of settlement and displacement monitoring marks and their significance to ground motion were evaluated. Finally, a threshold value curve for typhoon rainfall is proposed.

### 2 BASIC INFORMATION OF THE FIELD CASE

The field case discussed in this research is the campus of Huafan University in northeastern Taiwan. The University was constructed on the slope. For risk management and research on slope stability, a monitoring system was set up and data was collected for over ten years. The monitoring system includes the inclinometer, building tilt measurement, tiltmeters, crack gauges, water level observation wells, settlement and displacement monitoring marks, rebar strain gauges, concrete strain gauges and rain gauges. According to the records obtained from the rain gauges from 2003 to 2010, the average annual rainfall is about 4000mm, most of which is attributed to torrential rainfall concentrated in the period of typhoon season. The maximum monthly rainfall record is in October 2010 with 1208mm.

#### 2.1 Geological Condition

The base stratum of the site consists of the Miocene Mushan Formation. On the ground surface is 10 to 20 meters of

colluvium comprised of a bottom layer of sandstone (SS) and thin alternating layers of sandstone and shale (SS-SH). The attitude of the bedrock is strike in the east-west direction with the dip-anchor 10° to 20° toward south.

#### 2.2 Ground Motion Monitoring Results

##### 2.2.1 Settlement and Displacement Monitoring

Since 2001, hundreds of settlement and displacement monitoring marks were set up and recorded every six months. Some additional marks were gradually included over the years. Data was recorded until January 2011, and after ten years of monitoring, a total of 295 marks were collected. The accuracy of the investigation was controlled to within 1/5000 by the plane triangulation method with GPS (TRIMBLE 4800) for six fixed station points. Four traverse points were then laid within the survey area and double-checked for accuracy to be within 1/10000. The coordinates and elevation of each observation mark were then surveyed based on those traverse points. The displacement and settlement values were obtained by comparing the coordinates and elevation results of each survey to the initial results from the first survey. The data marks were then divided into two categories for buildings, and for roads and land.

##### 2.2.2 Settlement and Displacement Distribution

Figure 1 shows the results of the settlement distribution. The settlement marks around buildings are shown in solid triangle and the settlement marks for roads and other land are shown in solid circles, while the heaving points are shown in hollow circles. The values of settlement or heaving are discriminated into five levels from 5 to 25mm and are represented by different size circles. As indicated in Fig. 1, the maximum annual settlement is more than 20mm, distributed around the Hui-tsui building(B1), Chih-an building(B2) and Wu-Ming



building(B3). Although these values did not reach a dangerous level per the general management criteria, for some areas, the cumulated settlements reached over 10cm in the 10 years data. Moreover, when comparing the settlement distribution in Fig. 1 to the distribution of thickness of filled land, in the greater thickness of the filled land areas such as the Sport Ground(B4), the Basketball Court(B5) and Asoka Square(B6), the settlement is apparent. It is speculated that these higher settlement areas have something to do with the thicker fill. On the other hand, for the few heaving points like the upper slope of the Asoka Square, it is the result of the surface concrete pavement heaving caused by extrusion of the slope slide, not the ground surface condition.



Fig. 1 The settlement distribution diagram

Figure 2 shows the displacement tracks of each observation mark on the plan map. The scale of displacement has been enlarged to 200 times to highlight its tendency. It is shown in Fig. 2 that the main displacement direction is downward to the slope in the southwest or south direction. Meanwhile, the larger displacement is distributed, same as the aforementioned settlement distribution, around the areas of Hui-tsui building, Chih-an building and Wu-ming building. However, the upper slope of the Asoka Square shows movement in the upward direction to the slope. This also can be attributed to the aforementioned heaving phenomenon caused by extrusion of the slope slide, such that an overturning condition occurred in that area. The cracks created in the crown can also confirm this situation. Additionally, the direction of movement for the Sport court is different from the upper slope Dormitory building. That is because they are departing into different sliding blocks.

### 2.3 Correlation WITH rainfall

According to the results of the aforementioned settlement and displacement distribution, the most critical areas are concentrated in the Hui-tsui building, Chih-an building and Wu-ming building. As expected, the most significant contributing factor is rainfall. The correlation between settlement, displacement and, rainfall for the Hui-tsui building is discussed below.

The tendency of displacement with respect to time shown in Fig. 3 is generally similar to that of settlement vs. time shown in Fig. 4. Based on the increment tendency, both can be separated into four distinct time segments: (1) May 2001 to March 2002, (2) September 2004 to June 2006, (3) June 2007 to April 2009; (4) April 2010 to January 2011.

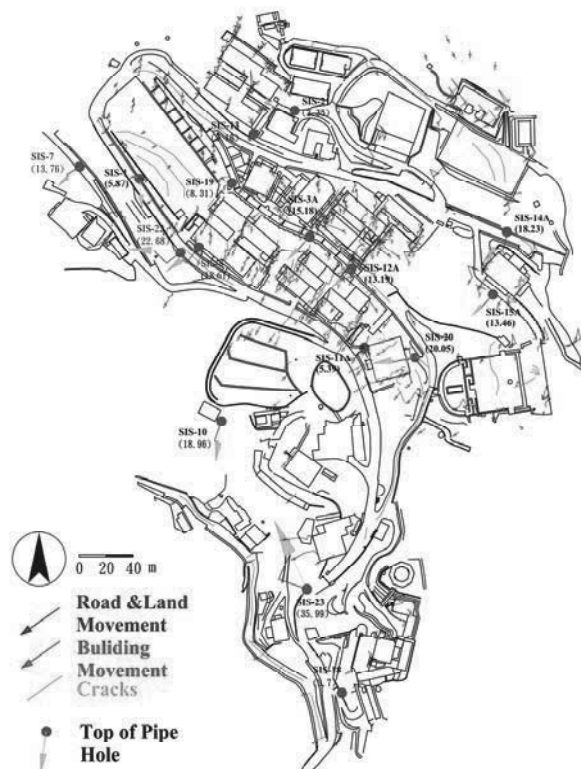


Fig. 2 displacement tracks and ground surface cracks distribution

When comparing the displacement and settlement time in Fig. 3 and Fig. 4 with the rainfall record, the displacement and settlement of the slope have a strong correlation with the rainfall record. In addition to the rainfall, another important influence factor to the displacement and settlement of the slope is the construction. For instance, within the third time segment, a new Library and Information Building were built with the excavation for the foundation at the toe of the slope. This may be the cause for the increased amount of displacement and settlement in the third time segment, despite the greater total accumulated rainfall in the second time segment (8973.5mm) versus the third (7241.5mm).

Aside from accumulated amounts, rainfall rate and duration also contribute to the threshold value that triggers displacement and settlement of the slope. Jeng and Sue (2008) illustrated that a rainfall threshold value of 800mm/month is able to trigger the displacement and settlement of the slope.

### 3 THE INCLINOMETER MONITORING

Many inclinometers have been installed starting the year 2000. Since then they have gradually settled in the test field, with some being damaged due to deformation. At present, 32 holes remain functional and are recording measurements. The results shows a sliding layer that deforms in depth from 14 to 15m. As seen from the core box the sliding occurs along the fracture layer.

### 4 COMPARISON THE RESULTS BETWEEN DISPLACEMENT MONITORING MARKS AND THE INCLINOMETER

The displacement monitoring marks are able to characterize the ground surface deformation and the inclinometer pipes can describe the ground deformation for the entire depth. To investigate the deformation of the slope, efforts were made by comparing the deformation of the top of the inclinometer pipes to the displacement monitoring marks. The comparison results shown in Fig. 2 indicated that the tendency of slope surface deformation obtained from both of these two data sets is

generally consistent. The primary slope deformation is toward the southwest and south direction, similar to the slope surface direction, which means the slope soil is generally moving downward along the slope.

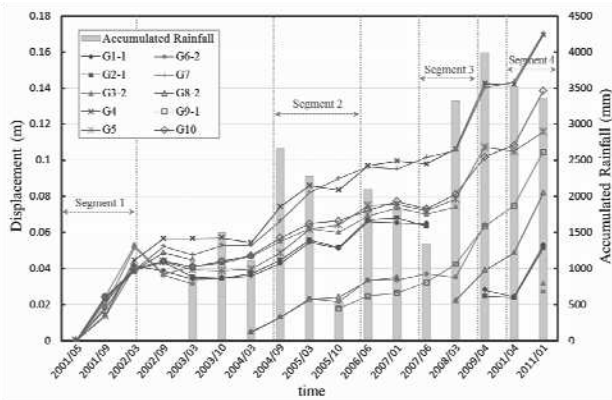


Fig. 3 Relation curves of displacement and rainfall for Hui-tsu building

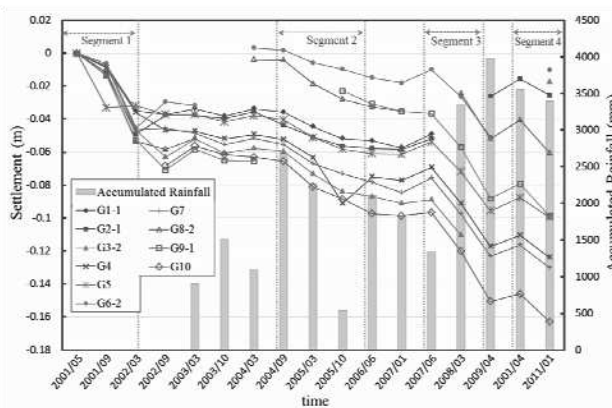


Fig. 4 Relation curves of settlement and rainfall for Hui-tsu building

5 SLOPE STABILITY ANALYSIS

After learning of the significant amount of slope deformation, there was concern for the integrity of the slope and any potentially hazardous contributing factors. To determine the slope stability, the limite equilibrium program - STABL was adopted and used for analysis. A simplified Bishop method with circular failure type was selected for the study. The input soil parameters were based on previous study (Jeng, 2003; Jeng and Li, 2009 ), as shown in Table 1. Areas with similar ground water variation and rainfall conditions were compared, and the crack distribution on the slope were used to assess potential failure areas.

Table 1 soils and rocks parameters

soils and rocks type	Cohesion (kPa)	Friction angle (°)	Unit weight (kN/m <sup>3</sup> )
Colluviums	18.45	29.92	19.31
sandstone and shale alternation	41.52	32.24	25.52
Sandstone	41.85	34.60	23.86

Figure 5 shows the slope stability analysis results for normal conditions. The safety factor is 2.17, which higher than the suggested value 1.5, remains within a stable state. However for rainfall conditions, when the ground water rises 3m, the safety factor decreases to 0.86. An unstable condition can then happen. Thus, it is concluded that the slope stability is significantly influenced by the rise in ground water during rainfall events.

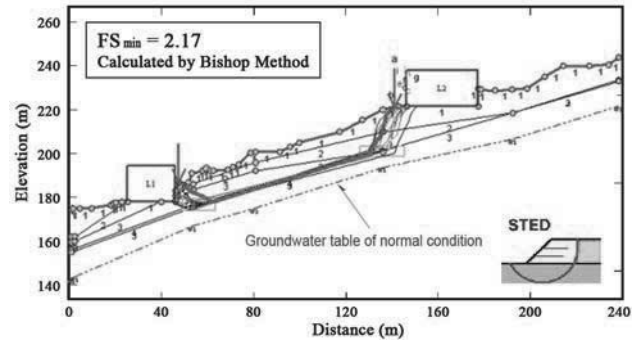


Fig. 5 Slope stability for normal condition (FS=2.17)

6 SLIDING BLOCKS DETERMINATION FROM SETTLEMENT AND DISPLACEMENT RESULTS

According to the inclinometer monitoring results provided by Jeng and Hsieh (2010), there are six sliding blocks within the slope. In that study, the sliding rate, depth and area of each block were presented. In addition to that information, this study evaluates the result of ground surface movement, including displacement direction and settlement, trend of ground water flow, and the distribution of ground surface cracks. A comprehensive evaluation was made to exam the previous sliding blocks study results. Fig.6 shows the finding which supports the presence of two sliding blocks. Among them, block No. A-1 is located in the area around Wu-Ming building, Asoca Square and the Chea-chau building; block No. A-2 is located in the area around Sport ground where there is 20m of fill. These two sliding blocks coincide with blocks R1 and L1 of the previous study (Jeng and Hsieh, 2010). Both blocks show movement in the shallow layer and are located in the active sliding areas. Numerous cracks can be found along the ground surface in these areas.

7 STABILIZE MEASURES AND THRESHOLD VALUE OF RAINFALL

According to aforementioned stability analysis results, it was learned that the rise of ground water in rainstorm conditions significantly impacts slope stability. Consequently, slope stability will be improved with the addition of drainage and drawdown systems and retaining structures. With budget and effectiveness in mind, the first step should focus on the area around the Wu-Ming building where the ground water and geological condition is least favorable. A detailed description of improvement steps includes :

1. Improvement of the ground surface drainage system for water runoff.
2. Installation of six catchpits with the horizontal drainage pipes, shown in Fig.7, to draw down the ground water level.
3. Filling of ground surface cracks to prevent seepage of water runoff into cracks.
4. Construction of bore piles and tiebacks with ground anchors behind the Wu-Ming building to strengthen the retaining structure for the toe of the slope.

Finally, for the safety management of the slope, threshold curves were established to illustrate the relationship between rainfall intensity and accumulation, and the observed slope deformation (Fig. 8). Looking ahead, these curves can be used for predicting slope stability before typhoons as it often brings significant amount of rainfall. The information correlating rainfall and slope stability improves slope management and risk assessment. To minimize the sloop disaster from occurring, the proposed approaches are believed to be beneficial to the community.

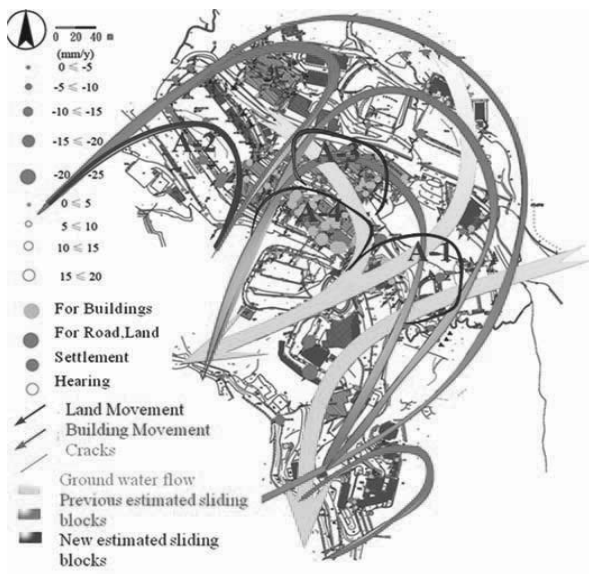


Fig. 6 Sliding blocks and movement distribution plane

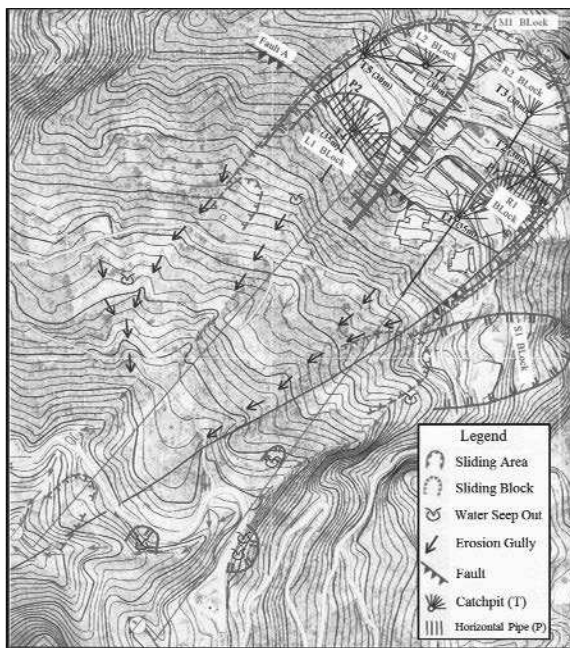


Fig. 7 Plan for catchpits location

## 8 CONCLUSIONS AND DISCUSSION

This paper discusses the displacement and settlement of the slope, evaluates the sliding block theory, and analyzes slope stability. After summarizing the results, stabilization measures

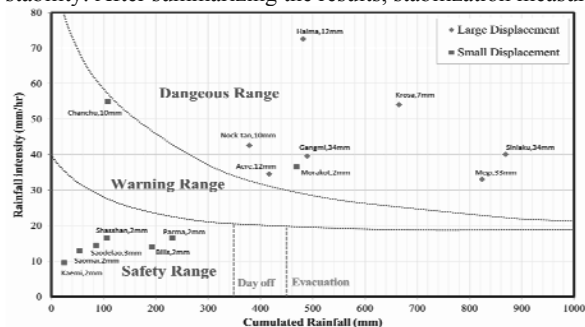


Fig. 8 Threshold value curves correlate with displacement

and rainfall threshold values were established. Based on the results, the following conclusions can be made:

1. The areas with the most significant settlement and displacement are located around the buildings of Hui-t sui, Zhian and Wu-Ming Building. Due to lack of slope stability, surface cracks appeared and several sliding surfaces have been observed.
2. The deformation of the top of the inclinometer pipes is consistent with the displacement monitoring marks. Findings indicate the primary slope deformation to be toward the southwest and south direction. In addition, rainfall was found to be the most significant factor for slope deformation and slope stability.
3. The results of the slope stability analysis show that an increase in ground water level is the most critical factor for slope stability.
4. The distribution of potential sliding blocks was examined by using slope displacement and settlement data, and the location of surface cracks. The sliding direction is strongly correlated to the direction of ground water flow. Depth or thickness of fill also contributes to slope sliding.
5. Several stabilization measures including catchpits with horizontal drainage pipes, bore piles and tieback ground anchors, and threshold value of rainfall are recommended to improve the slope stability. It was believed that the information presented is very important for slope disaster prevention.

## 9 REFERENCES

Dai F.C. & Lee C.F. 2002. Landslides on natural terrain— physical characteristics and susceptibility mapping in Hong Kong. *Mountain Research and Development*, 22(1), 40-46.

Hu I-Chou and Liao H. J. 2010. A Model of Slope Mitigation Priority for Alishan Mountain Road in Taiwan. *Journal of Performance for Constructed Facilities, ASCE*, 24(4), 373-381.

Jeng C.J. 2003. Study on Slope Stability Mechanism of Hua fan University by Using of Inclinometer Displacement and Limiting Equilibrium Stability Analysis. *Hua Fan Annual Journal*, 9, 115-127.

Jeng C.J. Chu B.L. Tsao S.P. Lin T.A. 2007. Matrix Suction of Unsaturated Colluvium Slope Influenced by Rainfall and Plant Condition : A case of Taiwan Hua fan University. *Wuhan University Journal of Natural Sciences*, 12(4), 689-694.

Jeng C.J. Su D.Z. 2008. Case study on the settlement and displacement monitoring results on a slope induced by natural hazards. *Proceedings of 3rd Taiwan-Japan Joint Workshop on Geotechnical Hazards from Large Earthquakes and Heavy Rainfall*. 119-130.

Jeng C.J. Li C.T. 2009. Case Study on the Numerical Analysis of the Building Foundation Excavation on the Dip-Slope. *Journal of Architecture*, (68), 147-162.

Jeng C.J. Hsieh T.Y. 2010. Case study on the sliding surface judgment for the monitoring slope. *Journal of Hua fan art and design*. 6, 1-14.

Jeng C.J. and Lin T.A. 2011. A Case Study on the In-situ Matrix Suction Monitoring and Undisturbed-sample Laboratory Test for the Unsaturated Colluvium Slope. *Soils and Foundations*. 51(2),321-331.

Wang H.M. and Yeh T.C. 2011. An Analysis on the Characteristics of Extreme Hourly Rainfall of Typhoon over Taiwan. *Meteorological Bulletin*, 48( 3) September, 1-14.

# Stability and movements of open-pit lignite mines in Northern Greece

## Stabilité et mouvements de terrain dans les mines de lignite à ciel ouvert en Grèce du Nord

Kavvadas M.

National Technical University of Athens, Greece

Agıoutantis Z.

Technical University of Crete, Greece

P. Schilizzi P.

Public Power Cooperation, Greece

Steiakakis C.

General Consulting Ltd "ISTRIA", Greece

**ABSTRACT:** This paper presents a case of a lignite mine in Northern Greece with excavated slopes exceeding 100-120m in depth in which substantial movement is occurring, with an average rate 10-20mm/day. The Mavropigi mine is very important for the power supply of Greece and uninterrupted operation is often critical, meaning that excavation is taking place on moving soil masses. The stability of the moving southeast slope is investigated and the information developed from an extensive monitoring campaign, with survey prisms, inclinometers and piezometers is presented. The use of the investigation data to evaluate the type of movement, the geometry of sliding surface and the effectiveness of remediation measures are analyzed in detail. The procedure of assessing the stability and safe slope operation during production, even with high rates of movement and the effect of precipitation are presented. It is shown that there are situations that mine slopes can move several meters laterally and still be operational without catastrophic failures.

**RÉSUMÉ :** On présente dans cet article une étude des mouvements de terrain dans une mine de lignite du nord de la Grèce. Dans cette mine à ciel ouvert de 100 à 120 m de profondeur, des glissements de pente (lents) sont observés : 10-20 mm/jour. L'exploitation de cette mine (Mavropigi) de lignite, primordiale pour la production d'énergie en Grèce, s'effectue sans interruption dans des pentes en mouvement permanent. Les problèmes de stabilité de la pente sud-est de la mine sont étudiés et les mesures effectués in situ à l'aide de différents appareillages (mesures topographiques, inclinomètres et piézomètres) sont présentés. L'analyse de l'ensemble des mesures est effectuée afin de caractériser le type de mouvement de terrain et la géométrie de la surface de glissement. Par ailleurs, l'efficacité des mesures adoptées pour stabiliser les pentes est analysée via les mesures effectuées sur le site. Une procédure permettant d'évaluer le risque de perte de stabilité pendant les phases d'exploitation (intensive) en tenant compte des effets défavorables des précipitations est proposée. On met ainsi en évidence des cas pour lesquels les pentes peuvent se déplacer latéralement de plusieurs mètres sans pour autant engendrer des ruptures majeures.

**KEYWORDS:** Slope movement, Coal open pit, Slope monitoring, Slope stability, Landslide.

## 1 INTRODUCTION

The Public Power Cooperation (PPC) operates a number of large open pit lignite mines in Northern Greece (Amyntaio-Ptolemais Basin). The Mavropigi mine has been mined since 2003 and at present the excavated slopes have reached depths exceeding 100-120m. Since 2011, the southeast slopes have shown persistent large horizontal movements at an average rate of 10-20mm/day, at times reaching more than 40-50mm/day affected by increased precipitation. The moving mass was estimated around 6Mm<sup>3</sup>. This paper presents a case of significant movements that occurred at the southeast slope (Fig. 1), and details the monitoring, evaluation and mitigation measures taken to safeguard mining operations which had to be uninterrupted for production management purposes.



Figure 1. Southeast slopes of Mavropigi lignite mine.

## 2 GEOLOGICAL AND GEOTECHNICAL CONDITIONS

The Mavropigi mine is in the sedimentary fill of the Ptolemais basin which includes terrestrial and lacustrine deposits of Miocene up to Pleistocene age, with abundant lignite horizons (Diamantopoulos, 2006). Near horizontal intercalations of Marls, Lignites, Stiff Clays and Sands are the predominant materials; from a geotechnical point of view they can be described as "Hard Soils – Soft Rocks". The main intercalations are Marl and Lignite. The Marl material is mostly classified as Elastic SILT or Organic SILT (MH-OH) per USCS (ASTM D2487). Locally in the Marl – Lignite intercalations, thin (few centimeters thick) beds of High Plasticity CLAY (CH) are found. These almost horizontal thin beds have very low residual shear strength and often act as slip surfaces. The mechanical properties of the different materials encountered in the area of Mavropigi are presented in Table 1. These parameters are assessed from triaxial, direct shear and ring shear tests performed on selected core samples and are used for the slope stability calculations of the Mine.

Table 1. Range of Geotechnical Properties of Mavropigi Mine Materials.

Parameters / Materials	Marl	Lignite	Clay (CH)
Unit weight $\gamma$ (kN/m <sup>3</sup> )	16-18	11-13	16-18
Effective Cohesion $c'$ (kPa)	50-150	150-200	5-50
Effective friction $\phi'$ (deg)	28-35	34-36	26-30
Residual Friction $\phi_r'$ (deg)	-	-	5-10

### 3 MONITORING OF SLOPE MOVEMENTS

At the end of 2010, tension cracks were observed at the crest of the Southeast mine slopes and visually observed horizontal transverse movements at the toe under prisms 5A3 and 6A4. Although this is usual in large and deep open pit mines, nevertheless, 20 prism monitoring stations, two inclinometers (KL-10, 11) and two piezometers (PM-10, 11) were installed on the slopes. The locations of the instruments are shown in Figure 2 together with the limits of the moving mass.

Prism measurement records were made available between January 2012 and up to the writing of this paper (Sept. 2012).

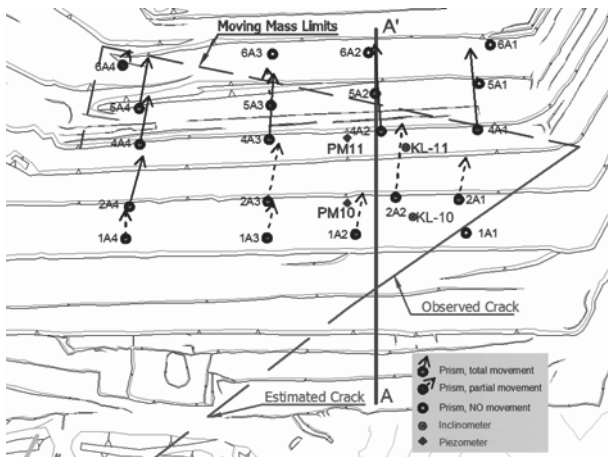


Figure 2. Monitoring equipment and trends on Southeast slopes

Initially the measurements were executed with a lower accuracy total station and only the “sloping distance” between the prism and the measurement base was evaluated. Due to the complexity and criticality of the situation, a new robotic total station of high accuracy (0.5cc) replaced the old one. With the new total station the movement vectors could easily be measured and evaluated. The use of the robotic total station eliminated the surveyor operation error and the high accuracy significantly reduced the horizontal and vertical angular measurement error.

Due to the high rate of movement, few measurements were taken from the inclinometers before they were sheared off. From inclinometer KL-10, six measurements were obtained in a period of one month which recorded a total displacement 100mm at 27m depth from ground surface. Inclinometer KL-11 recorded only three measurements in a period of 11 days, with maximum displacement 150mm at 9m depth. The two piezometers could only be measured twice due to operational reasons and recorded water table elevation at 18.4m in PM-10 and 9.9m in PM-11. A precise water table could not be estimated based on the piezometer measurements because of the number of measurements and since the faces of the slopes were found dry. Piezometric conditions and water pressures are very difficult to model with a high degree of accuracy in mines (Sullivan, 2007) mainly due to the presence of multiple perched aquifers. Figure 3 shows a geological cross section with the monitoring equipment and the failure surface location (white line). Dark zones indicate the lignite beds.

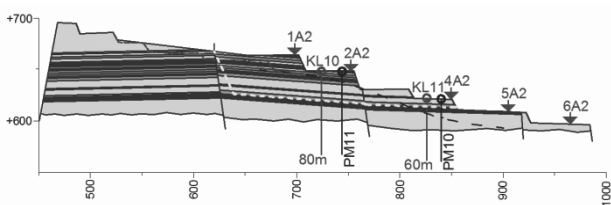


Figure 3. A-A' cross section with monitoring locations

### 4 EVALUATION OF SLOPE MOVEMENTS

The operation of Mavropigi mine is very important for the power supply of Greece and uninterrupted operation is often critical. Mining operations may take place even in moving slopes, as long as safety of personnel and equipment is satisfied. Zavodni (2000) states that “*mining operations can proceed safely with minimum interruption if failure mechanisms are understood and slopes are properly monitored*” even in moving slopes. The way to assess if a “moving slope” can be mined safely is to determine if the slope movement is regressive or progressive. A regressive movement is cyclic decelerated while a progressive movement exhibits overall acceleration without appreciable deceleration intervals (Zavodni, 2000). In regressive movements, mining operation can continue after incorporating a monitoring system. If monitoring data indicate a progressive type of movement the operations are in danger of imminent collapse. The question posed to the Geotechnical Engineer is to determine the type of movement that characterizes each particular slope. The failure mechanism needs to be understood and a sufficient quantity of qualitative measurements is required. In the literature, most case studies are analyzed after an incident and with adequate monitoring data and the type of movement is identified (Ryan & Call 1992). At the Mavropigi mine, decisions had to be made based on the day to day data becoming available without a priori having a large amount of data that could be used to determine the type of movement.

Initially, based on the geological model of the area, the visual observations of the cracks in the crest and the translational surface located by the inclinometers, a limit equilibrium model was analyzed to evaluate if the movement was possible and to back calculate the material properties of the shear surface. Based on back analysis (Figure 4) it was found that a sliding surface was possible with residual friction angle of  $\phi_r=7^\circ$  for the near horizontal surface and  $\phi^*=24^\circ$  for the back scarp. These values were considered to be the lower bounds since no water pressures were introduced and were in good agreement with the laboratory ones provided in Table 1 for the area.

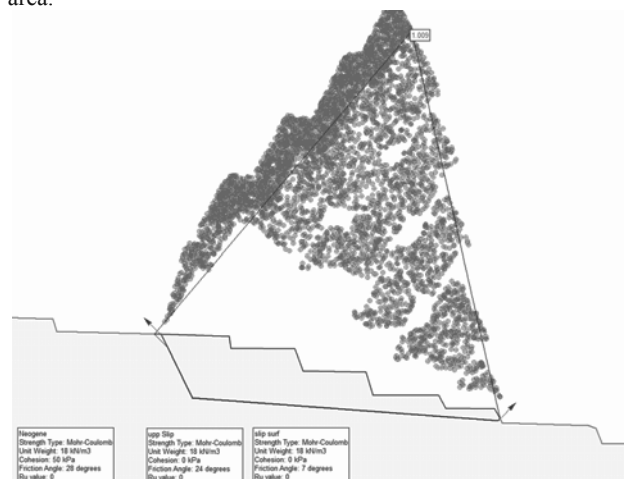


Figure 4. Back analysis of the sliding surface

From the geological model, the inclinometer readings and the back analysis it was found that the movement is taking place in a failure shear zone (thin high plasticity clay interlayer) with an inclination of about 4-5°. Based on this information an initial estimate was made that the movement could be of the regressive type based on the recommendations by (Zavodni and Broadbent, 1980), by which movements are deemed regressive when taking place on a surface with a lower angle in relation to the slope face inclination and the shear resistance (friction angle) of the material. Initial remediation measures consisting of excavating part of the top two benches were analyzed with the same data. Analysis showed that the FS became 1.06 which was considered

positive for reducing the rate of movement. The slope stability analysis was considered only indicative due to the complex nature of the sliding mass (fig 2) and greater emphasis was placed on slope monitoring.

The data were further analyzed to verify the regressive type of movement and to identify a possible onset of a progressive type of movement, leading to failure. One method to evaluate monitoring data is the inverse velocity measurement versus time. Based on this method, as described by (Rose and Hungr, 2007), when the inverse velocity of slope movement is plotted against time, failure is imminent as the trend line approaches zero values (velocity increases asymptotically). In Figure 5 the inverse velocity versus time is presented for prism 2A4.

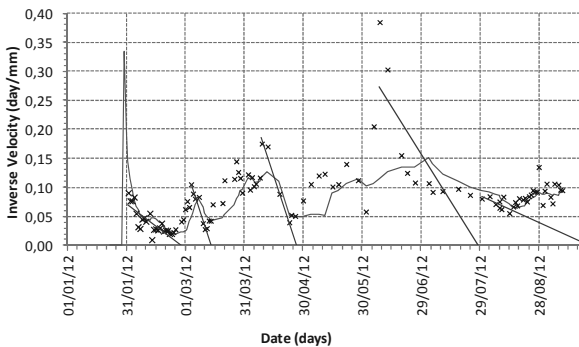


Figure 5. Inverse velocity versus time for prism 2A4

Figure 5 suggests that if this method is to be followed, at numerous times the mine slopes could be at imminent collapse. This is evaluated based on the extrapolation to zero of the regression lines for different time intervals (straight lines). For example the first imminent collapse could have been evaluated to have occurred on 01/03/12, which did not happen.

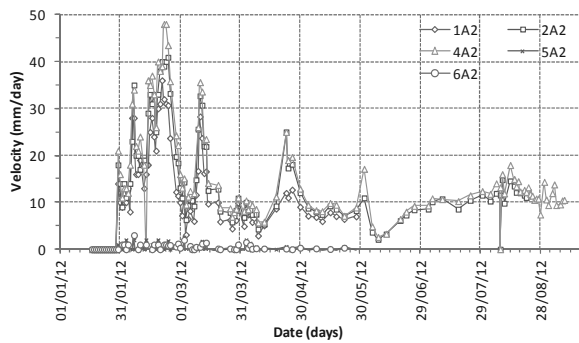


Figure 6. Velocity versus time for prisms of bench 2

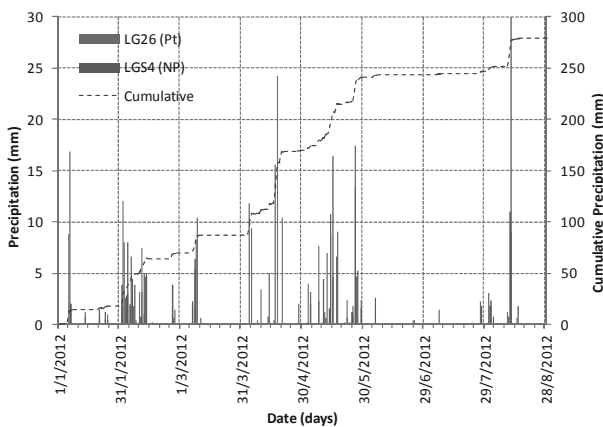


Figure 7. Precipitation versus time from two stations

Subsequently regression analysis presented times that failure could take place. This graph presents a situation where the

method could not work properly without evaluating other critical factors such as precipitation or excavation unloading.

Figure 6 presents velocity versus time for all prisms of bench 2 while figure 7 shows the daily and cumulative precipitation for two weather stations. The mine is located in between these stations with a distance of about 7km. No precipitation data at the mine were available.

From the evaluation of figures 6 and 7, a strong correlation between the precipitation and the increase of velocity is observed. Further observation of figure 6 provides information of a stick – slip mechanism and a regressive type of movement in which the velocity does not increase or decrease at a constant rate but undergoes abrupt changes. During and after heavy precipitation the water filled tension cracks provide an increasing driving force. As displacement continues, the width of the cracks increase and the water level drops with a dissipation of water pressure. This is a repetitive situation which modifies the velocity of the sliding mass. Beginning of February 2012 limited (day shift) remedial excavation was executed on bench 1 and above to reduce the weight of the sliding mass. Such excavation increased after March 2012 being conducted on 24hour shifts. As a result movement velocities were reduced after that date.

In retrospect the movement was of the regression type (or behaved in this respect due to the excavation at the top of the slope) as can be seen from the displacement measurements at bench 4 presented in Figure 8. In this graph the displacement at the bench is plotted versus time for four different prisms in different locations transversally placed on the slope (Figure 2).

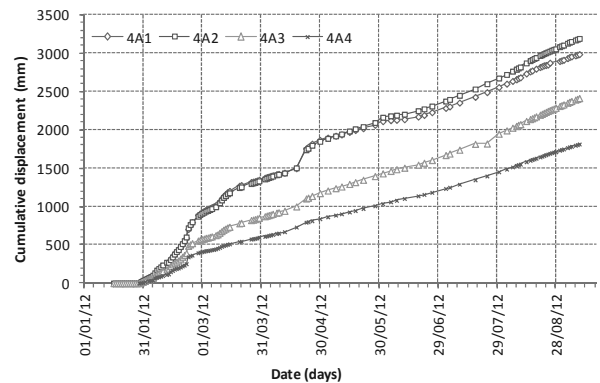


Figure 8. Cumulative displacement of prisms on bench 4

When the cumulative displacement becomes convex, movement acceleration is evident and a progressive type of movement can be inferred. When the cumulative displacement becomes concave then deceleration takes place. As can be seen from Figure 8 displacements “cyclically” change from convex to concave and back to convex meaning that this is of a mixed condition where the regressive type of movement prevails. Although the cumulative displacement of this slope for a period of 7 months is over 3m, the slope is still in a regressive type of movement and therefore mine operations continue.

## 5 GEOMETRICAL MOVEMENT INFORMATION

The dense grid of monitoring prisms together with the high accuracy of the robotic total station produced additional invaluable data for the moving mass. As can be seen from Figure 2 the vectors of motion are presented with arrows. The continuous arrows present monitoring information until the writing of this paper. The dashed arrows present monitoring data that were discontinued for operational reasons at different times. As can be seen from the arrows and the displacements at bench 4 (figure 8) the slope moves more to the east than to the west while both translation and rotation occurs at the same time. The reason for this complex movement can be explained taking

into account the sloping surface geometry and the kinematic conditions of the adjacent southwest slopes.

The southwest slopes can be considered in a regressive moving condition as well. The movement there occurs at a very deep seated slip surface which is, partly formed on the schist bedrock probably on top of an old "inactive" fault and partly on the Neogene formation. The movement of that deeper slide may be generating lateral forces that are applied on the moving mass at the southeast mine slopes.

The complex movement of the southeast slope is also affected by the inclination of the sliding surface where the southeast slopes are moving on. As was shown previously in section A-A', the shear surface was found to have an unfavorable inclination of about 4-5°. This unfavorable situation is not continuous transversely across the slope. This can be safely stipulated after careful evaluation of the vertical – horizontal displacement of different prisms in the same bench (figure 9). In this plot the abrupt change of measurements is due to maintenance of the prisms.

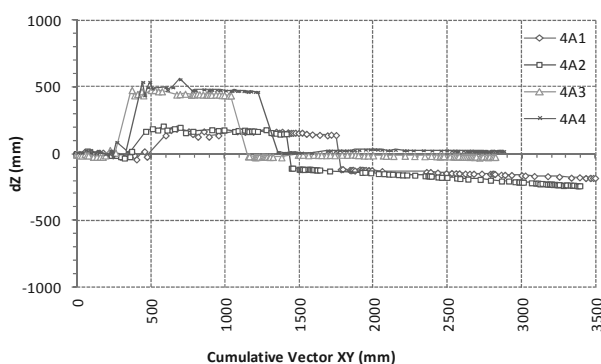


Figure 9. Vertical versus horizontal displacement

As can be seen from figure 9 and especially after about 1500mm of horizontal displacement, when no abrupt changes are recorded, the prisms at the east (4A1, 4A2) produce a downward movement with an angle of about 4-5°. The 4A2 prism which is located at cross section A-A' produces the same shear surface inclination as determined by the inclinometers. Further to the west the sliding surface becomes horizontal or even with slight favorable inclination. This sliding surface geometry is responsible for the increased movement to the east and the rotation of the moving mass.

This detailed evaluation of the moving mass could not be possible without the dense grid of measuring points and the high accuracy of the robotic total station. It is evident that with accurate monitoring data shear surface inclinations can be evaluated from surface measurements.

## 6 CONCLUSIONS

A case study of high horizontal movements recorded on operational surface mine slopes has been presented. The slopes have been moving with an average velocity of about 10-20mm/day and until today they have moved more than 3m.

The sliding mechanism was investigated and, based on back-analysis, it was determined that the southeast slopes of the mine are moving on top of a near horizontal shear surface with a residual friction angle of about 7°. As no water pore pressure was used in the analysis, this value is considered a lower bound, and coincides with values determined through lab experiments for similar material in the mine area. The slope stability analysis is considered only indicative due to the complex geometry of the moving mass. It is not possible to exactly model this mass with plain strain limit equilibrium methods.

Great emphasis was given in the monitoring program in which twenty prisms, two inclinometers and two piezometers were used. The surface monitoring of the prisms was greatly

enhanced when a high accuracy robotic total station was used. With the high accuracy of the robotic total station, movement vectors could easily and accurately be measured.

The measurements presented a complex type of movement of the slopes which most of the time was of the regressive type. The slope movement has been found to be greatly affected by the periodic precipitation and the infilling of the tension cracks.

Based on the regressive type of movement, the mining operation could continue and at the same time remedial measures taken with excavation of the top benches for unloading. This remediation decreased but did not stop slope movements. Although the slopes have moved more than 3m horizontally, they are still in operation without significant problems. Movements were found to be very sensitive to external conditions such as precipitation.

The increased accuracy of the prism measurements allowed the identification of the sliding surface inclination along the mine slopes. It was found that the sliding surface changed inclination transversely.

High mine slopes can be in operation even if they produce high rates of movement, as long as the sliding mechanism type is identified and continuously monitored. Remedial measures can be incorporated in the mine plan in order to reduce movements.

## REFERENCES

- ASTM D2487-98. *Standard Practice for Classification of Soils for Engineering Purposes (Unified Soil Classification System)*. American Society for Testing and Materials.
- Diamantopoulos, A., 2006. *Plio-Quaternary Geometry and Kinematics of Ptolemais Basin (Northern Greece): Implications for the Intra-Plate Tectonics in Western Macedonia*. Geologia Croatica, 59/1, Zagreb.
- Rose, N.D, Hungr, O., 2007. *Forecasting potential rock slope failure in open pit mines using the inverse-velocity method*. International Journal of Rock Mechanics & Mining Sciences, Vol. 44, pp. 308-320.
- Ryan, T. M. & Call, R. D., 1992. *Applications of rock mass monitoring for stability assessment of pit slope failures*. Rock Mechanics, Tillerson & Wawersik (eds), Balkema, Rotterdam.
- Sullivan, T. D., 2007. *Hydromechanical Coupling and Pit Slope Movements*. Slope Stability 2007, Potvin (ed), Australian Center for Geomechanics, Perth
- Zavodni, Z. M. and Broadbent, C. D., 1980. *Slope failure kinematics*. CIM Bulletin, Vol. 73, No. 816.
- Zavodni, Z. M., 2000. *Time-Dependent Movement of Open-Pit Slopes*. Chapter 8, Slope stability in surface mining, Hustrulid, McCarter, VanZyl (eds), Society for Mining, Metallurgy and Exploration.

# A web-based tool for ranking landslide mitigation measures

Un outil internet pour classer les techniques visant à diminuer le risque de glissements de terrain

Lacasse S., Kalsnes B.

*International Centre for Geohazards / Norwegian Geotechnical Institute (NGI), Norway*

Vaciago G.<sup>1</sup>, Choi Y.J.<sup>2</sup>, Lam A.<sup>3</sup>

<sup>1</sup>*Studio Geotecnico Italiano, Milano, Italy;* <sup>2</sup>*NGI Inc., Houston, TX USA;* <sup>3</sup>*GEO Civil Engineering Development Dept, Hong Kong, HKSAR*

**ABSTRACT:** As part of the European project SafeLand, a compendium of structural and non-structural mitigation measures for different landslide types in Europe was prepared, and the measures were assembled into a web-based "toolbox". The purpose of web-based toolbox is to assist decision-making and to guide the user in the choice of the most appropriate mitigation measures. The paper presents an overview of the toolbox features, mitigation measures considered and an example of the report for one application of the toolbox.

**RÉSUMÉ :** Parti intégrante du projet européen « SafeLand », un recueil des mesures d'atténuation structurelles et non structurelles pour les différents types de glissements de terrain en Europe a été établi. Les mesures d'atténuation ont été assemblées dans une "boîte à outils" utilisable via internet. Le but de la boîte à outils est d'aider la prise de décision et de guider l'utilisateur dans le choix des mesures de diminution des risques les plus appropriées. Le document présente un aperçu des fonctionnalités de la boîte à outils, des mesures de diminution des risques envisagées et un exemple de rapport pour une utilisation spécifique de la boîte à outils.

**KEYWORDS:** Landslide, Quantitative vulnerability evaluation, Intensity, Susceptibility

## 1 INTRODUCTION

As part of the research done in the European project SafeLand "Living with landslide risk in Europe: assessment, effects of global change, and risk management strategies", a compendium of structural and non-structural mitigation measures for different landslide types in Europe was prepared, and the measures were assembled into a web-based "toolbox". Emphasis was placed on providing a rational and flexible framework applicable to existing and future mitigation measures.

The purpose of web-based toolbox is to assist decision-making and to guide the user in the choice of the most appropriate mitigation measures.

The mitigation measures were classified into three categories, describing whether the mitigation measures addressed the landslide hazard, the vulnerability or the elements at risk themselves. The measures considered include structural measures reducing hazard and non-structural mitigation measures, reducing either the hazard, the vulnerability or the exposure of the elements at risk. The structural measures include surface protection and control of surface erosion; measures modifying the slope geometry and/or mass distribution; measures modifying surface water regime - surface drainage; measures modifying ground-water regime - deep drainage; measured modifying the mechanical characteristics of unstable mass; transfer of loads to more competent strata; retaining structures (to modify slope geometry and/or to transfer stress to competent layer); deviating the path of landslide debris; dissipating the energy of debris flows; and arresting and containing landslide debris or rock fall.

The non-structural mitigation measures, reducing either the hazard or the consequences: early warning systems; restricting or discouraging construction activities; increasing resistance or coping capacity of elements at risk; relocation of elements at risk; sharing of risk through insurance. The measures are described in the toolbox with fact sheets providing a brief description, guidance on design, schematic details, practical examples and references for each mitigation measure. Each of the measures was given a score on its ability and applicability for differ-

ent types of landslides and boundary conditions, and a decision support matrix was established.

The web-based toolbox organizes the information in the compendium and provides an algorithm to rank the measures on the basis of the decision support matrix, and on the basis of the risk level estimated at the site. The toolbox includes a description of the case under study and offers a simplified option for estimating the hazard and risk levels of the slide at hand. The user selects the mitigation measures to be included in the assessment. The toolbox then ranks, with built-in assessment factors and weights and/or with user-defined ranking values and criteria, the mitigation measures included in the analysis. The toolbox includes data management, e.g. saving data half-way in an analysis, returning to an earlier case, looking up prepared examples or looking up information on mitigation measures. The toolbox also generates a report and has user-forum and help features.

The paper presents an overview of the toolbox features, mitigation measures considered and an example of the report for one application of the toolbox. The reports in the reference list can be found on the SafeLand project website, [www.safeland-fp7.eu](http://www.safeland-fp7.eu). Much more details and the descriptions of each mitigation measure along with references for each can be found in the reports in the list of reference.

## 2 TOOLBOX FEATURES

The toolbox is organized to guide the user in ranking different mitigation measures and to assist in the decision-making about the most appropriate mitigation measures to select for a site. The toolbox suggests the ranking of mitigation measures for a given landslide situation. The toolbox offers an extensive menu of different mitigation measures, and the user selects those that he wishes to consider in the study at hand.

The toolbox documents "do's and don'ts" and "how to". It estimates relative costs, benefits, hazards, effectiveness and vulnerability of each measure to mitigate hazard and/or risk.



The toolbox offers a simplified option for estimating the hazard and risk levels of the slide at hand. The user selects the mitigation measures to be included in the assessment. The toolbox then ranks, with built-in assessment factors and weights and/or with user-defined ranking values and criteria, the mitigation measures included in the analysis.

The web-based toolbox does data management, generates a report and provides help to the user, as well as a user forum. The web-based toolbox has the following features:

- Algorithm to describe a case study, estimate the expected hazard and risk level and to rank, on an engineering judgment basis, the mitigation measures included in an analysis.
- Data management (e.g. save data half-way in analysis, return to an earlier case, look up prepared examples or look up in database for information on mitigation measures).
- Report generation function.
- User forum.
- Help function.
- User management, with password-protected user login.

The toolbox will probably always be in evolution, even after the SafeLand project is completed, as it has "dynamic" technical contents that need to be updated as experience grows and new information becomes available. At all times, the user has access to the toolbox with options to Create a new case, Open a saves case, View a case study, Save a current case, Save as, Delete a current case, and Print.

Several modern technologies were implemented in developing the toolbox. One of them includes desktop toolbar that can automatically be enabled, disabled or hovered to improve user-interface. These toolbar icons of 64 x 64 pixels were designed using graphic software.

### 3 DECISIONS IN TOOLBOX

#### 3.1 Risk classes and need for mitigation

The risk classes used in the toolbox are shown in Figure 1. Depending on a combination of levels of consequence and hazard selected by the user, three risk classes can be assigned by the toolbox: Low, Medium and High. In this simplified model, "High risk" represents an unacceptable risk that requires new site investigations, stability calculations and mitigation measures, "Medium risk" is a risk level that requires considering doing new site investigations and analyses. For "Low risk" situation, further risk reducing measures are not necessary.

Consequence Hazard	Low	Medium	High
High	Medium Risk	High Risk	High Risk
Medium	Low Risk	Medium Risk	High Risk
Low	Low Risk	Low Risk	Medium Risk

Figure 1. Risk classes in Toolbox of Mitigation measures.

#### 3.2 Ranking of measures

The selection of the most appropriate mitigation measures to be adopted in specific situations take into account the following:

(1) the factors that affect the hazard, in terms of the type, rate, depth and the probability of occurrence of the movement or landslide, such as, for example:

- the physical characteristics of the geo-system, including the stratigraphy and the mechanical characteristics of the materials, the hydrological (surface water) and the hydro-geological (groundwater) regime;
- the morphology of the area;
- the actual or potential causative processes affecting the geo-system, which can determine the occurrence of movement or landslides;

(2) the factors that affect the nature and the quantification of risk for a given hazard, such as the presence and vulnerability of elements at risk, both in the potentially unstable area and in the run-out area; and (3) the factors that affect the feasibility of specific mitigation measures, such as, for example:

- the phase and rate of movement at the time of implementation;
- the morphology of the area, accessibility and safety of workers and the public;
- environmental constraints, e.g. archeological, historical and visual values;
- pre-existing structures and infrastructure that may be affected directly or indirectly;
- capital and operating cost, including maintenance.

The user selects in the toolbox the mitigation measures to be considered. To rank the selected mitigation measures, a simple additive algorithm with weighted scoring factors for both default criteria and user-defined criteria in the toolbox was developed. The ranking ( $R_i$ ) is therefore done on the basis of the summation of weighted ( $w_i$ ) contributing factors ( $F_i$ ) for each evaluation criterion:

$$R_i = \sum w_i \cdot F_i \quad (1)$$

Where  $i$  are the mitigation measures selected by the user for analysis, from 1 to  $n$ ;  $w$  is the weighting factor proposed by the toolbox; the default value for all  $w_i$  at start is 1.0 and can be changed by the user; and  $F$  is the scoring factor proposed by the toolbox and which can be changed by the user

Values for  $F$  and  $w$  are proposed by the toolbox, based on a decision support matrix. The user can change the values of  $F$  and  $w$  according to his/her experience and/or engineering judgment. The user can also add additional factors  $F_i$  that will then be automatically included in the analysis.

The scoring factors ( $F_i$ ) for each mitigation measure offered as default in the toolbox are for the user to consider, adopt or modify during his/her assessment of the problem at hand. The scoring for all ranking parameters is on a scale of 1 to 10, where 1 describes the least favourable attribute (worst, lowest, poorest, most expensive), and 10 the most favourable attribute (best, highest, strongest, least expensive or not expensive). The scoring of 0 is used when the mitigation measure is inapplicable or inappropriate.

The weighting factor ( $w_i$ ) reflecting the relative importance of criteria or corresponding scoring factors is in the range of 0 (least) to 1 (most). The default value is set to zero, and the toolbox assigns a values of unity (1) as a function of the input provided by the user in the following technological criteria categories: type of movement, type of sliding material, depth of movement, rate of movement, groundwater, and surface water.

#### 3.3 Priority setting

At the end of the ranking process, the toolbox lists the ranking of the selected mitigation measures in the order of most appropriate to least appropriate measures. The calculated value for  $R_i$

is also given as well as which factor(s)  $F_i$  has the most significance on the result. The user can compare the ranking order and can go back to the previous steps and change the weighting and scoring factors, especially those with high effect on the ranking  $R_i$ , if necessary.

#### 4 CLASSIFICATION OF MITIGATION MEASURES

The Safeland partner Studio Geotechnico Italiano S.r.l. (SGI) prepared a "Compendium of tested and innovative structural, non-structural and risk-transfer mitigation measures for different landslide types" (SafeLand 1). This review was used as a basis for the selection and evaluation of the different mitigation measures included in the toolbox for landslide hazard and risk mitigation measures.

The classification of the mitigation measures was done in terms of the components of a risk assessment (hazard, vulnerability and elements at risk). Table 1 presents this classification. The classification system addresses three components of risk: hazard, vulnerability and elements at risk, where risk R can be expressed as:

$$R = H \cdot C = H \cdot V \cdot E$$

where H is the hazard or the probability of occurrence of an adverse event (landslide); C is the consequence(s); V is the vulnerability or the degree of loss of an element at risk for a given hazard; and E are the elements at risk.

To reduce (or mitigate) the risk, one can reduce the hazard or reduce the consequences (reduce the vulnerability or reduce the exposure of the elements at risk).

Table 2. Classification of mitigation measures (structural measures on top, non-structural measures on bottom)

Class	Component of risk addressed	Brief description	Notes and other terms used
Stabilization	Hazard (H)	Eng'g works to reduce the landslide probability of occurrence	Preventive, remedial, hard, soft, active stabilization.
Control	Vulnerability (V) (consequence)	Eng'g works to protect, reinforce, isolate the elements at risk from the landslide area	Preventive, hard, soft, passive stabilization.
Avoidance	Elements (E) (consequence)	Temporary or permanent reduction of exposure w/ warning systems, evacuation/-relocation, sheltering, land-use planning.	Reduction of the exposure of the elements at risk. Monitoring, early warning systems and civil protection procedures, often temporary, selective avoidance measures.
Tolerance	Elements (E) (consequence)	Awareness, acceptance and/or sharing of risk	Indirect reduction of the exposure of the elements at risk.

Within the general domain of the structural mitigation measures classified above as "stabilization", i.e. reduction of hazard, it is possible to consider a further subdivision in relation to the triggering factors and mechanisms that each measure addresses.

#### 5 MITIGATION MEASURES CONSIDERED

The toolbox includes near 70 structural mitigation measures and six non-structural mitigation measures. The structural measures are divided into ten categories and belong to the class of measures either reducing hazard or reducing consequences. The structural mitigation measures included are:

- A Structural measures reducing hazard
  - 1 Surface protection and control of surface erosion
    - 1.1 Hydro-seeding, turfing and trees/bushes
    - 1.2 Fascines/brush
    - 1.3 Geosynthetics
    - 1.4 Substitution - drainage blanket
    - 1.5 Beach replenishment, rip rap
    - 1.6 Dentition
  - 2 Modifying the slope geometry and/or mass distribution
    - 2.1 Removal of (actual or potentially) unstable soil/rock mass
    - 2.2 Removal of loose or potentially unstable blocks/boulders
    - 2.3 Removal of material from driving area
    - 2.4 Substitution in driving area with lightweight fill
    - 2.5 Addition of material to the area maintaining stability
  - 3 Modifying surface water regime - surface drainage
    - 3.1 Surface drainage works (ditches, channels, pipe works)
    - 3.2 Local re-grading to facilitate run-off
    - 3.3 Sealing tension cracks
    - 3.4 Impermeabilization (geo-membranes, impervious facing)
    - 3.5 Vegetation - hydrological effect
    - 3.6 Hydraulic control works (channel lining and check dams)
    - 3.7 Diversion channels
  - 4 Modifying groundwater regime - deep drainage
    - 4.1 Shallow trenches filled with free-draining material
    - 4.2 Deep trenches filled with free-draining material
    - 4.3 Sub-horizontal drains (conventional drilling)
    - 4.4 Sub-horizontal drains (directional drilling)
    - 4.5 Wells
      - 4.5.1 Small and medium dia. vertical wells (<800 mm)
        - 4.5.1.1 Relief of artesian pressure
        - 4.5.1.2 Under-drainage of perched aquifer
        - 4.5.1.3 Pumps
        - 4.5.1.4 Siphons
      - 4.5.2 Medium diameter vertical wells (1200-1500 mm)
      - 4.5.3 Large diameter vertical wells (>2000 mm)
      - 4.5.4 Caissons (>5-6 m) with gravity drainage
  - 4.6 Drainage tunnels, adits, galleries, with secondary drains
- 5 Modifying mechanical characteristics of unstable mass
  - 5.1 Vegetation - mechanical effects
  - 5.2 Substitution
  - 5.3 Compaction from surface
  - 5.4 Deep compaction (e.g. vibro-compaction)
  - 5.5 Mechanical deep mixing with lime and/or cement
  - 5.6 Low pressure grouting with chemical binder
  - 5.7 Jet grouting
  - 5.8 Modification of ground water chemistry
- 6 Transfer of loads to more competent strata
  - 6.1 Counterfort drains (trench drains)
  - 6.2 Piles
  - 6.3 Barrettes (diaphragm walls)
  - 6.4 Caissons - mechanical effects
  - 6.5 Soil nailing
  - 6.6 Dowels and harnessing
  - 6.7 Rock bolting
  - 6.8 Strand anchors
- 7 Retaining structures (to modify slope geometry and/or to transfer stress to competent layer)
  - 7.1 Reinforced soil structure
  - 7.2 Gabion walls
  - 7.3 Crib walls
  - 7.4 Dry stack masonry walls
  - 7.5 Mass concrete or masonry walls
  - 7.6 Reinforced concrete stem walls
- B Structural measures reducing consequences
  - 8 Deviating the path of landslide debris
    - 8.1 Deflection structure
    - 8.2 Debris flow/rockfall shed
  - 9 Dissipating the energy of debris flows
    - 9.1 Drop structure
    - 9.2 Debris-restraining structure
    - 9.3 Debris flow impediments

10 Arresting and containing landslide debris or rockfall

- 10.1 Debris-resisting barrier
- 10.2 Rock fall barrier
- 10.3 Rock fall net
- 10.4 Debris retention basin

The following non-structural mitigation measures, reducing either the hazard or the consequences (or vulnerability and exposure of elements at risk) or in some cases both hazard and consequence, are included in the toolbox:

- a Early warning systems
- b Restricting construction activities
- c Discouraging construction activities
- d Increasing resistance/coping capacity of elements at risk
- e Relocation of elements at risk
- f Sharing of risk through insurance

6 RANKING CRITERIA

Six criteria categories were implemented to rank the appropriateness of each mitigation measure: type of movement, type of sliding material, depth of movement, rate of movement, groundwater, and surface water. Table 3 lists the criteria used in the toolbox.

Table 3. Ranking criteria used for each mitigation measure

Ranking criterion	Descriptor
Type of movement	Falls Topples Slides Spreads Flows
Material type	Earth Debris Rock
Depth of movement	Superficial (< 0.5 m) Shallow (0.5 to 3 m) Medium (3 to 8 m) Deep (8 to 15 m) Very deep (> 15 m)
Rate of movement	Moderate to fast Slow Very slow Extremely slow
Groundwater	Artesian High Low Absent
Surface water	Rain Snowmelt Localized Stream Torrent River
Maturity of technology	
Reliability of performance	
Reliability in terms of uncertainty in design	
Reliability in terms of uncertainty in implementation	
Safety during construction	
Service life required (durability)	
Aesthetics	
Typical cost	

7 EXAMPLE RESULT

Table 4 presents a typical result of the ranking algorithm for a potential instability in a soft clay slope.

Table 4. Typical report from toolbox.

Rank	Category	Measure	Score	Most significant parameters *
1	Surface protection	Vegetated cover	66	Material/debris Type of movement/-flow
2	Surface protection	Surface drainage	65	Depth of movement Surface water/-stream
3	Surface protection	Infilling of cracks	62	Surface water/stream Rate of movement/-slow
4	Reducing consequence	Early warning system	36	Depth of movement/-superficial Material/rock

\* With respect to measure appropriateness

8 SUMMARY

The paper provides only a glimpse in the toolbox. One has to use it to actually see how it functions. The toolbox will be available at the Safeland web site in 2013.

The purpose of web-based toolbox is to assist decision-making and to guide the user in the choice of the most appropriate mitigation measures. The mitigation measures are classified into three categories, describing whether the mitigation measures addressed the landslide hazard, the vulnerability or the elements at risk themselves. The measures are described in the toolbox with fact sheets providing a brief description, guidance on design, schematic details, practical examples and references for each mitigation measure. Each of the measures was given a score on its ability and applicability for different types of landslides and boundary conditions, and a decision support matrix was established.

The web-based toolbox organizes the and provides an algorithm to rank the measures on the basis of a decision support matrix, and on the basis of the risk level estimated at the site.

9 ACKNOWLEDGMENTS

The SafeLand research was funded by the European Commission and the authors are thankful to all their partners for their remarkable cooperation throughout the project.

10 REFERENCES

SafeLand (2012). Deliverable D5.1. "Compendium of tested and innovative structural, non-structural and risk-transfer mitigation measures for different landslide types" (rev 1-Final dated 2011-03-31) prepared by Studio Geotechnico Italiano S.r.l. (SGI).  
 SafeLand (2012). Deliverable D5.2. " Toolbox of landslide mitigation measures" (rev 1-Final dated 2012-05-11) prepared by the Norwegian Geotechnical Institute (NGI).  
 SafeLand website. [www.safeland-fp7.eu](http://www.safeland-fp7.eu) .

# A Numerical Study of Granular Surge Flow through a Row of Baffles

## Une étude numérique des écoulements granulaires à travers une rangée de chicanes

Law R.P.H., Lam A.Y.T., Choi K.Y.

*Geotechnical Engineering Office, Civil Engineering and Development Department, The Government of the Hong Kong Special Administrative Region, Hong Kong, China*

**ABSTRACT:** A numerical study that utilizes three-dimensional discrete element method was undertaken to investigate the impact process and the dynamic interaction between granular surge flow and baffles. In the numerical analyses, the granular flow medium and the baffles were modelled as frictional spherical discrete elements and rigid square objects respectively. The location, velocity and forces acting on the individual discrete elements during the impact and interaction process were captured and recorded in the analyses. A detailed assessment of the numerical output data indicates that a single row of baffles is effective in reducing the kinetic energy and discharge of the granular surge flow.

**RÉSUMÉ :** Une étude numérique utilisant une approche par éléments discrets en 3D a été mise en oeuvre pour étudier le processus d'impact et l'interaction dynamique entre un écoulement granulaire et des chicanes. Dans cette étude, le milieu granulaire a été modélisé par des objets sphériques et les chicanes par les objets carrés. Les grains comme les chicanes sont considérées comme parfaitement rigides. L'emplacement, la vitesse et les forces agissant sur les éléments discrets au cours du processus d'impact et l'interaction ont été ainsi calculés. Une évaluation détaillée des données de sortie indique qu'une seule rangée de chicanes est efficace pour la réduction de l'énergie cinétique et l'évacuation de l'écoulement granulaire.

**KEYWORDS:** baffles, granular flow, discrete element method, energy dissipation, impact pulse, discharge.

## 1 INTRODUCTION

Granular surge flows such as debris flows and snow avalanches are dangerous natural hazards. Baffles have been employed to dissipate the kinetic energy of such flows and reduce the entrainment of channel bed deposits. Rows of baffles could be constructed across the flow path in order to reduce the flow velocity, the entrainment potential and dynamic impact force on downstream structures. Baffles constructed across the debris flow path are potentially more advantageous than the conventional rigid debris-resisting barriers because baffles are generally easier to construct without the need for extensive site formation works. However, the dynamic interaction of granular surge flow with baffles is still an emerging area of research to both the academics and the practitioners.

Discrete element method was introduced in geomechanics by Cundall and Strack in 1979 and was later adopted as a research tool by other researchers (e.g. Muir et al., 2008; Sibille et al., 2008; Thompson et al., 2009). The discrete element method is an appropriate and useful tool for modelling debris flow and snow avalanche because of the granular flow nature (Zwinger 2000; Nicot 2004; Hutter et al., 2005; Pudasaini & Hutter 2007) of these phenomena. In a previous study by Law 2008, a series of flume model tests and three dimensional discrete element analyses were conducted to investigate the impact behaviour of granular surge flow on a rigid barrier. The study has been extended to investigate granular surge flow through a row of baffles. This paper focuses on the numerical study of the impact process and the dynamic interaction between baffles and granular surge flow using the discrete element method.

## 2 NUMERICAL STUDY

### 2.1 Introduction

The granular medium was modelled as incompressible frictional discrete elements and the planar rigid surfaces were used to model the baffles and the ground surface. In the analyses, the location and velocity of the individual discrete elements together with the forces acting on each element were captured and recorded in order to study the impact process and the dynamic interaction between baffles and granular surge flow. The displacement of individual discrete elements is independent of one another, and they only interacted when coming into contact with each other or with the baffles and other rigid boundaries. The motion of each discrete element was calculated on the basis of the forces acting on it by the Newton's laws of motion. The displacements and rotations of the discrete elements were computed in the numerical analyses.

### 2.2 Numerical model setup and test procedure

Figure 1 shows the geometry of the flow path and the baffles. The granular medium comprises a total of 30,000 spherical discrete elements and all the discrete elements have a uniform diameter of 0.05m. The material density of each discrete element is 2,650 kg/m<sup>3</sup>. The discrete elements were not intended to simulate motion of individual particles in the granular medium. Instead, the macroscopic behaviour of the granular medium was represented by the contact behaviour between the discrete elements. Planar rigid surfaces were used to model the baffles and the ground surface.

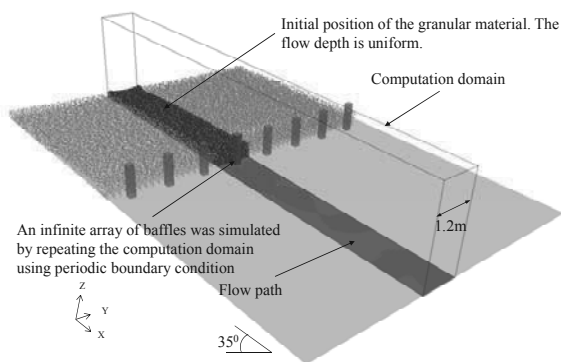


Figure 1. Numerical model setup

The length and width of the computation domain were 15m and 1.2m respectively. The slope gradient was chosen to be 35°. The plan area and the height of the individual baffle were 0.2m x 0.2m and 1m respectively. The baffle was located in the middle of the flow path. The periodic boundary condition (PBC) was applied along the y-direction (Figure 1) of the computation domain. With the PBC, discrete elements leaving one side of the computation domain in the y-axis will emerge on the opposite side with the same dynamic properties, such as velocity, force, etc. This boundary condition helps to reduce the computation time since the impact of granular flow medium on an array of baffles could be simulated using a single baffle and a reduced number of discrete elements (i.e. only the dark particles shown in Figure 1 need to be modelled). With reference to Chen 2009, a baffle spacing of 1m and the ratio of baffle spacing to element diameter of 20 were adopted in the analysis to prevent clogging of the discrete elements between the baffles.

Each numerical analysis is divided into two stages, namely the initial stage and the impact stage. At the initial stage, the granular medium comprising an assembly of discrete elements with random packing was placed on a rigid surface inclined at 35° as shown in Figure 1. The individual discrete elements stabilized itself under the action a body force, which was equivalent to gravity and acting perpendicularly downwards at the ground surface. The body force acting on the individual discrete elements was rotated to the vertical direction in the next stage to enable the granular medium to flow downslope under the action of gravity and impact the baffles. The initial thickness of the granular medium was uniform and chosen to be 0.5m before impacting on the baffles. At the impact stage, the granular medium was given an initial velocity of 8 m/s. The corresponding Froude number of the initial flow condition is close to 4 which fall within the range of Froude number of debris flow events reported by Hubl et al 2009.

### 2.3 Contact law applied in numerical model

The local rheology of the flow material was simulated by applying the contact law in the numerical model. The linear Hookean stiffness model was adopted for the discrete elements and the rigid planar surfaces in the numerical analyses. According to Crosta et al. 2001, the contact stiffness of the discrete element has negligible influence on the computed mobility of granular material. Given that the chosen stiffness value have only minimal influence on the computed result, the discrete element and wall stiffness used were both chosen to be 1x10<sup>8</sup> (N/m) such that the elements almost behave like a rigid body.

The relative translational and rotational motions between the discrete elements are mainly resisted by contact friction. The macroscopic friction angle of dry sand was measured to be 35° (Teufelsbauer et al. 2011, Chiou 2005, Pudasaini et al 2005 and 2007, Pudasaini and Hutter 2007). Based on field and laboratory tests conducted by Chau et al. 2002, Azzoni and Freitas 1995 and Robotham et al. 1995, the coefficient of restitution was chosen to be 0.5.

According to Calvetti and Nova 2004, the macroscopic friction angle of the granular medium is typically much less than 30° irrespective of the value of the contact friction angle adopted on spherical discrete elements without rolling resistance. Calvetti et al 2003 and Tamagnini et al 2005 emphasized the need to inhibit particle rotations and calibrate the particle contact friction angle based on the desired value of the macroscopic friction angle of the granular medium.

In the numerical analyses, a rolling resistance term was added in the calculation of rolling motion of discrete elements. The rolling resistance was calculated using a directional constant torque model elaborated by Ai et al 2011. The model applies a constant torque on a particle to represent the rolling friction. The direction of the torque was always against the relative rotation between the two contact entities. The torque between two in-contact spheres *i* and *j* can be expressed as:

$$M_{rel} = -(\omega_{rel} / |\omega_{rel}|) \mu_r R_i F_n \quad (1)$$

$$\omega_{rel} = \omega_i - \omega_j \quad (2)$$

where  $\omega_i$  = the angular velocities of sphere *i*;  
 $\omega_{rel}$  = the relative angular velocity between two elements;  
 $\mu_r$  = the rolling friction coefficient;  
 $F_n$  = the normal contact force; and  
 $R_r$  = the radius of the discrete element

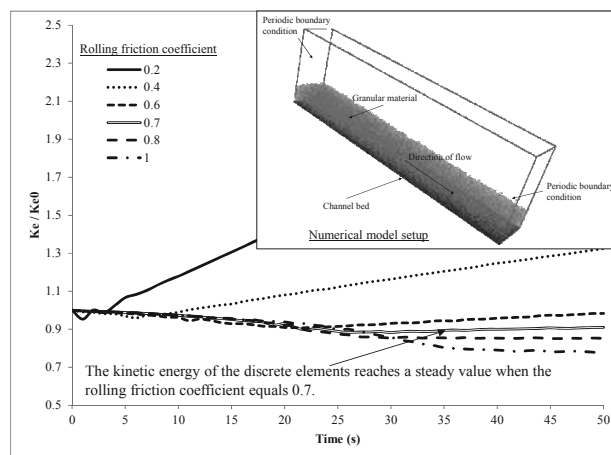


Figure 2. The effects of the rolling friction coefficient on the time history of the computed kinetic energy

A calibration exercise was carried out to identify the appropriate rolling friction coefficient for the numerical study. Figure 2 shows the numerical setup for the calibration work. The simulation box boundary was periodic in nature in order to allow the granular material to transport on the incline indefinitely. The granular material was given an initial velocity of 8m/s. By adopting a macroscopic friction angle of 35° (i.e. same as the channel inclination), a coefficient of restitution of 0.5 and trying different rolling friction coefficients (i.e.  $\mu_r = 0.2, 0.4, 0.6, 0.7, 0.8$  and 1) in the calibration exercise, the granular flow would eventually reach a steady kinetic energy.

Figure 2 shows the time history of the kinetic energy ( $k_e$ ) of all discrete elements relative to the computed  $k_e$  at time zero ( $k_{e0}$ ). The  $k_e$  is the sum of kinetic energy of all discrete elements. Based on the results of the calibration exercise, the granular flow could attain a steady velocity when the rolling friction coefficient reached a value of 0.7, which was chosen to be the appropriate rolling friction coefficient for the numerical study. The input parameters adopted is summarized in Table 1.

Table 1. Parameters adopted in the numerical study

Parameter	Magnitude
Slope angle	35°
Baffle dimension	0.2m x 0.2m x 1m
Particle diameter	0.05m
Density of each particle	2650kg/m <sup>3</sup>
Particle and wall stiffness	1x10 <sup>8</sup> (unit)
Contact friction angle	35°
Coefficient of restitution	0.5
Rolling friction coefficient	0.7
Approaching velocity	8m/s

### 3 COMPUTED RESULTS

#### 3.1 Flow Profile

Figure 3 shows the plan and side view of a number of snapshots recorded in the numerical analyses. The time difference between each snapshot is 0.012 second. The darker the particle colour, the lower was its velocity. A velocity reduction of the discrete elements immediately behind the baffles was observed on plane and Section A-A as shown in Figure 3.

In Figure 3a, at time = 0s, the particles at the front of the flow were just in contact with the baffle. In Figure 3b, at time = 0.012s, the dark region signified the slowing down of the discrete elements behind the baffle after impacting it. The boundary of the dark region where the momentum of the discrete elements was reduced by the baffle is marked by a white dashed line.

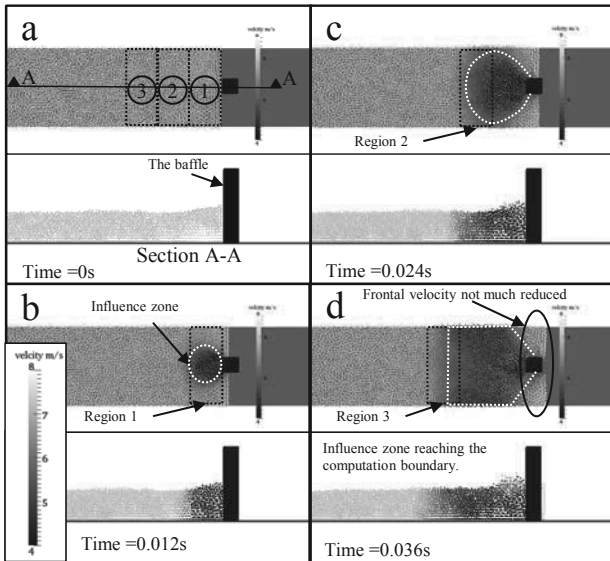


Figure 3. The snapshots showing the change of particle velocity during impact. The time difference between each snapshot is 0.012 second.

In Figure 3c, at time = 0.024s, the size of the dark region increased in size, and the dark region reached the computation boundary in Figure 3d. This indicates that the reduction of the momentum of the discrete elements behind each baffle was no longer localized, but a continuous zone of momentum reduction behind the row of the baffles. The presence of such a momentum reduction zone suggests that most discrete elements passing through the baffles will be decelerated by the flow resistance provided by the baffles. The only exception was the frontal discrete elements located between the baffles. As highlighted in Figure 3d, the velocity of the frontal discrete elements between the baffles was not reduced by the baffles. It is noted from the side view snapshots that the flow depth behind the baffle increases at the time of frontal impact. The

deceleration of the discrete elements was observed to be uniform over the flow depth.

In order to capture and record the dynamic behaviour of the discrete elements behind the baffles, three measurement regions (i.e. region 1, 2 and 3) as shown in Figure 3a were established. Each measurement region was 0.4m in length in the longitudinal direction. The unbalanced force, kinetic energy and discharge rate of the discrete elements within the measurement regions in the first 0.14 seconds of the impact process were recorded and presented as follows.

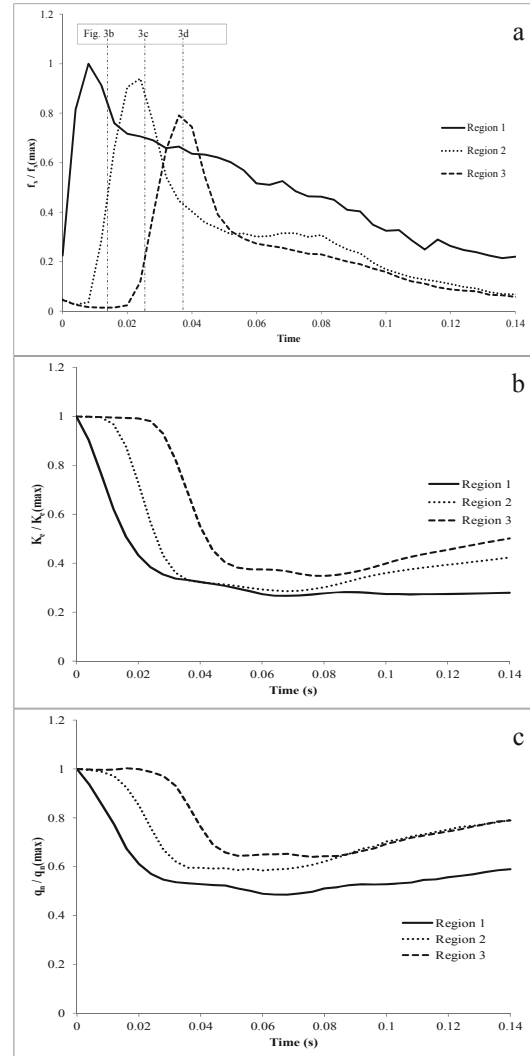


Figure 4. The computed  $f_x$ ,  $k_e$  and  $q_m$  of discrete elements located in region 1, 2 and 3 (please refer to Figure 3a for the location of the regions).

#### 3.2 Unbalanced force on discrete element close to the baffle

The unbalanced force ( $f_x$ ) is the sum of the unbalanced force of all discrete elements in the flow direction. When the granular flow approaches the baffles, a change in the normalized unbalanced force ( $f_x / f_{x(max)}$ ) with time is an indication of the internal stress experienced by the discrete elements due to the dynamic impact on the baffles. Figure 4a shows the relationship of ( $f_x / f_{x(max)}$ ) with time in region 1, 2 and 3. The built up and decline of  $f_x$  were recorded in the three measurement regions 1, 2 and 3 and presented in Figure 4a.

From Figure 4a, the duration of the peak  $f_x$  acting on the baffle was less than 0.01s, and the sequential peak  $f_x$  observed in all the three measurement regions had indicated the propagation of impact pulses in the opposite direction of the flow during frontal impact of granular flow on the baffles. By comparing Figure 3 and Figure 4a, it is observed that the

discrete elements located close to the edge of the dark region had the peak  $f_x$ . The impact pulse is therefore correlated to the propagation of the dark region where the discrete elements reduced their momentum notably. As the  $f_x$  decreased steadily with time after impact, the post-peak  $f_x$  was found to be less than 30% of the peak  $f_x$  after about 0.14s. This finding suggests the highly transient nature of the impact.

### 3.3 Energy dissipation and discharge

Figure 4b shows the relationship of the normalized kinetic energy ( $k_e/k_{e(max)}$ ) of the discrete elements with time in region 1, 2 and 3. The solid line, dotted line and dashed line represent the computed  $k_e/k_{e(max)}$  in region 1, 2 and 3 respectively. The  $k_e$  is the sum of the kinetic energy of all the discrete elements in a region. From Figure 4a and Figure 4b, it can be observed that  $k_e$  decreased much more rapidly with time than  $f_x$ . In region 1,  $k_e$  reduced to 30% of the peak  $k_e$  after less than 0.02s while  $f_x$  requires about 0.14s to reduce to 30% of its peak  $f_x$ . The magnitude of  $k_e$  rose gently following the rapid reduction.

Figure 4c shows the mean discharge rate ( $q_n$ ) of the discrete elements relative to the maximum computed  $q_n$  ( $q_{n(max)}$ ) in region 1, 2 and 3. Similar to the trend of  $k_e$ , the normalized discharge rate reduced with time. The reduction of the discharge rate was less rapid in comparison with the reduction of  $k_e$  shown in Figure 4b. A rising trend of  $q_n$  is observed following the reduction. It is interesting to note that both the  $k_e$  and  $q_n$  rose following the sharp reduction of their values. It is inferred that the deceleration effect caused by the baffles are more significant during the first impact (i.e. time before 0.04 second for regions 1 to 3) at which the impact pulse propagated along these regions. The trend of kinetic energy of these regions beyond 0.14 second is likely to be affected by the presence of various deposition mechanisms, such as runup, reflected wave, jet and hydraulic jump, etc (Armanini and Scotton 1993; Armanini 1997; Sun and Law 2012). Further research will be carried out to study the influence of these mechanisms on the computed kinetic energy and discharge. Based on the above observations of the first impact process, the baffles reduced the kinetic energy and the discharge of the discrete elements behind them effectively.

## 4 CONCLUSIONS

In this study, the three-dimensional discrete element method was used to analyse a granular surge flow through a row of baffles. The analysis focused on the short moment at which the first impact of the discrete elements on the baffles took place. The propagation of impact pulses in the upstream direction was observed at the moment of impact. The magnitude of the impact pulse decreased with the distance upstream from a row of baffles. The deceleration of the discrete elements was uniform over the flow depth at the moment of impact. More than half of the kinetic energy of the discrete element right behind the row of baffles was dissipated in less than 0.02s. The kinetic energy of the granular medium behind the row of baffles decreases more rapidly with time than the unbalanced force. Based on the findings of the analysis, a single row of baffles is effective in reducing the kinetic energy and discharge of the granular surge flow at the moment of impact.

## 5 ACKNOWLEDGEMENTS

This paper is published with the permission of the Head of the Geotechnical Engineering Office and the Director of Civil Engineering and Development, Government of the Hong Kong Special Administrative Region.

## 6 REFERENCES

- Ai J., Chen J.F., Rotter J.M. and Ooi J.Y. 2011. Assessment of rolling resistance models in discrete element simulations. *Powder Technology* 206 (2011) 269–282
- Armanini A., 1997, On the dynamic impact of debris flows, Recent developments on debris flows. Lecture Notes in Earth Science (Armanini and Michiue, Ed.). Berlin: Springer, 1997, vol. 64, p. 208-224.
- Armanini A., Scotton P., 1993, On the dynamic impact of a debris flow on structures, *Proceed. of XXV IAHR Congress, Tokyo Technical session B., debris flows and Landslides* 3:203-210
- Azzoni, A., and de Freitas, M. H. (1995). Experimentally gained parameters, decisive for rock fall analysis. *Rock Mechanics and Rock Engineering*, 28(2), 111-124.
- Calvetti F., Nova R. 2004. Micromechanical approach to slope stability analysis. In: Darve, F., Vardoulakis, I. (Eds.), *Degradation and Instabilities in Geomaterials, CISM Courses and Lectures No. 461*. Springer, Wien, pp. 235-254.
- Calvetti F., Viggiani G., Tamagnini C. 2003. A numerical investigation of the incremental behavior of granular soils. *Rivista Italiana di Geotecnica* 37 (3), 11-29.
- Chau K.T., Wong R.H.C. and Wu J.J. 2002. Coefficient of restitution and rotational motions of rockfall impacts. *International Journal of Rock Mechanics and Mining Sciences*, 39(1), 69-77.
- Chen F. 2009. Coupled Flow Discrete Element Method Application in Granular Porous Media using Open Source Codes. Doctoral Dissertations. University of Tennessee – Knoxville.
- Chiou M.C. 2005. Modelling dry granular avalanches past different obstructions: numerical simulations and laboratory analyses. *Dissertation, Technical University Darmstadt, Germany*
- Crosta G.B., Calvetti F., Imposimato S., Roddeman D., Frattin P. and Agliardi F. 2001. Granular flows and numerical modelling of landslides
- Cundall P.A. and Strack O.D.L. 1979. A distinct element model for granular assemblies. *Geotechnique* No 29, pp 47–65.
- Hubl J., Suda J., Prose D., Kaitna R. and Scheidl C. 2009. Debris flow impact estimation. *Proc. of the 11th Int. Sym. on Water Management and Hydraulic Engineering*, Macedonia, pp 139-148.
- Hutter K., Wang Y. and Pudasaini S.P. 2005. The Savage-Hutter avalanche model: how far can it be pushed? *Philos Transact A Math Phys Eng Sci*. No. 363, pp1507–1528.
- Law R.P.H. 2008. Investigations of Mobility and Impact Behaviour of Granular Flows. *MPhil. Thesis. Hong Kong University of Science and Technology*, 378 p. Hong Kong.
- Muir W.D. and Maeda K. 2008. Changing grading of soil: effect on critical states. *Acta Geotech* 3:3–14
- Nicot F. 2004. Constitutive modelling of snow as a cohesive granular material. *Granular Matter*. No 6, pp47–60.
- Pudasaini S.P., Hsiau S., Wang Y. and Hutter K. 2005. Velocity measurements in dry granular avalanches using particle image velocimetry-technique and comparison with theoretical predictions. *Phys Fluids* 17(9)
- Pudasaini S.P. and Hutter K. 2007. *Avalanche dynamics: dynamics of rapid flows of dense granular avalanches*. Springer, Berlin.
- Robotham M.E., Wang H. and Walton G. 1995. Assessment of risk from rockfall from active and abandoned quarry slopes. *Transactions - Institution of Mining & Metallurgy*, Section A, 104.
- Sibille L., Donze F.V., Nicot F., Chareyre B. & Darve F. 2008. From bifurcation to failure in a granular material: a DEM analysis. *Acta Geotech* 3:15–24
- Sun H.W. and Law R.P.H. 2012. A Preliminary Study on Impact of Landslide Debris on Flexible Barriers. *Technical Note No. TN 1/2012. Geotechnical Engineering Office, Hong Kong*, 42 p.
- Tamagnini C., Calvetti F., Viggiani G. 2005. An assessment of plasticity theories for modeling the incrementally nonlinear behavior of granular soils. *Journal of Engineering Mathematics* 52, 265-291.
- Teufelsbauer H., Wang Y., Pudasaini S.P., Borja R.I., Wu W. 2011. DEM simulation of impact force exerted by granular flow on rigid structures. *Acta Geotechnica* 6:119–133
- Thompson N., Bennett M.R. and Petford, N. 2009. Analyses on granular mass movement mechanics and deformation with distinct element numerical modelling: implications for large-scale rock and debris avalanches. *Acta Geotech* No 4, pp233–247.
- Zwinger T. 2000. Dynamik einer Trockenschneelawine auf beliebig geformten Berghängen. PhD Thesis, *Vienna University of Technology*. Austria.

# Full-Scale Field Monitoring of a Rainfall-Induced Sliding Slope in Hainan, China

## Étude en vraie grandeur d'un talus glissant soumis à des précipitations à Hainan en Chine

Li A.G., Qiu J.J., Mo J.F., Gao W.

*Shenzhen Geotechnical Investigation & Surveying Institute Co. Ltd., Shenzhen, China*

Tham L.G., Yan R.W.M.

*Department of Civil Engineering, The University of Hong Kong, Hong Kong, China*

**ABSTRACT:** This paper investigates the mechanism of rainfall-induced sliding slope through a study based on a full-scale field monitoring conducted in a sliding slope in Shimei Bay, Wanning City, Hainan, China, where some premium hotels and residential buildings are being built along a natural hillside slope. Due to the heavy rainfall in October, 2011, it was found that the hillside slope was sliding during the heavy rainfall. A number of instruments, including soil moisture probes, tensiometers, open standpipes and piezometers, inclinometers, and a rain gauge were installed in the slope. Field monitoring of the sliding slope was conducted during one dry and one wet seasons before the stabilization of the sliding slope. The paper mainly introduced the instrumentation system of field monitoring of the sliding slope. It also introduced the preliminary analysis of the variations of rainfall intensity, soil moisture content, matric suction, ground water level, slope deformation during the dry season of 2011 and the wet season of 2012 before the stabilization of the sliding slope.

**RÉSUMÉ :** Cet article étudie le rôle des précipitations sur une pente glissante via une étude basée sur un suivi sur le terrain à grande échelle, menée dans une pente glissante dans Shimei Bay, ville de Wanning, Hainan, en Chine, où certains hôtels de luxe et des bâtiments résidentiels sont en cours de construction, le long d'une la pente naturelle. En raison des fortes pluies en Octobre 2011, il a été constaté que la pente (colline) glissait pendant les fortes pluies. Un certain nombre d'instruments, y compris les sondes d'humidité, tensiomètres, bornes-fontaines, des piézomètres ouverts, inclinomètres, et une jauge de pluie ont été installés dans la pente. Le contrôle du glissement a été effectué pendant une saison sèche et une saison humide, avant la stabilisation de la pente. Cet article présente le système d'instrumentation mise en place sur le site. On présente également dans cet article l'analyse préliminaire sur des variations de l'intensité des précipitations, l'humidité du sol, succion matricielle, le niveau de la nappe phréatique et la déformation de la pente pendant la saison sèche de 2011 et la saison des pluies de 2012, avant la mise en place des renforcements du site.

**KEYWORDS:** field-monitoring ; sliding slope ; rainfall-induced ; strumentation.

## 1 INTRODUCTION

Rainfall-induced landslides are common in the tropical areas in China, especially in Southern China. Each year hundreds of landslides, occur during the rainy season. Many of these landslides have caused heavy damage and numerous fatalities. The majority of these landslides are associated with heavy rainfall. Hence, rainfall-induced slope failure becomes one of the most common types of landslides in Hong Kong (Lumb, 1962a, 1962b, 1975; Brand, et al. 1984; Au, 1998; Franks, 1999, Dai, et al. 1999, 2001; Li, et al. 2002, 2003, 2005a, 2005b, 2006).

Due to the new policy that China aims to build the southern island of Hainan into a top international tourism destination by 2020, the Hainan local government promises to boost development not only by expanding oil and gas exploration, offering more duty free services, developing logistics, reducing pollution, but also by improving transportation networks and infrastructure. Thus, more premium hotels, resorts, family-run hotels and residential buildings are being built along the east coast of the island.

In area of our study site, a lot of landslides were reported. A total of 4 landslides were recognized within the site. Site investigation was also carried out, which found that there was even a big landslide with a scar volume of 500000 m<sup>3</sup> just one kilometer away from the site. There was even a heavy debris flow, which almost damaged the newly built east fast train for Haikou to Sanya, which is just 5 kilometers away. As little research work was carried out in Hainan for the landslides, there

are even few documents for the landslides, only occasionally in the local newspapers.

In order to investigate the mechanism of rainfall-induced slope failure, a study is being carried out based on a full-scale field monitoring conducted in a sliding slope in Shimei Bay, Wanning City, Hainan, China, where some premium hotels and residential buildings are being built along a natural hillside slope.

Due to the heavy rainfall in October, 2011, it was found that the hillside slope was sliding during the heavy rainfall. The sliding slope was a gentle hillside, which was cut to accommodate a temporary road construction, and consisted mainly of residual soil, CDG and HDG. To characterize the soil properties of the sliding slope, a detailed site investigation was carried out prior to the instrumentation.

A number of instruments, including soil moisture probes, tensiometers, open standpipes and piezometers, inclinometers, and a rain gauge were installed in the slope. Site investigation included borehole drilling, soil sampling, field and laboratory tests was carried out. Field monitoring of the sliding slope was conducted during one dry and one wet seasons before the stabilization of the sliding slope. The pre-stabilized slope was monitored during the dry season of 2011 and the wet season of 2012. The stabilization of the sliding slope started before the end of the wet season in 2012.

Anti-sliding piles plus pre-stressed anchors were designed to stabilize the sliding slope. Other instruments including load cells and strain gauges were suggested to be installed in the



anchors and piles during the stabilization of the sliding slope. It was suggested that the post-stabilized slope should also be monitored for another dry season of 2012 and another wet season of 2013.

The paper mainly introduced the instrumentation system of fielding monitoring of the sliding slope. It also introduced the preliminary analysis of the variations of rainfall intensity, soil moisture content, matric suction, ground water level, slope deformation during the dry season of 2011 and the wet season of 2012 before the stabilization of the sliding slope.

## 2 SITE CONDITIONS

The site is a natural hillside terrain covered by a lot of vegetation. The section was originally a gentle slope and then it was cut to accommodate the footpath for the main road. Ground investigation work was carried out during instrument installation. The site ground as revealed by the ground investigation is mainly residual soil, completely decomposed granite (CDG) and highly decomposed granite (HDG), which are underlain by moderately decomposed granite (MDG) and slightly decomposed granite (SDG).

Laboratory tests were carried out on the soil samples obtained at the sliding slope during the site investigation. The soil, as revealed by site investigation, is completely decomposed medium-grained granite and can be classified as a very weak to weak, light brown to brown, silty/clayey sand. The laboratory program to characterize the soil properties included: (1) Bulk density, (2) Dry density, (3) Specific gravity, (4) Atterberg limits and (5) Particle size distribution.

Part of the laboratory tests results are summarized in Table 1.

Table 1. Soil properties for the sliding slope.

Bulk density (Mg/m <sup>3</sup> )	1.76~1.93
Dry density (Mg/m <sup>3</sup> )	1.44~1.54
Specific gravity	2.627~2.655
Void ratio	0.7314~0.8443
Porosity	0.42~0.46
Liquid limit (%)	31.5~44.3
Plasticity index (%)	12~23

## 3 INSTRUMENTATION SYSTEM

The instruments included soil moisture probes to measure volumetric water content, tensiometers to measure matric suction (negative pore water pressure), open standpipes and piezometers to measure ground water level and positive pore water pressure, inclinometers to measure the lateral ground movements, and a rain gauge to measure rainfall intensity.

The philosophy for instrumentation design was as follows: The moisture probes and tensiometers were installed in the shallow depth to monitor volumetric water content and matric suction in the unsaturated zone of the soil. The open standpipes and piezometers were installed in both the shallow depth and greater depth to monitor both perched and deep ground water or positive pore pressure in the saturated zone of the soil. The inclinometers were installed in the soil to monitor horizontal deformation of the sliding slope. The rain gauge was installed to monitor the specific rainfall intensity of the monitored sliding slope. Figure 1 shows instrumentation layout plan.

A total of six moisture probes were used to measure volumetric water contents inside different parts of the sliding slope (Figure 1). Three moisture probes were installed in borehole M1 (M1-1 (1m), M1-2 (2m) and M1-3 (3m)) at depths

of 1 m, 2 m and 3 m, respectively, at the toe of the slope. The other three moisture probes were installed in boreholes M3 (M3-1 (1m), M3-2 (2m) and M3-3 (3m)) at depths of 1 m, 2 m and 3 m, respectively, near the crest of the slope. A total of six tensiometers were used to measure matric suction at different locations of the sliding slope (Figure 1). Three of them were installed in boreholes T1 (T1-1 (1m), T1-2 (2m) and T1-3 (3m)) at depths of 1 m, 2 m, 3 m and 4 m, respectively at the toe of the sliding slope. The other three were installed in boreholes T3 (T3-1 (1m), T3-2 (2m) and T3-3 (3m)) at depths of 1 m, 2 m, 3 m and 4 m, respectively, near the crest of the sliding slope. A total of three open standpipes were used to measure ground water levels at different locations of the sliding slope (Figure 1). A total of three vibrating wire piezometers (P1, P2 and P3) were used to measure positive pore water pressures at different locations of the sliding slope (Figure 1). A total of three inclinometer tubes (IN1, IN2 and IN3) were used to measure the lateral ground movements at different locations of the sliding slope (Figure 1). One 0.5 mm “tipping bucket” rain gauge with internal logger was used to monitor the rainfall intensity of the monitored slope site automatically (Figure 1).

Ground water levels in the open standpipes were monitored manually with the help of a dipmeter. An automatic data acquisition system was set up for the sliding slope to monitor moisture content, matric suction, positive pore water pressure and horizontal deformation continuously. The automatic data acquisition system consists of sensors, cables, data loggers and power supplies. An instrumentation hut was constructed at the top of the sliding slope to house the data loggers and power supplies. The data loggers were configured to collect data at 15/30-min intervals and the data were transmitted to both the office in the site and the office in Shenzhen instantly via wireless data transition system.

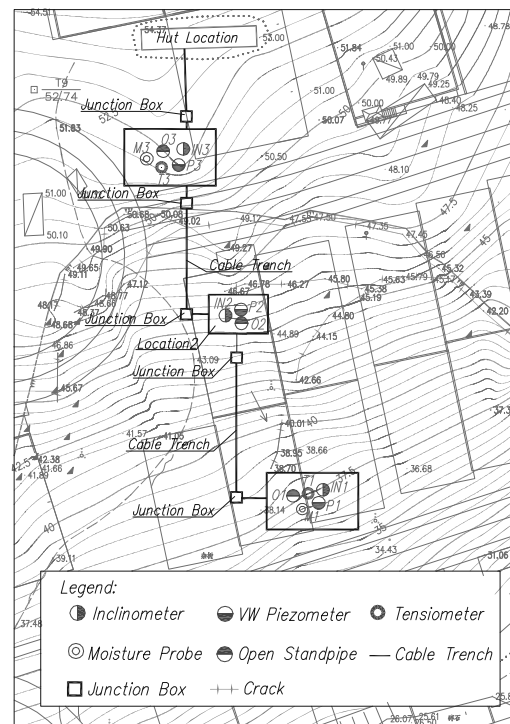


Figure 1. Boreholes and instrumentation layout plan.

#### 4 PRELIMINARY MONITORING RESULTS

##### 4.1 *Moisture Probes and Tensiometers*

Figures 2 and 3 show the variations of the volumetric water content and the matric suction of Borehole M3 at the crest of the sliding slope from November 2011 to June 2012. By examining the volumetric water content and the matric suction records and their comparison with daily rainfall in borehole M3 at the crest of the sliding slope during the above period (Figures 2 and 3), the following observations can be made:

(1) The volumetric water content increased due to rainfall infiltration in the wet season and decreased due to evaporation in the dry season. The matric suction decreased due to rainfall infiltration in the wet season and increased due to evaporation in the dry season.

(2) The volumetric water content at different depths was not uniform. Generally, the volumetric water content at a shallow depth was lower than that at greater depths during the dry season, while the volumetric water content at a shallow depth was higher than that at greater depths during the wet season. The matric suction at different depths was not uniform too. Generally, the matric suction at a shallow depth was higher than that at greater depths during the dry season, while the matric suction at a shallow depth was lower than that at greater depths during the wet season.

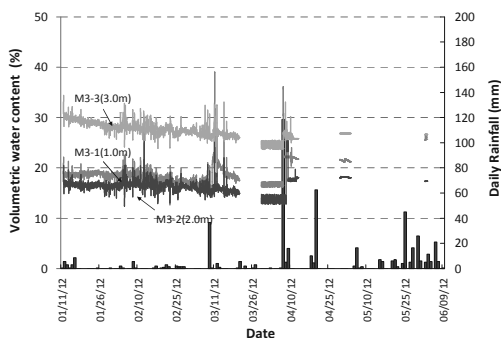


Figure 2. Variations of volumetric water content and daily rainfall from November 2011 to June 2012 in borehole M3 at the crest of the sliding slope.

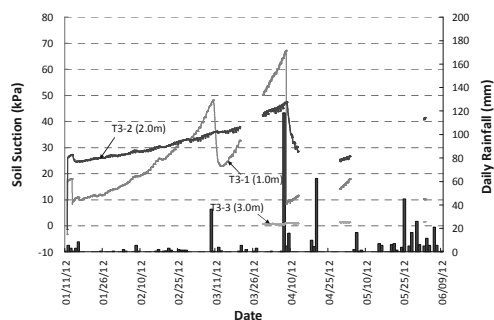


Figure 3. Variations of matric suction and daily rainfall from November 2011 to June 2012 in borehole M3 at the crest of the sliding slope.

##### 4.2 *Open Standpipes and Piezometers*

The monitoring of the three open standpipes was carried out by using a dipmeter. The monitoring of the open standpipes was to check the monitoring data of nearby installed piezometers. Figure 4 shows the variations of the ground water levels in Borehole P1 at the toe of the sliding slope from November 2011 to June 2012. By examining the ground water level records and comparing them with the daily rainfall data during the above period, the following observations can be made:

(1) The pore water pressure at P1-A was higher than that at P1-B. It probably implies that there was a perched water level in

the sliding slope and the permeability of the residual soil is higher than that of CDG.

(2) The groundwater level decreased around 6.0 m at both P1-A and P1-B.

(3) The rise of the groundwater level was sensitive to rainfall, and it was more sensitive at shallow depth. Furthermore, there was a time lag for monitoring the highest ground water level due to rainfall.

(4) The highest groundwater levels monitored in November, 2011 was probably due to the heavy rainfall during the wet season in 2011, which caused the landslide.

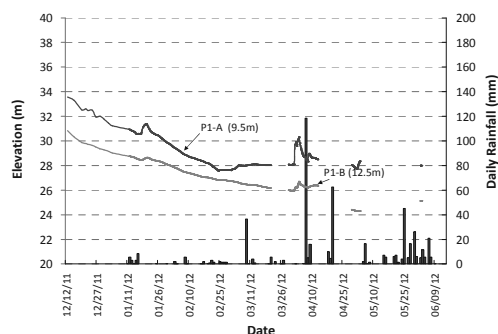


Figure 4. Variations of ground water level and daily rainfall from November 2011 to June 2012 in borehole P1 at the toe of the sliding slope

##### 4.3 *Inclinometers*

Figure 5 shows the monitored horizontal displacements from November 2011 to June 2012 in borehole IN1 at the toe of the sliding slope. By examining the monitored horizontal displacements during the above period, the following observations can be made:

(1) The maximum horizontal displacement from June 2011 to July 2012 in borehole IN1 at the toe of the sliding slope was about 10.0 mm (Figure 25).

(2) The monitored sliding slope was sliding slowly. It is believed that with rainfall infiltration, the matric suction in soils at shallow depth partially disappeared, which decreased the stability of this sliding soil slope.

(3) The decrease of groundwater level was up to 6.0 m during the dry season, however, the increase of groundwater level due to the heavy rainfall on April 7 was less than 1.0 m, therefore, the maximum horizontal displacement was insignificant.

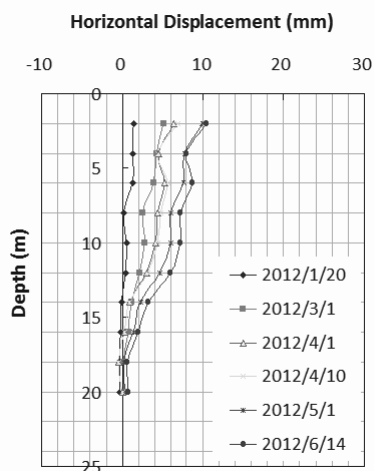


Figure 5. Horizontal displacements from November 2011 to June 2012 in borehole IN1 at the toe of the sliding slope

## 5 THE FAILURE OF THE MONITORING SLIDING SLOPE

As the client started the stabilization of the sliding slope using man-dug piles and anchors, it was found that it was very difficult to protect the monitored system. Therefore, automatic monitoring system for the sliding slope has to be given up. Instead, the sliding slope was being monitored manually during the stabilization of the sliding slope.

There are several rows of piles needed to be constructed during the stabilization and furthermore, there are a lot of excavations before the stabilization. Though many warning letters had been issued to the Contractor by the Consultant, before the completion of the stabilization works, due to a heavy rainfall on November 4, part of the sliding slope had completely collapsed, which caused the fifth landslide for the site.

The investigation of the fifth landslides was carried out later. It was found that the main reason for the landslide was the improper excavation. Some of the excavation has an angle of 45° to 50°. As the Contractor believed that the wet season would end and there would be no heavy rainfall in November 2012 just as in November 2011, improper excavation was carried out for the sliding slope.

Another very important reason for the failure of the improper excavated sliding slope may be due to the significant increase of the volumetric water content and the dramatic decrease of the matric suction of the sliding slope. It may be proved that negative pore-water pressure (or matric suction) plays a crucial role in the stability of unsaturated soil slope. With rainfall infiltration, the matric suction in soils at shallow depth would partially or completely disappear. Consequently, a slope failure may occur.

It is a pity that the automatic monitored system has to be abandoned due to the construction.



Figure 5. Failure of the sliding slope during a heavy rainfall on November 4, 2012.

## 6 CONCLUSIONS

From the study of the field monitoring of a monitoring sliding slope in Hainan, China and the failure of the sliding slope at last, the following conclusions can be made:

(1) The volumetric water content increased in the wet season and decreased in the dry season. Correspondingly, the matric suction decreased in the wet season and increased in the dry season.

(2) The variations of the volumetric water content and matric suction with time at different depths were different. Maximum variations often occurred near the ground surface. The large variations of volumetric water content and matric suction during rainy season at shallow depth may explain the

reason why so many slope failures occurred in this region during heavy rainstorms.

(3) The ground water level generally rose during the wet season and fell during the dry season. The rise of the ground water level occurred during heavy rainfall or long after the rainfall. The ground water level also decreased temporarily after the heavy rainfall.

(4) As the volumetric water content increased during the rainfall, the monitored slope was sliding slowly, though insignificantly. Furthermore, the monitored horizontal displacement during the monitored period was not significant, which is probably due to insignificant rise of the groundwater level in the sliding slope.

(5) It is believed that the main reason for the failure of the sliding slope was the improper excavation. It could also be due to the loss of the matric suction, which plays a crucial role in the stability of unsaturated soil slope.

## 7 ACKNOWLEDGEMENTS

The authors would like to thank China Resources Hainan Shimei Bay Tourism & Development Co., Ltd. for their providence of the site and especially their kind assistance during the installation of the instruments and the monitoring of the sliding slope in the field.

## 8 REFERENCES

- Lumb, P. (1962a). General nature of the soils of Hong Kong, Proc. Symp. Hong Kong Soils. Hong Kong, 19-32.
- Lumb, P. (1962b). Effect of rainstorms on slope stability, Proc. Symp. Hong Kong Soils. Hong Kong, 73-87.
- Lumb, P. (1975). Slope failures in Hong Kong. Q. J. Engng Geol. 8, 31-65.
- Brand, E.W., Premchitt, J. & Phillipson, H.B. (1984). Relationship between rainfall and landslides. Proceedings of the fourth International Symposium on Landslides. Canada, 1, 377-384.
- Au, S.W.C. (1998). Rain-induced slope instability in Hong Kong. Engineering Geology. 51, 1-36.
- Franks, C.A.M. (1999). Characteristics of some rainfall-induced landslides on natural slopes, Lantau Island, Hong Kong. Quarterly Journal of Engineering Geology. 32 247-259.
- Dai, F.C., Lee, C.F., Wang, S.J., & Feng, Y.Y. (1999). Stress-strain behavior of a loosely compacted volcanic-derived soil and its significance to rainfall-induced fill slope failures. Engineering Geology 53, 359-370.
- Dai, F.C. & Lee, C.F. (2001). Frequency-volume relation and prediction of rainfall-induced landslides. Engineering Geology 59, No. 3-4, 253-266.
- Li, A.G., Yue, Z.Q., Tham, L.G., Lee, C.F. & Law, K.T. (2002). Rainfall Infiltration at an Instrumented Cut Slope. 55th Canadian Geotechnical Conference, October 20-23, 2002, Ontario, Canada, 1159-1167.
- Li, A.G., Yue, Z.Q., Tham, L.G., Lee, C.F. & Law, K.T. (2003). Design and Installation of a Comprehensive Instrumentation System for a Slope in Hong Kong. Chinese Journal of Rock Mechanics and Engineering, 22 No. 5, 790-796. (In Chinese)
- Li, A.G., Yue, Z.Q., Tham, L.G., Lee, C.F. & Law, K.T. (2005a). Field Monitored Variations of Soil Moisture and Matric Suction in a Saprolite Slope. Canadian Geotechnical Journal. 42 13-26.
- Li, A.G., Tham, L.G., Yue, Z.Q., Lee, C.F. & Law, K.T. (2005b). Field Soil-Water Characteristics of Completely Decomposed Granite. Journal of Geotechnical and Geoenvironmental Engineering. 131 No.9 1176-1180.
- Li, A.G., Xiong, J.A., Nan, L. and Qiu, J. J. (2006). The Study of Rainfall-Induced Sliding of a Fill Slope in Shenzhen, China, The 10th IAEG Congress, 6-10 September 2006, Nottingham, United Kingdom.

# Estimation and Prediction of Debris Flow Potential Using Discrimination Analysis

## Estimation et prédiction du potentiel d'écoulement de boue utilisant une analyse discriminante

Lin M.L., Lin Y.S.

*Department of Civil Engineering, National Taiwan University, Taiwan*

**ABSTRACT:** Taiwan is situated at the juncture of tectonic plates, which caused complex and fragile geological condition with steep mountain terrain. Being frequently struck by typhoons and earthquakes, the landslide and debris flow hazard occurs frequently. In this research, the estimation model of regional debris flow potential was constructed based on the geo-morphological and hydrological conditions of the research area. For constructing the estimation model of debris flow potential, the Fisher's discrimination analysis was used. A study area of Nantou County in Central Taiwan was selected. Influence factors were identified and a database for both debris flow torrents and non-debris flow torrents were constructed. Estimation model was constructed using the Fisher's analysis by random sampling of the debris flow and non-debris flow torrents. The estimation model is validated and then used for prediction of debris flow potential. The final model can be determined by evaluating the estimation stability and prediction rate with each additional influence factor. The resulting potential estimation of the study area appears to be satisfactory. The influence factor stability of the Fisher's discriminant model and the prediction rate associated with the differences in influence factors were discussed.

**RÉSUMÉ :** Taiwan est situé à la jonction de plaques tectoniques, ce qui engendre un terrain escarpé avec des situations complexes et des conditions géologiques fragiles. L'île étant régulièrement frappée par des typhons et des tremblements de terre, des glissements de terrain et des écoulements de boue se produisent fréquemment. Pour cette étude, le modèle d'estimation des coulées de boue régionale potentiel a été construit sur la base des conditions géomorphologiques et hydrologiques de la zone de recherche. Pour la construction de celui-ci, l'analyse discriminante de Fisher a été utilisée. Une zone d'étude du comté de Nantou qui se situe au centre de Taiwan a été choisie. Les facteurs d'influence ont été identifiés et des bases de données pour les torrents d'écoulement de boue et torrents d'écoulement de non-boue ont été construites. Le modèle d'estimation a été construit en utilisant une analyse de Fisher par échantillonnage aléatoire des torrents d'écoulement de boue et des torrents d'écoulement de non-boue. Le modèle d'estimation est validé, puis utilisé pour la prédiction de potentiels écoulements de boue. Le modèle final peut être déterminé en évaluant l'estimation de la stabilité et la fréquence prédite avec chaque facteur d'influence additionnel. L'estimation résultante potentielle de la zone d'étude semble être satisfaisante. Le facteur d'influence de stabilité du modèle discriminant de Fisher et la fréquence prédite associée aux différences des facteurs d'influence ont été discutés.

**KEYWORDS:** debris flow, potential estimation, Fisher's discriminaton analysis, influence factor, prediction model.

## 1 INTRODUCTION

More than 70 percent of areas in Taiwan are in mountain region and with steep and fragile slopes. The earthquakes and heavy rainfall introduced by typhoons often induced significant landslide and debris flow hazards in Taiwan, which lead to significant loss of properties and lives. For effective mitigation of the debris flow hazards, it is important to evaluate the potential of debris flow torrents, which supports decision on mitigation measures and priority.

This research is based on the data of the 1,420 debris flow torrents published by Soil and Water Conservation Bureau in 2003. The fundamental data of the debris flow torrents for the study area of Nantou County in Central Taiwan were collected, and the basic database along with the related influence factors were established utilizing the geographic information system software, Arcview. The influence factors database included watershed area, stream length, hypsometric integral, stream mean slope, form factor, slope distribution, slope aspect and geology category, were extracted from the fundamental data. The statistic analysis was performed on all influence factors to discuss their significances. The multi-variant discrimination analysis was used to discriminate debris flows and non-debris flows. The analysis model was verified, and accordingly the potential of debris flow torrents in Nantou County was evaluated.

## 2 STUDY AREA AND FUNDAMENTAL DATABASE

The Nantou County located in central Taiwan is selected as the study area in this research, which has a large area with high mountains and rugged topography. The debris flow hazard in Nantou County came into great concern since 1996, when Typhoon Herb caused severe losses of properties and lives. In addition, severe debris flow hazard struck this area frequently after the Chi-Chi earthquake, 1999. According to the data published by Soil and Water Conservation Bureau (2003), the number of debris flow torrents reaches 199 in Nantou County, which are for the potential analysis. The distribution of the debris flow torrents and the study area are as shown in Figure 1. The fundamental database used for construction of related database for analysis include: the digital elevation model published in 1989 with a resolution of 40m x 40m, 1/500,000 Taiwan geology map produced by the Central Geological Survey in 1986, aerial photographs, topographical map. The primary geologic formations of the study area include slate, phyllite, sandstone, and shale. According to the engineering geology zonation proposed by Hung in 1997, the research area contents C zone (metamorphic rocks, metamorphic sandstone, shale, slate, phyllite), D zone (sedimentary rocks), E zone (lateritic tableland), and G zone (basin and plain). As shown in Figure 1. Study area and distribution of Debris Flow Torrents and Non-Debris Flow Torrents

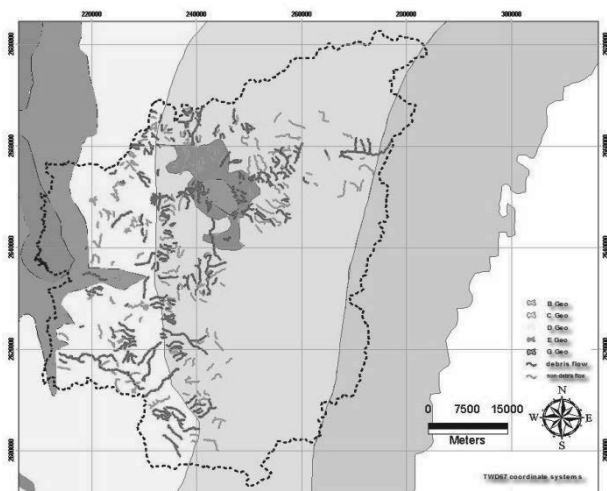


Figure 1, most of the debris flow torrents in Nantou County distribute in C zone and D zone.

In order to perform the discriminant analysis, database for both debris flow torrents and non-debris flow torrents are constructed as discussed in the followings:

a. Debris flow torrents: the debris flow torrents in research area are based on the debris flow torrents published by Soil and Water Conservation Bureau in 2003 in 1/5,000-scale. The total number of debris flow torrents in the research area is 199. The watershed of each debris flow torrent was generated using DEM accordingly.

b. Non-debris flow torrents: The procedures for establishing the non-debris flow torrents are to establish watersheds and streams based on the 1/25,000 topographic map and DEM, and are not debris flow torrents by SWCB (Lin, et al. 2003). The non-debris flow should be in the neighboring area of debris flow torrents and with similar geologic traits and watershed size. Accordingly, a total number of 175 non-debris flow torrents was generated in the research area. Cross examination of these torrents were performed by comparing the torrent distribution to the aerial photograph. The results appeared to be consistent, and the distribution of the non-debris flow torrents is as shown in Figure1.

### 3 INFLUENCE FACTORS AND THEIR SIGNIFICANCES

The necessary conditions for triggering debris flow include affluent debris materials, sufficient water supply, and appropriate geomorphological conditions. For evaluation of debris flow potential, the influence factors were selected based on the three conditions, and the database were generated. Based on previous researches (Lin, et al. 2003, Lin and Chen, 2005, and Lin and Wen, 2006), eight influence factors are selected as: watershed area, streams length, hypsometric integral, form factor of basin, stream mean slope, slope angle, slope aspect, and geology formation, respectively.

1. Watershed area: BA, in hectare. The watershed with larger area usually contributes more water, which is regarded as a factor related to the water supply.

2. Stream length: SL, in meter. Stream length means the largest length of the stream in the related watershed. The longer the stream length is, the larger the watershed area is. Stream length is also regarded as another factor of sufficient water supply.

3. Hypsometric Integral: HI, dimensionless. The hypsometric integral is determined from the integral of the basin's height versus area percentage curve, which is a characteristic of geomorphic evolution of the watershed. It also stands for terrain ruggedness and is regarded as a factor related to the abundance of debris material.

4. Form factor: Form factor, FF (dimensionless), is proposed by Horton in 1920, and is defined as the basin area divided by the square of stream length. A higher form factor suggests broader basin shape, and different basin shapes affect flow hydrograph of the stream (Robet and Raymond, 1978).

5. Stream mean slope: SMS, in degree. Stream slope is an important factor related to flow velocity; the steeper the slope is, the faster the stream flow. The stream mean slope serves as an indicator of appropriate slope conditions.

6. Slope aspect: N, NE, E, ES, S, SW, W, WN, in percentage of area ratio. Most debris flow disasters were triggered by typhoon or heavy rainfall. According to the landing path of typhoons, rain falls concentrated more on windward side. Strong wind also influences the weathering process. Slope aspect serves as an indicator of geomorphological condition.

7. Slope distribution: SD10(0°~10°), SD15(10°~15°), SD20(15°~20°), SD30(20°~30°), SD45(30°~45°), SD90(45°~90°), in percentage of area ratio. Steeper slope has a higher tendency of slope failure and leads to more debris material.

8. Geological formation: E1, E2, EO, Mj, Ml, MS, My, O1, O2, O3, P1, P2, Q2, Q3, Q0, as listed in Table 1, in area ratio percentage. Weak rock quality, complicated geologic structure, highly developed fault and fold, and intensive tectonic activity zone tend to provide abundant debris material. Different geological formation contributes to different material strength, degree of fracture, and soil type.

The influence factors were derived from fundamental data through performing spatial and hydrological analysis using GIS and the related database were established. The distributions and characteristics of the influence factors of debris flow torrents and non-debris flow torrents are compared and discussed.

Table 1. Geological formations of the study area

Category	Symbol	Rock Type
Metamorphic Rock (C Zone)	E1	Slate, interlaminations of slate and sandstone
	E2	Indurate sandstone with carbonaceous slate interbeds
	EO	Slate, phyllite, with sandstone interbeds
	Mj	Sandstone, shale
	Ml	Argillite slate phyllite sandstone interbeds
	MS	Sandstone, shale
	O1	Quartzitic sandstone, slate, graphitic shale
	O2	Argillite, indurate sandstone, slate
	Q2	Gravel, laterite, clay, sand
	Q3	Clay, sand, gravel
Sedimentary Rock (D Zone)	My	Sandstone, shale
	O3	Sandstone, shale
	P1	Shale, sandy shale, mudstone
	P2	Sandstone, mudstone, shale
	Q0	Sandstone, mudstone, shale, conglomerate (limestone)

During the analysis, it was found that the distribution of factors for different engineering geological region had different characteristics with significant effects on triggering of the debris flow; the potential analysis of the study area was conducted on whole area with combined geological zones, Zone C, and Zone D, respectively. The number of debris flow and non-debris flow torrents in Zone C are 99 and 95, and 54 and 54 in Zone D as shown in Figure 1. In order to conduct the statical analysis, the independency and significance level of each influence factor was checked using analysis of covariances and Pearson Test. A significance level of 0.1 with 90% of confidence was chosen, and it appeared that the influence factors selected were independent of each other. The resulting significant influence factors for the whole area, Zone C, and Zone D are listed in order of level of significance in Table 2. Due to the complexity of the geological characteristics when the whole area was

analyzed, the principal component analysis was performed on slope distribution and aspect distribution. In Table 2, the PS2 factor indicated a resulting principal component of slope for the whole area. As shown in Table 2, the significant factors are quite different for the whole area, Zone C, and Zone D except with the Hypsometric Integral, HI. This justified that the debris flow potential would be better understood if separate analysis were conducted for regions of different geological properties.

Table 2 The significant influence factors for different geological zones

Order of significance	Whole area	Zone C	Zone D
1	HI	HI	HI
2	PS2	E1	Mj
3	Q0	O1	FF
4	NE	WN	Q0
5	ES	MI	ES
6	My	SD10	O3
7	MI	-	SD10

#### 4 ESTIMATION MODEL OF DEBRIS FLOW POTENTIAL

In this research the multi-variant variables discrimination analysis is used to establish the differential function for debris flow torrents and non-debris flow torrents. The discrimination analysis is to form a linear combination of variables for each associated group to provide estimation values, where the coefficient of each individual variable represents its contribution to the associated group. The differential function of discrimination analysis defines the line which differentiates two groups, and its coefficients help to discriminate properties of each group. This research uses the commercial statistic software, SPSS, with Fisher's discrimination analysis, and analyses are performed for the whole area, Zone C and Zone D. Random sampling of the debris flow and non-debris flow torrents were used assuming normal distribution of each factor. For each analysis, the contributing influence factor was added following the order of significance, and the improvement of the rate of accuracy was checked with each additional factor. The definition of accuracy rate is expressed as the sum of accurately estimated debris flow torrents and non-debris flow torrents divided by the total number of torrents.

1. Whole area with combined geological zones: The analysis was performed over the whole area using 87 sets randomly sampled out of 199 and 175 debris and non-debris flow torrents. It was found that the HI appeared to be the most significant factor; the additional factors were added following the significant sequence of PS2, Q0, NE, ES, My, and MI, with accuracy rate of 78.9%, 81%, 82.2%, 82.2%, 83.3%, 84.5%, and 85.1%. The resulting discrimination function,  $y$ , is:

$$y = 5.108(HI) + 0.090(PS2) - 0.020(Q0) - 0.027(NE) - 0.065(ES) - 0.018(My) + 0.003(MI) - 1.911 \quad (1)$$

The accuracy rate increases more or less steadily with the additional parameters, but the trend is not significant with addition of NE, and the amount of increase in accuracy was not steady, suggesting different contribution of the parameters compared to their significance level.

2. Zone C: The analysis was performed for the Zone C using 40 sets randomly sampled out of 80 sets debris and non-debris flow torrents. It was found that the HI appeared to be the most significant factor; the additional factors were added following the significant sequence of E1, O1, WN, MI, SD10, with accuracy rate of 82.5%, 83.8%, 85.0%, 85.0%, 83.8%, and 83.8%. The resulting discrimination function,  $y$ , is:

$$y = 19.050(HI) + 0.018(E1) - 0.016(O1) + 0.009(WN) - 0.025(MI) + 0.082(SD10) - 11.388 \quad (2)$$

The accuracy rate increases with the additional parameters up till O1, and then remains the same and decreases. Thus, the amount of increase in accuracy does not increase beyond parameter O1. Although the rest of the parameters appear to be significant, they do not contribute to the estimation model

3. Zone D: The analysis was performed for the Zone D using 40 sets randomly sampled out of 54 sets debris and non-debris flow torrents. It was found that the HI appeared to be the most significant factor; the additional factors were added following the significant sequence of Mj, FF, Q0, ES, O3, and SD10, with accuracy rate of 61.3%, 70%, 68.8%, 75%, 80%, 80%, and 80%. The resulting discrimination function,  $y$ , is:

$$y = -5.070(HI) + 0.036(Mj) - 1.516(FF) - 0.015(Q0) - 0.083(ES) + 0.024(O3) + 0.009(SD10) + 4.731 \quad (3)$$

The accuracy rate increases with the additional parameters till ES and then remains the same. It suggests that the addition of O3 and SD10 parameters does not improve the accuracy rate, although both parameters are significant.

Observing the estimation models for the three regional analyses, the accuracy rate has a tendency to increase with the additional factors, and the HI factor appears to be the most effective factor in all three models. For all three models, the coefficient of each parameter indicates the contribution of the parameter, and is consistent with the variation in accuracy rate. However, the effectiveness of the influence factors is not fully in accord with the order of factor significance shown in Table 2. Therefore, the level of significance of the parameter could not be correlated to the contribution of the parameter to the estimation model.

#### 5 VALIDATION AND PREDICTION

In order to verify the feasibilities of the potential estimation model discussed previously, the data sets of debris flow torrents and non-debris flow torrents not used in developing the estimation models were used for validation and prediction. A total of 112 debris flow torrents and 87 non-debris flow torrents were used for the prediction of the whole area using Eq.1. A total of 40 sets of debris flow and non-debris flow torrents were used for the Zone C, and a total of 14 sets of debris flow and non-debris flow torrents were used for prediction using Eqs. 2, and 3, respectively. The prediction accuracy rates were compared to the estimation accuracy rates for whole area with combined geological zones, Zone C, and Zone D, as shown in Figure 2, Figure 3, and Figure 4, respectively.

From Figure 2, it was found that the accuracy rate for prediction increased steadily up to ES but then decreased with additional factor for whole area with combined geological zones compared to the estimation model. Therefore, the factors used for the model are only up to ES, and the model is rectified as:

$$y = 4.955(HI) + 0.090(PS2) - 0.0205(Q0) - 0.027(NE) - 0.065(ES) - 1.741 \quad (4)$$

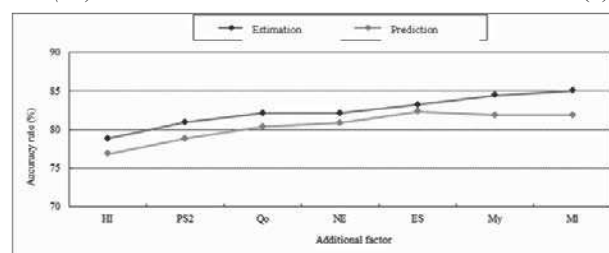


Figure 2. Accuracy rates of estimation and prediction for whole area

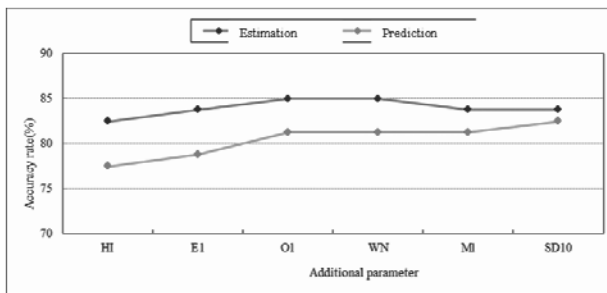


Figure 3. Accuracy rates of estimation and prediction for Zone C

The estimation accuracy rate is 83.3%, and the prediction accuracy rate is 82.4% with a difference of 0.9%.

From Figure 3, it was found that the accuracy rates for both estimation and prediction increased steadily with additional factor up to O1 but then varied for Zone C. It appears that the accuracy rate would become stable only with factors up to O1, and the model is rectified as:

$$y = 15.531(HI) + 0.019(E1) - 0.007(O1) - 9.255 \quad (5)$$

The estimation accuracy rate is 85.0%, and prediction accuracy rate is 81.3% with a difference of 3.7%.

From Figure 4, the accuracy rates varied for both estimation and prediction, but the accuracy rates increased steadily with additional factor up to ES for Zone D. It appears that the accuracy rate would become stable with the factors up to ES only, and the model is rectified as:

$$y = -5.685(HI) + 0.032(Mj) - 1.504(FF) - 0.015(Qo) - 0.085(ES) + 5.380 \quad (6)$$

The estimation accuracy rate is 80.0%, and the prediction accuracy rate is 78.6% with a difference of 1.4%.

For all three analyses, the prediction curves appear to be quite stable and approach the estimation curves with the similar trends. The resulting accuracy rates are satisfactory and the differences between prediction accuracy rate and estimation accuracy rate of all three models are all within 4%. Thus the discrimination functions used is good for differentiating debris flow torrents from non-debris flow torrents with satisfactory results. Comparing the three modified function equations, not all factors contributed effectively to the model for all three models. The prediction accuracy rate actually reduced if all the factors were included, which suggested over-fitting of the estimation models. Observing the number of factors used for the whole area prediction model is higher than the Zone C and Zone D, it may do to the complexity of multi-geological zones included. The accuracy rate of the Zone D analysis appeared to be lower than the other two analyses, which might due to less samples were available for estimation and prediction compared to number of samples in whole area and Zone C.

Based on the analysis results, the potential of debris flow torrent can be evaluated using distribution of the calculated discrimination function. The accumulated distribution density

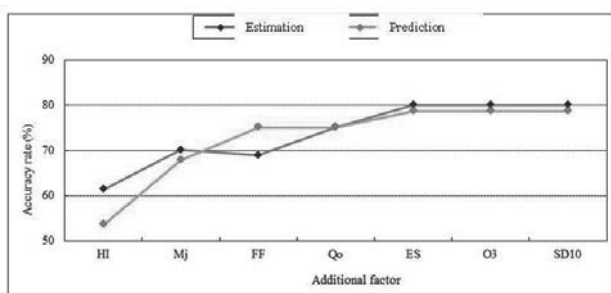


Figure 4. Accuracy rates of estimation and prediction for Zone D

of 30% and 70% values are selected as the boundary indicators for low-moderate and moderate-high potential. For the whole area analysis, the discrimination function value for 30% is 0.506 and 3.092 for 70%. Thus the debris flow torrents with discrimination values greater than 3.092 are classified as high potential and moderate potential when discrimination values range within 0.506 to 3.092. The debris flow torrents are considered as low potential when the values are less than 0.506. Similar procedures were applied to Zones C and D. For Zone C the discrimination value for 30% accumulation is 0.765, and 3.143 for 70% accumulation. The discrimination value for 30% accumulation is 0.325 and for 70% is -1.720 for Zone D. Thus the potential of debris flow torrents can be evaluated in all three analysis models.

## 6 CONCLUSIONS

In this research, the potential analysis of the debris flow torrents in Nantou County was performed using discrimination analysis. The influence factors included: watershed area, stream length, form factor, hypsometric integral, stream mean slope, slope distribution, slope aspect, and geological formation. Base on the previous discussions, most influence factors selected are within significance level. Among the factors used, the hypsometric integral appears to be the most important factor, which is a characteristic of geomorphic evolution of the watershed. The second most important factor is the geological properties of the analysis area. For all three models, the accuracy rates are about 80%, which suggests that the discrimination analysis provide satisfactory results. The accuracy rate for Zone D is slightly smaller than the accuracy rates for both the whole area and Zone C, which might due to smaller sample sizes in both estimation and prediction compared to the sample sizes of the whole area and Zone C. The final model could be determined based on the stability of accuracy rates in both estimation and prediction. However, not all the significant factors are contributing to the model effectively. The final potential of the debris flow torrents can be evaluated based on the values of discrimination function in all three models properly.

## 7 REFERENCES

- Hung J.J. 1997. Engineering Geology Zonation of Taiwan
- Lin M.L. and Chen T.C. 2005. Frame in renovation and feedback mechanism of database of potential debris flow torrents. SWBC-94-048 (Chinese)
- Lin M.L. and Lien H.P. and Hsieh C.L. 2003. Follow-up investigation and observation in developed tendency of potential debris flow torrents. SWCB-92-107. (Chinese)
- Lin M.L. and Wen H.Y. 2006. Field investigation and trend analysis of potential debris-flow rivers. *Sino-geotechnic*. 110, 45-54 (Chinese)
- Robert L.S. and Raymond J.K. 1978. *Landslide analysis and control*. Special Report 176, National Academy of Science, Washington, D.C. 17-27
- Taiwan Geology Map (1/500,000), 1986, Central Geological Survey

# Value of Landslide Investigation to Geotechnical Engineering Practice in Hong Kong

## Ingénierie des glissements de terrain à Hong Kong

Lo D.O.K., Lam H.W.K.

*Geotechnical Engineering Office, Civil Engineering and Development Department, Government of the Hong Kong SAR*

**ABSTRACT:** On average, about 300 landslides were reported to the Geotechnical Engineering Office (GEO) of the Civil Engineering and Development (CEDD) in Hong Kong each year. Over the years, GEO conducted landslide investigations to advance knowledge on slope performance and improve understanding of the causes and mechanisms of landslides. Landslide investigations have become an integral part of the Government's Slope Safety System in Hong Kong. Studies on notable landslides on man-made slopes have led to the use of more robust stabilisation measures for cut slopes, improved rock slope engineering practices, enhanced practices in the monitoring and maintenance of water-carrying services affecting slopes and improvement to drainage detailing. Studies on natural terrain landslides have allowed better understanding on the modes and mechanisms of failure. This also enables advancement in debris mobility assessment which is critical to natural terrain risk management. This paper highlights some key lessons learnt and observations made from selected landslide investigations and how this knowledge helps advance the geotechnical engineering practice in dealing with man-made slopes and natural terrain landslide hazards in Hong Kong.

**RÉSUMÉ:** En moyenne, environ 300 glissements de terrain sont signalés au Bureau Géotechnique (GEO) chaque année. Au fil des années, les enquêtes de glissements de terrain sont menées par le GEO et jouent un rôle clé dans l'avancement des connaissances sur la stabilité des pentes et la compréhension des causes et des mécanismes de glissements de terrain et sont devenus une partie intégrante du système de sécurisation des pentes à Hong Kong. Les études sur les glissements de terrain sur les pentes anthropiques ont conduit à l'utilisation de mesures plus robustes pour la stabilisation des pentes artificielles, l'amélioration des pratiques d'ingénieurs pour les pentes dans les matériaux rocheux et l'amélioration des pratiques de suivi. Les études sur les glissements de terrains naturels ont permis de mieux comprendre le mode et les mécanismes de défaillance. Cela permet également l'amélioration de l'évaluation des déplacements des boues, ce qui constitue un point essentiel dans la gestion des risques naturels. Ce document met en lumière certains des principaux enseignements tirés des observations faites à partir des enquêtes de glissements de terrain sélectionnés et comment cette connaissance contribue à l'avancement de la pratique de la géotechnique dans le traitement des pentes artificielles et naturelles à Hong Kong.

**KEYWORDS :** landslides, investigation, geotechnical engineering practice

### 1. INTRODUCTION

The rapid population growth in Hong Kong since the 1960s and substantial economic expansion has been accompanied by extensive civil engineering and building works, resulting in the formation of a considerable number of man-made slopes and retaining walls over the hilly territory. However, as there was very limited geotechnical control of slope formation in the old days, the stability of many of these slopes is therefore in doubt. Coupled with severe rainstorms and dense hillside development, Hong Kong is prone to landslide risk.

Following a number of landslide disasters in 1970s, the Hong Kong Government established the Geotechnical Control Office in 1977 (renamed as the Geotechnical Engineering Office (GEO) in 1991) to regulate geotechnical engineering works and slope safety in Hong Kong. This paper gives an overall review of the slope engineering practices that have been enhanced as a result of the landslide investigation (LI) findings.

### 2. GEOTECHNICAL STANDARDS AND PRACTICE

Setting geotechnical standards has been one of the GEO's functions. To date, some 300 guidance documents have been published covering standards of good practice for the investigation, design, construction and maintenance of slopes.

For public development projects, the prevailing Government policy stipulates that all permanent geotechnical works involving slopes and retaining walls as well as related activities, including investigations, designs and construction should be carried out in accordance with the prevailing standards. Details of the geotechnical works are required to be

submitted to the GEO for checking. In general, the standards for public development projects are also adopted for private building and civil engineering works in Hong Kong.

### 3. LANDSLIDE INVESTIGATION



Figure 1: The Kwun Lung Lau Landslide in July 1994

On average, about 300 landslides are reported to the GEO each year. Most of these occurred at man-made slopes affecting buildings, roads or pedestrian walkways. Many landslides which occurred in remote areas or in natural terrain were not reported. Prior to mid-1990s, the GEO conducted LI on few selected cases of technical interest or having significant consequence. The occurrence of a number of fatal landslides in the mid-1990s has highlighted the need to further enhance the landslide risk management strategy in



Hong Kong. Following the Kwun Lung Lau landslide of 23 July 1994 (Figure 1), which killed five people and seriously injured three others (Morgenstern & GEO 2000), the GEO introduced a number of new enhancement initiatives including a systematic LI programme. The scope of landslide investigations includes examination of all reported landslide incidents and in-depth studies of selected landslides to identify the causes of failure and necessary follow-up actions. The objectives of the systematic LI are to identify those slopes in need of early attention, and undertake forensic investigation of landslides that involve coroner inquests, legal actions or financial disputes. Through landslide investigations, the performance of the Government's slope safety system will be reviewed and areas for improvement identified. Landslide investigations help advance the understanding of causes and mechanisms of landslides and enhance slope engineering practices and the reliability of landslide preventive or remedial works.

The annual expenditure of the LI programme is about US\$3 million. Based on observations from LI, new guidelines are promulgated to improve the prevailing geotechnical practice. Some salient LI observations and improvements for soil cut slopes, rock slopes, retaining walls, fill slopes and natural hillside are described below.

#### 4. SOIL CUT SLOPES

Soil cut slopes formed or treated prior to 1990s typically involved trimming back to a less steep gradient without the provision of reinforcement or structural support. They are prone to degradation and vulnerable to the presence of local weaknesses in the groundmass. Large scale landslides involving such unsupported cut slopes are not uncommon. Notable examples are the Ching Cheung Road landslide in 1997 (Figure 2) and Shek Kip Mei failure in 1999 (Figure 3). The 1997 Ching Cheung Road landslide involved a failure volume of over 2,000 m<sup>3</sup>, resulting in the trapping of a motor car and temporary closure of a major route connecting east and west Kowloon for two months. The Shek Kip Mei failure involved a distressed volume of 6,000 m<sup>3</sup>, resulting in permanent evacuation of three housing blocks. Findings from investigation of such failures highlight the vulnerability of unsupported cut slopes to adverse geological features and hydrogeological conditions, which may be difficult to detect. A pragmatic approach of adopting more robust design solutions, such as the use of soil nailing was called for. A soil nailed slope tends to behave as an integral mass and is less sensitive to local adverse conditions as compared with an unsupported cut. The use of soil nailing has been widely adopted for upgrading of slopes in Hong Kong since mid 1990s.



Figure 2: The Ching Cheung Road Landslide in 1997

So far, there are 40 failures among some 7000 slopes installed with soil nails. None of these are major landslides

(volume  $\geq 50$  m<sup>3</sup>). This indicates that the use of soil nails is effective in averting large scale failure. These minor failures were mostly involved surface erosion or minor local detachment in the groundmass between soil nail heads. Lessons learnt from investigation of soil-nailed slope failures have led to enhanced understanding of the behaviour of soil-nailed slopes (e.g. the importance of soil-nail head), improved detailing of surface drainage provisions (e.g. provision of intersecting drains for long sloping grounds), and enhanced surface protection details. Advances have also been made in the design of soil nails, as promulgated in the Geoguide 7 (GEO 2008).



Figure 3: Laterally-persistent discontinuity infilled with slickensided kaolin and manganese oxide deposits at the 1999 Shek Kip Mei failure

#### 5. ROCK SLOPES

Major failures (volume  $\geq 50$  m<sup>3</sup>) involving rock slopes are not very common. Most of the landslides were rain-induced and structurally-controlled, involving build-up of cleft water pressure in rock joints. Other contributory factors such as presence of soft infill along discontinuities, slope deterioration, root wedging effect, etc were also noted. These failures highlight the importance of identifying adversely-orientated jointing system which could have implication to the stability of slopes in the design. With respect to minor rock slope failures such as rockfalls, the primary causes were due to presence of local adverse groundwater regimes and/or loose or unstable blocks. Many of the rockfalls were initiated by tree-root actions. Given the scale of the failure and the consequence of the failure in the urbanized setting in Hong Kong, rockfalls are difficult to guard against in design. A pragmatic approach is to provide suitable protective and mitigation measures such as rock mesh netting, rock fall fence and buffer zone where practicable. LI findings are incorporated in the relevant manuals and guidelines to enhance the rock slope engineering practice (GEO 2009).

#### 6. RETAINING WALLS

A few major landslides involving retaining wall failures had occurred in the past, the most notable one being the 1994 Kwun Lung Lau landslide. The landslide involved the a brittle collapse of a 100-year old masonry wall (Morgenstern & GEO 2000) releasing 1000 m<sup>3</sup> of debris causing 5 fatalities. No tell-tale sign was reported prior to the failure. The failure was triggered by saturation of the soil behind the masonry wall as a result of leakage from nearby defective buried water-carrying services. The incident highlighted the importance of regular inspection and maintenance of water-carrying services affecting slopes. Following the incident, a guidance document entitled "Code of Practice on Inspection and Maintenance of Water Carrying Services Affecting Slopes" was issued by the Government, setting out the recommended good practice for regular inspection and maintenance of water-carrying services affecting slopes.

Furthermore, the landslide investigation findings indicated that the failed wall was 10 m high but only about 0.8 m thick. The wall thickness is much less than that indicated in the record available. This incident highlighted the danger of slender masonry walls that are liable to fail in a brittle manner without any prior signs of distress, and the importance of verifying the wall thickness in stability assessment. This lesson learnt was incorporated in the guideline for stability assessment of old masonry walls (GEO 2004a).

## 7. FILL SLOPES

Following the disastrous failure of a fill slope at Sau Mau Ping in 1976, the Government appointed an Independent Review Panel to review the landslide problem and make recommendations on the design of fill slopes in Hong Kong. The Panel recommended, amongst others, that the minimum treatment of existing loose fill slopes should consist of removing the loose surface soil by excavating to a vertical depth of not less than 3 m and recompacting to an adequate standard, together with the provision of subsurface drainage behind the recompacted fill layer at the toe of the slope. Technical guidance on the treatment of existing loose fill slopes is given in relevant manual and technical circular (GCO 1984, GEO 2004b).

Up to 2012, about 260 loose fill slopes have been upgraded using the recompaction approach by the GEO. Between 1997 and 2012, a total of 18 landslides occurred on recompacted fill slopes. The primary causes of landslides of these incidents are:

- (a) Surface flow concentration
- (b) Leakage or bursting of water-carrying services
- (c) Inadequate subsurface drainage provisions

Discounting washout failures due to concentrated surface water flow or leakage of water-carrying services, landslides on recompacted fill slopes were generally ductile in nature and did not involve sudden and fast-moving debris as in liquefaction failure.

Enhancement measures have been implemented with reference to the lessons learnt from these landslides. For instance, the Code of Practice on Monitoring and Maintenance of Water Carrying Services Affecting Slopes, which was first issued in 1996, has been updated taking into account lessons learnt from landslides triggered by leakage or bursting of water-carrying services (ETWB 2006).

Detailing of slope drainage provisions has also been improved. Areas for improvement include provision of adequate movement joints for surface drainage channels and provision of filter pipes at upstream end of the subsurface drainage blankets behind the recompacted fill etc. The improvement measures were promulgated in the GEO Report Nos. 210 and 225 (Hui et al. 2007, Fugro 2008)

## 8. NATURAL HILLSIDE

Hong Kong has a land areas of about 1,100 km<sup>2</sup>. About 60% is natural terrain, over 30% of which has a slope gradient over 30°. Natural terrain landslides in Hong Kong are mainly rain-induced. Most of them occurred in remote areas while some affects developments. The GEO has been undertaking technical development works based on the study of natural terrain landslides since the early 1990s.

Based on observed runout distance of landslide debris, a set of simple and suitably conservative guidelines has been developed (Wong 2003) for initial screening purposes to assist planners, land administrators, project managers, etc. to review whether or not a given site is subject to natural terrain

landslide hazards. Where a site is shown to be potentially affected by landslide hazards, more refined criteria are then used to examine whether the proposed development meets the 'in-principle objection' criterion (i.e. relocate the proposed development or amend development layout), or the 'alert criteria' (i.e. carry out natural terrain hazard study and appropriate mitigation measures as part of the development).

In June 2008, Hong Kong was hit by a severe rainstorm. The short-duration rainfall intensity had a return period of about 1,000 years. The rainstorm triggered over 2,400 natural terrain landslides mainly on Lantau Island. Some of them affected developed areas and caused significant social disruption such as evacuation of houses and temporary closure of road sections. The GEO carried out systematic studies on some of these landslides. Detailed field mappings and in-depth landslide investigation provided valuable insights into the characteristics of natural terrain landslides.

Comparing the June 2008 landslides with past landslide records revealed that the 2008 landslides seem to 'cluster' around old ones. Up to 92% of the 2008 landslides occurred within 50 m of at least one past landslide, and 80% within two or more past landslides (Wong 2009). Although further work is needed to interpret this phenomenon, this sheds light on the prediction of regions of natural terrain that is more prone to failure and has implications in the determination of natural hillsides that warrant priority for the mitigation of landslide hazards.



Figure 4: Landslide on the hillside behind the Hong Kong University

Detailed landslide investigations on selected June 2008 landslides showed that past failures could have a significant implication to the scale of the landslides. Past failures could lead to extensive colluvial accumulations on hillside, which are susceptible to give rise to a laterally extensive and a much larger scale failure during heavy rainstorm than those in the past (Figure 4) (Maunsell 2009). If the debris of previous failures deposited along the drainage line, it could become 'entrainable', giving rise to a larger scale of a channelized debris flow (CDF) event (Figure 5) (AECOM 2009). In the 2008 rainstorm, significant entrainment was noted in many of the long runout CDFs with entrainment ratio up to 10 or higher (the entrainment ratio is the volume of additional material that has been entrained by a landslide expressed as a proportion of the source volume). The amount of the pre-existing 'entrainable' materials in a drainage line is dynamic and may change significantly after a rainstorm. This highlights the implications of the deposition of debris from past failures on occurrence of some large-scale failures in natural hillsides.



Figure 5: Yu Tung Road channelized debris flow

In general, the June 2008 landslide debris was found to be more mobile when compared with the previous historical natural terrain landslides in Hong Kong (Figure 6). About 20% of the June 2008 landslides have runout distances over 100 m, as compared with about 10% in past landslides that are observed from old aerial photographs.

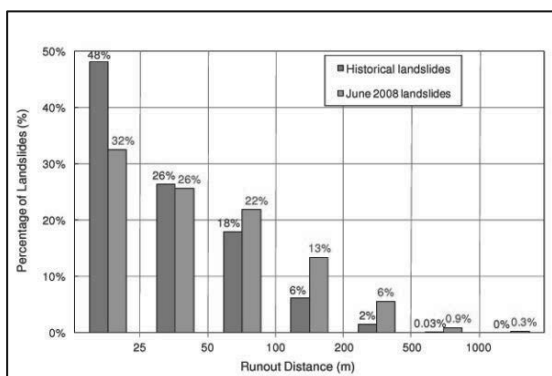


Figure 6: Distribution of landslide runout distance

Detailed studies on selected CDFs revealed that some of the CDFs with long runout generally involved debris with high water content, e.g. the failure near Yu Tung Road (Figure 5). After detaching from the source of failure, the debris mixes with a large amount of water along the drainage line, and results in higher debris mobility. LI revealed that a number of circumstances may lead to such ‘watery debris’, such as:

- (a) debris flows along a major drainage line with a large catchment and a long flow path;
- (b) debris flows occurring during heavy rain; and
- (c) debris flows along a main drainage line into which many tributaries of drainage lines are feeding.

To facilitate the modeling of debris mobility under such circumstances for natural terrain hazard studies, systematic back analyses were carried out on some selected long runout CDFs that occurred in June 2008 using a 2-D dynamic modelling algorithm, known as ‘debris mobility modeller’ (2d-DMM) program, as well as 3d-DMM in some cases, to refine the modeling parameters. Improved guidance on debris mobility modeling was promulgated by the GEO (2011).

## 9. CONCLUSIONS

The landslide investigations have brought insights into the causes, mechanisms and characteristics of landslides. The investigations enhance the understanding of the behaviour of man-made slopes and natural hillside under severe rainstorm

and the findings have helped to advance geotechnical engineering practices, and improve standards and design guidelines for enhancing the robustness of slope upgrading and landslide mitigation works.

## ACKNOWLEDGEMENTS

This paper is published with the permission of the Head of the Geotechnical Engineering Office and the Director of Civil Engineering and Development, Government of the Hong Kong Special Administrative Region.

## REFERENCE

AECOM Asia Co. Ltd. (2009) “Detailed Study of the 7 June 2008 Landslides on the Hillside above Yu Tung Road, Tung Chung” (GEO LSR No. 14/2009). GEO, CEDD, Hong Kong.

ETWB (2006). “Code of Practice on Monitoring and Maintenance of Water Carrying Services Affecting Slopes (Second Edition)”. Environment, Transport and Works Bureau, Hong Kong.

Fugro Scott Wilson Joint Venture (2008). “Review of Sub-surface Drainage Provisions for Recompacted Fill Slopes” (GEO Report No. 225). GEO, CEDD, Hong Kong.

GCO (1984). “Geotechnical Manual for Slopes” Geotechnical Control Office, Civil Engineering Services Department, Hong Kong.

GEO (2004a). “Guidelines for Assessment of Old Masonry Retaining Walls in Geotechnical Studies and for Action to be Taken on Private Walls” (GEO Circular No. 33). GEO, CEDD, Hong Kong.

GEO (2004b). “Fill Slope Recompaction – Investigation, Design and Construction Considerations” (GEO Technical Guidance Note No. 7). GEO, CEDD, Hong Kong.

GEO (2008). “Guide to Soil Nail Design and Construction” (Geoguide 7). GEO, CEDD, Hong Kong.

GEO (2009). “Enhancement of Rock Slope Engineering Practice Based on Findings of Landslide Studies” (GEO Technical Guidance Note No. 10). GEO, CEDD, Hong Kong.

GEO (2011). “Guidelines on the Assessment of Debris Mobility for Channelised Debris Flows” (GEO Technical Guidance Note No. 29). GEO, CEDD, Hong Kong.

Hui T.H.H., Sun H.W. & Ho K.K.S. (2007). “Review of Slope Surface Drainage with reference to Landslide Studies and Current Practice” (GEO Report No. 210). GEO, CEDD, Hong Kong.

Maunsell Geotechnical Services Limited (2009). “Detailed Study on the 7 June 2008 Landslide on the Natural Hillside behind Chow Yei Ching Building at the University of Hong Kong” (GEO LSR No. 3/2009). GEO, CEDD, Hong Kong.

Morgenstern N.R. & GEO (2000). “Report on the Kwun Lung Lau Landslide of 23 July 1994” (GEO Report No. 103). GEO, CEDD, Hong Kong.

Wong H.N. (2003). “Natural terrain management criteria - Hong Kong practice and experience.” *Proceedings of the International Conference on Fast Slope Movements - Prediction and Prevention for Risk Mitigation*, Naples, Italy, vol. 2.

Wong H.N. (2009). “Rising to the challenges of natural terrain landslides.” *Proceedings of the HKIE Annual Seminar on Natural Hillside: Study and Risk Mitigation Measures*, HKIE, Hong Kong, 15-54.

# Analyses of Seismic Slope Stability and Subsequent Debris Flow Modeling

Analysis de stabilité de pente sous sollicitation sismique et modélisation des écoulements de boues induits

Long X., Tjok K.-M.  
Fugro GeoConsulting Inc., Houston, Tx

**ABSTRACT:** Earthquake-triggered slope failures and subsequent submarine debris mass flow can cause severe consequences and jeopardize the integrity of offshore structures in the proximity. In this paper, a two-dimensional seismic slope stability analysis for an offshore liquefied slope site located in American Petroleum Institute (API) seismic zone 4 with layered stratigraphy is addressed. A nonlinear dynamic analysis using the stress-strain law of “hysteretic modeling” allowing for soil weakening under large strains was adopted to study flow failure instability. Laboratory tests were performed for the derivation of soil dynamic parameters and calibration of hysteretic soil model. Using “Constant-volume” constraints, the run-out distance of subsequent debris flow was also estimated.

**RÉSUMÉ :** Lors de séismes, les ruptures de pentes et les écoulements (de boue) sous-marin qui s’en suivent peuvent avoir des conséquences graves et compromettre l’intégrité des structures « offshore » voisines. Dans cet article, on présente une étude (2D) de stabilité d’une pente dans un site « offshore » liquéfiable, dans un zone sismique de niveau 4 (référentiel de l’American Petroleum Institute). Une analyse dynamique non-linéaire utilisant la loi « hysteretic modeling » (loi permettant la modélisation du radoucissement en grande déformation) a été adoptée pour étudier la rupture des pentes et les écoulements induits. Des tests de laboratoire ont été effectués afin d’identifier et de déterminer les paramètres numériques de la loi de comportement. En se plaçant dans le cadre des déformations à volume constant, la modélisation a permis d’estimer la distance parcourue par les écoulements de boues.

**KEYWORDS:** earthquake slope debris flow non-linear dynamic.

## 1 INTRODUCTION

Earthquakes are one of the major causes of submarine slides. Large shear stresses and deformations may be generated due to seismic vibrations and irrecoverable volume changes are accumulated accompanied by the rise of pore water pressure (i.e., decrease of effective stress) and cyclic degradation of shear strength. Liquefaction occurs when the effective stress equals zero and soil behaves as a liquid. The submarine debris mass flow following the onset of liquefaction and instability of liquefied slope can pose significant impact force and thus jeopardize the integrity of offshore structures in the flow path.

In this paper, a two-dimensional seismic submarine slope stability analysis is performed using commercial computer program FLAC (*Fast Lagrangian Analysis of Continua*) (Itasca, FLAC 7.0, an explicit finite difference program operating in the time domain. It simulates the behavior of soils which may subject to plastic flow when their yield limits are reached. The Finn Model- Byrne Formulation is implemented in the analysis to assess dynamic pore pressure generation and liquefaction potential. Based on “constant-volume” constraints, the run-out distance of subsequent debris flow was predicted using the one-dimensional subaqueous debris flow model BING (Imran and Parker, 2001).

## 2 TWO-DIMENSIONAL NON-LINEAR DYNAMIC ANALYSIS

The slope stability and liquefaction potential for a project site under seismic loading is assessed using FLAC for a two-dimensional non-linear dynamic analysis. The dynamic stress-strain behavior for the soil layers are simulated using a hysteretic model by means of a non-linear stress-strain backbone curve and the associated stress-strain loops that represent

the energy dissipated in the soil during seismic loading. Strain-controlled cyclic simple shear tests have been performed to determine dynamic soil parameters and calibration of hysteretic soil model.

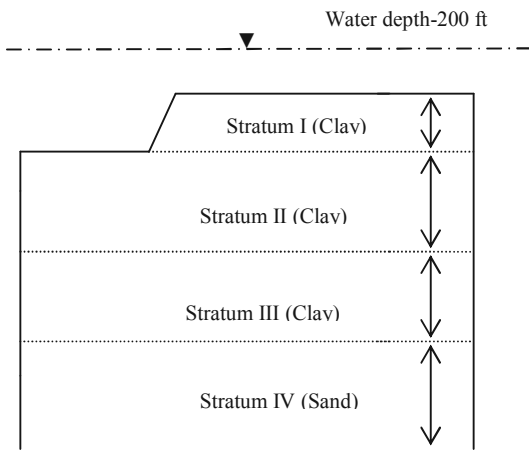
### 2.1 Site Condition

The site is located in International Organization for Standardization (ISO) seismic zone 4 (ISO 2004). Soil stratigraphy consists of soft to firm clay layers overlying dense fine sand. Based on the in situ suspension P (compression wave velocity)-S (shear wave velocity) logging and cone penetration test (CPT) data, the upper 33m (100ft) of the effective seabed is around 160 m/s (525 ft/s) and the site is classified as either American Petroleum Institute (API) criteria Type C or ISO criteria Type E.

Figure 1 below illustrates the soil stratigraphy at the study site. The subsurface conditions comprise of 50 m (160 ft) soft to firm clay underlain by a layer of dense to very dense fine sand down to 105 m (350 ft). The mean sea level is 61.0 m (200 ft) above seafloor. Due to soil erosion, a 20° slope is formed as detected from the geophysical multibeam bathymetric data. In light of variations of material parameters, three soil Strata, i.e., Stratum I, II and III, respectively, are defined within the clay sediment. For the study of effective stress analysis, four Strata with Stratum I, II and III for cohesive materials and Stratum IV for cohesionless sediment, are used. The soil parameters including submerged unit weight  $\gamma$ , average shear wave velocity  $V_s$ , cohesion  $c$ , and friction  $\phi$  for each stratum are also provided on the figure.

The laboratory test data from cyclic direct simple shear (CDSS) along with the generic curves of similar soil types (Seed & Idriss for sand) were used as guidance to develop hysteretic model for the analysis. Figure 2 presents the dynamic

soil characteristics used in the model as defined by the shear modulus degradation ( $G/G_{max}$ ) and damping ratio ( $D$ ) curves.



Stratum	Soil Parameters for Effective Stress Analysis
I (4.3m (14ft) thick)	$\gamma=726 \text{ kg/m}^3, V_s=122 \text{ m/s}, c=4.8 \text{ kPa}, \phi=15^\circ$
II (21.3m (70ft) thick )	$\gamma=807 \text{ kg/m}^3, V_s=186 \text{ m/s}, c=5.8 \text{ kPa}, \phi=20^\circ$
III (23.5m (76ft) thick)	$\gamma=888 \text{ kg/m}^3, V_s=300 \text{ m/s}, c=5.8 \text{ kPa}, \phi=20^\circ$
IV (58.0m (190ft) thick)	$\gamma=1000 \text{ kg/m}^3, V_s=335 \text{ m/s}, \phi=35^\circ$

Figure 1. Soil stratigraphy for the study site (Not to scale).

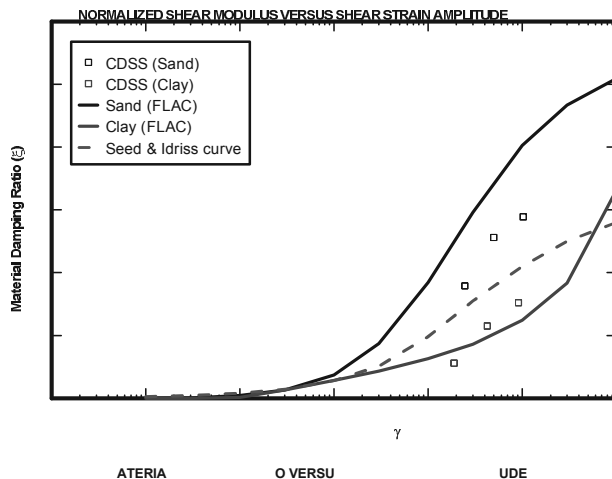
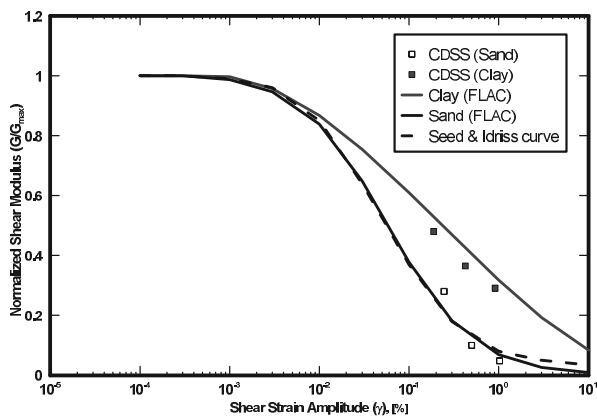


Figure 2. Soil dynamic characteristic curves

### 2.2 Characteristic of Earthquake Input Motion

The peak ground acceleration (PGA) of the earthquake motion is 0.48 g with a duration time of 40 sec. As indicated from the

power spectra of input velocity and input acceleration as shown on Figure 3, the highest frequency component of the input motion is less than 10 Hz with the majority of the frequencies are less than 6 Hz. The input motion is applied at the depth of 105m (350ft).

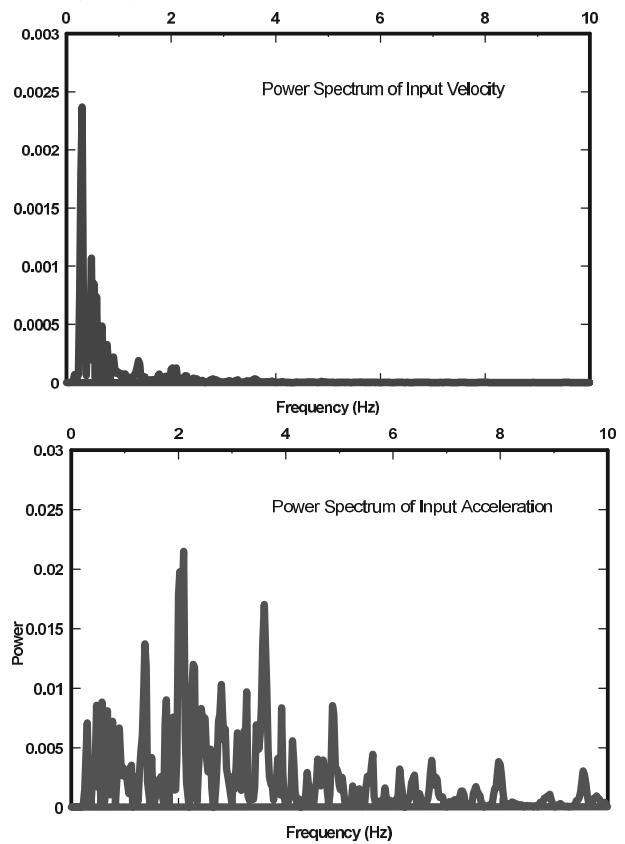


Figure 3. Acceleration time history and power spectrum of input motion.

### 2.3 Two-Dimensional Numerical Modeling

Kuhlemeyer and Lysmer (1973) state that for accurate representation of wave transmission through a model, the spatial element size,  $\Delta l$ , must be smaller than approximately one-tenth to one-eighth of the wavelength associated with the highest frequency component of the input wave, i.e.,  $\Delta l \leq \lambda/10$ , or  $\leq C_s/(10\Delta l)$ , where  $\lambda$  is the wavelength associated with the highest frequency component that contains appreciable energy; and  $C_s$  is speed of propagation associated with the mode of oscillation. Since the majority of the frequencies of input motion are less than 6.0 Hz, a 1.83m (6ft) x 1.83m (6ft) mesh size is selected for the modeling. The maximum frequency that can be modeled accurately for this element size is 6.7 Hz. The frequency of Dynamic excitation to the FLAC model was specified using the compliant-base deconvolution procedure (Mejia and Dawson, 2006). The input excitation was specified as a stress time history at the base of the model as a function of mass density  $\rho$ , shear wave velocity  $V_s$  at the half-space depth (105 m (350 ft) below seafloor) and input shear particle velocity  $v$ . Figure 4 demonstrates the FLAC mesh with rectangular and triangle shapes for this two-dimensional analysis. The free-field on vertical sides and quiet boundary conditions at the bottom are applied in the soil domain.

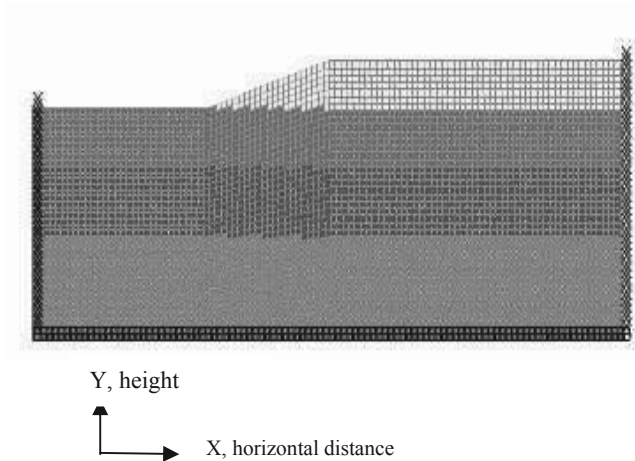


Figure 4. FLAC model for the modeling

The static equilibrium state at the time of the earthquake event is established to obtain the initial shear-stress distribution of the soil mass. The preliminary analysis, assuming undamped elastic-material, was performed to estimate maximum levels of cyclic shear strains and velocity levels throughout the model during the dynamic excitation. The maximum shear strain contour from the preliminary run is shown on Figure 5 indicating that the maximum elastic shear strains are smaller than 0.7 % throughout almost the entire modeled area. This range of shear strains is considered appropriate for inclusion of hysteretic damping based upon the dynamic characteristics of the soils as illustrated on Figure 2. The frequency range for the natural response of the elastic materials is calculated to be relatively uniform throughout the model, with a dominant frequency of approximately 3 Hz.

A fully coupled nonlinear seismic analysis is performed using the Mohr-Coulomb model to represent the soil layers, with additional hysteretic damping applied to simulate the non-linear soil dynamic behavior. Due to the fact that hysteretic damping does not completely damp high frequency component, a small amount of stiffness-proportional Rayleigh damping is also employed in the analysis.

The Finn-Byrne model is used for the liquefaction simulation by considering Strata I and II as liquefiable materials. Based on CPT/SPT correlations from in-situ CPT data and fine contents (Kulhawy and Mayne, 1990), the equivalent normalized SPT blow counts are assigned for the two strata. The automatic rezoning logic is applied in the analysis to correct for severely distorted mesh conditions developed during the simulation of earthquake shaking. The onset of liquefaction is identified by the cyclic pore-pressure ratio,  $u_e/\sigma'_c$ , where  $u_e$  is the excess pore pressure and  $\sigma'_c$  is the initial in-situ effective confining pressure. After the liquefaction, the soil shear strength is reduced to residual strength which is 30% of the original value.

The numerical analysis indicates the development of liquefaction and failure surface in the slope. Figure 6 displays the contours of maximum shear strain at the end of earthquake excitation (40 seconds). The contour of excess pore pressure ratio equaling 1 (onset of liquefaction) at 40 seconds is also marked in green line on Figure 6. Figure 7 shows the vertical and horizontal displacement histories at the slope crest. The negative sign for X and Y axes indicate the left direction and downward direction, respectively. the slope moves horizontally approximately 8.5m.

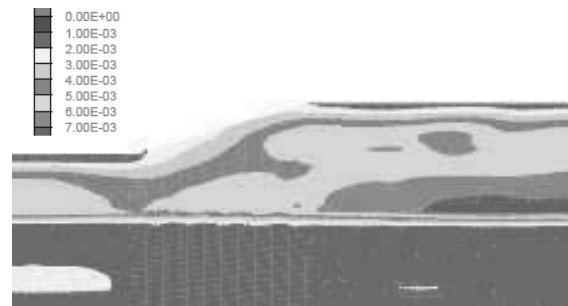


Figure 5. Maximum shear strain contours from undamped elastic analysis

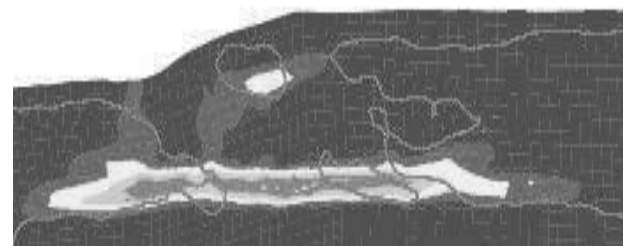


Figure 6. Shear strain contours and excess pore pressure ratio=1 contour at 40 seconds

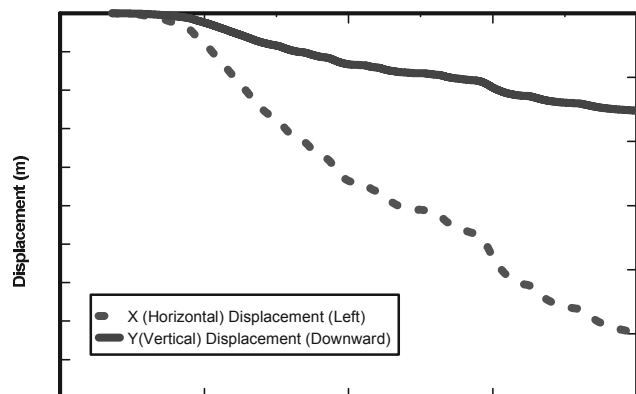


Figure 7. Horizontal (x) and vertical (y) displacement histories at crest of the slope

### 3 DEBRIS FLOW RUN-OUT DISTANCE

After the development of liquefaction and failure surface in the slope, debris flow can be triggered and the remolded mass during initial failure travels further downslope until the initial stored potential energy is dissipated by friction.

The debris flow run-out distance can be estimated using one- or two- dimensional numerical modeling of sediment-laden submarine flow. For this study, the one-dimensional (1-D) model *BING* assuming one phase flow and “constant volume” constraint. The required input for the simulation includes the bed profile over which the debris mass flow, the initial configuration of the pile of debris slurry, rheological parameters describing the debris slurry and numerical parameters to describe spatial and temporal discretization, run duration and

soil viscosity (Imran and Parker, 2001& 2001). The Herschel-Bulkley rheological model is used for the run-out distance prediction. In the absence of laboratory test data, the yield strength  $\tau_y$  of 1.5 kPa (30 psf) and reference strain rate  $\dot{\gamma}_r$  of 1/s were adopted using published relationships as shown on Figure 8 based on soil liquidity index LI (Locat and Lee, 2002).

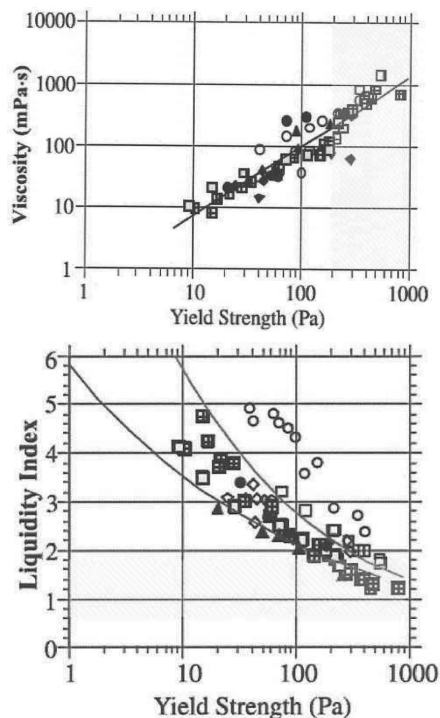


Figure 8. Relationship between yield strength, dynamic viscosity, and soil liquidity index (Reproduced from Locat and Lee, 2002)

Considering debris flow originated at the bottom of the slope and the flow origination mass length of around one-half of the sliding mass length, the estimated run-out distance is around 25 m from the toe of the liquefied slope. These mobilized debris flow mass may pose significant impact force against subsea infrastructure in the flow path, even lead to loss of foundation support.

#### 4 CONCLUSIONS

Dynamic slope instability due to earthquake excitation and subsequent submarine slides can cause mass gravity flow which may cause significant impact force or the loss of foundation support and thus pose great risk for the integrity of offshore structure along the flow path. This paper demonstrated the ability of using a fully coupled nonlinear effective stress analysis to simulate the development of liquefaction and the instability of liquefied slope. The prediction of run-out distance of subsequent debris flow was also discussed here. For practical application, it should be emphasized that the numerical model for assessing the run-out distance should be tested and calibrated with identified historic mass transport deposits (MTD) and geomorphologic conditions along study site.

#### 5 REFERENCES

American Petroleum Institute : Recommended practice for planning, designing and constructing fixed offshore platforms – working stress design, API RP 2A-WSD, twenty-first edition.2000.

International Organization for Standardization : ISO 19902- Petroleum and natural gas industries- fixed steel offshore structures, DIS version. 2004.

Imran J. and Parker J. 2001. BING, Subaqueous and subaerial finite source debris flow model.

ITASCA Consulting Group Inc. (2012). FLAC- Fast Lagrangian Analysis of Continua Dynamic Analysis.

Kuhlemeyer, R.L., and J.Lysmer. “Finite Element Method Accuracy for Wave Propagation Problems,” J.Soil. Mech. & Foundations, Div., ASCE, 99 (SM5), 421-427, May 1973.

Kulhawy, F.H. and Mayne, P.H. 1990. Manual on estimating soil properties for foundation design. Electric Power Research Institute, EPRI.

Locat, J. and Lee H. 2002. Submarine landslides: advanced and challenges, Canadian Geotechnical Journal, No. 39, 193-212.

Mejia, L.H. and Dawson, E.M. 2006. Earthquake Deconvolution for FLAC. FLAC and numerical modeling in geomechanics Proceedings of the 4<sup>th</sup> international FLAC symposium, Madrid, Spain.

# Quantitative risk assessment for earthquake-triggered landslides using Bayesian network

## Évaluation quantitative du risque associé aux glissements de terrain déclenchés par séisme en utilisant un réseau Bayésien

Nadim F., Liu Z.Q.

Norwegian Geotechnical Institute (NGI) / International Centre for Geohazards (ICG), Norway

**ABSTRACT:** Strong earthquakes in mountainous regions usually trigger many landslides that lead to damage and destruction. Separate investigations of single hazard processes (earthquake and landslide) might lead to a misjudgement of the risks associated with this type of cascading hazards. The assessment and mitigation of the risks require a multi-risk analysis approach that can account for the interactions among the threats and among the vulnerabilities to these threats. In this paper, a quantitative risk assessment model using Bayesian network is proposed to estimate the risk for the buildings exposed to the threat of earthquake-triggered landslides. A sensitivity analysis was done to identify the optimum and appropriate risk reduction strategy in a multi-hazard perspective.

**RÉSUMÉ :** De forts séismes dans les régions montagneuses déclenchent habituellement des nombreux glissements de terrain qui mènent à dommages et destruction. Si l'on traite les aléas singuliers séparément, par exemple un tremblement de terre et un glissement de terrain, une estimation erronée des risques associés à ce type d'aléas cascades peut être obtenue. L'évaluation et l'atténuation des risques nécessitent une approche multi-risques qui doit tenir compte des interactions entre les dangers et les vulnérabilités à ces dangers. L'article propose un modèle d'évaluation quantitative des risques en utilisant un réseau Bayésien pour estimer le risque aux bâtiments exposés aux glissements de terrain déclenchés par un séisme. Une analyse paramétrique a été réalisée pour identifier une stratégie optimale et appropriée pour réduire le risque dans une perspective multi-aléas.

**KEYWORDS:** Landslides, Earthquake, Quantitative risk assessment, Bayesian network

### 1 INTRODUCTION

Earthquake-triggered landslides are one of the most common secondary disasters caused by earthquake in mountainous areas. In the Wenchuan earthquake of May 2008, more than 15 000 landslides of various types were triggered in the steep mountain slopes (Huang 2008). The landslides caused more than 20 000 fatalities (Yin *et al* 2009) and caused extensive damage to housing settlements and irrigation channels (Tang *et al* 2011).

In earthquake-triggered landslide risk assessment, complex interactions are present between the earthquake and landslide threats. The vulnerabilities of the elements at risk are sometimes also correlated to the threats. Amplified risk resulting from hazard and vulnerability interactions has to be considered. Unfortunately, to date, the risk assessment involving multiple hazards is commonly done with independent analyses neglecting possible cascade effects (Marzocchi *et al* 2012) and standard approaches for dealing with the multi-risk situations are not available (Kappes *et al* 2012). In this paper, a quantitative risk assessment model using Bayesian network is proposed to estimate the risk for the buildings exposed to the threat of earthquake-triggered landslides.

### 2 BAYESIAN NETWORKS

A Bayesian network (BN), also called a belief network, Bayes net or casual network, is an increasingly popular method for reasoning under conditions of uncertainty and modelling uncertain domains. It has been applied to a number of civil and environmental engineering problems, ranging from avalanche risk assessment (Grêt-Regamey and Straub 2006), dam risk analysis (Smith 2006), earthquake risk management (Bayraktarli *et al* 2005; Bensi *et al* 2011), design of early warning system for landslide hazard mitigation (Medina-Cetina *et al* 2007) and environmental modelling and management (Aguilera *et al* 2011).

A BN is a probabilistic model based on directed acyclic graph

$$B_s = G(Z, E) \quad (1)$$

where  $B_s$  represents the structure of the network,  $Z$  is the set of random variables ( $Z_1, Z_2, \dots, Z_n$ ), and  $E \in Z \times Z$  is the set of directed arcs, representing the probabilistically conditional dependency relationships among random variables. Each variable  $Z_i$  can be defined in a discrete and finite outcome space (discrete random variable) or as a continuous outcome space (continuous random variable).

One important property of the Bayesian network is that the joint probability function of all random variables in the network can be factorized into conditional and unconditional probabilities implied in the network (Jensen 2007). Thus, the joint distribution can be expressed in the compact form as

$$P(z_1, z_2, \dots, z_n) = \prod_{i=1}^n P(z_i | pa(Z_i)) \quad (2)$$

where  $pa(Z_i)$  is the parent set of  $z_i$ . It should be noted that if child node  $z_i$  has no parents, then the equation reduces to the unconditional probability of  $p(z_i)$ .

A simple Bayesian network with five nodes and five arcs is illustrated in Fig.1. These nodes are: Magnitude ( $M$ ), Distance ( $D$ ), Seismic severity ( $S$ ), Landslide severity ( $L$ ), and Building damage ( $B$ ). These nodes are connected via the arcs:  $M-S$ ,  $D-S$ ,  $S-L$ ,  $S-B$  and  $L-B$ . The prior probability of  $B$ ,  $P(B = B_j)$  can be calculated by

$$P(B = B_j) = \sum_{i=1}^2 \sum_{j=1}^2 \sum_{k=1}^2 \sum_{m=1}^2 P(B = B_j, M = M_i, D = D_j, S = S_k, L = L_m) \quad (3)$$

where  $P$  = probability,  $B_j$  = no damage,  $M_1$  = small magnitude,  $M_2$  = large magnitude,  $D_1$  = small distance,  $D_2$  = large distance,  $S_1$  = low seismic severity,  $S_2$  = high seismic severity,  $L_1$  = low landslide severity,  $L_2$  = high landslide severity.



In this case, as both  $M$  and  $D$  are the parents of  $S$ ,  $S$  is the parent of  $L$ , and both  $S$  and  $L$  are the parents of  $B$ , the joint probability can be derived according to Eq. 2:

$$\begin{aligned}
 P(B = B_i, M = M_i, D = D_j, S = S_k, L = L_m) \\
 = P(M = M_i) \times P(D = D_j) \times P(S = S_k | M = M_i, D = D_j) \\
 \times P(L = L_m | S = S_k) \times P(B = B_i | S = S_k, L = L_m) \quad (4)
 \end{aligned}$$

where the (conditional) probabilities on the right hand side of the equation are quantified with available information (e.g., statistical data, expert knowledge, and physical approaches).

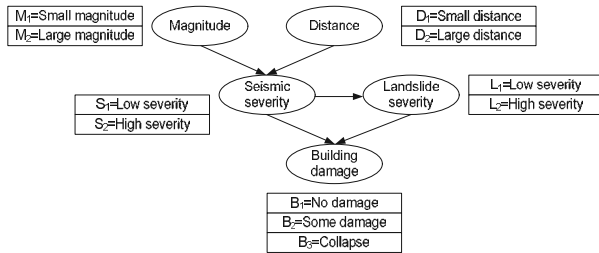


Fig. 1 A simple Bayesian network.

The BN allows one to enter evidence as input, meaning that probabilities in the network are updated when new information is made available, for instance, a case with a small magnitude and large distance. This information will propagate through the network and the posterior probabilities of  $B$ ,  $P(B = B_i)$  can be calculated as:

$$\begin{aligned}
 P(B = B_i | M = M_1, D = D_2) &= \frac{P(B = B_i | M = M_1, D = D_2)}{P(M = M_1, D = D_2)} \quad (5) \\
 &= \frac{\sum_{j=1}^2 \sum_{i=1}^2 P(B = B_i, S = S_j, L = L_i, M = M_1, D = D_2)}{\sum_{k=1}^3 \sum_{j=1}^2 \sum_{i=1}^2 P(B = B_k, S = S_j, L = L_i, M = M_1, D = D_2)}
 \end{aligned}$$

where the joint probabilities in the above equation are calculated with Eq. 3 on the basis of Baye’s theorem (Ang and Tang 2007).

### 3 BAYESIAN NETWORK FOR EARTHQUAKE-TRIGGERED LANDSLIDE RISK ASSESSMENT

According to the ISSMGE Glossary of Risk Assessment Terms, ‘Risk’ is the measure of the probability and severity of an adverse effect to life, health, property, or the environment. Quantitatively risk is the product of the threat times the potential worth of loss and can be expressed as:

$$Risk = Probability\ of\ Threat \times Worth\ of\ Loss \quad (6)$$

Otherwise expressed (e.g. Einstein 1997):

$$Risk = P(T) \times P(E|T) \times U(E) \quad (7)$$

where  $P(T)$  is probability of threat,  $P(E|T)$  is conditional probability of damage of the element(s) at risk exposed to threat, i.e. vulnerability, and  $U(E)$  is utility of element(s) at risk.

A comprehensive Bayesian network (modified after Einstein *et al* 2010) for estimating the risk of buildings in an assumed earthquake-triggered landslide case was built with an open-source MATLAB package BNT (Bayes Net Toolbox) (Murphy 2001) as shown in Fig. 2. There are 11 nodes and 16 arcs in the network. Each node is characterized by several discrete states as shown in Table 1.

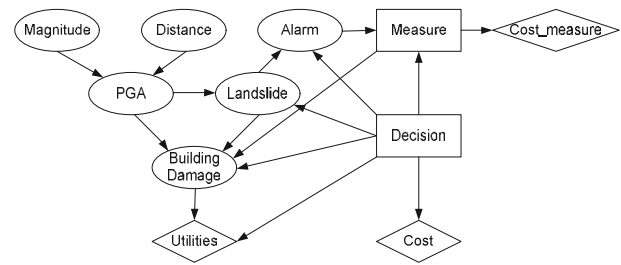


Fig. 2 Bayesian network for earthquake-triggered landslide risk assessment with possible decisions (modified after Einstein *et al* 2010).

Table 1 Nodes and their states of the Bayesian network in Fig. 2

Nodes	No. of states	States
Magnitude ( $M_w$ )	6	4.0-4.5-5.0-5.5-6.0-6.5-7.0
Distance (km)	6	22-25-28-31-34-37-40
PGA (g)	6	0-0.08-0.16-0.24-0.32-0.40-0.48
Landslide	2	Happens; Does not
Building damage	3	No damage; Some damage; Collapse
Alarm	2	Yes; No
Measure	2	Yes; No
Decision	4	Passive; Active; No action; Warning system
Cost measure	-	
Cost	-	
Utilities	-	

## 4 QUANTIFYING THE NETWORK

### 4.1 Seismic hazard

The seismic source is assumed as a line source in this study. Using the geometric characteristics of the source, the distribution of distances can be calculated as shown in Fig. 3.

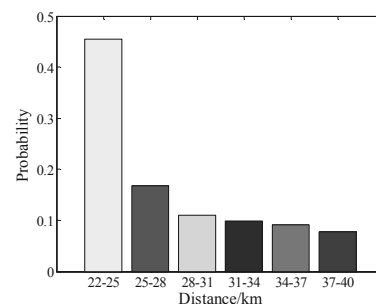


Fig. 3 Specification of the discrete probabilities of distance.

The annual probabilities for each range of  $M_w$  are calculated using the Gutenberg-Richter magnitude recurrence relationship (Gutenberg and Richter 1994), as shown in Fig. 4.

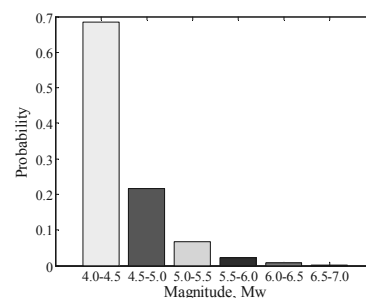


Fig. 4 Specification of the discrete probabilities of magnitude.

The conditional probabilities of PGA given the magnitude and distance to epicenter are calculated with the ground motion equation proposed by Ambraseys *et al* (2005), using Monte Carlo simulation in Microsoft Excel. The joint probabilities of

PGA are obtained based on inference of Bayesian network, as shown in Fig. 5

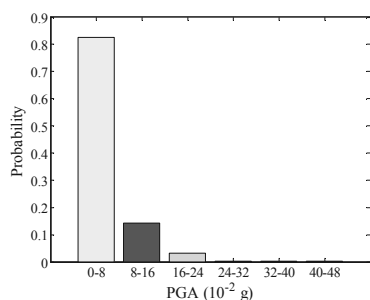


Fig. 5 Specification of the discrete probabilities of PGA.

#### 4.2 Landslide hazard

Approaches developed to assess the stability of slopes during earthquake fall into three general categories: (1) pseudo-static analysis, (2) stress-deformation analysis, and (3) permanent displacement analysis. In this paper, dynamic performance of slopes is modelled using permanent displacement analysis developed by Newmark (1965). The critical acceleration of a landslide block can be calculated by

$$a_c = (FS-1) g \sin \alpha \quad (8)$$

where  $FS$  is the static factor of safety;  $g$  is the acceleration of Earth's gravity; and  $\alpha$  is the angle of the sliding surface, which can generally be approximated as the slope angle.

The static factor of safety ( $FS$ ) for an infinite slope is

$$FS = c' / (\gamma z \sin \alpha \cos \alpha) + (1 - m \gamma_w / \gamma) \tan \phi' / \tan \alpha \quad (9)$$

where  $c'$  and  $\phi'$  are the effective cohesion and friction angle of the soil;  $z$  is the depth of the failure surface;  $\alpha$  is the slope angle;  $\gamma$  is the soil unit weight; and  $\gamma_w$  is the specific weight of water.

In the present study, the Newmark displacement is estimated using Eq. 10 reported by Ambraseys and Menu (1998):

$$\log D_n = 0.9 + \log [(1 - a_c / a_{max})^{2.53} (a_c / a_{max})^{-1.09}] \quad (10)$$

where  $D_n$  is the Newmark displacement in centimeters,  $a_c$  and  $a_{max}$  are critical acceleration and peak ground acceleration in  $g$ 's respectively.

The probability of slope failure as a function of Newmark displacement, as described by Jibson *et al* (2000) is estimated using the following equation

$$P(f) = 0.335 \times [1 - \exp(-0.048 \times D_n^{1.565})] \quad (11)$$

The soil and slope properties used in this study are shown in Table 2.

Table 2. Soil and slope properties.

Variable	Mean	St. Dev
$c'$ (N/m <sup>2</sup> )	10 000	2 000
$\phi'$ (degree)	30	2
$z$ (m)	2.5	0
$\alpha$ (degree)	35	0
$\gamma$ (N/m <sup>3</sup> )	27 500	0
$\gamma_w$ (N/m <sup>3</sup> )	10 000	0
$m$	0.4	0

The probabilities of slope failure computed by Eq. 11 for various ranges of PGA are listed in Table 3. Countermeasures made to landslide could reduce risk. Specifically, active actions can reduce the probability of slope failure, passive actions and warning system can reduce the vulnerability of element(s) at risk. The assumed probability of slope failure when active actions are taken is shown in Table 4.

Table 3. The probability of slope failure

PGA (10 <sup>-2</sup> g)	0-8	8-16	16-24	24-32	32-40	40-48
$P(f)$	0.124	0.256	0.305	0.328	0.339	0.346

Table 4. The probability of slope failure when active actions are taken

PGA (10 <sup>-2</sup> g)	0-8	8-16	16-24	24-32	32-40	40-48
$P(f)$	0.025	0.03	0.035	0.04	0.045	0.05

#### 4.3 Other nodes

In the case of a building subjected to a multi-hazard situation involving additive load effects (e.g. earthquake + landslide), the damage will be increased. Herein, the conditional probabilities of building damage are modified from Einstein *et al* (2010). For other nodes, we adopt from Einstein *et al* (2010). These probabilities (conditional probabilities) are shown in Tables 5-11.

Table 5. Four combinations of conditional probabilities of Building damage

Parent nodes	PGA		0-0.08		
	Measure		Yes		
	Decision	Passive	Does not Happens	Happens	Does not
Building damage	No damage	0.4	0.1	0.52	0.1
	Some damage	0.3	0.1	0.43	0.1
	Collapse	0.3	0.8	0.05	0.8

Table 6. Four combinations of conditional probabilities of Measure

Parent nodes	Alarm		Yes		
	Decision	Passive	Active	No action	Warning system
Measure	Yes	0	0	0	1
	No	1	1	1	0

Table 7. Four combinations of conditional probabilities of Alarm

Parent nodes	Landslide		Happens		
	Decision	Passive	Active	No action	Warning system
Alarm	Yes	0.5	0.5	0.5	0.9
	No	0.5	0.5	0.5	0.1

Table 8. Four combinations of conditional probabilities of Alarm

Parent nodes	Landslide		Happens		
	Decision	Passive	Active	No action	Warning system
Alarm	Yes	0.5	0.5	0.5	0.9
	No	0.5	0.5	0.5	0.1

Table 9. Conditional probabilities of Cost

Parent nodes	Cost		Warning system	
	Decision	Passive	Active	No action
Cost	-1250	-2000	0	-500

Table 10. Conditional probabilities of Utility

Parent nodes	Damage		Collapse	
	No damage	Some damage	No	Yes
Utilities	0	-10000	-20000	

Table 11. Conditional probabilities of Cost measure

Parent nodes	Measure		Cost measure	
	Yes	No	Yes	No
Cost measure	-1000	0		

## 5 RESULTS

The results obtained using the described Bayesian network of the entire risk assessment and decision are shown in Fig. 6. Different mitigation measures result in different utilities. The warning system, showing the lowest (negative) utility is the optimal mitigation measure.

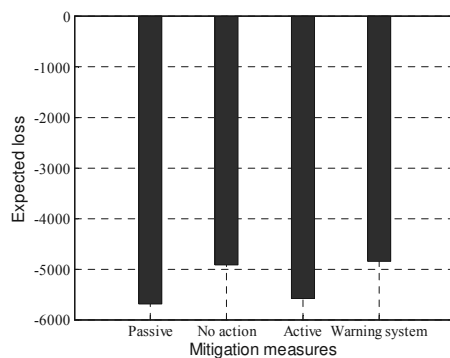


Fig. 6 Comparison of results for Passive countermeasure, No action, Active countermeasure, and Warning system.

This result is based on many parameters that can vary, for instance, the costs; the probability of slope failure or the reliability of the warning system. Therefore, sensitivity analyses were conducted to assess the effects of these variations on the results. Fig. 7 investigates the effect of changing the probability of landslide occurrence against different measures. As expected, for very low failure probabilities, no action is preferred; otherwise a warning system is the best choice, except for very high probabilities where active countermeasures are preferred. It is worth noting that this is only one example, and the sensitivity of the decision to other factors needs to be similarly investigated.

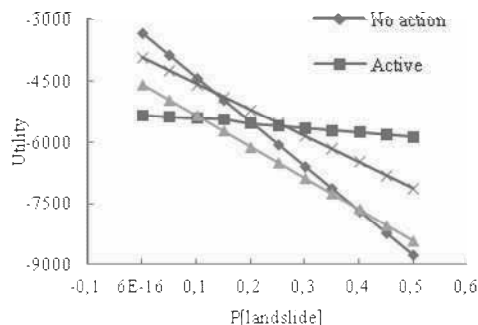


Fig. 7 Sensitivity analysis of the resulting risk arising from varying the probability of slope failure while employing different mitigation actions.

## 6 CONCLUSIONS

This paper presents a new model for evaluating the risks associated with earthquake-triggered landslides using a Bayesian network. The model considered the interactions between different threats in a systematic structure, and accounted for the uncertainties and expert judgments, which are always present in risk analysis. The results obtained in this study are a preliminary step in furthering the earthquake-triggered landslide risk assessment and similar multi-hazard risk assessments. Some of the subjective and empirical parameters in the model need to be further calibrated with the addition of objective data, experience and observations.

## 7 ACKNOWLEDGEMENTS

The research leading to these results has received funding from the European Community's Seventh Framework Programme [FP7/2007-2013] under Grant Agreement n° 265138 New Multi-Hazard and Multi-Risk Assessment MethodS for Europe (MATRIX).

## 8 REFERENCES

- Aguilera, P.A., Fernandez, A., Fernandez, R., Rumi, R., Salmeron, A. 2011. Bayesian networks in environmental modeling. *Environmental Modelling & Software* 26(12): 1376-1388.
- Ambraseys, N.N., Douglas, J., Sarma, S.K., Smit, P.M. 2005. Equations for the estimation of strong ground motions from crustal earthquakes using data from Europe and the middle east: horizontal peak ground acceleration and spectral acceleration. *Bulletin of earthquake engineering* 3:1-53.
- Ambraseys, N.N., Menu, J.M. 1988. Earthquake-induced ground displacements. *Earthq Eng Struct Dyn* 16:985-1006.
- Ang, A., H-S. Tang, W.H. 2007. Probability concepts in engineering, with emphasis on applications to civil and environmental engineering. 2<sup>nd</sup> Ed., John Wiley & Sons, Ltd.
- Bayraktarli, Y., Ulfkjaer, J., Yazgan, U., Faber, M. 2005. On the application of bayesian probabilistic networks for earthquake risk management. *9th International Conference on Structural Safety and Reliability (ICOSSAR 05)*, June 20-23, Rome.
- Bensi, M.T., Der Kiureghian, A., Straub, D. 2011. A Bayesian network methodology for infrastructure seismic risk assessment and decision support. *PEER Report* 2011/02.
- Einstein, H.H. 1997. Landslide risk - systematic approaches to assessment and management. Proc. Int'l Workshop on Landslide Risk Assessment. Landslide Risk Assessment, D. Cruden, R. Fell eds. Balkema.
- Einstein, H.H., Sousa, R.L., Karam, K., Manzella, I., Kvelsvik, V. 2010. Rock slopes from mechanics to decision making. *Rock Mechanics in Civil and Environmental Engineering*, Edited by Jian Zhao, Vincent Labiouse, Jean-Paul Dudt and Jean-Francois Mathier. London: CRC Press, 3-13.
- Grêt-Regamey, A., Straub, D. 2006. Spatially explicit avalanche risk assessment linking Bayesian networks to a GIS. *Natural Hazards and Earth System Sciences* 6(6):911-926.
- Gutenberg, B., Richter, C. F. 1944. Frequency of earthquakes in California. *Bulletin of the Seismological Society of America* 34:185-188.
- Huang, R.Q. 2008. Preliminary analysis of the development, distributions, and mechanisms of the geohazards triggered by the Great Wenchuan Earthquake, State Key Laboratory of Geohazards Prevention and Geological Environment Protection, Chengdu University of Technology, Chengdu, China.
- Jesen, F.V. 2007. Bayesian networks and decision graphs, Springer, New York.
- Jibson, R.E., Harp, E.L., Michael, J.A. 2000. A method for producing digital probabilistic seismic landslide hazard maps. *Eng Geol* 58:271-289.
- Kappes, M.S., Keiler, M., von Elverfeldt, K., Glade, T. 2012. Challenges of analyzing multi-hazard risk: a review. *Natural Hazards* 64:1925-1958.
- Marzocchi, W., Garcia-Aristizabal, A., Gasparini, P., Mastellone, M.L., Di Ruocco, A. 2012. Basic principles of multi-risk assessment: a case study in Italy. *Natural Hazards* 62:551-573.
- Medina-Cetina, Z., Nadim, F. 2008. Stochastic design of an early warning system. *Georisk: Assessment and Management of Risk for Engineered Systems and Geohazards* 2(4): 223-236.
- Murphy, K. 2001. The Bayes Net Toolbox for MATLAB. *Computing Science and Statistics* 33:1024-1034.
- Newmark, N.M. 1965. Effects of earthquake on dams and embankments. *Geotechnique* 15(2):139-160.
- Piteau, D.R., Martin, D.L. 1977. Slope stability analysis and design based probability techniques at Cassiar mine. *Bulletin of the Canadian Institution of Mining and Metallurgy*. 70:139-150.
- Smith, M. 2006. Dam risk analysis using Bayesian networks. *Proceedings of the 2006 ECI Conference on Geohazards*, June 18-21, Lillehammer, Norway.
- Tang, C., Zhu, J., Qi, X. 2011. Landslide hazard assessment of the 2008 Wenchuan earthquake: a case study in Beichuan area. *Canadian Geotechnical Journal* 48:128-145.
- Yin, Y.P., Wang, F.W., Sun, P. 2009. Landslide hazards triggered by the 2008 Wenchuan earthquake, Sichuan, China. *Landslides* 6: 139-152.

# Collapse behavior of slope due to change in pore water pressure

## Effondrement d'une pente à cause d'une variation de la pression interstitielle

Nakata Y., Kajiwara T., Yoshimoto N.  
Yamaguchi University, Ube, Japan

**ABSTRACT:** In 2010, a slope failure occurred due to heavy rain following an elevation in ground water level. Although a significant rainfall was experienced at the site in the previous year, there was no deformation with a similar elevation. In the past several collapses were recorded at the site due to heavy rain. Thus tests were performed using a plane strain compression apparatus to understand the deformation behavior of sand subjected to cyclic loadings in pore water pressure which were simulated the observed data on the collapsed slope. Rainfall records and data obtained from the observation well and extensometer were also shown. Finally lessons learned from the data were outlined.

**RÉSUMÉ :** En 2010, un glissement de terrain eu lieu après une élévation du niveau de la nappe phréatique à cause de fortes pluies. L'année précédente, bien que des précipitations légèrement plus fortes aient été enregistrées sur le site, il n'y eu pas de mouvement de terrain avec un niveau similaire de la nappe. Dans le passé, plusieurs effondrements ont été enregistrés à cause de fortes pluies. Des essais ont été effectués en utilisant un appareil de compression en déformation plane pour comprendre le comportement en déformation d'un sable soumis à des pressions interstitielles cycliques qui expliquent les données observées sur la pente effondrée en 2009-2011. Les relevés pluviométriques et les données obtenues dans un puits d'observation et à partir d'extensomètres sont également indiqués. Enfin on souligne les leçons tirées de l'ensemble de ces données .

**KEYWORDS:** slope stability, heavy rain, ground water level, pore water pressure, monitoring system, .

### 1 INTRODUCTION

Slope failures induced by heavy rainfall are one of the most destructive natural hazards and these have claimed untold numbers of lives and millions of dollars in infrastructure losses every year in many parts of the world. The rapid progress of global warming is already leading to changes in climate and related environmental problems. In line with global trends, temperatures in Japan are rising. At the same time active seasonal weather fronts carrying heavy clouds are resulting in increasingly heavy local downpours. As a result of these local downpours of torrential rain there is a national increase in geotechnical failures including slope failure and debris flows. These notable tendencies due to climate change have been increasingly recognized since the beginning of the 21st century.

In 2010, a slope failure due to heavy rain occurred at Hagi city in Yamaguchi Prefecture, which has been known as an unstable landslide area. In 2009, rainfall of significant intensity was experienced at the site, but there was no evident the deformation at that time. Additionally in the past, several collapses occurred at the site due to heavy rain. This means that several cycles of rise-and-fall of the ground water level have occurred at the site. The cycle could be linked to the cyclic changes of pore water pressure.

This paper firstly focuses on the cyclic change of pore water pressure. So far, there has been little research work done on cyclic loading of pore water pressure using triaxial compression apparatus (Ohtsuka & Miyata, 2001, and Orense et al., 2004). Therefore, in order to understand the deformation behavior of soil subjected to cyclic loading of pore water pressure, an experimental research using plane strain compression apparatus was carried out for sand specimens and the results are presented. Subsequently, the observed data on the collapsed slope in 2009-2011 is explained. Especially rainfall records and the data obtained from the observation well and extensometer

are shown. Finally, the lessons learned from the data are described.

### 2 DEFORMATION BEHAVIOR SUBJECTED TO CYCLIC CHANGE OF PORE WATER PRESSURE

#### 2.1 Plane strain compression test

In order to simulate the cyclic rise-and-fall of ground water level, experimental tests were performed by applying the cyclic change of pore water pressure in the specimen. In past researchers (Ohtsuka & Miyata, 2001, and Orense et al., 2004), tests were carried out using triaxial compression test apparatus applying monotonic loading of the pore water pressure. Thus, plane strain compression tests were adopted to reproduce stress condition closer to the site.

Each specimen was approximately 60mm wide, 160mm high and 80mm deep. Axial loading was applied through an electric motor from the top pedestal of the specimen. Confining and pore water pressures were applied by E/P transducers. All the external forces were controlled by a developed computer program. Grease was painted on the front and back planes of specimen in the direction of zero strain to minimize the friction. Note that the intermediate principal stress could not be measured in this study. Photos of the front plane of the specimen in the direction of zero strain were taken during the shearing process to observe local deformations.

The material used was Toyoura sand which has a higher permeability to propagate the quick change in pore water pressure and to keep the homogeneity of the effective stress condition. The material can be considered to show the relatively small compression deformation component. The specimens were prepared by air pluviation method with a constant falling height of 125mm. The specimen was formed in 5 layers with the falling height kept constant for each layer. As a result, the

initial relative density of specimens produced were 80%±3%. To saturate the specimen, de-aired water was flushed through the specimen and then a back pressure of 50 kN/m<sup>2</sup> was applied. All specimens were isotropically consolidated for 1 hour and then were sheared to reach maximum and minimum principal stress ratio of about 4.0. The cyclic change in pore water pressure was applied to the anisotropically consolidated specimen with constant amplitude. The principal stress difference was also kept constant by moving the top pedestal with constant axial deformation rate of 0.1%/min. The loading and unloading of the pore water pressure was conducted through a constant pressure increment of 1 kPa/min. After cyclic loading, monotonic loading of pore water pressure was applied to understand the strength of the specimen.

2.2 Cyclic deformation behavior due to pore water pressure

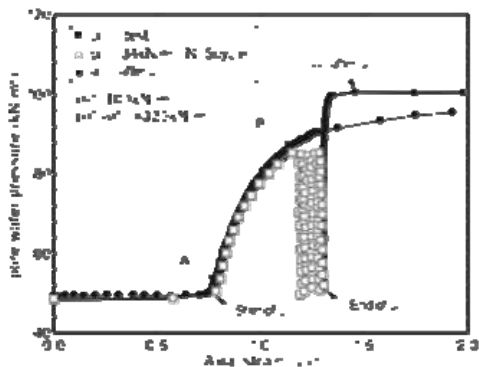


Figure 1 Deformation behavior due to cyclic and monotonic loadings of pore water pressure

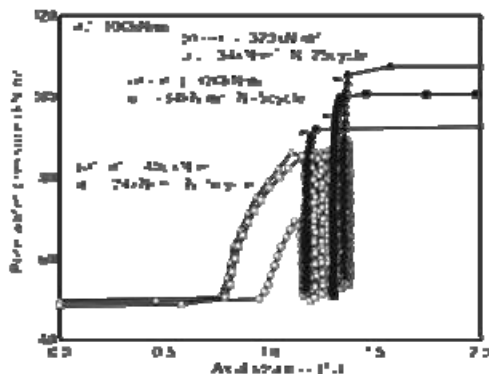


Figure 2 Effect of N and ( $\sigma_1/\sigma_3$ ) on the deformation behavior

Figure 1 shows the pore water pressure and axial strain relationship for the cyclic test under 100 kN/m<sup>2</sup> of the lateral pressure. The principal stress difference ( $\sigma_1 - \sigma_3$ ) was kept constant at 320 kN/m<sup>2</sup>. This value corresponded to the residual stress obtained from plane strain compression (PSC) test under 100 kN/m<sup>2</sup> of lateral pressure. The cyclic change in pore water pressure,  $u_{cyc}$  was the amplitude of 34 kN/m<sup>2</sup>. The maximum principal stress ratio reached corresponded to that of PSC test result at 100 kN/m<sup>2</sup>. The sand specimen generated 0.40% of axial distortion from 0.75% (A) to 1.15% (B) during the 1st loading of pore water pressure. After this, the specimen showed 0.15% of axial strain during the rest of the cyclic loading. For comparison, monotonic pore water pressure loading was applied as shown in the figure. The specimen subjected to cyclic pore pressure loading showed rigid-plastic behavior and reached a higher pore water pressure level than the monotonically-loaded specimen without any cyclic loading.

Figure 2 shows the cyclic loading test results with 100 kN/m<sup>2</sup> of lateral pressure. As the number of cycles increase, the axial deformation becomes larger during the cyclic loading.

Also, as the principal stress difference ( $\sigma_1 - \sigma_3$ ) is kept higher, the peak pore water pressure during the monotonic loading after the  $u_{cyc}$  process becomes lower. This is because the higher stress difference ( $\sigma_1 - \sigma_3$ ) is closer to the failure stress condition. After first loading, relatively small axial deformations were obtained irrespective of the amount of  $u_{cyc}$  and number of cycles N. This indicates that the cyclic loading of pore water pressure never lead to any larger deformation and failure.

2.3 Failure after cyclic change of pore water pressure

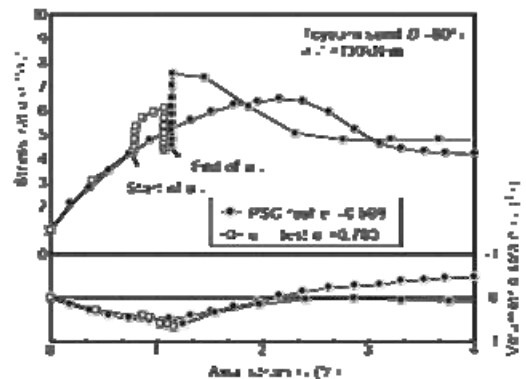


Figure 3 Stress-strain behavior from monotonic and cyclic loading of pore water pressure

Figure 3 shows the principal stress ratio  $\sigma_1/\sigma_3$  and axial strain relationship for the test results shown in Figure 1. The stress-strain curves before  $u_{cyc}$  loading are the same indicating good reproducibility of the specimen. Then, cyclic loading was initiated from the residual stress condition as described earlier. The sand subjected to the loading with  $u_{cyc} = 34$  kN/m<sup>2</sup> reaches a higher maximum stress ratio  $(\sigma_1/\sigma_3)_{max} = 7.5$  compared with  $(\sigma_1/\sigma_3)_{max} = 6.0$  for the conventional PSC test. The volume change during the cyclic loading is relatively small.

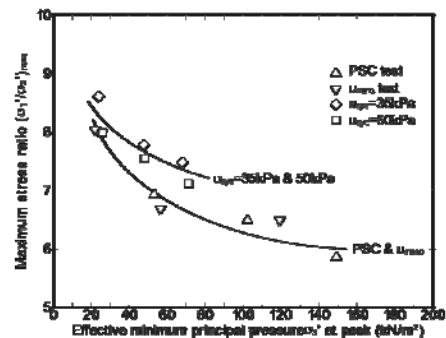


Figure 4 Stress dependency on peak stress ratio

Figure 4 shows the maximum stress ratio  $(\sigma_1/\sigma_3)_{max}$  plotted against the minimum principal stress at the peak stress condition. It can be seen that the value of  $(\sigma_1/\sigma_3)_{max}$  decreases as  $\sigma_3$  at peak increases. As generally well known the stress dependency on the peak stress has been observed. In addition, the results of the cyclic loading of pore water pressure shows a higher  $(\sigma_1/\sigma_3)_{max}$  than PSC tests. The results of the monotonic tests were similar with those of PSC test results. It can be recognized that the cyclic loading may induce the hardening and strengthening of the soil.

3 COLLAPSE BEHAVIOR OF SLOPE DUE TO GWL

The Kiyō District of Hagi City, Yamaguchi Prefecture has been known to be an unstable landslide area. The slope has geologic profile consisting of rhyolite and granite with a lower

permeability. Previous failures have occurred at the site in 1973, 1981, 1991 and 1994. In 2000, a landslide occurred as far as the lower debris flow barrier. In 2002 ground surface movements were observed without any apparent flow of soil mass. In order to monitor the stability of the slope, a monitoring system was installed since 1988 as shown in Figures 5 and 6. The main parameters measured were rainfall, ground water level (GWL) and slope movements using extensometers. The data were recorded remotely at the National Highways Bureau in Hagi. The system was upgraded in 2004 by installing inclinometers in the slope and debris barrier. In addition, a strain-gauged tell-tale system was installed across a crack in the barrier. The data logging and communications system was updated with wireless technology. The data has been automatically updated on a website. Moreover a mailing notification system has been installed in case of unusual conditions developing at the site.

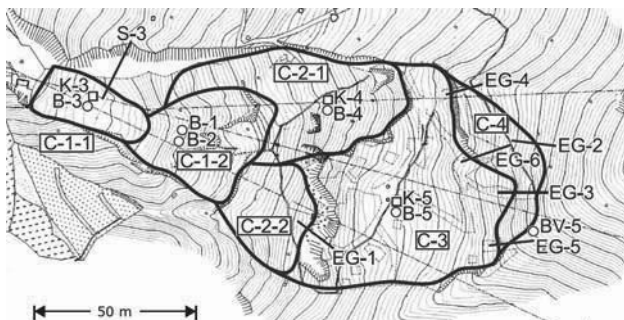


Figure 5 Plane view with failure blocks and measurement points (“C” represents failure block, “S” and “EG” are extensometers, “B” and “BV” are observation wells and “K” are for inclinometers)

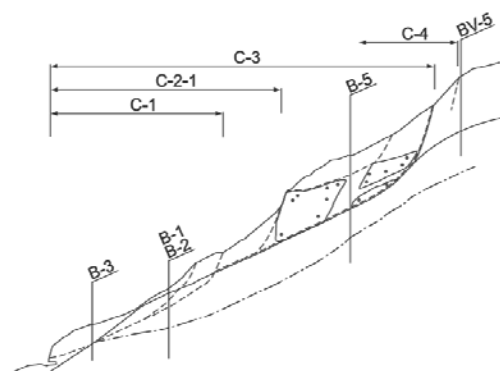


Figure 6 Cross section with failure block and measurement points

Three types of countermeasures were implemented to mitigate slope failure. Firstly the top third of the slope was covered with rubber sheeting to prevent inflow of rainwater. Secondly, water head relief tubes were installed below the area covered by the rubber sheets. And thirdly, a debris flow protection gallery was built over the road in front of the collapsed slope. This gallery was designed to resist an overburden of 4m thick of debris.

#### 4 RAINFALL RECORD AND FAILURE PROCESS

As shown in Figure 7, the rainfall commenced at 22:00 on 10/7/10 with a maximum recorded intensity of 25 mm/hr. At the time of failure, i.e. 5:00 on 10/7/14, the rainfall rate of 18 mm/hr on 7/12 led to a cumulative rainfall of 269mm. By 10:00 on 7/15 the accumulated rainfall was 351mm. The first failure occurred at 5:00 on 7/14 at the lower slope area C-1-2 over a slope length of 80m, width of 50m and depth of 2m. The total volume of the slip was 1600m<sup>3</sup>. The second failure occurred between 15:00 on 7/14 and 10:00 on 7/15 at Block C-2-1 over a slope length of 30m, width of 35m and depth of 2m. With these failures, the lower part of the slope was covered by a 2m to 3m

thick layer of debris. This layer was unstable and was liable to flow failure under future heavy rainfall. The upper part of the debris deposit had a vertical slope face. Also a visible continuous crack on the topside of block C-3 was discovered. This means higher potential for further movement of this block under the next heavy rainfall. So the stability of blocks C-2-2 and C-3 was worsened by the rainfall in July 2010.

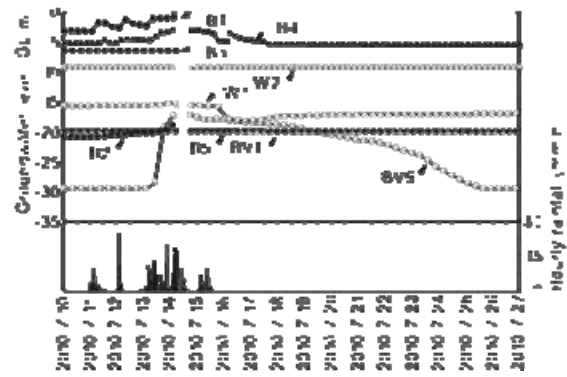


Figure 7 Variation of ground water level in July 2010

#### 5 GROUND WATER LEVEL RECORD

B1 and B2 were located in Block C-1-2. The elevation of GWL firstly occurred in B1 following the rainfall as shown in Figure 7. The GWL rose to within 0.51m below ground level (BGL). In the case of B2 the GWL rose to 18.54m BGL before the first failure, which represented a rise of 3m from the dry period. In previous failures in 1991 and 1994 similar GWL observations were made. It is therefore thought that the GWL was the trigger for the series of failures. The GWL in C3 had not apparently risen above normal levels.

BV-5 was located at the top of the slope and recorded a significant rise in GWL which correlated to the failure of C-3. During the dry period the GWL was at a depth of 29m. The GWL rose from 12:00 on 7/13 reaching a depth of 17.35m BGL at the initiation of failure and started to fall slowly again after 17:00 on 7/14. From 7/14 to 7/21 the rate of decrease was between 0.3m and 0.8m/day and from 7/22 to 7/25 the rate was 1.85m/day, finally reaching 29m BGL on 7/25. The movement of the extensometers stabilised when the ground water level dropped to 20m BGL. B4 was located at the top of the C-2-1 block. The GWL rose to 2.03m BGL which was a 3.5m rise. The rate of decrease was more than BV5 and on 7/17 it fell to 5m BGL. The major movement of Block C3 was considered to be the result of the earlier failure of C1-2 and C2-1 which effectively unloaded the toe of C3.

#### 6 GROUND MOVEMENT

Before the rainfall there were no indications of movement from the monitoring system located in Block C-3. However after the second failure, movement of the C-3 block was observed with rising GWL. After the first failure the monitoring system failed to work for a temporary period of time and was reinstated at 15:00 on 7/14. At this time it was noted that Block C-3 was moving at a rate of 30 mm/hr. This movement was monitored by the inclinometers at K-3. According to the inclinometer data, the slip surface was located at a depth of 20m. The movement at the surface was the same as that at depth, indicating that Block C-3 was moving as a single mass. From 7/15 the rate of movement decreased from 15 mm/hr to 1 mm/hr on 7/19, coming to a virtual halt on 7/22. This decrease correlated with the decrease in GWL. The S-3 extensometer became inactive due to the failure. No movement was observed by the extensometers EG1 and EG2 as shown in Figure 8. Movement was measured by EG3, EG4, EG5 and EG6 after 17:00 on 7/14 with greater than full-scale readings.

From 7/14 to 7/15 the rate of deformation was 5 mm/hr to 15 mm/hr and on 7/16 to 7/18 it reduced to 1 to 5 mm/hr. From 7/18 it gradually decreased. From 7/19 it reduced to 1mm/hr ceasing on the 7/22. The S-4 extensometer was set up on 7/17 because of the failure of C-2-1 and the enhanced risk of failure of the RHS of the slope. During the time the ground water level was going up, progression of displacement was not seen at all. Moreover, displacement between -17m and -20 m of the groundwater level was very remarkable. Furthermore, if the groundwater level falls lower than -23m, it can be considered that the movement of the block stopped in general.

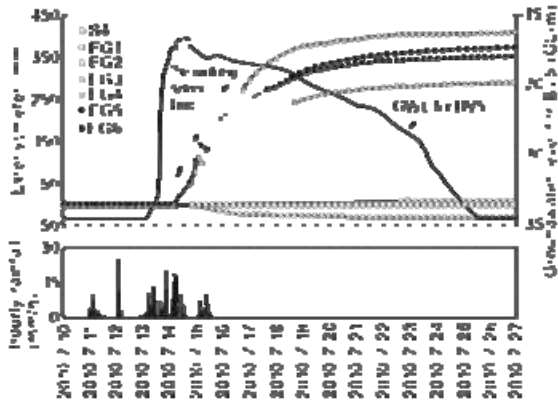


Figure 8 Data of extensometers observed in July 2010

6.1 Rainfall record in 2009

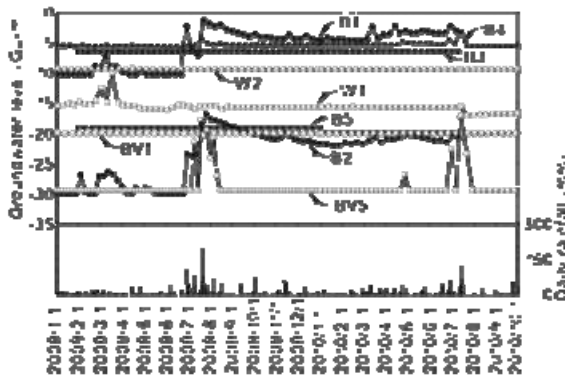


Figure 9 Rainfall record between 2009 – 2010

In 2009, a significant rainfall had been experienced at the same site as shown in Figure 9 with a maximum intensity of 62 mm/hr and cumulative intensity of 289mm over 3 days. However there was no evident of deformation at that time. The evidence indicates that it is difficult to predict the collapse solely by the rainfall forecast. The GWL in B1 in 2009 was 10m BGL compared to 3m BGL in 2010. The potential for slope failure in 2010 was therefore higher. The general tendency over the period 2009 to 2010 was for the GWL to be above normal.

6.2 Collapse behavior in 2011

Deformation of the slope was observed in 2011 due to the smaller rainfall shown in Figure 10. The rainfall in 2011 started on 6/27 and continued intermittently to 7/17. For 21 days, 4 major daily rainfall events were recorded; 60mm on 6/27, 40mm on 7/1, 30mm on 7/4 and 50mm on 7/8. The extensometer began to act on 7/1 before the GWL for BV5 elevated on 7/3. From this date, the deformation increased gradually and accelerated on 7/7, rising with the rapid increase in the GWL. During the ground water level rise and descent, the displacement of the C-3 block was recorded. The maximum displacement rate appeared during the water level rise while in 2010 it was during water level descent. This implies that the

timing of the warning official announcement would be earlier more for the next heavy rainfall.

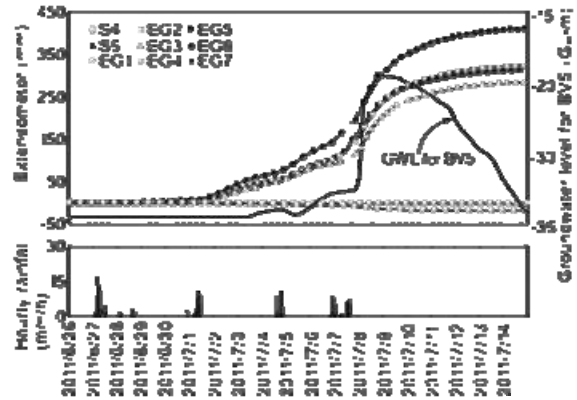


Figure 10 Data of extensometers observed at July in 2011

7 CONCLUSIONS

The paper focused on the evidence of collapse behavior for a slope due to heavy rain in 2010. In the past the site had experienced several collapses. An experimental research was performed to understand the deformation behavior of sand subjected to cyclic loading of pore water pressure using plane strain compression apparatus. Then the observed data on the collapsed slope in 2009-2011 was explained. Finally the lessons from the data were discussed.

- 1) The experimental test results showed that cyclic loading of pore water pressure never lead to any larger deformation and failure except the first loading. The rigid-perfectly plastic type behavior was observed for the sand specimen subjected to the cyclic changes in pore water pressure.
- 2) In 2009, a significant rainfall fell at the same site. However, there was no evidence of deformation at that time. This indicated that it was difficult to predict the collapse by the rainfall forecast only and a monitoring system is needed to predict any deformation.
- 3) The collapse behavior started at the surface layer of the toe part of the slope and then the movement of the major slip block correlated with the rise of ground water level behind the block. Therefore it is important to monitor the ground water level at the appropriate points to understand the collapse behavior.

8 ACKNOWLEDGEMENTS

The author gratefully acknowledges Mr. S. Yamada (Chugoku Regional Development Bureau, MLIT) for providing the monitoring data. This work was supported by Japan Society for the Promotion of Science KAKENHI, Grant-in-Aid for Scientific Research (B) 22360187.

9 REFERENCES

Ohtsuka S. and Miyata Y. 2001. Failure mechanism of clay in pore water pressure loading test. Landslide 37(4), 10-17 (in Japanese).  
 Orense R., Farooq K. and Towhata I. 2004. Deformation behavior of sandy slopes during rainwater infiltration. Soils and Foundations 44( 2), 15-30.

# Future evolution of slope stability analysis created by SPH method

## Évolution future de l'analyse de stabilité des pentes créé par la méthode SPH

Nonoyama H.  
Nagoya University, Japan

Yashima A., Moriguchi S.  
Gifu University, Japan

**ABSTRACT:** In this paper, the SPH (Smoothed Particle Hydrodynamics) method is applied to slope stability problems. This method can handle large deformation problems because it is based on the free mesh system. In addition, the constitutive models of geomaterials can be used directly. First, a simulation of a simple shear test is carried out to validate the SPH method. Then, slope stability analysis considering countermeasures is carried out. The numerical results are compared with results of the safety factors calculated by the Fellenius method. Based on the obtained results, the effectiveness of the SPH method for slope stability analysis is discussed.

**RÉSUMÉ :** Dans cet article, la méthode SPH (hydrodynamique des particules lissées) est appliquée à des problèmes de stabilité des pentes. La méthode peut traiter des problèmes de grandes déformations parce qu'elle est basée sur le système de maillage libre. En outre, les modèles de comportement des géomatériaux peuvent être utilisés directement. Dans un premier temps, une simulation d'essai de cisaillement simple a été réalisée afin de valider la méthode SPH. Ensuite, une analyse de stabilité des pentes considérant des contre-mesures a été réalisée. Les résultats numériques ont été comparés avec les résultats des facteurs de sécurité calculés par la méthode Fellenius. Sur la base des résultats obtenus, l'efficacité de la méthode SPH pour l'analyse de la stabilité des pentes a été discutée.

**KEYWORDS:** slope stability analysis, meshfree method, constitutive model

### 1 INTRODUCTION

In terms of the slope stability problems, design of structures and evaluation of countermeasures are carried out using a safety factor of slope obtained from circular slippage calculations at the practical level. In this approach, the safety factor of the slope is easily obtained from equilibrium of force. However, it is not possible to take into account of the deformation of slope. If it is possible to predict the deformation of slope, more detailed design of structures and evaluation of countermeasures can be facilitated. A lot of deformation analyses using the Finite Element Method (FEM) with developed constitutive models have been reported. It is, however, still difficult to solve large deformation problems using the FEM due to the distortion of the mesh. On the other hand, to solve such problems, various numerical approaches have been proposed, such as a modeling based on the computational fluid dynamics (CFD) and the discrete modeling (Cundall and Strack 1979). In the method based on CFD, it is not necessary to pay attention to mesh distortion, because the mesh is fixed in space. However, soils are assumed to be a kind of non-Newtonian fluids (Moriguchi 2005). Thus this modeling is an effective tool for flow problems, but is difficult to apply to static deformation problems. In addition, it is difficult to use constitutive models based on solid mechanics, because they cannot easily handle the history information of soils during deformation. The discrete modeling uses an assembly of discrete elements, and is inappropriate for dealing with constitutive models based on a continuum approximation.

Against these backgrounds, the purpose of this research is to express the large deformation behavior of geomaterials in the framework of continuum mechanics. The smoothed particle hydrodynamics (SPH) method, proposed by Lucy (1977) and Gingold and Monaghan (1977), is based on a mesh-free Lagrangian scheme, and is one of the effective numerical methods. The method can solve large deformation problems

without mesh distortion. Moreover, it can handle the governing equations and existing constitutive models for geomaterials, since it is based on a continuum approximation. The method has already been used to solve many types of geotechnical problems, and a number of interesting achievements have been published (e.g., Maeda et al. 2004, Bui 2007). From these achievements, it is shown that the SPH is applicable to geotechnical problems. However, as far as the introduction of the constitutive models of geomaterial into the SPH method, detailed discussions have not been carried out.

In this paper, the SPH method was applied to slope stability problems. In order to validate the method, a simulation of the simple shear test for elasto-plastic materials is carried out. Then, a slope stability analysis considering countermeasures is carried out. The numerical results are compared with the results of the Fellenius method. Based on the obtained results, the effectiveness of the SPH method for slope stability analysis is discussed.

### 2 NUMERICAL METHOD

#### 2.1 Basic theory of SPH method

In the SPH method, an object is expressed as an assembly of particles. If the motions of the particles are solved individually, the deformation behavior of the continuum cannot be represented by this technique. In order to treat an object as a continuum, a unique interpolation theory is used. This interpolation theory includes two key approximations: a kernel approximation and a particle approximation. The first step is a kernel approximation of the field functions. The kernel approximations are based on neighboring particles  $\beta$  located at points  $x^\beta$  within the support domain  $\kappa^d h$  of a smoothing function  $W$  for a reference particle  $\alpha$  located at point  $x^\alpha$ , as shown in Fig. 1. In the first step of the interpolation, we define a smoothed



physical quantity  $\langle f(x^\alpha) \rangle$  for the physical quantity  $f(x^\alpha)$  at the reference particle  $\alpha$  as follows:

$$\langle f(x^\alpha) \rangle = \int_{\Omega} f(x^\beta) W(r, h) dx^\beta \quad (1)$$

where  $r = |x^\alpha - x^\beta|$ ,  $h$  is the radius of the influence domain, and  $\Omega$  is the volume of the integral that contains  $x^\alpha$  and  $x^\beta$ .

In the second step of the interpolation, the physical quantity  $\langle f(x^\alpha) \rangle$  for the reference particle  $\alpha$  is expressed as the summation of the distribution of the assumed physical quantities  $f(x^\beta)$  for each particle. Thus, the physical quantity can be expressed in terms of  $N$  discrete points:

$$\langle f(x^\alpha) \rangle = \sum_{\beta} \frac{m^\beta}{\rho^\beta} f(x^\beta) W^{\alpha\beta} \quad (2)$$

where  $m^\beta$  is the mass, and  $\rho^\beta$  is the density of neighboring particles  $\beta$ .  $N$  is the numbers of neighboring particles in the support domain, and  $W^{\alpha\beta}$  is the smoothing function that expressed the contribution from the neighboring particles  $\beta$  to the reference particle  $\alpha$ . In this study, Cubic spline function (Swegle 1994) is used as the smoothing function. Equation (2) is a formula for evaluating a physical quantity via the SPH method. It is also possible to approximate the spatial gradient of a physical quantity in a similar way, using the spatial derivative of the smoothing function. The spatial derivative of Eq. (2) can be written as

$$\frac{\partial \langle f(x^\alpha) \rangle}{\partial x_i} = \sum_{\beta} \frac{m^\beta}{\rho^\beta} f(x^\beta) \frac{\partial W^{\alpha\beta}}{\partial x_i} \quad (3)$$

Based on the two-step interpolation procedure, it is possible to calculate any physical quantity and its special derivative of a physical quantity.

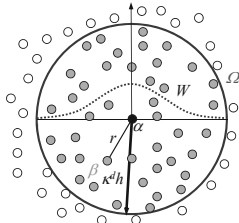


Figure 1. An image of basic concept of SPH method

## 2.2 SPH method based on the solid mechanics

The governing equations used in this study are based on solid mechanics. The equation of continuity and the equation of motion can be defined as follows,

$$\frac{d\rho}{dt} = -\rho \frac{\partial u_i}{\partial x_i} \quad (4)$$

$$\frac{du_i}{dt} = \frac{1}{\rho} \frac{\partial \sigma_{ij}}{\partial x_j} + F_i \quad (5)$$

where  $u_i$  is the velocity vector,  $\rho$  is the density,  $\sigma_{ij}$  is the stress tensor and  $F_i$  is the external force vector. Applying the SPH interpolation theories, the equations are expressed as follows:

$$\frac{d\rho^\alpha}{dt} = -\sum_{\beta} m^\beta (u_i^\beta - u_i^\alpha) \frac{\partial W^{\alpha\beta}}{\partial x_i} \quad (6)$$

$$\frac{du_i^\alpha}{dt} = \sum_{\beta} m^\beta \left( \frac{\sigma_{ij}^\alpha}{(\rho^\alpha)^2} + \frac{\sigma_{ij}^\beta}{(\rho^\beta)^2} + C_{ij}^{\alpha\beta} \right) \frac{\partial W^{\alpha\beta}}{\partial x_j} + F_i^\alpha \quad (7)$$

where  $C_{ij}$  is the summation of the artificial viscosity term (Monaghan and Gingold 1983) and the artificial stress term (Monaghan 2000; Gray et al. 2001). In order to introduce the artificial viscosity and the artificial stress, the numerical instability and the tensile instability are decreased (Swegle et al. 1995). Tensile instability, specifically the instability of the solution for tension deformation, is one of the problems with the SPH method for solid mechanics. In this study, the Drucker-Prager model (Drucker and Prager 1952) and the Super-subloading Yield Surface Modified Cam-clay model (Asaoka et al. 2000; 2002) are used in the deformation analysis of geomaterial to validate potential of the SPH method.

## 3 SIMULATION OF SIMPLE SHEAR TEST

In the validations of the SPH method for solid mechanics, a simulation of simple shear test under plane strain condition is carried out using Drucker-Prager model and Super-subloading Yield Surface Modified Cam-clay model. Calculated stress strain relation and stress paths are compared with the theoretical solution at the center of specimen. Figure 2 illustrates the numerical model used in the simulation. As the figure indicates, the specimen is a square object (10 cm by 10 cm). In the SPH method, numerical instabilities and errors tend to arise due to lack of calculation points. Therefore, a virtual area surrounded the specimen was used in this simulation. The solid line denotes the initial configuration of the specimen, and the dashed line denotes the configuration after deformation. In the simulation, the virtual area is forcibly deformed with a constant displacement to represent simple shear conditions, and the deformation of the specimen is calculated. Since a virtual area surrounded the specimen, only the scheme is employed in this validation. The parameters used in this simulation are summarized in Tables 1. As Table 1 indicates, seven different cases are considered in this simulation. In Cases 1, cohesive frictional material is used. In Cases 2 and 3, parameters of typical clay under two different values of the initial mean stress and initial overconsolidation ratio are used. In Cases 4 to 7, parameters of typical sand under three different values of the initial mean stress and degree of structure are utilized.

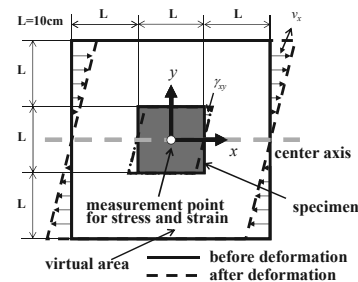


Figure 2. Numerical model

Figures 3 to 5 shows calculated stress-strain relation and stress paths at the center of the specimen. The theoretical solutions are also described in these figures for comparison. The solid line denotes the theoretical solutions, and plotted points indicate the obtained results. Based on the comparison, the results from the SPH scheme are in good agreement with the theoretical solution. Also, by introducing the Super-subloading Yield Surface Modified Cam-clay model (Asaoka et al. 2000; 2002) into the method, the softening with plastic compression behavior of structured soil and rewinding behavior of overconsolidated clay (Fig. 4) are expressed. Also, the softening behaviors with plastic compression of medium-dense sand and subsequent hardening behavior with plastic expansion (Fig. 5)

are expressed. It is summarized that the high performance elasto-plastic constitutive model can be introduced into the SPH method. Also, it is possible to simulate the various state of geomaterial, such as the clay and sand, using the SPH method.

Table 1. Material parameters

(a)Drucker-Prager model

Case		1
Young's modulus	$E$ [kPa]	1000.0
Poisson's ratio	$\nu$	0.33
cohesion	$c$ [kPa]	50.0
internal friction angle	$\phi$ [deg]	30.0
initial mean stress	$p_0$ [kPa]	98.0

(b) Super-subloading Yield Surface Modified Cam-clay model

Case		2	3	4	5	6	7
<b>&lt;elasto-plastic parameters&gt;</b>							
compression index	$\lambda$	0.200		0.052			
swelling index	$\kappa$	0.050		0.010			
critical state constant	$M$	1.40		1.0			
NCL intercept	$N$	2.20		1.98			
Poisson's ratio	$\nu$	0.3					
<b>&lt;evolution parameters&gt;</b>							
degradation index of overconsolidation	$m$	3.0		0.06			
degradation index of structure	$a$	0.5		2.2			
degradation index of structure	$b=c$	1.0					
<b>&lt;initial value&gt;</b>							
initial degree of overconsolidation	$1/R_0$	5.01	1.16	20.0			
initial degree of structure	$1/R_0^*$	5.0	1.40	10.0	23.6	39.0	
initial specific volume	$v_0$	2.20		1.95			
initial mean stress	$p_0$ [kPa]	98.1	294.3	20.0	98.1	196.2	294.3

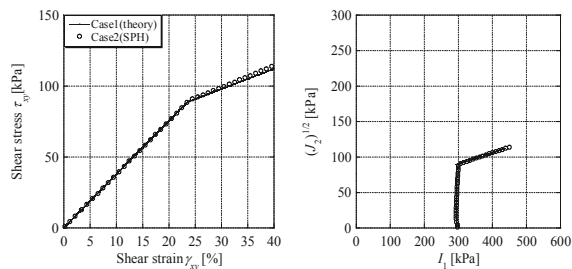


Figure 3. Drucker-Prager model (Case 1)

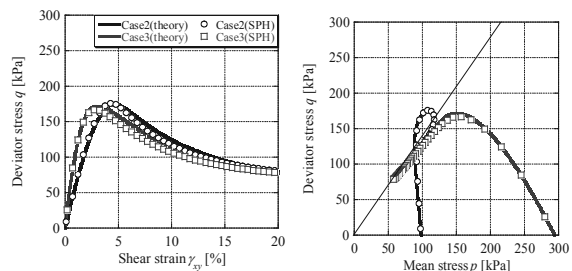


Figure 4. Super-subloading Yield Surface Modified Cam-clay model (Cases 2 and 3)

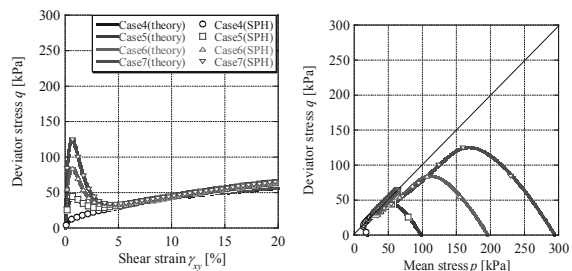


Figure 5. Super-subloading Yield Surface Modified Cam-clay model (Cases 4 to 7)

4 SLOPE STABILITY ANALYSIS CONSIDERING COUNTERMEASURES

A slope stability analysis considering countermeasures is carried out, using the Drucker-Prager model. Two types of countermeasures, such as top soil removal work and counterweight fill, are considered into these simulations. The numerical results are compared with results obtained using the safety factors calculated by the Fellenius method. Figure 6 illustrates the numerical models in Cases 1 to 8. The slope angle is 45 degrees and the model ground is cohesive. Also, as the figure shows, the displacements at the top of the slope are checked. The parameters used in this simulation are listed in Table 2. For the boundary conditions, the horizontal direction at the side wall of the slope was fixed, and the vertical direction is free. The horizontal and vertical directions at the bottom of the embankment are fixed. Fixed boundary particles are used to describe the walls. In order to take into account the effect of surface compaction, the internal friction angle of the counterweight fill material is set to 30 degrees. The effect of pore water pressure is not taken into account. The isotropic stress corresponding to static earth pressure is used as the initial stress.

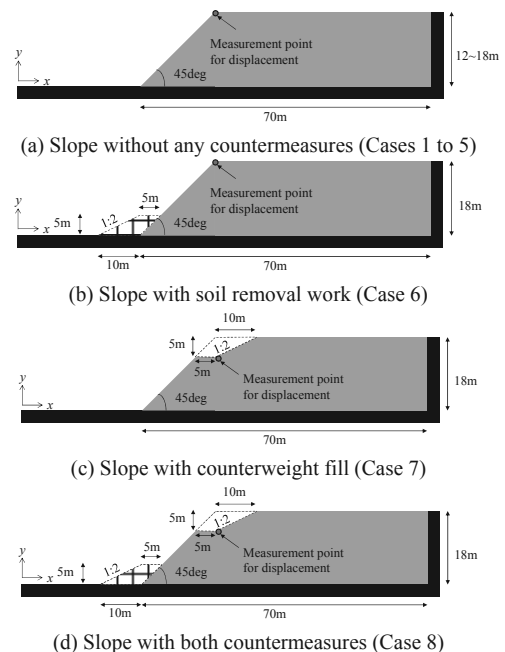


Figure 6. Numerical models.

Table 2. Material parameters.

Young's modulus	$E$ [MPa]	100.0
Poisson's ratio	$\nu$	0.30
cohesion	$c$ [kPa]	50
internal friction angle	$\phi$ [deg]	0.0
unit weight	$\gamma$ [kN/m <sup>3</sup> ]	19.6

Table 3. Safety factors obtained from the Fellenius method for each case.

Case	Countermeasures	Height of slope $H$ [m]	safety factor $F_s$
1	Without any countermeasures	12	1.24
2		14	1.01
3		15	0.91
4		16	0.86
5			0.75
6	Soil removal work	18	0.87
7	Counterweight fill		0.90
8	Both countermeasures		1.02

The safety factors obtained from the Fellenius method are listed in Table 3. As Table 3 indicates, the safety factors rise according to the order of case without any countermeasures,

case with soil removal work, case with counterweight fill, and case with both soil removal work and counterweight fill.

The distributions of accumulation of the maximum shear strain are shown in Fig. 7. As explained in above, boundary particles are used for the wall, but are not shown in these figures. Figure 8 shows the relationship between the safety factor and the value obtained by dividing the displacement  $\delta$  at the top of the slope by the height of the slope  $H$ . When the safety factor is larger than 1.0 (Cases 1 and 2), shear strain does not appear in the figures. However, when the safety factor is less than 1.0 (Cases 3 to 5), a distribution of circular shear strain can be seen. When the safety factor is close to 0.9, shear strain is observed but still large deformation cannot be observed. In particular, a crack forms at the crown of the slope, and block slippage is confirmed in the cases with the lowest safety factors. In the case without any countermeasures (Case 5), the shear strain is conspicuous and the slope is largely deformed. On the other hand, in the cases with countermeasures (Cases 6 to 8), the shear strain does not become more prominent and the displacements can be controlled as the safety factor increased. Thus, similar tendencies are observed in the results from the SPH method and the Fellenius method. In addition, while conventional circular slippage calculations are used to estimate the occurrence of rigid block slippage, the SPH method can estimate not only the stability, but also the effects of deformation. In Cases 3 and 7, the slope is not deformed, although the safety factor is less than 1.0. On the boundary between stable and unstable states, we consider that the slope is stabilized due to the redistribution of stress following an initial small deformation. The SPH method can estimate deformation and stability simultaneously. Moreover, it is capable of continuously predicting the deformation, even in a large deformation region. In other words, the SPH method can predict the entire deformation process of a geomaterial. Therefore, one may conclude that a variety of useful information about slope stability problems can be obtained via the SPH method.

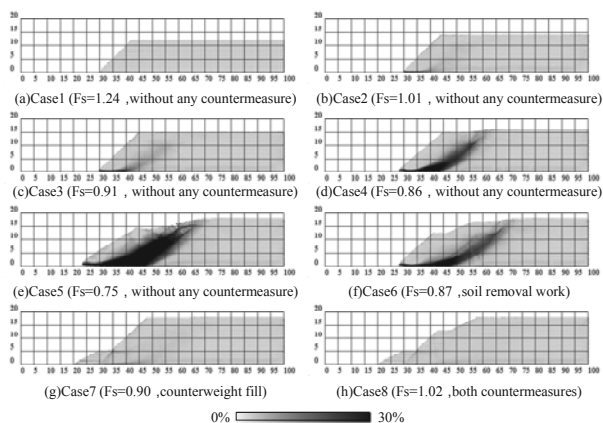


Figure 7. Distributions of accumulation of the maximum shear strain

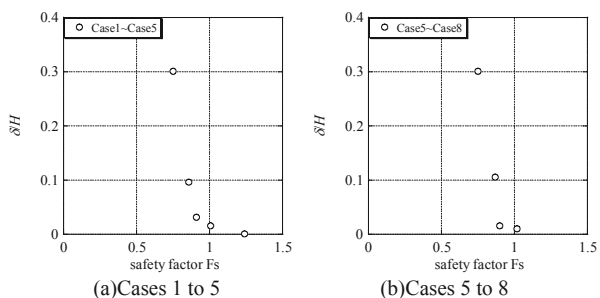


Figure 8. Relationship between safety factor and displacement at the top of slope.

## 5 CONCLUSION

In this study, introducing the constitutive model into the SPH method, deformation analyses of geomaterials were carried out. Firstly, in order to validate the method, the simulation of simple shear test of elasto-plastic material was simulated using two kinds of constitutive models of geomaterials. The numerical results were compared with the theoretical solutions. Then, a slope stability analysis considering countermeasures was carried out. The conclusions can be summarized as follows:

- The simulation of a simple shear test demonstrated that the SPH method could calculate the appropriate stress state of geomaterials using high performance elasto-plastic constitutive models.
- The SPH method was applied to slope stability analysis. The results indicated that the method was able to express the same safety factor tendencies obtained from the conventional circular slippage calculations. At the same time, the SPH method can simultaneously estimate both the deformation and stability. From the results of a slope stability analysis considering countermeasures, it can be inferred that the SPH method was capable of predicting the deformation and stability of slopes even in complex situations, such as simulations that include countermeasures.
- From a series of the numerical results, the SPH method was found to be applicable to slope stability analysis. Also, the SPH method has the potential to describe the deformation of geomaterials from the initial state to subsequent large deformations.

## 6 REFERENCES

- Asaoka A. et al. 2000. Superloading yield surface concept for highly structured soil behavior, *Soils and Foundations*, 40 (2), 99-110.
- Asaoka A. et al. 2002. An elasto-plastic description of two distinct volume change mechanisms of soils, *Soils and Foundations*, 42 (5), 47-57.
- Bui, H.H. 2007. Lagrangian mesh-free particle method (SPH) for large deformation and post-failure of geomaterial using elasto-plastic constitutive models, *Ph.D. Dissertation of Ritsumeikan University, Japan*.
- Cudall P.A. and Strack O.D.L. 1979. A discrete numerical model for granular assemblies, *Geotechnique*, 29 (1), 47-65.
- Drucker D.C. and Prager W. 1952. Soil mechanics and plastic analysis for limit design, *Quart. Appl. Math.*, 10 (2), 157-165.
- Gingold R.A. and Monaghan J.J. 1977. Smoothed particle hydrodynamics: theory and application to non-spherical stars, *Monthly Notices Roy. Astron. Soc.*, 181, 375-389.
- Gray J.P. et al. 2001. SPH elastic dynamics, *Comput. Methods Appl. Mech. Engrg.*, 190, 6641-6662.
- Lucy L.B. 1977. A numerical approach to the testing of the fission hypothesis, *Astron. J.*, 82, 1023-1024.
- Maeda K. and Sakai M. 2004. Development of seepage failure analysis procedure of granular ground with Smoothed Particle Hydrodynamics (SPH) method, *J. Appl. Mech.*, JSCE, 7, 775-786 (in Japanese).
- Monaghan J.J. and Gingold R.A. 1983. Shock simulation by the particle method SPH, *J. Comput. Phys.*, 52, 374-389.
- Monaghan J.J. 2000. SPH without a tensile instability, *J. Comput. Phys.*, 159, 290-311.
- Moriguchi S. 2005. CIP-based numerical analysis for large deformation of geomaterials, *Ph.D. Dissertation of Gifu University, Japan*.
- Swele J.W. et al. 1994. An analysis of smoothed particle hydrodynamics, *SAND93-2513, Sandia National Laboratories, Albuquerque, NM*.
- Swele J.W. et al. 1995. Smoothed particle hydrodynamics stability analysis, *J. Comput. Phys.*, 116(1), 123-134.

# Slope stability along a new road "Drisht –Drisht castle"

## Stabilité de pente le long de la nouvelle route "Drisht-Drisht castle"

Paçi E., Cullufi H., Dervishaj A.  
*Polytechnic University of Tirana, Albania*

**ABSTRACT:** Some slopes along the new road from the village Drisht center to the medieval castle entrance are located in a very disturbed tectonic zone. Due to overthrust geological processes the rock quality are extremely poor. In surface there are different active slides that due to water circulations especially during seismic events are very unstable and slide towards road pavements or cause side channel and culvert fills.

This article describes the numerical calculation concerning frequent normal conditions during construction and use of road and accidental condition during seismic events. Based in these calculations design solution are given. The calculations will be controlled by a back analysis algorithm. We have decided the upper and lower boundaries for the main results and we have made a sensitivity analysis that will show the influence of each parameter to the predicted results. So during maintenance time with same site tests results we can correct numerical parameters used in the model and predict long time behavior of the slope. In this manner we can also correct the future rehabilitation measures (if necessary) for the above mention road slope and other road slopes in similar conditions.

**RÉSUMÉ :** Certaines pentes le long de la nouvelle route allant du centre du village de Drisht à l'entrée du château médiéval sont situées dans une zone tectonique très perturbée. En raison de différents processus géologiques, la qualité de la roche est extrêmement médiocre. En surface, il existe différents glissements actifs qui, en raison de circulations d'eau lors d'événements sismiques, sont très instables et glissent vers chaussées et remplissent le canal longitudinal.

Cet article présente un calcul numérique (en conditions fréquentes – normales) pendant la construction et l'utilisation de la route. Les conditions accidentelles correspondant à des événements sismiques sont aussi traitées. Sur les bases des calculs effectués, des solutions techniques sont proposées. Les calculs sont contrôlés par un algorithme de "back analysis". Nous avons décidé les limites supérieure et inférieure pour les principaux résultats et nous avons fait une analyse de sensibilité qui montre l'influence de chaque paramètre. Ainsi, pendant le temps d'entretien du site, nous pouvons déterminer les paramètres numériques à utiliser dans le modèle pour prédire le comportement de la pente à long terme. Nous pouvons aussi proposer des mesures de réhabilitation futures (si nécessaire) pour la pente.

**KEYWORDS:** Slope stability, seismic events, weathering.

### 1 INTRODUCTION

The new road links the center of the village with a very famous medieval castle. It pass through a mauntainous area and need a lot of structures such as retaining walls, culverts, small bridges etc. The last part of the roads pass in a very steep slope where a year after the construction ware seen local slope failures.



Figure 1. Photo of local slope failures

The road width is 6m with 0.5 shoulders and a longitudinal concrete paved channel on the side of the mauntain. The road body is partly in filling and partly in cutting. The zone is one of

the wettest zone in Albania with a average rainfall of 1750mm/year. Due to lack of budget during the construction phase for finishing all the engineering measures and maintenance problems during exploitation phase local slope slides have occured after a period of 3 years.

#### 1.1 *Geological and geotechnical aspects*

The road to Drisht castle pass through a very disturbed tectonic zone. The study area takes part in subzone Cukali which, in the west and northwest is overthrust from the Albanian Alps zone , and in the southeast area is overthrust from Mirdita zone. Slope of the right side of the road represented by mainly constrained dark color old clays. Inside the clay mass can be meet compact sandstone layers bodies with dimensions up to 1 m in length, and up to 30 cm thickness and sandstone pieces measuring 5 to 10 cm with rounded shape and often alienated. These deposits are turbidits with a clayey - sandy cementation. They are too weak and are divided into small pieces. The above mention formation can be classified as very heterogonous flysch. Within the clay mass at the bottom of the slope (on the right side of the road) can be meet limestones olistolite size 5 to 10 meters above which are placed massive limestone rocks of Triassic geologic time.

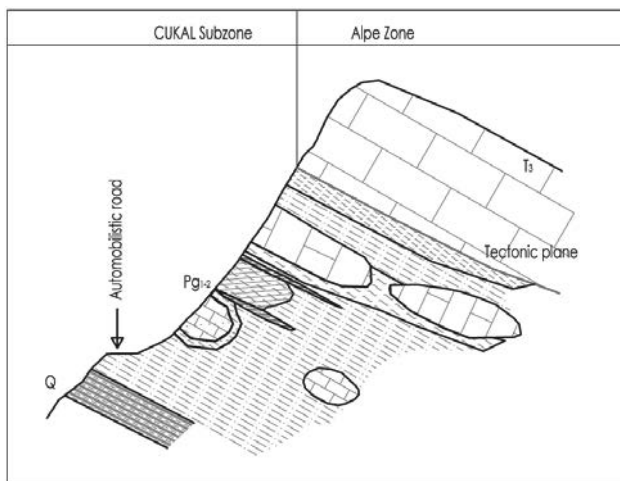


Figure 2. Schematic representation of the geological aspects of the slope

### 1.1.1 Geotechnical parameters

As given above we have identified two main type of terrain. The limestone rock formations with very good mechanical characteristics and flysch formations that are very weak rocks to soils.

These last rocks are described as rocks with relatively low strength and high deformability. They can be easily eroded by water, have a plastic behavior and poor stability on the slopes. Volume weight ranges from 2.2 - 2.6 g/cm<sup>3</sup>, porosity up to 35%, elasticity module  $2 \cdot 10^3 - 10^4$  daN/cm<sup>2</sup>, compression strength 5 - 25 daN/cm<sup>2</sup>, intact rock cohesion 20 - 100 kPa, internal friction angle <15°.

Based upon the lab test and empirical evaluation the main geotechnical parameters for unweathered formations used in the design are as follows

Table 1. Geotechnical main parameters

Layer	$\gamma_s$	$c$	$F$
Flysch/Clay	23	20-100	15
Limestone	26	400	45

## 2 MODELING OF THE SLOPE

### 2.1 FE 2D model

The slope stability analysis is made with finite element software Plaxis. The geometry and the layers are given in figure 3. For the calculation of sliding slopes should be distinguish the existing slides as well as those caused by changes in loading, reduction of parameters so first time slides. In finite element numerical calculations for the new slide slopes can not predefined a critical surface along its length the strength mobilized parameters progressively softened. The problem must pass in two stages, initially determining a critical sliding plan (if any) and then to give the soil strength mobilized parameters of this plan the residual parameters.

Through the first model we can determine the stability of the slope for a long time while the second model we can define the engineering measures (walls, piles, anchored wires, nails, etc.) and make the their design.

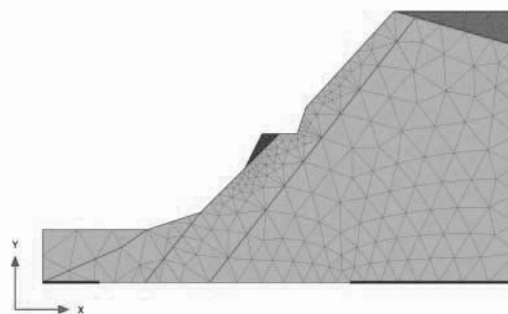


Figure 3. FE model of the slope

The soil is modeled as elasto-plastic material with yield criterion of Mohr-Coulomb. Advanced models with softening behavior would be more appropriate, but for lack of data (as well as the impossibility of accurate assessment of softening process) in our case can not be used. Weathering processes have been taken into account by dividing a surface layer in which the strength parameters gradually increase in depth until intact rock/soil values. In each analysis we took into account the initial natural stages as well as the following stages during the construction and the final stage during exploitation.

Influence of time, the accumulation of deformation, creep, brittle behavior that manifest same old overconsolidated clays, the formation of shear bands, influence of existing fissures, change of resistant parameters along the extent of the critical sliding surface, etc. in our model can not be taken in consideration. However, this modeling by taking the average parameters gives us practical results for the controls of the slope stability and dimensioning of retaining structures in the final limit state of the slope.

The fillings for road widening are reinforced with geogrids. Slope nailed wire mesh, anchors are simulated by applying a surface pressure perpendicular to the slope. The value of the pressure is taken such that the safety coefficient of the second model after application of this pressure to be 1.25. Plaxis program allows a sensivity analysis to see the influence of each parameter to the stability of the slope.

### 2.2 Water influence

The zone is one of the wettest zone in Albania with a average rainfall of 1750mm/year. It is well known that the rainfall precipitation degrade the soil properties due to progressive weathering. The weathered soil material has filled the longitudinal channel blocking the dewatering. The water infiltrate through existing fissures reducing significantly the soil parameters. The flysch/old clay formation have been separated into two soil layers. Upper surface layer that has been weakened as a result of rain water infiltrations and bottom layer of the terrain representing the intact formation. We haven't used an underground water level and thus a seepage calculation because in this type of formation we can not speak for a real water level. The water influence is taken into account only between the reduction of surface layer parameters and increase of the thickness of this layer at the end of the excavated slope, toe of the slope. For the surface layer geotechnical parameters that are used are the residual parameters  $c_r, F_r$ .

### 2.3 Seismic input

One of the reasons of slope instabilities are seismic events. So for the long term stability in the seismic zones is necessary to do also slope seismic loads analysis. Seismic input can be considered from time history of acceleration. These time

histories can be produced artificially or taken from records. In every case the accelerograms must be compatible with the acceleration spectra required by the codes.

For seismological and geotechnical applications real accelerograms are preferred because they are more realistic for frequency content, number of cycles, correct correlation between the vertical and horizontal components of ground motion and for the energy content in relation to the seismogenic parameters. In our case the site is near the zone of a seismic source that can generate earthquakes so we need to consider also near fault influence. However, in order to use a real accelerogram in near-fault conditions it is required for the time histories to include directivity effects and fling step, in other words they should refer to real, near-field earthquakes. So just for comparing the results we have also generated an artificial accelerogram taking account the near source effects.

Considering that we have been interested for the design of slope retaining structures the chosen accelerogram according to EC8 spectra is multiply by  $2 \cdot 1.4 / 1.146 \approx 2.45$  for being compatible with PGA taken from PSH analysis for  $T_R \approx 475$  years. The ground motion parameters are given below:

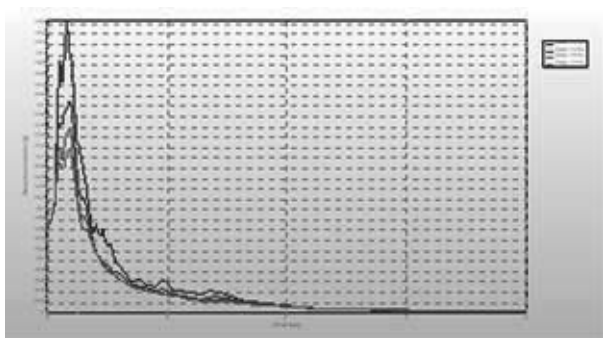


Figure 4. Acceleration response spectras

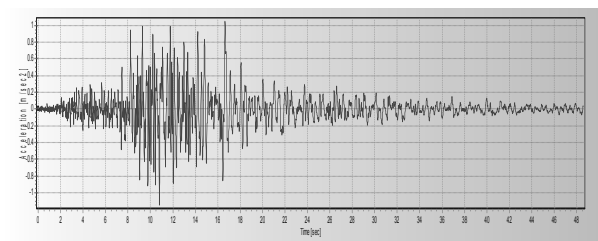


Figure 5. Time history of acceleration

PGA : 1.146m/sec<sup>2</sup> in t=10.790sec  
 PGV : 0.082m/sec in t=16.590sec  
 PGD : 0.020m in t=47.880sec  
 Vmax / Amax: 0.071sec. Predominant Period (Tp): 0.300sec

## 2.4 Results

From the analysis is seen that local instabilities occur before global instabilities. To overcome this problem the filling reinforcement with geogrids have been activated from the first stage of excavation before defining the critical sliding surface. In figure 6 are given the displacement of the road body fillings.

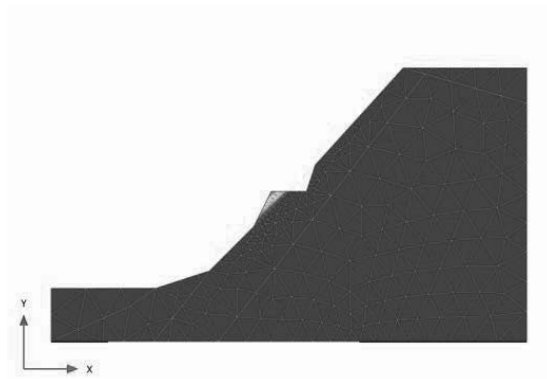


Figure 6. Local displacement

After that stage of local stabilization is done the global stability analysis. From analysis of the displacement and displacement incrementations we receive critical sliding surface shape and position as shown in Figure 7.

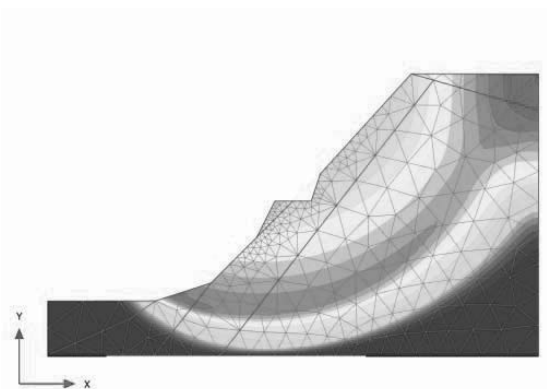


Figure 7. Total displacement

To simulate the critical sliding surface the "interface" element is activated with residual mechanical characteristics,  $c_r = 5 \text{ kPa}$ ,  $F_r = 10^\circ$

Since in site are not observed existing deep slides that affect the global stability of the slope conditioning the preexisting sliding surfaces the value of cohesion is not taken zero, thus improving also the numerical calculations. The displacement rate effect on residual strength parameters especially for seismic loading aren't taken in consideration.

In the case of application of a seismic load the safety coefficient for the second model decrease and wire anchored mesh of the slope should be strengthened, although for this case the coefficient of security can be taken close to 1. By sensitivity analysis of the parameters the cohesion changes are within small limits and their small changes doesn't affect the stability of the slope. The friction angle changes from peak values in those residual gives the greatest impact. These assessments we think correspond with the real monitored cases referred in literature. Since in the site is not implemented the wire anchored mesh the monitoring of weathering processes of slope materials in the future will give us the opportunity to correct resistance parameters values taken in the first analysis and reanalyze the slope stability.

## 3 CONCLUSIONS

Although the lack of data and the inability of finite element software with elasto-plastic modeling with Mohr-Coulomb yield criteria or softening criteria, to take into account the

numerous elements that affect the stability of slopes in soft rock / old clay the simulation of processes by means of two modeling even in the case of application of simple models of yield criteria gives practical good results for first time slides ultimate stage or when we have a reactivation of an existing surface of non-brutal slide. This modeling does not provide intermediate data for the developed process, giving the possibility to correct in time the analysis parameters, and provide in time appropriate engineering measures. In any case when it will be used it will be referred only to the final phase with residual parameters.

#### 4 ACKNOWLEDGEMENTS

The authors are very grateful for the help of Dr. Shkelqim Daja for the preparation of geological study.

#### 5 REFERENCES

- A.Anagnostopoulos 2011. The stability of natural cut slopes in stiff clays. Symposium of Landslide and Geoenvironment. Tirana,
- A.Federico and A.Murianni 2011, Empirical approaches to temporal prediction of slope failure. Symposium of Landslide and Geoenvironment. Tirana,
- Plaxis Reference Manual

# Landslides induced by the interaction of an earthquake and subsequent rainfall. A spatial and temporal model

Glissements de terrain induits par l'interaction d'un tremblement de terre suivi de précipitations.  
Un modèle spatio-temporel

Quan Luna B., Vangelsten B.V., Liu Z.Q., Eidsvig U., Nadim F.  
*Norwegian Geotechnical Institute (NGI) / International Centre for Geohazards (ICG), Norway*

**ABSTRACT:** The consideration of multiple hazards and their interaction to achieve risk reduction is a necessity since many regions are prone to different types of threats. However, this is neither simple and straightforward nor commonly undertaken at present since different natural hazards are usually analyzed individually and managed separately. A common example of this is the alteration of the density and locations of rainfall-induced landslides after an earthquake due to the extensive disturbance of surface strata. That implies an influence of the earthquake on the soil structure that alters the disposition towards landslides. Taking this into consideration, a model was developed that could give a rough spatial and temporal prediction of expected change in landslide hazard in an area following an earthquake. The model is able to describe the reduced impact of earthquakes with distance from epicentre as well as how the soil gradually regains its strength with time. These reductions are then applied to an equilibrium stability analysis in order to compute new Factors of Safety. Although analysis schemes can be proposed and software tools can be provided to facilitate many steps, a well-conceived and reflective approach to multi-hazard settings is still essential.

**RÉSUMÉ :** Etant donné que différentes régions sont sujettes à différents types de menace, l'étude de multiples facteurs de risque et de leur interaction est nécessaire afin de réduire le risque. Ce genre d'études est néanmoins rarement entrepris de nos jours puisque chaque risque naturel est usuellement analysé et traité séparément. Un exemple courant est l'évolution de la densité et de la localisation des glissements de terrain induits par des précipitations suite à un tremblement de terre en raison de l'importante perturbation des couches superficielles. Cela implique que l'influence des tremblements de terre sur la structure du sous-sol modifie la prédisposition aux glissements de terrain. Compte tenu de cela, un modèle de prédiction spatio-temporelle de la variation du risque de glissement de terrain dans une région donnée suite à un tremblement de terre a été développé. Le modèle est capable de décrire la diminution de l'impact des tremblements de terre en fonction de la distance à l'épicentre ainsi que la manière dont le sous-sol retrouve sa résistance initiale. Ces diminutions sont ensuite appliquées à une analyse de stabilité de façon à calculer de nouveaux facteurs de sécurité. Bien que des programmes d'analyses puissent être proposés et que des logiciels peuvent être fournis afin de faciliter de nombreuses étapes, une approche réfléchie et bien conçue des environnements à dangers multiples reste indispensable.

**KEYWORDS:** Landslide, Earthquake, Rainfall, Slope stability, Factor of Safety

## 1 INTRODUCTION

A multi-hazard analysis refers to the implementation of methodologies and approaches aimed at assessing and mapping the potential occurrence of different types of natural hazards in a given area. Analytical methods and mapping have to take into account the characteristics of the single hazardous events as well as their mutual interactions and interrelations (Delmonaco et al. 2006). The existence of relations between natural hazards and the potentially resulting consequences is an issue of increasing importance in multi-hazard studies (Kappes et al. 2010). The specific methods to deal with related hazards are as diverse as the terms and the phenomena falling into this category. However, a general approach can be applied where the investigation of the individual chain of one hazard triggering the next is performed (so-called cascading events).

Evidently, performing multi-hazard risk analysis is not a simple operation. Apart from the data requirements and time-consuming conduction of single-hazard risk studies that require know-how from different disciplines, many further aspects have to be considered. One important source of difficulty is the contrast in hazard characteristics. Hazards differ with respect to their properties such as time of onset, duration, physical properties and extent. As a result, the modelling approaches adjusted to the hazard specifics also contrast strongly (Bovolo et al 2009).

## 2 MODEL DESCRIPTION

The proposed model aims to compute and estimate the associated alteration in the landslide hazard following an earthquake event. The model describes the reduced impact of earthquakes with distance from epicentre as well as how the soil gradually regains its strength with time. This was achieved by analyzing the collected data on how seismic activity influences the critical rainfall intensity and duration needed to trigger landslides in the area impacted by the earthquake. Based on the gathered information the modelling objective was met by constructing three sub-models: A) Use empirical data to construct a sub-model linking rainfall threshold reduction as function of time after earthquake impact; B) Use empirical data to construct a sub-model linking rainfall threshold reduction as function of distance from epicentre and earthquake magnitude, C) Use an analytical hydrological model to link rainfall threshold reduction to changes in soil shear strength.

Sub-models A and B together form an empirical model for rainfall threshold reduction as a function of magnitude, distance and time after the earthquake. The model is based on the following assumptions:

- The effect of earthquake on the rainfall threshold reduction decays with distance from and time after the earthquake.
- The maximum rainfall threshold reduction (i.e. rainfall threshold reduction immediately after and at epicenter) is assumed to be a function of earthquake magnitude only.



- The temporal and spatial effects are independent and thus the spatial and temporal variations are treated separately in two different functions and multiplied to find the actual rainfall threshold reduction.
- The earthquake effect is included into the spatial model. The temporal model is a normalized model representing the remaining threshold reduction as a function of time after the earthquake.

According to the assumptions above, the threshold reduction for a given point in time and space is a product of the spatial model and the temporal model (Eq. 1):

$$\text{Threshold reduction (X, T, M)} = f_{\text{spatial}}(X, M) \cdot f_t(T) \tag{Eq.1}$$

In this model, X is the distance to the epicenter, T is the time after the earthquake and M is the earthquake magnitude. The purpose of the model is to relate the post-earthquake rainfall threshold to the pre-earthquake threshold using the derived threshold reduction function (Eq. 2):

$$\text{Post-earthquake threshold} = (1 - \text{Threshold reduction}(X, T, M)) \cdot \text{Pre-earthquake threshold} \tag{Eq.2}$$

The rainfall threshold changes referred to in the model is the numerical value of the mean rainfall intensity for a duration of one hour, i.e.  $\alpha$  in Eq. 3 below:

$$I = \alpha D^\beta \tag{Eq.3}$$

In this equation, I is the mean rainfall threshold intensity, D is the rainfall duration in hours and  $\beta$  is the slope of the threshold curve in log-log space.

### 2.1 Rainfall threshold reduction as function of time

Shou et al. (2011) modelled the effect of earthquake on the rainfall threshold reduction by an exponentially decaying function with time. The model parameter could be transferred to cumulative precipitation by using the annual mean precipitation. In the proposed model, the variations caused by other relevant parameters, such as slope angle and actual precipitation, are not treated explicitly; but model uncertainty is added to account for such variations. Shou et al. (2011) provided some data on the temporal effect of the Chi-Chi earthquake. No such data exist for the Wenchuan earthquake. From the available data it appears that the temporal behavior is site-dependent. However, Shou et al. (2011) used a model representing the average of three sites in Taiwan. Model uncertainty was introduced by two curves representing uncertainty bands. The uncertainty bands represent deviations of  $\pm 50\%$  from the average curve in a semi-log coordinate system.

Figure 1 shows the variation of the normalized rainfall threshold reduction with time for three different locations in Taiwan together with the average curve and uncertainty bands. The figure illustrates the long-term effects after the Chi-chi earthquake.

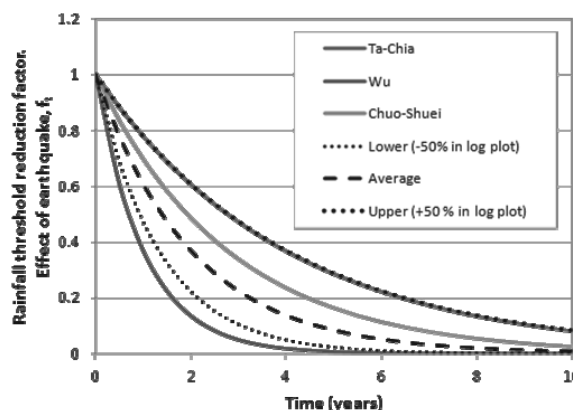


Fig. 1 Remaining rainfall threshold reduction (i.e. rainfall threshold reduction factor) as a function of time for three locations in Taiwan (colored curves) as well as an average curve and curves representing model uncertainty (black curves).

### 2.2 Rainfall threshold reduction as function of distance and earthquake magnitude

The rainfall threshold reduction as a function of earthquake magnitude and distance from the epicenter is based on the following relations and assumptions:

- For the spatial variation, the effect of earthquake on the rainfall threshold reduction is assumed to decay exponentially with distance from the epicenter/fault. This assumption is based on observations after the Chi-Chi earthquake by Khazai & Sitar (2003).
- The maximum “influence radius” of an earthquake is a function of the magnitude. The function described by Keefer (1984) is applied. This function describes the maximum distance from epicenter for seismically induced landslides as a function of earthquake magnitude. It was further assumed that at for a distance equal to the influence distance of the earthquake, the rainfall threshold reduction was 1/100 of the rainfall threshold reduction at distance 0.
- The model for maximum rainfall threshold reduction as a function of magnitude is assumed to increase with increasing magnitude.

Based on the above mentioned relations, a conceptual model for rainfall threshold reduction as a function of earthquake magnitude and distance from epicenter may be established as illustrated in Figure 2.

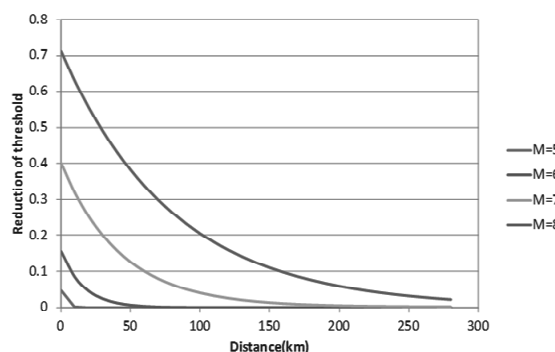


Fig. 2 Reduction of rainfall threshold caused by earthquake as a function of magnitude and distance

### 2.3 Linking rainfall threshold reduction and reduction of soil shear strength

Post-earthquake soil strengths may be lower than pre-earthquake (static) strengths for zones that are susceptible to

strength loss. As time passes, the progression of soil self-healing will result in increased shear strength compared to shortly after the earthquake. Temporal changes of soil properties are known to have an effect on the rainfall thresholds required to trigger landslides (Tang et al. 2009). Due to the decreased soil strength, landslide-triggering rainfall thresholds decrease compared with their pre-earthquake values (Lin et al. 2004).

A proposed methodology is presented for estimating temporal changes in soil strength related to landslide-triggering rainfall thresholds after an earthquake over a wide area (a few square kilometers). This methodology is based on response analysis with a deterministic, spatially distributed model that combines a 1-D transient infiltration model with a safety-factor analysis for calculating rainfall threshold.

After an earthquake, an abundance of loose landslide debris can be present on the hillslopes. The potential failure surface typically lies at or near the contact between the relatively permeable colluvium and the relatively impermeable underlying bedrock. The thickness of the soil cover is small compared with the length of slope, thus the infinite slope stability model can be performed to evaluate slope stability. Limit equilibrium conditions are reached at a certain depth when the mobilized shear stress (a function of soil unit weight, failure surface depth and slope angle) equals the soil shear strength, given by the Mohr-Coulomb failure criterion (Eq. 4):

$$\frac{\tan \phi'}{\tan \alpha} + \frac{c' - \gamma_w \psi \tan \phi'}{\gamma_s d_b \sin \alpha \cos \alpha} = 1 \quad \text{Eq.(4)}$$

where  $c'$  and  $\phi'$  are the effective cohesion and friction angle of the soil,  $d_b$  is the depth of the failure surface,  $\alpha$  is the slope angle,  $\gamma_s$  is the soil unit weight,  $\gamma_w$  is the specific weight of water, and  $\psi$  is the pressure head at the failure surface.

The limiting value of the pressure head which leads a slope with given geometrical characteristics and soil properties to limit equilibrium conditions can be calculated from Equation 5 as:

$$\psi_{lim} = \frac{c'}{\gamma_w \tan \phi'} + \frac{\gamma_s}{\gamma_w} d_b \cos^2 \alpha \left( 1 - \frac{\tan \alpha}{\tan \phi'} \right) \quad \text{Eq.(5)}$$

For a saturated soil cover, the evolution of the pressure head with time and depth inside the slope is governed by the following one-dimensional conservation equation (Eq. 6) (Iverson 2000):

$$\frac{\partial \psi}{\partial t} = D \frac{\partial^2 \psi}{\partial Z^2} \quad \text{Eq.(6)}$$

where  $Z$  is the depth of the point considered with respect to an horizontal reference plane;  $D = D_0 / \cos^2 \alpha$  and  $D_0$  is the hydraulic diffusivity of the soil.

Two factors,  $f_s$  and  $f_i$ , which are respectively reduction factors of soil shear strength and critical rainfall intensity, are now introduced. It is assumed that the effective cohesion and tangent of effective internal friction angle have the same reduction factor  $f_s$ . The reduction factor of critical rainfall intensity is calculated by dividing the reduced rainfall intensity  $I_{reducrit}$  due to soil shear strength reduction by the original critical rainfall intensity  $I_{critic}$  (Eq. 7):

$$f_i = \frac{I_{reducrit}}{I_{crit}} \quad \text{Eq.(7)}$$

For sandy soil, where the cohesion is zero, i.e.  $c = 0$ , an approximation solution is given by Eq. 8:

$$f_i = \frac{\frac{\gamma_s}{\gamma_w} d_b \left( 1 - \frac{\tan \alpha}{f_s \tan \phi'} \right) - (d_b - d_w)}{\frac{\gamma_s}{\gamma_w} d_b \left( 1 - \frac{\tan \alpha}{\tan \phi'} \right) - (d_b - d_w)} \quad \text{Eq.(8)}$$

### 3 RESULTS

#### 3.1 Study area: MATRIX virtual region

The case presented below is used to demonstrate the capabilities of the model in terms of hazard assessment. It is not a validation of the performance of the model. The case partly makes use of artificial data (including the digital elevation model) and partly typical engineering values (as for the soil parameters and rainfall intensity). A digital elevation model (DEM) has been developed for demonstration of the landslide hazard model (Fig. 3)

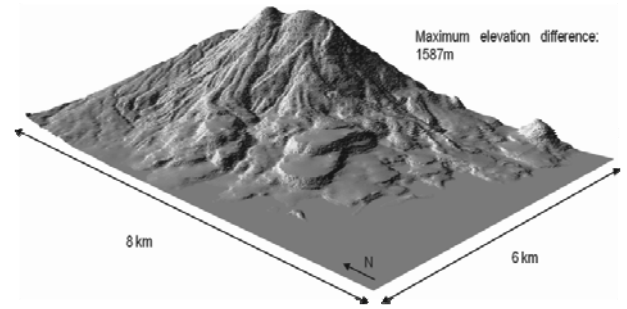


Fig. 3 3D representation of digital elevation model (DEM) for the case study region.

#### 3.2 Reduction factor for critical rainfall intensity

Figure 4 shows the results of the reduction factor inside the virtual region for a sandy soil where the earthquake event has a magnitude of 6.98 with a fault length of 3.08 km. The time span after the earthquake is assumed to be 45 days.

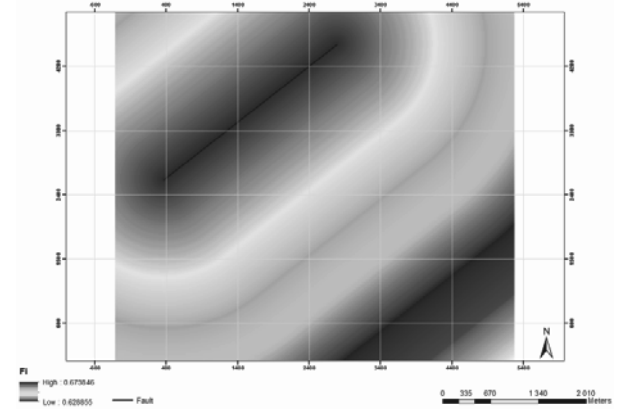


Fig. 4 Rainfall threshold reduction factor ( $f_i$ ) as a function of time, magnitude and distance to the fault.

The temporal model represents the remaining threshold reduction as a function of time after the earthquake. The remaining threshold reduction is represented by a normalized function with values between 0 and 1. Value 1 corresponds to the maximum rainfall threshold reduction (i.e. the rainfall threshold reduction immediately after the earthquake) and value 0 corresponds to no remaining rainfall threshold reduction (i.e. after long time, when the occurrence of the earthquake has no effect on the rainfall threshold.) The effect from the earthquake on the rainfall threshold reduction is included in the spatial model.

### 3.3 Reduction factor of the soil shear strength

A quantitative assessment of the relationships between different factors (i.e. slope angle, failure depth and water table depth) and reduction factor of soil shear strength due to earthquake was performed. Figure 5 shows the areal distribution of the reduction factor of the soil shear strength considering a rainfall intensity of 120 mm a day. The bedrock is assumed to be much less permeable than the soil cover. Soil depth varies from 4 to 7 m depending on the type of soil and topographic characteristics inside the virtual region.

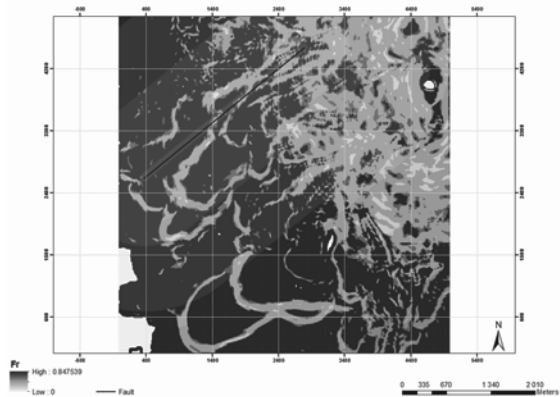


Fig. 5 Spatial distribution of the soil shear strength reduction factor ( $f_r$ ).

### 3.4 Slope stability assessment including the reduction factors

A two dimensional equilibrium stability analysis based on the infinite slope model was carried out in order to compute the new factors of safety that included the reduction factors. The mean values of the logarithmic distributions functions of the input parameters were applied in the analyses. A constant porosity of 42% and an evapotranspiration of 5 mm/day were selected throughout the area. Five different friction angles were used for the different soil types: 30, 32, 34, 36, 38°. Figure 6 shows the results of the stability analysis considering the reduction of the soil strength after an earthquake.

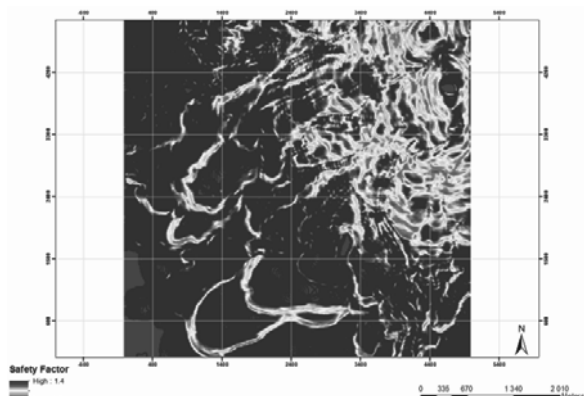


Fig. 6 Stability analysis considering the loss of strength of soil due to the perturbations caused by a magnitude 6.98 earthquake.

## 4 CONCLUSIONS

A natural system is not just the sum of its components but is the result of many interacting parts. Hence, a multi-hazard assessment should address evolving characteristics in space and time. These characteristics can, for analysis purposes, be analyzed as the alteration of the susceptibility and the triggering mechanism. A multi-hazard assessment offers the advantage to consider a slightly larger part of the overall system. The major challenge is to identify the relationships among the interacting factors and establish the respective links.

For this reason, a model that includes the reduction of the soil strength parameters induced by the strong motion of an earthquake was developed and implemented. A virtual case study was performed to assess the behavior of the model and its parameters. This was achieved by calculating two reduction factors that represented the reduction of rainfall threshold in space and time, and the reduction of the soil strength due to prevailing conditions.

There are still some limitations regarding the model and further validation needs to be done. A thorough calibration of the reduction factors should be done locally and the possibility of using real events that are well documented should be considered. However, despite its limitations, the model provides a practical approach to assess the prospective outcomes of future hazards and their interactions. Thus the model contributes to increasing the knowledge required for the protection of the people at risk and their assets.

## 5 ACKNOWLEDGEMENTS

The research leading to these results has received funding from the European Community's Seventh Framework Programme [FP7/2007-2013] under Grant Agreement No 265138 New Multi-Hazard and MulTi-RIsK Assessment MethodS for Europe (MATRIX).

## 6 REFERENCES

- Bovolo, C. I., Abele, S. J., Bathurst, J. C., Caballero, D., Ciglan, M., Eftichidis, G., Simo, B. 2009. A distributed framework for multi-risk assessment of natural hazards used to model the effects of forest fire on hydrology and sediment yield. *Computers & Geosciences* 35(5): 924 - 945.
- Delmonaco, G., Margottini, C., Spizzichino, D. 2006. ARMONIA methodology for multi-risk assessment and the harmonisation of different natural risk maps. *Deliverable 3.1.1, ARMONIA*
- Iverson, R. M. 2000. Landslide triggering by rain infiltration. *Water Resources Research*, 36(7), 1897-1910.
- Kappes, M., Keiler, M., Glade, T. 2010. From single- to multi-hazard risk analyses: a concept addressing emerging challenges. In Malet, J.-P., Glade, T. & Casagli, N. (Eds.), *Mountain Risks: Bringing Science to Society*. Proceedings of the International Conference, Florence. CERIG Editions, Strasbourg, 351-356.
- Keefer, D. K. 1984. Landslides caused by earthquakes. *Geological Society of America Bulletin*, v 95, pp. 406 - 421.
- Khazai, B., Sitar, N. 2003. Evaluation of factors controlling earthquake-induced landslides caused by Chi-Chi earthquake and comparison with the Northridge and Loma Prieta events. *Engineering Geology*, 71, pp. 79 - 95.
- Lin, C.W., Shieh, C. L., Yuan, B. D., Shieh, Y. C., Liu, S. H., and Lee, S. Y. 2004. Impact of Chi-Chi earthquake on the occurrence of landslides and debris flows: example from the Chenyulan River watershed, Nantou, Taiwan. *Engineering Geology*, 71, 49-61
- Shou, K. J., Hong, C.Y., Wu, C.C., Hsu, H. Y., Fei, L. Y., Lee, J. F., Wei, C. Y. 2011. Spatial and temporal analysis of landslides in Central Taiwan after 1999 Chi-Chi earthquake. *Engineering Geology*, 123, pp. 122 - 128.
- Tang, C., Zhu, J., Li, W. L. 2009. Rainfall-triggered debris flows following the Wenchuan earthquake. *Bulletin of Engineering Geology and the Environment*, 68, 187-194.

# Analyse des glissements de terrains en région urbanisée

## Analysis of landslides in urban regions

Rahhal M.E.

*Université Saint Joseph, Beyrouth, Liban*

Hajal M.

*Université Libanaise, Beyrouth, Liban*

Seoud J.P.

*GSC Consultants, Beyrouth, Liban*

Rafie E.

*STS Consultants, Beyrouth, Liban*

**RÉSUMÉ:** Des glissements de terrains importants ont eu lieu au pays du cèdre. La topographie montagneuse du Liban, la présence des aquifères et les fouilles réalisées pour les travaux de construction sont à l'origine du risque élevé de glissements de terrains. Un objectif principal visé par cette étude est de comprendre les facteurs causant ces instabilités. Deux études de cas bien documentés sont analysées. Les glissements ont lieu dans des formations argileuses à l'interface au-dessus de formations plus rigides composées de marne argileuse ou de roche calcaire. On observe aussi les glissements dans des alternances de banc calcaire fracturé et couche d'argile intercalée. Des conclusions intéressantes sur le comportement des sols à la rupture sont avancées. Les résultats escomptés devront compléter une cartographie éventuelle des cas de glissement à travers le Liban.

**ABSTRACT:** Important landslides took place in the land of cedar. Lebanon's mountainous topography, the presence of aquifers and excavations for construction are at the origin of the high risk of landslides. A main objective of this study is to understand the factors causing these instabilities. Two well-documented case studies are analyzed. Landslides occur in clay formations at the interface over more rigid formations composed of clayey marl or limestone. There are also landslides in alternating fractured limestone bench and intercalated clay layer. Interesting conclusions on the behavior of soil at failure are proposed. The expected results should help in achieving a possible landslide cases mapping throughout Lebanon.

**KEYWORDS:** landslide, marly clay, shale

**MOTS-CLÉS:** glissement de terrains, argile marneuse, schiste argileux

## 1 INTRODUCTION

Le Liban a connu ces dernières années des hivers avec des pluies particulièrement abondantes. Ces intempéries sont à l'origine de plusieurs cas d'instabilité des terrains surtout en régions montagneuses parfois très proches du littoral densément habité. La densité moyenne de la population libanaise est de 450 habitants par km<sup>2</sup>, ce chiffre étant beaucoup plus élevé sur la côte méditerranéenne et diminuant en altitude. L'urbanisation couvre donc aujourd'hui une grande superficie du pays du cèdre. En janvier 2013, la tempête qui a frappé le pays a laissé des dégâts énormes avec des glissements menaçant des habitations dans plusieurs régions. Mais l'activité humaine due à l'urbanisation se manifestant par les fouilles réalisées pour les travaux de construction vient aussi se conjuguer aux facteurs naturels déclenchant les glissements.

La répartition spatiale des mouvements relève de la topographie et de la géologie (Carrara et al. 1995). Leur occurrence est très marquée par les variations climatiques mais peut aussi être liée à des secousses sismiques ou encore être induite par les activités humaines. Le glissement est défini par le déplacement de terrains meubles ou rocheux et peut être identifié par un état d'activité (Cruden et Couture 2011). Selon la géométrie de la surface de rupture, deux types principaux de glissements sont distingués: d'abord, le glissement plan où la ligne de rupture suit généralement une couche mince ayant de mauvaises caractéristiques mécaniques et sur laquelle s'exerce souvent l'action de l'eau (couche savon). Ensuite, le glissement plutôt rotationnel où la surface de glissement est plus ou moins circulaire; ce mouvement étant caractérisé par l'existence d'une zone de départ (Abramson et al. 2002). Le passage de l'état de stabilité à l'état d'instabilité (Dikau et al. 1996) relève de causes nombreuses: externes (l'érosion, les séismes, les surcharges

d'un ouvrage); et internes (l'augmentation de la pression interstitielle, l'altération d'une roche). Souvent aussi, les causes sont conjuguées. Les matériaux affectés sont très variés (Fletcher et al. 2002), mais globalement la présence d'argile en forte proportion est toujours un élément défavorable. Au Liban, le rôle de l'eau est reconnu comme le facteur déclenchant des glissements en l'absence du facteur tectonique. Il y a aussi les excavations réalisées qui deviennent un facteur déstabilisant. Beaucoup de techniques ont été développées afin de minimiser l'impact des glissements de terrains (Popescu 2002). Une analyse des facteurs causant les instabilités de pentes au Liban a été réalisée (Rahhal et al. 2003). Un travail de cartographie des mouvements de terrains a aussi été entrepris (Rahhal et al. 2004). Enfin, des études probabilistes sont aussi conduites dans le but de comprendre la sensibilité des paramètres géotechniques dans l'évaluation de la stabilité des pentes. (Rahhal and Abou Rached 2005; Rahhal 2006; Benarroch et al. 2011).

Cet article présente une analyse étoffée de deux glissements, survenus au nord de Beyrouth dans deux régions densément peuplées. La compréhension du comportement des sols est une étape fondamentale lors de l'analyse d'un glissement de terrain.

## 2 CAS DU GLISSEMENT DE ESSFIRÉ

### 2.1 Localisation et contexte

Essfiré est une bourgade au nord du Liban, d'altitude moyenne 1100 mètres. Elle est située à 120 km de la ville de Beyrouth. En mars 1998, le sol à Essfiré a glissé, suite à la fonte de la neige accumulée. Ce glissement montré dans la Figure 1 sera l'objet de cette étude. La région a déjà connu dans son

histoire plusieurs glissements depuis les années soixante. La zone glissée a 70m de largeur, et 835m de longueur. Le profil de la pente a été tracé entre les cotes 960 et 1170 mètres. La pente à la cote 960m a un angle de 18°, elle commence à s'atténuer peu à peu, pour atteindre 12° au milieu du glissement, et arrive enfin à 10° au sommet, aux alentours de la cote 1170m.



Figure 1. Vue globale du glissement dans le centre de la bourgade Essfiré. Le mouvement entre les maisons est indiqué par la flèche.

## 2.2 Données géotechniques

Pour pouvoir identifier les différentes couches de sol constituant la région glissée, une analyse détaillée des forages réalisés s'avère être indispensable. Le profil du sol qui a glissé peut être représenté par 3 couches principales: une première couche en surface constituée d'une argile sableuse avec du gravier; une seconde couche en profondeur formée d'une argile marneuse; et enfin, une troisième couche constituant le substratum rocheux. Les propriétés géotechniques minimales et maximales des deux couches argileuses sont présentées dans le Tableau 1.

Tableau 1. Plage de valeurs pour les propriétés des couches d'argile sableuse et d'argile marneuse.

Propriété	Argile sableuse	Argile marneuse
Limite de liquidité (%)	30-52	21-67
Limite de plasticité (%)	12-24	7-35
Pourcentage de fines (%)	31-96	42-83
Pourcentage d'argile (%)	9-42	9-52

La couche superficielle du sol est formée principalement d'une argile sableuse d'épaisseur variable allant de 1 à 13m. Les essais de cisaillement direct réalisés permettent d'attribuer à cette couche d'argile sableuse les valeurs moyennes de cohésion et d'angle de frottement suivantes:  $c = 20 \text{ kN/m}^2$  et  $\phi = 22^\circ$ . Par ailleurs sa perméabilité mesurée est  $k = 8 \times 10^{-5} \text{ cm/s}$ . En dessous de la couche d'argile sableuse, se trouve une couche d'argile marneuse d'épaisseur variant entre 1.5 m et 8 m. Les essais de cisaillement direct réalisés sur cette argile marneuse donnent les valeurs moyennes de cohésion et d'angle de frottement suivantes:  $c = 46 \text{ kN/m}^2$  et  $\phi = 18.5^\circ$ . Une perméabilité représentative de cette couche d'argile marneuse est donnée par  $k = 7 \times 10^{-6} \text{ cm/s}$ . L'indice de plasticité de 22 % laisse supposer un taux et un potentiel de gonflement pour cette argile marneuse assez élevés. En cas de saturation de cette argile, elle pourrait gonfler considérablement, et sa cohésion risquerait de diminuer. Cette couche d'argile jouerait donc en cas de saturation, le rôle d'une couche savon. Sachant que pendant la période des forages, aucune nappe n'a été détectée, cela laisserait supposer que ces valeurs sont «à sec». Enfin, le substratum rocheux a été

trouvé à des profondeurs variant entre 5 m et 17m. Ce rocher est moyennement fracturé et fissuré, et ses fractures sont remplies d'argile. Sous l'effet des pluies et des infiltrations d'eau dans le sol, la saturation d'argile comblant les fissures entraînerait leur gonflement, ce qui exercerait une importante pression latérale dans le rocher, et augmenterait le risque de détachement du rocher de l'argile qui est en dessus.

## 2.3 Calcul et analyse de la stabilité

Une analyse du profil de sol obtenu laisserait présager les causes éventuelles qui ont déclenché le glissement. La couche d'argile marneuse, en cas de saturation pourrait très bien jouer le rôle de couche savon pour cette pente. Le glissement s'étant produit au mois de mars, la fonte des neiges a un rôle à jouer dans la saturation du sol. La nature gonflante de cette argile et son grand potentiel d'effondrement renforcent la théorie de la couche savon; ce qui nous laisse deviner une surface de rupture potentielle qui se trouverait au niveau de l'argile marneuse. Ceci valide l'existence d'un glissement plan dû à une couche saturée aux faibles propriétés mécaniques qui glisserait sur une discontinuité. Le problème serait donc a priori un problème d'eau. Ayant considéré la saturation de la couche d'argile marneuse comme étant la cause du glissement, il a été décidé de répartir le profil en 3 couches: une première couche d'argile sableuse (couche 1), une deuxième couche d'argile marneuse non saturée (couche 2) qui perd de ses propriétés mécaniques, et enfin une dernière couche qui représente le substratum rocheux (couche 3). L'analyse qui suit va considérer donc deux périodes, selon que la couche d'argile marneuse soit non saturée (période sèche) ou saturée (période humide), pour observer l'évolution du coefficient de sécurité entre ces deux périodes de l'année.

### 2.3.1 La période sèche

Cette période est la période d'été en principe, où il n'existe pas d'eau dans le sol. Pendant la période d'été, quand les forages ont été réalisés, l'argile marneuse n'a pas de partie saturée. Les propriétés mécaniques à considérer seront celles trouvées lors de la réalisation des essais sur des échantillons tirés à partir des forages exécutés. La surface de rupture a été prédéfinie à l'avance. Ainsi durant la période sèche, les coefficients de sécurité obtenus suivant quatre méthodes de calcul (Fellenius, Bishop, Janbu, Morgenstern-Price) sont de l'ordre de 3.

### 2.3.2 La période humide

Cette période est normalement caractérisée par les mois d'hiver et du début du printemps, où les fortes pluies, et la fonte des neiges ont un effet sur l'approvisionnement du sol en eau, et la saturation de ses couches. Les propriétés mécaniques à observer pour l'argile marneuse saturée en profondeur sont:  $\phi_u = 0$ , et une valeur réduite de la cohésion  $C_u$  sera considérée. La saturation de l'argile marneuse entraînant son gonflement et une diminution de ses propriétés cohésives, plusieurs itérations seront effectuées sur cette valeur en la diminuant constamment, afin de trouver la valeur critique de la cohésion qui entraînerait la rupture, et la chute du versant. La surface de rupture a été prédéfinie à l'avance, comme étant parallèle à la discontinuité entre le rocher et le sol. Une variation en diminution de la cohésion donne les valeurs de coefficients de sécurité montrés dans le Figure 2. Les cohésions qui induisent la rupture pour les différentes méthodes de calcul varient entre 23 et 29 kPa. Le coefficient de sécurité diminue presque linéairement avec la cohésion tel que montré dans la Figure 2. D'autre part, en considérant une cohésion de 26 kPa pour l'argile marneuse saturée, l'équilibre des forces pour une même tranche a été analysé, et l'évolution des forces sur cette tranche entre période sèche et période humide a été calculée. L'analyse des résultats montre une diminution moyenne de 33 % de la résistance au cisaillement à l'interface roche/sol dans les conditions humides.

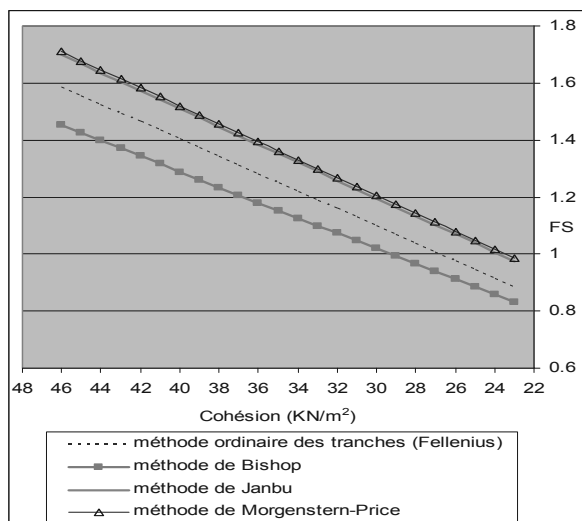


Figure 2. Evolution du coefficient de sécurité en fonction de la cohésion en période humide pour différentes méthodes de calcul.

### 3 CAS DU GLISSEMENT DE ANTELIAS

#### 3.1 Localisation et contexte

Le deuxième glissement de terrain analysé est survenu en Avril et Mai 2006 à Antélias, une ville sur le littoral au nord de Beyrouth, emportant une partie de la route Faouar Antélias-Raboueh (Figure 3 et Figure 4). La synthèse des levés géologiques, des sondages de reconnaissance et des constatations sur le site, permet de schématiser le site comme suit. Dans la partie supérieure du glissement (cote 130m) et le sommet de la fouille Mission La Vie (cote 95m), la surface du sol a une pente de 15° dans la direction Ouest-25°-Sud. Dans sa partie inférieure, la surface se poursuit avec une pente 15° dans la direction Ouest-45°-Sud pour arriver sur un plat artificiel ayant servi d'aire de stockage de déchets à la cote 86m. Dans la zone de glissement, le pendage ne peut être mesuré en surface car le rocher n'y affleure pas, mais des sondages indiquent que le toit du rocher a un pendage de 14° dans la direction Nord-78°-Ouest. Les relevés piézométriques montrent que la zone de glissement est imbibée d'eau; Elle est alimentée par un aquifère et par les égouts défailants le long de la route.



Figure 3. Route Faouar Antélias-Raboueh coupée par le glissement.



Figure 4. Le glissement de Antélias vers la fouille Mission la Vie. L'ouverture de la fouille serait un facteur déclenchant

#### 3.2 Données géotechniques

Dans la zone de glissement, on rencontre de haut en bas 3 couches, à savoir: D'abord, à la surface, une couche d'éboulis et de dépôts quaternaires alluviaux formée de silts argilo-sableux et caillouteux. Cette couche s'étend jusqu'à la surface et a une épaisseur moyenne de 7m. Ensuite, une couche d'argile silteuse fortement surconsolidée (schiste argileux ou shale), de couleur brun chocolat. Son épaisseur est variable entre 0,5 et 4m avec une moyenne de 1,5m. L'épaisseur semble croître en allant vers le Nord. Enfin, le substratum rocheux calcaire, altéré et fissuré. Cette roche est relativement perméable (10 à 20 lugeons) et sert de drain aux argiles qui la surmontent. En termes de caractéristiques mécaniques, la couche de surface a un angle de frottement  $\phi=25^\circ$  et une cohésion  $c=20$  kPa. Cette couche n'intéresse pas le glissement. La deuxième couche (schiste argileux) est responsable du glissement. En effet, dans leur état naturel ces schistes argileux sont très résistants, avec une cohésion de plusieurs centaines de kN/m<sup>2</sup>. Cependant, mis en contact prolongé avec l'eau, ils sont fortement absorbants et leurs propriétés mécaniques se dégradent fortement, jusqu'à provoquer un glissement à leur surface. Deux échantillons de ce schiste argileux ont été testés (essais CU) pour en déduire un angle de frottement  $\phi_{cu}$  et une cohésion  $C_{cu}$ . Les résultats sont les suivants: Essai 1 ( $I_c = \text{indice de consistance} = 0,803$ ;  $\phi_{cu} = 15^\circ$ ;  $C_{cu} = 44$  kPa); Essai 2 ( $I_c = \text{indice de consistance} = 0,725$ ;  $\phi_{cu} = 17^\circ$ ;  $C_{cu} = 46$  kPa). Les caractéristiques ci-dessus ne représentent pas en réalité les caractéristiques des schistes argileux lors du glissement et ce, pour deux raisons, à savoir: Premièrement,  $\phi_{cu}$  et  $C_{cu}$  représentent les caractéristiques mesurées à court terme; or quand les sols argileux sont soumis à des contraintes de cisaillement pendant un temps assez long, les particules le long de la ligne de glissement potentielle se réorientent progressivement (fluage); il en résulte un affaiblissement des caractéristiques du sol le long de cette ligne et elles tendent vers les "caractéristiques résiduelles" en grande déformation. Ces dernières sont estimées, aux deux tiers des caractéristiques mesurées ( $IP=17\%$ ), soit:  $\phi_{rcu} = 2/3 \phi_{cu}$  et  $C_{rcu} = 2/3 C_{cu}$ . Deuxièmement, si en plus de l'affaiblissement dû au fluage, on permet au schiste argileux fortement absorbant de se saturer d'eau et de gonfler (gonflement 5,6 et 7,8%), il s'affaiblit encore plus pour tendre vers des caractéristiques minimales  $\phi_{mecu}$  et  $C_{mecu}$  qui sont essentiellement fonction de l'indice de consistance  $I_c$ . Cependant, en surface de la couche de schiste argileux, directement en contact avec l'eau, l'indice de consistance  $I_c$  peut atteindre 0,5 formant ainsi une pellicule de quelques centimètres extrêmement affaiblie (couche savon). En appliquant les deux réductions (caractéristiques résiduelles et

caractéristiques minimales) aux deux échantillons, pour obtenir les caractéristiques des schistes argileux le long de la ligne de glissement, nous obtenons: pour l'essai 1 ( $\phi_{m\text{cu}} = 10^\circ$  et  $C_{m\text{cu}} = 2,8$  kPa) et pour l'essai 2 ( $\phi_{m\text{cu}} = 11^\circ$  et  $C_{m\text{cu}} = 4,8$  kPa).

Pour une couverture de 7m de sol, de densité 2, la résistance au cisaillement au toit de la couche de schiste argileux (shale) serait de 26,3 à 30,7 kPa. Ces valeurs se recoupent assez bien avec celles dans la littérature pour des argiles raides et shales à long terme, soit une résistance au cisaillement de 20 à 40 kPa.

### 3.3 Calcul et analyse de la stabilité

Une estimation des forces dues à la pression de l'eau dans les fissures montre que celles-ci sont très faibles comparées aux forces actives de gravité qui provoquent le glissement et aux forces passives de cohésion qui le freinent (de l'ordre de 4 à 5%). Ces faibles forces de pression d'eau n'ont d'importance pour le glissement que si les forces actives de gravité et les forces passives de cohésion s'équilibrent à peu de chose près, c'est-à-dire si les forces actives de gravité seules sont très légèrement inférieures aux forces passives de cohésion (période sèche stable) mais en y ajoutant les forces actives de poussée d'eau, elles deviennent légèrement supérieures aux forces de cohésion (fortes précipitations).

Le glissement plan se fait sur le toit des shales, qui dans la direction du glissement (Ouest 13° Sud) faisant un angle de 25° avec la ligne de plus grande pente, a une pente de 12°7. En effet, il ne peut se faire dans les couches de surface (éboulis et dépôts quaternaires) car l'angle de frottement  $\phi = 20^\circ$  est supérieur à la pente 12°7 et il ne peut se faire dans la masse des shales ou au contact shale-rocher car dans ces zones, le schiste argileux a un indice de consistance supérieur à 0,725 donc des caractéristiques résiduelles  $\phi_{cu} \geq 10^\circ$  et  $C_{cu} \geq 29,3$  kPa entraînant une résistance au glissement supérieure aux forces actives de gravité. Sur le toit des schistes argileux (couche savon), les contraintes de cisaillement dues au poids des sols de surface, sur un élément de pente 12°7, sont en moyenne de 30 kPa.

Pour équilibrer ces forces actives, le toit des schistes argileux devrait avoir en moyenne une résistance au cisaillement de 30 kPa, or les schistes argileux mis en présence d'eau de façon prolongée, atteignent leur état minimal, c'est-à-dire une résistance au cisaillement de 26,3 à 30,7 kPa. Ce calcul montre que les forces actives et passives s'équilibrent sensiblement (le coefficient de sécurité étant très voisin de 1) et que le glissement peut se produire. Si aux forces actives nous ajoutons les faibles forces dues aux pressions d'eau dans les fissures, il devient alors très probable que le glissement s'active comme il a été constaté après de fortes précipitations. En admettant une résistance moyenne au cisaillement égale 28,5 kPa, les coefficients de sécurité sont: Absence de précipitations,  $F = 28,5/30 = 0,95$ ; incertitude sur le glissement. Fortes précipitations: poussées de l'eau = 1,8 kPa par mètre carré de glissement:  $F = 28,5/31,8 = 0,9$ ; le glissement est presque certain. Le bilan des forces, présenté ci-dessus, néglige les forces de butée au pied du glissement comme cela est effectivement le cas après ouverture de la fouille Mission La Vie.

La question qui se pose naturellement est de savoir si l'ouverture de la fouille a contribué au glissement, sachant que le sol avait été très affaibli par les écoulements d'eaux usées. Pour y répondre nous avons évalué les forces de butée au pied du glissement, avant ouverture de la fouille. Pour une fouille de 7m de hauteur en moyenne et 30m de long environ, la force de butée est de 50000 kN, soit une contrainte moyenne tangentielle sur le plan de glissement (estime à  $10.000\text{m}^2$ ) de 4,75 kPa. En admettant une résistance moyenne au glissement de 28,5 kPa, l'ensemble des forces passives serait égal à  $28,5 + 4,75 = 33,25$  kPa, soit une sécurité  $F = 33,25/30 = 1,1$ ; ce qui signifie que le glissement n'aurait probablement pas eu lieu. Il semblerait donc que l'ouverture de la fouille Mission La Vie ait contribué au glissement bien que faiblement, la raison essentielle étant

l'affaiblissement du sol par les eaux usées. En définitive, nous pouvons affirmer que le glissement est dû à deux causes, l'une majeure et l'autre mineure, à savoir: la cause majeure est due à l'imbibition en surface, et pendant une période prolongée, des schistes argileux qui se situent à 7m sous la surface du sol. Cette imbibition est due aux pertes en continu des égouts vétustes le long de la route Fouar Antélias-Raboueh. Elle réduit très fortement la résistance du sol le ramenant dans un état à la limite du glissement (sécurité  $F = 1.1$ ). Quant à la cause mineure: le sol étant à la limite du glissement, l'ouverture de la fouille qui enlève la faible butée en pied du glissement (15% des forces résistantes) le fragilise encore plus, rendant le glissement possible à la moindre force active supplémentaire.

## 4 CONCLUSION

Les deux glissements sont plans: le sol glissé subit une translation, formant un bloc non ou peu fissuré. Le glissement se fait sur le toit de formations argileuses affaiblies par l'eau et sensiblement parallèles au toit du rocher. Pour le deuxième glissement, l'ouverture de la fouille en aval constitue un élément de déclenchement supplémentaire. L'effet néfaste des propriétés mécaniques affaiblies des argiles est expliqué.

## 5 REFERENCES

- Abramson L.W., Lee T.S., Sharma S. and Boyce G.M. 2002. *Slope stability and stabilization methods, Second edition*. John Wiley & Sons, USA.
- Benarroch A., Hernandez M.A. and Manzanilla R. 2011. Evaluation of sensitivity of the geotechnical parameters in the analysis of slope stability, *Proceedings of the 64<sup>th</sup> Canadian Geotechnical Conference*, Toronto, Ontario, Canada, Volume 3: 2633-2639.
- Carrara A., Cardinali M., Guzzetti F. and Reichenbach P. 1995. *GIS-based techniques for mapping landslide hazard*. Edited by A. Carrara and F. Guzzetti. Kluwer Academic Publishers, Dordrecht, Netherlands.
- Cruden D.M and Couture R. 2011. The working classification of landslides: material matters, *Proceedings of the 64<sup>th</sup> Canadian Geotechnical Conference*, Toronto, Ontario, Canada, Volume 3: 2540-2546.
- Dikau R., Brunsden D., Schrott L. and Ibsen M.L. 1996. *Landslide Recognition: Identification, Movement and Causes*. John Wiley & Sons, England.
- Fletcher L., Hungr O. and Evans S.G. 2002. Contrasting failure behavior of two large landslides in clay and silt. *Canadian Geotechnical Journal*, 39(1), 46-62.
- Popescu M.E. 2002. Landslide causal factors and landslide remedial options. *Keynote Lecture. Proceedings of the third international conference on landslides, slope stability and safety of infrastructures*, Singapore: 61-81.
- Rahhal M.E., Nini R. and Favre J.L. 2003. Analysis of factors causing slope instabilities, *Proceedings of the 56<sup>th</sup> Canadian Geotechnical Conference*, Winnipeg, Manitoba, Canada, Volume 2: 368-375.
- Rahhal M.E., Nini R. and Favre J.L. 2004. Une Approche Simple de la Cartographie du Risque du Glissement de Terrains. *Proceedings of the 57<sup>th</sup> Canadian Geotechnical Conference*, Québec, Canada, Session 5C: 13-18.
- Rahhal M.E. and Abou Rached, Z. 2005. Reliability Analysis of Slope Stability Involving Generalized Slip Surfaces. *Proceedings, 9<sup>th</sup> International Conference on Structural Safety and Reliability*, ASCE Geo-Institute Risk Assessment and Management Committee, Università di Roma La Sapienza, Rome, ITALY, Millpress 2005 Eds, pages: 985-992.
- Rahhal, M.E., 2006. Geotechnical Understanding of Probabilistic Landslides Appraisal Approaches. *Proceedings 5<sup>th</sup> International Conference on Computational Stochastic Mechanics*, Rhodes, GREECE, Millpress 2007 Eds, pages: 559-568.

# A smart adaptive multivariable search algorithm applied to slope stability in locating the global optima

Un algorithme adaptatif multivariable de recherche d'optimum global appliqué à la stabilité des pentes

Saha A.

Irrigation & Waterways Department, Govt. of West Bengal, Kolkata, India

**ABSTRACT:** The paper addresses the topic of single objective optimisation of a three dimensional real-world problem and introduces a hybrid technique of an iterative random population search within a geometrically shrinking hypercube and a sort of simplified Design of Experiments (DOE). A 'population' of design variables are generated and augmented with the multivariable objective function, and the design variables pertaining to the local optima are perturbed by a factor ( $\Delta k$ ) sequentially in both positive and negative directions to create  $2(2^N-1)$  offspring in the neighbourhood of local optima to hopefully produce some better progeny. The 'fittest' perturbed offspring decides a new contracted search interval for the consecutive generation according to a geometric decay rule commensurate with the generation number. A 'simple hill-climbing' strategy in Artificial Intelligence context is followed subsequently and the loop is continued to produce fresh generations of refined offspring till the outcome converges to the global optimum. The method is applied in searching the critical slip-surface of a vulnerable soil-slope and it was revealed that the optimum found by this method is superior to that found by traditional and non-traditional (genetic algorithms) optimization techniques while using much less computational resources.

**RÉSUMÉ:** L'article traite de l'optimisation à une seule fonction objectif pour un problème réel tridimensionnel et introduit une technique hybride de recherche itérative à partir d'une population aléatoire au sein d'un hyper cube de taille décroissante, selon une méthode simplifiée de plan d'expérience. Une "population" de variables de design est générée, et étendue grâce à la fonction objectif multi variable. Les variables de design correspondant à l'optimum local sont alors perturbées par un facteur ( $\Delta k$ ) de manière séquentielle dans les directions à la fois positives et négatives pour créer  $2(2^N-1)$  individus de génération suivante dans le voisinage de cet optimum, dans l'espoir de produire une meilleure génération. La génération perturbée la plus satisfaisante selon l'objectif définit un nouvel intervalle de recherche, de taille réduite pour la génération suivante, selon une règle de décroissance géométrique en rapport avec le rang de génération. Une stratégie simple de plus grande pente dans un contexte d'intelligence artificielle est suivie pas à pas et une boucle produit de nouvelles générations améliorées jusqu'à ce que le résultat converge vers l'optimum global, indépendamment de la population initiale. La méthode est appliquée à la recherche de la surface de glissement critique d'un sol en pente vulnérable. Il a été constaté que l'optimum trouvé par cette méthode est plus critique que celui donné par les méthodes traditionnelles et non traditionnelles (algorithmes génétiques) et de plus, cette méthode est moins exigeante en terme de capacité de calcul.

**KEYWORDS:** hybrid technique, random population search, optimization algorithm, slope stability.

## 1 INTRODUCTION

The stability of slopes has received wide attention due to its practical importance in the design of excavations, embankments, and dams. There are numerous methods available for stability analysis and the majority of analyses performed in practice still use traditional limit equilibrium approaches. By the advent of computers, the use of optimization techniques in locating the critical slip surface has been a major topic for the researchers. Duncan (1996) presented a comprehensive review of both limit equilibrium and finite-element analysis of slopes. Malkawi et al (2001) developed an effective approach for locating the critical circular slip surface based on Monte-Carlo techniques. Non-traditional optimization algorithms simulating processes drawn from nature like genetic algorithm (GA) and simulated annealing (SA) have proved to be efficient in locating the global optima. GA mimics the principles of Darwin's natural selection and survival of the fittest rule, in which an optimum solution evolves through a series of generations of population and has the super ability of global convergence and parallel searching. SA is the stochastic evolution of thermodynamic state of slow cooling of molten metals to achieve a crystalline absolute minimum energy state, where a perpetual decreasing sequence of temperature controls the reproduction rate, which is very efficient in neighborhood search. Li et al (2009), Author (2011) proposed hybrid global search procedures combining GA with SA. While summarizing

the state of the art techniques for evolutionary algorithm (EA) parameter tuning, T. Beielstein (2003) exclaims that "*real world optimization problems allow only a few preliminary experiments to find good EA settings. As the commonly used 'one factor at a time approach' is considered as inefficient and ineffective, we recommend DOE methods*". The present paper introduces a new Soft Computing algorithm- a hybrid technique of an iterative *random population based search embedded with simulated annealing (SA) features within a geometrically shrinking hypercube coupled with simplified Design of Experiments (DOE)*.

## 2 APMA-A NOVEL OPTIMIZING TOOL

A smart adaptive population based multivariable function optimization algorithm proposed herein, and referred to as APMA hereinafter, is a simple yet robust optimization procedure basically of heuristic nature. Before plunging into details, a fitness function is defined to maintain uniformity over various problem domains and to map the 'goodness' of the objective function (here FOS) value to a fitness value. The fitness of an individual is calculated as the worst objective function objective function (FOS) value of the whole population subtracted from the individual's objective function value. Hence, this fitness function is computed for the individual as  $F_i = \max. \{f(x)_j | j = 1, 2, \dots, n\} - f(x)_i$ . Where; 'n' is the population



size.  $f(x)_i$  is the objective function (here FOS of  $i^{\text{th}}$  individual). The technique is known as windowing as it eliminates the worst individual (FOS)-the probability comes to zero, and stimulates the better ones.

Within the random generated set of population (n) of design multivariable (N-dimensions or feature vectors),  $f(x_i, y_i, z_i, \dots, w_i)$  within wide deterministic search boundaries for each variable, and subsequent objective function evaluations, the minimum is located. With a view to exploit the search space neighbourhood

the N-multivariable set  $f(x_{i_{\min}}, y_{i_{\min}}, z_{i_{\min}}, \dots, w_{i_{\min}})$  creating this minimum is perturbed by a factor ( $\Delta k$ ) sequentially in both directions (positive as well as negative directions)  $f(x_{i_{\min}} \pm \Delta k), (y_{i_{\min}} \pm \Delta k), (z_{i_{\min}} \pm \Delta k), \dots, (w_{i_{\min}} \pm \Delta k))$  to

$$2 \sum_{i=1}^{i=N} {}^N C_i = 2 \sum_{i=1}^{i=N} \frac{N!}{(i!)(N-i)!} = 2(2^N - 1)$$

create offspring  $\{ \text{Where, } N! = N.(N-1).(N-2) \dots \dots 3.2.1 \}$  in the neighbourhood of the local minimum in an attempt to generate some superior offspring. Hence, for a three variable function (like slope-stability problem)  $f(x_i, y_i, z_i)$ , a population (of n individuals) are randomly generated and their local minimum  $f(x_{i_{\min}}, y_{i_{\min}}, z_{i_{\min}})$  located for the first generation.

Thereafter, this local minimum is perturbed initially in the positive direction and function evaluations are made at  $f(x_{i_{\min}} + \Delta k), (y_{i_{\min}}, z_{i_{\min}}); f(x_{i_{\min}}, (y_{i_{\min}} + \Delta k), z_{i_{\min}}); f(x_{i_{\min}}, y_{i_{\min}}, (z_{i_{\min}} + \Delta k)); f(x_{i_{\min}} + \Delta k), (y_{i_{\min}} + \Delta k), z_{i_{\min}}); f(x_{i_{\min}}, (y_{i_{\min}} + \Delta k), (z_{i_{\min}} + \Delta k)); f(x_{i_{\min}} + \Delta k), (y_{i_{\min}} + \Delta k), (z_{i_{\min}} + \Delta k)); f(x_{i_{\min}} + \Delta k), (y_{i_{\min}} + \Delta k), (z_{i_{\min}} + \Delta k));$

and finally in the negative direction, by changing the sign of  $\Delta k$  in above expressions. Hence, apart from objective function evaluations of all n number of population individuals in each generation, the algorithm requires further function evaluations at  $2(2^N-1)$  points around the local minimum of each generation. Now as fresh generations are produced, often different selection pressures of reproduction are needed at successive generations. Hence, the choice of a value of the sequential perturbing factor ( $\Delta k$ ) becomes of paramount importance, in a sense that if it is too large it will be adequate in the first phase of the search but not in the final phase and vice versa if it is too small. Further, this  $\Delta k$  is likely to be different for different design variables commensurate with their individual feasible search intervals. As such, the situation calls for some sort of normalization of  $\Delta k$  in initial phase for application in various problem domains, and further it should possess the flexibility of shrinking itself automatically in successive generations according some decay rule in compliance with the selection pressure criteria. In this study, this perturbing parameter is defined as  $\Delta k = \kappa.(x_i^U - x_i^L) \Delta_i$ , where,  $\kappa$  is a problem specific constant; to be fixed after some initial trials.  $x_i^U$  and  $x_i^L$  are the upper and lower bounds of a design variable and  $\Delta_i [=G_i(1-r)^{(G_i-1)}]$  is the size reduction parameter, where,  $G_i$  is the generation number and 'r' a constant less than unity. As the number of design variables (N-dimensions) increases, more trials are needed for fixing the value of  $\kappa$ . The 'fittest' perturbed offspring

$f(x_{i_{\min}}^p, y_{i_{\min}}^p, z_{i_{\min}}^p, \dots, w_{i_{\min}}^p)$  of the  $i^{\text{th}}$  generation decides a new contracted search interval for the consecutive generation, wherein the value each design variable corresponding to the fittest perturbed offspring is assigned the central value of the interval. The two new extreme bounds of the fresh search interval is the product of the positive and negative value of this central value and the size reduction parameter,  $\Delta_i$ . Thus, if the local minimum objective function of the previous generation be

$$f(x_{(i-1)_{\min}}^p, y_{(i-1)_{\min}}^p, z_{(i-1)_{\min}}^p, \dots, w_{(i-1)_{\min}}^p), \text{ the current (that is, } i^{\text{th}} \text{ search interval becomes, } \left[ \left\{ x_{(i-1)_{\min}}^p \pm G_i(1-r)^{G_i-1} x_{(i-1)_{\min}}^p \right\}, \left\{ y_{(i-1)_{\min}}^p \pm G_i(1-r)^{G_i-1} y_{(i-1)_{\min}}^p \right\}, \left\{ z_{(i-1)_{\min}}^p \pm G_i(1-r)^{G_i-1} z_{(i-1)_{\min}}^p \right\}, \dots, \left\{ w_{(i-1)_{\min}}^p \pm G_i(1-r)^{G_i-1} w_{(i-1)_{\min}}^p \right\} \right]$$

A new population of random variables (of size n) is again generated from scratch within the new reduced stochastic search interval and again objective function evaluations are made for each set of new random variables so generated. The generated set replaces the initial one and the loop is continued to produce fresh generations of refined offsprings till the outcome converges to the global optima.

### 2.1 APMA efficacy checked with benchmark test functions

With a view to examine the performance of the algorithm, APMA is initially applied to some benchmark unconstrained global optimization test functions like Goldstein-Price's function, Hartman's function, Beale's function, Perm's function, Booth's function, Bohachevsky's function (A. Hedar), Six hump camel's back function and Xin-She-Yang's function (X.-S. Yang, 2010) and promising results were obtained. APMA successfully captured all the four optima of the multimodal Himmelblau function (Deb K., 2000):  $f(x_1, x_2) = (x_1^2 + x_2 - 11)^2 + (x_1 + x_2^2 - 7)^2$ , [the optima being (-2.805, 3.131); (-3.779, -3.283); (3.584, -1.848); (3,2)] in each and every simulation run while finally converging to the global minimum at (3,2) [The simulation runs has been done with  $\kappa=80-90\%$  &  $r=0.10$ ]. The method may be regarded as a basic thrust of 'Artificial Intelligence', that is to get the computer to perform tasks fast and automatically. The method is independent of the initial vector and as no specific search direction is used in this method, this random search method is expected to work efficiently in many classes of problems.

### 3 THE PROBLEM DEFINITION

A problem cited by Spencer (1967) is chosen for analysis. The problem parameters, soil-data and search boundaries are depicted in Fig.1. In the search process, the three independent design variables are the abscissa (CX) and ordinate (CY) of the circle centre and the depth factor ( $N_d$ ) of the circular failure surface. The base width (B) and height (H) of slope are assumed as 60 meters and 30 meters respectively.

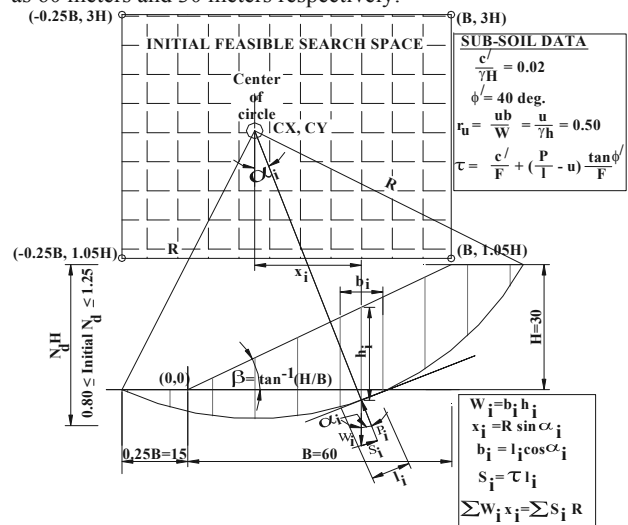


Fig.1. Initial variable bounds of the tri-variable & soil data used in search for critical circle-The Slope-Stability problem definition.

The radius  $R=f\{CX, CY, N_dH\}$ . Based on a few trials, the feasible bounds of the design variables, has been identified as: -

$0.25B \leq CX \leq B$ ,  $1.05H \leq CY \leq 3H$ ,  $0.80 \leq N_d \leq 1.25$ . In the widely used limit equilibrium methods of slope analysis, the potential slip surface and the sliding mass are divided into segments or slices. The FOS, (F) is related to the total height of the slope H, the effective subsoil parameters  $c'$ ,  $\phi'$  and  $\gamma$ , the pore pressure ratio  $r_u (= u/\gamma h)$ , the individual slices of width  $b_i$ , height  $h_i$  and  $\alpha_i$ -the inclination of slice on the failure arc with the horizontal, by the following equation (Bishop, 1955):

$$F = \frac{\sum_{i=1}^n \left[ \left\{ \left( \frac{c'}{\gamma H} \right) \left( \frac{b_i}{H} \right) + \left( \frac{b_i}{H} \right) \left( \frac{h_i}{H} \right) (1 - r_u) \tan \phi' \right\} \frac{\sec \alpha_i}{1 + \tan \alpha_i \tan \phi'} \right]}{\sum_{i=1}^n \left( \frac{b_i}{H} \right) \left( \frac{h_i}{H} \right) \sin \alpha_i}$$

A modest population size (n) of 20 is adopted. The design variables of the fittest population genre (local FOS<sub>min</sub>) is perturbed sequentially by a factor  $\Delta k$  in both directions, resulting in  $2(2^3-1)=14$  ‘offsprings’. **Initial value of  $\Delta k$  is fixed at 5% of the search interval** for each variable after some initial trials. Hence,  $\Delta k$  works out to be  $3.75 [= .05x\{(60.00)-(-15.00)\}]$  for  $x_i$ -the abscissa of the slip-circle centre,  $3.225 [= .05x(94.50-30.00)]$  for  $y_i$ -the ordinate of the slip-circle centre and  $0.0225 [= .05x(1.25-0.80)]$  for  $z_i$ -the depth factor of the slide (refer Fig.2). **This  $\Delta k$  is further shrunk in successive generations by multiplying it with the size reduction parameter,  $\Delta_i = G_i(1-r)^{(G_i-1)}$** . Again, the objective function evaluations are made for the perturbed individuals and the minimum of these 14 points is located. This local minimum point (offspring) acts as the ‘mother’ of the next generation, and the corresponding design variables acts as the mean of the search space of next generation.

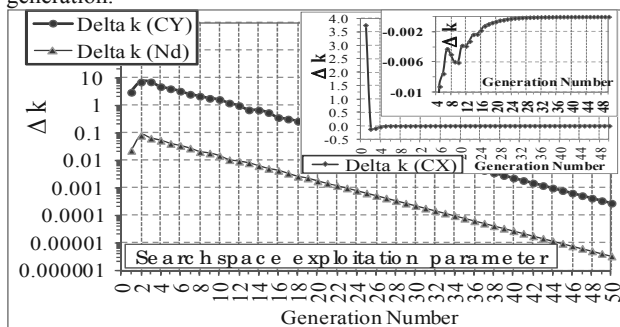


Fig.2. Search space exploitation in line with Design of Experiments.

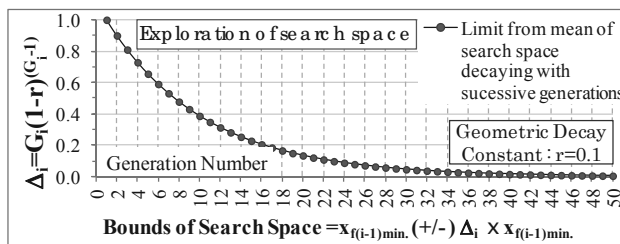


Fig.3. Search space exploration analogous to simulated annealing schedule by contraction of search boundary in successive generations.

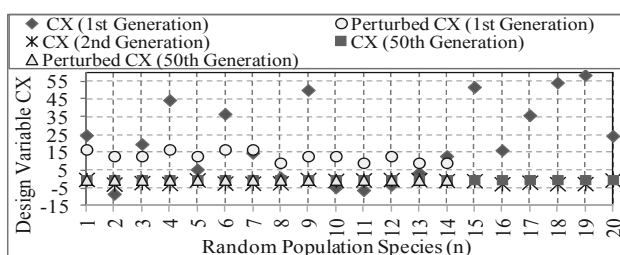


Fig.4. Initial deterministic search space turns heuristic at 2<sup>nd</sup> Generation—a quick shift towards the best part of search space.

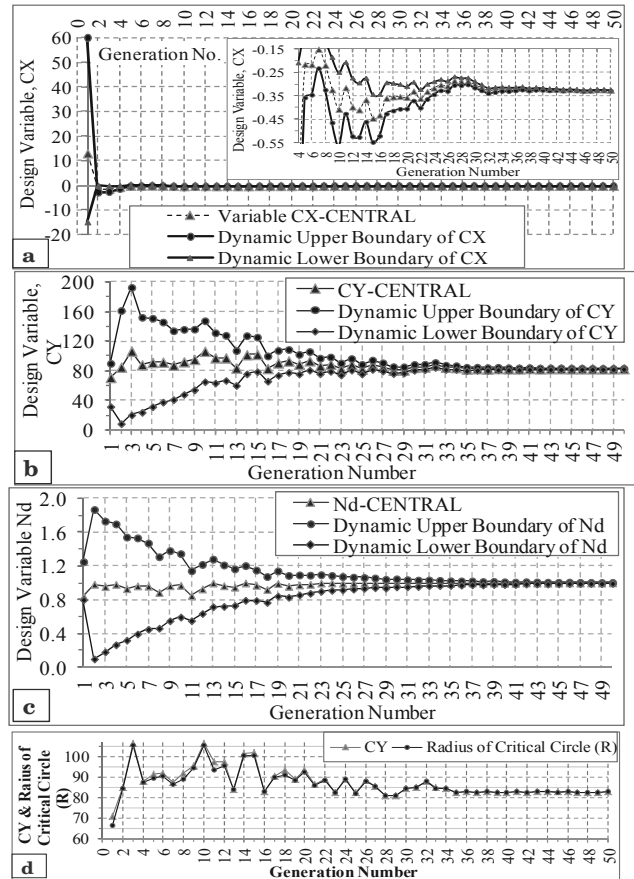


Fig.5. Robust movement of variable bounds along with the central value of tri-variables (CX, CY,  $N_d$ ) shown in (a), (b), (c) respectively. In (a), a further close-up view from 2<sup>nd</sup> generation is shown. From (d) it emerges that  $R \approx CY$  for critical circle.

#### 4 COMPUTER SIMULATION & GRAPHICAL DEPICTION OF THE SMART ADAPTIVE PROCESS

Fig.3 shows how the limit of search boundary shrinks towards the mean (that is, the central value or the best point of the preceding generation) of the search space. Fig.4 shows a typical result of 1<sup>st</sup>, 2<sup>nd</sup> and 50<sup>th</sup> randomly generated population along-with the perturbed population set of 1<sup>st</sup> and 50<sup>th</sup> generations. **It may be noted that initial wide deterministic search space turns heuristic at 2<sup>nd</sup> generation with a quick shift towards the best part of search space.** Fig.5(a) to (c) depict the robust movement of variable bounds along with the central value of the three design variables (CX, CY &  $N_d$ ), illustrating the generate-and-test heuristic search technique that exploit domain-specific knowledge. It emerged that whatever be the initial search bounds specified deterministically, the algorithm adjusts itself to move to the best part of search space in the immediate 2<sup>nd</sup> generation. It is revealed that **the bounds of CX are drastically reduced (Fig.5a), and that of CY &  $N_d$  are radically expanded (Fig.5b&c) in immediate 2<sup>nd</sup> generation**, and thereafter the bounds move steadily with successive generations that are guided by the mean of the search space, while maintaining a heuristic character. It emerged that the value of radius of critical circle (R) almost merges with the ordinate (CY) of the critical slip circle (Fig.5d). Fig.6 depicts the change in average fitness, standard deviation and variance of fitness function of population with successive generations. The variance of fitness decreases steadily with increasing generations maintaining its randomness. Fig.7 shows the maximum fitness of each generation vs. search space size reduction parameter in log-log scale. Fig.8 portrays the stochastic movement of Min. FOS in successive generations to converge to global optimum, wherein results of five simulation runs are superimposed. The inherent

stochastic nature of the algorithm showing value convergence with increasing generations is reflected in all the results.

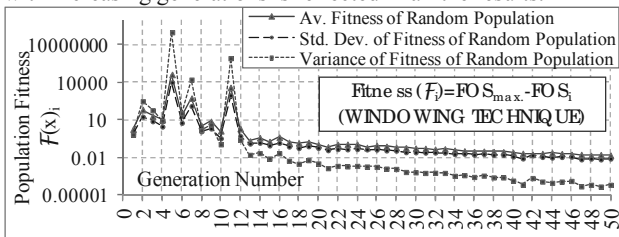


Fig.6. Change in average fitness, standard deviation & variance of population fitness function with successive generations.

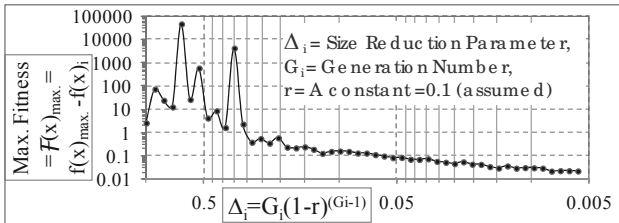


Fig.7. Max<sup>m</sup> fitness of each gen. vs. search space size red. parameter.

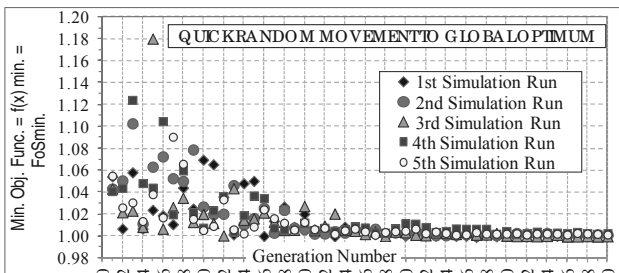


Fig.8. Stochastic movement of Min. FOS (obj. func.) in successive gens. to converge to global optimum (Results of five simulation runs).

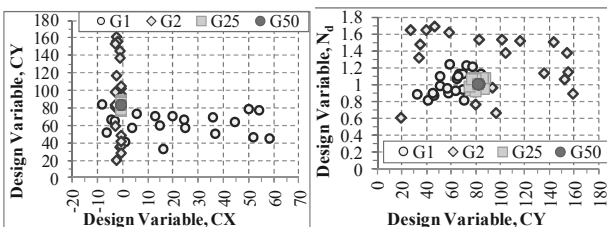


Fig.9. CX vs. CY & CY vs. N<sub>d</sub>: The artificial intelligent character depiction. Fast random movement of candidate solutions to best part of the search space with increasing generations.

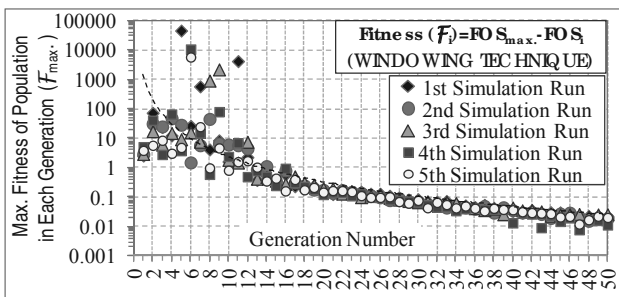


Fig.10. Stochastic decrease of maximum fitness in successive generations (Results of five simulation runs superimposed).

Fig.9 depicts the artificial intelligent character of the algorithm wherein a fast random movement of candidate solutions with increasing generations to best part of the search space is noticed. Fig.10 shows the stochastic decrease of maximum fitness in successive generations in 5 simulation runs. Fig.-11 gives the validation of results against other studies reported in literature.

## 5 CONCLUSIONS

A global population based search procedure (APMA) is developed and successfully applied to slope-stability problem. It does not require problem specific knowledge in searching the critical slip-surface of a soil-slope and is a heuristic technique based on the ‘generate-and-test’ strategy. Diverse aspects are presented to demonstrate its efficiency and robustness. The spectrum of application area of APMA is widespread as it is a direct search method where no specific search direction is used and multivariable functions, both continuous and discontinuous can be handled. Function value evaluations at discrete points only enable it to handle non-differentiable functions at ease. The beauty of the process is that, it handles a number of designs in each simulation run. The result of some simulation runs revealed minimum factor of safety obtained by APMA is less than that found by directed grid search, variational method, GA and GA-SA hybrid.

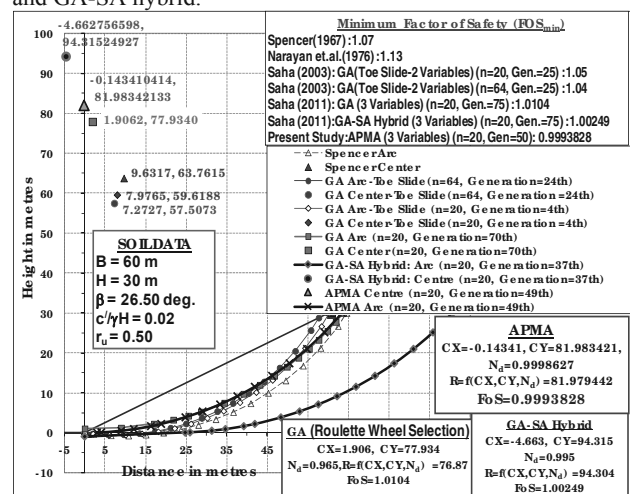


Fig.11. Comparison of results obtained by various methods.

## 6 REFERENCES

A.Hedar. Test function web pages, [http://www-optima.amp.i.kyoto-u.ac.jp/member/student/hedar/Hedar\\_files/TestGO\\_files/Page364.htm](http://www-optima.amp.i.kyoto-u.ac.jp/member/student/hedar/Hedar_files/TestGO_files/Page364.htm)  
 Bishop A.W. 1955. “The use of slip circles in the stability analysis of slopes”, *Geotechnique*. Vol.-5, 7-17.  
 Deb Kalyanmoy 2000. *Optimization for Engineering Design, Algorithms and Examples*, Prentice Hall, New Delhi, India.  
 Duncan J.M. 1996. State of the art: limit equilibrium and finite-element analysis of slopes, *Journal of Geotec. Eng., ASCE*, 122(7), 577-596.  
 Li K.S., Z. Shangguan, H. Duan, Y Liu, M. Luan 2009. Searching for critical failure surface in slope stability analysis by using hybrid genetic algorithm, *Geomechanics and Engg.*, 1(1), 85-96.  
 Malkawi A.H., Hassan W.F., and Sarma S.K. 2001. Global search method for locating general slip surface using Monte Carlo techniques, *Journ. of Geotech. & Geoenv. Engg.*, 127(8), 688-398.  
 Narayan C.G.P., Bhatkar V.P. & Ramamurthy T. 1976. Slope stability analysis by variational method, *Indian Geotech. J.*, Vol.- 6, 68-90.  
 Saha Abhijit 2003. Genetic algorithm based search in slope stability analysis, *Proc. of 12<sup>th</sup> Asian Regional Conference in Soil Mech. & Geotechnical Engg.*, Singapore, Vol.-I, 981-984.  
 Saha Abhijit 2011. Genetic algorithm based search coupled with Boltzmann selection in locating the critical surface in slope stability, *Proc. of 14<sup>th</sup> Asian Regional Conference in Soil Mech. & Geotechnical Engg.*, Hong Kong, Paper No.-115.  
 T. Beielstein 2003. *Tuning evolutionary algorithms/Overview & Comprehensive Introduction*. Tech. Report 148/03, Universität Dortmund, Germany.  
 Spencer E. 1967. *A method of analysis of the stability of embankments assuming parallel inter-slice forces*, *Geotechnique*, London, Vol.- 17, 11-26.  
 X.-S. Yang 2010. *Test problems in optimization, in: Engineering Optimization: An Introduction with Metaheuristic Applications (Eds Xin-She Yang)*, John Wiley & Sons.

# Soil slope stability of hydropower reservoirs - from geological site investigation to design of mitigation measures

## La stabilité des talus de réservoirs hydroélectriques - de l'investigation géologique du site à la conception de mesures d'atténuation

Saurer E., Prager C., Marcher T.  
*ILF Consulting Engineers, Rum/Innsbruck, Austria*

**ABSTRACT:** Many reservoir slopes are affected by different types of instabilities during the first impoundment, due to reservoir level fluctuations and due to earthquakes. These potential failure processes are caused by complex hydro-mechanically coupled processes, which in most cases cannot be fully assessed during the design stage due to a limited knowledge of the soil behaviour and properties. Thus, for the site selection and the design of power storage plants, especially for the risk assessment and mitigation of potentially unstable soil slopes, a systematic methodology for the selection of the appropriate stability measures is presented. Based on case studies from both engineering projects and literature, a methodological approach and a decision matrix for the design of appropriate mitigation measures depending on the failure mode and size of the potentially instable slope are proposed.

**RÉSUMÉ :** Un grand nombre de talus à proximité des réservoirs sont affectés par différents types d'instabilités en raison des fluctuations des niveaux de réservoir et en raison de tremblements de terre. Ces procès potentiels de défaillance sont causés par des transformations complexes hydromécaniques, qui dans la plupart des cas, ne peuvent être entièrement évalués au cours de la phase de conception en raison d'une connaissance limitée sur le comportement et des propriétés des sols. Ainsi, pour la sélection des sites et la conception des installations de stockage d'énergie, il est essentiel de tenir compte des expériences antérieures et d'appliquer ces connaissances à la conception de nouvelles installations pour créer une stratégie d'évaluation des risques et d'atténuation. Ici une méthode pour la sélection des mesures de la stabilité appropriées en fonction du mode de défaillance est fournie. Basé sur des études de projets et de la littérature une méthodologie systématique et une matrice de décision pour la conception de mesures d'atténuation appropriées en fonction du mode de défaillance et la taille de la pente potentiellement instables sont proposées.

**KEYWORDS:** soil slope stabilization, mitigation measures, decision matrix

## 1 INTRODUCTION AND FRAMEWORK

### 1.1 *Reservoir slope instabilities (causes, triggers)*

Concerning site selection studies for a water storage reservoir, particular focus has to be placed on the assessment of terrain stability, especially in the dam area but also along the reservoir slopes.

In general, failures are related to changes of stability parameters of natural slopes or artificial cuts. Related to reservoirs, the disturbance may be caused by water level changes (due to first impoundment and/or recurring water level fluctuations during operation) which may cause catastrophic (uncontrollable) slope failures of all sizes. According to Riemer 1995, the causes and triggers of soil displacements include, e.g.

- change of consistency due to saturation (fine soils)
- change of effective stresses (pore pressure)
- groundwater flow (steady and transient flow)
- external erosion, e.g. caused by waves
- internal erosion (suffosion, subrosion)

At the design stage of a reservoir, these processes have to be considered in order to assess the slope stability. Commonly, slope failures are only treated when they affect the serviceability (storage volume loss, operational restrictions, land use along shoreline, water quality) or failure of a reservoir and its surroundings.

### 1.2 *Slope stability assessment and risk management*

Extensive literature reviews of landslides and reservoirs as well as detailed case studies have been carried out by many authors (e.g. in Riemer 1995). In particular deep-seated rock slides have been monitored and investigated intensively, and monitoring

results have been reported over the last decades (Leobacher and Liegler 1998, Tentschert 1998, Jäckli 1996, Watson et al. 2006, Barla et al. 2010).

Moreover, process based investigation methods and monitoring measures have been developed (Keusen 1998, Zangerl et al. 1999, Leobacher and Blauhut 2010).

The issue of slope stability, in particular for dam safety, during rapid drawdown and earthquake loading and has been studied widely (e.g. ICOLD 1980, Casagrande 1937, Sherard 1963, Alonso and Pinyol 2009). Besides the stability assessment, (e.g. according to Casagrande 1937), it is expected that engineers are able to make a statement not only on stability but also on the consequences of potential mass movements.

Following the stability assessment, a risk management plan may be produced. Whereas several research projects on landslide risk management have been undertaken (e.g. ICG 2009 and 2011), only few data concerning slope stability in the vicinity of water reservoirs are publically available.

Here, an overview of a systematic approach to assess the slope stability before and after reservoir impoundment with particular consideration of earthquake and rapid drawdown conditions and a proposal for a customized toolbox for slope stabilization in cohesive and granular soils are provided.

## 2 SLOPE STABILITY ASSESSMENT

A possible flowchart for the slope stability assessment is provided in Figure 1. The individual steps are described in the subchapters below.

### 2.1 Site selection

The site selection process for hydropower reservoirs is driven by the need to optimise decision criteria which are initially mainly of an economic nature.

In the best case, several sites are shortlisted based on economic factors followed by comparisons of options and more detailed feasibility studies including detailed geological and geotechnical investigations and designs.

### 2.2 Geological and hydrogeological model

A geological and hydrogeological model may be developed using the following investigation techniques (selection):

- geological site mapping, incl. structural geological surveys;
- remote sensing and terrain analyses (e.g. optical images, LiDAR, DEMs);
- hydrogeological field surveys (mapping of springs, surface flow systems incl. discharge measurements, recharge and infiltration characteristics);
- groundwater measurements, tests and monitoring (spring parameters e.g. EC, T and discharge, stage-discharge stream gauges, groundwater elevation gauges, piezometers/hydraulic heads, tracer tests, hydrochemical and isotopic analyses, etc.);
- core drillings with in-situ measurements and tests (e.g. core SPTs, geophysical borehole logs, geotechnical and hydraulic tests, e.g. packer tests, water pressure tests, dilatometer tests) and (un)disturbed rock/soil sampling;
- geophysical surveys (surface and borehole seismics);
- slope monitoring (geodetic surveys, inclinometer measurements and others).

Based on these data, a comprehensive rock mass model may be established, which in turn constitutes the basis for the subsequent steps (see Figure 1).

### 2.3 Geotechnical model and assessment of actual slope stability

Based on the geological model (incl. results from lab and field tests), characteristic soil parameters and a geotechnical model are defined. “Characteristic” soil properties may be i) obtained from field and lab tests and/or ii) back calculated from the geological model, (taking into account the soil strata and slope inclinations). In the latter case an assumption on earthquake loads which have already been acting on the slope has to be made and included in the back analyses. When using back calculations it is assumed that the slope is in limit equilibrium. Ideally both approaches should be combined.

These calculations yield values for the assessment of the actual slope stability. However, these assessments are commonly based on geological and geotechnical models of limited accuracy due to a limited number of available results from laboratory and field tests. Therefore, the “real” soil parameters are to be verified at the latest at the stage of the first impoundment of a reservoir.

### 2.4 Assessment of slope stability under changed boundary conditions

The boundary conditions of reservoir slopes may change drastically due to impoundment and rapid drawdown

Therefore the back calculated geotechnical slope model (see above) has to be adapted to these changed boundary conditions and the slope stability has to be reassessed. From this analysis four different scenarios may be obtained (see Figure 1):

In the best case, the slope stability is not affected by the new boundary conditions at all. This is the case when the failure plane is located entirely above the shoreline.

The remaining three cases may be assessed according to i) the size and shape of the potential landslide mass and ii) the acceptance of the consequences of a failure.

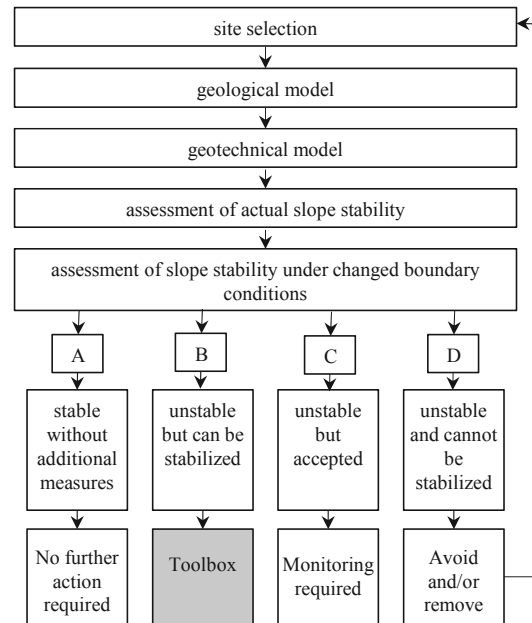


Figure 1: Flow chart for the assessment of slope stability (explanations, see text).

The decision whether a potential slope failure is acceptable depends on various criteria: If the slope stability deteriorates, proof has to be provided that the safety of the dam and its surroundings are not affected. This means that the size and the velocity of potential landslides do not cause critical tsunamis overtopping the dam.

For this proof and the risk assessment, the slope deformation behaviour has to be evaluated according to the types shown in Figure 2. While deformation types 1 and 2 are commonly unproblematic and type 3 requires a sound risk assessment, the stick-slip behaviour of type 4 landslides is much more difficult to predict. Such deformation behaviour requires intensive monitoring and a fundamental knowledge of the soil properties (Barla et al. 2010, Leobacher and Liegler 1998, Zangerl et al. 1999).

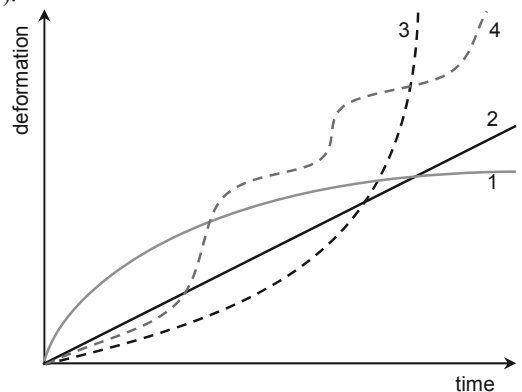


Figure 2: slope kinematics (temporal deformation types): (1) decreasing slope velocity; (2) constant velocity; (3) accelerating and failing slope; (4) episodic accelerated slope (after Keusen 1998)

Planning any mitigation measures depends on the geometry and depth of landslides. Concerning this, the classification of landslide thickness (according to BAFU 2009 and ICG 2011) is shown in Table 1.

Table 1: Landslide categories as a function of the depth of movement (acc. to BAFU, 2009 and ICG 2011).

Category	Depth of movement [m]	
	BAFU 2009	ICG 2011

Superficial	0 - 2	< 0.5
Shallow		0.5 - 3
Medium	2 - 10	3 - 8
Deep	> 10	8 - 15
Very deep	> 30	> 15

Depending on the findings from the above mentioned work packages (Ch. 2.1. to 2.4) four possible slope scenarios and respective measures may be differentiated (Figure 1):

- A) stable without additional measures, no further action is required.
- B) unstable due to changed boundary conditions and cannot be stabilized with feasible measures. However, the slope instability may be avoided by flattening the slope by massive earth works.
- C) unstable due to changed boundary conditions but the consequences of the instability do not affect the serviceability of the reservoir and are therefore acceptable and do not affect the serviceability of the facility.
- D) potentially unstable due to changed boundary conditions but can be stabilized with additional stabilization measures: for this case a toolbox is presented in Table 2; depending on the geometry, of the potential slide and its failure mode, the required measures may be chosen.

### 3 MITIGATION MEASURES

#### 3.1 Superficial and shallow landslide mitigation measures

Shallow landslide (i.e. < 3m thick, see table 1) mitigation measures aim to prevent surface erosion and to improve the drainage capacity of the uppermost meters. Appropriate measures comprise, e.g.:

- drainage trenches, to reduce the length of drainage path and hence erosion; they may be lined with geotextiles and combined with drainage tubes;



Figure 3: reservoir slope featuring drainage trenches above the storage level.

- wave protection, to prevent soil from external erosion



Figure 4: Wave protection measure (stone wall) in an impounded reservoir.

- cultivated crib walls;
- geomembranes, along with soil nailing, gabion mattresses and/or blocks as surface erosion protection, especially for fine-grained soils; nails are used primarily to stabilize the geotextile and secondarily to stabilize the soil itself;
- geomembranes, along with flat gabions, as erosion protection measure.

Protection in the vicinity of road cuts above the shoreline comprises gabion walls and soil nailing, used as artificially steepened natural slope measure.

#### 3.2 Medium to deep seated landslide mitigation measures

By installing a defined grid of geotextile wrapped stone columns, the shear strength of the soil may increase and the length of the drainage path in the soil can be shortened. Both effects increase the slope stability. Also, by means of local soil substitution with material of higher shear strength and permeability, the stability and erosion protection are improved.

Supporting embankments may be used to prevent erosion and to stabilize deep seated potential slip circles. Such embankments have already been successfully applied to stabilize unstable slopes of operating hydropower facilities.

If subaquatic soil instabilities (i.e. below the reservoir water level) are accepted, which may be acceptable if they do not influence the serviceability of the reservoir, but the shore above water level has to be protected, a pile wall at the height of the maximum water level may be installed as a protection measure.

#### 3.3 Very deep seated landslide mitigation measures

Very deep seated (i.e. > 15 m thick, see table 1) landslides generally require cost-extensive mitigation and monitoring measures such as drainage drillings and adits (Bonzanigo et al. 2007, Zangerl et al. 2010).

### 4 COMBINATIONS OF MEASURES

In order to find feasible and appropriate combinations of mitigation measures, Table 2 presents a matrix of scenarios (scenarios 1 to 7).

- Scenario 1 represents possible combinations of protection measures below storage level to prevent superficial mass movements and erosion.
- Scenarios 2 to 7 combine mitigation measures against potential superficial instability with medium to deep seated mass movements. Whereas in scenario 2 flattening of the upper part of the slope reduces the driving force of a potential instability, in scenario 3, the increase of the safety level is obtained by increasing the resisting force at the toe of the slope. Note that for scenario 3 the safety against surface erosion is given when using accordingly graded fill material. In contrast, when combining measures as shown in scenario 4, measures for both failure mechanisms have to be designed individually. This may also be the case for scenario 5.
- The most drastic measure is hence the soil replacement depicted as scenario 6, whereas in scenario 7 the goal is that the safety of the slope above the impoundment level remains, without taking into consideration the stability below the measure.

Table 2: Matrix of combinations. +: appropriate measure/combination. ° inappropriate measure/combination.

1	2	3	4	5	6	7	Scenario	
+	°	°	°	°	°	°	drainage trench	superficial instability
+	°	°	°	°	°	°	wave protection	
+	+	°	+	+	°	°	geomembranes with gabion mattresses	
+	+	°	+	+	°	°	geomembranes with soil nailing	
+	+	°	+	+	°	°	cultivated protection walls	
°	+	°	°	°	°	°	flatten slope geometry by soil removal	shallow to medium deep seated instability
°	°	+	°	°	°	°	flatten slope geometry by support fill	
°	°	°	+	°	°	°	Deep soil nailing	
°	°	°	°	+	°	°	soil improvement (e.g. vibro replacement)	
°	°	°	°	°	+	°	soil replacement	
°	°	°	°	°	°	+	pile wall	
°	°	°	°	°	°	°		

## 5 RESIDUAL RISK ASSESSMENT

The residual risk from a potential mass movement has to be analysed independently from mitigation measures. This is due to the fact that the mitigation measures are designed for a certain defined load (e.g. design earthquake). However, remaining residual risks may comprise events larger than the design event and resulting slope instabilities. Thus, also the impacts of such instabilities on both the safety of the dam and reservoir (probability and consequences of overtopping) have to be assessed.

For this both empirical approaches (Fritz et al. 2003, Heller 2007) and numerical models (e.g. Grilli and Watts 2005) may be applied.

## 6 MONITORING MEASURES

Slope stability behaviour can be monitored a) pointwise, b) linear and c) areally and can be measured in-situ and/or by remote sensing methods (see Sect. 8 References). Point data can be obtained through triangulation, levelling, GPS surveys, wire extensometer, joint- or crackmeter, laser distance meter and water level gauge measurements. Line data may be obtained from inclinometer, extensometer and Trivec measurements and/or from fibre optic sensing techniques. The deformation field of a surface of a landslide can be obtained by photogrammetry, terrestrial or satellite based radar interferometry and terrestrial or airborne laser scanning. A variety of these monitoring methods has already been successfully applied to some well-documented reservoir slopes (e.g. Leobacher and Liegler 1998, Tentschert 1998, Watson 2006, Zangerl et al. 2009, 2010).

## 7 CONCLUSION

Assessment of slope stability of potential reservoir sites requires interdisciplinary knowhow, comprising intensive field investigations and sound determination of soil characteristics. Data thus obtained enable the assessment of slope stability (due to changed boundary conditions) and the design of appropriate mitigation measures.

For the design phase, possible scenarios of mitigation measures are described and presented in a matrix form. These measures serve as a basis during later design phases and during execution when the stabilization measures are allocated to the appropriate slopes in the reservoir according to the corresponding refined geological model and boundary conditions.

The scenarios 1 to 7 (Table 2) may be applied to different slope conditions (Figure 1: A to D), i.e. areas with acceptable slope stability, areas where near-surface stabilization measures are required, and areas with shallow to deep seated mass movements which have to be stabilized.

On the basis of available geological surface and subsurface data (field survey, geophysics, drillings) representative geological slope cross sections are established in order to illustrate, evaluate and assess the current and future slope stability in the individual regions. These geological sections and geotechnical data are used to for stability calculations.

Due to the repeated water level fluctuations, some areas may experience erosion and landslide processes (landslides, flow processes), especially in areas with large granular or cohesive soil layers. Stability studies including all load cases (including earthquakes) have to be carried out. If the safety calculation without stabilization measures returns an insufficient safety factor, measures required to achieve the required level of safety have to be determined. The goal of constructing mitigation measures is that the slopes for the mentioned load combinations (including earthquake load) remain stable.

For the monitoring of slope stability during the construction and operating phase, instrumental measurements of selected slope areas are required. These include both episodic campaigns and permanent measurements, e.g. geodetic surveys, levelling and inclinometer measurements.

## 8 REFERENCES

- Alonso E. & Pinyol N. (2009). *Slope stability under rapid drawdown*. 1<sup>st</sup> Italian Workshop on Landslides 11 - 27, Naples
- BAFU, 2009: Schutz vor Massenbewegungsgefahren, Technische Richtlinie als Vollzugshilfe, Entwurf 09.09.2009. – Bundesamt für Umwelt BAFU, 90 pp., Bern.
- Barla, G., Antolini, F., Barla, M., Mensi, E., Piovano, G. (2010). *Monitoring of the Beauregard landslide (Aosta Valley, Italy) using advanced and conventional techniques*. Engineering Geology, 116, 218-235.
- Eberhardt E., Bonzanigo L., Loew S. (2007): *Long-term investigation of a deep-seated creeping landslide in crystalline rock. Part II. Mitigation measures and numerical modelling of deep drainage at Campo Vallemaggia*. Can. Geot. J., 44/10, 1181-1199.
- Casagrande, A. (1937). *Seepage through dams*. Contributions to soil mechanics, 1925-1940. Boston Society of Civil Engineers.
- Fritz, H. M., Hager, W. H., Minor, H.-E. (2003). Landslide generated impulse waves. Experiments in Fluids 35, 505-532.
- Grilli, S. T. & Watts, P. (2005). Tsunami generation by submarine mass failure. I: Modeling, experimental validation and sensitivity analyses. II: Predictive Equations and case studies. J. Waterw. Port Coast. Ocean Eng. 131(6), 283-310.
- Heller, V. (2007). *Landslide generated impulse waves: Prediction of near field characteristics*. ETH Diss. No. 17531
- ICG (2009) *SafeLand – Living with landslide risk in Europe: Assessment effects of global change, and risk management strategies*. 7<sup>th</sup> Framework Programme Cooperation Theme 6 Environment, Sub-Activity 6.1.3 Natural Hazards, Deliverable 5.2 Toolbox of landslide mitigation measures, 47 pp.
- ICG (2011) *SafeLand – Living with landslide risk in Europe: Assessment effects of global change, and risk management strategies*. 7<sup>th</sup> Framework Programme Cooperation Theme 6 Environment, Sub-Activity 6.1.3 Natural Hazards, Deliverable 5.1 Compendium of tested and innovative structural, non-structural and risk-transfer mitigation measures for different landslide types, 340 pp.
- ICOLD (1980). *Deterioration of dams and reservoirs. Examples and their analysis*. ICOLD, Paris, Balkema, Rotterdam.
- Jäckli, H. (1996). *Durch Spiegelschwankungen des Stausees Wägital beeinflusste Kriechbewegungen*. Instabile Hänge und andere risikorelevante natürliche Prozesse. in: Oddson B. (ed.), *Instabile Hänge und andere risikorelevante natürliche Prozesse*, 219-226, Birkhäuser.
- Keusen, H.R. (1998) *Warn- und Überwachungssysteme (Frühwarndienste)*. Fan-Forum, Zollikofen, 1-40.
- Leobacher, A., Liegler, K. (1998) *Langzeitkontrolle von Massenbewegungen der Starraumhänge des Speichers Durlaßboden*. Felsbau 16/3, 184-193.
- Leobacher, A., Blauhut, A. (2010). Gerlos power station/Gmünd dam – stabilization of a reservoir slope (Grasegger slope). Geomechanics and Tunneling 3, 462-469.
- Riemer, W. (1995). *Keynote lecture: Landslides and reservoirs*. in: Bell (ed.), *Landslides*, pp. 1973-2004. Balkema, Rotterdam.
- Sherard, J.L., Woodward, R.J., Gizienski, S.F. & Clevenger, W.A. (1963). *Earth and earth-rock dams*. Wiley&Sons.
- Tentschert, E. (1998). *Das Langzeitverhalten der Sackungshänge im Speicher Gepatsch (Tirol, Österreich)*. Felsbau 16/3, 194-200.
- Watson, A.D., Martin, C.D., Moore, D.P., Steward, W.G. Lorig, L.J. (2006) *Integration of Geology, Monitoring and Modelling to Assess Rockslide Risk*. Felsbau 24/3, 50-58.
- Zangerl C., and others, 2009: Landslide failure and deformation mechanisms, investigation and monitoring methods. - in: Veulliet E. et al (eds.), *Sustainable Natural Hazard Management in Alpine Environments*, 135-178, Springer.
- Zangerl C., Eberhardt E. & Perzmaier S., 2010: Kinematic behaviour and velocity characteristics of a complex deep-seated crystalline rockslide system in relation to its interaction with a dam reservoir. - Engineering Geology 112/1-4, 53-67.

# Landslide stabilization by piles: A case history

## Stabilisation des glissements de terrain par des pieux : un cas d'étude

Şengör M.Y.

*Yuksel Project Co. Inc., Ankara, Turkey*

Ergun M.U., Huvaj N.

*Middle East Technical University, Ankara, Turkey*

**ABSTRACT:** During the foundation excavation of an industrial plant in Eskişehir, Turkey, a landslide occurred in the neighbouring slope, and consequently, the excavation had to be stopped. The instability occurred in a natural slope which had an average slope angle of 9-13 degrees. The aerial extent of the slide mass was 400 m by 115 m. The material in the slope was 7 to 20 meter-thick colluvium (slide debris), which constitutes a historic landslide mass, underlain by a gravelly sandy silty clay matrix containing limestone blocks, weathered tuff and tuff. Soil profile and location of the slip surface were determined through a site investigation program including nine boreholes and inclinometers. A back analysis was carried out and shear strength parameters of the slope forming materials were determined. Slope stability analyses were carried out, stabilization alternatives were evaluated and slope stabilization by piled retaining walls was considered as the most feasible alternative. The analyses and design procedure for the piles will be presented together with a summary of existing analyses and design methods for landslide stabilizing piles.

**RÉSUMÉ :** Pendant les excavation des fondations d'un site industriel à Eskişehir, en Turquie, un glissement de terrain a eu lieu dans un talus voisin, et par conséquent, les travaux ont été arrêtés. L'instabilité s'est produite dans un terrain naturel présentant une pente moyenne de 9 – 13 degrés. Les dimensions en plan du glissement étaient de 400 m par 115 m. Le matériau du glissement était composé de colluvions, sur 7 à 20 m d'épaisseur, qui constituaient une masse de glissement postérieur. Les colluvions reposaient sur une argile graveleuse et sablo-limoneuse contenant des blocs de calcaire, du tuf sain et du tuf altéré. La coupe géotechnique du site et la localisation de la surface de glissement ont été mises en évidence par une campagne d'investigations incluant neuf forages et inclinomètres. Les paramètres de résistance au cisaillement des terrains en place ont été déterminés par une rétro-analyse. Suite aux études de stabilité des pentes et à l'examen des systèmes de renforcement alternatifs, la solution de stabilisation par une paroi en pieux s'est avérée comme la plus judicieuse. Les analyses et la procédure de dimensionnement pour ces pieux vont être présentées en même temps qu'un résumé des analyses et des méthodes de calcul existantes sur la stabilisation des glissements par pieux.

**KEYWORDS:** landslide, piles, inclinometer.

### 1 INTRODUCTION AND SOILS AT THE SITE

Instability occurred in a natural slope which had an average slope angle of 9-13 degrees, during excavation works near the toe. The aerial extent of the slide mass was 400 m by 115 m. The construction site was located at the toe of this sliding mass (Figure 1). The slope movement had a NW-SE direction. The material in the slope was 7 to 20 meter-thick colluvium (slide debris), which constitutes a historic landslide mass, underlain by gravelly sandy silty clay layers with limestone blocks, weathered tuff and unweathered tuff at different borehole locations. The colluvium was also composed of pieces of limestone cobbles and blocks in a clayey silty matrix.

It was observed that the slide debris lies on tuff. The pliosen age tuffs are approximately 100 m thick and lies on limestone. In the borehole descriptions the tuff layer at the upper levels are weathered to highly weathered condition and can be considered as a transition between rock and soil and identified as a layer of stiff clay. Samples from this weathered tuff had natural water content 19-43% (high natural water content such as 43% was obtained near the shear surface at about 20 m depth at borehole SK9). Since this material can be considered clay-like, Atterberg limits are determined LL=45-49%, PI=11-28% (for the material near the shear surface LL=49-66% and PI=27-36%), fines content=34-74% and clay-size fraction was 23-57%, and the material can be classified as CL, ML, GC and SC. The natural unit weight of samples were 20-21 kN/m<sup>3</sup>. Unconfined compressive strength of this material was 30-240 kPa and UU triaxial tests gave  $c_u$ =13-44 kPa and  $\phi_u$ =11-22°. Since the

residual shear strength will be of interest in this reactivated landslide case, direct shear tests were carried out on limited number of undisturbed samples taken from near the shear surface in order to find the residual friction angle. 46 mm diameter specimens were sheared undrained without submerging in water, then sheared continuously and slowly to reach residual condition. From the lab tests it was concluded that the 100 and 250 kPa undrained shear strength for tuffaceous clay and clayey tuff are reasonable values. Drained friction angle of slope debris/colluvium was 15-20 degrees, and tuffaceous clay taken from near the shear surface had 10.2 degrees residual friction angle.

#### 1.1 Soil Profile and The Mechanism of the Slope Movement

The sliding mass has grown progressively backward into the slope as multistage rupture surfaces from the toe of the landslide developed. First, the tension crack (scarp) C1 has been observed while excavation works were going on. Then, within about 15 days, there were total of four major tension cracks (visible scarps) (C1 to C4 in Figures 1 and 2) and one meter horizontal and vertical movements have been observed at the ground surface. Fifty days after the start of the first scarp, a small road located at the slope was observed to move 15 m downslope and 4 m in vertical direction.

Nine boreholes are opened at a line of NW-SE direction which is also the direction of the movement and inclinometers are also placed in these boreholes. In all boreholes except SK7, SK8 (at the toe) and SK6; the top layer is slope debris and



below that tuffs sometimes in clayey state and sometimes in harder state are encountered.

## 2 ANALYSES AND RESULTS

In this section the types of the analyses, the results of the back-analyses of the landslide movement and then the stabilization works will be presented.

### 2.1 Back-Analyses and the Shear Strength Parameters

In all boreholes inclinometer readings were taken, and the depth of the slip has been determined. As it is a fast movement, all inclinometer pipes were sheared by the landslide (except SK-3 and SK-8) shortly after they are placed. These depths were considered as the depth of the slip surface. The cross section of the landslide were prepared according to the borehole data and inclinometer readings and the scarps of the progressive slips. The positions of the slope debris and tuff layers and also the scarps of the progressive failure slides are shown in Figure 2. The shear surface passes mostly through the colluvium material in the upper half of the sliding mass, whereas it passes near the contact between the colluvium and tuff (more within the tuff) in the lower half of the sliding mass. There was no groundwater level, however in stability analysis to be on the safe side some water level is considered.

It was not easy to take samples from the sliding mass near the shear surface, therefore only a limited number of soil samples were tested in the laboratory. Determination of the soil parameters at the sliding surface of a landslide at the limit equilibrium state by the back analyses of the movement is a widely used method. In this method the  $c$  and  $\phi$  parameter couples are determined which give a factor of safety value of one at the sliding surface. In the back analyses the cohesion and angle of friction parameter couples for the tuff and the slope debris layers are identified. In this case the number of the unknowns is four. They are decreased progressively using a methodology given below.

At the first stage, the back analyses of sliding surfaces of C3 and C4 were performed. By this way the parameters for the slope debris were determined as  $c'=5.6$  kPa and  $\phi'=15.7^\circ$ ,  $E'=35$  MPa are used in the analyses.

At the second stage, calculations for sliding surfaces of C1 and C2 were performed. The above parameters were used for slope debris, and the shear strength parameters for the tuff layers were determined. The parameters for the weathered tuff layer at the sliding level are assessed as  $c'=0$  kPa and  $\phi'=9.2^\circ$ . But these parameters were not suitable to use for the whole tuff layers. Table 1 summarizes the parameters used in the analyses.

Table 1. Material properties used in analyses

Material	Drained			Undrained	
	$c'$ (kPa)	$\phi'$ ( $^\circ$ )	$E'$ (MPa)	$c_u$ (kPa)	$E_u$ (MPa)
Slope debris	5.6	15.7	35	60-75	20
Weathered tuff (first 3 m)	0	9.2		100	60
Unweathered tuff	20	25	60	250	130

Undrained triaxial compression and consolidated drained direct shear tests were performed on the debris and tuff soil samples from the boreholes which are located between the slope debris and tuff layers. The results of these tests show that the internal friction angle for the slope debris and for the clay soil originated from tuff are  $15$  to  $20^\circ$  and  $10.2^\circ$  respectively. This findings support the results of the back analyses.

### 2.2 Slope Stabilization by Piles

Piles used in slope stabilization are subject to lateral force caused by the movement of surrounding soil, and they are called "passive piles" (Viggiani 1981; Poulos 1995). One of the major issues in the design of these piles is the magnitude of the force on the pile. Since this is related to the soil movement and soil movement is influenced by the presence of piles, the interaction between the passive piles and the soil is quite complicated. There exists a number of empirical, analytical, and numerical methods available in the literature about the design of piles used in slope stabilization (Brinch Hansen 1961, De Beer 1977, Fukuoka 1977, Ito and Matsui 1977, Sommer 1977, Winter et al. 1983, Popescu 1991, Reese et al. 1992). Some of these methods are pressure or displacement-based and some of them are numerical methods, such as finite element and finite difference (Kourkoulis et al., 2012).

In the pressure or displacement based methods, the pile is modeled as a beam supported by springs at its sides. A single laterally loaded pile is considered, and the ultimate soil-pile resistance is correlated with the undrained shear strength for clays, and with the overburden stress and friction angle for sands. In these methods group effects are taken into account by using reduction factors. Although spring constants are dependent on pile deflection, or the movement of the soil, they are typically assumed constant. In the current study this approach is used.

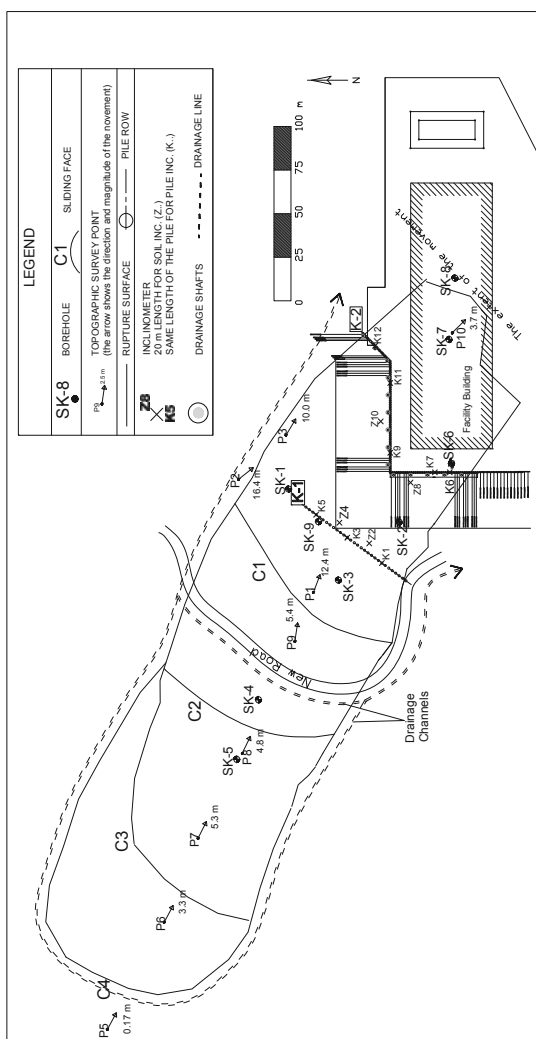


Figure 1. General layout plan

The general design procedure consists of two main steps: Step 1: Provision of the required total lateral force needed to increase the factor of safety of the slope to the desired value (based on analysis of the unreinforced slope). Step 2: Calculation of loading on piles and pile lateral capacity.

In the last few years, 3-dimensional finite-element and finite-difference methods are becoming increasingly popular. Using these methods complex geometries and complicated phenomenon such as soil arching, pile group effects, nonlinearity of soil and pile could be modeled. Use of 3D numerical methods is still not very attractive to practitioner engineers because of the long computational time and learning effort. Kourkoulis et al. (2012) developed a hybrid solution to the problem, combining the benefits of accurate 3D finite element simulation with the simplicity of widely accepted analytical techniques.

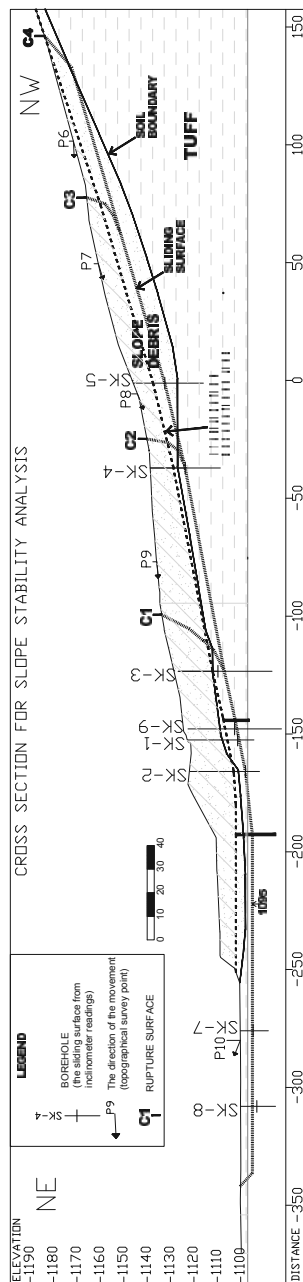


Figure 2. Cross section for the analyses

## 2.2 Stabilization Works for Foundation Excavation and Prevention of the Slope Movements

As a result of the preliminary works it is understood that the diameter of the stabilizing passive piles should be 1.2 m and more than single pile row would be needed. The depth of the sliding mass was 20 m at the centerline. It was not possible to stabilize this amount of soil mass by two rows of piles only. So stabilizing excavations were needed to decrease the amount of sliding mass (about half of the sliding depth was removed-see Figure 2), and then the following piled analyses were performed.

1. Slope Stability (GEOSLOPE 6.02, SLIDE 5.014) / Structural Analyses (SAP 2000, V8.4)

2. Finite Element Method (PLAXIS 2D, V8.6)

In this stabilization program, one row of stabilizing piles are placed at an upper level (Pile Row K1 in Figure 1). The lower row of piles (Pile Row K2 in Figure 1) will also have a function of retaining wall for the facility. To decrease the moment and the displacements of the piles in this second row, permanent ground anchorages were planned at the top beam of the piles.

The most critical issue in the analyses were the excavation works for the foundation of the facility which would be performed after the stabilizing works were completed. Because of the excavations just behind the second row of the piles, the pile displacements and the moments were increasing for both row of piles. This critical concept was best configured in 2D finite element analyses (figure 3).

## 2.3 Finite Element and Limit State Analyses

The place of the two rows of the stabilizing piles is shown in the plan view in Figure 1. In the analyses the construction stages were excavations for stabilization, the construction of the piles and the foundation excavations to the 1095 m elevation just in front of the K2 Pile Row. For the drained analyses of the K1 pile row it was found that the pile head displacement as 18 cm, the shear force as 468 kN/m and the bending moment as 1240 kN.m/m. The same values for the K2 pile row were 10.8 cm, 387 kN/m and 970 kN.m/m, respectively.

The horizontal peak ground acceleration at the construction site was accepted as 0.25g and accordingly the seismic stability of the stabilizing system was also checked. The slope stability analyses of the final stage of the works were repeated for a horizontal seismic ground acceleration of 0.125g.

The cohesive soil exerts a pressure on the piles when it tries to pass between the piles forming a failure mechanism. This pressure being related to the undrained cohesion of the soil and is a limit value to be checked (see Eq. 1). This equation is valid for  $s \geq 3d$  where  $s$  is the pile center-to-center spacing and  $d$  is the pile diameter. If  $s < 3d$  there will be a reduction up to a factor of 0.5.

$$p = c_u k D \quad (1)$$

Active and passive lateral earth pressures are represented by spring constants  $k$  above and below sliding surface. The  $k$  values for this case were 1.30 for the passive side of the lower level (K2) piles and 1.34 and 0.86 for the passive and active side of the upper level (K1) piles. These are lower than the limit values (Ergun, 2000).

## 3 CONCLUSION

A long landslide which progresses backwards had occurred because of the foundation excavations of an industrial plant which coincided with the toe of a historic landslide. The construction works were stopped, and the landslide was investigated through boreholes. The clayey debris (colluvium) containing limestone cobbles and boulders had slid over

plastic tuffs. Back analyses and the laboratory tests were performed for the determination of the shear strength parameters at the sliding surface. Two rows of stabilizing piles were designed through the sliding mass and the structural analyses and also FE analyses of these piles were performed independently.

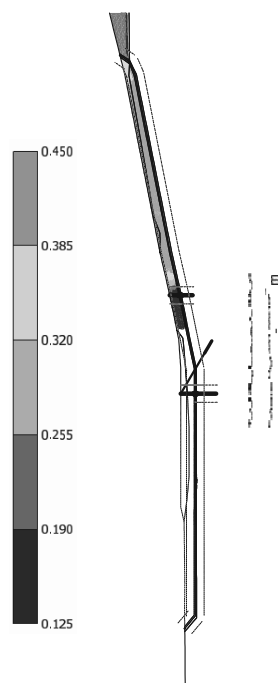


Figure 3. Total displacements plot of FE analysis

10 to 15 m deep excavations were performed for the first stage of the stabilization works. The upper level piles (K1) were 12 m in length and 1.2 m in diameter. Center to center spacing of piles were 2.5 m. The total number of stabilizing piles is 30 covering a longitudinal length of 72 m reaching the South edge of the landslide. The 2nd row of stabilizing piles (K2) was also used as the retaining walls of the facility. The 1.2 m diameter bored reinforced concrete piles are placed with 1.25 m spacing in this row. The pile lengths are 17 m. The total length of the pile row is 137 m in plan view passing over the South edge of the landslide.

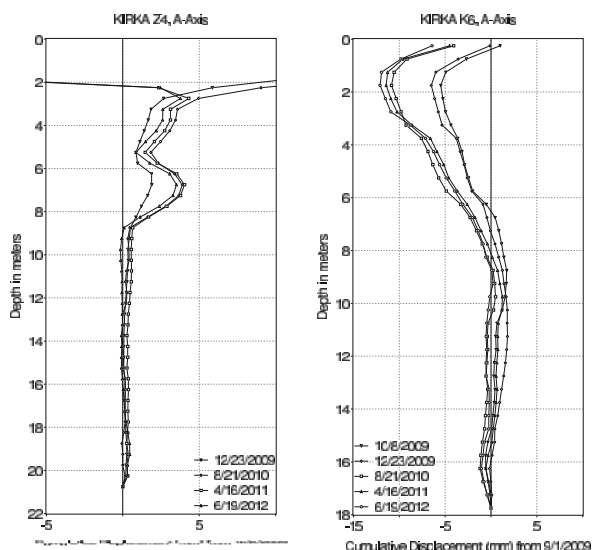


Figure 4. Cumulative displacements (mm) at Z4 (soil) and K6 (pile) inclinometers

The permanent ground anchors were constructed at the head beam of the piles with 1.25 m spacing, 30 to 35 m in length and inclined at 30 and 45 degree to the horizontal.

No drainage system was planned in the sliding mass. Instead surface drainage was implemented as reinforced concrete drainage channels at the edges of the landslide and at the upper levels of the new road. Behind the retaining walls of the construction site 0.60 m diameter vertical drainage shaft between the piles were planned and the collected groundwater was transferred to the water drainage system of the facility.

The deformations of the system are controlled by the 12 inclinometers (8 in the soil, 4 in the piles) at each stage of the construction works. There are no displacements in three years (Figure 4).

#### 4 REFERENCES

Brinch Hansen, J. 1961. The Ultimate Resistance of Rigid Piles against Transversal Forces. *Bulletin of the Danish Geotechnical Institute* (12).

De Beer, E. 1977. Piles Subjected to Static Lateral Loads. Proceedings, 9th I.C.S.M.F.E., Specialty Session 10, Tokyo.

Ergun, M.U. (2000), "Stabilization of Landslides using Piles", Landslides in Research, Theory and Practice, Proceedings of the 8th International Symposium on Landslides, Vol.1, pp:513-518, Cardiff, 2000.

Fukuoka, M., "The Effects of Horizontal Loads on Piles due to Landslides", Proceedings, 9th I.C.S.M.F.E., Specialty Session 10, Tokyo, 1977

Ito, T. and Matsui, T., "The Effects of Piles in a Row on the Slope Stability", Proceedings, 9<sup>th</sup> I.C.S.M.F.E., Specialty Session 10, Tokyo, 1977

Kourkoulis, R. Gelagoti F., Anastasopoulos I, and Gazetas, G. (2012) Hybrid Method for Analysis and Design of Slope Stabilizing Piles, *Journal of Geotechnical and Geoenvironmental Engineering*, v138(1), pp:1-14.

Popescu, M.E., "Landslide Control by Means of a Row of Piles", Slope Stability Engineering, Thomas Telford, pp: 389-394, London, 1991

Poulos, H. G. (1995). "Design of reinforcing piles to increase slope stability." *Can. Geotech. J.*, 32(5), 808-818.

Reese, L., Wang, S., and Fouse, J. "Use of Shafts in Stabilizing a Slope", Slopes and Embankments-II A.S.C.E., Specialty Session, 1992

Sommer, H., "Creeping Slope in a Stiff Clay", Proceedings, 9th I.C.S.M.F.E., Specialty Session 10, Tokyo, 1977

Viggiani, C., "Ultimate Lateral Load on Piles Used to Stabilize Landslides", Proceedings, 10th I.C.S.M.F.E., Vol.3, pp: 555-560, Stockholm, 1981

Winter, H., Schwarz, W. and Gudehus, G., "Stabilization of Clay Slopes by Piles", Proceedings, 8th European Conference on S.M.F.E., pp: 545-550, Helsinki, 1983

# Landslide Susceptibility Mapping Using Bayesian Conditional Probability Model at An Linh Commune, Tuy An District, Phu Yen Province, Vietnam

Élaboration de la carte de risques de glissement de terrain sur la commune de An Linh, district de Tuy An, province de Phu Yen, à l'aide d'un modèle Bayésien de probabilité conditionnelle

Son N.T.

*Tuy Hoa Industrial College, Phu Yen Province, Vietnam*

Ha P.T.S.

*Faculty of Geology and Petroleum Engineering, Ho Chi Minh City University of Technology, Ho Chi Minh City, Vietnam*

Son L.M.

*flatGEO Consulting Co., Ltd.*

**ABSTRACT:** Landslide phenomenon at An Linh commune, Tuy An district, Phu Yen province is more and more severe year after year. The prediction of a highly landslide susceptibility zone will support the government and local residents to save their properties. In this paper the authors carried out the landslide susceptibility mapping at An Linh commune using the deterministic approach with knowledge-driven methods and the stochastic approach with data-driven methods. The deterministic approach is conducted using traditional survey, field investigation, geophysical survey... to evaluate not only geotechnical properties of rock and soil materials but also the mechanism of landslide phenomenon in the studied area. The stochastic approach with probability methods is chosen to evaluate the weights of influence factors such as the elevation, aspect, slope angle, distance to roads and distance to drainages, geology and topographical wetness index of the materials. Landslide susceptibility zonation is developed using the model of Bayesian conditional probability with different criteria for weighting factor calculation integrated with GIS analytical tools. Landslide susceptibility maps from different models are validated with the current landslide inventory to select the most reasonable model for the study area.

**RÉSUMÉ :** Les glissements de terrain sont devenus de plus en plus fréquents sur la commune de An linh, district de Tuy An, province de Phu Yen, au cours des dernières années. Les auteurs ont réalisé une carte de risques de glissement de terrain sur la commune An Linh selon une approche déterministe fondée sur une connaissance experte et à l'aide d'une approche stochastique basée sur les données. L'approche déterministe est conduite à partir des méthodes de reconnaissance, d'observation du terrain, de prospection géophysique... afin de quantifier non seulement les propriétés géotechniques du sol et de la roche mais aussi le mécanisme de glissement de terrain dans la région concernée. L'approche stochastique fondée sur les modèles statistiques est choisie pour évaluer le poids de facteurs d'influence comme l'altitude, l'aspect, la pente, la distance aux cours d'eau, la distance aux voies routières, et au drains, les paramètres géologiques, et l'indice de l'humidité des sols. Le zonage des risques de glissement de terrain a été développé en utilisant un modèle de probabilité conditionnelle de Bayes avec différents critères de calcul du poids des variables, en intégrant les outils analytiques de SIG. Les cartes de risques élaborées selon ces modèles ont été validées à l'aide de l'inventaire des glissements actuels afin de choisir le modèle le plus approprié pour ce site.

**KEYWORDS:** Landslide susceptibility; Bayesian conditional probability; Stochastic model.

## 1 INTRODUCTION

The study area locates at An Linh commune, Tuy An district, Phu Yen province in the south central coast of Vietnam (see Fig. 1).

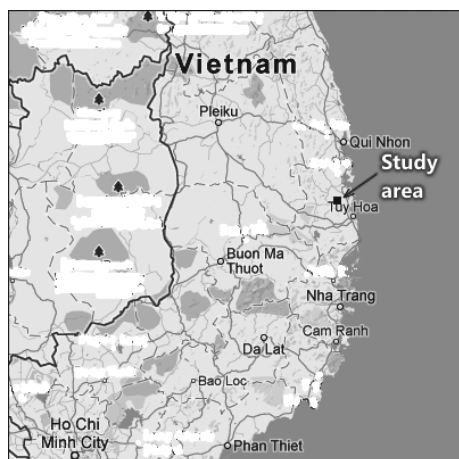


Figure 1. Location of the study area

During the past few years, landslides often occur in the study area after heavy and long rains. This phenomenon damages roads and construction works and results in serious cracks in the residential areas that in turn affect to human lives. Therefore the landslide prediction is an urgent task for scientists to support the government in planning and save human lives of local residents.

### 1.1 Geographic characteristics

An Linh area which has hill and mountain landscape locates on the eastern side of Van Hoa highland whose elevation of 12 ~ 500m. In that area, hills are rounded and have steep slopes, decorated by narrow valleys which follow along north-south direction. The ground surface which inclines to the north is a bare area with basaltic boulders or cobbles. This topographic landscape is favorite for erosion progress and stimulate landsliding and cracking process.

The study area belongs to the monsoon tropical region with oceanic climate. The annual precipitation is approximate 2000mm. Especially in the rainy season the precipitation can reach 70 ~ 80% the annual precipitation. Furthermore, the precipitation concentrates in a short time – only one or two months at the end of a year.

Water systems strongly develop with Cai river and Ho Lo river in the west and the east respectively. Both rivers form a hydrological network distributed evenly in the study area.

### 1.2 Geological characteristics

A general stratigraphy of the study area composes of following formations:

Table 1. Brief description of geological formations

Formation	Composition
Phong Hanh formation (ε - Sph)	Quartzite of blocky structure, quartz-sericite schist
Mang Yang formation (T <sub>2</sub> my)	Boulders, cobbles, sandstone, siltstone and claystone, blocky structure, thick bedding
Kon Tum formation (N <sub>2</sub> kt)	Green, dark grey, greenish grey basalt, bubble or porosity structure, fracturing; diatomite, clay with diatomite, basalt with interbedded clay
Dai Nga formation (N <sub>2</sub> - Q <sub>1</sub> đn)	Greenish grey, dark grey basalt, blocky structure, fracturing
Quaternary formation	Boulders, cobbles, gravel, sand, silt, clay

### 1.3 Landslide characteristics

Landslide occurs mainly at low areas with elevations less than 200m and gentle slopes (slope angles vary from 5° to 20°) in heavily weathered rocks which compose of clay, swelling clay with diatomite... Landscape after sliding forms terraces with many fractures on the ground surface. Landslide exposures usually locate at positions associated with hydrological factors. There are water flows at the toe of slopes in massive landslides. The shear strength of soils within landslide areas is rather low (cohesions vary from 12 to 17kPa, friction angles from 10° to 13°).

### 1.4 Landslide causes

The fieldwork study shows some of causes of landslides in the study area:

- Heavy landslides usually occur at geological structures which compose of clay, clay with diatomite underlying thin heavily weathered basaltic layers. Soils and rocks at landslide areas are different in permeability, swelling, strength (weak soils overlay hard rocks).
- The erosion process occurs at the toe of slopes and piping develops due to the surface run off and underground water flow.
- Heavy and long rains cause rocks and soils swelling or liquefaction that in turn cause the volume change suddenly.
- Human activities also take part in the landslide trigger: the forest clearance, reservoir and rice field preparation... Those activities result in losing strength at the toe of slopes.

## 2 LANDSLIDE SUSCEPTIBILITY MAPPING

### 2.1 Theoretical Background

Nowadays there are two common groups of methods for landslide prediction:

- a) Knowledge-driven methods: those methods are based on experiences of experts and rely on empirical relationships.
- b) Data-driven methods: those methods analyse collected data and establish models based on the inherent relationship of data. This approach, especially, Bayesian conditional probability method will be applied for the landslide susceptibility mapping in this research. In Bayesian conditional

probability method, the likelihood of event D given the presence of factor B can be expressed as the prior probability:

$$P\{D|B\} = \frac{P\{D \cap B\}}{P\{B\}} = P\{D\} \frac{P\{B|D\}}{P\{B\}} \quad (1)$$

On the contrary, the unlikelihood of event D given the presence of factor B is the probability:

$$P\{\bar{D}|B\} = \frac{P\{\bar{D} \cap B\}}{P\{B\}} = P\{\bar{D}\} \frac{P\{B|\bar{D}\}}{P\{B\}} \quad (2)$$

- where
- $P\{D|B\}$  the likelihood of event D given the presence of factor B
  - $P\{\bar{D}|B\}$  the unlikelihood of event D given the presence of factor B
  - $P\{B|D\}$  the likelihood of factor B given the presence of event D
  - $P\{B|\bar{D}\}$  the likelihood of factor B given the absence of event D
  - $P\{D \cap B\}$  the probability of the presence of both event D and factor B
  - $P\{B\}$  the probability of the presence of factor B

If there are more datasets (more B factors) involved in the mapping prediction and those datasets are conditionally independent to each other with respect to a set of landslide occurrences, the Bayesian conditional probability of event D is expressed by the following formula:

$$P\{D|(B_1 \cap B_2 \cap \dots \cap B_n)\} = \frac{e^{(\log it\{D\} + \sum W^k)}}{1 + e^{(\log it\{D\} + \sum W^k)}} \quad (3)$$

where

$$\log it\{D\} = \ln \frac{P\{D\}}{1 - P\{D\}} \quad (4)$$

$$W^+ = \log \frac{P\{B|D\}}{P\{B|\bar{D}\}} \quad (5)$$

$$W^- = \log \frac{P\{\bar{B}|D\}}{P\{\bar{B}|\bar{D}\}} \quad (6)$$

$W^k$ : positive weight ( $W^+$ ) or negative weight ( $W^-$ ) of factor B depending on the presence or absence of factor B

The total weight of all B factors at each pixel on the prediction map is the sum of  $W^k$ , in which  $W^k$  will be the positive weight  $W^+$  if the factor B is present or negative weight  $W^-$  if B is absent.

The contrast of weight is:

$$C_w = W^+ - W^- \quad (7)$$

### 2.2 Landslide susceptibility mapping

After the landslide survey at the end of year 2010, 142 landslide occurrences are recorded in which 103 positions are used for the landslide susceptibility prediction by Bayesian conditional probability and 39 occurrences are used for the validation. The location of 103 landslide occurrences is presented in Fig 2. Black plus symbols on this figure are landslide occurrences.

There are seven factors chosen for the calculation of the landslide probability: elevation (DEM), slope direction (ASPECT), slope angle (SLOPE), geology (GEO), distance to road (DTR), distance to drainage (DTD), topographical wetness

index (TWI). Each factor is classified into several classes; the positive and negative weights of each class for each factor are calculated using an open-source software ILWIS (Integrated Land and Water Information System). To each factor, a class trigger for positive or negative weight is chosen at the class whose contrast reaches the highest value (see highlight classes in Table 2).

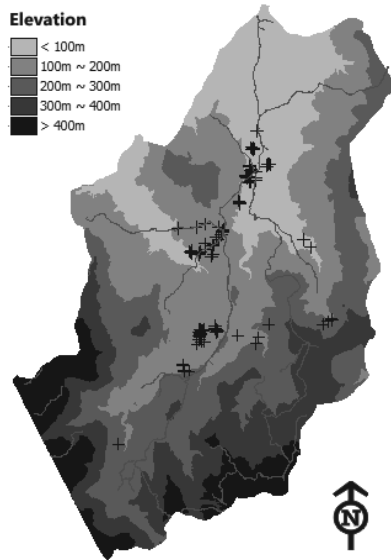


Figure 2. Landslide inventory map for modelling (103 points)

Table 2. Weight values of classes from parameters

Parameter	Value	W <sup>+</sup>	W <sup>-</sup>
DEM	100m ~ 200m	0.620	-0.488
ASPECT	West	0.470	-0.121
SLOPE	0° ~ 10°	0.073	-0.078
GEO	Claystone, sandstone with diatomite	1.009	-1.960
DTR	< 100m	0.758	-0.274
DTD	300m ~ 400m	0.881	-0.180
TWI	4 ~ 6	0.137	-0.077

The flow chart of the procedure for landslide susceptibility mapping by Bayesian conditional probability is shown in Fig. 3.

Weights of seven factor maps are calculated and expressed as weight maps and displayed in Fig. 4 to Fig. 10.

The Bayesian conditional probability map is derived from seven factor maps using the formula (3). However the slicing of this probability map into landslide susceptibility zones is not applicable because the ranges of landslide probability on different probability maps from different methods are totally different. Therefore the probability pattern is sliced into susceptibility zones using the ranking of predicted probability value instead of predicted value itself (Chung and Fabbri, 2003). A pixel of highest probability will be assigned the highest rank and pixel of lowest probability will be the lowest rank. After ranking all pixels within the study area, the landslide zoning could be carried out using predefined threshold values of different zones: high, moderate and low susceptibility.

In the study area, those threshold values are 15%, 25% and 60% for the high, moderate and low susceptibility area respectively. The landslide susceptibility map is presented in Fig. 11.

### 2.3 Validation

The landslide susceptibility map is validated by using 39 heavy landslide occurrences (white plus symbols on Fig. 12). Among them there are 31 points classified as high landslide susceptibility (80% accuracy).

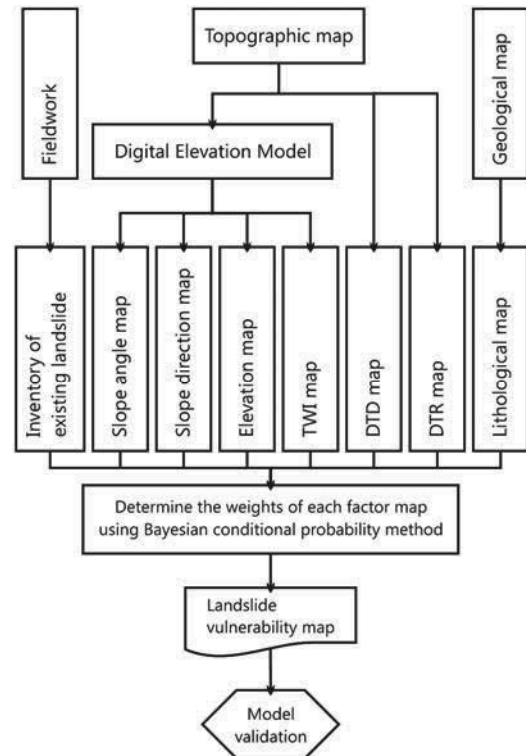


Figure 3. Procedure of landslide susceptibility mapping

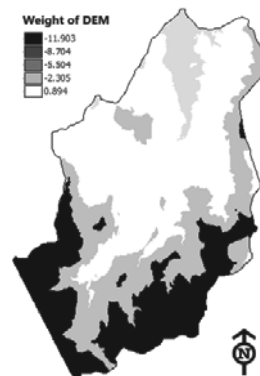


Figure 4. Weight of elevation factor

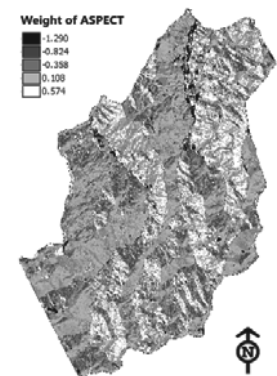


Figure 5. Weight of aspect factor



Figure 6. Weight of slope angle factor

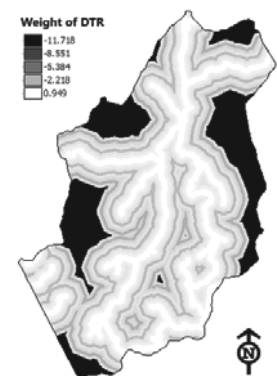


Figure 7. Weight of DTR factor

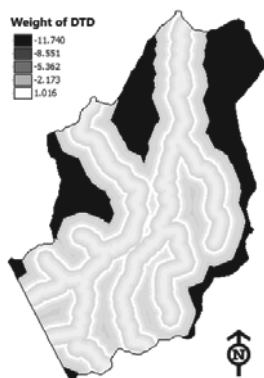


Figure 8. Weight of DTD factor

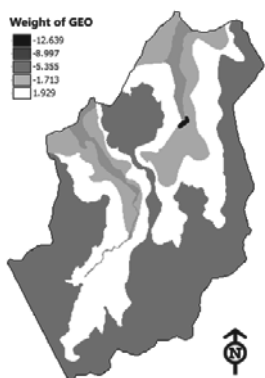


Figure 9. Weight of geological factor

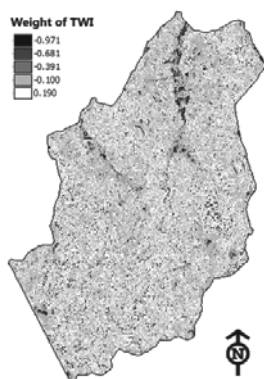


Figure 10. Weight of TWI factor

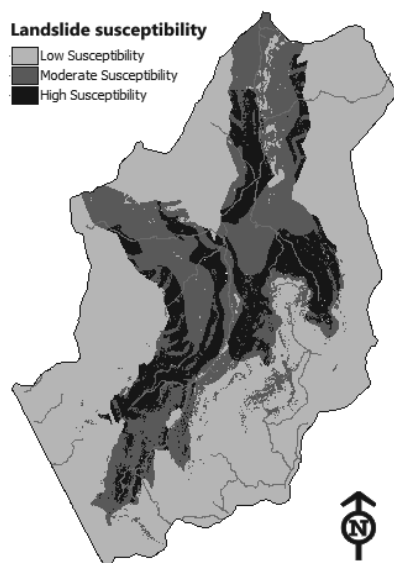


Figure 11. Landslide susceptibility map

### 3 CONCLUSION

a) The landslide susceptibility map shows that most of landslide occurrences concentrate at the areas of low elevation (100~200m), gentle slopes (slope angles vary from 5° to 20°), high TWI values (high water accumulation).

b) Landslides are also triggered due to the road construction. The roadway cuts into the slope faces and reduces the stability of slopes. Landslides occurs near the road construction sites (approximate 100m far from roads).

c) Landslides also distribute along the east-west direction which coincides with the direction of narrow valleys of steep slopes in the study area.

d) The results of Bayesian conditional probability model and the fieldwork survey show that landslides occur usually in soil layers with high proportion of clay and diatomite clayey soils which are heavily weathered.

e) The Bayesian conditional probability model gives the reliable result of landslide susceptibility for the study area. The validation was conducted for 39 heavy landslide positions which show that there are 31 positions (80% accuracy) located in the high landslide susceptibility zone.

f) The reliability of this model could be improved year after year when new landslide occurrences are updated annually in the landslide inventory.

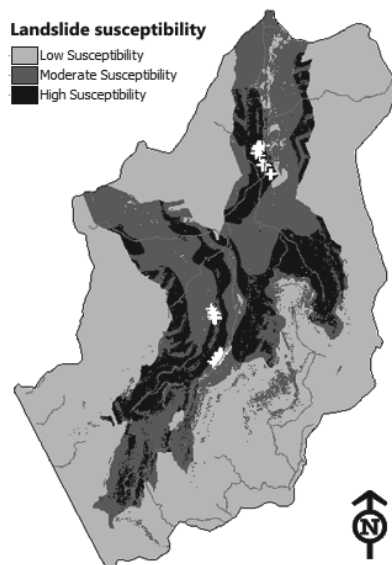


Figure 12. Landslide location for model validation (39 points)

### 4 REFERENCES

Bonham-Carter G.F. 1994. *Geographic Information Systems for Geoscientists: Modelling with GIS*, Volume 13 (Computer Methods in the Geosciences). Pergamon.

Brett G. Dickson et al. 2006. Mapping the Probability of Large fire Occurrence in Northern Arizona, USA. *Landscape Ecology* (21), 747-761.

Chung C.F. and Fabbri A.G. 1999. Probabilistic Prediction Models for Landslide Hazard Mapping. *Photogram Engineering Remote Sensing* (65), 1389-1400.

Chung C.F. and Fabbri A.G. 2003. Validation of Spatial Prediction Models for Landslide Hazard Mapping. *Natural Hazards* (30), 451-472.

Lee S., J. Choi, K. Min. 2002. Landslide Susceptibility Analysis and Verification Using the Bayesian Probability Model. *Environmental Geology* (43), 120-131.

Raul Romero-Calcerrada et al. 2008. GIS analysis of spatial patterns of human-caused wildfire ignition risk in the SW of Madrid (Central Spain). *Landscape Ecology* (23), 341-354.

# Influence of Ground Motion Variability on Seismic Displacement Uncertainty

## Influence de la variabilité des mouvements de terrain sur l'incertitude des déplacements en régime sismique

Strenk P.M.

Golder Associates, Inc., Reno, Nevada, USA

Wartman J.

University of Washington, Department of Civil and Environmental Engineering, Seattle, Washington, USA

**ABSTRACT:** A series of probabilistic seismic displacement analyses were performed to understand how material property variability coupled with systematic changes in the type and complexity of ground motion variability affect the displacement prediction uncertainty of the Newmark rigid-block method.

**RÉSUMÉ:** Une série d'analyses probabilistes des déplacements en régime sismique ont été effectués pour comprendre comment les variations des propriétés des matériaux couplées avec le type et la complexité des variabilités des mouvements de terrain affectent les incertitudes dans les prédictions de déplacement avec la Méthode des blocs rigides de Newmark.

**KEYWORDS:** Newmark, displacement, seismic, probabilistic, ground motion, variability, uncertainty, Monte Carlo

### 1 INTRODUCTION

Seismic slope deformation methods are used to make predictions of earthquake-induced permanent displacements in natural slopes and man-made dams and embankments. The predictive capability of well-established methods such as rigid-block (Newmark 1965) and decoupled (Makdisi and Seed 1978) procedures, however, are often associated with a high-degree of uncertainty which is a consequence of both parametric and modeling sources of variability. Parametric variability describes a method's sensitivity to the range of input parameters (e.g., shear strength, groundwater and earthquake ground motions) and is a function of the number of input parameters as well as the amount of variability in each parameter. Modeling variability is related to how well the method captures the actual physical mechanism of seismic-induced deformation when all input parameters are fully known. Although the majority of deformation-based method available today have a common conceptual origin in the sliding-block model proposed by Newmark (1965), differences in their analytical formulation, procedural structure, underlying assumptions and mathematical or regression functional form can result in different predictive capabilities and sensitivities to parametric variability (Strenk and Wartman 2011).

In seismic slope deformation analyses, parametric variability comes from parameters characterizing the seismic demand (earthquake ground motions) and those characterizing the slope's seismic resistance (represented by the seismic yield coefficient,  $k_y$ , which is a function of the slope geometry, shear strength and groundwater conditions). In a probabilistic framework, the interplay between these two sources of parametric variability can make evaluating their relative contributions to total displacement uncertainty a difficult task. The main focus of this study is to examine how ground motion variability influences the prediction uncertainty of the Newmark (1965) rigid-block method. To that end, a series of probabilistic seismic slope deformation analyses were performed on an idealized slope for a scenario earthquake event. Displacement uncertainty was quantified for several scenarios designed with increased levels of ground motion variability. Variability in the seismic resistance of the slope was also included. In this approach, realistic levels of variability in both seismic

resistance and demand are systematically changed to evaluate their collective effect on displacement prediction uncertainty.

### 2 PROBABILISTIC DISPLACEMENT ANALYSIS

Performing a rigid-block analysis consists of the following steps: (1) a limit-equilibrium pseudostatic slope stability analysis to compute  $k_y$ ; and (2) characterization of the earthquake-induced shaking at the site. The seismic yield coefficient represents the minimum acceleration required to initiate down-slope displacement of a slide mass. In the rigid-block method, earthquake shaking is characterized by acceleration time-histories that represent a rock outcropping condition which is consistent with the concept of slide mass rigidity assumed by Newmark (1965). Each of these analyses was implemented in a probabilistic framework using Monte-Carlo simulation. All simulations were performed for 1000 iterations using Latin-Hypercube sampling of the input distributions.

The idealized slope model has a height of 20 m with a slope face inclined at an angle of 18 degrees. The failure surface shown in Figure 1 is intended to represent a first-time, shallow translational landslide. Shear strength of the landslide material (unit weight,  $\gamma = 20 \text{ kN/m}^3$ ) was assumed to be controlled by the peak friction angle ( $\phi'_{peak}$ ) only.

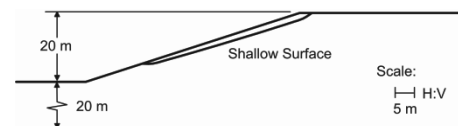


Figure 1. Cross-section of the idealized slope model with a shallow failure surface (maximum thickness of 2 m).

The scenario earthquake used for this analysis is the 1994 Northridge event (moment magnitude,  $M_w = 6.7$ ), in California, USA. The slope was assumed to be located 28 km to the northwest of the epicenter. Based on the assumed site location, acceleration time histories were selected from recording stations that recorded the Northridge event. Four stations were selected: (1) Lake Hughes 12A (LHA); (2) Castaic-Old Ridge Road (ORR); (3) Vasquez Rock Park (VAS); and (4) Newhall-West



Pico Canyon Road (WPI). These time-histories were rotated to their fault-normal/parallel components and only the fault-normal components were used in the analysis.

### 3 GROUND MOTION VARIABILITY

Shaking experienced at the hypothetical site was characterized using published ground motion prediction equations (GMPE) using a pseudo-probabilistic approach to model variability in the ground motions. In this approach, the Abrahamson and Silva (2008) GMPE was used to obtain a median acceleration response spectrum and the intra-event component of standard deviation ( $\sigma$ ) (i.e., single-event variability) for the median prediction. Variability was modeled by varying the number of standard deviations ( $n_\sigma$ ) around the median spectrum ( $n_\sigma = 0$ ) as a normally-distributed random variable ranging from  $n_\sigma = -3$  to  $+3$ . The use of a normal distribution achieves symmetry in the range of  $n_\sigma$  generated while preserving the underlying log-normal distribution of the spectral ordinates. Different target response spectra were obtained by multiplying  $n_\sigma$  by the intra-event standard deviation and adding or subtracting this from the median spectrum. The median,  $\pm 1\sigma$  and  $\pm 3\sigma$  spectra are shown in Figure 2; the *PGA* ranges from 0.07 g to 1.15 g with a median value of 0.28 g. A rock outcropping condition was simulated by assuming a shear wave velocity over 30 m ( $v_{s30}$ ) of 1100 m/s and depth of rock of 0 m (ground surface).

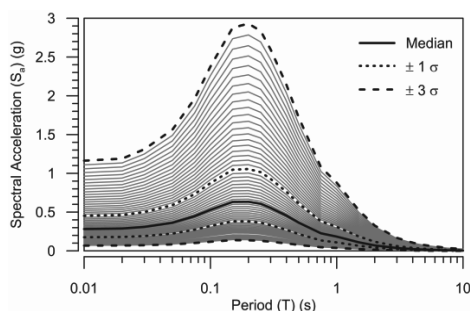


Figure 2. Illustration of the range of acceleration response spectra for the hypothetical site

To understand how ground motion variability affects the displacement uncertainty, the pseudo-probabilistic approach described above was implemented in the seismic displacement analysis in a systematic way by performing multiple probabilistic analyses for four different scenarios. These scenarios were designed to progressively increase in their inherent complexity by introducing different types of ground motion variability to the seismic displacement analysis. The four scenarios evaluated are described below.

**No variability** – This is a baseline condition with no variability where the ground motion is held at a constant intensity. Each parent motion (LHA, ORR, VAS, WPI) was spectrally-matched to the median target response spectra generating four separate motions each with a *PGA* of 0.28 g. All spectral-matching was performed using a wavelet-based algorithm developed by Mukherjee and Gupta (2002).

**Variable intensity** – For this scenario, variability in the ground motion intensity is introduced. Using the median spectrally-matched motions from the previous scenario, in this approach, variation in intensity is modeled by simple uniform-scaling to the target  $\pm 3\sigma$  *PGA* values generated from the pseudo-probabilistic approach. For each parent motion, a suite of 1000 *PGA*-scaled acceleration time-histories were generated.

**Variable intensity and frequency** – For this case, additional variability in form of richer ground motion frequency content is combined with the variation of intensity. This form of variability was introduced by considering the variation of spectral acceleration ( $S_a$ ) with period ( $T$ ) provided by the full target response spectra. Variability in the frequency content is

modeled in an approximate manner through variation of the spectral shape and bandwidth of the response spectra between the  $\pm 3\sigma$  bounds (Figure 2). This additional variability was achieved by spectrally-matching a single parent ground motion to randomly-selected response spectrum between  $\pm 3\sigma$  bounds generated from the pseudo-probabilistic approach. For each parent motion, 1000 spectra-compatible acceleration time-histories were generated.

**Variable, intensity, frequency and waveform** – In this approach, additional variability is introduced by using all four parent ground motions in the spectral-matching process. Since the wavelet-based spectrally-matching algorithm generally maintains the non-stationary characteristics of the parent motions, this scenario provides variability in the core waveforms that are propagated through the displacement analysis. To accomplish this, randomly selected parent motions are paired with randomly selected response spectra (between the  $\pm 3\sigma$  bounds generated from the pseudo-probabilistic approach) and spectrally-matched. A total of 1000 spectra-compatible acceleration time-histories were generated that incorporate all four parent ground motions.

### 4 SEISMIC DISPLACEMENT NON-LINEARITY

While the intended purpose of this study is to examine ground motion variability, Strenk and Wartman (2011) demonstrated that predictive uncertainty of common seismic displacement methods is also a function of a slope's relative degree of stability. In the context of Newmark's sliding block analogy, the stability of a slope with respect to sliding is defined as the ratio of a slope's ability to resist sliding ( $k_y$ ) over the peak value of the earthquake-induced acceleration (*PGA*) and is referred to as the acceleration ratio ( $k_y/PGA$ ). For a variety of simplified, equation-based methods and even more complex decoupled methods, a highly-nonlinear relationship exists between the acceleration ratio and displacement ( $\delta$ ); this is illustrated in Figure 3.

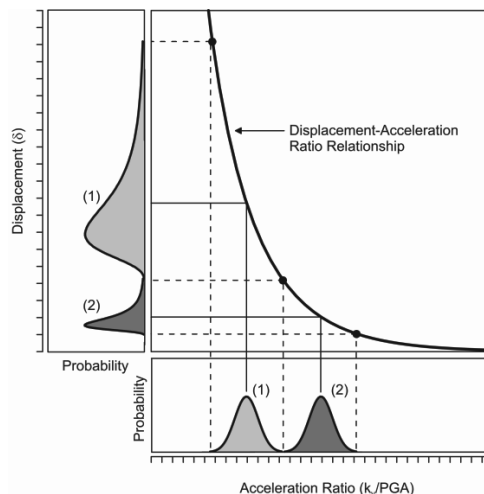


Figure 3. Illustration of the relationship linking the position of the acceleration ratio distribution to displacement prediction uncertainty.

Non-linearity is a consequence of Newmark's modeling decision to approximate the physical mechanism of earthquake-induced displacement after the inherently non-linear dynamic behavior of a sliding-block system. This inherent non-linearity manifests itself through the calculation procedure of "double-integrating" the acceleration time-history in excess of  $k_y$  (Newmark 1965) to compute the permanent displacement. In a probabilistic framework, non-linearity was observed to have a strong influence on how parametric variability (in seismic resistance and demand) is propagated through the analysis and can lead to varying degrees of displacement uncertainty (Strenk

and Wartman 2011). This relationship is characterized by a threshold behavior whereby nominal changes in acceleration ratio are greatly amplified into large changes in predicted displacement and hence uncertainty (Figure 3).

In order to capture this, multiple simulations were performed with the purpose of generating three different distributions of  $k_y$ , targeted to have low, moderate and high median values. To do this, probability distributions of  $\phi'_{peak}$  were systematically varied through the pseudostatic analysis to control the slope's seismic resistance; these distributions are referred to as "low", "moderate" and "high" strength and are illustrated in Figure 4a.

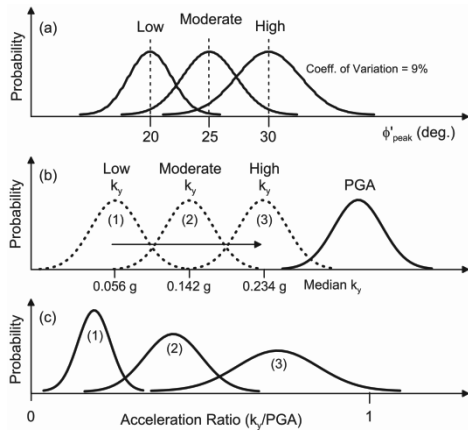


Figure 4. Illustration of the relationship between the  $k_y$  and  $PGA$  distributions and the resulting  $k_y/PGA$  distributions. Corresponding distributions of  $\phi'_{peak}$  are shown for the three strength conditions.

By holding the distribution of  $PGA$  constant and varying the  $k_y$  distributions (Figure 4b), sampling of acceleration ratios was targeted to concentrate along different portions of the  $k_y/PGA$  scale (Figure 4c). For each ground motion variability scenario, three separate simulations for each strength condition were performed. This approach allowed displacement uncertainty to be quantified along different regions of displacement-acceleration ratio relationship and provided insight into how both method non-linearity and ground motion variability affect the level of prediction uncertainty.

## 5 DISPLACEMENT ANALYSIS RESULTS

Statistical measures of central tendency and spread were calculated for the displacement data obtained from the Monte-Carlo simulations of the different scenarios of ground motion variability. Overall, the displacement data was observed to be positively skewed as a result of several sources including inherent distributional assumptions (e.g. log-normal GMPE), truncation at prescribed limits (e.g.  $k_y$  below zero cannot exist, no  $k_y/PGA$  greater than 1) and method non-linearities (Figure 3). Non-parametric statistics based on percentiles that are less sensitive to data asymmetry and were used to describe the data.

For this study, uncertainty in the displacement predictions was assessed using the interquartile range ( $IQR$ ). This parameter represents the range of the middle 50% of the displacement data and is calculated as:

$$IQR = P_{75} - P_{25}$$

where,  $P_{75}$  and  $P_{25}$  are the 75<sup>th</sup> and 25<sup>th</sup> percentiles of the data. Interquartile range data is summarized in Table 1 for the different ground motion variability scenarios and strength conditions.

Table 1. Summary of displacement interquartile range for the different types of ground motion variability and strength conditions

Ground Motion Variability	Displacement $IQR$ (cm)			
	LHA	ORR	VAS	WPI
<b>No Variability</b>				
Low Strength	8.2	7.5	9.1	9.4
Moderate Strength	0.4	0.5	0.9	0.8
High Strength	0.1	0.1	0.2	0.2
<b>Varied intensity</b>				
Low Strength	14.6	12.9	15.9	16.4
Moderate Strength	2.3	2.0	3.4	3.0
High Strength	0.7	0.7	1.3	1.0
<b>Varied intensity-frequency</b>				
Low Strength	15.3	13.9	17.1	17.5
Moderate Strength	2.6	2.3	3.9	3.5
High Strength	0.8	0.9	1.5	1.3
<b>Varied intensity-frequency-waveform (all 4 motions)</b>				
Low Strength			16.7	
Moderate Strength			3.0	
High Strength			1.0	

## 6 DISCUSSION

The seismic displacement results presented in Table 1 demonstrate that the combined variability from both ground motions and the soil properties have a marked influence on displacement prediction uncertainty. For the scenarios evaluated, uncertainty is also observed to increase as variability in the intensity, frequency content and waveform are incrementally introduced into the probabilistic seismic displacement analysis.

### 6.1 No Variability

For this scenario, displacement uncertainty is due *entirely* to the variability in the seismic resistance, specifically the  $k_y$  distributions. With no variability in the ground motions, the displacement-acceleration ratio relationship ( $\delta-k_y/PGA$ ) plots as a smooth, monotonically-increasing line; the  $\delta-k_y/PGA$  relationship for the LHA parent motion is shown in Figure 5. At low acceleration ratios, this relationship is highly non-linear which causes parametric variability of  $k_y$  to be magnified into large displacement uncertainty ( $IQR$  of 8 to 9 cm at the low strength) that progressively reduces as the relative stability of the slope increases (moderate to high strength conditions). This is consistent with the median  $k_y/PGA$  that increases from about 0.20, 0.51 and 0.83 for the low, moderate and high strength  $k_y$  distributions. For this scenario, the  $\delta-k_y/PGA$  relationship for the LHA motion is similar to that for the other parent motions which is due to the fact that all four motions were spectrally matched to the same median response spectrum and thus predict a similar response.

### 6.2 Varied Intensity

For this scenario, variability in  $k_y$  and intensity of the ground motions contribute to the overall displacement uncertainty. As these are scaled motions, the frequency content is constant in the displacement analysis of each parent motion. The  $\delta-k_y/PGA$  relationship for the LHA motion is compared to the case of no ground motion variability in Figure 5. Significant scatter is observed in the  $\delta-k_y/PGA$  relationship and the displacement uncertainty for each parent motion is higher than that for the case of no ground motion variability. By including variability in the shaking intensity, the displacement  $IQR$  is observed to increase by a factor of nearly 2 for the low strength condition. The  $IQR$  increases by factors of 4 and 5 for the moderate to high strength conditions.

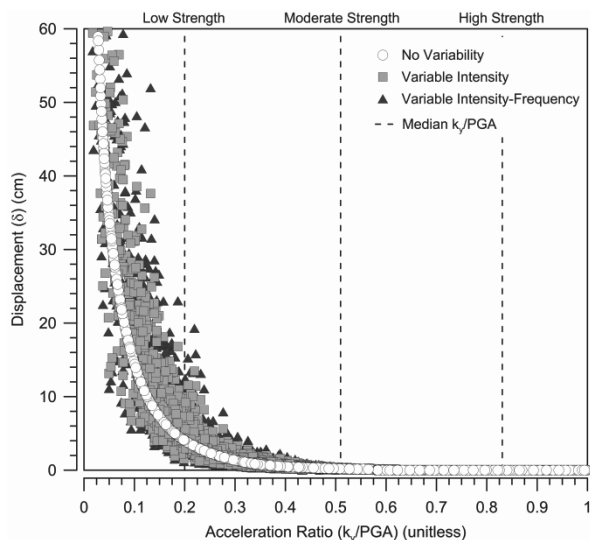


Figure 5. Comparison of the  $\delta$ - $k_y/PGA$  relationships for the LHA parent motion for the different ground motion variability scenarios

From this it may be inferred that the displacement uncertainty for marginally stable slopes is more sensitive to variability in the site conditions (i.e., input parameters that feed into  $k_y$ ) while slopes with greater relative stability are more sensitive to ground motion variability. This suggests that for weaker slopes, greater resources and effort should be focused on constraining the variability of the subsurface conditions, whereas for more stable slopes the focus should be on characterizing the earthquake ground motions.

### 6.3 Varied Intensity and Frequency

When additional variability from frequency content is introduced into the analysis, marginal increases in the displacement uncertainty are observed. This is indicated by the slight increase in scatter in the  $\delta$ - $k_y/PGA$  data shown in Figure 5. For the four parent motions, displacement uncertainty increases by a factor of about 1.2, this is substantially less change than that observed when variability in intensity was introduced into the analysis. This is consistent with research that has demonstrated the efficiency of intensity ground motion parameters (e.g.,  $PGA$ , peak ground velocity,  $PGV$  and Arias Intensity,  $I_a$ ) over frequency content parameters for correlating with displacement predictions (Saygili and Rathje 2008).

While the range of response spectra simulated in the analysis (Figure 2) do show variations in their spectra shape, the peak spectral acceleration between the  $\pm 3\sigma$  bounds remains constant at a predominant period ( $T_p$ ) of about 0.2 s. This characteristic as well as the frequency-smoothing affect that spectral-matching has on the output motions could explain the marginal increase in displacement uncertainty. It is likely that displacement uncertainty would increase had the  $T_p$  of the simulated response spectra been allowed to take on a range of values. If, for example, the sub-model for site-conditions (specifically  $v_{s,30}$ ) in the Abrahamson and Silva (2008) GMPE had been modeled as a random variable this would have generated more diverse spectral shapes and hence additional variability in the ground motions. If this technique is implemented in a probabilistic analysis it should be compatible with the underlying assumptions of the method being used. For example, the Newmark (1965) rigid-block model assumes that the slope and slide mass are a non-deformable, rigid body. As such it would be inappropriate to use motions spectrally-matched to a response spectrum for site conditions representative of soft soil as this implies that the slope and slide mass can respond dynamically to the motions. In this case, decoupled-type analyses such as Makdisi and Seed (1978) would be appropriate.

### 6.4 Variable Intensity, Frequency and Waveform

When the intensity, frequency and waveform are varied, the combined affect yields displacement uncertainty that is marginally different from the previous case. Similar to frequency, introducing more diverse waveforms has little effect on the prediction uncertainty. However, it is interesting to note that  $IQR$  for this scenario is sometimes greater or less than the  $IQR$  for the individual parent motions. This is related to the wavelet-based spectral-matching process where the parent motion is decomposed, scaled up/down using wavelets and re-assembled such that modified time-history is compatible with the spectrum and non-stationary characteristics of the parent motion are preserved. Thus, even though the response spectra varies between  $\pm 3\sigma$  bounds using only one parent motion yields a suite of spectra-compatible motions that have very similar non-stationary characteristics. This explains the systematic differences between the four parent motions for three previous ground motion variability scenarios. For example, the non-stationary characteristics of the VAS and WPI motions are such that when input into the “double-integration” computation of the rigid-block method, regardless of being scaled or spectrally matched, systematically yield higher median displacements and more prediction uncertainty than motions LHA and ORR. When all four motions are propagated through the displacement analysis, the effects of individual motions are tempered and a more average displacement response is computed. This average response, however, is not necessarily more precise than using a single parent motion.

## 7 CONCLUSIONS

Systematically increasing ground motion variability (and complexity) in the probabilistic displacement analysis showed a trend of increased displacement uncertainty. For the idealized slope, this trend was consistent across a range of relative stabilities (low, moderate and high). Ground motion variability had its most pronounced affect on displacement uncertainty at low acceleration ratios as a consequence of the non-linear  $\delta$ - $k_y/PGA$  relationship. Of the four scenarios considered, variability in ground motion intensity alone has the greatest impact on the displacement prediction uncertainty. When additional variation in frequency content and waveform is introduced, only minimal changes in uncertainty are observed. These results suggest that displacement uncertainty may be adequately characterized through simple scaling of ground motion intensity and that the effort required to create variability in both intensity and frequency through spectral-matching may be of limited utility. Also, the use of multiple parent motions in a displacement analysis can overcome potential biases introduced by individual motions, but may not always lead to more constrained prediction uncertainty.

## 8 REFERENCES

- Abrahamson N.A. and Silva W.J. 2008. Summary of the Abrahamson & Silva NGA ground motion relations. *Earthquake Spectra* 24, 67-97.
- Makdisi F. I. and Seed H. B. 1978. Simplified procedure for estimating dam and embankment earthquake-induced deformations. *Journal of Geotechnical Engineering Division* 104(GT7), 849-867.
- Mukherjee S. and Gupta V.K. 2002. Wavelet-based generation of spectrum-compatible time-histories. *Soil Dynamics and Earthquake Engineering* 22(9-12), 799-804.
- Newmark N.M. 1965. Effects of earthquakes on dams and embankments. *Géotechnique* 15(2), 139-160.
- Strenk P.M. and Wartman J. 2011. Uncertainty in seismic slope deformation model predictions. *Engineering Geology* 122(1-2), 61-72.
- Saygili G. and Rathje E.M. 2008. Empirical predictive models for earthquake-induced sliding displacements of slopes. *Journal of Geotechnical and Geoenvironmental Engineering* 134(6), 790-803.

# A new approach to assess the potential for flow slide in sensitive clays

## Une nouvelle approche pour évaluer le potentiel d'écoulement des argiles sensibles

Thakur V., Degago S.A., Oset F., Dolva B.K., Aabøe R.  
Geotechnical section, Norwegian Public Roads Administration

**ABSTRACT:** Sensitive clays could constitute a major threat to nearby infrastructure due to potential flow slides. A key question is if all sensitive clays have the same potential to retrogress to the same extent and the significance of remoulded shear strength ( $c_{ur}$ ) in flow slides. This paper proposes a new approach to assess the potential for flow slides and in doing so presents a new laboratory test procedure referred to as the quickness test. The test focuses on remoulded behaviour of sensitive clays in terms of a numerical value referred to as quickness ( $Q$ ). Sensitive clay samples were collected from three different landslide locations. The quickness test was used to demonstrate why sensitive clays with  $c_{ur} > 1$  kPa are not susceptible to flow slides. Based on this study, it is possible to state that a  $Q < 15\%$  or  $c_{ur} > 1$  kPa seems to be the threshold limit above which the extent of the retrogression of a landslide is limited to the initial slide. This criteria has been supported using data available from several Norwegian landslides in sensitive clays.

**RÉSUMÉ :** Les argiles sensibles pourraient constituer une grave menace pour les infrastructures en raison de coulées potentielles. Une question clé est de savoir si toutes les argiles sensibles ont un potentiel de rétrogression équivalent et de d'estimer l'amplitude de la résistance de cisaillement remaniée ( $c_{ur}$ ) des les coulées. Cet article propose une nouvelle approche pour évaluer le potentiel de coulées et présente ainsi une nouvelle procédure de laboratoire appelée le test de rapidité. Le test se concentre sur le comportement de l'argile sensible remaniée en termes de valeur numérique dénommée rapidité ( $Q$ ). Des échantillons d'argiles sensibles ont été recueillis à partir de trois sites différents où il y a eu des glissements de terrain. Le test de rapidité a été utilisé pour démontrer pourquoi les argiles sensibles avec  $c_{ur} > 1$  kPa ne sont pas sujettes à des coulées. Sur la base de cette étude, il est possible d'affirmer que  $Q < 15\%$  ou  $c_{ur} > 1$  kPa semble être le seuil au-delà duquel l'ampleur de la rétrogression d'un glissement de terrain est limitée à la rupture initiale. Ce critère se base sur des données disponibles à partir de plusieurs glissements de terrain dans les argiles sensibles norvégiens.

**KEYWORDS:** Flow slide, sensitive clays, quickness, remolded shear strength, landslide.

### 1 INTRODUCTION

Soft sensitive clays are normally associated with loss of stability as well as substantial ground deformation, which can lead to structural damage and jeopardize the overall stability of an area. It is worth mentioning the statement by Bishop in 1973 that "Rotational slips alone may cause damage to services and property, but seldom involve loss of life. It is the subsequent development into a flowslide which has been responsible in each case where disaster has occurred". In the sensitive clay deposits of Scandinavia and eastern Canada, landslides are particularly destructive, due to the possibility of small landslides initiating a flow slide, which may involve massive soil movements in the order of millions of cubic meters.

For flow slides to occur after an initial slide, it is important that at least the following two criteria are fulfilled (Tavenas et al. 1983):

- The slide debris should be sufficiently remoulded.
- The slide debris should be able to flow out of the slide area if remoulded.

There may be additional factors, such as the topography and the stability of the area behind the initial slide zone. However, if the two criteria mentioned above are not fulfilled, then vast landslides, such as those listed in Table 1, are unlikely to occur. An overview of Norwegian landslides as shown on Table 1 clearly indicates that soft sensitive clays must be handled carefully. However, the term 'sensitive clay' encompasses a wide range of clays depicting significant variations in engineering behaviour such as the remoulded shear strength

( $c_{ur}$ ). Therefore, a key question is whether all sensitive clays have the same potential to create flow slide and the significance of  $c_{ur}$  for occurrence of flow slide? Answer to this question has a direct relevance in the selection of an appropriate safety level for constructions, measures and in hazard mapping.

A relationship between the  $c_{ur}$  and the soil sensitivity ( $S_t$ ) as well as between  $c_{ur}$  and the liquidity index ( $I_L$ ) has been used to evaluate the potential for flow slides in sensitive clays. Mitchell and Markell (1974) suggest a direct relationship between  $c_{ur}$ ,  $S_t$  and the retrogression distance ( $L$ ). They suggest that landslides with an  $L > 100$  m are observed for  $c_{ur} < 1$  kPa. Retrogression was zero for  $c_{ur} > 1$  kPa. Leroueil et al. (1983) and Locat and Demers (1988) presents correlations between  $c_{ur}$  and  $I_L$ . The correlations are  $c_{ur} = (I_L - 0.21)^2$  and  $c_{ur} = 1.46 I_L^{-2.44}$  respectively. These showed that sensitive clays with  $I_L > 1.2$  are susceptible to flow slides. This finding is also supported by the landslide data presented in Table 1. It must be noted that, according to the correlations  $I_L > 1.2$  is only possible when  $c_{ur}$  is less than 1 kPa. In other words, the findings by Mitchell and Markell (1974), Leroueil et al. (1983), Tavenas et al. (1983) and Locat and Demers (1988) are in line with each other. Based on the landslide data, Lebus et al (1983) also suggested that  $c_{ur} < 1$  kPa may define the threshold limit for occurrence of flow slides.

$I_L$  and  $c_{ur}$  based criteria have been widely adopted to study the flow slide potential of sensitive clays. However, the measurement of  $I_L$  demands determination of three parameters a priori, i.e. liquid limit ( $w_l$ ), plastic limit ( $w_p$ ) and natural water content ( $w$ ). Notably the conventional thread-rolling method of

determining  $w_p$  has a significant drawback as it can easily be biased by subjective judgement. Also,  $c_{ur}$  is usually measured using the fall-cone test, a point based measurement system, which may not necessarily be representative of a large soil volume.

Keeping this in view this paper proposes a new test procedure, the quickness test, to evaluate the flow slide potential of sensitive clays. In contrast to the conventional  $c_{ur}$  and  $I_L$  based approaches, the quickness test is a soil volume based approach and has an added advantage of qualitative description that provides a better visualisation with respect to understanding of flow slides.

Table 1 Selected large landslides in Norwegian sensitive clays.

No.	Year	Landslide	$L_R$ [m]	$c_{ur}$ [kPa]	$S_t$ [-]	$I_L$ [-]	$I_P$ [%]
1	2012	Byneset	300	0.12	120	3.8	4.8
2	2010	Lyngen	230	0.35	50	1.5	12
3	2009	Kattmarka	300	0.24	63	2.9	8
4	1978	Rissa	1200	0.24	100	2.2	6
5	1974	Baastad	930	0.53	35	1.8	8
6	1967	Hekseberg	230	0.25	100	2.4	4
7	1965	Selnes	700	0.35	100	2.3	7
8	1959	Furre	215	0.2	85	1.3	6
9	1953	Bekkelaget	145	0.2	130	2.4	9
10	1953	Borgen	165	0.7	100	1.2	20
11	1953	Ullensaker	250	0.35	42	1.9	6.7
12	1893	Verdalen	2000	0.2	300	2.2	5

\* $L_R$  = Retrogression distance

## 2 THE QUICKNESS APPROACH

In this section, a simple test known as the quickness test is presented. The quickness test aims to provide the basis for a physical understanding of flow behaviour of fully remoulded sensitive clays using a new type of geotechnical engineering test. Additional description on the test methodology can be referred to Thakur and Degago (2012).

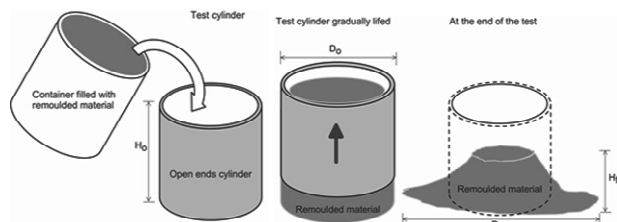


Figure 1. Quickness test procedure (Thakur and Degago, 2012).

### 2.1 Test procedure

The quickness test is a simple procedure that is performed by filling an open ended cylinder with remoulded sensitive clay, then slowly lifting the cylinder, and finally measuring the deformation (height and lateral spreading) as the material is subjected to flow due to its own weight. The test concept is similar to the slump test for concrete that is used to measure the consistency of freshly mixed concrete. Two different cylinder sizes were used. The dimensions were the diameter ( $D_o$ ) = 65 mm and height ( $H_o$ ) = 45 mm for the small cylinder, and  $D_o$  = 100 mm and  $H_o$  = 120 mm for the large cylinder. The large cylinder has the same size as the cylinder used for the standard

proctor tests. Figure 1, taken from Thakur and Degago (2012), shows the concept of the proposed quickness test. The thoroughly remoulded material is placed into the cylinder, levelled off, and allowed to flow outward as the cylinder is slowly lifted upward with minimum disturbance to the sample. The difference in height between the cylinder and the slumped material ( $H_o - H_f$ ) is measured. The outward flow spread diameter ( $D_f$ ) is also noted. The quickness ( $Q$ ) in % is defined as  $[1 - H_f / H_o] \times 100$ .

### 2.2 The tested material

Quickness tests were performed on several sensitive clay samples taken from three different locations in the central Norway. One of the landslides, Lersbekken, have been studied and presented in Thakur and Degago (2012). In this work a similar approach is presented for two new landslide locations Byneset and Olsøy. These sites have been studied extensively in connection to landslide hazards. Laboratory index properties of the sampled material are presented in Table 2. Liquid limit ( $w_L$ ),  $c_{ui}$  and  $c_{ur}$  of the tested material were obtained using the fall-cone method as described by the National Standard NS 8015 in Norway.

Table 2 Properties of the tested materials from three different landslide locations

Properties	Lersbekken	Byneset	Olsøy
Sampling depth ( $H$ ) [m]	6 – 10	4 – 12	4 – 15
Clay fractions (< 2 $\mu$ m) [%]	30	30 – 55	50 – 65
Water content ( $w$ ) [%]	22 – 34	27 – 48	28 – 38
Plasticity index ( $I_P$ ) [%]	5 – 7	3 – 15	3 – 10
Liquidity index ( $I_L$ ) [-]	0.7 – 2.0	0.9 – 5.4	0.6 – 3
Undisturbed undrained			
shear strength ( $c_{ui}$ ) [kPa]	12 – 58	5.2 – 72	60 – 100
Remoulded undrained			
shear strength ( $c_{ur}$ ) [kPa]	0 – 2	0 – 3	0 – 2.1
Sensitivity ( $S_t$ ) [-]	16 – 29	4 – 400	30 – 100
Over consolidation ratio ( $OCR$ ) [-]	1.8 – 2.0	1.1 – 3.3	2 – 4

## 3 TEST RESULTS AND OBSERVATIONS

Quickness tests were performed on more than 60 different samples extracted from Lersbekken, Byneset and Olsøy landslide locations. A series of pictures taken during the quickness test on two Byneset clay samples, with  $c_{ur} = 0.1$  kPa and  $c_{ur} = 1.0$  kPa, are shown in Fig. 2. The figure shows slump and spread observed at selected stages of the tests given as the percent ratio of the height lifted to the cylinder height ( $H_o$ ).

Previous observations during a quickness test conducted on Lersbekken clay showed that sensitive clays with  $c_{ur} \approx 0.5$  kPa were not as fluid as they were originally assumed and sensitive clays with  $0.5 \text{ kPa} < c_{ur} < 1.0 \text{ kPa}$  were semisolid in nature (Thakur and Degago, 2012). In line with this observations, the Byneset and Olsøy clay samples with  $c_{ur} < 0.2$  kPa, seemed to be more like a soup as reported by Mitchell and Soga (2004). The registered collapse of the remoulded material was negligible when the remoulded sensitive clay had  $c_{ur} > 1.0$  kPa.

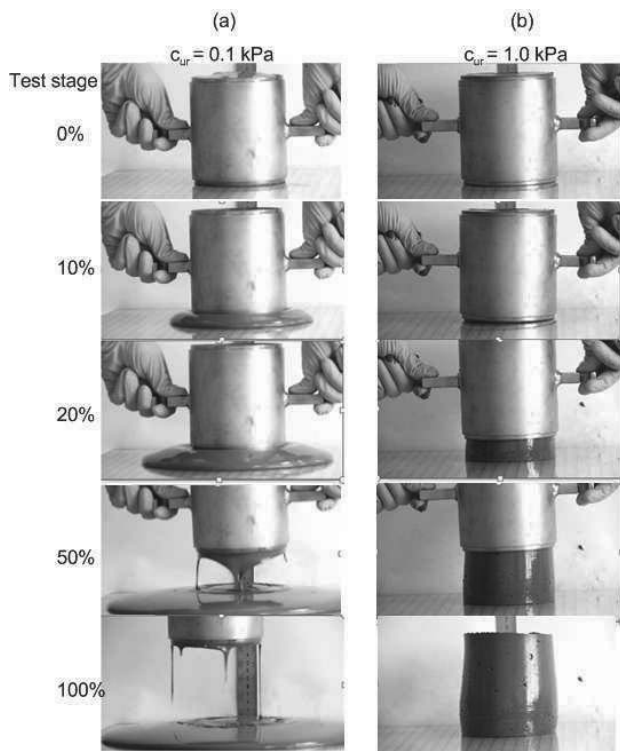
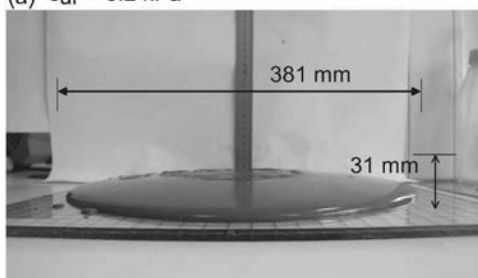


Figure 2. Slump and spread observed from the start to the end of the Quickness tests for remoulded Byneset clays (a)  $c_{ur} = 0.1$  kPa and (b)  $c_{ur} = 1.0$  kPa.

A typical flow and spread behaviour of two remoulded clays from the Olsøy site are presented in Figure 3. The tests on Olsøy clay shows that the remoulded material with  $c_{ur} < 0.2$  kPa seemed to be more like a soup, Figure 3(a). As the  $c_{ur}$  increases from 0.2 kPa towards 1 kPa, the remoulded material increasingly showed less viscous behavior and for a  $c_{ur} > 1.0$  kPa little or no flow is observed, Figure 3(b). This simple test indicates why soft sensitive clays with a  $c_{ur} > 1$  kPa are less likely subjected to a large retrogression or run-out.

(a)  $c_{ur} = 0.2$  kPa



(b)  $c_{ur} = 1.2$  kPa

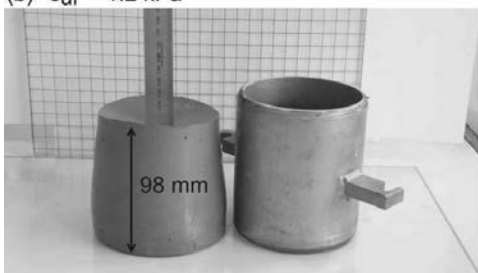


Figure 3. Flow and spread behaviour of the two remoulded Olsøy clays having (a)  $c_{ur} = 0.2$  kPa and (b)  $c_{ur} = 1.2$  kPa.

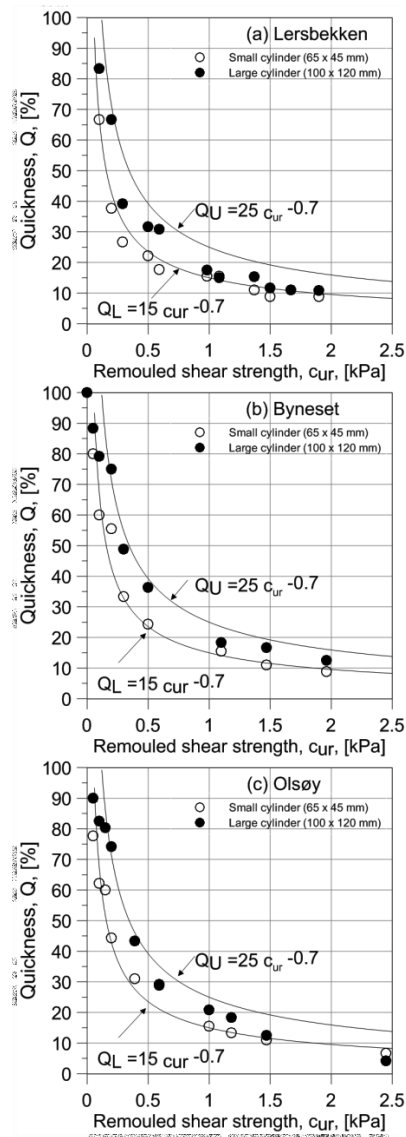


Figure 4.  $Q$  versus  $c_{ur}$  values registered on soil samples taken from a) Lersbekken b) Byneset and c) Olsøy landslide locations.

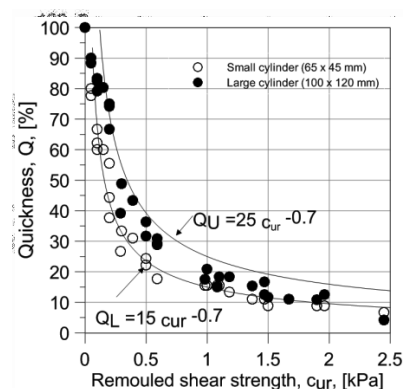


Figure 5. Compilation of  $Q$  versus  $c_{ur}$  values registered on soil samples taken from the three landslide locations.

Apparently, the flow behaviour of the Lersbekken, Byneset and Olsøy clay is identical. Figure 4 presents  $Q$  versus  $c_{ur}$  for various sets of tests on the Lersbekken, Byneset and Olsøy clays performed with two different cylinder sizes, 100 mm x 120 mm, 65 mm x 45 mm. For the major area of interest, i.e. clay samples with  $c_{ur} > 1.0$  kPa, material flow was not registered irrespective of the size of the test cylinders. Accordingly, this

study recommends using a cylinder size 100 mm x 120 mm and proposes some correlations based on this cylinder size because this cylinder size is readily available in connection with the standard proctor test. The Figures presents the lower and the upper bound  $Q$  values observed for various  $c_{ur}$  of the tested material. A combined plot is shown in Figure 5 where all the data from the three landslide locations are plotted together.

Thakur and Degago (2012) suggests considering the lower bound quickness in evaluating flow slide potentials since it provides a conservative estimate. It can be noticed from the quickness test results (Figure 4 and 5) that all Lersbekken, Byneset and Olsoy materials have nearly identical responses and the lower bound  $Q = 15\%$  corresponds to  $c_{ur} = 1$  kPa for all the three sensitive clays.

#### 4 SUITABILITY OF QUICKNESS TEST

Suitability of quickness value ( $Q$ ) as compared to remoulded shear strength ( $c_{ur}$ ) in relation to assessment of flow behaviour of materials is briefly discussed.

Fluidity of sensitive clays is difficult to interpret by small numerical values of  $c_{ur}$  because a seemingly small change could imply significant alteration in flow behaviour of clay. For example, a significant change in the flow behaviour of the sensitive clay from the Lersbekken site is observed for a small variation of  $c_{ur}$ , i.e. from 0.5 to 0.2 kPa. In this case, the significant behavioural change is reflected by the quickness test visually as well as numerically  $Q$  varies from 32% to 67% (Thakur and Degago, 2012). The quickness test amplifies the small range of  $c_{ur}$ , i.e. from 0 to 2.0 kPa, to a larger scale, 0 to 100%. Quickness test therefore gives a better visualisation of the flow behaviour of sensitive clays where small  $c_{ur}$  values have large implications in regards to understanding the potential for retrogressive landslides.

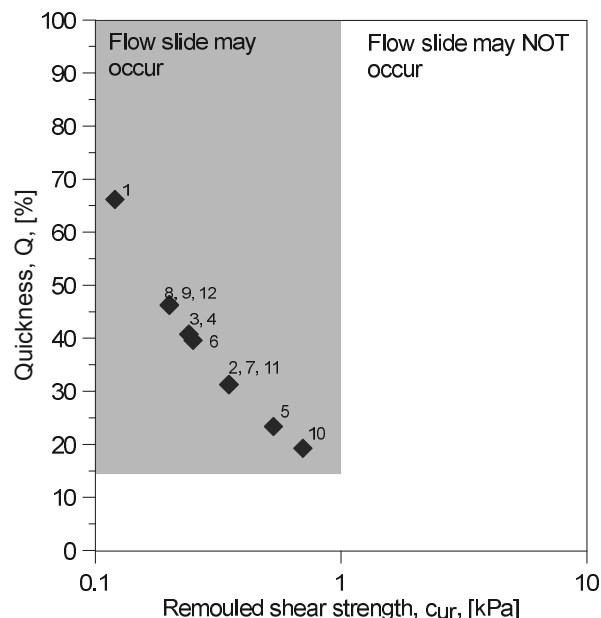


Figure 6. Estimated  $Q$  values for Norwegian landslides given in Table 1 and quickness based criteria for occurrence of flow slides.

In general, both  $c_{ur}$  and  $Q$  principally explains the same soil characteristic through different test approaches. The fall-cone test is a point specific method calibrated against the undrained shear strength of soil under undisturbed and remoulded state; whereas, the quickness test gives a value that is representative of the volume of the material tested. In contrast to the fall-cone test, the quickness test has an added advantage of qualitative

description that can provide a better visualization with respect to understanding flow slide (Thakur and Degago, 2012).

#### 5 ASSESSMENT OF FLOW SLIDE POTENTIALS

Significance of quickness test is illustrated in relation to assessment of potential for flow slides using the Norwegian landslides given in Table 1. In doing so the  $Q$  values for each landslides is estimated based on the corresponding  $c_{ur}$  values and using a lower bound correlation shown in Figure 5 ( $Q = 15 c_{ur}^{-0.7}$ ). The estimated  $Q$  values of the Norwegian landslides are shown in Figure 6 where the numbers corresponds to the landslide numbers as listed in Table 1.

Based on the quickness test results and the data from the Norwegian landslides, two distinct regions are shown in the Figure 6. These regions depict the potential for occurrence of flow slides based on  $Q$  values. Accordingly, large flow slides are less likely to occur when  $Q < 15\%$  (or  $c_{ur} > 1$  kPa) and in this case the slide will be limited to an initial slide only. However, for  $Q > 15\%$  (or  $c_{ur} < 1$  kPa), a flow slide is possible. Based on the retrogression length ( $L_R$ ) of the Norwegian landslides studied in this work,  $15\% < Q < 25\%$  (or  $0.5$  kPa  $< c_{ur} < 1$  kPa) mostly corresponds to a flow slide with  $L_R < 250$  m while  $Q > 25\%$  (or  $c_{ur} < 0.5$  kPa) corresponds to a flow slide with  $L_R > 250$  m. Effort is being made to establish a correlation between  $L_R$  and  $Q$  using several landslide data, however at this stage no specific recommendation is made.

#### 6 CONCLUSIONS

This paper presents a new laboratory procedure that focuses on remoulded behaviour of sensitive clays in terms of a numerical value referred to as quickness ( $Q$ ). The quickness test was used to demonstrate why sensitive clays with  $c_{ur} > 1.0$  kPa are not susceptible to flow. This particular study shows that a  $Q < 15\%$  or  $c_{ur} > 1.0$  kPa seems to be the threshold limit where the extent of the retrogression of a landslide is limited to the initial slide.

#### 7 ACKNOWLEDGEMENT

National research program “Natural hazards: Infrastructure, Floods and Slides (NIFS)”, by the Norwegian Public Roads Authority, Norwegian Water Resources and Energy Directorate and Norwegian National Railways Administration and Mrs. Olga Lapkovski are acknowledged for their support.

#### 8 REFERENCES

Lebuis J., Robert J.-M. and Rissmann P. 1983. “Regional mapping of landslide hazard in Quebec”, In Proceedings of the Symposium Slopes on Soft Clays, SGI Report 17, 205–262.

Leroueil S., Tavenas F. and Le Bihan J.P. 1983. “Propriétés caractéristiques des argiles de l’est du Canada”, Canadian Geotechnical Journal 20,681–705.

Locat J. and Demers D. 1988. “Viscosity, yield stress, remoulded strength, and liquidity index relationships for sensitive clays”, Canadian Geotechnical Journal 25,799–806.

Mitchell R. J. and Markell A. R. 1974. “Flow slides in sensitive soils. Canad. Geotech. J. 11 (1), 11–31.

Tavenas F., Flon P., Lerouil S. and Lebuis J. 1983. “Remolding energy and risk of slide retrogression in sensitive clays”, Proc. Symp. Slopes on Soft Clays, Linköping, Swedish Geotechnical Institute (SGI) Report 17, 423 – 454.

Thakur V. and Degago S.A. 2012. “Quickness of sensitive clays”, Géotechnique Letters 2 (3), 87-95.

# Landslide risk assessment in the Göta river valley: effect of climate changes

L'évaluation des risques de glissement de terrain dans la vallée de la rivière Göta :  
effet des changements climatiques

Tremblay M., Svahn V., Lundström K.  
Swedish Geotechnical Institute, Linköping and Gothenburg, Sweden

**ABSTRACT:** The predicted effects of the ongoing climate change such as increased precipitation and longer dry periods are expected to result in an increased frequency of landslides in Sweden. In order to meet this challenge, the Swedish Government commissioned the Swedish Geotechnical Institute (SGI) to investigate and assess the landslide risk in the Göta river valley, which is one of the Swedish valleys with the highest landslide frequency and where consequences of a landslide could be severe due to the number of large industrial sites as well as residential areas and infrastructure. A mapping of the landslide risk considering both present conditions and the effects of a future climate change has been performed. The investigation shows that climate change will increase the risk of landslides in the valley. However, it also shows that high level of risk is already estimated in many areas which can be affected even in today's climate.

**RÉSUMÉ :** Les effets prévus du changement climatique en cours, comme l'augmentation des précipitations et des périodes sèches plus longues devraient se traduire par une augmentation de la fréquence des glissements de terrain en Suède. Afin de relever ce défi, le gouvernement suédois a chargé l'Institut suédois de géotechnique (SGI) d'étudier et d'évaluer le risque de glissement de terrain dans la vallée de la rivière Göta, qui est une zone à haute fréquence de glissement de terrain et une zone particulièrement vulnérable en raison du nombre de grands sites industriels ainsi que des zones résidentielles et des infrastructures. Une étude des risques de glissement de terrain considérant à la fois les conditions actuelles et les effets d'un changement climatique à venir a été effectuée. L'étude montre que le changement climatique augmente les risques de glissements de terrain dans la vallée, mais elle montre aussi que le niveau de risque est déjà élevé dans de nombreuses parties de la vallée, même dans le climat actuel.

**KEYWORDS:** landslides, risk assessment, climatic changes, mapping.

## 1 INTRODUCTION

The Göta river valley is situated in the southwest of Sweden and runs from Lake Vänern in the north to Gothenburg in the south, Figure 1. It is one of the areas in Sweden which is most frequently affected by landslides. Each year, several landslides of various size and character occur in this region. The landslides are generally small and shallow, however, a number of large landslides have occurred during the past century, some of them with human casualties and extensive property damages (e.g. Alén et al. 2000; Hultén et al. 2007). One reason for the high frequency of landslides in the Göta river valley is its geological history. The deep clay layers were formed during and after the latest glaciation period and in some parts reach a thickness up to 100 meters. The Göta river has overtime cut deep into the clay, forming the prerequisites for landslides. As the clays were mainly deposited in a marine environment, quick clay is therefore widespread in the area. The total length of the river is about 100 km.

The valley has a long history of human activities resulting in settlements, industries, shipping and harbours. Roads and railroads of national importance follow the river bank for kilometres, and environmentally hazardous activities and contaminated sites are common. More than 100,000 people live in the valley and the river is also the fresh water source for about 700,000 people. Due to the relatively high exploitation of the area, the consequences of a landslide in the Göta river valley can therefore be very severe.

The Göta river has suffered from many landslides over the years that have been documented. Parts of the most populated areas in the valley have earlier been investigated for mapping

the risk of landslides, but in order to predict the effect of climate changes, the Swedish Government has commissioned the Swedish Geotechnical Institute to investigate and map landslide risks in the whole valley.

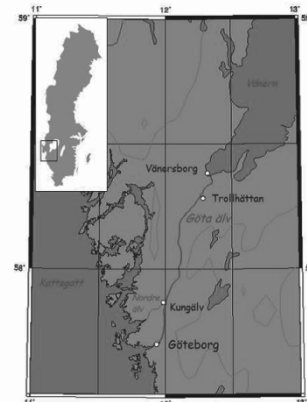


Figure 1. Location of the Göta river

## 2 METHODOLOGY OF RISK MAPPING

The concept of risk used in these investigations refers to a combination of the *probability* that an event might happen in a given area and the *consequence* of this event occurring.

Risk is defined as a combination of these two parameters:  
 $Risk = Probability \times Consequence$



A landslide risk analysis thus includes three separate parts:

- the estimation of the probability for a landslide to occur,
- the determination of the consequences of such a landslide,
- the combination of these two factors resulting in a risk map.

Landslide probability is based on the calculation of the safety factor using conventional stability analysis. By studying the uncertainties in a number of parameters used in the calculation of the safety factor in a given area, the probability of a failure occurring in this area is estimated. The probability is therefore directly dependent on the safety factor and the variation in different parameters such as slope geometry, shear strength and density of the soil, etc. The probability of landslide occurrence is divided into five probability classes from "negligible probability of landslide" (probability class S1) to "substantial probability of landslide" (probability class S5).

The impact of a landslide in an area, i.e. damage to life, property and environment, is also defined in five consequence classes, from "minor damages" (consequence class K1) to "catastrophic damages" (consequence class K5). The assessment of the consequences of a landslide takes into account the damage that a possible landslide would cause. Extent of the damage is assumed to be in proportion to how the land is used for dwelling, industries, infrastructure and other facilities and activities. Of course, the size of the landslide is important for the assessment of the consequences, both on land and in the river, and it is affected by the presence of quick clay in the area as well as the topography of the slope. In earlier investigations, the consequences were described following a scale with incremental effects, but in the present project the financial aspects have been added on the impact assessment in order to more systematically compare the consequences of landslides in different areas, affecting different functions in the society.

The combination of landslide probability classes and landslide consequence classes results in an expression of the risk of landslide. Landslide risk class is expressed as a pair of numbers that reflects the consequences of a landslide (K) and its probability to happen (S). A total of 25 risk classes may be obtained from the risk matrix, see Figure 2, and they are clustered into three risk levels (low, medium, high) in order to simplify the risk mapping. The different levels of risk of landslides involve different requirements for geotechnical actions including the need of detailed stability investigations and eventually protective measures.

Probability class	S5	5/1	5/2	5/3	5/4	5/5	Low risk level Medium risk level High risk level
	S4	4/1	4/2	4/3	4/4	4/5	
	S3	3/1	3/2	3/3	3/4	3/5	
	S2	2/1	2/2	2/3	2/4	2/5	
	S1	1/1	1/2	1/3	1/4	1/5	
		K1	K2	K3	K4	K5	Consequence class

Figure 2. Risk matrix used in the present investigation.

The landslide risk map is obtained by overlaying the probability map and the consequence map and combining them into risk levels. The results of the risk analysis is finally presented in colored maps representing the three risk levels (low, medium and high) as shown in Figure 3. Areas with no landslide risk, e.g. areas with visible bedrock, are omitted from the risk map.

**Landslide probability**



**Landslide consequences**



**Risk**

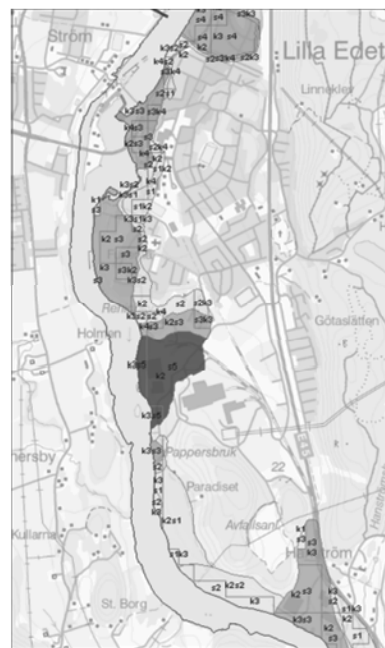


Figure 3. Principle of landslide risk mapping: probability map and consequence map are combined into a risk map.

### 3 EFFECTS OF CLIMATE CHANGE

Climate change is generally expected to result in increased frequency of natural disasters. In order to limit the damages and meet the new threat that a changing climate will mean for society, it is necessary to work both proactively to identify risks and to protect exposed areas by improving the quality of planning with regard to the new situation. SGI has for several years and on several occasions drawn attention to the geotechnical impacts of climate change. The analysis was summarized in an action plan for climate adaptation work and reported in various publications including the report "Geotechnical conditions for an increased flow of lake Vänern to the Göta River", SGI Varia 565 (Hultén et al, 2006).

Expected climate change in the Göta river valley over the coming 100 years includes gradually increase of yearly mean temperature and precipitation, see Figure 4 and 5, resulting in a higher mean water level in the river. The climate change will also result in an increase in most intensive rainfall events, an increased number of high and low discharges from the Lake Vänern due to increased inflow during autumn/winter and decreased inflow during spring/summer, and finally increased 100-year flows in Göta river tributaries (Bergström et al., 2011).

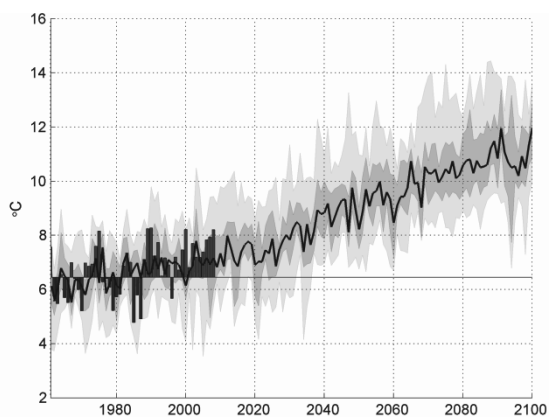


Figure 4. Calculated increase in temperature in the Göta river valley, based on 16 climate scenarios. The historical observations are shown as bars. The dark shaded area shows the 25-75 percentiles and the light shaded area the maximum and minimum values. The black line is the median value (after Bergström et al, 2011).

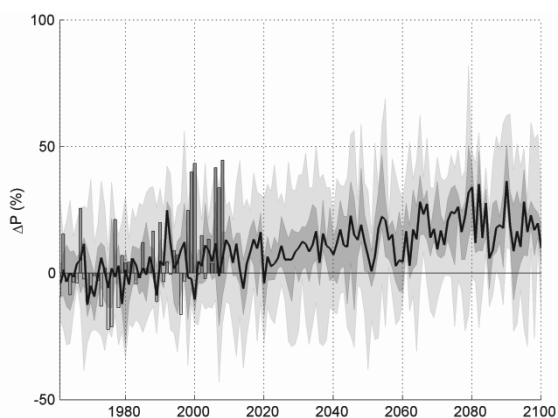


Figure 5. Calculated increase in precipitation in the Göta river valley, based on 16 climate scenarios. The historical observations are shown as bars. The dark shaded area shows the 25-75 percentiles and the light shaded area the maximum and minimum values. The black line is the median value (after Bergström et al, 2011).

A closer study of the results from the different climate scenarios which were performed in the present investigation

shows a significant increase in precipitation during the autumn/winter period, which means that the amount of water coming to the Göta river through discharge from the lake Vänern will increase, increasing the risk of erosion and the risk of landslides along the river.

The forecast produced by the different climate scenarios also shows reduced quantities of water during the drier spring/summer periods in the Vänern basin. This means that a lower water level is expected in the Göta river during these periods and thus an increased risk of landslides due to the decreased stabilizing effect of the water in the river. However, the water level in the Göta river is controlled by the presence of electric power plants along the river and is regulated by court statements and different agreements between the electricity producers and the authorities. Therefore, only minor changes of the highest or lowest water levels are expected to occur due to climate change. However, the mean water flow will increase over longer period, causing erosion along the river.

Studies of the changes in groundwater levels have shown that the expected variations are about 0,5 m in the area which means a minor effect on the total stability (see Blied and Persson, 2011).

An extensive study of the impact on the erosion process has also been conducted in this project. The results show that a number of river sections will be affected by the increase of flow in the valley resulting in an increase of erosion (see Rydell et al., 2011).

### 4 WORK DONE IN CURRENT INVESTIGATION

#### 4.1 Stability conditions

To improve the basis for stability calculations, a detailed topographical model of the area has been set up. The model includes topography from a laser scanning on land and a multibeam scanning of the topography of the river bottom.

Existing studies, surveys, maps, charts and other relevant material were collected from various stakeholders and analyzed. Inventory was also made regarding the older material from a stability study in 1962, and other SGI investigations.

To get an overview of ongoing work and a reasonable amount of stability studies, the river valley has been divided into 10 different areas. For all of these areas, a number of sections were chosen and studied using traditional methods to estimate the stability conditions in the current situation. Thereafter, the impact of climate change on the stability was assessed and quantified. A total of 240 sections along the river have been studied including over 2500 field investigation tests and laboratory testing on about 4000 soil samples.

Erosion of the Göta River is a very important factor associated with increased risk of landslides. Cooperation with universities, government agencies and other appropriate bodies was established early in the project in order to plan the study and investigation work necessary for the implementation of the mandate.

Mapping of quick clay areas has also been a major topic studied in this project since it is a primordial parameter needed for a better prediction of the size of expected landslides. Improved investigation methods have been tested and implemented in the project.

#### 4.2 Consequences of landslides

In order to perform a complete risk analysis, elements that may be affected by a possible landslide have been analyzed and taken into account. Among the major elements included in the study are human life, residential properties and infrastructures as well as contaminated soils. Extensive work has been performed for inventory, compilation and report of the selected

elements for impact assessment (see Andersson-Sköld et al, 2011).

#### 4.3 Data processing and databases

Information, data and results from different studies must be organized in an orderly manner to allow for quick access to all materials. For this purpose, a GIS database was built up to simplify data processing and to enable work with the large amount of information acquired during the project.

### 5 R&D IN CURRENT INVESTIGATION

The investigation included a comprehensive risk analysis to be performed in a rather large area with many factors to be taken into account. The methodology chosen for the investigation using a risk matrix was developed and used in previous landslide analysis.

The commission stipulates that the investigation is expected to result in a complete risk analysis along the Göta river together with a general increase of knowledge regarding landslide analysis and risk mapping. A number of working studies were therefore initiated to study and improve different methods used in this kind of analysis. The Research and Development efforts have mainly been concentrated on mapping of input parameters, understanding of the erosion process, the estimation of probability of landslide and new routines for assessment and presentation of impact of landslides in different areas.

The assignment, which in addition to studying the current situation should also take into account increased flow and runoff conditions in the river valley, asked for a study of the climate changes at a regional level.

The research and development linked to the commission was mainly needs-driven and provided direct assistance in the investigation. Research on mapping and handling of quick clay is an example of efforts which provided valuable knowledge for the investigation. A method based on field measurements has been improved and implemented in the project for classification and mapping of sensitive and quick clays.

Efforts have also been made to try to understand and predict the impact of climate changes on prevailing groundwater conditions. These changes are expected to affect both the mean value of the groundwater level and its variations in time.

Even though it has been the object of a number of earlier analysis and studies, the ongoing erosion in the Göta river valley is still incompletely known. Better knowledge has been acquired and improved models have been developed for both the bottom erosion and erosion of the slopes at the waterline. Analysis and measurements of erosion and sediment transport coordinated with the determination of bathymetric and topographic conditions have been performed in this project. The R&D-work has also included studies of boat related erosion and the use of advanced numerical models.

### 6 RESULTS AND REPORTING

The results of the project are presented in two different forms:

- a series of 34 reports in which the results from the different R&D groups are presented including study of groundwater, erosion, methodology of probability analysis, methodology for estimation of consequences, mapping of quick clay, etc.
- a final report in three parts including general discussions and recommendations, a complete presentation of the methods used in the investigation and finally risk maps covering the whole valley, see Swedish Geotechnical Institute (2012) or SGI's website: [www.swedgeo.se](http://www.swedgeo.se).

As expected, the investigation shows that climate changes will increase the risk of landslides in the Göta river valley. However, it also shows that high level of risk is already estimated in many areas which can be affected even in today's climate. Both the risk for landslide in the present climate conditions and the effect of the climate change in form of new estimation of risk in the future are presented in the final report.

The investigation also leads to a general presentation of protective and preventive measures which could be taken in different parts of the valley. Examples of practical measures that have to be considered are excavations, backfills, soil reinforcement and erosion protection. Besides a rough estimation of the costs of protective measures, the report also includes recommendations regarding different monitoring activities which should be regularly performed along the river.

### 7 REFERENCES

- Alén, C., Bengtsson, P.-E., Berggren, B., Johansson, L. & Johansson, Å. (2000). Skredriskanalys i Göta älvdalen – Metodbeskrivning. (In Swedish). Swedish Geotechnical Institute, Report 58, Linköping.
- Andersson-Sköld, Y. (2011). Metod för inventering och värdering av konsekvenser till följd av skred i Göta älvdalen samt Metodik konsekvensbedömning - Känslighetsanalys, klassindelning och applicering av metodik i hela utredningsområdet. (In Swedish). Swedish Geotechnical Institute, Göta älvtredningen delrapport 12 & 13, Linköping.
- Bergström, S., Andreasson, J., Losjö, K., Stensen, B. & Wern, L. (2011) Hydrologiska och meteorologiska förhållanden i Göta älvdalen. (In Swedish). Swedish Geotechnical Institute, Göta älvtredningen delrapport 27, Linköping.
- Blied, L. och Persson, H. (2011). Bedömd förändring av maximala grundvattennivåer i Göta älvdalen till följd av förändrat klimat. (In Swedish). Swedish Geotechnical Institute, Göta älvtredningen delrapport 9, Linköping.
- Hultén, C., Andersson-Sköld, Y., Ottosson, E., Edstam, T. & Johansson, Å. (2007). Case studies of landslide risk due to climate change in Sweden, International geotechnical conference on climate change and landslides, Ventnor, Isle of Wight. Proceedings 2007, pp 149-157.
- Hultén, C., Edstam, T., Arvidsson, O. & Nilsson, G. (2006). Geotechnical conditions for increased drainage from Lake Vänern to River Göta. (In Swedish). Swedish Geotechnical Institute, SGI Varia 565, Linköping.
- Rydell, B., Persson, H., Blied, L. & Rankka, W. (2011). Erosionsförhållanden i Göta älv. (In Swedish). Swedish Geotechnical Institute, Göta älvtredningen delrapport 1, Linköping.
- Swedish Geotechnical Institute (2012). Landslide risk in the Göta river valley in a changing climate. Final Report Part 1-3, Swedish Geotechnical Institute, Linköping.

# Deformation and water seepage observed in a natural slope during failure process by artificial heavy rainfall

Déformation du sol et infiltration d'eau observées le long d'une pente naturelle pendant le processus de glissement du a de fortes pluies artificielles

Uchimura T., Gizachew G.  
 Department of Civil Engineering, University of Tokyo, Tokyo, Japan

Wang L., Nishie S., Seko I.  
 Chuo Kaihatsu Corporation, Tokyo, Japan

**ABSTRACT:** Monitoring and early warning is one of the most effective ways toward reduction of disasters induced by landslides due to heavy rainfall. The authors has developed a simple and low-cost early warning system which measures tilting angles on the surface and/or in the ground of a slope, as well as volumetric water contents in the ground. Unlike conventional sensing devices, measurement with tilt sensors is simple and easy, but the translation of the obtained data of tilting angle is still under consideration. The authors conducted an artificial rainfall test on a natural slope of weathered and loose andesite deposit in order to observe its prefailure behaviours. The tilt angles and volumetric water contents were measured during the deformation and failure process. The tilt sensors showed tilting rates between 0.1 and 0.5 degree / hour before failure. In addition, there was a unique relation between the deformation and the water content, which is independent of the time history of the artificial rainfall. Simple shear tests were also conducted to observe the prefailure deformation of an unsaturated soil. These observations will give us ideas on the warning criteria for slope failure based on monitoring of tilting angle and water contents.

**RÉSUMÉ :** Donner l'alerte au plus tôt est sûrement la solution efficace pour réduire l'ampleur des désastres induits par les glissements de terrain dus à des chutes massives de pluie. Un système d'alerte simple et à bas-coût qui mesure les angles d'inclinaison de la surface du sol et/ou dans la terre, ainsi que le volume d'eau absorbé est proposé. Contrairement aux appareils conventionnels, la mesure avec les sondes de l'inclinaison est simple et facile, mais la traduction des données obtenues est encore à l'étude. Un test de chute de pluie artificielle sur une pente naturelle d'andésite durcie et dégagée pour observer les comportements des pré-fractures a été réalisé. L'orientation de l'inclinaison ainsi que le volume d'eau ont été mesurés pendant la déformation de la surface. Les sondes ont révélé des pentes comprises entre 0,1 et 0,5 degré/heure avant glissement. De plus, une relation unique indépendante de la durée de la chute de pluie artificielle est établie entre la déformation du sol et le contenu d'eau. Des tests de cisaillement ont aussi été effectués pour observer la déformation des pré-fractures d'un sol non saturé. Ces observations nous donnent des informations sur les critères d'alerte pour prévenir un glissement de terrain.

**KEYWORDS:** landslide, slope failure, monitoring, early warning.

## 1 INTRODUCTION

There is a long history in prevention and mitigation of rainfall and/or scouring-induced landslides. Mechanical countermeasures to prevent slope failure, like retaining walls and ground anchors, have been widely used. However, they are expensive and it is not realistic to apply such mechanical measures for all of these slopes with potential risk, because most of landslide occurs in small scale, but a large number of slopes. Therefore, careful monitoring of slope behaviors and consequent early warning is reasonable as alternatives.

The authors have proposed and developed an early warning system for slope failures, as one of feasible countermeasures (Figure 1) (Uchimura, et. al. 2010 & 2011a). The system consists of minimum number of low-cost sensors on a slope, and the data is transmitted through wireless network. Thus, the system is low-cost and simple so that the residents in risk areas can handle it to protect themselves from slope disasters.

There are several publications which report incremental deformation of slopes before failure due to heavy rainfall (Ochiai, et. al. 2004, Orense, et. al. 2003 & 2004). These behaviors can be used as criteria of early warning for slopes disasters. Extensometers and borehole inclinometers are conventional and widely used devices to detect such displacements of slopes. But, these devices require high skills and equipments for installation and operation, resulting in a respectable cost.

Therefore, the proposed early warning system uses tilt sensors to detect abnormal deformation of slopes as shown in

Figure 1. The surface tilt sensor is installed with a rod inserted into the slope surface for a depth of 0.5 or more. It has a MEMS tilt meter (nominal resolution = 0.04 mm/m) to measure the tilting angle in the surface layer of the slope. The obtained tilt angle is equivalent to shear deformation of the surface layer, which can be translated to the surface displacement if the tip of rod reaches the intact base layer.

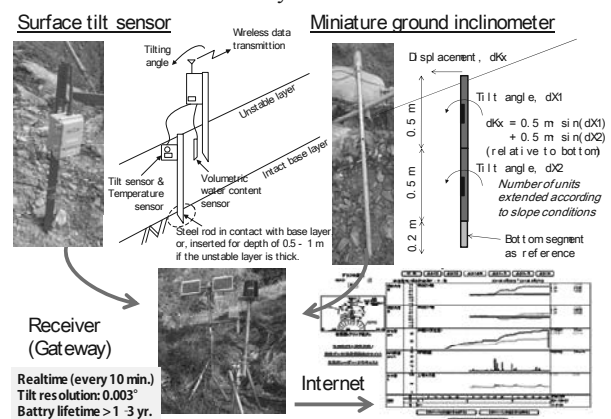


Figure 1. Tilt sensor units and wireless monitoring system

The miniature ground inclinometer consists of stainless steel pipe segments with a length of 50cm or 1m and outer diameter of 25 mm. The segments are connected to each other by a

flexible mechanism, so that the device moves together with the ground displacement. A sensor unit covered by a small aluminum cylindrical case is installed in each segment. The sensor unit contains the MEMS tilt meter and a geomagnetic sensor (digital compass, nominal resolution = 0.5 deg) to detect the direction of unit. Each unit also contains a microcontroller chip, which control the sensors, and transfer the control commands and the obtained data to the next units by serial interfaces. A significant advantage of this device is that it can be installed quickly into the slope ground being blown with a hammer, as its diameter is as small as 25 mm. Besides, it can be installed into a deeper layer of slopes (3-5 m) by connecting the segments as many as needed.

Unlike conventional sensing devices, such as borehole inclinometer and extensometer which measures displacements of slope, measurement with tilt sensors is simple and easy. However, the translation of the obtained data of tilting angle is still under consideration. It is because there are few case histories of early warning with tilt sensors compared to those with conventional sensors. Therefore, it is essential to observe the behaviors of tilt angles in prefailure stages of slopes.

## 2 SLOPE FAILURE TESTS BY ARTIFICIAL RAINFALL

An artificial rainfall test was conducted on a natural slope of weathered and loose ( $N_d < 10$  for 10 cm of penetration by portable dynamic cone penetration tests) andesite deposit in order to observe its prefailure behaviour. The site is located on an unstable slope in Taziping, Sichuan Province, China. Figure 2 shows the cross-section and photo of the site together with the instruments. The slope angle is around 18 degrees, and its lower end was excavated for a depth of 1.4 m with an angle of 40 degrees. The deposit contains some big rocks with diameter of 300 mm or more. The particle size distribution of component finer than 100 mm is show in Figure 2. It is a sandy material containing some gravel and fine particles.

Figure 2 also shows surface tilt sensors (T50-1, T50-2, T200, and T300), and miniature ground inclinometer (K50 and K150). The number in the notation of each sensor represents the distance from the bottom end of slope in cm. Each rod of the surface tilt sensors was inserted into the ground by 75 cm. Each miniature ground inclinometer consists of 2 segments with a length of 500 mm.

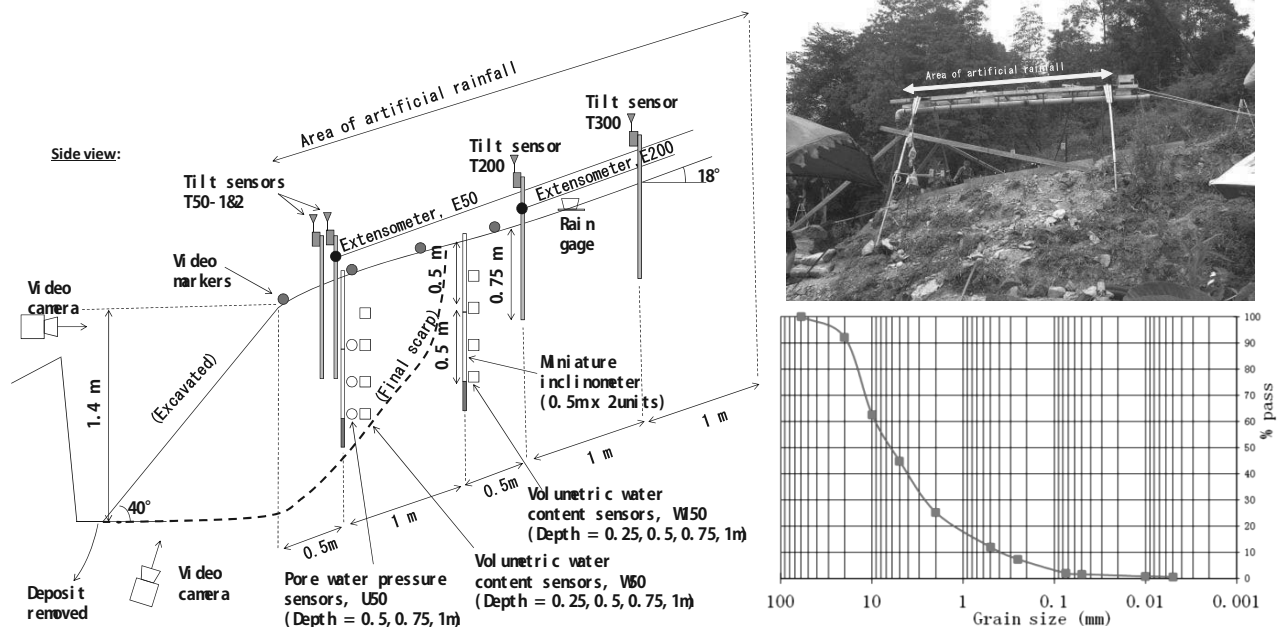


Figure 2. Cross-section, photo, and particle size distribution (finer part than 100 mm) of the site for the artificial rainfall test.

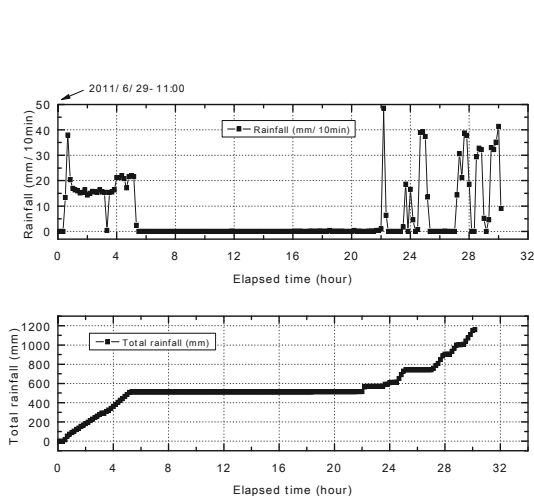


Figure 3. Records of the artificial rainfall.

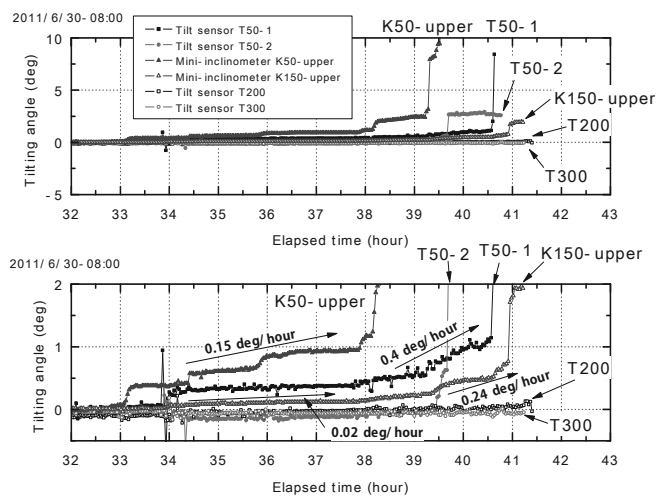


Figure 4. Tilting angles on the slope.

Artificial heavy rainfall was given as shown in Figure 3. The rainfall intensity fluctuated due to restriction of water supply, but around 500 mm of total of rain was applied in the first day, and 700 mm was given in the second day.

Major deformation was observed in the second day, and the slope failed progressively from the bottom with scarp angle of 40 to 50 degrees. The final shape of scarp is shown with thick broken line in Figure 2.

Figure 4 shows the changes in tilting angles detected by the tilt sensors due to the rainfall in the second day. Tilt angles of the upper segment are shown for the miniature ground inclinometers. The nearer to the bottom of slope, the more tilting angles are observed. The tilting rate for each sensor is between 0.1 and 0.5 degree / hour before failure. It is also remarkable that K150-upper, 150 cm apart from the bottom of slope, started to tilt slowly in the early stage, when the failure was observed only at the bottom scarp. This suggests that the sensor detected slight effects of the failure event at some distance of the sensor position. This behaviour is not visible to human eyes because its tilting rate was only 0.02 degree / hour.

Figure 5 shows the behaviours of the tilting angle of the upper unit of the miniature inclinometer, K50, at 50 cm from the bottom of slope. This represents the average shear deformation of the soil layer between depth of 0 and 50 cm. Besides, Figure 5 also shows the volumetric water content at a depth of 50cm at a position of 50 cm from the bottom of slope. The volumetric water content repeated to increase and decrease corresponding to the intermissive rainfall and drainage stages.

Figure 6 plots the tilting angle versus the volumetric water contents of Figure 5. This represents relationships between the shear deformation and water content. The deformation increased when the water content was high corresponding to rainfall, although some additional deformation was also recorded due to removal of soil which dropped and deposited in front of the bottom of slope.

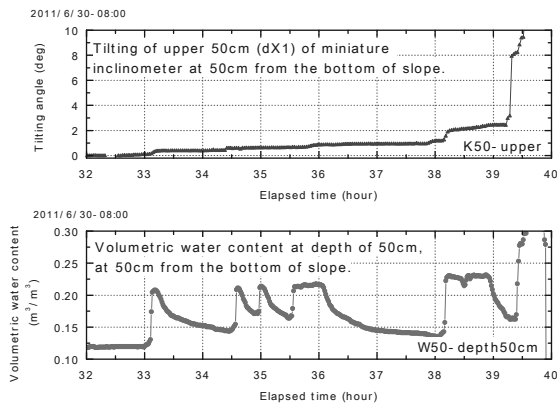


Figure 5 Time histories of tilting angles and volumetric water contents at 50 cm from the bottom of slope.

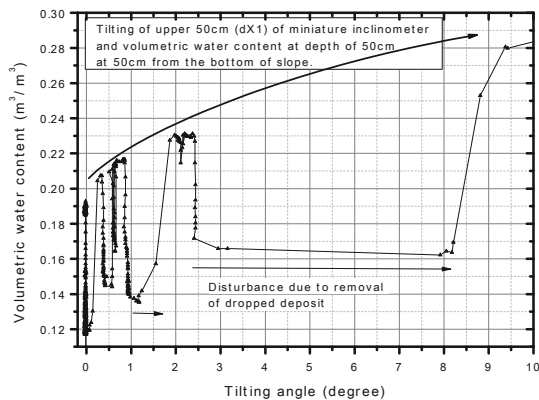


Figure 6 Tilting angles versus volumetric water contents at 50 cm from the bottom of slope.

A unique relation between the deformation and the water content can be drawn as an envelope of the plot, as indicated in Figure 6, which is independent of the time history of the artificial rainfall. Similar behaviours was be also observed in laboratory model tests on slip surface of unsaturated soil under constant shear stress and cyclic water infiltration/drainage processes (Uchimura et. al. 2011b).

### 3 SIMPLE SHEAR TESTS ON SLIP SURFACE

A series of simple shear tests were conducted on unsaturated sandy soil specimens to observe their prefailure behaviors more precisely. Figure 7 shows the arrangement of the testing device. Edosaki Sand ( $D_{max} = 2$  mm,  $D_{50} = 0.23$  mm, fine content = 6 %,  $G_s = 2.665$ ,  $e_{max} = 1.685$ ,  $e_{min} = 0.578$ ) was compacted into a disc shape with a diameter of 60 mm and a height of 20 mm, and a relative density of  $D_r = 70$  % with initial volumetric water content of 7 %. The specimen is surrounded by a stacked layers made of Teflon, which has low friction coefficient, to reduce the effect of friction. The specimen was loaded with 60 kPa of vertical confining pressure. And then, 15, 24, 30 kPa of constant shear stress was applied, which corresponds to 0.25, 0.4 and 0.5 of stress ratio, respectively. These three stress ratio simulate the stress state on the slip surface for gentle, medium, and steep slopes. Then, water was injected into the specimen from the top and bottom surface through ceramic discs with a constant injection rate of 310 ml/hr, which corresponds to a rainfall intensity 110 mm/hr fall on the top area of the specimen.

Figure 8 shows the obtained volumetric water contents and shear strain during the water infiltration process. It seems that there are three patterns of deformation and failure processes. In the case with stress ratio of 0.25 (gentle slope), the shear deformation increases with water infiltration, but it converged to a limited value not showing failure. On the other hand, in the case of steep slope with stress ratio of 0.5, the strain started to increase with a similar rate to that in the case of gentle slope, but it suddenly yielded at incremental volumetric water content of around 7 % and shear strain of around 1.7 %, followed by a quick deformation with high strain rate.

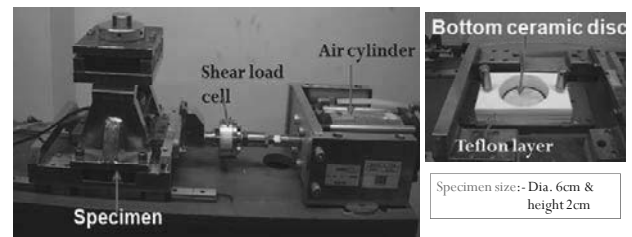


Figure 7 Equipments for direct shear tests.

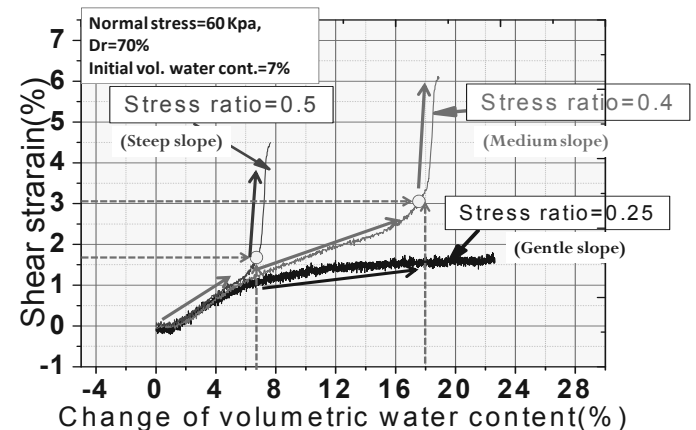


Figure 8 Shear strain versus volumetric water content under 3 values of constant stress ratio.

The behavior in the case of medium slope with stress ratio of 0.4 was more complicated. The strain started to increase with a similar rate to those in the other cases, but it slowed down when the change of volumetric water content was between around 7 % and 18 %. And then, it yielded, followed by a quick deformation with high strain rate.

The reason for the slowing down of strain rate observed in the case of medium slope could be explained with the behaviors of suction. The authors developed a miniature suction sensor to measure the suction in the specimen (Figure 9). A tiny metal pipe ( $\phi 1.5 \text{ mm} \times 4 \text{ mm}$ ) with small hole is wrapped with a micro-porous membrane. One end of the pipe is connected to a water pressure transducer via a plastic tube, while the other end is closed. The membrane allows water to pass through, but prevent air to pass by capillary effect. Thus, the pipe with the membrane works just like a miniature ceramic cup. Properties of a similar membrane are studied by Nishimura et. al. (2011). Due to its small size, the miniature suction sensor can be installed with minimum disturbance to deformation and water seepage in the specimen as seen in Figure 9.

Figure 10 shows relationships between the suction and the change of volumetric water content measured in another specimen during water infiltration process. The suction decreases with fast rate until the change of volumetric water content reaches around 4.5 %. Then, the decreasing rate of suction slowed down.

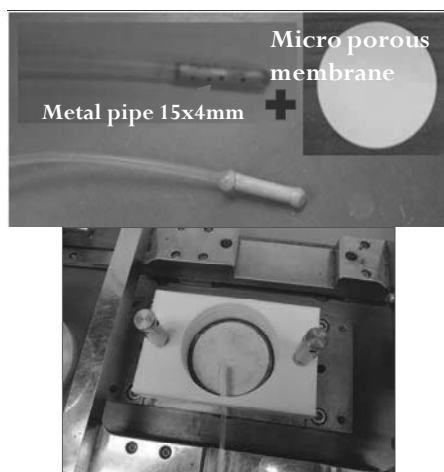


Figure 9 Miniature suction sensor with microporous membrane.

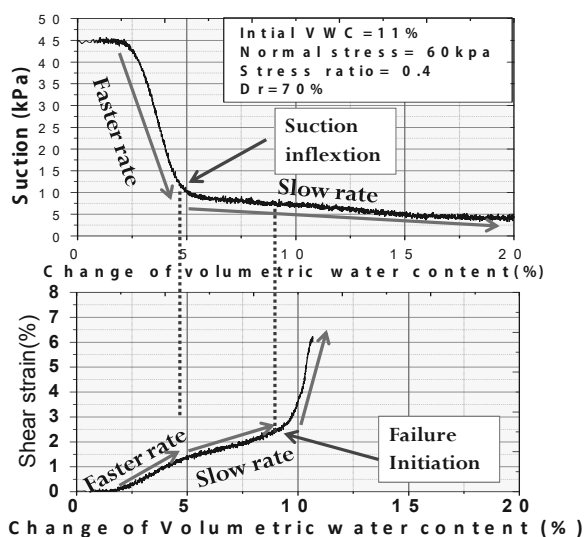


Figure 10 Relations among volumetric water content, suction, and shear strain.

The strain rate of the specimen also slowed down at the same change of volumetric water content. Thus, this behavior can be

explained with the suction-water characteristics curve (SWCC) of the soil. Finally, the specimen yielded at higher change of volumetric water content, corresponding to lower suction.

This observation suggests that a tentative slowing down of slope deformation does not always mean stabilization of slope.

#### 4 CONCLUSIONS

A slope failure test with an artificial rainfall was conducted on a natural slope. The tilt sensors installed into the slope showed tilting rates between 0.1 and 0.5 degree / hour. These values of tilting rate could be used as criteria of early warning for slope disasters.

The deformation proceeded when the water content was high corresponding to rainfall, while it is less progressive when the water content is low. Similar behaviours were also observed in model test in laboratory, where an unsaturated soil layer was sheared under constant shear stress with cyclic water infiltration and drainage. It seems that there is a unique relation between the deformation and the water content, which is independent of the time history of the artificial rainfall. These results suggest a possibility of combined monitoring of tilting angle and water contents for more precise comprehension of the status of slopes.

The results of direct shear tests on unsaturated soil under constant shear stress and constant water injection rate suggest that there are three patterns of deformation and failure processes corresponding to the slope angle. In a case of medium slope, the strain rate may slow down due to the SWCC of the soil even though water is injected with a constant rate. However, it does not always mean that the slope is getting stable.

#### 5 ACKNOWLEDGEMENTS

These researches are supported by Grants-in-Aid for Scientific Research of Japan Society for the Promotion of Science (JSPS), Joint Research Projects/Seminars by JSPS, and International Cooperate Project of Chinese Ministry of Science and Technology.

#### 6 REFERENCES

Ochiai, H., Okada, Y., Furuya, G., Okura, Y., Matsui, T., Sammori, T., Terajima, T., and Sassa, K. (2004): A fluidized landslide on a natural slope by artificial rainfall, *Landslides*, Vol. 1, No. 3, pp. 211-219.

Orense R.P., Towhata I., and Farooq K. (2003): Investigation of failure of sandy slopes caused by heavy rainfall, *Proc. Int. Conf. on Fast Slope Movement-Prediction and Prevention for Risk Mitigation (FSM2003)*, Sorrento.

Orense R.P., Farooq K., and Towhata I. (2004): Deformation behavior of sandy slopes during rainwater infiltration. *Soils and Foundations* 44(2):15-30.

Uchimura, T., Towhata, I., Trinh, T. L. A., Fukuda, J., Bautista, C. J. B., Wang, L., Seko, I., Uchida, T., Matsuoka, A., Ito, Y., Onda, Y., Iwagami, S., Kim, M. S., and Sakai, N. (2010): "Simple monitoring method for precaution of landslides watching tilting and water contents on slopes surface", *Landslides*, (Published online: 17 October 2009)

Uchimura, T., Wang, L., Qiao, J.-P., and Towhata, I. (2011a). Miniature ground inclinometer for slope monitoring, *Proc. of The 14th Asian Regional Conference on Soil Mechanics and Geotechnical Engineering*, ATC3 Session.

Uchimura, T., Suzuki, D., and Seo, H.-K. (2011b): Combined monitoring of water content and displacement for slope instability, *Proc. of 4th Japan-Korea Geotechnical Workshop*, Kobe, pp. 67-72.

Nishimura, T., Koseki, J., Fredlund, D.G., and Rahardjo, H. (2011): Microporous Membrane Technology for Measurement of Soil-Water Characteristic Curve, *Geotechnical Testing Journal*, Vol. 35, No. 1, Paper ID GTJ103670.

# Study on field detection and monitoring of slope instability by measuring tilting motion on the slope surface

## Détection et surveillance in situ des phénomènes d'instabilités de pente par mesure locale des mouvements de surface

Wang L., Nishie S., Seko I.  
Chuo Kaihatsu Corporation, Tokyo, Japan

Uchimura T.  
University of Tokyo, Japan

**ABSTRACT:** Monitoring and early warning is one of the most effective methods toward reduction of disasters induced by landslides and slope instabilities, but the traditional methods such as multiple borehole inclinometers or extensometer are expensive and unsuitable to zoning monitoring. To overcome the above weaknesses, a simple and low-cost early warning system was developed for slope failure and landslide (Uchimura et al. 2009). The developed tilt sensor is easy to install and it can monitor slope deformation by means of a tilting MEMS module angle which embedded in the sensor, and transfers real time data via wireless network. The warning system with its developed equipments has been deployed in several actual slopes for validation of field performance in Japan and China. In this paper, the authors will show that the developed system and sensor can successfully detect the situation of slope and landslide, and issue useful information that allows residents to avoid slope failure or landslide disasters. Based on the results of field case studies, the developed low-cost sensor unit and real-time warning system are considered particularly effective against rainfall-induced slope failure or landslides and its general use is recommended.

**RÉSUMÉ :** Une surveillance constante associée à un dispositif rapide d'avertissement est une solution efficace pour lutter contre les désastres et les pertes humaines liés aux glissements de terrain ou aux ruptures de pentes. Cependant, les équipements traditionnels tels que les inclinomètres ou extensomètres installés par forage sont généralement d'un coût prohibitif et sont peu adaptés à une surveillance plus généralisée du territoire. Un nouveau système plus flexible et de coût plus réduit a été proposé par Uchimura et al. (2009). Il incorpore des micro-inclinomètres de type MEMS faciles d'installation qui permettent d'estimer les mouvements de surface. Les données peuvent être transmises en temps réel via réseau sans fil. Ce système a été déployé sur plusieurs sites en Chine et au Japon. A partir des données recoltées sur ces sites, il est démontré que ce système est efficace et fiable dans l'estimation et la détection précoce des glissements de terrain, et qu'il permet d'obtenir des renseignements cruciaux pour prévenir leur poursuite ou pour réduire les dégâts occasionnés.

**KEYWORDS:** landslide, slope failure, monitoring, early warning.

## 1 INTRODUCTION.

Typical measures to prevent slope failure are retaining walls and ground anchors which improve safety factor against failure. These measures have been widely used everywhere in the world and its effectiveness has been confirmed. However, the traditional methods take a lot of cost, as a result that a limited application can be used only for large scale slopes. In fact, most of landslide occurs at small scale slopes, but with a large number. It is not realistic to apply mechanical reinforcement measures for these slopes with potential risk.

Rainfall-induced slope failures are one kind of the most destructive natural hazards. Many slope failures have been observed to occur during or immediately after rainfall. For a wide range slope safety monitoring, a problem in the first was that the equipments were high-cost; this is a problem that

disaster prevention measures was difficult for implementation into developing countries. The cost issues should be overcome for a purpose of widespread use; another is that a simple and effective real-time monitoring becomes necessary.

The authors have proposed an early warning system for sediment disasters, as one of more feasible countermeasures for small-scale slope failures. The system measures minimum number of items by using the developed smart sensor units; the measured data is transferred through wireless network. Thus, the system is low-cost and simple enough so that the residents in risk areas can handle it to protect themselves from slope disasters (Uchimura et al. 2009).

## 2 A LOW-COST AND SIMPLE WARNING SYSTEM.

A simple and low-cost early warning sensor unit was developed that only two parameters of the volumetric water content of soil and the inclination of slope or landslide were focused, and its applicability and effectiveness were tested on model slopes under artificial heavy rainfall (Uchimura et al. 2009). The sensor unit works with batteries, and transfers real time data via wireless network, and installation is simple and easily to control so that non-expert residents in risk area can handle it by themselves, even in developing countries. Figure 1 shows the basic concept of the wireless monitoring unit using for early warning system.

### 2.1 RF (Radio Frequency) wireless data transmit method

Figure 2 shows the outline of wireless monitoring and early warning system for slope failure. The system is designed to be wireless, that is, each unit works autonomously with

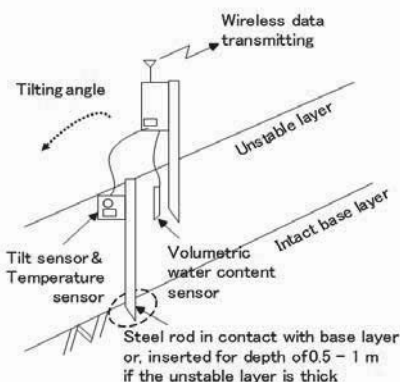


Figure 1. Wireless tilt sensor unit with water content sensor.



microcomputer with independent power supply by batteries or

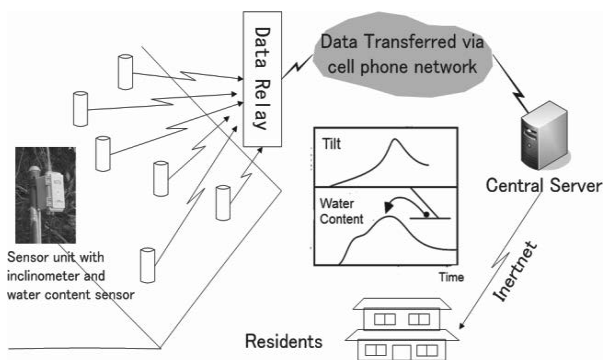


Figure 2. Outline of wireless monitoring units and early warning system for slope failure.

solar cells. Radio modems operated in the 429 MHz ISM band for Japan, 434 MHz ISM band for E.U. countries and China.

The sensor units measure the condition of the slope periodically every 10 minutes for example. The data is transferred to a gateway unit, which is also placed near the slope, by using low power radio communication modules. The data transmitting distance is 300-600 meters under typical conditions in the field. The gateway unit collects the data from all the sensor units, and sends them to a data server on internet through a mobile phone network. Thus, the data can be browsed anywhere and anytime on web site. The data is processed by the server, and any abnormal phenomena of the slope can be detected and used for a precaution of failure, and then issue an evacuation warning.

### 2.2 MEMS inclinometer technology embedded to sensor unit

The proposed system measures the inclination on the slope surface and the volumetric water content in the slope. A MEMS tilt module (nominal resolution = 0.04 mm/m = 0.0025 degree) is embedded in each sensor unit. The tilt module is a 3D-MEMS-based dual axis inclinometer that provides sensor unit grade performance for leveling applications. The measuring axes of the sensing elements are parallel to the mounting plane and orthogonal to each other. Low temperature dependency, high resolution, power-saving and low noise, together with robust sensing element design, if we keep on leveling installation, this MEMS type inclinometer is ideal choice for slope failure sensors.

### 2.3 Saving power designed based on 16-bit ultra-low-power MCU

In order to reach the purpose of a low-cost and simple warning system, the choice of CPU controller become very important. 16-bit Ultra-Low-Power MCU with ultralow power consumption being very suitable to no commercial power supply region was selected.

A long-term sensor unit power consumption test (not include Micro SD) was started on July 7, 2008, the interval time of data sampling and transmit was 10 minutes. 4 cells alkaline batteries were installed in the test sensor unit. Figure 3 shows the relation of battery voltage and elapsed time, the test unit has been worked for 3.5 years.

## 3 FIELD VALIDATION FOR SIMPLE SLOPE MONITORING AND LANDSLIDE IN JAPAN AND CHINA.

### 3.1 A case of detection on Three Gorge Dam landslide failure in China

Prototype of the developed monitoring system has been established on a side slope of Three Gorge Dam region, the

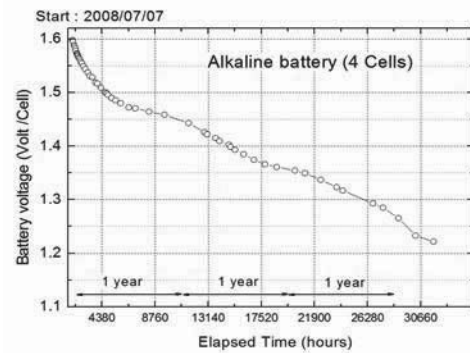


Figure 3. Sensor unit long-term power consumption test.

world largest dam in China, since 2008. The site named Sai Wan-Ba is located on the right side of the dam lake, near Wenzhou Ward, 80 km eastward from Chongqing City (Figure 4). Several landslide blocks were found by geological investigations.

The time histories of the tilting angles in X-axis and Y-axis, the volumetric water content at a depth of 30 cm on the ground surface, and the record of precipitation are shown in Figure 5 and Figure 6 respectively.

A consecutive movement of a sliding block shown in Figure 5 was observed for a long period. A quick movement of tilt sensor was detected at a heavy rainfall event on June 6-7, 2009; a large scale of landslide disaster nearby observation point 2

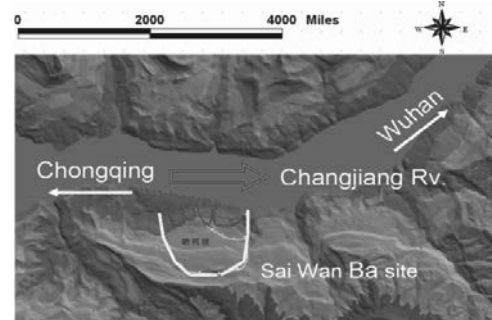


Figure 4. Location of Sai Wan Ba landslide site.

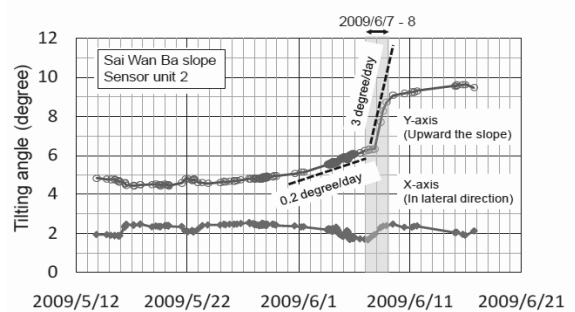


Figure 5. Time history of tilting angle & precipitation by sensor unit 2.

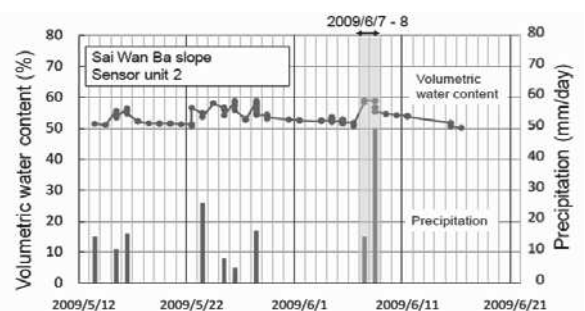


Figure 6. Time history of volumetric water content & precipitation by sensor unit 2.

was happened on 8 June shown in Figure 7, and this landslide disaster caused the slope of observation point 2 inclined gradually at the same time. As a result, there was almost two day for taking refuge before the landslide happened.



Figure 7. New landslide on June 7, 2009.

1.1 Monitoring of a slope failure site for secondary disaster prevention in Japan

Another field detection result of a slope failure site along a national road in Kyushu of Japan is shown in Figure 8. This slope consists of strongly weathered granite, and it was failed due to a heavy rainfall in July of 2009. The slope was excavated to have a gradient of 45 degrees for disaster relief work, and was monitored with three sensor units. Heavy rainfall caused a second failure, and a local part of slope including the sensor unit fallen down. Figure 9 shows the records of tilt sensor of the unit, in directions toward and laterals to the slope, respectively. Specially, the tilting in Y-axis (lateral direction) showed

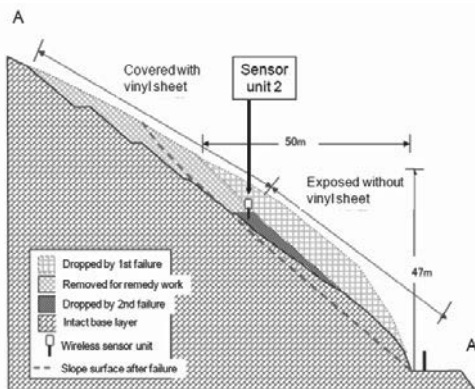


Figure 8. Sketch of failed slope along highway

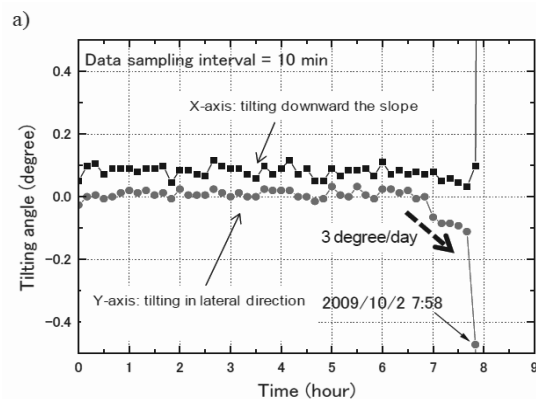


Figure 9. Tilt angle change just before the second failure.

extraordinary behaviors 50 minutes before the second failure.

Its tilting rate was around 3 degrees per day (0.12 degrees per hour). As this second failure took place adjacent to the location of the sensor unit 2, the behaviors of the slope before and after the failure was detected by the monitoring system. The site manager got aware of the extraordinary behaviors of the data from sensor unit 2, and he stopped the disaster relief work and the road service to avoid large loss successfully.

1.2 Field evaluation for developed tilt sensors to traditional extensometers based on in-site measuring

Another in-site measurement results were showed in Figure 10 to Figure 11a-e, a heavy rainfall on July 2011 caused a slope failure along local national road in Kyushu of Japan.

For the road earthwork construction, an emergency monitoring system using multiple borehole inclinometers, extensometers, tilt sensors and rain gauge has been set up at

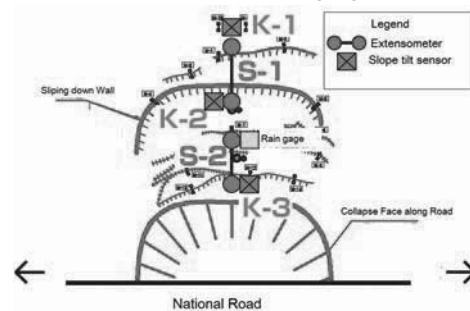


Figure 10. A field site of failed slope along national road in Japan

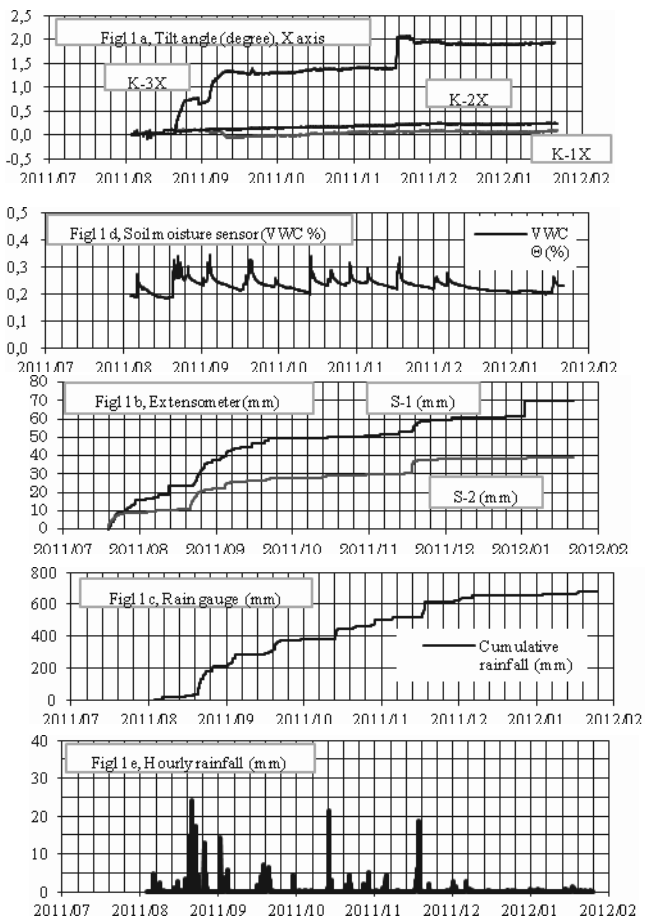


Figure 11. Time histories vs. measuring values.

slope failure site. For validating developed tilt sensor with field extensometers data, the three tilt sensors were installed nearby

fixed pole of extensometers moving point shown in Figure 10. In this field site, other 4 boring surveys have been carried out and multiple borehole inclinometers were installed, two of the tilt sensors (K-2, 3) were just set up nearby the survey boring holes. According to the result of boring survey, a landslide slip surface, which depth was 17m, was found shown in Figure 12.

Figure 10a-b show the time histories of tilt sensor inclination alone extensometer wire direction (tilt sensor x axis) and the extensometer movement(S-1, S-2), Figure 10c shows the result of cumulative rainfall value by rain gauge. Figure 10d shows the result of volume water content by FCH2O water content

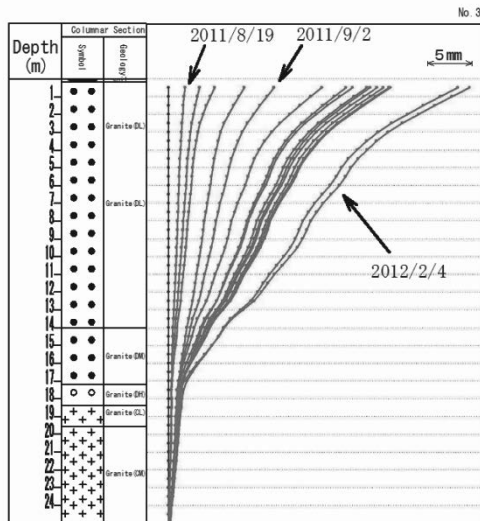


Figure 12. The result of multiple borehole inclinometers.

sensor.

The normal case, the fix pole of tilt sensor was inserted into earth of slope surface at the depth of 1.0 meter, so that the inclination of tilt sensor means average movement of the slope surface. The inclinations of tilt sensors especially tilt sensor K-3, and movement of extensometers were increased with rainfall and showed a strong correlation each other based on the results of Figure 10a-e.

Figure 13 shows the relation of slope movement (mm) by extensometer(S-1) vs. inclination (degree) by tilt sensor (K-3). Based on the result, the almost linear relationship between extensometer and tilt sensor was obtained except for the storms period of August, October and November, 2011.

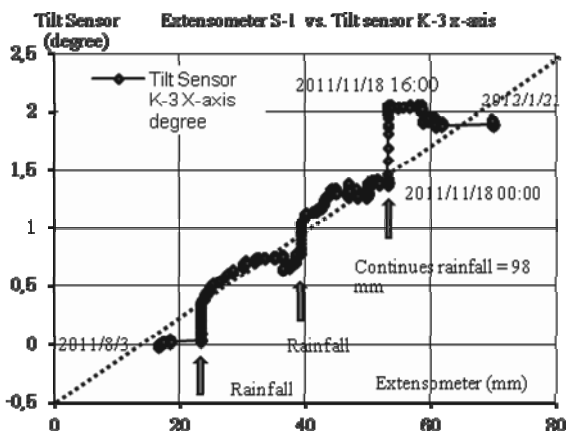


Figure 13. The relation of slope movement vs. tilt angle.

Another important result is that between heavy rainfall start and landslide initiation, the value of extensometer seems no any change but the tilt sensor inclination has reacted quickly, for example, the heavy rainfall on 18 November 2011, that hourly rainfall reached 20mm and continues rainfall reached 96mm, run continuously for 16 hours, during this period, the inclination of tilt sensor was increased but the value of extensometer

showed no any change (Figure 13). The tilt sensor measures a local change of slope surface, and the extensometer measures a whole movement of slope failure or landslide. The failure of slope starts from local and enlarges to whole area usually, so that this result should be considered as an important slope pre-failure phenomenon, which can let warning system to issue useful information to residents to avoid slope failure or landslide disaster in advance.

## 2 CONCLUSION

Based on above case histories and field validation result, a low-cost and simple monitoring method of measuring tilting motion on these slope surface is effective and proposed for precaution of rainfall-induced slope failure and landslides; The tilt sensor unit with MEMS inclinometer module and wireless module is very save power and installed easily. At a side slope of Three Gorge Dam in China, consecutive movement of a sliding block was observed for a long period.

A quick movement was detected at a heavy rainfall event, in which a tilting rate of about 3 degrees per day was continued for 2 days. This event includes a slope failure and significant displacement in a wide area including the position of the sensor unit.

At a slope failure site along a national road in Japan, the slope surface showed abnormal tilting behaviors 30 to 50 minutes before failure. The tilting rate was around 3 degrees per day, although it continued for only 50 minutes before failure. Such behaviors could be used as a signal for early warning.

Furthermore, between heavy rainfall and landslide initiation, the tilt sensor inclination has reacted quickly than extensometer value; it can be considered that the tilt sensor unit is effective tool for early warning system.

## 3 ACKNOWLEDGEMENTS

The present study has been supported by the research funding supplied by JSPS of Japanese government as well as the Science Academy of China. These research assistants are deeply acknowledged by the authors.

## 4 REFERENCES

- Orense R.P., Towhata I., Farooq, K. 2003. Investigation of failure of sandy slopes caused by heavy rainfall. *Proc. Int. Conf. on Fast Slope Movement-Prediction and Prevention for Risk Mitigation (FSM2003)*, Sorrento.
- Towhata, I., Uchimura, T. and Gallage, C.P.K. 2005. On early detection and warning against rainfall-induced landslide. *Proc. of The First General Assembly and The Fourth Session of Board of Representatives of the International Consortium on Landslides (ICL)*. Washington D.C., Springer, pp.133-139.
- Uchimura, T., Towhata, I., Wang, L. and Seko, I. 2008. Simple and Low-Cost Wireless Monitoring Units for Slope Failure. *Proc. of the First World Landslide Forum, International Consortium on Landslides (ICL)*. Tokyo, pp. 611-614.
- Uchimura, T., Towhata, I., Wang, L. and Seko, I. 2009. Development of Low-cost Early Warning System of Slope Instability for Civilian Use. *Proc. of 17th ISSMGE*. Alexandria, Vol. 3, pp.1897-1900.
- Uchimura, T., Wang, L., Qiao, J.P., and Towhata, I. 2011. Miniature ground inclinometer for slope monitoring. *Proc. of the 14th Asian Regional Conference on Soil Mechanics and Geotechnical Engineering*, Hongkong.

# The physical vulnerability of roads to debris flow

## La vulnérabilité physique des routes aux coulées de boue

Winter M.G., Smith J.T.

*Transport Research Laboratory (TRL), Edinburgh, United Kingdom*

Fotopoulou S., Pitolakis K.

*Aristotle University of Thessaloniki, Thessaloniki, Greece*

Mavrouli O., Corominas J.

*Technical University of Catalonia, Barcelona, Spain*

Agyroudis S.

*Aristotle University of Thessaloniki, Thessaloniki, Greece*

**ABSTRACT:** The physical vulnerability of roads to debris flow is expressed through fragility functions that relate flow volume to damage probabilities. Fragility relations are essential components of quantitative risk assessments (QRA) and allow for the estimation of risk within a consequence-based framework. This paper describes fragility curves produced in order to provide the conditional probability for a road to be in, or to exceed, a certain damage state for a given debris flow volume. Preliminary assessments were undertaken by means of a detailed questionnaire. Fragility curves have been defined for three damage states for high speed (reported herein) and for low speed roads (to be reported later) in order to cover the typical characteristics of roads vulnerable to debris flow. The probability of any given damage state being met or exceeded by a debris flow of a given volume ( $10\text{m}^3$  to  $100,000\text{m}^3$ ) was derived from the mean of the responses received. The development of the fragility curves is described and data issues discussed.

**RÉSUMÉ :** La vulnérabilité physique des routes aux coulées de boue s'exprime à travers des fonctions de fragilité qui mettent en rapport le débit volumique et les probabilités de dommages. Les relations de fragilité sont des composantes essentielles des évaluations quantitatives de risques (QRA) et permettent d'estimer le risque au sein d'un cadre basé sur les conséquences. Cet article décrit les courbes de fragilité produites afin d'indiquer la probabilité conditionnelle qu'une route se trouve, ou dépasse, un certain état d'endommagement pour un débit volumique donné de boue. Des évaluations préliminaires ont été réalisées au moyen d'un questionnaire détaillé. Des courbes de fragilité ont été définies pour les trois états d'endommagement pour les routes à grande vitesse (présentées dans ce document) et pour les routes à petite vitesse (qui feront l'objet d'un rapport ultérieur) afin de couvrir les caractéristiques typiques des routes vulnérables aux coulées de boue. La probabilité d'atteinte ou de dépassement d'un état d'endommagement donné en présence d'une coulée de boue d'un volume donné ( $10\text{m}^3$  à  $100\,000\text{m}^3$ ) a été dérivée de la moyenne des réponses reçues. L'élaboration des courbes de fragilité est décrite et les problématiques liées aux données sont abordées.

**KEYWORDS:** Landslides, debris flows, hazard, risk, probability, fragility, QRA.

## 1 INTRODUCTION

Fragility curves are a graphical means of describing the physical vulnerability of elements at risk to a given hazard. They give the conditional probability of a particular element at risk to be in, or to exceed, a certain damage state as a result of a hazard of a particular type or intensity (Mavrouli & Corominas 2010). Fragility relationships are essential components of quantitative risk assessments (QRA) as they allow for the estimation of risk within a consequence-based framework.

For the purposes of this work the element at risk is a road and the hazard is debris flow. Damage probabilities have been assigned for specific debris flow volumes; these should not be confused with the probability of event occurrence. Fragility curves have been produced which indicate the probability of a debris flow of a given volume exceeding each of three damage states. To the best of the Authors' knowledge this is the first time that fragility curves have been developed for the effects of debris flow on roads. Fragility relationships are widely adopted in seismic 'expected loss' and risk assessments, being a valuable tool to explicitly assess the vulnerability of structures to earthquake hazard (Pitolakis et al. 2006).

While several possible approaches were available, including analytical and empirical ones, for the development of fragility curves, it was decided that expert engineering judgement should be used due to a lack of a comprehensive empirical dataset as well as the complex nature of the problem.

This paper describes the questionnaire sent to experts globally to collect data for the fragility curve development. It

also describes the analysis and interpretation of the data collected, and its validation using real world examples.

## 2 METHODOLOGY

### 2.1 Road characterisation

Many different classifications of roads could be considered, covering numerous key factors such as construction type, stiffness, and traffic speed. However, in order to reduce the questionnaire to a reasonable size some simplification was needed. Primarily it was decided that, for the purposes of this exercise, all roads could be considered to be relatively stiff and brittle (the low strain stiffness of even an unbound pavement is such that it is likely to behave in a stiff, brittle manner). In order to further simplify the analysis roads have been divided into low and high speed roads, characterized as follows:

- High speed: speed limit between 80 and 110km/h and one or more running lane in each direction, most likely in conjunction with a hardstrip or hard shoulder.
- Local (or low speed) roads: speed limit typically  $<50\text{km/h}$  on a single-carriageway (one lane for each traffic direction) or single-track. This category is intended to encompass both paved (bituminous, unreinforced or reinforced concrete) and unpaved constructions.

The gap between the speed limits of the two classes of road, reflects the transition between local roads and high speed roads, which is by no means geographically consistent. This reflects reality – in some countries and regions certain road geometries are more closely aligned with the definition of local roads and

in others they are more closely aligned with the definition of high speed roads. The results reported here are for high speed roads.

### 2.2 Damage states

Representative damage states associated with the consequences of a debris flow of a given volume intersecting a road were defined. The damage states considered in the questionnaire are defined in Table 1 and range from the type of damage that is unlikely to significantly affect the passage of vehicles, at least on high speed roads, to that which causes longer term damage and restrictions to the speed and/or passage of traffic.

Respondents to the survey were requested to use their expert judgement to assess the probability of each damage state being exceeded (Table 2) for a given event size. Respondents were asked to use the qualitative descriptors ‘Highly Improbable’ and ‘Extremely Likely’ with caution, and only where an extensive, high quality dataset supports the classification.

Table 1. Damage state definition.

Damage State	High Speed Roads
P1 (Limited damage)	Encroachment limited to verge/hardstrip
P2 (Serious damage)	Blockage of hardstrip and one running lane
P3 (Destroyed)	Complete blockage of carriageway and/or repairable damage to surfacing

Table 2. Description of probabilities.

Qualitative Descriptor	Description	Value for Analysis
Highly improbable	Damage state almost certainly not exceeded, but cannot be ruled out	0.000001
Improbable (remote)	Damage state only exceeded in exceptional circumstances	0.00001
Very unlikely	Damage state will only be exceeded in very unusual circumstances	0.0001
Unlikely	Damage state may be exceeded, but would not be expected to occur under normal circumstances	0.001
Likely	Damage state expected to be exceeded under normal circumstances	0.01
Very likely	Damage state expected to be exceeded	0.1
Extremely likely	Damage state is almost certainly exceeded	1.0

## 3 RESULTS

The questionnaire was sent to 176 experts; 47 responses (27%) were received from 17 countries: UK (34%), Greece (23%), other European countries (26%), Asia (4%), Australasia (4%), North America (4%) and the Middle East (2%). The respondents’ backgrounds were Academia (32%), the Commercial Sector (51%) and Government Bodies (17%).

## 4 ANALYSIS

### 4.1 Preliminary fragility curves

It is a relatively straightforward matter to construct preliminary fragility curves from the average of the probability responses at each volume, at each damage state and for both high speed roads and local roads as illustrated in Figure 1. These curves have the basic attributes of typical fragility curves. In broad terms these curves and the data that underpin pass the sense test. The curves generally show that landslides of a given volume are associated with higher probabilities of exceeding a certain damage state when they affect local roads than when they affect high speed roads, as would be expected. In addition, the curves for high speed roads generally show little effect at small landslide volumes, below a few hundred cubic metres.

It is noticeable that the mean probabilities do not reach unity for any of the curves. This implies that the damage states as defined can never be met or exceeded with complete certainty. However, this is an inevitable function of using the average of the responses, as the maximum possible response coincides with the desired termination point of each curve (a volume at which exceeding the given damage state is inevitable and the probability is unity). Further stages of analysis were undertaken to interrogate and better understand the data.

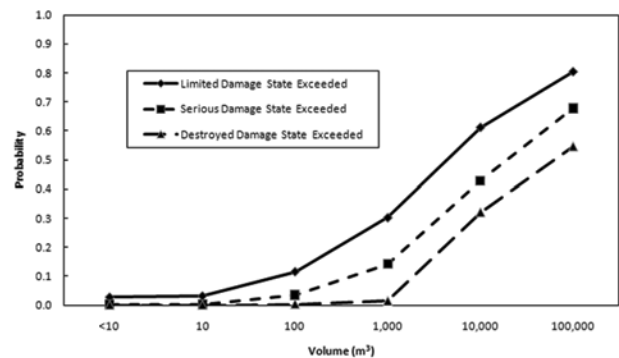


Figure 1. Preliminary fragility curves for high speed roads.

### 4.2 Curve fitting

Standard Excel<sup>TM</sup> curves were fitted (third order polynomial for Limited Damage and fourth for Severe Damage and Destroyed states). This gave better separation of the individual curves than is shown in Figure 1, and there was greater contrast between the results for high speed and local roads (Pitilakis & Fotopoulou 2011). This technique allows a degree of extrapolation of the data to higher volumes/probabilities. However, over application of such extrapolation tends to distort the curves at lower volumes.

### 4.3 Manual extrapolation

The data presented in Figure 1 may be manually extrapolated by a further logarithmic cycle by visually judging the appropriate value of probability at 1,000,000m<sup>3</sup> in order to maintain the broad appearance and trend of the curves. It is noticeable that, even when the volume is increased to 1,000,000 m<sup>3</sup> in this way none of the fragility curves reach unity; only that for Limited Damage for local roads reaches a value of around 0.95.

### 4.4 Weighting the data

Clearly the experience of the respondents is a critical metric in terms of understanding, evaluating, analysing and interpreting these data. The respondents were asked to assess their experience on a scale of zero (no experience) to 10 (extensive experience). The scores of this self-assessment weight towards the higher end of the range, as might be expected from a sample of respondents who were selected for their known expertise in this area. It thus seems potentially appropriate to place a greater confidence in the responses received from those who reported that their level of experience was higher than the average and a number of approaches is possible.

Firstly, a weighting approach may be taken. However, care is needed to ensure that the sample is weighted rather than the individual responses; otherwise bias will be introduced into the results. (Weighting the individual responses will, depending upon the precise approach taken, either increase or decrease the individual probabilities contained within the questionnaires for those with higher expertise and the converse for those with lower levels of expertise. There is no logical justification for such a change and this should therefore be avoided.) Weighting the sample may be done as follows

$$p = \frac{\sum_{i=1}^n p_i E_i}{\sum_{i=1}^n E_i} \quad (1)$$

where  $p$  = weighted mean probability of a particular damage state being exceeded;  $p_i$  = the individual responses of the probability of a particular damage state being exceeded;  $E_i$  = the individual responses in terms of self-assessed experience; and  $n$  = the number of responses.

However, there does remain a question as to what a weighted average means and statistical advice (Sexton, pers. comm.) indicates that the results should be treated with a degree of caution.

This yields fragility curves with lower probabilities of given damage states being exceeded by a given event volume than those derived from the full data set (Figure 2). This may indicate that either those with less experience overestimate, or those with greater expertise underestimate, potential damages.

The second approach involves rejecting the data from those respondents reporting less experience, leaving only that from those who assessed themselves as more experienced in this area. Statistical advice (Sexton, Pers. Comm.) indicates that approximately only scores from the upper 25% of the available range should be examined. This implies that the analysis should be undertaken for those judging their experience level as eight or above (33% of respondents). However, plotting the data led to a rather confused picture and to the conclusion that the 16 responses corresponding to the 33% of respondents reporting their experience level to be eight or above were insufficient to present a coherent picture. As for the weighting approach the resulting fragility curves yield lower probabilities of given damage states being exceeded by a given volume of event than those derived from the full data set.

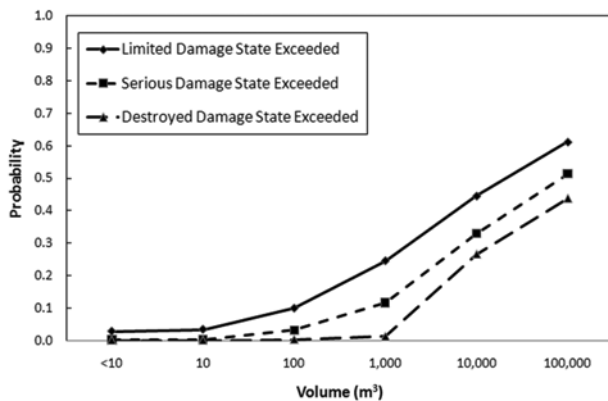


Figure 2. Weighted fragility curves: top, local roads; bottom, high speed roads.

## 5 INTERPRETATION

The curves illustrated in Figure 1 do not stretch between zero and unity. Even when manually extrapolated to a landslide volume of  $1,000,000\text{m}^3$  the curves do not reach unity as would be expected if they had been derived from by modelling in which such an outcome would have been constrained.

Using the current approach it is inevitable that the mean probability of each damage state being reached or exceeded is less than unity unless all of the respondents return such a value. This then begs the question of how to account for such an inevitable, and seemingly contradictory, facet of the results. It is straightforward to 'force' the curves to reach to unity by a ratio approach (the forced probability at any value of landslide volume,  $p_{if} = p_i \cdot [1/p_n]$  where  $p_i$  is the mean probability and  $p_n$  is the mean probability at the maximum landslide volume).

In order to determine whether such an approach can be justified one must examine the more detailed responses of the respondents to the questionnaire and in particular the responses

of those where a probability of unity was assigned to the combinations of landslide volume and damage state. These data illustrate, as might be anticipated, that the number of responses assigning a probability of unity increases markedly with landslide volume while decreasing with increased damage state severity. Most importantly, for high landslide volumes, the majority of respondents give unity for the likelihood of a given damage state being reached or exceeded, lending justification to 'forcing' the curves to reach unity.

As discussed, the preliminary fragility curves of Figure 1 can be forced to unity, and manually extrapolated to the next order of magnitude in terms of landslide volume (i.e.  $1,000,000\text{m}^3$ ). The next logical step is to combine these two actions as illustrated in Figure 3. The curves illustrated therein conform to the 's'-shape generally perceived as being the correct form for fragility curves. Notwithstanding this, one would normally expect that the curves for different damage states would reach unity at different landslide volumes; that they do not is a function of the type of analysis undertaken and it seems reasonable, as none of the curves reach unity, to force them all to such a level at the highest volume considered.

Geographical variations and variations potentially caused by respondents' backgrounds (Academic, the Commercial Sector, and Governments) were investigated. It was concluded that the datasets were generally too small to draw definitive conclusions albeit that the data appeared to suggest that:

- Responses for the UK exhibited slightly higher probabilities for larger landslide volumes compared to those for the 'Rest of the World'.
- The responses for Academia exhibited slightly higher probabilities for larger landslide volumes compared to those for the Commercial Sector.

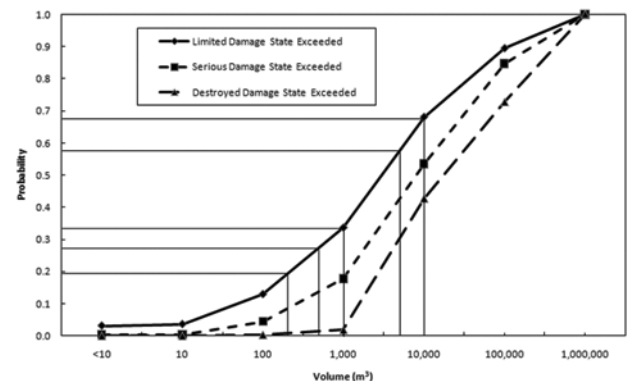


Figure 3. Fragility curves for high speed roads 'forced' to unity and manually extrapolated to the next order of magnitude of debris flow volume. Lines for Limited Damage at 200, 500, 1,000, 5,000 and  $10,000\text{m}^3$  are also shown.

## 6 VALIDATION

The comments received from respondents generally supported the use of curves of the form illustrated in Figure 3 and events from Scotland in the UK and the Republic of Korea are considered here. Figure 4 illustrates hypothetically-shaped curves in which the numbers given relate to a  $5,000\text{m}^3$  event on a high speed road (Figure 3). The probabilities ( $p$ ) of the damage being equal to or greater than a given level are:

- Damage greater than or equal to 'Limited',  $p = 0.6$ .
- Damage greater than or equal to 'Serious',  $p = 0.4$ .
- Damage greater than or equal to 'Destroyed',  $p = 0.3$ .

The discrete, or conditional, damage state probabilities (i.e. the probabilities of the occurrence of a given damage state) are estimated from the probabilities given above:

- Probability of no damage =  $1.0 - 0.6 = 0.4$ .
- Probability of 'Limited' damage =  $0.6 - 0.4 = 0.2$ .
- Probability of 'Serious' damage =  $0.4 - 0.3 = 0.1$ .
- Probability of 'Destroyed' damage state =  $0.3$ .

Note that the conditional probability of the ‘Destroyed’ damage state is always equal to the probability of that state being exceeded. Vulnerability assessment using fragility curves is, of course, probabilistic in nature and the models used in their construction – in this case based upon expert judgment – have inherent uncertainties. Accordingly, the validation examples are not expected to precisely predict the observed damages.

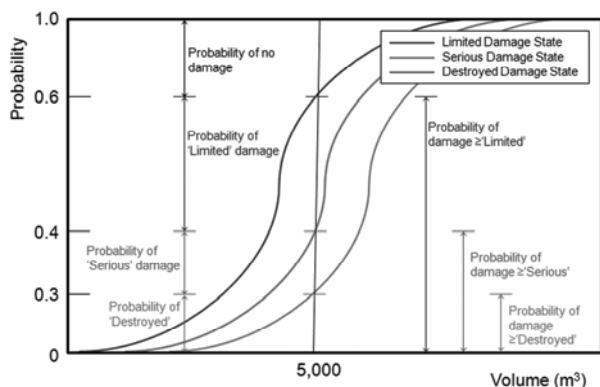


Figure 4. Hypothetical fragility curves: the numbers relate to a 5,000m<sup>3</sup> event on a high speed road (see Figure 3) and show conditional probabilities and those of a given event exceeding a damage state.

### 6.1 A85 Glen Ogle, Scotland

In August 2004 two debris flow events occurred at Glen Ogle blocking the A85 strategic road, culverts and other drainage features, and necessitated a full repair to the road pavement, safety barriers and parapets. Some 20 vehicles were trapped by the events and 57 people were airlifted to safety; one vehicle was swept away in the latter stages of the event (Winter et al. 2005, 2006, 2009). The smaller southerly and larger northerly events were estimated to have deposited around 3,200m<sup>3</sup> and 8,500m<sup>3</sup> in their respective debris lobes having been triggered by smaller translational slides of around 285m<sup>3</sup> and 280m<sup>3</sup> (Milne et al. 2009). These figures are believed to exclude material deposited on the road and it seems reasonable therefore to round these figures up to around 5,000m<sup>3</sup> and 10,000m<sup>3</sup>. This illustrates the uncertainty when dealing with debris flow volumes between the amount mobilised and that deposited at road level.

Figure 4 shows how these event volumes plot on the fragility curves. For the smaller (5,000m<sup>3</sup>) event the conditional probabilities for no damage, ‘Limited’, ‘Serious’ and ‘Destroyed’ damage states are 0.4, 0.2 (0.6), 0.1 (0.4) and 0.3 (0.3) (the probabilities of the damage states being met or exceeded are given in parentheses); for the larger (10,000m<sup>3</sup>) event the conditional probabilities are around 0.3, 0.15 (0.7), 0.15 (0.55) and 0.4 (0.4). Certainly the damage caused by the larger event would have been described as ‘Destroyed’ using the scheme considered here and the probability of this state being 0.4 seems to be broadly in line with observations in its immediate aftermath, affecting a road length of around 200m. Similarly the damage caused by the smaller event, although significantly less in terms of physical damage to the infrastructure, would also be classified as ‘Destroyed’ and this seems to broadly reflective the probability of 0.3 (Figure 4).

### 6.2 Chuncheon National Highway, Republic of Korea

Debris flows of around 500m<sup>3</sup> to 1,000m<sup>3</sup> were evident at the Chuncheon National Highway Tunnel Portals (Lee & Winter, 2010). For an event of this volume (1,000m<sup>3</sup>) the conditional probabilities of the damage states no damage, ‘Limited’, ‘Serious’, and ‘Destroyed’ are 0.7, 0.1 (0.3), 0.18 (0.2), and 0.02 (0.02) (Figure 4).

Only very minor damage was incurred and this reflects the small volumes and the combined conditional probabilities of 0.8 for no damage and of the ‘Limited’ damage. The road was not

open at the time of the event and there is every possibility of both further and larger events that have the potential to meet or exceed higher damage states.

## 7 CONCLUSIONS

A survey of experts was conducted to develop of preliminary fragility curves for the effects of debris flows on roads.

Included in the questionnaire was the opportunity for the respondents to make ‘free text’ responses to defined questions. Their responses have been used, in part, to determine the form of analysis. Consequently the proposed fragility curves have been extrapolated to include events one order of magnitude greater than the largest considered in the questionnaire. In addition, this form of determining fragility curves renders it almost impossible for the probabilities to range from zero to unity; according the proposed fragility curves have been stretched to ensure such a spread.

The derived fragility curves have been compared to known events in Scotland (UK) and the Republic of Korea. In general the curves tend to give results that might be deemed ‘sensible’ with probabilities of around 0.3 to 0.8 being suggested for the known damage states. Exceptions to this occur when detailed site characteristics introduce complexities that are not, and could not be, accounted for in the analysis.

Notwithstanding this, the method of data acquisition and the perceived interpretations of the questionnaire for this first approach raise some interesting issues that will be explored in a later paper. Continued efforts are needed, potentially including the use of modelled and empirical data.

## 8 ACKNOWLEDGEMENTS

The work described in this paper was (partially) supported by the European Commission through the project “SafeLand – Living with landslide risk in Europe: Assessment, effects of global change, and risk management strategies” of EU’s 7th Framework Programme. Their support is gratefully acknowledged. The TRL authors gratefully acknowledge additional funding from Transport Scotland.

## 9 REFERENCES

- Lee, S.-G. & Winter, M.G. 2010. The effects of debris flow in the Republic of Korea and some issues for successful management and mitigation. In A.L. Williams, G.M. Pinches, C.Y. Chin, T.M. McMorran & C.I. Massey (eds.), *Geologically Active: Proceedings, 11th IAEG Congress*, 1243-1250. London: CRC Press.
- Mavrouli, O. & Corominas, J. 2010. Rockfall vulnerability assessment for reinforced concrete buildings, *Natural Hazards and Earth System Sciences* 10, 2055-2066.
- Milne, F. D., Werritty, A., Davies, M. C. R. & Browne, M. J. 2009. “A recent debris flow event and implications for hazard management”, *Quarterly Journal of Engineering Geology and Hydrogeology* 42, 51-60.
- Pitilakis, K., Alexoudi, M., Argyroudis, S., Monge, O. & Martin, C. 2006. Earthquake risk assessment of lifelines. *Bulletin of Earthquake Engineering* 4, 365-390.
- Pitilakis, K. & Fotopoulou, S. (Eds.) 2011. Physical vulnerability of elements at risk to landslides: methodology for evaluation, fragility curves and damage states for buildings and lifelines. SafeLand Deliverable 2.5. ([www.safeland-fp7.eu](http://www.safeland-fp7.eu))
- Winter, M. G., Macgregor, F. & Shackman, L. (Eds.) 2005. Scottish Road Network Landslides Study, 119p. Trunk Roads: Network Management Division Published Report Series. Edinburgh: The Scottish Executive.
- Winter, M. G., Heald, A. P., Parsons, J. A., Macgregor, F. & Shackman, L. 2006. Scottish debris flow events of August 2004, *Quarterly Journal of Engineering Geology and Hydrogeology* 39, 73-78.
- Winter, M.G., Macgregor, F. & Shackman, L. (Eds.) 2009. *Scottish road network landslides study: implementation*: 278p. Transport Scotland Published Report Series. Edinburgh: Transport Scotland.

# Inspection and Capacity Assessment of Anchored Slopes

## Inspection et évaluation des capacités des pentes renforcées par ancrage

Yeh H.n-S., Wang C.-S., Wei C.-Y.  
*Taiwan Area National Freeway Bureau, MOTC*

Lee S.-M., Ho T.-Y., Hsiao C.-A., Tsai L.-S.  
*CECI Engineering Consultants, Inc., Taiwan*

**ABSTRACT:** In Taiwan, anchors were first used in the Techi Dam for slope protection in 1970s. Since then, anchors were often used for stabilizing slopes in the construction of roads or communities. Lots of anchor experience of engineering practices have been accumulated in the past 40 years, however, it still remains some problems to be solved. In particular, after the failure of anchored slope at station 3.1K of Highway No. 3 in 2010, the function of existing anchors and the safety of anchored slopes have raised lots of concern. This paper introduces examining items, methods and processes of functional inspection of existing anchors. Also, results of 16 functional inspection of existing anchors in western Taiwan are presented. It is expected that the concepts and suggestions described in this article would be helpful for an engineer in gaining the ability of the analysis of slopes so that the more effective design can be developed for such a problem in the future.

**RÉSUMÉ :** A Taiwan, les renforcements par ancrages ont d'abord été utilisé dans le barrage Techi pour la protection des talus dans les années 1970. Depuis lors, les ancrages étaient souvent utilisés pour la stabilisation des pentes dans la construction de routes. Beaucoup d'expérience dans les pratiques d'ingénierie d'ancrages a été accumulées au cours des 40 dernières années. Cependant, il reste encore quelques problèmes à résoudre. En particulier, après la rupture d'une pente ancrée à la station 3.1k de la route n°3 en 2010, l'efficacité des ancrages existants et la sécurité des talus ancrées ont soulevé beaucoup d'inquiétude. Cet article présente l'examen des ancrages, des méthodes et des processus de contrôle du fonctionnement des ancrages existants. En outre, les résultats d'inspection de 16 talus renforcés par ancrages existants dans l'ouest de Taiwan sont présentés. Il est prévu que les concepts et les suggestions décrits dans cet article soit utilisable par un ingénieur via l'acquisition d'outils d'analyse des pentes de sorte qu'une conception plus efficace puisse être développé à l'avenir.

**KEYWORDS:** Landslides, anchor, lift-off test, anchor inspection, maintenance and management.

### 1 INTRODUCTION

Taiwan's area is approximately 3,600,000 hectare, and of it moderately flat area comprises about 26% while sloped and forested land make up the remaining 74%. Therefore Taiwan is mostly mountainous with lesser plains topography, though in the recent decade with the economic growth and the pursuit of comfort and ease of transportation, the trend of developing public infrastructure such as roadways and public facilities is moving toward hillsides and slopes.

Ground anchoring usage over steep slope has its certain advantages. Ground anchoring technique originated since the 1970s in Taiwan. Since 1988, Northern Taiwan Second Highway construction had begun, as its alignment laid predominantly among mountainous ranges and slopes, this type of method had proved itself to be an effective technique under such natural constraints and coupled with rapid economic growth, many new projects had begun to adopt this method in many sloped terrain community developments. Until today, ground anchorage technique has proven to be a reliable method and have been widely used, as well as the design and field installation has vastly improved since its earlier days. However, there are still many ground anchoring failure instances in recent years, one of which is the quite high profiled case of the 1997 Xizhi Lincoln Mansions disaster and 2010 National Highway No. 3 at 3.1k accident. Both failure cases are considered ground anchoring accidents and attributed to parallel landslide as the cause.

According to Briaud et al.(1998), Bruce and Wolfhope (2007), Liao et al. (2011), Ho et al.(2011), Jeng et al.(2011) and various domestic and foreign ground anchoring case studies, failure instances involved most commonly pre-stressed losses.

The main cause of that include 1) free section of tendon(unbounded tendon) rusted and cracked, 2) ground anchoring wedges rusted or had sub-standard quality, 3) Installation did not conform to the specification, as the steel tendon had not gone far enough into the earth, 4) change of terrain layer, and 5) ground cave in at bottom of the bearing plate.

After the National Highway No. 3 incident involving ground anchoring failure, see Figure 1, a complete study had done on ground anchor inspection and assessment. Even so, the findings of the study were routine and not consistent among the investigators. This article will introduce and explain the currently most adopted ground anchoring inspection, procedure, and assessment. In addition, this article will propose a new way of ground anchoring assessment, in hoping to establish a standardized quantitative analysis procedure for professional reference.



Figure 1. National Highway No. 3 at 3.1k accident



## 2 INSPECTION ITEMS AND PROCEDURE

Ground anchoring inspection and assessment is aimed to analyze and understand the performance of existing anchors and the impact to the site and its surrounding.

### 2.1 Inspection items

Currently there are some initial inspection items including: exterior inspection, anchor head inspection, endoscopy inspection and Lift-off test, the four major items will be explained in detail later.

### 2.2 Inspection procedure

Inspection procedure is as indicated in Figure 2. First gather basic data from all sloped terrains for ground anchor index, then remove all outgrowth on the slope, and check the entire ground anchors for outside appearance, pressure bearing integrity and water seepage status. According to the gathered data and inspection results, select the most typical anchor in characteristics of all anchors, remove the concrete casing to examine the anchor head and steel tendon closely, and record findings. After examining the anchor, use the findings to select partial ground anchors for endoscopy inspection to examine steel tendon corrosion and proceed with Lift-off Test, in order to understand the existing ground anchor Residual load( $T_r$ ). Lastly, based on sloped terrain basic data and findings of various test results, evaluate in totality the ground anchors current capacity. If ground anchor capacities no longer meet the requirement of original specifications or there are other anomalies present which render the anchors inappropriate for continuing usage, then a proposal is required to improve or remediate the situation, including refurbishment, remedy, reinforcement or reconstruction as required.

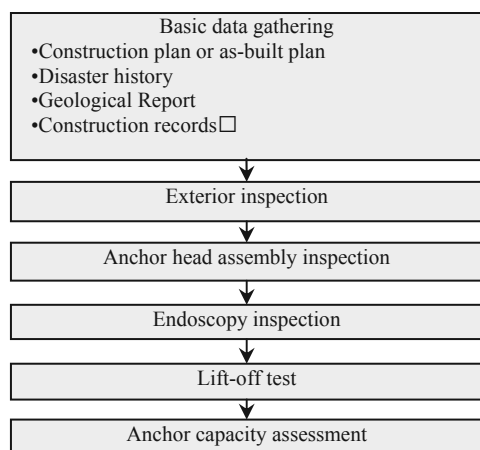


Figure 2. Ground anchor capacity assessment flowchart

## 3 CAPACITY INSPECTION METHOD

Various inspection category results can be used to provide as the basis for evaluating the capacity of anchors, summary of each categories is as follows:

### 3.1 Exterior inspection

Prior to knocking off the ground anchor concrete protected seats, obtain as-built drawings to mark off each and every anchors with numeric identifications. Visually inspect, investigate and record all anchor protected seats and load bearing structure system conditions. Visual inspection should emphasize on 1) anchor head protected seat hammer knocking test and the quality of sound whether solid or hollow, 2) visually inspect exterior of anchor protected seat for any damages, 3) between anchor head and load bearing structure,

look for any sign of separation, rotation, or even detachment, 4) Whether subsoil below shows sign of cave-in for the load bearing structure and 5) anchor head proximity has sign of efflorescence or ground water seepage, and all visual inspection should be carefully documented.

### 3.2 Anchor head assembly inspection

Anchor head assembly includes locking mechanism(wedges and screw head), load bearing plate and angle plate, as such parts tend to have anomalies. When inspecting anchor head assembly, carefully select a representative anchor head, after the removal of concrete protected seat, visually inspect the corrosive state of the anchor heads. After removal of anchor head protected seat the following category of items need to be recorded: load bearing plate dimension, angle plate dimension, load bearing plate angle, anchor head dimension, steel tendon style and remaining length data.

At this stage visual inspection should emphasize on 1) anchor head wedges and steel tendon corrosion, 2) anchor head assembly and water seepage condition and 3) steel tendon interior shortening, and all inspection should be recorded in detail.

### 3.3 Endoscopy inspection

Endoscopy can be used to inspect the backside of anchor head and free section of steel tendon, to determine whether the steel tendon is corroded, broken or free section has water inside. Entire inspection process should be video recorded to allow further inspection and study back in the lab. The equipment used is as shown in Figure 3.

Besides inspecting steel tendon status, this stage should measure the steel tendon length of free section. The measuring technique is to use a stainless steel rod to insert into the anchor free section portion until the rod can not be inserted further, as Figure 4 indicated. Then record the length of the rod which was inserted, as such length can be taken as the exposed section length.

Endoscopy inspection should emphasize on 1) steel tendon corrosion level, 2) steel threads loosened condition, 3) free-section concrete condition, 4) any concrete casting pipes and 5) interior moisture level or any water seepage, all inspection processes should be done carefully and in detail.

### 3.4 Lift-off test

After locking in load bearing of ground anchors, it's possible that due to creep at the bond end, wedges not properly function which would reduce or increase the loading capacities. To measure the change of loading capacities after lock-in, typical lift-off test is conducted, as shown in Figure 5. Lift-off test is aimed at finding the remaining load capacity of anchor( $T_r$ ), and the reason being when tensile load is greater than the anchor remaining capacity, anchor will demonstrate obvious displacement increase, from which can be taken to evaluate the remaining capacity of ground anchors, as shown in a standard test curve in Figure 6. Ground anchor residual load( $T_r$ ) divided by ground anchor original designed load capacity ( $T_w$ ) is the remaining load capacity ratio.



Figure 3. Equipment installation and operation

#### 4 GROUND ANCHOR CAPACITY ASSESSMENT PROCEDURE AND CASE STUDY

For the purpose of quantitative assessment on the ground anchor capacities, and with regard to the ground anchors performance on the sloping terrain application is the goal of this procedure. Based on the inspection and assessment items, this article shall introduce a new set of ground anchor capacity assessment procedure, in hoping to establish a standardized way to quantitatively evaluate and assess ground anchoring. Such procedure shall comprised of exterior inspection, anchor head

inspection, endoscopy inspection and lift-off test. The findings based on Table 1 distribution is point based. The total score will then be carried to Table 2 to evaluate ( $\beta$ ) and classification. Sloped terrain performance and ground anchoring total capacity shall be classified based on Table 2 standards. Ground anchoring total performance assessment classified as A or B grade, respectively, will be given corresponding effective rehabilitation to ensure the full and reliable capacity of the ground anchors.


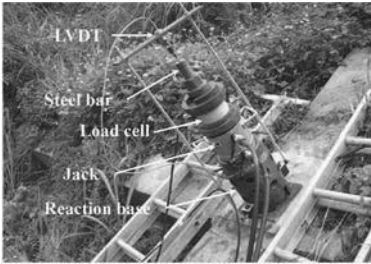
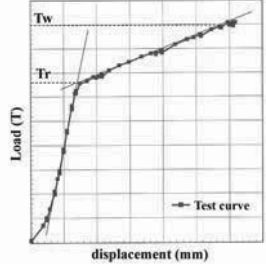
		
Figure 4. Free section exposed portion length investigation	Figure 5. Lift-off test installation	Figure 6. Lift-off test curve diagram

Table 1. Score of anchor capacity assessment

item	scoring	Content of inspection	Weight	subtotal
Exterior inspection	10	Buckled or detached.	0	
		Greater than 2mm separation from bearing plate or water corrosion is severe.	0.25	
		Anchor head protected seat and bearing plate separation is less than 2mm.	0.50	
		Anchor head protected seat surrounded by water seepage, efflorescence or anchor seat outside is slightly damaged or water corrosive level is moderate.	0.75	
		No observable anomalies or water quality is normal.	1.0	
Anchor head assembly inspection	15	Assembly came apart(clamp became loosened, steel tendon shrinkage or broken)	0	
		Anchor head surface appeared rusted and cracked, spread over 50% of the surface, steel tendon section is deformed due to corrosion.	0.25	
		Anchor head surface appeared rusted and cracked, but spread less than 50% of the surface.	0.50	
		Slightly corroded or water seepage. Anchor head appeared rusted, but the depth of the rust is quite thin, not measurable or lesser than 0.1mm.	0.75	
		No corrosion or water seepage is present.	1.0	
Endoscopy inspection	30	Steel tendon broken or steel threads became loosened and completely rusted.	0	
		Steel tendon appeared dark brownish, the surface already appeared corral-like or lumpy or rusted surface spread over 90%.	0.15	
		Steel tendon appeared dark brownish, the surface is rough, but not appearing corral-like or lumpy or rusted surface is between 50~90%.	0.45	
		Steel tendon appeared light brownish, but the surface is smooth and shining or rusted surface is between 10~50%.	0.75	
		No anomaly presence or rusted surface is below 10%.	1.0	
lift-off test	45	Detached, steel tendon broken or $Tr=0$ .	0	
		$Tr > 1.2Tw$ or $Tr \leq 0.2Tw$	0.33	
		$0.2Tw < Tr \leq 0.5Tw$	0.67	
		$0.5Tw < Tr \leq 0.8Tw$	0.75	
		$0.8Tw < Tr \leq 1.2Tw$	1.0	
Single ground anchor capacity assessment( $\beta$ )				
Total score of anchor capacity assessment( $\alpha$ )				

Remark: 1. If any of the items in categories 1,2,3,4 assessed a score of 0, such ground anchor shall be deemed as defective, and the total score of the anchor shall be zero.  
2. When a sloped terrain of which 1/3 of the ground anchors inspected has reach over 90% rusted surface under the examination of endoscopy, but the lift-off test revealed remaining capacity falls into the range  $0.8Tw < Tr \leq 1.2Tw$ , additional investigations in the field and test data is recommended to determine whether the slope may have a tendency to slide.

Table 2. Ground anchor assessment classifications

Individual capacity assessment		Total capacity assessment	
$\beta$	class	$\alpha$	class
0	X. Defective		
$\beta \leq 30$	A. Worst	$\alpha \leq 30$	A. Worst
$30 < \beta \leq 55$	B. Unacceptable	$30 < \alpha \leq 55$	B. Unacceptable
$55 < \beta \leq 80$	C. Acceptable	$55 < \alpha \leq 80$	C. Acceptable
$80 < \beta$	D. Normal	$80 < \alpha$	D. Normal

Ground anchor inspection items will be measured with apparatus, which is the best and most direct way to understand the existing conditions of the anchors and remaining bearing capacities. These values usually will be referred to while performing sloping reinforcing analysis. Of course the anchor capacity cannot and should not base solely on the lift-off test result. There are other factors such as ground condition below the anchors for possible cave-ins, steel tendon or anchor head surface appeared rusted and cracked. When a sloped terrain of which 1/3 of the ground anchors inspected has reach over 90% rusted surface under the examination of endoscopy, but the lift-off test revealed remaining capacity falls into the range  $0.8T_w < Tr \leq 1.2T_w$ . Such conditions should be cross referenced with other data like field observations and inspections and evaluate in totality whether the slope has a tendency to slide. This article brings forth various anchor evaluations by which will address the possible different scenarios that might be overlooked otherwise. In order to validate the practicality of Table 1, this article takes 16 slopes and conduct a simulating calculation for them. The results are as shown in Table 3 and 4. The results and classifications are consistent, thus prove the validity of this assessment procedure and its practicality.

Table 3. Case study of Single ground anchor capacity assessment

No. of anchors	S4-1	S4-2	S4-3	S4-4	S4-5
Exterior inspection	7.5	7.5	7.5	7.5	7.5
Anchor head assembly inspection	11.25	11.25	11.25	11.25	11.25
Endoscopy inspection	22.5	30	22.5	30	30
Lift-off test	33.75	45	33.75	45	45
$\beta$	75.0	93.8	75.0	93.8	93.8
$\alpha$	86.3				
Class of lift-off test	C	D	C	D	D
Class of $\beta$	C	D	C	D	D
Class of $\alpha$	D				

5 CONCLUSION

Based on collected statistical data, 90% ground anchor failure are resulted at the anchor head proximity and free section part of the steel tendon. This article had gathered data which initially showed free section was not completely filled with concrete for nearly 85% of the ground anchors being examined, therefore making it the most prevalent shortcoming. To avoid anchors becoming defective which leads to disaster, anti-corrosive remedy should be done promptly.

This article only took 16 areas of sloping terrain to gather data on ground anchors for inspection and assessment as explained previously. This evaluation procedure demonstrates that the four categories assessment: inspecting the exterior aspect of the anchor, the anchor head examination, endoscopy inspection and lift-off tests is a logical process in finding

shortcomings. In the future it is bound to have additional data available added to and revised upon, and would become a valuable systematic way for the engineering industry to adopt widely across.

Table 4. Case study of anchored slope capacity assessment

Slope No.	lift-off test			Total capacity	
	Amounts	Tr(%)	Class	Scoring	Class
S1	6	88.2	D	83.9	D
S2	5	77.8	C	55.3	C
S3	6	35.6	B	38.9	B
S4	5	88.2	D	86.3	D
S5	5	65.5	C	77.2	C
S6	4	35.6	B	54.2	B
S7	3	52.9	C	60.2	C
S8	3	70.2	C	63.6	C
S9	4	43.3	B	62.9	C
S10	3	85.1	D	87.9	D
S11	3	108.6	D	74.7	C
S12	8	69.5	C	64.8	C
S13	7	71.2	C	61.6	C
S14	5	55.6	C	62.0	C
S15	8	53.5	C	68.4	C
S16	7	47.7	B	52.9	B

6 REFERENCES

Briaud J.L., Powers W.F. and Weatherby D.E. 1998. Should grouted anchors should have short tendon bond length. Journal of Geotechnical and Geoenvironmental Engineering 124(2), ASCE, New York.

Bruce D.A. and Wolfhope J. 2007. Rock anchors for north American dams: the national research program bibliography an database. Institution of Civil Engineers, Ground Anchorages and Achored Structures in Service, London, England, U.K., 481-491.

Liao H.J. and Cheng S.H. 2011. Failure cases of anchors and anchored slopes in Taiwan", Proc. of the 5th Cross-strait Conference on Structural and Geotechnical Engineering, Hong Kong.

Ho T.Y., Hsiao C.A. and Tsai L.S. 2011. Present situations and improvement suggestions of existing anchors in Taiwan. Sino-Geotechnics 130, 43-54.

Jeng C.J., Chen Y.C., Chen R., Yang P.J. and Lin Y.C. 2011. Discussion and recommendation on performance influence of current permanent ground anchor factors through case study. Sino-Geotechnics 130, 19-30.

Liao J.T., Wu T.H., Chen C.W. and Lu C.H. 2011. Discussion on Establishment of prestressed ground anchor maintenance and management system. Sino-Geotechnics 130, 79-90.

# 2011 Seoul Debris Flow and Risk Analysis

## Coulée de boue à Séoul en 2011 et analyse des risques

Yune C.-Y., Kim G., Lee S.W., Paik J.

*Department of Civil Engineering, Gangneung-Wonju National University*

**ABSTRACT:** A series of debris flow events occurred around 8:00 to 8:50 a.m. on July 27, 2011 in the Umyeon Mountain area located in central Seoul, Korea. Umyeon Mountain is a relatively small one with a height of 250m and slopes with the average angle of around 15°. Due to the debris flows with runout distances ranging from 300m to 1,000m, 16 people were killed and more than 150 houses had been damaged in the area. In this work, we seek to understand the physical characteristics of the initiation and propagation behavior of debris flows from field investigation in the area and the analysis of rainfall data collected by AWS (Automatic Weather Stations) rain gauges. Field investigation shows that about 33 debris flows occurred in the Umyeon Mountain area and most of these debris flows were initiated from small slope failures induced by high-intensity rains. The application of landslide hazard map which has been recently developed by taking slope angle and direction, strength of soil, hazard record, rainfall condition and plantation into account demonstrates its good performance to highlight areas that are vulnerable of heavy-rainfall-induced slope failure and the resulting debris flow disasters.

**RÉSUMÉ :** Une série de coulées de boue s'est produite vers 8h00 ~ 8h50 le 27 Juillet 2011 dans la région du mont Umyeon situé dans le centre de Séoul, en Corée. La montagne Umyeon est relativement petite avec une hauteur de 250m et des pentes à angle moyen d'environ 15°. En raison de ces coulées de boue sur une distance allant de 300 à 1000m, 16 personnes ont été tuées et plus de 150 maisons ont été endommagées dans la région. Dans cette étude, nous chercherons à comprendre les caractéristiques physiques de l'initiation et du développement de la propagation des coulées de boue à partir d'une enquête sur place dans la zone concernée et de l'analyse des informations de précipitations recueillies par les pluviomètres de l'AWS (« Automatic Weather Stations », Station météorologique automatique). L'enquête sur place montre que près de 33 coulées de boue ont eu lieu dans la région du mont Umyeon et la plupart de ces coulées de boue ont pris naissance à partir de petites ruptures de pente provoquées par des pluies très intenses. L'application de la carte des risques de glissement de terrain qui a été récemment mise au point en prenant en compte l'angle et la direction des pentes, la résistance du sol, l'historique des désordres, les conditions des précipitations et des plantations démontre sa bonne performance pour mettre en évidence les zones qui sont vulnérables à des ruptures de pente provoquées par de fortes pluies et des catastrophes résultant de ces coulées de boue.

**KEYWORDS:** debris flows, field investigation, rainfall, hazard map

## 1 INTRODUCTION

Most of the debris flow hazard has been concentrated during the rainy season from June to August in Korea. In 2011, there were Typhoon Meari (22 June to 27 June), Typhoon Muifa (28 July to 9 August) and the seasonal rain front that stayed in the middle part of the Korean peninsula. They poured much more rainfall compared to the average value, and eventually led to debris flows around the country (Yune and Jun, 2011). A series of debris flow events occurred around 8:00 to 8:50 a.m. on July 27, 2011 in the Umyeon Mountain area located in southern part of Seoul, Korea.

Debris flows which generally contain more than 50% of granular materials larger than sand particles flow fast (Johnson and Rahn, 1970; Hutchinson, 1988). Because of their fast movement, it is very hard to take refuge, even though people recognize beforehand the outbreak of the debris flow. Between 8:00 to 8:50 a.m. on July 27, 2011, many debris flows occurred simultaneously at Umyeon Mountain in Seoul where there had been a previous debris flow event in 2010 caused by Typhoon Kompasu. Because the mountain is located at the center of a dense residential area in Seoul, the hazard had a great impact on the society compared to debris flows that occur in rural areas, and it led to careful scrutiny of the hazard area and the causes of debris flows.

In this research, a site survey on the debris flow at Umyeon Mountain was carried out to analyze the causes of the event, and rainfall records were also collected to investigate the triggering characteristics of the rain. In addition, risk analysis based on the hazard map of the landslide and debris flow was performed.

## 2 2011 SEOUL DEBRIS FLOW

### 2.1. Overview of Umyeon Mountain

Located in southern part of Seoul (Fig. 1) with the height of 312.6 m above the sea level, Umyeon Mountain includes lots of eco-friendly facilities, such as natural ecological park and mineral spring which can be easily accessed by local residents. It has a main ridge formed from the northeast to the southwest, including several valleys perpendicular to the main ridge. Most of the mountain consists of highly-weathered banded gneiss with subordinate granitic gneiss. Directions in ENE- and NW to NNW-striking faults are predominant with strike- or normal-slip sense. The groundwater level in the basin seems high because six mineral springs are located side by side at the altitude of 220 to 250 meters on the slope. Field observation of Son et al. (2012) also showed that groundwater level at locations where debris flows initiated reaches to the surface so that surface runoff occurs at the continuous rainfall condition of more than 250 mm, even if there is no significant antecedent rainfall. In

2010, regional intensive rainfall following Typhoon Kompasu caused a few landslides, and some of them developed as debris flows at the northern valleys in Umyeon Mountain (Fig. 2). However, the damage in 2010 was not great compared with the debris flow hazard in 2011.



Figure 1. Location of Umyeon Mountain

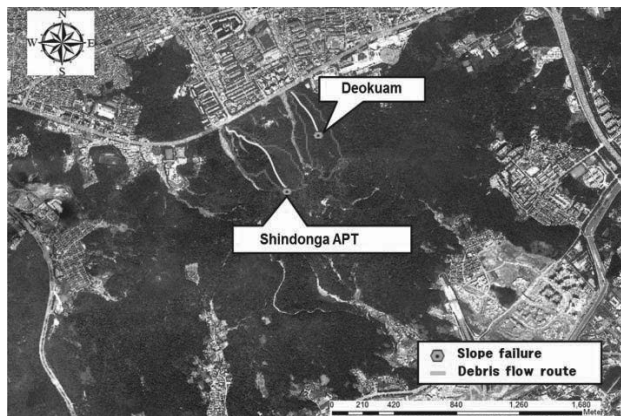


Figure 2. Locations of Slope Failures and Debris Flows around Umyeon Mountain in 2010

### 2.2. Field Survey

Field survey was performed to get data, such as longitude/latitude and topographical/geotechnical characteristics in places where debris flows were initiated, transported, and accumulated using a portable GPS, a laser ranger, and a clinometer. Based on the data from field survey, coordinates regarding initiation zones and debris flow routes were indicated on an aerial photograph around Umyeon Mountain as shown in Fig. 3. In this figure, the initiation slope failures are marked by blue dots, and debris flow routes are marked by yellow lines. Orange dots and green dots are also the initiation slope failure at the boundary and inside of air force base at the summit of the mountain, respectively. Most of the debris flows were initiated by slope failure and flowed down the valley. It was determined that they occurred simultaneously in the whole Umyeon Mountain area. The total number of slope failure that initiated debris flow was about 150. Based on the outlet in which the debris flows accumulated, the number of debris flows was about 33.

When we classified debris flows by direction, it was found that many of the slope failures occurred on the southern slope but many of the debris flows occurred on the northern slope. The debris flows moving towards the south were channelized debris flows which flowed down the valley and merged together. On the other hand, debris flows on the northern slope were hillslope debris flows which moved rapidly without being confined in an established channel. Therefore, the northern

slope has fewer initiation zones but more debris flows compared to the southern slope.

The field survey result showed that the average moving distance of debris flows in Umyeon Mountain was about 615m, ranging from 95 to 1,584m. Also, the average gradient of initiation slopes was about 27 degrees, ranging from 11 to 37 degrees. The initiation volume of the slope failure was measured from 73 to 4,000 m<sup>3</sup>.

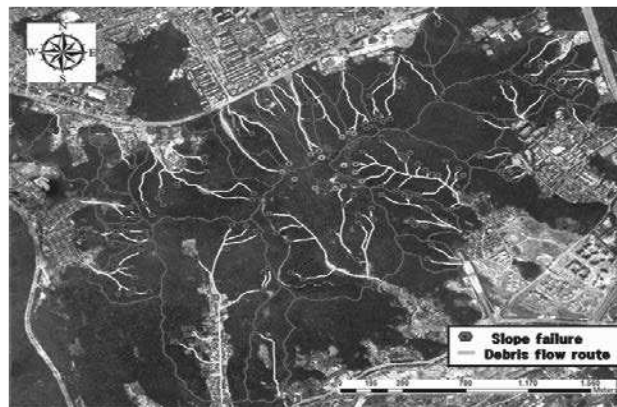


Figure 3. Locations of Slope Failures and Debris Flows around Umyeon Mountain in 2011

### 2.3. Rainfall Conditions

Korea Meteorological Administration (KMA) reported that the torrential heavy rain which triggered landslides at Umyeon Mountain in 2011 was due to unstable atmospheric conditions mainly determined by cold and dry air from inland China along with the hot and humid air masses from the strong Southwestern wind alongside the Western North Pacific subtropical high (Fig. 4).

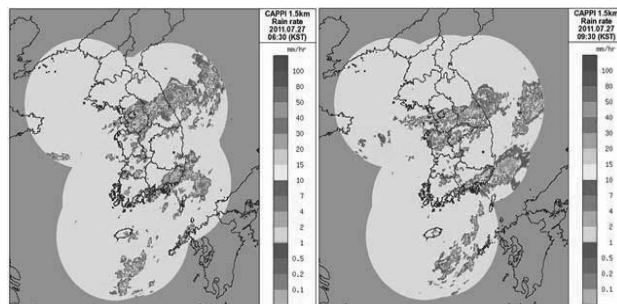


Figure 4. Spatial patterns of rainfall in Korea peninsula by KMA

There are two automatic weather stations (AWSs) operated by KMA near Umyeon Mountain as shown in Fig. 5. Namhyeon and Seocho stations are located at west and northeast part of Umyeon Mountain, respectively. Rainfall records from Namhyeon and Seocho stations were analyzed as daily and cumulative rainfall for 2 months as shown in Fig. 6. The cumulative rainfall for 2 months before debris flow event was 1,489.5mm and 1,105.0 mm at Namhyeon and Seocho station, respectively. Those values were comparable to the average annual rainfall in Seoul (1,450.5 mm). A significant amount of rainfall (681.5 mm at Seocho station) was concentrated during the period from 21 June to 18 July which was 10 to 36 days before the occurrence of the debris flows. Then there was no rainfall up to 4 days before the debris flow event and 88.5 mm of rainfall was recorded 1 to 3 days before debris flow. On the day of the debris flows, 359 mm and 281 mm of rainfall at Namhyeon and Seocho station were recorded. Unlike neighboring Gwanak Mountain, which is primarily

composed of granite, the geological structure of Umyeon Mountain is made up of gneiss. Therefore, the prolonged rainfall one month prior to the debris flow event might have caused saturation of the ground and made it more vulnerable to collapse. Average return period of rainfall for the duration of one hour and more was about 120 and 20 year for the Namhyeon and Seocho stations, respectively.

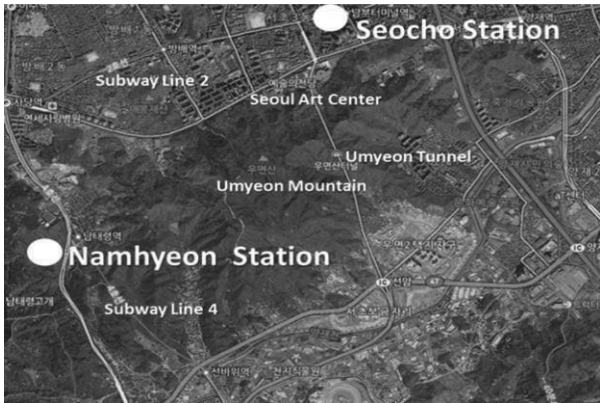


Figure 5. Locations of automatic weather stations around Umyeon Mountain

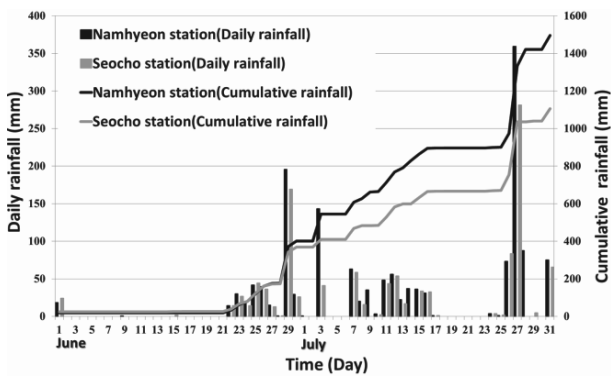


Figure 6. Locations of automatic weather stations around Umyeon Mountain

### 3 RISK ANALYSIS

#### 3.1 Landslide susceptibility assessment

There are two general approaches for landslide susceptibility assessment. The first approach is based on a physical mechanism and the second is based on a statistical method. In this work, statistical model developed in Gangneung-Wonju national university was used (Lee et. al., 2012). This model can directly yields the probability of landslide because the equation of the model was derived from logistic regression. The landslide susceptibility map is created by using GIS data which includes geomorphological characteristics, soil properties, rainfall, vegetation, and forest fire history. Figure 7 shows the landslide susceptibility map which was made with 329 mm of accumulated rainfall for 3 days, and the field survey result which included the initial slope failure and flow path of the debris flows was overlaid. As shown in figure 7, most of the slope failures were occurred in highly susceptible regions for landslide.

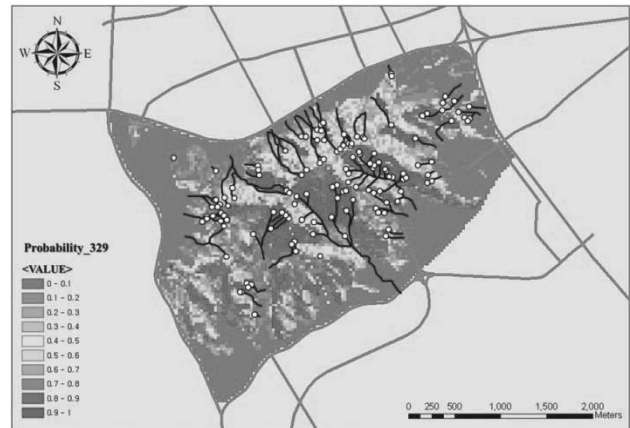


Figure 7. Landslide susceptibility map with field survey results

#### 3.2 Debris flow risk assessment

A methodology for the evaluation of debris flow risk in a watershed incorporated with GIS was proposed in this work. This model predicts the debris flow hazard risk on any given watershed. The model was developed using statistical analysis of debris flow hazard data in Korea from 2005 to 2011. These data was obtained from field surveys, disaster reports on national roads of Korea, aerial photos, and digital maps. Each set of data in the database includes geomorphologic factors influencing debris flow size, rainfall information, bedrock types, and run out distance of the debris. Figure 8 shows flow chart of the methodology.

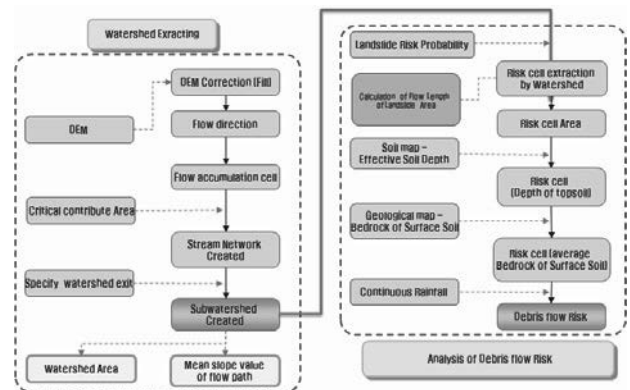


Figure 8. Flow chart of the debris flow risk assessment

Debris flow hazard probability is calculated by equation (1).

$$\text{Debris flow hazard probability} = \text{Logit}(p) \quad (1)$$

where  $\text{Logit}(p) = -5.4 - 1.3E-5 \times (\text{area indicating landslide probability higher than } 50\% \times \text{depth of surface soil}) + 0.005 \times (\text{amount of continuous rainfall}) + 4.522 \times (\text{bedrock type}) + 2.1E-8 \times (\text{mean slope of flow path-area of watershed})$ . Table 1 shows the data and data acquisition method used in the model.

Based on the analysis of DEM (Digital Elevation Map) of Umyeon Mountain, 31 watersheds can be generated as shown in Figure 9. The probability of debris flow hazard for individual watershed in Umyeon Mountain is summarized in Table 2. As shown in Table 2, most of the watershed where debris flow took place showed high probability for the debris flow hazard except one watershed (Seonbawi) where debris flow hazard did not occur. Unlike the other watersheds, the bedrock of Seonbawi watershed was granite and the bedrock condition might be one of the important factor in the occurrence of debris flow. These results confirmed the applicability of the developed risk assessment model for the landslide and debris flow hazard.

Table 1. Data of the debris flow hazard occurrence

Dataset	Data acquisition
Potential landslide area ( )	Landslide susceptibility map
Depth of top soil (m)	Soil classification map
Possible sediment area ( )	Field survey, DEM
Mean slope gradient of flow path(°)	Field survey, DEM
Watershed area( )	GIS tool, DEM
Rainfall(mm)	AWS
Bedrock type	Geological map
Mean flow distance(m)	GIS tool, DEM

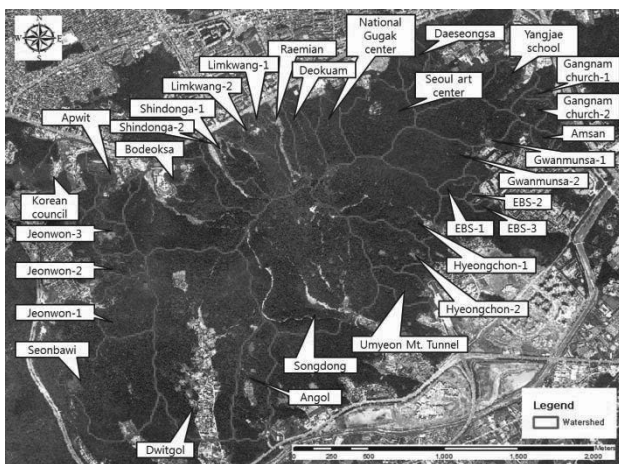


Figure 9. Watersheds in Umyeon Mountain

Table 2. The probability of debris flow hazard for individual watershed

Watershed	Prob.	Watershed	Prob.
Raemian	84%	EBS-1	77%
Limkwang-1	72%	EBS-2	70%
Limkwang-2	76%	EBS-3	71%
Shindonga-1	87%	Gwanmunsa-1	96%
Shindonga-2	87%	Gwanmunsa-2	97%
Hyeongchon-1	99%	Amsan	73%
Hyeongchon-2	92%	Gangnam church-1	71%
Jeonwon-1	94%	Gangnam church-2	79%
Jeonwon-2	80%	Yangjae school	84%
Jeonwon-3	75%	Daeseongsa	79%
Bodeoksa	99%	Seoul art center	96%
Apwit	69%	National gugak center	87%
Korean Council	73%	Dwitgol	99%
Songdong	99%	Angol	90%
Umyeon Mt. tunnel	83%	Seonbawi	17%
Deokuam	85%		

#### 4 CONCLUSIONS

A series of debris flow events occurred around 8:00 to 8:50 a.m. on July 27, 2011 in the Umyeon Mountain area located in Seoul, Korea. Field survey on the debris flow at Umyeon Mountain was carried out to understand the comprehensive situation of the hazard. The field survey result showed that debris flows occurred all around Umyeon Mountain and the average moving distance of debris flows was about 615m, ranging from 95 to 1,584m. Also, the average gradient of initiation slopes was about 27 degrees, ranging from 11 to 37 degrees. The initiation volume of the slope failure was measured from 73 to 4,000 m<sup>3</sup>.

In addition, risk analysis based on the hazard map of the landslide and debris flow was performed. Risk assessment of the landslide hazard showed the most of the slope failures were occurred in highly susceptible regions for landslide. And debris flow risk assessment also showed that the most of the watershed experienced debris flow hazard showed high probability of debris flow occurrence. And these results confirmed the applicability of the developed risk assessment model for the landslide and debris flow hazard.

#### 5 ACKNOWLEDGEMENT

This research was supported by the Basic Science Research Program through the National Research Foundation of Korea (NRF) funded by the Ministry of Education, Science and Technology (2012014940).

#### 6 REFERENCES

- Hutchinson, J. 1988. Morphological and geotechnical parameters of landslides in relation to geology and hydrogeology, 5th. Int. Symp. on Landslides 1, 3-35.
- Johnson, A.M. and Rahn, P. 1970. Mobilization of debris flows, Z. Geomorphology 9, 168-186.
- Lee, S.-W., Kim, G.-H., Yune, C.-Y., Ryu, H.-J., and Hong, S.-J. 2012. Development of Landslide-Risk Prediction Model through Database Construction, Journal of Korea Geotechnical Society 28(4) 23-33. (in Korean)
- Son, S.-H., Choi, B. and Paik, J. 2012. Characteristics of rainfall and groundwater table in a small forested watershed of Mt. Umyeon, Proceedings of 38th Korea Society of Civil Engineering Conference and Civil Expo 2012, Chonnam National University, Korea, October 24-26
- Yune, C.-Y. and Jun, K.J. 2011. National investigation on the landslides and debris flows in 2011, Korea, River and Road in Mountain Area, Vol. 4, Special publication, 15-19.

# General Report of TC209 Offshore Geotechnics

## Rapport général du TC209 Géotechnique marine

Jewell R.A.  
Fugro GeoConsulting

**ABSTRACT:** This general report introduces the discussion session organized by ISSMGE Technical Committee 209 (TC209) “Offshore Geotechnics”. The main topics include offshore wind projects, pipelines and seabed structures, seabed soils, coastal and nearshore work, and pile foundations.

**RÉSUMÉ :** Ce rapport général introduit la séance de discussion organisée par le Comité Technique 209 (TC209) “Géotechnique Offshore” de la SIMSG. Les principaux thèmes abordés sont les projets d’éoliennes offshore, les pipelines et structures sous-marines, les sols sous-marins, les travaux côtiers et nearshore et les fondations sur pieux

**KEYWORDS:** offshore, caisson, piles, pipes, cyclic load, stability diagram, lateral load, tests, numerical analysis, bearing capacity

### 1 INTRODUCTION.

The organizers of the 18th International Conference “Challenges and Innovations in Geotechnics” have implemented important changes to the conference format. One is the inclusion of Offshore Geotechnics at this main ISSMGE forum. Second is the focus given to the technical committees.

This general report covers the session organized by the ISSMGE Technical Committee 209 (TC209) “Offshore Geotechnics” chaired by Philippe Jeanjean. Participation by TC209 at this 18<sup>th</sup> conference includes the 2<sup>nd</sup> ISSMGE McClelland Lecture by Mark Randolph, this discussion session and a workshop on recent research and development on piles under cyclic loading.

The main difference in offshore geotechnics arises from the conditions and environment offshore. There is a stark contrast in access for site investigation, soil sampling, field testing, installation and observation. Activities offshore often require new tools. Soft soil conditions at seabed level are encountered in deepwater, frequently with high carbonate content, unusual mineralogy or biogenic activity. Combined and cyclic loading usually dominate design, whether caused by waves and currents acting on structures or by repeated expansion and contraction of pipelines on the seabed. Large displacement is a feature of the installation and operation of seabed pipelines. Many of the above features of offshore geotechnics are discussed in papers to this session.

This general report has been organized into five main subject areas: Offshore Wind; Pipelines and Seabed Structures; Seabed Soils; Coastal and Near Shore work; Pile Foundations.

Since papers on the cyclic loading of piles will be presented and discussed at the TC209 workshop, these are highlighted in this general report but will not be presented during the discussion session. The main focus for presentations will be Offshore Wind and large displacement as encountered with Offshore Pipelines.

Only a limited selection of papers will be presented at the discussion session. All the papers are in the proceedings and many will be presented at the poster session. Participants are strongly encouraged to attend the TC209 workshop where the cyclic behavior and design of piles will be presented and debated based around papers to this session.

### 2 OFFSHORE WIND.

#### 2.1 Site investigation

Project development, engineering design and project construction are three main phases for offshore wind farms. A major challenge is to minimize geotechnical risk for foundation engineering. In current practice, geotechnical risk is addressed mainly during the engineering design phase P2 in Table 1. Ben-Hazzine and Griffiths (2013) suggest that risk management may be improved through more extensive geophysical survey and preliminary site investigation during the project development phase P1. The authors highlight various sources of geotechnical risk such as inherent soil variability, measurement errors and “transformation errors” caused by simple empirical interpretation of data.

Table 1. Timing of Geotechnical Work for Offshore Windfarms (Ben-Hazzine and Griffiths, 2013)

Phase	Common			Proposed		
	P1	P2	P3	P1	P2	P3
Desk study	X			X		
Geophysical survey		X		X		
Preliminary investigation		X		X		
Full investigation		X			X	
Assurance & validation			X			X

Phases: P1 = Development, P2 = Design, P3 = Construction

Muir Wood and Knight (2013) use experience from 15 offshore wind farm projects in the UK to illustrate the manner in which geotechnical risk was managed and to define categories of poor, mediocre and good practice (or *vice versa*).

Poor practice includes appointment of the foundation design team after site investigation is completed, insufficient planning and poor interpretation of geophysical and geotechnical surveys. Mediocre practice often involves incorrect scope for geophysical and geotechnical surveys causing extra cost and increased risk. On projects with good practice the foundation design team was appointed at the start of the project and specified the site investigation work. The ground models were



developed and refined over multiple phases of geotechnical and geophysical investigation. The authors conclude that a formal approach to risk management with staged investigations and early appointment of the foundation design team is the best practice.

## 2.2 Wind turbine performance

A wind energy project involves several disciplines within civil engineering. The complex interaction between the turbine and the supporting structure governs the dynamic behaviour. Analysis is required of the structural modal parameters that influence fatigue of a wind turbine. Indeed, continuous monitoring of modal frequencies and damping ratios during the operational life of a wind turbine can provide early warning of the onset of structural damage.

Damgaard et al. (2013) assess instrumentation data from 30 offshore wind turbines in the North Sea. The measured modal frequency and damping ratio are found to vary with time. However, the observed magnitude and pattern of change with time might result from scour erosion or backfilling around the monopile structure. This highlights that the dynamic interaction between an operating turbine and the supporting structure may be affected by changes with time of the local seabed level, something that could be reduced by scour protection.

## 2.3 Foundation systems

The power capacity of a wind turbine, typically in the range 2MW to 5MW, but increasing toward 10MW in future, determines the required height above mean sea level and the maximum horizontal and vertical loads to be supported. Deeper water increases the moment arm for both wind and wave loading and often signifies larger design storms. There are many novel features to the required foundation engineering as discussed in papers to this session, Table 2.

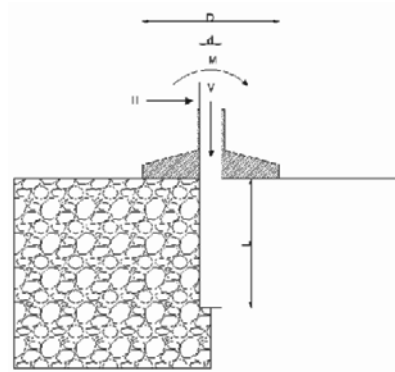
Table 2. Papers on Foundation Systems for Offshore Wind.

	SINGLE LOAD		CYCLIC LOAD	
Shallow Foundation	Arroyo et al	A		
Monopile			Roesen et al	E.1g; A
Caisson	Kim et al	E.c; A	Versteede et al	A
Hybrid (pile/caisson)	Arshi et al	E.1g; A		

E = Experimental (E.1g lab floor; E.c centrifuge);  
A = Analysis

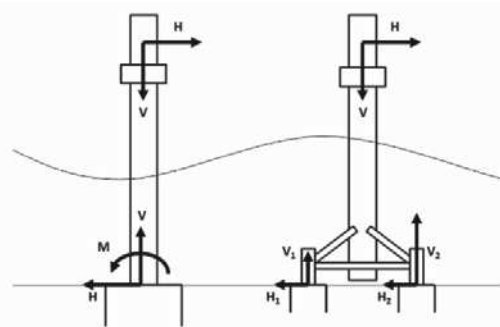
In brief résumé, shallow foundations and monopiles generally provide efficient support for wind turbines. However, these foundations are less effective when the moment load to be resisted increases due to larger turbines and/or deeper water. One approach is to improve the capacity by combining a monopile and shallow foundation, Figure 1. Alternatively, a caisson can support combined vertical, horizontal and moment loading at seabed level. Three or four caissons may be combined to support a structure where greater load carrying capacity is required, Figure 2.

The issues for foundation engineering discussed in the papers include: (1) the impact of the loading path and loading direction on safety factor and use of a single failure envelope; (2) improved performance by combining a shallow foundation and monopile; (3) the incremental displacement of cyclically loaded monopiles; and, (4) assessment of simultaneous pore water pressure generation and dissipation for caissons under storm loading.



(Arshi et al, 2013)

Figure 1. Hybrid Monopile and Shallow Foundation.



(Versteede et al, 2013)

Figure 2. Monopod and Multipod Foundations.

### 2.3.1 Bearing capacity analysis

The assessment of bearing capacity for offshore wind turbine foundations differs from onshore practice in several respects. The issues include: (a) separate correction factors in analysis for shape, depth, load inclination and eccentricity that are cumbersome and prone to calibration error; (b) use of separate partial factors on loads and resistances as in DNV-OS-J101 when the difference between favourable and detrimental effects can be subtle; and (c) simultaneous application of two major horizontal loads from wind and wave acting in separate directions. Arroyo et al highlight these issues and question the suitability of the conventional design approach for offshore wind foundations (Arroyo et al 2013).

A more satisfactory framework for capacity checks would be through failure-envelopes as detailed in the paper. Arroyo et al examine a synthetic design example to illustrate their case using the geometry of a Thornton Bank GBS and a set of derived loading parameters, Figure 3. The complex interaction between horizontal and moment loading, and the impact of different directions for wind and wave loading are illustrated by the authors using Figure 4 and the results in Table 3.

It is conventional to increase both detrimental loads at the same time, so that the load increment causing the limit to be reached is in the same direction as the reference combined load. The authors consider the cases where only wind or wave loading is increased. Such analysis might be used to assess the impact of any error in the assessment of those loads. Because of the greater influence on moment of wind loading, the analysis shows that an underestimate 21% (in this case) in the wind load would be sufficient to cause failure compared with an underestimate 50% for the wave load, Table 3.

Arroyo et al (2013) conclude that failure envelopes offer a powerful framework for analysis of shallow foundation capacity; the approach is particularly well suited for offshore wind structures that require refined design in the face of considerable uncertainty.

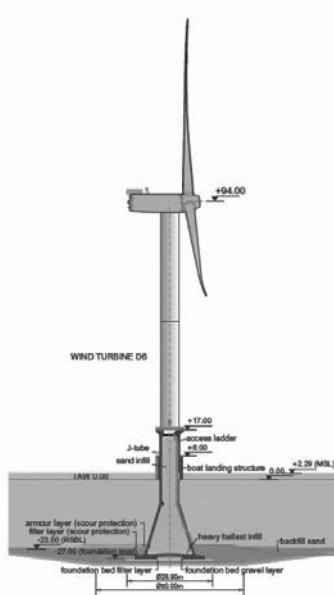
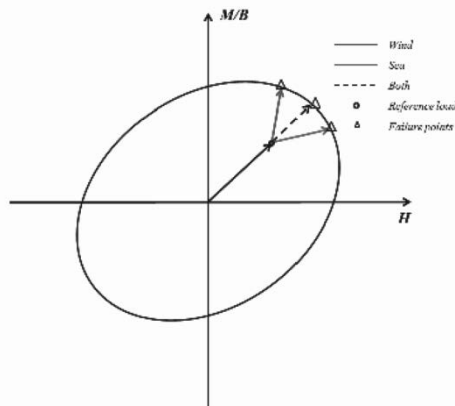


Figure 3. Thornton Bank GBS (after Peire et al 2009).



(Arroyo et al 2013)

Figure 4. Incremental loading paths to failure.

Table 3. Results of analysis on incremental load to failure.

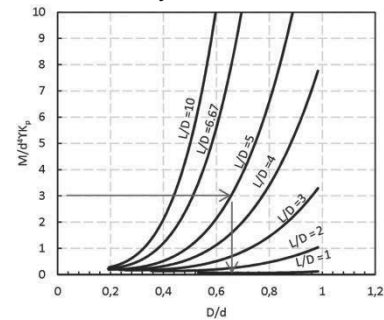
Hypothesis	Hr (MN)	Hr / Hi	$\Delta H$ (%)
Sea	14.1	1.4	50
Both	11.6	1.15	15
Wind	10.5	1.04	21

### 2.3.2 Hybrid foundations

When considered as a monopile design, the addition of a shallow footing at seabed level may be thought of as adding “fixity” to the monopile “head” thereby generating improved resistance and stiffness to lateral loading, Figure 1. A simplified design analysis would assess the limiting moment capacity of the shallow foundation acting alone and include the equal and opposite moment resistance to the analysis of the monopile. The shallow foundation not only increases load carrying capacity but also reduces the bending moment supported by the monopile, by about 25% in the example cited by Arshi et al (2013).

Experimental modelling of these hybrid systems at 1g and in the centrifuge are described together with numerical and analytical work. The significance of the geometric ratio of footing to pile diameter, and pile length to pile diameter is demonstrated and a form for design charts proposed, Figure 5. Some tests on caisson/monopile combinations are noted and indicate additional benefit due to the lateral load resistance of

the caisson. Centrifuge tests are currently underway to define better the benefit of caisson versus simple shallow foundation in such hybrid foundation systems.



(Arshi et al 2013)

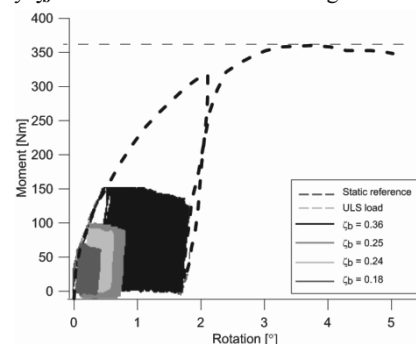
Figure 5. Moment resistance chart for hybrid foundations.

### 2.3.3 Lateral displacement due to cyclic loading

The focus above is the limit resistance of offshore wind tower foundations subject to a single application of combined loading. In practice, the structures are subject to several episodes of extreme loading caused by major storms and a great number of cycles of low amplitude loading from normal wind and wave conditions. The latter source of repeated loading may cause fatigue or serviceability problems (Roesen et al. 2013).

The authors report a series of 1g laboratory tests on monopiles in sand subject to one-way cyclic loading over more than 50,000 cycles. One limitation in these 1g tests is a more rigid pile compared with a typical prototype, but the trend of results should be similar. The cyclic loading is described by two non-dimensional ratios: the maximum moment compared with the static moment capacity  $\zeta_b = M_{max}/M_{static}$  in the range  $1 > \zeta_b > 0$ ; and the ratio of the minimum to the maximum moment  $\zeta_c = M_{min}/M_{max}$  which has a value 1 for a static test, 0 for one-way loading (the case examined by Roesen et al) and -1 for two way cyclic loading.

The pile displacement is measured by the rotation  $\theta$  at the soil surface. The results of a static load test and the measured displacement in one-way cyclic load tests ( $\zeta_c = 0$ ) with load intensity  $\zeta_b = 0.2$  to 0.4 are shown on Figure 6.



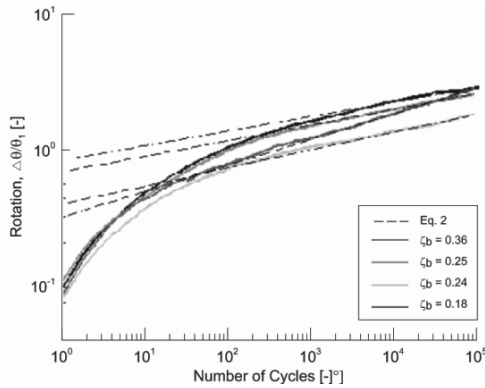
(Roesen et al 2013)

Figure 6. Static and cyclic one-way loading tests on model monopiles.

The incremental rotation due to one-way cyclic loading may be quantified with respect to the rotation caused by the first, single loading  $\Delta\theta_N = \theta_N - \theta_1$ . Tests with different loading intensity may then be compared through the non-dimensional form  $\Delta\theta_N/\theta_1$  as shown on Figure 7.

The test data are compared with a simple power law  $(\Delta\theta_N/\theta_1) = aN^b$ , where  $a$  and  $b$  are empirical constants found from testing. The power law seems to provide a reasonable asymptotic limit for the data after about 1000 or more load repetitions, Figure 7. The value of the constant  $a$  is found to vary almost linearly with the applied load magnitude  $\zeta_b$ . The slope of accumulating displacement with repeated loading, the constant  $b$ , appears to be a function of the combination of

monopile and sand parameters, presumably including the installation process. The rate of accumulation appears not to depend markedly on the applied load magnitude. The analysis in §6.2 suggests that the data might also fit with a natural logarithm through to low numbers of cycles ( $\Delta\theta_N / \theta_1$ ) =  $c \cdot \ln(N)$ .

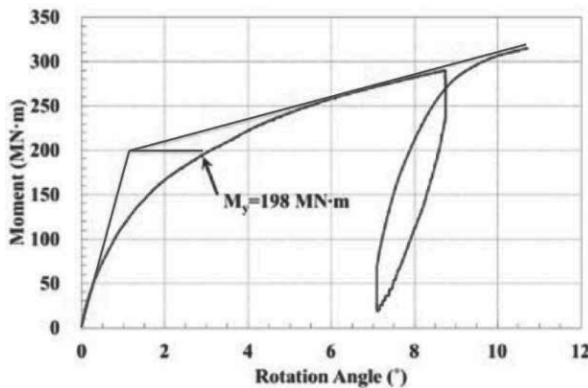


(Roesen et al 2013)  
Figure 7. Monopile rotation versus number of cycles.

### 2.3.4 Caisson foundations

A centrifuge test of a caisson in sand is reported by Kim et al. (2013). The caisson response to single combined load to failure is measured and numerical analysis applied. The test details are provided elsewhere and it is not clear whether the 1/70<sup>th</sup> scale caisson was installed by suction during the centrifuge test or before testing. Soil material from the proposed site is used to model a planned prototype caisson foundation. The measured response of the modelled prototype 15.5m diameter 10.5m long caisson is shown on Figure 8 in terms of applied moment versus rotation.

The authors report a parametric analysis using FLAC to show the significant influence of the assumed elastic modulus and cohesive strength parameters assumed for the soil.



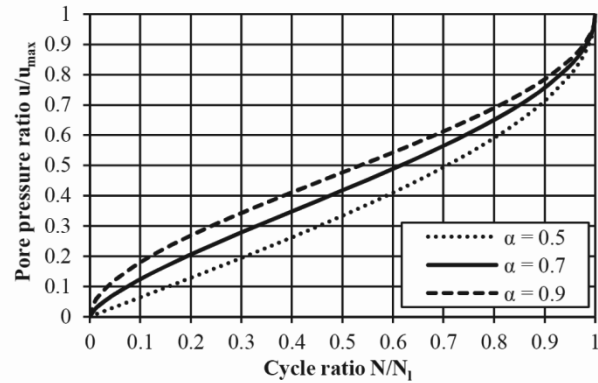
(Kim et al 2013)  
Figure 8. Measured moment-rotation for prototype caisson.

The offshore design standard DNV-OS-J101 (DNV, 2011) requires structures to resist a 50 year design storm considering both peak loads and the entire history of cyclic loading. It is this latter requirement that is tackled by Versteede et al (2013) for the case of caisson foundations in sand.

Because a full analysis of cyclic loading of caissons in sand is not practically feasible with current numerical methods, the authors develop an analysis to provide insight into the competing processes of excess pore water pressure generation and dissipation during the design storm. The analysis breaks the storm into several packages of cyclic loading (magnitude, number of cycles and time). The excess pore water pressure generated at each point in the soil by the package of cyclic loading is computed analytically and input into the numerical analysis. The dissipation and redistribution of pore water pressure during the time period is computed numerically. The

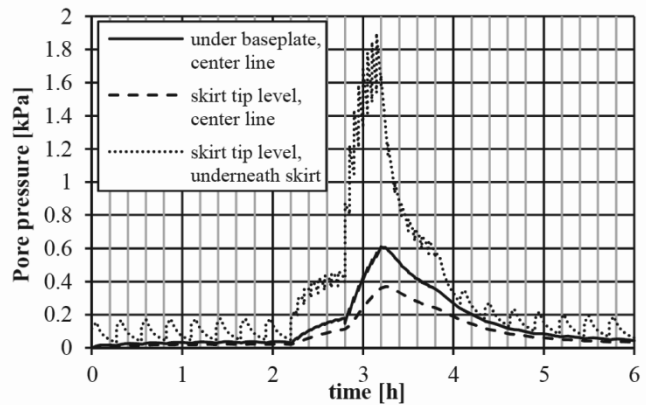
process is repeated for the next package of cyclic loading, and so on.

The analysis for pore pressure generation uses two relations for the sand material. First the measured cyclic shear strength versus number of cycles to liquefaction,  $N_i$ , from cyclic laboratory tests; second an empirical formula linking pore water pressure generation to number of load cycles, Figure 9. Liquefaction occurs at  $u/u_{max} = 1$  when  $N/N_i = 1$ .



(Versteede et al 2013)  
Figure 9. Generation of excess pore water pressure.

The results of a 3D analysis for a caisson foundation are reported to illustrate the method, Figure 10. The 20m diameter by 10m length caisson is subjected to a 6 hour design storm of 2160 waves. These are split for analysis into 5 individual load packages. The direction of wind and wave loading is assumed to be aligned. The results illustrate the asymmetric nature of pore water pressure generation that has potential consequences for possible differential settlement and tilting of the caisson.



(Versteede et al 2013)  
Figure 10. Example of excess pore water pressure below a caisson.

Versteede et al (2013) conclude that the model is useful in predicting areas beneath the caisson prone to the development of excess pore pressure. However, the analysis does not predict liquefaction behaviour or compute settlement, nor does it allow for load redistribution in the caisson due to the changing effective resistance in the soil during the design storm. There is further development work to be done.

### 3 PIPELINES AND LARGE DISPLACEMENT.

A challenging feature for offshore pipelines is the large displacement that can occur during installation and service. Large displacement is particularly extreme for laying pipe on a soft seabed. Large displacement also results from multiple cycles of heat expansion and contraction of the operating pipeline. This requires engineering design to avoid localized

pipe distortion and over-stress irrespective of the sea bed soil type. A less discussed cause of large displacement is where a pipeline crosses a seismic fault; here it is movement of the ground with respect to the pipe that causes gross distortion. Fault crossings occur both onshore and offshore.

The geotechnical analysis for large displacement requires suitable tools and numerical models and both have developed significantly in recent years. A variety of large displacement numerical methods with 3D capability are commercially available for design purposes. Similarly, constitutive models for soft clay that account for competing strain rate and strain softening effects, and competing pore pressure generation and dissipation, are available for designers. Specific numerical elements to model the large displacement interaction between a pipe and the surrounding soil are also currently under development for practical application in design (SAFEBUCK JIP). However, the constitutive and numerical modeling for large displacement in dense sand is less well advanced.

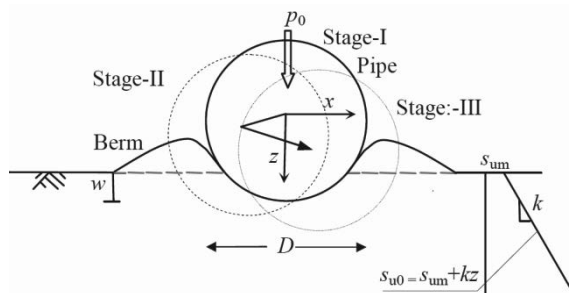
Pipe buckling and pipe walking is usually assumed to occur between fixed seabed structures. There may be scope for permitting the seabed structures to move horizontally to help accommodate axial pipe displacement.

Several of these topics are described in four papers to the discussion session.

### 3.1 Dynamic embedment of offshore pipelines

Dutta et al (2013) examine pipe laying and dynamic embedment using Coupled Eulerian Lagrangian (CEL) methods available in ABAQUS software. Progressive degradation of undrained shear strength with plastic shear strain is included using the model of Einav and Randolph (2005). Similar analysis by Wang et al (2010) used remeshing and small strain (RITSS analysis).

The simplified problem is illustrated in Figure 11. A pipe is penetrated monotonically into a soft clay sea bed under self-weight (submerged weight of pipe). The pipe is then cycled laterally by a displacement  $u/D = \pm 0.05$ , in the  $x$  direction of Figure 11, under constant self-weight vertical load. This causes additional pipe penetration.



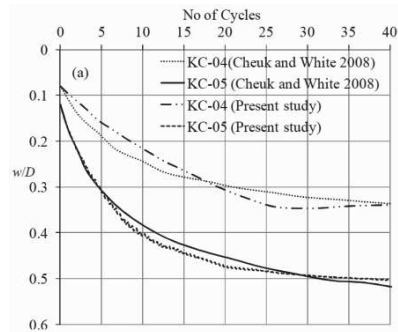
(Dutta et al 2013)

Figure 11. Pipe penetration of a seabed.

The analysis uses the same dimensions, soil parameters and loading sequence as the first stage of two pairs of centrifuge tests by Cheuk and White (2008) on a light and heavier pipe. The progressive pipe penetration and magnitude of horizontal resistance caused by cyclic lateral displacement is computed. The penetration of the pipe with cycles of lateral displacement is shown in Figure 12 for one pair of pipe tests.

Current practice is to estimate separately the embedment due to pipe laying and due to dynamic effects. The initial embedment on pipe laying involves temporary overload at the touch down point. Typically the pipe weight is increased by a "lay factor" and the initial pipe penetration under monotonic loading is computed for this higher load. The effect of small amplitude cyclic lateral motion is incorporated using a "dynamic embedment factor" that multiplies up the initial monotonic pipe lay embedment to determine a final estimated pipe embedment. The centrifuge tests and analysis here did not

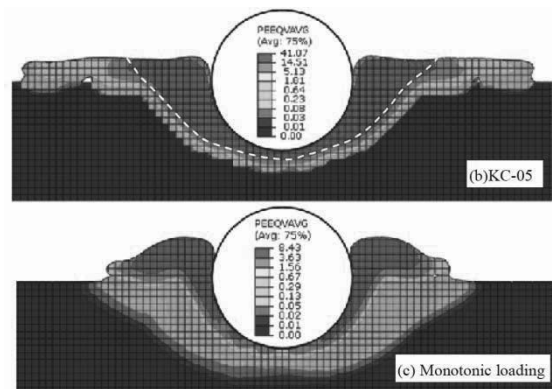
incorporate initial overloading of the pipe, but the forty cycles of lateral loading resulted in a dynamic embedment factor of the order 4 to 5, within the range often assumed in practice.



(Dutta et al 2013)

Figure 12. Static and dynamic pipe penetration of a seabed.

As shown previously by Wang et al (2010), the analysis provides insight into the size of the zone of highly sheared and softened soil around the pipe and the shape of the berms formed by pipe penetration. The results in Figure 13 are for the heavier pipe and show dynamic pipe penetration and monotonic pipe penetration to the same depth (increased vertical load). The comparison is striking. Dynamic embedment causes more extensive plastic strain softening in the soil, coloured red, and wider and flatter berms than generated by monotonic pipe penetration. The latter could be important for the analysis of initial lateral breakout of the pipe. Dynamic embedment affects the magnitude of pipe penetration, the zone of soil remoulding and the shape of the berms formed.



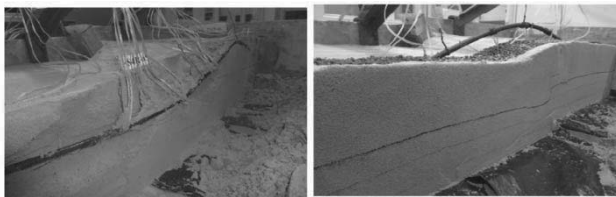
(Dutta et al 2013)

Figure 13. Dynamic and monotonic pipe penetration of a soft seabed.

### 3.2 Pipeline fault crossing

Damage is caused to pipelines that cross a seismic fault that subsequently displaces. Rupture of oil or gas pipelines can cause fire and environmental risk. For critical pipelines, the magnitude and direction of localized fault displacement should be assessed and appropriate engineering implemented to avoid pipe rupture due to ground movement.

Moradi et al completed centrifuge tests on buried steel pipe subject to an upward thrust fault at  $30^\circ$  to the vertical in the direction of the pipe. A fault displacement 70mm was applied across an 8mm diameter buried pipe with 0.4mm wall thickness tested in a centrifuge at 40g. In one test the pipe is simply buried in the compacted sand. A low density and light weight loose backfill was used in the second test. The axial and bending strain in the pipe was measured in both tests. The light backfill allowed the pipe to buckle and displace over a greater length considerably reducing the damage to the pipe. The pipe embedded in the sand suffered more localized deformation and damage, as illustrated by the photos post testing, Figure 14.



(Moradi et al 2015)

Figure 14. Pipe response to shear fault displacement in a centrifuge.

### 3.3 Seabed structures that displace horizontally

The sea bed in deep water is generally soft and often requires large shallow foundations to support seabed facilities. If some movement could be tolerated the size could be reduced. Further, if the structure connects with a pipeline subject to walking or other axial force, there may be merit in allowing the structure to slide horizontally to help relieve concentrated load.

Bretelle and Wallerand (2013) examine the design for a shallow foundation that displaces horizontally in a cyclic fashion, as might be caused by repeated pipe expansion and contraction. The influence of soil softening, foundation settlement and potential change in stiffness with time is examined through relatively straightforward analysis. The authors conclude that shallow foundations designed to displace horizontally could be useful for subsea pipeline networks.

### 3.4 Large displacement in dense sand

While numerical analysis for large deformation is increasingly amenable for engineering design, a relatively simple constitutive model for dense sand that provides stable large deformation analysis is still subject to study. Li et al (2013) propose a Critical State Mohr Coulomb (CSMC) model: deformation up to peak strength is elastic and thereafter dense sand dilates (including non-associated flow) and reduces in strength to the critical state angle of friction. The concept of the state parameter defined by Been and Jeffries (1985) is used.

A key objective is analysis for punch through of a spudcan footing in dense sand overlying soft clay. Li et al (2013) have not reached that target. However, development of the model starkly highlights non-uniform deformation and preferential shear band formation in dense sand post peak that makes data acquisition (lab tests) and model calibration such a challenge.

In analysis for bearing capacity of a circular plate on uniform sand, the authors found that the elastic stiffness of the sand influences bearing capacity by as much as 50% over the realistic range, reminiscent of rigidity index in penetration problems. Stiffness was found to have greater impact than dilation angle. The analysis for bearing capacity is described in terms of a combined bearing capacity factor  $N_{q\gamma}$  that applies across the range from  $N_q$  alone to  $N_\gamma$ . The proposed formula for  $N_{q\gamma}$  includes soil stiffness and dilation angle along with peak friction angle, foundation size, soil unit weight and surcharge.

## 4 SEABED SOILS.

The three papers on soil properties cover diverse topics. Ho et al (2013) describe undrained cyclic triaxial compression tests on isotropically consolidated Singapore Marine Clay. The focus is the behavior of the clay when it is sheared monotonically to failure after cycling. The tests show that when the current mean effective stress in the sample reduces below half the original preconsolidation pressure,  $p/p_c \leq 0.5$ , due to cyclic loading, some increase in mean effective stress commences at higher stress ratio in each cycle. At mean effective stress  $p/p_c \geq 0.6$  (first few cycles) the mean effective stress of the clay always reduces. This behavior is similar to normally versus over consolidated clay. The final effective stress path for monotonic triaxial compression to failure after cycling similarly depends on the mean effective stress  $p/p_c$  at the end of

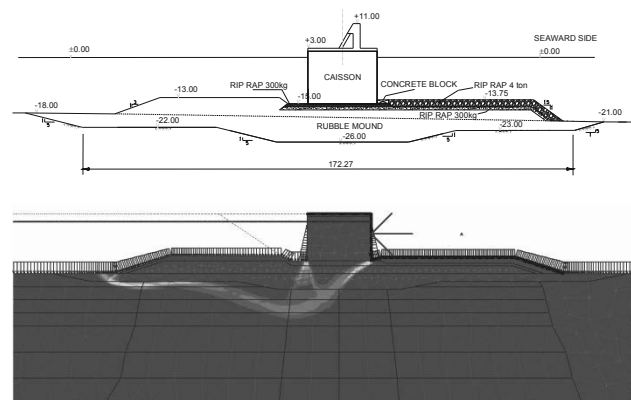
cycling. However, the shear strength is found to be largely independent of the previous number of load cycles and the strain amplitude.

Kim and Safdar (2013) report cyclic direct simple shear tests on compacted silty sand to define the limiting cyclic stress ratio versus number of cycles for two initial void ratios.

Tyldesley et al (2013) describe site investigation to define parameters for wind farm foundation design on a deep deposit of carbonate clayey silt till in Ontario Canada. This onshore site investigation demonstrates the use of insitu tests and shear wave velocity measurement, interpreted together with laboratory tests, to assemble knowledge on soil strength and stiffness properties.

## 5 COASTAL AND NEARSHORE WORK.

There are three papers on diverse topics. Madrid et al (2013) describe site investigation, cyclic laboratory tests and numerical analysis for the stability of a caisson breakwater in about 20m to 25m depth of water. The caissons are founded on a rubble mound infilling a large zone where the deep underlying soft clay soil was removed, Figure 15.



(Madrid et al 2013)

Figure 15. Caisson breakwater and stability analysis for wave impact.

There is much detail in the paper on soil testing and soil properties, loading cases for various phases of project construction and hydrodynamic testing to determine dynamic uplift. A good description is provided on the way cyclic loading and shear strength reduction were treated for design.

Relic footprints from earlier jack-up activity can occur next to the location for new shallow foundations. Ballard and Charue (2013) describe a study on a circular zone of remoulded soft clay ( $S_r = 2$ ) with a diameter equal to the size of the square mudmat and with soft clay thickness of half that size. The limiting envelope for combined moment and horizontal resistance is computed for a range of applied vertical load ( $V/V_{ult}$ ), and a range of distance between the mudmat and the remoulded zone/footprint that causes the moment and horizontal resistance to be reduced, as well as  $V_{ult}$ . 2D and 3D analyses show very substantial benefit from the 3D geometry in this case.

A detailed design and project record for installation of large diameter, buried HDPE pipes in a nearshore environment prone to seismic loading is described by Bellezza et al (2013). Details for the case history and the various code requirements considered in design are documented. Initial measurements are provided on the vertical deflection of the installed pipes.

## 6 PILE FOUNDATIONS.

A lack of code guidance on capacity, stiffness and displacement for cyclically loaded piles is being addressed by collaborative research including the original GOPAL study and the current SOLCYP project, supplemented by individual research work. Several papers to this session report on SOLCYP results from instrumented field tests, calibration chamber and centrifuge

tests. SOLCYP will be presented and discussed at the TC209 workshop and recorded for publication. Therefore only some key aspects are described below to avoid duplication.

There are four axial load magnitudes: the mean  $Q_{\text{mean}}$  and the half-amplitude of the cyclic load  $Q_{\text{cyclic}}$  define the maximum  $Q_{\text{max}} = Q_{\text{mean}} + Q_{\text{cyclic}}$  and the minimum  $Q_{\text{min}} = Q_{\text{mean}} - Q_{\text{cyclic}}$  pile loads. These loads are typically referenced to the ultimate pile capacity in tension  $Q_T$  or compression  $Q_{UC}$ . The ultimate capacity and the capacity under cyclic load is determined at a limiting displacement (0.1D or less) or due to an increasing rate of displacement; either continuing displacement after a static load increment or the cyclical displacement rate (mm/cycle).

### 6.1 Stability diagram: cyclic axial loading

The stability diagram is a non-dimensional map for cyclic pile behavior. The diagram in Figure 16 is for axial tension tests on model driven piles in dense sand in a calibration chamber (Silva et al, 2013). A similar diagram is found for the equivalent field test data (Rimoy et al, 2013). The chart defines the region of stable cyclic load combinations for a number of load cycles to be resisted. One way loading ( $Q_{\text{mean}} > Q_{\text{cyclic}}$ ) is more stable. The dashed line shows the limit of valid load combinations.

Puech et al (2013) provide the equivalent stability diagrams for cyclic compression loading of bored piles in dense sand from field and centrifuge tests. The field tests by Benzaria et al (2013a) are shown on Figure 17. The results from centrifuge model tests are very similar. Note that only one-way loading was tested and the data should not be extrapolated beyond.

While bored piles in stiff clay have lower ultimate resistance compared with driven piles, cyclic compression tests on bored piles in over-consolidated clay indicate a much larger range of stable load combinations compared with piles in dense sand (Benzaria et al, 2013b).

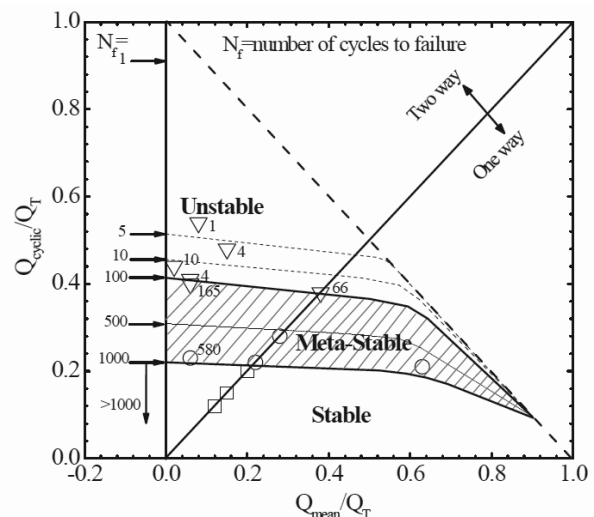
Information on deformation can be included on the stability diagram as shown by Rimoy et al (2013) for field tests under cyclic axial tension on driven piles in sand, Figure 18. The data on the accumulation of displacement with cycling shows mostly stable behavior that suddenly degrades near the limiting number of cycles, a rather "brittle" behavior under tensile load.

A consistent observation for driven piles in dense sand is that stable cycling increases the ultimate capacity when tested subsequently. This is attributed to densification with some relaxation in lateral effective stress around the pile, as measured in the exceptional data of Silva et al. (2013). Conversely, strong cyclic loading (as would lead to instability) acts to reduce the ultimate axial pile capacity that can be mobilized subsequently.

Data on large axial pile tests in silt on a 4.2m long test pile are also interpreted in a stability diagram by Chen et al (2013).

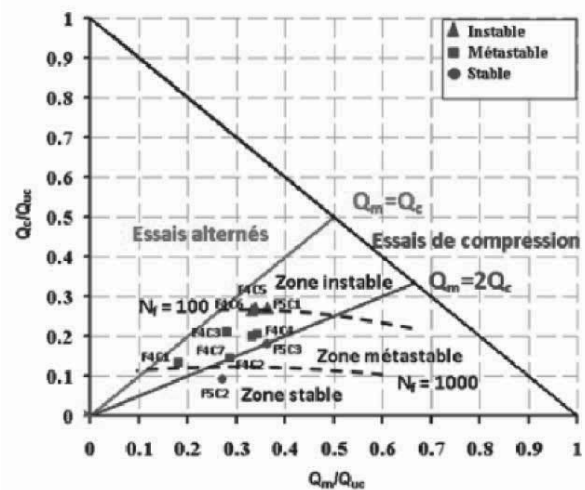
### 6.2 Cyclic lateral loading

Rosquoët et al (2013) report data on lateral displacement for model driven piles in sand tested under one-way loading at 40g in a centrifuge. As in §2.3.3, but for displacement rather than rotation, the lateral displacement  $y_N$  compared with the first load displacement  $y_1$  [ $\Delta y_N = y_N - y_1$ ] is linked with the number of cycles. A logarithmic form  $\Delta y_N / y_1 = c \cdot \ln(N)$  fits the data well where  $c$  varies with the amplitude of cyclic load and the maximum lateral load (equivalent to  $2Q_{\text{cyclic}} / Q_{\text{max}}$  in the axial terminology above, written as  $DF/F$  by Rosquoët et al). Based on their test data the authors suggest  $c = 0.1(DF/F)^{0.35}$  as a general fit, but sand and pile properties might also be important.



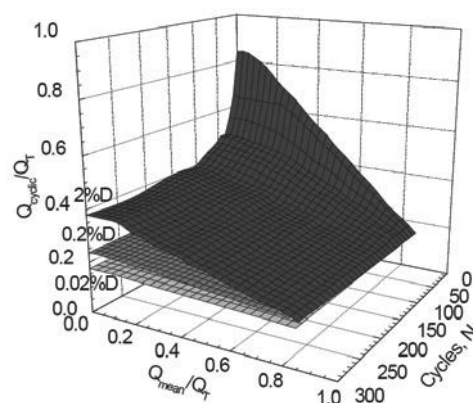
(Tsuha et al (2012) calibration chamber tests)

Figure 16: Stability diagram: tension tests on model driven piles in sand.



(Puech et al, 2013)

Figure 17: Stability diagram: field compression on bored piles in sand.



(Rimoy et al, 2013 field tension tests on driven piles in sand)

Figure 18: Stability diagram: accumulated displacement.

The natural logarithm form has the advantage of fitting the data through to low numbers of cycles (recall §2.3.3). Rosquoët et al (2013) also note that the maximum moment in the pile does not increase significantly with lateral cyclic loading. Finally, the work to extend  $p$ - $y$  analysis for laterally loaded piles failed to capture the measured behavior beyond the first few cycles.

### 6.3 Extension of *t-z* analysis to cyclic loading

Burlon et al (2013) extend static *t-z* analysis for piles in sand to the case of tensile and compressive cyclic load and compare the results with centrifuge test data. The analysis turns out not yet to be practical as four new parameters are introduced that require measurement in cyclic pile tests. Even then, the fit with the test data is good only for relatively few load cycles.

### 6.4 Plugging of open-ended displacement piles

Laboratory tests on sand to measure pile plugging, using PIV observations, are described by Lueking and Kempfert (2013). The fully plugged limit IFR=0 was not achieved in the tests. The results of 2D Plaxis analysis are reported to investigate the mechanism of plugging. Based on this study, the authors propose two largely empirical calculation methods for the analysis of end-bearing for open-ended, partially plugged piles.

### 6.5 Cyclic pressuremeter tests

Reiffsteck et al (2013) report new work on the application of Ménard and self-boring pressuremeter tests to measure the change in soil properties with cyclic loading and, potentially, liquefaction resistance. Data are reported for several sites where cyclic pile tests were completed (SOLCYP). The authors emphasise the importance of a high quality borehole and the need for at least 50 cycles of repeated load to characterize the shear modulus. Soil horizons susceptible to liquefaction could be identified by large volume expansion. The acquisition of pore water pressure data during the test would greatly improve the test control (data on drainage/rate effects) and interpretation.

### 6.6 Osterberg cell testing

The general reporter is not aware of recent cyclic pile tests using O-Cell technology (Osterberg, 1989). A two level O-Cell test arrangement, for example, permits end bearing to be eliminated from cyclic axial compression tests on piles.

## 7 CONCLUSIONS.

As demonstrated by papers to this session, the practical challenges of offshore geotechnics actively drive forward the development of soil mechanics and geotechnical engineering. This is partly due to more extreme loading and deformation than usually encountered onshore. The fruits of this research and development are of great value for the overall understanding and practice of geotechnical engineering. That is why offshore geotechnics should remain part of this key ISSMGE conference.

## 8 ACKNOWLEDGEMENTS

The author would thank TC209 Chairman Philippe Jeanjean for the invitation to prepare this General Report, and colleagues J.C. Ballard, P. Peralta and V. Whenham for valuable support.

## 9 REFERENCES

Arroyo M., Abadias D., Alcoverro J. and Gens, A. 2013. Shallow foundations for offshore wind towers. *Proc. 18th ICSMGE*, Paris.  
 Arshi H.S., Stone K.J.L., Vaziri M., Newson T.A., El-Marassi, M., Taylor R.N. and Goodey R.J. 2013. Modelling of monopile-footing foundation system for offshore structures in cohesionless soils. *Proc. 18th ICSMGE*, Paris.  
 Ballard J.C. and Charue N. 2013. Influence of jack-up footprints on mudmat stability - How beneficial are 3D effects? *Proc. 18th ICSMGE*, Paris.  
 Been, K. and Jefferies, M.G. (1985). A state parameter for sands. *Géotechnique*, Vol. 35(2), pp. 99-112.  
 Bellezza I., Mazziari F., Pasqualini E., D'Alberto D. and Caccavo C. 2013. Design and installation of buried large diameter HDPE pipelines in a coastal area. *Proc. 18th ICSMGE*, Paris.

Ben-Hassine J. and Griffiths D.V. 2013. Geotechnical Exploration for Wind Energy Projects. *Proc. 18th ICSMGE*, Paris.  
 Benzaria O., Puech A. and Le Kouby A. 2013a. Essais cycliques axiaux sur des pieux forés dans des sables denses. *Proc. 18th ICSMGE*.  
 Benzaria O., Puech A. and Le Kouby A. 2013b. Essais cycliques axiaux sur des pieux forés dans l'argile surconsolidée des Flandres. *Proc. 18th ICSMGE*, Paris.  
 Bretelle S., Wallerand R. Fondations Superficielles Glissantes pour l'Offshore Profond – Méthodologie de Dimensionnement. *Proc. 18th ICSMGE*, Paris.  
 Burlon S., Thorel L. and Mroueh H. 2013. Proposition d'une loi *t-z* cyclique au moyen d'expérimentations en centrifugeuse. *Proc. 18th ICSMGE*, Paris.  
 Chen R.P., Ren Y., Zhu B. and Chen Y.M. 2013. Deformation behavior of single pile in silt under long-term cyclic axial loading. *Proc. 18th ICSMGE*, Paris.  
 Cheuk, Y.C. and White, J.D. (2008). Centrifuge modelling of pipe penetration due to dynamic lay effects. *Proc. Int. Conf. on Offshore Mechanics and Arctic Engineering*, Portugal. OMAE2008-57923.  
 Damgaard M., Andersen J.K.F., Ibsen L.B. and Andersen L.V. 2013. Time-Varying Dynamic Properties of Offshore Wind Turbines Evaluated by Modal Testing. *Proc. 18th ICSMGE*, Paris.  
 DNV-OS-J101 (2011). Design of Offshore Wind Turbine Structures. Det Norske Veritas (DNV) Offshore Standard, September 2011.  
 Dutta S., Hawlader B. and Phillips R. 2013. Numerical investigation of dynamic embedment of offshore pipelines. *Proc. 18th ICSMGE*.  
 Einav, I. and Randolph, F.M. (2005). Combining upper bound and strain path methods for evaluating penetration resistance. *Int. J. Numer. Meth. Engng.*, Vol. 63, pp. 1991-2016.  
 Ho J., Goh S.H. and Lee F.H. 2013. Post Cyclic Behaviour of Singapore Marine Clay. *Proc. 18th ICSMGE*, Paris.  
 Kim D.J., Youn J.U., Yee S.H., Choi J., Choo Y.W., Kim S., Kim J.H., Kim D.S. and Lee J.S. 2013. Centrifuge test and numerical modelling for a suction bucket monopod foundation. *Proc. 18th ICSMGE*, Paris.  
 Kim J.M. and Saffar M. 2013. Behaviour of marine silty sand subjected to long term cyclic loading. *Proc. 18th ICSMGE*, Paris.  
 Li X., Hu Y. and White D. 2013. A large deformation finite element analysis solution for modelling dense sand. *Proc. 18th ICSMGE*.  
 Lueking J. and Kempfert H.-G. 2013. Plugging Effect of Open-Ended Displacement Piles. *Proc. 18th ICSMGE*, Paris.  
 Moradi M., Galandarzadeh A. and Rojhani M. 2013. The new remediation technique for buried pipelines under permanent ground deformation. *Proc. 18th ICSMGE*, Paris.  
 Muir Wood A. and Knight P. 2013. Site investigation and geotechnical design strategy for offshore wind development. *Proc. 18th ICSMGE*.  
 Osterberg, J.O. 1989. New Device for Load Testing Driven Piles and Drilled Shafts Separates Friction and End Bearing. *Proc. Int. Conf. on Piling and Deep Foundations*, London, A.A. Balkema, p. 421.  
 Peire, K., Nonneman, H. & Bosschem E. (2009) Gravity Base Foundations for the Thornton Bank Offshore Wind Farm. *Terra et Aqua*, No. 115, pp. 19-29  
 Puech A., Benzaria O., Thorel L., Garnier J., Foray P., Silva M. and Jardine R. 2013. Diagrammes de stabilité cyclique de pieux dans les sables. *Proceedings 18th ICSMGE*, Paris.  
 Reiffsteck P., Fanelli S., Tacita J.L., Dupla J.C. and Desanneaux G. 2013. Utilisation des essais d'expansion cyclique pour définir des modules élastiques en petites déformations. *Proc. 18th ICSMGE*.  
 Rimoy S., Jardine R. and Standing J. 2013. Displacement response to axial cyclic loading of driven piles in sand. *Proc. 18th ICSMGE*.  
 Roesen H.R., Ibsen L.B. and Andersen L.V. 2013. Experimental Testing of Monopiles in Sand Subjected to One-Way Long-Term Cyclic Lateral Loading. *Proc. 18th ICSMGE*, Paris.  
 Rosquoët F., Thorel L., Garnier J. and Chenaf N. 2013. Pieux sous charge latérale : Développement de lois de dégradation pour prendre en compte l'effet des cycles. *Proc. 18th ICSMGE*, Paris.  
 Silva M., Foray P., Rimoy S., Jardine R., Tsuha C. and Yang Z. 2013. Influence des chargements cycliques axiaux dans le comportement et la réponse de pieux battus dans le sable. *Proc. 18th ICSMGE*.  
 Tyldesley M., Newson T., Boone S. and Cariveau R. 2013. Characterization of the geotechnical properties of a carbonate clayey silt till for a shallow wind turbine foundation. *Proc. 18th ICSMGE*.  
 Verstele H., Stuyts B., Cathie D. and Charlier, R. 2013. Cyclic loading of caisson supported offshore wind structures in sand. *Proc. 18th ICSMGE*, Paris.  
 Wang, D., White, D. J. and Randolph, M. F. (2010). Large deformation finite element analysis of pipe penetration and large-amplitude lateral displacement. *Canadian Geotech. Jnl.*, Vol. 47, pp. 842-856.

# Shallow foundations for offshore wind towers

## Fondations superficielles pour des installations éoliennes maritimes

Arroyo M., Abadías D., Alcoverro J., Gens A.

*Dep. of Geotechnical Engineering and Geosciences, Technical University of Catalonia, Barcelona, Spain*

**ABSTRACT:** Direct foundations are present in about 25% of the installed offshore wind power towers. The peculiarities of this type of structure are well known: high dynamic sensitivity, complex couplings between environmental actions, machine operation and structural response, complex installation and maintenance, difficult site investigation. There is a clear need for optimized foundation design tools that would enable cost reduction and a more detailed assessment of the risk of every installation. One such tool is likely to be the systematic use of failure envelopes for capacity checks. The paper explores the benefits of such an approach with various realistic design examples.

**RÉSUMÉ :** Les fondations superficielles interviennent dans la réalisation de 25% des structures éoliennes maritimes. Les particularités de ce type de structures sont bien connues: haute sensibilité dynamique, couplages complexes entre les actions environnementales, le fonctionnement de la machine et la réponse structurelle, installation et maintenance difficiles, investigation géotechniques onéreuses. Un besoin évident d'optimisation des outils de conception est nécessaire pour permettre la réduction des coûts et une évaluation plus détaillée du risque de chaque installation. Le recours systématique à des enveloppes de rupture pour les justifications de la capacité portante des fondations peut bien être un tel outil. Ce papier explore les avantages d'une telle approche avec divers exemples de conception réalistes.

**KEYWORDS:** direct foundation, capacity, offshore, energy, wind farms

### 1 INTRODUCTION

Offshore wind is an increasingly large contributor to the energy production mix of several European countries, particularly those bordering the North and Baltic seas. An exponential increase in installations is currently anticipated in this region. It is reasonable to expect that other regions of the world will follow suit.

Offshore wind turbines (OWT) are generally larger than those installed on land, with 3 to 5 MW of nominal capacity being now the norm, but with turbines of up to 10 Mw coming soon to the market. Rotor diameters of more than 100 m and nacelle locations 80 m above mean sea level are common. The result is a relatively lightweight and slender structure, supporting a rotating machine finely tuned to maximize power production while minimizing structural loading.

While initial OWT installations took place near shore (< 10 km) at locations with relatively shallow water depths (< 20 m), current developments are clearly located offshore (10 -100 km from the nearer coast) with water depths of 20-50 m being typical. Several floating support concepts are now being developed; however, commercial installations are still always supported by some kind of fixed structure. For these, the foundation of choice would depend in any case on the particular site conditions, construction equipment availability and, to a certain extent, local traditions.

To this date pile foundations have been largely dominant, mostly as single large (4-6 m diameter) monopile installations, and lately also as smaller (1-2 m) piles for jackets and tripods. However, examining the industry databases (e.g. Burton et al 2011) it appears that at the end of 2011 about 25% of the installed power was supported by direct foundations or gravity base substructures (GBS). Most of these GBS installations took place in relatively shallow waters, but there are some examples already at larger distances from the coastline and in deeper waters. Perhaps the most significant is the Thornton Bank I

project, 27 km offshore Zeebrugge in Belgium, where 6 OWT of 5 Mw were installed in water depths of 20-30 m. The foundation design for this installation was described by Peire et al (2009) and its outline is reproduced here in Figure 1. These are large (44 m height; 23.5 m base diameter) concrete shells, floated into place and later ballasted with a mixture of sand and olivine with the base at 4 m below the original seafloor level. The geotechnical profile at the site comprises medium and high density sands and stiff tertiary clays.

### 2 DESIGN ISSUES FOR DIRECT OWT FOUNDATIONS

There are several specific standards dealing with OWT. Perhaps the highest ranked is IEC 61400-3 (2009) which, from the point of view of structural design, establishes design cases and site ambient load specification procedures, introduces a safety format and gives broad indications about structural design procedures. However, detailed specification of structural and foundation design procedures is deliberately referred to other documents, like the ISO 1990X offshore standard series or DNV-OS-J101 (2010).

As might be expected, the indications given by such standards are, on the one hand, firmly based in conventional design practice when being specific, and somewhat elusive with problems that lack a clear conventional solution. An example of the later is the consideration of fatigue or foundation failure under cyclic loading. An example of the former is the consideration of foundation bearing capacity which, for shallow foundations, follows a conventional superposition and correction procedure not very different from those outlined by Brinch-Hansen (1970) or Vesic (1975).

When designing foundations for OWT, there will be of course issues of geotechnical capacity under extreme loads. However the design drivers might be sometimes related to other considerations, such as dynamic characteristics of the whole



structure (Van der Temple and Molenaar, 2002) or displacement limits imposed by operating constraints (e.g. foundation tilting limits of 0.25° - 0.5° are sometimes quoted). However, even if we narrow our focus to bearing capacity considerations there are reasonable grounds to question the suitability of the conventional design approach.

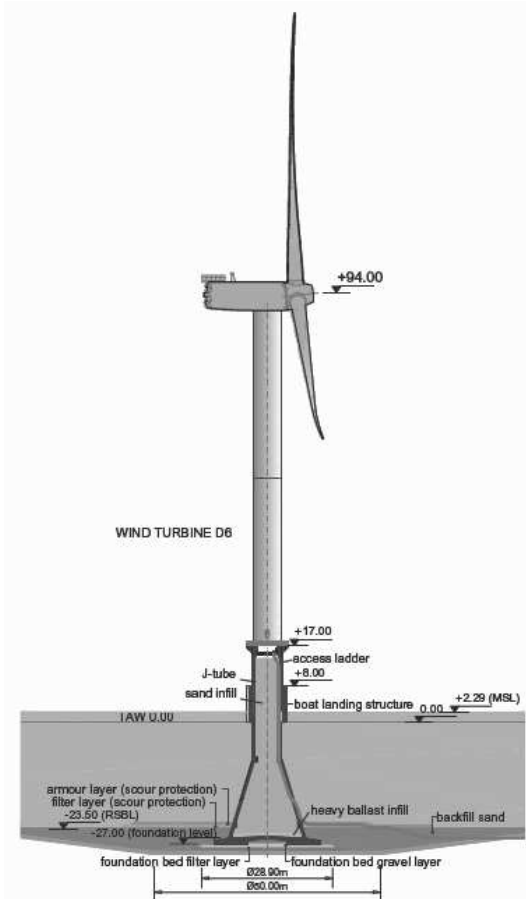


Figure 1. Thornton Bank GBS (Peire et al., 2009).

Indeed there are several aspects of the traditional approach to bearing capacity that are poorly suited to deal with OWT. Firstly, using separate corrections for shape, depth, load inclination, load eccentricity is cumbersome and prone to calibration error if the effects that are being corrected for are not truly independent. This is perhaps the reason behind the large scatter between inclination factor formulations (Siefert & Bay-Gress; 2000); that uncertainty is particularly undesirable for structures, like OWT, that are mostly designed to sustain horizontal loads.

Secondly, the traditional approach to bearing capacity quickly leads to conundrums when the security format (as is the case for most modern codes, like DNV-OS-J101) is based on separate partial factors for loads and resistances. As discussed in detail by Lesny (2007) the same action might have a detrimental or favourable effect depending on which other actions are being simultaneously considered. Also it is fairly evident that a traditional bearing capacity check is far from eliminating the most likely path towards failure.

Finally, it is very difficult to generalize the traditional approach to cases when two major horizontal loads (wind, wave) are acting in separate planes. All these problems are best dealt with if the traditional approach to capacity checks is replaced by a failure-envelope based one.

### 3 FAILURE ENVELOPES

#### 3.1 Concept

Failure envelopes were introduced (Butterfield & Tiof, 1979) as an alternative to classical bearing capacity analyses. They were based on the concept of interaction diagram, which was applied to the system of loads acting on the foundation. Most developments to date –but not all–, refer to the case in which that system can be reduced to loads acting within a plane ( $V, H, M$ ) –where  $M$  represents the moment acting within the plane,  $M$  normalised by a characteristic foundation dimension,  $M/B$ .

Failure envelopes are implicit in the traditional approach to bearing capacity. However, it was clearly appreciated from the beginning that an explicit failure envelope was useful to link previously separate checks on different foundation failure modes (e.g. sliding and bearing capacity) into a coherent view. Failure envelopes offered advantages also from the experimental viewpoint, because they provide a clearer framework for experimentation, even suggesting new, more efficient, procedures (like “swipe” tests).

Failure envelopes are also attractive because they can fit well with generalized force-displacement foundation models (“macroelements”; Nova and Montrasio, 1991) that are used to compute foundation displacements and represent an economical solution to non-linear soil-structure interaction studies. Finally, failure envelopes are interesting because they enable a more coherent approach to foundation safety.

#### 3.2 Safety considerations

Already Georgiadis (1985) clearly identified as one major advantage of failure envelopes that they allow a very natural consideration of the influence of different loading paths. To do that, it is important to distinguish between the reference design load state and incremental loading paths (Figure 2).

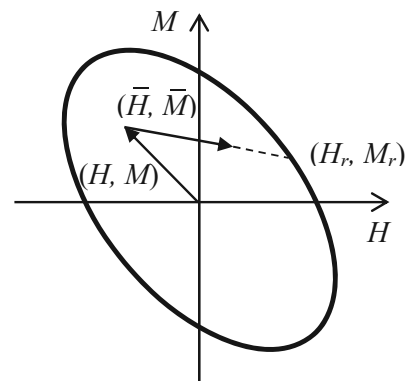


Figure 2. Schematic load envelope illustrating a reference design load and one incremental load path

Any load system ( $V, H, M$ ) shall remain within the failure envelope. It is however convenient to establish a non-dimensional safety measure. To do so a simple approach is, for any incremental loading direction, to obtain the crossing point with the failure envelope ( $V_r, H_r, M_r$ ) and then define a generalized safety factor,  $SF$ , as

$$SF_{(\bar{V}, \bar{H}, \bar{M})}(V, H, M) = 1 + |\lambda_r| \quad (1)$$

$$(V_r = V + \lambda_r \bar{V}, H_r = H + \lambda_r \bar{H}, M_r = M + \lambda_r \bar{M}) \quad (2)$$

It is thus made explicit the fact that safety is not only dependent on the initial design situation but also on the incremental loading path. This definition includes, as a particular case, the traditional safety factors against bearing capacity (the incremental load direction and the reference

design load are collinear) or sliding (incremental loading direction collinear with the Horizontal component of the reference design load). Another particular case included is that of “plastic overturn”, a prescribed check for breakwater design in Spanish regulations (Puertos del Estado, 2005) in which the lever arm of the horizontal loading is maintained (i.e. the incremental load is aligned with the the Horizontal and Moment components of the reference load).

### 3.3 Example formulations

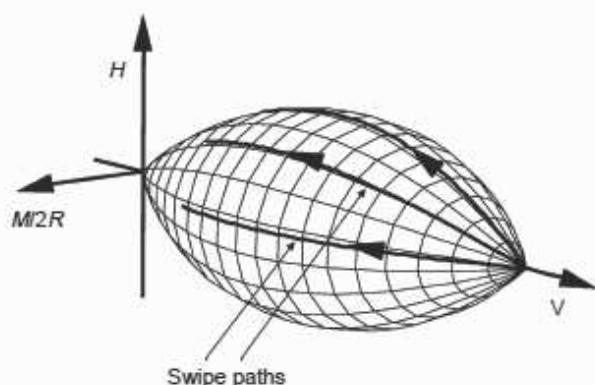


Figure 3 Failure envelope by Gottardi et al (1999)

There are many failure envelopes in the literature. For foundations failing without drainage at the soil-foundation interface Gourvenec & Randolph (2011) offer an excellent review. For the example below a sand profile is assumed and drained conditions are reasonable. In these circumstances a convenient expression for a failure envelope is that proposed by Gottardi et al. (1999) (Figure 3)

$$F(V, H, M) = \left(\frac{h}{h_0}\right)^2 + \left(\frac{m}{m_0}\right)^2 - 2a\left(\frac{hm}{h_0 m_0}\right) - (4v(1-v))^2 = 0 \quad (3)$$

Where  $(a, h_0, m_0)$  are shape factors, empirically determined as  $(-0.22, 0.12, 0.09)$  for quartzitic sand, and we use a non-dimensional notation in which  $v = V/V_0$ ,  $h = H/V_0$ ,  $m = M/(DV_0)$  and  $D$  is the foundation diameter. The normalizing factor  $V_0$  is the maximum load (i.e. centered vertical) that the foundation can sustain. Here that maximum load is computed assuming no embedment and introducing the bearing capacity factor  $N_\gamma$  from Bolton & Lau (1993) into

$$V_0 = \frac{1}{2} \gamma D N_\gamma \left(\frac{\pi D^2}{4}\right) \quad (4)$$

It is worth noting that (a) it is relatively straightforward to generalize expression (3) to more complex loading situations – e.g. Lesny 2010- although the experimental base for adjusting the parameters in those circumstances is somewhat scarce, (b) that the shape of (3) above has proven rather resilient and very similar expressions have been found to fit well other foundation test results in materials like carbonate sand or even clay (Martin & Houlsby, 2001), as long as the contact surface remains drained. Of course the choice of  $V_0$  would change according to the material and foundation shape.

## 4 EXAMPLE APPLICATION

To illustrate the argument we propose an example, synthetic but realistic. The case is developed using the characteristics of the gravity base substructure built at Thornton Bank (Peire et al. 2009) and the design loading specified for a Baltic windfarm development site, Kriegers Flak (Bulow et al, 2009). This reference gives some basic characteristics for the OWT superstructure (Table 1).

Table 1 Super-structure characteristics

Rated power	5 MW
Rotor diameter	126 m
Nacelle height above msl	90 m
Nacelle-rotor weight	4.1 MN
Tower weight	3 MN

The same reference also includes resultants from ambient loads for a range of depths and load hypothesis (e.g. extreme, fatigue). Using these data, Table 2 has been computed for a 30 m depth case and extreme load scenario. It appears that, in this particular case, 80% of the total horizontal thrust is due to sea action, but this load is the source of less than 20% of the overturning moment at foundation level. This might partly reflect the fact that at that particular site sea current is relatively strong, lowering the action line of sea forces.

These ambient loads should be combined with the OWT selfweight. Using the Thornton Bank design like a template for substructure shape, the relevant characteristics of that part of the OWT are those listed in Table 3. As usual with gravity base OWT, the dead weight of the substructure is significantly larger than that of the superstructure. Combining all environmental actions and structure selfweight the resultant load combination acting at the foundation level is  $(H, V, M) = (10.1; 44.5; 284.3)$  in MN and MNm. This will be the reference design load state in this example.

Table 2 Ambient loading parameters

Parameter / load	Unit	Value
Total thrust, H	MN	10.1
Total overturning moment, M	MNm	284.3
Wind thrust, H <sub>w</sub>	MN	2.03
Wind arm lever, b <sub>w</sub>	m	120
Sea thrust, H <sub>s</sub>	MN	8.07
Sea arm lever, b <sub>s</sub>	m	5

Table 3 Thornton Bank type substructure characteristics

Parameter / load	Unit	Value
Base diameter	m	23,5
Concrete weight	MN	30
Fill weight	MN	38
Buoyant volume	m <sup>3</sup>	2965

From that reference state we probe the failure surface alongside three different incremental loading paths. One will correspond to a simultaneous and proportional increase of all ambient actions (the “plastic overturn” case). The other two hypothesis would correspond to increases of just one of the

ambient horizontal actions, (sea, wind) while the other remains constant. These hypotheses would, for instance, naturally follow from any circumstance in which the estimates of wind and wave carry different uncertainties. Figure 4 illustrates graphically the meaning of these load directions in an idealised section of the failure envelope at constant  $V$ .

For this check we use the failure envelope of Gottardi et al described above. The soil profile below the foundation is characterised by a friction angle of  $33^\circ$  and submerged weight of  $10 \text{ kN/m}^3$ . These values might correspond well to the characteristic values of a medium-dense sand profile, frequently encountered in North Sea locations. It is assumed that the foundation base is perfectly rough.

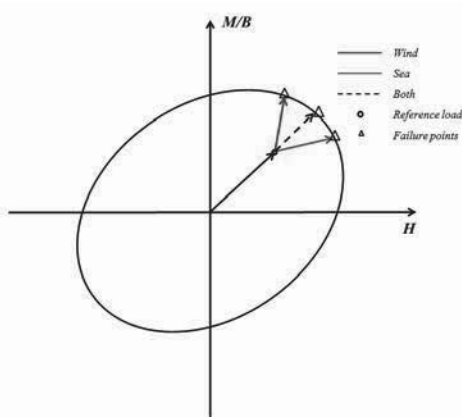


Figure 4 Incremental load paths in the example

Table 4 Example: results

Hypothesis	$H_r$ (MN)	$H_r / H_i$	$\Delta H$ (%)
Sea	14.1	1.4	50
Both	11.6	1.15	15
Wind	10.5	1.04	21

Some relevant results from the computation are presented in table 4. For each incremental loading path a failure point is identified in the envelope, with values ( $H_r$ ,  $M_r$ ). In the table the value  $H_r$  corresponding to each loading path is reported in the first column. In the second column this value is normalized by the reference state horizontal load. This corresponds to the generalized safety factor defined above, which, only for the hypothesis in which both loads are simultaneously increasing, coincides with the “plastic overturn” safety factor of ROM 0.5-05. As a reference the value required for that safety factor in breakwaters is commonly above 1.3 (Puertos del Estado; 2005).

For the other two load hypothesis in which only one environmental action is increased no similar reference exists to judge on the computed safety factor. For these cases it is perhaps more meaningful the number in the third column of Table 4, where the difference between failure and reference thrust is expressed as a percent of the reference ambient load that is increasing. In the case computed, a 21% error in the reference estimate of wind thrust would result in foundation failure, whereas it would be necessary a 50% underestimate of the hydrodynamic thrust to fail the foundation.

The previous computations have always been made under the hypothesis of increased thrust and constant lever arm. This can be interpreted as action magnitude uncertainty. Alternative hypothesis dealing with lever arm uncertainty can be equally set up with relative ease. Note, finally, that most geotechnical uncertainty can be lumped in the  $V_0$  estimate to achieve a relatively straightforward approach to reliability evaluation.

## 5 CONCLUSION

Failure envelopes offer a powerful framework to analyze shallow foundation capacity problems. They seem particularly suitable for offshore wind towers, where refined design in the face of large load uncertainties is likely to be a frequent situation.

## 6 ACKNOWLEDGEMENTS

The research on direct foundations for offshore wind towers described in this paper was partly funded by the company ACCIONA ENERGY within the framework of the CENIT-AZIMUT project supported by the Spanish Ministry of Science.

## 7 REFERENCES (TNR 8)

- Brinch-Hansen J. (1970). A revised and extended formula for bearing capacity. *Danish Geotechnical Institute Bulletin*, n° 28, 5-11
- Bülow, L., Jorgensen, L. and Gravessen, H. (2009) *Kriegers Flak Offshore Wind Farm. Basic data for conceptual design of foundations*. March 2009, Vattenfall Vindkraft AB
- Burton, T., Sharpe, D., Jenkins, N. and Bossanyi, E. (2011) *Wind Energy Handbook, 2nd Edition*, John Wiley & Sons, Chichester, UK
- Butterfield R., Ticof J. (1979). The use of physical models in design (discussion). *7th European Conference on Soil Mechanics and Foundation Engineering*, Brighton, UK, Vol.4, 259-2
- Georgiadis, M (1985) Load-path dependent stability of shallow footings, *Soils & Foundations*, 25,1, 84-88
- Gottardi, S., Houlsby, G.T. y Butterfield, R. (1999) Plastic response of circular footings on sand under general planar loading, *Géotechnique* 49, No. 4, 453-469
- Gourvenec, S. y Randolph, M. (2011) *Offshore geotechnical engineering*, Spon Press, New York
- DNV (2010) DNV-OS-J101 *Design of offshore wind turbine structures*
- IEC 61400-3 (2009) International standard *Wind turbines –Part 3: Design requirements for offshore wind turbines*. International Electrotechnical Commission
- Lesny, K. (2010) *Foundations for offshore wind turbines : tools for planning and design*, VGE, Essen
- Lesny, K. (2007) Design approaches of Eurocode 7 and their effect on the safety of shallow foundations, *ICASP10, Applications of statistics and probability in Civil Engineering*, Taylor & Francis
- Martin, C., M., Houlsby, G. T. (2001) - Combined loading of spudcan foundations on clay: numerical modeling. *Géotechnique*, 51, No. 8, pp. 687 – 699
- Nova R. y Montrasio L. (1991). Settlements of shallow foundations on sand. *Géotechnique*, vol.41(2), 243-256.
- Peire, K., Nonneman, H. & Bosschem E. (2009) Gravity Base Foundations for the Thornton Bank Offshore Wind Farm. *Terra et Aqua*, N. 115, pp. 19–29
- Puertos del Estado (2005) ROM 0.5-05 *Recomendaciones Geotécnicas para Obras Marítimas y Portuarias*, [http://www.puertos.es/es/programa\\_rom/rom\\_05\\_05.html](http://www.puertos.es/es/programa_rom/rom_05_05.html)
- Sieffert, J.G., y Bay-Gress, Ch. (2000). Comparison of the European bearing capacity calculation methods for shallow foundations; *Geotechnical Engineering, Institution of Civil Engineers*, Vol. 143, pp. 65-74
- Van der Tempel, J. y Molenaar, D.P. (2002) Wind turbine structural dynamics – a review of the principles for modern power generation, onshore and offshore, *Wind Engineering*, 26,4, 211-220
- Vesic, A. S. (1975) Bearing capacity of shallow foundations, Ch. 3 in Winterkorn H.F. & Fang H.Y., *Foundation Engineering Handbook*, Van Nostrand Reinhold

# Modelling of monopile-footing foundation system for offshore structures in cohesionless soils

Modélisation d'un système de fondation superficielle isolé pour sur les structures maritimes dans les sols pulvérulents

Arshi H.S., Stone K.J.L.  
University of Brighton, UK

Vaziri M.  
Ramboll UK Limited, UK

Newson T.A., El-Marassi M.  
University of Western Ontario, Canada

Taylor R.N., Goodey R.J.  
City University London, UK

**ABSTRACT:** While monopiles have proven to be an economically sound foundation solution for wind turbines, especially in relatively shallow water, their installation in deeper water and in hard ground may require a more complex foundation design in order to satisfy the loading conditions. One approach is that foundation systems are developed which combine several foundation elements to create a 'hybrid' system. In this way it is possible to develop a foundation system which is more efficient for the combination of vertical and lateral loads associated with wind turbines while maintaining the efficiency and simplicity of the design. Previous studies have reported the results of single gravity tests of the hybrid system where the benefits of adding the footing to the pile are illustrated. This paper presents experimental results on the performance of skirted and unskirted monopile-footings. A simplified design approach based on conventional lateral pile analysis is presented.

**RÉSUMÉ :** Alors que les fondations de type monopile se sont révélées être une solution économiquement viable pour les fondations d'éoliennes, en particulier dans les eaux relativement peu profondes, leur installation dans des eaux plus profondes et dans un sol dur peut exiger une conception plus complexe afin de satisfaire les conditions de chargement. Une approche possible est que les systèmes de fondations développés combinent plusieurs éléments de fondation pour créer un système hybride. De cette manière, il est possible de développer un système de fondation plus efficace vis à vis des charges verticales et latérales associées aux éoliennes, tout en maintenant une conception efficace et simple. Des études antérieures sous gravité simple ont montré l'efficacité d'un système hybride en combinant une semelle et un pieu. Cet article présente des résultats expérimentaux sur la performance de systèmes avec et sans pieu pour des semelles. Une approche de conception simplifiée basée sur l'analyse classique d'un pieu sous charge latérale est présentée.

**KEYWORDS:** Hybrid monopile footing, offshore piles, laterally loaded piles, wind turbine foundations

## 1 INTRODUCTION

Due to the needs of on-going developments in the oil and energy sector, the design of offshore foundations is constantly evolving. In the hydrocarbon extraction sector, exploration and development is moving in to ever deeper water resulting in ever more challenging geotechnical conditions. Similarly the expansion of the offshore wind sector involves the development of deepwater sites, together with requirements for heavier high capacity turbines. Conventional offshore foundations are not always economical or practical for this new generation of turbines, and there remains a requirement to develop foundation solutions which can better satisfy future developments in the offshore wind sector.

The foundations of a typical offshore wind turbine are subjected to combined loading conditions consisting of the self-weight of the structure ( $V$ ), relatively high horizontal loads ( $H$ ) and large bending moments ( $M$ ). The preferred foundation system to date has been the monopile, which has the advantage that it can be employed in a variety of different soil conditions. However, a disadvantage in the use of monopiles in deep water sites is that the system can be overly compliant. For sites with intermediate water depths, it may be possible to stiffen the lateral response of the monopile at the mudline.

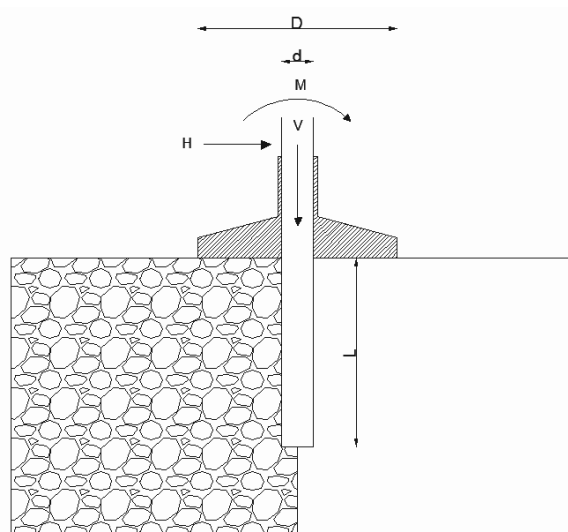


Figure 1. Schematic illustration of the prototype hybrid system.

One such approach to increase the lateral resistance of a monopile is the 'hybrid' monopile-footing system. As schematically represented in Figure 1, this foundation system

comprises of a circular footing attached to the monopile at the mudline. A 2-D analogy of this system is that of a retaining wall with a stabilising base (Powrie and Daly, 2007). The role of the footing is to provide a degree of rotational restraint at the pile head, leading to an improvement in the lateral resistance of the pile. It has also been shown that the use of a relatively thick pile cap leads to an increase in the lateral resistance through the development of passive soil wedges (Mokwa, 1999), in a similar way to the behaviour of skirted foundations (Bransby and Randolph, 1998).

Analysis of the hybrid system would involve both lateral pile analysis and bearing capacity analysis. The lateral response of piles is well reported in the literature and various methods of analysis have been proposed by numerous researchers, such as Matlock and Reese (1960), Broms (1954), Poulos (1971), Reese *et al.* (1974), Randolph (1981), Duncan *et al.* (1994) and Zhang *et al.* (2005). Where the plate diameter is relatively small, the system is similar to a single capped pile, for which methods have been developed for analysing the influence of the pile and pile cap under axial loading (Poulos and Randolph, 1983), and the effect of the pile cap on the lateral performance of single piles has also been investigated by others (Kim *et al.*, 1979), (Mokwa and Duncan, 2001: 2003), (Maharaj, 2003).

The bearing capacity problem has also been investigated under different loading conditions relevant to offshore foundations, see for example references Houslsby and Puzrin (1999), and Gourvenec and Randolph (2003).

## 2. EXPERIMENTAL INVESTIGATIONS

The potential performance of the hybrid system was investigated in single gravity studies (Stone *et al.* (2007)) and is illustrated in Figure 2. These studies suggested that the additional rotation restraint provided by the footing can result in a stiffer lateral response of the pile and greater ultimate lateral load. The degree of restraint at the pile head was dependent on the size of the footing, the initial contact between the soil and the footing and the stiffness of the soil beneath the footing. Observations of heaved and displaced soil in front of the edge of the footing also suggested that a degree of passive soil resistance is likely to be generated under the lateral movement and rotation of the footing.

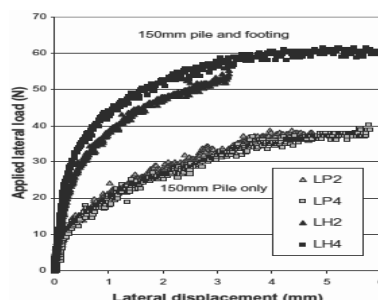


Figure 2. Lateral load response of the hybrid system (after Stone *et al.* 2007).

Arshi (2011), and Arshi and Stone (2012) reported the results of a comprehensive series of single gravity tests carried out on the foundation system where the elements affecting the overall performance of the foundation system was investigated in depth. It was reported that the size for the footing has a direct effect on the overall lateral load bearing capacity of the foundation system. Furthermore it was reported that the ratio between the vertical and horizontal load has a significant effect on the lateral performance of the foundation system where larger vertical loads tend to improve the lateral load bearing capacity of the hybrid system. The connection between the

footing and the pile was also investigated where it was suggested that the hybrid foundation system tends to be more effective if vertical movements are allowed at the pile-footing connection. This movement allows the footing to act independently from the pile where the positive contact between the footing and the soil underneath is solely controlled by the vertical load acting on the footing.

Table 1. Notations for skirted hybrid foundations system

ID	Footing size (mm)	Skirt length (mm)	Dead load (N)	Footing to pile connection
P.W0	-	-	0	-
P.F80.W1.FR	80	-	100	Slipping
P.F80.S1.W1.FR	80	-	100	Slipping
P.F80.S2.W1.FR	80	-	100	Slipping
P.F80.S3.W1.FR	80	-	100	Slipping

More recent single gravity tests are presented in Figure 3 where skirts with different lengths have been added to the footing. The tests were conducted in sand and the results indicate that the presence of the skirts has a relatively significant contribution on the lateral load capacity of the system. The results show that adding the skirts to the footing and increasing the skirt length tends to increase the lateral load bearing capacity of the foundation system by about 50% in comparison to a non-skirted hybrid system. It is also apparent that footings with very short skirts do not tend to show any ‘apparent’ additional advantage to that without the skirt. This could be due to the fact that the stresses around the skirt induced by the soil are very small at 1g. Further studies in the centrifuge are in the taking place to investigate the effect of the skirts and the results will be reported soon.

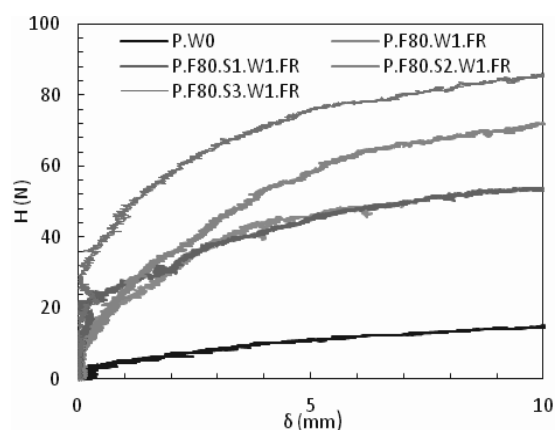


Figure 3. Load vs. deflection plot for the hybrid system with skirts.

Stone *et al.* (2011) reported the results of a series of centrifuge tests in sand. The results of the combined vertical and lateral loading tests are best represented through plots of lateral load versus lateral displacement. Figure 4 shows a plot of the lateral load versus lateral displacement for the monopile-footing (HL 1) and single pile (PL 1) with a vertical load of 600N at 50 g. It is apparent from this plot that the initial lateral stiffness of the monopile-footing and pile are similar for the first 1–1.5mm of lateral displacement. However the monopile-footing continues to exhibit a stiffer response than the single pile as the lateral displacement increases. Further analyses of these data provided information on the redistribution of bending moment in the pile due to the plate.

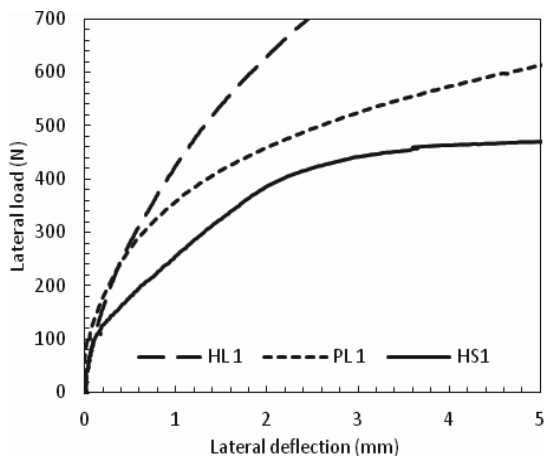


Figure 4. Load deflection graph for centrifuge tests carried out on the hybrid system (after Stone *et al.* 2011).

In Figure 5, the bold lines represent the bending moments at 5% and 20% of the maximum deflection for the pile only case and the dashed lines show the behaviour of the hybrid system. The results show that adding the footing to the pile reduces the bending moment at any given deflection, and as a result increases the moment capacity of the system at any given applied lateral load. The results indicate about 25% improvement in the bending moment for at both deflections.

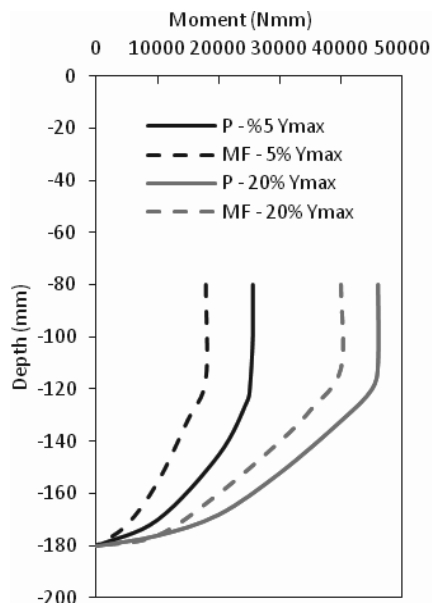


Figure 5. Bending moment distribution along the pile length for the hybrid system.

### 3. ANALYSIS

Whilst some advanced numerical modelling of monopiled footings has been undertaken (El-Marassi *et al.* 2008; Stone *et al.* 2010; Arshi *et al.* 2011; Arshi and Stone 2012), the method presented here utilises conventional lateral pile analysis methodology where the hybrid system is idealised to a lateral pile with a resisting moment applied at the mudline. The resisting moment capacity provided by the footings were estimated analytically using conventional bearing capacity theory and applied at the mudline acting in the opposite direction to the loading. This approach only considers the ultimate condition of the system and does not allow the moment

developed by the footing to be generated as a function of the footing rotation.

The results generated by this approach are illustrated in Figure 6 where it is shown how different pile to footing diameter increases the moment capacity of the piles, where this variation lies between a fully free and a fully fixed pile.

The dashed lines in Figure 6 show the ultimate moment capacities of the hybrid system. Although this method successfully leads to obtaining the ultimate load bearing capacity of the hybrid degree of rigidity (D.O.R 75%, 50% and 25% showing the ultimate capacity of the system when 75%, 50% and 25% of the ultimate moment at pile head is applied to the free headed pile) of the system are shown as a benchmark for comparing how different pile to footing diameters relate to the fully fixed moment. As apparent in Figure 6, increasing the size of the footing tends to increase the lateral load bearing capacity. As the footing size increases, it gets close to the fully fixed head condition. This also indicates that there for a given pile diameter and length, there ought to be a footing size after which increasing the footing size further will not enhance the lateral load bearing capacity of the foundation system.

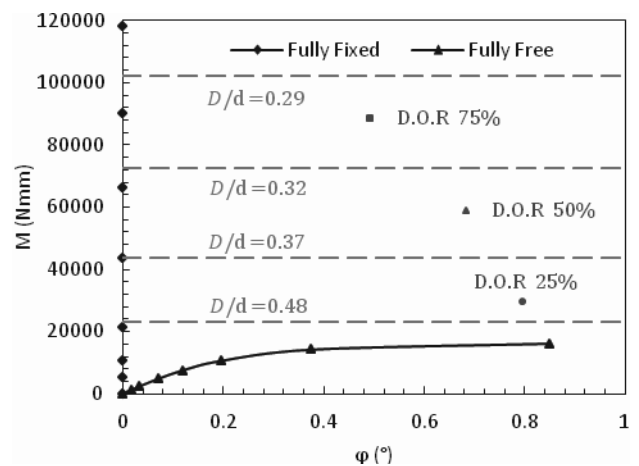


Figure 6. Moment vs. rotation plot for the hybrid system with different pile to footing ratios.

In addition to this, design charts have been developed which relate the pile embedment length to pile and footing diameters. Numerous design charts have been developed covering a wide range of pile diameters, pile lengths, footing diameters and normalized moment capacities an example of which is shown in Figure 8 where the  $L/D$  ratios vary from 1 to 10 and the footing to pile diameter ratios varies from 0 to 1. The moment capacity of the hybrid system has been normalised and is shown against footing to pile diameter ratio. The lines in between represent different pile embedment depth where for a given moment capacity the designer could utilise this graph to choose the appropriate pile length as well as pile and footing diameters. It is also notable that for any given value of normalized moment capacity the designer has the option of choosing a short pile relatively large footing diameter, or long pile with relatively small footing diameter. The flexibility in this design approach is beneficial in particular designing the hybrid system in difficult soil conditions.

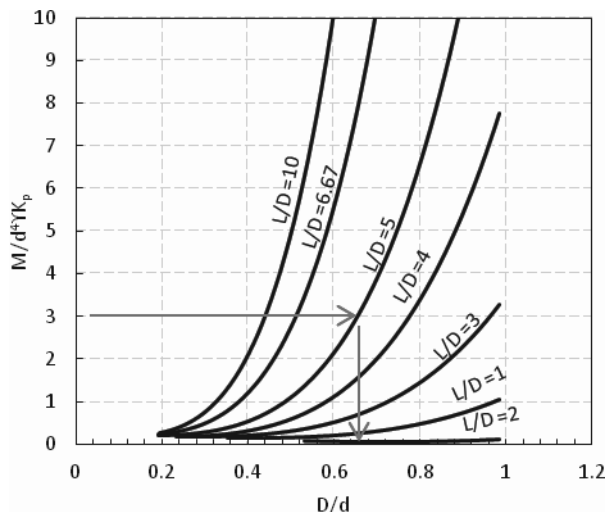


Figure 7. Example of a design chart for the hybrid system developed using analytical and numerical methods.

#### 4. DISCUSSION & CONCLUSION

It is apparent that the ultimate lateral response of a single monopile foundation can be enhanced by the presence of a footing resulting in a greater ultimate lateral capacity. This improvement was observed at both load versus deflection as well as the bending moment versus depth plots. Whilst the effect on the initial lateral stiffness may not be significant, the lateral stiffness beyond this initial movement was significantly enhanced through the presence of the footing.

The effect of adding skirts to the hybrid system has been shown to further increase the lateral performance of the hybrid system, and centrifuge tests are planned to investigate the skirted system in more detail.

A simple analytical approach using conventional lateral pile analysis methods is presented from which preliminary design charts can be generated. This approach can be developed to generate realistic design charts where the lateral capacity of the hybrid system is related to the development of bearing capacity coupled to the lateral resistance of the pile shaft.

#### 5. REFERENCES

- Arshi HS. (2011). Structural behavior and performance of skirted hybrid monopile-footing foundations for offshore oil and gas facilities. *Proceedings of the Institution of Structural Engineers: Young Researchers Conference '11*. London: IStructE Publications, 8.
- Arshi HS, Stone KJL and Newson TA. (2011). Numerical modelling on the degree of rigidity at pile head for offshore monopile-footing foundation systems. *9<sup>th</sup> British Geotechnical Association Annual Conference, London*.
- Arshi HS and Stone KJL. (2011). An investigation of a rock socketed pile with an integral bearing plate founded over weak rock. *Proceedings of the 15<sup>th</sup> European Conference of Soil Mechanics and Geotechnical Engineering*. Amsterdam: Ios Pr Inc, 705 – 711.
- Arshi HS. (2012). A new design solution for increasing the lateral resistance of offshore pile foundations for wind turbines located in deep-water. *Proceedings of the Institution of Structural Engineers: Young Researchers Conference '12*. London: IStructE Publications, 10.
- Arshi HS and Stone KJL. (2012). Lateral resistance of hybrid monopile-footing foundations in cohesionless soils for offshore wind turbines. *Proceedings of the 7<sup>th</sup> International Conference on Offshore Site Investigation and Geotechnics*. London: Society for Underwater Technology, 519 – 526.
- Bransby MF and Randolph MF. (1998). Combined loading of skirted foundations. *Géotechnique*. 48(5), 637–655.
- Broms BB. (1964). Lateral resistance of piles in cohesionless soils. *ASCE Journal of the Soil Mechanics and Foundation Division*. 90(SM3), 123-156.
- Duncan JM, Evans LT and Ooi PS. (1994). Lateral load analysis of single piles and drilled shafts. *ASCE Journal of Geotechnical Engineering*. 120(6), 1018-1033.
- El-Marassi M, Newson T, El-Naggar H and Stone KJL. (2008). Numerical modelling of the performance of a hybrid monopile-footing foundation. *Proceedings of the 61<sup>st</sup> Canadian Geotechnical Conference, GeoEdmonton 2008*. Edmonton, (Paper No. 480), 97 – 104.
- Gourvenec S and Randolph M. (2003). Effect of strength non-homogeneity on the shape of failure envelopes for combined loading of strip and circular foundations on clay. *Géotechnique*. 53(6), 575–586.
- Houlsby GT and Puzrin AM. (1999). The bearing capacity of a strip footing on clay under combined loading. *Proc. R. Soc. London Ser. A*. 455, 893–916.
- Kim JB, Singh LP and Brungraber RJ. (1979). Pile cap soil interaction from full scale lateral load tests. *ASCE Journal of Geotechnical Engineering*. 105(5), 643-653.
- Maharaj DK. (2003). Load-deflection response of laterally loaded single pile by nonlinear finite element analysis. *EJEG*.
- Matlock H and Reese LC. (1960). Generalized solutions for laterally loaded piles. *ASCE Journal of Soil Mechanics and Foundations Division*. 86(SM5), 63-91.
- Mokwa RL. (1999). Investigation of the Resistance of Pile Caps to Lateral Loading. *Ph.D Thesis*. Virginia Polytechnic Institute, Blacksburg, Virginia.
- Mokwa RL and Duncan JM. (2001). Experimental evaluation of lateral-load resistance of pile caps. *ASCE Journal of Geotechnical and Geoenvironmental Engineering*. 127(2), 185 - 192.
- Mokwa RL and Duncan JM. (2003). Rotational restraint of pile caps during lateral loading. *ASCE Journal of Geotechnical and Geoenvironmental Engineering*. 129(9), 829 - 837.
- Poulos HG. (1971). Behaviour of laterally loaded piles: Part I-single piles. *ASCE Journal of the Soil Mechanics and Foundations Division*. 97(SM5), 711-731.
- Poulos HG and Randolph MF. (1983). Pile group analysis: a study of two methods. *ASCE Journal of Geotechnical Engineering*. 109(3), 355-372.
- Powrie W, and Daly MP. (2007). Centrifuge modelling of embedded retaining wall with stabilising bases. *Geotechnique*. 57(6), 485-497.
- Randolph MF. (1981). The response of flexible piles to lateral loading. *Géotechnique*. 31(2), 247-259.
- Reese LC, Cox WR and Koop FD. (1974). Analysis of laterally loaded piles in sand. *Offshore Technology Conference*. Vol. II (Paper No. 2080), 473-484.
- Stone KJL, Newson TA and Sandon J. (2007). An investigation of the performance of a 'hybrid' monopile-footing foundation for offshore structures. *Proceedings of 6<sup>th</sup> International on Offshore Site Investigation and Geotechnics*. London: SUT, 391-396.
- Stone KJL, Newson TA and El Marassi, M. (2010). An investigation of a monopile-footing foundation. *International Conference on Physical Modelling in Geotechnics, ICPMG2010*. Rotterdam: Balkema, 829-833.
- Stone KJL, Newson TA, El Marassi M, El Naggar H, Taylor RN, and Goodey RA (2011). An investigation of the use of bearing plate to enhance the bearing capacity of monopile foundations. *International Conference on Frontiers in Offshore Geotechnics II - ISFOG*. London: Taylor and Francis Group, 623-628.
- Zhang L, Silva F and Grismala R. (2005) Ultimate lateral resistance to piles in cohesionless soils. *Journal of Geotechnical and Geoenvironmental Engineering*. Vol. 131(1), 78–83.

# Influence of jack-up footprints on mudmat stability – How beneficial are 3D effects?

Influence des dépressions laissées par les jack-ups sur la capacité portante des mudmats – quels sont les effets bénéfiques d'une analyse en 3D?

Ballard J.-C., Charue N.  
*Fugro GeoConsulting Belgium*

**ABSTRACT:** Jacket platforms are piled into the seabed but need to be supported temporarily by mudmats during installation. They sometimes need to be located next to seabed features such as pug marks formed by previous deployments of jack-up rigs. These features may influence the bearing capacity of the mudmats. This is a 3D problem for which simplified approaches are unsatisfactory, simplified 2D plane strain simulations can lead to over-conservative results. This paper presents a project example in very soft clay for which the software package Plaxis 3D has been successfully used. The presence of a pug mark was found to degrade significantly the yield surface in the VHM load space. A comparison between 2D and 3D analyses shows that the beneficial 3D effects are substantial, especially when the pug mark is located at the corner of the mudmat. The zone of influence of the pug mark is also much more limited when the problem is modelled in 3D.

**RÉSUMÉ :** Les plateformes de type « Jacket » sont fondées sur pieux mais nécessitent d'être supportées temporairement pendant l'installation par des mudmats (fondations de type superficiel). Ces jackets sont parfois situées à proximité de dépressions laissées par l'installation antérieure de jack-ups. Ces dépressions peuvent influencer la capacité portante des mudmats. Il s'agit d'un problème 3D typique pour lequel aucune solution simplifiée n'existe. Une approche 2D (en état plan de déformation) peut même mener à des résultats trop conservatifs. Cet article présente un exemple dans de l'argile molle pour lequel la suite de logiciels Plaxis a été utilisée avec succès. Les conclusions sont les suivantes : la présence des dépressions modifie singulièrement la surface de rupture dans l'espace VHM. Une comparaison entre les approches 2D et 3D montre que les avantages à faire appel au 3D sont substantiels, spécialement quand la dépression est située à proximité du coin du mudmat. La zone d'influence de la dépression est aussi bien plus limitée lorsque le problème est modélisé en 3D.

**KEYWORDS:** Pug mark, mudmat, stability, VHM, 2D, 3D, Finite Element Analysis, soft clay, remoulded, jack-up, mesh

## 1 INTRODUCTION

Jacket platforms are the most common type of offshore structure in the offshore hydrocarbons industry (Dean, 2010). They consist of open-framed steel structures made of tubular leg chords, horizontal bracing, and diagonal bracing. These structures are piled into the seabed but need to be supported temporarily by mudmats during installation. Mudmats are essentially flat stiffened metal plates attached to legs or the lower braces. In soft soils, mudmats can cover the entire surface between the legs to maximise the bearing area. They are generally subjected to combined Vertical, Horizontal and Moment (VHM) loads induced by the jacket weight, wind, waves and currents.

Jacket platforms are not always installed on a virgin seabed and are sometimes located next to features such as pug marks formed by previous deployments of jack-up rigs. A jack-up is a mobile, self-elevating offshore platform consisting of a hull and three or more retractable legs passing through the hull (McClelland et al, 1982). A unit moves onto location, sets its legs onto the seabed, and raises its hull out of the water. The legs are supported on independent foundations called spudcans. Penetration and extraction of spudcans in soft grounds create zones of remoulded soil and seabed depressions (Hossain et al, 2012). These seabed features potentially influence the bearing capacity of the mudmats and need to be accounted for in the stability verification.

Mudmats subjected to combined VHM loads and located next to a jack-up footprint is a 3D problem for which simplified approaches for analysis do not exist. Simplified 2D plane strain simulations are generally performed but they can lead to over-

conservative results. This type of problem is better analysed by means of 3D Finite Element (FE) analyses.

This paper presents a project example in very soft clay for which the software package Plaxis 3D (Plaxis, 2011) has been used successfully. The analysis allowed confidence to be established for the selected location of the mudmat with respect to a pug mark. In contrast, a simplified 2D analysis suggested that the proximity of the mudmat to the pug mark was unacceptable.

It is shown for this particular example how the presence of a pug mark degrades the yield surface in the VHM load space. 3D analyses are compared with 2D analyses to quantify the beneficial 3D effects for different pug mark locations.

## 2 PROBLEM GEOMETRY AND SOIL CONDITIONS

A 30 m by 30 m square mudmat is considered. The mudmat is located next to a circular pug mark of 30 m in diameter. Analyses were performed for 2 positions of the mudmat. The first position considers a pug mark located along the width of the mudmat while the second position considers a pug mark located at the corner of the mudmat, as illustrated on Figure 1. The distance  $d$  between the edges of the mudmat and the pug mark is varied in the analysis.

Soil conditions in this example consist of very soft clay. The soft deposit is considered to be 15 m thick and underlain by stiffer soils, which are not modelled. The intact undrained shear strength increases linearly with depth according to  $s_u = 4 + 0.8z$  (in kPa), where  $z$  is the depth below ground level in meter. This gives a strength heterogeneity  $\kappa = 6$  where  $\kappa = kB/s_{u0}$ ,  $k$  is the



shear strength gradient,  $B$  the mudmat width and  $s_{u0}$  the undrained shear strength at mudline.

A cylinder of soil with remoulded properties is considered to model the pug mark. This cylinder extends to the bottom of the soft layer. A 30 m diameter cylinder corresponds approximately to a 15 m diameter spudcan. The remoulded zone created by the penetration and extraction of a spudcan has indeed been observed to be of the order of 2 times the spudcan diameter (Hossain, 2012). On removal of the jack-up unit, the spudcans leave depressions at the site. The depth and configuration of the depression depends on several factors including soil strength, spudcan final penetration, amount of soil backfill during installation, etc. A seabed depression of 2 m is considered in this paper. To keep the model geometry simple, a horizontal depression with vertical walls is modelled, as illustrated in Figure 1. A remoulded undrained shear strength profile  $s_{ur} = 2 + 0.4z$  (in kPa), where  $z$  is the depth in meter below original ground level, is considered within the pug mark area.

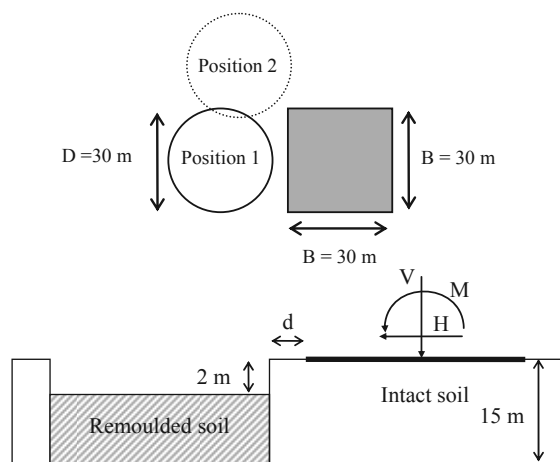


Figure 1. Problem geometry: plan view and cross-section

### 3 FINITE ELEMENT MODEL

2D plane strain and 3D FE simulations were carried out using Plaxis (Plaxis, 2011). The 2D analyses only consider a pug mark along the width of the mudmat while the 3D analyses consider two positions for the pug mark: along the width and at the corner.

An example of 3D finite element mesh is shown on Figure 2. Similar mesh discretization was adopted for the different analyses. The external boundaries were set sufficiently remote so as not to intercept the different failure mechanisms.

Preliminary analyses were first performed for the base case without a pug mark and for which analytical and/or numerical solutions exist. The aim was to check for any effects due to mesh size on the accuracy of the solution. A compromise was found between the accuracy of the solution and computational time. It is estimated that the over-estimation of the true solution due to discretization errors was maximum 10% for the selected mesh, which was judged to be reasonable.

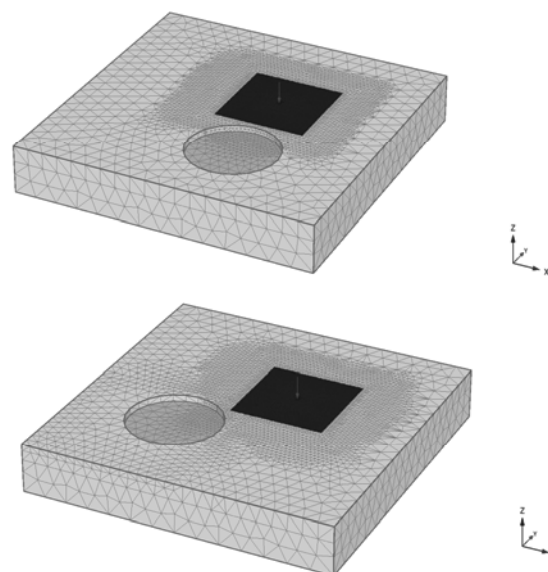


Figure 2. 3D Finite Element meshes

The soil is modelled as an isotropic elasto-perfectly plastic continuum, with failure described by the Mohr-Coulomb yield criterion. It is assumed to behave “undrained” and is characterized by a cohesion equal to the undrained shear strength  $s_u$  with  $\phi_u=0$ . The elastic behaviour was defined by a Poisson’s ratio  $\nu=0.495$ , and a constant ratio of Young’s modulus to undrained shear strength  $E/s_u=300$  for both undisturbed and remoulded clays.

The strength of the mudmat/clay interface is modelled using an interface factor  $\alpha$ , where the maximum shear stress at the interface  $\tau_{max} = \alpha s_u$ . The “rough” and “smooth extremes of interface strength correspond to  $\alpha = 1$  and  $\alpha = 0$  respectively. An intermediate roughness was assumed with  $\alpha = 0.5$ , which is a typical assumption for steel/soft clay interface. A no-tension condition allowing separation of the mudmat from the seabed was permitted at the mudmat/clay interface.

The jacket mudmat is modelled as a 30 m by 30 m rigid plain square plate. The seabed is assumed to be perfectly flat below the mudmat.

### 4 DESIGN PROCESS

The vertical load  $V$  from the mudmat and jacket structure is generally known and well-defined. It should typically be limited to a maximum of 50% the uniaxial vertical capacity. Then, for a given mobilisation ratio of the uniaxial vertical capacity  $v = V/V_{ult}$ , the stability verification consists of ensuring that there is adequate factor of safety on the ‘live’ loading  $M$  and  $H$ . This can be performed by comparing design load combinations to the MH failure envelope. The higher the mobilisation of the uniaxial vertical capacity, the lower the moment and horizontal capacity, i.e. the MH failure envelope shrinks with increasing  $v$ .  $M$  and  $H$  loads are applied in the direction of the pug mark centre, namely perpendicular to the side of the mudmat or along its diagonal.

The presence of a pug mark with remoulded soil conditions in the vicinity of a mudmat has two adverse effects. First, it affects the moment and horizontal capacities for a given  $v$ . Second, it reduces  $V_{ult}$  and therefore increases  $v$ , reducing further the moment and horizontal capacities.

## 5 RESULTS AND DISCUSSION

## 5.1 2D Analyses

The accuracy of the 2D FE model was verified by computing the uniaxial vertical capacity and comparing with results published in the literature. An interface factor at the mudmat/soil interface  $\alpha = 1$  was assumed for this comparison. A normalized vertical capacity  $V_{ult}/s_{uo}B = 10.45$  was found. This compares well with the analyses results published by Salgado (2008) who found 10.42 using ABC program (Martin, 2004). When the interface factor is reduced to  $\alpha = 0.5$ , the vertical capacity  $V_{ult}/s_{uo}B$  reduces to 9.8.

The MH failure envelope for the case without pug mark is shown on Figure 3 assuming a vertical load  $V$  so that  $v = 0.4$ , which is equivalent to a safety factor of 2.5 on the uniaxial vertical capacity. The results are plotted in a non-dimensional way:  $M/s_{uo}B^2$  versus  $H/s_{uo}B$ . This case is for an inter-distance  $d = 2$  m (i.e.  $d/B = 0.07$ ).

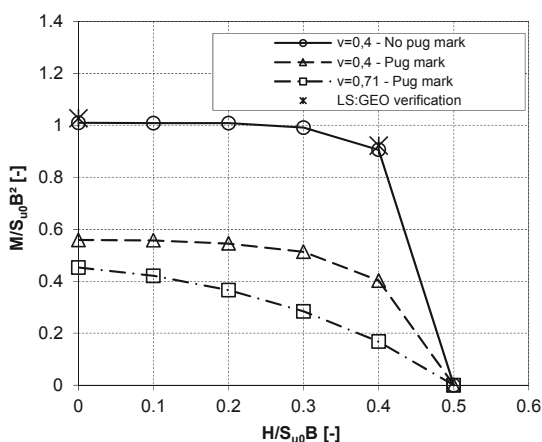


Figure 3. Influence of pug mark on MH failure envelope

A few comparison runs were performed with Limitstate:Geo v2 (Limstate, 2009). Limitstate:Geo is designed to analyze the ultimate limit (or “collapse”) state for a wide variety of geotechnical problems. The current version is however limited to 2D plane strain analyses. The ultimate limit state is determined using the Discontinuity Layout Optimization (DLO) algorithm (Smith & Gilbert, 2007). The agreement with the FE results is found to be excellent.

The effect of the pug mark on the MH failure envelope is significant. The normalized uniaxial vertical capacity  $V_{ult}/s_{uo}B$  is reduced to 5.5 leading to a mobilisation ratio  $v = 0.71$  instead of 0.4 (i.e. a safety factor of 1.4 instead of 2.5). The moment capacity is reduced by 55% to 80% depending on the applied horizontal load.

The inter-distance between the mudmat and the pug mark was then progressively increased and results are presented on Figure 4. The maximum moment capacity increases progressively with the inter-distance towards the capacity obtained for the case without a pug mark. From an inter-distance  $d/B = 0.2$ , the difference in mobilisation ratio of the vertical capacity does not affect the maximum moment capacity and, at an inter-distance  $d/B = 0.5$ , the pug mark has no effect at all.

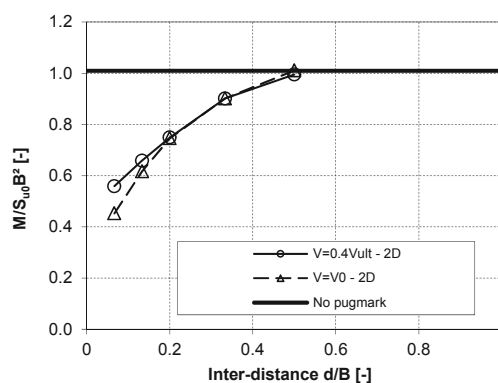


Figure 4. Influence of pugmark / mudmat inter-distance on maximum moment capacity – 2D analyses

## 5.2 3D Analyses

The accuracy of the 3D FE model was also checked by computing the uniaxial vertical capacity for a square footing resting on soft clay, with  $s_u$  constant with depth and  $\alpha = 1$ , and comparing with available literature results. A normalized vertical capacity  $V_{ult}/s_{uo}B^2 = 5.96$  was found. This compares well with the results published by Gourvenec et al. (2006) who found 6.02. When the interface factor is reduced to  $\alpha = 0.5$  and  $s_u$  increases with depth (as defined in Section 2), the vertical capacity  $V_{ult}/s_{uo}B^2$  is about 9.1, which is slightly lower than the 2D plane strain capacity.

Similarly to the 2D plane strain FE analyses, the MH failure envelope for the case without a pug mark assumes a vertical load  $V$  so that  $v = 0.4$ . As discussed above and shown on Figure 1, the 3D analyses consider two positions for the pug mark: along the width and at the corner of the mudmat. The results are plotted on Figures 5 and 6 for the first and second positions, respectively, using the following non-dimensional groups:  $M/s_{uo}B^3$  and  $H/s_{uo}B^2$ . This case is for an inter-distance  $d = 2$  m (i.e.  $d/B = 0.07$ ). The moment capacity is not affected for small mobilisation ratios of the horizontal capacity. However, when  $H/s_{uo}B$  approaches 0.5, the failure mechanism switches rapidly from a general shear mechanism to a sliding mechanism.

For the first position (along the width), the effect of the pug mark on the MH failure envelope is noticeable but not as significant as for the 2D plane strain simulations. The normalized uniaxial vertical capacity  $V_{ult}/s_{uo}B^2$  is reduced to only 8.4 leading to a mobilisation ratio  $v = 0.44$  instead of 0.4 (i.e. a safety factor of 2.29). The moment capacity is reduced by 20% to 28% depending on the applied horizontal load. There is very little difference in the results between a vertical mobilisation factor of 0.4 and 0.44 (Figure 5).

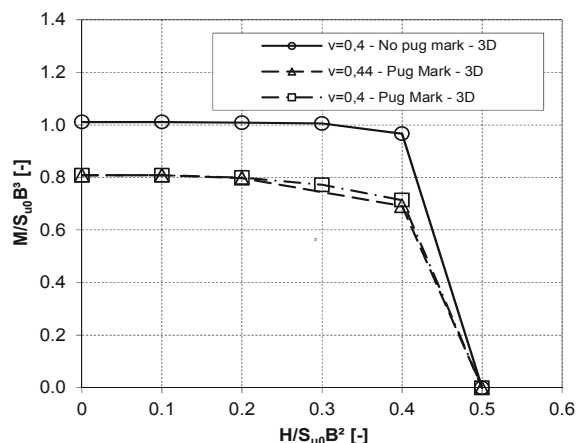


Figure 5. Influence of pug mark on MH failure envelope – Position 1 (along width of mudmat)

For the second position (at the corner), the normalized uniaxial vertical capacity is not affected, meaning that the safety factor for a pure vertical load remains 2.5. The moment capacity is only reduced by 1 to 3 % (Figure 6) depending on the applied horizontal load. This is a negligible difference.

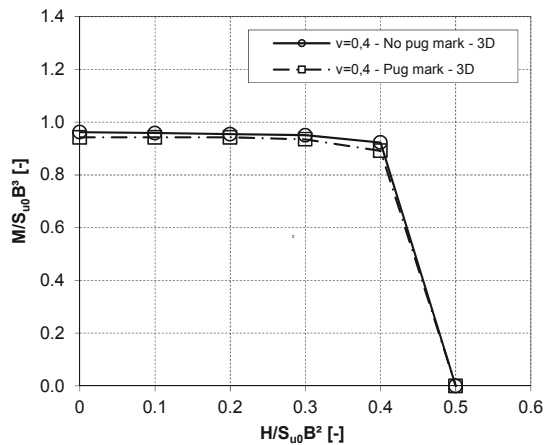


Figure 6. Influence of pug mark on MH failure envelope – Position 2 (at mudmat corner)

Similarly to the 2D plane strain approach, the inter-distance between the mudmat and the pug mark was progressively increased for the position of the pugmark along the width of the mudmat and the results are presented on Figure 7. The maximum moment capacity increases progressively with the inter-distance towards the capacity obtained for the case without pug mark. From an inter-distance  $d/B = 0.25$ , the pug mark has no effect anymore. This result illustrates the benefit of considering a more realistic 3D analysis when facing this kind of problem. The inter-distance required to have no influence of the pug mark in the 3D model is half the inter-distance required in the 2D plane strain model.

Finally, Figures 5 and 6 allow the comparison of the effect of the orientation of the moment and the horizontal loads on the MH envelope. The moment capacity for the loads in the direction of the corner is about 5% lower than for the case where the loads are towards the width of the mudmat. This geometrical effect is however limited.

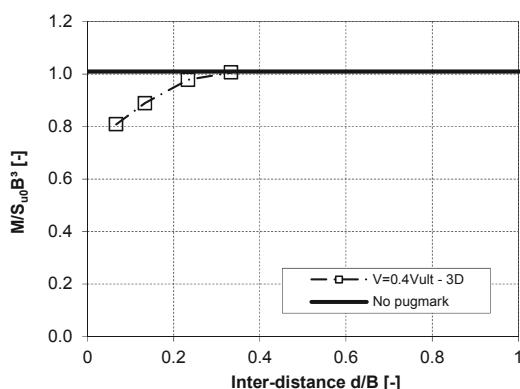


Figure 7. Influence of pugmark / mudmat inter-distance on maximum moment capacity – 3D analyses

### 5.3 Conservativeness of 2D Analyses

Simplified 2D plane strain and more realistic 3D simulations give similar results if the pug mark is not considered.

In the case where the pug mark is located along the width of the mudmat, the MH failure envelope is degraded in both 2D and 3D analyses. However, the effect is significantly larger in the 2D analyses for which the moment capacity is reduced by

55% to 80% depending on the applied horizontal load. In the more realistic 3D analyses, the moment capacity is only reduced by 20 to 28%. When the pug mark is located at the corner of the mudmat, the 3D analyses show very little impact on the mudmat capacity.

The analyses show also that the distance of influence of the pug mark on the mudmat stability is 2 times less in 3D compared to 2D analyses. The maximum moment capacity is not affected from an inter-distance  $d/B = 0.25$  in 3D analyses while the distance is  $d/B = 0.5$  in 2D analyses.

## 1 CONCLUSION

The presence of a pug mark has been found to degrade significantly the yield surface of a square mudmat in the VHM load space. However, a comparison between simplified 2D plane strain and 3D analyses has shown that the beneficial 3D effects are substantial. If the pug mark is located along the width of the mudmat, the more realistic 3D model shows that the moment capacity is only reduced by 20 to 28% depending on the applied horizontal load. The impact of the pug mark is significantly larger when a more simplified 2D plane strain approach is followed. Moreover, in the particular example treated in this paper, it was observed that a pug mark located at the corner of the mudmat does not influence its stability. The zone of influence of the pug mark is also much more limited when the problem is modeled in 3D and the orientation of a complex VHM loading scheme can be considered in the global stability. Simplified 2D plane strain simulations can lead to over-conservative results for this particular problem.

## 6 ACKNOWLEDGEMENTS

The authors acknowledge the permission of Fugro GeoConsulting to publish this work and the guidance and review provided by Dr Richard Jewell.

## 7 REFERENCES

- Dean E.T.R. 2010. *Offshore geotechnical engineering – Principles and practice*. Thomas Telford, London.
- Gouverneec S., Randolph M.F. and Kingsnorth O. 2006. Undrained bearing capacity of square and rectangular footings. *Int. J. Geomech.* 6, N°3, 147-157.
- Hossain M.S., Dong D., Gaudin C. and Kong V.W. 2012. *Skirted spudcans and perforation drilling for installation of spudcans close to existing footprints*. Proceedings of the 7<sup>th</sup> Intern.Conf. Offshore Site Investigation and Geotechnics, London.
- Salgado R. 2008. *The Engineering of Foundations*. McGraw-Hill, New-York.
- Plaxis 2011. *Finite element code for soil and rock analyses*, Version 2011. Plaxis BV. Delft, Netherlands.
- Limitstate Ltd 2009. *Geotechnical software for stability analysis, Version 2*. Limitstate Ltd. Sheffield, UK.
- Smitts C. and Gilbert M. 2007. *Application of discontinuity layout optimization to plane plasticity problems*. Proc. of the Royal Society A.
- Martin C.M. 2004. *User guide for ABC – Analysis of bearing capacity*. Department of Engineering Science, Oxford University, Oxford.

# Design and installation of buried large diameter HDPE pipelines in a coastal area

## Project et installation de tuyaux enterrés de grand diamètre en zone côtière

Bellezza I., Mazzier F., Pasqualini E.  
Dep. SIMAU – Università Politecnica delle Marche, Ancona, Italy

D'Alberto D., Caccavo C., Serrani C.  
SPS - Società Progettazione Servizi s.r.l., Ancona, Italy

**ABSTRACT:** The present paper deals with the main geotechnical aspects of the design and installation of two adjacent HDPE large diameter pipelines along the Adriatic Sea (Italy) coastline. The pipelines -270 m in length and 2 m in diameter - are conceived as buried collectors of polluted runoff water, to convey to sanitation prior to discharge into the sea. Considering that pipes are below the water table uplift analysis is detailed, showing three possible approaches in static conditions, whereas in seismic conditions a method is proposed that include the build-up of pore-water pressures during earthquake. As far as prediction of vertical deflection is concerned, the backfill loosening due to sheet piles extraction has been modelled by assuming no compaction (dumped backfill). Despite this assumption, theoretical short term deflection represents a lower bound of measured deflections.

**RÉSUMÉ :** Cet article décrit les principales problématiques géotechniques du projet et de l'installation de deux tuyaux enterrés adjacents de grand diamètre sur le littoral adriatique italien. Les tuyaux – longs de 270 m - ont la fonction de collecteurs enterrés pour l'eau de ruissellement polluée, pour permettre sa dépollution avant du déchargement dans la mer. En considérant que les tuyaux se trouvent au-dessous du niveau de la nappe d'eau on a analysé le problème du possible soulèvement en conditions statiques utilisant trois différentes méthodes. En conditions sismiques on a proposé une méthode qui considère le développement de pressions interstitielles positives excessives durant le tremblement de terre. L'ovalisation du tuyau a été calculée par une méthode de littérature en considérant un remblai sans compactage pour tenir compte de l'extraction des palplanches utilisées pendant l'excavation de la tranchée. Les valeurs calculées de l'ovalisation initiale représente un limite inférieur de l'ovalisation mesurée.

Keywords : uplift, pipe of large diameter, deflection

## 1 INTRODUCTION

Urban and infrastructural development often involves vulnerable areas such as coastlines. To prevent pollution of the sea from runoff water of a nearby urban area and crowded roads a system of buried collectors are to be built along a stretch of the Italian shoreline of the Adriatic Sea. In such a way, the collected runoff water will be conveyed to sanitation before discharging into the sea. A preliminary hydraulic study allowed to define different drainage basins, and for each basin an adequate collector is required. This paper deals with the design and execution of the first part of the system, concerning a collected water volume of about 1300 m<sup>3</sup>, for which the designers opted to realise the collectors by two adjacent buried pipelines of 2000 mm in internal diameter and 270 m long.

The design and execution of geotechnical works in coastal area must in general face regulatory requirements, environmental and aesthetic concerns, public attention.

As far as engineering problems are concerned, the designer must take into account the objective difficulties connected with the critical location (e.g., underwater excavation, tidal and storm waves, risk of uplift). For the specific case, additional constraints are represented by the closeness of the working area to an important railway (Figure 1), and consequent limited accessibility for materials and machinery. Moreover, local authorities required to minimize the working area, avoiding the occupancy of the beach for the overall length of the collectors through the entire duration of the works. To comply with this requirement, a staged execution was envisaged.

## 2 OUTLINE OF THE DESIGN

### 2.1 Pipe material

Corrugated HDPE pipes were selected (Table 1). HDPE offer in general significant advantages in terms of costs, corrosion resistance, ease of handling and jointing over more traditional materials such spheroidal cast iron. The selected HDPE pipes are manufactured in modules 6.0 m long (less than other materials, e.g., cast iron) which allowed solving the problem linked to area accessibility. In particular with the use of 6 m long modules it is possible to reach the beach area passing through a narrow railway underpass. For longer pipe modules, a more expensive marine transportation would be requested.

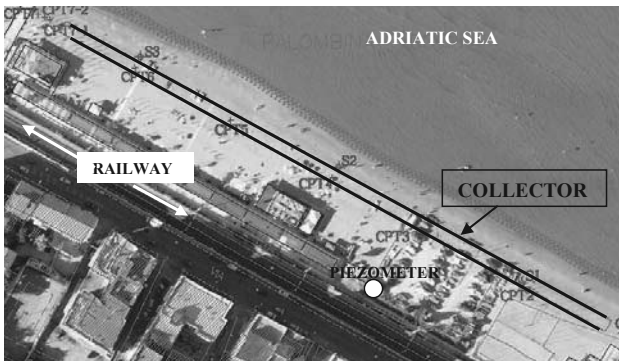


Figure 1. Plan view of the working area

Table 1. HDPE Pipe properties

Parameter	
Weight for unit length (kN/m)	2
External diameter (mm)	2240
Internal diameter (mm)	2000
Moment of Inertia (mm <sup>4</sup> /mm)	45899
Young modulus short term(MPa)	1185
Young modulus long term (MPa)	288

## 2.2 Underwater excavation

The soil stratigraphy is essentially composed by a sandy layer 3.5-4.0 m thick overlying a cohesive bed. An open standpipe piezometer installed close to the working area (Fig.1) indicated that the groundwater table is located 1.0-1.5 m below the ground level. Fig.2 shows a typical CPT profile with the characteristic values of geotechnical parameters obtained by laboratory and in situ tests.

Considering the large pipe diameter, the bedding layer and a minimum soil cover to counteract buoyancy (as detailed later), an excavation depth of at least 4.70 m was necessary. Moreover, a minimum inclination of 0.5% to the horizontal is required to ensure gravity flow. This results in an excavation depth ranging from 4.7 m to 6.0 m from ground surface.

Various techniques were considered for the excavation. Unsupported trench with inclined sidewalls was excluded due to excessive breadth to ensure stability and the need for continuous dewatering by well-points. Other equally suitable technologies, (e.g., soil freezing), were incompatible with the budget.

The selected solution consisted in a 6.1 m wide trench supported by strutted sheet piles, embedded in the impervious clay layer. The total length of the sheet piles varied between 8 m and 10 m as depending on excavation depth. Sheet piling allowed retaining the vertical trench walls, minimizing seepage into the trench and protecting the working area from tidal and storm waves (the top of sheet piles was +1 m above g.l., Fig. 2).

To comply with the requirement of minimizing occupation of the area, the installation of the collectors (270 m) was realized in four distinct segments (i.e. the excavation in a zone starts only after the work in the previous zone is completed). For the first segment, sheet piles were preliminarily installed to enclose a rectangular excavation zone, creating a continuous barrier to groundwater along the entire perimeter. For the subsequent segments, the presence of the installed pipes prevented to create rectangular hydraulic barrier by sheet piles only. Therefore, cast-in-place concrete waterproof screens were designed around the protruding edge of the pipes to block seepage due to extraction of sheet piles from the adjacent completed segment.

## 2.3 Pipe uplift

During the service phase the pipelines are expected to be only rarely filled by runoff water but permanently submerged by groundwater and then subjected the buoyancy. Consequently, the design shall be checked against failure by uplift.

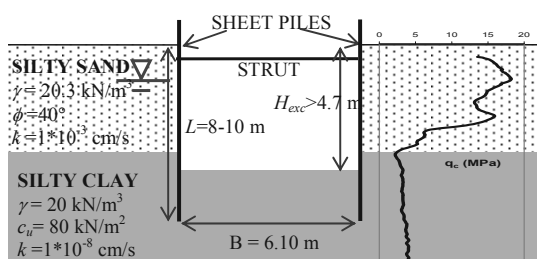


Figure 2. Simplified sketch of the excavation geometry with geotechnical soil characterization and a typical cone resistance profile.

According to Italian Building Code (NTC, 2008), as well as Eurocode 7 (2004), for any mass potentially subjected to the failure mechanism, the following inequality must be satisfied:

$$V_d \leq G_d + R_d \quad (1)$$

where  $V_d$  is the design destabilizing action acting upwards (obtained by a partial factor  $\eta_1 = 1.1$  in static conditions),  $G_d$  is the design stabilizing permanent action including the weight of the mass subjected to uplift (obtained by a partial factor  $\eta_2 = 0.9$  in static conditions) and  $R_d$  is the design soil resistance by friction along the vertical contours of the assumed block.

Considering the closeness of pipes to the sea (Fig. 1) it can not be excluded that in the future a portion of the soil above the pipe can be eroded. To confer protection against erosion a cast-in-place concrete slab (6.05 m wide and variable thickness) is realized above the pipes, as illustrated in Figure 3. This solution allows also to increase the average unit weight of the material above the pipes and enlarge the size of the block subjected to uplift. Finally, it represents a protection against accidental damage due to anthropic activities and the superficial sand layer enables to continue the recreational use of the beach.

In the application of Eq. (1) different approaches can be adopted to calculate the term  $V_d$  and in  $G_d$ . Eurocode 7 indicates a total stress analysis for uplift problems (EC7, 2004 §10.2). According to this approach,  $V_d$  is the upward resultant of pore water pressure acting on the lower boundary of the assumed block. Consistently,  $G_d$  includes the total weight of the soil block above the pipes. However, following this approach, the resultant of pore water pressure acting downwards is multiplied by a partial safety factor ( $\eta_1 = 1.1$ ) different to that applied to the vertical upward resultant ( $\eta_2 = 0.9$ ). This results in a violation of the “single source principle” enunciated by Eurocode 7 (EC7, §2.4.2). According to this principle, when destabilising and stabilising permanent actions come from a single source, “a single partial factor may be applied to the sum of these actions or to the sum of their effects”. Based on the above considerations, in the second approach the destabilizing action is assumed to be the buoyancy force on the two submerged pipes (i.e. the weight of the water displaced by the pipes  $W_w$ ). Consistently,  $G_d$  includes the submerged weight of the block above the pipes. Finally, a third approach can be used in which the destabilizing action is assumed to be the resultant buoyant force of the submerged pipes, i.e. the algebraic sum of weight of displaced water  $W_w$  and weight of pipes  $W_p$  (WSSC, 2008). This latter approach implies that the check against failure by uplift is automatically verified when  $W_w < W_p$ .

The three approaches described previously are applied assuming the simplified sliding surface shown in Fig. 3, which implies a failure mechanism involving pipes, slab and soil above and between the pipes as well (hatched zone in Fig.3). The results were obtained for the worst-case scenario of complete erosion of the superficial sand layer ( $h_3 = 0$  in Fig 3) and minimum cover thickness above the pipes ( $h_1 + h_2 = 0.5$  m,  $s = 0.6$  m). The unit weight of concrete and saturated soil were 23.5 kN/m<sup>3</sup> and 20.3 kN/m<sup>3</sup> respectively.

The  $R_d$  term was calculated as the sum of the friction forces along the vertical planes on each side of the assumed block (BC, B’C’, DE, D’E’)

$$R_d = \gamma' K_s \frac{\tan \delta_{BC}}{\eta_3} s^2 + \gamma' K_s \frac{\tan \phi_k}{\eta_3} \left[ (s + h_1 + h_2 + R_e)^2 - s^2 \right] \quad (2)$$

where  $\delta_{BC}$  is the interface friction angle between concrete and the sandy soil ( $\delta_{BC} = 30^\circ$ ),  $\phi$  is the shear resistance angle of the granular backfill,  $\eta_3 = 1.25$  is the partial safety factor applied to the shear strength parameters. The angle  $\phi_k$  after backfilling is assumed to be  $40^\circ - 42^\circ$ , but a reduced value of  $38^\circ$  is assumed in eq. (2) owing to potential loosening induced by sheet pile

extraction.  $K_s$  is the lateral earth pressure coefficient assumed conservatively equal to 0.5 by neglecting the effect of compaction.

Results of static analysis of uplift failure (Table 3) indicate that, as expected, the second and third approaches are less conservative in static conditions; however they appear to better represent the physical reality (i.e. the destabilizing force on a fully submerged pipe is independent of the depth below the water table).

In seismic conditions, Italian Building Code (NTC, 2008 §7.11.1) requires that Eq. (1) shall be checked using  $\eta_1 = \eta_2 = I$ , which result in uniqueness of the approach in seismic analysis (i.e. the difference between  $G_d$  and  $V_d$  is the same using a total stress analysis or an effective stress analysis).

Using a pseudo-static approach the vertical inertial force  $F_V$  acting on pipes, soil, concrete is assumed upwards and proportional to relevant weights by the seismic coefficient  $k_v$  ( $=0.046$ ) defined in Italian Building Code (NTC, §7.11.3.5.2).

It is well recognized that in the presence of earthquake, a build-up of pore water pressures can occur with respect to static conditions. A simplified procedure to account for this phenomenon is the introduction of the pore-pressure coefficient  $r_u = \Delta u / \sigma'_{v0}$  assumed constant with depth (e.g. Ebeling and Morrison, 1992; Kramer, 1996). Accordingly, the unit weight of water and submerged soil are given by:

$$\gamma_{we} = \gamma_w + r_u \gamma' = \gamma_w + r_u (\gamma_{sat} - \gamma_w) \quad (3)$$

$$\gamma'_e = \gamma' (1 - r_u) = (\gamma_{sat} - \gamma_w) (1 - r_u) \quad (4)$$

For  $r_u = 1$  soil liquefaction occurs which implies that (a) upward action acting on pipes is proportional to  $\gamma_{we}$  ( $= \gamma_{sat}$ ) instead of  $\gamma_w$ , and (b) the submerged weight of the soil block and soil resistance  $R_d$  vanish.

In seismic analysis the coefficient  $r_u$  shall be selected on the basis on seismic input (magnitude and maximum acceleration), as well as soil characteristics. In the analyzed case the presence of a coarse backfill (gravel) around the pipes (Fig.3) is expected to strongly limit the build-up of pore water pressure. Hence, the seismic analysis of uplift are performed assuming  $r_u = 0$  and  $r_u = 0.1$ . Results of seismic analysis shown in Table 3 indicate that also for  $r_u = 0.1$  the inequality (2) is satisfied.

## 2.4 Pipe deflection

Flexible conduits fail by excessive deflection rather than by rupture of the pipe wall. It is necessary, therefore, to estimate the deflection of this type of conduit and to establish limits of allowable deflection for the proposed installation.

Table 3. Uplift analysis

Action (kN/m)	Static conditions			Seismic conditions	
	appr.1	appr.2	appr.3	$r_u = 0.1$	$r_u = 1$
$V_d$	174.1	86.6	82.3	86.6	159.9
$W_{pipes}$	4.0	4.0	-	4.0	4.0
$W_{soil}$	87.6	44.4	44.4	40.0	0
$W_{slab}$	85.3	49.0	49.0	45.3	11.6
$F_v$	0	0	0	-8.1	-8.1
$G_d$	159.2	87.7	84.1	81.2	7.5
$R_d$	15.6	15.6	15.6	13.4	0
$R_d + G_d$	174.8	103.3	99.7	94.6	7.5

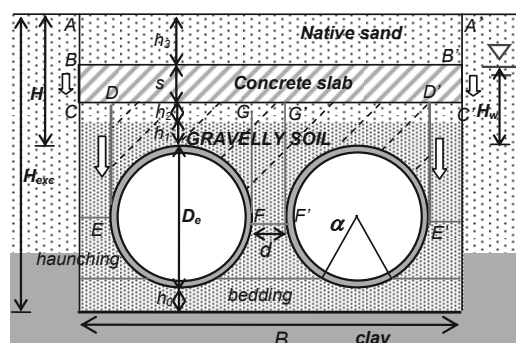


Figure 3. Details of pipe installation

For flexible conduits the vertical deflection  $\Delta y$  mainly depends on the actual load acting on the pipe and the stiffness of the backfill at the side of the pipes whereas the contribute of pipe stiffness is generally small (i.e. Rogers et al. 1995). In the specific case, the presence of two pipes as well as of the concrete slab makes the analysis more complex than the classical solutions available in the literature.

### 2.4.1 Load on pipes

According to Young and Trott (1984), the pair of pipes can be considered as equivalent to a single pipe of overall width  $D'$  where  $D' = 2D_e + d$ . The load on  $D'$  is calculated by taking the lesser of the two values obtained by the complete ditch condition ( $P_1$ ) and the positive projection condition ( $P_2$ ). This load is taken as being shared equally by the two pipes.

The load acting on a pipe (stiffer than side fill) in a trench with a partially submerged homogeneous backfill (see Fig.3) is given by Bulson (1985):

$$P_1 = \frac{B^2 \gamma}{2\lambda} \left[ 1 - \exp\left(-\lambda \frac{2H}{B}\right) \right] - \frac{B^2 \gamma_w}{2\lambda} \left[ 1 - \exp\left(-\lambda \frac{2H_w}{B}\right) \right] \quad (5)$$

where  $\lambda$  is a coefficient ranging from 0.11 to 0.19 depending on soil type,  $\gamma$  is the total unit weight of backfill. In the analysed case actual backfill unhomogeneity is accounted for by assuming a weighted average unit weight ( $\gamma_{av}$ ).

For a positive projection conduit the  $P_2$  value depends on the relative settlement between the soil prism above the pipe and the adjacent soil, which determines positive or negative arching. In the specific case, the presence of the slab prevents the occurrence of complete ditch or projection conditions. Moreover, considering that the ratio  $H/D'$  is very small, it is reasonable to neglect arching. Therefore, the value of  $P_2$  is assumed to be the weight of overlying prism of width  $D'$ .

Obviously, the maximum deflection is expected to occur at the section with the maximum cover (3.30 m) with the lowest groundwater level (-1.60 m below g.l.). With reference to Figure 3, for  $h_1 = 1$  m,  $s = 0.30$  m,  $h_2 = 1.7$  m,  $h_3 = 0.3$  m,  $H_w = 1.7$  m  $\gamma_{av} = 20.85$  kN/m<sup>3</sup>  $\lambda = 0.19$ ,  $P_1$  and  $P_2$  are calculated as 281 kN/m and 264 kN/m, respectively. Following the suggestion of Young and Trott (1985), the load acting on a single pipe ( $P$ ) is taken as 132 kN/m.

### 2.4.2 Backfill

A large part of ability of flexible pipes to support vertical load must be derived from the passive pressures induced as the sides move outward against the soil. Therefore, any attempt to analyse the behaviour of the flexible conduits must take into account the soil at the sides as an integral part of the structure, since such a large proportion of the total supporting strength is attributable to the side material.

Considering that compactive effort is restricted by the geometry of the trench and the difficult in compacting underneath the pipe in the haunch zone (Fig.3), as well as the

sensitivity of installed flexible pipe to compaction of material around it, a clean gravelly soil has been selected as structural backfill (i.e. the part of backfill that extends from the base of the bedding to a maximum of 30 cm above the pipe, as shown in Fig.3). This coarse-grained soil is preferred over native silty sand for easy of compaction, high earth pressure response and stability when saturated and confined. The same material – well compacted - has been used also as bedding soil (Fig.3).

#### 2.4.3 Calculation of pipe deflection

The pipe deflection is predicted by the method of Spangler (1941) or Iowa formula, although it is well recognized that this method contains some debatable assumptions.

$$\Delta y = \frac{D_L \cdot K \cdot P}{EJ/R^3 + 0.061E'} \quad (6)$$

where  $\Delta y$  = vertical deflection of pipe (m);  $P$  = vertical load on the pipe (MN/m);  $EJ$  = flexural pipe stiffness (MNm<sup>2</sup>/m);  $R$  = mean radius of the pipe (m);  $D_L$  = time-lag factor (-);  $K$  = bedding constant ( $K = 0.1$  for bedding angle  $\alpha = 60^\circ$ , see Fig.3).  $E'$  = horizontal modulus of soil reaction (MPa).

Considering the absence of vehicular loading and the prevalent recreational use of the site, live loads have been neglected. In design the sheet pile extraction is accounted for using the value of  $E'$  relevant to a dumped backfill (Table 4). In long term analysis a time lag factor of 1.5 and a reduced pipe stiffness are considered (see Table 1). With the above assumptions short term and long-term deflections are calculated as 10.1 cm and 20.5 cm, respectively.

Numerous authors have reported that pipes have been distorted by 10-20% and still continue to perform adequately. Therefore the theoretical deflections have been considered acceptable, but a monitoring activity was planned during installation.

### 3 COMPARISON OF ACTUAL AND THEORETICAL DEFLECTIONS

The large diameter of pipelines allowed accessibility and direct measurement of vertical diameter at prescribed positions during the various stages of installation (structural backfilling, slab, final backfilling and sheet piles extraction). The trend of measured vertical deflection versus time is not monotonic, showing an initial small deflection, followed by a slight decrease, a sharp increase and a final stabilisation. The observed trend can be ascribed to the variation of the acting loads (backfill height and groundwater level) and the different lateral support offered by the soil before and after the extraction of sheet piles. Therefore, for the comparison between actual and theoretical deflections, only the stabilised values are considered because they better represent the service conditions of the pipes, with the groundwater level certainly above the crown of the pipes.

With reference to a pipe stretch 45 m long the vertical deflections were measured in sections spaced 3 m apart. Final (stabilized) deflections are shown in Fig. 4. In spite of a quite uniform cover height the measured deflections vary considerably along the pipeline with a minimum of 7 cm to a maximum of 15 cm. This behaviour can be attributed mainly to inherent differences in compacting the soil beside the pipes and variable effect of sheet pile extraction. Moreover, variability in stiffness of native soil can influence the overall response owing to the closeness of pipes to trench sides.

Considering that measurements refer to a design cover height ranging from 2.15 m to 2.37 m, the vertical deflection is calculated by (6) for an average cover height  $H = 2.26$  m. The load on pipe ( $P = 104$  kN/m) is calculated following the suggestion of Young and Trott (1984) discussed previously. The groundwater level was assumed at 1.6 m below the ground

surface ( $H_w = 0.66$  m) based on measurement in the nearby piezometer. As shown in Fig. 4, the theoretical deflection calculated by Spangler method is lower than the actual average deflection. This can be ascribed to effect of sheet pile extraction which results in a loosening of backfill and a probable increase of the load on pipes to due to negative arching.

Table 4. Values of  $E'$  for a clean coarse-grained soil (Howard, 1977)

Degree of compaction	dumped	slight	moderate
$E'$ (MPa)	1.4	6.9	13.8

### 4 CONCLUSIONS

In the present paper some aspects of design and installation of two adjacent large diameter pipelines along the Adriatic Sea coastline in Italy are described.

Uplift analysis is detailed, showing three possible approaches which lead to different results in static conditions, whereas in seismic condition a unified approach is proposed that account for build-up of pore-water pressures.

As far as prediction of vertical deflection is concerned, in the analyzed case the backfill loosening due to sheet piles extraction has been modelled by assuming no compaction (dumped backfill). Despite this assumption, theoretical short term deflection represents a lower bound of measured deflections.

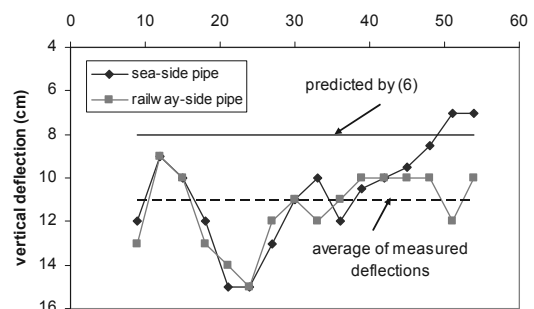


Figure 4. Comparison between measured and predicted short-term deflections

### 5 REFERENCES

- Bulson P.S. (1985) "Buried Structures. Static and Dynamic strength". Chapman & Hall ed., London.
- Ebeling, R.M., Morrison, E.E. (1992). "The seismic design of waterfront retaining structures". *Technical report ITL-92-11*. Washington, DC. US Army Corps of Engineers.
- EC7 (2004). Eurocode 7: Geotechnical design – Part 1: General Rules. European Committee for Standardization.
- Howard A.K. (1977) "Modulus of soil reaction values for buried flexible pipeline". *J. of Geotech. Eng. Div. ASCE* 103 (1), 33-43.
- Kramer, S.L. (1996). *Geotechnical Earthquake Engineering*. Pearson Education Inc. New Jersey.
- NTC (2008). Norme Tecniche per le Costruzioni. D.M. 14/01/2008. (in Italian).
- Rogers C.D., Fleming P.R., Loepky M.W. and Faragher E. (1995) "Structural performance of profile-wall drainage pipe – stiffness requirements contrasted with results of Laboratory and Field Test". *Transportation Research Record*, 1514, 83-92.
- Spangler M. G. (1941) The structural design of flexible pipe culverts". *Bul. 153*. Iowa Engineering Experiment Station, Ames, Iowa.
- Young O.C., Trott J.J. (1984). *Buried rigid pipes: structural design of pipelines*. Elsevier Applied Science Publishers. London-New York.
- WSSC (2008) Pipeline Design Manual. Part Three - Common Design Guidelines. Washington Suburban Sanitary Commission. [www.wsscwater.com/home/jsp/misc/siteMap.faces](http://www.wsscwater.com/home/jsp/misc/siteMap.faces)

# Geotechnical Exploration for Wind Energy Projects

## Compagnes géotechniques destinées aux parcs éoliens

Ben-Hassine J.

*Renewable Energy Systems Americas Inc., Broomfield, Colorado, USA*

Griffiths D.V.

*Colorado School of Mines, Golden, Colorado, USA*

**ABSTRACT:** Wind energy projects are often fast-paced and cover large terrains. Such conditions result in increased geotechnical risks and require specially adapted geotechnical exploration and data analysis techniques that are designed to manage risks at different stages of project development. Use of geophysical methods, in addition to the traditional subsurface exploration methods, is generally required to collect design critical data. During the early stages of project development, using quick qualitative geophysical methods can prove advantageous for finalization of wind farm layout and preliminary foundation design. However, as project plans progress, a more thorough geotechnical investigation is required. At all stages of a project, an understanding of the available geotechnical tools, along with their associated risks and cost implications is essential to minimize the likelihood of design changes that result in cost over runs. This paper presents geotechnical exploration methods used at different stages of project development and discusses key geotechnical parameters for wind turbine foundation design, available geotechnical tools, and the degree of confidence associated with these tools. The paper makes an attempt to present an exploration approach that is optimized for efficiency and risk.

**RÉSUMÉ :** Les projets d'énergie éolienne sont souvent réalisés dans un contexte d'exécution rapide et couvrent des terrains de grandes envergures. Ces conditions présentent des risques géotechniques accrus et nécessitent des compagnes d'exploration géotechnique et des techniques d'analyse de données spécialement bien adaptées pour gérer les risques à différentes étapes du projet. Le recours à des techniques géophysiques en plus des méthodes d'exploration traditionnelle est généralement requis pour obtenir les données critiques. Durant les premières étapes du projet, le recours à des méthodes géophysiques qualitatives et rapides peut s'avérer plus avantageux pour établir " la faisabilité du projet, " le plan d'implantation du projet et la conception préliminaire des fondations. Toutefois, dans les étapes plus avancées, une étude géotechnique plus poussée doit être réalisée. A toute étape, une connaissance adéquate des méthodes géotechniques disponibles, des risques et coûts qui leurs sont associés est essentielle pour minimiser l'éventualité de changements à la conception résultant en dépassement de coûts. Cet article est un essai de présenter une approche d'exploration optimisant l'efficacité et le risque.

**KEYWORDS:** geotechnical exploration, risk management, wind energy, efficiency.

## 1 INTRODUCTION

The period leading up to an operational wind energy plant starts several years before construction and can be divided into three overlapping phases: project development, engineering design, and project construction (Figure 1). During the development phase, various risk types and sources are evaluated and decisions are made to maintain, modify, or abandon the project. During the engineering design phase, decisions are made to refine the design while maintaining acceptable levels of risk. Any subsequent changes to the design typically result in additional cost. This paper focuses on geotechnical risks, particularly how such risks are being addressed currently and how this process may be improved. The objective is to assess risks and catch flaws as early as possible in the project development phase while there are still opportunities to make changes before significant development funds are spent. As in all large expenditure projects, early decisions have the greatest impact on financial performance. The motivation of this paper is to minimize the cost of civil infrastructure related to wind energy projects (turbine foundations, access roads and facilities such as the substation and the operation and maintenance building) through a rational redistribution of the geotechnical exploration effort. It has been estimated that civil infrastructure accounts for 4 to 10% of the total wind energy project cost. Given the thin profit margins of wind energy projects, a 2% saving can make the difference between whether a project goes ahead or is shelved.

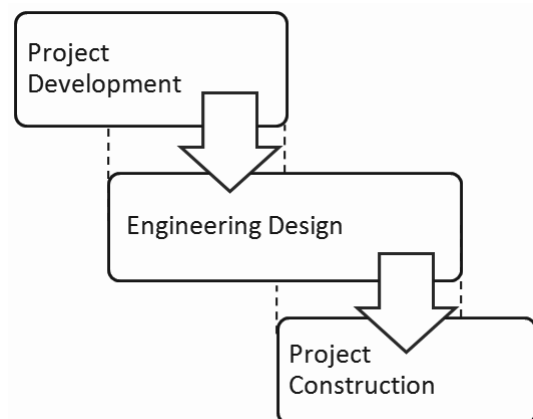


Figure 1. Overlapping phases leading up to a wind energy plant.

## 1 PROJECT REALISATION PHASES

All three project phases (development, design, and construction) involve some level of geotechnical risk assessment and management, with most of this effort currently focused at the engineering design phase. Current and proposed activities related to geotechnical risk assessment for each phase are described below.



### 1.1 Project Development Phase

During the project development phase, the developer is usually focused on wind resource assessment, land agreements, power purchase agreements, and identifying potential investors. The geotechnical aspect is secondary and is typically limited to site visits and reporting of surficial characteristics such as terrain topography, accessibility, proximity to bodies of water, etc. The initial environmental permitting effort presents an opportunity to identify geotechnical conditions that carry cost implications as most environmental permitting efforts include an evaluation of geo-environmental conditions. However, the development phase of a wind project rarely includes geotechnical field investigation activities. However, the development phase is the most opportune time to identify significant geotechnical risks. The findings of a preliminary geotechnical investigation conducted during the development phase rarely render the project non-pursuable. However, preliminary geotechnical investigations are critical to proper planning and allocation of risks to the appropriate stakeholders. The achievement of the benefits of this proposed shift can be formalized through techniques such as geostatistics, Bayesian updating, statistical inference and neural networks (Christian et al. 2006 and Lin and Hung 2011). An immediate benefit of a more holistic development phase exploration is to focus the detailed exploration effort on the critical issues or portions of the project area. In addition to desk studies, recommended development phase exploration techniques include:

- Geophysical surveys using seismic methods such as Multi-Analysis of Surface Waves (MASW) at all proposed turbine locations, possibly excluding locations where rock is at the surface. An MASW survey provides depth profiles of shear and compression wave velocities. The information is used to gain an insight into site stratigraphy and to estimate elastic moduli needed to verify foundation stiffness requirements. The MASW survey, conducted at the project development phase, helps to identify soft locations or locations with potential difficulties as an aid to micrositing of turbines. This exercise lessens the likelihood of needing very large foundations or performing costly ground modifications at soft sites. MASW surveys are also quick and relatively low cost, making them the ideal qualitative tool that is suited for the development phase.
- Preliminary geotechnical exploration borings using a limited number of traditional SPT, SCPT, CPT, or DMT borings spread over different portions of the project area. Exploration pits may also be used along planned access road alignments. Information obtained through site visits and review of available published information and online maps can be used to decide on the locations of the preliminary borings so that the captured range of variability is as wide as possible. Information from the preliminary exploration is used to assess the type and range of variability of site geomaterials, to identify potential foundation types and to plan the full investigation. For example, if a gravity base (shallow) foundation is deemed feasible, an effort should be made at the project development stage to assess the depth range of the stationary groundwater table in order to decide if buoyancy will be a design consideration. If soft materials are encountered requiring consideration of deep foundations, the depth of borings during the full investigation can be adjusted.
- The preliminary geotechnical exploration should also include electrical and thermal resistivity testing as this input is critical to sizing the electrical collection system which is associated with a significant share of project cost.

### 1.2 Engineering Design Phase

During this phase, a full geotechnical investigation must be carried out to finalize the design. The full geotechnical study is designed to complete the investigation and to fill the gaps remaining after the preliminary exploration. The full investigation should confirm and refine the assessment of the

risks identified during the preliminary investigation and should assess any additional risks that may be uncovered. At a minimum, standard practice includes at least one exploratory boring at every turbine location extending to a depth of interest not less than the largest base dimension of the structure (DNV/Risø 2002, GL 2010). For a typical shallow foundation used to support wind turbines, the explored depth is 1 to 1.5 times the foundation diameter. Common current practice is to perform geophysical testing during the full investigation phase at a limited subset (approximately 10%) of turbine locations. In the proposed redistribution of effort, a more extensive geophysical survey is recommended at the development phase. A non-exhaustive list of risks that should be assessed as early as possible during the development and preliminary design phases (but prior to the final design phase) is shown in Table 1. Geotechnical exploration activities help in identifying these risks but are not the sole resource.

Table 1. Non-exhaustive list of potential wind farm geotechnical and geo-environmental risks (in no particular order).

No.	Risk	Identification tools
1	High groundwater	Drilling, excavation pits, monitoring wells and permeability testing.
2	Flooding, storm surge, tsunami	Records, maps
3	Shallow bedrock / blasting	Visual, drilling, MASW
4	Slope stability & landslides	Visual, geologic study
5	Mine subsidence	Records, LiDAR, maps
6	Coal seams	Drilling, records
7	Karst subsidence, caves & voids	Records, drilling, LiDAR, maps, type of underlying rock, groundwater regime
8	Shrink/swell (expansive) soils	Laboratory testing
9	Frost heave	Records, climatic data
10	Permafrost	Records, climatic data
11	Freeze-thaw	Climatic records
12	Collapsible soils	Laboratory testing
13	Excessive consolidation / tilt	Laboratory testing
14	Aggressive environments: high sulfates, high salinity, corrosion	Laboratory testing
15	Alkali-Silica Reaction (ASR)	Testing, local information
16	Peat bogs and soft grounds	Visual, drilling, MASW
17	High seismicity / liquefaction	Exploration, design codes
18	Hurricanes	Records, design codes
19	Volcanic activity	Records, geologic study
20	Scarcity of gravel / road base	Visual, local information
21	Buried pipelines & infrastructure	Records
22	Forest logging roads	Drilling, excavation pits
23	Drifting sands	Visual, local information
24	High soil electrical resistivity	Field and lab testing
25	High soil thermal resistivity	Field and lab testing

### 1.3 Project Construction Phase

During the construction phase, geotechnical activity is typically limited to quality assurance testing which serves to confirm and ensure that the design assumptions remain valid. This is the phase where risks missed during the earlier phases may become apparent with the potential for project cost overruns.

Rarely would geotechnical input in this phase result in cost savings. However, *value engineering* where the balance of plant (BOP) contractor is provided an opportunity to redesign is becoming more popular. Value engineering often occurs shortly before construction or as the BOP contractor is mobilizing to construct the project. Ironically, the likely reason for value engineering is the tendency of the original designer to err on the conservative side because of compressed schedules and/or lack of substantive geotechnical basis of design at the end of the development phase, creating opportunities for the BOP contractor to cut costs at the last minute.

### 1.4 Summary of Current and Proposed Practice

Table 2 shows a summary of current and proposed practice. The essence of the proposed redistribution of the geotechnical exploration effort is to advance the geophysical survey and the preliminary investigation to the development phase (P1). Details of the geotechnical activities for the proposed redistribution are shown in Table 3.

Table 2. Common and proposed geotechnical effort.

Phase	Common			Proposed		
	P1	P2	P3	P1	P2	P3
Desk study	X			X		
Geophysical survey		X		X		
Preliminary investigation		X		X		
Full investigation		X			X	
Assurance & validation			X			X

Phases: P1 = Development, P2 = Design, P3 = Construction

Table 3. Wind farm realization phases and proposed geotechnical activities.

Phase	Proposed minimum geotechnical activities
Development	<ul style="list-style-type: none"> <li>• Desk study:                             <ul style="list-style-type: none"> <li>○ Often required for permitting but can be useful in planning preliminary investigation</li> </ul> </li> <li>• Geophysical Survey                             <ul style="list-style-type: none"> <li>○ All turbine locations except possibly sites where rock is at the surface</li> <li>○ Useful for micrositing</li> </ul> </li> <li>• Preliminary Investigation                             <ul style="list-style-type: none"> <li>○ Drilling at a subset of turbine locations distributed strategically to capture maximum variability</li> <li>○ Excavation pits along potential access road alignment</li> <li>○ Electrical and thermal resistivity testing</li> <li>○ Limited laboratory testing</li> </ul> </li> </ul>

Design	<ul style="list-style-type: none"> <li>• Full Investigation                             <ul style="list-style-type: none"> <li>○ Drilling at all turbine locations</li> <li>○ Extensive laboratory testing</li> <li>○ Fill all gaps to form design basis</li> </ul> </li> </ul>
Construction	<ul style="list-style-type: none"> <li>• Construction QA/QC                             <ul style="list-style-type: none"> <li>○ Confirm validity of design assumptions</li> <li>○ Ensure compliance with design requirements</li> </ul> </li> </ul>

## 2 SOURCES OF UNCERTAINTY

Wind energy projects differ from most traditional projects in that they cover large terrains. Wind turbines are typically placed 5 to 10 rotor diameters apart to optimize energy extraction (Denholm et al. 2009). Nowadays, typical rotor diameter for large wind turbine generators is around 120 meters, signifying turbine spacing of 0.5 to 1 kilometer just for energy extraction efficiency. Therefore, wind turbines are too far apart to consider any relationship between ground conditions from one turbine location to another. This is separate from regional or larger scale characteristics which may be applicable to the project area or portions of it, such as those related to different geologic settings or terrains. Turbine structures themselves are also unique due to the nature of loading they impart to foundations and supporting soils in terms of type, magnitude and variation. Thus, in addition to increased uncertainty due to essentially independent conditions at turbine locations, these projects also require parameters unique to these structures such as those needed to ensure adequate foundation stiffness.

Generally, there are three main sources of uncertainty in a geotechnical design property: i) inherent soil variability, ii) measurement error, and iii) transformation error (see Baecher and Christian 2003, Phoon and Kulhawy 1999). Often, a design parameter is not measured directly in-situ or in a laboratory test but is calculated based on other measured properties. Two of the above sources (inherent variability and measurement error) are associated with the measured property. The third source is associated with uncertainty in the selected transformation model, i.e., the empirical or theoretical relationship used to calculate the design property from the measured properties. Point estimates, as well as spatial variability of various shear strength, mechanical and index properties, are available in the literature (e.g., Lee et al. 1983). This information can be used to select the test methods that result in lowest variability depending on the soil type. In this section, uncertainty sources are discussed in more detail as they relate to wind energy projects.

### 2.1 Uncertainty Due to Inherent Soil Variability

Inherent soil variability is related to the natural geologic processes that produced the soil and should not include the influence of deterministic trends (e.g., trends due to depth), mixing of soils from different geologic units, or measurement errors. In the case of wind projects, inherent variability should be considered at each individual turbine location.

Another source of uncertainty is related to spatial variability extending vertically and horizontally to dimensions of influence. Uncertainty related to spatial variability is affected by the scale of fluctuation or correlation distance which is an important statistical parameter loosely defined as the distance within which the values of a given parameter are significantly correlated (Fenton and Griffiths 2008). Due to the often layered nature of soils, the correlation distance is typically shorter in the vertical direction than in the horizontal direction. Engineering design practice, including that within the wind energy industry, considers single (or point) variables to represent properties of an

entire soil mass. Thus, in designing a shallow foundation for a wind turbine, for example, traditional practice assumes an infinite horizontal correlation length where a single value is assumed for the soil in each layer. Furthermore, while focus is on variation in the vertical direction, geotechnical exploration rarely goes beyond one boring at the center of the foundation unless there is strong reason to believe conditions are non-uniform in the lateral directions, such as in cavitate terrain. Thus, knowledge of the vertical spatial variation is often limited to the line of the boring. On the other hand, knowledge in the horizontal direction is limited to the observation and verification of the exposed foundation bearing surface. This is very limited information but standard practice. This is also why at least two forms of exploration should be carried out at each turbine location: a traditional boring and a seismic survey (MASW).

## 2.2 Uncertainty Caused by Measurement Error

Measurement uncertainty is related to the equipment being used, in-situ or laboratory test procedures, and random data scatter. Naturally, measurement error is different for different test procedures. Reported measurement error data have been summarized for various laboratory and field tests by various investigators (e.g. Phoon and Kulhawy 1999). It is worthwhile to note that the highest variability attributed to in-situ test measurement error is that corresponding to the Standard Penetration Test (SPT). The error introduced by sample size is sometimes considered as a measurement error. Normally, the greater the number of data points or sample size, the smaller the error. However, beyond a rather low number of samples, it is more important to capture the full range of variability than to obtain more data points. There are numerous simplified rules to estimate standard deviation and variability based on the range and number of samples (Tippett 1925, Withiam et al. 1997, Whitman 2000 and Foye et al. 2006). For this reason, the effort to capture the full range of variability as early as possible is very important to the early assessment of risks.

## 2.3 Uncertainty Caused by Transformation Error

Transformation or model errors are introduced when test measurements are used to calculate the desired design properties using empirical or theoretical relationships. The sources of the error include the fitting errors in the case of empirical equations and the simplification/idealization errors in the case of theoretical relationships. The transformation errors for several design properties (undrained shear strength, effective stress friction angle, Young's modulus, horizontal stress coefficient, etc.) have been compiled (e.g. Phoon and Kulhawy 1999) for various laboratory and in-situ test methods. Noteworthy remarks from these compilations include:

- Higher variability (as expressed in higher coefficients of variation) result for sand properties obtained through correlations with SPT blow counts, especially if "universal" empirical relationships are used; i.e., relationship not calibrated to a specific geology. Hence, "local knowledge" seems to be important for interpretation of SPT results.
- Higher variability is typically obtained for sand properties than for clay properties.

## 3 CONCLUSIONS

Wind energy projects are almost always developed and built under compressed schedules where project realization phases overlap. They also cover large terrains that involve wide variability of geotechnical and geo-environmental conditions. For these reasons, geotechnical risks must be addressed as early as possible during the development phase to avoid overlooking fatal hazards that can shelve or financially devastate the project. This paper proposes to conduct extensive, low cost and quick

geophysical surveys during the development phase to help with turbine micro-siting and to gain an insight into the variability of the entire project area. The paper lists potential hazards that should be assessed and discusses sources of geotechnical uncertainty and how they relate to wind energy projects.

## 4 ACKNOWLEDGEMENTS

The author would like to acknowledge his employer, Renewable Energy Systems Americas Inc, for support in the preparation and presentation of this paper.

## 5 REFERENCES

- Christian, J.T. and Baecher, G.B. 2006. The meaning(s) of statistical inference in geotechnical practice, *Proceedings of the 2006 GeoCongress*, ASCE, Atlanta, GA, 26 Feb. – 1 Mar., 2006.
- Lin, C.P. and Hung, Y.C. 2011. Parameter estimation and uncertainty analysis incorporating engineering judgment and Bayesian inversion, *Proceedings of Georisk 2011*, ASCE, Atlanta, GA, Jun. 26-28, 2011.
- DNV/Risø 2002. *Guidelines for the Design of Wind Turbines*. 2<sup>nd</sup> edition. Copenhagen.
- GL (Germanischer Lloyd) 2010. *Guidelines for the Certification of Wind Turbines*. Edition 2010.
- Denholm P., Hand M., Jackson M. and Ong S. 2009. Land-Use Requirements of Modern Wind Power Plants in the United States. *National Renewable Energy Laboratory*. Technical Report 4NREL/TP-6A2-45834.
- Baecher G.B. and Christian J.T. 2003 *Reliability and Statistics in Geotechnical Engineering*, John Wiley & Sons, New York.
- Phoon K. K., Kulhawy H. 1999a. characterization of geotechnical variability. *Canadian Geotechnical Journal* 36, 615-624.
- Lee I.K., White W. and Ingles, O.G. 1983 *Geotechnical Engineering*, Pitman, Boston.
- Fenton G.A. and Griffiths D.V. 2008. *Risk Assessment in Geotechnical Engineering*. John Wiley & Sons, New York.
- Phoon K.K., Kulhawy H. 1999. Evaluation of Geotechnical Property Variability. *Canadian Geotechnical Journal* 36, 625-639.
- Tippett, L.H.C. 1925. On the extreme individuals and the range of samples taken from a normal population. *Biometrika* 17(3/4), 364-387.
- Withiam, J.L., et al. 1997. *Load and Resistance Factor Design (LRFD) for Highway Bridge Substructures*, Federal Highway Administration, Washington, D.C.
- Whitman, R.V. 2000. Organizing and evaluating uncertainty in geotechnical engineering, *J. Geotech. Geoenviron. Eng., ASCE* 126(7), 583-593.
- Foye, K.C. Salgado, R. and Scott, B. 2006. Assessment of variable uncertainty for reliability-based design of foundations, *J. Geotech. Geoenviron. Eng., ASCE* 132(9), 1197-1207.

# Essais cycliques axiaux sur des pieux forés dans des sables denses

## Cyclic axial load tests on bored piles in dense sands

Benzaria O.

Fugro GeoConsulting, Nanterre, France – IFSTTAR, Paris, France

Puech A.

Fugro GeoConsulting, Nanterre, France

Le Kouby A.

IFSTTAR, Paris, France

**RÉSUMÉ :** Dans le cadre du projet national SOLCYP, cinq pieux forés instrumentés ont été installés dans les sables denses des Flandres. Deux pieux de 8 mètres de fiche et 420 mm de diamètre ont été soumis à des séries d'essais de chargements statiques et cycliques axiaux en compression. Cette communication présente les résultats les plus significatifs des essais statiques conventionnels et des essais cycliques en compression.

**ABSTRACT:** As part of the national project SOLCYP, five bored piles were installed in dense Flanders sands. Two 8m long, 420mm diameter instrumented piles were submitted to extensive series of static and cyclic load tests in compression. This paper presents key results from conventional static tests and cyclic one-way tests in compression.

**MOTS-CLÉS :** SOLCYP, pieux forés, sables denses, chargements cycliques.

**KEYWORDS :** SOLCYP, bored piles, dense sands, cyclic loading.

## 1 INTRODUCTION

Le projet national SOLCYP (Puech et al., 2012) a pour objectif principal le développement d'une méthodologie pour le dimensionnement des pieux soumis à des chargements cycliques. Dans ce cadre, des essais sur pieux réels ont été conduits sur deux sites expérimentaux du Nord de la France: le site de Merville constitué d'argile des Flandres et le site de Loon-Plage constitué de sables denses. Sur le site de Loon-Plage ont été installés cinq pieux forés et deux pieux métalliques battus.

Les résultats obtenus sur les pieux battus et forés de Merville ont été partiellement publiés (Benzaria et al., 2012, 2013 ; Puech et Benzaria, 2013). Cette communication est centrée sur les résultats des essais statiques et cycliques en compression exécutés sur les pieux forés sur le site de Loon-Plage.

## 2 SABLE DES FLANDRES

Le site expérimental se situe sur la commune de Loon-Plage (59) près de Dunkerque dans le Nord de la France. Il se caractérise par une couverture de remblais récents (0-0,6m) et d'argile sableuse (0,6-2,2m) sous laquelle on rencontre la formation de sable des Flandres. La nappe phréatique au moment des essais se situait à environ 2m sous le niveau du terrain naturel.

Une campagne spécifique d'investigations a été réalisée au droit du plot d'essais comportant 4 essais au piézocône (CPTu), 2 essais au pressiomètre Ménard (PMT), 3 carottages continus et une série d'essais de laboratoire sur carottes (Figures 1 et 2). Le sable est un sable siliceux très fin ( $D_{50}$  voisin de 0,15mm) et mal gradué (coefficient d'uniformité  $CU=0,98$ ). La formation est latéralement homogène et se caractérise par des valeurs de résistance au cône  $q_n$  croissant de 5 à 40MPa vers 8 m de profondeur pour se stabiliser ensuite entre 30 et 50MPa jusque vers 11,5m. Entre 12 et 16,5m se trouve une couche d'argile molle qui fait brutalement chuter les caractéristiques mécaniques. L'interprétation des CPT par la méthode de Jamiolkowski et al. (2003) (Figure 2) conduit à un indice de densité  $I_D$  compris entre 0,7 et 0,9 (sable dense à très dense).

Une série d'essais triaxiaux monotones a donné un angle de frottement interne  $\phi_{cv}$  voisin de  $31^\circ$  en bon accord avec les valeurs trouvées par Kuwano sur le sable de Dunkerque (Kuwano, 1999 ; Jardine et Standing, 2000)

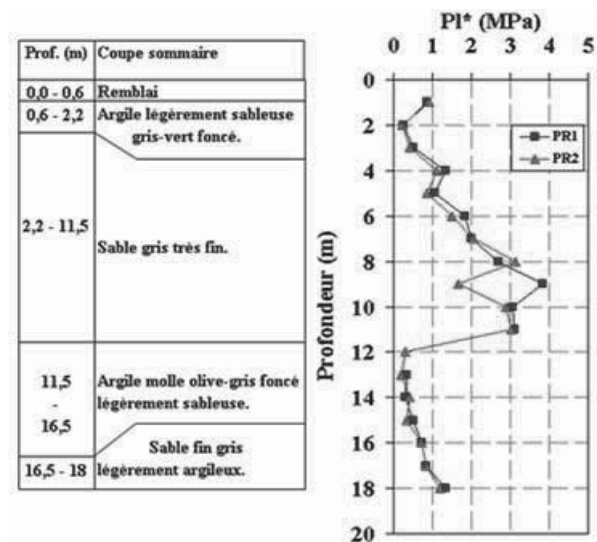


Figure 1. Profils stratigraphiques et pressiométriques à Loon-Plage

## 3 INSTALLATION ET CHARGEMENT DES PIEUX

Les deux pieux, F4 et F5, sont géométriquement identiques ( $D=420$ mm, fiche 8m). Ils ont été exécutés par l'entreprise Botte Fondations à l'aide d'une tarière à axe creux vissée dans le sol sans extraction notable de matériau (Figure 3a) puis extraite sans dévissage tandis que le béton est injecté simultanément par l'axe creux. Les pieux sont équipés d'un train d'extensomètres amovibles de type LCPC introduits dans

un tube de réservation positionné entre les armatures (Figure 3b).

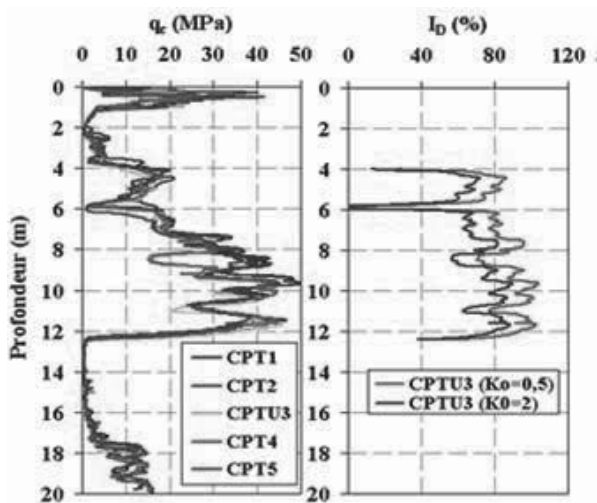


Figure 2. Profils pénétrométriques à Loon-Plage : résistance au cône  $q_c$  et indice de densité  $I_D$ .

Les pieux ont été testés trois mois environ après leur mise en place. Les programmes de chargement comportaient des essais statiques de référence à paliers d'une heure selon la norme NF P 94-150, des essais de chargement rapides (réduction des paliers à 3mm) et des essais de chargements cycliques axiaux de type répété. Une description plus précise des modes de chargement est indiquée dans Benzaria et al. (2012).

La caractérisation complète d'un chargement cyclique suppose la définition des paramètres suivants :

$Q_m$ : valeur moyenne de la charge sous chargement cyclique,

$Q_c$ : demi-amplitude du chargement cyclique,

$Q_{max}$ : charge maximale ( $Q_{max} = Q_m + Q_c$ )

$N$ : nombre de cycles (les essais ont été conduits à la rupture ou à grand nombre de cycles  $N > 1000$ )

$f$ : fréquence des cycles (en général 0,5Hz)

$Q_u$ : capacité statique ultime selon le mode considéré.

L'essai est dit répété si  $Q_c < Q_m$  et alterné si  $Q_c > Q_m$ .

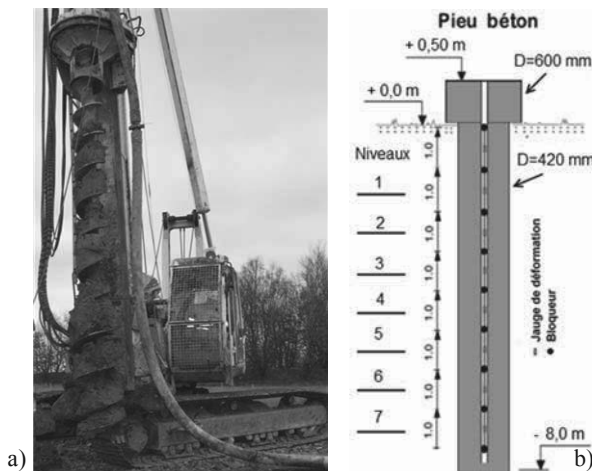


Figure 3. a) réalisation d'un pieu foré à l'aide d'une tarière à axe creux b) schéma d'instrumentation d'un pieu foré à l'aide d'extensomètres amovibles de type LCPC

Le dispositif de chargement des pieux est similaire à celui utilisé pour les pieux de Merville et décrit dans Benzaria et al. (2012).



Figure 4. Dispositif d'essais de chargement utilisé à Loon-Plage

#### 4 ESSAIS STATIQUES

La Figure 5 montre la courbe charge-déplacement en tête obtenue pour l'essai statique de référence sur le pieu F4, vierge de tout chargement, ainsi que la courbe de mobilisation de l'effort en pointe et la courbe de fluage (représentant la vitesse de déplacement du pieu lors de chaque palier de chargement).

On note :

- une rupture de type ductile,
- une entrée du pieu en grands déplacements pour un déplacement en tête de l'ordre de 5% du diamètre. La charge de rupture  $Q_{uc}$  conventionnelle pour 10% de déplacement de la tête (42mm) peut être estimée à environ 1 100kN,
- une charge de fluage  $Q_F$  vers 850kN soit  $Q_F/Q_{uc} \approx 0,77$ ,
- une mobilisation de l'effort de pointe retardée puis quasi linéaire jusqu'à 8% de déplacement relatif de la tête laissant préjuger d'une croissance de l'effort de pointe au-delà de la valeur conventionnelle à 0,1D.

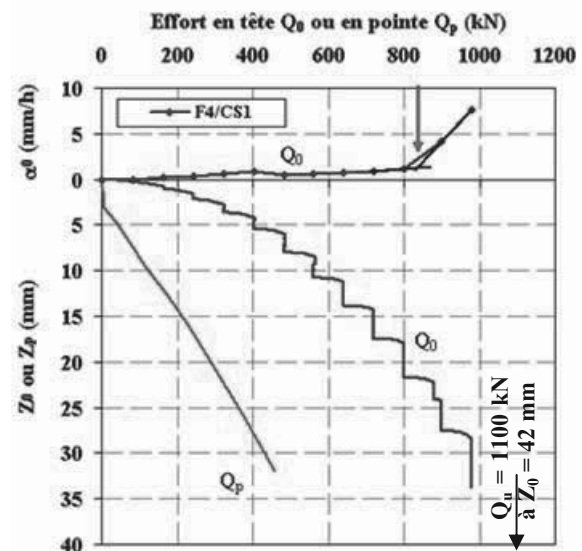


Figure 5. Essai statique de référence sur le pieu F4. Courbes de charge-déplacement en tête, de mobilisation de l'effort de pointe et de fluage.

Les mesures extensométriques ont permis de déterminer la distribution des charges le long du pieu (par éléments de 1m) ainsi que les courbes locales de mobilisation du frottement latéral selon la procédure décrite dans Benzaria et al. (2012). Les courbes locales de transfert de charges (dites aussi courbes t-z) sont données sur la Figure 6 pour les seuls niveaux correspondant au sable des Flandres. La mobilisation du frottement est très progressive : le déplacement local à la

rupture est de l'ordre de 3 à 5% du diamètre du pieu. Le caractère ductile de la rupture est confirmé. Les frottements sont modestes ( $f < 45\text{kPa}$ ).

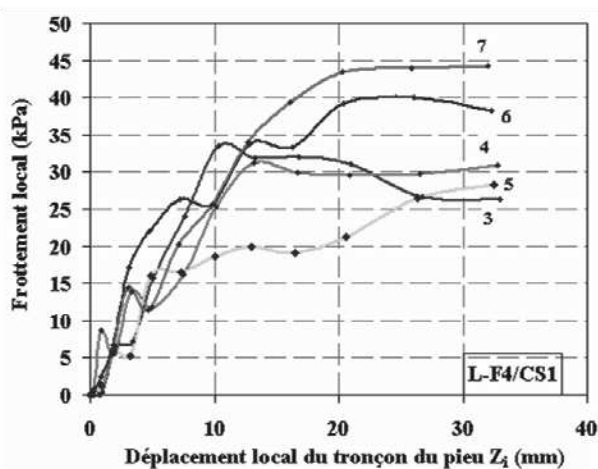


Figure 6. Courbes de mobilisation des frottements locaux obtenues lors de l'essai statique de référence sur le pieu F4.

## 5 ESSAIS CYCLIQUES

### 5.1 Essais cycliques sur pieu vierge

La Figure 7 représente la séquence d'essais de chargements réalisés sur le pieu F5 vierge de tout chargement. Leurs caractéristiques sont données dans le Tableau 1

Tableau 1 : Caractéristiques des chargements appliqués au pieu F5  
C : cyclique  $Q_{uc}$  : 1100 kN (pieu F1)

Test F5-	Type	Date	f (Hz)	$Q_m / Q_{uc}$	$Q_c / Q_{uc}$	N
Installation		25/11/11				
CC1	C	08/03/12	0,5	0,36	0,27	14
CC2	C	08/03/12	0,5	0,27	0,09	5000
CC3	C	08/03/12	0,5	0,36	0,18	280

L'essai CC1 a été réalisé avec un taux de chargement relativement modeste ( $Q_{max}/Q_{uc} = 0,63$ ). Il a été arrêté prématurément en raison de l'instabilité d'un pieu de réaction mais il est manifeste que la rupture était imminente après seulement 14 cycles. La rupture est définie pour un déplacement cyclique permanent de la tête du pieu de 3% du diamètre soit 12mm.

L'essai CC2, enchaîné avec un taux nettement plus faible ( $Q_{max}/Q_{uc} = 0,35$ ), a pu être conduit à 5000 cycles mais pour un déplacement additionnel permanent de plus de 16mm.

L'essai CC3 ( $Q_{max}/Q_{uc} = 0,54$ ) a provoqué un déplacement supplémentaire de 6mm pour seulement 280 cycles.

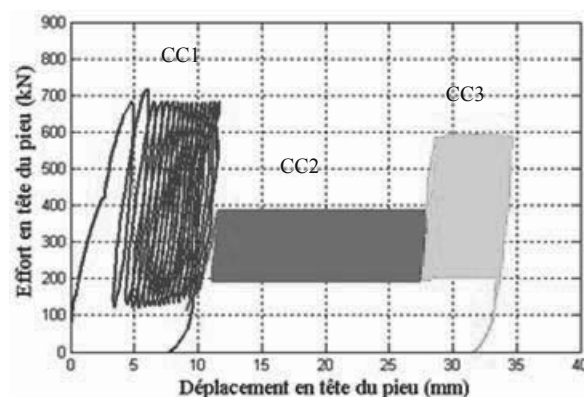


Figure 7. Courbes charges-déplacements en tête obtenues lors des essais de chargements réalisés sur le pieu F5.

Il est à noter que la vitesse d'évolution des déplacements en tête pour un nombre de cycles donné augmente avec le taux de chargement. Cependant pour chacun des essais cette vitesse décroît avec le nombre de cycles (Figure 8). Cette observation peut paraître contradictoire avec le constat de rupture.

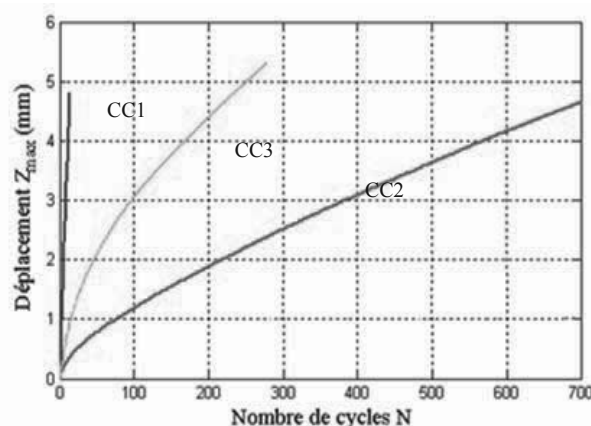


Figure 8. Courbes déplacement en tête en fonction du nombre de cycles obtenues lors des essais de chargements réalisés sur le pieu F5.

Une observation fine des phénomènes générés par les chargements cycliques sur un pieu dans un sable permet de mieux comprendre cet apparent paradoxe. Les cycles provoquent une succession de petits glissements relatifs sol-pieu dont le cumul détermine le déplacement global. La vitesse de déplacement est fonction de l'amplitude et du niveau de chargement mais ces paramètres conditionnent également l'évolution du frottement qui peut se détériorer (cycles sévères) ou s'améliorer (petits cycles). Sur un pieu sollicité en traction, la vitesse initiale se modifie pour conduire vers la rupture de plus en plus rapide ou vers la stabilisation (Tsuha et al., 2012). La rupture peut être indifféremment définie de manière conventionnelle (par exemple 0,1D) ou en terme de déplacement acceptable. Sur un pieu en compression, le déplacement s'accompagne d'une mobilisation progressive de l'effort de pointe de sorte que dans tous les cas le pieu tend vers la stabilisation. Il en résulte que le critère de rupture doit être défini en terme de déplacement acceptable et non de manière conventionnelle. Le critère peut être alors atteint aussi bien en phase de vitesse de déplacement croissante que décroissante. Dans le premier cas, le nombre de cycles amenant à la rupture est faible. Dans le deuxième cas il peut être très élevé. On peut alors introduire la notion de zones instables et métastables (e.g. Puech et al, 2013).

## 5.2 Effet de l'histoire des chargements

La Figure 9 montre l'histoire des chargements du pieu F4, détaillée dans le Tableau 2.

L'essai CC1 a été exécuté après que le pieu ait été amené à la rupture (essai S1). Malgré son faible taux de chargement ( $Q_{max}/Q_{uc} = 0,31$ ) le critère de rupture est atteint avant 2000 cycles. La capacité post cyclique (essai R1) ne semble toutefois pas affectée par cette série de cycles de faible amplitude.

Tableau 2 : Caractéristiques des chargements appliqués au pieu F4  
S : statique conventionnel R : statique rapide C : cyclique

Test F4-	Type	Date 2012	f (Hz)	$Q_m / Q_{uc}$	$Q_c / Q_{uc}$	N
Installation		25/11/11				
CS1	S	01/03/12				
CC1	C	02/03/12	0,5	0,18	0,13	1819
CR1	R	02/03/12				
CC2	C	02/03/12	0,5	0,36	0,18	200
CC3	C	02/03/12	0,5	0,36	0,27	200
CC4	C	02/03/12	0,5	0,47	0,25	100
CC5	C	02/03/12	0,5	0,45	0,36	200
CR2	R	02/03/12				
CR3	R	27/03/12				

Une série de quatre essais d'amplitudes et taux moyens croissants (CC2 à CC5) est ensuite enchaînée, provoquant des déplacements significatifs (environ 25mm pour seulement 700 cycles cumulés). L'essai statique rapide R2 indique que la rigidité du pieu a fortement augmenté. L'essai statique R3 confirme ce résultat et montre que la capacité post cyclique du pieu est maintenant de 1480 kN soit un accroissement de 27% par rapport à l'essai S1 sur le pieu vierge.

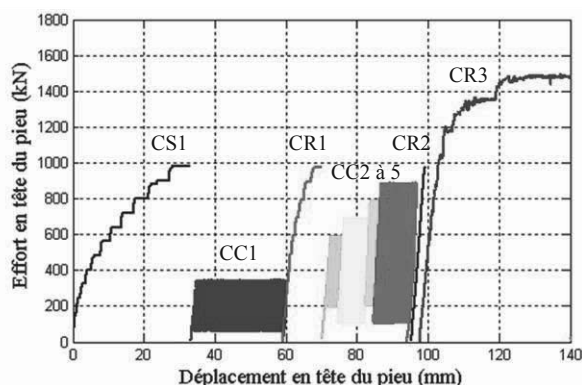


Figure 9. Courbes charge-déplacement en tête obtenues lors des essais de chargements réalisés sur le pieu F4.

## 6 CONCLUSIONS

On a présenté les résultats des essais statiques et cycliques en compression effectués sur les pieux forés à la tarière creuse installés sur le site de Loon-Plage constitué de sable dense des Flandres.

Sous chargement statique la rupture est ductile et la mobilisation du frottement nécessite des déplacements globaux et locaux importants entre 3 et 5% du diamètre du pieu.

Le comportement cyclique est très fortement dépendant de l'histoire des chargements. D'une manière générale, les pieux forés apparaissent très sensibles aux chargements répétés. Des déplacements importants peuvent être générés avant de pouvoir bénéficier d'une capacité en pointe suffisante pour stabiliser le pieu. La rupture doit donc être définie par un critère en déplacement et non de manière conventionnelle.

Une interprétation plus approfondie des résultats reste à proposer après traitement complet des autres données recueillies (essais alternés et essais en traction) et en liaison avec le comportement mécanique du sable des Flandres.

## 7 REMERCIEMENTS

Les résultats présentés dans cette communication ont été acquis dans le cadre du Projet National Français SOLCYP. SOLCYP est un projet de recherche sur le comportement des pieux soumis à des sollicitations cycliques, regroupant 12 entreprises et bureaux d'études du génie civil et 6 organismes universitaires et de recherche. Il est piloté par l'IREX et financé par les partenaires, l'Agence Nationale de la Recherche, le Ministère de l'Écologie, du Développement Durable et de l'Énergie et la Fédération Nationale des Travaux Publics. Les auteurs remercient les partenaires du projet d'avoir autorisé la publication de ces données.

## 8 REFERENCES

- AFNOR. 1999. NF P 94-150-2. Norme Française. Sols: Reconnaissance et Essais – Essai statique de pieu sous effort axial – Partie 1: en compression et Partie 2: en traction.
- Benzaria O., Puech A., and Le Kouby A. 2012. Cyclic axial load-tests on driven piles in overconsolidated clay, *Offshore Site Investigation and Geotechnics*, SUT, London
- Benzaria A., Puech A. et Le Kouby A. 2013. Essais cycliques axiaux sur des pieux forés dans l'argile des Flandres. *Proceedings 18th ICSMGE, Paris*
- Jamiolkowski, M.B., Lo Presti, D.C.F. & Manassero, M. 2003. Evaluation of Relative Density and Shear Strength of Sands from CPT and DMT. *Soil Behavior and Soft Ground Construction*, ASCE, GSP No. 119, 201-238.
- Jardine, R.J., Standing, J.R.: OTO 2000. 008 - Pile Load Testing Performed for HSE Cyclic Loading Study at Dunkirk, France; Volume 1".
- Kuwano R. 1999. "The stiffness and yielding anisotropy of sand." PhD thesis, University of London (Imperial College).
- Puech A., Canou J., Bernardini C., Pecker A., Jardine R., and Holeyman A. 2012. SOLCYP: a four year JIP on the behavior of piles under cyclic loading. *Offshore Site Investigation and Geotechnics*, SUT, London
- Puech A. et Benzaria O. 2013. Effet du mode de mise en place sur la réponse statique et cyclique de pieux dans l'argile surconsolidée des Flandres. *Proceedings 18th ICSMGE, Paris*
- Puech A., Benzaria O., Thorel L., Garnier J., Foray P. et Jardine R. 2013. Diagrammes de stabilité cyclique de pieux dans les sables. *Proceedings 18th ICSMGE, Paris*
- Tsuha C.H.C., Foray P.Y., Jardine R.J., Yang Z.X., Silva M., Rimoy S. 2012. Behaviour of displacement piles in sand under cyclic axial loading. *Soils and Foundations* 52(3), June 2012, 393–410,

# Essais cycliques axiaux sur des pieux forés dans l'argile surconsolidée des Flandres

Cyclic axial load tests on bored piles in overconsolidated Flanders clay

Benzaria O.

Fugro GeoConsulting, Nanterre, France - IFSTTAR, Paris, France

Puech A.

Fugro GeoConsulting, Nanterre, France

Le Kouby A.

IFSTTAR, Paris, France

**RÉSUMÉ :** Dans le cadre du projet national SOLCYP, quatre pieux forés instrumentés ont été installés dans l'argile fortement surconsolidée des Flandres. Ces pieux de 13 mètres de fiche et 420mm de diamètre ont été soumis à des séries d'essais de chargements statiques et cycliques axiaux. Cette communication présente les principaux résultats des essais statiques conventionnels et des essais cycliques en compression répétés et alternés.

**ABSTRACT:** As part of the national project SOLCYP, four bored piles were installed in the high OCR Flanders clay. The 13m long, 420mm diameter instrumented piles were submitted to extensive series of static and cyclic load tests. This paper presents key results from conventional static tests and cyclic one-way and two-way tests in compression.

**MOTS-CLES:** SOLCYP, pieux forés, argile surconsolidée, chargements cycliques.

**KEYWORDS :** SOLCYP, bored piles, overconsolidated clay, cyclic loading

## 1 INTRODUCTION

Le projet national SOLCYP (Puech et al., 2012) a pour objectif principal le développement d'une méthodologie pour le dimensionnement des pieux soumis à des chargements cycliques. Dans ce cadre, des essais sur pieux réels ont été conduits sur deux sites expérimentaux du Nord de la France: le site de Merville constitué d'argile des Flandres et le site de Loon-Plage constitué de sable dense. Sur le site de Merville ont été installés quatre pieux métalliques battus, quatre pieux forés et deux pieux vissés moulés.

Un précédent article (Benzaria et al., 2012) était consacré à la description du contexte expérimental et à la présentation des résultats obtenus sur les pieux battus. Cette communication présente les résultats des essais statiques et cycliques exécutés sur les pieux forés.

## 2 ARGILE DES FLANDRES

Le site expérimental se situe sur la commune de Merville (59) dans le Nord de la France. Il se caractérise par une couverture de limons sableux à argileux de 3,5m d'épaisseur dans lequel fluctue la nappe phréatique (-2m environ lors des essais) sous laquelle on rencontre la formation d'argile des Flandres, particulièrement homogène sur toute la zone, et d'une puissance de 40m environ.

L'argile des Flandres, géologiquement comparable à l'argile de Londres et à l'argile de Boom, s'est déposée il y a 50 millions d'années (Eocène) dans un golfe marin qui couvrait toute la zone Nord de la France, de la Belgique et du Sud Est de l'Angleterre. Elle a été recouverte par des formations tertiaires dont la sédimentation s'est poursuivie jusqu'au Pleistocène supérieur. Le niveau du sol se situait alors probablement à 200m au-dessus du niveau actuel. Les formations sus-jacentes se sont érodées. Le processus d'érosion a été suivi au Quaternaire par le dépôt d'alluvions du Flandrien. Le matériau a été soumis à des cycles de chargement/déchargement et à des processus périglaciaires qui associés à des phénomènes de cimentation

chimique et de vieillissement ont fortement conditionné son degré de surconsolidation (OCR) apparent (Josseaume, 1998)

L'argile des Flandres présente des caractéristiques voisines de celles des argiles de Londres et de Boom (Borel et Reiffsteck, 2005) :

- faible teneur en eau (de l'ordre de 30%)
- forte plasticité (IP voisin de 50)
- forte fissuration notamment au-delà de 5m de profondeur

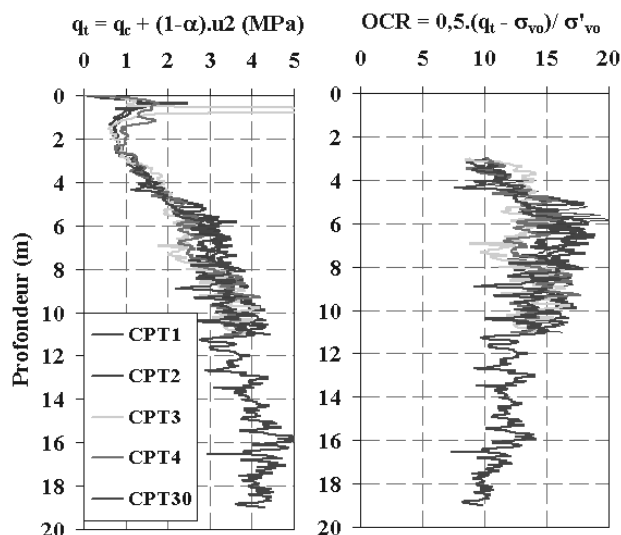


Figure 1. Profils de résistance au cône  $q_t$  et OCR sur le site de Merville

Une campagne spécifique d'investigations a été réalisée au droit du plot d'essais comportant des essais au piezocône (CPTU), des essais au pressiomètre Ménard (PMT), des carottages continus et une série d'essais de laboratoire sur carottes.



L'OCR a été estimé à partir du CPT et de la relation de Mayne (1991) :  $OCR = k \cdot (q_t - \sigma_{v0}) / \sigma'_{v0}$  avec  $k=0,5$ . Le facteur  $k$  est fonction du type de matériau. La valeur de 0,5 a été retenue car elle donne des valeurs d'OCR compatibles avec l'épaisseur de surcharge supposée et le gradient de  $q_n = q_t - \sigma_{v0}$  dans l'argile profonde (au-delà de 8m). A noter que pour l'argile de Londres, Powell et al., 1989 suggèrent des valeurs de  $k$  supérieures à 1.

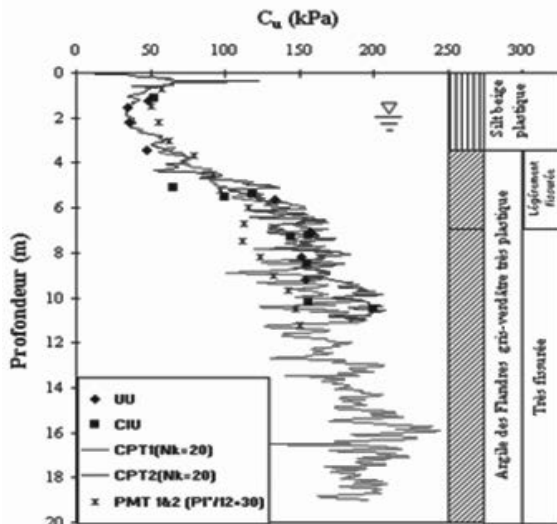


Figure 2. Conditions de sol au niveau du plot d'essais de Merville

Les essais triaxiaux de type UU (non consolidé, non drainé) ou CIU (consolidé isotropiquement, non drainé) montrent des ruptures prématurées de type fragile, caractéristiques de ce type d'argile plastique fissurée et fortement surconsolidée. La rupture se caractérise par la formation de plans de cisaillement contenant des particules réorientées, comme noté par Bond et Jardine (1991). Les valeurs de la résistance au cisaillement non drainée  $C_u$  sont corrélées à la résistance au cône par un facteur  $N_{kt}$  élevé,  $[N_{kt} = (q_t - \sigma_{v0}) / C_u = 20]$ , compatible avec la nature du matériau. Les valeurs de pression limite pressiométrique nette sont assez bien reliées à  $C_u$  par la relation d'Amar et Jezequel (1998) :  $C_u = p_l^* / 12 + 30$ , avec  $C_u$  en kPa et  $p_l^*$  en MPa

### 3 INSTALLATION ET CHARGEMENT DES PIEUX

Les quatre pieux sont géométriquement identiques ( $D=420$ mm, fiche 13m). Ils ont été exécutés à l'aide d'une tarière à axe creux vissée dans le sol sans extraction notable de matériau (Figure 3a) puis extraite sans dévissage tandis que le béton est injecté simultanément par l'axe creux. La partie basse est munie d'un manchon télescopique. Les pieux sont équipés d'un train d'extensomètres amovibles de type LCPC introduits dans un tube de réservation positionné entre les armatures (Figure 3b).

Les pieux ont été testés deux mois après leur mise en place. Les programmes de chargement comportaient des essais statiques de référence à paliers d'une heure selon la norme NF P 94-150 (1999), des essais de chargement rapides (réduction des paliers à 3mm) et des essais de chargement cycliques axiaux de type répété ou alterné. Une description plus précise des dispositifs (Figure 4) et modes de chargement est indiquée dans (Benzaria et al., 2012).

La caractérisation complète d'un chargement cyclique suppose la définition des paramètres suivants :

$Q_m$ : valeur moyenne de la charge sous chargement cyclique,

$Q_c$ : demi-amplitude du chargement cyclique,

$Q_{max}$ : charge maximale ( $Q_{max} = Q_m + Q_c$ )

$N$  : nombre de cycles (les essais ont été conduits à la rupture ou à grand nombre de cycles  $N > 1000$ )

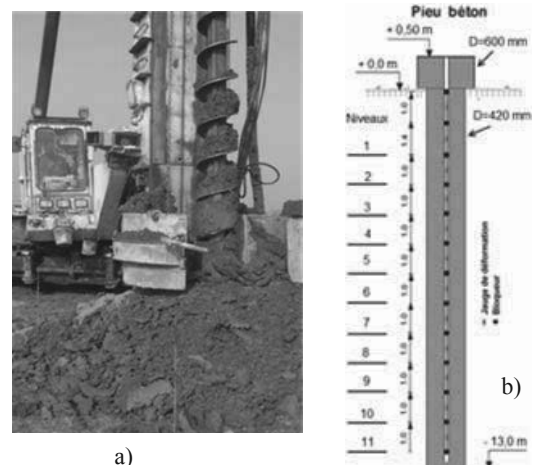


Figure 3. Pieux forés a) tarière à axe creux. b) schéma d'instrumentation à l'aide d'extensomètres amovibles de type LCPC.



Figure 4 : Dispositif de chargement des pieux en compression.

$f$  : fréquence des cycles (en général 0,5Hz)

$Q_u$  : capacité statique ultime selon le mode considéré.

L'essai est dit répété si  $Q_c < Q_m$  et alterné si  $Q_c > Q_m$ .

### 4 ESSAIS STATIQUES

La Figure 5 montre la courbe charge-déplacement en tête obtenue pour l'essai statique de référence sur le pieu F1, vierge de tout chargement, ainsi que la courbe de fluage représentant la vitesse de déplacement du pieu lors de chaque palier de chargement.

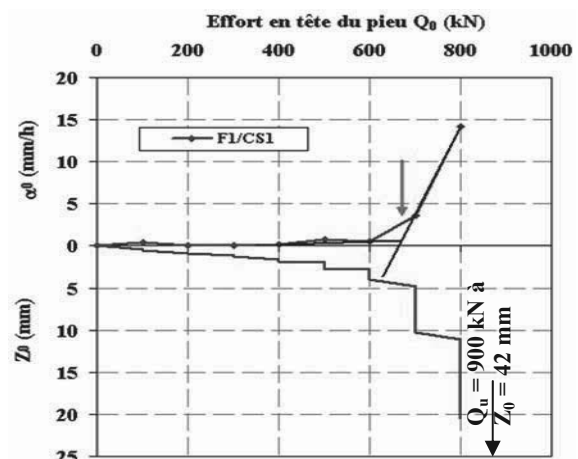


Figure 5. Courbe charge-déplacement en tête et courbe de fluage obtenues pour l'essai statique de référence sur le pieu F1.

On note :

- une rupture de type ductile (contrairement aux observations de Benzaria et al., 2012 sur le pieu battu) ;
- une entrée du pieu en grands déplacements pour un déplacement en tête de l'ordre de 3% du diamètre. La charge de rupture  $Q_{uc}$  conventionnelle pour 10% de déplacement de la tête peut être extrapolée avec confiance à 900kN ;
- une charge de fluage  $Q_F$  nette vers 670kN soit  $Q_F/Q_{uc} \approx 0,75$ .

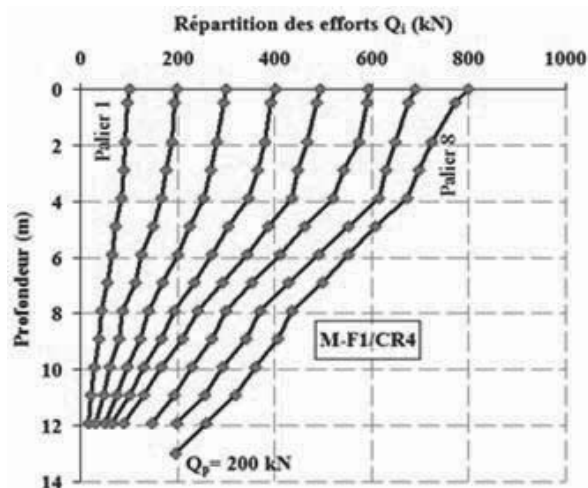


Figure 6. Distributions des charges obtenues pour l'essai statique de référence sur le pieu F1.

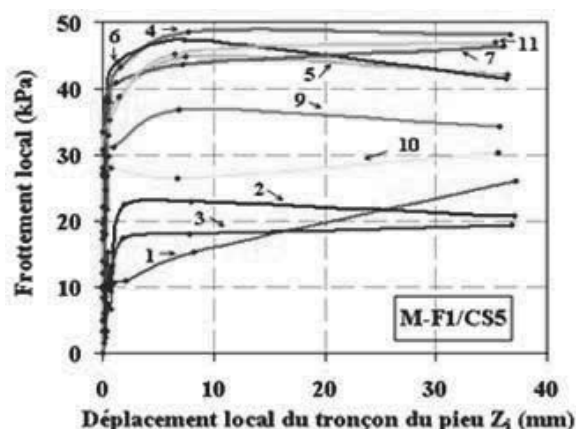


Figure 7. Courbes locales de mobilisation du frottement latéral obtenues pour l'essai statique de référence sur le pieu F1.

Les mesures extensométriques ont permis de déterminer la distribution des charges le long du pieu (Figure 6) ainsi que les courbes locales de mobilisation du frottement latéral selon la procédure décrite dans Benzaria et al. (2012). Les courbes locales de transfert de charges (dites aussi courbes t-z) sont données sur la Figure 7. La mobilisation du frottement est très rapide (entre 1 et 2%) du diamètre du pieu. Le caractère ductile de la rupture est confirmé. Les frottements sont modestes ( $f < 50$ kPa) et très inférieurs à ceux observés sur les pieux métalliques battus installés sur ce même site.

## 5 ESSAIS CYCLIQUES

### 5.1 Essais cycliques répétés

La Figure 8 représente la séquence d'essais de chargements réalisés sur le pieu F2. Leurs caractéristiques sont données dans la Tableau 1.

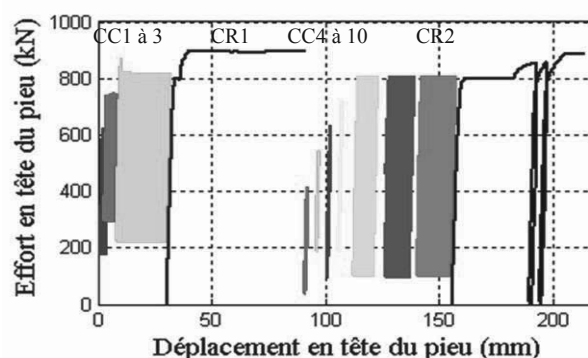


Figure 8. Courbes charge-déplacement en tête obtenues lors d'essais de chargements statiques et cycliques sur le pieu F2.

On observe que :

- le taux de chargement maximal contrôle la réponse du pieu ;
- lorsque ce taux demeure inférieur à un seuil critique, les déplacements restent non significatifs y compris pour de grands nombres de cycles ( $N > 1000$ ). Les boucles d'hystérésis sont fermées (Figure 9) ;
- lorsque le seuil critique est franchi, le pieu cumule rapidement des déplacements le conduisant vers la rupture. Les essais CC3, CC8, CC9 et CC10 ont dépassé 12mm (3%D) de déplacement cyclique permanent considéré comme critère de rupture (Figure 8) ;
- le seuil critique est très voisin de  $Q_{max}/Q_{uc} = 0,9$
- les chargements cycliques, y compris lorsqu'ils conduisent à la rupture, n'ont pas significativement affecté la capacité statique du pieu.

Tableau 1 : Caractéristiques des chargements appliqués au pieu F2  
C : cyclique R : statique rapide  $Q_{uc} = 900$ kN (pieu F1)

Test F2-	Type	Date	f (Hz)	$Q_m/Q_{uc}$	$Q_c/Q_{uc}$	N
Installation		16/03/2011				
CC1	C	16/05/2011	0,5	0,50	0,25	3408
CC2	C	17/05/2011	0,5	0,58	0,25	4834
CC3	C	17/05/2011	0,5	0,58	0,33	2021
CR1	R	17/05/2011				
CC4	C	17/05/2011	0,5	0,25	0,20	1013
CC5	C	17/05/2011	0,5	0,40	0,20	1000
CC6	C	17/05/2011	0,5	0,40	0,30	1088
CC7	C	17/05/2011	0,5	0,50	0,30	602
CC8	C	17/05/2011	0,5	0,50	0,40	81
CC9	C	17/05/2011	0,1	0,50	0,40	24
CC10	C	17/05/2011	0,5	0,50	0,40	85
CR2	R	17/05/2011				

La comparaison des essais CC9 et CC10 effectués à mêmes taux de chargement met en outre en évidence un effet de fréquence dans le domaine proche de la rupture : la rupture est accélérée lorsque la fréquence diminue.

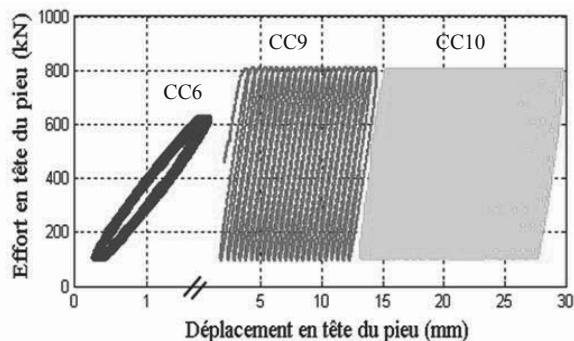


Figure 9. Courbes charge-déplacement en tête obtenues d'essais de chargements réalisés sur le pieu F2.

### 5.2 Essais cycliques alternés

Neuf essais cycliques alternés ont été effectués sur le pieu F3. Les caractéristiques de ces essais sont telles que  $Q_m/Q_{uc} < 0,2$  et  $0,2 < Q_c/Q_{uc} < 0,5$ . Pour des raisons de montage hydraulique (deux vérins en opposition de phase), il n'a pas été possible d'appliquer une charge maximale  $Q_{max}$  supérieure à  $0,7 Q_{uc}$ .

Tous les essais effectués dans ces conditions sont du type stable avec des boucles d'hystérésis fermées comme illustré sur la Figure 10.

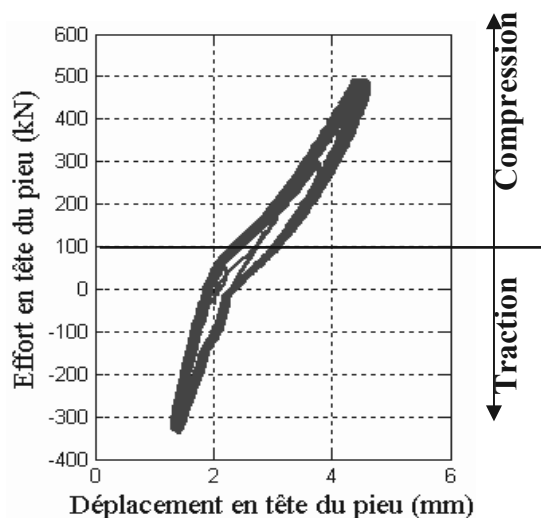


Figure 10, Courbe charge-déplacement en tête obtenue lors de l'essai de chargement CC9 réalisé sur le pieu F3.

### 5.3 Notion de stabilité cyclique

L'ensemble des résultats obtenus en compression pure et en compression alternée (mais également en traction pure et en traction alternée) suggèrent que pour le type de matériau et de pieu considéré il existe deux zones de fonctionnement bien différenciées :

- une zone dans laquelle les chargements cycliques même en grand nombre ( $N > 1000$ ) ont peu d'effet sur le comportement du pieu : accumulation non significative des déplacements permanents, rigidité cyclique constante ;
- une zone dans laquelle le pieu évolue très rapidement vers la rupture.

La zone de stabilité cyclique est étendue mais pourrait être affectée par le caractère répété ou alterné des chargements.

L'analyse complète des résultats et la définition de critères de rupture précis devrait permettre de proposer ultérieurement des diagrammes de stabilité cyclique au sens de Poulos (1988) ou Karlsrud et al. (1986)

## 6 CONCLUSIONS

On a présenté des résultats d'essais statiques et cycliques en compression pure et alternée effectués sur des pieux forés à la tarière creuse installés sur le site de Merville constitué d'argile surconsolidée des Flandres.

Sous chargement statique la rupture n'est pas fragile contrairement aux observations faites sur les pieux battus. Les frottements mobilisés sont nettement inférieurs (Benzaria et al., 2012).

Il semble exister sous chargement cyclique une zone étendue à l'intérieur de laquelle la stabilité est assurée pour un grand nombre de cycles. Le seuil critique, au moins pour les essais répétés, semble voisin de  $Q_{max}/Q_{uc} = 0,9$ . Les chargements cycliques, y compris lorsqu'ils conduisent à la rupture, n'affectent pas significativement la capacité statique du pieu.

Un article à cette même conférence (Puech et Benzaria, 2013) analyse le comportement statique des deux types de pieux battus et forés en liaison avec la nature et le comportement mécanique de l'argile des Flandres.

## 7 REMERCIEMENTS

Les résultats présentés dans cette communication ont été acquis dans le cadre du Projet National Français SOLCYP. SOLCYP est un projet de recherche sur le comportement des pieux soumis à des sollicitations cycliques, regroupant 12 entreprises et bureaux d'études du génie civil et 6 organismes universitaires et de recherche. Il est piloté par l'IREX et financé par les partenaires, l'Agence Nationale de la Recherche, le Ministère de l'Écologie, du Développement Durable et de l'Énergie et la Fédération Nationale des Travaux Publics. Les auteurs remercient les partenaires du projet d'avoir autorisé la publication de ces données.

## 8 REFERENCES

- AFNOR. 1999. NF P 94-150-2. Norme Française. Sols: Reconnaissance et Essais – Essai statique de pieu sous effort axial – Partie 1: en compression et Partie 2: en traction.
- Benzaria O., Puech A and Le Kouby A. 2012. Cyclic axial load-tests on driven and bored piles in overconsolidated clay, *Offshore Site Investigation and Geotechnics*, SUT, London.
- Bond A.J. and Jardine R.J. 1991. Effects of installing displacement piles in a high OCR clay. *Géotechnique*, 41(3) 341-363.
- Borel S. and Reiffsteck P. 2006. Caractérisation de la déformabilité des sols au moyen d'essais en place. *Géotechnique et Risques Naturels*, LCPC, GT81.
- Josseume H. 1998. Propriétés mécaniques de l'argile des Flandres à Dunkerque et Calais. *Revue Française de Géotechnique*, N°84.
- Karlsrud, K., Nadim F. and T. Haugen (1986). Piles in clay under cyclic loading: Field tests and computational modeling. Proc., 3rd int. Conf. on Nun. Meth. In offshore Piling, 165-190, Nantes, France, May 1986.
- Mayne P.W. 1986. CPT indexing of in situ OCR in clays. Proceedings ASCE Spec. Conf. "In situ 86", Blacksburg, Virginia.
- Powell J.J.M., Quaterman R.S.T. and Lunne T. 1989. Interpretation and use of piezocone test in UK. *Proc. Geotechnology Conference: penetration testing in UK, Birmingham*, Thomas Telford, London.
- Puech A., Canou J., Bernardini C., Pecker A., Jardine R., and Holeyman A. 2012. SOLCYP: a four year JIP on the behavior of piles under cyclic loading. *Offshore Site Investigation and Geotechnics*, SUT, London.
- Puech A. et Benzaria O. 2013. Effet du mode de mise en place sur la réponse statique de pieux dans l'argile surconsolidée des Flandres. *Proceedings 18th ICSMGE, Paris*.

# Fondations superficielles glissantes pour l'offshore profond – Méthodologie de dimensionnement

## Deep Offshore Sliding Footings – Design Methodology

Bretelle S.  
GHD, Perth, Australie

Wallerand R.  
Subsea7, Paris, France

**RÉSUMÉ :** Les caractéristiques géotechniques des sols rencontrés en offshore profond conduisent de manière récurrente à des fondations de très grandes dimensions. Ceci induit des difficultés d'installation qui stimulent la recherche de solutions audacieuses pour les fondations dont le dimensionnement intègre des sollicitations horizontales transitoires. Les efforts horizontaux résultent de conditions transitoires pour les pipelines (arrêt et redémarrage de l'exploitation induisant des changements de température dans les pipelines). Ceux-ci induisent un glissement de la fondation. Ces efforts horizontaux étant variables dans le temps, le sol est soumis à des sollicitations cycliques. Cet article détaille les différentes étapes proposées pour le dimensionnement des fondations glissantes, destinées au support des structures liées aux pipelines, en prenant en compte les effets de la dégradation cyclique sur la capacité portante, et l'évaluation des tassements.

**ABSTRACT:** Due to the geotechnical characteristics of offshore deep-water soils, footing size can become very large. This may induce installation challenges, which in turn stimulates smart design solutions allowing for horizontal displacement of the footing. Horizontal loads results from flow lines expansion during start-up and shut-down of the production, as large temperature changes will induce dilatation. If horizontal loads are above the horizontal capacity of the footing, the foundation will slide. Horizontal loads varying with time, soil cyclic loadings are induced. This paper presents the different steps of the design for the proposed concept, allowing the footing to slide. This design includes cyclic soil degradation effects on bearing capacity and settlements.

**MOTS-CLÉS:** Offshore, fondation, glissante, pipeline, cyclique, dégradation, tassement.

**KEYWORDS:** Offshore, footing, sliding, pipeline, cyclic, degradation, settlement.

### 1 INTRODUCTION

Les caractéristiques géotechniques des argiles molles rencontrées en offshore profond conduisent de manière récurrente à des fondations de très grandes dimensions. Ceci induit des difficultés d'installation qui stimulent la recherche de solutions audacieuses pour les fondations dont le dimensionnement intègre des sollicitations horizontales transitoires.

Les efforts horizontaux résultent des sollicitations horizontales transitoires. C'est le cas notamment des structures intermédiaires ou des structures fin de ligne, qui permettent la connexion entre les pipelines et les différents éléments de l'architecture du champ (puits, risers, manifolds). Les efforts appliqués à ces structures sont transmis au sol par l'intermédiaire de fondations superficielles faites de tôles d'acier. Les efforts verticaux proviennent du poids propre de la structure, de la section de conduite qu'elle supporte, des différents connecteurs et vannes associées. Les efforts horizontaux sont eux provoqués par la dilatation ou la contraction de la conduite (arrêt et redémarrage de l'exploitation induisant des changements de température et de pression dans les pipelines). Ceux-ci induisent un glissement de la fondation (le coefficient de sécurité au glissement est inférieur à 1). Ces efforts horizontaux étant variables dans le temps, le sol est soumis à des sollicitations cycliques.

L'évaluation des effets résultants de la dégradation cyclique des propriétés des sols (ici la résistance au cisaillement) permettra d'assurer que la fondation reste stable sous efforts verticaux et moments.

L'évaluation des tassements est nécessaire. Le cisaillement cyclique (environ 2000 cycles sur la durée de vie de l'ouvrage)

est source de tassements spécifiques, qui sont dus aux déplacements répétés de la fondation.

Cet article détaille les différentes étapes proposées pour le dimensionnement des fondations glissantes, destinées au support des structures liées aux pipelines, et posées sur des argiles molles.

### 2 COMPARAISON PIPELINES-FONDATIONS

Le tableau 1 rappelle les concepts d'interaction sol-pipeline et sol-fondation. Il permet d'illustrer les différences entre les comportements admis pour les pipelines et ceux généralement requis pour les fondations superficielles (White - Cathie 2010).

Les grandes familles de différences qui sont décrites ci-dessous affectent directement la perception du dimensionnement, qui intègre naturellement les déplacements pour les pipelines, et qui par contre recommande des coefficients de sécurité importants sur la capacité portante (incluant les efforts horizontaux) des fondations pour se prémunir des déplacements.

Pour ce qui concerne les pipelines, il peut s'avérer économiquement impossible d'empêcher le pipeline de se déplacer, en l'enfouissant par exemple, sur des dizaines de kilomètres, et à des profondeurs d'eau de plus de 1000m. Par contre, des modèles d'interaction sol-pipeline intégrant le déplacement permettent d'optimiser les dimensions des pipelines (les épaisseurs des tubes en particulier).

Pour ce qui concerne les fondations, même liées aux pipelines, il reste d'usage de les dimensionner sans autoriser leur déplacement.

Ce choix conduit à des fondations de très grandes dimensions, en particulier sur les argiles marines en grande

profondeur. Il pose aussi des problèmes structuraux au niveau de la connexion du pipeline et de la fondation.

Tableau 1. Comparaison des comportements admis pour les pipelines et pour les fondations.

Paramètre	Pipeline	Fondation
Géométrie de l'interface sol-fondation	Incertaine, la pénétration dépend des méthodes d'installation, de la forme du fond marin	Connue, contrôlée
Critère de dimensionnement en service	Déplacement autorisé, lois de comportement spécifiques	Fixe, déplacements minimales de la fondation
Sol	Perturbé pendant l'installation et les cycles	Similaire à l'état initial
Charges	La réponse du pipeline est affectée par l'interaction avec le sol	Les charges ne sont pas affectées par le sol de fondation
Méthodes de dimensionnement	Non disponible (ou encore contestées), les hypothèses de sol enveloppes (hautes ou basses) doivent être considérées	Disponibles, les hypothèses de sol basses sont conservatives pour la stabilité

### 3 DIMENSIONNEMENT SOUS CHARGES PERMANENTES

La première étape traite du dimensionnement sous charges permanentes qui requiert un coefficient de sécurité supérieur à 1 avec la prise en compte concomitante des efforts verticaux et moments (Cathie 2008).

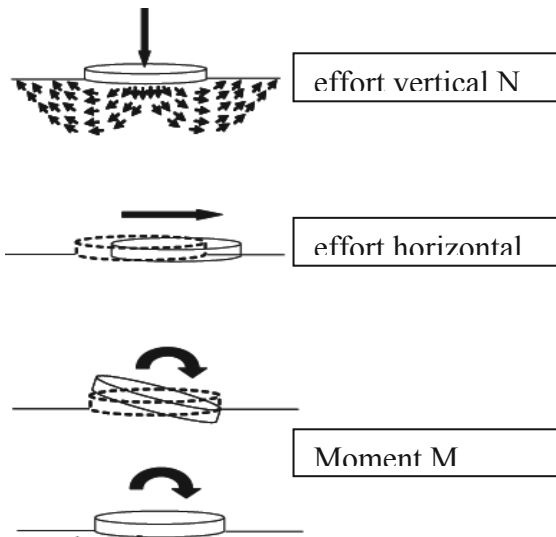


Figure 1 : Mécanismes de rupture

La stabilité au sens usuel du terme doit être assurée. Les charges permanentes sont essentiellement liées au poids de la structure.

La problématique du dimensionnement des fondations superficielles connaît de nombreux développements récents et il existe une normalisation (ISO 19901-4 2011) afférente. Celle-ci permet la prise en compte de manière concomitante des efforts verticaux N, horizontaux T ainsi que des moments M.

On rappelle en préambule les principes du dimensionnement intégrant ces efforts M, N, T, sous la forme d'enveloppes 3D (Randolph 2005).

Les mécanismes de rupture sont rappelés sur la figure 1.

L'approche traditionnelle de dimensionnement de fondations superficielles consiste à simplifier le chargement (M, N, T) en un chargement (N, T) appliqué sur une surface réduite. Cette approche conduit à des surdimensionnements quand ils sont comparés à des calculs par éléments finis tridimensionnels.

L'approche proposée dans l'API-ISO permet l'utilisation d'enveloppes de rupture 3D, utilisant les valeurs de :

- ✓ Nult charge verticale de rupture sous chargement vertical seul (M=0 et T=0) ;
- ✓ Tult charge horizontale de rupture sous chargement horizontal seul (M=0 et N=0) ;
- ✓ Mult moment de renversement ultime en condition de renversement seul (T=0 et V=0).

La surface limite dans l'espace (N/N<sub>ult</sub>, M/M<sub>ult</sub>, T/T<sub>ult</sub>) est alors définie par des calculs spécifiques 3D ou disponibles dans certaines références pour des formes de fondation types. Un exemple est proposé sur la figure 2.

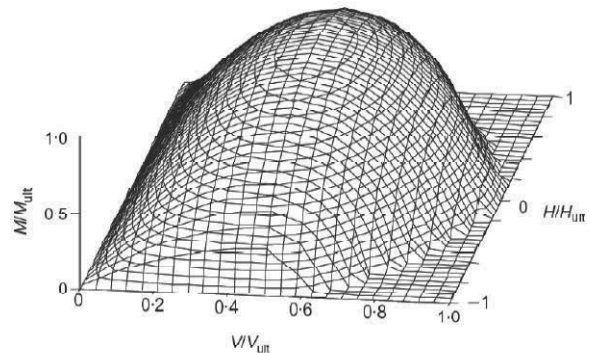


Figure 2 : Enveloppe de rupture (Gourvenec 2007)

### 4 DIMENSIONNEMENT SOUS CHARGES HORIZONTALES

Les efforts horizontaux résultent de conditions transitoires pour les pipelines (arrêt et redémarrage de l'exploitation induisant des changements de température dans les pipelines).

Un coefficient de sécurité suffisant doit être obtenu pour que la fondation soit stable (pas de rupture sous charges verticales et moments), tout en autorisant son déplacement horizontal.

L'évaluation présentée dans cet article se limite au cas des argiles molles trouvées dans les grands fonds.

#### 4.1 Vérifications de stabilité

L'évaluation des effets résultants de la dégradation cyclique des propriétés des sols (ici la résistance au cisaillement) se décompose en trois étapes :

- ✓ Une évaluation des contraintes de cisaillement est effectuée sous la fondation le long de surfaces de rupture ;
- ✓ l'effet des cycles est intégré en utilisant des résultats usuels d'essais de laboratoire caractérisant la dégradation cyclique ;
- ✓ une vérification de la stabilité de la fondation est effectuée le long des surfaces de rupture précédentes, avec les caractéristiques réduites déterminées précédemment.

#### 4.1.1 Évaluation des contraintes de cisaillement

Il est suggéré d'utiliser un programme de calcul aux éléments finis pour obtenir les contraintes de cisaillement sous la fondation.

Il n'est pas requis d'utiliser un modèle autorisant des grands déplacements (2 à 3 mètres sont observés pour les pipelines), ni

de représenter fidèlement les cycles (les structures concernées subissent 1000 à 5000 cycles), ce qui nécessiterait des temps de calculs importants et des outils complexes.

La modélisation proposée ici applique un effort vertical représentatif du poids de la structure, et un effort horizontal « à la rupture », c'est-à-dire saturant les contraintes de cisaillement à l'interface sol fondation.

La figure 3 présente un modèle type de calcul.

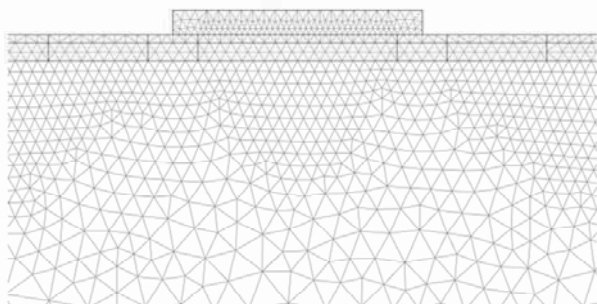


Figure 3 : Modèle de calcul

Ce calcul permet de déterminer l'étendue des zones sollicitées sous la fondation et les contraintes de cisaillement appliquées au sol de fondation.

A partir de ce calcul, on détermine le taux de cisaillement moyen ( $\tau$ ) à différentes profondeurs sous la fondation (en général de 0 à B, où B est la largeur de la fondation).

#### 4.1.2 Dégradation cyclique

La dégradation cyclique est déterminée à partir d'essais de laboratoire cycliques, qui permettent d'obtenir des enveloppes de dégradation en fonction du nombre de cycles.

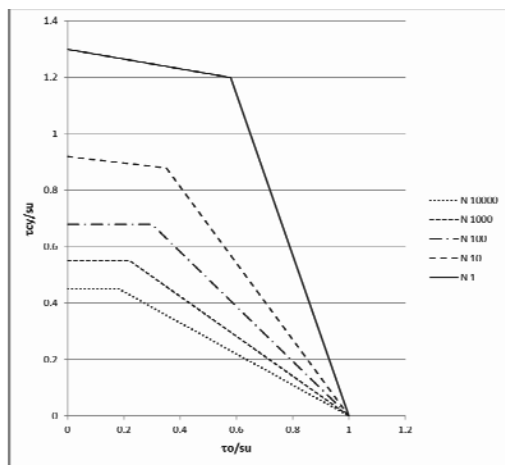


Figure 4 : Dégradation cyclique (Argile de Drammen, OCR=1, d'après Andersen 2004)

On lit sur l'axe horizontal le rapport  $\tau_0/s_u$  et sur l'axe vertical le ratio  $\tau_{cy}/s_u$ . Le nombre de cycles correspond aux différentes courbes sur l'abaque.

Les notations suivantes sont utilisées :

$\tau_0$  = cisaillement moyen sans cycles

$\tau_{cy}$  = cisaillement dégradé, après N cycles

$s_u$  = résistance au cisaillement moyen

#### 4.1.3 Vérification de la stabilité après dégradation cyclique

Le calcul présenté en 4.1.1 peut être repris en modifiant les valeurs de  $S_u$  pour tenir compte de la dégradation cyclique.

Le coefficient de sécurité obtenu est alors représentatif de la stabilité de la fondation après un grand nombre de cycles.

#### 4.2 Calculs des tassements

L'évaluation des tassements (élastique, consolidation, fluage) est nécessaire. Le cisaillement cyclique (environ 2000 cycles sur la durée de vie de l'ouvrage) est source de tassements additionnels, qui sont dus aux déplacements répétés de la fondation. Les tassements additionnels suivants sont considérés :

- ✓ Tassements induits par le chargement cyclique de l'argile profonde (données de triaxiaux DSS publiées),
- ✓ Dégradation de la couche en contact avec la fondation du fait du glissement répété,
- ✓ Erosion par les bords de la fondation (cause potentielle de réduction de la surface effective sous la fondation).

##### 4.2.1 Tassements élastiques, consolidation, fluage

Les tassements élastiques de consolidation et de fluage peuvent être déterminés à partir des méthodes usuelles analytiques, ou à partir du modèle éléments finis décrit plus haut (avec des modèles de type Soft Soil pour Plaxis).

##### 4.2.2 Réduction cyclique du module d'élasticité

Pour les tassements cycliques, il faudra tenir compte :

- ✓ Des déformations dues aux cycles ;
- ✓ Du développement de surpressions interstitielles dû aux cycles.

Dans les deux cas, on utilisera les résultats des calculs décrits plus haut, et les enveloppes obtenues par essais de laboratoire.

Les notations suivantes sont utilisées (différentes de celles du chapitre précédent) :

$\tau_{av}$  = cisaillement moyen sans efforts horizontaux

$\tau_{cy}$  = cisaillement moyen avec efforts horizontaux

$s_u$  = résistance au cisaillement moyen

La figure 5 présente des résultats types pour la détermination des déformations ( $\gamma$ ) dues au cisaillement cyclique.

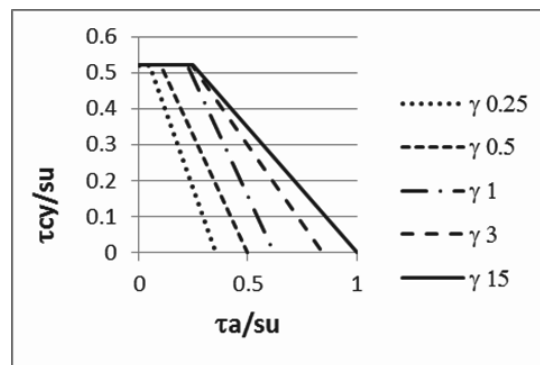


Figure 5 : Déformations moyennes de cisaillement cyclique (Argile de Drammen, OCR=1, d'après Andersen 2004)

La déformation ci-dessus est multipliée par l'épaisseur de la couche concernée pour obtenir le tassement supplémentaire.

La figure 6 présente l'augmentation de pression interstitielle en fonction du nombre de cycles.

La déformation supplémentaire est alors obtenue par :

$$\varepsilon = (\Delta u / \sigma'_v) * \sigma'_v / M$$

Avec

$\Delta u / \sigma'_v$  : lu sur la figure 6

$\sigma'_v$  : contrainte effective verticale

M : module de déformation

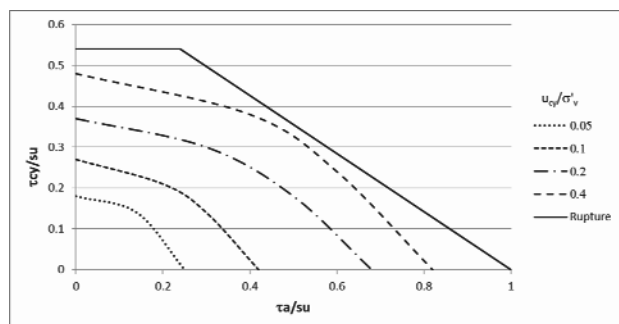


Figure 6 : augmentation de pression interstitielle due au cisaillement de 1000 cycles (Argile de Drammen, OCR=1, d'après Andersen 2004)

#### 4.2.3 Dégradation de la couche de contact

La couche de contact (les 20 à 30 cm d'argile directement en contact avec la face inférieure de la fondation) subit de façon répétée un état de rupture, sous l'effet du glissement.

Cet état de rupture reste en général confiné au niveau de cette couche d'interface, car une couche de meilleures caractéristiques (crouete) est souvent présente entre 0 et 2 m de profondeur. La crouete agit comme une barrière de protection qui limite le transfert des ruptures par cisaillement vers les couches inférieures.

Il est très difficile, voire impossible de modéliser le processus cyclique dans cette couche supérieure, du fait des redistributions de contraintes entre les bords et le centre de la fondation et bien entendu du fait des sollicitations cycliques.

Il est donc proposé de retenir une approche simplifiée qui considère les différents aspects de la dégradation.

Le modèle éléments finis décrit plus haut permet de considérer le moment maximum qui sollicite la fondation, associé au poids de la fondation et à l'effort horizontal qui sature le frottement au niveau de l'interface. Ce calcul peut être mené avec les caractéristiques « intactes » dans la couche de contact, puis avec les caractéristiques remaniées dans cette même couche.

La comparaison directe des résultats permet d'estimer un tassement et une rotation supplémentaire à considérer dans le dimensionnement.

#### 4.2.4 Erosion par les bords

La concentration de contraintes est un phénomène bien connu qui dans ce cas particulier peut créer des tassements supplémentaires par érosion près des angles.

Les skis ont depuis longtemps apporté une réponse appropriée en relevant les bords pour limiter l'effet de l'angle.

Les fondations glissantes devront comporter un dispositif similaire pour éviter de racler progressivement toute une bande de sol.

L'estimation par le calcul de ce phénomène reste à développer, par contre, les conséquences peuvent être évaluées en retirant arbitrairement les éléments de sol de l'interface sous une partie de la fondation. On pourra enlever les éléments sur une bande correspondant au mouvement calculé des pipelines qui se connectent sur la fondation, puisque ce mode de comportement est disponible dans les modèles de pipelines.

Une autre méthode, moins pénalisante consiste à reprendre les résultats du calcul avec les moments présentés au paragraphe précédent 4.2.3, pour déterminer les contraintes dans la couche d'interface.

En comparant ces contraintes à la contrainte ultime ( $N_c * S_u$ )

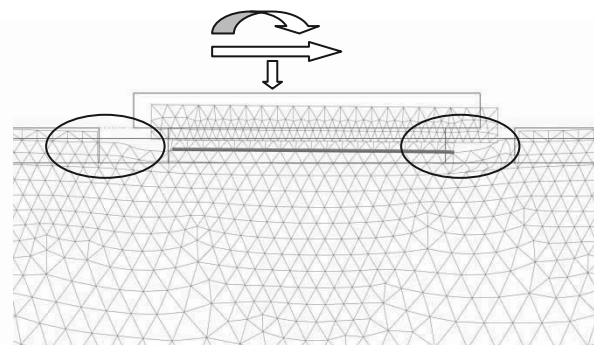


Figure 7 : Exemple de calcul avec dégradation sous les bords (cercleées).

## 5 CONCLUSION

Cet article a détaillé les différentes étapes proposées pour le dimensionnement des fondations glissantes, destinées au support des structures liées aux pipelines, dans des conditions géotechniques d'argiles grands fonds.

Le tassement à long terme et sous un nombre de cycle représentatif de la vie de la structure sera obtenu par cumul des différentes valeurs de tassements calculées suivant la démarche proposée. La stabilité de la structure sera ainsi assurée, et son fonctionnement ne sera pas altéré par les tassements ou rotations dus au chargement cyclique.

## 6 REMERCIEMENTS

Je tiens à remercier mon mari et mon fils pour leur patience pendant la période de rédaction de cet article, ainsi que pour leur relecture.

Bien entendu, cet article n'aurait pas vu le jour sans mon expérience en France, à Terrasol pour la maîtrise des fondamentaux géotechniques, chez Saipem, pour l'ouverture Internationale et offshore, chez Cathie Associates pour la pratique continue des projets liés aux grands fonds et enfin en Australie, où GHD me donne l'opportunité de travailler sur des grands projets d'infrastructure.

## 7 REFERENCES

- Andersen 2004 Cyclic clay data for foundation design of structures subjected to wave loading International Conf. on "Cyclic behaviour of Soils and Liquefaction Phenomena" Keynote lecture CBS04, Bochum, Germany.
- Cathie et Al. 2005 Pipeline Geotechnics State of the Art.
- Cathie et Al 2008 Design of sliding foundations for subsea structures.
- Gourvenec, S. (2007), Shape Effects on Capacity of Rectangular Footings Under Combined Load, *Géotechnique*, 57(8), pp. 637–646.
- ISO 19901-4 2003 modified 2011 API RP2GEO Geotechnical and foundation design considerations.
- Randolph et Al - 2005 Challenges of offshore geotechnical engineering.
- White, D., Cathie, D.N. 2011, 'Geotechnics for subsea pipelines', *Frontiers in Offshore Geotechnics II*, The Netherlands, CD, pp. 87-123.

# Proposition d'une loi t-z cyclique au moyen d'expérimentations en centrifugeuse

## Proposal of cyclic t-z law by means of centrifuge experiments

Burlon S., Thorel L.

Université Paris-Est, IFSTTAR, Département GERS, Paris, France

Mroueh H.

LGCgE, Lille, France

**RÉSUMÉ :** Cet article propose une extension de la loi t-z de Frank et Zhao (1982) pour le calcul des déplacements d'un pieu soumis à des charges axiales cycliques. Les potentialités de cette nouvelle loi sont présentées et une comparaison est effectuée entre des résultats expérimentaux issus d'essais en centrifugeuse pour quatre pieux soumis à des charges cycliques et des résultats numériques obtenus au moyen de cette nouvelle loi. Pour chaque cas, le déplacement de la tête de pieu en fonction du nombre de cycles de chargement est analysé. Une discussion est menée pour mieux cerner l'influence de chaque paramètre de la nouvelle loi t-z cyclique développée et envisager les développements futurs à mettre en œuvre.

**ABSTRACT:** This paper includes an extension of the t-z law proposed by Frank and Zhao (1982) for the displacements calculation of a pile subjected to cyclic axial loads. The potential of this new law are presented and a comparison is made between experimental results obtained from centrifuge tests for four piles subjected to cyclic loads and numerical results obtained by this new law. For each case, the displacement of the pile head according to the number of load cycles is analyzed. A discussion is conducted to better understand the influence of each parameter of the new cyclic t-z law and to consider future developments to implement.

**MOTS-CLÉS :** Fondation profonde, charge axiale, sollicitations cycliques, centrifugeuse, loi t-z.

**KEYWORDS:** Deep foundations, axial load, cyclic load, centrifuge tests t-z curve.

## 1 INTRODUCTION

Le comportement des pieux soumis à des charges axiales monotones peut être appréhendé par des calculs mettant en œuvre des lois d'interaction locale de type t-z. Ces lois permettent, pour chaque section d'un pieu, d'associer le déplacement relatif de l'interface sol-pieu à la contrainte de cisaillement mobilisée. Cette approche de calcul du comportement des pieux est généralement mise en œuvre, comme le recommande l'Eurocode7 Partie 1 (Eurocode 7 2005), lorsque les exigences de la structure portée en termes de déplacement sont essentielles. En France, ces lois sont très largement utilisées et s'appuient essentiellement sur les propositions de Frank et Zhao (1982) à la fois pour les sols fins et les sols grenus. Elles sont toutefois limitées au cas de charges axiales monotones ne dépassant la charge de fluage du pieu et ne permettent pas de rendre compte des phénomènes observés dans le cas où le pieu est soumis à des charges cycliques (fondations d'éoliennes, de structures pétrolières, etc.). Toutefois, des lois t-z cycliques, développées notamment pour l'ingénierie pétrolière, existent pour rendre compte des effets de tels chargements (Chin et Poulos 1992 et Randolph 1986).

Sur la base de ces lois, cet article propose une extension de la loi t-z formulée par Frank et Zhao. Les aptitudes de cette nouvelle loi, pour rendre compte des phénomènes de durcissement ou de radoucissement cyclique ou de rochet et de relaxation (Lemaître et Chaboche 2009), sont présentées à l'échelle locale. Une comparaison entre des résultats expérimentaux issus d'essais sur modèles réduits centrifugés pour quatre pieux soumis à des charges cycliques et des résultats numériques obtenus au moyen de cette nouvelle loi est ensuite proposée. Cette comparaison concerne l'évolution du déplacement en tête de pieu en fonction du nombre de cycles. Une discussion des résultats est ensuite présentée de manière à mieux cerner l'influence de chaque paramètre de la nouvelle loi t-z cyclique développée et à esquisser les développements futurs à mener.

## 2 MISE AU POINT D'UNE LOI T-Z CYCLIQUE

### 2.1 Principes

Dans sa version la plus générale, la loi t-z cyclique entre le frottement  $q_s$  et le déplacement tangentiel  $u_t$  est traduite par l'équation 1. Les neuf paramètres de cette loi sont présentés dans le tableau 1.

$$q_s(u_t) = q_{s,i} + A(-1)^{n_{\text{cyl}}+1} \left[ \left( q_{s,0} + \Delta q_s \left( 1 - e^{-\frac{u_{ti}}{\alpha}} \right) \right) \left( 1 - e^{-R \left| \frac{u_t - u_{ti}}{\alpha} \right|} \right) + \left[ \beta e^{-\frac{u_{ti}}{\alpha}} |u_t - u_{ti}|^\delta e^{-\left| \frac{u_t - u_{ti}}{\gamma} \right|^\delta} \right] \right] \quad (1)$$

Les paramètres auxiliaires A et R sont définis de la manière suivante :

- le paramètre A contrôle l'augmentation de la raideur de l'interface sol-pieu lors des déchargements. Cette augmentation est d'autant plus importante que le déchargement est réalisé à un niveau de chargement élevé ;
- le paramètre R gère l'augmentation de la raideur de l'interface sol-pieu à chaque inversion de cycle. Il comprend les paramètres  $\rho$  et  $\xi$  définis dans le tableau 1.

Lors du premier cycle de chargement, la relation entre le frottement  $q_s$  et le déplacement relatif  $u_t$  peut être simplifiée :

$$q_s = q_{s,0} \left( 1 - e^{-\frac{u_t}{\alpha}} \right) + \beta u_t^\delta e^{-\left( \frac{u_t}{\gamma} \right)^\delta} \quad (2)$$

Le second terme comprenant les paramètres  $\beta$ ,  $\delta$  et  $\gamma$  traduit le durcissement monotone. Il est maximal lorsque le



déplacement relatif  $u_t$  atteint la valeur  $\gamma$ . En l'absence de durcissement, la relation se simplifie sous la forme suivante :

$$q_s = q_{s0} \left( 1 - e^{-\frac{u_t}{\alpha}} \right) \quad (3)$$

On peut remarquer que le paramètre  $\alpha$  correspond au déplacement relatif de l'interface sol-pieu permettant de mobiliser environ 63 % du frottement maximal en l'absence de durcissement. Pour des chargements monotones, les paramètres  $q_{s0}$  et  $\alpha$  peuvent être déterminés respectivement selon la norme française d'application de l'Eurocode 7 (AFNOR 2012) relative aux fondations profondes et selon les lois de Frank et Zhao (1982) (Figure 1). Les autres paramètres sont à caler sur des essais cycliques de chargements de pieu. Actuellement, ils ne peuvent pas être déduits à partir de propriétés usuelles du sol comme le module pressiométrique, la pression limite ou la résistance de cône.

Tableau 1. Définition des paramètres de la loi t-z cyclique

Paramètres généraux	
$i$	nombre d'inversion de cycle de chargement ( $i \geq 1$ )
$q_{s,i}$	frottement mobilisé à l'inversion de charge ( $q_{s,i} = 0$ pour $i = 1$ )
$u_{t,i}$	déplacement relatif de l'interface sol-pieu au cycle $i$ ( $u_{t,i} = 0$ pour $i = 1$ )
$u_{ts} = \sum  u_{t,i} - u_{t,i-1} $	somme des valeurs absolues des déplacements relatifs
Paramètres auxiliaires	
$A = abs \left  \frac{q_{s,i} - (-1)^{(n_{cycl} + 1)} (q_{s0} + \Delta q_s (1 - e^{-u_{ts}/\varepsilon}))}{(q_{s0} + \Delta q_s (1 - e^{-u_{ts}/\varepsilon}))} \right $	
$R = e^{-(n_{cycl}-1)\xi} + \rho (1 - e^{-(n_{cycl}-1)\xi})$	
Mobilisation du frottement sous chargement monotone – 2 paramètres	
$q_{s0}$ [kPa]	frottement mobilisable sous chargement monotone pour de grands déplacements
$\alpha$ [cm]	paramètre de mobilisation du frottement (plus ce paramètre est faible, plus le déplacement pour mobiliser un frottement important est faible et plus l'interface sol-pieu est rigide)
Radoucissement/durcissement monotone – 3 paramètres	
$\gamma$ [cm]	paramètre fixant le déplacement pour laquelle le durcissement est maximal
$\beta$ [kPa]	paramètre contrôlant l'amplitude du durcissement
$\delta$	paramètre de calage égal à 2
Phénomènes cycliques – 4 paramètres	
$\Delta q_s$ [kPa]	amplitude de radoucissement ou de durcissement cyclique
$\varepsilon$ [cm]	paramètre contrôlant la vitesse de radoucissement ou de durcissement cyclique
$\rho$	paramètre contrôlant l'adaptation, l'accommodation et le rochet ou la relaxation
$\xi$	paramètre contrôlant la vitesse d'adaptation, d'accommodation et de rochet ou de relaxation

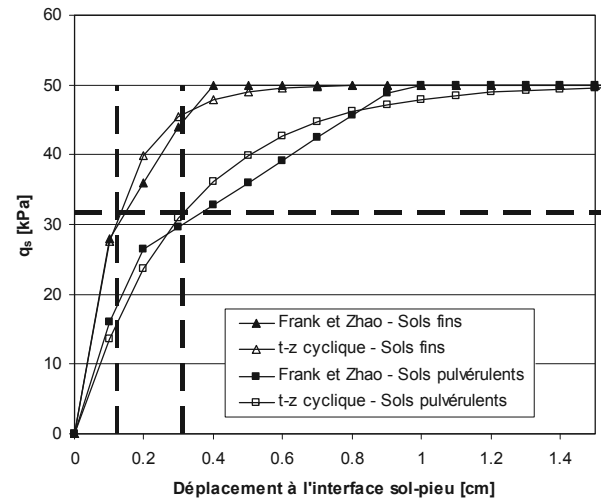
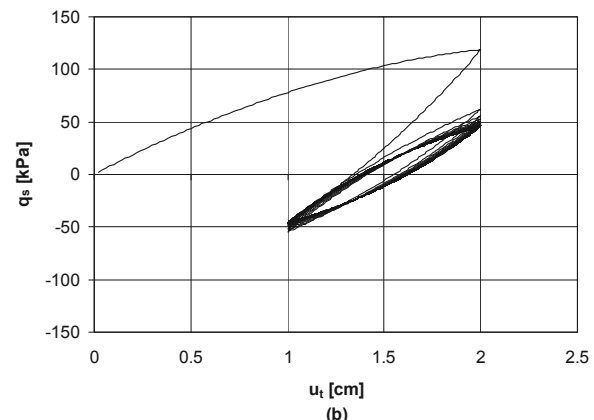
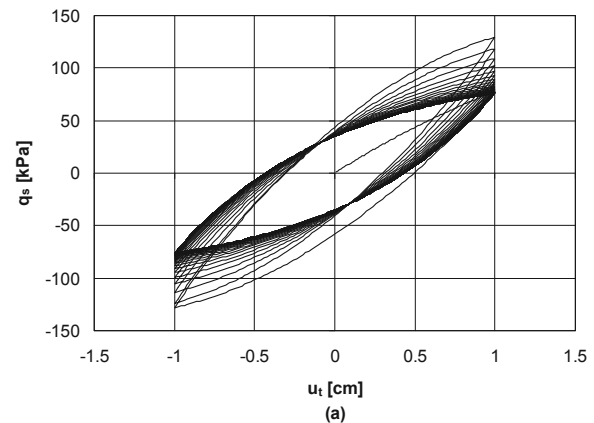


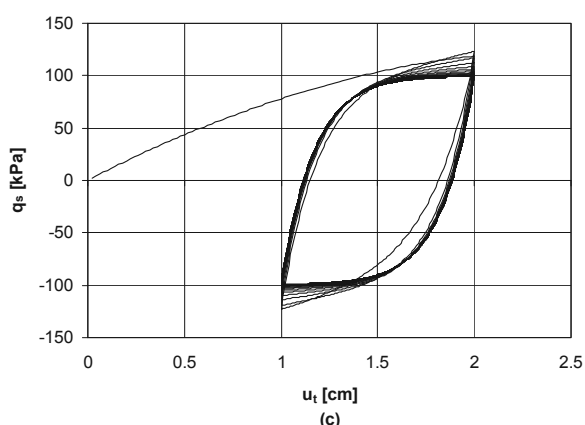
Figure 1. Comparaison entre la loi de Frank et Zhao et la loi t-z cyclique pour une sollicitation monotone.

## 2.2 Potentialités de la loi t-z cyclique

La loi t-z cyclique a été élaborée de manière à rendre compte les principaux phénomènes cycliques observés lors d'essais de cisaillement cyclique en laboratoire :

- le durcissement ou le radoucissement cyclique pour des essais de cisaillement en déplacement symétrique (Figure 2a) ;
- la relaxation ou non pour des essais de cisaillement en déplacement non symétrique (Figures 2b et 2c) ;
- le rochet plus ou moins important pour des essais de cisaillement en contrainte non symétrique.





Figures 2. Modélisation d'essai de cisaillement suivant différentes conditions (a : déplacement symétrique, b : déplacement non symétrique – relaxation, c : déplacement non symétrique – relaxation nulle)

### 2.3 Comportement de la base du pieu

La loi utilisée pour modéliser l'enfoncement de la base d'un pieu  $u_p$  a été développée sur le même modèle que la loi précédente. Elle est formulée directement en termes d'effort axial mobilisable sous la base du pieu et comprend neuf paramètres dans sa version la plus évoluée. Pour des chargements monotones, les paramètres  $Q_{p0}$  et  $\alpha$  sont toujours calés respectivement selon la norme française d'application de l'Eurocode 7 relative aux fondations profondes (AFNOR 2012) et selon les lois de Frank et Zhao (1982).

Un paramètre complémentaire  $p_r$  (variant entre 0 et 1) a été introduit de manière à prendre en compte le fait que la pointe d'un pieu sollicitée axialement peut se trouver au-dessus de sa position d'origine. Plus il est faible, moins l'effort mobilisé sous la pointe du pieu, tant que ce dernier est au-dessus de sa position initiale, est important (Figure 3).

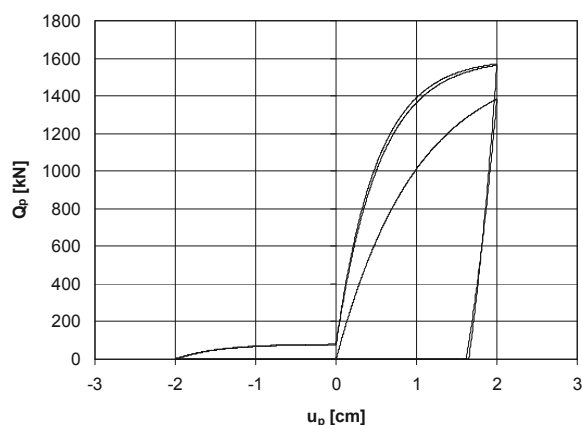


Figure 3. Modélisation de la mobilisation de l'effort de pointe

## 3 PRÉSENTATION DES ESSAIS EN CENTRIFUGEUSE

Le modèle réduit considéré, à l'échelle du  $1/23^{\text{ème}}$ , est soumis à une accélération centrifuge de  $23 \times g$ . Les propriétés du sable sont les suivantes (Jardine *et al.* 2009, Andria-Ntoanina *et al.* 2010) :  $\rho_{\text{dmin}} = 1395\text{-}1408 \text{ kg/m}^3$ ,  $\rho_{\text{dmax}} = 1755 \text{ kg/m}^3$ ,  $\rho_s = 2650 \text{ kg/m}^3$ ,  $d_{10} = 0,15 \text{ mm}$ ,  $d_{50} = 0,207\text{-}0,210 \text{ mm}$ ,  $d_{60} = 0,23 \text{ mm}$  et  $CU = 1,49\text{-}1,43$ . Le pieu modèle a les caractéristiques suivantes : forme cylindrique « pointe » plate, diamètre de 18 mm, longueur de 590 mm, fiche de 560 mm, barreau d'aluminium de masse totale 0,405 kg, rugosité à l'état « neuf » définie par  $R_t = 112 \mu\text{m}$ ,  $R_a = 25,9 \mu\text{m}$  soit  $R_t/d_{50} = 0,54$  et  $R_a/d_{50} = 0,13$ , rugosité à l'état « usé » (après 10 essais) définie par  $R_t = 90 \mu\text{m}$ ,  $R_a = 23,9 \mu\text{m}$  soit  $R_t/d_{50} = 0,44$ ,  $R_a/d_{50} = 0,12$ . Les massifs sont

reconstitués par pluviage de sable sec dans un conteneur double (Figure 4).

Les expérimentations réalisées comprennent deux séries d'essais monotones permettant de déterminer la résistance ultime du pieu en compression ( $Q_p$ ) et en traction ( $Q_s$ ). Quatre essais cycliques ont ensuite été réalisés : la charge atteint d'abord la valeur  $V_m$  puis oscille entre  $V_{\text{max}} = V_m + V_c$  et  $V_{\text{min}} = V_m - V_c$  (Tableau 2).

Tableau 2. Programme de chargement des essais cycliques

	$V_m/Q_p$	$V_c/Q_p$
Essai 1 (traction cyclique)	-0,33	0,05
Essai 2 (traction cyclique)	-0,133	0,133
Essai 3 (cyclique alterné – compression dominante)	0,3	0,4
Essai 4 (cyclique alterné)	0	0,133

## 4 ANALYSE DES RÉSULTATS OBTENUS

### 4.1 Présentation des résultats

Les paramètres de calcul (Tableau 3) sont calés sur les deux essais monotones en traction (Figure 4) et en compression (Figure 5) en supposant le module de Young du pieu égal à 10 GPa et sur l'essai cyclique 3 qui présente le comportement *a priori* le plus complexe à modéliser.

Tableau 3. Propriétés des paramètres de la loi t-z pour le frottement axial et pour la résistance de pointe

Frottement axial		Résistance de pointe	
$q_{s0}$	102 kPa	$Q_{p0}$	1615 kN
$\alpha$	1 cm	$\alpha$	0,1 cm
$\beta$	30 kPa	$\beta$	
$\gamma$	1,8 cm	$\gamma$	
$\delta$	2	$\delta$	
$\Delta q_s$	- 83 kPa	$\Delta Q_p$	300 kN
$\varepsilon$	25 cm	$\varepsilon$	5 cm
$\rho$	20	$\rho$	6
$\xi$	0,05	$\xi$	0,1
		$p_r$	0,05

### 4.2 Analyse des résultats

La figure 6 propose, pour les quatre essais, la comparaison entre les résultats expérimentaux et les résultats numériques. Expérimentalement, la rupture du pieu est obtenue pour les essais 2, 3 et 4 avec un défaut de résistance à la traction du sol. Pour l'essai 1, alors que l'effort de traction appliqué est plus important de tous les essais réalisés, la rupture n'a pas été atteinte pour le nombre de cycles effectués. Il est néanmoins très probable que le nombre de cycles effectués est insuffisant. Pour l'essai 3, la rupture en compression peut être observée puisque l'enfoncement du pieu est supérieur à 10 % de son diamètre. Les efforts de traction atteints traduisant la rupture du pieu pour les essais 2, 3 et 4 sont très différents : 1204,6 kN, 843,22 kN et 317 kN. Ce résultat montre que le frottement mobilisable le long du fût du pieu, après un grand nombre de cycles de chargement, varie en fonction du chargement appliqué. Dans l'état actuel, la loi t-z proposée n'est pas en mesure de rendre compte ce phénomène car les paramètres  $\Delta q_s$  et  $u_s$  ne traduisent pas suffisamment les effets des cycles sur la résistance de l'interface.

Les résultats obtenus indiquent toutefois que le modèle développé rend compte de manière plutôt satisfaisante des déplacements du pieu lors des premiers cycles de chargement. Pour des nombres de cycles élevés, les tendances restent plutôt bien appréhendées même si les amplitudes de déplacement ne sont pas correctes.

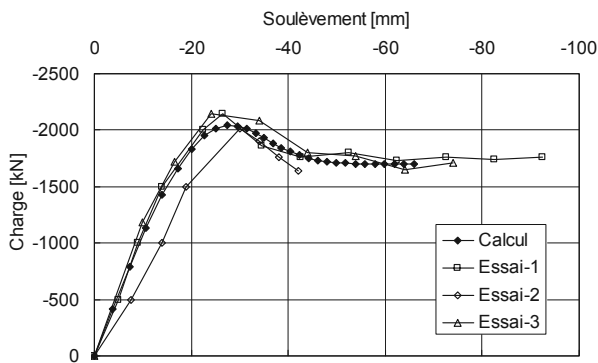


Figure 4. Modélisation de l'essai de traction

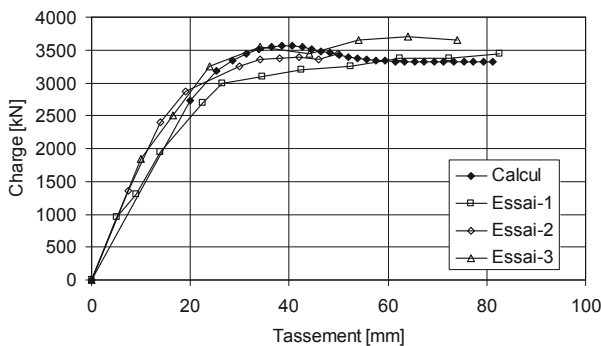


Figure 5. Modélisation de l'essai de compression

## 5 CONCLUSION

Une loi d'interaction  $t$ - $z$  cyclique a été développée pour le calcul des pieux sous charge axiale. Des tentatives de validation ont été effectuées en confrontant des résultats numériques obtenus avec cette loi et des expérimentations en centrifugeuse pour des chargements cycliques en traction et en compression alternés ou non. Des améliorations significatives restent à apporter. Les premiers résultats sont encourageants car ils traduisent au moins dans leurs grandes lignes les principaux comportements du pieu.

## 6 REMERCIEMENTS

Les résultats présentés dans cette communication ont été acquis dans le cadre du Projet ANR et du Projet National Français SOLCYP (SOLlicitations Cycliques sur les Pieux).

## 7 REFERENCES

Eurocode 7 – Part 1. (2004) *Calcul Géotechnique – Partie 1: Règles Générales*. Comité Européen de Normalisation, Bruxelles.

Frank, R. et Zhao, S. (1982). Estimation par les paramètres pressiométriques de l'enfoncement sous charge axiale de pieux forés dans des sols fins. *Bulletin Liaison Laboratoire Ponts Chaussées* 119 17-24.

Chin J. T. and Poulos H. G. (1992) Cyclic axial loading analyses: a comparative study. *Computers and Geotechnics*, 13, 137-158.

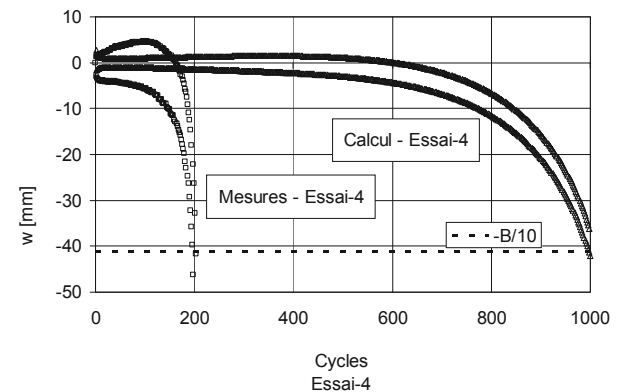
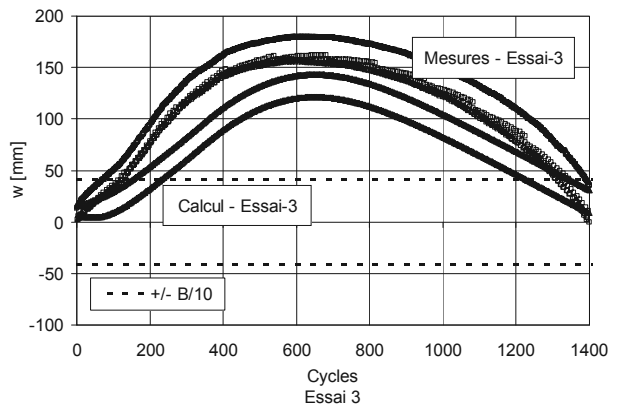
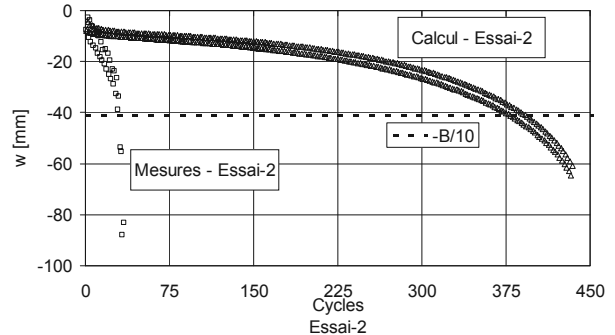
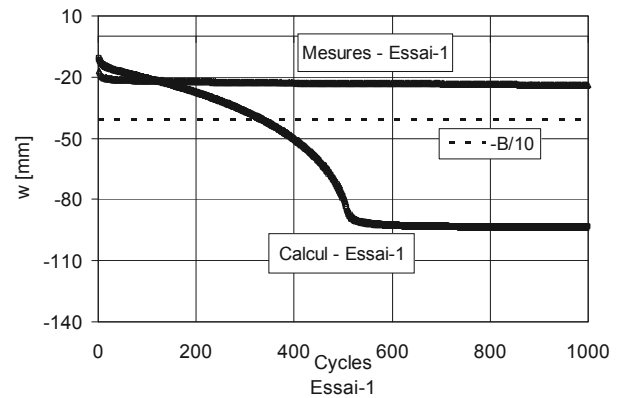
Randolph M.F. (1986) RATZ: Load transfer analysis of axially loaded piles, *Report Geo: 86033*, Department of Civil Engineering, The University of Western Australia.

Lemaître, J. et Chaboche, J.L. (2009). *Mécanique des Matériaux Solides* (éd. 2ème). Paris: Dunod.

AFNOR. (2012) Dimensionnement des fondations profondes. *Norme NF P 94-292*, Paris.

Jardine R.J., Zhu B.T., Foray P. & Dalton, C.P. (2009). Experimental arrangements for the investigation of soil stresses developed around a displacement pile. *Soil and Foundations* 49(5): 661-673.

Andria-Ntoanina I., Canou J. et Dupla J.-C. (2010) Caractérisation mécanique du sable de Fontainebleau NE34 à l'appareil triaxial sous cisaillement monotone. *Rapport SOLCYP*, 23p.



Figures 6. Modélisation des quatre essais cycliques ( $w$  : déplacement axial du pieu  $\rightarrow > 0$  : tassement  $\leftarrow < 0$  : soulèvement)

# Deformation behavior of single pile in silt under long-term cyclic axial loading

## Comportement d'un pieu isolé sous chargement axial cyclique de longue durée dans un limon

Chen R.P., Ren Y., Zhu B., Chen Y.M.

*MOE Key Laboratory of Soft Soils and Geoenvironmental Engineering, Zhejiang University, Hangzhou, China*

**ABSTRACT:** Evaluating the response of piles to cyclic loading is a crucial part in the design of piled-embankment over soft ground. In this paper, a series of large-scale model tests were performed to investigate the response of pile in silt under cyclic axial loading. Heavily instrumented piles were used in the tests. The study is focused on the accumulation of permanent displacement of the piles under long-term cyclic loading. Piles were tested at different cyclic loading levels and subjected up to 50,000 cycles of loading in each test. The accumulated settlement was found to be strongly dependent on the characteristics of the applied cyclic loads. The piles were found not to produce any increase in accumulated settlement if the cyclic loading amplitude is less than a certain threshold value. A simple method is proposed to predict the accumulated settlement of single pile due to very large number of loading cycles. The idea of a cyclic deformation diagram for analyzing the influence of characteristics of cyclic loads on the deformation behavior was also developed.

**RÉSUMÉ :** L'évaluation de la réponse des pieux vis-à-vis d'un chargement cyclique est un élément essentiel dans la conception des remblais sur sols mous. Dans cet article, une série d'essais sur maquette à grande échelle a été réalisée pour étudier la réponse de pieux sous chargement axial cyclique dans le limon. L'étude est centrée sur l'accumulation des déplacements permanents des pieux sous chargement cyclique de longue durée. Les pieux ont été testés à différents niveaux de charge cyclique et soumis à 50000 cycles pour chaque test. Les tassements accumulés sont fortement dépendants des charges cycliques appliquées. Aucune augmentation de tassements n'est constatée si l'amplitude de chargement cyclique est inférieure à un certain seuil. Une méthode simple est proposée pour prédire le tassement cumulé d'un pieu isolé en fonction d'un très grand nombre de cycles de chargement. L'idée d'un diagramme de déformation cyclique pour analyser l'influence des caractéristiques des charges cycliques sur le comportement en déformation a également été développée.

**KEYWORDS:** Pile; model test; accumulated settlement; cyclic loading

## 1 INTRODUCTION

Piles are commonly used to support high-speed railway embankment in soft ground, which are exposed not only to the heavy loads from superstructure self-weight, but also to the long-term "one-way" cyclic loads induced by high-speed trains throughout their service life. However, available design experiences on the long-term response of the pile in silt to cyclic axial loading are very limited, due to the fact that the existing data obtained from laboratory tests and field measurement are insufficient. This results in uncertainty in the design and always leads to an over-conservative design of the pile foundation.

The response of pile subjected to cyclic loading is very complex and model test is the most effective and reliable way to study it and its influencing factors. Laboratory and field tests (Chan and Hanna 1980; Lee and Poulos 1991; Karlsrud et al. 1993) have shown that there are two main effects of cyclic axial loading on piles: (1). a reduction in load capacity and pile-soil system stiffness; (2). an increase in settlement of piles. Poulos (1989) reviewed several cyclic loading tests performed in sand and stated that the accumulation of permanent displacement with increasing load cycles was expected to dominate under "one-way" cyclic loading, particularly if "strain-softening" behavior can occur at the pile-soil interface. The accumulation of the permanent displacement principally depends on the cyclic load level. Briaud and Felio (1986) analyzed the published data and concluded that a load threshold exists above which failure occurs by plunging due to cyclic loading and the value of this threshold is 80% of the ultimate pile capacity on average.

In previous studies, most of the piles were loaded less than 500 cycles of loading. There have been few researches on the response of pile to long-term cyclic loading at present.

This paper describes the results of a series of large-scale model tests on single stiff piles in saturated silt to study the accumulation of permanent displacement of the piles. The tests have been performed using heavily instrumented model piles. A simple method for predicting the accumulation of permanent displacement of pile to long-term cyclic axial loading is proposed. The idea of a cyclic deformation diagram for analyzing the influence of characteristics of cyclic loads on the deformation behavior was also developed.

## 2 DESCRIPTIONS OF EXPERIMENTS

### 2.1 Test site and soil characteristics

The present large-scale model tests were carried out in a big soil tank at Zhejiang University (Fig 1). This soil tank has a dimension of 15×5m in plan view and a depth of 6m.

The soil used in the tests is low cohesive silt. Grading tests showed that the soil contains 10% sand, 85% silt and 5% clay. The characteristics of the soil are summarized in Table 1. Laboratory tests show that the prepared soil had an average water content of 28.5% and an effective internal friction angle of 30°.



Figure 1. The big soil tank at Zhejiang University

Table 1. Main soil properties

Property	Value
D <sub>50</sub> particle size (mm)	0.032
Specific gravity, G <sub>s</sub>	2.69
Plastic limit, W <sub>L</sub>	22.6
Liquid limit, I <sub>L</sub>	31.7
Plasticity index, PI	9.1

### 2.2 Model pile

The used instrumented model pile was closed-ended steel tube pile with an outer diameter (*d*) of 168 mm, a wall thickness of 7 mm. The pile had a cone-shaped tip end with a cone angle of 60°. The model pile was designed to be assembled from four segments to give a full length of 4.2 m. The instrumentation consisted of axial load cells (ALC), total pressure transducers (TPT) and pore pressure transducers (PPT).

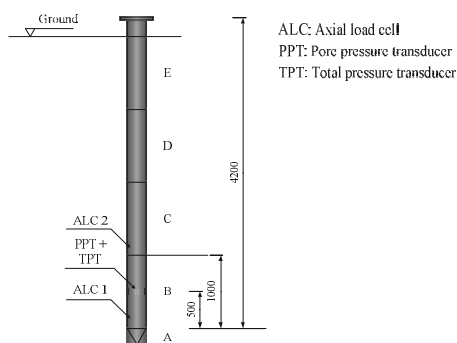


Figure 2. Schematic diagram of the model pile (Unit: mm)

### 2.3 Characteristics of cyclic loading

The characteristics of the applied cyclic load are uniquely defined using two independent parameters:

$$SLR = P_s / P_u \quad (1)$$

$$CLR = P_c / P_u \quad (2)$$

in which  $P_u$  refers to the static ultimate capacity of the pile in compression, and  $P_s$  is the minimum in a load cycle and  $P_c$  is the cyclic load amplitude. In present study,  $P_s$  and  $P_c$  simulated the self-weight from the superstructure and the cyclic load induced by the high-speed trains, respectively. A visual interpretation of the load ratios is given in Fig. 3.

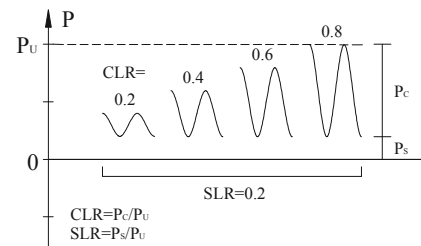


Figure 3. The characteristics of cyclic loading

In this study, the cyclic load frequency of 3Hz was used for the tests and the sampling frequency was of 50 Hz.

## 3 TEST RESULTS

### 3.1 Accumulated settlement

The overall pattern of accumulated settlement of the pile with SLR of 0.3 is presented in Fig. 4 by normalizing the accumulated permanent displacement *s* by the pile diameter *d*. The values of the CLR in this series ranged from 0.1 to 0.6. It can be found that the ways in which displacement developed is highly dependent on the amplitudes of cyclic load which can be represented by the cyclic load ratio (CLR).

In the test with the smallest CLR of 0.1, extreme small permanent displacement, of approximately 0.04%*d* was produced in the first three cycles and remained nearly constant from cycle No. 3 to 50,000. For the CLR's ranging from 0.2 to 0.5, the permanent accumulated displacement increased gradually with the increasing number of cycles and also with the increasing magnitude of cyclic load. For the tests with the CLR of 0.2, 0.3, 0.4 and 0.5, the permanent displacements at the end of the tests were 0.15%*d*, 0.35%*d*, 0.56%*d* and 1.26%*d*, respectively. The permanent displacement increased rapidly at initial stage and had the highest rate of displacement increase in the first few cycles, and then it kept increasing continuously with a decreased rate of displacement increase and seemed to increase without a final and constant value. For the test with very large cyclic load, such as CLR=0.6, the pile head moved downward in a very "unstable" way marked by a quick plunging during the test and the pile failed with a total accumulated displacement of 10%*d* in 2,147 cycles.

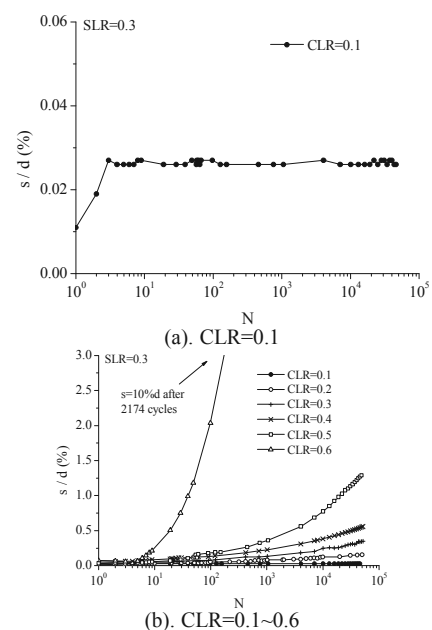


Figure 4. Normalized permanent displacement (*s/d*) with number of cycles (SLR=0.3)

The aforementioned patterns of behavior shown in Fig. 4 can also be found in other tests with SLR of different values. The accumulated displacement for each test fell qualitatively into any of the three distinct patterns shown in Fig. 4:

(1) no accumulated displacement, as exhibited during the test with CLR of 0.1;

(2) continuing displacement, as exhibited during the tests with CLR ranging from 0.2 to 0.5;

(3) failure, as exhibited during the test with CLR of 0.6.

For the first case, the pile-soil system seems not to be influenced by the cyclic loading and is in elastic range; only small accumulated displacement was produced during the first few cycles. For the second case, the pile-soil system was influenced to some degree and partially entered plastic range; the pile head showed continuing downward movement without any apparent limit and the accumulation of displacement depended on both of cyclic load level and number of load cycles, and high cyclic load level and large number of cycles produced larger permanent displacement. For the last case, the cyclic loading had brought severe damage to the pile-soil system and the pile fully entered the plastic range; the pile head moved continuously downward at a rapid rate up to the end of the test and a plunging failure might occur in some cases.

Thus, to divide the accumulated displacement responses for the tests with a given SLR two critical values of CLR are defined here, named minimum cyclic load ratio (MCLR) and failure cyclic load ratio (FCLR), respectively. For CLR smaller than the MCLR, the pile was in elastic range; for CLR greater than the FCLR, the damage to the pile-soil system was severe and the always caused "failure".

The MCLR was found to be of 0.1 in all the tests and shown to be unaffected by the SLR, and it can be inferred that if the applied cyclic loads remained less than 10% of the ultimate pile static capacity, the response of the pile can be considered to be total elastic and the permanent displacement was negligible after first several cycles.

The FCLR was found to be of 0.5 for the tests with SLR ranging from 0.2 to 0.4. However, in the case of the test with SLR of 0.1, the pile produced large permanent displacement with CLR of 0.4, and it showed the tendency that lesser cyclic loads were required to cause large permanent displacement for the pile with very small SLR. Briaud and Felio (1986) reviewed the previous cyclic load tests and concluded that a threshold of peak load ratio (CLR+SLR) existed above which large permanent displacement occurred and the value of that threshold was about 0.8 on average. However, the tests results suggest that the large permanent displacement depended more on the magnitude of the cyclic load rather than the peak cyclic load. It can be inferred from the results that large permanent displacement occurred if the magnitude of the applied cyclic load exceeds the 50% of the ultimate pile static capacity.

### 3.2 Prediction method

To investigate the evolution of the permanent displacement in the tests in which the permanent displacement are identified as "continuing displacement", the results are replotted on double logarithmic scales and the evolution of the permanent displacement is evaluated in terms of the dimensionless ratio

$$\frac{\Delta s(N)}{s_s} = \frac{s_N - s_0}{s_s} \quad (3)$$

which expresses the magnitude of the permanent displacement  $\Delta s(N)$  caused by cyclic loading in terms of the displacement  $s_s$  that would occur in a static load test when the load is equivalent to the maximum cyclic load (as defined by  $(SLR + CLR) \times P_u$ ). The  $s_0$  and  $s_N$  refer to the permanent displacement in first and  $N$ 'th cycle, respectively.

The results, plotted in Fig. 5, show that the trend in the data follows the exponential behavior which appears as straight lines in double logarithmic axes. This suggests that the permanent displacement due to cyclic loading can be predicted by the following power model:

$$\frac{\Delta s(N)}{s_s} = AN^b \quad (4)$$

where  $A$  and  $b$  are two parameters. It is observed in Fig. 5 that all slopes are almost equal. This suggests that  $b$  is independent of the load characteristics within the observed range. It is introduced into (4) to represent the influence of load characteristics on parameter  $A$  in the following form:

$$A = a(SLR + 1)^m (CLR)^n \quad (5)$$

where  $a$ ,  $m$  and  $n$  are three calibration parameters. Clearly, when  $CLR = 0$ , then  $A = 0$  and no accumulated displacement will occur under static load. Also, when  $SLR = 0$  then  $A = a(CLR)^n$  indicates that the accumulated displacement depends only on CLR. Thus, substituting (5) into (4) gives the following model for accumulated permanent displacement:

$$\frac{\Delta s(N)}{s_s} = a(SLR + 1)^m (CLR)^n N^b \quad (6)$$

The expression in Equation (6) was fitted to the data in Fig. 5 to empirically determine values of these parameters and back-calculated parameters  $a$ ,  $m$ ,  $n$  and  $b$  for the tests are 0.054, 0.68, 1.24 and 0.23. The predicted results are shown by the dotted lines in Fig. 5 and it appears that the influences of the load characteristics on permanent displacement are reflected well in the prediction. The closeness of the fit up to  $5 \times 10^4$  cycles indicates that, in the absence of further experimental data, it might be reasonable to extrapolate beyond  $N > 5 \times 10^4$ . Further data are, of course, required to confirm this hypothesis.

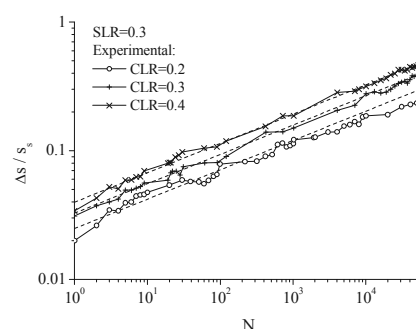


Figure 5. Measured and predicted accumulated displacement  
The dotted lines are obtained using Equation (6)

## 4 CYCLIC DEFORMATION DIAGRAM

Poulos (1988) proposed the idea of cyclic stability diagram to investigate the capacity degradation caused by cyclic loading. In this study, similar concept is used and the idea of a diagram named cyclic deformation diagram is developed. The cyclic deformation diagram for the model piles is shown in Fig. 6. In the diagram, the aforementioned three types of displacement response are represented by different symbols. Therefore, three main regions can be identified on the diagram shown in Fig. 6:

(1) A stable (elastic) region I in which the cyclic loading has no influence on the pile responses and the displacement response is the type of "no accumulated displacement".

(2) A serviceability region II in which the cyclic loading has some influence on the pile response and the displacement response can be identified as “continuing displacement”.

(3) A unstable region III in which cyclic loading causes severe damage for the pile to produce very large permanent displacement and in some cases a plunging failure occurs.

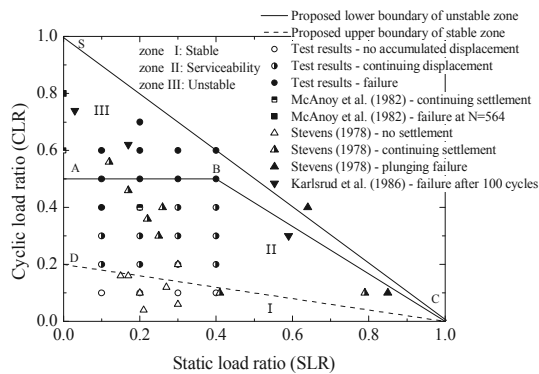


Figure 6. Cyclic deformation diagram for pile in silt ( $N=50,000$ )

The upper boundary to the cyclic permanent displacement is the straight line (CS:  $SLR+CLR=1$ ) that represent the combinations of SLR and CLR necessary to cause a failure of pile without cyclic effects being considered. The other two lines plotted in this diagram represent the approximate boundaries between the stable region, the serviceability region and the unstable region. These lines are defined by the following relations:

Upper boundary of stable zone (line AB and BC):

$$\begin{cases} CLR = 0.5 & 0 \leq SLR \leq 0.4 \\ 1.2CLR + SLR = 1 & 0.4 < SLR \leq 1.0 \end{cases} \quad (7)$$

Lower boundary of unstable zone (line DC):

$$5CLR + SLR = 1, \quad 0 \leq SLR \leq 1 \quad (8)$$

Fig. 6 also plots the other test results of field or model tests on axial cyclically loaded pile. It can be seen that these proposed lines are consistent with the experimental data and thus it is indicated that the proposed three regions are capable of reasonably identifying the deformation behavior of pile under various load combinations. A diagram such as shown in Fig. 6 represents the permanent displacement of a pile for a specified number of cycles,  $N$ . As  $N$  increases, the stable region will remain unchanged and the unstable region may increase as the permanent displacement increases.

In the pile design, it is very convenient to determine the deformation behavior of the pile to cyclic loading using this diagram. The most conservative design is to have the cyclic loads in the stable region which means that pile will not be affected by cyclic loading and issues of the permanent displacement can be totally ignored. If the designed cyclic load is in the serviceability region, the permanent displacement accumulates in “stable” way and depends on both of the number of cycles and the load characteristics; and it can be predicted using the proposed simple method mentioned above. For a safe design, it should avoid the cyclic load to be in the unstable region in which cyclic loading will result in very large permanent displacement and even a plunging failure.

## 5 CONCLUSION

A series of tests were conducted on large-scale model piles subjected to long-term cyclic axial loading. The deformation behavior of the piles in silt to cyclic loading was investigated.

The evolution of permanent displacement highly depends on the magnitude of cyclic load. In general, the accumulation of permanent displacement increases with increasing cyclic load amplitude and increasing number of cycles. However, the pile behaves in an elastic manner and does not accumulate any deformation after the first few cycles of loading if the magnitude of cyclic load is less than 10% of the ultimate pile capacity. Very large permanent displacement, even plunging failure, occurs when magnitude of cyclic load exceeds 50% of the ultimate pile capacity. This suggests that the magnitude of the cyclic load be kept below 50% of the ultimate capacity to avoid large permanent displacement in the design.

These results provide a better understanding of the deformation behavior of pile in silt to long-term cyclic axial loading, and can be used to optimize the designs of pile foundations that resist cyclic loads in service.

## 6 ACKNOWLEDGEMENTS

The work was supported by the National Natural Science Foundation of China (Grant Nos. 51225804 and U1234204).

## 7 REFERENCES

- ASTM 2010. D2487-10. Standard Practice for Classification of Soils for Engineering Purposes (Unified Soil Classification System). ASTM International.
- Briaud J.L and Felio G.Y. 1986. Cyclic axial loads on piles: Analysis of existing data. Canadian Geotechnical Journal, 23, 362-371.
- Chan S.F. and Hanna T.H. 1980. Repeated loading on single piles in sand. Journal of Geotechnical Engineering Division, 106, 171-188.
- Karlsrud K., Nadim F. and Haugen T. 1986. Piles in clay under cyclic axial loading-field tests and computational modeling. Proc., 3rd Int. Conf., Numerical Methods in Offshore Piling, Nantes, France, 165-190.
- Karlsrud K., Nowacki F. and Kalsnes B. 1993. Response in soft clay and silt deposits to static and cyclic loading based on recent instrumented pile load test. Proc. SUT Int. Conf, Kluwer, Dordrecht, 549-584.
- Lee C.Y. and Poulos H.G. 1991. Tests on model instrumented grouted piles in offshore calcareous soil. Journal of Geotechnical Engineering, 117, 1738-1753.
- McAnoy R.P.L., Cashman A.C. and Purvis D. 1982. Cyclic tensile testing of a pile in glacial till. Proc., 2nd Conf., Numerical Methods in Offshore Piling, Austin, Tex., 257-292.
- O’Riordan N., Ross A. and Allwright R. 2003. Long-term settlement of piles under repetitive loading from trains. Transportation geotechnics, Thomas Telford, London, 67-74.
- Poulos H. G. (1988). “Cyclic stability diagram for axially loaded piles.” Journal of Geotechnical Engineering, 114, 877-895.
- Poulos H.G. 1989. Cyclic axial loading analysis of piles in sand. Journal of Geotechnical Engineering, 115, 836-852.
- Stevens J.B. 1978. Prediction of pile response to vibratory loads. Proc., 10<sup>th</sup> OTC Conf., Houston, Tex., Vol. 3, 2213-2223.

# Time-Varying Dynamic Properties of Offshore Wind Turbines Evaluated by Modal Testing

Étude expérimentale de l'évolution temporelle des propriétés dynamiques d'éoliennes maritimes

Damgaard M., Andersen J.K.F.  
*Vestas Turbines R&D, Denmark*

Ibsen L.B., Andersen L.V.  
*Department of Civil Engineering, Aalborg University, Denmark*

**ABSTRACT:** Modal frequencies and damping ratios of civil engineering structures are often used as damage-sensitive features, since changes in the dynamic characteristics of the structures may indicate structural damage. For offshore wind turbine structures, the modal parameters are influenced by environmental impacts that change boundary conditions, irreversible soil deformations and inherent structural properties. The excitation frequencies related to the environmental loads and the passage of blades past the tower are so low that a proper estimate of the modal parameters are needed in order to avoid strong resonance of the wind turbine structure. In this paper, free vibration tests and a numerical Winkler type approach are used to evaluate the dynamic properties of a total of 30 offshore wind turbines located in the North Sea. Analyses indicate time-varying eigenfrequencies and damping ratios of the lowest structural eigenmode. Isolating the oscillation oil damper performance, moveable seabed conditions may lead to the observed time dependency.

**RÉSUMÉ:** Les fréquences modales et les taux d'amortissement des structures de génie civil sont souvent utilisés comme indicateur de dommages car l'évolution de la réponse dynamique des structures peut indiquer des dégâts structuraux. Pour des structures comme les éoliennes maritimes, les paramètres modaux sont influencés par la déformation irréversible des sols, les propriétés structurelles inhérentes et les conditions environnementales qui peuvent changer les conditions aux limites. Les fréquences d'excitations liées aux charges environnementales et aux passages des pales sont si basses qu'une estimation correcte des paramètres modaux est nécessaire pour éviter une forte résonance de la structure de l'éolienne. Dans cet article, des tests vibratoires et une approche numérique du type Winkler sont utilisés afin d'évaluer les propriétés dynamiques de 30 éoliennes maritimes situées en mer du Nord. Les analyses révèlent le changement des fréquences propres et des taux d'amortissement de la plus basse fréquence propre structurelle en fonction du temps. En isolant la performance de l'amortisseur oscillant à huile, les changements de conditions du fond marin peuvent démontrer une dépendance temporelle.

**KEYWORDS:** Free vibration; modal; offshore wind turbine;  $p$ - $y$  curve; scour; winkler approach.

## 1 INTRODUCTION

Recently, offshore wind turbine towers and blades have increased significantly in height and length, respectively, with only a small increase in weight. Therefore, the dynamic response of the wind turbine structure occurs in a frequency range close to the excitation frequencies related to environmental and structural harmonic loads. In this context, sufficient geometrical and material damping in the structure and soil are required to counteract large amplitudes of vibration. Especially for wind parks characterised by a large degree of wind-wave misalignment, a proper estimate of the inherent damping is needed due to low aerodynamic forces out of the rotor plane.

The aim of this paper is to investigate the time-varying eigenfrequency  $f_1$  and inherent modal damping  $\delta_1$  of the lowest eigenmode  $\Phi^{(1)}$  for offshore wind turbines installed on a monopile foundation. Experimental modal analysis of offshore wind turbines have been studied by several researchers. Based on free vibration tests, Tarp-Johansen *et al.* 2009 and Damgaard *et al.* 2011 have used "rotor-stop" tests to determine each damping contributor to the measured inherent modal damping  $\delta_1$  of an offshore wind turbine. Versteijlen *et al.* 2011 and Devriendt *et al.* 2012 used the same modal approach to obtain reliable damping estimates. In addition, Versteijlen *et al.* 2011 considered operational modal analysis in order to include the aerodynamic effects on the structure. The theory has been widely used for civil engineering structures like bridges and buildings. However, in the last years the application of

operational modal analysis on wind turbines has been published in many excellent papers, see for instance Hansen *et al.* 2006 and Tcherniak *et al.* 2010. A thorough data processing of more than 650 free vibration tests on 30 offshore wind turbine structures are presented in the paper. The variation in the dynamic properties is supported by a numerical Winkler approach that estimates the modal parameters for different environmental conditions.

## 2 STRUCTURE AND SITE CONDITIONS

A total of 30 Vestas V90-3MW turbines located in the North Sea are considered. Each tower is installed on a monopile connected by a grouted transition piece to the tower base. The tower height is approximately 60 m, the monopile diameter 4.3 m and the water depth 8 m w.r.t. LAT. For each turbine an oscillation damper is placed in the top of the tower. It consists of a pendulum partly immersed in highly viscous oil, capable of oscillating in the horizontal directions. The soil consists mainly of cohesionless soil in the top layers with friction angles  $\phi_k$  higher than 30° followed by cohesive soils with undrained shear strength  $c_u$  higher than 90 kPa.

## 3 MODAL PARAMETER ESTIMATION

By use of two accelerometers placed in the nacelle, the modal parameters of each wind turbine are experimentally estimated



from the acceleration decay when the turbine generator shuts down and the blades pitch out of the wind, see Figure 1. Hence, assuming that the wind turbine structure behaves as a single-degree-of-freedom (SDOF) system, the eigenfrequency  $f_1$  and modal damping  $\delta_1$  are determined by least-squares fitting of a linear function to the zero crossings and to the natural logarithm of the rate of decay of the vibration, respectively. It should be noticed that a wind turbine structure has two closely spaced modes occurring at nearly identical frequencies (Damgaard *et al.* 2012), where vibrational energy is transferred from the highest to the lowest damped mode. Hence, for the damping estimation of each free vibration test it is ensured that the acceleration of the structure only takes place in the fore-aft direction  $y$ .

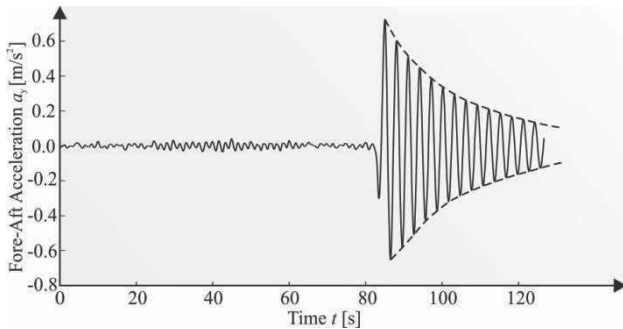


Figure 1. Raw output acceleration signal during a “rotor-stop”.

### 3.1 Winkler Approach

Offshore wind turbines supported by pile foundations are subjected to lateral cyclic loads. The load-deflection behaviour is often evaluated by a Beam on Nonlinear Winkler Foundation (BNWF) model due to its computationally efficiency and practical versatility. The tower and pile are modelled as Bernoulli-Euler beams and the soil-structure interaction is incorporated via so-called  $p$ - $y$  curves suggested by DNV 2011, see Fig. 2. The soil consists of a series of independent soil layers with smooth horizontal boundaries, *i.e.* no shearing can be transmitted across the boundaries. Rather than modelling the soil as a number of discrete springs connected to the element nodes, this paper uses a consistent approach, where the soil is modelled as a continuous spring over each element. The nodal forces are then obtained via numerical integration. The reader is referred to Damgaard *et al.* 2011 for more information about the computational model.

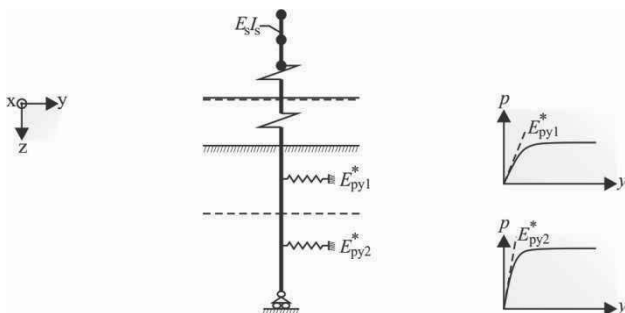


Figure 2. Beam on nonlinear Winkler foundation (BNWF) model.

#### 3.1.1 Soil Damping Estimation

In general, attenuation of wave propagation in the soil is determined from geometric damping, *i.e.* the radiation of waves into the subsoil, and material damping caused by the slippage of soil grains with respect to each other. However, extensive studies of wind turbines on a homogeneous or layered ground made by Andersen 2008 show that geometric dissipation is

insignificant at frequencies below 1 Hz. From the continuum mechanics it is known that material damping is related to the relative motion of material points, and the energy dissipation is frequency-dependent. For a given frequency and deformation level, the soil material damping can be approximated to an equivalent viscosity. Based on a static deformation analysis, using the Winkler approach, the following procedure is used to determine the soil damping ratio  $\zeta_{soil}$  of the lowest eigenmode  $\Phi^{(1)}$ :

- A 10-minutes time-domain simulation of the wind turbine structure is conducted for a power production situation with a normal turbulence model (IEC 2005) using the aeroelastic code FLEX (Øye 1996). A correct estimate of the structural eigenfrequency  $f_1$  in the FLEX model is ensured by extending the tower until the eigenfrequency  $f_1$  of the Winkler model is reached.
- Based on the maximum overturning moment at the tower/foundation interface from the FLEX simulation and including wave loads, the horizontal pile deformation in each nodal point below the seabed is evaluated.
- Assuming a load-displacement cycle after the generator shuts down, as indicated in Figure 3a, the irreversible soil deformations are a measure of energy dissipation. Hence, the energy dissipation in Figure 3a can be transformed to an equivalent viscous damping model as shown in Figure 3b.
- Using the theory of linear structural dynamics, the soil damping  $\zeta_{soil}$  of the lowest eigenmode  $\Phi^{(1)}$  is determined from the global damping matrix  $C$ , the angular eigenfrequency  $\omega_1$ , the eigenmode  $\Phi^{(1)}$  and the modal mass  $M_1$  given by

$$\zeta_{soil} = \frac{\Phi^{(1)T} C \Phi^{(1)}}{2\omega_1 M_1} \quad (1)$$

The virgin curve in Figure 3a is determined by the  $p$ - $y$  curve formulation given by DNV 2011. The unloading phase is determined by the initial stiffness  $E_{py}^*$ . Assuming separation between the pile and the soil, a shear drag  $p_{drag}$  is introduced. For cohesionless soils, the shear drag depends on the vertical effective stress  $\sigma_v$  (Ovesen *et al.* 2006) given by  $p_{drag} = 0.6D \sigma_v$ , whereas for cohesive soils the undrained shear strength  $c_u$  must be considered, *i.e.*  $p_{drag} = 0.7Dc_u$ .

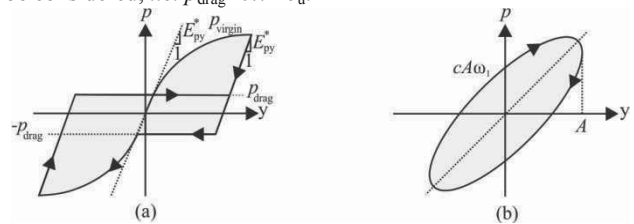


Figure 3. Hysteresis Loop Method (Nielsen 2004): (a) Load-displacement curve after the wind turbine generator shuts down, (b) Hysteresis loop implied by viscous damping in a harmonic motion with the amplitude  $A$  and the angular eigenfrequency  $\omega_1$ .

## 4 INTERPRETATION OF RESULTS

Experimental modal testing of 30 offshore wind turbines in the period 2006-2011 is presented in Figure 4a and Figure 4b in terms of the modal damping  $\delta_1$  and the eigenperiod  $T_1$  of the lowest eigenmode  $\Phi^{(1)}$ , respectively. Using a lognormal probability distribution, the 5% quantile of the modal damping  $\delta_1$  and the eigenperiod  $T_1$  are estimated to 0.11 and 2.94 s, respectively. This corresponds to an eigenfrequency  $f_1$  of 0.34 Hz. As indicated in Figure 4a and Figure 4b, the scatter of the estimated parameters is high. Increasing the R-square value from 0.95 to 0.99, meaning that the fit of the acceleration amplitude peaks and zero crossings explains 99% of the total variation in the data about the average, seems to reduce the scatter to a certain extent, see Figure 4c and Figure 4d. Overall,

a tendency of decreasing modal damping and eigenfrequency is observed for increasing acceleration level. High structural accelerations induce irreversible soil deformations and thereby soil damping activation. However, the oil damper performance is characterised by optimal damping for low levels of accelerations, which may explain the observed behaviour. In addition, distinct non-linear soil behaviour occurs for high accelerations, which reduces the secant stiffness  $E_s$  and thereby the eigenfrequency  $f_1$ .

An almost identical mean value and standard deviation of the modal parameters have been observed for each wind turbine. Hence, the variation of the modal parameters in Figure 4c and Figure 4d might be caused by the following conditions:

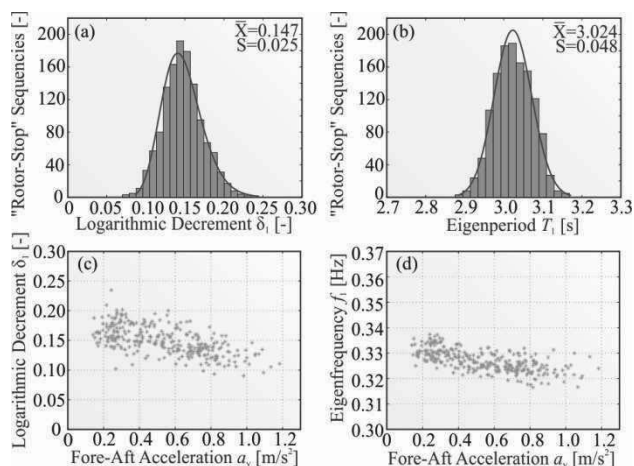


Figure 4. Free vibration tests for a total of 30 offshore wind turbines: (a) Damping histogram, (b) Eigenperiod histogram, (c) Damping vs. acceleration level, (d) Eigenfrequency vs. acceleration level.

- Tower damper performance
- Tidal variation
- Wind variation
- Temperature dependent modal parameters
- Moveable seabed and scour around the foundation

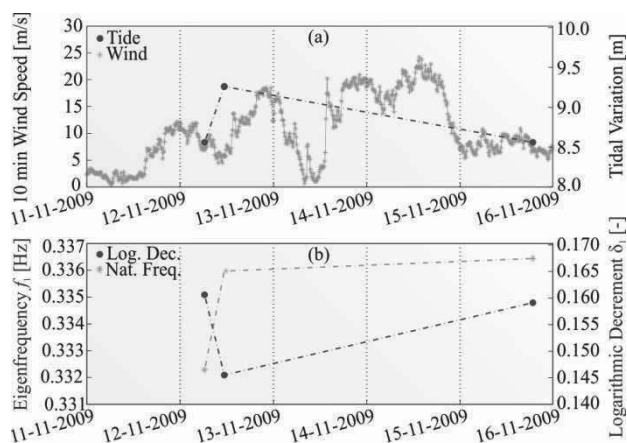


Figure 5. Selected turbine investigation: (a) Tidal and wind variation as a function of time, (b) Modal parameters as a function of time. Data are collected with same acceleration level and slope of generator speed.

It has been observed that the mass pendulum of the tower damper in some tests moves exactly with a phase identical to the phase of the wind turbine, resulting in almost no additional damping. To eliminate the variation of the tower damper performance, data for each turbine is investigated for the same slope of generator speed when the blades pitch out of the wind and for the same acceleration level. As an example, Figure 5 shows the comparison of the measured 10-minutes wind speed

and tidal variation together with the modal parameters for a selected turbine. One one-year measurements of the tidal levels at the wind park show only a maximum difference between highest and lowest astronomical tide of 2 m. It might then be assumed that the tidal variation at the wind park has negligible impact on the magnitude of the modal parameters. The same conclusion can be drawn regarding the variation in the wind speed and temperature during the tests. The aerodynamic damping is very low, when the blades pitch out of the wind, and a temperature change from  $-73^\circ$  to  $93^\circ$  only changes the Young's modulus of elasticity  $E_{\text{steel}}$  with 5% (Nielsen 2004). Based on a Winkler model this corresponds to a change in the eigenfrequency  $f_1$  of only 0.5%. In conclusion, assuming that the tower damper contributes with the same damping value in Figure 5b, the time-dependent modal parameters might be caused by erosion of soil particles near the monopile foundation.

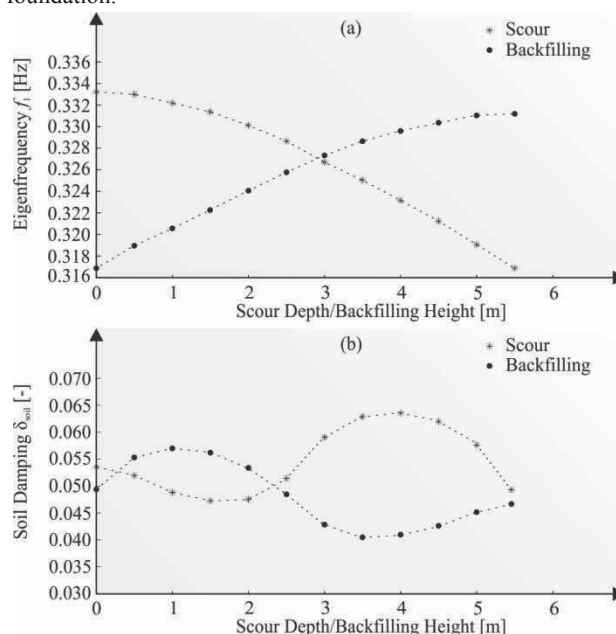


Figure 6. Scour and backfilling analysis based on a Beam on Nonlinear Winkler Foundation model: (a) Eigenfrequency  $f_1$  as a function of scour depth and backfilling height, (b) Soil damping  $\delta_{\text{soil}}$  as a function of scour depth and backfilling height.

### 1.1 Scour and Backfilling

When a pile is installed in a loose sedimentary bed, a scour hole will form around the pile. The phenomenon is of high importance, since the structural eigenfrequency and soil damping contribution will change and in worst case lead to fatigue damage and, eventually, failure. Based on experimental tests, Sumer *et al.* 1992 stated that the mean value of the equilibrium scour depth for a vertical cylinder in steady current is given by  $1.3D$ , where  $D$  is the diameter of the cylinder. However, for combined current and wave conditions the scour depth is difficult to determine, since wave action tends to reduce the scour depth (Høgedal and Hald 2005).

As no scour protection is present for the investigated wind turbine structures in this paper, the variation of the eigenfrequency  $f_1$  and soil damping  $\delta_{\text{soil}}$ , caused by sediment transportation at seabed, is estimated using a Winkler approach. Different scour depths and backfill heights are considered for a wind speed of 13 m/s with maximum depth and height equal to  $1.3D$ , respectively. The vertical effective stress  $p_0$  is reduced linearly with depth to a depth equal to  $3D$  below the base of the current scour hole. As expected, Figure 6a shows a decreasing eigenfrequency  $f_1$  for increasing scour depth. Assuming cohesionless backfill material with a friction angle  $\phi_k$  of  $28^\circ$ ,

the eigenfrequency  $f_1$  tends to increase for increasing backfill height. The material soil damping  $\delta_{\text{soil}}$  highly depends on the pile deflection and the initial stiffness  $E_{\text{py}}^*$  for each soil layer, see Figure 3. However, the pile deflection at the base of the scour hole only increases to a certain scour depth, and the initial stiffness  $E_{\text{py}}^*$  depends on the strength of each soil layer and the scour depth. Hence, for increasing scour depth the pile deflection and initial soil stiffness might increase or decrease relative to each other. This may in turn explain the observed behaviour of the soil damping  $\delta_{\text{soil}}$  in Figure 6b.

Over a period of time the relative density  $I_d$  of the backfill material might be increased due to the presence of waves inducing depth compaction (Sørensen *et al.* 2010). Hansson *et al.* 2005 have reported friction angles above 40° for Frederikshavn sand. Figure 7 shows the eigenfrequency  $f_1$  and soil damping  $\delta_{\text{soil}}$  as a function of the strength of the backfill material after the scour hole is replaced by the backfill material.

In conclusion, the Winkler approach shows a variation of the eigenfrequency  $f_1$  caused by sediment transportation at the seabed level of 8%. The model indicates a soil damping  $\delta_{\text{soil}}$  in the range of 0.05-0.08 logarithmic decrement. Hence, comparing these results with the experimental findings in Figure 5, the time-varying modal parameters of the investigated offshore wind turbines might be caused by sediment transportation at seabed.

## 2 CONCLUSION

Wind energy is a rapidly growing interdisciplinary field that involves many different disciplines within civil engineering. The dynamic behaviour of the wind turbine structure is determined by a complex interaction of components and sub-systems. A full understanding of the structural modal parameters is crucial in order to assess the fatigue damage accumulation during the lifetime of the wind turbine structure.

Experimental and numerical investigations of the dynamic properties of offshore wind turbine structures installed on a monopile foundation have been presented in this paper. Based on a total of 665 free vibration tests, time-varying modal parameters are observed, which is supported by a Winkler approach. Several interesting observations can be made:

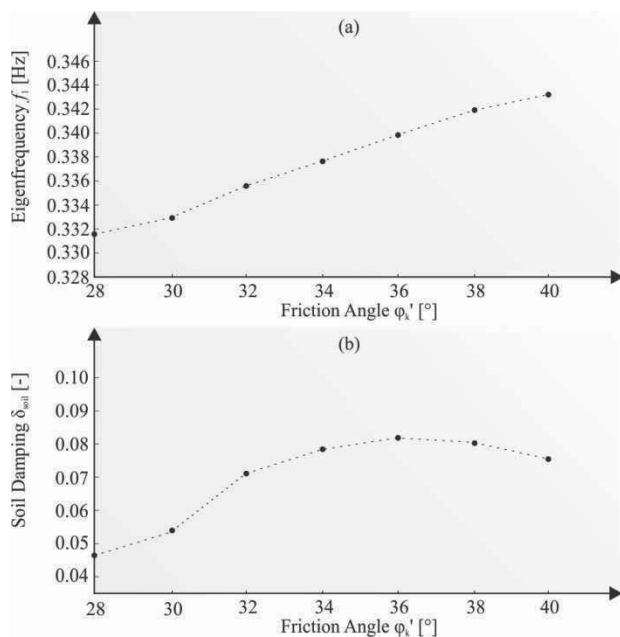


Figure 7. Strength of backfilled material based on a Beam on Nonlinear Winkler Foundation model: (a) Eigenfrequency  $f_1$  as a function of the friction angle  $\phi_k'$  of the backfill material, (b) Soil damping  $\delta_{\text{soil}}$  as a function of the friction angle  $\phi_k'$  of the backfill material.

- Experimental testing indicates a high variation in the eigenfrequency  $f_1$  and the modal damping  $\delta_1$ . A 5% quantile of 0.11 logarithmic decrement is observed, which corresponds very well with the findings for each considered turbine.
- Eliminating the tower damper performance tends to reduce the large variation of the modal parameters. However, distinctly time-varying eigenfrequencies  $f_1$  and modal damping values  $\delta_1$  are still obtained.
- A Beam on a Winkler foundation model indicates that the observed time-dependencies might be caused by sediment transportation at seabed. Scour development and backfilling change the eigenfrequency  $f_1$  with 8%, and the soil damping  $\delta_{\text{soil}}$  varies in the range 0.05-0.08.

## 3 ACKNOWLEDGEMENTS

The authors are grateful for the financial support from the research project Cost Effective Monopile Design.

## 4 REFERENCES

- Andersen L.V. 2008. Assessment of Lumped-Parameter Models for Rigid Footings. *Computers and Structures*. 88, 1333-1347.
- Damgaard M, Ibsen L.B, Andersen L.V. and Andersen J.K.F. 2012. Natural Frequency and Damping Estimation of an Offshore Wind Turbine Structure. *Proc. of the 20th Int. Offshore and Polar Engineering Conf.*, Rhodes, Greece. 300-307.
- Damgaard M, Ibsen L.B, Andersen L.V., Andersen J.K.F. and Andersen P. 2012. Damping Estimation of Prototype Bucket Foundation for Offshore Wind Turbines Identified by Full Scale Testing. *Proc. of the 5th Int. Operational Modal Analysis Conf. (IOMAC)*, Guimarães, Portugal, 300-307.
- Devriendt C., Jordaens P.J., De Sitter G. and Guillaume P. 2012. Damping Estimation of an Offshore Wind Turbine on a Monopile Foundation. *Proc. of the EWEA 2012 Conf.*, Copenhagen.
- DNV 2011. *Design of Offshore Wind Turbine Structures*. Det Norske Veritas AS.
- Hansen M.H., Thomsen K., Fuglsang P., and Knudsen T. 2006. Two Methods for Estimating Aeroelastic Damping of Operational Wind Turbine Modes from Experiments. *Wind Energy*. 9, 179-191.
- Hansson M., Hjort T.H. and Thaarup M. 2005. Data Report 0408 Frederikshavn Sand. Technical Report, Aalborg University.
- Høgedal M. and Hald T. 2005. Scour Assessment and Design for Scour for Monopile Foundations for Offshore Wind Turbines. *Copenhagen Offshore Wind*, Copenhagen.
- IEC 2005. *International Standard. Wind Turbines – Part 1: Design Requirements*. European Committee for Electrotechnical Standardization, Brussels.
- Nielsen S.R.K. 2004. *Linear Vibration Theory*. Aalborg Tekniske Universitetsforlag, Denmark.
- Ovesen N.K., Fuglsang L. and Bagge G. 2006. *Lærebog i Geoteknik*. Polyteknisk Forlag, Denmark.
- Sumer B.M., Fredsøe J., and Christiansen N. 1992. Scour Around a Vertical Pile in Waves. *Journal of Waterway, Port, Coastal and Ocean Engineering*, ASCE. 117, 15-31.
- Sørensen S.P.H., Ibsen, L.B. and Frigaard P. 2010. Experimental Evaluation of Backfill in Scour Holes around Offshore Monopiles. *Proc. of the 2nd Int. Symposium on Frontiers in Offshore Geotechnics*, Perth, Australia.
- Tarp-Johansen N.J., Andersen L., Christensen E.D., Mørch C., Kallešø B. and Frandsen S. 2009. Comparing Sources of Damping of Cross-Wind Motion. *The European Offshore Wind Conference & Exhibition*, Stockholm.
- Tcherniak D., Chauhan S., Rosseth M., Font I., Basurko J. and Salgado O. 2010. Output-Only Modal Analysis on Operating Wind Turbines: Application to Simulated Data. *European Wind Energy Conf.*, Warsaw, Poland.
- Versteijlen W.G., Metrikine A.V., Hoving J.S., Smid E. and De Vries W.E. 2011. Estimation of the Vibration Decrement of an Offshore Wind Turbine Support Structure Caused by its Interaction with Soil. *Proc. of the EWEA Offshore 2011 Conf.*, Amsterdam.
- Øye S. 1996. *FLEX 5 User Manual*. Lyngby.

# Numerical investigation of dynamic embedment of offshore pipelines

## Étude numérique de l'ancrage dynamique de conduites enterrées maritimes

Dutta S., Hawlader B.  
Memorial University, St. John's, Canada.

Phillips R.  
C-CORE, St. John's, Canada.

**ABSTRACT:** Pipelines are one of the key components of offshore oil and gas development programs. Deep water pipelines are often laid on the seabed and penetrate into soil a fraction of their diameter. High operating temperature and pressure generate axial stress that could buckle the pipeline laterally. The embedment and formation of soil berm have a significant effect on lateral resistance. The embedment of a pipeline depends on stress concentration at the touchdown point (TDP) and dynamic laying effects. In this study, large deformation finite element modelling of dynamic penetration of offshore pipeline is presented. The Coupled Eulerian Lagrangian (CEL) technique is used to develop finite element model. The pipe is first penetrated into the seabed followed by a small amplitude cyclic lateral motion. Results from the finite element models are compared with centrifuge test results. High plastic shear strain is obtained around the pipeline during cyclic loading which causes significant pipe embedment. The shape of soil berm is different from that of monotonic pipe penetration.

**RÉSUMÉ :** Les conduites enterrées sont un des éléments clés des programmes de développement de pétrole et de gaz. Des conduites enterrées en eau profonde sont souvent mises sur le plancher océanique et pénètrent dans le sol sur une fraction de leur diamètre. La température et la pression de fonctionnement élevées génèrent une contrainte axiale qui peuvent déformer la conduite latéralement. L'ancrage et le sol encaissant ont un effet significatif sur la résistance latérale. L'enfouissement d'une conduite dépend des concentrations de contraintes et des effets dynamiques de la pose. Dans cette étude, une modélisation par éléments finis en grande déformation de la pénétration dynamique de la conduite est présentée. Une technique de type Eulérien Lagrangien (CEL) est utilisée pour développer le modèle éléments finis. Le tuyau est d'abord mis en place dans le fond marin puis subit un mouvement cyclique de faible amplitude latérale. Les résultats des modèles éléments finis sont comparés avec les résultats d'essais en centrifugeuses. D'importantes valeurs de la déformation plastique sont obtenues autour de la canalisation lors du chargement cyclique ce qui nécessite un ancrage suffisant de la conduite. La forme du sol encaissant est différente de celle du tuyau mis en place statiquement.

**KEYWORDS:** pipelines, dynamic embedment, clay, large deformation analysis.

## 1 INTRODUCTION

As-laid pipelines are commonly used in deepwater. During installation the as-laid pipeline could be penetrated a fraction of its diameter into the seabed (Bruton et al. 2006), and a soil berm could be formed. The soil around the pipelines provides not only the thermal insulation and hydrodynamic stability to the pipe but also resistance to pipeline walking and lateral buckling during high operating temperature and pressure. Accurate assessment of as-laid pipe embedment is extremely difficult. Depending upon sea state, vessel conditions, pipe stiffness and soil conditions, the pipeline might experience both in-plane and out-of-plane cyclic motion during installation (Westgate et al. 2010, 2012), which causes dynamic embedment of the pipeline.

The penetration of a pipeline under static load can be obtained using bearing capacity theory, analytical solution or finite element techniques. In the current engineering practice, two additional factors are used to estimate the embedment of pipelines: (a) additional vertical force near the TDP (the point where the pipe first touches the soil) due to catenary effects and (b) dynamic lay effects. A number of methods have been proposed in the past to estimate these factors (Carneiro et al. 2010, Oliphant and Yun 2011). For example, Randolph and White (2008) proposed an empirical equation to calculate the touchdown lay factor ( $f_{lay}$ ) using pipe submerged weight, bending rigidity, horizontal component of effective tension, lay angle, water depth and seabed stiffness. The embedment factor for dynamic lay effects ( $f_{dyn}$ ) varies between 2 and 10 (Lund 2000, Bruton et al. 2006). This wide range of variation in this factor makes the assessment of pipe embedment very difficult.

During installation, both vertical and lateral pipe motions can soften the seabed soil near the pipe. Soil softening/remolding together with water entrainment can reduce the undrained shear strength of soil. Field observation (Westgate et al. 2010) and physical modeling using geotechnical centrifuge (Cheuk and White 2011) show that the horizontal cyclic motion, although small amplitude, has a significant effect on pipe embedment.

The main purpose of this study is to conduct large deformation finite element (FE) analysis for dynamic events during the installation of pipeline. Coupled Eulerian Lagrangian (CEL) technique is adopted in the analysis using ABAQUS FE software. Four FE models are developed for two different soils: kaolin and high plasticity clays (plasticity index for kaolin is 34 and for high plastic clay is 100-130, Cheuk and White 2011). The results are compared with the centrifuge test results available in the literature.

## 2 PROBLEM DEFINITION.

The problem considered in the present finite element (FE) modelling is shown in Fig.1. During laying, offshore pipelines usually penetrate vertically into the seabed due to its self-weight and catenary effect near the touchdown zone (TDZ). The vessel movement from wave loading could cause small amplitude cyclic motions in the  $x$ -direction. As the pipeline is under a vertical load ( $p_0$ ), the lateral movement in the  $x$ -direction could cause additional vertical penetration as shown by Stage-II and III in Fig. 1.

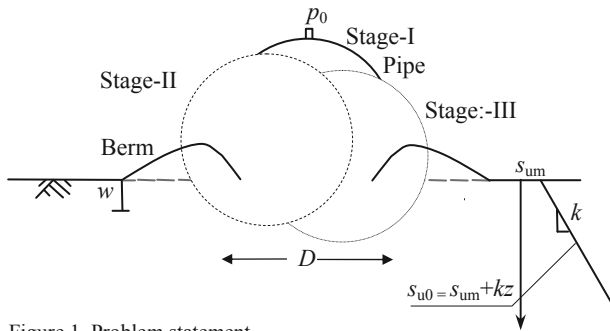


Figure 1. Problem statement.

### 3 FINITE ELEMENT MODELLING.

ABAQUS 6.10 EF-1 is used in the present finite element analysis. As the embedment of pipe in the seabed is large deformation problem, the conventional finite element techniques in Lagrangian approach cannot simulate the complete process realistically as numerical difficulties are generally encountered for such large displacements. Therefore, in this study the Coupled Eulerian Lagrangian (CEL) technique currently available in ABAQUS FE software is used. In CEL, the soil flows through the fixed mesh without having any numerical issues. The FE modeling using CEL for pipe embedment into the seabed is presented by the authors previously (Dutta et al. 2012 a&b). A soil domain of  $8\text{m} \times 3\text{m} \times 0.04\text{m}$  (length  $\times$  height  $\times$  thickness) is used in this study. The soil is modelled as Eulerian elements and the pipe is modelled as Lagrangian elements. The 1.5 m void space above the soil is required to accommodate the displaced soil mass (Eulerian materials) during pipe displacement. Zero velocity boundary conditions are applied at all faces of the Eulerian domain to make sure that Eulerian materials are within the domain and cannot move outside. However, at the seabed-void interface, no boundary condition is provided so that the soil can flow to the void. That means, the bottom of the model is restrained from any vertical movement, while all the vertical faces are restrained from any lateral movement. The pipe is modeled as a rigid body. During penetration, especially in cyclic loading, the remolding of soil near the pipe could cause significant reduction in undrained shear strength. Smooth pipe/soil interface condition is used for the present analysis. Mesh sensitivity analysis is also performed and an optimum mesh size of  $0.04\text{m} \times 0.04\text{m}$  is used (Dutta et al. 2012 a).

The loading is performed in three different stages. First, the geostatic conditions are applied to bring the seabed to in-situ condition. Second, the pipe is penetrated applying a vertical load ( $p$ ) which is the combined effect of submerged unit weight of the pipe and laying effects. In the third step, 40 cycles of small amplitude ( $\pm 0.05D$ ) lateral displacement are applied using displacement boundary conditions under the constant vertical load  $p_0$ . Plastic shear strain develops near the pipe during penetration. In the present FE analyses the degradation of undrained shear strength as a function of plastic shear strain is adopted using the following model (Einav and Randolph 2005 Wang et al. 2009 and Zhou and Randolph 2009).

$$s_u = [\delta_{rem} + (1 - \delta_{rem}) \exp(-3\xi/\xi_{95})] s_{u0} \quad (1)$$

where  $\delta_{rem} = 1/S_r$ ,  $S_r$  is the soil sensitivity,  $\xi$  is the accumulated equivalent plastic shear strain,  $s_{u0}$  is the intact undrained shear strength of soil and  $\xi_{95}$  is the accumulated plastic shear strain at 95% undrained shear strength degradation. The variation of  $s_{u0}$  with depth is shown in Fig. 1 and the von-Mises yield criteria is adopted.

In this study four cases are simulated and the results are compared with centrifuge test results of Cheuk and White (2008). Two tests (KC-04 & KC-05) are in kaolin clay and two

(HP-06 & HP-07) are in high plasticity clay. Table 1 shows the parameters used in the FE analyses. The vertical load  $p$  for initial static penetration and during cyclic motion are also shown in Table 2.

Table 1. Parameters for finite element modelling.

Pipe	Soil Properties	
	Kaolin Clay	High Plasticity Clay
Pipe diameter, $D$ (mm)	800	
Lateral displacement during cyclic motion	$\pm 0.05D$	
Undrained modulus of elasticity, $E_u$	$500s_u$	$500s_u$
Poisson's ratio, $\nu_u$	0.495	0.495
Undrained shear strength at mudline, $s_{um}$ (kPa)	0.75	0.40
Gradient of shear strength increase, $k$ (kPa/m)	1.6	2.5
Submerged unit weight of soil, $\gamma'$ (kN/m <sup>3</sup> )	6.0	3.0
Remoulded soil sensitivity, $S_r$	4.0	1.7
Accumulate absolute plastic shear strain for 95% degradation of soil strength, $\xi_{95}$	10	10

Table 2. Centrifuge test conditions (Cheuk and White 2011).

	KC-04	KC-05	HP-06	HP-07
Pipe vertical load, $p$ (kN/m)	1.17	2.23	1.47	2.61
Initial static embedment, $w_{in}/D$	0.08	0.12	0.10	0.22
Pipe vertical load at cyclic motion, $p_0$ (kN/m)	1.13	2.17	1.43	2.52

### 4 RESULTS.

The pipe was initially penetrated under a static vertical load  $p$ . The initial static embedment ( $w_{in}$ ) for this load is shown in Table 2. After initial penetration a small amplitude cyclic lateral load is applied (e.g. Fig. 2 for KC-05,  $u$  = pipe lateral displacement) to simulate the first 40 cycles (Stage-I) of centrifuge tests. The normalized lateral resistance for KC-05, where  $s_{u0(i)}$  in the horizontal axis is the intact undrained shear strength at pipe invert, is shown in Fig. 3(a) and compared with centrifuge test results Fig.3(b). The lateral resistance is slightly higher than that obtained in centrifuge test. This might be due to the limitation of the soil shear strength degradation model (Eq. 1). It is very difficult to measure and model the behaviour of soil near the pipeline under cyclic loading. However, using this simplified model (Eq. 1) in ABAQUS CEL the lateral resistance during cyclic movement is reasonably simulated.

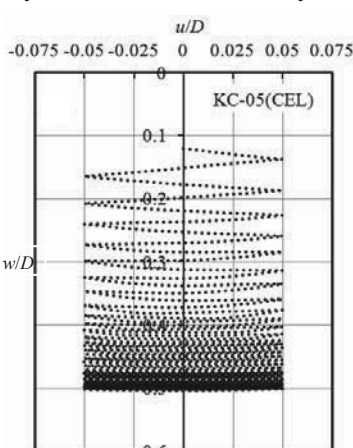


Figure 2. Pipe embedment during lateral motions

Figures 4(a),4(b) and 4(c) show the lateral resistance for other three simulations. As shown, the shape of the lateral resistance plot is different, which mainly depends on soil shear strength profile, shear strength degradation, sensitivity of soil, and applied vertical load. The depth of the invert of the pipe normalized by pipe diameter ( $D$ ) with number of load cycle is shown in Fig. 5 for comparison the centrifuge test. the present FE model reasonably simulates the embedment

of the pipe with the soil parameters listed in Table 1. Figure 5(a) shows that the depth of embedment does not increase



significantly after 20-30 load cycles for kaolin clay. However, the pattern is somehow different for high plastic clay as shown in Fig. 5(b) where the pipes continue to penetrate even after 20-30 load cycles.

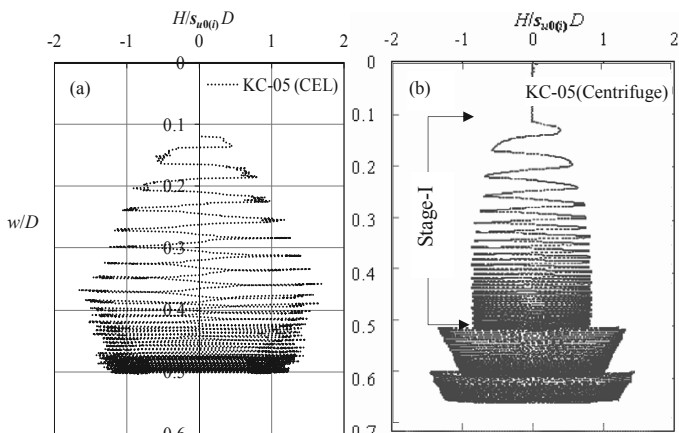


Figure 3. Test KC-05 (a) present study (b) centrifuge test.

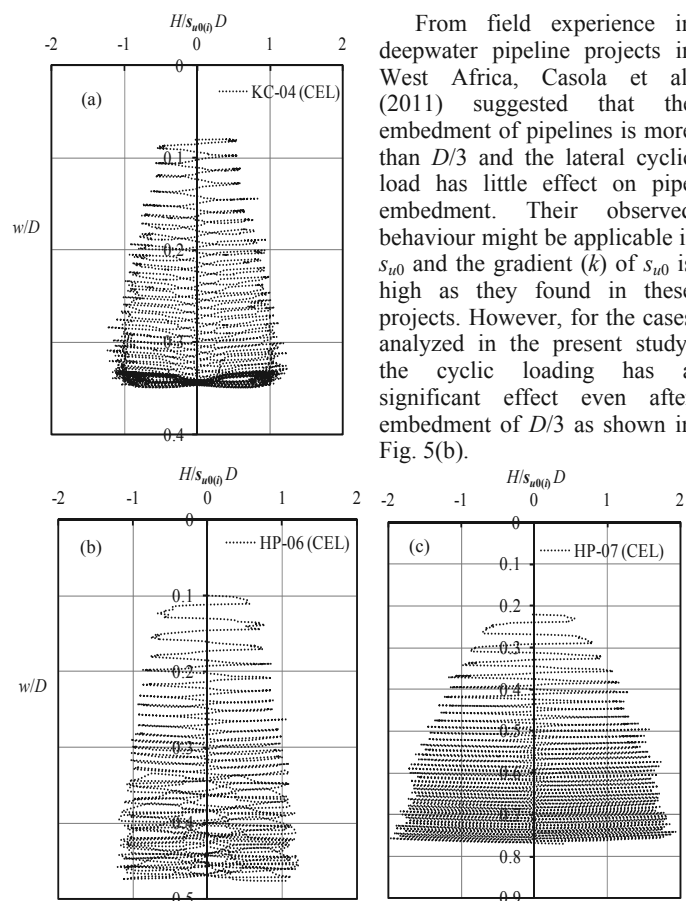


Figure 4. FE results (a) KC-04 (b) HP-06 and (d) HP-07.

## 5 DYNAMIC EMBEDMENT

In the current engineering practice the effects of laying and dynamic embedment are assessed separately. The lay effect on vertical load ( $p$ ) is obtained by multiplying the submerged unit weight of the pipe by an empirical lay factor ( $f_{lay}$ ). The monotonic embedment ( $w_{mon}$ ) for this load  $p$  is calculated using the bearing capacity theory. The effect of small amplitude cyclic lateral motion is incorporated using another empirical factor known as dynamic embedment factor ( $f_{dyn}$ ). Finally, the total embedment ( $w_f$ ) is calculated as  $w_f = f_{dyn} w_{mon}$ . In some projects

(e.g. Oliphant and Yun 2011) a combined empirical factor ( $=f_{lay} \times f_{dyn}$ ) is also used that accounts for both laying and dynamic effects. Table 3 shows the calculated values of  $f_{dyn}$  for the four tests simulated in this study. Analyzing field data of a 200 km offshore pipeline in shallow to deep water, Oliphant and Yun (2011) showed that an average value of  $f_{dyn}$  of approximately 7 could be used for estimation of pipeline embedment. Lund (2000) suggested that the value of  $f_{dyn}$  in the field varies between 2 and 10.

## 6 EQUIVALENT PLASTIC STRAIN AND BERM SHAPE.

During penetration the soil around the pipeline is softened as a function of plastic shear strain as shown in Eq. 1. The equivalent plastic shear strain at the end of penetration for two

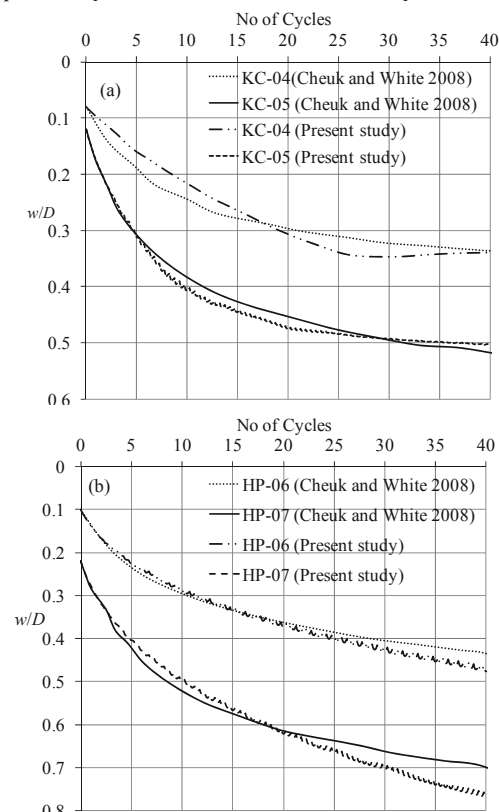


Figure 5. Pipeline embedment with horizontal cyclic motions (a) Kaolin clay (b) High plasticity clay.

cases (KC-04 and KC-05) are shown in Figs. 6(a) & 6(b). A significant plastic strain ( $>500\%$ ) is developed near the pipe. The white broken lines in Figs. 6(a) & 6(b) show the boundary above which the equivalent plastic shear strain is greater than  $\xi_{95}$  ( $=10$ ). That means 95% degradation of undrained shear strength occurred in the soil above this line (see Eq. 1). In other words, the undrained shear strength of the soil in the zone above this line is almost near the remoulded undrained shear strength. In order to show the effects of lateral cyclic loading on penetration, an analysis is performed for monotonic penetration as shown in Fig. 6(c). The geometry and soil property used in this analysis is same as KC-05 in Fig. 6(b), except the pipe moved monotonically downward to the depth of final embedment in KC-05 using a displacement boundary condition. The shear strain and berm formation for monotonic penetration is shown in Fig. 6(c). The equivalent plastic shear strain near the pipe in monotonic loading is significantly lower (Fig. 6c) than that obtain in lateral cyclic loading (Figs. 6a&b). The maximum plastic shear strain developed near the pipe in cyclic loading is almost 5 times higher than that of monotonic loading. Also the maximum equivalent plastic shear strain is less than  $\xi_{95}$ , which means that the shear strength reduction due to softening is less

than 95%. The softening has a significant effect on the shape of the berm and soil movement around the pipe. The highly softened displaced soil mass formed flat berms on the top of the seabed extended over a large distance in cyclic loading. In addition, the soil is in contact with the pipe almost up to the top of the berm. However, for monotonic loading the displaced soil mass formed a berm mainly near the pipe and the berm height is more than that of in cyclic loading. That means, the soil deformation in monotonic and cyclic loading is significantly different.

In a parametric study Dutta et al. (2012 b) showed that the effect of softening on the vertical penetration resistance in monotonic loading is not very significant, which is because of less plastic strain developed near the pipe. However, for cyclic loading huge plastic strain is developed in a zone near the pipe which causes significant reduction in undrained shear strength. That means, the zone of considerable softening is higher in cyclic loading. As in offshore the small amplitude lateral cyclic loading near the touchdown zone is commonly encountered from the motion of the vessel, the analyses for cyclic motion with strain softening behaviour of soil will provide more accurate results.

Table 3. Dynamic embedment factor,  $f_{dyn}$ .

	KC-04	KC-05	HP-06	HP-07
Initial static embedment ( $w_{in}/D$ )	0.08	0.12	0.10	0.22
Final embedment ( $w/D$ )	0.34	0.50	0.48	0.77
$f_{dyn}$	4.25	4.16	4.8	3.5

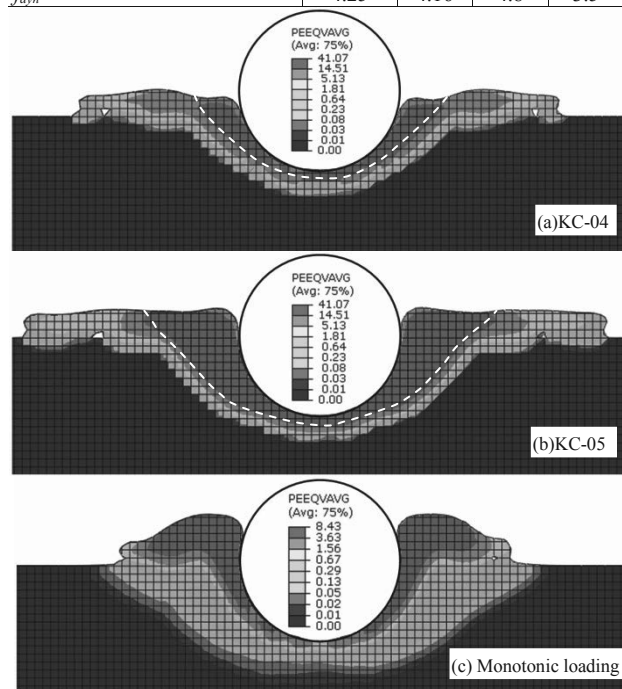


Figure 6. Equivalent plastic strain.

## 7 CONCLUSION

Large deformation finite element analyses are conducted to assess the embedment of as-laid offshore pipelines in clay. The effects of small amplitude cyclic lateral loading are investigated. The following conclusions can be drawn from this study.

- The Coupled Eulerian Lagrangian (CEL) method currently available in ABAQUS FE software can simulate the pipeline embedment.
- The plastic shear strain near the pipeline in cyclic loading is significantly higher than that of in monotonic loading.

- The shape of the berm depends on type of loading; spread over a large area in cyclic and mounted near the pipe in monotonic loading.
- The softening of soil in a zone near the pipe is significantly higher in cyclic loading compared to monotonic loading.
- Forty cycles of small amplitude lateral loading increased the embedment by a factor of 4-5 of initial static embedment. The embedment is higher in initial loading cycles.

## 8 ACKNOWLEDGEMENTS

The work has been funded by C-CORE, MITACS and NSERC Discovery grant which is greatly acknowledged.

## 9 REFERENCES

- Bruton, D., White, D., Cheuk, C. And Bolton, M. (2006). Pipe/soil interaction behaviour during lateral buckling, including large amplitude cyclic displacement tests by the Safebuck JIP. *Proc. Offshore Technology Conference*, Houston, Texas, USA. OTC 17944.
- Carneiro, D. Gouveia, J. and Parrilha, R. 2010. Feedback analysis of pipeline embedment over as-laid survey results. *Proc. Int. Conf. on Offshore Mechanics and Arctic Engineering*, Shanghai, China. OMAE2010-20410.
- Casola, F., El-chayeb, A., Greco, S. and Carlucci, A. 2011. Characterization of pipe soil interaction and influence on HP/HT pipeline design. *Proc. Int. Conf. on Offshore and Polar Engineering Conference*, Hawaii, USA, pg:111-121.
- Cheuk, Y.C. and White, J.D. 2008. Centrifuge modelling of pipe penetration due to dynamic lay effects. *Proc. Int. Conf. on Offshore Mechanics and Arctic Engineering*, Estoril, Portugal. OMAE2008-57923.
- Cheuk, Y.C. and White, J.D. 2011. Modelling the dynamic embedment of seabed pipelines. *Géotechnique* 61 (1), 39-57.
- Dutta, S., Hawlader, B. and Phillips, R. 2012a. Finite element modeling of vertical penetration of offshore pipelines using Coupled Eulerian Lagrangian approach. *Proc. Int. Conf. on Offshore and Polar Engineering Conference*, Rhodes, Greece, pg:343-348.
- Dutta, S., Hawlader, B. and Phillips, R. 2012b. Strain softening and rate effects on soil shear strength in modeling of vertical penetration of offshore pipelines. *Proc. Int. Pipeline Conference*, Alberta, Canada. IPC2012-90233.
- Einav, I. and Randolph, F.M. 2005. Combining upper bound and strain path methods for evaluating penetration resistance. *Int. J. Numer. Meth. Engng.*, 63:1991-2016.
- Lund, K.H. 2000. Effect of increase in pipeline soil penetration from installation. *Proc. Int. Conf. on Offshore Mechanics and Arctic Engineering*, New Orleans, USA. OMAE2000-PIPE5047.
- Oliphant, J. and Yun, J.G. 2011. Pipeline embedment prediction using as-laid data. *Proc. Int. Conf. on Offshore Mechanics and Arctic Engineering*, Rotterdam, The Netherlands. OMAE2011-50095.
- Randolph F.M. and White J.D. 2008. Pipeline embedment in deep water: Processes and quantitative assessment. *Proc. Offshore Technology Conference*, Houston, Texas, USA. OTC 19128.
- Wang, D., White, J.D. and Randolph, F.M. 2009. Numerical simulations of dynamic embedment during pipe laying on soft clay. *Proc. Int. Conf. on Offshore Mechanics and Arctic Engineering*, Hawaii, USA. OMAE2009-79199.
- Westgate, J.Z., White, J.D. and Randolph, F.M. 2010. Pipeline laying and embedment in soft fine-grained soils: Field observations and numerical simulations. *Proc. Offshore Technology Conference*, Houston, Texas, USA. OTC 20407.
- Westgate, J.Z., White, J.D. and Randolph, F.M. 2012. Modelling the embedment process during offshore pipe laying on fine-grained soils. *Canadian Geotechnical Journal* (accepted).
- Zhou, H. and Randolph, M. F. (2009). Numerical investigations into cycling of full-flow penetrometers in soft clay. *Géotechnique*, 59 (10), 801-812.

# Post Cyclic Behaviour of Singapore Marine Clay

## Le comportement post-cyclique de l'argile marine de Singapour

Ho J., Goh S.H., Lee F.H.  
*National University of Singapore*

**ABSTRACT:** In this paper, the post-cyclic behaviour of remoulded Singapore Marine Clay is examined. Cyclic triaxial tests, followed by monotonic loading to failure, were performed on normally consolidated specimens (38mm diameter by 76mm height) within a cyclic strain range of approximately 0.7% to 1.4%. Results herein reveal that the effective stress paths under post-cyclic monotonic loading may take on different forms depending on the mean effective stress state of the specimen at the end of the cyclic loading phase. By normalizing the mean effective stress ( $p'$ ) against the effective consolidation pressure ( $p_c'$ ) of the specimen, the effective stress paths during the post-cyclic monotonic loading may be approximately grouped into three different regimes, according to the normalized mean stress ( $p'/p_c'$ ). Within each normalized mean stress regime, the monotonic soil response is independent of the effective consolidation pressure, the cyclic strain amplitude and number of cycles applied during cyclic loading. The results suggest that the normalized mean stress after cyclic loading may be an important parameter in determining the subsequent stress path under undrained monotonic loading to failure.

**RÉSUMÉ :** Dans ce papier, le comportement post-cyclique de l'argile marine remaniée de Singapour est étudié. Des essais triaxiaux cycliques suivis de chargement monotone jusqu'à la rupture ont été effectués pour des déformations cycliques comprises entre 0,7% et 1,4% sur des échantillons normalement consolidés. Les résultats démontrent que les chemins de contrainte durant le chargement monotone post-cyclique peuvent être de formes différentes et dépendent de l'état de contrainte moyenne effective de l'échantillon à la fin de la phase du chargement cyclique. En normalisant la contrainte moyenne effective ( $p'$ ) par la contrainte de consolidation ( $p_c'$ ), les chemins de contrainte pendant le chargement monotone post-cyclique peuvent être regroupés en trois différents groupes selon la contrainte moyenne normalisée ( $p'/p_c'$ ). Dans tous les cas, la réponse monotone du sol est indépendante de la contrainte effective de consolidation, de l'amplitude de la déformation cyclique et du nombre de cycles appliqué pendant le chargement cyclique. Les résultats suggèrent que la contrainte moyenne normalisée après le chargement cyclique pourrait être un paramètre important pour déterminer, sous chargement monotone non-drainé, les chemins de contrainte jusqu'à la rupture.

**KEYWORDS:** Post-cyclic clay behaviour, Mean effective stress, Cyclic stress reversal

### 1 INTRODUCTION

Previous studies have shown that, during undrained compression loading, the effective stress path of a normally consolidated clay after cyclic loading is similar to the effective stress path of an overconsolidated clay (Hyde and Ward 1985, Matsui et al. 1992, Yasuhara et al. 1992). Researchers have adopted different frameworks in the analysis of the post-cyclic undrained shear strength of clays. One common approach is to estimate the undrained shear strength based on the maximum shear strain during the applied cyclic loading (Thiers and Seed 1969, Sangrey and France 1980). Another method of analysis is to relate the post-cyclic undrained shear strength with the apparent overconsolidation ratio induced by the cyclic loading (Matsui et al. 1992, Yasuhara et al. 1992). Apart from the post-cyclic undrained shear strength, this induced apparent overconsolidation ratio from cyclic loading was also used to determine how the subsequent monotonic effective stress path approaches the critical state line (Yasuhara et al. 1992).

However, one possible limitation in past studies is the relatively fast rates of cyclic loading used, which typically ranges from 0.5Hz to 1 Hz. At such loading rates, it is uncertain if excess pore pressure in the clay specimens will be able to dissipate. For this reason, the reliability of pore pressure measurements during cyclic loading phase may be doubtful. Fast loading rates on normally consolidated clays during undrained triaxial tests prevents equilibration of excess pore pressure within test specimens, which results in a higher pore pressure within the middle one-third portion of the specimen

(Wood 1982). This can lead to errors in effective stress calculations. Few attempts had been made to overcome the issue of unequalized pore pressures during cyclic loading. For example, Matsui et al (1992) the specimen to stand in an undrained state for 1 hour after cyclic loading and prior to post-cyclic monotonic loading to allow for equalization of pore pressures. On the other hand, Diaz-Rodriguez et al (2000) used a longer equalization period of 12 hours. Another approach is to allow drainage before post-cyclic loading to allow for pore pressures accumulated during cyclic loading to be dissipated (Yasuhara et al. 1992). The drawback of this approach is that it alters the pore pressures within specimens, leading to discontinuities in effective stress paths between the cyclic loading and post-cyclic loading phases. Intuitively, the effective stress response of a clay undergoing cyclic loading should be indicative of its post-cyclic behavior if post-cyclic monotonic loading is conducted immediately after cyclic loading. Due to possible errors effective stress measurements and discontinuities between cyclic and post-cyclic effective stress paths, a direct comparison between the cyclic and post-cyclic behavior of clays has hitherto not been possible. This objective of the study reported herein is to re-visit the issue of post-cyclic behaviour of soft clay, while ensuring adequate equilibration of excess pore pressure.

### 2 CYCLIC AND POST CYCLIC TESTING PROGRAM

A series of two way strain-controlled undrained cyclic triaxial tests were performed on remoulded specimens (38mm diameter by 76mm height) of normally consolidated Singapore Upper



Marine Clay, the standard properties of which have been reported by Tan (1983). After cyclic loading, the specimens were immediately subjected to standard consolidated undrained triaxial monotonic loading to failure. According to Ho et al. (2012), when undrained cyclic triaxial tests on clays are conducted at a sufficiently slow rate for pore pressure equilibration, intrinsic strain rate effects on pore pressure measurements, effective stress paths and stress-strain relationships are negligible. Since the focus of this study is not on strain rate effects, all tests were conducted at relatively slow rates. Both mid-plane and base pore pressure transducers were used and pore pressure equilibration is considered to be achieved when both transducers produce similar excess pore pressure measurements. All cyclic and post-cyclic triaxial tests were performed using the GDS Enterprise Level Dynamic Triaxial Testing System. Table 1 shows the experimental matrix. Experimental data presented in this study was recorded at 2-second intervals.

Table 1. Experimental Matrix.

No	Effective Consolidation Pressure, $p_c'$ (kPa)	Cyclic Amplitude		Period (min)	No. of Cycles
		Amplitude (mm)	Strain (%)		
1	50	-	-	-	0
2		-	-	-	5
3		-	-	-	10
4		1	≈1.4	10	15
5		1	≈1.4	10	20
6		1	≈1.4	10	100
7	100	-	-	-	0
8		-	-	-	2
9		-	-	-	3
10		-	-	-	4
11		1	≈1.4	14	5
12		1	≈1.4	14	6
13		1	≈1.4	14	20
14		1	≈1.4	14	30
15		1	≈1.4	14	100
16	200	-	-	-	0
17		-	-	-	2
18		-	-	-	3
19		-	-	-	4
20		1	≈1.4	60	5
21		1	≈1.4	60	6
22		1	≈1.4	60	10
23		1	≈1.4	60	30
24		1	≈1.4	60	100

### 3 EXPERIMENTAL RESULTS AND DISCUSSION

#### 3.1 Cyclic Loading

Normalized stress plots and stress-strain relationships during the cyclic tests are summarized in Figure 1. The stress path parameters, i.e. deviator stress ( $q$ ) and mean effective stress ( $p'$ ), are normalized against the effective consolidation pressure ( $p_c'$ ) for easy comparison between specimens subjected to different consolidation pressures. Post-cyclic effective stress paths are included in Figure 1. The critical state line is also plotted based on data from monotonic triaxial compression tests where the effective angle of friction for Singapore Upper Marine Clay is found to be 25.4 degrees. The initial yield locus and the state boundary surface are assumed to be elliptical.

For Singapore Upper Marine Clay specimens subjected to the same effective confining pressure, the stress paths and stress-strain relationships shown on Figure 1 for different number of applied cycles are similar, reflecting consistency among the specimens. Due to positive excess pore water

pressure generated during cyclic loading, the mean effective stress generally decreases during the reloading phase of each cycle. However, after a certain number of load cycles, the mean effective stress is observed to increase at the later part of the loading, just before the maximum deviator stress is reached, as illustrated in Figure 2. The turning point marking this change in mean effective stress is hereby termed as "stress reversal" point. These stress reversal points correspond to a decrease in shear-induced excess pore water pressure, which would seem to imply dilative behavior. As the stress reversal points appear after the normalized mean effective stress decreases beyond a certain value, post-cyclic monotonic tests are conducted after different number of load cycles to investigate the factors governing the onset of this stress reversal behaviour.

#### 3.2 Post-cyclic Loading

Normalized stress plots and stress-strain relationships during the post-cyclic monotonic tests are summarized in Figure 3, for the tests listed in Table 1. From Figure 3, the form of the effective stress paths under post-cyclic monotonic loading depends on the normalized mean effective stress state of the specimen at the start of the post-cyclic loading phase. These post-cyclic effective stress paths may be approximately grouped into three different regimes, according to the normalized mean effective stress.

When the normalized mean effective stress state of the clay specimen at the start of post-cyclic monotonic loading is greater than 0.6, stress reversal is generally absent and post-cyclic shearing shows either a decrease or no change in mean effective stress. This is akin to that of lightly over-consolidated and normally consolidated clays which tend to increase in density when sheared.

On the other hand, when the normalized mean effective stress state of the clay specimen at the start of post-cyclic monotonic loading falls below 0.5, stress reversal becomes evident and the effective stress path becomes similar to that of heavily over-consolidated clays.

Within the range of 0.5 to 0.6, the effective stress path is approximately vertical indicating that this is a boundary zone between occurrence or otherwise, of stress reversal.

Unlike the effective stress paths, the normalized stress-strain relationships are relatively similar. The post-cyclic undrained strength is almost equal to that without cyclic loading. This means that the undrained shear strength of Singapore Upper Marine Clay is not significantly influenced by cyclic loading. This observation agrees with the findings of Yasuhara et al. (1992).

#### 3.3 Effect of Cyclic Strain Amplitude

In this section, the results of four additional tests conducted at a lower strain amplitude are presented; the aim being to investigate whether strain amplitude has any effect on the stress reversal. Table 2 summarizes the four additional tests conducted.

Table 2. Additional Cyclic and Post-cyclic Tests.

No	Effective Consolidation Pressure, $p_c'$ (kPa)	Cyclic Amplitude		Period (min)	No. of Cycles
		Amplitude (mm)	Strain (%)		
1	100	0.5	≈0.7	14	10
2					15
3					20
4					110

Figure 4 presents the normalized stress plots and stress-strain relationships obtained from the additional tests. As the applied cyclic strain amplitude for these four tests has reduced by half to 0.7%, the number of load cycles required to reach the same mean effective stress state as previous tests with strain amplitude of 1.4% has increased proportionally. However, as Figure 4 shows, the post-cyclic effective stress paths of these four tests can still be categorized under the three normalized mean effective stress regimes previously discussed. The boundaries of these three regimes remain the same despite the

increase in number of load cycles and reduction in applied cyclic strain amplitude. This implies that the form of the effective stress paths of Singapore Upper Marine Clay under post-cyclic monotonic loading is dependent primarily on the mean effective stress state at the end of the cyclic loading phase.

#### 4 CONCLUSIONS

The effective stress paths of Singapore Upper Marine Clay under post-cyclic monotonic loading takes on three different forms depending on the mean effective stress state of the specimen at the end of the cyclic loading phase. Although it is commonly accepted that the undrained post-cyclic effective stress path of a normally consolidated clay is similar to the effective stress path of an overconsolidated clay (Matsui and Abe 1981, Hyde and Ward 1985, Yasuhara et al. 1992), this study shows that this condition holds only when the normalized mean effective stress state of the clay specimen at the start of

post-cyclic monotonic loading falls below 0.5. When the normalized mean effective stress state of the clay specimen at the start of post-cyclic monotonic loading is greater than 0.6, the effective stress path of the specimen still follows that of lightly over-consolidated and normally consolidated clays. Within each of these normalized mean effective stress regimes, the post-cyclic clay behavior is governed by the normalized mean effective stress after cyclic loading and independent of the effective consolidation pressure, the cyclic strain amplitude and number of cycles applied during cyclic loading.

Furthermore, stress reversal points observed during cyclic loading phase becomes evident when mean effective stress state of the clay specimen at the start of post-cyclic monotonic loading falls below 0.5. Thus, the occurrence of stress reversal during cyclic loading is indicative of dilative behavior and post-cyclic monotonic loading in this regime exhibits effective stress path of an overconsolidated clay.

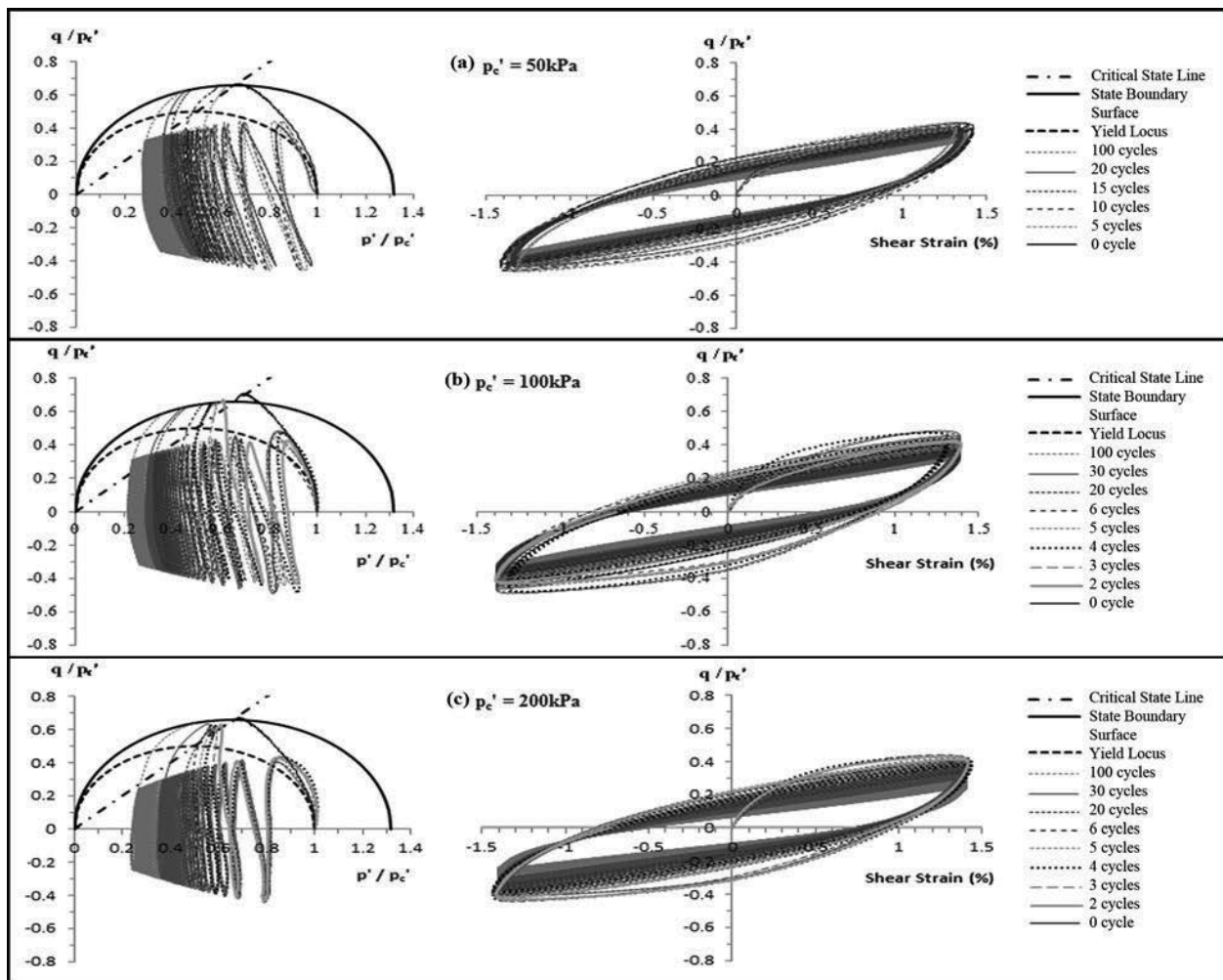


Figure 1. Effective Stress Paths and Stress-Strain Relationships for (a)  $p_c' = 50\text{kPa}$ , (b)  $p_c' = 100\text{kPa}$ , and (c)  $p_c' = 200\text{kPa}$ .

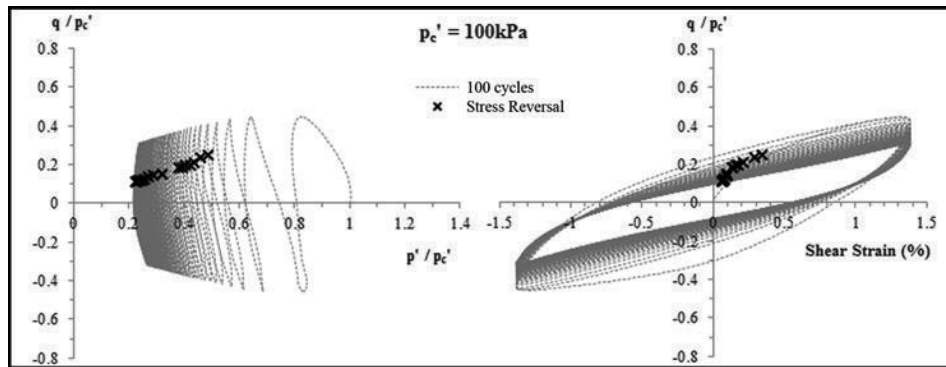


Figure 2. Stress Reversal Points.

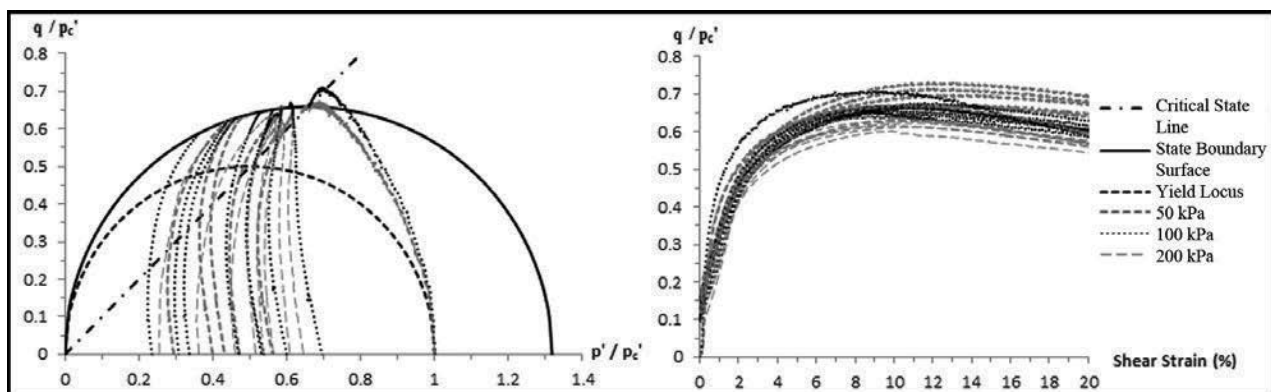


Figure 3. Post-cyclic Effective Stress Paths and Stress-Strain Relationships.

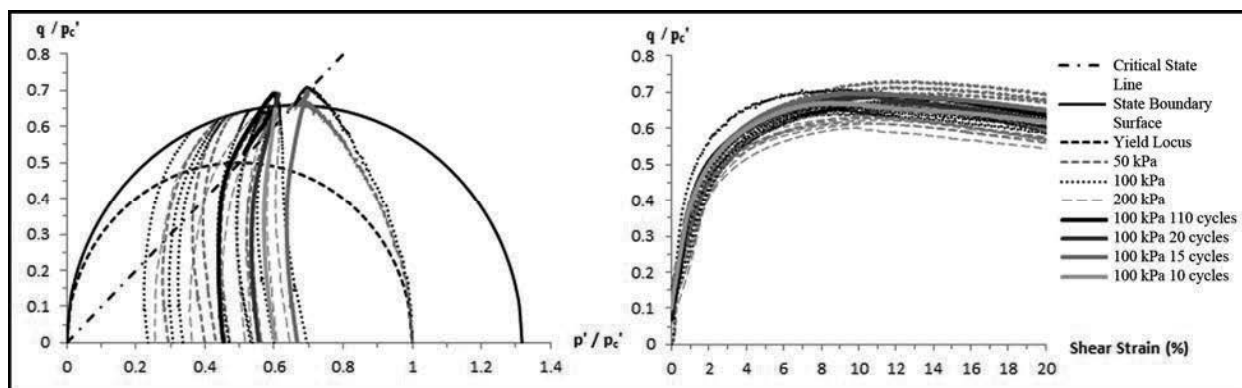


Figure 4. Post-cyclic Effective Stress Paths and Stress-Strain Relationships for Post-Cyclic Tests at 0.7% Cyclic Amplitude.

## 5 ACKNOWLEDGEMENTS

The authors are grateful to National University of Singapore for the provision of laboratory facilities, without which the research will not be possible. In particular, the main author will like to thank National University of Singapore for the research opportunity given through the award of research scholarship.

## 6 REFERENCES

Diaz-Rodriguez J.A., Moreno P. and Salinas G. 2000. Undrained shear behavior of Mexico City sediments during and after cyclic loading. Proc. 12th World Conference on Earthquake Engineering, 1652-1660.

Ho J.H., Kho Y., Goh S.H. and Lee F.H. 2012. Cyclic triaxial testing of soft clays. Proc. 25th KCCNN Symposium on Civil Engineering, 347-350.

Hyde A.F.L. and Ward S.J. 1985. A pore pressure and stability model for a silty clay under repeated loading. *Géotechnique* 35 (2), 113-125.

Tan S.L. 1983. Geotechnical properties and laboratory testing of soft soils in Singapore. Proc. 1st International Seminar on Construction Problems in Soft Soils, 1-47.

Thiers G.R. and Seed H.B. 1969. Strength and stress-strain characteristics of clays subjected to seismic loading conditions. Proc. ASTM STP 450, 3-56.

Wood, D.M. 1982. Laboratory investigations of the behaviour of soils under cyclic loading: a review. In: Soil mechanics – Transient and cyclic Loads, eds. Pande, G.N. and Zienkiewicz, O.C. John Wiley & Sons Ltd, Chichester.

Yasuhara K., Hirao K. and Hyde A.F.L. 1992. Effects of cyclic loading on undrained strength and compressibility of clay. *Soils and Foundations* 32 (1), 100-116.

# Centrifuge test and numerical modeling for a suction bucket monopod foundation

Essai en centrifugeuse et la modélisation numérique d'une fondation de type : caisson à succion

Kim D.J., Youn J.U., Jee S.H., Choi J.  
*Hyundai Engineering and Construction, Seoul, Korea*

Choo Y.W., Kim S., Kim J.H., Kim D.S.  
*Department of Civil and Environmental Engineering, KAIST, Daejeon, Korea*

Lee J.S.  
*Department of Civil and Environmental Engineering, Wonkwang University, Iksan, Korea*

**ABSTRACT:** A centrifuge load test for a preliminary design of a monopod suction bucket foundation was performed. The target site was the Yellow Sea of Korea and the prototype foundation was a steel monopod caisson with a diameter of 15.5m for a 3MW turbine. The seabed conditions comprised of a dense silty sand above layers of sandy silt were reproduced to a model soil profile using soil samples collected at nearby seashores. Horizontal load and overturning moment were applied and monitored in the test, with vertical load being simulated by self-weight of the bucket model. Series of numerical analysis were performed in order to validate test conditions and compare the effects of soil parameters.

**RÉSUMÉ :** Un test de chargement en centrifugeuse pour étudier le design préliminaire d'une fondation de type « caisson à succion » a été réalisé. Le site cible était la mer Jaune de Corée et la fondation prototype était un caisson unique en acier caisson de 15.5 m de diamètre pour une éolienne de 3 MW. La stratigraphie du fond marin, sable limoneux dense et limon sableux, a été reproduite pour faire un profil de sol modèle en utilisant des échantillons de sol prélevés sur le rivage à proximité. Un chargement horizontal et un moment de renversement ont été appliqués et contrôlés pendant l'essai, le chargement vertical était simulé en utilisant le poids propre du modèle. La modélisation numérique a été réalisée afin de valider les conditions d'essai et de comparer les effets du choix des paramètres de sol.

**KEYWORDS:** Suction bucket foundation, Monopod bucket foundation, Offshore wind, Centrifuge Test, Numerical Modeling

**MOTS-CLÉS :** Caisson à succion, Caisson de fondation, Éolienne Offshore, centrifugeuse, modélisation numérique

## 1 INTRODUCTION

Suction bucket (also termed as suction caisson or suction pile) has been considered as a viable alternative to conventional foundations for offshore wind turbines, because it has features appropriate for installing large foundations in offshore environment with minimal environmental problems (Byrne and Houlby 2003, Houlby et al. 2005, Villalobos 2006, LeBlanc et al. 2009, Hung and Kim 2012, Oh et al. 2012). In Korea, major offshore wind farm projects are planned in the Yellow Sea near the south western coast of Korea. The soil profiles are mainly composed of layers of silty sand and sandy silt.

A preliminary design was performed for field testing of suction bucket foundations, and centrifuge load tests were performed to verify and compare alternative designs. In this paper, a centrifuge test for a steel monopod with a diameter of 15.5 m and a length of 10.5 m is described. Expected horizontal load combined with moment load was applied in the test.

Numerical analyses were performed to validate the centrifuge test model conditions such as model weight and soil boundary distance. In addition, the effects of soil parameters such as elastic modulus, internal friction angle, dilation angle, cohesion and wall interface friction angle, on foundation behaviour were evaluated.

## 2 CENTRIFUGE MODELING

A centrifuge test was performed with a geotechnical centrifuge at KAIST (Korea Advanced Institute of Science and Technology) in South Korea. It has a maximum capacity of 240 g-ton and 5 m radius (Kim et al. 2012). Detailed description of the centrifuge test for this study can be found in Choo et al. (2012) and Kim et al (2013). The procedures and results are briefly described here.

The soil conditions at the target site were replicated in the model soil container for the centrifuge test. Natural soil samples collected at the Western coastal areas near the target site were used after verifying that the properties of model materials were comparable the soil samples from the target site (Figure 2). The model profile was formed in two layers of dense silty sand and medium dense sandy silt up to the depth of 32 m, which was about two times the diameter of the foundation.

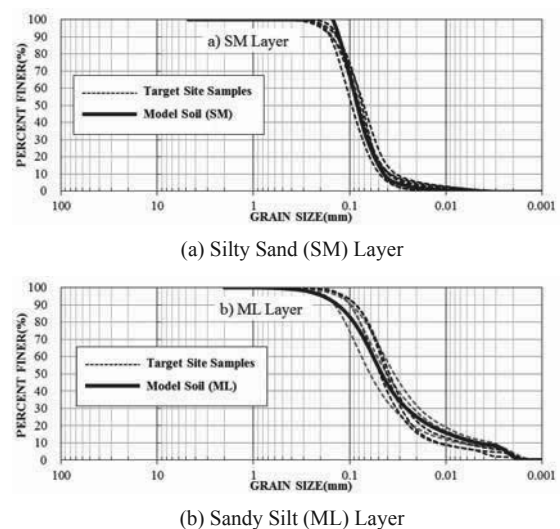


Figure 1. Comparison of grain size distributions between target site samples and model soil

A 1/70 scaled model was used for the test. Horizontal load by a displacement controlled actuator was applied and

monitored at the model tower which was located at 33.0 m height from the foundation top in prototype scale. The horizontal displacement of the tower was measured at multiple points so as to calculate the horizontal displacement and rotation of the foundation.

The load – displacement curve of the test are shown in figure 2. The load is presented in moment, which is the horizontal load multiplied by the vertical eccentricity of the load from the foundation top. The displacement is shown in terms of the rotation of the foundation. Gradual decrease in the slope was observed and the method by Villalobos (2006) was used to define the yield load, which was 198 MN-m.

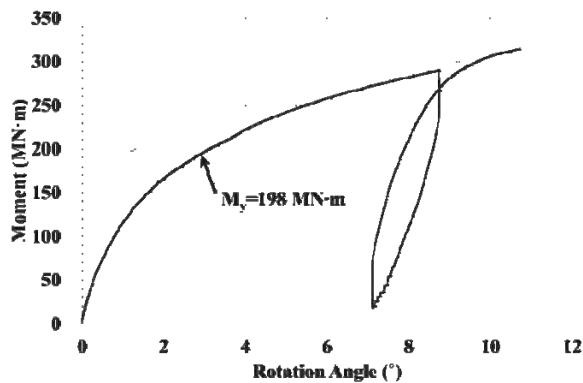


Figure 2. Moment – rotation angle curve of the centrifuge test

The model and nearby soil after the test are shown in Figure 3. Tilting of the foundation by the horizontal and moment load induced several mm of heave in the passive side and 20 to 30 mm of subsidence behind the bucket. Positions of the model before and after the load test are shown in Figure 4.

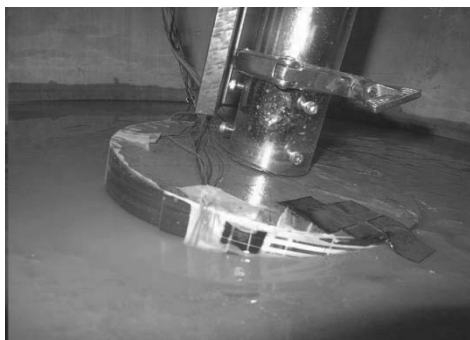


Figure 3. Model and nearby soil after the test

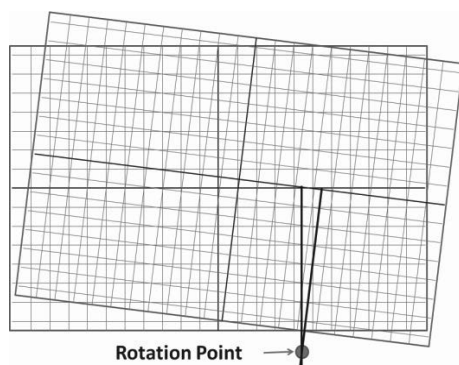


Figure 4. Comparison between positions before and after the test

### 3 NUMERICAL ANALYSIS

#### 3.1 Model setup and analysis procedures

Numerical modeling in this study was performed using FLAC 3D V 5.0 based on the finite-difference method and explicit scheme (Itasca, 2012). The numerical model was modified from a model used in Kim et al. (2013) and detailed descriptions are given for modeling and analysis procedures.

Soil elements were modeled by Mohr-Coulomb failure criterion with linear elasticity up to plastic yield and the bucket body and tower parts were modeled by linear elastic solid elements. In order to represent the load conditions, a solid circular tower was additionally modeled on top of the bucket top lid and horizontal displacement was applied on the top face of the tower. Half section model mesh and boundary conditions were used for the analysis because of the symmetry of the foundations and load conditions. Approximately 4800 elements were used in the model. Actual steel deformation properties were used in the analysis ( $E = 200 \text{ GPa}$ ,  $\nu = 0.30$ ). The mesh for the analysis is shown in Figure 5.

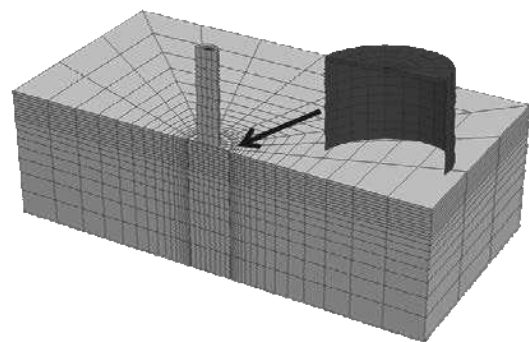


Figure 5. Mesh for numerical model (Bucket body shown in magnified scale)

The base properties for the model are shown in Table 1. The submerged unit weight of the steel used for the bucket body was modified from actual value, because the weight of the centrifuge model bucket was increased by the connection between the bucket body and the vertical rod.

Table 1. Base properties for numerical analysis

Items	Parameters		
	Bucket	SM Layer	ML Layer
Submerged unit weight ( $\gamma_{sub}$ , $\text{kN/m}^3$ )	75.9	9.50	8.60
Elastic modulus ( $E$ , MPa)	200,000	10	10
Poisson ratio ( $\nu$ )	0.3	0.3	0.3
Internal friction angle ( $\phi$ )	-	33.7	34.5
Dilation angle ( $\psi$ )	-	11.7	0
Cohesion ( $c$ , kPa)	-	16.1	5.2
Friction angle between bucket wall and soil ( $\delta$ , )	-	22.5	-
Coefficient of earth pressure at rest ( $K_0$ )	-	0.5	0.5

Bottom face nodes were fixed in vertical displacement, and side face nodes were fixed in horizontal displacement. Coulomb criterion interface elements were applied in contacting faces between the bucket body and soil in order to model sliding and separation behaviour. Shear and normal stiffness values were set to 200 MPa/m which was larger than ten times the elastic modulus of surrounding soil (Itasca, 2005).

The analysis was run in three stages. The first stage simulated the initial  $K_0$  soil condition. The second stage simulated the installation of the bucket in the soil. The third stage was the loading stage where the top of the loading tower was horizontally moved in every step and unbalanced forces were calculated as the resistance of the foundation.

The ramping algorithm was used for the loading velocity control, in which the loading velocity was linearly increased with step to  $u_{d,max}$  per step ( $1 \times 10^{-6}$  m/step in this study) till prescribed steps were run and kept constant afterwards (Itasca, 2012).

### 3.2 Analyses and results

Cases considered in this study are summarized in Table 2 and a plot of displacement contour for C2 case is shown in Figure 6.

Table 2. Analysis cases

Items	Values
A1. Reference case	Parameters in Table 1
A2. Bucket weight and vertical load	Bucket weight 2220 kN Vertical load 5750 kN
B1. Horizontal boundary distance from model center (5D for reference case)	2D
C1, C2. Elastic modulus of SM layer (E, MPa)	20, 5.0
D1, D2. Internal friction angle ( $\phi$ )	38.7, 28.7
E1. Dilation angle ( $\psi$ )	3.7
F1. Cohesion (c, kPa)	0.1
G1. C2 + F1	

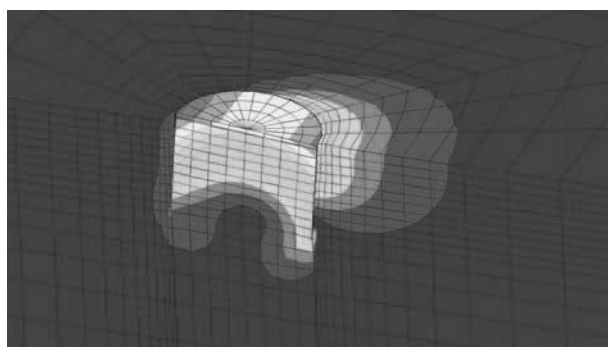


Figure 6. Contour of displacement for case C2

The prototype of the centrifuge test was modeled with larger thickness in the wall and the top plate than the preliminary design due to limitations in fabrication. The vertical rod and the connecting part between the bucket body and the rod were designed to have sufficient stiffness and strength for the centrifuge. These resulted in a heavier prototype and vertical load than the target structure in the preliminary design. Therefore, the effect of heavier structure weight was analyzed in the numerical analysis. The load – displacement curve is shown in Figure 7. Slight decrease in the resistance was observed for the reduced weight and vertical load, after around  $0.003 \sim 0.005D$ .

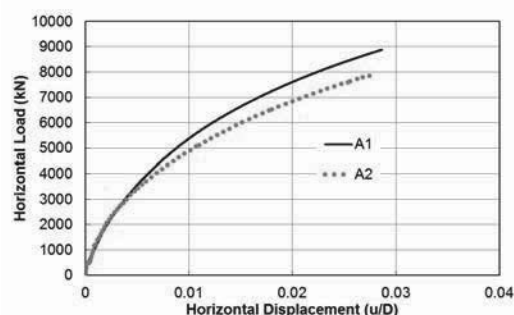


Figure 7. Load – displacement curves for different foundation weight and vertical load

The centrifuge model soil container had a radius of 447.5 mm, which was about two times the diameter of the model foundation. The results between 2D and 5D horizontal boundary distances are compared in Figure 8. The difference was negligible between the horizontal boundary distances considered.

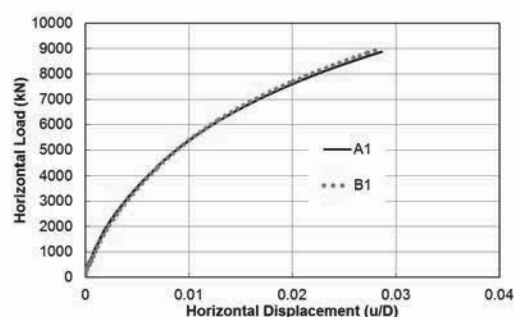


Figure 8. Load – displacement curves for different horizontal boundary distances

Different elastic moduli resulted in a noticeable variation in the slopes of the curves (Figure 9). Therefore, proper estimation of the elastic modulus and application in the numerical model are thought to be important for the load – displacement behaviour in the conditions of this study.

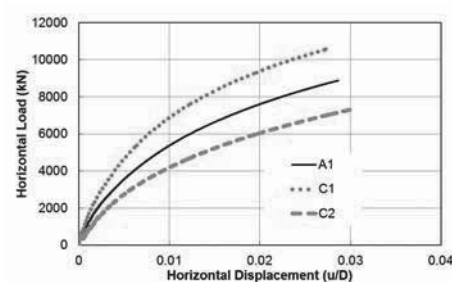


Figure 9. Load – displacement curves for different elastic moduli of the silty sand layer

The effect of variations in the internal friction angle and dilation angle of the silty sand layer was considered (Figure 10). Slight changes in slopes were observed after around  $0.005 \sim 0.01D$ , but they were found to be relatively small in the displacement range considered in this study.

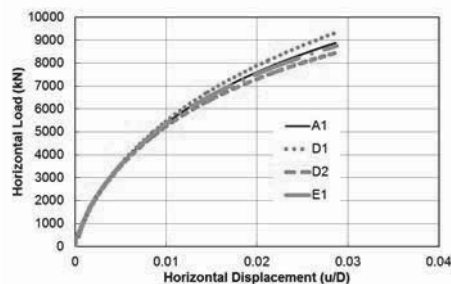


Figure 10. Load – displacement curves for different internal friction angles and dilation angles of the silty sand layer

The resistance was affected by the cohesion of the surrounding soil (Figure 11).

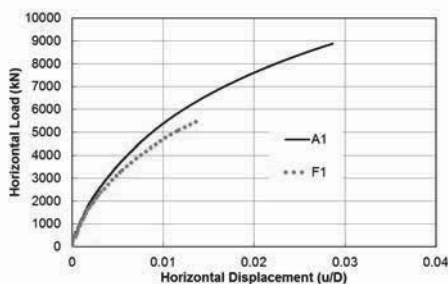


Figure 11. Load – displacement curves for different cohesions of the silty sand layer

Figure 12 shows the result when the elastic modulus and cohesion were decreased from the reference values. The curve is closer to the centrifuge test result than others. However, this does not mean that this set of parameters are the actual properties, but provides a guide on which parameters are more influential than others and how the numerical model can be improved. Further researches are needed to model the nonlinearity and the dependency on confining stress of elasticity of the silty sand layer.

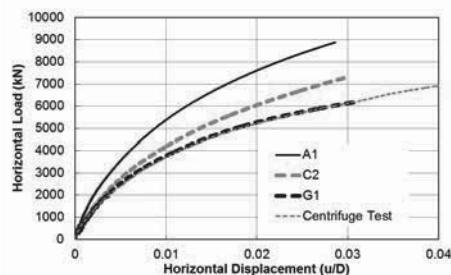


Figure 12. Comparison of load – displacement curves for the centrifuge test result and numerical model

#### 4 CONCLUSIONS

The load – displacement behaviour of a monopod suction bucket foundation was studied by a centrifuge test and numerical modeling. The centrifuge model test was performed with a model soil which represented key soil characteristics of the target site. Horizontal load combined with overturning moment was applied according to the preliminary design of an offshore wind tower. In the centrifuge test, the foundation and

soil behaviour was observed for a wide load range from the initial to the post-yield load, so that the foundation design be verified and improved based on the test result. A series of numerical modeling were performed to validate the centrifuge test condition and study the effects of soil parameters on the load-displacement curves. It was found that the increased weight and vertical load provided slight increase in the resistance. The effect of the limited horizontal boundary distance in the tested centrifuge model was analysed to be minimal. Soil parameters such as elastic modulus and cohesion were found to have significant impacts than other factors in this study on the load – displacement behaviour of the monopod foundation in the silty sand layer. Refinement of the numerical model related to these parameters and elaborate estimation of them are important for realistic modeling of the foundation behaviour.

#### 5 ACKNOWLEDGEMENTS

This study was supported by a grant from the Offshore Wind-energy Foundation System (OWFS) R&D program (10 CTIP E04) of Korea Institute of Construction & Transportation Technology Evaluation and Planning funded by Ministry of Land, Transport and Maritime Affairs and Hyundai Engineering and Construction, Co., Ltd.

#### 6 REFERENCES

- Byrne B.W. and Houlsby G.T. 2003. Foundations for offshore windturbines, *Philosophical Transactions of the Royal Society of London, Series A: Mathematical and Physical Sciences*, 361 (1813), 2909-2930.
- Choo Y.W., Kim D.J., Kim S., Kim J.H., Kim D.S., Jee S.H. and Choi J.H. 2013. Centrifuge Tests of Monopod and Tripod Bucket Foundations for Offshore Wind Turbine Tower. *Proc. of Asiafuge 2012*, Indian Institute of Technology Bombay, Mumbai, India.
- Houlsby G.T., Ibsen L.B. and Byrne B.W. 2005. Suction caissons for wind turbines, *Frontiers in Offshore Geotechnics : ISFOG*, 75-93.
- Hung L.C. and Kim S.R. 2012. Evaluation of vertical and horizontal bearing capacities of bucket foundations in clay, *Ocean Engineering*, 52, 75-82.
- Itasca. 2012. *FLAC(Fast Lagrangian Analysis of Continua) 3D User's Manual*, Itasca Consulting Group, Minneapolis, MN.
- Kim D.J., Choo Y.W., Kim S., Kim J.H., Choi H.Y., Kim D.S., Lee M.S. and Park Y.H. 2013. Bearing capacity of monopod bucket foundations for offshore wind tower via centrifuge and numerical modeling, *Journal of the Korean Geotechnical Society*, under review. (in Korean)
- Kim D.J., Choo Y.W., Lee J.S., Kim D.S., Jee S.H., Choi J., Lee M.S. and Park Y.H. 2013. Numerical Analysis of Cluster and Monopod Suction Bucket Foundation, *OMAE2013-10480*, under review.
- Kim, D.S, Kim, N.R., Choo, Y.W., and Cho, G.C. (2012), "A newly developed state-of-the-art geotechnical centrifuge in South Korea," *KSCSE Journal of Civil Engineering*, 17 (1), 77-84 (doi:10.1007/s12205-013-1350-5).
- LeBlanc C., Ahle K., Nielsen S. A. and Ibsen L. B. 2009. The monopod bucket foundation, Recent experience and challenges ahead. *European Offshore Wind 2009 Conference & Exhibition*, Stockholm, Sweden.
- Oh M.H., Kwon O., Kim K.S. and Jang I. 2012. Economic feasibility of bucket foundation for offshore wind farm. *Journal of the Korea Academia-Industrial cooperation Society*, 13 (4), 1908-1914.
- Villalobos F.A. 2006. *Model Testing of Foundations for Offshore Wind Turbines*. Ph.D. Dissertation, University of Oxford, UK.

# A large deformation finite element analysis solution for modelling dense sand

## Solution d'analyse par éléments finis d'une large déformation pour la modélisation de sable dense

Li X.<sup>1,2</sup>, Hu Y.<sup>1</sup>, White D.<sup>1</sup>

<sup>1</sup> University of Western Australian, Perth, Australia

<sup>2</sup> Beijing Jiaotong University, China

**ABSTRACT:** To capture the softening behaviour of dense sand, an extended Mohr-Coulomb model was developed using a critical state framework. The model extends Bolton's correlations to capture dilatancy and peak strength, and is compatible with the remeshing and remapping strategies used in large deformation finite element analysis. This model is initially being used to simulate the behaviour of sand layers during foundation and spudcan penetration into uniform and stratified soils, but is applicable to a variety of problems that cannot be accurately simulated using conventional M-C plasticity alone.

**RÉSUMÉ :** Pour attraper le comportement s'adoucissant de sable, un modèle de Mohr-Coulomb étendu a été développé en utilisant un cadre critique d'état. Le modèle étend les corrélations de Bolton pour capturer la dilatance et la résistance de pic, et est compatible avec les stratégies de remaillage et remappage. Ce modèle est initialement utilisé pour simuler le comportement des couches de sable lors de la pénétration du caisson vers les sols feuilletés. Donc, il sera applicable à une variété de problèmes qui ne sont pas bien capturés en utilisant la plasticité M-C conventionnel.

**KEYWORDS:** Critical state; Large deformation analysis; Remeshing and mapping algorithm; Dilation; Shear band; Biaxial test.

### 1 INTRODUCTION

Sand can display dilation and strain-softening during shearing under certain stress and relative density conditions. There are numerous constitutive models developed to capture these characteristics (Manzari and Dafalias 1997; Li et al. 1999). However, to be able to implement such a constitutive model into finite element software for large deformation analysis, a relatively simple model is essential with the minimum of control variables involved. This is to ensure that the large deformation analysis can be kept stable.

Large deformation of sand has not been analysed widely since large deformation doesn't occur in general when a conventional foundation is placed on sand. However, when foundations – such as the spudcan foundations beneath offshore drilling rigs – are placed on sand overlying clay in offshore design, it is more likely for the sand layer to experience large deformation (Yu et al. 2010). Although large deformation of layered soils has been studied extensively for stiff clay over soft clay soils using large deformation FE analysis (LDFE) and centrifuge tests, fewer LDFE studies for sand over clay conditions have been executed since to date no suitable modelling approach exists for efficient simulation of the large strain behaviour of sand.

This paper describes an investigation into the dependency of bearing capacity on the large strain shearing characteristics of sand. An extended Mohr-Coulomb (MC) model was developed, which features strain-dependent hardening and softening using a critical state framework. The model uses state dependent dilatancy and friction angles. The controlling relations have been calibrated for a number of well-characterised sands, demonstrating that the model is a practical approach that can capture the specific responses of particular soils. The model was implemented in LDFE analysis (Hu and Randolph 1998a, 1998b) using the remeshing and interpolation technique with small strain model (RITSS).

The results of LDFE/RITSS with the extended MC model show that the volumetric and softening behaviour of sand has a significant influence on the penetration resistance of foundations during large penetration. When a shear band forms in sand, its dilatancy angle reaches zero and the sand finds the critical state. For foundations on uniform sand, this model shows how the variation in the bearing capacity factors  $N_q$  and  $N_\gamma$  is linked to density and initial stress state, as well as the fundamental strength property, the critical state friction angle.

The extended CSMC model coupled with LDFE shows great potential to capture sand behaviour through large deformations in a simple and efficient computational framework.

### 2 CRITICAL STATE MOHR-COULOMB (CSMC) MODEL

#### 2.1 State dependent dilatancy angle and friction angle

Using the critical state concept, Been and Jefferies (1985) proposed a state parameter,  $\Psi$  to identify the current soil density state and to predict the subsequent shearing behaviour. The state parameter,  $\Psi$  is defined as:

$$\Psi = e - e_c \quad (1)$$

where  $e$  is the current void ratio;  $e_c$  is the critical state void ratio at current stress. The state parameter  $\Psi$  can be used to indicate the current volume change tendency of the sand and be linked to the dilation angle (Jefferies 1993; Manzari and Dafalias 1997; Li et al. 1999; Li 2002).

Been and Jefferies (1985) reported that both the peak friction angle  $\phi_p$  and dilatancy angle  $\psi$  decrease with increasing  $\Psi$ . This idea also can be extended to loose sand where negative dilatancy (or contraction) occurs. A simple single parameter relation can be written as:

$$\tan \psi = -A\Psi \quad (2)$$

where  $A$  is a constant and is suggested as 1.2 (Li et al. 2013). The parameter  $A$  serves as a scale factor to the dilatancy angle, and it influences dilatancy angle in both the negative and positive regions of the state parameter  $\Psi$ , i.e. both dense and loose sands.

For a better fit to experimental data, a three-parameter relation can be written as:

$$\tan \psi \approx A(1 - \exp^{\text{sign}(\Psi)m|\Psi|^n}) \quad (3)$$

where  $m$ ,  $n$  are constants;  $n$  is a parameter controlling the curve shape;  $m$  is a parameter majorly influenced the curve shape with positive state parameter, i.e. loose sand.

Bolton (1986) linked peak friction and dilation angles by:

$$\phi_p \approx \phi_c + a\psi \quad (4)$$

where  $\phi_c$  is critical friction angle;  $a$  is a constant. However, the value of  $a$  varies with soil stress condition and soil type (Li et al. 2003). Thus, the energy equation proposed by (Taylor 1948) is preferred here:

$$\tan \phi = \tan \phi_c + \tan \psi \quad (5)$$

Combining Eqs. 3 and 5, the relation between the mobilized friction angle and soil state parameter  $\Psi$  is illustrated in Fig. 1 with the variation of parameter  $A$ . The current state-dependent dilatancy angle and friction angle can be substituted into any modified Mohr-Coulomb (MC) model such as the hyperbolic MC model (Abbo and



Sloan 1995). This extension allows the MC model to capture soil hardening and softening behavior based on a critical state concept.

### 3 MODEL CALIBRATION

To implement state-dependent dilatancy and friction angles in the extended Mohr-Coulomb model developed here, the following parameters must be selected through the model calibration process (see Li et al. 2013 for further details):

(1) *Soil critical state line (CSL)*. A power relation (Li and Wang 1998) can be more accurate than the conventional log-linear CSL for sand under a confining pressure no more than 2MPa:

$$e_c = e_r - \lambda \left( \frac{p'}{p_a} \right)^\xi \quad (6)$$

where  $e_c$  is the critical void ratio at mean effective stress  $p'$ ;  $e_r$  is the critical void ratio as mean effective stress diminishes to zero;  $p_a$  is a reference pressure taken as,  $p_a = 101$  kPa (atmospheric pressure) for convenience;  $p'$  is the mean effective stress;  $\lambda$  is the slope of CSL in  $e$  versus  $(p'/p_a)^\xi$  plane, which is similar to the conventional compression index;  $\xi$  is a dimensionless constant. In this paper,  $\lambda$  is also termed as compression index and  $\xi$  is termed as compression power for convenience. For sand,  $\xi$  is typically 0.75 and the compression index can be estimated as  $0.01C_u$  where  $C_u$  is the coefficient of uniformity of sand;  $e_r$  is estimated as  $0.85 \times e_{\max} + 0.15 \times e_{\min}$  where  $e_{\max}$  and  $e_{\min}$  are the maximum and minimum void ratios of the sand.

(2) *Dilatancy parameter  $A$  for Eq. 2 or dilatancy parameters  $A$ ,  $m$ ,  $n$  for Eq. 3*. For Eq. 2,  $A = 1.2$  can be selected. For Eq. 3,  $m$ ,  $n$  can be estimated as 3.5, 0.75 respectively.  $A$  is to be calibrated by experimental data and is typically in the range of 0.3 to 1.0.

(3) *Young's modulus  $E$  and Poisson's ratio  $\nu$* . The stiffness of sand varies with void ratio and stress state. Good predictions can be made using the following equation (Hardin and Richart 1963; Wang et al. 1990; Li et al. 1999; De and Basudhar 2008):

$$E = E_0 \frac{(2.97 - e)^2}{1 + e} \sqrt{\frac{p'}{p_a}} \quad (7)$$

where  $E_0$  is suggested as 6~10 MPa (Carraro et al. 2009). The bulk and shear moduli,  $K$  and  $G$  can be calculated by the usual elastic relations from  $\nu$  and  $E$ .

## 4 IMPLEMENTATION OF CSMC IN LDFE

### 4.1 LDFE with RITSS technique

Large deformation FE (LDFE) analysis is conducted by remeshing and interpolation technique with small strain (RITSS) (Hu & Randolph 1998a, b). This approach is coupled with a finite element package named AFENA (Carter & Balaam, 1995). To avoid large mesh distortion and achieve large deformation simulation, a series of small strain analysis increments (using AFENA) are combined with fully automatic remeshing of the entire domain, followed by interpolation of all field variables (such as stresses and material properties) from the old mesh to the new mesh.

During the mapping of field variables, some mapping error is inevitable. The fewer number of variables that must be carried to describe the current material state, the less error will be introduced after each mapping, thus the more accurate and convergent the large deformation analysis. When CSMC constitutive model is implemented to the LDFE/RITSS, void ratio  $e$  is the only extra variable required to be interpolated in addition to the stress field. Thus, numerical stability can be kept.

In the mesh generation/remeshing algorithm, the angle in one triangle element is limited in the range of 26~111°. Two criteria are used to trigger mesh refinement: (1) the distortion ratio  $\rho$  (which is the shortest distance from the mid node to a straight line joining the corner nodes, divided by the length of that straight line) exceeding

0.02; (2) the ratio between the maximum and minimum element edge lengths exceeding 100.

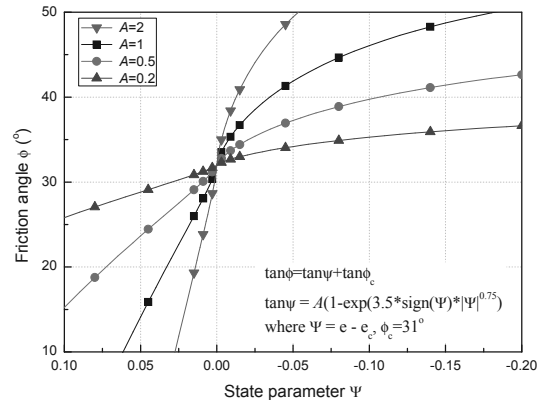


Fig. 1 Effect of parameter  $A$  on friction angle  $\phi$

### 4.2 Biaxial test

The calibration of the model parameters is illustrated using a single element simulation of a triaxial test and by a fully meshed simulation of a biaxial test, both in Ottawa sand (Alshibli et al. 2003). The close match of the prediction and the experimental data for a single element triaxial test provides the model parameters  $A = 0.36$ ,  $m = 8$ ,  $n = 0.75$  (Fig. 2).

When the calibrated parameters were applied to the bi-axial element test conditions, a much lower peak is observed (Fig. 3). However, if the dilatancy angle is increased, as the parameter  $A$  in equation 2 is raised from 0.36 to 0.6, the CSMC model shows a similar peak as the experimental data (Fig. 3). Bolton (1986) has also suggested that the dilatancy angle in plane strain test is about 1.6 times of that in triaxial test. This shows that different parameters might be needed for triaxial and biaxial test conditions. In the biaxial test, the softening behaviour is captured very well.

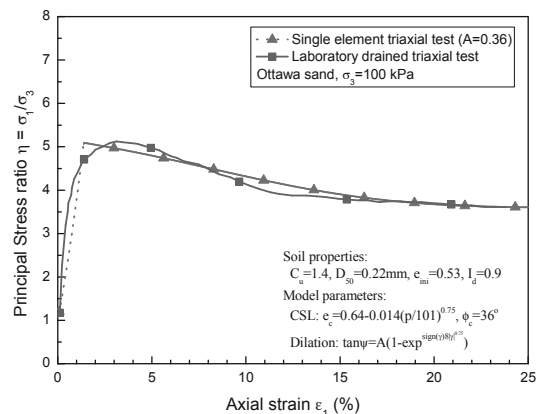


Fig. 2 Model calibration by single element triaxial test

Fig. 4 depicts the shear band formed in a biaxial test using the CSMC model. A single shear band is formed first at ~2% axial strain. Subsequently, a double shear band begins to form at ~3% axial strain and evolves gradually. This phenomenon is consistent with the observation in Alshibli et al. (2003).

The soil in the shear band yields and dilates gradually to the critical void ratio for this stress level, which is 0.61. The dilatancy angle decreases continuously until the soil reaches the critical state, mobilising  $\phi_c$ . However, the soil outside the shear band remains at the initial void ratio, i.e. 0.54. The local strain in the shear band exceeds the external strain. The single element simulation (Fig. 2) shows a much slower decrease in the principal stress ratio after the peak than the biaxial test (Fig. 3). This confirms that the measured axial strain in laboratory tests that undergo localisation is only an apparent value (Fig. 4).

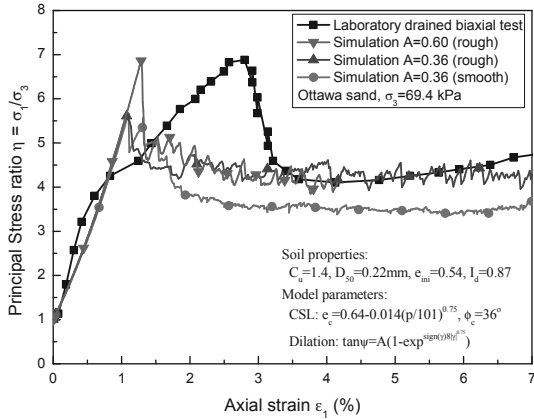


Fig. 3 Biaxial test result of Ottawa sand simulated by FEM

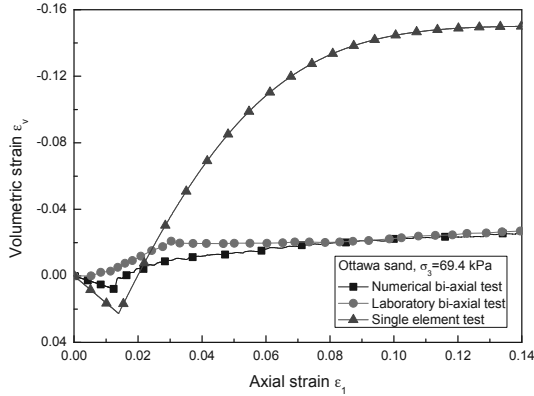


Fig. 4  $\epsilon_v$ - $\epsilon_1$  relation in biaxial test

Strain localization is critical in explaining some laboratory test results where after the peak, the deviatoric stress,  $q$ , often decreases to a stable value much earlier for axial strain than volume strain (Samieh and Wong 1997; Salgado et al. 2000; Alshibli et al. 2003). In Alshibli et al. (2003), the stress starts to oscillate around a stable value after 10% axial strain, whilst the volume strain continuously increases even over 25% axial strain. Once a “central” shear band of soil at the critical state is formed, the apparent shear strength of whole sample reaches the critical value. However the volume of whole sample still increases with yielding of soil at the margins of the shear band (Fig. 5).

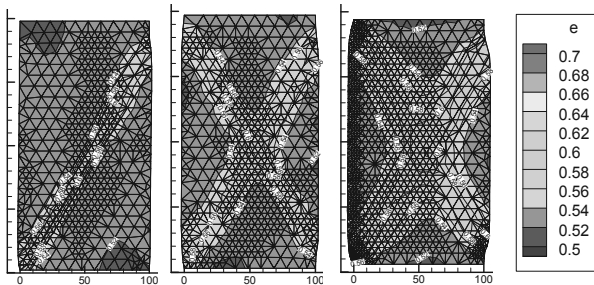


Fig. 5 Void ratio field: (a)  $\epsilon_1=2\%$ ; (b)  $\epsilon_1=3\%$ ; (c)  $\epsilon_1=9\%$

The geometry of the specimen affects the shearing behavior. Biaxial simulation results with different sample aspect ratios are shown in Fig. 6. The  $\sigma_1$ - $\epsilon_1$  relation is nearly identical in all three cases. However, the  $\epsilon_v$ - $\epsilon_1$  relation is dependent on the aspect ratio of the soil specimen and the shape of shear band formed.

5 BEARING CAPACITY OF A FOUNDATION ON SAND

The bearing capacity of circular plate on sand is analyzed by both limit analysis (using the ABC program, Martin 2004) and LDFE. In soil with self-weight the bearing capacity factor  $N_\gamma$  is often coupled with  $N_q$  although the two parts are not simply superposable. An  $N_q$ - $N_\gamma$  bounding index  $\xi$  is defined as:

$$\xi = \frac{\gamma D}{q_{surf}} \tag{8}$$

where  $\gamma D$  is a representative self-weight stress beneath the footing and  $q_{surf}$  is the surface surcharge. The coupled  $N_q$  and  $N_\gamma$  bearing capacity can be characterized by an integrated bearing capacity  $N_{q\gamma}$  that varies with  $\xi$  and is defined as:

$$N_{q\gamma} = \frac{q_u}{q_{surf}} \tag{9}$$

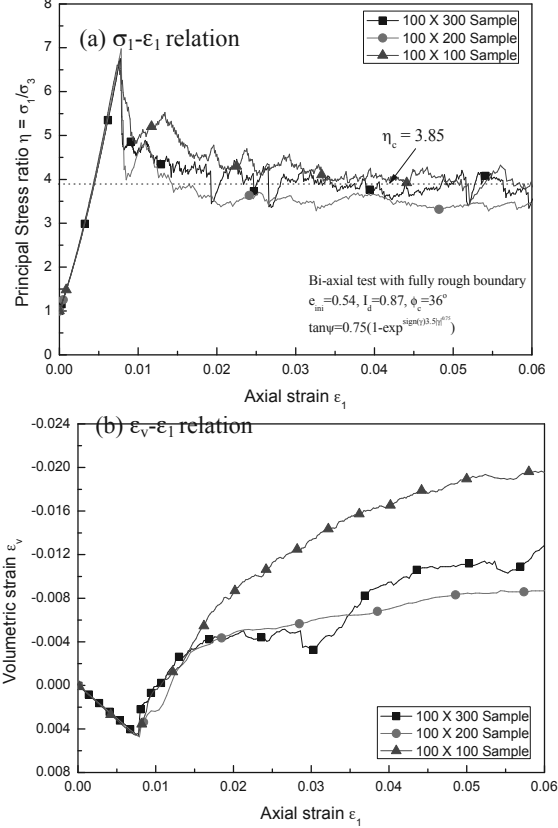


Fig. 6 Effect of sample geometry on biaxial shearing behaviour

Limit analysis using ABC shows that the integrated  $N_{q\gamma}$  factor for a rough circular foundation can be approximated as (Fig. 7):

$$N_{q\gamma} = e^{2\pi \tan \phi} \left( 1 + 0.48 \tan \phi \frac{\xi}{1 + 0.0025 \xi} \right) \tag{10}$$

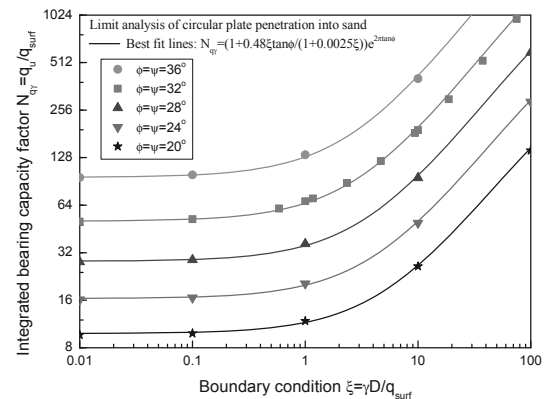


Fig. 7 Coupled bearing capacity factor  $N_{q\gamma}$  for a circular foundation

Referring to Fig. 7, the integrated  $N_{q\gamma}$  factor approaches a constant value with the decrease of the  $N_q$ - $N_\gamma$  bounding index  $\xi$ . That ultimate value,  $e^{2\pi \tan \phi}$ , can be regarded as  $N_q$ . Similarly, the integrated  $N_{q\gamma}$  of rough strip foundation can be calculated as,

$$N_{qY} = \exp^{5\pi \tan \phi} \left(1 + 0.91 \tan \phi \frac{\xi}{1 + 0.0025\xi}\right) \quad (11)$$

However, plasticity limit analysis involves certain assumptions: (1) an associated flow rule, i.e.  $\psi = \phi$ ; (2) rigid plastic strength. The FEM method can consider the effect of soil stiffness and soil dilatancy angle on bearing capacity factor and the CSMC model allows the progressive changes in strength and stiffness during bearing failure to be captured.

Calculations of the  $N_q$  bearing capacity factor for a circular plate on weightless sand have been performed using LDFE and the MC model. The results show that both stiffness and dilatancy angle have a significant influence on the soil bearing capacity. The bearing capacity factor  $N_q$  varies by up to 50% for a realistic range of stiffness. The variation of  $N_q$  induced by the variation of dilatancy angle is no more than 15%. An empirical relation can be drawn for the estimation of  $N_q$ , as:

$$N_q = (0.6 - 0.06 \ln \frac{q_{surf}}{E}) e^{2\pi \tan \phi} \quad (12)$$

For the plate on weighted sand, the integrated  $N_{qY}$  is found to vary with soil stiffness, soil weight, soil dilatancy angle and soil dimension (as shown in Fig. 8). The FEM results (Fig. 9) show that the integrated  $N_{qY}$  approaches its ultimate value  $N_q$  if  $\xi$  is smaller than 2, as follows:

$$N_q = \left(\text{atan} \frac{0.015E}{\gamma D} + 0.3\right) (0.65 + \sin \psi) \exp^{2\pi \tan \phi} \quad (13)$$

For all the cases, the integrated bearing capacity factor can be written as (seeing Fig. 8),

$$N_{qd} = \frac{0.45E}{q_{surf}} \frac{d}{D} e^{\tan \phi} \quad (14)$$

$$N_{qd} \leq N_q \left(0.95 + 0.009 \left(\frac{E}{\gamma D}\right)^{0.5} \tan \phi \frac{\xi}{1 + 0.02\xi}\right)$$

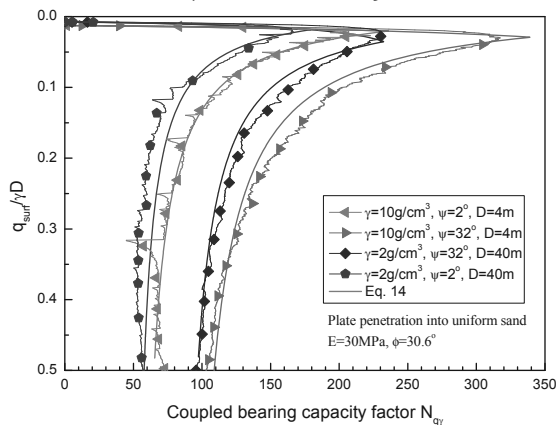


Fig. 8 Integrated bearing capacity factor  $N_{qY}$

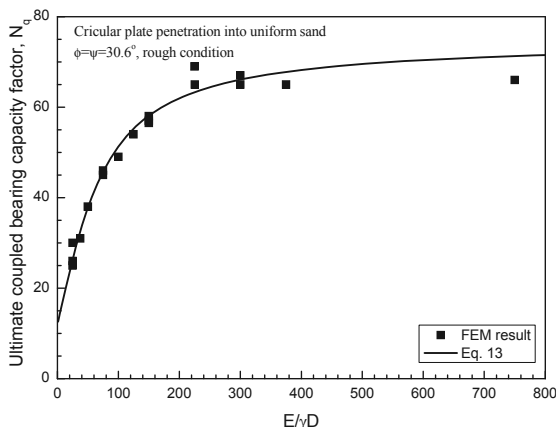


Fig. 9 Ultimate value of integrated bearing capacity factor  $N_q$

## 6 CONCLUSION

In this paper, the classic Mohr-Coulomb (MC) model is extended to simulate soil hardening and softening behaviour based on critical state (CS) soil mechanics. Friction and dilation angles are linked with soil state parameter in an MC model. This new critical state Mohr-Coulomb (CSMC) model is verified by single element tests and large deformation finite element (LDFE) analysis using the RITSS method. The newly developed CSMC model can be easily applied to large deformation analysis and shows good stability.

## ACKNOWLEDGEMENTS

This research is supported by The National Basic Research Program of China (973 Program, No. 2012CB026104) and the ARC Discovery Project DP1096764. The third author is supported by an ARC Future Fellowship and Shell.

## REFERENCES

- Abbo, A.J. and Sloan, S.W. 1995. A Smooth Hyperbolic Approximation to the Mohr-Coulomb Yield Criterion. *Computers and Structures* 54(3): 427-441.
- Alshibli, K.A. Batiste, S.N. and Sture S. 2003. Strain localization in sand: plane strain versus triaxial compression. *Journal of Geotechnical and Geoenvironmental Engineering*, 129(6): 483-494.
- Been, K. and Jefferies, M.G. 1985. A state parameter for sands. *Geotechnique*, 35(2): 99-112.
- Been, K., Jefferies, M.G., and Hachey, J. 1991. The critical state of sands. *Geotechnique*, 41(3), 365-381.
- Bolton, M.D. 1986. The strength and dilatancy of sands. *Geotechnique*, 36(1): 65-78.
- Carter, J.P. and Balaam, N.P. 1995. AFENA users manual: Geotechnical Research Center, University of Sydney.
- Hu, Y.X. and Randolph, M.F. 1998a. H-adaptive FE analysis of elastoplastic non-homogeneous soil with large deformation. *Computers and Geotechnics*, 23(1-2): 61-83.
- Hu, Y. & Randolph, M. F. 1998b. A practical numerical approach for large deformation problems in soil. *Int. J. Numerical and Analytical Meth. Geomech.* 22(5): 327-350.
- Li X. Hu, Y.X. and White, D. 2013. Development of a critical state hyperbolic Mohr-Coulomb model for sand in large deformation FE analysis. Submitted to *Geotechnique*.
- Li, X.S., Dafalias, Y.F., and Wang, Z.L. 1999. State-dependent dilatancy in critical-state constitutive modelling of sand. *Canadian Geotechnical Journal*, 36(4): 599-611.
- Ling, H.I. and Yang, S. 2006. A unified sand model based on critical state and generalized plasticity. *J. of Eng. Mech.*, 132: 1380-1391.
- Manzari, M.T., and Dafalias, Y.F. 1997. A critical state two-surface plasticity model for sands. *Geotechnique*, 47(2): 255-272.
- Martin, C.M. 2004. ABC – Analysis of Bearing Capacity. <http://www.eng.ox.ac.uk/civil/people/cmm/software>.
- Riemer, M.F. and Seed, R.B. 1997. Factors affecting apparent position of steady-state line. *Journal of Geotechnical and Geoenvironmental engineering*, 123(3): 281-287.
- Richard F., Wendell, H., Michael, M. and Gioacchino, V. Strain localization and undrained steady state of sand. *Journal of Geotechnical and Geoenvironmental Engineering*, 122(6): 462-473.
- Samieh, A.M. and R.C.K. Wong. 1997. Deformation of Athabasca oil sand in triaxial compression tests at low effective stresses under varying boundary conditions. *Canadian Geotech. J.*, 34: 985-990.
- Taylor, D.W. 1948. *Fundamentals of soil mechanics*. Wiley. New York.
- Verdugo, R., and Ishihara, K. 1996. The steady state of sandy soils. *Soils Foundation*, 36(2): 81-91.
- Wang, Z.L., Dafalias, Y.F. and Shen, C.K. 1990. Bounding surface hypoplasticity model for sand. *Journal of Engineering Mechanics*, ASCE, 116(5): 983-1001.
- Salgado R., Bandini, P. and Karim, A. 2000. Shear strength and stiffness of silt sand. *Journal of Geotechnical and Geoenvironmental Engineering*, 126: 451-461.
- Yu, L., Hu, Y.X., Liu, J., Randolph, M. and Kong, X.J. 2012. Numerical study of spudcan penetration in loose sand overlying clay. *Computers and Geotechnics*, 46: 1-12
- Carraro, H. Prezzi, M. and Salgado, R. 2009. Shear strength and Stiffness of sands containing Plastic or Nonplastic Fines. *Journal of Geotech. and Geoenvironmental Engineering*, 135(9): 1167-1178.

# Plugging Effect of Open-Ended Displacement Piles

## Prise en compte de l'effet de bouchon pour les pieux battus ouverts

Lüking J.

HOCHTIEF Solutions AG, Civil Engineering Marine and Offshore, Hamburg, Germany

Kempfert H.-G.

Institute of Geotechnics and Geohydraulics, University of Kassel, Kassel, Germany

**ABSTRACT:** During jacking an open-ended displacement pile the soil is entering through the pile toe into the profile. This plug can close up the pile toe completely. Because of this the pile can be treated approximately as a fully closed-ended displacement pile and is able to mobilize an additional base resistance. Indeed the soil-mechanical processes and the different factors of influence on the plugging effect are mostly unknown. This report is based on research work and investigated the influence of different factors on the plugging effect and hence the change in the load-bearing behaviour mainly in non-cohesive soils using experimental, numerical and statistical methods. All investigations show that a fully plugged soil inside the pile could not be identified and disproved the classical model representation of a fully plugged pile toe. The load transfer in the plug takes place by compression arches, which are mainly influenced by the pile diameter and the soil density. Finally, based on these results a practical calculation method is suggested.

**RÉSUMÉ :** Lors de la mise en place d'un pieu battu ouvert, le terrain est susceptible de pénétrer dans le pieu par son pied de manière plus ou moins importante. Suivant le degré de pénétration du sol dans le pieu, celui-ci peut être considéré comme ouvert ou fermé et une résistance supplémentaire peut alors être mobilisée. Ce papier propose une étude des processus de pénétration du terrain dans les pieux battus ouverts pour des sols non cohésifs. La variation de capacité portante des pieux induite par ces processus est analysée selon des points de vue expérimentaux, numériques et statistiques. Toutes les investigations réalisées montrent que l'effet de bouchon complet n'existe pas et qu'un pieu battu ouvert ne peut pas être considéré comme véritablement fermé. L'effet de bouchon correspond à la formation de « voûtes » à l'intérieur du pieu. Enfin, une méthode de prévision de la capacité portante intégrant ces processus est proposée.

**KEYWORDS:** open-ended displacement pile, plugging effect, pile bearing capacity, pile foundation.

## 1 INTRODUCTION

Open-ended displacement piles are piles, which are open at the pile toe like pipe piles, H-profiles or composed of sheeting piles. During the piling process (jacking, impact driving, vibrating or pressing) the soil is entering into the pile tube. Between the opposite inner shaft areas a plug can occur, which is able to mobilize an additional toe resistance. This toe resistance depends on the soil parameters, the pile geometry and the stress distribution.

Open-ended displacement piles are often used in harbour constructions or as foundations for offshore wind plants (i.e. monopiles or jackets).

Technical standards like API or others assume a fully plugged open-ended displacement pile and treat this plug in a monolithic way. However the soil-mechanical process and the different factors of influence on the plugging effect are mostly unknown.

Starting with a short state of the art this paper summarizes laboratory tests, numerical and statistical calculations and recommends new experience values for the bearing capacity of open-ended displacement piles.

These research results are based on the works described in Lüking 2010 and also Lüking and Kempfert 2012.

## 2 STATE OF THE ART

The bearing capacity of the plug can be evaluated by the values IFR (Incremental Filling Ratio) after Bruzy et al. 1991 or the PLR (Plug Length Ratio) after Paik and Lee 1993, see Eq.1 and Eq.2.

$$IFR = \Delta h_p / \Delta d_e \quad (1)$$

$$PLR = h_p / d_e \quad (2)$$

These values describe the incremental and the absolute ratio of the height of the plug  $h_p$  to the pile embedded depth  $d_e$ .

An IFR = 1 means that the surface of the plug does not penetrate into the soil during driving in comparison to the last measurement. Only the pile penetrates into the soil. This means that no plugging effect takes place.

In contrast an IFR = 0 means that the surface of the plug penetrates into the soil with the same value as the pile. In this case the pile is fully plugged and all the soil has to be displaced sideways.

The IFR will be measured during driving by a sounding line. The PLR is only measured after finishing the driving and gives only an average value for the plug development. This is problematic in layered soils.

The highest radial displacement  $u_R$  and radial stresses  $\sigma'_R$  occur by an IFR = 0. In this case the soil is fully plugged which means that the soil resistance is the same like the toe resistance of the profile. Then the plug could be treated like a monolith and is comparable to a closed-ended pile. With an increasing IFR the radial displacement and the radial stresses are decreasing. If the IFR lies between 0 and 1 the soil is partially plugged. The changeover from a full plug to a partial plug and no plugging is steady and the statuses cannot easily be distinguished. Figure 1 gives an overview of the described context after White et al. 2005.

The maximum pile diameter in which a plugging effect could occur is about 1.5 m, see Jardine et al. 2005.

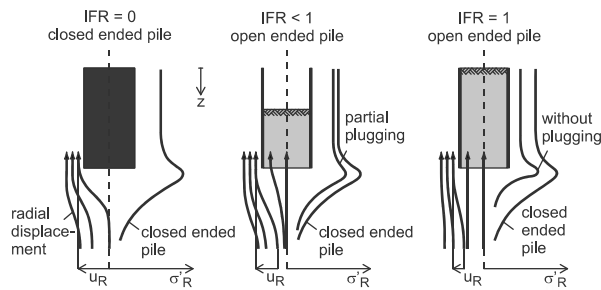


Figure 1. Distribution of the radial displacement  $u_R$  and the radial stress  $\sigma_R$  on the pile shaft depending on different IFR after White et al. 2005

### 3 EXPERIMENTAL INVESTIGATIONS

#### 3.1 General

Different experimental investigations were carried out. The next section gives a short overview of the laboratory test program before the results are discussed. A detailed description and a documentation of all test results is given in Lüking 2010.

#### 3.2 Model Tests and Particle Image Velocimetry Tests

In the first test series a test pile of two pipe piles was constructed. Both piles were only connected at the top. In all the test pile had the following geometry: outer pile diameter 19 cm and inner pile diameter 16 cm. The pile embedded depth after driving the test pile into a sand box was about 140 cm. After this a static pile test loading was carried out.

This test pile was equipped with different strain gauges. Based on the measured strain  $\epsilon$  the inner shaft friction  $q_{is}$ , the outer shaft friction  $q_s$  and the pile toe pressure  $q_b$  could be calculated. By means of a special constructed cone-penetration-test (lab-CPT) the change in density and the displacement effect of the pile installation could be examined.

In the second test series Particle Image Velocimetry (PIV) tests were carried out. The PIV method is a contact free measurement, in which displacement vectors can be identified. Basics to this method can be found in Raffel et al. 2007.

The test pile in the second test series had an outer pile diameter of 60 mm and a wall thickness of 2 mm. It was driven behind an acrylic glass to an embedded depth of 50 cm. Figure 2 gives a perspective view of both test series which were mainly carried out in non-cohesive soils.

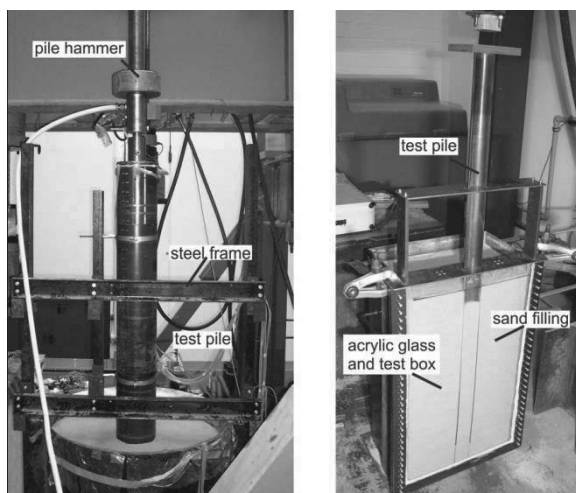


Figure 2. Perspective view of a) test pile of the first test series and b) test pile of the second test series (PIV)

#### 3.3 Results of the experimental test series

In general the experience on the pile bearing behaviour regarding different influence factors could be confirmed. With

an increasing relative density and increasing stress level the pile bearing capacity is also increasing.

The change in density around the test pile was lower in dense sands than in loose sands, which could be identified by different tests with the lab-CPT. The base resistance of the lab-CPT inside the soil plug was up to 80 MPa. A higher density of the soil tends to a higher IFR. Nevertheless the IFR does not converge to a fixed value. It was increasing and also decreasing during driving which means that the soil inside was plugging and loosening again. This phenomenon was also identified during the static pile test loading. However during both test series the value never reached IFR = 0. The minimum was IFR = 0.2. This means that only a partially plugged soil could occur and based on this the concept of a monolithical soil plug should be analyzed critically.

Figure 3 shows the distribution of the inner and outer shaft friction at different load levels from the first test series. The outer shaft friction is increasing with higher pile length as expected. In contrary the inner shaft friction is very high on a length which approximate two pile diameters. Above this the inner shaft friction in section 1 and 2 is very low and it looks approximately independent of the load level. The increasing of the inner shaft friction in section 3 is an indication for a (partial) plugging effect of the soil.

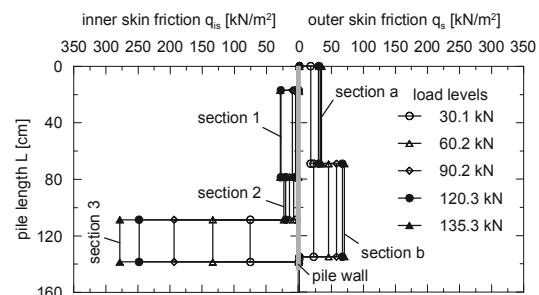


Figure 3. Distribution of the inner and outer shaft friction  $q_{is}$  and  $q_s$  for different load levels in non-cohesive soils.

Figure 4 shows the vertical displacement of the soil on the lowest two pile diameters exemplary for the second test series.

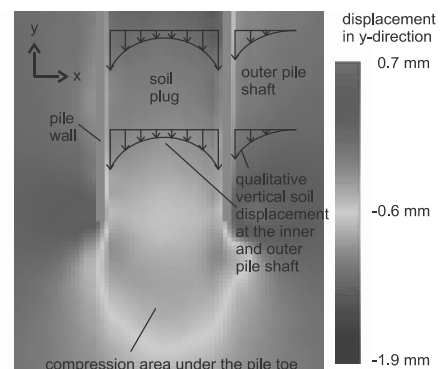


Figure 4. Distribution of the vertical displacements in the soil at the pile toe in the second test series in non-cohesive soils.

There an inhomogeneous distribution could be identified. Near the inner pile shaft the vertical displacement is much higher than in the middle of the soil plug. This distribution occurs during driving independently of all investigated boundary conditions in the second test series. It is another indication that the load transfer takes place by the inner shaft friction and not by an additional base resistance underneath the soil plug. This assumption can also be supported by the comparable distribution of the inner and outer shaft frictions, see also in Figure 3. For a monolithical approach the vertical displacement had to be more constant which could not be observed. Furthermore the tests show that these results in non-cohesive soils cannot be transferred easily to cohesive soils. It

looks like that two different mechanisms are active which are not comparable.

## 4 NUMERICAL INVESTIGATIONS

### 4.1 General

The experimental works were further investigated by finite element calculations. The experimental test loadings as well as test loadings with bigger pile diameter were recalculated. The numerical calculation software PLAXIS 2D - Version 9.0 was used. A rotation-symmetric, 2-dimensional FE-model was built. The simulation of the soil displacement during jacking was considered by the method of Dijkstra et al. 2006. A detailed calculation description and the verification of the numerical model is given in Lükling 2010.

Finally the numerical results confirmed the results of the experimental tests quantitatively and qualitatively.

### 4.2 Results of the numerical calculations

Figure 5 shows the distribution of the inner skin friction for different inner pile diameters ( $D_i = 0.45$  m up to  $D_i = 3.95$  m) of a pile which is embedded in the soil of about  $d_c = 10$  m. The soil is non-cohesive and has a “dense” relative density (cone penetration resistance of about  $q_c \approx 20$  MPa). The settlement for the mobilization of the skin friction was about  $s = 4.2$  cm.

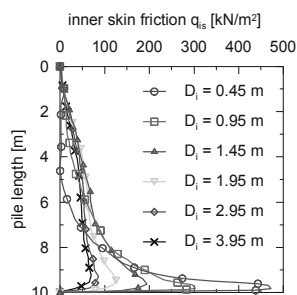


Figure 5. Distribution of the inner skin friction  $q_{is}$  under variation of the inner pile diameter  $D_i$  at a pile embedded length of  $d_c = 10$  m and a pile settlement of about  $s = 4.2$  cm

At low pile diameter ( $D_i = 0.45$  m) the results show a good agreement in the distribution to the experimental works, compare Figure 3 with Figure 5.

Furthermore the results show that the inner skin friction for lower pile diameters is significantly higher at a length of approximately two pile diameters. On the upper part of the pile length no skin friction was mobilized. With an increasing pile diameter the peak value of the skin friction is reduced and is transferred to the upper part of the pile. At pile diameters of about 3 m or 4 m the distribution of the inner skin friction is comparable to the outer skin friction. The changeover from a raised inner skin friction to a more constant inner skin friction is continuous. Calculations show that this changeover depends mainly on the pile diameter and the relative density of the soil, see Lükling 2010. The distribution of the inner skin friction is also valid at “loose” relative density ( $q_c \approx 10$  MPa).

Figure 6 shows the numerical results for the orientation of the stress trajectories and for the load transfer depending on the pile diameter in a “dense” relative density of a non-cohesive soil. The left part of each pile shows the derived load transfer based on the stress trajectories which are shown on the right part. In general all results show a rotation of the stress trajectories near the pile toe and also at the pile wall. With increasing distance from the pile wall to the middle of the soil plug the rotation is reducing. Also this depends mainly on the pile diameter.

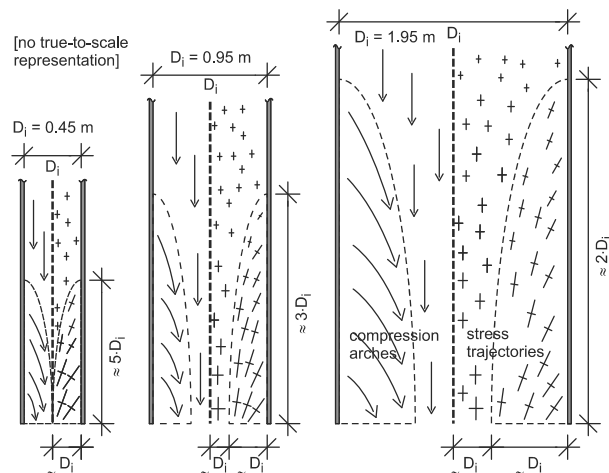


Figure 6. Numerical results for the orientation of the stress trajectories (right part of each pile) and the derived load transfer (left part of each pile) for different pile diameters in a “dense” relative density of a non-cohesive soil

The orientation of the stress trajectories suggests a compression arch, which is in analogy to the load transfer mechanism of the outer skin friction, see Kempfert 2009.

At low pile diameters these compression arches can be overlapped and results in another support. Because of this the inner skin friction can increase significantly which is also shown in the numerical and experimental results, compare Figure 5 and Figure 3. With increasing pile diameter the height of the compression arches is also increasing. This load transfer could also be identified in “loose” relative density.

Finally the results suggest that the load transfer takes place over an inner skin friction which is based on compression arches inside the soil. No fully plugged soil inside an open-ended displacement pile could be identified which would legitimate to treat the plug in a monolithic way.

## 5 CALCULATION METHODS

### 5.1 General

Based on the new knowledge two feasible methods for calculating the bearing capacity of open-ended displacement piles are suggested. The values were verified statistically to a large extend with calculation method 1 up to a pile diameter of  $D = 1.6$  m in cohesive and non cohesive soils and with calculation method 2 up to a pile diameter of  $D = 1.2$  m in non-cohesive soils. All histograms of the statistical verifications can be found in Lükling 2010.

### 5.2 Calculation Method 1

Calculation method 1 is based on an analysis of 28 static and 59 dynamic pile loading tests with pile diameters up to  $D = 1.6$  m. This method derived new adaptation factors which are linked to the values of experience of the EA-Pfähle 2012. The basic equation for calculating the pile resistance is given in Eq.3.

$$R_k = \eta_b \cdot q_{bk} \cdot A_b + \eta_s \cdot q_{s,k} \cdot A_s \quad (3)$$

- $R_k$ : characteristic pile resistance
- $\eta_b$ : adaptation factor for the pile toe, see Eq.4
- $q_{b,k}$ : characteristic pile toe pressure after EA-Pfähle 2012
- $A_b$ : pile base area (contact area of the pile and the bottom area of the soil plug)
- $\eta_s$ : adaptation factor for the pile skin, see Eq.5
- $q_{s,k}$ : characteristic pile skin friction after EA-Pfähle 2012
- $A_s$ : outer shaft area of the pile

The best compliance for the adaption factors was found by a hyperbolic correlation, see Eq.4 and 5.

$$\eta_b = 0.95 \cdot e^{-1.2 \cdot D_a} \quad (4)$$

$$\eta_g = 1.1 \cdot e^{-0.63 \cdot D_a} \quad (5)$$

$D_a$ : outer pile diameter

### 5.3 Calculation Method 2

Calculation method 2 is based on an analysis of 28 static pile loading tests with pile diameters up to  $D = 1.2$  m. In contrary to calculation method 1 this method derived new values of experience for each part of pile resistance for the 10 % and the 50 % quantile. Eq.6 gives the basic equation.

$$R_k = q_{is,k} \cdot A_{is} + q_{ak} \cdot A_a + q_{s,k} \cdot A_s \quad (6)$$

- $R_k$ : characteristic pile resistance
- $q_{is,k}$ : characteristic inner pile skin friction after Table 1
- $q_{a,k}$ : characteristic pile toe pressure of the pile contact area after Table 2
- $q_{s,k}$ : characteristic outer pile skin friction after Table 3
- $A_{is}$ : inner shaft area of the pile
- $A_a$ : contact area of the pile
- $A_s$ : outer shaft area of the pile

This method is valid for pile diameters from 0.3 m up to 1.2 m only in non-cohesive soils. The first values of the experiences in the following tables are the 10 % quantile and the second are the 50 % quantile.

Table 1. Values of experience for the characteristic inner shaft friction  $q_{is,k}$  depending on the pile settlement and the resistance of the CPT

Settlement $s$	Characteristic inner shaft friction $q_{is,k}$ [kN/m <sup>2</sup> ] at a cone penetration resistance $q_c$ [MN/m <sup>2</sup> ]		
	7.5	15	≥ 25
$s = 0.035 \cdot D_a$	15/κ ÷ 35/κ	35/κ ÷ 55/κ	50/κ ÷ 67.5/κ
$s = 0.1 \cdot D_a$	30/κ ÷ 50/κ	60/κ ÷ 80/κ	90/κ ÷ 100/κ

with  $\kappa = 2 \cdot \text{PLR}$ , see Eq. 2

Table 2. Values of experience for the characteristic pile toe pressure  $q_{a,k}$  depending on the pile settlement and the resistance of the CPT

Settlement $s$	Characteristic pile toe pressure $q_{a,k}$ [kN/m <sup>2</sup> ] at a cone penetration resistance $q_c$ [MN/m <sup>2</sup> ]		
	7.5	15	≥ 25
$s = 0.035 \cdot D_a$	650 ÷ 1.200	1.300 ÷ 1.750	1.750 ÷ 2.800
$s = 0.1 \cdot D_a$	1.100 ÷ 2.000	2.000 ÷ 3.000	2.800 ÷ 4.800

Table 3. Values of experience for the characteristic outer shaft friction  $q_{s,k}$  depending on the pile settlement and the resistance of the CPT

Settlement $s$	Characteristic outer shaft friction $q_{s,k}$ [kN/m <sup>2</sup> ] at a cone penetration resistance $q_c$ [MN/m <sup>2</sup> ]		
	7.5	15	≥ 25
$S_g^*$	15 ÷ 25	30 ÷ 50	50 ÷ 70
$s = 0.1 \cdot D_a$	20 ÷ 30	35 ÷ 60	55 ÷ 75

with  $S_g^* [\text{cm}] = 0.5 \cdot R_{s,k} [\text{MN}] \leq 1 [\text{cm}]$

### 5.4 Comparable Calculations

Figure 7 gives an overview of the calculation results of both methods compared with the results of the pile load tests.

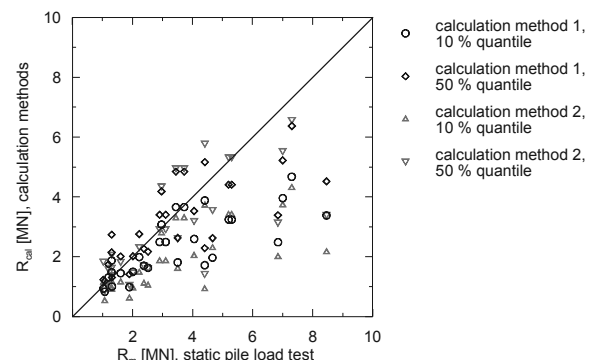


Figure 7. Calculation results for the characteristic pile resistance  $R_{cal}$  of both calculation methods in comparison to results  $R_m$  of static pile load tests

Figure 7 shows that the requirements of the calculation methods for the 10 % and 50 % quantile are fully accomplished. Further calculations and variations of parameters are given in Lükling 2010.

### 6 SUMMARY

The load transfer inside a plug of an open-ended displacement pile was investigated by experimental, numerical and statistical methods. It was shown that the load transfer takes place by compression arches. A fully plugged soil could not be identified.

### 7 REFERENCES

API RP 2A-WSD 2007. *Recommended Practice for Planning, Designing and Constructing Fixed Offshore Platforms - Working Stress Design*, 21st Edition, American Petroleum Institute, Washington

Brucy F., Meunier J. and Nauroy J.-F. 1991. *Behavior of Pile Plug in Sandy Soils during and after Driving*. Proceedings of the 23rd Offshore Technology Conference, OTC 6514, Vol. 1, pp 145-154

Dijkstra J., Broere W., and van Tol A. F. 2006. *Numerical Investigation into Stress and Strain Development around a Displacement Pile in Sand*. Proceedings of the 6th European Conference on Numerical Methods in Geotechnical Engineering. NUMGE 06, pp 595-600

Empfehlungen des Arbeitskreises „Pfähle“ EA-Pfähle 2012. Empfehlungen des Arbeitskreises „Pfähle“; 2. Edition, Ed. Arbeitskreis „Pfähle“ of the German Society of Geotechnics. Ernst & Sohn. Berlin

Jardine R. J., Chow F. C., Overy R. F. and Standing J. R. 2005. *ICP Design Methods for Driven Piles in Sands and Clays*. Thomas Telford, London

Kempfert H.-G. 2009. Pfahlgründungen. Chapter 3.2 in: *Grundbau-Taschenbuch*. 7th edition. Part 3. Ernst & Sohn. Berlin. pp 73-277

Lükling J. 2010. *Tragverhalten von offenen Verdrängungspfählen unter Berücksichtigung der Pfropfenbildung in nichtbindigen Böden*. Schriftenreihe Geotechnik, University of Kassel, Issue 23.

Lükling J. and Kempfert H.-G. 2012. *Untersuchung der Pfropfenbildung an offenen Verdrängungspfählen*. Bautechnik 89, Issue 4, pp 264-274.

Paik K.-H. and Lee S.-R. 1993. *Behavior of Soil Plugs in Open-Ended Model Piles Driven into Sands*. Marine Georesources and Geotechnology, Vol. 11, pp 353-373

Raffel M., Willert C., Wereley S. and Kompenhans J. 2007. *Particle Image Velocimetry - A Practical Guide*. Second Edition, Springer-Verlag, Berlin Heidelberg New York

White D. J., Schneider J. A. and Lehane B. M. 2005. *The Influence of Effective Area Ratio on Shaft Friction of Displacement Piles in Sand*. Proceedings of the International Symposium on Frontiers in Offshore Geotechnics, Balkema, Rotterdam, pp 741-747

# A simplified procedure to assess the dynamic stability of a caisson breakwater

## Une procédure simplifiée pour évaluer la stabilité dynamique d'une digue en caissons

Madrid R., Gens A., Alonso E., Tarrago D.

Dep. of Geotechnical Engineering and Geosciences, Technical University of Catalonia, Barcelona, Spain

**ABSTRACT:** The paper describes a simplified method of analysis used to evaluate the stability of a caisson breakwater to sea wave actions. An intensive laboratory program was performed in order to evaluate the static and dynamic characteristics of the foundation soil. Anisotropic and isotropic consolidated cyclic triaxial tests and cyclic simple shear tests were used to define the cyclic interaction diagram for the foundation soil. The possibility of foundation cyclic mobility due to wave loading and their effect on the breakwater stability was examined combining the cyclic interaction diagram with the results of finite element analysis. The potential reduction in soil strength is then incorporated into a conventional stability analysis. The procedure is illustrated by a specific application to a caisson breakwater that is part of the extension works of the Barcelona Harbour.

**RÉSUMÉ :** L'article décrit une méthode simplifiée pour évaluer la stabilité d'une digue verticale sous l'action de la houle. Les caractéristiques statiques et dynamiques de la fondation ont été évaluées à l'aide d'un programme intensif de tests en laboratoire, qui inclut des essais triaxiaux cycliques isotrope et anisotrope et des essais de cisaillement simple cycliques dans le but d'établir le diagramme d'interaction cyclique du sol. La possibilité d'une mobilité cyclique de la fondation sous l'action de la houle et son effet sur la stabilité de la digue ont été examinés en combinant le diagramme d'interaction cyclique ainsi obtenu avec une analyse numérique par Éléments Finis. La réduction potentielle de la résistance du sol est ensuite incorporée dans une analyse de stabilité conventionnelle. La procédure est illustrée par une application spécifique à une digue en caissons qui fait partie des travaux d'extension du port de Barcelone.

**KEYWORDS:** cyclic tests, interaction diagrams, liquefaction, caisson breakwater, wave loading, stability.

## 1 INTRODUCTION

Two new breakwaters and a large container area, immediate to a new quay, are the main development works of the ongoing extension of Barcelona harbour. A plan view of the new breakwaters and quays is shown in Figure 1.

Breakwaters have a total length of 6.8 km. The East breakwater is of a rubble mound type whereas the South breakwater involves two different types: rubble mound and vertical caissons. This paper refers to the caissons section that has a total length of 1.7 km constructed in water depths that range from 20m to 25m. Most of the foundation soil immediately under the breakwaters consists of weak sediments of clayey silts and silty clays belonging to the pro-deltaic deposits of the Llobregat River.

The paper describes summarily the main geotechnical features of the foundation ground with special attention given to undrained strength parameters. The bases for the static design of the breakwater are then briefly presented. Finally, a description of the cyclic resistance of the foundation soil is described in terms of an interaction diagram; this information is then used in a simplified assessment of the stability of the breakwater under storm conditions incorporating the potential strength reduction due to cyclic loading.

## 2 SOIL PROFILE CHARACTERISTICS

A representative soil profile at the location of breakwaters is shown in Figure 2. It consists of: i) upper silts and clays, brown and grey in colour, although dark colours occasionally appear when organic matter content increases. The thickness of this deposit underneath the breakwaters is about 50 m. Sandy and silty sand inter-stratifications, were often found, specially in the

upper levels of the layer. ii) an intermediate layer of gravels and sands, whose thickness is about 7 m; some silt partings were also detected. iii) a lower level of clays whose identification properties are similar to the upper clay unit, although it is a denser soil. The maximum thickness of this layer is 14 m. iv) a lower layer of gravels and sands; it includes several clays and sands stratifications.

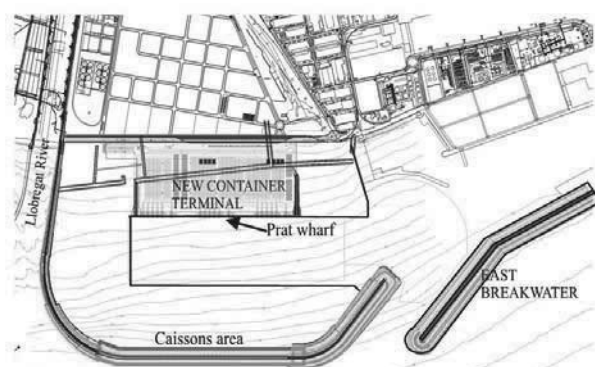


Figure 1. Plan view of the new breakwaters and new container areas of the Barcelona harbour. The location of the caisson breakwater is indicated.

Closer to the coast line, an upper deltaic sand deposit of increasing thickness, laid on top of the upper stratum of soft silty clays, appears. As it would be expected from a deltaic environment the transitions between this sand deposit and the upper clays are neither sharp nor regular. This sand deposit is 15 m thick at the shore line but it practically disappears at the breakwater location and it is not considered further in this paper.



Some of the geotechnical indices and properties obtained during the site investigations are shown in Figure 3. The fine grained materials classify mainly as CL (low plasticity clays) and ML (low plasticity silts). Water content commonly exceeds the liquid limit in the upper part of the soft silty clay unit, but at lower levels it is close to the plastic limit, an indication of the self weight consolidation of the sediments. Void ratios range between 0.8 and 1.0 in the upper clay stratum. Dry densities vary from 1.2 Mg/m<sup>3</sup> at the upper clay levels to 1.8 Mg/m<sup>3</sup> at deeper locations.

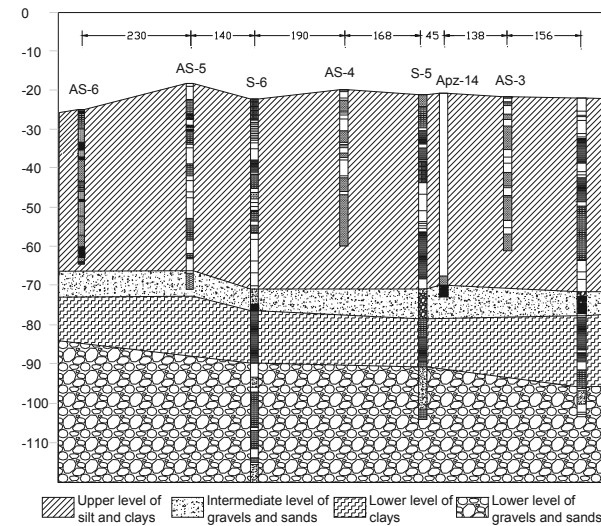


Figure 2. Soil profile under the caisson breakwater

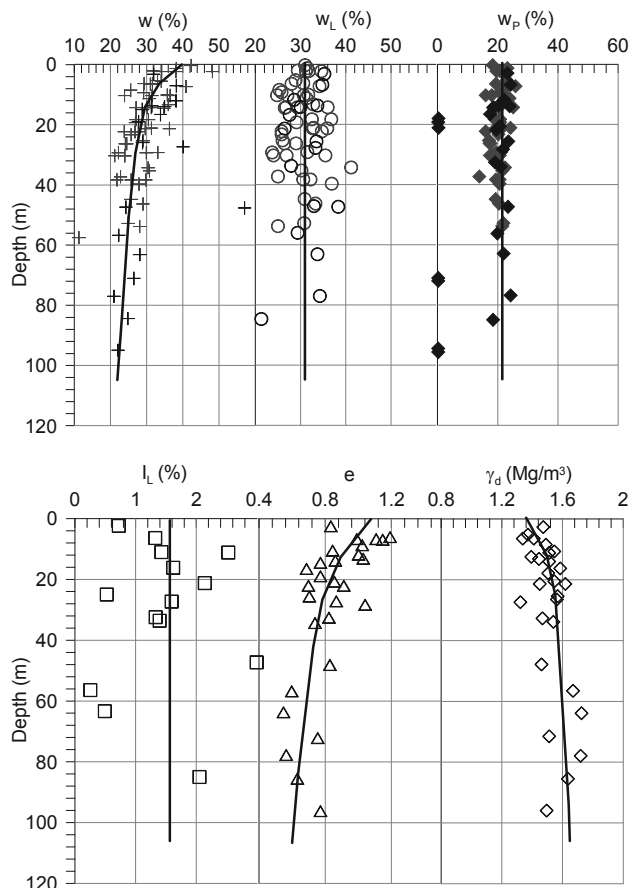


Figure 3. Basic soil properties

In the low permeability foundation soils, stability is controlled by the undrained shear strength ( $c_u$ ). In the normally

consolidated range, this parameter is largely proportional to the consolidation effective vertical stress. Undrained shear strength has been examined by means of laboratory and in situ tests.

Unconfined compression tests of clay samples provided a value of  $c_u=0.215\sigma'_v$ . However, sample disturbance and suction loss may lead to an underestimation of the real value (e.g. Tsuchida, 2000). Simple shear tests performed by NGI provided a value of  $c_u=0.25\sigma'_v$ , quite consistent with the results of CPTU tests. Anisotropically consolidated triaxial tests (compression and extension) yielded a range of  $c_u=0.21 - 0.33 \sigma'_v$ , the larger values associated with compression tests. A summary of results obtained is presented in Figure 4. The unusually large values of undrained strength obtained in some vane tests were probably due the occasional presence of sand lenses or laminations.

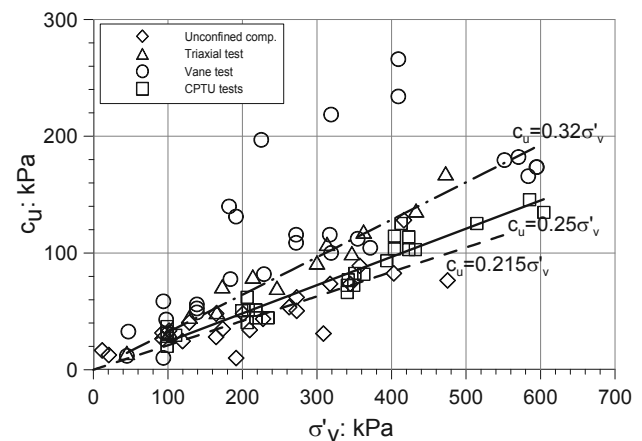


Figure 4. Undrained shear strength. Summary of results

It was also found that specimens sheared under normal effective stresses reproducing in situ stress conditions showed somewhat higher strength ratios than specimens consolidated to higher effective stress values. This is an indication of some modest overconsolidation/structure effects due to natural creep or aging phenomena. However, the additional stresses applied by the caissons and fills will take the soil in situ to a normally consolidated state. Therefore, a conservative attitude is favoured for the selection of the undrained stress ratio. The static design of the breakwater was eventually performed using a value of  $c_u=0.25\sigma'_v$ .

### 3 BREAKWATER DESIGN

The conventional breakwater design was performed using finite element analysis as the most efficient method to consider automatically the variation of undrained shear strength throughout all stages of construction. The following phases were considered: i) dredging and bench construction on the new soil surface, ii) caisson placement and filling, iii) construction of the superstructure, and iv) backfill behind the caissons to create a new quay zone. Although all potential limit states were considered, it should be pointed out that the use of finite element analysis readily identifies the most critical failure mechanism at every stage of the analysis. It should also be noted that the gain in undrained shear strength during each one of the construction phases was a critical feature with respect to the stability of the subsequent construction phase.

The wave and uplift forces due to storm loading in the different phases of construction are listed in Table 1. They were derived from physical model tests using the specific breakwater design. Wave forces depend on two factors: the height of the superstructure that provides the surface on which the wave impact acts and the wave height that in turn depends on the intensity of the storm. It can be observed that the wave height (and hence the storm intensity) is lower in Phase II. This is due to the temporary character of this Phase that makes it less likely

that an extremely large storm will occur during that limited period. Probability analysis based on available time series provides the design storm to be used in each particular stage.

For each construction stage, a variety of factors of safety were used to assess the degree of stability of the breakwater affecting either loads or soil strength parameters. In the former case, wave caisson weight and storm wave loads were considered both jointly and separately. The values of safety factors were assessed in relation with the perceived uncertainty of the parameters involved. Thus, a higher factor of safety was demanded when only the wave action was considered due to the much larger uncertainty of the load magnitude associated with the storm. In fact, uncertainty affects both storm intensity and the actual effect on the caisson. The final design of the breakwater is depicted in Figure 5. Note the wide rockfill bench required for stability. An example of the failure mechanism in a particular instance of the analysis is shown in Figure 6.

Table 1. Wave and uplift forces acting on the caissons breakwater at different phases of construction

Phase	Shoulder height (m)	Wave height (m)	Wave period (s)	Wave force (kN/m)	Force height (m)	Dynamic uplift (kN/m)
II	No	5	9	1036.3	9.48	525.1
III	+6	5.91	12.7	1436.1	10.36	878.2
IV	+11	8.04	12.7	748.9	6.10	766.2

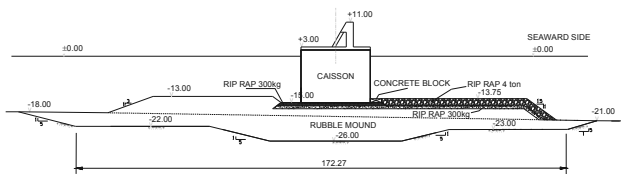


Figure 5. Design of the caisson breakwater.

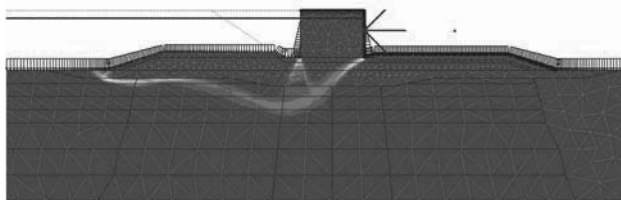


Figure 6. Failure mechanism for Phase III under storm loading.

#### 4 CYCLIC SHEAR STRENGTH

However, breakwaters are also subjected to cyclic wave loading. Storms are the primary source of energy that may cause cyclic mobility or, in extreme conditions, liquefaction of foundation soils. Even if such extreme events do not occur, undrained shear strength may be lower after a severe episode of cyclic loading. Consequently, clay behaviour under cyclic loading was also investigated in the laboratory by performing cyclic simple shear and triaxial tests (on isotropically and anisotropically consolidated specimens). Data from simple shear tests were favoured because they appear to correspond more closely to the actual breakwater foundation conditions during storm loading.

Results from these tests can be usefully summarized using interaction diagrams such as that shown in Figure 7. This diagram shows a relationship between the normalized average shear stress  $\tau_a/\sigma'_{vc}$ , normalized cyclic shear stress  $\tau_{cy}/\sigma'_{vc}$  and the number of cycles to reach the cyclic mobility criteria. Also, results obtained from simple shear testing on the plastic Drammen clay (Goulois et al, 1985) are shown for reference.

Failure occurs for a given combination of normalized cyclic and average shear stress. Figure 7 shows the approximate bounds of these combinations for two different loading conditions (40 impacts and 1000 impacts). The normalised cyclic shear stress  $\tau_{cy}/\sigma'_{vc}$ , for low values of the normalized average shear stress, is close to 0.17 for 40 cycles and to 0.10 for 1000 cycles. A second static bound is provided by the relationship  $\tau_{cy}/\sigma'_{vc} + \tau_a/\sigma'_{vc} = 0.25$ , which is based on the previous discussion on static undrained strength.

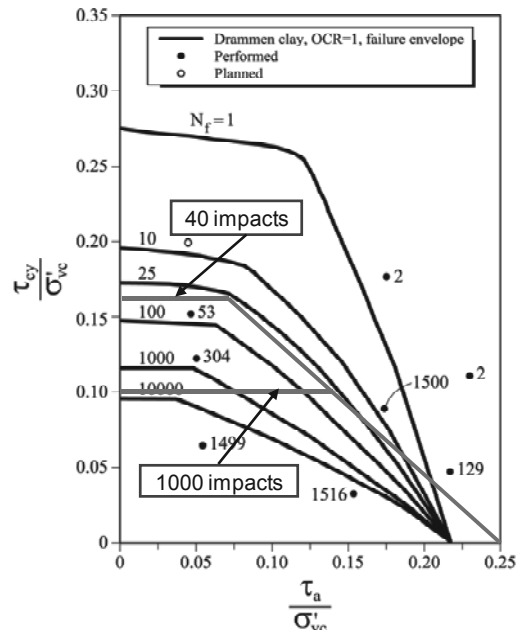


Figure 7. Interaction diagram from direct simple shear tests (NGI, 2002).

#### 5 SIMPLIFIED ANALYSIS USING THE INTERACTION DIAGRAM

An example of the simplified stability analysis concerning Phase III of construction is presented in this section. The design storm established for this Phase is summarised in Table 2 that contains the number of waves of different heights corresponding to a succession of storm intensities with different durations and different significant wave heights.

It is assumed that the design storm can be represented as the application of a number of wave impacts of a certain magnitude. Then, a static analysis can be used to identify areas in the foundation soil where the stress state exceeded the criteria of unstable stress defined by the interaction diagram. Naturally, to use the information contained in the interaction diagram, it is necessary to transform the variable wave loads of the storm into a series of cycles of uniform magnitude. This transformation always involves, to a certain extent, a degree of uncertainty and approximation. It is therefore advisable to adopt a measure of conservatism.

With this approach, two loads intensities were selected from the wave magnitudes shown in Table 2: a large load of 1011.5 kN/m and a smaller load of 341.6 kN/m. The former is assumed to act forty times and the latter five thousand times. The limit criteria corresponding to those two numbers of cycles have been indicated in Figure 7.

Now, it is possible to compute, using a conventional static finite element analysis and applying the corresponding wave loads, the points at which such criteria are exceeded, indicating the possibility that, in those zones, a degree of cyclic mobility occurs with a potential reduction of the undrained shear strength. A quite conservative assumption is that the operational undrained shear strength reduces to the residual value of  $c_u$ . The foundation zones affected are shown in Figures 8 and 9. They

are quite similar in the two cases and affect only a quite limited area of the foundation soil.

Table 2. Characteristics of the design storm

Wave height (m)	Number of waves				Wave force (kN/m)	Force height (m)
	H <sub>s</sub> = 3m (24 h.)	H <sub>s</sub> = 4m (24 h.)	H <sub>s</sub> = 5m (24 h.)	H <sub>s</sub> = 5.9m (24 h.)		
1-2	3124	1661	593	150	213.4	9.77
2-3	2203	1693	720	199	341.6	10.28
3-4	848	1133	626	198	475.0	10.62
4-5	195	545	427	161	685.0	10.65
5-6	28	194	236	111	825.4	10.74
6-7	2	52	108	66	870.5	10.80
7-8	0	11	41	34	920.0	10.00
8-9	0	2	13	16	1011.5	10.36
9-10	0	0	3	6	1410.1	11.46
10-11	0	0	1	2	1528.0	11.15
11-12	0	0	0	1	1559.3	11.38

Finally, a new stability analysis is performed with the new distribution of undrained shear strength of the foundation soil for the two cases considered. The analysis also considers the influence of the dynamic uplift caused by the storm loading, derived from the physical model tests carried out for this particular breakwater design. The results, in terms of factor of safety for strength reduction, are shown in Table 3. It can be seen that consideration of cyclic loading has a moderate but noticeable impact on the factor of safety. Given the exceptional character of the design storm and the conservative assumptions made in the analysis, the factor of safety obtained was considered adequate for accepting the design.

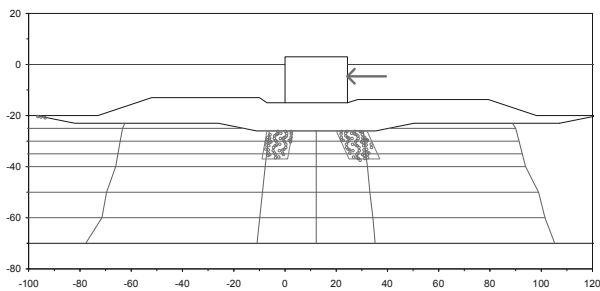


Figure 8. Foundation zones exceeding the interaction diagram criterion. Wave load = 341.6 kN/m and 1000 cycles.

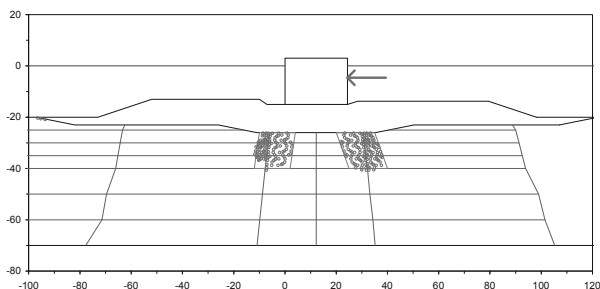


Figure 9. Foundation zones exceeding the interaction diagram criterion. Wave load = 1011.5 kN/m and 40 cycles.

Table 3. Computed factors of safety (on strength parameters)

Consideration of cyclic loading	Factor of safety	
	Wave force = 341.6 kN/m 1000 impacts	Wave force = 1011.6 kN/m 40 impacts
Yes	1.48	1.18
No	1.55	1.40

## 6 CONCLUDING REMARKS

A key design feature of a breakwater is the assessment of the stability of the breakwater when subject to extreme storms. This is particularly the case for caisson breakwaters in which the effects of wave action are significantly stronger than for the classical rubble mound type. A proper consideration of the dynamic effects would require the performance of a full dynamic analysis. Here, a simplified stability analysis is proposed that takes into account the potential reduction of the shear strength of the soil due to cyclic loading. It is based on the experimental determination of the interaction diagrams that provide criteria to identify the conditions for which the soil can undergo cyclic mobility and strength degradation. The corresponding strength reduction is then taken into account in conventional stability analyses. The procedure has been illustrated by a specific application to a caisson breakwater that is part of the extension works of the Barcelona Harbour.

## 7 ACKNOWLEDGEMENTS

The authors are grateful for the technical and financial support provided by APB (Autoritat Portuaria de Barcelona).

## 8 REFERENCES (TNR 8)

Goulois, A.M., Whitman, R.V., and Hoeg, K. (1985). Effect of sustained shear stress on the cyclic degradation of clay. *Proceeding, Symposium on Strength Testing of Marine Sediments*, R.C. Chaney and K.R. Demars, eds., ASTM STP 883, ASTM, Philadelphia, 336-351.

NGI. (2002). Laboratory Testing. Geotechnical Testing Report. March 2002.

Tsuchida, T. (2000). Evaluation of undrained shear strength of soft clay with consideration of sample quality. *Soil & Foundations* 40, No 3, 29-42.

# The new remediation technique for buried pipelines under permanent ground deformation

Une nouvelle technique de pose des conduites enterrées soumises à des déformations permanentes du sol

Moradi M., Galandarzadeh A., Rojhani M.

Department of Soil Mechanics and Foundation Engineering of Collage of Civil Engineering, University of Tehran

**ABSTRACT:** One part of lifelines is buried pipelines such as gas, water and oil pipelines. Permanent ground deformation such as fault crossing and lateral spreads is one of the more important threats for pipelines. In this research, a new remediation technique for buried pipeline system subject to permanent ground deformation is proposed. Also this new technique has been evaluated by centrifuge modeling of buried pipelines subjected to concentrated PGD. In proposed technique, the high porosity gravels are used as low-density backfill to fill the trench around the pipe near the susceptible area to PGD, thereby reducing soil resistance and soil-pipe interaction forces and also pipeline strains. Previously, the expanded polystyrene (EPS) geofoam proposed to reduce density of pipelines backfill. However, the high porosity gravel is better than expanded polystyrene geofoam from many cases such as workability to construct, environmental effect, durability and cost. In this technical paper, described the proposed technique and also two centrifuge modeling have been done to evaluate its performance. The comparisons of responses of remediated pipeline with unremediated pipeline have been shown that the proposed technique is effective considerably.

**RÉSUMÉ :** Une partie des réseaux nécessaires au transport du gaz, de l'eau et du pétrole est constituée de conduites enterrées. Les déformations permanentes du sol dues à des tassements ou à des mouvements latéraux sont l'une des menaces les plus importantes pour les conduites enterrées. Dans cet article, une nouvelle technique de pose des conduites enterrées soumises à des déformations permanentes du sol est proposée. Cette nouvelle technique a été évaluée par des essais en centrifugeuse sur des canalisations enterrées soumises à des déformations permanentes du sol. Pour la technique proposée, des matériaux sableux dont la porosité est élevée sont utilisés pour le remplissage des tranchées. Ils réduisent les efforts induits par l'interaction sol-tuyau. Auparavant, c'est le polystyrène expansé geofoam qui était utilisé. Le matériau proposé est meilleur que le polystyrène expansé geofoam en ce qui concerne la mise en œuvre, l'effet sur l'environnement, la durabilité et le coût. Dans ce papier, la technique proposée est décrite ainsi que deux modèles en centrifugeuse réalisés pour évaluer sa performance. Les résultats obtenus montrent que la technique proposée est plus efficace que celle utilisée précédemment.

**KEYWORDS:** Centrifuge Modeling, Faulting, Lifelines, Pipeline, Earthquake

## 1 INTRODUCTION

Buried pipelines often serve as lifelines in that they may carry resources that are essential to the support of human life and this is the reason to retain them in serviceable condition in every situation. Among various kinds of natural hazards, earthquakes happen to be the most serious threats for lifelines serviceability. They can damage lifelines through faulting, permanent ground deformation (PGD) and deformations due to seismic wave's propagation. Faulting can affect pipelines in various ways (Fig. 1) and cause severe damages (Fig. 2) depending on faulting movement direction.

Considering mentioned hazards, lots of statistical, analytical and numerical studies have been conducted since 1970s in order to predict pipelines response and vulnerability level and also to investigate methods of damage mitigation; but it has been a difficult and somehow impossible way to evaluate theoretical and analytical research results due to loss of accurate and efficient records about pipelines response to faulting in actual case histories of earthquakes (Choo et al. 2007). In order to compensate such a gap, studies turned towards applying experimental and physical modeling of this phenomenon. Since 2003, significant researches have been started in U.S.A. and Japan with support of companies and institutes such as Tokyo Gas Company, US lifelines Agency, National Science Foundation in U.S.A, Earthquake Engineering Research Center and etc. Most of mentioned conducted studies have been focused on strike-slip faulting. So, still there is lack of studies

on normal and reverse faultings' effects and this puts them in prime importance of research priority.

Herein, the authors investigated the pipeline response due to reverse faulting and also investigated the use of high porosity gravel as low-density backfill in pipeline response. It is expected that low-density backfill for will reduce soil-pipe interaction and reduce the pipe strain.

Table 1. Centrifuge Facility Properties

Property	Unit	Quantity
Exerted acceleration	g	5 – 130
Acceleration accuracy	g	+ 0.2
Rotational velocity range	rpm	38 – 208
Rotation radius	m	3
Maximum model weight (up to 100 g)	kg	1500
Maximum model weight (up to 150 g)	kg	500

### 1.1 Faulting simulator split box

Experimental setup provision in order to use in centrifuge instrument has its own limitations; for instance, weight and dimensions of the box is thoroughly tied to the used centrifuge facility properties and it is of prime importance for the box to have the minimum weight and dimensions possible together with having enough strength for high magnitude forces caused due to high exerted accelerations. Regarding these limitations, the group-7000 aluminum alloy which has low density and high strength is used to build up the faulting simulator split box in

this study. Outer dimensions of the box are 102×76×68 cm (l×w×h) and the inner dimensions are 96×70×23 cm. The split line of the box which is the faulting line itself, makes the angle of 30° from the vertical direction. The box setup is assembled and fixed on a 4 cm thick aluminum block of 15 cm width that can bear the hydraulic jack caused 5 ton horizontal force and high magnitude vertical force which is exerted due to high accelerations. Holes have been cut in the two ending walls of the box as the backrests for studied structures such as pipelines. Regarding lack of space in the centrifuge basket, the motivating system and the other constituents of the simulator must occupy the minimum space possible.

Moving mechanism has been designed to be enough stable during the faulting movement and also can bear the high magnitude unbalanced forces derived from soil-structure friction.

A wedge-sliding mechanism has been applied for the box movement to direct the faulting through the 30° specified direction and prevent from any strike between fixed and moving parts of the split box. The wedge-sliding mechanism is consisted of two rails installed with the angle of 30° from the vertical direction and high level force tolerating ball bearings to guide the movement as desired. Sliding the wedge forward and backward, the moving part of the box would have an upward-downward movement (Fig. 4). Considering the high magnitude forces and weight increase in high order accelerations, the moving system has been chosen of hydraulic type to be strong enough and less space occupying. The velocity and displacement control can be done by means of electronic hydraulic valves with a satisfactory level of accuracy and reliability. The hydraulic pressure generator is installed out of the centrifuge basket to save a significant amount of space and is connected to the inside basket moving system by means of hydraulic pipe and rotary joints.

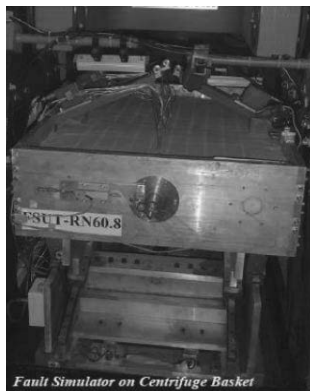


Figure 4. General View

### 1.2 Scaling laws

The scaling laws used for this modeling are indicated as below (Table 2).

Table 2. Scaling laws for centrifuge testing

Parameter	Model / Prototype	Dimensions
Length	1/N	L
Strain	1	1
Stress	1	ML-1T-2
Acceleration	N	LT-2
Axial Rigidity	1/N2	MLT-2
Flexural Rigidity	1/N4	ML3T-2

### 1.3 Soil properties

Soil material used in first test is chosen to be the granular soil of standard Firoozkough 161 sand. Soil material used in second test is high porosity gravel with low density. The density

of low-density soil is equal to 50% of Firoozkough soil density. (Table 3)

Table 3. Properties of Firoozkough and low-density Soil

Sand type	$G_s$	$e_{max}$	$e_{min}$	D50 (mm)	FC	$C_u$	$C_c$
Firoozkough 161	2.65	0.874	0.548	0.27	1 %	2.58	0.88
Low-Density	1.3	-	-	3	~0%	-	-

### 1.4 Instrumentation

Two types of instruments containing strain gauge and linear variable differential transformers (LVDTs) were installed in the model. The strain gauges are installed in axial and circumferential directions on the

pipelines with the number of 26 in 7 stations. Strain gauges are placed in a way that axial and bending strains could be measured separately. Strain gauges are of the high strain type and are connected in the quarter bridge form.

Three LVDTs of the whole 5 ones are installed on the surface of the pipeline to record the deformation profile and the 2 other ones measure the axial displacement of the two endings of the pipeline. Apart from above, colorful grids were being used on the surface and between the soil layers.

## 2 RESULTS

Two tests were conducted in this study. In the first one, a stainless steel pipe with diameter of 8.0 mm and wall thickness of 0.4 mm which buried in Firoozkough sand was subjected to a 70 mm reverse faulting with the acceleration of 40g. In the second experiment, the stainless steel pipe with 8.0 mm diameter and 0.4 mm wall thickness which buried in low-density gravel was subjected to the reverse faulting with 40g acceleration. The properties of model and prototype are indicated in Table 4.

Table 4. Properties of model/prototype for conducted tests

	1st Test		2nd Test	
	Model	Prototype	Model	Prototype
Pipeline Diameter (m)	0.008	0.320	0.008	0.32
Pipeline Wall Thickness (m)	0.0004	0.016	0.0004	0.016
Faulting Magnitude (m)	0.070	2.8	0.070	2.8
Backfill	Firoozkough 161		High Porosity Sand (Low Density)	
Faulting Type	Reverse (60%)		Reverse (60%)	

Following figures illustrate the deformations of pipeline and soil during the faulting process. In Figs. 9 and 10 bending and axial strains before pipe failure versus distance from the faulting in 2nd test are presented.

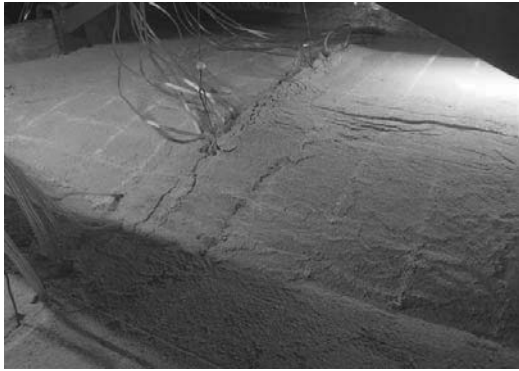


Figure 5. Surface Observation of 1st test

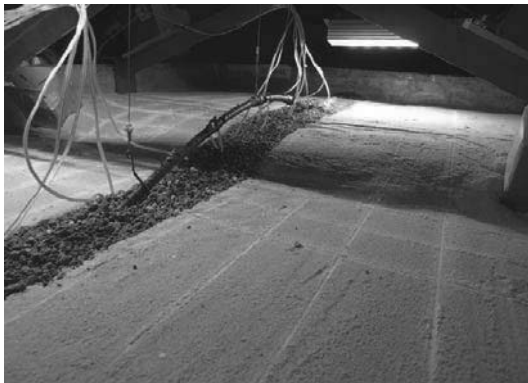


Figure 6. Surface Observation of 2nd test



Figure 7. Section Observation of 1st test

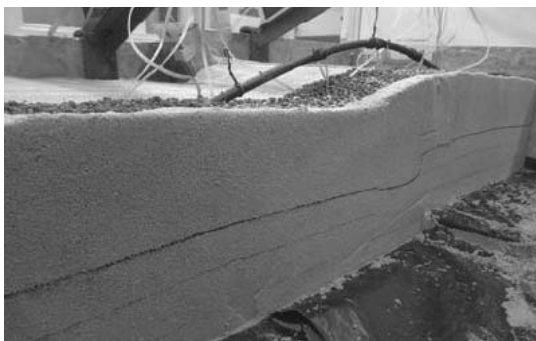


Figure 8. Section Observation of 2nd test

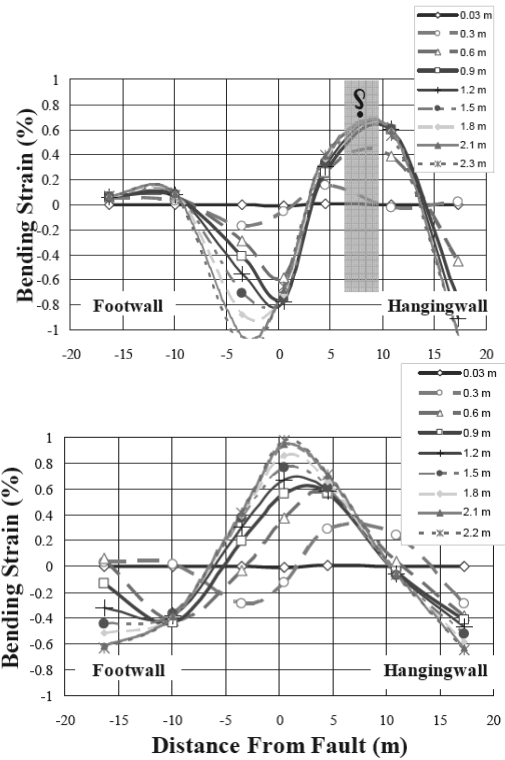


Figure 9. Bending strain during faulting- (Top: 1<sup>st</sup> test, Down: 2<sup>nd</sup> test)

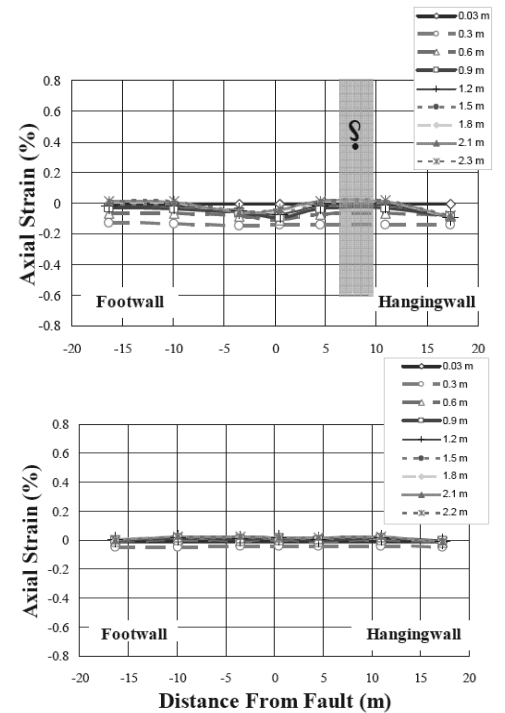


Figure 10. Axial strain during faulting- (Top: 1<sup>st</sup> test, Down: 2<sup>nd</sup> test)

### 3 CONCLUSIONS

In this article the report of establishment of the first geotechnical centrifuge in Iran and its initial application in buried pipelines modeling subjected to faulting are presented. Also, a brief summary of the modeling details, related scaling laws and used facilities and instruments are described. Reported in this experimental study are the axial and bending strains diagrams of steel pipe versus distance from the normal faulting before pipe failure for the first time in the literature. Pipe failure happened almost at 3 cm in model or 1.2 m in prototype offset.

The use of light weight material to fill pipeline trench is an affective technique to improve pipeline response to PGD. This technique changes the pipeline response from wrinkling to beam buckling which is a better deformation mechanism. In this mechanism the deformation of pipeline is distributed along the pipeline, despite of wrinkling mechanism which the deformation concentrated on two points. Also in beam buckling mechanism, the axial strain of pipeline is very small and the maximum bending moment reduced and transferred to the middle of pipeline. Choo et al. (2007) also investigated the use of light weight material (polystyrene blocks) to remediate the behavior of buried pipeline under normal faulting. They found that this technique improved the performance of pipeline under PGD condition.

#### 4 REFERENCES

- O' Rourke, M., Gadicherla, V., and Abdoun, T., (2003). "Centrifuge Modelling of Buried Pipelines", ASCE, Earthquake Engineering;
- Rojhani, M., Ebrahimi, M.H., Moradi, M., and Ghalandarzadeh, A., (2010). "Building the Faulting Simulator Split Box for Geotechnical Centrifuge Modeling", 4th International Congress of Geotechnical Engineering and Soil Mechanics in Iran, Tehran, Iran.
- Taylor, R. N., (1995). Geotechnical Centrifuge Technology, Chapman & Hall Press.
- Woo Choo, Y., Abdoun, T. H., O'Rourke, M., and Ha, D., (2007). "Remediation for buried pipeline systems under permanent ground deformation", Soil Dynamics and Earthquake Engineering.
- Wood, D. M., (2004)

# Site investigation and geotechnical design strategy for offshore wind development

## Investigation géotechniques et stratégie de conception pour le développement d'éoliennes maritimes

Muir Wood A.  
DONG Energy

Knight P.  
Parsons Brinckerhoff

**ABSTRACT:** The development of multi billion euro Offshore Wind Farms presents geotechnical engineers with the opportunity to create comprehensive detailed ground models incorporating a large variety of geotechnical hazards. However the political structure of renewable energy projects often leads to a fragmented development team, with no one party appointed for the whole design process. Inexperienced clients are often commissioning surveys because they think that they want to do a survey rather than for an engineering reason. This leads to unclear specification, and a resulting survey that does not add the expected value to the project. The authors demonstrate in this paper how site investigation and ground modelling practices that are followed as routine in the design cycle of onshore projects can be adapted and applied to add significant value to offshore renewable projects. This paper seeks to set out a structure for development of the ground model for offshore wind projects, and demonstrates how clients can ensure their surveys are adding value to the design strategy for their projects.

**RÉSUMÉ :** Grâce au développement très coûteux de fermes éoliennes en mer, les ingénieurs géotechniciens, ont l'opportunité de concevoir des modèles de sol détaillés et exhaustifs qui peuvent rendre compte d'un large éventail de risques géotechniques. Cependant la structure politique conduit au fait que les projets concernant les énergies renouvelables se trouvent bien souvent menés par diverses équipes de conception sans véritable coordination. Des clients inexpérimentés ont souvent recours à des sondages dans le seul but de faire des sondages et non pour des raisons techniques. Cela conduit à avoir des cahiers des charges souvent imprécis qui n'apportent rien à la valeur attendue du projet. Les auteurs démontrent dans cet article comment les études de terrain et les pratiques de modélisation du terrain utilisées systématiquement dans les projets sur terre peuvent être adaptées et appliquées aux projets en mer et peuvent augmenter leur valeur considérablement. Cet article propose une structure de développement des modèles terrestres pour les champs d'éolienne en mer et démontre comment les clients peuvent s'assurer que leurs sondages valorisent les stratégies de conception de leurs projets.

**KEYWORDS:** geotechnical hazard management, site investigation strategy, ground model development, offshore wind farm

## 1 INTRODUCTION

The offshore wind industry in Northern Europe started with the development of small demonstration projects. In recent years these have significantly increased in size, and many of the current projects are now multi billion euro investments, with development times in excess of five years. The industry can demonstrate many examples of how lessons learnt and knowledge gained from the earlier projects have been incorporated into the recent larger projects, ultimately leading to lower capital and operational expenditure per MW of power generated.

Through this process the design methodology and codes (e.g. DNV 2011) which were originally predominately based on the experience of offshore oil and gas infrastructure have also continued to develop and there are many examples of good practice in current projects. However, for geotechnical site investigations this learning process has not been completely positive. It leads to a tendency to base the scope of the investigation on a specification for a previous projects, rather than on what is most appropriate for the site and specific development.

The authors have been involved in the design of over 15 projects, which when built will total more than 8GW of power. A review of these projects shows that they have all spent comparable money on site investigation - typically approximately 1% of the project capital costs (which on the current large projects leads to investigations costing in excess of €30M). However the success of the investigations in managing

the geotechnical risks and bringing value to the projects is extremely variable.

## 2 EXAMPLE PROJECTS

Typical problems that the authors have experienced are: investigations not planned to mitigate project specific geotechnical hazards; poor recording and interpretation of geological information; planning of surveys not based on the results of proceeding investigations/studies; and surveys not specified by the foundation designers.

Some specific examples of good and poor practice on projects are detailed in the following sections. The project names have not been stated however the approximate construction cost of each project is given.

### 2.1 *Poor practice*

#### 2.1.1 *Project 1 – value ~€2bn*

The site investigation comprised site wide sub-bottom geophysical survey with three rounds of geotechnical works: (1) met mast borehole; (2) site wide boreholes; (3) seabed CPTs on every foundation location. Extensive advanced lab testing and down hole geophysical methods and pressuremeter tests were undertaken.

Issues included: the detailed designer was appointed after the site investigation was completed; insufficient time was allowed for the interpretation of the geophysical and geotechnical



surveys; early CPT refusal and lack of boreholes on location meant that insufficient information was collected at many locations; and, the advanced cyclic testing undertaken was not optimised for the design load being applied to the soil.

The above issues meant that stratigraphy was not certain for the full foundation depth leading to very conservative design and uncertain driveability.

#### 2.1.2 *Project 2 – value ~€0.3bn*

The site investigation comprised a site wide sub-bottom geophysical survey with several rounds of geotechnical works comprising CPTs and boreholes.

The primary issue was the detailed designer being appointed after the site investigation was specified. The boreholes were not deep enough and insufficient information was gathered about the bedrock.

The developer had to commission another round of geotechnical investigation to gather further information for design and risk mitigation, which resulted in project delays and additional costs.

#### 2.1.3 *Project 3 – value ~€1.5bn*

The site investigation comprised a site wide sub-bottom geophysical survey with staged geotechnical works comprising CPTs and boreholes. Extensive advanced lab testing and down-hole geophysical methods and pressuremeter tests were undertaken.

Again, the detailed designer was appointed after site investigation had been undertaken, resulting in an insufficient number of boreholes to allow an efficient design.

#### 2.1.4 *Project 4 – value ~€0.1bn*

The site investigation comprised a site wide sub-bottom geophysical survey with staged geotechnical works comprising CPTs and boreholes.

The specification for the surveys was directly copied by the client from one of their previous projects in very different geology, and the detailed designer was appointed after the site investigations had been undertaken. This resulted in the geophysical techniques not being suitable for the geology and the developer had to repeat the geophysical survey to an enhanced specification.

### 2.2 *Mediocre practice*

#### 2.2.1 *Project 5 – value ~€1bn*

The site investigation comprised sub-bottom geophysical survey with one round of geotechnical investigation comprising full depth CPTs and boreholes.

The geophysics was incorrectly scoped, so when planning the geotechnical campaign, the detailed designer could not utilise the geophysics. The project programme was also compressed, meaning the geotechnical campaign was carried out in one stage.

More value, cost savings and mitigation of geotechnical risks could have been achieved with a collaborative geophysical and geotechnical interpretation and a staged geotechnical campaign with ground model development.

#### 2.2.2 *Project 6 – value ~€1bn*

The site investigation comprised sub-bottom geophysical survey with one round of geotechnical investigation comprising full depth CPTs and boreholes with geophysical borehole logging.

Again, the geotechnical campaign was carried out in one stage with the scope being developed whilst offshore. A more cost effective survey could have been achieved with a staged geotechnical campaign with ground model development.

### 2.3 *Good practice*

#### 2.3.1 *Project 7 – value ~€2bn*

The site investigation comprised sub-bottom geophysical survey with multi-stage geotechnical investigation comprising CPTs and boreholes. Extensive advanced laboratory testing was undertaken.

The foundation designer was involved in the specification of the surveys, and a ground model was developed based on collaborative geophysical and geotechnical interpretations. The geotechnical investigations were specified considering the confidence in the ground model and the foundation design.

#### 2.3.2 *Project 8 – value €1.5bn*

The site investigation comprised sub-bottom geophysical survey with multi-stage geotechnical investigation comprising CPTs and boreholes.

The early geophysics identified a considerable geological hazard which was successfully mitigated (Liingaard et al. 2012) through ground model development based on collaborative geophysical and geotechnical interpretations. A multi-stage geotechnical investigation allowed the detailed designer to develop a specific design method and scope the investigations to verify the variations from design codes.

## 3 SUGGESTED APPROACH

The above projects highlight the issues regarding quality and more importantly the effectiveness of the geotechnical investigations. There are common problems with scoping and management of site investigations. The offshore wind industry should look to the experience gained on projects in other fields of engineering, especially the lessons learnt by large onshore infrastructure projects. In particular they should: consider more formal approaches to the management of geotechnical risk; accept that a staged site investigation will deliver the most cost effective results; and, consider a contracting structure that brings the detailed designer onto the project from a very early stage.

### 3.1 *Management of geotechnical risk*

Managing ground risks solely through the traditional practice of thorough site investigation will not lead to the most cost effective project. Simply undertaking the most detailed site investigation that the budget will pay for leads to investigations being undertaken that are not specifically targeting the unknowns that are truly affecting the project, and also does not allow for the fact that the acceptable level of risk at construction is very different depending on the project developer and their attitude towards risk.

Developers should therefore seek to apply a more formal approach of managing geotechnical risk so that the site investigation specifically targets the unique project hazards. Clayton (Clayton, 2001) suggests formal processes for managing geotechnical risk, these have been adapted to form the recommended process detailed in Figure 1.

Figure 1 shows a design team led approach to planning, undertaking and reviewing effective site investigations. The design team identifies all hazards affecting the project (design, installation, operation and decommissioning). An assessment is made of the significance of those hazards in consultation with all project stakeholders. The site studies/investigations are planned to specifically target the hazards. The results are studied and the residual hazards reviewed. The consultation is repeated with the stakeholders and the need for further investigation evaluated.

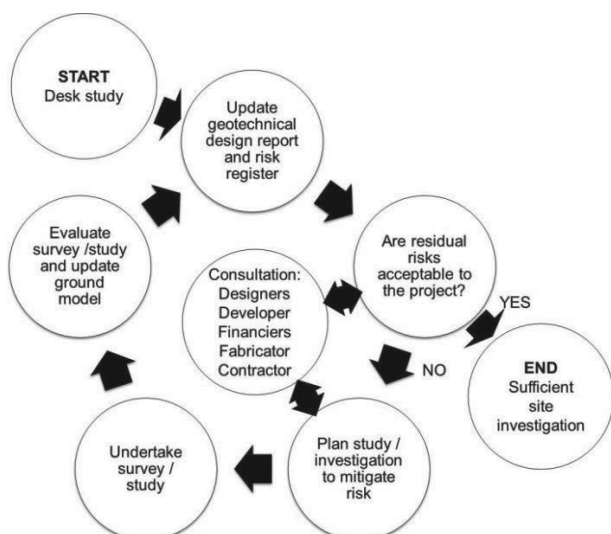


Figure 1. Risk based approach to managing geotechnical hazards

In managing this risk based approach it is essential that the designers appreciate that developers will have different acceptable levels of risk (Figure 2). This level of risk will depend on developers' sources of funding, project timescale and contracting/procurement strategy. The acceptable level of risk will also change as a project develops.

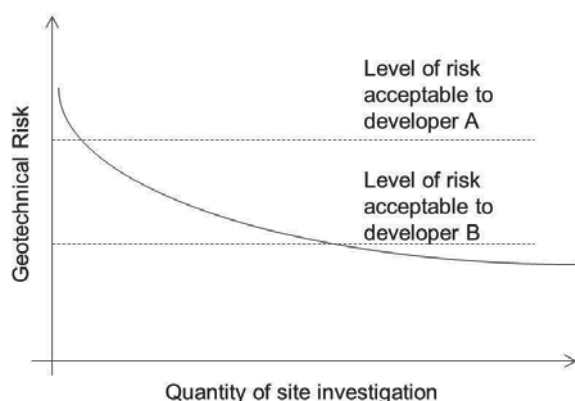


Figure 2. Acceptable level of geotechnical risk to a developer

### 3.2 Staged site investigations

All of the projects reviewed in Section 2 had separate stages of site investigation comprising a geophysical followed by a geotechnical campaign. However the good practice projects had a multistage geotechnical campaign. Eurocode 7 (EC7) (BS EN 1997-2:2007) states that “Ground investigations should normally be performed in phases depending on the questions raised during planning, design and construction”. The code goes on to define two distinct phases of investigation – preliminary investigation and design investigation.

The multistage geotechnical investigation allows for a comparatively cheap ground-truthing geotechnical campaign early in the design process. This campaign gives the designer sufficient information to confirm the expected ground model and develop a preliminary design solution. The design investigation will then be significantly more effective, since it can utilise the most effective methods of investigation for the ground conditions, and fit the foundation type and dimensions that are being designed.

The strategy outlined in Figure 1 will be most effective when repeated several times; designers should be wary of trying to understand all ground based hazards in one stage of geotechnical investigation. A simple preliminary investigation

combined with the existing understanding of the site will often provide the best value to the developer at an early stage.

### 3.3 Develop contracting structure that allows early appointment of the designer

Many of the example projects detailed in Section 2 had ineffective site investigations because the detailed designer for the foundations was not appointed until after all site investigations had been completed. These projects appointed engineers solely to organise and supervise a single phase of site investigation who were not otherwise engaged in planning or design of the project. “This practice inhibits continuity or integration of project development, with the prospect that the site investigation will not be coupled with other features of the project planning process and will, in consequence, not provide adequate answers to vital questions and will not allow consideration of innovative methods of working”. This quote from Muir Wood (Muir Wood 2000) is just as applicable to offshore wind farm developments as it is to the tunnelling projects it was originally written to describe.

Instead developers should seek to engage a designer at the start of the development phase, who has the competence and ability to provide the geotechnical engineering for the whole project. This allows the foundation design and the scope of the site investigation to develop with the project, which mitigates project risks and delivers cost effective site investigations.

This is the approach taken by most infrastructure projects of equal size and complexity to these offshore wind developments. As these projects have demonstrated, this does not prevent the use of different project procurement mechanisms, provided that mechanisms such as novation are available to the developer.

## 4 APPLIED EXAMPLE

The strategy detailed in Section 3 is being applied to the first project of the Hornsea Round 3 development area as follows.

### 4.1 Engineering contract setup

For this project, the developer – DONG Energy is using in-house engineers to undertake the geotechnical design and engineering. This capability is supplemented by the use of additional consultants appointed to the projects for long term positions. This setup gives an integrated approach to engineering and development. Different parts of the project will have different procurement strategies; where the developer chooses not to progress the detailed design in house the design for that element will be contracted to another party, with the original in-house design team maintained in a reviewing capacity.

### 4.2 Desk study

Prior to the desk study, no geotechnical design parameters were available. The principal geotechnical risks at this stage are shown in Table 1. At this point, the site investigations cannot be specified as the foundation type, ground conditions and design requirements are not understood.

Table 1. Design parameters and primary geotechnical risks prior to desk study

Design parameter	Geotechnical risks
None	Unknown site constraints
	Unknown design constraints
	Unknown construction constraints

Following completion of a desk study which includes a review of geological information, design requirements and possible foundation types and construction considerations,

geotechnical design information is available and project specific geotechnical risks can be identified, as shown in Table 2. At this point the design parameters have been selected based on geological memoirs and nearby site investigations. The undrained shear strength of the main clay unit has been used as an example to show how the design inputs change as more information is collected.

Table 2. Design undrained shear strength of main clay unit and primary geotechnical risks following desk study

Design parameter	Geotechnical risks
125 to 350 kPa	No wind farm specific ground information
	Presence of regional geohazards
	Several foundation types possible

The design information and project risks are reviewed at this stage. Referring to Figure 2, this level of design information and risk may be acceptable to some clients, in which case the design and construction risks will be managed with a conservative and uncertain design, or passed onto a third party with large financial consequences. However in this case, to confirm the ground conditions and add confidence to the design, site investigation works were specified.

#### 4.3 Geophysical survey

A site wide sub-bottom geophysical survey was carried out. The primary objectives were to: identify the geological units present; identify any unexpected geological features; and, collect information to allow preliminary geotechnical boreholes to be positioned.

#### 4.4 Preliminary geotechnical survey

A preliminary geotechnical survey consisting of seabed CPT and composite CPT and sampling boreholes was carried out. The primary objectives were to: validate the desk study and geophysical survey; collect information for ground model development including in situ testing and sampling in the primary units; and, identify unexpected ground conditions and risks.

Following completion of the preliminary geotechnical site investigation, the results were interpreted and a ground model produced.

#### 4.5 Ground model development

The ground model was developed using a collaborative geophysical and geotechnical approach. The engineering units were identified and geotechnical parameters selected using the CPT and laboratory testing results. Wind farm specific ground information is now known, and the regional geohazards understood, allowing preliminary design to commence. The design parameters and risks (Table 3) have been refined, resulting in a more efficient foundation.

Table 3. Design undrained shear strength of main clay unit and primary geotechnical risks following preliminary site investigation and ground model development

Design parameter	Geotechnical risks
Low: 145 kPa	Local variation in site geology
Mean: 240 kPa	Advanced design parameters unknown
High: 325 kPa	

#### 4.6 Design team and stakeholder review

The confidence and expected accuracy of the geotechnical interpretation and risks were reviewed by the design team and stakeholders. It was decided that there was sufficient knowledge

of the site to progress the design and construction planning and manage the geotechnical risks.

Some of the project infrastructure will be designed and developed by others. There is now sufficient knowledge of the site to be able to define a contract ground model baseline, and enable the risk to third parties of unknown ground conditions to be appropriately handled.

#### 4.7 Future geotechnical survey

The residual project risks are not acceptable for the finalisation of detailed design. To obtain this information, a small number of sampling boreholes (to obtain samples for advanced laboratory testing) complemented by one CPT to the expected foundation depth (to identify local variability and confirm the units present) will be carried out. Subsequent investigation may be required depending on the results of this investigation and the developer's acceptable risk.

## 5 CONCLUSIONS

Offshore wind projects in their early stages present considerable challenges to engineers managing the geotechnical hazards given the large complexity, cost and time scale of the projects.

A review of the site investigations undertaken for various projects highlights repeated mistakes leading to inefficient site investigations; namely the site investigations not being planned to mitigate project specific geotechnical hazards and surveys not being specified by the foundation designers.

Lessons must be learnt from the wider construction industry, including: the need for formal approaches to the management of geotechnical risk; acceptance that a staged site investigation will deliver the most cost effective results; and, considering a contracting structure that brings the detailed designer onto the project from a very early stage.

The authors have proposed an engineer led approach for managing geotechnical risks, where the design team and stakeholders are actively involved in assessing and mitigating the geotechnical risks, allowing the geotechnical foundation design and site investigation to develop with the project and ensuring that survey work is specified to directly control project risks.

These principles are being applied to the first project of the Hornsea Round 3 development area, where design and construction risks are being mitigated early with a relatively small amount of site investigation works.

## 6 REFERENCES

- BS EN 1997-2:2007. *Eurocode 7 Geotechnical design – Part 2: Ground Investigation and testing*
- Clayton C.R.I. 2001. *Managing geotechnical risk: improving productivity in UK building and construction*. Institution of Civil Engineers and Thomas Telford, London.
- Det Norske Veritas AS. 2011. *Offshore Standard DNV-OS-J101 Design of Offshore Wind Turbine Structures*. Det Norske Veritas, Oslo.
- Liingard M.A. Mygind M. Thomas S. Clare M. and Pickles A. 2012. *Evidence of tertiary intrusive rock at the West of Duddon sands offshore wind farm*. Society for Underwater Technology Proceedings of the 7th International Conference, London 2012, 145-152.
- Muir Wood A.M. 2001. *Tunnelling: management by design*. E&FN Spon, London.

# Diagrammes de stabilité cyclique de pieux dans les sables

## Cyclic stability diagrams for piles in sands

Puech A., Benzaria O.  
*Fugro GeoConsulting, Nanterre, France*

Thorel L., Garnier J.  
*IFSTTAR, Nantes, France*

Foray P., Silva M.  
*3S-R, Grenoble, France*

Jardine R.  
*Imperial College, London, UK*

**RÉSUMÉ:** Cette communication rassemble des diagrammes de stabilité cyclique obtenus dans des sables siliceux denses et par des moyens expérimentaux variés : essais in situ sur pieux réels, essais sur pieux modèles en grande chambre d'étalonnage et essais sur pieux modèles centrifugés. Elle couvre le cas des pieux battus en traction et celui des pieux forés en compression. Les diagrammes cycliques de stabilité sont des outils précieux pour une première estimation de l'effet des chargements cycliques sur le comportement axial des pieux.

**ABSTRACT:** This paper gathers cyclic stability diagrams obtained from various experimental sources: in situ tests on actual piles, laboratory tests on model piles in a large calibration chamber and model piles in a centrifuge. Driven piles in tension and bored piles in compression are addressed. Cyclic stability diagrams are useful tools for a preliminary assessment of the effects of cyclic loadings on the behaviour of piles.

**MOTS-CLÉS:** pieu battu, pieu foré, chargement cyclique axial, diagramme de stabilité cyclique

**KEYWORDS:** driven pile, bored pile, axial cyclic loading, cyclic stability diagrams

## 1 INTRODUCTION

Le concept de diagramme de stabilité cyclique pour représenter de manière synthétique la réponse des pieux soumis à des chargements cycliques axiaux a été introduit dans les années 80 par Karlsrud et al. (1986) pour les argiles et par Poulos (1988) pour les sables.

Ce concept se révèle particulièrement utile pour juger en première estimation de l'effet potentiel des chargements cycliques sur la réponse des pieux (Jardine et al., 2012)

On dispose en pratique de peu d'éléments dans les sables. La présente communication propose des diagrammes cycliques applicables aux pieux battus et aux pieux forés dans les sables denses.

## 2 ESSAIS EN TRACTION

### 2.1 Essais de Dunkerque (ICL)

Sept pieux tubulaires en acier à base ouverte non instrumentés ont été testés par l'Imperial College de Londres (ICL) sur un site de sable marin dans le secteur Industriel Ouest du port de Dunkerque, France (Jardine & Standing, 2000). Le profil du sol est caractérisé par 3 m de remblai hydraulique sur du sable des Flandres. Le sable est composé principalement de quartz (84%), d'albite et microcline (8%) et de débris de coquillages CaCO<sub>3</sub> (8%). Les profils pénétrométriques ( $q_c$ ) du site varient entre 10 et 35 MPa selon la profondeur et l'emplacement. La densité relative est en moyenne d'environ 75%. Des essais de cisaillement direct et triaxiaux indiquent un angle de frottement de pic  $\phi'$  de 35 à 40° et une valeur d'état critique  $\phi'_{cv} \sim 32^\circ$ . Des renseignements supplémentaires sur les caractéristiques du site et les essais de laboratoire réalisés sont présentés par Jardine et al. (2006).

Les essais cycliques ont utilisé les installations du projet GOPAL (Parker et al., 1999). Au total 21 essais statiques et 14 essais cycliques ont été effectués sur les six pieux de réaction du projet GOPAL. Ces pieux ont été battus jusqu'à une profondeur d'environ 19 m avec une relation espacement/diamètre du pieu d'environ 15. Leur diamètre est de 457 mm.

Plusieurs séries de chargements cycliques ont été appliquées, entrecoupées d'essais statiques référentiels en traction, la plupart d'entre eux avec des cycles uniquement en traction pour mieux individualiser la distribution des charges entre la pointe et le frottement latéral.

La réponse des pieux au chargement cyclique est décrite dans Jardine & Standing, 2012 ; Tsuchi et al., 2012; Rimoy et al., 2013.

### 2.2 Essais en chambre d'étalonnage (3SR-ICL-SOLCYP)

Dans le cadre d'une coopération entre l'Imperial College de Londres (ICL), le Laboratoire 3SR de l'Université de Grenoble et le Projet SOLCYP, plusieurs séries d'essais ont été réalisées sur un pieu modèle instrumenté dans la chambre d'étalonnage du laboratoire 3SR de Grenoble. L'objectif initial était de tenter de reproduire à une échelle de laboratoire et dans un environnement contrôlé les résultats obtenus par Jardine et Standing, 2000 sur les pieux battus dans le sable de Dunkerque.

La chambre de calibration a une hauteur de 1,5m et un diamètre de 1,2m. Dans sa paroi intérieure, une membrane en latex et une couche de graisse en silicone ont été mises comme système d'anti frottement pour avoir un meilleur contrôle des conditions  $K_0$  du sol. Un système d'isolation permet d'effectuer les essais à une température constante comprise entre 18 et 19°.

Le sable utilisé est le sable de Fontainebleau NE34, ( $d_{50} = 0,2$  mm,  $\gamma_{max} = 17,2$  kN/m<sup>3</sup> et  $\gamma_{min} = 14,2$  kN/m<sup>3</sup>). Pour l'ensemble des essais présentés, ce sable été mis en place par pluviation en obtenant un indice de densité relative compris entre 0,65 et 0,70. Le massif de sable est soumis à une pression

verticale appliquée sur la surface du massif de 150 kPa, correspondant à une résistance de pointe pénétrométrique  $q_c$  de 20 à 23 MPa.

Le pieu modèle instrumenté a été développé par ICL et est décrit en détail dans Jardine et al (2009). C'est un pieu à base fermée de 36 mm de diamètre, instrumenté en 3 niveaux le long du fût pour mesurer les contraintes tangentielles et radiales dans la surface du pieu. Chaque niveau d'instrumentation inclut aussi un capteur de force. Pour les derniers essais réalisés, il a été équipé d'un capteur de force en pointe.

L'installation initiale du pieu a été effectuée jusqu'à une profondeur d'environ 1 m par des cycles d'enfoncement successifs de 5 à 20 mm à une vitesse de 0,2 mm/s, suivis d'une décharge complète, de façon à simuler les effets d'un processus de battage.

Le programme expérimental a inclus quatorze essais cycliques autant sous contrôle de déplacement que sous contrôle en charge pour des cycles alternés et non-alternés (seulement en traction).

Une première partie des résultats concernant les essais de chargement cyclique a été présentée par Tsuha et al. (2012). On trouvera de plus amples informations dans Rimoy et al., 2013

### 2.3 Critères de rupture

L'application de cycles sur un pieu installé dans du sable provoque une succession de petits glissements relatifs sol-pieu dont le cumul détermine le déplacement global. La vitesse de déplacement initiale est fonction de l'amplitude  $Q_c$  et du niveau de chargement maximal  $Q_{max}$  mais ces mêmes paramètres conditionnent également l'évolution du frottement qui peut se détériorer pour des cycles de grande amplitude ou s'améliorer pour des cycles de faible amplitude (Tsuha et al., 2012). Sur un pieu sollicité en traction, la vitesse initiale se modifie pour :

- soit conduire vers la rupture : dans ce cas la vitesse s'accroît. La rupture peut être définie de manière conventionnelle (par exemple pour un déplacement de la tête du pieu de 0,1D) ou lorsque se produit une accélération brutale du taux de déplacement ;
- soit conduire vers la stabilisation : la vitesse décroît continuellement jusqu'à passer en dessous d'un seuil où on peut considérer que les déplacements cumulés deviennent non significatifs.

### 2.4 Diagrammes de stabilité cyclique

La caractérisation complète d'un essai de chargement cyclique suppose la définition des paramètres suivants :

- $Q_m$  : valeur moyenne de la charge sous chargement cyclique,
- $Q_c$  : demi-amplitude du chargement cyclique,
- $N_f$  : nombre de cycles conduisant à la rupture,
- $N$  : nombre de cycles appliqués en l'absence de rupture,
- $f$  : fréquence des cycles (en général 0,5Hz)

L'essai est dit répété (one-way) si  $Q_c < Q_m$  et alterné (two-way) si  $Q_c > Q_m$ . On définit de plus :

$Q_u$  : capacité statique ultime selon le mode considéré ( $Q_{ut}$  en traction et  $Q_{uc}$  en compression).

Il est pratique de présenter les résultats d'essais de chargements cycliques dans un diagramme où chaque série de chargement est identifiée par le couple de paramètres normalisés  $Q_m/Q_u$  et  $Q_c/Q_u$ . Ce type de représentation permet de bien visualiser les zones de fonctionnement sous chargements répétés et sous chargements alternés. Si on affecte chaque point du nombre de cycles  $N_f$  ayant provoqué la rupture ou du nombre de cycles  $N$  appliqué sans provoquer la rupture on peut définir des zones de « stabilité » ou d'« instabilité » du pieu. On voit que la taille de ces zones dépend du (des) critère(s) de rupture choisis.

On reproduit sur les Figures 1 et 2 les diagrammes cycliques obtenus pour les essais de Dunkerque (Jardine and Standing,

2012) et pour les essais en chambre de calibration (Tsuha et al., 2012).

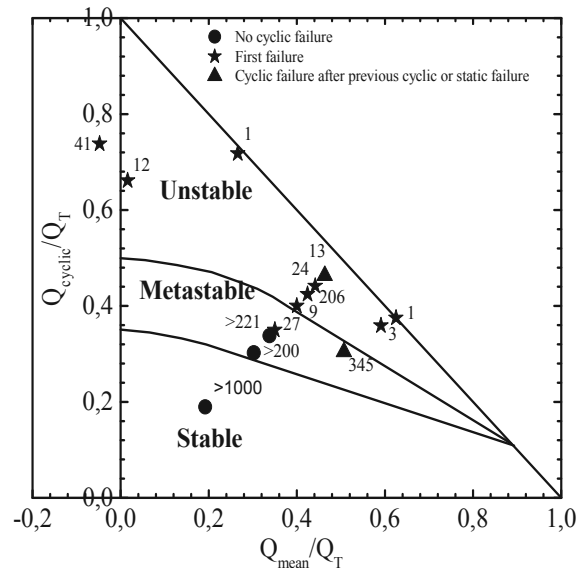


Figure 1 : Diagramme de stabilité cyclique des pieux battus de Dunkerque (d'après Jardine and Standing, 2012)

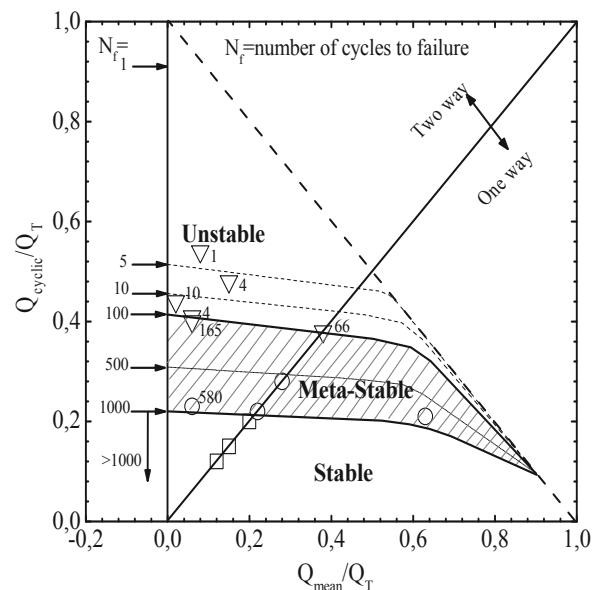


Figure 2 : Diagramme de stabilité cyclique des pieux modèles en chambre de calibration (d'après Tsuha et al., 2012)

Pour ces deux diagrammes, la rupture est atteinte lorsque le déplacement de la tête du pieu atteint 0,1D. La zone *instable* caractérise les essais ayant atteint le critère de rupture avant 100 cycles. La zone *stable* correspond à une zone de faible amplitude de chargement cyclique dans laquelle les pieux ont été soumis à plus de 1000 cycles sans accumuler de déplacements significatifs (pour les deux types de pieux) ou pour lesquels la vitesse de déplacement était inférieure à 1mm pour 1000 cycles (pieux de Dunkerque). Entre ces deux zones se situe une zone qualifiée de *métastable* dans laquelle les pieux atteignent la rupture entre 100 et 1000 cycles ou développent des taux de déplacement pouvant faire craindre des ruptures au-delà de 1000 cycles.

Il est intéressant de mentionner que les trois zones de stabilité resteraient inchangées si on adoptait un critère de rupture à  $0,03 D$  comme pour les pieux en compression ci-après.

### 3 ESSAIS EN COMPRESSION

#### 3.1 Essais de Loon-Plage (SOLCYP)

Dans le cadre du projet national SOLCYP (Puech et al., 2012) des essais sur pieux réels ont été conduits sur le site de Loon-Plage constitué de sables denses. Cinq pieux forés et deux pieux métalliques battus ont été installés et soumis à des séries de chargements statiques et cycliques. Les résultats obtenus sur les pieux forés sont présentés dans Benzaria et al. (2013).

Le site expérimental se situe sur la commune de Loon-Plage (59) près de Dunkerque dans le Nord de la France. Il se caractérise par une couverture de remblais récents (0-0,6m) et d'argile sableuse (0,6-2,2m) sous laquelle on rencontre la formation de sable des Flandres.

Le sable est un sable siliceux très fin ( $D_{50}$  voisin de 0,15mm) et mal gradué (coefficient d'uniformité  $CU=0,98$ ) très proche de celui rencontré sur le site voisin des essais ICL (même origine). La formation est latéralement homogène et se caractérise par des valeurs de résistance au cône  $q_n$  croissant de 5 à 40 MPa vers 8 m de profondeur pour se stabiliser ensuite entre 30 et 50 MPa jusque vers 11,5m. L'interprétation des CPT conduit à un indice de densité  $I_D$  compris entre 0,7 et 0,9 (sable dense à très dense).

Une série d'essais triaxiaux monotones a donné un angle de frottement interne  $\phi'_{cv}$  voisin de  $31^\circ$  en bon accord avec les valeurs trouvées sur le sable de Dunkerque (Jardine et Standing, 2000).

Les deux pieux F4 et F5 sont géométriquement identiques ( $D=420\text{mm}$ , fiche 8m). Ils ont été exécutés à l'aide d'une tarière à axe creux vissée dans le sol sans extraction notable de matériau puis extraite sans dévissage tandis que le béton est déversé simultanément par l'axe creux. Les pieux sont équipés d'un train d'extensomètres amovibles de type LCPC introduits dans un tube de réservation positionné entre les armatures.

Les pieux ont été testés trois mois environ après leur mise en place. Les programmes de chargement comportaient des essais statiques de référence à paliers d'une heure selon la norme NF P 94-150, des essais de chargement rapides (réduction des paliers à 3mm) et des essais de chargement cycliques axiaux de type répété à la fréquence de 0,5Hz. Une description plus précise des modes de chargement est indiquée dans Benzaria et al. (2012).

#### 3.2 Essais sur modèles réduits centrifugés (SOLCYP)

Une campagne d'expérimentations sur modèles réduits centrifugés a été réalisée sur la centrifugeuse géotechnique de l'IFSTTAR à Nantes (Guefrech et al., 2012). Les pieux d'élanement 31 sont réalisés à l'échelle  $1/23^{\text{ème}}$ . Leur diamètre est de 18 mm. Leur surface est parfaitement rugueuse. Ils sont mis en place selon un procédé non refoulant consistant essentiellement à mettre le sable en place par pluviation alors que le pieu est déjà pré-positionné dans le conteneur. Cette technique simule un pieu moulé en place comme les pieux forés à la tarière creuse du site de Loon-Plage.

Le sable de Fontainebleau NE34 sec est en tout point identique à celui utilisé au laboratoire 3SR pour les essais en chambre d'étalonnage et présente des propriétés physiques et mécaniques très voisines de celle du sable des Flandres.

On s'intéresse dans ce qui suit à une série d'essais réalisés dans un massif à forte densité ( $I_D \approx 0,7$ ) à la fréquence de 1Hz. Seuls les essais de chargement cyclique en compression répétée sont analysés.

#### 3.3 Critère de rupture

La définition de critères de rupture en compression est plus délicate qu'en traction. En effet, quelle que soit la vitesse de déplacement initiale (sur les premiers cycles), les déplacements tendent globalement vers la stabilisation. Cette observation est commune aux pieux in situ (Benzaria et al., 2013) et aux pieux modèles (Guefrech et al., 2012). En effet, même s'il y a dégradation rapide du frottement, le déplacement du pieu provoque une mobilisation progressive de l'effort de pointe qui ralentit progressivement les tassements.

Le critère de rupture ne peut alors être défini de manière conventionnelle (e.g.  $0,1D$ ) mais doit s'exprimer en termes de déplacement cyclique acceptable. Ce critère pourra être franchi sur les tous premiers cycles en cas de chargement très sévère (avec une vitesse de déplacement forte voire croissante) mais plus généralement au bout d'un nombre de cycles plus ou moins important et avec une vitesse de déplacement décroissante.

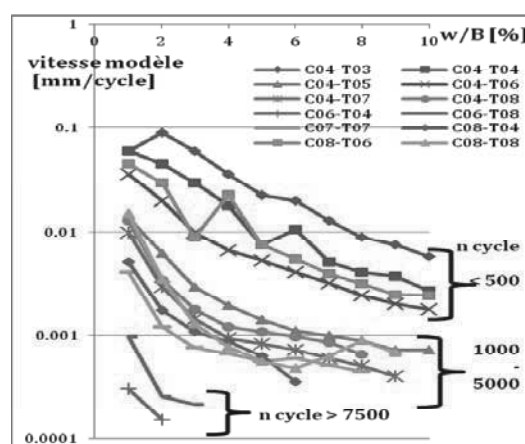


Figure 3 : Vitesses de déplacements des pieux en compression pour les essais en centrifugeuse

L'analyse des vitesses de déplacement effectuée sur les pieux modèles centrifugés illustre les phénomènes en jeu (Figure 3). On distingue trois familles d'essai : a) les essais pour lesquels un tassement de  $0,1D$  est atteint en moins de 500 cycles et qui présentent une décroissance permanente de la vitesse de tassement ; b) ceux pour lesquels ce tassement est atteint entre 1000 et 5000 cycles avec une vitesse de tassement qui semble se stabiliser ; c) ceux pour lesquels la vitesse de tassement devient rapidement très faible ( $< 0,5$  mm pour 1000 cycles). L'évolution vers des déplacements importants est alors improbable.

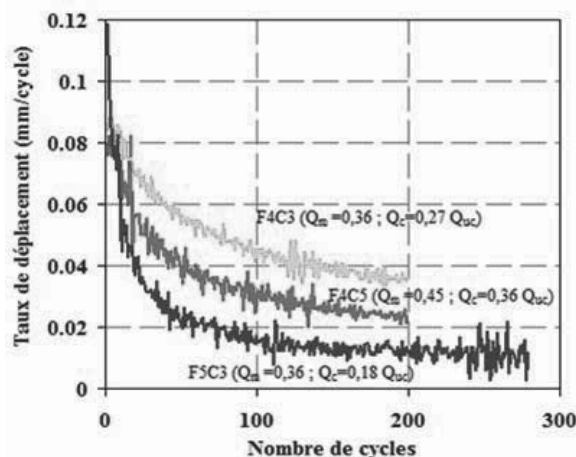


Figure 4 : Vitesses de déplacement des pieux en compression pour les essais de Loon-Plage

La Figure 4 montre le même type d'évolution des vitesses de déplacement pour les pieux de Loon-Plage.

### 3.4 Diagrammes de stabilité cyclique

On présente sur les Figures 5 et 6 les diagrammes de stabilité cyclique obtenus pour les essais cycliques en compression sur pieux forés de Loon-Plage et les pieux moulés en centrifugeuse.

Pour ces deux diagrammes, la rupture est définie pour un déplacement du pieu de 0,03 D. La zone *instable* caractérise les essais ayant atteint le critère de rupture avant 100 cycles. La zone *stable* correspond à une zone de faible amplitude de chargement cyclique dans laquelle les pieux n'ont pas atteint le critère de rupture et les vitesses de déplacement sont faibles. Entre ces deux zones se situe la zone qualifiée de *métastable* dans laquelle les pieux atteignent la rupture entre 100 et 1000 cycles.

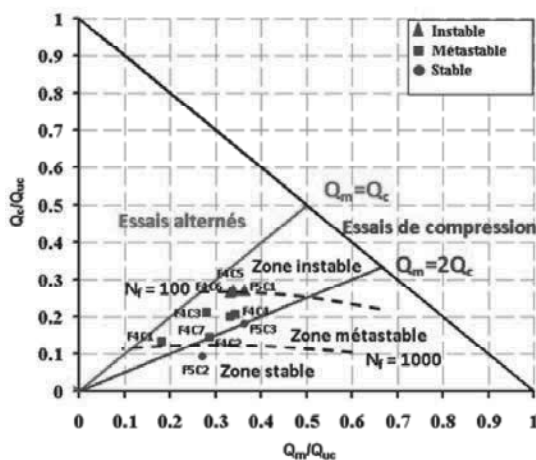


Figure 5 : Diagramme de stabilité cyclique pour les pieux forés de Loon-Plage

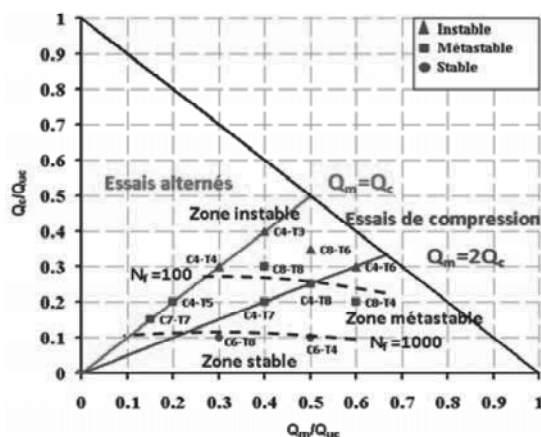


Figure 6 : Diagramme de stabilité cyclique pour les pieux moulés en centrifugeuse

On constate une bonne concordance entre les deux diagrammes. Il est recommandé de ne pas extrapoler les données dans le domaine des essais alternés. Les données disponibles (non montrées ici) indiquent en effet une forte réduction des zones métastable et stable dans le domaine alterné.

## 4 CONCLUSION

Cette communication rassemble des diagrammes de stabilité cyclique obtenus dans des sables siliceux denses et par des

moyens variés : essais in situ sur pieux réels, essais sur pieux modèles en chambre d'étalonnage et essais sur pieux modèles centrifugés. Elle couvre le cas des pieux battus en traction et celui des pieux forés en compression.

Les diagrammes cycliques de stabilité sont des outils précieux pour juger de la sévérité des chargements cycliques sur le comportement axial des pieux.

L'attention est attirée sur la difficulté de définir des critères de rupture significatifs, notamment en compression. L'interprétation des diagrammes ne peut être dissociée des critères choisis pour les élaborer.

## 5 REMERCIEMENTS

La rédaction de cette communication a été rendue possible par la collaboration de nombreux chercheurs et organismes. Les auteurs remercient tous leurs collègues impliqués dans ces recherches et les différents organismes ayant autorisé la publication des résultats.

## 6 REFERENCES

- AFNOR.1999. NF P 94-150. Norme Française. Sols: Reconnaissance et Essais – Essai statique de pieu sous effort axial – Partie 1: en compression et Partie 2: en traction
- Benzaria O., Puech A., and Le Kouby A. 2012. Cyclic axial load-tests on driven piles in overconsolidated clay, *Offshore Site Investigation and Geotechnics*, SUT, London
- Benzaria A., Puech A. et Le Kouby A. 2013. Essais cycliques axiaux sur des pieux forés dans des sables denses. *Proceedings 18th ICSMGE*, Paris
- Guefrech A., Rault G, Chenaf N., Thorel L., Garnier J., Puech A. 2012. Stability of cast in place piles in sand under axial cyclic loading . *Proc. 7<sup>th</sup> Int. Conf. Offshore Site investigation and Geotechnics*. London. 12-14 sept. pp.329-334.
- Jardine, R.J. and Standing, J.R. 2000. Pile load testing performed for HSE cyclic loading study at Dunkirk, France. Two Volumes. *Offshore Technology Report OTO 2000 007; Health and Safety Executive*, London. 60p and 200p.
- Jardine, R.J., Standing, J.R. & Chow, F.C. 2006. Some observations of the effects of time on the capacity of piles driven in sand. *Geotechnique*, 56 (4), 227-244.
- Jardine, R., Bitang, Z., Foray, P., & Dalton, C. 2009. Experimental Arrangements for Investigation of Soil Stresses Developed around a Displacement Pile. *Soils and Foundations*, 49(5), 661–673.
- Jardine, R.J. and Standing. 2012. Field axial cyclic loading experiments on piles driven in sand. *Soils and Foundations*, 52(4), 723–736.
- Jardine R, Puech A and Andersen K. 2012. Cyclic loading of offshore piles: potential effects and practical design. *Proc.7th Int. Conf. on Offshore Site Investigations and Geotechnics*, SUT., London.
- Karlsrud K., Nadim F. and Haugen, T. 1986. Piles in clay under cyclic axial loading - Field tests and computational modeling. *Proc. 3<sup>rd</sup> Int. Conf. on Numerical Methods in Offshore Piling*, Nantes, France
- Parker, E. J., Jardine, R.J., Standing, J.R. and Xavier, J. 1999. Jet grouting to improve offshore pile capacity. *Offshore Technology Conference*, Houston, OTC 10828.
- Poulos H.G. 1988 Cyclic stability diagram for axially loaded piles. *Journal of Geot. and Geoenv. Eng.* 114 (8): 877-895 .
- Puech A., Canou J., Bernardini C., Pecker A., Jardine R., and Holeyman A. 2012. SOLCYP: a four year JIP on the behavior of piles under cyclic loading. *Offshore Site Investigation and Geotechnics*, SUT, London
- Rimoy S., Jardine R. and Standing J. 2013. Displacement response to axial cyclic loading of driven piles in sand. *Proceedings 18th ICSMGE*, Paris
- Tsuha, C., Foray, P., Jardine, R., Z.X., Y., Silva, M., & Rimoy, S. 2012. Behaviour of displacement piles in sand under cyclic axial loading. *Soils and foundations*, 52(3), 393–410.

# Utilisation des essais d'expansion cyclique pour définir des modules élastiques en petites déformations

## Determining small strain elastic modulus using cyclic expansion tests

Reiffsteck P., Fanelli S., Tacita J.-L.  
*Univ Paris Est, IFSTTAR GER, Paris, France*

Dupla J.-C.  
*Univ Paris Est, Marne-la-Vallée, Navier Géotechnique*

Desanneaux G.  
*CETE de l'Ouest, LRPC Saint Brieuc, France*

**RÉSUMÉ :** Depuis trente ans, la réalisation d'essais d'expansion cycliques réalisés en trous préforés ou forés à l'avancement sur différents sites expérimentaux a permis de disposer d'une base assez importante de cas. La qualité de ces résultats permet de dériver des paramètres de déformabilité à des taux de déformation faibles. Ces essais cycliques ont été réalisés au pressiomètre Ménard et au pressiomètre autoforeur. Un peu moins d'une dizaine de sites ont été étudiés permettant d'observer le comportement de matériaux sableux et argileux normalement consolidés et surconsolidés. Cette communication présente le matériel utilisé ainsi que les procédures suivies. Le programme d'essai composé de plusieurs phases de cycles d'amplitude variable a été proposé dans les années quatre-vingt. On observe une évolution du module en fonction du nombre de cycles, de la nature du matériau et du rapport de l'amplitude et de la position moyenne avec la contrainte horizontale en place. Une synthèse des résultats des essais obtenus sur ces sites est présentée.

**ABSTRACT:** For thirty years, realization of cyclic expansion tests carried out in borehole pockets drilled using a separate tool or integrate in the probe, on different experimental sites allowed to have a rich database. The quality of these results allows to derive stress-strain parameters at low strain level. These cyclic tests were carried out using Menard and self-boring pressuremeters. A little less than ten sites were studied covering the behavior of sandy and clayey materials normally consolidated or overconsolidated. This paper will present the equipment used and procedures applied. Usually, the test program, which was proposed in the eighties, consists of several phases of cycles of variable amplitude. One can observe a shift of the module depending on the number of cycles, the nature of the material and the ratio of the amplitude and the mean position compared to the at rest horizontal stress. A summary of test results obtained on these sites is presented.

**MOTS-CLÉS :** comportement cyclique, essais d'expansion de cavité, pressiomètre autoforeur, pressiomètre Ménard

**KEYWORDS:** cyclic behavior, cavity expansion test, Self-boring pressuremeter, Ménard pressuremeter.

## 1 INTRODUCTION

Avec le matériel d'essai pressiométrique Ménard, il est possible de réaliser des essais d'expansion par palier (norme NF P94-110-1) et des essais cycliques (norme NF P94-110-2) (AFNOR, 1999 et 2000). Ces derniers essais comportent un cycle réalisé par paliers, dans les mêmes conditions que l'essai pressiométrique Ménard objet de la norme NF P 94-110-1. L'essai d'expansion classique, dans les conditions de forages préconisées par la norme NF P 94-110-1 et avec le protocole de chargement proposé, ne donne pas de résultats utilisables directement dans une étude de la déformabilité des ouvrages notamment lorsque la connaissance des modules en petite déformation est nécessaire (Combarieu et Canépa, 2001).

Les essais avec boucle de déchargement-rechargement permettent de déterminer un module cyclique de déformation. Les valeurs obtenues sont intermédiaires entre les modules en petites déformations obtenus au laboratoire, ou avec des essais de propagation d'ondes in situ, et les modules Ménard usuels (Les pressiomètres Louis Menard, 1960, Borel et Reiffsteck, 2006). Toutefois, un seul cycle est insuffisant pour cerner l'évolution des caractéristiques du sol sous chargement cyclique (Dupla et Canou, 2003). L'étude présentée, réalisée dans le cadre du projet national SOLCYP (projet de recherche sur le comportement des pieux soumis à des sollicitations cycliques, voir le site [www.pnsolcyp.org](http://www.pnsolcyp.org) pour plus d'information), comporte des essais multi-cycles réalisés avec la technique de la sonde mise en place dans un trou pré-foré ou foré à l'avancement.

## 2 DISPOSITIF EXPÉRIMENTAL

Le principe de l'essai consiste à mesurer l'évolution du volume injecté lors de l'application de cycles de pression.

### 2.1 Matériel

La mesure de la variation de volume en fonction des cycles se fait soit par mesure du volume d'eau injecté, soit par mesure du déplacement d'un palpeur (Figure 1a et b). L'idée étant de pouvoir réaliser des essais avec une sonde pressiométrique mise en œuvre par autoforage ou dans un pré-forage de type Ménard (AFNOR, 2000).

Le matériel utilisé développé par l'entreprise Jean Lutz SA est un contrôleur pression volume (CPV) (de type PREVO), capable de piloter des électrovannes par un ordinateur de type PC via une application spécifique.



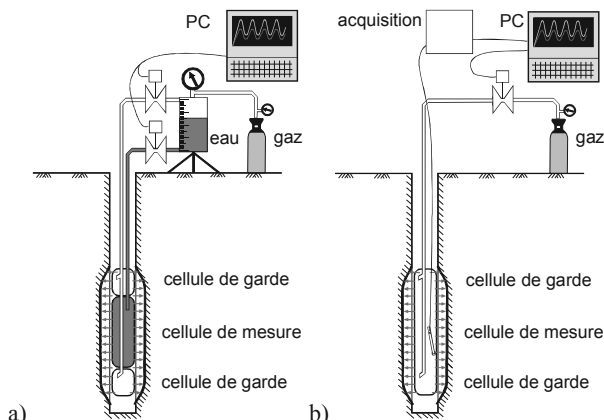


Figure 1. Architecture de l'essai cyclique (a) au pressiomètre Ménard, (b) au pressiomètre autoforeur

Le principe de fonctionnement est le suivant. Les différentes opérations manuelles sont réalisées, soit directement sur le CPV, soit par le programme. Le pilotage en cyclique est réalisé sur la base d'un fichier d'essai acceptant tout type de signal, harmonique ou multifréquence. Le suivi se fait en temps réel sur un onglet graphique ou sur le tableau de valeur.

### 2.2 Méthode d'essai

Durant les années 70, l'Association pour la Recherche en Géotechnique Marine rassemblant différentes entreprises, bureaux d'étude et établissements de recherche dans le domaine a mené une campagne, sur plusieurs sites, d'essais cycliques au pressiomètre. Les détails des expérimentations sont rassemblés dans plusieurs rapports et articles du Symposium sur la pressiométrie et ses applications en mer tenu en 1982 à Paris (Jézéquel et le Méhauté, 1982 ; Puech et al., 1982). Trois types d'essais furent réalisés ; nous présentons les deux mis en œuvre dans la présente étude :

- essai de chargement cyclique entre deux bornes de pression  $p_M$  et  $p_m$  (Figure 2 a),
- essais de chargement entre deux bornes de pression variables, dont la moyenne est cependant constante, la borne inférieure restant supérieure à  $p_0$  la pression des terre au repos (Figure 2 b).

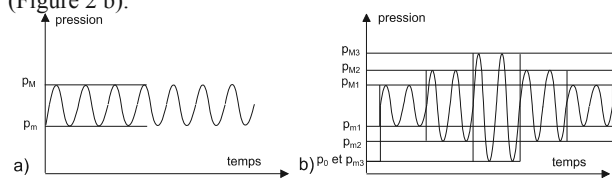


Figure 2. Différents types d'essais cycliques

Les paramètres retenus pour les essais cycliques découlent de la méthode proposée (cf. ci avant) : essai à pression contrôlée ; adaptation de la fréquence au type de sol pour tenter de rester drainé, niveau de sollicitation : 0,8 ( $R_c = \Delta p_{cyc} / p'_0$ ) ; fréquence : 0,01 à 0,05 Hz et nombre de cycles égal à 50.

La pression initiale  $p_m$  utilisée pour démarrer l'essai est définie comme la contrainte horizontale en place (pression des terres de repos) (effective de préférence) et la pression maximale  $p_M$  est égale à  $(1+0,8)p_m$  (Dupla et Canou, 2003). La pression  $p_m$ , qui a été prise égale à  $p_0$ , a été définie à partir des résultats d'essais d'expansion de type Ménard antérieurs par la méthode proposée par Briaud (1992).

### 2.3 Définition des modules

L'intérêt de réaliser des cycles avec le pressiomètre pour obtenir des modules en petites déformations est apparu très tôt (Les pressiomètres Louis Menard, 1960). Dès l'origine, plusieurs modules ont été définis à partir des courbes expérimentales.

Dans la première zone désignée comme « élastique », le module atteint une valeur quasi indépendante du niveau de déformation. Il est appelé module « initial »  $G_0$ .

Les courbes en partie monotone sont décrites par un module « sécant » ( $G_{s,1}$ ) défini par la pente de la droite reliant l'origine au point actuel et en partie cyclique, un autre module sécant ( $G_{p,N}$ ) déterminé par la pente de la droite reliant les deux points d'inversion du cycle N. Les modules maxima des cycles sont calculés avec la relation (avec les notations de la Figure 3) :

$$G_{p,N} = \frac{\Delta p}{\Delta V / V_m}$$

La boucle parcourue dans ces séquences de déchargement/remise en charge est de forme ellipsoïdale. Elle représente l'énergie dissipée en déformation plastique. L'évolution de l'inclinaison des cycles ou module au cours des cycles permettra d'évaluer le comportement du sol. On peut évaluer le durcissement ou l'adoucissement cyclique et l'accumulation de déformation, la stabilisation ou la relaxation ou l'effet rochet.

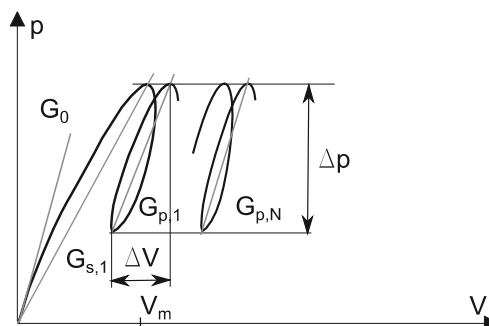


Figure 3. Calcul des modules des cycles

Le mode d'interprétation est basé sur l'évolution de l'aire caractéristique des boucles de chargement déchargement ainsi que du module sécant des boucles d'hystérésis (Figure 3).

## 3 ESSAIS CYCLIQUES

### 3.1 Essais du LRPC de Saint Brieuc

À la fin des années 70, le laboratoire des Ponts et Chaussée de Saint Brieuc a réalisé plusieurs campagnes d'essais d'expansion cyclique au pressiomètre autoforeur (modèle PAF76 de diamètre 132 mm). Ces essais comportaient une centaine de cycles voire plusieurs milliers de cycles (durée de 24 à 72 heures). Ils ont été réalisés sur deux sites principaux Cran et Plancoët (Le Méhauté et Jézéquel, 1980).

#### 3.1.1 Site de Plancoët

Le site est constitué d'une parcelle plane en bordure de la rivière Arguenon. Le sol est constitué de sols fins très lâches : silts en surface (0 à 4 m), sables fins ensuite (surtout de 6 à 9 m) puis des argiles (de 10 à 12 m) avec quelques inclusions de graviers et de sables. Le substratum est à 15 m. La nappe fluctue en fonction des saisons entre 0,30 et 1,50 m.

#### 3.1.2 Site de Cran

La plaine alluviale de la Vilaine en aval de Redon est une vallée sédimentaire de près de 2 km de large. On y rencontre un dépôt d'argile sur une épaisseur de 10 à 20 m, reposant sur une couche de sable et de galets qui recouvre le substratum rocheux. À Cran, la rive droite est constituée par un dépôt d'argile molle marine de 17 m d'épaisseur reposant sur un substratum rocheux (schiste et phanites).

### 3.2 Essais du projet Solcyp

Des tests de validation ont été effectués sur trois sites : Gosier, Cran et Merville. Les deux derniers sites ont fait l'objet de nombreuses études dans le cadre de recherches programmées par les Laboratoires des Ponts et Chaussées. Les caractéristiques qui ont présidé au choix, ont été une relative homogénéité d'ensemble sur une profondeur minimale de 5 à 10 m.

#### 3.2.1 Site de Gosier

Les premiers essais avec le nouveau matériel ont été entrepris sur le site de Gosier en Guadeloupe situé dans une zone potentiellement liquéfiable, instrumentée et étudiée dans le cadre du projet ANR Belle Plaine. Des essais pressiométriques Ménard (par paliers) ont été réalisés pour compléter les profils obtenus au pénétromètre statique à pointe électrique et définir les pressions  $p'_0$  à utiliser puis deux sondages pressiométriques cycliques ont été réalisés.

La figure 4a présente les courbes de la pression imposée corrigée en fonction de la variation volumique obtenue pour 4 essais de la série MC2. Après une première partie qui correspond à la montée à la charge moyenne en monotone, la phase cyclique entre  $p_M$  et  $p_m$  montre la tendance à la stabilisation de quasiment tous les essais, même si celle-ci n'a jamais été atteinte. Apparemment, l'essai à la profondeur 7 m montre une accumulation importante de déformation volumique (couche d'argile molle).

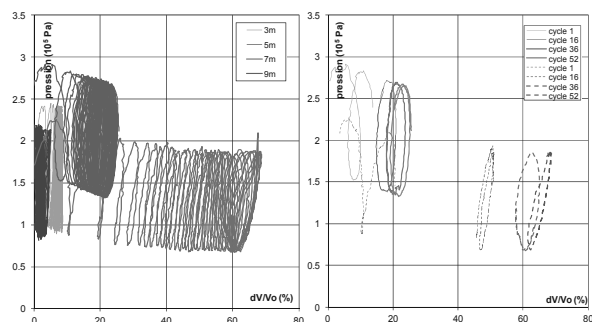


Figure 4. a et b Essais d'expansion cycliques pré-forés site de Gosier

#### 3.2.2 Site de Cran

Les essais réalisés en 2011 ont été placés à proximité des séries réalisées en 1979.

À la profondeur 2 m, la courbe d'essai présentée sur la Figure 5a montre une accumulation de volume élevée (de l'ordre de 900 cm<sup>3</sup>) conduisant à la conclusion que le test a été effectué dans la couche molle et que la pression initiale déduite des études précédentes a été surestimée. Le signal obtenu représenté sur la Figure 5a est assez bruité car l'amplitude de la plage de pression est faible, et une interaction entre l'asservissement de l'eau et l'air n'a pu être corrigée à temps dans le pilotage.

#### 3.2.3 Site de Merville

Sur le site expérimental de Merville (Nord), on rencontre à 1,5 m environ de la surface, une couverture de limons peu plastiques, affectée par le battement de la nappe et de 1,5 à 42 m de profondeur, l'argile (surconsolidée) des Flandres de l'Yprésien.

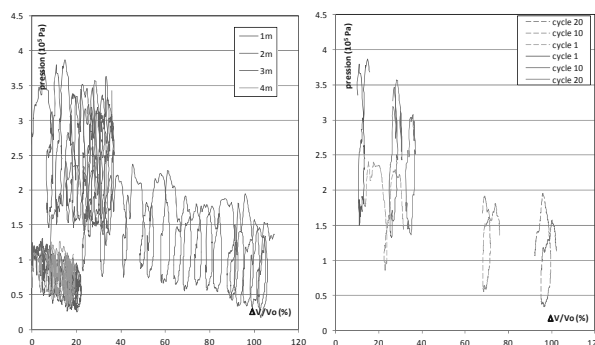


Figure 5. a et b Essais d'expansion cycliques autoforés site de Cran

Un sondage au pressiomètre autoforeur avec des essais cycliques à 6, 8 et 12 m, en alternance avec des essais d'expansion monotone croissante à 5, 7 et 11 m, a été réalisé (Figure 6 et Figure 7a). Les trois premiers essais cycliques ont été réalisés avec la même amplitude fixée à partir des essais d'expansion monotones. Le dernier essai a été réalisé avec une amplitude basée sur l'essai à 11 m.

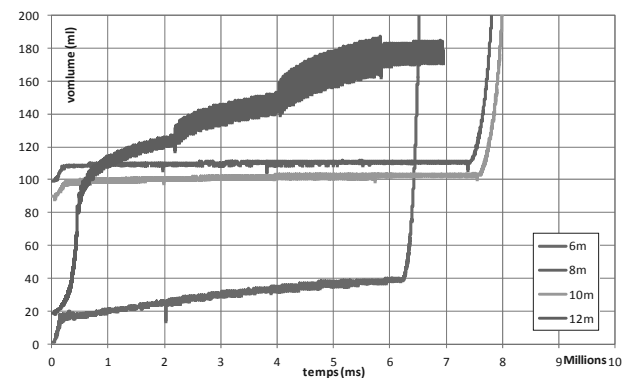


Figure 6. Essais d'expansion cycliques autoforés multi-amplitude site de Merville

Les amplitudes de 60 kPa ont abouti à des résultats peu précis car d'une part la source de pression était réglée à une pression trop forte et de ce fait l'électrovanne de la chambre tampon avait du mal à réguler et d'autre part cette valeur est faible et de l'ordre de grandeur de la précision de l'asservissement. Il est donc nécessaire d'adapter les amplitudes aux profondeurs et de réévaluer la méthode de détermination de celle-ci.

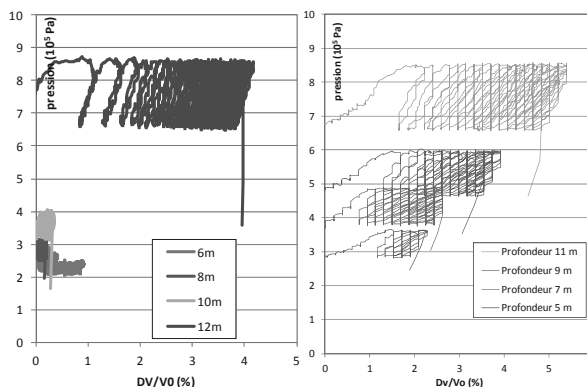


Figure 7. a et b Essais d'expansion cycliques (a) autoforés et (b) pré-forés site de Merville

À proximité immédiate un sondage au pressiomètre Ménard avec un perforage d'un mètre à la tarière hélicoïdale avec des essais cycliques à 5, 7 et 11 m permet de disposer de résultats comparables (figure 7).

#### 4 DISCUSSIONS

Un premier constat est que le signal obtenu représenté sur les Figure 4 à 7 est plus bruité que celui donné dans les articles de Jézéquel et Le Méhauté (1982) car l'asservissement par contrôleur pression volume à vis à bille en vitesse de volume (2%/mn) est plus stable qu'un asservissement en pression par électrovanne. Les cycles obtenus présentent des points singuliers à méplats et non de rebroussement.

Les différentes expérimentations ont montré qu'il faut réaliser un minimum de 50 cycles pour obtenir une évolution claire du module sécant et qu'il n'est pas possible de se limiter à quelques cycles – 3 à 10 par exemple – pour obtenir des résultats représentatifs. A noter que l'évolution du module sécant de 50 à 500 cycles est de 10% en moyenne et de 500 à 5000 de 3%.

Même si les différences de protocole dues à la mise au point de ces matériels et essais ne permettent pas une comparaison détaillée, les accumulations volumiques constatées sont du même ordre de grandeur avec les différents modes de mise en œuvre. La qualité du pré-forage est essentielle pour permettre un essai avec un volume injecté initialement minimal. Sur deux sites (Gosier et Cran) indépendamment du mode de mise en œuvre, l'accumulation importante de déformation à certains niveaux a permis de localiser les couches susceptibles d'une chute de caractéristiques importante lors de l'application de sollicitations cycliques (figures 4 et 5).

Tableau 1. Caractéristiques des essais

Site	Forage	Sol	z (m)	$G_{p,1}$ ( $10^5$ Pa)	$a_{M0}$ (%)	$G_{p,50}/G_{p,1}$	
Plancoët	8-3	silt	2	5,19	0,5	1,6	
			16-1	3	3,46	1	1,8
			7-3	2	1,08	5	3
	8-3	sable	7	9,98	0,5	2,2	
			16-1	7	6,49	1	2
			7-3	7	2,69	5	3,3
			8-3	11	8,58	0,5	1,43
16-1	argile	11	6,47	1	1,9		
		7-3	11	3,75	5	2,1	
Cran 1	C1	argile	moy	29,9	1,67	1,15	
	C2	argile	moy	20	0,99	1,09	
Gosier	C2-PMT	sable	7	51,6	0,5	1,60	
			9	13,9	3,5	1,41	
Cran 2	A0-PAF	argile	1	60,8	10	2,71	
			2	25,6	12	1,59	
Merville	PAF	argile	6	426	0,8	2,01	
			12	294	3,5	1,93	
Merville	PMT	argile	5	145	0,6	1,37	
			11	255	0,9	1,21	

Lors de tous les essais, une stabilisation des déformations moyennes des cycles en fonction du nombre de cycle a pu être observée. Selon le type de sol, les cycles tendent à se redresser plus ou moins fortement, comme cela semble être le cas pour les sables de Plancoët et l'argile de Merville.

Les séries d'essais multi-amplitude permettent d'obtenir des courbes d'évolution du module cyclique en fonction de la profondeur et de l'amplitude des cycles pour différentes natures de sol (figure 6 et tableau 2).

Tableau 2. Évolution du module sur plusieurs amplitudes

Site	Outil	z (m)	$G_{p,50}/G_{p,1}$ de la phase			
			1	2	3	4
Plancoët	PAF	1	1.83	1.08	0.8	1.27
Merville	PAF	12	1,93	0,99	0,87	0,98
	PMT	11	1,21	0,94	1,42	1,06

On observe une évolution très similaire sur le site de sols lâches de Plancoët et sur le site d'argile raide de Merville : une évolution importante pour la première amplitude, puis une quasi stabilisation pour les autres amplitudes

#### 5 CONCLUSION

Les différentes campagnes de sondages avec essais cycliques mono ou multi amplitudes ont montré l'intérêt de cet essai pour cerner l'évolution du module de cisaillement en fonction du nombre de cycle et le potentiel de l'essai à localiser les horizons susceptibles de liquéfaction.

Il reste à mieux préciser les conditions d'essais pour avoir des jeux de données comparables et si possible disposer de la mesure de la pression interstitielle au niveau de la membrane pour estimer les accumulations potentielles de pression ou adapter la vitesse d'essais afin de rester drainé.

#### 6 REMERCIEMENT

Les auteurs désirent remercier le projet national SOLCYP ainsi que le ministère de l'Environnement de l'Énergie, du Développement Durable et de la Mer pour le financement de cette action de recherche ainsi que leurs collègues O. Malassingne et A. le Kouby.

#### 7 RÉFÉRENCES

- AFNOR (1999) Essai pressiométrique Ménard – partie 2 Essai avec cycle, NF P94-110-2, Reconnaissance et essais, pp. 43.
- AFNOR (2000) Essai pressiométrique Ménard – partie 1 Essai sans cycle, NF P94-110-1, Reconnaissance et essais, pp. 43.
- Borel S., Reiffsteck Ph., (2006) Caractérisation de la déformabilité des sols au moyen d'essais en place. LCPC Paris, pp. 132.
- Briaud, J.L., (1992). The Pressuremeter, A. A. Balkema, Rotterdam, Netherlands.
- Combarieu O., Canépa Y. (2001) L'essai cyclique au pressiomètre, BLPC, 233, 37-65.
- Dupla, J.C., Canou J. (2003). Cyclic pressuremeter loading and liquefaction properties of sands, Soils and Foundations, Vol. 43(2), 17-31.
- Jézéquel J.F., Le Méhauté A. (1982) Essais cycliques au pressiomètre autoforeur, Symposium sur la pressiométrie et ses applications en mer, Paris, Éditions Technip, 221-233.
- Le Méhauté A. Jézéquel J.F., (1980) Essais cycliques au pressiomètre autoforeur, Rapports des LPC, FAER 1-05-09-22, 29 pages
- Les Pressiomètres Louis Ménard (1960) Phase de déchargement des essais pressiométriques, Etude théorique et applications, Circulaire 3 pages
- Puech A., Brucy F., Ma E., (1982) Calcul de la capacité axiale des pieux de fondations marines à partir du pressiomètre autoforeur, Symposium sur la pressiométrie et ses applications en mer, Paris, Éditions Technip, 373-388.

# Displacement response to axial cyclic loading of driven piles in sand

## Réponse en déplacement au chargement cyclique axial de pieux battus dans le sable

Rimoy S., Jardine R., Standing J.  
Imperial College London

**ABSTRACT:** Interactive axial cyclic loading stability charts have been developed to guide the assessment of axial cyclic capacity degradation of piles driven in sands. Less guidance is available regarding displacement accumulation and cyclic stiffness response at full scale. This paper focuses on axial cycling experiments of six full-scale steel open-ended pipe-piles at a marine sand site in Dunkerque, France. Multiple suites of cyclic loading were applied, interspersed with reference static tension capacity tests. The piles' stable, meta-stable and unstable capacity responses are identified with reference to a site-specific normalised cyclic interaction stability diagram. The stiffness response and rates of accumulated displacement associated with each style of cycling are reported. It is shown that under stable loading, the piles' cyclic stiffnesses remain constant or decline marginally. Similar trends are observed with meta-stable tests up to onset of an eventual cyclic failure, after which stiffness degrades rapidly. Unstable tests displayed shorter periods of modest change before marked losses of cyclic stiffness. The patterns of accumulated displacement growth show more complex relationships with the cyclic loading parameters that can be expressed in multi-surface 3-D plots.

**RÉSUMÉ :** Des diagrammes interactifs de stabilité cyclique ont été développés afin d'évaluer la dégradation cyclique des pieux battus dans les sables. Peu de données sont disponibles à échelle réelle en ce qui concerne les déplacements. Cet article s'intéresse aux essais cycliques axiaux de six pieux tubulaires en acier à base ouverte dans un site de sable marin à Dunkerque. Plusieurs séries de chargement cyclique ont été appliquées, entrecoupées d'essais statiques référentiels en traction. Les réponses stable, méta-stable et instable de capacité des pieux sont identifiées en relation avec un diagramme normalisé de stabilité cyclique. La réponse en termes de rigidité et de taux de déplacement accumulé associée à chaque type de chargement cyclique est ensuite présentée. On montre que sous un chargement stable, la rigidité cyclique reste constante ou diminue légèrement. On observe des tendances similaires dans les essais méta-stables jusqu'à l'apparition d'une éventuelle rupture cyclique, après laquelle la rigidité se dégrade rapidement. Les essais instables ont montré de courtes périodes de léger changement avant de fortes pertes de rigidité cyclique. Les schémas de croissance des déplacements cumulés montrent des relations avec les paramètres de charge cyclique plus complexes qui peuvent être exprimées dans des représentations 3-D.

**KEYWORDS:** axial cyclic loading/ pile stiffness/ accumulated displacements/ offshore engineering/ renewable energy  
**MOTS-CLÉS:** chargement cyclique axial/rigidité du pieu/déplacements cumulés/ingénierie offshore/énergies renouvelables

### 1 INTRODUCTION

The axial cyclic response of driven pile foundations can be critical in the design of offshore oil and gas platforms, and multi-piled wind turbines, towers and pylons. Lateral and moment loads imposed by wind or wave action can be large compared to self-weights, leading to multiple modes of axial and lateral cyclic loading on the foundation piles. Lateral loading model tests have been reported that tracked the gradual rotation and stiffness of monopiles (Leblanc et al. 2010); however less guidance is available on full-scale displacement accumulation and stiffness responses under axial cycling.

Jardine et al. (2012) reviewed the potential effects of cyclic loading on offshore pile foundations and considered how these may be addressed in practical design for a range of geomaterials. They note that loads vary with platform weight, water depth, metocean environment and structural form. Of the 15 field research studies they identified, only one concerned silica sands, that at Dunkerque, France reported by Jardine & Standing (2000, 2012). Merritt et al. (2012) describe how the most severe tens or hundreds of cycles imposed in storms are the most critical to pile performance. The Jardine & Standing (2000) field study investigated behaviour up to 1000 cycles.

Karlsrud et al. (1986), Poulos (1988) and Jardine & Standing (2000) have used cyclic stability diagrams to guide the assessment of pile axial cyclic behaviour. These consider the interaction effects of cyclic and mean loads (normalised by static capacity before cycling) and the number of cycles applied. Such interaction diagrams may be zoned to identify a cyclically stable (S) region where there is no reduction of load capacity after N cycles, a meta-stable (MS) region where some reduction of load capacity occurs after N cycles and an unstable (US) region where cyclic failure develops within a small specified number of cycles. Jardine & Standing (2012) used a similar

scheme in interpretation of their field tests at Dunkerque (Figure 1) where multiple cyclic loading tests performed that were interspersed with reference static tension capacity ( $Q_T$ ) tests. This paper focuses on further interpretation of the same axial cycling experiments. The axial static and cyclic stiffness responses are discussed and the accumulated cyclic displacement trends associated with each mode of cycling are examined, referring to the site specific normalised cyclic interaction stability diagram.

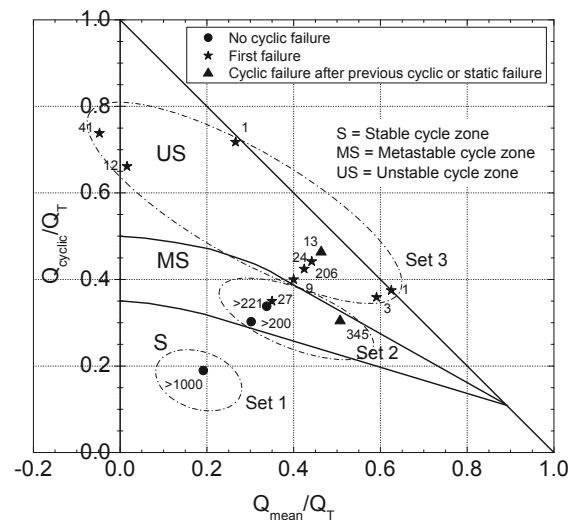


Figure 1. Axial cyclic interaction diagram for the full-scale pile tests in Dunkerque silica marine sands (Jardine & Standing 2012).



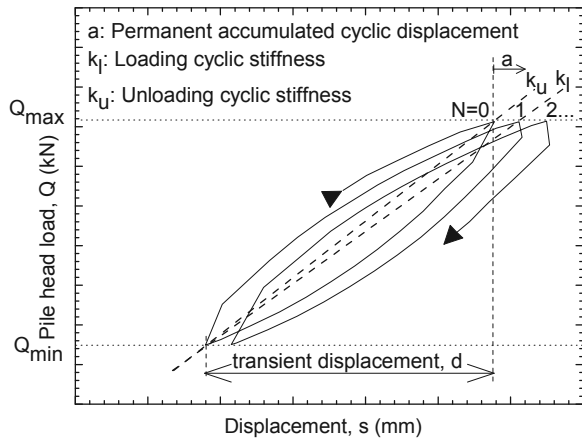


Figure 4. Illustration of the stiffness and displacement parameters used in the analyses

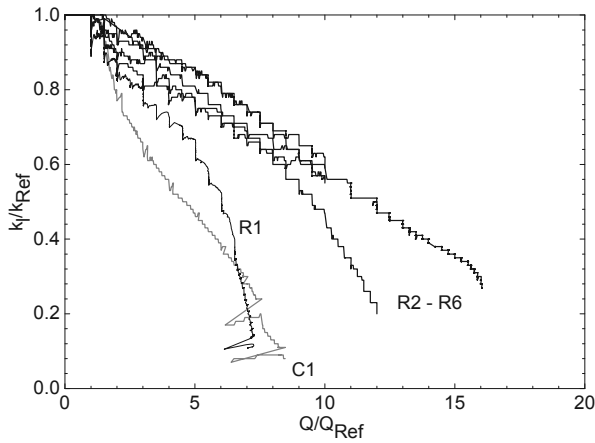


Figure 5. Pile stiffness from the first-time axial static monotonic tension loadings normalised by the reference stiffnesses against normalised load

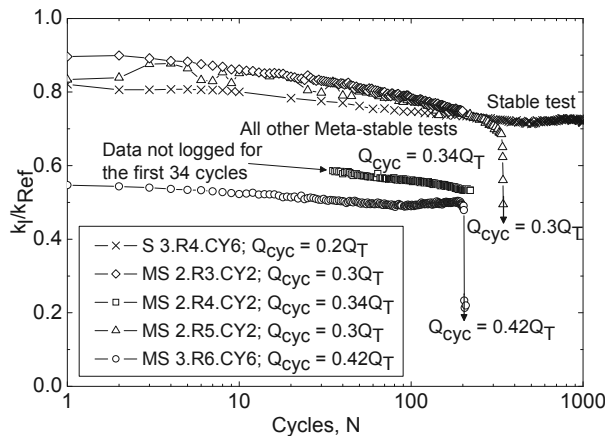


Figure 6. Axial cyclic loading stiffness  $k_l$  responses normalised by  $k_{Ref}$  against number of cycles for the stable and meta-stable tests.

The loading stiffness  $k_l$  degradation trends for the unstable tests (Set 3 of Figure 1) are shown on Figure 7. By definition, these tests failed with sudden stiffness loss after relatively few cycles. However, even these piles retained most of their initial stiffnesses until within  $\sim 10$  cycles of final failure. Seemingly anomalous stiffness behaviour is observed towards failure in some one-way meta-stable and unstable loading tests when stiffnesses are defined from the unloading cycle phase  $k_u$ , Figure 8. This reversal in normalised stiffness results from an increased opening-up of the load-unload hysteresis loops as

cyclic failure approaches with more plastic displacements accumulating on the loading loops leading to the progressively decreasing secant loading stiffnesses and apparently stiffer behaviour on unloading as cyclic loading approaches failure.

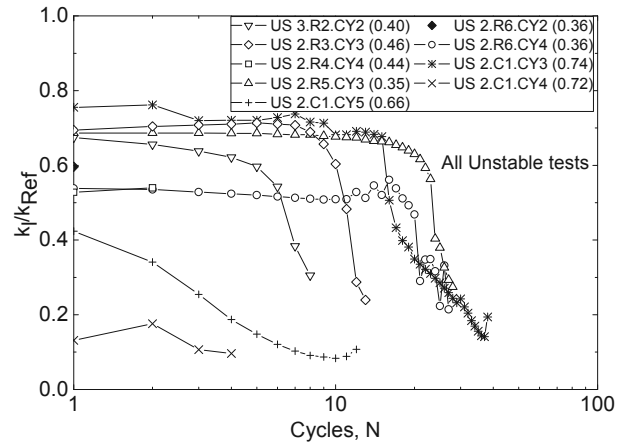


Figure 7. Axial cyclic loading stiffness  $k_l$  responses normalised by  $k_{Ref}$  against number of cycles for the unstable tests.

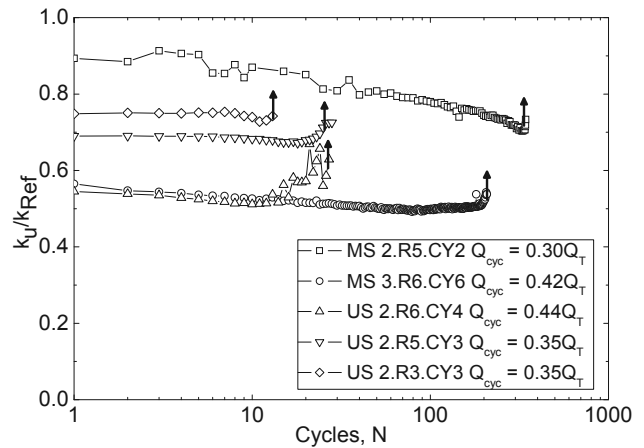


Figure 8. Axial cyclic unloading stiffness  $k_u$  responses normalised by  $k_{Ref}$  against number of cycles for selected metastable and unstable tests.

### 4.3 Accumulated cyclic displacements

The patterns of pile head displacement accumulation for the stable and meta-stable cyclic tests are shown on Figure 9. Also shown are the reference lines related to the predefined thresholds for stable, metastable and unstable accumulated displacements rates. An almost static accumulated displacement trend was observed in the single fully stable loading test 3.R4.CY6. The meta-stable tests 2.R3.CY2 and 2.R4.CY2 developed higher, but steady displacement rates  $> 1\text{mm}/100\text{cycles}$  while the other two meta-stable tests 2.R5.CY2 and 3.R6.CY6 displaced by  $> 1\text{mm}/10\text{cycles}$ . A range of responses is evident for the unstable loading tests summarised in Figure 10 which develop displacement rates  $> 1\text{mm}/10\text{cycles}$ .

While the cyclic stiffness patterns varied principally as a function of the applied cyclic amplitudes  $Q_{cyclic}$ , the accumulated cyclic displacement patterns depended on both the normalised mean ( $Q_{mean}/Q_T$ ) and cyclic ( $Q_{cyclic}/Q_T$ ) loads. Rimoy et al. (2013) demonstrate the interactive effects of the loading components  $Q_{cyclic}$  and  $Q_{mean}$  by considering the accumulated displacements developed after 3, 10, 30, 100, 200, and 300 cycles to produce tentative 3D surfaces equivalent to displacements of 2%, 0.2% or 0.02% pile diameter, Figure 11. The accumulated displacement trends flatten progressively as  $N$  increases. The zero cyclic effect boundary was set at  $Q_{cyclic}/Q_T =$

0.1 following centrifuge studies by Julio (2009). No displacements are expected to accrue due to cycling below this level; further full-scale specific investigation of this lower threshold is required.

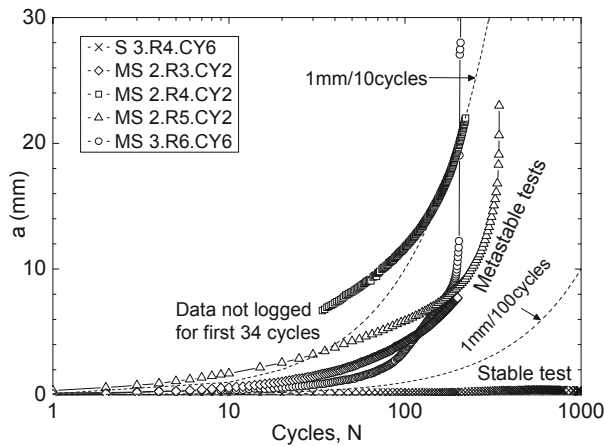


Figure 9. Accumulated cyclic displacements for the stable and meta-stable loading tests

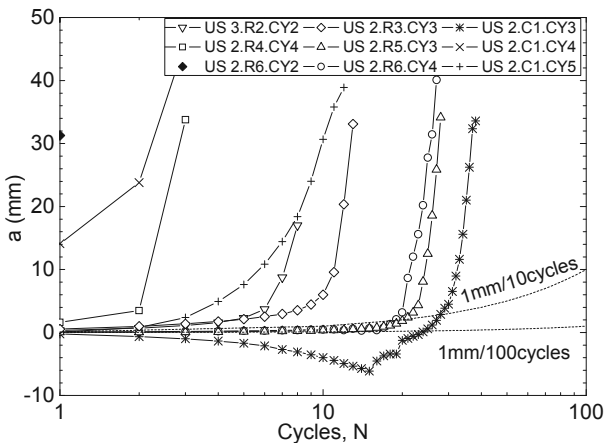


Figure 10. Permanent accumulated cyclic displacements response for the unstable tests

## 5 SUMMARY AND CONCLUSIONS

The analysis presented of the axial cyclic loading load–displacement, stiffness and accumulated displacements responses seen in tests on steel open-ended pipe piles driven in silica sand indicate the following.

- (1) Axial load–displacement behaviour is highly non-linear, even at relatively low levels of loading.
- (2) The piles' cyclic stiffnesses generally remained within 20% of those observed under initial static loading until cyclic failure was approached.
- (3) The patterns of accumulated displacements depended on both the mean and cyclic normalised loading levels.
- (4) While displacements accumulate rapidly over just a few cycles in the unstable zone, extended cycling in the stable zone led to minimal (and stabilising) accumulated displacements and axial capacity gains (Jardine et al (2006) meta–stable tests showed intermediate behaviour.

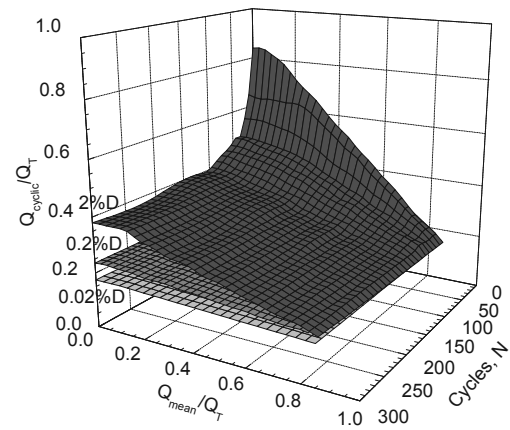


Figure 11. 3D plot for accumulated cyclic displacements equivalent to 0.02%D, 0.2%D and 2%D.

## 6 ACKNOWLEDGEMENTS

The above research was funded by the EU (through the GOPAL project) and Health and Safety Executive (HSE) of UK. We gratefully acknowledge the Port Autonome de Dunkerque for providing the test site. The field testing was conducted in conjunction with Precision Monitoring Control Ltd. of Teesside UK. The first author has been supported by the Commonwealth Scholarship Commission during the writing of this paper.

## 7 REFERENCES

- Chow F.C. 1997. *Investigations into displacement pile behaviour for offshore foundations*, PhD thesis, University of London (Imperial College).
- Jardine R.J. & Standing J.R. 2000. *Pile load testing performed for HSE cyclic loading study at Dunkirk, France*. Two volumes. Offshore Technology Report OTO2000 007; Health and Safety Executive, London. 60p and 200p.
- Jardine, R.J., Standing, J.R., & Chow, F.C. 2006. Some observations of the effects of time on the capacity of piles driven in sand. *Geotechnique* 56(4): 227-244.
- Jardine R.J. & Standing J.R. 2012. Field axial cyclic loading experiments on piles driven sand. *Soils and foundations* 52(4): 723 - 736.
- Jardine R.J., Puech A. & Andersen K. H. 2012. Cyclic loading of offshore piles: Potential effects and practical design. *Proceedings of the SUT 7th International Conference on Offshore Site Investigation and Geotechnics*, London, UK, pp. 59 - 97.
- Julio R.M.H. 2009. *Comportement des pieux et des groupes de pieux sous chargement latéral cyclique*. These de doctorat, Ecole Nationale des Ponts et Chaussées, Paris, France.
- Karlsruh K., Nadim F. & Haugen T. 1986. Piles in clay under cyclic axial loading field test and computational modelling. *Proceedings of the 3rd International Conference on Numerical Methods in Offshore Piling*, Nantes, France, pp. 165 - 190.
- Leblanc C., Houslyby G.T., & Bryne B.W. 2010. Response of stiff piles in sand to long-term cyclic lateral loading. *Geotechnique* 60(2): 79-90.
- Merritt A.S., Schroeder F.C., Jardine R.J., Stuyts B., Cathie D. & Cleverly D. 2012. Development of pile design methodology for an offshore wind farm in the North Sea. *Proceedings of the SUT 7th International Conference on Offshore Site Investigation and Geotechnics*, London, UK, pp. 439 - 447.
- Parker E. J., Jardine R.J., Standing J.R. & Xavier J. 1999. Jet grouting to improve offshore pile capacity. *Offshore Technology Conference, Houston, OTC 10828* 1: 415 - 420.
- Poulos H.G. 1988. Cyclic stability diagram for axially loaded piles. *Journal of Geotechnical and Geoenvironmental Engineering*, 114(8): 877-895.
- Rimoy S., Jardine R., and Standing J. 2013. Displacement response to axial cycling of piles driven in sand. *Geotechnical Engineering*, 165 (GE1): 1 - 16.

# Experimental Testing of Monopiles in Sand Subjected to One-Way Long-Term Cyclic Lateral Loading

Étude expérimentale de monopiles dans le sable soumis à un chargement cyclique transversal non alterné

Roesen H.R., Ibsen L.B., Andersen L.V.  
Aalborg University, Aalborg, Denmark

**ABSTRACT:** In the offshore wind turbine industry the most widely used foundation type is the monopile. Due to the wave and wind forces the monopile is subjected to a strong cyclic loading with varying amplitude, maximum loading level, and varying loading period. In this paper the soil-pile interaction of a monopile in sand subjected to a long-term cyclic lateral loading is investigated by means of small scale tests. The tests are conducted with a mechanical loading rig capable of applying the cyclic loading as a sine signal with varying amplitude, mean loading level, and loading period for more than 60 000 cycles. The tests are conducted in dense saturated sand. The maximum moment applied in the cyclic tests is varied from 18% to 36% of the ultimate lateral resistance found in a static loading test. The tests reveal that the accumulated rotation can be expressed by use of a power function. Further, static tests conducted post cyclic loading indicate that the static ultimate capacity increases with the magnitude of cyclic loading.

**RÉSUMÉ:** Dans l'industrie éolienne offshore, le type de fondation le plus largement utilisé est la monopile. En raison de la force des vagues et du vent, la monopile est soumise à une charge cyclique élevée dont l'amplitude, le niveau de charge maximale et la périodicité varient. Dans cet article, l'interaction sol-pieu d'une monopile implantées dans du sable et soumises à un chargement latéral cyclique est étudiée au moyen d'essais à échelle réduite. Les tests sont effectués avec une grue de chargement mécanique capable d'appliquer un chargement cyclique sinusoïdal avec amplitude, niveau moyen et période de chargement variable pendant plus de 60 000 cycles. Les tests sont effectués dans du sable dense saturé. Le moment maximum appliqué durant les essais cycliques varie de 18% à 36% de la résistance latérale ultime obtenue lors d'essais de chargement statique. Les essais montrent que la rotation accumulée peut être exprimée par l'utilisation d'une fonction de puissance. En outre, des essais statiques menés après le chargement cyclique indiquent que la capacité statique ultime augmente avec le niveau du chargement cyclique.

**KEYWORDS:** Experimental, wind turbine foundation, monopile, long-term cyclic loading, dense sand.

## 1 INTRODUCTION

In the offshore wind turbine industry, the most widely used foundation type is the monopile, i.e. a large diameter stiff pile. During the lifetime of a wind turbine, the monopile foundation is subjected to few load cycles with large amplitudes, caused by the strong storms, and also to millions of lateral load cycles with low or intermediate amplitudes due to the wave loading. This loading may cause failure in the fatigue or serviceability limit states, FLS and SLS respectively (Wichtmann et al. 2008). The cyclic loading might induce a change in the soil stiffness and a permanent accumulated rocking rotation (tilt) of the turbine. Due to the efficiency of the wind turbine, strict demands for the rotation and the stiffness of the entire structure are normally made and thus, the change in stiffness and rotation becomes key issues in the design. However, the current design guidance, DNV (2011), on this long-term loading is limited and a procedure for designing large diameter piles is yet to be fully expressed and confirmed. The development of a reliable design method requires verification and for that in-situ and large-scale testing is by far the best tool. However, this is also the most expensive and time-consuming tool. Therefore, the recent choice for evaluating the cyclic behaviour has been numerical modelling and small scale testing. Several authors has investigated this e.g. Niemunis et al. (2005), Achmus et al. (2005), Peng et al. (2006), LeBlanc et al. (2010) and Achmus et al. (2011). However, the research has mainly been based on cyclic triaxial tests, FEM-calculations and 1g experimental setups in dry sand.

In this paper, a 1g testing rig for modelling the environmental loading on a stiff monopile foundation in dense saturated sand is described and the results from four one-way

cyclic loading tests are presented. The purpose of the cyclic tests is to evaluate the influence of the number of load cycles,  $N$ , on the accumulated rocking rotation of the pile at seabed, under long-term cyclic loading with constant frequency but different loading amplitude and mean loading level.

The characteristic of the cyclic loading can be described by the ratios  $\zeta_b$  and  $\zeta_c$  as defined by LeBlanc et al (2010).  $\zeta_b$  expresses the magnitude of the loading as the ratio between the maximum load in a load cycle and the maximum static lateral capacity,  $\zeta_b = M_{max}/M_{static}$ .  $\zeta_b$  will take a value between 0 and 1. The cyclic load ratio  $\zeta_c$  defines the direction of the loading on the basis of the minimum and maximum load in a load cycle,  $\zeta_c = M_{min}/M_{max}$ .  $\zeta_c$  will take the value 1 for a static test, 0 for one-way loading, and -1 for two-way loading.

## 2 EXPERIMENTAL MODEL TESTS

The 1g small scale tests are carried out at the geotechnical laboratory at Aalborg University, Denmark. In the tests an open ended aluminium pipe pile is used. The pile is scaled approximately 1:50 in relation to a typical offshore monopile. In Table 1 the dimensions of the model pile are presented.

Table 1. Dimensions of the open ended aluminium pipe pile.

Diameter $D$ (mm)	Embedded length $L$ (mm)	Wall thickness $t$ (mm)	Load eccentricity $e$ (mm)
100	500	5	600



The bending stiffness of the model pile is similar to a scaled prototype steel pile, however, the behaviour of the pile during loading also depends on the stiffness of the surrounding soil. According to Poulos and Hull (1989) a pile behaves flexible if  $L > L_c$  and rigidly if  $L < L_c/3$ , where  $L_c$  is a critical length defined by Eq. 1.  $E_p I_p$  is the bending stiffness of the pile and  $E_s$  is Young's modulus of elasticity of the soil.

$$L_c = 4.44 \left( \frac{E_p I_p}{E_s} \right)^{0.25} \quad (1)$$

Due to the low stresses in the soil at 1g small scale testing, the stiffness is also low. From previous testing and numerical modelling an estimated soil stiffness of 4 MPa can be used for the sand in the test setup (Roesen et al. 2010). With use of Eq. 1 the model pile is thereby found to behave rigidly during lateral loading. In comparison a prototype steel monopile with  $D = 5$  m and  $t = 0.07$  m installed in sand with  $E_s = 70$  MPa is found to behave rigidly with a slenderness ratio  $L/D = 3$  and behave flexible with  $L/D = 9$ . Thus, for the examined slenderness ratio ( $L/D = 5$ ) the model pile experiences a more rigid behaviour than the prototype pile. Nevertheless, the results obtained in the small scale model tests can be used as underlying basis for understanding the monopile behaviour during lateral cyclic long-term loading.

The test setup consists of a cylindrical sand container with an inner radius of 2.00 m and a height of 1.20 m surrounded by a loading frame equipped for both static and cyclic loading. The setup is an improvement of the system presented in Roesen et al. (2012) which originally is based on the setup presented by LeBlanc et al. (2010). A cross-sectional sketch and a photo of the system are shown in Figure 1 and 2. The pile is installed in the middle of the container by use of a mechanical motor with installation velocity of 0.02 mm/s. The container holds up to 0.90 m dense saturated sand with 0.30 m highly permeable gravel underneath. In the bottom a drainage system with perforated pipes ensures homogeneous in- and outflow of water.

The cyclic loading system is a simple load controlled system based on a lever arm, weight hangers with applied masses,  $m_1$ ,  $m_2$ , and  $m_3$ , wires, and an electric motor controlling the rotation of weight  $m_1$ . The rotation causes an oscillating motion on the lever and thereby a cyclic loading on the pile. The system is thereby capable of providing sinusoidal loading to the pile for more than 60 000 load cycles. The rotational frequency of the motor is set to 0.1 Hz to be in agreement with environmental wave loading (Peng et al. 2006).

Initially, when the mass  $m_1 = m_2 = 0$ , the mass  $m_3$  is chosen to outbalance the system. Depending on the weights chosen for  $m_1$  and  $m_2$  the system is capable of providing both one- and two-way loading with varying  $\zeta_b$  and  $\zeta_c$ , i.e. different direction, amplitude, and mean loading level. The loading is applied through steel wires attached to the pile 600 mm above soil surface. Hence, the pile experiences both horizontal and moment loading. In both sides of the pile a HBM U2A 100 kg load cell is attached measuring the actual force applied to the pile throughout the whole test. The displacement of the pile is measured using three WS10-125-R1K-L10 displacement transducers from ASM GmbH. The transducers, D1, D2, and D3 are mounted 600 mm, 375 mm, and 155 mm above soil surface, respectively. The rocking rotation,  $\theta$ , and displacement of the pile at soil surface is found by use of linear regression of the three measurements assuming rigid pile behaviour. The data sampling rate is 2 Hz.

Before conducting any cyclic tests a static loading test is performed. The static test is conducted displacement controlled by use of a motor with a loading rate of 0.02 mm/s. The displacement is actuated 600 mm above soil surface, i.e. the same height as the loading in the cyclic loading tests. The pile is loaded to a rotation of 2°, unloaded, and reloaded to failure. The static test is used as a reference for the ultimate lateral

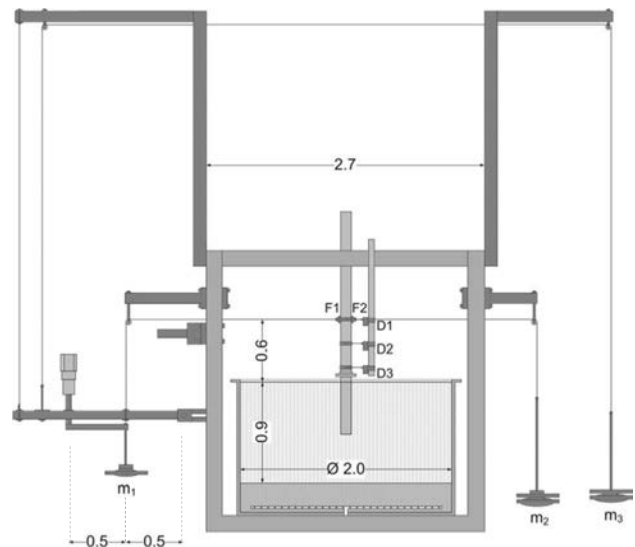


Figure 1. Sketch of the test setup. F1 and F2 refer to the two load cells, D1, D2, and D3 refer to the three displacement transducers and  $m_1$ ,  $m_2$ , and  $m_3$ , refer to the weights applied on the load hangers. All measurements are in meters.



Figure 2. Test setup for cyclically long-term loaded monopiles.

Table 2. Test programme with relative soil densities,  $D_r$ , loading characteristics, and number of cycles,  $N$ .

Test No.	Type	$D_r$ (%)	$\zeta_b$	$\zeta_c$	$N$	Static test after cyclic loading
1	Static	78.56	-	-	-	-
2	Cyclic	87.76	0.18	0.03	50 894	yes
3	Cyclic	85.38	0.24	0.10	51 732	no
4	Cyclic	87.87	0.25	-0.01	50 960	yes
5	Cyclic	91.70	0.36	0.03	60 224	yes

resistance and the maximum resistance obtained is interpreted as the ULS load on the pile.

In total four long-term cyclic loading tests are performed, each with more than 50 000 load cycles. The tests are conducted with  $m_1 = m_2$ , i.e. one-way loading with the target  $\zeta_c = 0$ . The magnitudes of the loading in the cyclic tests are chosen to reflect realistic loading conditions for FLS and SLS loading, which according to LeBlanc et al. (2010) is approximately 30% and 40% of the ultimate limit state loading (ULS), respectively. Thus, the target maximum moment applied in the cyclic loading tests are defined as 20%, 25%, 30% and 40% of the maximum static lateral resistance, i.e.  $\zeta_b$  is chosen in the interval 0.2 to 0.4. In Table 2 a summary of the testing programme with the obtained loading characteristics is presented.

In general the magnitude of the loading is seen to be a little less than expected. This result verifies the importance of measuring the actual force on the pile as some of the applied load is lost in the system due to friction. For three of the tests the cyclic load ratio,  $\zeta_c$ , is seen to be close to zero which is in agreement with the target loading.

In order to investigate the influence of cyclic loading on the ultimate lateral resistance static loading tests were performed after the cyclic loading.

### 2.1 Soil Conditions

The tests are conducted using saturated Aalborg University Sand No. 1 (Baskarp Sand No.15). In Table 3 the properties of the sand are summarised.

Table 3. Properties of Aalborg University Sand No. 1

Specific grain density	Maximum void ratio	Minimum void ratio	50%-quantile	Uniformity coefficient
$d_s$	$e_{max}$	$e_{min}$	$d_{50}$	$U = d_{60}/d_{10}$
(-)	(-)	(-)	(mm)	(-)
2.64	0.858	0.549	0.14	1.78

Prior to each test the sand is prepared by use of an initially upward gradient of 0.9 followed by mechanical vibration with a rod vibrator. The obtained homogeneity and compaction of the sand is verified by conducting three cone penetration tests (CPT) with a laboratory cone; one in the middle of the container and two in a distance 400 mm from the centre in the active and passive side of the pile, respectively. The relative densities of the sand,  $D_r$ , are derived in accordance to Ibsen et. al (2009) where the laboratory cone is correlated with in-house triaxial tests on the same sand type. The mean values of the relative densities found prior to each experiment are presented in Table 2 together with the characteristic of the tests themselves.

## 3 TEST RESULTS

Initially, the static loading test is used as a reference test for the ULS moment capacity and thus the choice of maximum moment loading in the cyclic tests. The moment-rotation relationships obtained in both the static and the cyclic tests are presented in Figure 3. The static test clearly defines a maximum moment capacity of 360 Nm which is interpreted as the ULS load. In all the cyclic tests the rotation obtained in the first loading cycle follows the static reference test cf. Figure 3. This verifies the use of the static test as a reference for the loading despite the difference in relative densities of the soil cf. Table 2. Even though the cyclic loading system is an improvement of the system presented in Roesen et al. (2012) the maximum moment loading in the cyclic tests are seen to decrease a little during the test. Therefore, the characteristics of the cyclic loading,  $\zeta_b$  and  $\zeta_c$  cf. Table 2, are calculated as mean values over the whole test and  $\zeta_b$  is seen to be lower than the target value.

In Figure 4 the rotation of the pile,  $\theta$ , at soil surface as a function of the number of cycles,  $N$ , for test no. 2 is presented. The figure shows the cyclic response during loading and the rotation is seen to accumulate throughout the entire test. Similar results are obtained in the three other tests. In the evaluation of the accumulated rotation the maximum values of the rotation are used, i.e. the rotation marked with dark grey in Figure 4. As seen in Figure 3 the rotation in the first loading cycle is equal to the rotation obtained in the static reference test. Thus, in order to evaluate the influence of the cyclic loading only the accumulated rotation,  $\Delta\theta(N) = \theta_N - \theta_1$ , is investigated.  $\theta_N$  is the rotation obtained at the  $N^{\text{th}}$  loading cycle and  $\theta_1$  is the rotation obtained in the first loading cycle.

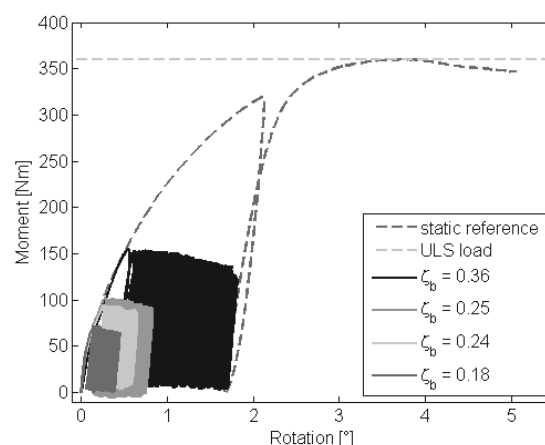


Figure 3. Moment-rotation relationships of the static reference test and the four cyclic loading tests.

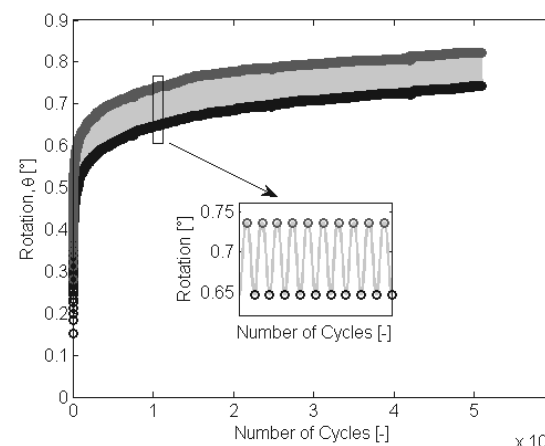


Figure 4. Rotation of the pile at soil surface as a function of the number of cycles in the test with  $\zeta_b = 0.25$ . Maximum and minimum values of the rotation are indicated by dark grey and black colouring.

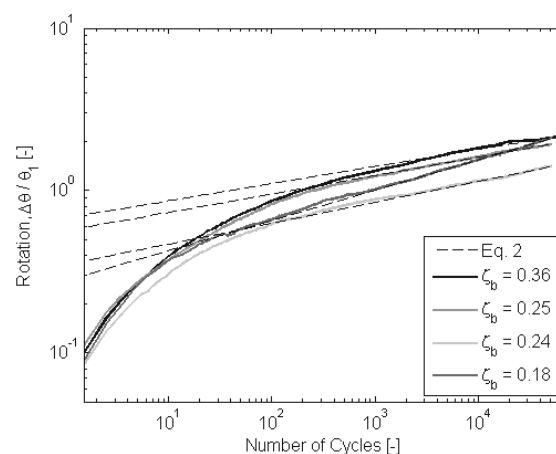


Figure 5. Normalised accumulated rotation as a function of the number of cycles for the four cyclic tests.

In Figure 5 the accumulated rotation obtained in all four cyclic tests are presented. The rotations are normalised with respect to the rotation obtained in the first loading cycle. The accumulated rotations of the stiff pile are fitted with a power function as suggested by several authors, e.g. Long and Vanneste (1994), Peralta and Achmus (2010), and LeBlanc et al. (2010). The fitted expression is given by Eq. 2 and shown as the dotted black lines in Figure 5.

$$\frac{\Delta\theta}{\theta_1} = a N^b \quad (2)$$

$a$  and  $b$  are dimensionless constants determined empirically from the tests. The results from the long-term one-way loading cf. Figure 5 shows a general good agreement with the power function even though deviations in the first 1000 cycles are observed. The values for the power  $b$  are found to be similar for all the tests with values in the range of 0.11 to 0.18. These values are found to be smaller than the value of 0.31 as presented by LeBlanc et al. (2010). The results for the constant  $a$  cf. Figure 6 indicates that  $a$  depends linearly of the magnitude of the loading  $\zeta_b$  which is in agreement with the findings in LeBlanc et al. (2010).

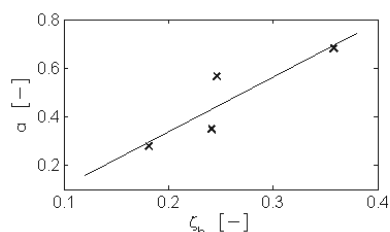


Figure 6. Fitted empirical constant  $a$  as a function of the loading magnitude  $\zeta_b$  in the four cyclic tests.

The influence of the cyclic loading on the static lateral capacity is evaluated by means of the results from the three static tests performed post cyclic loading cf. Figure 7. The maximum moments obtained indicates that the lateral capacity depends on the cyclic loading and increases with increasing load magnitude.

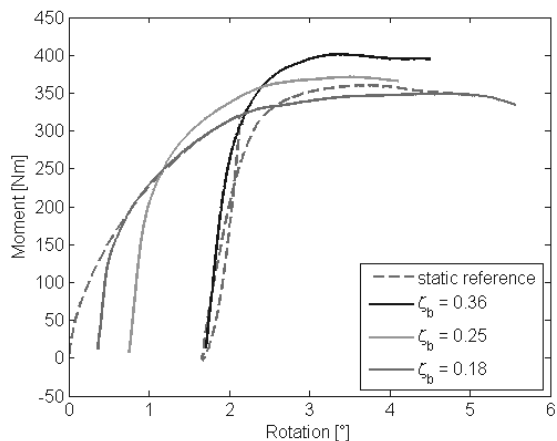


Figure 7. Moment-rotation relationships obtained in the static tests post cyclic loading compared with the reference static test.

#### 4 CONCLUSION

This paper presents a description of a 1g laboratory small scale test setup for modelling laterally long-term cyclic loading of a stiff pile in saturated dense sand. A static loading test and four one-way cyclic loading tests with maximum moment loading equal to 18% to 36% of the maximum static capacity are presented. The purpose of the tests is to evaluate the influence of the number of load cycles on the accumulated rocking rotation of the pile at seabed during long-term cyclic loading. In addition the effect of the cyclic loading on the static lateral capacity is evaluated by means of static loading tests conducted post cyclic loading.

All the tests are carried out with an open ended aluminium pipe pile scaled approximately 1:50 in relation to a typical monopile foundation for an offshore wind turbine. In the four

cyclic tests more than 50 000 load cycles are applied to the pile. When evaluating the cyclic tests the accumulated rotation normalised with respect to the rotation obtained in the first loading cycles is used. The results reveal that the accumulation of rotation during long-term cyclic loading can be described by use of a power function. Further, the maximum moments obtained in the static tests conducted post cyclic loading indicates that the lateral capacity depends on the cyclic loading and increases with increasing load magnitude.

The entire test setup is still in the initial phase of testing and can be improved even more. Thus, the findings inhere must be evaluated further and supplemented with additional testing with varied loading characteristics, i.e. varied  $\zeta_b$  and  $\zeta_c$  for both one- and two-way loading.

#### 5 ACKNOWLEDGEMENTS

This research is associated with the EUDP programme “Monopile cost reduction and demonstration by joint applied research” funded by the Danish energy sector. The financial support is sincerely acknowledged.

#### 6 REFERENCES

- Achmus, M., Abdel-Rahman, K. and Peralta, P. 2005. On the design of monopile foundations with respect to static and quasi-static loading. *Copenhagen Offshore Wind 2005*.
- Achmus, M., Albiker, J. and Abdel-Rahman, K. 2011. Investigations on the behaviour of large diameter piles under cyclic lateral loading. In: *Frontiers in Offshore Geotechnics II - Gourvenev & White* (eds), Taylor & Francis Group, LLC.
- DNV 2010. Offshore standard DNV-OS-J101: Design of offshore wind turbine structures, *Technical report DNV-OS-J101*, Det Norske Veritas.
- Ibsen, L. B., Hanson, M. Hjort, T. and Taarup, M. 2009. MC-parameter Calibration of Baskarp Sand No. 15, *DCE Technical Report No. 62*. Department of Civil Engineering, Aalborg University
- LeBlanc, C., Houlsby, G. and Byrne, B. 2010. Response of stiff piles to long-term cyclic lateral load, *Géotechnique*, 60 (2), pp. 79-90.
- Long J. H. and Vanneste G. 1994. Effects of Cyclic Lateral Loads on Piles in Sand. *Journal of Geotechnical Engineering*, 120 (1), pp. 225-244.
- Niemunis, A., Wichtmann, T. and Triantafyllidis, T. 2005. A high-cycle accumulation model for sand, *Computer and Geotechnics*, 32 (4), pp. 245-263.
- Peng, J.-R., Clarke, B. G. and Rouainia, M. 2006. A device to Cyclic Lateral Loaded Model Piles, *Geotechnical Testing Journal* 29 (4) pp. 1-7.
- Peralta, P. and Achmus, M. 2010. An experimental investigation of piles in sand subjected to lateral cyclic loads, *7th International Conference on Physical Modeling in Geotechnics*, Zurich, Switzerland.
- Poulos H., and Hull T. 1989. The Role of Analytical Geomechanics in Foundation Engineering. *Foundation Engineering.: Current Principles and Practices*, 2, pp. 1578-1606.
- Roesen, H. R., Thomassen, K., Sørensen, S. P. H., and Ibsen, L. B., 2010. Evaluation of Small-Scale Laterally Loaded Non-Slender Monopiles in Sand *DCE Technical Report No. 91*, Aalborg University, Department of Civil Engineering.
- Roesen, H. R., Ibsen, L. B., and Andersen, L. V. 2012. Small-Scale Testing Rig for Long-Term Cyclically Loaded Monopiles in Cohesionless Soil, *Proceedings of the 16th Nordic Geotechnical Meeting*, Copenhagen, 9-12 May, 2012, vol. 1/2, p.435-442..
- Wichtmann, T., Niemunis, A. and Triantafyllidis, T. 2008. Prediction of long-term deformations for monopile foundations of offshore wind power plants. *11th Baltic Sea Geotechnical Conference: Geotechnics in Maritime Engineering*, Gdansk, Poland.

# Pieu sous charge latérale : développement de lois de dégradation pour prendre en compte l'effet des cycles

Pile cyclic lateral loading: Development of degradation laws for describing the cyclic effect

Rosquoët F.

Laboratoire LTI (AE3899), Amiens, France

Thorel L., Garnier J., Chenaf N.

LUNAM Université, IFSTTAR, Nantes, France

**RÉSUMÉ :** A l'origine, le dimensionnement des pieux sous une charge latérale supposait que le sol est entièrement à l'état de rupture (calcul aux états limites). Les méthodes de calcul ont progressé et le dimensionnement est maintenant réalisé en déplacement mais sans possibilité de tenir compte de l'effet des cycles de chargement (sauf dans le cas des ouvrages offshore). Pour corriger cette lacune, nous proposons deux méthodes : une méthode globale basée sur le déplacement en tête de pieu et sur le moment maximum, et une méthode locale basée sur les courbes P-y. Pour la méthode globale, nous montrons que l'effet des cycles sur le déplacement est essentiellement lié au rapport entre l'amplitude de la charge cyclique et la charge maximale. Nous proposons une loi de type logarithme donnant le déplacement relatif en fonction du nombre de cycles. On notera que l'effet des cycles sur le moment maximum est faible. La méthode locale est basée sur l'interaction entre le sol et le pieu permettant de relier directement la réaction latérale du sol P et le déplacement du sol y. Nous introduisons un coefficient d'abattement qui permet de prendre en compte l'effet des cycles en modifiant la réaction des courbes P-y statiques.

**ABSTRACT:** Generally, the design of pile under lateral cyclic loads supposed that the soil is completely in the state of failure (limit states calculation). However, the calculation methods progressed and the design can be executed in displacement and at maximum bending moment. To analyse the cyclic effect we propose two methods: the global method is based on pile head displacement and maximum bending moments and local method is based on P-y curves. For the global method, we propose an empirical law to evaluate pile head displacements at application point. A simple power function of  $DF/F$  and a logarithm function of the number of cycles are proposed to calculate pile head displacements under cyclic loading from the displacement values under applied monotonic loads. We show that the effect of the cycles on the bending moments is weak. Local methods are based on the soil reaction profile, P and the pile lateral displacement, y called P-y curves. We propose a reduction coefficient then applied to the monotonic P-y curves to take the cyclic effect on the soil degradation into account.

**MOTS-CLES :** Comportement sous chargements cycliques – Séismes

**KEYWORDS:** Pile under lateral cyclic load – Seism

## 1 INTRODUCTION

Le chargement latéral cyclique des pieux est généralement le résultat des sollicitations mécaniques engendrées par les vagues, le vent sur des structures offshore, l'amarrage de bateaux sur des quais, des surcharges variables ou des dilatations thermiques. Il est caractérisé par quatre paramètres qui sont la charge maximum appliquée F ; l'amplitude de la variation de la charge DF ; le nombre de cycles n et le type de chargement (non-alterné ou alterné).

L'utilisation des modèles réduits de pieux permet de réaliser des études paramétriques et ainsi améliorer notre compréhension de ces phénomènes à multiples variables. Une meilleure connaissance et quantification de la réponse des pieux sous charge latérale cyclique permettra d'optimiser leurs dimensionnement pour ce type de sollicitation mécanique.

La modélisation physique des structures géotechniques en centrifugeuse est une technique assez répandue (Garnier 2001) et a déjà été appliquée à l'étude de pieux sous charge latérale cyclique dans le sable (Rosquoët 2004, Rakotonindriana 2009) ou dans l'argile (Khemakhem 2012). La centrifugation des modèles réduits est indispensable pour assurer le respect des conditions de similitude qui imposent qu'un modèle à l'échelle 1/n soit testé sous une accélération centrifuge égale à n fois la gravité terrestre.

Un important programme de recherche est en cours en France sur les pieux sous charge cycliques (Projet national SOLCYP). Les travaux décrits ci-dessous s'intègrent dans ce programme et concernent les charges latérales cycliques. Le but final de ces études est de proposer une méthode rationnelle de

dimensionnement des pieux soumis à de telles sollicitations et d'évaluer l'influence du chargement latéral cyclique sur les éléments qui permettent de dimensionner le pieu, c'est-à-dire le déplacement horizontal en tête y, le moment maximum M ou encore les relations entre la réaction du sol P et le déplacement horizontal du pieu y, appelées « courbes P-y ».

L'étude se limite aux cas où les cycles dégradent la réaction du sol et aux charges cycliques de service. Le pieu modélisé peut être considéré comme un pieu souple. La partie du pieu située à une profondeur supérieure à 3 fois la longueur de transfert  $l_0$ , n'a théoriquement plus d'influence sur la réponse due à une charge en tête (Frank 1999). De fait, dans cette étude, on admettra que l'effet des cycles se manifeste essentiellement dans les couches de surface, à des profondeurs inférieures à 4 ou 5 fois le diamètre du pieu. A titre de comparaison, l'API (2002) fixe cette profondeur limite à  $z/B = 2,625$  pour des sables, soit 1,89 m dans notre cas.

## 2 DISPOSITIF ET MÉTHODE EXPÉRIMENTALE

Les essais ont été effectués dans des massifs secs homogènes de sable de Fontainebleau NE34 de poids volumique  $16 \text{ kN/m}^3$  (indice de densité  $I_D = 86 \%$ ) reconstitués par pluviation. Le pieu modèle au 1/40<sup>ème</sup> est mis en place à 1g par battage dans les massifs préalablement reconstitués. Ce pieu modèle est testé sous une accélération de 40 g. Il représente un pieu grandeur réelle de 0,72 m de diamètre, de 12 m de longueur de fiche ayant une rigidité à la flexion de  $476 \text{ MN.m}^2$  (Figure 1). Il est instrumenté par 20 paires de jauges de déformation collées sur

deux génératrices diamétralement opposées permettant de déterminer à tout moment le profil des moments fléchissants.

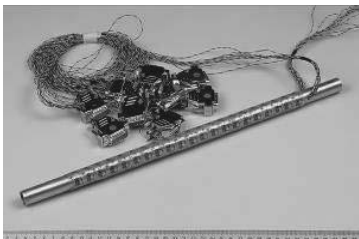


Figure 1. Pieu modèle instrumenté de 18mm de diamètre.

Un servo-vérin horizontal placé sur un bâti rigide fixé sur le conteneur d'essai permet d'appliquer le chargement à 40 mm au-dessus du sol. Deux capteurs de déplacement (d'une course de 100 mm) fixés par l'intermédiaire d'une rotule à 20 mm et de 65 mm au dessus du sol permettent de connaître le déplacement au point d'application de la charge (Figure 2). L'effort est mesuré à l'aide d'un capteur de force, d'une capacité maximale de 500 daN. Pour le chargement unidirectionnel non alterné (traction uniquement), un câble assure la liaison entre le capteur et le pieu modèle.

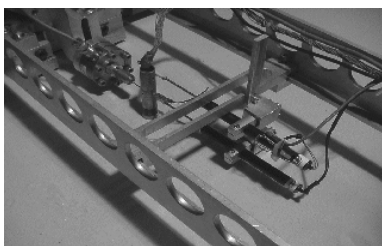


Figure 2. Détail du dispositif de chargement avec les capteurs de déplacement.

Dans le cas d'un chargement cyclique de type non alterné, l'effort est toujours appliqué dans le même sens, la charge variant entre  $F$  et  $F - DF$ .

### 3 MÉTHODE GLOBALE

#### 3.1 Déplacement en tête

L'effet des cycles sur l'évolution du déplacement en tête au point d'application de la charge (figure 3) est fortement dépendant de l'amplitude des cycles ( $DF$ ) et du chargement maximal ( $F$ ).

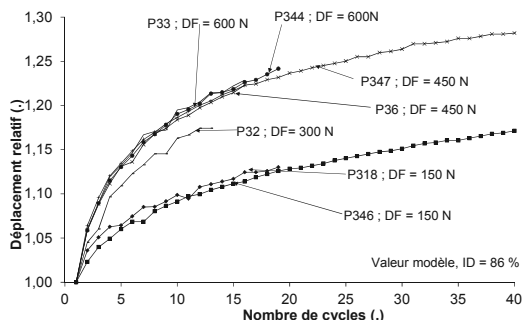


Figure 3. Evolution des déplacements relatifs sous la charge maximale ( $F = 960$  kN) en fonction du nombre de cycles pour différentes amplitudes  $DF$ .

Comme déjà observé par d'autres auteurs, une loi logarithmique représente très correctement la relation entre le déplacement relatif et le nombre de cycles (Eq. 1) :

$$\frac{y}{y_1} = 1 + b \ln(n) \tag{1}$$

où  $y_n$  est le déplacement au cycle  $n$ ,  $y_1$  le déplacement à la fin du chargement statique,  $b$  un coefficient positif adimensionnel et  $n$  le nombre de cycles (Figure 3).

L'interpolation des courbes est réalisée par la méthode des moindres carrés. Pour tous les cas étudiés, les valeurs expérimentales sont proches de la loi logarithmique choisie (coefficient de corrélation  $R^2 = 0,98$ ). Le coefficient «  $b$  » dépend de l'amplitude des cycles. Lorsque l'amplitude des cycles  $DF$  tend vers 0, nous sommes dans le cas d'un essai de fluage puisque la charge est constante et égale à  $F$ . Nous avons observé que le déplacement induit par le fluage peut être négligé, par conséquent, le coefficient «  $b$  », est dans ce cas proche de 0.

L'évolution du déplacement relatif en fonction du nombre de cycles, pour chaque essai réalisé, peut être caractérisée par ce coefficient «  $b$  ». On note  $\sigma_b$  l'incertitude liée à la mesure de ce déplacement. En supposant que les incertitudes sur le déplacement relatif soient toutes de même amplitude nous pouvons calculer les incertitudes sur la constante «  $b$  » de la fonction logarithmique (Rosquoët 2004).

Tableau 1. Estimation de  $b$  et de l'incertitude  $\sigma_b$  associée.

Essai	Nombre de cycles	$F$ (kN)	$DF$ (kN)	$b$ (.)	$\sigma_b$ (.)
P33	14	960	960	0,082	0,019
P344	14	960	960	0,081	0,017
P36	18	960	720	0,078	0,017
P347	40	960	720	0,075	0,01
P32	15	960	480	0,071	0,021
P318	25	960	240	0,044	0,017
P346	40	960	240	0,049	0,01

Il apparaît (Tableau 1), que le coefficient «  $b$  » est strictement croissant avec l'amplitude  $DF$ . Il est possible de représenter les variations de «  $b$  » par une fonction puissance. La figure 4 montre la courbe d'évolution du coefficient «  $b$  » en fonction du rapport entre l'amplitude et la charge maximale appliquée ( $DF/F$ ), permettant ainsi de rendre adimensionnelle l'amplitude des cycles.

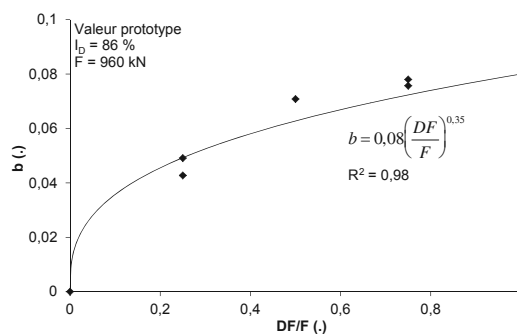


Figure 4. Evolution du coefficient «  $b$  » en fonction de  $DF/F$ .

L'expression du coefficient «  $b$  » défini sur la figure 4 en fonction de  $DF/F$  permet de compléter l'équation (2) pour ainsi donner le déplacement en tête pour un cycle  $n$  donné.

$$\frac{y}{y_1} = 1 + 0,08 \times \ln(n) \times \left( \frac{DF}{F} \right)^{0,35} \tag{2}$$

Le tableau 2 présente les valeurs proposées dans la littérature pour le paramètre  $b$ , que l'on peut appeler paramètre de dégradation.

Tableau 2. Plages des valeurs de b proposées dans la littérature.

Auteurs	Sol	Pieux testés	Nombre de cycles	Paramètre de dégradation
Hettler (1981)	Sable sec	Rigides / 1g		0,2
Bouafia (1994)	Sable sec	Rigides Centrifugés	5	0,18 < b < 0,25
Lin et Liao (1999)	Divers sables	Pieux in situ	100	0,02 < b < 0,24
Verdure et al. (2003)	Sable sec dense	Flexibles Centrifugés	50	0,04 < b < 0,18
Rakotonindriana (2009)	Sable sec dense	Flexibles Centrifugés	500	0,12
Li et al. (2010)	Sable sec dense	Rigides Centrifugés	100 à 1000	0,17 < b < 0,25
Peralta (2010)	Sable sec	Flexibles 1-g	10000	0,21

Au regard des expressions de « b » proposées dans la littérature et des résultats des études réalisées par Rosquoët (2004) et Rakotonindriana (2009), nous retenons une valeur moyenne de b de 0,1. Finalement nous proposons pour l'expression de l'évolution du déplacement en tête en fonction du nombre de cycles et de l'amplitude (Eq. 3) :

$$\frac{y_n}{y_1} = 1 + 0,1 \times \ln(n) \times \left( \frac{DF}{F} \right)^{0,35} \quad (3)$$

### 3.2 Moment maximum

Le moment maximum est l'un des paramètres dimensionnant et il est important d'examiner son évolution lors de chargements cycliques (Figure 5).

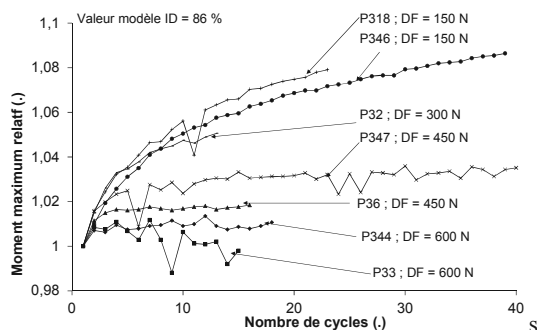


Figure 5. Evolution des moments maximums relatifs en fonction du nombre de cycles pour différents rapports DF/F.

Comme pour les déplacements relatifs, il est possible d'interpoler l'évolution du moment maximum relatif en fonction du nombre de cycles par une fonction de type logarithmique (Eq. 4) :

$$\frac{M_n}{M_1} = 1 + a \ln(n) \quad (4)$$

L'effet des cycles sur le moment maximum s'avère faible, inférieur à 8 % pour 15 cycles (Rosquoët, 2004) et à 12 % pour 75000 cycles (Rakotonindriana, 2009). De plus, nous avons montré que les valeurs du coefficient représentant l'effet des cycles sur le moment maximum sont du même ordre de grandeur que l'incertitude sur ce coefficient (tableau 3). Par conséquent, dans le cas d'un sable sec et dense, nous proposons à ce stade d'appliquer une majoration forfaitaire de 10% au moment maximum observé sous la charge statique F (solution conservative).

 Tableau 3 : Estimation de a et de l'incertitude  $\sigma_a$  associée (F = 960 kN,  $I_D = 86\%$ ).

Essai	Nombre de cycles	DF/F (.)	a (.)	$\sigma_a$ (.)
P33	14	1	0	/
P344	14	1	0	/
P36	18	0,75	0,0047	0,0038
P347	40	0,75	0,0069	0,0052
P32	15	0,5	0,019	0,017
P318	25	0,25	0,026	0,014
P346	40	0,25	0,025	0,006

## 4 MÉTHODE LOCALE

Comme déjà proposé par plusieurs auteurs et adopté dans les règles API, nous admettons qu'il est possible de modéliser l'effet des cycles, sur les courbes P-y, par une diminution de la réaction P (pour un déplacement y donné) dans les couches de surface. Cette approche présente l'avantage de pouvoir être mise en œuvre avec tout logiciel de calcul de pieu sous charge latérale statique. Pour quantifier l'influence des cycles sur la « dégradation » du sol nous introduisons un coefficient d'abattement  $r_c$  qui dépend a priori de cinq paramètres : la profondeur z, le déplacement du pieu y, le nombre de cycles n, la charge appliquée F et l'amplitude des cycles DF.

### 4.1 Méthode itérative pour déterminer un coefficient d'abattement $r_c$

Le coefficient d'abattement  $r_c$  des courbes P-y statiques va être déterminé à l'aide d'un calcul itératif par calage progressif entre les données expérimentales (état du pieu au 15<sup>ème</sup> cycle) et les données calculées par le logiciel Pilate (courbe P-y statique abattues d'un coefficient r).

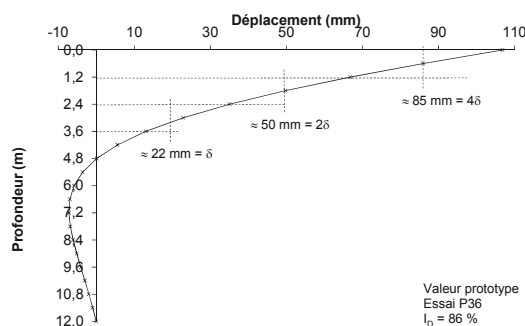


Figure 6. Evolution du déplacement en fonction de la profondeur.

Pour une profondeur comprise entre 0 et 3,6 m, si l'on note  $\delta$  le déplacement du pieu au niveau de la couche comprise entre 2,4 et 3,6 m, on constate que le déplacement est proche de  $2\delta$  entre 1,2 et 2,4 m et  $4\delta$  entre 0 et 1,2 m (Figure 6).

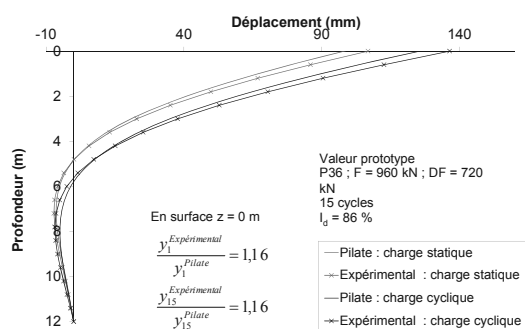


Figure 7. Evolution du déplacement en fonction de la profondeur.

Dans un premier temps, les coefficients d'abattement  $r_c$  sont déterminés par calage sur les données expérimentales obtenues sur le déplacement de la tête du pieu en fonction du nombre de cycles. Pour représenter l'effet des cycles, les courbes P-y

statiques de surface (jusqu'à 3,6 m) sont affectées d'un facteur  $r_c$  sur la réaction  $P$  inférieur à 1 et croissant avec la profondeur.

Compte tenu du constat tiré de la figure 6, on impose que le coefficient  $r$  soit égal à  $1 - 4\Delta$  entre 0 et 1,2 m ;  $1 - 2\Delta$  entre 1,2 et 2,4 m et  $1 - \Delta$  entre 2,4 et 3,6 m (avec  $\Delta$  un coefficient strictement positif tel que  $1 - \Delta$  soit inférieur ou égal à 1). Par itération, nous recherchons la valeur de  $\Delta$  qui conduit au rapport correct entre le déplacement au 15<sup>ème</sup> cycle  $y_{15}$  et le déplacement du pieu sous la charge maximum  $y_1$  (Figure 7).

La même procédure a été utilisée pour les autres cas, de charge maximum de 960 kN, d'amplitude des cycles variant entre 960 et 240 kN. Il est possible d'exprimer le coefficient  $r$  en fonction du rapport d'amplitude de la variation de la charge sur la charge  $DF / F$ , pour les couches de surfaces entre 0 et 5B (Figure 8).

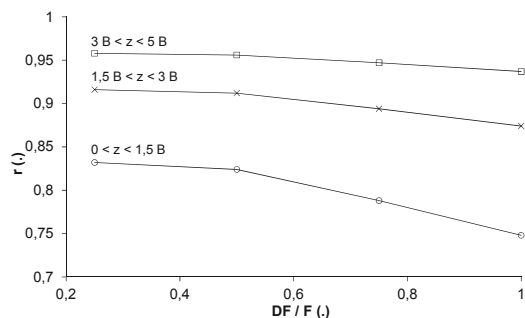


Figure 8. Evolution du coefficient  $r_c$  en fonction de  $DF / F$  (pour 15 cycles).

L'extrapolation des courbes de la figure 8 permet de déterminer des expressions simples du coefficient  $r_c$  en fonction du rapport  $DF / F$  pour les trois couches de surfaces (Tableau 4).

Tableau 4 : Extrapolation par des droites de l'évolution du coefficient  $r_c$  en fonction de  $DF / F$  (pour 15 cycles).

Profondeur $z$	Expression de $r_c$ en fonction de $DF / F$
$0 < z < 1,5B$	$r = 0,87 - 0,12 \frac{DF}{F}$
$1,5B < z < 3B$	$r = 0,94 - 0,058 \frac{DF}{F}$
$3B < z < 5B$	$r = 0,97 - 0,029 \frac{DF}{F}$

## 5 COMPARAISON MÉTHODE GLOBALE / MÉTHODE LOCALE POUR LE DÉPLACEMENT EN TÊTE.

Un exemple de comparaison entre les deux méthodes est donné sur la figure 9 pour l'essai sur un pieu dans un sable dense ( $I_D = 86\%$ ) et des cycles caractérisés par  $F = 960$  kN et  $DF = 720$  kN.

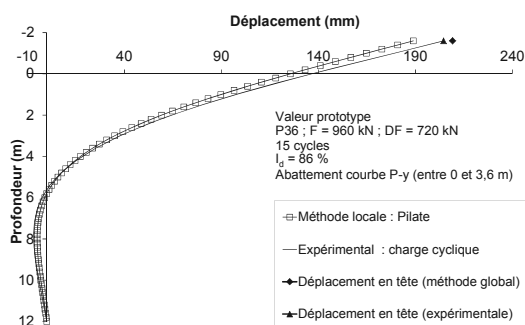


Figure 9. Evolution du déplacement en fonction de la profondeur.

L'écart entre la méthode globale déduite de la relation présentée dans le tableau 4 et la courbe expérimentale est de 2% soit de l'ordre de grandeur de l'incertitude sur la mesure du

déplacement (l'incertitude sur le déplacement est de 0,104 mm, l'écart entre méthode locale et expérimentale est de 0,112 mm).

## 6 CONCLUSION

Une nouvelle analyse de l'étude paramétrique réalisée à l'IFSTTAR sur un pieu soumis à une charge latérale cyclique dans un sable sec et dense (Rosquoët 2004) et complétée par la suite (Rakotonindriana 2009, Khemakhem 2012) permet de proposer de nouvelles méthodes de dimensionnement des pieux sous chargement latéral cyclique. Une méthode globale, basée sur une loi logarithmique en fonction de  $DF/F$  permet de donner le déplacement en tête pour un nombre de cycles  $n$  donné. On notera que l'effet des cycles sur le moment maximum, dans le cas d'un sable sec et dense, est négligeable.

Une méthode locale basée sur l'abattement des courbes  $P-y$  statiques a été réalisée. Des calculs itératifs ont permis de valider la modélisation de l'effet des cycles sur le déplacement et sur les moments par une modification des courbes  $P-y$  d'un facteur  $r_c$  croissant entre 0 et 5B (soit entre 0 et 3,6 m). Des expressions simples ont été proposées permettant de déterminer ce facteur  $r_c$  à partir du rapport  $DF / F$ .

On note, pour finir une bonne concordance des résultats obtenus par les deux méthodes. Toutefois si la méthode globale est utilisable pour un très grand nombre de cycles ( $> 500$ ), la méthode locale n'est valide que pour une quinzaine de cycles et pour des chargements cycliques non alternés.

## 7 REFERENCES

- API - American Petroleum Institute. 2002. *Recommended Practice for Planning, Designing and Constructing Fixed Offshore Platforms - Working Stress Design*. RP 2AWS, Washington, DC.
- Bouafia A. 1994. Etude expérimentale du chargement latéral cyclique répété des pieux isolés dans le sable en centrifugeuse. *Canadian Geotechnical Journal*, Vol. 31, n°5, 740-748.
- Frank R. 1999. *Calcul des fondations superficielles et profondes*. Editions Technique de l'Ingénieur et Presse des Ponts et Chaussées. Paris.
- Garnier J. 2001. Modèles physiques en géotechnique I-Evolution des techniques expérimentales et des domaines d'application. *Revue Française de Géotechnique*. N°97. 3-29.
- Hettler. A. 1981. Verschiebungen starrer und elastischer Gründungskörper in Sand bei monotoner und zyklischer Belastung. *Institut für Boden-und Felsmechanik der Universität Karlsruhe*, Heft Nr. 90.
- Khemakhem M. 2012. Etude expérimentale de la réponse aux charges latérales monotones et cycliques d'un pieu foré dans de l'argile. *Thèse de Doctorat. Ecole Centrale de Nantes Université de Nantes*. 336 p.
- Lin S.S. & Liao J.C. 1999. Permanent strains of piles in sand due to cyclic lateral loads. *Journal of Geotechnical and Geoenvironmental Engineering*, Vol. 125, n°9, 798-802.
- Li Z. Haigh S. K. & Bolton M. D. 2010. Centrifuge modelling of mono-pile under cyclic lateral loads. *7th International Conference on Physical Modelling in Geotechnics*. Zurich. Vol. 2, 965-970.
- Peralta P. and Achmus M. 2010. An experimental investigation of piles in sand subjected to lateral cyclic loads. *7th International Conference on Physical Modelling in Geotechnics*. Zurich. Vol. 2, 985-990.
- Rakotonindriana M. H. J. 2009. Comportement des pieux et des groupes de pieux sous chargement latéral cyclique. *Thèse de doctorat. Ecole Nationale des Ponts et Chaussées*. 381p.
- Rosquoët F. 2004. Pieux sous charge latérale cyclique. *Thèse de Doctorat. Ecole Centrale de Nantes Université de Nantes*. 305 p.
- Verdure L. Levacher D. & Garnier J. 2003. Effet des cycles sur le comportement d'un pieu isolé dans un sable dense sous chargement latéral. *Revue Française de Génie Civil*. 7/2003. 1185-1210.

# Behavior of marine silty sand subjected to long term cyclic loading

Comportement du sable limoneux marin soumis à une charge cyclique de longue durée

Safdar M., Kim J.M.

*Pusan National University, Busan, South Korea*

**ABSTRACT:** The foundations for offshore wind turbines are demanding due to the dynamic nature of the offshore loading. A greater understanding of the behavior of wind turbine foundation soil, will certainly lead to the stable construction of foundations which in turn, will make offshore wind farms a more feasible part of the solution to the global energy problem. This paper presents the results of cyclic direct simple shear test (CDSS) to explain the long term cyclic behavior of marine silty sand. Cyclic behavior of marine sand are based on the number of loading cycles, cyclic shear strain amplitude, relative density, and cyclic stress ratio. These results are modeled and can be applied to design offshore wind turbine foundations.

**RÉSUMÉ :** Les fondations pour les éoliennes offshore sont principalement exigeante en raison de la nature dynamique du chargement offshore. Une meilleure compréhension du comportement de l'éolienne des sols de fondation, va certainement conduire à la construction des fondations stables qui à leur tour, feront de parcs éoliens en mer un rôle plus possible de la solution au problème mondial de l'énergie. Ce document présente les résultats d'essai de cisaillement cyclique directe simple (CDSS) pour expliquer le comportement cyclique à long terme de sable limoneux marin. Comportement cyclique de sable marin sont basés sur le nombre de cycles de charge, cyclique d'amplitude de contrainte au cisaillement, la densité relative et du taux de contrainte cyclique. Ces résultats sont modélisés et peut être appliquée à la conception fondations d'éoliennes off-shore.

**KEYWORDS:** *Cyclic Loading, Offshore Wind Turbine, CDSS, Cyclic Stress Ratio*

## 1 INTRODUCTION

Understanding the behavior of offshore marine sand subjected to long term cyclic loading is very vital in solving several offshore geotechnical problems. Several researchers have studied behavior of clay and sand subjected to cyclic loading.

(Vucetic et al. 1988) studied the degradation of marine clays under cyclic loading. (D. Wijewickreme et al. 2005) studied the cyclic loading response of loose air-pluviated Fraser river sand. (K.H. Andersen 2009) investigated in detail, the bearing capacity of the soil under cyclic loading, and stated that the cyclic shear strength and the failure mode under cyclic loading depend on the stress path and the combination of average and cyclic shear stresses. Safdar et al., 2013, studied the cyclic behavior of marine silty sand subjected to symmetrical cyclic loading. Different approaches have been made as an attempt to include cyclic loading in the design procedure of offshore wind turbine foundation (Soren et al. 2012).

### 1.1 Stress controlled CDSS test

Constant volume direct simple shear (DSS) test is a reliable method for measuring undrained shear strength of undisturbed or compacted soil samples. The DSS test is most similar to the CU triaxial test in that samples are consolidated prior to shearing. The simple shear is the test condition that only normal and shear stress acting on top face of a specimen is defined, whereas the displacement constraints exist for the other boundaries: The bottom face of specimen is theoretically fixed, and the radial strain on specimen is zero.

The CDSS test procedure is based on that of a constant-volume direct simple shear testing of soils, which has been studied extensively for half a century and is described in the standard ASTM D6528-07. The sample is consolidated under a

normal load within a wire-reinforced membrane (in this study) or a stack of thin rings that provide lateral confinement.

Once consolidation is complete, a horizontal shear force is applied to one end of the sample. The sample height is continuously maintained during shear to ensure constant volume. Rather than measuring pore pressures, which would require complete saturation of the sample, the pore pressure response is inferred from the change in vertical stress which is monitored throughout the test (Baxter et al 2010). In this way changes in applied vertical stress ( $\Delta\sigma_v$ ), which are required to keep the sample height constant, are assumed to be equal to the excess pore water pressure ( $\Delta u$ ) that would develop if the test were truly undrained with pore pressure measurements (Finn, 1985, Dyvik et al. 1987).

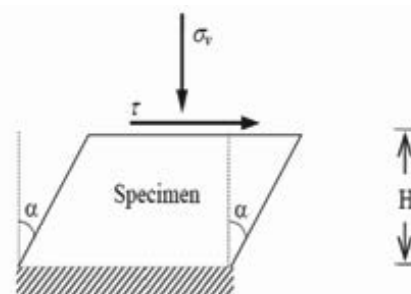


Figure 1 Simple Shear Condition, (Dyvik et al 1987)



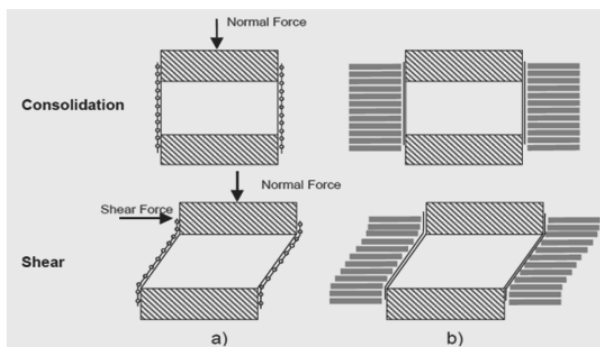


Figure 2 (a). Wire Reinforced Membrane (b). Stacked Rings (Baxter et al 2010)

The cyclic shear response of natural low-plastic Fraser River silt was investigated using constant-volume direct simple shear (DSS) testing (Wijewickreme 2010). Maria V. Sanin et al., (2011) studied the cyclic shear response of undisturbed and reconstituted Fraser River Silt. A soil can be subjected to many different stress conditions, being purely cyclic stress, static or average stress, or a combination of both. Andersen (2009) shows this clearly in a study on Drammen clays at the NGI. Drammen clays samples are tested in cyclic triaxial and cyclic simple shear conditions for different combinations of static and cyclic shear stresses. In this study cyclic simple shear tests have been performed with static or average shear stress,  $\alpha = 0$  or symmetrical cyclic loading.

### 1.2 Sample Preparation

Air Pluviation with dry compaction approach was developed to produce samples of the silty sand with consistent heights and initial relative densities. The equipment used consists of the shear box having bottom cap, two o-rings, wire-reinforced membrane, top cap, triaxial pressure panel, and compacting hammer. Sample diameter is 63.5mm and height is varied from 20 to 25 mm to maintain height to diameter ratio less than 0.4, in order to fulfill the ASTM D6528-07 criteria. In this study marine silty sand is obtained from the West coast of South Korea. Specific gravity of material tested is  $G_s = 2.65$ . Marine silty sand has minimum voids ratio of 0.74 and maximum voids ratio of 1.18. Details of properties of soil tested are given in Table 1.

Table 1 Properties of marine silty sand.

Properties of Soil Tested	
Min. Voids Ratio	0.74
Max. Voids Ratio	1.18
Coefficient of Uniformity	1.8 mm
$D_{10}$	0.08 mm
$D_{30}$	0.09 mm
$D_{60}$	0.14
USCS	Silty Sand (SM)
Specific Gravity ( $G_s$ )	2.652

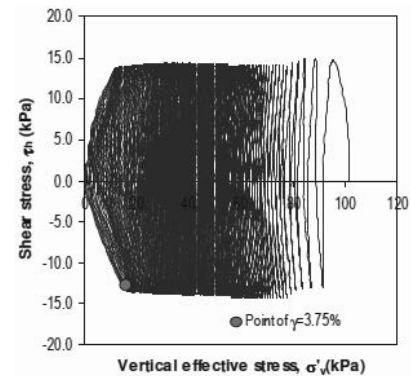


Figure 3 Stress-path responses of NC Fraser River silt under constant volume cyclic DSS loading ( $\sigma'_v = 97$  kPa; CSR = 0.20;  $\alpha=0$ ; OCR = 1.0) (Maria V. Sanin et al., 2011).

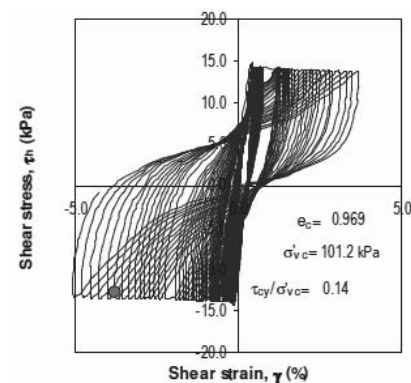


Figure 5 Constant volume cyclic DSS test on undisturbed Fraser River Delta silt. ( $\sigma'_v = 100$  kPa, CSR = 0.14) (Maria V. Sanin et al., 2011).

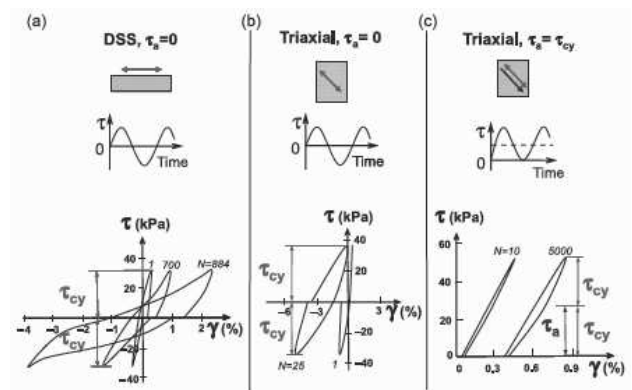


Figure 5 Stress-strain behavior under different loading conditions (Andersen, 2009)

### 1.3 Testing Program

The laboratory testing program for this study was designed to analyze the behavior of marine silty sand when subjected to cyclic loads for different combinations of parameters such as cyclic stress ratio, no. of loading cycles and relative density.

For marine silty sand, the tests were performed at a frequency of 0.1 Hz. Effect of Relative Density ( $D_r$  %) for 65, and 70 percent is studied for various CSR and no. of loading cycles. Marine silty sand has minimum voids ratio of 0.74 and maximum voids ratio of 1.18. Specific gravity of  $G_s=2.65$ .

To produce in-situ ( $K_0$ ) stress conditions, a vertical consolidation stress must be applied to the sample prior to shearing. Applied vertical stresses simulate the loads from overburden material located over the soil sample. For marine

silty sand, a normal consolidation stress of 100 kPa was applied in one step for all the specimens.

1.4 *Cyclic Direct Simple Shear test results*

Several researchers have used different shear strain failure criteria such as 3%, 4%, 5% and 7.5%. A shear strain failure condition was used for tests performed on marine silty sand and the failure criterion was established as 4% double amplitude shear strain. The results of a test are shown in Figure 6, 7 and 8. Figure 8 shows the applied cyclic shear stress of +/- 12 kPa (CSR = 0.12). Figure 6 shows the development of shear strain throughout the test, which reaches 4% double amplitude shear strain at nearly 205 cycles.

8 CDSS tests were conducted, 4 tests at voids ratio of 0.898 (Dr 65%) and CSR range of 0.10, 0.12, 0.14, and 0.16. 4 tests at voids ratio of 0.847 (Dr 70% and CSR range of 0.10, 0.12, 0.14, and 0.20. All the tests were conducted at nominal initial effective confining stress of 100 kPa to provide a basis for comparison between tests. In case of 70% relative density, Figure 6 shows the degradation curve and development of shear strain with increasing number of cycles. In a general sense, marine silty sand specimens seem to exhibit gradual increase in shear strain and degradation of shear stiffness with increasing number of load cycles. Typical stress paths and stress-strain curves of tests conducted on marine silty sand specimens are presented in Figures 7 and 8 respectively.

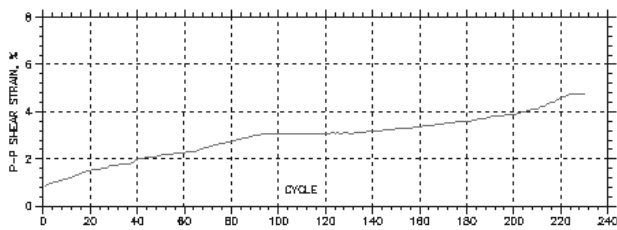


Figure 6 Peak-Peak Shear Strain vs No. of Loading cycles for ( $\sigma'_v = 100$  kPa, CSR=0.12 and Dr (%) = 70).

Figure 6 shows that samples having relative density of 70% reached 2% cyclic double amplitude cyclic shear strain after 42 cycles and 205 to reach failure.

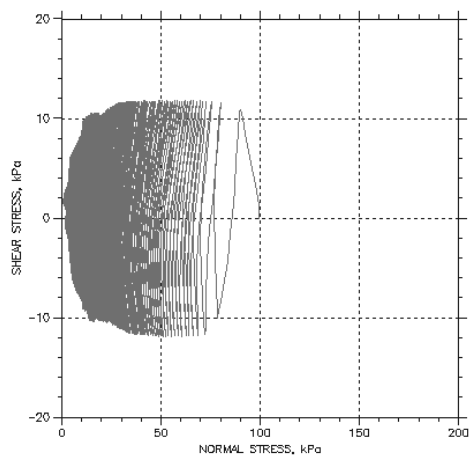


Figure 7 Stress Path During constant volume cyclic DSS loading of silty sand for ( $\sigma'_v = 100$  kPa, CSR=0.12 and Dr (%) = 70).

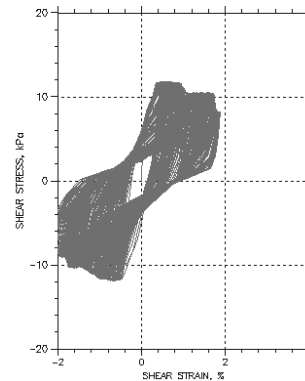


Figure 8 Stress-strain response of marine silty sand under constant volume cyclic DSS loading ( $\sigma'_v = 100$  kPa; Dr (%) = 70, CSR = 0.12;  $\alpha = 0.0$ ; OCR = 1.0).

In case of 65% relative density, Figure 9 shows the degradation curve and development of shear strain with increasing number of cycles. Typical stress paths and stress-strain curves of tests conducted with 65% relative density on marine silty sand specimens are presented in Figures 10 and 11 respectively.

It was observed that specimens having higher relative densities require higher no. of loading cycles to reach 4% double amplitude cyclic shear strain and specimens having lower relative density reach to failure in smaller no. of loading cycles. In case of higher cyclic stress ratio (CSR) the soil samples reached the failure criterion in few no. of loading cycles.

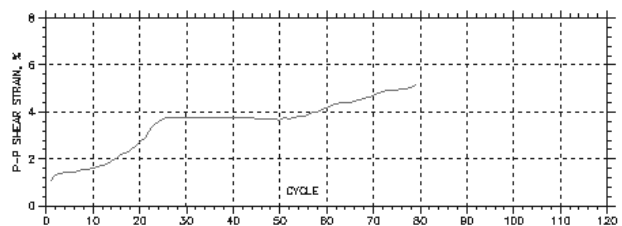


Figure 9 Peak-Peak Shear Strain vs No. of Loading cycles for ( $\sigma'_v = 100$  kPa; Dr (%) = 65, CSR = 0.12;  $\alpha = 0.0$ ; OCR = 1.0).

Figure 9 shows that samples having relative density of 65% reached 2% cyclic double amplitude cyclic shear strain after 15 cycles and 57cycles to reach failure.

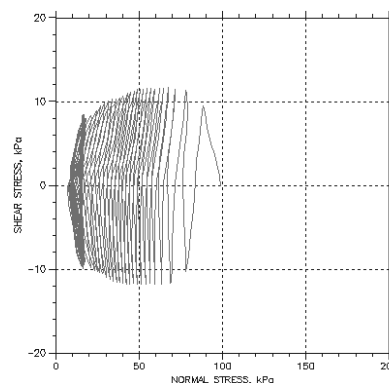


Figure 10 Stress Path During constant volume cyclic DSS loading of silty sand for ( $\sigma'_v = 100$  kPa; Dr (%) = 65, CSR = 0.12;  $\alpha = 0.0$ ; OCR = 1.0).

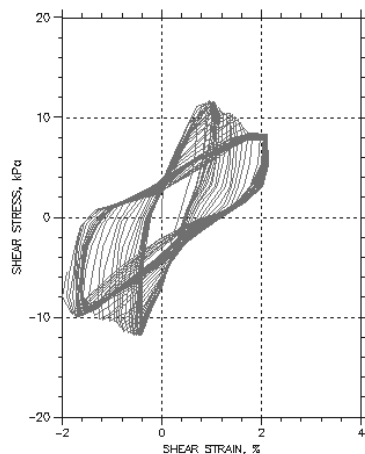


Figure 11 Stress-strain response of marine silty sand under constant volume cyclic DSS loading ( $\sigma'_v = 100$  kPa;  $Dr$  (%)= 65,  $CSR = 0.12$ ;  $\alpha = 0.0$ ;  $OCR = 1.0$ ).

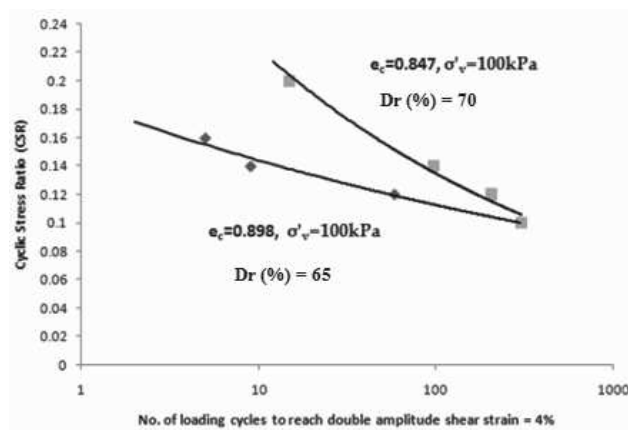


Figure 12 CSR versus No. of Loading cycles to reach double amplitude shear strain of 4% for marine silty sand

Figure 12 shows the number of loading cycles versus cyclic stress ratio that reach shear strain of 4%. As expected, samples having higher value of cyclic stress ratio and/or low relative density fail at a small number of loading cycles. It is found in this particular study that the number of loading cycles required to reach the threshold strain is not much different for two relative densities after 300 loading cycles. The trends are little different from the previous study reported (Fig. 13) in which the curves are almost parallel even in high number of cycles.

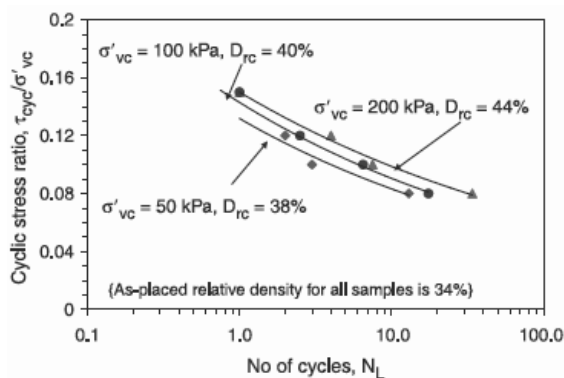


Figure 13 Effect of stress densification on cyclic resistance of loose air-pluviated sand (Wijewickreme et al., 2005)

Samples having 70% relative density and subjected to CSR of 0.12 reached cyclic double amplitude of 4% shear strain at nearly 205 cycles. In case of samples having 65% relative density and subjected to CSR of 0.12 reached cyclic double amplitude of 4% at nearly 57 cycles.

## 2 SUMMARY AND CONCLUSIONS

The constant volume cyclic shear response of marine silty sand was examined using data from CDSS tests. The intent was to compare the shear response of the silty sand specimens under different relative densities. samples having higher value of cyclic stress ratio and/or low relative density fail at a small number of loading cycles. It is found in this particular study that the number of loading cycles required to reach the threshold strain is not much different for two relative densities after 300 loading cycles. The trends are little different from the previous study reported in which the curves are almost parallel even in high number of cycles.

## 3 ACKNOWLEDGEMENT

This research is supported by the Ministry of Land, Transport and Maritime Affairs, Korea 2010 research grant (2010 Construction Technology Innovation Program, 10-CTIP-E04).

## 4 REFERENCES

Andersen K.H 2009. Bearing capacity under cyclic loading- offshore, along the coast, and on land. The 21st Bjerrum Lecture presented in Oslo, 23 November 2007". *NRC Research Press* Web site (www.cgj.nrc.ca)

Baxter C.D.P, Bradshaw A.S., Ochoa-Lavergne M. and Hankour R. 2010. DSS Test Results using Wire-Reinforced Membranes and Stacked Rings. *GeoFlorida 2010 ASCE*.

Boulanger R.W & Seed R.B. 1995. Liquefaction of sands under Bidirectional monotonic and cyclic loading. *Journal of Geotechnical Engineering ASCE* Vol. 121, No. 12 pp. 870-878.

Bjerrum, L., and Landva, A. 1966. Direct simple-shear tests on a Norwegian quick clay. *Geotechnique* 16(1), 1-20.

Dyvik, R., Berre, T., Lacasse, S., and Raadim, B. 1987. Comparison of truly undrained and constant volume direct simple shear tests. *Geotechnique* 37(1), 3-10.

Idriss, I. M., and Boulanger, R. W. 2008. Soil liquefaction during Earthquakes. Monograph MNO-12, *Earthquake Engineering Research Institute, Oakland, CA*.

Maria V. Sanin, Wijewickreme D. 2011. Cyclic shear response of undisturbed and reconstituted Fraser River Silt. *Pan-Am CGS Geotechnical Conference*.

Safdar M., Kim, J.M. (2013). "Cyclic Behavior of Marine Silty Sand" *Electronic Journal of Geotechnical Engineering (EJGE)* Vol.18A, pp. 209-218.

Soren K. N., Amir Shajarati, K.W.Sorenson, L.B. Ibsen 2012. Behaviour of Dense Frederikshavn sand during cyclic Loading. *DCE Technical Memorandum No. 15*

Vucetic M. & Dobry R. 1988. Degradation of marine clays under cyclic loading. *Journal of Geotechnical Engineering ASCE* Vol. 114, No. 2 pp. 133-149.

Wijewickreme D. 2010. Cyclic shear response of low plastic Fraser River silt. *Proceedings of the 9th U.S. National and 10th Canadian conference on Earthquake Engineering*

Wijewickreme D., Sanin M.V. and Greenaway G.R. (2005) Cyclic shear response of fine-grained mine tailings. *Canadian Geotechnical Journal* Vol. 42 pp. 1408-1421

Wijewickreme, D., Sriskandakumar, S., and Byrne, P. 2005. Cyclic loading response of loose air-pluviated Fraser River sand for validation of numerical models simulating centrifuge tests. *Canadian Geotechnical Journal* 42(2), 550-561.

# Influence des chargements cycliques axiaux dans le comportement et la réponse de pieux battus dans le sable

Influence of cyclic axial loads in the behaviour and response of driven piles in sand

Silva M., Foray P.  
*Laboratoire 3SR, Grenoble, France*

Rimoy S., Jardine R.  
*Imperial College London, London, UK*

Tsuha C.  
*University of Sao Paulo, Sao Paulo, Brazil*

Yang Z.  
*Zhejiang University, Zhejiang, China*

**RÉSUMÉ:** Cet article présente un nouveau diagramme de stabilité cyclique pour le frottement latéral ainsi que l'effet sur la capacité en traction des pieux modèle instrumentés soumis à des chargements cycliques axiaux suite à une large série d'essais en chambre d'étalonnage dans du sable siliceux. Les mesures locales des contraintes dans le sol (verticales, radiales et orthoradiales) à différentes distances de l'axe du pieu, ainsi que les mesures tangentielles et radiales à l'interface sol-pieu, permettent une analyse détaillée de l'évolution des chemins de contraintes locaux autour du pieu et au sein du massif lors des chargements cycliques et post-cycliques.

**ABSTRACT:** This paper presents a new cyclic stability diagram for the lateral friction and the effect on the tensile capacity of instrumented model piles subjected to axial cyclic loading across a wide range of calibration chamber testing in silica sand. Local measurements of stresses in the soil mass (vertical, radial and orthoradial) at different distances from the axis of the pile, as well as shear and radial stresses at the soil-pile interface, provide a detailed analysis of the evolution of local stress paths around the pile and the soil mass during cyclic and post-cyclic loading.

**MOTS-CLÉS:** Chambre d'étalonnage, chargement cyclique axial, interaction sol-pieu, diagramme de stabilité cyclique.

## 1 INTRODUCTION

Des fondations sur pieux de plateformes de pétrole/gaz et des turbines éolienne/marémotrice peuvent être soumises à des chargements cycliques de très longue durée en raison des conditions environnementales. Les longs pieux battus, installés par des cycles de charge-décharge, subissent une dégradation sévère du frottement lors de leur installation (Lehane et al. 1993, Kolk et al. 2005). Celle-ci peut être compensée par un phénomène de « cicatrisation » avec le temps (« ageing »), observé dans des expériences in-situ (Chow et al 1998, Jardine et al. 2006). Selon leur finalité (fondation d'ouvrages offshore ou d'éoliennes), ces pieux sont ensuite souvent soumis à des sollicitations cycliques de service (houle, vibrations) qui affectent également leur frottement. La réponse cyclique de l'interface sol-pieu a été étudiée en laboratoire à l'aide de pieux modèle dans des chambres d'étalonnage pressurisées (Chan & Hanna 1980, Al-Douri & Poulos 1994, Chin and Poulos 1996, Le Kouby et al. 2004). Ces essais ont montré que la contrainte de cisaillement décroît d'autant plus que l'amplitude des déplacements tangentiels augmente. Jardine et al. (2006) ont montré à partir des essais in-situ réalisés à Dunkerque (Chow et al. 1998) qu'alors que des cycles de grande amplitude dégradent la capacité du pieu en frottement, des cycles non alternés de faible amplitude accélèrent les effets bénéfiques du phénomène de « cicatrisation » (augmentation de la capacité avec le temps). Le Kouby et al. (2004) donnent des résultats similaires sur un pieu modèle de 20 mm de diamètre.

L'étude présentée ici a pour but de donner une meilleure compréhension, à une échelle de laboratoire et dans un environnement contrôlé, des résultats obtenus sur des pieux réels à Dunkerque par Jardine & Standing (2000), en mesurant, grâce à une instrumentation exceptionnelle de la chambre d'étalonnage et du pieu, les chemins de contraintes locaux, le long du pieu et au sein du massif lors des différentes phases d'installation, de repos et de chargement statique et cyclique du pieu. Ce travail fait partie d'un programme de recherche

commun entre le laboratoire 3SR et Imperial College London, ainsi que du projet National SOLCYP.

## 2 DISPOSITIF EXPÉRIMENTAL

### 2.1 La chambre d'étalonnage

La grande chambre d'étalonnage du Laboratoire 3S-R a été adaptée de façon à maîtriser les conditions environnementales (température, pression, alimentation électrique) sur des périodes de longue durée (plusieurs mois), afin de pouvoir mesurer les phénomènes de « cicatrisation » du frottement après cyclage et après une longue période de repos. Une isolation complète de la cuve ainsi qu'un système de chauffage/refroidissement des parois ont été réalisés de façon à minimiser les variations de température dans la cuve. La pressurisation des membranes a été conçue pour fonctionner en cas de panne du réseau.

La chambre d'étalonnage de Grenoble est composée de trois éléments cylindriques de 50 cm de hauteur et d'un diamètre interne de 1.2 m. Le fond de la chambre et le couvercle supérieur sont constitués de plaques rigides d'une épaisseur de 100 mm. Une pression verticale d'environ 150 kPa est imposée par une membrane en caoutchouc remplie d'eau, qui est fixée sous le couvercle supérieur et contrôlée par un système d'interface eau/air. Une membrane en latex de 2 mm d'épaisseur a été installée sur la paroi interne de la chambre afin de mieux fournir des conditions  $K_0$  au bord de la cuve. Une couche de graisse de silicone entre cette membrane et la paroi de la chambre permet de réduire le frottement entre le mur et la masse de sable et d'assurer une meilleure homogénéité des contraintes à l'intérieur du sol.

Un système d'isolation thermique formé de serpentins en cuivre autour de la cuve permet de travailler avec une température presque uniforme entre 18 et 19 degrés.

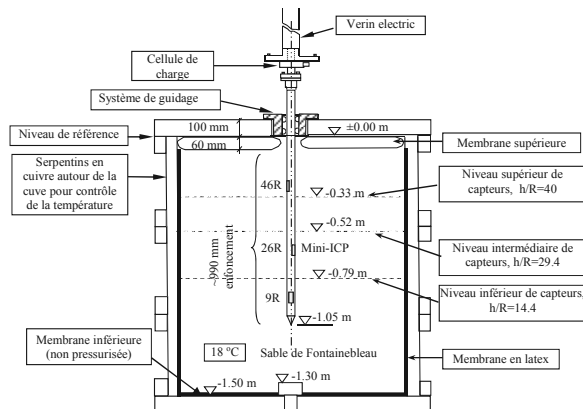


Figure 1: Modifications apportées à la chambre d'étalonnage du laboratoire 3S-R.

Pour les essais présentés ici, la chambre d'étalonnage a été remplie avec du sable siliceux de Fontainebleau NE34 commercialisé par l'entreprise Sibelco. En utilisant une technique de remplissage par pluviage, nous obtenons une densité du massif moyennement dense à dense,  $D_r=72\%$ . Le tableau 1 montre les propriétés mécaniques du sable.

Tableau 1: Propriétés mécaniques du sable NE34

$G_s$	$D_{10}$ (mm)	$D_{50}$ (mm)	$D_{60}$ (mm)	$e_{max}$	$e_{min}$	$\gamma_{max}$ ( $kN/m^3$ )	$\gamma_{min}$ ( $kN/m^3$ )
2.65	0.150	0.210	0.230	0.90	0.51	17.2	14.2

Plusieurs essais pénétrométriques ont été effectués sur des échantillons de sable NE34 sous 150 kPa avec une résistance en pointe quasi-constante de  $21 \pm 2$  MPa. Des détails supplémentaires sur les propriétés mécaniques du sable sont décrits dans Yang et al. (2010).

## 2.2 Le pieu d'essai Mini-ICP

Le pieu utilisé correspond au pieu modèle Mini-ICP développé par l'Imperial College London et décrit par Jardine et al. 2009. C'est un pieu tubulaire en acier à base fermée de 36mm de diamètre avec un cône solide de  $60^\circ$  à sa pointe. Il est composé de trois niveaux d'instrumentation (ou clusters) identifiés selon leur distance à la pointe en: A (9R), B (24) et C(44), R étant le diamètre du pieu. Chacun de ces clusters contient une cellule de charge axiale, qui peut être utilisée pour calculer la moyenne de frottement dans le fût du pieu; un capteur de contraintes en surface (SST: surface stress transducer) pour mesurer la contrainte totale radiale et la contrainte de cisaillement; un capteur de température MEMS et un inclinomètre. À partir de l'essai ICP03, une cellule de charge axiale a été ajoutée près de la pointe du pieu pour mieux séparer les contributions de la pointe et du frottement latéral dans la capacité totale du pieu.

Le pieu a été installé jusqu'à une profondeur finale de 0.98m par fonçage avec des cycles de charge-décharge en simulant la dégradation des efforts radiaux comme dans une installation par battage. La vitesse de pénétration varie entre 0.5 et 2 mm/s et l'amplitude des cycles d'enfoncement successifs est de 5, 10 ou 20 mm. La décharge de chaque cycle a été menée jusqu'à obtenir une charge en tête du pieu nulle.

## 2.3 Mesure des contraintes dans le massif

36 mini-capteurs Kyowa et TML de capacités variant de 500 kPa à 7 MPa selon leur distance au pieu, ont été mis en place sur trois niveaux comportant chacun douze capteurs, de façon à mesurer les contraintes verticales, radiales et orthoradiales sur des rayons concentriques à des distances de 2R à 16R. Leur étalonnage sous chargement cyclique a été effectué à Imperial College en suivant le protocole établi par Zhu et al 2009. La réponse de chaque capteur est représentée par une série de courbes d'hystérésis selon l'histoire de charge précédente.

## 3 PROGRAMME EXPÉRIMENTAL

Après une certaine période de cicatrisation post-installation, un premier essai en compression et un essai en traction ont été effectués pour définir la capacité du pieu avant les chargements cycliques. Plusieurs séries d'essais de faible et de haut niveau de chargement cyclique ont ensuite été effectuées, ainsi que des essais de traction pour évaluer l'effet des charges dans la réponse du pieu à l'arrachement.

Les essais cycliques ont été caractérisés selon deux paramètres de charge;  $Q_{cyclic}$  et  $Q_{mean}$  correspondant respectivement à la moitié de l'amplitude de chaque cycle et à la valeur moyenne de charge. Les essais de faible niveau en charge ont été effectués sous chargement contrôlé (FC), uniquement en traction (non alterné). Ces essais ont mobilisé jusqu'à 60% de la capacité totale du pieu en tension,  $Q_t$ . Les cycles de charge de haut niveau alternés (compression et traction) ont été conduits en déplacement contrôlé (DC). Les cycles ont été appliqués à une fréquence relativement basse, allant de moins de 0,5 cycles par minute pour les essais alternés, à presque 2,5 cycles par minute pour les essais de faible charge.

Des essais de traction statique post-cyclique ont été réalisés, avec un taux de déplacement de 0,01 mm/s, afin de vérifier les capacités à l'arrachement disponibles après chaque chargement cyclique. Comme indiqué par Jardine et al (2006), les essais préalables peuvent influencer sur les capacités développées lors des essais ultérieurs. Le tableau 2 résume les différentes séries d'essais cycliques réalisées.

Tableau 2: Programme d'essais de chargement cyclique

ID	N of cycles	Description	$Q_{cyclic} / Q_T$	$Q_{mean} / Q_T$
ICP1-OW1 (FC)	1000	0 à -4,0 kN	0,22	0,22
ICP1-TW1 (DC)	100	-4 à 5 mm	0,41	0,06
ICP2-OW1 (FC)	1000	0 à -3,0kN	0,12	0,12
ICP2-OW2 (FC)	1000	0 à -4,8 kN	0,20	0,20
ICP2-OW3 (FC)	500	0 à -6,8 kN	0,28	0,28
ICP2-TW1 (DC)	100	-2,0 à 3,0 mm	0,48	0,15
ICP3-OW1 (FC)	100	0 à -9,6 kN	0,38	0,38
ICP3-TW1 (FC)	287	-5,0 à +8,0kN	0,54	0,08
ICP3-TW2 (FC)	199	-5,0 à +5,0kN	0,40	0,06
ICP3-TW3 (FC)	50	-5,0 à +7,0 kN	0,44	0,02
ICP3-TW4 (FC)	37	-5,0 à +10,0kN	0,44	0,02
ICP4-OW1 (FC)	7000	0 à -3,5 kN	0,15	0,15
ICP4-TW1(FC)	600	-4,0 à +4,0kN	0,23	0,06
ICP4-OW2 (FC)	50	-2,3 à -4,6 kN	0,21	0,63

OC = cycles non alternés, et TC = cycles alternés

## 4 RÉSULTATS DES ESSAIS CYCLIQUES NON ALTERNÉS À FAIBLE AMPLITUDE

### 4.1 Evolution des contraintes le long du pieu et au sein du massif

Les mesures de contrainte effectuées au sein du massif et le long du pieu permettent de préciser les mécanismes conduisant à l'amélioration ou à la dégradation du frottement. La Figure 2 montre l'évolution des contraintes radiales dans le sol à différentes distances du pieu. On constate une décroissance de ces contraintes radiales avec le nombre de cycles, plus accentuée lors de cycles alternés. La même situation est vérifiée avec les contraintes radiales le long du pieu, accentuée lors des grands cycles mais avec des amplitudes plus grandes. On remarque également dans la Figure 2, que le chargement statique effectué entre les deux séries de cycles entraîne une nette augmentation des contraintes près du pieu après les petits cycles (effet de la dilatance).

La distribution des contraintes dans le massif du sol à différentes distances de l'axe du pieu a été interprétée par Jardine et al. 2012 en utilisant l'information des capteurs.

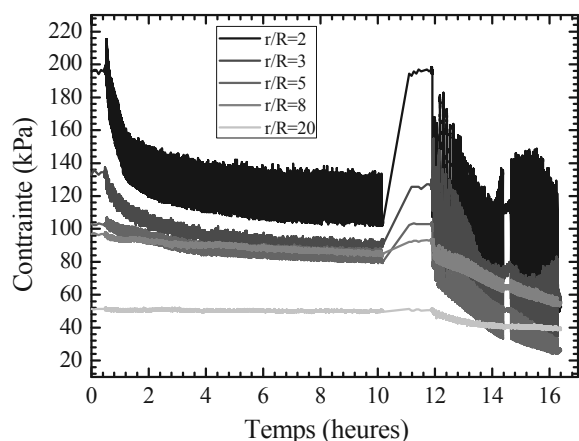


Figure 2: Evolution des contraintes radiales dans le sol : De 0 à 9,6h : 1000 cycles non alternés de faible amplitude (ICP1-OW1) ; de 10,4 à 14,7h : 100 cycles alternés de grande amplitude (ICP01-OW1).

La mesure simultanée des contraintes radiales et tangentielles permet de tracer les chemins de contraintes suivis par le sol au contact du pieu. Les petits cycles non alternés, tels que ceux représentés sur la Figure 3 pour les trois niveaux le long du pieu, provoquent un déplacement des chemins de contraintes vers la gauche, traduisant une tendance à la contractance de l'interface et donc sa densification. C'est cette densification qui produit ensuite une augmentation de la dilatance et l'amélioration de la capacité. Lorsque l'amplitude de ces cycles non alternés augmente, les cycles s'approchent de la droite de rupture en traction (Yang et al 2010).

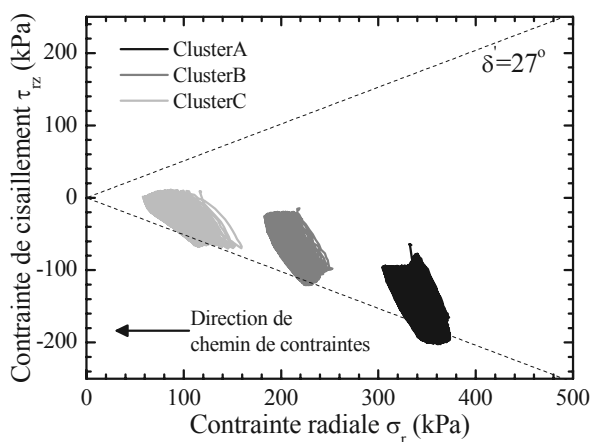


Figure 3: Chemins de contraintes à la surface du pieu. Essai Mini-ICP2. Cycles non alternés de faible amplitude.

A l'inverse, les chemins de contraintes des grands cycles alternés traversent l'équivalent d'une « ligne de changement de phase » et produisent des alternances de dilatance/contractance et une désorganisation du sol autour de l'interface. On peut remarquer qu'on retrouve pour ces chemins de contraintes la forme en « ailes de papillon » qu'on observe lors d'essais de cisaillement cyclique à volume constant ou à rigidité normale contrôlée (Fakharian & Evgin 1997, Mortara et al. 2007).

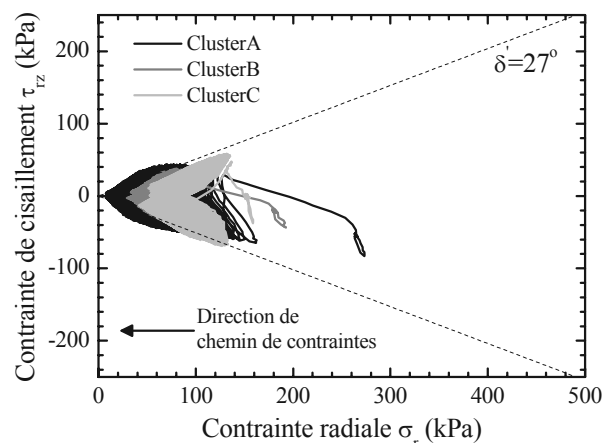


Figure 4: Chemins de contraintes à la surface du pieu. Essai Mini-ICP4. Cycles alternés de forte amplitude.

#### 4.2 Capacité du pieu à l'arrachement avant et après chargement

Le tableau 3 montre les essais statiques effectués après chaque essai cyclique pour évaluer l'effet de ceux-ci sur la capacité à l'arrachement.

Tableau 3: Programme d'essais de chargement cyclique

Essai	Essai précédent (selon Tableau II)	$Q_r$ (kN)	Variation entre essais (%)
ICP1-T1	1ère compression	9,2	-
ICP1-T2	ICP1-OW1	10,8	17,4%
ICP1-T3	ICP1-TW1	4,9	-54,6%
ICP2-T1	1ère compression	12,1	-
ICP2-T2	ICP2-OW1	13,2	9,1%
ICP2-T3	ICP2-OW2	14	6,1%
ICP2-T4	ICP2-OW3	13,7	-2,1%
ICP2-T5	ICP2-TW1	8,7	-36,5%
ICP3-T1	1ère compression	12,5	-
ICP3-T2	ICP3-OW1	10,9	-12,8%
ICP3-T3	ICP3-TW1,2,3,4	4,8	-56,0%
ICP4-T1	1ère compression	11,5	-
ICP4-T2	ICP4-OW1	13,9	20,9%
ICP4-T3	ICP4-TW1	5,5	-60,4%
ICP4-T4	ICP4-OW2	6	9,1%

Comme indiqué, selon l'amplitude de la charge cyclique, il est possible d'obtenir une augmentation de la résistance, ce que proposent Jardine et al (2006) dans des essais sur le terrain.

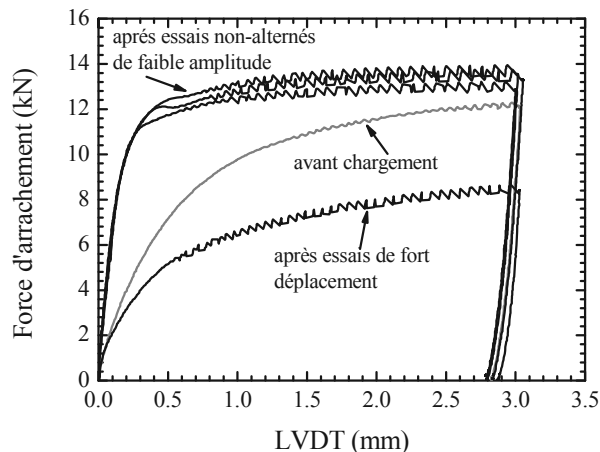


Figure 5: Courbes force d'arrachement-déplacement du pieu avant et après application des cycles Essai ICP2.

Les essais d'arrachement avant et après l'application de cycles, présentés dans la Figure 5 pour les essais Mini-ICP2, montrent clairement que l'application des cycles non alternés de

faible amplitude améliore la capacité du pieu en raison de la densification de l'interface, alors que les cycles de grande amplitude avec passage de la traction à la compression produisent une nette dégradation de cette capacité due à la désorganisation de l'interface.

#### 4.3 Diagramme de stabilité cyclique

Une première partie des résultats concernant les essais de chargement cyclique a été résumée par Tsuha (2012). On a analysé l'évolution du frottement latéral du pieu et sa stabilité selon le nombre et le type de cycles appliqués (réversibles ou non réversibles), l'amplitude et la valeur moyenne de la charge. La Figure 6 montre le diagramme de stabilité cyclique établi à partir de la totalité des essais réalisés. Trois zones ont été identifiées pour le comportement du pieu.

- Stable, correspondant à une zone de faible amplitude au niveau de la charge et où le pieu peut être soumis à plus de 1000 cycles sans accumuler une déformation importante.
- Métastable, correspondant à une déformation importante ou une rupture entre 100 et 1000 cycles.
- Instable, correspondant à une rupture obtenue en moins de 100 cycles.

La rupture cyclique a été définie comme ; i) un déplacement permanent atteignant 10% du diamètre (i.e. 3.6 mm), ou ii) un taux de déplacement montrant une augmentation forte, en considérant comme « lent » un taux inférieur à 1 mm/10<sup>4</sup> cycle, et « rapide » un taux supérieur à 1 mm/100 cycle.

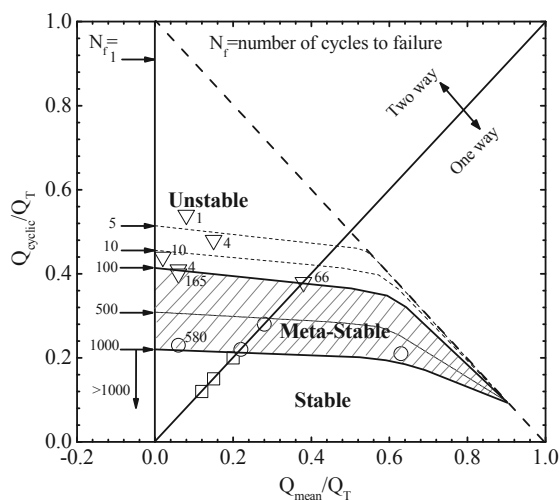


Figure 6: Diagramme de stabilité cyclique essais ICP1-4 (d'après Tsuha et al., 2012)

## 5 CONCLUSION

La mesure des chemins de contraintes le long de pieux instrumentés avec précision, ainsi que ceux au sein du massif de sol au voisinage du pieu, permet de mieux appréhender les mécanismes gouvernant la dégradation ou l'amélioration du frottement lors de sollicitations cycliques. Elle permet en particulier de faire le lien entre les états « stable », « métastable » et « instable » dans les diagrammes classiques de stabilité cycliques et le comportement élémentaire des interfaces par rapport à leur « ligne de transformation de phase » ou « droite caractéristique ».

L'ensemble des essais effectués jusqu'à présent montre que l'application d'un grand nombre de petits cycles non alternés produit une densification de l'interface sol-pieu, favorisant le développement d'une dilatance lors d'un chargement ultérieur et donc une amélioration de la capacité du pieu à l'arrachement.

A l'inverse les grands cycles alternés produisent une désorganisation de l'interface et une diminution de la dilatance

lors d'un chargement ultérieur et une dégradation de la capacité à l'arrachement. Ce phénomène est analogue à celui conduisant à une dégradation du frottement le long des pieux battus lors de leur installation.

## 6 RÉFÉRENCES

- Al-Douri R. and Poulos H.G. 1994. Cyclic Behaviour of Pile Groups in Calcareous Sediments. *Soils and Foundations* 34, 49-59.
- Chan S. and Hanna T. H. 1980. Repeated loading on single piles in sand. American Society of Civil Engineers. *Journal of the Geotechnical Engineering Division* 106 (2), 171-188.
- Chin J. T. and Poulos H.G. 1996. Tests on model jacked piles in calcareous sand. *Geotechnical Testing Journal* 19(2), 164-180.
- Chow F.C., Jardine R.J., Bruzy F., Nauroy J.F. 1998. Effects of time on capacity of pipe piles in dense marine sand. *Journal of Geotechnical and Geoenvironmental Engineering* 124(3), 254-264.
- Fakharian K. and Evgin E. 1997. Cyclic simple-shear behavior of sand-steel interfaces under constant normal stiffness condition. *Journal of Geotechnical and Geoenvironmental Engineering* 123(12), 1096-1105.
- Foray P., Tsuha C.H.C., Silva M., Jardine R.J. et Yang Z. 2010. Stress paths measured around a cyclically loaded pile in a calibration chamber. Proc. Int. Conf. on Physical Modelling in Geomechanics, ICPMG 2010, Zurich, Switzerland.
- Jardine R.J. and Standing J.R. 2000. Pile load testing performed for HSE cyclic loading study at Dunkirk, France. Two Volumes. Offshore Technology Report OTO 2000 007. Health and Safety Executive, London. 60p and 200p.
- Jardine R.J., Chow F., Overy R., Standing J. 2005. ICP Design Methods for Driven Piles in Sands and Clays, Thomas Telford.
- Jardine R.J., Standing J.R., Chow F.C. 2006. Some observations of the effects of time on the capacity of piles driven in sand. *Géotechnique* 56 (4), 227-244.
- Jardine R.J., Zhu B.T., Foray P., Dalton C.P. 2009. Experimental arrangements for the investigation of soil stresses developed around a displacement pile. *Soil and Foundations* 49(5), 661-673.
- Jardine R., Zhu B., Foray P., Yang Z., 2012. Interpretation of stress measurements made around closed-ended displacement piles in sand. *Géotechnique*. Accepted.
- Kolk H.J, Baaijens A.E, Vergobbi P., 2005. Results of axial load tests on pipe piles in very dense sands: the EURIPIDES JIP Proc. 1st Int. Symposium on Frontiers in Offshore Geotechnics, ISFOG 2005, Perth, W.A., pp. 661- 667.
- Lehane B. M., Jardine R. J., Bond A. J., Frank R., 1993. Mechanisms of shaft friction in sand from instrumented pile tests. *Journal of Geotechnical Engineering* 119(1), 19-35.
- Le Kouby, A., Canou, J., and Dupla, C. 2004. Behaviour of model piles subjected to cyclic axial loading. *Cyclic Behaviour of Soils and Liquefaction Phenomena*: 159-166. Triantafyllidis (ed).
- Mortara G., Mangiola, A., Ghionna, V.N. 2007. Cyclic shear stress degradation and post-cyclic behaviour from sand-steel interface direct shear tests. *Canadian Geotechnical Journal* 44(7), 739-752.
- Tsuha C.H.C., Foray P., Jardine R.J., Yang Z.X., Silva M., Rimoy S. 2012. Behaviour of displacement piles in sand under cyclic axial loading. *Soils and Foundations* 52(3), 393-410.
- Yang Z.X., Jardine R.J., Zhu B.T., Foray P., Tsuha C.H.C., 2010. Sand grain crushing and interface shearing during displacement pile installation in sand. *Géotechnique* 60(6), 469-482.
- Zhu B.T., Jardine R.J., Foray P., 2009. The use of miniature soil stress measuring sensors in applications involving stress reversals. *Soils and Foundations* 49(5), 675-688.

# Characterization of the geotechnical properties of a carbonate clayey silt till for a shallow wind turbine foundation

Caractérisation des propriétés géotechniques d'un silt argileux carbonaté glaciaires pour une fondation superficielle d'éolienne

Tyldesley M., Newson T.

*Geotechnical Research Centre, Department of Civil Engineering, University of Western Ontario, Ontario, Canada*

Boone S.

*Golder Associates Ltd., London, Ontario, Canada*

Carriveau R.

*Intelligence Research Group, Department of Civil Engineering, University of Windsor, Ontario, Canada*

**ABSTRACT:** Wind energy is a major source of renewable energy and is projected to capture 11% of the energy generation capacity for Ontario by 2018. A number of problems that the energy industry currently faces stem from a lack of understanding of cyclic loading of Ontario soils and a paucity of regional regulatory guidance for site investigation and design methods for wind turbine foundations. A multi-disciplinary research project is underway to integrate laboratory testing, field monitoring and numerical modeling of a commercial wind turbine on a shallow foundation. This paper describes an initial part of the study to characterize the geotechnical properties of the clayey silt till soils on the site. Emphasis has been placed on comparison of different *in situ* and laboratory methods, and correlations for determining key geotechnical parameters for wind turbine foundation design.

**RÉSUMÉ :** L'énergie éolienne est une source importante d'énergie renouvelable et doit permettre de satisfaire 11 % de la capacité de production d'énergie de l'Ontario d'ici 2018. Un certain nombre de problèmes auxquels l'industrie de l'énergie est actuellement confrontée provient d'un manque de connaissances des sols de l'Ontario sous charges cycliques et de directives réglementaires régionales pour les méthodes d'investigation et de conception des fondations d'éoliennes. Un projet de recherche multidisciplinaire est en cours pour intégrer les tests en laboratoire, l'instrumentation et la modélisation numérique d'une éolienne commerciale sur fondation superficielle. Cet article décrit la partie initiale de l'étude pour caractériser les propriétés géotechniques du silt argileux glaciaire du site. L'accent a été mis sur la comparaison de différentes méthodes *in situ* et en laboratoire ainsi que les corrélations pour déterminer les paramètres géotechniques clés pour la conception de fondation d'éoliennes.

**KEYWORDS:** wind turbine, clay, till, shallow foundation, soil-structure interaction, elastic, anisotropy, *in situ*, geophysical.

## 1 INTRODUCTION

### 1.1 Wind energy and turbine design in Canada

Wind is a major source of renewable energy and is projected to capture 11% of the energy generation capacity for Ontario by 2018 (CANWEA, 2011). However, to achieve this expansion some major technical and policy issues must be addressed by the Canadian wind sector. Some of these issues are associated with the construction and design of foundations for wind turbines. Foundations for onshore wind turbines usually consist of large gravity bases and monopiles (e.g. DNV/Risø, 2002). The geometry and foundation type depends on the wind climate, power regulation philosophy, physical characteristics of the machine, uplift criteria, required foundation stiffness and geotechnical characteristics of the site (Bonnett, 2005). The critical analyses for design include bearing capacity and overturning resistance, horizontal and rotational displacements, and dynamic soil-structure interaction (Harte et al., 2012).

Although there has been much recent research associated with foundations for offshore wind turbines (e.g. Byrne and Houlsby, 2003), the literature on onshore systems is still relatively sparse. Consequently, despite similar issues for wind turbine foundations across the industry, there is often diverse interpretation of design codes and understanding of the behavior of foundations (Morgan and Ntambakwa, 2008). This can lead to quite different foundation designs on different wind farms with the same turbines and comparable geotechnical profiles. This issue is exacerbated in Canada, since there is currently no regional regulatory guidance for site investigation and design methods for wind turbine foundations. Hence it is not surprising

that rather generic approaches have developed for site investigation and design, which are relatively crude and can lead to quite conservative designs. To capture more wind energy, the industry is continuing to develop larger turbines and is considering more marginal sites in terms of geotechnical characteristics, which will only complicate the current situation.

### 1.2 Project overview and objectives

A number of the above issues are being addressed as part of a multi-disciplinary research project that includes an integrated laboratory testing, field monitoring and numerical modeling program investigating the behaviour of a fully operational Canadian commercial wind turbine throughout its service life. The equipment installed on the turbine will enable an integrated, life cycle assessment of the wind turbine and its foundation. This paper describes the portion of the study that involves preliminary characterization of the geotechnical properties of the wind farm site. In particular, a comparison between the *in situ* testing, laboratory testing and commonly used correlations are presented. It is anticipated this process will guide future projects on clayey silt tills in Ontario and provide cost effective site investigation and design methods for turbine foundations.

## 2 SOIL PROFILES & MATERIAL CHARACTERISATION

### 2.1 Wind farm and geological environment

The wind farm is located in a simple geographical and environmental area in the Great Lakes region of Southern Ontario. The farm has horizontal axis 2.3 MW turbines with an



80 m hub height and triple bladed rotors with a 93 m diameter. The tower has a typical tapered tubular steel design and is founded on a 16 m diameter hexagonal reinforced concrete shallow foundation at 3.6 m depth. The site is underlain by carbonate-rich clayey silt tills that are a ubiquitous feature of the Great Lakes basins and is located at the confluence of four major geological deposits. These consist of the Port Stanley and Tavistock tills, glaciolacustrine sand and gravel, and glaciolacustrine clayey silt. These materials were laid down in the Port Bruce Stade (c. 14,800 years bp.) during the re-advance of the Laurentide Ice Sheet of the Late Wisconsin. These subglacial lodgement tills are calcareous and fine-grained, suggesting that the ice overrode and incorporated fine-grained glaciolacustrine sediments deposited during the previous Erie Interstade. This has created approximately 40-45 m thickness of clayey silt tills with interbedded glaciolacustrine sediments. The bedrock is shale with limestone-dolostone-shale interlayers.

## 2.2 Overview of site investigation

The site investigation was designed to establish detailed stratigraphic and geotechnical characteristics for the soils beneath the wind turbine foundation. Forty metre deep boreholes were drilled on the site to evaluate the soil profile, perform *in situ* tests and collect high-quality samples for laboratory testing. A track-mounted drill was used for the drilling activities. Three boreholes were drilled 10-16 m adjacent to the turbine foundation (to ensure minimal stress change from the foundation). The wash boring method was used for two of the holes and the PQ coring method for the other hole. The boreholes were drilled to depths of twice the foundation diameter and were spaced at 3 m to allow for later cross-hole geophysical testing. Thin-wall Shelby tube sampling was completed to obtain minimally disturbed samples for the laboratory testing. *In situ* testing adjacent/in to the boreholes consisted of SPT, field shear vane, cross-hole geophysics and seismic SCPTu, and was conducted to depths of 30 m. To complement the *in situ* test results, laboratory tests were conducted for soil classification and geotechnical properties.

## 2.3 Soil description and basic properties

This deposit can be separated into three zones: a heavily weathered oxidized upper crust from 0–1.5 m, a partially weathered lower crust that transitions from an oxidized to an unoxidized state from 1.5–4.5 m and an unweathered clay till below 4.5 m to greater than 40 m depth. The intensity of fissuring in the upper crust is very intense and the deposit becomes nearly unfissured below 4.5 m. The fissures are vertically dipping planar joints striking at right-angles. The fissure spacing at 1.5 m depth is 15 cm and this increases to 0.6-1.2 m at 4.5 m depth. The variation in moisture contents and the Atterberg limits with depth are shown in Figure 1.

The upper crust zone of this deposit is weathered, mottled brown-grey or brown-green with a stiff to very stiff consistency. This weathered zone generally has higher moisture contents (22-32%) due to the infiltration of surface water into the fissures of the clay. The underlying lower crust is prevalently brown in colour and has a very stiff consistency and relatively lower natural moisture content (16-20%). At several locations this layer has clayey silt, sandy clay and silt seams. A soil colour change occurs from brown to grey between 3 and 4 m below the ground surface. Below the crust, the unweathered till extends beyond the maximum depth of sampling. This zone is characterized by a uniform grey appearance, a stiff to very stiff consistency and relatively uniform moisture contents (16-24%).

Atterberg test results (Table 1) indicate that the material can be classified as CL-ML to CL (silty clay or low plasticity clay). There is an increase in liquid limit and plasticity towards the upper crust and the clay content is also found to increase near the surface, leading to little change in activity (0.5).

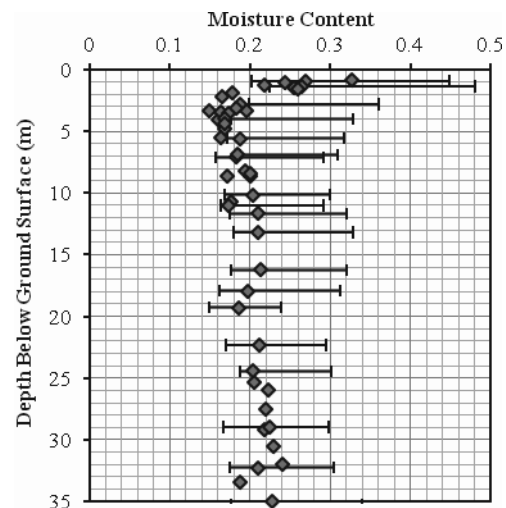


Figure 1. Moisture contents and Atterberg limits with depth.

The liquidity index ( $I_L$ ) is found to range from 0.2 to 0.4 in the virgin till, is below zero in the lower crust and ranges from 0.15 to 0.25 in the upper crust. The bulk unit weights of the profile are generally uniform and range from 20.3 to 21.6 kN/m<sup>3</sup>.

Table 1. Atterberg Limits and Particle Size Distributions.

Layer	Liquid Limit (%)	Plastic Limit (%)	Clay (%)	Silt (%)	Sand (%)
Upper Crust	46	21	40	45	15
Lower Crust	34	19	29	49	20
Unweathered Till	30	17	31	45	21

Semi-quantitative XRD shows that the unweathered till is predominantly composed of quartz/feldspar (39%), carbonate (25-35%), mica/illite (16%), chlorite/kaolinite (7%) and trace minerals. In the 2 micron range the minerals are dominated by illite, calcite and chlorite. The lower crust has a similar composition, with more quartz/feldspar (49%), lower carbonate (22%), mica/illite (18%), chlorite/kaolinite (7%) and swelling clay (2%) and other trace minerals. In similar deposits (Quigley and Obunbadejo, 1974) downwards leaching has removed carbonates from the near surface and redeposited lower in the crust. Table 2 shows the values of total carbonates, dolomite and calcite (from the gas evolution method) in the three zones, confirming the removal of carbonates from the near surface.

Table 2. Carbonate Contents in the Soil Profile.

Layer	Total Carbonates (%)	Dolomite (%)	Calcite (%)	C/D ratio
Upper Crust	0	0	0	-
Lower Crust	19.9	6.2	13.7	2.2
Unweathered Till	24.8	6.2	18.6	3.0

## 2.4 Compressibility and strength properties

In common with other tills around the world the compressibility, permeability and strength characteristics of this material are generally a function of the clay content. Estimates of undrained shear strength ( $s_u$ ) using various methods are

shown in Figure 2. All of the profiles show that the values of  $s_u$  are relatively constant with depth below 7 m and are in the range of 100-130 kPa. The lower crust material (2-4.5 m) increases in strength rapidly, in excess of 250 kPa and the upper crust material has a similar strength to the lower till. The usual hierarchy of strengths is seen for the different methods, due to the different modes of shearing. However, the field vane (FSV) shows higher values than the triaxial compression (CIU) test. This is likely due to partial drainage and problems rotating the vane slowly enough for an undrained state. Two estimates have also been determined from the CPT (Mayne, 2007):

$$s_u = (q_t - \sigma_{vo})/N_{kt} \quad (1)$$

$$s_u = \Delta u/B_q \cdot N_{kt} \quad (2)$$

where  $N_{kt}$  is a cone factor (taken as 15),  $\Delta u$  is the excess pore pressure and  $B_q$  is the ratio of excess pore pressure to the net cone resistance ( $q_t - \sigma_{vo}$ ). The approach based on excess pore pressures appears to give better estimates for the strengths, but the cone would be anticipated to provide lower values than CIU triaxial, since the shearing mode is a complex combination of triaxial compression/extension and plane strain. The depth of the foundation base and one base diameter (B) are also shown.

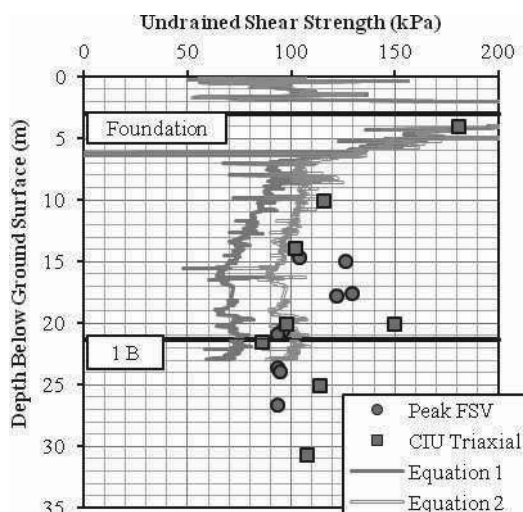


Figure 2. Undrained shear strength with depth.

From oedometer testing, average compression index ( $c_c$ ) for the three layers was found to be 0.072 and average recompression index ( $c_r$ ) was 0.008, giving a ratio of 0.12, which is in the usual range in the literature. The values of the two indices are quite low and are typical for sandy clays/silts, and the values from the crustal material are lower than those for the weathered till.

The pre-consolidation pressures ( $\sigma_{vp}'$ ) from oedometer tests have been estimated using the method of Boone (2011) and the corresponding overconsolidation ratio (OCR) is shown in Figure 3. This shows low OCRs in the weathered till, with a relatively small increase in the crustal material, up to an OCR of 4. Another estimate of OCR is shown using the relationship of Ladd et al. (1977), equation (3), with  $m = 0.8$  and the ratio of undrained shear strength (from CIU triaxial testing) to the *in situ* vertical effective stress [ $s_u/\sigma_{vo}'$ ] $_{nc} = 0.22$ :

$$\frac{[s_u/\sigma_{vo}']_{oc}}{[s_u/\sigma_{vo}']_{nc}} = OCR^m \quad (3)$$

This shows similar values of OCR at depths below 15 m, but much higher OCR values for shallower depths, up to an OCR of 15 at 4 m. Two further estimates of over-consolidation ratio have been made using the CPT data with expressions for the

preconsolidation pressure ( $\sigma_{vp}'$ ), after Mayne (2007):

$$\sigma_{vp}' = 0.33 \cdot (q_t - \sigma_{vo})^\mu \quad (4)$$

$$\sigma_{vp}' = 0.161 \cdot G_0^{0.478} \cdot \sigma_{vo}'^{0.42} \quad (5)$$

where  $G_0$  is the small-strain stiffness determined from the seismic cone data,  $\mu$  takes a value of 0.85 for silts and  $q_t$  is the cone tip pressure. These relationships show similar characteristics to the previous estimates, with the small-strain expression closely following the oedometer derived data and the CIU triaxial derived data following the CPT expression. Interestingly, the ratio of undrained shear strength to the *in situ* vertical effective stress in the upper crust [ $s_u/\sigma_{vo}'$ ] $_{oc}$  shows quite high values of 2.7-3.4, dropping to 0.3 at depth. This suggests values of  $K_0$  in excess of 1 and as high as 2.4 in the crust.

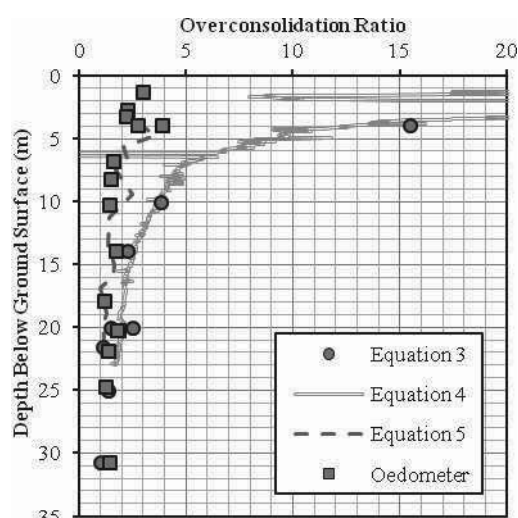


Figure 3. Overconsolidation ratio with depth.

## 2.5 Small-strain stiffness properties

Small-strain stiffness ( $G_0$ ) is presumed to be a function of the void ratio, stress history and ratio of horizontal (h) to vertical stresses (v). It is also thought to be related to the soil macro-fabric and can often display cross-anisotropic characteristics (where the vertical axis is an axis of radial symmetry). The characterization of cross-anisotropic elastic materials can be reduced to five independent elastic moduli ( $E_h$ ,  $E_v$ ,  $\nu_{vh}$ ,  $\nu_{hh}$  and  $G_{hh}$ ; Pennington et al., 1997). *In situ* and laboratory estimates of small-strain stiffness often use measurements of shear wave velocity ( $V_s$ ) travelling and polarized in different directions to determine shear modulus. Hence various methods of determining *in situ* elastic moduli provide often provide different components of the elastic stiffness tensor  $G_{o(ij)}$ .

Estimates of the small-strain stiffness ( $G_0$ ) from different *in situ* tests are shown in Figure 4. This includes cross-hole geophysics, seismic cone and two correlations; one using standard CPT output parameters (Long and Donohue, 2010) and one based on soil properties (Hardin and Black, 1969):

$$V_s = 1.961 \cdot q_t^{0.579} \cdot (1+B_q)^{1.202} \quad (6)$$

$$V_s = (159-53.5e_0) \cdot OCR^{0.18/2} \cdot \sigma_{vo}'^{0.25} \quad (7)$$

where  $V_s$  is the shear wave velocity,  $e_0$  the *in situ* void ratio, small-strain shear modulus  $G_0 = \rho \cdot V_s^2$  and  $\rho$  is density. The values of  $G_0$  appear to generally increase with depth and range from 50 to 350 MPa, with the majority of values being between 75 and 150 MPa. The cross-hole measurements were made with an axial hammer system and thus provide estimates of  $G_{ohv}$ ; these values are generally constant with depth and give the

highest *in situ* estimates of shear modulus. The seismic cone provides estimates of  $G_{ovh}$  and these values are lower than those of the cross-hole testing. The Long and Donohue (2010) CPT correlation (from equation 6) shows comparable variations in  $G_0$  with depth and falls between the two other *in situ* test datasets. However the Hardin and Black (1969) method based on OCR and overburden (equation 7) shows much higher estimates of  $G_0$  (despite using the lower values of OCR from Figure 3).

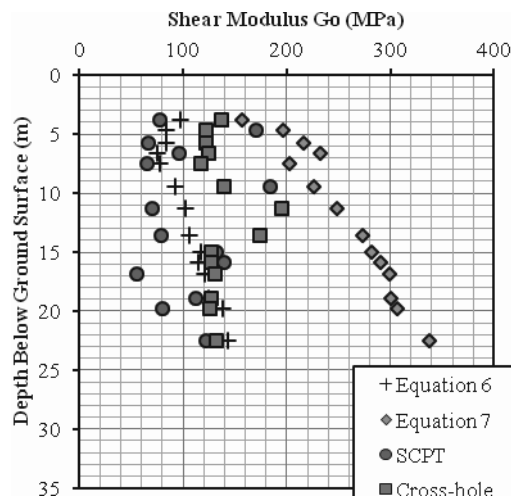


Figure 4. Small-strain shear modulus with depth.

Similar variations in the elastic shear moduli ( $G_{ovh}$  and  $G_{ohv}$ ) have been observed with *in situ* tests previously (Pennington et al. 1997). These would be expected to be equal for a perfectly cross-anisotropic material. However, the different travel times may result from the averaging of the shear wave velocity through layered strata (for vertical travel), compared to lateral wave velocity through the stiffest layers. This leads to cross-hole measurements tending to measure the stiffest layers, rather than the average stiffness for SCPT measurements.

### 3 DISCUSSION

The design of gravity base foundations for onshore wind turbines requires accurate estimates of strength parameters for bearing capacity and stiffness parameters for displacements, within at least 1B of the founding level. The adoption of the most appropriate methods for site investigation to determine these parameters is debated in the industry and various published correlations are commonly used. Unfortunately many of these correlations have been previously developed for geologically young and relatively simple materials, and their applicability beyond their original databases can be uncertain.

The different methods of determining the undrained shear strengths show the crustal materials are quite strong, particularly near the founding depth, with undrained shear strength of up to 300 kPa reducing to 100 kPa at the crust base. Given the relatively high  $c_v$  (and permeability) and field vane values, there is a possibility that the CPT and vane estimates may be artefacts due to partial drainage. The crustal zone also has fissuring related to drying/wetting and frost action, and field shearbox tests on similar materials have indicated that bulk strengths can reduce considerably, and therefore representative values may be closer to 60-80 kPa (Lo, 1970). However, whether crustal fissures and associated strength changes are significant for such large shallow foundations is questionable.

Since overconsolidation ratio is often used as a component of correlations to determine geotechnical parameters, accurate estimation is important. Overconsolidation in tills is often attributed to loads from the overlying ice, however if drainage is inhibited, then only a small degree of consolidation will occur.

The measurement of preconsolidation pressure in tills using laboratory testing has been found to be quite difficult due to the high pressures often required to fully define compression curves and the effects of sample disturbance (which lead to under-estimation of  $\sigma_{vp}'$ ). The difficulties with this process are evident in the wide range of estimates for OCR shown in Figure 3.

Stiffness anisotropy is often evident in soils from *in situ* and laboratory measurements. The data in Figure 4 shows the general difficulties in choosing appropriate estimates of the small-strain stiffness ( $G_0$ ). Indeed cross-anisotropy in till may be difficult to justify, since sub-glacial shear and consolidation could have effects on the anisotropy of the *in situ* stress and fabric. Rocking stiffness ( $k$ ) for circular surface loads (radius,  $R$ ) is estimated using equation 8, (DNV/Risø, 2002):

$$k = \frac{8R^3G}{3(1-\nu)} \quad (8)$$

where  $\nu$  is Poisson's ratio and  $G$  is the shear modulus determined from the shear modulus ratio  $G/G_0$  that corrects the stiffness for degradation due to strain level (this is typically 0.25 for the presumed strain levels of  $10^{-3}$  for wind turbines). Manufacturers recommend criteria for rocking stiffness to ensure the natural frequency of the turbine remains above the main excitation frequencies. The range of small-strain moduli in Figure 4 indicate rocking stiffnesses from 50 to 170 GNm/rad, which is in excess of typical requirements of 40 GNm/rad, but still represents quite a significant range of stiffness.

### 4 CONCLUSIONS

There is currently little guidance for choosing cost effective site investigation methods and interpreting the results for this type of geotechnical structure on glacial tills in Ontario. It is anticipated that the completion of this project will provide some of the missing knowledge and insight required in this area.

### 5 ACKNOWLEDGEMENTS

We wish to acknowledge the support of NSERC, Golder Associates, Michael Cookson, JJ Davis, and Paul Dawson.

### 6 REFERENCES

- Boone S. 2011. A critical reappraisal of preconsolidation pressure interpretations using the oedometer test. *Can Geo J.* 47 (3), 281-296.
- Bonnett D. 2005. Wind turbine foundations: loading, dynamics and design. *The Structural Engineer*, 83 (3), 41-45.
- Byrne B. and Houlby. G. 2003. Foundations for offshore wind turbines. *Phil Trans: The Royal Society*, 361 (1813), 2909-2930.
- CANWEA. 2011. *The Economic Impacts of the Wind Energy Sector in Ontario 2011-2018*. ClearSky Advisors Inc. Report, pp 46.
- DNV/Risø. 2002. *Guidelines for Design of Wind Turbines*, 2nd Edition.
- Hardin B.O. and Black W.L. 1969. Vibration Modulus of Normally Consolidated Clay; Closure. *J. SMF. ASCE*, 95 (SM6), 1531-1537.
- Harte, M., Basu, B. and Nielsen R. 2012. Dynamic Analysis of Wind Turbines Including Soil-Structure Interaction. *Engineering Structures*, 45, 509-518.
- Ladd C.C., Foott R., Ishihara K., Schlosser F. and Poulos H.G. 1977. Stress-deformation and strength characteristics: SOA report. *Proc., 9th Int. Conf. on Soil Mech and Found Eng.*, Tokyo, 2, 421-494.
- Lo K.Y. 1970. The operational strength of fissured clays. *Geotechnique* 20 (1), 57-74.
- Long M. and Donohue S. 2010. Characterisation of Norwegian marine clays with combined shear wave velocity and CPTU data. *Can Geo J.* 47 (7), 709-718.
- Mayne P. 2007. NCHRP Synthesis 368. 2007. *Cone Penetration Testing. A Synthesis of Highway Practice*. National Cooperative Highway Research Program, TRB: Washington, D.C.
- Pennington D. S., Nash D. F. T. and Lings M. L. 1997. Anisotropy of  $G_0$  shear stiffness in Gault clay. *Géotechnique*. 47 (3), 391 - 398.
- Quigley R. M. and Ogunbadejo T. A. 1974. Soil weathering, soil structure and engineering properties. *Soil Microscopy*, 165-178.

# Cyclic loading of caisson supported offshore wind structures in sand

## Chargement cyclique des éoliennes offshore soutenues par des caissons à succion en sable

Versteele H.

Cathie Associates SA/NV, Diegem, Belgium (formerly Université de Liège, Liège, Belgium)

Stuyts B., Cathie D.

Cathie Associates SA/NV, Diegem, Belgium

Charlier R.

Université de Liège, Liège, Belgium

**ABSTRACT:** With the number of offshore wind turbines in Europe growing rapidly, offshore wind farm developers are looking for support structures which are relatively light, easy to produce and install and are suited for water depths in excess of 30m. Suction caissons could offer a solution for these requirements. Since cyclic environmental loads form an important part of the loading conditions, the cyclic degradation of the caisson capacity needs to be evaluated in detail. During storm events, pore pressure build-up inside and around the caisson can lead to degradation of capacity and stiffness. To date, there are no generally accepted material models which combine generation and dissipation of pore pressure with the mechanical response of the sand. Existing methods for analyzing pore pressure build-up are reviewed. Subsequently, a numerical model is proposed which captures the phenomena of pore pressure generation and dissipation around the caisson. Pore pressure increases under storm load cycles are calculated from cyclic laboratory tests and are added to existing pore pressures in the numerical model. The influence of cyclic loading history and drainage effects on the caisson performance is assessed using the 3D FE model. Implications for suction caisson design in sand are outlined.

**RÉSUMÉ :** Vu la croissance rapide du nombre d'éoliennes offshore en Europe, les développeurs des parcs éoliens offshore sont intéressés par des structures combinant légèreté, facilité de fabrication et qui sont adaptées à des profondeurs d'eau supérieures à 30m. Les caissons à succion répondent à ces critères. Comme les charges environnementales cycliques constituent une partie importante du chargement total, la dégradation cyclique de la capacité portante du caisson doit être évaluée en détail. Lors de tempêtes, l'accumulation de pressions d'eau interstitielle à l'intérieur et autour du caisson peut induire une dégradation de la capacité et de la raideur. A ce jour, il n'existe pas de modèle de matériau unanimement accepté qui combine génération et dissipation de pression interstitielle et comportement mécanique du sable. Les méthodes existantes d'analyse de génération de pression interstitielle sont examinées dans un premier temps. Ensuite, un modèle numérique intégrant les principaux mécanismes de génération et dissipation de ces surpressions autour du caisson est introduit. L'augmentation de pressions interstitielles résultants des charges cycliques dues aux tempêtes est estimée de manière indirecte sur base des résultats d'essais cycliques en laboratoire; ces surpressions sont ensuite ajoutées aux pressions interstitielles existantes dans le modèle numérique. L'influence de l'historique de chargement cyclique et des conditions de drainage est évaluée à l'aide du modèle éléments finis 3D. Enfin, les implications de ces résultats pour la conception de caissons à succion sont exposées.

**KEYWORDS:** suction caisson, cyclic loading, liquefaction analysis, offshore wind turbine, marine geotechnics

## 1 INTRODUCTION

### 1.1 Suction caisson as foundations for offshore wind turbines

The European Wind Energy Association expects that the installed offshore wind capacity within the EU will increase from 4GW to 40 GW by 2020 (EWEA 2011) requiring the installation of approximately 6000 6MW turbines located ever further offshore in consequently deeper waters. Due to the demanding working conditions at sea and the limited availability of offshore installation vessels, the foundation system typically accounts for up to 25-30 % of the total cost of an offshore wind farm. This makes the choice and design of the foundation an important factor in the overall cost effectiveness of offshore wind farms.

Offshore wind farm developers are thus looking for support structures which are relatively light, easy to produce and install and are suited for water depths in excess of 30m. Suction caissons could offer a solution for these requirements.

A suction caisson is a steel structure consisting of a circular top plate with peripheral vertical skirts (Figure 1). In operation it is similar to a skirted gravity foundation, but the skirt length is significant compared to the diameter.

Installation of the caisson is achieved in two phases. After initial penetration under the self-weight of the caisson, water is

pumped out. The induced pressure difference pushes the caisson into the soil, while the induced seepage forces and reduced effective stress near the skirt tips facilitate penetration.

Advantages of the caisson include a potentially lower cost than equivalent piled foundations (Senders 2008) and relatively easy installation and removal, not restricted by water-depth.

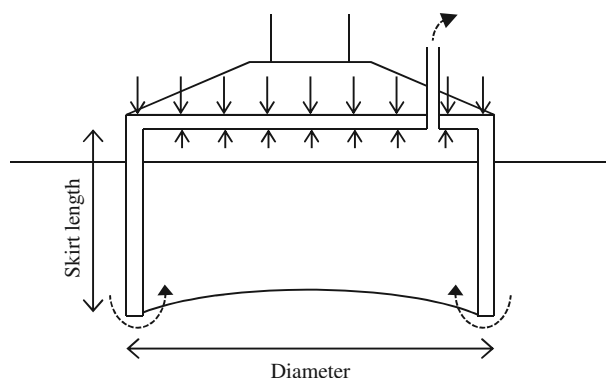


Figure 1: Cross-section sketch of a suction caisson and installation principle

### 1.2 Loads on offshore wind turbines

The foundation must resist loads caused by the weight of the structure, the operation of the turbine, currents, wind and wave action. Incoming waves exert a cyclic horizontal force (and moment) on the foundation, which in the case of offshore wind turbines may be a significant proportion of the weight of the structure. A vertical weight of 6MN and a horizontal wave loading of up to 3MN are realistic values for a 3.5MW turbine (Houlsby et al. 2005).

The offshore design standard DNV-OS-J101 (DNV 2011) specifies that the structure must be able to resist a 50-year design storm (a storm with a probability of occurrence of 1/50 during one year), where not only the peak loads, but the entire history of cyclic loading affects the stability of the structure. For the cyclic loading assessment, the irregular wave loading is usually converted into an idealized, equivalent design storm.

### 1.3 Structural configuration

Caissons could support offshore wind turbines in two ways, based on mode of load transfer to the soil (Figure 2). A monopod foundation consists of a single caisson and is suited for shallow waters. In deeper water, the increased moments acting on the caisson would require a very large caisson. In that case a tripod (three caissons) or quadripod (four caissons) structure could be economical, as moment loads are converted into a vertical push and pull action on the individual caissons.

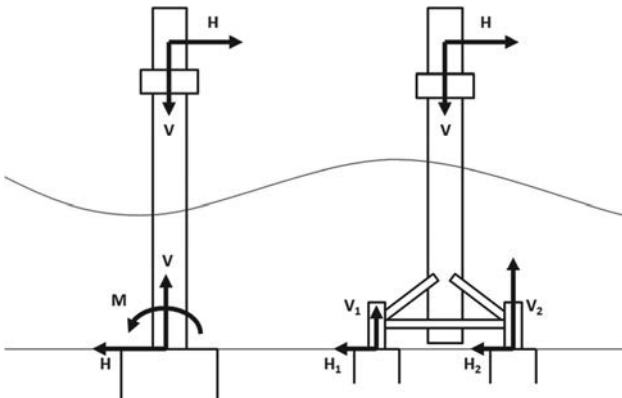


Figure 2: The monopod and multipod concept and reaction forces on the caissons

### 1.4 Scope of work

The aim of this paper is to examine the effect of cyclic loading during a design storm on both the monopod and multipod and to produce a model which is suitable for engineering practice. The presented model is still under development, and is considered a starting point for more sophisticated approaches.

## 2 CYCLIC DEGRADATION OF SOILS AND FOUNDATIONS

### 2.1 Pore pressure build up in sand under cyclic loading

Cyclic shearing of sand degrades the soil structure and causes a tendency to densify. This is the case even for very dense sands that are dilative under monotonic loading conditions (Seed and Idriss 1980, Andersen and Berre 1999).

Under undrained conditions, volume changes are prevented by the low compressibility of water, so normal stresses carried by the soil will be transferred to the pore water, thus increasing the pore water pressure in the sample as illustrated in Figure 3. The decrease in effective stress furthermore causes a progressive increase in average shear strain. Failure occurs when the generated pore pressure reaches a critical value  $u_{max}$ .

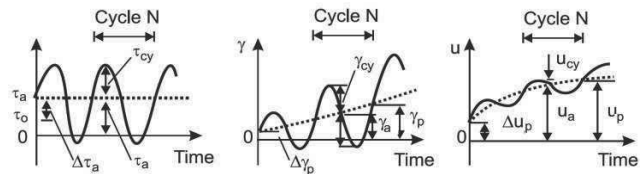


Figure 3: Behaviour of sand under cyclic loading (after Andersen and Berre 1999)

The intensity of cyclic loading is expressed in terms of the cyclic shear stress ratio, the ratio of cyclic deviatoric stress amplitude over mean effective stress. This formulation is convenient for the interpretation of triaxial test results and for implementation in the finite element procedure.

$$CSR = q_{cy}/p'_o \quad \text{with } q = \sigma_1 - \sigma_3 \quad (1)$$

Based on several cyclic tests at different CSR, cyclic shear strength curves can be established, expressing the number of cycles required to induce failure  $N_f$  as a function of the CSR and Dr.

The cyclic shear strength depends on the relative density and the initial shear stress in the sample. The set of curves used in this study was presented by Lee and Focht (1975) in their investigation of the liquefaction potential at the Ekofisk site, North Sea. The curves for this typical dense North Sea sand are redrawn in Figure 4.

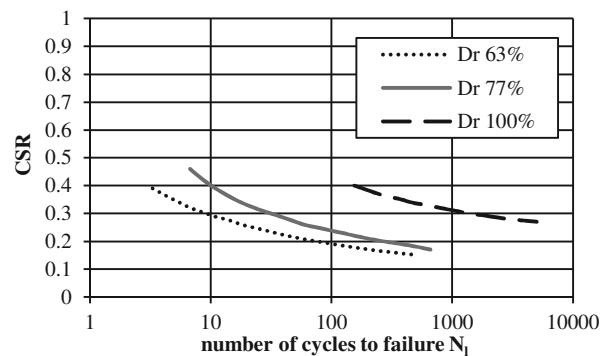


Figure 4: Cyclic shear strength curves for dense North Sea sand at the Ekofisk site (after Lee and Focht 1975)

The build-up of pore pressure in samples can be described by the empirically determined pore pressure generation function given in Eq. 2 and plotted in Figure 5. The empirical constant  $\alpha$  depends on the soil properties and is on average equal to 0.7 (Rahman et al. 1977). As it is cyclically loaded, the soil sample evolves from the initial, undisturbed state at  $N = 0$  to a state of liquefaction at  $N = N_f$  and  $u = u_{max}$ .

$$\frac{u}{u_{max}} = \frac{2}{\pi} \arcsin \left[ \left( \frac{N}{N_f} \right)^{1/2\alpha} \right] \quad (2)$$

### 2.2 Drainage conditions

In laboratory tests soil samples are brought to failure under undrained conditions. However, in situ loading conditions may be fully or partially drained, depending on the combination of soil permeability, frequency of the loading and drainage conditions.

For offshore turbines founded on sand, the high permeability and relatively slow wave loading results in the dissipation or redistribution of a significant part of the generated pore pressure

during the cyclic loading itself. This effect becomes more important as the soil permeability increases and the loading frequency diminishes. Not taking into account the simultaneous dissipation leads to overestimation of the generated pore pressure and potentially to overconservative design.

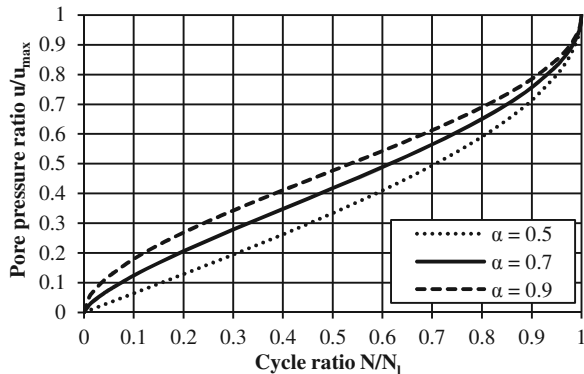


Figure 5: Pore pressure generation function.

### 2.3 Liquefaction of foundations

The definition of failure of a foundation due to liquefaction requires special attention. Not all parts of the soil under a foundation will fail at the same time or will fail at all. Some intensely loaded zones may liquefy completely or partially, while other zones may still be intact.

Taiebat (1999) discussed the problem and proposed the following definitions. *Total failure* of a foundation-soil system under cyclic loading is defined as the condition where the soil mass deforms continuously under the ambient and cyclic loads applied to the foundation, resulting in bearing capacity failure. *Partial failure* involves large permanent displacements during cyclic loading. Some elements of the soil liquefy and lose their strength, but overall, the soil mass remains stable.

Due to the complexity of the problem, numerical analysis is often the preferred method to assess to what extent the foundation capacity is degraded.

## 3 EXISTING NUMERICAL METHODS

There are at least two approaches to numerical modelling of offshore foundation liquefaction. In the first approach an appropriate constitutive model is used to capture cyclic stress-strain behaviour of the soil. Many such models exist and they can successfully reproduce soil behaviour in laboratory conditions (e.g. bounding surface plasticity, multi-surface plasticity). However, the number of required parameters and calculation time are two obstacles that up to now have limited application of these models to analysis of boundary value problems in engineering practice.

The second approach is simpler and consists of improving a conventional (possibly slightly modified) constitutive model by incorporating the effects of cyclic loading separately, based on a set of laboratory tests. A rigorous review of the work by researchers who followed this approach to analyze offshore foundations subjected to wave loading is given by Taiebat (1999).

## 4 IMPLEMENTED METHOD

The proposed method follows the second approach and is based on the work by Rahman et al. (1977), Taiebat (1999) and to a lesser extent Lee & Focht (1975) and Verruijt & Song (1991).

The calculation procedure is as follows: undrained pore pressure increases are calculated analytically, at regular time

intervals in the FE analysis. At each node, the pore pressure at the end of the previous interval (which includes effects of all previous loading) is converted into an equivalent number of cycles using Eq. 2. The increase in pore pressure during next interval (containing a number of load cycles) can then be calculated from Eq. 2, assuming the CSR is constant during this interval.

After the pore pressure and effective stress in the FE analysis are updated accordingly, the dissipation analysis continues over the length of the considered time interval. This is done in a coupled Biot-type consolidation analysis in the FE package Abaqus.

The total design storm consists of a number of load parcels, during which the cyclic load (and thus the CSR) is assumed to have a constant average and amplitude. The load parcels are subdivided in a number of steps and the process of updating the pore pressure and subsequent consolidation is repeated for every subdivision, tracing the average pore pressure response (excluding oscillations within each load cycle) over the entire load history of the design storm.

## 5 APPLICATION TO SUCTION CAISSONS

In two case studies the influence of cyclic loading history and drainage effects on the caisson performance is assessed using the proposed model. Realistic forces acting on the foundation are estimated from the loads outlined in section 1.2 and a simplified load histogram is adopted. Corresponding realistic caisson dimensions are found by applying the bearing capacity equation (DNV 1992) for the tripod caisson and the formula proposed by Byrne and Houlsby (2003) for the monopod caisson. In both cases the sand is represented by an isotropic elastic material model with Mohr-Coulomb plasticity.

### 5.1 Leeward caisson of a tripod

#### 5.1.1 Model

Initially the horizontal load, divided over three caissons, is neglected. The resulting axisymmetric problem only considers vertical cyclic loading on the individual caisson due to weight of the structure and overturning moments as this is the most important load component. The histogram consists of 3 load parcels of 2000 seconds each, applying 200 load cycles at 60% of the maximum load in the first and last parcel and 200 cycles at maximum loading in the middle parcel.

#### 5.1.2 Results

An example of calculated pore pressure response within and around a 8x8m caisson is shown in Figure 6. First of all it is clear that the abrupt increases (generation) and gradual decreases (dissipation) are an approximation for the real behaviour.

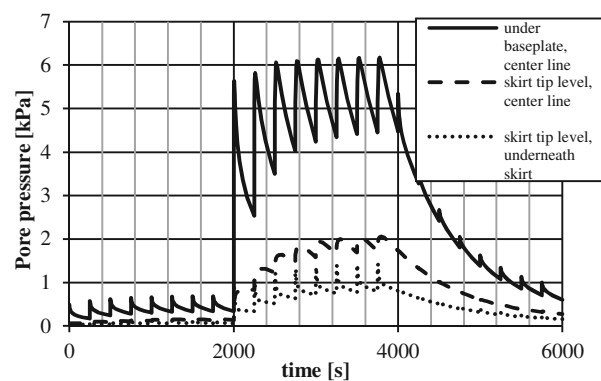


Figure 6: Example of excess pore pressure history, tripod caisson

The analysis predicts liquefaction of the soil near the skirt tips and build-up of pore pressure inside the caisson during the second load parcel. Stress redistribution towards the baseplate will cause an additional increase in pore pressure inside the caisson. The abrupt increase at  $t = 2000$ s is due to the nonlinear dependency of generated pore pressure on the CSR, which increases at the start of the second load parcel. Much of the pore pressure is dissipated by the end of the last load parcel, even though cyclic loading continues (at 60% of the second parcel). As the pore pressure dissipates, settlements due to the cyclic loading are expected.

The discretization of cyclic loading in load parcels and subsequently in subdivisions affects the accuracy of the analysis, but the results seem to converge as the number of subdivisions is increased. Where short drainage paths or high CSR values are involved, sufficiently short steps are required. The rate of pore pressure dissipation is affected by the length of the skirts. Longer skirts result in slower dissipation and higher potential for pore pressure accumulation inside the caisson.

## 5.2 Monopod

### 5.2.1 Model

The monopod caisson (20x10m) is subjected to three degree of freedom loading, including a horizontal and moment load. A 3D FE model of half the caisson is sufficient, taking advantage of the plane of symmetry formed by the vertical and the direction of aligned wind and wave loading. A six hour design storm, consisting of 2160 waves in five load parcels, was adopted.

### 5.2.2 Results

The five load parcels are distinguishable in the pore pressure response plotted in Figure 7 and peak pore pressure occurs right after the peak of the storm. The permanent horizontal load due to wind and/or current causes an asymmetric cyclic shearing in the example, so the observed peak pore pressure (4 kPa) does not occur on the center line. The consequences, such as potential differential settlements and tilting of the turbine, should be examined in a more advanced analysis.

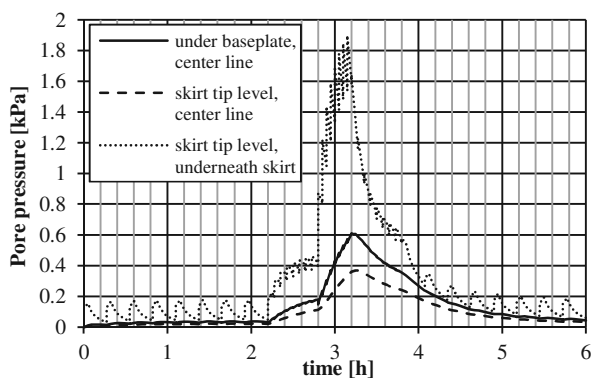


Figure 7: Example of excess pore pressure history, monopod caisson

## 6 CONCLUSIONS AND FURTHER DEVELOPMENTS

A pore-pressure generation and dissipation model has been developed to study the effect of cyclic loading on suction caissons in sand. Example analyses have shown that the proposed model can be successfully applied to the study of suction caissons, both in 2D and in 3D. However, the model needs further improvement to allow prediction of the complete liquefaction behaviour, including settlements, of a caisson.

The model can be used to predict which areas are prone to pore pressure build-up, estimate the rate of pore pressure build-up and to some extent how fast this pore pressure is dissipated.

Analysis of the type presented here may be useful to assess the geotechnical and structural risks related to cyclic loading of caissons in sand such as:

- reduction in caisson bearing capacity due to generated pore pressures;
- caisson foundation stiffness reductions;
- pore pressure induced total and differential settlements for offshore wind turbine structures;
- analysis of the effect of scour on pore pressure gradients.

The model can be improved to reflect more realistic soil behaviour. As some zones underneath the suction caisson liquefy, the load is transferred to other parts of the foundation. This leads to secondary pore pressure increases which are not yet considered in the presented model.

If sufficient soil data are available, the cyclic shear strength curves could include dependency on the relative density and initial shear stresses in the soil.

Finally, a large part of the vertical load on suction caissons is taken by friction between the caisson skirts and the soil. A systematic study of the influence on the liquefaction potential would be interesting.

## 7 ACKNOWLEDGEMENTS

The work described in this paper was performed as a part of the author's master thesis (Versteede 2012), supervised by professor Charlier (Université de Liège), whose guidance is gratefully acknowledged. Development of the model and calculations were performed at, and with support of Cathie Associates SA/NV.

## 8 REFERENCES

- Andersen K.H. and Berre T. 1999. Behaviour of a dense sand under monotonic and cyclic loading. *Proceedings of the 12<sup>th</sup> ECSMGE*, Vol 2, Geotechnical Engineering for Transportation Infrastructure, 667-676
- Byrne B.W. and Houlsby G.T. 2003. Foundations for offshore wind turbines. *Phil. Trans. R. Soc. Lond.*, Vol 361, 2909-2930
- DNV 1992. Classification notes No 30.4 – foundations. *Det Norske Veritas*, Norway
- DNV 2011. Design of offshore wind turbine structures, Offshore Standard DNV-OS-J101, *Det Norske Veritas*, Norway
- EWEA 2011. Wind in our sails – The coming of Europe's offshore wind energy industry. <http://www.ewea.org>
- Houlsby G.T., Ibsen L.B. and Byrne B.W. 2005. Suction caissons for wind turbines. *Proc. International Symposium on Frontiers in Offshore Geotechnics (ISFOG)*, Taylor & Francis Group, Perth, Australia
- Lee K.L. and Focht J.A. 1975. Liquefaction potential at Ekofisk tank in North Sea. *Journal of Geotechnical Engineering Division, ASCE*, 101(GT1), 1-18
- Rahman M.S., Seed H.B. and Booker J.R. 1977. Pore pressure development under offshore gravity structures. *Journal of Geotechnical Engineering Division, ASCE*, 103(GT12), 1419-1436
- Seed H.B. and Idriss I.M. 1980. On the importance of dissipation effects in evaluating pore pressure changes due to cyclic loading. *International Symposium on Soils under Cyclic and Transient Loading, Swansea*, 569-570
- Senders M. 2008. Suction caissons in sand as tripod foundations for offshore wind turbines. *Ph.D.*, The University of Western Australia, Australia
- Taiebat H.A. 1999. Three dimensional liquefaction analysis of offshore foundations. *Ph.D. Thesis*, The University of Sydney, Australia
- Verruijt A. and Song E.X. 1991. Finite element analysis of pore pressure build-up due to cyclic loading. *Deformation of soils and displacement of structures, Proc. 10<sup>th</sup> European Conference on Soil Mechanics and Foundation Engineering*, 277-280
- Versteede H. 2012. Cyclic loading of suction caisson foundations for offshore wind turbines. *M.Sc. Thesis*, Université de Liège, Belgium

# General Report of TC 211 Ground Improvement

Rapport général du TC 211  
Amélioration des sols

Huybrechts N.

*Belgian Building Research Institute, BBRI & KU Leuven, Belgium*

Denies N.

*Belgian Building Research Institute, BBRI, Belgium*

**ABSTRACT:** The present General Report highlights the significant contributions of the papers of the Session of the XVIII ICSMGE dedicated to Ground Improvement. All papers that have been reviewed are referred (in bold) in the General Report in order to provide a balanced overview of the entire Technical Session.

This General Report discusses the latest developments and current researches in the field of Ground Improvement (GI) works. The various GI techniques are classified considering the recent classification proposed by Chu et al. (2009). The papers are then tackled according to the described GI technique and with regard to the topics that are assessed: execution process, mechanical characterization of the treated material (in laboratory or in situ), case history, Quality Assurance/Quality Control (QA/QC) activities and design aspects. Conceptual works and numerical modeling are supported by laboratory and field investigations - with in situ monitoring and large scale tests. Finally, other references on the topics discussed are also given in the report.

**RESUME :** Le présent rapport général met en évidence les contributions significatives des articles de la session « amélioration des sols » de la 18<sup>ème</sup> CIMSG. Tous les articles revus ont été référencés (en gras) dans le rapport général de manière à fournir une vue d'ensemble équilibrée du contenu de cette session.

Ce rapport discute des derniers développements et des recherches actuelles dans le domaine des travaux d'amélioration des sols. Les différentes techniques sont classées selon la récente classification proposée par Chu et al. (2009). Les articles sont ensuite abordés en tenant compte de la technique d'exécution décrite et du sujet choisi par les auteurs : procédé d'exécution, caractérisation mécanique du matériau traité (en laboratoire ou in situ), cas pratique, activités de contrôle et d'assurance du point de vue de la qualité et aspects liés au dimensionnement. Les approches de conception et la modélisation numérique sont supportées par des recherches en laboratoire et par l'expérience de chantier – apportée par le monitoring in situ et par les essais en grandeur réelle. Finalement, d'autres références concernant le domaine de l'amélioration des sols sont aussi indiquées.

**KEYWORDS:** ground improvement/reinforcement, deep mixing, drainage, geosynthetics, grouting, inclusions, vacuum consolidation

## 1 INTRODUCTION

Ground improvement (GI) is one of the major topics in geotechnical engineering. With regard to the world population growth and in response to the expansion needs of our society, it has become a fast growing discipline in civil engineering as an alternative allowing construction on soft/weak/compressible soils. Various specialized ground improvement conferences have been frequently held in the past and recent years such as the International Symposium on Ground Improvement organized by the Technical Committee 211 of the ISSMGE and recently held in Brussels (Denies and Huybrechts, 2012) especially with more than 140 papers and 7 General Reports focusing on GI works. A number of books covering various topics on ground improvement have been also published in the past. Most of them are referred in Chu et al. (2009). During the last decades the importance of the ground improvement market has enormously increased. New methods, tools and procedures have been developed and applied in practice. In order to support this evolution in a scientific way, research programs have been and are being carried out worldwide, leading to more and better insights and delivering the basis for the establishment of design methods, quality control procedures and standards. As a result, many technical papers on GI works were published in journals and conference proceedings. It is not possible to mention all. Separate lists are given on the TC211 website ([www.bbri.be/go/tc211](http://www.bbri.be/go/tc211)). Major GI techniques have been

documented by the Working Groups of TC211 and are currently available on this website.

TC211 adopts a classification system as shown in Table 1 in Chu et al. (2009) with the following categories (and methods):

- A. GI without admixtures in non-cohesive soils or fill materials (dynamic compaction, vibrocompaction,...)
- B. GI without admixtures in cohesive soils (Replacement, preloading, vertical drains, vacuum consolidation,...)
- C. GI with admixtures or inclusions (Vibro replacement, stone columns, sand compaction piles, rigid inclusions,...)
- D. GI with grouting type admixtures (Particulate and chemical grouting, Deep mixing, jet grouting,...)
- E. Earth reinforcement (geosynthetics or MSE, ground anchors, soil nails,...)

This classification is based on the broad trend of behaviors of the ground to be improved and whether admixture is used or not. In the following sections, the papers of the Session of the XVIII ICSMGE dedicated to GI works will be reviewed according to this classification and with regard to the topics that are assessed: execution process, mechanical characterization of the treated material, case history, QA/QC activities and design aspects. It can already be noted that there is no paper considering GI without admixtures in non-cohesive soils (category A) in the present Technical Session.



## 2 GI WITHOUT ADMIXTURES IN COHESIVE SOILS

In the present Technical Session, six papers can be put in the category B: GI without admixtures in cohesive soils. They are mainly related to the subject of consolidation acceleration by vertical drains combined with surcharge or Vacuum. The interest seems to be oriented to the approach of “smear”. **Parsa-Pajouh et al. (2013)** address this delicate topic so difficult to model due to the lack of field parameters. According to the authors, the smear zone varies between 1.6 and 7 times the drain radius or 1 to 6 times the mandrel equivalent diameter. Numerical models are used within the framework of case studies. Parameters studies confirm their validity. As a result of their researches, it is recommended to assess the smear zone on the basis of trial construction with the help of back calculation process.

**Chai and Carter (2013)** present a theoretical approach of Prefabricated Vertical Drains (PVD) and consolidation combining vacuum pressure and surcharge loading. Using Hansbo's (1981) solution, consolidation parameters of the smear zone and the undisturbed zone were derived using a simple equation. Adopting an average well resistance and with some approximation, the dimensionless parameter  $\mu$  quantifying the effects of PVD spacing, smear zone and well resistance can be expressed. The study was performed in uniaxial consolidation condition, which is not in agreement with the real isotropic character of deformation under Vacuum. Moreover, the classical assumption of uniform smear zone cannot be measured. However the pore pressure measurements of the tested samples are in extreme close concordance with the prediction confirming the validity of the approach and the selected parameters.

**Indraratna et al. (2013)** treat similar subject in conjunction with a real construction site in the Port of Brisbane where the consolidation of thick Holocene clays was performed with PVD's under surcharge and/or Vacuum loading. Variable drain spacing was selected and analytical solutions were proposed. For the excess pore pressure dissipation, the same equation as in Chai and Carter (2013) was adopted. The results demonstrate that Vacuum combined with preloading would speed up consolidation compared to preloading alone. Moreover, Vacuum results in isotropic consolidation increasing the stability of the surcharge fill (decreasing lateral displacements).

In a similar way, **Lee et al. (2013)** have also studied the effect of the smear zone for a consolidation case history in Busan (South Korea). Modification of Hansbo's analysis is proposed to study the degree of consolidation considering the properties of the soil within the smear zone.

As another case history, **Islam and Yasin (2013)** present an application of PVD's coupled with preloading used for the construction of a large container yard in Bangladesh. The soil profile consists of 4 to 6 m thick silty clay, 8 to 10 m of sand and silt and 16 m of clayey silt. On the basis of design requirements, GI of the upper soft clay layer was considered essential. Five alternatives were assessed and compared. A solution combining PVD and preloading was adopted for this site. The settlement under preloading was monitored during the consolidation phase. Pre and post consolidation SPT tests are presented to illustrate the efficiency of the technique. It is believed that dynamic compaction although economical would not have been technically feasible due to the clayey nature of the upper fill. However, dynamic replacement in the upper 4 m with densification of the lower silty sand might have been technically and financially optimal.

For their part, **Jebali et al. (2013)** have assessed the theory of Carillo using three different oedometer tests carried on Tunis soft soil. Oedometer tests were conducted, conventionally (NF P94-90-1) for the first test, with a vertical drain allowing only radial drainage for the second one and finally with a drain

allowing vertical and radial drainage for the last one. Defining  $C_r$  and  $C_v$  as the radial and vertical coefficients of consolidation and  $K_r$  and  $K_v$  as the coefficients of radial and vertical permeability, they observed that the often-made assumption of the equality between the ratio's  $C_r/C_v$  and  $K_r/K_v$  is only valid at high levels of stress conditions. Moreover, on the basis of experimental results, the authors demonstrated that the global degree of consolidation computed with respect of the Carillo's theory can lead to underestimated consolidation times.

The paper of **Weihrauch et al. (2013)** describes a combination of GI methods for the improvement of roads in the Hafencity area in Hamburg. Indeed, in the Hamburg Harbour area, many roads are lifted with almost 3 m to ensure safety in case of flooding. Special measures are necessary when the subsoil contains compressible layers. At the Hongkongstrasse, three different construction methods have been applied, namely:

- installation of PVD and preloading with sand (settlements of more than 30 cm have been measured);
- filling with lightweight aggregate: expanded clay (almost no settlement was observed);
- pile supported embankment including geogrid-reinforced sand layer (measurements are discussed in another paper).

The different aspects of each method are described. The conclusion is that when comparing different methods, not only the absolute costs must be ascertained, but also the project specific reconstruction, protection and follow-on measures, as well as the time and flexibility for individual measures, and their technical feasibility under local conditions.

## 3 GI WITH ADMIXTURES OR INCLUSIONS

### 3.1 Rigid inclusions

Moving towards category C, GI with admixtures or inclusions, the paper presented by **Kirstein and Wittorf (2013)** is an interesting transition between categories B and C. Indeed, the authors describe the improvement of soft fat clay using rigid inclusions combined with vertical drains, preloading and the use of geotextile. The aim of the project was the construction of a bridge for a new road in Germany including 1.5 to 7 m high embankments. Vertical drains were first used to accelerate the consolidation under the embankments (preloading condition). Even using 600 kN/m woven geotextiles, vertical settlement of around 1.5 m and horizontal displacement up to 27 cm were measured throughout one year of monitoring. Because the bridge could not tolerate residual settlements, Controlled Modulus Columns (CMC) were designed and executed. The design of the transition interface between the bridge and the embankment, referred as the Load Transfer Platform (LTP), was confirmed by the monitoring.

**Ciri3n et al. (2013)** set the constructive procedures and bases of design of rigid inclusions including the LTP. The ASIRI guidelines (IREX, 2012) were not yet published at the time of preparation of this paper. The paper highlights the difference with pile foundation. In rigid inclusion solutions, there is no mechanical link between the pile and the structure. A LTP is usually placed between the inclusions and the structure. This distribution layer spreads the acting loads from the structure towards the underlying soil-inclusions setup. As indicated by the authors, isolated or continuous footings can possibly be used to directly transmit the loads to the soil-inclusions setup. This GI technique can also be applied for embankments and landfills.

The following paper constitutes a good transition with the next topic concerning stone columns. According to **Carvajal et al. (2013)**, dealing with the design of Column Supported Embankments (CSE), a clear distinction has to be made between rigid inclusions (e.g. concrete type columns) characterized by a brittle behavior in its Ultimate Limit State

(ULS) and stone columns (made of gravel and sand) which demonstrate a ductile behavior in its Serviceability Limit State (SLS) due to its compressibility and drainage characteristics (influence of the consolidation process on the design). Due to the brittle behavior of concrete type columns, larger safety factors have to be introduced, certainly for very slender elements. The General Reporters fully agree that similar approaches cannot be applied for very slender concrete type columns and for stone columns. However it has to be remarked that it is not common to consider stone columns as drainage elements.

### 3.2 Stone columns

In the present Technical Session, **Vlavianos et al. (2013)** propose technical solutions for the design of a road project in the Region of Western Greece. The geology of the site consists of soft silty clays and silty sands with high liquefaction susceptibility. The high ground water table and the seismicity of the area result in a design solution including GI. The installation of stone columns followed by preloading was selected. For the design of the bridge embankments and the pile foundations for bridge piers, a comparative parametric study was performed with or without stone columns. As discussed by the authors, the main aim of the preloading was the increase of the undrained shear strength of the superficial fine-grained soil layer. With the installation of the stone columns, the following requirements were met:

- increase of the general stability of the embankments;
- increase of the bearing capacity;
- reduction of the internal forces in the classical pile foundations;
- acceleration of the consolidation process;
- mitigation of the liquefaction susceptibility.

Although “stone columns” is nowadays a well-known GI method, installation effects arising during the execution still remains poorly understood. In order to investigate this question, **Klimis and Sarigiannis (2013)** describe the numerical analysis of the installation of stone columns with a diameter of 0.8 m and a depth of 23 m by means of the FLAC 3D Finite Difference code. The excavation stage has been modeled in one unique step and the realization of the stone column as follows:

- a) vibration and compaction, modeled by the application of an equivalent radial pressure against the internal wall of the cylindrical excavation;
- b) filling with a linear elastic geomaterial.

This numerical sequence was necessary to correctly determine the area in the surrounding soil influenced by the installation of the stone column and hence to assess with more accuracy the effective diameter of this latter.

**Poon and Chan (2013)** present another methodology to design stone columns. In this analysis, stone columns are replaced by equivalent strips, as illustrated in Fig. 1. The equivalent friction angle of the strips is dependent of the stress concentration ratio which is defined as the ratio of the average applied vertical stress within stone column to the average vertical stress of the surrounding soil at the same level. A method is proposed to compute this ratio by means of an axisymmetric Finite Element Model (FEM) containing one column and the surrounding soil. Numerical results obtained with this methodology (2D FEM with strips) have been compared with the results of a 3D FEM and with the results of a conventional 2D FEM analysis in which the entire soil is represented by a single block with equivalent properties. The authors conclude that the strip model is preferable to the block model for the assessment of the horizontal displacements. Further research is still necessary to investigate the question of the equivalent strength of the interface in the 2D strip method.

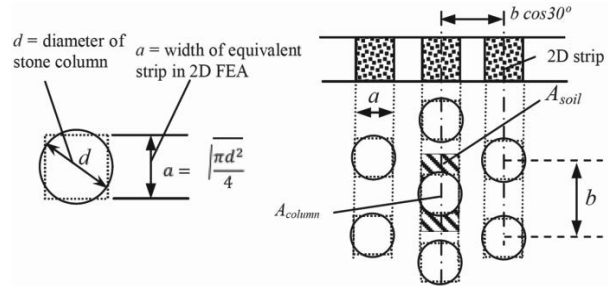


Figure 1. 2D stone column strips, from Poon and Chan (2013)

### 3.3 Geotextile confined columns

Rigid inclusions are a common GI technique for foundations of embankments in soft soils. Nevertheless, when the soft soil does not provide enough lateral support, the columns can be encased with a geotextile. The following papers mainly focus on the geotextile confined columns, also defined as geocased granular columns (GEC's).

**Castro et al. (2013)** describe and compare analytical and numerical analyses considering the behavior and the performances of geotextile confined columns (GEC's). Parametric studies of the settlement reduction and stress concentration show the efficiency of GEC's for GI purposes. This efficiency is mainly related to the contrast of stiffness between the encasement and the soil. As another conclusion, it is found that the settlement reduction is nearly the same for different replacement ratios but decreases with the applied load. Finally, columns with smaller diameter are better confined.

If GEC's are often used to reduce settlements induced by the construction of large embankments on soft soils, up to now no rational displacement based design approach has been introduced. For the purpose of investigating this question, **Galli and di Prisco (2013)** first review the most common design standards and then focus on the interaction between the embankment and the geocased columns. The main contribution of the paper resides in the consideration of the deformable base of the embankment. Indeed, real embankments are characterized by a deformable base, as illustrated in Fig. 2. As a consequence, different values of settlement are expected for the top of the column ( $u_c$ ) and for the soil ( $u_s$ ) at the base of the embankment. As explained by the authors, vertical stresses are redistributed at the base of the embankment between the internal zone of the cell (above the column characterized by an average stress  $\sigma_i$ ) and the external one (a circular crown above the soil, characterized by an average stress  $\sigma_e$ ) due to the arch effect. Shear stresses are then activated at the GEC-soil interface, and differential settlements are expected even at the top of the embankment.

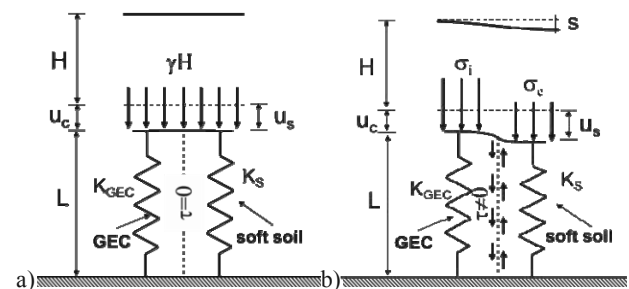


Figure 2. Mechanical response of the system in case of (a) rigid and (b) deformable embankment, from Galli and di Prisco (2013)

**Hataf and Nabipour (2013)** have designed a reduced-scale model in such a way to identify the parameters governing the behavior of the GEC's installed in clayey soils. As a result, they propose to encapsulate only the upper half of the column.

### 3.4 Geosynthetic reinforced column or pile supported embankment – the use of geogrids

Another way to use geosynthetic material for GI application is the design of geogrids for the support of embankment, land levees, yards and structure foundations (slabs and superficial isolated or continuous footings).

Investigating the use of geosynthetics for reinforcement under ground mass collapse, **Ponomaryov and Zolotozubov (2013)** compare the method outlined in British Standard BS 8006 and several design approaches with numerical calculations. On the basis of experimental elongation results, they introduce the ratio of actual tensile force to deformation. Computational assumptions are proposed for the description of the mechanisms of stress-strain development in the reinforced ground mass. The authors finally present a comparison between experimental measurements and the results of seven different methods used for the calculation of the tensile force in the geosynthetic, its deflection and the surface settlement.

**Mihova and Kolev (2013)** analyze the benefit of a geosynthetic reinforced pad of crushed stone used for the foundation of a hall in Sofia over soft saturated soil. Field tests were performed to estimate the E-moduli before and after improvement. The authors also conducted Finite Element analysis to model the consolidation process and to confirm the design stability under static and seismic conditions.

**Dimitrievski et al. (2013)** present a history case of soil reinforcement with geosynthetics for the construction of a six-storey structure in Ohrid (Republic of Macedonia). Multi layers geogrids were designed and the effects of the geostatic, hydrostatic and dynamic loading conditions were studied with the help of FEM calculations. The validity of the analysis was demonstrated with the help of in situ measurements obtained for a close similar structure.

### 3.5 Sand compaction piles (SCP's)

In the sand compaction pile (SCP) method, sand is fed into the ground through a casing pipe and is compacted by vibration, dynamic or static compaction to form columns. In practice, SCP's are mainly used to prevent liquefaction and reduce settlement with similar success in sandy and clayey soils. With the help of laboratory and field tests, **Burlacu et al. (2013)** investigate the potential of columns made of loess-sand-bentonite mixture for the reinforcement of collapsible loess deposits in Romania. Indeed, as explained in the paper of **Alupoae et al. (2013)**, these collapsible soils require GI works. They are characterized by high water sensitivity: when its water content increases, important deformations in the soil can be observed. In such a way to illustrate this phenomenon, the authors present a case study of differential settlement of buildings founded on loess sensitive to wetting. In spite of the good realization and control of the foundation, important differential settlements were measured thereafter as a result of the defective rainwater recovery system.

### 3.6 Microbial methods

The use of microbially induced carbonate precipitation (MICP) to cement cohesionless soils has recently received substantial attention from geotechnical researchers. The most common MICP mechanism is hydrolysis of urea. MICP via ureolytic hydrolysis relies on microbes to generate urease enzyme, which then serves as a catalyst for the calcium carbonate ( $\text{CaCO}_3$ ) precipitation reaction. If it is to date well known that the mechanical properties of the treated soils are directly correlated to the amount of ( $\text{CaCO}_3$ ) precipitation, a gray area still remains concerning the influence of the original nature of the granular material on the resulting properties of the treated soil. Within the framework of a laboratory campaign, **Tsukamoto et al.**

**(2013)** investigate the influence of the relative density of sand samples on the MICP. As a result of their study, the MICP tends to increase as the relative density of the soil decreases. Nevertheless, considering the results of triaxial tests, maximum principal stress differences were obtained for the samples with the highest relative density. In light of these results, this technique seems to be very promising for the future but due to the bioplugging (permeability reduction) of the granular material and to the generation of toxic product (ammonium salt); soil stabilization using ureolytic MICP remains currently unusual. According to **Hamdan et al. (2013)**, the use of plant derived urease to induce the carbonate cementation could be the solution to avoid these drawbacks.

## 4 GI WITH GROUTING TYPE ADMIXTURES

### 4.1 Deep Mixing Method (DMM) and soil stabilization

The deep mixing method (DMM) is nowadays a worldwide accepted GI technology. In this method, the ground is in situ mechanically (and possibly hydraulically or pneumatically) mixed while a binder, based on cement or lime, is injected with the help of a specially made machine. Numerous reviews and recent progresses of the DMM are referred in Denies and Van Lysebetten (2012). In the recent years, the DMM is undergoing rapid development, particularly with regard to its range of applicability, cost effectiveness and environmental advantages, as illustrated by the papers of this paragraph.

In the deep mixing projects, the design can be based on laboratory mixing tests. Soil-cement samples are then prepared and tested to study the mechanical properties of the stabilized soil. But, up to now, many laboratories prepared these samples without standardized procedure. Actually, molding techniques have a great influence on the mechanical characteristics of the stabilized material. According to **Grisolia et al. (2013)**, this influence is strictly correlated to the workability of the soil-cement mixture and this latter can be quantified with the measurement of the torque required to turn an impeller in the mixture. Five molding techniques have been studied and the authors propose the abacus illustrated in Fig. 3 to define the range of applicability of these techniques in function of this torque.

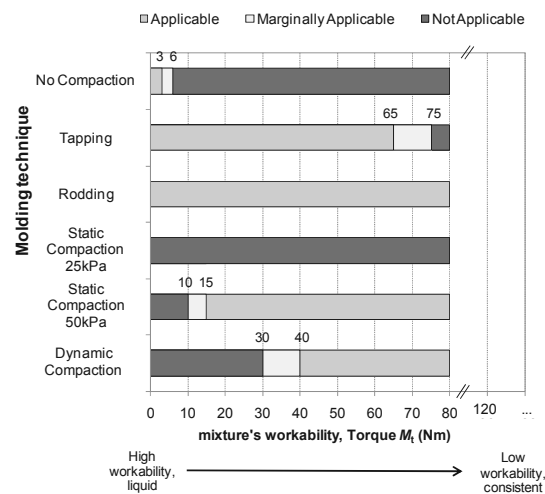


Figure 3. Ranges of applicability of the different molding techniques, from Grisolia et al. (2013)

The applicability of each molding technique was evaluated by an “Applicability index”, related to “densest specimens with the highest strength” and “results repetitiveness”.

Since several decades, DMM has been used for GI works. But in recent years, this technique has been increasingly used

for structural applications. Standardized guidelines for the design of this kind of applications are not currently available. If the previous work allows the construction of standardized and international test procedures for laboratory mix samples, the Quality Control (QC) of the execution process is generally based on the results of Unconfined Compressive Strength (UCS) tests performed on cored material. As part of the semi-probabilistic design approach presented in Eurocode 7, it is thus essential to define the UCS characteristic value that can be taken into account in the design. **Denies et al. (2013)** discuss the definition of this value. In the first category of approaches, the characteristic strength is defined as an X% lower limit value computed either on the basis of a statistical distribution function or based on the cumulative frequency curve of the original experimental dataset of UCS values obtained from tests on cored samples. A second approach to determine the UCS characteristic value is the use of the average value of the dataset in combination with a safety factor. For the first category of approaches, a value for the X% has to be defined. Actually, one major issue is the representativeness of the core samples with regard to the in situ executed material. For the purpose of investigating this question, the authors present the results of a study on the influence of soil inclusions and then they discuss the topic of the scale effect with regard to large scale UCS tests.

The following papers concern the investigation of the mechanical properties of the soil mix material under the field of laboratory or in situ experiments and with the help of numerical modeling.

In such a way to investigate the properties of the soil mix material, **Szymkiewicz et al. (2013)** have carried out a parametric study on lab soil-cement mixtures. The influences of the particle size, the clay content and the water content on the strength of the material were considered. They propose an abacus relating the UCS of the specimens to the cement content. Six zones are identified in the abacus depending on the nature of the soil. In addition, the authors also propose a formula valid for granular soils for the estimation of the UCS at 28 curing days. This formula takes into account the water, the cement and the fine contents.

In a similar way, **Correia et al. (2013)** have performed laboratory tests to study the improvement of soft clayey silt with high organic content by mixing it with a binder made up of 75% Portland cement (PC) and 25% blast furnace slag. They first give a formula for the assessment of the UCS at 28 days in function of the binder content and the liquidity index (LI) of the soil. A normalized UCS is then introduced as follows:  $UCS_{LI} = UCS \times LI$ . In a second step, the applicability of the normalized UCS approach is analyzed for seven other cement-stabilized soft soils with successful result.

If the water/cement (w/c) ratio is often used in attempt to understand soil-mix properties, it can be found limited since in practice execution is mostly performed in soils in the presence of water (unsaturated or saturated conditions). A well-adapted governing parameter could be then the porosity/cement index defined as the ratio of porosity to the volumetric cement content ( $n/C_{iv}$ ). **Rios et al. (2013)** highlight the influence of this index on the mechanical properties of cemented Porto silty sand. Unique trend was obtained between the UCS and an adjusted porosity/cement ratio ( $n/C_{iv}^{0.21}$ ), proposed by the authors. Similar observation was also made with indirect tensile strength. Triaxial tests resulted in two peak strength envelopes for each predetermined ( $n/C_{iv}^{0.21}$ ) and finally, oedometer tests establish this ratio as the governing parameter of the behavior of the soil-cement specimen in one-dimensional compression in lieu of the cement content or the initial void ratio.

A major advance in DMM could be found in the contribution of **Yi et al. (2013)** with the investigation of the carbonation of reactive magnesia (MgO) for soil stabilization. Nowadays, Portland cement (PC) is the most common binder used in the

deep mixing applications. However, there are significant environmental impacts associated with its production in terms of high energy consumption and CO<sub>2</sub> emissions. In their laboratory study, reactive MgO was used as a binder and the MgO-soil samples were carbonated by CO<sub>2</sub> to improve the mechanical properties of the soil and reduce the CO<sub>2</sub> emission. As an evident result, the UCS values of the uncarbonated MgO-stabilised soils were much lower than those of the PC-stabilised soils; both mixes took ~28 days to finish most of their strength development. Nevertheless, the carbonation process significantly increased the UCS of MgO-stabilised soils in a very short time, this latter fast reaching the UCS value of the 28-day PC-stabilised soils, indicating that it could be used to support a structure just after the completion of the carbonation procedure.

Another type of binder largely used for soil stabilization is lime. **Mesri and Moridzadeh (2013)** discuss the results of a laboratory study focusing on the improvement of the Brenna clay (high plastic lacustrine clay of North Dakota) by adding lime. Lime contents varying between 3 and 10 % of the dry weight of the clay have been considered. The authors observed a decrease of the measured pH with time and an increase of the Liquid Limit and the Plasticity Index with time when 5 % of lime was added. Adding 3 to 8 % of lime, the residual friction angle (in drained conditions) increases between 3 to 6 %. Unfortunately the laboratory test results were not compared with full scale test results.

Extensive laboratory tests have been performed by **Szendefy (2013)** for the purpose of determining the effect of lime stabilization on 21 Hungarian clayey soils. In addition, some in situ stabilized soils have also been analyzed. According to his study, the improvement of the clayey soil with the lime is mainly related to the coagulation of the clay particles related to the cation exchange. Indeed, during the stabilization with lime, Ca<sup>2+</sup> ions attach to the surface of clay particles. As a result of this high charging, the clay particles coagulate resulting in a material characterized by an increased internal friction angle. The pozzolanic reaction would play then a secondary role in the stabilization.

Soil stabilization can also be performed with fiber reinforcement, such as discussed in **Madhusudhan and Baudet (2013)**. In their study, laboratory tests have been performed to determine the influence of adding polypropylene fibers on the shear strength characteristics of completely decomposed granite (CDG). In Hong Kong, CDG is regularly used for landscaping and as green cover of existing shotcrete slopes. The test results clearly indicate an important increase of the UCS when adding 0.5% of fibers and compacting the CDG at the water content close to the optimum Proctor value. In triaxial drained tests, the addition of fibers seems to increase the shear strength of the CDG and its stiffness. Dilation is also reduced.

In Singapore, laboratory tests have been performed by **Xiao et al. (2013)** in order to determine the characteristics of the Singapore upper marine clay when mixed with 20 to 50% Portland cement (PC) and up to 0.32% fibers of different types. As a result of their study, strength and ductility of cement-treated clay were improved by fiber reinforcement. There is an optimum fiber content with regard to performance and workability of the material. Polyvinyl alcohol (PVA) fibers are generally more efficient than polypropylene (PP) fibers except for low cement and water contents. The length of the fibers has a significant effect on the ductility of the cement-treated clay for both fiber types. Concerning the strength, the influence of the fiber length is more significant for PVA reinforcement than for PP reinforcement.

**Cuira et al. (2013)** present the results of numerical models simulating an axial Static Load Test (SLT) on a soil-cement column. Numerical and experimental results are compared with the help of three Finite Element models and one simplified

semi-analytical model. Numerical results are in agreement with the experimental observations all along the SLT but especially regarding to the fracture pattern: structural failure localized in the upper part of the column. This numerical study highlights the nonlinear behavior of the soil-mix material. In comparison with classical “rigid” piles, the contrast of strength (and stiffness) between the column and the soil is lower and has a huge influence on the global behavior.

Originally, DMM was developed for GI applications in soft clays and organic soils. But more recently, it was also dedicated to various structural and environmental applications such as illustrated by the following case histories.

Recently, the DMM has been chosen for several Hungarian railway projects involving soft soils, such as the restoration of the “Sárrét” railway line crossing an area where the subsoil consists of soft chalky silt. For the foundation of a 4m high embankment, two DMM were taken into account: the mass stabilization and the soil-cement columns. **Koch and Szepesházi (2013)** firstly describe results of laboratory tests on chalky silt samples mixed with cement for different w/c contents. Both DMM are then assessed using 3D-FEM considering the site requirements in term of stability and settlement.

In a similar way, DMM have been widely used in Japan for the improvement of soft clays and organic soils. **Matsui et al. (2013)** introduce the concepts of an hybrid application of soil-cement columns combined with soil mix walls (SMW) designed for the foundation of an embankment. The concept is illustrated in Fig. 4. The authors propose a conceptual method allowing the control of ground deformation and ensuring an optimization of the volume of treated soil. The method is supported by 2D-FEM and in situ monitoring is performed for the validation of the concept.

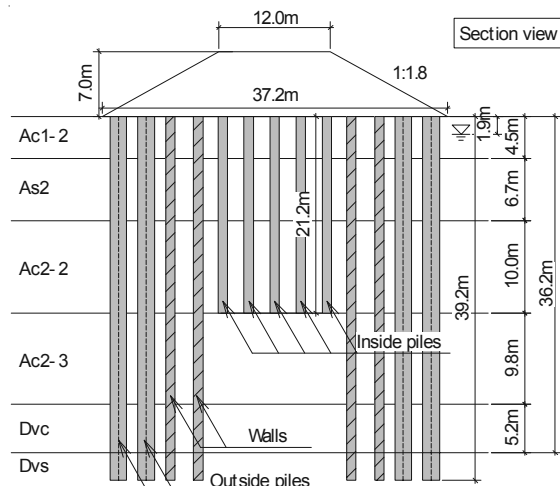


Figure 4. GI with soil-cement columns and SMW, from Matsui et al. (2013)

In Lund (southern Sweden) a new generation synchrotron radiation facility, called MAX IV, is under construction. According to **Lindh and Rydén (2013)**, it should be 100 times more efficient than any existing comparable synchrotron radiation facility in the world. For this kind of facility, the vibration requirements are very stringent. Various alternatives were discussed and simulated during the conception. The optimum solution was achieved with a four meter thick layer of stabilized soil below the concrete foundation. A combination of quicklime and ground granulated blast furnace slag (GGBFS) was found to be in agreement with both design and construction requirements.

**Jeanty et al. (2013)** describe the use of the CSM and the Trenchmix methods for the realization of SMW. Both techniques are explained in details and different applications are

presented, namely: settlement reduction, improvement of slope stability, reduction of active pressure on retaining walls and decrease of liquefaction susceptibility. The two last topics are then illustrated with case histories.

Other case history tackles the topic of liquefaction susceptibility restrained with the DMM. **Yamashita et al. (2013)** deal with the measurements performed underneath a piled raft completed with SMW to reduce the risks of liquefaction. It concerns a 12-storey office building. The load distribution between piles, SMW and the surrounding soil has been monitored during a period of three years. After the end of the construction, settlements of 20 mm have been recorded, as illustrated in Fig. 5. As another result, 70 % of the load was taken by the piles, 14 % by the SMW and 15% by the soil, as shown in Fig. 6. The measurements also learned that the Tohoku earthquake of March 2011 had almost no influence on the settlements and on the load distribution.

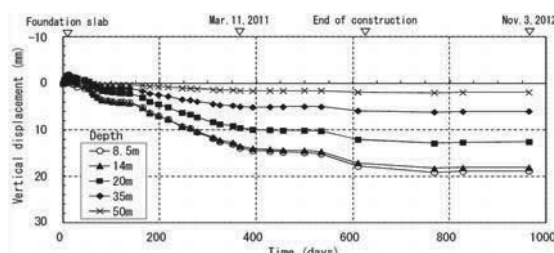


Figure 5. Measured vertical ground displacements below raft, from Yamashita et al. (2013)

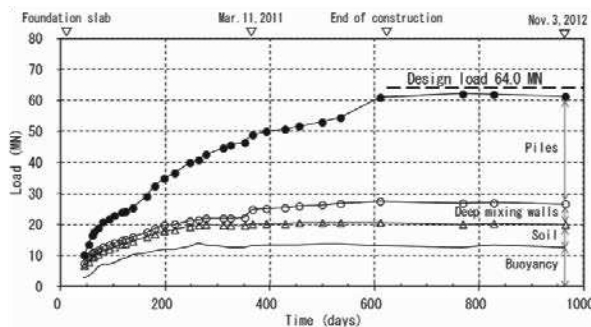


Figure 6. Time-dependent load sharing between raft and piles, from Yamashita et al. (2013)

If the foundation of embankments and buildings are become both common applications of the DMM, underpinning with soil mix material constitutes an interesting emerging technique, such as illustrated in the following paper.

Traditional DMM are commonly restricted for underpinning, limitations being mainly related to the capacity of the machine to pass existing foundation structures as reinforced slabs or footings, the reduced working spaces and the possible low headroom conditions. **Melentijevic et al. (2013)** present a case history of underpinning of an existing floor slab in an industrial building using DMM. The soil-cement columns were installed with the new Springsol® tool. After the realization of a contact grouting between the slab and the soil, the slab and the contact grouting layer are cored. The spreadable Springsol® tool is then introduced into the gap. Finally, its blades are opened and the soil-cement column is executed until the predetermined depth. The conception is supported by numerical modeling and QA/QC aspects of the project are related to the testing of core and wet grab samples.

#### 4.2 Use of stabilized dredged material for construction

As previously discussed in Chu et al. (2009), dredging and land reclamation have increasingly become important parts of construction activities that involve heavily geotechnical knowledge. If dredging provides low cost construction material,

it is sometimes necessary to resort to additional GI methods in order to obtain a product meeting the design requirements. The following paper illustrates how GI and dredging are complementary construction processes.

**Loh et al. (2013)** present considerations in the design and construction of a containment bund made of modified geotextile tubes (M-GT) filled with cement-mixed soil. In the port of Singapore, dredged soil mixed with cement was used as in-fill material in the M-GT's and as the core of a large geotextile containment bund, as illustrated in Fig. 7. Field instrumentation and monitoring were carried out with the help of strain measurements, hydrographic survey, inclinometers and extensometers during and after the construction to verify the design and the performance of the system.

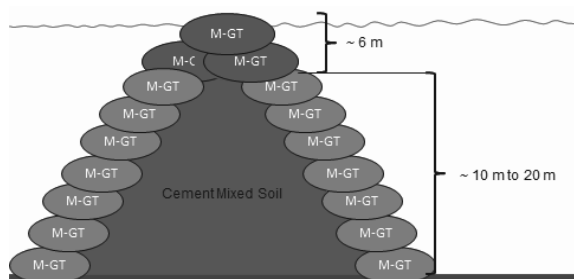


Figure 7. Geotextile containment bund, from Loh et al. (2013)

#### 4.3 Recent advances in the jet grouting applications

If special devices have been developed in the past to measure the diameter of the jet grout columns executed in situ, considerable effort should be made in the understanding of the physical processes governing this parameter. **Bzówka et al. (2013)** analyze excavated jet grout columns. The experimental results are used to model the bearing capacity of the columns by means of the Z-soil software. Indeed, although the jet grout columns have been realized in compacted medium sand underlain by stiff clay, almost all columns had an irregular shape influencing its bearing capacity.

In the grouting applications, the bleed capacity is another indicator of grout effectiveness, since it is representative of the volume of voids filled by cement. The grout's water-to-cement ratio (W/C) and the maximum cement grain size ( $d_{max}$ ) are two important parameters controlling the cement grout bleed capacity. **Pantazopoulos et al. (2013)** provide some insights on the effect of grout bleed capacity on the mechanical properties of ordinary and microfine cement grouted sands, in conjunction with the effect of the W/C ratio. They demonstrate that the distinction between stable and unstable grouts (see EN 12715) may not be an indicator of grout effectiveness since similar effects may be produced by both stable and unstable grouts: e.g. same coefficients of permeability were obtained for a bleed capacity ranging from 5 (stable) to 30 % (unstable suspension). Bleed capacity correlates very well with some grouted sand properties (i.e. unconfined compression strength and cohesion) and not at all with other properties (i.e. internal friction angle and damping ratio).

## 5 EARTH REINFORCEMENT

### 5.1 Geosynthetics

Centrifuge tests have been performed by **Bo et al. (2013)** in order to study the reinforcement of low plastic brown weathered shale with polypropylene fibers for the construction of an embankment. Vertical and horizontal displacements deduced from the centrifuge tests have been compared with those obtained from FEM analyses. Both approaches demonstrate the contribution of the fibers on the stability.

In a similar way, **Tabarsa and Hajiesmaeilian (2013)** have studied the influence of sand encapsulated non-woven geotextile (sandwich technique) on the stability of clay embankment. Using FLAC 2D Finite Difference model, the authors highlight the efficiency of the method with regard to the geotextile-reinforced and the unreinforced embankments.

### 5.2 Vegetation methods

A significant element in the reclamation of landfills is the reinforcement and biological stabilization of the slopes which can be very sensitive to surface erosion. According to **Koda and Osinski (2013)**, landfill stability improvement activities can be divided in two phases: the first one consists in the technical reclamation of the landfill and the second one is the biological restoration of the vegetation cover. For both phases, the authors argue it is possible to use recyclable materials such as fly ash or sewerage sludge. They discuss the improvement of slope stability of a solid waste disposal with the help of this approach. On the one side, fly ashes can be considered as impermeable and present good compaction properties. Mixed with cohesive soil, it could be therefore used for the capping of the waste disposal. On the other side, the sewerage sludge protects the seeds from erosion and excessive drying. Moreover the sewerage sludge presents a high nutrition content supporting the development of the vegetation cover. Unfortunately, no information is given in the paper concerning the installation procedures of the fly ashes and sewerage sludge and how the influence of vegetation can be introduced in the stability calculations.

## 6 CONCLUSIONS

In the present General Report, 47 papers of the Technical Session on GI of the XVIII ICSMGE are reviewed. It can be noted that 40% of these papers deal with Deep Mixing and soil stabilization, proving the huge interest in these techniques. Similar percentage was already observed in the Proceedings of the TC211 IS-GI 2012 (Denies and Huybrechts, 2012) but this is not surprising, as these methods constitute outstanding and cost-effective sustainable construction processes.

Finally, beyond the choice of the GI solution, the necessity of monitoring was also highlighted by several authors of this Technical Session. For example, **van der Stoel et al. (2013)** discuss a well-documented case history concerning the realization of two deep excavations in the courtyards of a historical building in Amsterdam. Based on 2D FEM calculations, an extensive monitoring program has been proposed and performed (including levelling point measurements, inclinometers and the use of a permanent webcam). Thanks to this monitoring process the consequences of two important accidents during the execution of the excavations could be limited as much as possible. Most important was that the time delay remained very small. The authors conclude that the costs of the meticulous and proactive monitoring were minor in comparison with the potential costs of a delayed opening of the hotel.

If ground improvement is really become an efficient and controllable cost-effective alternative to classical foundation technique, measure still remains treasure.

## 7 ACKNOWLEDGEMENTS

The authors wish to thank the chairmen of the TC211 Jan Maertens and Serge Varaksin for their contribution to the review of the papers of the Technical Session on GI works.

## 8 REFERENCES

- Alupoae, D. Aşucei, V. and Răileanu, P. 2013. Time - dependent behaviour of foundations lying on an improved ground.
- Bo, L., Linli, J., Ningyu, Z. and Sinong, L. 2013. Centrifugal and numerical analysis of geosynthetic-reinforced soil embankments.
- Burlacu, C., Olinic, E., Manea, S. and Uță, P. 2013. Compacted soil columns for foundations on collapsible soils. Laboratory and in-situ experimental study.
- Bzówka, J., Juzwa, A. and Wanik, L. 2013. Selected problems connected with the use of the jet grouting technique.
- Carvajal, E., Vukotić, G., Sagasetta, C. and Wehr, W. 2013. Column Supported Embankments for Transportation Infrastructures: Influence of Column Stiffness, Consolidation Effects and Cyclic Loading.
- Castro, J., Sagasetta, C., Cañizal, J., Da Costa, A. and Miranda, M. 2013. Foundations of embankments with encased stone columns.
- Chai, J.-C. and Carter, J. P. 2013. Consolidation theory for combined vacuum pressure and surcharge loading.
- Chu, J., Varaskin, S., Klotz, U. and Mengé, P. 2009. Construction Processes, *Proceedings of the 17<sup>th</sup> International Conference on Soil Mechanics and Geotechnical Engineering, 5-9 October 2009, Alexandria, Egypt, M. Hamza et al. (Eds.), IOS Press, Amsterdam*, Vol. 4, pp. 3006-3135.
- Cirión, A., Paulín, J., Racinais, J. and Glandy, M. 2013. Displacement rigid inclusions. *Proceedings of the 18<sup>th</sup> ICSMGE*, Paris, France.
- Correia, A.A.S., Venda Oliveira, P.J. and Lemos, L.J.L. 2013. Prediction of the unconfined compressive strength in soft soil chemically stabilized.
- Cuira, F., Costa d'Aguiar, S., Grzyb, A., Pellet, F., Mosser, J.F., Guimond-Barrett, A. and Le Kouby A. 2013. Numerical modeling of a soil-mixing column behavior and comparison with a full-size load test.
- Denies, N. and Huybrechts, N., editors. 2012. *Proceedings of the International Symposium of ISSMGE - TC211. Recent research, advances & execution aspects of ground improvement works. 31 May-1 June 2012, Brussels, Belgium (www.bbri.be/go/tc211)*.
- Denies, N. and Van Lysebetten, G. 2012. General Report. Session 4 – Soil Mixing 2 – Deep Mixing. *Proceedings of the International Symposium of ISSMGE - TC211. Recent research, advances & execution aspects of ground improvement works. 31 May-1 June 2012, Brussels, Belgium (www.bbri.be/go/tc211)*.
- Denies, N., Van Lysebetten, G., Huybrechts, N., De Cock, F., Lameire, B., Maertens, J. and Vervoort, A. 2013. Design of Deep Soil Mix Structures: considerations on the UCS characteristic value.
- Dimitrievski, Lj., Ilievski, D., Dimitrievski, D., Bogoevski, B. and Strasheski, A. 2013. Method of improvement of the subsoil under Adora facility – Ohrid, Republic Of Macedonia.
- Galli, A. and di Prisco, C. 2013. Geocased columns: toward a displacement based design.
- Grisolia, M., Leder, E. and Marzano, I.P. 2013. Standardization of the molding procedures for stabilized soil specimens as used for QC/QA in Deep Mixing application.
- Hamdan, N., Kavazanjian, E. and O'Donnell, S. 2013. Carbonate Cementation via Plant Derived Urease.
- Hataf, N. and Nabipour, N. 2013. Experimental investigation on bearing capacity of geosynthetic encapsulated stone Columns.
- Indraratna, B., Rujikiatkamjorn, C. and Geng, X. 2013. Performance and Prediction of Vacuum Consolidation Behavior at Port of Brisbane.
- IREX. 2012. *Projet national ASIRI. Recommandations pour la conception, le dimensionnement, l'exécution et le contrôle de l'amélioration des sols de fondation par inclusions rigides. Presses des Ponts. France.*
- Islam, M. S. and Yasin, S. J. M. 2013. Improvement of a Clay Deposit using Prefabricated Vertical Drains and Pre-loading - A Case Study.
- Jeanty, J.M., Mathieu, F. and Benhamou, L. 2013. Importance and practical examples of inertial soil improvement.
- Jebali, H., Frikha, W. and Bouassida, M. 2013. Assessment of Carillo's theory for improved Tunis soft Soil by geodrains.
- Kirstein, J. F. and Wittorf, N. 2013. Improvement of soft fat clay using rigid inclusions and vertical drains.
- Klimis, N.S. and Sarigiannis, D.D. 2013. Interaction of stone column and surrounding soil during its construction: 3D numerical analysis.
- Koch, E. and Szepesházi, R. 2013. Laboratory tests and numerical modeling for embankment foundation on soft chalky silt using deep-mixing.
- Koda, E. and Osinski, P. 2013. Assessment of bio-mechanical reinforcement materials influencing slope stability, based on numerical analyses.
- Lee, C., Choi, Y., Lee, W. and Hong, S. J. 2013. Evaluation of Vertical Drain-enhanced Radial Consolidation with Modified Analytical Solution.
- Lindh, P. and Rydén, N. 2013. Adjusting the soil stiffness with stabilisation to minimize vibration at Maxlab IV – a synchrotron radiation facility in Sweden.
- Loh, C.K., Chew, S.H., Tan, C.Y., Lim, S.K. and Lam, J.P.W. 2013. Construction and Performance of Containment Bund Using Geotextile Tubes Filled With Cement Mixed Soil in Singapore.
- Madhusudhan, B.N. and Baudet, B.A. 2013. Reinforcement of completely decomposed granite with discrete fibres.
- Matsui, H., Ishii, H. and Horikoshi, K. 2013. Hybrid Application of Deep Mixing Columns Combined with Walls as a Soft Ground Improvement Method Under Embankments.
- Melentijevic, S., Arcos, J.L. and Oteo, C. 2013. Application of cement deep mixing method for underpinning.
- Mesri, G. and Moridzadeh, M. 2013. Lime Remediation of Reactivated Landslides.
- Mihova, L. and Kolev, Ch. 2013. Improvement of the Soil under the Concrete Pavement of a Plant's Hall.
- Pantazopoulos, I.A., Atmatzidis, D.K., Basas, V.G. and Papageorgopoulou, S.K. 2013. Effect of Grout Bleed Capacity on the Engineering Properties of Cement Grouted Sands.
- Parsa-Pajouh, A., Fatahi, B. and Khabbaz, H. 2013. Numerical Analysis to Quantify the Influence of Smear Zone Characteristics on Preloading Design in Soft Clay.
- Ponomaryov, A. and Zolotozubov, D. 2013. Technique of reinforced soil base calculation under fall initiation in ground mass.
- Poon, B. and Chan, K. 2013. Stress Concentration Ratio and Design Method for Stone Columns using 2D FEA with Equivalent Strips.
- Rios, S. and Viana da Fonseca, A. 2013. Porosity/cement index to evaluate geomechanical properties of an artificial cemented soil.
- Szendefy, J. 2013. Impact of the soil-stabilization with lime.
- Szymkiewicz, F., Le Kouby, A., Reiffsteck, P., Mosadegh, A. and Tacita, J.-L. 2013. Laboratory parametric study of the Deep Mixing material.
- Tabarsa, A.R. and Hajiesmaeilian, S. 2013. Investigation of failure analysis of clay reinforced with sand encapsulated.
- Tsukamoto, M., Inagaki, Y., Sasaki, T. and Oda, K. 2013. Influence of relative density on microbial carbonate precipitation and mechanical properties of sand.
- Van der Stoep, A.E.C., Vink, D. and Bouma, J. 2013. Conservatoriumhotel Amsterdam, geotechnical design and monitoring.
- Vlavianos, G.J., Marinelli, A.K., Andrianopoulos, K. and Foti, S. 2013. Bridge foundation on very soft alluvia with stone column ground improvement.
- Weihrauch, S., Oehrlein, S. and Vollmert, L. 2013. Subgrade improvement measures for the main rescue roads in the urban redevelopment area HafenCity in Hamburg.
- Xiao, H.W., Lee, F.H., Zhang, M.H., Yeoh, S.Y. 2013. Fiber Reinforced Cement Treated Clay.
- Yamashita, K., Wakai, S. and Hamada, J. 2013. Large-scale Piled Raft with Grid-Form Deep Mixing Walls on Soft Ground.
- Yi, Y.L., Liska, M., Unluer, C. and Al-Tabbaa, 2013. A. Initial investigation into the carbonation of MgO for soil stabilisation.

# Time-dependent behaviour of foundations lying on an improved ground

## Temps-comportement dépendant de fondations reposant sur un sol amélioré

Alupoae D., Aşucei V., Răileanu P.

"Gheorghe Asachi" Technical University of Iasi, Faculty of Civil Engineering and Building Services, Department of Roads and Foundations, 43 Dimitrie Mangeron Bd, 700050, Iasi, Romania

**ABSTRACT:** The paper presents some aspects concerning time-dependent behaviour of the improved foundation soils. The foundation soils can develop favourable or inappropriate resistance properties under the loads submitted by constructions. Engineers and investors encounter more and more difficult foundation soils, in their desire to efficiently use the construction sites. In this case, physical and mechanical properties of the soil have to be improved, in order to sustain the infrastructure and structure of a building. The paper reviews some improvement methods, after presenting difficult foundation soils from Iaşi area. The paper presents a case study regarding problems caused by difficult foundation soils that are present in the region, during the operating period of structures. The presence of water in the foundation soil created a negative impact in its behaviour, which led to differential settlements and, consequently, the buildings were switching from their initial vertical position. The study also analyzes time-dependent settlements of a construction. Finally the paper presents some conclusions resulting from studies both bibliographic and practical.

**RÉSUMÉ :** Le document présente quelques aspects concernant le comportement en temps des sols améliorés pour les fondations. Le terrain de fondation peut avoir un comportement favorable ou par contre défavorable sous l'action des charges donner par les constructions. Pour utiliser efficacement les terrains des constructions, les ingénieurs et les investisseurs rencontrent souvent des sols de fondation de plus en plus difficile. Dans ce cas, les propriétés physiques et mécaniques du sol doivent être améliorées, afin d'assurer des bonnes conditions d'appuis pour l'infrastructure et la structure d'un bâtiment. Le document passe en revue les sols de fondation difficiles de la zone de Iaşi et des méthodes de les améliorées. Il est aussi présenté une étude de cas concernant les problèmes qui peuvent apparaitre au cours de la période d'exploitation de structures, a cause des ces sols de fondation difficiles. La présence de l'eau dans le terrain de fondation a eu un impact négatif sur son comportement, ce qui a produit des tassements différentiels, ca veut dire que les bâtiments furent commutés de leur position initiale, verticale. Pour conclure, le document présente des conclusions issues de l'étude bibliographique et pratique à la fois.

**KEYWORDS:** leaning structure, expansive clay, loess, differential settlement.

### 1 INTRODUCTION

As a result of the analysis performed over time on a large variety of soils and taking into account soil behaviour in the presence of external factors, the foundation soils can be divided in two categories, considering their capacity to support loads from constructions: good and difficult foundation soils.

The entire existence of the building system depends on the stability and strength of the foundation soil and this is the main reason why a special interest is given to the second category of soils and therefore to the specific issues that must be considered in the design, execution and operating period of a construction.

### 2 DIFFICULT FOUNDATION SOILS

The sites that have a construction soil with good geotechnical characteristics are rapidly decreasing. Large urban areas are a particular problem because, due to the lack of space, it is necessary to reconsider the possibility of placing a building on a soil that was unsuitable for constructions until now.

#### 2.1 Difficult foundation soils - classification

These soils are classified as follows:

- macroporous soils (present large cavities in their structure and have the ability to suffer large settlements when are subjected to a wetting process);
- collapsible soils (are characterised by the fact that when in high humidity develop large deformations);

- liquefiable soils (especially non-cohesive soils consisting of saturated fine sand which under the action of a dynamic load suddenly loose their shear strength);
- expansive soils (cohesive soils such as clays, which change their volume when water content varies);
- soils that during the freezing and thawing phenomena change their structure and properties;
- peaty soils (organic matter is present in its structure, have a high and very high compressibility and a low shear strength);
- eluvium (formed as a result of decomposition and alteration of existing rocks);
- saline soils (are characterized by the settlement phenomena that occurs during a long lasting wetting);
- fillings (occur as a result of unconsolidated alluvial deposits) (Iliesi 2012).

#### 2.2 Methods of soil improvement

Given the frequency of soils that present unfavourable characteristics for constructions over time were developed methods to improve their mechanical properties, such as:

- soil compaction which can be made on surface (rolling, dynamic, cushions) or in depth (columns, pre-wetting, dynamic);
- chemical soil stabilization (cementation, silicization, jet grouting, bentonite etc.);
- electrochemical methods (electrophoresis and electroosmosis);
- thermal treatment of soils.



The case study refers to the problems that can occur with an improved foundation soil. The method used for improvement is soil replacing (soil cushion).

### 3 CASE STUDY

Within the areas with difficult foundation soils, Iași City is the largest urban settlement located in the eastern part of Romania. The city lies at the contact between Jijia Meadow and the Moldavian Plateau. The landscape is varied, forming a region consisting of eroded hills crossed by Bahlui plateau.

#### 3.1 Soil types in the studied area

Studies performed over the last decades into the existing terraces of the region show that almost 70% from the current area of the city have medium and low suitability for construction purpose, this reason being more or less a natural barrier for city expansion. Theoretical and practical solutions offered for solving the issues caused by these types of soils present a special interest in the current context (Vieru 2010). Among these types of soils there are two specific categories: loess and expansive soils.

The different types of soils existing in the studied area have either a normal behaviour under loads, or an atypical one.

Therefore, upper and medium terraces consist of a succession of coarser sediments at the bottom followed by a loess soil sensitive to wetting. Loess layer is yellow-brown with variable thickness from 8.00 m to 15.00 m lying in the highest areas of the city. Loess deposits usually consist of silty clay and clayey silt.

The loess of Iași region has medium plasticity with the liquid limit  $LL = 30 \div 50\%$ . Grain-size distribution is:  $25 \div 29\%$  clay,  $43 \div 47\%$  silt and  $24 \div 32\%$  sand. Regarding the uniformity coefficient, the loess of Iași City is considered to have a good uniformity (Ciornei & Răileanu 2000).

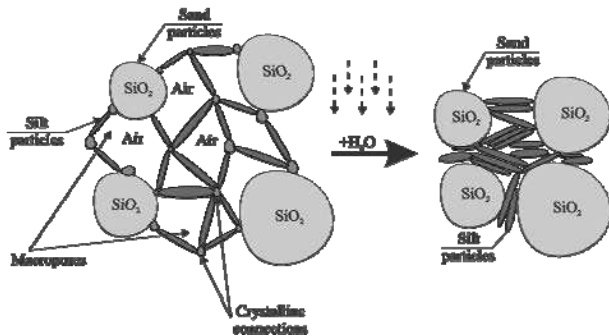


Figure 1. Structural rearrangement for collapsible soils

Bahlui Meadow is characterized as a mixture of sand and gravel layers at the base of the stratification, followed by a layer of fat swelling and shrinking clay. The sand layer has a thickness of almost 4.00 m and the clay is between 5.00 m and 6.00 m. This clay is actually the foundation soil from the area, requiring good knowledge of soil characteristics.

As far as the soil properties are concerned, Bahlui clay falls within the category of high swelling and shrinking soils. Climatic conditions of the area, with temperatures decreasing in the summer with  $10^{\circ}\text{C} \dots 20^{\circ}\text{C}$  from day to night and heavy rainfall, lead to changes in soil volume. To avoid foundation deterioration the minimum foundation depth has been set at -2.00 m, as deep as the effects of seasonal variations in moisture content and temperature may not be felt (NE 001-96 1996).

Other factors influencing the volume variation are:

- soil activity – volume variation is influenced by molecular and electro-molecular phenomena reflected by adhesive and capillary water, their size depending on the mineralogical nature

of the particles making up the clay fraction and the nature of the absorbed ions;

- hydro-geological conditions – groundwater is present both through deep under pressure aquifers and also through free flow ones. Deep layers have a high mineralization, being intercepted only by drilling. They have an ascending nature, sometimes an artesian one. Shallow drillings revealed the presence of captive water with low mineralization, which can be used locally;

- layer thickness – the thicker the layer is, the bigger its swelling;

- moisturized area – if the wet surface under an existing building is insignificant, the deformations increase and the probability of deterioration grows (Alupoae et al. 2011).

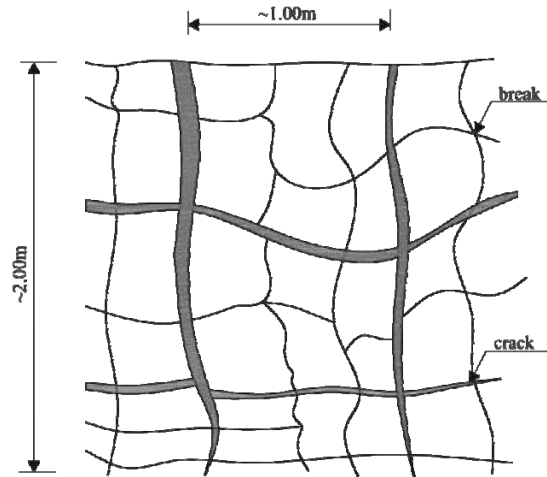


Figure 2. Contraction breaks and cracks

#### 3.2 On site situation

The case study follows a residential area placed on one of the hills in Iași City, Romania. The increase of water content inside the foundation soil determined a differential settlement and the buildings placed on site were switched from their initial vertical position.

##### 3.2.1 Data regarding the constructions from the studied area

The constructions were built during two different time frames:

- Stage 1 – between 1994 and 1998, consists of a two section building 22.0 x 12.0 meters (Section I and Section II), has a total ground surface of 530 m<sup>2</sup>, a structure made of reinforced concrete frames placed on network of foundation beams. The foundation rests on a soil cushion, 1.0 meter thick. In 1998 the foundation system was checked and the results showed that the soil cushion placed under the foundation had a degree of compaction of 95.15%. Thus it can be stated that the operations of soil improvement using mechanical means were correctly carried out. On site, a layer of loess, sensitive to wetting, was intercepted in drillings up to 9.0 meters from the ground surface. Under the soil cushion the thickness of the loess layer is about 5.0 ÷ 6.0 meters.
- Stage 2 – the construction of Section III started in 2001, with a built area of about 850 m<sup>2</sup> and a structure and height similar to the initial sections. This section is not entirely finished and the main problem is the fact that no systematization works are carried out. Also, the systems of rainwater collection and disposal are not finished. Because of this, in 2010 a movement was observed.

After the initial observations, measures have been taken to analyze the technical condition of the building and to establish the necessary actions to ensure a proper exploitation for the constructions.



Figure 3. Photos showing on site displacements

### 3.2.2 Causes that led to differentiated settlements

The main cause that led to settlements on the studied case was determined by the increased humidity in the foundation soil. This happened as a result of a deficient vertical systematization: no sidewalks, there were no gradients on site to discharge the water and also there were not built ditches and surface drainage systems. The lack of systematization works led to rainwater infiltrations in the filling layer above the soil cushion used as an improving method for the loss soil on the site. Water bags were formed in the filling layer which supplied the permanent moisture on the layer above the cushion. The humidity of the cushion became 3.14% higher than the optimum compaction humidity (19.40%). Also the filling layer recorded higher values for humidity: 25.07% ÷ 27.52%.

Table 1. Humidity evolution on the site – filling layer

Section	Humidity 1998 [%]	Average humidity 1998 [%]	Humidity 2010 [%]	Average humidity 2010 [%]	Increase of humidity [%]
I	16.98 ÷ 29.16	24.78	19.57 ÷ 30.07	25.83	+4.20
II	17.18 ÷ 24.15	22.45	22.99 ÷ 32.85	26.90	+19.80
III	---	---	18.31 ÷ 33.04	24.40	---

Table 2. Humidity evolution on the site – soil cushion

Section	Humidity 1998 [%]	Average humidity 1998 [%]	Humidity 2010 [%]	Average humidity 2010 [%]	Increase of humidity [%]
I	21.15 ÷ 24.15	21.29	16.37 ÷ 23.81	20.53	-3.70
II	17.11 ÷ 23.69	20.63	18.40 ÷ 24.45	21.77	+5.50
III	---	---	17.61 ÷ 20.64	19.03	---

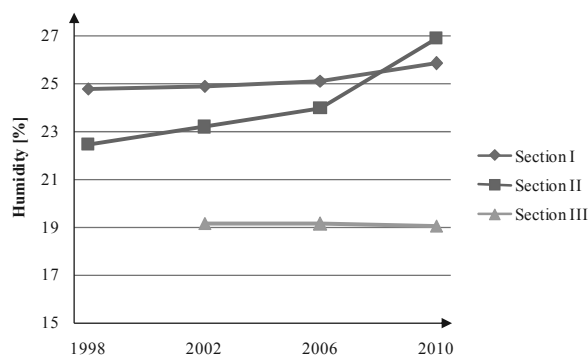


Figure 4. Humidity variation on the site, in the filling layer, for the three sections of the building

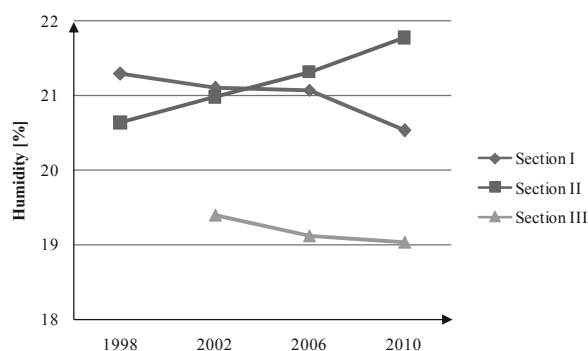


Figure 4. Humidity variation on the site, in the earth pillow, for the three sections of the building

Table 3. Humidity evolution on the site – surrounding area

Section	Humidity 1998 [%]	Average humidity 1998 [%]	Humidity 2010 [%]	Average humidity 2010 [%]	Increase of humidity [%]
I	20.70 ÷ 33.42	26.85	18.90 ÷ 29.36	22.30	-20.0
II	20.70 ÷ 33.42	26.85	18.90 ÷ 29.36	22.30	-20.0

Topographic measurements were made, on the site, for verifying settlements that appeared due to moistening of the foundation soil. By analyzing the results obtained after four cycles of measurements, the following conclusions can be drawn:

- for section I the measured values of settlements are insignificant. This happened because the values fall within the margin of error of the measurements and also because the variations determined at the markers considered stationary must be taken into consideration;
- for section II were found higher values of the settlements at the joint between section II and III. This occurs where the surface water penetrated the ground and produced a pronounced moistening of the foundation soil;
- for section III were also found higher values of the settlements at the joint between section II and III. This occurs where the surface water penetrated the ground and produced a pronounced moistening of the foundation soil.

Established settlements have small values and pose no danger to the behaviour of the building in time. Relative settlements have also small values,  $3.65 \cdot 10^3$  millimetres, much lower than the admissible relative settlement, which is, according to Romanian Standards, 0.001 millimetres.

The settlement speed decreases from 0.213 mm/day, after 9 days, to 0.061 mm/day after 22 days and further to 0.006 mm/day after 83 days. This led to the conclusion that settlements are slowing down.

### 3.2.3 Proposed solutions

Continuous monitoring of building settlements and conducting topographic readings at least every three months until the constructions are stabilized.

Efficient vertical and horizontal systematization can be done by making sidewalks, gradients for water discharge, ditches and surface drains.

For stopping water infiltration in the foundation soil is mandatory to check utility networks and repair them where is necessary.

## 4 CONCLUSIONS

Difficult foundation soils are frequently found on sites located in large urban areas.

Over time, a series of methods and techniques for improving the difficult foundation soils were developed. The implementation of this methods and techniques must take into consideration the soil characteristics intercepted on the site.

In the case of loess soils that are improved using soil cushions a good vertical and horizontal systematization is required to drain the rainwater or the water from other surface sources and to avoid the appearance of settlements.

## 5 ACKNOWLEDGEMENTS

This paper was realised with the support of POSDRU CUANTUMDOC “DOCTORAL STUDIES FOR EUROPEAN PERFORMANCES IN RESEARCH AND INNOVATION” ID79407 project funded by the European Social Fund and Romanian Government.

## 6 REFERENCES

- Alupoae D. Baron A. Rotaru A. and Răileanu P. 2011. *Geomorphological characteristics of the Bahlui riverbed soils in the metropolitan area of Iasi city, Romania*, 11<sup>th</sup> International Scientific Conference VSU’, VI 141-146.
- Ciornei A. and Răileanu P. 2000. *How to dominate the macroporous soil sensitive to wetting*. Junimea, Iași.
- Iliesi A.T. 2012. *Geotechnical risk when building on collapsible soils*. PhD. Thesis. Iași.
- Vieriu F. 2010. *The study of Sarmatian clay and covering formations from Iași City, seen as foundation soils*. PhD Thesis. Iași.
- NE 001-96. 1996. *Design and building execution on high swelling and shrinking soils*.

# Centrifugal and numerical analysis of geosynthetic-reinforced soil embankments

## Etude par centrifugeuse et analyse numérique des remblais renforcés par géotextile

Bo L., Linli J., Ningyu Z., Sinong L.

School of Civil Engineering and Architecture, Chongqing Jiaotong University, Chongqing, China

**ABSTRACT:** Centrifuge models and numerical analysis of geosynthetic-reinforced and unreinforced soil embankments are presented. The results obtained from the centrifuge tests were compared with those from the numerical analysis. It is found that the filamentous fiber (polypropylene) is effective in constraining lateral displacement and reducing vertical settlement for the case of geosynthetic-reinforced soil embankments. Also, the distribution of stress in the geosynthetic-reinforced soil embankment is significantly ameliorated compared with the unreinforced. The presence of geosynthetic filamentous fibers in reticular structure provides the reinforced soil embankments strength to resist crack.

**RÉSUMÉ :** Dans cet article, les résultats de modèles de centrifugeuse et les analyses numérique des remblais renforcés par géotextile et non-renforcés sont présentés. Les résultats obtenus à l'aide de la centrifugeuse sont comparés avec ceux des analyses numériques. Les fibres filamenteux (polypropylène) sont efficaces pour restreindre les déplacements latérales et réduire les tassements verticaux dans le cas du remblais renforcé. De plus, la répartition des contraintes dans le remblai renforcé est améliorée de façon significative comparé avec celle du remblai non-renforcé. La présence des fibres dans une structure réticulaire dans le remblai renforcé donne une résistance contre la fissuration.

**KEYWORDS:** Embankment ; Geosynthetic-reinforcement ; Centrifuge test ; Numerical analysis

## 1 INTRODUCTION

The concept and design theory of reinforced soil were proposed by the French engineer Henri Vidal from model tests in the 1960s. The reinforcement materials include metal strips, concrete slabs, bamboo ribs and geosynthetic materials, etc. Now-a-days, geosynthetics was commonly used in reinforcing soil owing to its easy-controlled properties of structure type and size, strength, impermeability, acid dissolution and durability.

“Cohesion” of filamentous fiber reinforced soil comes from friction between soil and fibers, as well as the constraint force of the fiber network. The magnitudes of CBR and unconfined compressive strength(UCS) increase with augment of filamentous fibers linearly(Xiong Youyan 1989). Soil reinforced with continuous filamentous fibers is obviously effective in reducing the vertical deformation of sand under the vertical pressure; it is superior in reducing horizontal tension than geogrids(A.F.L.Hyde and M.Ismail 1988). In recent years, this technique has applied successfully by reinforcing the embankment using filamentous fibers in embankment projects, and datum are available from researches (Bao Chenggang and Ding Jinhua 2012). However, the interaction micro-mechanism of interface between soil and filamentous fibers is still unclear (Tang Chaosheng, Shi Bin and Gu Kai 2011, Jie Yuxin and Li Guangxin 1999).

In this paper, the behavior of geosynthetic-reinforced embankments has been explored using centrifugal and finite element modeling. The objectives of this paper include: (1) to probe the mechanism of filamentous fibers in improving the stability of the embankment, and (2) to examine the effectiveness of filamentous fiber reinforcement.

## 2 CENTRIFUGE TESTS

Centrifuge model testing, because of its ability to reproduce same stress levels, same deformation and same failure mechanism in an 1/n scale model as in a full-scale prototype, is widely used in studying geotechnical problems. Jie Yuxin and Guang-Xin Li studied the stability of cohesive soil slope and fiber-reinforced soil slope with different densities through centrifugal model tests; Yang Xiwu and Ouyang Zhongchun

obtained the deformation behavior of embankments which reinforced with various fiber styles. It should be pointed out that idealized conditions may be created in centrifuge models carefully to avoid problems caused by stress errors, boundary effects, particle scale effects and geometrical scale effects.

### 2.1 Centrifuge tests—Equipment and procedure

#### 2.1.1 Equipment

In the present study, centrifuge model tests were performed using the TLJ—60 centrifuge in Chongqing Jiaotong University. The main parameters of the centrifuge are indicated in Table 1.

Table 1. The main parameters of the centrifuge

Characteristic	Value
Maximum volume weight	60g·t
Maximum load	600kg(100g) 300kg(200g)
Effective radius	2.0m
Maximum acceleration	200g
Acceleration control accuracy	±0.5%F·S
Model box size	600mm×350mm ×500mm

#### 2.1.2 Model scale

Due to the inherent symmetry of the embankment about its centerline, only one half of it was modeled. In order to simulate the actual project accurately and satisfy the boundary effects, 1:90 scale centrifuge model was constructed. Fig.1 shows the details of test model and its full-scale prototype.

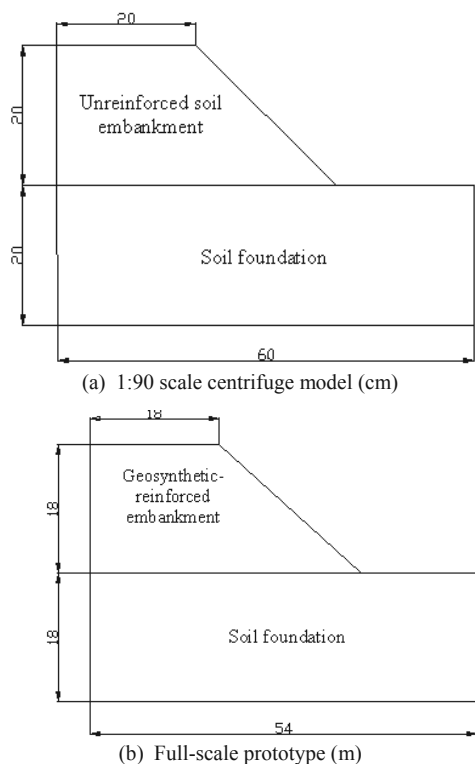


Figure 1. Arrangement of model for centrifuge test and its prototype

2.1.3 Parameters of soil and fiber

( 1 ) The physical parameters of the soil

Table 2 gives the parameters of the brown weathered shale that obtained from compaction test and liquid and plastic limit combined test.

Table 2. Brown weathered shale material properties

Optimm water content (%)	Maximm dry density (g/cm <sup>3</sup> )	Liquid limit (%)	Plastic limit (%)	Plasticity index
8.9	2.15	26.928	20.193	6.735

Before the centrifuge test, soil sample was experienced airing and grinding, then sieved by 6mm sieve to remove impurities.

( 2 ) The parameters of the fiber

Polypropylene fiber with 19mm length was proposed to construct the fiber reinforced soil embankment model. Table 3 gives the triaxial test strength of the embankment soil with the fiber ratio of 1 ‰, 2 ‰ and 3 ‰ respectively.

Table 3. Embankment soil material parameters

Embankment soil	Cohesion(kPa)	Friction angle(degrees)
Unreinforced soil	49.167	34.077
19mm-0.1%-Polypropylene-reinforced soil	94.005	35.717
19mm-0.2%-Polypropylene-reinforced soil	138.294	36.362
19mm-0.3%-Polypropylene-reinforced soil	228.356	35.951

2.1.4 Deformation measuring

An array of pins was installed on the front face of the embankment model as deformation marker. This was used for measuring the model vertical and horizontal displacement from coordinate difference between beginning of test and the end of test through the front perspex window. Fig.2 shows the details of the marked model.

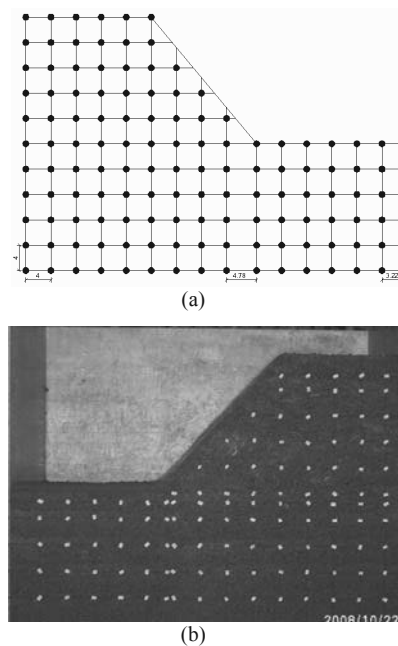


Figure 2. The marked model

2.2 Centrifuge tests—summary of results

2.2.1 Comparison analysis of deformation and displacement

In this section, the results obtained from unreinforced embankment test are compared with the results obtained from reinforced embankment test. The deformation of unreinforced embankment was slightly larger than the deformation of reinforced embankment. The settlements under the shoulder of the unreinforced embankment and the slope gradient were considerably greater than those of reinforced embankment. Two cracks on the top of the unreinforced embankment and (heave) beyond the toe of the unreinforced embankment were observed at the end of the centrifuge tests. Fig.3 and Fig.4 show the displacement vectorgraph of unreinforced and reinforced embankment respectively. From the close comparison between unreinforced and reinforced embankments, it is evident that fiber reinforcement reduced the displacement of embankment, and enhanced the embankment obviously.

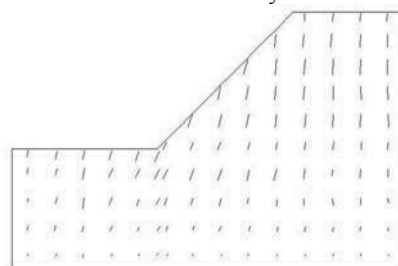


Figure 3. Deformation of the unreinforced model

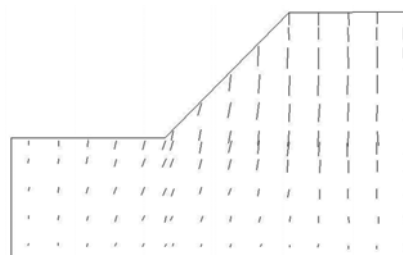


Figure 4. Deformation of geosynthetic-reinforced model

2.2.2 Comparison analysis of settlement

The maximum lateral displacement of unreinforced model was 72cm, which located in the distance of 8m from the toe of the embankment. The maximum settlement was 48.6cm, which located in the distance of 10.8m from the centerline; For reinforced case, the maximum lateral displacement emerged in the distance of 8.2m from the toe of the embankment with 35cm, and the maximum settlement was 41.2cm (located in the distance of 10.4m from the centerline). It is safely to conclude that the maximum displacement of both unreinforced and reinforced embankment approximately close to the same point, whereas the maximum lateral displacement of reinforced embankment is approximately equal to 48.6% of the maximum lateral displacement of unreinforced embankment and the maximum settlement of reinforced embankment is approximately equal to 84.8% of the maximum settlement of unreinforced embankment.

The comparison between computation analysis and centrifuge tests of the embankment discloses that fibers help to resist the lateral thrust and lateral deformation of the embankment effectively. This is due to the fact that fibers unified the overall redistribution of stress and reduced asymmetric settlement of embankment.

3 FINITE ELEMENT MODELLING

3.1 Assumptions of computing

In the analysis presented in this paper, the unreinforced and reinforced embankments are modeled using the Drucker-Prager constitutive model (D-P model).

Two-dimensional plane strain models were constructed with boundary conditions similar to those of centrifuge models. The modeling based on follow assumptions: (1) taking geotextile reinforced soil as homogeneously isotropic material, the parameters obtained from triaxial tests; (2) without considering the influence of temperature to embankment; (3) consolidation was completed under its gravity, and without considering the impact of pore pressure.

3.2 Parameters

Table 4. Material parameters specified for the finite element analysis

Characteristic	Unreinforced embankment	Polypropylene-reinforced embankment (19mm-0.1%)	Foundation
Density (kg/m <sup>3</sup> )	2150	2180	2150
Cohesion (kPa)	49.167	94.005	49.167
Friction angle(degrees)	34.077	35.717	34.077
Poisson's ratio	0.27	0.23	0.27
Depth of embankment(m)	18	18	36

3.3 Displacement comparison

The computed results indicated that the values of deformation and stress as well as its fluctuation range were marginally less for reinforced embankment than for unreinforced embankment. The maximum lateral displacement of unreinforced model was 79.442cm (located in the distance of 11.4m from the toe of the embankment), and the maximum settlement was 51.498cm (located in the centerline); The maximum lateral displacement of reinforced model was 38.246cm (located in the distance of 11.4m from the toe of the embankment), and the maximum settlement was 48.318cm (located in the centerline). Fig.5 and

Fig.6 present computed displacement and stress contours of the unreinforced and reinforced models respectively.

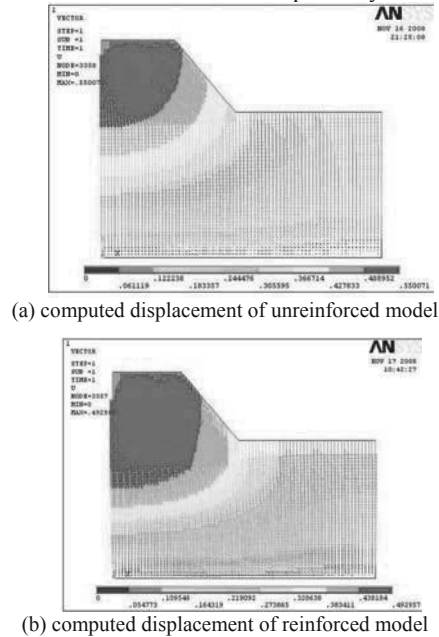


Figure 5. Computed displacement of unreinforced and reinforced model

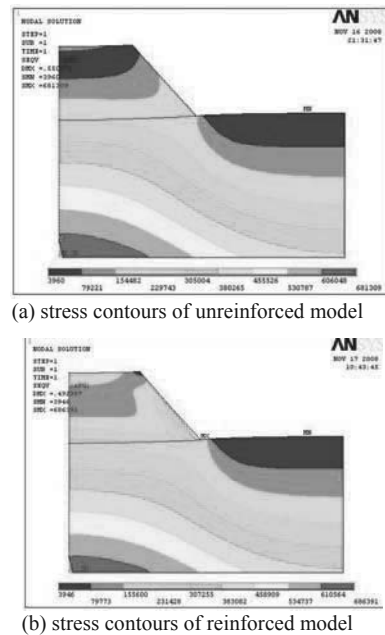


Figure 6. Stress contours of unreinforced and reinforced model

4 RESULTS AND COMPARISONS

Fig.7 shows the variation of lateral displacement and vertical displacement of unreinforced embankment from centrifuge tests. Superimposed on the measured variation are the variations computed by numerical modeling analysis. It can be seen from Fig.7 that there is a close agreement between the observed and computed displacements for centrifuge test and numerical analysis.

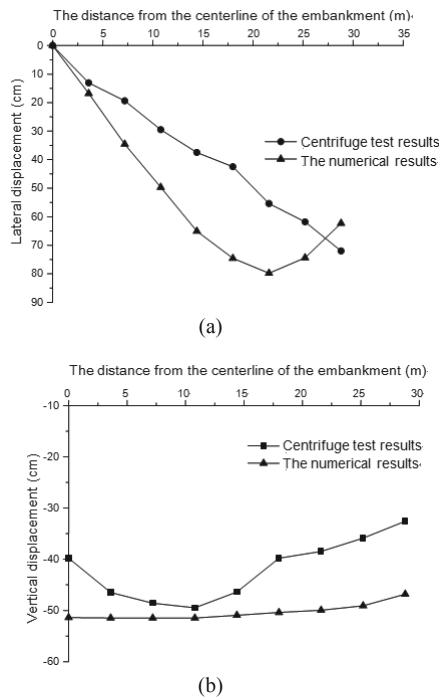


Figure 7. measured and computed displacement of unreinforced model

The comparison between the computed and observed displacement both in the horizontal direction and in the vertical direction for the reinforced embankment are shown in Fig.8. The computed displacement is quite close to the observed values for both lateral displacement and vertical displacement.

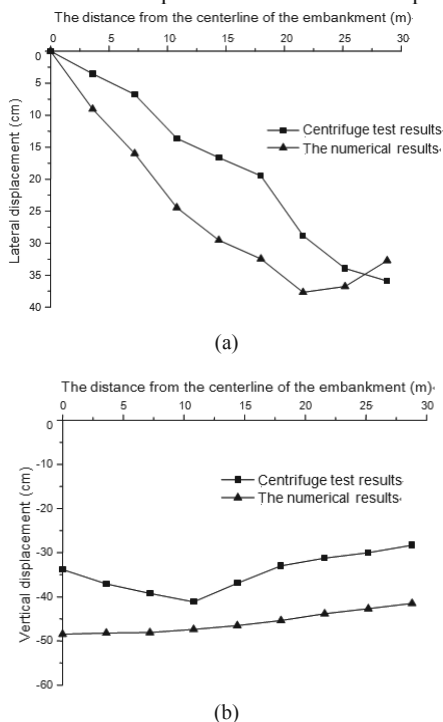


Figure 8. Measured and computed displacement of reinforced model

The behavior of reinforced embankment and unreinforced embankment was successfully investigated using centrifuge modeling and finite element analysis. The comparisons between the centrifuge tests and computed results indicated the utility of fibers can enhance overall stability of embankment. For the case of reinforced embankments with fibers, it was found that the deformation, the magnitude of stress, and their variation range was considerably less than those for unreinforced case. Also, the fiber reinforcement constrained the lateral displacement

effectively, and the distribution of stress and deformation was harmonious comparing with the unreinforced.

When using geosynthetic fibers to reinforce embankment, it also shows two advantages: (1) reinforced embankment can resist cracks due to the network of intertwined fibers, and(2) the fiber reinforced soil is closer to a homogeneous, isotropic material than unreinforced soil.

## REFERENCES

- Vidal, M.H. 1978. The development and future of reinforced earth. *Proceedings of a Symposium Reinforcement at the ASCE Annual Convention*. Pittsburgh, Pennsylvania, 1-61.
- Xiong Youyan.1989. *Geosynthetic-reinforced soils*. Chongqing Highway Science Research Institute, Chongqing, China.
- Tang Chaosheng, Shi Bin and Gu Kai. 2011. Microstructural study on interfacial interactions between fiber reinforcedment. *Journal of Engineering Geology*19(4), 610-614.
- Jie Yuxin and Li Guangxin. 1999. A study on colculation method of textsol. *China Civil Engineering Journal*2(5), 51-55.
- Bao Chenggang and Ding Jinhua. 2012. Researches and applications of fiber reinforced soils. *Soil Engineering and Foundation*26(1), 80-83.
- Jie Yuxin, Li Guangxin and Chen Lun. 1998. Study of centrifugal model tests on textsol and cohesive soil slopes. *Chinese Journal of Geotechnical Engineering*20(4), 12-15.
- Yang Xiwu and Ouyang Zhongchun. 2000. Experimental study on the strengthened sreep slopes. *China Civil Engineering Journal*33(5), 88-91.

# Compacted soil columns for foundations on collapsible soils. Laboratory and in-situ experimental study

Colonne de sols compactés utilisées pour des fondations sur sols effondrables.  
Étude expérimentale menée en laboratoire et in-situ

Burlacu C., Olinic E., Manea S.

Technical University of Civil Engineering Bucharest, Department of Soil Mechanics and Foundations

Uță P.

SC Geosond SA Bucharest

**ABSTRACT:** Moisture-sensitive or collapsible soils are materials with high porosity that under the loads transmitted by the foundations present additional settlements once the soil is saturated. This category includes loess deposits and other high silt content soils with uneven porosity. A method often used for foundation on these soils is the realization of local loessoid material compacted columns. According to the Romanian legislation, it is forbidden to use granular material in loessoid soils. A compromise may be reached by using a mixture of granular material and local loessoid soil in columns. This paper presents the experimental laboratory program aiming to achieve an optimal mixture of local material (loess) and monogranular sand in order to improve the values of the mechanical soil parameters while keeping the permeability coefficient values as low as possible. This objective can be achieved by adding bentonite. On the experimental polygons, 1:5 scale compacted soil columns were made using a dynamic penetrometer. The aim of the dynamic penetration tests performed in the center and between the columns was to obtain results concerning the improvement of the mechanical characteristics of the columns and the foundation soil.

**RÉSUMÉ :** Les sols effondrables sont des matériaux avec une porosité élevée, qui, suite à la saturation, présentent des tassements supplémentaires sous l'effet des charges transmises par les fondations. Cette catégorie inclue les dépôts de loess et d'autres sols ayant un contenu élevé de silt avec une porosité irrégulière. Une des méthodes de fondation souvent utilisée sur ce type de sols est la réalisation de colonnes de matériel loessique compacté. Bien que la législation roumaine interdise l'utilisation de matériaux sableux dans des sols loessiques, ceux-ci peuvent toutefois être utilisés pour la réalisation de colonnes dans un mélange avec du sol loessique. Cet article présente un programme expérimental de laboratoire qui vise à réaliser un mélange optimal de matériaux loessiques avec du sable pour améliorer les valeurs des paramètres mécaniques du sol, en maintenant toutefois les valeurs du coefficient de perméabilité le plus bas possible. On peut atteindre cet objectif par l'addition de bentonite. Dans le cadre d'un programme expérimental, on a réalisé des essais à l'aide d'un pénétromètre dynamique sur des colonnes de sol compacté à une échelle de 1:5. Le but des essais de pénétration dynamique a été d'obtenir des résultats concernant l'amélioration des caractéristiques mécaniques des colonnes et du terrain de fondation.

**KEYWORDS:** collapsible soils, compacted soil columns, dynamic penetration test, soil mixtures.

## 1 INTRODUCTION

Moisture-sensitive or collapsible soils are unsaturated macroporous cohesive soils that, upon saturation with water, undergo sudden and irreversible changes of the internal structure, reflected by additional settlements with collapsing character and decreases in the values of geotechnical parameters of mechanical behaviour (NP 125: 2010).

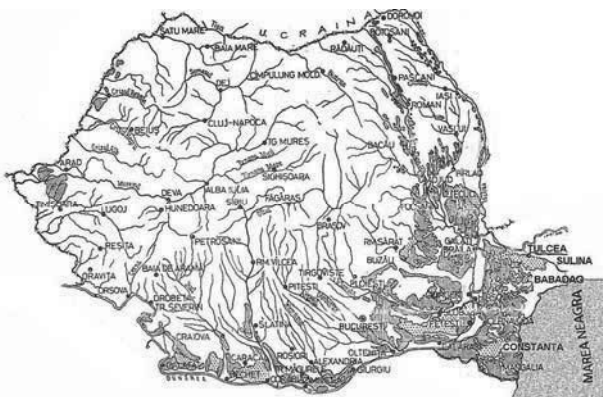


Figure 1. Collapsible soil spreading in Romania (Bally, Antonescu 1971)

In Romania, moisture-sensitive soils cover about 19% of the country's territory (approx. 40.000 km<sup>2</sup>) and it is common particularly in the eastern part of the country (Figure 1).

In order to characterize a soil as moisture sensitive, it must meet at least one criterion regarding the physical characteristics and one criterion regarding the mechanical behaviour, the main criteria being the following:

A. Criteria regarding physical characteristics:

- ratio of silt fraction: 50 – 80%
- degree of saturation:  $S_r < 0,8$
- porosity in natural state:  $n > 45\%$

B. Criteria regarding mechanical behaviour:

- the index of the additional settlement caused by saturation under a loading of 300 kPa (in oedometric test):  $i_{m300} \geq 2\%$ .

## 2 IMPROVEMENT METHODS FOR COLLAPSIBLE SOILS

Difficult foundation soil improvement methods are continuously progressing, not only quantitatively, but also qualitatively, as a result of both the development of new technologies and the recognition of economic and environmental protection benefits of modern methods.

A significant number of techniques aimed at improving the mechanical characteristics of difficult foundation soils have



been developed. Methods are divided into two wide categories (Schlosser 1997):

- physical methods – soil improvement technologies, by which soil structure is mainly improved in what concerns contacts between particles by additives or by reducing porosity in order to increase the tamping state - physical characteristics improvement methods;
- mechanical methods – soil reinforcing technologies, by which structural elements are introduced in the ground in order to increase the mechanical strength – mechanical characteristics improvement methods.

Classification of results sought by difficult foundation soil improvement (Kirsch, Sonderrmann 2003):

- increasing density and shearing strength
- reducing compressibility
- influencing permeability in order to reduce infiltrated water flow or to speed up consolidation process
- improving homogeneity.

### 3 LABORATORY TESTS

In the experimental programme, various mixtures of loessoid material with different natural mineral materials have been proposed, in view of eliminating moisture sensitiveness, improving geotechnical parameters of mechanical behaviour and limiting permeability (Burlacu 2012).

To this purpose, a series of mixtures have been proposed: loess with sand 1-2 mm ( $C_u = 1.5$ ) and loess with sand and bentonite powder addition in two variants of mixture. The obtained mixtures are presented below:

Mixture 1: 80% loess + 20% sand (1-2 mm);

Mixture 2: 60% loess + 40% sand (1-2 mm);

Mixture 3: 50% loess + 40% sand (1-2 mm) + 10% bentonite;

Mixture 4: 50% loess + mixture from (40% sand (1-2 mm) + 10% bentonite);

The difference between the last two mixtures consisted in the way they were mixed. In the first case, all the three materials were simultaneously mixed and then water was added to reach different degrees of humidity in order to perform the normal Proctor test. In case of the last mixture, the sand was first mixed with the bentonite and with water and then, after this mixture had dried, it was also mixed with the loess (Olinic 2012).

As a first step, the optimal compaction characteristics of the proposed mixtures were determined and then, based on the compacted samples, the compressibility and shearing mechanical characteristics and the possible moisture-sensitivity of the compacted material were determined. The samples used for carrying out the mechanical tests were the ones surrounding the optimum compacted sample. In order to reach uniform results, the variation of the density in dry condition depending on the height of the compacted sample was analyzed and confirmed (Figure 2). This is why a certain sampling order was followed.

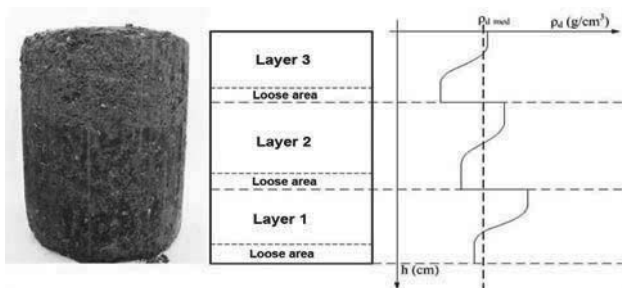


Figure 2. Dry density theoretical variation depending on the height of the compacted sample.

As a result of the Proctor test outcome analysis (Figure 3), it has been observed that along with adding up and increasing the

percentage of sand in the mixture (from 20% to 40%), the maximum density in dry condition increases. At the same time, the optimal compaction moisture of the mixtures decreases

The synthesis of the oedometre compressibility tests depending on the oedometric moduli values indicated that the same values  $E_{oed\ 200-300}$  could be obtained for the mixture containing an addition of sand of 20%, at smaller humidity values and at a better tamping state than in case of the natural loess samples. This trend disappeared once the percentage of sand in the mixture was increased (40%). In what concerns samples with bentonite, similar values of oedometric moduli were obtained at a better tamping state that in case of medium loess samples, but at a reduced tamping state than in case of samples with sand, which was also confirmed by the values obtained following Proctor tests.

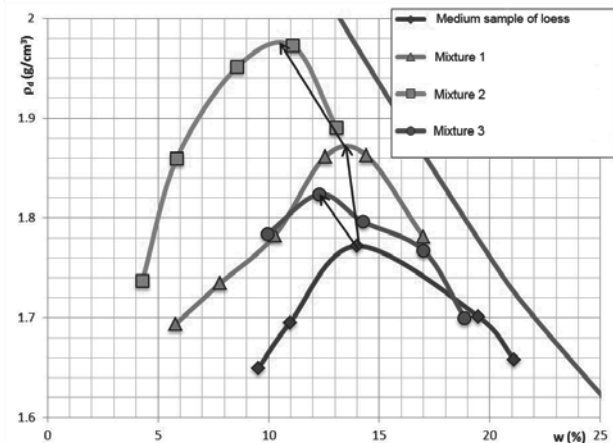


Figure 3. the results of the Proctor trial for all the mixtures obtained.

If, in case of mixture 3, the Proctor diagram has a maximum point ( $\rho_{dmax}, w_{opt}$ ), in case of mixture 4, the same tamping state was obtained for humidity values between 11% and 15%.

The Proctor diagram resulted for mixture 4 indicated that sample 3 could have represented a maximum point. Therefore, in order to validate the results, tests on this sample were carried out again and similar values were obtained (Figure 4). Given that, humidity plays a key role in the real scale compaction process, the last indication regarding mixture 4 is important because it allows compaction at humidity values belonging to higher humidity domains.

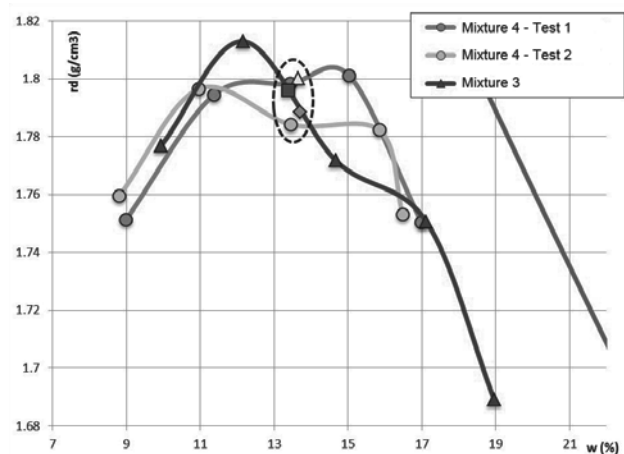


Figure 4. Results of Proctor test for mixtures 3 and 4.

As to the values of the permeability coefficient, these have been of the order of  $10^{-5}$  cm/s for the average loess sample rising up to values of  $10^{-4}$  cm/s in case of the mixture containing 40% sand, while in case of the mixtures containing an addition of bentonite, the measured values were below  $10^{-9}$  cm/s.

#### 4 IN SITU TESTS

In-situ tests first aimed at identifying the effect of the cone shape on: the rate at which the cone advances in the ground, the tamping of the surrounding ground and the compaction degree of the material in the column body. Three types of cones with a diameter of 7 cm were made. (Figure 5).



Figure 5. Cones made: a) C1 – 30°; b) C2 – 60°; c) C3 – hemisphere.

##### 4.1 Column execution technology

Collapsible soils improvement by soil columns is regulated by normative C29 - 85. The experimental polygon met the column execution methodology described in the normative but adapting it to the equipment that has been newly proposed for their execution (LMSR-Hk dynamic penetrometer).

Column execution steps are: column hole execution, filling by fill material portions and fill material compaction until rejection.

The fill material portion was set for a column with a diameter of 7 cm and for a height of the compacted material of 21 cm (3 diameters), resulting 1,5 kg of material having optimal compaction humidity.

Successive tests regarding the obtained compaction degree indicated that rejection (compaction stopping) was reached after an advance of maximum 7mm/blow.

##### 4.2 Optimal cone shape

On the experimental polygon, columns were executed by using the three types of cones. Figure 6a presents the blow number variation per an advance of 10 cm in DPM tests performed in the centre of the columns and Figure 6b presents the same tests carried out at a distance of 2 diameters towards the column.

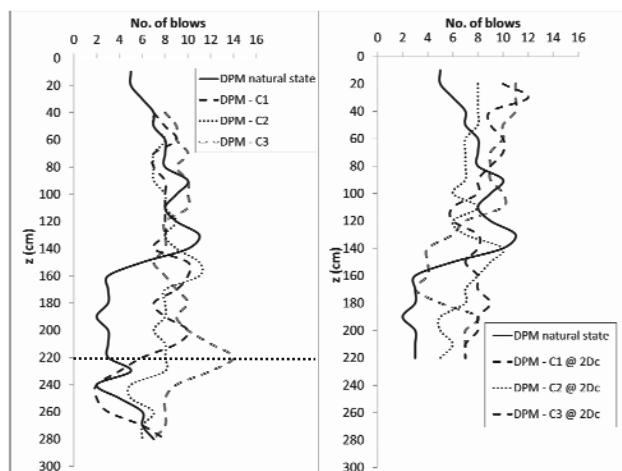


Figure 6. Results of DPM tests carried out in the centre of the columns and at a distance of 2Dc (14cm) towards the columns.

In case of DPM tests carried out in the centre of the columns, the results obtained were similar for all the columns. Therefore, an optimal shape of the cone that leads to a better compaction of the column body could not be found.

Then, for determining the cone with a wider influence radius, DPM tests were carried out at a distance of  $2D_c=14$  cm towards the columns. These tests indicated [as expected given its shape (the smallest angle at the top)], that cone no. 1 ( $30^\circ$ ) had the greatest influence on the tamping state of the soil around the column.

The tests indicated that cone 1 shape ( $30^\circ$ ) was optimal for soil columns execution.

##### 4.3 Compacted loess columns

Therefore, 2 m long columns were executed, arranged as an equilateral triangle network (Figure 7) with a distance of  $3D_c - 21$  cm between the columns.

After finishing the group of columns, average dynamic penetration tests were conducted both between the columns and at different distances towards them.

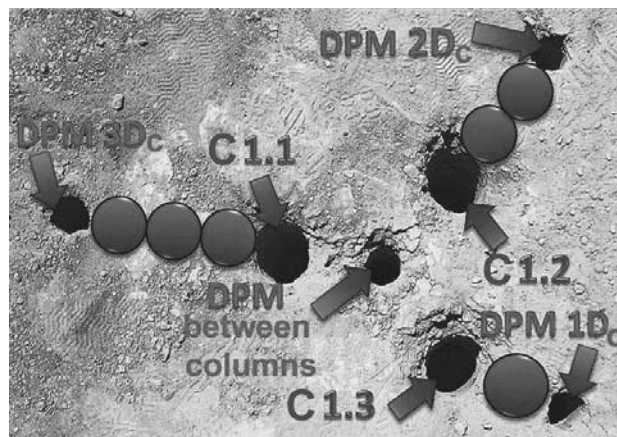


Figure 7. Columns and DPM tests disposal.

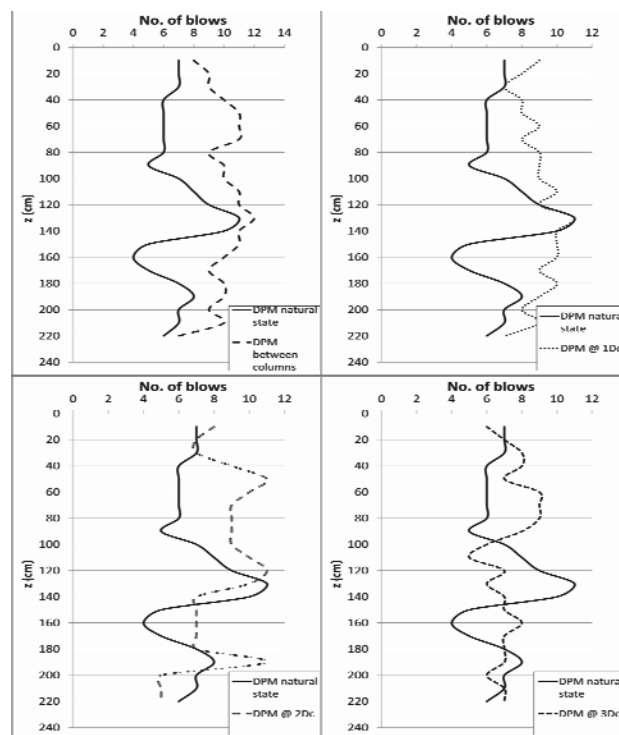


Figure 8. DPM tests results: a) between the columns; b) @ 1Dc; c) @ 2Dc; d) @ 3Dc.

It may be observed that, at a distance of  $3D_c$  near the columns, the improvement effect has no longer been perceived (Figure 8d). When the DPM test was carried out in the centre of the column group (Figure 8a), the improvement effect recorded an obvious increase.

#### 4.4 Loess and sand mixture compacted columns

Finally, on the experimental polygon columns of 60% local material (loess) and 40% sand were executed. For the execution of these columns, cone 1 (30°) was also used as rammer.

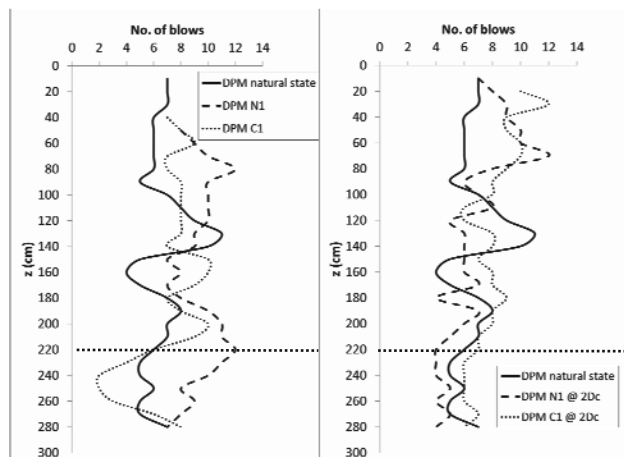


Figure 9. DPM tests results for the column executed from a mixture of loess and sand (N1): a) DPM in the centre of C1 and N1 columns; b) DPM at 2Dc towards C1 and N1 columns

Figure 9a indicates that the results of the DPM tests carried out in the centre of the column executed from a mixture of loess and sand are better than those of the column made entirely of loess. Moreover, it may be noticed that, unlike the compacted loess column, the one made of mixture led to the improvement of the material under the column's body.

Nevertheless, the results of the medium dynamic penetration test carried out near the columns at a distance of 2Dc (~14 cm) indicate that the tamping effect is higher than in case of the loess column.

## 5 CONCLUSIONS

Laboratory tests aimed at identifying a mixture of loess and natural mineral materials, with better mechanical characteristics and with reduced permeability compared to the one the loess has in its natural state. From all the solutions proposed (compacted loess, mixture of loess and sand and mixture of loess, sand and bentonite) the last one (mixture 4 - sand and bentonite, mixed with loess after drying) seems to be the optimal one due to the wide domain in which optimal compaction parameters are reached.

Concerning mechanical characteristics, no significant differences seem to exist between the analysed mixtures, but one can notice that water sensitivity is significantly reduced and that, compared to the flooded loess, the values obtained are significantly better.

In-situ tests, performed with a penetrometer, simulated the execution of loess columns and of loess with compacted sand columns, at a scale of 1:5. Both the quality of the material in the column body and the effect on the surrounding ground were verified by typical tests. The sand improves the mechanical behaviour of the material in the column body, without significantly exceeding the mechanical behaviour of natural loess that has not been flooded.

By executing columns of compacted local material with natural mineral materials, the mechanical behaviour of the columns - loess complex that has not been flooded does not improve, but this technique leads to some nuclei capable of reducing the negative effect of the accidental flooding of loess.

## 6 REFERENCES

- Bally R.J. and Antonescu I. 1971. *Loessoid soils in constructions*. Tehnica Publishing House, Bucharest. (in Romanian)
- Burlacu C. 2012. *Contributions to improvement solutions for weak foundation soils*. PhD Thesis. Technical University of Civil Engineering Bucharest, Romania.
- Kirsch K. and Sondermann W. 2003. *Geotechnical engineering handbook, Volume 2: Procedures, Chapter 2.1. Ground improvement*, 1 - 50. Ernst & Sohn, Berlin, Germany.
- Olinic E. 2012. Personal communication.
- Schlosser. 1997. *Exposé sur la thème: Amélioration et renforcement des sols*. Proceedings of the Fourteenth International Conference on Soil Mechanics and Foundation Engineering, Volume 4, 2445 - 2466, Hamburg, Germany.
- NP 125:2010. *Normative for foundation of buildings on moisture - sensitive, collapsible soils*. (in Romanian)

# Selected problems connected with the use of the jet grouting technique

## Certains problèmes liés à l'application de la technologie d'injection de jet

Bzówka J., Juzwa A., Wanik L.  
*The Silesian University of Technology, Gliwice, Poland*

**ABSTRACT:** The paper presents selected problems connected with the use of the jet grouting technique. It is one of the most popular methods for subsoil strengthening, enhancement for existing foundation, vertical and horizontal waterproof cut-off walls. Columns made using this method feature a high bearing capacity (very high friction on the shaft). The newest achievements of the numerical explanation of the interaction between jet grouting columns and subsoil are presented in the paper. The created models will be used to verify engineering methods of jet grouting columns dimensioning. Computational analyses are conducted using software based on the finite element method (Z\_Soil).

The computational model describes the interaction between a group of jet grouting columns and soil. The main element of this analysis consists of selection and calibration of computational model of the "group of jet grouting columns – subsoil" interaction. The model space is divided into three zones: columns, soil and the contact layer formed between the columns and the soil massif. The computational model allows for a plastic character of deformation under load and especially for a non-linearity of contact zone. The description of shape of a shaft surface of jet grouting columns is very difficult, so the fractal theory is used to describe this shape. Fractal and box dimensions are used to estimate the irregular surface. This model allows a precise selection of formation parameters, like the injection rod pull out velocity and number of rotations, injection pressure and the water/cement ratio, which define the geometry of jet grouting columns.

**RÉSUMÉ :** Cet article présente quelques problèmes liés à l'utilisation de la technique d'amélioration des sols : le jet grouting. Cette technique est une de méthodes les plus utilisées pour renforcer le sous-sol, les fondations déjà existantes et on s'en sert aussi comme les parois verticales et horizontales étanches (imperméables à l'eau). Les colonnes réalisées par cette méthode se caractérisent par la grande capacité portante (coefficient de frottement très élevé sur la surface latérale). Dans cet article, on présente les découvertes les plus récentes liées aux modélisations numériques de l'interaction entre les colonnes de jet et du sol. Les modèles développés seront utilisés pour vérifier les méthodes d'ingénierie et pour dimensionner les colonnes de jet grouting. Les analyses numériques sont effectuées par les programmes basés sur la méthodes des éléments finis (Z\_Soil).

Le modèle de calcul décrit l'interaction entre un groupe de colonnes de jet grouting et le sol. L'apport le plus important de cette analyse réside dans le choix et le calage du modèle de calcul pour l'interaction « groupe de colonnes de jet grouting – sol ». L'espace du modèle est divisé en trois zones: colonnes, sol et couche de contact formée entre les colonnes et le massif du sol. Le modèle de calcul permet d'avoir des déformations plastiques et en particulier de déformation non-linéaire de la zone de contact.

La description de la forme des surfaces latérales de ces colonnes est extrêmement difficile, alors on a introduit la théorie de fractales pour la décrire. Les dimensions de type fractal et de boîte, sont utilisées pour estimer la surface latérale irrégulière des colonnes. Ce modèle permet de choisir d'une manière précise des paramètres de formation des colonnes tels que: vitesses - de rotation et d'avancement en descente de la tige de forage, le nombre de rotation, la pression de coulis injecté, rapport eau/ciment, qui définissent la géométrie des colonnes de jet grouting.

**KEYWORDS:** jet grouting technique, interaction between columns and subsoil, shape and dimensions of jet grouting column.

### 1 JET GROUTING COLUMNS INTERACTION WITH SUBSOIL

The jet grouting method is frequently used in the engineering practice. It may be used for nearly all types of soils, both natural and man-made. It does not work only for a subsoil built of organic soils. The method consists in a high-pressure injection into the subsoil of an injectant stream (most often being a cement grout), which cuts and disintegrates the soil body, forming – after binding with soil fractions – a petrified soil-cement composite of any geometrical form, e.g. close to a column cylinder shape. This solution – because of the speed of performance and very good parameters of subsoil strengthening – is frequently used to strengthen a weak subsoil under high transport embankments or bridge abutments (Bzówka 2009; Juzwa 2012b; Modoni and Bzówka 2012).

To explain the interaction between the jet grouting columns and the strengthened subsoil it is suggested to apply numerical methods and to build models reflecting the operation of a single column and the interaction of jet grouting columns group in

transferring the load to deeper soil layers. A solution is sought, which would allow optimising design solutions of jet grouting columns, would ensure safety of a structure designed this way and at the same time would contribute to the works costs cutting. The authors emphasise especially as precise as possible reflection of real conditions, existing on a site.

A single column and a group of columns are the subject of numerical and in situ analysis. A single column is an idealised form, seldom existing in practice. However, the analysis of its behaviour is a starting point to make models more realistic and built of a group of columns. For the needs of analysis of interactions occurring between jet grouting columns strengthening a weak subsoil and the soil body numerical models were constructed, considering the environment division into three material zones: the soil-cement material of jet grouting columns – the contact layer – the subsoil (Bzówka 2009, 2010).

Because of a physical inhomogeneity and of a complicated geometrical arrangement the finite element method was used to

build models and the Z\_Soil software was used for computations. An elastic – ideally plastic model of Coulomb – Mohr boundary surface with non-associated law of flow were adopted to describe the mechanical behaviour of the soil environment and the jet grouting columns material.

To perform computer simulations it is necessary to give the following parameters: angle of internal friction  $\Phi$ , angle of dilatancy  $\Psi$ , cohesion  $c$ , modulus of elasticity  $E$  and Poisson's ratio  $\nu$ . Values of parameters for soils building the model subsoil were taken based on in situ tests on a test site. The following values were taken, for sand:  $E = 55.5$  MPa,  $\nu = 0.3$ ,  $\Phi = 31.8^\circ$ ,  $c = 1$  kPa, for a cohesive soil interbedding:  $E = 33.8$  MPa,  $\nu = 0.3$ ,  $\Phi = 18.0^\circ$ ,  $c = 30$  kPa. The value of angle of dilatancy was introduced from the range of values  $\Psi = (0.35-0.40) \cdot \Phi$ . Determination of material parameters for a cement–soil material depends on the subsoil ground characteristics, cement type in the grout, the method of columns performance. To determine them it is necessary to take core samples from the column performed (Fig. 1). These samples are then tested for uniaxial and triaxial compression. For the needs of this study 10 samples were tested for each case, obtaining results of significant scatter (Bzówka 2009). A statistical analysis of result values was carried out and after approximation with the first type regression function the following parameters were taken for calculations:  $E = 9888$  MPa,  $\nu = 0.186$ ,  $\Phi = 59.3^\circ$ ,  $c = 1772$  kPa. Values of soil parameters ( $E$ ,  $\nu$ ,  $\Phi$ ,  $c$ ) were taken for the contact zone based on CPT sounding performed in this area. Their values equal to soil parameters reduced by 1/3.



Figure 1. Core samples for strength tests (Bzówka, 2009).

A 2D model was built cutting from the space around columns an area large enough, allowing idealisation of boundary conditions. Boundary conditions were taken in the form of: full fixing of the base of the half–space cut and partial fixing, allowing a vertical shift, on side surfaces of the half-space

In the model of a flat system a group of 3 columns was taken, each of them 4.0 m long and 0.8 m in diameter, arranged at a distance of 2.5 m, while the subsoil is stratified. Division into quadrilateral isoparametric elements was assumed. The grid was concentrated in the area of contact zone. An incremental load (uniform for all columns) was applied to such system, reflecting a real transport embankment 4.0 m high, laid at fixed intervals in layers 0.5 m thick.

The image of system deformations caused by columns loading is presented for two stages in Fig. 2. Corresponding stresses are shown in Fig. 3. The stress maps perfectly show the range of transition zone, which parameters affect the distribution of internal forces values in the system (Bzówka et al. 2012; Juzwa 2012a).

## 2 GEOMETRY OF JET GROUTING COLUMNS

The shape of columns made by the jet grouting technique, due to specific nature of this technology, is very diversified and difficult to predict. It depends inter alia on the type and condition of soils making the subsoil, the injection system used (single, double or triple) and on technological parameters (injection pressure, size and shape of injection nozzles, speed of injection rod pulling out and rotations and others) (Wanik and Bzówka 2012).

To determine precisely the geometry of jet grouting columns they are excavated, making their measurement and macroscopic visual inspection possible. The shaft may have various shapes (Fig. 4) depending on the aforementioned factors.

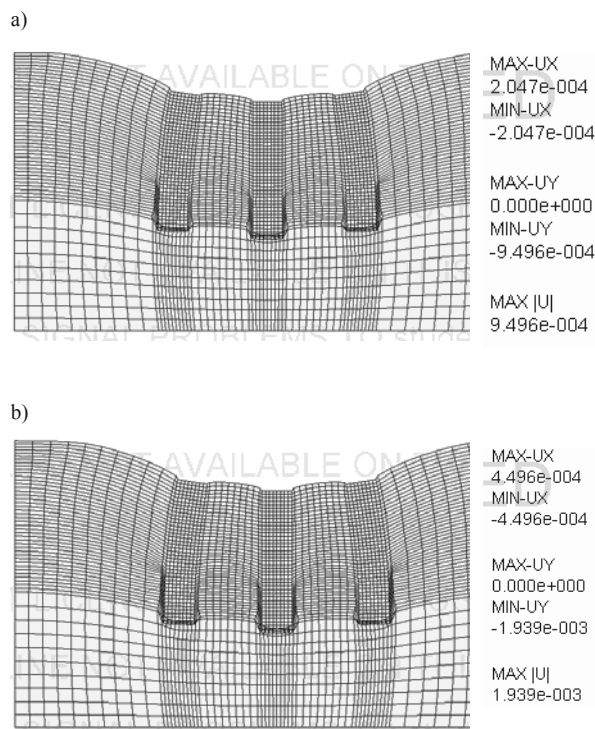


Figure 2. Model deformations [m] under influence of the load of embankment: a)  $h=2.0$  m; b)  $h=4.0$  m high (Z\_Soil) (Bzówka et al. 2012; Juzwa 2012a).

Fractal theories may be used to describe an irregular surface of jet grouting columns. Using a fractal and a box dimension it is possible to describe better an irregular shaft surface of a jet grouting column, its shape and roughness. A more precise description of roughness and geometrical parameters of soil particles allows a more detailed determination of such properties as: porosity, density and shear strength (Bzówka and Skrzypczyk 2011).

The paper presents an example of fractal dimension and box dimension calculation for an excavated jet grouting column made in a single system (see Fig. 6÷8). Results of studies presented in papers (Kawa and Wieczorek 2005; Wanik 2012a, 2012b; Wanik and Bzówka 2012) have been used.

The described jet grouting column was made in average compacted medium sand, under which a stiff silty clay was situated. After column excavating and cleaning, an irregular shaft surface was disclosed and also a clear change of column diameter on the boundary of two layers forming the subsoil (see Fig. 5).

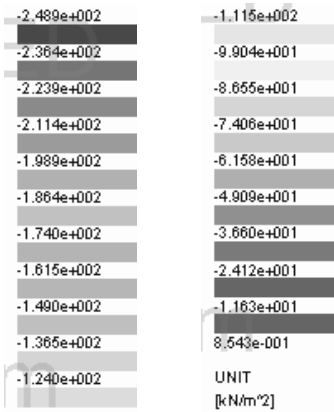
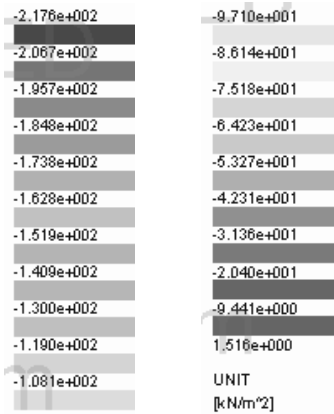


Figure 3. Map of vertical stresses of the model under influence of the load of embankment: a)  $h=2.0$  m; b)  $h=4.0$  m high ( $Z_{Soil}$ ) (Bzówka et al. 2012; Juzwa 2012a).

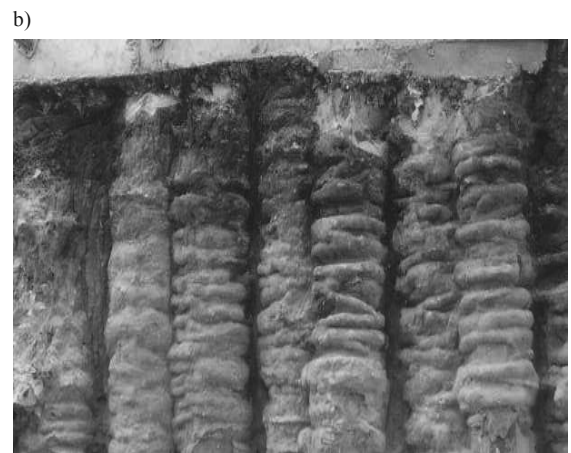


Figure 4. Different shapes of excavated jet grouting columns (photos: J. Bzówka, and K. Wanik).



Figure 5. Structure of excavated jet grouting column (photo: J. Bzówka).

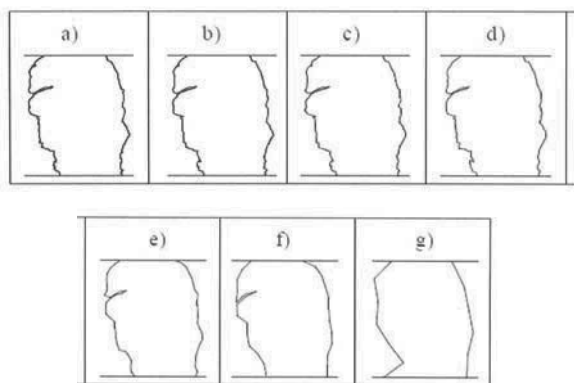


Figure 6. Method for determining fractal dimension for column (Kawa and Wiczorek 2005; Wanik 2012a).

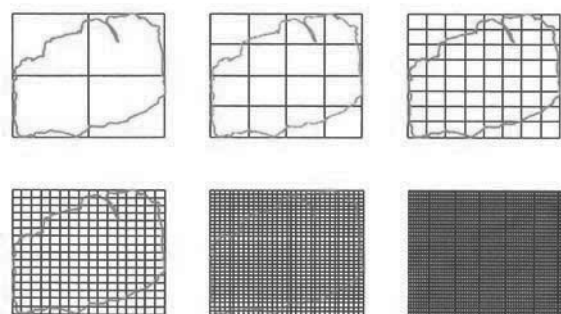


Figure 7. Method for determining box dimension for column (Kawa and Wiczorek 2005; Wanik 2012a).

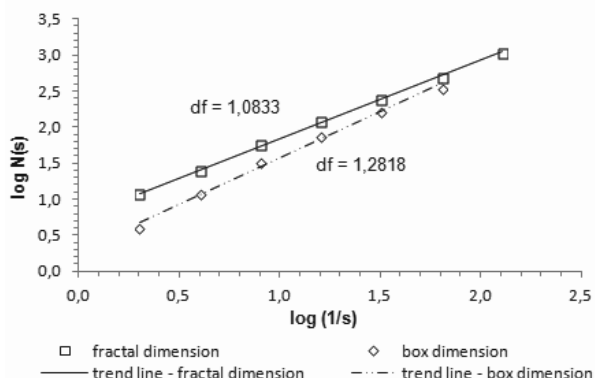


Figure 8. Fractal dimension and box dimension for jet grouting column.

### 3 SUMMARY

Issues presented in the paper show the scale of problems related to the representation of actual interaction of jet grouting columns with the surrounding subsoil. Theoretical models require repetitions and calibration, making the obtained results realistic. It is especially important to determine the thickness and parameters of the contact zone formed at the contact of column material and the subsoil.

The shape and dimensions of formed jet grouting columns depend on the type and condition of soils building the subsoil and on technological parameters of columns forming, such as: the injection pressure, the injection rod pulling out and rotation speed, the density of injected cement grout as well as the number and size of injection nozzles.

A large number of factors affecting geometry and hence related columns bearing capacity and the soil-cement material strength causes problems in designing. To verify geometry of columns made it is necessary to perform excavations and to measure the diameter, circumference shape and to assess the shaft structure. Mathematical issues from the field of fractal and box dimension allow creating a clear description of a complicated shape of jet grouting columns shaft.

### 4 ACKNOWLEDGEMENT

The co-Authors: Anna Juzwa and Lidia Wanik received a grant of the DoktorIS project – a scholarship program for innovative Silesia region co-financed by the European Union of the European Social Fund.

### 5 REFERENCES

Bzówka J. 2009. Interaction between jet grouting columns and subsoil. Monograph published by the Silesian University of Technology, Gliwice (in Polish).

Bzówka J. 2010. FEM analysis of interaction of jet grouting column with subsoil. Scientific Conference on Natural and Technical Problems of Environmental Engineering – Soil parameters from in situ and laboratory tests, Poznań 27-29 September 2010, 445–455.

Bzówka J. and Juzwa A. and Wanik L. 2012. Selected problems of jet grouting application. *Inżynieria Morska i Geotechnika*, No. 4, 514–519 (in Polish).

Bzówka J. and Skrzypczyk J. 2011. Fractal dimensions in geotechnics. Proc. of the 9<sup>th</sup> International Conference on New Trends in Statics and Dynamics of Buildings, 20-21 October 2011, Bratislava, Slovakia, 21–24 (in Polish).

Juzwa A. 2012a. Computational description of interaction between group of jet grouting columns and subsoil. Monograph: *Experimental and theoretical tests in Civil Engineering* published by the Silesian University of Technology, Gliwice, 67–74 (in Polish).

Juzwa A. 2012b. Subsoil strengthening by using jet grouting technology. 9<sup>th</sup> fib International PhD Symposium in Civil Engineering, Karlsruhe Institute of Technology, Germany, 22-25 July 2012.

Kawa K. and Wiczorek W. 2005. Fractals application in geotechnics. Master thesis, The Silesian University of Technology, Faculty of Civil Engineering, Gliwice (in Polish).

Modoni G. and Bzówka J. 2012. Analysis of foundations reinforced with jet grouting. *ASCE-Journal of Geotechnical and Geoenvironmental Engineering*.

Wanik L. 2012a. Application of fractals to describe shape of jet grouting columns. Monograph: *Experimental and theoretical tests in Civil Engineering* published by the Silesian University of Technology, Gliwice, 133–141 (in Polish).

Wanik L. 2012b. Fractal and box dimensions in description of jet grouting columns geometry. *Inżynieria Morska i Geotechnika*, No. 4, 432–434 (in Polish).

Wanik L. and Bzówka J. 2012. Influence of various factors on geometry of jet grouting columns. *Zeszyty Naukowe Politechniki Rzeszowskiej, Budownictwo i Inżynieria Środowiska*, z.59 (3/12/IV), No. 283, t. 4, 117–124 (in Polish).

# Column Supported Embankments for Transportation Infrastructures: Influence of Column Stiffness, Consolidation Effects and Cyclic Loading

Remblais sur sols renforcés avec de colonnes ballastées pour les infrastructures de transport: Influence de la rigidité des colonnes, des effets de consolidation et du chargement cyclique

Carvajal E., Vukotić G.  
Kellerterra S.L., Madrid, Spain

Sagaseta C.  
University of Cantabria, Santander, Spain

Wehr W.  
Keller Holding GmbH, Offenbach, Germany

**ABSTRACT:** Ground improvement methods based on column-type elements are analyzed regarding the influence of the column properties on serviceability and safety of the Column Supported Embankments (CSE). Particularly, treatments made by rigid inclusions are analyzed and compared with stone columns. Stiffness of column-type elements determines the design and risks involved. Rigid inclusions are analyzed according to the recent French national project ASIRI. In the case of these elements, a considerable mobilization of negative skin friction and punching effects governs their behavior in the Ultimate Limit State, which represents a non-ductile mechanism of failure. Whereas stone columns present a ductile behavior determined in the domain of Serviceability Limit State (SLS). It is pointed out, that possible damages on CSE systems may extend settlement stabilization due to the consolidation process, if no drainage elements are adopted. It is also noted that risks related to rigid columns in the SLS under cyclic loading, may be decisive in the design of CSE composed by low-heights embankments. Briefly, it could be stated that rigid inclusions present higher risks, increasingly when their diameters are smaller than 30 cm.

**RÉSUMÉ :** On analyse les méthodes d'amélioration des sols avec des colonnes pour la fondation des remblais sur sols mous. En particulier, on analyse les inclusions rigides selon les recommandations du récent projet national français ASIRI, et on présente la comparaison avec des colonnes ballastées. La rigidité de la colonne détermine la conception et les risques associés. Dans le cas des inclusions rigides, une mobilisation considérable du frottement négatif et la portance résultante gouvernent leur comportement dans l'état limite ultime, ce qui représente un mécanisme non-ductile de rupture. Au contraire, les colonnes ballastées présentent un comportement ductile déterminée dans le domaine de l'état limite de service. Il a été observé que les risques de colonnes rigides dans les ELS peut être retardés à moins que on installe quelques éléments de drainage. On a remarqué aussi que les risques associés aux inclusions rigides soumises aux chargements cycliques peuvent être décisives pour remblais de faible hauteur. Ainsi, les inclusions rigides présentent des risques plus élevés, de plus en plus lorsque leur diamètre est plus petit que 30 cm.

**KEYWORDS:** Load Transfer Platform, geosynthetic, embankment, rigid inclusion, stone columns, risk, stiffness, arching effect

## 1 INTRODUCTION

Column Supported Embankments (CSE) represent an innovative solution for transport infrastructure over soft soils, in order to reduce execution time and general earthworks. Hence, the use of low-height embankments based on column-type elements tends to be preferred, whenever possible, instead of direct soil replacement or preloading with or without vertical drains. Recently, the use of CSE is increasing, and consequently growing interest in developing reliable and unified criteria for their design and construction is observed.

However, due to the possibility of application of a wide range of ground improvement techniques, further risk assessment has to be done. Risks and reliability related to CSE could be largely analyzed considering the influence of column stiffness in Ultimate and Serviceability Limit States. Furthermore, column stiffness also affects consolidation process and the system behavior against cyclic or dynamic loading, very often decisive for safety and serviceability.

## 2 COLUMNS SUPPORTED EMBANKMENT SYSTEMS

### 2.1 Type of columns

Typical elements of CSE systems are shown in Figure 1. Initially, reinforced piles with concrete cap were applied, in order to absorb the largest load of embankment as possible. In

order to optimize the solution, ground improvement methods have been increasingly used in the last years.

Ground improvement methods should intent not to take the entire action by the supporting elements, but only the difference between the required and existing bearing capacity without improvement (Wehr et al. 2012). This is applicable to stone and sand columns, which take important part of the foundation load, and make the most of soil confinement to ensure its own capacity. These two types of columns accelerate the consolidation process and do not need any embedment to transfer the loads to stiffer soil layers; thereby they can be considered as authentic ground improvements.

On the other side, the columns made by the addition of bonding agents, mortar or concrete into the ground, do not accelerate consolidation. The improvement introduced by such columns mainly consists of the load transfer to the stiffer layers in the same way as piles, thus, to ensure their correct application the largest embedment is frequently desired.

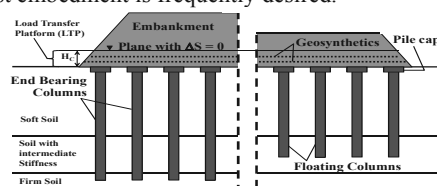


Figure 1. Elements of Column Supported Embankment Systems



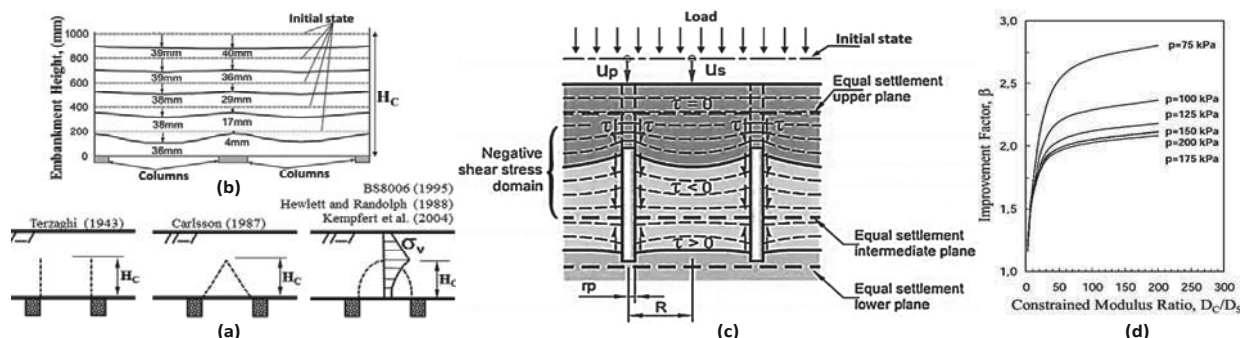


Figure 2. Mechanism of load transfer in the CSE: (a) approaches of arching-effect shape; (b) results of laboratory test performed by Chen et al. (2008); (c) load transfer mechanism proposed by Combarieu (1974, 1988); (d) influence of confined modulus on improvement factor (Kirsch 2004).

These kinds of columns, with predominantly round cross-sections of 25 cm to 80 cm diameter, are denominated Rigid Inclusion according to the French national research project ASIRI (Améliorations de Sols par Inclusions Rigides). Rigid inclusions may be arranged in a regular grid, although, due to horizontal stresses sometimes have to be distributed in wall or panel form in order to overcome slope and internal instability.

### 2.2 Load Transfer Platform

The design and operation of CSE is largely influenced by the load transmission mechanism toward the columns, through a Load Transfer Platform (LTP) laid out at the base of embankment. LTPs are generally composed by a layer of compacted granular material that in many cases has to be reinforced by geosynthetics, or composed by layers treated with hydraulic binder.

LTP behavior is essentially determined by two parameters. The efficacy or efficiency  $E$ , defined as the ratio between load on the column head  $Q_p$  and the total load on the surrounding soil within a unit cell ( $W + Q$ ), where  $W$  is the weight of embankment and  $Q$  is the force due to surcharge on the surface; and the critical Height  $H_c$ , which indicates the height of embankment where differential settlements in between column head and middle of the grid are negligible. As stated by several authors,  $E$  and  $H_c$  depend on many factors such as column rigidity, shear strength of LTP layers, spacing between columns, and soft soil stiffness (Zaeske and Kempfert 2001, Okay 2010).

Most theoretical methods focus on the requirements of the geosynthetic within LTPs for piled embankments, considering a void between rigid elements. The geosynthetic takes the load that remains in the middle of columns and delivers it to the column heads by means of membrane effect. Consequently almost all load is acting on the columns heads. According to these methods only a minor part or even any soil reaction is considered. Several guidelines or recommendations documents deal with these methods (BS8006 2010, EBGeo 2010, Nordic Handbook 2005). Such approaches could be classified according to the shear stress form-distribution that governs the mechanism of arch load-transfer and differential settlements within the LTP (Han and Colling 2005), see Figure 2a. According mentioned approaches  $H_c$  varies from 0.7 to 1.6 times the clear distances between columns ( $s - a$ ).

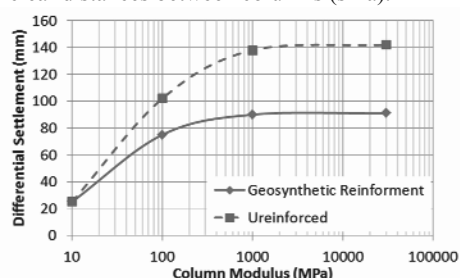


Figure 3. Influence of column modulus on the differential settlements within Load Transfer Platform (Gangakhedar 2004).

Otherwise, the method proposed by Combarieu (1974, 1988), and adopted in the ASIRI Recommendations, deals not only with the load transfer into LTP but also along the entire length of rigid columns. Furthermore, ASIRI project's recommendations are based on various physical and numerical modelling (Jenck 2005, Chevalier et al. 2008).<sup>1°</sup>

Figure 2c shows the mechanism of load transfer proposed in the ASIRI, where differential settlements between soil and columns produce negative skin friction in the upper part of the column; at certain depth where settlements are the same in soil and columns, the skin friction is equal to zero, and below this neutral plane the load in the columns is transferred through positive skin friction and tip resistance. It can be noted that such mechanism is quite similar to those exhibited by the combined pile-raft foundations (CPRF).

## 3 INFLUENCE OF THE COLUMN CHARACTERISTICS

### 3.1 Columns stiffness

Unfortunately, so far there is not any analytical method (commonly used) that takes into account the variation of column stiffness, and accordingly numerical modelling usually have to be performed to analyze the influence of column stiffness. However, even the most relevant numerical modelling that can be found in the literature has no focus on the risks and suitability aspects related to the column stiffness.

Kirsch (2004) analyzed the influence of the ratio between confined modulus of columns and soil on the improvement factor  $\beta$  (ratio of settlements with and without improvement). Results indicate that confined modulus ratios beyond 40 to 50 do not suppose considerable increments on improvement factor  $\beta$ , (Figure 2d). Similarly, Gangakhedar (2004) performed a numerical analysis of the influence of Young's modulus of the columns, on the differential settlements at the base of geosynthetic reinforced embankment. Figure 3 shows that differential settlements increase with increasing column modulus. Although it can be noted that there exists a greater increase of differential settlements when modulus are higher than those usually obtained for stone columns, of about 80 to 120 MPa, and that differential settlements tends to be much higher with the increase of column modulus if no geosynthetic reinforcement is considered.

Therefore, the cost-operating inefficiency of columns may be stated when column modulus are higher than 120 MPa, or modulus ratio are larger than 40 to 50, approximately. If columns rigidity exceeds this limits, CSE system requires an increase on the capacity of geosynthetic-reinforcement and the additional improvement is negligible.

It is well known that stone columns have a load-carrying mechanism by lateral bulging, whereas rigid inclusions transmit the load by skin friction and punching effect on their tip and head. In the latter case, the usual amount of differential settlement obtained in the column head implies a behavior controlled by its ultimate limit state (ULS), and governed by mobilization of negative skin friction. Figure 3 depicts that such

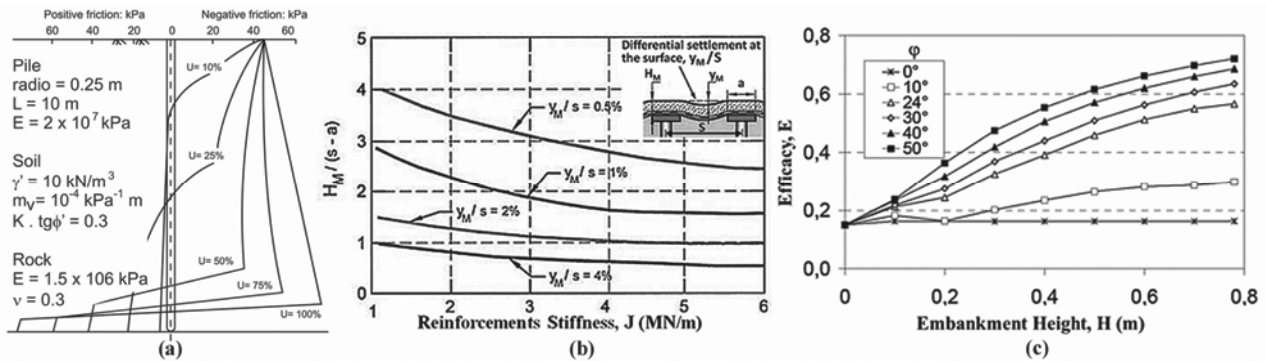


Figure 4. (a) Estimation of evolution of negative skin friction with degree of consolidation (Alonso et al. 1984); (b) chart for geosynthetic design based of allowable differential settlement (Lawson 2000); (c) influence of height and friction angle of embankment on Efficacy factor (Jenck 2005).

deformation in the head of rigid inclusions may suppose the failure state, as settlements may reach levels corresponding to large percent of column diameter. Furthermore, the punching failure in the head and toe of columns occurs immediately after the application of embankment load, and associated risk increases with smaller diameters of rigid inclusion, being quite sensitive to the variation of the soil parameters also.

On the other side, flexible elements like stone columns tend to reduce the punching effects at the base of embankment. In this case the system gives a ductile behavior, whereas, due to column compressibility and its drainage characteristics, the ultimate limit state is reached after large deformation and at the end of consolidation. Therefore, the behavior of such system takes place in the domain of serviceability limit state (SLS).

Wehr et al. (2012) proposed three categories of increasing risks, in order to assess the reliability of ground improvement methods according to their ductility and sensitivity to the variation of soil and materials parameters, taking as a reference the standards DIN 1054 and Eurocode 7. Thus, regarding to columns-type elements, flexible columns with small risks (stone columns, vibro compaction, sand columns) are in category A; rigid columns with diameter larger than 30 cm, which presents an average risk, are in category B; and rigid inclusions with diameters less than 30 cm and non-ductile behavior, which represent a high risk, are in category C.

### 3.2 Consolidation process

The addition of cement agents disables the drainage capacity of rigid columns, whereby settlements stabilization is obtained only due to a high load concentration on the columns. However, during the consolidation of pore pressures produced by the remaining part of embankment load that act on the soil, an important negative skin friction is generated in the part of columns above the neutral plane, very similar to piles, but without any capacity and structural connections. Consequently, the risk should be assessed due to possible reduction or loss of the load concentration on columns (or efficiency factor) along the lifetime of the CSEs. This situation could occur if certain loss of arching effect happens, as a consequence of possible LTPs deteriorations, e.g. due to internal failure of geosynthetic-reinforcement. In this case, the consolidation would occur in the long term, according to the permeability of the natural soil.

Moreover, it would involve the evolution of neutral plane over the time, dominated by the increase of negative friction. Figure 4a shows an example of this complex mechanism reported by Alonso et al. (1984).

In the case of stone columns, the rapid settlements stabilization is expected due to their drainage capability. Castro and Sagaseta (2009) analyzed the evolution of stress concentration on the stone columns, showing that in the very beginning entire load is carried by the soil, and the final load concentration on the columns is obtained after consolidation (Figure 5). However, after short period of consolidation,

effective stress of soil tends to increase, and additionally provides greater confinement to the columns. Such results suppose an improvement of the whole column-soil system.

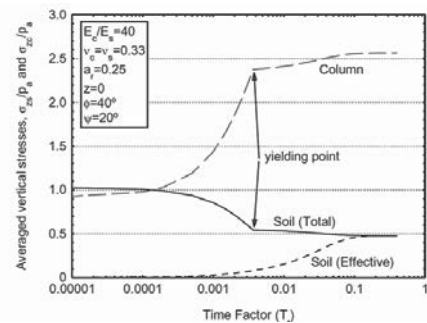


Figure 5. Time development of soil and column stresses, (Castro and Sagaseta 2009)

## 4 GENERAL ASPECTS OF SAFETY VERIFICATION

There is a range of recommendations that attempt to unify design of LTPs composed by geosynthetic-reinforcement layers, basically used in piled embankments (BS8006 2010, EBGE0 2010, Nordic Handbook 2005). However, the design of column-type elements is redirected to typical pile standards. As it was mentioned in section 2.2, it has to be emphasized, that these recommendations deal with systems where almost entire load is transferred to bearing elements heads, hence negative skin friction is practically negligible. According to what has been stated here about the higher level of risk exhibited by the rigid inclusions with small diameter, the most important safety aspects of such elements will be commented.

### 4.1 Large-height embankment

The ASIRI recommendations define two different situations:

Domain 1: if the ULSs are not guaranteed without improvement, rigid inclusions are used to ensure the global stability, and bearing capacity of rigid inclusions for both ULSs and SLSs have to be checked, similarly to the French Eurocode 7 application for piles.

Domain 2: if the ULSs are analyzed for the situation without improvement, then rigid inclusions are used as settlement reducers, and only SLSs have to be proceeded.

Taking into account the ASIRI recommendations, it could be distinguished that when the CSE system comprises embankments with more than 3 to 5 m height, the design is usually focused to guarantee the ULSs. Regarding to the external bearing capacity (GEO) for rigid inclusions, the most important checks against the permanent loads will be punching at their heads and tips, as well as the horizontal stresses, bending moments and shear stresses due to slope failures. Buckling effects have to be checked when soft soil has pressuremeter modulus smaller than 3 MPa.

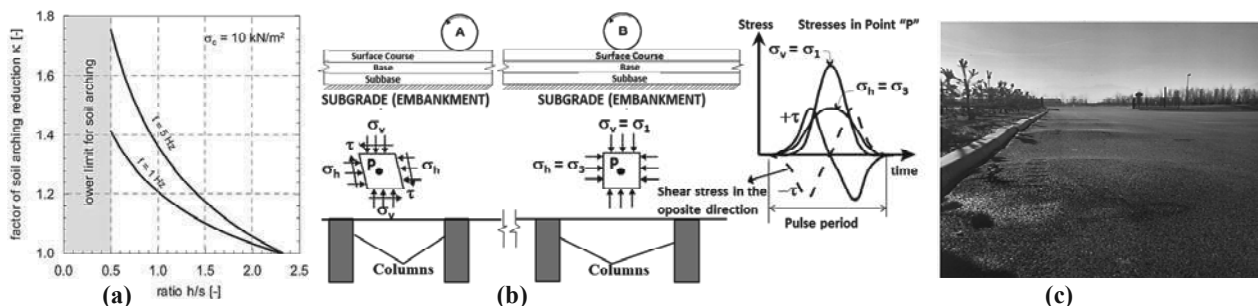


Figure 6. (a) Factor of soil arching reduction (Heitz et al. 2008); (b) stress conditions in the subgrade due to moving load on the pavement surface; (c) pavement deformation due to hard-point effects associated with the presence of rigid inclusions.

Regarding to the structural bearing capacity (STR), a minimum compressive strength of 7 MPa has to be adopted, and no shear stress is allowed for unreinforced columns smaller than 30 cm. Besides, if tension can develop, for Domain 1 the rigid inclusions have to be reinforced, whereas for Domain 2 only an adequate tensile strength of concrete could be adopted.

On the other hand, Katzenbach et al. (2012) have compared the safety checks outlined in the ASIRI recommendations with other guidelines for similar foundation systems usually used in Germany (CSV, CRPF), according to the partial safety factor approach. They reported that ASIRI has lower values of safety factors than those the compared guidelines indicate.

#### 4.2 Low-height embankment

In the case of embankments with heights less than 3 meters, the design is usually aimed to guarantee the SLSs, according to the Domain 2. Basically, the geometry of the CSE systems has to be set to avoid excessive deformation in the surface of the embankments, in order to allow an adequate traffic operation. For this objective Lawson (2000) proposed the chart depicted in Figure 4b, for the design of the height and geosynthetic-reinforcement of LTP layers considering the columns as hard points, and according to typical thresholds adopted in transport projects related to differential settlements.

The differential settlements also depend on the LTP strength. Figure 4c shows the analysis of Jenck (2005) related to the influence of the height of the embankment and the strength of unreinforced LTPs in terms of friction angle. Results indicate that efficiency factor  $E$  increase with height of embankments until a maximum value similar to the critical height  $H_c$ . Also, it can be seen that when LTP is composed by materials with friction angle less than 20 degree the efficiency factor is drastically reduced, and practically negligible when  $\phi = 0$ .

So far it is not fully analyzed the behavior of CSE against the cyclic loading of traffic. Heitz et al. (2008) have demonstrated that the arching mechanism to transfer load of LTP can only be formed in a very limited extent if geosynthetic reinforcement is not placed. Based on laboratory model tests under cyclic loading, they proposed a soil arching reduction factor,  $\kappa$ .

Figure 6a shows this factor depending on the ratio of fill height and column spacing  $h/s$ , the frequency  $f$  and amplitude of the cyclic load  $\sigma_c$ . For rigid inclusion application negative influence of the traffic loading has to be considered during construction and operation stages. Figure 6b illustrates that cyclic loading of traffic can generate the rotation of principal stresses in the subgrade layers, which could cause severe damages to the rigid inclusions and pavement serviceability in the long term, especially for low-height embankments.

Finally, Figure 6c shows an example of pavement deformation due to a combination of the effects mentioned.

#### 5 CONCLUSIONS

The influence of columns stiffness commonly used on the Column Supported Embankment (CSE) systems has to be rigorously investigated in order to establish the implications on the safety and serviceability issues. The facts that indicate the higher risks of rigid inclusions compared with flexible ground

improvement methods like stone columns are exposed, especially when diameters of rigid inclusions are smaller than 30 cm. Moreover, the requirements of LTPs in terms of strength and thickness, has to be more strict for rigid inclusion comparing with stone columns, in order to ensure the arching load transfer in the long term behavior of the CSEs, for both static and cyclic loading.

#### 6 REFERENCES

- Alonso E. Josa A. and Ledesma A. 1984. Negative skin friction on piles: a simplified analysis and prediction procedure. *Geotechnique* 34. No. 3. pp 341-357.
- ASIRI National Project. 2012. Recommendations for the design, construction and control of rigid inclusion ground improvements.
- British Standard 8006. 2010. Code of practice for strengthened/reinforced soils and other fills. British Standard Institution. London.
- Castro J. and Sagaseta C. 2009. Consolidation around stone columns. Influence of column deformation. *Int. J. Num. Anal. Meth. Geomech.* 33(7): 851-877. doi:10.1002/nag.745.
- Chen Y. M. Cao W. P. and Chen R. P. 2008. An experimental investigation of soil arching within basal reinforced and unreinforced piled embankments. *Geotex. and Geom.* 26. 164-174.
- Chevalier B. Combe G. and Villard P. 2008. Modélisation discrète: étude du report de charge. Rapport 3-08-4-01.
- Combarieu O. 1988. Amélioration des sols par inclusions rigides verticales. Application à l'édification des remblais sur sols médiocres. *Revue française de géotechnique* No. 44. pp 57-79.
- EBGEO. 2011. Recommendation for design and analysis of earth structures using geosynthetic reinforcement. Ernst & Sohn. Berlin.
- Gangakhedar R. 2004. Geosynthetic reinforced piled-supported embankments. Master thesis. University of Florida.
- Han J. and Collin J.G. 2005. Geosynthetic Supported System over Pile Foundations". *ASCE. G.S.P.* 130-142. pp. 3949-3953
- Heitz C. Lüking J. and Kempfert H.G. 2008. Geosynthetic reinforced and pile supported embankments under static and cyclic loading. *Proceedings EuroGeo 4*. Edinburg. United Kindom.
- Jenck O. 2005. Le renforcement des sols compressibles par inclusions rigides verticales. Modélisation physique et numérique. Thèse de Doctorat. INSA Lyon.
- Kirsch F. 2004. Experimentelle und numerische Untersuchungen zum Tragverhalten von Rüttelstopfsäulen. Dissertation am Institut für Grundbau und Bodenmechanik. Heft 75. Braunschweig.
- Katzenbach R. Bohn C. Wehr J. 2012. Comparison of safety concepts for soil reinforcement methods using concrete columns. Technische Universität Darmstadt. Institut und Versuchsanstalt für Geotechnik.
- Lawson C. R. 2000. Serviceability limits for low-height reinforced piled embankment. *Proceedings GeoEng 2000*. Melbourne. Australia.
- NGG. 2005. Nordic Handbook – Reinforcement soil and fills, Nordic Geotechnical Society. Stockholm
- Okay U.S. 2010. Etude expérimentale et numérique des transferts de charge dans un massif renforcé par inclusions rigides. Application à des cas de chargements statiques et dynamiques. PhD in the scope of ASIRI. INSA Lyon and Université Claude Bernard.
- Wehr W. Topolnicki M. And Sonderman W. 2012. Design Risks of ground improvement methods including rigid inclusions. *International Symposium – Ground improvement*. Brussels.
- Zaesck D. and Kempfert H.G. 2001. Wirkungsweise von unbewehrten und unbewehrten mineralischen Tragschichten über pfahlartigen Gründungselementen. Universität Gh Kassel. Heft 10.

# Foundations of embankments using encased stone columns

## Fondations de remblais avec des colonnes ballastées entourées de géotextile

Castro J., Sagaseta C., Cañizal J., Da Costa A., Miranda M.  
*University of Cantabria, Santander, Spain*

**ABSTRACT:** Stone columns are a common improvement technique for foundations of embankments in soft soils. When the soft soil does not provide enough lateral support, the columns are encased with a geosynthetic. This paper presents a closed-form solution to study soft soil improvement, both reduction of settlement and consolidation time, by means of encased stone columns. An end-bearing column and its surrounding soil, is modelled in axial symmetry under a rigid and constant load. Soil is assumed as elastic but plastic strains are considered in the column. An elasto-plastic behaviour is also considered for the encasement by means of a limit tensile strength. Parametric studies of the settlement reduction and stress concentration show the efficiency of encasing the columns, which is mainly ruled by the encasement stiffness compared to that of the soil. The analytical results are in good agreement with numerical analyses. Finally, the encasement length is analysed using the closed-form solution.

**RÉSUMÉ:** Les colonnes ballastées sont une technique d'amélioration de sol pour les remblais en sols mous. Lorsque le sol mou ne fournit pas assez de soutien latéral, les colonnes sont entourées avec un géosynthétique. Cet article présente une solution analytique pour étudier l'amélioration des sols mous, la réduction des tassements ainsi que le temps de consolidation, au moyen des colonnes entourées en géotextile. Une colonne ne reprenant les efforts que par la pointe et le sol environnant sont modélisés en axisymétrie sous une charge constant. Le comportement du sol est supposé élastique mais les déformations plastiques sont considérées dans la colonne. Un comportement élasto-plastique est également pris pour le géosynthétique au moyen d'une résistance à la traction limite. Des études paramétriques de la réduction du tassement et de concentration de contraintes montrent l'efficacité de l'enveloppe géosynthétique des colonnes, ce qui est principalement régie par la rigidité de l'enveloppe géosynthétique par rapport à celle du sol. Les résultats analytiques présentent une bonne concordance avec les analyses numériques. Finalement, la longueur de l'enveloppe géotextile est analysée en utilisant la solution basée sur une cellule élémentaire constituée d'une colonne et d'un volume élémentaire de sol.

**KEYWORDS:** soft soils, ground improvement, encased stone columns, analytical solution, numerical analyses.

### 1 INTRODUCTION

Stone columns, either by the vibro-replacement or vibro-displacement methods, are one of the most common improvement techniques for foundation of embankments or structures on soft soils. The inclusion of gravel, which has a higher strength, stiffness and permeability than the natural soft soil, improves the bearing capacity and the stability of embankments and natural slopes, reduces total and differential settlements, accelerates soil consolidation and reduces the liquefaction potential. Alteration of the natural soft soil caused by stone column installation (Guetif et al. 2008, Castro and Karstunen 2010) is not usually considered in their design.

Stone columns may not be appropriate in very soft soils that do not provide enough lateral confinement to the columns. It is generally accepted that those are soils with undrained shear strengths below 5-15 kPa (Wehr 2006). To increase the lateral confinement of the columns, and consequently their vertical capacity, encasing the columns with geotextiles has proved to be a successful solution in recent years.

A high tensile stiffness of the encasement is recommended as it will be shown in this paper; and therefore, other geosynthetics, such as geogrids, are also used to encase the column (Sharma et al. 2004, Gniel and Bouazza 2009). However, geogrids do not act as a filter and do not avoid contamination of the column with fines.

The development of encased stone columns as a ground improvement technique has come with an increasing number of studies in the last decade. However, most of the research is done using numerical methods (e.g. Murugesan and Rajagopal 2006, Malarvizhi and Ilamparuthi 2007, Smith and Filz 2007, Yoo 2010, Lo et al. 2010) and there are very few analytical solutions available in the literature (Raithel and Kempfert 2000, Pulko et al. 2011). That recently motivated the authors to develop a new closed-form solution to study the deformation and consolidation

around encased stone columns (Castro and Sagaseta 2011). That solution is an extension of another previous analytical solution developed for non-encased stone columns (Castro and Sagaseta 2009).

This paper analyses the main features of that closed-form solution, showing its limitations and range of applicability, the influence of the key parameters for routine design and a comparison with numerical analyses.

### 2 CLOSED-FORM SOLUTION

#### 2.1 Model

The vertical capacity of the columns is a fundamental issue when the applied load is concentrated on the columns. Therefore, column encasement is very useful in those cases (Murugesan and Rajagopal 2010, Khabbazian et al. 2010); but also under distributed loads, such as tanks or embankments, because the increase of lateral confinement reduces the settlement.

The authors' closed-form solution (Castro and Sagaseta 2011) is limited to distributed uniform loads because it is based on a "unit cell" model, i.e. only one column and its surrounding soil are studied in axial symmetry. Furthermore, the column is assumed to be fully penetrating in the soft soil and the applied load is considered as rigid, i.e. uniform settlement. The area of soft soil,  $A_b$ , that is improved by each column,  $A_c$ , is generally expressed by the area replacement ratio,  $a_r = A_c/A_b$ , but sometimes is also defined in terms of the relation between diameters or radii,  $N = r_i/r_c = 1/\sqrt{a_r}$ .

The solution is developed for a horizontal slice at a depth  $z$  of the unit cell, and consequently, shear stresses between slices at different depths are not considered (Figure 1). The overall

behaviour of the whole unit cell is obtained by means of integration of the solution at the different depths.

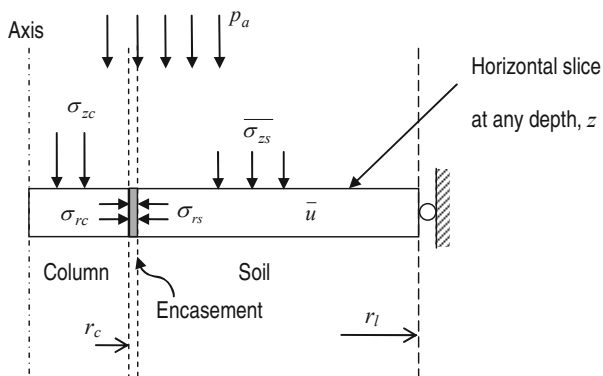


Figure 1. Analytical model.

## 2.2 Consolidation

The analysis of consolidation around encased stone columns as a fully coupled problem is difficult to deal with. As a simplifying assumption, the solution uses the average value of the excess pore pressure along the radius,  $\bar{u}$ , which is a simple way of getting a reasonably accurate solution. The details of this kind of approach can be found in Castro and Sagaseta (2009). Multiple instantaneous load steps may be considered. The column (drain) is considered to be fully permeable, which is doubtful for conventional stone columns but is reasonable if the columns are coated with a geotextile. In this way, consolidation around encased stone columns is studied using any conventional solution for radial consolidation (e.g. Barron 1948) and a modified coefficient of consolidation that accounts for the influence of column and encasement.

## 2.3 Encasement

The encasement is modelled as a cylindrical shell of negligible thickness around the column. Therefore, it is valid for different types of coating, such as geotextiles, geogrids... Encasement behaviour is supposed to be linear elastic-perfectly plastic and characterized by a tensile stiffness,  $J_g$ , and a maximum tensile strength,  $T_{g,max}$ . During column installation, the encasement is pre-stressed to an initial tensile stress,  $T_{g,i}$ . The encasement tensile stress obtained with the analytical solution is the increment from that value,  $\Delta T_g$ .

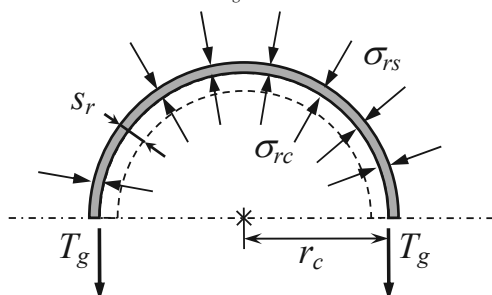


Figure 2. Equilibrium and compatibility conditions of the encasement.

The encasement is compressed in vertical direction, and as it can only take tension, it does not have any influence in vertical direction. Its equilibrium and compatibility conditions (Figure 2) are those of a thin tube under internal,  $\sigma_{rc}$ , and external pressure,  $\sigma_{rs}$ .

$$\sigma_{rc} = \frac{T_g}{r_c} + \sigma_{rs} \quad (1)$$

$$T_g = J_g \frac{s_r}{r_c} \quad (2)$$

where  $s_r$  is the radial displacement of the interface.

Combining these two equations, the radial equilibrium between soil and column at their interface depends on the encasement properties (stiffness and radius) and its radial expansion.

$$\sigma_{rc} = \frac{J_g s_r}{r_c^2} + \sigma_{rs} \quad (3)$$

Those simple equations (Eq. 2 and 3) show how the encasement influence depends on its stiffness and radius.

## 2.4 Formulation

The detailed formulation of the solution can be found in Castro and Sagaseta (2009, 2011). Three different possible phases are identified: (a) soil, column and encasement in the elastic range, (b) column yielding and (c) encasement yielding, which will occur after column yielding in a real situation.

A sensible design should cause yielding of the column but not of the encasement. Therefore, the last phase of the solution may not be considered and it is just necessary to check that the tensile stress of the encasement does not exceed its strength.

The solution considers just one instantaneous load step, but it is quite straightforward to generalize it for multiple loading steps (Castro and Sagaseta 2008), taking the initial stresses as the final ones of the previous load step. However, modelling the real loading steps is only necessary to study the consolidation process but not for the final values as it gives the same results.

## 2.5 Drained solution

The studied closed-form solution models the consolidation process. However, consolidation around stone columns, especially if the columns are coated with a geotextile, may be nearly as fast as the loading pace, which means that for these cases drained condition is a more reasonable assumption.

In any case, depending on the soil permeability and the loading pace, the real behaviour is between drained condition and an undrained loading followed by consolidation. Fortunately, both cases yield very similar final values as can be shown numerically.

Nonetheless, analytical solutions use simplifying assumptions that have different consequences in each situation. The most evident example is disregarding the elastic strains in the column once it has reached its active state. This assumption gives acceptable results for non-encased columns or when the consolidation process is modelled but not if drained conditions are considered for encased columns (Castro and Sagaseta 2011). Hence, in that last case it is necessary to account for those elastic strains in the column (Pulko et al. 2011).

## 3 PARAMETRIC STUDY AND NUMERICAL ANALYSES

### 3.1 Numerical model

Numerical simulations are included in the parametric study to evaluate the accuracy of the closed-form solution and the influence of its simplifying assumptions, such as neglecting the shear stresses and using an average pore water pressure along the radius. Coupled numerical analyses of the unit cell were performed using the finite element code Plaxis v8.6 (Brinkgreve 2007). For comparison purposes, the same boundary conditions and material properties of the analytical solution were chosen for the numerical models. Therefore, a rigid plate was set on top

of the unit cell, the soil was modelled as elastic and the encasement and the column as elastic-perfectly plastic.

### 3.2 Stress concentration

The ratio between the vertical stress on the column and on the soil is usually called the stress concentration factor ( $SCF = \sigma_{zc} / \sigma_{zs}$ ) and gives an idea of the part of the applied load that the soil transfers to the column. Figure 3 shows its variation with time. The vertical stresses on the soil and on the column may vary with the radius, and therefore, their averaged values are used to calculate the  $SCF$ .

A higher encasement stiffness provides a better lateral confinement to the column, and hence, the column supports a higher load. A good agreement is found between the analytical and the numerical results. However, as it happens for the stone column solution (Castro and Sagasta 2009), the agreement for low degrees of consolidation (<30%) is not very good due to inherent assumptions of Barron's solution.

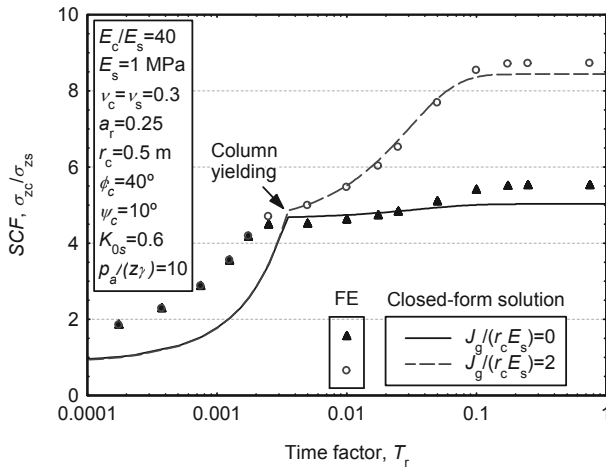


Figure 3. Stress concentration on the column with time.

### 3.3 Settlement reduction

The settlement reduction decreases with the applied load,  $p_a$ , from an elastic value,  $\beta^e$ , and approaches a plastic one,  $\beta^p$ , at the same rate as plastic strains develop in the column (Figure 4). The applied load is normalized by the initial vertical stress because column yielding depends on that factor,  $p_a/(L\gamma'_s)$ .

On the other hand, the settlement reduction introduced by the encasement is nearly the same for different area replacement ratios (Figure 5), which means that column encasement is equally useful for different area replacement ratios, yet columns of smaller diameters are better confined. In Figures 4, 5 and 6, the numerical results validate the accuracy of the analytical solution, but the agreement gets slightly worse as the tensile stiffness of the encasement increases. Hence, the only assumption that has a slightly noticeable effect in the results is neglecting the elastic strains in the column during its plastic deformation. A future improvement of the analytical solution including those elastic strains is currently being developed.

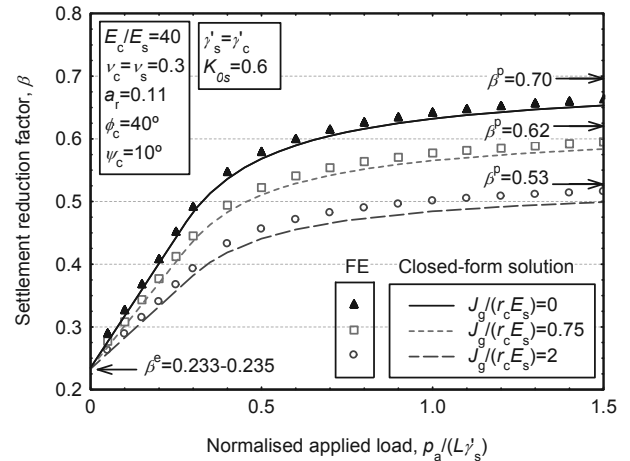


Figure 4. Settlement reduction. Influence of the applied load.

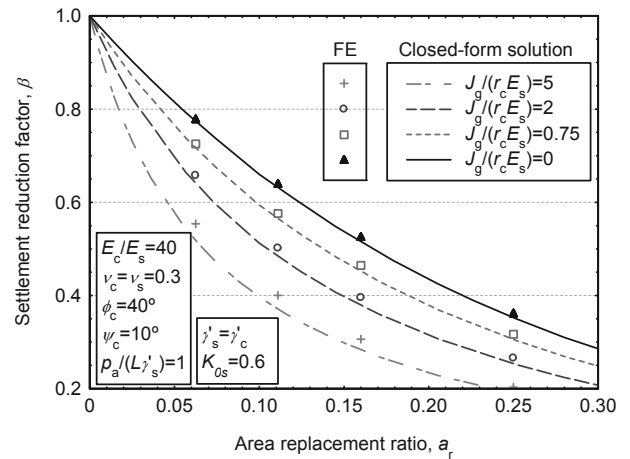


Figure 5. Settlement reduction. Influence of the encasement stiffness for different area replacement ratios.

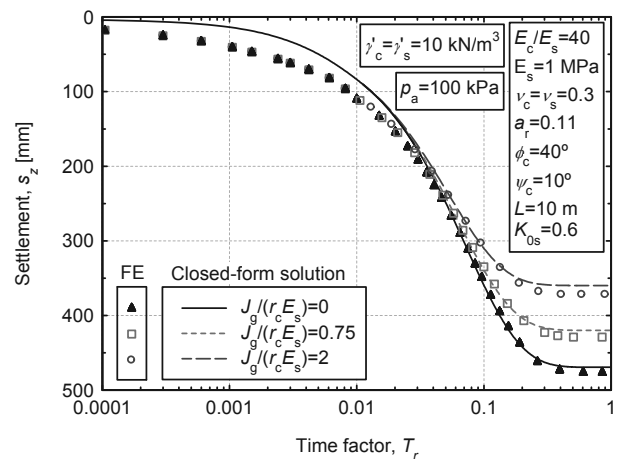


Figure 6. Time-settlement curve.

### 3.4 Encasement length

The effectiveness of encasing the columns in reducing the settlement is directly related to the tensile stress of the encasement, which provide lateral support to the column. Some authors (e.g. Khabbazian et al. 2010, Gniel and Bouazza 2009, Murugesan and Rajagopal 2006) have proposed a partial encasement of the columns, limiting it to the upper part where

the initial lateral stresses are lower. Then, the analysis focuses on the length of the column that should be encased. Here, a preliminary study of the encasement length is presented using the authors' closed-form solution.

The closed-form solution provides the vertical strain of the column at different depths. Figure 7 shows that those strains are higher at shallow depths and linearly decrease with depth, as initial horizontal stresses increase. If the column is encased, those strains are lower but follow a similar pattern. Therefore, encasing the columns is more effective in their upper part but that varies linearly with depth and there is not a critical length of the encasement that should specifically be used.

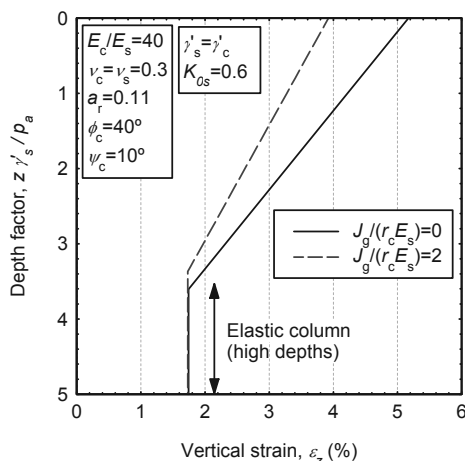


Figure 7. Vertical strain at different depths.

#### 4 CONCLUSIONS

The main features of a closed-form solution, recently developed by the authors (Castro and Sagaseta 2011), to study soft soil improvement, both reduction of settlement and consolidation time, by means of encased stone columns are presented. The analytical solution pretends to be a simple and useful tool for design. Therefore, only a unit cell, i.e. an end-bearing column and its surrounding soil, is modelled in axial symmetry under a rigid and constant load.

Parametric studies of the settlement reduction and stress concentration show the efficiency of encasing the columns, which is mainly ruled by the encasement stiffness compared to that of the soil. Therefore, encasing stone columns is recommended in very soft soils and the encasement should be stiff enough. Besides, the settlement reduction decreases with the applied load. Column encasement is equally useful for common area replacement ratios but columns of smaller diameters are better confined.

The results of the closed-form solution agree well with numerical analyses. The only assumption of the solution that has a slightly noticeable effect in the results is neglecting the elastic strains in the column during its plastic deformation. Therefore, including those elastic strains is an improvement of the presented solution under development.

Finally, a preliminary analysis of the encasement length shows that is more efficient to encase the columns in the upper part, as expected, but there is not a critical length of the encasement that should specifically be used.

#### 5 ACKNOWLEDGEMENTS

The work presented is part of a research project on "An integrated calculation procedure for stone columns, considering the influence of the method of installation", for the Spanish Ministry of Science and Innovation (Ref.: BIA2009-13602).

#### 6 REFERENCES

- Balaam N.P. and Booker J.R. 1981. Analysis of Rigid Rafts supported by Granular Piles. *International Journal for Numerical and Analytical Methods in Geomechanics* 5: 379-403.
- Barron R.A. 1948. Consolidation of fine-grained soils by drain wells. *Transactions ASCE* 113: 718-742.
- Brinkgreve R.B.J. 2007. *Plaxis finite element code for soil and rock analysis*, 2D, version 8. Rotterdam: Balkema.
- Castro J. and Karstunen M. 2010. Numerical simulations of stone column installation. *Canadian Geotechnical Journal* 47(10): 1127-1138.
- Castro J. and Sagaseta C. 2008. Influence of stone column deformation on surrounding soil consolidation. In M. Karstunen and M. Leoni (ed.), *Proc. of the 2nd International Workshop on Geotechnics of Soft Soils, Glasgow*, pp. 333-338. Leiden: Balkema.
- Castro J. and Sagaseta C. 2009. Consolidation around stone columns. Influence of column deformation. *International Journal for Numerical and Analytical Methods in Geomechanics* 33: 851-877.
- Castro J. and Sagaseta C. 2011. Deformation and consolidation around encased stone columns. *Geotextiles and Geomembranes* 29, 268-276.
- Gniel J. and Bouazza A. 2009. Improvement of soft soils using geogrid encased stone columns. *Geotextiles and Geomembranes* 27: 167-175.
- Guétif, Z., Bouassida, M. and Debats, J.M. 2007. Improved soft clay characteristics due to stone column installation. *Computers and Geotechnics* 34(2): 104-111.
- Kempfert H.-G. 2003. Ground improvement methods with special emphasis on column-type techniques. In: *Proceedings of the International Workshop on Geotechnics of Soft Soils-Theory and Practice, SCMEP, Noordwijkerhout, Netherlands*, pp. 101-112.
- Khabbazian M., Kaliakin V.N. and Meehan C.L. 2010. Numerical study of the effect of geosynthetic encasement on the behaviour of granular columns. *Geosynthetics International* 17: 132-143.
- Lo S.R., Zhang R. and Mak J. 2010. Geosynthetic-encased stone columns in soft clay: A numerical study. *Geotextiles and Geomembranes* 28: 292-302.
- Malarvizhi S.N. and Ilamparuthi K. 2007. Comparative study on the behaviour of encased stone column and conventional stone column. *Soils and Foundations* 47: 873-885.
- Murugesan S. and Rajagopal K. 2006. Geosynthetic-encased stone columns: Numerical evaluation. *Geotextiles and Geomembranes* 24: 349-358.
- Murugesan S. and Rajagopal K. 2010. Studies on the Behavior of Single and Group of Geosynthetic Encased Stone Columns. *Journal of Geotechnical and Geoenvironmental Engineering* 136: 129-139.
- Pulko B. and Majes B. 2005. Simple and accurate prediction of settlements of stone column reinforced soil. In: *Proceedings of the 16<sup>th</sup> International Conference on Soil Mechanics and Geotechnical Engineering, Osaka, Japan*, vol. 3, pp. 1401-1404.
- Raithel M. and Kempfert H.G. 2000. Calculation models for dam foundations with geotextile coated sand columns. In: *Proceedings of the International Conference on Geotechnical & Geological Engineering, GeoEngg-2000, Melbourne*.
- Sharma S.R., Phanikumar B.R. and Nagendra, G. 2004. Compressive load response of granular piles reinforced with geogrids. *Canadian Geotechnical Journal* 41: 187-192.
- Smith M. and Filz G. 2007. Axisymmetric numerical modeling of a unit cell in geosynthetic-reinforced, column-supported embankments. *Geosynthetics International* 14: 13-22.
- Wehr J. 2006. The undrained cohesion of the soil as criterion for the column installation with a depth vibrator. In: *Proceedings of the International Symposium on vibratory pile driving and deep soil vibratory compaction, TRANSVIB 2006, Paris*.

# Consolidation theory for combined vacuum pressure and surcharge loading

## Théorie de la consolidation sous l'action combinée du vide et d'un pré-chargement

Chai J.-C.

*Saga University, Japan*

Carter J. P.

*The University of Newcastle, Australia*

**ABSTRACT:** A theory describing the consolidation of a uniform clayey deposit with and without prefabricated vertical drain (PVD) improvement under the combination of a vacuum pressure and a surcharge load has been developed and expressed as closed-form equations. For the case of a soil layer without PVD improvement, both one-way and two-way drainage boundary conditions are considered. Laboratory consolidation tests using combinations of vacuum pressure and surcharge load were conducted under oedometer conditions with vertical or radial drainage. The measured excess pore water pressures are compared with values predicted by the theory presented in the paper. It has been demonstrated that the theory is valid and can be used for designing preloading projects that involve the combination of a vacuum pressure and a surcharge load.

**RÉSUMÉ :** Une théorie décrivant la consolidation d'un dépôt argileux uniforme avec et sans amélioration par drains verticaux préfabriqués (DVP) sous l'action combinée du vide et d'un pré-chargement a été développée avec un système fermé d'équations. Pour le cas d'une couche de sol sans amélioration par DVP, des conditions aux limites drainantes par un côté et par deux côtés sont considérées. Des essais de consolidation au laboratoire sous des conditions oedométriques ont été réalisés sous vide et pré-chargement avec des drains verticaux ou radiaux. La surpression interstitielle mesurée est comparée avec les valeurs prévues par la théorie présentée dans le présent article. Il a été démontré que la théorie est valable et peut être utilisée pour définir des projets de pré-chargement qui impliquent l'utilisation combinée du vide et d'un pré-chargement.

**KEYWORDS:** consolidation, vacuum pressure, embankment, laboratory test, soft clay

## 1 INTRODUCTION

Preloading a soft clayey deposit with the combination of a vacuum pressure and a surcharge load (embankment fill) has several advantages, such as increasing the preloading pressure and reducing lateral displacements of the deposit, etc. (e.g., Chai et al. 2006). Its use in engineering applications has increased in recent years (e.g., Kelly and Wong 2009; Hirata et al. 2010; Indraratna et al. 2011).

Vacuum consolidation has different characteristics compared with consolidation induced by direct application of a surcharge load (Chai et al. 2009). For a soil deposit without any improvement in consolidation performance that might result from the installation of prefabricated vertical drains (PVDs), when a vacuum pressure is applied water is drained out of the soil layer only at the boundary where that vacuum pressure is applied. This applies for both cases of one-way and two-way drainage conditions. However, for a deposit with one-way drainage constrained to deform under one-dimensional (1D) conditions, the final state is a uniform vacuum pressure distribution throughout the deposit and consequently zero flow rate. But for a deposit with two-way drainage, at the bottom boundary the excess pore water pressure is fixed at zero and effectively no vacuum pressure can be applied at this location, and so the final state involves the steady flow of pore water toward the boundary at which the vacuum pressure is applied. Considering these complicating factors, Chai and Carter (2011) recently derived a consolidation theory for soils subjected to vacuum pressure. However, their theory cannot be applied directly for cases that involve a combination of vacuum pressure and surcharge loading, and therefore there is a need to develop a reliable theory for such cases.

This paper presents a newly developed consolidation theory applicable to soils subjected to a combination of vacuum pressure and surcharge loading. This theory is applicable to the

case of a uniform soil deposit with or without PVD improvement. Predictions obtained using this theory are compared with the results of laboratory tests conducted under oedometer conditions, for cases that involve both vertical and radial drainage conditions, with the latter designed to simulate the consolidation of a deposit improved by PVDs. It has been shown that the theory is valid and can be used for designing preloading projects that involve a combination of vacuum pressure and surcharge loading.

## 2 CONSOLIDATION THEORY

### 2.1 Uniform layer without PVDs

Under the same assumptions as those made in Terzaghi's 1D consolidation theory (Terzaghi 1943), the governing equation and the boundary conditions for the generation and dissipation of excess pore water pressure in a saturated soil layer under a combination of vacuum pressure and surcharge load are as follows:

$$c_v \frac{\partial^2 u}{\partial z^2} = \frac{\partial u}{\partial t} \quad (1)$$

$$u(0, t) = -p_{vac} \quad (2)$$

$$\frac{\partial u(H, t)}{\partial z} = 0 \text{ for } t > 0 \text{ (one-way drainage)} \quad (3)$$

$$u(H, t) = 0 \text{ for } t > 0 \text{ (two-way drainage)} \quad (3a)$$



where  $z$  = the spatial coordinate;  $t$  = time;  $u$  = the excess pore water pressure;  $c_v$  = the coefficient of consolidation of the soil;  $p_{vac}$  = the magnitude of the applied vacuum pressure at  $z = 0$ ; and  $H$  is the thickness of the deposit.

With the presence of a vacuum pressure, the final state is not a condition with zero excess pore pressure in the deposit. Therefore, the solution to the governing equation must consist of two parts, namely the steady state solution ( $Y(z)$ ) and the transient solution ( $v(z,t)$ ) (Chai and Carter 2011). With the boundary condition defined by Eq. (2),  $u(z, t)$  can be expressed in the following form:

$$u(z, t) = -p_{vac}Y(z) + p_{vac}v_1(z, t) + p_s v_2(z, t) \quad (4)$$

where  $p_s$  = the magnitude of the applied surcharge load. The term  $-p_{vac}Y(z)$  is the final steady state excess pore water pressure distribution and  $(p_{vac} v_1(z, t) + p_s v_2(z, t))$  is the time-dependent component of the excess pore water pressure.

### 2.1.1 One-way drainage

For this case the excess pore water pressure distribution is given by:

$$u = -p_{vac} + (p_{vac} + p_s) \cdot \left( \frac{4}{\pi} \sum_{n=1}^{\infty} \frac{1}{2n-1} \sin(a_n z) e^{-a_n^2 c_v t} \right) \quad (5)$$

where  $a_n = (2n-1)\pi/(2H)$ . In this case,  $Y(z) = 1$ , and the  $v_1(z, t) = v_2(z, t)$  and its expression is given in the last set of parentheses of Eq. (5). The average degree of consolidation is given by:

$$U = 1 - \frac{8}{\pi^2} \sum_{n=1}^{\infty} \frac{1}{(2n-1)^2} e^{-\frac{c_v t}{4H^2} (2n-1)^2 \pi^2} \quad (6)$$

### 2.1.2 Two-way drainage

In this case the excess pore water pressure distribution in the soil is given by:

$$u(z, t) = -p_{vac} \left( 1 - \frac{z}{H} \right) + \frac{2}{\pi} \sum_{n=1}^{\infty} \left[ \frac{p_{vac} + p_s}{n} \sin(\lambda_n z) + \frac{p_s}{n} \sin(\lambda_n (H - z)) \right] e^{-\lambda_n^2 c_v t} \quad (7)$$

where  $\lambda_n = n\pi/H$ . The average degree of consolidation is given by:

$$U(t) = 1 - \frac{8}{\pi^2} \sum_{n=1}^{\infty} \frac{1}{(2n-1)^2} e^{-\frac{c_v t}{H^2} (2n-1)^2 \pi^2} \quad (8)$$

## 2.2 Uniform layer with PVD improvement

The theory for a PVD-improved soil deposit is derived here for the case of one-way drainage conditions using a unit cell model, as shown in Fig. 1. The governing equation for consolidation is as follows:

$$\frac{\partial u}{\partial t} = c_h \left[ \left( \frac{\partial^2 u}{\partial r^2} \right) + \frac{1}{r} \left( \frac{\partial u}{\partial r} \right) \right] \quad (9)$$

where  $r$  = the radial distance and  $c_h$  = the coefficient of consolidation in the horizontal direction. The boundary conditions are:

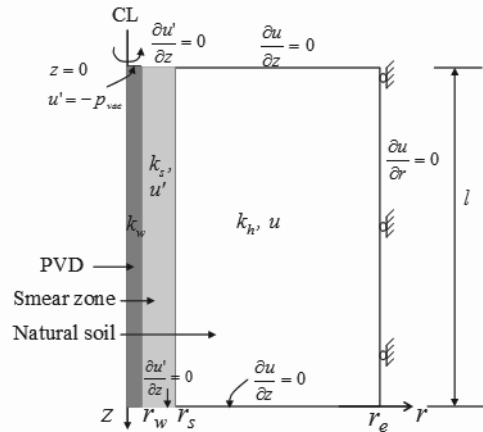


Figure 1. Unit cell model and boundary conditions

$$\frac{\partial u(r_e, z, t)}{\partial r} = 0 \quad (10)$$

$$\frac{\partial u(r, 0, t)}{\partial z} = 0, \quad \frac{\partial u'(r, 0, t)}{\partial z} = 0 \quad (11)$$

$$\frac{\partial u(r, l, t)}{\partial z} = 0, \quad \frac{\partial u'(r, l, t)}{\partial z} = 0 \quad (12)$$

$$u'(r_w, 0, t) = -p_{vac} \quad (13)$$

where  $u$  and  $u'$  = the excess pore water pressures in the undisturbed zone and the smear zone, respectively (Fig. 1),  $z$  = depth from the ground surface,  $r_w$  = equivalent radius of a PVD, and  $r_e$  = radius of the unit cell. The solutions for  $u$  and  $u'$  can be expressed as:

$$u(r, z, t) = -p_{vac} + (p_{vac} + p_s)v(r, z, t) \text{ for } (r_s < r \leq r_e) \quad (14)$$

$$u'(r, z, t) = -p_{vac} + (p_{vac} + p_s)v'(r, z, t) \text{ for } (r_w < r \leq r_s) \quad (15)$$

where  $r_s$  = radius of the smear zone. The additional conditions for getting explicit expressions for  $v$  and  $v'$  are the following water flow continuity conditions.

- (1) The total inflow of pore water through the boundary of a cylinder with a radius of  $r$  has to be equal to the change in volume of the hollow cylinder with outer radius of  $r_e$  and inner radius of  $r$ .
- (2) The pore water flow into the PVD from a horizontally cut soil slice is equal to the change of vertical flow rate in the PVD.

At the interface between the smear zone and the undisturbed zone, the radial flow rate from the undisturbed zone is equal to the flow rate into the smear zone.

With these conditions and using the same assumptions as those adopted in obtaining Hansbo's (1981) solution, it can be shown that the expressions for  $v(r, z, t)$  and  $v'(r, z, t)$  are as follows:

$$v'(r, z, t) = \frac{k_h}{k_s \cdot r_e^2 \cdot \mu} \left[ \frac{r_e^2 \ln \frac{r}{r_w} - \frac{r^2 - r_w^2}{2}}{+ \frac{k_s}{k_w} (n^2 - 1)(2lz - z^2)} \right] \exp\left(\frac{-8T_h}{\mu}\right) \text{ for } (r_w \leq r \leq r_s) \quad (16)$$

$$v(r, z, t) = \frac{1}{r_e^2 \cdot \mu} \left[ \frac{r_e^2 \ln \frac{r}{r_s} - \frac{r^2 - r_s^2}{2} + \frac{k_h}{k_s} \left( \frac{r_e^2 \ln s}{- \frac{r_s^2 - r_w^2}{2}} \right) \right] \exp\left(\frac{-8T_h}{\mu}\right) \text{ for } (r_s < r \leq r_e) \quad (17)$$

where:  $n = r_e/r_w$ ,  $s = r_s/r_w$ ,  $k_h$  and  $k_s =$  the hydraulic conductivities in the horizontal direction of the undisturbed zone and the smear zone respectively,  $k_w =$  the hydraulic conductivity of the drain (PVD),  $l =$  the drainage length of a PVD, and  $T_h = c_v t / (4r_e^2)$ . Parameter  $\mu$  represents the effects of PVD spacing, smear zone and well resistance. Adopting an average well resistance and with some approximation, the expression for  $\mu$  is as follows (Hansbo 1981):

$$\mu = \ln(n/s) + (k_h/k_s) \ln(s) - \frac{3}{4} + \frac{2l^2 \cdot k_h}{3r_w^2 k_w} \quad (18)$$

The average degree of consolidation ( $U_h$ ) of the unit cell is (Hansbo 1981):

$$U_h = 1 - \exp(-8T_h / \mu) \quad (19)$$

### 3 COMPARISON OF TEST RESULTS AND PREDICTIONS

Laboratory consolidation tests involving the combination of a vacuum pressure and a surcharge load have been conducted under oedometer conditions with both vertical and radial drainage (the latter to simulate the effects of PVD drainage), and the measured excess pore pressures have been compared with the predicted values.

#### 3.1 Test details

Figures 2(a) and (b) show the set-up of the tests, with vertical (V-test) and radial (R-test) drainage conditions, respectively. During testing, the settlement, the excess pore water pressure at the bottom of the sample (V-test) or the middle height of the consolidation ring (R-test), and the horizontal earth pressure at the middle height of the consolidation ring can be measured. For the R-test, the centre drainage porous stone tube has an outer diameter of 8 mm, which is inserted into a predrilled hole at the center of a sample with a filter paper placed between the soil sample and the tube. The soil samples were re-consolidated from Ariake clay slurries under a surcharge pressure of 20 kPa.

Two series of tests, V-tests and R-tests, were conducted. Here only one test from each series has been chosen to compare with the values predicted by the theory presented above. In the case of the V-test, the test with one-way drainage conditions has been selected, because for two-way drainage conditions no pore water pressures were measured with the device used. The two series of tests were conducted at different times and different soil samples were used. Some of available soil properties as well as the test conditions are listed in Table 1. In this table, the vertical effective stress,  $\sigma'_{v0}$ , indicates that the soil sample was first consolidated under  $\sigma'_{v0}$  (simulating the initial effective stress of the soil sample at a specified depth in the deposit) and then the consolidation test was conducted by applying additional incremental consolidation pressures (vacuum pressure and surcharge load).

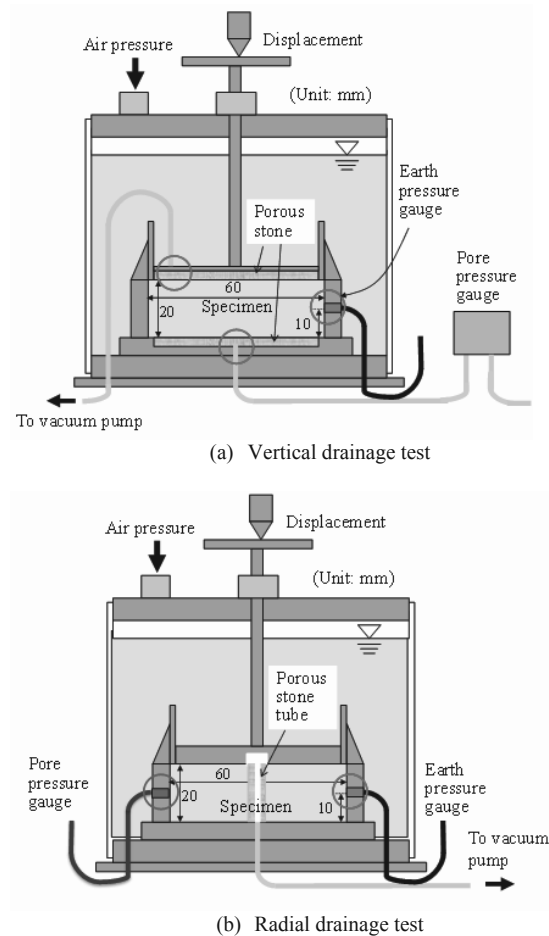


Figure 2. Sketch of the set-up of the tests

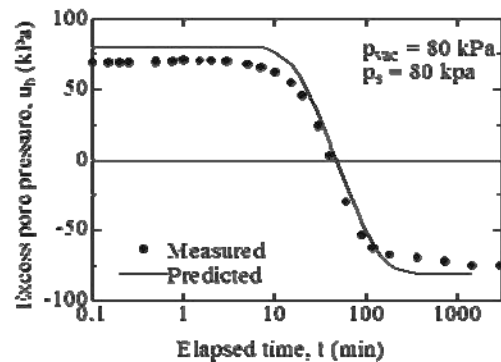


Figure 3. Comparison of predicted and measured  $u_b$  values

#### 3.2 Comparison of measured and predicted pore pressures

##### 3.2.1 V-test

After initial consolidation under  $\sigma'_{v0} = 40$  kPa, the thickness of the sample was 18.7 mm (or compression of about 1.2 mm). Further, under 80 kPa vacuum pressure and 80 kPa surcharge load, the additional compression was about 3.2 mm. Since the thickness of the sample is also the vertical drainage path length, in the predictions an average sample thickness of 17.2 mm was adopted. Comparison of the measured and the predicted excess pore water pressures at the bottom of the sample ( $u_b$ ) is shown

Table 1. Some soil properties and test conditions

Test	Soil	Plasticity limit, $W_p$ (%)	Liquid limit, $W_L$ (%)	Coefficient of consolidation $c_v$ or $c_h$ (m <sup>2</sup> /min)	$C_c$	$e_{0\clubsuit}$	$\sigma'_{v0}$ (kPa)	$p_{vac}$ (kPa)	$p_s$ (kPa)
V-test	Ariake clay-1	60.3	120.5	$2.3 \times 10^{-5} \#$	0.75	2.5	40*	80	80
R-test	Ariake clay-2	56.8	120.3	$5.0 \times 10^{-6}$	-	-	0	80	80

\*: Initial vertical effective stress in the sample; #: The value was obtained by fitting the measured consolidation rate;  $\clubsuit$ : After pre-consolidation under 20 kPa pressure.

in Fig. 3. Except for the fact that the measured initial value of  $u_b$  of about 72 kPa is slightly lower than the 80 kPa applied surcharge load, the prediction almost matches the measured data. The slightly lower initial  $u_b$  value may indicate that the specimen was not 100% saturated.

Although two-way drainage test was not conducted, using the same soil parameters as for one-way drainage test, and assuming the thickness of the soil sample is 20 mm, the predicted excess pore water pressure ( $u$ ) distribution within the sample at different elapsed times are given in Fig. 4 to demonstrate the capacity of the proposed theory.

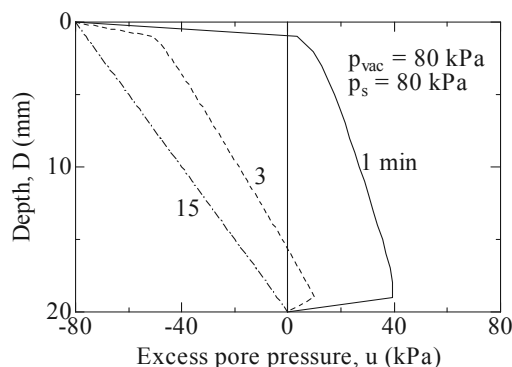


Figure 4. Predicted  $u$  variation in soil sample under two-way drainage boundary condition

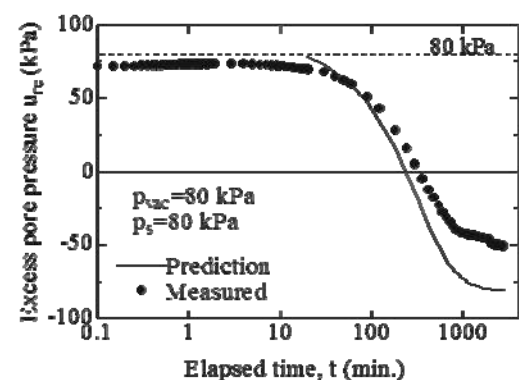


Figure 5. Comparison of predicted and measured  $u_{re}$

### 3.2.2 R-test

The geometric parameters required to calculate the predictions for this case are:  $r_e = 30$  mm;  $r_w = 4$  mm; and  $l = 20$  mm. The assumed radius of the smear zone,  $r_s = 7$  mm; the hydraulic conductivity ratio,  $k_h/k_s = 5$ ;  $k_h = 10^{-9}$  m/s; and  $k_w = 10^{-4}$  m/s. In the case of radial drainage, with Eqs. (16) and (17) the initial condition of a uniform excess pore water pressure ( $u_0$ ) distribution in a unit cell is not satisfied (which is a particular limitation of this theory). These equations only ensure that the average initial value of  $u_0$  is the same as the applied value. The predicted initial value at the periphery of the sample (unit cell) is higher than the applied value. The predicted values are compared with the measured data from the time at which the predicted value at the periphery was equal to the applied initial value. In the physical test at the corresponding time, the pore

water pressure at the periphery of the sample starts to reduce. Comparison of the excess pore water pressures at the periphery of the sample ( $u_{re}$ ) is given in Fig. 5. For this case, during the consolidation period the measured excess pore water pressure initially decreased but then increased for a brief period before finally exhibiting further dissipation. Furthermore, the measured final excess pore water pressure did not reach the applied vacuum pressure of 80 kPa. Nevertheless, the trends of both the measured and the predicted dissipation curves are similar.

From the above comparisons, it can be seen that the theory provides reasonable predictions of the measured soil behaviour and so it should be able to be used reliably for designing preloading projects that adopt a combination of vacuum pressure and surcharge load to consolidate the soil deposit.

## 4 CONCLUSIONS

A consolidation theory, expressed in closed-form equations, for soil consolidation under the combination of a vacuum pressure and a surcharge load has been developed for a uniform clayey deposit with and without prefabricated vertical drain (PVD) improvement. For cases without PVD improvement, both one-way and two-way drainage boundary conditions have been considered.

Laboratory consolidation tests were conducted, adopting a combination of vacuum pressure and surcharge loading under oedometer conditions with both vertical and radial drainage. The excess pore water pressures measured in these test were compared with values predicted by the suggested theory. It has been demonstrated that the theory is valid and can be used for designing preloading projects that adopt a combination of vacuum pressure and surcharge load to pre-consolidate soft soil deposits.

## REFERENCES

Chai, J. C., Carter, J. P. and Hayashi, S. 2006. Vacuum consolidation and its combination with embankment loading. *Canadian Geotechnical Journal* 43(10), 985-996.

Chai, J.-C., Matsunaga, K., Sakai, A. and Hayashi, S. 2009. Comparison of vacuum consolidation with surcharge load induced consolidation of a two-layer system. *Géotechnique* 59(7), 637-642.

Chai, J.-C. and Carter, J. P. 2011. *Deformation analysis in soft ground improvement*. Springer, p. 247.

Hansbo S. 1981. Consolidation of fine-grained soils by prefabricated drains. *Proceedings of 10th International Conference on Soil Mechanics and Foundation Engineering*, Stockholm 3, 677-682.

Hirata, M., Kitoh, M., Yamada, K., Iizuka, A. and Arai, K. 2010. Deformation behavior and counter measures of expressway embankment on super-soft ground. *Journal of Japan Society of Civil Engineers* 66(2), 356-369 (in Japanese).

Indraratna, B., Rujikiatkamjorn, C., Ameratunga, J. and Boyle, P. 2011. Performance and Prediction of Vacuum Combined Surcharge Consolidation at Port of Brisbane. *Journal of Geotechnical and Geoenvironmental Engineering ASCE* 137(5), 550-554.

Kelly, R. B., Wong, P. K. 2009. An embankment constructed using vacuum consolidation. *Australian Geomechanics* 44(2), 55-64.

Terzaghi K. 1943. *Theoretical soil mechanics*. New York, John Wiley and Sons.

# Displacement rigid inclusions

## Inclusions rigides refoulées

Ciri6n A., Paul6n J.  
*Soletanche-Bachy-CIMESA, Mexico*

Racinais J.  
*Menard, France*

Glandy M.  
*Soletanche-Bachy-Pieux, France*

**ABSTRACT:** In soils with poor mechanical properties and in areas where the generation of excavation debris is an issue, given the restrictions regarding its disposal, the solutions of massive soil improvement with displacement rigid inclusions solve both needs. In this paper we describe the basis of the constructive procedure of displacement rigid inclusions. We explain the concept of improvement with this kind of inclusions; we itemize the bases of their design, and describe their construction sequence, highlighting the controls during the execution to ensure quality.

**RÉSUMÉ:** Dans les sols ayant des propriétés mécaniques faibles comme dans les zones où l'élimination des matériaux produits des travaux représente un problème, les Inclusions Rigides avec refoulement de sol donnent des solutions à ces deux situations. L'article explique le concept des solutions d'amélioration des sols en utilisant la technique des Inclusions Rigides, donne les bases du dimensionnement, et décrit la séquence de construction des inclusions Rigides en insistant sur les contrôles utilisés pour assurer la qualité finale.

**KEYWORDS:** soft soil, rigid inclusion, displacement of soil, excavation debris.

### 1 INTRODUCTION

When studying what type of foundation is best suited to withstand the shock that a new building (structure) will impose on the soil, it is necessary to check not only the limit conditions for failure, but also the limit conditions of service, including total and differential settlements.

Being successful in the choice and design of the type of foundation to be built largely depends on the control of two variables: load and settlement. Nevertheless, there are additional parameters that also play an important role in the decision process, such as the cost of the foundation with respect to the total cost of the project, construction time and —increasingly— the impact on the environment.

The foundations based on rigid inclusions (system structure massive soils improvement) have experienced a boom in recent years, especially in works on large areas subjected to uniform vertical loads. While this is not a new concept (wooden inclusions were used since prehispanic times in Mexico —see Auvinet, G., 2006—), there is now specialized equipment capable of building concrete rigid inclusions following special procedures that not only achieve higher production results, but also greater depths and better loadbearing capacities. They also respect strict quality controls. This gives us the possibility to propose foundations based on the installation of grids of rigid inclusions made of poor concrete that meet specific technical requirements regarding load bearing capacities and the reduction of settlements. They are also attractive: economically and for their constructive feasibility, as well as for their reduced construction times and the quality of their execution.

Displacement inclusions in particular have the great advantage of not generating construction debris, which benefits the environment and reduces or eliminates the cost of its removal. In soils with a large frictional component, the ratio of voids surrounding the inclusion is reduced by the incorporation of the concrete so that the relative compactness of the material

increases, as well as the perimeter friction of the inclusion-ground. The construction process of the displacement rigid inclusion guarantees quality control in the execution, so the concrete is placed continually and safe from contamination.

### 2 BASES OF DESIGN

The goal is to install a set of inclusions in soils with low bearing capacity and/or highly compressibility to create a layer of compound soil-inclusions material that has better mechanical properties.

The improvement or reinforcement of soils with rigid inclusions is commonly used to ensure bearing capacity and/or reduce settlements in the following types of work:

- Slabs,
- Superficial footings (isolated or continuous),
- Embankments, landfills,
- Work or storage yards.

The solution is characterized by the fact that the traditional mechanical link between the pile and the structure in deep or mixed foundations does not exist. A distribution layer, also called a Load Transfer Platform (LTP), is usually placed between the inclusions and the structure to be supported, and this is what marks the difference between piles and inclusions.

The distribution layer spreads the acting loads on the slab or other covering surface towards the underlying soil-inclusions setup. The system described is configured as shown in Figure 1. If there are concentrated vertical loads from one column, isolated or continuous footings can be used to directly transmit the loads to the soil-inclusions setup.

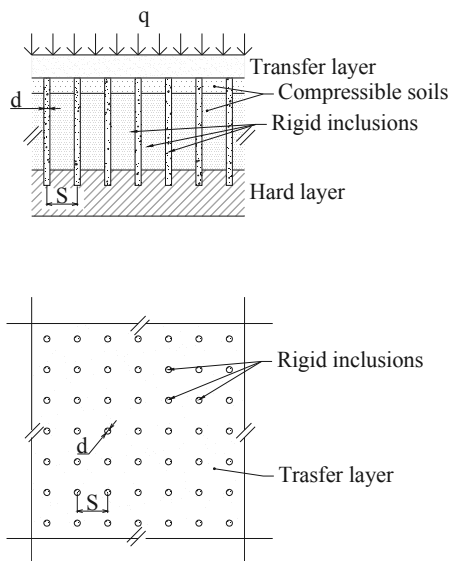


Figure 1. Inclusion under a load uniformly distributed on the surface. Side and top views.

In this case the LTP may not be required and a significant portion of the load from the superstructure will be supported by the grid of inclusions and the remainder will be supported by the soil surrounding the inclusions —see Figure 2—.

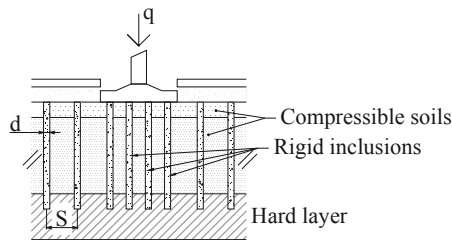


Figure 2. Model setup of inclusions under an acting strut load on a footing. Side view.

In the same way that the inclusion-soil system supports vertical loads —uniformly distributed or concentrated— from buildings, this application can be extended to the case of embankments and landfills in which the system will receive the weight of the material that forms the embankments or landfills. A particular case occurs when the embankment or landfill is significantly high and the soil reinforced with inclusions participates in its stabilization —see Figure 3—.

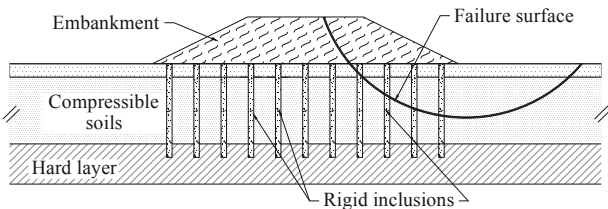


Figure 3. Inclusions that help stabilize an embankment or landfill constructed on the surface.

The inclusions will generally be subjected to the action of vertical forces caused by discharges from the building or due to the weight of the embankment or landfill. However, in cases where the inclusions participate in the stabilization of embankments or landfills, or when they are subjected to the action of seismic forces, the generation of lateral forces will also have to be taken into account in the design.

Several approaches and ways of analyzing and designing inclusions have been developed. Some of them have been recently brought together in the ASIRI (*Amélioration des Sols par Inclusions Rigides*—see ASIRI National Project, 2012—).

### 3 CONSTRUCTIVE SEQUENCE

The equipment used for the construction of displacement rigid inclusions kind must circulate over a flat working platform, drained and stable, generally constructed of granular material. The inclusions are built from this platform.

The drilling equipment consists of a crane supported on caterpillars with a cab for the operator and a mast that supports a cylindrical auger of a defined length. The auger is hollow and has a special geometry —see Figures 4a, 4b—, capable of displacing soil laterally when drilling. This is the most important feature of displacement rigid inclusions because the surrounding soil becomes laterally compressed. Lateral friction increases in the case of mainly granular soils or soils with a large content of sand.

At the bottom part of the tip there is a hinged lid that remains closed during the drilling phase to prevent the entry of material into the inner tube and which opens to allow the exit of the concrete to form the inclusions.

Besides the necessary drilling equipment there has to be a concrete pump which feeds the upper side of the drilling tool through flexible hoses.

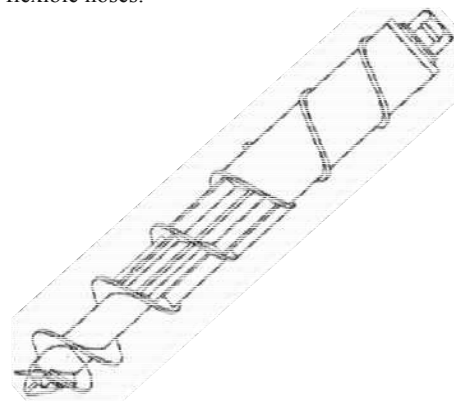


Figure 4a. Diagram of the typical point of the hollow auger for displacement rigid inclusions.

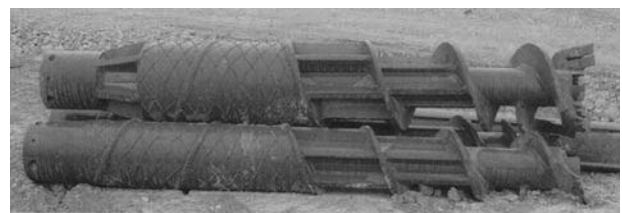


Figure 4b. Point of the hollow auger for displacement rigid inclusions developed for Soletanche-Bachy, RefSol system.

With the topographic location of the inclusion to be built, the process begins by placing the mast of the crane upright and lowering the auger into the ground. A rotor torque and a descending vertical force are applied to the auger to cut, penetrate and displace the soil laterally. This action is performed continuously until the drill reaches the specified depth —see Figure 5A—.

At this point, the concrete is pumped from the tank of the pump through a flexible hose to the upper part of the hollow auger to fill it completely and to generate sufficient pressure on the concrete.

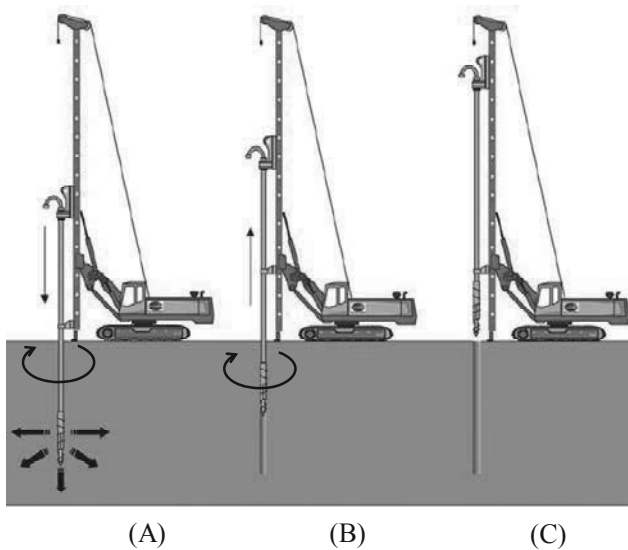


Figure 5. Execution sequence of a displacement rigid inclusion.

Then the auger is lifted a few centimeters from the soil at the bottom of the perforation, which causes the lid at the lower end of the auger to open. The concrete, subject to pressure, pours into the bottom of the hole, filling it. While still pouring concrete and controlling the pressure, at this point the operator lifts the auger continuously by means of a rotor torque and a vertical pulling force —see Figure 5B—. This process continues until the auger is fully above ground —see Figure 5C—. The concrete is poured continuously from the bottom of the perforation until it reaches the level defined as the head of inclusion, which can be between the working platform level and a few dozen centimeters below it.

Throughout the process of building an inclusion (Figures 5A, 5B and 5C) real time and continuous monitoring of the parameters that intervene in its execution are done with electronic devices located in the cab of the crane. They detect the signals sent by various sensors installed at strategic points of the construction equipment. Through this monitoring, the operator has control of the different construction parameters and can ensure the quality of the construction of the inclusion at all times and along its entire height. Among the parameters controlled are: the drilling depth, the pressure and the volume of the concrete, the upward and downward speeds, rotation and the auger's torque.

The equipment is also able to store the record of the controls for each inclusion, to be processed later on a personal computer. Continuous records are obtained along the depth (see Figure 6).

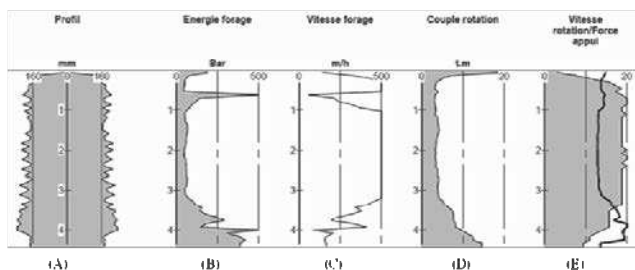


Figure 6. Record of monitoring in continuous real time: (A) Inclusion profile (mm), (B) Perforation energy (bar), (C) Perforation speed (m/h), (D) Rotation torque (t.m), (E) Rotation speed / Bearing force.

The start and stop of the concrete pump is wirelessly controlled by the crane operator from the cab. The speed at which the auger advances, the rotor torque, the rotation speed and down force or extracting force of the auger is controlled manually through the hydraulic system of the crane.

The procedure described is a clean process that leaves practically no perforation debris on the work platform. There are also no vibrations or damage to the surface layers, which makes working in areas adjacent to sensitive structures possible. Additionally, the method is capable of achieving high industrial production compared with traditional methods of pile construction.

For quality control, it is also necessary to carry out strength tests on samples of the concrete used. There will be as many tests as are needed or as required by local regulations. The common values of resistance to compressive strength of the concrete used for the construction of displacement rigid inclusion range from 10 to 15 MPa at 28 days, with modulus of elasticity usually set between 5,000 and 10,000 MPa, although higher resistance and rigidity levels can be used according to the needs of each project.

The commercial diameters of displacement rigid inclusion construction range between 250 and 500 mm and can reach depths of up to 30 m.

To guarantee the quality of the implementation and the design criteria, this construction procedure has been certified by the international bureau of control and certification Bureau Veritas.

#### 4 CONCLUSIONS

Soil improvement and reinforcement with displacement rigid inclusions kind solves a great number of foundations in which not only increasing bearing capacity, reducing settlements or ensuring slope stability play an important role, but where also cost and execution times are factors to be considered.

Given the type of auger used in the construction these inclusions are defined as displacement inclusions where the surrounding soil is displaced and laterally compressed at the moment of drilling, which increases the compactness of soils whose frictional component is significant.

During construction of displacement rigid inclusion there is real-time monitoring of parameters such as drilling depth, pressure and volume of the poured concrete, advancement speed and auger rotation, downward force of the rotor torque of the auger, which ensures a high quality control of the construction. Due to the advantages provided by the design of soil improvement systems with rigid inclusions, plus the geotechnical and environmental benefits of displacement rigid inclusions, numerous projects worldwide are being approached with this technique.

#### 5 REFERENCES

- Auvinet, G. (2006). "Rigid inclusions in Mexico City soft soils: history and perspectives", International Symposium "Rigid inclusions in difficult soft soil conditions", Instituto de Ingeniería, UNAM, Cd. de México.
- Combarieu, O. (1988). "Amélioration des sols par inclusions rigides verticales – Application à l'édification des remblais sur sols médiocres". *Revue Française de Géotechnique* N° 44, 5779.
- ASIRI National Project (2012). "Recommendations for the design, construction and control of rigid inclusion ground improvements". Bureau Veritas. "Cahiers des charges CMC".
- Bureau Veritas. "Cahiers des charges Refsol".



# Prediction of the unconfined compressive strength in soft soil chemically stabilized

## Prévision de la résistance à la compression non confinée dans sols mous chimiquement stabilisés

Correia A.A.S.; Venda Oliveira P.J., Lemos L.J.L.  
*Department of Civil Engineering – University of Coimbra, Portugal*

**ABSTRACT:** The chemical stabilization of soils is a ground improvement technique consisting on the mechanical mixing of the in situ natural soil with binders. The chemical stabilization of soils can be applied with either slurries (wet method) or powder (dry method) binders. When the stabilizing binders are mixed with the soil, physico-chemical interactions take place and are responsible for the stabilization effect, which has a major influence on the mechanical behaviour of the improved material. This stabilizing effect is dependent on a range of parameters which should be analysed through a long and extensive laboratory and field trial test program, as stated in the european standard (EN 14679:2005). In order to minimize the number of tests during the optimization process, this paper presents a simple method to predict the unconfined compressive strength, which is independent of the binder content and state (powder or slurry). The method is successfully applied to a wide range of soils, showing its versatility (Correia, 2011). Applying the generalised relationship of the method, it is possible to predict the unconfined compressive strength for any binder content and state from one single unconfined compression test.

**RÉSUMÉ :** La stabilisation chimique de sols est une technique de l'amélioration des sols qui consiste en le mélange mécanique dans situ du sol naturel avec liants. La stabilisation chimique de sols peut être appliquée avec coulis (méthode mouillée) ou poudre (méthode sec) liants. Quand les liants stabilisateurs sont mélangés avec le sol, ils produisent interactions physique-chimique lesquels sont responsables pour l'effet de la stabilisation, qui a une influence majeure sur le comportement mécanique du matériel améliorée. Cet effet stabilisateur est dépendant d'une gamme de paramètres qui devraient être analysés à travers d'un long et étendu programme d'essais en laboratoire et sur terrain, comme énoncé dans la norme européenne (EN 14679:2005). Pour minimiser le nombre d'essais pendant le processus de l'optimisation, cet article présente une méthode simple de prédire la résistance à la compression simple, qui est indépendant du contenu de liant et état (poudre ou coulis). Le méthode est appliquée avec succès à une grande gamme de sols, montrant sa versatilité (Correia, 2011). Appliquant la version généralisée du méthode, c'est possible prédire la résistance à la compression simple pour tout contenu de liant et état basé d'une seule essais à la compression simple.

**KEYWORDS:** chemical stabilization, unconfined compression test, soft soils, strength prediction.

### 1 INTRODUCTION.

Over the last few decades, infrastructure requirements and land occupation policies have demanded construction on soils with poor geotechnical properties (in particular, soft soils). These soils are usually characterized by low strength and high compressibility, demanding from geotechnical engineers new and challenging solutions to overcome these undesirable engineering characteristics. One of the ground improvement techniques that have been used with success in practice is the chemical stabilization, where the natural soil is mechanically mixed in situ with binders (usually called Mass Stabilization, or, Deep Mixing when applied in depth). This technique has given good results when applied to soft soils, becoming a prominent subject nowadays, rapidly growing and wide spreading around the world due to its technical and economical benefits when compared with other ground improvement techniques.

At first the chemical stabilization of soils used the quicklime as the hardening agent. Later on, the use of Portland cement has permanently been outpacing the use of quicklime, not only because Portland cement is readily available at reasonable cost but also because cement is more effective than quicklime (Horpibulsuk et al 2011, Åhnberg 2006, Lorenzo and Bergado 2004, Kitazume and Terashi 2002). However, additives such as granulated blast furnace slag, fly ash, gypsum and silica dust, among others, may be used specially for the improvement of soft soils with high water content or organic soils (Kitazume and Terashi 2002, Edil and Staab 2005).

The chemical stabilization of soils can be applied with either slurries (wet method) or powder (dry method) binders. When the stabilizing binders are mixed with the soil, physico-chemical interactions take place and are responsible for the stabilization effect, which has a major influence on the mechanical behaviour of the improved material. This stabilizing effect is dependent on a range of parameters which should be analysed through a laboratory and field trial test program, as stated in the european standard (EN 14679:2005).

The fundamental mechanical properties of cement based admixed soft soils have been experimentally investigated by many researchers (Correia 2011, Åhnberg 2006, Hernandez-Martinez 2006, Lorenzo and Bergado 2006 and 2004, Horpibulsuk et al 2004, Kamruzzaman 2002, Horpibulsuk 2001, Miura et al 2001, Uddin et al 1997, Locat et al 1996). Most of these previous investigations mainly focus on the influence of the water content and binder content, as well as on the ratio between them. Based on some of these parameters, Horpibulsuk et al (2003 and 2011) and Lorenzo and Bergado (2006) have introduced phenomenological models for predicting laboratory strength development in cement based stabilized soft soils. This paper presents a new simple model which aims to predict the laboratory strength (expressed by the unconfined compression test) for various combinations of water content and cement content. This model intends to minimize the number of laboratory tests needed to specify the quantity of cement and water to be admixed with the soft soil. Although the model is



developed for a particular soft soil, its versatility is demonstrated for a wide range of soils. A generalized strength equation is presented, which allows the strength prediction based, at lower limit, on a single unconfined compression test.

## 2 EXPERIMENTAL TESTS

### 2.1 Materials

Table 1 presents the geotechnical and chemical properties of the soft soil deposit of “Baixo Mondego” (located near Coimbra city, Portugal), used in the study. In general, the soil is predominantly clayey-silt with a high organic matter content, which has a strong influence on some characteristics of the soil, namely, low unit weight, high plasticity, high natural water content, high void ratio, low undrained shear strength and high compressibility although this fact is not consistent with the grain size distribution, particularly due to the low clay content, (Coelho 2000, Venda Oliveira et al. 2010).

Table 1. Principal properties of the soft soil of “Baixo Mondego”.

Natural water content, $w_{nat}$ (%)	80
Unit weight, $\gamma_{sat}$ (kN/m <sup>3</sup> )	14.6
Natural void ratio, $e_{nat}$ (-)	2.1
Clay fraction (%)	8-12
Silt fraction (%)	71
Sand fraction (%)	17-21
Density, $G$ (-)	2.55
Organic matter content, OM (%)	9.3
Liquid limit, $w_L$ (%)	71
Plastic limit, $w_P$ (%)	43
Undrained shear strength, $c_u$ (kPa)	< 25
CaO (%)	0.74
SiO <sub>2</sub> (%)	62
Al <sub>2</sub> O <sub>3</sub> (%)	16
Fe <sub>2</sub> O <sub>3</sub> (%)	4.8
MgO (%)	1.1
pH (-)	3.5

The binders used in the present study to produce stabilized “Baixo Mondego” soft soil samples were a Type I Portland cement, designated CEM I 42.5 R (EN 197-1 2000), and a blast furnace granulated slag, here simply designated as SLAG. These two binders, on a dry weight proportion of 75/25 as proposed by Correia (2011), were thoroughly mixed to obtain a uniform binder. The binder added to the soil was defined by the parameter binder content,  $a_w$  (ratio of the dry weight of binder used in the mixture to the dry weight of the soil). The composition and the specific surface of the binders are presented in Table 2.

Table 2. Composition and specific surface of the binders.

	CEM I 42.5R	SLAG
CaO (%)	63.02	37.02
SiO <sub>2</sub> (%)	19.70	38.74
Al <sub>2</sub> O <sub>3</sub> (%)	5.23	11.59
Fe <sub>2</sub> O <sub>3</sub> (%)	2.99	0.85
MgO (%)	2.38	6.75
Specific surface, $S$ (m <sup>2</sup> /kg)	321.5	363.0

### 2.2 Chemical stabilization of the soft soil of “Baixo Mondego”

In order to evaluate the influence of the water content and binder content on the chemical stabilization of the soft soil of “Baixo Mondego”, several samples were prepared for various water contents (equivalent to a liquidity index  $I_L$  of 1.35, 1.96 and 2.49) and binder contents (from 9 to 27, step 3). The laboratorial procedure to produce stabilized samples followed

the laboratory procedure presented in EuroSoilStab (2001) with the modifications proposed by Correia (2011). During the curing time, fixed as 28 days, all samples were subjected to a vertical pressure of 24 kPa and stayed submerged in a water tank at a controlled temperature (20±2°C). After this period, the samples were submitted to the unconfined compression test in order to evaluate its strength ( $q_{u\ max}$ ).

Table 3 and Figure 1 summarizes the main results of the chemical stabilization of the soft soil of “Baixo Mondego”. The results show that, as expected, the unconfined compressive strength increases with the binder content and with the decreasing of the water content (or liquidity index). As the binder content increases, more binder is admixed with the soil allowing the construction of a stronger skeleton matrix. As the water content increases the void ratio also increases, promoting the particles’ spacing with obvious reflects on the fabric of the stabilized soil and on its strength.

Table 3. Unconfined compressive strength results of the chemical stabilization of the soft soil of “Baixo Mondego”.

$I_L$ (-)	$a_w$ (%)	$q_{u\ max}$ (kPa)
1.35	9	209
	12	644
	15	1143
	18	1618
	21	1831
	24	1936
1.96	27	1995
	9	118
	15	694
	21	1266
	27	1383
2.49	9	90
	15	552
	21	965
	27	1032

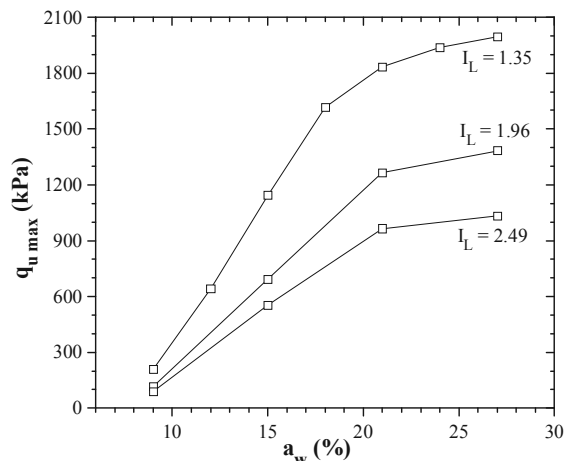


Figure 1. Unconfined compressive strength results of the chemical stabilization of the soft soil of “Baixo Mondego”.

From Figure 1 it can be seen that the curves for different liquidity index exhibit a similar shape (are homothetic). Thus the unconfined compressive strength ( $q_{u\ max}$ ) can be normalised by the liquidity index ( $I_L$ ) multiplying both parameters ( $q_{uL} = q_{u\ max} \times I_L$ ). Figure 2 presents these results which are well fitted by a linear logarithmical regression. This is a simple way to predict the unconfined compressive strength at 28 days of curing time for the cement based stabilized softy soil in study. As it is a linear regression it only requires two test data made for different binder contents.

In order to validate this simple method, it will be applied to other soft soils as presented in the next section.

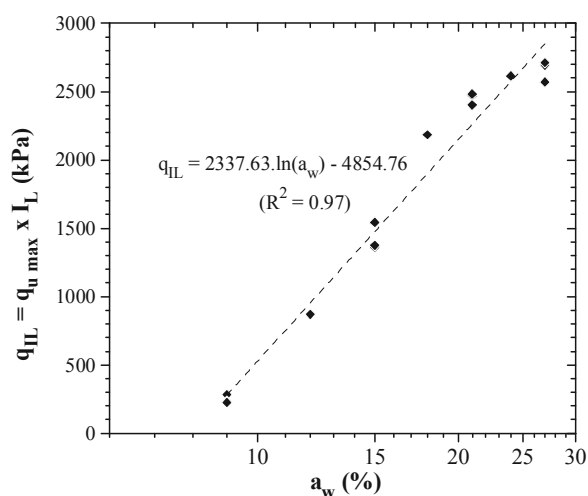


Figure 2. Normalized unconfined compressive strength results of the chemical stabilization of the soft soil of "Baixo Mondego".

### 3 DATA FROM OTHER CEMENT BASED STABILIZED SOFT SOILS

Table 4 presents the main results of 7 other cement based stabilized soft soils whose geotechnical properties are described in Horpibulsuk (2001) and Kawasaki et al (1981). Figure 3 presents the results of the unconfined compressive strength normalized by the liquidity index, from which it can be concluded that each cement based stabilized soft soil has its normalization (fitting curve). Thus the method here proposed is versatile as it is valid for other soft soils.

Table 4. Unconfined compressive strength results of cement based chemical stabilization of other 7 soft soils (Horpibulsuk 2001, Kawasaki et al 1981).

Soft soil	$I_L$ (-)	$a_w$ (%)	$q_{u \max}$ (kPa)
Ariake clay	1.0	10	833
		15	1798
	1.5	10	434
		15	1286
		20	2343
		20	1736
Tokyo clay	1.0	10	1085
		20	4941
		30	6072
Chiba clay	1.0	10	2063
		20	4189
		30	5894
Kangawa clay	1.0	10	1068
		20	3120
		30	5047
Aichi clay	1.0	10	887
		20	1889
		30	2159
Osaka clay	1.0	10	595
		20	1707
		30	1976
Hiroshima clay	1.0	10	748
		20	2436
		30	3952

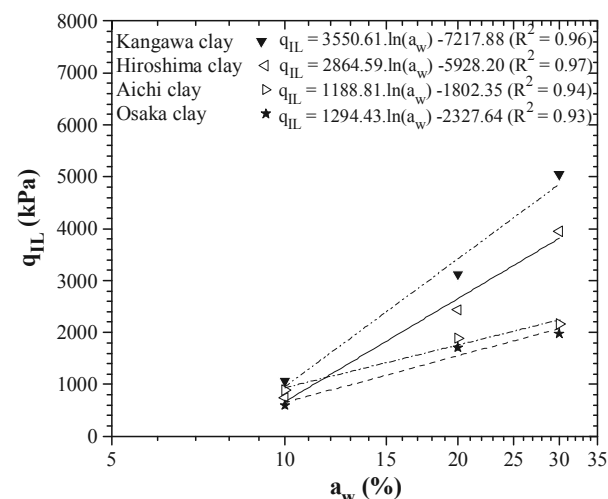
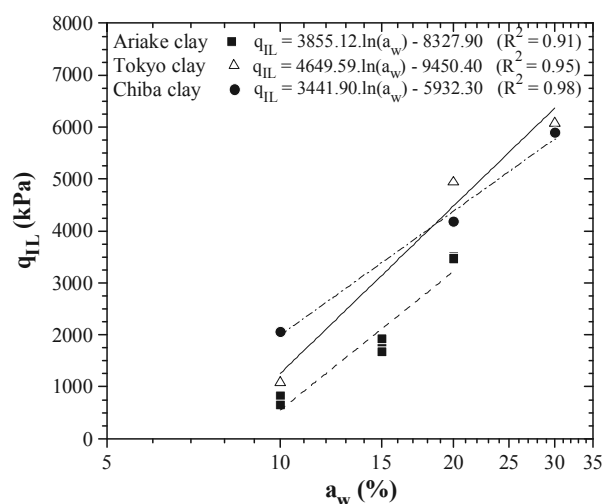


Figure 3. Normalized unconfined compressive strength for other cement based stabilized soft soils.

### 4 GENERALIZING THE PROPOSED METHOD

As it was observed in Figures 2 and 3, the method proposed can be applied satisfactory to a wide range of soft soils. However, each cement based stabilized soft soil has its own fitting parameters (see the equations for  $q_{IL}$  in Figures 2 and 3), different for each soil.

In order to find a generalized strength equation, independent of the soft soil, the  $q_{IL}$  data of a particular soft soil was normalized by the unconfined compressive strength defined for a liquidity index of 1.0 and for a constant binder content (it was considered the value 18% for all soft soils),  $q_{IL=1}(a_w=18\%)$ . For each soft soil, this last value was evaluated from the fitting curves presented in Figures 2 and 3. All data are presented in Figure 4, where it can be seen that the values are in a narrow linear band, fitted relatively well by a linear logarithmical regression ( $R^2 = 0.94$ ). Thus, the method proposed in this paper seems to be independent of the soft soil type, being valid for the prediction of the unconfined compressive strength at 28 days of curing time of cement based stabilized soft soils, which is helpful for the laboratory optimization process of the chemical stabilization. The number of unconfined compression tests required can be reduced to one if it is applied the generalized equation and the binder content chosen is 18%.

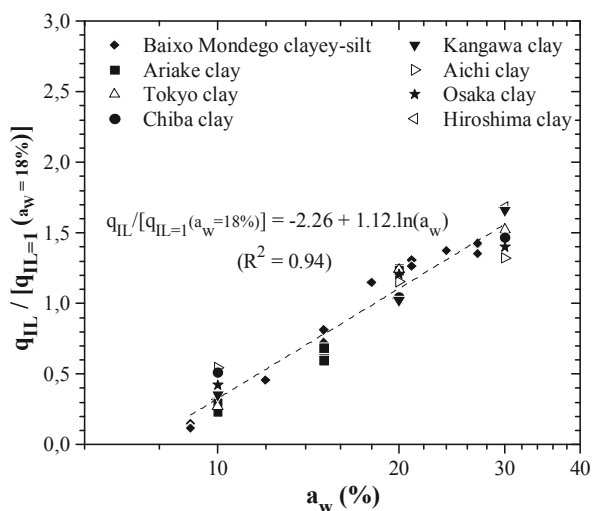


Figure 4. Generalized strength equation for the unconfined compressive strength of cement based stabilized soft soils.

## 5 CONCLUSION

The paper presents a new simple method to predict the unconfined compressive strength at 28 days of curing time of cement based stabilized soft soils, whatever be the water content and binder content. The method was initially developed for the soft soil of “Baixo Mondego” chemically stabilized, and then was successfully applied to a wide range of cement based stabilized soft soils. Thus, this new method seems to be independent of the soft soil, which allows the definition of a general relationship (presented in Figure 4). At limit, the number of unconfined compression tests required can be reduced to one if it is applied the generalized equation and the binder content chosen is 18%. The method proposed in this paper is helpful for the laboratory optimization process of the chemical stabilization at the pre-design stage.

## 6 ACKNOWLEDGEMENTS

The authors would like to express their thanks to CIMPOR for supplying the binders used in the work and to the institutions that supported the research financially: University of Coimbra, CIEC and FCT (PTDC/ECM/101875/2008).

## 7 REFERENCES

- Åhnberg H. 2006. Strength of stabilised soils – a laboratory study on clays and organic soils stabilised with different types of binder. PhD Thesis, University of Lund, Sweden.
- Coelho P.A.L.F. 2000. *Geotechnical characterization of soft soils. Study of the experimental site of Quinta do Foja*, MSc Dissertation, University of Coimbra (in portuguese).
- Correia A.A.S. 2011. *Applicability of deep mixing technique to the soft soils of Baixo Mondego*, Ph.D. Dissertation, University of Coimbra, Portugal (in Portuguese).
- Edil T.B. and Staab D.A. 2005. *Practitioner’s guide for deep-mixed stabilization of organic soils and peat. Final Report*. The National Deep Mixing Research Program, Project Number NDM302, p. 60.
- EN 197-1 2000. *Cement - Part 1: Composition, specifications and conformity criteria for common cements*. IPQ, Portuguese edition from April of 2001, 35 p.
- EN 14679 2005. *Execution of special geotechnical works – deep mixing*. CEN, English version, April of 2005, p. 52.
- Eurosoilstab 2001. *Development of design and construction methods to stabilise soft organic soils. Design guide soft soil stabilization*. CT97-0351, EC Project No. BE 96-3177, Industrial & Materials

- Technologies Programme (BriteEuRam III), European Commission, p. 94.
- Hernandez-Martinez F.G. 2006. *Ground improvement of organic soils using wet deep soil mixing*. PhD Thesis, University of Cambridge, United Kingdom.
- Horpibulsuk S. 2001. *Analysis and assessment of engineering behavior of cement stabilized clays*. PhD Dissertation, Saga University, Saga, Japan.
- Horpibulsuk S., Runglawan R. and Suddeepong A. 2011. Assessment of strength development in blended cement admixed Bangkok clay. *Construction and Building Materials*, Vol. 25, No. 4, p. 1521-1531.
- Horpibulsuk S., Miura N. and Bergado D.T. 2004. Undrained shear behavior of cement admixed clay at high water content. *Journal of Geotechnical and Geoenvironmental Engineering*, ASCE, Vol. 130, No. 10, p. 1096–1105.
- Horpibulsuk S., Miura N. and Nagaraj T.S. 2003. Assessment of strength development in cement-admixed high water content clays with Abrams' law as a basis. *Géotechnique*, Vol. 53, No. 4, p. 439 – 444.
- Kamruzzaman A.H.M. 2002. *Physico-chemical and engineering behavior of cement treated Singapore marine clay*. PhD Thesis, Department of Civil Engineering, National University of Singapore.
- Kawasaki T., Niina A., Saitoh S. and Honjyo Y. 1981. Deep mixing method using cement hardening agent. *Proceedings of the 10th International Conference on Soil Mechanics and Foundation Engineering*, Vol 3, p. 721-724.
- Kitazume M. and Terashi M. 2002. *The deep mixing method – principle, design and construction*. Edited by Coastal Development Institute of Technology, Japan. Balkema.
- Locat J., Trembley H. and Leroueil S. 1996. Mechanical and hydraulic behaviour of a soft inorganic clay treated with lime. *Canadian Geotechnical Journal*, Vol. 33, p. 654 – 669.
- Lorenzo G.A., and Bergado D.T. 2004. Fundamental parameters of cement-admixed clay- New approach. *Journal of Geotechnical and Geoenvironmental Engineering*, ASCE, Vol. 130, No. 10, p. 1042-1050.
- Lorenzo G.A., and Bergado D.T. 2006. Fundamental characteristics of cement-admixed clay in deep mixing. *Journal of Materials in Civil Engineering*, ASCE, Vol. 18, No. 2, p. 161-174.
- Miura N., Horpibulsuk S. and Nagaraj T.S. 2001. Engineering behavior of Cement stabilized clays at high water content. *Soils and Foundations*, Vol. 41, No. 5, p. 33-45.
- Uddin K., Balasubramaniam A.S. and Bergado D.T. 1997. Engineering behavior of cement-treated Bangkok soft clay. *Geotechnical Engineering Journal*, Southeast Asian Geotechnical Society, Vol. 28, No. 1, p. 89-119.
- Venda Oliveira P.J., Lemos L.J.L., and Coelho P.A.L.P. 2010. Behavior of an atypical embankment on soft soil: field observations and numerical simulation. *Journal of Geotechnical and Geoenvironmental Engineering*, ASCE, Vol. 136, No. 1, p. 35-47.

# Modélisation numérique du comportement d'une colonne de soil-mixing et confrontation à un essai de chargement en vraie grandeur

Numerical modeling of a soil-mixing column behavior and comparison with a full-size load test

Cuira F.  
TERRASOL, Paris, France

Costa d'Aguiar S.  
SNCF I&R, Paris, France

Grzyb A., Pellet F.  
INSA, Lyon, France

Mosser J.-F.  
SOLETANCHE BACHY, Rueil-Malmaison, France

Guimond-Barrett A., Le Kouby A.  
IFSTTAR, Paris, France

**RÉSUMÉ :** Cet article présente les résultats d'un travail de modélisation numérique visant à simuler un essai de chargement axial sur une colonne de sol-ciment, réalisée par soil-mixing en voie humide. Quatre modèles ont été bâtis dans le cadre de ce travail : trois modèles en éléments finis, et un modèle semi-analytique simplifié. Les résultats des quatre modèles sont confrontés à ceux obtenus par un essai de chargement monotone en vraie grandeur, réalisé sur une colonne de sol – mixing de 400 mm de diamètre et 5 m de hauteur, mise en œuvre dans un sol limoneux à sablo-graveleux. Ces résultats permettent notamment de reproduire le mode de rupture observé lors de l'excavation de la colonne, et mettent en évidence la nécessité de modéliser correctement le comportement non linéaire du matériau sol-ciment qui influe significativement sur le comportement global, à la différence des pieux « rigides ».

**ABSTRACT:** This article shows the results of a numerical modelling study aiming at simulating an axial load test on a soil-cement column, carried out using the wet soil-mixing method. Four models were built as part of this study: three finite element models and one simplified semi-analytical model. The results from the four models were compared with those from a full-size monotonic load test, performed on a Ø400 mm diameter and 5m high soil-mixing column, installed in silty to sandy-gravelly soils. These results allow to reproduce the failure mode observed during the column excavation, by emphasizing the need of an accurate modelling of the non-linear soil-cement material which has a significant influence on the general behaviour, unlike with "rigid" piles.

**KEYWORDS:** Numerical modelling, soil reinforcement, Soil-mixing, load test.

## 1 INTRODUCTION

La technique du soil mixing permet d'améliorer les caractéristiques d'un sol meuble par mélange mécanique *in situ* avec un liant hydraulique. Le sol initialement présent sur le chantier est alors valorisé comme un matériau de construction, avec le double intérêt de diminuer les déchets (sols excavés) et de réduire la consommation de matériaux et d'énergie.

Le procédé Springsol® utilise un outil ouvrant, pour réaliser des colonnes de sol-ciment de diamètre variable, ce qui limite au maximum l'impact des travaux sur les existants. Ce procédé offre des perspectives aussi bien dans le domaine de la maintenance des plateformes ferroviaires (possibilité de renforcer les structures ferroviaires sans avoir à déposer les voies), que dans celui du renforcement des fondations existantes (empreinte des forages sur les structures limitée au diamètre de l'outil fermé).

Cette souplesse et le caractère économe en déchets et en matériaux permettent au procédé Springsol de répondre aux nouvelles exigences environnementales et économiques des projets. C'est donc dans le but de développer ces solutions que Soletanche Bachy, la SNCF et Terrasol collaborent au sein du projet de recherche RUFEX (Renforcement et réUtilisation des plateformes et Fondations Existantes) avec l'IFSTTAR, l'INSA de Lyon et l'Ecole des Ponts ParisTech.

Cet article présente les résultats d'un travail de modélisation numérique d'un essai de chargement monotone conduit jusqu'à la rupture sur une colonne de soil mixing réalisée sur un chantier de validation du projet RUFEX.

## 2 ESSAI DE CHARGEMENT EN VRAI GRANDEUR

Un essai de chargement sur une colonne de soil-mixing de 400 mm de diamètre et 5 m de hauteur a été réalisé sur le site expérimental du projet Rufex situé sur la commune de Vernouillet (78). Le contexte géotechnique est caractérisé par des remblais en surface suivis d'une couche de limon sableux reposant sur un sable graveleux. Aucune nappe phréatique n'a été rencontrée lors des reconnaissances. Le Tableau 1 récapitule les caractéristiques géo-mécaniques issues des essais réalisés.

Tableau 1. Caractéristiques géotechniques des sols du site.

Nature	Limon sableux	Sable graveleux
Profondeur du toit (m)	0,5	3,5
Pression limite nette $pl^*$ (MPa)	1	2,5
Module pressiométrique $E_m$ (MPa)	10	20
Cohésion $c'$ (kPa)	2	0
Angle de frottement ( $^\circ$ )	27	37

La colonne testée a été forcée avec l'outil Springsol®. Le malaxage du sol avec le liant hydraulique (ciment de type CEM III) a été effectué *in situ* par voie humide. La quantité de ciment injectée dans la colonne sous forme de coulis était d'environ 230 kg / m<sup>3</sup>.

L'essai de chargement a été réalisé 90 jours après l'installation de la colonne, avec des paliers de chargement de 50 kN maintenus pendant 30 min. La courbe de chargement obtenue est présentée sur la Figure 1. Le chargement a été arrêté pour une charge maximale de 400 kN, lorsque le tassement de la tête de la colonne a dépassé 40 mm (1/10<sup>ème</sup> du diamètre).

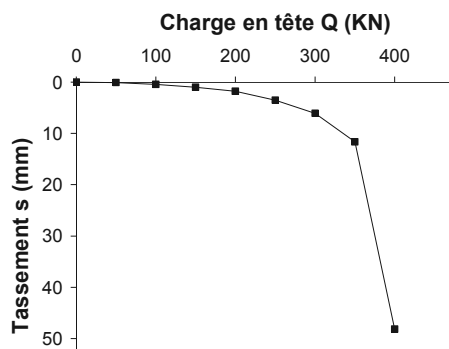


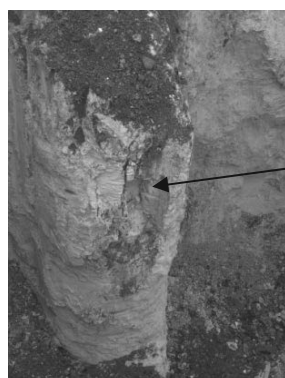
Figure 1. Courbe de chargement sur colonne de soil-mixing.

Après 180 jours, l'excavation de la colonne testée a permis de distinguer une partie supérieure (de 0 à 2,5 m) constituée de limon traité et une partie inférieure composée de sable traité. Une zone de transition faite d'un mélange de limon et de sable traité a été observée entre 2,5 et 3,5 m. Des fragments de la colonne ont été prélevés, carottés en laboratoire, et soumis à des essais mécaniques pour déterminer la résistance et le module de déformation du matériau constitutif de la colonne (Tableau 2).

Tableau 2. Résultats des essais en laboratoire sur les éprouvettes provenant de la colonne excavée.

Nature	Limon traité (1)	Transition (2)	Sable traité (3)
Profondeur (m)	0,5 - 2,5	2,5 - 3,5	3,5 - 5,0
Résistance Rc (MPa)	3,7	7,6	11,9
Module local E <sub>50</sub> (MPa)	1280 Rc	1280 Rc	1280 Rc
Angle de frottement (°)	42	42	42
Cohésion (kPa)	700	1700	2800

Vers 1 m de profondeur, la colonne de limon traité apparaît particulièrement fissurée et fracturée (Figure 2), ce qui fait suggérer que la rupture s'est produite au sein du matériau constitutif de la colonne. Ce constat est conforté par le fait que la portance de la colonne (estimée à partir des résultats des essais pressiométriques) était a priori supérieure à sa résistance interne (estimée à partir des résultats des essais sur les éprouvettes carottées).



Zone de limon traité fissurée et fracturée vers 1 m de profondeur

Figure 2. Excavation de la colonne après l'essai de chargement.

### 3 MODÉLISATION DE L'ESSAI DE CHARGEMENT : MODÈLES ÉLÉMENTS FINIS

Le résultat de l'essai de chargement est utilisé comme référence pour l'évaluation de quatre modèles numériques dont trois basés sur un traitement complet en éléments finis. Ces modèles sont construits selon la coupe schématique suivante (Figure 3) et sur la base des paramètres donnés dans les Tableaux 1 et 2.

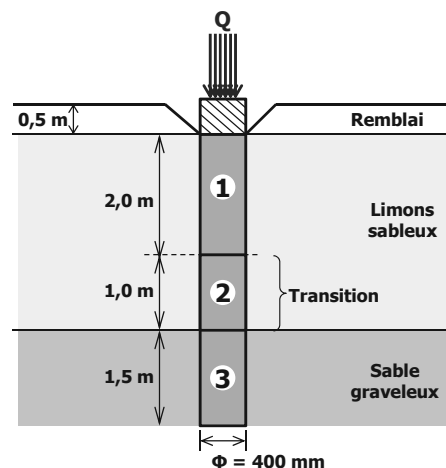


Figure 3. Coupe de calcul retenue

#### 3.1 Modèle 1 (logiciel GEFDyn)

Ce modèle est bâti à l'aide du logiciel éléments finis GEFDyn. Il s'agit d'un modèle tridimensionnel où la colonne est modélisée par des éléments volumiques à 8 nœuds formant un quart de cylindre de 400 mm de diamètre et 5 m de long, noyé dans un milieu continu de 20 m de profondeur. Des éléments d'interface ont été introduits entre la structure de la colonne et les éléments de sol.

Le modèle de comportement choisi est un modèle linéaire élastique parfaitement plastique avec un critère de rupture de Mohr Coulomb (noté MC par la suite) pour les différents matériaux (sol et colonne). La loi de l'interface est celle d'Aguiar et al (2011) dont la formulation est basée sur les mêmes hypothèses de comportement que le modèle dit de Hujieux (1985) qui se révèle très adapté au comportement non linéaire des sols. La richesse de ce type de modèle réside dans la possibilité, en fonction des paramètres de la surface de charge et du type d'érouissage, de modéliser des comportements qui peuvent aller du simple « élastique parfaitement plastique » à un comportement élasto-plastique à érouissage déviatorique et volumique. Pour le présent calcul, les paramètres de l'interface sont choisis de manière à représenter une surface de charge de Mohr Coulomb avec un comportement élastique parfaitement plastique. L'angle de frottement à l'interface a été choisi égal à celui du sol environnant. Cela est justifié par le mode de réalisation de la colonne (malaxage local) qui produit une interface rugueuse mobilisant ainsi un mécanisme de rupture mettant en jeu la résistance intrinsèque du sol (Figure 4).



Figure 4. Etat de la surface d'un tronçon de colonne excavée

### 3.2 Modèle 2 (logiciel ABAQUS)

Le modèle 2 est bâti sous le logiciel ABAQUS. Il s'agit d'un modèle axisymétrique qui intègre une loi de comportement avancée de type « Drucker-Prager » modifiée avec cap (DPC). Ce modèle permet de prendre en compte l'effet d'écroutissage du sol, l'historique de contraintes, ainsi que l'effet de compaction en pointe sous la colonne. La surface de charge est composée de trois parties : une limite de rupture en cisaillement de type Drucker-Prager, un cap elliptique, et une zone de transition (Figure 5).

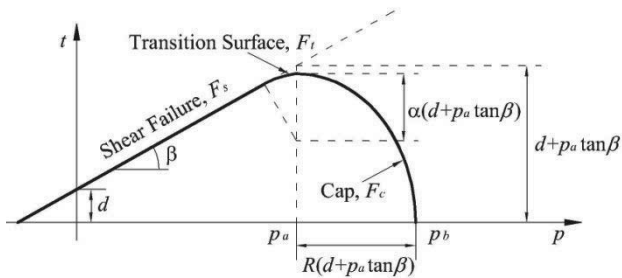


Figure 5. Loi de Drucker-Prager modifiée avec cap (DPC)

Les paramètres  $\beta$  et  $d$  s'expriment en fonction de l'angle de frottement interne  $\varphi$  et la cohésion  $c$  à l'aide de la relation (1) :

$$\tan \beta = \frac{6 \sin \varphi}{3 - \sin \varphi} \quad \text{et} \quad d = \frac{18c \cos \varphi}{3 - \sin \varphi} \quad (1)$$

Les autres paramètres sont choisis soit par calage, soit d'une manière forfaitaire sur la base d'éléments bibliographiques. En particulier, le paramètre  $p_b$  qui délimite la surface d'écroutissage, doit en toute rigueur être calé sur le résultat d'un essai de consolidation isotrope. Dans le présent exercice, ce modèle (DPC) a été considéré pour caractériser le comportement des sables graveleux. Pour les autres matériaux (colonne et limons sableux), il a été retenu une loi linéaire élastique parfaitement plastique avec critère de rupture de Mohr Coulomb (MC). Pour la définition de la loi DPC dans les sables graveleux, les paramètres suivants ont été considérés :  $R = 0,10$ ,  $\alpha = 0,01$  et  $p_b$  fonction de la déformation volumique plastique selon la loi d'écroutissage des sables d'Ottawa (Helwany 2000). Enfin, des éléments d'interface ont été introduits avec une loi MC.

### 3.3 Modèle 3 (logiciel PLAXIS)

Le 3<sup>e</sup> modèle est un modèle axisymétrique bâti sous le logiciel PLAXIS. Les éléments utilisés sont des éléments triangulaires à 15 nœuds et 30 degrés de liberté. Pour le sol et la colonne, on choisit une loi de contraintes-déformations de type « HSM » (Hardening Soil Model - Figure 6) qui est une loi hyperbolique tenant compte de l'écroutissage en cisaillement et en compression.

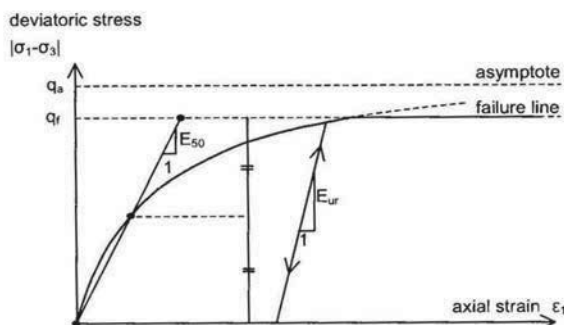


Figure 6. Principe de la loi HSM sous PLAXIS

Ce modèle permet par ailleurs de tenir compte de la variation du module de déformation sécant  $E_{50}$  (à 50% de la contrainte de rupture) avec l'état de contraintes. Cette variabilité est contrôlée par un paramètre « puissance » noté  $m$ , qu'on prend usuellement égal à  $m = 0,5$  pour le sol en place (le module sécant est proportionnel à la racine de la contrainte appliquée). Pour la colonne, ce paramètre est pris égal à  $m = 0$  (pas de variation du module sécant avec l'état de contraintes). Enfin, cette loi est combinée avec un critère de rupture de type Mohr Coulomb.

Des éléments d'interface ont été par ailleurs introduits sur toute la frontière de la colonne avec une loi de contraintes-déformations et un critère de rupture identiques à ceux des sols environnants.

### 3.4 Mise en œuvre et résultats

Pour les trois modélisations réalisées, les données géotechniques ont été complétées par les valeurs du module de déformation sécant  $E_{50}^{h/2}$  à mi-épaisseur dans chaque couche :  $E_{50}^{h/2} = 25$  MPa pour les limons sableux et  $E_{50}^{h/2} = 100$  MPa pour les sables graveleux. La Figure 7 présente la courbe de chargement simulée à l'aide des trois modèles présentés ci-dessus. Une très bonne concordance est observée entre la modélisation et les mesures jusqu'à 300 kN (75% de la charge de rupture mesurée). Les modèles 2 et 3 mettent en évidence un palier de rupture net situé entre 350 et 400 kN, ce qui correspond, à 10% près, au palier obtenu par l'essai de chargement sur site.

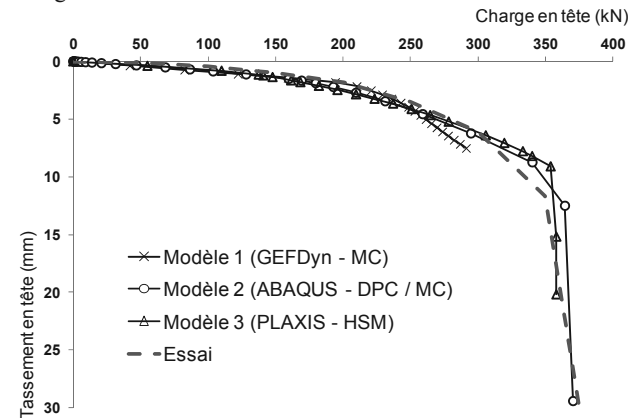


Figure 7. Simulation de la courbe de chargement par modélisation numérique en éléments finis

Dans les modèles 2 et 3, le palier de rupture obtenu correspond au développement d'une zone de plastification « conique » dans la partie supérieure de la colonne vers 1 m de profondeur (Figure 8). Ce constat est corroboré par les observations faites sur site lors de l'excavation de la colonne.

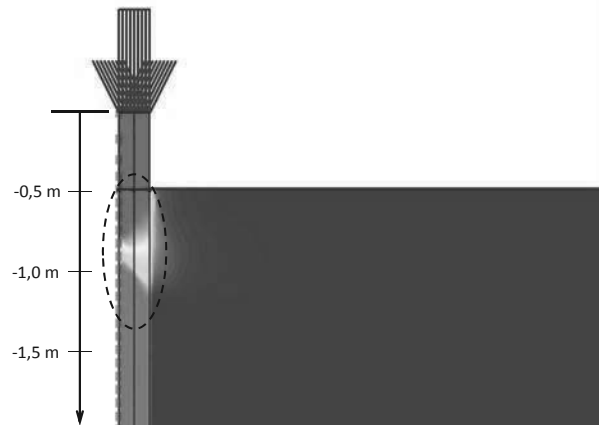


Figure 8. Développement d'un mécanisme de rupture localisé dans la colonne (modèle 3)

#### 4 MODÈLE SEMI-ANALYTIQUE SIMPLIFIÉ

##### 4.1 Principe du modèle

On utilise à présent un modèle semi-analytique simplifié basé sur la méthode dite « t-z » : la colonne est assimilée à une poutre verticale travaillant en compression axiale, tandis que le frottement latéral  $\tau$  et la contrainte en pointe  $q$  suivent une loi de mobilisation de Frank et Zhao (1982), et sont donc fonctions du déplacement vertical de la colonne  $w$ . Chaque loi est caractérisée à l'aide de deux paramètres : un paramètre de pente ( $K_t$  ou  $K_p$ ) et une contrainte unitaire limite ( $q_s$  ou  $q_p$ ). Ces lois sont couramment utilisées en France pour estimer le tassement d'un élément de fondation profonde, et se révèlent très efficaces dans les exercices de calage par rapport à un essai de chargement en vraie grandeur.

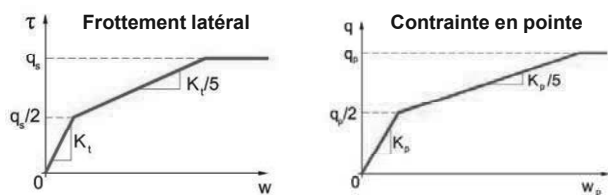


Figure 9. Lois de mobilisation de type Frank et Zhao

Les courbes de mobilisation ci-dessus sont combinées avec la loi de comportement de la colonne, qui relie la contrainte appliquée  $\sigma$  au taux de déformation axiale de la colonne  $\epsilon$ . A la différence des pieux « classiques » pour lesquels le contraste de rigidité pieu/sol est tel que l'essentiel des tassements est obtenu en pointe, la particularité d'une colonne de soil-mixing réside dans un contraste de rigidité colonne/sol plus faible et une sensibilité notable de la raideur globale en tête vis-à-vis du comportement local. Ces éléments ont justifié le recours à une loi de contrainte-déformation non linéaire pour la colonne : il a été retenu une loi de forme hyperbolique (Figure 10) construite à l'aide de deux paramètres : le module sécant  $E_{50}$  et la résistance à la compression simple  $R_c$ . Lors du présent exercice, cette loi s'est révélée apte à retranscrire le comportement observé, à la différence d'une loi linéaire élastique.

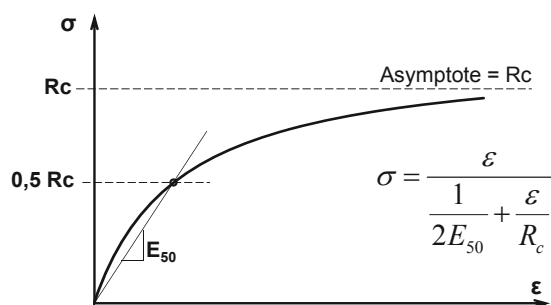


Figure 10. Loi de contrainte-déformation retenue pour la colonne

##### 4.2 Mise en œuvre

La loi de contrainte-déformation de la Figure 10 est construite à partir des paramètres ( $E_{50}$ ,  $R_c$ ) qui figurent dans le Tableau 2.

Les paramètres de pente des lois de Frank et Zhao (Figure 9) s'obtiennent par corrélation avec le module pressiométrique  $E_M$  :  $K_t = 0,8 E_M / B$  et  $K_p = 4,8 E_M / B$ , où  $B$  désigne le diamètre de la colonne. Ensuite, pour le choix du frottement latéral limite  $q_s$ , deux hypothèses enveloppes sont examinées : la première est celle d'un contact béton/sol pour laquelle la valeur de  $q_s$  s'obtient par corrélation avec la pression limite  $pl^*$  ; la deuxième hypothèse est celle d'un contact sol/sol pour laquelle la valeur de  $q_s$  est celle du cisaillement limite de Mohr Coulomb :  $q_s = \tan(\phi^*) \cdot K_0 \cdot \sigma_v'$ , avec  $K_0 = 0,5$  et  $\sigma_v'$  la contrainte verticale effective initiale à l'interface de la colonne. Enfin, la contrainte limite en pointe  $q_p$  est prise égale à 4 MPa.

#### 4.3 Résultats

La Figure 11 présente les résultats obtenus (courbe de chargement). Deux cas ont été étudiés : cas d'un comportement linéaire élastique de la colonne ( $E = E_{50}$ ), et cas d'un comportement non linéaire ( $E = f(\sigma)$ ) selon la loi décrite dans la Figure 10. Pour chaque cas, deux situations sont examinées : frottement de type sol/sol ( $q_s = f(\sigma_v')$ ) et frottement de type béton/sol ( $q_s = f(pl^*)$ ). Les résultats obtenus confirment la pertinence d'une loi de comportement non linéaire pour le matériau constitutif de la colonne, et montrent que le choix d'un frottement de type « sol/sol » est plus représentatif du comportement réel observé. Avec ces hypothèses, le résultat du modèle semi-analytique se révèle très concordant avec celui de l'essai de chargement jusqu'au palier de rupture. Celui-ci est obtenu par plastification en tête de la colonne (contrainte appliquée proche de la résistance à la compression simple  $R_c$ ).

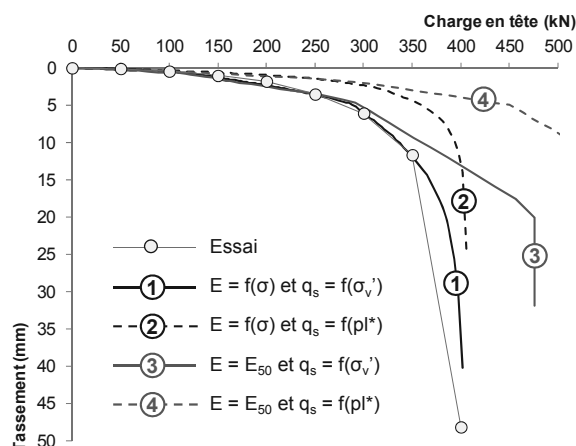


Figure 11. Courbe de chargement – Modélisation analytique simplifiée

#### 5 CONCLUSION

Les enseignements tirés de l'essai de chargement en vraie grandeur ont permis d'orienter le choix des paramètres d'entrée des différents outils numériques développés dans le cadre du projet RUFEX. Les résultats obtenus, tant par les modèles numériques que par le modèle semi-analytique, permettent de bien reproduire le comportement observé lors de l'essai, aussi bien sur le comportement avant rupture que sur le mode de rupture. Ils mettent en évidence la nécessité de modéliser correctement le comportement non linéaire du matériau sol-ciment qui influe significativement sur le comportement global, à la différence des pieux « rigides ».

#### 6 REMERCIEMENTS

Les auteurs tiennent à remercier la DGCIS (Direction Générale de la Compétitivité et des Services) et les Conseils Généraux de la Région Ile de France et 93 qui cofinancent cette recherche.

#### 7 REFERENCES BIBLIOGRAPHIQUES

D'Aguiar, S. C., A. Modaressi-Farahmand-Razavi, J. A. dos Santos, and F. Lopez-Caballero (2011). *Elastoplastic constitutive modeling of soil-structure interfaces under monotonic and cyclic loading*. Computers and Geotechnics 38(-), 430447.

Frank, R. & Zhao, S. R. (1982), *Estimation par les paramètres pressiométriques de l'enfoncement sous charge axiale des pieux forés dans les sols fins*, Bull. Liaison Labo. P. et Ch. 119 :17-24.

Helwany S. 2000 *Applied Soil Mechanics with ABAQUS Applications*, J. WILEY & SONS, INC pp. 61-67

Hujeux, J. C. (1985). *Une loi de comportement pour le chargement cyclique des sols en génie parasismique*, pp. 278–302. V. Davidovici, Presses ENPC.

# Design of Deep Soil Mix Structures: considerations on the UCS characteristic value

## Dimensionnement des structures en soil mix : considérations sur la valeur caractéristique UCS

Denies N., Van Lysebetten G., Huybrechts N.  
*Belgian Building Research Institute, BBRI, Belgium*

De Cock F.  
*Geotechnical Expert Office Geo.be, Belgium*

Lameire B.  
*Belgian Association of Foundation Contractors ABEF, Belgium*

Maertens J.  
*Jan Maertens bvba & KU Leuven, Belgium*

Vervoort A.  
*KU Leuven, Belgium*

**ABSTRACT:** Since several decades, the deep soil mix (DSM) technique has been used for ground improvement works. But in recent years, this technique has been increasingly used for structural applications. Standardized guidelines for the execution and the design of this kind of applications are not currently available. For the purpose of developing such guidelines, mechanical characteristics of DSM material were investigated. Within the framework of a Flemish regional research program (IWT 080736), DSM material from 38 Belgian construction sites, with various soil conditions and for different execution processes, has been tested. Internationally QA/QC activities are commonly related to tests on core samples for the determination of the Unconfined Compressive Strength (UCS) and the modulus of elasticity (E) of the material. Both values allow an approach of the design which takes into account the bending characteristics (EI), the deformation (E), the arching effect (UCS) and the structural resistance (UCS) of the element. For the semi-probabilistic design approach presented in Eurocode 7, a “characteristic value” of the UCS has to be defined as part of the design of DSM structures. The present paper discusses the definition of this value.

**RÉSUMÉ :** Depuis plusieurs décennies, la technique du soil mix est utilisée comme procédé d'amélioration du sol. Mais ces dernières années, elle est de plus en plus utilisée pour des applications structurelles. Aucune directive n'est actuellement disponible pour l'exécution et le dimensionnement de telles applications. De manière à développer de telles directives, les caractéristiques mécaniques du matériau soil mix ont été investiguées. Dans le cadre d'un programme de recherche financé par l'IWT, l'agence gouvernementale flamande pour l'innovation, des échantillons de soil mix de 38 sites de construction ont été testés pour différents types de sol et différents systèmes. La qualité du matériau soil mix est généralement contrôlée à l'aide d'essais, réalisés sur des échantillons carottés in situ, par lesquels sont déterminés la résistance à la compression simple (UCS) et le module d'élasticité (E) du matériau. Ces deux grandeurs permettent une approche du dimensionnement tenant compte de la rigidité flexionnelle (EI), des déformations (E), de l'effet de voûte (UCS) et de la résistance structurelle (UCS) de l'élément. Au vue de l'approche semi-probabiliste de l'Eurocode 7, il est important de définir la valeur caractéristique de la résistance du soil mix (UCS) à prendre en compte dans le dimensionnement. Le présent article discute de la définition de cette valeur caractéristique.

**KEYWORDS:** Deep soil mix wall, structural design, ucs characteristic value

### 1 INTRODUCTION

The Deep Soil Mix (DSM) process was introduced in the 70's in Japan and in the Scandinavian countries. Since several decennia, DSM has been known as a ground improvement (GI) technique. According to the classification of GI methods adopted by the ISSMGE TC 211, DSM can be classified as ground improvement with grouting type admixtures. Numerous reviews and recent progresses of the DSM technique are referred in Denies and Van Lysebetten (2012). The results of national and European research programs have also been published in multiple interesting reports (such as Eurosoilstab 2002), while the European standard for the execution of deep mixing “Execution of special geotechnical works – Deep Mixing” (EN 14679) was published in 2005. Most of these research projects focused on the global stabilization of soft cohesive soils such as clay, silt, peat and gyttja (result of the digestion of the peat by bacteria). More recently, DSM is increasingly being used for structural applications such as soil mix walls (SMW) for the retaining of soil and water in the case of excavations.

In the DSM process, the ground is mechanically mixed in place, while a binder, based on cement, is injected. For SMW applications, the DSM cylindrical columns or the rectangular

panels are placed next to each other, in a secant way. By overlapping the different soil mix elements, a continuous SMW is realized. Steel profiles are inserted into the DSM fresh material to resist the shear forces and bending moments. The main structural difference between SMW and the more traditional secant pile walls is the constitutive DSM material which consists of a soil – cement mixture instead of concrete.

Elements such as piles or diaphragm walls only comprise standardized components and their characteristic strength can be defined by the strength class of concrete. The design approach for the DSM material is very different since the existing soil is used as an essential component of the final product. Moreover, the DSM strength depends not only on the soil type, but also on the DSM technique, the amount and the type of binder, etc.

Within the framework of the BBRI “Soil Mix” project initiated in 2009 in collaboration with the KU Leuven and the Belgian Association of Foundation Contractors (ABEF), numerous tests on in situ DSM material have been performed. A good insight has been acquired with regard to mechanical characteristics that can be obtained with the CVR C-mix<sup>®</sup>, the TSM and the CSM systems in several Belgian soils as reported in Denies et al. (2012). BBRI information sheets (BBRI, 2012a and b) have been published for the purpose of helping contractors to improve the quality control (QC) of their finished



product, but guidance rules for the design of SMW are still lacking in particular for the determination of a “characteristic value” representative of the strength of the soil mix material. Neither in the Eurocode 7 nor in the European standards for grouting (EN 12715), jet-grouting (EN 12716) or deep-mixing (EN 14679), specifications are given for the internal strength of the material.

In practice, Quality Assurance (QA) and Quality Control (QC) activities are commonly related to tests on core samples for the determination of the Unconfined Compressive Strength (UCS) and the modulus of elasticity (E) of the material. Both values allowing an approach of the design taking into account the bending characteristics (EI), the deformation (E), the arching effect (UCS) and the structural resistance (UCS) of the element. For engineering purposes and as part of the semi-probabilistic design approach presented in Eurocode 7, it is thus essential to define the UCS characteristic value that can be taken into account in the design of DSM structures. The following paragraphs discuss the definition of this value.

## 2 DETERMINATION OF THE UCS CHARACTERISTIC VALUE OF DSM MATERIAL

### 2.1 On the basis of an X% lower limit value

The first methodology consists in the calculation of the characteristic strength as the X% lower limit on the basis of a statistical distribution function. Nevertheless, in practice, the wrong assumption is often made that the datasets of UCS values of soil mix material are normally distributed (see Fig. 1a). The characteristic UCS value is then erroneously calculated as the X% lower quantile of the normal distribution with parameters corresponding to the dataset. Moreover, this often results into negative and thus useless characteristic UCS values. The mathematically correct solution would be to apply the best fitting standard distribution function, for example a lognormal distribution in case the distribution is skewed and/or does not contain subpopulations. The X% lower limit can then be calculated on the basis of this theoretical distribution function, as illustrated in Denies et al. (2012) for a lognormal distribution (see Fig. 1b). Possibly, a factor  $\beta$  has to be added to the values to obtain an optimal fit with a normal distribution after transformation. However, this way of working is probably too complex to apply in practical situations.

The second methodology to determine the X% lower limit is based on the cumulative frequency curve of the original experimental dataset and thus independent of any theoretical distribution function. Note that to apply this method, enough data points have to be available (for an accurate determination of the 5% lower limit without extrapolation, at least 20 samples are necessary). This approach seems rather simple but any other method probably results in a large uncertainty. Figure 2 presents the cumulative frequency curve for the UCS values of the dataset illustrated in Fig. 1.

### 2.2 On the basis of an average value with safety factor

A second approach to determine the UCS characteristic value is the use of the average value of the dataset in combination with a safety factor:

$$f_{c,k} = \alpha \overline{q_{uf}} \tag{1}$$

where  $\overline{q_{uf}}$  is the mean UCS value and  $\alpha$  a factor representing a certain confidence and safety level ( $\alpha < 1$ ).

In the formalized design approach (DIN 4093, August 2012) used in Germany, the UCS characteristic value is defined as the minimum value of three parameters:

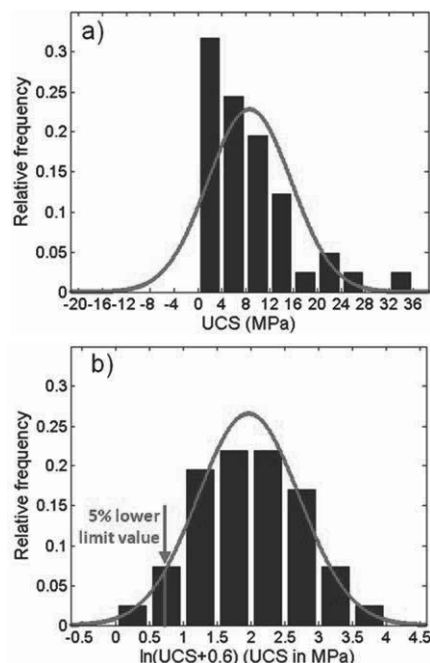


Figure 1. a) Distribution of the UCS values of 41 cores of DSM material from a site in Gent (Belgium) and the corresponding theoretical Gaussian curve. b) Distribution of the logarithm of the UCS values increased with  $\beta = 0.6$  from the same site and the corresponding Gaussian curve. The vertical line indicates the 5% lower limit value, after Denies et al. (2012).

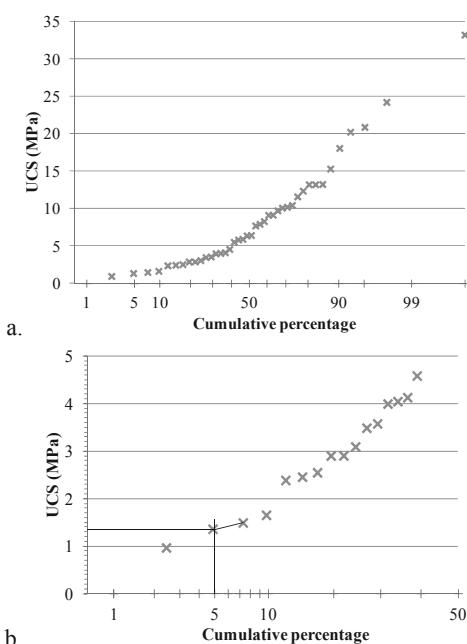


Figure 2. Cumulative frequency curve of all UCS values of the dataset from the site in Gent: a) Full curve. b) Zoom on the part below 50%: presentation of the construction for the evaluation of the 5% lower limit value.

$$f_{c,k} = \min(f_{m,min} ; \alpha f_{m,mittel} ; 12 \text{ MPa}) \tag{2}$$

where  $f_{m,min}$  is the minimum UCS value and  $f_{m,mittel}$  the arithmetic mean UCS value from a series of at least 4 samples.  $\alpha$  is determined in function of  $f_{c,k}$ :  $\alpha$  equals 0.6 for  $f_{c,k} \leq 4$  MPa and 0.75 for  $f_{c,k} = 12$  MPa (linear interpolation is required for intermediate values). This method is described in more detail by Topolnicki and Pandrea (2012).

If the characteristic value  $f_{c,k}$  is smaller than 4 MPa, additional creep tests have to be conducted with a load of  $f_{c,k}/2$  as described in the annex B of the DIN 4093.

The design strength for calculations with the concept of partial safety factors is then computed as follows:

$$f_{c,d} = 0.85 \frac{f_{c,k}}{\gamma_m} \quad (3)$$

where 0.85 is a factor to consider permanent situations and  $\gamma_m$  is the material safety factor as defined in Eurocode 7 (1.5 for permanent and temporary load cases and 1.3 for accidents). For temporary situations, the design strength is computed without the 0.85 coefficient.

As reported in Topolnicki and Pandrea (2012), if independent and separate design calculations are performed for compressive and shear stresses (i.e. no 3D stress analysis), the maximum allowed compressive stress is  $0.7 \times f_{c,d}$  and the maximum allowed shear stress is  $0.2 \times f_{c,d}$ .

For comparison with the previous version of the DIN 4093 (published in September 1987), Table 1 presents cumulated safety factors on material strength ( $f_{m,mittel}$ ) and equivalent global safety factors ( $(\gamma_m \times \gamma_{G,Q}) / (\alpha \times 0.85 \times (0.7 \text{ or } 1))$ ) computed with the new DIN 4093 for permanent design situations. An increase in the number of test samples has no effect on the safety factors.

Table 1. Cumulated safety factors on material strength ( $f_{m,mittel}$ ) and equivalent global safety factors in permanent design situation according to DIN 4093 – August 2012 ( $\gamma_m = 1.5$ ).

	For $\alpha=0.6$	For $\alpha=0.75$
With 3D analysis		
<b>Cumulated safety factor</b>	<b>2.94</b>	<b>2.35</b>
Permanent actions ( $\gamma_G=1.35$ )		
<b>Equivalent global safety factor</b>	<b>3.97</b>	<b>3.18</b>
Variable actions ( $\gamma_Q=1.50$ )		
<b>Equivalent global safety factor</b>	<b>4.41</b>	<b>3.53</b>
Without 3D analysis		
<b>Cumulated safety factor</b>	<b>4.20</b>	<b>3.36</b>
Permanent actions ( $\gamma_G=1.35$ )		
<b>Equivalent global safety factor</b>	<b>5.67</b>	<b>4.54</b>
Variable actions ( $\gamma_Q=1.50$ )		
<b>Equivalent global safety factor</b>	<b>6.30</b>	<b>5.04</b>

For comparison, in the previous version of the DIN 4093 (September 1987), the design value was computed as follows:

$$f_{c,d} = \frac{f_{m,mittel}}{5} \quad (4)$$

for samples with UCS values expected larger than 5 MPa and tested according to the DIN 1048 standard for concrete material, or with the help of:

$$f_{c,d} = \frac{q'_u}{3} \quad (5)$$

for samples with UCS values expected smaller than 5 MPa and tested according to the DIN 18 136 for soil material.  $q'_u$  is the UCS value computed according to the DIN 18136.

Considering the safety factor of 5 and the reduction factor of 0.7 related to the 3D character of the loading, the previous version of the DIN 4093 resulted in a global safety factor of 7.14.

For this second approach based on an average value with safety factor, Denies et al. (2012) have remarked that first, the definition of the most suitable mean (arithmetic mean, median,

etc.) should depend on the type of the distribution of the dataset. Second, problems may arise with limited number of samples, skewed populations and in the presence of subpopulations.

Figure 3 compares the UCS characteristic value computed with the help of the cumulative frequency curve (CC method) or with respect to the DIN approach. The ratio of the two characteristic values is presented as a function of the number of tested samples for each considered dataset. Minimum 20 samples are necessary in order to conduct the statistical analysis on the cumulative frequency curve. As observed in Fig. 3, the UCS characteristic value is always greater when computed with the help of the cumulative frequency curve (all the values are larger than 1). In Fig. 3, results are given for two different X% lower quantiles: X = 5% and 10%. Indeed, for the first category of approaches (based on the lower limit value), a value for the X% has to be defined. A more detailed analysis is necessary to determine if a 5% lower limit, as often stated in Eurocode 7, is a representative characteristic value for the strength of the soil mix material. Actually, one major issue is the representativeness of the core samples with regard to the in situ executed DSM material.

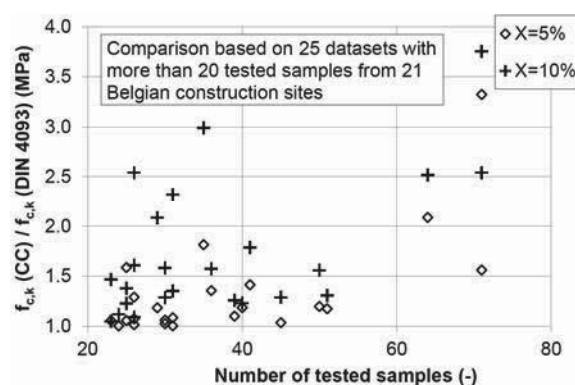


Figure 3. Ratio of the characteristic values ( $f_{c,k}$  (CC) and  $f_{c,k}$  (DIN4093)) as a function of the number of tested samples.

### 3 INFLUENCE OF THE UNMIXED SOIL INCLUSIONS

There is mainly the question of the influence of unmixed soft soil inclusions on the mechanical behaviour of the DSM material. Indeed, as a natural material (i.e. soil) is being mixed, it is to be expected that the entire wall is not perfectly mixed and homogeneous: inclusions of unmixed soft soil are present. As a result, Ganne et al. (2010) have proposed to reject all test samples with soil inclusions  $> 1/6$  of the sample diameter, on condition that no more than 15% of the test samples from one particular site would be rejected. This possibility to reject test samples results from the reflexion that a soil inclusion of 20 mm or less does not influence the behaviour of a soil mix structure. On the other hand, a soil inclusion of 20 mm in a test sample of 100 mm diameter significantly influences the test result. Of course, this condition is only suitable if one assumes that there is no soil inclusion larger than  $1/6$  of the width of the in situ DSM structure. For the purpose of studying this question, 2D numerical simulations were performed at KU Leuven with the aim to quantify the effect of soil inclusions on the DSM strength and stiffness. The following parameters are being considered: size, number, relative position and percentage of soil inclusions. The results of this study are presented in Vervoort et al. (2012) and Van Lysebetten et al. (2013). As illustrated in Fig. 4, they confirm that DSM samples with soft soil inclusions larger than  $1/6$  have a considerable influence on the deduction of the engineering values. Based on this numerical analysis, the “rule of  $1/6$ ” as proposed by Ganne et al. (2010) seems to be justified.

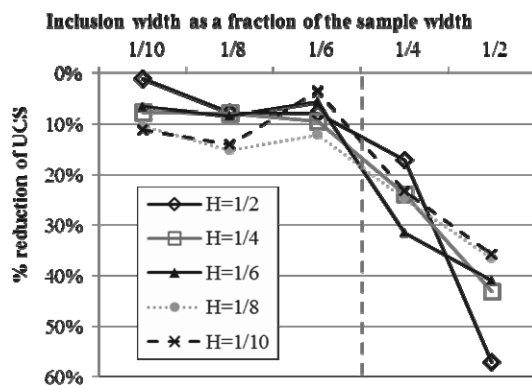


Figure 4. Influence of the dimensions of the soil inclusions on the UCS of soil mix material. Results of 2D numerical simulations performed with the help of the Universal Distinct Element Code UDEC of Itasca®. Details of the model are available in Van Lysebetten et al. (2013). H is the ratio between the height of the soil inclusion width and the sample diameter.

#### 4 INFLUENCE OF THE SCALE EFFECT

Apart from traditional core samples (with a diameter around 10 cm), large scale UCS tests were conducted on rectangular blocks with approximately a square section, with a width corresponding to the width of the in situ SMW (about half a meter) and with a height approximately twice the width (Vervoort et al. 2012). The results of all the tests performed in KU Leuven are presented in Fig. 5 for various soil conditions and different execution systems: the CSM and the TSM.

As observed in Fig. 5, a linear relationship is observed between the test results obtained from the typical core samples and the large rectangular blocks. Although there is a scatter in the test results, the UCS of the full-scale blocks is about 70% of the average UCS of the typical core samples. It is to note that similar conclusion was observed for DSM columns in Japan (CDIT 2002).

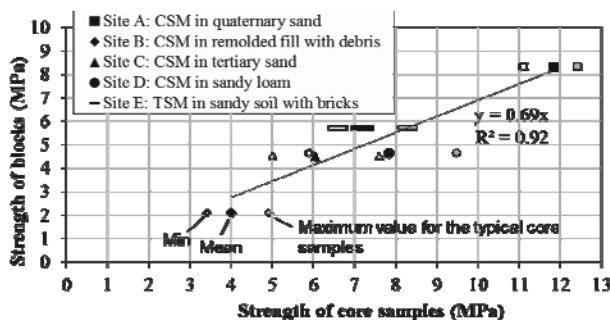


Figure 5. Scale effect: relationship between the results of UCS tests on typical cylindrical core samples (10 cm diameter) and on large rectangular blocks tested in KU Leuven (after Vervoort et al. 2012).

#### 5 CONCLUSIONS

Based on the results of the BBRI ‘Soil Mix’ project, a Belgian design methodology for the DSM structures is currently developed. On the one hand to determine the UCS characteristic value of the DSM material and on the other hand to design the SMW as a retaining wall according to the requirements of the Eurocode 7. According to the results presented in this paper, the calculation of the UCS characteristic value should consider:

- the number of tested core samples,
- the possibility to use a statistical approach (based on the cumulative curve) or an approach such as in the DIN,

- the determination of the X% lower quantile for DSM material (in case of statistical calculation),
- the presence of the unmixed soft soil inclusions potentially considering the rule of 1/6 (Ganne et al. 2010),
- the scale effect (with regard to the full-scale factor of 0.7),
- the possibility of 3D analysis,
- and the time effects (with the help of creep test or based on experience with similar technique and soil conditions).

The curing and creep phenomena are currently investigated within the framework of the BBRI ‘Soil Mix’ project. Indeed, while SMWs were previously used only for temporary excavation support, permanent retaining and bearing applications with soil mix are increasingly applied in Belgium. For the evolution of the UCS value with time, it is suggested to consider the value of the UCS at 28 days as the value of reference for the strength of the DSM material.

#### 6 ACKNOWLEDGEMENTS

This research is financially supported by the Agency for Innovation by Science and Technology of the Flemish Region IWT (BBRI ‘Soil Mix’ project, 2009-2013).

#### 7 REFERENCES

- BBRI. 2012a. Infofiche. Pariois de type “Soil mix” de type 1 : parois faites de colonnes. *BBRI information sheet 56.5*, [www.bbri.be](http://www.bbri.be), July 2012 (in Dutch and French).
- BBRI. 2012b. Infofiche. Pariois de type “Soil mix” de type 2 : parois faites de panneaux. *BBRI information sheet 56.6*, [www.bbri.be](http://www.bbri.be), July 2012 (in Dutch and French).
- CDIT. Coastal Development Institute of Technology. 2002. *The Deep Mixing Method – Principle, Design and Construction*. Edited by CDIT, Japan. A. A. Balkema Publishers/Lisse/Abingdon/Exton (PA)/Tokyo.
- Denies, N. and Van Lysebetten, G. 2012. General Report – Session 4 – SOIL MIXING 2 – DEEP MIXING. *International Symposium of ISSMGE - TC211. Recent research, advances & execution aspects of ground improvement works*. N. Denies and N. Huybrechts (eds.). 31 May-1 June 2012, Brussels, Belgium, Vol. I, pp. 87-124.
- Denies, N., Huybrechts, N., De Cock, F., Lameire, B., Vervoort, A., Van Lysebetten, G. and Maertens, J. 2012. Soil Mix walls as retaining structures – mechanical characterization. *International Symposium of ISSMGE - TC211. Recent research, advances & execution aspects of ground improvement works*. 31 May-1 June 2012, Brussels, Belgium, Vol. III, pp. 99-115.
- DIN 4093:2012-08. Design of ground improvement – Jet grouting, deep mixing or grouting. August 2012 (in German).
- Eurosoilstab. 2002. Development of design and construction methods to stabilise soft organic soils. *Design Guide Soft Soil Stabilisation*. EC project BE 96-3177.
- Ganne, P., Huybrechts, N., De Cock, F., Lameire, B. and Maertens, J. 2010. Soil mix walls as retaining structures – critical analysis of the material design parameters. *International conference on geotechnical challenges in megacities, June 07-10, 2010, Moscow, Russia*, pp. 991-998.
- Topolnicki, M. and Pandrea, P. 2012. Design of in-situ soil mixing. *International Symposium of ISSMGE - TC211. Recent research, advances & execution aspects of ground improvement works*. 31 May-1 June 2012, Brussels, Belgium, Vol. III, pp. 309-316.
- Van Lysebetten G., Vervoort A., Denies, N., Huybrechts, N., Maertens, J., De Cock, F. and Lameire B. Numerical modeling of fracturing in soil mix material. *International Conference on Installation Effects in Geotechnical Engineering, March 24 – 27, 2013, Rotterdam, The Netherlands*.
- Vervoort, A., Tavallali, A., Van Lysebetten, G., Maertens, J., Denies, N., Huybrechts, N., De Cock, F. and Lameire, B. 2012. Mechanical characterization of large scale soil mix samples and the analysis of the influence of soil inclusions. *International Symposium of ISSMGE - TC211. Recent research, advances & execution aspects of ground improvement works*. 31 May-1 June 2012, Brussels, Belgium, Vol. III, pp. 127-135.

# Method of improvement of the subsoil under Adora facility – Ohrid, Republic Of Macedonia

## Méthode d'amélioration du sous-sol sous le bâtiment Adora – Ohrid, République de Macédoine

Dimitrievski L.

*Faculty of Civil Engineering, Skopje, Republic of Macedonia*

Ilievski D., Dimitrievski D., Bogoevski B., Strasheski A.

*GEING Krebs und Kiefer International and others ltd. Skopje, Republic of Macedonia*

**ABSTRACT:** Adora residential building is a 6-storey structure, built nearby Ohrid Lake (Ohrid, Republic of Macedonia). The foundation depth of the building is approximately 1,5 m (foundation construction – foundation slab). The foundation soil consists of soil materials which have a poor strength properties and low bearing capacity. The ground water table (GWT) on the location is on 1,0 m bellow the ground surface. On such geotechnical conditions a big settlements are expected. Therefore, a project on soil improvement was prepared. Several preliminary solutions were considered, but most appropriated was the one which involves geosynthetic reinforcement as subsoil improvement measure. In order to evaluate the settlements, performance of the building, axial forces developed in the geogrids and stress-strain condition in the subsoil during static and dynamic loads, detailed analyses were conducted. The software models developed in Plaxis 2D clearly showed the effectiveness on the applied measures for soil improvement.

**RÉSUMÉ :** le bâtiment de résidence Adora est-une construction de 6 étages, bâti à coté du lac d'Ohrid (Ohrid, République de Macédoine). La profondeur des fondations du bâtiment est d'environ 1,5 m (construction de fondation – dalle de fondation). Le sol de fondation est composé de sols de mauvaise qualité et faible capacité portante. La nappe phréatique (NP) du site est située 1,0 m en dessous de la surface de sol. Avec ces conditions géotechniques des tassements du sol sont attendus. Un projet d'amélioration des sols a donc été préparé. Plusieurs solutions préliminaires ont été considérées, mais la plus appropriée est celle qui implique le renforcement par géosynthétiques, comme mesure d'amélioration du sous-sol. Des analyses détaillées ont été menées afin d'évaluer les tassements du sol, la construction du bâtiment, les forces axiales développées dans le géogrid et la relation contrainte-déformation dans le sous-sol sous chargements statique et dynamique. Les modèles logiciels développés dans Plaxis 2D montrent clairement l'efficacité des mesures appliquées pour l'amélioration des sols.

**KEYWORDS:** soil improvement, geogrid, geotextile

## 1 INTRODUCTION

Adora residential building is foreseen to be built on a site which has very poor geomechanical properties or in other words the geotechnical conditions on the site are very unfavorable. In such cases always major problems are low bearing capacity of the subsoil and large differential settlements. The city of Ohrid is located in active seismic area which is classified in the 9<sup>th</sup> seismic zone according to MCS. Moreover, on the site there are layers of loose uniform sand. Having in mind these two facts a liquefaction becomes also a serious danger for the structure. In order to adopt a solution for soil improvement and to check the liquefaction potential of the soil, comprehensive analyses were conducted.



Figure 1. Excavation pit on a site

## 2 GEOLOGICAL SITE PROPERTIES

According to the geological formations on the site, there are present sediments from the Quaternary period (Pleistocene epoch), i.e. lake and swamp sediments, represented with gravel, sand, sandy clays, silt, different types of clay and clayey-silty sediments, as well as occasional presence of peat. The sediments are well sorted, so that they have heterogenic particle size distribution and heterogenic mineralogy composition, i.e. they are fine to medium gravels and sands; fine silty sands, sandy clays and soft lake/swamp clays with low to medium plasticity. The thickness of these sediments varies between 50.0 – 80.0 m. According to the hydrogeological properties, they belong to the group of low permeability sediments with interparticle porosity. A closed type of springs with free level is present in the sediments, at depth to 20.0 m with GWT = 5.0 – 7.0 m, and with permeability  $k = nx10^{-4} - nx10^{-5}$  m/s.

Also there is a closed type of springs under pressure (artesian springs) at depth from 20.0 – 60.0 m with discharge of  $Q = 1.0 - 5.0$  l/sec.

From engineering geological point of view, these sediments belong to the group of weathered rocks, well placed and sorted with heterogenic particle size distribution, low compacted, with smooth surfaces, fully saturated with water. In other words they present materials with poor physical and mechanical properties that have different strength and deformability parameters.

## 3 GEOMECHANICAL SITE PROPERTIES

The site for construction of the new building is located approximately 200 m from the shore of Ohrid Lake, so, as it was mentioned before, the soils found on the site are with

sediment nature. In order to get precise geotechnical profile of the ground, extensive geotechnical field investigations were conducted. On the other hand, soil samples were taken for laboratory testing. With such extensive scope of field investigations, clear view of the ground profile was obtained.

Based on the performed field investigation works, it was concluded that the site is composed of different layers of sedimentary soils. With foreseen depth of the boreholes, no bedrock was detected. On this site there is vast variety of soil materials, from gravels and sands to silts and clays. Because of the high heterogeneity of the ground profile, layers are grouped into two extinguishing layers. The surface layers are low plasticity clays and clayey sands, which are highly compressive and they are present up to approximately 2.0 m from the surface. While the next deeper layer is clayey sand with higher compaction than the previous layer, and they are present up to 10.0 m from the surface. It is supposed that this second layer continues up to depth for which loading stresses have impact on the settlements.

According to the conducted field and laboratory tests, present soil materials are loose and they have very poor strength properties. In addition, the level of ground water table is very high, approximately 1.0 m from the ground surface, because of the nearby Ohrid Lake.

Table 1. Geomechanical properties

Soil	Fill Material	CL/SFc	SFc
$\gamma$ (kN/m <sup>3</sup> )	22.0	18.4	18.5
$c$ (kN/m <sup>2</sup> )	0.0	15.0	10.0
$\varphi$ (°)	35.0	10.0	20.0
Mv (kPa)	80000.0	5000.0	10000.0
SPT	/	4	13

Considering all these facts, it is obvious that ground improvement is necessary under the foundation of the new construction. Moreover, the problem with the settlements is inevitable, so the serviceability of the construction is also an important issue.

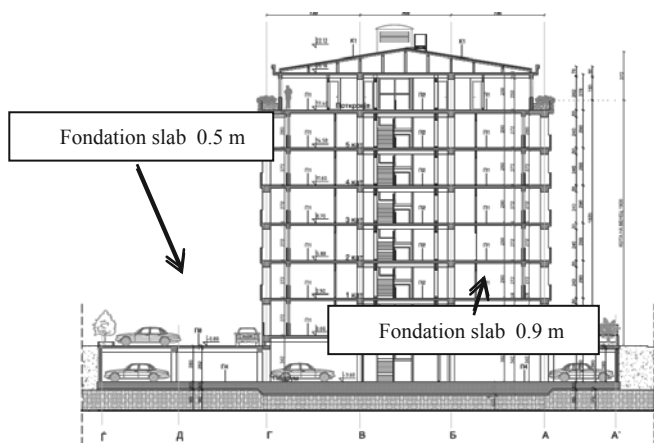


Figure 2. Adora building – cross section

#### 4 CONSTRUCTION DETAILS

The Adora building is built on the site which is very close to the Ohrid Lake. The superstructure of the building has 5 floors and the substructure has 1 floor (see Figure 2). The substructure is extended out of the superstructure and it is actually a parking lot. The size of the superstructure in plan view is 52.0x22.0 m, and the total size of the building (including the extensions of the

substructure) is 69.0x41.5 m. The foundation slab under the superstructure is 0.9 m thick and on the extension parts it is 0.5 m thick. The contact pressure transferred on the subsoil varies in range between 100 kPa (on cross-sections in the middle of the building) and 20 kPa (on cross-sections in the extensions).

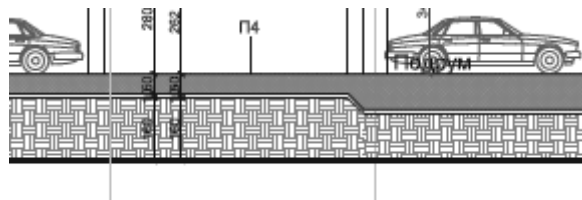


Figure 3. Cross section of the foundation structure

#### 5 THE SOLUTION

As it was mentioned before, the improvement of the subsoil was done by means of soil replacement and usage of geosynthetic materials.

Because of the foundation level of -1.5 m from the ground surface and the depth of soil replacement of 2.0 m, total of 3.5 m deep foundation pit was excavated. The excavation pit was done by constructing 2:1 slopes. In addition, dry conditions for execution of the construction works in the excavation pit were ensured by dewatering the excavation by extraction wells. On the other hand the excavation pit had greater dimensions in plan view, 2.0 m greater than the contours of the foundation slab. Hence the loading stresses can be spread in the fill material by angle of max 45°.

Table 2. Properties of the geotextile

Raw material	PP multicolored/PET
Method of production	Mechanically bonded
Weight	≥ 300 gr/m <sup>2</sup>
Thickness under 2 kPa load	≥ 3 mm
Ultimate tensile strength	Longitudinal ≥ 4.0 kN/m Transversal ≥ 7.5 kN/m
Strain at ultimate tensile strength	Longitudinal 120% (±40%) Transversal 80% (±40%)
CBR puncture resistance	≥ 1300 N (-300 N)
Opening size O90	0.10 mm (±0.02 mm)
Water permeability index normal to the plane	85 x 10 <sup>-3</sup> m/s (-15 x 10 <sup>-3</sup> m/s)

##### 5.1 Geotextile

At the bottom of the excavation pit, geotextile was used to ensure separation of the fill material from the subsoil. By the separation, it is meant that the geotextile will prevent mixing of the different soils, but it will enable complete water permeability, so with this, complete preservation of the properties of the later placed fill materials will be ensured. Used geotextile has the physical and mechanical properties, listed in the Table 2.

The geotextile was placed all over the bottom of the excavation pit as well as on the excavation slopes. The overlap of two adjacent panels is 60 cm, and it completely wraps the fill material up. Used geotextile with the properties given in the Table 2 has the ability to withstand burst and puncture, and has enough tensile strength to serve a separation function, without being destroyed.

## 5.2 Geogrids and fill material

For increasing the bearing capacity of the subsoil under the foundation slab, geogrids are inserted as reinforcement. For reinforcement three layers of geogrids with different properties are placed in the fill material at different elevations.

The first layer of the geogrids was installed under the middle section of the building where the contact pressure has maximum mean value up to  $P=100$  kPa. The geogrids installed on this position give the geotextile an additional tensile strength, as well as bursting and puncturing resistance.

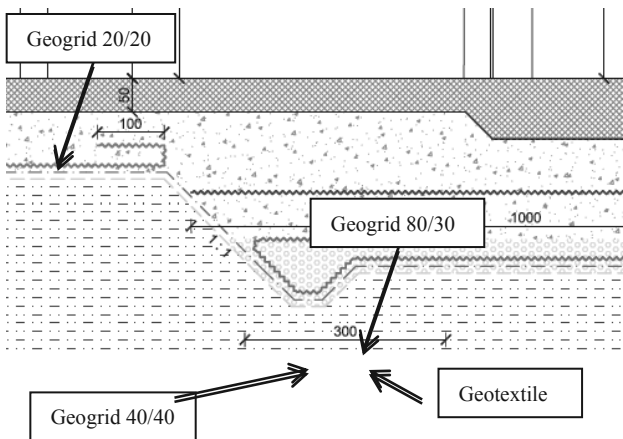


Figure 4. Cross section of the soil improvement measures

On other hand this first layer provides initial stiffness of the low lifts of the fill material. The overlap of two adjacent panels is 50 cm and anchoring length of 3.0 m. The properties of the first layer of geogrid are shown in the Table 3.

Table 3. Properties of the geogrid 40/40 (first layer of geogrids)

Raw material	PP
Coating	Polymer
Weight	~ 330 gr/m <sup>2</sup>
Ultimate tensile strength	Longitudinal $\geq 40$ kN/m Transversal $\geq 40$ kN/m
Tensile strength at 2% strain	Longitudinal $\geq 16$ kN/m Transversal $\geq 16$ kN/m
Tensile strength at 5% strain	Longitudinal $\geq 32$ kN/m Transversal $\geq 32$ kN/m
Strain at nominal tensile strength	Longitudinal $< 7\%$ Transversal $< 7\%$
Mesh size	40 x 40 mm

Over this geogrid a layer of drainage fill material was placed with thickness of 50 cm. This material has particle size from 16 to 32 mm.

This layer of drainage fill material is foreseen to reduce the possibility of liquefaction. So in case of earthquake, the building up of the pore water pressure will be reduced by draining the water from the subsoil layers into the drainage layer placed with the subsoil replacement works.

Over this drainage fill material, another geogrid was placed but this time with higher strength properties. The use of this geogrid is to reinforce the fill material as well as to ensure additional stiffness, which is gradually increasing from the

bottom of the excavation pit up to the foundation slab. Furthermore, this geogrid will ensure reaching of the requested modulus of compressibility of the upperlayers of fill material. The properties of the second layer of geogrid are shown in the Table 4.

Table 4. Properties of the geogrid 80/30 (second layer of geogrids)

Raw material	PET
Coating	Polymer
Weight	~ 350 gr/m <sup>2</sup>
Ultimate tensile strength	Longitudinal $\geq 80$ kN/m Transversal $\geq 30$ kN/m
Ultimate tensile strength at 3% strain	Longitudinal $\geq 22$ kN/m
Ultimate tensile strength at 5% strain	Longitudinal $\geq 40$ kN/m
Strain at nominal tensile strength	Longitudinal $< 8.5\%$ Transversal $< 8.5\%$
Mesh size	20 x 20 mm

On top of the second geogrid two lifts of fill material are done with thickness of 30 cm, total of 60 cm. The required modulus of compressibility on top of these two layers of fill material should be at least 100 MPa and minimum 98% compaction after Proctor. The fill material is crushed stone base aggregate.

On the extended parts of the building where the contact pressure has maximum mean value up to  $P=20$  kPa, also a geogrids is installed. This geogrid has an ultimate tensile strength of 20 kN/m in both directions. The overlap of two adjacent panels is 60 cm and the anchoring length is 1.0 m. After installation of this geogrid the fill material is placed and compacted in 30 cm thick lifts. The final layer of the fill material at the extended parts of the building should reach at least 80 kPa and minimum 98% compaction after Proctor.

After completion of the earth works ground improvement measures were completely finished. So the works for hydro insulation and constructing the structure commenced.

Table 5. Properties of the geogrid 40/40 (first layer of geogrids)

Raw material	PP
Coating	Polymer
Weight	~ 190 gr/m <sup>2</sup>
Ultimate tensile strength	Longitudinal $\geq 20$ kN/m Transversal $\geq 20$ kN/m
Tensile strength at 2% strain	Longitudinal $\geq 8$ kN/m Transversal $\geq 8$ kN/m
Tensile strength at 5% strain	Longitudinal $\geq 18$ kN/m Transversal $\geq 18$ kN/m
Strain at nominal tensile strength	Longitudinal $< 7\%$ Transversal $< 7\%$
Mesh size	40 x 40 mm

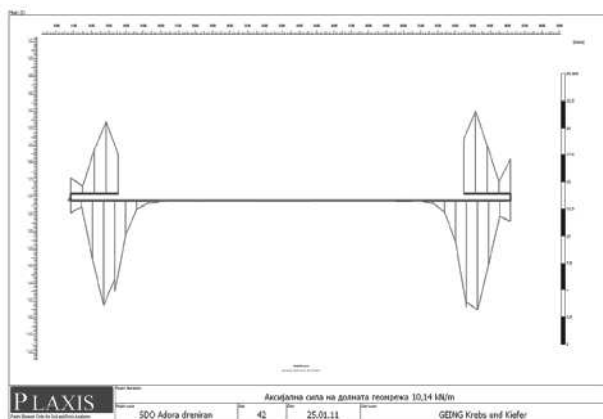


Figure 5. Axis forces in geogrid 80/30 (first layer of geogrids)

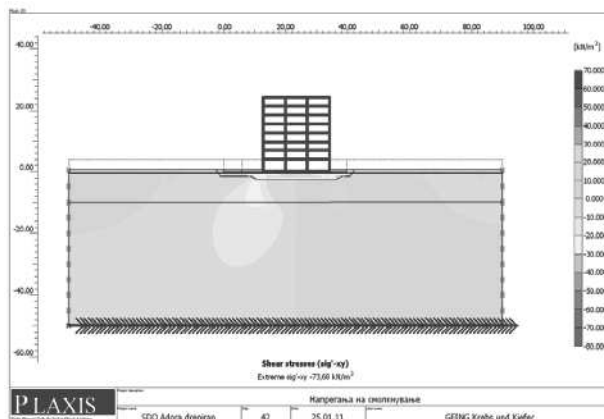


Figure 7. Shear stresses distribution

## 6 GEOTECHNICAL ANALYSES

In order to adopt the measures for improvement of the subsoil, detailed analyses were conducted. These analyses involve flow net analyses, analyses of soil-structure interaction due to geostatic and dynamic load as well as analyses of the liquefaction potential of the subsoil. The ground model was developed according to the adopted soil properties shown in the Table 1, and also the exact geometry of the structure was applied to the model. Most of the analyses were carried out in Plaxis 2D software using finite element method.

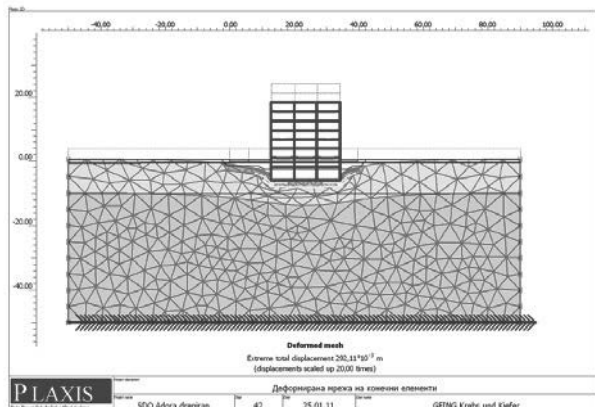


Figure 6. Plaxis model of the Adora building

The Plaxis model was subjected to several load cases which involves geostatic, hydrostatic and dynamic load. The analyses are conducted with and without applied geosynthetics under the construction. Comparing the results of analyses of both models it was obvious that improvement of the subsoil using geosynthetics is fully justified.

The maximum total settlements of the subsoil after the construction of the hotel are estimated at 30 cm. The estimated differential settlements during the seismic analyses were 0.1 cm. The maximum axial forces developed in the geogrids for geostatics load case are 13,86 kN/m in the middle geogrid and 10,14 kN/m in the lowest geogrids. When the model is subjected to dynamic loads (seismic activity) the axial force in the middle geogrid 35,17 kN/m and in the lowest geogrid the axial force is 19,12 kN/m.

Additional analyses were carried out in order to estimate a liquefaction potential of the subsoil. These analyses were necessary due to the presence of saturated, uniform sand in the subsoil which has a relative density in the range of  $D_r=15-40\%$ . The results showed that the subsoil has a liquefaction potential.

## 7 CONCLUSION

In the last 2,5 years this is the second bigger project of soil improvement using geosynthetics in the Ohrid area. The first, very similar, case was soil improvement under the new Hotel Park 2,5 years ago. The two buildings are approximately 2.0 km apart. On a basis of a obtain data from monitoring of the buildings settlements it can be concluded that the total settlements of both buildings are below the initially estimated settlements.

For example, for monitoring of the settlements of the Hotel Park 8 survey points were positioned. Those points initially were measured after placing them (during the fundaments constructing), later in the time of constructing the structure and after finishing of the whole construction. The first initial measurement of the elevation of the fixed points was undertaken on 11.07.2011, and the last one on 23.03.2012.

In both cases cost-benefit analyses conducted during the designing process showed that soil improvement using geosynthetics is most economical method in such geotechnical conditions. Regardless the economic aspect this method has a major advantage which is a very short period of installation.

## 8 REFERENCES

- Brinkgreve, R. & Vermeer P. 1998. Plaxis Finite Element Code for Soil and Rock Analyses.
- Geing-KuK. 2011. Geomechanical report for construction of residential building in Ohrid. Skopje Geing Kuk.
- Geing-KuK. 2011. Project on improvement of the foundation soil under the residential building in Ohrid. Skopje Geing Kuk.
- Robert M. Koerner. 1997. Designing with Geosynthetics. Fourth edition. Prentence-Hall, Inc.

# Geoencased columns: toward a displacement based design

## Colonnes renforcée par géotextiles: vers une conception basée sur le déplacement

Galli A., Prisco di C.  
*Politecnico di Milano*

**ABSTRACT:** As is largely testified by the scientific literature, in the last decade geoencased columns have become a quite common alternative solution to standard stone columns. This is essentially due to the possibility of employing reinforcements to better the mechanical response of the inclusions without reducing their drainage efficiency. Although GEC are often used to reduce settlements induced by the construction of large embankments on soft soils, up to now a rational displacement based design approach has not yet been introduced. This is thus the final objective of this paper, that, by starting from a critical review of the standards presently available, will illustrate the results of a series of finite difference numerical analyses. The unit cell of an ideal reinforced soil embankment placed on a soft soil stratum will be accounted for and the effect of the main geometrical/mechanical parameters, as well as the response of the system during the construction stages, is discussed.

**RÉSUMÉ :** Comme il est largement connu dans la littérature de ces vingt dernières années, les colonnes en matériaux granulaires renforcée par géotextiles (GEC) sont devenues une solution très utilisée par rapport aux colonnes ballastées standard. Cela est essentiellement dû à la possibilité d'employer des renforts pour améliorer la réponse mécanique des inclusions sans réduire leur efficacité de drainage. Bien que les GEC soient souvent utilisées pour réduire les tassements induits par la construction de remblais importants sur sols mous, une approche rationnelle de conception basée sur le déplacement n'a, jusqu'à présent, pas encore été mise en place. Cela est donc l'objectif final de cette étude, qui, en partant d'une analyse critique des normes actuellement disponibles, illustrera les résultats d'analyses numériques aux différences finies. Une cellule élémentaire d'un remblai idéal de sol renforcé placé sur un sol mou sera prise en compte et l'effet des principaux paramètres géométriques et mécaniques et la réponse du système au cours des différentes étapes de la construction seront discutés.

**KEYWORDS:** geoencased granular columns, geotextiles, numerical analyses, displacement based design, earth reinforced structures.

### 1 INTRODUCTION.

As it is well documented in the literature (see e.g. Raithel et al. 2005), since mid-nineties the use of geoencased granular columns (GEC) as foundations of earth structures on soft and very soft soils has been progressively increased. GECs have both mechanical and hydraulic functions: they work not only as reinforcement inclusions, capable of preventing the global collapse of the foundation and reducing differential settlements within the structure, but they work additionally as vertical drains, thus reducing the consolidation time of the soft soil.

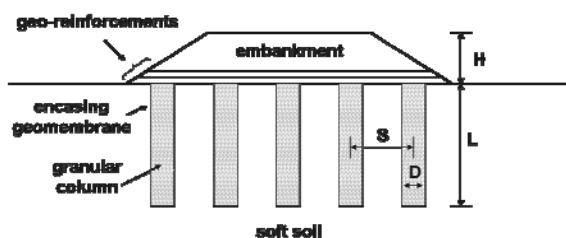


Figure 1. sketch of an earth embankment on GECs.

The GEC foundation system is composed of an array of granular columns of length  $L$  and diameter  $D$ , placed at a regular spacing  $S$  below an embankment of height  $H$  (Figure 1). The columns are encased by a geotextile with the double aim of reinforcing the column and filtering to prevent the clogging of the column itself. At the base of the embankment, to redistribute vertical stresses, several layers of geotextile are also inserted during the construction. The effectiveness of this foundation system has been clearly proved both on real scale data (see e.g.

Kempfert 2003, where the response of the system is analyzed by varying the spacing among columns and of the stiffness of the encasing geotextile), and by means of numerical and experimental researches (Murugesan and Rajagopal 2006, di Prisco and Galli 2011). The fundamentals of the mechanical behavior of the system is therefore quite well understood. Nevertheless, common design standards are still based on too simplified approaches, unable of capturing the actual mechanical complexity of the system in particular, the interaction between embankment and columns (this point will be tackled in further details in the following section by critically reviewing the most used design standards). Conversely to traditional deep foundation systems (like reinforced concrete piles or jet-grouted columns which can be considered axially rigid with respect to the surrounding soil), GECs are axially deformable inclusions, whose axial deformability is strictly coupled with the stiffness of the surrounding soil. Moreover, since this latter is very often characterized by a very low permeability and high deformability, its mechanical response should be modeled by properly taking into account the hydro-mechanical coupling (for the sake of brevity, this aspect will however be disregarded in the following).

In the present paper the attention will be initially focused on a critical review of the most common design standards. Then an engineering displacement based approach will be briefly introduced, and some numerical analyses, with the particular aim of studying the distribution of differential settlement at the top of the embankment, which are generally neglected by the design approaches, will be presented.



2 REVIEW OF DESIGN STANDARDS

The two most common design standards available for the design of earth embankment on GECs are the British Standard BS 8006 (1995) and the German Standard EBGEO (Chapter 6.9; 2003). Both of them assume the column to be rigid and, estimate the vertical stress distribution at the base of the embankment to be independent of the mechanical interaction with the foundation (i.e. the GEC and the soft soil). From an engineering point of view, however, the vertical stress redistribution at the base of the embankment is the main parameter governing (i) the design of the reinforcement layers (see Figure 1) and (ii) the evaluation of the differential settlements.

According to BS8006, the vertical stress redistribution does not depend on the mechanical properties of the embankment. In particular, the average vertical stress acting at the column's top (in the following this quantity will be called  $\sigma_i$ ) is determined only as a function of the geometry (H, S, D), as was suggested by the approach proposed by Martson (1913) for buried pipes (see also Jones et al., 1990). The estimation of the average vertical stress  $\sigma_e$  acting on the soft soil is instead obtained by means of empirical expressions, depending on the full or partial formation of the arch effect, as a function of the ratio between height H and difference S-D. According to EBGEO, on the contrary, a rather complex analytical procedure, based on the work proposed by Zaeske (2001), is employed to describe the arch effect. This takes into account the geometry (H, S, D) and the friction angle of the granular material constituting the embankment, and imposes the equilibrium of one central slice of a vault shell of the arch that it is supposed to develop within the embankment. No estimation of the vertical stress  $\sigma_i$  at the top of the column is provided. For the sake of brevity, the analytical expressions have not been reported here; for further details, see BS8006 and EBGEO (Chapter 6.9).

As far as the evaluation of settlements is concerned, the procedure prescribed by EBGEO follows the work proposed by Ghionna and Jamiolkowski (1981) and consists in subdividing the length L of the column in slices (each one of them is then assimilated to an axisymmetric triaxial soil sample). The following hypotheses are assumed: (i) the granular soil in the column is at critical state (i.e. no changes in volume are possible for the column), (ii) no relative settlement are considered between the column and the soil. These two hypotheses introduce very strong simplifications that can lead to unphysical results. The second one, in particular, makes impossible the superficial differential settlements to be estimated.

2.1 Parametrical analyses

In this section parametrical analyses on the values of  $\sigma_e$  obtained by employing BS8006, as well as some results concerning the evaluation of the settlement and of the tensile force in the encasing geo-membrane computed according to EBGEO, are presented. In particular, the effect of the embankment height H and of the material friction angle  $\phi'$  is investigated for increasing values of the relative spacing S/D, and by taking into account several diameters D of the column (the authors are aware of the fact that some values of D and S/D considered are unrealistic, nevertheless they have been chosen in order to test even the asymptotic trend of the design approaches).

2.1.1 Stress on the soft soil at the base of the embankment

Figure 2 shows the values of  $\sigma_e$  computed according to BS8006, and highlights that unphysical results of  $\sigma_e < 0$  are obtained for low values of the relative spacing S/D, independently of the embankment height H. This result could in general lead to an overestimation of the arch effect and thus to an unsafe design of the georeinforcement layers at the base of the embankment.

The arch effect tends to vanish for increasing values of S/D, and the value of  $\sigma_e$  tends to the weight  $\gamma H$  of the embankment.

The corresponding values of  $\sigma_i$  computed according to BS8006 (not reported here for the sake of brevity) are independent of S/D, and only slightly dependent on H.

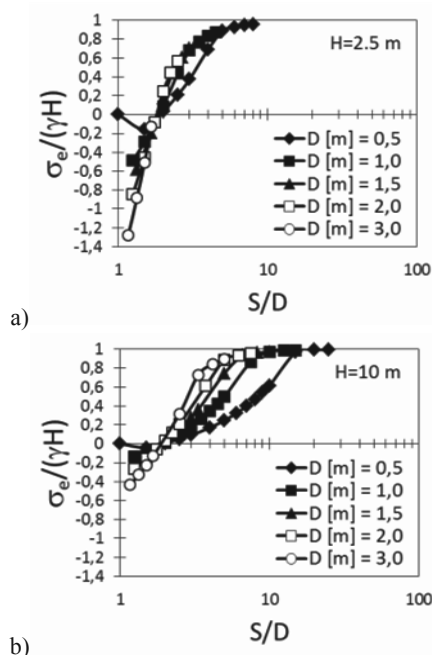


Figure 2. Evaluation of the stress  $\sigma_e$  according to BS8006: (a) H=2.5m and (b) H=10m.

It can be easily demonstrated that  $\sigma_e$  and  $\sigma_i$  (if computed according to BS8006) do not even satisfy the total equilibrium along the vertical direction with respect to the weight of the embankment, and that the values of the tensile force in the geosynthetic layers at the base of the embankment computed according to BS8006 are not continuous with increasing H (Moraci and Gioffrè 2010).

2.1.2 Settlements and tensile force in the encasing membrane

With reference to the values of the mechanical parameters listed in Table 1 (taken from an example of application proposed by EBGEO), in this paragraph a parametrical analyses on the values of the settlement is presented, for increasing values of the embankment weight  $\gamma H$  and by taking into account several values of stiffness J of the encasing geomembrane. The values of the column length L and of the relative spacing S/D are here considered to be constant and equal to 10 m and 2, respectively (with  $D=80$  cm and  $S=1.6$ m).

Table 1. Values of the mechanical properties of the materials considered in the analyses.

	Embankment	Column	Soft soil
Unit weight (kN/m <sup>3</sup> )	20	19	15
Friction Angle (°)	-	35	15
Cohesion (kPa)	-	-	10
Young modulus (kPa), at a reference pressure of 100kPa	-	-	750
Poisson coefficient (-)	-	-	0.4

As it is evident from Figure 3a (where, for the sake of generality, the value of s has been normalized with respect to L), the presence of the encasing geomembrane induces a stiffening effect of the foundation system, thus reducing the expected value of the total settlement (which is considered, according to the adopted hypotheses, to be uniform and coincident with the settlement s at the top of the embankment). The numerical procedure, however, for low values of  $\gamma H$  (i.e. shallow or light embankments) leads to unrealistic results, for

which negative settlements (i.e. uplift) are obtained. This meaningless result is obtained even for a nil value of the stiffness  $J$  of the encasing geomembrane. This essentially derives from the assumption concerning the soil within the column which is imposed to be at the critical state along the entire column (similar results have been observed even for other values of  $L$  and  $S/D$ , but they have not been reported here for the sake of brevity). This is evident when the tensile force  $T_g$  in the encasing geomembrane along depth  $z$  of the column is considered (Figure 3b, where the case of a shallow embankment is analyzed): at the base of the column the vertical stress is not sufficient to induce an active state of stress, and the only possibility for the column to satisfy the hypothesis of critical state is to reduce its radius, thus inducing a compression (i.e.  $T_g < 0$ ) in the encasing geomembrane.

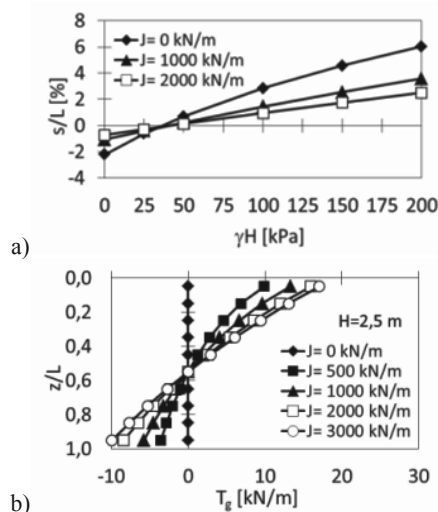


Figure 3. EBGEO: evaluation of (a) settlements and (b) tensile force in the encasing geomembrane.

### 3 A DISPLACEMENT BASED DESIGN APPROACH

In order to overcome the above cited limitations, a consistent and physically based design would require a fully displacement based approach. As was theoretically outlined by Galli and di Prisco (2011), with reference to a single axisymmetric cell (i.e. to a single column together with the surrounding soft soil), the foundation system can be assumed to be composed by two coupled springs, one representing the GEC and the second representing the surrounding soft soil. The two springs work in parallel if and only if the base of the embankment can be considered to be rigid and no differential settlements to arise (Figure 4a). Under this hypothesis, the vertical stress at the base of the embankment is thus uniformly distributed (in Figure 4a  $\gamma$  stands for the unit weight of the granular material constituting the embankment), no differential settlement are observed at the top of the embankment, and no shear stresses develop at GEC-soil interface. The values of vertical stress both in the column and in the soil then can be assumed to depend exclusively on the axial stiffness of the column ( $K_{GEC}$ ) and on the vertical compressibility of the soft soil (represented in Figure 4a by a global stiffness  $K_S$ ).

Real embankments, however, are characterized by a deformable base (Figure 4b), and different values of settlement are expected for the top of the column ( $u_c$ ) and for the soil ( $u_s$ ) at the base of the embankment. Consequently: (i) vertical stresses are redistributed at the base of the embankment between the internal zone of the cell (above the column, characterized by an average stress  $\sigma_i$ ) and the external one (a circular crown above the soil, characterized by an average stress  $\sigma_e$ ) due to the so called arch effect, (ii) shear stresses are

activated at GEC-soil interface, and (iii) differential settlements are expected even at the embankment top.

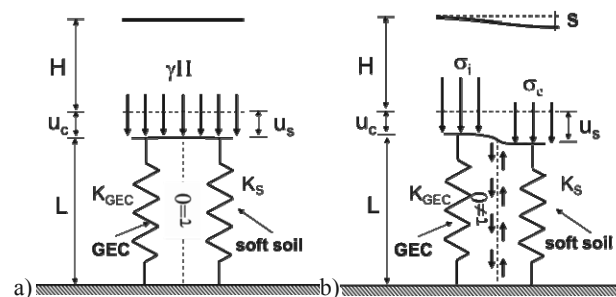


Figure 4. Mechanical response of the foundation system in case of (a) rigid and (b) deformable embankment.

From a modeling point of view, by assuming an engineering approach based on generalized variables, the mechanical behavior of the embankment can be described by means of a generalized constitutive relationship between the average stresses at the base of the embankment and the differential settlements (assumed to be uniform) between the column and the soil:

$$\sigma_i - \sigma_e = f(u_s - u_c), \quad (1)$$

where the values of  $\sigma_i$  and  $\sigma_e$  must satisfy the equilibrium with respect to the weight of the embankment on the unit cell

$$\sigma_i \cdot D^2 + \sigma_e \cdot (S^2 - D^2) = \gamma H \cdot S^2. \quad (2)$$

The constitutive relationship  $f$  can be in general assumed to be described by means of a non-linear curve, whose average stiffness depends (i) on the geometry of the system ( $S$ ,  $D$ ,  $H$ ), (ii) on the mechanical properties of the granular material constituting the embankment and (iii) on the geo-reinforcements at the base of the embankment. Its limit value corresponds instead to the activation of a failure mechanism within the embankment. Depending on the formation of the arch effect, either a “punching” failure mechanism, or a “dome” failure mechanism, with no (or very limited) superficial differential settlements, might develop (Figure 5a-b).

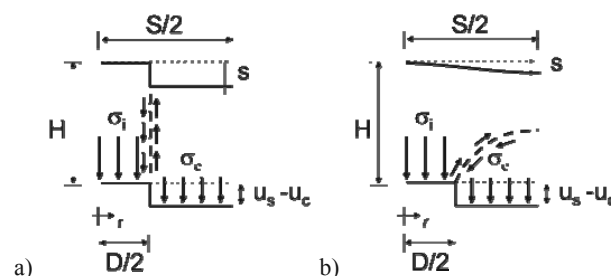


Figure 5. Failure within the embankment: (a) punching mechanism and (b) domed mechanism due to arch effect.

The pattern of superficial differential settlement  $s=s(r)$  could then be formally described by a transfer function, ranging from a discontinuous function (in case of punching), to a smooth function (in case of formation of the arch effect).

### 4 NUMERICAL ANALYSES ON SETTLEMENT PROFILE

In order to investigate the settlement distribution  $s(r)$  at the top of the embankment for increasing values of  $H$ , some preliminary finite difference numerical analyses have been performed by means of the commercial code FLAC. An axisymmetric geometry has been chosen in order to model the cell, and the simplifying hypothesis of rigid column has been

assumed; the mechanical behavior of both the materials constituting the embankment and the soft soil has been modeled by assuming an elastic perfectly plastic relationship with a non-associated Mohr-Coulomb failure condition. For the embankment, two different types of material have been considered: a loose sand ( $\phi=20^\circ$ , with no dilatancy) and a compacted sand ( $\phi=40^\circ$ , with dilatancy  $\psi=10^\circ$ ). In both cases, for the sake of simplicity the unit weight  $\gamma$  is assumed to be equal to  $20 \text{ kN/m}^3$ , the Young modulus equal to  $3 \text{ MPa}$  and the Poisson coefficient equal to  $0.25$ . No friction has been considered at soil-column interface. For the soft soil, for the sake of simplicity a dry condition has been assumed (i.e. no hydro-mechanical coupling has been modeled). The values of the mechanical parameters are listed in Table 1. Consistently with the parametrical analyses previously discussed, the length  $L$  of the column is  $10 \text{ m}$  and its diameter  $D$  is  $80 \text{ cm}$ . Two ratios  $S/D$  have been considered, and the settlement distribution  $s(r)$  has been normalized at each stage for the current value of  $H$ .

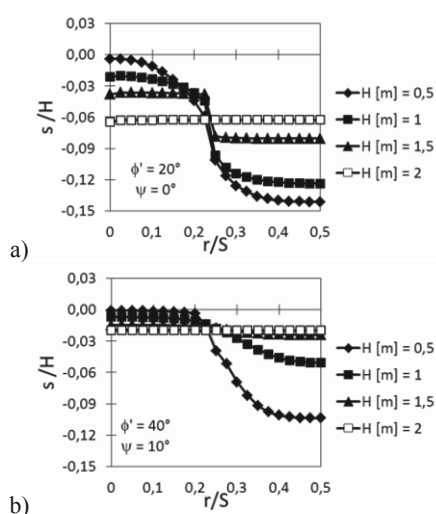


Figure 6. Normalized superficial settlements for  $S/D=2$ : (a) loose and (b) dense material.

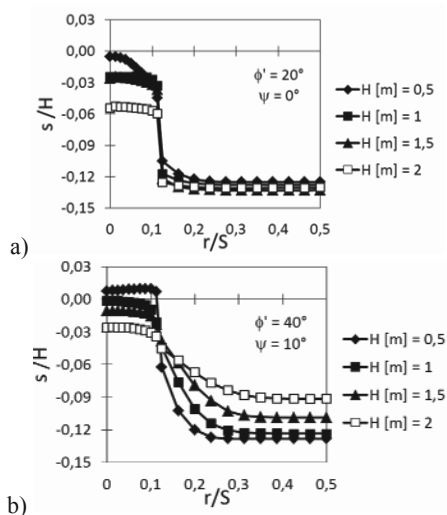


Figure 7. Normalized superficial settlements for  $S/D=4$ : (a) loose and (b) dense material.

Figures 6 and 7 describe the evolution of  $s(r)$  at the top of the embankment during the construction stages. It appears clearly that the settlement profile ranges from a well localized punching failure mechanism to a smooth distribution of settlements for increasing  $H$  (witnessing the progressive mobilization of the arch effect). The influence of relative spacing  $S/D$  and of the mechanical properties of the embankment (in terms of both  $\phi'$  and  $\psi$ ) is opposite: an increase in  $S/D$  tends to localize the

failure, whilst an increase in  $\phi'$  and  $\psi$  tends to smoothen the settlement profile.

## 5 CONCLUSIONS

The paper critically discussed some results obtained according to the usual Design Standards, and proved that in some cases these approaches lead to unrealistic results. The codes, moreover, disregard the estimation of relative settlements at the top of the embankment, which is actually one of the most important parameters describing the efficiency of the foundation. A consistent, displacement based conceptual framework for describing the behavior of the system has been formulated, and some preliminary numerical analyses have been shown. These latter, in particular, showed on the contrary that the top settlement profile is remarkably affected by both the geometry and the mechanical properties of the embankment.

## 6 ACKNOWLEDGEMENTS

The Authors want to acknowledge TENCATE and ITASCA Italy for financially supporting the research.

## 7 REFERENCES

- British Standard BS 8006. 1995. Code of practice for strengthened/reinforced soils and other fills. *British Standards Institution*, London, UK pp.176.
- di Prisco C. and Galli A. 2011. Mechanical behaviour of geo-encased sand columns: small scale experimental tests and numerical modeling. *Geomechanics and Geoengineering: An International Journal* 6(4), 251–263
- EBGEO. 2003. Empfehlung 6.9 (2003). Bewehrte Erdkörper auf punktoeder linienförmigen Traggliedern, Kapitel 6.9 für die Empfehlungen für Bewehrungen aus Geokunststoffen, EBGEO, DGGT (German Geotechnical Society).
- Galli A. and di Prisco C. 2011. Un modello concettuale per la progettazione di colonne granulari georinforzate a fondazione di rilevati artificiali (in Italian). *XXIV Convegno Nazionale di Geotecnica*, 231–246.
- Ghionna V.N. and Jamiolkowski M. 1981. Colonne di ghiaia (in Italian). *X Ciclo di conferenze dedicate ai problemi di meccanica dei terreni e ingegneria delle fondazioni: Metodi di miglioramento dei terreni*. Politecnico di Torino, Atti dell'Istituto di Scienza delle Costruzioni, n.507, pp.1-63.
- Jones C.J.F.P., Lawson C.R., Ayres D.J. 1990. Geotextile reinforced piled embankments. *Geotextiles Geomembranes and Related Products*, Den Hoedt (ed.) © 1990 Balkema, Rotterdam, ISBN 90 6191 119 2, pp 155-160.
- Kempfert H.G. 2003. Ground improvement methods with special emphasis on column-type techniques. *Int. Workshop on Geotechnics of Soft Soils-Theory and Practice- SCMEP*.
- Marston A. and Anderson A.O. 1913. The theory of load on pipes ditches and tests of cement and clay drain tile and sewer pipes. *Bulletin 31. Iowa Engineering Experiment Station*, Iowa State College, Ames, Iowa.
- Moraci N. and Giofrè D. 2010. La progettazione di rilevati su terreni compressibili rinforzati con geosintetici (in Italian). *Rivista Italiana di Geotecnica*, vol. 3/10, 67-100.
- Murugesan, S. and Rajagopal, K. 2006. Geosynthetic encased stone columns: Numerical Evaluation. *Geotextiles and Geomembranes*, Vol. 24, 349-358.
- Raithel M., Kirchner A., Schade C. and Leusink E. 2005. Foundation of Constructions on Very Soft Soils with Geotextile Encased Columns - State of the Art. *Proceedings ASCE Geo-Frontiers 2005*.
- Zaeske D. 2001. Zur Wirkungsweise von unbewehrten und bewehrten mineralischen Tragschichten über pfahlartigen Gründungselementen, Schriftenreihe Geotechnik. Universität Kassel, Heft 10.

# Design prediction of the strengthened foundation base deformation by field tests data

La prèvision de calcul des déformations de la base des fondements reportès à partir des recherches prises en nature

Gotman A., Gotman N.  
*BashNIIstroy, Ufa, Russia*

**ABSTRACT:** The paper presents the solution of the complicated practical geotechnical problem of the skeleton structure foundation strengthening. The strengthening was done due to change of the spatial arrangement of a building and essential load increase. The experience of a foundation strengthening with jet grouted piles is described based on results of the base deformations monitoring. The main design principles of the foundations under strengthening are given. The results of the deformation design prediction based on jet grouted piles test and the base deformation measuring are presented.

**RÉSUMÉ :** Dans cet article on présente la solution d'un problème géotechnique pratique compliqué du renforcement des souches d'un bâtiment en carcasse construit sur les sols de fondation dangereux à cause du karst, en raison du changement lors de la construction de la conception de plan et de volume du bâtiment et de l'accroissement signifiant de charge. L'expérience est décrite du renforcement des souches par des papillons d'injection de forage sur la base des résultats du monitoring des déformations des sols de fondation. Les résultats sont présentés des pronostiques prévisionnelles des sols de fondation des souches renforcées à la base des essais des papillons d'injection de forage et de la mesure des déformations du sol de fondation.

**KEYWORDS:** foundation strengthening, settlements, pile vertical load test

## 1 INTRODUCTION

Design prediction of the strengthened foundation base deformation by field tests data was executed for the new shopping centre located in Ufa (Russia). The 500x250m shopping center was designed as a skeleton one-storey building with column spacing 16x8 m. The building construction was started in April, 2007, then restarted in June, 2009 and finished in 2010. Since May, 2008 till August, 2009 the construction at site has been not performed. In 2007...2008 the foundations and the most part of the bearing structures have been constructed. During construction time, the building part was changed (by investor's demand). The column spacing was increased (8x16m to 16x16m or 12x16m) and foundation loads to the moment of construction stoppage 1,2...1,5 times increased the design ones. After construction restarting, other changes of building frame design have taken place. At the significant area the number of stories and floor loads have been increased. As a result, all these changes provoked 30...70% increase of the foundation loads and the further foundation strengthening.

## 2 ENGINEERING-GEOLOGICAL CONDITIONS

Under the foundation base stiff clays, tough and soft loams occur underlain with water saturated medium coarse sand and gravel at the depth of 8...10 m. (table 3). Maximum predicted ground water level is 2 m under the foundation base. The building site applies to the third category of stability about karst deformations and is divided into sections according to extent of their risk in accordance with Russian Codes. At this site, areas are located that are classified according to their karst risk as potentially not dangerous and potentially dangerous (fig.1) with the probable design diameter of karst hole 7 m. Due to site severe engineering-geological conditions characterized with lack of homogeneity and karst risk, the following foundations were designed: post- and strip foundations on the bed; piled foundations with the in-situ raft (pile groups); strip foundations on the bed and piled foundations

with the strip in-situ raft reinforced considering a karst hole formation.

Severe engineering-geological conditions of site demanded foundation settlement observation and expert investigation of construction.

## 3 TECHNICAL EVALUATION OF THE STRUCTURAL CONCEPT ON FOUNDATION STRENGTHENING

When design working out and the way of the foundations strengthening selecting, the following was taken into attention.

1. To the moment of the strengthening design development, the building was 1,5 years. In axes 1...15' the bearing structures were completely constructed and at the rest part of the area foundations, columns and floors of the ground floor were built.

2. According to monitoring results (table 1), it was stated that to the moment of strengthening design development (August 2009), the settlements on the whole were stabilized. The settlements of the column foundations with the loads exceeding the design ones already in the process of construction were 6...10cm; the settlements of the rest foundations were 3...4 cm. The settlements data were used to evaluate the coefficients of subgrade reaction of strip- and post foundations bases that demanded strengthening (fig.2, table 2).

Taking into account that the significant part of the structures was constructed and more than half of the base loads have already been transferred, when selecting the method of the foundation strengthening the minimum digging out and dismantling (drilling, cutting, etc.) of the existing foundation should have been provided. Method of strengthening with jet grouted piles was selected with loads transfer from the building through the connection of the reinforced concrete column with the in-situ raft rested on piles.

Table 1

Mark number (fig. 1)	Dates of measurement (days) and settlements (mm) from the moment of last measuring												Settlement for 958 days of observation, mm	Strengthening	Foundation type
	Settlement for the previous period, mm	24. 11. 2007	20. 02. 2008	10. 04. 2008	07. 05. 2008	02. 09. 2008	15. 04. 2009	16. 11. 2009	20. 01. 2010	16. 05. 2010	16. 06. 2010	09. 07. 2010			
		7	88	50	27	118	225	217	63	116	31	23			
M7	0	0	1,8	8,0	3,7	0	0	0,5	0	2,1	0	0	16,1	-	post
M14	0	0	2,6	5,8	0	0,9	0	9,7	0,5	1,2	0	0	20,7	-	strip
M26	1	0	0	1,9	2,5	0	2,1	0,7	0	0,9	0	0	9,1	-	strip
M27	1	0	5,4	14,0	6,1	5,9	9,2	21,5	17,0	3,3	0	0	83,4	-	strip
M29	0	0	6,2	11,7	5,2	2,3	10,2	13,8	2,1	1,2	0	0	52,7	-	strip
M31	50	0	0	0	1,4	8,5	7,7	21,8	2,0	1,3	0	0	92,7	JGP	post

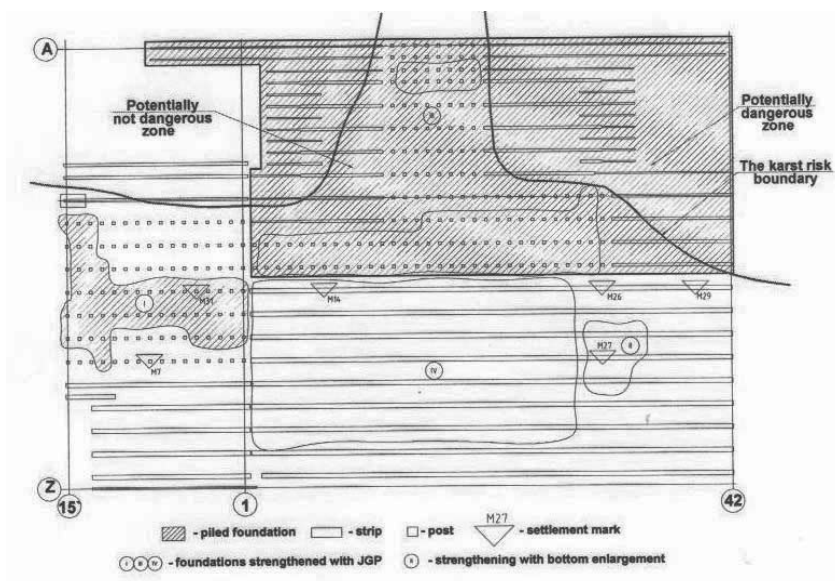


Fig.1. Combined plan of foundations, strengthening constructions and settlement marks

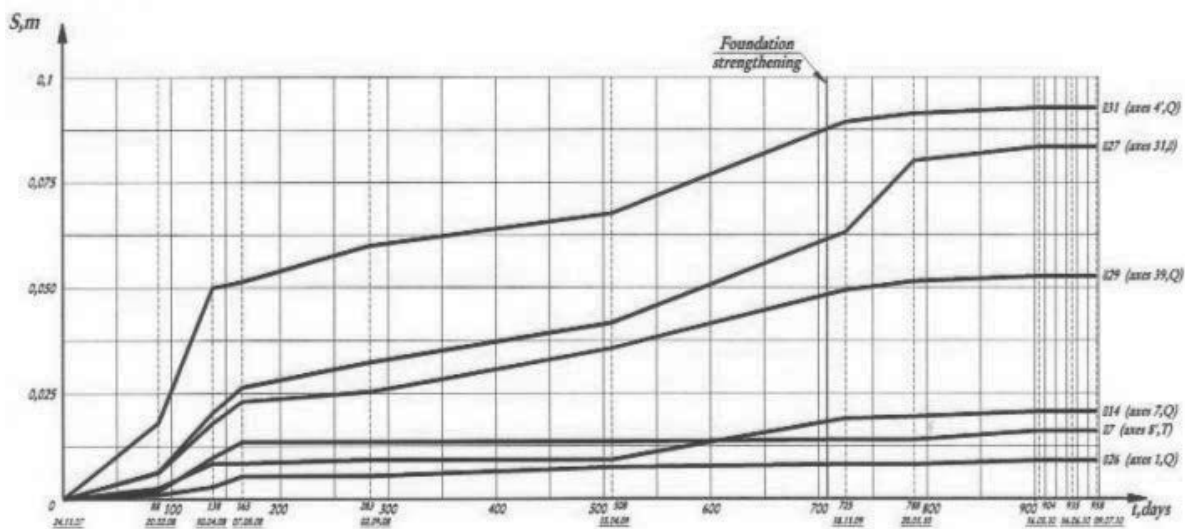


Fig. 2. Monitoring results of foundations settlements

Table 2

Mark number (fig. 1)	Foundation type	Settlement before construction restart, mm	Base pressure before construction restart, kH/m <sup>2</sup>	Coefficient of subgrade reaction, kH/m <sup>3</sup>
M7	post	13,5	64	4700
M14	strip	9,3	114	12200
M26	strip	5,4	114	20000
M27	strip	25,5	114	4400
M29	strip	25,0	114 </td <td>4500</td>	4500
M31	post	60,0	144	2400

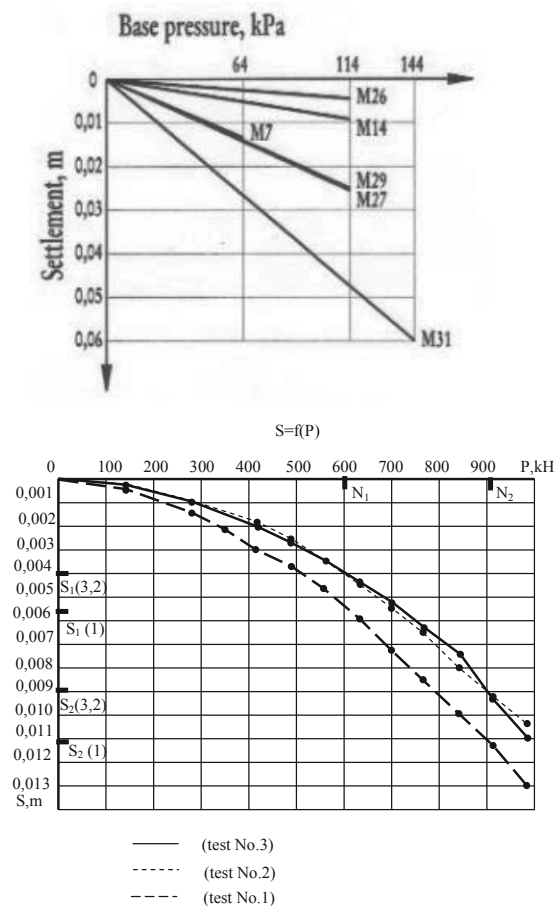


Fig.3. Diagrams of field investigations

a – base pressure-settlement of post- and strip foundations; b– load-settlement of test piles

Table 3

Engineering-geological element	Soils	$I_L$	$\rho, \text{t/m}^3$	$\varphi, \text{grad.}$	E, MPa
1	clay	0,1	1,838	16	17(10)
2	clay	0,63	1,59	11	5
3	loams	0,34	1,85	13	12
4	loams	0,64	1,89	11	8
5	sand	-	1,9	29	20
6	gravel	-	2,09		$R_{0,5} = 0,5 \text{ MPa}$

425 mm diameter and 10...11 m length jet grouted piles were deepened into gravel soil to the depth of 1 m and more. To evaluate the pile design load, the pile vertical load test of trial piles with the diameter 425 mm, 10,6 m length (pile No. 1), 10,88 m length (pile No. 2) and 11,5 length (pile No. 3) (table 3) have been carried out. The piling was realized with the unit SBU 100 GA50. The engineering-geological characteristics of soils are presented in table 3.

Pile vertical load tests have been carried out according to standard method. The limit resistances while testing reached 980 kH. Figure 3 presents diagrams of pile tests.

Considering different structural concepts of the foundations and the building, analysis have been carried out according to these features and four types of the foundations strengthening have been suggested (see figures 1 and 4).

I. Strengthening of *post foundations* of a building in axes 15' – 1. Practically all extra load is taken into account to be transferred to jet grouted piles, i.e. the load is not transferred to post foundation, as the construction of the reinforced concrete raft strengthening is not absolutely stiff.

That's why only insignificant part of the extra load is transferred to the foundation base, so the foundation in combination with the strengthening construction and piles behaves as combined piled foundation.

II. Strengthening of *strip foundations without piles* by means of geometrical dimensions increase with use of technology "HILTI".

III. Strengthening of *pile group foundations* with increased loads was carried out by means of jet grouted piling around the raft and including them into pile group behavior through the reinforced concrete slab fixed with the column and the raft (with the anchors HILTI). With such method of strengthening jet grouted piles start to work in a pile group together with the driven piles.

IV. Strengthening of *foundations without piles* in axes 1 – 29 was carried out by means of insignificant part of load transfer to the foundation. Jet grouted piling use is based on insufficient reinforcing with in situ reinforced concrete strip under the columns, the load of which is more than twice increased compared to design one. Such strengthening construction partially loads the existing foundation including it into work. The jet grouted piles together with the foundation accept the ultimate design load. Pile strengthening is carried out along the whole length of the strips, as otherwise the different stiffness of the strip base will lead to its deterioration.

Irrespective of strengthening type, the main design requirement is continuation of foundations loading only after completion of all works on strengthening considering the terms of strength increase of in-situ concrete of structures.

#### 4 THE MAIN DESIGN PRINCIPLES

Analysis of foundation strengthening has been carried out considering the deformability of the foundation base and jet grouted piles. Due to special features of constructions of the foundations under strengthening and different extent of works completion on above foundations structures construction, the following design assumptions were taken.

While the building *post foundations* strengthening in axes 1'...15', analyses of loads transferred to the foundation after its strengthening were carried out i.e. when construction restarting considering the loads after the building starting (fig.5). Analysis of the column joint and strengthening construction was done for the total design load. Deformability indices of the foundation base and jet grouted piles quantitatively evaluated with the coefficients of subgrade reaction of the foundation base under strengthening and pile stiffness respectively, were determined

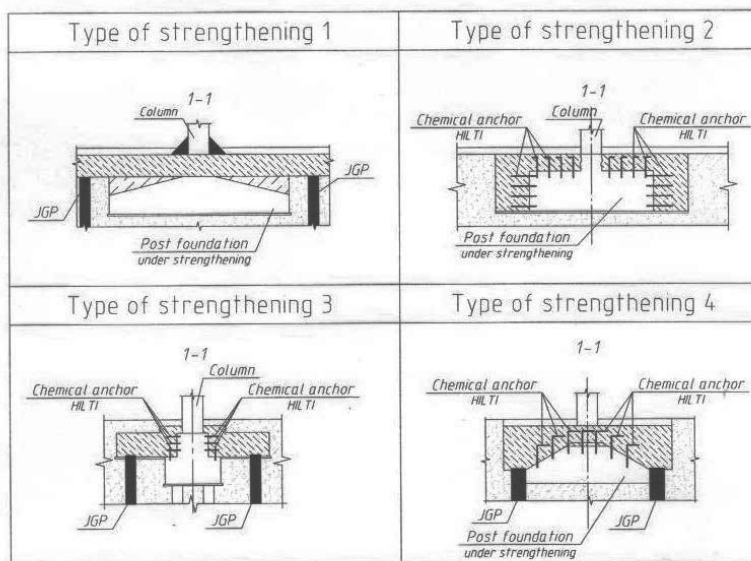


Fig.4 Types of foundation strengthening with jet grouted piles (technical decision)

by results of pile test at site and monitoring of post foundations settlement (tables 2, 4). While analysis of the number of jet grouted piles, the total load was taken to be transferred to those piles, so the coefficient of subgrade reaction of the foundation base under strengthening was taken to be equal 0.

When *piled foundations* strengthening with jet grouted piles, analyses have been carried out for the total design load. Pile stiffness was determined by data of pile vertical load test of the driven- and jet grouted piles.

The authors of the paper made predictions of the foundation settlement in axes 1' 15', P-S due to foundations load increments, strengthened with the jet grouted piles after the construction restart. The deformations are calculated with regard for the different deformability of the post foundation base and a pile. The coefficient of subgrade reaction in the post foundation base (settlement marks M7 and M31 in fig.1) was determined by results of settlements monitoring (table 2, fig.3a) and stiffness coefficient of jet grouted piles – by tests data (table 4, fig. 3b). The design scheme is presented in fig.5. By results of analysis of the base deformation of the most loaded post foundations strengthened with the jet grouted piles, the settlements after the construction restart with regard for the total load were 13,8 and 12 mm, respectively. At present, when the construction of the shopping center is completed, but the building is not put into operation, the measured base deformations of these foundations are 10,5 and 5 mm, respectively. Such conformity of predicted and measured deformations confirms the efficiency of the base strengthening and high accuracy of the analysis methods based on in-place tests.

Table 4

Test number (table 3)	Pile (JGP) length, m	Pile (JGP) length in soil, m	Pile settlement according to test, mm	Stiffness ratio of pile (JGP) base, kN/m $K = \frac{N_2 - N_1}{S_2 - S_1}$
1	10,6	10	13	50000
2	10,88	10,58	11	60000
3	11,50	11,10	10,35	60000

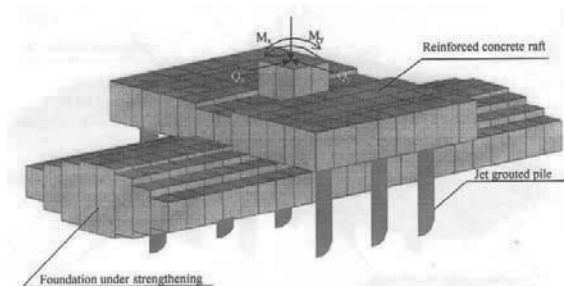


Fig.5. Design diagram of foundation strengthening (strengthening types 1 and 4)

## 5 CONCLUSION

1. The complicated practical geotechnical problem of strengthening of the skeleton building foundations under construction, the necessity of which was provoked by change of space-planning decision in the process of construction is solved.

Within one 500x250 m building, four types of foundations have been designed: post foundations on the bed without karst protection; strip foundations on the bed designed for 7 m diameter karst hole; piled foundations in kind of pile groups of driven piles without karst protection and pile group foundations combined with karst protected reinforced concrete strips on piles.

2. Four types of foundations strengthening has been developed with the use of jet grouted piles taking into attention loads increase compared to design, acting (already imposed) loads and foundations settlements at the moment of their strengthening, structural concepts of foundations and the extent of karst risk of the base.

3. Analysis of strengthening constructions and base deformations was carried out according to data of jet grouted piles vertical load test and settlements measurements of the foundations under strengthening.

4. The results of the strengthened foundations settlements measurement after the building implementation showed the good precision with analysis data. This proves the correctness of the taken structural and design schemes.

# Standardization of the molding procedures for stabilized soil specimens as used for QC/QA in Deep Mixing application

Normalisation des procédures pour la production d'éprouvettes de sols stabilisés utilisées dans les processus de QC/QA pour des applications de « Deep Mixing »

Grisolia M., Leder E., Marzano I.P.

Department of Civil and Environmental Engineering (DICEA), "Sapienza" University of Rome

**ABSTRACT:** An international collaborative research has been undertaken to establish common understanding of the key issues involved in Quality Control/Quality Assurance (QC/QA) of Deep Mixing technique and propose international standards on design, execution and execution control. The aim of the study is to investigate the influence of the laboratory procedures on the mechanical properties of stabilised soil specimens and develop an innovative method to select the appropriate molding technique. A large laboratory testing program was carried out on seven types of heterogeneous natural soils, as found in Rome, and on Kawasaki clay stabilised with Portland cement. Thirty soil-binder mixtures with different workability were prepared using five different molding techniques, varying initial water content of the soils, water to cement ratio and binder amount. Unconfined compression tests have been carried out systematically on over 800 specimens. The applicability of different molding techniques in function of the workability of the mixture has been investigated and from the results it was possible to define an "applicability index" and therefore the range of applicability for each technique in function of the mixture's workability.

**RÉSUMÉ:** Une étude internationale a été entreprise dans le but de définir des orientations communes pour les procédures QC/QA liés aux travaux effectués par « Deep Mixing » et proposer des normes internationales relatives à la conception, l'exécution et le contrôle des opérations. Le but de cette étude est d'étudier l'effet des procédures de laboratoire pour la réalisation des éprouvettes de sols stabilisés et de développer une méthode innovante pour sélectionner à chaque fois la technique de réalisation appropriée. Un vaste programme d'essais en laboratoire a été réalisé en analysant plus de trente mélanges différents de ciments et sols à partir de huit sols naturels de Rome et Tokyo. Cinq techniques de réalisation ont été utilisées pour la confection d'éprouvettes testées avec des essais de compression simple. L'applicabilité des différentes techniques de réalisation a été étudiée selon l'usinabilité du mélange. A partir des résultats, il a été possible de définir un index d'applicabilité et donc un champ d'application de chaque technique en fonction de l'usinabilité du mélange.

**KEYWORDS:** Deep mixing, workability, laboratory procedures, operational abaci.

## 1 INTRODUCTION

The Deep Mixing Method is a widely spread in situ ground improvement technique using different kind of binders to enhance mechanical and physical properties of soils (Terashi 1997; CDIT 2002).

Laboratory mixing tests are essential to QC/QA processes and performed to obtain the mechanical and physical properties of stabilized soil samples. The laboratory test results provide crucial information for the estimation of the mix design and in-situ properties to utilize in the geotechnical design. (Bruce et al. 2000; Larsson 2005; Marzano et al. 2009; Terashi and Kitazume 2011; Filz et al. 2012). At the moment many laboratories produce and test soil-binder specimens without a standard procedure, therefore the results for the same soil-binder mixture could be very different and not usefully compared. In fact molding techniques have a great influence on the mechanical and physical properties of the stabilized soil specimens (Grisolia et al. 2012; Marzano et al. 2012). This influence is strictly correlated to the workability of the soil-binder mixture defined as the property of the mixture of being easily mixed in the bowl and placed in the mold. High workability refers to liquid type mixtures (easier to place and handle), while low workability to sticky and stiff type ones.

Workability represents diverse characteristics of fresh mixture that are difficult to measure quantitatively, because a soil-binder mixture is a complex material with a wide range of particle sizes and time-dependent properties. The definition of a parameter representative of the mixture's workability and an univocal method for the evaluation of the mixture's workability are currently not available (Koehler and Fowler, 2003) even if

such parameter could be well related to consistency when considering mixtures made up of cohesive soils.

A new method for the evaluation of the mixture's workability was introduced and applied in the study. It is based on the measure of the torque required to turn an impeller in soil-binder mixture through a commercial device which is applied directly on the mixer. This method has the advantage to provide the possibility of measuring the workability for each mixable mixture, independently on the type of the materials used.

Furthermore, the study develops a procedure to select, through an "applicability index" function of the initial mixture workability, the molding technique that provides densest specimens with highest strength and results repetitiveness in order to obtain very useful reference values to set specification limits to be achieved in field applications (ratio between laboratory and field target strength is reported for instance by JGS 0821-2000 and EuroSoilStab 2002).

## 2 MATERIALS AND METHODS

The experimental work consisted in a laboratory investigation on the effect of different molding techniques on the unconfined compressive strength,  $UCS$  (measured according to the JIS A 1216:2009) and wet density,  $\gamma$  (defined as the specimen's weight divided by the volume of the mold) of cement stabilised soil specimens under various mixing conditions.

### 2.1 Materials

Eight types of natural soils stabilised with Portland cement added in wet or dry form were used. The tests were performed on: Kawasaki Clay ( $KC$ ), manmade Silty Deposit ( $SD$ ), Silty



clayey Sand (*SS*), Sand and Gravel (*SG*), Pliocene Clay (*PC*), Black Pozzolana (*BP*), Red Pozzolana (*RP*) and Argillified Tuff (*AT*). For each soil, different mixtures were produced, varying the initial water content and keeping constant the cement content,  $a_c$  (defined as the weight of the introduced dry cement divided by the dry weight of the soil to be stabilized). Specimens with 5 cm diameter and 10 cm height were employed. Each soil was sieved through a 9.5mm sieve, so that the maximum grain size of the soil sample would be less than 1/5<sup>th</sup> of the inner diameter of the mold. The properties of the soil-binder mixtures analyzed are shown in Table 1.

Table 1. Soil properties and Testing conditions.

Soil type	Gravel-Sand-Silt-Clay	Water content, $w_n$ (%)	Cementitious grout	Workability parameter, Torque, $M_t$ (Nm)
<i>KC</i>	0-14-42-44	72	$w/c = 0$	5,32
		66		8,47
		60	$a_c = 5\%$	17,40
		60		29,00
		60	$a_c = 20\%$	40,00
		54		61,00
		54	$a_c = 30\%$	75,00
		49		96,00
		49	$a_c = 20\%$	96,00
		49		120,00
<i>SD</i>	18-24-34-24	20	$a_c = 10\%$	13,55
		30		4,81
		40		2,23
<i>SS</i>	22-40-20-18	35	$w/c = 1$	9,08
		40		4,88
		45		3,76
<i>SG</i>	33-40-14-13	6	$w/c = 1$	11,28
		8		5,11
		10		3,51
<i>PC</i>	00-00-64-36	50	$a_c = 10\%$	10,16
		60		5,76
		70		2,34
<i>BP</i>	08-49-38-05	25	$w/c = 0,5$	6,97
		30		2,37
		35		0,21
<i>RP</i>	11-58-24-07	20	$w/c = 0,5$	8,34
		26		1,60
		32		1,08
<i>AT</i>	02-47-39-12	44	$w/c = 0,5$	8,22
		48		0,60
		53		0,20

## 2.2 Laboratory procedures and testing methods

A Hobart type mixer apparatus was adopted. After placing the natural soil in the mixer, the water content was adjusted to the desired value by adding water. Before adding the binder the soil was homogenised by mixing. The grout made of Portland cement (PC) and water or the PC in dry form was then added to the soil and mixed for ten minutes according to JGS 0821 (2000).

Using a commercial device applied directly on the kitchen mixer apparatus, it was measured the torque required to turn the impeller in a soil-binder mixture just before the molding phase. According to the proposed method the workability was expressed as a torque ( $M_t$ ) applied to mix certain amount of soil-binder mixture ( $V_m$ ) with set impeller shape ( $S_h$ ) and rotational speed ( $R_s$ ). In the study were assumed the following parameters:  $V_{m0} = 3dm^3$ ;  $S_{h0} = "K"$  shape;  $R_{s0} = 10rpm$ .

Since the kitchen mixer has a planetary motion, the test was undertaken continuously on the whole mixture therefore giving more reliable outputs. For each completed revolution it was possible to measure the Torque, and for the test it was decided to set the number or revolution to 10, to obtain more accurate measures.

Afterwards the stabilized soil was placed into plastic molds in three layers and compacted using several molding techniques (Figure 1):

– No Compaction (namely *N.C.*): It simply consisted in placing the stabilized soil into the mold with a spoon.

– Tapping, namely (*TA.*): For each layer, the mold was tapped against the floor 50 times.

– Rodding, (namely *RO.*): It consisted in tamping each layer with a 8mm diameter steel rod for 30 times and eventually pushing down the material attached to the rod.

– Static Compaction (namely *S.C.25* and *S.C.50*): Each layer was statically compressed for 10 seconds by using a heavy rod, 49 mm in diameter. 25 or 50 kPa pressure were applied.

– Dynamic Compaction (namely *D.C.*): Each layer was compacted by a falling weight (1.5 kg) using a special apparatus. Fall height was set at 10 cm, number of blows at 5.

These techniques are those currently used in most of the laboratory all over the world (JGS 0821, 2000; EuroSoilStab, 2002; Kitazume et al. 2009).

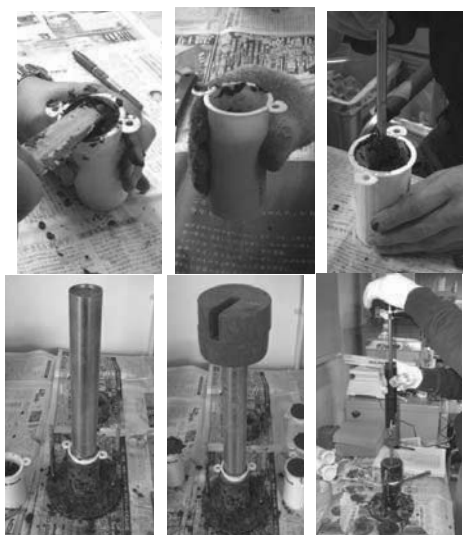


Figure 1. Molding techniques used: a) *N.C.*, b) *TA.*, c) *RO.*, d) *S.C.25*, e) *S.C.50*, f) *D.C.*

To prevent water evaporation from the specimen each mold was covered with the sealant and stored in special curing tanks at 95% relative humidity. To reduce the effect of the time of rest between the hydration of binder and completion of molding on the specimens properties, according to Kitazume et al. (2009), all the stabilized soil was molded in less than 45 minutes from binder hydration. After curing times of 28 days, the specimens were removed from the molds and then subjected to unconfined compression tests at a rate of 1.0 mm/min. Unconfined compression tests were conducted on triplicate samples for each case (mixture type and molding technique) analyzed.

## 3 RESULTS

The applicability of a molding technique was evaluated by the “Applicability index”, which is related to “densest specimens with the highest strength” and “results repetitiveness”.

For the same mixture a well made specimen has low cavities/bubbles/voids amount and therefore higher wet density ( $\gamma$ ) if compared to a bad made one. Furthermore it was indeed observed that the specimens produced by different molding techniques could have similar wet density but very different unconfined compressive strength (*UCS*) values. For that reason the *N*-parameter was introduced to condense the indications given by both parameters,  $\gamma$  and *UCS*, into one. *N* is defined as the mean of the normalized unconfined compressive strength ( $UCS_N$ ) and the normalized unit weight ( $\gamma_N$ ) as reported in the Eq. 1. The  $UCS_N$  and  $\gamma_N$  values for a given molding technique

and mixture were calculated by dividing the UCS and  $\gamma$  by the maximum values ( $UCS_{max}$  and  $\gamma_{max}$ ) obtained from all the employed molding techniques. The normalizations are necessary to allow direct comparison between two parameters with different unit of measurements. According to the Eq. 1 the  $N$  parameter values range between 0 and 1. In order to define a criteria for the choice of the applicable techniques, it was set the acceptable limit of  $0.9N$  considering a variation of 10 % from the maximum  $N$  value.

$$N = \text{Average} [ UCS_N ; \gamma_N ] \quad (1)$$

The Figure 2 shows as example the  $N$  parameters vs. torque values obtained for all the analyzed soil-binder mixtures molded by the Rodding technique. From the figure clearly appears that for all the measured mixtures workability the  $N$  values are above the set limit as an expression of the high quality of the specimens realized by Rodding.

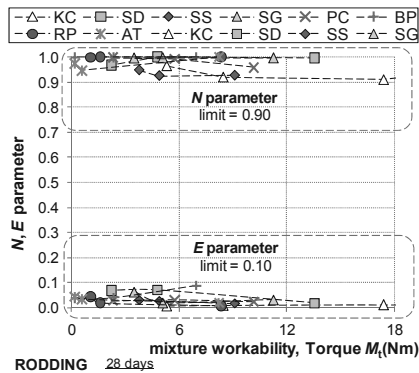


Figure 2. Applicability of Rodding technique considering the  $N$  and  $E$  parameters.

Despite the  $N$ -parameter is a good indicator of the applicability of a molding technique, to take into account that the applicability should be also related to the “repeatability” of the tests results the  $E$ -parameter was introduced. Repeatability means that the results related to the specimens produced by a specific molding technique should have a low “scatter” or relative error. Unconfined compression tests was conducted on triplicate samples for each case analyzed, therefore it was possible to evaluate the relative error on the unconfined compressive strength and wet density values for the different mixtures types and molding techniques.  $E$  is defined as the mean of the relative error on the UCS and  $\gamma$  values as reported from Eq. 2. According to its definition also this parameter ranges between 0 and 1. To set a criteria to select the applicable techniques, some literature works were taken into account. For the accuracy or repeatability of the experiments, Richards and Reddy (2010) claimed that a standard deviation of 10 % was not unheard of in geotechnical testing. Al-Tabbaa et al. (2012) also reported an error of 5 – 15% for laboratory mixed specimens tested with unconfined compression tests. Therefore even for the  $E$  parameter the acceptable limit was set equal to 10% of  $E$ .

$$E = \text{Average} [ E_{UCS} ; E_{\gamma} ] \quad (2)$$

The results obtained from the specimens molded by the Rodding technique in terms of  $E$  vs. torque values are shown in Figure 2 as example. It can be clearly seen that also for the  $E$  parameter all the obtained values are below the set limit, expression once again of the high repeatability of the tests results obtained from the specimens molded by the Rodding technique.

In order to take into account the different aspects of a well made specimen, expressed by the  $N$  and  $E$  parameter, an index of applicability  $I_A$  defined in Eq. 3 was introduced.

$$I_A = \frac{N}{1+E} \quad (3)$$

According to the Eq. 3 and to the  $N$  and  $E$  parameters definitions, also the  $I_A$  values range between 0 and 1. To obtain a target value for the choice of the applicable techniques, the limit values given for the two different parameters  $N$  and  $E$  were introduced in the Eq. 3. A target value of  $I_A = 0.82$  was then obtained.

The Figure 3 shows an example of the  $I_A$  vs. mixtures workability graph obtained for all the analyzed soil-binder mixtures molded by the Rodding technique.

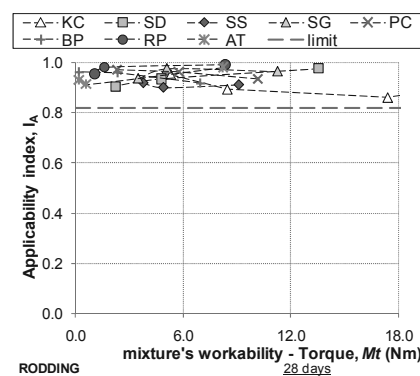


Figure 3. Applicability index of Rodding technique.

The figure show that Rodding is applicable for all the measured mixtures workability since  $I_A$  values are all above the set target limit. From the results it is possible to see a very good trend of the  $I_A$  despite the fact that data were obtained from mixtures based on different types of soil (cohesive and granular types), with different grout dosage and water contents. The results obtained also from other techniques show that the  $I_A$  is strictly dependent on the workability of the mixture among other factors.

The results related to the No Compaction technique are shown in Figure 4. It clearly appears that this technique is applicable for  $M_t < 3Nm$  and not applicable for  $M_t > 6Nm$ . In the range  $M_t = 3\div 6Nm$  it is not possible to obtain univocal indication from the data, therefore this technique have been considered marginally applicable in this workability interval.

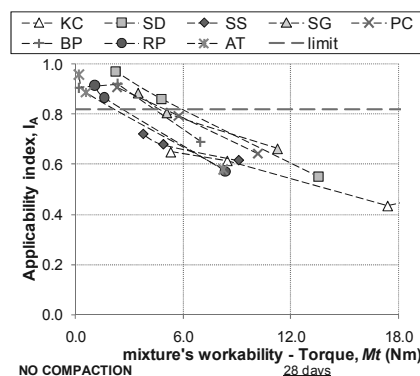


Figure 4. Applicability index of No Compaction technique.

Similar graphs to the ones shown in Figures 3 and 4 were also obtained for the other molding techniques used in the study. From these graphs it was possible to determine for each molding technique the ranges of workability in which they are

applicable, marginally applicable and not applicable. The results are summarized in the operational abacus of Figure 5.

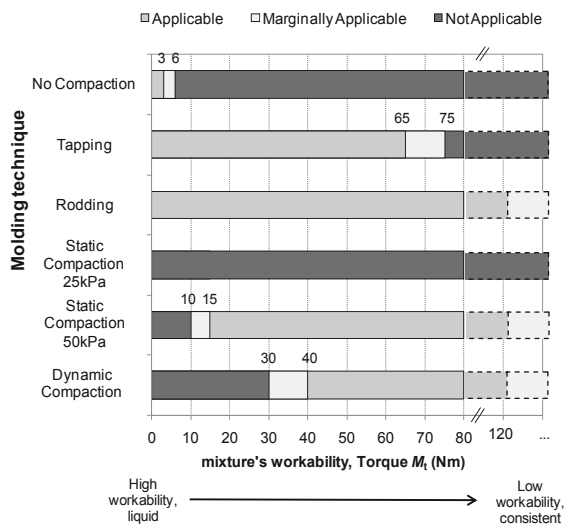


Figure 5. Ranges of applicability of the different molding techniques.

To allow the standardisation and the use of the method a “calibration curve” was elaborated by drawing the torque versus the water content ( $w$ ) of an easily available kind of soil such as kaolin clay using the set of mixer related parameter  $V_{m0}$ ,  $S_{h0}$  and  $R_{s0}$  (Figure 6).

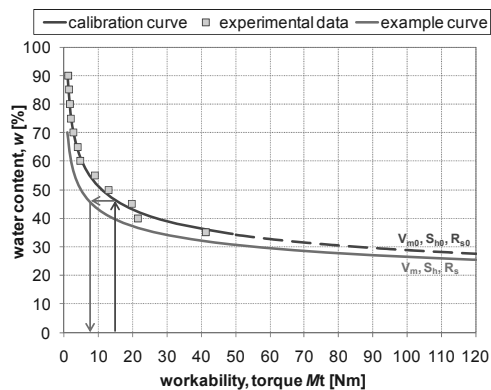


Figure 6. Calibration curve.

By using different set of parameters ( $V_m$ ,  $S_h$  and  $R_s$ ), function of the mixer type and torque evaluation procedure, other curves can be drawn in the same graph. Therefore for each molding technique the range of applicability (expressed by torque values) corresponding to the used set of parameter can be graphically obtained from the calibration curve, as shown in Figure 6.

By mean of the abaci of Figures 5 and 6, it would be possible to select for every kind of mixable soil-binder mixture the molding technique that gives high quality specimens in a very quick and easy way only by measuring the workability of the material.

#### 4 CONCLUSIONS

The results of the large laboratory study performed on eight types of natural soils confirm that the mixture’s “workability” has a great influence on the mechanical and physical properties of the stabilised soil specimens. The results provide very useful operational abaci to select the molding technique that produces high quality specimens in function of the soil-binder mixture’s workability.

The results obtained represent a useful data set for the correct selection of the molding technique for different kind of soils and mixing conditions headed for the international standardisation. This study represents a significant step forward towards the definition of highly required guidelines for the molding procedures of stabilised soil specimens as used in QC/QA processes for Deep Mixing applications.

#### 5 ACKNOWLEDGEMENTS

The authors wish to thank Prof. Masaki Kitazume for his help and suggestions throughout the study. The Soil Stabilization Group of the Port and Airport Research Institute (JP) is also acknowledged for the helps during the tests and for providing part of the data.

#### 6 REFERENCES

Al-Tabbaa, A., Liska, M., McGall, R., Critchlow, C. 2012. Soil Mix Technology for Integrated Remediation and Ground Improvement: Field Trials. IS-GI Brussels 2012, Belgium.

Bruce, D.A., Bruce, M.E., Di Millio, A.F. 2000. Deep Mixing: QA/QC and Verification Methods. Grouting Sol Improvement, Geosystems Including Reinforcement. 4th Intl Conf. Ground Improvement Geosystems. Helsinki, Finland, pp. 11-22.

CDIT, Coastal Development Institute of Technology 2002. *The Deep Mixing Method - principle, design and construction*. A.A. Balkema Publishers, Lisse, Abingdon, Exton (PA), Tokyo, p. 123.

EuroSoilStab, 2002. *Development of design and construction methods to stabilise soft organic soils*. Design Guide Soft Soil Stabilization. EC project BE96-3177, 94p.

Filz, G., Adams, T., Navin, M., Templeton, A.E. 2012. Design of Deep Mixing for Support of Levees and Floodwalls. 4th Intl. Conf. on Grouting and Deep Mixing, Marriott New Orleans, LA, US.

Grisolia M., Kitazume M., Leder E., Marzano I.P., Morikawa Y. 2012. Laboratory study on the applicability of molding procedures for the preparation of cement stabilised specimens. IS-GI Brussels 2012, Belgium

JGS 0821-00 2000. *Practice for Making and Curing Stabilised Soil Specimens Without Compaction* (Translated version). Geotechnical Test Procedure and Commentary, Japanese Geotechnical Society.

Kitazume, M., Nishimura, S., Terashi, M., Ohishi, K. 2009. International Collaborative Study Task 1: Investigation into Practice of Laboratory Mix Tests as Means of QC/QA for Deep Mixing Method. International Symposium on Deep Mixing & Admixture Stabilization, Okinawa, Japan.

Koehler, E.P., and Fowler, D.W. 2003. *Summary of Concrete Workability Test Methods*. Research Report, International Center for Aggregates Research The University of Texas at Austin.

Larsson, S. 2005. State of Practice Report – Execution, monitoring and quality control. Intl. Conf. on Deep Mixing - Recent Advances and Best practice, Stockholm, Sweden.

Marzano I.P., Al-Tabbaa A., Grisolia M. 2009. Influence of sample preparation on the strength of cement-stabilised clays. Intl. Symp. on Deep Mixing & Admixture Stabilization, Okinawa, Japan.

Marzano I.P., Leder E., Grisolia M., Danisi C. 2012. Laboratory study on the molding techniques for QC/QA process of a Deep Mixing work. 3<sup>rd</sup> International Conference on New Developments in Soil Mechanics and Geotechnical Engineering, Near East University, Nicosia, North Cyprus. ISBN 975-8359-28-2.

Richards, K. S., Reddy, K. R., 2010. True triaxial piping test apparatus for evaluation of piping potential in earth structures. *Geotechnical Testing Journal*, 33(1): 1-13.

Terashi, M. 1997. Deep mixing method Brief state of the art. 14th International. Conference on Soil Mechanics and Foundation Engineering. Tokyo

Terashi, M., and Kitazume, M. 2011. QA/QC for deep-mixed ground: current practice and future research needs. *Proc. of the Institution of Civil Engineers – Ground Improvement* 164 (3), 161-177.

# Analysis of Floating Pile Capacity in Improved Ground for Thi Vai Port, Vietnam

## Analyse de la capacité de pile flottante dans un sol amélioré du port Thi Vai, Vietnam

Hai N.M., Tuong N.K.

Faculty of Civil Engineering, Thu Dau Mot University, Vietnam

Long P.D., Nhon P.V.

Vietnamese Society of Soil Mechanics and Geotechnical Engineering, Vietnam

**ABSTRACT:** A static loading programme was performed to respond to total and effective stress analysis of floating pile capacity in improved ground at Thi Vai Port approximately 90 km southeast of Ho Chi Minh City, Vietnam. The soil profile consists of an about 15 to 23 m thick deposit of soft, normally consolidated, compressible clay deposited on dense to compact sand. Scheme of soil improvement was imposed, consisting of wick drains installed at a spacing of 1.5 m through the clay to the sand and placing to 4.7 m thick surcharge. After removal of the surcharge, two square precast concrete piles, 400 mm diameter, were driven to depths of 16 and 22 m and the static loading tests were performed reaching the pile capacities after piles driven about 14 and 23 days, respectively. The capacity of the 16 and 22 m pile measured are about 450 and 1,100 kN at maximum movements of about 5 and 6 mm, respectively. The tests indicate a good agreement between measurements and analysis of total stresses, and the correlation coefficient,  $N_{KT}$ , between CPTU pore pressure adjusted cone stress and vane shear stress is about 18 instead of 12 through 16 as used for the Project.

**RÉSUMÉ :** Un programme de chargement statique a été réalisé pour répondre à l'analyse des contraintes totale et effective de la capacité du pieu flottant dans un sol amélioré au port de Thi Vai à environ 90 km au sud-est de Ho Chi Minh-Ville, Vietnam. Le profil de sol est constitué d'un dépôt de 15 à 23 m d'épaisseur d'argile souple compressible normalement consolidé, déposé sur un sable dense et compact. Le schéma d'amélioration des sols a été imposé, composé de drains verticaux installés à une distance de 1,5 m à travers l'argile au sable et à la mise à 4,7 m d'épaisseur en supplément. Après l'élimination de la surcharge, deux piles carrées en béton préfabriqué de 400 mm de diamètre ont été installés à des profondeurs de 16 à 22 m et les essais de chargement statique ont été réalisés pour atteindre les capacités de pieux après ce que des pieux sont mis en place environ 14 et 23 jours, respectivement. La capacité de la pile 16 et 22 m mesurée est d'environ 450 et 1100 kN aux mouvements maximum d'environ 5 et 6 mm, respectivement. Les tests montrent un bon accord entre les mesures et l'analyse des contraintes totales, et que le coefficient de corrélation,  $N_{KT}$ , entre la pression interstitielle CPTU ajustée la contrainte cône et la contrainte de cisaillement est d'environ 18 au lieu de 12 à 16 comme utilisés pour le projet.

**KEYWORDS:** soil improvement, static loading test, total stress analysis, effective stress analysis.

## 1 INTRODUCTION

The Thi Vai Container Port is built on an improved ground over a 470 m by 600 m area along the Thi Vai River approximately 90 km southeast of Ho Chi Minh City. The soil profile consists of deltaic sediments of about 15 to 23 m of soft, normally consolidated, highly compressible clay on a thick layer of dense to compact sand. The highest water level is at Elev. +4.0 m, which requires raising the ground elevation by about 2 m to Elev. +5.0 m to avoid flooding. To reduce settlement after construction, wick drains were installed with a spacing of 1.5 m through the clay to the sand and a temporary surcharge was added raising the surface to Elev. +7.6 m, an additional 2.0 m of fill height. The surcharge was removed after 80 % to 90 % of the consolidation settlements had developed and the expected future ground settlement shall not exceed 200 mm over a period of 20 years, which included secondary compression. After removal of surcharge, two 400 mm square precast piles driven into 16 and 22 m depth to serve for test and design of building foundations.

This paper presents the methods used for analysis of the pile capacity based on total and effective stress approaches, details of the results from the tests on 16 and 22 m piles, and discusses the merits of each method.

## 2 SOIL PROFILE

The soil profile is indicated in Figures 1 and 2. Figure 1 shows the results of a typical CPTU sounding pushed at the site before driving test piles.

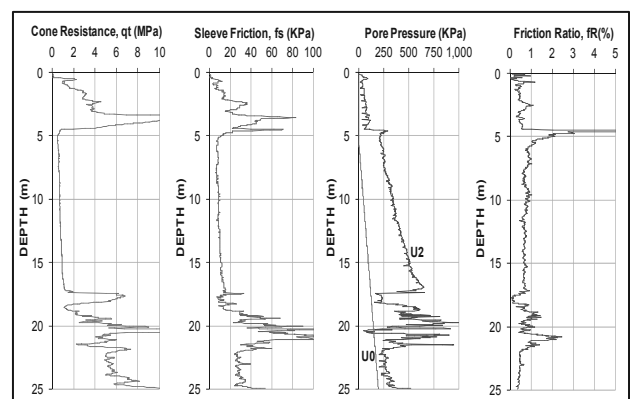


Figure 1. Diagram of CPTU sounding pushed before construction start

Figure 2 presents distribution of the grain size, water content, consistency limits, and the distribution of the undrained shear strength in the clay from a field vane. The field vane demonstrates the clay to be very soft above 10 m depth and soft below. Total saturated density is about  $1,600 \text{ kg/m}^3$  throughout the clay (from  $w_n = 61 \%$ ). The density of the sand above and below the clay is estimated to  $2,100 \text{ kg/m}^3$  (from  $w_n = 24 \%$ ) and  $1,800 \text{ kg/m}^3$  (from  $w_n = 22 \%$ ), respectively.

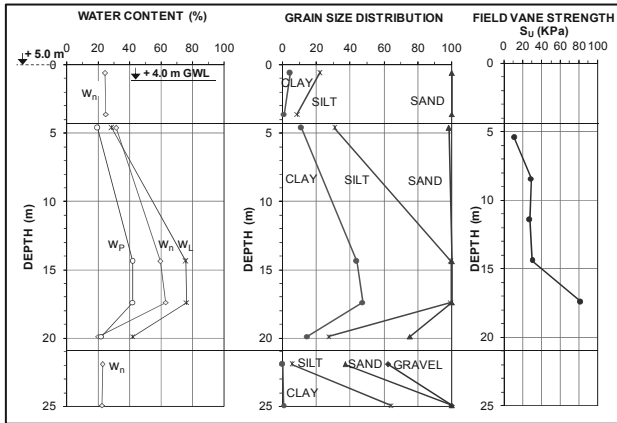


Figure 2. Water content and Atterberg Limits, grain size distribution, and field vane strength

### 3 SOIL IMPROVEMENT AND MEASUREMENTS

Figure 3 shows the location of SS8 settlement benchmark was installed on the original ground surface before the placing of the fill. Pore pressure measurement was performed by piezometer tips installed at depths of 6.5 m and 15.2 m. Settlement distribution with elevations was measured by means of extensometer gages placed at elevations of +5 m, -1.6 m, -5.9 m, -10.3 m and -17 m in the clay. Figure 4 also indicates location of field soil tests and test piles.

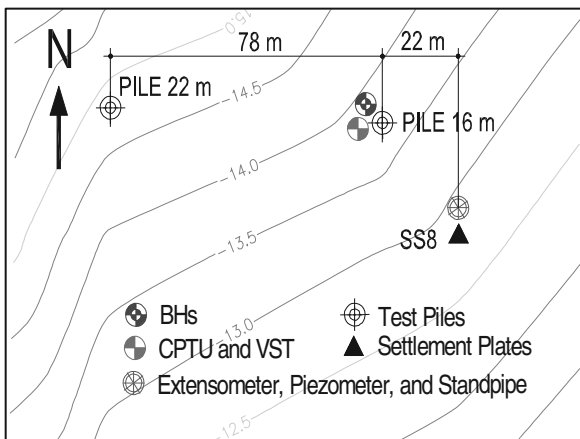


Figure 3. Locations of test piles, borehole, CPTU, VST, and field instrumentation

Figure 4 shows the settlements measured at SS8 plate near the tested piles. Day 0 is March 12, 2009 and the total settlement measured after completed removal of surcharge was about 2.15 m. Removal of surcharge at the 22 and 16 m pile was completed on August 22, 2011 and September 9, 2011, respectively. 15 and 60 days after removal of surcharge, the 22 and 16 m test pile was driven on September 6, 2011 and November 8, 2011, respectively, to serve for test and design of building foundation.

Figure 5 shows the settlement distribution with depth as measured at extensometer station, next to the SS8 at 4.6, 8.9, 13.3, and 20 m depths below the original ground surface from August 29 through June 30, 2011. The extensometer station had to be removed on June 30, 2011 before the test pile driven. The four settlements anchors were referenced to the presumed zero for the fifth anchor point placed at 20 m depth. The settlement distribution is almost linear from the fill surface to zero at 15 m depth.

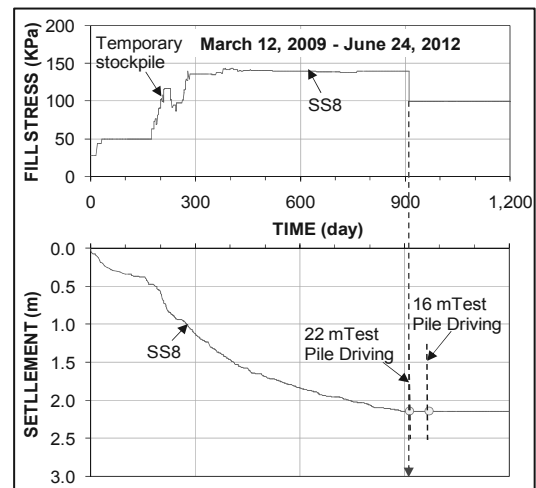


Figure 4. Fill stress versus settlement

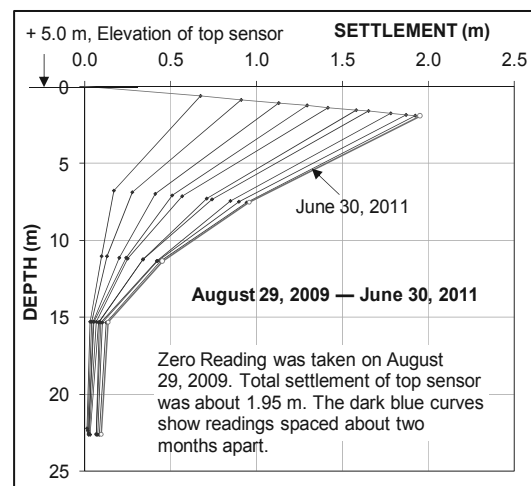


Figure 5. Distribution of settlement versus depth

Figure 6 shows the pore pressures measured at Elev. -1.5 m and -10.2 m from August 29, 2009, through September 23, 2011. The Piezometer had to be removed before driving the test piles. As shown in Figure 6, the pore water pressures seem to be equal to the hydrostatic pressures after removing the surcharge.

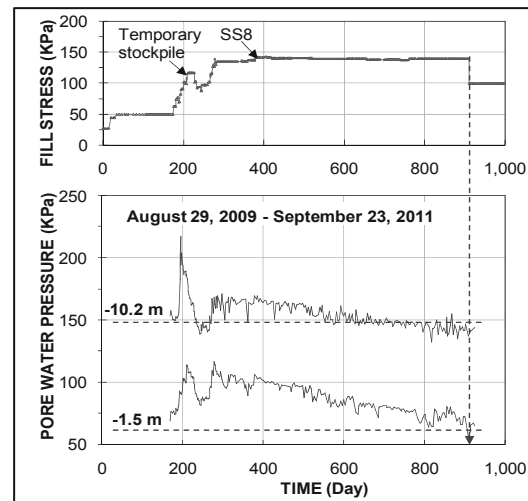


Figure 6. Pore water pressure versus fill stress

## 4 ANALYSIS OF PILE CAPACITY

### 4.1 Total stress approach ( $\alpha$ Method)

The so-called alpha method is a most common method to calculate shaft resistance in total stress approach, which correlates the shaft resistance,  $r_s$ , to the undrained shear strength of the clay,  $S_u$ , via an adhesion reduction coefficient,  $\alpha$ , as the undrained shear strength of the soil increased:

$$r_s = \alpha S_u \quad (1)$$

For field CPTU tests, Lunne et al. (1985) proposed a method to indirectly estimate the  $S_u$  versus corrected cone resistance ( $qt$ ) as:

$$S_u = (qt - \sigma_{v0})/Nkt \quad (2)$$

Where,  $Nkt$  is known as an empirical cone factor and  $\sigma_{v0}$  is the total overburden stress.

The records of undrained shear strength from the field vane test are substituted to Eq. (2) to determine  $Nkt$  as shown in Figure 7.

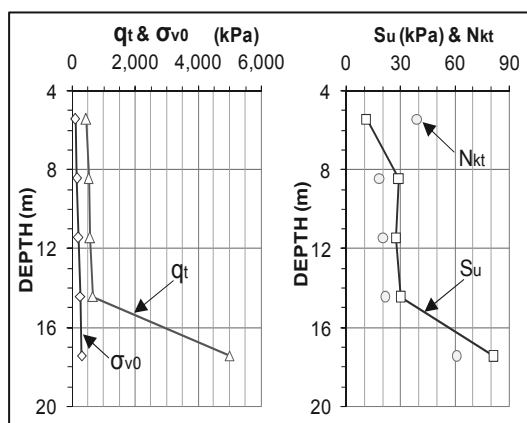


Figure 7. Correlation between cone stress and field vane strength

To improve total stress approach, Randolph and Murphy (1985) considered ratio of the undrained strength to the effective overburden stress,  $\sigma'_{v0}$  (stress history) and proposed a reduction coefficient incorporated into the API 1987 edition (excluding the effects of the pile length) as:

$$\alpha = 0.5(S_u/\sigma'_{v0})^{0.50} \text{ for } (S_u/\sigma'_{v0}) \leq 1 \quad (3a)$$

$$\alpha = 0.5(S_u/\sigma'_{v0})^{0.25} \text{ for } (S_u/\sigma'_{v0}) > 1 \quad (3b)$$

The effects of the pile slenderness (ratio of the embedment pile length,  $L$ , to the pile width,  $B$ ) also were considered by Murff (1980), Kraft et al. (1981), Semple and Rigden(1984), Randolph and Murphy (1985). The unit shaft resistance proposed from two alternative combinations of undrained shear strength and effective stress was refined in the API 1993 edition as shown in Eq. (4) and (5).

$$r_s = 0.5(S_u)^{0.50} (\sigma'_{v0})^{0.50} \quad (4)$$

$$r_s = 0.5(S_u)^{0.75} (\sigma'_{v0})^{0.25} \quad (5)$$

Kolk and van der Velde (1996) suggested an updated version incorporated directly length effects and the unit shaft resistance was determined in Eq. (6):

$$r_s = 0.55(S_u)^{0.7} (\sigma'_{v0})^{0.3} (40B/L)^{0.2} \quad (6)$$

The  $Nkt$  values in Figure 7 determined correlation between cone stresses and field vane strengths are used to determine the  $S_u$  of CPTU test and calculate the unit shaft resistance according to Eq. 1 and Eqs. 4 - 6.

The results are plotted in Figure 8 versus the accumulated unit shaft resistance for the full dissipation of excess pore pressures. For 5 m thick fill sand layer above the clay layer surface, the effective stress analysis is applied with a coefficient  $\beta$  of 0.3 and indicates the bearing capacity of this layer is about 97 KN.

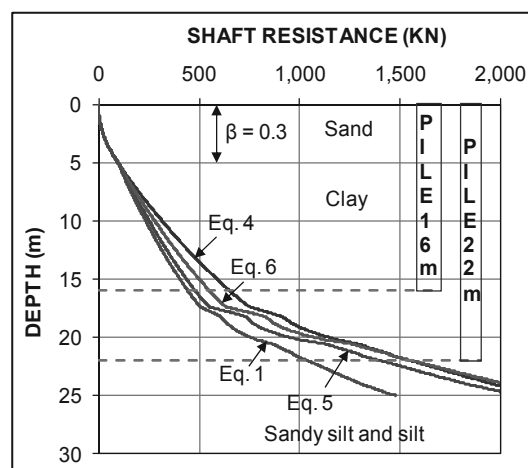


Figure 8. The accumulated shaft resistances versus depth

### 1.1 Effective stress approach ( $\beta$ Method)

The effective stress approach for evaluating the pile capacity, Burland (1973) developed a simple equation written as:

$$r_s = K \tan \delta \sigma'_{v0} = \beta \sigma'_{v0} \quad (7)$$

Where,  $K$  is the lateral earth-pressure coefficient,  $\delta$  is the constant volume friction angle, and  $\beta = K \tan \delta$  is Bjerrum-Burland coefficient.

Two direct CPTU methods typical of effective stress approach are method of Eslami and Fellenius (1997) and Takesue et al. (1998). In the Eslami and Fellenius CPTU method, the cone stress is transferred to an apparent "effective" cone stress,  $q_E$ , by subtracting the measured pore pressure,  $U_2$ , from the measured total cone stress,  $q_t$ , the unit shaft and toe resistance is obtained from:

$$r_s = C_s q_E \quad (8)$$

Where,  $C_s$  is the side correlation coefficient determined from the soil profile chart which uses both cone stress and sleeve friction.

For method of Takesue et al. (1998), the unit pile shaft resistance,  $r_s$ , is estimated from the measured sleeve friction,  $f_s$ , which is scaled up or down depending on the magnitude of the measured excess porewater pressures during penetration,  $\Delta U$  ( $\Delta U = U_2 - U_0$ ). The data used to derive the correlation were obtained from both bored and driven pile foundations in clays, sands, and mixed ground conditions.

$$r_s = f_s (\Delta U / 1250 + 0.768) \text{ for } \Delta U < 300 \text{ kPa} \quad (9a)$$

$$r_s = f_s (\Delta U / 200 - 0.5) \text{ for } 300 < \Delta U < 1,250 \text{ kPa} \quad (9b)$$

The results of the effective stress analysis are presented in Figure 9. For fill layer above clay surface, the analysis is made the same as above total stress analysis.

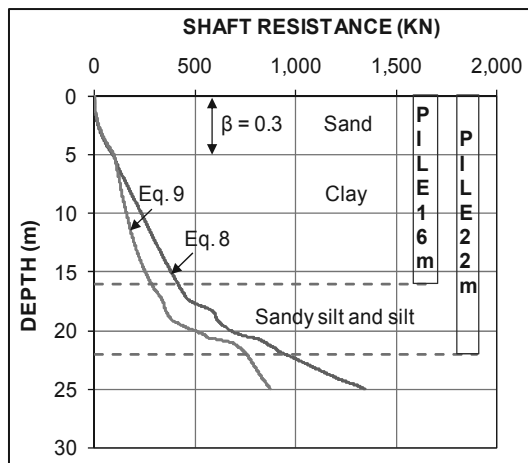


Figure 9. The accumulated shaft resistances versus depth

### 1.2 Pile test results and evaluation of approaches

The static loading tests for the 22 and 16 m Pile were performed after piles driven about 23 and 14 days, respectively. The 22 and 16 m were tested on September 29, 2011 and November 22, 2011. The load-movement curves of the two tested piles in Figure 12 indicate the ultimate loads of the plunging failures at 1,100 and 459 kN, respectively.

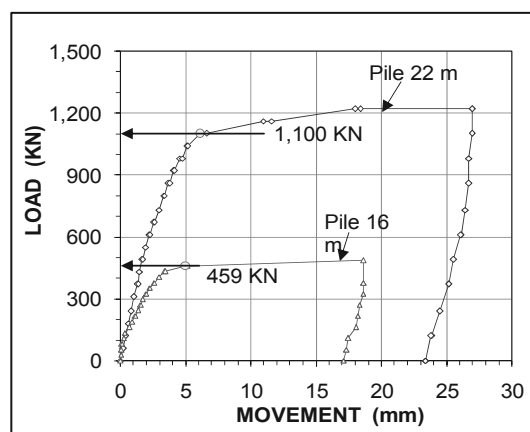


Figure 10. Pile-head load-movement curves of two static loading tests performed on 22 and 16 m pile.

Normally, the plunging failures of the test piles are found when the pile toe is in soft clay as in the subject case and the pile toe resistance can be disregarded when evaluating the analysis methods. Performance of two approaches are evaluated basing on ratio of the estimated capacities,  $Q_p$ , to the measured capacities,  $Q_m$ . Table 1 shows the performance evaluation of two approaches for the measured pile capacities.

Table 1. Evaluation on performance of the total and effective approach for predicting the pile capacity.

	Pile 16 m ( $Q_p/Q_m$ )	Pile 22 m ( $Q_p/Q_m$ )
Total stress approach		
Eq. 1	0.967	0.949
Eq. 4	1.422	1.416
Eq. 5	1.048	1.280
Eq. 6	1.203	1.423
Effective stress approach		
Eq. 8	0.915	0.884
Eq. 9	0.624	0.688

## 5 SUMMARY AND CONCLUSION

The total and effective stress analysis on two tested piles driven in improved ground of Thi Vai Port is performed and summarized as:

- For total stress approach, the analysis indicates the alpha method with a reduction coefficient incorporated into the API 1987 edition gave the best agreement.
- For effective stress approach, the analysis shows the Eslami and Fellenius method (1997) is approximately the same as the measurements.
- For two approaches, the total stress approach is the better agreement.
- Correlation coefficient,  $N_{KT}$ , between CPTU pore pressure adjusted cone stress and vane shear stress is about 18.

## 6 REFERENCES

API (1987) Recommended practice for planning, designing, and constructing fixed offshore platforms, API RP2A, 17th edn. American Petroleum Institute, Washington.

API (1993) Recommended practice for planning, designing and constructing fixed offshore platforms—working stress design, API RP2A, 20th edn. American Petroleum Institute, Washington.

Cai G., Songyu L., Liyun T., Guangyin D. 2009. Assessment of direct CPT and CPTU methods in predicting the ultimate bearing capacity of single piles. *Eng Geol* 104:211–222.

Eslami A., Fellenius B.H. 1997. Pile capacity by direct CPT and CPTU methods applied to 102 case histories. *Can Geotech J* 34:886–904.

Fellenius B.H. 2008. Effective stress analysis and set-up for shaft capacity of piles in clay. *ASCE Geotechnical Special Publication, GSP180*:384–406.

Karlsrud K., Haugen T. 1981. Cyclic loading of piles and pile anchors, field model tests at Haga. Norwegian Geotechnical Institute Research Report.

Kolk H.J., van der Velde E. 1996. A reliable method to determine the friction capacity of piles driven into clays. In: Proceedings of the 28th annual offshore technology conference, Houston, pp 337–346.

Lunne, T., Christoffersen, H.P. and Tjelta, T.I. 1985. Engineering use of Piezocone data in North Sea Clays. Proceedings XI ICSMFE, San Francisco.

Murff D. 1980. Pile capacity in a softening soil. *Int J Numer Anal Methods Geomech* 4:185–189.

Randolph M.F., Murphy B.S. 1985. Shaft capacity of driven piles in clay. In: Proceedings of the 17th annual offshore conference, Houston, pp 371–378.

Semple R.M., Rigden W.J. 1984. Shaft capacity of driven pipe piles in clay. In: Proceedings of the on analysis and design of deep foundations, San Francisco, pp 59–79.

Takesue, K., Sasao, H., Matsumoto, T. 1998. Correlation between ultimate pile skin friction and CPT data. *Geotechnical Site Characterization (2)*: 1177–1182. Rotterdam: Balkema.

# Carbonate Cementation via Plant Derived Urease

## Cimentation carbonatée par l'utilisation d'uréase issue de plantes

Hamdan N., Kavazanjian Jr. E., O'Donnell S.

*School of Sustainable Engineering and the Built Environment, Arizona State University, Tempe, AZ 85287-5306; PH: (480) 965-3997*

**ABSTRACT:** The use of plant-derived urease enzyme to induce calcium carbonate ( $\text{CaCO}_3$ ) cementation has been demonstrated through laboratory column tests. Benefits of the use of plant-derived urease over the use of microbially-generated urease to induce carbonate cementation include the small size of the enzyme, which permits penetration into finer grained soils and makes the process less sensitive to biopugging, and the availability of 100% of the carbon in the substrate for conversion to  $\text{CaCO}_3$ . The laboratory column tests employed both Ottawa 20-30 silica sand and finer-grained F-60 silica sand. The laboratory column specimens were prepared in a variety of manners and showed varying degrees of cementation and carbonate yield. Triaxial tests performed on cemented specimens showed significant strength increases over non-cemented specimens. These tests confirm the feasibility of using plant-derived urease to induce carbonate cementation in sand and provide valuable insight into the factors that must be considered in developing practical applications for ureolytic carbonate precipitation using plant-derived urease enzyme.

**RÉSUMÉ :** La cimentation de sable par du carbonate de calcium ( $\text{CaCO}_3$ ) produit par l'enzyme uréase obtenue à partir de plantes a été réalisée en laboratoire. Les avantages d'utiliser de l'uréase obtenue de plantes plutôt que de l'uréase produite microbilogiquement pour produire la cimentation carbonatée sont la petite taille de l'enzyme qui permet la pénétration dans les sols fins et rend le processus moins sujet au colmatage biologique et la disponibilité à 100% du carbone présent dans le substratum pour conversion en  $\text{CaCO}_3$ . Des essais en colonnes ont été réalisés sur deux sables de silice dits Ottawa 20-30 et F-60 (plus fin). Les échantillons ont été préparés de différentes manières et ont atteint des degrés de cimentation variés et des productions de carbonate différentes. Les résultats des essais de compression triaxiale sur des échantillons cimentés et des échantillons non-cimentés indiquent que les premiers sont beaucoup plus résistants. Ces essais confirment que l'uréase obtenue à partir de plantes peut être utilisée pour induire une cimentation carbonatée dans les sables. De plus ces essais ont permis de d'identifier les facteurs à considérer pour développer des applications pratiques pour l'utilisation de la précipitation carbonatée « uréolytique » en utilisant l'uréase issue de plantes.

**KEYWORDS:** carbonate, cementation, urease, calcite, soil improvement

## 1. INTRODUCTION

### 1.1 Background

The potential for using plant-derived urease enzyme to cement sands by inducing calcium carbonate ( $\text{CaCO}_3$ ) precipitation has been demonstrated through a series of laboratory column tests on two different gradations of silica sand. The use of microbially induced carbonate precipitation (MICP) to cement cohesionless soils has recently received substantial attention from geotechnical researchers (Burbank et al. 2012, Chou et al. 2011, Dejong et al. 2010, Harkes et al. 2010, van Paassen et al. 2010). The MICP mechanism most often discussed in the literature and most advanced in terms of field application is hydrolysis of urea (ureolytic hydrolysis). MICP via ureolytic hydrolysis relies on microbes to generate urease enzyme, which then serves as a catalyst for the precipitation reaction. The use of plant-derived urease (enzymatic ureolytic hydrolysis) to induce  $\text{CaCO}_3$  precipitation eliminates the need for microbes in the  $\text{CaCO}_3$  precipitation process.

Besides eliminating the need to nurture urease-producing microbes, enzymatic ureolytic hydrolysis offers several other advantages over ureolytic MICP. Applications of ureolytic MICP on clean sands in laboratory column tests and limited field tests have encountered significant practical difficulties, including biopugging (permeability reduction accompanying induced mineral precipitation) and generation of a toxic waste product (ammonium salt) (Harkes et al. 2010, van Paassen et al. 2008). Biopugging not only limits the distribution of

precipitation agents within the soil but also makes flushing of the waste product from the soil a difficult, energy intensive task. Due to these limitations, mass stabilization of soil using ureolytic MICP remains problematic. Furthermore, the microbes that produce the urease enzyme cannot readily penetrate the pores of soils smaller than medium to fine sand, limiting the minimum grains size of soils amenable to ureolytic MICP to clean fine sands or coarser graded soils. The small size (on the order of 12 nm) of the urease enzyme suggests that  $\text{CaCO}_3$  precipitation by enzymatic ureolytic hydrolysis will be less susceptible to bio-pugging and will be able to penetrate finer grained soils, perhaps into the silt-sized particle range, compared to MICP processes.

### 1.2 Sustainability of Ground Improvement Practices

Finding effective solutions to ground improvement challenges is becoming increasingly complex due to sustainability considerations. Established materials and methods often need to be either replaced or supplemented by innovative materials and environmentally-friendly practices to address sustainability considerations. One example of a common building material that poses significant sustainability concerns is Portland cement. Portland cement is widely used in ground improvement applications. Unfortunately, Portland cement production is extremely energy intensive and a major source of emissions of carbon dioxide ( $\text{CO}_2$ ), as well as of sulfur and nitrogen oxides. MICP has been explored recently as an alternative to Portland cement for ground improvement. Reductions in the use of



Portland cement through either direct substitution or complementary use of MICP could contribute considerably towards reduction in CO<sub>2</sub> emissions. Research suggests that cementation using MICP can address a number of important geotechnical problems in granular soils, including slope stability, erosion and scour, under-seepage of levees, the bearing capacity of shallow foundations, tunneling, and seismic settlement and liquefaction (DeJong et al. 2010, Harkes et al. 2010, Kavazanjian and Karatas 2008, van Paassen et al. 2010).

### 1.3 Ureolytic MICP

MICP attempts to create a cemented soil mass by precipitating calcium carbonate from the pore fluid such to form cementation bonds at the interparticle contacts (van Paassen et al. 2010, DeJong et al. 2006). Karatas et al. (2008) have identified several mechanisms for MICP. The MICP mechanism that has garnered the most attention and is most advanced in terms of development is ureolytic hydrolysis, or ureolysis (Chou et al. 2011, DeJong et al. 2006, van Paassen et al. 2010, Whiffin et al. 2007). Ureolytic MICP has typically been accomplished using a technique best described as biogrouting (Harkes et al. 2010, van Paassen et al. 2010), wherein bacteria and nutrients are mixed in a tank ex-situ and then injected into the soil followed by a fixation fluid to foster microbial attachment to soil particles and, finally, by a calcium-laden cementation fluid. Ureolytic MICP by stimulation of indigenous bacteria has also been reported in the literature (Burbank et al. 2012).

### 1.4 Agricultural Urease

Urease is a widely occurring hexameric protein found in many microorganisms, higher order plants, and some invertebrates. The enzyme is approximately 12 nm in dimension (Blakely & Zerner 1984). The small size of a solubilized urease enzyme affords it a distinct advantage over carbonate cementation methods that employ ureolytic microbes in cases that require penetration into very small pore spaces as nearly all known bacteria are greater than 300 nm in diameter, with the majority in the range of 500-5000 nm. Several families of common plants are very rich in urease, including some varieties of beans, melons and squash, and the pine family (Das et al. 2002). Extraction of urease enzyme from most urease containing plants has been shown to be very simple (Srivastava et al. 2001) and the enzyme is readily available from laboratory suppliers.

It is well-established that urease can occur as both an intra- and extra-cellular enzyme (Ciurli et al. 1996, Marzadori et al. 1998). Free soil urease (i.e. urease not bound to any living organism), generally derived from dead and decaying microorganisms and possibly from plant sources, readily occurs apart from the host microorganism and, upon absorptive association with soil particles, can persist for long periods of time without degradation or loss of function (Pettit et al. 1976). By contrast, exogenously added urease (i.e. urease added as a free enzyme) has a limited lifespan and its activity and function decrease with time (Marzadori et al. 1998, Pettit et al. 1976). This limited lifespan is potentially advantageous in some engineering applications as the enzyme can naturally degrade thereby eliminating long term impacts to the ecosystem.

## 2. METHODS

### 2.1 Ottawa 20-30 Sand

Laboratory column tests were conducted using plant derived urease to induce CaCO<sub>3</sub> precipitation in Ottawa 20-30 sand. These tests were carried out in 6"x 2" (152 mm x 51 mm) acrylic tubes and membrane-lined 2.8" x 6" (71 mm x 152 mm) split molds (for creating specimens for triaxial testing). Three acrylic tubes and two columns for triaxial testing were filled with 20-30 Ottawa silica sand (mean grain size 0.6 mm,

coefficient of uniformity 1.1) and treated as follows: tube #1: the sand was dry pluviated via funnel at ≈3" (76 mm) drop height and then received 5 applications of a cementation solution containing urea and calcium chloride mixed with 1.4g/L enzyme (total solution volume ≈ 300 ml); tube #2: sand was added in same manner as tube #1 and then received 2 applications (≈ 150 ml total) of the same cementation solution mixed with 1.4g/L enzyme; tube #3: the lower-third of tube was filled with sand and dry enzyme (≈ 3g), the remainder of the tube contained dry pluviated sand without enzyme, and the tube then received 2 applications (≈ 150 ml) of the cementation fluid with no enzyme added. The cementation fluid composition was based upon stoichiometry and experience with microbial urease cementation, e.g. DeJong et al. (2007), Whiffin et al. (2008).

Approximately 100 mL of a pH=7.8 solution containing 383 mM urea (reagent grade, Sigma-Aldrich), 272 mM CaCl<sub>2</sub>-2H<sub>2</sub>O (laboratory grade, Alfa Aesar) was used for the first application in each acrylic tube. Subsequent applications employed approximately 50 mL of a pH=7.6 solution containing 416 mM urea and 289 mM CaCl<sub>2</sub>-2H<sub>2</sub>O. Solution concentrations, while variable, were formulated within a reasonably similar range as a matter of convenience. In each application, the cementation fluid was poured into the top of the acrylic tube with the bottom closed off. The cementation fluid was allowed to stand, loosely covered, in the acrylic tube for at least 24 hours and then drained out the bottom of the cylinder. The next application followed immediately after drainage was complete. Drainage was accomplished by puncturing the base of the cylinder with a 20-gauge needle. When drainage was complete, the needle was removed and the puncture was plugged with a dab of silicone. Occasionally, the needle became plugged and an additional needle was inserted through the base. The triaxial columns were filled with sand in the same manner as tube 1 and then received 2 applications (each application ≈ 250 ml) of cementation solution with 1.4g/L enzyme.

In each application of cementation fluid, the fluid was added until it rose to approximately ½-inch (12-mm) above the soil line. After 2 applications, tubes #2 and #3 were allowed to air dry for several days and then analyzed. Experimentation with tube #1 was continued for several more days as three more batches of cementation fluid were applied. The last 2 applications of cementation fluid were allowed to slowly drain through the needle in the base immediately after application rather than sit for 24 hours (drainage rate ≈10-25ml/hour). The triaxial columns were allowed to stand for at least a week after the second cementation fluid application and then drained.

After drainage was complete, the triaxial columns were moved to a triaxial testing device. After draining the specimens from the acrylic tubes and after the completion of the triaxial tests, all samples were triple washed with de-ionized water. Tubes #2 and #3 were separated in 3 layers, while tube #1 was separated into six layers (for better resolution). Each layer from the specimens in the acrylic tubes and the entire mass of the triaxial specimens were acid washed to determine CaCO<sub>3</sub> content by oven drying for 48 hours, weighing, digesting with warm 1M HCl, washing, drying, and reweighing to determine carbonate mineral content.

Several of the cemented specimens were analyzed for mineral identification using X-Ray Diffraction (XRD). Samples were ground in an agate mortar and pestle and powdered onto a standard glass slide for analysis. Scanning electron microscopy (SEM) imaging was performed on intact cemented chunks of material with an Agilent 8500 Low-Voltage SEM (LV-SEM). A LV-SEM is a field emission scanning electron microscope capable of imaging insulating materials, such as organic and biological substances without the need for a metal coating and without causing radiation damage to samples.

### 2.2 Ottawa F-60 Sand

A triaxial column was prepared using Ottawa F-60 silica sand (mean grain size 0.275 mm, coefficient of uniformity 1.74) to

investigate enzymatic ureolytic  $\text{CaCO}_3$  precipitation in a finer grained material. The specimen was prepared in the same manner as described for the triaxial columns for the Ottawa 20-30 sand. The cementation fluid for the first of the two applications contained approximately 2.0 g/L enzyme, 400 mM urea (reagent grade, Sigma-Aldrich), 300 mM  $\text{CaCl}_2 \cdot 2\text{H}_2\text{O}$  (laboratory grade, BDH) at  $\text{pH}=7.7$ . The fluid for the second application contained 1 M urea- $\text{CaCl}_2 \cdot 2\text{H}_2\text{O}$  solution at  $\text{pH}=7.8$  without any enzyme. After the test, the triaxial specimen was washed and subject to acid digestion in the same manner as the Ottawa 20-30 triaxial specimens.

### 3. RESULTS

#### 3.1 Acrylic Tubes

Approximately 100 ml of cementation solution was delivered per application for the first application in each acrylic tube. However, the amount of solution the tube would accept was notably reduced in subsequent applications, when less than 75 ml was typically required to fill the tubes to  $\approx \frac{1}{2}$  inch (12 mm) above soil line. At the conclusion of the experiment, precipitation was visible along the entire length of tubes 1 and 2. Internally the cementation was variable, with some highly cemented zones and other zones with little to no cementation.

Tube 1 yielded mostly small, loose chunks of sand with strong effervescence upon digestion. Most of this column appeared un-cemented and exhibited unusually viscous behavior when wet. A fairly large (compared to column diameter) piece of strongly cemented sand (not breakable without tools) formed in the deepest layer of tube 1. Tube 2 had many small chunks of weakly cemented sand with strong effervescence upon digestion. Tube 3 had little to no precipitation in the top layer (i.e. this layer did not show any indication of carbonate upon acid digestion.) The deepest layer of tube 3 contained many pieces of weakly cemented sand that effervesced strongly upon digestion. The middle layer of tube 3 contained a few pieces of cemented sand that effervesced moderately upon digestion. The results from the acid washing are presented in Table 1.

Table 1. Results from *Experiment Set 1* using 20-30 Ottawa silica sand

Summary of Results					
Tube #	Layer	Weight Change via Digestion	Amt. of $\text{CaCO}_3$ (g)	Total Amt. $\text{CaCO}_3$ (g)	Theor. Max $\text{CaCO}_3$ (g)
1	1	11%	3.57	11.8	$\approx 14.5$
	2	3.8%	1.67		
	3	2.7%	1.73		
	4	2.1%	1.40		
	5	2.3%	1.74		
	6	2.0%	1.64		
2	1	0.76%	0.63	2.07	$\approx 4.35$
	2	0.65%	0.69		
	3	0.49%	0.75		
3	1	0.23%	0.31	3.57	$\approx 4.35$
	2	0.58%	0.63		
	3	1.7%	2.63		

The theoretical maximum  $\text{CaCO}_3$  content is the stoichiometric maximum balanced on initial concentrations. The primary experimental differences between the tests are (1) the number of applications of cementation fluid and (2) the manner in which the urease was delivered. The results indicate that there is greater carbonate precipitation with increasing number of applications, as expected. The data show more precipitation in (or on) the top layer of tubes 1 and 2 but not in tube 3, as the enzyme was physically confined to the lower-third layer in tube

3 during sample preparation. In the top layer of tube 3, where no urease was mixed with the sand, carbonate precipitation was nearly undetectable. There was no visual evidence of precipitation and practically no measurable change in weight of this layer after acidification (weight change = 0.23%). In the bottom layer of tube 3, where 3 g of dry enzyme was mixed with the soil, there was a weight change of 1.7% following acid washing. The middle layer of this specimen had a minor change in weight (0.58%), possibly due to uneven distribution of the layers during preparation or splitting of the specimen or to upward migration of urease from the bottom layer.

XRD analysis, presented in Figure 1, confirms that calcite is the mineral phase present in the cemented soil chunks. LV-SEM images, presented in Figure 2, show silica (quartz) sand particles cemented with calcium carbonate and various morphological features associated with the cementation process on the silica surface.

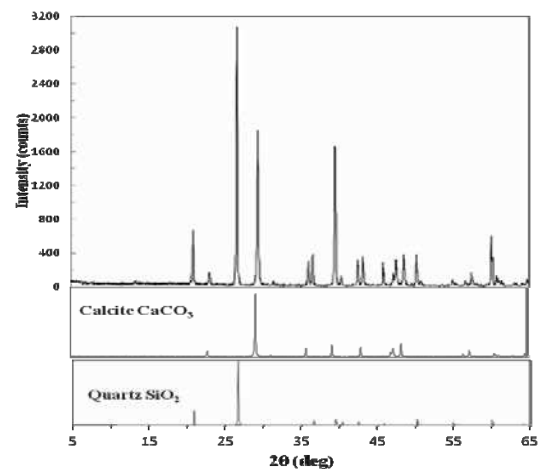


Figure 1. XRD results from cemented sand sample (top plot). Quartz & calcite standards (middle & bottom plot, respectively).

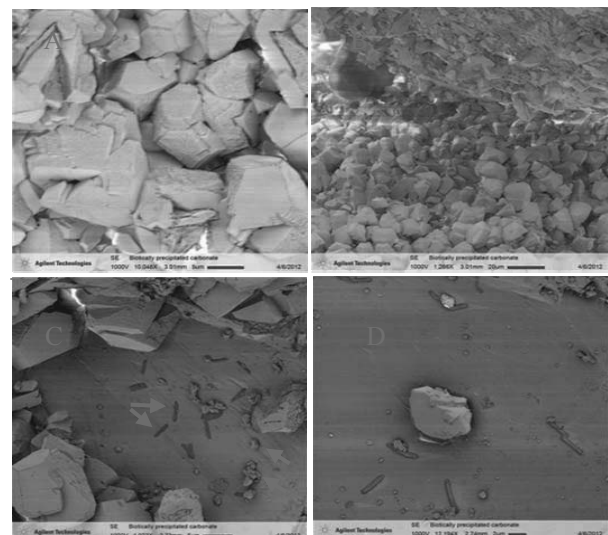


Figure 2. LV-SEM images a.) Well-grown and cementing calcite crystals; b.) Cementing calcite crystals at inter-particle contact; c.) Indentation of quartz surface (blue arrows) and nucleation of calcite crystals (red arrows); d.) Calcite crystal growing on quartz surface.

#### 3.2 Triaxial Columns

The three triaxial sand columns (2 Ottawa 20-30 sand columns and 1 Ottawa F-60 sand column) were tested in drained triaxial compression prior to acid digestion. All three columns were able to stand upright after removal of the split mold. The results

of the triaxial compression tests performed on the 20-30 Ottawa sand are presented in Figure 3 and the results for the F-60 Ottawa sand are presented in Figure 4. The carbonate cement content for one of the 20-30 silica sand columns was 2.0% CaCO<sub>3</sub> (by weight). The carbonate content of the other 20-30 Ottawa sand column could not be quantified due to unintended sample loss. The carbonate cement content for the finer grained F-60 Ottawa sand was 1.6% CaCO<sub>3</sub> (by weight). The results show substantial strength increase for all 3 sand columns tested.

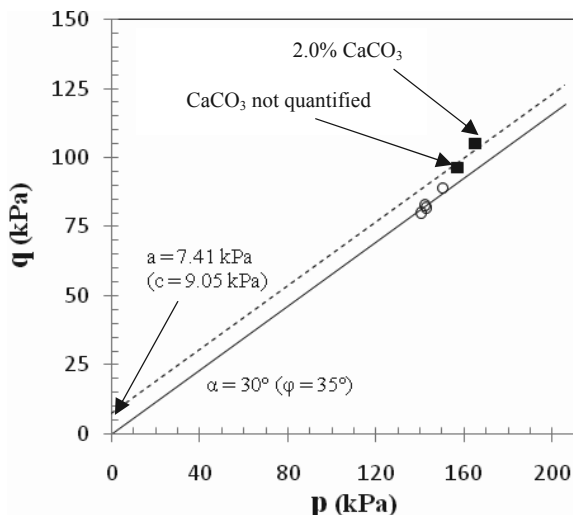


Figure 3. p-q plot failure envelopes for 20-30 silica sand: ■ Cemented ( $D_r = 60\%$ ); ○ Uncemented ( $D_r = 60\%$ )

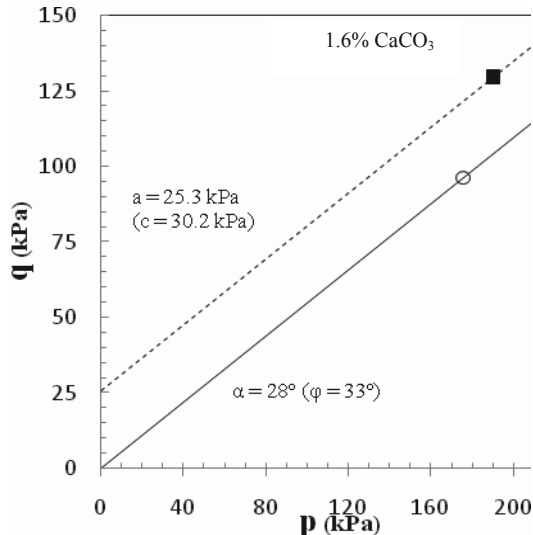


Figure 4. p-q plot failure envelopes for F-60 silica sand: ■ Cemented ( $D_r = 35\%$ ); ○ Uncemented ( $D_r = 37\%$ );

#### 4. CONCLUSION

Sand column tests at Arizona State University have shown that agriculturally-derived urease can be used to induce calcium carbonate precipitation in sand. Sand columns were developed using Ottawa 20-30 and F-60 sand and three different preparation methods: dry pluviation followed by percolation of a calcium-urease-urea cementation solution, pluviation into a calcium-urease-urea cementation solution, and mixing the sand with urease prior to pluviation with a calcium-urea solution. Cementation was observed in all of the columns. XRD and SEM testing confirmed that calcium carbonate (specifically calcite) was the cementing agent. Acid digestion showed that increased applications yielded correspondingly greater

carbonate precipitation. The quality of cementation, as determined by the effort needed to break apart cemented chunks of sand, varied depending on the sampling location within the column. Triaxial test results on cemented columns showed substantial strength increase over non-cemented columns at the same relative density.

#### 5. REFERENCES

- Baumert, K.A., Herzog, T., Pershing, J., 2005. Navigating the Numbers Greenhouse Gas Data & International Climate Policy *World Resources Institute*
- Blakely, R.L. and Zerner, B., 1984. Jack Bean Urease: The First Nickel Enzyme. *Journal of Molecular Catalysis* 23, 263–292.
- Burbank, M., Weaver, T., Lewis, R., Williams, T., Williams, B. and Crawford, R. 2012. Geotechnical Tests of Sands Following Bio-Induced Calcite Precipitation Catalysed by Indigenous Bacteria *ASCE JGGE* 132, DOI: 10.1061/(ASCE)GT.1943-5606.0000781.
- Chou, C.W., Seagren, E.A., Aydiyek, A.H., and Lai, M. 2011. Biocalcification of Sand through Ureolysis. *JGGE* 137, 1179–1189.
- Ciurli S., Marzadori C., Benini S., Deiana S. and Gessa C., 1996. Urease from the soil bacterium *Bacillus pasteurii*: Immobilization on Ca-polygalacturonate. *Soil Biol. & Biochem.* 28, 811-817.
- Das, N., Kayastha, A.M. and Srivastava, P.K., 2002. Purification and characterization of urease from dehusked pigeonpea (*Cajanus cajan* L.) seeds. *Phytochemistry* 61 (5), 513-521.
- DeJong, J.T., Fritzges, M.B., and Nusslein, K. 2006. Microbially Induced Cementation to Control Sand Response to Undrained Shear. *ASCE JGGE* 132, 1381–1392.
- DeJong, J.T., Mortensen, B.M., Martinez, B.C., and Nelson, D.C., 2010. Bio-mediated soil improvement. *Ecological Engineering* 197-210.
- Harkes, M. P., van Paassen, L. A., Booster, J. L., Whiffin, V. S., and van Loosdrecht, M. C. M. 2010. Fixation and distribution of bacterial activity in sand to induce carbonate precipitation for ground reinforcement. *Ecological Engineering* 36 (2), 112–117.
- Karatas, I., 2008. Microbiological Improvement of the Physical Properties of Soils. PhD. Dissertation, Department of Civil, Environmental, and Sustainable Engineering Arizona State University, Tempe, AZ.
- Kavazanjian, E. and Karatas, I., 2008. Microbiological Improvement of the Physical Properties of Soil, *6<sup>th</sup> International Conference on Case Histories in Geotech. Eng.*, Arlington, VA August 11-16.
- Krogmeier, M.J., McCarty, G.W. and Bremner, J.M., 1989. Phytotoxicity of foliar-applied urea. *Proc. Natl. Acad. Sci., USA* 86, 8189–8191.
- Marzadori, C., Miletto, S., Gessa, C. and Ciurli, S., 1998. Immobilization of jack bean urease on hydroxyapatite: urease immobilization in alkaline soils. *Soil Biol. & Biochem.* 30 (12), 1485-1490.
- Pettit N. M., Smith A. R. J., Freedman R. B. and Burns R. G., 1976. Soil urease: activity, stability, and kinetic properties. *Soil Biol. & Biochem.* 8, 479-484.
- Srivastava, P.K. and Kayastha, A.M., 2001. Characterization of gelatin-immobilized pigeon pea urease and preparation of a new urea biosensor. *Biotechnology and Applied Biochemistry* 34, 55-62.
- van Paassen, L.A., Ghose, R., van der Linden, T.J.M., van der Star, W.R.L., and van Loosdrecht, M.C., 2010. Quantifying Biomediated Ground Improvement by Ureolysis: Large-Scale Biogrout Experiment. *ASCE JGGE* 136, 1721–1728.
- van Paassen, L.A., Daza, C.M., Staal, M., Sorokin, D.Y. and van Loosdrecht, M.C., 2008. In situ soil reinforcement by microbial denitrification. *1st Int. Conf. on Bio-Geo-Civil Engineering*, Netherlands, 124-133, June 23-25.
- Whiffin, V.S., van Paassen, L.A., and Harkes, M.P., 2007. Microbial Carbonate Precipitation a Soil Improvement Technique. *Geomicrobiology* 24, 1-7.

# Experimental investigation on bearing capacity of geosynthetic encapsulated stone columns

## Étude expérimentale sur la capacité portante des colonnes de pierre géosynthétiques encapsulées

Hataf N., Nabipour N.

*Department of Civil and Environmental Engineering, Shiraz University, Shiraz, Iran*

**ABSTRACT:** Civil engineers have developed different soil improvement techniques in recent decades to improve the bearing capacity of soft soils loaded by foundations and reduce soil settlement. A method for increasing the bearing capacity of foundation soil is the use of stone columns. However, one of the major weaknesses in use of stone columns in loose soils is lack of confinement. Using geosynthetic reinforcement to compensate low confinement pressure in these soils, is a solution to this problem. This paper presents the results of an experimental study on the improvement of the bearing capacity of stone columns reinforced by geosynthetics. In this study the influences of three variables have been investigated, including: surrounding soil types (i.e. clay and sand), stone column aggregate size and length of reinforcement. Having mentioned these variables, the results showed that encapsulating stone column with geosynthetic is more effective in cohesive soil compared to granular soil. The results of the experiments revealed that the coarser the aggregate the better behavior is expected for the stone column. The results also showed that, reinforcing half height of stone columns is the optimal encapsulating length.

**RÉSUMÉ:** Ces dernières décennies, les ingénieurs civils ont développé différentes techniques pour l'amélioration de la capacité portante du sol mou ainsi que celles des fondations. Une des techniques couramment utilisée permettant l'augmentation de la capacité portante des sols et des fondations est l'utilisation des colonnes de pierre. Cependant, l'une des grandes faiblesses de l'utilisation de colonnes de pierre dans les sols mous est le manque de confinement. L'utilisation de renforts géosynthétiques permet de compenser pour la faible pression de confinement. Cet article présente les résultats d'une étude expérimentale sur l'amélioration de la capacité portante des colonnes de pierre renforcées par des méthodes géosynthétiques. Dans cette étude, l'influence de trois variables ont été étudiées, notamment: le type de sol environnant (i.e. argile et sable) ainsi que la longueur de l'armature de renforcement. Les résultats démontrent que l'emploi de la colonne en pierre avec encapsulation géosynthétique est plus efficace dans un sol consistant comparé aux sols granulaires. De plus, les résultats de ces expériences ont révélé que plus la rugosité de l'agrégat augmente, plus le comportement des colonnes de pierres est amélioré. Finalement, les résultats indiquent que la longueur d'encapsulation optimale est atteinte en renforçant la hauteur médiane des colonnes de pierre.

**KEYWORDS:** stone column, bearing capacity, geosynthetic, reinforcement.

### 1 INTRODUCTION.

In recent years with increasing in population density in specific locations, the value of land has increased significantly. This has made the use of areas with soft soils inevitable.

Due to the lack of bearing resistance in these soils, different methods of soil improvement techniques, including stone columns as a method of strengthening the loose soil are used.

Stone columns behavior has been studied experimentally, theoretically and numerically by many researchers (Bergado and Teerawattanasuk 2008, Guetif et al. 2007, Castro and Sagasetta 2011)

However, one of the major weaknesses in use of stone columns in loose soils is lack of confinement. This leads researchers and practitioners to use geosynthetics to increase confinement of column, compensating the scarcity of studding around reinforced stone columns (Malarvizhi and Ilamparuthi 2007, Gniel and Bouazza 2009, Gniel and Bouazza 2010). In this study the parameters affecting the behavior of reinforced stone columns have been investigated. These parameters are reinforced length, column material and surrounding soil type.

### 2 LABORATORY SETTINGS

Since the focus of this research was on the laboratory results, the physical model, is described, firstly.

#### 2.1 Test apparatus

A cylindrical tank (height=1.0 m and dia.=1.0m) filled with soil was used as the soil environment. Stone column run in the middle of the tank. The static loading system consists of a loading arm and weights were used (Razavi and Hataf, 2003) to determine the bearing capacity of a circular foundations resting on stone column, Figure 1.

#### 2.2 Soil tested

To test and evaluate the behavior of reinforced stone columns in loose soil, two soil types were used, a clay soil as cohesive soil and a sandy soil as granular soil.

Physical properties of the soils are listed in Table 1.

#### 2.3 Specimens preparation

To prepare the soil and column, first two 10 cm soil layers has been poured in the tank and compacted using 20 strokes caused by dropping a 50 N weight attached to a wooden handle from a distance of 40 cm as the substrate layer. The next layers were compacted with 10 strokes from 10cm distance to provide loose soil.

To prepare the stone column an open ended hollow cylindrical pipe with a diameter of a little more than the diameter of the stone column was used. After that the cylinder was placed at its position and the surrounding was filled slowly with soil.



Figure 1. Laboratory setting for model testing.

Table 1. Physical properties of the soils tested.

Parameter	Clay	Sand
Friction Angle	26.0	35.0
Cohesion (KN/m <sup>2</sup> )	5.0	0.0
Unit weight(KN/m <sup>3</sup> )	15.0	16.0
Liquid Limit(%)	44.5	-
Plasticity Index (%)	20.0	-

Then until reaching up to the surface level the stone column filled with stone aggregates in 10 cm layers. After filling each layer the cylinder pulled out about 10 cm and aggregates were poured in and compacted with 40cm length rod.

Three types of aggregates were used to fill the stone columns. These are shown in Figure 2.

Stone columns with no reinforcement, half-length reinforcement and full-length reinforcement were prepared for testing. A commercially available geogrid was used for reinforcement.

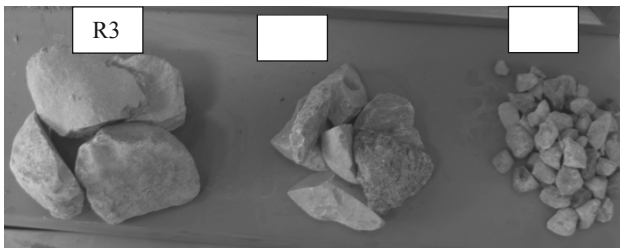


Figure 2. Different aggregates used as stone columns materials.

### 3 TEST RESULTS

Test results as load settlement curves for stone columns embedded in cohesive and granular soils are illustrated in Figures 3 and 4. In this figures f-Ri, h-Ri and no-Ri stand for full-length, half-length and no reinforced column, respectively.

Loads were normalized to maximum load obtained for unreinforced column in each case and settlements were normalized to radius of stone column.

As it can be seen from these figures it is obvious that reinforcement improve the bearing capacity of stone columns in both cohesive and granular soils. The reinforcement however is more effective in cohesive soil than in granular soil.

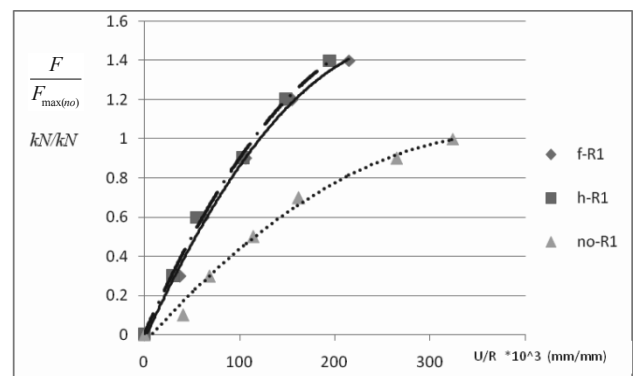
Further numerical studies (not presented here) showed that the effect of viscosity is reduced with the increase in cohesion of soil which in turn caused increase in the confining pressure of surrounding soil. Therefore this results in decrease in stone column material to spread out within the surrounding soil.

The most important variable in this study was to experimentally and practically examine the optimal length of

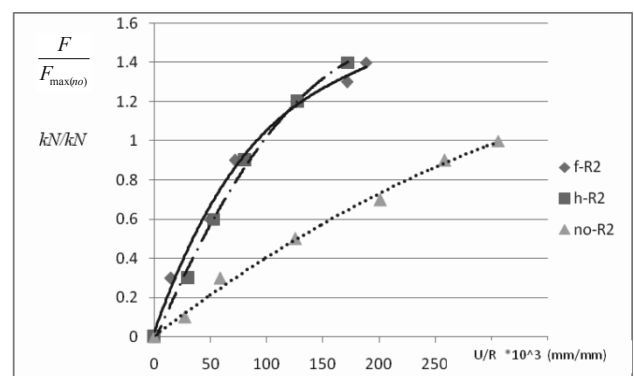
reinforcement for optimal strength. This was achieved by changing the length of reinforcement compared to the column length as full-length, half-length and non-reinforced.

Test results indicated that in both types of surrounding soils and for all sizes of column aggregate materials, it is enough to reinforce only half length of the column to achieve desired bearing improvement. However the Improvement rate in cohesive soils is more noticeable. This can be related to the fact that the confining pressure in the bottom of the column is higher than that in the upper parts of the column due to higher overburden pressure. By increasing the confining pressure in the upper parts of the column by installing reinforcement, the radial strain reduces and as the result, it reduces the side contact pressure between the soil and stone column. This in turn causes just vertical distribution of the stresses to the layer below the column and not distributing of stresses to the surrounding soil. This obviously causes more vertical deflections in the below layers of soil and less in the upper layers.

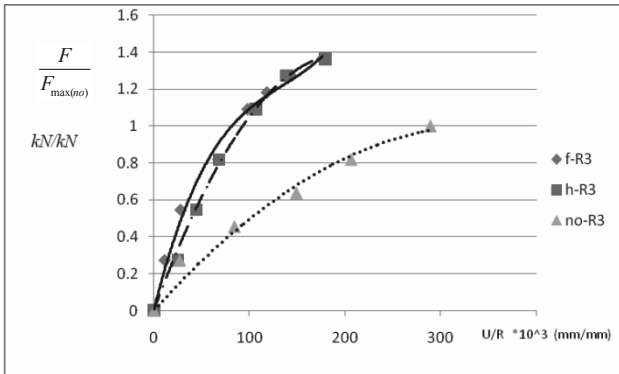
In the half-length reinforced column by increasing in stresses, a small amount of inflation on the side layers are observed which results in increase in lateral soil friction and so the stresses spreads over a larger surface of the soil and it results the deflection not to increase below the column but spread in larger area homogeneously.



3-a fine aggregate material

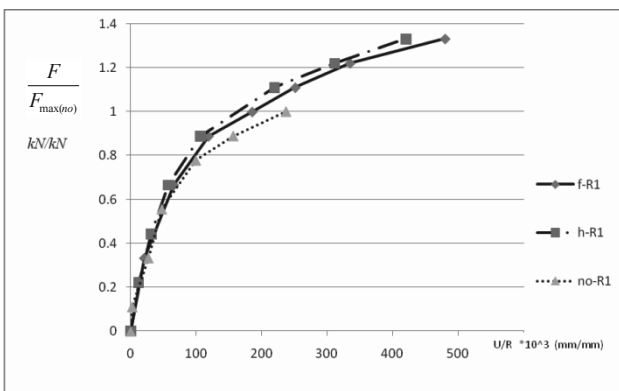


3-b medium aggregate material

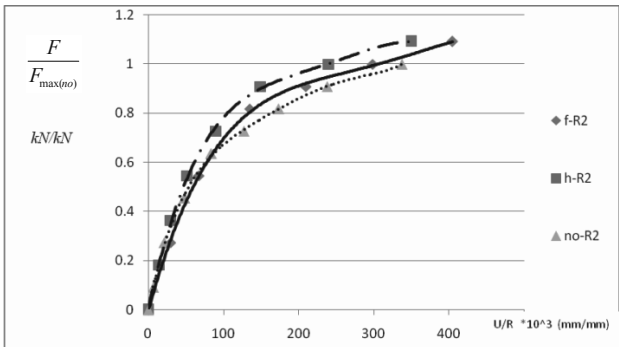


3-c coarse aggregate material

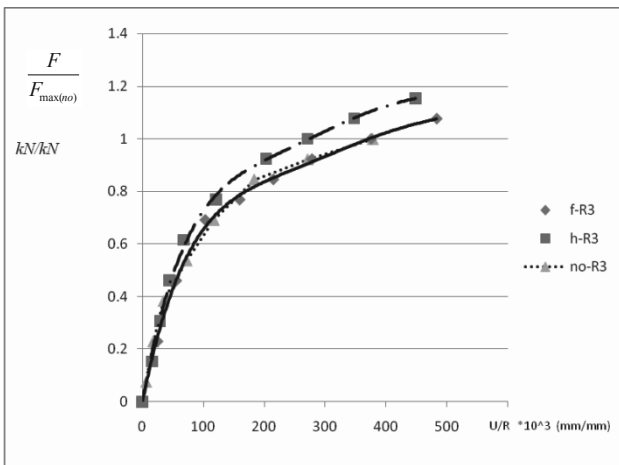
Figure 3. Test results for stone columns embedded in cohesive soil.



4-a fine aggregate material



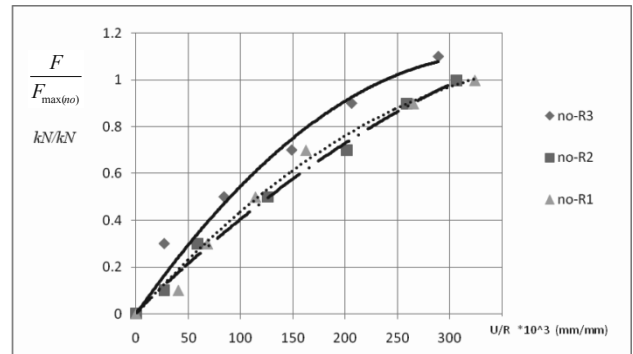
4-b medium aggregate material



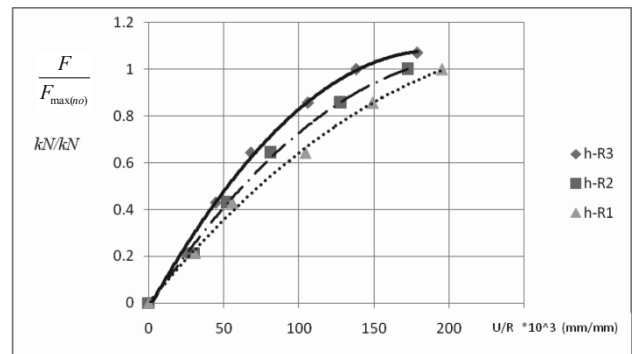
3-c coarse aggregate material

Figure 4. Test results for stone columns embedded in granular soil.

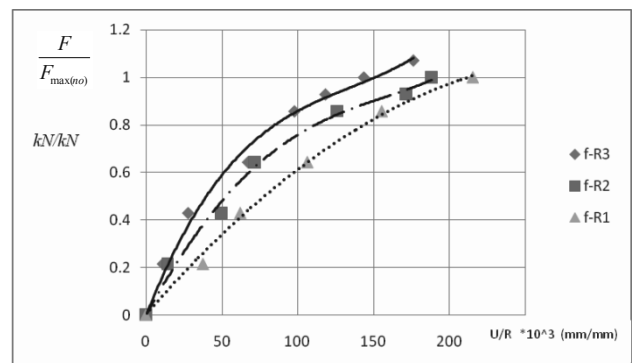
As it was mentioned earlier one of the variables in this study was the size of the column aggregate materials. The results of tests on the same stone column conditions but with different size of stone column materials are illustrated in Figure 5 and 6 for cohesive and granular surrounding soils, respectively. It can be seen that keeping all conditions constant, there was an increase in bearing resistance of the column with increasing grain size dimension of column material. However the improvement due to the use of geosynthetic reinforcement was the same for all column material sizes.



5-a non-reinforced stone column

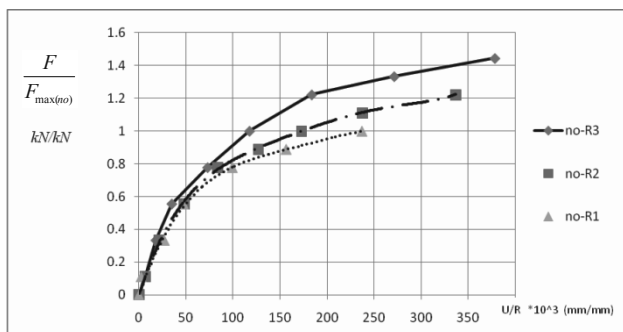


5-b half-length reinforced column

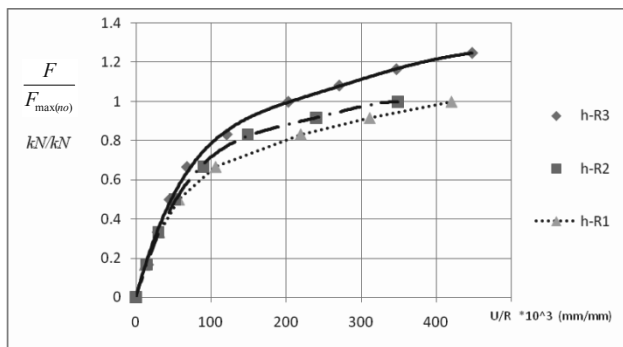


5-c full-length reinforced column

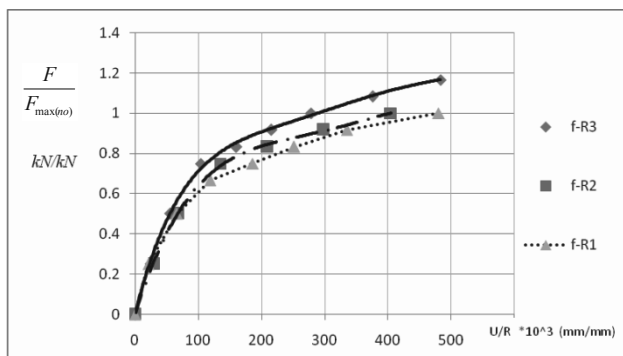
Figure 5. Test results for different stone columns materials embedded in cohesive soil.



6-a non-reinforced stone column



6-b half-length reinforced column



6-c full-length reinforced column

Figure 6. Test results for different stone columns materials embedded in granular soil.

#### 4 CONCLUSION

One of the recent methods for increasing the bearing capacity of foundation soil is the use of vertical stone columns. Stone columns consist of a stiffer material or aggregates, compared to the surrounding soils, which are usually vibrocompacted into the soil. These columns increase the bearing capacity of the soil significantly. Compared to concrete or steel piles inclusion, for soil improvement, this technique is more economical and needs to be studied further. However, one of the major weaknesses in use of stone columns in loose soils is lack of confinement. This leads to use reinforcement to compensate low confinement pressure in these soils. Because of the lack of experimental studies on the behavior of reinforced stone columns, an experimental study has been performed. It was shown that the use of stone columns improves the soil bearing capacity, significantly. The results showed that encapsulating stone column with geosynthetic is more effective in cohesive soils compared to granular soils. Three types of stone column materials were used with different aggregate dimensions. The results of the experiments revealed that the coarser the aggregate the better behavior is expected for the stone column. Although the increase in grain size should not be more than two percent of stone column diameter. On the other hand, the

behavior of stone column encapsulated by geosynthetic in its entire length was compared to partially encapsulated stone column behavior. The results showed that, reinforcing half height of stone columns in both types of soils, especially in clay, is the optimal encapsulating length. This finding is significant regarding the economical and efficiency of use of stone columns as a soil improvement technique.

#### 5 REFERENCES

- Bergado, D.T. and Teerawattanasuk, C. 2008. 2D and 3D numerical simulations of reinforced embankments on soft ground. *Geotextiles and Geomembranes*, 26, 39–55.
- Castro, J., Sagaseta, C. 2011. Consolidation and deformation around stone columns: Numerical evaluation of analytical solution. *Computers and Geotechnics* 38,354–362.
- Guetif, A. Z., Bouassida, M., Debats, J. M. 2007. Improved soft clay characteristics due to stone column installation. *Computers and Geotechnics* 34,104–111.
- Gniel, J., and Bouazza, A. 2009. Improvement of soft soils using geogrid encased stone columns. *Geotextiles and Geomembranes* 27, 167–175.
- Gniel, J., and Bouazza, A. 2010. Construction of geogrid encased stone columns: A new proposal based on laboratory testing. *Computers and Geotechnics*, 28, 108–118.
- Hataf, N. and Razavi, M. R., 2003. Model Test and Finite Element Analysis of Ring Footings on Loose Sand. *Iranian J. of Science & Technology*, 27(B1), transaction B, 1-11.
- Malarvizhi, S. N. and Ilamparuthi, K. 2007. Comparative study on the behaviour of encased stone column and conventional stone column. *Soils and Foundations*, 47 (5), 873–885.

# Performance and Prediction of Vacuum Consolidation Behavior at Port of Brisbane

## Avantages et prédictions de comportement due a la consolidation sous vide au port de Brisbane

Indraratna B., Rujikiatkamjorn C., Geng X.

*Centre for Geomechanics and Railway Engineering, University of Wollongong, Wollongong City, NSW Australia, ARC Centre of Excellence in Geotechnical Science and Engineering, Australia*

Ameratunga J.

*Coffey Geotechnics, 47 Doggett Street, Newstead, QLD. 4006, Australia*

**ABSTRACT:** Due to a projected increase in trade activities at the Port of Brisbane, new berths on Fisherman Islands at the mouth of the Brisbane River will be constructed in the outer area (235ha) close to the existing port facilities via land reclamation. A vacuum assisted surcharge load in conjunction with prefabricated vertical drains was chosen to reduce the required consolidation time. The features of the combined vacuum and surcharge fill system and the construction of the embankment are described in this paper. A comparison of the performance of the vacuum combined surcharge loading system with a standard surcharge fill emphasizes the obvious advantages of vacuum consolidation. Field data is presented to show how the embankment performed during construction. An analytical solution for radial consolidation incorporating both time-dependent surcharge loading and vacuum pressure is employed to calculate the settlements and associated excess pore pressures of the soft Holocene clay deposits.

**RÉSUMÉ :** L'augmentation des activités de commerce au port de Brisbane nécessite la construction, à proximité des terminaux existants, de nouveaux postes de quais dans les îles Fisherman à l'embouchure de la rivière de Brisbane sur une superficie de 235 Ha gagnée sur la mer. Un chargement sous vide contrôlé, associé à des drains préfabriqués, a été appliqué pour réduire le temps de consolidation. L'article décrit les caractéristiques de la technique de consolidation sous vide associée au chargement par remblaiement et la construction du remblai. Une comparaison entre la consolidation sous vide associée au remblaiement et le pré chargement classique montre clairement les avantages en faveur de la consolidation sous vide. Les données enregistrées sur le site illustrent le comportement du remblai durant la consolidation. Une solution de consolidation horizontale tenant compte du chargement et de la pression sous vide est présentée en vue de prédire le tassement et l'excès de la surpression interstitielle du dépôt d'argile molle de l'Holocène.

**KEYWORDS:** consolidation, soil improvement, vertical drains, vacuum.

## 1 INTRODUCTION

The Port of Brisbane is one of the Australia's largest commercial ports located at the entrance of the Brisbane River at Fisherman Islands. With demand in commercial activities, a new outer area (235ha) is being reclaimed for major expansion to maximise the available land, and to provide the maximum number of berths suitable for container handling for servicing regional importers and exporters. In this area, the soil profile mainly consists of compressible clay deposits over 30m in thickness with very low undrained shear strength (<15 kPa at shallow depth). The strength of dredged mud had a much lower strength depending on the placement time and the thickness of capping material. Without surcharge preloading, it is estimated that the consolidation time could be more than 50 years with overall settlements of 2.5-4.0m. Therefore, vacuum consolidation with prefabricated vertical drains (PVDs) was suggested to accelerate the consolidation process and to minimise lateral deformation adjacent to the Moreton Bay Marine Park (Indraratna et al. 2011).

The effectiveness of the vacuum preloading assisted by PVDs has been illustrated by Chu et al. (2000) and Chai et al. (2005). In this technique, vacuum pressure can propagate to a greater depth of the subsoil via PVD length. Also, extended consolidation time due to stage construction can be minimized (Indraratna et al. 2005). The surcharge fill height can be reduced by several metres, if a vacuum pressure (at least 70 kPa) is applied and sustained (Rujikiatkamjorn et al. 2008). The embankment construction rate can be increased and the number of construction stages can be reduced (Yan and Chu 2003). Once the soil has increased its stiffness and shear strength due to consolidation, the post-construction settlement will be significantly less, thereby eliminating any risk of differential settlement of the overlying infrastructure (Shang et al. 1998). To the authors' knowledge, there is no comprehensively

reported case history where both the conventional surcharge preloading and vacuum technique have been applied in the same area with distinct variation of drain types and spacing.

In this paper, the performance between the vacuum and non-vacuum areas has been compared based on the measured settlements, excess pore pressures and lateral displacements. The influences of drain spacing, drain types and type of soil improvement are discussed based on the observed degree of consolidation. The analytical solutions for radial consolidation considering both time dependent surcharge loading and vacuum pressure are proposed to predict the settlement and associated excess pore pressure.

## 2 GENERAL DESCRIPTION OF EMBANKMENT CHARACTERISTICS AND SITE CONDITIONS

At the Port of Brisbane, to evaluate the performance of the vacuum consolidation system with the non-vacuum system (PVD and surcharge load), a trial area (S3A) shown in Fig. 1 was partitioned into WD1-WD5 (Non-vacuum areas) and VC1-VC2 (Vacuum areas). After placing the dredged fill, the mud was capped off with a 2-3m layer of dredged sand, which acted as a working platform for PVD installation machine, whilst serving as a drainage layer.

The upper Holocene sand beneath the reclaimed dredged mud was about 2m thick, followed by the Holocene clay layer with different in thickness from 6m to 25m. A Pleistocene deposit containing highly over-consolidated clay underlies the softer Holocene clay layer. Site investigation techniques including cone penetration/piezcone tests, dissipation tests, boreholes, field vane shear tests and oedometer tests were carried out to assess the relevant consolidation and stability design parameters. The water contents of the soil layers were similar to or exceed their liquid limits. The vane tests show that the undrained shear strength of the reclaimed dredged mud and



the Holocene clays were from 5 to 60 kPa. The compression index changed from 0.1 to 1.0. The coefficient of consolidation in vertical direction is similar to that in horizontal direction ( $c_h$ ) for the remoulded dredged mud layer, while  $c_v/c_h$  is about 2 for the Holocene clay layer.

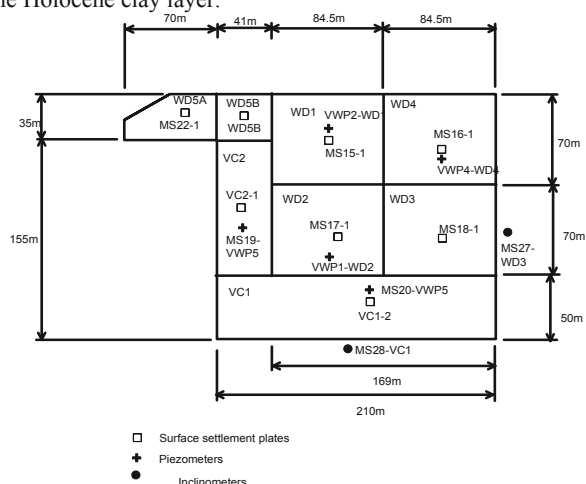


Figure 1. Site layout for S3A with instrumentation plan

The surcharge preloading system was adopted for the inner areas (WD1-WD5) while, in the outer area (VC1 and VC2) close to the Marine Park, the technique of vacuum combined preloading was selected to control lateral displacement in order to minimise disturbance of the nearby marine habitats. Stringent design criteria were adopted for the design and construction of embankment over the soft Holocene deposits: (a) Service load of 15-25 kPa, (b) maximum residual settlement less than 250 mm over 20 years after treatment. The surcharge embankment heights varied from 3.0m to 9.0m. Based on the design criteria, Table 1 presents the PVD characteristics and treatment types applied to each section. In the non-vacuum areas, both circular and band shape drains were established in a square pattern at a spacing in the range of 1.1-1.3m. The length of PVDs changed from 6m to 27.5m across the site as shown in the Table 1. Table 1. PVD characteristics and improvement scheme

	Drain type	Drain spacing	Fill height (m)	Treatment scheme
WD1	Circular drains	1.1	5.2	Surcharge
WD2	Circular drains	1.3	7-7.2	Surcharge
WD3	Band drain Type -A	1.1	4.3-4.6	Surcharge
WD4	Band drains Type -A	1.3	6.1	Surcharge
WD5A	Band drains Type -B	1.2	3.3	Surcharge
WD5B	Band drains Type -B	1.1	5.5	Surcharge
VC1	Circular drains	1.2	3.2	Surcharge+ vacuum
VC2	Circular drains	1.2	2.8	Surcharge+ vacuum

The inevitable variation in drain lengths was attributed to the non-uniform clay thickness. Wick drains (Band Drain Type-A and Band Drain Type-B) had dimensions of 100mm x 4mm, and the circular drains had an internal diameter of 34mm. The Authors have deliberately omitted the commercial brand names of all PVDs used. To monitor the ground behaviour, comprehensive instruments were installed e.g. settlement plates, vibrating wire piezometers, magnetic extensometers, and inclinometers. In the vacuum area, only circular drains were employed at a spacing of 1.2m in conjunction with a High Density Polyethylene (HDP) membrane, horizontal perforated

pipes and the pumps that represent the vacuum system. The horizontally pipes offered the desired uniform distribution of suction beneath the membrane. The measured suction varied from 60 kPa to 75 kPa, and no air leaks were observed during vacuum application that ensured the intact seal provided by the membrane. A vacuum pressure of 70kPa was applied after 40 days.

### 3 INTERPRETATION OF FIELD RESULTS

The embankment performances including settlements and excess pore pressures together with the staged construction of the embankments are depicted in Fig. 2. It would be observed that the trends are very comparable where the settlement occurred more quickly at the early stage of consolidation. The amount of final settlement depends on the clay thickness and embankment height. The highest settlement was measured in the WD4 area having the greatest clay thickness (19-26m), whereas the lowest settlement was in the WD5A area in which the clay layer was relatively thin (8-12m).

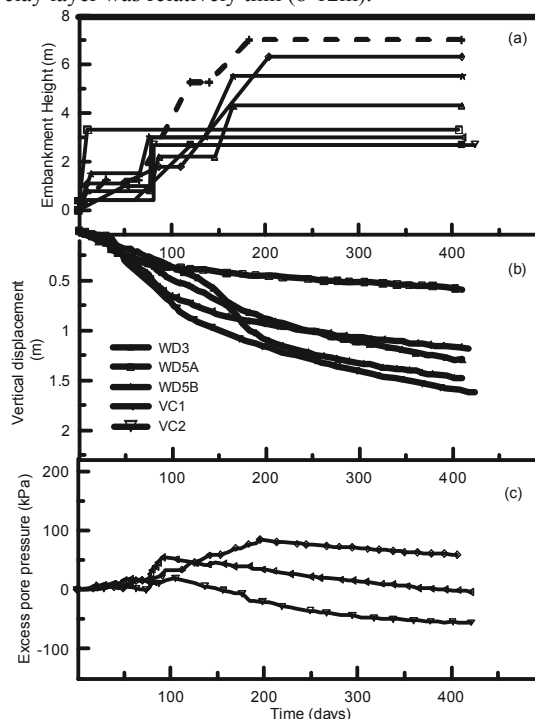


Figure 2. Embankment responses (a) staged construction, (b) settlements and (c) excess pore pressures

The measured lateral displacement normalized to total change in applied stress (vacuum plus surcharge load) for two inclinometer locations is shown in Fig. 3. For WD3 area, the total surcharge height was 90 kPa, whereas for VC1 area the reduced surcharge pressure of 40 kPa was complemented with a vacuum pressure of 65 kPa. The lateral displacements clearly lessen in the Holocene sand due to its greater stiffness. Fig. 3 indicates that the lateral movements are effectively controlled to minimise the disturbance in the adjacent Moreton Bay Marine Park, due to the isotropic consolidation by vacuum pressure.

### 4 SETTLEMENT AND EXCESS PORE PRESSURE PREDICTIONS

In order to analyse the radial consolidation caused by vertical drains, the unit cell theory has been employed to predict the settlement and excess pore pressure. A unit cell theory was introduced by Barron (1948) and Richart (1957) for surcharge preloading alone. Lekha et al. (1998) further extended the radial consolidation by including time-dependent surcharge loading. Indraratna et al. (2005) introduced the unit cell analysis for vacuum preloading under instantaneous loading while Geng et al. (2012) proposed analytical solutions under time-dependent

surcharge preloading. During embankment construction, the surcharge fill is increased at a prescribed rate to reach the desired height. Therefore, the time-dependent loading due to the filling would be more realistic than an instantaneous loading, especially during the stages of embankment construction. In this section, the embankment load is assumed to be a ramp loading: i.e., the embankment load ( $\sigma_t$ ) increases linearly with time up to a maximum value ( $\sigma_1$ ) within time  $t_0$  and is constant thereafter (Fig. 4a). The vacuum is applied at  $t=t_{vac}$ . Figure 4b shows the unit cell adopted for analytical solutions with boundary conditions (Fig. 4c).

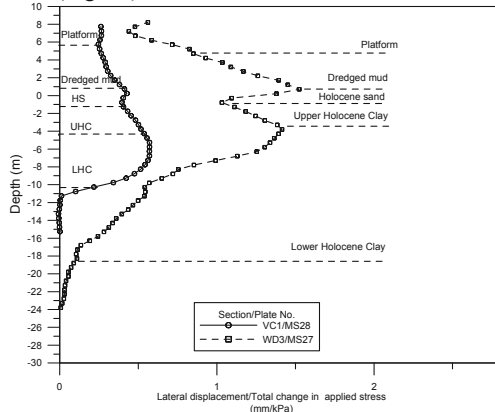


Figure 3. Comparison of lateral displacements at the embankment toe in vacuum and non-vacuum area after 400 days (Indraratna et al. 2011)

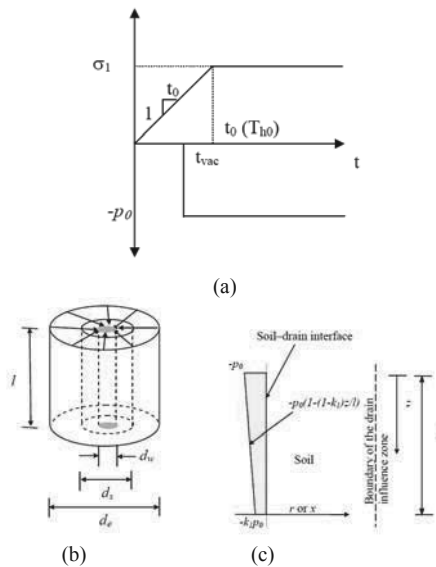


Figure 4. (a) time-dependent surcharge loading, (b) unit cell including smear zone, and (c) boundary conditions with vacuum distribution (after Indraratna et al. 2011)

The excess pore pressure due to radial consolidation considering smear effect under time-dependent surcharge can be expressed by (Indraratna et al. 2011):

$$\bar{u}_L = \frac{\mu d_e^2}{8c_h t_0} \left( 1 - \exp\left(\frac{-8c_h t}{\mu d_e^2}\right) \right) \sigma_1 \quad \text{for} \quad 0 \leq t \leq t_0 \quad (1)$$

$$\bar{u}_L = \frac{\mu d_e^2}{8c_h t_0} \left( 1 - \exp\left(\frac{-8c_h t_0}{\mu d_e^2}\right) \exp\left(\frac{-8c_h (t - t_0)}{\mu d_e^2}\right) \right) \sigma_1 \quad \text{for} \quad t > t_0 \quad (2)$$

Recently, Indraratna et al. (2005) proposed that the excess pore pressure dissipation due to vacuum pressure alone could be determined from:

$$u_{vac} = 0, \quad t < t_{vac} \quad (3)$$

$$u_{vac} = p_0 \exp\left(\frac{-8c_h (t - t_{vac})}{\mu d_e^2}\right) - p_0, \quad t \geq t_{vac} \quad (4)$$

$$\mu = \left[ \ln\left(\frac{n}{s}\right) + \frac{k_h}{k_s} \ln(s) - \frac{3}{4} + \pi \frac{2k_h}{3q_w} l^2 \right] \quad (5)$$

$$n = d_e / d_w \quad (6)$$

$$s = d_s / d_w \quad (7)$$

where,  $d_e$  = the diameter of soil cylinder dewatered by a drain,  $d_s$  = the diameter of the smear zone,  $d_w$  = the equivalent diameter of the drain,  $k_s$  = horizontal soil permeability in the smear zone and  $q_w$  = drain discharge capacity.

The excess pore pressure at a given time  $t$  can be calculated based on the Equations (2) to (7). For normally consolidated clay, the settlement ( $\rho$ ) can now be determined by the following equation:

$$\rho = \frac{HC_c}{1 + e_0} \log\left(\frac{\sigma'}{\sigma'_i}\right) \quad (8)$$

where,  $\rho$  = settlement at a given time,  $C_c$  = compression index, and  $H$  = compressible soil thickness.

In order to calculate excess pore pressures and associated settlements, Equations (1)-(8) are employed using parameters in Table 2. For the completely remoulded dredged mud that was reclaimed from the seabed and the Upper Holocene Sand the ratio  $k_h/k_s$  was assumed to be unity. For the upper and lower Holocene clay, the ratios of  $k_h/k_s$  and  $d_s/d_w$  were 2 and 3, respectively, in accordance with the laboratory observation described by Indraratna and Redana (1998).

The embankment load was applied according to a staged construction (unit weight of  $20 \text{ kN/m}^3$ ). Settlement and associated excess pore pressure predictions were calculated at the embankment centreline using Eqs. 1-8. It is noted that, at the beginning of each subsequent stage, the initial in-situ effective stress was calculated based on the final degree of consolidation of the previous stage. In vacuum areas, a suction pressure of 65 kPa was employed.

Figures 5 and 6 present the predicted settlement and associated excess pore pressure with the measured data in Areas WD1 and VC1, where the total applied load (vacuum and surcharge = 120-130kPa) and clay thickness (20-23m) are comparable. Overall, the comparisons between prediction and field observation show that the settlement and associated pore water pressure can be predicted very well. In vacuum areas, the degree of consolidation was more than 90% after 13 months, whereas that in the non-vacuum area was less than 85%. This confirms that, at a given time, the vacuum combined preloading would speed up consolidation compared to a surcharge preloading alone. This is because in non-vacuum areas, a staged embankment construction had to be adopted to avoid any undrained failure in the remoulded dredged layer.

Table 2. Soil properties for each layer

Soil layer	Soil type	$C_c/(1+e_0)$	$c_h$ (m <sup>2</sup> /yr)	$k_h/k_s$	$s=d_s/d_w$
1	Dredged Mud	0.235	1	1	1
2	Upper Holocene Sand	0.01	5	1	1
3	Upper Holocene Clay	0.18	2	2	3
4	Lower Holocene Clay	0.2	1.9	2	3

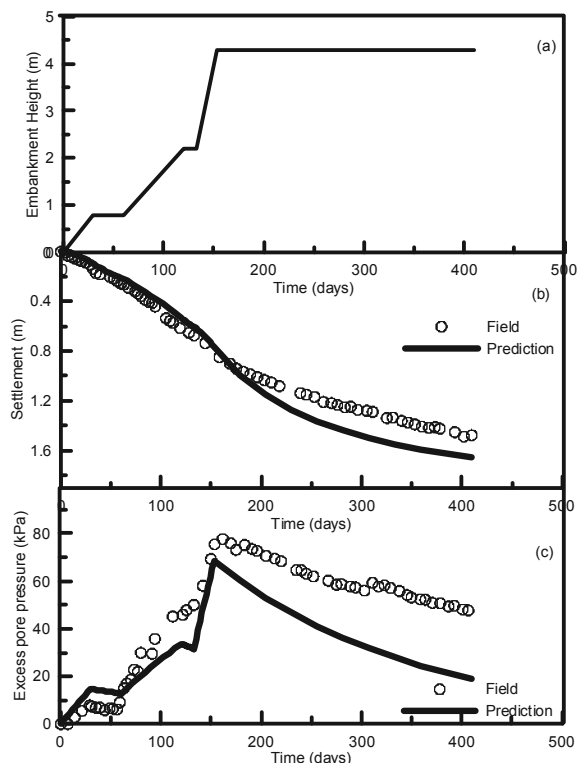


Figure 5. WD1 area: (a) stages of loading, (b) surface settlements at the embankment centreline and (c) excess pore pressures at 9.2m deep

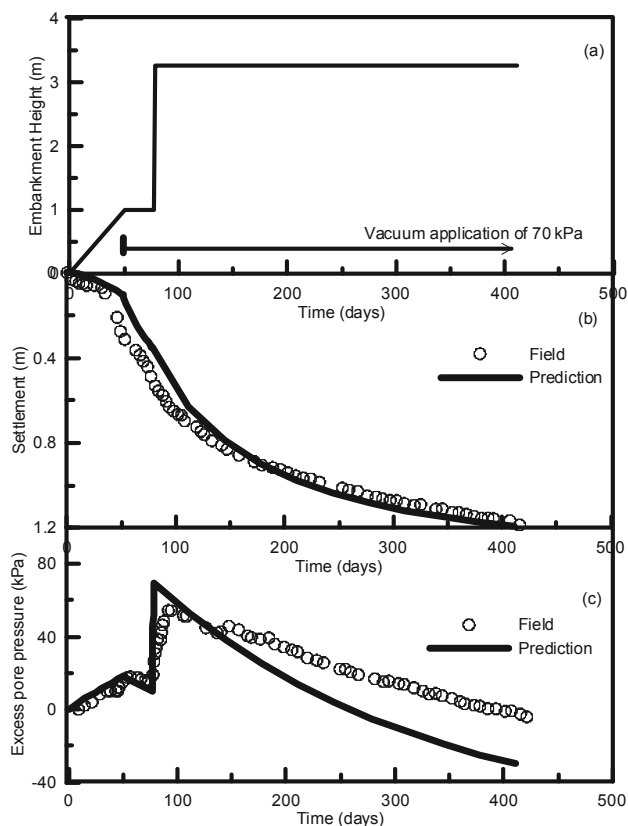


Figure 6. VC1 area: (a) stages of loading, (b) surface settlements at the embankment centreline and (c) excess pore pressures at 14.1m deep (Indraratna et al. 2011)

5 CONCLUSIONS

A system of vertical drains with vacuum preloading is an effective method for speeding up soil consolidation. The performance of 2 treatment schemes at the Port of Brisbane was

analysed and discussed. The dredged materials from the seabed were placed in the reclaimed area. A total of 8 areas were selected to examine the performance of vacuum consolidation, and the vertical drain spacing varied from 1-1.3m for 3 different drain types. The vacuum application induces an inward lateral movement, whereas the conventional surcharge fill creates outward movement. When the vacuum pressure combined with surcharge fill is employed, the overall lateral movement is decreased due to the isotropic consolidation induced by vacuum pressure. From a stability point of view, vacuum pressure reduces the ratio of lateral displacement to surcharge fill height at any given time.

The unit cell theory considering time-dependent surcharge load and vacuum application was employed to predict the settlement and associated excess pore pressure, which provided a good agreement with the field measurements. After 1 year, the degree of consolidation in the vacuum areas was much higher than the non-vacuum areas for the same total stress.

6 ACKNOWLEDGEMENTS

Writers acknowledge the support of the Port of Brisbane Corporation, Coffey Geotechnics and Austress Menard. The research funding from the Australia Research Council is acknowledged. The assistance of Prof. A.S. Balasubramaniam of Griffith University, Daniel Berthier of Austress Menard, Prof Harry Poulos, Cynthia De Bok, Tine Birkemose and Chamari Bamunawita of Coffey Geotechnics is appreciated. Most of the contents reported in this paper are also described in greater detail in a number of and ASCE Journal of Geotechnical and Geoenvironmental Engineering.

7 REFERENCES

Barron, R. A. 1948. The influence of drain wells on the consolidation of fine-grained soils. Diss., Providence, U S Eng. Office.  
 Chai, J.C., Carter, J.P., and Hayashi, S. 2005. Ground deformation induced by vacuum consolidation. *Journal of Geotechnical and Geoenvironmental Engineering*, 131(12):1552-1561.  
 Chu, J. Yan, S.W., and Yang, H. 2000. Soil improvement by the vacuum preloading method for an oil storage station. *Geotechnique*, 50(6): 625-632.  
 Geng, X. Y., Indraratna, B. and Rujikiatkamjorn, C. (2012). Analytical solutions for a single vertical drain with vacuum and time-dependent surcharge preloading in membrane and membraneless systems. *International Journal of Geomechanics*, ASCE, 12(1), 27-42.  
 Indraratna, B., and Redana, I. W. 1998. Laboratory determination of smear zone due to vertical drain installation. *J. Geotech. Eng., ASCE*, 125(1): 96-99.  
 Indraratna, B., Sathananthan, I., Rujikiatkamjorn C. and Balasubramaniam, A. S. 2005. Analytical and numerical modelling of soft soil stabilized by PVD incorporating vacuum preloading. *International Journal of Geomechanics*, 5(2). 114-124.  
 Indraratna, B., Rujikiatkamjorn, C., Ameratunga, J., and Boyle, P. 2011. Performance and Prediction of Vacuum Combined Surcharge Consolidation at Port of Brisbane. *J. of Geotechnical & Geoenvironmental Engineering*, ASCE, 137 (11), 1009-1018.  
 Richart, F.E. 1957. A review of the theories for sand drains. *Journal of the Soil Mechanics and Foundations Division*, ASCE, 83(3): 1-38.  
 Rujikiatkamjorn, C., Indraratna, B. and Chu, J. 2008. 2D and 3D numerical modeling of combined surcharge and vacuum preloading with vertical drains. *International Journal of Geomechanics*, 8(2): 144-156.  
 Shang, J.Q., Tang, M., and Miao, Z. 1998. Vacuum preloading consolidation of reclaimed land: a case study. *Canadian Geotechnical Journal*, 35: 740-749.  
 Yan, S.W. and Chu, J. 2003. Soil improvement for a road using a vacuum preloading method. *Ground Improvement*, 7(4): 165-172.

# Improvement of a Clay Deposit using Prefabricated Vertical Drains and Pre-loading. A Case Study

Amélioration d'un massif d'argile à l'aide de drains verticaux préfabriqués et de pré-chargement. Une étude de cas

Islam M.S., Yasin S.J.M.

Bangladesh University of Engineering and Technology, Dhaka, Bangladesh

**ABSTRACT:** Construction of a Container Terminal covering an area of 153,000 m<sup>2</sup> is underway at Chittagong sea port in Bangladesh, situated on the right bank of the Karnaphuli river at its confluence with the Bay of Bengal. The sub-soil at the site consisted of a 4 to 6 m thick clay layer with random zones of soft to stiff clay (CL). This was underlain by a 10 m thick loose to medium dense silt/fine sand (SM) layer below which a loose clayey silt layer existed beyond 30 m depth. The unconfined compressive strength, void ratio and compression index of the soft clay zones varied in the ranges of 12~16 kPa, 0.8~1.2 and 0.2~0.3, respectively. The targeted use of the land required improvement of the sub-soil. This paper presents the design considerations, comparison of required time and cost of alternative options, effectiveness of the adopted measure and the achieved improvement of the engineering properties. Actual consolidation settlements were up to 600 mm over a period of about 30 days with PVD and pre-load. The effectiveness of the available theories of consolidation settlement under vertical and radial drainage, in the design of the ground improvement measures, has been demonstrated.

**RÉSUMÉ :** La construction d'un terminal à conteneurs d'une superficie de 153.000 m<sup>2</sup> est en cours en ville portuaire de Chittagong au Bangladesh, située sur la rive droite de la rivière Karnaphuli à sa confluence avec le golfe du Bengale. Le sous-sol sur le site se composait d'une couche de 4 à 6 m d'épaisseur d'argile avec des zones aléatoires d'argile molle à raide (CL). Cela a été superposée à une épaisseur de 10 m limon / sable fin (SM) lâche à dense, une couche en dessous de laquelle une couche limon argileux lâche existait au-delà de 30 m de profondeur. La résistance à la compression, l'indice des vides et l'indice de compression des zones d'argile molle varient dans les plages de 12 à 16 kPa, 0.8 ~ 1.2 ~ 0.3 et 0.2, respectivement. L'utilisation obligatoire de ces terres requiert l'amélioration du sous-sol. Cet article présente la conception, la comparaison du temps nécessaire et le coût des options alternatives, l'efficacité de la mesure adoptée et de l'amélioration obtenue des propriétés mécaniques. Les tassements de consolidation réels ont été de 600 mm sur une période d'environ 30 jours avec PVD et pré-chargement. Dans la conception de l'amélioration des sols, l'efficacité des théories existantes de tassement de consolidation en vertu de drainage vertical et radial a été démontré.

**KEYWORDS:** Clay, Ground improvement, Pre-loading, PVD

## 1 INTRODUCTION

Chittagong sea port, the largest sea port of Bangladesh is situated on the right bank of the Karnaphuli river at its confluence with the Bay of Bengal. The port, that once handled mostly bulk cargo is gradually shifting its operational mode to handle increasing volume of container traffic. In this regard, Chittagong Port Authority (CPA) is implementing a project for construction of backup facilities at New Mooring behind berths 4 and 5. The site is locally known as 'NCT' (New-Mooring Container Terminal). The project area is about 153,000 m<sup>2</sup> which is planned to accommodate stacking yard for containers, passage for truck and trailer movement, tracks for Gantry Crane, electrical substation etc.

A comprehensive geotechnical investigation was carried out at the site to assess the sub-soil condition, decide on the necessity of improvement and determine relevant design parameters for the envisaged improvement methodology. The soil profile in the project area, consisted of a 4 to 6 m thick soft to medium stiff clay layer, underlain by a 10 m thick loose to medium dense silt/fine sand layer below which a loose clayey silt layer existed to more than 30 m depth.

To keep conformity with the earlier constructed adjacent yard, it is considered that the area will be paved with interlocking block (ILB) except the RMG (Rail Mounted Gantry) and RTG (Rubber Tyred Gantry) tracks which will be pile founded. On the basis of design requirements and geotechnical characteristics, improvement of the upper soft clay layer was considered essential to eliminate the possibility of differential settlement within the yard as well as between pile founded structures (i.e. jetty and RMG, RTG tracks) and yard.

From an study of several alternatives, Prefabricated Vertical Drain (PVD) with pre-loading was adopted as the ground improvement measure for the site. Improvement measures have been completed on a part of the project area. The settlement under preloading with PVD has been monitored using settlement plates. Field and laboratory tests have also been conducted to evaluate the effectiveness of the adopted measures in terms of change of soil properties. This paper presents the geotechnical characteristics of the sub-soil in the area, the design considerations and a comparison of cost of several alternative improvement methods. From the limited data, that has so far been available, comparison of some engineering properties before and after preloading has also been made.

## 2 SITE LOCATION AND TOPOGRAPHY

The site for the container yard is in a tidal plain at a narrow strip between Chittagong hilly uplands and the Bay of Bengal. Geologically it is a recent alluvium formed by the material carried by the river Karnaphuli and its tributaries from the upper tertiary hills. Figure 1 shows the site map with grid lines. About half of the land, the eastern side (segments marked 1, 2, 3 and 4) had been used as jetty yard for more than 50 years and housed storage sheds for general cargo, road and railway tracks. The other half (western part, segments marked 1A, 2A, 3A and 4A) contained a city road, a residential area of CPA containing one/two storey building, ponds, play ground, open land, village dwellings etc. Different parts of this western side had different elevations with 1~3 m ditches. Because of earlier diverse use of the land, there was little possibility of homogeneity of the upper soil layer in the area.

### 3 SUB-SOIL CHARACTERISTICS

A total of 67 exploratory boreholes were drilled in the area to gather information about sub-soil type and characteristics. The borehole locations were carefully decided to make them distributed over the entire area as well as to cover zones of different land use (i.e. pond, road, houses etc.). The borehole that are referred here are marked by grid points as shown in Figure 1. The boreholes, approximately 100 mm in diameter, were drilled using water flush aided by chiselling. Twelve boreholes were of 30.5 m depth and the rest were of 15.0 m depth below the existing ground level. Standard Penetration Tests (SPT) were made at 1.5 m interval. Undisturbed samples were retrieved from cohesive layers by pushing conventional 76 mm external diameter thin-walled Shelby tubes. Disturbed samples were also collected from the SPT spoon (conventional split spoon) from cohesive and cohesionless soil layers at different depths for visual-manual identification of the layers as well as for laboratory testing.

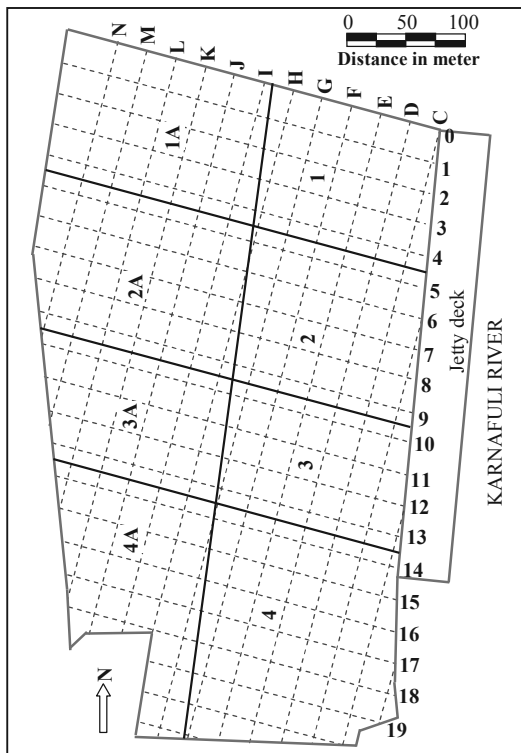


Figure 1 Site map showing grids and loading blocks.

In general, the sub-soil at the site is found to consist of a layer of 'soft to medium stiff silty clay' extending from the ground surface to about 4 to 6 m depth. This layer is underlain by a 10 m thick 'loose to medium dense fine sand/silt' layer. A 'clayey silt' layer is encountered below the fine sand/silt layer which extend beyond the maximum depth of investigation (i.e., about 30 m from surface). Thus, up to a depth of 30 m the sub-soil at the site is idealized to have three distinct layers (top silty clay layer, intermediate fine sand/silt layer and bottom clayey silt layer). In a small number of boreholes medium dense sand was encountered near the ground surface instead of the clay layer, which was probably a fill during past use of the land. Figure 2 presents the field SPT-N values at different depths for the explored borehole locations and the stratigraphy.

silt', the field SPT-N values ranged between 5 and 27 except in one borehole where a 'sandy silt' layer existed.

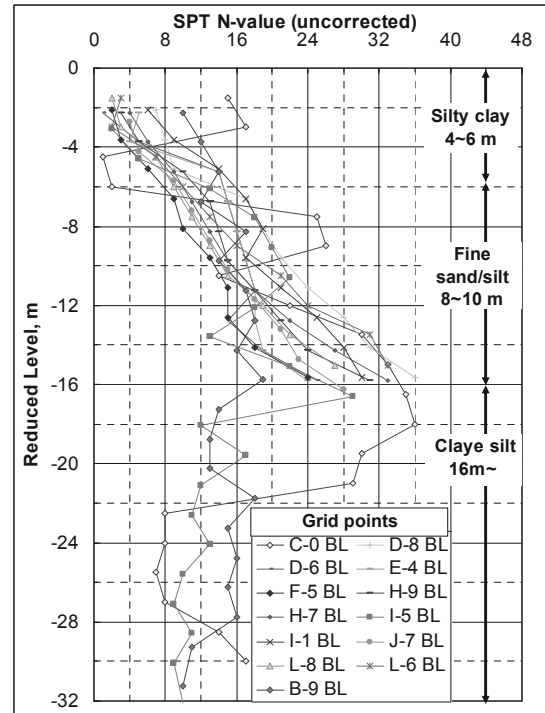


Figure 2 General ground profile and variation of SPT with depth.

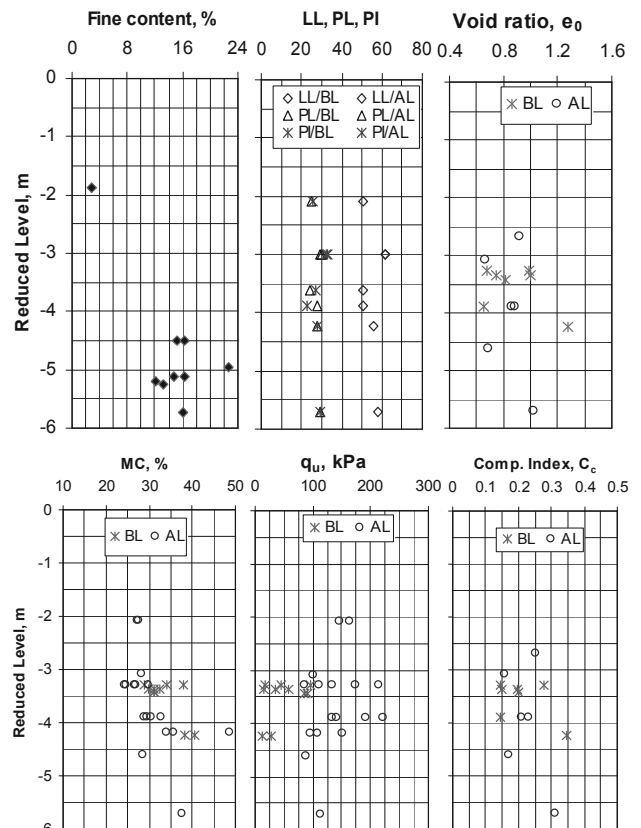


Figure 3 Variation of index, strength and deformation properties of the upper clay deposit with RL (BL=Before loading, AL=After loading).

Extensive laboratory tests have been conducted on samples of top silty clay layer (BRTC, BUET Report, 2009) and some of the results are presented in Figure 3. The layer may be

characterized as having  $LL=50\sim60$ ,  $PL=20\sim30$ ,  $PI=20\sim30$ ,  $NMC=20\sim35\%$ . According to Unified Soil Classification System (USCS), the soil in this layer is mostly plastic-silty clay of low plasticity (CL), though a few samples were found to be clay of high plasticity (CH). On the USCS chart, the data points lie just above A-line. The dry unit weight varied in the range of  $13\sim15 \text{ kN/m}^3$  and the range of void ratio was  $0.80\sim1.20$ . The variation of these properties can be seen from Figure 3. The layer also has some organic content is about  $1.4\sim4.0\%$ . The values of the coefficient of consolidation in the vertical direction,  $C_v$  were mostly within  $3.1$  to  $25.2 \text{ m}^2/\text{year}$  and at some location as low as  $0.79 \text{ m}^2/\text{year}$ .

#### 4 DESIGN OF GROUND IMPROVEMENT METHOD

It was decided by CPA, that the project will be carried out by local contractors. Therefore, capacity, experience, equipments etc. of local contractors were to be considered in the design of the yard. Furthermore, ground improvement was to be completed for the entire project site within one year. Hence, the area was divided into four blocks and time for improvement for each block was 3 months. An area adjacent to the north boundary of the site was earlier developed for similar purpose, by a foreign contractor, where dynamic temping was used for ground improvement and interlocking block pavement was made. To keep similarity with the earlier part, interlocking block pavement was decided for this yard too.

The presence of very soft to medium stiff silty clay at various locations within the site indicated strong possibility of substantial total and differential settlement unless effective measures for improvement of sub-soil are undertaken before the construction of pavement for the Container Yard. Therefore, effective measures for improvement of sub-soil before the construction of pavement were considered essential in order to avoid/minimize future problems.

The necessity and extent of the ground improvement measures are judged with an objective to reduce the differential settlement and maintenance operations considering the maximum load from stacking of containers on the entire area (i.e.  $p=52 \text{ kN/m}^2$ ). It should be understood that a solution, for which there will be no future settlement, will lead to high cost and time for completion and thus may not be practical. The load on the RTG tracks from the gantry is estimated to be  $77.5 \text{ kN/m}^2$ . The extent of improvement and design of pavement system at the site is targeted to keep maintenance option with minimal disruption. For RTG and RMG tracks and other facilities, suitable deep/shallow foundations will be considered so that they do not undergo relative settlement with respect to jetty top.

Five alternatives, that appeared to be feasible for local contractors, were assessed. These are- (i) preloading (ii) sand drain with surcharge (iii) PVD with surcharge and (iv) dynamic

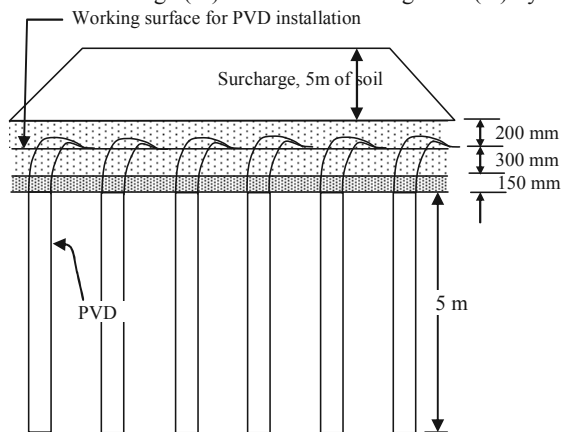


Figure 4 Details of the ground improvement work. temping and (v) soft pocket identification, removal and

compacted backfilling. Table 1 presents the comparison of cost and completion time for different methods. Both time and cost depends to some extent on the number of equipments mobilized and source of material, particularly the surcharge (max. 5 m of soil considered). Considering the capacity of local contractors minimal engagement of equipments and dredge sand from the Karnaphuli river were considered. Though dynamic temping/compaction appeared to be very prospective in terms of time and cost, it posed the risk of damaging the adjacent yard and structures. Finally, PVD with surcharge was adopted as the ground improvement measures, mainly because of reduced time in PVD driving compared to sand drain installation, though PVD is an imported material. Also this method was considered advantageous over other methods in bringing the clay layer to a state where differential settlement potential will be reduced as it will automatically take care of soft zones and bring the soft and stiff zones to closer soil properties in terms of deformation and strength.

Since, from  $e\text{-log}(p)$  curves, most of the samples of the upper clay layer was found to be normally consolidated, the total consolidation settlement under the working loads ( $52 \text{ kPa}$ ) without improvement was calculated using  $S_c = \sum \Delta e \cdot H$ ,  $\Delta e = C_c / (1 + e_0) \log(\Delta p + p'_0) / p'_0$  and  $p'_0 = \sum \gamma H$  where,  $e_0$  = initial void ratio,  $p'_0$  = effective past maximum overburden pressure,  $\gamma$  = effective unit weight of soil,  $H$  = thickness of the compressible layer. The estimated settlement for different borehole locations varied from about  $140 \text{ mm}$  to  $570 \text{ mm}$ . This variation is due to difference in  $e_0$ ,  $C_c$  and layer thickness. In these estimations,  $\Delta p$  is calculated as  $\Delta p = \sigma_0 [1 - \{1 + (r/z)^2\}^{-1.5}]$  where  $\sigma_0$  = Intensity of stress applied on the surface,  $r$  = radius of the loaded area,  $\Delta p$  = increase in stress at depth  $z$  from the centre of the loaded area. This expression for  $\Delta p$  is obtained by integration of Boussinesque's equation that gives the stress at a point within a semi-infinite, homogeneous, isotropic, weightless, elastic half-space for a point load on the surface (Bowels, 1988). Estimated time to achieve this consolidation ( $U_{av} \approx 99\%$ ) varied from about 50 days to more than 700 days for different borehole locations. The time was determined using Terzaghi's one dimensional consolidation theory with double drainage and constant initial pore pressure distribution using the equations (Das, 1983):

$$U_{av} = 1 - \sum_{m=0}^{\infty} \frac{2}{M^2} e^{-M^2 T_v}, \quad T_v = \frac{C_v t}{H^2} \quad \text{and} \quad M = \frac{\pi}{2}(2m+1)$$

It was intended to apply a surcharge with PVD such that a maximum of  $25 \text{ mm}$  of total settlement remains to occur in future under the working loads expecting a differential settlement of not more than  $12 \text{ mm}$ . Estimation of required time to achieve this level of consolidation was made considering both vertical and radial drainage (Carillo, 1942) as  $U = 1 - (1 - U_v)(1 - U_r)$  where  $U_v$  and  $U_r$  are the average degree of consolidation respectively for vertical and radial drainage. The average degree of consolidation for radial drainage was calculated using the following as

$$U_r = 1 - e^{-\frac{8T_r}{m}} \quad \text{where} \quad T_r = \frac{C_{vr} t}{d_e^2}$$

$$m = \frac{n^2}{n^2 - S^2} \ln\left(\frac{n}{S}\right) - \frac{3}{4} + \frac{S^2}{4n^2} + \frac{k_h}{k_s} \left(\frac{n^2 - S^2}{n^2}\right) \ln(S)$$

$$n = \frac{d_e}{d_w} \quad \text{and} \quad S = \frac{d_s}{d_w}$$

The equivalent diameter of PVD was calculated following Hansbo (1979) as

$$d_w = \frac{2(b+t)}{\pi}$$

where,  $b$  is the width and  $t$  is the thickness of PVD. Considering smear effect  $S$  was chosen between  $1.0$  and  $1.2$ . The effective diameter of soil column around the PVD was taken as  $d_e = 1.06s$ ,  $s$  = PVD spacing in triangular pattern.

For all the calculations horizontal permeability is taken as

the same as the vertical permeability. From the calculations it appeared that for 5 m surcharge and PVD the target settlement would occur within 10 to 50 days in different locations.

Table 1 Comparison of estimated cost and completion time for different ground improvement methods.

Method	Time (month)	Cost (million USD)	Comments
Preloading	36	1.96	Reliable Better assessment of improvement Long time required for improvement
Sand drain with surcharge	20	3.29	Relatively less reliable Installation of drains takes long time
PVD with surcharge	14	3.24	Reliable Good control of field operation Vibration may damage adjacent facilities
Dynamic compaction	11	2.04	High noise pollution Assessment of improvement needs lot of field tests
Soft pocket identification, removal and improvement, compacted backfilling	12	7.25	Relatively less reliable Assessment of improvement is difficult Highly dependent on field monitoring and control

The PVD used were of 100 mm width, 3 mm thick placed 1m c/c in triangular pattern. Other properties - Drain: Water discharge capacity  $90 \times 10^{-6}$  m<sup>3</sup>/s, and  $60 \times 10^{-6}$  m<sup>3</sup>/s respectively at 10 and 350 kPa ( $i=0.5$ ); Core: Tensile strength 700 N; Filter jacket: Apparent Opening size (AOS) 90  $\mu$ m, Grab tensile strength 400 N, Elongation at break 50%, Puncture resistance 130 N, Burst strength 800 kN/m<sup>2</sup>, Permeability  $2 \times 10^{-4}$  m/s. Details of the ground improvement work is shown in Figure 4.

5 ASSESSMENT OF GROUND IMPROVEMENT

Monitoring of settlement has been made using settlement plates placed at 25 m grid as shown in Figure 1. After preloading exploratory boreholes were made at selected locations with field SPT and laboratory tests were conducted on collected undisturbed samples.

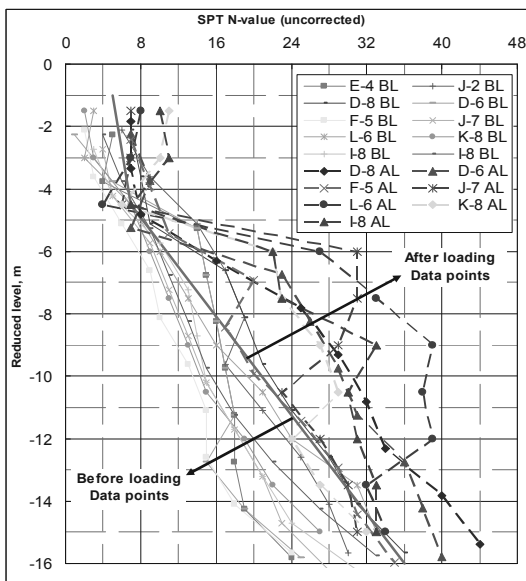


Figure 5. Variation of SPT-N value before and after loading.

Figure 5. compares the Field SPT-N values at several spots before and after preloading. It can be observed that in the upper silty clay layer the SPT-N values has become twice or more up to about 3m depth. At about 4~5m, which is the boundary between the clay and sand/silt layer the SPT-N values have not

changed. The field SPT-N values are found to increase significantly in the 'fine sand/silt' layer up to about 12 m.

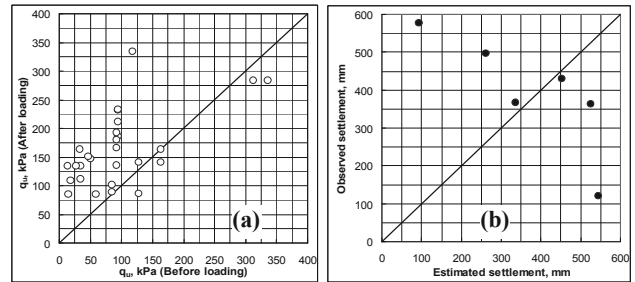


Figure 6 Comparison of (a) unconfined compressive strength and (b) observed and estimated settlement .

The unconfined compressive strength of the upper clay layer before and after preloading can be seen on Figure 6(a) for different locations and depths. In general the unconfined compression strength has increased at most of the spots. However, the magnitude of increase is not same. A few data points lie below the 45 degree line, that apparently shows to have reduction in strength but quite unlikely. The reason for these discrepancies may be the variation of non-plastic silt content in the layer.

In Figure 6(b) the recorded settlements are plotted against the estimated settlement for some of the grid points. Out of the six locations (for which estimates were made) four appear to match reasonably well. For one location the observed settlement is about five times the estimated value, which may be due to presence of localized sand lenses. On the other hand for another location the observed settlement is one-fifth of the estimated value, which may be due to clogging or disturbance of the clay during drain installation. Conclusive comments regarding the variation may be made when data from the remaining project work become available.

6 CONCLUSIONS

The following conclusions can be made based on the design and field monitoring of the ground improvement work:

- 1) Due to the application of the surcharge with PVD the consolidation settlement could be achieved within the stipulated time.
- 2) Both the SPT-N value and unconfined compressive strength were found to increase satisfactorily due to application of preload with PVD.
- 3) The available theories of 1-D consolidation and combined vertical and radial consolidation used in the design of ground improvement for the project site using PVD and preload appeared to have been fairly applicable. Predicted and observed settlement matched reasonably.

7 ACKNOWLEDGEMENTS

This research work was carried out in connection with the consultancy services provided to CPA through BRTC, BUET. The authors would like to express their sincere thanks to CPA and Contractor's personnel involved in the project.

8 REFERENCES

Bowels, J.E. (1988) Foundation Analysis and Design, 4th edn., McGraw-Hill Book Company.  
 BRTC, BUET Report (2009) Sub-soil investigation and ground improvement measures for construction of backup facilities behind berth 4 & 5 at New Mooring Container Terminal (NCT), CPA, Chittagong.  
 Carillo, N.J. (1942) Simple two- and three- dimensional cases in the theory of consolidation of soils. Journ. Math. and Phy.(21),pp.1-5.  
 Das, B.M. (1983) Advanced Soil Mechanics, International edn., McGraw Hill  
 Hansbo, S.(1979) Consolidation of clay by band-shaped prefabricated drains, Ground Engineering,(12),5,pp.16-25.

# Importance et applications des inclusions de grande inertie

## Importance and practical examples of inertial soil improvement

Jeanty J.M., Mathieu F., Benhamou L.  
*Soletanche-Bachy, RUEIL-MALMAISON, France.*

Berthelot P.  
*Bureau Veritas, Paris, France.*

**RÉSUMÉ :** Les techniques traditionnelles d'amélioration des sols par inclusions visent le plus souvent à renforcer l'aptitude du massif à reprendre les charges verticales auxquelles il est soumis, moyennant des déformations acceptables par les ouvrages. Elles peuvent également avoir pour objectif d'améliorer la résistance aux efforts horizontaux, et plus généralement aux sollicitations à dominante déviatorique, dans le cadre de problématiques liées aux séismes (traitements anti-liquéfaction), à la stabilité générale (remblais sur sols compressibles), à la réduction des poussées sur des ouvrages de soutènement, au poinçonnement du sol sous de fortes surcharges (effets de bord), ... La réalisation d'inclusions à forte inertie, sous forme de tranchées parallèles ou de réseaux de tranchées, est une réponse particulièrement bien adaptée à ces problématiques d'amélioration des sols. Une manière élégante de construire ces inclusions sans perturber les structures existantes consiste à traiter le sol en place en y incorporant un liant hydraulique, par application des techniques de soil mixing les plus récentes. Après une présentation de ces méthodes, la communication proposée met en évidence le rôle fondamental joué par l'inertie des inclusions, par des considérations fonctionnelles et par divers exemples d'application.

**ABSTRACT:** Conventional soil reinforcement techniques as rigid inclusions mainly report vertical loadings to the substratum layer with an induced settlement. They can also improve soil resistance regarding lateral forces as those related to earthquakes (liquefaction hazard), or slope stability for embankments on soft soil foundation. They can reduce active pressure on retaining walls. The appropriate design answer to those issues is to create strong inertia inclusions based on a trench geometry with either a parallel or a crossed frame arrangement. Last but not least, an even better technique to build those inclusions with a reduced environment impact consists in treating in situ soil by adding cement. This article presents different soil mixing projects and explains how strong inertia trenches are relevant.

**MOTS-CLÉS:** amélioration de sols, sol-mixing, sol-ciment, inclusions rigides, inertie, liquéfaction, soutènement, poussée des terres, tassement, tranchées de sol-mixing.

**KEYWORDS :** soil reinforcement, soil mixing, rigid inclusions, slope stability, retaining wall, liquefaction, seismic, active pressure, Bouassida approach, settlement, soil mixing caissons, soil mixing trench, crosswalls.

### 1 INTRODUCTION

Le soil mixing profond est une technique développée dans les années 1970 en Europe du Nord et au Japon, initialement pour résoudre des problématiques liées au comportement des sols compressibles. Cette technique consiste à améliorer les caractéristiques d'un sol en le mélangeant en place avec un liant hydraulique.

La déstructuration des terrains et l'incorporation du liant s'effectue par des moyens mécaniques, en utilisant un outil dont la géométrie et le mouvement dans le terrain définissent les dimensions des éléments de sol traité.

La mise en œuvre de cette technique a longtemps fait appel à l'utilisation d'outillages simples ou multiples, rotatifs à axe vertical, munis de pales latérales de géométries très variées. Des outils de type tarière simple ou tarières multiples avec inversion des sens de rotation entre forage descendant et malaxage / compactage en remontant sont aussi utilisés. Des colonnes réalisées par jet-grouting peuvent aussi être apparentées au sol-mixing.

Plus récemment, durant la dernière décennie, de nouveaux procédés de soil mixing avec des outils à axe horizontal ont fait leur apparition : haveuses et trancheuses. Ces procédés ont permis de repousser les limites du soil mixing en élargissant la méthode au traitement d'une plus large gamme de sols et présentant des atouts en termes de caractéristiques et d'homogénéité.

Le soil mixing se distingue depuis l'origine des autres procédés d'améliorations des sols en ce sens qu'il permet de réaliser, à l'extrême, des réseaux d'inclusions isolées (pour l'exécution desquelles des outillages de type tarière peuvent être suffisants) ou des traitements dans la masse (utilisation d'outillages de type multitarière ou haveuse pour réaliser des "pavés" de sol traité), mais c'est dans la réalisation d'éléments linéaires de grande inertie, de type refend ou écran continu (susceptible à la fois de jouer un rôle porteur et d'assurer une fonction soutènement moyennant l'incorporation d'armatures métalliques), voire de réseaux orthogonaux, permettant de confiner le sol en place, que le soil mixing trouve sa véritable originalité et ses développements les plus prometteurs.

Généralement apparenté aux réseaux d'inclusions plutôt qu'aux traitements dans la masse, il s'en distingue pourtant de façon fondamentale, non seulement par les aspects géométriques précédemment évoqués, mais encore par ses propriétés mécaniques. Cela ne permet de le classer ni dans la catégorie des inclusions souples (colonnes ballastées, dont la résistance en compression est nulle en l'absence d'étreinte latérale de la part du sol avoisinant), ni dans la catégorie des inclusions rigides, dont la résistance en compression, qu'il s'agisse de métal, de béton ou de mortier, est au contraire indépendante de l'étreinte exercée par le sol et pour lesquelles la résistance en compression simple est par conséquent le paramètre déterminant pour le dimensionnement.

Au contraire, les propriétés du soil mixing sont bel et bien celles d'un sol amélioré, même s'il ne s'agit généralement pas d'un



traitement uniforme de l'ensemble du massif de fondation, dont le critère de rupture n'est autre que le critère de Coulomb, qui lui permet de bénéficier à la fois :

- .d'une résistance intrinsèque indépendante de l'étreinte (terme de cohésion) ;
- .d'une augmentation de résistance avec la profondeur en fonction de l'étreinte latérale du sol (terme de frottement).

En termes de déformations, ses propriétés sont également intermédiaires entre celles généralement attribuées aux inclusions rigides et souples ce qui conduit naturellement à le ranger dans la catégorie inédite des "inclusions semi-rigides".

Le tableau qui suit résume les ordres de grandeurs usuels de la résistance à la compression  $F_c$  et du module de déformation  $E_y$ .

Renforcement	Inclusion rigide	Inclusion semi-rigide	Inclusion souple
$F_c$ (MPa)	5 à 500	0.5 à 5	0
$E_y$ (GPa)	3 à 200	0.2 à 3	0.04 à 0.08

### 1.1 Mélange par haveuse

Le procédé met en œuvre un outillage appelé « Cutter Soil Mixing » (CSM), dérivé de la technologie utilisées sur des machines de type haveuse ou hydrofraise. Deux tambours spécialement conçus pour cette application et entraînés en rotation par des moteurs hydrauliques de fort couple, sont utilisés pour déstructurer et mélanger le sol en place. Une buse d'injection située entre ces moteurs permet l'incorporation d'un fluide. Le mélange ainsi réalisé est ensuite déplacé soit au dessus des tambours dans le sens descente ; soit au dessous dans le sens remontée.

Les inclusions construites avec cet outillage jusqu'à des profondeurs de quelques dizaines de mètres, sont de section rectangulaire (longueur courante 2,80 m ; épaisseurs 500 à 1000 mm). Elles peuvent être utilisées unitairement (on parle alors de barrettes) ou disposées de manière contiguës afin de constituer des parois continues (Figure 1).

Certains outillages plus perfectionnés sont munis d'un dispositif de mesure inclinométrique, permettant de mesurer et de corriger en temps réel la position de l'outil lors de la construction d'une inclusion.

Le fluide injecté peut être de différents types : il peut s'agir d'un fluide facilitant le forage, remplacé en phase remontée par un mélange eau-ciment (appelé aussi coulis de ciment). Il est également possible d'injecter directement un coulis pendant le forage, la phase de remontée étant alors utilisée pour parfaire le mélange.

Le type et la quantité de liant utilisée permettent d'atteindre une large gamme de caractéristiques (résistance, perméabilité, cohésion, module de déformation), en fonction de la nature des sols en place.

Pour les outillages les plus perfectionnés, les volumes injectés ainsi que les énergies de malaxage sont contrôlés et ajustés en temps réel grâce à un système informatique embarqué dans la cabine de la machine. Tous les paramètres opératoires sont enregistrés afin d'être restitués sous forme de rapports.

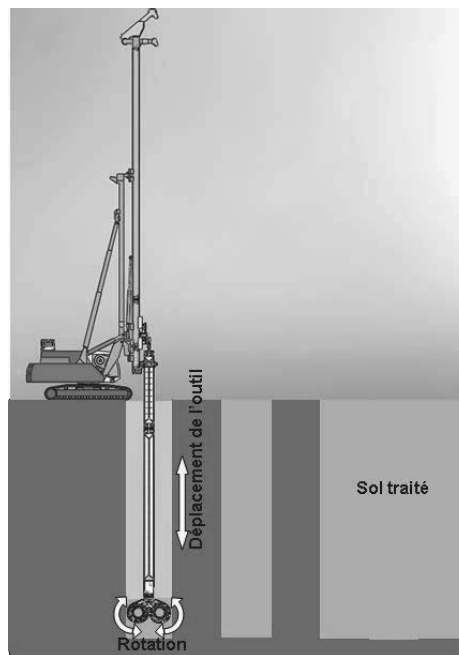


Figure 1 : Principe de construction de parois avec le procédé CSM.

Enfin, divers types d'armatures peuvent être mis en place dans le matériau encore frais, permettant ainsi de réaliser des ouvrages de soutènement provisoire ou à caractère permanent.

### 1.2 Mélange par trancheuse

Les machines de type trancheuse mettent en œuvre une chaîne avec outils de coupe et de malaxage. La chaîne est guidée par une lame travaillant dans un plan vertical dans le sol. L'ensemble de l'outillage présente une certaine similitude visuelle avec une tronçonneuse. L'action de cette lame, combinée à l'incorporation d'un fluide, permet de construire des tranchées de sol traité en place (Figure 2).

Suivant les cas, le liant hydraulique peut être injecté sous la forme d'un coulis ou incorporé au mélange sous forme pulvérulente, auquel cas une adjonction d'eau est généralement réalisée afin de faciliter l'action des outils.

Les tranchées construites de cette manière sont continues, et toutes les couches de sol sont uniformément mélangées. L'épaisseur de l'inclusion est de l'ordre de 0.3 à 0.5 m pour une profondeur maximale d'environ 10 mètres.

De manière analogue au procédé par havage, le procédé par trancheuse s'accompagne d'un dispositif de contrôle-qualité embarqué, permettant le pilotage de la machine, le respect des paramètres de traitement ainsi que les enregistrements nécessaires pour l'émission de rapports.

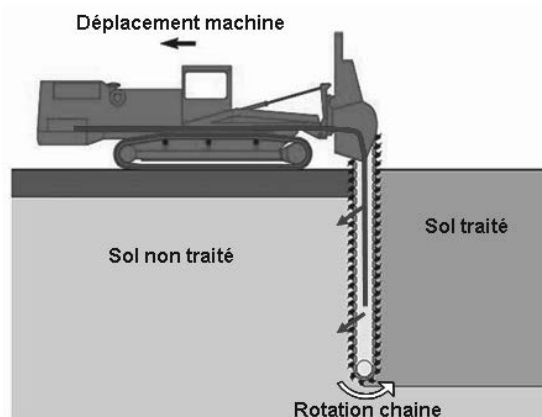


Figure 2. Principe de construction d'une tranchée.

## 2 DOMAINES D'APPLICATION

Les tranchées de sol traité en place peuvent être parallèles à une seule direction ou constituer une trame selon deux directions en général perpendiculaires. Le premier cas correspond à une problématique avec une direction privilégiée de sollicitation, le second avec deux directions de sollicitation d'égales probabilités.

Différents domaines d'application selon le type de renforcement recherché méritent d'être distingués.

.Domaine 1 : Reprise de charges surfaciques, permettant un traitement plus réparti qu'avec des inclusions rigides (ce qui permet de limiter fortement l'effet de "point dur" qui conditionne sinon le ferrailage du dallage ou du radier sus-jacent et l'épaisseur du matelas de répartition).

A noter que le caractère "2D" du procédé permet en outre de procéder à des calculs plus rigoureux que les approches traditionnelles, utilisant par exemple les coefficients de capacité portante de Bouassida (Bouassida, 2002) (qui permettent de traiter le cas d'une semelle de fondation sur sol renforcé par une tranchée), ainsi que des modèles de calcul numérique en déformation plane pour le calcul du tassement (ce qui ne serait pas acceptable pour un réseau d'inclusions isolées).

Un exemple d'application récent est donné par le chantier de Saint-Roch (06), consistant à renforcer le sol sous un remblai SNCF par un réseau de tranchées longitudinales.

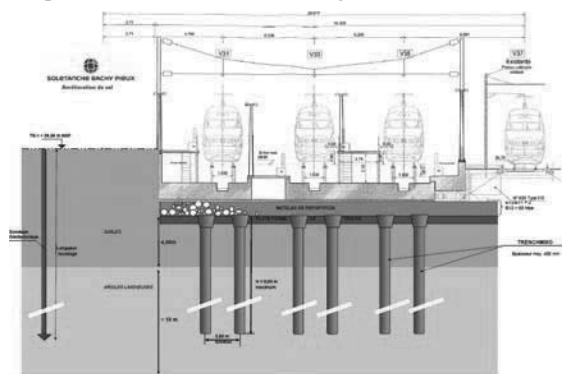


Figure 3. Coupe type SNCF St Roch (06).

.Domaine 2 : Renforcement du sol dans les zones où le champ de contraintes est à dominante déviatorique.

La justification des réseaux d'inclusions repose en général sur des justifications de portance effectuées en partie courante de la surface chargée, là où le risque de rupture du massif de sol est insignifiant dans la mesure où le champ de contraintes est généralement de type plutôt oedométrique. Le plus souvent, aucune justification particulière n'est demandée dans les zones soumises à de fortes contraintes déviatoires mobilisant de façon significative la résistance au cisaillement du sol (périphérie des zones de stockage par exemple), et corrélativement susceptibles de mobiliser les inclusions en flexion.

Un exemple de ce type est donné par les zones latérales des remblais de forte hauteur reposant sur des sols compressibles. Alors, une combinaison judicieuse d'inclusions isolées en partie centrale et de refends sous la partie latérale a pu être préconisée et mise en œuvre par différents auteurs (réf. Filz G. & Al, Kitazume M.).

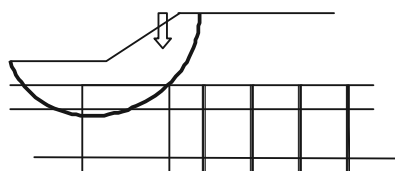


Figure 4. Diagramme de grand glissement.

.Domaine 3 : Réduction des poussées exercées sur les écrans de soutènement.

Les inclusions isolées agissent par limitation du tassement derrière le soutènement et allègement des contraintes verticales dans le massif de sol par transfert partiel sur les inclusions, tandis que les inclusions de forte inertie ajoutent à cet effet celui d'une diminution "directe" des contraintes de poussée par mobilisation du frottement sur les refends autostables.

Un exemple d'application significatif est celui du rempiètement du quai poste 7 du Transmanche (Calais), pour lequel le premier mode de comportement s'avérait inefficace en raison d'un contraste de rigidités verticales insuffisant entre le sol en place et les inclusions, et où seul l'effet inertiel permettait donc de réduire la poussée de façon significative (cf chapitre 3.1).

.Domaine 4 : Traitement anti-liquéfaction des sols sous sollicitation sismiques.

Il a été montré (réf. Seed) que certaines méthodes de justification des réseaux d'inclusions disjointes reposaient à tort sur un effet de transfert sur ces dernières des contraintes de cisaillement induites par le séisme.

Ces méthodes reliaient en effet l'efficacité des inclusions à leur module de cisaillement, en ignorant le fait que leur élancement induit en général un mode de déformation en flexion largement prépondérant par rapport au mode de déformation par cisaillement, à l'instar des poutres sur appuis élastiques de la résistance des matériaux.

C'est donc bien l'inertie et non la rigidité qui constitue le facteur clé dans l'efficacité de ce type de traitement, ce qui conduit là encore à privilégier les réseaux d'inclusions de forte inertie. Le traitement de type "quadrillage" est souvent qualifié à tort de "confinement", alors que c'est bien l'effet "inertiel" qui est recherché, le double réseau d'écrans orthogonaux permettant avant tout de réaliser un traitement isotrope dont l'efficacité est ainsi rendue indépendante de la direction des ondes sismiques.

Un exemple particulièrement représentatif est donné par le chantier de l'extension de la préfecture de Fort-de-France, pour lequel s'ajoutait, à la problématique du traitement de terrains fortement liquéfiables sur une grande hauteur, celle de l'écoulement post-liquéfaction induit par le pendage significatif du substratum, ce qui rendait nécessaire la mise en œuvre d'un réseau autostable (cf chapitre 3.2).

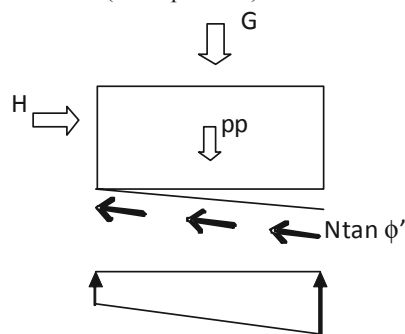


Figure 5. Stabilité. Principaux efforts dans le plan d'un refend.

## 3 EXEMPLES D'APPLICATION

### 3.1 Renforcement de sol derrière un soutènement

La mise en place de tranchées de soil-mixing de grande inertie à l'arrière d'un écran de soutènement permet la réduction des poussées du terrain sur l'écran lui-même.

Une optimisation de la reprise des efforts de poussée conduit à installer des éléments d'inertie maximale (concentration des efforts pour des déplacements limités). Des éléments isolés sont bien moins efficaces en terme d'inertie globale.

C'est ce principe qui a été proposé et retenu pour les travaux de reconstruction du poste transmanche n°7 à Calais.

La mise en place de refends de Geomix (Méthode par havage spécifique à l'entreprise) perpendiculairement à l'axe du quai (figure 6) a permis de réduire la section des palplanches à mettre en œuvre dans le cadre des travaux d'approfondissement du quai.

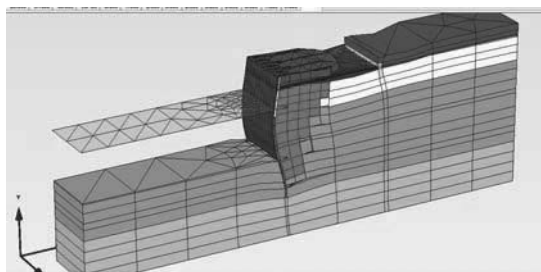


Figure 6. Vue 3D du renforcement derrière le rideau du quai existant.

Le massif de sol traité reprend la poussée des terres et les palplanches à l'avant ne reprennent plus que la poussée d'eau. La stabilité du massif renforcé par les éperons de sol mixing est vérifiée vis-à-vis du non-basculement, du non-glisement, et de la non extrusion entre tranchées.

L'autre partie des vérifications a consisté à établir la cohésion homogénéisée du massif de sol, variable de 45 à 85 kPa pour ce projet.

La solution de base en barrettes isolées apportait une cohésion homogénéisée moyenne de l'ordre de 24 kPa, attestant la bien moindre performance des renforcements disjoints par rapport à la disposition en refends de grande inertie.

### 3.2 Traitement anti-liquéfaction

Les dégâts engendrés par le dernier séisme significatif de novembre 2007 en Martinique ont nécessité la reconstruction de la préfecture de Fort de France (bâtiments type R+4).

Le contexte géotechnique du site montre un fort potentiel de liquéfaction des alluvions à dominante sablo-limoneuse de faible caractéristique ( $PI^* \sim 0,3$  MPa,  $Em \sim 2,2$  MPa), sur une épaisseur variable de 9 à 18 m correspondant à la pente du substratum.

En réponse à l'appel d'offres, l'entreprise a proposé une solution variante pour répondre à la fois aux problématiques de liquéfaction et d'écoulement post-liquéfaction des sols sur la pente du substratum.

Un nouveau type de fondations basé sur un quadrillage en sol mixing sous l'emprise totale des bâtiments (environ 36 m x 40 m) a été conçu (figure 7).

Les tranchées Geomix, d'épaisseur 0,50 m, sont espacées d'environ 4.5 m entre axes. Par leur forte inertie (par comparaison aux inclusions rigides) et à leur géométrie, les déformations des panneaux sont limitées pendant l'épisode sismique. Le cisaillement additionnel du sol et les efforts horizontaux provenant de la structure se concentrent sur les bandes Geomix. Le traitement de confinement permet ainsi de limiter le cisaillement et le développement de pressions interstitielles dans le sol confiné non traité. Le risque de liquéfaction est évité.

Les caissons anti-liquéfaction servent également en phase service de fondation aux bâtiments par l'intermédiaire d'une dalle de transfert. Ils ont donc aussi le rôle de réduction des tassements sous la structure en situation statique.

Le phénomène d'écoulement post-liquéfaction a provoqué de nombreux dégâts lors du séisme de Kobé au Japon en 1995. Sur le site de la préfecture de Fort-de-France, ce risque est accru par une pente importante du substratum (dénivelé de 9 m sur une

longueur de seulement 40 m). Les inclusions isolées de faible inertie ne peuvent résister à ce phénomène.

Cette première technique, mise en œuvre entre octobre 2010 et janvier 2011 représente un vrai pas en avant dans l'approche des fondations pour les Départements d'Outre Mer.

Plus largement, il s'agit d'une solution technique innovante, reposant sur un procédé propre à Solétanche Bachy et qui répond efficacement aux problématiques des clients en sites sismiques.

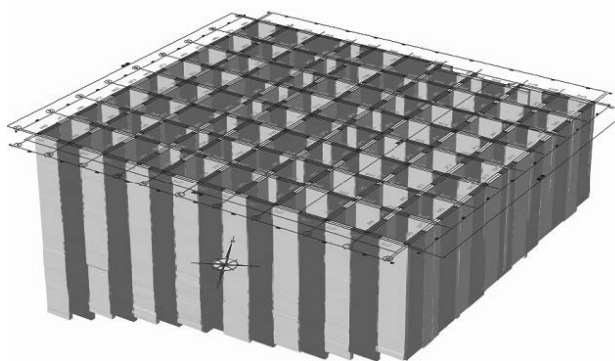


Figure 7. Vue en 3D des fondations en caisson.

## 4 CONCLUSION

Les quelques exemples présentés dans l'article, représentatifs de différents domaines d'application, ont permis de mettre en évidence la nécessité de privilégier non pas tant la rigidité que l'inertie des réseaux d'inclusions : la mise en œuvre de refends, de parois continues ou de caissons "semi-rigides", réalisés au moyen de techniques récemment développées pour étendre le domaine d'application du procédé "soil mixing", permet ainsi dans bien des cas d'apporter à des problèmes complexes une réponse particulièrement pertinente.

## 5 REFERENCES

- The deep mixing method. *Coastal Development Institute Tokyo, June 2002.*
- Lebon S.P.. New Methods in European Deep mixing – A contractor's perspective on the developing challenges of execution. *Deep Mixing 2005, Stockholm.*
- Benhamou L. and Mathieu F.. Geomix Caissons against liquefaction. *ISSMGE - TC 211 International Symposium on Ground Improvement IS-GI Brussels, 2012.*
- Bouassida Mounir et Belgacem Jellali. Capacité portante ultime d'un sol renforcé par une tranchée. *Revue française de génie civil volume 6. No 7 – 8/2002.*
- Corneille S. and Ré A.. Trenchmix : une technique d'amélioration de sols qui contribut au développement durable. *Revue Travaux n°854, Juillet 2008.*
- Filz G and al.. Design of Deep Mixing for support of levees and floodwalls. *4<sup>th</sup> International Conference of Grouting and Deep Mixing, New Orleans, 2012.*
- Kitazume M. Application of physical modelling for investigating ground failure pattern. *Physical Modelling in Geotechnics 6<sup>th</sup> ICPMG 2006. London ISBN 0-415-41586-1.*
- Gueguin M and al. A homogenization approach for evaluating the longitudinal shear stiffness of reinforced soils: column vs. cross trench configuration. *International Journal of Solids and Structures, November 8th 2011.*
- R B Seed & Al. Recent advances in soil liquefaction engineering : A unified and consistent framework. *26<sup>th</sup> Annual ASCE Los Angeles Geotechnical Spring seminar. Queen Mary presentation 2003.*
- Shinkawa N. and Bessho N. Application examples of Deep Mixing Method as Aseismic Measures. *International Symposium on Deep Mixing & Admixture Stabilization, Okinawa 2009.*

# Assessment of Carillo's Theory for Improved Tunis Soft Soil by Geodrains

## Évaluation de la théorie de Carillo pour les sols mous de Tunis améliorés par géodrains

Jebali H., Prikha W., Bouassida M.

Université Tunis El Manar, Geotechnical Engineering Research Team, École nationale d'ingénieurs de Tunis (ENIT)

**ABSTRACT:** This paper presents an experimental study carried out on undisturbed cored samples of Tunis soft soil extracted at 17.25 m depth at the lagoon of Séjoui. Three types of oedometer tests had been performed: first type was a standard test on Tunis soft soil, the second was an oedometer test on the same soil improved by a prefabricated vertical drain MebraDrain 88 (Mb88) type and the third test is similar to the second test in which vertical drainage was prevented. Then, the assessment of Carrillo's theory is studied by quantifying the effect of radial and vertical consolidation from the observed global degree of consolidation of improved Tunis soft soil specimens by geodrains.

**Résumé:** Ce papier présente une étude expérimentale réalisée sur des échantillons intacts du sol mou de Tunis prélevés à 17,25 m de profondeur de la marécage de Séjoui. Trois types d'essais oedométriques ont été effectués : le premier est un test standard sur le sol mou de Tunis, le second était un essai oedométrique sur le même sol amélioré par un drain vertical de type MebraDrain 88 (MB88); le troisième test est similaire au deuxième test dans lequel seulement le drainage radial a été favorisé. Ensuite, l'évaluation de la théorie de Carrillo est étudiée en quantifiant l'effet de la consolidation radiale et verticale sur le degré de consolidation global.

### 1. INTRODUCTION

Considerable attention has been recently devoted worldwide to the problem of building structures on highly compressible saturated soils and to the development of soil improvement techniques for increasing stability, reducing settlements, and accelerating consolidation of soft soils.

Prefabricated vertical drains (PVD) with preloading method was considered the most used improvement technique to accelerate the consolidation of soft soils and, consequently, to increase their bearing capacity.

The commonly used consolidation theory for designing PVD's is the unit cell model, e.g., Barron (1948), Hansbo (1981) and Terzaghi (1943). Because the solutions considering both vertical and radial drainage are complicated, those most used in practice ignore the effect of vertical drainage, such as Barron's theory. Barron (1948) developed solutions for two types of boundary conditions at the surface of improved soil such as: (i) "free vertical strain," resulting from a uniform distribution of vertical load, and (ii) "equal vertical strain", which results from imposing the same vertical deformation. However, in some cases, the vertical drainage by PDV has a considerable effect on the degree of consolidation of improved soil; Terzaghi (1943) suggested the well known simple method for one-dimensional (1D) vertical consolidation condition.

Furthermore, for most cases in practice, the soil is not homogeneous, and the deformation of PVD improved soil

does not occur in 1D condition. Carrillo's theoretical solution (1942) is used to combine the vertical and radial drainage effects to predict the global degree of consolidation  $U$ :

$$(1 - U) = (1 - U_r)(1 - U_v) \quad (1)$$

$U_r$  and  $U_v$  are respectively the radial and the vertical average degree of consolidation.

Theoretically speaking, Carillo's formula (Eq 1) is only valid for instantaneously applied loading.

The consolidation of soft soil is related to the dissipation of excess pore pressure generated by the surcharge load. For radial consolidation problem with centered vertical drain in oedometer cell, the governing differential equation of excess pore pressure is (Parakash et al, 1996):

$$\frac{\partial(\Delta u^r)}{\partial t} = C_r \left( \frac{\partial^2(\Delta u^r)}{\partial r^2} + \frac{1}{r} \frac{\partial(\Delta u^r)}{\partial r} \right) \quad (2)$$

$C_r$  is the coefficient of radial consolidation of soft soil and  $\Delta(u^r) = \Delta u(r, t)$  is the excess of pore pressure at radius  $r$  and time  $t$ .

Solution of equation (2) that uses the condition of equal vertical strain without smear effect is given by (Barron, 1948):

$$U_r = 1 - \exp\left(-\frac{8T_r}{F(n)}\right) \quad (3)$$

The smear zone is defined as the remolded zone of soil immediately adjacent to the drain.  $F(n)$  is a Barron's function given by :

$$F(n) = \left( \frac{n^2}{n^2 - 1} \right) \ln(n) - \left( \frac{3n^2 - 1}{4n^2} \right) \quad (4)$$

"n" is the drain spacing ratio given by:

$$n = \frac{D}{d_w} \quad (5)$$

D and  $d_w$  denote the equivalent diameters of unit cell and of PVD, respectively.

$T_r$  is the dimensionless time factor of consolidation due to radial drainage is written in function of time t:

$$T_r = \frac{C_r \times t}{D^2} \quad (6)$$

For vertical consolidation problem, the differential equation of one-dimensional consolidation for the excess pore pressure is written (Terzaghi, 1943):

$$\frac{\partial(\Delta u^z)}{\partial t} = C_v \left( \frac{\partial^2(\Delta u^z)}{\partial z^2} \right) \quad (7)$$

$\Delta(u^z) = \Delta u(z, t)$  is the excess of pore pressure depending of the depth z and time t;

$C_v$  is the coefficient of vertical consolidation.

Solution of the differential equation (7) is the vertical degree of consolidation  $U_v$  as follows:

-  $U_v < 50\%$ :

$$U_v = 2\sqrt{\frac{T_v}{\pi}} \quad (8)$$

-  $U_v > 50\%$ :

$$U_v = 1 - \frac{8}{\pi^2} \exp\left(-\frac{T_v \pi^2}{4}\right) \quad (9)$$

$T_v$  denotes the time factor of vertical drainage:

$$T_r = \frac{C_v \times t}{H^2} \quad (10)$$

H is the drainage distance that is equal half of the thickness of specimen.

## 2. STUDIED SOIL

Tunis soft soil specimens used in this study were obtained from the Sejoumi's lagoon at depth of 17.25 m. The extracted sample is grey coloured, it has a characteristic smell and contains shell debris. From grain size analysis performed by hydrometer and sieving in accordance with standards NFP 94-056 and NFP 94-057, (AFNOR, 1995), it was found that Tunis soft soil presents 85 % of particles

with dimension less than 80  $\mu\text{m}$ , it also includes a high fraction of silt.

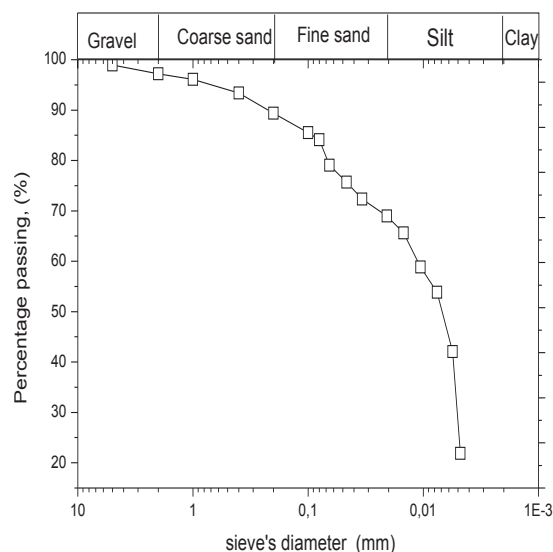


Figure 1. Gradation curve of Tunis soft soil

## 3. CONSOLIDATION TESTS

Three series of consolidation tests were carried out on the Tunis soft soil in oedometer cells. These tests involved applied increments of vertical load to the specimen and measurements of the settlement. For each increment of loading, the decrease of the thickness of the sample versus time is recorded. Duration of the applied increment of load depends on the soil and its consolidation characteristics.

The range of applied stress depends on the range of effective stress which is needed in the consolidation analysis of the studied. When the primary consolidation at prescribed load level is completed (200 kPa) the sample is unloaded in one or several steps until the increment of load of 25 kPa is dismantled and the swelling of specimen can be measured. The applied vertical load is doubled at each increment until reaching the maximum required load (50, 100, 200,400,800 kPa). The specimen is again unloaded. At the end of the test, the sample is careful removed and its thickness and water content are measured. Series 1 (VD): It corresponds to a standard oedometer test performed according to NF P94-90-1 standard (French Standard, 1997). This test is carried out on a cylindrical sample of saturated soil with 70 mm diameter and 19 mm thickness. The soil sample is enclosed in a metal ring and is placed on a porous stone. The loading cap has also a porous stone, so the sample is sandwiched between two porous stones at the top and bottom of the sample to allow vertical drainage (VD).When preparing the sample, filter papers are placed between the soil and the porous stones. The sample is then placed in the consolidation cell and the unit cell. Water is added into the cell around the sample, so the sample remains saturated during the test.

Series 2 (RD): It corresponds to an oedometer test performed on Tunis soft soil improved by a single geodrain (Mebradrain 88) of sizes (thickness = 0.5 cm, width = 1cm and length= 19 mm). In these tests only

radial drainage (RD) is allowed, vertical drainage is prevented by mean of an impervious membrane which covers the porous stone at the top and the bottom levels of the specimen.

Series 3 (V&RD): It corresponds to an oedometer test performed on Tunis soft soil improved by a single of geodrain (Mebradrain 88) type sized as that used in series 2. In these tests the vertical drainage radial drainage are allowed.

Results of the three series of tests presented in Figure 2 show the variation of void ratio  $e$  in function of the effective stress plotted in the logarithmic scale for loading-unloading – reloading sequences for three series of tests.

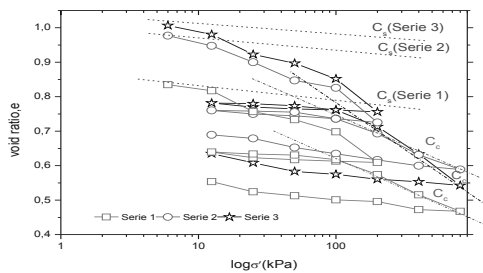


Figure 2. Oedometer curves obtained from three experimental series

Compression  $C_c$  and the swelling  $C_s$  indices, obtained from the three series of tests (VD, RD and VR&D) were determined from oedometer curves and summarized in table 1. Notice that the compression index obtained from series 3 (VR&D) is roughly the double of that recorded in series 1 (VD) and 2 (RD). This can be explained by the allowed vertical and radial drainage paths from which follows enhanced consolidation of the compressible soil. From Table 1, it is understood the swelling is only attributed to vertical infiltration of water with sample unloaded.

Table 1: Values of compression and swelling indices

Serie of tests	1 : VD	2 : RD	3 : V&RD
$C_c$	0.16	0.16	0.30
$C_s$	0.022	0.022	0.023

#### 4. STUDY OF THREE DIMENSIONAL CONSOLIDATION:

##### 4.1 Coefficients of consolidation:

Coefficients of vertical and radial consolidation  $C_v$  and  $C_r$  are determined from the evolution in time of settlement for each increment of loading (from 50 to 800 kPa). From the results obtained for series 1 and 2:  $C_v$  and  $C_r$  were determined by the logarithmic method; which use the plot of thickness of sample versus the logarithmic of time:  $\log(t)$  (Casagrande, 1938).

##### 4.2 Coefficient of permeability

Vertical and radial hydraulic conductivities (permeability coefficients  $k_v$  and  $k_r$ ) are determined by the variable head permeability test. In fact, oedometer apparatus (in series 1 and 2) is equipped with a conventional measuring device (tubes connected to the base of the specimen). The measurements are performed for different levels of applied load from 100 kPa to 800 kPa (100, 200, 400 and 800 kPa).

Figure 9 shows opposite variations of the ratios  $C_r/C_v$  and  $k_r/k_v$  when the consolidation stress varies from 100 to 800 kPa. In this range, ratio  $C_r/C_v$  varies from 36 to 12 and ratio  $k_r/k_v$  varies from 4 to 12. Obtained results show that the assumption made e.g.  $C_r/C_v = k_r/k_v$  is only valid at high levels of consolidation stress (Jia and Chai, 2010).

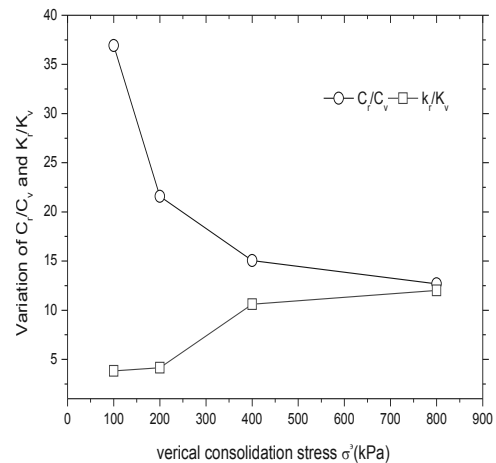


Figure 3. Ratios  $k_r/k_v$  and  $C_r/C_v$  versus consolidation stress

##### 4.3 Degree of consolidation:

In this paper, the global degree of consolidation  $U(t)$  is predicted by two methods. The first one uses the measured settlement at different levels of applied load in series 3 (case of vertical and radial drainage, VR&D):

$$U(t) = \frac{s(t)}{s_{\infty}} \quad (11)$$

$s(t)$  and  $s_{\infty}$  denote respectively the settlements at given time and at the end of consolidation.

The second method consists in calculating  $U$  by the Carillo's equation (1). The radial degree of consolidation  $U_r$  is estimated from the experimental results of series 2 (case of radial consolidation RC) and equations (7) and (9). The vertical consolidation  $U_v$  is obtained from recorded results in series 1 (case of vertical consolidation VC) by using equation (2).

Figures 4a and 4b illustrate the variation of global degree of consolidation  $U$  in function of time for vertical consolidation stress of 400kPa and 800 kPa.

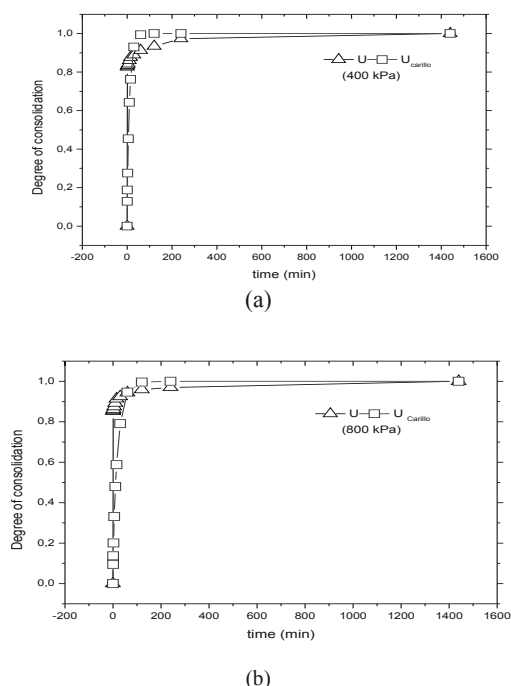


Figure 4. Variation of global degree of consolidation

For applied loads (100, 200, 400 and 800 kPa), it is noted that the degree of consolidation as predicted by the Carillo's theory reaches 100% for a time less than 24 hours, while the degree of consolidation  $U$ , estimated from equation (11) by using measurements of serie 3 results, reaches 100% in 24 hours.

One can also remarks that by using the Carillo's theory a lower degree of consolidation which starts from 10% is obtained, however when using measurements of in series 3 simple approximate methods, higher degrees of consolidation starting from 70% are obtained. Comparing between recorded and predicted global degree of consolidation  $U$ , it follows that the evolution of  $U$  predicted by the Carrillo's theory are overestimated with respect to that deduced from recorded settlement from series 3. The final global consolidation degree  $U$  is identical by using the two methods.

## CONCLUSION

This paper presented an experimental study conducted on Tunis soft clay, in which three types of oedometer tests were executed: a standard oedometer test; an oedometer test on specimen soil improved by an element of geodrain and test a similar test to the second one by preventing the vertical drainage. From measurements coefficients of permeability  $k_v$  and  $k_r$  were determined by the variable head permeability test. In addition, coefficients of vertical and radial consolidation  $C_v$  and  $C_r$  were determined from the evolution in time of settlement at different levels of consolidation stress. Comparison between the ratios  $k_r/k_v$  and  $C_r/C_v$  demonstrated that equality between the two ratios only happens at high level of stress consolidation, contrarily to the common assumption made in previous studies. Predictions of the global degree of consolidation showed that the Carillo's theory leads to overestimated results with respect to predictions from recorded settlements. Further, the effect of vertical and radial consolidations

from the observed global consolidation of improved Tunis soft soils was discussed.

## Acknowledgement:

Authors gratefully appreciate the help provided by Mrs. S. Boussetta during the experimental work carried out at the soil mechanics laboratory of the National Engineering School of Tunis.

## References

- Barron A., (1948). «Consolidation of fine grained soils by drains wells», American Society of Civil Engineers, Journal of Soil Mechanics, Volume 73, pp 718-743.
- Carillo N., (1942). «Simple two-and three-dimensional cases in the theory of consolidation of soils», Journal of Mathematics and Physics, Volume, n°1, pp 1-5.
- Casagrande A. (1938) Notes on soil mechanics-first semester. Harvard University 1-29.
- Guofu.Z and Jian-Hua, (2001). "Design charts for vertical drains considering construction time". Canadian Geotechnical Journal. 38: 1142–1148.
- Hansbo, S. (1981). Consolidation of fine-grained soils by prefabricated drains. Proceedings of 10th International Conference on Soil Mechanics and Foundation Engineering, Stockholm, Balkema, Rotterdam, 3, pp. 677-682.
- Indraratna. B, and Rujikiatkamjorn .C. (2006) "Predictions and Performances of Prefabricated Vertical Drain Stabilized Soft Clay Foundations". Proceedings of the Symposium on Rigid Inclusions in Difficult Soft Soil Conditions International Society for Soil Mechanics and Geotechnical Engineering (ISSMGE TC36).
- Jia, R. and Chai, J. C. (2010). Effect of strain distribution pattern on interpreting CRS consolidation test results. Proceedings of the Fourth Japan-China Geotechnical Symposium, Okinawa, Japan, 29-36.
- Kjellman W. (1948). Accelerating construction of fine-grained soils by means of card board wicks. In Proceedings of the 2nd International Conference on Soil Mechanics and Foundation Engineering, Rotterdam. Vol. 2, pp. 302–305.
- Kjellman W. (1948). Discussion: "Consolidation of fine-grained soils by drain wells" by R.A. Barron. Transactions, ASCE, 113 (2346): 748–751.
- Parakash .K, Sridharan . A and Asha, SR (1996). Consolidation behavior of clayey soils under radial Drainage. Geotech.Test. J, ASTM, 19 (4), 421-431.
- Sridhar, G and Robinson, G (2011) "Determination of radial coefficient of consolidation using log t method". International Journal of Geotechnical Engineering (373-381).
- Terzaghi, K. 1943. Theoretical soil mechanics. Wiley, New York.
- Tyn Myint-U. 1980. Partial differential equations of mathematical physics. Elsevier, North Holland.

# Improvement of soft fat clay using rigid inclusions and vertical drains

## Amélioration d'une argile plastique molle par inclusions rigides et drains verticaux

Kirstein J.F.

BVT DYNIV GmbH; Germany

Wittorf N.

Ingenieurbüro Dr. Lehnert und Wittorf; Germany

**ABSTRACT:** In the case of a new road crossing in Germany with 1.5 to 7.0 m high embankments nearby the Danish border particularly soft clays were found 13 to 20 m deep below sea level. The undrained shear strength of the clay varied between 7 and 20 kN/m<sup>2</sup>. The water content was almost 100 % and the organic matter below 6 %. The consolidation coefficient  $C_v < 0.3$  m<sup>2</sup>/year is characteristics of a fat clay which requires a long time or tight spacing of vertical drains to consolidate. Due to stability risks, vertical wick drains were installed at a 0.5 m spacing in the part of the highest embankments, which were built in three load steps, each time waiting for 60 to 80 % consolidation degree before loading the next step. Even using 600 kN/m woven geotextiles, a total vertical settlement of around 1.5 m and up to 27 cm horizontal deformation were measured throughout one year of monitoring. These deformations were too high for the existing and running highway in the middle of the new projects. Therefore, full displacement concrete columns (rigid inclusions system CMC) were installed up to 22 m deep with load transfer platforms installed on top the inclusions. In order to improve the installation process of the rigid inclusions, additional vertical drains were installed in the soft soil before the inclusions. Within the first two years, the area supported by the rigid inclusion experienced less than 2 cm of deformation, a proportionally small amount compared to the deformations recorded in the wick drain consolidation parts of the project.

**RÉSUMÉ :** Pour un projet d'une nouvelle route sur des remblais de 1,5 à 7,0 m de hauteur en Allemagne près de la frontière danoise, des argiles particulièrement molles ont été trouvés de 13 à 20 m de profondeur sous le niveau de la mer. La résistance au cisaillement de l'argile varie entre 7 et 20 kN / m<sup>2</sup>. La teneur en eau est proche de 100% et la matière organique inférieure à 6%. Le coefficient de consolidation  $C_v < 0,3$  m<sup>2</sup> / an montre une argile plastique qui nécessite un long temps ou un réseau de drains verticaux très serrés pour la consolidation. En raison de calculs de stabilité, les drains verticaux ont été installés avec un espacement de 50 cm dans la partie des remblais les plus hauts, qui ont été construits en trois étapes de chargement, avec pour chaque étape des périodes d'attente de 60 à 80% degré de consolidation avant de la prochaine étape de chargement. Même avec l'utilisation de géotextiles de 600 kN/m, des tassements verticaux de 1.5 m et des déformations horizontales jusqu'à 27 cm ont été mesurés pendant une année de surveillance. Ces déformations sont trop importantes pour l'autoroute existante en exploitation près du nouveau projet. Des inclusions rigides (système CMC) ont été installées jusqu'à 22 m de profondeur avec différents matelas de répartition placés au dessus des colonnes. Afin d'améliorer le processus d'installation des inclusions rigides supplémentaires, des drains verticaux ont été installés dans le sol mou avant l'installation des colonnes. Au cours des deux premières années de construction, la zone supportée par les inclusions rigides a eu moins de 2 cm de déformation, une déformation relativement petite comparé avec celles enregistrées dans des zones du projet consolidées par des drains verticaux.

**KEYWORDS:** soil improvement, Controlled modulus columns (CMC), vertical drains

### 1 INTRODUCTION AND DESCRIPTION OF THE PROJECT

Large areas nearby the northern sea are nearly flat with elevations slightly above or under the sea level. Soft soil of silt, clay, mud and peat reach between five and twenty meters from the surface, before glacial sands are encountered.

The existing west coast highway B5 near the German city of Husum will be widened from two to three lanes in the future in order to improve traffic. The crossing between B5 and B202 was designed as a bridge project with high embankments located on the unconsolidated soft soils, typical at the flat coastal region near the North Sea.

All traffic constructions bring new loads in form of dead- and live-loads to these soft soils. Without soil improvement methods large long-time settlements will occur, which often causes damages to the road during the construction or later on.

The traffic on the highways B5 and B202 in the site had to be maintained during the construction period and the existing road could not tolerate additional stability risks or settlements, especially when the 1.5 to 7 m high embankments are built directly beside the traffic. There are different stages to look at, but we will focus only on the western part with the highest dam nearby the bridge.



Figure 1. detail of the highest embankment west with the bridge abutment over the highway B5 (CMC close to bridge and coloured areas with vertical drains and preloading)



Due to stability and settlement calculations the foundation works took place according to the following sequence of works and according to the figure 2 below:

1. Installation of vertical drains in different spacings from a one meter thick sand working platform.
2. Preloading with three load steps with a distance of 30 m security and working space from the bridge and existing highway B5. (A)
3. The measured consolidation settlements shown in figure 8 fit with the given predictions according to figure 7. An additional strong woven geotextile layer of 600 kN/m tensile strength between the embankment and vertical drains had very little influence on the vertical inclinometer results with 27 cm of deformation as shown in figure 9.
4. After waiting for 1.3 m settlement (figure 8) a part of the embankment and preload was temporarily rebuilt in order to install the controlled modulus Columns CMC. (B)
5. The preload was brought back to the edge of the foundation systems between CMC and vertical drains in order to optimize the settlement behaviour.(C)
6. Installation of deep foundations for the bridge took place on driven concrete piles with additional sleeves sockets in the soft soils.
7. The CMC were installed between the driven piles afterwards, free of vibrations.

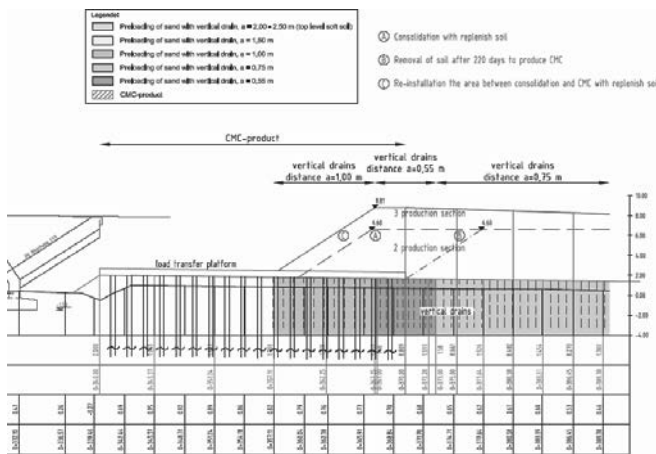


Figure 2. steps of consolidation and construction

The working sequence with different steps was necessary because of stability calculations and the wide influence of the settlements during the consolidation. The CMC brought the following advantages:

- short installation period to complete the project on time
- the vibration free technique allows to work close to the piles of the bridge
- The settlements of the embankment support on CMC with a stiff load transfer platform are compatible with the bridge abutment

## 2 SOIL-PARAMETERS

After the first part of the soil investigations with several borings (BS) and cone penetration tests (CPT) it was clear that there was a problem of stability and consolidation time due to the presence of fat clay in the upper soft soil layer. The project can be modelled with two layers of soft soils divided by a loose sand layer in between. This reaches 13 m up to 22 m in the deepest parts from the surface.

The undrained shear strength  $c_u$  in the soft soil from the results of shear vane tests multiplied with factors of 0.5 to 0.65 are linked to the plasticity according to Bjerum standard DIN

4094-4, Part 4 (Deutsche Institut für Normung 2002). In addition to borings, several laboratory testing ( water content, organic matter and plasticity index ) as well as several load-settlement tests were performed.

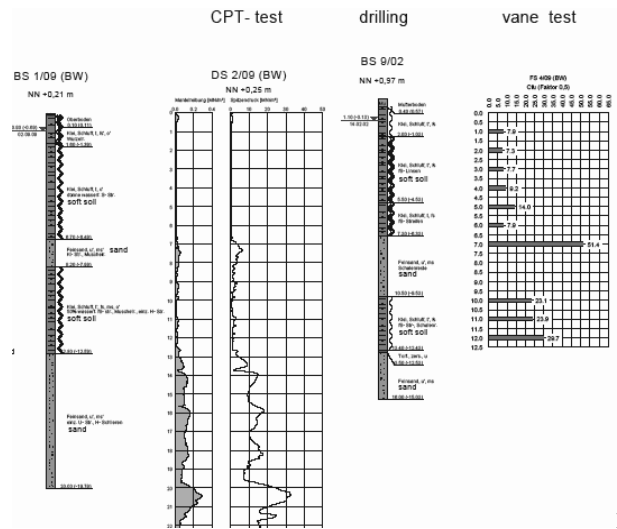


figure 3. boring, cone penetration test and shear vane test in the detail area bridge west

The vane tests showed an undrained shear strength of  $c_u = 6$  to  $8 \text{ kN/m}^2$  near the bridge and an undrained shear strength of  $c_u = 12$  to  $20 \text{ kN/m}^2$  in other parts of the project. This was one more reason to select a CMC foundation nearby the bridge in the area of the lowest undrained shear strength.

Following this decision and the results of soil investigation and laboratory the geotechnical engineers assumed an undrained shear strength of  $c_u = 12 \text{ kN/m}^2$  in vertical drain areas. The representative soil parameters for the calculation of consolidation and stability in the project are given in the following table.

Table 1 . soil parameters for the calculation of consolidation and stability in the coloured drain areas

soil properties / soil	density $\gamma_k/\gamma_k'$ [ $\text{kN/m}^3$ ]	shear strength $\phi'_k$ [grade]	Cohesion $C'_k$ $C_{u,k}$ [ $\text{kN/m}^2$ ]	Modulus $E_{s,k}$ [ $\text{MN/m}^2$ ]	Consolidation coefficient $c_v$ [ $\text{m}^2/\text{s}$ ]
fill sand	18/10	30,0	---	60	$6,0 \cdot 10^{-1}$
soft soil, clay [top level]	14/4	17,5	15 12	0,8	$8,0 \cdot 10^{-9}$
soft soil, silt top level	15/5	20,0	10 12	0,8	$2,0 \cdot 10^{-8}$
sand	18/10	27,5	---	25	$2,5 \cdot 10^{-3}$
soft soil, silt (Bottom level)	16/6	20,0	10 20	2,0	$1,0 \cdot 10^{-7}$

## 3 SOILIMPROVEMENT TECHNIQUES

### 3.1 Vertical drains

Prefabricated vertical drains were installed in different spacings with lengths between 15 m (corresponding to the conditions in figure 3) and 22 m in other parts of the project. It was necessary

to pass the intermediate sandlayer in order to place the vertical drains in the glacial sand below the second layer of soft soil. The small spacings in this project were justified by the step loading and the presence of fat clay in the upper layer of soft soil with special low permeability and corresponding primary consolidation coefficient.

### 3.2 *Controlled Modulus Columns CMC*

The controlled modulus columns CMC are well adapted to installation in soft soils. The full displacement auger acts as a casing and maintain the right borehole diameter over more than two meter length. Concrete pressure and adequate volume are monitored and maintained throughout the concreting phase, which is very critical in very soft soils. The typical piling standards give a minimum limit of 15 kN/m<sup>2</sup> undrained shear strength to use for cast-in-place-concrete.

By the standard DIN EN 12699 (Deutsche Institut für Normung 2001) above  $c_u = 15 \text{ kN/m}^2$  the minimal distance between full displacing elements is linked to the undrained shear strength of the soils. Critical distance is only relevant during the concrete curing period.

Compared to vibrating techniques, CMC are usually faster to install and can be performed in softer soils with lower undrained shear strength. There are several references with CMC-installation directly adjacent to freshly grouted CMC under  $c_u < 15 \text{ kN/m}^2$  conditions. In this project the CMC have been first successfully checked under conditions with the lowest  $c_u$ -values by integrity tests and dynamic pile tests. Loads larger than 500 kN could be tested with a factor of safety larger than 2 FOS on the CMC, drilled into the glacial sand layer.

On part of the project, the process of installing additional CMCs close to nearby fresh CMC was improved through the installation of vertical drains in-between the CMC. Immediately after the CMC installation the water starts to flow out of the vertical drain even at the top of the sandy working platform. A continuous flow for several hours up to one day and the volume of water collected show an efficient fast additional consolidation.

Compared with other CMC areas the heave of the working platform and the excessive over-consumption of concrete, normally increasing with the thickness of softsoil, could be reduced by the additional intermediate vertical drains.



Figure 4. installation of CMC combined with vertical drains and pore-water on the platform

## 4 CALCULATIONS AND PREDICTIONS

### 4.1 *Consolidation and stability calculations in the areas receiving vertical drains*

Initially, a total settlement of 1.29 m was calculated in the area west of the bridge. The time-settlement curves for both primary and secondary consolidation are shown below on figure 5.

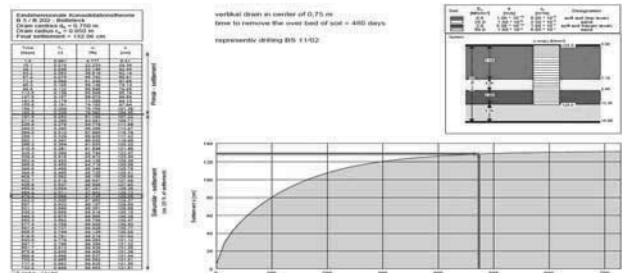


Figure 5. 129 cm of settlements within ½ year of primary consolidation with vertical drains spacing of 0.75 m

The stability calculations are based on undrained shear strength  $c_u$  and required to build the embankment in three steps of loading with berms and twice waiting for the sufficient degree of consolidation necessary. According to (Chaumeny, Kirstein and Varaksin 2008) the shear strength was calculated using the following relation to the degree of consolidation:

$$\tau = U (\sigma \tan \phi' + c) + (1-U) c_u \quad (1)$$

- U: degree of consolidation
- $\sigma$ : total load at a given depth
- $\phi'$ : internal friction angle
- c: final drained cohesion
- $c_u$ : undrained shear strength

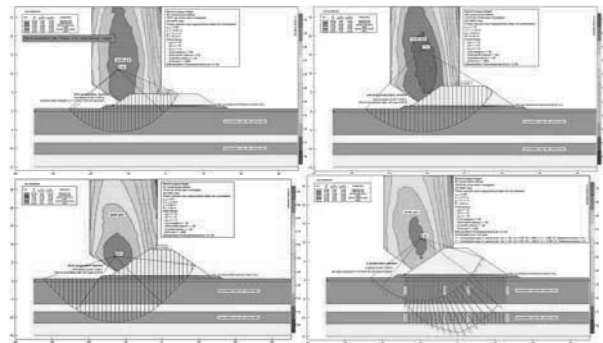


Figure 6. stability calculation of three loading steps and control calculation of the final situation

For this project  $c = c_u$  in formula (1) as improvement  $\Delta c_u$  was added to the basic  $c_u$  value in the stability calculations.

$$\Delta c_u = U \sigma \tan \phi' \quad (2)$$

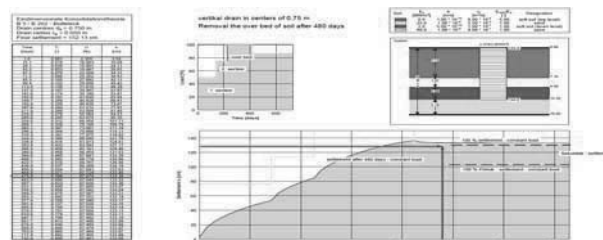


Figure 7. settlement calculations with the three load steps

Field measurements and the stability analysis in final configuration based on  $\phi'$ , c and porewater pressure were in good agreement with the calculations using the improved undrained shear strength.

### 4.2 *Controlled Modulus Columns CMC*

Due to the presence of very soft soils, the CMC are designed to take the full load of the embankment, neglecting the small load bearing capacity of the soil in between the inclusions. With 500 kN characteristic load per CMC, the calculated settlement at the top of each CMC is very similar to the settlement of the piles under the bridge.

Nevertheless, below the embankment, there is no concrete slab or rigid structure like for the foundation of the bridge. Reinforced earth with galvanized steel was designed to hold the large horizontal forces of active earth pressure. Because of the large geotextile deformations during the consolidation period, as shown in the following monitoring results, the decision was made to use a stronger more rigid construction with nearly no deformation. Compared with plastic geotextiles, the steel grid material has only very small elastic deformations, and as a result limiting the horizontal deformations of the embankment. Through the addition of some gravel in parts of the sandy load transfer platform LTP, the friction between LTP and CMC was greatly increase and nearly no deformation was necessary to mobilize the friction of the LTP.

## 5 MONITORING RESULTS

### 5.1 Wick drains

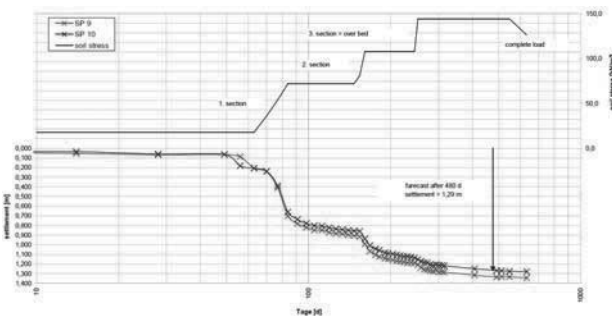


Figure 8. measurement at the settlement plates SP 9 und SP10.

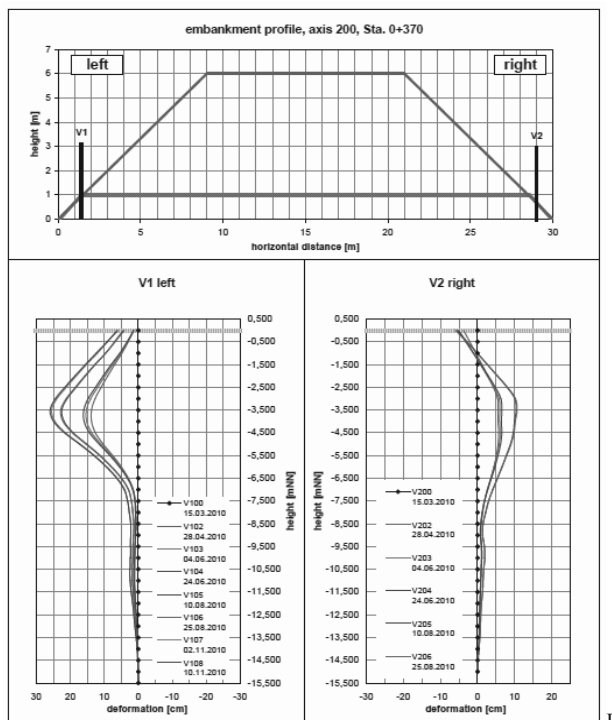


Figure 9. vertical inclinometer results at the 7 m high damm with drains and 600 kN/m woven geotextile

The measured settlements during the consolidation process in figure 8 follow very closely the predictions shown in figure 7. An additional strong geotextile layer of 600 kN/m tensile strength between the embankment and the vertical drains had 27 cm of deformation measured with vertical inclinometers.

### 5.2 Controlled Modulus Columns CMC

Several measurement systems were installed between the CMC and the reinforced earth in the load transfer platform. The instruments show an almost perfect full stress concentration of the load on the CMC and less than one centimetre of horizontal deformation. Figure 10 shows the cross section and the 5 vertical deformation measurements over a period of 2 years. The horizontal inclinometer was laid across six marked CMC-columns (figure 1 and figure 9). A settlement of one centimetre of the top of the CMCs and two centimetres in-between CMC in the reinforced earth steel construction were measured. There was a good agreement between the calculated values of the settlement and the results of the monitoring.

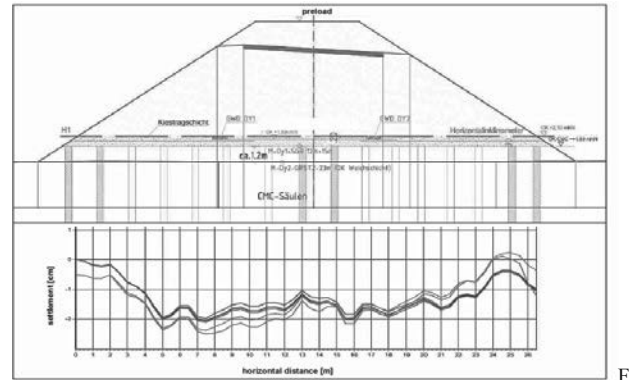


Figure 10. horizontal inclinometer results with around 1 cm of CMC settlements and 2 cm of reinforced earth settlements

## 6 SUMMARY AND CONCLUSIONS

Soft and fat clay were found at the B5 / B202 road crossing. Additional soil investigations and laboratory tests were performed to be able to complete a proper design, regarding stability and consolidation time.

Oedometer consolidation tests allowed to precisely predict the movements during the consolidation processes that were accelerated by the use of vertical drains at different spacings. Large deformations of up to 1.5 m of settlements and 27 cm of horizontal displacement were experience and closely match the calculations and show that it was the right decision not to place the highest embankment directly on the softest soil beside the bridge over the running traffic on the highway B5.

Vibration free CMC in combination with reinforced earth allowed to construct this high embankment with less than two centimetre differential settlements to the piled bridge.

With a careful planning of the work within the overall construction schedule, detailed design combined with an extensive monitoring program, economic soil improvement techniques can be combined with deep foundations in one project even on very soft soil can be treated successfully.

## 7 REFERENCES

- DIN Deutsches Institut für Normung, 2002, DIN 4094-4: Subsoil – field testing – part 4 : Field vane test.
- DIN Deutsches Institut für Normung, 2001, DIN EN 12699: Execution of special geotechnical work - Displacement piles; German version J-L Chaumeny, J.F.Kirstein, S. Varaksin, 2008, An experience of consolidation of extremely soft mud for one of Europe’s largest projects “The AIRBUS A-380” factory in Hamburg, Glasgow.

# Interaction of stone column and surrounding soil during its construction: 3D numerical analysis

Interaction d'une colonne ballastée et du sol environnant pendant sa construction : analyse numérique 3D

Klimis N.S.

*Civil Engineering Department, Democritus University of Thrace (DUTH), Xanthi, Greece*

Sarigiannis D.D.

*AUTH, MSc DIC*

**ABSTRACT:** This work deals with a simulation of a construction sequence of a stone column in two distinct stages: a) a one stage excavation and b) a multi-stage backfilling of the column stone excavation with crushed gravel at ascending steps of 1m. Simulation of this procedure is attempted using a 3D model which represents the stone column and the surrounding soil. Analysis is carried out using a numerical code, called FLAC3D, based on finite differences. The mathematical model incorporates geometry and boundary conditions of the problem, profile of soil layers with their physical, deformational and mechanical properties and their constitutive laws, as well as, initial conditions of stresses and deformations of subsoil stratum of the examined area. Special emphasis is given to simulation of an harmonically imposed vertical loading of the vibrating column, into an equivalent static vertical loading and subsequently into an equivalent radial pressure against internal wall of the cylindrical excavation of the constructed stone column. Results clearly denote that there is a strong interaction of the complex system in the kinematical and stress field, which satisfactorily justifies modification of the final diameter of the constructed stone column compared to the theoretical proposed diameter.

**RÉSUMÉ :** Ce travail se réfère à une simulation numérique de la séquence de construction d'une colonne ballastée, en deux étapes séparées : a) une étape unique d'excavation, et b) plusieurs pas successifs de remblayage de l'excavation cylindrique de la colonne ballastée, avec du matériau granulaire écrasé, à des pas montants de 1m. La simulation est effectuée à l'aide d'un modèle 3D qui représente la colonne ballastée et le sol environnant. Le code numérique utilisé est FLAC3D et il est basé sur le modèle des différences finies. Le modèle mathématique intègre la géométrie et les conditions limites du problème, le profil du sol avec leurs propriétés physiques, mécaniques et de déformation, ainsi que leurs lois de comportement et les conditions initiales de la région examinée. Une attention particulière est donnée à la simulation d'un chargement harmonique vertical imposé à la colonne vibrante, à un chargement équivalent vertical statique, et par la suite, à une pression équivalente radiale exercée sur l'intérieur de l'excavation cylindrique de la colonne ballastée construite. Les résultats démontrent clairement l'interaction prononcée du système complexe, qui justifie aisément le grossissement du diamètre construit par rapport au diamètre théorique conçu lors du dimensionnement du projet.

**KEYWORDS:** stone column, excavation, multi-stage backfilling, Flac3D, interaction, complex system, diameter.

## 5 INTRODUCTION – SCOPE OF THE WORK

The present work focuses on the investigation of kinematic and strain interaction of a complex system consisting of a single column stone and the surrounding soil, during the excavation stage and the backfilling stage with crushed gravel.

The scope of this work is the investigation and a possible explanation of the problem concerning modification of the constructed stone column diameter, versus the theoretical (design) one, taking into account the procedure of the stone column construction, its geometrical characteristics and the geotechnical model representing the surrounding soil and its physical, deformational and mechanical properties.

In the framework of this work, a summary of geological, geophysical, geotechnical and seismological data are presented in a succinct way in the following chapters, for the examined area, based on a number of corresponding projects performed in the recent past. After a short technical description of the stone column constructing procedure adopted for this project, the numerical model is determined and numerical analyses results are presented, in an attempt to explain the deduced discrepancy between “constructed” and “designed” stone column diameter. The examined area is located in the wide bed of a river in northern Greece, prone to liquefy, where a bridge is founded.

## 2. GEOLOGICAL AND SEISMOLOGICAL DESCRIPTION OF THE SITE

According to geological and geotechnical data, resulting from preceding investigation projects on this area, the surface is

covered by deposits that belong to the Quaternary and is subdivided into: a) river deposits (RD) consisting of silty sands, clay-silty sands, gravels and locally cobbles of gneiss or marble, and b) alluvial deposits (AL), consisting mainly of sands with a largely fluctuating percentage of clays, silts and gravels, of a thickness ranging from 12 to almost 55m.

The geological bedrock of the examined site consists of rocks of the alpic age and belongs to the Rodopic Mass, consisting mainly of biotitic gneisses (gn) interpolated by amphibolites and marbles green-gray coloured. The upper part of the gneissic rockmass appears intensively weathered to totally weathered, consisting thus the weathering zone of 2 to 4m of thickness. The permeability of different geological formations is quite heterogeneous: the riverbed deposits, mainly gravel consisting (RDg) are a rather permeable soil formation ( $k \geq 10^{-3} m/sec$ ), whilst alluvial deposits present a rather low permeability ( $10^{-7} \leq k \leq 10^{-5} m/sec$ ).

As for the seismological data, the examined site belongs to zone I of low seismic hazard, with a horizontal free-field peak ground acceleration value:  $a_{max}=0.16g$ , according to the most recent Hellenic map of seismic zones, valid from 1/1/2004.

## 3. GEOTECHNICAL CHARACTERIZATION

According to the entity of the geotechnical and geophysical investigation programs performed on the broad area (geotechnical boreholes, CPTs and Cross-Hole tests), it results that the prevailing soil formation are alluvial deposits consisting

of sands to silty sands, with a high degree of heterogeneity, characterized by USCS as SP, SW, SM, SM-SP, SM-SW. In some cases they appear as clayey sand (SC) to sandy clay (CL), whereas in other cases, they turn out to be gravel layers, such as: GP, GW, GM, GP-GM. According to the almost 200 SPTs performed, the mean value of blows was calculated about 23, with a standard deviation of  $\pm 11$ . The whole area, where the bridge is founded, has been initially divided into three sub-regions represented each by a different geotechnical design section (ITSAK & Gazetas 2003), and finally a design geotechnical section has been attributed to each bridge pier (Edafomichaniki 2007) used for dynamic analyses purposes.

From various simplified design geotechnical sections, each per bridge pier, it has been chosen one, for the needs of the present project, corresponding to a precise pier of the bridge, as being the most representative of the area, but not the most conservative one. The soil profile used in the present work, can be described as follows:

Layer S<sub>1A</sub> (0 to 2m): loose to medium dense gravels with sand and sand or silty sand with local presence of gravels (GP, SW-SM, SP):  $N_{SPT} \cong 22$ ,  $\gamma=20.5\text{kN/m}^3$ ,  $\phi^{\circ}=36^{\circ}$ ,  $c^{\circ}=3\text{kPa}$ ,  $E_s=10\text{MPa}$ ,  $\nu=0.33$

Layer S<sub>1B</sub> (2 to 5m): medium dense gravels with sand and sand to silty sand with local presence of gravels (GP, SW-SM, SP):  $N_{SPT} \cong 23$ ,  $\gamma=20.5\text{kN/m}^3$ ,  $\phi^{\circ}=37^{\circ}$ ,  $c^{\circ}=5\text{kPa}$ ,  $E_s=12\text{MPa}$ ,  $\nu=0.32$

Layer S<sub>2A</sub> (5 to 12m): medium dense gravels with silt and sand to silty sand with presence of gravels (GM-GP, SP-SM, SM):  $N_{SPT} \cong 25$ ,  $\gamma=21.0\text{kN/m}^3$ ,  $\phi^{\circ}=39^{\circ}$ ,  $c^{\circ}=6\text{kPa}$ ,  $E_s=16\text{MPa}$ ,  $\nu=0.31$

Layer S<sub>2B</sub> (12 to 19m): medium dense silty gravels, silty sand with presence of gravels to silty sand (GM-GP, SP-SM, SM):  $N_{SPT} \cong 28$ ,  $\gamma=21.0\text{kN/m}^3$ ,  $\phi^{\circ}=40^{\circ}$ ,  $c^{\circ}=8\text{kPa}$ ,  $E_s=20\text{MPa}$ ,  $\nu=0.30$

Layer S<sub>3A</sub> (19 to 23m) and layer S<sub>3B</sub> (23 to 35m): medium dense clayey sand-gravels mixture to sandy clay with gravels, or silty sand-gravels mixture (GC-GM, SM, CL):  $N_{SPT} \cong 26$ ,  $\gamma=21.2\text{kN/m}^3$ ,  $\phi^{\circ}=37^{\circ}$ ,  $c^{\circ}=12\text{kPa}$ ,  $E_s=15\text{MPa}$ ,  $\nu=0.31$ .

From 35 to almost 48m the weathering zone of the gneissic bedrock or highly weathered gneiss is met.

#### 4. METHODOLOGICAL APPROACH

The analysis was carried out with FLAC 3D numerical code of finite differences.

##### 4.1 Modeling Procedure

By considering the construction of a stone column in the above soil profile, simulation of two distinct stages of the construction of a stone column is attempted using a three-dimensional (3D) model which represents the stone column and the surrounding soil. Simulation of soil materials is realized by a 3-dimensional polyhedral grid with use of the finite difference method. The mathematical model adopted, incorporates geometry and boundary conditions of the problem, the profile of soil layers, physical, deformational and mechanical properties, constitutive laws for the geomaterials, as well as, initial conditions of stresses and deformations of the subsoil stratum of the area under study.

Geometry of the problem is simplified to axial symmetry. A vertical plane through stone column axis is a plane of symmetry for the analysis. Model grid is shown in figure (1). Coordinate axes are located with origin at the base of the grid, whereas y-axis is oriented along vertical column axis and upward. The initial grid is assigned by 5.0m and 50 units in x-direction, by 5.0m and 50 units in z-direction and by 28.0m and 56 units of in y-direction. A Mohr-Coulomb constitutive model elastoplastic behavior is assigned to all zones of soil surrounding stone column, whilst linear elastic one is assigned to stone column backfilling crushed material. Boundary conditions consist of roller boundaries along the external grid sides of column axis and a fixed base. Equilibrium conditions for initial stresses are

based on earth pressure coefficient at rest  $K_0=v/(1-v)$ , where  $\nu$ : Poisson's ratio.

The modeling sequence consists of the following stages:

Stage I : Initial stresses

Establish equilibrium conditions to initialize stresses

Stage II : Excavation

Stone column excavation at full penetration depth was decided to be numerically simulated in one and only stage, since in reality, excavation was accomplished in about 30 min for a typical stone column of the project, and also, because no steps of excavation during its construction, could be discretized.

Stage III : Stone Column Construction

In reality, construction of cylindrical stone columns of the project with a theoretical diameter  $D=0.8\text{m}$  and a length  $L=23.0\text{m}$ , is realized by ascending steps of 0.5m; at each step, the crushed geomaterials are driven through the top of the stone column downwards (top feed method), and then, the vibrational torpedo is sunk into the excavated cyclic area, reaches the top of the crushed material and starts vibrating harmonically at a frequency of 30Hz, in order to achieve an harmonically applied normal stress of 30 to 35MPa. However, our choice of computational ascending steps to simulate stone column construction was of 1.0m, since an initial comparative study between 0.5m and 1.0m ascending steps, revealed no significant differences, whereas computational time difference was important. Therefore, Stage III is sub-divided in two distinct calculation steps, ever after named as "Sub-stage IIIa and IIIb"

Sub-stage IIIa : Simulation of Vibration and Compaction

Based on the construction procedure concerning the one stage of excavation of the stone column to be realized, which affects significantly the mechanical properties of the surrounding zone, a weak zone boundary has been created, by reducing  $\phi^{\circ}$  &  $c^{\circ}$ , in a distance of 0.60m surrounding column lateral sides, in order to simulate relaxation due to excavation. The width of the weak zone, the reduced values of the mechanical parameters and the elastic deformation modulus, resulted from a "trial and error" back calculating procedure, based on the quantity of the crushed material measured in situ, during the construction of a stone column of the project. Namely, we tried to match the increase of the "as built" diameter of the examined stone column, in agreement with the quantity of the crushed material used for the construction of the stone column, by adjusting the values of mechanical and deformational parameters of the disturbed zone. Vertical normal stress, harmonically applied on top of filling crushed material in order to compact the crushed fill material, per numerical ascending step of the stone column construction, is transferred as a lateral pressure "p" to simulate subjected compressive lateral loads of material due to gravel compaction, in terms of an "equivalent static" lateral (radial) pressure, as explained in the following paragraph.

Sub-stage IIIb : Simulation of Crushed Stone Material filling

This sub-stage simulates filling of the stone column crushed material taking under consideration the preceding compaction procedure. In order to maintain the shape of the "deformed diameter" per constructed step of the stone column, crushed fill material, considered as a linear elastic one, it has been attributed a very high modulus of elasticity, avoiding thus a rebound of the plastic lateral displacements obtained from sub-stage IIIa.

##### 4.2 Assessment of equivalent lateral static loading

It is widely known in Mechanics, that a dynamic system responds to an harmonic external loading, according to the following equation:

$$u(f) = u_{st} \frac{1}{\sqrt{[1 - (f/f_1)^2]^2 + 4\zeta^2}} \quad (1)$$

where,  $u(f)$ : dynamic displacement,  $u_{st}$  : equivalent static displacement ( $=P/K$ ),  $\omega$ : frequency of the input motion,  $\omega_1$ :

predominant frequency of the system (herein: the soil column overlying gneissic bedrock), and  $\zeta$ : damping ratio of the system.

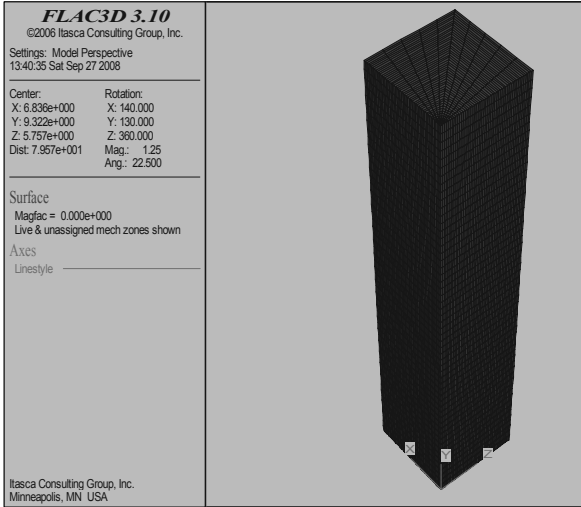


Figure 1. Model grid used for 3D numerical analyses.

From equation (1), it results that ratio  $u(f)/u_{st}$  is greater than 1.0 when  $f/f_1 < 1.0$ , and vice versa, when  $f/f_1 \gg 1.0$ . In this last case, it results:

$$u(f)/u_{st} \cong \frac{1}{(f/f_1)^2} < 1 \quad (2)$$

Based on the aforementioned, in order to use an “equivalent static” loading instead of a dynamic or harmonic one, we need to use a coefficient  $b(f)$ , defined as in equation 2. As  $b(f)$  is proportional to  $u(f)/u_{st}$ , it is evident that it will be inversely proportional to loadings, i.e. the ratio  $P_{st}/P(f)$ . Therefore:

$$b(f) \cong \frac{P(f)}{P_{st}} = \frac{1}{\sqrt{[1 - (f/f_1)^2]^2 + 4\zeta^2}} \quad (3)$$

In the present problem, it can be assumed approximatively, that:

$$f_1 \cong \frac{V_{La}}{4H} \cong \frac{3V_s}{8H} \quad (4)$$

where,  $V_{La}$ : wave velocity according to Lysmer ( $V_{La} \approx 1.5V_s$ ),  $V_s$ : shear wave velocity, and  $H$ : depth of the soil column overlying the gneissic bedrock.

Consequently, for the examined case, where a mean depth of the soil column is admitted as:  $H=30\text{m}$  and  $V_{S30} \approx 250\text{m/sec}$ , the predominant frequency of the system for vertically induced harmonic external loading, can be roughly approximated, as:

$$f_1 \approx \frac{3 \times 250\text{m/s}}{8 \times 30\text{m}} = 3\text{ Hz} \quad (5)$$

For input motion frequencies ranging from 20 to 35Hz (mean estimated value of 30Hz) and mean estimated value of damping ratio  $\zeta=20\%$  (Mylonakis et al 2006), equation (3) results  $b \approx 0.15$ , which represents a reductional coefficient due to the frequency of the input motion. It is estimated that due to a large number of uncertainties of the system, and also because the examined system is not a single degree freedom oscillator, it would be wiser to impose a factor of safety of 2.0, resulting thus to a design coefficient  $b_{design} = b \times 2 = 0.3$ . Accordingly, it results that  $P_{st} \approx 30\%P_{cyclic}$ .

Based on the above, vertical harmonic loading imposed by a hydraulic vibrating torpedo, can be calculated via cyclic normal stress (30 to 35MPa) applied through the edge of the vibrating

column of a diameter  $d=0.40\text{m}$ . The vertical harmonic loading, is calculated, as follows:

$$P_{cyclic} = q_{cyclic} \frac{\pi d^2}{4} = 30 \times \frac{3.14 \times 0.4^2}{4} = 3.768\text{MN} \quad (6)$$

providing thus an equivalent static vertical loading  $P_{st} \approx 30\%P_{cyclic} = 0.3 \times 3.768 \approx 1.13\text{MN}$ , and an equivalent vertical normal stress that is estimated to compact vertically the crushed fill material of the stone column at every step of construction:

$$\sigma_{z,st} = \frac{1130 \times 4}{3.14 \times 0.8^2} \cong 1777\text{kPa} \quad (7)$$

According to linear elastic theory, earth pressure coefficient at rest, equals to:  $k_0 = \nu/(1-\nu) = 0.3/(1.0-0.3) \approx 0.429$ , and then the equivalent radial (horizontal) static normal stress is estimated  $\sigma_h = 0.429 \times 1777 \approx 762\text{kPa}$ .

For the numerical analyses performed, for the deeper part of the stone column it was adopted a radial pressure of 750 to 800kPa, whereas, it has been progressively reduced as ascending steps of stone column construction were getting close to the head of the stone column at free surface until it has almost been nullified in the last step.

## 5. NUMERICAL ANALYSIS IMPLEMENTATION & RESULTS

Developing a step by step simulation of a stone column construction (excavation, filling & compaction), analysis results are mainly concentrated to the plasticity limits of soil strength and to the outwards lateral displacement of the stone column excavated sides due to gravel compaction. Plasticity indicators for shear or tension are divided at a present plastic yield indicator with symbol (-n) or a past plastic yield indicator with symbol (-p). Outwards lateral displacement are being recorded at every depth level of the stone column, in different grid points with distance of 0, 30cm, 60cm and 100cm of the excavated sides of the stone column.

Figure (2) shows plasticity indicators generated due to the excavation at full penetration depth. It can be seen that one step column excavation, has no remarkable effect at inwards horizontal displacements. At this case, plasticity limits of soil strength developed in a distance of 0.20-0.40m surrounded excavated sides. Inwards horizontal displacements of the excavation are limited in a range of 4-5mm with maximum values appearing at deeper levels of excavation.

Sub-stages IIIa & IIIb simulate the compaction/filling of crushed stone material and interaction of the above to surrounding soil. Figures (3) and (4) exhibit plasticity indicators for two different construction depths from 16m to 15m and from 1m up to the head of the stone column (free soil surface) respectively. Although, most of plastic indicators, reveal a past plastic yield (indicator -p) in shear or tension, plasticity disturbance of the soil is generated in a remarkable distance of 1.0 to 1.2m surrounding column sides for the first example and in almost the entire surface area of the surrounding soil at the second one. Low initial stress state at free soil surface, leads to a remarkable plastic yield over limit close to the stone column head, even though equivalent static normal radial stress is very low. Concerning lateral outwards displacement of stone column excavated sides, due to gravel compaction/filling, shows that values between 10 and 20cm keep well at a distance of 100cm of the excavated sides. Indicatively, outwards radial displacement values (at excavated sides) for depths at 22.5m, 11.0m and 1.0m are in a size of 23cm, 12cm and 20cm respectively. In general terms, outwards horizontal displacements are eliminated at distances more than 60cm of excavated sides.

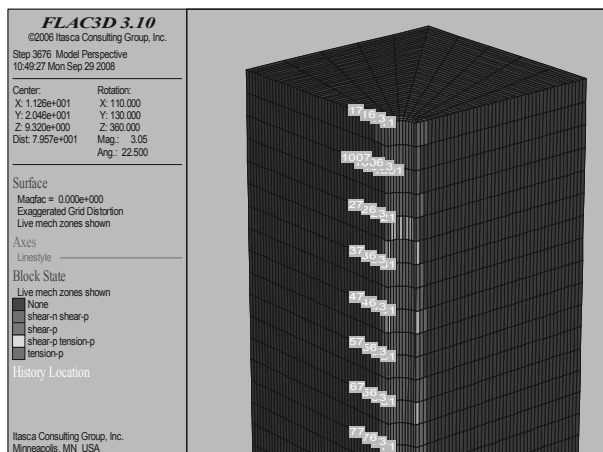


Figure 2. Plasticity zones during the one stage excavation of the examined stone column

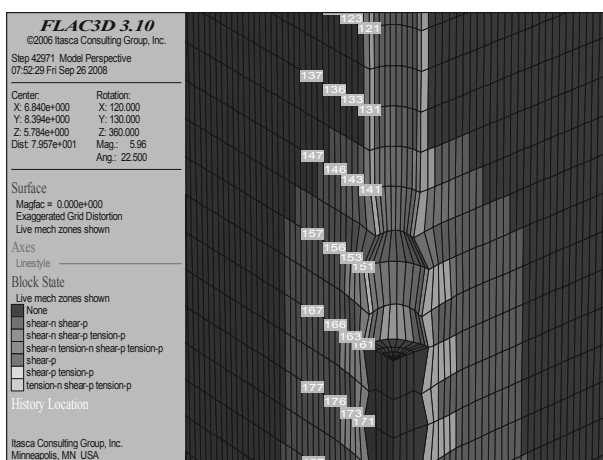


Figure 3. Plasticity zones during multi-stage filling of the stone column with crushed geomaterial at depth of 16 to 15m simulated by an equivalent static radial pressure (sub-stage IIIa, 8<sup>th</sup> ascending step of construction of the examined stone column)

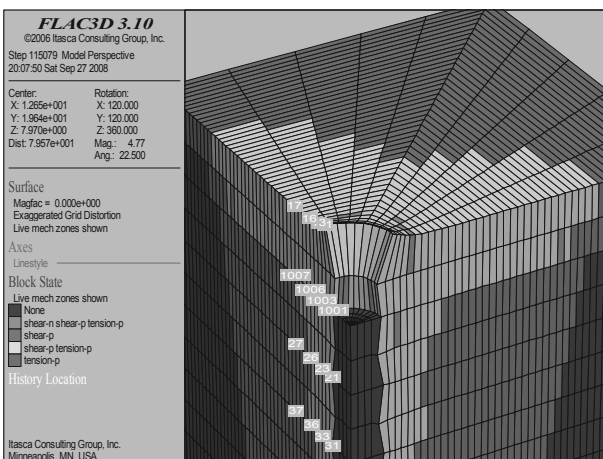


Figure 4. Plasticity zones during multi-stage filling of the stone column with crushed geomaterial at depth of 1m to head of the stone column, simulated by an equivalent static radial pressure (sub-stage IIIa, 23<sup>rd</sup> final ascending step of construction of the examined stone column)

## 6. CONCLUDING REMARKS

For the needs of the present project it has been decided to adopt a rather simple, yet representative, soil profile corresponding to a bridge pier, where typical stone columns of 0.8m diameter and 23m length are constructed, in order to improve foundation soil behaviour. The complex system consisting of a stone column

and the surrounding soil is numerically analyzed with FLAC3D numerical code based on finite differences.

The numerical code used considered the procedure of construction, as well as, its effects on the surrounding soil, and simulated at its best, the physical procedure of the stone column construction, in a rational and well documented way.

Excavation stage is simulated in one and unique stage, whereas, construction of a stone column is simulated by a multi-stage complex procedure divided in two distinct calculating steps. Those are identified as two sub-stages per ascending step of construction: a) vibration and compaction, materialized by application of an equivalent radial pressure against the internal wall of the cylindrical excavation and b) stone column filling with a linear elastic geomaterial assigned a high elastic modulus of compressibility, due to the compaction procedure, preventing a rebound of the induced radial displacements of the first sub-stage.

Commenting the outcome of numerical analyses performed, the following points can be outlined:

1. after completion of excavation stage, the plastic zones developed around the cylindrical excavation are limited, same as horizontal displacements, ranging from some millimeters to only a few centimeters,
2. once excavation procedure is completed, it has been documented via a “trial and error” back calculating procedure, that a zone of about 60cm is seriously disturbed, affecting notably the mechanical and deformational parameters of the surrounding soil,
3. the stage of construction of the stone column has been simulated by a multi-stage procedure of ascending steps of 1m and application of an equivalent static radial pressure, as defined in §4.2, progressively reduced as ascending construction steps approached the head of the stone column at the free surface,
4. horizontal inelastic displacements in the limit of the side wall of the cylindrical excavation range between 10 and 20cm, resulting thus in an expansion of the constructed diameter, compared to the theoretical one as designed.

## 7. REFERENCES

- Edafomichaniki s.a. 2007. Egnatia Odos s.a., section of Nestos bridge and road access on it (14.1.2/14.2.1). Geotechnical Final Design Study (boreholes GT1 to GT5).
- Itasca Consulting Group Inc. FLAC3D v3.10: Fast Lagrangian Analysis of Continua. User’s Manual version 3.10.
- Itsak and Gazetas G. 2003. Study of seismic response and evaluation of liquefaction risk. *Issue 1*, pp 73.
- Mylonakis G., Nikolaou S. and Gazetas G. 2006. Footings under seismic loading: Analysis and design issues with emphasis on bridge foundations. *Soil Dyn. Earthquake Eng.*, 26(9), 824-853.

# Laboratory tests and numerical modeling for embankment foundation on soft chalky silt using deep-mixing

Essais au laboratoire et modélisation numérique de la fondation d'un remblai sur un limon crayeux mou des sols améliorés par malaxage en profondeur

Koch E., Szepesházi R.

*Széchenyi István University, Győr, Hungary*

**ABSTRACT:** The deep-mixing is nowadays world-wide accepted method as a ground treatment technology to improve the permeability, strength and deformation properties of soils. Binders, such as lime or cement are mixed in-situ with the soil by rotating mixing tools. The method is undergoing rapid development, particularly with regard to its range of applicability, cost effectiveness and environmental advantages. The paper describes the results of laboratory tests on chalky silt samples mixed with cement of different content. The influence of the different mixing parameters on the unconfined compression strength and deformation modulus is shown and evaluated. Typical results of the laboratory tests were used in numerical modeling with PLAXIS 3D as input parameters to study the behavior of a 4 m high embankment constructed on this soil improved by deep mixed columns with different spacing and diameters. The parameters of the soil improvement technique were analyzed to study their influence on the settlement and the stability of the embankment. The trends of the calculation outputs are shown and evaluated.

**RÉSUMÉ :** Pour l'amélioration de la perméabilité, de la résistance et des caractéristiques de déformation des sols mous la malaxage est considéré comme une technique courante, préconisée partout. La procédure consiste à malaxer, par rotation, les liants: la chaux ou/et le ciment et le sol in-situ à l'aide de l'outil de malaxage par rotation. Grâce à la diversité technique et aux possibilités d'application de l'appareillage, ainsi que ses avantages économiques, tout en respectant les intérêts de l'environnement, cette technologie approuve un développement continu même dans nos jours. L'étude a pour but de faire connaître les résultats des essais au laboratoire réalisés sur des éprouvettes prélevées du sol traité avec les liants: la chaux et le ciment, dont la teneur par éprouvettes était variable. L'analyse des résultats de ces essais a mis à l'évidence l'influence des divers paramètres de malaxage sur la résistance à la compression simple et sur le modul de déformation du sol traité. Ces résultats nous ont rendu possible d'appliquer le programme d'éléments finis PLAXIS 3D, en vue d'étudier une digue de 4m de hauteur, reposant sur des colonnes de sol traité, ayant une disposition variable et des diamètres différents. Le but de cette étude était de fournir un moyen de calcul qui permet le suivi des tassements et la stabilité de la digue, en fonction de la variation des paramètres de malaxage.

**KEYWORDS:** deep mixing, laboratory test, numerical modeling

## 1 INTRODUCTION

Road and railway embankments have often been constructed on soft, saturated, organic subsoil. In the future this type of construction is suspected to increase, due to environmental and land management considerations. The low strength and the high compressibility together with the low permeability and the high creep potential result in stability problems, extremely large settlements with prolonged consolidation times, and long term secondary compression. One of the solutions to avoid these problems is deep-mixing stabilization of the subsoil.

The development of deep-mixing was started in Sweden and Japan in the late 1960's with the application of a single mixing tool to produce column-type elements (Figure 1.). Since then, new technologies using different mixing tools or binder types have been introduced. Lately, another technology; mass stabilization, based on Finnish research is gaining acceptance, where the whole soil mass is treated normally to a depths of 2 to 4 m (Figure 2.).

The goal of deep-mixing is to improve the soil characteristics, e.g. increase the shear strength and/or reduce the compressibility, by mixing the soil with some type of chemical additives that react with the soil. The improvement occurs due to ion exchange at the clay surface, bonding of soil particles and/or filling of voids by chemical reaction products.

Mass stabilization is preferred if the subsoil is very poor e.g. peat, organic clay or soft clay deposits, and the thickness of the mass to treat is less than 5 m, the height of the embankment is low, and the main purpose of the treatment is to increase stability (Allu Stabilisation System). If the main purpose is to reduce settlements and the weak soil is thicker than 5 m;

approximately 60 cm diameter single columns are used. With this technology the treated depths can be increased up to 40 m (Moseley and Kirsch, 2004, Logar, 2012).

Recently, the use of deep-mixing technology has been planned on several Hungarian railway projects. The „Sárrét” railway line rehabilitation is one of these projects; the railroad crosses an area where the subsoil is soft chalky silt. Both deep-mixing technologies could be applied on this site. This paper describes the preparation of their use at this project. Firstly, the mechanical properties of the improved soil were investigated in the laboratory, then, the effectiveness of the technology as embankment foundation was evaluated with the PLAXIS 3D finite element program using the laboratory test results.

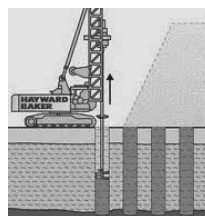


Figure 1.  
Column-type deep-mixing

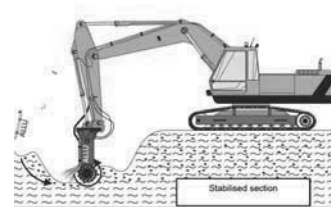


Figure 2.  
Mass stabilization



## 2 LABORATORY TEST RESULTS

### 2.1 Parameters of deep-mixing technologies

The quality of the mixed depends on the applied binder type and quantity as well as the ratio of water to binder in the mixture. These quantities can be expressed by volume or weight. It is essential that the water content of the original soil is considered when calculating the water content of the slurry.

The binder quantity is described with the cement factor ( $\alpha$ ), and the in-place cement factor ( $\alpha_{inpl}$ ):

- $\alpha = m_{cement} / V_{soil} = \text{binder weight} / \text{soil volume} [\text{kg}/\text{m}^3]$ ,
- $\alpha_{inpl} = m_{cement} / V_{mix} = \text{binder weight} / \text{mixture volume} [\text{kg}/\text{m}^3]$ .

The water content of the soil is described with

- $w_T / c = m_{w,mix} / m_{cement} = \text{the total water-cement ratio} [-]$ .

The quality of the mixture is generally described with two parameters:

- $q_u = \text{the unconfined compressive strength} [\text{MPa}]$ ,
- $E = \text{the Young's modulus} [\text{MPa}]$ .

These mechanical properties are generally measured at 7, 14, 28, 42 and 90 days after mixing, because the strengthening of the improved soft fine grained soils is a long process, but the qualifying parameter is generally the 28 day unconfined compression strength [Filz et. al., 2003].

### 2.2 Properties of the chalky silt soil before treatment

Based on the laboratory tests, the main parameters of the original chalky silt are listed in Table 1.

The soil changes its color if its water content changes: the in-situ moist soil is pale yellow, while it turns light grey when drying. It has high lime content; the texture has small roots and organic threads, and high sensitivity. Based on laboratory tests, it is classified as highly plastic silt (MH).

Table 1. Soil properties of the chalky silt soil in „Sárrét”

$w_L$	$w_p$	$I_p$	$w$	$e$	$E_s$	$E_{s,ur}$	$c_\alpha$	$\lambda^*$
%	%	%	%	-	MPa	MPa	-	-
72.1	54.4	17.7	71.1	2.08	2.1	15	0.0015	0.038

### 2.3 Data of chalky silt mixtures

In the testing program the use of both deep-mixing technologies was investigated. Thirteen different mixtures were prepared by varying  $\alpha$  and  $w_T / c$  parameters (Table 2). Mixtures P1-P3 were made with low water contents and with slightly-varying cement contents. Mixtures 1-5 were prepared with lower water contents but highly varying cement contents. The mixtures 6-10 were made with a little bit greater water contents and with cement contents varied in the similar range. Since the water content of the original soil was high the addition of water was less significant in comparison to cement. The cement content dominated the behavior of the mixture.

### 2.4 Evaluation of stabilized soil parameters

In Figure 3, the increase of unconfined compressive strength with time is shown. As expected, the strength increases with time, but the hardening/strengthening rate is different from that of the concrete. The strength is less than 2.0 MPa for cement content of 50-300 kg/m<sup>3</sup>. Generally, 0.5-2.0 MPa 28-day unconfined compressive strength is required for column-type deep-mixing, and somewhat lower strength for mass stabilization (Moseley and Kirsch, 2004). The data presented in figure three indicate that:

- 4 tested mixtures (P2, 1, 6 and 7) which have a cement content of 125 kg/m<sup>3</sup> or less did not reach 200 kPa unconfined compressive strength, but 3 of them would be acceptable for a mass stabilization, only P2 with a cement content of 50 kg/m<sup>3</sup> should be considered as too weak,

- the 28-day unconfined compressive strength of mixtures 2, 3 and 8 (cement content = 150-175 kg/m<sup>3</sup>) was about 330 kPa, and for 90 days it increased to 500 kPa (50 %). These mixtures could be accepted for mass stabilization,
- the 28-day unconfined compressive strength of the rest of the samples with cement contents of 200-300 kg/m<sup>3</sup> were 500-2000 kPa with a 90-day to 1000-3000 kPa (50-100 %). These would be acceptable for column-type deep-mixing.

Table 2. Parameters of the mixtures

mix-ture	$w_T/c$	$\alpha$	$\alpha_{inpl}$	$q_u$ kPa				
				7	14	28	42	90
	-	kg/m <sup>3</sup>	kg/m <sup>3</sup>	day				
P1	6.8	102	96	70	80	70	93	104
P2	13.5	51	49	12	17	11	18	17
P3	3.4	204	187	303	418	567	727	980
1	5.3	127	120	58	69	92	88	93
2	4.4	153	144	196	235	343	334	430
3	3.8	178	166	301	297	312	380	598
4	2.7	254	231	655	878	1351	1384	1900
5	2.2	305	274	1037	1487	2125	2853	2991
6	6.8	108	97	81	71	94	82	117
7	5.5	134	120	81	92	165	174	246
8	4.5	162	144	196	231	334	424	508
9	3.4	214	188	370	542	910	1024	1559
10	2.7	268	231	508	670	1162	1458	1952

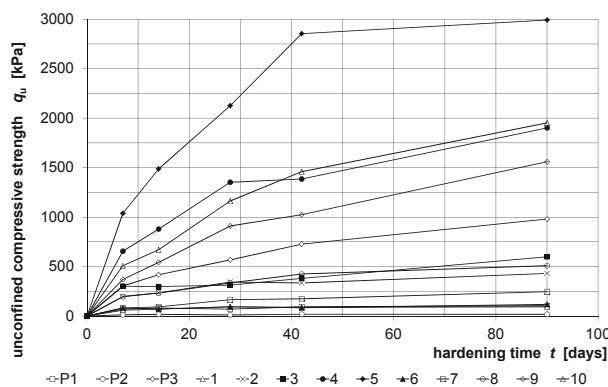


Figure 3. Measured hardening/strengthening of chalky silt mixtures

Figure 4 shows the relationship between the 28-day unconfined compressive strength ( $q_u$ ) and in-place cement factor ( $\alpha_{inpl}$ ). The exponential trendline fits the points well with  $R^2=0.97$ . The chalky silt responded well to cement addition.

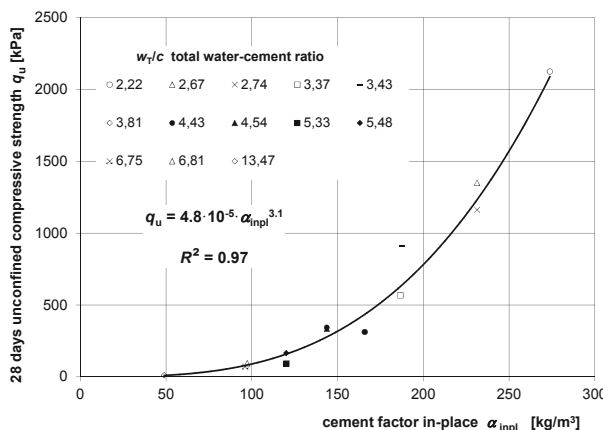


Figure 4. Measured relationship between  $q_u - \alpha_{inpl}$

Figure 5 shows how the 28-day unconfined strength depends on total water-cement ratio. Samples with high water content

show very low strength, and improvement of soil with  $w_T/c > 8$  is not possible. When  $w_T/c < 4$  the strength increased rapidly with decreasing water-cement ratio, but this also means the soil is very sensitive to changes in its properties. Since the total water-cement ratio hardly changes, it is clear that the role of cement factor is significant.

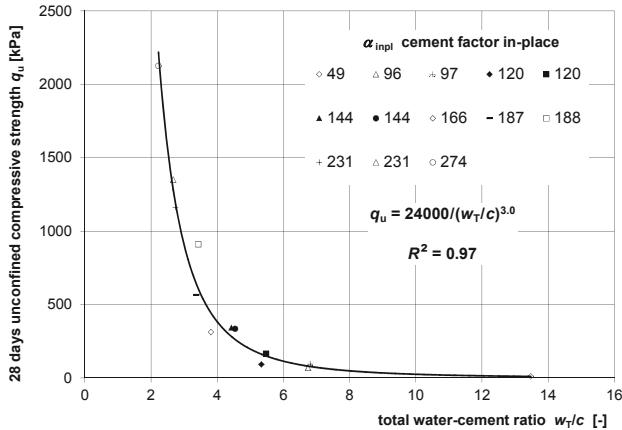


Figure 5. Measured relationship between  $q_u - w_T/c$

Figure 6 shows the relationship between the unconfined strength and the Young's modulus. It can be seen that the trend-line fits very well. In this respect, the chalky silt of „Sárrét” behaves as expected: the modulus is proportional to unconfined strength. The equation from the figure can be simplified to

$$E_u = 70 \cdot q_u \quad (1)$$

where the units are both in kPa.

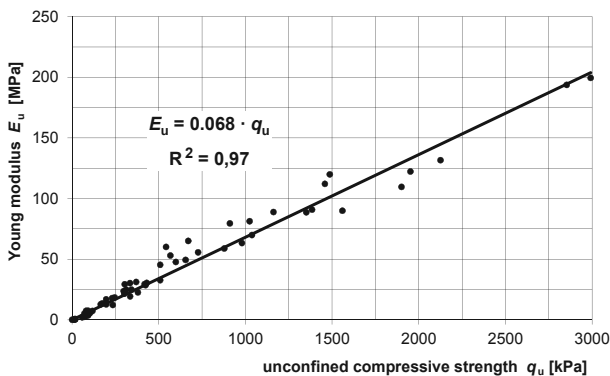


Figure 6. Measured relationship between  $q_u - E$

### 3 MODELING OF DEEP-MIXING TECHNOLOGIES

#### 3.1 Site evaluation

The second part of our research program was to apply a calculation method and give some guidelines for design. Both technologies (column-type and mass stabilization) were studied for expected design conditions at the Sárrét site. Variation in soil layering, soil strength and compression parameters, and embankment height will dictate the choice of technology. The PLAXIS 3D program was used to assess the effect of stabilization on stability and settlement.

The geometry of the embankment and the parameters of the untreated soil are shown in figure 7. Groundwater level was assumed to be even with the ground surface. Sandy-gravel, suitable for structural fill, was used for embankment material. A 3-m wide, 52.5 kPa distributed load was placed on top of the ballast during the stability analysis.

Column diameters were 60 cm, with a 5.0-m uniform length extending into the gravel layer. The columns were placed in  $2.0 \times 2.0$ -m and  $3.0 \times 3.0$ -m square grids (Figure 8). In order to

model partial mass stabilization, 1.8-m diameter equivalent columns were placed in  $2.4 \times 2.4$ -m,  $3.6 \times 3.6$ -m and  $5.4 \times 5.4$ -m square grids (Figure 9.). Total mass stabilization has been analyzed by modeling the treated soil as a homogeneous composite of mixed and in-situ soils with averaged strength properties.

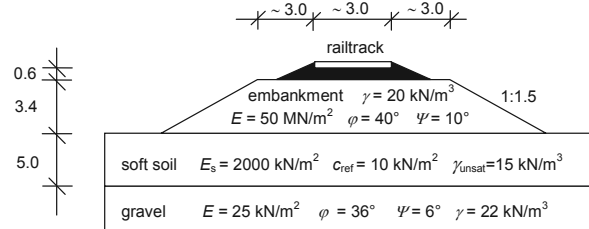


Figure 7. The model geometry and soil properties

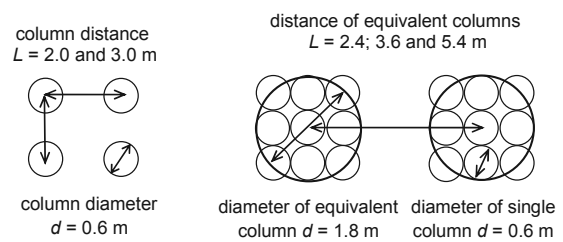


Figure 8. Column-type deep-mixing

Figure 9. Partial mass stabilization

The unconfined compressive strength of the 5 mixtures was used for modeling as base parameters (Table 2). Strength assigned to the column material in the analysis was assumed to be half of the unconfined compressive strength measured in the laboratory. In PLAXIS, this strength is represented by the cohesion ( $c_{ref}$ ). Based on laboratory tests, Young's modulus for the columns was 70 times the unconfined compressive strength. The value of Poisson's ratio was  $\nu = 0.2$ .

Table 2. Mechanical parameters of the mixtures

Mohr-Coulomb	mixture				
	1.	2.	3.	4.	5.
$E_{ref}$ kN/m <sup>2</sup>	7000	1500	20000	40000	70000
$q_u$ kN/m <sup>2</sup>	100	200	300	600	1000
$c_{ref}$ kN/m <sup>2</sup>	50	100	150	300	500

The analysis modeled the construction and load stages in five steps:

- placement of deep-mixing soil material,
- construction of initial 2-m high embankment in 30 days,
- construction of final embankment height in 30 days,
- final state (consolidation up to 5 kPa pore pressure).
- stability analysis considering traffic load.

#### 3.2 Analysis of settlement reduction

The results were evaluated by plotting the calculated settlements versus the unconfined strength of improved soil elements (Figure 10.). The following conclusions can be drawn:

- with increasing strength all technologies reduce settlement, but the effectiveness depends significantly on column diameter and spacing,
- there is a relation between column spacing and  $q_u$ . If  $q_u$  is too small, the column spacing is no longer effective, no matter how close. At a higher  $q_u$ , the column spacing scheme is efficient,
- for partial and total mass stabilization settlements reduce rapidly as  $q_u$  increases, up to 0.4 MPa. Beyond this value, the improvement is much less significant,

- 60-cm diameter column-type improvements reduce the settlements linearly with increasing unconfined strength, but not very markedly,
- 60-cm diameter columns are more effective in 2.0×2.0-m grid spacing than in 3.0×3.0-m, although the settlements are halved at  $q_u = 1$  MPa for the larger grid as well,
- there is little difference between the reduction curves of the 60-cm diameter columns in 2.0×2.0-m grid spacing and of the 1,8-m diameter equivalent columns made in 5.4×5.4-m grid spacing,
- the improvement with 1,8 m diameter equivalent columns in 3.6×3.6 m grid spacing is dramatic, the settlements are halved at about  $q_u = 0,2$  MPa,
- total mass stabilization can be the most effective technology. Even for very small unconfined strengths ( $q_u = 0.1$  MPa) the settlements are reduced to one-fourth.

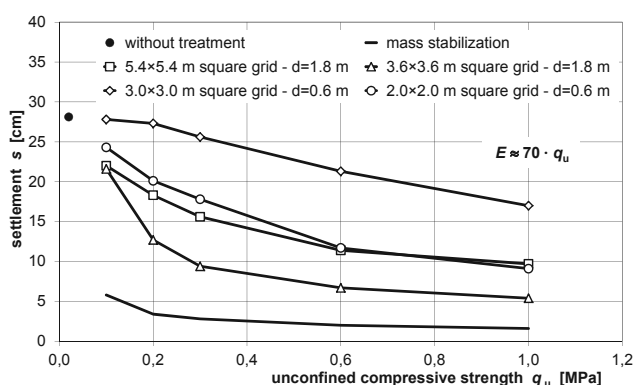


Figure 10. Calculated relationship between  $s - q_u$

### 3.3 Stability analysis

The influence on sliding stability was evaluated by plotting safety factor as a function of unconfined strength (Figure 11.). For untreated soil,  $SF = 1.18$  and it could be significantly increased with even a slight amount of treatment.

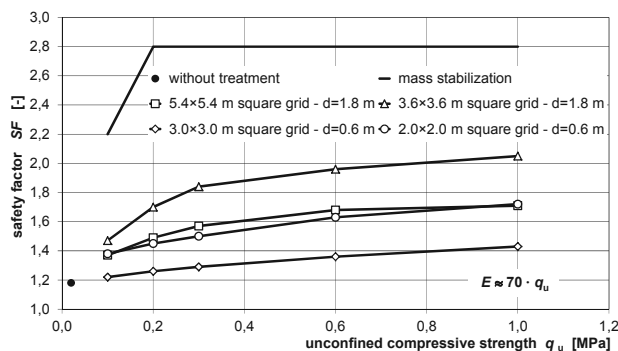


Figure 11. Calculated relationship between  $SF - q_u$

The results can be summarized in the following:

- the lines for different diameters and grid spacing are very similar (except for mass stabilization),
- the four lines show that for  $q_u > 0.5$  MPa, improvement is not necessary,
- the 0.6-m diameter columns with 3-m grid spacing is the least effective just reaching  $SF = 1.4$  value with the maximum strength investigated,
- the most effective technology to insure stability is the partial mass stabilization. With 1.8-m diameter equivalent columns and 3.6-m grid spacing, the required  $SF = 1.35$  value can be achieved with even small unconfined strength,
- the line for total mass stabilization shows a very different behavior. It generates a high safety factor even for small

strength values, but quickly reaches a plateau. Beyond this point the mechanics of the stability failure changes with the failure surface travelling through the embankment slope only.

## 4 CONCLUSIONS

For road and rail embankment foundations, soil improvement is a frequently-used technique. Column-type deep-mixing and mass stabilization are effective soil improvement technologies to reduce settlements increase safety against slope failure. To prepare new railway rehabilitation projects the usability of both methods was investigated on a special soil type: chalky silt in Sárret (Hungary).

While the underlying chemistry may be complex, the performance of the mixed material can be evaluated by standard laboratory and field tests. Laboratory tests have clearly demonstrated that the Sárret chalky silt is suitable for improvement by cement. While it cures relatively slowly, an adequate strength is reached in about 40 days. Unconfined strengths up to 1,0 MPa can be reached by adding relatively small amounts of cement. Its uniform and predictable response to treatment allows the engineer to design the field improvement. For example, the relationship between unconfined strength and total water-cement ratio can be described with simple equations. The Young's modulus of the chalky silt can be calculated as 70 times the unconfined strength.

Finite element modeling was used to study the effectiveness of the mixing improvement. Column-type and mass stabilization scenarios were analyzed using strength and compressibility values from laboratory test results. Both technologies showed reductions in settlement and increase in stability. Based on the figures presented, the effectiveness of various solutions can be evaluated at the first design stages easily and rapidly. Using the trends from the figures, an optimal solution can then be arrived at during the detailed design phase by making only some calculations with PLAXIS for the actual design conditions.

In the future, a further refinement of the proposed method can be achieved by assessing and involving the cost-effectiveness of the alternatives in the design.

## 5 REFERENCES

- Allu Stabilisation System, <http://www.allu.net/products/stabilisation-system>
- Brinkgreve R.B.J., Vermeer P.A. (2010): *PLAXIS-Finite element code for soil and rock analyses*, Plaxis 3D. Manuals, Delft University of Technology & Plaxis bv, The Netherlands.
- Dumas, C. et. al. (2003): *Innovative Technology for Accelerated Construction of Bridge and Embankment Foundations in Europe*, FHWA-PL-03-014, 2003, pp. 6-13.
- Filz, G.M., Hodges, D.K., Weatherby, D.E. and Marr, W.A. (2005): *Standardized Definitions and Laboratory Procedures for Soil-Cement Specimens Applicable to the Wet Method of Deep Mixing*, GSP 136 Innovations in Grouting and Soil Improvement, ASCE Geo-frontiers, Reston, Virginia, pp.1-13.
- Hayward Baker, (2010) Geotechnical Construction, Construction Techniques, <http://www.haywardbaker.com/WhatWeDo/Techniques/default.aspx>
- Logar, J. (2012), *Ground Improvement State of the Art in South Eastern Europe*, 2. Symposium Baugrundverbesserung in der Geotechnik am 13. und 14. September 2012 an der TU Wien, pp. 19-46.
- Moseley, M.P., Kirsch, K. (2004): *Ground Improvement*, Taylor and Francis, London, pp. 57-92, 331-428.

# Assessment of bio-mechanical reinforcement materials influencing slope stability, based on numerical analyses

## Évaluation des matériaux de renforcement bio-mécaniques qui influencent la stabilité des pentes par des analyses numériques

Koda E., Osinski P.

*Department of Geotechnical Engineering, Warsaw University of Life Sciences - SGGW, Warsaw, Poland*

**ABSTRACT:** The article is an answer proposal for the conclusion stated in European regulations regarding the environment friendly and more sustainable development, which among others includes utilising secondary and recycled material in order to obtain durable and stable cuttings and embankments. Bearing in mind that the slope stability and erosion control on embankments are the issues rising the nowadays geotechnics awareness through all around the world, the paper content provides the alternative engineering solutions to such problems. The techniques proposed in the paper mainly consist of the proper vegetation cover implementation on embankment slopes, the reinforcement of earth structures by utilising geotextiles and a combination of those two. Additionally, it is presented how secondary materials could be used as a vegetation development accelerating and enhancing material. In order to prove the reliability and efficiency of such activities the laboratory material tests and numerical modeling of slope failures were conducted.

**RÉSUMÉ :** L'article est une proposition de réponse à la conclusion énoncée dans les règlements européens concernant l'environnement de développement favorable et plus durable, ce qui comprend entre autres l'utilisation des matériaux de récupération et de recyclage afin d'obtenir des déblais et remblais stables et durables. Il est admis que la stabilité des pentes et le contrôle de l'érosion sur les remblais sont des problèmes qui apparaissent comme des priorités pour la géotechnique actuelle. Le papier propose des solutions d'ingénierie à ces problèmes. Les techniques proposées dans le document se composent principalement de la mise en œuvre de couverture végétale sur les talus, le renforcement des structures en terre en utilisant par géotextiles et une combinaison des deux. En outre, il est présenté comment les matériaux secondaires pourraient être utilisés comme un développement de la végétation accélérant et en améliorant le matériau. Afin de prouver la fiabilité et l'efficacité de telles activités, les essais de matériaux en laboratoire et la modélisation numérique des ruptures de pente ont été effectuées

**KEYWORDS:** slope stability, reinforcement, vegetation cover, recycled materials, landfill.

### 1 INTRODUCTION.

The most significant element of the embankment type landfill reclamation process is the reinforcement and biological stabilisation of slopes, which are very sensitive to several destabilisation processes like i.e surface erosion. The landfill stability improvement activities are divided into phase 1 - technical reclamation (implementation of civil engineering techniques), and phase 2 - biological restoration (establishment of the vegetation cover). For both of them it is highly recommended to use such recyclable materials as sewage sludge and fly ash as a landfill reinforcement filling (CEN/BT, 2009).

In 2012, in Poland the production of fly-ashes from the coal combustion was 18.5 mln tones. The amount of slag and ashes disposed on Polish landfills and usable for the road embankment construction and land reclamation is 261.8 mln tons. Furthermore, the annual production of sewage sludge in Poland is also significant - 500 000 tones, and could be successfully utilised in landfill reclamation process, as a rich in nutrients fertilizer (Koda et al 2012). The combination of carefully selected types of fly-ash, sewage sludge, soil and vegetation cover can be excellent alternative for the heavy engineering activities for the landfill slopes reinforcement. All the presented solutions are based on the analyses conducted at the Radiowo landfill site located near Warsaw.

### 2 SITE DESCRIPTION

The Radiowo landfill (embankment type) was established in 1962. It covers approximately 15 ha and the altitude is 60 m high. No protection system against the environmental pollution was introduced into the surrounding area at the start of the landfill operation.

The municipal solid waste was disposed there up to the early 90's. The local landslides treatment, changes in further exploitation, and the reinforcement treatment were required. Since 1993 only non-composted waste from the compostory plant has been disposed there (approximately 300 tons/day). The remediation works on the landfill have been carried out since 1994. They include: slopes forming and planting, stability improvement solution, mineral capping, bentonite cut-off wall as a limitation of the groundwater pollution and a peripheral drainage.

The in situ and laboratory tests for Radiowo landfill has been performed since 1993. The field investigation consists of settlement measurements, geotechnical tests of waste, back analysis (as well as slope failure tests), quality tests of sealing (capping layer and vertical barrier) and filter materials. In the Radiowo landfill case, the morphological composition of waste creates an additional factor influencing the mechanical parameters. The organic matter content for non-composted waste is ca. 5 %. A location map involving cross sections selected for slope stability analyses is presented in Figure 1.

Nowadays, the landfill site is planning to be adopted as a winter sports activity complex. The construction plan has already been accomplished and accepted by a legal body, which is a requirement when considering new development plan for contaminated sites (for more detail please refer to Koda 2012).

### 3 UTILISATION OF ANTHROPOGENIC MATERIALS

One of the elements of the landfill reclamation process is the construction of capping system. It is a landfill surface cover protecting against the rainfall infiltration (limitation of leachate penetration). It provides good establishment conditions for the vegetation cover, and significantly enhances slopes stability.

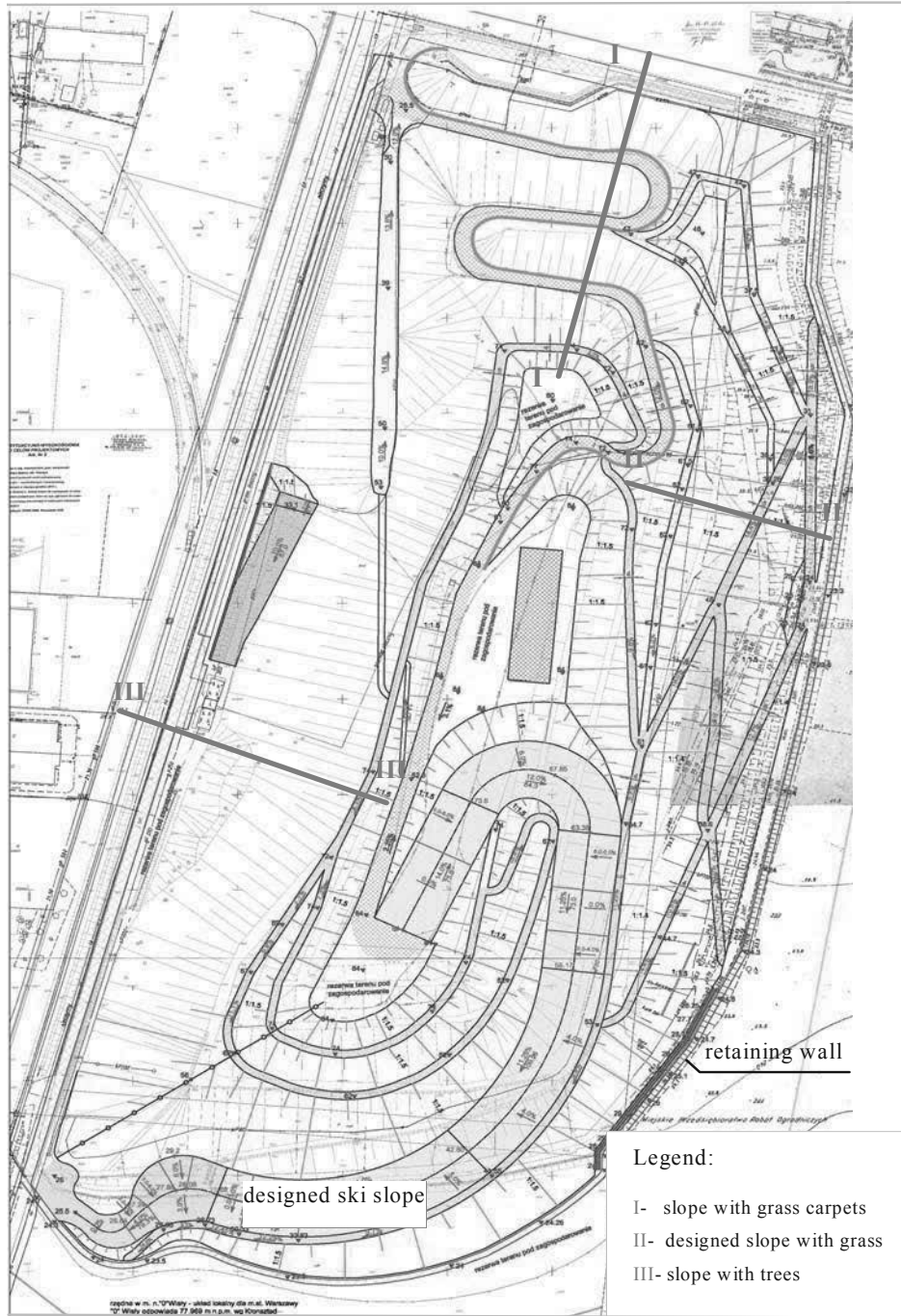


Figure 1. Current development plan of Radiowo landfill, and location of cross-section for slope stability analyses.

Because of its appropriate geotechnical properties like impermeability and good compaction conditions, fly-ashes mixed with cohesive soil are a great material for the capping system. Recently it was recommended to use geomembrane instead of mineral barriers to insulate the surface of the landfill, however there are lots of disadvantages like decreasing slope stability or slowing down the bio-chemical decomposition of waste. Applying mineral capping systems (made of ashes and sewage sludge), in many cases resulted in enhanced fermentation processes (Koda 2011).

The fly-ash is basically a by product of the coal combustion process in power plants. The mineral and chemical composition is determined by mineral elements present in coal. These minerals are: iron oxides, carbonates and clayey minerals. The properties of the fly-ash mainly depend on shape and size distribution of its particles. The bulk density of ashes contains in the range of 2000-2500 kg/m<sup>3</sup>.

The reason for this is some of the particles are filled with gas. The chemical reactions proceeding during the coal combustion process produce mineral phases stated in Table 1.

Table 1. Mineral phases of the fly-ash (Koda and Osinski 2011).

Mineral phases	% content of total mass
Glass	60-83
Millite	4-25
Quartz	4-18
Hematite	0.5-2
Magnetite	1-7
Coke	0.5-5

The additional anthropogenic component which also presents high usability in terms of slope surface reinforcement is sewage sludge (Katsumi et al. 2010). The mineral elements of

the sewage sludge are developing slowly and are not exposed to the erosion processes. This kind of material is hazardous when disposed but when treated by vegetation and additives it is safely absorbed and utilized by plants. Additionally it has to be mentioned that sewage sludge supply is free of charge. The mixture is applied by hydraulic seeders supplied with high pressure pumps, which enables spraying on different soil/material types. The advantage of using sewage sludge is that seeds are protected from the erosion and excessive drying. The viscosity of the sludge and its mixing ability with other components, assure even and smooth protection cover, and moreover, high adhesion to the sprayed surface. The most significant advantage of using the sewage sludge is the nutrition content, essential for the vegetation cover establishment. Especially the undrained sludge is rich in microelement, nitrogen, phosphorus, potassium and organic matter. Some of them are highly valuable for plants (Koda 2011), however cannot exceed normative values of dry mass. The usability of ashes and sewage sludge for the geotechnical purpose is determined by several physical and mechanical properties such as: capacity index in saturated conditions, grain-size distribution, maximum dry bulk density, swelling, internal friction angle, and passive capillarity.

#### 4 VEGETATION COVER AS A RELIABLE METHOD OF SLOPE STABILITY IMPROVEMENT

Beyond described activities for the slope stability and erosion control improvement purpose on the Radiowo landfill, there were also bio-engineering techniques applied with additional use of geosynthetics. Due to the usability assessment of the compost, from organic waste as an enhancing material for the grass carpets, an experimental plot was established within the compostory plant area (Koda, 2012). A composite (grass carpet) consisting of three elements was constructed: reinforcing material, substrate and grass seeds mixture was prepared. As a reinforcing material the geotextile (G) and geogrid (Gs) was used. A reinforcing material task was to connect particular elements of the carpet, improving the shear strength and hydraulics conditions, and also an increase of erosion control on landfill slopes. A porous structure of geotextile and geogrid enhances establishment of the root zone deeper into the surface.

During the selection of reinforcing material the mechanical properties and the stock was considered. The polypropylene materials guarantee long term durability and resistance to aggressive environmental conditions. A seeding suspension consisted of a mixture of three types of grass seeds: lawn type (MT), pasture type (MP) and "gazon" type grass seeds (G). A substrate consisted of sand and compost mixture in three different volumetric proportions: 1P/1K- 1:1 (1 measure of sand + 1 measure of compost), 1P/2K- 1:2 (1 measure of sand + 2 measures of compost), and K- pure substrate (100% compost). The scheme of experimental plot is presented in Figure 2.

Additionally an application of already described fly-ash and sewage sludge suspension on such slopes to accelerate the establishment of a green cover was also provided. The grass carpets were introduced in order to maintain the observation and to conduct further research on how does such solution influence conditions of slopes. The assessment of the effectiveness of bio-engineering activity on landfill slopes were undertaken after 1, 2, 6, and 10 years of the experiment duration. The result of the observation confirms the reinforcing purpose of the method, as even after 10 years of grass carpets establishment the slopes are evenly covered with plants, while on the slopes where only traditional method of planting was applied, the slope conditions are significantly worse. Additionally, the numerical analyses involving the influence of reinforcing layer also proved the correctness of applied method on slope of section I-I marked on Figure 1 where location map is provided. For the results please refer to Table 3.

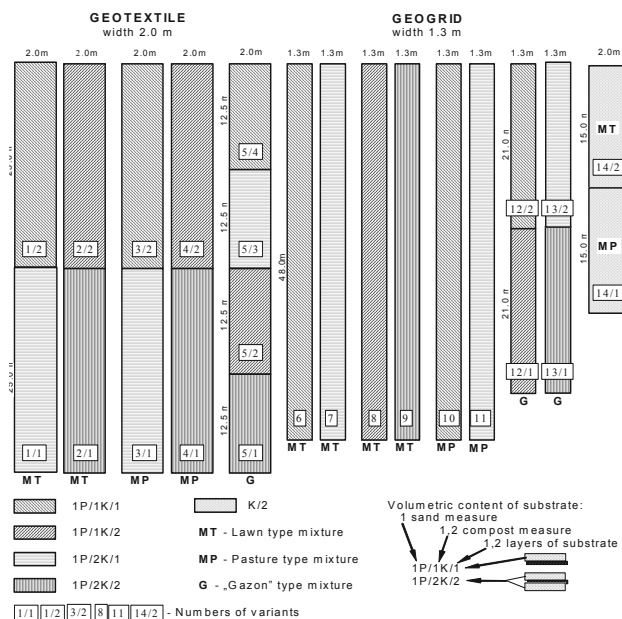


Figure 2. Scheme of the experimental plot established at Radiowo landfill slopes (Koda 2011).

The additional solution improving the slope stability is a proper establishment of high trees and shrubs on slopes (Coppin and Richards 1990, Norris and Greenwood 2003, Clark et al. 2003). Such activity was also conducted for Radiowo landfill site. Comprehensively analysed plant species were selected in terms of root system characteristics and assimilation ability in such specific ecosystem as contaminated land (Coppin and Richards 1990, Greenwood 2006).

In the present study, slopes where the vegetation cover was applied, have been assessed to see whether implementation of plants affected the resulting stability significantly. Firstly, however the geotechnical parameters of waste had to be determined. For such purpose back analyses, CPT and WST tests were conducted on site. The back-stability analysis by the Bishops', Swedish (GEO-SLOPE program) and FEM (Z-SOIL numerical program) methods were performed for three chosen cross-sections of Radiowo landfill slopes and were applied for the shear strength parameters verification. The results are listed in Table 2.

Table 2. Shear strength parameters for municipal solid waste (Koda, 2011)

Material	$\gamma$ [kN/m <sup>3</sup> ]	$\phi$ [°]	c [kPa]	Method
non-composted waste	11.0	20	25	failure tests, CPT, WST
non-composted waste + sand	12.0	25	23	failure tests, CPT, WST
old municipal waste	14.0	26	20	back-analysis CPT, WST

The computations of factor of safety including vegetation cover influencing slope stability were conducted with use of General Greenwood Method. Greenwood (2006) developed an equation, based on the limit equilibrium method, where parameters of plants existing on the slope are considered. These parameters are: root reinforcement forces, wind forces, or the mass of vegetation, or related to these, changes in the pore water pressure. In Slip4EX the Factor of Safety can be calculated by using several equations developed by Greenwood (2006), however in this study the Greenwood General Method was used, as it presents similar characteristics to other methods used in this study. A powerful equation of FOS concerning a vegetation influence, proposed by Greenwood is as follows:

$$F = \frac{\Sigma[(c' + c'_v)l + ((W + W_v)\cos\alpha - (U + \Delta U_v)l - ((U_2 - \Delta U_{2v}) - (U_1 + \Delta U_{1v}))\sin\alpha - D_w \sin\alpha(\alpha - \beta) + T \sin\Theta)\tan\phi']}{\Sigma[(W + W_v)\sin\alpha + D_w \cos(\alpha - \beta) - T \cos\Theta]} \quad (1)$$

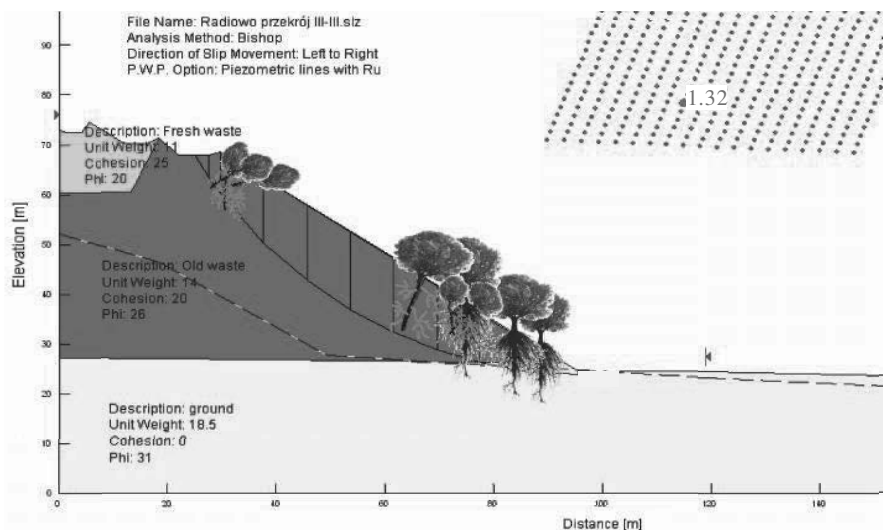


Figure 3. Numerical analysis of slope stability including the influence of vegetation cover (cross-section III-III please refer to Figure 1).

where all the parameters indexed with v mean changes according to vegetation influence. Additionally such parameters like  $D_w$  (wind force),  $T$  (tensile root strength) are also included in the equation. This method was basically developed to assess the stability of slope according to the soil reinforcement by anchors or geotextiles, or vegetation effects. By using the Slip4Ex spreadsheet (Greenwood 2006), it is possible to assess how the distribution and type of vegetation can influence the Factor of Safety. After full establishment and grow of proposed plants the numerical analyses of slope stability were conducted. A distribution of high vegetation cover on analysed slope (cross-section III-III) is presented in Figure 3.

Firstly the numerical analyses were conducted for bare slopes. The computations were based on Bishop method which was employed during analyses performed in GeoStudio2007 software. The second step was to determine factor of safety influenced by plants.

The results obtained proved that the factor of safety for the slopes covered with plant was improved as much as 20%. The initial results of numerical modeling for bare slopes has presented unstable condition, however long term monitoring proved that no signs of failure were noticed. The only reliable explanation for such state could be a presence of well developed vegetation on slopes. The example of results of numerical analyses for slope stability for bare and vegetated slopes is presented in Table 3.

Table 3. Comparison of numerical analyses of factor of safety for bare and vegetated slopes

Cross Section	Factor of safety	
	Bare slope Bishop method	Vegetated slope Greenwood method
I-I	1.30	1.38
II-II	1.35	1.42
III-III	1.15	1.32

## 5 CONCLUSIONS

The instability of slopes is one of the most significant problem concerning reclamation processes of landfill sites. The partial solution for this issue is presented in the paper. There are available methods, which are relatively simple, efficient, and cost effective. The use of fly ash and sewage sludge for the reclamation of the surface of landfill is an alternative. It also solves the problem of the ash storage which, from the economical and environmental point of view, is very positive.

The reinforcement of slope does not require only heavy engineering methods, basic solution as a proper selection and implementation of plants is always worth consideration. It is definitely cost effective, environment friendly and reasonable technique accelerating landfill reclamation works. Furthermore, other waste material like compost could be a great substitute of humus for the surface reclamation layer establishment. The compost could be used for reinforced grass carpets production, which positively influences the erosion control on slopes, a factor which often determines processes of slope failure.

## 6 REFERENCES

CEN/BT WG2003 2009. *Earthworks*. Final report Feb. 2009.

Clark L.J., Whalley W.R, and Barraclough P.B. 2003. How do roots penetrate strong soil? *Plant and Soil*, 255, 93–104.

Coppin, N. J., and Richards, I. G. 1990. *Use of vegetation in civil engineering*. CIRIA – Butterworths, London.

Greenwood, J.R. 2006. SLIP4EX – A Program for Routine Slope Stability Analysis to Include the Effects of Vegetation, Reinforcement and Hydrological Changes. *Geotech. and Geol. Eng.*, No. 24 (3), 449-465.

Katsumi T., Inui T., and Kamon M. 2010. Sustainable geotechnics for reuse of by-products. *Proc. of the 6th Inter. Congress on Env. Geotech.*, New Delhi Vol. 1, 302-317.

Koda E. 2011. *Stability and pollutant transport from remediated landfills with the use of Observational Method*. SGGW Press, Warsaw, Scient. public. No 384 [In Polish].

Koda E. 2012. Development plan of Radiowo landfill site, a ski slope construction. *X Conf. "For city and environment-waste management issues"*, Warsaw, 110-117 [In Polish].

Koda E. and Osinski P. 2011. Slope erosion control with the use of fly-ash and sewage sludge. *Ann. Warsaw Univ. Life Scien., Land Reclam.* No. 43 (1), 1-12.

Koda E., Osinski P., and Głazewski M. 2012. Use of fly-ash and sewage sludge for the erosion control on sanitary landfill slopes. *GeoCongress 2012, - State of the Art and Practice in Geotechnical Engineering*. ASCE GSP No 225, 3873- 3890.

Norris, J.E. and Greenwood, J.R. 2003 Root reinforcement on unstable slopes in Northern Greece and Central Italy. *Inter. Conf. on Problematic Soils, Nottingham*, 414-418.

# Evaluation of Vertical Drain-enhanced Radial Consolidation with Modified Analytical Solution

## Évaluation de la consolidation radiale améliorée par des drains verticaux par une solution analytique modifiée

Lee C., Choi Y., Lee W.

*School of Civil, Environmental, and Architectural Engineering, Korea University*

Hong S.J.

*Technology Research & Development Institute, Daelim Industrial Co., Ltd.*

**ABSTRACT:** The installation of vertical drains accelerates the consolidation process by reducing the drainage path and predominating horizontal flow within the soft deposits. However, the radial consolidation of the vertical drain installed into the soft ground is governed by the permeability of a smear zone. Modification of Hansbo's analysis is proposed to analyze the degree of consolidation on a horizontal plane by considering the properties of the soil within the smear zone in this study. A parametric study is carried out to investigate the effects of the soil properties on the proposed analysis. The proposed equation is observed to be relatively insensitive to the uncertainty of the horizontal permeability ratio between the undisturbed and smear zones. The validity of the proposed analysis is examined by comparison with the settlement data from a field measurement. It is revealed that the proposed analysis provides a reliable prediction on the consolidation rate of soft ground installed PVD.

**RÉSUMÉ :** L'installation de drains verticaux accélère le processus de consolidation en réduisant les chemins de drainage et d'écoulements horizontaux prédominant dans les dépôts mous. Toutefois, la perméabilité de la zone d'influence détermine le degré de la consolidation radiale induite par les drains verticaux installés dans les sols mous. Une modification de l'analyse de Hansbo est proposée dans cette étude pour analyser le degré de consolidation dans un plan horizontal en considérant les propriétés du sol dans la zone d'influence. Une étude paramétrique est notamment menée pour étudier les effets des propriétés du sol sur l'analyse proposée. L'observation montre que l'équation proposée est relativement insensible à l'incertitude du rapport entre perméabilités horizontales entre les zones non perturbées et les zones d'influence. La validité de l'analyse proposée est examinée par comparaison avec les données de tassement d'une mesure sur site. Il s'est révélé que l'analyse proposée fournit une prévision fiable sur le taux de consolidation des drains verticaux installés dans les sols mous.

**KEYWORDS:** Permeability, Radial consolidation, Smear zone, Vertical drain

## 1 INTRODUCTION

The radial consolidation flow into the vertical drain induces a reduction in the flow channel and an increase in flow rate approaching the drain. It causes that the hydraulic head is dramatically decreased as the distance to the drain decreases. Therefore, the permeability of drain and soil near the drain control the rate of consolidation by the vertical drain. Since the permeability of drain is generally designed to be larger enough than that of soil, it is known that the well resistance is negligible if the discharge capacity exceeds the required discharge capacity (Holtz et al. 1987, Lo 1991). On the other hand, the installation of vertical drains induces a soil disturbance in the vicinity of the mandrel. The disturbed zone, called smear zone, is an area where has reduced permeability and increased compressibility comparing with an undisturbed soil. Reduced permeability in the disturbed zone governs the rate of consolidation, because the hydraulic head loss in soil near the drain further increases when the permeability decreases.

Many researchers insisted that the soil adjacent to the drain is remolded, and several researches were investigated the smear effect by obtaining the permeability of the disturbed zone from the permeability of remolded clay (Tavenas et al. 1983, Bergado et al. 1991, Hird and Moseley 2000, Sathanathan and Indraratna 2006). In this study, modification of Hansbo's solution is proposed to evaluate the degree of radial consolidation, considering the consolidation characteristics of remolded clay. Characteristics of the modified solution are discussed, in comparison with Hansbo's solution. And the consolidation settlement predicted by the modified solution is compared with measured settlement data in the field.

## 2 MODIFIED ANALYTICAL SOLUTION

Hansbo's (1981) solution has been widely used to evaluate the consolidation behavior with vertical drain. It is simple and accurate as compared with other rigorous solutions and numerical analysis (Onoue 1988, Lo 1991). According to Hansbo (1981), the average degree of radial consolidation ( $\bar{U}_r$ ) by vertical drain is

$$\bar{U}_r = 1 - \exp(-8T_h / \mu_s) \quad (1)$$

where,  $\mu_s = \ln(d_s/d_w) + (k_h/k_s - 1) \ln(d_s/d_w) + \pi \cdot z(2L - z)(k_h/q_w) - 0.75$ ,  $T_h$  is a time factor ( $= c_h \cdot t/d_c^2$ ),  $c_h$  is the coefficient of horizontal consolidation in the field,  $d_c$  is the circular diameter influenced by the drain,  $d_w$  is the drain diameter,  $k_h$  is the coefficient of horizontal permeability in the undisturbed zone,  $k_s$  is the coefficient of horizontal permeability in the disturbed zone,  $d_s$  is the disturbed zone diameter,  $L$  is the drainage path length, and  $q_w$  is the drain discharge capacity.

Hansbo's analysis is based on the horizontal flow characteristics of the undisturbed zone ( $k_h$  or  $c_h$ ) to evaluate the radial consolidation. However, it is difficult to obtain due to the anisotropy of permeability and difference between laboratory and field measurement values (Bergardo et al. 1991, Chai and Miura 1999).

The consolidation characteristics of the disturbed zone are homogeneous and isotropic due to the disturbance (Lo 1991). To analyze the radial consolidation based on the consolidation characteristics of disturbed zone, Hansbo's solution is modified in this study. Since Hansbo's solution assumes an equal vertical strain, the ratio of horizontal permeability between the undisturbed and disturbed zones ( $k_h/k_s$ ).



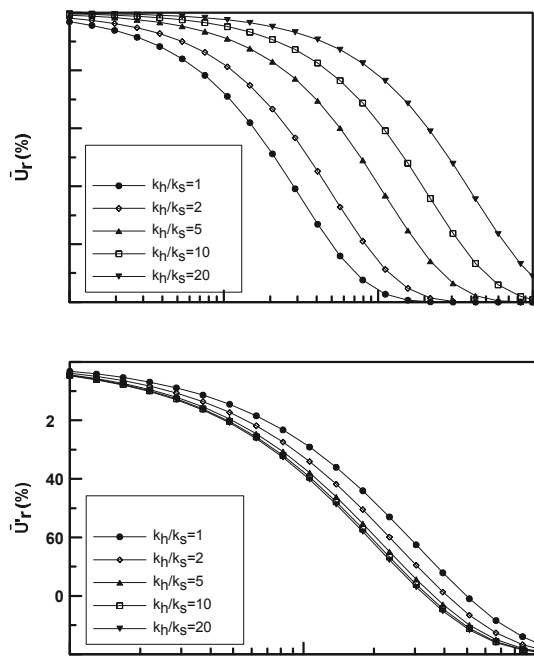


Figure 1. Effect of  $k_h/k_s$  on the degree of consolidation: (a) Hansbo's method, (b) Proposed method

is the same as the consolidation coefficients ratio between the undisturbed and disturbed zones ( $c_h/c_{hs}$ ). By using this condition, rearranged the average degree of radial consolidation ( $\bar{U}'_r$ ) is

$$\bar{U}'_r = 1 - \exp(-8T_{hs} / \mu'_s) \quad (2)$$

where,  $\mu'_s = \ln(d_s/d_w) + [\ln(d_c/d_s) + \pi \cdot z(2L-z)(k_h/q_w) - 0.75] / (k_h/k_s)$ ,  $T_{hs}$  is a time factor based on  $c_{hs}$ .

The permeability reduction in the disturbed zone, frequently represented as  $k_h/k_s$ , is important factor for the vertical drain-enhanced consolidation. The effect of  $k_h/k_s$  on the analysis results is investigated both Hansbo's solution and modified solution. Figure 1 shows the effect of  $k_h/k_s$  on  $\bar{U}'_r - T_{hs}$  and  $\bar{U}'_r - T_{hs}$  curves. Other factors are maintained as a constant value ( $d_c/d_w=25$ ,  $d_s/d_w=5$ ), and well resistance is ignored.

As shown in Figure 1(a), the rate of consolidation by Hansbo's method is continuously retarded with increasing in  $k_h/k_s$ . However, the consolidation rate by proposed method (Figure 1(b)) is slightly speeded up and finally converged with increasing in  $k_h/k_s$ , because the rate of vertical drain-enhanced consolidation is governed by the permeability of disturbed zone (Basu and Prezzi 2007).

### 3 APPLICATION (BUSAN NEW-PORT SITE)

The consolidation behavior in Busan New-port site is analyzed to verify the proposed analysis. The rate of consolidation settlement is evaluated by Hansbo's solution and modified solution, and these results are compared with observed settlements in field.

#### 3.1 Soil properties of clay layers

The profiles of clay layer properties (Busan New-port) are shown in Figure 2. The natural water content ( $w_n$ ) and liquid limit ( $w_L$ ) vary 35~75% and 40~80%, respectively. The plastic limit ( $w_p$ ) exists in relatively narrow range from 20 to 30%.

Table 1. Void ratio and compression index of each clay layer

Property	Layer 1		Layer 2		Layer 3	
	U	R	U	R	U	R
$e_L$	1.81		2.22		1.35	
$e_0$	1.65	1.32	1.95	1.46	0.94	0.78
$C_c$	0.84	0.46	1.04	0.57	0.57	0.34
$c_v$ ( $10^{-4}$ cm <sup>2</sup> /sec)	7.1	3.8	13.0	4.8	22.0	5.0

Note. U: undisturbed clay, R: remolded clay

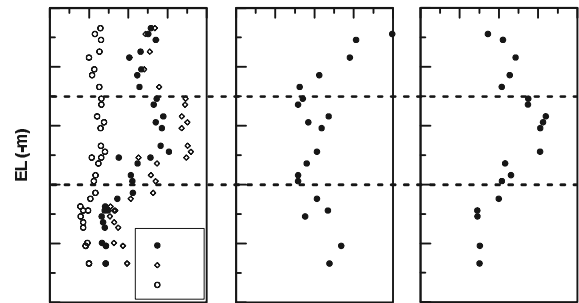


Figure 2. Profiles of soil properties

Although OCR at shallow depth is slightly larger than 1, the clay layers can be presumed normally consolidated. Busan clay can be divided into upper and lower clay layers based on EL - 30m.

#### 3.2 Consolidation properties of each clay layer

In this study, the clay layers of Busan New-port are divided into 3 layers for the consolidation analysis based on the soil properties. The consolidation tests were carried out for 50 samples for the natural clay and 3 samples for the remolded clay to figure out the consolidation characteristics of clay layers. Table 1 shows the void ratio, compression index ( $C_c$ ) and coefficient of consolidation ( $c_v$ ) representing the each clay layer.

#### 3.3 Extent of the disturbed zone

In this study, several assumptions are made to evaluate the extent of the disturbed zone: 1) the soil adjacent to the drain is completely remolded. Therefore, the void ratio of the clay adjacent to the drain is the same as that of the remolded clay at the same effective stress level; 2) the void ratio reduction due to the disturbance around the drains occurs faster than the consolidation settlement under a surcharge load. Therefore, ground settlement that occurred without applying the surcharge load is mainly caused by the void ratio reduction due to the disturbance; 3) the extent of the disturbed zone and the variation of the void ratio within the disturbed zone are a invariable property with depth; 4) the shape of disturbed zone is a circular cross section. With these assumptions, the extent of the disturbed zone is evaluated from measured ground settlement, which occurred in the interval between PVD installation and a surcharge loading.

Burland (1990) suggested that the  $e$ -log  $\sigma'_v$  relation for the remolded clay:

$$e_r = e_L (A - B \log \sigma'_v) \quad (3)$$

where,  $e_r$  is the void ratio of the remolded clay,  $e_L$  is the void ratio at the liquid limit,  $\sigma'_v$  is a vertical effective stress (kPa), and A and B are constants. For Busan clay, the values of A and B are 1.224 and 0.256, respectively (Hong 2011). Therefore, the

void ratio reduction ( $\Delta e$ ) due to the disturbance can be evaluated from the liquid limit and the natural water content.

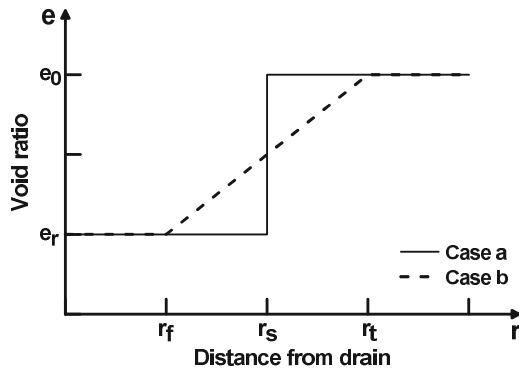


Figure 3. Variations of void ratio in disturbed zone

Figure 3 shows two possible variations of the void ratio with radial distance from the center of the drain. Case a assumes a constant permeability or void ratio within the disturbed zone ( $r_s$ ). However, most studies (Onoue et al. 1991, Indraratna and Redana 1998, Shin et al. 2009) were consistently insisted a decrease in the permeability or the void ratio within the disturbed zone, although there are some differences in shape of variation (e.g. linear, bilinear, and parabolic). To consider variation of the permeability or the void ratio within the disturbed zone, case b assumes that the void ratio linearly increases from the value equal to  $e_r$  at the outer boundary of the fully disturbed zone ( $r_f$ ) to the initial void ratio ( $e_0$ ) of the undisturbed soil at the outer boundary of the transition zone ( $r_t$ ). For cases a and b, the volume changes due to the disturbance induced by PVD installation can be expressed as:

$$\Delta V = \pi \cdot r_s^2 \cdot H \cdot \Delta e / (1 + e_0) \quad \text{Case a (4)}$$

$$\Delta V = \pi \cdot [(r_f^2 + r_f \cdot r_t + r_t^2) / 3] \cdot H \cdot \Delta e / (1 + e_0) \quad \text{Case b (5)}$$

where,  $\Delta e$  is the void ratio reduction due to the disturbance, and  $H$  is the thickness of the target clay layer.

Figure 4 shows the ground elevation and total ground settlement during the entire period of the improvement. The measured settlement that occurred between the PVD installation and surcharge loading is 85.6 cm. This ground settlement could be occurred by the two reasons: 1) void ratio reduction within the disturbed zone; and 2) consolidation settlement in the undisturbed zone due to the sand mat. The consolidation settlement in the undisturbed zone is calculated as 13.8 cm by using Zeng and Xie's solution (1989). Therefore, the ground settlement caused by the void reduction within the disturbed zone is 71.8 cm.

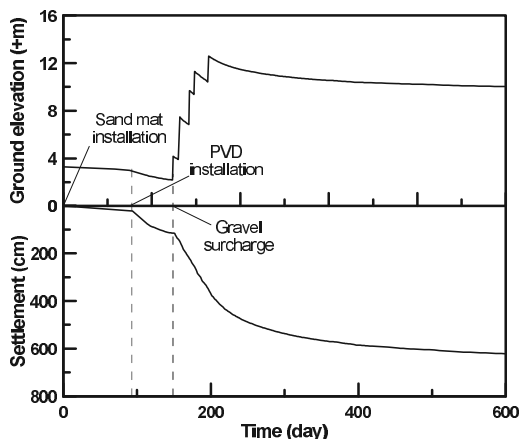


Figure 4. Ground level and settlement of Busan New-port site

Table 2. Analysis conditions

Case	Analytical condition	
	Hansbo's method	Proposed method
1	No disturbance, $c_h = c_v$	No disturbance, $c_h = c_v$
2	$c_h = c_v$ in disturbed zone, $c_h = 2c_v$ in undisturbed zone	No disturbance, $c_h = c_{hs}$
3	$c_h = c_v$ in undisturbed zone, $k_h/k_s = 2.5$	$c_h = c_{hs}$ in disturbed zone, $k_h/k_s$ or $k_h/k_f = 2.5$
4	$c_h = c_v$ in undisturbed zone, $k_h/k_s = 5.0$	$c_h = c_{hs}$ in disturbed zone, $k_h/k_s$ or $k_h/k_f = 5.0$
5	$c_h = c_v$ in undisturbed zone, $k_h/k_s = 10.0$	$c_h = c_{hs}$ in disturbed zone, $k_h/k_s$ or $k_h/k_f = 10.0$

The extent of the disturbed zone ( $r_s$ ) for case a is easily calculated as 21.6 cm based on 71.8 cm of the ground settlement. However, it is hard to calculate the values of  $r_f$  and  $r_t$  for case b because both  $r_f$  and  $r_t$  values are variables. For the linear spatial variation, previous studies suggested that the  $r_f$  is approximately 1.0~1.6 $r_m$  (Onoue et al. 1991, Hird and Moseley 2000, Sharma and Xiao 2000), where  $r_m$  is the equivalent radius of the mandrel. In this study, since the  $r_f$  is assumed to be 1.0 $r_m$  (8.0 cm), calculated value of  $r_t$  is 4.1 $r_m$ .

### 3.4 Consolidation analysis

The consolidation rate of Busan New-port is predicted using both Hansbo's method and proposed method. To evaluate effect of consolidation properties, parametric study is performed for a set of different conditions, as shown in Table 2. In case of proposed method, two possible permeability variations within disturbed zone are considered. Based on the PVD property,  $d_w=6$ ,  $d_c=135$ cm, and  $q_w=15$ cm<sup>3</sup>/sec are used for analysis.

Figure 5 shows the rate of consolidation settlement predicted by both Hansbo's method and proposed method, and the measured settlement for the layer located above EL -30 m. The average degree of consolidation ( $\bar{U}$ ) is calculated by using Carillo's suggestion (1942), and then the consolidation settlement is calculated by considering the non-linear relationship between the consolidation settlement and the degree of consolidation.

As shown in Figure 5(a), Hansbo's analysis for cases 1 and 2 overestimate the settlement rate compared with the measured one because the coefficient of horizontal consolidation in the disturbed zone is assumed to be the same as  $c_v$ . All cases do not fit well with the measured settlement. To obtain the best result by Hansbo's analysis, it is necessary to know proper values of  $c_h$  and  $k_h/k_s$ . However, the suitable  $k_h/k_s$  ratio appears to vary with the assumed  $c_h$  value.

Proposed analysis (Case a) results show in Figure 5(b). The settlement rate at a certain time is underestimated to compare with the measured settlement, since the extent of disturbed zone is evaluated relatively large compared with the real condition due to an assumption for a constant permeability or void ratio within the disturbed zone. Basu et al. (2006) suggested the simplified  $\mu_s$  for the linear spatial variation in disturbed zone (Case b). Using this suggestion, the settlement rate for case b is calculated by the proposed method, as shown in Figure 5(c). Case 4 ( $k_h/k_f = 5.0$ ) is well matched with measured settlement within 100 days, and then case 3 ( $k_h/k_f = 2.5$ ) shows good agreement with the measured settlement after 100 days. Since the typical value of  $c_h/c_v$  could be larger than 1.0 in nature, the  $k_h/k_f$  is presumed larger than 3.0, based on the consolidation test results. The slightly underestimation of the settlement rate predicted with the presumed  $k_h/k_f$  value may occur due to the difference in the surcharge schedule. In the analytical solution,

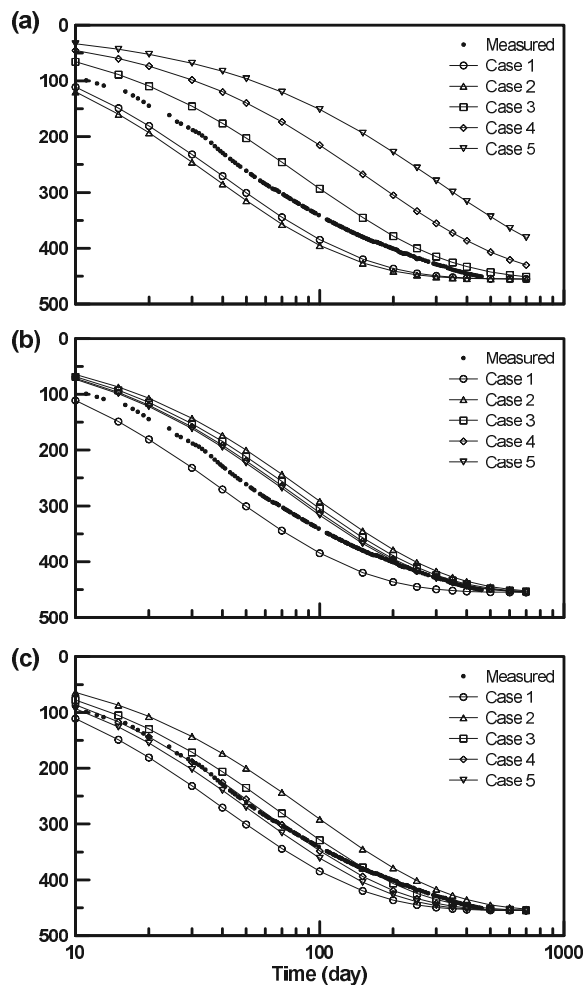


Figure 5. Measured and predicted settlement rate for the layer above EL -30m: (a) Hansbo's method, (b) Proposed method with case a, (c) Proposed method with case b

the surcharge load is assumed to be applied all at once, while, in the field, the surcharge load is applied incrementally.

#### 4 CONCLUSION

In this study, the radial consolidation enhanced by the vertical drain is discussed with the analytical method existed, and the modified solution is suggested. Through parametric study and comparison between the calculated and measured settlement rates, the results are summarized as follows.

As the degree of disturbance increases, Hansbo's analysis shows that the time factor  $T_h$  increases for a certain degree of radial consolidation. However, the time factor for proposed analysis ( $T_{hs}$ ), which corresponds to a certain degree of radial consolidation, slightly decreases as the degree of disturbance increases. Furthermore, proposed analysis gives the almost identical  $\bar{U}_r - T_{hs}$  curves when the  $k_h/k_s$  value becomes larger than 20.

For Busan New-port site, the extent of the disturbed zone is evaluated using two possible void ratio variations within the disturbed zone. When a constant permeability or void ratio within the disturbed zone is assumed, the extent of the disturbed zone  $r_s$  is estimated to be  $2.7r_m$ . For the linear spatial variation within the disturbed zone, the extent of the transition zone  $r_t$  is estimated to be  $4.1r_m$  with the same equivalent radius between fully disturbed zone and mandrel ( $r_f = 1.0r_m$ ).

The settlement rate predicted by the proposed analysis is well matched with the measured field settlement when the  $k_h/k_f$  ratio is 2.5 with a linear spatial distribution of the permeability

within the disturbed zone. The proposed method has advantages to evaluate the extent of disturbed zone and it is less influenced by the disturbance effect than Hansbo's method.

#### 5 REFERENCES

- Basu D., Basu P., and Prezzi M. 2006. Analytical solutions for consolidation aided by vertical drains. *Geomechanics and Geoengineering: An International Journal* 1(1), 63-71.
- Basu D. and Prezzi M. 2007. Effect of the smear and transition zones around prefabricated vertical drains installed in a triangular pattern on the rate of soil consolidation. *Journal of Geomechanics* 7(1), 34-43.
- Bergado D.T., Asakami H., Alfaro M.C., and Balasubramaniam A.S. 1991. Smear effects of vertical drains on soft Bangkok clay. *Journal of Geotechnical Engineering* 117(10), 1509-1530.
- Burland J.G. 1990. On compressibility and shear strength of natural clay. *Geotechnique* 40(3), 329-378.
- Carillo N. 1942. Simple two and three dimensional cases in the theory of consolidation of soils. *Journal of Mathematics and Physics* 21(1), 11-18.
- Chai J.C. and Miura N. 1999. Investigation of factors affecting vertical drain behavior. *Journal of Geotechnical and Geoenvironmental Engineering* 125(3), 216-226.
- Hansbo S. 1981. Consolidation of fine-grained soils by prefabricated drains. *Proceedings of 10th International Conference on Soil Mechanics and Foundation Engineering*, Stockholm, Sweden, Vol.3, 677-682.
- Hird C.C. and Moseley V.J. 2000. Model study of seepage in smear zones around vertical drains in layered soil. *Geotechnique* 50(1), 89-97.
- Holtz R.D., Jamiolkowski M.B., Lancellotta R., and Pedroni S. 1987. *Performance of prefabricated band-shaped drains*. Construction Industry Research and Information Association (CIRIA) Report, Research project 364.
- Hong S.J. 2011. *Evaluation of geotechnical properties of Busan Newport clay*, Doctoral thesis, Korea University.
- Indraratna B. and Redana I.W. 1998. Laboratory determination of smear zone due to vertical drain installation. *Journal of Geotechnical and Geoenvironmental Engineering* 124(2), 180-184.
- Lo D.O.K. 1991. *Soil improvement by vertical drains*, Doctoral thesis, University of Illinois at Urbana-Champaign.
- Onoue A. 1988. Consolidation by vertical drains taking well resistance and smear into consideration. *Soils and Foundation* 28(4), 165-174.
- Onoue A., Ting N.H., Germaine, J.T., and Whitman, R.V. 1991. Permeability of disturbed zone around vertical drains. *Proceedings of 1991 ASCE Geotechnical Engineering Congress*, Boulder, Colorado, Vol. 2, 879-890.
- Sathanathan I. and Indraratna B. 2006. Laboratory evaluation of smear zone and correlation between permeability and moisture content. *Journal of Geotechnical and Geoenvironmental Engineering* 132(7), 942-945.
- Sharma J.S. and Xiao D. 2000. Characterization of a smear zone around vertical drains by large-scale laboratory tests. *Canadian Geotechnical Journal* 37(6), 1265-1271.
- Shin D.H., Lee C., Lee J.S., and Lee W. 2009. Detection of smear zone using micro-cone and electrical resistance probe. *Canadian Geotechnical Journal* 46(6), 719-726.
- Tavenas F., Jean P., Leblond P., and Leroueil S. 1983. The permeability of natural soft clays. Part II: Permeability characteristics. *Canadian Geotechnical Journal* 20(4), 645-660.
- Zeng G.X. and Xie K.H. 1989. New development of the vertical drain theories. *Proceedings of 12th International Conference on Soil Mechanics and Foundation Engineering*, Rio de Janeiro, Brazil, Vol.2, 1435-1438.

# Adjusting the soil stiffness with stabilisation to minimize vibration at Maxlab IV – Asynchrotron radiation facility in Sweden

Ajustement de la rigidité du sol par stabilisation pour minimiser les vibrations à Maxlab IV, un centre de rayonnement synchrotron en Suède

Lindh P.  
*Peab Anläggning AB, Sweden*

Rydén N.  
*Lund University, Sweden*

**ABSTRACT:** In Lund a new next-generation synchrotron radiation facility are under construction, MAX IV. This facility requires extraordinary techniques for the earthworks at site. The vibration requirements are very stringent compared to traditional earthwork standard. The tolerance is 26 nm (1 s rms above 5 Hz) and this requires a very good damping from external and internal vibrations. Different solutions were discussed and simulated during the design phase and the best performance was achieved with a four meter thick layer of stabilised soil below the concrete foundation. The soil consists of clay till with high clay content. During the design phase many different binder combinations were tested to meet the design criteria regarding seismic modulus. In order to achieve a monolith the binders' setting time was critical since the soil is stabilised in 0.35 meter layers were the next layer are mixed into the layer below. The binder to best meet both design and construction requirements were a combination of quicklime and ground granulated blast furnace slag (GGBFS).

**RÉSUMÉ :** Un nouveau centre de rayonnement synchrotron de dernière génération, MAX IV, est en cours de construction à Lund. Ce centre nécessite des techniques exceptionnelles pour les travaux de terrassement sur le chantier. Les exigences de vibrations sont très strictes par rapport à la norme de terrassement traditionnel. La tolérance est de 26 nm (valeur efficace 1 s rms au-dessus de 5 Hz), ce qui nécessite un très bon amortissement des vibrations internes et externes. Des solutions différentes ont été discutées et simulées au cours de la phase de conception et la meilleure performance a été réalisée avec une couche épaisse de quatre mètres de sol stabilisé en dessous de la fondation en béton. Le sol se compose de till argileux à forte teneur en argile. Au cours de la phase de conception, de nombreuses combinaisons de liants différents ont été testées pour répondre aux critères de conception concernant le module sismique. En raison de la réalisation d'un monolithe, le temps de durcissement était critique puisque le sol est stabilisé en couches de 0,35 mètre dont la couche suivante est mélangée dans la couche de dessous. Le liant qui répondait le mieux aux exigences à la fois de conception et de construction était une combinaison de chaux vive et de laitier granulé de haut fourneau (SLGHF).

**KEYWORDS:** Soil stabilisation, seismic testing, vibration, P-wave.

## 1 INTRODUCTION

Max-lab is a Swedish facility for materials research based on synchrotron radiation. The new version, Max IV, will be 100 times more efficient than any now existing comparable synchrotron radiation facility in the world. The location of the new Max-lab is placed just outside the city of Lund in southern Sweden. The geology consists of 12 to 16 meters of soil (clay till) on top of the bedrock. Close to Max IV runs a major highway which will introduce ground vibrations. Since the facilities are sensitive to vibrations an extensive measurement program of background vibrations were executed.

Several foundation alternatives were discussed and some of them were tested with FEM-simulations to determine which alternative that fulfilled the requirement of damping both external and internal vibrations. The alternative that best fulfilled external and internal damping was a 4 meter thick stabilised layer underneath the concrete slab.

### 1.1 Geotechnical testing

The pre-investigation of the geology included geotechnical sounding as well as geophysical measurements as well as core drilling through the soil layers down into the bedrock. After the in-situ investigation and evaluation a geological model for the site was developed. From this model minor excavations were performed for soil sampling. The soils were classified and an extensive testing was performed to evaluate which binder or binder combination that was optimal for the soils. The major parts of the soils were clay till with layers of silty sand till.

Three different binders were tested, lime; cement and slag. The slag was ground granulated blast furnace slag (GGBFS). The clay till contained up to 40% clay and the sandy silt till has low clay content. The high clay content indicated that lime should be used to break up the clay. However, lime alone would not work with the sandy silt till. The clay till from this area have been tested in a earlier study and the combination of lime and slag was discovered to be efficient in this type of soil (Lindh, 2004). Two different binder recipes were chosen from the initial laboratory testing;

- Cement/slag (80/20)
- Lime/slag (50/50)

During the construction phase of the mock-up, cement and slag were chosen due to the current weather conditions and the time schedule for the mock-up. During the seismic testing of the mock-up cracks were found in the stabilized material. The results indicated that the cracks were introduced during construction of the stabilised layers. The layer in question was milled 50 mm down into the layer below to ensure interaction between layers. The binder's working period was not sufficient to guarantee that the next layer could be milled into the stabilised bottom layer without causing cracks. This resulted in a change of binder to a combination of lime and slag (50/50).

FE-calculations as well as seismic measurements performed on the mock-up showed that a shear wave velocity needed to be at least 900 m/s in the stabilised soil. In this case it corresponds to a compression wave velocity (P-wave) of 1430 m/s. The seismic velocity testing was performed according to a methodology developed at Lund University and tested on

cement stabilised soils (Rydénet *et al.*, 2006). New samples were prepared to measure the early strength development, see Figure 1. After more than 1200 hours the samples were removed from the plastic mould that supported the samples during compaction and in the beginning of the curing period of the samples. This resulted in a small drop in P-wave velocity.

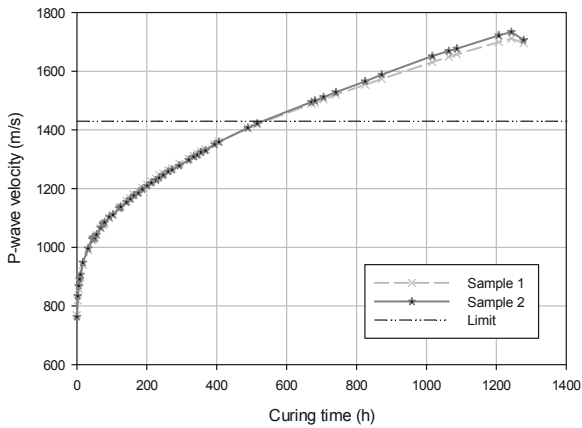


Figure 1. The figure shows the development of compressive wave velocity with time. The drop in velocity after 1240 hours is caused by removing the samples from the plastic mould.

The seismic measurements of the prepared samples were performed several times every 24 hours for the first 400 hours. In Figure 2 the measured frequency is shown together with higher frequency modes.

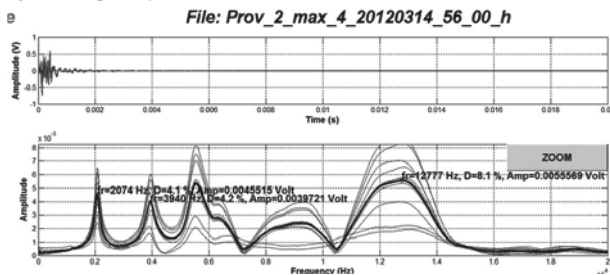


Figure 2. Different frequency modes for sample number 2 after 56 hours curing. The lowest frequency peak corresponds to a fundamental mode longitudinal resonance frequency of 2074 Hz which corresponds to a P-wave velocity of 1043 m/s.

The longitudinal resonance frequency of 2074 Hz corresponds to a P-wave velocity of 1043 m/s for sample 2. The samples needed approximately 500 hours of curing in 20 degree Celsius to meet the requirements regarding P-wave velocity.

## 2 IN-SITU MEASUREMENTS

The quality testing in-situ was done both as ordinary testing with binder content, MCV, pulverization and  $E_{vib}$  measurement with the compaction roller. The testing procedure also included sampling from the stabilised soil when the mixer had made two mixing passes. The stabilised soil that would be tested was excavated and transported to a field laboratory for compaction in plastic moulds. After compaction the P-wave velocity was measured and compared with the laboratory mixed samples. Most of the production samples (PS) were stored in room temperature to ensure the same conditions compared with the laboratory compacted samples.

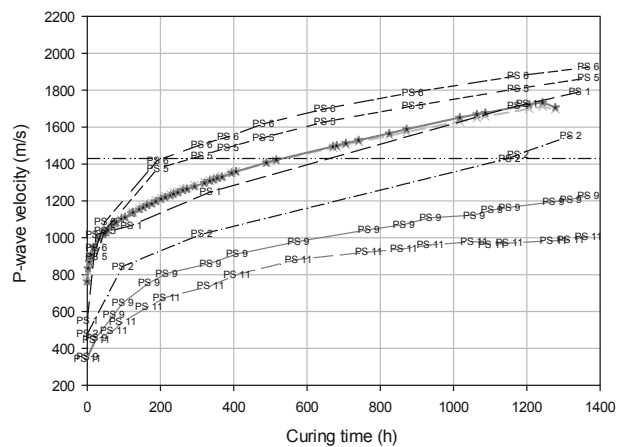
There was a great variation in the development of P-wave velocity versus curing time for different samples, see Figure 3.

The causes of this variation were a combination of different parameters such as;

- Variation in water content
- Variation in density
- Variation in grading (clay content)
- Variation in the degree of pulverization

In order to study the development of P-wave at different temperatures two pairs of specimens were manufactured. One pair was stored in room temperature and the other pair was stored at outside temperature. The difference in P-wave development is shown in Figure 3. The different samples are denoted PS9 and PS11 in the figure. The sample PS 9 was stored at room temperature and the sample PS 11 was stored at outside air temperature.

Figure 3. Development of compressive wave velocity with time for



reference and production samples.

The production sample denoted PS9 required more than 2400 hours achieving the limit value of 1430 m/s and the sample PS 11 did not achieve the required limit. However, storing a specimen in an outside air temperature is not fully correct compared to the in situ conditions due to larger volume of stabilised soil and in the in-situ case the heat transfer is one dimensional. It does however give an idea of how low temperature will affect the stabilised soil in-situ.

An example of the in situ seismic measurements is shown in Figure 4.

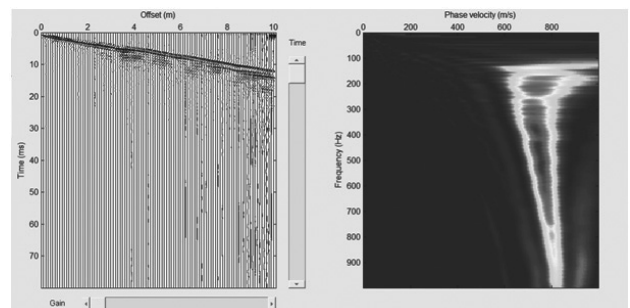


Figure 4. A result from seismic in-situ measurement along the surface of the stabilised layer is presented in the figure. The top layer has almost reached a surface wave velocity ( $\sim 0.92V_s$ ) of 800 m/s at the time for measurement. The target shear wave velocity after curing is 900 m/s.

The in-situ measurement of the stabilised soil is performed with the same equipment as used for sample testing. However, the in-situ testing involves the whole volume and gives a true value of the stabilised soils' performance. The seismic testing will be followed up in future with testing on the concrete slab.

### 3 CONCLUSIONS

Soil stabilisation with binders increases the stiffness (E-modulus) of the soil and thereby changes the resonance frequency of the soil. In this project the soil stabilisation has been a key issue to meet the requirements regarding vibrations in a cost effective way. It has been proven that it is possible to achieve a homogenous stabilised monolithic ring with a circumference of 528 meters and a depth of 4 meters.

The homogeneity of the stabilised material is a result of an extensive testing program in both laboratory and full scale. The binders' working period has also been an important issue to ensure a crack-proof construction.

It has also been shown that seismic testing works very well for both laboratory and in-situ testing of stabilised soils.

### 4 ACKNOWLEDGEMENTS

The authors acknowledge Peab Anläggning AB for the opportunity to publish this data.

### 5 REFERENCES

- Lindh P. 2004. Compaction- and strength properties of stabilised and unstabilised fine-grained tills. Lund University. Department of Building and Environmental Technology. Division of Soil Mechanics and Foundation Engineering. LUTVDG/TVGT-1013 / Swedish Geotechnical Institute, SGI. Report 66
- Rydén N., Ekdahl U. and Lindh P. 2006. Quality Control of Cement Stabilised Soil Using Non-destructive Seismic Tests. Advanced testing of fresh cementitious materials, Stuttgart, August 3-4, 2006 / DGZfP - Proceedings BB102-CD (Deutsche Gesellschaft für Zerstörungsfreie Prüfung e.V.) Lecture 34.



# Construction and Performance of Containment Bund Using Geotextile Tubes Filled With Cement Mixed Soil in Singapore

La construction et la performance de la digue de confinement utilisant des tubes géotextiles remplis de terre mélangée au ciment à Singapour

Loh C.K.

*Maritime and Port Authority of Singapore (MPA), Singapore*

Chew S.H., Tan C.Y.

*Department of Civil Engineering, National University of Singapore (NUS), Singapore*

Lim S.K.

*Housing and Development Board (HDB), Singapore*

Lam J.P.W.

*Surbana Corporation Pte Ltd, Singapore*

**ABSTRACT:** In a major port development project in Singapore, a containment bund using modified geotextile tubes (M-GT) filled with cement mixed soil has been constructed. The main purpose of this bund is to create a containment area to contain any sediment plumes due to construction activities (i.e. dredging activities, dumping activities and sand-filling activities). The containment bund also serves as a retaining structure to retain dredged materials during the sand-key construction and other port expansion works. This paper presents the key consideration in the innovative design and construction of a geotextile containment bund. In addition, instead of usual sand fill, the dredged soil mixed with cement was used as the fill material in this bund. Among the challenges faced in this project were the great water depth of this containment bund location (>25m) and high traffic volume in Singapore water course as the site is next to the existing operating port terminal. Extensive field instrumentation and monitoring were carried out during and post construction phase to verify the design, as well as ascertain the performance of the geotextiles containment bund system.

**RÉSUMÉ :** Dans un important projet de développement portuaire à Singapour, une digue de confinement utilisant des tubes géotextiles modifiés (M-GT) et remplis de terre mélangée au ciment, a été construite. Le but principal de cette digue est de créer une zone de confinement afin de contenir les débris de sédiments provenant des travaux de construction (c'est-à-dire travaux de dragage, de déversement et de remplissage au sable). La digue de confinement sert également de structure de retenue pour retenir les matériaux de dragage lors de la construction de la tranchée d'étanchéité et d'autres travaux d'extension de port. Cette étude présente le facteur clé dans la conception innovatrice et la construction d'une digue de confinement en géotextiles. En outre, au lieu du remplissage au sable habituel, le sol dragué est mélangé avec du ciment avant d'être utilisé comme matière de remplissage dans cette digue. Parmi les défis relevés durant ce projet étaient la grande profondeur des eaux à l'emplacement de la digue de confinement (> 25m) et le volume du trafic maritime dans les eaux de Singapour vue que le site se trouve à proximité du terminal portuaire existant. Des instrumentations et mesures approfondies ont été menées pendant et après la phase de construction pour vérifier la conception, de même que la performance du système de digue de confinement en géotextiles.

**KEYWORDS:** Geotextile tubes, containment bund, cement mixed soil.

## 1 INTRODUCTION

A containment bund consisting of modified geotextile tubes (M-GT) filled with cement mixed soil has been constructed for a major port development project in Singapore. This containment bund forms part of the Pasir Panjang Terminal Phase 3 & 4 Expansion Project, which is located at the Southern part of Singapore water (Figure 1). During the project construction phase, this bund serves as a retaining structure to retain dredged materials and at the same time contains any sediment plumes arises from construction activities from being transported towards the nearby forest reserve area by currents. This containment bund, termed as a geotextile containment bund, is being constructed by systematically stacking of modified geotextile tubes (M-GT) and filling of cement mixed dredged soil. A typical cross section of the geotextile containment bund is shown in Figure 2.

A "geotextile tube" is a tubular container (diameter 1m to 10m) that is formed in-situ, on land or in water, by hydraulically filling the tube with sand or dredged material (Pilarczyk, 2000) and Lawson, 2006). On the other hand, "geotextile container" is made of geotextile sheet laid onto a split-bottom barge, filled mechanically with sand or other fill material, and sewn the top opening to form into a closed "container". The barge will then

move to the desired position, and the bottom of the barge will open allowing the containers to sink into the sea at the intended location. The volume of these containers can range from 100m<sup>3</sup> to 800m<sup>3</sup>.



Figure 1 Location of project site in Singapore (Google image)



The modified geotextile tube (M-GT) introduced in this paper is an innovative application, which combines the structure / shape of a “geotextile tube” and the method of installation of a “geotextile container”. The diameter of M-GT is 5m and the length is 25m (limited by barge length). The theoretical maximum volume of M-GT is 490m<sup>3</sup>. However, for practical reasons, the filled volume is only about 290m<sup>3</sup> or 60% filled in this project.

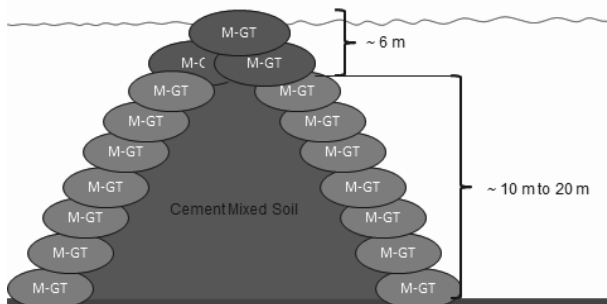


Figure 2 Typical cross section of geotextile containment bund

Two geotextile containment bunds were constructed in this project. The length of bund 1 is 500 m and bund 2 is 1800 m. Bund 1 was constructed first in order to provide a staging ground for other construction activities at the site. The layout and length of the bunds are shown in Figure 3.

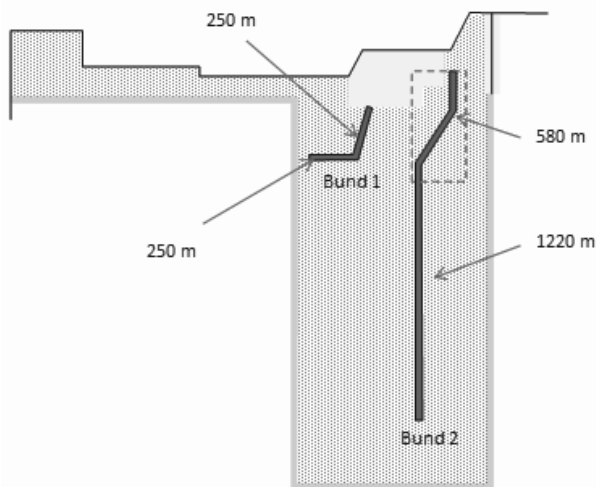


Figure 3 Length of geotextile containment bund 1 and 2 (Plan view)

## 2 DESIGN AND CONSTRUCTION OF GEOTEXTILE CONTAINMENT BUND

In the design of this bund, there are a few stability criteria that have to be fulfilled: Stability against hydraulic force of waves and current, local stability against sliding failure, local stability against slip failure, settlement and deformation. The tensile strength of the geotextile material is one of the major design parameters. This is because the installation of the tubes at water depth of 25m is deemed to be ‘extreme’ in the field installation of geotextile tubes and containers.

The installation process of the M-GT consists of five (5) main phases, namely:-

1) Filling of the M-GT – The dredged material mixed with cement, known as cement mixed soil, is being pumped into the modified geotextile tube via the inlet ports that are available at the top face of the M-GTs.

2) Opening of split-hopper barge – the bottom of the split-hopper barge opens slowly to allow the exit of the filled M-GTs through its opening. High tension in geotextile is expected to be experienced at this stage.

3) Free-falling of M-GTs onto the seabed – Air pockets inside the tube or container during free-falling would exert certain forces onto the geotextile and cause higher strain (Pilarczyk 2000). Tensions are generated in the tube due to the balancing of these forces, fill weight, buoyancy, drag, etc. (Lawson, 2006).

4) Impacting onto the seabed – At the point of impact, the kinetic energy of the falling tube is converted to elastic energy, which will reshape the tube, from a cone shape into a transitional cylindrical shape and eventually into a semi-oval shape or rectangular shape (Pilarczyk, 2000).

5) Stabilized phase of the M-GTs – The final shape of the tube attained depends on a number of interrelated factors such as the volume of fill, internal shear resistance of the fill material and the stiffness of the geotextile material (Lawson, 2006).

There are a number of equations and formulas available for the determination of the tension development in some of the stages mentioned above. The equations used in the design of M-GT in this project can be found in Chew et al. (2010).

The construction sequence of the bund is illustrated in five steps (Figure 4(a) to (e)).

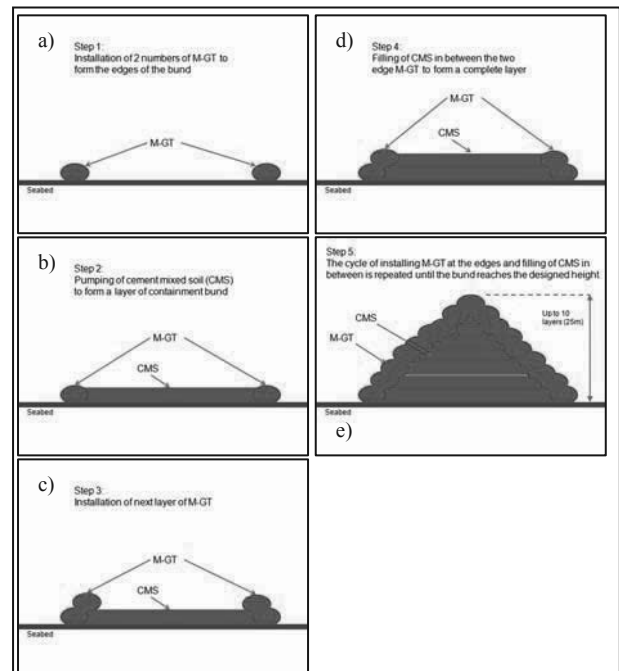


Figure 4 (a) to (e) Construction sequence of geotextile containment bund (cross-section view)

## 3 USE OF CEMENT MIXED SOIL (CMS) AS IN-FILL MATERIAL

Discarded soil from other excavation projects on land or sea in Singapore, and dredged materials from port extension works have been mixed with cement to form into Cement Mixed Soil (CMS), and was used as in-fill material in the M-GTs and as the core of the geotextile containment bund as shown in Figure 2. In order to satisfy the stability criteria of the geotextile containment bund, the cement mixed soil has to achieve a design value of unconfined compressive strength  $q_u$  of 200kN/m<sup>2</sup>. After taking into account of soil variability and the factor between the laboratory test result and in-situ achieved results, the targeted in-situ unconfined compressive strength is state as 1.3x200, which is 260kN/m<sup>2</sup>.

## 4 PERFORMANCE OF CONTAINMENT BUND

The performance of the bund has been monitored during and after the construction through an extensive instrumentation plan.

A total of 28 numbers of M-GTs were instrumented and monitoring at various stages of the installation process. One of the key parameters was that monitored closely is the strain development of the M-GT at different stages. The results of the monitoring during the installation process were presented by Chew et al. (2011) and it showed that high tensile forces of about 180kN/m were recorded at the bottom of M-GT during the impact onto the seabed.

Hydrographic survey was used to monitor the shape of the installed M-GTs, which is one of the performance indicators of this design. The accuracy of the installation was determined by using survey results conducted before and after the dumping of the instrumented M-GTs. The overall construction progress of the bund was also tracked using hydrographic surveys that were conducted every 5 days. The profile of the bund can be plotted using the survey results as shown in Figure 5, which shows one of the completed bund.

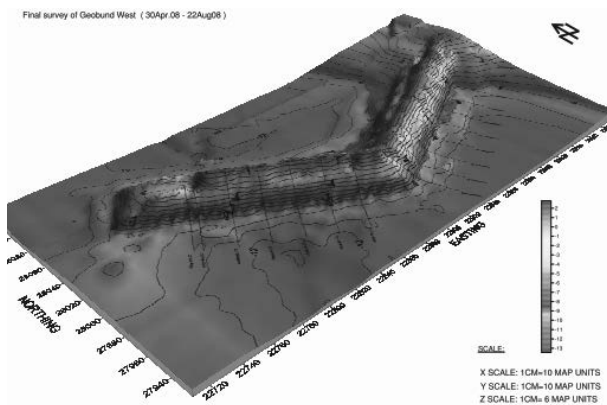


Figure 5 Profile of completed bund 1

After the completion of the bund, a total of 11 instrument clusters have been installed to monitor the performance of the containment bund during other construction activities such as the filling of dredged soil behind the containment bund and soil improvement works for the dumped material within the containment bund.

Out of the 11 instrumented clusters, 6 of them were placed at the top of the bund and the remaining was installed to monitor the slope of the bund by using a staging. The cross section of the instrument clusters is given in Figure 6.

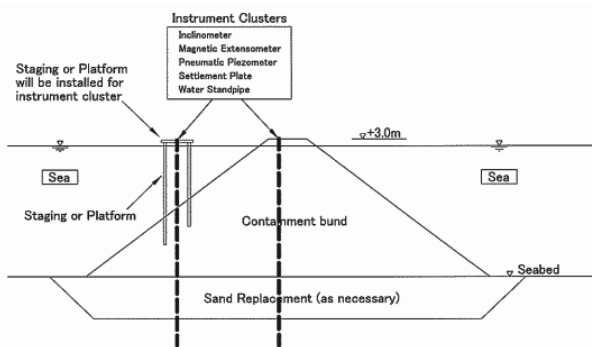


Figure 6 Instrumentation cluster installed in the containment bund

The results from the inclinometers installed at the top and side faces of the bund are discussed here. The location of the inclinometer is at CH. 1370 (Figure 7). The lateral deformation in the section perpendicular to the centre line of the bund is plotted in Figure 8 for both top and side inclinometer.

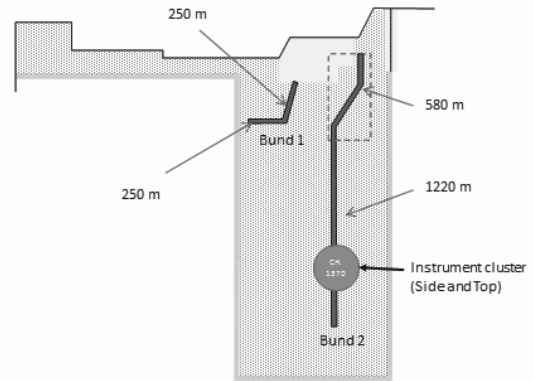


Figure 7 Location of inclinometers at CH. 1370 of the bund (Plan view)

The inclinometer readings show that the maximum deformation of the bund centre is 10mm at elevation of -8.5m (Figure 8a). The measurement was taken at 911 days after the completion of the bund at that location. This shows that the containment bund has remained stable throughout the period of other construction activities that occurred during this period.

Figure 8b shows the lateral deformation at the sides of the bund, which was also found to be within 10mm, where the maximum deflection occurred close to the bottom of the bund. Higher lateral deformation of up to 30mm was also recorded by the inclinometer at elevation above the bund (i.e. -5m to +10m). The lateral movement above the surface of the bund (side inclinometer) indicates that the dredged filled material has been placed onto the sides of the bund and at the same time being treated.

The settlement measured by extensometers installed on the top and side instrumentation clusters and settlement plates at the top of the bund are given in Table 1. The settlement readings showed that the geotextile containment bund filled with cement mixed soil has remained stable and performed as expected throughout the construction period of this project.

Table 1 Settlement of containment bund

Elevation	Settlement (mm)		
	Extensometer (Center)	Extensometer (Side)	Settlement plate
Top	---	---	11
-3.0 CD	24	---	---
-6.0 CD	26	40	---
-9.0 CD	25	29	---
-12.0 CD	17	23	---
-15.0 CD	18	8	---

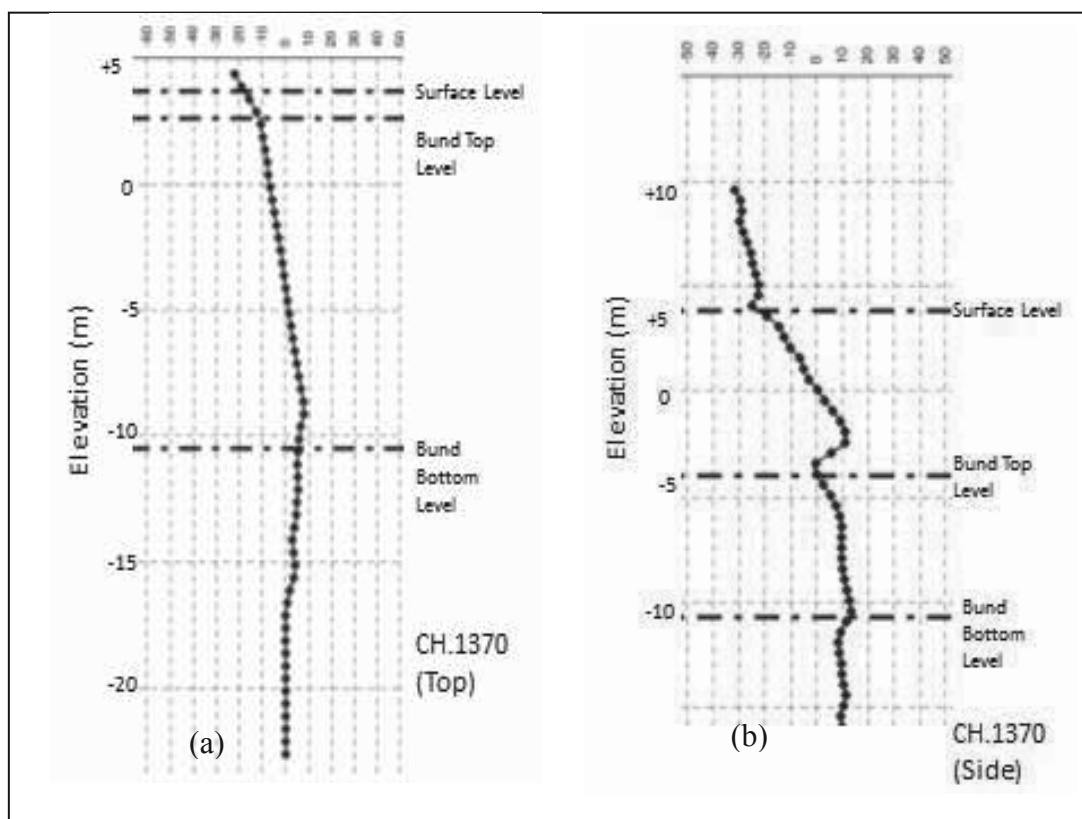


Figure 8 Lateral deformations measured from inclinometer at: (a) top of the bund. (b) side of the bund

## 5 CONCLUSION

The construction of the geotextile containment bund using modified geotextile tubes (M-GT) filled with cement mixed soil (CMS) has been completed successfully over a total length of 2.3 kilometres in Singapore. Field measurements of lateral deformations and settlements showed that the bund has performed well within the design limits and expectations. The innovative use of discarded soil from other excavation projects on land or sea via mixing with cement is proven to be a good fill material. This CMS material was shown to be able to achieve highly uniform and well controlled properties, and deemed to be suitable as in-fill material for geotextile tubes and the core portion of a containment bund.

## 6 REFERENCES

- Chew, S.H., Tan, C.Y., Loh, C.K., Lim, S.K., Lam, J.P.W. 2011. Design and Construction of Containment Bund using Geotextile Tubes in Singapore. *The 14th Asian Regional Conference on Soil Mechanics and Geotechnical Engineering*, Hong Kong
- Chew, S.H., Tan, C.Y., and Tan, H.W.A. 2010. Application of Geotextile Containment System in Coastal, Beach and River Restoration Projects. *The 1st International GSI-Asia Geosynthetic Conference*, Taiwan.
- Lawson, C. 2006. Geotextile containment for hydraulic and environmental engineering. *The 8th International Conference on Geosynthetic*, Yokohama, Japan.
- Pilarczyk, K.W 2000. *Geosynthetic and Geosystems in Hydraulic and Coastal Engineering*. Balkema, Rotterdam.

# Reinforcement of completely decomposed granite with discrete fibres

## Renforcement de granite complètement décomposé avec des morceaux fibres

Madhusudhan B.N., Baudet B.A.

*The University of Hong Kong, Hong Kong*

**ABSTRACT** :The use of discrete fibres as reinforcing material for soils has been researched by many, e.g. Gray and Al-Refeai (1986), Maher and Ho (1994), Crockford et al. (1993), Santoni et al. (2001), Consoli et al. (2009a), but these studies have been generally done independently and have not always been consistent. Silva dos Santos et al. (2010) used data gathered through many years of study to develop a framework of behaviour for a poorly graded quartzitic sand reinforced with polypropylene fibres. In Hong Kong, the construction industry has used reinforcement with continuous fibres for some time, but it is mainly applied to landscaping of otherwise stabilised slopes, for example as a green cover on an existing shotcreted slope. Using randomly distributed short discrete fibres in Hong Kong completely decomposed granite (CDG) could help stabilise the soil while keeping the density low enough to allow growth of vegetation. It is not guaranteed, however, that a well graded residual soil like CDG would behave in the same way as sands used by previous researchers. Laboratory tests have been carried out on completely decomposed granite using short discrete polypropylene fibres as a reinforcing material. The fibres are randomly distributed in the soil. It was found that the fibres increase the unconfined compressive strength of the CDG prepared at its maximum dry density by up to tenfold for fibre contents less than 1%. The behaviour of the fibre-CDG mixture during drained triaxial compression changed from dilative to compressive, with more effects at low confining pressures. These tests seem to indicate that discrete fibres could be considered for improving the performance of CDG.

**RÉSUMÉ** : L'utilisation de fibres pour renforcer les sols ont déjà fait l'objet de nombreux travaux de recherche e.g. Gray and Al-Refeai (1986), Maher and Ho (1994), Crockford et al. (1993), Santoni et al. (2001), Consoli et al. (2009a), mais ces études ont été généralement faites indépendamment et elles n'ont pas toujours été synthétisées. Silva dos Santos et al. (2010) ont utilisé les données obtenues au cours d'années de recherche pour développer un modèle de comportement pour un sable quartzitique uniforme renforcé avec des fibres en polypropylène. A Hong Kong, l'industrie de la construction a utilisé des fibres continues comme moyen de renforcement depuis longtemps, mais l'application se limite à l'aspect paysager de pentes déjà stabilisées, par exemple pour la plantation de surfaces de pentes recouvertes de béton projeté. L'utilisation de fibres courtes distribuées de façon aléatoire dans le granite complètement décomposé de Hong Kong (CDG) pourrait aider à stabiliser le sol tout en gardant sa densité assez basse pour permettre à la végétation de pousser. Il n'est pas garanti cependant qu'un sol résiduel a la distribution granulométrique bien calibrée comme le CDG se comportera de la même façon que les sables utilisés par les chercheurs précédents. Des essais de laboratoire ont été faits sur du granite complètement décomposé en utilisant du béton projeté et des fibres courtes en polypropylène comme matériau de renforcement. Les fibres sont distribuées de façon aléatoire dans le sol. On a trouvé que les fibres ont pour effet de multiplier par presque dix fois la résistance en compression simple du CDG préparé à sa densité sèche optimale, pour une teneur en fibres de moins de 1%. Le comportement du mélange CDG-fibres lors de l'essai triaxial drainé en compression est passé de dilatant à contractant avec plus d'effet aux pressions faibles. Les essais paraissent indiquer que l'utilisation de fibres courtes pourrait être considérée pour améliorer la performance du CDG.

**KEYWORDS**: laboratory tests ; reinforced soils ; residual soil

## 1 INTRODUCTION

Adding fibres to soil can be an effective way of strengthening it, by providing tensile strength at high strains. The factors influencing the effectiveness of the fibre-reinforced soils are a) the type of soil and its deformation behaviour; b) the type of fibre and its specifications (fibre length, fibre content and its aspect ratio). A careful study of the mechanics of the fibre-reinforced soil will help practising and design engineers to understand better its behaviour under different loading conditions.

Hong Kong is a modern city with growing population, so that engineers are pressed to optimise land utilisation. The topology of Hong Kong has led to urban development on natural or man-made slopes. Conventional methods of stabilising slopes such as shotcreting the whole face of the slope (current practice) are neither cost effective nor environmentally friendly and alternative sustainable methods are being sought after.

Many researchers have produced a large body of research on the performance of discrete fibres with soils (Gray and Al-Refeai, 1986; Maher and Ho, 1994; Crockford et al., 1993; Santoni et al., 2001; Consoli et al., 2009a), but these studies

have been generally done independently and they have not always been consistent (Silva dos Santos et al., 2010). This paper presents initial results from laboratory tests performed on completely decomposed soil reinforced with discrete fibres.

## 2 MATERIALS AND METHODS

Completely decomposed granite was used as the host soil. It originates from in-situ weathering of the parent igneous rock, and is one of the most common geo-materials in Hong Kong. The short discrete fibres used in the tests presented here were similar to those used by Silva dos Santos et al. (2010).

### 2.1 *Materials tested*

The completely decomposed granite (CDG) host soil was obtained from a construction site near Beacon Hill, Hong Kong. Completely decomposed residual soils are well-graded in nature as the tropical climate has weathered the parent rock to a material comprising gravel and sand grains down to silt and clay-sized particles. Coarser particles are usually of quartz origin owing to its high chemical resistance while finer particles are most likely other primary hydrous minerals, such as

kaolinite and feldspar (Yan and Li, 2012). The grain size distribution (shown in figure 1) reflects that the soil has 16% particles finer than 63 $\mu$ . The specific gravity of the soil was found to be 2.65. From Standard Proctor compaction tests, the maximum dry density of the soil was determined as 1.93Mg/m<sup>3</sup> with an optimum moisture content of 12.3%. Tests on particles finer than 425 $\mu$  indicated the plastic and liquid limits to be 25.6% and 35.6% respectively. Using the Unified Soil Classification System (USCS) the soil can be classified as clayey sand of low plasticity (SC-CL).

The fibres used are short filaments made of polypropylene similar to those used by Silva dos Santos *et al.* (2010). They are chemically inert and have uniform characteristics, with a relative density of 0.91, a tensile resistance of 120MPa, an elastic modulus of 3GPa and a range of linear deformation at rupture between 80% and 170%. The dimensions of the fibres used in the tests were 0.023mm in diameter and 24mm long (Silva dos Santos *et al.*, 2010). After performing a series of unconfined compression tests on CDG reinforced with a range of fibre contents (0.3 – 1%), it was decided to continue the study with 0.3% of fibre per weight in the triaxial tests.

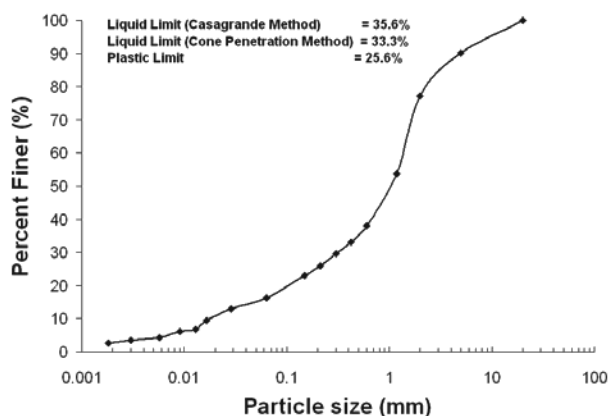


Figure 1. Particle size distribution of CDG.

## 2.2 Testing apparatus, methods and sample preparation

### 2.2.1 Uniaxial Compression Test

Unconfined compression tests on CDG and CDG+fibre soils were performed in a uniaxial compressive testing machine. The particle sizes passing 2mm diameter sieve were used for preparing specimens in a 38mm diameter; 76mm height mould at maximum dry density and optimum moisture content. The compression tests were performed at 0.5mm/min in all cases.

### 2.2.2 Triaxial Testing

Drained triaxial tests were performed using a conventional triaxial apparatus with a computer controlled GDS cell and back pressure controllers. The shearing tests were performed with a constant effective stress on specimens of both unreinforced and reinforced (with polypropylene fibres) CDG soil.

The soil was first soaked in water with a deflocculating agent and left for air drying, then it was sieved to constituent particle sizes so that the samples could be prepared in exact proportion as shown in figure 1, discarding particles above 5mm. Loose specimens were prepared, avoiding macro-voids and taking care of minimising membrane penetration. The specimens of 76mm diameter and 152mm height were prepared in a sample preparation mould.

The samples were saturated under back pressure and the effective confining pressures ranged from 100 to 500kPa. Saturation was monitored in each test, ensuring Skempton *B* values of at least 0.92 throughout the testing programme. The axial strains were measured outside the cell using a standard displacement transducer. The triaxial tests were run at a low

axial strain rate of 0.01% per minute to ensure no excess pore pressure development within the sample (this was checked by measurement at the opposite end of specimen). The membrane and area corrections were made as per the recommendations proposed by La Rochelle *et al.* (1988). The void ratios are calculated averaging from that obtained by the initial density of the sample and the final moisture content, taking account of the measured volume change in all the stages. In all tests the difference in specific volume compiled was less than 0.02.

## 3 TEST RESULTS

### 3.1 Unconfined compressive strength

Representative unconfined compression test results on pure CDG and CDG + 0.5% fibre are presented in figure 2. The plot clearly shows that the specimens of reinforced CDG yielded at very high strain, contributing an additional tenfold strength to the soil. On the other hand unreinforced CDG yielded at very low strength (131kPa) and low strain.

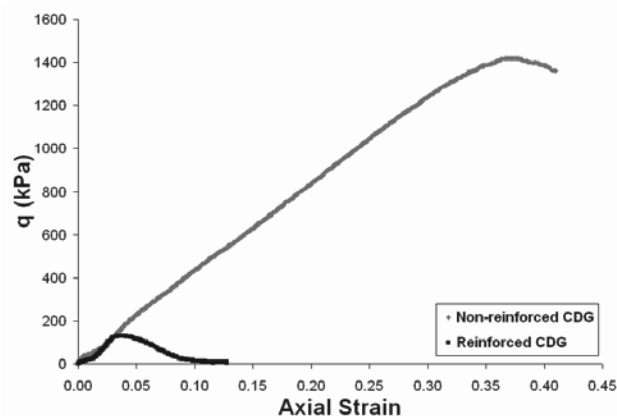


Figure 2. Unconfined compression of CDG and fibre-reinforced CDG.

### 3.2 Triaxial shearing

Triaxial drained tests were performed on isotropically consolidated specimens of pure CDG and reinforced CDG (Table 1). Some specimens were over-consolidated by a ratio of OCR=5 before being sheared. Details of the tests are shown in Table 1 (UR and R refer to unreinforced and reinforced specimens respectively).

Table 1. Summary of the triaxial tests.

Test	$v_0$	$v_c$	$p_c$ (kPa)	OCR
UR 100	1.42	1.32	112.0	5
UR 200	1.42	1.37	210.4	1
UR 500	1.48	1.32	499.6	1
R 100	1.58	1.36	98.9	5
R 200	1.43	1.32	202.9	1
R 500	1.58	1.41	499.4	1

The void ratios determined after consolidation (before shearing) were found to vary between 0.32 and 0.37 for pure CDG specimens and 0.32 and 0.42 for CDG-fibre specimens. Only dense specimens were prepared for the test programme. Looser specimens were difficult to prepare due to the presence of macro-voids which caused an initial collapse of the specimen, resulting in void ratios after consolidation within the same range as those for the dense specimens.

The stress-strain and volumetric responses during shearing are shown in figure 3. The stress-strain response (figure 3a) shows that the reinforced specimens generally have higher

strength and higher initial stiffness at the beginning of shearing, when compared to their unreinforced counterparts. However the reinforced specimens that mobilised their full strength only did so at shear strains in excess of 20%. The unreinforced specimens on the other hand either reached a constant stress by 20% strain or they showed strain-softening, depending on their consolidation history. Unlike the other reinforced specimens, R100 kept gaining strength and never reached critical state even at large strains (about 50%). This may be due to the over-consolidation history of the specimen, which may have released some of the tension in the fibres prior to shearing. The peak strengths of reinforced CDG were calculated to be 1.76 (100kPa), 1.29 (200kPa) and 1.26 (500kPa) times that of the pure CDG.

Similar behaviour on fibre-reinforced sands is reported by Consoli *et al.*, 2007, Consoli *et. al* (2005) and Silva dos Santos *et al.* (2010). For example Silva dos Santos *et al.* (2010) found that the effect of fibres depends on the effective stress at which they are sheared, reducing marginally with increasing effective stress. For sands, it is already reported that at low effective stress, adding fibres contributes to reducing the degree of dilation in the reinforced specimens (Silva dos Santos *et al.*, 2010). The persistent strain hardening behaviour (figure 3a, R100) was also observed by Consoli *et. al* (2005) on Botucatu residual soil, however their data were limited to strains of about 25%. In the present study, the specimens were sheared to strains up to 50% and it is clear that the strain hardening behaviour of specimens R200 and R500 stopped beyond  $\varepsilon_s > 35\%$  to reach a critical state. The governing mechanism for the strain hardening behaviour of R100 specimen might therefore be due either to the effect of low effective stress or to the effect of over-consolidation, or a combined effect.

The effect of the fibres on the volumetric response of the reinforced CDG in comparison seems to be that of restricting the degree of dilation in the specimen sheared at lower effective stresses, while at higher effective stress this effect is not so evident (figure 3b). The over-consolidated specimen of reinforced CDG shows a different volumetric response i.e. it tends to dilate after 20% shear strain even though it is expected that reinforcement will impede dilation. This behaviour is again either due to over-consolidation or to low effective confining stress. Previous findings on Botucatu residual soils (Consoli *et. al.*, 2005) and other pure sands may be extrapolated to normally consolidated CDG, but the effect of over-consolidation is new and more test results are required to explain it within the critical state framework.

The stress-dilatancy behaviour of CDG (black symbols) and reinforced CDG (grey symbols) samples tested at different effective stress are shown in figure 4. All normally consolidated specimens, reinforced and unreinforced, show a typical frictional behaviour. The pure CDG specimens converge to a unique frictional critical state stress ratio ranging from  $M=1.57$  to  $M=1.61$ . The reinforced CDG specimens tested at effective stresses of 200 and 500kPa converged to a critical stress ratio of  $M = 1.83$ . For the lower effective stress of 100kPa (R100), the specimen reached a higher stress ratio of  $M = 2.14$ , which is similar to what was found by Silva dos Santos *et al.* (2010) on fibre-reinforced sand. The over-consolidated specimens, UR100 and R100, did not follow the frictional trend but showed much less volumetric deformation up to critical state, which was also observed in the stress-strain behaviour. This may have been caused by locking of the fibres during compression and swelling prior to shearing.

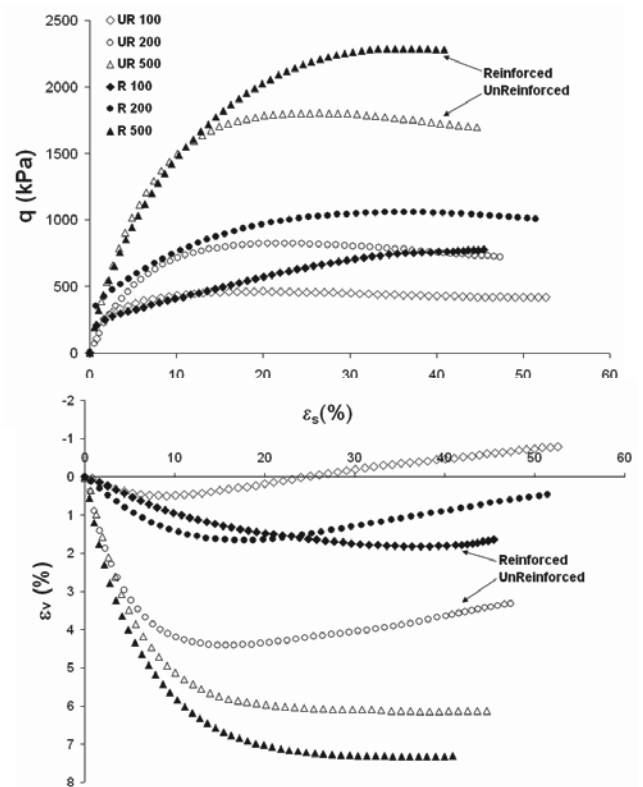


Figure 3. Stress-strain-volumetric response of CDG and fibre-reinforced CDG sheared at different effective confining stresses.

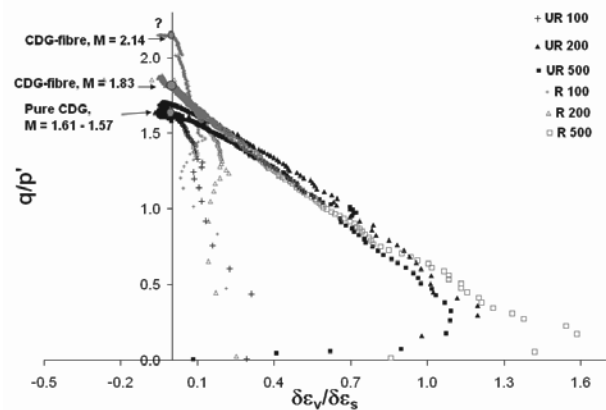


Figure 4. Stress-dilatancy response of CDG and fibre-reinforced CDG.

The deviatoric stress and corresponding mean effective stress in the test that reached a stable critical state are plotted in a  $q$ - $p'$  plane in figure 5. These points form a critical state envelope for the pure CDG with a critical state gradient  $M=1.57$ . This is found to be consistent with critical stress ratio  $M = 1.57 - 1.61$ , obtained from the stress-dilatancy plot (figure 4). The end of test points are also plotted for the reinforced specimens but no attempt has been made in this paper to define the critical state envelope for fibre-reinforced CDG because at low stresses, the deviatoric stress does not stabilise (figure 3a). More tests are required over a larger range of stresses to do so, as was done by Silva dos Santos *et al.* (2010) who found that the critical state lines of the unreinforced and reinforced specimens converge at large stresses of the order of 5MPa.

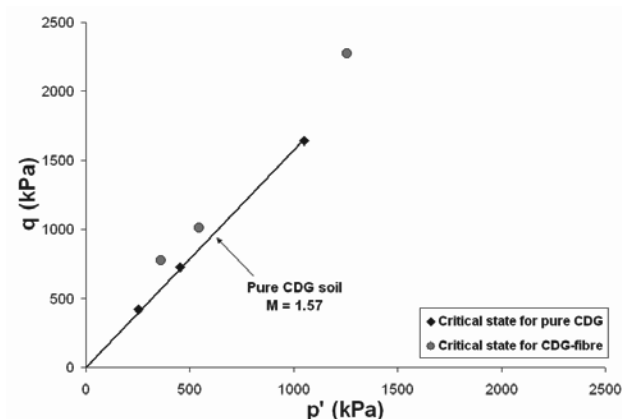


Figure 5. Critical states and end of test points for CDG and fibre-reinforced CDG in  $q$ - $p'$  plane.

#### 4 CONCLUDING REMARKS

The results presented indicate that using discrete fibres can be an effective means of reinforcing CDG, specifically at low effective stresses. The unconfined compressive strength tests showed a tenfold increase in strength with 0.5% fibres content in the soil prepared at maximum dry density and optimum moisture content. In triaxial drained tests, adding fibres seems to increase the shear strength by up to two times the strength of the unreinforced specimens, as well as its initial stiffness. Dilation was also found to be reduced. Unique critical states were reached for the unreinforced CDG and reinforced CDG tested at high effective stress. The stress-dilatancy was found to be frictional for all normally consolidated specimens, but with different critical state stress ratios ( $M$ ) for the fibre-reinforced specimens depending on their effective confining stress. Initial results also seem to indicate that the over-consolidation ratio affects the performance of the reinforced CDG, noticeably in the stress-dilatancy response, but more work is needed to confirm it.

#### 5 ACKNOWLEDGEMENTS

The authors wish to acknowledge Ku Hei Man, Gloria (final year project student 2012, The University of Hong Kong) for providing the Unconfined compressive test results. The financial support provided by Hong Kong Research Grant Council GRF No.70211 is gratefully acknowledged.

#### 6 REFERENCES

- Altuhafi F.N. and Coop M.R. (2011). Changes to particle characteristics associated with the compression of sands. *Géotechnique* 61, No. 6, 459–471.
- BS 1377:1990. Methods of test for soils for civil engineering purposes. British Standards Institution, London
- Consoli N.C., Casagrande M.D.T. and Coop M.R. (2005). Effect of fiber reinforcement on the isotropic compression behavior of a sand. *J. Geotech. Geoenviron. Engng, ASCE* 131, No. 11, 1434–1436.
- Consoli N.C., Heineck K.S., Casagrande M.D.T. and Coop M.R. (2007). Shear strength behavior of fiber-reinforced sand considering triaxial tests under distinct stress paths. *J. Geotech Geoenviron. Engng, ASCE* 133, No. 11, 1466–1469.
- Consoli N.C., Casagrande M.D.T., Thomé A., Dalla Rosa F. and Fahey M. (2009a). Effect of relative density on plate tests on fibre-reinforced sand. *Géotechnique*, 59, No. 5, 471–476.
- Consoli N.C., Festugato L. and Heineck K.S. (2009b). Strainhardening behaviour of fibre-reinforced sand in view of filament geometry. *Geosynthetics Int.* 16, No. 2, 109–115.
- Crockford W.W., Grogan W.P. and Chill D.S. (1993). Strength and life of stabilized pavement layers containing fibrillated polypropylene. *Transpn Res. Rec.* 1418, 60–66.
- Gray D.H. and Al-Refeai T. (1986). Behavior of fabric versus fiber reinforced sand. *J. Geotech. Engng, ASCE* 112, No. 8, 804–826.
- Lee I.K. and Coop M.R. (1995). The intrinsic behaviour of a decomposed granite soil. *Geotechnique* 45 (1), 117–130.
- Maher M.H. and Ho Y.C. (1994). Mechanical properties of kaolinite/fiber soil composite. *J. Geotech. Engng, ASCE* 120, No. 8, 1381–1393.
- Santoni R.L., Tingle J.S. and Webster S.L. (2001). Engineering properties of sand–fiber mixtures for road construction. *J. Geotech. Geoenviron. Engng, ASCE* 127, No. 3, 258–268.
- Silva Dos Santos A.P., Consoli N.C. and Baudet B.A. (2010). The mechanics of fiber-reinforced sand. *Géotechnique*, 60, No. 10, 791–799.
- Yan W.M. and Li X.S. (2012). Mechanical response of medium-fine-grained decomposed granite in Hong Kong. *Engineering Geology* 129-130 (2012) 1–8.

# Hybrid Application of Deep Mixing Columns Combined with Walls as a Soft Ground Improvement Method Under Embankments

Application hybride de la méthode de « Deep Mixing » sur des colonnes combinées à des murs en tant que méthode d'amélioration des sols mous sous remblais

Matsui H., Ishii H., Horikoshi K.  
 Technology Center, Taisei Corporation, Yokohama, JAPAN

**ABSTRACT:** In this paper, we introduce the concepts and general functions of a hybrid application of deep mixing columns combined with walls. This new method for improving the soft ground under embankments helps control ground deformation. We briefly describe a case in which the method was applied under an embankment 7 m in height. The method effectively restricted the induced deformation of the ground surface to a target level, not only under the embankment but also adjacent to the embankment toes. Two-dimensional finite element analysis was adopted to the case and found effective for simulating the performance. Also proposed is a design flow for the new method to efficiently determine the best arrangement of deep mixing columns and walls. Numerical parametric studies were carried out to compare the new method with conventional methods.

**RÉSUMÉ :** Dans cet article, nous présentons les concepts et les fonctions générales de l'application hybride de méthode de « Deep Mixing » sur des colonnes combinées à des murs. Cette nouvelle méthode d'amélioration de sols mous sous remblais aide à contrôler la déformation du terrain. Nous décrivons brièvement un cas dans lequel la méthode a été appliquée sous un remblai d'une hauteur de 7 m. La méthode a permis de limiter efficacement la déformation induite de la surface du sol à un niveau cible, non seulement sous le remblai, mais aussi dans les zones adjacentes aux pieds de talus. Une analyse par éléments finis en deux dimensions a été appliquée à ce cas et s'est avérée efficace pour simuler les performances. Une méthode d'optimisation est également proposée en vue de déterminer de manière efficace la meilleure disposition des colonnes et des murs. Des études paramétriques numériques ont été menées pour comparer la nouvelle méthode avec les méthodes classiques.

**KEYWORDS:** soft ground improvement method, finite element analysis, deep mixing method

## 1 INTRODUCTION

Deep mixing methods have been widely used in Japan for the foundation systems of embankments constructed on soft clayey ground, and various low improvement ratio arrangements have been proposed (Miki and Nozu 2004, Ishikura et al. 2009, Miki et al. 2011). Typical of recent applications is to achieve limited soil improvement—around 10-20%—through an arrangement of soil improvement columns. This reduces the volume of soil that must be improved and limits the ground settlement under the embankments. Moreover, embankment construction in urban areas requires strict control of ground deformation, especially in the areas adjacent to the embankment toes.

The authors propose a new hybrid application of deep mixing columns combined with walls (Tsutsumi et al. 2009) as a method of improving the soft ground under embankments to control ground deformation. In this paper, the concepts and general functions of the method are introduced. The paper then describes a case in which the method was applied under a tall embankment 7 m in height. Two-dimensional finite element analysis was adopted to simulate the performance. Also proposed is a design flow for the new method that efficiently determines the best arrangement of deep mixing columns and walls. Finally, numerical parametric studies were carried out to compare the new method with conventional methods.

## 2 CONCEPTS AND GENERAL FUNCTIONS OF A HYBRID APPLICATION OF DEEP MIXING COLUMNS COMBINED WITH WALLS

The basic concept of this method is to place deep mixing walls in the ground directly under the embankment slopes, which

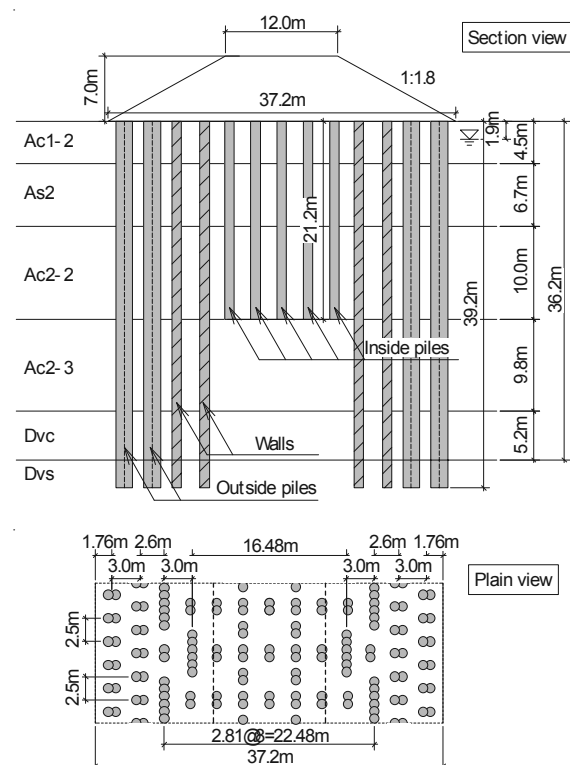


Figure 1. Geological profile and arrangement of the deep mixing columns and walls at the construction site where the method was applied.



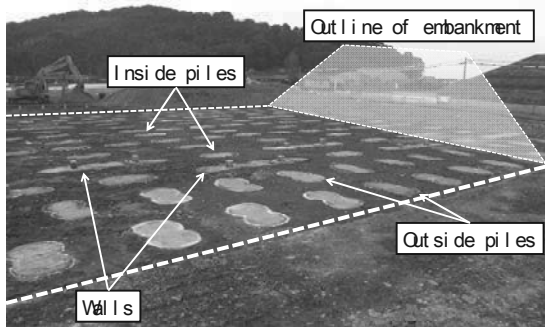


Figure 2. Ground surface after soil improvement.

bear the embankment loads as well as the lateral movement of the soft ground. Deep mixing piles are placed inside and outside the walls to restrict vertical and horizontal deformation caused by the embankment.

Figure 1 shows an example of the arrangement of deep mixing columns and walls at a site. The function and placement of each pile and wall are explained below.

**Inside piles:** Columns placed in the ground directly under the crown of the embankment. This part transfers the load from the center part of the embankment to the deep layer.

**Walls:** Walls are placed in the ground under the edges of the embankment crown. This part bears a large part of the embankment load and prevents the soil from moving.

**Outside piles:** Columns placed in the ground directly under the embankment slopes. This part transfers the load of the embankment slopes.

This method is designed to economically satisfy the limit value of settlement by optimizing and minimizing these parts in the design.

### 3 TRIAL EMBANKMENT

#### 3.1 Work outline

The effectiveness of this method was demonstrated in a road construction project along the Ariake Sea in Kumamoto Prefecture. The soft clay at the construction site was about 40 m thick, so a large volume of settlement could be expected after constructing an embankment 7m in height. Some parts of the proposed road were close to residential buildings. Therefore, a limit value for deformation was set not only for the embankment but also for the area adjacent to the embankment, as described below.

**Embankment:** Settlement since the start of service is equal to or lower than 300 mm.

**Adjacent area:** Lateral and horizontal displacement since the start of construction is equal to or lower than 20 mm.

During the design stage, many of the arrangements were compared using two- and three-dimensional effective stress analysis. After considering all of the above, the arrangement shown in Fig. 1 was determined to be optimal. Each column had a design strength of 1.0MN/m<sup>2</sup>, and the arrangement had an improvement ratio of 18.5%.

Before the embankment was constructed, settlement plates and pressure gauges were installed for the purpose of taking measurements. The ground surface after soil improvement is shown in Fig. 2.

#### 3.2 Result of construction

Figure 3 shows the settlement history of the ground surface at the center of the embankment. The same figure also shows a similar settlement history, observed at a trial embankment nearby with no subsoil treatment. In the improvement case, 200mm of settlement occurred one year after embankment construction. Subsequently, settlement converged in both cases. Table 1. Material properties used for numerical model

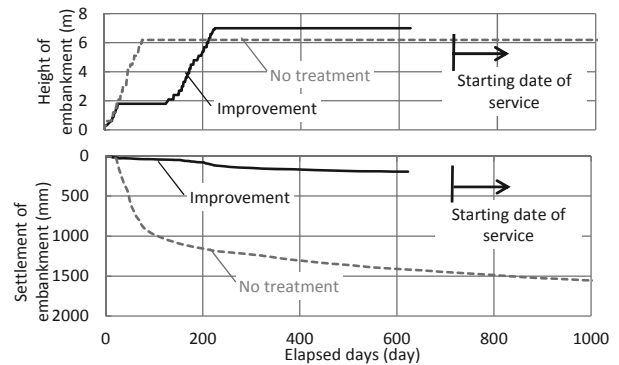


Figure 3. History of ground surface settlement in at the center of the embankment.

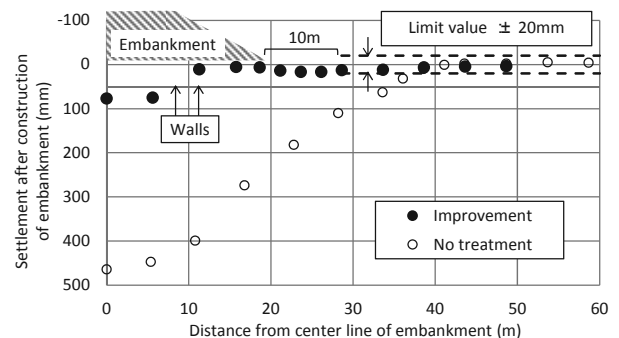


Figure 4. Distribution of ground surface settlement after construction of the embankment.

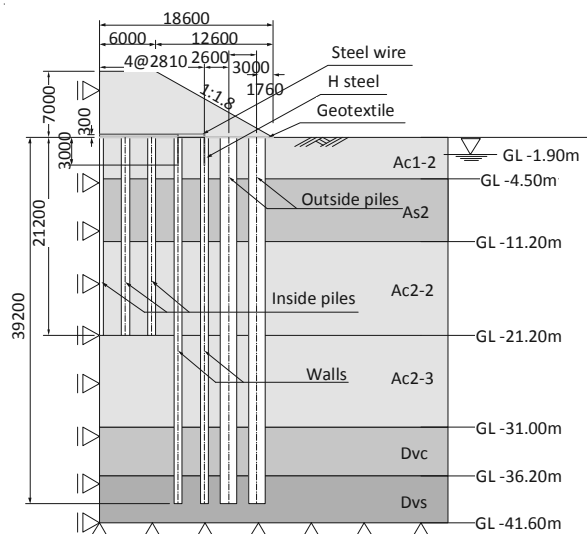


Figure 5. Section view of the numerical model.

Figure 4 shows the settlement history for a one-year period after the construction road was removed. In the improvement case, large walls prevented deformation under the embankment, keeping the settlement around the embankment below the limit value. The vertical strain measured in the walls is shown in Fig. 7; this, too, was kept below the fracture strain value.

#### 3.3 Back-analysis

To investigate the applicability of two-dimensional effective stress analysis under actual construction conditions, the geological profile and mechanical properties of the deep mixing columns were analyzed using Plaxis 2D Ver.9.02.

The numerical model is shown in Fig. 5. Due to the symmetry of the embankment, only half of the geometry was considered for the model. The distance from the embankment

	Unit weight $\gamma_i$ (kN/m <sup>3</sup> )	Effective cohesion $c'$ (kN/m <sup>2</sup> )	Effective angle of friction $\phi'$ (deg.)	Deformation modulus $E$ (kN/m <sup>2</sup> )	Initial void ratio $e_0$	Consolidation yield stress $p_c$ (kN/m <sup>2</sup> )	Compression index $\lambda$	Expansion index $\kappa$	Critical state parameter $M$	Poisson's ratio $\nu$	Coefficient of permeability $k$ (cm/sec)
Embankment	19.0	10.0	35.0	28,000	-	-	-	-	-	0.25	$1.00 \times 10^{-3}$
Ac1-2	14.6	10.0	36.4	1,720	2.13	36.8	0.289	0.029	1.48	0.35	$1.30 \times 10^{-6}$
As2	18.7	-	-	28,000	-	-	-	-	-	0.25	$1.00 \times 10^{-3}$
Ac2-2	14.3	10.0	36.2	6,380	2.53	146.1	0.665	0.067	1.47	0.35	$3.00 \times 10^{-7}$
Ac2-3	15.1	10.0	33.0	7,130	2.00	178.5	0.408	0.041	1.33	0.35	$2.30 \times 10^{-7}$
Dvc	15.8	10.0	33.0	6,510	1.21	215.7	0.149	0.015	1.33	0.35	$1.40 \times 10^{-9}$
Dvs	19.0	-	-	70,000	-	-	-	-	-	0.35	$1.00 \times 10^{-3}$
Columns	19.0	-	-	367,000 – 718,000*1	-	-	-	-	-	0.20	$1.40 \times 10^{-9}$ – $1.00 \times 10^{-3*2}$

\*1 The deformation modulus of the deep mixing columns was derived from quality verification tests, which reduced dependence on the improvement ratio.

\*2 The coefficients of permeability of the deep mixing columns are same as those for each layer.

toe to the lateral boundary is 80m. As a boundary condition of deformation, the bottom surface was fixed. The side surface was free vertically and fixed horizontally. As a drainage condition, excess pore water pressures at the ground surface and bottom surface were set to zero.

The soil layer is modeled as an elasto-plastic material using the Sekiguchi-Ohta model (Sekiguchi and Ohta 1977). The sand layers and deep mixing columns are modeled as a linear elastic material. The embankment is modeled as an elasto-plastic material using the Mohr-Coulomb model. Table 1 lists the model parameters used for the analysis.

The history of the embankment construction was modeled by building up the elements. In converting from actual three-dimensional ground to the two-dimensional numerical model, the deformation modulus of the deep mixing columns was reduced according to the improvement ratio and the coefficient on permeability for deep mixing columns was set to the value for each layer of ground.

The following figures are for the sake of comparison and analysis: Figure 6 shows the history of ground-surface settlement at the center of the embankment; Fig.7 shows the distribution of ground-surface settlement after construction of the embankment; Fig. 8 shows the horizontal displacement and vertical strain of the walls. The settlement history and displacement of the ground surface and walls are quantitatively evaluated using two-dimensional analysis. However, a clear difference in the vertical strain exists at greater depths. In the numerical models, the deformation modulus of walls less than 21 m in height is lower than that of walls greater than 21 m in height as per the arrangement of the deep mixing columns. This is thought to be the cause of the difference in vertical strain. Individual material properties are effective for evaluating the strain distribution of walls.

#### 4 DETERMINING THE OPTIMUM ARRANGEMENT OF DEEP MIXING COLUMNS

In this method, the piles and walls are effectively arranged according to the limit values of deformation in the embankment and the adjacent area. Due to the countless combinations of planar arrangements and improvement depths, arbitrary parametric studies require considerable time to identify optimum arrangement. Therefore, the following 3-step method is proposed for determining the optimum arrangement.

1) Determine the planar arrangement: First, walls are placed in the ground under the edges of the embankment crown. Next, inside and outside piles are arranged equidistantly by an amount not less than the necessary improvement ratio  $\alpha$ , defined as

$$\alpha = \gamma \cdot H / q_{uck} \quad (1)$$

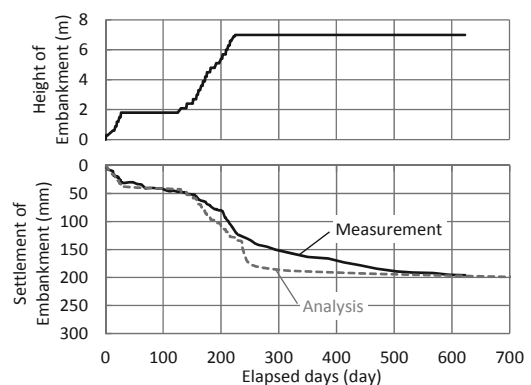


Figure 6. Settlement history of ground surface in center of the embankment

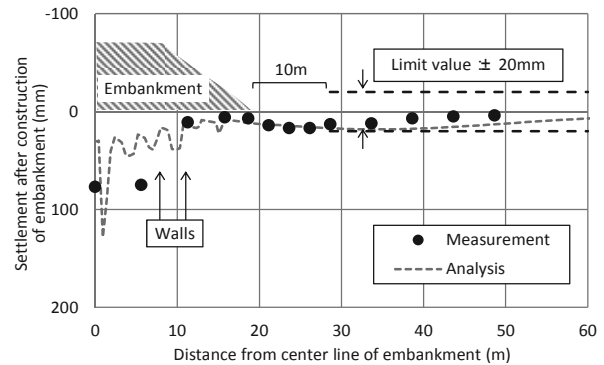


Figure 7. Distribution of ground surface settlement after construction of the embankment

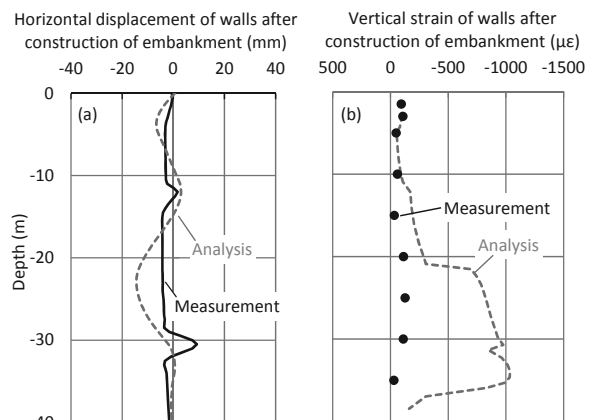


Figure 8. (a) Horizontal displacement of walls (b) Vertical strain in walls

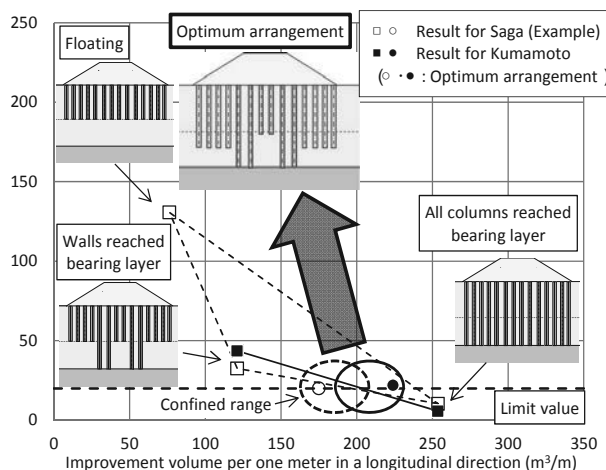


Figure 9. Example of confining the range of consideration and the result of the consideration for in-situ construction in Kumamoto

in which  $\gamma$  is the unit weight of the embankment,  $H$  is the height of the embankment and  $q_{uck}$  is the design strength of the deep mixing columns.

2) Confine the range of consideration: For the planar arrangement noted above, the deformation of three arrangements with different improvement depths (as shown in Fig. 9) is calculated. The relation between the improvement volume and the deformation of the three arrangements is illustrated in Fig. 9. The range of consideration is narrowed by comparing with the limit value of deformation in the adjacent area.

3) Identify the optimum arrangement: The optimum arrangement in the range noted above is the arrangement with the lowest improvement volume that satisfies the limit value.

Figure 9 shows the results of a search for the optimum arrangement in areas along the Ariake Sea in Saga Prefecture. Figure 9 also shows the results of a search in Kumamoto as an example of an arbitrary parametric study. The positional relation between both cases is fitted and the results indicate the effectiveness of the search method.

## 5 COMPARISON WITH CONVENTIONAL METHODS

To confirm the effect of displacement suppression, a hybrid arrangement is compared with conventional columns arrangements as well as an arrangement in which the columns are equidistant and narrowly spaced.

Under the same geological conditions and embankment height as in the Kumamoto case, the settlement of the embankment and at a point 10 m from the embankment toes of each arrangement were calculated using two-dimensional analysis.

Figure 10 shows the relation between individual settlement values and improvement volumes per meter in the longitudinal direction. Regarding settlement of the embankment, the settlement of the hybrid arrangement and the equidistant arrangement are lower than the arrangement under the slopes, confirming the effect of displacement suppression. For the settlement at a point 10 m from the embankment toes, the hybrid arrangement is the lowest among same improvement volumes. When the limit value of settlement in the adjacent area is 20 mm, the hybrid arrangement is more effective than conventional methods in reducing the improvement volume.

## 6 CONCLUSIONS

On-site measurements confirmed the method's effectiveness in suppressing displacement. The validity of deformational estimation using two-dimensional effective stress analysis also

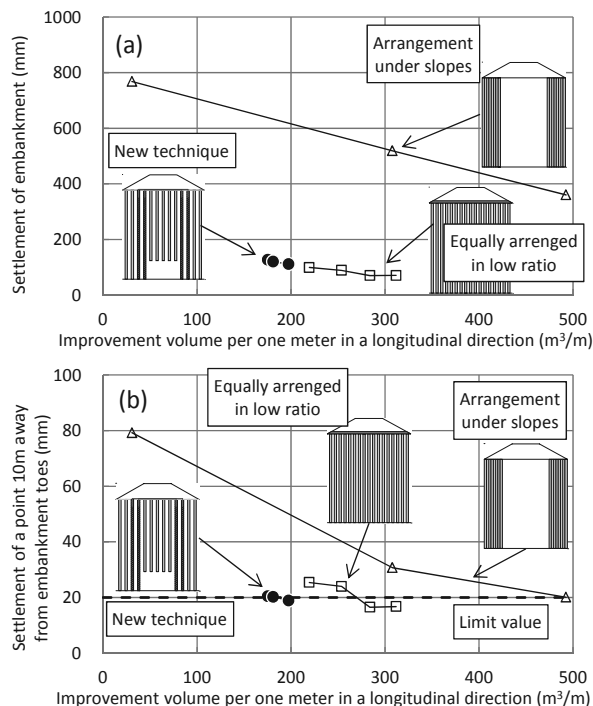


Figure 10. (a) Settlement of embankment (b) Settlement at a point 10 meters from the embankment toes.

was confirmed. However, little difference was seen in the estimation of stress and strain distribution in the walls. Using individual material properties for the walls, however, is effective. The two examples of searching for the optimum arrangement using the method proposed in this paper confirmed the method's effectiveness. Analytical comparison of the new method with conventional methods also confirmed the economic efficiency of the new method.

## 7 ACKNOWLEDGEMENTS

The development of this column link method is the result of collaborative research involving the Public Works Research Institute, Japan, and thirteen private corporations in Japan. The authors are particularly grateful for the kind assistance of Shouichi Tsutsumi (PWRI), Hirota Kawasaki (Shimizu Corp.), Shouichi Tsukuni (Takenaka Civil Eng. & Const. Co., Ltd.), and Naotoshi Shinkawa (Fudo Corp.).

## 8 REFERENCES

- Miki, H. and Nozu, M. 2004. Design and numerical analysis of road embankment with low improvement ratio Deep Mixing method, *Geotechnical Engineering for Transportation Projects*, Vol. 2, 1935-1402.
- Ishikura, R. Ochiai, H. and Matsui, H. 2009. Estimation of settlement of in-situ improved ground using shallow stabilization and floating-type columns, *Proceedings of 17<sup>th</sup> International Conference on Soil Mechanics and Geotechnical Engineering*, 2394-2398.
- Miki, H. Okochi, Y. and Makino, M. 2011. Evaluation of constraint effect of DMM with varied shape and arrangement of stabilized bodies using centrifuge model test, *Proceedings of Indian Geotechnical Conference*, 501-504.
- Tsutsumi, S. Sawamatsu, T. Iso, Y. and Oshita, T. 2009. Centrifuge model experiment of new improvement type in deep mixing method with steel tied by cable for lateral flow, *Deep mixing 2009 Okinawa symposium*.
- Sekiguchi, H. and Ohta, H. 1977. Induced anisotropy and time dependency in clays, Constitutive equations of soils, *Proceedings of 9<sup>th</sup> International Conference on Soil Mechanics and Foundation Engineering*, 229-238.

# Application of cement deep mixing method for underpinning

## Application de colonnes de sol-ciment pour travaux de reprise en sous œuvre

Melentijevic S., Arcos J.L.  
Grupo Rodio-Kronsa, Madrid, Spain

Oteo C.  
Universidad de A Coruña, A Coruña, Spain

**ABSTRACT:** This paper presents a case history of the application of wet deep soil mixing columns for underpinning of the existing floor slab of an industrial building, which settled due to different encountered post-constructive pathologies related to ground conditions. The soil-cement columns were constructed with the application of the new developed Springsol<sup>®</sup> tool that permits the underpinning of existing foundations, infrastructure transport platforms and embankments, as well as working in limited spaces and under low headroom conditions. The quality control regarding laboratory testing of core and wet grab samples is reported. Design procedure and the finite element analysis that verify settlement calculations are described. The FEM is focused on the axisymmetric numerical modeling in Plaxis.

**RÉSUMÉ :** Cet article présente une étude de cas de réalisation de colonnes de sol mixing par voie humide pour la reprise en sous œuvre du dallage d'un bâtiment industriel, ayant tassé après sa construction à cause de pathologies du sol. Les colonnes de sol-ciment ont été réalisées avec la méthode Springsol<sup>®</sup>, qui permet la reprise en sous œuvre de fondations existantes, d'infrastructures de transports et de remblais, à partir d'emprises étroites et sous faible gabarit. Les contrôles de qualité réalisés en laboratoire sur des éprouvettes carottées et sur des prélèvements frais y sont présentés. Le mode de dimensionnement ainsi que les analyses par éléments finis pour estimer les tassements sont également décrits. Les calculs EF ont été réalisés avec le code Plaxis en axi-symétrie.

**KEYWORDS:** deep mixing, soil-cement columns, Springsol<sup>®</sup>, underpinning, FEM.

### 1 INTRODUCTION

In order to reduce settlements, increase bearing capacity of natural ground and improve the overall stability, different ground improvement techniques can be put into practice, but not all of them can be applied for underpinning projects. The limitations for the applications are mainly related to capacity of the machinery to pass existing foundation structures as reinforced slabs or footings, and insufficient working spaces and/or low headroom conditions.

The soil-cement deep mixed columns for ground improvement of soft soils have an extensive application for different geotechnical projects due to their higher strength and lower compressibility than the untreated natural soft soil. The application of traditional deep mixing methods, both wet and dry, was very restricted for the underpinning of existing foundations, improvement of existing embankments and infrastructure platforms, due to the form and dimensions of the mixing tool.

With objective to present new wet deep soil mixing system called Springsol<sup>®</sup> a case history with its application in underpinning project is reported in this paper. To prevent further settlements and guarantee bearing capacity of the foundation of the industrial building that presented various post-constructive pathologies, the Springsol<sup>®</sup> deep mixing columns were proposed as an alternative method to basic project underpinning solution comprising jet-grouting, traditional tuba-manchette grouting and micropiles for different areas of the building. Due to its technical, economic and environmental advantages, soil-cement columns were accepted and executed as a global solution. In the following chapters the main characteristics of the Springsol<sup>®</sup> system will be described as well as the analysis of the solution adopted and performed for this project. Some recent applications of the Springsol<sup>®</sup> technique are given in Melentijevic et al., 2012.

### 2 SPRINGSOL<sup>®</sup> SOIL CEMENT COLUMNS

Springsol<sup>®</sup> device was originally developed for improvement of soils under existing railways due to its spreadable form (Innotrack 2009, Le Couby 2010). The folded tool is introduced through the casing to the required depth at the beginning of the column head. Once it reaches the end of the casing and penetrates the underlying soft soil, the blades spread out forming the soil-cement column down to the required depth.

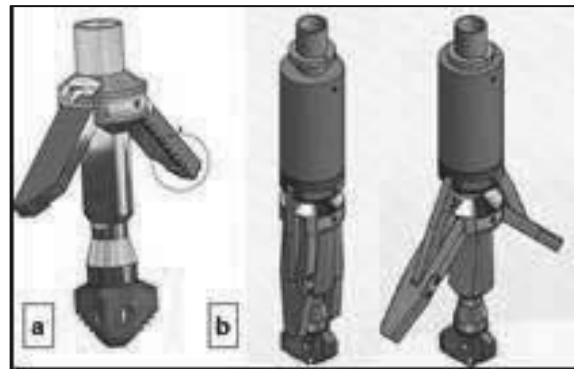


Figure 1. The Springsol<sup>®</sup> spreadable tool: (a) original and (b) modified.

At present, Springsol<sup>®</sup> columns permit an application in ground improvement for underpinning of existing foundations (both slabs and footings), paving, embankments and subbase below infrastructures (both highways and railways). Originally it was developed to form columns of 400 mm diameter. Due to continuous necessity for construction of soil-cement columns of larger diameters the Springsol<sup>®</sup> soil mixing tool has technically evolved into the new modified version, permitting achievement of different column diameters ranging from 400 to 700 mm. The modified tool also includes the automatic system for opening and closing blades thus having the possibility to form variable

diameter along the column depth. Figure 1 shows the nowadays available original and modified improved Springsol<sup>®</sup> tool. The folded tool is of a diameter of 150 and 165 mm for the original and modified version respectively.

Some of the advantages of the method are:

- No pollution of the subgrade layer with the cement slurry, due to insertion of the casing that enables the recovery of spoil.
- The spoil collection with the system installed at the base of the mast of the drilling rig, connected to the peristaltic pump drawing the spoil directly to the container.
- The high production rate.
- Working under difficult execution conditions and limitations, i.e. under low headroom conditions and within reduced spaces.
- Execution with small batching plants and small drilling rigs in reduced limited spaces, etc.

The quality of soil-cement columns regarding their homogeneity and strength is influenced by two parameters:

- Im (rev/m) - blade rotation number determining the mixing efficiency defined as a total number of mixing blades passing along one meter of tool penetration, and
- li (kg/m<sup>3</sup>) - cement quantity introduced per m<sup>3</sup> of the treated soil.

Table 1. Springsol<sup>®</sup> columns performance and geo-mechanical parameters.

Parameter	
Diameter (mm)	400-700
Water / Cement ratio	0.6-1.2
Penetration velocity (cm/min)	15-50
Im (rev/m)	min 350
li (kg/m <sup>3</sup> )	150-350
UCS (MPa)	0.5-6.0
E <sub>50</sub>	(50-500) UCS
Shear strength	20-40% UCS
Bending strength	8-15% UCS

The general execution parameters and geo-mechanical characteristics (unconfined compressive strength - UCS, stiffness modulus – E<sub>50</sub>, shear and bending strength) of the soil-cement columns executed by the Springsol<sup>®</sup> device are given in Table 1. These data are established on experiences gained on different projects and field tests carried out recently in Spain (Melentijevic et al 2012, Melentijevic et al 2013). These findings on geo-material properties are in agreement with worldwide published information on deep mixed columns (Bruce 2001, CDIT 2002, etc.).

### 3 PROJECT DETAILS AND ADOPTED GROUND IMPROVEMENT SOLUTION

In this chapter an example of application of the Springsol<sup>®</sup> technique for underpinning is presented. The industrial building in the central Spain presented different post-constructive pathologies regarding differential settlements of floor slabs and pavements as a consequence of poorly compacted anthropic fill material. The main structure (walls and columns) were founded on a natural ground, and due to its adequate geotechnical characteristics did not present any pathology. The shallow foundation on a natural ground was performed after a massive excavation of superficial layers of natural soil, applying the

same material for construction of a fill without its appropriate compaction.

The affected area included more than 8000 m<sup>2</sup> with the installation of more than 2500 soil-cement columns. The length of soil-cement columns ranged from 5.50 m to 8.00 m in function of the thickness of the man-made fill, with the total length of columns of more than 15000 meters. Due to the form of the Springsol<sup>®</sup> tool, the columns were embedded approximately 20 cm in the natural ground. The columns of a 400 mm diameter, performed with the originally developed tool, were distributed in a square grid pattern ranging from 1.50 m to 2.00 m in function of the surcharge to be transmitted from the slab. The performed solution is schematically presented in Figure 2.

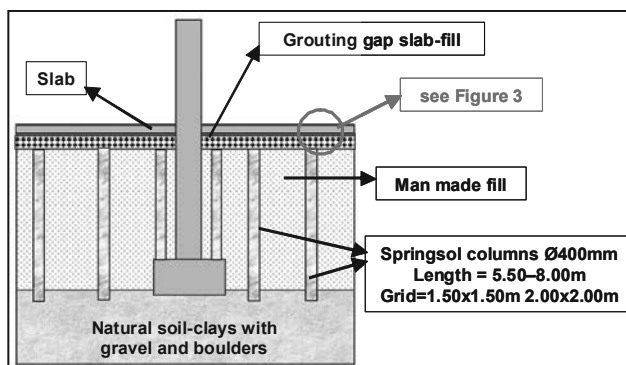


Figure 2. Cross section of the ground treatment solution.

The post pathology site investigation consisted of 46 dynamic penetration tests and 5 drilled boreholes with standard penetration tests, executed from the working platform, i.e. the existing floor slab level. The natural ground, detected at the depth of 5.50 to 8.00 m from the surface, consisted of clays of high consistency with gravels and boulders, with the N<sub>20</sub>>40 (DPSH). The overlying treated loose man made fill was formed of clays with gravels (N<sub>20</sub><10) proceeding from the natural ground after a massive excavation for the foundation of the main structure elements.

The soil treatment solution included following steps:

- Coring of the existing slab (diameter = 62 mm) for grouting of the gap between slabs and fill.
- Contact grouting between the slab and the fill in order to fill gaps due to settlement of badly compacted man made fill.
- Coring of the existing slab and contact grouted gap (diameter = 182 mm) for the passage of the spreadable tool.
- Execution of Springsol<sup>®</sup> columns (diameter = 400 mm).
- Filing the gaps of coring the existing slab.

Visual description of the executed steps previously mentioned is shown in Figure 3.

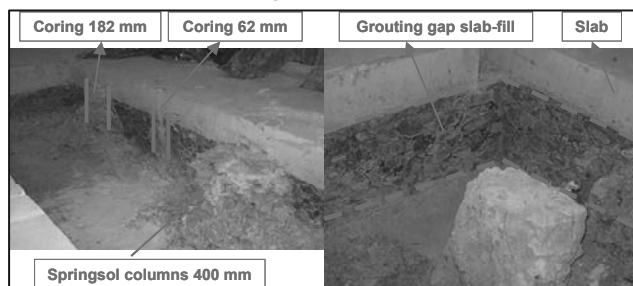


Figure 3. Visual control of the excavated treatment area.

#### 4 GEOMATERIAL SOIL-CEMENT COLUMN CHARACTERIZATION

The cement used for the construction of soil-cement columns was of the Portland type CEM I 52.5 SR. The slurry mix was of a Cement / Water type with the relation 1/1. The average penetration rate for the construction of columns was 30 cm/min with the rotation velocity of 50 to 55 rpm and the average cement consumption of 350 kg/m<sup>3</sup>.

The unconfined compressive strength tests (UCS) were performed both on drilled core samples and wet grab samples (cylinder dimensions height / diameter > 2), both of them usually being the main mean of the quality control of wet deep mixing methods. Three core samples were taken from different soil-cement trial test columns, 21 days after the completion of the soil-cement columns. The samples were cored at a distance of 110 mm to 120 mm from the centre of columns. The overall average total core recovery was more than 97% for all soil-cement columns. Wet grab samples were taken in the half an hour after execution of columns and were tested at same age as core samples. The UCS tests were also used to determine the stiffness modulus  $E_{50}$  (secant value of Young's modulus of elasticity determined at 50% of UCS).

The UCS values of wet grab samples after 7 days varied from 1.4 to 3.9 MPa, while UCS values for drilled core samples on 28 days ranged from 2.2 to 4.4 MPa and axial failure strain values varied from 1 to 1.2 %. Stiffness modulus values determined from UCS tests varied from 270 to 330 MPa, with the average relationship between  $E_{50}$  and UCS resulting in approximately 100.

Some of the drilled core samples extracted from soil-cement trial test columns is presented in Figure 4. It can be observed uniformly treated Springsol<sup>®</sup> columns.

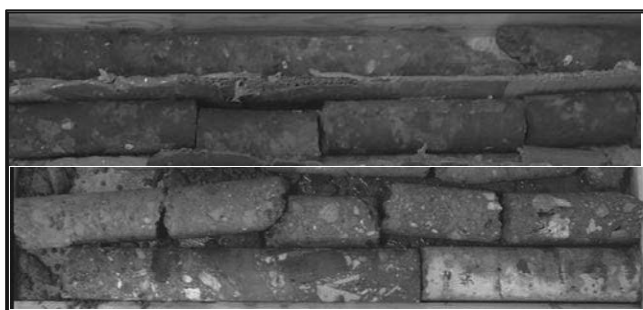


Figure 4. Drilled core samples of soil-cement columns.

#### 5 NUMERICAL MODEL

##### 5.1 General data

When using finite element analysis to model deep mixed columns installed in a periodic pattern, the problem is usually modelled in a 2D axisymmetric model, referred as a unit cell model. The homogenization equivalent model is usually not used due to lack of access to column stresses.

The radius of the unit cell depends on the grid spacing:

$$R_{eq} = \frac{s}{\sqrt{\pi}} \quad (1)$$

where:  $R_{eq}$  is the radius of the unit cell and  $s$  is the grid spacing.

In this project different square grid patterns (grid spacing varying from 1.50 to 2.00 m) depending on the surcharge of the slab (ranging from 10.00 to 20.00 kN/m<sup>2</sup>) are taken into account.

In this study the commercial finite element code used for 2D modelling is Plaxis (version 8.6). Both the soft soil and the soil-cement column behaviour are modelled by the elastic-plastic Mohr-Coulomb failure criterion, while the slab is characterized

by the elastic law. The load transfer layer formed by grouting the gap within the contact gravel layer below the existing slab of the approximate thickness of 20 cm is modelled by the Mohr-Coulomb law. Geotechnical parameters of each material (LTL-load transfer layer, CU-upper clay layer, CM-medium clay layer, NSC-natural soil clay layer, SC-soil cement column) used in the numerical analysis are given in Table 2.

The cross section of the FE model is presented in Figure 6 showing the geometry and soil layers used in analysis, as well as the finite element mesh.

Table 2. Material parameters.

Parameter	LTL	CU	CM	NSC	SC
Thickness (m)	0.2	4.0-6.5	1.5	>4.5	
Density (kN/m <sup>3</sup> )	22	16	17	18	20
Cohesion (kPa)	500	5	10	20	500
Friction angle (°)	40	18	20	22	35
Young's modulus (MPa)	300	2.5	5.0	50	300
Poisson ratio	0.2	0.3	0.3	0.3	0.2

##### 5.2 Results

Figure 6 present the employed mesh in the FEM model, and the results regarding vertical displacements and axial stresses for the case of the grid spacing of 1.50 m corresponding to the surcharge of 20 kN/m<sup>2</sup>.

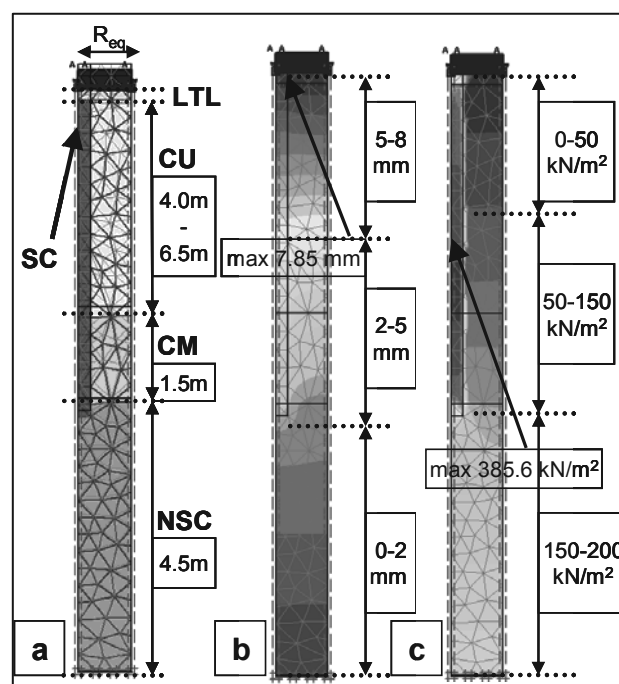


Figure 6. Numerical modeling results for reinforced soil. (a) Geometry of the unit cell - mesh and model dimensions. (b) Vertical displacements. (c) Axial stresses.

The homogenized settlements as well as negligible differential settlements due to high rigidity of the load transfer layer, formed by grouting the layer of gravel below the slab, and soil-cement columns can be observed in Figure 6-b.

The maximum allowable axial stresses in soil-cement columns defined by the UCS value and verified by the FEM analysis was not exceeded for different cases of grid spacing, surcharge and column lengths taken into consideration in the project.

The comparative study of the maximum vertical displacement, in cases without and with the soil improvement for different grid meshes is shown in Figure 7. The significant settlement reduction with the applied soil improvement can be observed in function of grid spacing and for different thicknesses of the soft soil layer.

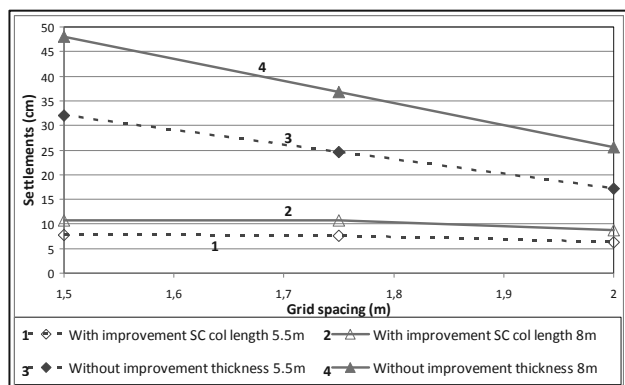


Figure 7. Maximum vertical displacements.

The numerical calculations were also analyzed in terms of load and settlement efficiency (ASIRI 2012) in order to determine the effectiveness of the soil improvement method. The load efficiency ( $E_L$ ) is defined as a ratio of a transmitted load to the head of a soil-cement column and the total load acting on the unit cell. The settlement efficiency ( $E_{set}$ ) represents the reduction of a settlement by a soil-cement column compared to the settlement of the unit grid without ground improvement. They are represented by the following equations:

$$E_L = \frac{Q_p}{W+Q} \quad (2)$$

$$E_{set} = 1 - \frac{S_M}{S_0} \quad (3)$$

where:  $Q_p$  is the load acting on the head of soil-cement column,  $W$  is the dead load of the load transfer platform and  $Q$  is the force of the surcharge applied to the slab.  $S_M$  is the settlement of the soil reinforced by soil-cement columns measured at the surface of the load transfer platform and  $S_0$  is the settlement of the natural soil without ground improvement.

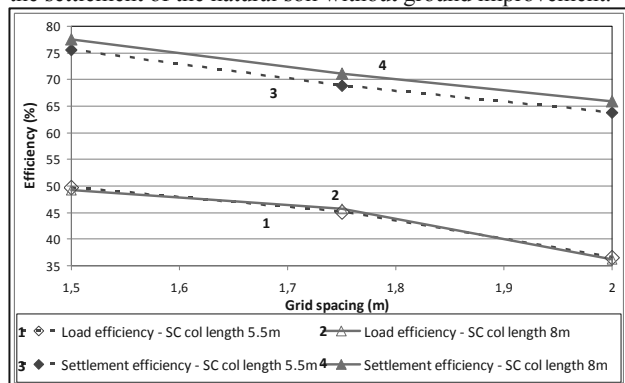


Figure 8. Load and settlement efficiency.

The results of the load and settlement efficiency are given in Figure 8 in terms of different grids adopted in the project for different surcharge loads and for different column length in function of the thickness of the soft layer. Both terms of

efficiency have the same tendency. The load efficiency ranges from 36 to 50 %, while the settlement efficiency varies between 64 and 78 %. The difference of approximately 25 to 30 % between load and settlement efficacy relationships is observed.

It is important to emphasize that the estimated settlements obtained by the analysis by FEM were in accordance with the observed settlements after ground improvement by the performance of soil-cement columns and re-loading of the slab of the industrial building.

## 6 CONCLUSIONS

The general application of the wet deep mixing method by the Springsol<sup>®</sup> system for ground improvement of existing paving, embankments and subbase below railways and roads, and underpinning of existing structures is presented. The case history of underpinning of existing industrial building, which settled due to poorly compacted anthropic fill, with the use of the Springsol<sup>®</sup> system is reported.

The design procedure and the estimation of settlements by the finite element method (Plaxis commercial code) based on axisymmetric model is in concordance with the monitored settlements. The general homogenized nature of settlements, as well as insignificant differential settlements are achieved by the good interaction of the performed soil-cement column and load transfer layer formed by grouting of the layer of gravel below the slab. The evaluation of efficiency of the soil treatment by soil-cement columns, in terms of load and stress efficiency, is determined confirming its effectiveness.

## 7 ACKNOWLEDGEMENTS

The authors wish to thank to the personnel of Grupo Rodio-Kronsa for their technical assistance, especially to Juan Ignacio López, Juan Manuel Dimas, Francisco Martín and Esteban Casado. Also, the collaboration and provision of all necessary information by the Proprietary of the Industrial building is highly appreciated.

## 8 REFERENCES

- ASIRI National Project 2012. Recommendations for the design, construction and control of rigid inclusion ground improvements.
- Bruce D.A. 2001. An introduction to deep mixing methods as used in geotechnical applications, Volume III: The verification and properties of treated ground. U.S. Department of Transportation, Federal Highway Administration, report FHWA RD-99-167.
- CDIT (Coastal Development Institute of Technology), Japan. 2002. The Deep Mixing Method, A.A. Balkema.
- Innotrack. Project N° TIP5-CT-2006-031415. 2009 Subgrade reinforcement with columns. Part 1 Vertical columns, Part 2 Inclined columns.
- Le Kouby A., Bourgeois E. & Rocher-Lacoste F. 2010. Subgrade Improvement Method for Existing Railway Lines – an Experimental and Numerical Study. *EJGE* Vol. 15: 461-494
- Melentijevic S., Martin F. & Prieto L. 2013. Execution of Springsol<sup>®</sup> deep mixed columns: field trials. *International Conference Installation Effects in Geotechnical Engineering, Rotterdam. The Netherlands. 24-27 March 2013*: accepted for publishing.
- Melentijevic S., Prieto L. & Arcos J.L. 2012. Aplicaciones de columnas suelo-cemento tipo Springsol<sup>®</sup>. *9º Simposio Nacional de Ingeniería Geotécnica. Cimentaciones y Excavaciones Profundas. Proc. Symp. Sevilla. 17-19 October 2012*: 255-268.
- Plaxis BV. 2008. Plaxis 2D Manual - version 8. www.plaxis.nl.

# Lime Remediation of Reactivated Landslides

## Traitement à la chaux pour la stabilisation des glissements réactivés

Mesri G.

*University of Illinois at Urbana-Champaign, Urbana, Illinois 61801, U.S.A.*

Moridzadeh M.

*Montgomery Watson Harza, Chicago, Illinois, U.S.A*

**ABSTRACT:** Lime improvement of frictional resistance was examined using samples of Brenna Clay Formation from North Dakota. The montmorillonitic stiff clay samples had a natural water content, plastic limit, liquid limit, clay size fraction, fully softened friction angle, and residual friction angle, respectively, in the range of 42 to 85%, 20 to 40%, 62 to 154%, 60 to 95%, 14 to 24°, and 7 to 9°. Immediately after introduction of hydrated lime, pH increased to a range of 12.2 to 12.7; within hours, however, pH began to decrease. Whereas there was a large increase in plastic limit, the liquid limit response to lime treatment was dependent on the effective confining pressure. Lime treatment increased fully softened friction angle by 5 to 10° at effective normal stress of 100 kPa and by 3 to 5° at 300 kPa. Lime treatment increased the residual friction angle by 3 to 6° at both 100 kPa and 300 kPa.

**RÉSUMÉ:** L'amélioration par addition de chaux de la résistance en frottement est examinée sur des échantillons de la formation d'argile de Brenna dans le Dakota du Nord. Les échantillons d'argile raide montmorillonitique ont une teneur en eau, une limite plastique, une limite liquide, une fraction de dimension argileuse, un angle de frottement après remaniement et un angle de frottement résiduel respectivement de l'ordre de 42 à 85%, de 20 à 40%, de 62 à 154%, de 60 à 95%, de 14 à 24°, et de 7 à 9°. Immédiatement après l'addition de chaux hydratée, le pH augmente à des valeurs de 12,2 à 12,7 mais commence ensuite à décroître dans les heures qui suivent. L'augmentation de la limite de plasticité suite au traitement à la chaux est importante, l'augmentation de la limite de liquidité dépend cependant de la pression de confinement. Le traitement à la chaux augmente l'angle de frottement après remaniement de 5 à 10° sous une contrainte effective normale de 100 kPa et de 3 à 5° sous 300 kPa. Le traitement à la chaux augmente l'angle de frottement résiduel de 3 à 6° autant sous une pression de 300 kPa plutôt que de 100 kPa.

**KEYWORDS:** Brenna clay, frictional resistance, lime treatment, landslides.

## 1 INTRODUCTION

The effectiveness of lime treatment of soils has been commonly evaluated in terms of improved workability and increased undrained unconfined stiffness and compressive strength, in connection to road and airfield construction (Bell 1996). Soil improvement is expected to result from the flocculation of clay minerals and cementing action of lime-soil chemical reactions. On the other hand if the objective of lime treatment is to improve long-term stability of first-time or reactivated landslides in stiff clays and shales, permanent changes in the size and shape of clay particles must be realized to increase drained frictional resistance. Lime-soil interactions that may produce less platy and larger soil particles begin and continue with time under the highly alkaline pH environment. For Brenna clay samples treated with lime, measurements of pH as an indicator of chemical environment, Atterberg plastic limit and liquid limit as indirect measures of changes in particle size and shape, and fully softened friction angle and residual friction angle, were used to examine possible mechanisms of lime-soil interactions. The main variables, in addition to soil mineralogy, are soil water content, lime content, and duration of lime-soil interactions.

## 2 LIME-SOIL INTERACTION

When dry hydrated lime is thoroughly mixed with a wet soil, lime is consumed, in the absence of carbonation, through two mechanisms: (a) part of the lime particles is adsorbed on soil particles during the mixing process, and (b) part of the remaining lime is dissolved in the soil porewater. The solubility of calcium hydroxide in water is rather small (0.75 g/l). Therefore, the maximum lime content as percent of dry weight

of soil that can dissolve in the porewater during the mixing process is quite small and a function of soil water content (only 1.5% of lime for 5% lime content at soil water content of 100%). Dissociation of hydrated lime to (OH)<sup>-</sup> and Ca<sup>2+</sup> leads to a rise in the pH. If enough lime is left, after satisfying the adsorption, soil porewater becomes saturated and pH increases to approximately 12.3 to 12.4. Under the strong alkaline condition, soil mineral particle surfaces become unstable and begin to dissolve in the porewater. Simultaneously, under the elevated pH condition, adsorbed lime particles begin to attack the soil particle surfaces at the points of contact.

Dissolved silica and alumina react with the dissociated calcium hydroxide and form new compounds. As the dissolved hydrated lime is used up in the chemical reactions with silica and alumina, the remaining free lime, if any, dissolves in the porewater and pH is maintained at 12.3-12.4. The dissolution of soil particles and local attack of adsorbed lime on the particle surfaces continue at the initial rate until all free lime is completely consumed. Thereafter, pH begins to decrease as the dissociated calcium hydroxide is used up in the chemical reactions with dissolved silica and alumina. This has been confirmed by pH measurements and chemical analyses conducted by Clare and Cruchley (1957) and Diamond et al. (1964). Dissolution of soil particle surfaces continues at a decreasing rate, becoming insignificant as pH drops to values probably less than around 9 (Eades and Grim 1960, Eades et al. 1962, Hunter 1988). The reaction products begin to harden or crystallize as pH decreases. A calcium hydroxide particle is attached to more than one soil particle, connecting them together and producing silt- and sand-sized flocs and agglomerates (Diamond et al. 1964, Verhasselt 1990). The Atterberg plastic limit increases, often dramatically, because large amount of water is enclosed within the flocs and



agglomerates. In other words, only part of the porewater contributes to plasticity. This is similar to diatoms with poriferous particles in soils such as the Mexico City clay, and andosols containing allophane in which water is trapped within soil aggregates (Mesri et al. 1975, Terzaghi et al. 1996). Both soils display unusually high plastic limits. In summary, total lime content,  $l_c$ , is used up through adsorption,  $l_{ca}$ , and dissolution,  $l_{cd}$ .

The time-dependent manifestation of adsorbed lime is a gradual chemical reaction of calcium hydroxide with soil particle surfaces. As the reaction products continue to form and later harden or crystallize at the reaction sites of adsorbed lime particles, they improve soil particle connections within the flocs and agglomerates that may mature into porous soil aggregates (Baver 1956). The proposed concept of lime particle adsorption on soil particles is somewhat similar to physical adsorption of calcium hydroxide molecules proposed by Diamond and Kinter (1965). However, considering that a clay-sized hydrated lime particle may contain  $10^{11}$  molecules of  $Ca(OH)_2$ , a more significant time-dependent chemical reaction of adsorbed lime with soil particle surfaces is expected for adsorbed lime particles than for adsorbed lime molecules. Richardson et al. (1994) have mentioned layers of  $Ca(OH)_2$  sandwiched between silicate layers.

particle size decreases and therefore, surface area increases,  $l_{ca}$  increases. Lime content consumed through adsorption is probably also related to the soil water content as it influences dispersion of soil particles and facilitates thorough mixing to allow full distribution and intimate contact between lime and soil particles, degree of pulverization of hydrated lime, and the intensity of mixing.

Because the solubility of calcium hydroxide in water is very small, for typical soil water contents a very small lime content is required to saturate the porewater. However, experience indicates that pH remains below 12.3-12.4 for lime contents far in excess of that required for the saturation of porewater. This behavior appears to suggest that lime adsorption must be satisfied before lime is dissolved in the porewater to increase the pH. Zolkov (1962) considered it as remarkable that in spite of the very small solubility of lime in water, large amount of lime was required "to bring the pH of the soil slurry to 12.6."

Most of the chemical reaction products have a layer structure, have high surface area, and a particle morphology that has been described as thin plates, foils, and rolled up sheets (Diamond et al. 1964; however sometimes fibers or laths occur which could contribute to particle interlocking, Richardson et al. 1994). On the other hand, adequate but not excessive lime attack may improve morphology of existing soil particles by producing ragged, irregular, frosted or serrated particles and following proper compaction connect them by the new reaction products. These features are expected to improve mechanical behavior of soils.

Because some of the reaction products during the stabilization process are amorphous and hydrated, drying of lime-treated soils during stabilization is likely to result in some irreversible dehydration as well as irreversible aggregation.

### 3 BRENNA FORMATION

The highly plastic lacustrine clays of Lake Agassiz lead to slope instability along the banks of the Red River that separates Grand Forks, North Dakota from East Grand Forks, Minnesota, as it flows north to Lake Winnipeg in Manitoba, Canada (Mesri and Huvaj 2004). The clays of the Red River slopes are the glacio-lacustrine deposits of glacial Lake Agassiz that is believed to have existed from 13,000 to 8,500 years before present, during the Late Wisconsin Glacial Episode of the Pleistocene Epoch (Quigley 1980).

The Brenna Formation, which is characterized as a uniform, soft to firm, dark grey, glacio-lacustrine clay with little or no visible stratification, is full of slickensided surfaces. The major source of sediment for the Brenna Formation was the highly plastic montmorillonitic Pierre Shale bedrock (Quigley 1968, Baracos 1977). The clay size fraction of Brenna Formation ranges from 60 to 95% (Arndt 1977). This unit is divided into Lower Brenna and Upper Brenna members. The natural water content, plastic limit and liquid limit of Lower Brenna are in the range of 42 to 69%, 20 to 40%, and 62 to 103%, respectively, and the corresponding range for Upper Brenna are 60 to 85%, 27 to 38%, and 107 to 154%, respectively. Samples of both Lower Brenna and Upper Brenna were used in the present investigation.

### 4 TESTS ON LIME-TREATED BRENNIA CLAY

Drained direct shear tests on lime-treated Brenna clay were performed using reconstituted specimens. Drained multiple reversal direct shear tests on precut specimens were used to measure residual shear strength, and drained direct shear tests on uncut specimens were used to measure fully softened shear strength. Air dry Brenna clay was pulverized until all of a representative sample passed the no. 200 US standard sieve.

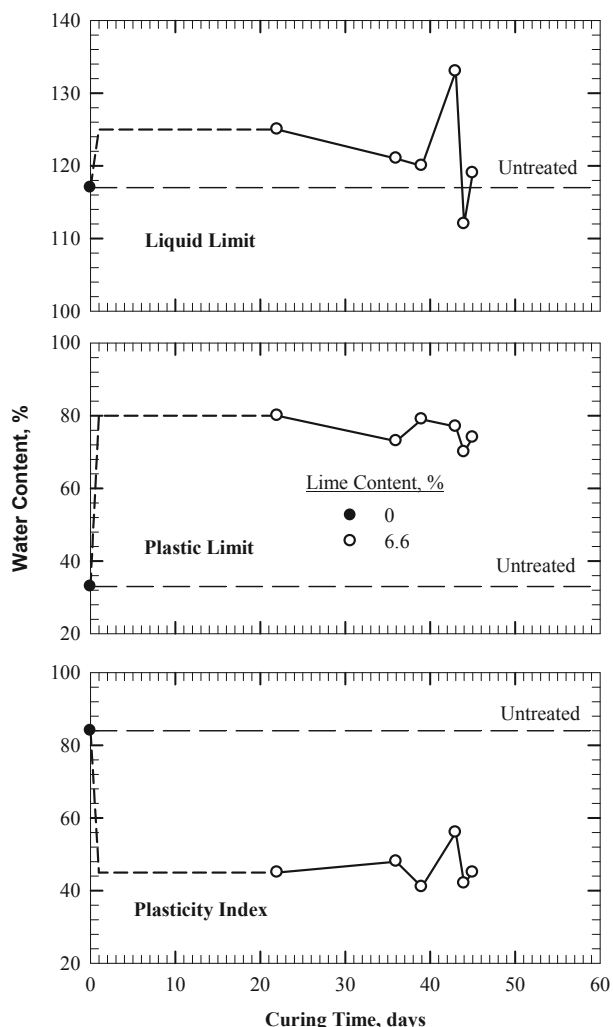


Figure 1. Lime-Brenna clay interaction under effective confining pressure

The lime content required to fully satisfy adsorption is mainly related to soil particle size and shape and therefore, the mineralogy of soil solids (Goldberg and Klein 1952, Eades and Grim 1960) and degree of dispersion or aggregation. As soil

The pulverized clay was mixed with dry hydrated lime, and was thoroughly rehydrated using distilled water. Two halves of the pre-cut specimen were formed by remolding or compaction and separately consolidated inside the top and bottom halves of the shear box using the procedure described by Mesri and Cepeda-Diaz (1986) and Mesri and Huvaj-Sarihan (2012). The consolidation pressure ranged from 100 to 450 kPa, and shear displacement rate was in the range of  $3.3 \times 10^{-4}$  to  $5 \times 10^{-4}$  mm/min.

Lime content as a percent of dry weight of clay ranged from 0 to 10%, and water content was in the range of 30 to 274%. In a few direct shear tests, dry hydrated lime was sprinkled on the exposed shear surface or on the top and bottom, of the direct shear specimen to examine lime diffusion.

For one series of direct shear specimens with lime content of 6.6%, liquid limit and plastic limit were determined at the end of the test. These data are shown in Fig. 1. For another series of lime-treated Brenna clay samples with lime content of 2, 5 and 9% and water content of 80, 100, 150 and 230%, pH and Atterberg limits were measured as a function of time. These samples were sealed; however, they were not subjected to confining pressure. The pH measurements are shown in Fig. 2, and the liquid limit and plastic limit at lime content of 5% and water contents of 80 and 100% are shown in Fig. 3.

The data on residual friction angle and fully softened friction angle from drained direct shear tests are summarized in Table 1. All index tests and direct shear tests reported here were performed at laboratory temperature of  $20 \pm 2^\circ\text{C}$ .

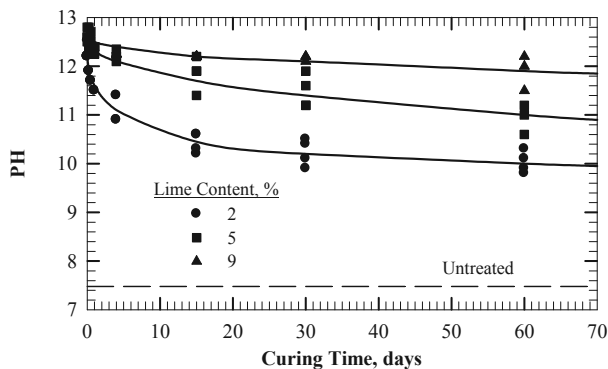


Figure 2. pH measurements of lime-Brenna clay

## 5 INTERPRETATION OF THE MEASUREMENTS

The pH measurements on lime-treated Brenna clay, such as those in Fig. 2 as well as others, show that immediately after introduction of lime, pH increases to a range of 12.2 to 12.7; shortly thereafter, however, pH begins to decrease. This observed behavior suggests that either within hours no free lime is left to dissociate to maintain pH above 12, or dissociated  $(\text{OH})^-$  is simultaneously consumed by the silica and alumina dissolved from Brenna minerals. Nevertheless, during the 60 day observation period, pH remained above 9 suggesting continued lime-clay chemical reactions.

The rather immediate large increase in plastic limit above that of the untreated Brenna clay, such as observed in Figs. 1 and 3 results from flocculation and agglomeration of lime-treated clay, especially as the water content is reduced during the plastic limit measurements. Rapid chemical attack of adsorbed lime on clay particles contributes to the production of porous flocs and agglomerates that entrap water.

When the curing of lime-Brenna clay takes place unconfined, liquid limit dramatically increases above the liquid limit of untreated clay (Fig. 3); whereas when curing takes place under an imposed effective stress condition, such as the  $\sigma'_n$  in

the range of 100 to 450 kPa in the direct shear tests, there is a minor increase in liquid limit (Fig. 1). The interpretation of this significant observed behavior appears to be that when aluminosilicates form in unconfined condition, they hydrate fully, thus holding significant amount of water that contributes to the high liquid limit. On the other hand when lime-clay reaction products form under effective confining pressure, either the resulting aluminosilicates do not hydrate much or they experience irreversible dehydration through consolidation, thus resulting in little change in the liquid limit. The implication of this behavior, which is under more detailed examination, is significant for both laboratory study of lime-soil interaction to improve frictional resistance as well as field application of lime to remediate reactivated landslides.

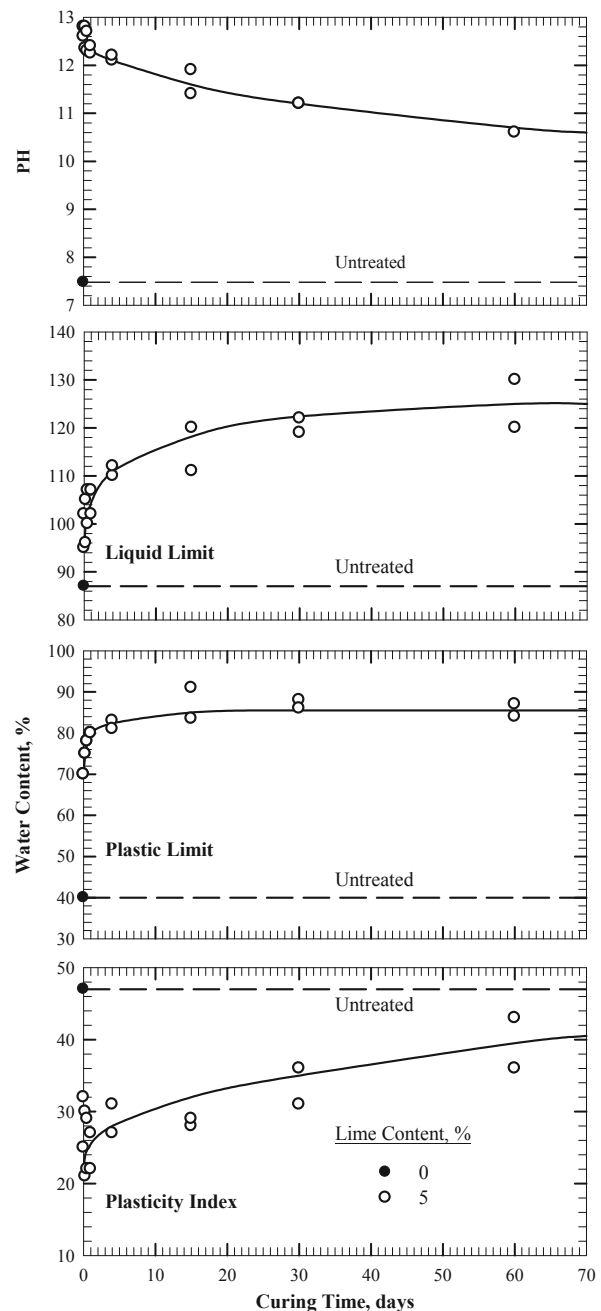


Figure 3. Lime-Brenna clay interaction under unconfined condition

The fully softened friction angle and residual friction angle of stiff clays and shales decrease with the increase in effective normal stress (Mesri and Shahien 2003, Mesri and Huvaj-Sarihan 2012). The secant friction angles of Brenna clay in

Table 1 correspond to effective normal stresses of 100 kPa and 300 kPa. Lime treatment of Brenna clay increased fully softened friction angle by 5 to 10° at effective normal stress of 100 kPa, and by 3 to 5° at 300 kPa. Lime treatment increased the residual friction angle by 3 to 6° at both 100 kPa and 300 kPa. These results suggest formation of stable clay aggregates through the lime-clay chemical reactions. These increases in frictional resistance were realized with lime contents in the range of 3 to 8% and treatment periods of 2 to 8 weeks. The detailed correlation between improvement in frictional resistance of Brenna clay as well as other stiff clays and shales, with lime content and with duration of treatment, is under further investigation with additional index and direct shear tests, including scanning electron observations of reaction products.

Table 1. Frictional resistance of lime-treated Brenna clay

Sample	I <sub>c</sub> (%)	Curing (days)	w <sub>0</sub> (%)	[φ <sup>°</sup> <sub>fs</sub> ] <sub>s</sub> <sup>100</sup>	[φ <sup>°</sup> <sub>fs</sub> ] <sub>s</sub> <sup>300</sup>	[φ <sup>°</sup> <sub>rs</sub> ] <sub>s</sub> <sup>100</sup>	[φ <sup>°</sup> <sub>rs</sub> ] <sub>s</sub> <sup>300</sup>
1	0.0	0	67	15	14	9	7
2 <sup>a</sup>	0.0	0	111	24	-	9	6
3 <sup>b</sup>	3.0	7	74	-	-	-	7
4	3.0	11	98	17	-	11	9
5 <sup>a</sup>	3.0	28	30	-	-	11	8
6 <sup>b</sup>	3.0	54	74	-	-	-	9
7 <sup>c</sup>	4.0	1	74	-	-	11	-
8	5.0	11	109	20	-	11	11
9 <sup>a</sup>	5.0	7	111	29	-	15	10
10 <sup>a,d</sup>	5.0	120	111	34	-	13	-
11	5.0	40	274	-	17	-	12
12	5.0	56	274	-	-	12	12
13	6.6	3	75	20	18	13	13
14	6.6	8	97	18	-	15	-
15	6.6	14	75	-	-	13	13
16	6.6	26	64	20	-	11	-
17	6.6	26	77	-	21	-	11
18	6.6	-	105	-	18	-	16
19 <sup>c</sup>	8.0	0.4	74	-	-	16	-
20 <sup>a</sup>	10.0	180	111	36	-	-	-

**Notes:**

- a- Lower Brenna was used for these specimens.
- b- Lime was sprinkled on top and bottom of the sample to investigate the treatment caused by lime diffusion.
- c- Lime was sprinkled on the shear surface.
- d- Lime-treated sample was stored for 120 days before being placed in the shear box.

For the 27<sup>th</sup> Avenue slide in Grand Forks, North Dakota (Mesri and Huvaj 2004), with entire slip surface in Brenna clay at residual condition, 5% lime content treatment of fifty percent of the slip surface increases computed factor of safety from 1.00 to the range of 1.26 to 1.37 (φ<sub>r</sub><sup>°</sup> = 7 to 8° increases to φ<sub>r</sub><sup>°</sup> = 12°). This level of lime remediation effort is expected to have a significant effect on rate of movement of the slide.

A combination of horizontal directional drilling (HDD), mechanical deep mixing (MDM) with augers and paddles, and dry jet mixing (DJM), together with signal receivers at the ground surface, is being investigated for introducing lime into clay along a pre-existing slip surface. The longest crossing of HDD to date has been 2000 m and borehole diameter of up to 160 mm.

## 6 CONCLUSIONS

Remediation of the montmorillonitic Brenna clay from North Dakota using lime contents of 3 to 8% and treatment periods of 2 to 8 weeks increased drained fully softened friction angle by 3 to 10° and drained residual friction angle by 3 to 6°, in the

effective normal stress range of 100 to 300 kPa. The increase in drained frictional resistance suggests formation of stable clay aggregates through lime-clay chemical reactions under the highly alkaline pH 12.5 to 9.8 environment measured over a period of 8 weeks. The measurements of liquid limit as an indicator of changes in particle size and shape resulting from lime treatment must be carried out on samples cured under an effective stress condition rather than sealed but unconfined. Unconfined lime treatment results in a significant increase in liquid limit, thus underestimating the decrease in plasticity index and associated increase in frictional resistance resulting from lime remediation.

## 7 REFERENCES

- Arndt B.M. 1977. *Stratigraphy of offshore sediment Lake Agassiz-North Dakota, Report of Investigation No. 60*. North Dakota Geological Survey.
- Baracos A. 1977. Compositional and structural anisotropy of Winnipeg soils – a study based on scanning electron microscopy and X-ray diffraction analysis. *Can. Geotech. J.*, 14 (1), 125-143.
- Baver L.D. 1956. *Soil Physics, 3<sup>rd</sup> edition*. John Wiley & Sons, London.
- Bell F.G. 1996. Lime stabilization of clay minerals and soils. *Engineering Geology* 42, 223-237.
- Clare K.E. and Cruchley A.E. 1957. Laboratory experiments in the stabilization of clays with hydrated lime. *Géotechnique* 7 (2), 97-111.
- Diamond S. and Kinter E.B. 1965. Mechanisms of soil-lime stabilization: an interpretive review. *Highway Research Record* 92, 83-102.
- Diamond A, White J.L. and Dolch W.L. 1964. Transformation of clay minerals by calcium hydroxide attack. In: Bradley, W.F.(Ed.), *Proc. 12<sup>th</sup> Int. Conf. Clays and Clay Minerals*. Pergamon Press, New York, 359-379.
- Eades J.L. and Grim R.E. 1960. Reaction of hydrate lime with pure clay minerals in soil stabilization. *Highway Research Record* 262, 51-63.
- Eades J.L., Nichols F.P. and Grim R.E. 1962. Formation of new minerals with lime stabilization as proven by field experiments in Virginia. *Highway Research Board* 335, 31-39.
- Goldberg I. and Klein A. 1952. Some effects of treating expansive clays with calcium hydroxide. *ASTM Special Publication 142, Symp. on Exchange Phenomenon in Soils*, 112-128.
- Hunter D. 1988. Lime-induced heave in sulphate-bearing clay soils. *J. Geotech. Engrg.* 1114 (2), 150-167.
- Mesri G. and Cepeda-Diaz A.F. 1986. Residual shear strength of clays and shales. *Géotechnique* 36 (2), 269-274.
- Mesri G. and Huvaj N. 2004. Residual shear strength mobilized in Red River slope failures. *Proc. 9<sup>th</sup> Int. Symp. on Landslides, Brazil*, 925-931.
- Mesri G. and Huvaj-Sarihan N. 2012. Residual shear strength measured by laboratory tests and mobilized in landslides. *J. Geotech. and Geoenviron. Engrg.* 138 (5), 585-593.
- Mesri G., Rokhsar A. and Bohor B.F. 1975. Composition and compressibility of typical samples of Mexico City clay. *Géotechnique* 25 (3), 527-554.
- Mesri G. and Shahien M. 2003. Residual shear strength mobilized in first-time slope failures. *J. Geotech. and Geoenviron. Engrg.* 129 (1), 12-31.
- Quigley R.M. 1968. Soil mineralogy, Winnipeg swelling clays. *Can. Geotech. J.*, 5 (2), 120-122.
- Richardson I.G., Brough A.R., Groves G.W. and Dobson C.M. 1994. The characterization of hardened alkali-activated blast-furnace slag pastes and the nature of the calcium silicate hydrate (C-S-H) phase. *Cement Concrete Res.* 24 (5), 813-829.
- Terzaghi K., Peck R.B. and Mesri G. 1996. *Soil Mechanics in Engineering Practice, 3<sup>rd</sup> edition*. John Wiley & Sons, New York, 549 p.
- Verhasselt A. 1990. Lime-cement stabilization of wet cohesive soils. *Proc. 6<sup>th</sup> Int. Symp. on Concrete Roads, Madrid*, 67-76.
- Zolkov E. 1962. Influence of chlorides and hydroxides of calcium and sodium on consistency limits of fat clay. *Highway Research Record* 309, 109-115.

# Improvement of the Soil under the Concrete Pavement of a Plant's Hall

## Amélioration du terrain d'assise sous la dalle en béton d'une halle d'usine

Mihova L.

University of Architecture, Civil Engineering and Geodesy, Sofia, Bulgaria,

Kolev Ch.

Todor Kableshkov University of Transport, Sofia, Bulgaria,

**ABSTRACT:** The geological profile of the ground for the construction of a hall of the "Stilmet" plant in Sofia includes soft saturated soils. The improvement is developed of the natural ground by constructing a geosynthetic reinforced pad of crushed stone. To determine the mechanical parameters of the improved soil ground, in situ tests have been performed and settlement/load relationships and E modulus values have been obtained. A numerical model is made of the ground by the finite element method. The undrained short term stability and the consolidation long term stress-strain process of the improved soil ground are investigated.

**RÉSUMÉ :** Le profil géologique du terrain d'assise, prévu pour la construction d'une halle de l'usine "Stilmet" à Sofia, contient des sols peu solides, imbibés d'eau. On a effectué une amélioration du terrain d'assise naturel par la mise en place d'une semelle en pierres concassées, armée de matériaux géosynthétiques. Pour définir les paramètres mécaniques de la fondation consolidée, on a exécuté des essais in situ et l'on a obtenu la relation affaissement-charge, ainsi que le module E. On a établi un modèle numérique suivant la méthode des éléments finis. La stabilité à court terme (non drainé) et l'évolution des contraintes et déformations (consolidation) des sols améliorés sont étudiés.

**KEYWORDS:** soft saturated soil, geosynthetics, reinforced foundation pad, FEM

## 1 INTRODUCTION

The design of reinforced earth structures to replace natural soft soils is a modern practice in geotechnical engineering of improving the foundation ground. High bearing capacity and low ground deformation values are obtained by applying a foundation pad constructed of layers of hard soil, like compacted crushed stone, and of geosynthetic reinforcement. The required thickness of the reinforced pad is much smaller compared to unreinforced soil replacements. Some projects based on this way of soil improvement are realized in Bulgaria in the recent years (Mihov Y. and Mihova L. 2012, Kolev Ch. and Mihova L. 2012).

This paper presents some investigations of the improvement of soft saturated ground under the hall of the "Stilmet" plant in Sofia, which specializes in producing aluminum elements. The geological profile includes uncompacted non-homogeneous fillings at a depth of up to 4 m and soft clays at a depth of up to 10 m. The design of the ground improvement by the reinforced pad involves the following steps: (1) Choosing the thickness of the pad and the number of reinforced layers, based on FE analysis of various configurations of reinforced soil replacement; (2) Construction of an experimental improved ground area and realization of "in situ" settlement/load tests, using a circular steel plate with a diameter of 300 mm; (3) FE modeling using the actual mechanical parameters, and analyzing the stress-strain behavior and the stability of the improved ground; (4) Realization of the improvement of the hall's ground, and verifications of its deformation behavior using plate settlement/load tests.

## 2 GEOTECHNICAL CONSIDERATIONS

The "Stilmet" plant hall, whose area is 3000 m<sup>2</sup>, is being constructed near halls of the same kind (Fig. 1). It has a frame steel structure with spread footings constructed after a 4-meter-

deep strip excavation in three longitudinal axes. The pavement of the hall is made of fibre concrete with a thickness of 20 cm. The equipment of the hall is composed of steel shelves, each being supported at 8 points, and each being 12 m high and weighing 12 tons. Longitudinal beams on the concrete pavement of the hall transform the point loading into striped. The seismic loads on the pavement are obtained by performing a dynamic analysis of the shelf structures.

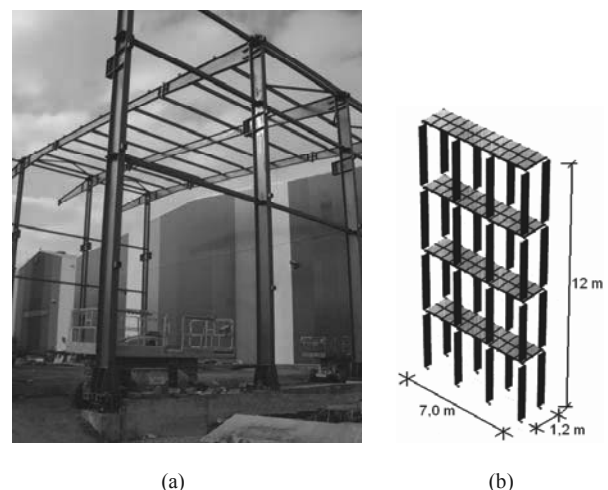


Figure 1. Steel hall structure (a) and equipment shelf (b).

### 2.1 Geological profile

The geological profile is shown in figure 2, and the properties of the different layers are summarized in table 1. The water level is 1.5 m under the surface. The high water level requires analysis of both the undrained short-term stability and the consolidated long-term stress-strain behavior of the soil ground. The ground

is being examined at a depth of up to 10 m, where solid clay lies.

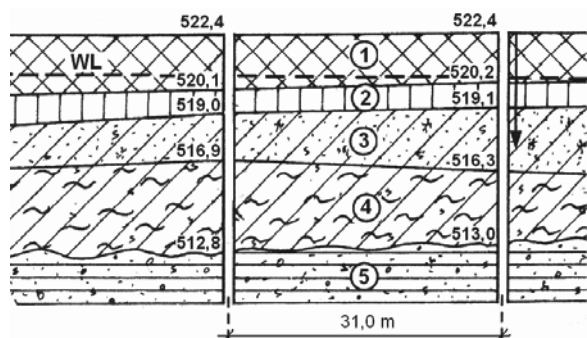


Figure 2. Geological profile

Table 1. Average values of the soil layers characteristics.

No.	Soil type	$e$	$\gamma$ kN/m <sup>3</sup>	$c'$ kPa	$\phi'$ deg	$E$ MPa
1	Top soil	1,35	1,45	11,0	8,0	3,5
2	Black clay	1,30	1,62	15,0	5,0	3,5
3	Brown clay	0,95	1,86	32,5	7,0	8,5
4	Silty clay	1,41	1,70	11,0	5,0	6,0
5	Sandy clay	0,82	1,89	32,5	18,5	15,0

### 2.2 Structure of the reinforced crushed stone pad

Investigations about the stress-strain behavior of the improved soil ground with various thickness values of the crushed stone pad, various numbers and various stiffness values of the geosynthetic layers have been carried out in advance by FEM models. The optimal structure of reinforced pad with regard to mechanical behavior of improved soil is obtained (fig. 3).

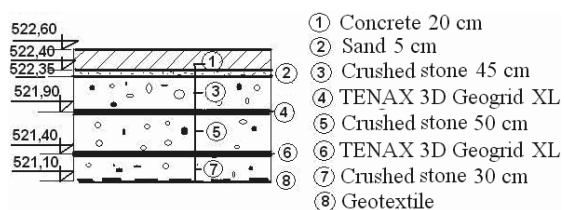


Figure 3. Structure of the reinforced crushed stone pad

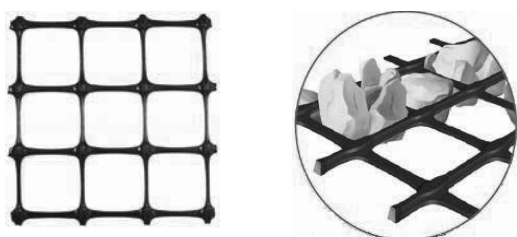


Figure 4. TENAX 3D Geogrid XL (www.tenax.net)

The pad should be built of stone particles sized 0–85 mm, and should be 1.3 m thick. The reinforcement is composed of two polypropylene TENAX 3D geogrid XL layers which have particularly large concave shaped ribs that enhance the interaction mechanism between grids and stone particles by restricting the horizontal movement of particles (fig. 4). Technical characteristics of the geogrids are: bi-axial stiffness

900/600 kN/m at 0.5% strain and coefficient of friction soil/geogrid 1.2 (www.tenax.net).

### 3 FIELD TESTING PROCEDURE

To determine the E-modulus of the improved ground, a field test program is performed. It includes the construction of the reinforced pad of area 150 m<sup>2</sup> and an application of a static loading by rigid plate of dimension 30 cm at the following four stages of construction: (1) After compaction of the natural ground; (2) After building the first layer of crushed stone with a thickness of 30 cm; (3) After placing the first geogrid layer and building the second crushed stone layer with a thickness of 50 cm; (4) At the end of the pad construction. At each stage three loading/unloading cycles are applied by steps of 0.05 MPa and settlement/load curves are obtained. The  $E$ -modulus of total settlement and the  $E_c$ -modulus of their elastic part are estimated, and the results are shown in table 2. The settlement/load curves for the first and the last stage of pad construction are shown in figure 6. The moduli values increase more than five times after the soil ground improvement.



Figure 5. Construction of the experimental reinforced crushed stone pad

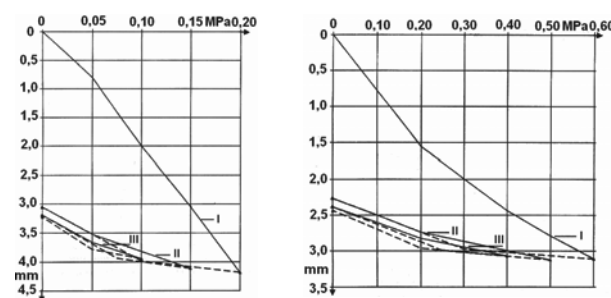


Figure 6. Settlement/load curves for the plate loading tests

Table 2. Values of the  $E$ -moduli of the soil ground at field testing

No.	Stage of the pad construction	$E$ MPa	$E_c$ MPa
1	Compaction of the natural ground	10,0	33,0
2	The first 30-cm-thick stone layer	25,7	60,0
3	The first geogrid layer and the second 50-cm-thick stone layer	44,3	121,0
4	The end of the pad construction	57,7	181,0

## 4 NUMERICAL ANALYSES

### 4.1 Finite element model

Plane-strain finite element model of the improved ground is made (fig. 7). The behavior of soil is modeled as Mohr-Coulomb material. Linear bar elements that only have tensile strength are used for the geogrids. The concrete pavement is modeled by using linear beam elements. Interface elements are included for modeling the interaction between the soil and the structure elements.

The loading of the pavement is assumed as uniformly distributed with a value of 30 kPa for combination of dead and live static loads and with a value of 45 kPa for seismic load combination. Before the pavement loading calculations, the initial condition of gravity loading is formed by the  $k_0$ -procedure. The construction stages of consecutive excavation and the replacement of the soil are simulated by means of phases of calculation with various FE meshes. An impermeable bottom boundary of the FE model is assumed in consolidation analysis.

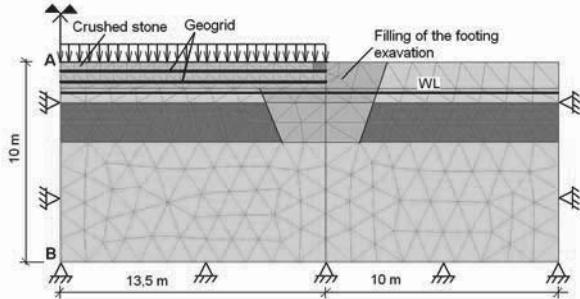


Figure 7. Finite element model

### 4.2 Results from FE analyses

#### 4.2.1 Consolidation of the ground at dead and live loads

The consolidation process is investigated, and 3 years and 4 months is the time of the pore pressure dissipation. The maximum value of the pavement settlement is 2.62 cm at point A (fig. 7) and this value corresponds to the end of the consolidation process. The distribution of the vertical displacements is shown in figure 8.

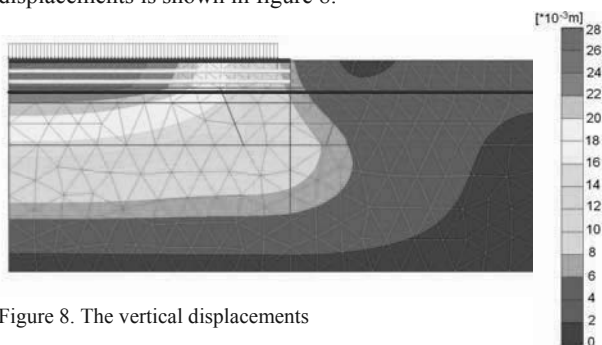


Figure 8. The vertical displacements

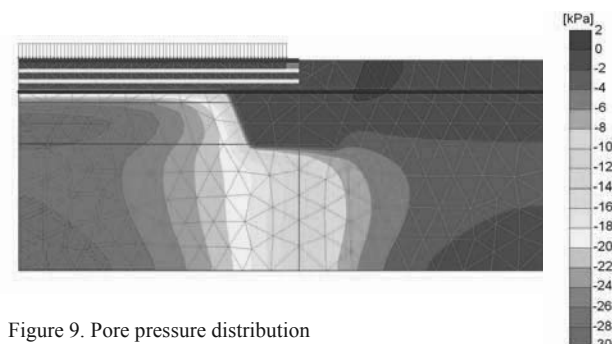


Figure 9. Pore pressure distribution

The maximum pore pressure values are obtained immediately after the load application, and its distribution is represented in figure 9. It is evident that in all clayed soils under the pavement the pore pressure increases up to the value of the applied load. The 29.6 kPa maximum value of pore pressure is calculated at point B situated at the bottom of the field. The consolidation curves pore pressure vs. distance at 18 time steps are shown in figure 10 for the cross section A – B. Step number 6 is related to the loading completion.

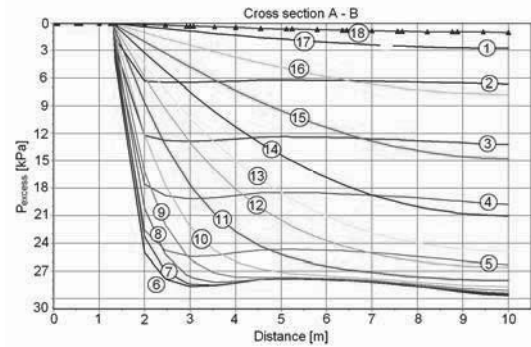


Figure 10. The curves pore pressure vs. distance

The membrane forces of geogrids, caused by vertical loading, reduce the normal stresses under it. The maximum value of the normal stresses on the soft subsoil at the bottom of the crushed pad is 52.3 kPa. Figure 11 presents the tensile forces in geogrids.

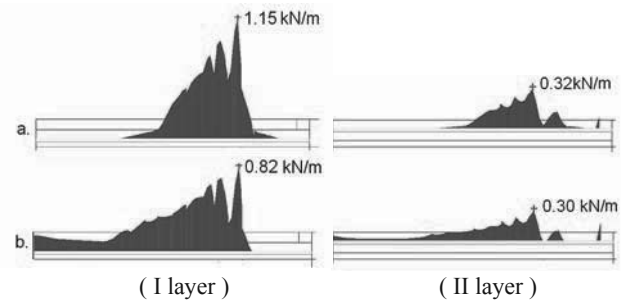


Figure 11. The forces in geogrids at time moments: (a) at a pavement loading; (b) at the end of consolidation

#### 4.2.2 Stability of the ground at seismic load combination

The undrained analysis is performed and the lateral displacements are estimated. The vectors of the total displacements are shown in figure 12. The maximum horizontal displacement is 1.4 cm and it occurs at depth of 4 m under the crushed stone filling of the foundation excavation. The zones of lateral displacements are located, as shown in figure 13, and the stability of the ground is provided.

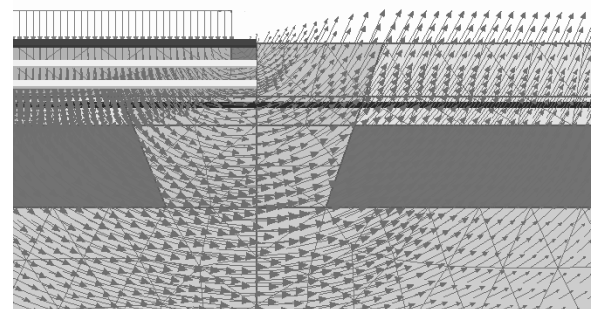


Figure 12. The vectors of the total displacements

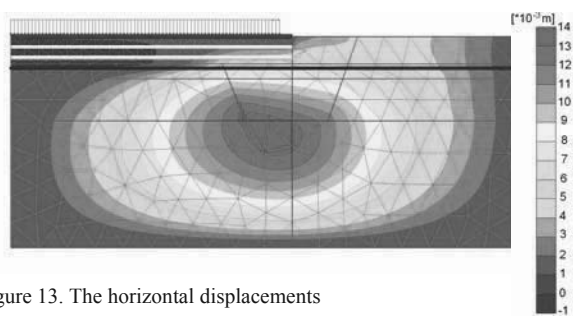


Figure 13. The horizontal displacements

The stability of the ground has been estimated using the  $\varphi, c$ -reduction method. The coefficient of stability has a value  $F_s = 3.42$  for deep slide surface.

## 5 CONCLUSION

The required thickness of reinforced crushed stone pad is about two times smaller compared to the unreinforced pad. The improvement of the ground by replacing of the soft foundation soil by the reinforced crushed stone pad is an effective modern technology which decreases excavation works and increases the heartedness of the foundation soil.

## 6 REFERENCES

- Mihov Y. and Mihova L. 2012. Finite element analysis of reinforced foundation soil. Proc. 2nd International Scientific Meeting, Tuzla.
- Kolev Ch. and Mihova L. 2012. Project for improvement of a soft soil under the foundation slab of a building in Haskovo. (unpublished). TENAX 3D Geogrid XL, [www.tenax.net](http://www.tenax.net).

# Effect of Smear on Strength Behavior of SCP-Reinforced Soft Ground

## Effet de comportement de l'étalement de force du SCP- Sol mou renforcé

Mir B.A.

*Deptt. of Civil Engineering, National Institute of Technology Srinagar- 190006, Kashmir, India*

Juneja A.

*Deptt. of Civil Engineering, Indian Institute of Technology Bombay, Mumbai-400076, MH, India*

**ABSTRACT:** Sand columns traditionally known as sand compaction piles-(SCPs) have been used to increase the load carrying capacity of soft clays and accentuate consolidation during preloading. Installation of SCPs is known to cause disturbance due to smear in a limited zone of the soil surrounding the SCP. In this study, conventional triaxial tests have been performed on 200mm long and 100mm-diameter clay samples installed with SCP to simulate the strength behaviour of composite ground under different confining pressures ranging from 50kpa to 575kpa. The SCPs were prepared using area replacement ratio of 6.25 to 64% and compacted using pneumatic compactor. The smear zone was created by using a rough casing to drill the hole. The results seem to suggest that the stress-strain behaviour of the clay was influenced by the presence of smear zone. The effect of smear zone on SCP was investigated by observing the change in pore pressure during undrained shear strength of the composite ground. The natural fabric of the soil was destroyed adjacent to the SCPs and the shear-induced pore pressures were less in composite specimens with smear-effect. In addition, as the area replacement ratio was increased, both the stiffness and the strength of the specimen increased.

**RÉSUMÉ :** Des colonnes de sable traditionnellement connues comme piles de compactage (SCPs) de sable ont été utilisées pour augmenter la capacité portante des argiles molles et accentuer la consolidation au cours du préchargement. L'installation de MCS est connue pour causer des perturbations dues au frottis dans une zone limitée du sol entourant le SCP. Dans cette étude, les essais triaxiaux conventionnels ont été réalisés sur les échantillons d'argile, de 100 mm de long et de 200 mm de diamètre, installés avec SCP pour simuler le comportement de la résistance du terrain composite sous différentes pressions de confinement allant de 50 kPa à 575 kPa. Les MCS ont été préparés à l'aide du coefficient de remplacement de 6,25 à 64 %, et compactées au pneumatique. La zone de souillure a été créée en utilisant une enveloppe rugueuse pour percer le trou. Les résultats donnent à penser que le comportement de contrainte-déformation de l'argile a été influencé par la présence de la zone de souillure. L'effet de zone de souillure sur SCP a été examiné en observant le changement de pression interstitielle au cours de la consolidation et de la résistance au cisaillement du sol composite. Le tissu naturel du sol a été détruit adjacent à la SCP et les pressions interstitielles induites par cisaillement étaient inférieures dans les échantillons composites avec un effet de maculage. En outre, lorsqu'on augmente le ratio de remplacement du frottis, la rigidité et la résistance de l'échantillon augmentent.

**KEYWORDS:** Sand compaction pile, installation effects, smear, soft ground

**MOTS-CLÉS :** Sable tas de compactage, les effets de l'installation, les frottis, sol mou

## 1 INTRODUCTION

Soft ground is widely distributed especially along the coastal area, having large potential for settlement with low inherent shear strength. In the recent years, improvement of soft soils has been extensively implemented for the various development projects all over the world due to extremely limited stable construction sites. Granular piles such as sand compaction piles (SCPs) are considered as cost-effective and alternative solution to the problem of stability and settlement posed by construction on soft ground. The insertion of SCPs into soft clay has been shown to have a positive effect on the load carrying capacity of the clay, resulting in a composite soil mass that has greater shear strength and improved stiffness compared to the unreinforced clay. Sand compaction pile (SCP) is a method of constructing large diameter sand column in the ground. This method of ground improvement has been widely used for rapid improvement of soft ground, and also in near-shore regions for land reclamation works (e.g. Aboshi and Suematsu 1985, Bergado and Balasubramniam 1994). In India, the granular columns have been used to improve ground for container freight station at Navi Mumbai and the construction of dry dock at Pipavav shipyard (Raj and Dikshith 2009). Many researchers (e.g. Bergado et al. 1991, Juneja and Mir 2011) have investigated the effect of SCP installation on disturbance to the surrounding soil. The extent of the disturbed or smear zone can

affect the engineering behaviour of the composite ground. The disturbance in this zone depends upon the column diameter and the tools used in the installation (e.g. Singh and Hattab 1979, Madhav et al. 1993). Shear induced pore pressures were found to be less in specimens which had the smear zone surrounding the sand column. However, pore pressures began to increase close to failure due to rearrangement of soil particles (Mir 2010). Laboratory and field tests previously conducted to determine the extent of the disturbance caused by pile driving into soft clay deposits have demonstrated that the natural structure of the clay around the pile is excessively disturbed (Randolph et al. 1979, Xu et al. 2006). It was observed that the diameter of the severely disturbed or remoulded ground around a driven closed-ended casing was about 1.4 times the diameter of the casing. Recently, Weber et al. (2010) compared the smear zone around model SCPs to that observed around driven piles. It was observed that the smear zone around SCPs installed on the centrifuge extended up to 1.2 to 1.4 times the SCP diameter. Dissipation of the excess pore pressures often results in increase in the shear strength. Aboshi et al. (1979) observed up to 50% increase in the undrained strength in about one month after the SCP installation at test sites in Japan. Matsuda et al. (1997) also reported an increase in strength of the composite SCP ground within three months of the SCPs installation.



In this study, the effect of smear zone on strength of model SCP installed in 100mm diameter and 200mm long clay specimens is investigated using conventional triaxial compression tests under different confining pressures ranging from 50kPa to 575kPa. The composite specimen were prepared by driving a small diameter PVC casing into the sample and then backfilling the cavity with sand column after removing the casing. The casing was roughened using sand glued to its outer walls prior to insertion to replicate the smearing effect. The SCPs were prepared using area replacement ratio of 6.25 to 64% and compacted using pneumatic compactor. SCPs of different diameters (25-80mm) were used to investigate the improvement in the load-carrying capacity of the specimens. The effect of smear zone on SCP was investigated by observing the change in pore pressure during consolidation and undrained shear strength of the composite ground. The test results suggest that, tress-strain behavior of the clay was influenced by the presence of smear zone. The natural fabric of the soil was destroyed adjacent to the SCPs with smear zone which in turn affected pore pressure response of the composite soil sample. Shear induced pore pressures were less in soil specimens with smear-effect, but this difference was not apparent when 80mm diameter SCP with smear zone was used. In addition, as the reinforcement area ratio increased, both the stiffness and the shear strength of the specimen increased. Thus, sand compaction piles currently stand as one of the most viable and practical techniques for improving the mechanical properties of soft clays.

2. EXPERIMENTAL WORK

2.1. Materials and methods of sample preparation

The test specimens were prepared in 450mm long and 250mm diameter stainless steel cylindrical mould. Deaired clay slurry was consolidated on the laboratory floor, first under its own self-weight and later under surcharge of 211- to 404 kN/m<sup>2</sup> applied in stages on top of the clay surface using a custom designed pneumatic load frame (Fig.1).



Slurry consolidation Specimen trimming Final specimen size  
Figure 1. Consolidation set-up on the laboratory floor

Upon completion of the 1-D consolidation, the block of clay was extruded and trimmed into three 100mm diameter cylindrical specimens using soil lathe. Up to 3 specimens could together be prepared using this mould. The experimental program consisted of 20 tests on composite clay with sand column. The specimens were held in split cylindrical moulds and a smooth PVC casing slowly pushed along its length to form a cylindrical hole at the centre. The hole was backfilled with fine sand ( $d_{50}=0.3\text{mm}$ ) compacted in layers at 90% relative density using a pneumatic compactor (Fig. 2). Sand column

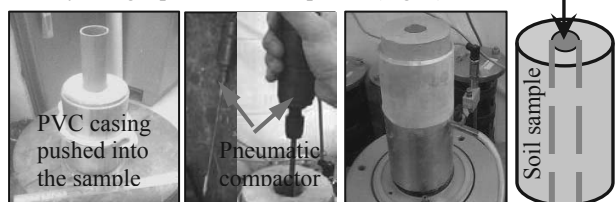


Figure 2. Preparation of composite specimen  
Diameter of the sand column varied between 25- and 80mm in the specimens. This corresponds to an area replacement ratio,  $a_s$

(Aboshi et al. 1979) that ranges between 6.25- and 64%. The smear zone was created by using a rough casing painted with a paste of coarse sand ( $d_{50} = 1.3\text{mm}$ ) to drill the hole. Thickness of the smear zone was taken equal to the thickness of the paste. The effect of smear beyond this zone was ignored. After preparing the sand column, the ends of the specimen were covered with a thin circular rubber sheets having a central hole. Diameter of the hole was slightly less than that of the sand column so as to only permit radial drainage. Two deaired porous stones were then placed at the two ends of the specimen and the entire assembly mounted on the triaxial chamber. Table 1 shows properties of the clay used in this study. The ratio of the diameter of sand column with smear zone to the diameter of sand column without smear zone ( $d_s/d$ ) was about 1.1 to 1.2 in all tests, which compares well with the values reported by the previous researchers (e.g. Indraratna and Redana, 1998; amongst others). The specimen was enclosed in a rubber membrane and the chamber filled with water. The soil samples were then isotropically consolidated under mean effective stress,  $p'$  which varied between 50 and 575 kN/m<sup>2</sup>.

Table 1 Properties of kaolin clay

Clay (%)	Silt (%)	Liquid limit (%)	Plastic limit (%)	Shrinkage limit (%)	$G_s$
75	25	49	23	16	2.64

3. RESULTS AND DISCUSSIONS

Consolidated undrained triaxial tests were performed on 200mm long and 100mm diameter cylindrical samples prepared from remoulded and reconsolidated commercially available kaolin clay installed with SCP. Table 2 shows the details of the soil specimens prepared for testing. In the table, OCR is defined as the ratio of the isotropic preconsolidation pressure,  $p_{0'}$  to  $p'$ .  $p_{0'}$  was taken equal to the higher of either  $p'$  or the mean effective stress after 1D consolidation,  $p'$  estimated using the equation (Wroth 1984):

$$p' = \sigma'_v [1 - 0.67 \sin \phi'] \tag{1}$$

where  $\phi'$  is the effective angle of friction (e.g. Schofield and Wroth 1968). The load-deformation data was analyzed using the unit cell arrangement proposed by Balaam et al. (1977). In this method, the column and surrounding clay are assumed to act as a single element with equivalent distributions of stresses and strains in composite specimens. Figures 3a-b show results of deviator stress,  $q$  plotted against axial strain,  $\epsilon_a$ . As can be seen, all samples reached peak deviator stress ( $q_{max}$ ) at 6 to 10% axial strain. Figures 3a-b also show that the ultimate strength exhibit transient peaks in some tests. This was expected since these soil samples were overconsolidated prior to the shearing. In few tests on normally consolidated clays,  $q$  decreased after passing  $q_{max}$  because of instability of the failed samples at high confining pressure.

Table 2 Experimental program

Test No	$\sigma'_v$ (kPa)	$d_s$ (mm)	Smear zone	$p'_o$ (kPa)	$p'$ (kPa)	OCR
S1	404	24.6	×	285	95	3
S1	404	24.6	×	285	146	2
S1	404	24.6	×	300	299	1
S1	264	29	✓	187	95	2
S1	264	29	✓	187	145	1.3
S1	264	29	✓	300	289	1
S2	211	31.7	×	450	450	1
S2	211	31.7	×	200	197	1
S2	211	31.7	×	149	50	3
S2	211	35.7	✓	450	434	1
S2	211	35.7	✓	200	195	1
S2	211	35.7	✓	149	49	3
S3	211	40	×	375	374	1
S3	211	40	×	575	575	1
S3	211	40	×	149	71	2.1
S3	211	45.2	✓	575	572	1
S3	211	45.2	✓	375	372	1
S3	211	45.2	✓	149	68	2.2
S4	211	80	×	149	144	1
S4	211	80	✓	149	142	1

\*:  $\sigma'_v$  = Vertical stress at end of 1D loading,  
 #:  $d_s$  = Equivalent diameter of sand column,  
 \$:  $p'_o$  = Preconsolidation pressure,  
 \*\*:  $p'$  = Mean effective stress at end of consolidation,

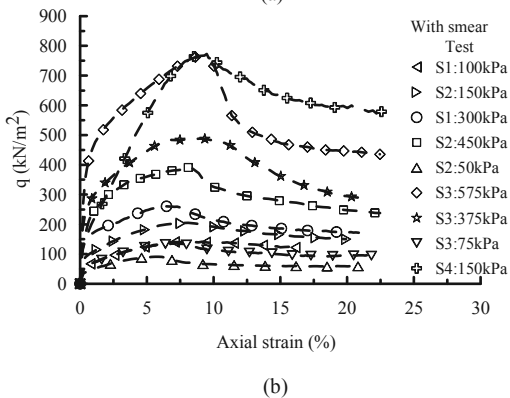
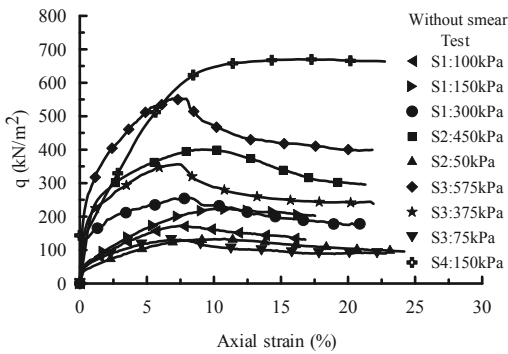


Figure 3a-b Deviator stress versus axial strain relationship for: (a) Samples without smear zone; and (b) Samples with smear zone.

The undrained shear strength ( $s_u$ ) of composite specimen was taken equal to  $\frac{q_{max}}{2}$ , and the effect of stress history induced

over consolidation on undrained strength ratio  $\frac{s_u}{p}$  was expressed as:

$$\left(\frac{s_u}{p'}\right)_{OC} = a(OCR)^m \quad (2)$$

where  $a$  is the normalized undrained shear strength of NC soil equal to  $\left(\frac{s_u}{p'}\right)_{NC}$  for  $OCR=1$ , and  $m$  is an empirical exponent equal to  $\left(1 - \frac{\kappa}{\lambda}\right)$ ,  $\kappa$ ,  $\lambda$  are soil model parameters

obtained from triaxial testing. Using test data, undrained shear strength ( $s_u$ ) of composite ground was expressed in the following form:

$$\left(\frac{s_u}{p'}\right) = 0.44(OCR)^{0.99} \text{ - without smear} \quad (3)$$

$$\left(\frac{s_u}{p'}\right) = 0.33(OCR)^{0.90} \text{ - with smear effect} \quad (4)$$

The evidence of the smear zone was not significant on the ultimate undrained shear strength when 25mm and 30mm diameter sand columns were used. What was surprising is that the effect of smear was apparent on the ultimate shear strength when 80mm diameter sand columns were used. It seems clear that the presence of smear zone has reduced the ultimate undrained shear strength by 25%. In addition, as the area replacement ratio was increased, both the stiffness and the shear strength of the composite samples also increased. Figure 4 show results of Skempton's (1954) pore pressure parameter,  $a$ , plotted against axial strain,  $\epsilon_a$ . As seen, the A-factor in specimens with smear effect was less from early stage of shearing even when the specimens had the same OCR. This was expected because the smear zone did not permit the pore pressures to dissipate within the SCP. However, there was a marginal increase in a-factor after passing  $q_{max}$ .  $a_f$  of these samples was between 0.7 and 1.1 which is typical for normally consolidated clays.

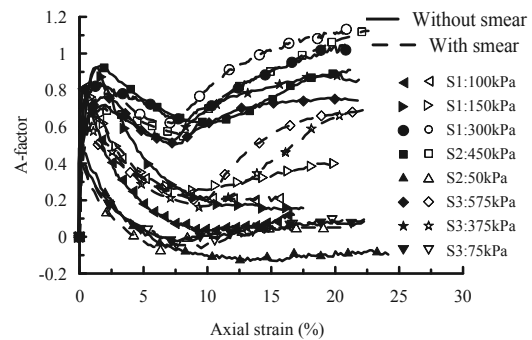


Figure 4. Variation of Skempton's parameter A with axial strain for samples with and without smear zone.

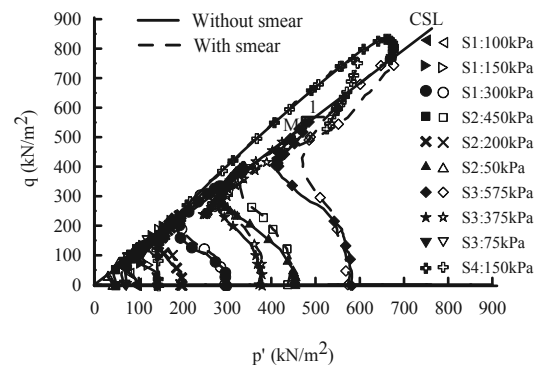


Figure 5. Effective stress paths for samples without smear and with smear zone  
 Figure 5 show the effective stress path in  $p'$ - $q$  stress space.

The figures show that the shear induced pore pressures were found to be less in specimens which had the smear zone surrounding the sand column. Due to the smear zone, these pore pressures within the SCP were reduced because the water was not permitted to flow towards the column during shearing.

This was also evident from Scanning Electron Microscope (SEM) images (Fig. 6a-b) taken on post shear tests of specimens with and without smear. The images of samples with and without the smear zone show differences in the microstructure. The clay minerals in the smear zone appear to be closely packed with reduced pore space. 7.5 mm x 7.5 mm x 7.5 mm air dried samples were prepared at room temperature for the SEM images.

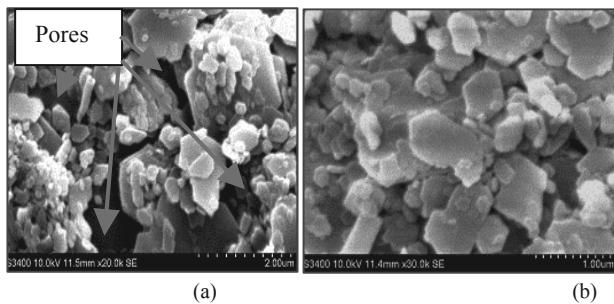


Figure 6. SEM images: (a) Composite samples without smear zone; and (b) Composite samples with smear zone.

#### 4. CONCLUSIONS

The strength behavior of composite ground reinforced with sand compaction piles has been studied using 20 consolidated undrained triaxial tests. Vertical stress of the sand column was examined when the composited specimens were tested to failure in conventional triaxial tests. The test results suggest that the stress-strain behavior of the clay was influenced by the presence of smear zone. It seems clear that the presence of smear zone has reduced the ultimate undrained shear strength by 25%. SEM images indicated that the natural fabric of the soil was destroyed adjacent to the SCPs with smear zone which in turn affected pore pressure response of the composite soil sample. Specimens sheared with smear effect appear closely packed and more homogeneous with partly discernible particle systems, while specimen without smear condition indicate a distinct division between smaller intra-aggregate pore spaces and the larger inter-aggregate voids. Shear induced pore pressures were less in soil specimens with smear-effect because the water was not permitted to flow towards the column during shearing. It was postulated that the difference in the behavior of smear and non-smear specimens was because that the pore pressure measurements were taken within the sand column. This difference was not apparent when 80mm diameter SCP with smear zone was used. These changes affect the effective horizontal stress in the clay and hence the load carried by the individual sand columns.

#### 5. ACKNOWLEDGEMENT

The first author would like to acknowledge the financial support from the Indian Institute of Technology Bombay (IITB) in the form of research scholarships.

#### 6. REFERENCES

- Aboshi, H. and Suematsu, N. (1985). Sand compaction pile method: State-of-the art paper. *Proceedings of the 3<sup>rd</sup> International Geotechnical Seminar on Soil Improvement Methods*, Nanyang Technological Institute, Singapore.
- Aboshi, H., Ichimoto, E., Enoki M. and Harada, K. (1979). Composer: method to improve characteristics of soft clays by inclusions of large diameter sand column. *Proceedings of the International Conference on Soil Reinforcement: Reinforced Earth and other Technique*, Paris, Vol. 1, 211-216 (1979).
- Asaoka, A., Kodaka, T. and Nozu, M. (1994). Undrained shear strength of clay improved with sand compaction piles. *Soils and Foundations*, Vol. 34, No. 4, 23-32.
- Balaam, N.P., Brown, P.T. and Poulos, H.G. (1977). Settlement analysis of soft clays reinforced with granular piles. *Proceedings of the 5<sup>th</sup> Southeast Asian Conference on Soil Engineering*, Bangkok, 81-91.
- Bergado, D. T. and Balasubramniam, A. S. (1994). Laboratory testing of prefabricated vertical drains (PVD). *Geotechnical Engineering Journal*, Vol. 25, No. 1, pp.1.
- Indraratna, B. and Redana, I. W. (1998). Laboratory determination of smear zone due to vertical drain installation. *Journal of Geotechnical Engineering, ASCE*, Vol. 124, No. 2, 180-184 (1998).
- Juneja, A. and Mir, B. A. (2011). "Effects of Sand Compaction Pile Installation on Surrounding Soft Soil". *Proc. of National Conference on Recent Advances in Ground Improvement Techniques (RAGIT-2011)*, pp. 1-10, CBRI Roorkee, India.
- Madhav, M. R., Park, Y. M. and Miura, N. (1993). Modelling and Study of Smear Zones around Band Shaped Drains. *Soils and Foundations*, Vol. 33, No. 4, 137-149.
- Matsuda, H., Fujiwara, Takahasi, S. and Kitayama, M. (1997). Influence of SCP driving on the behaviour of clay. *Ground improvement geosystems: Densification and reinforcement*, Thomas Telford London, 233-238.
- Mir, B. A. (2010). *Study of the influence of smear zone around sand compaction pile on properties of composite ground*. Ph.D. Thesis, IIT Bombay.
- Singh, G. and Hattab, T. N. (1979). A laboratory study of efficiency of sand drains in relation to methods of installation and spacing. *Geotechnique* 29(4), 395-422.
- Skempton, A. W. (1954). The pore-pressure coefficients A and B. *Geotechnique* 4(4), 143-147
- Raj, D. and Dikshith, C.V. (2009). Vibro replacement columns for shipyard infrastructure at Pipavav, Gujarat, India. *Proceedings of the International Symposium on Ground Improvement Technologies and Case Histories*, GeoSS, Singapore, 763-769.
- Randolph, M. F., Carter, J. P. and Wroth, C. P. (1979). Driven piles in clay-the effects of installation and subsequent consolidation. *Geotechnique* 29(4), 361-393.
- Schofield, A. N. and Wroth, C. P. (1968). *Critical State Soil Mechanics*. MacGraw-Hill, London, p. 218.
- Xu, X. T., Liu, H. L. and Lehane, B. M. (2006). Pipe pile installation effects in soft clay. *Proceedings of the Institution of Civil Engineers, Geotechnical Engineering* 159, Issue GE4 pp. 285-296.
- Weber, T. M., Plotze, M., Laue, J., Peschke, G. and Springman, S. M. (2010). Smear zone identification and soil properties around stone columns constructed in-flight in centrifuge model tests. *Geotechnique* 59(3), 197-206.
- Wroth, C. P. (1984). The interpretation of in-situ soil tests. *Geotechnique* 34(4), 449-489.

# Bio-mediated soil improvement utilized to strengthen coastal deposits

## Amélioration du sol biologiquement négociée utilisée pour renforcer les dépôts côtiers

Montoya B.M., Feng K., Shanahan C.  
North Carolina State University, Raleigh, NC, USA

**ABSTRACT** - Vital coastal lifelines can be vulnerable during large storm events. Large wave action and high sea levels erode the sandy soil that supports coastal infrastructure, including highways, structures, pipelines, and other utilities. Damage from these events can result in severe property damage, loss of revenue, and large repair costs. Natural bio-geochemical methods can be used to reinforce the erodible sandy soil to help prevent damage to the infrastructure. Utilizing naturally-occurring biological metabolic activity, calcium carbonate cementation can be induced *in situ* to bind the sand grains together, thereby improving the strength and stiffness of the soil and in turn preventing erosion of the coastal deposits. Microbial induced carbonate precipitation (MICP) has been shown to be an effective method to improve the soil behavior in saturated conditions subjected to undrained monotonic and seismic loading in both laboratory and centrifuge tests. Applying this proven natural treatment technique to unsaturated coastal soils can improve the soil's resiliency during large storm events. Results indicate that the strength of the unsaturated soils increase from intermittent surficial treatments. Rigid-walled soil column tests were conducted to evaluate the effectiveness of treating sandy soils by flooding the surface of the soil with the appropriate microbes and nutrients and allowing free drainage. Clean fine sand, typical of coastal dune deposits, was used in the soil column tests. The strength of the cemented sand was evaluated using unconfined compression tests. A discussion of upscaling the results from the laboratory tests to application *in situ* to improve the resiliency of coastal infrastructure is also presented herein.

### 1. INTRODUCTION

Vital coastal lifelines can be vulnerable during large storm events. Large wave action and high sea levels erode the sandy soil that supports coastal infrastructure, including highways, structures, pipelines, and other utilities. Damage from these events can result in severe property damage, loss of revenue, and large repair costs. The outer banks of North Carolina have seen several hurricanes in recent years (Irene in 2011, and Sandy in 2012) which have inflicted damage to vital coastal lifelines as illustrated in Figures 1 and 2.

Natural bio-geochemical methods can be used to reinforce the erodible sandy soil to help prevent damage to the infrastructure. Utilizing naturally-occurring biological metabolic activity, calcium carbonate cementation can be induced *in situ* to bind the sand grains together, thereby improving the strength and stiffness of the soil and in turn preventing erosion of the coastal deposits. Microbial induced carbonate precipitation (MICP) has been shown to be an effective method to improve the soil behavior in saturated conditions subjected to undrained monotonic and seismic loading in both laboratory and centrifuge tests (Montoya et al., 2013, Mortensen and DeJong, 2011, DeJong et al., 2006). Applying this proven natural treatment technique to unsaturated coastal soils can improve the soil's resiliency during large storm events. Results indicate that the strength of the unsaturated soils significantly increase from intermittent surficial treatments. Rigid-walled soil column tests were conducted to evaluate the effectiveness of treating sandy soils by flooding the surface of the soil with the appropriate microbes and nutrients and allowing free drainage. Clean fine sand, typical of coastal dune deposits, was used in the soil column tests. Changes in the strength of the sand from the unsaturated cementation treatments was evaluated using unconfined compression tests. A discussion of upscaling the results from the laboratory tests to application *in situ* to improve the resiliency of coastal infrastructure is also presented herein.



Figure 1. A section of Highway 12 at the edge of Rodanthe, N.C. undermined by erosion due to the storm surge and wave action during Hurricane Irene. (Photo: News & Observer, Aug. 31, 2011)



Figure 2. High ocean waves from Hurricane Sandy lap against Highway 12 and erode the underlying sand. (Photo: News & Observer, Nov. 14, 2012)

## 2. MATERIALS AND METHODS

### 2.1. Sand and Specimen Preparation

Four soil column specimens were prepared by dry pluviation to a target relative density of 40%. The soil column specimens had a 50.8 mm (2 in) diameter and an aspect ratio of 2:1. Ottawa 50-70 sand was used for the initial cementation trials, because of the published results with the sand (DeJong et al., 2006, Mortensen and DeJong, 2011, Montoya et al., 2013, Martinez et al., 2013). A summary of the sand characteristics is listed in Table I.

Table I. Ottawa 50-70 Sand characteristics

	Ottawa 50-70 Sand Characteristics
$D_{50}$ (mm)	0.22
$C_u$	1.4
$C_c$	0.9
$G_{max}$	2.65
$e_{min}$	0.55
$e_{max}$	0.87
Mineralogy	Quartz
Shape	Round

### 2.2. Biological Treatment Process

*Sporosarcina pasteurii* (ATCC 11859), a urea hydrolyzing bacterium, was grown at 30 °C in an Ammonium-Yeast Extract medium (ATCC 1376: 0.13 mol l<sup>-1</sup> Tris buffer (pH=9.0), 10 g l<sup>-1</sup> (NH<sub>4</sub>)<sub>2</sub>SO<sub>4</sub>, and 20 g l<sup>-1</sup> yeast extract). Individual ingredients were autoclaved separately and mixed together post-sterilization. The growth medium was inoculated with the *S. pasteurii* stock culture and incubated aerobically at 30 °C in a shaking water bath (200 rpm) for approximately 40 hrs before harvesting at a final optical density (OD<sub>600</sub>) of 0.8-1.0. Cultures were centrifuged at 4000 g for 10 min in 15 mL volumes and washed in fresh growth medium. Harvested bacteria were stored in the centrifuge vials at 4 °C for a maximum of 2 days.

Urea-calcium cementation media was used to induce ureolytic-driven calcite precipitation. A summary of the components and concentrations are presented in Table II.

Table II. Chemical recipe for cementation media

Chemical	Chemical Concentration (M)
Urea	1.0
CaCl <sub>2</sub>	0.25

Cementation treatments were performed by flooding the top surface of the soil column, and allowing the cementation media to freely drain through the sand (Figure 3). Bacteria were introduced into the soil during the initial cementation flush. Calcium chloride was not included in the initial treatment with the bacteria to prevent precipitation during inoculation. Cementation treatments were repeated every 3 to 6 hours. Two pore volumes of nutrients were used in each treatment flush (concentrations of nutrients presented in Table II). The cementation treatments were repeated for a total of 40 times.

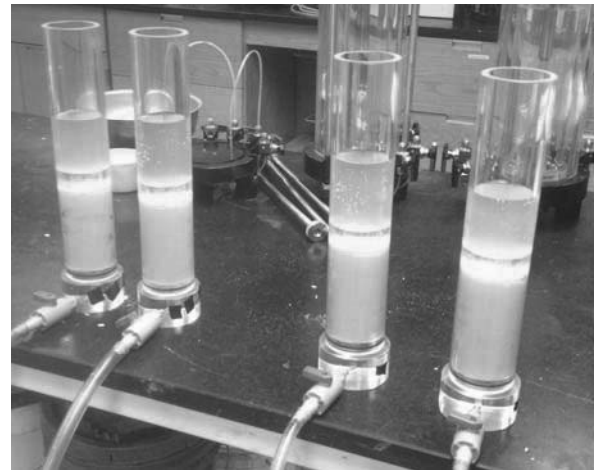


Figure 3. Initial biological flush through soil columns. Cementation flushes allowed to free drain through pluviated soil.

### 2.3. Specimen Shearing

After cementation was completed, the specimen was flushed with water to remove residual chemicals from the cementation treatments. The cemented sand was removed from the soil columns. The cemented soil columns were then subjected to unconfined compression tests until failure. A GeoJac automated load actuator was used to perform the unconfined compression test.

### 2.4 Mass of Calcium Carbonate Measurements

The mass of calcium carbonate was determined post-test using methods outlined in ASTM D4373, *Standard Test Method for Rapid Determination of Carbonate Content in Soils*. At the end of the cementation treatments, oven dried cemented sands are dissolved in hydrochloric acid and the resulting pressure generated from the dissolution of calcium carbonate is measured. The generated pressure is equated to an equivalent mass of calcium carbonate. The percentage of mass of calcium carbonate is expressed as the mass of calcium carbonate divided by the mass of soil (not including calcium carbonate).

## 3. RESULTS

### 3.1 Calcium Carbonate Content in Soil Columns

Mass of calcium carbonate was taken in the top and bottom of the cemented soil column, which are reported in Table III. As indicated in Table III, the mass of calcite in the four soil columns is relatively small compared to published results from other MICP treatment studies (Weil et al., 2011). However, the cementation within the soil column was extremely uniform, as indicated by the mass of calcium carbonate of the top and bottom samples (Table III).

Table III. Summary of Mass of Calcium Carbonate

Soil Column	Mass of CaCO <sub>3</sub> (%)
1 (top)	0.082
1 (bottom)	0.081
2 (top)	0.102
2 (bottom)	0.103
3 (top)	0.070
3 (bottom)	0.068
4 (top)	0.070
4 (bottom)	0.068

### 3.2 Cemented Sand Compressive Strength

Unconfined compression tests were performed on the cemented soil columns (Figure 4 and Figure 5). As mentioned, the mass of precipitated calcium carbonate is relatively small compared to published results from other MICP treatment studies; however even at low mass of calcium carbonate levels, unconfined compression tests were able to be performed on the cemented sand columns. A summary of the compression test results are listed in Table IV.

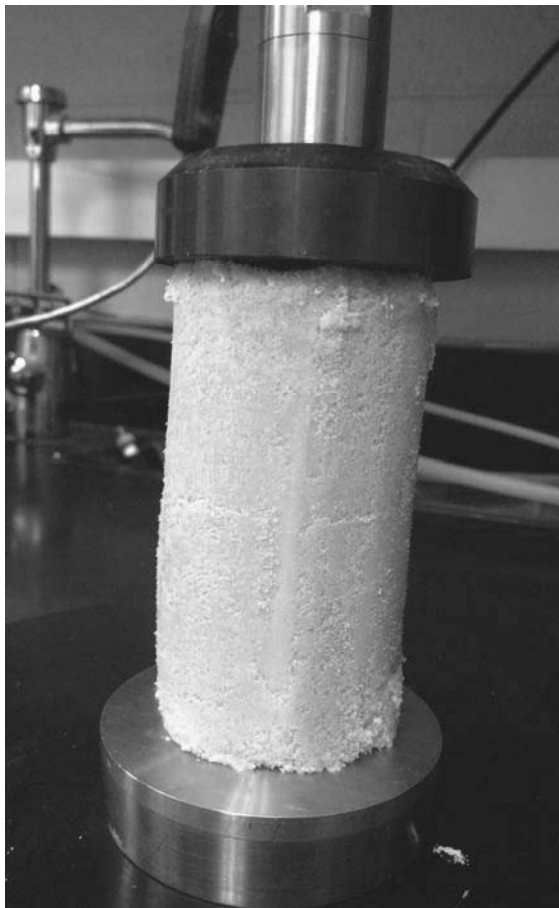


Figure 4. Cemented soil column mid-test during the unconfined compression test.



Figure 5. Failed cemented soil column at the end of the unconfined compression test.

Table IV. Summary of Compressive Strength

Soil Column	Unconfined Compressive Strength (kPa)
1	5.2
4	5.4

As indicated in Table IV, unconfined compression tests were performed on only two of the four columns. Two of the soil columns were not able to be tested because they were disturbed during extraction from the soil column walls. The cemented soils were especially vulnerable because of the low levels of cementation. To rectify the tendency for disturbance, the soil in the remaining columns was extracted from the soil column walls by creating vertical slices through the acrylic walls and allowing the soil to be removed through the sliced opening.

The unconfined compressive strength of the cemented sand columns was about 5 kPa. Other studies found that MICP treated Ottawa 50-70 sand could get compressive strengths of about 170 to 350 kPa at higher levels of cementation (Faison and Mahin, 2012).

The angle of the failure plane in soil columns 1 and 4 was about 63 degrees from the horizontal. This failure plane angle is representative of soil with a friction angle of 36 degrees. Untreated Ottawa 50-70 sand has a friction angle of about 33 degrees (Montoya, 2012). Based on previous work, MICP treated sand with a friction angle of 36 degrees is typical of sand treated to a shear wave velocity of 400 m/s (Montoya, 2012). An approximate shear wave velocity of 400 m/s corresponds to the strength data, indicating the cemented soil columns represent lightly cemented sand.

For use as a treatment process for coastal sand deposits, an appropriate level of MICP cementation should be used. A high enough level of cementation should be used to resist induced shear loads from waves and storm surges, and a low enough level of cementation so that native wildlife, such as birds, burrowing animals, and dune grass, can still interact with the coastal deposits. Further work will include upscaling the

treatment process using a wave tank to identify optimum ranges of cementation for treatment of coastal deposits.

#### 4. CONCLUSIONS

MICP can be used to reinforce sandy coastal deposits to improve the resiliency of vital lifelines during large storm events. Soil columns of clean fine sand were treated with MICP, and resulted in lightly cemented sand. The lightly cemented sand had an increase in strength, as demonstrated with the unconfined compression tests, and increase in friction angle. The free-draining treatment process was designed to be similar to likely treatment processes of unsaturated surficial sands in situ. This treatment process provided uniform levels of cementation throughout the height of the soil column. The light levels of cementation achieved in the soil columns provide an increase in shear strength while still allowing for birds, burrowing animals, and dune grass to interact with the coastal deposits. Future work involves investigating the optimal range of MICP cementation to provide enough strength to resist the loads from large storm events while continuing to support the coastal ecology.

#### 5. REFERENCES

- ASTM D4373, *Standard Test Method for Rapid Determination of Carbonate Content in Soils*
- DeJong, J.T., Fritzges, M.B., and Nüsslein, K. (2006) "Microbial Induced Cementation to Control Sand Response to Undrained Shear", *ASCE Journal of Geotechnical and Geoenvironmental Engineering*, Vol. 132, No. 11, pp. 1381-1392.
- Faison, H., and Mahin, S.A. (2012). "Microbial induced calcite precipitation in partially saturated soils." *PEER 2011/10 – Earthquake Engineering for Resilient Communities: 2011 PEER Internship Program Research Report Collection*, December.
- Martinez, B.C., DeJong, J.T., Ginn, T.R., Mortensen, B.M., Barkouki, T.H., Hunt, C., Tanyu, B., Major, D. (2013) "Experimental Optimization of Microbial Induced Carbonate Precipitation for Soil Improvement", *ASCE Journal of Geotechnical and Geoenvironmental Engineering*, in press.
- Montoya, B.M. (2012) *Bio-Mediated Soil Improvement and the Effect of Cementation on the Behavior, Improvement, and Performance of Sand*, Doctoral Dissertation, University of California, Davis, pp. 238.
- Montoya, B.M., DeJong, J.T., and Boulanger, R.W. (2013) "Seismic Response of Liquefiable Sand Improved by Microbial Induced Calcite Precipitation", *Geotechnique*. in review.
- Mortensen, B.M., and DeJong, J.T. (2011). "Strength and Stiffness of MICP Treated Sand Subjected to Various Stress Paths", *ASCE GeoFrontiers 2011: Advances in Geotechnical Engineering*, Geotechnical Special Publication 211, pp. 4012-4020.
- Weil, M.H., DeJong, J.T., Martinez, B.C., Mortensen, B.M., Waller, J.T. (2012). "Seismic and Resistivity Measurements for Real-Time Monitoring of Microbially Induced Calcite Precipitation in Sand." *ASTM Geotechnical Testing Journal*, Vol. 35, No.2.

# Effect of Grout Bleed Capacity on the Engineering Properties of Cement Grouted Sands

## Effet de la capacité de ressuage de coulis de ciment sur les propriétés mécaniques des sables injectés

Pantazopoulos I.A., Atmatzidis D.K., Basas V.G., Papageorgopoulou S.K.

*Geotechnical Engineering Laboratory, Department of Civil Engineering, University of Patras, Greece*

**ABSTRACT:** Grouts of three different cement types, each at four different cement gradations, with W/C ratios ranging from 0.6 to 3.0 and bleed capacities ranging up to 70% were injected into two different sands. Permeability, unconfined and triaxial compression and resonant column tests were conducted to investigate the influence of grout bleed capacity on the engineering properties of cement grouted sands. Cement grouting resulted in (a) permeability coefficient values as low as  $10^{-8}$  cm/s, (b) unconfined compressive strength in the range of 1MPa to 35MPa, (c) cohesion in the range of 100kPa to 1400kPa, (d) improvement of the internal friction angle by up to  $5^\circ$ , (e) higher shear modulus by up to 25 times and (f) improved damping ratio by up to 10 times. Bleed capacity is an indicator of sand void volume filled with solidified grout but its degree of correlation with the static and dynamic properties of the grouted sands ranges from very good to negligible.

**RÉSUMÉ :** On a injecté des coulis de trois types de ciments différents, chacun avec quatre dosages en ciment différents, avec un rapport eau/ciment variant de 0.6 à 3.0, et une capacité de ressuage se situant jusqu'à 70% lorsque injectés, dans deux sables différents. On a effectué des essais de perméabilité, de compression simple et triaxiale et de colonne résonnante pour étudier l'influence de la capacité de ressuage des coulis sur les propriétés mécaniques des sables injectés. L'injection du ciment a résulté en: a) des valeurs de coefficients de perméabilité aussi faible que  $10^{-8}$  cm/s, b) une compression simple de 1MPa à 35MPa, c) une cohésion de 100kPa à 1400kPa, d) une augmentation de l'angle de frottement jusqu'à  $5^\circ$ , e) un module de cisaillement jusqu'à 25 fois plus élevé, f) une augmentation du coefficient d'amortissement jusqu'à 10 fois plus élevé. Le ressuage des coulis est un indicateur du volume des vides du sable remplis de coulis solidifié mais son degré de corrélation avec les propriétés statiques et dynamiques des sables cimentés varie de très bonnes à négligeables.

**KEYWORDS:** cement grout, bleed capacity, permeability, strength, shear modulus, damping ratio

## 1 INTRODUCTION

Improvement of the mechanical properties and behavior of soils by permeation grouting using cement suspensions is frequently required in order to assure the safe construction and operation of many structures. The grout water-to-cement ratio (W/C) and the maximum cement grain size ( $d_{max}$ ) are two important parameters controlling the cement grout bleed capacity and, consequently, the effectiveness of cement grouts in terms of the percentage of soil voids volume filled by grouting. Although the bleed capacity of cement grouts has been frequently quantified, its correlation with the engineering properties of the grouted sand has not been investigated so far.

Scope of this presentation is to provide some insights on the effect of grout bleed capacity on permeability, unconfined compressive strength, shear strength parameters and dynamic properties of ordinary and microfine cement grouted sands, in conjunction with the effect of the grout W/C ratio.

## 2 MATERIALS AND PROCEDURES

For the purposes of this investigation, a Portland, a Portland-composite and a pozzolanic cement (CEM I, CEM II/B-M and CEM IV/B according to Standard EN 197-1) were used. Each cement was pulverized to produce three additional cements with nominal maximum grain sizes ( $d_{max}$ ) of 40 $\mu$ m, 20 $\mu$ m and 10 $\mu$ m and average Blain specific surface values of 567, 720 and 928 $m^2/kg$ , respectively. Cements with  $d_{max}=10\mu$ m can be considered as "microfine" according to Standard EN 12715 ( $d_{95}<20\mu$ m and specific surface over 800 $m^2/kg$ ). Also, cements with  $d_{max}=20\mu$ m have adequately small characteristic grain sizes to be considered, marginally, as "microfine". Typical gradations of these cements are presented in Figure 1.

All suspensions tested during this investigation were prepared using potable water since it is considered appropriate for

preparing cement-based suspension grouts. The W/C ratio of the suspensions was set equal to 0.6, 0.8, 1.0, 2.0 and 3.0 by weight, in order to test both stable and unstable suspensions in terms of bleed capacity. A superplasticizer (patented new generation of admixture based on polycarboxylate chemistry) at a dosage of 1.4 % by weight of dry cement was used to improve grout properties. All suspensions were prepared using high speed mixers. As recommended by the superplasticizer producer,

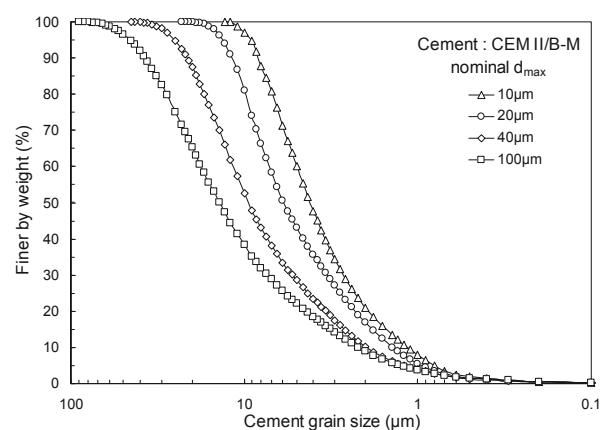


Figure 1. Typical cement gradations.



Table 1. Bleed capacity values (%) of all cement grouts

d <sub>max</sub>	W/C				
	0.6	0.8	1.0	2.0	3.0
100µm	5-10	17-19	16-39	44-60	60-70
40µm	5-7	11-15	10-26	42-55	56-68
20µm	N/T	N/T	0-4	25-37	43-49
10µm	N/T	N/T	0-2	7-26	38-42

N/T: Not tested

the total amount of cement, 70 % of the water and the superplasticizer dosage were mixed for 5 min. Then, the rest of the water was added and mixing continued for another 5 min. Bleed capacity measurements were conducted for all cement suspensions used and the results are summarized in Table 1.

According to Standard EN 12715, a suspension is stable when it has a bleed capacity of not more than 5 % after 120 min from preparation. It can be observed that a W/C ratio of about 0.6 was required to obtain stable suspension of the coarse cements (d<sub>max</sub>=100µm and 40µm) while microfine cement suspensions were stable for a W/C ratio of 1.0

The soils used were clean, uniform, limestone sands with angular grains and were grouted at a dense (relative density approximately 90%) and dry state. Two different sand gradations were used with grain sizes limited between sieve sizes (ASTM E11) Nos. 10-14 and 14-25 (d<sub>15</sub> size of 1.5mm and 0.8mm, respectively) in order to allow grouting by both the coarse- and fine-grained suspensions. The angle of internal friction of the sands was 42.2° and 42.6°, respectively.

Laboratory equipment, similar to the arrangement described in ASTM D4320-84, was used to produce small-size grouted sand specimens, with a height of 112mm and a diameter of 50mm, ready for testing (Pantazopoulos et al. 2012). Injection was stopped when the volume of the injected grout was equal to two void volumes of the sand in the molds. After 24 h, the specimens were extracted from the split molds and cured in a humid room for 28 days before testing.

Grouted specimens were tested in unconfined compression at a displacement rate equal to 0.1%/min. Hydraulic conductivity tests were performed according to the procedure described by Head (1986) for permeability testing in a triaxial cell with two back-pressure systems. Drained triaxial compression tests were conducted under confining pressures of 100, 200 and 400kPa and axial strain rate equal to 0.1%/min, without initial saturation and consolidation. The dynamic properties of the grouted sands were investigated at confining pressures up to 400kPa by conducting torsional resonant column tests for a shear strain range, γ, of approximately 5\*10<sup>-5</sup> % to 5\*10<sup>-2</sup> %. Testing procedures and interpretation of raw data complied with well established methods (Pantazopoulos and Atmatzidis 2012). For comparison, similar tests were conducted on clean sands.

### 3 COEFFICIENT OF PERMEABILITY

The coefficient of permeability values of all grouted sands tested are presented in Figure 2 with respect to W/C ratio, bleed capacity and maximum cement grain size of the suspensions. The coefficient of permeability decreases considerably (by about 5 orders of magnitude) as the W/C ratio decreases from 3 to 0.6 and attains a value of about 10<sup>-7</sup> to 10<sup>-8</sup>cm/s indicating practically impermeable materials. The permeability of the grouted sands appears not to be affected by the cement grain size. Evaluation of the permeability of the grouted sands in terms of grout bleed capacity indicates a similar trend as with the W/C, but allows some observations to be made in terms of the effect of cement grain size. For cement grouts with d<sub>max</sub> equal to 100µm and 40µm, the coefficient of permeability of the grouted sands attained values in the range of 10<sup>-7</sup> to 10<sup>-8</sup>cm/s and 10<sup>-3</sup> to 10<sup>-4</sup>cm/s, for grout bleed capacity ranging from 6%

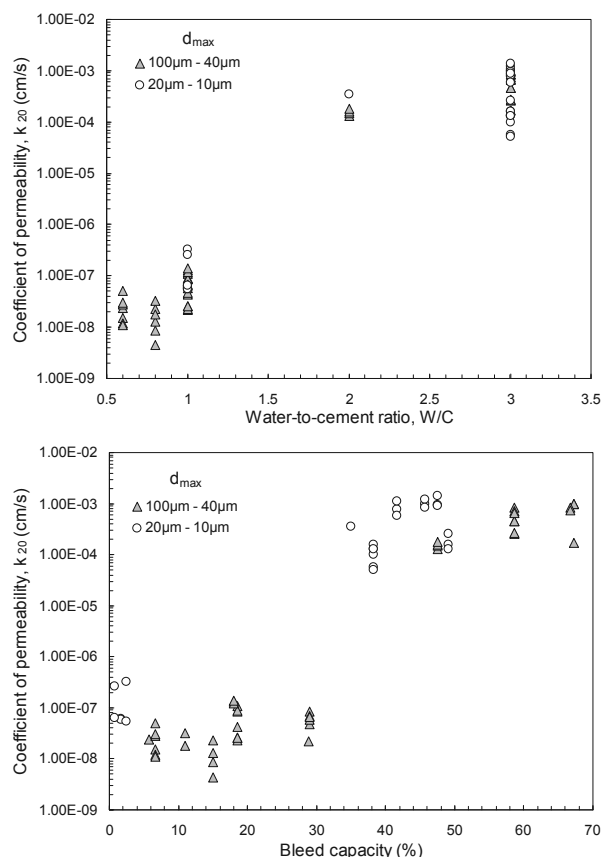


Figure 2. Effect of grout W/C ratio and bleed capacity on the permeability of cement grouted sands.

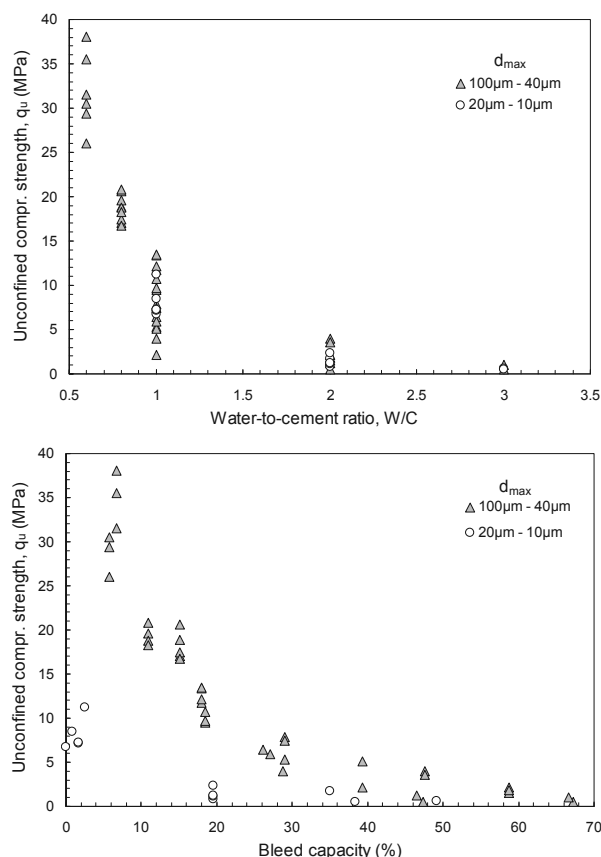


Figure 3. Effect of grout W/C ratio and bleed capacity on the unconfined compression strength of cement grouted sands.

to 30% and from 48% to 68%, respectively. Sands injected with microfine cement grouts ( $d_{max}=20\mu\text{m}$  and  $10\mu\text{m}$ ) obtained, generally, higher coefficients of permeability, by half to one order of magnitude, compared to sands grouted with the coarser cement suspensions, for similar bleed capacities. This is reasonable and can be attributed to the increased amount of coarse-grained cement needed to obtain the same bleed capacity with suspensions of microfine cements. It should also be noted that (a) similar coefficient of permeability values ( $10^{-7}$  to  $10^{-8}$  cm/s) are obtained when injecting with stable or unstable suspensions for bleed capacity values up to 30% and (b) for higher bleed capacity values, the coefficient of permeability of the grouted sand decreases dramatically but remains in the range of  $10^{-4}$  to  $10^{-3}$  cm/s.

#### 4 UNCONFINED COMPRESSION STRENGTH

The results presented in Figure 3 indicate that the unconfined compression strength of the grouted sands increases significantly with decreasing W/C ratio of the grouts, as verified by other research efforts (i.e. Dano et al. 2004) and seems not to be affected by cement grain size. However, the effect of cement grain size can be clearly demonstrated in terms of grout bleed capacity. The unconfined compression strength of the grouted sands is very well correlated with grout bleed capacity of both the coarse-grained cements ( $d_{max}=100$  and  $40\mu\text{m}$ ) and the microfine cements ( $d_{max}=20$  and  $10\mu\text{m}$ ) but, definitely, microfine cement grouts with the same bleed capacity as cement grouts yield significantly lower grouted sand strength. As with permeability, this can be attributed to the increased amount of coarse-grained cement needed to obtain the same bleed capacity as microfine cement suspensions.

#### 5 SHEAR STRENGTH

The shear strength of the grouted sand specimens is expressed in terms of internal friction angle and cohesion, by applying the Mohr-Coulomb failure criterion. As indicated in Figure 4, the internal friction angle ranged from  $40^\circ$  to  $50^\circ$  and the effect of W/C ratio, bleed capacity and cement grain size appear to be insignificant. In general, the internal friction angle of the grouted sands was up to  $5^\circ$  higher than the value obtained for clean sands. The cohesion of the grouted sands is strongly affected both by the W/C ratio and by the bleed capacity of the grouts. As shown in Figure 5, the cohesion values of the grouted sands ranged from 600kPa to 1450kPa, from 300kPa to 500kPa and from 50kPa to 250kPa, for W/C ratios equal to 1, 2 and 3, respectively. Furthermore, grouted sands injected with stable grouts (bleed capacity values less than 5%) obtained the highest cohesion values ranging from 1200kPa to 1450kPa. Increased bleed capacity values (unstable suspensions) in the range of 15% to 65%, leads to an almost linear decrease of the cohesion values from 800kPa to 100kPa. The effect of cement grain size on grouted sand cohesion, as shown in Figure 5, where the microfine cements exhibit higher values of cohesion than the coarse-grained cements, by 40% to 150%, is misleading since the suspensions used had different bleed capacities for the same W/C ratio. For example, at W/C ratio equal to 1, the microfine cement suspensions are stable (bleed capacity  $< 4\%$ ) and fill the sand voids with cement more completely and uniformly than the coarse cement suspensions with W/C=1 (bleed capacity  $> 16\%$ ).

#### 6 SHEAR MODULUS

Presented in Figure 6 are typical results obtained for the shear modulus,  $G$ , of grouted sands at a confining pressure equal to 50kPa and shear strain equal to  $10^{-5}\%$ . The effect of confining pressure is not pronounced for the grouted sands tested (Pantazopoulos and Atmatzidis 2012). As shown in Figure 6, the shear modulus values decrease, from 4.1GPa to

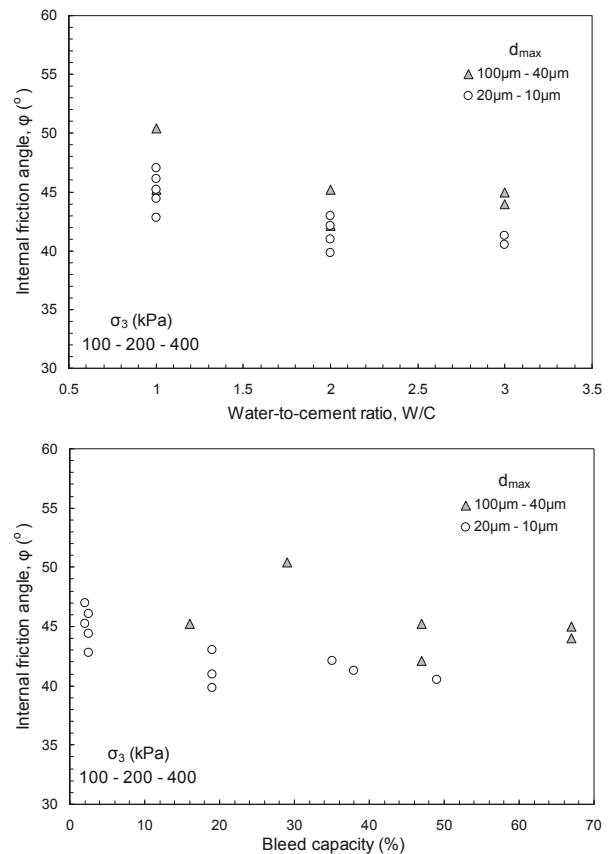


Figure 4. Effect of grout W/C ratio and bleed capacity on the internal friction angle of cement grouted sands.

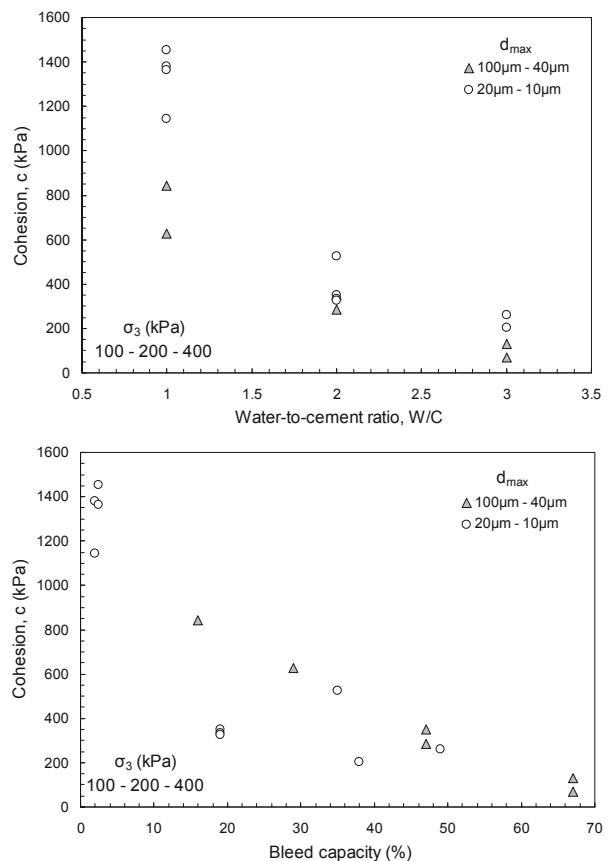


Figure 5. Effect of grout W/C ratio and bleed capacity on the cohesion of cement grouted sands.

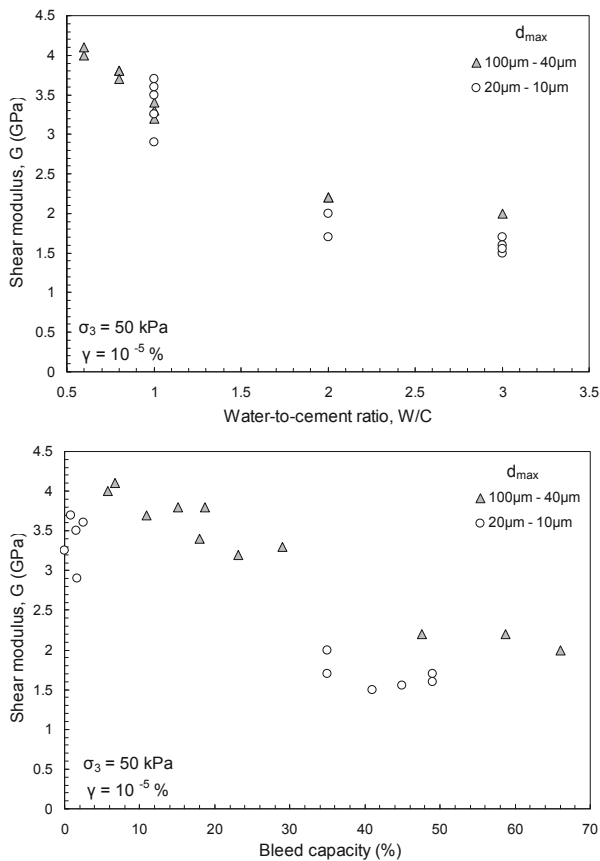


Figure 6. Effect of grout W/C ratio and bleed capacity on the shear modulus of cement grouted sands.

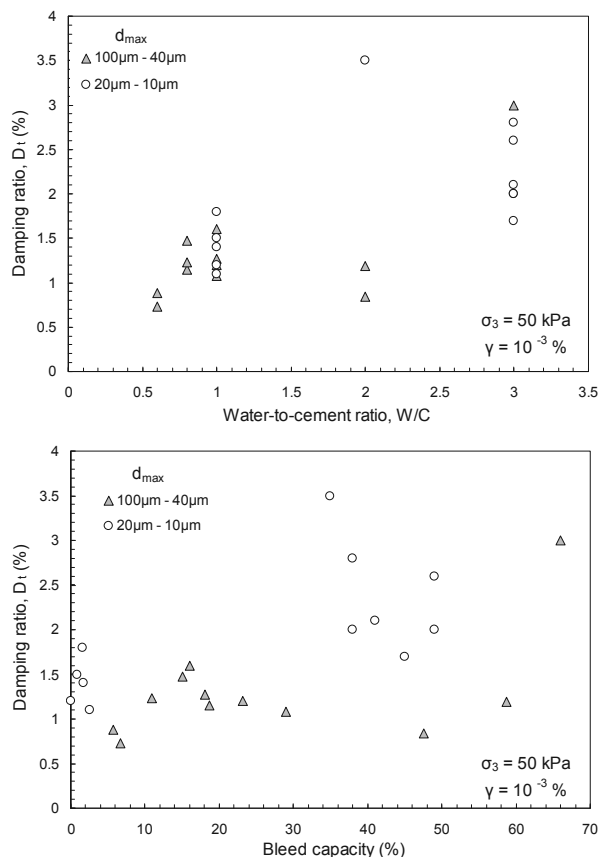


Figure 7. Effect of grout W/C ratio and bleed capacity on the damping ratio of cement grouted sands.

1.5 GPa, with increasing W/C ratio, from 0.6 to 3. The shear modulus values of the clean sands did not exceed 170MPa, indicating an improvement up to 25 times by grouting. The effect of grout bleed capacity on the shear modulus of grouted sand is clearly depicted in Figure 6, where it can be observed that above a bleed capacity value of about 30%, the shear modulus of the grouted sand decreases sharply by about 40%. Cement grain size seems to have a measurable effect on the shear modulus values of the grouted sands. For similar bleed capacity values, the sands grouted with microfine cement grouts have lower shear modulus values, by 15% to 30%, compared to sands grouted with coarse-grained cement grouts.

### 7 DAMPING RATIO

The damping ratio values of the grouted sands are presented in Figure 7 for a confining pressure equal to 50kPa and shear strain equal to  $10^{-3}$ %. The effect of shear strain and confining pressure on the grouted sand damping ratio has been presented elsewhere (Pantazopoulos and Atmatzidis 2012). In general, the values obtained ranged from 0.5% to 8.0%, increased with increasing shear rate (from  $5 \cdot 10^{-5}$ % to  $5 \cdot 10^{-2}$ %) and decreased with increasing confining pressure (from 50kPa to 400kPa). The grout W/C ratio has a measurable effect on the damping ratio values of the grouted sands, which have a tendency to increase with increasing W/C ratio. The effect of grout bleed capacity on the damping ratio of the grouted sand appears to be less dominant, mainly for coarse-grained cements. For microfine cements there is a tendency for the damping ratio of the grouted sands to increase with increasing bleed capacity of the grouts. Even though the available data are limited, grouted sands injected with stable grouts (bleed capacity less than 5%) of microfine cements indicated damping ratios lower by 50% than those for grouting with unstable grouts. The damping ratios of the clean sands (for confining pressure and shear strain equal to 50kPa and  $10^{-3}$ %, respectively) did not exceed 0.5%, indicating an improvement up to 10 times by grouting.

### 8 CONCLUSIONS

Based on the results obtained and the observations made, the following major conclusions may be advanced:

1. Bleed capacity is an indicator of grout effectiveness, since it is representative of the soil void volume filled by cement.
2. The distinction between stable and unstable grouts may not be an indicator of grout effectiveness since similar effects may be produced by both stable and unstable grouts.
3. Bleed capacity values correlate very well with some grouted sand properties (i.e. unconfined compression strength, cohesion) and not at all with other properties (i.e. damping ratio, internal friction angle).

### 9 ACKNOWLEDGEMENTS

The information reported herein is part of research project PENED-03ED527, co-financed by the European Social Fund (75%) and the Greek Ministry of Development (25%).

### 10 REFERENCES

Pantazopoulos I.A., Markou I.N., Christodoulou D.N., Droudakis A.I., Atmatzidis D.K., Antiohos S.K., Chaniotakis E. 2012. Development of microfine cement grouts by pulverizing ordinary cements. *Cement and Concrete Composites* 34, 593-603.  
 Head K.H. 1986. *Manual of soil laboratory testing*. vol.3. Pentech Press Ltd, London.  
 Pantazopoulos I.A. and Atmatzidis D.K. 2012. Dynamic properties of microfine cement grouted sands. *Soil Dynamics and Earthquake Engineering* 42, 17-31.  
 Dano C., Hicher P-Y, Tailliez S. 2004. Engineering properties of grouted sands, *Journal of Geotechnical and Geoenvironmental Engineering* 130, 328-338.

# Numerical Analysis to Quantify the Influence of Smear Zone Characteristics on Preloading Design in Soft Clay

Analyses numériques pour quantifier l'influence des caractéristiques de la zone endommagée sur la conception de préchargement dans les argiles molles

Parsa-Pajouh A., Fatahi H., Khabbaz B.

School of Civil and Environmental Engineering, University of Technology Sydney (UTS), Sydney, Australia

**ABSTRACT:** In this paper, the effects of uncertainties of smear zone characteristics induced by installation of prefabricated vertical drains on the preloading design are numerically investigated. FLAC 2D finite difference software with additional developed subroutines has been employed to conduct the numerical simulations. The finite difference analyses have been verified using a case study. Furthermore, a comprehensive parametric study is conducted to investigate the influence of smear zone permeability and extent on the model predictions. Results of this study indicate that the assumptive properties for smear zone characteristics may result in inaccurate predictions of ground deformations and pore water pressures. This may lead to early removal of the surcharge in the construction process causing excessive post construction settlement. It is recommended to practising engineers to use results of trial preloading to back calculate the required smear zone characteristics in the early stages of embankment construction to optimize the design.

**RÉSUMÉ :** Dans cet article, les effets des incertitudes des caractéristiques de la zone endommagée induites par l'installation des drains verticaux préfabriqués sur la conception du préchargement sont étudiés par une méthode numérique. Le logiciel de différences finies FLAC2D avec sous-programmes additionnels a été utilisé afin de réaliser les simulations numériques. Les analyses de différences finies ont été vérifiées à l'aide d'une étude de cas. Par ailleurs, une étude paramétrique approfondie est effectuée afin d'investiguer l'influence de la perméabilité de la zone endommagée sur les prédictions du modèle. Les résultats de cette étude montrent que les propriétés supposées pour les caractéristiques de la zone endommagée peuvent entraîner des prédictions incorrectes de déformations du sol et de pressions interstitielles. Cela peut conduire à un retrait précoce de la surcharge dans le processus de construction engendrant un tassement post-construction excessive. Il est recommandé aux ingénieurs d'utiliser les résultats de l'essai de préchargement afin de calculer les caractéristiques requises de la zone endommagée pour optimiser la conception.

**KEYWORDS:** FLAC, numerical analysis, preloading, smear zone, vertical drain

## 1 INTRODUCTION

Finding efficient ground improvement techniques to modify the soft soil properties, considering the project time limitation and the construction cost has been a continuous challenge for the construction companies. Various ground improvement methods have been proposed to improve the strength properties of the soft soil. In the last two decades, employing prefabricated vertical drain (PVD) assisted preloading has been recognised as a very efficient ground improvement method for sites with deep soft soil deposits (Holtz et al. 1991; Shang et al. 1998; Indraratna et al. 2005). Installation of the prefabricated vertical drains using mandrel, induces disturbance of the soil surrounding the drain, resulting in a smear zone of reduced permeability adversely affecting the consolidation process. Predicting the soil behaviour surrounding the drain requires an accurate estimation of the smear zone properties. Generally, two major parameters are proposed to characterise the smear zone; the permeability ( $k_s$ ), and the extent ( $r_s$ ) of the smear zone. Figure 1 illustrates the cross section of prefabricated vertical drains surrounded by smear zone, which are installed in rectangular pattern. Determining both the smear zone extent and its permeability is a challenging task. According to literature, very diverse values are reported for the permeability ratio ( $k_h/k_s$ ) and extent ratio ( $r_s/r_m$ ), which are illustrated in Figure 2. The proposed range shows that the extent of the smear zone ( $r_s$ ) may vary between 1.6 to 7 times of the drain radius ( $r_w$ ) or, 1.0 to 6 times of mandrel equivalent diameter ( $r_m$ ). The proposed range for the permeability ratio ( $k_h/k_s$ ) is 1.3 to 10, where  $k_h$  is the horizontal permeability of the intact soil.

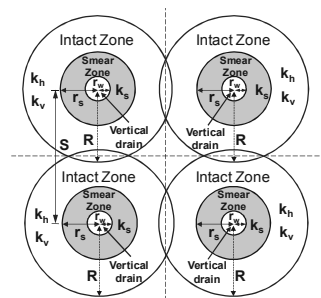


Figure 1. Cross section of PVD surrounding by smear zone

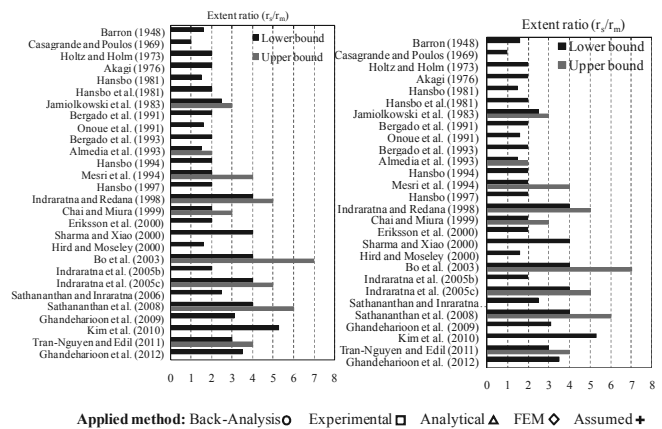


Figure 2. Proposed values for smear zone characteristics

It can be observed that wide ranges are proposed for  $k_h/k_s$  and  $r_s/r_m$  and there is no definite method to predict these parameters precisely to be used by practising engineers. The assumptive properties for smear zone characteristics may result in

inaccurate predictions of the ground behaviour. This can lead to early removal of surcharge in construction process resulting in excessive post construction settlement. Therefore, it is essential to study the influence of the uncertainties in the smear zone size and its permeability on the preloading design to improve the performance of soft deposits. Thus, a numerical code using FLAC 2D has been developed in this study to investigate the uncertainties of PVD smear zone characteristics on the preloading design which can be used to back calculate smear zone characteristics for actual preloading projects.

## 2 NUMERICAL MODELLING

In the present study, FLAC 2D v6.0 has been employed to model the PVD assisted preloading process focusing on smear zone uncertainties. Required new subroutines have been written using the built-in programming language FISH (FLACish) to tailor analyses to suit specific needs for the parametric study, giving the following unique advantages to the developed code for this study; (i) automatic mesh generation process by entering the required parameters to modify the grid pattern inside and outside the smear zone; (ii) ability to change different parameters such as the model dimensions, vertical drain properties, subsoil profile, smear zone characteristics and preloading conditions; (iii) the option to define the exact location of desired points to generate and plot any future history graphs; and (iv) automatic solving process based on the modified input data. Chittagong Sea Port in Bangladesh with 3.0 m high embankment on 9 m deep soft clay, has been selected for the numerical simulations and verification of the developed code and subroutines.

### 2.1. Case Study: Chittagong Sea Port in Bangladesh

According to Dhar et al. (2011), a container yard has been constructed at Chittagong Port, the largest sea port in Bangladesh, for handling loaded containers. The site is located on the bank of Karnafully river beside the Bay of Bengal in the Indian Ocean. The yard covers an area of 60,700 m<sup>2</sup> and was designed to support a container load producing a contact pressure of approximately 56 kPa. Geotechnical investigations revealed the presence of a soft to very soft clayey silt/silty clay deposit with a thickness of approximately 7 m (Figure 3).

Preloading with prefabricated vertical drains was adopted to preconsolidate the compressible soft deposits, which was followed by the field monitoring. Vertical drains were installed down to the depth of approximately 9 m below the ground level in square patten to cover the full depth of the soft clay. A surcharge load consisting of 3.0 m high fill of sand was placed for preloading. Surcharge material was placed in two layers of approximately equal thickness. The sides of the surcharge load were kept vertical along the boundaries of the area using sand bags and brick stacks. Figure 3 shows a profile detailing the ground improvement work schematically. In addition, Figure 4 shows the construction history of the embankment.

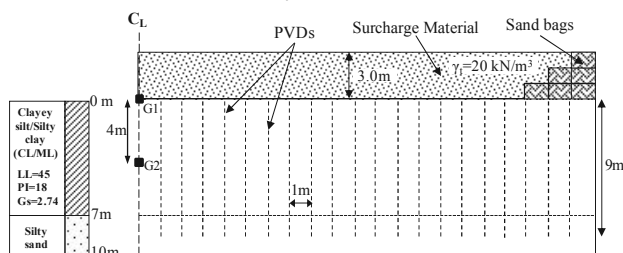


Figure 3. Cross section of constructed embankment

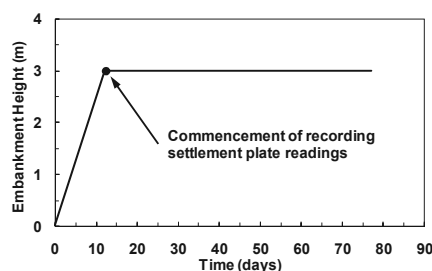


Figure 4. Construction history (Chittagong Port embankment)

FLAC 2D numerical code incorporating modified Cam-Clay constitutive soil model has been employed to simulate Chittagong Port preloading process applying plane strain conditions. The zero excess pore water pressure has been considered along the vertical drains and the ground surface boundary to model the PVD and surface drainage, respectively. Adopted soil properties in the numerical analysis are summarised in Table 1.

Table 1. Adopted soil properties (after Dhar et al. 2011)

Layer	Soil type	M	λ	κ	v	e <sub>o</sub>	γ <sub>s</sub> kN/m <sup>3</sup>	k <sub>h</sub> 10 <sup>-9</sup> m/s	k <sub>h</sub> / k <sub>v</sub>
Clayey Silt	Soft soil	0.94	0.13	0.026	0.3	1.28	14.0	2.31	1.5

The equivalent plane-strain permeability ( $k_{hp}$ ) proposed by Indraratna and Redana (2000) has been used in the numerical analysis.

$$(k_{hp}/k_h) = 0.67 / [(\ln(n)-0.75)] \quad (1)$$

$$(k_{sp}/k_{hp}) = \beta / [(k_{hp}/k_h) [(\ln(n/s)+(k_h/k_s) \ln(s)-0.75)]-\alpha] \quad (2)$$

$$\alpha = 2(n-s)^2 / [3(n-1)n^2] \quad (3)$$

$$\beta = [2(s-1) / (n-1)n^2] * [n(n-s-1)+1/3 (s^2+s+1)] \quad (4)$$

where,  $k_h$  and  $k_{hp}$  are axisymmetric and plane-strain horizontal permeability values of intact zone respectively,  $k_s$  and  $k_{sp}$  are axisymmetric and plane-strain permeability values of smear zone, respectively,  $\alpha$  and  $\beta$  are geometric coefficients,  $n$  is the spacing ratio equal to  $B/b_w$  where  $B$  and  $b_w$  are equivalent plane-strain radius of the influence zone and radius of the drain respectively, and  $s=r_s/r_w$ . The value of  $k_h$  needs to be determined first (laboratory or field), then  $k_{hp}$  can be calculated using Equation (1). When  $k_{hp}$  is known,  $k_{sp}$  can be obtained from Equation (2). The discretised plane-strain finite-difference mesh composed of quadrilateral elements is shown in Figure 5, where only half of the trial embankment is considered by exploiting symmetry.

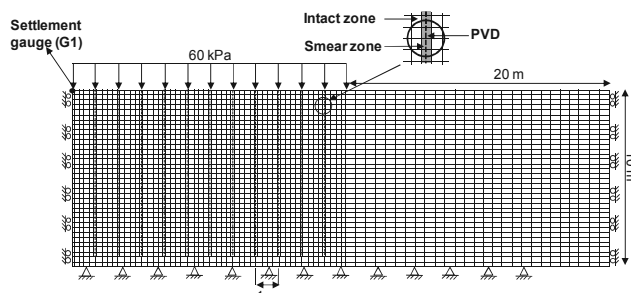


Figure 5. Sample of mesh grid pattern for Chittagong Port embankment considering the smear

Numerical results are compared with the field measurements in Figure 6. According to Figure 6, FLAC predictions are in a good agreement with the field measurements considering  $k_h/k_s=2$  and  $r_s/r_m=3$ . The primary consolidation settlement is

predicted to be approximately 258 mm. As illustrated in Figures 4 and 6, the field settlement is measured immediately after placing the surcharge to the full height of 3 m (after 12 days).

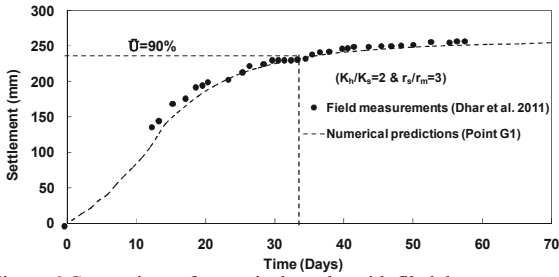


Figure 6. Comparison of numerical results with field data

### 3 PARAMETRIC STUDY AND DISCUSSION

Parametric studies have been conducted to investigate the influence of the smear zone characteristics on the preloading design simulating Chittagong Port case study with the details presented in the previous section. For this purpose,  $k_h/k_s$  (permeability ratio) and  $r_s/r_m$  (extent ratio) have been changed from 2 to 5. Figure 7 illustrates the parametric study results for settlement-time relationships.

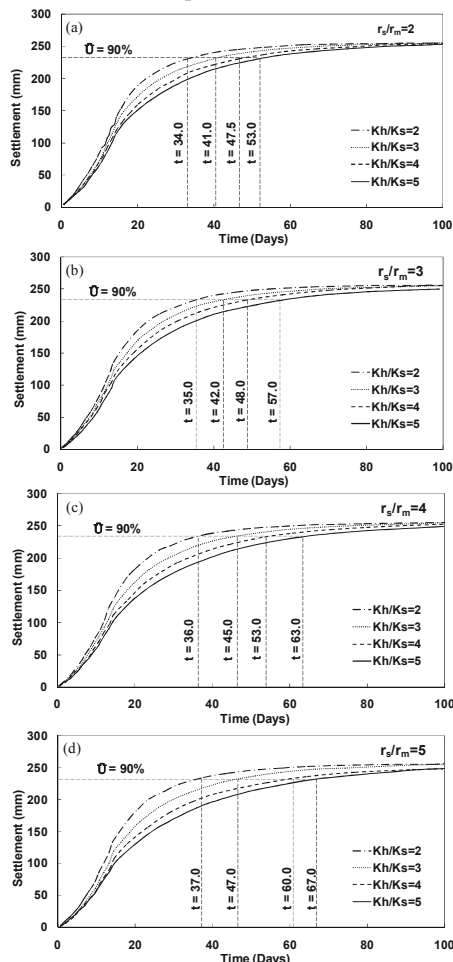


Figure 7. Parametric study results for Chittagong port case history at point G1; (a)  $r_s/r_m=2$ ; (b)  $r_s/r_m=3$ ; (c)  $r_s/r_m=4$ ; and (d)  $r_s/r_m=5$

According to Figure 7, the settlement curves are converged to a unique value of approximately 258 mm, which is the primary consolidation settlement. The required time to obtain 90% of primary consolidation settlement (232 mm) has been considered to investigate the effect of smear zone properties on consolidation process. According to Figure 7a, the minimum time of 34 days is needed to achieve 90% degree of consolidation, considering  $k_h/k_s=2$  and  $r_s/r_m=2$ . When smear

zone properties are  $k_h/k_s=5$  and  $r_s/r_m=5$ , the required time would be the maximum and equal to 67 days, which is approximately twice longer than the minimum (see Figure 7d). According to the settlement curves in Figure 7, the influence of smear zone permeability variations is more critical when the smear zone extent ratio is larger. For instance the required time to obtain 90% degree of consolidation has been increased by 56% (from 34 days to 53 days) changing the permeability ratio from 2 to 5 considering the extent ratio equal to 2, while this boost is 80% (from 37 days to 67 days) for extent ratio of 5.

The general trend in Figures 7(a)-7(d) shows that changing the permeability ratio in a smaller range results in large variations of the required time to obtain 90% degree of consolidation considering a constant extent ratio. According to Figure 7(a), the consolidation time is increased by 23% by varying the permeability ratio from 2 to 3, while this change is 17% and 12% when the permeability ratio is changed from 3 to 4 and 4 to 5, respectively.

Figure 8 illustrates the numerical parametric study results investigating the influence of the smear zone properties on the excess pore water pressure (EPWP) dissipation. Graphs are plotted for point G2 located at the depth of 4 m (see Figure 3). Figure 8 confirms that increasing the permeability and extent ratios prolongs the pore water pressure dissipation process considerably. According to Figure 8, the permeability ratio is more critical parameter than the extent ratio, although the influence of extent ratio variation on the consolidation time can not be neglected. For example, according to Figure 8b, there is 160% difference between the predicted excess pore pressure values after 34 days (90% of the field degree of consolidation) for  $k_h/k_s=2$  (EPWP=13 kPa) and  $k_h/k_s=5$  (EPWP=34 kPa), while keeping  $r_s/r_m=3$ .

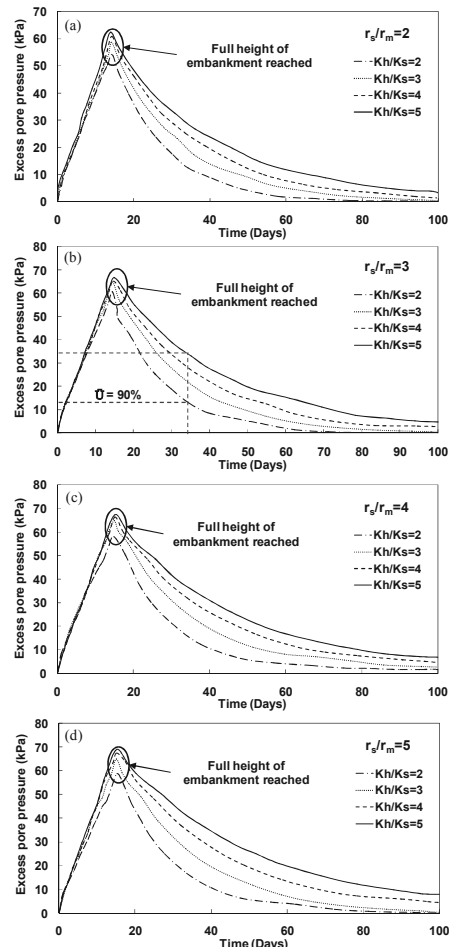


Figure 8. Effect of smear zone properties on excess pore water pressure dissipation for Chittagong port case history at point G2

The required time to obtain 90% degree of consolidation for different smear zone properties is illustrated in Figure 9 using parametric study results, which presents a better interpretation of the effects of the smear zone properties on consolidation time. According to Figure 9, the consolidation time significantly depends on the smear zone permeability and extent. For example, assuming  $r_s/r_m=2$ , for the case with  $k_h/k_s=2$  and  $k_h/k_s=5$ , the required times to obtain 90% degree of consolidation are approximately 33 days and 53 days, respectively, indicating 60% difference. It can be noted that the difference is more significant for larger values of  $r_s/r_m$ .

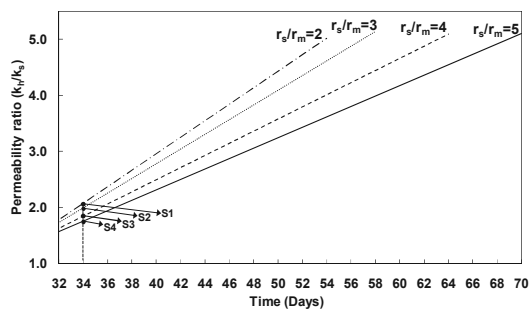


Figure 9. Predicted time to obtain 90% degree of consolidation

Figure 9 clearly indicates that the smear zone extent ratio ( $r_s/r_m$ ) is an important parameter influencing the consolidation time and cannot be neglected. Varying  $r_s/r_m$  in the range of 2 to 5, assuming  $k_h/k_s$  as a constant parameter can influence the required consolidation time by more than 25%. Combined effects of uncertainties in the smear zone extent and permeability will result in momentous changes of consolidation time. Results presented in Figure 9 indicate that the influence of uncertainties in  $r_s/r_m$  becomes more important when permeability of smear zone decreases.

According to the back calculation results presented in Figure 6, the predicted settlement curve is in the best agreement with the field measurements considering smear zone properties of  $k_h/k_s=2$  and  $r_s/r_m=3$ . The required time to obtain 90% degree of consolidation for this condition is equal to 34 days, which is highlighted as point S2 in Figure 9. A vertical line is plotted from  $t_{90\%}=34$  days, which intersects the set of lines at points S1, S2, S3 and S4. Smear zone properties at these points are summarised in Table 2.

Table 2. Back calculated smear zone properties to achieve  $t_{90\%}=34$  days

Point	S1	S2	S3	S4
$k_h/k_s$	2.10	2.0	1.85	1.75
$r_s/r_m$	2	3	4	5

Numerical analyses applying developed FLAC code have been conducted to compare the settlement and excess pore water pressure variations against the consolidation time. Different combinations of smear zone extent and permeability may result in the same  $t_{90\%}=34$  days and predictions are presented in Figure 10.

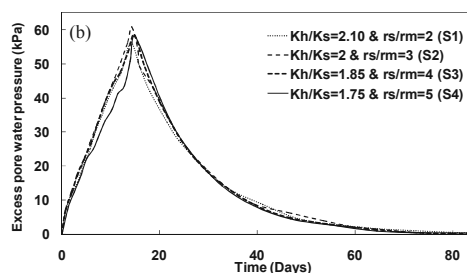
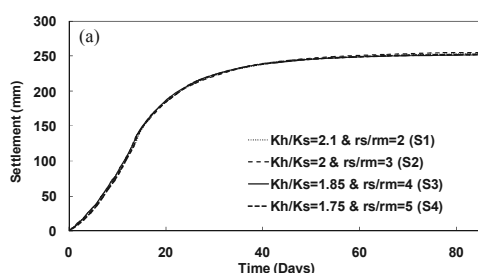


Figure 10. FLAC analysis results for points in Table 2 (a) Settlement variation; (b) Excess pore water pressure dissipation

Figure 10 shows that the curves for the settlement variations and the excess pore water pressure dissipations with time follow the same trend for points S1, S2, S3 and S4. Therefore, smear zone properties of any of these points can be adopted for the practical design purposes.

#### 4 CONCLUSIONS

Preloading time during consolidation process can significantly be affected by formation of the smear zone in the vicinity of the prefabricated vertical drains (PVDs). Smear zone is a reduced permeability area induced by mandrel insertion that halts the consolidation process. Available literature proposes a wide range for the smear zone extent and permeability and yet there is no definite prediction method that can be used to estimate the extent of smear zone and its permeability to be used in the design procedure. In this study, numerical analyses have been employed to investigate the effects of uncertainties of smear zone characteristics on the preloading design. FLAC 2D software has been employed to develop a numerical code assisting with the parametric study and back calculating smear zone properties. The verification exercise on Chittagong port case history confirms the validity of the developed numerical code. According to the parametric study results the properties of the smear zone have key roles on the required consolidation time to achieve a certain soil strength and stiffness satisfying both bearing capacity and settlement design criteria. Therefore, accurate estimation of the properties of smear zone based on the soil type and the installation method is vital for the ground improvement projects adopting PVD assisted preloading. Results of this study indicate that assumptive properties for smear zone characteristics may result in inaccurate predictions of ground deformations and pore water pressures. This can lead to early removal of surcharge in construction process resulting excessive post construction settlement. Thus, it is recommended to practising geotechnical engineers to back calculate the smear zone properties using a trial construction similar to the future construction procedure.

#### 5 REFERENCES

Dhar, A. S., Siddique, A. and Ameen, S. F. 2011. Ground improvement using pre-loading with prefabricated vertical drains. *International Journal of Geoenvironment Case Histories*, 2(2), 86-104.

Holtz, R.D., Jamiolkowski, M.B., Lancellotta, R. and Pedroni, R. 1991. Prefabricated vertical drains: design and performance. *CIRIA, Butterworth-Heinemann*, London.

Indraratna, B. and Redana, I. W. 2000. Numerical modeling of vertical drains with smear and well resistance installed in soft clay. *Canadian Geotechnical Journal*, 37(1), 132-145.

Indraratna, B., Rujikiatkamjorn, C. and Sathanathan, I. 2005. Analytical and numerical solutions for a single vertical drain including the effects of vacuum preloading. *Canadian Geotechnical Journal*, 42(4), 994-1014.

Shang, J.Q., Tang, M. and Miao, Z. 1998. Vacuum preloading consolidation of reclaimed land: a case study. *Canadian Geotechnical Journal*, 35(5), 740-749.

# Construction of virtual sites for reliability-based design

## Construction de sites virtuels à des fins de conception fiabiliste

Phoon K.K.

National University of Singapore, Singapore

Ching J.

National Taiwan University, Chinese Taipei

**ABSTRACT:** This paper presents the construction of “virtual sites” using multivariate normal distributions calibrated from actual soil property databases. By doing so, the actual magnitude of uncertainty reduction from conducting better/more soil tests can be estimated realistically, rather than theoretically.

**RÉSUMÉ:** Cet article présente la construction de "sites virtuels" en utilisant des distributions normales à plusieurs variables calibrées à partir de bases de données de propriétés de sols réels. Par cette méthode, la réduction réelle de l'incertitude que l'on peut obtenir en augmentant le nombre et/ou la qualité des essais de sol peut être estimée de manière réaliste, et non plus seulement théorique.

**KEYWORDS:** virtual site; uncertainties; soil properties; correlation; site investigation; reliability-based design.

### 1 INTRODUCTION

This paper presents the concept of a “virtual site”; the purpose is to emulate site investigation efforts as realistically as possible. It is not possible to emulate every aspect of a real site at present. In this paper, the scope is to reproduce the information content arising from a typical mix of laboratory and field tests conducted in a site for the purpose of estimating a design undrained shear strength ( $s_u$ ) for clays and friction angle ( $\phi$ ) for sands. The critical feature here is the consistent and realistic coupling of different test data, which is achieved using multivariate normal distributions. Data from different tests will be correlated, because they are measuring the same mass of soil, although they could be measuring different aspects of soil behavior under different boundary conditions and over different volumes. The purpose of developing a virtual site is not to replace actual site investigation. The purpose is to quantify the uncertainty reduction in  $s_u$  and  $\phi$  by incorporating the test results from better and/or more tests.

The idea of simulating a “virtual site” is not new. For example, Jaksa et al. (2005) and Goldsworthy et al. (2007) used three dimensional random fields and Monte Carlo simulation to simulate the spatially variable elastic modulus of a “virtual” site. Each spatially variable realization constitutes a plausible full information scenario. Site investigation is then carried out numerically by sampling the continuous random field at discrete locations. The site investigation data so obtained constitute the typical partial information scenario commonly encountered in practice. The goal of these studies was to quantify the difference in the designs based on these full and partial information scenarios. In this paper, the virtual site simulation is based on multivariate normal distributions that couple soil parameters such as  $s_u$ , overconsolidation ratio, standard penetration test N-value, cone tip resistance, and Atterberg limits. The distinct features of this paper are: (a) a more realistic bag of multivariate information containing both laboratory and field data and (b) the probability model is constructed from an actual database of clays and sands. These features are critical to the objective of this paper, which is to quantify the uncertainty reduction in  $s_u$  and  $\phi$  by incorporating the test results from better and/or more tests. This objective is only achievable if the information contained in the virtual site is comparable to that contained in a real site, not merely pertaining

to a single laboratory/field parameter, but to a group of parameters that are correlated in a realistic way. By doing so, it is possible to evaluate the *actual* merits of reliability-based design approximately, rather than elaborate on the theoretical merits widely discussed in previous studies. This paper summarizes the current development of such virtual sites.

### 2 MULTIVARIATE GEOTECHNICAL DATA

Multivariate information is usually available in a typical site investigation. For instance, when undisturbed samples are extracted for oedometer and triaxial tests, SPT and/or piezocone test (CPTU) may be conducted in close proximity. Moreover, data sources such as the unit weight, plastic limit (PL), liquid limit (LL), and liquidity index (LI) are commonly determined from relatively simple laboratory tests on disturbed samples. These data could be correlated, and these correlations can be exploited to reduce the coefficient of variation of a design parameter. The impact on RBD is obvious. This section presents statistical characterization of multivariate geotechnical data.

Most soil parameters are not normally distributed, because they are positive valued. Let  $Y$  denote a non-normally distributed soil parameter. One well known cumulative distribution function (CDF) transform approach can be applied to convert  $Y$  into a standard normal variable  $X$ :  $X = \Phi^{-1}[F(Y)]$ , where  $\Phi(\cdot)$  is the CDF of a standard normal random variable, and  $F(\cdot)$  is the CDF of  $Y$ . A set of multivariate soil parameters  $\underline{Y} = (Y_1, Y_2, \dots, Y_n)'$  can be transformed into  $\underline{X} = (X_1, X_2, \dots, X_n)'$ . By definition,  $X_1, X_2, \dots, X_n$  are *individually* standard normal random variables. It is crucial to note here that *collectively*  $(X_1, X_2, \dots, X_n)'$  does not necessarily follow a multivariate normal distribution even if each component is normally distributed. Even so, recent studies by Ching et al. (2010) and Ching and Phoon (2012a) showed that the multivariate normal distribution is an acceptable approximation for selected parameters of clays, and Ching et al. (2012b) arrived at the same observation for selected parameters of sands.

The multivariate normal probability density function for  $\underline{X} = (X_1, X_2, \dots, X_n)'$  can be defined uniquely by a correlation matrix:



$$f(\underline{X}) = |C|^{-\frac{1}{2}} (2\pi)^{-\frac{n}{2}} e^{-\frac{1}{2}\underline{X}'C^{-1}\underline{X}} \quad (1)$$

where  $C$  is the correlation matrix. For  $n = 3$ , the correlation matrix is given by:

$$C = \begin{bmatrix} 1 & \delta_{12} & \delta_{13} \\ \delta_{12} & 1 & \delta_{23} \\ \delta_{13} & \delta_{23} & 1 \end{bmatrix} \quad (2)$$

between  $X_i$  and  $X_j$  (not equal to the correlation between the original physical variable  $Y_i$  and  $Y_j$ ). It is clear that the full multivariate dependency structure of a normal random vector only depends on a correlation matrix ( $C$ ) containing bivariate correlations between all possible pairs of components, namely  $X_1$  and  $X_2$ ,  $X_1$  and  $X_3$ , and  $X_2$  and  $X_3$ . It is not necessary to measure  $X_1$ ,  $X_2$ , and  $X_3$  *simultaneously*. The practical advantage of capturing multivariate dependencies in any dimension (i.e., any number of random variables) using only bivariate dependency information is obvious.

It is simple to obtain realizations of *independent* standard normal random variables  $\underline{U} = (U_1, U_2, U_3)'$  using library functions in many softwares. Realizations of *correlated* standard normal random variables  $\underline{X} = (X_1, X_2, X_3)'$  can be obtained using  $\underline{X} = L\underline{U}$ , in which  $L$  is the lower triangular Cholesky factor satisfying  $C = LL'$ . Finally, each soil parameter is obtained using  $Y_i = F^{-1}[\Phi(X_i)]$ .

## 2.1 Complete multivariate information (structured clays)

A multivariate database of  $Y_1 = LI$  (liquidity index),  $Y_2 = s_u$ ,  $Y_3 = s_u^{re}$  (remolded undrained shear strength),  $Y_4 = \sigma'_p$  (preconsolidation stress), and  $Y_5 = \sigma'_v$  (effective vertical stress) is compiled in Ching & Phoon (2012a). There are 345 data points of structured clays from 37 sites worldwide, covering a wide range of sensitivity,  $LI$ , and clay types, with simultaneous knowledge of  $(Y_1, Y_2, \dots, Y_5)'$ . The OCR values of the data points are generally small, mostly less than 4. Fissured and organic clays are mostly left out of the database. Because  $s_u$  values depend on stress state, strain rate, sampling disturbance, etc., all  $s_u$  values are converted into mobilized  $s_u$  values following the recommendations made by Mesri and Huvaj (1997). The marginal probability density functions (PDF) for  $(Y_1, Y_2, \dots, Y_5)'$  and their statistics (mean of  $Y_i = \mu_i$ , COV of  $Y_i = V_i$ , mean of  $\ln(Y_i) = \lambda_i$ , standard deviation of  $\ln(Y_i) = \xi_i$ ) are summarized in Table 1.

For lognormal  $Y$ , the CDF transform is:

$$X_i = [\ln(Y_i) - \lambda_i] / \xi_i \quad (3)$$

The transformed  $(X_1, X_2, \dots, X_5)'$  are individually standard normal random variables. The correlation matrix  $C$  for  $(X_1, X_2, \dots, X_5)'$  is shown in Table 2, and  $(X_1, X_2, \dots, X_5)'$  is assumed to be multivariate normal with the correlation matrix listed in the table.

The multivariate normal distribution is employed to simulate samples of  $(LI, s_u, s_u^{re}, \sigma'_p, \sigma'_v)$ , shown in Figure 1 together with the calibration database. Not only the correlations among the original random variables ( $LI, s_u, s_u^{re}, \sigma'_p, \sigma'_v$ ) are shown but the correlations among their derived (normalized) quantities, including  $S_t = s_u/s_u^{re}$ ,  $OCR = \sigma'_p/\sigma'_v$ ,  $s_u/\sigma'_v$ , are also shown. The multivariate normal distribution performs adequately, as the simulated samples closely mimic the correlation behaviors of the calibration database, even for those with nonlinear trends, e.g.  $LI-s_u^{re}$  and  $LI-S_t$  correlations.

Table 1. Distributions and statistics of  $(Y_1, Y_2, \dots, Y_5)'$  for structured clays (Source: Ching & Phoon 2012a).

Distribution	Mean	COV	Mean of	stdev of
--------------	------	-----	---------	----------

				$\ln(Y_i), \lambda_i$	$\ln(Y_i), \xi_i$
$Y_1 = LI$	Lognormal	1.25	0.49	0.122	0.459
$Y_2 = s_u$	Lognormal	31.01kN/m <sup>2</sup>	0.95	3.051	0.898
$Y_3 = s_u^{re}$	Lognormal	2.51kN/m <sup>2</sup>	1.52	0.226	1.191
$Y_4 = \sigma'_p$	Lognormal	105.82kN/m <sup>2</sup>	0.98	4.311	0.835
$Y_5 = \sigma'_v$	Lognormal	66.63kN/m <sup>2</sup>	0.80	3.891	0.823

Table 2. Correlation matrix  $C$  for  $(X_1, X_2, \dots, X_5)'$  for the five selected parameters of structured clays (Source: Ching & Phoon 2012a).

	$X_1 (LI)$	$X_2 (s_u)$	$X_3 (s_u^{re})$	$X_4 (\sigma'_p)$	$X_5 (\sigma'_v)$
$X_1 (LI)$	1.000	-0.083	-0.824	-0.176	0.280
$X_2 (s_u)$	-0.083	1.000	0.276	0.915	0.801
$X_3 (s_u^{re})$	-0.824	0.276	1.000	0.365	0.453
$X_4 (\sigma'_p)$	-0.176	0.915	0.365	1.000	0.850
$X_5 (\sigma'_v)$	0.280	0.801	0.453	0.850	1.000

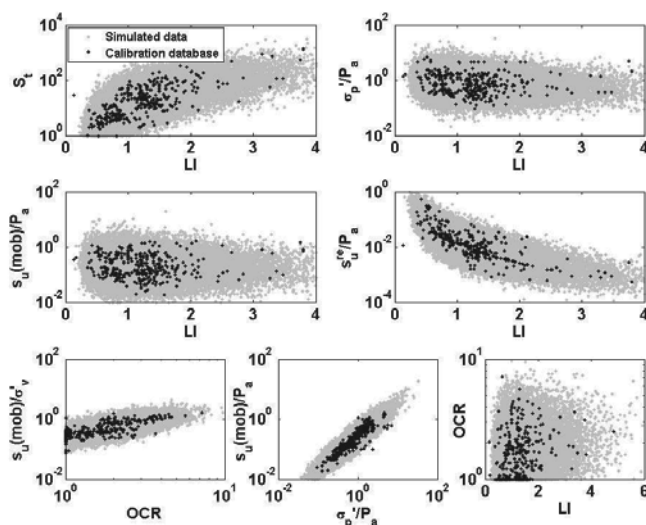


Figure 1. Comparisons between the calibration database and the simulated data points (Source: Ching & Phoon 2012a).

## 2.2 Incomplete multivariate information (unstructured clays)

Ching et al. (2010) presented another clay database containing four soil parameters:  $Y_1 = OCR$ ,  $Y_2 = s_u$  from CIUC test,  $Y_3 = q_T - \sigma_v$  (net cone resistance), and  $Y_4 = N_{60}$  (SPT N corrected for energy efficiency). The range of OCR of this database is wider – from 1 to 50. However, only bivariate data on  $(Y_1, Y_2) = (OCR, s_u)$ ,  $(Y_3, Y_2) = (q_T - \sigma_v, s_u)$ , and  $(Y_4, Y_2) = (N_{60}, s_u)$  are available. Bivariate data on  $(Y_1, Y_3) = (OCR, q_T - \sigma_v)$ ,  $(Y_1, Y_4) = (OCR, N_{60})$ , and  $(Y_3, Y_4) = (q_T - \sigma_v, N_{60})$  are missing, i.e., the bivariate correlations  $\delta_{ij}$  are only partially known. Given that complete bivariate information is not available, it is not possible to apply the aforementioned CDF transform approach directly. It is accurate to say that although it is common to measure more than two soil parameters in a site investigation, it is uncommon to establish correlations between *all possible pairs* of soil parameters.

To deal with this difficulty of incomplete bivariate correlations, Ching et al. (2010) constructed a multivariate normal distribution using a Bayes net model which prescribed a dependency structure based on some postulated but reasonable conditional relationships between the soil parameters. They considered  $Y_1 = OCR$  as a given number and the remaining soil parameters  $(Y_2, Y_3, Y_4)'$  are lognormally distributed random variables. Hence,  $\ln(Y_2) = \ln(s_u) = \lambda_2 + \xi_2 X_2$ ,  $\ln(Y_3) = \ln(q_T - \sigma_v) = \lambda_3 + \xi_3 X_3$ , and  $\ln(Y_4) = \ln(N_{60}) = \lambda_4 + \xi_4 X_4$ , in which  $X_i$  are standard normal random variables. The simulation of  $(Y_1, Y_2, Y_3, Y_4)'$  starts from OCR. The undrained shear strength,  $Y_2$ , is next simulated using this OCR sample and the SHANSEP model (Ladd and Foott 1974):

$$\ln(s_u) = 0.64 \ln(\text{OCR}) + \ln(\sigma'_{v0}) - 0.874 + 0.237U_1 \quad (4)$$

where 0.237 is the standard deviation of the transformation uncertainty, and  $U_1$  is standard normal. The third step is to simulate  $N_{60}$  and  $q_T - \sigma_v$  using the  $s_u$  sample:

$$\ln(N_{60}) = 1.633 \ln(s_u) - 0.403 \ln(\sigma'_{v0}) - 3.845 + 0.456U_2 \quad (5a)$$

$$\ln(q_T - \sigma_v) = \ln(s_u) + 2.54 + 0.34U_3 \quad (5b)$$

where 0.456 and 0.34 are the standard deviations of the transformation uncertainties, and  $U_2$  and  $U_3$  are standard normal. Figure 2 shows the correlation plots for the simulated  $\{\text{OCR}, s_u, N_{60}, q_T - \sigma_v\}$  for a case where OCR is uniformly distributed over [5, 24].

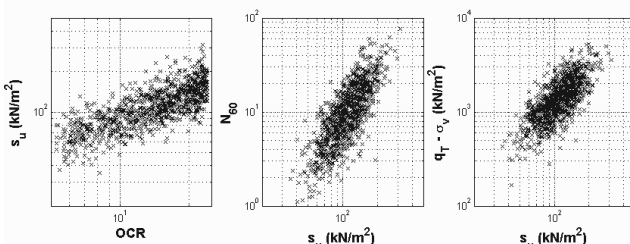


Figure 2. Correlation plots for  $\{\text{OCR}, s_u, N_{60}, q_T - \sigma_v\}$  samples.

Based on the results of Ching et al. (2010), Phoon et al. (2012) further assumed OCR to be lognormal with a reasonable COV = 0.25. Under this assumption, they showed that the underlying standard normal variables ( $X_1, X_2, X_3, X_4$ ) have the correlation matrix shown in Table 3. The correlation matrix in Table 3 should be suitable for unstructured clays covering a fairly wide range of OCR.

Table 3. Correlation matrix C for ( $X_1, X_2, X_3, X_4$ ) for the four selected parameters of unstructured clays (Source: Phoon et al. 2012).

	$X_1$ (OCR)	$X_2$ ( $s_u$ )	$X_3$ ( $q_T - \sigma_v$ )	$X_4$ ( $N_{60}$ )
$X_1$ (OCR)	1.000	0.554	0.355	0.395
$X_2$ ( $s_u$ )	0.554	1.000	0.642	0.714
$X_3$ ( $q_T - \sigma_v$ )	0.355	0.642	1.000	0.458
$X_4$ ( $N_{60}$ )	0.395	0.714	0.458	1.000

### 2.3 Incomplete multivariate information (clean sands)

Ching et al. (2012b) presented a study that is very similar to Ching et al. (2010) but for clean sands. The study was based on a database containing five selected parameters of normally consolidated clean sands:  $Y_1 = \phi_{cv}$  (critical state friction angle),  $Y_2 = I_R$  (dilatancy index, see Bolton 1986),  $Y_3 = \phi_p$  (peak secant friction angle),  $Y_4 = (q_c/P_a)/(\sigma'_v/P_a)^{0.5} = q_{c1}$  (corrected cone resistance), and  $Y_5 = (N_1)_{60}$  (SPT N corrected for energy efficiency and overburden stress). They considered  $Y_1 = \phi_{cv}$  and  $Y_2 = I_R$  as given numbers and the remaining soil parameters ( $Y_3, Y_4, Y_5$ ) are random variables:  $Y_3$  is normal, while  $Y_4$  and  $Y_5$  are lognormal. Hence,  $Y_3 = \phi_p = \mu_3 + \mu_3 V_3 X_3$ ,  $\ln(Y_4) = \ln(q_{c1}) = \lambda_4 + \xi_4 X_4$ , and  $\ln(Y_5) = \ln[(N_1)_{60}] = \lambda_5 + \xi_5 X_5$ , in which  $X_1$  are standard normal random variables. If we further assume  $\phi_{cv}$  and  $I_R$  are normal with reasonable standard deviations of  $3^\circ$  and  $1^\circ$ , respectively, i.e.,  $Y_1 = \phi_{cv} = \mu_1 + 3X_1$  and  $Y_2 = I_R = \mu_2 + X_2$ , and also assume independence between  $\phi_{cv}$  and  $I_R$ , it can be shown that the underlying standard normal variables ( $X_1, X_2, X_3, X_4, X_5$ ) has the correlation matrix shown in Table 4. The correlation matrix in Table 4 should be suitable for normally consolidated clean sands.

Table 4. Correlation matrix C for ( $X_1, X_2, X_3, X_4, X_5$ ) for the five selected parameters of clean sands (Source: Ching et al. 2012b).

	$X_1$ ( $\phi_{cv}$ )	$X_2$ ( $I_R$ )	$X_3$ ( $\phi_p$ )	$X_4$ ( $q_{c1}$ )	$X_5$ [( $N_1$ ) <sub>60</sub> ]
$X_1$ ( $\phi_{cv}$ )	1.000	0.000	0.642	0.491	0.536
$X_2$ ( $I_R$ )	0.000	1.000	0.642	0.491	0.536
$X_3$ ( $\phi_p$ )	0.642	0.642	1.000	0.764	0.835
$X_4$ ( $q_{c1}$ )	0.491	0.491	0.764	1.000	0.638
$X_5$ [( $N_1$ ) <sub>60</sub> ]	0.536	0.536	0.835	0.638	1.000

### 2.4 Undrained shear strengths under various test procedures

The undrained shear strength ( $s_u$ ) of a clay is not a constant. In particular,  $s_u$  of a clay evaluated by different test procedures are different because these tests may have different stress states, stress histories, degrees of sampling disturbance, and strain rates. Ching & Phoon (2013) constructs the multivariate normal distribution of the  $s_u$  values from seven  $s_u$  tests (CIUC, CK<sub>0</sub>UC, CK<sub>0</sub>UE, DSS, VST, UU, UC) based on a large clay database consisting data points from 146 studies. Many  $s_u$  data points are associated with a known test mode (6310 points), a known OCR (4584 points), and a known plasticity index (PI) (4541 points). The geographical regions cover Australia, Austria, Brazil, Canada, China, England, Finland, France, Germany, Hong Kong, Iraq, Italy, Japan, Korea, Malaysia, Mexico, New Zealand, Norway, Northern Ireland, Poland, Singapore, South African, Spain, Sweden, Thailand, Taiwan, United Kingdom, United States, and Venezuela. The clay properties cover a wide range of OCR (mostly 1~10, few studies OCR > 10, but nearly all studies are with OCR < 50) and a wide range of sensitivity  $S_t$  (sites with  $S_t = 1$ ~tens or hundreds are fairly typical).

An important step for the construction of the multivariate distribution is to convert all  $s_u$  data points in the database into the following standardized form:

$$s_{u,NC,1\%,PI20}/\sigma'_v = (s_u/\sigma'_v)/(b_{OCR} \cdot c_{rate} \cdot d_{PI}) \quad (6)$$

where  $s_{u,NC,1\%,PI20}$  is the undrained shear strength of a NC clay with PI = 20 subjected to a 1% per hour strain rate;  $b_{OCR}$ ,  $c_{rate}$ , and  $d_{PI}$  are modifier factors that adjust the reference normalized undrained shear strength for overconsolidation ratio, strain rate, and plasticity. Table 5 shows these factors (Ching et al. 2013; Ching & Phoon 2013). The standardized  $s_{u,NC,1\%,PI20}/\sigma'_v$  is denoted by  $Y_{\text{test mode index}}$ . The test mode indices are respectively 1, 2, 3, 4, 5, 6, and 7 for CIUC, CAUC, CAUE, DSS, FV (field vane), UU, and UC. Hence, there are seven random variables ( $Y_1, Y_2 \dots Y_7$ ). Table 6 shows the statistics of  $Y_i$ . The  $Y$  data points for each test mode are roughly lognormally distributed, i.e.,  $X_i = [\ln(Y_i) - \lambda_i]/\xi_i$  is roughly standard normal. Given a test mode  $i$ , the scatter in the  $Y_i$  data points, quantified by the COV in Table 6, may be due to measurement errors in  $s_u$  and global inherent variability in  $s_u$  ( $s_u$  from different geographic locales) as well as the transformation uncertainties associated with the standardization steps for PI, strain rate, and OCR.

The  $Y_i$  data points are converted to standard normal variables  $X_i = [\ln(Y_i) - \lambda_i]/\xi_i$ . Table 7 shows the correlation matrix C for ( $X_1, X_2, \dots, X_7$ ). The estimated correlation coefficients  $\delta_{ij}$  are quite sensible. The four triaxial compression (TC) test modes ( $X_1, X_2, X_6, X_7$ ) seem mutually highly correlated ( $\delta_{ij} > 0.8$ ), with the exception of ( $X_6, X_7$ ) having  $\delta_{ij} = 0.59$ . The CAUE test mode ( $X_3$ ) has weak correlation with TC test modes ( $\delta_{ij} < 0.5$ ), probably because it imposes a different stress state from TC tests. The correlation coefficients between FV and TC are relatively weak as well ( $\delta_{ij} \leq 0.63$ ). Such relatively low correlation between FV and TC may be due to the fact that the FV test has several distinct aspects (stress state, drainage boundaries, strain rate, and failure mode). It is interesting that the correlation between FV and DSS is high ( $\delta_{ij} = 0.73$ ).

Table 5  $b_{OCR}$ ,  $c_{rate}$ , and  $d_{PI}$  factors (Source: Ching et al. 2013).

Factor	Test type	Formula
$b_{OCR}$	CIUC	$\text{OCR}^{0.602}$
	CAUC	$\text{OCR}^{0.681}$

	CAUE	$OCR^{0.898}$
	DSS	$OCR^{0.749}$
	VST	$OCR^{0.902}$
	UU	$OCR^{0.800}$
	UC	$OCR^{0.932}$
$c_{rate}$		$1.0+0.1 \times \log_{10}(\text{strain rate}/1\%)$
$d_{PI}$	CIUC	$(PI/20)^0 = 1$
	CAUC	$(PI/20)^0 = 1$
	CAUE	$(PI/20)^{0.178}$
	DSS	$(PI/20)^{0.0655}$
	VST	$(PI/20)^{0.124}$
	UU	$(PI/20)^0 = 1$
	UC	$(PI/20)^0 = 1$

Table 6 Statistics of Y data points (Source: Ching et al. 2013).

	# pts.	Mean	COV	Mean of $\ln(Y_i), \lambda_i$	Stdev of $\ln(Y_i), \xi_i$
$Y_1$ (CIUC)	637	0.404	0.316	-0.955	0.315
$Y_2$ (CAUC)	555	0.350	0.318	-1.090	0.280
$Y_3$ (CAUE)	224	0.184	0.324	-1.748	0.355
$Y_4$ (DSS)	573	0.241	0.399	-1.468	0.277
$Y_5$ (FV)	1057	0.275	0.416	-1.363	0.372
$Y_6$ (UU)	435	0.243	0.504	-1.523	0.463
$Y_7$ (UC)	387	0.223	0.611	-1.640	0.523

Table 7 Correlation matrix C for  $(X_1, X_2, \dots, X_7)'$  (Source: Ching & Phoon 2013).

	$X_1$ (CIUC)	$X_2$ (CAUC)	$X_3$ (CAUE)	$X_4$ (DSS)	$X_5$ (FV)	$X_6$ (UU)	$X_7$ (UC)
$X_1$ (CIUC)	1.00	0.84	0.47	0.72	0.63	0.88	0.85
$X_2$ (CAUC)	0.84	1.00	0.39	0.78	0.35	0.7*	0.6*
$X_3$ (CAUE)	0.47	0.39	1.00	0.45	0.41	0.4*	0.3*
$X_4$ (DSS)	0.72	0.78	0.45	1.00	0.73	0.6*	0.5*
$X_5$ (VST)	0.63	0.35	0.41	0.73	1.00	0.64	0.46
$X_6$ (UU)	0.88	0.7*	0.4*	0.6*	0.64	1.00	0.68
$X_7$ (UC)	0.85	0.6*	0.3*	0.5*	0.46	0.68	1.00

\* insufficient data pairs, estimated based on judgments

### 3 REDUCING UNCERTAINTY IN DESIGN PARAMETER WITH BETTER AND/OR MORE TESTS

As mentioned earlier, it is simple to simulate virtual site investigation data  $(Y_1, Y_2, \dots, Y_n)'$ . First, obtain realizations of independent standard normal random variables  $\underline{U} = (U_1, U_2, \dots, U_n)'$  using library functions in many softwares. Realizations of correlated standard normal random variables  $\underline{X} = (X_1, X_2, \dots, X_n)'$  can be obtained using  $\underline{X} = \underline{L}\underline{U}$ , in which L is the lower triangular Cholesky factor satisfying  $C = \underline{L}\underline{L}'$ . Finally, each soil parameter is obtained using  $Y_i = F^{-1}[\Phi(X_i)]$ . For lognormal distribution,  $Y_i = \exp(\lambda_i + \xi_i \times X_i)$ . Figures 1 & 2 already showed the simulated data  $(Y_1, Y_2, \dots, Y_n)'$ . This section will further discuss how to use the simulated data to quantify the uncertainty reduction in  $s_u$  and  $\phi$  by incorporating the test results from better and/or more tests.

This is illustrated below using results presented in Figure 2. The histogram of the simulated  $s_u$  data for the same virtual site is given in the left plot of Figure 3, showing the simulated  $s_u$  data when no site-specific tests are conducted. Let us consider a site investigation program consisting oedometer, CPTU, and SPT N tests. Suppose the test results show that OCR is within [9.5,13.1],  $N_{60}$  within [7,9], and  $q_T - \sigma_v$  within [1100kN/m<sup>2</sup>,1350kN/m<sup>2</sup>]. Based on the above information, the conditional samples of  $s_u$  can be easily obtained by filtering out samples satisfying  $OCR \in [9.5,13.1]$ ,  $N_{60} \in [7,9]$ , and  $q_T - \sigma_v \in [1100kN/m^2,1350kN/m^2]$  simultaneously from the population at large. The  $s_u$  values associated with this filtered set of (OCR,  $s_u$ ,  $N_{60}$ ,  $q_T - \sigma_v$ ) values are therefore the conditional  $s_u$  samples. The histogram of these conditional samples is

shown in the right plot of Figure 3. It is clear that the uncertainty in  $s_u$  is significantly reduced, given the information from better and/or more tests.

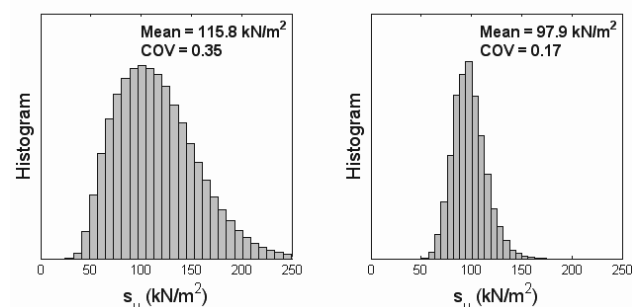


Figure 3. Histograms of the (conditional)  $s_u$  samples.

### 4 CONCLUSION

The construction of “virtual sites” are demonstrated in this paper using multivariate normal distributions calibrated from actual soil property databases. By doing so, it is possible to evaluate the reduction in the uncertainties associated with design parameters as a function of better and/or more tests. The practical goal is to establish an actual (not theoretical) link between the cost of a site investigation program and the potential design savings accrued from reliability-based design.

### 5 REFERENCES

Bolton, M.D. 1986. The strength and dilatancy of sands. *Geotechnique* 36(1), 65-78.

Ching, J., Phoon, K. K. and Chen, Y.C. 2010. Reducing shear strength uncertainties in clays by multivariate correlations. *Canadian Geotechnical Journal* 47(1), 16-33.

Ching, J. and Phoon, K.K. 2012a. Modeling parameters of structured clays as a multivariate normal distribution, *Canadian Geotechnical Journal* 49(5), 522-545.

Ching, J., Chen, J.R., Yeh, J.Y., and Phoon, K.K. 2012b. Updating uncertainties in friction angles of clean sands. *ASCE Journal of Geotechnical and Geoenvironmental Engineering* 138(2), 217-229.

Ching, J. and Phoon, K.K. 2013. Multivariate distribution for undrained shear strengths under various test procedures, submitted to *Canadian Geotechnical Journal*.

Ching, J., Phoon, K.K., and Lee, W.T. 2013. Second-moment characterization of undrained shear strengths from different test modes, to appear in *Geotechnical Special Publication honoring Professor F. H. Kulhawy*.

Goldsworthy, J.S., Jaksa, M.B., Fenton, G.A., Griffiths, D.V., Kaggwa W.S., and Poulos, H.G. 2007. Measuring the risk of geotechnical site investigations. *Proc. Geo-Denver 2007*, Denver.

Jaksa, M.B., Goldsworthy, J.S., Fenton, G.A., Kaggwa, W.S., Griffiths, D.V., Kuo, Y.L., and Poulos, H.G. 2005. Towards reliable and effective site investigations. *Géotechnique* 55(2), 109-121.

Ladd, C.C. and Foott, R. 1974. New design procedure for stability in soft clays. *ASCE Journal of Geotechnical Engineering Division* 100(7), 763-786.

Mesri, G. and Huvaj, N. 2007. Shear strength mobilized in undrained failure of soft clay and silt deposits. *Geotechnical Special Publication 173*, ASCE, Reston.

Phoon, K.K., Ching, J., and Huang, H.W. 2012. Examination of multivariate dependency structure in soil parameters. *GeoCongress 2012 – State of the Art and Practice in Geotechnical Engineering (GSP 225)*, ASCE, Reston, 2012, 2952-2960.

# Technique of reinforced soil base calculation under fall initiation in ground mass

## Technique du compte armé les raisons du sol à l'apparition des échecs à le massif du sol

Ponomaryov A., Zolotozubov D.  
Perm national research polytechnical university,

**ABSTRACT:** On the basis of carried out investigations, the authors obtained stress and strain development mechanisms of the reinforced ground mass depending on the properties of soils, the characteristics of the reinforcing elements, the depth of their location and their number. The obtained mechanisms allowed to propose the calculation methodology of the reinforced base surface settlement in the territories expose to deformation. To evaluate the proposed method, it was compared with previously obtained results of the experiments and calculations carried out with the help of BS8006, Giroud, Perrier, R.A.F.A.E.L methods and PLAXIS and Sofistik programs.

**RÉSUMÉ :** À la base des études accomplies les auteurs ont reçu les mécanismes du développement de l'effort et l'effort de la masse affermie de la raison en fonction des propriétés des sols, les particularités des éléments du renforcement, la profondeur de leur situation et leur nombre. Les régularités reçues ont permis de proposer la méthode du compte le dépôt de la surface des raisons armées sur les territoires exposés aux déformations. Pour estimer la méthode proposée, c'était en comparaison d'aparavant résultats acquis des expériences et calculs accomplis avec l'aide de BS8006, Giroud, Perrier, les méthodes R.A.F.A.E.L et PLAXIS et les programmes Sofistik.

**KEYWORDS:** reinforced soils, fall in ground mass, technique of calculation.

### 1 INTRODUCTION

When laying foundations of buildings and structures in areas prone to possible vertical deformations (for instance, karstic and technogenic dolines), it is necessary to provide measures to prevent emergency situations.

The choice of measures depends on the type of security – perfect or partial. When it is sufficient to provide only partial security, geosynthetic material reinforcement of a ground base is most commonly used. It is connected with the fact that ground reinforcement is more economical as compared with other methods. In the majority of case reinforcing of the bases by geosynthetic materials apply at building automobile and railways. Besides at building on karstic territories it is expedient to reinforce geosynthetic materials of the bases low-charged constructions, for example, low-rise buildings.

In Russia ground base reinforcement has not been used widely so far due to various factors, including both the increase in the cost of construction connected with the use of geosynthetics and sufficiently large amount of excavation works.

High quality geosynthetic materials themselves are not cheap, and large volumes of excavation arise from the need of a sufficiently deep placement of reinforcing layers. However, the use of local materials and a well-tried technology of reinforced base laying, as well as the increase in the safe upkeep of buildings, give a good economic effect.

### 2 EXPERIMENTAL INVESTIGATIONS

Effective use of geosynthetics for reinforcement under ground mass collapse is possible with the joint account of such factors as physical and mechanical properties of foundation soil, tensile properties of geosynthetics, the depth of reinforcing layers and their number. The optimal choice of these parameters requires rather complex calculations taking into account load – elongation dependences. The existing methods (the method outlined in the British Standard BS 8006, section 8.4 (BSI, 1995 – Fig. 1), the method of Giroud et al (1990), the method of Perrier (1985); R.A.F.A.E.L. – method (Blivet et al, 2002) do not consider the actual tensile force – relative deformation ratio.

They are applied for single-layer reinforcement. Being used to solve geotechnical problems, software packages that implement numerical methods give great inaccuracy, but at the same time they allow to calculate more quickly and check more types of reinforcement including those of multi-layer reinforcement.

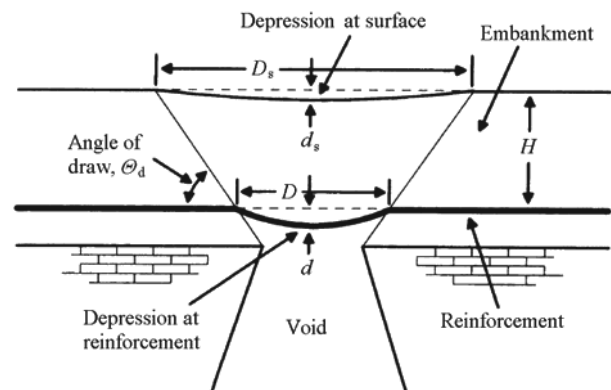


Figure 1. BS 8006: Parameters used to determine reinforcement.

The study of reinforced bases under ground mass collapse conducted by the authors allowed to obtain the mechanisms of stress – strain development in the reinforced ground mass depending on the foundation soil properties, the characteristics of the reinforcing elements, their depth and quantity. The results of S. Schwerdt's investigations were also used in the study.

On the basis of the mechanisms obtained we proposed the technique for calculating the reinforced base surface settlement in areas prone to deformation. As in the above-mentioned methods, the calculations were carried out for single-layer reinforcement, but at the same time the change in elongation of the geosynthetic reinforcing material depending on the load was taken into account. To do calculations using this method it is necessary to have load – elongation dependences which are obtained when testing geosynthetics at rupture, in accordance with ISO 10319:2008 (Fig. 2).

In the course of our studies we were doing experiments with account of the current Russian regulations enabling to apply tensile-testing machines to ensure the constant rate of bottom

clamp sinking, the constant strain rate or the fixed rate of load increase (similar to ISO 10319:2008) with relative error indications of breaking load  $\pm 1.0\%$ , with absolute error indications of elongation  $\pm 1.0\text{ mm}$ , with an average rupture duration regulated from  $(30 \pm 15)$  to  $(60 \pm 15)$  sec.

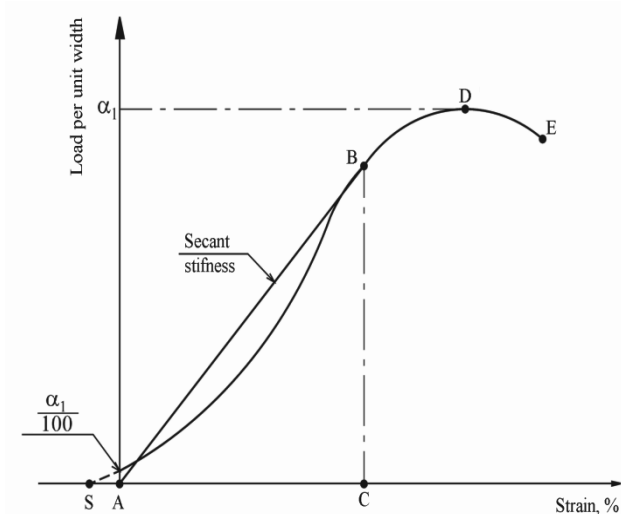


Figure 2. Typical load-elongation curve.

In practice, we had to build these relationships using the results obtained with the help of the tensile-testing machine that provided the constant rate of bottom clamp sinking (Fig. 3, 4).

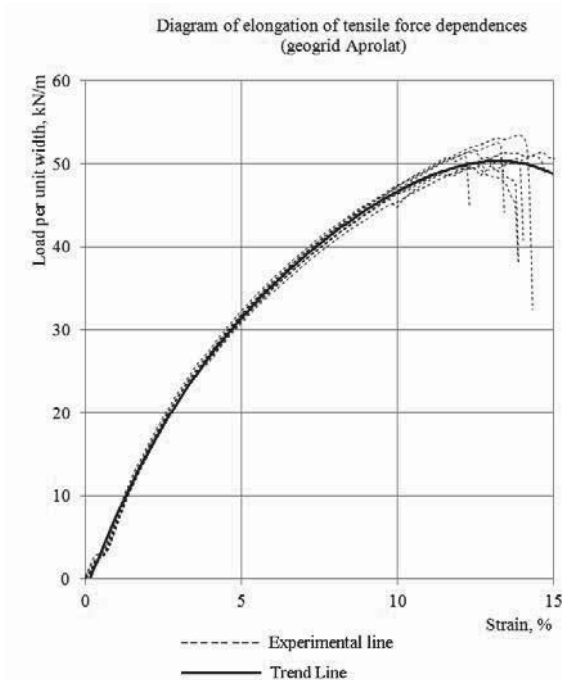


Figure 3. Example of elongation-load curve according to the test results.

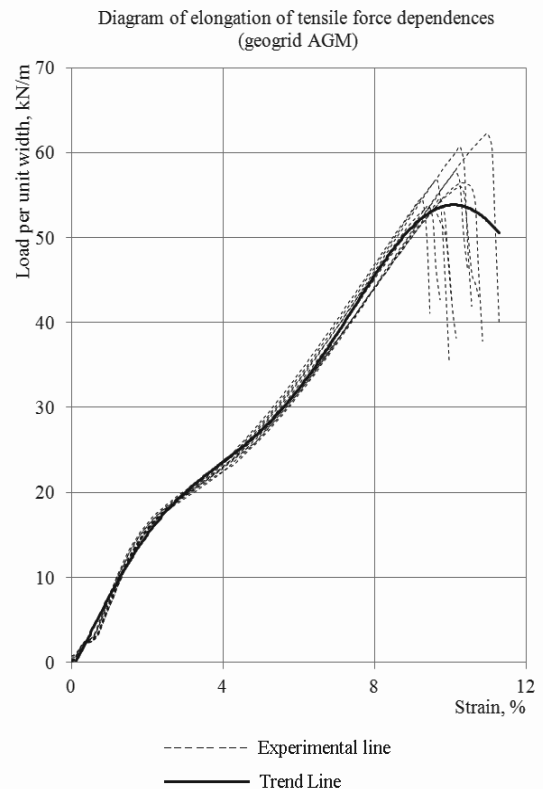


Figure 4. Example of elongation-load curve according to the test results.

The obtained dependences were used in the calculations done with the help of both numerical methods (PLAXIS program) and the developed technique.

### 3 TECHNIQUE OF REINFORCED SOIL BASE CALCULATION

The design scheme of the proposed method is shown in Figure 5.

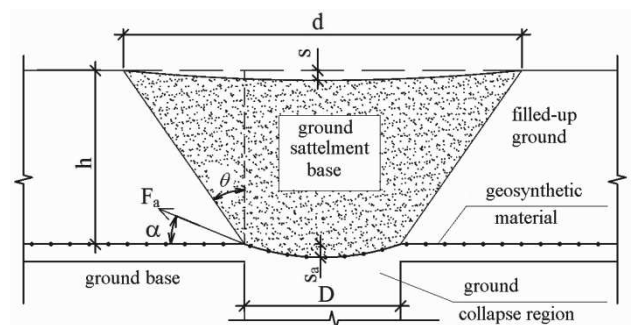


Figure 5. Design diagram of reinforced ground settlement under earth collapse.

In this method the following assumptions allowing to use formulas well-known in soil mechanics for the calculation of stresses in ground bases were made:

- the reinforced ground mass is in an equilibrium (stabilized) state before the ground collapse formation;
- the reinforcing layer is located in the homogeneous ground;
- the stress-strain state is considered at that moment when the marginal state of the ground mass is reached;
- the deformation form of the ground mass above the reinforcing interlayer has a sectional view of a trapezoid;
- the geosynthetic material does not stretch beyond the collapse region;
- the arch effect is not taken into account.

The algorithm for calculating the proposed technique is based on the tensile force dependence in the geosynthetics  $F_a$  on the size and shape of the collapse, the reinforcing interlayer depth, the surface load and geosynthetic material elongation. Our studies showed that the tensile force – elongation dependence is determined most accurately with the use of the formula similar to that in the BS 8006 standard

$$F_a = 0,5 \cdot k \cdot (\gamma \cdot h + q) \cdot D \cdot \sqrt{1 + \frac{1}{6 \cdot \varepsilon_a}}, \quad (1)$$

where  $k$  is the coefficient taking into account the supposed form of the collapse (for the rectangular collapse – plane problem – it is equal to 1). In the British standard BS 8006 the value of 0.67 for the axisymmetric case is given, but studies showed that higher convergence with the experimental results was obtained when  $k = 0.78$ ;  $\varepsilon_a$  is the specific elongation of the geosynthetic material depending on the tensile force in the reinforcing interlayer, which is determined according to the graphs (for example, as shown in Fig. 2);  $h$  is the depth of the reinforcing layer, m;  $\gamma$  is the specific weight of the ground, which is located above the reinforcing interlayer,  $\text{kN/m}^3$ . If there are ground layers having different specific weight values and located above the reinforcing interlayer, it is necessary to make the following replacement in the formula

$$\gamma \cdot h = \sum_{i=1}^n \gamma_i \cdot h_i \quad (2)$$

where  $n$  is the number of ground layers above the reinforcing interlayer,  $\gamma_i$  is the specific weight of the  $i$ -th ground layer,  $h_i$  is the height of the  $i$ -th ground layer;  $q$  is the equivalent surface load on the reinforcing layer,  $\text{kN/m}$ . Its calculation depends on the surface load amount by analogy with the calculation of the additional pressure (tension) in the ground mass, as well as on the load type, the load area-to-collapse region ratio, the surface load location with respect to the ground collapse;  $D$  is the collapse length (diameter), m.

The main problem when calculating by this method is that at the initial calculation stage we are aware of neither the tensile force  $F_a$ , nor the specific elongation of the geosynthetic material  $\varepsilon_a$  because the actual dependence of the elongation on the tensile load is not taken into account in the formula (1). That's why, we used the successive approximations method accurate to 5%. The received value  $\varepsilon_a$  is used to determine the maximum deflection  $s_a$  of the reinforcing material

$$s_a = \sqrt{3/8 \varepsilon_a D^2}. \quad (3)$$

To calculate the maximum ground surface settlement, the following formula is used,

$$s = \left( \frac{D}{2h \cdot \tan\theta} \right)^2 s_a, \quad (4)$$

where  $\theta$  is the inclination angle of the slip plane to the vertical. The values  $\theta$  depend on the characteristics of the backfill soil. Since it is necessary to determine the maximum surface settlement by the current Russian regulations, in practical calculations  $\theta = \varphi$  is taken. In case the ground layers located above the reinforcing interlayer have different  $\varphi$  values, the following value is used.

$$\theta = \bar{\varphi} = \frac{\sum_{i=1}^n \varphi_i \cdot h_i}{\sum_{i=1}^n h_i} \quad (5)$$

The obtained value of the surface settlement  $s$  is compared with the normative or design values for this construction

project. If the condition  $s \leq s_u$  is not satisfied, then a geosynthetic material with different characteristics is selected and the calculation is done again.

To evaluate the proposed method, its comparison with the results of the experiments and calculations performed by other methods (BS8006, Giroud, Perrier, R.A.F.A.E.L.) as well as PLAXIS and Sofistik programs was carried out. Due to the fact that we were not able to do model experiments in Russia, the data for comparison were taken from Schwerdt's works.

Table 1. Results of calculations

Calculation method	Tensile force in geosynthetic material, $\text{kN/m}$	Deflection of geosynthetic material, mm	Surface settlement, mm
Experiment	105	90	30
BS8006	64	240	30*
Giroud	215.5	90*	30*
Perrier	120	90	90
R.A.F.A.E.L.	95.8	120	–**
PLAXIS	103	160	–
Sofistik	113	130	–***
Proposed method	114.5	107	34

\*-These are initial data according to the indicated methods.

\*\*-Negative values are received.

\*\*\*-The Sofistik program does not allow to determine the surface settlement.

#### 4 REFERENCES

- Blivet et. al. 2002. Design method for geosynthetics as reinforcement for embankment subjected to localized subsidence. Delmas; Gourc; Girard (ed): *Geosynthetics 7*. ICG. Swets & Zeitlinger.
- BS 8006: 1995. *Code of Practice for Strengthened/Reinforced soil and Other Fill*, British Standard Institution. Section 8. Design of embankment with reinforced soil foundation on poor ground, 98–121.
- Giroud J.P., Bonaparte R.; Beech J.F. 1990. Design of Soil Layer-Geosynthetic Systems overlying Voids. *Geotextiles and Geomembranes*. 9Jg, H. 1., 11-50.
- Schwerdt, S. 2003. Die Ueberbrueckung von Erdeinbruechen unter Verwendung von einlagig verlegten Geogittern - Vergleich zwischen Versuchsergebnissen und den Ergebnissen von analytischen und numerischen Berechnungen. *Geotechnik*, 26, 95-105.
- Schwerdt, S., Naciri, O., Jenner, C.G. 2004. Performance of aggregates in geogrid-reinforced soils used for protection against surface collapse into underground voids. *EuroGeo 3: Geosynthetics conference*, Munich, Germany, 483-488.
- Pappiau Ch., Baraize E.; Perrier H. 1995. Motorway level fortification above carstic cavities. *Geotextiles – Geomembranes rencontres*. Tome 1, 93-99.
- Paul A., Schwerdt S. 2001. Untersuchungen zur Ueberbrueckung von Tagesbruechen und Erdfaelen durch Einbau einer einlagigen Geokunststoffbewehrung. *Proc. 7. Informations- und Vortragstagung Kunststoffe in der Geotechnik*. Muenchen, 251-257.
- Ponomaryov, A.B., Zolotozubov, D.G. 2010. Effect of reinforcing material depth on bearing capacity of foundation under ground collapse. *Herald of Civil Engineers*, 2 (23), 100-104.
- Zolotozubov, D.G., Ponomaryov, A.B. 2009. Structural protection of ground bases under collapse initiation in karst areas. *Herald of Volgograd State University of Architecture and Civil Engineering. Section: Construction and architecture* 15 (34), 15-18.



# Stress Concentration Ratio and Design Method for Stone Columns using 2D FEA with Equivalent Strips

Ratio de concentration de contraintes et méthode de conception pour les colonnes ballastées en utilisant une analyse aux éléments finis 2D avec des bandes équivalentes

Poon B., Chan K.  
GHD Geotechnics, 57-63, Herbert Street, Artarmon, NSW, Australia

**ABSTRACT:** This paper presents an approach for the prediction of vertical and horizontal displacements of soft ground treated with stone columns in a 2D finite element analysis (FEA). This involved modeling the columns as strips with appropriate strip width, spacing and smeared properties based on stress concentration ratio. Charts to assess the equivalent 2D column stress concentration ratio are provided for the design of full depth and floating columns under the influences of various key parameters. The accuracy of the proposed 2D strip model is investigated by comparing the results with a baseline 3D and axi-symmetric FEA. It is found that the proposed strip model is preferable over the conventional approach using composite block properties to represent the improved soil.

**RÉSUMÉ :** Cet article représente une approche pour la prédiction des déplacements verticaux et horizontaux de sols mous traités avec des colonnes ballastées par une analyse aux éléments finis (FEA) en 2D. Cela implique la modélisation des colonnes en tant que bandes avec une largeur de bande appropriée ainsi que l'espacement et les propriétés des zones d'influence basées sur le ratio de concentration de contrainte. Les graphiques pour évaluer le ratio 2D équivalent de concentration de contraintes sont donnés pour la conception des colonnes profondes et flottantes sous l'influence de divers paramètres. La précision du modèle de bande 2D proposé est étudiée en comparant les résultats avec une base en 3D et d'une analyse aux éléments finis axisymétrique. Il se trouve que le modèle de bande proposé est préférable à l'approche conventionnelle qui utilise les propriétés d'un bloc composite pour représenter le sol amélioré.

**ORDS:** Stone column, stress concentration, ground improvement, numerical analysis.

## 1 INTRODUCTION

Conventionally, the design of stone columns involves the prediction of settlements using a composite material approach in which equivalent strength and deformation parameters are derived using semi-empirical correlation to represent the entire improved soil. While these approaches have been accepted as reasonable methods for settlement prediction, they are less certain for the prediction of horizontal displacement. This paper presents a design approach where stone columns are idealised as equivalent strips in 2D finite element analysis (FEA). The stress distribution between the stone column and surrounding soil is essential for determining the strength parameter of the equivalent strips. A series of design curves for the stress concentration are presented to facilitate parameter derivation in practice. The accuracy of the 2D strip model is investigated by comparing the results with the 3D and axi-symmetric FEA.

## 2 IDEALISED 2D MODELLING APPROACH

For the modeling of stone columns in 2D FEA, the width of the stone column strips can be made to be equal to the width of an equivalent square for the cross-sectional area (Figure 1). The spacing of the strips is equal to the actual spacing,  $b$ , for square column arrangement and  $\sqrt{3}b/2$  for equilateral triangular arrangement. Mohr-Coulomb model is used for the stone columns with Poisson's ratio of 0.3, which is taken to be the same as the soil itself. The equivalent Young's modulus  $E_{eq}$  and the cohesion  $c_{eq}$  of the strips can be calculated based on weighted average approach as given by Eq 1.

$$E_{eq} \text{ (or } c_{eq}) = \frac{E_{soil} \text{ (or } c_{soil}) \cdot A_{soil} + E_{column} \text{ (or } c_{column}) \cdot A_{column}}{A_{soil} + A_{column}} \quad (1)$$

where  $A_{soil}$  and  $A_{column}$  are the areas of the soil and column inside a unit cell within the 2D strip as shown in Figure 1.

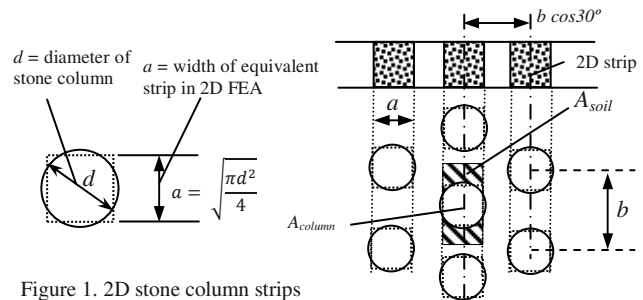


Figure 1. 2D stone column strips

The equivalent friction angle  $\phi_{eq}$  of the strips can be derived based on force equilibrium approach as given by

$$\tan(\phi_{eq}) = \frac{A_{soil} \tan(\phi_{soil}) + n \cdot A_{column} \tan(\phi_{column})}{A_{soil} + n \cdot A_{column}} \quad (2)$$

The determination of  $\phi_{eq}$  requires a presumption of stress concentration,  $n$ , which is defined as the ratio of the average applied vertical stress within stone column to the average applied vertical stress of the surrounding soil at the same level. Section 3 presents an appraisal for this parameter. Note that the present 2D FEA is an elasto-plastic analysis in which the decay of excess pore pressure with time was not taken into account.

## 3 STRESS CONCENTRATION OF STONE COLUMN

This section presents a series of elasto-plastic solutions in charts for the stress concentration ( $n$ ) of stone columns founded on (i) rigid boundary and (ii) infinite compressible soil materials. The solutions were obtained based on axisymmetric FEA using PLAXIS software programme for a "unit cell" consisting of a stone column and the surrounding soil within a column's zone of influence. Interface elements were introduced at the soil-column contact to allow for slippage. The interface strength was assumed to be 70% of the original soil strength ( $R_{int} = 0.7$  in PLAXIS). Note that the interface properties have minimal effect on the results as the stone column is in triaxial state.



3.1 Stone columns on rigid base

Figure 3b presents the calculated  $n$  with depth for a particular case where embankment load is applied on stone columns that are founded on rigid base. The selected column configuration and parameters are shown in Figure 2. Note that the embankment fill was modeled as soil elements and the arching stresses developed above the column have been accounted for in the FEA model.

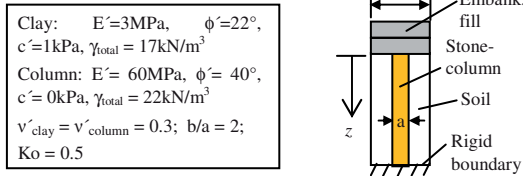


Figure 2. Stone column on rigid base

If the column and soil were appraised as elastic materials, the calculated  $n$  (dash line in Figure 3b) increases from 5 at the top of column, which is consistent with design chart solution provided in FHWA (1983) for embankment supporting columns, to about 14 at depth, which is commensurate with the equal strain solution (soil and column settle at the same rate at depth) given by Balaam and Poulos (1982).

When the column and soil are modeled as Mohr-Coulomb materials, yielding elements begin to form at the column top after a small load (~20kPa) is applied, leading to a reduction in stress concentration. The yielding of the column (hence the reduction of  $n$ ) progresses downwards through the column as the applied load level increases (see the solid curves in Figure 3b). Figure 3a shows the stress state of the unit-cell model after the application of maximum embankment load. It indicates that most yielding elements are confined within the column periphery. The soil is generally elastic and therefore the soil friction angle has little influence on the solution.

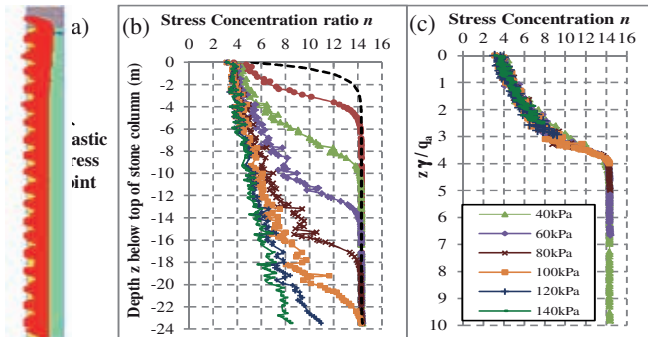


Figure 3. Stone column with rigid base (elasto-plastic solution)

Figure 3c shows a normalised plot in which the depth of the column,  $z$ , was normalized by  $q_a/\gamma$ , where  $q_a$  is the applied fill stress and  $\gamma$  is the total unit weight of the soil. It is found that the normalised stress concentration curves for the different load levels ( $\geq 40$ kPa) lie on a single curve. The turning point of the normalized curve corresponds to the transition from the upper yielding zone to the lower non-yielding zone, which occurs at different  $z$  for the different  $q_a$ . For example, point A in Figure 3c occurs at  $z/\gamma a = 4$ . When  $q_a = 40$ kPa and  $\gamma = 17$ kN/m<sup>3</sup>,  $z = 9.5$ m (B in Fig 3b). Conversely, when  $q_a = 60$ kPa,  $z \approx 14$ m (Point C).

Figure 4 presents a series of normalised curves for the  $n$  value under different modulus ratios, column spacing and friction angles of the stone column. For a given column spacing ratio and friction angle, the stress concentration is higher for higher modulus ratio  $E_c/E_s$ . Conversely, for the columns with a given modulus ratio, the extent of the yielding zone, and hence the reduction of stress concentration, is greater as the spacing ratio increases even though the maximum stress ratio in the columns is ultimately similar. This occurs because there is less confinement for the spaced columns, leading to greater yielding zone and stress reduction within columns. A comparison of the corresponding curves in Figures 4a and 4b shows that the loss

of stress concentration due to yielding is more severe for column material having a lower angle of internal friction.

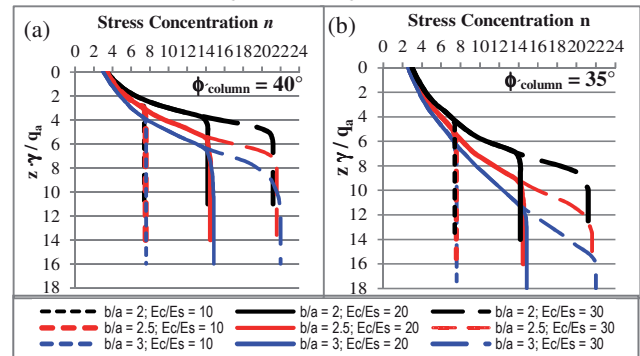


Figure 4. Stone column with rigid base

3.2 Stone columns on compressible soils (elastic appraisal)

For stone columns founded on compressible soil, the elastic FE solution has indicated that there exists a lower equal settlement plane, below which the columns move more than the soil to mobilise positive skin resistance of the soil. More load is transferred from the column to the surrounding soil and therefore the stress concentration  $n$  reduces (see Figure 5a).

Figure 5b shows a plot of normalised distance from the column base  $y/a$  ( $y$  and  $a$  defined in inset in Figure 5b) versus stress concentration reduction ratio  $r (= n/n_{max})$  for the corresponding elastic FEA results given in Figure 5a. The  $n_{max}$  is the maximum computed  $n$  value based on elasticity as shown in Figure 5a. The FEA results for  $r$  near the column base can be approximated by the following logarithmic relationship.

$$r = 1 - \frac{1}{m} \left[ \log \left( \frac{\xi}{y/a} \right) \right] \quad (\text{for } y/a \leq \xi) \quad (3)$$

where  $\xi$  is the influenced zone (also normalized by the column diameter  $a$ ) that is measured from the base of the column to the equal settlement plane (where  $r = 1$ ). The magnitude of  $m$  controls the rate of reduction of  $r$  with  $y/d$ . The higher the  $m$  the more rapid reduction of  $r$  would be towards the column tip.

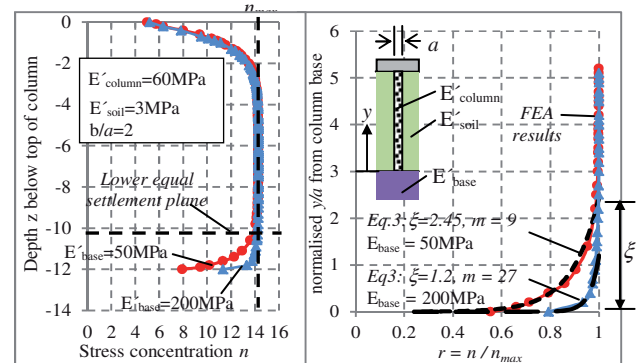


Figure 5. Stone column with compressible base -elastic solution

Figure 5b indicates that as the Young's modulus  $E_{base}$  of the soil beneath the columns increases, the extent of  $\xi$  reduces. Also, the ratio  $r$  reduces more rapidly towards the column tip (i.e.  $m$  increases) as  $E_{base}$  increases. Figure 6 presents the computed  $\xi$  and  $m$  for the different  $E_{base}/E_{column}$  and  $E_{base}/E_{soil}$  ratios based on elastic FEA. The following points can be drawn:

- The influenced zone  $\xi$  at the column base reduces as  $E_{base}/E_{column}$  increases. The reduction may be approximated by a straight line in  $\xi$  vs.  $\log(E_{base}/E_{column})$  plot. Curves 1 and 4 in Figure 6a delineate such relationships for column spacing  $b/a$  of 3 and 2, respectively. A curve in between representing  $b/a = 2.5$  has not been shown for clarity of the figure. Note that these curves can apply to cases where  $E_{base}/E_{soil} \geq 10$  as  $E_{soil}$  has negligible effect on the shape of  $r$  under this condition. For a particular  $b/a$  ratio, the  $\xi$  shows a

lower value as  $E_{base}/E_{soil}$  reduces to less than 10, although the trend of reduction with  $\log(E_{base}/E_{column})$  remains linear and parallel with that for  $E_{base}/E_{soil} \geq 10$  (curves 2 & 3, 5 & 6 in Figure 6a).

- The rate of reduction of  $r$  towards the column tip, represented by the  $m$ , has been found to increase linearly with  $E_{base}/E_{column}$ . Curve 7 in Figure 6b shows such relationship and is applicable for cases with different  $b/a$  ratio up to 3 (limit of parametric range) and with  $E_{base}/E_{soil} \geq 10$ . Curves 8 and 9 delineate the corresponding curves for cases with  $E_{base}/E_{soil} = 2$  and 1.

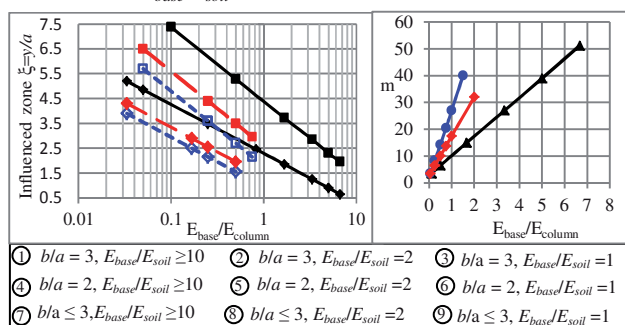


Figure 6. Stone column with compressible base -elastic solution

### 3.3 Stone columns on compressible soils - elasto-plasticity

The effect of compressible base on stress concentration  $n$  is now discussed based on Mohr Coulomb model. In particular, the soils surrounding and below the stone columns have been appraised alternatively using (i) effective shear strength ( $c, \phi$ ) and (ii) undrained shear strength  $s_u$ .

Figure 7a shows the computed  $n$  under different fill loads for the same case as in Figure 2, except that the column is founded on compressible soil that is represented by  $c-\phi$  materials. The stress concentration curves initially follow identical paths as those shown in Figure 3b until they intercept the lower equal settlement plane and thereafter trace along the curve of the elastic solution at the column base. To explain this stress transfer mechanism, the material stress state of the model at the end of simulation (under 140kPa fill stress) is presented (inset in Figure 7a). As before, yielding of the column follows a top-down process. While there is significant yielding of the column due to high stress ratio, there is little yield in the surrounding soil especially towards the column base because of sufficient confinement even with an adopted soil friction angle as low as  $22^\circ$ . Since the soil is elastic, the reduction of  $n$  due to the compressible elastic base soil can be superimposed directly onto the aforementioned reduction due to yielding of column.

Figure 7b presents the results for the case where  $s_u = 30\text{kPa}$  has been adopted for the soils surrounding and below the column. Significant yielding occurs in the soils, which has altered the shape of the stress concentration curves towards the column base as compared to that of the  $c-\phi$  soils. However the differences are not great and for the purpose of assessing  $n$ , the problem can be idealised by assuming that there is no failure in the surrounding soil so that its behavior is essentially elastic.

### 3.4 Procedure for assessing stress concentration

The following procedure for assessing the stress concentration of the stone columns under fill embankment may be proposed:

**Step 1** – Assessing the stress concentration  $n$  along column depth by using charts such as Figure 4, which have accounted for the influence of load level, column spacing, modulus ratio of column and surrounding soil, and yield of the stone column.

**Step 2** – Assess the influence of the compressible base soil on  $n$  based on elasticity by the following equation:

$$n = n_{max} \times r \quad (4)$$

where  $r$  is the stress concentration reduction ratio given in Eq. 3, which is a function of  $\xi$  and  $m$  given in Figure 6.  $n_{max}$  is the maximum elastic  $n$  value below the turning point of each normalised  $z/\gamma q_a - n$  curve in Figure 4.

**Step 3** – Superimpose the solution from Step 2 onto that of Step 1. Thereby, the final  $n$  along the depth of the column is the lower of the two solutions at the same depth.

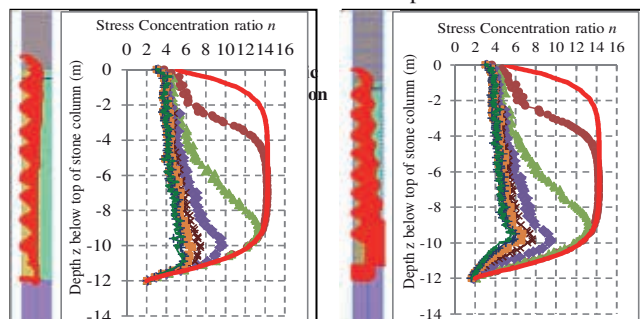


Figure 7. Stone column on compressible (a)  $c-\phi$  and (b)  $s_u$  soil

## 4 COMPARISON WITH FULL 3-D MODELLING

The accuracy of plane strain idealisation of stone columns using equivalent strips in 2D FEA was investigated under self-weight load imparted by a 6m high embankment with 2H:1V batter. The analyses undertaken for the investigation include: *Analysis 1* - Full 3D FEA of embankment over stone columns modeled by solid elements; *Analysis 2* - Axisymmetric FEA of a unit cell consisting stone column; *Analysis 3* - 2D plane strain FEA with the stone columns modeled as strips; and *Analysis 4* - 2D FEA with the soil and columns modeled as equivalent block. The 2D and 3D FEA were carried out using software programme PLAXIS 2D and PLAXIS 3D, respectively.

Table 1 summarises the adopted parameters for all analyses. The 3D FEA is considered a baseline model that comprises a 13m long segment of embankment over soft clay treated with stone columns which are founded on compressible soil. The analysis was repeated with the 0.9m diameter stone columns spaced at 1.7m, 2m and 2.5m in triangular pattern. The 3D FE mesh is shown in Figure 8. The stone columns are modeled using 15 nodes wedge element with interface elements at the column-soil contact. Two cases of interface strength of 100% and 67% of the surrounding soil strengths have been considered.

Table 1. FEA Model Parameters

Analysis	$b/d$	$a_r$	Stone Column Parameters
1,2 3D FEA	2.0,	0.26,	$E_{col}=50\text{MPa}, c_{col}=0\text{kPa}, \phi_{col} = 40^\circ$
	2.3,	0.19,	
	2.9	0.12	
3 - 2D FEA (strips)	2.0	0.26	$E_{strip}=26\text{MPa}, c_{strip}=1\text{kPa}, \phi_{strip} = 36.5^\circ - 38^\circ$ along shaft ; $= 35.5^\circ$ near base
	2.3	0.19	$E_{strip}=22\text{MPa}, c_{strip}=1\text{kPa}, \phi_{strip} = 35.5^\circ - 37^\circ$ along shaft ; $=34^\circ$ near base
	2.9	0.12	$E_{strip}=18\text{MPa}, c_{strip}=1\text{kPa}, \phi_{strip} = 34.5^\circ - 35.5^\circ$ along shaft; $= 33^\circ$ near base
4 - 2D FEA (equiv. block)	2.0	0.26	$E_{block}=6\text{MPa}, c_{block}=1\text{kPa}, \phi_{block} = 30^\circ$
	2.3	0.19	$E_{block}=6\text{MPa}, c_{block}=1\text{kPa}, \phi_{block} = 30^\circ$
	2.9	0.12	$E_{block}=6\text{MPa}, c_{block}=1\text{kPa}, \phi_{block} = 30^\circ$

Soil surrounding columns are  $E_{soil} = 3\text{MPa}, c_{soil} = 2\text{kPa}, \phi_{soil} = 26^\circ$ ;

Soil beneath columns are  $E_{base} = 3\text{MPa}, c_{soil} = 5\text{kPa}, \phi_{soil} = 28^\circ$

In Analysis 3, a 2D plane strain idealisation of the stone columns using equivalent strips was investigated. The strips are divided into several segments, each of which has different strength properties that correspond to the varying stress concentration along the column depth. The dimension and spacing of the 2D strips are as per those outlined in Figure 1.

Analysis 4 presents a conventional 2D approach in which the entire treated soil is represented by a single block with the

equivalent properties,  $\phi_{block}$ ,  $c_{block}$  and  $E_{block}$  derived based on the semi-empirical relationships given by Madhav, 1996.

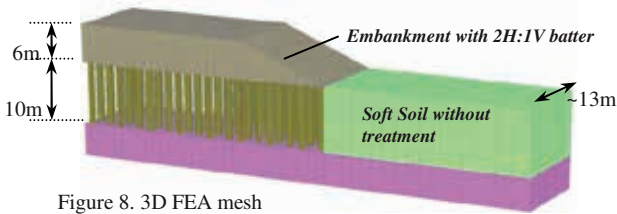


Figure 8. 3D FEA mesh

The baseline 3D model (Analysis 1) and the 2D strip model (Analysis 3) show similar deformation mechanisms of the stone columns, which can be broadly divided into three zones (see Fig 9a, 9b): Zone 1 away from the fill batter where columns underwent vertical deformation by “bulging”; Zone 2 just behind the crest of the fill batter where columns underwent both vertical and horizontal deformation by “bulging” and “leaning”; and Zone 3 beneath the fill batter where columns underwent mainly leaning. This numerical prediction of the deformation appears to be consistent with the results of the centrifuge model test carried out by Stewart and Fahey (1994). The maximum settlement of the embankment occurs in Zone 2 just before the crest of the fill batter (more than that in Zone 1). This is presumably due to the concurrence of bulging and leaning deformation mechanisms of the stone columns. Conversely, the columns in Zone 3 exhibit the maximum horizontal displacement and are likely due to the prevailing leaning deformation of the stone columns.

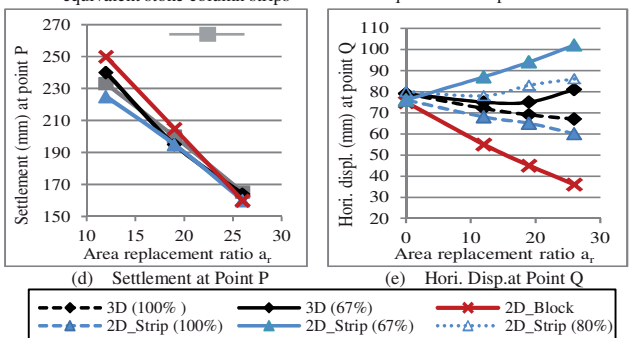
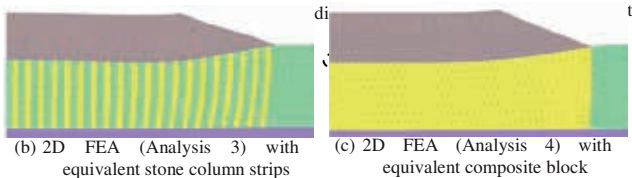
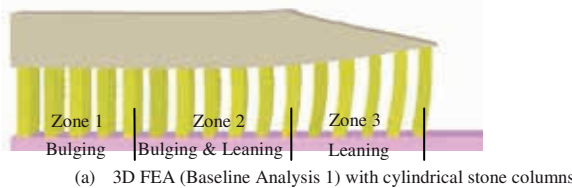


Figure 9. Comparison of FEA results

Figure 9c presents the deformation predicted by the conventional 2D FEA using composite block material (Analysis 4). This method is unable to capture the bulging and leaning deformation of the stone columns. The maximum settlement occurs at the centre of the embankment (i.e. in Zone 1) as opposed to in Zone 2 as predicted by the baseline 3D FEA and the proposed 2D FEA using equivalent strips.

Figure 9d shows a plot of predicted settlements at points P versus area replacement ratio  $a_r$ . All analyses give comparable results, indicating that all the different FE methods are commensurable in terms of settlement prediction under axially symmetric load condition.

Figure 9e presents the predicted horizontal displacement at point Q. The following points are drawn from the results:

- When original soil strengths are used for the interface properties, the result of the 2D strip model (curve 1) compares well with that of the 3D baseline model (curve 2). Both results show a trend of reducing horizontal displacement with  $a_r$ .
- When the interface strength of the columns in the 3D model are reduced to 67% of the soil strengths, the result (curve 3) indicates an initial drop off in horizontal displacement with  $a_r$ , but increases again once  $a_r > 20\%$ . This is due to increasing proportion of yielding elements in the remolded soil as the columns draw closer to each other.
- The application of the same interface strength reduction (67% of surrounding soil strength) in the 2D equivalent strip model has caused excessive yield in the remolded soil and led to increased horizontal displacement with  $a_r$  (curve 4). A better fit to the 3D solution is by changing the interface strength to 80% of the surrounding soil strength (curve 5). Evidently, there needs a regime to determine an equivalent interface strength for the strip model. This merits further research.
- The 2D block model result (curve 6) under-predicts the horizontal displacement when compared with the 3D baseline model predictions. This indicates that the use of isotropic soil properties in the 2D block model, which were derived based on semi-empirical relationships originally for settlement prediction under axially loading condition, have overestimated the reduction in lateral spreading underneath the embankment batter. The use of equivalent strips in the 2D strip model is able to capture the interaction between the soil and the stone column, leading to a better agreement for the lateral deformation with the 3D baseline solution.

## 5 CONCLUSIONS

This paper presents a 2D FEA approach for analysing the response of stone columns under embankment loading. The stone columns are modeled as equivalent strips with the  $c_{eq}$  and  $E_{eq}$  of the strips calculated based on weighted average area approach, and the  $\phi_{eq}$  derived based on force equilibrium method, which requires a presumption of stress concentration ratio of the stone column. For convenience, charts to assess the stress concentration ratio have been generated for full depth and floating stone columns. The solutions cover key parameters including load levels, column spacing ratio,  $E_{column}/E_{soil}$  ratio  $E_{base}/E_{column}$  ratio,  $E_{base}/E_{soil}$  ratio and column friction angles.

The accuracy of the proposed 2D strip model has been investigated by comparing the results of the 3D baseline FEA and the conventional composite approach. It has been shown that the proposed strip model is preferable over the conventional approach for the prediction of horizontal displacement. However, further research is needed to develop a regime to determine equivalent interface strength in the 2D strip method.

## 6 REFERENCES

Balaam, N.P. and Poulos, H.G. 1982. The behavior of foundations supported by clay stabilized by stone columns. *Proc. 8th European Conf. on Soil Mechanics and Foundation Engineering, Helsinki*.  
 FHWA. 1983. U.S. Department of Transportation Federal Highway Administration (Dec, 1983) – *Design and Construction of Stone Columns*, Vol 1. Report No. FHWA/RD-83/026.  
 Madhav, M.R. and Nagpure, D.D. 1996. Design of granular piles for embankments on soft ground. *Proc. 12th SE Asian Geot. Conf.*, Kuala Lumpur. 1: 285-290  
 Stewart, D.P. and Fahey, M. (1994). Centrifuge modelling of a stone foundation system, Seminar on ground improvement techniques, Perth, Curtin Printing Services, 1: pp 101-111.

# Porosity/cement index to evaluate geomechanical properties of an artificial cemented soil

## Le paramètre porosité/ciment pour l'évaluation des propriétés géomécaniques d'un sol cimenté artificiellement

Rios S., Viana da Fonseca A.  
*Faculty of Engineering of the University of Porto*

**ABSTRACT:** This paper highlights the importance of the porosity/cement index on the evaluation of the geomechanical properties of soil-cement mixtures as a contribution to analyse these materials. This index is defined as the ratio between porosity and volumetric cement content combining the degree of compaction with the cement content. The relevance of these two parameters is defined by an exponent to the volumetric cement content which changes with the type of soil. This paper results from a broad experimental program with unconfined compression tests, indirect tensile tests, triaxial tests and oedometer tests, which were all analysed by this index adjusted by a specific exponent value. The (tensile and compression) strength, the (elastic and initial tangent) stiffness, as well as the compressional behaviour are conveniently represented by this index and a different behaviour is observed when this index is changed.

**RÉSUMÉ :** L'importance du paramètre porosité/ciment dans l'évaluation des propriétés géomécaniques des mélanges sol-ciment est présentée dans cet article comme une contribution pour l'analyse de ces matériaux. Ce paramètre est défini comme le rapport entre la porosité et la teneur volumique en ciment. L'importance relative entre la porosité et la teneur en ciment est introduite en introduisant un exposant à la teneur volumique en ciment dépendant du type de sol. Les résultats d'un vaste programme expérimental incluant essais de compression simples, essais de traction indirect, essais triaxiaux et essais œdométriques sont présentés et analysés par ce paramètre ajusté par un exposant spécifique. La résistance à la compression et à la traction, la rigidité élastique et tangente initiale, ainsi que le comportement en compression sont bien représentés par l'intermédiaire de ce paramètre et un comportement différent est observé si le paramètre est modifié.

**KEYWORDS:** soil-cement, porosity/cement index, tensile strength, compression strength, compressional behaviour.

## 1 INTRODUCTION

Soil-cement mixtures are very interesting for the construction of road and railway platforms, especially in the noble layers of subgrade as well as in transition zones between embankment and concrete structures, where good mechanical properties are required. This solution, not only concurs to improve those characteristics, but also leads to a significant reduction in the economic and environmental costs of these works. Despite these advantages this method has not a generalized application in Portugal due to the lack of design methodologies based on mechanical parameters.

There are several factors affecting the behaviour of cemented soils, such as the type of cement and cement content, the curing time and stress, the water content and porosity. Seeking for a ratio that would reflect the influence of some of these parameters Consoli et al. (2007) presented an index property defined as the ratio of porosity to the volumetric cement content, called porosity/cement ratio ( $n/C_{iv}$ ). Some previous attempts have been made, such as the degree of cementation proposed by Chang and Woods (1992) that concerns the percentage of voids filled with cement, being this parameter developed for sands. Lorenzo and Bergado (2004) have also presented the ratio of the after curing void ratio to the cement content ( $e_o/A_w$ ) proving to be quite interesting for clay mixtures with high values of water and cement content.

Another available parameter is the water/cement ratio used for concrete. However, soil-cement mixtures for road or railway platforms are usually cured in a non saturated condition, which makes the previous ratio inadequate in the analysis of these mixtures behaviour. The main difference between soil-cement mixtures and concrete (besides the cement content) is that during the curing of concrete all voids are completely full of

water and therefore concrete stress-strain behaviour is not dependent on the void ratio but on the water content. In opposition, soil-cement mixtures currently executed in embankments and transport platforms have curing water content lower than the saturation water content and so their compressibility will be related to its porosity. Moreover, while concrete has an almost linear behaviour for a wide range of deformations, soil-cement mixtures have a clear non-linear behaviour since very small strains as a result of the progressive degradation of the cemented structure. Therefore, even if the soil-cement mixture is saturated after the maximum strength has been achieved (i.e. after curing) the curing void ratio still has a very important role on the mechanical behaviour of the mixture.

The influence of the porosity/cement ratio on strength and stiffness parameters is described in Consoli et al. (2012) providing the comparison between two different materials mixed with Portland cement: well graded Porto silty sand and uniform Osorio sand. An advance analysis on the compression and shearing behaviour of cemented Porto silty sand through this parameter is described in Rios et al. (2012).

This paper summarizes some geomechanical properties of cemented Porto silty sand through this index in terms of strength (unconfined, tensile and triaxial), stiffness (initial tangent and unload-reload) and one-dimensional compression.

## 2 MATERIALS AND SPECIMEN PREPARATION

A well graded soil, classified as silty sand (SM) in the unified classification system (ASTM, 1998) was used in this study. The soil is derived from weathered Porto granite which is abundant in Northern Portugal (Viana da Fonseca et al., 2006). Its particle specific gravity is 2.72, and it contains around 30% fines,



although a low plasticity index was obtained ( $I_p = w_L - w_p = 34\% - 31\% = 3\%$ ). From the particle size distribution curve presented in Figure 1 an average diameter  $D_{50}$  equal to 0.25 mm was obtained, as well as uniformity and curvature coefficients of 113 and 2.7 respectively. A high strength Portland cement (CEM I 52.5R) of grain density equal to 3.15 was used as the cementing agent in order to speed up the laboratory tests.

The experimental program is performed with specimens made by the mixture of silty sand, Portland cement and tap water that is compacted statically in three layers in a stainless steel mould. For each specimen, a quantity of fines equal to the weight of cement to be introduced was removed from the soil, in order to have the same grain size distribution curve in the mixture of soil-cement as in the soil itself. Following this procedure the dry density of the soil was also constant throughout the study even though the cement content changed. The specific gravity of the cement-soil mixture was calculated as a weighted average of those of the soil ( $G_s = 2.72$ ) and of the cement ( $G_s = 3.15$ ), and thus it was different for different cement contents.

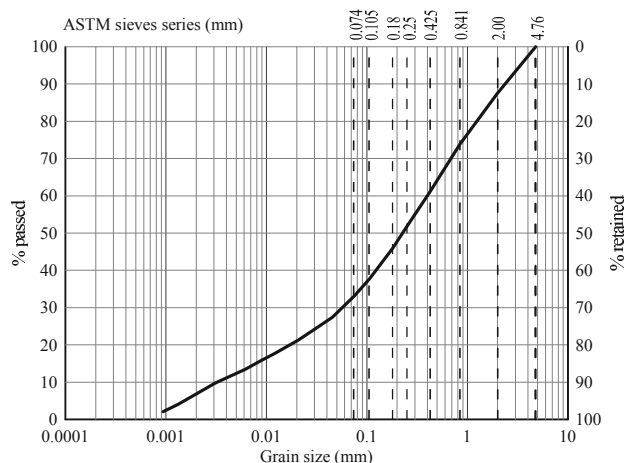


Figure 1. Grain size distribution curve

### 3 STRENGTH PARAMETERS

#### 3.1 Unconfined compression strength

Strength properties of the cemented sand were evaluated in different ways by means of unconfined compression tests, indirect tensile tests, as well as triaxial tests. First, several specimens moulded to have different cement contents (2%, 3%, 5% and 7%) and dry unit weights (16.4, 17.2, 18.0 and 18.8 kN/m<sup>3</sup>) were tested in unconfined compression in a total of 16 tests. In these tests, the water content was kept equal to 12%. The representation of the unconfined compression strength (UCS) and the ratio of porosity to the volumetric cement content ( $n/C_{iv}$ ) revealed that some adjustment was needed and therefore, an exponent was added to  $C_{iv}$ . This exponent was defined as the value that provides the best correlation coefficient with the data, which, for this material, was found to be 0.21 – Eq. (1).

$$UCS \text{ (kPa)} = 4E+09 (n/C_{iv}^{0.21})^{-4.296} \quad (1)$$

This exponent seems to depend on the type of soil as other authors have found different coefficients when working with different soils (Consoli et al., 2007, 2011): an exponent of 0.28 was found in a residual soil from sandstone (Botucatu soil), while a value of 1.0 was found in an uniform sand (Osorio sand). Based on this parameter, named adjusted porosity/cement ratio ( $n/C_{iv}^{0.21}$ ), the results of different tests were analysed.

#### 1.1 Tensile strength

Taking into account the possibility of shrinkage in cemented materials, the evaluation of the tensile strength is of utmost importance. In that sense, indirect tensile tests following the standard EN 13286-42 (CEN, 2003) were performed on similar specimens whose results were plotted against  $n/C_{iv}^{0.21}$  for which Eq. (2) was obtained,

$$R_{tb} \text{ (kPa)} = 2E+09 (n/C_{iv}^{0.21})^{-4.719} \quad (2)$$

The results showed that the indirect tensile strength ( $R_{tb}$ ) was about 11% of the UCS. In Figure 2 both  $R_{tb}$  and UCS are plotted against  $n/C_{iv}^{0.21}$  in different scales for comparison. It is clear that both trends are very similar (except for the absolute values) corroborating the convenience of the adjusted porosity/cement ratio.

In Consoli et al. (2011), where the data from these tests is plotted together with data from other two soils, it is shown that for the three soils a decrease in porosity promotes an increase in the tensile strength as a consequence of the higher number of contact points between particles which improves the cementation. Also for the other two soils, a unique correlation was found between the adjusted porosity/cement ratio and the indirect tensile strength, the exponent of the ratio depending on the soil.

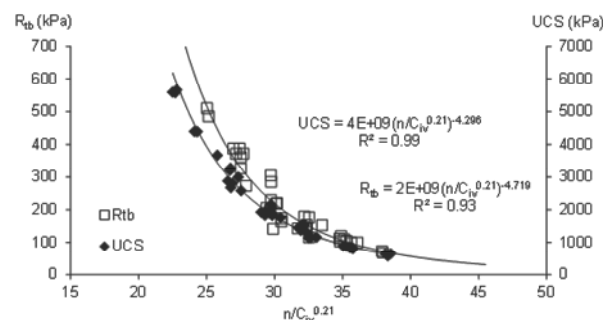


Figure 2. Indirect tensile strength and unconfined compression strength against the adjusted porosity/cement ratio

#### 3.2 Triaxial tests

Drained triaxial compression tests were performed over soil-cement specimens, which were moulded to have two different adjusted porosity/cement ratios ( $n/C_{iv}^{0.21} = 36$  and 29) corresponding respectively to UCS of 800 kPa and 2000 kPa. For these ratios, two moulding conditions were defined characterized by cement content and dry unit weight while the water content remains constant and equal to 12%. For the first ratio ( $n/C_{iv}^{0.21} = 36$ ), 2 and 4% cement contents were considered which lead to dry unit weights of 16.7 and 15.4 kN/m<sup>3</sup>, respectively. For the second ratio ( $n/C_{iv}^{0.21} = 29$ ) higher strength was needed, so 5 and 7% of cement contents were assumed with 17.0 and 16.4 kN/m<sup>3</sup> of dry unit weight. The tests were performed at three different effective confining pressures (30, 80 and 250 kPa) over specimens moulded in four moulding points, comprising 12 tests (Table 1).

The stress-strain curves (see Figure 3 as an example) clearly evidence that the specimens with  $n/C_{iv}^{0.21} = 29$  have higher peak deviator stresses than the specimens with  $n/C_{iv}^{0.21} = 36$  independently of the cement content. Adding cement to the sand had the effect of increasing the shear strength by up to five times for the adjusted porosity/cement ratio of 36 and tenfold for the adjusted porosity/cement ratio of 29. All specimens initially compressed, followed by significant dilation, which was associated to a peak strength, before strain softening. This is typical of cemented soils, with the maximum rate of dilation taking place right after the peak strength (Viana da Fonseca 1998). The peak strength corresponds to the onset of significant

breakage in the cement, while dilation involves particle rearrangement that is only possible after bonding breakage. Assuming only compressive volumetric deformations up to the point of zero dilation, beyond this point yielding exists, which indicates that the onset of cement breakage is progressive starting even before peak. However, being the peak strength not frictional but controlled by the cement yielding, then most destructuration may take place only at peak.

Table 1. Moulding conditions of the specimens for the triaxial tests

Moulding Point	%C	$\gamma_d$ (kN/m <sup>3</sup> )	$e_0$	w (%)	$n/C_{iv}^{0.21}$	UCS (kPa)	$\sigma'_c$ (kPa)
1	2	16.6	0.61	12	36	800	30
	2	16.5	0.62	12	36	800	80
	2	16.7	0.60	12	36	800	250
2	4	15.4	0.74	12	36	800	30
	4	15.7	0.71	12	36	800	80
	4	15.5	0.73	12	36	800	250
3	5	16.9	0.59	12	29	2000	30
	5	17.0	0.58	12	29	2000	80
	5	17.0	0.58	12 <td 29	2000	250	
4	7	16.3	0.66	12	29	2000	30
	7	16.5	0.63	12	29	2000	80
	7	16.7	0.61	12	29	2000	250

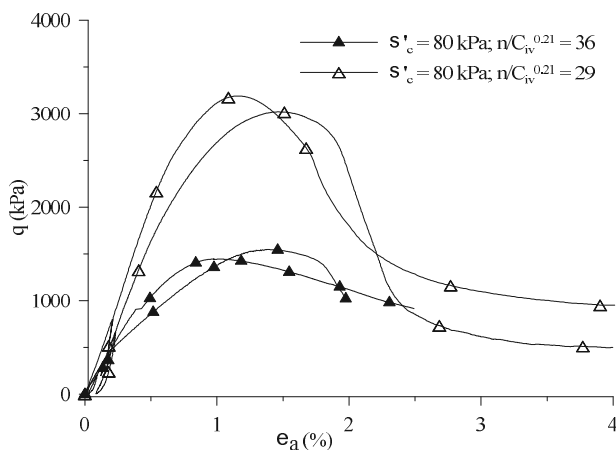


Figure 3. Stress-strain curves for the confining pressure of 80 kPa.

All the cemented specimens tested in triaxial tests suffered strain localisation. Therefore, it becomes difficult to rely on the local instrumentation at strain levels close and after the peak, but especially at ultimate conditions. In that sense, the stress invariants such as the deviator stress ( $q$ ) and the mean effective stress ( $p'$ ) were not considered representative of the stress state and thus, the stresses acting on the shear plane were calculated by the procedure used by Gasparre (2005) based on the Mohr circles and taking into account the post rupture analysis described by Burland (1990).

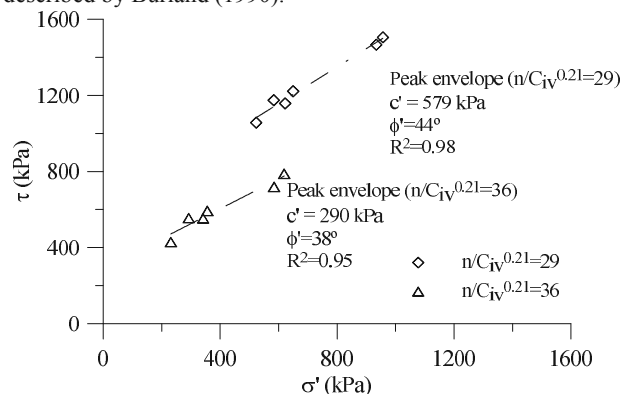


Figure 4. Peak strength envelopes by adjusted porosity/cement ratio.

In Figure 4 the stresses acting on the plane are plotted on a ( $\sigma'$ ,  $\tau$ ) graph for peak conditions from which the correspondent strength parameters were obtained. The points are assigned to each adjusted porosity/cement ratio ( $n/C_{iv}^{0.21}$ ) expressed before. It is interesting to notice that for peak conditions two strength envelopes were obtained depending on the index ratio. The adjusted porosity/cement ratio influences the peak angle of friction and cohesion intercept, being the peak envelope for the index  $n/C_{iv}^{0.21}=29$  higher than that for the index equal to 36. This could have been predicted from moulding characteristics as each ratio corresponds to different UCS.

## 4 STIFFNESS PARAMETERS

### 4.1 Initial tangent stiffness

The unconfined compression tests were performed with local measurement of deformation using LDT's and so the stiffness modulus could be evaluated. An initial tangent modulus ( $E_{ti}$ ) was then calculated based on the linear part of the stress-strain curve. Plotting this modulus against the adjusted porosity/cement ratio for the 16 tests presented above, as Figure 5 shows, it can be concluded that the general adjustment of the data is quite reasonable.

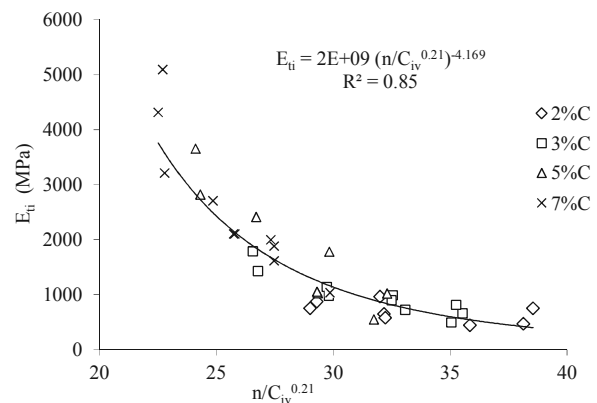


Figure 5. Indirect tensile strength and unconfined compression strength against the adjusted porosity/cement ratio

As expected, stiffness parameters are more scattered than strength parameters because strain measurements are always more sensitive to non-homogeneities of the specimen and anchors are introduced in the specimen in single reference points. On the contrary, strength measurements capture more easily an average value of the whole specimen.

### 4.2 Unload-reload moduli

In the triaxial compression tests reported above, a small static cycle was performed during shearing, between 30% and 15% of the expected peak deviatoric stress. These loads were selected to avoid soil yielding before the cycles so the modulus could be assumed elastic. Figure 6 summarizes the results of the unload-reload moduli ( $E_{ur}$ ) obtained for the two adjusted porosity/cement ratio. The values of  $E_{ur}$  obtained from these triaxial tests are higher than the initial tangent modulus ( $E_{ti}$ ) obtained in the unconfined compression tests presented in Figure 5. This can be considered expected because  $E_{ur}$  is usually assumed to follow an elastic pattern, if performed at low ranges of cyclic stress, while in the initial monotonic loading path some compliance errors of strain gauges may be presented. This graph also evidences a clear and almost discrete increase in the stiffness modulus values for the specimens with  $n/C_{iv}^{0.21}=29$  (5% and 7% cement contents) in comparison with the specimens with distinct ratio  $n/C_{iv}^{0.21}=36$  (2% and 4% cement contents). This could be even clearer if the instrumentation

would perform in a completely satisfactory way for the highest cemented mixtures (for 5% and 7% of cement content).

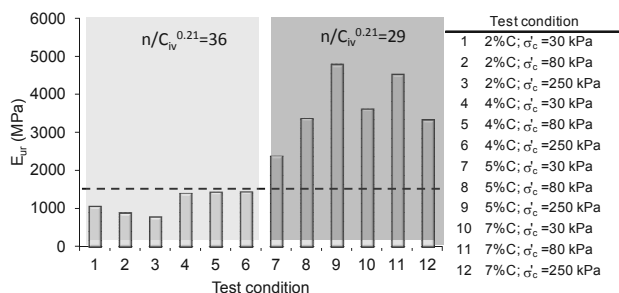


Figure 6. Stiffness modulus obtained in the unload-reload cycles.

### 5 COMPRESSIBILITY PARAMETERS

One-dimension compression tests in oedometer cells with constant rate of deformation (CRD) were performed over soil-cement specimens in the four moulding conditions presented in Table 1. The preparation of the different mixtures for these tests followed the same procedure of the other tests, as expressed briefly in section 2. Due to the size of the mould, the static compaction was performed in one layer, although the soil was placed in several stages followed by tapping. For the calculation of the mean effective stress ( $p'$ ) in each test the value of the coefficient of earth pressure at rest ( $k_0$ ) was considered equal to 1 due to the high compaction degree that the specimens were subjected during moulding (>80% of the Modified Proctor test). Figure 7 shows two of those tests, corresponding to two different porosity cement ratios, indicating that these compressibility curves do not seem to converge.

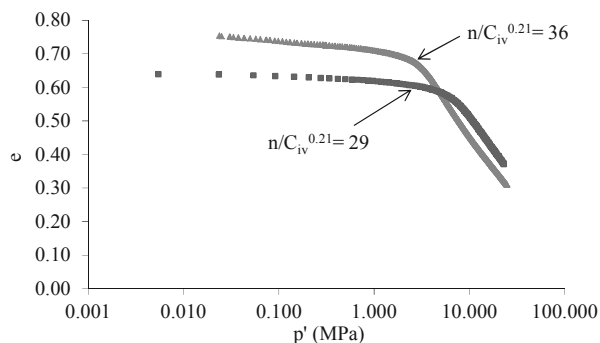


Figure 7. Void ratio against mean effective stress for two different porosity/cement ratios

However, plotting the tests performed over specimens with the same porosity cement ratio, a unique compressibility line was obtained. The same has happened for the other two tests with the other porosity cement ratio of 36. On the contrary, when specimens with the same cement content but different void ratio were represented no unique line was obtained. These results indicate that this ratio can better reproduce the behaviour in one-dimensional compression than the cement content or initial void ratio alone.

### 6 CONCLUSIONS

This paper presented a great number of data from different tests. Together, they allowed a better understanding of the artificially cemented soil used in this work. Compressive and tensile strength, strength envelopes, stiffness parameters and one-dimensional behaviour were some of the most important issues studied. The adjusted porosity/cement ratio revealed to be very consistent and useful for the analysis of the unconfined

compression strength since a unique trend was obtained between this variable and  $n/C_{iv}^{0.21}$ . A similar trend was obtained for the indirect tensile strength performing tests over specimens moulded in the same conditions. The comparison of the two curves provided a relationship between indirect and compressive strength of about 11%.

The strength envelope values of the cemented specimens tested in triaxial compression were obtained through a procedure based on the Mohr's circles analysis to solve the lack of representativeness of principal stress analysis due to non correspondence of the real localised shear locus. In fact, strain localisation is unavoidable in these very stiff materials, and consequently, the global stress-strain measurements are no longer representative of the conditions throughout the shearing process. Two peak strength envelopes were obtained for each  $n/C_{iv}^{0.21}$  ( $n/C_{iv}^{0.21}=36$ :  $\phi^*=30^\circ$  and  $c^*=253$  kPa;  $n/C_{iv}^{0.21}=29$ :  $\phi^*=39^\circ$  and  $c^*=589$  kPa), showing once again the convenience of this ratio for the analysis of these mixtures behaviour.

This ratio also seems to be very useful to reproduce the one dimensional compression behaviour of the mixture, since for each  $n/C_{iv}^{0.21}$  a single line was obtained for higher stresses.

### 7 ACKNOWLEDGEMENTS

This research was developed under the activities of FCT (Portuguese Foundation for Science and Technology) research unit CEC, in FEUP [PTDC/ECM/ 099475/2008], and financed by the European Community (QREN/UE/FEDER), Operational Program for Competitive Factors "COMPETE".

### 8 REFERENCES

ASTM 1998. D 2487-98 Standard practice for classification of soils for engineering purposes (Unified Classification System)

Burland J. B. 1990. On the compressibility and shear strength of natural clays. *Geotechnique* 40(3), 329-378.

CEN 2003. EN 13286-42 - Unbound and hydraulic bound mixtures. Test method for the determination of the indirect tensile strength of hydraulically bound mixtures, Comité Européen de Normalisation

Chang T. S. and Woods R.D. 1992. Effect of particle contact bond on shear modulus. *Journal of Geotechnical and Geoenvironment Engineering* 118(GT8), 1216-1233.

Consoli N.C., Viana da Fonseca A., Cruz R., Rios S. 2011. Voids/Cement ratio controlling tensile strength of cement treated soils. *Journal of Geotechnical and Environmental Engineering*, 137(11), 1126-1131 (doi:10.1061/(ASCE)GT.1943-5606.0000524)

Consoli N.C., Viana da Fonseca A., Rios S., Cruz R. and Foini A. 2012. Parameters controlling stiffness and strength of artificially cemented soils. *Geotechnique* 62(2), 177-183 (doi: 10.1680/geot.8.P.084)

Consoli N.C., Foppa D., Festugato L. and Heineck K. 2007. Key Parameters for Strength Control of Artificially Cemented Soils, *Journal of Geotechnical and Geoenvironmental Engineering* 133(2), 197-205.

Gasparre A. 2005. Advanced laboratory characterisation of London Clay. PhD dissertation presented to the University of London

Lorenzo G. and Bergado D. 2004. Fundamental parameters of cement-admixed clay - New Approach. *Journal of Geotechnical and Geoenvironmental Engineering* 130(10), 1042-1050.

Rios S., Viana da Fonseca A. and Baudet B. 2012. The effect of the porosity/cement ratio on the shearing behaviour of cemented soil. *Acta Geotechnica* (accepted)

Viana da Fonseca, A. 1998. Identifying the reserve of strength and stiffness characteristics due to cemented structure of a saprolitic soil from granite. The Geotechnics of Hard Soils - Soft Rocks, Evagelista and Picarelli (eds), Balkema, Rotterdam

Viana da Fonseca A., Carvalho J., Ferreira C., Santos J.A., Almeida F., Pereira E., Feliciano J., Grade J. and Oliveira A. 2006. Characterization of a profile of residual soil from granite combining geological, geophysical and mechanical testing techniques. *Geotechnical and Geological Engineering* 24, 1307-1348

# Compressive Strength of Fiber-Reinforced Lightly-Cement Stabilized Sand

## Résistance à la compression des sables renforcées par fibres et ciment

Sadek S., Najjar S., Abboud A.

Department of Civil and Environmental Engineering, American University of Beirut

**ABSTRACT:** The stabilization of soils using cementing agents has long gained acceptance and is well established in geotechnical engineering practice. Furthermore, adding discrete fibers to the cement-treated soil has been shown to improve the soil's response to loading and its overall engineering behavior. Limited studies of the behavior of fiber-reinforced cemented sand in the laboratory indicated that the addition of cement and fibers results in an increase in the strength of the composite, especially at high fiber contents and lengths. Cemented sands were found to be brittle compared to un-cemented sands, with the brittleness decreasing with the inclusion of fibers. The objective of this paper is to investigate the effect of randomly distributed fiber reinforcements and cement addition on the response of sandy soils. To achieve this objective, the behavior of cement/fiber-reinforced sands was studied using unconfined compression tests. The parameters that were varied are [1] the cement content (0.5% and 1%), [2] the fiber content (0%, 0.25%, 0.5%, and 1.0%), and [3] fiber lengths (6, 12 and 20 mm). The results of the tests were used to quantify the degree of improvement in strength and stiffness due to the addition of fibers and cement to the cohesionless sand.

**RÉSUMÉ:** La stabilisation des sols en utilisant des agents de cimentation a longtemps été accepté et est bien établie dans la pratique de la géotechnique. De plus, l'ajout de fibres discrètes au sol-ciment a été démontré effectif pour améliorer la réponse du sol au chargement et son comportement mécanique global. Seules quelques études existent où le comportement des sols renforcés par des fibres et ciment a été étudié au laboratoire. Elles ont indiqué que l'addition de ciment et de fibres engendrent une augmentation de la résistance du composite, en particulier à des teneurs en fibres et des longueurs élevées. Les sables cimentés ont été jugés fragiles par rapport aux sables non cimentés; cette fragilité diminue avec l'inclusion de fibres. L'objectif de cet article est d'étudier l'effet de renforts en fibres distribuées de façon aléatoire et l'ajout de ciment sur la réponse des sols sableux. Pour atteindre cet objectif, le comportement de sables enforcés par ajout de ciment / fibres a été étudiée par des essais de compression non confinée. Les paramètres qui ont été variées sont [1] la teneur en ciment (0,5% et 1%), [2] la teneur en fibres (0%, 0,25%, 0,5%, et 1,0%), et la longueur des fibres [3] (6, 12 et 20 mm). Les résultats des tests ont été utilisés pour quantifier le degré d'amélioration de la résistance et de rigidité due à l'ajout de fibres et de ciment au sable pulvérulent.

**KEYWORDS:** fiber-reinforced sand, cement stabilized sands, fibers, cement, unconfined compressive strength.

## 1 INTRODUCTION

The geotechnical and materials/pavement engineering fields are witnessing an increasing interest in exploring soil improvement schemes that are based on the addition of stabilizing agents such as synthetic or natural fibers and/or cementing agents for various applications. The objective is to produce a composite material with improved engineering properties that could be used in lieu of good quality construction material that is typically obtained through non-sustainable and environmentally problematic activities such as quarrying. The composite material with its improved engineering properties could be used to replace conventional base and sub-base material under pavements, or to support foundations of "light" structures or infrastructure, which otherwise could not be adequately supported by the natural soil. The improved material could also be used as backfill behind earth retaining walls and reinforced or stabilized slopes.

The experimental data that is available in the literature for fiber/cement reinforced sands is relatively limited (Maher and Ho 1993, Consoli et al. 1998, Kaniraj and Havanagi 2001, Sobhan and Mashnad 2002, and Consoli et al. 2002). There is a need for designing and implementing a comprehensive experimental testing program that is aimed at investigating the behavior of fiber/cement reinforced sands systematically. To achieve this objective, the behavior of cement/fiber reinforced sands was studied in the laboratory using unconfined compression tests. The parameters that were varied in this study are [1] the cement content (0.5% and 1%), [2] the fiber content (0%, 0.25%, 0.5%, and 1.0%), and [3] fiber lengths (6, 12 and 20 mm). The results of the tests were used to quantify the degree of improvement in strength, stiffness, and ductility due to the addition of fibers and cement to the cohesionless sand.

## 2 EXPERIMENTAL PROGRAM

Twenty unconfined compression tests on fiber/cement reinforced sands were conducted as part of this study.

### 2.1 Material Properties

The sand used in this study is Ottawa Sand with the properties shown in Table 1. The sand classifies as a *poorly graded sand (SP)* according to the Unified Soil Classification System.

The fibers (Fig. 1) chosen for the reinforcement are polypropylene fibers, typically used as secondary reinforcement of lightweight concrete and mortar mix designs. They were adopted because they are available in several lengths, they can be mixed with soil-cement mixtures and satisfy efficiently the intended role of reinforcement. The fibers have a specific gravity of 0.91 g/ml, a tensile strength of 0.38 kN/mm<sup>2</sup> and a young modulus of 3.5 kN/mm<sup>2</sup>. Fiber lengths of 6 mm ±1, 12 mm ±1 and 20 mm ±1 were used in the testing program. The nominal diameter of the fibers was determined in the lab under an electronic microscope to be in the order of 0.1 mm.

Table 1. Table caption (TNR 8), numbered consecutively. Tables placed below caption. TNR 8 for text and numbers in Table.

Soil Property	Value
$D_{10}$ (mm)	0.22
$D_{30}$ (mm)	0.31
$D_{60}$ (mm)	0.42
Coefficient of uniformity ( $D_{60}/D_{10}$ )	1.95
Coefficient of curvature ( $(D_{30})^2/(D_{60}*D_{10})$ )	1.04
Maximum and minimum void ratios ( $e_{max}, e_{min}$ )	(0.75, 0.49)
Specific gravity	2.65



The cement used in this study is normal Portland cement type I. The same sources of cement and sand were used for all the specimens to eliminate all risk of material discrepancy.

## 2.2 Sample Preparation

The specimens used in the UCS tests were prepared in cylindrical PVC split molds to facilitate the extraction of the sample after formation. For a given test, the material quantities were determined based on the target fiber content, cement content, and sand density. Initially, the sand and cement were mixed in dry conditions before adding 5% by weight of water necessary for the hydration of the cement and blending of the mixture. The fibers were then mixed thoroughly with the sand-cement to obtain a final homogenous mix with well-distributed and untangled fibers. It is to be noted that all the mixing was done manually since the use of a mechanical mixer could result in tangling and clodding of the fibers and their segregation from the soil mixture. Each layer was then compacted into the mold to the required height under the effect of a compaction tool which was specifically designed for the purpose. The top surfaces of the 1<sup>st</sup> and 2<sup>nd</sup> layers were scratched prior to putting the new material for the subsequent layer in order to obtain, to the extent possible, a homogenous specimen and eliminate the risk of weak shear planes at the contact surface between two layers.

A curing time of  $8 \pm 1$  days was chosen to allow the cement enough to time to set. Since the curing time is not a parameter which was studied in the testing program, the period of 8 days was chosen as an average time which provides a significant period for curing without unduly prolonging the overall time needed for each test.

## 2.3 Unconfined Compression Strength Tests

The UCS tests were performed according to ASTM D2166 with specimens having a diameter of 5.5 cm and a height of 11 cm giving an acceptable height to diameter ratio of 2. The machine used in the tests is a HUMBOLDT HM-3000 loading frame fully automated and computer software-controlled. The vertical deformation is recorded by an LVDT, while the resisting axial load is recorded by load cells of different capacities. The rate of application of the strain is 0.05 cm/min. The data were recorded automatically every 4 seconds and the test was continued until failure occurred or when the axial strain exceeded 15%.

## 3 TEST RESULTS AND ANALYSIS

Results from twenty unconfined compression tests on fiber/cement reinforced sands are presented in this paper. The tests were restricted to lightly cemented sands (cement content = 0.5% and 1.0%) that were reinforced with fibers of different lengths (6mm, 12mm, and 20mm) at different fiber contents (0%, 0.25%, 0.5%, and 1.0%). The analysis of the tests includes an assessment of the stress-strain behavior and the dependency of the unconfined compressive strength on the reinforcement parameters (fiber content, fiber length, and cement content).

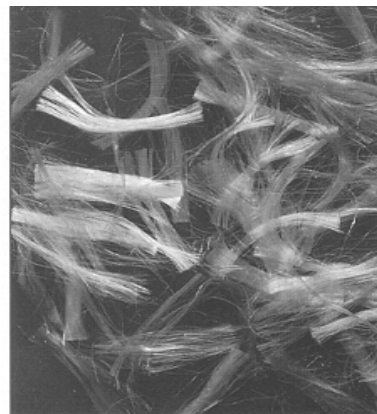


Figure 1. Polypropylene fibers used in the experiments.

## 3.1 Stress-Strain Response

The stress-strain response of specimens that were stabilized with a cement content of 0.5% is presented in Figs. 2a, 2b, and 2c for fiber contents of 0.25%, 0.5%, and 1.0%, respectively. The response of specimens that were reinforced with a cement content of 1.0% is similarly presented in Figs. 3a, 3b, and 3c. On each of the plots, stress-strain curves are presented for different fiber lengths (6mm, 12mm, and 20mm) and for the specimen that was prepared with no fibers.

For specimens that were reinforced with a cement content of 0.5% (Fig. 2), the stress strain curves indicate a consistent increase in stress with strain up to a maximum peak stress value at which failure occurs. The value of the peak and the post peak behavior are a function of the cement content, fiber content, and fiber length. The failure mode as indicated by the value of the strain at failure and by the post peak response is found to be more ductile as the fiber content increased from 0% to 1.0%. In addition, for a given fiber content, ductility was found to improve as the length of fibers increased from 6mm to 20mm.

For the higher cement content of 1.0% (Fig. 3), the behavior of the composite specimens was found to be more brittle compared to their lightly cemented counterparts. The inclusion of fibers added some ductility to the mode of failure, but this effect was minor for the smaller fiber contents (0.25% and 0.50%). The improvement in the mode of failure was only evident in the higher fiber content of 1.0% at all fiber lengths and for the intermediate fiber content of 0.5%, but only at the larger fiber length of 20mm.

## 3.2 Effect of Fiber/Cement on Stiffness

The stress-strain response at the onset of loading in Figs. 2 and 3 could be used as a measure of stiffness for the fiber/cement reinforced specimens. For the smaller cement content, results on Fig. 2 indicate that the stiffness of the specimens was not affected by the addition of fibers except for cases involving the longest fibers (20mm) with fiber contents of 0.25% and 0.50% where the stiffness was found to be improved. For cases involving fibers with a high fiber content of 1.0%, no improvements were observed in the stiffness, irrespective of the fiber length.

A slightly different behavior was observed for the higher cement content of 1.0% where slight improvement in stiffness were observed for the shorter fibers at the smaller fiber contents, with the improvements in stiffness vanishing for the longest fiber and the highest fiber contents, where slight reduction in stiffness was actually observed. This indicates that fibers could result in a softer initial response for higher cement contents, higher fiber content, and longer fibers.

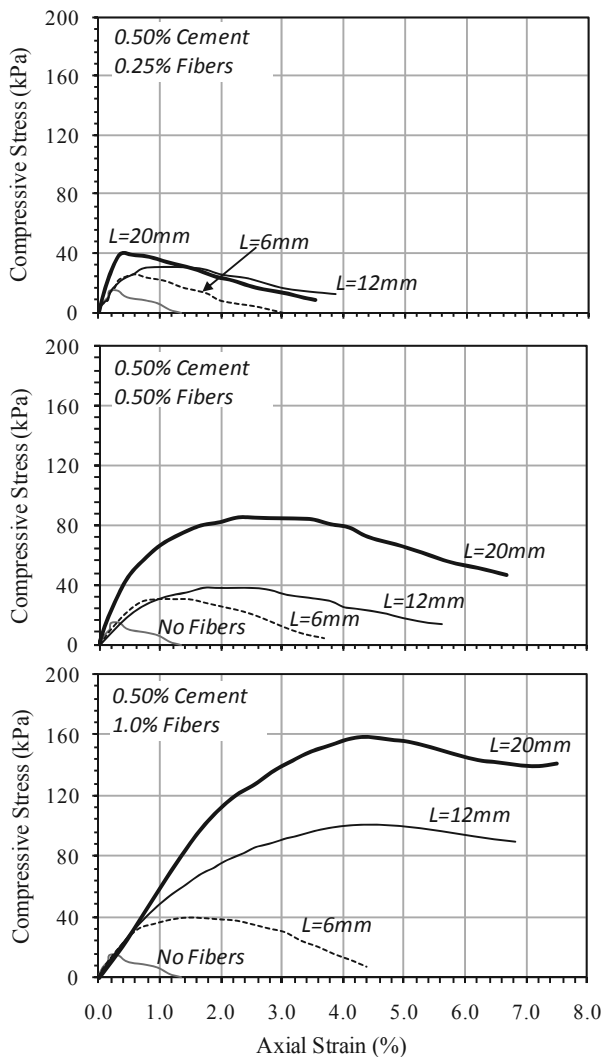


Figure 2. Stress-strain response for cement content of 0.5%.

### 3.3 Effect of Fiber Content on UCS

For a given cement content, the stress-strain curves in Figs. 2 and 3 indicate that the unconfined compressive strength increases as the fiber content increases. The unconfined compressive strength for each test was computed and plotted as a function of the fiber content in Figs. 4a and 5a for cement contents of 0.5% and 1.0%, respectively. For the two cement contents and for all fiber lengths, results indicate a consistent increase in the unconfined compressive strength with fiber content. For a cement content of 0.5%, the UCS increased from about 15 kPa (no fibers) to about 40 kPa (1.0% fibers) for the shortest fiber length of 6mm, and from 15 kPa (no fibers) to about 160 kPa (1.0% fibers) for the longest fiber length of 20mm. For the larger cement content of 1.0%, the UCS increased from about 50 kPa (no fibers) to about 112 kPa and 178 kPa, for the shortest and longest fibers at 1.0% fiber content, respectively.

In order to obtain a quantitative measure of the degree of improvement in the unconfined compressive strength, the ratio of the UCS with fibers to the UCS without fibers was computed and plotted versus the fiber content in Figs. 4b and 5b. These results indicate that the cement content played a significant role in defining the improvement ratio, with the ratio varying from 2 (smallest fiber content and fiber length) to 10 (largest fiber content and fiber length) for a cement ratio of 0.5%, and from about 2 to 4 for the larger cement ratio of 1.0%.

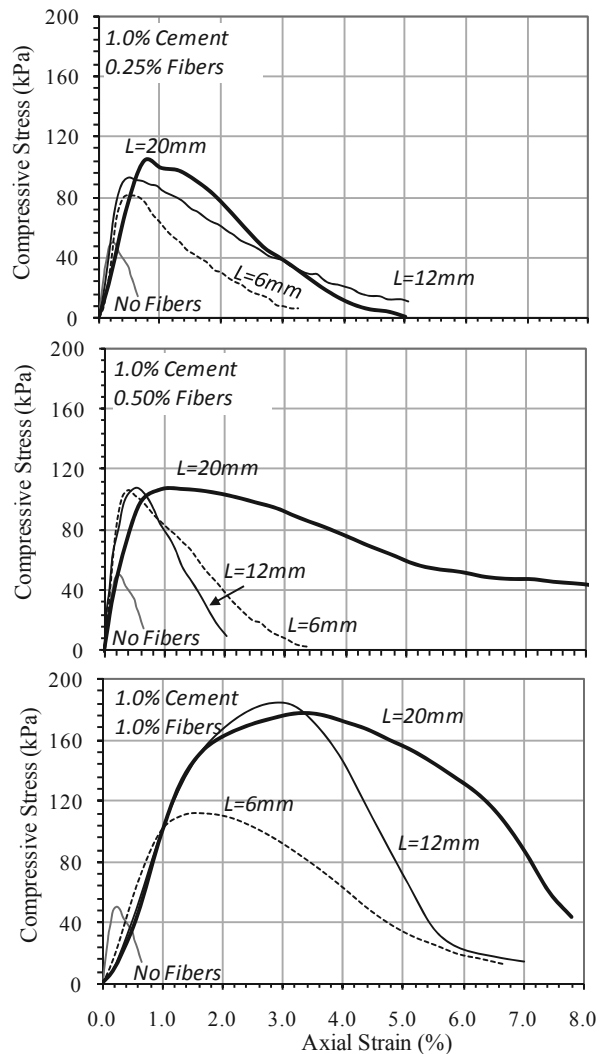


Figure 3. Stress-strain response for cement content of 1.0%.

### 3.4 Effect of Fiber Length on UCS

The effect of the fiber length on the stress-strain response and on the improvement in the UCS is evident in Figs. 2 to 5 and is found to be dependent on the cement content. For a cement content of 0.5%, as the fiber length increases, the unconfined compressive strength increases and the strain at failure increases, indicating improved ductility. The effect of fiber length was found to be more evident at higher fiber contents compared to lower fiber contents. For example, for the small fiber content of 0.25%, the improvement ratio in the UCS increased slightly from 1.7 to 2.6 (for fiber length of 6mm and 20mm) compared to the dramatic increase from 2.6 to 10.6 (for fiber length of 6mm and 20mm) for the larger fiber content of 1.0%.

For the larger cement content of 1.0%, the effect of fiber length on the unconfined compressive strength becomes smaller. For the smaller fiber contents of 0.25% and 0.5%, the difference in the measured values of the UCS is relatively insignificant, with improvement ratios varying in the narrow range of 1.6 to 2.0 (fiber content of 0.25%) and 2.1 to 2.15 (fiber content of 0.50%) for the shortest and longest fibers, respectively. For the largest fiber content of 1.0%, the improvement ratio increases from 2.2 to 3.7, as the fiber length increases from 6mm to 20mm.

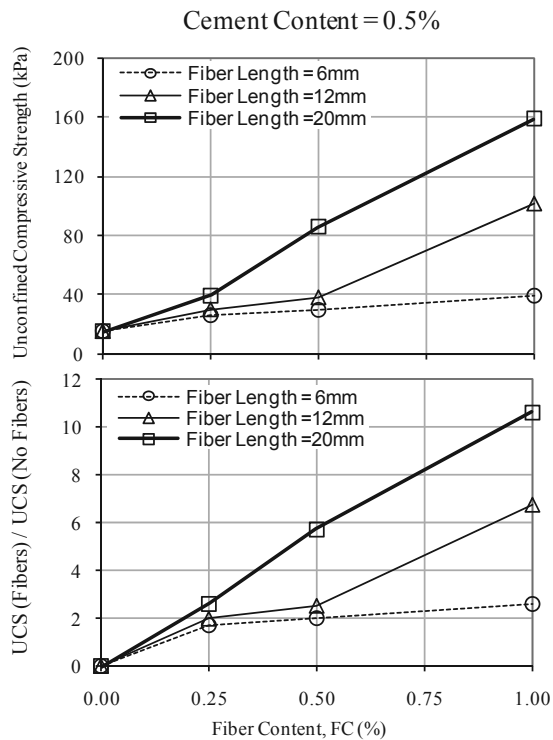


Figure 4. Improvement in UCS for cement content of 0.5%.

### 3.5 Effect of Cement Content on UCS

The range of the cement content that was chosen in this study (0.5% to 1.0%) is indicative of lightly-cemented sands. However, the results presented in Figs. 2 to 5 indicate a clear difference in the performance of the composite specimens that were stabilized with 0.5% cement and specimens stabilized with 1.0%, particularly with regards to the contribution of the fibers to the improved compressive strength.

For specimens that were not reinforced with fibers, the increase in cement content from 0.5% to 1.0% increased the unconfined compressive strength from 15 kPa to 50 kPa. With the addition of fibers, results showed that the UCS could be improved by more than 10 times for a cement content of 0.5% but only to 3.7 times for the cement content of 1.0%, indicating a decreased relative efficiency of the fibers at improving the compressive strength as the cement ratio increases.

It should be noted however that the actual maximum value (largest fiber content and fiber length) of the unconfined compressive strength was still higher (about 185 kPa) for the cement content of 1.0% compared to the maximum value (159 kPa) measured for the cement content of 0.5%. For the smaller fiber contents and fiber lengths, the values of the UCS for the cement content of 1% were all higher than those of the 0.5% at the same fiber content and fiber length, indicating that the magnitude of the improved UCS was larger for the higher cement content.

## 4 CONCLUSION

Based on the results of 20 unconfined compression tests that were conducted in this study on fiber-reinforced lightly-cemented sands, the following conclusions can be drawn:

1. The behavior of specimens with higher cement contents is more brittle compared to specimens with lower cement contents. However, brittleness decreased with the inclusion of fibers and the energy absorption capacity increased as the fiber content and length increased.
2. For the smaller cement content, the stiffness of the specimens was not affected by the addition of fibers, except for the cases of 20mm fibers with fiber contents

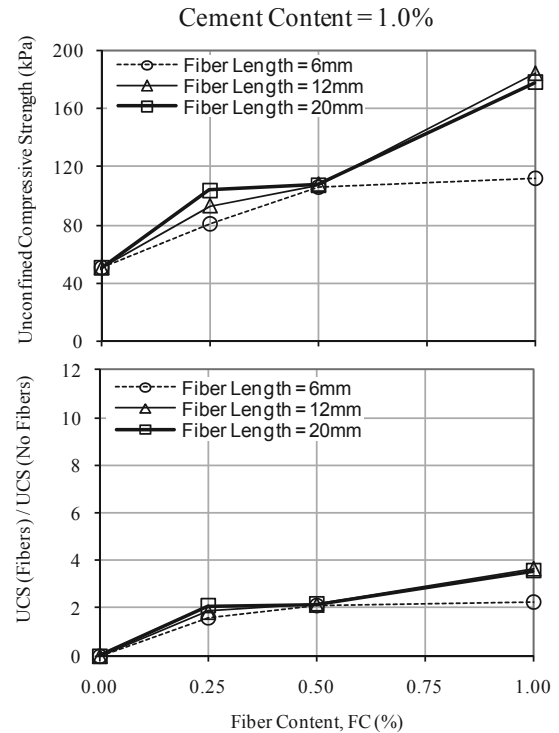


Figure 5. Improvement in UCS for cement content of 1.0%.

of 0.25% and 0.50%, where the stiffness was found to be improved. For the higher cement content fibers could result in a softer initial response particularly for higher fiber contents and longer fibers.

3. For the both cement contents used, results indicated a consistent increase in the unconfined compressive strength with fiber content. The cement content played a significant role in defining the improvement ratio of the UCS, with the ratio varying from 2 (smallest fiber content and fiber length) to 10 (largest fiber content and fiber length) for a cement ratio of 0.5%, and from about 2 to 4 for the larger cement ratio of 1.0%.
4. For a cement content of 0.5%, as the fiber length increased, the UCS increased and the strain at failure increased, indicating improved ductility, with the effect of fiber length being evident at higher fiber contents compared to lower fiber contents. For the larger cement content of 1.0%, the effect of fiber length on the unconfined compressive strength was less significant.

## 5 ACKNOWLEDGEMENTS

The authors would like to acknowledge the support of the Lebanese National Council for Scientific Research (LNCSR) for funding this research program.

## 6 REFERENCES

- Maher M.H. and Ho Y.C. 1993. Behavior of fiber-reinforced cemented sand under static and cyclic loads. *American Society for Testing and Materials* 16, 330-338.
- Kaniraj S.R. and Havanagi V.G. 2001. Behavior of cement-stabilized fiber-reinforced fly ash-soil mixtures. *Journal of Geotechnical Engineering* 127, 574-584.
- Consoli et. al. 1998. Influence of fiber and cement addition on behavior of sandy soil. *Journal of Geotechnical Engineering* 124, 1211-1214.
- Consoli et. al. 2002. Engineering behavior of a sand reinforced with plastic waste. *Journal of Geotechnical Engineering* 128, 462-472.
- Sobhan K. and Mashnad M. 2002. Tensile strength and toughness of soil-cement-fly-ash composite reinforced with recycled high-density polyethylene strips. *Journal of Materials in Civil Engineering* 14, 177-184.

# Conservatoriumhotel Amsterdam, geotechnical design and monitoring

## Conservatoriumhotel Amsterdam, conception géotechnique et instrumentation

Stoel van der A.E.C.

CRUX Engineering BV Amsterdam & Universiteit Twente

Vink D., Bouma J.

CRUX Engineering BV Delft

**ABSTRACT:** This article deals with the geotechnical design of the building pit and the foundation restoration of the Conservatoriumhotel Amsterdam. It involves a selection of results of analytical and Plaxis calculations and damage predictions regarding vibrations and settlements. The second part of the paper deals with the execution of the works and the important role of a pro-active monitoring-system and careful communication with all stakeholders. It briefly outlines the monitoring plan, type and results of the monitoring and the risk management during implementation. Some measurement results are compared with predictions and two calamities that occurred during the construction will be specifically addressed. This will clearly show the added value of monitoring and active risk management, that eventually has led to the successful completion of this project in 2011.

**RÉSUMÉ :** Cet article traite de la conception géotechnique de la tranchée couverte du bâtiment et reprise en sous œuvre des fondations du Conservatoriumhotel Amsterdam. Il s'agit d'une sélection de résultats de calculs analytiques et Plaxis et des prévisions concernant les dommages dus aux vibrations et les tassements induits. La deuxième partie de l'article traite de l'exécution des travaux et le rôle important que la surveillance pro-active et de la communication prudent avec toutes les investisseurs. Le plan d'instrumentation est brièvement décrit ainsi que le type et le suivi, des résultats et de la gestion des risques lors de la mise en œuvre. De plus les résultats des mesures sont comparés aux prévisions. Deux sinistres qui se sont produits lors de la construction seront abordés. La valeur ajoutée de l'instrumentation est montrée ainsi que la gestion active des risques qui a finalement conduit à la réussite de ce projet en 2011.

**KEYWORDS:** geotechnical design, building pit, Plaxis, monitoring, restoration

## 1 INTRODUCTION

In Amsterdam, at Van Baerlestraat 27, the stately listed building of the "Rijkspostspaarbank" (Imperial Bank, see Figure 1) is situated. It was originally built between 1899 and 1901 by Imperial architect, D.E.C Knuttel. The building was previously reassigned to function as Sweelinck Conservatory and was since 2008 radically converted into a luxurious hotel, including over 9000 m<sup>2</sup> of five star hotel and 85 parking facilities. This conversion has been one of the most expensive (more than 30 million euro) hotel refurbishments ever.

This renovation required a number of radical structural changes that led to a complex task with regard to the geotechnical design. The most important of these tasks was realising a two level parking / basement including a (-3) swimming pool in the courtyard of the existing building. Special attention had to be paid to the many historical details in the buildings that were incorporated in the new design and had to be preserved. In addition, the building location is flanked by two tram lines and the Van Gogh Museum and Rijksmuseum and the Royal Concert Hall, resulting in numerous logistic restrictions.

## 2 SOIL CONDITIONS

At the location, the typical Amsterdam soil profile (Figure 2) is found. The top layer of the first meters below surface level consists of Anthropogenic sand. Below this top layer the Holocene deposits are found until a depth of about 10-15 m below surface level. The Holocene formation can be divided (from top to bottom) into peat, clay, silty sand, clay and peat. The Holocene lies on top of the Pleistocene sands which are divided by an intermediate silty, clayey sand layer. The phreatic water level is found about 0.4 m below surface level.



Figure 1. Aerial photo of the building Stradivarius

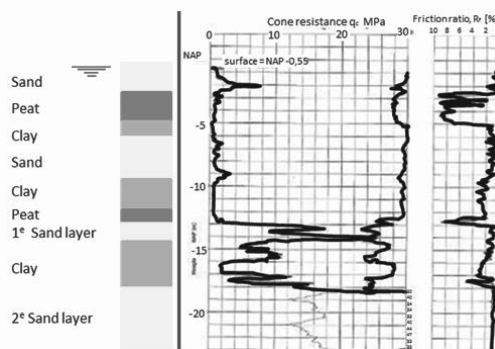


Figure 2. Amsterdam soil conditions

### 3 CONSTRUCTION AND BUILDING LAYOUT

In Figure 3, 4 and 7 the lay out of the building and building pit are shown. Because of the very deep excavation next to the pile foundation of the existing building, much precaution had to be paid to settlements and angular distortion (damage) of this listed building. Also, the bending moments in the existing wooden piles were a major concern. This resulted in a staged excavation as shown in Figure 4. Note the different excavation levels of the two excavations A and B, which cause an asymmetrical load situation and displacements. An extra complication was that the building site could only be accessed through a narrow entrance in the eastern part.

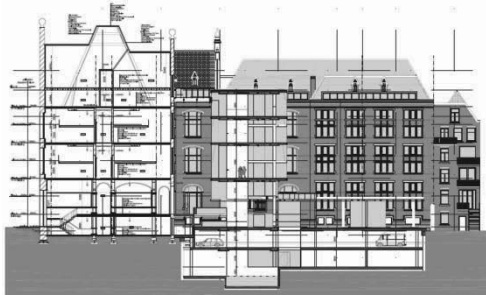


Figure 3. Section C-C: new situation (note swimming pool at -3)

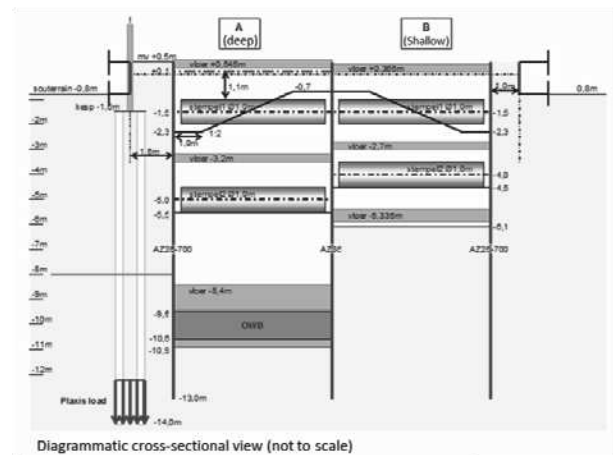


Figure 4. Schematic cross-section C-C, NAP = reference level

### 4 GEOTECHNICAL DESIGN

Because of the asymmetrical excavation and the need to assess soil and building deformations, 2D FEM Plaxis calculations were performed. In Figure 5 an example of the used model for section C-C is shown (see Figure 7). Based on the deformations and stresses resulting from this model, the vertical deformations and inclination of the existing building were determined, see Figure 6. The sheet piles and struts were designed in such an iterative way that the damage prediction resulted in an acceptable damage class (see Table 1).

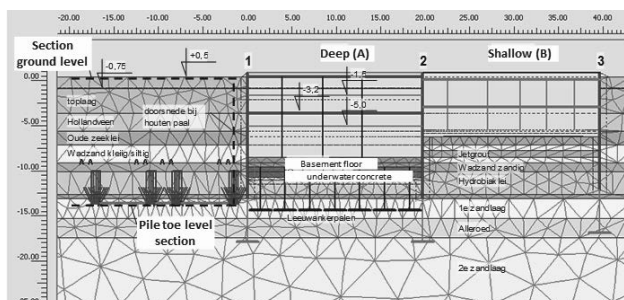


Figure 5. Plaxis geometry section C-C, shallow excavation NAP -6,1m.

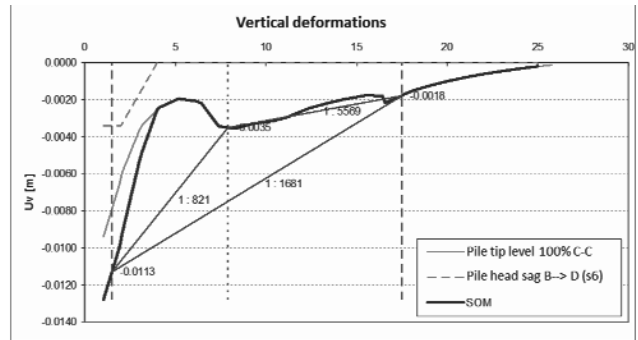


Figure 6. Vertical deformations in building, section C-C.

Because of the proximity of the existing building, full of marble stairs and exquisite tiles that had to be preserved, all the applied foundation system were vibration free: the sheet piles AZ26 were pushed and the Hek-piles were screwed.

Table 1. Results damage prediction sect. C-C (based on BRE regulation / Netzel 2010)

$u_v$	L/H	$\beta$	$E_h$	$\Delta/L$	$\epsilon_{tot}$	Damage class
m	-	-	%	-	-	-
-0.0113	1:1605	0.066	0.0002	0.00088	-	Slight (minor aesthetic damage)

L/H = Ratio depth/height of the building  $\Delta$  = Vertical deflection  
 $\beta$  = Relative angular distortion  $\epsilon_h$  = Horizontal strain  
 $\epsilon_{tot}$  = Total building strain  $u_v$  = vertical displacement

### 5 MONITORING

#### 5.1 General

Because of the sensitive nature of the existing building and the high complexity of the execution of the works, an extensive monitoring program was implemented. Figure 7 shows a general overview including the position of the levelling point (bolts) and inclinometers. By measuring the inclination of the sheet piles, an excellent comparison could be made between predictions and execution for all stages of the works. The leveling points were mainly used to verify whether the inclination indeed resulted in the predicted building deformation. This is particularly useful because some deviation from the predictions is not uncommon.

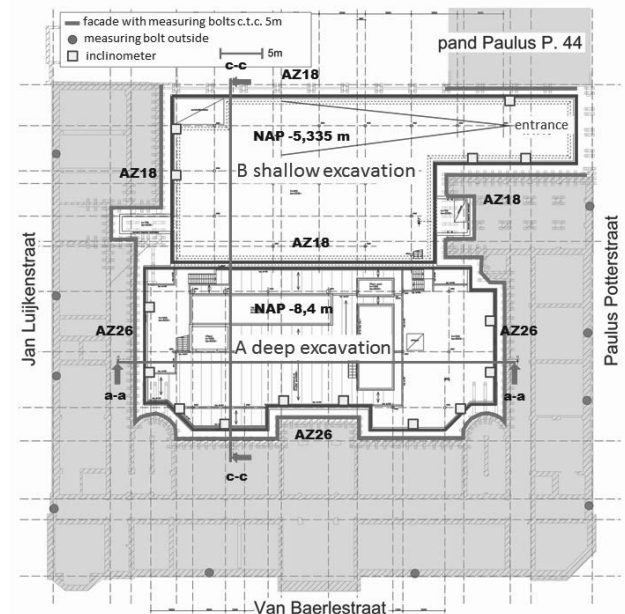


Figure 7. Overview leveling points (bolts) and inclinometers.

The monitoring proved to be particularly valuable because of the occurrence of two incidents during construction.

### 5.2 Incident 1

Incident 1 occurred during the excavation of building pit A. The situation at that time is illustrated by Figure 8 (by a recommendable, remotely operable, permanent webcam!) and Figure 9.



Figure 8 Overview building pit (at the time of incident)



Figure 9. Top view building pit (at the time of incident; © Google)

To limit the displacements the execution sequence has been that, after placement of the sheet piles and the excavation for the NAP -1,5m and -5,0m struts, the water table was first set up again before wet excavation to NAP -10,5m commenced. After hardening of the underwater concrete floor, the water table was lowered again. It was then timely discovered that the -5,0m struts and girder were not in position, see Figure 10. Pumping was stopped immediately to access the situation.

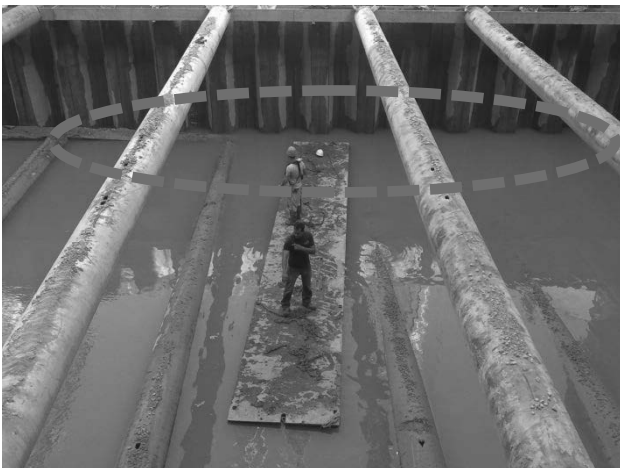


Figure 10. Situation at 2<sup>nd</sup> level girder (collapsed during excavation)

In order to be able to inspect the girder and struts, the water table had to be lowered further than calculated (-6,5m without strut). It was found that, probably because of excavating under the girder, it's consoles were removed, thus causing it to 'hang by a tread'. Because of the extensive monitoring and modelling, an alternative model could be made very quickly based on actual deformations, from which it could be concluded that the deformations resulting from the mitigating measures stayed within acceptable boundaries, see Figure 11. Thus, within three weeks and without significant delay in construction, the strut and girder could be repaired allowing for further excavation of the pit.

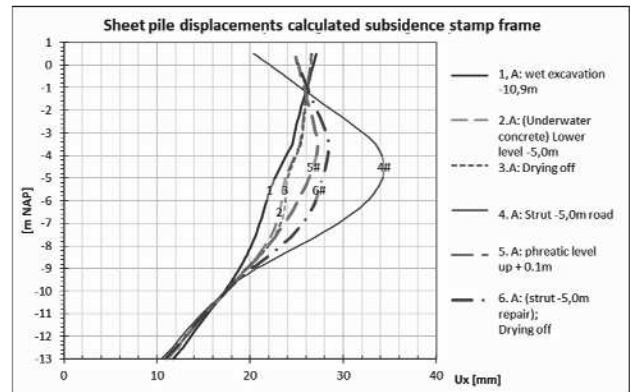


Figure 11. Inclinometer & predictions after incident at girder/strut -5.0m

### 5.3 Incident 2

Incident 2 occurred during the excavation of the entrance at building pit B. The situation is illustrated by Figures 12 (before) and 13 (after excavation). At the left side of the pictures, a listed building at Paulus Potterstraat 44 (PP44) is located. During the excavation of building pit B, this building started to settle, as can be seen in Figure 15. The main concern however was that the side at the entrance settled significantly more than the opposite side, thus potentially causing damage.

In November 2009 the monitoring showed that the settlement rate increased alarmingly. The frequency of monitoring was immediately increased and owner, contractor, consultants, insurer and the municipality intensively discussed a solution. This was found in a combination of allowing more deformation as long as no damage resulted from frequent building inspection and, more importantly, the remedial measure of pre-stressing the NAP -4,0m strut with 150 kN/m. The last measure resulted in a stabilisation of deformations that has held up to now. No damage to PP44 was detected.



Figure 12. Building pit at PP44 before incident



Figure 13. Building pit at PP44 during incident

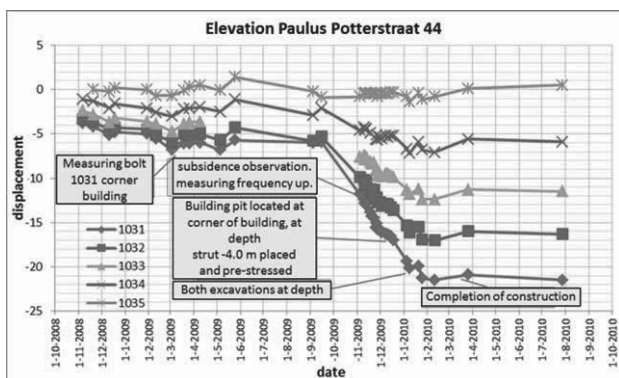


Figure 14. Displacement of building Paulus Potterstraat 44

#### 5.4 Costs

The (interest)cost of a delayed opening of the hotel have been estimated at least at €50.000,- a week. The additional costs of the additional monitoring and damage risk assessment have however, as compared to a basic monitoring program, not exceeded €100.000. When no information would have been available after one of the calamities, construction could have been stopped for months.

### 6 COMPLETED WORKS

The works have been completed in 2011, not only resulting in one of the most luxurious hotels in Amsterdam, but also in a construction of both geotechnical as well as aesthetic beauty. It won the 2012 Dutch Renovation 'Golden Phoenix' award for the most effective reuse of existing property stocks. An impression of the completed work is given in Figure 14 to 16. Figure 19 shows the impressive swimming pool at -3 level, right next to the over 110 years old existing pile foundations.

### 7 CONCLUSIONS

The renovation of the former Rijkspostspaarbank Amsterdam to luxury five star Conservatoriumhotel has been very successful from a geotechnical perspective. Through a sophisticated geotechnical design and a detailed risk analysis of the distortions of the building before construction, combined with a meticulous and proactive monitoring and excellent communication during execution, two major incidents have not

led to significant additional costs and/or delays. The investments that have been necessary to achieve this have been minor compared to the potential cost of the delay that would have resulted from the lack of information without such a system.



Figure 15. Finished construction – atrium new-old



Figure 16. Finished inside construction



Figure 17. Finished outside construction



Figure 18. Finished swimming pool at -3 level

### 9 ACKNOWLEDGEMENTS

The authors wish to express their gratitude to the client Alrov Group and IQNN Vastgoed, structural engineer Van RossumRaadgevendIngenieurs, contractor Strukton NV and foundation subcontractor Van 't Hek for their contributions to this paper.

### 10 REFERENCES

Netzel, H.D., Building Response Due to Ground Movements, Delft University Press, March 2009, Pages 320, ISBN978-1-58603-995-0  
 Van der Stoel, A.E.C. D. Vink & J. Bouma, Van RijkspostspaarbanknaarvijfsterrenConservatoriumhotel; deel 1 geotechnischontwerpConservatoriumhotel Amsterdam, Geotechniek, jaargang 16, no. 4, augustus 2012 (in Dutch)  
 Van der Stoel, A.E.C. D. Vink & J. Bouma, Van RijkspostspaarbanknaarvijfsterrenConservatoriumhotel; deel 2 Monitoring en uitvoeringConservatoriumhotel Amsterdam, jaargang 16, no. 5, december 2012 (in Dutch)



# Impact of the soil-stabilization with lime

## Impact de la stabilisation des sols à la chaux

Szendefy J.  
BUTE, Budapest, Hungary

**ABSTRACT:** The protection of environment and economical consideration demands giving the usage of internal soils preference over external materials. Soil-stabilization with lime increase the bearing capacity and treats the properties of cohesive soils due to chemical reactions. During a soil-stabilization with lime, the  $\text{Ca}^{2+}$  ions introduced into the soil attach to the surface of the clay particles, replacing the cations located there previously. Due to the high charging of the  $\text{Ca}^{2+}$  ions, the clay particles coagulate. The coagulation exerts a decisive effect on the soil structure, resulting the plasticity index in a shifting towards a certain zone. This effect leads to the elimination of the silt and clay particles, resulting in an intensive reduction surface of the particle of the stabilizations. Due to the coagulating particles, the friction angle increases, and also the value of cohesion becomes higher. The addition of lime results consequently in a growth of the compression strength of the soil, leading to an increased load bearing capacity. In order to define the internal friction angle ( $\Phi$ ) and the cohesion ( $c$ ), triaxial compression test were done with ten different kind of soils. The soil-stabilization with lime were made with 2 %, 4 %, and 6% additional lime, the temporal aspect has been investigated in ages of 1, 7, and 28 days. In case of admixing an ideal quantity of lime, the soils are shifting towards the value of  $\Phi=40^\circ$ . The extent of growth of the cohesion did not show as clear tendency as the friction angle, but give back a significant increasing. Contrary to the literature, I regard to remark that the positive impacts of soil-stabilization with lime is basically a result of the cation exchange, while the puzzolan reaction playing only a secondary role. It is also important to remark that the lime stabilization of soils is not only suitable for the drying up of soaked soils. With the application of a planned and properly executed stabilization, load bearing capacity of ballast materials can be achieved with local soils regarded or qualified as unsuitable. Accordingly, the ballast and pavement layers can be effectively reduced, and the quantity of delivered external materials minimized.

**RÉSUMÉ :** Les considérations environnementales et économiques font préférer l'utilisation des matériaux locaux aux matériaux extérieurs transportés sur place. Avec ses processus chimiques, la stabilisation des sols à la chaux permet une augmentation de la portance des sols argileux et une amélioration de leurs propriétés. Lors des processus de stabilisation, les ions  $\text{Ca}^{2+}$  remplacent les cations qui s'attachent à la surface des grains d'argile. Les grains d'argile s'agglomèrent à cause de la haute charge des ions  $\text{Ca}^{2+}$ . L'agglomération provoque un changement important dans la structure du sol et, en conséquence, l'indice de plasticité du sol se décale vers une certaine zone. Cet effet élimine les grains d'argile et de limon diminuant ainsi radicalement la surface des grains du sol stabilisé. À cause de l'agglomération des grains, les valeurs de l'angle de frottement interne et de la cohésion augmentent. En ajoutant de la chaux, la compressibilité des sols diminue, en conséquence la portance des sols augmente. Afin d'établir le changement des valeurs de l'angle de frottement interne ( $\Phi$ ) et de la cohésion ( $c$ ) nous avons effectué des essais triaxiaux sur différents sols. Nous avons stabilisé les sols en ajoutant 2%, 4% et 6% de chaux et nous avons mesuré l'effet du temps avec des essais effectués à l'âge de 1 jour, 7 jours et 28 jours. Dans le cas d'une addition de quantité optimale de chaux la valeur de l'angle de frottement interne est de  $40^\circ$ . Dans le cas de la cohésion, il a été impossible de démontrer une tendance, mais une augmentation importante a pu être observée dans tous les cas. Contrairement à la bibliographie technique sur les essais lors de la stabilisation des sols à la chaux, l'agglomération causée par l'échange de cations a un rôle dominant, tandis que les réactions pouzzolanes ont plutôt un rôle secondaire. Il est important de souligner également que la stabilisation des sols à la chaux n'a pas pour seule application le séchage des sols mouillés ou humidifiés. En utilisant une formule bien établie, une portance équivalente au gravier peut être atteinte avec les sols locaux, ainsi les sols locaux qualifiés de non-utilisables peuvent être finalement convenables pour la construction routière. En conséquence l'épaisseur de l'assises de chaussée et celle de la structure de la chaussée peuvent être diminuées efficacement, et la quantité des matériaux extérieurs transportés peut être minimisée.

**KEYWORDS:** soil stabilization with lime, cation exchange, bearing capacity

### 1 INTRODUCTION

The road vehicle and railway traffic are increasing worldwide that require a permanent extension of the infrastructure. In addition to the extension, the high load bearing and economical operation are required in new infrastructure and rehabilitation investments. To satisfy the above demands, the expectation towards pavements, bedding and subsoil is increasing continuously. Similar tendencies can also be experienced at industrial and commercial buildings e.g. their industrial floors, service-roads and parking area.

According to the Hungarian code (ÚT 2-1-222-2002), the above high requirements can essentially be satisfied by granular

soils; the application of transient and cohesive soils are limited. Another argument prevailing against the use of locally transient and cohesive soils is the fact that their characteristics are extraordinarily influenced by rainfall: their workability is decreasing rapidly and their load bearing capacity becomes practically zero. Consequently, they may upset a strict time schedule due to the drastically abbreviated execution times, so their application result significant risks.

The omission of local materials and the delivery and use of extraneous ones arises questions related not only to costs but also to environment protection and to the preservation of national property. The excavation of extraneous materials cause



damages on nature, and the transportation of thousands and millions m<sup>3</sup> of materials to infrastructure and industrial plants also results considerable load to the environment. Beyond the above effects, this significant transportation also abrades, damages and amortizes the already existing infrastructure.

## 2 GENERALLY ABOUT THE SOIL-STABILIZATION WITH LIME

The soil-stabilization with lime is a successful and widespread procedure for several decades in the USA and Western Europe, while this technology is applied in Hungary and in the neighboring countries only for the drying of sodden earthworks. The research work was performed with Hungarian soils, with the aim of supporting the work of designers and contractors to use local soils as high bearing capacity layer and to reduce the thickness of bedding and floors.

Mainly cohesive soils are used to be stabilized with lime, however transient and clayey silty gravely soils can be stabilized satisfactory based on my research. Therefore I modified a figure of a generally used literature (Mitchell & Hooper, 1961.) about the types of suitable soils for stabilization with lime with the modern machineries.

My suggestion based on my laboratory tests and field experience is shown in red in Figure 1.

The stabilized layer can be built of materials mixed in situ or at a distant site, however the soil is generally not moved but worked in at the location of its original place, transforming it into a layer of sufficient load bearing capacity. Bedding and pavement layers are built on to the stabilized layer to achieve the full layer system of a road, runway or industrial floor. However in case of roads exposed to a lower traffic, forestry or agriculture roads, the stabilized layer may also used as pavement.

During the construction of the stabilized layer, the required quantity of lime is spread over the previously executed surface by a truck provided with a dosing head. The quantity of the lime is 8-60 kg/m<sup>2</sup> depending on the thickness of stabilization and on the type of soil. Subsequently the soil is mixed with the lime by a remix machine. In case the process of stabilization requires water, the modern remix machinery is able to add water through the mixing head. Following mixing, the layer is compacted, and the required ground level provided.

The lime improves the soil characteristics through chemical reactions. Chemical reactions start with the mixing and may take several decades. The chemical reactions during the soil stabilization with lime are as follows:

- dissolution of the lime – reduction of the water content;
- cation exchange-coagulation;
- puzzolan reaction-cementation;
- carbonatization – development of limestone.

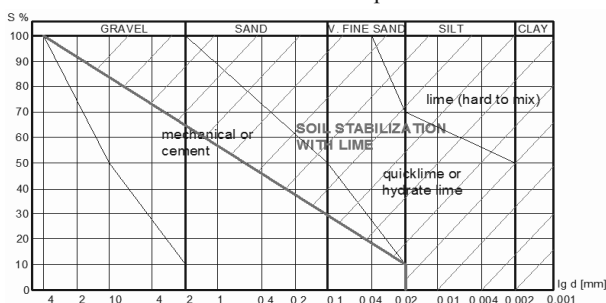


Figure 1. Delimitation of grain size distribution areas from the point of view of soil-stabilization with lime (Kézdi, 1967., Szendefy, 2008.)

## 3 DELINEATION OF MY RESEARCH

During the research 21 soils were measured in the laboratory of Budapest University of Technology and Economics. The origin soil properties of the measured soils are listed in the Table 1. For the verification of the laboratory tests some in-situ stabilization were analyzed as well.

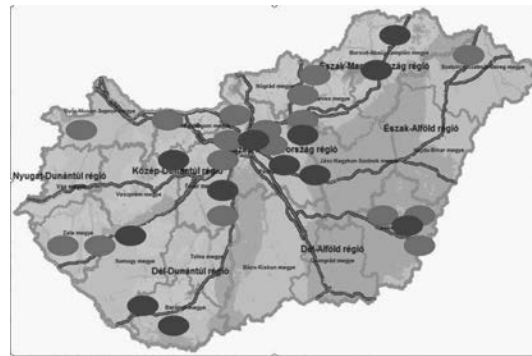


Figure 2. Red spots show the origin of the soils for laboratory measurements, blue spots show in-situ bearing measurements

After the literature 2, 4, 6% quick lime was added for the soils. The quantity of the lime is the percent of the dried soil. Some measurements was done with hydrate lime as well, but the final determinations are given in quick lime, because it contains only the agent (CaO), which is the unit of necessary active agent

My laboratory and field work included soil mechanics parameters (plasticity, grain size, permeability, Proctor-test, swelling), bearing capacity measurements (triaxial compression test, CBR test, durability test) and geological tests (X-ray, derivatograph, pH).

The soils were dried to the laboratory air humidity, than were determined their moisture content and were determined the quantity of the added lime. The lime and the required water were mixed during 15 minutes than left it rest 45 minutes. After resting they were remixed and compacted with Proctor-machine. After compaction the mixtures were left for curing in waterproof package.

To measure the time effect of soil-stabilization with lime I made measurements 1 hour, 1 day, 3 days, 7 days, 14 days and 31 days after compaction.

I can show only a part of my research because the compass of the article.

## 4 ALTERATION OF THE SOIL STRUCTURE

The clue of soil-stabilization with lime is an alteration of the structure of soil caused by lime. Through the admission of lime, the cohesive soils become crumbly, characterized by a reduced plasticity.

### 4.1. Alteration of plasticity

Several researchers pointed out that the plasticity index of soils decreases even if a very low quantity of lime is added (Wang, 1963., Jan, & Walker, 1963., Kézdi, 1967., Nemesdy, 1983.)

They explain the reduction of the plasticity index with a slight reduction of the liquid limit and with the drastic increase of the plastic limit.

As I saw the clue of stabilization in the alteration of the soil structure, I have performed experiments to find the exact mechanism of changes of the plasticity index, and processed literature data.

During the experiments, several soil types were tested (Ip = 6.4 - 69.2 %), admixing 2 % - 4 % - 6 % of lime at different ages.

Table 1. Origin soil physics parameters

Sign of soil	Plasticity index [%]	Grain size < 0.1mm [%]	Friction angle [°]	Cohesion [kPa]
T1	22,0	88,4	10.5	61.7
T2	18,5	76,6	22.4	88.3
T3	50,0	96,4	11.9	117
T4	12,3	87,6	25.6	72.9
T5	33,5	98,7	11.4	37.6
T6	61,5	99,3	18.2	123
T7	43,4	98,8	22.8	114.8
T8	22,9	90,5		
T9	-	36,8		
T10	69,2	99,5		
T11	34,4	94,1	26.9	124
T12	47,5	-		
T13	-	70,2		
T14	-	41,2		
T15	38,5	-	14.5	104.5
T16	34,8	92,8	20.9	82.5
T17	24,8	88,2		
T18	8,8	76,1		
T19	29,1	91,8		
T20	6,4	74,2		
T21	27,0	-		

The analysis of the results shows that the liquid limit ( $w_l$ ) is shifting towards the zone of  $w_l = 35 - 45$  %, irrespective of the initial values. The high values of the liquid limit decrease drastically, those situated near the zone practically stagnate, and a slight increase was experienced at the low liquid limit values. Similarly to the plastic limit ( $w_p$ ) a tendency of shifting towards a certain zone can be experienced, similarly to the behavior of the liquid limit. This zone is situated at  $w_p = 25 - 35$  %. The plastic limit is generally increasing, however in case of fat clays having high plasticity limit stagnation or decrease can be experienced.

The alteration of Atterberg-limits in the value of the plasticity index ( $I_p$ ) also leads to shifting towards a zone (Figure 3). The value of plasticity index is shifting to the zone delimited by  $I_p = 5 - 15$  %, corresponding to very fine sand and silt type soils, according to the description of the bound soils.

An investigation of the temporal aspects of the impact shows that the above tendencies appear during the first hour following mixing, however the most extreme alteration of the parameters could be measured appr. on day 7. The following period was characterized by stagnation, with slight shifts in case of certain soils toward the properties of an untreated soil.

#### 4.2. Alteration of the grain distribution

The process of increased crumbliness and the more granular soil experienced at the plasticity index were tried to be delimited by an investigation of the grain size distribution. During the grain size distribution test and hydrometration of soil samples treated

with lime, the soil particles settled very rapidly. The settling process took 5-15 minutes.

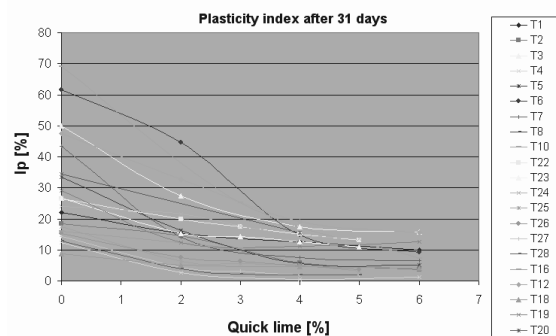


Figure 3. Alteration of the plasticity index plotted against lime dosage

This rapid sedimentation process produces the grain size distribution curve characterizing soils treated with lime. The section situated above hydrometration of the curve shows a picture identical with that of an untreated soil, plunging however at the section below 0.063 mm. The stabilized soils maintain this character later on, with the only difference that also the proportion of particles of above 0.063 mm becomes slightly higher. These alterations are visualized in Figure 4.

As was suspected this intensive coagulation that is not characteristic for the hydrometration of soils of natural stratification is triggered by the cation exchange taking place during lime stabilization. In order to prove it, the hydrometration was performed with a 15 months old sample, by means of admixing a significant quantity of dispersive material (sodium hexametaphosphate) to the mixture prepared in the measuring glass. During the test, a long lasting, continuous precipitation could be experienced as usual for natural soils. The obtained curve of grain size distribution is indicated in Figure 4 in purple color, showing a high conformity with the curve of an untreated soil.

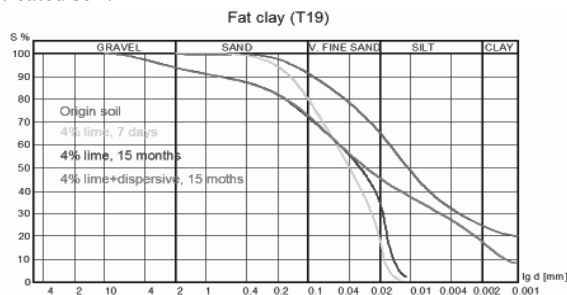


Figure 4. Alteration of the grain size distribution caused by a lime treatment of medium clay soil

It can be observed with the lapse of time that the more frequent presence of particles of above 0.063 mm of particle diameter can be explained with two other chemical processes of the lime stabilization: the cementation and carbonatization. The investigation of particles of above 0.063 mm by means of microscope and X-ray diffraction demonstrated the presence of aluminates and silicates leading to cementation, together with carbonatized limestone particles.

The results obtained from the investigation of plasticity and the grain size distribution show that the particles of a treated soil coagulate, cohere, resulting from the cation exchange. This coagulation creates a strong connection between the soil particles that cannot be dissolved by water, rendering it durable in the soil.

The coagulation is able to eliminate one of the biggest disadvantages of bound soils, i.e. the relatively high particle surface binding high quantities of water. The high level of water intake reduces namely the shearing strength and consequently the load bearing capacity of the soils.

## 5 ALTERATION OF THE LOAD BEARING CAPACITY OF THE SOIL

Drying and working in soils are facilitated by the addition of lime which is very important to constructors. Therewith the important to designers is an intensive increase of the load bearing capacity based on the effect of lime exerted on the soil structure. The load bearing capacity of soils is determined by their parameters related to shearing strength and deformation.

### 4.3. Alteration of the parameters related to shearing strength

In order to define the internal friction angle ( $\Phi$ ) and the cohesion ( $c$ ), I have performed triaxial compression test over a long range of the above mentioned soils. Similarly to the previous procedures added lime was 2 %, 4 %, and 6 %, the temporal aspect has been investigated in ages of 1, 7, and 31 days.

The evaluation of the measurement results shows a growth of the values of friction angle and cohesion. At the 1 day old samples the growth showed a fully disordered picture, then the alteration of value „ $\Phi$ ” shift towards a single zone as the boundaries of consistency at the age of 31 days. In case of admixing an ideal quantity of lime, the soils are shifting towards the value of  $\Phi=40^\circ$ . A growth can also be measured at lower lime quantities, however its extent does not reach the value of  $40^\circ$  that can be regarded as maximum, while the addition of an excessive lime quantity results in a stagnation or decrease. The curve fitted to the measurement results is visualized in Figure 5.

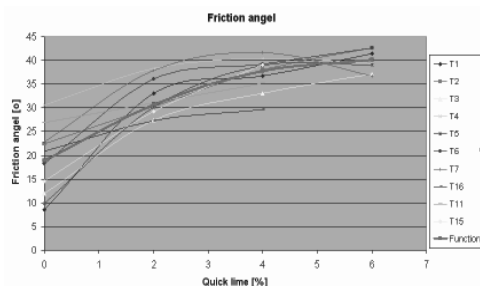


Figure 5. Increase of the friction angle at an age of 28 days, plotted against the quantity of lime

The equation of the fitted curve based on 10 different soil can be expressed with the following function:

$$\Phi = -0,589 M^2 + 7,07 M + 18,9 \quad (1)$$

where

$\Phi$  - internal friction angle

$M$  - added lime quantity

With the use of the function, the fitting to the points could be expressed with the value of  $R^2=0.77$ .

The function does not work at  $M=0\%$  and it is limited to  $M=8\%$ , which is the rationality quantity of added quick lime.

The extent of growth of the cohesion did not show a consistency similar to the previous one. The improvement amounted generally to several hundreds of per cent, with 150 % experienced in the worst case (Figure 6).

The above demonstrated alterations of the shearing parameters have been measured at an age of 28 days, when only the impact of the cation exchange prevailed to a significant extent among the chemical processes taking place during stabilization.

Further alterations triggered by the puzzolan reaction have been tested on a sample taken at an age of 15 months. According to the results of measurement, no changes could be experienced at the friction angle of the stabilization, it maintained its value of  $\Phi=40^\circ$ , however the value of the cohesion increased to  $c = 787$  kPa, from the value of  $c = 343$  kPa measured at an age of 28 days. The alteration of the shearing parameters clearly demonstrates the cementation effect of the puzzolan reaction.

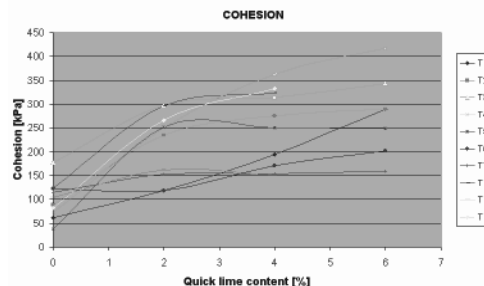


Figure 6. Increase of the cohesion at an age of 28 days, plotted against lime quantity

## 6 CONCLUSIONS

During a soil stabilization with lime, the  $\text{Ca}^{2+}$  ions introduced into the soil attach to the surface of the clay particles, replacing the cations located there previously. Due to the high charging of the  $\text{Ca}^{2+}$  ions, the clay particles coagulate. The coagulation exerts a decisive effect on the soil structure, resulting the plasticity index in a shifting towards a certain zone. This effect leads to the elimination of the silt and clay particles, resulting in an intensive reduction surface of the particle of the stabilizations.

Due to the coagulating particles, the friction angle increases, and also the value of cohesion becomes higher. The addition of lime results consequently in a growth of the compression strength of the soil, leading to an increased load bearing capacity.

Contrary to the literature, I regard to remark that the positive impacts of lime stabilization of the soil is basically a result of the cation exchange, while the puzzolan reaction playing only a secondary role.

It is also important to remark that the lime stabilization of soils is not only suitable for the drying up of soaked soils. With the application of a planned and properly executed stabilization, load bearing capacity of ballast materials can be achieved with local soils regarded or qualified as unsuitable. Accordingly, the ballast and pavement layers can be effectively reduced, and the quantity of delivered external materials minimized.

## 7 REFERENCES

- Boromissza T. 1999. Hungarian design rules of concrete pavements. *Közlekedési és mélyépítési szemle (évfolyam, szám, oldalak) (in Hungarian)*
- Bowles XXX: *Engineering Properties of Soils and their Measurement* Filep Gy. 1988. *Chemistry of soils*. Akadémiai kiadó, Budapest
- Jan M. A., Walker R. D. 1963. Effect of Lime, Moisture and Compaction on a Clay Soil. *Highway Research Record* 29, 1-12.
- Kézdi Á. 1967. *Stabilized earthroads*. Akadémiai Kiadó, Budapest
- Little D.N. 1999: *Evaluation of Structural Contribution of Lime Stabilized Soils and Aggregates, Summary of Findings*, 1999 National Lime Association
- Lohmeyer G., Ebeling K. 2001. *Building of industrial floors*. Magyar Építőanyagipari Szövetség Építésügyi (in Hungarian)
- Mitchell J.K., Hooper D.R. 1961. Influence of Time Between Mixing and Compaction on Properties of a Lime-Stabilized Expansive Clay, *Highway research Board* 304, 14-31.
- Nemesdy E. 1983. *Building technology of road pavements*. Tankönyvkiadó, Budapest (in Hungarian)
- Szendefy J. 2008. Impact of soilstabilization with lime to the structure and bearing capacity of internal soils, *Geotechnic conference, Ráckeve (in Hungarian)*
- ÚT 2-1-222-2002, *Útügyi Műszaki Előírás: General Rules of Geotechnical Design of Roads (in Hungarian)*
- Wang J. W. H. 1963. Comparative Studies on the Effects of Hydraulic, Calcitic and Dolomitic Limes and Cement in Soil Stabilization, *Highway Research Record* 29, 42-54.

# Etude paramétrique en laboratoire du matériau Deep Soil-Mixing

## Laboratory parametric study of the Deep Mixing material

Szymkiewicz F., Le Kouby A., Reiffsteck P., Mosadegh A., Tacita J.-L.  
IFSTTAR, boulevard Newton, Champs-sur-Marne, F-77447 Marne la Vallée Cedex 2

**RÉSUMÉ :** Le Deep Soil-Mixing consiste à mélanger mécaniquement un liant hydraulique avec le sol en place en vue d'améliorer ses propriétés mécaniques. En France, de nouvelles exigences concernant la méthode et le matériau sont apparues à mesure que son champ d'applications s'est étendu. Dans cette communication, le travail de recherche entrepris à l'IFSTTAR est présenté. Il a consisté à mener en laboratoire une étude paramétrique, en réalisant des mélanges dits "de référence". Trois sables et cinq sols fins ont été traités (à l'état pur ou mélangés entre eux) en faisant varier à chaque fois les quantités de ciment et d'eau, afin d'observer l'influence de la granulométrie, de l'argilosité et de la quantité d'eau présente dans le mélange sur la résistance. Les retombées de ce travail sont la proposition d'abaques reliant la résistance au dosage en ciment et au rapport C/E, et des formules permettant pour les sols grenus de prédire la résistance à 28 jours en fonction du pourcentage de fines dans le sol et du dosage en ciment.

**ABSTRACT:** The Soil-Mixing consists in mixing a hydraulic binder into the soil mechanically in order to improve its mechanical properties. In France, these new applications imply new requirements on the method as well as on the material. In this paper, the research work undertaken at IFSTTAR is presented: it consisted in carrying out a parametric study on reference mixtures. Three sands and five fine soils were treated with different cement and water contents to observe the influence of particle size, clay content and the amount of water present in the mixture on its strength. Benefits of this work is the proposal of abaci connecting the strength of the material to its cement content and cement / water ratio (C / E), and formulas allowing the prediction, for granular soils, of the strength of the material at 7 and 28 days depending on the percentage of fines in the soil and on the cement content.

**MOTS-CLÉS:** Deep Mixing, sol, ciment, résistance, compression simple, abaque.

**KEYWORDS:** Deep Mixing, soil, cement, strength, unconfined compression, abacus.

## 1 INTRODUCTION

La méthode du Deep Mixing présente de nombreux avantages (respect de l'environnement, exécution facile et rapide ainsi que coût faible) qui ont grandement contribué à étendre son domaine d'applications (amélioration des sols, confinement des pollutions et réalisation d'éléments structurels). Ces nouvelles applications nécessitent une meilleure compréhension de la méthode et du matériau. Les caractéristiques du matériau Deep Mixing (en particulier l'homogénéité et la continuité) sont de plus en plus étudiées, au fur et à mesure que le domaine d'application s'agrandit. De même, des méthodes de prédiction de la résistance du matériau sont en cours de développement.

Babasaki et al. (1996) citent quatre facteurs qui influencent la croissance de la résistance du matériau: les caractéristiques du liant, la nature et l'état du sol rencontré, le malaxage et les conditions de cure. Porbaha et al. (2000) affirment qu'il est communément admis que la résistance du sol traité au ciment augmente avec le temps, de la même façon qu'un béton. De nombreuses études ont été menées pour proposer des formules en ce qui concerne la prédiction de la résistance du matériau. Bruce (2001) et Topolnicki (2004) ont proposé des relations générales reliant le gain de résistance à la nature du sol à traiter, ainsi que des plages de résistances atteignables pour ces mêmes sols après 28 jours de cure. En outre, des formules ont été proposées pour prédire la résistance du matériau à partir d'un ou plusieurs facteurs énoncés par Babasaki et al. (1996). Pour les bétons, des lois portant sur le développement de la résistance et dépendant uniquement du rapport ciment sur eau du mélange étudié ont été établies. Ces lois ont été testées sur le Soil-Mixing, mais se sont avérées inadéquates.

Mais d'autres formules ont été proposées, en tenant compte du ciment, de l'eau et / ou du contenu en fines du sol traité. Cependant, il n'existe toujours pas de formule largement applicable pour estimer la résistance du matériau et intégrant tous les facteurs qui devraient être pris en compte (CDIT, 2002), car au jour d'aujourd'hui, aucune norme internationale n'existe pour la préparation des échantillons de sol traités en laboratoire (Kitazume et al., 2009). De plus, certaines formules ne peuvent être appliquées qu'à un site particulier, tandis que d'autres ne peuvent être appliquées qu'à certains sols.

Cet article présente les résultats d'une étude paramétrique exhaustive ayant mis l'accent sur la résistance du matériau Deep Mixing. Des relations liant la résistance aux paramètres du Deep Mixing ainsi qu'un abaque pouvant servir au dimensionnement d'ouvrages sont proposées.

## 2 PROGRAMME EXPERIMENTAL

### 2.1 Matériaux

Les sols testés au cours de cette étude vont des sables purs aux argiles pures, avec des limons et des sols artificiels reconstitués à partir de sable de Fontainebleau mélangé avec de l'argile ou du Silica Flour, afin de permettre l'étude de l'impact de la nature et de la quantité des fines sur la résistance du matériau Deep Mixing. Le tableau 1 présente les principales caractéristiques des sols testés.

Tableau 1. Principales caractéristiques granulométriques et valeurs au bleu de méthylène (VBS) des sols utilisés

Soils	d <sub>60</sub> (mm)	d <sub>30</sub> (mm)	d <sub>10</sub> (mm)	Percent passing 2 mm	Percent passing 80 µm	Percent passing 2 µm	VBS
Fontainebleau sand (SF)	0,22	0,18	0,15	100	0,1	0	0,01
Triel sand	0,38	0,23	0,13	89,2	2,33	0	0,1
Fréjus sand	0,5	0,23	0,07	94,25	11,8	0	0,2
Silica Flour (SilicaF)	0,028	0,011	0,004	100	95,2	≈ 5	0,14
Silt TGV	-	-	-	100	98,9	19	2,3
Silt Vémars	-	-	-	96,8	82	30	4
kaolinite Soka (kaoS)	-	-	-	100	100	82	1,25
kaolinite de Provins	-	-	-	100	100	92	6,67
illite du Puy	-	-	-	100	95,1	56	5,4
illite Arvel	-	-	-	100	100	76	5,9
Montmorillonite Arvel	-	-	-	100	100	53	28

Les sols artificiels sont nommés par l'abréviation citée entre parenthèses dans le tableau 1 : par exemple, un sol artificiel fait de 75% de sable de Fontainebleau et 25% de kaolinite Soka sera nommé SF75-kaoS25. Plus de détails sur tous ces sols peuvent être trouvés dans Szymkiewicz (2011).

Le ciment utilisé pour ce programme expérimental est un ciment de haut fourneau contenant au moins 85% de laitier de haut fourneau, avec le reste de clinker Portland et un peu de gypse (Classement Européen: "HRC" CEM III / C 32,5 N CE PM-ES NF). Ce ciment présente une résistance à développement lent, et son temps de prise initial est de 4 heures après hydratation.

## 2.2 Malaxage, coulage et conservation

Les sols ont été traités avec des teneurs en ciment diverses allant de 70 à 400 kg/m<sup>3</sup>, couvrant ainsi toute la gamme usuelle de dosages des applications Deep Mixing. Sol et ciment ont d'abord été soigneusement mélangés à sec et manuellement, afin d'obtenir une consistance uniforme. Ils sont mis dans le malaxeur et l'eau est ajoutée. La teneur en eau du mélange ( $w_i$ ) a été choisie afin d'obtenir un matériau auto-plaçant, ce qui signifie qu'il doit être suffisamment fluide pour s'écouler sous son propre poids. Ainsi,  $w_i$  doit être au moins égale à la limite de liquidité du mélange (Szymkiewicz et al., 2012 b).

Le matériau est ensuite malaxé pendant 5 minutes pour les sols non cohérents et pendant 10 minutes pour les sols cohérents. Le mélange est ensuite coulé dans des moules cylindriques de 52 mm de diamètre, et, pour éviter les bulles d'air dans les échantillons, piqué et vibré.

Les moules sont ensuite bouchés et scellés dans un sac hermétique contenant une humidité relative élevée. Ceux-ci sont conservés à une température de  $20 \pm 3$  ° C jusqu'à la date d'essai (7, 14, 21, 28, 56 et 90 jours).

Le test de compression simple a été choisi principalement pour sa fiabilité et son utilisation internationale. La charge verticale statique a été appliquée à une vitesse constante de 0,3 mm min<sup>-1</sup>. Le déplacement axial externe a été mesuré à l'aide d'un LVDT. Plus de détails peuvent être trouvés dans Szymkiewicz et al. (2012 a).

## 2.3 Représentativité des résultats

De nombreux essais sur tout type de sol ont été effectués, afin d'évaluer la répétitivité, reproductibilité et la répétabilité des résultats (figure 1). La figure 1a montre que la méthode de réalisation des éprouvettes et leurs conditions de cure assurent une bonne répétitivité et reproductibilité des résultats, puisque deux mélanges (Fontainebleau C 265 et C 320) ont été répétés en suivant exactement la même procédure, le lendemain, par le même opérateur (Fontainebleau C 320) et par un autre opérateur

(Fontainebleau C 265). La figure 1b montre que la répétitivité des tests est assurée: le coefficient de variation est égal à 7% pour le Puy du Argile, et égale à 9,3% pour les sols sableux.

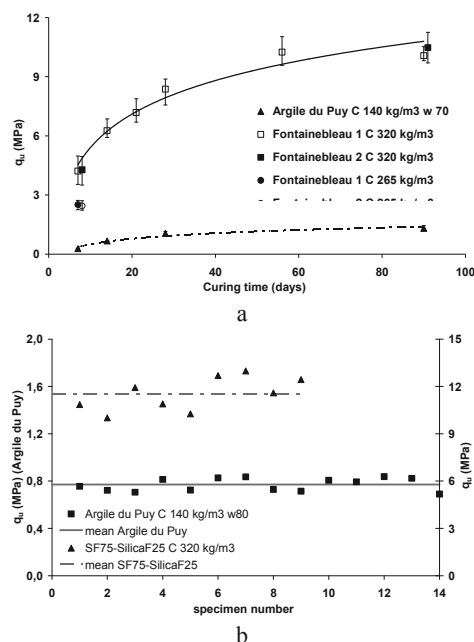


Figure 1. Représentativité des résultats : répétibilité et reproductibilité (a) et répétitivité (b).

## 3 RÉSULTATS ET ANALYSES

### 3.1 Effet du ciment et des fines sur la résistance des sols granulaires non plastiques

Consoli et al. (2010) ont proposé une fonction puissance (Eq. 1) comme étant la plus adaptée à la relation expérimentale entre la résistance à la compression simple ( $q_u$ ) et le dosage en ciment (C).

$$q_u = a \times C^b \quad (1)$$

où  $a$  est un paramètre exprimé en kPa et  $b$  un paramètre sans dimension. Les deux sont des paramètres expérimentaux.

Szymkiewicz et al. (2012 a) ont observé la même relation pour différents sols reconstitués ou naturels et non plastiques. Ils ont également observé que les paramètres expérimentaux  $a$  et  $b$  sont fonction (au bout de sept jours de cure) du paramètre  $C_{63}$ , qui représente le pourcentage de fines dans le sol. Ainsi, ils ont

proposé une formule (Eq. 2) permettant de prédire la résistance du matériau Deep Mixing constitué d'un sol non plastique et de ciment, connaissant le  $C_{63}$  du sol, le dosage cible en ciment  $C$  (%), et les teneurs en eau initiale et finale  $w_i$  et  $w_f$  du matériau. Comme les résultats in situ et obtenus en laboratoire sont très comparables dans le cas de sols granulaires, une telle formule peut être utilisée directement pour des applications sur site.

$$q_{u28} = \frac{w_f}{w_i} \times 64.032 \times C^{1.777-0.171 \ln C_{63}} \times C_{63}^{0.544} \quad (2)$$

### 3.2 Effet du ciment, de l'eau et des fines sur la résistance des sols plastiques

Pour les sols cohérents (c'est-à-dire argileux ou limoneux), cependant, il n'est pas si simple d'analyser l'influence du ciment et des fines.

Tout d'abord, alors que la teneur en eau nécessaire pour obtenir un matériau auto-plaçant ne varie pas beaucoup dans le cas des sols strictement non plastiques (puisque les particules de sol sont inertes à l'eau), celle-ci est très variable lorsque des particules d'argile sont présentes dans le sol. D'autre part, le domaine optimal d'ouvrabilité du matériau Deep Mixing (défini par Szymkiewicz et al. (2012) comme la teneur en eau comprise entre les limites de liquidité et de floculation du sol traité (figure 2a)) est très faible dans le cas d'un sol non plastique, tandis qu'au contraire pour les sols traités plastiques, il peut être très important. En outre, le domaine d'ouvrabilité des sols évolue en fonction de la quantité de ciment ajoutée et le type de sol rencontré.

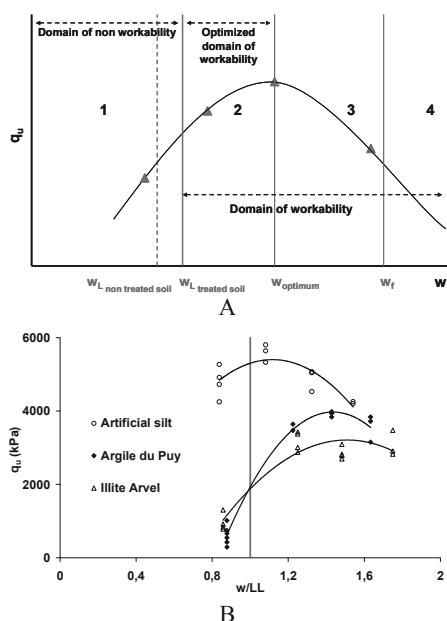


Figure 2. Représentation du domaine d'ouvrabilité (a) et détermination de la teneur en eau optimale (b) du matériau Deep Mixing.

Enfin, des essais sur éprouvettes ayant 28 jours ont également montré l'existence d'une teneur en eau optimale, indépendante de la teneur en ciment du mélange, mais fonction de l'indice de plasticité du sol d'origine (figure 2b). Par conséquent, il est presque impossible de dissocier le dosage en ciment de l'eau lors de l'étude des sols plastiques traités au ciment.

De plus, les sols plastiques présentent une cohésion qu'il est très important de prendre en compte, puisqu'elle apporte un gain de résistance supplémentaire. Pour déterminer l'effet de cette cohésion, des sols constitués de sable et de particules fines non plastiques d'une part, et de sable et de particules fines

plastiques d'autre part, en différentes proportions, ont été traités, à différents dosages en ciment. Les résultats ont montré que, pour un dosage en ciment constant, les sols traités faits de sable à 75% et de particules fines à 25% sont plus résistants que les sols purs traités. Ceci peut s'expliquer en partie par une optimisation de la distribution granulométrique, ce qui augmente la densité du matériau. Cependant, les particules plastiques participent aussi à l'augmentation de la résistance du matériau, via un apport de cohésion non drainée supplémentaire. Les résultats ont montré que cette résistance supplémentaire due à cette cohésion diminue avec l'augmentation de la teneur en ciment. Entre 210 et 320 kg/m<sup>3</sup> de ciment, les particules d'argile cessent d'avoir un effet bénéfique sur la résistance et peuvent commencer à être considérées comme un agent polluant.

Néanmoins, la fonction reliant la résistance au ciment pour les sols plastiques peut encore être exprimée comme une fonction puissance : le paramètre  $b$ , défini précédemment, diminue à mesure que le pourcentage de fines dans le sol augmente (comme pour un sol non plastique, d'ailleurs) jusqu'à ce qu'il atteigne 1. Ensuite, la relation devient linéaire (Eq. 3), de la forme :

$$q_u = c + a \times C^b \quad (3)$$

avec  $b$  toujours égal à 1, et  $a$  et  $c$  des paramètres expérimentaux exprimés en kPa.

Les paramètres  $c$  et  $a$  varient en fonction de la nature du sol (figure 3a), de même qu'en fonction du temps de cure. Cependant, aucune relation logique ne peut être proposée. La teneur en eau initiale du matériau semble quant à elle n'influencer que le paramètre  $c$  (figure 3b).

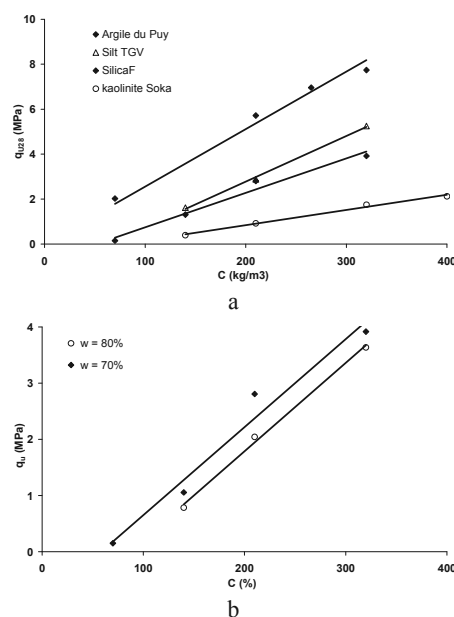


Figure 3. Relation résistance – dosage en ciment pour 4 sols plastiques (a) et pour un sol plastique à différentes teneurs en eau (b).

Dans le cas du Deep Mixing, où le matériau doit être suffisamment fluide pour être auto-plaçant,  $c$  est toujours nul ou négatif. Il existe donc un dosage seuil en ciment qui conditionne le succès du traitement au ciment d'une argile.

On voit bien qu'il est nécessaire de continuer les travaux en se focalisant sur les sols plastiques, puisqu'aucune formulation générale n'a encore pu être proposée qui permettrait de prédire la résistance du matériau.

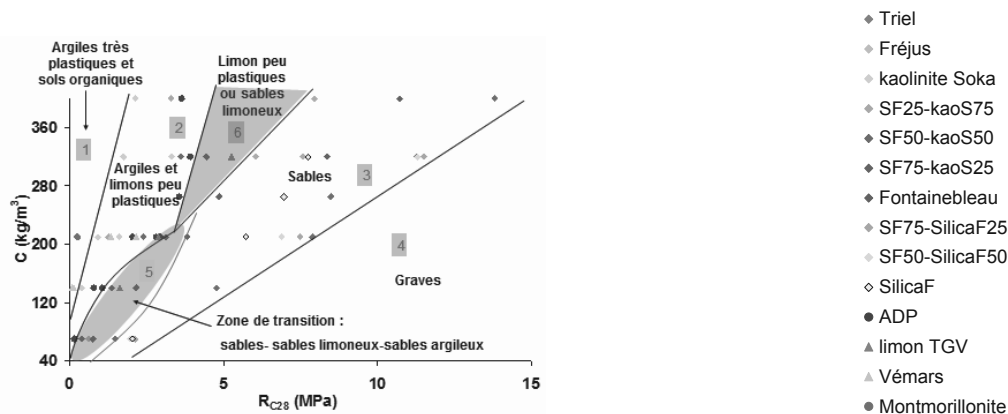


Figure 4. Abaque résistance – dosage en ciment pour un matériau Deep Mixing auto-plaçant.

### 3.3 Proposition d'un abaque Résistance – Dosage en ciment

Au cours de cette étude, 57 mélanges à partir de 14 sols et 6 dosages en ciment différents ont été réalisés et testés à chaque âge. Un des objectifs de cette étude était la réalisation d'abaques afin d'aider les ingénieurs à déterminer le dosage en ciment nécessaire à la réalisation des travaux à partir de la résistance mécanique nécessaire du matériau. Ces 57 points peuvent donc être placés dans le plan  $C = f(R_{C28})$  pour obtenir un premier abaque (figure 4), qui n'intègre pas de manière précise l'influence de l'eau, mais en tient compte tout de même de manière générale, puisque les mélanges testés ont été réalisés à des teneurs en eau s'étalant de la limite de liquidité à la limite de floculation. Nous avons choisi comme résistance de référence la  $R_{C28}$ , ce qui est toujours très parlant pour les industriels car elle est la référence utilisée pour les bétons, et aussi car c'est la résistance la plus grande que nous puissions prédire pour les mélanges à base de sols grenus. Cet abaque a été validé en la confrontant à des résultats obtenus sur site par des entreprises françaises.

Six zones peuvent être clairement identifiées sur cet abaque : la première représente le domaine des sols très plastiques et des sols organiques. La seconde représente celui des sols moyennement ou peu plastiques, qu'ils soient argileux ou limoneux, tandis que les troisième et quatrième sont dédiées aux sables et graves. Les graves traitées n'ont pas pu être testées en laboratoire, du fait de la petite taille des éprouvettes, qui n'aurait pas assuré une bonne représentativité du matériau. Deux zones un peu particulières se détachent : ce sont les zones 5 et 6 qui sont des zones dites de transition. Elles représentent les résultats présentés au paragraphe 3.1.

## 4 CONCLUSION

Dans cette communication, le travail de recherche mené à l'IFSTTAR depuis plusieurs années, de concert avec les différents acteurs du Deep Mixing français, est présenté. Une relation (validée par des retours chantier et des éléments bibliographiques) est proposée, qui permet de prédire la résistance des sols non plastique traités au ciment selon la méthode du Deep Mixing, c'est-à-dire avec une teneur en eau initiale suffisante pour que le matériau créé soit auto-plaçant, en connaissant seulement la granulométrie du sol, le dosage cible en ciment, et la teneur en eau initiale du mélange (ce qui sous-entend que les paramètres d'exécution sont contrôlés tout au long du chantier).

L'étude montre que la transition d'un sol non plastique à un sol plastique se fait de manière logique, en gardant la même forme de relation entre la résistance finale et le dosage en ciment, même si la nature même des particules argileuse fait que l'eau

et le temps auront un impact beaucoup plus important sur les sols plastiques que sur les sols purement grenus. L'existence d'optimums, en ce qui concerne le couple teneur en eau – dosage en ciment, permet néanmoins d'affirmer qu'il sera bientôt possible de proposer une formulation générale, à un âge donné.

Un abaque, réalisé à partir de cette étude et validé grâce à des retours chantier, est proposé : il permet, de manière simple, de déterminer le dosage en ciment à utiliser afin de s'assurer de l'obtention de la résistance mécanique requise, en fonction de la nature du sol rencontré.

Les perspectives de ce travail sont donc la poursuite de l'étude des sols argileux traités, ainsi que le développement d'une méthode de dimensionnement des ouvrages en matériau Deep Mixing, en mettant l'accent sur l'étude de l'homogénéité du matériau sur site.

## 5 REFERENCES

- Babasaki, R., M. Terashi, T. Suzuki, A. Maekawa, M. Kawamura and E. Fukazawa (1996). Factors influencing the strength of improved soil, Grouting and Deep Mixing. 2nd International Conference on Ground Improvement Geosystems
- Bruce, D. A. (2001). "Practitioner's guide to the deep mixing method." *Ground Improvement* 5(3): 95-100.
- CDIT. (2002). The Deep Mixing Method – Principle, Design and Construction. The Netherlands: A.A. Balkema Publishers.
- Consoli, N.C., Caberlon Cruz, R., Floss, M.F., & Festugato, L. (2010). Parameters controlling tensile and compressive strength of artificially cemented sand. *Journal of Geotechnical and Geoenvironmental Engineering*, 136, 759–763.
- Kitazume, M., & Nishimura, S. (2009). Influence of specimen preparation and curing conditions on unconfined compression behaviour of cement-treated clay. Deep Mixing'09, Japan.
- Porbaha, A., Shibuya, S., & Kishida, T. (2000). State of the art in deep mixing technology, Part III: Geomaterial characterization of deep mixing. *Ground Improvement*, 4, 91–110.
- Szymkiewicz, F. (2011). Evaluation des propriétés mécaniques du matériau Soil-Mixing (PhD Thesis). Paris: Université Paris-Est.
- Szymkiewicz, F., Guimond-Barrett, A., Le Kouby, A. & Reiffsteck, P. (2012 a) "Influence of grain size distribution and cement content on the strength and aging of treated sandy soils". *European Journal of Environmental and Civil Engineering*, 16, 7, pp 882–902.
- Szymkiewicz, F., Tamga, F-S., Le Kouby, A. & Reiffsteck, P. (2012 b), "Optimization of the strength and homogeneity of the deep mixing material by mean of the determination of the workability limit and optimum water content", *Canadian Geotechnical Journal*, submitted.
- Topolnicki, M. (2004). Chapter 9: In situ soil mixing. In M.P.M.K. Kirsch (Ed.), *Ground Improvement* (pp. 331–423). Abingdon, UK: Spon Press.

# Investigation of failure analysis of clay reinforced with sand encapsulated

## Enquête sur l'analyse des défaillances d'argile renforcé avec du sable enrobe

Tabarsa A.R.

*Faculty of Engineering, Golestan University, Gorgan, IRAN*

Hajjesmaeilian S.

*Islamic Azad University, Science and Research, IRAN.*

**ABSTRACT:** The paper includes discussions on the theory studies and numerical analysis as to stability of slopes reinforced with geotextile encapsulated with lenses of sand. In this study, given the laboratory research conducted on clay reinforced with geotextile encapsulated with lenses of sand, which showed in the high confining stresses due to the suitable interaction of clay and sand particles with geotextile, significant improvement is obtained in shear strength. Considering these results, based on the stability importance of slopes in the engineering projects and optimization, and increasing slopes stability, this technique is used as a reinforcement method in the clay slopes using various methods of reinforcement and the effect of various conditions such as the number of layers of reinforcement, confining pressures has been considered. In the study the numerical finite difference using software FLAC 2D has been applied. The results showed that the slopes with higher height the Sandwich technique to typical reinforcement with geotextile increases factor of stability safety under different studied scenarios because of improvement of intermediate behavior weakness by thin sand layers and the amount of factor of stability safety has been also enhanced, increasing the number of reinforcement layers.

**RÉSUMÉ :** Le document comprend des discussions sur les études théoriques et l'analyse numérique que les pentes stability of renforcés par des géotextiles encapsulés avec des lentilles de sable. Dans cette étude, compte tenu de la recherche en laboratoire menées sur de l'argile renforcée avec géotextile encapsulés avec des lentilles de sable, qui a montré dans les fortes contraintes de confinement en raison de l'interaction appropriée d'argile et de sable avec géotextile, une amélioration significative est obtenue dans la résistance au cisaillement. Compte tenu de ces résultats, basés sur l'importance de la stabilité des slopes in les projets d'ingénierie et d'optimisation, et d'augmenter la stabilité des pentes, cette technique est utilisée comme une méthode de renfort dans les pentes argileuses en utilisant diverses méthodes de renforcement et de l'effet de diverses conditions telles que le nombre de couches de renfort, des pressions de confinement a été pris en compte. Dans l'étude de la différence finie numérique à l'aide du logiciel FLAC 2D a été appliqué. Les résultats ont montré que les pentes à plus forte hauteur de la Technique du sandwich à renfort typique avec un facteur de sécurité augmente géotextile stabilité sous différents scénarios étudiés en raison de l'amélioration de la faiblesse comportement intermédiaire par des couches de sable fin et la quantité de facteur de sécurité de stabilité a été améliorée également, l'augmentation du nombre de couches de consolidation.

**KEYWORDS:** sandwich technique, reinforced soil, factor of safety, stability

## 1 INTRODUCTION

In non-reinforced backfills are constructed using natural materials the constraints from poor materials used, methods and non-favorable environmental and geotechnical conditions on the project site created failures or adverse conditions in the backfill.

Intensity and scope of the failures may be increased to some extent that to impact the general and stability and complete servicing the intended project. In addition in some exceptional cases the project needs stimulate the engineers to consider construction of backfills with special dimensions in slope or height and stability against particular loadings such as earthquake. For example construction of road or rail backfills with more height or backfills with steep (in places due to limited land, the possibility of Transverse extension of backfill base missing) can be considered as specific items. In each of the above mentioned cases the Construction of reinforced backfills with particular materials is felt, to be able to bear external factors effects as well as to have suitable stability in environmental and geotechnical conditions.

In the last three decades, Geosynthetics is widely used with high tension resistance to the soil reinforcement in geotechnical engineering. Makes using thereinforces provides soil tension resistance in the soil and thus reduce lateral deformation of soil and increase overall stability of reinforced soil structures (Abiera, H.O. 1991).

In past decades, mostly the reinforced soil technique has been applied using coarse materials as backfill (Backfill materials). Recently, due to economic considerations, the backfill material with low quality and local access has been used successfully (Bergado et al. 2008). Although you need to determine the geotechnical properties for reinforcement elements and backfill materials to design reinforced soil system, but the mechanism of interaction of soil - reinforcement element, plays an important role.

To consider soil interaction mechanisms – reinforcement element, studies have been done using direct shear and tension tests by various researchers (Zhenggui Wang and Werner Richwien 2002).

In the reinforced clay Soil, the contact resistance is low and consequently, failure in interface occur prior to the reinforcement tension strength to the final extent. Thus, a large percentage of the tension strength of reinforcement not mobilized at failure and cannot be used (Jewell, R.A and Wroth, C.P. 1987).

Experimental results show that the shear stress around reinforcement is high and decreases rapidly with distance from its surface. Thus in the reinforced soil structures with low quality backfill material it is possible that a thin layer with granular material containing high resistance around the reinforcement will be used to control high shear stresses near the reinforce and in the interface (Ghiassian and Jahannia 2004). This method improves the stress transfer mechanism due to a



better interface properties which is called sandwich technique (sandwich technique), In fact, the basis of this method is to provide a thin layer of sand with high strength on both sides of Geotextile, in order to improve the shear strength and deformation behavior of the reinforced clay soil (Unikrishnan.N, Rajagopa.K and.Krishnaswamy,N.R. 2001).

1.1 Studies on clay reinforced

The Studies of Unikrishna et al. (2001) on the reinforced clay with lens of sand (sandwich technique) did show that adding sand improves reinforced soil strength properties. Sand lens thickness, humidity and type of geotextile was paid attention.

Abdi et al. (2009) during large-scale direct shear tests, studied the resistance improvement due to provide the thin layers of sand on either side of the geogrid (sandwich technique) in the clay and reported the results of the study as follows.

- given the Figure (1) one can understand that providing a thin layer of sand with high strength on both sides of reinforcer is very effective to improve plasticity and resistance of clay soils.

- using the buried geogrid system in the sand of fine granular soil (sandwich technique) increases the shear resistance impressively. The buried geogrid system in the sand is more effective on the internal friction of soil and less effective on the coefficient of cohesion.

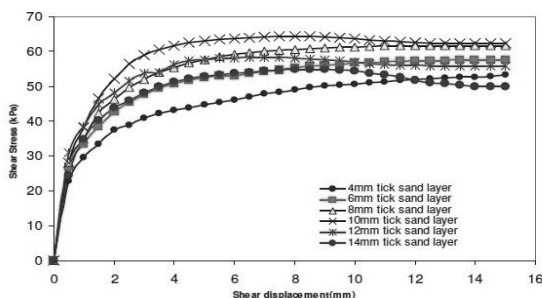


Figure 1. The relationship between shear stress - shear displacement under confining stress 75 kPa with different thicknesses of sand layers. (Abdi et al., 2009)

Abdi and Arjmand (2011) carried out various experiments on the pullout test on reinforced clay with geogrid encapsulated with thin layers of sand. The Samples have been prepared at the optimum moisture content and maximum dry density weight which have been obtained from Standard density testing Proctor. One-way geogrids used with a sand layer, 6, 10 and 14 mm in thickness. Experimental results showed that the encapsulated geogrid in thin sandy layers increases reinforced clay pullout resistance under the pullout conditions. The results showed that the maximum resistance to pullout increased with confining pressure and the optimal thickness of layer of sand is the same for all normal stresses.

Studies of Tabarsa and Radmehr (2011) on the reinforced clay with lens of sand (sandwich technique) yielded the following results. According to this research the increasing reinforcement layers caused to increase ultimate strength. Also improved the recovery of samples increasing confining stress from 100 to 550 kPa and to confining stress 300 kPa the improvement trend increases and then decreases. (Figure 2)

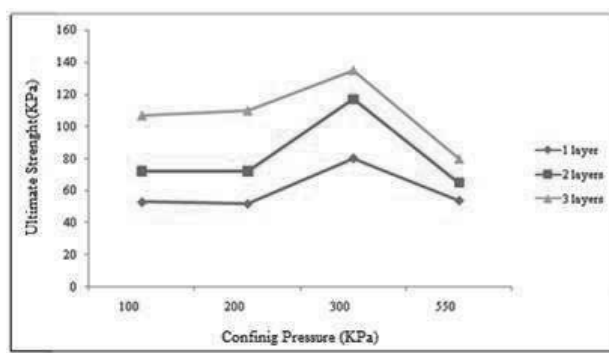


Figure 2. Effect of confining pressure on the reinforced sample, with geotextile and sand in 4 mm thick. (Tabarsa and Radmehr 2011)

Given the abovementioned forms it can be perceived that sample plasticity diminishes increasing the thickness of the layer of sand. Also, recovery percentage of resistance has increased slightly increasing the thickness of the sand in low confining stresses. And in high confining stresses (550 kPa) the high resistance percentage has increased significantly and therefore it can be stated that the high confining stresses impact on the sand performance in the composite system desired result is achieved. Because of the angle of high internal friction of the sand. The Results and research, suggest few studies on the subject of numerical simulation techniques for soil slopes stability analysis which the research has been done in this direction.

2 MODELING AND NUMERICAL ANALYSIS

FLAC software is based on the finite differential method. Finite differential methods used in various engineering issues. Its application in the soil and rock mechanics is common because one can model the big displacements and stresses of soil and rock masses. In the research FLAC 2D software has been used.

3 CHARACTERISTICS OF THE STUDIED MATERIALS

In this study, to analysis the slope stability, the behavioral models Mohr - Coulomb is used. Also nonwoven geotextile have been used for modeling the slopes.

Table 1. details the parameters considered in this study

soil	Density, kg/m <sup>3</sup>	Bulk module, kg/m <sup>2</sup>	Shear module, kg/m <sup>2</sup>	Dilation, degree	Cohesion, kg/m <sup>2</sup>	Angle of internal friction, degree
clay	2000	2E6	3E6	0	20000	15
sand	2000	3E7	4E7	15	2000	39

4 GEOMETRIC PROPERTIES OF SLOPES

In the analysis, four types of slope with different heights of 6, 9, 12 and 15 m with the same slope of 56 degrees have been considered. The method of geotextiles arrangement is shown in Figure 3 in the sandwich technique for the slope 12 meters.

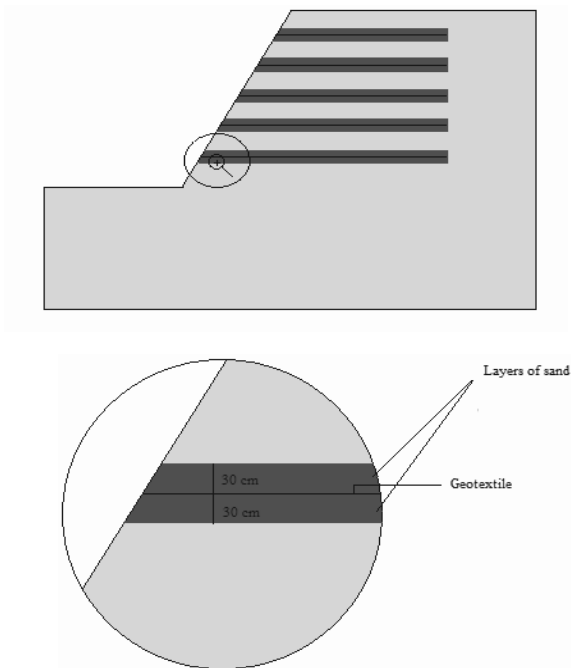


Figure 3. slopes 12-meter, reinforced with sandwich technique

### 5 HOW TO MODEL

First defining the model geometry and then required parameters are considered for different scenarios of various materials.

Given the importance of the boundary conditions on the both sides the slope is anchored in the horizontal direction (x) and in downwardslope horizontal and vertical directions (x, y) are anchored. Then geotextiles with distances equal to 1.5 m with the same length have been modeled. And following given the characteristics of the geotextiles, the suitable interaction parameters are involved between soil and geotextile. Then thin layers of sand with equal 30 cm thickness are considered to simulate the effect of sandwich technique in reinforcement process on the border between the reinforcement element and the clay soil (geotextile), given the different distances between the layers.

### 6 THE RESULTS OF NUMERICAL MODELING

After modeling and static analysis using software it evaluates and compares the factor of stability safety in slopes for different heights and different modes of reinforcement as follows.

#### 6.1 Results of static analysis on slopes with different heights

According to the analysis results, finite differences of reinforced clay slopes are shown as 6, 9, 12, 15 m, factors of safety in different states of reinforcement as computed (figures 4 and 5) and includes three modes 1- clay Model (C), 2 - clay with geotextile (CG), 3 - Sandwich Technique (CGS)

According to the output of numerical modeling analysis and the results shown in the above graphs, adding layers of sand on both sides of geotextiles (sandwich technique) increases significantly factors of safety at different height (6, 9, 12, 15 m). In Figure 6 this technique has a greater impact on stability of clay slopes in above heights and further increases the factor of stability safety.

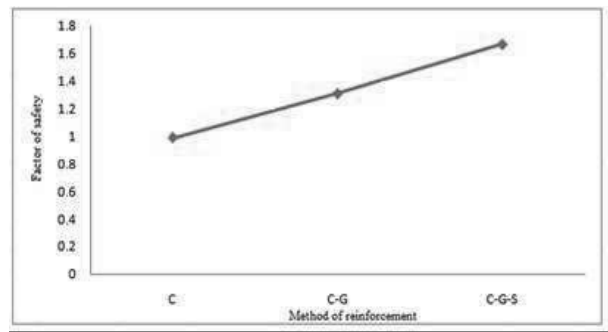


Figure 4. Comparison of factors of safety in 9 m slope

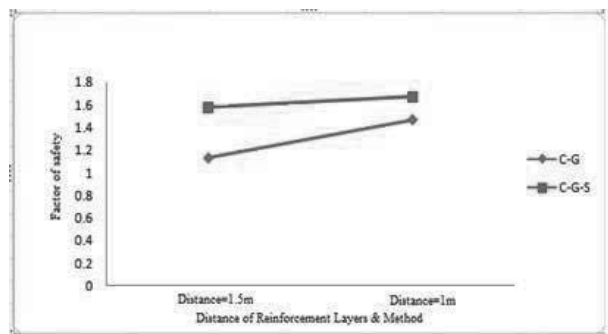


Figure 5. Comparison of factors of safety in 12 m slope for geotextile distances intervals in both 1 and 1.5 meter

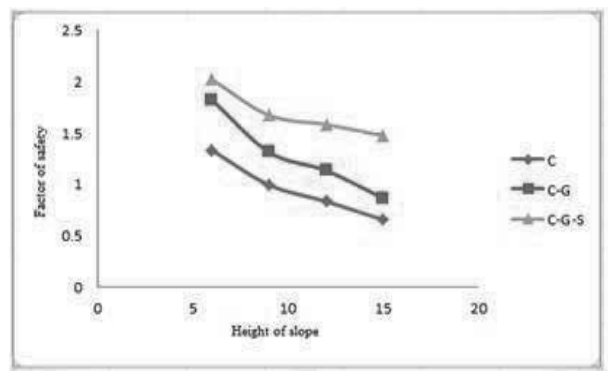


Figure 6. Comparison factors of safety of slop different heights in various states of reinforcement

### 7 CONCLUSION

- Analyses showed that the sandwich technique is an effective method of stabilizing clay slopes for engineers and results of the numerical analysis carried out in vitro studies are consistent with the sandwich technique.

- Sandwich technique is used in clay soils where have the poor and weak interaction with the geotextiles.

- given the acceptable development of a factor of safety using the sandwich technique we can make or design slopes with more height and slope in the engineering projects.

- sandwich technique in the more heights has more impact in the factor of safety increase, because of confining pressure increase and consequently getting better interaction condition between sand and geotextile.

- The factor of stability safety will be increased, increasing number of reinforced layers in the sandwich technique.

## 8 ACKNOWLEDGEMENT

At the end we thank sincerely for cooperation of dear friends Mr. Amir Gharib and Mohsen Mosivand.

## 9 REFERENCES

- Abiera H.O. 1991. Mechanically stabilized earth using tensar,bamboo and steel grid reinforcements with weathered Bangkok clay as backfill , *M. Eng. Thesis*,No.Gt-90-21 ,Asian institute of technology, Bangkok,Thailand.
- Bergado,D.T, Sampaco,C.L, Shivashankar,R, Alfaro,M.C, Anderson,L.R. and Balasubramaniam, A.S. 2008. Performance of a welded wire wall with poor quality backfill on soft clay, *In proceedings of ASCE*.
- Zhengui .W and Werner .R . 2002. A study of soil-reinforcement interaction friction .,*Journal of Geotechnical and Geoenvironmental Engineering*, 128 (1),92-94.
- Jewell. R.A. and Wroth, C.P. 1987. Direct shear test on reinforced sand., *Geotechnique* 37 (1), 53-68.
- Unnikrishnan.N, Rajagopal.K and Krishnaswamy,N.R. 2002. Behavior of reinforced clay under monotonic and cyclic loading ., *Geotextile and Geomembrances* (20),117-133.
- Abdi.M.R. and Arjomand M.A. 2011. Pullout tests conducted on clay reinforced with geogrid encapsulated in thin layers of sand., *Geotextiles and Geomembranes*, 1 – 8.
- Tabarsa,A.R. and Radmehr.M. 2011. Influence of geotextile encapsulated with sand on behavior clay reinforced., *research report*, Iran.
- Abdi.M.R and Sadnejad. M.R and Arjomand. M.A. 2009. Strenght enhancement of clay by encapsulating geogrids in thin layers of sand., *Geotextiles and Geomembranes* 27 ,447- 455
- Ghiassian.H and Jahannia.M. 2004. Influence of encapsulated geogrid-sand suestem on bearing capacity and settlement characteristics of reinforced clay. , *International Journal of Civil Engineering*, Vol.2,No.1.

# Influence of relative density on microbial carbonate precipitation and mechanical properties of sand

L'influence que la densité relative du sol donne dans précipitation du carbonate microbienne et propriétés de la mécanique

Tsukamoto M.

Kawasaki Geological Engineering Co., Ltd. (Formerly Public Works Research Institute), Minato-ku, Tokyo, Japan

Inagaki, T. Sasaki, Y.

Public Works Research Institute, Tsukuba, Ibaraki, Japan

Oda K.

Osaka University, Suita, Osaka, Japan

**ABSTRACT:** There exists a ground improvement technology that uses calcium carbonate precipitated from carbon dioxide generated by microbial metabolism and calcium sources in the pores of soil. It is known that the mechanical properties of the improved grounds correlate with the amount of calcium carbonate precipitation, but it is unclear how soil density influences calcium carbonate precipitation and the mechanical properties of the improved soil. Toyoura sand specimens of three relative densities are used to precipitate calcium carbonate through microbial metabolism. The injection-improved test and the triaxial test (consolidated-drained condition) are conducted to investigate calcium carbonate precipitation and the mechanical properties of the soil. The results show clearly that more calcium carbonate precipitation occurs in soil with lower relative density, but that in soil with higher relative density, the mechanical properties strengthen as calcium carbonate precipitation increases.

**RÉSUMÉ :** Dans la nature, il existe des micro-organismes qui capturent le dioxyde de carbone et les ions calcium présents dans la terre pour ensuite rejeter du carbonate de calcium. Ces dernières années, en s'appuyant sur le fonctionnement de ces micro-organismes, une technique renforçant la résistance du sol a été développée. Dans le cadre du développement d'une technologie qui renforce le sol à l'aide de métabolisme microbien, la présente étude a mis en évidence expérimentalement que l'influence de la densité relative du sol exerce un effet bénéfique. Tout d'abord, à travers une série de tests de cisaillement, le comportement au cisaillement du sol renforcé par le métabolisme de ces micro-organismes a été mis en avant. Ensuite, il s'est avéré que plus la densité relative du sol était petite, plus la quantité de carbonate de calcium déposée était importante. Cependant, nous avons aussi compris que plus la densité relative du sol était grande, plus les effets renforçant la résistance du sol étaient visibles.

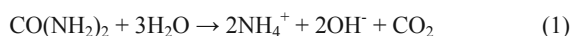
**KEYWORDS:** micro-organism, ureolysis, soil improvement, mechanical properties, triaxial test, calcium carbonate

## 1 INTRODUCTION

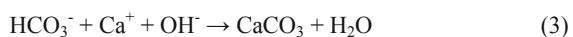
To ensure the efficient maintenance of civil engineering structures, which is an issue, ground improvement technologies can be applied to reinforce existing structures. Ground improvement technology that uses calcium carbonate precipitated from carbon dioxide generated by microbial metabolism and calcium sources in the pores of soil is expected to be applicable to ground directly under existing structures because the viscosity of the injected grout is low (Wiffen et al. 2007). It is known that the mechanical properties of grounds improved through the use of this method correlate with the amount of calcium carbonate precipitation (Inagaki et al. 2011), but it is unclear how the relative density of the soil influences the precipitation and the mechanical properties of the improved soil.

In this study, we used *Sporosarcina pasteurii* (ATCC11859) to stimulate microbial metabolism via the following reactions. Our aim was to investigate the relationship between the soil's mechanical properties and calcium carbonate precipitation in three types of Toyoura sands that were compacted by microbial metabolism.

(Ureolysis)



(Calcium carbonate precipitation)



In the tests, microbial broth and a nutrient mixture were injected into the Toyoura sand specimens with three relative densities to improve compaction. In addition, we carried out a triaxial test (consolidated-drained [CD] condition) on the improved specimens. Then, we examined the influence of the relative density of the soil on calcium carbonate precipitation and the soil's mechanical properties.

## 2 TEST METHODS

### 2.1 Method for production of specimens

A half-split mold made of PVC, 15 cm in height and 5 cm in diameter, was used to create the specimens (Fig. 1 and Photo 1). Silicone grease was applied on the internal surface of the mold to prevent the generation of water paths along the wall. Toyoura sands having the physical properties listed in Table 1 were used to create the specimens, and the molds were filled with sand using the air-drop method. The specimens had a relative density of  $Dr = 15\%$  ( $\rho_d = 1.372 \text{ g/cm}^3$ ),  $Dr = 60\%$  ( $\rho_d = 1.504 \text{ g/cm}^3$ ), and  $Dr = 85\%$  ( $\rho_d = 1.589 \text{ g/cm}^3$ ). The specimens were checked for weight and density, fitted with a collar on top, and saturated with distilled water supplied from the bottom. The surface of the specimen of  $Dr = 15\%$  sank significantly during the hydraulic filling. This settlement was measured using vernier calipers, and it was confirmed that the relative density after hydraulic filling was about  $Dr = 30\%$ .

2.2 Curing method (nutrient injection process)

After saturation, 250 ml of microbial broth was injected into each specimen. The microbial broth was made by planting *Sporosarcina pasteurii* in the medium described in Table 2. After confirming that the broth had completely permeated the specimen, 200 ml of the nutrient mixture described in Table 3 was injected into the specimen at 12 h intervals for specified cycles.

Table 1. Physical properties of Toyoura sand

Soil particle density $\rho_s$ ( $g/cm^3$ )	Water content (%)	Max. grain diameter (mm)	50% diameter on the grain size diagram $D_{50}$ (mm)	Fine fraction content (%)	Max. dry density $\rho_{dmax}$ ( $g/cm^3$ )	Min. dry density $\rho_{dmin}$ ( $g/cm^3$ )	Soil suspension pH
2.623	0.0	0.425	0.177	0.6	1.645	1.333	6.3

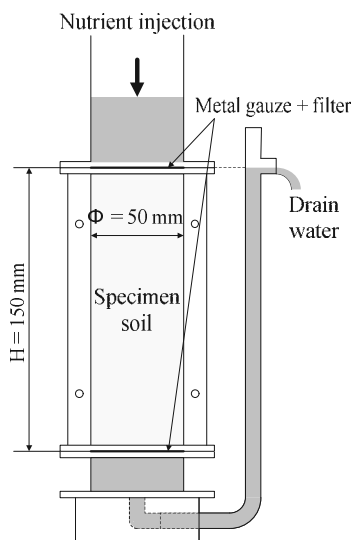


Figure 1. Schematic diagram of the mold



Photo 1. Photo of the mold

Table 2. Composition of medium

Name of reagent	Added amount
0.13 M Tris (pH = 9)	0.13 mol = 15.75 g
Yeast extract	20 g
(NH <sub>4</sub> ) <sub>2</sub> SO <sub>4</sub>	10 g
Distilled water	1 L

Table 3. Composition of nutrient mixture

Name of reagent	Added amount
Nutrient broth	3 g
NH <sub>4</sub> Cl	10 g
NaHCO <sub>3</sub>	2.12 g
Urea	0.5 mol = 30.03 g
CaCl <sub>2</sub>	0.5 mol = 55.49 g
Distilled water	1 L

The mold was cured in a room with a constant temperature set at 22°C. The nutrient mixture that had been injected previously and that remained in the pore was pushed out and drained to maintain the saturated state of the specimen in the mold.

Approximately 12 h after the specified cycles of nutrient injection were completed, 300 ml of distilled water was injected to wash away the nutrient mixture remaining in the pore.

As Table 4 shows, 15 specimens were made. The nutrient mixture was injected into these specimens at various frequencies in order to diversify the amount of CaCO<sub>3</sub> precipitation at each relative density. In addition, three specimens were only saturated with distilled water, and not injected with the broth and nutrient mixture, in order to examine the strength of the Toyoura sand itself.

Table 4. Test cases

Case	Specimen No.	Frequency of nutrient injection (Total injection amount ml)	Curing time (hours)	Initial dry density $\rho_d$ ( $g/cm^3$ )	Initial relative density Dr (%)	CaCO <sub>3</sub> Precipitation ( $kg/m^3$ )
Dr30	Dr30-N	—	—	1.423	33.2	—
	Dr30-P1	2(400)	24	1.428	35.2	32.24
	Dr30-P2	4(800)	48	1.414	30.2	63.72
	Dr30-P3	8(1600)	96	1.416	30.8	141.92
Dr60	Dr30-P4	12(2400)	144	1.414	30.4	225.53
	Dr60-N	—	—	1.513	62.6	—
	Dr60-P1	2(400)	24	1.504	59.9	28.11
	Dr60-P2	4(800)	48	1.504	60.0	51.77
Dr85	Dr60-P3	8(1600)	96	1.504	59.9	130.61
	Dr60-P4	12(2400)	144	1.504	60.0	212.11
	Dr85-N	—	—	1.589	84.9	—
	Dr85-P1	2(400)	24	1.589	85.0	27.12
Dr85	Dr85-P2	4(800)	48	1.589	85.0	57.38
	Dr85-P3	8(1600)	96	1.589	84.9	117.13
	Dr85-P4	12(2400)	144	1.589	85.0	198.55

2.3 Triaxial test method

Triaxial tests (CD condition) were conducted using the specimens produced by the method explained in 2.2. To reduce disturbance caused by the demolding/shaping of specimens, the specimens were frozen in the mold after the free water was removed. The specimens that featured high CaCO<sub>3</sub> precipitation were also frozen to equalize test conditions. The frozen specimens were removed from the molds and shaped to 10 cm in height and 5 cm in diameter. The shaped specimens were measured to check the diameter and height and then placed in a triaxial cell and defrosted under a negative pressure of 30 kPa. The defrosting time was set at about 1.5 h, which was the approximate time needed for stabilization of the axial displacement caused by contraction in the process of defrosting. We measured the diameter and the height of the defrosted specimens, covered them with a cell cover, and saturated them with degassed distilled water via the double-negative pressure method. The back pressure was increased to 200 kPa, and effective consolidation stresses of  $\sigma_c' = 100 \text{ kPa}$  were applied for isotropic consolidation. After consolidation, we confirmed that the  $B$  values in all the specimens were 0.95 or higher. Then, axial compression was performed at a strain rate of 0.5%/min. The axial force was measured by the load cell inside the cell, axial strain was measured by the displacement gauge outside the cell, cell pressure and back pressure were measured by the water pressure gauge, and the volume change was measured by the low-capacity differential pressure gauge.

After the triaxial tests were completed, the specimens were dried in a furnace and weighed, and the  $\text{CaCO}_3$  precipitation in each specimen was then obtained by measuring the decrease in mass resulting from  $\text{CaCO}_3$  decomposition by hydrochloric acid.

### 3 TEST RESULTS

#### 3.1 Relationship between the amount of nutrient mixture injected and the $\text{CaCO}_3$ precipitation

Figure 2 shows the relationship between the amount of nutrient mixture injected and the  $\text{CaCO}_3$  precipitation. The quantity of  $\text{CaCO}_3$  precipitation is given per unit volume of the test specimen.

The tendency for  $\text{CaCO}_3$  precipitation to increase as the injections of the nutrient mixture increased can be confirmed for each relative density. When the total injection of the nutrient mixture is less than 800 ml, the differences among specimens with different densities is unclear. When more than 800 ml of the nutrient mixture is injected, the differences among the specimens with different densities are observed. It is confirmed that lower the relative density, the more  $\text{CaCO}_3$  precipitates. This is because the low relative density increases the amount of microbes and nutrients absorbed by the test specimen.

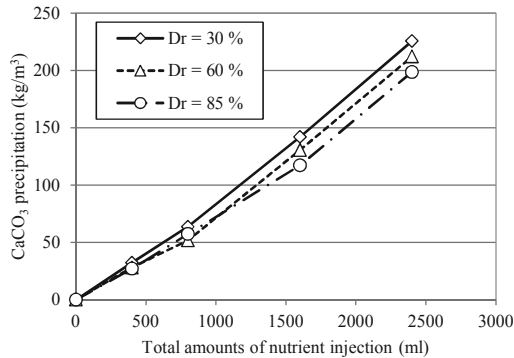


Figure 2. Total amounts of nutrient mixture injected and  $\text{CaCO}_3$  precipitation

#### 3.2 Relationships among axial strain, principal stress difference, and volumetric strain

Figure 3 shows the principal stress difference–axial strain curves and volumetric strain–axial strain curves. Toyoura sands of each relative density saturated only with distilled water (unconsolidated) and those injected with 800 ml of the nutrient mixture and  $\text{CaCO}_3$  precipitation of 51.8–63.7  $\text{kg/m}^3$  are shown in Fig. 3. Photo 2 shows the solidified test specimen after shear.

It can be confirmed that the solidification caused by the  $\text{CaCO}_3$  precipitation leads to an increase in the maximum principal stress. In specimens with about the same  $\text{CaCO}_3$  precipitation, the higher relative density of the soil, the increase in the maximum principal stress difference is the greater. Strain softening behavior is observed when the principal stress difference reaches the maximum in the solidified test specimen. A residual state occurs when axial stress reaches 5% or more; then, the principal stress difference is constant at every relative density, and its value shows no difference at each relative density. It is thought that the principal stress difference becomes equality in the residual domain because the test specimen is sheared along the sliding surface. Photo 2 also shows a shearing plane along the sliding surface. The increase in the volumetric strain on the expansion side is confirmed clearly in the solidified test specimens when the axial strain is small at each relative density in comparison with the unconsolidated test specimens, and the ratio of increase becomes small around an axial strain over 5%.

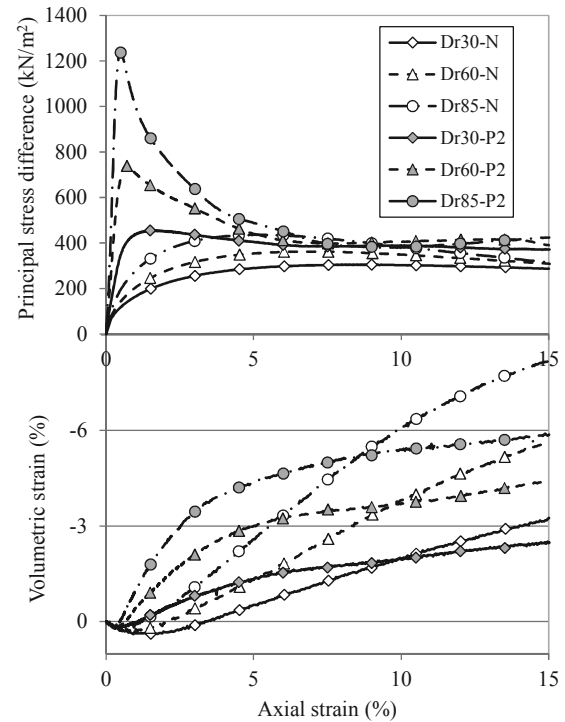


Figure 3. Relationships among axial strain, principal stress difference, and volumetric strain ( $\sigma'_c = 100 \text{ kPa}$ )



Photo 2. Condition of the test specimen after shear

#### 3.3 Relationship between $\text{CaCO}_3$ precipitation and maximum principal stress difference

Figure 4 shows the relationship between  $\text{CaCO}_3$  precipitation and the maximum principal stress difference. There is no change in the maximum principal stress difference when  $\text{CaCO}_3$  precipitation is less than 30  $\text{kg/m}^3$  at each relative density. At precipitation levels greater than 30  $\text{kg/m}^3$ , the maximum principal stress difference increases monotonically depending on  $\text{CaCO}_3$  precipitation. The increase in strength is remarkable in test specimens have higher relative density but little  $\text{CaCO}_3$  precipitation. In the case of  $\text{Dr} = 85\%$ , in comparison with  $\text{Dr} = 30\%$  and  $\text{Dr} = 60\%$ , the maximum principal stress difference increases even as  $\text{CaCO}_3$  precipitation stays at the same level.

#### 3.4 Relationship between $\text{CaCO}_3$ precipitation and secant modulus

Figure 5 shows the relationship between  $\text{CaCO}_3$  precipitation and the secant modulus. The secant modulus was calculated from the principal stress difference at the axial strain of 0.4%. At each relative density, there is little change when  $\text{CaCO}_3$  precipitation is less than 30  $\text{kg/m}^3$ , however, when  $\text{CaCO}_3$  precipitation is more than 30  $\text{kg/m}^3$ , the secant modulus increases linearly according to the increase in  $\text{CaCO}_3$  precipitation.

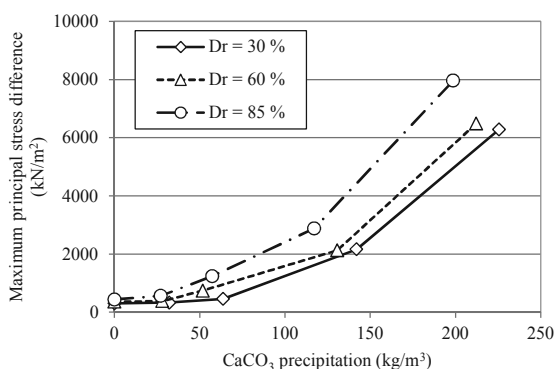


Figure 4. Relationship between CaCO<sub>3</sub> precipitation and maximum principal stress difference

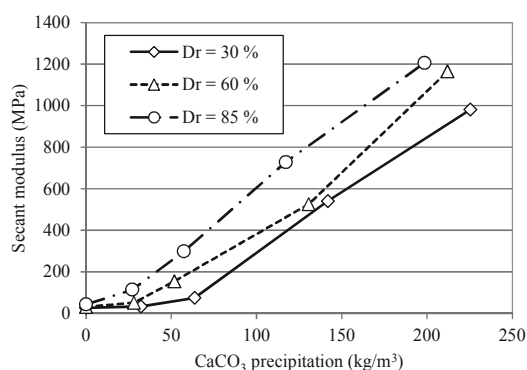


Figure 5. Relationship between CaCO<sub>3</sub> precipitation and secant modulus (axial strain 0.4%)

### 3.5 Relationship between CaCO<sub>3</sub> precipitation and axial strain at maximum principal stress difference

Figure 6 shows the relationship between CaCO<sub>3</sub> precipitation and axial strain at the maximum principal stress difference. For each relative density, when CaCO<sub>3</sub> precipitation is less than 60 kg/m<sup>3</sup>, the axial strain at the maximum principal stress difference increases linearly according to the increase in precipitation. When CaCO<sub>3</sub> precipitation is more than 60 kg/m<sup>3</sup>, the axial strain at the maximum principal stress difference remains in the vicinity of 0.5% and shows no difference at each relative density.

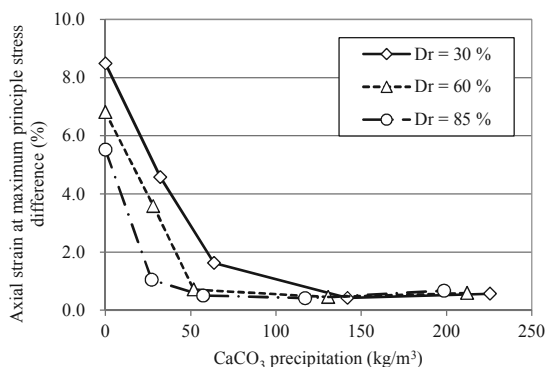


Figure 6. Relationship between CaCO<sub>3</sub> precipitation and axial strain at maximum principal stress difference

### 3.6 Relationship between CaCO<sub>3</sub> precipitation and residual stress

Figure 7 shows the relationship between CaCO<sub>3</sub> precipitation and residual stress. The residual stress indicates the minimum principal stress difference, less than axial strain 15%, after the maximum principal stress difference.

There is little change in the residual stress at each relative density up to about 30 kg/m<sup>3</sup> of CaCO<sub>3</sub> precipitation in

comparison with a case of no precipitation. It is confirmed that the residual stress increases as the CaCO<sub>3</sub> precipitation increases at precipitation levels of more than 30 kg/m<sup>3</sup>. The specimens for each relative density show no difference at CaCO<sub>3</sub> precipitation levels less than 60 kg/m<sup>3</sup>, and it is unclear whether a difference is observed at precipitation levels greater than 60kg/m<sup>3</sup>.

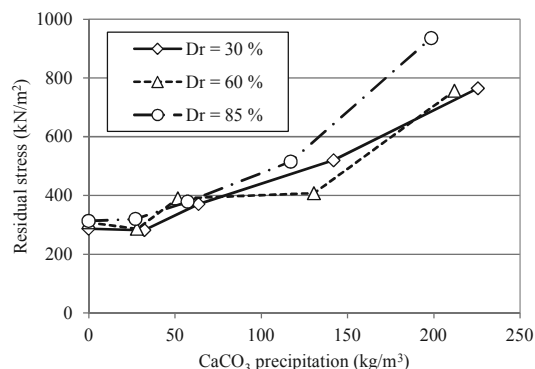


Figure 7. Relationship between CaCO<sub>3</sub> precipitation and residual stress

## 4 CONCLUSION

We investigated the influence of the relative density of soil on CaCO<sub>3</sub> precipitation by microbial metabolism and on the soil's mechanical properties. The results of our experiment are as follows:

- The CaCO<sub>3</sub> precipitation tends to increase as the relative density of the soil decreases.
- The maximum principal stress difference increased monotonically with the CaCO<sub>3</sub> precipitation at each relative density. The secant modulus increased linearly.
- The increase in the maximum principal stress difference was remarkable in soils with high relative density.
- The axial strain at the maximum principal stress difference decreased depending on CaCO<sub>3</sub> precipitation in specimens of all relative densities and became constant regardless of CaCO<sub>3</sub> precipitation when it approached 0.5%.
- The residual stress increased monotonically depending on CaCO<sub>3</sub> precipitation, but the differences among the relative densities are unclear.
- A meaningful difference is not seen in the mechanical properties of the soil among specimens with no precipitation and those with CaCO<sub>3</sub> precipitation up to 30 kg/m<sup>3</sup>.

These results indicate that when applying this injection solidification technique in the field, the density of the existing ground will affect the strength increase. Therefore, like a conventional compaction method used in construction, this method would require a combination examination beforehand in order to confirm extreme expression characteristics.

Because the axial strain at the maximum principal stress difference becomes constant regardless of density when CaCO<sub>3</sub> precipitation becomes constant, we suggest that the approximate strength of the soil can be estimated using the secant modulus.

We will investigate the influence of soil density on a permeability change attributable to solidification by microbe metabolism in the future.

## 5 REFERENCES

Victoria S. W., Leon A. P. and Marien P. H. 2007. Microbial carbonate precipitation as a soil improvement technique. *Geomicrobiology Journal* 24, 417-423.

Y. Inagaki, M. Tsukamoto, H. Mori, S. Nakajima, T. Sasaki and S. Kawasaki. 2011. A centrifugal model test of microbial carbonate precipitation as liquefaction countermeasure. *Japanese Geotechnical Journal* 6, No. 2, 157-167.

# The reinforcement of soils by dispersed oversized particles

## Le renforcement des sols par les particules trop grandes non réparties uniformément

Vallejo L.E., Lobo-Guerrero S., Seminsky L.F.

Department of Civil & Environmental Engineering, University of Pittsburgh, Pittsburgh PA, USA

Caicedo B.

Departamento de Ingenieria Civil & Ambiental, Universidad de los Andes, Bogota, Colombia

**ABSTRACT:** Soils containing dispersed large particles (greater than # 4 sieve) form part of many engineered fills, glacial tills, debris flows, and residual soil deposits. Very little is known about the effect that the large particles have on the shear strength of the soil-large particles mixtures. In this study, the influence of the large particles on the shear strength of the mixtures was evaluated experimentally and numerically. The experimental analysis used direct shear tests on simulated granular materials containing large dispersed particles. The numerical analysis used the Discrete Element Method (DEM). The laboratory and the DEM simulation results indicated that the shear strength of the mixtures increased with the concentration ( $C_a$ ) of the simulated large particles in the mixtures. Also, this study established that the shear strength of the simulated granular materials with dispersed large particles,  $S_c$ , can be obtained if one uses the following relationship:  $S_c = S_m (1 + M C_a)$ . In this relationship,  $S_m$  is the shear strength of the simulated soil matrix in which the large particles are dispersed, and  $M$  is a constant that varied between 1 and 2 for the numerical and laboratory analyses.

**RÉSUMÉ :** Les sols contenant des particules dispersées de grande taille (supérieure à tamis # 4) constituent la majorité des remblais, argiles glacières à blocs, des coulées d'éboulis et des dépôts résiduels de sol utilisés dans la construction. Peu de travaux existent sur l'effet que les grosses particules ont sur la résistance au cisaillement des mélanges de particules de sol de grande taille. Dans cette étude, l'influence des grosses particules sur la résistance au cisaillement des mélanges a été évalué expérimentalement et numériquement. L'analyse expérimentale utilisée essais de cisaillement direct sur simulées matériaux granulaires contenant de grandes particules dispersées. L'analyse numérique utilisé la méthode des éléments discrets (DEM). Les essais en laboratoire et les résultats des simulations ont indiqué que la résistance au cisaillement des mélanges augmente avec la concentration ( $C_a$ ) des particules de grandes tailles simulées. En outre, cette étude a établi que la résistance au cisaillement des matériaux granulaires simulées avec des grosses particules dispersées,  $S_c$ , peut être obtenu si l'on utilise la relation suivante:  $S_c = S_m (1 + M C_a)$ . Dans cette relation,  $S_m$  c'est la résistance au cisaillement de la matrice du sol simulé dans lequel les grosses particules sont dispersées, et  $M$  est constante qui varie entre 1 et 2 pour les analyses numériques et de laboratoire.

**KEYWORDS:** granular mixtures, shear strength, laboratory tests, DEM analysis.

## 1 INTRODUCTION.

Materials forming part of natural slopes and engineered fills have a distinct structure, this consisting of a mixture of a soil matrix (sand) and large particles of gravel that are dispersed (fragments do not interact) in the soil matrix. The rock fragments are composed of materials larger than the No. 4 sieve (Magier and Ravina, 1982; Poesen and Lavee, 1994; Fragaszy et al. 1992; Budiman, et al., 1995 and Vallejo 1989, 2001) (Fig 1). Soil Mechanics has dealt mainly with the study of three main soil types: sands, silts, and clays. However, mixtures of soils such as those shown in Fig. 1 are more commonly found in nature and in earth construction projects than pure sands, silts and clays. Since the determination of the mechanical properties (i.e. shear strength) of mixtures such as those depicted in Fig. 1 has heretofore received scant attention, such an investigation is indeed called for. This study reports on the mechanisms involved with the shear strength of simulated granular materials with dispersed oversized particles.

## 2 LABORATORY TESTING PROGRAM

### 2.1 Equipment and simulated granular materials

For the purpose of understanding the mechanisms involved in the shear strength of granular materials with dispersed large particles an open face, two-dimensional direct shear apparatus.



Figure 1. Natural slope in Wisconsin made of a soil-rock mixture

was used (Fig. 2) This apparatus is called the Plane stress Direct Shear Apparatus (PSDSA) (Vallejo, 1991). The granular matrix will be simulated by a mixture of wooden sticks. Wooden sticks are strong and can be easily shaved into polygons as their cross sectional areas. These polygons resemble the profiles of actual



granular materials (Fig. 3). The wooden sticks forming the granular matrix will have 3 different average diameters. These will be equal of 6, 4, and 2.7 mm. Thus, the granular matrix as a whole will be made of sticks having an average diameter equal to 4.2 mm. The oversized large particles will be simulated by rough wooden circular cylinders with a diameter equal to 12 mm. The irregular sticks as well as the circular cylinders have a length equal to 25 mm. The mixture of wooden sticks and cylinders were placed inside two U forms that comprise the box in the Plane Stress Direct Shear apparatus (PSDSA) (Figs. 2 and 3). The area inside the two U forms is a square area with sides measuring 7.6 cm in length. The open face of the shear apparatus formed by the two U forms allows the recording of the changes taken place in the mixture during shearing. Two proving rings measure the normal and shear forces applied to the mixtures. Dial gauges measure the normal and shear displacements. The changes in fabric experienced by the mixture as well as the interaction between the granular matrix and the large particles during shear was recorded using digital photographs of the open face of the PSDSA .

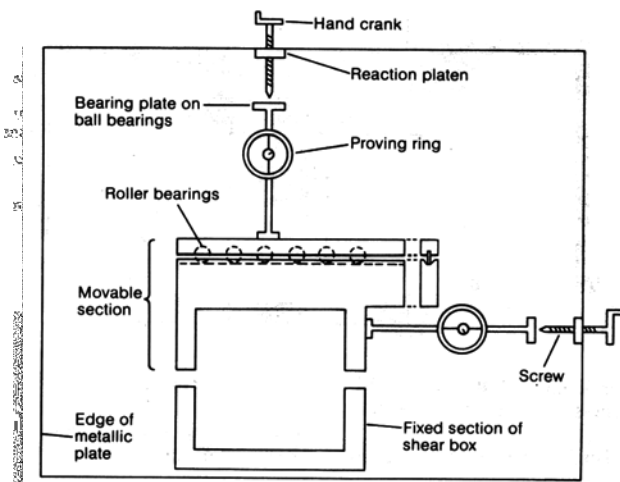


Figure 2. The Plane Stress Direct Shear Apparatus (PSDSA) (Vallejo, 1991)

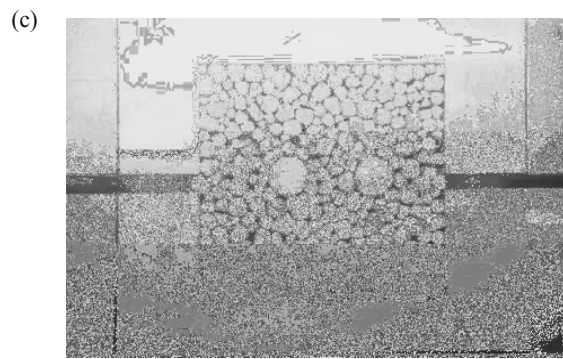
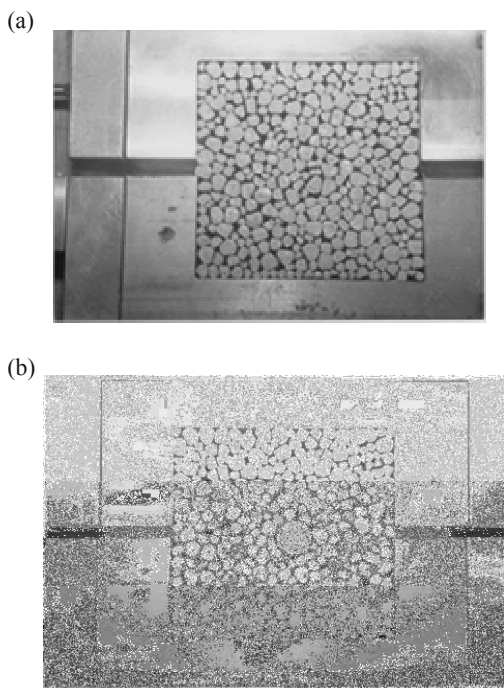


Figure 3. Simulated granular mixture in the PSDSA before shearing: (a) sample with no oversized particles, (b) sample with one oversized particle, (c) sample with two oversized particles.

### 2.2 Direct shear testing in the PSDSA

The simulated granular mixtures depicted in Fig. 3 were subjected to shear in the PSDSA. The shear testing of the mixtures were carried out using two normal stresses. These were equal to 99.6 and 199.3 kPa. The rate of shearing of the mixtures was equal to 2mm/min. Fig. 4 shows the shear stress versus the horizontal displacement relationships for the sample containing the matrix alone and the samples with one and two 12 mm in diameter cylinders representing the large particles (Fig.3).

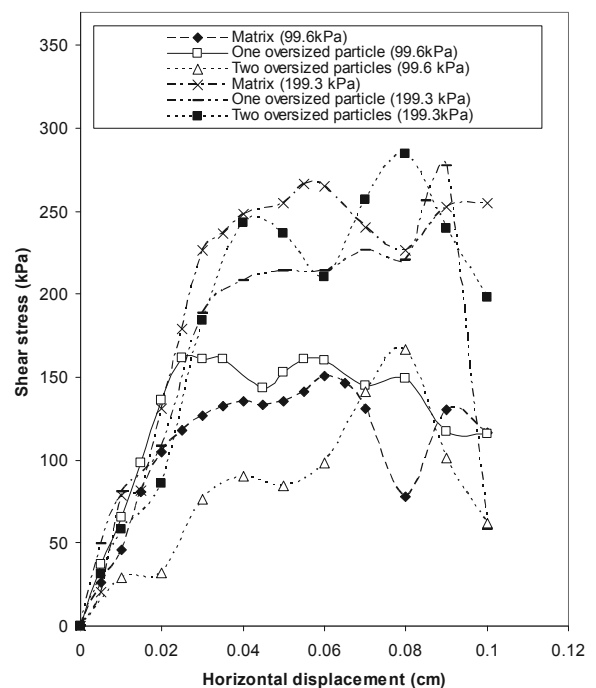


Figure 4. Shear stress versus horizontal displacement for the samples tested in the PSDSA

The peak values of the shear stress plots of Fig. 4 have been used to plot the shear strength versus the area concentration of the large cylinders in the sample. This area concentration is equal to the cross sectional area of the large cylinders in the mixture divided by the area of the whole mixture (7.62 cm x 7.62 cm) (Fig. 3). The resulting plot is shown in Fig. 5. This figure shows that the shear strength of the mixture increases as the number of large cylinders increases in the mixture. An equation that represents this increase is of the form:

$$S_c = S_m (1 + 2C_a) \quad (1)$$

where  $S_c$  is the shear strength of the mixture,  $S_m$  is the shear strength of the matrix, and  $C_a$  is the area concentration of the large cylinders in the mixture. The results of Fig. 5 and Eq. (1) indicate that the overall shear strength of the simulated granular mixtures increases with an increase in the number of the large cylinders. Thus, in the case of real sand-gravel mixtures, it is expected that the shear strength of these mixtures will increase with the volume concentration of the gravel in the mixtures.

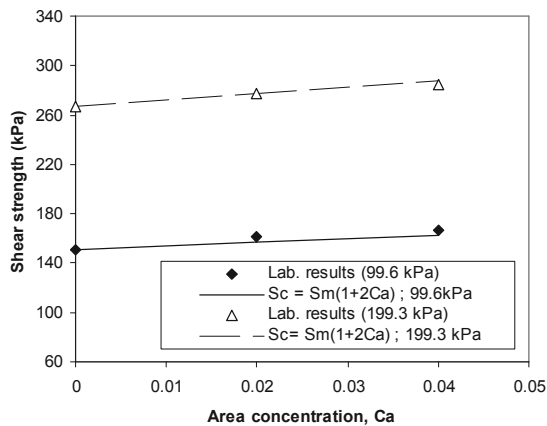


Figure 5. Shear strength of the simulated granular mixtures in function of the area concentration of the large cylinders in the mixture.

### 3 ANALYSIS OF THE LABORATORY RESULTS USING THE DISCRETE ELEMENT METHOD (DEM)

#### 3.1 Configuration of the samples

The PFC<sup>2D</sup> program produced by Itasca (Itasca Consulting Group Inc., 2002) was used for the simulation of the direct shear tests on granular material with dispersed oversized particles. The first step on the configuration of the sample was the construction of the shear box. The box had two sections each with a width of 6 cm and a height of 1.5 cm. The two sections were placed on top of each other and after the circular particles were generated inside the box, the gap between the two sections was maintained at 0.5 mm. The depth of the sample was assumed to be equal to 1 m. The shear and normal stiffness of the walls forming the box were set to  $1 \times 10^9$  N/m. The coefficient of friction between the circular particles and the walls was set to 0.7.

After the construction of the box, 1000 particles representing the granular matrix and having a diameter of 0.63 mm were generated inside the box. The density of the particles was set to  $2,500 \text{ kg/m}^3$ , their normal and shear stiffness were set to  $1 \times 10^8$  N/m. Their positions were randomly chosen by the program, having the limitation of no overlap between particles. A normal gravity field ( $9.8 \text{ cm/sec}^2$ ) was used during the simulation. In order to simulate the dispersed oversized particles, 52 particles of diameter equal to 0.63 mm were removed and replaced by an oversize particle measuring 5 mm. If an additional oversize particle was needed to be placed in the sample, the same number of smaller particles were removed and replaced by another large particle of 5 mm in diameter (Fig. 6). The tests were run under a constant normal compressive load equal to  $2 \times 10^4$  N. After the normal compressive force was applied to the sample, the shearing started by moving the upper section of the shear box to the left with a constant velocity of 0.44 mm/sec.

The tests ended when the horizontal displacement was equal to 5 mm. Also, using a subroutine available in the PFC<sup>2D</sup> code, one can obtain the value of the shear stress in function of the horizontal deformation. In this study, the peak shear resistance that was measured in the simulation represents the shear strength of the mixture.

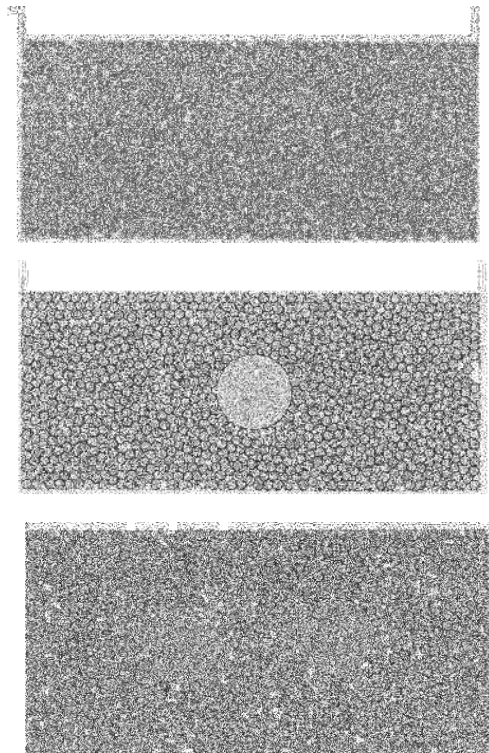


Figure 6. Simulated samples using DEM that contained zero, one, and two large dispersed particles.

#### 3.2 Results of the simulations

The DEM simulations of the direct shear tests were carried out on mixtures having zero, one, and two oversized particles. Figs 7 shows typical DEM results for the samples with zero, one and three oversized particles. These figures show the force chains and their intensity (the thicker the force chains, the bigger are the force chain value, their maximum values are shown on top of the figures) for the samples with 3.5 mm of horizontal displacement.

An analysis of Fig. 7 indicates that the larger force chains which were compressive in nature were directed toward the large particles and were transmitted to them by the smaller surrounding particles. When the horizontal displacement in the simulated test reached a 3.5 mm value, the force chains were inclined at about 45 and 135 degrees with respect to the horizontal axis of the cross sectional area of the large particles. It is usually assumed that when samples of granular materials with oversized particles are subjected to either compressive or direct shear stress conditions, the smaller particles in the mixture distribute the loads uniformly around the perimeter of the bigger particles. This uniform load distribution produces low compressive stresses on the bigger particles which allows them to survive without breakage (Fragaszy et al., 1992). The results shown by Fig. 7 indicate that this is not the case. Under direct shear, the smaller particles concentrate on the oversized particles, large compressive forces that are exerted on a small section of the perimeter of the large particles. These high concentrated compressive forces exerted by the smaller particles

on the large particles have also been found by Cheng and Minh (2009) to be effective in granular mixtures. The peak shear stress values obtained during the shearing of the mixtures shown in Figs. 6 and 7 were plotted against the area concentration of the large cylinders in the mixture. The result of the plot is shown in Fig. 8.

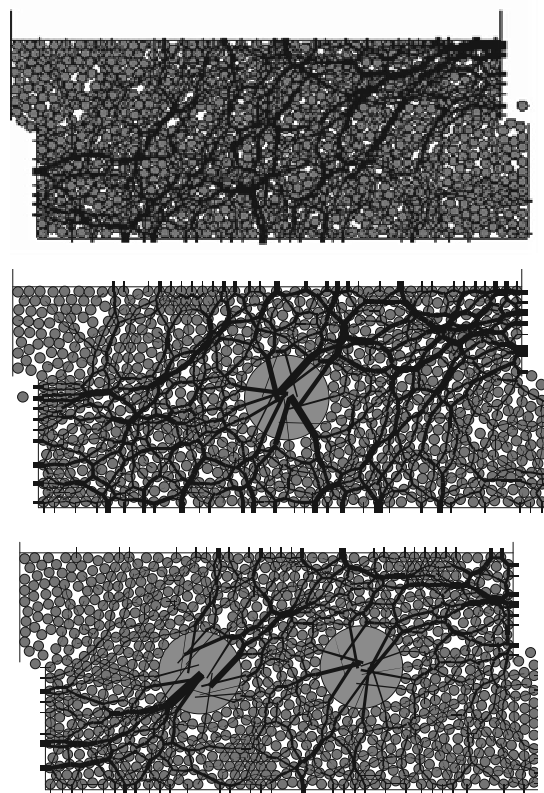


Figure 7. Force chains in the samples with zero, one and two large particles at a horizontal shear displacement equal to 3.5 mm.

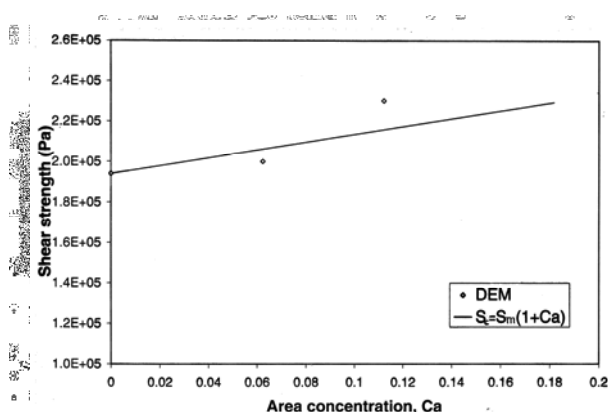


Figure 8. Shear strength versus the area concentration of the large cylinders in the simulated granular mixture.

An analysis of Fig. 8 indicates that the presence of the large cylinders in the mixture has a reinforcing effect. That is, as the number of large cylinders increase in the mixture, its shear strength also increases. The best fit line shown in Fig. 8 has an equation of the form:

$$S_c = S_m (1 + C_a) \quad (2)$$

which is very similar to Eq. (1).

It should be noted that the DEM simulations did not represent exactly the shape of the particles forming part of the laboratory experiments. Also, the sizes of the particles used in the laboratory experiments were different than those used in the DEM simulations. However, the general results of the laboratory tests are corroborated by the DEM simulations. In addition, the DEM simulations help to explain the way internal forces are transmitted through the particles in the laboratory experiments. Thus, for the case of real sand-gravel mixtures, it is expected that the shear strength of these mixtures will increase with the volume concentration of the gravel in the mixtures. Also, it should be noted that for the case of embankments and natural slopes, the effectiveness of the oversized particles on the shear strength of the mixtures forming these structures will depend upon if the large particles are located on or near the critical failure surface (Fig.1).

#### 4 CONCLUSIONS

In the present study the shear strength of simulated granular mixtures made of granular matrix in which large particles are embedded was carried out using laboratory and numerical analyses. Results from using both approaches indicated that the presence of the large particles has a reinforcing effect in the mixtures. That is, the greater the number of the large particles in the mixture, the greater is the shear strength of the mixtures.

#### 5 ACKNOWLEDGEMENTS

The work described herein was supported by Grants No. CMS: 0124714 and CMS: 0301815 to the University of Pittsburgh from the National Science Foundation, Washington, D.C. This support is gratefully acknowledged

#### 6 REFERENCES

Budiman, J.S., Mohamadi, J., and Bandi, S. (1995). Effect of large inclusions on liquefaction of sands. In: *Static and Dynamic Properties of gravelly Soils*, Evans, M.D., and Fragaszy, R.J. (eds), *ASCE's Geotechnical Special Publication No. 56*: 48-63.

Cheng, Y.P. Minh, N.H. (2009). DEM investigation of particle size distribution effect on direct shear behavior of granular agglomerates. *Powders and Grains 2009*, M. Nakagawa (Editor), American Institute of Physics, New York, 401-404.

Fragaszy, R.J., Su, J., Sidiqqi, F.H., and Ho, C.L. (1992). Modeling strength of sandy gravel. *Journal of Geotechnical Engineering*, ASCE, 118(6):920-935.

Itasca Consulting Group, Inc. (2002). *PFC2D (Particle Flow Code in Two Dimensions) version 3.0*. Minneapolis.

Magier, J. and Ravina, I. (1982). Rock fragments and soil depth as factors in land evaluation of Terra Rossa. *Soil Science Society of America (SSSA) Special Publication No. 13*: 13-30.

Poesen, J., and Lavee, H. (1994). Rock fragments on top soil: significance and processes. *Catena*, 23(1-2): 1-28.

Vallejo, L.E. (1989). An extension of the particulate model of stability analysis for mudflows. *Soils and Foundations*, 29 (3):1-13.

Vallejo, L.E. (1991). A plane stress direct shear apparatus for testing clays. *ASCE Geotechnical Special Publication No.27 (II)*: 851-862.

Vallejo, L.E. (2001). "Interpretation of the limits in shear strength in binary granular mixtures." *Canadian Geotechnical Journal*, 38:1097-1104.

# Analysis of Displacements of GPA in Normally Consolidated Soft Soil

## L'analyse des déplacements des GPA dans le sol mou Normalement consolidé

Vidyaranya B.

Research Scholar, Osmania University, Hyderabad, India

Madhav M.R.

Professor Emeritus, JNT University, & I.I.T., Hyderabad, India

**ABSTRACT:** Granular piles (GP) offer most effective and economical solution for ground improvement due to their drainage, densification and reinforcement actions, GPs mitigate liquefaction induced damages. An anchor placed at the base of the granular pile and attached to the footing by a cable or rod transfers the applied pullout force to the bottom of the GP termed as Granular Pile Anchor (GPA). The effective stresses in a normally consolidated saturated soil increase linearly with depth. Consequently, the undrained strength and the deformation modulus of the soil increase linearly with depth. Analysis of the displacements of granular pile anchor is presented considering the influence of the linearly increasing undrained modulus of soil and of the GPA with depth on the load – displacement response of the GPA. A parametric study quantifies effects of the length to diameter ratio of GPA, and the relative stiffness of the GP with respect to that of in situ soil at ground level, on the variations of tip and top displacements of GPA with applied load, variation of shear stresses and pullout load with depth, etc.

**RÉSUMÉ :** Pieux granulaires (GP) offrent une solution plus efficace et économique pour amélioration des sols en raison de leur drainage, la densification et des actions de renforcement, les médecins généralistes atténuer les dommages induits par liquéfaction. Un point d'ancrage placé à la base du pieu granulaire et fixée à la semelle par un câble ou une tige transfère la force de traction appliquée sur le fond de la GP qualifiée de mouillage pieu granulaire (GPA). Les contraintes effectives dans un sol normalement consolidé saturé augmente linéairement avec la profondeur. Par conséquent, la résistance non drainée et le module de déformation du sol augmente linéairement avec la profondeur. L'analyse des déplacements de l'ancrage empiement granulaire est présentée compte tenu de l'influence de plus en plus le module linéaire non drainée du sol et de l'GPA avec la profondeur de la réponse force - déplacement du GPA. Une étude paramétrique de quantifier les effets de la longueur par rapport au diamètre de l'GPA, et la rigidité relative du GP par rapport à celle du sol in situ au niveau du sol, sur les variations de pointe et des déplacements supérieurs de GPA avec la charge appliquée, la variation de cisaillement contraintes et la charge de retrait avec la profondeur, etc

**KEYWORDS:** Granular pile anchor, modulus of deformation, homogenous ground, displacements, load transfer.

### 1 INTRODUCTION.

Granular piles (GP) offer most effective and economical solutions in soft marine clays to counter-act low undrained shear strength and stiffness of the deposits. GPs improve the performance of ground by reinforcement, densification, increasing bearing capacity and resistance to liquefaction by increasing strength and stiffness of ground. GPs are ideally suited as they form elements of low compressibility and high shear strength. The effective stresses in a normally consolidated saturated soil increase linearly with depth. As a result the undrained shear strength and deformation modulus of the soil also increase linearly with depth. The increase in modulus of soil and granular material with depth result in reduced load-displacements response and increased confinement pressure.

The functional utility of the GP in compression is extended by placing an anchor at its base to transfer the pullout load or uplift forces to the base and the assembly is termed as Granular Pile Anchor (GPA). Granular pile treated expansive soil adjusts itself to changes in moisture better than an untreated-soil (Phani Kumar *et al.*, 2004). White *et al.* (2001) studied the application of reinforced geopiers for resisting tensile loads and settlement control. Lillis *et al.* (2004) reported results from in situ tests on pullout response of GPA. Kumar *et al.* (2004) present results from laboratory and field tests on pullout response of GPA in cohesive and cohesionless soils. A linear analysis of displacements of GPA is presented by Madhav *et al.* (2008).

### 2 PROBLEM DEFINITION

A granular pile of length,  $L$ , and diameter,  $d$ , with the soil and pile material characterized by moduli of deformation  $E_s$  and  $E_{gp}$ , and unit weights of  $\gamma_s$  and  $\gamma_{gp}$ , respectively is considered (Fig.1). A force,  $P_o$ , applied at the base of GPA is resisted by the shear stress,  $\tau$ , acting along the periphery of the pile. The force and the stresses acting on the GPA are depicted in Figure 2a. The stresses transferred to the in situ soil are shown in Figure. 2b. The non-homogeneities of deformation moduli of soil,  $E_s$  and granular material,  $E_{gp}$  (Fig. 3 & 4) are defined by the parameters,  $\alpha_s$  &  $\alpha_{gp}$ , to quantify the rate of increase of deformation moduli of in-situ soil and granular material with depth. The Poisson's ratio of the soil is  $\nu_s$ . In order to evaluate the upward displacements of the elements of the soil adjacent to the GPA

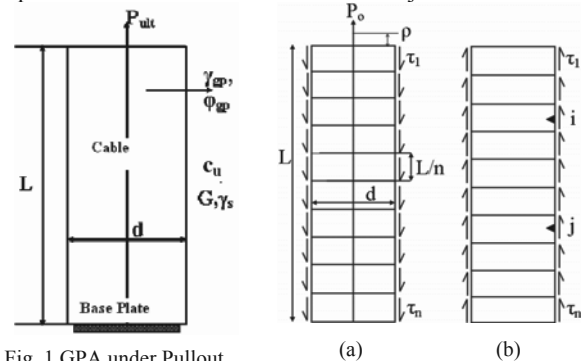


Fig. 1 GPA under Pullout

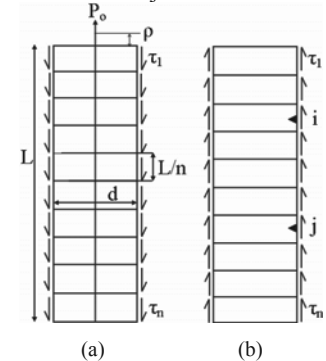


Fig. 2 Forces and Stresses acting on GPA and Soil.

due to the boundary stresses,  $\tau$ , the GPA surface is divided in to 'n' elements of length,  $\Delta L (=L/n)$ . The stress acting on a typical

element, j, is  $\tau_j$ . The displacement at the centre of an element, i, due to stresses acting on element, j, are obtained by the method described by Poulos and Davis (1980).

Integrating numerically, the Mindlin's equation for a point load in the interior of a semi-infinite elastic continuum over the cylindrical periphery of the element, the displacement,  $\rho_{s,ij}$ , of the soil adjacent to the centre of the i<sup>th</sup> element due to stress,  $\tau_j$ , acting on the element, j, considering deformation modulus,  $E_s$ , of the soil, increases linearly with the depth as

$E_s(z) = E_{s0} \left(1 + \alpha_s \frac{z}{L}\right)$  is obtained as

$$\rho_{s,ij} = \frac{d}{E_{s0}} \cdot \frac{I_{s,ij}}{\left(1 + \alpha_s \left(\frac{z_i}{L}\right)\right)} \cdot \tau_j \quad (1)$$

where  $I_{s,ij}$  is the soil displacement influence coefficient. The total soil displacement,  $\rho_{s,i}$ , adjacent to node 'i' due to stresses on all the elements of the GPA, is obtained by summing up all the displacements at node 'i', as

$$\rho_{s,i} = \frac{d}{E_{s0}} \sum_{j=1}^n \frac{I_{s,ij}}{\left(1 + \alpha_s \left(\frac{z_i}{L}\right)\right)} \tau_j \quad (2)$$

The vertical soil displacements adjacent to all the nodes are collected to arrive at

$$\{\rho_s\} = \frac{d}{E_{s0}} [I_s] \{\tau\} \quad (3)$$

where  $\{\rho_s\}$  and  $\{\tau\}$  are respectively the soil displacement and stress vectors of size, n, and elements of the matrix  $[I_s]$  are  $I_{s,ij} = \frac{I_{s,ij}}{\left(1 + \alpha_s \left(\frac{z_i}{L}\right)\right)}$  - non-dimensional soil displacement influence coefficient of GPA, where  $Z'_i = \frac{z_i}{L}$  - normalized depth at i<sup>th</sup> element.

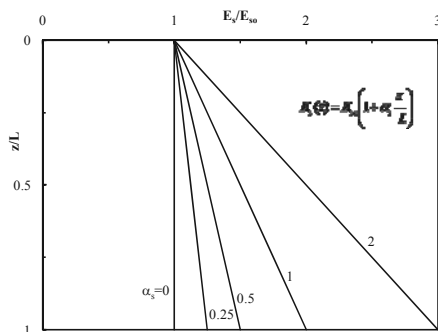


Fig. 3 Variation of  $E_s$  with Depth – Effect of  $\alpha_s$

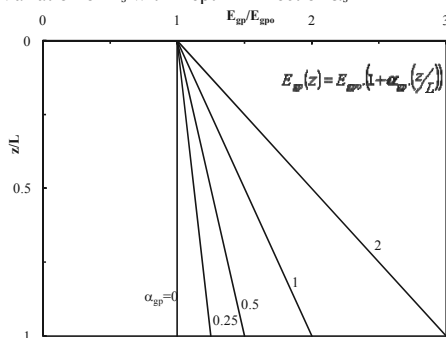


Fig. 4 Variation of  $E_{gp}$  with Depth – Effect of  $\alpha_{gp}$

### 2.1 DISPLACEMENTS OF GPA

The vertical displacements of GPA are obtained considering it to be compressible. Figure 5 depicts the stresses on an infinitesimal element of GPA of thickness,  $\Delta z$ . Poulos and Davis (1980) have established that lateral/radial stresses have negligible effect on the vertical displacements. Considering the deformation modulus of the granular material,  $E_{gp}$ , to increase linearly with depth, z, as

$$E_{gp}(z) = E_{gp0} \left(1 + \alpha_{gp} \left(\frac{z}{L}\right)\right) \quad (4)$$

The equilibrium of forces in the vertical direction reduces to

$$\frac{d\sigma_z}{dz} + \frac{4}{d} \tau = 0 \quad (5)$$

where  $\sigma_z$  is the normal stress in to the GPA. The stress-strain relationship for GPA material, is

$$\sigma_z = E_{gp} \epsilon_z = -E_{gp} \frac{d\rho_{gp}}{dz} \quad (6)$$

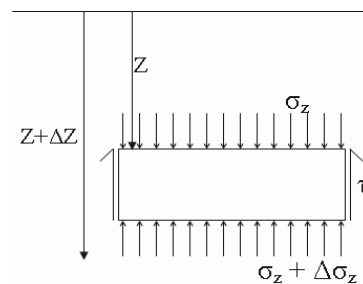


Fig. 5 Stresses acting on an Infinitesimal Element

where  $\epsilon_z$  and  $\rho_{gp}$  are respectively the axial strain and GPA displacement. Substituting for modified  $E_{gp}$  the stress-strain Equation 6 is modified as

$$\sigma_z = E_{gp} \epsilon_z = -E_{gp0} \left(1 + \alpha_{gp} \left(\frac{z}{L}\right)\right) \frac{d\rho_{gp}}{dz} \quad (7)$$

Differentiating Equation 7 with respect to depth, z,

$$\frac{d\sigma_z}{dz} = -E_{gp0} \left[ \left(\frac{\alpha_{gp}}{L}\right) \frac{d\rho_{gp}}{dz} - E_{gp0} \left(1 + \alpha_{gp} \left(\frac{z}{L}\right)\right) \frac{d^2\rho_{gp}}{dz^2} \right] \quad (8)$$

On simplification the differential Equation 8 becomes

$$\frac{d\sigma_z}{dz} = -E_{gp0} \left[ \left(\frac{\alpha_{gp}}{L}\right) \frac{d\rho_{gp}}{dz} + \left(1 + \alpha_{gp} \left(\frac{z}{L}\right)\right) \frac{d^2\rho_{gp}}{dz^2} \right] \quad (9)$$

Combining Equations 5 and 9 simplify

$$-E_{gp0} \left[ \left(\frac{\alpha_{gp}}{L}\right) \frac{d\rho_{gp}}{dz} + \left(1 + \alpha_{gp} \left(\frac{z}{L}\right)\right) \frac{d^2\rho_{gp}}{dz^2} \right] + \frac{4}{d} \tau = 0 \quad (10)$$

Equation 10 is solved along with the boundary conditions: at  $z = 0$  (i.e. at the top of GPA)  $P = 0$  (Free boundary) and at  $z = L$  (tip of the GPA),  $P = P_0$  (the applied load). Equation 10 written in finite difference form reduces to

$$\left\{ \frac{\alpha_{gp}(\rho_{gp,i-1} - \rho_{gp,i+1})}{L} + (1 + \alpha_{gp} z'_i) \frac{(\rho_{gp,i-1} - 2\rho_{gp,i} + \rho_{gp,i+1})}{(\Delta z)^2} \right\} \frac{4}{E_{gpo} d} \tau_i = 0 \quad (11)$$

where  $\Delta z = (L/n)$  – length of differential element of GP. Rearranging the terms in Eq. 11

$$\frac{n^2}{L^2} \left\{ \frac{\alpha_{gp}}{2n} (\rho_{gp,i-1} - \rho_{gp,i+1}) + (1 + \alpha_{gp} z'_i) (\rho_{gp,i-1} - 2\rho_{gp,i} + \rho_{gp,i+1}) \right\} - \frac{4}{E_{gpo} d} \tau_i = 0 \quad (12)$$

Eq. 12 is written as

$$\left\{ a_i \cdot \rho_{gp,i-1} - 2b_i \cdot \rho_{gp,i} + c_i \cdot \rho_{gp,i+1} \right\} - \frac{4L^2}{n^2 \cdot E_{gpo} \cdot d} \tau_i = 0 \quad (13)$$

where  $a_i = \left( 1 + \alpha_{gp} z'_i - \frac{\alpha_{gp}}{2n} \right)$   $b_i = \left( 1 + \alpha_{gp} z'_i \right)$   $c_i = \left( 1 + \alpha_{gp} z'_i + \frac{\alpha_{gp}}{2n} \right)$

$a_i$ ,  $b_i$  and  $c_i$  are displacement influence coefficients.

$\rho_{gp,i}$  and  $\tau_i$  are respectively the displacement at the centre of node ‘i’ and the shear stress on the interface of element, ‘i’, of the GPA. Eq. 13 is written for nodes  $i = 2$  to  $(n-1)$ . Invoking the first boundary condition,  $P=0$  implies  $\sigma_z=0$  and hence strain,  $\epsilon_z=0$ , leads to i.e.,

$$\rho_{gp,1} = \rho_{gp,1'} \quad (14)$$

where  $\rho_{gp,1'}$ —displacement at the imaginary node 1’ above the GPA (Fig. 2a). Eqs. 13 and 14 are combined to arrive at the finite difference equation for node ‘1’, as

$$\left\{ a_1 \cdot \rho_{gp,1'} - 2b_1 \cdot \rho_{gp,1} + c_1 \cdot \rho_{gp,2} \right\} - \frac{4L^2}{n^2 \cdot E_{gpo} \cdot d} \tau_1 = 0 \quad (15)$$

Eq. 15 reduces to

$$\left\{ (a_1 - 2b_1) \rho_{gp,1} + c_1 \cdot \rho_{gp,2} \right\} - \frac{4L^2}{n^2 \cdot E_{gpo} \cdot d} \tau_1 = 0 \quad (16)$$

All the equations for nodes 1 to  $(n-1)$  are collated as

$$[L'_{gp}] \{ \rho_{gp} \} - \frac{4L^2}{E_{gp} \cdot n^2 \cdot d} \{ \tau \} = 0 \quad (17)$$

where  $[L'_{gp}]$  is the displacement coefficient matrix.

The pile displacements equations for nodes 1 to  $(n-1)$  are collated and summarized in Eq. 17. The pile displacement influence coefficients are

$$\begin{bmatrix} (a_1 - 2b_1) & c_1 & 0 & \dots & \dots & \dots & \dots & 0 \\ a_2 & -2b_2 & c_2 & 0 & \dots & \dots & \dots & 0 \\ 0 & a_3 & -2b_3 & c_3 & 0 & \dots & \dots & 0 \\ 0 & 0 & a_4 & -2b_4 & c_4 & 0 & \dots & 0 \\ \dots & \dots & \dots & \dots & \dots & \dots & \dots & \dots \\ \dots & \dots & \dots & \dots & \dots & \dots & \dots & \dots \\ \dots & \dots & \dots & \dots & \dots & \dots & \dots & \dots \\ \dots & \dots & \dots & \dots & \dots & a_{n-1} & -2b_{n-1} & c_{n-1} \end{bmatrix} \quad (18)$$

Considering the compatibility of displacements in soil and GPA

$$\{ \rho_S \} = \{ \rho_{gp} \} \quad (19)$$

Combining Eqs. 3 and 17 with Eq. 19

$$[L'_{gp}] \frac{d}{E_{so}} [L'_S] \{ \tau \} - \frac{4L^2}{E_{gpo} \cdot n^2 \cdot d} \{ 1 \} \{ \tau \} = 0 \quad (20)$$

where  $\{ 1 \}$  is the unit vector.

### 3 RESULTS AND DISCUSSION

Equation 20 is solved for the displacements in GPA. The displacements generated along the GPA length are extrapolated to obtain the top,  $\rho_0$ , and the tip,  $\rho_L$ , displacements considering the 1<sup>st</sup>, 2<sup>nd</sup> and 3<sup>rd</sup> elements for the top and  $n-2$ ,  $n-1$  and  $n^{\text{th}}$  elements for the tip displacements in the GPA, respectively. The results are presented for the following ranges of parameters.  $L/d$ : 5, 10, 25 and 50;  $K$ : 10 to 10,000; Poisson’s ratio,  $\nu_s$ : 0.5,  $\alpha_s = 0, 0.25, 0.5, 1$  and 2; and  $\alpha_{gp} = 0, 0.25, 0.5, 1$  and 2.

The influence of  $\alpha_s$  on the variation of the shear stresses with depth is presented in Figure 6 for  $L/d=10$ ,  $K=50$ ,  $\nu_s=0.5$  and  $\alpha_{gp}=0, 0.5$  and 1. The variations of the shear stresses with depth are magnified at top as shown in Figure 6(b). The variations of shear stresses with depth are very similar for both values of  $\alpha_s = 0$  and 0.5 and decrease with increasing values of  $\alpha_{gp}$ . The shear stresses at the tip decrease from 6.65 to 5.63 and from 5.25 to 4.39 for  $\alpha_s = 0$  & 0.5 with  $\alpha_{gp}$  increasing from 0 to 1 respectively. On the contrary, the shear stresses at the top increase from 0.35 to 0.41 and 0.77 to 0.86 for  $\alpha_s = 0$  & 0.5 with  $\alpha_{gp}$  increasing from 0 to 1 respectively.

The variations of shear stresses with depth as a function of  $\alpha_{gp}$  are presented in Figure 7 for  $L/d=10$ ,  $K=50$ ,  $\nu_s=0.5$  and for  $\alpha_s = 0, 0.5$  and 1.0. The plots are magnified for the stresses at the top in Figure 7(b). The variation of shear stresses with depth for  $\alpha_{gp} = 0$  & 0.5 are very similar for all  $\alpha_s$ .

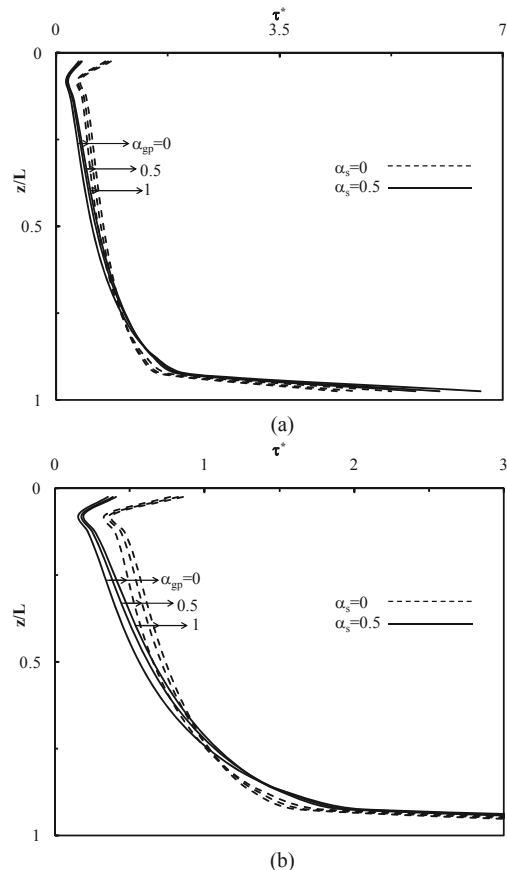


Fig. 6 Normalized shear stress,  $\tau^*$  vs. Depth,  $z/L$  for  $L/d = 10$ ,  $K=50$  &  $\nu_s=0.5$  – (a) Effect of  $\alpha_s$  &  $\alpha_{gp}$ . (b) Enlarged at top.

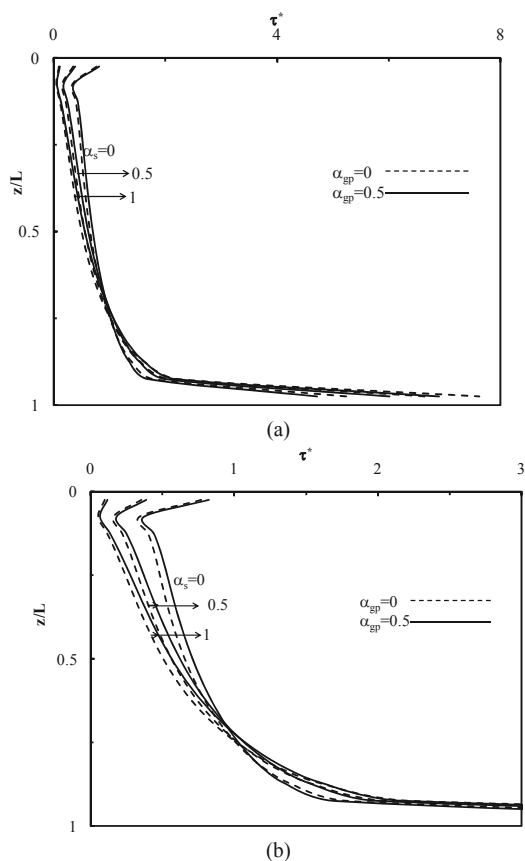


Fig. 7 Normalized shear stress,  $\tau^*$  vs. Depth,  $z/L$  for  $L/d = 10$ ,  $K=50$  &  $v_s=0.5$  – (a) Effect of  $\alpha_s$  &  $\alpha_{gp}$ . (b) Enlarged at top.

The variations of normalized tip displacements with depth for  $\alpha_s = 0$  ( $E_s$  constant with depth) and 0.5 are presented in Figure 8 for  $L/d=10$ ,  $K=50$ ,  $v_s=0.5$  and  $\alpha_{gp}=0, 0.5$  and 1. The displacement coefficients decrease with  $\alpha_{gp}$  at the tip, and increase at the top with  $\alpha_{gp}$  for  $\alpha_{gp}$  increasing from 0 to 1. The variation of  $I_U$  with depth is relatively large for smaller values of  $\alpha_{gp}$  compared to that for  $\alpha_{gp}=1$ . The displacement coefficient at the tip decreases from 1.91 to 1.47 for  $\alpha_s=0$  and from 1.732 to 1.34 for  $\alpha_s=0.5$ .  $I_U$  decreases by about 30% for  $\alpha_s=0.5$  in comparison to that for  $\alpha_s=0$  (homogenous soil).

The influence of  $\alpha_{gp}$ , the rate of increase of deformation modulus of granular material with depth on the variations of the displacement coefficients,  $I_U$  with depth for varying  $\alpha_s$  from 0 to 1,  $L/d=10$ ,  $K=50$  and  $v_s=0.5$  is presented in Figure 9. The displacement coefficient,  $I_U$ , for  $\alpha_s=0$ , at the tip decreases from 1.91 to 1.8 and increases from 1.12 to 1.17 for  $\alpha_{gp} = 0$  and 0.5 respectively. Similarly for  $\alpha_s=0.5$  and 1, the displacements at the tip decrease from 1.47 to 1.39 and 1.14 to 1.10 while at the top they increase from 0.87 to 0.90 and 0.71 to 0.74 for  $\alpha_{gp} = 0$  & 0.5 respectively.

#### 4 CONCLUSION

Analysis of the GPA under the influence of the non-homogeneities of the deformation moduli of the soil and granular material is presented in this paper. The shear stresses near the top of GPA are significantly less for  $\alpha_s$  increasing with depth. Displacements reduce for the deformation moduli parameters of soil and granular material increasing linearly with depth ( $\alpha_s=0.5$  &  $\alpha_{gp}=0.5$ ). The displacements reduce by 30% with depth for  $\alpha_s=0.5$  and 6% for  $\alpha_{gp}=0.5$  in comparison to those for  $\alpha_s=0$  and  $\alpha_{gp}=0$  respectively.

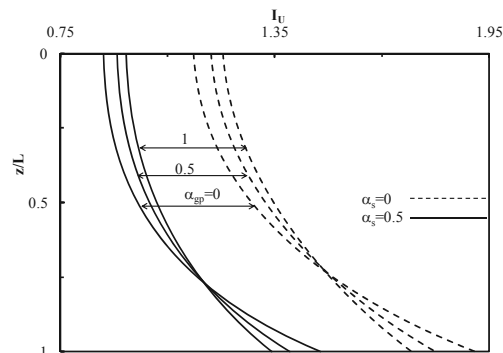


Fig. 8 Normalized displacement coefficient,  $I_U$  vs. Depth,  $z/L$  for  $L/d=10$ ,  $K=50$  &  $v_s=0.5$  – Effects of  $\alpha_s$  &  $\alpha_{gp}$ .

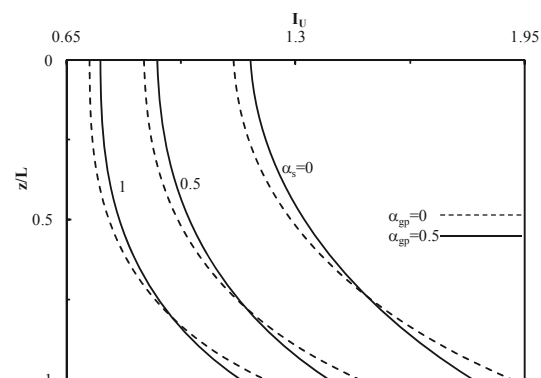


Fig. 9 Normalized displacement coefficient,  $I_U$  vs. Depth,  $z/L$  for  $L/d=10$ ,  $K=50$  &  $v_s=0.5$  – Effect of  $\alpha_{gp}$  &  $\alpha_s$ .

#### 5 REFERENCES

- Kumar P., Ranjan G. & Saran S. (2004). Granular Pile System for Strengthening of Weak Sub-Soils –A Field Study. International Conf. on Geosynthetics and Geov. Engg, Bombay, 217-222.
- Lillis, C., Lutenegeger, A.J & Adams, M. (2004). Compression and Uplift of Rammed Aggregate Piers in Clay. Geosupport: ASCE/GEO Geotechnical Special Publication no. 14, 497-507.
- Madhav, M.R., Vidyananya, B. & Sivakumar, V. (2008). Linear Analysis and Comparison of Displacements Granular Pile Anchors. J. Ground Improvement, Issue 161, 31- 41.
- Phanikumar, Sharma, R.S., Srirama Rao, A. & Madhav M.R. (2004). Granular Pile Anchor Foundation (GPAF) System for Improving the Engineering Behavior of Expansive Clay Beds. Geotechnical Testing J., ASTM, Vol.27(3), 1-9.
- Poulos, H.G. & Davis, E.H. (1980). Pile Foundation Analysis and Design. John Wiley and Sons, New York, 397.
- White, D., Wissmann, K., & Lawton, E. (2001). Geopier Reinforcement for Transportation Application. Geotechnical News : 63-68.

# Bridge foundation on very soft alluvia with stone column ground improvement

## Fondation de pont sur alluvions très mous et amélioration du sol avec des colonnes ballastées

Vlavianos G.J., Marinelli A.K.

*Ministry of Development, Competitiveness, Infrastructure, Transport and Networks, Greece*

Andrianopoulos K.

Foti S.

*Geosynolo Ltd.*

**ABSTRACT:** The present paper proposes technical solutions for a road design project comprising both bridges and high embankments in the Region of Western Greece, where major geotechnical issues had to be dealt with. The very low P-y reaction of the soft silty clays and the eventual liquefaction of the silty sand layers embedded within the foundation soil, the high ground water table and the high seismicity of the area, led to the decision to improve the top part of the natural soil given the necessity for an acceptable solution in terms of both dimensions and cost. Among other possible methods of soil improvement, the application of stone columns followed by preloading was selected. A comparative parametric stability analysis of the bridge embankments and the pile foundations for bridge piers, with or without the presence of stone columns, quantified the benefits from the proposed ground improvement method and verified that the completion of this project is feasible within acceptable performance, safety and cost limits.

**RÉSUMÉ :** La communication propose des solutions techniques pour l'élaboration d'un projet de route qui comprend des ponts et des remblais de grande hauteur dans la région de la Grèce occidentale où il a fallu faire face à des problèmes géotechniques importants. La très faible résistance des argiles limoneuses molles aux sollicitations horizontales et la liquéfaction éventuelle des couches du terrain formées de sables limoneux qui sont contenues dans le sol de la fondation, la nappe phréatique élevée et la haute séismicité de la région, ont conduit à la décision d'améliorer la partie supérieure du sol naturel en prenant en considération la nécessité de trouver une solution acceptable en ce qui concerne les dimensions et le coût. Parmi d'autres méthodes d'amélioration du sol, il a été choisie l'utilisation des colonnes ballastées suivie d'un préchargement du sol. Une analyse paramétrique comparative de stabilité des remblais des ponts et des fondations des piliers des ponts avec ou sans la présence des colonnes ballastées, quantifient les bénéfices obtenus par l'utilisation de la méthode d'amélioration du sol proposée et vérifie que l'achèvement de ce projet est réalisable avec une performance acceptable en termes de sécurité et de coûts

**KEYWORDS:** road project, bridge foundation, soft alluvia, liquefaction, ground improvement, stone column, preloading.

### 1 INTRODUCTION

A significant project for road infrastructure is currently under way in western Greece, prefecture of Aitolokarnania, concerning the construction of a 13,1km part of a public provincial road connecting the municipality of Astakos to the bridge of Gouria.

Owner of the project is the Greek State and the Supervising Authority is the Directorate of Studies for Road Works, General Directorate of Road Works, Ministry of Development, Competitiveness, Infrastructure, Transport and Networks. Following the necessary competitive procedure, the design of the project was assigned to a joint scheme of specialized design offices, covering the involved scientific areas.

This paper focuses on the technical solutions proposed for the geotechnical issues that arose with reference to the stability of embankments and bridge foundation.

### 2 PROJECT OVERVIEW

The importance of this project lies in its expected contribution to the improvement of road access towards western Aitolokarnania and mainly the touristic zone of Astakos-Mytikas-Palairos. It is also anticipated to take over some of the traffic load of other local axis and to support the increase in use of an existing tunnel nearby. What is more important though, is the expected traffic load assumption for the shipbuilding and industrial zone of Astakos, which in the future will be the base for development in the whole area.

The realization of the project will improve the accessibility of the area and will facilitate road connection between cities and existing or planned infrastructure, decreasing time demands and improving safety and comfort requirements

This road axis under study forms a part of the connection of Astakos and the port of Platygiali with the major motorway of "Ionia Odos", passing through the bridge of Gouria and the existing tunnel of Saint Elias. The road section is 11,0m wide (1 lane per direction). From geotechnical point of view, it is to be mentioned that the whole project comprises 6 bridges (15-105m long) and a significant length of embankments between 2 and 7 meters high.

Major geological and geotechnical issues that arise for the last 10km of the road are related to the very low altitude of the ground and the lack of inclination, the high ground water table, the insufficient drainage system and the presence of silty clays and sands, often with high content of organics. The whole situation is aggravated by the liquefaction potential of the silty sand layers embedded within the foundation soil, in connection with the high seismicity of the area.

During the preliminary design stages, it became obvious that the most significant geotechnical problems for the realization of the project would be related to the load bearing capacity of the soil, the expected subsidence under static loading and the eventual liquefaction phenomena.

### 3 GEOTECHNICAL CONDITIONS

The area where the bridge foundation will be constructed consists of soft and compressible saturated alluvial soils, while the water table is located at ground level. The prevailing



geotechnical conditions at these areas can be simplified in two main profiles.

**Soil profile I (Fig. 1)** is encountered in the majority of the bridge sites. Its main characteristic is the surficial layer of fine-grained medium plasticity soil. According to the geotechnical exploration results, this soil layer consists mainly of low to medium plasticity silts (ML) and clays (CL), with thin layers of high plasticity silts (MH), fat clays (CH) and organic clays (OL). The thickness of this layer varies between about 22.5 to 35m. Below this layer, to the depth of 40m, either a medium to dense non-cohesive soil unit (SC, SM) or a dense cohesive soil unit (CL) are present. Rock or any other rock-like geological formation was not encountered at any of the locations explored.

Profile I	Profile II
ML, CL, MH, CH, OL $\gamma=17-19\text{kN/m}^3$ , $c_u=10-30\text{kPa}$ , $E_s=0.5-3\text{MPa}$ , $q_t=0.5-4.3\text{MPa}$ , $FC=49-100\%$ , $PI=4-48\%$ 22.5-35m	ML, CL, MH, CH, OL same as Profile I 7m
	SM $\gamma=17-19\text{kN/m}^3$ , $q_t=4.5\text{MPa}$ , $N_{sp}=18$ , $FC=7-20\%$ 15m
	22.5-35m
SC, SM or CL $\gamma=21\text{kN/m}^3$ , $E_s=12-18\text{MPa}$ , $c_u=65-100\text{kPa}$ or $\phi=34-35^\circ$ 40m	SC, SM or CL $\gamma=21\text{kN/m}^3$ , $E_s=12-18\text{MPa}$ , $c_u=65-100\text{kPa}$ or $\phi=34-35^\circ$ 40m

Figure 1: Representative geotechnical profiles

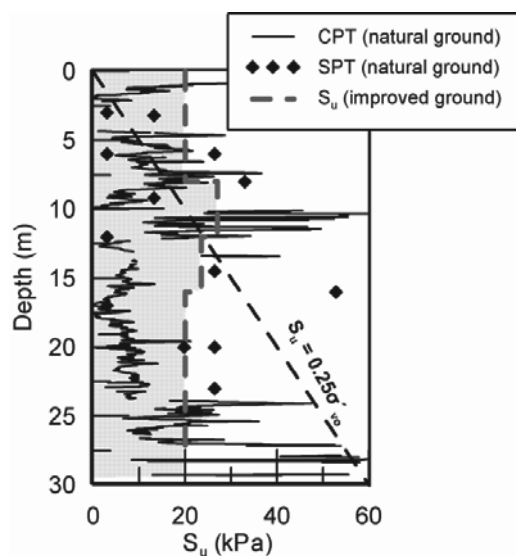


Figure 2: Distribution of undrained shear strength with depth for profile I conditions, before and after the improvement

Figure 2 presents an estimation of the undrained shear strength of the surficial fine-grained soil unit of Profile I, based on the results of typical CPT & SPT recordings. An estimation of undrained shear strength for normally consolidated clays is also presented, based on Jamiolkowski et al. (1985) (see Eq.1):

$$S_u = 0.25 \sigma'_{vo} \quad (1)$$

where  $\sigma'_{vo}$  is the geostatic effective vertical stress. Comparing these two estimations, it is concluded that the surficial fine-grained layer is normally or even at some depths under-consolidated, with low values of undrained shear strength. Thus, the bearing capacity of this formation is considered low and significant settlements are expected during loading, with the necessary consolidation time to exceed the acceptable time limits (horizontal coefficient of consolidation ranging between

$c_h=7 \times 10^{-7} - 9 \times 10^{-6} \text{ m}^2/\text{sec}$  based on CPTu dissipation tests). The lateral resistance of this layer is also considered very low, leading to large horizontal displacements and structural forces, especially during seismic loading.

With regard to the seismic response, profile I belongs to group type S1 according to EC8. The average shear wave velocity  $V_{s,30}$  generally ranges between 85 and 140m/sec, as computed from the CPT recordings:

$$G_{\max,0} = (q_t - \sigma_v) \times 0.0188 \times 10^{0.55I_c + 1.68} \quad (2)$$

where  $I_c$  is a soil behavior type index (Robertson, 2009). Thus, special study is required for the definition of the seismic action, which will take into account the non-linear response of the soil layers and the dependence of soil moduli and internal damping on cyclic strain amplitude.

**Profile II (Fig. 1)** represents the soil conditions prevailing at one bridge site. The soil conditions resemble those of Profile I, with the exception of an 8m thick layer of loose silty sand that interrupts the surficial fine-grained formation. This non-cohesive formation (SM according to USCS) is relatively close to ground surface (at the depth of 7m), while it is classified as non-plastic, with fines content between 7 and 20% and potentially liquefiable under seismic conditions.

A preliminary liquefaction analysis with NCEER methodology (Youd et al. 2001) for CPT recordings revealed that this non-cohesive formation is liquefiable. As shown in Fig. 4, the factor of safety against liquefaction is well below unity for the silty sand layer, revealing its high liquefaction potential. Hence, although this soil layer presents higher stiffness ( $V_{s,30}=140\text{m/s}$ ) and bearing capacity for static loading, as compared to the clay layer, its liquefaction potential deteriorates its mechanical properties. Thus, during earthquake loading, loss of bearing capacity, lateral stiffness degradation and settlements are expected to occur, increasing this way superstructure displacements and structural forces. Furthermore, Profile II is now characterized as Group type S2 according to EC8 and special study is needed to define the seismic action and the exact liquefaction potential.

#### 4 DESIGN CONCEPT

As a result of the existing poor soil conditions, the foundation of the foreseen bridge piers on surface foundations was excluded and was replaced by a group of piles with a rigid pile cap. However, due to the high seismicity of the area, the very low P-y reaction of the soft silty clays and the eventual liquefaction of the silty sand layer led to extreme internal forces of the piles and increased dis-proportionally the cost of the project. Hence, the necessity of an acceptable solution in terms of both dimensions and cost, led to the decision to improve the top part of the natural soil.

Among a number of possible methods of soil improvement that were examined, it was decided to proceed with the application of gravel piles followed by preloading. Plastic drains are also prescribed to act as secondary drainage system for greater soil depths.

The main aim of pre-loading was to increase the undrained shear strength of the surficial fine-grained soil unit. The improved undrained shear strength (when the increase of effective stress due to surcharge exceeded 10% of its initial value), was estimated according to Eq. 4:

$$S_{u,f} = S_{u,0} \text{OCR}^{0.8} \quad (3)$$

with  $S_{u,0}$  reflecting the anticipated undrained shear strength for normally consolidated clays (see Eq. 2). The increase of effective vertical stress at each depth was computed according to the well known Westergaard solutions, taking into account the increase of soil stiffness at upper layers, where gravel pile installation accompanies pre-loading. The effect of pre-loading reduces with depth, while a percentage of the surcharge load is used for the increase of OCR, due to the distribution of the external load between gravel piles and original soil. Despite that, the anticipated increase of undrained shear strength at upper layers (i.e. at layers that are crucial for the overall safety

of the bridge embankments) is considered substantial, while its secondary effects such as the acceleration of consolidation at layers that were found under-consolidated and the reduction of downdrag forces at piles (i.e. by allowing the consolidating soil to settle before construction) increase its efficiency. The prescribed pre-loading embankment were wider from the bridge embankment / pile cap by 2.5-3.0m at each side, in order to apply uniform stress at the area of interest, while its height generally varies between 3 and 7m.

Stage construction of pre-loading embankment was decided (with height increments between 1.5-2.0m), due to the poor soil conditions, followed by continuous settlement and pore-pressure dissipation recordings. Figure 2 presents the anticipated final (after improvement) distribution of  $S_u$  with depth for the CPT recording presented in Section 3.

Gravel pile installment is prescribed ahead of pre-loading, consisting of 0.80m diameter piles in a 1.80 x 1.80m square arrangement (denoting replacement percentage equal to  $a_s = 0.78 \times (0.8/1.8)^2 = 15.4\%$ ). Gravel pile length varies between 8 and 13m, depending on soil conditions.

The installation of gravel piles increased the mechanical properties of the upper cohesive fine-grained layers and subsequently increased the general stability of bridge & pre-loading embankments. The following equivalent strength parameters were used (Van Impe & De Beer, 1983):

$$c_{eq} = (1-a_s) S_{u,f} \quad (4a)$$

$$\tan\phi_{eq} = [na_s / (na_s + 1 - a_s)] \tan\phi_1 \quad (4b)$$

where  $c_{eq}$  &  $\phi_{eq}$  denote the equivalent cohesion & friction angle of the composite system respectively,  $\phi_1$  denotes the friction angle of gravels (assumed equal to  $42^\circ$ ),  $a_s$  denotes the replacement ratio (equal to 0.154) and  $n$  denotes the ratio of the load taken by the gravel pile versus the surcharge load. The contribution of geostatic stresses is omitted; while outside the embankment limits (where no surcharge is applied)  $n$  equals 1.0. The improved shear strength of the composite system, combined with the increase of the undrained shear strength due to pre-loading proved adequate for the construction of the bridge embankments with acceptable factor of safety under both static and seismic conditions (e.g. the static F.S. increased from 0.64 to 1.51 for a representative height of 4m).

Note that, besides the improvement of shear strength characteristics, the inclusion of gravel columns combined with pre-loading has altered the seismic ground response relative to free-field. In order to take into account this effect, the shear wave velocity and the spring stiffness in P-y curves of the relevant soil layers were appropriately increased. Namely, the formula presented by Baez & Martin (1993) was used for the estimation of the maximum shear modulus of the composite system:

$$G_{max,eq} = G_{max,i} a_s + G_{max,p} (1-a_s) \quad (5)$$

where  $G_{max,eq}$  is the maximum equivalent shear modulus,  $G_{max,i}$  is the maximum shear modulus of the fine-grained layer after pre-loading,  $G_{max,p}$  is the maximum shear modulus of the gravel pile and  $a_s$  is the replacement ratio (here 0.154). The maximum shear modulus of the fine-grained layer after pre-loading was computed as follows (Weiler, 1988):

$$G_{max,i} = G_{max,o} OCR^{0.5} \quad (6)$$

where  $G_{max,o}$  is the maximum shear modulus of unimproved soil, as computed by Eq. 2. The maximum shear modulus of the gravel pile was computed assuming a dense configuration ( $e=0.55$ ). Figure 3 presents the shear wave velocity profile of the composite system for the CPT recording of Fig. 1. The average shear wave velocity  $V_{s,30}$  for this profile increased from 86 to 140m/s, reflecting stiffer ground conditions. This increase was also implemented to the P-y curves, by increasing the horizontal subgrade reaction coefficient  $k$ . The increase was assumed proportional to the ratio  $G_{max,eq}/G_{max,o}$ , while for the

unimproved soil coefficient  $k$  was computed according to DIN4014 for bored cast-in-place piles.

For the case of Profile II, where a non-cohesive liquefiable layer is present, the gravel piles are expected to act as a countermeasure against liquefaction. The gravel piles will be constructed via bottom-feed vibro-replacement, while a proper gradation curve range is prescribed in order to ensure the effective drainage of earthquake-induced excess pore-pressures. During vibro-replacement, the non-cohesive layer is expected to be densified and increase its resistance to liquefaction. Based on Mizuno et al. (1987), the average measured tip resistance is expected to increase between gravel piles from 4.5MPa to 9.5MPa, providing an adequate liquefaction resistance. Figure 4 compares results from the preliminary (before improvement) and the detailed (after ground improvement) liquefaction study, which show the minimization of liquefaction potential. The densification of the non-cohesive layer due to pre-loading and the potential dissipation of excess pore pressures were conservatively ignored. It is noted that even if densification was ignored, drainage through gravel piles would retain excess pore pressure ratio  $r_u$  well below 0.5, as computed according to Seed & Booker (1977) and Bouckovalas et al. (2011) for the given characteristics and gravel pile geometry.

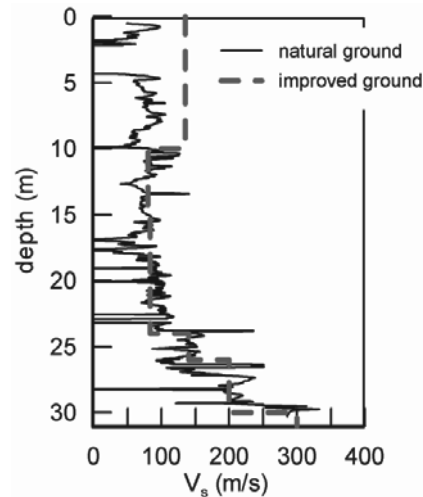


Figure 3: Distribution of shear wave velocity with depth for profile I, before and after the improvement

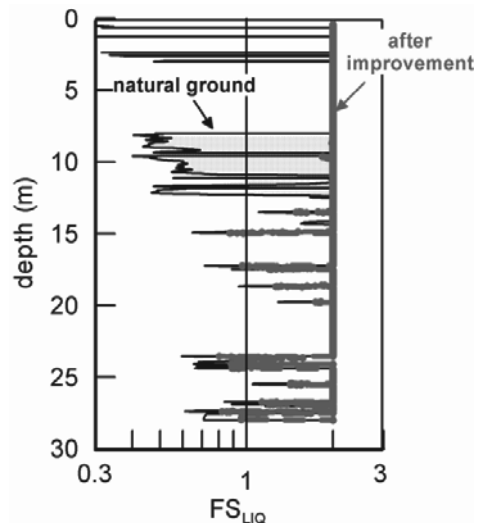


Figure 4: Factor of safety against liquefaction for Profile II, before (preliminary results) and after improvement (detailed study).

Finally, consolidation process is expected to be accelerated with the presence of gravel piles. Excess pore pressures for each loading stage are expected to diminish within 19 days, assuming conservatively only radial flow towards the gravel piles and

horizontal coefficient of consolidation equal to  $c_h=7 \times 10^{-7} \text{m/s}^2$ . The actual consolidation time is expected to be even lower, considering the actual 2D water flow, the presence of horizontal layers of higher permeability and the additional discharge from the secondary pipe drains that are prescribed.

## 5 SEISMIC GROUND RESPONSE ANALYSES

Besides ground improvement, detailed ground response analyses were also crucial for the successful completion of the project. Since, both Profile I & II belong to group type S1 & S2 according to EC8, special study was necessary to define the proper seismic action and the exact liquefaction potential. Thus, 1D equivalent linear analyses were performed with the equivalent-linear frequency domain method (e.g. Schnabel et al. 1972). Modulus reduction and hysteretic damping curves were used as a function of cyclic strain amplitude (Vucetic & Dobry, 1991), and introduced the non-linear behavior of soil layers in ground response analyses, according to its layers' plasticity index. According to EC8 provisions, three different accelerograms were used, which cover a wide range of frequencies and are representative of the seismic region.

Shear wave velocities of the improved ground were computed according to Eq. 5, while the peak ground acceleration at bedrock outcrop was calibrated to 0.24g, according to the Greek Annex of EC8 for the area under investigation. Since no bedrock was found, artificial bedrock was used at the end of each borehole, while the bedrock shear wave velocity was assumed to range between 300 and 550m/s, providing a high impedance ratio compared with the soil column characteristics. Thus, radiation damping was conservatively minimized. Fig. 5 shows representative results from ground response analyses conducted in Profile II. Significant de-amplification of the seismic motion is observed, due to the flexibility of the soil column but also due to the non-linearity exhibited by the soil layers. The computed peak ground acceleration at ground surface ranges between 0.20 to 0.24g, significantly lower from the 0.32g required by EC8 for the flexible soil type D. Thus, the structural forces due to seismic loading were significantly reduced, while the factor of safety against liquefaction was substantially increased.

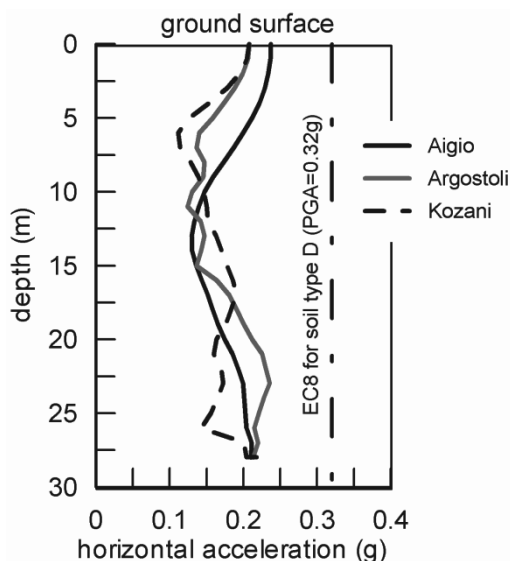


Figure 5: Distribution of peak ground acceleration with depth for Profile II using three different accelerograms.

## 6 CONCLUSION

The present paper presents details of the technical solution proposed for a road design project in Western Greece, where major geotechnical issues had to be dealt with for the

foundation of bridges and high embankments. Geotechnical investigations revealed very poor soil conditions consisting of silty clays and sands, often with high content of organics, and high ground water table that locally appeared on the ground surface. As a result, the foundation of foreseen bridge piers on surface foundations was excluded and was replaced by a group of piles with a rigid pile cap. Among a number of possible methods of soil improvement that were examined, it was finally decided to proceed with the application of stone columns followed by preloading. This way, the following were accomplished:

- increase of the general stability of the bridge embankments
- increase of the bearing capacity of foundation soil layers
- reduction of internal forces of piles
- acceleration of the stage of primary consolidation of silty clay-sands and
- reduction of the liquefaction potential of sandy layers.

All of the above effects were verified by site-specific computations and implemented to the design of the relevant works

## 7 ACKNOWLEDGEMENTS

Authors acknowledge the assistance of Harris Lamarinis, Civil Engineer M.Sc. on the geotechnical investigations and the preliminary liquefaction analyses.

## 8 REFERENCES (TNR 8)

- Baez J.I., Martin G.R.1993., Advances in the design of vibro systems for the improvement of liquefaction resistance, Symposium on Ground Improvement. Vancouver
- Bouckovalas G., Papadimitriou A., Niarchos D., Tsiapas D. 2011, Sand fabric evolution effects on drain design for liquefaction mitigation, *Soil Dynamics & Earth. Eng.*, 31, 1426-1439
- Jamiolkowski M., Ladd C., Germaine J.T., Lancellota R. 1985. New developments in field and laboratory testing of soils. *IX Intern. Conf. on SMFE*, Vol. 1, 57-154.
- Mizuno Y., Suematsu N. & Okuyama K., 1987. Design method of sand compaction pile for sandy soils containing fines. *Journal of JSSMFE*, 53-56
- Robertson P.K. 2009. Interpretation of cone penetration tests – a unified approach. *Can. Geotech. J.*, 46, 1337-1355
- Schnabel P.B., Lysmer J. and Seed H.B. 1972. SHAKE: a computer program for earthquake response analysis of horizontally layered sites. Report EERC 72-12, Earthquake Engineering Research Center, Univ. of California, Berkeley
- Seed HB, Booker JR. 1977. Stabilization of potentially liquefiable sand deposits using gravel drains. *Journ. of Geotech. Eng., ASCE*, 103 (GT7). 757-768
- Van Impe W., De Beer E. 1983. Improvement of settlement behavior of soft layers by means of stone columns. *Proc. 8<sup>th</sup> European Conf. of SMFE*, Vol. 1, 309-312
- Vucetic M, Dobry R. 1991. Effect of soil plasticity on cyclic response. *Journal of Geotech. Eng. ASCE*, 117 (1), 89-107
- Weiler W.A. 1988. Small strain shear modulus of clay. *Proc. ASCE Conf. on Earth. Eng. & Soil Dyn. II*, New York, 331-335
- Youd et al. 2001. Liquefaction resistance of soils: Summary report from the 1996 NCEER and 1998 NCEER/NSF workshops on evaluation of liquefaction resistance of soils. *Journal of Geotech & Geonv.*, ASCE, 127 (10), 817-833

# Subgrade improvement measures for the main rescue roads in the urban redevelopment area HafenCity in Hamburg

Mesures d'amélioration du sol de fondation des principales routes de secours dans la zone du réaménagement urbaine de la HafenCity à Hamburg

Weihrauch S., Oehrlein S.

*Grundbauingenieure Steinfeld und Partner GbR, Hamburg*

Vollmert L.

*BBG Bauberatung Geokunststoffe GmbH & Co. KG, Espelkamp*

**ABSTRACT:** The level of many streets in Hamburg's HafenCity is being raised by around 3 m to ensure safety from flooding. The marshy soils in this area— mainly clay (a soft clay) and peat – necessitate the use of different foundation-soil improvement concepts for the limitation of settlement; these have to take account of the surrounding infrastructure (buildings, river-bank structures, services). The Honkongstrasse serves as a good example of such concepts. Stress and deformation measurements were carried out on the site, in which the concept of a "pile-supported, geogrid-reinforced sand sub-base layer" was used; this paper reports on the results.

**RÉSUMÉ:** Dans le quartier d'HafenCity à Hamburg, la plupart des routes seront surélevées jusqu'à 3 mètres pour atteindre le niveau de protection contre les eaux. Les sols en place, d'origine marécageuse, sont constitués d'argile et de tourbe. Du fait de l'hétérogénéité des sols, et en fonction des ouvrages existants (bâtiments, murs de rive, tuyaux enterrés), différentes approches ont été appliquées pour améliorer les sols et limiter les tassements. Dans cette communication, le cas d'étude de la rue « Hongkong » sera présenté. Dans ce projet, des géogrilles sont utilisées en renforcement d'une couche de forme sableuse pour la répartition des contraintes. Une instrumentation complète a été mise en place. Des mesures de contraintes et de déformation ont été effectuées. Les résultats de cette instrumentation sont présentés dans cette communication.

**KEYWORDS:** urban redevelopment, soil improvement, geogrid, piled embankment, expanded clay, pre-loading

## 1. INTRODUCTION

At the HafenCity in Hamburg, previously part of the harbour area, the current inner-city area south of the historic warehouse district is being extended by some 40 % to a total of 157 hectares (Figure 1). 5,500 dwellings for 12,000 residents are to be constructed, along with office space for 40,000 employees.

In the course of these infrastructure projects, the trafficked areas – with the exception of the quay and embankment promenades – are being raised from the current MSL +5 m to MSL +7.5 m to + 8.0 m, to make them safe for flood events.



Figure1: City-planning concept of the HafenCity Hamburg (as of January 2008)

The soil conditions around today's Honkongstrasse (formerly Magdeburger Strasse) are typical for the HafenCity Hamburg. Fill material of low bearing capacity overlies soft organic layers of clay and peat which in turn overly firm sands (Figure 2). Raising the level of the road embankment by approximately 3.0 m would have resulted in long-term settlements of between 300 and 400 mm, and significant differential settlements would have been expected.

The following subgrade-improvement methods are used to limit settlement in the HafenCity:

- pre-emption of settlement with a sand pre-loading layer and vertical drains
- use of lightweight materials (expanded clay)
- construction of a piled, geogrid-reinforced sand layer

The choice of method depends largely on the local boundary conditions. On the Honkongstrasse site, all three methods were used on different sections. Measurements of stresses and deformations were carried out on the section with the piled, geogrid-reinforced sand layer. The paper therefore concentrates in greater detail on this method.

## 2. METHOD DESCRIPTION AND CONCEPT

### 2.1 Sand pre-loading layer and vertical drains

If the local boundary conditions e.g. space available, existing and planned services, local structures (buildings, river-bank structures, sewers) and the time constraints permit, the use of a sand pre-

loading layer and vertical drains to pre-empt settlements is an economical standard method.

To accelerate consolidation, vertical drains are installed in the area to be loaded. The planned, elevated cross-section is then constructed, and an additional 2.0 to 3.0 m thick sand pre-load is placed.

The consolidation of the weak organic layers is monitored over time using settlement gauges.

After the time required for settlement (usually at least three months), during which no further construction takes place, the sand pre-load is removed to the agreed planned height and the structure passes out of the responsibility of the earthworks contractor.

## 2.2 Use of lightweight aggregates (expanded clay)

In areas where pre-emption of settlement is impractical because of local structures or services, lightweight aggregates are often used. These materials significantly reduce settlements resulting from the raising of ground levels.

For forecast residual settlements of around 50 to 70 mm, the lightweight materials are placed to a depth of around MSL + 2 m.

The expanded-clay layer is wrapped in a nonwoven geotextile to prevent particle displacement and leaching-in of soil.

The use of expanded clay is regulated in the "Merkblatt über die Verwendung von Blähton als Leichtbaustoff im Untergrund von Straßen" of the Forschungsgesellschaft für Straßen- und Verkehrswesen (FGSV).

## 2.3 Construction of a piled, geogrid-reinforced sand layer

### 2.3.1 Construction method and system chosen

The system is characterised by vertical columns (lime-cement treated gravel, unreinforced) and an overlying sand layer horizontally reinforced with geogrids. Use is made of the arching effect of the overburden sandy soil while the foundation soil acts as a bedding layer. In contrast to concrete slabs on (reinforced concrete-) piles, in which the individual elements are very stiff in comparison to the surrounding soils, there is a pronounced interaction between the columns, geogrid and the foundation soil in the system described here.

In contrast to the methods described under 2.1 and 2.2, the foundation soil in this system is only subjected to low additional stresses. The major part of the vertical stresses is transferred in a concentrated manner by the vertical columns into the firm foundation soil. The system settlements remain proportionally very small both during and after the construction phase.

When correctly designed, the system possesses significant reserves of bearing capacity, so that subsequent interventions and changes within limits in the foundation soil have no influence on the serviceability of the structure.

The placement grid of the supporting elements should be designed to transfer the geogrid loads in an orthogonal manner. For Hongkongstrasse, this resulted in a rectangular grid with a spacing of 2.3 m normal to the embankment axis and 2.5 m in the axial direction; the diameter of the elements was 0.6 m (Figure 2). Reinforced-concrete columns with continuous steel reinforcement were used at the edge of the structure to cope with a bending moment (e.g. should any excavation be required at a later date) as a result of lateral pressure.

The geogrid-reinforcement is installed 150 mm above the columns in order to guarantee adequate safety against shear during the construction phase, and in case of large settlements. The reinforcement is placed at right angles to the placement grid, so that the layers are cross-laid in the longitudinal and transverse directions of the embankment.

In the transverse direction, the constructive situation leaves practically no room to anchor the geogrid. The design requirement

of a short-term tensile strength of 400 kN/m is therefore assigned to two layers, which are wrapped round at the edges of the structure, and overlapped in the upper layer.

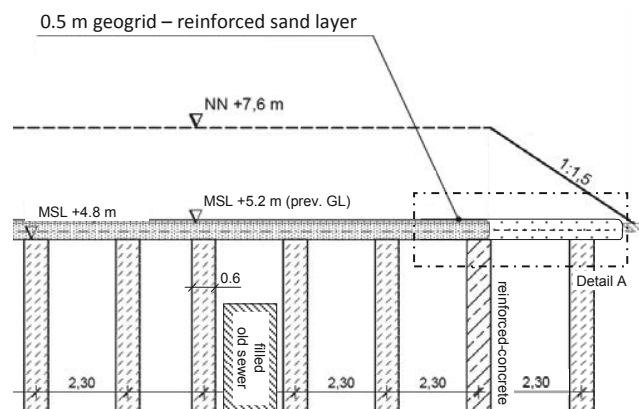


Figure 2: Cross section – piled sand layer

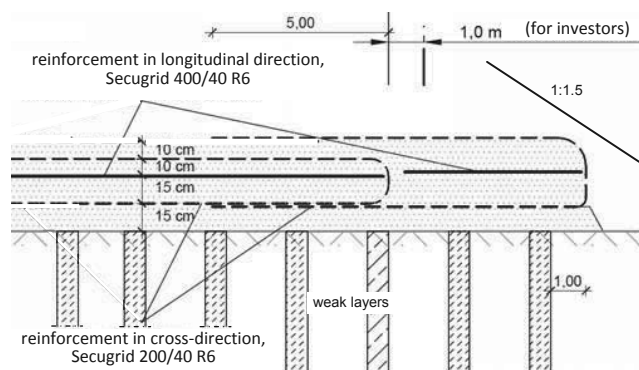


Figure 3: Detail A – sketch of system showing reinforcement placing (vertical scale greater than horizontal)

### 2.3.2 Points of constructive relevance near Hongkongstrasse

To avoid the risk of subsequent construction activity of investors endangering or destroying sections which have already been built, an area of 1.0 m of the traffic section must be able to be removed. Fill which intrudes into investor areas must also be removable.

In order to prevent any damage to the embankment-support system, the geogrid-reinforced fill layer was built with sufficient overlap (Figure 3). The outer section can thus be removed in the course of normal earthworks.

### 2.3.3 Design and verifications

The design of the support system is performed for the columns and the geogrid-reinforced fill layer in co-ordination with one another.

The columns are designed for the total load, and the contribution of the subsoil to load bearing and subgrade reaction between the columns is neglected.

The geogrid-reinforced layer was designed according to a verification concept which has already been used and proven itself several times in HafenCity Hamburg. The limit bearing capacity was first verified in accordance with a suggestion from Kempfert et al. (1997). A conservative value for subgrade reaction was used. This verification procedure does not enable any deformations to be inferred.

However, verification of serviceability and of deformation limitation is compulsory for all construction projects in the HafenCity Hamburg. A complementary design procedure was

therefore adopted, using a method developed and extended from EBGeo, which at the time of planning was only available in its 2004 draft stage. This extended design method was verified for similar subsoil and loading conditions (Vollmert et al., 2006). The anticipated further settlements at the level of the reinforcement were estimated at less than 50 mm after termination of construction.

Comparisons with the current EBGeo (2010), available in its final form now that construction is complete, show that the design and verification of the system is sufficiently robust to cater even for the special case "Loss of Subgrade Reaction" in Load Case 3.

It must however be noted, that extreme changes in subgrade-reaction conditions – such as its total loss – will result in load redistribution in the sub-base layer. The long-term influence of these on the serviceability can currently not be finally estimated and is the subject of research. Taking serviceability aspects into account, a conservative, realistic estimate of foundation conditions is therefore critical in the design of such subsoil-improvement projects.

### 2.3.4 Accompanying measurement

The selection of the subgrade-reaction value at the underside of the reinforced layer is therefore a critical starting parameter for design. Values for this are usually derived from the stiffness modulus of the subgrade and the thickness of the weak soil layers. The actual reaction is, however, a variable whose value depends on, among other things, the soil improvement during the construction phase, consolidation processes, the stiffness of the geogrid-reinforced foundation layer and the sub-base layer.

In order to obtain further information on the subgrade reaction and the actual behaviour of the structure, it is necessary to investigate such structures in-situ. During the development of Hongkongstrasse, boundary conditions for monitoring with a measurement system were ideal, as not only the foundation soil conditions, but also the geometric conditions and the alterations anticipated in the medium term (development of the investor areas and resulting encroachments into the stress distribution in the structure) were seen as exemplary for the particular situation of HafenCity Hamburg.

The objective of the measurement programme is therefore the investigation and measurement of

- the state of stress in the geogrid
- the development of soil arching, taking construction and operational conditions into account
- the proportions of the load allocated to the supports and the weak layer
- the influence of variations in water-table level in the foundation soil, and
- the deformation situation at foundation level.

## 3. CONSTRUCTION AND MEASUREMENTS RESULTS

### 3.1 Sand pre-loading layer and vertical drains

After the necessary clearing away of foundations, the removal of old services and the search for unexploded ordinance, in the southern part of Hongkongstrasse, vertical drains were hydraulically driven into the foundation soil. Plastic strip drains with a width  $b$  of around 100 mm were used.

In installing the strip drains it was required to ensure that a depth of soft soil of around  $d = 1.0$  m remained under the drains as a natural barrier to the lower groundwater aquifer (lower sands).

After this, the sand layer (including any pre-load) was placed. Sand with a silt content  $\leq 5\%$  by weight, a uniformity coefficient  $U$  of approx. 2 and a rating of Z0 in accordance with the LAGA guidelines was to be used. The sands were compacted in layers to at least medium compaction density.

Below the level at which the sand was laid, settlement-measuring rods, each adjustable in length and with a base plate (1 m x 1 m) were installed, and these were continuously monitored while the pre-load was in place. A plot of settlement against time is shown in Figure 4.

### 3.2 Use of lightweight aggregate (expanded clay)

Lightweight aggregate in the form of expanded clay was used in the northern area of Hongkongstrasse.

Various active services crossed the construction area and it had to be ensured that these were not damaged during the excavation of trenches, around 3.5 m deep. In the area of the services, the expanded clay was installed in so-called big bags as a foundation for the services. In the remaining areas, the expanded clay was placed, spread, and compacted in layers to the design height (base of sand protection layer) (Figure 5).

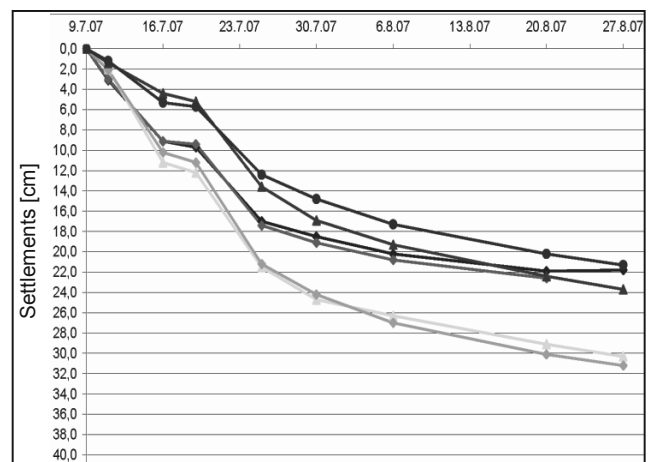


Figure 4: Development of settlement during loading phase

### 3.3 Piled, geogrid-reinforced sand base layer

#### 3.2.1 Construction

For the required design working load of 500 kN, partial-displacement bored columns with a diameter of 420 mm and an unreinforced, fresh-in-fresh tapered cast cap C25/30 with a cap diameter of 600 mm were installed by GKT Spezialtiefbau GmbH working for Eggers Umwelttechnik GmbH.

High-strength, high-modulus geogrids Secugrid 200/40 R6 and Secugrid 400/40 R6 were used to reinforce the sand base-layer. The construction of the geogrid-reinforced sand layer had to be carried out with overlap. A length of grid from the lower layer, which was laid across the width of the base layer, was rolled and stored at the edge of the fill. After the lengthwise reinforcement and the fill had been placed, the stored roll was pulled up, wrapped round the fill, and overlapped by the length required in the design calculations (Figure 6). For a workmanlike placing it is therefore necessary to ensure that the roll overlaps are arranged in a staggered pattern in order to avoid distortion and twisting of the geogrids.

The results of the measurements have been published by Weihrauch et al. (2010) indicating the expected performance as well as meeting the deformation requirements as given by the design.



Figure 5: Placing of expanded clay

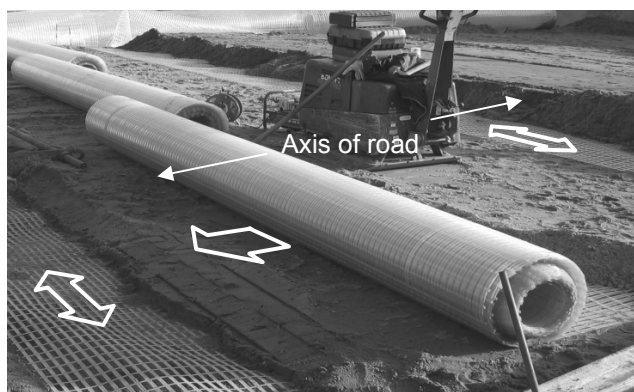


Figure 6: Laying of the geogrid

#### 4. CONCLUDING REMARKS

Three quite different methods of soil improvement techniques were used in the area of Hongkongstrasse. The prime objective of the soil improvement is, in all cases, the reduction of subsequent settlements in order to guarantee the serviceability of the trafficked areas under operating conditions.

The decisive factors in the choice of construction method are the local conditions, the time constraints, and the economic conditions applicable to the section being planned or built.

Settlement pre-emption with vertical drains and a sand pre-load requires a relatively long lead time. Significant associated settlements must be expected in the immediate vicinity; in the case of existing buildings or services these will usually have to be classified as unacceptable. On the other hand, the foundation soil remains more or less undisturbed in its stratification and composition, and is free of construction elements.

In contrast to this, soil improvement using expanded clay, i.e. a lightweight aggregate, involves only very small additional settlements. This method is therefore advantageous mainly at the interface with existing structures, and with existing roads. Because of the cohesionless nature and the low compressive strength of expanded clay, difficulties can be experienced later if services and anchorage layers are installed, or reconstruction work carried out.

With its columns and the geogrid layers, the pile-supported base-course method contains the most construction components. Depending on the construction process of the columns, this method can be used even close to existing structures. Particularly in cases of large fill depths – and these are typical of the HafenCity – services can be constructed at a later date without problems. And the structure can be continued without a break in the adjoining construction section; building over existing elements

such as pipes is not a problem. Perforation of the geogrid-reinforced base, e.g. by anchor layers, is possible in principle.

The sandfill material can be assumed to incur the lowest cost as regards the pure construction costs of the structure. Under the conditions applying at the HafenCity, the pile-supported, geogrid-reinforced method is usually somewhat cheaper to construct than an expanded-clay fill layer. Absolute costs must be ascertained taking into account project-specific reconstruction, protection and follow-on measures. In addition to the cost aspect, the time flexibility for individual measures, and their technical feasibility under local conditions, are decisive criteria.

The authors wish to thank HafenCity Hamburg, Eggers Umwelttechnik GmbH and Tilman Kaden Landschaftsbau, Bad Segeberg for their support and permission for publication.

Thanks are due to NAUE GmbH & Co. KG for providing the instrumented geogrids and technical support.

#### 5. REFERENCES

- EBGEO – Empfehlungen für den Entwurf und die Berechnung von Erdkörpern mit Bewehrungseinlagen aus Geokunststoffen. (Recommendations for Design and Analysis of Earth Structures using Geosynthetic Reinforcements) 2. Auflage 2010. Hrsg. DGGT. Verlag Ernst & Sohn, Berlin.
- Kempfert, H.-G., Stadel, M. & Zaeske, D. (1997): Berechnung geokunststoffbewehrter Tragschichten über Pfahlelementen. Bau-technik 74 (1997), Heft 12
- Vollmert, L., Kahl, M., Giegerich, G. & Meyer, N. (2007): In-situ verification of an extended calculation method for geogrid reinforced load distribution platforms on piled foundations. XIV European Conference on Soil Mechanics and Geotechnical Engineering (ECSMGE), Madrid, September 2007
- Weihrauch, S., Oehrlin, Vollmert, L. (2010): Baugrundverbesserungsmaßnahmen in der HafenCity Hamburg am Beispiel des Stellvertreterprojektes Hongkongstraße. Vortragsband zur 31. Baugrundtagung der DGGT, München, 3. – 6. November 2010

# Fiber Reinforced Cement Treated Clay

## Fibro-ciment renforcé argile traitée

Xiao H.W., Lee F.H., Zhang M.H., Yeoh S.Y.  
National University of Singapore, Singapore

**ABSTRACT:** Cement-treated soil has been used widely in ground improvement for several decades. However, its behavior, especially at high cement content, is highly brittle. Previous studies have shown that addition of both fibers and cement in soil improvement seems to be more efficient and attractive than adding fibers or cement alone. This paper presents an experimental study on fiber-reinforced cement-treated marine clay. Two different types of fibers and fiber lengths as well as different fiber contents (0.0%-0.32%) will be investigated with cement content ranging from 20%-50% and water content ranging from 100%-167%. The experiment results indicate that the strength and ductility of cement-admixed marine clay improve significantly with increasing fiber content until an optimum fiber content is reached. It was found that the factors affecting the behavior of fiber-reinforced cement-treated marine clay, such as fiber content, type and cut length and cement soil mix ratio, are not independent. In general, for water content not higher than 100% and cement content higher than 20%, using 12-mm polyvinyl alcohol fiber was found to give higher strength and better ductility than polypropylene or shorter fibers.

**RÉSUMÉ :** Des études précédentes ont démontré que l'incorporation de fibres et du ciment dans l'amélioration de sol semble être plus efficace et attrayante qu'en ajoutant seulement les fibres ou le ciment. Cet écrit présente une étude expérimentale de l'argile marine traitée au ciment et renforcée avec fibres. Deux différents types et longueurs de fibres de même que des teneurs en fibre différentes (0.0%-0.32%) seront examinés avec une teneur en ciment qui s'étend de 20%-50% et d'eau qui s'étend de 100%-167%. Les résultats de l'expérience indiquent que la résistance et la ductilité du ciment-sol sont améliorées de manière significative avec le contenu croissant de fibres jusqu'à ce qu'une teneur en fibre optimale soit atteinte. Il a été trouvé que les facteurs qui affectent le comportement de l'argile marine traitée au ciment et renforcée avec fibres, tel que la teneur en fibres, la longueur et le type de fibre et la proportion du mélange du sol-ciment, ne sont pas indépendants. En général, pour une teneur en eau ne dépassant pas les 100% et une teneur en ciment de plus de 20%, il a été constaté que l'utilisation de la fibre d'alcool de polyvinyl de 12mm offre une plus haute résistance et une meilleure ductilité que le polypropylène ou des fibres plus courtes.

**KEYWORDS:** fiber reinforcement, cement treated soil, brittleness index, compressive strength

## 1 INTRODUCTION

Cement-treated soil has been used widely in ground improvement during the past forty years and is becoming more attractive and efficient method for soil treatment due to its economy, availability and feasibility. However, cement-treated soil, especially at high cement content, tends to be brittle. Previous studies have shown that fiber-reinforcement increases the strength and ductility while decreasing the stiffness of the soil (e.g., Gray & Ohashi 1983). Recent studies have also shown that incorporation of both fibers and cement in soil improvement seems to be more efficient than fibers or cement alone (e.g., Maher and Ho 1993, Consoli et al. 1998). Maher and Ho's work presented a basic study of the mechanical behavior of artificially cemented sand reinforced with randomly distributed glass fibers.

The use of randomly distributed fiber as a new reinforcement material for cement-treated soil has been receiving increasing attention in recent years (e.g., Consoli et al. 2003, Khattak and Alarshidi 2006, Tang et al. 2007, Park 2009; Consoli et al 2011; Ud-din et al. 2011). Previous research works, however, have focused mainly on low cement content ( $\leq 10\%$ ), sand or sandy soil and particular fiber. In this paper, different fiber types (PP & PVA), fiber lengths (6 & 12mm) and fiber contents (0.0%-0.32% by volume of mixture) will be investigated with different cement and water contents for Singapore marine clay treatment. The specimens were made in laboratory and tested with unconfined compression loading. The strength and ductility of the FRCT marine clay specimens were then analyzed based on the experiment results.

## 2 EXPERIMENT INVESTIGATIONS

The materials used in the study are Singapore upper marine clay, type I Ordinary Portland cement, and fibers. The constituents of the clay are 24.13% of colloid, 21.77% of clay,

47.71% of silt and 6.39% of very fine to medium sand. Two different fibers were used, namely polypropylene (PP) and polyvinyl alcohol (PVA) fibers. PVA fibers are commonly used in concrete reinforcement to improve the tensile and flexural strength of concrete. The properties of the fibers are given in Table 1. A naphthalene-based superplasticizer (Rheobuilder 1000) was used in some mixtures for workability purpose.

Table 1 Physical and mechanical properties of fibers

Fiber Type	Length (mm)	Diameter (micron)	Aspect ratio	Tensile strength (MPa)	Elastic modulus (GPa)	Density (kg/m <sup>3</sup> )
PP6	6	26	231	540	7	910
PP12	12	26	462	540	7	910
PVA6	6	26	231	1600	40	1300
PVA12	12	38	316	1500	40	1300

The cement soil mix ratio will be expressed in the form of S:C:W wherein S is mass of soil solid, C the mass of cement and W the mass of water at the point of mixing. The cement content  $A_w$  is defined as the ratio of mass of cement to the mass of soil solid. The water content  $C_w$  is defined as the ratio of mass of water to the total mass of soil solid and cement. In this study, the cement content ranges from 20 to 50% by weight of soil solid while the water content ranges from 100 to 167% by weight of cement and soil solid. The fiber content is defined as the ratio of volume of fiber to the total volume of the mixture at the point of mixing, and ranges from 0 to 0.32%. The ductility of the fiber-reinforced cement-treated (FRCT) soil is designated herein by the brittleness index (BI), which is defined as the ratio of the peak strength to the strength at a prescribed post-peak strain.



The natural marine clay was first mixed with the prescribed amount of water to achieve 100% moisture content and remoulded. Cement slurry with the water-cement ratio needed to achieve the desired mix ratio was then added to marine clay in a Hobart Mixer and mixed at a rotational speed of 125rpm for around 5 minutes. The fiber was finally added to cement soil mixing and mixed for another 10 minutes. For mixtures with water content of 100%, the superplasticizer was used to improve their workability. The dosage of the superplasticizer was 1.13-2.27l/100kg soil+cement solids. The mixture was placed into a 50mm (diameter) by 100mm (height) cylindrical polyvinyl chloride (PVC) split-mould. No compaction was applied during placement. Specimens were then submerged in distilled water within their split-moulds without loading for curing. The specimens were then taken out after 7 days for unconfined compression testing. The test procedure followed those prescribed in ISO/TS 17892 (2004). The strain rate used for the unconfined compression test was 1.32%/min.

### 3 EXPERIMENT RESULTS AND ANALYSIS

#### 3.1 Stress strain behavior

Figure 1 shows the typical stress strain behavior of FRCT soil specimens under unconfined compression. Compared to purely cement-treated soil, fiber reinforcement increases the strength and ductility significantly, the ductility increasing with fiber content.

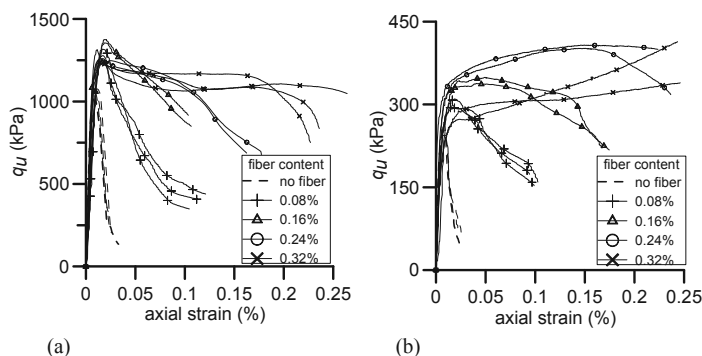


Figure 1. Stress strain behavior for FRCT soil specimens with 6mm long fiber. (a) 50% cement content and 100% water content; (b) 50% cement content and 167% water content.

#### 3.2 Effect of fiber content

Figures 2-3 present the effect of fiber content on peak strength and brittle index of FRCT soil specimens. As Figure 2a shows, for both PP and PVA reinforced specimens with mix ratio 2:1:3 (cement content 50%, water content 100%), the peak strength increases with fiber content until a certain fiber content (0.16-0.24%), after which it decreases slightly. A similar trend is also observed in Figure 2b for specimens with mix ratio 2:1:5 (cement content 50%, water content 167%).

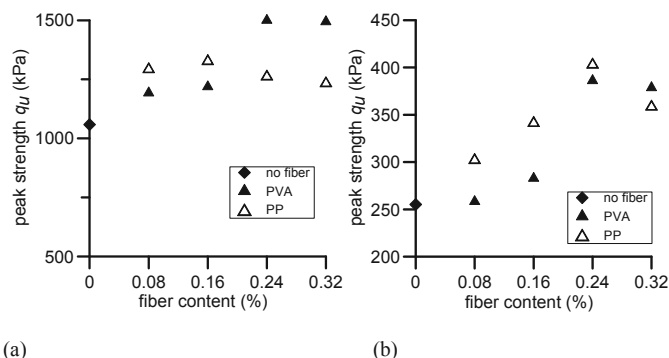


Figure 2. Effect of fiber content on strength for FRCT soil specimens. (a) Specimens with mix ratio 2:1:3 (cement content 50%, water content 100%); (b) Specimens with mix ratio 2:1:5 (cement content 50%, water content 167%).

Figures 3a-3b show that the BI, evaluated at four different axial strain levels between 2% and 20%, reduces significantly with both PP and PVA fiber content for specimens with mix ratio 2:1:3. A similar trend is also observed from Figures 3c-3d for specimens with mix ratio 2:1:5. At higher fiber content, that is, higher than 0.32% for mix ratio 2:1:3 and 0.24% for mix ratio 2:1:5, the results were very scattered due to the poor workability of the mix, which can be observed in Figure 1b. Hence, with current mixing condition, the optimum fiber content, taking into account performance and workability, is 0.32% and 0.24% for specimens with mix ratio 2:1:3 and 2:1:5 respectively. For mix ratios 2:1:4, 20:7:27 and 5:1:6, the optimum fiber content is 0.24%.

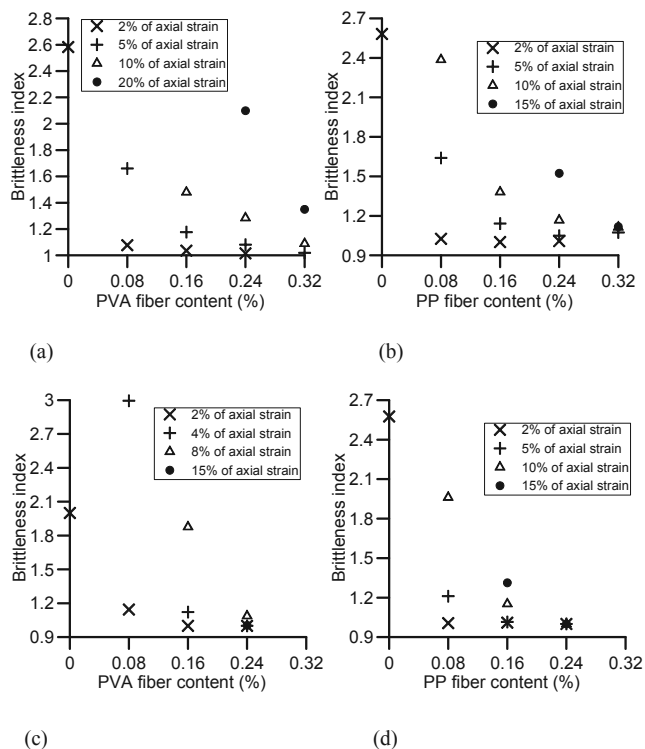


Figure 3. Effect of fiber content on ductility for FRCT soil specimens. (a) PVA reinforced specimens with mix ratio 2:1:3 (cement content 50%, water content 100%); (b) PP reinforced specimens with mix ratio 2:1:3 (cement content 50%, water content 100%); (c) PVA reinforced specimens with mix ratio 2:1:5 (cement content 50%, water content 167%); (d) PP reinforced specimens with mix ratio 2:1:5 (cement content 50%, water content 167%).

3.3 Effect of fiber length

For 12mm fiber reinforcement, 0.08% and 0.16% fiber content was used. It was found that 0.16% fiber reinforcement is much better than 0.08% fiber reinforcement (see Figure 4). Hence, only results of 0.16% fiber content were compared. Figure 5 presents the effect of fiber length on the strength and ductility of the FRCT soil. It can be seen from Figure 5a that for PVA-reinforced specimens, 12mm fiber confers distinctly higher strength than 6-mm fibers. For PP fibers, the difference in peak strength is small.

Figure 5b shows that for specimens with different mix ratio and a given type of fiber (PVA), longer fibers consistently give a lower BI than shorter fibers; the difference increasing with strain level. Similar trend is also observed in specimens reinforced by PP fibers. Therefore, the effect of fiber length on ductility of FRCT soil is significant for both PP and PVA fiber type.

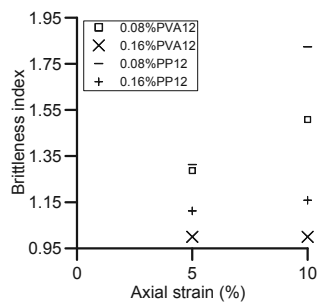
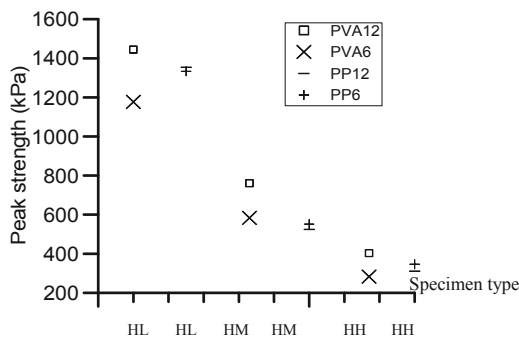
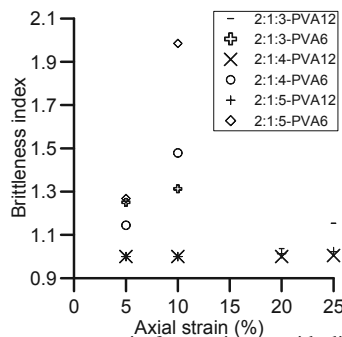


Figure 4. Ductility of RFCT soil with 0.08% and 0.16% 12mm long fiber (50% cement and 100% water content).



(a) Comparison in peak strength for specimens with 50% cement content, 100%-167% water content, and 0.16% of 12mm or 6 mm long fiber (HL, HM, HH denote cement and water content, see Table 2).



(b) Brittleness versus strain for specimens with different mix ratio and 0.16% of 12mm or 6mm long fiber.

Figure 5. Effect of fiber length on strength and ductility for RFCT soil specimens.

3.4 Effect of fiber type

For simplicity and convenience, FRCT soil specimens are categorized in Table 2 according to their cement content and water content together with their performance at optimum fiber

content. As discussed in the previous section, the optimum short fiber content is 0.32% for mix ratio 2:1:3 while it is 0.24% for mix ratio 2:1:4, 2:1:5, 20:7:27 and 5:1:6. For long fiber, the optimum fiber content is 0.16%.

Figures 6-7 present the effect of fiber type on the strength and BI of the FRCA soil. It can be seen from Table 2 and Figure 6 that 12mm PVA fiber reinforcement always gives higher strength than 12mm PP fiber reinforcement due to PVA's higher strength. For water content at and below 133% and cement content not less than 35%, 6mm PVA fiber reinforcement gives higher strength than 6mm PP fiber reinforcement due to the same reason above. For low cement content (20%) and low water content (100%) or high cement (50%) and high water content (167%), short PP fiber gives slightly higher strength than short PVA fiber.

Table 2. Peak strength and BI of specimens with different mix ratios and fiber types, at optimum fiber content.

Mix proportion	2:1:3	2:1:4	2:1:5	20:7:27	5:1:6	
A <sub>w</sub> (%)	50	50	50	35	20	
C <sub>w</sub> (%)	100	133	167	100	100	
category	high A <sub>w</sub> , low C <sub>w</sub> (HL)	high A <sub>w</sub> , mid C <sub>w</sub> (HM)	high A <sub>w</sub> & C <sub>w</sub> (HH)	mid A <sub>w</sub> , low C <sub>w</sub> (ML)	low A <sub>w</sub> & C <sub>w</sub> (LL)	
Peak strength (kPa)	SF	1494 (PVA), 1240 (PP)	752 (PVA), 632 (PP)	386 (PVA), 405 (PP)	1053 (PVA), 874 (PP)	455 (PVA), 471 (PP)
	LF	1445 (PVA), 1354 (PP)	761 (PVA), 628 (PP)	403 (PVA), 313 (PP)	NA	NA
Ductility	SF	PVA>PP	PVA=PP	PVA=PP	PVA=PP	PVA<PP
	LF	PVA>PP	PVA=PP	PVA>PP	NA	NA
Performance	PVA>PP	PVA>PP	PVA ≈ PP (short) PVA>PP (long)	PVA>PP	PVA<PP	

Note: SF and LF denotes short and long fiber respectively

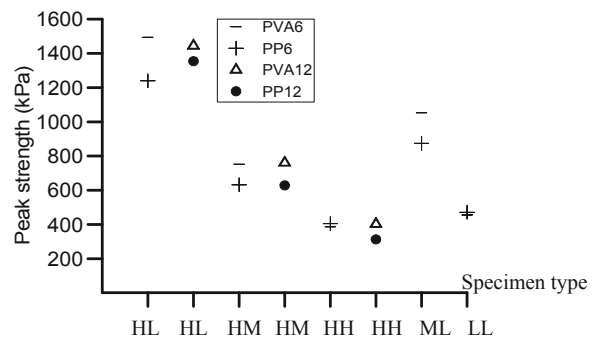
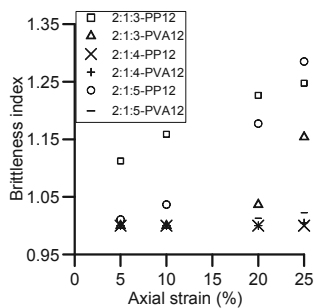


Figure 6. Effect of fiber type on strength of RFCT soil specimens with 20%-50% cement content, 100%-167% water content, 0.24-0.32% of 6mm long fiber or 0.16% of 12mm long fiber.

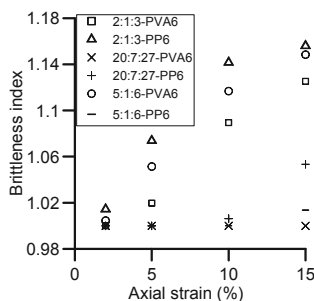
For 12mm fiber reinforcement, Figure 7a shows that for specimens with high cement content (50%) and low or high water content (100% or 167%), PVA fiber gives lower BI values at four different strain levels between 5%-25% than PP fiber. For specimens with high cement content and mid high water content (133%), no fiber type effect is observed. This may

be explained as below. For high cement content and low water content, there is stronger interaction between PVA fiber and cement-soil body due to PVA's higher strength, which results in higher ductility in long PVA fiber reinforced soil specimens. For high cement and water content, there is high PP fiber concentration due to PP's higher aspect ratio, which induces lower ductility in long PP fiber reinforced soil specimens.

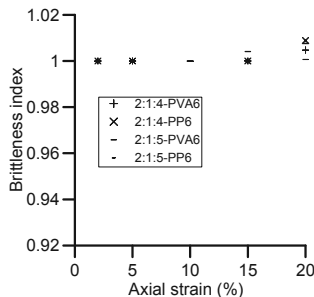
For 6mm fiber reinforcement, Figure 7b shows that for low water content (100%) and high cement content (50%), PVA fiber gives lower BI values at four different strain levels between 2%-15% than PP fiber. For low cement content (20%) and low water content, PVA gives higher BI values than PP fiber. This suggests that short PP fiber interacts with cement-soil body better than PVA fiber of the same length, at low cement and water content. Figures 7b-7c also show that for mid-high cement (35%) and low water content or high cement and mid to high water content, fiber type effect is very small. Therefore, short PVA fiber generally gives ductility not lower than PP fiber except for low cement content and low water content.



(a) Brittleness index versus strain for 12mm long fiber reinforcement (fiber content, 0.16%).



(b) Brittleness index versus strain for 6mm long fiber reinforcement (low water content, 100%; cement content, 20%-50%; fiber content 0.24-0.32%).



(c) Brittleness index versus strain for 6mm long fiber reinforcement (mid to high water content, 133%-167%; high cement content, 50%; fiber content, 0.24%).

Figure 7. Effect of fiber type on ductility for RFCT soil specimens with 20%-50% cement content, 100%-167% water content, fiber cut length 6-12mm and 0.16-0.32% fiber.

In summary, as Table 2 shows, by considering of the strength and ductility of FRCT soil specimens, PVA fiber reinforcement is generally better than PP fiber except for low cement content and water content.

#### 4 CONCLUSIONS

Based on the results and analysis, the main conclusions may be drawn as below.

The strength and ductility of cement-treated marine clay was improved significantly by fiber reinforcement. There is optimum fiber content, considering performance and workability of cement-treated soil specimens. PVA fiber reinforcement is generally better than PP fiber reinforcement except for low cement content and water content.

It was observed that the fiber cut length has significant effect on the ductility of cement-treated soil. However, the cut length effect on strength for PP fiber reinforcement is much smaller than that for PVA fiber reinforcement.

#### 5 ACKNOWLEDGEMENTS

This research is supported by the National Research Foundation Singapore under its Competitive Research Programme (CRP Award No. NRF-CRP 6-2010-03).

#### 5 REFERENCES

Consoli, N.C., Prietto, P.D.M., Ulbrich, L.A. 1998. Influence of fiber and cement addition on behavior of sandy soil. *Journal of Geotechnical and Geoenvironmental Engineering* 124 (12), 1211–1214.

Consoli, N.C., Vendruscolo, M.A., Prietto, P.D.M. 2003. Behavior of plate load tests on soil layers improved with cement and fiber. *Journal of Geotechnical and Geoenvironmental Engineering, ASCE* 129 (1), 96–101.

Consoli, N.C., Zortea, F., Souza, M., Festugato, L. 2011. Studies on the dosage of fiber-reinforced cemented soils. *Journal of Materials in Civil Engineering, ASCE* 23 (12), 1624-1632.

Gray, D.H., Ohashi, H. 1983. Mechanics of fiber reinforcement in sand. *Journal of Geotechnical Engineering* 109 (3), 335–353.

ISO/TS 17892, 2004. Geotechnical investigation and testing - Laboratory testing of soil. International Organization for Standardization, Edition 1, Part 7-9.

Khattak, M. J., & Alrashidi, M. 2006. Durability and mechanistic characteristics of fiber reinforced soil-cement mixtures. *International Journal of Pavement Engineering* 7(1), 53-62.

Maher, M.H., Ho, Y.C. 1993. Behavior of fiber-reinforced cement sand under static and cyclic loads. *Geotechnical Testing Journal* 16 (3), 330–338.

Park, S. S. 2009. Effect of fiber-reinforcement and distribution on unconfined compressive strength of fiber-reinforced cemented sand. *Geotextiles and Geomembrane* 27, 162-166.

Tang, C., Shi, B., Gao, W., Chen, W. and Cai, Y. 2007. Strength and mechanical behavior of short polypropylene fiber reinforced and cement stabilized clayey soil. *Geotextiles and Geomembranes* 25 (3), 194–202.

Ud-din S., Marri A. and Wanatowski D. 2011. Effect Of high confining pressure on the behaviour of fibre reinforced sand. *Geotechnical Engineering Journal of the SEAGS & AGSSEA* 42(4), 69-76.

# Large-scale Piled Raft with Grid-Form Deep Mixing Walls on Soft Ground

Comportement en vraie grandeur d'une fondation mixte radier-pieux établie dans un sol meuble amélioré par quadrillage de mélange profond de sol

Yamashita K., Wakai S., Hamada J.

*Research & Development Institute, Takenaka Corporation, Chiba, Japan*

**ABSTRACT:** This paper offers a case history of a large-scale piled raft supporting a twelve-story building founded on liquefiable sand underlain by soft cohesive soil in Tokyo. The building, 55.7 m in height above the ground surface and measuring 120 m by 100 m in plan, is a steel-framed structure with a base isolation system of laminated rubber bearings. An assessment of a potential of liquefaction during earthquakes indicated that the loose clayey sand between depths of 5 and 15 m had a potential of liquefaction during earthquakes with the peak horizontal ground acceleration of  $3.0 \text{ m/s}^2$ . Therefore, a piled raft combined with grid-form deep cement mixing walls was employed to cope with the liquefiable sand and also to reduce settlements of the soft cohesive soil below the sand. To confirm the validity of the foundation design, field measurements were carried out on the foundation settlements, the axial loads of the piles, the contact pressures between raft and soil and the pore-water pressure beneath the raft from the beginning of construction to 11 months after the end of construction.

**RÉSUMÉ :** Cet article présente une étude de cas en vraie grandeur d'une fondation mixte radier-pieux d'un bâtiment à douze niveaux construit à Tokyo. Cette fondation est établie dans une couche de sable liquéfiable reposant sur une couche de sol cohérent et meuble. Le bâtiment, qui fait 120 m par 100 m dans le plan et 55.7 m en hauteur au-dessus du sol, a une structure métallique en portiques. Il est isolé à sa base par un système d'appareils d'appui en élastomère fretté. Le potentiel de liquéfaction estimé du sable argileux entre 5 et 15 m de profondeur serait atteint sous une accélération horizontale maximum de  $3.0 \text{ m/s}^2$ . Pour pallier à ce phénomène et réduire le tassement de la couche sous-jacente de sol cohérent et meuble, une fondation mixte radier-pieux a été adoptée en combinaison avec l'amélioration, en forme de quadrillage, de la couche de sable par mélange profond. L'article discute le comportement de cette fondation sur la base d'une série de mesures sur site, qui se sont poursuivies depuis le début jusqu'à onze mois après la fin de la construction du bâtiment. Le dimensionnement de cette fondation est estimé convenable considérant les mesures de tassement, des forces axiales sur pieux, des contraintes sur le sol et de la pression de l'eau interstitielle sous le radier.

**KEYWORDS:** piled raft foundation, deep cement mixing wall, soft ground, field measurements, settlement, load sharing

## 1 INTRODUCTION

In recent years there has been an increasing recognition that the use of piles to reduce raft settlements can lead to considerable economy without compromising the safety and performance of the foundation (Poulos, 2001). Detailed investigations of many high-rise buildings founded on piled rafts in Germany have been carried out (Katzenbach et al. 2000). Piled raft foundations have been used for many buildings in Japan and the settlement and the load sharing between raft and piles have been carefully investigated for the selected buildings (Yamashita et al. 2011a; Yamashita et al. 2011b). It has become necessary to develop more reliable seismic design methods for piled rafts, particularly in highly seismic areas such as Japan.

This paper offers a case history of a large-scale piled raft supporting a twelve-story building founded on liquefiable sand underlain by soft cohesive soil in Tokyo. To cope with the liquefiable sand and also to reduce settlements of the soft cohesive soil below the loose sand, piled raft foundation combined with grid-form deep cement mixing walls was employed. To confirm the validity of the foundation design, field measurements were carried out on the foundation settlements, the axial loads of the piles, the contact pressures between the raft and soil and the pore-water pressure beneath the raft from the beginning of construction to 11 months after the end of construction. During the construction period, the 2011 off the Pacific coast of Tohoku Earthquake struck the site of the building. The effects of the earthquake on the settlement

and the load sharing between the raft and the piles are also discussed.

## 2 BUILDING AND SOIL CONDITIONS

The twelve-story office building is located in Tokyo, 0.3 km southeast from the twelve-story residential building (Yamashita et al., 2011b). Figure 1 shows a schematic view of the building and the foundation with a soil profile. The building, 55.7 m in height above the ground surface and measuring 120 m by 100 m in plan, is a steel-framed structure with a base isolation system of laminated rubber bearings. The foundation levels were between depths of 3.6 and 7.2 m.

The subsoil consists of an alluvial stratum to a depth of 44 m below the ground surface, underlain by a diluvial very dense sand. The ground water table appears approximately 3 m below the ground surface. The soil profile down to a depth of 15 m is made of fill which consists of loose clayey sand, sandy clay and rubble. Between the depths of 15 to 44 m, there lie very soft to medium silty clay which is slightly overconsolidated with an OCR of 1.3 or higher. The shear wave velocities derived from a P-S logging were 150 m/s at the foundation levels and 290 m/s in the dense sand below the depth of 44 m.

## 3 FOUNDATION DESIGN

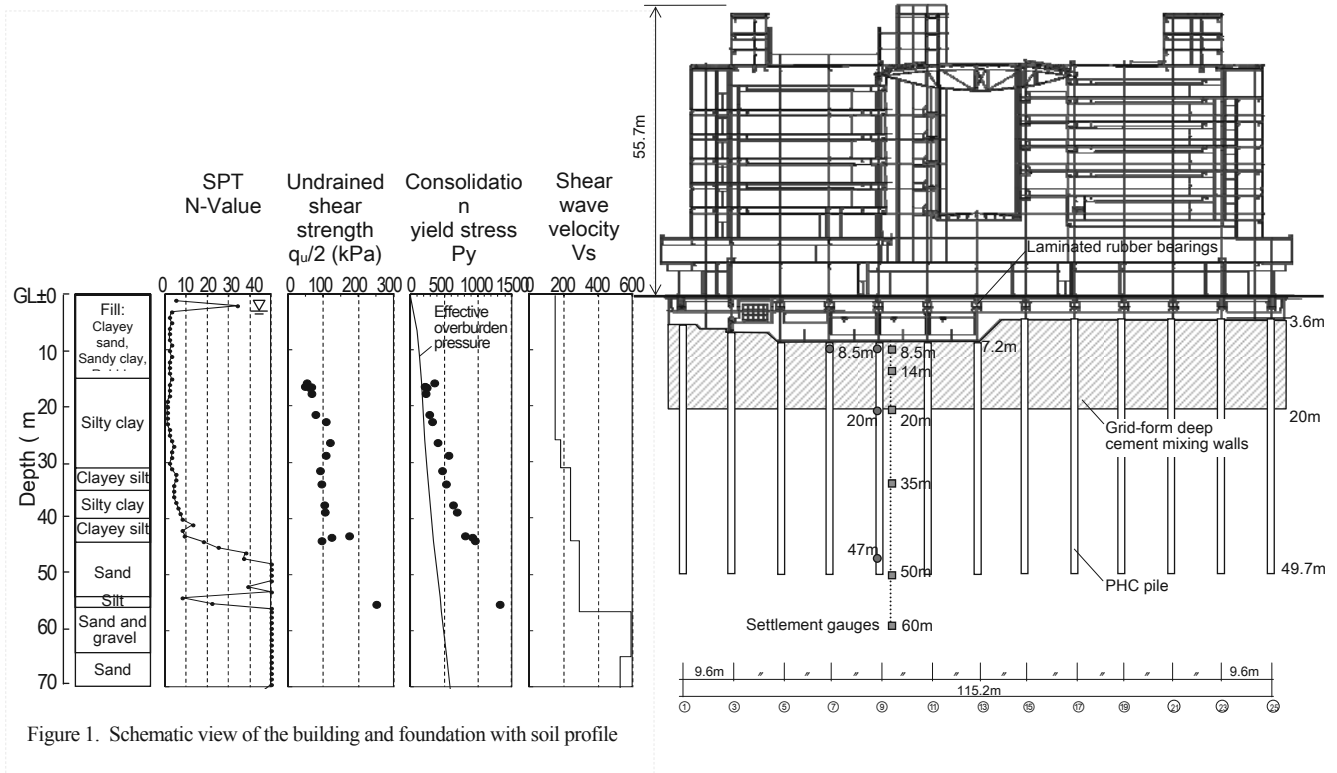


Figure 1. Schematic view of the building and foundation with soil profile

### 3.1 Ground improvement

An assessment of a potential of liquefaction during earthquakes indicated that the loose clayey sand between the depths of 5 to 15 m had a potential of liquefaction during earthquakes with the peak horizontal ground acceleration of  $3.0 \text{ m/s}^2$ . The foundation level was between depths of 3.6 and 7.2 m, therefore, grid-form deep cement mixing walls were introduced to cope with the liquefiable clayey sand below the raft. Figure 2 shows the grid-form deep cement mixing walls constructed by TOFT method. The high-modulus soil-cement walls confine loose sand so as not to cause excessive shear deformation to the loose sand during earthquakes. The effectiveness of the TOFT method for the prevention of liquefaction was confirmed during the 1995 Hyogoken-Nambu earthquake (Tokimatsu et al., 1996).

### 3.2 Design of piled raft

The average contact pressure over the raft is 187 kPa. To improve bearing capacity of the raft, the grid-form deep cement mixing walls were extended to the depth of 20 m with the bottom being embedded in the silty clay with undrained shear strength of 100 kPa or higher. Furthermore, to reduce the settlement and the differential settlement to an acceptable level, 180 pre-tensioned spun high-strength concrete (PHC) piles of 0.6 to 1.2 m in diameter were used. The pile toes were embedded in the very dense sand below the depth of 44 m enough to ensure the toe resistance as well as the frictional resistance. The pile was constructed by inserting the precast piles into a pre-augered borehole filled with mixed-in-place soil cement. Figure 3 shows a layout of the piles and the grid-form deep cement mixing walls.

## 4 INSTRUMENTATION

The locations of the monitoring devices are shown in Figs. 3 and 4. Four piles, P1, P2, P3 and P4, were provided with a couple of LVDT-type strain gauges at depths of 8.5 m (near pile head), 20.0 m and 47.0 m (near pile toe) from the ground

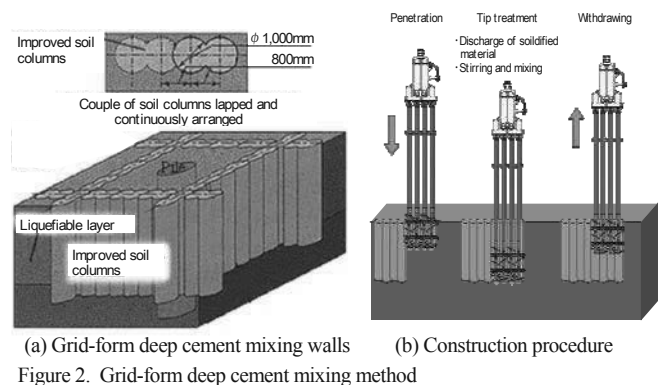


Figure 2. Grid-form deep cement mixing method

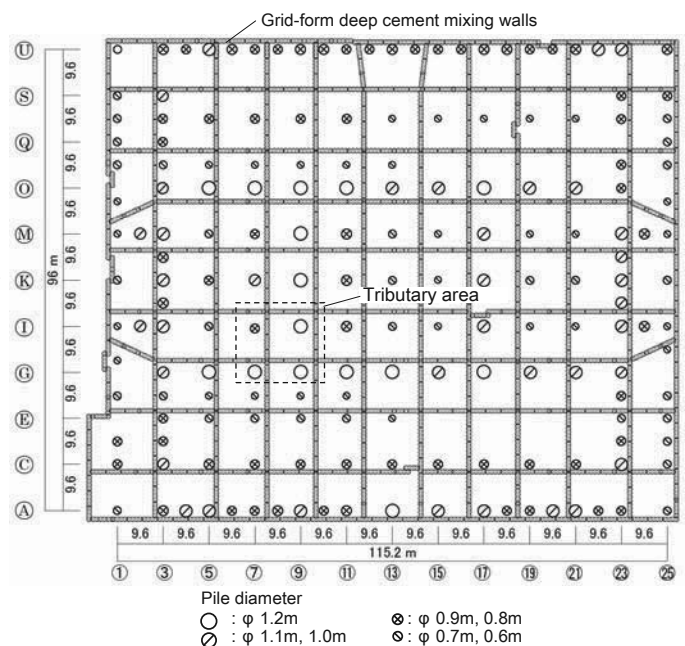


Figure 3. Layout of piles and grid-form deep cement mixing walls

surface. In the tributary area of the instrumented piles, six earth pressure cells and one piezometer were installed beneath the raft at the depth of 7.2 m. Earth pressure cells E1-E3 were installed on the intact soil and earth pressure cells D1-D3 were installed on the deep mixing walls. The vertical ground displacements below the raft were measured by differential settlement gauges. LVDT-type transducers were installed beneath the raft at depths of 8.5 m, 14.0 m, 20.0 m, 35.0 m and 50.0 m to measure the relative displacements to a reference point at a depth of 60.0 m. The settlements of the foundation were measured at the monitoring points on the raft by an optical level. The measurement of the vertical ground displacements was begun during the excavation for the foundation construction. The measurement of the axial loads of the piles, the contact pressures and the pore-water pressure beneath the raft was begun just before the casting of the 0.6-m thick foundation slab.

## 5 RESULTS OF MEASUREMENTS

### 5.1 Foundation settlement

Figure 5 shows the measured vertical ground displacements below the raft. The measured ground displacement at the depth of 8.5 m after the casting of the foundation slab, was approximately equal to the foundation settlement. The foundation settlement increased considerably just before the end of construction (November 15, 2011) due to the water pouring into the underground pits. Thereafter, the foundation settlement became stable and reached 21 mm 11 months after the end of construction (November 3, 2012). Figure 6 shows the settlement profile of the raft measured by the optical level just before the end of construction. The measured settlements were 12 to 24 mm and the maximum angular rotation of the raft was 1/1400 radian which satisfied the design requirements.

### 5.2 Pile load and contact pressures

Figure 7 shows the development of the measured axial loads of piles P1-P4. The axial loads also increased considerably just before the end of construction due to the water pouring. Thereafter, the pile-head loads reached 4.7-11.2 MN in November, 2012. Figure 8 shows the distribution of the measured axial loads on pile P1. Since the piles were surrounded by the deep mixing walls to a depth of 20.0 m, the skin friction of the pile shaft between the depths of 8.5 m and 20.0 m was quite small. The average skin friction between the depths of 20.0 m and 47.0 m was 76 kPa. The ratio of the pile-toe load to the pile-head load was 0.21 in November, 2012. Figure 9 shows the development of the measured contact pressures between the raft and the soil and the pore-water pressure beneath the raft. The measured contact pressures between the raft and the intact soil seemed to reach a state of equilibrium in early stage of the construction, while those between the raft and the deep mixing walls increased with construction loading in the same way as the axial loads of the piles. The measured contact pressures between the raft and the deep mixing walls were 137-180 kPa and those between the raft and the intact soil were 66-72 kPa just before the end of construction. The measured pore-water pressure was approximately 40 kPa.

### 5.3 Load sharing between raft and piles

Figure 10 shows the time-dependent load sharing among the piles, the soil, the deep mixing walls and the buoyancy in the tributary area of the instrumented piles shown in Fig. 4. The sum of the measured pile-head loads and the raft load in the tributary area varied from 61.3 to 62.0 MN after the end of construction, which was generally consistent with the design load of 64.0 MN. Figure 11 shows the ratios of the load carried

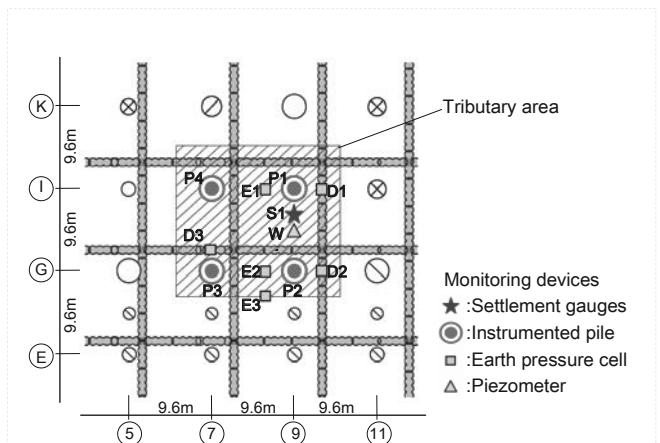


Figure 4. Locations of monitoring devices

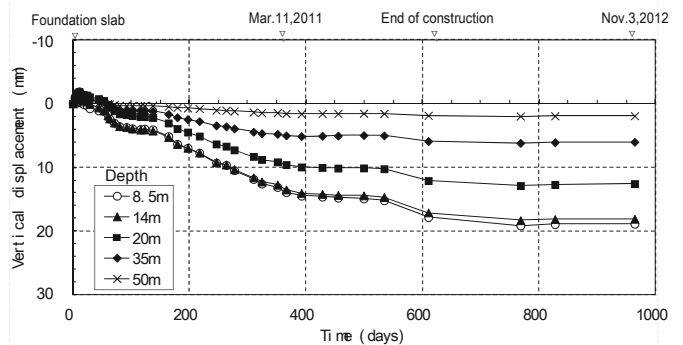


Figure 5. Measured vertical ground displacements below raft

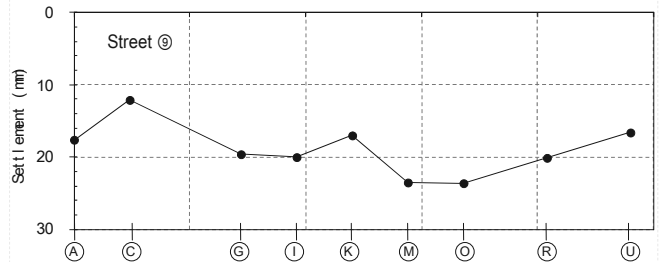
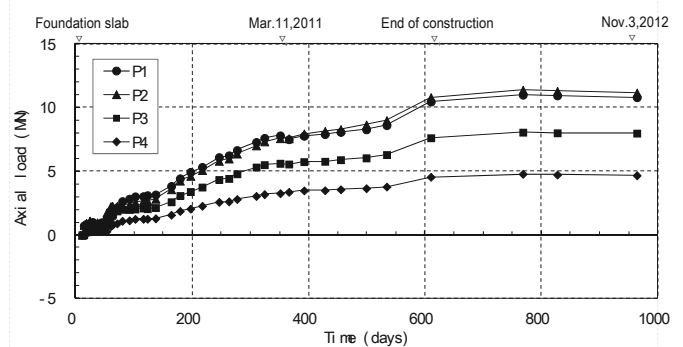
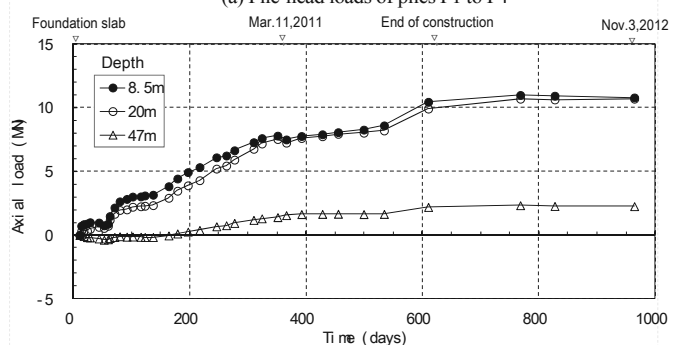


Figure 6. Measured settlement profile of raft



(a) Pile-head loads of piles P1 to P4



(b) Axial loads of pile P1

Figure 7. Measured axial loads of piles

by the piles to the effective load and that to the total load in the tributary area versus time. The ratio of the load carried by the piles to the effective load was estimated to be 0.70 just before the end of construction and increased only slightly to 0.71 in November, 2012. Meanwhile, the ratio of the effective load carried by the deep mixing walls to the effective load was 0.14 and the ratio of that carried by the intact soil to the effective load was 0.15 in November, 2012.

#### 5.4 Effects of earthquake on settlement and load sharing

On March 11, 2011, nine months before the end of construction, the 2011 off the Pacific coast of Tohoku Earthquake struck the site of the building. At the site of the twelve-story residential building, the peak horizontal ground acceleration of  $1.75 \text{ m/s}^2$  was observed (Yamashita et al. 2012). Although the contact pressures between the raft and the deep mixing walls were increased markedly as shown in Fig. 9(a), no significant changes in the foundation settlement or the load sharing between the raft and the piles were observed after the earthquake, as shown in Figs. 5 and 11.

### 6 CONCLUSIONS

Field measurements were carried out on the foundation settlement and the load sharing between the raft and the piles for the large-scale piled raft with the grid-form deep cement mixing walls on soft ground in Tokyo. The foundation settlement reached 21 mm and the ratio of the load carried by the piles to the effective load in the tributary area was estimated to be 0.71 11 months after the end of construction. During the construction period, the 2011 off the Pacific coast of Tohoku Earthquake struck the site of the building. Based on the measurement results, no significant changes in the foundation settlement or the load sharing were observed after the earthquake. Consequently, it is confirmed that a large-scale piled raft, combined with grid-form deep mixing walls, works effectively in grounds consisting of liquefiable sand and soft cohesive soil.

### 7 ACKNOWLEDGEMENTS

The authors are grateful to Messrs. H. Matsuzaki, H. Nagaoka of Takenaka Corporation and Mr. N. Nakayama (formerly of Takenaka Corporation) for their contribution to the foundation design.

### 8 REFERENCES

Katzenbach, R., Arslan, U. and Moormann, C. 2000. Piled raft foundation projects in Germany. Design applications of raft foundations, Hemsley J.A. Editor, Thomas Telford, 323-392.  
 Poulos, H.G. 2001. Piled raft foundations: design and applications, Geotechnique 51, No.2, 95-113.  
 Tokimatsu, K., Mizuno, H. and Kakurai, M. 1996. Building damage associated with geotechnical problems, Special Issue of Soils & Foundations, 219-234.  
 Yamashita, K., Yamada, T. and Hamada, J. 2011a. Investigation of settlement and load sharing on piled rafts by monitoring full-scale structures", Soils & Foundations, Vol.51, No.3, 513-532.  
 Yamashita, K., Hamada, J. and Yamada, T. 2011b. Field measurements on piled rafts with grid-form deep mixing walls on soft ground, Geotechnical Engineering Journal of the SEAGS & AGSSEA, Vol.42, No.2, 1-10.  
 Yamashita, K., Hamada, J., Onimaru, S. and Higashino, M. 2012. Seismic behavior of piled raft with ground improvement supporting a base-isolated building on soft ground in Tokyo, Soils & Foundations, Vol.52, No.5.

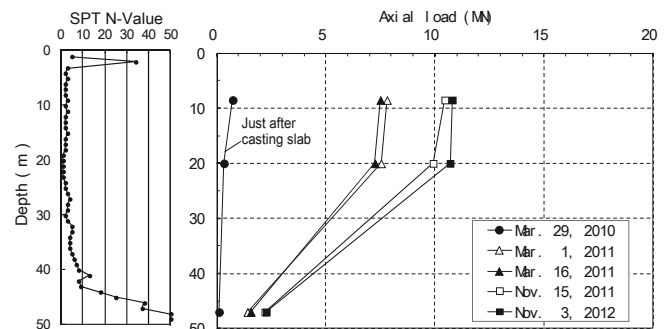
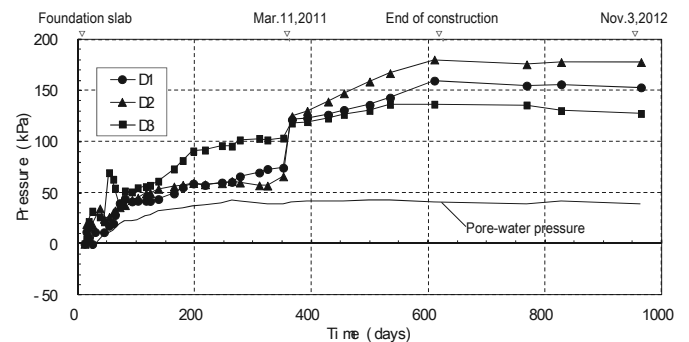
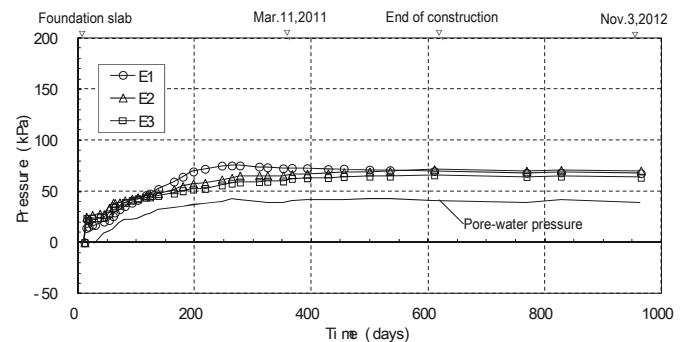


Figure 8. Axial load distribution on pile P1



(a) Contact pressures between raft and deep mixing walls



(b) Contact pressures between raft and soil

Figure 9. Measured contact pressures and pore-water pressure beneath raft

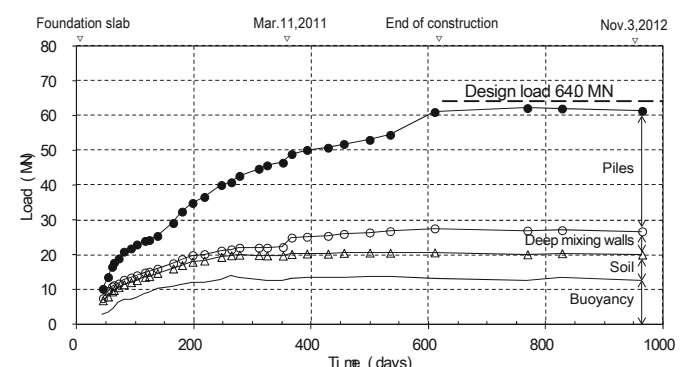


Figure 10. Time-dependent load sharing between raft and piles in tributary area

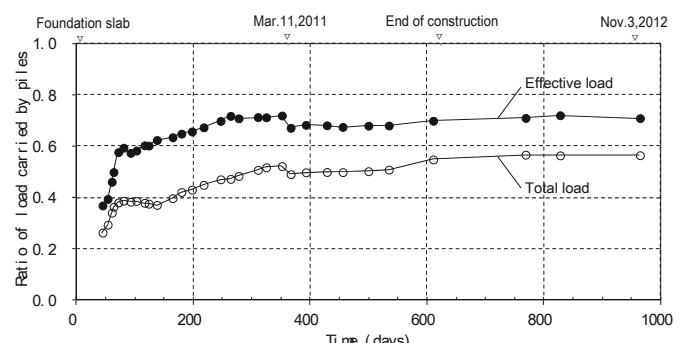


Figure 11. Ratios of pile load to effective load and total load in tributary area

# Initial investigation into the carbonation of MgO for soil stabilisation

## Premières investigations sur la carbonatation de MgO utilisé pour la stabilisation des sols

Yi Y.L.

*Institute of Geotechnical Engineering, Southeast University, China, and Department of Engineering, University of Cambridge, Cambridge, UK*

Liska M., Unluer C., Al-Tabbaa A.

*Department of Engineering, University of Cambridge, Cambridge, UK*

**ABSTRACT:** While Portland cement (PC) is the most widely used binder for soil stabilisation, there are significant environmental impacts associated with its production in terms of high energy consumption and CO<sub>2</sub> emission. Hence, the development of new low carbon foot-print alternative cements has been encouraged. In this paper, reactive magnesia (MgO) was used as a soil stabilisation binder and the MgO-stabilised soils were carbonated by gaseous CO<sub>2</sub> to improve the mechanical properties of the soil and reduce the CO<sub>2</sub> emission. The mechanical and microstructural properties of the carbonated MgO stabilised soils were investigated by using unconfined compressive testing, x-ray diffraction (XRD) and scanning electron microscopy (SEM). The results showed that the strength development rates of carbonated MgO-stabilised soils were much faster than those PC- and MgO-stabilised soils, and the unconfined compressive strength of highly carbonated MgO-stabilised soils was close to that of 28-day ambient cured PC-stabilised soils. The XRD and SEM results indicated that nesquehonite (MgCO<sub>3</sub>·3H<sub>2</sub>O) was the main product of the carbonated MgO-stabilised soils and responsible for the significant strength development.

**RÉSUMÉ :** Alors que le ciment Portland est le liant le plus utilisé pour la stabilisation des sols, il y a d'importants impacts environnementaux associés à sa production en termes de consommation d'énergie élevée et d'émission de CO<sub>2</sub>. Par conséquent, le développement de nouveaux ciments alternatifs à basse teneur en carbone a été encouragé. Dans cet article, la magnésie réactive (MgO) a été utilisée comme liant pour la stabilisation des sols et les sols stabilisés à la magnésie ont été carbonatés par du CO<sub>2</sub> gazeux afin d'améliorer les propriétés mécaniques des sols et de réduire les émissions de CO<sub>2</sub>. Les propriétés mécaniques et microstructurelles des sols stabilisés à la magnésie et carbonatés ont été étudiées en utilisant des essais de compression simples, la diffractométrie de rayons X (DRX), et la microscopie électronique à balayage (MEB). Les résultats montrent que le développement de la résistance des sols stabilisés à la magnésie et carbonatés était beaucoup plus rapide que celui du ciment Portland avec prise à l'air ambiant et celui des sols stabilisés à la magnésie. Ils ont également montré que la résistance à la compression uniaxiale des sols stabilisés à la magnésie et carbonatés était proche de celle des sols stabilisés au ciment Portland avec prise à l'air ambiant pendant 28 jours. Les résultats des DRX et MEB ont indiqués que la nesquehonite (MgCO<sub>3</sub>·3H<sub>2</sub>O) était le produit principal des sols stabilisés à la magnésie et carbonatés, et responsable de la forte augmentation de la résistance.

**KEYWORDS:** soil stabilisation, reactive MgO, carbonation, unconfined compressive strength, microstructure.

## 1 INTRODUCTION

Soil-cement mix technology is one of the most widely used ground improvement methods, with Portland cement (PC) being the most commonly employed binder (Sherwood 1993, Bergado et al. 1996, Al-Tabbaa, 2003). However, there are significant environmental impacts associated with the production of PC in terms of high energy consumption and CO<sub>2</sub> emissions (0.85t CO<sub>2</sub>/t PC), and hence is responsible for 5-8% of anthropogenic CO<sub>2</sub> emissions worldwide (WBCSD, 2002; IPCC, 2004).

In order to reduce the usage of PC, new alternative cements have been encouraged. Reactive magnesia (MgO) cements recently emerged as a more sustainable alternative to PC (Harrison 2008). Reactive MgO is generally calcinated from magnesite (MgCO<sub>3</sub>) at temperatures of ~700-800°C and should not be confused with dead burned MgO manufactured at a temperature higher than 1400°C, which is known to cause an unsoundness problem in PC due to its delayed hydration behavior (Shand, 2006).

Extensive research has been conducted at the University of Cambridge since 2004 into the reactive MgO cements, as detailed in Al-Tabbaa (2013). Reactive MgO hydrates, much faster than dead burned MgO, to form brucite (Mg(OH)<sub>2</sub>). Although brucite has a very limited binding ability, it could carbonate to form one or more of the hydrated magnesium carbonates, namely nesquehonite (MgCO<sub>3</sub>·3H<sub>2</sub>O), hydromagnesite (Mg<sub>5</sub>(CO<sub>3</sub>)<sub>4</sub>(OH)<sub>2</sub>·5H<sub>2</sub>O) and/or dypingite

(Mg<sub>5</sub>(CO<sub>3</sub>)<sub>4</sub>(OH)<sub>2</sub>·4H<sub>2</sub>O). The hydration of MgO and carbonation of brucite both are expansive reactions, which significantly fill available pores. These hydrated magnesium carbonates also form well ramified networks of massive crystals with a very effective binding ability resulting in substantial and rapid strength increase. For example, in porous construction blocks, they significantly outperformed corresponding PC blocks with strengths of 200-300% higher (Liska 2009; Unluer 2012). High levels of carbonation have been achieved in full-scale porous blocks trial production (Liska et al. 2012a and b), reabsorbing most of the CO<sub>2</sub> generated during the decomposition of the magnesite.

In this paper, reactive MgO was initially used as a soil stabilisation binder and the MgO-soil samples were carbonated by CO<sub>2</sub> gas to improve the mechanical properties of the soil and reduce the CO<sub>2</sub> emission. This initial work is thereafter complemented by investigating the impact of relevant variables including soil type, soil water content, binder content and carbonation method (Yi et al., 2012), as well as by using a laboratory-scale auger to model the installation of carbonated soil-MgO deep mixed columns (Yi et al. 2013).



## 2 MATERIALS AND METHODS

### 2.1 Binders, soils and sample preparations

A model soil was used, namely a slightly clayey silty sand, consisting of 90% sharp sand, 5% kaolin clay and 5% silica flour. The sharp sand (obtained from Ridgeons, Cambridge, UK), had a D<sub>50</sub> of 0.8 mm and coefficient of uniformity of 4.3, and the kaolin clay (obtained from Richard Baker Harrison, Ilford, UK) had a liquid limit of 51% and plastic limit of 30%. The silica flour was obtained from David Ball Group, Cambridge. The water content of the soil was 10%. Reactive MgO (obtained from Richard Baker Harrison, Ilford, UK) and PC (obtained from Castle Cement, UK) were applied at 13% dry content to the soil. The reactive MgO had the following oxide composition: MgO: 97.2%, CaO: 1.2%, SiO<sub>2</sub>: 1.2%, Al<sub>2</sub>O<sub>3</sub>: 0.2% and Fe<sub>2</sub>O<sub>3</sub>: 0.2%, while the PC had: CaO: 63.6%, SiO<sub>2</sub>: 13.6%, Al<sub>2</sub>O<sub>3</sub>: 10.2%, Fe<sub>2</sub>O<sub>3</sub>: 2.7%, SO<sub>3</sub>: 6.9%, MgO: 0.6% and K<sub>2</sub>O: 0.9%.

The sharp sand, kaolin clay and silica flour were initially mixed and homogenised for 5 minutes in a bench-top food mixer after which water was added and the mixing continued for further 5 minutes. The MgO was then applied to the model soil and the entire system was then mixed twice for 5 minutes with an inspection inbetween the two intervals. The homogenised mix was then placed in cylindrical moulds, with 50 mm diameter and 100 mm height, applying consistent moderate compaction in three layers by rodding and eliminating any trapped air pockets. The samples were demoulded ~1 hour later, then placed in the triaxial apparatus and subjected to the carbonation procedures detailed below. A subset of MgO and PC stabilised samples was also cured in their moulds under “ambient” conditions, of 20±2°C and 95±3% relative humidity, for 1, 7, 28 and 90 days.

### 2.2 Carbonation procedure and testing

A triaxial apparatus was used to permeate pressurised gaseous CO<sub>2</sub> through the MgO-treated soil as shown in Figure 1. The samples were subjected to 400 kPa confining pressure and then followed by upward permeation of the gaseous CO<sub>2</sub>. First, the CO<sub>2</sub> outflow tap was open during the carbonation process, and the inflow CO<sub>2</sub> pressure was maintained at a low value of 20 kPa to reduce leakage. However, the CO<sub>2</sub> leakage was still serious, and hence only four carbonation periods were conducted using this method, which were 0.75, 1.5, 3 and 6 hours. Thereafter, the carbonation process was modified: the CO<sub>2</sub> outflow tap was closed two minutes after turning on the CO<sub>2</sub> inlet while keeping the inlet open therefore maintaining the CO<sub>2</sub> pressure at the 200 kPa level for the designated carbonation periods: 0.75, 1.5, 3, 6, 12, 24, 48 and 96 hours. Besides, a subset of samples carbonated for 24 hours using this method was then cured under ambient conditions for 7, 28 and 90 days.



Figure 1. The triaxial cell used for MgO-stabilised soil carbonation.

In addition, an incubator, with 20% CO<sub>2</sub> concentration (1 bar) at 20±2°C and relative humidity of 95±3%, was also used to carbonate MgO-stabilised soils for comparison purposes. The carbonation periods were 12, 24, 48, 96 and 168 hours (7 days). A subset of samples carbonated for 7 days using this method were then cured under ambient conditions for 28 and 90 days.

All the samples were tested in triplicate for their unconfined compressive strength (UCS) at a constant displacement rate of 1.14 mm/min. X-ray diffraction analysis (XRD) and scanning electron microscopy (SEM) were conducted for selected mixes.

## 3 RESULTS AND DISCUSSIONS

### 3.1 Unconfined compressive strength

Figure 2 shows the UCS of MgO-stabilised soils carbonated using different carbonation methods. The MgO-stabilised soils carbonated in an incubator, which is generally used to carbonate the MgO-based construction blocks (Liska 2009; Unluer 2012), took ~96 hours of carbonation to reach a maximum UCS value (~8 MPa). While those carbonated in triaxial cell with 200 kPa CO<sub>2</sub> stationary showed similar strength development behavior but with much faster rate, whereby after ~3 hours the stabilised soil also reached a similar maximum UCS value. The UCS of the MgO-stabilised soils carbonated in triaxial cell with 20 kPa CO<sub>2</sub> flow through for 45 minutes was much lower than those with 200 kPa CO<sub>2</sub> stationary, mainly due to the lower CO<sub>2</sub> pressure of the former (Yi et al. 2012). However, the attained strength is approximately the same regardless of the CO<sub>2</sub> pressure applied and its concentration. Figure 2 indicates that there is no need to keep the CO<sub>2</sub> flowing through the sample during the carbonation process, which causes CO<sub>2</sub> leakage.

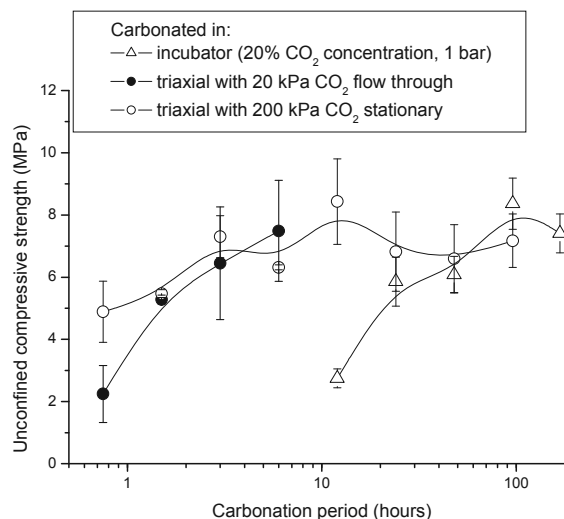


Figure 2. UCS of MgO-stabilised soils carbonated in incubator, triaxial cell with 20 kPa CO<sub>2</sub> flow through and 200 kPa CO<sub>2</sub> stationary.

Figure 3 presents the UCS of uncarbonated MgO- and PC-stabilised soils and carbonated MgO-stabilised soils cured under ambient conditions. It is evident that the UCS values of the uncarbonated MgO-stabilised soil are much lower than those PC-stabilised soils, and both of the two mixes took ~28 days to finish most of their strength development. Comparing of Figure 2 and Figure 3 indicates that the carbonation significantly increased the UCS of MgO-stabilised soils in a very short time, and the UCS of highly carbonated MgO-stabilised soils was close to that of the 28-day PC-stabilised soils, which was ~10 times that of 28-day uncarbonated MgO-stabilised soils. However, the ambient curing period did not affect the strength of carbonated MgO-stabilised soil significantly, indicating the carbonated MgO-stabilised soil could be used to support a structure just after the completion of the carbonation procedure.

This is confirmed by the results of laboratory-scale auger installed soil-MgO deep mixed columns (Yi et al. 2013).

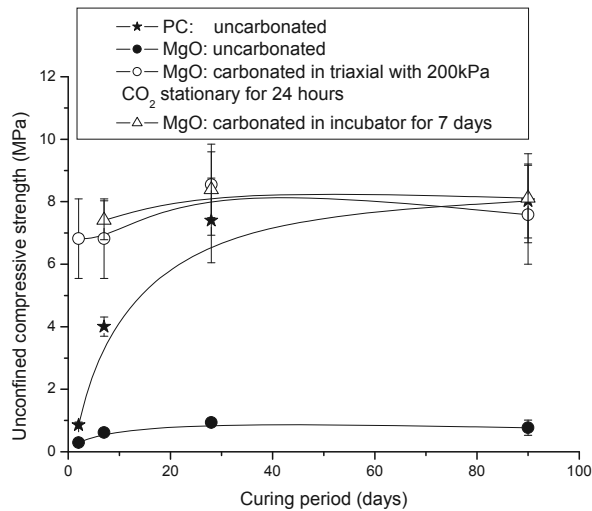


Figure 3. UCS of uncarbonated MgO- and PC-stabilised soils and carbonated MgO-stabilised soils versus ambient curing period.

### 3.2 X-ray diffraction

Figure 4 shows the XRD diffractograms of the MgO-stabilised soils ambient cured for 28 days (uncarbonated) and carbonated in incubator for 12 hours and 7 days, the MgO-stabilised soils carbonated in triaxial cell with 20 kPa CO<sub>2</sub> flow through for 45 minutes, 3 hours and 6 hours, as well as the MgO-stabilised soils carbonated in triaxial cell with 200 kPa CO<sub>2</sub> stationary for 45 minutes, 3 hours and 4 days. Two strong brucite (Mg(OH)<sub>2</sub>) peaks and a weak MgO peak are detected for the 28-day ambient cured MgO-stabilised soil (Figure 4a). For the carbonated samples, the disappearance of the brucite peak together with the gradually weakening of the MgO peak suggest the carbonation of the MgO resulting in the formation of nesquehonite (MgCO<sub>3</sub>·3H<sub>2</sub>O). With no other changes in the mineralogy, this correlates with the rapid and significant strength development of carbonated MgO-stabilised soils.

Additionally, the MgO peak was detected in all the carbonated MgO-stabilised soils, including those carbonated in an incubator for 7 days and in a triaxial cell with 200 kPa CO<sub>2</sub> stationary for 4 days, which were much stronger than that in the 28-day ambient cured sample. These results indicated that the water content (10%) was not enough for all the MgO (13%) to carbonate to form nesquehonite. Hence the MgO content should be linked to the water content of the soil, as well as its porosity.

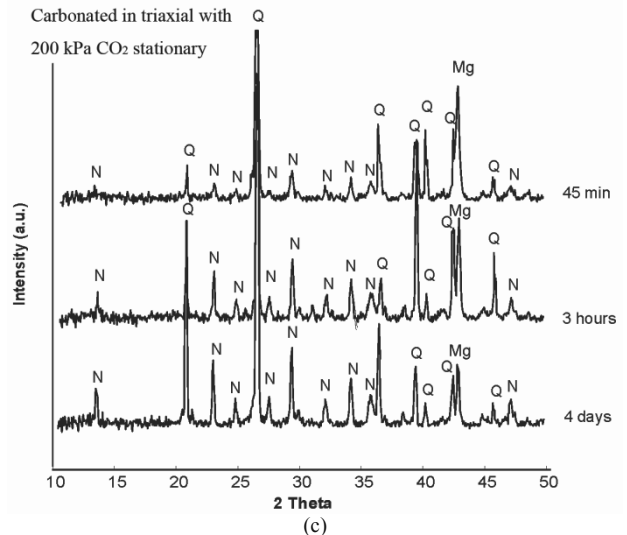
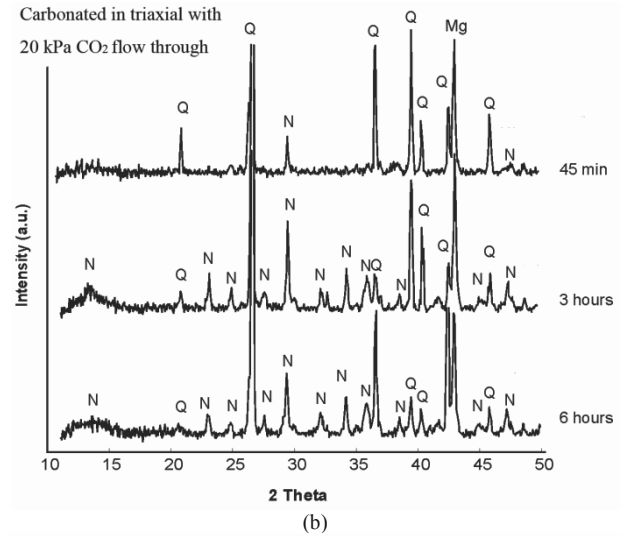
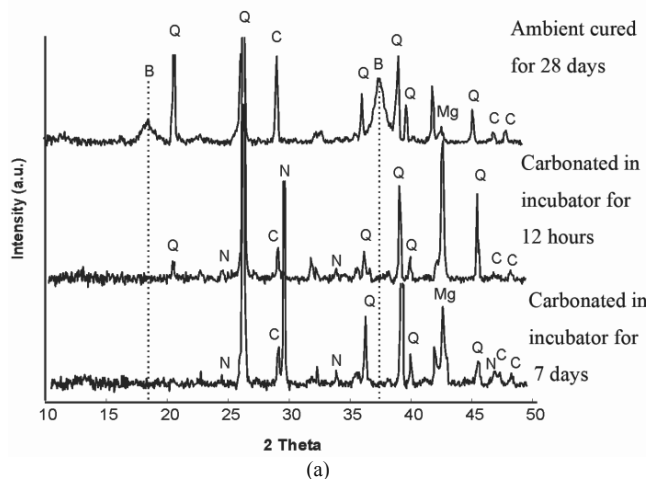
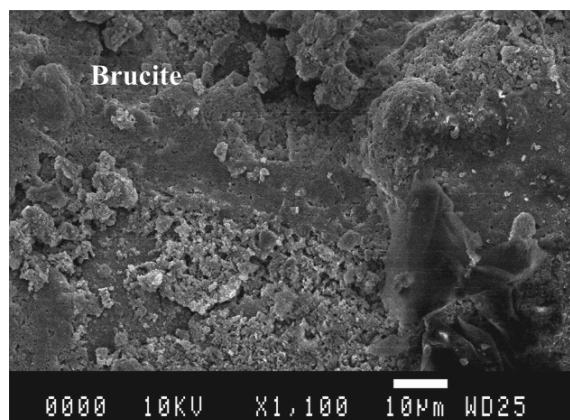


Figure 4. XRD diffractograms of MgO-stabilised soils: (a) ambient cured for 28 days and carbonated in incubator; (b) carbonated in triaxial cell with 20 kPa CO<sub>2</sub> flow through; and (c) carbonated in triaxial cell with 200 kPa CO<sub>2</sub> stationary. The abbreviations stand for: B-Brucite, C-Calcite, Mg-MgO, N-Nesquehonite, Q-Quartz.

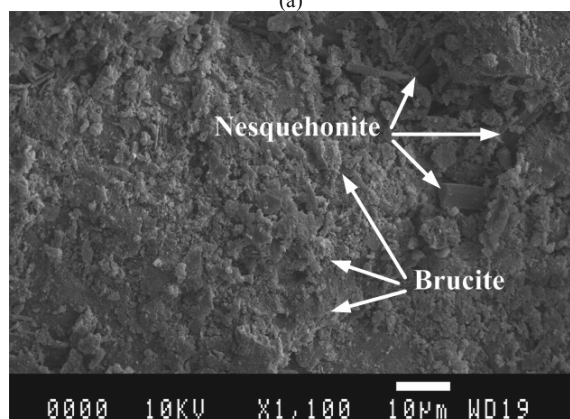
### 3.3 Scanning electron microscopy

Typical SEM micrographs of the MgO-stabilised soils ambient cured for 28 days (uncarbonated), carbonated in triaxial cell with 200 kPa CO<sub>2</sub> stationary for 45 minutes and 4 days, as well as that carbonated in an incubator for 7 days are shown in Figure 5.

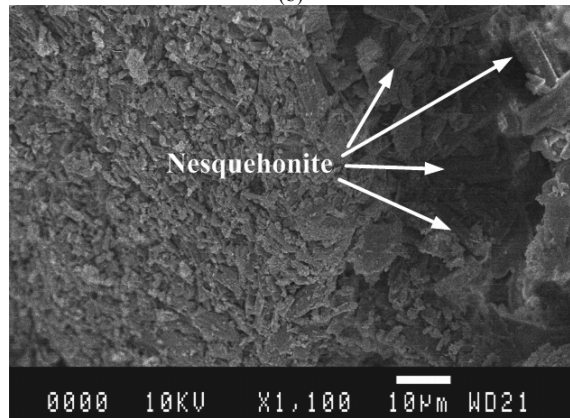
The 28-day ambient cured sample (Figure 5a) exhibits the presence of brucite, which has a very limited binding ability due to its poorly interconnected structure (Liska 2009; Unluer 2012). All the carbonated MgO-stabilised soils (Figure 5b, c and d) display formation of nesquehonite, consistent with the XRD results. Besides, brucite was also observed in Figure 5b confirming that there was only partial carbonation at 45 minutes, and which then disappeared at 4 days (Figure 5c) confirming that the carbonation proceeded to a high degree.



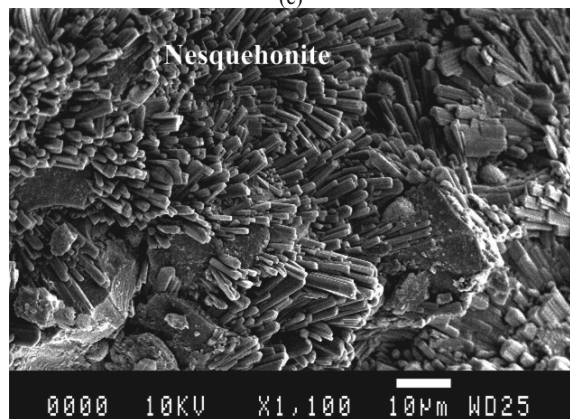
(a)



(b)



(c)



(d)

Figure 5. Scanning electron micrographs of the MgO-stabilised soils: (a) ambient cured for 28 days (uncarbonated); carbonated in triaxial cell with 200 kPa CO<sub>2</sub> pressure for (b) 0.75 hours and (c) 4 days; (d) carbonated in incubator for 7 days.

#### 4 CONCLUSION

The results showed that the carbonation significantly increased the strength of MgO stabilised soil, and the UCS of highly carbonated MgO stabilised soil was close to that of the 28-day ambient cured PC-stabilised soil, which was ~10 times that of 28-day uncarbonated ambient cured MgO-stabilised soil. The carbonation of MgO stabilised soil in the triaxial cell with high CO<sub>2</sub> pressure happened much faster than in the incubator, the former could be finished in a few hours while the latter took a few days. Dissimilar to the uncarbonated ambient cured MgO- or PC-stabilised soil, the UCS of highly carbonated MgO stabilised soil did not increase with ambient curing period. The XRD and SEM results indicated that nesquehonite, one of the hydrated magnesium carbonates, was the main product of the carbonated MgO in soil.

#### 5 ACKNOWLEDGEMENTS

The experimental work presented in this paper was carried out at the Geotechnical & Environmental Laboratory, Department of Engineering, University of Cambridge, in the academic year 2009-2010 when the first author was a visiting researcher there. The funding from CSC, NSSFC (51279032) and MOST (2012BAJ01B02-01) of China is gratefully acknowledged. The authors sincerely appreciate the French abstract translation by Marine Deruelle.

#### 6 REFERENCES

Al-Tabbaa A. 2003. Soil mixing in the UK 1991-2001: state of practice report. *Ground Improvement* 7 (3), 117-126.

Al-Tabbaa A. 2013. Reactive magnesia cements. Chapter 19 in *Eco-Efficient Concrete* (Torgal, Jalali, Labrincha & John, Ed), Woodhead Publishing, in-press.

Bergado D.T., Anderson L.R., Miura N. and Balasubramaniam A.S. 1996. *Soft ground improvement in lowland and other environments*. ASCE, New York.

Harrison A.J.W. 2008. Reactive magnesium oxide cements. *United States Patent*, 7347896.

Intergovernmental Panel on Climate Change. 2004. Sources of CO<sub>2</sub>. In *IPCC Special Report on Carbon Dioxide Capture and Storage*. IPCC, Geneva, Switzerland, 77-103.

Liska M. 2009. Properties and applications of reactive magnesia cements in porous blocks. *PhD Thesis*, University of Cambridge, UK.

Liska M., Al-Tabbaa A., Carter, K. and Fifield J. 2012a. Scaled-up commercial production of reactive magnesia pressed masonry units. Part I: Production. *Construction Materials* 165 (4), 211-223.

Liska M., Al-Tabbaa A., Carter K. and Fifield J. 2012b. Scaled-up commercial production of reactive magnesia pressed masonry units. Part II: Performance. *Construction Materials* 165 (4), 225-243.

Shand M.A. 2006. *The Chemistry and Technology of Magnesia*. Wiley, New York.

Sherwood T.P. 1993. *Soil stabilization with cement and lime: state of the art review*. HMSO Books, London.

World Business Council for Sustainable Development. 2002. The cement sustainability initiative-our agenda for action. *WBCSD, Conches-Geneva*, Switzerland.

Unluer C. 2012. Enhancing the carbonation of reactive magnesia cement-based porous blocks. *PhD Thesis*, University of Cambridge, UK.

Yi Y. L., Liska M., Unluer C. and Al-Tabbaa A. 2012. Carbonating magnesia for soil stabilisation. *Canadian Geotechnical Journal*, submitted.

Yi Y.L., Liska M., Unluer C., Akinyugha, A. and Al-Tabbaa A. 2013. Preliminary laboratory-scale model auger installation and testing of carbonated soil-MgO columns. *ASTM Geotechnical Testing Journal*, in-press.

# Innovative solutions in the field of geotechnical construction and coastal geotechnical engineering under difficult engineering-geological conditions of Ukraine

Solutions innovantes dans le domaine de la construction géotechnique et de la géotechnique côtière dans des conditions géotechniques complexes en Ukraine

Zotsenko M., Vynnykov Y.  
*Poltava National Technical University, Poltava, Ukraine*

Doubrovsky M., Oganesyanyan V.  
*Odessa National Maritime University, Odessa*

Shokarev V.  
*State Research Institute of Building Constructions, Zaporog'e, Ukraine*

Syedin V., Shapoval  
*Academy of Civil Engineering and Architecture, Dnipropetrovsk, Ukraine*

Poizner M.  
*ChernomorNIiproekt, Odessa, Ukraine*

Krysan V.<sup>1</sup>, Meshcheryakov G.<sup>2</sup>  
*<sup>1</sup>"RemBud", Dnipropetrovsk, Ukraine ; <sup>2</sup>Engineering Center Transzvuk, Odessa, Ukraine*

**ABSTRACT:** This paper contains the research findings of reinforced soil cement properties manufactured by drilling mixing method. Application of soil cement for solution of specific geotechnical problems is considered herein in terms of specific examples. In the field of coastal geotechnical engineering the hybrid coastal hydraulic engineering structures and sheet piling using reinforced concrete semi-shells have been developed. Full-scale physical simulation of pressing-in and removal of steel piles is carried out using a modular coordination pile-pressing system.

**RÉSUMÉ :** Cet article présente les résultats de l'étude des caractéristiques de matériau renforcé sol-ciment fabriqué par forage et mélange en place. L'utilisation de mélange sol-ciment pour la résolution de certains problèmes géotechniques est considérée à partir d'exemples précis. Dans le domaine de la géotechnique côtière, des ouvrages mixtes côtiers et maritimes ont été construits, ainsi que des pieux à rainures, fabriqués en utilisant des demies coques en béton armé. La simulation physique à grande échelle des processus d'enfoncement et d'extraction des pieux en acier est réalisée par application d'un système de coordination modulaire d'enfoncement des pieux.

**KEYWORDS:** soil cement, drilled pile, roll displacement of buildings, pile-pressing system.

## 1 DRILLED PILES IN UNSTABLE SOILS

Drilled piles installation in unstable soils is specified by conditions to secure wellbore stability prior to concrete placing. We know some well-drilling methods in such soils under protection of well casing being removed at concrete placing or under drilling mud protection followed by underwater concreting. SOLETANCHE METHOD of drilled piles installation is now very much in evidence as well. It involves the cored screw dipping into the soil to the projected drilling depth and feeding of concrete mixture through such screw under pressure with simultaneous screw lifting.

However the aforesaid methods have their faults, specifically:

- application of well casings results in considerable increasing of works costs, and in some cases it's not possible to remove well casings. Moreover floated soil may escape from drill hole into the well casing thus damaging neighboring buildings and constructions;
- the way to install reinforcement cage into the piles manufactured by SOLETANCHE technology seems rather problematic, whereas drifting sand penetration to the drill hole at drilling is not improbable;
- drilling under the drilling mud and underwater concreting prevents floated soil escaping into the well casing, but on the other hand, makes material quality control more complicated and increases labor intensity.

Mixed technology of drilled piles manufacturing provides primarily manufacturing of soil-cement elements (SCE) with dia. 0.8-1.2 m using drilling mixing method or jet method (Van Impe 2005, Bruce 2000, Larsson 2003). As soon as the soil concrete reaches 30% of its rated capacity, a well hole shall be drilled along the element's center line up to the projected drilling depth, so that the width of a soil concrete shell around it amounted to 150 mm. It serves to protect a drill hole against ingress of water and/or unstable soil for a specific period. Reinforcement cage is mounted in a dry drill hole and the concreting is performed.

The soil cement shells also provide increasing of bearing capacity of composite drilled piles at vertical and horizontal load actions owing to SCE which provide the contact surface between a pile and the soil.

The development works for manufacturing of 8 meter long composite drilled piles were carried out in conditions of bedding of water-saturated loess clay soils.

The following factors were determined in process of the research conducted:

- prism strength and concrete content in soil cement in the samples taken from the pile shaft after 28 days of concrete damp curing ( $\sigma$ , mPa),
- SCE diameter (D, mm),
- drill well cross section in SCE (D', mm),
- availability of loose soil cement in drill hole bottom
- drill hole water flow 2 hours prior to surveillance (h, mm),

- concrete content in soil cement using method of estimation of part of hydrated cement as for the time of research conducting ( $\Delta$ , %),
- visual inspection of reinforcement cage mounting,
- testing of concreting sampling.

Four average piles were selected from a pile field consisting of 256 piles, which data are specified in Figure 1 (1 – fill-up ground, 5-6 – flow loamy soils, 7 – semisolid clays) and in Table 1.

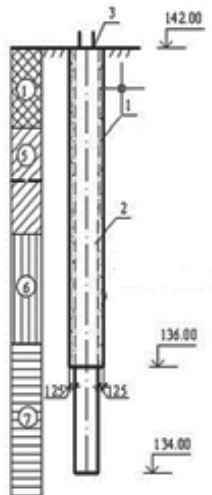


Figure 1 – Composite pile diagram: 1 – soil cement shell, 2 – cast-in-place reinforced concrete pile, 3 – reinforcement cage.

Table 1. Test piles installation indices

No	$\sigma$ , mPa	D, mm	$\Delta$ , %	D', mm	h, m
1	3.4	801	22	512	0.1
2	3.7	786	21.4	524	0.05
3	3.2	790	20	518	-
4	3.5	793	20.6	510	0.1

Findings of pilot works related to installation of composite drilled piles in soil cement shells testifies the following:

- soil cement elements buried in the clay-pans correspond to the design size and properties. In 7 days after their installation they can be lightly drilled and hold wellbore walls in flow clay-bearing soils;
- up to 10 cm of loose soil cement remains in drill holes and can be compacted using earth rammer and impregnated with fluid soil cement;
- drill hole water flow makes ca. 20l per hour, what just insignificantly influences the results of drill hole concreting;
- reinforcement cage mounting and drill hole concreting can be easily performed.

## 2 SOIL CEMENT PILES

Prism strength of soil cement manufactured by drilling mixing method or jet method without using of reinforcing chemical additives makes 1,5...4 mPa depending on water and cement content (M. Zotsenko, Yu. Vynnykov, 2011). In many instances such material strength seems insufficient for manufacturing of underground supporting frames, so there is a necessity to increase the soil cement strength.

This problem can be solved having applied reinforcing of soil cement structures with steel reinforcement. Correspondence of thermal-expansion coefficients of these materials apart from rather high grip of reinforcement on soil cement as well as its high waterproofing capacity is deemed to be the ground for collaboration of soil cement and steel reinforcement.

Effect of reinforcement on soil concrete strength was studied in vitro by testing of pile models of scale 1:4. Models dimensions made up 100 x 100 x 400 mm (Fig. 2). 4 series each per 6 samples were investigated. Samples of the first series were not reinforced, while the samples of the following series were reinforced 1,13%, 2,03% и 3,14% ( $P_r$ ,%) correspondingly. End surfaces of reinforcement cages were equipped with supporting plates with longitudinal reinforcement bars rigidly fastened thereto. Reinforcement protective coating made 20 mm.



Figure 2. Axial compression testing of test samples

Soil cement was produced in vitro using the drilling mixing method, i.e. no stabilization of loess soil-water-cement mixture was carried out. M400 Portland cement content amounted to 20% by weight of soil skeleton. The soil-water-cement ratio with consideration for soil natural humidity made up W/C (Water/Cement) = 2.7. At that its slump of concrete cone flowability amounted to 11 cm.

Properties of constructive materials used in the above experiment are shown in Table 2.

Table 2. Materials mechanical properties

Reinforcement properties		Soil cement properties	
$E_s$ , mPa	$R_{sc}$ , mPa	$E_s$ , mPa	$R_b$ , mPa
210000	225	2000	1.12

All samples were subject to the axial compression test, during which the average values of their bearing capacity were determined, see Table 3.

Table 3. Values of bearing capacity of soil cement prisms

Series No.	Section reinforcement percent $\mu$ , %	Average values of bearing capacity N, kN	Coefficient of variation, v
1	0.00	11.20	0.21
2	1.13	42.50	0.19
3	2.01	62.70	0.17
4	3.14	84.00	0.18

Definition of bearing capacity of steel soil cement prisms by materials was performed using two methods to select the most acceptable one for calculation of structural analysis of steel soil cement structures.

The first method of testing the axially loaded elements' strength with given dimensions, reinforcement quantity and loads is equated as

$$N = \varphi(R_b A + R_{sc} A_{s,tot}), \quad (1)$$

where  $N$  is a required axial force;  $\varphi$  – coefficient equal to 0,92 in this case;  $R_b$  – prism strength of soil cement;  $A$  – normal prism section area of 0,01 m<sup>2</sup>;  $R_{sc}$  – reinforcement rated compressing strength equal to 225 mPa;  $A_{s,tot}$  – total area of main reinforcement.

Rated values of abovementioned indices, as well as model bearing capacity and expected bearing capacity of full-scale piles are shown in Table 4.

Table 4. Bearing capacity of soil cement prisms and piles by materials (using the first calculation method)

Series No.	$\rho_f$ , %	$A_{s_s}$ , mm <sup>2</sup>	$N$ , kN	$N$ , kN full-scale pile
1	0.00	0	11.20	179
2	1.13	113	33.70	661
3	2.01	201	51.91	1019
4	3.14	314	75.30	1478

The second method constitutes the method of calculation of oblique loaded reinforced concrete elements in accordance with deformation model in the stress-strain state in its supercritical stage. Axial compression figures its special case. Dynamic pile formula for definition by material of standard cross-section is given by

$$N_U = A_b \left[ AR_b \eta_U + \frac{R_b \eta_U (K - \eta_U)}{1 + (K - 2)\eta_U} \right], \quad (2)$$

where  $A$ ,  $\eta_U$ ,  $K$  are bearing capacity coefficients.

Table 5 illustrates the bearing capacity of steel soil cement prisms and expected bearing capacity of soil cement piles.

Table 5. Bearing capacity of soil cement prisms and full-scale piles (determined by the second method)

Series Nos.	$A$	$\eta_u$	$K$	$N_u$ , kN	$N$ , kN, full-scale piles
1	0	1	1.70	11.20	179
2	1.54	1.40	1.70	32.20	635
3	2.73	1.60	1.70	52.41	1033
4	4.27	1.79	1.70	81.68	1616

Figure 3 contains relationship: bearing capacity of steel soil cement samples – ratio of standard cross-section reinforcement. It also contains relationships determined analytically according to the aforementioned methods.

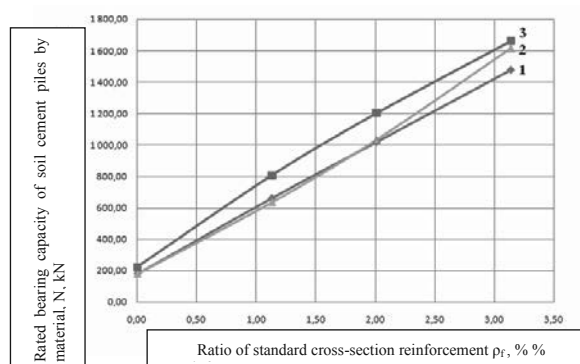


Figure 3. Relationship between bearing capacity of soil cement piles by material  $N$  and ratio of standard cross-section reinforcement  $\rho_f$  based on the following data: 1 – calculation by the first method, 2 – calculation by the second method, 3 – according to in vitro data.

On basis of the research performed it may be concluded as follows:

- Application of longitudinal reinforcement enables to considerably increase the soil cement strength;
- Comparison of data of analytical calculations of soil cement strength with in vitro data showed that the described methods of reinforced concrete structures calculation can be used for calculation of steel soil cement structures strength;
- As for the two above calculation methods the calculation according to the deformation model shall be given preference, since it is aimed at calculation of structures at combined loading. Moreover this method seems to be less sensitive to soil cement parameter variability.

### 3 USE OF SOIL CEMENT FOR REGULATION OF SETTLEMENT SPEED OF BUILDINGS AT RECTIFYING THEIR ROLL DISPLACEMENT

The method of soil drilling out from bottom of less subsided foundations for rectifying of roll displacement of buildings is widely used in Ukraine. For this purpose underworking of the bottom with help of horizontal drill holes of variable diameters is usually performed (V. Shokarev, V. Shapoval, 2009).

Technological parameters calculation for underworking of soil under foundation (diameter and pitch of drill holes) is carried out by formula

$$S = d \cdot t, \quad (3)$$

where  $S$  is the required settlement for rectifying of roll displacement of a building;  $d$  – drill hole diameter;  $t$  – pitch of a drill hole.

Possessing the research findings related to changing of zero-air dry unit weight ( $\rho_d$ ) under bottom of foundation and experimental data on critical density of soil ( $\rho_{cr}$ ) – vertical pressure relationship we can determine the soil layer depth, where drilling of horizontal drill holes and soil structure destruction will be carried out

$$h = \frac{S}{1 - \rho_d / \rho_{cr}}. \quad (4)$$

Time of conditional stabilization of building's settlement shall be determined by formula

$$T = \frac{tg \rho}{V}, \quad (5)$$

where  $V$  is the value of conditional stabilization equal to 0.143 cm per day.

Influence coefficient  $tg \rho$  shall be determined by quotation

$$tg \rho = \frac{S - S_1}{\ln t / t_1}, \quad (6)$$

where  $S$ ,  $S_1$  means the value of building's settlement received according monitoring data;  $t$ ,  $t_1$  means time interval between monitoring stages.

If stabilization of building's settlement during rectifying of its roll displacement takes place prior to fulfillment of required settlement, additional breaking up of soil under foundation bottom shall be necessary. In order to forecast the time of stabilization of building's settlement after fulfillment of required settlement the soil cement mortar using drilling mixing technology shall be fed to the foundation bottom. It allows to reduce the building's settlement speed and to achieve the required value.

#### 4 INNOVATIVE SOLUTIONS FOR COASTAL HYDRAULIC ENGINEERING

A new structure of the retaining wall has been worked out to provide, firstly, resistance to heavy loads stipulated by soil pressure behind the coastal sheet piled wall and, secondly, simplifying of construction technology for deep water quay wall due to absence of traditional anchor devices. Retaining wall (Fig. 4) includes steel sheet piles installed along the structure, soil backfilling behind the wall and transversal sheet piled rows (counterforts) connected with axial wall. Counterforts are made of sheet piles of different length and have a shape of rectangular trapezoid. The length of the sheet piles in counterforts is decreased according to the distance from the axial wall and width of the transversal rows is increased downwards. Sheet piles' heads are joined by the cap. In such structure the idea of counterforts is not only to increase a rigidity of the retaining wall while withstanding the applied loads but also to reduce effectively soil pressure behind the wall.

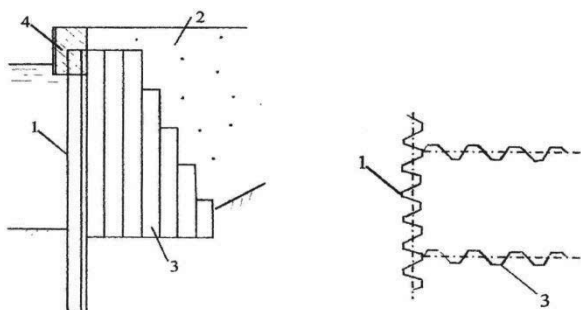


Figure 4. Sheet piling wall with counterforts: a – cross-section; b – plan. 1 – axial sheet piling; 2 – soil backfilling; 3 – sheet piled counterforts; 4 – cap.

A new construction of the bulkhead is worked out to increase the bearing capacity of the coastal protection wall or quay wall as well as to reduce their material consumption (Fig. 5). The structure incorporates the front wall and soil backfilling behind it. Anchor bearers are made of “comb” type as several small anchor plates fixed along the rigid core. Anchor force is taken by all plates of the comb simultaneously. It provides increasing of the bearing capacity both of the anchorage and of the structure in whole (keeping the same material consumption for the anchorage as at the traditional solutions with one large anchor plate). On the other hand proposed structure may provide decreasing of the material consumption (keeping the same structure's bearing capacity as at the known facilities).

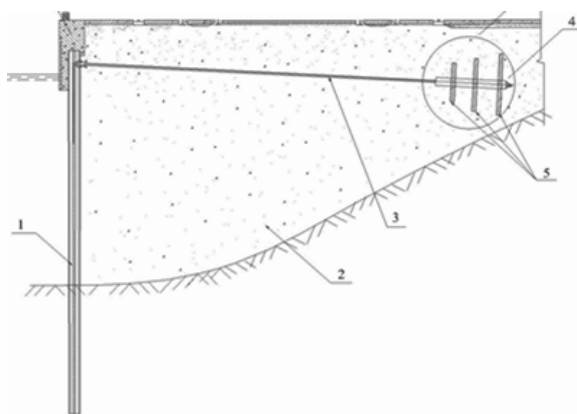


Figure 5. Anchored bulkhead with anchor bearer of new “comb” type: 1 – sheet piling; 2 – backfilling; 3 – tie-rod; 4 – rigid core; 5 – anchor plates.

The basic research for full-scale physical modeling on press-in and extraction equipment was based on the Modular Piling System. This multifunctional equipment has been developed with the intended purpose of implanting prefabricated construction elements using the press-in method. The piling system is equipped with the original hydraulic piling machine (Fig. 6) with wedge-operated clamps (testing devise) and a modular coordinating skidding system (MKS).

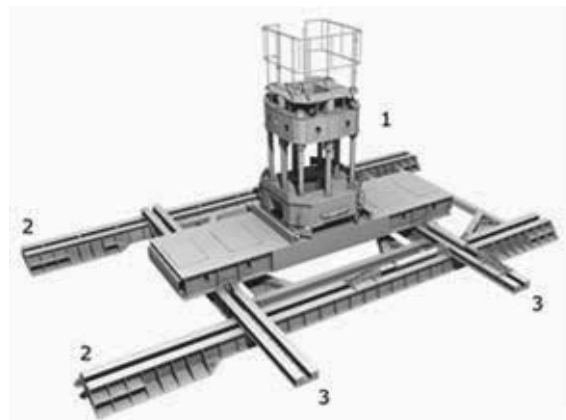


Figure 6. Modular section of the piling system MKS: 1 – press-in piling machine; 2 – longitudinal guides (skid tracks); 3 – transverse guides (cross slide).

In terms of its impact capability the piling machine is completely quiet and vibrations in the ground are at an absolute minimum allowing for the machine to work on certain highly sensitive ground areas, extremely small spaces, and in historical preservation areas. The strategic technological advantages of the piling system are high productivity, precision and quality control.

Depending on the features of the project, location of the piles in terms of engineering and geological conditions of the site, pressing construction elements into the ground could be provided with the flow-line and coordinating installation methods.

#### REFERENCES

- Bruce D.A. An introduction to the deep soil mixing methods as used in geotechnical applications. Report FHWA-RD-99-138 / D.A. Bruce. – U.S. Dept. of Transportation, Federal Highway Administration, 2000. – 143 p.
- Characteristics of manmade stiff grounds improved by drill-mixing method / M. Zotsenko, Yu. Vynnykov, I. Lartseva, V. Shokarev, V. Krysan // Proc. of the 15<sup>th</sup> European Conf. on Soil Mechanics and Geotechnical Engineering “Geothechnics of Hard Soils – Weak Rocks”. – Athens. – 2011. – P. 1097 – 1102.
- Deep mixing research results in under water conditions / [W.F. Van Impe, R.D. Verástegui Flores, P.O. Van Impe et. al.] // Proc. of the 16th Intern. Conf. on Soil Mechanics and Geotechnical Engineering (Osaka, 2005). – Millpress Science Publishers Rotterdam, 2005. – V. 3. – P. 1275 – 1278.
- Larsson S. Mixing processes for ground improvement by deep mixing. Doctoral thesis / S. Larsson. – Stockholm: Royal Institute of Technology, 2003. – 218 p.
- Stress-strain state of the system “base-strip foundation” at elimination of excessive tilts of buildings / V. Shokarev, V. Shapoval, V. Chaplygin, R. Samchenko, D.Volkov // Proceedings of the 17th International Conference on Soil Mechanics and Geotechnical Engineering, Alexandria, Egypt, 2009. - Published by IOS Press under the imprint Millpress, 2009. – V. 1. – P. 680-683.